ECCM21

02-05 July 2024 | **Nantes - France**

Proceedings of the 21st European Conference on Composite Materials





Vol 3

Material and Structural Behavior Simulation & Testing

WWW.ECCM21.ORG

UNDER THE PATRONAGE OF:

ESCM European Society For Composite Materials

Association pour les Matériaux Composites AMAC

EuCIA The European Voice of Composites

WITH THE SUPPORT OF:

RÉGION PAYS DE LA LOIRE

ORGANIZED BY:

CENTRALE NANTES

Nantes Université

SUPPORTING PARTNER:

JEC CONNECTING THE WORLD WITH COMPOSITES

Edited by:

Prof. Christophe BINETRUY
ECCM21 Conference Chair
Institute of Civil Engineering and Mechanics (GeM)
Centrale Nantes
Nantes Université

Prof. Frédéric JACQUEMIN
ECCM21 Conference Co-Chair
Institute of Civil Engineering and Mechanics (GeM)
Nantes Université

Published by:

The European Society for Composite Materials (ESCM) and the Ecole Centrale de Nantes.

©2024 ECCM21/The publishers
The Proceedings are published under the CC BY-NC 4.0 license in electronic format only, by the Publisher. The CC BY-NC 4.0 license permits non-commercial reuse, transformation, distribution, and reproduction in any medium, provided the original work is properly cited. For commercial reuse, please contact the authors. For further details please read the full legal code at:
http://creativecommons.org/licenses/by-nc/4.0/legalcode

These Proceedings have an ISBN (owned by the Publisher) and a DOI (owned by the Ecole Centrale de Nantes).

ISBN: 978-2-912985-01-9
DOI: 10.60691/yj56-np80

The Authors retain every other right, including the right to publish or republish the article, in all forms and media, to reuse all or part of the article in future works of their own, such as lectures, press releases, reviews, and books for both commercial and non-commercial purposes.*

Disclaimer:

The ECCM21 organizing committee and the Editors of these proceedings assume no responsibility or liability for the content, statements and opinions expressed by the authors in their corresponding publication.

Editorial

This collection contains the proceedings of the 21st European Conference on Composite Materials (ECCM21), held in Nantes, France, July 2-5, 2024. ECCM21 is the 21st in a series of conferences organized every two years by the members of the European Society of Composite Materials (ESCM). As some of the papers in this collection show, this conference reaches far beyond the borders of Europe.

The ECCM21 conference was organized by the Nantes Université and the Ecole Centrale de Nantes, with the support of the Research Institute in Civil and Mechanical Engineering (GeM).

Each volume gathers contributions on specific topics:

Vol 1. Industrial applications
Vol 2. Material science
Vol 3. Material and Structural Behavior – Simulation & Testing
Vol 4. Experimental techniques
Vol 5. Manufacturing
Vol 6. Multifunctional and smart composites
Vol 7. Life cycle performance
Vol 8. Special Sessions

Nantes, the birthplace of the novelist Jules Verne, is at the heart of this edition, as are the imagination and vision that accompany the development of composite materials. They are embodied in the work of numerous participants from the academic world, but also of the many industrialists who are making a major contribution to the development of composite materials. Industry is well represented, reflecting the strong presence of composites in many application areas.

With a total of 1,064 oral and poster presentations and over 1,300 participants, the 4-day event enabled fruitful exchanges on all aspects of composites. The topics that traditionally attracted the most contributions were fracture and damage, multiscale modeling, durability, aging, process modeling and simulation and additive manufacturing.

However, the issues of energy and environmental transition, and more generally the sustainability of composite solutions, logically appear in this issue as important contextual elements guiding the work being carried out. This includes bio-sourced composites, material recycling and reuse of parts, the environmental impact of solutions, etc.

We appreciated the high level of research presented at the conference and the quality of the submissions, some of which are included in this collection. We hope that all those interested in the progress of European composites research in 2024 will find in this publication sources of inspiration and answers to their questions.



Prof. Christophe BINETRUY
ECCM21 Conference Chair
Institute of Civil Engineering and Mechanics (GeM)
Centrale Nantes
Nantes Université



Prof. Frédéric JACQUEMIN
ECCM21 Conference Co-Chair
Institute of Civil Engineering and Mechanics (GeM)
Nantes Université

Under the Patronage of:

ESCM
European Society For Composite Materials

Association pour les Matériaux Composites

EuCIA
The European Voice of Composites

Organized by:

CENTRALE NANTES

Nantes Université

With the support of:

RÉGION PAYS DE LA LOIRE

Supported by:

EMC2

JEC
CONNECTING THE WORLD WITH COMPOSITES

Sponsored by:

Bronze Partner:

BRUKER

INSTRON

MatchID
Metrology beyond colors

Other partners:

CAPACITÉS
De la recherche à l'innovation

CARBON AXIS

CETIM

Depestele

EikoSim

ELSEVIER

FAIRMAT

metravib
material testing

NOVITOM

Quantiflex
simulations

Surface Measurement Systems
World Leader in Sorption Science

Hosting Organizations

Conference chairs

Prof. Christophe BINETRUY
ECCM21 Conference Chair
Institute of Civil Engineering and Mechanics (GeM)
Centrale Nantes
Nantes Université

Prof. Frédéric JACQUEMIN
ECCM21 Conference Co-Chair
Institute of Civil Engineering and Mechanics (GeM)
Nantes Université

International Scientific Committee

Malin Akermo (Sweden)
Remko Akkerman (Netherlands)
Andrey Aniskevich (Latvia)
Leif Asp (Sweden)
Emmanuel Baranger (France)
Janice Barton (UK)
Johnny Beaugrand (France)
Andrea Bernasconi (Italy)
Christophe Binetruy (France)
Thomas Bohlke (Germany)
Alain Bourmaud (France)
Nicolas Boyard (France)
Joël Breard (France)
Richard Butler (UK)
Baris Caglar (Netherlands)
Pedro Camanho (Portugal)
Pierpaolo Carlone (Italy)
Paolo Andrea Carraro (Italy)
Valter Carvelli (Italy)
Nuno Correia (Portugal)
Gergely Czél (Hungary)
Clemens Dransfeld (Netherlands)
Sylvain Drapier (France)
Klaus DRECHSLER (Germany)
Andreas ECHTERMEYER (Norway)
Paolo Ermanni (Switzerland)
Martin Fagerström (Sweden)
Ewald Fauster (Austria)
Julien Ferec (France)
Antonio Ferreira (Portugal)
Bodo Fiedler (Germany)
Stefanos Giannis (UK)
Nathalie Godin (France)
Carlos Gonzalez (Spain)
Sotirios Grammatikos (Norway)
Christoph Greb (Germany)
Emile Greenhalgh (UK)
Gianmarco Griffini (Italy)
Stephen Hallett (UK)
Nahiene Hamila (France)
Roland Hinterhoelzl (Austria)
Martin Hirsekorn (France)
Darko Ivančević (Hungary)
Frédéric Jacquemin (France)
Mikko Kanerva (Finland)
Luise Karger (Germany)
Vassilis Kostopoulos (Greece)
Theodosia Kourkoutsaki (Germany)
Thomas Kruse (Germany)
Ugo Lafont (France)
Jacques Lamon (France)
Frédéric Laurin (France)
Antoine Le Duigou (France)
Stepan Lomov (Belgium)
Theodoros Loutas (Greece)
Staffan Lundstrom (Sweden)
António Marques (Portugal)
David May (Germany)
Véronique Michaud (Switzerland)
Jörg Mussig (Germany)
Thomas Neumeyer (Germany)
Philippe Olivier (France)
Alkiviadis Paipetis (Greece)
Federico Paris (Spain)
Chung Hae Park (France)
John-Alan Pascoe (Netherlands)
Alessandro Pegoretti (Italy)
Ton Peijs (UK)
Rob Pierce (Denmark)
Soraia Pimenta (UK)
Silvestre Pinho (UK)
Gerald Pinter (Austria)
Connie Qian (UK)
Marino Quaresimin (Italy)
Andrew Rhead (UK)
Paul Robinson (UK)
Essi Sarlin (Finland)
Yentl Swolfs (Belgium)
Sofia Teixeira du Freitas (Netherlands)
Julie Teuwen (Netherlands)
Ole Thomsen (UK)
Stavros Tsantzalis (Greece)
Konstantinos Tserpes (Greece)
Albert Turon (Spain)
Julien van Campen (Netherlands)
Wim Van Paepegem (Belgium)
Anastasios Vassilopoulos (Switzerland)
Ignaas Verpoest (Belgium)
Michael Wisnom (UK)
Dimitrios Zarouchas (Netherlands)
Daiva Zeleniakiene (Lithuania)
Dan Zenkert (Sweden)

Local Organizing Committee

Suresh Advani
Romain Agogué
Sylvain Chataigner
Sébastien Comas-Cardona
Sofiane Guessasma
Suzanne Laïk
Philippe Le Bot
Mael Peron
Luisa Silva
Vincent Sobodka
Alexandre Ripoche
Elena Syerko

Table of Contents

Click on **CONTENTS** on the right side to return to the table of contents

AUTHORS'S INDEX | *COUNTRY*	TOPIC	ARTICLE TITLE	PAGE
ABREU FILHO Marco A. | *PORTUGAL*	Durability, ageing, environmental effects	Experimental and numerical analyses on the thermal distribution within hybrid FRP sandwich panels under different climatic conditions	**976**
ACOSTA CORREA Jose David | *UNITED KINGDOM*	Poster	Promises and challenges of using electrical resistance change to detect damage in carbon fibre composite laminates	**435**
AHMADVASHAGHBASH Sina | *BELGIUM*	Bio-inspired designs	Intermittent Interfaces in Fiber-Reinforced Composites: Optimising the Balance Between Strong and Weak Fibre-Matrix Interfaces	**1085**
AL-RAMAHI Nawres | *SWEDEN*	Poster	Analysis of electrical performance of carbon fiber composites for heat generation in deicing applications	**1091**
ANTONIOU Alexandros | *GREECE*	Buckling & stability	A novel test load frame for characterizing the buckling resistance of thick sandwich panels	**808**
AOKI Ryoma | *JAPAN*	Fatigue	Numerical prediction of fatigue damage progress and residual strength after fatigue in composite pressure vessel	**1099**
ARRESE Ainhoa | *SPAIN*	Poster	Characterization of fatigue-driven delamination in mode	**1113**
ATHIRA ANIL KUMAR Athira Anil | *UNITED KINGDOM*	Textile composites	Implementation of Second-Order Homogenisation using Shell Elements for Woven Composites	**1120**
AZADI Shain | *ITALY*	AI-based methods	Delamination classification in composite plates using guided waves and 1D-CNN	**101**
BAEK Jeong-Hyeon | *SOUTH KOREA*	Multiscale modeling	Prediction of Mechanical Behavior of Carbon Fiber Braided Composites: A Multi-Scale Simulation-Based Progressive Failure Model	**191**
BA El Hadji Amadou | *FRANCE*	Sandwich structures	Influences of mechanical and water aging on changes in mechanical behavior and damage mechanisms on sandwich structures used as windturbine blades in marine environment (EMR)	**840**
BANGARU Ashish Kumar | *DENMARK*	Fatigue	Understanding fatigue delamination crack growth in a wind turbine rotor blade through an element testing	**1132**
BENDER Marcel | *AUSTRIA*	Textile composites	Influence of Fluid Properties on Transverse Fabric Compressibility During In-Situ Impregnation	**1140**
BOLD Jens | *GERMANY*	Keynote Lecture	Analytical and Numerical Modeling of Aramid Honeycomb Cores	**826**
BOND Emily | *UNITED KINGDOM*	Lightning Strike, fire behavior and fire retardance/ resistance of composites	Finite Element Modelling of Lithium-Ion Battery Fires on Composite Structures	**1**

Table of Contents

AUTHORS'S INDEX | *COUNTRY*	TOPIC	ARTICLE TITLE	PAGE
BONE Jasmine | *UNITED KINGDOM*	Durability, ageing, environmental effects	Micromechanical Property Characterisation of Water Absorption in Carbon Fiber Epoxy Composites using Nanoindentation	1148
BRUYNEEL Michael | *BELGIUM*	Fracture and damage	Modelling coupons at dome area of composite pressure vessels: from a 2D-shell to a 3D-solid formulation, with comparison to test results	109
BUTLER Richard | *UNITED KINGDOM*	Joining & joints	An efficient method to predict skin-stiffener debonding in post-buckled panels	207
CANTWELL Wesley | *UNITED ARAB EMIRATES*	Maintainance & repair	The Repair of Interlaminar Fracture in Thermoplastic-matrix Composites	32
CAPRETTI Monica | *ITALY*	Hybrid composites	On Design and Optimization of Flax and Hybrid Composite Tubular Structures Subject to Axial Crushing	847
CARDONA Carlos | *LUXEMBOURG*	Fracture and damage	Mechanical behaviour of bamboo fibres at the micro scale by applying digital image processing analysis	1156
CARMINE Contaldi | *DENMARK*	Fracture and damage	A semi-analytical model for crack kinking out of the interface of bimaterial anisotropic layers	1172
CHANDRAKAR Prateek | *INDIA*	Buckling & stability	Stochastic thermal buckling investigation of optimized variable stiffness composite laminates incurred internal flaws	199
CHAO Luo | *JAPAN*	Multiscale modeling	Multiscale study on nonlinear properties of cellulose nanofiber-reinforced thermoplastic polymer composite filaments	214
CHARKIEH Ahmad Shawki | *BELGIUM*	Short & long fibre composites	Mechanical performance of 3D printed fibre-reinforced triply periodic minimal surfaces structures	39
CHAUDHARY Amit | *INDIA*	Fracture and damage	A new semi-discrete continuum damage modelling framework for composites with focus on open-hole compression failure	443
CHEBBO Hussein | *FRANCE*	Durability, ageing, environmental effects	Accelerated ageing of a pultruded FRP composite PA6/GF: Characterisation and modelling of hygrothermal ageing	1164
CILENTO FABRIZIA | *ITALY*	Material by design	Investigation on GNP layer as protection against high thermal fluxes in CFRP composites	1204
CORREA Elena | *SPAIN*	Interfaces	Experimental and numerical comparison of fibre/matrix debond extension in ultra-thin plies after tension-tension cyclic loading	1178
DADABO Koami Pierre | *FRANCE*	Multiscale modeling	Eshelby's inhomogeneity problem in complete Mindlin's first strain gradient elasticity theory	775
DAGHIA Federica | *FRANCE*	Keynote Lecture	Mechanism-based modelling of the viscoelastic response of a unidirectional composite ply: validation of a new transversely isotropic model through analytical and numerical homogenisation	113
DE ANTUNES E SOUSA Guilherme | *PORTUGAL*	Poster	Cork-based Composite Materials Suitable to Protect Type I Hydrogen Tanks	783

Table of Contents

AUTHORS'S INDEX | *COUNTRY*	TOPIC	ARTICLE TITLE	PAGE
DEBARRE Antoine | *FRANCE*	Fracture and damage	Experimental and numerical study of the mechanical behaviour of an oxide/oxide ceramic-matrix-composite at high temperature	358
DEMIR Serdar | *TURKIYE*	Poster	THE INFLUENCE OF THE CRUSH PLUGS ON THE ENERGY ABSORPTION OF CARBON/EPOXY COMPOSITE CIRCULAR TUBES UNDER AXIAL CRUSHING	675
DEMOULIN Leyne | *FRANCE*	Fracture and damage	Identification of local to global mechanical properties of clear wood peeled veneers from off-axis tensile tests using full-field local displacement measurements	451
DEYDIER Maxime | *FRANCE*	Fracture and damage	Design assessment of composite patch repair on steel structures based on toughness tests using a newly designed non-standard "equivalent interface" specimen	984
DIMASSI Adli | *GERMANY*	Sandwich structures	Investigating load introduction methods for aircraft floor panels made of foam core sandwich	458
DOITRAND Aurélien | *FRANCE*	Fracture and damage	Simulation of transverse cracking and subsequent acoustic emission in laminates	118
DORIAT Aurélien | *FRANCE*	Durability, ageing, environmental effects	Thermo-Oxidation Aging of Carbon-Fiber Reinforced Epoxy Polymer Composite under High-Speed Air Flow	992
DROUIN Thomas | *FRANCE*	Fracture and damage	Thermo-mechanical study of oxide/oxide CMCs using in-situ micro-ct tests and digital volume correlation	1182
DUBARY Nicolas | *DENMARK*	Fracture and damage	On the use of modeling to assist experimental issues and method development for compressive characterization determination of pultruded carbon fiber specimen	464
DUSHIMIMANA Aloys | *PORTUGAL*	Durability, ageing, environmental effects	Modelling of short- and long-term bond behavior in concrete structures strengthened with externally bonded CFRP composites	683
ECKRICH Maximilian | *GERMANY*	Topological optimization	Anisotropic topology optimization considering multiaxial fiber orientations for composite truss structures with improved intersection point design	8
ELMAS Sinem | *TURKIYE*	Poster	Annealing Effects on Mechanical Performance and Failure Characteristics of CF/PEKK Aerospace Composites: A Thorough Exploration	691
ERIVES ANCHONDO Ruben | *DENMARK*	Fracture and damage	Influence of large-scale fibre bridging in the crack growth rate of mixed-mode delamination of a unidirectional glass-epoxy composite	1196
FACHTAN Robin | *GERMANY*	Design of parts	Robust skin: a multidisciplinary approach to robust membrane wing design for sustainable urban mobility	1211
FAN Jialiang | *SWISS*	Joining & joints	Fatigue Investigation of Self-healing Adhesives for Wind Turbine Applications	1219
FARROKHABADI Amin | *BELGIUM*	Acoustic Emission & ultrasonic method	Investigation of energy absorption and ultrasound-based damage response of 3D printed composite star hourglass shaped lattice structures	1339

Table of Contents

AUTHORS'S INDEX | *COUNTRY*	TOPIC	ARTICLE TITLE	PAGE
FAWAZ Arij | *FRANCE*	Durability, ageing, environmental effects	Moisture Absorption Comparison Between Bulk Adhesives and Adhesively Bonded Joints in different environments	1227
FERNANDES Pedro | *PORTUGAL*	Topological optimization	Topology optimization and numerical modelling of structural batteries	1235
FERNBERG Patrik | *SWEDEN*	Fracture and damage	Modelling of transverse cracking resistance reduction at elevated temperatures and after isothermal heat treatments	1245
FIKRY M. J. Mohammad | *JAPAN*	Fracture and damage	Suppression of delamination in CFRP laminates with ply discontinuities using polyamide mesh material	471
FINAZZI Daniele | *BELGIUM*	Short & long fibre composites	Tensile behaviour of short glass fibre-reinforced polyamide-6: combined effect of temperature, moisture content and strain rate	122
FIORE Vincenzo | *ITALY*	Poster	Effect of alternating salt fog and dry conditions on the behavior of flax fiber reinforced epoxy composites	479
FOTOUHI Sakineh | *FRANCE*	Poster	Finite element modelling of composite materials under impact loading, challenges and potential ways forward.	855
FUJITA Yuki | *UNITED KINGDOM*	Short & long fibre composites	Failure prediction of injection-moulded short-fibre composites: characterisation and prediction from coupons to components	1737
GERMAN Guillaume | *FRANCE*	Durability, ageing, environmental effects	Aging mechanisms of ceramic matrix composites	485
GERRITZEN Johannes | *GERMANY*	AI-based methods	Direct Parameter Identification for Highly non-linear Strain Rate Dependent Constitutive Models using Machine Learning	1252
GIBHARDT Dennis | *GERMANY*	Durability, ageing, environmental effects	Effects of Temperature, Water Absorption, and Weak Interphase Strength on the Damage Tolerance of GFRP	697
GIORDANO Michele | *ITALY*	Structural health monitoring and control	Hierarchical highly electrically conductive nanocomposites for strain sensing device in Structural Health Monitoring	386
GIRARD Hugo | *FRANCE*	Fracture and damage	Fiber-matrix interface fracture characterization by the Coupled Criterion and dual-vision system	366
GIUSEPPE ROMANO Giuseppe | *UNITED KINGDOM*	Poster	On the transverse shear failure in unidirectional fibre-hybrid composite laminae using periodic microstructures	705
GOMEZ Arturo | *DENMARK*	Multiscale modeling	Multi-scale level prediction of crack growth in wind turbine blade shear-web joints applying cohesive zone modelling	734
GORDE Shubham Shahaji | *GERMANY*	Short & long fibre composites	Warpage modelling of carbon fibre-reinforced SMC components in automotive applications	1260
GORTNER Florian | *GERMANY*	Lightning Strike, fire behavior and fire retardance/ resistance of composites	Development of translucent epoxy-based Sheet Molding Compounds with flame retardant properties for aircraft applications	492

Table of Contents

AUTHORS'S INDEX | *COUNTRY*	TOPIC	ARTICLE TITLE	PAGE
HACKER Gereon | *GERMANY*	Fatigue	An Energy Conserving Cycle Jump and Load Application Technique for High-cycle Fatigue Simulations under General Loading Conditions	713
HAILUN ZHOU Hailun | *UNITED KINGDOM*	Topological optimization	Topology optimization method based on minimal surface lattice structure for the lightweight design	61
HAO Jianqun | *BELGIUM*	Structural health monitoring and control	Remaining useful life prediction of flax fibre composites under creep load by acoustic emission and deep learning	1269
HASAN Tarikul | *PORTUGAL*	Durability, ageing, environmental effects	Durability under hygrothermal exposure of vacuum infused GFRP composites produced with polyester and vinyl ester resins	1277
HASAN Tarikul | *PORTUGAL*	Durability, ageing, environmental effects	Effects of thermal cycles and thermal ageing on the mechanical and thermomechanical behaviour of vacuum infused GFRP composites	1285
HASELBACH Philipp Ulrich | *DENMARK*	Multiscale modeling	Quantifying the accuracy of different modelling techniques and element types to predict the structural performance of the DTU 12.6m wind turbine blade	1293
HAWKINS Aidan | *UNITED KINGDOM*	Fracture and damage	Investigating Homogenisation, Mechanical Performance and Compression After Impact of Double-Double Laminates	130
HEDVARD Michelle | *GERMANY*	Fracture and damage	Numerical method for fracture modelling of lattice interface materials in composite structures	226
HERMASSI Nahed | *FRANCE*	Poster	Effects of continuous glass fiber incorporation to recycled PA6 polymer: An interfacial approach	1301
HIGUCHI Ryo | *JAPAN*	Integrated testing and modelling of composite structures	Effects of ply thickness and 0-degree layer ratio on failure mode and strength of notched composite laminates: Experiment and high-fidelity simulation	1310
HIRSEKORN Martin | *FRANCE*	Multiscale modeling	Multi-scale modeling of time-dependent thermal expansion and chemical shrinkage during the curing process of polymer matrix composites	232
HO-NGUYEN-TAN Thuan | *SOUTH KOREA*	Forming & stamping	An effective simulation method for the laminated composite fan blade structure with fiber-draping analysis	500
HORN Alexander | *DENMARK*	Sandwich structures	Temperature-dependent changes in thermo-plastic sandwich core properties and failure mechanisms using short four-point tests with short specimens	1318
HOSOI Atsushi | *JAPAN*	Joining & joints	Enhancement of Interlaminar Fracture Toughness by Micro-Bridging at Crack Tip in Bonded Dissimilar Materials	506
HOSSEIN ABADI Ramak | *BELGIUM*	Multiscale modeling	Numerical fiber reorientation modeling for in-plane shear behavior of woven thermoplastic composite laminates	1000
HUAIXIANG Sun | *CHINA*	Fracture and damage	Structural damage identification of composite reinforced siding panels based on machine learning	718

Table of Contents

AUTHORS'S INDEX | *COUNTRY*	TOPIC	ARTICLE TITLE	PAGE
HUANG Weizhao | *JAPAN*	Durability, ageing, environmental effects	Structural health monitoring of CFRTP under thermo-oxidative ageing by non-destructive vibrational method	138
ISHAN MANOJ Ishan | *INDIA*	Joining & joints	Novel joint interface design strategies for strength improvement in fdm printed single lap adhesive joints	726
ISOZAKI Minori | *JAPAN*	Joining & joints	Comprehensive Evaluation for Joint Strength of Ultrasonic-Welded CFRTP involving Interface and Resin Strengths	512
JACKSTADT Alexander | *GERMANY*	Hybrid composites	Revisiting Constrained-layer Damping in Hybrid Lightweight Laminates: Characterisation, Modelling and Design Guidelines	1323
JADHAV Prakash | *INDIA*	Dynamic	Wear analysis of microstructure image-based 3D models to help design the best abradable coating composition.	146
JEON Min-Hyeok | *SOUTH KOREA*	Fracture and damage	Compressive energy absorption of 3D printed continuous fiber reinforced composite with different printing path	519
JEON Na-Hyun | *SOUTH KOREA*	Buckling & stability	Study on buckling behavior of composite sandwich structure with 3D-printed corrugated core under hydrostatic pressure	741
KANDARE Everson | *AUSTRALIA*	Lightning Strike, fire behavior and fire retardance/ resistance of composites	Engineered mycelium for fireproofing flammable composite materials and structures.	1331
KASHTALYAN Maria | *UNITED KINGDOM*	Multiscale modeling	Effect of stiffness variation in the adhesive on performance of composite-metal tubular joints	1347
KAWAI Masamichi | *JAPAN*	Fatigue	Fatigue Notch Sensitivity of Woven CFRP Laminate Under Different R-ratio Loadings - Experiment and Modeling -	753
KHANDAR SHAHABAD Peiman | *TURKIYE*	Design of parts	Design and fabrication of variable stiffness composite laminates with enhanced dynamic behavior	524
KHAN Kamran A. | *UNITED ARAB EMIRATES*	Multiscale modeling	FLEXURAL RESPONSE OF REAL WOVEN COMPOSITE ENABLED VIA XCT-DRIVEN FINITE ELEMENT MODELING	246
KIM Doyoung | *SOUTH KOREA*	Poster	Challenges in characterizing and modeling 3D woven composites	532
KITAMOTO Kazuya | *JAPAN*	Poster	Modeling Moisture-induced Deformation in CFRP Based on Two-Phase Diffusion Theory	761
KLEIN Timothée | *FRANCE*	Interfaces	Virtual testing of the transverse cracking mechanisms of thin ply thermoplastic and thermoset matrix laminated composites under cryogenic thermomechanical loading	816
KOBEISSI Alaa | *FRANCE*	Fracture and damage	Static and fatigue multi-axial traction/torsion loading of 3D reinforced composite materials	1005
KONDAGUNTA Nagendra Gopal | *INDIA*	Sandwich structures	Vibration analysis of syntactic foam core sandwich composites using an exact state-vector formulation	536

Table of Contents

AUTHORS'S INDEX | *COUNTRY*	TOPIC	ARTICLE TITLE	PAGE
KORFF Maximilian | *GERMANY*	Design of parts	Sustainable Integration Strategy for Recycled Carbon Fiber Nonwovens within CFRP Boss Structures for Pressure Vessels	**544**
KOYANAGI Jun | *JAPAN*	Fatigue	Numerical simulation for fatigue failure by randomly variable loadings for a viscoelastic material based on entropy damage criterion	**252**
KRAUKLIS Andrejs | *NORWAY*	Durability, ageing, environmental effects	Modular framework for lifetime prediction of composite materials affected by the environment	**1354**
KUDO Natsuko | *JAPAN*	Fatigue	Numerical simulation of fatigue damage accumulation of orthotopically viscoelastic CFRP laminates considering temperature elevation caused by energy dissipation	**1012**
KULKARNI Anish Niranjan | *LATVIA*	Textile composites	FE modeling of damage development in hybrid carbon/ steel fiber textile composites using fracture mechanics and cohesive zone approach	**1362**
KUMAR Manish | *INDIA*	Fracture and damage	A Kinematically Enriched Directed Continuum Damage Mechanics Approach to Model Low-Velocity Impact Damage in Composites	**550**
KWAK Minjun | *SOUTH KOREA*	Poster	Physics-informed neural network for efficient prediction of the mechanical behaviour of short fiber-reinforced composites	**257**
LAMMING François | *FRANCE*	Poster	Comprehensive Analysis of Fatigue and Creep Relationships in Thermoplastic Composites: Towards Innovative Structural Design Approaches.	**1369**
LARQUEMIN Tiffany | *FRANCE*	Poster	Numerical Modelling and Experimental Comparison of a Tensile Test on Flax Roving	**1375**
LASEN Matias | *NETHERLANDS*	Fatigue	Hybrid Paris-Erdogan laws estimation from high frequency testing in T700/M21 composites	**218**
LAURENTZI Aretxabaleta | *SPAIN*	Dynamic	Design, manufacturing and testing of 3D printed variable-stiffness laminates for optimum dynamic response	**1107**
LECOINTRE Lea | *JAPAN*	Poster	Lightning strike induced and impact induced delamination investigation using advanced Non-Destructive Testing methods	**1383**
LEE Se-Min | *SOUTH KOREA*	Dynamic	Revolutionizing Airbag Deployment Predictions: Study of Dynamic Properties of TPO and PP in Automotive Safety Modeling	**263**
LIEBAU Alex | *GERMANY*	Lightning Strike, fire behavior and fire retardance/ resistance of composites	Investigation how the Flame-Retardant Content Affects the Mechanical Properties of GFRP for Lightweight Ship Constructions	**558**
LIN Lanhui | *FRANCE*	Poster	Translaminar fracture behavior of hybrid woven-ply PEEK thermoplastic laminates under isothermal and kerosene flame exposure	**378**

Table of Contents

AUTHORS'S INDEX | *COUNTRY*	TOPIC	ARTICLE TITLE	PAGE
LI Runze | *UNITED KINGDOM*	AI-based methods	A two-level machine learning model for failure prediction of an original Z-beam wing box concept	270
LIU Qingchuan | *CHINA*	Poster	The research of the residual stress influence on unidirectional composite materials mechanical properties through micromechanical analysis.	566
LIU Shichen | *NETHERLANDS*	Hybrid composites	Hot-pressing of uncured metal-composite laminates: A numerical study on simultaneous deformation	69
LI Xi | *NETHERLANDS*	Fracture and damage	Interlaminar Fracture Behaviour of Emerging Laminated-Pultruded CFRP Plates for Wind Turbine Blades under Different Loading Modes	372
LI Zhongyu | *CHINA*	Hybrid composites	Impact behavior of hybrid CFRP-elastomer-metal laminates in comparison with conventional fiber-metal laminates impacted with different energies	1390
LORIMER Tobias | *NEW-ZEALAND*	Design of parts	Biaxial Testing of FRP Laminates Optimised Using a Range of Common Failure Criteria – Development of a Biaxial Testing Apparatus	1399
LU Maria Morissa | *PHILIPPINES*	Durability, ageing, environmental effects	The effects of ageing tests on the flexural performance of flax fibre composites	863
LYU Weibang | *CHINA*	Lightning Strike, fire behavior and fire retardance/ resistance of composites	Metallization of carbon nanotube films and their application in the lightning strike protection of CFRPs	1407
MA Dayou | *ITALY*	Dynamic	A comprehensive investigation on the impact resistance of composites with nanoparticles	353
MAHENDRAN Arunjunai Raj | *AUSTRIA*	Short & long fibre composites	Investigating the mechanical performance of bio-composites containing long natural fibers: A study on environmentally friendly chemical and physical treatments for natural fiber reinforcement	1415
MARCINIAK Roland | *GERMANY*	Dynamic	Design and analysis of CFRP crash tubes for energy absorption in eVTOLs	574
MARQUET Loïc | *FRANCE*	Fracture and damage	Analysis of the effects of AFP singularities by multi-instrumented tests on plane and open-hole coupons	1422
MARQUEZ-COSTA Juan-Pablo | *FRANCE*	Durability, ageing, environmental effects	Modelling of oxidation gradients of epoxy-diamine networks on both sides of the glass transition temperature: Towards the prediction of degradation of thermo-mechanical properties	1430
MARTON Gergő Zsolt | *HUNGARY*	Poster	The effect of pattern width on the properties and behavior of interfacially engineered composites with designed failure	1438
MAZIZ Ammar | *FRANCE*	Fracture and damage	NEXTCOPV. Impact Behavior of Carbon Fiber/ Epoxy Composite Overwrapped Tanks in Cryogenic Environments	1444

Table of Contents

AUTHORS'S INDEX | *COUNTRY*	TOPIC	ARTICLE TITLE	PAGE
MEEMARY Bilal | *FRANCE*	Structural health monitoring and control	Mechanical impact of embedded sensors in filament wound thermoplastic composite rings: numerical and experimental analyses	1453
MEHDIKHANI Mahoor | *BELGIUM*	Fracture and damage	Micromechanical modeling of transverse cracking with different methods for generating fiber distributions	1461
MICHELE Gulino | *ITALY*	Joining & joints	Effect of the surface morphology on the mode I fracture toughness in Metal-Composite Joints with 3D Printed Titanium Substrates	1469
MIOT Stephanie | *FRANCE*	Sandwich structures	A new sandwich solution combining CMC and ceramics for the liner of radioactive waste disposal cells	767
MIRANDA Mario | *UNITED KINGDOM*	Multiscale modeling	Multiscale modelling of a novel wingbox structure with increased bend-twist coupling	276
MIRANDA Riccardo | *ITALY*	Poster	Optimization of anodizing process parameters to improve adhesion between fiber reinforced polymers and 3D-printed metal substrates with macroscopic pins	582
MITSUBAYASHI Seiji | *JAPAN*	Poster	Improvement of Impact Energy of Cellulose Nanofiber-added CFRP by Water Absorption under High Temperature and Pressure Conditions	590
MOLLAH Md Tusher | *DENMARK*	Multiscale modeling	Computational Fluid Dynamics Modelling of Vacuum-Assisted Resin Infusion in Composite Sandwich Panels during Wind Turbine Blade Manufacturing	281
MÖLLMANN Imke | *GERMANY*	Sensing and actuation	Non-structurally damaging film-based sensors for in-situ manufacturing pro-cess and curing monitoring of fibre-reinforced composites	596
MOREIRA AROUCHE Marcio | *NETHERLANDS*	Fatigue	Effect of temperature and saltwater ageing on the fatigue delamination of a glass fiber reinforced polymer (GFRP)	289
MOREL Claire | *FRANCE*	Fracture and damage	Analytical and numerical shear-lag models describing probabilistic ruptures in ceramic matrix mini-composites.	295
MOSLEH Yasmine | *NETHERLANDS*	Durability, ageing, environmental effects	Effects of In-Service Environments and Hygrothermal Ageing on Tensile Response of Structural Biocomposites: A Comparative Study of Flax and Glass Epoxy Composites	1477
MUJIKA Faustino | *SPAIN*	Fracture and damage	Decomposition of fracture modes in asymmetric double cantilever beam and asymmetric end notched flexure tests	1486
NEZAMI Aamir Anwar | *India*	Sandwich structures	Stress Analysis of Thick Laminated Composite and Sandwich Plates Using Higher Order Zigzag Theory	1493
NIKOLAOU Christos | *BELGIUM*	Multiscale modeling	Analytical and numerical modeling of thermal strains of composites	612
NOURY Philippe | *NORWAY*	Durability, ageing, environmental effects	Environmental Effects on Mechanical Properties of Composites Materials – A New Recommended Practice	1501
OLENA Karpenko | *NETHERLANDS*	Fatigue	A Study on Fatigue Resistance and Structural Integrity in Web-Core Composite Bridge Deck Panels	1018

Table of Contents

AUTHORS'S INDEX | *COUNTRY*	TOPIC	ARTICLE TITLE	PAGE
PANTALEONI Alessia | *ITALY*	Lightning Strike, fire behavior and fire retardance/ resistance of composites	Sustainable green coating for natural fibers: a flame retardant approach to PLA-based composites	393
PANTEA AFSHARI Pantea | *UNITED KINGDOM*	Multiscale modeling	Effective Properties of Magnetostrictive Composites Through Numerical Homogenisation	1507
PERRUCHOUD Valentin | *NETHERLANDS*	Fatigue	Pre-straining, an effective strategy to improve fatigue life and mitigate cyclic ratcheting of flax FRP composites for their use in structural applications	1512
PETRO Julia | *AUSTRIA*	Durability, ageing, environmental effects	Numerical modeling of aging effects based on the mechanical behavior of functionally graded materials	897
PIANI Riccardo | *ITALY*	Dynamic	Crashworthiness performances of an innovative cylindrical tri-axial braided carbon fibre composite	400
PINTO Rochele | *LITHUANIA*	Fracture and damage	Investigation of basalt fibre reinforced epoxy composites using star-like polymers	413
POLLAK Maximilian | *AUSTRIA*	Poster	Process simulation chain combined with a structural simulation to capture the actual process-induced effects and 'as-built' characteristics	1520
POLYZOS Efstratios | *BELGIUM*	Multiscale modeling	Analytical and numerical modeling of the effective specific heat of composites	620
PONTEFISSO Alessandro | *ITALY*	Structural health monitoring and control	Electrical monitoring of bonded joints	628
PORS Guillaume | *FRANCE*	Structural health monitoring and control	Nondestructive inspection of thick, multi-layered thermoplastic composite pipes	636
POURAHMADI Emad | *CANADA*	Short & long fibre composites	Effect of in-situ consolidation on the in-plane elastic moduli of Carbon/PEEK thermoplastic composites made by Automated Fiber Placement (AFP) process	419
PUPURS Andrejs | *LATVIA*	Fracture and damage	Analysis of micro-damage evolution in induction-cured thermoset composites	1529
QI Jiangwei | *CHINA*	Interfaces	The Scale Effect of Crashworthiness of Composite Tube: Experimental and Simulation Study	301
RADTKE Albrecht | *GERMANY*	Fracture and damage	Enhanced Analytical Modeling of Crack Propagation in Through-Thickness Reinforced Composite Laminates	1535
RAHARD Mathis | *FRANCE*	Durability, ageing, environmental effects	Modelling the mechanical behaviour of a Carbon/ Carbon composite material for aeronautical structures under the influence of its environment	1542
RAN Maojing | *CHINA*	Dynamic	Nonlinear Dynamic Response of 2.5D Woven SiC/ SiC Ceramic Matrix Composites: Experimental and Numerical Investigation	1026
RAN Maojing | *CHINA*	Dynamic	Nonlinear Dynamic Response of 2.5D Woven SiC/ SiC Ceramic Matrix Composites: Experimental and Numerical Investigation	1550

Table of Contents

AUTHORS'S INDEX | *COUNTRY*	TOPIC	ARTICLE TITLE	PAGE
RASTAK Mohammadali | *CANADA*	Hybrid composites	Bending Response of Hybrid Aluminum/Thermoplastic Composite Tube Using Four-Point Bending Test	154
RATKOVIĆ Jakov | *CROATIA*	Fracture and damage	Impact induced progressive damage modelling in woven fibre reinforced composites considering strain rate sensitivity	1558
RAYYAAN Rishad | *UNITED KINGDOM*	Joining & joints	Enhancing the repair performances of glass/epoxy wind-turbine blades using a novel resistance-welding approach	1560
REKIK Houssem Eddine | *SAUDI ARABIA*	Poster	Numerical and Experimental Investigation of Diffusion of Carbondioxide in High-Density Polyethylene and Subsequent Rapid Gas Decompression	1034
RHARDANE Abderrahmane | *FRANCE*	Lightning Strike, fire behavior and fire retardance/ resistance of composites	A numerical-experimental methodology to determine the temperature-dependent thermophysical properties of carbon fiber reinforced composite materials exposed to fire	1568
ROBERT Gilles | *FRANCE*	Short & long fibre composites	Mechanical Characterization and modeling of fiber reinforced polyamides in contact with coolant	1042
RODRIGUES Jhonny | *PORTUGAL*	Sensing and actuation	Temperature distribution estimation using Neural Networks in Composite materials manufacturing: a Soft computing approach	746
RODRIGUEZ Jon | *SPAIN*	Sandwich structures	3D printing of foamed PLA with variable mechanical properties for optimised lightweight sandwich cores	1584
ROHRMÜLLER Benedikt | *GERMANY*	Multiscale modeling	Experimental and numerical probabilistic multiscale investigation of short-fiber reinforced polymers	907
SÁNCHEZ-CARMONA Serafín | *SPAIN*	Fatigue	Tension-compression cyclic behaviour of ultra-thin 90º ply blocks in CFRP laminates	162
SANTOS Bruno Pereira | *UNITED KINGDOM*	Fracture and damage	Arrest of unstable compressive cracks in fibre-reinforced polymers using ply-discontinuities	1591
SATO Mio | *JAPAN*	Durability, ageing, environmental effects	Micro-scale FEA for clarifying the relationship between entropy generation and residual strength of polymer composites	1597
SCHMIDT Sandra | *GERMANY*	Short & long fibre composites	The behavior of paper composites under compressive load	1750
SCHMIDT Tim | *GERMANY*	Multiscale modeling	Guideline Development for Structural Modeling of Textile-Based Composites for the Numerical Permeability Prediction	167
SCHRÖDER Leon | *GERMANY*	Hybrid composites	Efficient Approach to the Dimensioning of Hybrid Metal-FRP Interference Fitted Connections with High Circumferential Speed	912
SEIFFERT Jan | *FRANCE*	Structural health monitoring and control	Integration of carbon fiber and fiber optical sensors in continuous fiber-reinforced additively manufactured parts	1603
SENA-CRUZ José | *PORTUGAL*	Durability, ageing, environmental effects	Durability of pultruded GFRP composites under natural weathering and accelerated laboratory ageing	1611

Table of Contents

AUTHORS'S INDEX | *COUNTRY*	TOPIC	ARTICLE TITLE	PAGE
SERGI Claudia | *ITALY*	Dynamic	Effects of temperature and electro-spun veils on the low velocity impact response of basalt/epoxy composites tested with different impactor masses and impact energies	309
SERNA MORENO María Del Carmen | *SPAIN*	Buckling & stability	Buckling of a [±45]S laminate in a compression-compression biaxial test with a cruciform specimen	315
SEYEDNOURANI Mahsa | *TURKIYE*	Automated placement technologies	Mechanical Performance and Damage Analysis of Multi-Jointed Carbon Fiber-Reinforced Thermoset Composites Under Transverse Impact and Low-Temperature Conditions Assisted with Acoustic Emission Analysis	921
SHAHIDI Kaveh | *TURKIYE*	Poster	Design and damage assessment in earthquake resistant composite pipe joints	1619
SHARMA Akash | *BELGIUM*	Poster	Investigating the Mode-I Failure behavior of Thick Adhesive Joints using a coupled computational/ experimental approach	928
SHARMA Atul | *UNITED KINGDOM*	Poster	Advancing Understanding of Eddy Currents in Carbon Fiber Reinforced Composites using Through-Transmission Technique	1126
SHENGHAO ZHANG | *CHINA*	Textile composites	Effects of braiding architectures in the mechanical properties and damage mechanisms of 3D braided composites	936
SHIFERAW Tsilat | *FRANCE*	Multiscale modeling	Multiscale Modeling and Experimental Assessment of Damping in Unidirectional Fiber Reinforced Composites	1048
SHIVAIE KOJOURI Ali | *BELGIUM*	Fracture and damage	Experimental evaluation of the T-stress impact on the crack trajectory in thick adhesive joints under mode I loading	1627
SHUBHAM - | *INDIA*	Fracture and damage	Integration of Johnson-Cook Rate-Dependent Constitutive Model for Improved Prediction of Unidirectional Glass-Epoxy Composites Ballistic Response	644
SINDHE NARAYANA RAO Nithya | *GERMANY*	Design of parts	A double-wall CFPR hydrogen storage and distribution system as a structural component in aircraft applications	1635
SKENDER Ana | *CROATIA*	Maintainance & repair	Mechanical properties of CIPP: A comparative analysis of testing methods, sample geometry, and liner materials	869
SÖLLINGER Georg | *AUSTRIA*	Fracture and damage	DESIGN AND TEST OF A WITNESSING COUPON FOR FILAMENT-WOUND TOW PREG CFRP PARTS	1055
SONG Xinling | *FRANCE*	Multiscale modeling	Tomography-based numerical reconstruction of fiber bundle and response of microstructural characteristics to mechanical behavior	792
SØRENSEN Bent F. | *DENMARK*	Fracture and damage	Design approach using damage tolerant composites materials with rising fracture resistance (R-curve behaviour)	800
SORRENTINO Luigi | *ITALY*	Maintainance & repair	Assessment of the impact performance of repaired thermoplastic laminates	1644

Table of Contents

AUTHORS'S INDEX | *COUNTRY*	TOPIC	ARTICLE TITLE	PAGE
STEWART Christian | *UNITED KINGDOM*	Textile composites	Damage Tolerance of 3D Woven Composites	652
SUBRAMANIYAN VENKAT Swami | *GERMANY*	Buckling & stability	Impact of pre-existing delamination defects on the evolution of buckling in composites	877
SUNDER Sruthi | *GERMANY*	Lightning Strike, fire behavior and fire retardance/ resistance of composites	Investigating the trade-off effects of inorganic phosphate/silicate flame retardant content on the fire performance and post-fire flexural mechanics of epoxy/ glass fiber composites	78
SYMONS Digby | *NEW-ZEALAND*	Design of parts	Analysis and Optimization of a CFRP Mountain Bicycle Frame	47
SZEDERKÉNYI Bence | *HUNGARY*	Poster	Investigation of continuous fiber-reinforced triply periodic minimal surfaces (TPMS) for high-performance energy absorption applications	1651
SZPOGANICZ Eduardo | *GERMANY*	Tests in severe conditions	Determination of damage onset of thin-ply carbon-fiber composites in cryogenic environments	656
TAILLEUR Alexy | *FRANCE*	Multiscale modeling	A generalized global-local defect/damage initiation model for launcher composite structures pre-sizing	1659
TAKASHIMA Risa | *JAPAN*	Multiscale modeling	Prediction of mechanical properties of thermoplastic resins considering molding conditions	1669
TAZI Mohamed Amine | *FRANCE*	Bio-inspired designs	Reinforcement of damaged steel beams using flax fiber reinforced polymer patches	944
TEMPELIS Antonios | *DENMARK*	Poster	Water droplet impact simulations and prediction of liquid erosion damage for wind turbine blades	85
TOEPFER Friedrich | *GERMANY*	Design of parts	Physical-Virtual Testing Methodology for Efficient Property Determination of Tailored Fiber-Reinforced Composite Structural Vanes for Future Jet Engines	55
TOMURO Ryo | *JAPAN*	Topological optimization	Production of continuous carbon fiber reinforced thermoplastic composites by anisotropic topology optimization and 3D printing	1677
TSAI Jia-Lin | *TAIWAN*	Poster	Characterizing the mechanical behaviors of graphene nanocomposites using molecular dynamics simulation	16
TSIVOURAKI Niki | *GREECE*	Structural health monitoring and control	Vibration-based progressive fatigue damage detection and classification for thermoplastic coupons under population and operational uncertainty	604
ULLAH Zahur | *UNITED KINGDOM*	Fracture and damage	Finite Fracture Mechanics fracture criterion for free edge delamination	1063
VACANDARE Julie | *FRANCE*	Poster	Mechanical behavior of carbon fibers reinforced PEEK laminates under fire conditions	176
VAN PAEPEGEM Wim | *BELGIUM*	Keynote Lecture	Effect of hydrothermal ageing of E-glass fibres on the interfacial bonding strength of E-glass fibre/epoxy in static and fatigue loading	1685
VEREECKE Jean | *FRANCE*	Composites for Hydrogen Storage	Investigating the Permeability of CFRPs for Liquid Hydrogen Storage	321

Table of Contents

AUTHORS'S INDEX | *COUNTRY*	TOPIC	ARTICLE TITLE	PAGE
VINOGRADOV Vladimir | *UNITED KINGDOM*	Fracture and damage	Analysis of laminates with transverse cracks and induced delaminations: stress distribution, effective properties and energy release rate	1070
WALTER Melissa | *GERMANY*	Lightning Strike, fire behavior and fire retardance/ resistance of composites	Heterogeneously distributed flame retardants in fibre-reinforced epoxies: Novel manufacturing process and tailored flame tests	93
WANG Yu | *FRANCE*	Poster	Micro–meso scale numerical approach for yarn considering the damage behavior and its friction analysis	664
WANG Yushen | *UNITED KINGDOM*	Material by design	Towards Highly Homogeneous Heating of Self-regulating Heating Nanocomposites	1698
WANG Zhenyi | *FRANCE*	Sandwich structures	Mechanical performance analysis of 3D printing PLA/ flax composite sandwich with different core geometries	1078
WANG Zhiyu | *JAPAN*	Poster	A dual-scale model for tensile properties analysis of CFRTP-SMC based on micropolar peridynamic method	330
WATANABE Takeshi | *JAPAN*	Fatigue	Material characterization on temperature dependency of fatigue stiffness degradation of CFRP laminate manufactured by filament winding using three-point bending test	885
WITTICH Hans | *GERMANY*	Fracture and damage	Thermoset and glass fiber composite flexibilization using partially reacted substructures (PRS)	952
WITZMANN Jean-Marc | *GERMANY*	Poster	Initial Tests of CCLT – A timber sandwich structure with COMBOO core	1706
WUNDERLE Fabian | *GERMANY*	Poster	Development of design guidelines for adhesive bond lines of segmented wind power rotor blades	427
XUE Peng | *JAPAN*	Material by design	stochastic analysis of spatial inhomogeneity of carbon fiber paper reinforced thermoplastics using monte carlo method	338
XU Zhiyuan | *NETHERLANDS*	Bio-inspired designs	Bio-inspired 3D-printed microstructure for crack arresting in bio-based epoxy matrix	1711
YAMAMOTO Tatsuto | *JAPAN*	Poster	Mechanical characterization of hybrid reinforced polypropylene composites with talc fillers and cellulose nanofibers	1718
YANG Zhikun | *GERMANY*	Poster	Development of a modular and flexible construction system for a self-supporting and modular bridge formwork made of fibre-reinforced plastics	968
YAN Yan | *FRANCE*	Poster	Simulation of self-heating in unidirectional composite material under fatigue loading observed by infrared thermography	960
YAZDANI SARVESTANI Hamidreza | *CANADA*	Bio-inspired designs	Biomimetic Architected Ceramics: Enhancing Interfacial Properties and Energy Absorption through Surlyn-Alumina Composites	23
YERRAMALLI Chandrasekher | *INDIA*	Short & long fibre composites	Laser ablation mechanism and damage prediction in fiber reinforced polymer composites	1724

Table of Contents

AUTHORS'S INDEX | *COUNTRY*	TOPIC	ARTICLE TITLE	PAGE
YILDIRIM Ceren | *TURKIYE*	Structural health monitoring and control	Comprehensive Analysis of Damage Progression in High-performance Thermoplastic Composites through Multi-Instrumental Structural Health Monitoring Approaches	**1731**
YOU Chao | *CHINA*	Fatigue	Fatigue Failure Mechanisms and Lifing Method of 2.5D CMCs under Combined Loading	**890**
YU Guoqiang | *CHINA*	Structural health monitoring and control	Residual strength monitoring of ceramic matrix composites based on damage self-sensing method	**346**
ZHANG Weijie | *CHINA*	Poster	Evaluation of 3D woven near-net-shaped composite I-sections: fabric design, manufacture, and mechanical properties	**28**
ZHU Keyu | *CHINA*	Sandwich structures	The investigation of double impact positions on impact behavior of composite sandwich structure	**240**
ZIMMERMANN DE ALMEIDA Otavio | *FRANCE*	Fatigue	Interlaminar shear fatigue of carbon/epoxy laminates	**1744**
ZIMMERMANN Urs | *SWISS*	Design of parts	Basic structural design of fiber reinforced components based on open source software	**184**

FINITE ELEMENT MODELLING OF LITHIUM-ION BATTERY FIRES ON COMPOSITE STRUCTURES

Emily Bond[1], James Sterling[1], Francesco De Cola[2], Emer McAleavy[3], Adrian Murphy[1] and Scott L.J. Millen[1]

[1] School of Mechanical and Aerospace Engineering, Queen's University Belfast, Ashby Building, Belfast, BT9 5AH, Northern Ireland, UK Email: ebond04@qub.ac.uk
[2] WAE Technologies Limited, Grove, Wantage, Oxfordshire, OX12 0DQ Email: francescodecola@gmail.com
[3] Artemis Technologies Limited, Concourse 2, Queen's Road, Belfast, BT3 9DE Email: emer.mcaleavy@artemistechnologies.co.uk

Keywords: Carbon Fibre-Reinforced Polymer (CFRP), Finite Element Analysis (FEA), Lithium-Ion Battery Thermal Runaway, Battery Enclosure, Intumescent Coatings

Abstract
The use of composite materials, for lightweighting, and lithium-ion batteries (LIB), for electrification, has expanded across the transportation industry. A common failure mechanism for LIBs is thermal runaway (TR), i.e. when a battery enters a state of uncontrolled, self-heating which can result in very high temperatures, smoke, and even battery fire. Battery fire containment is generally achieved with metallic structures, but to-date Carbon Fibre Reinforced Polymer (CFRP) containment structures have not been investigated. This paper presents Finite Element (FE) models to assess thermal and mechanical damage and failure during and after a lithium-ion battery (LIB) thermal runaway (TR) event impinging on a CFRP composite specimen. A loading approach is developed using published experimental data for a cylindrical 18650 LIB fire. A trio of sequential simulations including heat transfer, thermo-mechanical and Compression after Thermal Runaway (CaTR) models are linked with python scripts to transfer damage states. Results have shown, for unprotected specimens, the presence of thermal damage from a single cell runaway can potentially reduce the residual strength by 20%. Application of a 0.5 mm coating reduced the thermal damage area from 10,587 mm^2 to 1431 mm^2.

1. Introduction

The use of composite materials, for lightweighting, and lithium-ion batteries (LIB), for electrification, has expanded significantly in aerospace, maritime, and automotive sectors. The combination of these technologies presents new and emerging design challenges. Carbon Fibre Reinforced Polymer (CFRP) composites are more susceptible to thermal damage (softening, deformation, and failure) than traditional metallic structures due to lower thermal conductivity [1].

Thermal runaway (TR) describes the phenomenon when a battery enters a state of uncontrolled, self-heating which can result in very high temperatures, smoke, and even battery fire [2–4]. While TR mechanisms are largely well known, containment of such events is less well understood, but remains a prominent safety concern. It is standard practice for batteries to be housed in a metal enclosure, typically aluminium or steel, which contains the batteries and enables extinguishment in the event of TR. However, the interest in composite battery enclosures has been growing in recent years, as a means of lightweighting battery assemblies.

Research on the effects of fire on composite structures is relatively well established [5,6]. However, research on the effects of battery fires on composite structures is less well developed [1]. Due to the

inherent susceptibility of composites to thermal damage, barrier coatings have been proposed with the potential to protect these structures. While there exists a range of protective coating types each with advantages and disadvantages, intumescent and gel coatings have become a common choice due to their flame-retardant properties [6–9]. Intumescent coating systems, when expanded, provide a low thermal conductivity protective layer that limits heat transfer to the underlying composite structure [7]. Intumescent coatings have been used to protect composite structures from the effects of fire but none are recorded to have been tested under exposure to a battery fire, whether experimentally or computationally [6].

This work develops finite element (FE) models of thermal loading experienced during an 18650 battery thermal runaway event on composite specimens. Experimental data for a cylindrical cell fire was studied and used to define representative thermal loading patterns and behaviours for single-cell load cases. Once validated, the loading profile was applied to a composite specimen to appraise thermal damage, predict the reduction in residual strength and assess the merits of an intumescent coating.

2. Methodology

A trio of sequential simulations; heat transfer modelling, thermo-mechanical modelling and Compression after Thermal Runaway (CaTR) were established to model and predict damage to composite structures during and post thermal runaway fire, as shown in Figure 1.

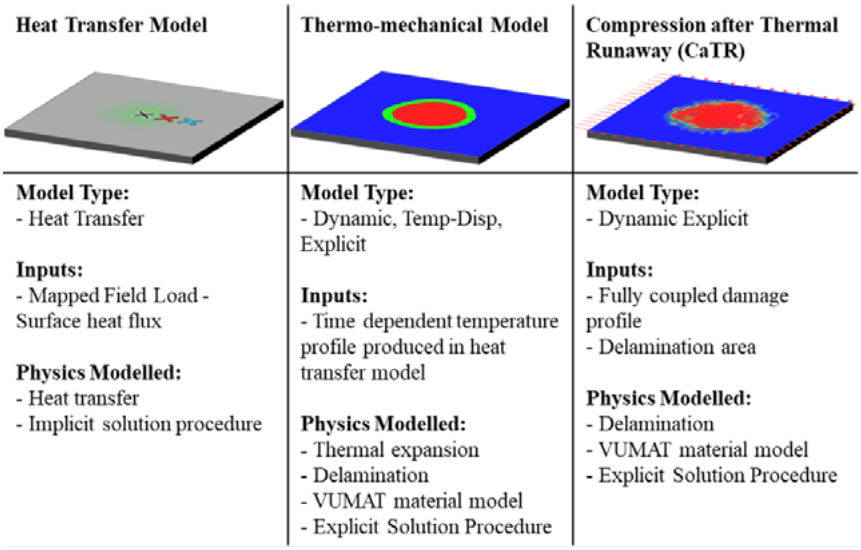


Figure 1. Model flow scheme

Prior to the modelling of composite structural damage a validated loading approach was required. Therefore, a representative loading profile, varying both spatially and temporally, for a single-cell 18650 runaway event was created based on data from Shen [10] and Zhang et al. [2]. This was applied to a 6061-T6 aluminium alloy specimen. The heat flux distribution was applied to the model using a mapped analytical field, with more details given by Sterling et al. [1]. Three thermocouples, attached to the rear of the specimen, at 0 mm, 50 mm, and 100 mm from the centre of the specimen were used to check the accuracy of the loading profile. The accuracy of this loading approach is shown in Figure 2.

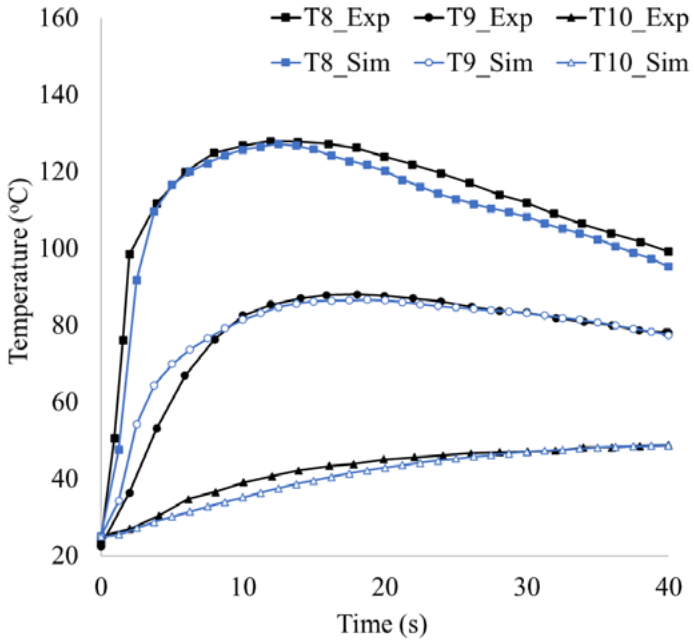


Figure 2. Comparison of measured (from ref. [11]) and predicted back face temperature on aluminium plate

It can be seen there is generally good agreement between the measured and predicted temperature peaks with some discrepancy around three seconds into the simulation. The predictions can still be considered acceptable given that no two fires will be identical there will be some inherent variation in results from test to test. Once this loading approach had been created and validated, it could then be applied to composite specimens.

2.1 Heat Transfer Model

Firstly, modelling of the heat transfer behaviour, due to heat flux loading, was completed. All models in this work replicated the specimen geometry used in preceeding experimental work by Zhang et al. [2]. The specimen measured 400 mm x 400 mm x 4.704 mm and was meshed with DC3D8 8-node linear brick solid heat transfer elements. The laminate stacking sequence was $[45/0/-45/90]_{4s}$. Temperature dependant material properties for the CFRP used are shown in Table 1, from ref. [12].

Table 1. Temperature dependent CFRP material properties

Temperature (°C)	Density (kg/m^3)	Specific Heat (J/kg°C)	Thermal Conductivity		
			Fibre (W/m.K)	Transverse (W/m.K)	Through-Thickness (W/m.K)
25	1520	1065	8.00	0.67	0.67
500	1520	2100	4.39	0.34	0.34
800	1100	2100	2.61	0.18	0.18
1000	1100	2171	1.74	0.10	0.10
3316	1100	2500	1.74	0.10	0.10
3334	1.11	5875	1.74	0.10	0.10

2.1.2 Intumescent coating modelling

The intumescent coating used in this work was derived from the work of Mouritz et al. [6] with properties shown in Table 2.

Table 2. Intumescent coating material properties from ref. [6].

Property	Material State	Value
Thermal conductivity (W/m°C)	Virgin	0.4
	Intumesced/Charred	$3.00 \times 10^{-4}T + 0.1$
Specific heat capacity (J/kg °C)	Virgin	2200
	Intumesced	$1.5T + 3000$
Density (kg/m^3)	Virgin	1392

2.2 Thermo-mechanical modelling

A thermo-mechanical model, was completed with a dynamic, temperature-displacement, explicit analysis step in Abaqus/Explicit using C3D8RT elements. The temperature profile from each node of each element of the FE mesh in the heat transfer simulation was transferred using Python scripts, as discussed in previous works [12,13]. Intralaminar damage was captured using a VUMAT material model developed by Millen et al. [14], with material properties shown in Table 2.

Table 2. Mechanical properties for thermo-mechanical model [14]

Temperature (°C)	E_1 (MPa)	E_2=E_3 (MPa)	G_{12}=G_{13} (MPa)	G_{23} (MPa)	ν_{12}= ν_{13}	ν_{23}	α11 (x10^{-8})	α22= α33 (x10^{-5})
25	161,000	11,400	5170	3980	0.32	0.44	1.8	3
200	161,000	9120	4136	3184	0.32	0.44	5.4	5.25
260	161,000	114	41.36	31.84	0.32	0.44	5.4	5.25
600	161,000	5.7	2.068	1.592	0.32	0.44	5.4	5.25
3316	161,000	5.7	2.068	1.592	0.32	0.44	5.4	5.25

This temperature distribution was then transferred to structural models to predict mechanical damage (i.e., fibre/matrix failure or delamination), considering strain and heating rates, with a VUMAT subroutine. Finally, CaTR simulations were completed, after damage mapping with python scripts, to determine the residual strength of the specimen.

2.3 Compression after Thermal Runaway (CaTR)

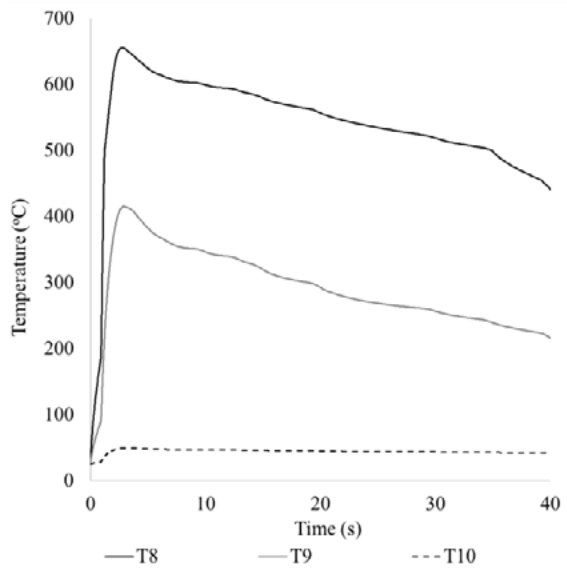
CaTR was completed using Abaqus/Explicit. Boundary conditions in the CaTR models were derived from the typical compression-after-impact (CAI) arrangement. As such, the side of the specimen opposite the compression load was fixed in all directions. The two sides perpendicular to loading were constrained to avoid buckling. The intralaminar and interlaminar damage from the preceeding thermo-mechanical model was transferred to the the CaTR using the same approach proposed in ref. [15].

3. Results

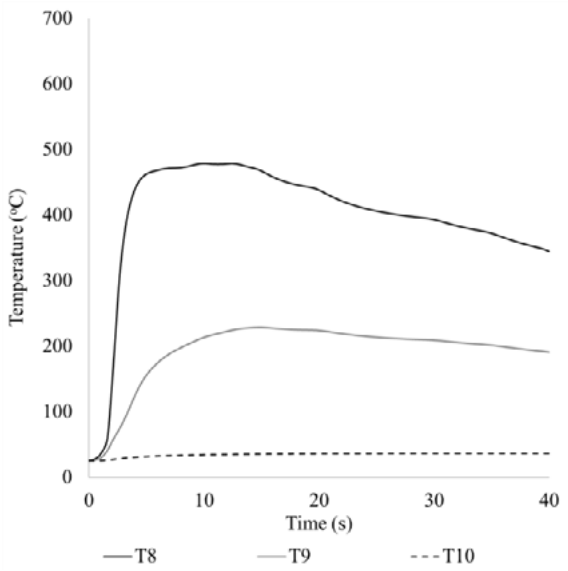
3.1 Thermal damage

Figure 3 shows the thermocouple measurements and predicted damage profiles for both unprotected and protected composite specimens. In the unprotected case, Figure 3a, the temperature rises rapidly at approximately 14,000 °C/min reaching a peak of 656 °C. This temperature then gradually drops as the flux from the battery runaway decreases and conduction and emissivity occur. Alternatively, in Figure 3b it can be seen that the addition of a 0.5 mm thick intumescent coating reduced the peak temperature to 479 °C (~5500 °C/min).

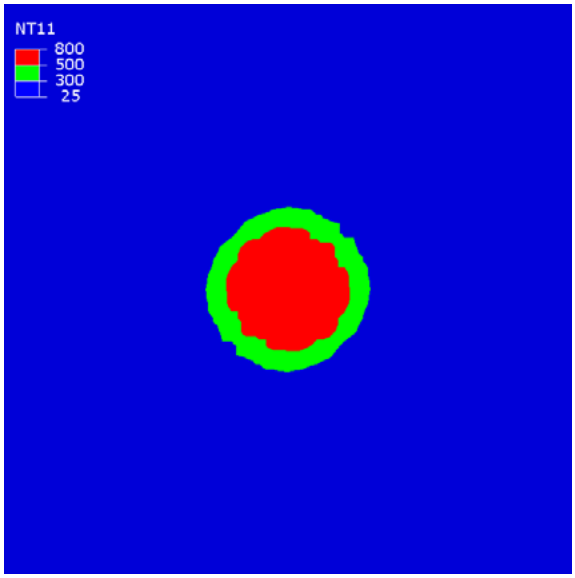
Looking at the predicted thermal damage area, a similar trend is observed, where the addition of an intumescent coating reduces the overall damage. In the unprotected case the moderate damage area (areas where 300 °C ≤ T < 500 °C) was 10,587 mm^2 and extended four plies deep or 0.588 mm while the severe damage area (areas where T ≥ 500 °C) was 5413 mm^2 and was confined to the top ply. The addition of a 0.5 mm thick intumescent coating eliminated the severe damage area and reduced the moderate thermal damage area to 1431 mm^2.



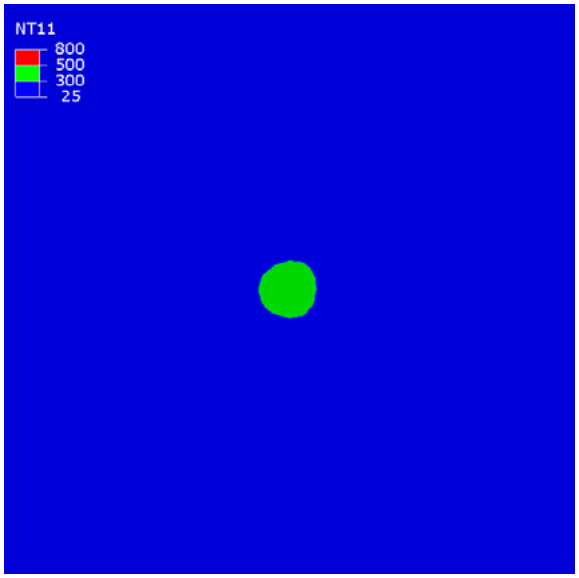
a) Thermocouple measurements on unprotected composite specimen



b) Thermocouple measurements on protected composite specimen



c) Top surface predicted thermal damage profile on unprotected composite specimen



d) Top surface predicted thermal damage profile on protected composite specimen

Figure 3. Thermocouple measurements and predicted damage profiles for both unprotected and protected composite specimens

3.2 Mechanical damage

In the thermo-mechanical models, delamination was the dominant failure mode. Under the influence of a single-cell runaway event, the predicted delamination area and depth were 9930 mm^2 and six plies

(0.88 mm), respectively. This represented an increase of 6% over the moderate thermal damage area predicted previously. The delamination depth was two plies or 0.3 mm deeper than the predicted moderate thermal damage, due to the combined effects of mechanical and thermal strains.

3.2 CaTR results

Figure 4 compares the CaTR strength after a single cell exposure and the strength of an undamaged specimen. The strength of the undamaged specimen was 333 MPa but after a single cell runaway event this reduced to 265 MPa.

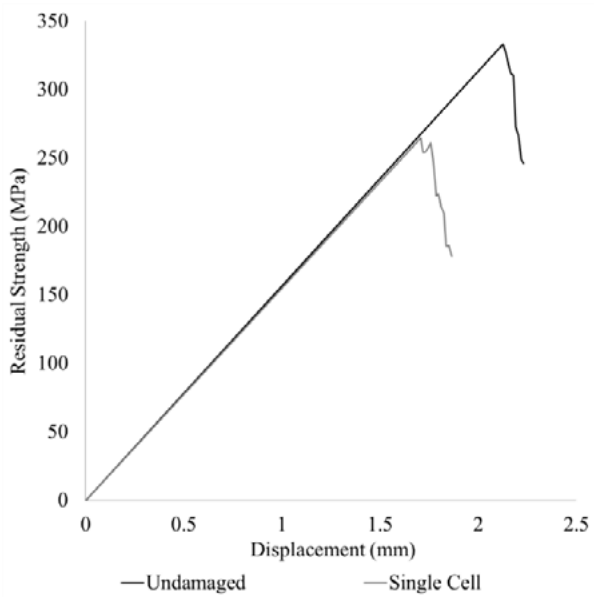


Figure 4. CaTR plots for undamaged and single cell specimens

4. Conclusions

The models presented herein have been used to predict thermal and mechanical damage during and after a cylindrical 18650 lithium-ion battery thermal runaway fire on a composite specimen. A thermal loading profile was developed, based on published experimental data, which could replicate the spatial and temporal variation of the fire. Initial validation was completed on an aluminium plate specimen before being applied to a typical aerospace composite. Results have shown, for unprotected specimens, the presence of damage from a single cell runaway can potentially reduce the residual strength by 20%. An intumescent coating was also modelled in heat transfer simulations, with material properties derived from literature. Application of a 0.5 mm coating reduced the thermal damage area from 10,587 mm^2 to 1431 mm^2 following a single cell thermal runaway event. Further details of the models used herein and results can be found in ref. [1].

References

[1] Sterling J, Tattersall L, Bamber N, De Cola F, Murphy A, Millen SLJ. Composite Structure Failure Analysis Post Lithium-Ion Battery Fire. Eng Fail Anal 2024;160. https://doi.org/10.1016/j.engfailanal.2024.108163.

[2] Zhang Y, Kong D, Ping P, Zhao H, Dai X, Chen X. Effect of a plate obstacle on fire behavior of 18650 lithium ion battery: An experimental study. J Energy Storage 2022;54. https://doi.org/10.1016/j.est.2022.105283.

[3] Zhang Y, Mei W, Qin P, Duan Q, Wang Q. Numerical modeling on thermal runaway triggered by local overheating for lithium iron phosphate battery. Appl Therm Eng 2021;192:116928. https://doi.org/10.1016/j.applthermaleng.2021.116928.

[4] Lamb J, Orendorff CJ, Steele LAM, Spangler SW. Failure propagation in multi-cell lithium ion batteries. J Power Sources 2015;283:517–23. https://doi.org/10.1016/j.jpowsour.2014.10.081.

[5] Mouritz AP, Feih S, Kandare E, Mathys Z, Gibson AG, Des Jardin PE, et al. Review of fire structural modelling of polymer composites. Compos Part A Appl Sci Manuf 2009;40:1800–14. https://doi.org/10.1016/j.compositesa.2009.09.001.

[6] Mouritz AP, Feih S, Kandare E, Gibson AG. Thermal–mechanical modelling of laminates with fire protection coating. Compos B Eng 2013;48:68–78. https://doi.org/10.1016/j.compositesb.2012.12.001.

[7] Vahabi H, Laoutid F, Mehrpouya M, Saeb MR, Dubois P. Flame retardant polymer materials: An update and the future for 3D printing developments. Materials Science and Engineering: R: Reports 2021;144. https://doi.org/10.1016/j.mser.2020.100604.

[8] Zhu Y, Zhang F, Xing L, Xie W, Cheng Y. Construction and verification of a heat transfer model for intumescent coatings. Prog Org Coat 2022;167. https://doi.org/10.1016/j.porgcoat.2022.106868.

[9] Kovács Z, Pomázi Á, Toldy A. Development of Multifunctional Flame-Retardant Gel Coatings for Automotive Applications. Coatings 2023;13. https://doi.org/10.3390/coatings13020345.

[10] Shen J. Experimental Study on the Inhibition of Lithium Battery Combustion and Explosion in Different Atmospheric Nitrogen Environment. 2021.

[11] Zhang Y, Kong D, Ping P, Zhao H, Dai X, Chen X. Effect of a plate obstacle on fire behavior of 18650 lithium ion battery: An experimental study. J Energy Storage 2022;54:105283. https://doi.org/10.1016/j.est.2022.105283.

[12] Millen SLJ, Murphy A. Understanding the influence of test specimen boundary conditions on material failure resulting from artificial lightning strike. Eng Fail Anal 2020;114. https://doi.org/10.1016/j.engfailanal.2020.104577.

[13] Foster P, Abdelal G, Murphy A. Modelling of mechanical failure due to constrained thermal expansion at the lightning arc attachment point in carbon fibre epoxy composite material. Eng Fail Anal 2018;94:364–78. https://doi.org/10.1016/j.engfailanal.2018.08.003.

[14] Millen SLJ, Murphy A, Catalanotti G, Abdelal G. Coupled thermal-mechanical progressive damage model with strain and heating rate effects for lightning strike damage assessment. Applied Composite Materials 2019;26:1437–59. https://doi.org/10.1007/s10443-019-09789-z.

[15] Millen SLJ, Xu X, Lee J, Mukhopadhyay S, Wisnom MR, Murphy A. Towards a virtual test framework to predict residual compressive strength after lightning strikes. Compos Part A Appl Sci Manuf 2023;174. https://doi.org/10.1016/j.compositesa.2023.107712.

ANISOTROPIC TOPOLOGY OPTIMIZATION CONSIDERING MULTIAXIAL FIBER ORIENTATIONS FOR COMPOSITE TRUSS STRUCTURES WITH IMPROVED INTERSECTION POINT DESIGN

Maximilian Eckrich[1], Peter A. Arrabiyeh[1], Anna M. Dlugaj[1], David May[1]

[1]Leibniz-Institut für Verbundwerkstoffe GmbH,
Erwin-Schrödinger-Str. 58, 67663 Kaiserslautern, Germany
Email: maximilian.eckrich@leibniz-ivw.de, Web Page: http://www.ivw.uni-kl.de

Keywords: Topology Optimization, BESO, Fiber Placement

Abstract
Modern fiber placement technologies for continuous fiber reinforced polymer composites allow for manufacturing of parts with complex shapes and load-adapated fiber orientation. For design of corresponding structures, anisotropic topology optimization is promising as it results in very light truss-structures with optimized fiber orientation. However, most anisotropic topology optimization approaches are limited towards exclusively unidirectional fiber orientations that are not suitable for intersection points with multiaxial stress states. Therefore, a bi-directional evolutionary structural optimization approach that uses unidirectional fiber orientations at regions with unidirectional stress states and biaxial fiber orientations where needed is developed. Results show that the proposed topology optimization approach produces fiber orientations at intersection points that are more suitable for manufacturing by fiber placement technologies such as Wet Fiber Placement compared to optimization with purely unidirectional fiber orientations. In addition, by adding a second fiber orientation at intersection points during the optimization procedure the probability for inter-fiber failure at those regions is reduced.

1. Introduction

Wet Fiber Placement (WFP) is a novel fiber placement process in which continuous fiber rovings are in-line impregnated with a thermoset resin system, conveyed to a placement head by a system of driven rollers, and – almost tension-free – placed directly into cavities of a mold. After placement, the molds can be demounted and transferred to a press for curing of the final part by applying temperature and pressure [1]. Since the freshly impregnated rovings are rather limp compared to preimpregnated tapes they can be placed in curved pathways [2], which allows for load-adapted placement and manufacturing of complex-shaped parts.

For design of such complex-shaped, lightweight structures, topology optimization is a promising approach. While material optimization and topology optimization have been combined by a wide number of researchers to account for the anisotropic material properties of continuous fiber reinforced polymer composites (CFRPC), those approaches are, in many cases, limited to exclusively unidirectional fiber orientations. Topology optimization usually results in truss structures, in which the trusses carry unidirectional tension or compression loads, whereas the intersection points between the individual trusses are subject to more complex, multiaxial stress states. For such regions, a unidirectional fiber orientation is not reasonable. Therefore, anisotropic topology optimization based on unidirectional fiber orientations may yield a design that is not feasible for manufacturing and for load transfer at intersection points. To overcome these issues a bi-directional evolutionary structural optimization

(BESO) procedure that accounts for unidirectional but also biaxial fiber orientations is developed and studied on benchmark test cases.

2. Materials

In our topology optimization procedure, we distinguish between solid, CFRPC material and void material representing the elements that are removed from the design space. For CFRPC we assume the material properties presented in Table 1. For the void material, we consider a Young's modulus of E_{Void} = 0.0001 MPa and a Poisson's ratio μ_{Void} = 0.3. [3]

Table 1. Elastic material properties for CFRPC [3].

E_{11} (MPa)	E_{22} (MPa)	E_{33} (MPa)	G_{12} (MPa)	G_{13} (MPa)	G_{23} (MPa)	μ_{12}	μ_{13}	μ_{23}
140,000	9,000	9,000	5,000	5,000	3,000	0.3	0.3	0.4

While it is not a direct objective of the optimization procedure, we also evaluate failure criteria for the optimized structures. For this Puck's failure criteria [4] is used together with the strength values provided in Table 2 [3].

Table 2. Strength values for CFRPC [3].

$R_{\parallel}^{t}$ (MPa)	$R_{\parallel}^{c}$ (MPa)	$R_{\perp}^{t}$ (MPa)	$R_{\perp}^{c}$ (MPa)	$R_{\perp\parallel}$ (MPa)
1750	1200	40	175	60

3. Methods

3.1. Anisotropic BESO

For topology optimization we use the anisotropic BESO procedure as presented in [5]. In this, the topology optimization problem is formulated as a compliance minimization subject to a volume constraint [5]:

$$\text{min:} \qquad \boldsymbol{C} = \frac{1}{2}\boldsymbol{F}^{\boldsymbol{T}}\boldsymbol{U} \tag{1}$$

$$\text{subject to:} \qquad V^{*} = \sum_{i=1}^{N} v_i x_i \tag{2}$$

In those equations, $\boldsymbol{C}$ is the compliance, which is the objective function to be minimized, $\boldsymbol{F}$ are the applied forces, and $\boldsymbol{U}$ the displacements. Furthermore, V^{*} is the target volume fraction of the design space that should be filled by CFRPC material, v_i is the volume of element i and x_i is its relative density. The relative density can either take values of 1 for CFRPC material or 0.001 for void material [5]. The decision, whether an element will contain CFRPC or void material is based on the element sensitivity α_i that can be calculated according to Eq. 3 [6]:

$$\alpha_i = -p\frac{E_i}{x_i} \tag{3}$$

In Eq. 3, E_i is the element strain energy that is directly obtained from finite element analysis (FEA) and p is a constant that is called penalty exponent. In the BESO procedure, the element sensitivities are filtered spatially and by their history from previous iterations. In this study the filtering scheme as described in [6] is applied. The BESO procedure starts with a design space completely filled with CFRPC material. The volume fraction of the CFRPC material is then subsequently decreased according to Eq. 4 [5]:

$$V_k = V_{k-1}(1 - ert) \text{ for } V_k > V^* \quad (4)$$

Here, ert is an evolution rate to be specified. Based on the volume fraction of the current iteration V_k a sensitivity threshold value α_{th} is determined using a bisection method [7]. Elements with a sensitivity that is larger than the threshold are assigned CFRPC material, while the other elements are assigned void material. When the target volume fraction is reached, the optimization procedure continues until a convergence criteria for the objective function is met [5].

In order to account for anisotropic material properties, the BESO procedure is coupled with computer aided internal optimization (CAIO) [8]: In each iteration of BESO, the elements are not only switched between CFRPC and void material, but their material orientation is aligned with the direction of the maximum absolute principal stress in the element. More detailed descriptions for this can be found in [5,6].

3.2. Consideration of biaxial fiber orientations

In order to consider not only unidirectional fiber orientations, but also biaxial fiber orientations at regions were this is necessary, we consider models that are build from two layers of shell elements as shown in Fig. 1 for the example of a plate clamped at its left end and subject to a vertical force at its right bottom corner. The first layer will be denoted as “master layer”. On this, we will perform most of the calculations needed for the anisotropic BESO procedure. The second layer referred to as “slave layer”, on the other hand will be only activated at regions of multiaxial stress states in order to add a second fiber orientations at such areas. Both layers are ideally connected by using a tie-constraint. For a symmetric laminate, a symmetry boundary condition (not shown in Fig. 1) can be added optionally. [3]

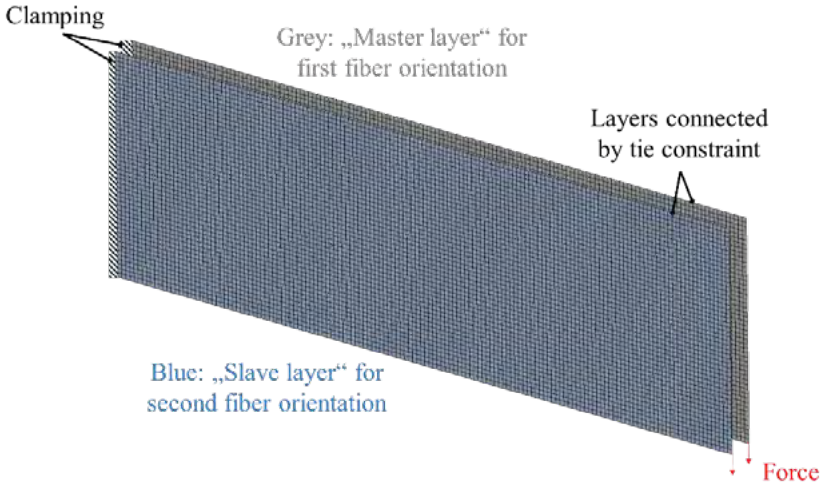


Figure 1. Finite element model of a plate consisting of two shell element layers.

To decide at which regions a second fiber orientation should be introduced, we define a variable sr that describes the stress ratio of an element i in the master layer m [3]:

$$sr_i = \frac{|\sigma_{I_{i,m}}|}{|\sigma_{II_{i,m}}|} \quad (5)$$

In Eq. 5, $\sigma_{I_{i,m}}$ is the first principal stress of element i in the master layer m and $\sigma_{II_{i,m}}$ is its second principal stress. Elements for which sr_i is smaller than a threshold sr_{th} are saved in a list and considered

as candidate elements for adding a second fiber orientation by activation of the corresponding element in the slave layer. To create smooth regions in which a second fiber orientation is added, the candidate elements are filtered: The slave layer element is only activated for candidate elements if more than half of the surrounding CFRPC elements in the master layer are also candidate elements. [3]

Of course activation of elements in the slave layer increases the overall volume fraction of CFRPC material in the design space. To account for this and to guarantee, that the overall CFRPC volume fractions between different optimization results are equal for comparability, we extent the variable space for the relative element density x_i: The relative element density x_i will therefore be 0.001 for void elements, 1 for elements in the master layer with unidirectional fiber orientation (corresponding slave element is deactivated) and 2 for elements in the master layer with biaxial fiber orientation (corresponding slave element is activated). The relative element densities are then considered in Eq. 2 for calculation of the solid material volume fraction. The volume fraction is only calculated based on the elements in the master layer. [3]

By choice of the threshold value sr_{th} the amount of material with a second fiber orientation can be controlled. However, large values for sr_{th} in an early stage of the optimization procedure – at which many regions with multiaxial stress states exist compared to a truss-like structure at a later stage of the optimization process – can lead to optimization instabilities, as "more material is removed" with respect to the plane design space in order to meet the volume fraction criteria. To avoid those, we start the optimization procedure with sr_{th} = 1 and subsequently increase sr_{th} after the target volume fraction is reached according to Eq. 6 [3]:

$$sr_{th,k} = sr_{th,k-1} + ert_{sr} \quad \text{for} \quad (sr_{th,k} < sr_{th}^{*} \; and \; V_{k-1} = V^{*}) \tag{6}$$

In this, $sr_{th,k}$ is the threshold value in iteration k and $sr_{th,k-1}$ is the threshold value from the previous iteration. ert_{sr} is an evolution rate for the stress ratio threshold and sr_{th}^{*} is a target value for the threshold. [3]

While in the master layer the element orientations are aligned with the direction of the maximum absolute principal stresses, a second (different) fiber orientation is required at regions of multiaxial stress states. To calculate the fiber orientation angle in the slave layer we utilize composite net theory, which is considered one of the first tools for design of composite structures [9]. By this we can simply calculate the fiber orientation angle of an active element in the slave layer by [3]:

$$\beta_2 = \arctan\left(-\frac{\sigma_{II_{i,m}}/\sigma_{I_{i,m}}}{\tan\beta_1}\right) \tag{7}$$

Where $\sigma_{II_{i,m}}$ and $\sigma_{I_{i,m}}$ are the principal stresses in the underlying element of the master layer, β_1 is the fiber orientation angle of the underlying element in the master layer and β_2 is the fiber orientation angle of the corresponding element in the slave layer [3].

Activation of elements in the slave layer s with a second fiber orientation of course affects the stress state and the strain energies obtained for the corresponding elements in the master layer m. To account for this Eqs. 3, 5, 7 are replaced by Eqs. 8, 9, 10 in case that the slave layer element is activate for a corresponding master element [3]:

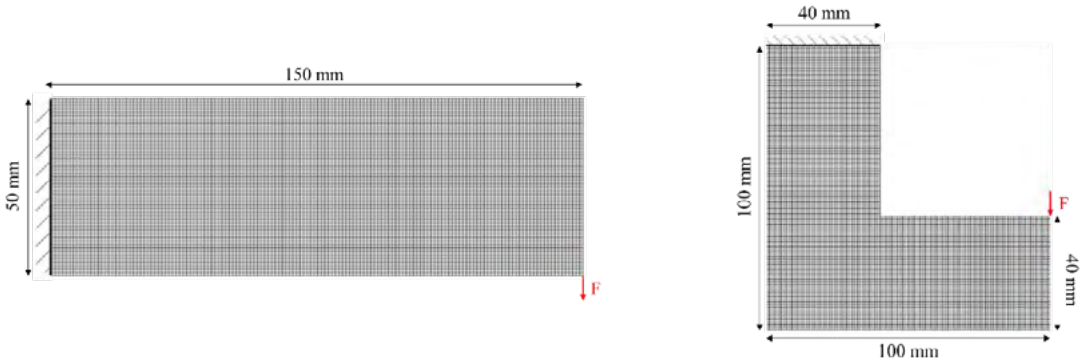
$$\alpha_{i,m} = -p\frac{(E_{i,m} + E_{i,s})}{x_{i,m}} \tag{8}$$

$$sr_i = \frac{|\sigma_{I_{i,m}}|}{|\sigma_{I_{i,s}}|} \tag{9}$$

$$\beta_2 = \arctan\left(-\frac{\sigma_{I_{i,s}}/\sigma_{I_{i,m}}}{\tan\beta_1}\right) \tag{10}$$

3.3. Test cases

Two numerical test cases are shown in order to evaluate the optimization procedure. The first one is a beam clamped on its left end and subject to a vertical force on its bottom right corner, the second one is a L-shaped cantilever (Fig. 2). For both test cases, a filter radius of 4 mm and a target volume fraction of 40% is used. As the parameter sr_{th}^* affects how much material with a second fiber orientation is added, for this parameter the values 1 (exclusively unidirectional optimization), 4, 6, 8, 10, and 12 are tested. [3]

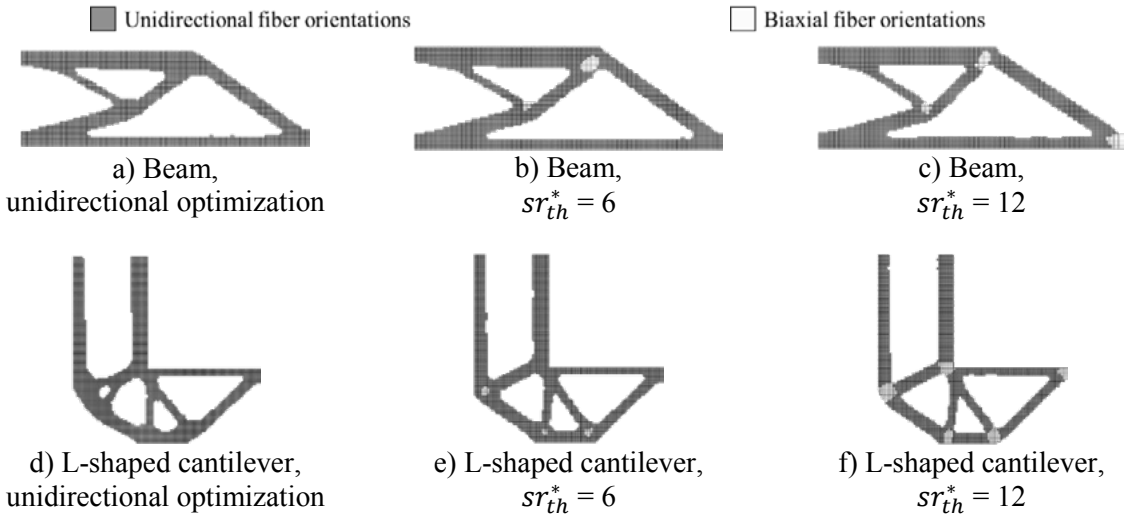


a) Beam test case b) L-shaped cantilever test case

Figure 2. Numerical test cases for topology optimization [3].

4. Results

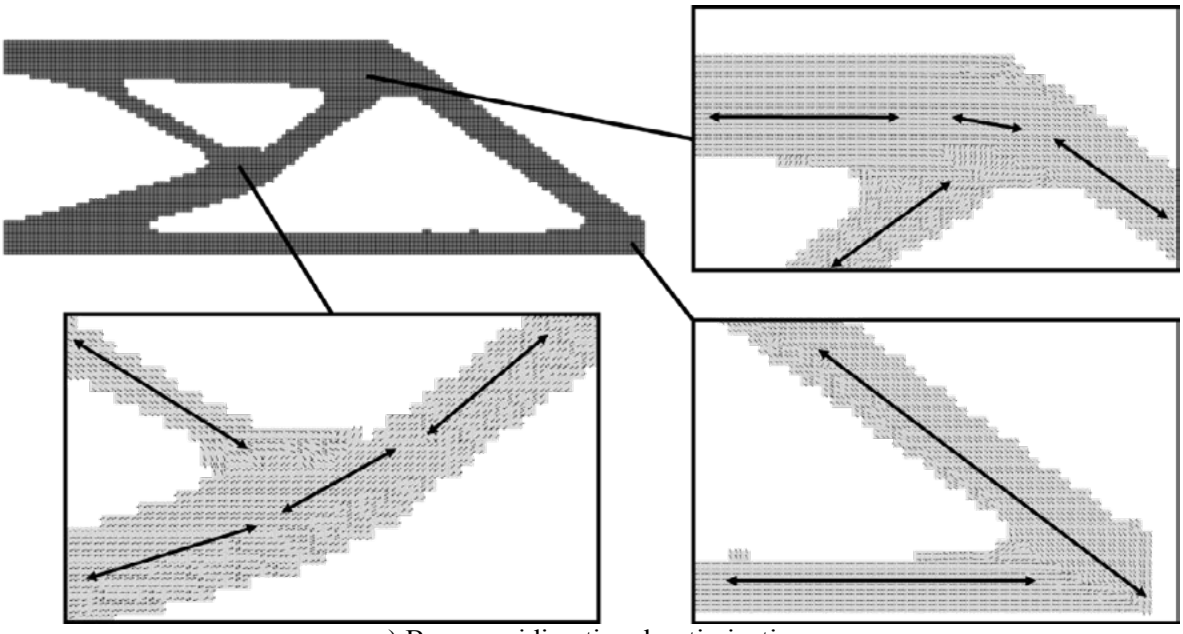
In the following, selected results from our studies are presented. For more detailed results, the reader is referred to [3]. Fig. 3 shows the material distribution for the optimization results considering sr_{th}^* values 1, 6, and 12. In this, the dark grey colored elements represent unidirectional fiber orientations and the light grey colored elements represent regions where a second fiber orientation is added. From Fig. 3, it can be obtained that, as expected, increasing values for sr_{th}^* lead to more and larger regions at which a second fiber orientation is added.



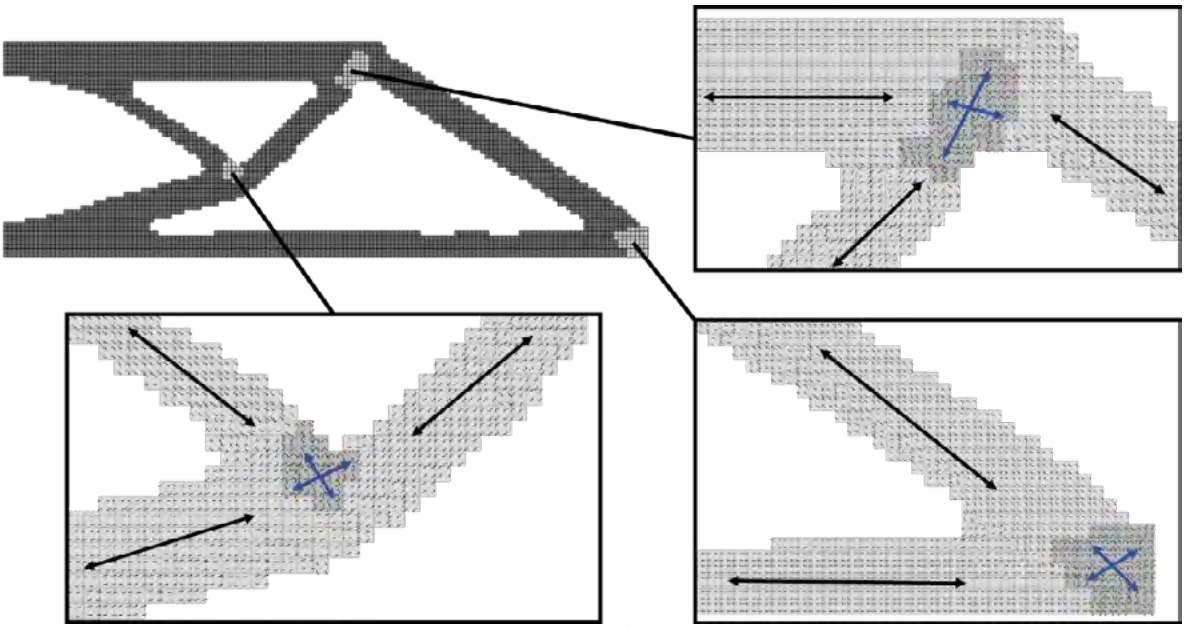
a) Beam, unidirectional optimization
b) Beam, sr_{th}^* = 6
c) Beam, sr_{th}^* = 12
d) L-shaped cantilever, unidirectional optimization
e) L-shaped cantilever, sr_{th}^* = 6
f) L-shaped cantilever, sr_{th}^* = 12

Figure 3. Optimization results and material distribution [3].

At the example of the beam test case, the fiber orientation distributions at intersection points are studied in more detail in Fig. 4 by comparing the unidirectional optimization result and the result for sr_{th}^{*} = 12. Regarding the unidirectional optimization result, the fiber orientations at intersection points are dominated from the higher stressed truss member. Therefore, there is no fiber continuity at intersection points and it is unclear, how the fiber bundles should be placed in the WFP process. For the biaxial optimization result on the other hand, the fiber orientations obtained indicate, that overlapping fiber bundles should be placed above each other. This is considered a feasible design, as by that small placement radii, that would very likely lead to placement defects [2], are avoided.



a) Beam, unidirectional optimization



b) Beam, sr_{th}^{*} = 12

Figure 4. Fiber orientations at intersection points for beam test case.

While it is not a direct objective of the optimization process, the biaxial fiber orientations are also found to be beneficial for structural strength. Fig. 5 shows the results for fiber failure (FF) stress exposure

factors and inter-fiber failure (IFF) stress exposure factors utilizing Puck's failure criteria at the example of the L-shaped cantilever considering a load of 2000 N [3]. Regarding FF stress exposure, there is little difference between the unidirectional and biaxial optimization result – in both cases FF stress exposure factors can be considered uncritical. However, the optimization considering exclusively unidirectional fiber orientations leads to critical IFF values > 1 at all intersection points. Therefore, the resulting fiber orientation is not feasible to achieve sufficient strength. IFF stress exposure is clearly improved when adding a second fiber orientation during topology optimization (Fig. 5 e) and f)). Therefore, the approach leads to designs that require less redesign in such regions compared to topology optimization considering only one fiber orientation.

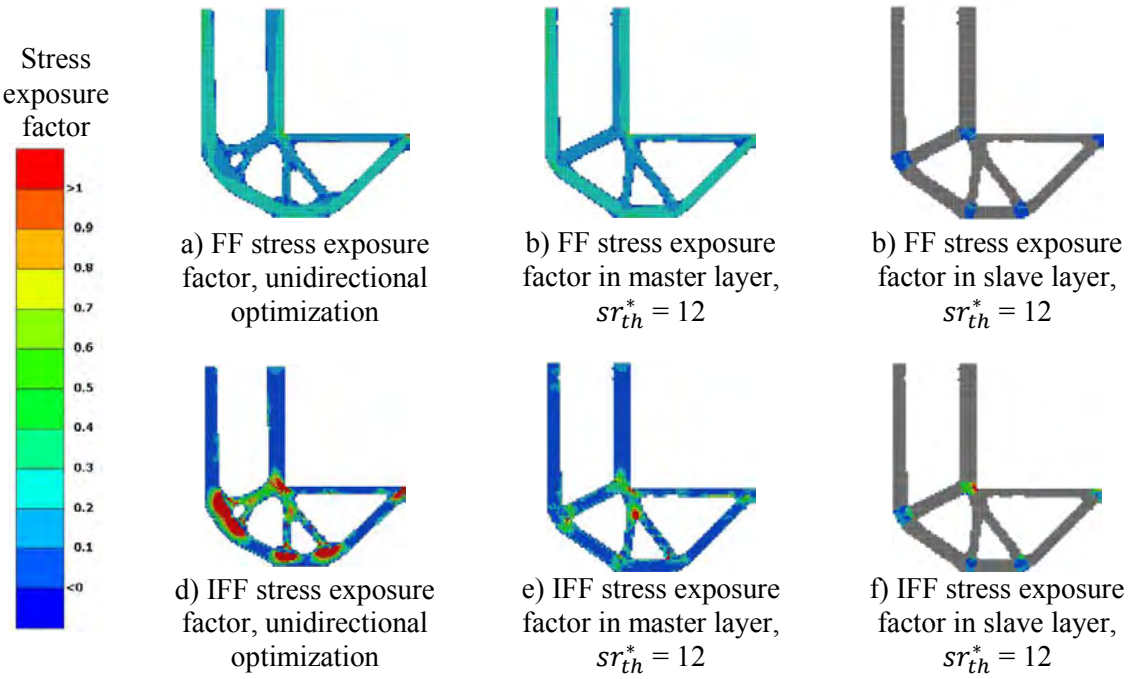


Figure 5. FF and IFF stress exposure factors for L-shaped cantilever test case.

In [3], the impact of adding a second fiber orientation on structural compliance is also discussed. It was found that the approach can lead to improved structural compliance, but whether an improvement is achieved depends on the specific test case and also on the target volume fraction.

5. Conclusions

In this study, an anisotropic BESO algorithm that adds a fiber orientation at regions in which a multiaxial stress state is present is developed. The choice where a second fiber orientation is added is made based on the stress state within the finite elements. It could be shown that a parameter describing the stress ratio in the finite elements can be used to control the number and size of regions in which a second fiber orientation is added. From numerical test cases, it was observed that the fiber orientation distribution at intersection points is improved regarding the manufacturability of topology-optimized structures and also structural strength is improved by reducing the probability of inter-fiber failure.

Acknowledgments

The project "TopComposites – Topology-optimized and resource efficient composites for mobility and transport" is funded by the Federal Ministry of Education and Research (Funding reference 03XP0259).

References

[1] D. May, M. Domm, P. Mitschang. Wet fiber placement: A novel manufacturing technology for continuous fiber reinforced polymer composites. *Journal of Composite Materials*, 52(4):521-533, 2019.

[2] M. Eckrich, P. A. Arrabiyeh, A. M. Dlugaj, D. May. Placement defects in thermoset-impregnated rovings deposited along curved paths. *Polymer Composites*, 44(6):3634-3645, 2023.

[3] M. Eckrich, P. A. Arrabiyeh, A. M. Dlugaj, D. May. An anisotropic topology optimization procedure for continuous fiber reinforced polymer structures with biaxial fiber layout for improved intersection point design. *Composite Structures*, 337:118064, 2024.

[4] A. Puck and H. Schürmann. Failure analysis of FRP laminates by means of physically based phenomenological models. *Composites Science and Technology*, 62(12-13):1633-1662, 2002.

[5] K. Mehl, S. Schmeer, N. Motsch-Eichmann, P. Bauer, I. Müller, J. Hausmann. Structural Optimization of Locally Continuous Fiber-Reinforcements for Short Fiber-Reinforced Plastics. *Journal of Composites Science*, 5(5):118, 2021.

[6] M. Eckrich, P. A. Arrabiyeh, A. M. Dlugaj, D. May. Structural topology optimization and path planning for composites manufactured by fiber placement technologies. *Composite Structures*, 289:115488, 2022.

[7] Z. H. Zuo and Y. M. Xie. A simple and compact Python code for complex 3D topology optimization. *Advances in Engineering Software*, 85:1-11, 2015.

[8] C. Mattheck, A. Baumgartner, R. Kriechbaum, F. Walther. Computational methods for the understanding of biological optimization mechanisms. *Computational Materials Science*, 1(3):302-312, 1993.

[9] D. Klein, W. Malezki, S. Wartzack. Introduction of a computational approach for the design of composite structures at the early embodiment design stage. In *International Conference on Engineering Design, ICED 15*, Milano, 2015.

CHARACTERIZING THE MECHANICAL BEHAVIORS OF GRAPHENE NANOCOMPOSITES USING MOLECULAR DYNAMICS SIMULATION

Jia-Lin Tsai[1] and Po-Ying Tseng[2]

[1]Department of Mechanical Engineering, National Yang Ming Chiao Tung University, Hsinchu, Taiwan
Email: jialin@nycu.edu.tw
[2]Department of Mechanical Engineering, National Yang Ming Chiao Tung University, Hsinchu, Taiwan
Email: tsengpoying0405@gmail.com

Keywords: molecular dynamics simulation, graphene, nanocomposites, mechanical behaviors

Abstract
The study aimed to characterize the mechanical behaviors of graphene nanocomposites using molecular dynamics (MD) simulation. Both monolayer graphene and multilayer graphene were considered as reinforcement in the epoxy matrix. The influences of surface functionalization and graphene waviness on the behaviors of the nanocomposites were also examined. The moduli of the nanocomposites were evaluated from simple tension simulation. In order to explicate the load transfer efficiency between the graphene and the surrounding matrix, the local stress of the graphene was calculated. Moreover, the pullout simulations were also carried out to characterize the interfacial behavior of the graphene and the epoxy matrix. Results indicated that the increase in the number of graphene layers reduced the Young's moduli of the nanocomposite. The reduction of moduli for the nanocomposites was attributed to the poor interfacial properties.

1. Introduction

In recent years, with the advancement of nanotechnology, nano-materials with the characteristics of high surface area-to-volume ratio have been applied in composite materials, forming nanocomposites. Graphene with excellent mechanical properties has been introduced in nanocomposites as reinforcement. In graphene nanocomposites, graphene often exhibited a multilayered or curved morphology [1-3], and these different forms of graphene may influence the mechanical properties of the nanocomposite. Moreover, the mechanical properties of nanocomposites are closely related to the interfacial properties between the reinforcement and surrounding matrix. Thus, understanding the influence of the graphene morphology and the interfacial properties between nano-reinforcements and the matrix on the mechanical properties of nanocomposites has become an essential topic in the society of nanocomposites [4-6]. This study utilized MD simulations to investigate a model of multilayer graphene/epoxy resin nanocomposites. By analyzing mechanical properties, and local stress distribution on graphene, we aimed to understand the effects of different forms of graphene on the moduli of nanocomposites and further explore the underlying physical mechanisms.

2. Molecular dynamics simulation

2.1. Generation of atomistic model

In MD simulation, the atomistic interactions between molecular were described using potential function. In this study, the Polymer Consistent Force Field (PCFF) [7] potential was adopted to model the bonded and non-bonded interactions. This is because that this potential has been widely used in MD models for epoxy resin and graphene [8, 9]. Regarding the epoxy resin molecular chains, a structure representing a cross-linked resin with a crosslink density of 50% was constructed using 9 EPON862® resins and 3 TETA® hardeners [10]. For multilayer graphene, the initial stacking was done in an A-B-A configuration. Concerning surface modification of graphene, carboxyl (-COOH) and amine (-NH2) groups were introduced based on experimental measurements [9], with

modification proportions of 4.7% and 9.7%, respectively. The modification proportion was defined as the number of functional groups divided by the number of carbon atoms in a single-layer graphene. The Large-scale Atomic/Molecular Massively Parallel Simulator (LAMMPS) [11] was utilized for MD simulations.

In the MD simulation, the atomistic models for graphene/epoxy nanocomposites need to be established. The graphene length and width in x and y directions was 100 Å and 21 Å, respectively, with periodic boundaries in the y direction. The graphene was placed in the middle of the simulation cell, and constraints were applied to maintain its rigidity and to prevent the effect of external forces. Epoxy resin molecules were randomly distributed throughout the cell. The length of the cell in the y direction was then compressed to 150 Å, and the density in the z direction is compressed to approximate experimental values under NVT ensemble at 800 K. Subsequently, the temperature was reduced from 800 K to 300 K within 90 ps under NPT ensemble at zero atmospheric pressure, and the constraints on graphene were removed. Finally, the system was equilibrated at 300 K for 300 ps to reach a stable state of the graphene/epoxy resin nanocomposite model. Figure 1 illustrates the atomistic model for the nanocomposites containing monolayer, two-layer and four layer graphene. In these atomistic models, the volume fractions of graphene were the same.

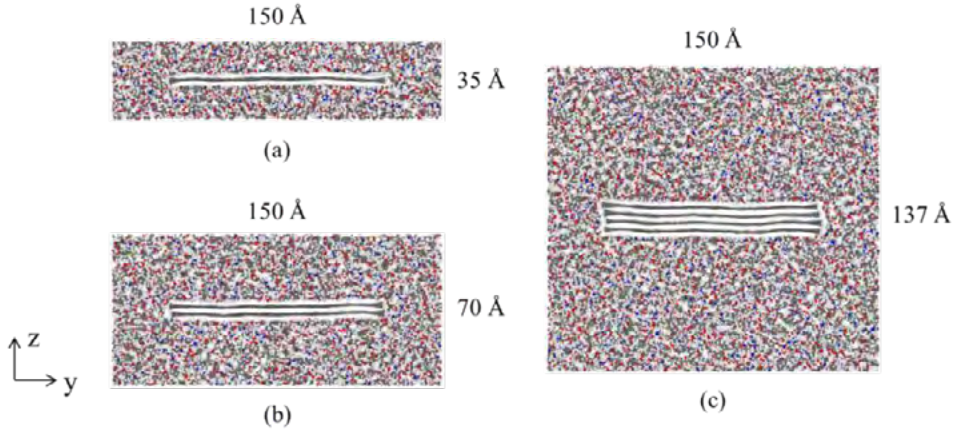


Figure 1. Atomistic model of graphene nanocomposites
(a) monolayer (b) two layers (c) four layers

On the other hand, for the nanocomposites with wavy graphene, the sinuous form of graphene was described using a sine function to quantify the degree of curvature of graphene as follows

$$z = a\sin\left(\frac{2\pi x}{L}\right) \tag{1}$$

where a is the amplitude and L is the wave length of the sine function. The waviness ratio of graphene is defined as α=a/L. In this study, α = 0.05, 0.1 and 0.15 were considered. By following the equilibrium procedure described early, the atomistic models of nanocomposites with two-layer wavy graphene were generated as shown in Figure 2.

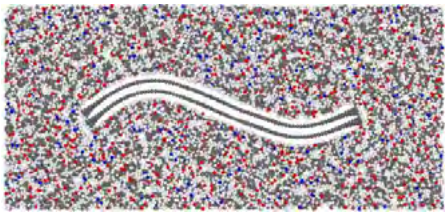


Figure 2. Atomistic model of wavy graphene nanocomposites (α = 0.1)

2.2. Simple tensile simulation

The mechanical properties of the nanocomposites were characterized through tensile loading simulation. The atomistic model was placed under the NPT ensemble with zero pressure in all directions and the temperature was reduced from 300 K to 0.1 K within 40 ps. Subsequently, equilibrium was conducted at 0.1 K for 10 ps to obtain a nanocomposite model close to absolute zero. Next, an amount of strain was applied in the graphene plane direction (y-direction) of the simulation cell. Each time a strain of 0.005 was applied, stress relaxation was performed simultaneously in the x and z directions, followed by a 50 ps equilibration process. This process was repeated for uniaxial tensile simulation until the strain reached 2%, and the corresponding stress of the nanocomposites was recorded for each strain. Stress was calculated using the Virial stress [12] which calculated the average stress components in all directions of the simulation cell. However, to further investigate the load transfer efficiency and mechanism between graphene and epoxy resin within the nanocomposites, it is necessary to perform local stress calculations. Lutsko [13] and Cormier et al. [14] developed the Lutsko stress, which calculated the average stress within a chosen Lutsko volume to analyze the local stress distribution in the materials. In this study, the local stress within graphene was calculated and the load transfer efficiency was defined as the ratio of the average Lutsko stress to the Virial stress along the tensile direction of the nanocomposites.

2.3. Pullout simulation

To further investigate the influence of the interfacial properties on the load transfer between graphene and epoxy resin, we also conducted graphene pull-out simulations and calculated the corresponding average interfacial shear stress. This simulation methodology was used by many researchers to explore load transfer behaviors between different materials [15-17]. The pullout simulation involved the calculation of the graphene pull-out energy, which was defined as

$$U_{pullout} = U_2 - U_1 \tag{2}$$

Where U_2 is the energy when the graphene was completely pullout. On the other hand U_1 is the energy, when the graphene was fully embedded with the nanocomposites. Figure 3 depicts snapshots before and after the pull-out process of two-layer graphene. Based on the pullout energy, the averaged interfacial stress was then evaluated as

$$\tau_i = \frac{U_{pullout}}{wL^2} \tag{3}$$

where w and L denote the width and length of the graphene, respectively.

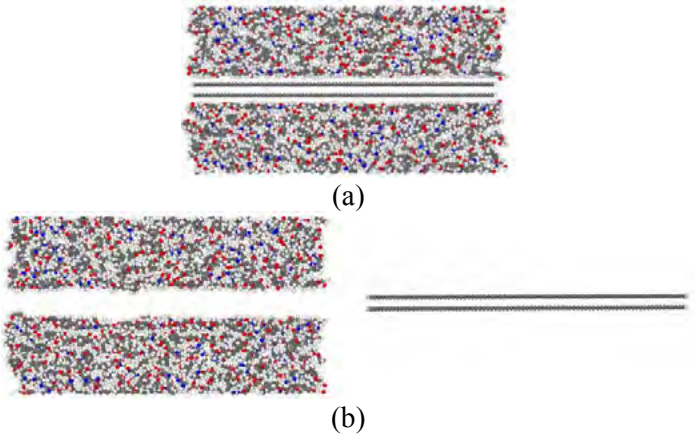


Figure 3. Schematic of graphene pull-out simulation
(a) Before graphene pull-out, (b) After graphene pull-out

3. Results and discussion

The results of the Young's moduli for different numbers of layers and levels of curvature are presented in Table 1. It can be observed that surface modification can effectively enhance the mechanical properties of the nanocomposite material compared to the unmodified case. Specifically, for single-layer graphene, the Young's modulus increases from 8.48 GPa to 10.26 GPa after modification. Regarding the number of layers, it is noticeable that as the number of graphene layers increases, the Young's moduli of the nanocomposite material decreases, indicating that aggregation of graphene reduces the mechanical properties of the nanocomposite. When the curvature increases, regardless of modification, there is a significant decrease in the Young's moduli of the nanocomposite material. For unmodified single-layer graphene, the Young's modulus decreases by nearly 50% at $\alpha = 0.15$, indicating a significant impact of this curvature effect on the mechanical properties of the nanocomposites. Additionally, comparing the α values from 0 to 0.15 for one-layer, two-layer, and four-layer graphene, it can be observed that as the α value increases, the difference in Young's moduli in terms of different-layer graphene nanocomposite materials is becoming minor. At $\alpha = 0.15$, there is no significant difference in the Young's moduli between single-layer and multi-layer graphene nanocomposite materials. For the practical applications, when using graphene, it is essential to maintain its flatness to achieve a more significant enhancement in the Young's moduli of the nanocomposites.

Table 1. Young's modulus of graphene nanocomposites

Layer number	Young's modulus of nanocomposite (GPa)							
	Pristine graphene				Functionalized graphene			
	α=0	α=0.05	α=0.1	α=0.15	α=0	α=0.05	α=0.1	α=0.15
1	8.48	5.97	5.13	4.38	10.26	8.43	6.69	5.43
2	6.64	6.48	5.28	4.35	8.29	6.89	6.60	5.21
4	5.86	5.70	5.03	4.42	7.22	5.92	5.52	4.72

Table 2. Load transfer efficiency of nanocomposites with four layer graphene

	Pristine graphene		Functionalized graphene	
	outermost layer	inner layer	outermost layer	inner layer
Average Lutsko stress(GPa)	0.384	0.278	0.909	0.386
Load transfer efficiency	4.22	3.05	7.97	3.39

Load transfer efficiency of nanocomposites with four layer graphene is listed in Table 2. It can be seen that the outer layer of graphene exhibits better load transfer efficiency than the inner layer. This may

be due to the phenomenon of loss of stacking between layers during stretching, as mentioned in previous literature [18], where the shear strength between graphene layers is lower than the shear strength at the polymer/graphene interface, resulting in reduced load transfer efficiency for the inner layers of multi-layer graphene. In addition, Table 2 illustrates that surface modification can significantly increases the load transfer efficiency of the outer layer of graphene from 4.22 to 7.97. However, the increase in load transfer efficiency for the inner layer of graphene is lower, only rising from 3.05 to 3.39. This phenomenon demonstrates that surface modification can effectively enhance the load transfer between the outer layer of graphene and the epoxy resin, with a lower increase in efficiency for the inner layer. The stress values of the inner and outer layers of four-layer graphene were averaged and the corresponding load transfer efficiency was calculated. The results for the four layer case were compared with the results for one and two layers in Table 3. It can be observed that single-layer graphene has a higher load transfer efficiency compared to multi-layer graphene, primarily because of the lower load transfer efficiency of the inner layers in multi-layer graphene. These results can explain the reduction in the Young's moduli of the nanocomposites with multi-layer graphene.

Table 3. Load transfer efficiency of nanocomposites

	Pristine graphene			Functionalized graphene		
	1 layer	2 layer	4 layer	1 layer	2 layer	4 layer
Average Lutsko stress(GPa)	0.796	0.380	0.331	1.413	0.822	0.648
Load transfer efficiency	5.65	3.92	3.64	8.94	6.63	5.68

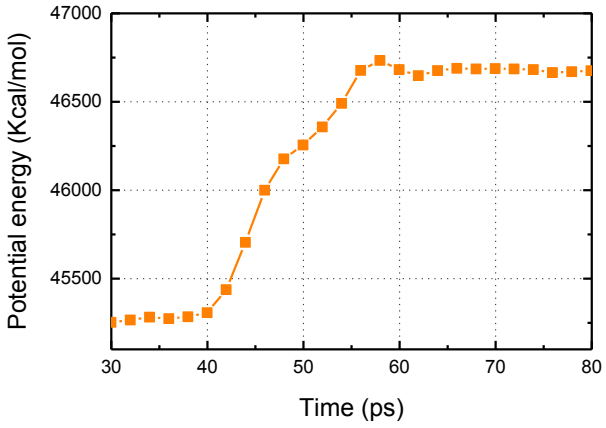


Figure 4. Energy variations during graphene pull-out simulation

Figure 4 shows the variation of potential energy during the pull-out process. Subtracting the potential energy U_1 before 40 ps from the potential energy U_2 after 60 ps yielded the graphene pull-out energy, and the corresponding interfacial shear stress is listed in Table 4. The results indicate that the interfacial shear stress between graphene and epoxy resin decreases with an increase in the number of graphene layers. For single-layer graphene, the interfacial shear stress is 46.4 MPa, whereas for four-layer graphene, it decreases to 39.2 MPa. This further demonstrated that adding single-layer graphene to epoxy resin can result in better mechanical properties as compared to multi-layer graphene.

Table 4. Interfacial shear stress in graphene nanocomposites

Layer number	Pullout energy (Kcal/mol)	Interfacial shear stress (MPa)
1	1397	46.4
2	1234	40.9
4	1182	39.2

4. Conclusions

The mechanical properties of graphene nanocomposites were examined using MD simulation. The moduli of the nanocomposites were calculated and the load transfer efficiency between the graphene and the surrounding matrix was evaluated. Moreover, the pullout simulations were also carried out to characterize the interfacial behavior of the graphene and the epoxy matrix. Results illustrated that the increase in the number of graphene layers reduced the Young's moduli of the nanocomposite, which was mainly due to the low load transfer efficiency of the graphene inner layer. The pullout simulation revealed that the interfacial shear stress of the multilayer graphene was lower than that of the monolayer graphene. In addition, graphene surface functionalization can effectively improve the load transfer efficiency between graphene and epoxy matrix, thereby improving the Young's moduli of the nanocomposites, wherein the enhancement of the outermost layer is more significant than the inner layer. In addition, the phenomenon that wavy graphene would dramatically reduce the Young's modulus of the graphene nanocomposite was observed in our simulation.

Acknowledgments

This research was supported by National Science and Technology Council of Taiwan, which was awarded to National Yang Ming Chiao Tung University.

References

[1] I. M. Inuwa, A. Hassan, S. A. Samsudin, M. H. Mohamad Kassim, and M. Jawaid. Mechanical and thermal properties of exfoliated graphite nanoplatelets reinforced polyethylene terephthalate/polypropylene composites. *Polymer Composites*, vol. 35: pp. 2029-2035, 2014.

[2] J. Shang, Y. Chen, Y. Zhou, L. Liu, G. Wang, X. Li, J. Kuang, Q. Liu, Z. Dai, H. Miao, L. Zhi, and Z. Zhang. Effect of folded and crumpled morphologies of graphene oxide platelets on the mechanical performances of polymer nanocomposites. *Polymer*, vol. 68: pp. 131-139, 2015.

[3] J.-E. An and Y. G. Jeong. Structure and electric heating performance of graphene/epoxy composite films. *European Polymer Journal*, vol. 49: pp. 1322-1330, 2013.

[4] J. C. Huang. Carbon black filled conducting polymers and polymer blends. *Advances in Polymer Technology: Journal of the Polymer Processing Institute.* vol. 21: pp. 299-313, 2002.

[5] M. Okamoto and S. S. Ray. Polymer/clay nanocomposites. *Encyclopedia of nanoscience and nanotechnology*. vol. 8: pp. 791-843, 2004.

[6] M. Moniruzzaman and K. I. Winey. Polymer nanocomposites containing carbon nanotubes. *Macromolecules*. vol. 39: pp. 5194-5205, 2006.

[7] H. Sun, S. J. Mumby, J. R. Maple, and A. T. Hagler. An ab initio CFF93 all-atom force field for polycarbonates. *Journal of the American Chemical society*. vol. 116: pp. 2978-2987, 1994.

[8] T.-Y. Wang and J.-L. Tsai. Investigating thermal conductivities of functionalized graphene and graphene/epoxy nanocomposites. *Computational Materials Science*. vol. 122: pp. 272-280, 2016.

[9] M.-W. Lee, T.-Y. Wang, and J.-L. Tsai. Mechanical properties of nanocomposites with functionalized graphene. *Journal of composite materials.* vol: pp. 3779-3789, 2016.

[10] H. Shin, S. Yang, S. Chang, S. Yu, and M. Cho. Multiscale homogenization modeling for thermal transport properties of polymer nanocomposites with Kapitza thermal resistance. *Polymer*. vol. 54: pp. 1543-1554, 2013.

[11] S. Plimpton. Fast parallel algorithms for short-range molecular dynamics. *Journal of computational physics*. vol. 117: pp. 1-19, 1995.

[12] D. Tsai. The virial theorem and stress calculation in molecular dynamics. *The Journal of Chemical Physics*. vol. 70: pp. 1375-1382, 1979.

[13] J. Lutsko. Stress and elastic constants in anisotropic solids: Molecular dynamics techniques. *Journal of applied physics.* vol. 64: pp. 1152-1154, 1988.

[14] J. Cormier, J. Rickman, and T. Delph. Stress calculation in atomistic simulations of perfect and imperfect solids. *Journal of Applied Physics*. vol. 89: pp. 99-104, 2001.

[15] K. Liao and S. Li. Interfacial characteristics of a carbon nanotube–polystyrene composite system. *Applied physics letters*. vol. 79: pp. 4225-4227, 2001.

[16] M. Li, H. Zhou, Y. Zhang, Y. Liao, and H. Zhou. The effect of defects on the interfacial mechanical properties of graphene/epoxy composites. *RSC advances.* vol. 7: pp. 46101-46108, 2017.

[17] A. Alian and S. Meguid. Molecular dynamics simulations of the effect of waviness and agglomeration of CNTs on interface strength of thermoset nanocomposites. *Physical Chemistry Chemical Physics*. vol. 19: pp. 4426-4434, 2017.

[18] Y.-J. Wan, L.-C. Tang, L.-X. Gong, D. Yan, Y.-B. Li, L.-B. Wu, J.-X. Jiang, G.-Q. Lai. Grafting of epoxy chains onto graphene oxide for epoxy composites with improved mechanical and thermal properties. *Carbon* vol. 69: pp. 467-480, 2014.

BIOMIMETIC ARCHITECTED CERAMICS: ENHANCING INTERFACIAL PROPERTIES AND ENERGY ABSORPTION THROUGH SURLYN-ALUMINA COMPOSITES

Ehsan Azad[1,2], Hamidreza Yazdani Sarvestani[2]*, Behnam Ashrafi[2]*, Frajad Shadmehri[1], Mehdi Hojjati[1]

[1]Concordia Center for Composites, Department of Mechanical, Industrial, and Aerospace Engineering, Concordia University, Montreal, QC H3G 1M8, Canada
Email: ehsan.azad@concordia.ca, farjad.shadmehri@concordia.ca, mehdi.hojjati@concordia.ca
[2]Aerospace Manufacturing Technology Center, National Research Council Canada, Montreal, QC H3T 2B2, Canada
Email: hamidreza.yazdani@nrc-cnrc.gc.ca, behnam.ashrafi@nrc-cnrc.gc.ca

Keywords: Bioinspired ceramics; Interfacial strength; Microstructure engineering.

Abstract
Ceramic materials, known for their strength, often lack the flexibility and energy absorption required for diverse applications. This study dives into the static and cyclic flexural properties, including energy absorption, stiffness, and strength, of bioinspired ceramic-polymer composites. Specifically, we explore how different micro-patterns influence these properties. Utilizing ultra-short pulsed picosecond lasers in a subtractive manufacturing process, we engrave an array of micro-patterns onto alumina tiles, mimicking the designs found in natural armors. These laser-engraved tiles are then layered with an interlayer of Surlyn®, a commercial monomer, to create the composites. Our findings highlight the intricate relationship between the composites' performance and the bioinspired surface patterns. Certain macro architectures result in significant improvements in energy absorption, with enhancements of up to 85%. These improvements are attributed to mechanisms such as crack deflection, interfacial friction, and plastic deformation of the soft phase. This research not only advances our understanding of natural armor structures but also lays the groundwork for a new era of ceramic composites with superior properties.

1. Introduction

Ceramics are vital materials across various industries, prized for their exceptional thermo-mechanical properties, hardness, durability, and low electrical conductivity. However, their inherent brittleness presents a significant challenge, limiting their damage tolerance. Despite efforts to enhance impact resistance and toughness through strategies like nano-material dispersion and microstructure control, significant improvements have been elusive [1-5].

In materials like nacre, significant energy dissipation occurs due to inelastic deformations around cracks, a primary toughening mechanism. Complex interfaces in natural materials lead to outstanding combinations of stiffness, strength, and toughness. For instance, the heterogeneous architecture of beetle cuticles initiates localized toughening mechanisms, enhancing mechanical performance while reducing weight [6-10].

Recent efforts have integrated bioinspired architectures with ceramics to achieve optimized stiffness, strength, and toughness balances. However, unlocking the full potential of bioinspired materials requires scalable manufacturing technologies capable of producing complex structures [11-15]. To address this, we've developed a digital manufacturing platform enabling precise control over 3D architecture, including micro-pattern cut depth. This platform fabricates multilayered ceramic composites with bioinspired hard building blocks and soft interlayers. Through experimental investigation, we compare the static and cyclic mechanical performance of these ceramics with and

without patterns. This innovative approach yields a new class of ceramics offering predictable, high-performance responses, essential for advanced composite development [16-18].

2. Materials and Methods

2.1. Material Fabrication

High-tolerance nonporous alumina ceramic tiles (96-99.8% Al_2O_3, 3875 kg/m^3 density, McMaster-Carr, No. 8462 K45) with a thickness of 635 µm serve as the rigid component. A 100 µm thick Surlyn® thermoplastic film acts as the soft polymer interface between the ceramic tiles. Four beams are created by circular diamond saw-cutting the ceramic tiles, each measuring 25 mm wide and 114 mm long. Laser machining is performed on the tiles before lamination, using established parameters for alumina laser machining. An Ytterbium picosecond fiber laser (YLPP-25-3-50-R, IPG Photonics, USA) with 50 W maximum average power, emitting 3 ps pulses at 1030 nm wavelength, is used. The laser can operate at up to 1.83 MHz repetition rate and generates a Gaussian beam profile.

A 45° oriented micro-pattern (Figure 1a) and a hexagonal pattern penetrating the entire ceramic thickness with 5 mm length (Figure 1b) are applied. The micro-patterns, designed for precise surface engraving, achieve a depth of 20 µm in a single pass with a 200 µm kerf width matching the spacing between patterns. Each beam consists of two ceramic tile layers with the same engraved hexagonal pattern and an intermediate Surlyn® layer. One group of beams includes micro-patterns, while the others do not. Components are assembled using vacuum bagging and subjected to a 5-hour heat treatment at 146 °C for proper bonding and desired properties.

2.2. Experimental Setup

All specimens undergo 3-point bending tests with an 80 mm fixed span length (Figure 1e). In static tests, a constant displacement control at 1.3 mm/min rate is applied until 12 mm deflection. For cyclic tests, a combined control strategy is used. Loading phase maintains a 6 mm/min rate for 1 mm/cycle over 12 cycles. The control mode transitions to load control during unloading to capture specimen behavior under cyclic loading, providing a comprehensive assessment of material response in static and cyclic conditions.

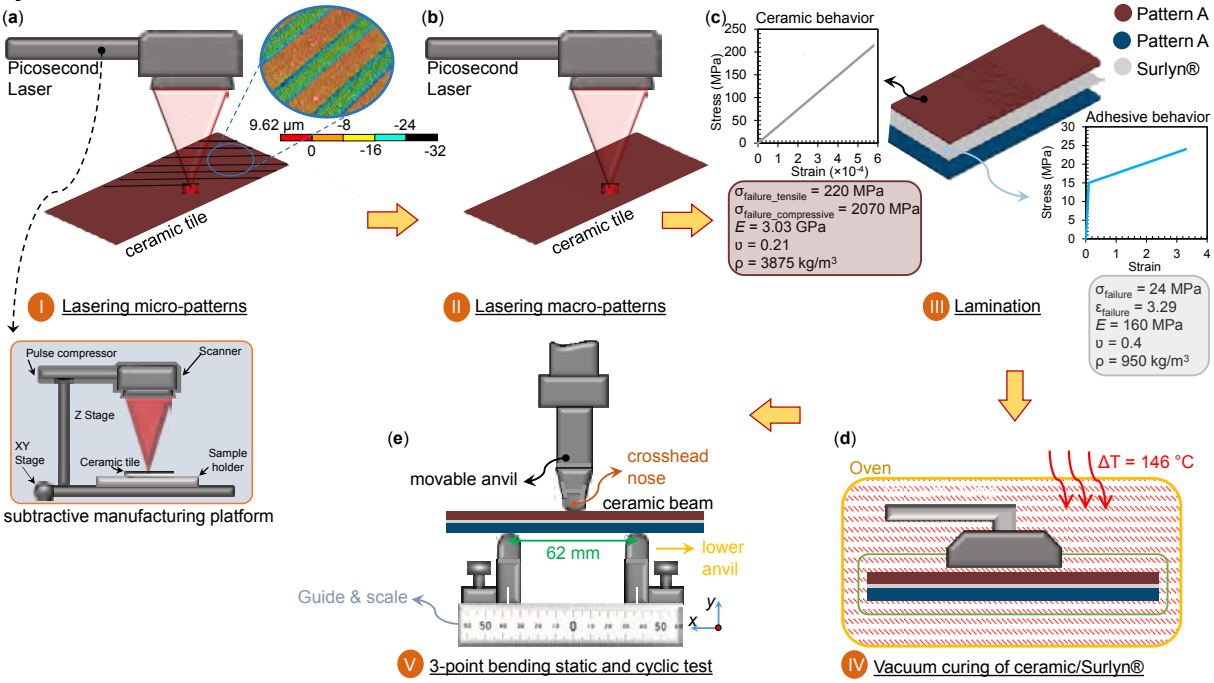


Figure 1. The manufacturing process of the bi-layer architectured ceramic beams: (**a**) Micro-patterning of ceramic tiles using the picosecond laser and subtractive manufacturing platform, (**b**) Macro-patterning of ceramic tiles using the picosecond laser, (**c**) Lamination of ceramic tiles and

commercial monomer Surlyn, (**d**) Vacuum bagging and curing of ceramic composite beams, and (**e**) Configuration for static and cyclic 3-point bending tests.

3. Results and Discussion

The architectured ceramic beams were subjected to 3-point bending static load testing to evaluate the impact of stacking sequences (Back-to-back (BB), Side-down (SD), Side-up (SU), and Face-to-face (FF)), along with micro-patterns, on their mechanical performance. The main parameters assessed included maximum load, flexural stiffness, and energy absorption. The energy absorbed by the structures in the static analysis was determined by the area under the force-displacement curves, while the cyclic analysis was represented by the loop area.

3.1. Static Loading

Figure 2 shows how micro-patterns significantly enhance the ceramics' mechanical properties under static load. Micro-patterns improve energy absorption, with Ceramic FF increasing by up to 140%. Maximum load is also boosted, with Ceramics SD and FF increasing by up to 140% and 130%, respectively. Flexural stiffness sees notable improvements, particularly in Ceramics FF (up to 300%) and SD (up to 80%).
Enhancements stem from:

1. Enhanced interfacial bonding: Micro-patterns strengthen bonding between ceramic units, improving cohesion and robustness.
2. Optimized stress distribution: Specific micro-patterns disperse stresses more evenly, reducing localized failure risk and improving overall strength and stiffness.

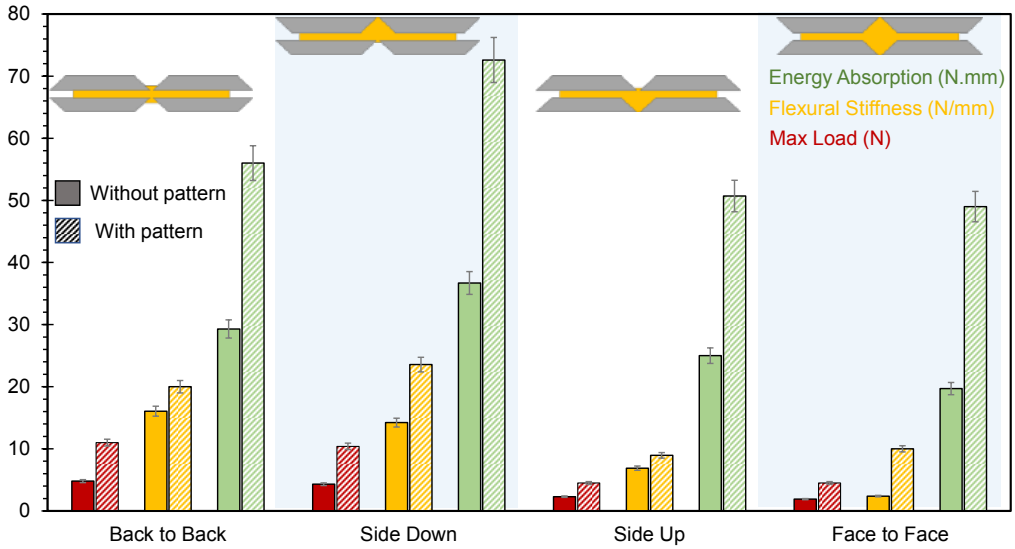


Figure 2. Static 3-point bending mechanical performance of the architectured ceramic beams with different stacking sequences (Back-to-back (BB), Side-down (SD), Side-up (SU), and Face-to-face (FF)) and micro-patterns: Maximum load, flexural stiffness, and energy absorption of the ceramics under static load with and without micro-patterns.

3.2. Cyclic Loading

Figure 3 illustrates the hysteresis force-deflection curves of architectured ceramic beams with varying stacking sequences (BB, SD, SU, and FF) and micro-patterns. Introducing micro-patterns on ceramic surfaces generally enhances the cyclic mechanical performance of the multilayered ceramic beams, improving both energy absorption and stiffness. However, the extent of this enhancement varies among the different stacking sequences. Notably, micro-patterns had a significant impact on Ceramics FF and SU, where Surlyn primarily influences the mechanical characteristics (controlled by shear force), emphasizing their role in these enhancements. For instance, the total cyclic energy absorption for

Ceramic FF increased by up to 85%, whereas for Ceramic BB, this improvement was only 14%, as shown in Figure 3. Several factors contribute to the varying improvements in cyclic mechanical performance with the introduction of micro-patterns:

Interfacial bonding enhancement: Micro-patterns promote better bonding between ceramic units and the Surlyn matrix, improving load transfer and energy dissipation. This bonding is particularly beneficial for Ceramic FF, enhancing adhesion and interaction between layers.

Crack deflection and propagation: Certain micro-patterns, like grooves or ridges, act as crack arrestors, deflecting cracks and preventing propagation. Ceramic FF may benefit more from crack deflection mechanisms due to its configurations.

Stress redistribution: Micro-patterns redistribute stress concentrations, preventing localized high-stress areas that could lead to failure. Ceramics FF, SU, and SD with intricate micro-patterns may show more significant improvements in stress redistribution compared to Ceramic BB.

Energy dissipation pathways: Micro-patterns create additional pathways for energy dissipation, allowing the material to absorb more energy before failure. Unique patterns on Ceramic FF offer effective pathways for energy dissipation.

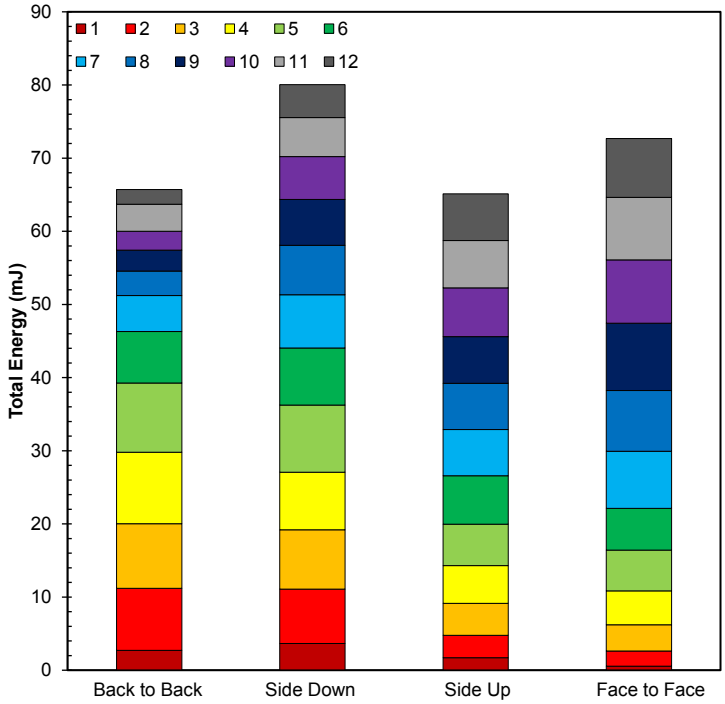


Figure 3. Cyclic 3-point bending mechanical performance of the architectured ceramic beams with different stacking sequences (BB, SD, SU, and FF) with micro-patterns: Total energy absorption as well as energy absorption, flexural stiffness, and plastic deformation of each cycle.

After cyclic 3-point bending tests, each ceramic system exhibited plastic deformation, evident in the increase in residual deflection with each cycle. Up to the third cycle, all ceramic groups, micro-patterned or not, showed similar levels of plastic deformation. Beyond this point, Ceramics BB and SD underwent significantly greater plastic deformation, indicating enhanced energy dissipation mechanisms and damage accumulation. Conversely, Ceramics FF and SU displayed higher durability and resistance to plastic deformation but lower energy dissipation capabilities under cyclic bending. Micro-patterned specimens exhibited comparable plastic deformation levels but at higher load capacities, suggesting improved interfacial strength and stress distribution.

4. Conclusion

In this study, we investigated bioinspired ceramic-polymer composites' static and cyclic flexural properties using an advanced subtractive manufacturing platform. Alumina tiles were engraved with

micro patterns and stacked with Surlyn® interlayers to create the composites. Micro-patterns significantly improved properties, enhancing energy absorption, maximum load, and flexural stiffness. Ceramic FF showed up to 85% more cyclic energy absorption due to crack deflection, better bonding, stress distribution, and energy dissipation. Cyclic behavior insights showed FF's stability, SD and BB's higher energy dissipation potential, and BB's initial energy absorption loss. In summary, micro-patterns further improved properties, particularly in energy absorption and bonding. This study highlights tailoring ceramic properties for various applications by choosing stacking sequences and micro-patterns carefully.

Acknowledgment

Financial support from National Research Council Canada (NRC) and Natural Sciences and Engineering Research Council of Canada (NSERC) is gratefully acknowledged.

References

[1] Evans, A.G., Perspective on the development of high-toughness ceramics. Journal of the American Ceramic society, 1990. 73(2): p. 187-206.
[2] Otitoju, T.A., et al., Advanced ceramic components: Materials, fabrication, and applications. Journal of industrial and engineering chemistry, 2020. 85: p. 34-65.
[3] Sun, J., et al., Macro-micro-nano multistage toughening in nano-laminated graphene ceramic composites. Materials Today Physics, 2022. 22: p. 100595.
[4] Bouville, F., et al., Strong, tough and stiff bioinspired ceramics from brittle constituents. Nature materials, 2014. 13(5): p. 508-514.
[5] Ritchie, R.O., The conflicts between strength and toughness. Nature materials, 2011. 10(11): p. 817-822.
[6] Yazdani Sarvestani, H., et al., Bioinspired stochastic design: tough and stiff ceramic systems. Advanced Functional Materials, 2022. 32(6): p. 2108492.
[7] Gao, K., et al., Friction and wear behavior of bioinspired composites with nacre-like lamellar and brick-and-mortar architectures against human enamel. Journal of Materials Science & Technology, 2022. 128: p. 133-141.
[8] Barthelat, F., Z. Yin, and M.J. Buehler, Structure and mechanics of interfaces in biological materials. Nature Reviews Materials, 2016. 1(4): p. 1-16.
[9] Fatehi, E., et al., Accelerated design of architectured ceramics with tunable thermal resistance via a hybrid machine learning and finite element approach. Materials & Design, 2021. 210: p. 110056.
[10] Katz, Z., et al., Bioinspired Hierarchical Ceramic Sutures for Multi-Modal Performance. Advanced Materials Interfaces, 2023: p. 2300098.
[11] Rahimizadeh, A., et al., Engineering toughening mechanisms in architectured ceramic-based bioinspired materials. Materials & Design, 2021. 198: p. 109375.
[12] Sarvestani, H.Y., et al., Multilayered architectured ceramic panels with weak interfaces: energy absorption and multi-hit capabilities. Materials & Design, 2019. 167: p. 107627.
[13] Sarvestani, H.Y., et al., Architectured ceramics with tunable toughness and stiffness. Extreme Mechanics Letters, 2020. 39: p. 100844.
[14] Yazdani Sarvestani, H., et al., Interlocking design, programmable laser manufacturing and testing for architectured ceramics. Scientific Reports, 2022. 12(1): p. 17330.
[15] Beausoleil, C., et al., Deep and high precision cutting of alumina ceramics by picosecond laser. Ceramics International, 2020. 46(10): p. 15285-15296.
[16] Esmail, I., et al., Engineered net shaping of alumina ceramics using picosecond laser. Optics & Laser Technology, 2021. 135: p. 106669.
[17] Amsellem, W., et al., Deep precision machining of SiC ceramics by picosecond laser ablation. Ceramics International, 2023. 49(6): p. 9592-9606.
[18] Behbahani, R., et al., Machine learning-driven process of alumina ceramics laser machining. Physica Scripta, 2022. 98(1): p. 015834.

EVALUATION OF 3D WOVEN NEAR-NET-SHAPED COMPOSITE I-SECTIONS: FABRIC DESIGN, MANUFACTURE, AND MECHANICAL PROPERTIES

Weijie Zhang[1,a], Yiding Li[1,b], Junru Li[1,c] and Shibo Yan[1,d]
[1] School of Aeronautic Science and Engineering, Beihang University, Beijing, China, 100191;
[a] Email: zhangweijie@buaa.edu.cn; [b] Email: leading@buaa.edu.cn ;[c] Email: lijunru@buaa.edu.cn
[d] Email: shiboyan@buaa.edu.cn

Keywords: 3-Dimensional reinforcement; Damage tolerance; Weaving; I-sections; weave pattern

Abstract

The design of composite I-sections in aerostructures faces a significant challenge with conventional laminates because they are prone to delamination under out-of-plane loads. This study investigates the design, manufacture, and mechanical properties of 3D woven near-net-shaped composite I-sections to address this issue. The study also compares their advantages with equivalent laminates and examines the influence of weave patterns on their mechanical behavior. Specimens were manufactured using the vacuum-assisted resin transfer molding technique, and quasi-static tensile, compressive, and bending tests were conducted to assess the properties of I-sections with three different weave patterns. It finds that the ultimate strength and damage tolerance of the 3D woven I-sections is superior to that of the laminated counterparts, and different weave patterns play a significant effect in damage mode and load-bearing capacity. In addition, using 3D woven preforms to manufacture composite I-sections also exhibits shortened production time in terms of layup and resin infusion.

1. Introduction

Delamination is common in traditional laminated composites when subjected to out-of-plane loads due to weak interlaminar properties. This poses significant challenges in designing and manufacturing aerostructures like clips, airframe joints, or aeroengine vanes, prone to catastrophic failures under operational loads [1]. 3D woven composites provide better structural integrity and higher strength due to interlaced yarns [2].

3D woven composites are gaining popularity in the aerospace industry due to their superior mechanical properties, cost-effectiveness, and high production efficiency. They are ideal for structural components such as fan blades and casings in aeroengines and have potential for other structures. Various composite manufacturing techniques, including z-pinning [3], braiding [4, 5], and weaving [2], have been employed to improve the load-bearing capacity of structures typically dominated by interlaminar strength. Different methods for composite manufacturing have their limitations. For example, z-pinning is effective against mode I crack only. Braiding can reduce structural stiffness due to fiber waviness. 3D woven composites, however, offer advantages in near-net-shaped manufacturing and mechanical properties, especially with 3D angle-interlock and orthogonal weaving techniques.

The design of bifurcated preforms using 3D weaving is categorized into on-loom [6] and off-loom [7] methods. On-loom methods weave preforms directly without the need for unfolding but have size and thickness limitations. Off-loom methods involve unfolding flat-woven fabrics to form near-net-shaped structures, with ongoing research to improve mechanical properties through fabric pattern design. Recent advancements [8-10] in off-loom design methodologies, particularly through 3D angle interlock and orthogonal weaving, have significantly improved the in-plane mechanical properties by increasing the fraction of straight fibers. Research [10, 11] has shown that 3D woven bifurcated structures, such as T-joints and I-sections, exhibit improved structural performance, including better damage tolerance and ultimate strength than traditional laminated counterparts.

To further promote the application of 3D woven composites, extensive research has been conducted on evaluating their mechanical properties, focusing on the effects of weave pattern design. Innovations in yarn orientation and weave patterns at the junctions of these structures have led to notable enhancements in strength and failure resistance, crucial for preventing crack initiation and propagation under operational loads.

2. Materials, manufacture, and experiment setup

The I-section composites in this study were formed using near-net-shaped preforms, which were woven with three distinct regions using a Jacquard loom. The preforms were bifurcated during the forming process (**Figure 1** left)to create flanges and a web. The key to designing this structure is in the appropriate bifurcation design, which is achieved by reinforcing the bifurcated region with separate non-through-thickness binders. The composites were fabricated using the VaRTM process.

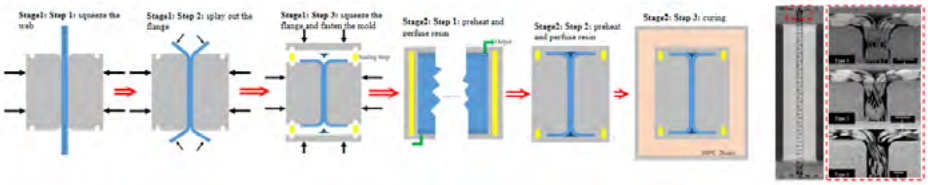


Figure 1. Schematic representation of the I-section manufacturing process.

This study explores the mechanical properties of different bifurcation techniques by manipulating the arrangement of weft yarns in the bifurcation region. Three distinct weft yarn paths were incorporated to create crossed or entangled weft structures, resulting in different mechanical properties (Figure 1 right). Types 1, 2, and 3 represent unchanged weft yarn order, crossed weft yarns, and entangled pattern weft yarns respectively. The areal density of three types of 3D woven preforms are 3474 g/m^2, 3481 g/m^2, and 3394 g/m^2. Ten layers of 400 g/m^2 plain-woven fabrics made of T700 spread tows were used as a control group for specimen manufacturing, due to availability in the lab.

We studied the mechanical behavior of 3DWOC near-net-shaped I-sections under three loading conditions: tension, compression, and bending. Tension and compression tests simplified the out-of-plane loads experienced by the I-sections, while the bending test approximated the anticipated distributed aerodynamic force on the web. We used a 10kN universal testing machine with a uniform loading rate of 1mm/min. Three specimens were tested for Type 1, Type 2, Type 3, and Type L at a constant room temperature and relative humidity until the specimen fractured.

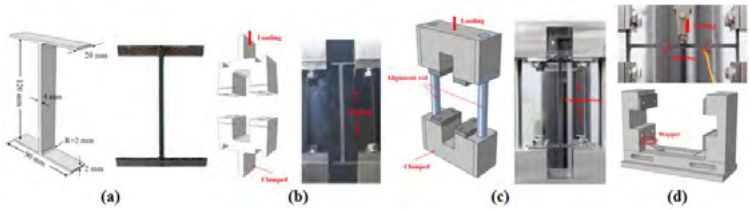


Figure 2. Testing layout for composite I-sections; (a) Specimen dimensions; (b) Tensile test layout; (c) Compressive test layout; (d) Bending test layout.

3. Results and discussion

3.1. Load-displacement responses

Representative load-displacement responses for the four types of I-sections under tension, compression, and bending are plotted in **Figure 3** The mean value derived from three sets of valid data of the initial stiffness, damage onset load, and ultimate failure load are compared in **Table 1**, where the initial damage load is defined as the first significant load drop and the ultimate failure load is defined as the maximum load. Good consistency in load-displacement responses under all three loading conditions was observed for the four types of specimens

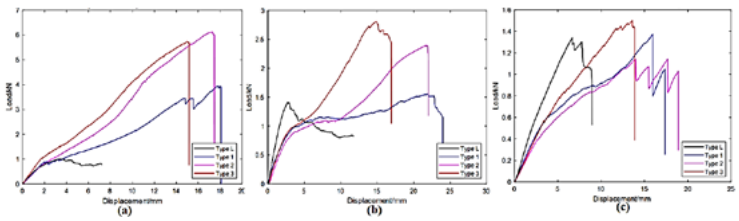


Figure 3. Load-displacement responses for each test; (a) Tension; (b) Compression; (c) Bending.

Table 1. Stiffness, initial, and ultimate failure loads (averaged) of the four types of specimens.

Test	Type	Initial Stiffness (N/mm)	Initial damage load (N)	Ultimate failure load (N)
Tension	1/2/3/**L**	460/478/629/**500**	836/778/911/**412**	3481/6481/5392/**1027**
Compression		411/338/415/**665**	414/557/745/**1255**	1345/2166/2724/**1441**
Bending		184/151/148/**242**	423/375/451/**525**	1255/1297/1471/**1302**

The 3D woven specimens have enhanced damage tolerance and increased load improvement potential after initial damage. Compared to laminates, 3D woven composite I-sections have much higher loading-bearing capacity. During the compressive test, the Type L specimen experienced a notable drop in compressive load after ultimate failure followed by persistent load fluctuations throughout the stage. Type 2 and Type 3 specimens saw their compressive loads increase during the damage-evolving stage. Under bending loads, the Type L specimen has a higher initial stiffness of 242N/mm and a smooth curve. The 3D woven specimens have lower initial stiffness but can withstand different ultimate loads. Type 3 shows the best ultimate strength with a 13% increase.

3.2. Characterization of failure modes

Neat matrix cracking, yarn transverse cracking, delamination, and yarn rupture are the primary failure modes of the four types of specimens. The nomenclature utilized to denote these failure modes are outlined in **Table 2**. The failure mode of laminated I-section Type L in tensile test is delamination. The delamination starts from the noodle and extends to the web and flange until the test parts fail. The primary difference in the fiber architecture between Type 1 and Type L is the presence of binder yarns. The binder yarns in the 3D orthogonal woven specimens enhance the preform integrity, resulting in a higher ultimate strength than the Type L specimens.

Table 2. Nomenclature of failure modes in the test.

Damage type	Neat matrix crack	Yarn transverse crack	Delamination	Yarn ruptures
Code	C	Cy	D	R

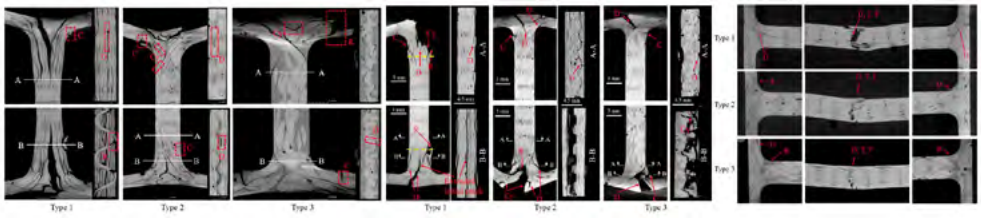


Figure 4. The images from μCT scan of fractured tension (left), compression (middle), and bending (right) specimens

The failure mode of 3D woven I-section Type 2 under tension has limited delamination propagation due to the crossing structure of the weft yarns in the noodle. Type 2 only showed transverse cracking in the flange. Similarly, Type 3 exhibited matrix cracking and delamination in the junction, but tightly entangled weft yarns limited the delamination propagation and improved the ultimate strength of the I-section. The 3D woven specimens with through-thickness yarns and featured weft yarn paths improved the structures' ultimate strength and damage tolerance under tension. Type 1 and Type 2/3 with binder and crossed-weft yarns limited the crack propagation, with crossed-weft yarns being more effective. Type 2/3 maintained the webs' integrity, and the fracture of flanges led to ultimate failure rather than propagated cracks of Type 1/L.

The images from the μCT scans of the fractured compression specimen are shown in **Figure 4** (middle). Delamination occurs similarly in the three types of 3D woven specimens. In Type 1, severe delamination occurs along the weft yarn interfaces extending to the web's middle plane. Neat matrix cracks, transverse cracks, and yarn fractures occur around the top and bottom binders in the web. (marked with yellow dashed lines in **Figure 4**(middle-a)). Type 2 and Type 3 specimens both had minor delamination along weft yarns in section A-A. Crossed weft yarns in section B-B prevented initial cracks from propagating but caused resin-rich regions leading to neat matrix cracking. Overall, both types showed similar failure modes including neat matrix cracks, minor delamination, and yarn ruptures.

μCT results show that Type 3 noodle specimens with intricate cross structures have better load-bearing capacity and less damage area than other weft yarn architectures.

CT scan images of the three types of 3D woven specimens after bending tests are shown in **Figure 4** (right). The 3D woven specimens had damages in the noodles and middle of the web, with delamination along weft yarns, transverse cracks within warp yarns, and ruptures of the weft yarns. The three types of 3D woven specimens in the noodle showed different failure modes. Failures were observed in Type 1, while Type 2 and Type 3 showed matrix cracks and slight delamination in resin-rich areas. Noodle failures do not determine the ultimate failure of the structures. However, 3D woven I-sections may show enhanced ultimate strength due to delamination resistance in the junctions. All noodle failures occurred near the top flanges, which withstand the tensile stress caused by bending loads.

4. Conclusions

This study explored the use of 3D woven composite I-sections for aeronautical applications. Three types of I-sections with junction variations were tested for mechanical properties. Results showed that adding binder yarns and crossed weft yarns improved strength and damage tolerance under pull-off load. The test results show that the ultimate strength of the three tests has been enhanced by 531%, 89%, and 13% respectively using different designs, compared with 2D counterparts. Crossing weft yarns is more effective in maintaining the integrity of webs, limiting crack propagation, and improving load-bearing capacity. This means manipulating yarn paths can help tailor the mechanical properties of I-section composites. Moreover, the 3D woven specimens exhibited superior damage tolerance and ultimate strength compared to the laminated specimens, as well as a fast production cycle. This highlights the potential of 3D weaving technology in the development of high-performance composite structures.

Acknowledgments

This research did not receive any specific grant from public, commercial, or not-for-profit funding agencies.

References

[1] Verma KK, Padmakara G, Gaddikeri KM, Ramesh S, Kumar S, Bose S. The key role of thread and needle selection towards 'through-thickness reinforcement' in tufted carbon fiber-epoxy laminates. Composites Part B: Engineering. 2019;174.
[2] Yan S, Zeng X, Brown L, Long A. Geometric modeling of 3D woven preforms in composite T-joints. Textile Research Journal. 2017;88(16):1862-75.
[3] Zhou J, Shi Y, Zuo Y, Shan C, Gu Z. Experimental investigation into influences of Z-pin and deltoid on structural properties and damage tolerance of CFRP T-joints. Composites Part B: Engineering. 2022;237.
[4] Zhang W, Yan S, Yan Y, Li Y. A parameterized unit cell model for 3D braided composites considering transverse braiding angle variation. Journal of Composite Materials. 2021;56(3):491-505.
[5] Li Y, Yan S, Yan Y, Zhang W. Modelling of the compressive behavior of 3D braided tubular composites by a novel unit cell. Composite Structures. 2022;287.
[6] Zhou Y, Li H, Deng Z. Mathematical modelling of complicated 3D woven fabrics. The Journal of The Textile Institute. 2021;113(1):25-32.
[7] Soden JA, Weissenbach G, Hill BJ. The design and fabrication of 3D multi-layer woven T-section reinforcements. Composites Part A: Applied Science and Manufacturing. 1999;30(3):213-20.
[8] Umair M, Shaker K, Javaid MU, Hussain M, Kashif M, Nawab Y. Effect of weaving patterns on damage resistance of 3D woven jointless T and H shaped reinforcements. Mechanics of Advanced Materials and Structures. 2020;29(1):104-17.
[9] Lyu L, Liu W, Guo J, Wei C-y, Zhao Y-p, Qian Y-f, et al. Compression properties of three-dimensional I-shaped woven composites with basalt fiber filament tows. Journal of Engineered Fibers and Fabrics. 2019;14.
[10] Yan S, Zeng X, Long A. Experimental assessment of the mechanical behaviour of 3D woven composite T-joints. Composites Part B: Engineering. 2018;154:108-13.
[11] Yan S, Zeng X, Long A. Effect of fibre architecture on tensile pull-off behaviour of 3D woven composite T-joints. Composite Structures. 2020;242.

THE REPAIR OF INTERLAMINAR FRACTURE IN THERMOPLASTIC-MATRIX COMPOSITES

T. Khan[1], R. Umer[2] and W.J. Cantwell[3]

[1]Department of Aerospace Engineering, Khalifa University of Science and Technology,
PO Box 127788 Abu Dhabi, United Arab Emirates
Email: Tayyab.khan@ku.ac.ae, Web Page: https://www.ku.ac.ae/college-people/tayyab-khan
[2]Department of Aerospace Engineering, Khalifa University of Science and Technology,
PO Box 127788 Abu Dhabi, United Arab Emirates
Email: Rehan.umer@ku.ac.ae, Web Page: https://www.ku.ac.ae/college-people/rehan-umer
[3]Department of Aerospace Engineering, Khalifa University of Science and Technology,
PO Box 127788 Abu Dhabi, United Arab Emirates
Email: Wesley.cantwell@ku.ac.ae, Web Page: https://www.ku.ac.ae/college-people/wesley-cantwell

Keywords: Repair 1, delamination 2, thermoplastic 3, fracture 4, Elium 5

Abstract
In this study, pre-cracked carbon fiber-reinforced composite laminates based on an infusible thermoplastic resin (Elium®) were manufactured via the vacuum-assisted resin transfer molding process. These pre-cracks were subsequently repaired using a hot press by heating the laminates above the glass transition temperature of the cured liquid thermoplastic resin. The Mode I interlaminar fracture toughness (G_{Ic}) was investigated by conducting a series of double cantilever beam (DCB) tests and the precise contribution of each processing parameter towards the measured fracture toughness was determined using an analysis of variance (ANOVA) approach. The bonding mechanisms were investigated through microscopic analyses and X-ray Computed Tomography (XCT) and the mechanical performance of the repaired composites was also investigated through four-point bending tests.

1. Introduction

Thermoplastic-matrix composites have, at times, attracted significant interest from the aerospace industry for use in load-bearing aircraft parts. Thermoplastic-matrix composites are typically associated with a high impact resistance, superior solvent resistance, the possibility to recycle, and relatively good formability characteristics. Limitations to the greater use of these materials in aircraft composites are linked to the high melting temperature of the polymeric matrix and its elevated melt viscosity. For example, poly-ether-ether-ketone, a semi-crystalline thermoplastic that has attracted significant attention over the years has a processing temperature of between 380 and 400°C, excluding it from many traditional manufacturing processes [1,2]. Producing large, potentially complex structures using this material is, therefore, challenging. Attempts to overcome these challenges have resulted in the recent development of liquid resin systems, such as Elium® from Arkema, with a very low melt viscosity, rendering it compatible with out-of-autoclave techniques such as RTM/VARTM as well as the possibility of being cured at room temperature [3-5]. A number have studies have recently highlighted the ease of manufacturing of Elium-based composites as well as their resulting mechanical properties. Thermoplastic-matrix composites also offer the benefit of ease of repair since the polymer can be softened at elevated temperatures, leading to molecular interdiffusion across the crack or delamination. It is well–established that strong molecular bonds can be formed via an interdiffusion mechanism with the associated movement and entanglement of chains across the interface precipitating crack-healing and toughness restoration [6,7]. Research has shown that polymer molecules diffuse across the crack

boundary via a mechanism termed reputation that was first proposed by de Gennes [6] and later investigated by Doi and Edwards [7].

Currently, there is very little information on the interdiffusion and crack-healing mechanisms that take place in Elium®-based composites at elevated temperatures. Having such information available would enable engineers to potentially repair damaged composites, such as wind turbine blades that have been impacted during operational service.

In this study, the possibility of repairing carbon fiber reinforced polymer (CFRP)/Elium® laminates containing delamination is investigated. Here, cracked laminates are repaired under different pressures and temperatures for different time periods and the resulting toughness of the interface is measured by conducting Mode I double cantilever beam (DCB) tests at quasi-static rates of loading.

2. Experimental Procedure

The reinforcement material used in this investigation was based on a 2x2 twill weave carbon fibre fabric with an areal density of from Gurit Ltd. The fabrics were infused with a low viscosity thermoplastic polymer (Elium 1880 from Arkema, China) and an benzoyl per oxide initator was used to trigger the polymerization process. Further details regarding these constituent materials are given elsewhere [8].
Pre-cracked laminates, suitable for double cantilever beam (DCB) testing, were manufactured using the vacuum assisted resin transfer molding technique, Figure 1. Here, twelve layers of the carbon fabric were stacked in preparation for resin infusion. A nylon film was placed at the interface between the 6th and 7th plies in order to create a pre-crack for subsequent testing, Figure 1. The polymer film covered approximately 75% of the total length of the plate, thereby allowing sufficient area for subsequent repair. Resin infusion was undertaken at 23°C, then allowed to cure for 24 hours and finally post-cured at 60°C for 24 hours. Double cantilever beam test specimens with length and width dimensions of 250 × 20 mm respectively were removed from the plates using a diamond slitting wheel. Futher details of the manufacturing process are given elsewhere [8].

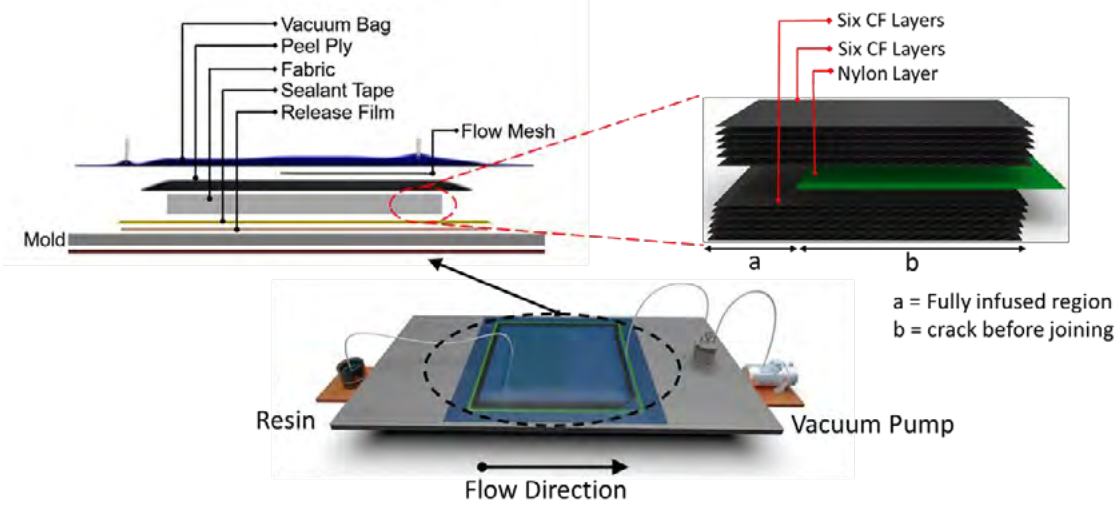


Figure 1. Schematic of the VARTM process and the position of the artificial defect [8].

The test samples containing very long artificial pre-cracks were healed in a Meyer hot press for different periods of time and at different temperatures and pressures. Here, an 80 mm long aluminum foil was inserted at the mid-plan to act as a pre-crack, leaving sufficient area for subsequent repair. The specimens were subsequently healed at temperatures of 150, 180, and 210°C for periods of 30, 60, and 90 minutes at pressures of 4.7, 7.0, and 9.3 bar. After the healing process was completed, the press was opened and the specimen was left to cool.

Mode I DCB testing was conducted according to the ASTM D5528-13 standard. The tests were conducted on an Intron-5969 universal testing at a crosshead displacement rate of 5mm/minute. The load (P) and resulting crosshead displacement (δ) were recorded during each test. The Mode I interlaminar fracture toughness (G_{Ic}) was determined using the following equation:

$$G_{Ic} = \frac{3P\delta}{2b(a+|\Delta|)} \quad (1)$$

Where b is the specimen width, a is the crack length and Δ represents a correction factor to account for the fact that the beam halves do not act as if they are fully built-in at the crack tip [9]. The experimental results were also corrected for large displacements.

3. Results and Discussion

Inspection of the DCB samples after being subjected to a healing process indicated that in all cases, the application of pressure and temperature for different periods of time resulted in the formation of a bond between the upper and lower portions of the test sample. This bond was primarily created due to the flow of the polymer resin across the interface at higher temperature. Figure 2 shows the polymer melt flow across the interface in the repaired specimens. DCB tests were then conducted to measure the Mode I interlaminar fracture toughness and edge views of several samples are presented in Figure 3.

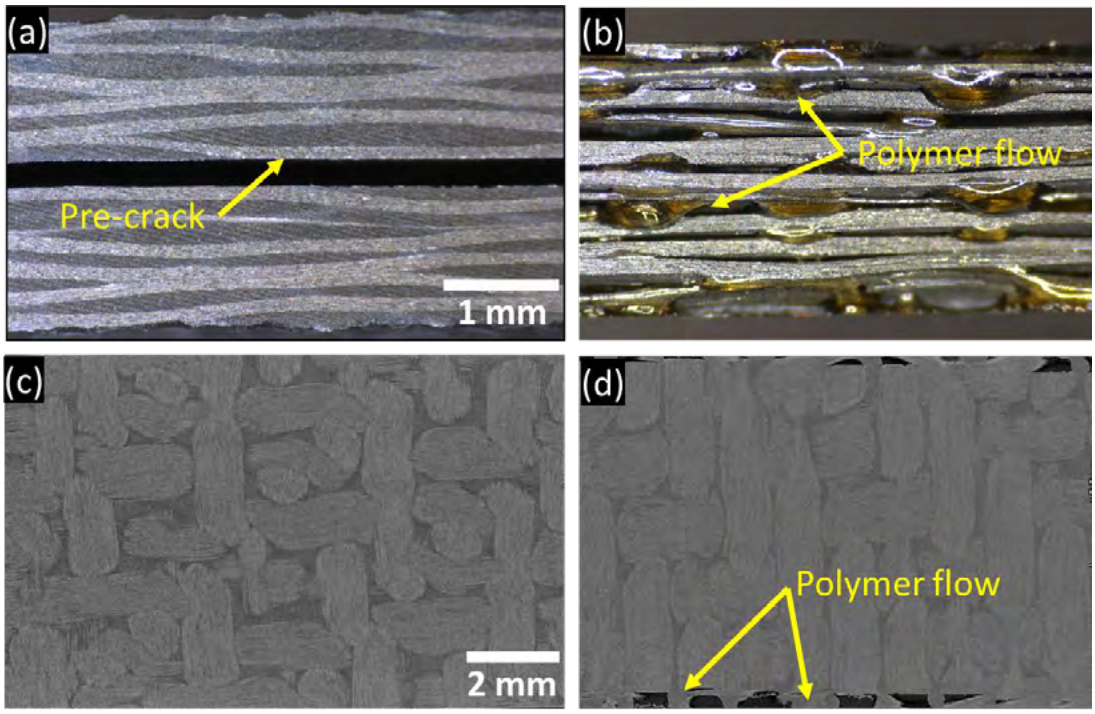


Figure 2. (a) Cross-sectional optical micrograph a pre-cracked specimen, (b) Cross-sectional optical micrograph of the specimen repaired at 210C for 90 min., (c) Raw XCT image of the reference specimen (top view), and (d) Raw XCT image of the specimen repaired at 210C for 90 min.

Figure 3 clearly highlights an increase in fiber bridging as the healing temperature is increased. The presence of fiber bridging is known to increase the stability of the crack and also increase the measured fracture toughness. During delamination growth, fibers on the upper and lower sides of the interface are pulled out and the fracture surface is stabilized. This increases the resistance to failure, leading to an increase in the interlaminar fracture toughness. Many studies have reported fiber bridging to significantly improve the delamination resistance of composites [10,11].

Figures 3c and 3d show that these samples healed at 180°C and 210°C exhibited greater levels of fiber bridging relative to their S150 counterparts. The amount of fiber bridging was also observed to increase with time for a given healing temperature.

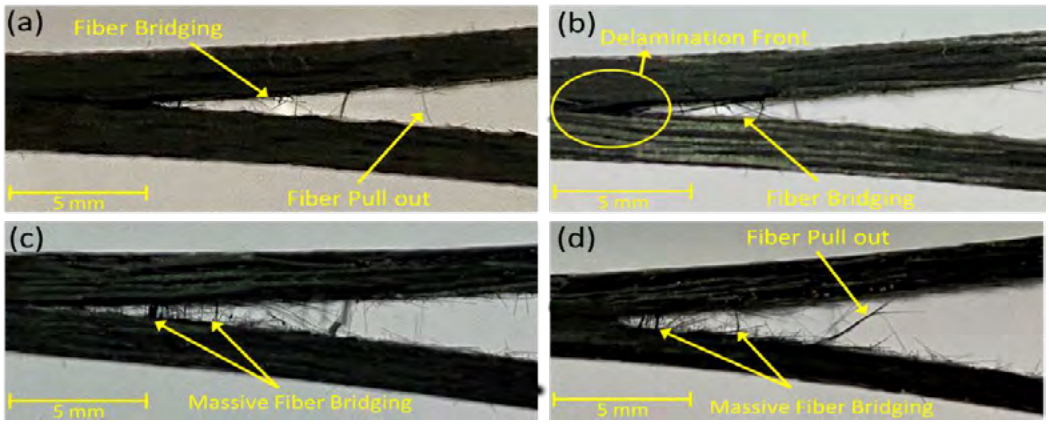


Figure 3. Edge view of DCB specimens showing the crack front in the following samples (a) S_O (b) S150-90-4, (c) S180-90-2 and (d) S210-90-3.

Table 1 summarizes the resulting values of Mode I interlaminar fracture toughness, G_{Ic}. Included for comparison is the average value measured following tests on as-manufactured DCB samples, i.e. the baseline value. From the table, it is clear that The contribution of each of these processing parameters to the measured interlaminar fracture toughness was identified using an ANOVA analysis. The ANOVA analysis showed that temperature and time contributed 84 % and 12 %, respectively, whereas the applied pressure was shown to have only a small effect (Figure 4a). Additionally, the ANOVA interaction plots shown in Figure 4b revealed that the effect of temperature was independent of other parameters (i.e., time and pressure). In other words, the repair of the specimens could be optimized by changing the temperature while keeping other two parameters constant.

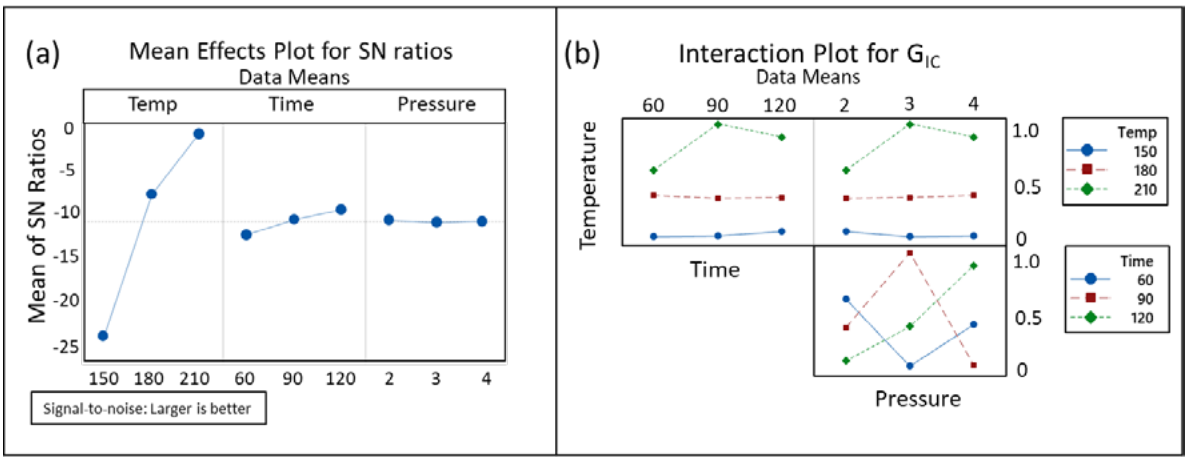


Figure 4. Main effects plot for G_{IC}, and (b) Interaction plot for G_{IC}.

Table 1. Average values of the different healing temperatures, times and pressures.

Specimen Code	Temperature (°C)	Time (min)	Pressure (Bar)	G_{Ic} (J/m^2)
S150-30-2	150	30	2	19
S150-60-3	150	60	3	60
S150-90-4	150	90	4	69
S180-30-3	180	30	3	67
S180-60-4	180	60	4	422
S180-90-3	180	90	3	406
S210-30-4	210	30	4	521
S210-60-2	210	60	2	625
S210-90-3	210	90	3	749
S_o	–	–	–	**1160**

As noted above the value of G_{Ic} exhibited a strong dependency on the contact time, t, increasing continuously as the sample was exposed to high-temperature healing. The effect of healing time was investigated more closely via a series of experiments conducted at 210°C involving healing times ranging from 10 to 120 minutes whilst being subjected to a constant pressure of 4 bar. The resulting variation of G_{Ic} with the square root of the healing time $t^{1/2}$ (in seconds) is shown in Figure 5 where a reasonably linear relationship between these two parameters is evident. This linear increase in G_{Ic} with $t^{1/2}$ aligns well with de Gennes's interdiffusion theory [6] and Wool's crack healing theory [7]. Based on these theories, the interlaminar fracture toughness is related to the healing time by the following relation:

$$G_{Ic} = G_{Ic}^{*} \, (t/\tau)^{1/2} \tag{2}$$

Where, G_{Ic}^{*} is the fracture toughness of the base material and τ is the reptation time.

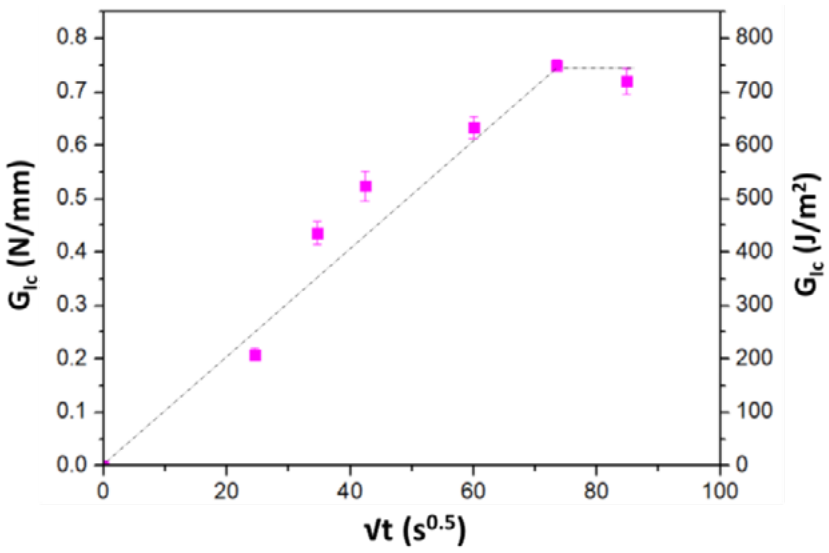


Figure 5. The plot of G_{Ic} vs. $\sqrt{t}$ ($s^{0.5}$) for specimens healed at 210°C at 4 bar.

This repair technique was also utilized to repair artificial cracks representing impact-induced delamination. The performance of the repaired laminates was investigated by subjecting them to four-point bending tests and an ANOVA analysis. The mechanical tests revealed that the samples repaired at the same optimum parameters exhibited the highest residual flexural strength (96%) of the pristine specimens [12]. A dominant delamination failure mode was observed in all the repaired specimens. As all the specimens were observed to fail in an opening mode at the crack tip during the flexural tests, their residual strength was compared to the G_{IC} values. Based on Figure 6, a linear increase in the residual strength was observed as the fracture toughness was increased. In addition, both the fracture toughness and the residual flexural strength were increased by increasing the repair time.

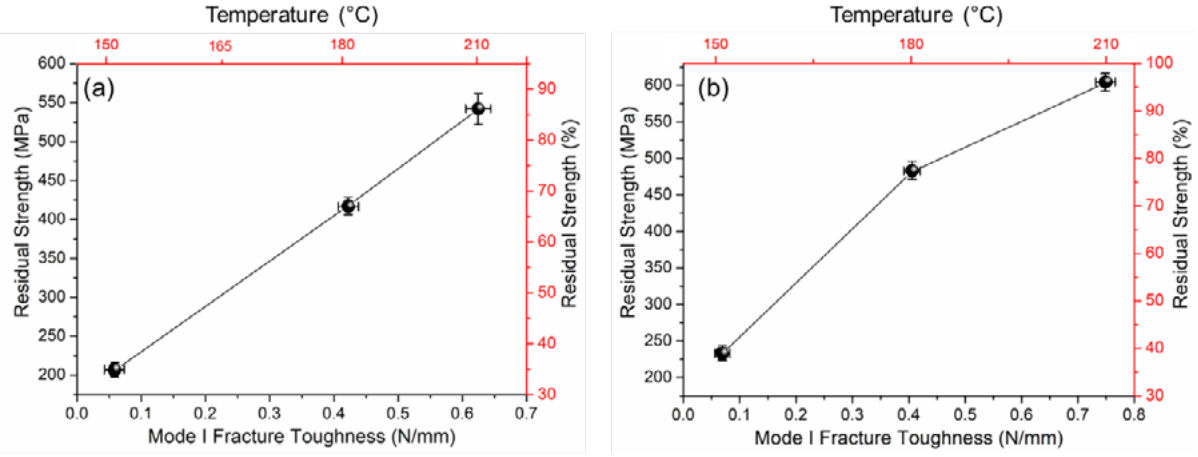


Figure 6. Residual strength as a function of the Mode I fracture toughness for specimens repaired for (a) 60 min and (b) 90 min [12].

3. Conclusions

This possibility of repairing delamination-type cracks in an infusible thermoplastic-matrix composite has been investigated experimentally through a series of DCB tests. Optical micrographs of test samples after healing showed that the level of healing was influenced by both temperature and time. In contrast, the level of applied pressure had very little effect on the quality of the interface. It is believed that the bonding mechanism responsible for removing the crack was associated with the interdiffusion of the polymeric molecules across the crack, as well as chain bridging and interface bonding. The Mode I fracture toughness of the healed DCB specimens was high at 750 J/m^2, corresponding to approximately 65% of the value of the standard reference specimens. An observation of the test sample during fracture highlighted the presence of significant fiber bridging, which failure mechanism that served to increase the interlaminar fracture toughness and stabilize the crack front. Finally, the measured interlaminar fracture toughness exhibited a linear relationship with the square root of the healing time ($t^{1/2}$), agreeing with the predictions of earlier interdiffusion crack healing theories.

Acknowledgments

This publication is based on work supported by the Khalifa University of Science and Technology internal grants CIRA-2020-007 and FSU-2019-08. The authors are also grateful to Arkema, China for providing the Elium® resin.

References

[1] K. Fujihara, Z.-M. Huang, S. Ramakrishna and H. Hamada. Influence of processing conditions on bending property of continuous carbon fiber reinforced PEEK composites. *Composites Science and Technology,* volume 64: 2525-2534, 2004.

[2] P. Davies, W. Cantwell, C. Moulin and H.H. Kausch. A study of the delamination resistance of IM6/PEEK composites. *Composites Science and Technology*, volume 36: 153-166, 1989.

[3] M. E. Kazemi, L. Shanmugam, D. Lu, X. Wang, B. Wang, and J. Yang. Mechanical properties and failure modes of hybrid fiber reinforced polymer composites with a novel liquid thermoplastic resin. Elium®. *Compos. Part A Appl. Sci. Manuf.*, volume 125: 105523, 2019.

[4] S. K. Bhudolia, P. Perrotey, and S. C. Joshi. Mode I fracture toughness and fractographic investigation of carbon fibre composites with liquid Methylmethacrylate thermoplastic matrix. *Composites Part B Engineering.* volume 134: 246–253, 2018.

[5] S. K. Bhudolia, G. Gohel, K. F. Leong, and R. J. Barsotti. Investigation on Ultrasonic Welding Attributes of Novel Carbon/Elium® Composites. *Materials (Basel)*, volume 13: p. 1117, Mar. 2020.

[6] P. G. de Gennes, Reptation of a Polymer Chain in the Presence of Fixed Obstacles. *J. Chem. Phys.*, vol. 55: 572–579, 1971.

[7] M. Doi and S. Edwards. *The Theory of Polymer Dynamics*. Oxford University Press, 1988.

[8] T. Khan, M.S. Irfan, W.J Cantwell, R. Umer Crack healing in infusible thermoplastic composite laminates. Composites Part A: Applied Science and Manufacturing, volume 156, 106896, 2022.

[9] J. G. Williams. Large Displacement and End Block Effects in the 'DCB' Interlaminar Test in Mode I and II. *Journal of Composite Materials,* volune 21: 330–347, 1987.

[10] Y. Gong, B. Zhang, L. Zhao, J. Zhang, N. Hu, and C. Zhang. R-curve behaviour of the mixed-mode I/II delamination in carbon/epoxy laminates with unidirectional and multidirectional interfaces. *Composite Structures*, volume 223: 110949, 2019.

[11] F. Naya, G. Pappas, and J. Botsis. Micromechanical study on the origin of fiber bridging under interlaminar and intralaminar mode I failure. *Composite Structures*, volume 210: 877–891, 2019.

[12] T Khan, MA Ali, M.S. Irfan, W.J Cantwell, R Umer. Visualization and investigation of healing mechanism in carbon fiber reinforced Elium® composites. Journal of Thermoplastic Composite Materials. 2023;36(10):3966-3989. doi:10.1177/08927057221145551.

MECHANICAL PERFORMANCE OF 3D PRINTED FIBRE-REINFORCED TRIPLY PERIODIC MINIMAL SURFACES STRUCTURES

Ahmad Sh. Charkieh[1,2] (*),Yifan Zhu[1,2], Lincy Pyl[1]

[1]Department of Mechanics of Materials and Constructions (MeMC), Vrije Universiteit Brussel (VUB), Pleinlaan 2, B-1050, Brussels, Belgium
(*)Email: ahmad.shawki.charkieh@vub.be, memc.research.vub.be/nl

[2]VLAIO, Ellipsgebouw, Koning Albert II Laan 35, 1030 Brussels

Keywords: TPMS structures, 3D printed, gyroid, stiffness, mechanical behavior, energy absorption.

Abstract

This study focuses on geometric optimization of short-fiber composite 3D printed Triply Periodic Minimal Surfaces (TPMS) structures. It evaluates their performance in compression, assesses their energy absorption capabilities, and examines the impact of geometric grading.
Owing to its material versatility and support for complex geometries, the fused filament fabrication (FFF) 3D printing technique is used to print a set of TPMS structures. This experimental study covers a series consisting of a strut-based canonical lattice structure in addition to skeletal and sheet gyroid TPMS structures, with attention to the influence of relative density grading and cell size grading.

1.Introduction

Additive manufacturing (AM), facilitating the production of geometrically challenging customized components from digital input, has seen intriguing developments, including the production of lattice structures [1]. The production of low-density, strong lattice cores opens the door to the implementation of such design in sandwich structures providing promising lightweight load-bearing units [2]. Demonstrating a uniform stress distribution throughout the material and enhanced energy absorption with minimal surface area, Triply Periodic Minimal Surfaces (TPMS) structures exhibit superior strength-to-weight ratios [3]. Grading, which is limited and less achievable in conventional lattices, holds promise in design and fabrication of functionally enhanced TPMS structures, featuring anisotropy and controlled deformation characteristics [3][4]. Studying compression and energy absorption characteristics of the core serves as a foundation preceding our broader investigation into hybrid sandwich structures.

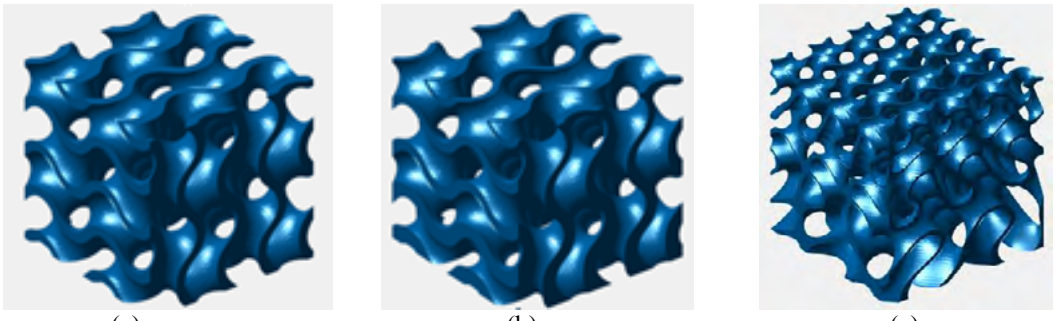
©2024 | 3_CHARKIEH_Ahmad Shawki_WKLKB.pdf

2. Methodology

2.1 Design

The designs chosen for this study include the strut-based lattice, in the form of an octet lattice structure, in addition to skeletal and sheet gyroid TPMS structures. The octet truss lattice is a complex three-dimensional lattice structure made of interconnected octahedral and tetrahedral units, where the repeating pattern ensures both structural stability and the ability to bear loads [2]. TPMS, which are mathematical surfaces with zero mean curvature at every point, are here studied in the form of skeletal and sheet structures. Skeletal gyroid TPMS structures are made up of interconnected struts or beams, resembling a skeletal framework. On the other hand, sheet gyroid TPMS structures have more continuous surfaces, creating a sheet-like geometry with minimal thickness.

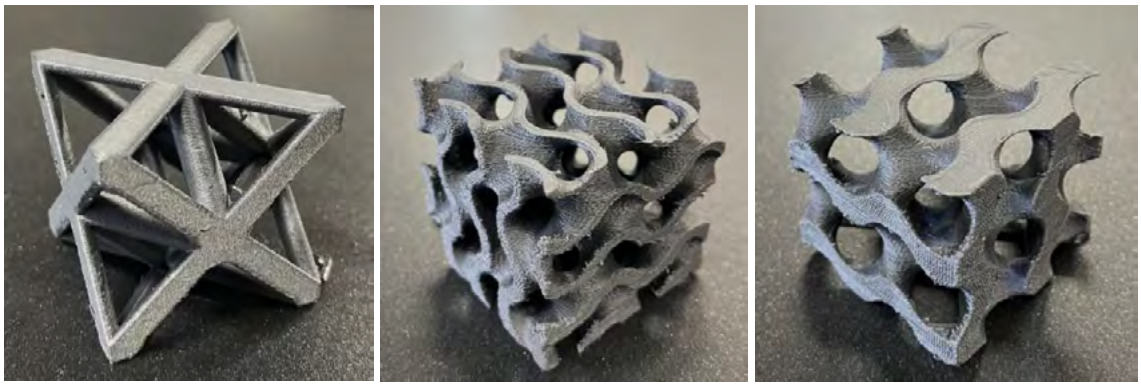
Following the design and the production of the preliminary prints, the structures undergo optimization in cell size, and specific weight, which is defined as the weight per unit volume of a substance. The gradation applied to these structures is along their vertical dimension with the printing direction. By introducing this variation in the strut size or thickness, the relative density of the structure can be tailored to achieve application-specific mechanical behaviors. Optimization of gyroid structures has shown a promising avenue for enhancing energy absorption capacity through gradation using both conventional fabrication and additive manufacturing [5][6]. In this study, the best performing structure between the three initial uniform designs undergoes gradation in cell size and specific weight. Two uniform TPMS structures are produced and studied in compression to find the stiffer structure, and as a result, this better performing geometry was graded. This helps understand the effect of gradation and the potential for improvement in terms of stiffness and energy absorption. Starting initially with uniform TPMS design as shown in figure 1-a, a new structure was created by employing gradation, with a specific weight ranging from 0.5 at one extreme to 0.2 at the other as shown in figure 1-b. In another specimen the gradation ratio used for relative density was also applied to the cell size, as shown in figure 1-c. The gradation implemented ensured that the total material volume remained consistent between the uniform and graded structures. The purpose was to optimize the distribution of material throughout the structure to enhance its performance.



(a) (b) (c)

Figure 1. Sheet gyroid TPMS design
(a) Uniform | (b) Relative density gradation | (c) Cell size gradation

The samples were created through fused filament fabrication using a Prusa i3 MK3S+. The layer height was set to 0.2 mm, ensuring precision in each layer, at a controlled printing speed of 40 mm/s. Following supplier's recommendation, the nozzle and print bed temperatures were set to 285°C and 100°C, respectively, to ensure proper filament flow and adhesion. The filament material used is polycarbonate with short carbon fiber reinforcement. All the samples are made up of an array of unit cells and have dimensions of 5x5x5 cm^3. Figures 2 depicts the 3D printed samples.

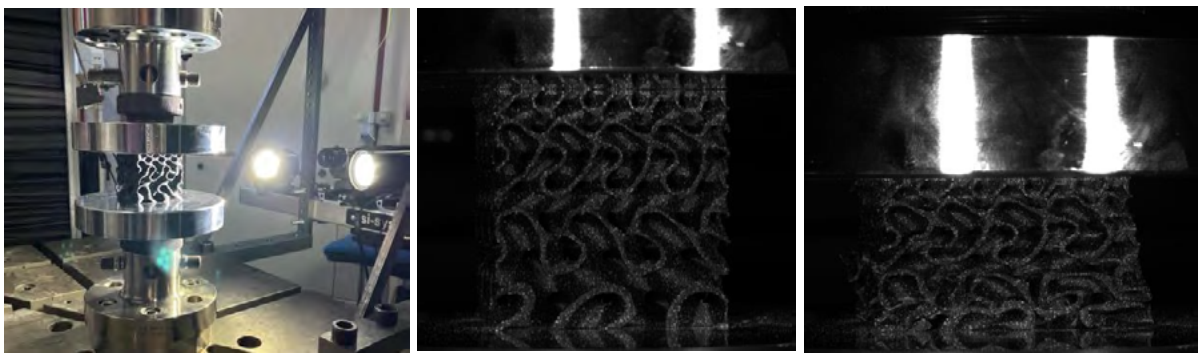


(a) (b) (c)

Figure 2. 3D printed samples analyzed in this article
(a) Octet | (b) Sheet gyroid TPMS | (c) Skeletal gyroid TPMS

2.1 Testing

The investigation of the compressive properties of the 3D-printed samples was carried out experimentally using an Instron 5885 electromechanical testing system. The compression tests were performed perpendicular to the build direction and according to the ASTM D695 standard [7]. The quasi-static compression tests were displacement controlled at a rate of 1 mm/min. A stereo digital image correlation (DIC) system was employed for the strain measurement with two 24 megapixels Basler cameras. Figure 3 shows the test set-up for the compression of a sheet TPMS with cell size gradation. White paint was sprayed evenly across the surface of the structures, forming a random pattern of contrasting specks, as seen on the specimens in figures 3-b and 3-c. The speckle serves as a reference to measure displacement during testing. A thorough comparison is established to compare strut-based lattices to TPMS structures, in terms of compressive strength and energy absorption with focus on the effect of grading.



(a) (b) (c)

Figure 3. Deformation monitoring in compression by DIC.
(a) Compression test and DIC set-up | (b) Test sample before loading | (c) Test sample after loading

3. Results

The data obtained from both the Instron electromechanical testing system and DIC were post-processed. The strut-based lattice is compared to the TPMS structures giving insights into both compressive strength and energy absorption capacities of these structures. The following results were normalized and rescaled using Eq (1) to facilitate comparison and analysis. The normalization is applied to each property studied, such as E modulus, SEA, or ultimate strength, across all tested specimens, with **x** representing the selected property value, $\mathbf{min}\ (\boldsymbol{x})$ indicates the minimum value of this property observed among all the tested specimens and $\mathbf{max}(\boldsymbol{x})$ comes from the highest value. $\boldsymbol{x'}$ is the normalised and rescaled value and it falls between 0 and 1. In terms of strain, the maximum value shown is 1, which in full scale refers to an upper limit of 20% strain in the structure.

$$\boldsymbol{x'} = \frac{\boldsymbol{x} - \mathbf{min}\ (\boldsymbol{x})}{\mathbf{max}(\boldsymbol{x}) - \mathbf{min}\ (\boldsymbol{x})} \tag{1}$$

Given its porous structure, the octet truss structure exhibited the lowest stiffness, compared to sheet and skeletal TPMS structures. The uniform sheet TPMS structure scoring 0.2 outperformed the skeletal structure scoring 0.08. This can be attributed to the improved load distribution and material efficiency in sheet structures. The continuous shell geometry in the sheet structure promotes a more uniform stress distribution, minimizing the likelihood of localized stresses and failure. Figure 4 shows that sheet TPMS structures tend to withstand higher stresses compared to the other two structures reflecting its promising strength as well. While TPMS structures show a ductile behavior, the octet trusses in this case can be classified as brittle according to Gibson and Ashby reproduced curves [8]. An octet structure consists of interconnected beams or struts that are prone to sudden failure following straight crack propagation, in contrast to tortuous propagation in TPMS structures. Plate-based structures have been proven to outperform truss lattices in terms of Young's modulus [1], and TPMS sheet structures are akin to plate lattices. As lateral expansion of the octet is not prohibited by the boundary conditions, stress concentrations around the hinges initiated shear failure.

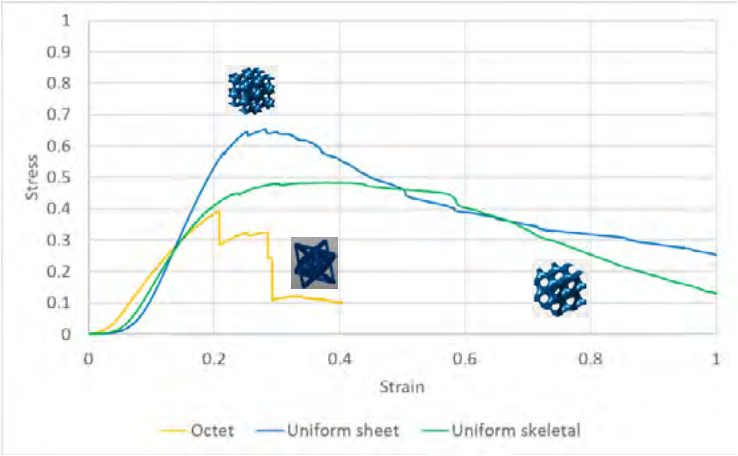


Figure 4. Normalized stress-strain curve of the uniform structures under quasi-static compression

Building on previous results where sheet TPMS structures showed superior performance, it was chosen to undergo gradation in relative density and cell size. Figure 5 depicts the normalized stress-strain curves for a uniform sheet TPMS structure, a TPMS that underwent relative density gradation (RD-sheet), and another with cell size gradation (CS-sheet). Referring to the same figure and to table 1, the TPMS structure with cell size gradation shows no improvement in stiffness, but rather a minor decrease. The change in the cell size throughout the height of the specimen may have altered the load distribution, where smaller cells deformed redistributing the loads to more voluminous cells below, which is shown in figure 3-c. On the other hand, gradation in relative density shows potential with a substantial increase in stiffness of around 400%, from a Young's modulus of 0.2 before gradation to around 1 post gradation. This is attributed to the material distribution gradient within the specimen. Strategically redistributing the material density can be useful in tailoring the load distribution and optimizing the load-bearing capacity.

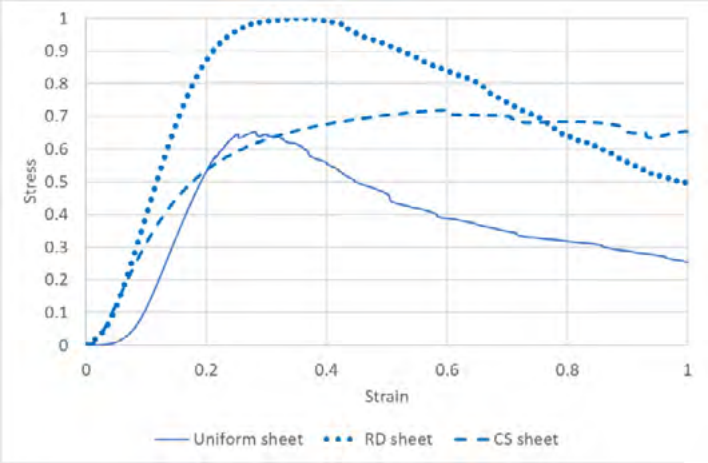


Figure 5. Normalized stress-strain curve of the sheet TPMS structures under quasi-static compression

For energy absorption calculations, it is a common practice in literature to transform load-displacement curves into engineering stress-strain curves. The energy absorption (EA) per unit volume is determined by the numerical integration of the stress-strain curve during compression, consisting of the area under the curve. Energy absorption capacity is highly influenced by localized densification [6][9].

Energy absorption: $$EA = \int \boldsymbol{\sigma}(\boldsymbol{\varepsilon})\boldsymbol{d\varepsilon} \quad (2)$$

where σ, the engineering stress, denotes the ratio of applied force $\boldsymbol{f}(x)$ to stressed area, and ε is the engineering strain which is the ratio of the displacement to the total height of the sample.

The Specific Energy Absorption (SEA) is defined as the work per unit mass when the material is quasi-statically compressed [9]. By examining table 1 and its visualization in figure 6, it is observed that gradation in sheet TPMS structures notably enhances the energy absorption with around 200% increase, which is consistent with literature findings on the effect of gradation [10]. By optimizing the material distribution within the structure, critical regions can be reinforced to withstand higher stresses, improving the overall structural robustness. The structures thus effectively absorb and dissipate energy, withstanding a larger stress envelope while undergoing deformation. However, this gradation effect is not as pronounced in skeletal TPMS structures, where the increase in energy absorption is relatively minimal. While sheet TPMS owe their superior performance to the continuous shell-like topology, skeletal TPMS structures are closer to strut-based structures featuring larger voids throughout its cells.

While gradation in cell size of sheet TPMS improved specific energy absorption substantially, there is no improvement in the mechanical properties. Load bearing capacity of larger cells and deformation in smaller cells balance each other, leading to a plastic behavior. As the smaller cells deform, the structure can sustain the loads for a longer duration, which delays the drop in stresses. Consequently, this results in a larger envelope under the stress-strain curve as shown in the stress-strain plot in figure 5.

Table 1 and figure 6 summarize the results of all tested structures, normalized and falling between 0 and 1, with 1 being for the highest scoring structure in each category. The results consist of the Young's modulus (**E**), the ultimate strength (**σ**) and the specific energy absorption (**SEA**).

Table 1. Mechanical properties and energy absorption capacity of tested structures – normalized (0-1)

Specimen	*E*	σ	SEA
Octet	0	0	0
Sheet TPMS	0.2	0.15	0.47
Skeletal TPMS	0.07	0.43	0.4
RD-sheet	**1**	**1**	**0.9**
RD-skeletal	0.09	0.71	0.49
CS-sheet	0.07	0.24	1

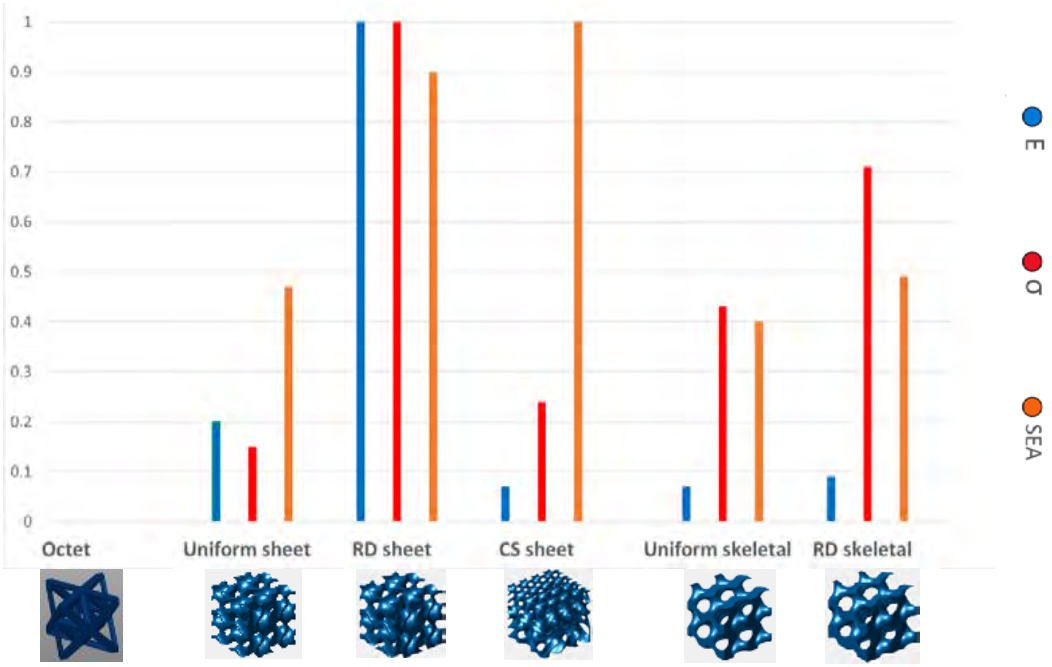


Figure 6. Overview of the mechanical performance and energy absorption of tested structures

4. Conclusion

The observed mechanical behavior in compression of the tested structures can be attributed to the intricate interplay between the lattice topology and material distribution employed in the design process. The octet truss structure exhibited the lowest stiffness displaying a brittle behavior, while the sheet TPMS structure showed superior performance due to improved load distribution and material efficiency.

Gradation in relative density notably enhanced the performance of sheet TPMS structures, particularly in stiffness and energy absorption. However, while gradation in cell size improved energy absorption thanks to the larger area under the stress-strain curve because of larger plastic deformations, it didn't lead to improvements in Young's modulus and ultimate strength in compression. Overall, these findings underscore the importance of material distribution and gradation strategies in optimizing the mechanical performance of lattice structures.

Exploring the potential of TPMS lattices with gradation could offer exciting avenues for tailoring mechanical properties to meet specific performance requirements. The influence of relative density gradation and morphological variations on the structural response to loading conditions can lead to diverse mechanical behaviors optimized for different applications. While our study demonstrates the influence of gradation on the mechanical properties and energy performance, future research could delve into targeted functional gradation to explore the versatility and tunability of TPMS-based lattice structures for various engineering applications.

References

[1] Zhu, Y., Polyzos, E., & Pyl, L. (2024). Stiffness optimisation of sandwich structures with elastically isotropic lattice core. Thin-Walled Structures, 195, 111408. https://doi.org/10.1016/j.tws.2023.111408

[2] Ashby, M. (2011). Hybrid materials to expand the boundaries of material-Property Space. Journal of the American Ceramic Society, 94(s1). https://doi.org/10.1111/j.1551-2916.2011.04559.x

[3] Wu, Y., Fang, J., Wu, C., Li, C., Sun, G., & Li, Q. (2023). Additively manufactured materials and structures: A state-of-the-art review on their mechanical characteristics and energy absorption. International Journal of Mechanical Sciences, 246, 108102. https://doi.org/10.1016/j.ijmecsci.2023.108102

[4] Al-Ketan, O., Lee, D.-W., Rowshan, R., & Abu Al-Rub, R. K. (2020). Functionally graded and multi-morphology sheet TPMS lattices: Design, manufacturing, and mechanical properties. Journal of the Mechanical Behavior of Biomedical Materials, 102, 103520. https://doi.org/10.1016/j.jmbbm.2019.103520

[5] Wallat, L., Selzer, M., Wasmuth, U., Poehler, F., & Nestler, B. (2022). Energy absorption capability of graded and non-graded sheet-based gyroid structures fabricated by microcast processing. Journal of Materials Research and Technology, 21, 1798–1810. https://doi.org/10.1016/j.jmrt.2022.09.093

[6] Park, S.-Y., Kim, K.-S., AlMangour, B., Grzesiak, D., & Lee, K.-A. (2022). Compressive deformation behavior and energy absorption characteristic of additively manufactured sheet cocrmo triply periodic minimal surface lattices. Journal of Materials Research and Technology, 18, 171–184. https://doi.org/10.1016/j.jmrt.2022.02.086

[7] ASTM Standard ASTM D695-15, 2016, "Standard Test Method for Compressive Properties of Rigid Plastics," ASTM International, West Conshohocken, PA, 2016, DOI: 10.1520/D0695-15, www.astm.org

[8] Ashby, M. F., & Gibson, L. J. (1997). Cellular solids: structure and properties. Press Syndicate of the University of Cambridge, Cambridge, UK, 175-231.

[9] Tancogne-Dejean, T., Spierings, A. B., & Mohr, D. (2016). Additively-manufactured metallic micro-lattice materials for high specific energy absorption under static and dynamic loading. Acta Materialia, 116, 14–28. https://doi.org/10.1016/j.actamat.2016.05.054

[10] Wang, Q., Li, Z., Zhang, Y., Cui, S., Yang, Z., & Lu, Z. (2020). Ultra-low density architectured metamaterial with superior mechanical properties and energy absorption capability. Composites Part B: Engineering, 202, 108379. https://doi.org/10.1016/j.compositesb.2020.108379

ANALYSIS AND OPTIMIZATION OF A CFRP MOUNTAIN BICYCLE FRAME

Digby D. Symons[1] and James Krippner[2]

[1]Department of Mechanical Engineering, University of Canterbury, Christchurch, New Zealand
Email: digby.symons@canterbury.ac.nz,
Web Page: https://profiles.canterbury.ac.nz/Digby-Symons/about
[2] Department of Mechanical Engineering, University of Canterbury, Christchurch, New Zealand
Email: Jameskrippner@hotmail.com

Keywords: Finite element analysis; Optimization; Sports engineering; Carbon fibre; Design

Abstract
Bicycles must resist loads without failure or excessive deflection but also be lightweight. Constructing a bicycle frame from carbon fibre rather than metal allows design freedom to maximally benefit from the higher specific strength and stiffness of the composite material. However, determining the best composite lay-up is non-trivial. This paper presents a case-study computational optimization of a CFRP mountain bicycle frame. Multiple load cases were considered (impact, jumping, pedalling and cornering) with a combined weighted compliance value as the objective to minimise. Key constraints were a maximum frame mass and a factor of safety (FOS) greater than two for each load case. Laminate stresses were determined by finite element analysis with ply failure predicted by the Hoffman criterion. The analysis was validated by comparison with a published test to failure of a similar composite frame. An initial design had excessive strength under some load cases (FOS of up to 7) and deflections of up to 10 mm. After optimization, all FOS were within a range of 2 to 3.5 and deflections were less than 6 mm. Although load-case definition and weighting remain significant subjective manual tasks this case study demonstrates the benefit of computational optimization for a designer of a composite bicycle.

1. Introduction

Off-road cycling is a sport that is demanding of both athlete and equipment. Bicycles must endure a range of high-magnitude load scenarios without failure or excessive deflection but also be as light as possible. Constructing a bicycle frame from carbon fibre reinforced plastic (CFRP) allows much more design freedom than metal tube construction and an opportunity to take advantage of carbon fibre's high specific strength and stiffness. However, determining the best distribution of composite material is a non-trivial task. This paper presents a case study investigation into the use of computational optimization of the composite laminate lay-up for a frame of a full-suspension “mountain” bicycle (Figure 1). The aim is to maximise stiffness whilst achieving adequate strength and low weight.

2. Methods

2.1. Load cases

Although some standards do exist for bicycle design, e.g. [1,2], they do not define a full set of operating load cases that can be used to optimize the design of a high-performance off-road bicycle. Indeed, such loads, along with resulting composite lay-ups, may be industrial proprietary knowledge and thus unpublished. Consequently, the load cases used for this case study were partly determined from first principle analysis of the bicycle and cyclist system with reference to published data where available. In general it is intended that this bicycle design be suitable for up to ASTM “condition 4” cycling (i.e.

jumps under 1.22 m and speeds under 40 km/h) [1]. Four main scenarios were considered: frontal impact, jump landing, pedalling and cornering. Key assumptions included:

- A rider mass limit of m = 120 kg
- Factor of safety (FOS) > 2 for all load cases
- Fatigue life > 100,000 cycles for repeated load cases
- Maximum seat post extension of 400 mm, minimum insertion of 120 mm

A FOS of 2 was selected because carbon fibre composites fracture without yield and consequently a failure could be potentially catastrophic for the rider. Fatigue life was determined from the ASTM Standards for mountain bicycles [2] resulting in an allowable stress/strength value of 0.55 for quasi-isotropic laminates [3] to be applied to repeated load cases. The load cases are summarized in Table 1.



Figure 1. Full-suspension mountain bicycle.

2.1.1 Frontal impact

The frontal impact load case was based on a published test by Santa Cruz Bicycles [4] in which a CFRP full-suspension mountain bicycle frame failed at a force of approximately 9000 N applied between the front fork axle and the crank axle (bottom bracket).

2.1.2 Jump landing

The jump landing load case assumes a total drop height of 1.22 m with a constant landing force resisted by compression of the rider's legs through a distance of 0.24 m; this gives a total force of 5.1mg = 6000 N applied vertically to the crank axle. These values are in good agreement with measured jump landing forces [5] and also match Pole Bicycles' internal testing procedure [6].

2.1.3 Seated pedalling fatigue

This load case simulates the fatigue loading of a 120 kg rider pedalling while seated. The repeated force is taken as the complete weight, mg = 1200 N, of the rider acting on the seat. This force is in agreement with the ASTM standard for Condition 3 mountain bike use [2], as well as Pole Bicycles' test procedure [6]. The load is applied with 400 mm of seatpost extension for the given maximum assumption and 70 mm rearward according to the ASTM test specification [2], with the virtual seat post constrained 120 mm into the frame to give the minimum insertion depth. As this load is cyclic, the actual load to be applied is: 1200 N / 0.55 = 2200 N.

2.1.4 Maximal pedalling

This load case simulates the overloading of a 120 kg rider applying maximal torque during a race start. In previous work [7] the forces applied to the frame by cyclists in a racing standing start were calculated as 2.1*mg* at the left pedal and -0.5*mg* at the right pedal (or vice versa). As this maximal load is not expected to occur often fatigue amplification was not applied.

2.1.5 Cornering fatigue

This load case simulates the fatigue loading of high-speed cornering. A 10 m radius corner and speed of 10 m/s were assumed [8] giving a centripetal acceleration of approximately 1*g*. The corresponding horizontal centripetal force acts simultaneously with the vertical rider weight. To allow for the possibility of the rider's centre of mass not being aligned with the plane of the bicycle frame whilst cornering the centripetal and weight forces were treated as separate horizontal and vertical forces applied at the crank axle. Since this load case is repeated, the actual loads applied are each: mg / 0.55 = 1.8mg = 2200 N.

Table 1. Summary of load cases.

Load Case	Description	Parameters	Optimization weighting
1	Frontal impact	4500 N between fork and crank axles	0.1
2	Jump landing	6000 N vertically at crank axle	0.1
3	Seated pedalling fatigue	2200 N vertically on virtual saddle	0.1
4A & 4B	Maximal pedalling	2500 N vertically at left/right pedal -600 N vertically at right/left pedal	0.4
5A & 5B	Cornering fatigue	2200 N vertically at crank axle +/- 2200 N horizontally at crank axle	0.3

2.2. Frame loads

To determine the forces applied to the frame front triangle (Figure 2) during load cases 1-5, the bicycle-rider system and rear suspension mechanism were each analysed in static equilibrium. This firstly allowed ground reaction forces to be found; subsequently chain tension and suspension pivot contact forces were calculated.

2.3. Material properties

The material properties for the carbon fibre prepreg to be used in the frame were adapted from the Gurit SE 84LV datasheet [9] with reference to standard properties [10]. Two materials were used: 300 gsm HEC unidirectional and 200 gsm RC200T 3K weave HEC with assigned properties as listed in Table 2.

2.4. Initial frame design

A candidate bicycle frame geometry was defined using SolidWorks (Dassault Systèmes) software (Figures 1 & 2). To define an initial frame lay-up the thickness of carbon fibre laminate required for a FOS of 2 under load case 1 was determined by an approximate hand calculation. The load applied through the front fork axle and bottom bracket was assumed to be resisted only by bending in the circular cross-section of the 58 mm diameter down tube. For an approximately isotropic 0/90°, +/-45° lay-up of Gurit 200 gsm RC200T 3K twill weave HEC [9] this gave a required wall thickness of 2.9 mm. The initial laminate design adopted was therefore a quasi-isotropic carbon fibre lay-up of thickness 2.8 mm (12 0.23 mm plies of RC200T weave) in the main tubes and 5.5 mm (24 plies of RC200T weave) in reinforced areas around bearings (suspension, pedal cranks, steering) and the seatpost (Figure 2). The mass of this initial design was 1.1 kg.

Table 2. Material properties.

Property	Description	300 GSM HEC UNIDIRECTIONAL	200 GSM RC200T 3K WEAVE HEC
	Cured ply thickness (mm)	0.3	0.23
E1	Longitudinal Modulus (MPa)	130000	61000
E2	Lateral Modulus (MPa)	8300	61000
NU12	Poisson's Ratio	0.26	0.06
G12	In-plane Shear Modulus (MPa)	5600	5200
G1Z	Transverse Shear Modulus in 1Z Plane (MPa)	5600	4100
G2Z	Transverse Shear Modulus in 2Z Plane (MPa)	3000	3300
XT	Allowable longitudinal tensile stress (MPa)	2458	719
XC	Allowable longitudinal compressive stress (MPa)	1354	759
YT	Allowable lateral tensile stress (MPa)	39.2	662
YC	Allowable lateral compressive stress (MPa)	1354	731
S	Allowable in plane shear stress (MPa)	86.6	74.8

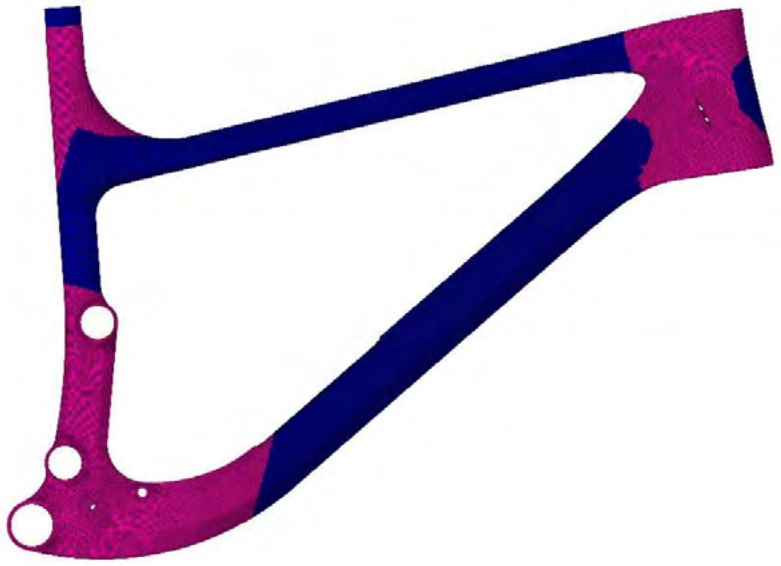


Figure 2. Frame front triangle design showing initial boundaries of reinforced areas.

2.5. Finite element analysis

Calculation of laminate stresses was performed using the HyperWorks (Altair Engineering) finite element analysis programme [11]. The frame geometry was imported as a surface and meshed with shell elements. Ply failure was predicted using the Hoffman composite failure criterion.

2.5.1 Boundary conditions

The frame was constrained in all 6 degrees of freedom via RBE3 (load-transfer) semi-rigid body elements between the upper and lower headsets to simulate the fork constraint. RBE3 elements distribute

the load applied at the independent node while allowing local deflections [11]. Each suspension pivot, the bottom bracket, and the seat mounting interface were also connected with RBE3 elements.

2.5.2 Mesh convergence study

A mesh convergence study was conducted to determine the required element size for accurate results. Both maximum nodal displacement and minimum composite strength ratio were considered for load case 5. A suitable mesh density was determined when the results did not change by more than 0.1% while further decreasing element size. Convergence occurred at 83400 nodes, with a 2 mm nominal mesh element size (Figure3).

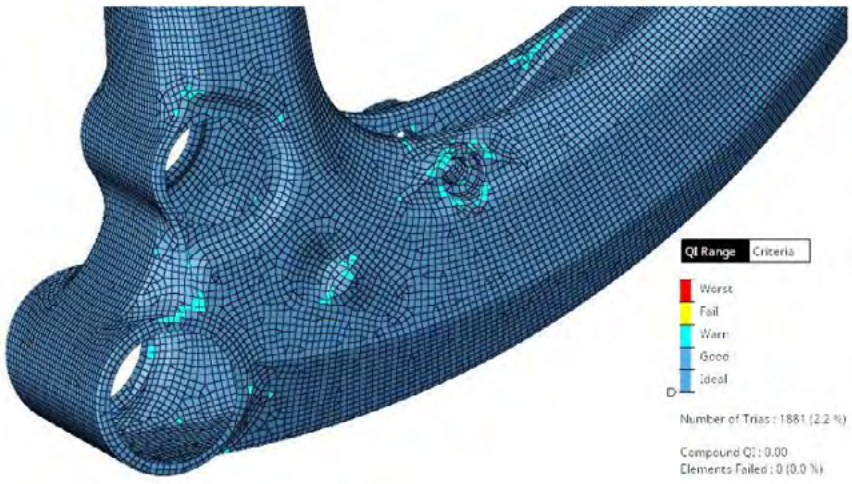


Figure 3. Detail of finite element mesh in the bottom bracket area.

2.5.3 Validation

The finite element modelling approach was validated by comparison of predicted strength with the published Santa Cruz test to failure of a similar composite frame [3].

2.6. Optimization

The multiple load cases considered present a multi-objective optimization problem. This was tackled by assigning selected weights to each load case and using a weighted compliance value as the objective to minimise. Stiffness under maximal pedalling loads was selected as most important and the largest weight (0.4) was therefore assigned to load case 4. To further prioritise the lateral stiffness of the frame a weight of 0.3 was assigned to cornering (load case 5) whilst the remaining load cases were assigned weights of 0.1 (Table 1). Key constraints for optimization were that the frame mass did not exceed that of the initial design (1.1 kg) and that a factor of safety (FOS) of at least two was achieved for each load case. Optimization of lay-up was performed using the HyperWorks (Altair Engineering) software in two steps: an ideal free-size optimization and a subsequent manufacturable size optimization to produce a practical laminate with discrete ply thicknesses and boundaries.

2.6.1 Free-size optimization

Free-size optimization was used to determine the ideal thickness of specific ply orientations and types in each element of the model, in particular allowing unidirectional plies to be used in the lay-up. For this optimization the design variables were defined as the thickness of plies in each element. A “super-ply” concept was adopted, in which each available fibre orientation was assigned to a super-ply whose thickness was free-sized. In addition the “smear” option was used in order to neutralise the effect of stacking sequence (giving an ABD stiffness matrix that is stacking sequence independent and assumes a symmetric lay-up) [12].

Plies of +/-45 and 0/90 3K twill weave; and 0, 45, 90, and -45 degree unidirectional fibres were used. Lay-up constraints were used so that, for each element, the +/-45° unidirectional plies should be balanced, the surface 3K twill weave plies should have a minimum thickness of 0.23 mm each, and the total laminate thickness should be >1.6 mm. The unidirectional plies were balanced to minimise the effects of warping. The twill weave constraints were added to keep a surface aesthetic/protective layer intact. The total minimum thickness was defined to keep some strength in the non-structural regions to mitigate impact damage, e.g. rock strikes. The responses measured at each iteration were the mass of the frame (< 1.1 kg), the composite failure index for each ply in each element (strength ratio > 2) and the compliance of the frame under each load case. The objective of the optimization was to minimise the combined weighted compliance value.

2.6.2 Size optimization

Following the Free-Size Optimization a Size Optimization was performed to define a practical (i.e. manufacturable) laminate with discrete ply thicknesses and boundaries. This took the lay-up schedule generated by the free-size optimization and refined the thickness and boundaries of each ply. The thicknesses of the 300 gsm unidirectional plies and 200 gsm 3K woven fabric were defined to be 0.3 mm and 0.23 mm, respectively.

3. Results and discussion

3.1. Initial laminate & validation

For the initial frame lay-up the HyperWorks calculation gave a minimum composite strength ratio of 2.1 at the joint of the headtube and downtube for load case 1 (an applied load of 4500 N between the front fork axle and bottom bracket). This magnitude and location were in good agreement with the failure at 9000 N in the Santa Cruz test [3] and was therefore considered an adequate validation of the overall approach. The initial design was found to have adequate strength under all load cases with a minimum FOS of 2.1 (load case 1) but an excessive maximum of 7.0 (load case 5). The greatest deflection was under load case 1 with a magnitude of 10 mm.

3.2. Optimization

The free-size and subsequent size optimization resulted in adjusted displacements and FOS values for all load cases. These are plotted in Figs. 4 & 5, respectively. Small increases in displacement and FOS are seen after the final size optimization step due to the additional constraints applied to produce a manufacturable lay-up. After optimization deflections for all load cases were reduced, the largest to less than 6 mm. In particular, the average stiffness for cornering and pedalling (load cases 4 &5) increased by 30%. The optimized FOS for all load cases are in the range of 2 to 3.5. The final optimized total laminate thickness is plotted in Figure 6.

Table 3. Displacement and strength for all load cases, initial and optimized laminates.

Load Case	Description	Initial laminate design		Free-Size Optimization		Size Optimization	
		Max. Disp. (mm)	Min. FOS	Max. Disp. (mm)	Min. FOS	Max. Disp. (mm)	Min. FOS
1	Frontal impact	10.0	2.14	5.53	2.10	5.95	2.02
2	Jump landing	1.58	2.54	1.61	2.05	1.67	2.01
3	Seated pedalling	5.32	2.60	2.89	1.97	3.25	2.05
4A	Max. Pedal Left	2.22	4.37	1.72	2.34	1.73	2.47
4B	Max. Pedal Right	1.33	5.69	0.83	3.54	0.87	3.61
5A	Cornering Left	1.45	6.94	1.20	3.00	1.19	3.37
5B	Cornering Right	1.44	6.92	1.19	3.28	1.17	3.28

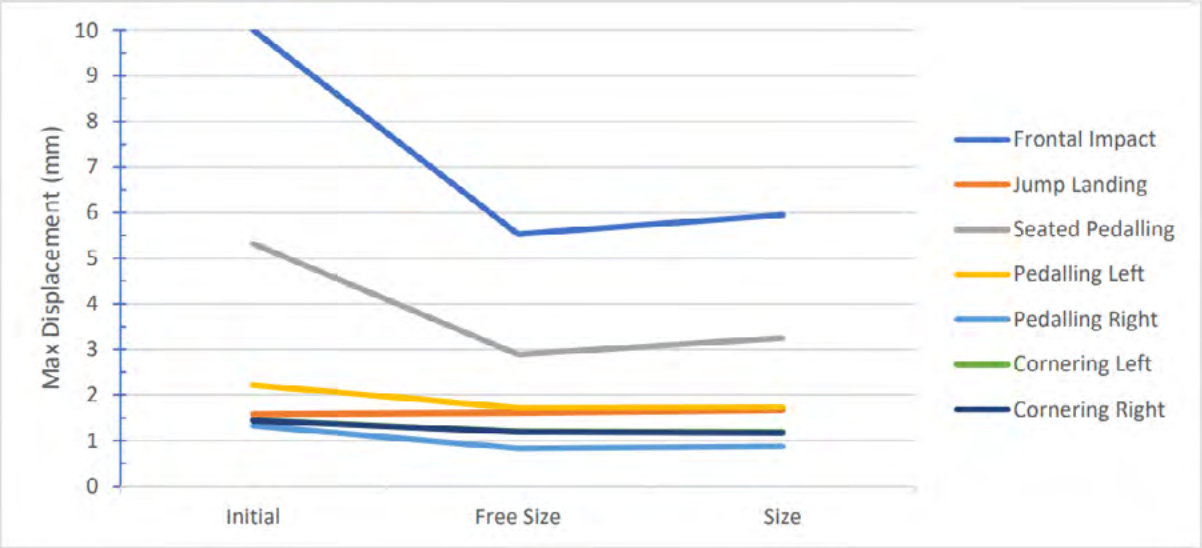


Figure 4. Maximum displacement (mm) under each load case for initial and optimized lay-ups.

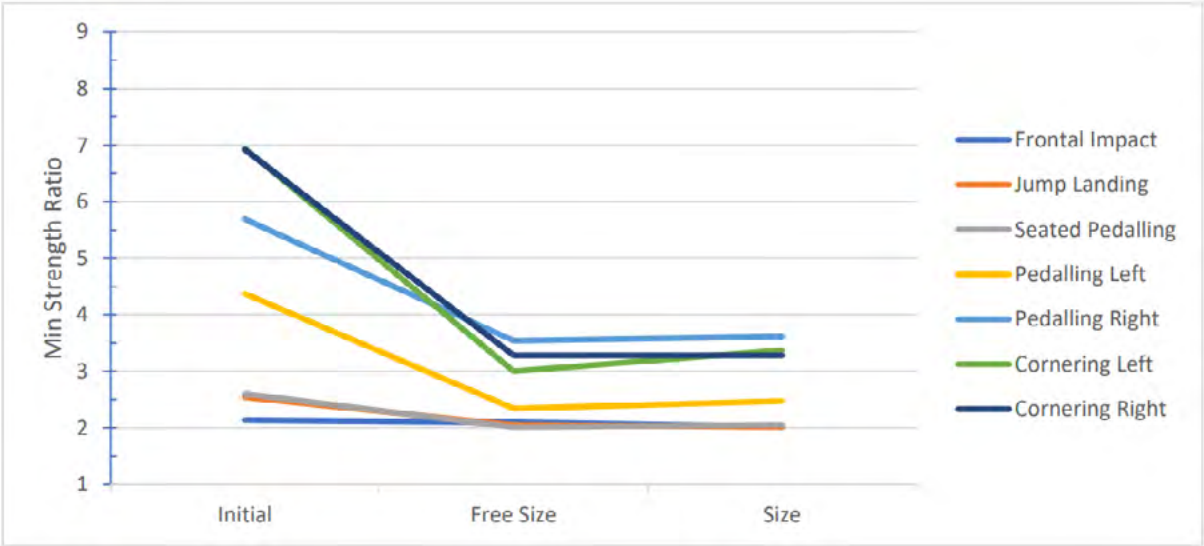


Figure 5. Minimum strength ratio (FOS) under each load case for initial and optimized lay-ups.

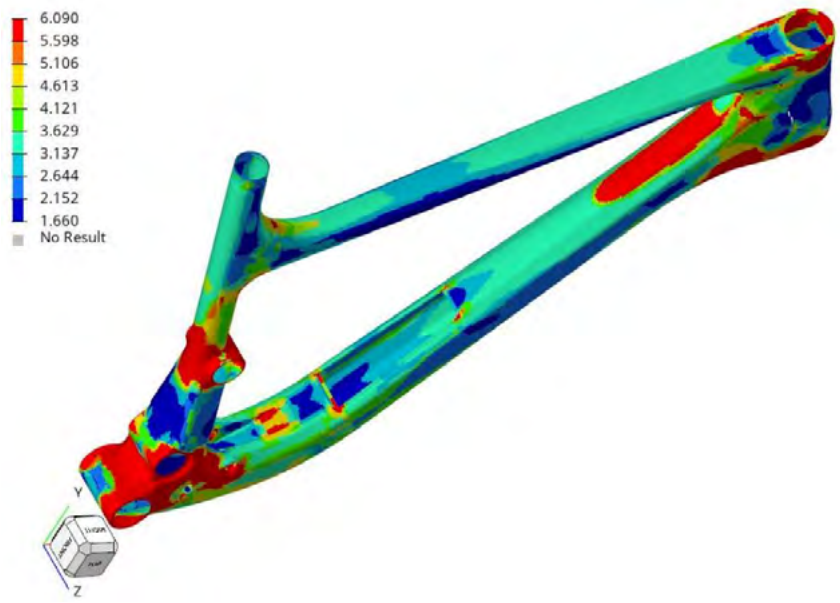


Figure 6. Total laminate thickness (mm) after size optimization.

4. Conclusions

The optimization process carried out for this case study has produced a laminate design that maximises stiffness whilst achieving adequate strength and low weight. Although load-case definition and weighting remain significant subjective manual tasks, the case study demonstrates the benefit of computational optimization for designers of composite bicycles.

References

[1] ASTM International. *F2043-13 - Standard Classification for Bicycle Usage*. ASTM International, West Conshohocken, 2018.
[2] ASTM International. *F2711-19 - Standard Test Methods for Bicycle Frames*. ASTM International, West Conshohocken, 2019.
[3] S. Zhou and X. Wu. Fatigue life prediction of composite laminates by fatigue master curves. *Journal of Materials Research and Technology*, 8(6):6094-6105, 2019.
[4] M. Levy. *Santa Cruz Bicycles - Test Lab. Pinkbike,* 23 February 2012. [Online]. Available: https://www.pinkbike.com/news/santa-cruz-bicycles-test-lab.html. [Accessed 28 September 2021]
[5] W. Niu, T. Feng, C. Jiang and M. Zhang. Peak Vertical Ground Reaction Force during Two-Leg Landing: A Systematic Review and Mathematical Modeling. *BioMed Research International*, 2014(126860), 2014.
[6] Pole Bicycles. *EFBE Tri-Test® Gravity.* 11 May 2021. [Online]. Available: https://polebicycles.com/efbe-tri-test-gravity-the-gold-standard-test-for-gravity-frames/. [Accessed 18 May 2022]
[7] D. Symons. Loading and structural stiffness of tandem bicycle frames. *Sports Engineering*, 27(12), 2024.
[8] Trailism. Trail Turn Design. [Online]. Available: https://trailism.com/trail-turn-design/ . [Accessed 16 May 2022].
[9] K. Cadd, *SE 84LV General Datasheet.* Gurit, Wattwil, 2021.
[10] I. M. Daniel and O. Ishai. *Engineering Mechanics of Composite Materials 2nd Edition*. Oxford University Press, 2005.
[11] Altair Engineering. *Altair HyperMesh*, 2021 [Online]. Available: https://2021.help.altair.com/2021/hwdesktop/hm/index.htm [Accessed 11 April 2024].
[12] Altair Engineering. *Simulating Composites using OptiStruct*, Altair Engineering, 2014.

PHYSICAL-VIRTUAL TESTING METHODOLOGY FOR EFFICIENT PROPERTY DETERMINATION OF TAILORED FIBER-REINFORCED COMPOSITE STRUCTURAL VANES FOR FUTURE JET ENGINES

F.Töpfer[1], N.Hanisch[1], S.Spitzer[1,4], L.Schröder[1], L.Bittrich[2,3], A.Spickenheuer[2,3], M.Gude[1]

[1] Institute of Lightweight Engineering and Polymer Technology, TUD Dresden University of Technology, Holbeinstrasse 3, 01307 Dresden , Germany
Email: friedrich.toepfer@tu-dresden.de, Web Page: http://tu-dresden.de/mw/ilk
[2] Leibniz-Institut für Polymerforschung Dresden e.V., Hohe Straße 6, 01069 Dresden, Germany
Email: spickenheuer@ipfdd.de, Web Page: www.ipfdd.de/tfp-technologie
[3] Complex Fiber Structures GmbH, Wigardstr. 21, 01097 Dresden, Germany
Email: bittrich-lars@ipfdd.de, Web Page: https://www.complex-fiber-structures.de/
[4] Chair of Lightweight Design, Universität Rostock, Albert-Einstein-Str. 2, 18059 Rostock, Germany
Email: sebastian.spitzer@uni-rostock.de, Web Page: https://www.cld.uni-rostock.de

Keywords: Tailored Fiber Placement, variable-axial, structural vane, jet engine

Abstract
This paper presents a virtual-physical testing methodology for the design and dimensioning of a variable-axial structural guide vane manufactured by Tailored Fibre Placement (TFP). Within the context of a jet engine, a validation pyramid based on the building block approach is developed, considering different levels of complexity from coupon- up to system-level. Both virtual and physical sections of the validation pyramd are defined. Focussing on the coupon- and element-level, a method to determine a material model for the TFP structural vane is proposed, considering the complex environment of the jet engine. A work flow for the specific TFP element-specimen design process using the software EDOstructure for variable-axial components is developed.

1. Introduction

The use of lightweight materials in the aerospace sector can significantly contribute to the European Union's ambitious goal of reducing CO2 emissions by 75% by 2050 [1]. This potential is especially evident when employing innovative technologies such as TFP to produce stress-adapted structures [2]. However, designing novel tailored, variable-axial (VA) carbon fibre reinforced polymer (CFRP) structures presents complex challenges. The assessment of their load-bearing capacity is particularly demanding due to the intricate relationship between geometry, composition, and the manufacturing process [3]. Figure 1 illustrates the evolution of the intermediate case (IMC) in the Rolls-Royce Pearl engine architecture: transitioning from the traditional function-separated intermediate case on the left, through the newer generation of IMC with a function-integrated metallic design in the center, to a future architecture featuring a hybrid metal-composite design on the right [4]. In this hybrid design, CFRP is utilised in areas where load transmission is indirect and straightforward, while metal is employed in regions subjected to complex loads due to its isotropic properties.

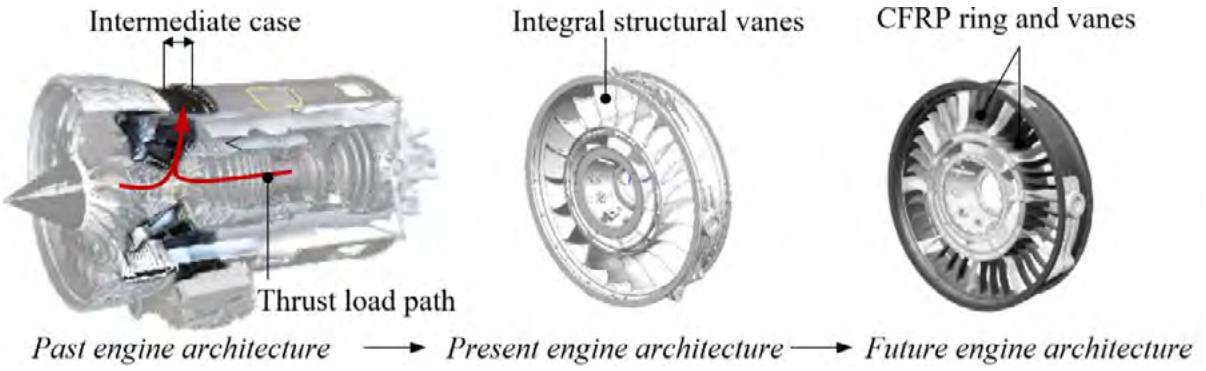


Figure 1. Intermediate cases of Rolls-Royce jet engines [4]

In order to increase the efficiency of the Engineering Design Process, it is essential to use reliable mechanical properties that take the influence of TFP process into account. For a complex system such as a jet engine and its different scales, the material scale provides important input parameters for the higher scales that follow. Furthermore, the modelling of tailored structures proves to be challenging when conventional simulation software is used [4, 5].
The TFP technology, designed for creating curvilinear fiber patterns, was invented and developed at the Leibniz Institute for Polymer Research Dresden e.V. [6] and is shown in Figure 2 [5]. The adjustable process parameters are the stitch width, stitch distance (R-value), oscillating movement of the roving placement, roving distance, number of layers and the deposit radius.

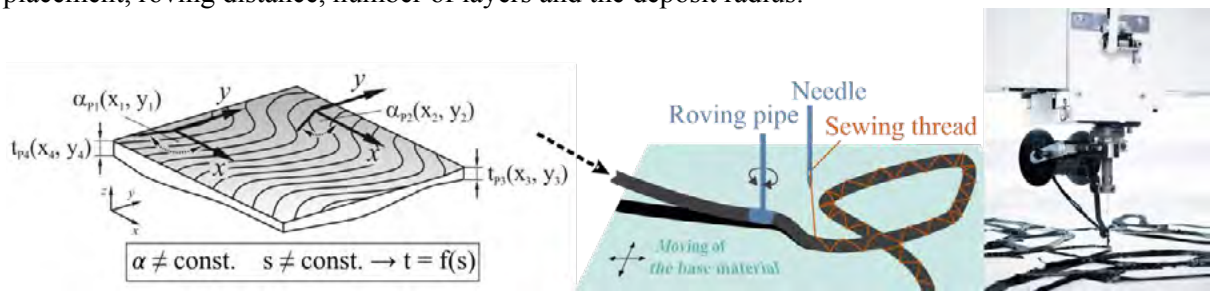


Figure 2. Principle of a VA composite design (left), TFP manufacturing principle (center), and TFP fibre placement head (right) [5]

Preliminary experimental research on how TFP process parameters affect the tensile modulus and strength was carried out by Spickenheuer [7]. Uhlig et al. demonstrated in one work [8] that variations in TFP parameters significantly influence local fiber volume content and in-plane waviness of composite materials. In a further work [9] they concluded, that the stiffness reduction due to the TFP process is minor compared to a unidirectional (UD) material, but can be significant for strength properties.

2. Development of a physical-virtual testing methodology

This paper presents a virtual-physical testing methodology to efficiently determine the material properties of variable-axial structural vanes for future jet engines. The developed validation strategy is based on the building block approach [10] as shown in Figure 3.Various levels are defined in a validation pyramid (VP) to determine the material model at the coupon- and element-level, analyse the structural behaviour from the virtual component- to system-level, and validate the numerical models with a physical test campaign extedning from the physical element- to system-level. This work specifically focuses on the two lower levels—coupon and element—which provide critical input parameters for the subsequent levels. The levels above the element level are included in the VP for completeness only.

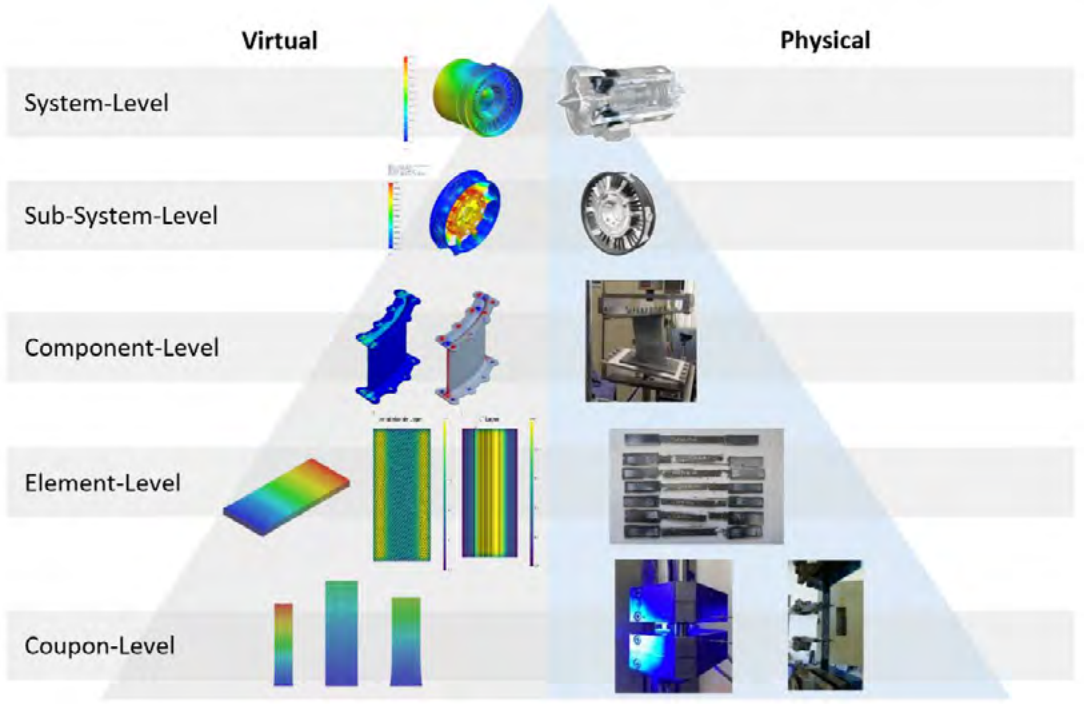


Figure 3. Virtual-physical validation pyramid

For VA structures, it is necessary to capture the influence of the TFP process parameters on the material properties. On the coupon-level, the material parameters are determined to define the initial material model. Two material models are determined: one without the TFP influence considered, which serves as a baseline, and another one with TFP influence considered. By that, a knock-down factor is determined for the TFP process influence on the material properties. Subsequently, the component simulation is solved in Ansys APDL with an isotropic shell model including load and boundary conditions as an input. The result file .rst format is the compatible file format for the TFP component strcutrual vane design process. Here, a specific TFP software called EDOstructure from Complex Fibre Structures GmbH [11] is used (version 1.0.2193). A vane TFP pattern is realised, which is used to derive an element specimen design. The pattern is exported as a DXF file and transmitted to Hightex Verstärkungsstukturen GmbH [12] to manufacture the specimen. Furthermore, the element test is performed and the initial material models are calibrated. Finally, the calibrated material model is implemented in the vane simulation model and further analysis can be performed. The process flow chart is shown Figure 4.

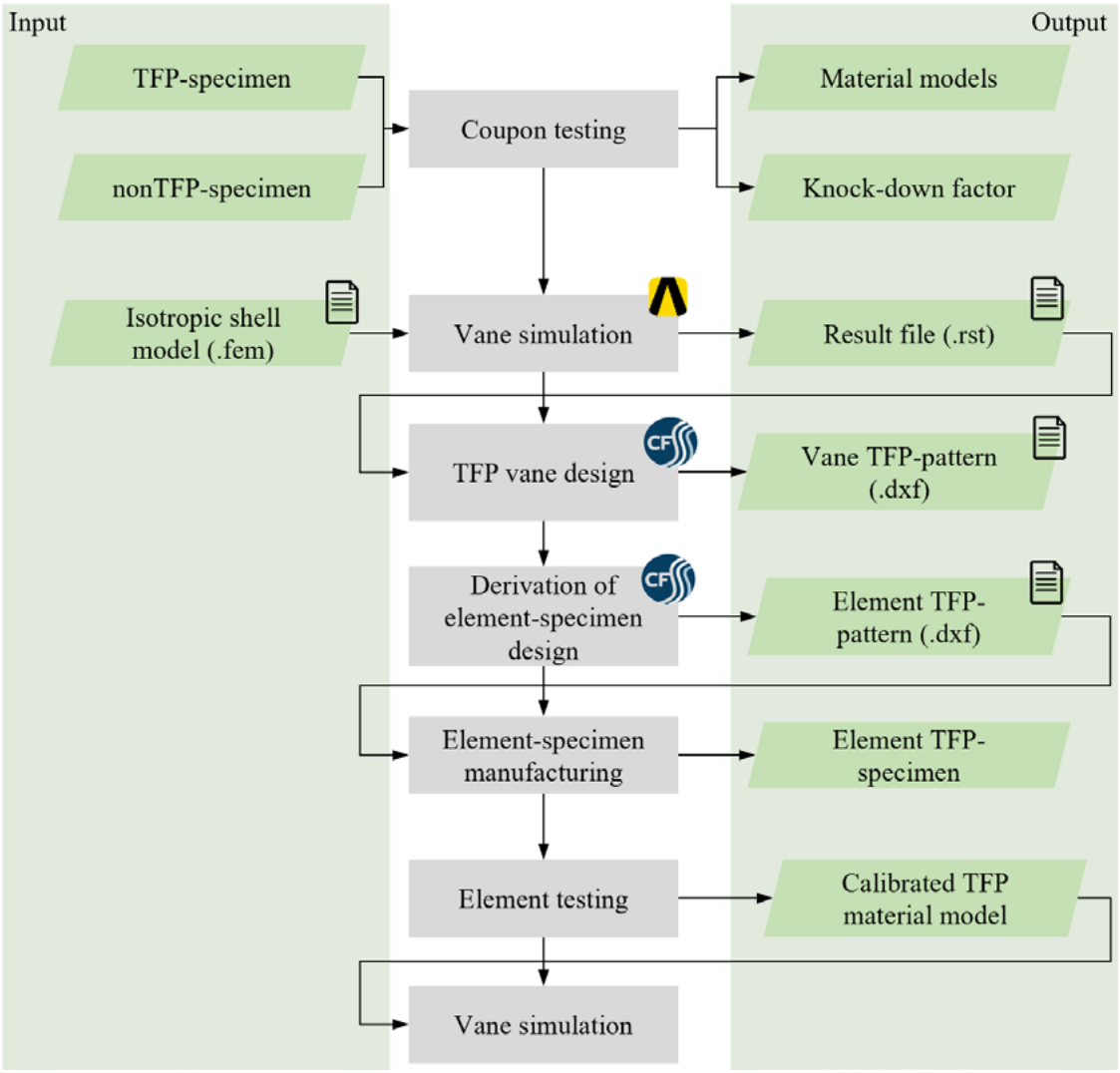


Figure 4. Process flow chart for the determination of the TFP material model

3. Results

Specific TFP element-specimens were designed, considering component, sub-system- and system-level factors (cf. Figure 5). The design parameters were derived from the component model. From the sub-system, relevant interface information was obtained, and from the engine system, load and boundary conditions were extracted. An isotropic shell model was developed and solved; its solution was imported into EDOstructure. The VA pattern for the vane was generated, and a specific design feature, referred to as the S-curve, was identified. To accurately map the fibre orientations on the mesh of the vane finite element (fe) model, a mesh size equal to half of the roving width was selected.

Subsequently, a simple specimen model was created to project the S-curve pattern from the vane onto a plate model. Load and boundary constraints were appropriately set, and the .rst file was imported into EDOstructure to verify the directional field and generate the DXF pattern for producing the TFP element-specimen.

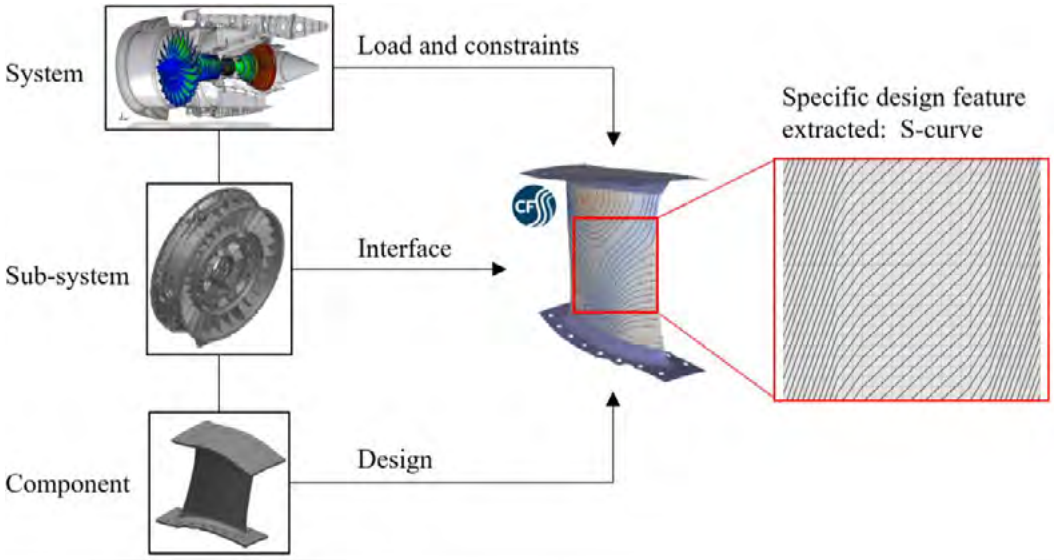


Figure 5. TFP element design determination considering component, sub-system and system-level

The pattern was modified by Hightex into a manufacturing-oriented design, and the adaptations were retransferred and mapped onto the specimen model by re-importing an HGT DXF file into EDOstructure. The preform for the TFP element-specimen was produced and infiltrated using a Resin Transfer Moulding plate tool. The consolidated plate was cut by a water jet into the specimens. The process of designing the specimen and plate preform, as well as the actual preform, is shown in Figure 6. The green frame marks the TFP specimen.

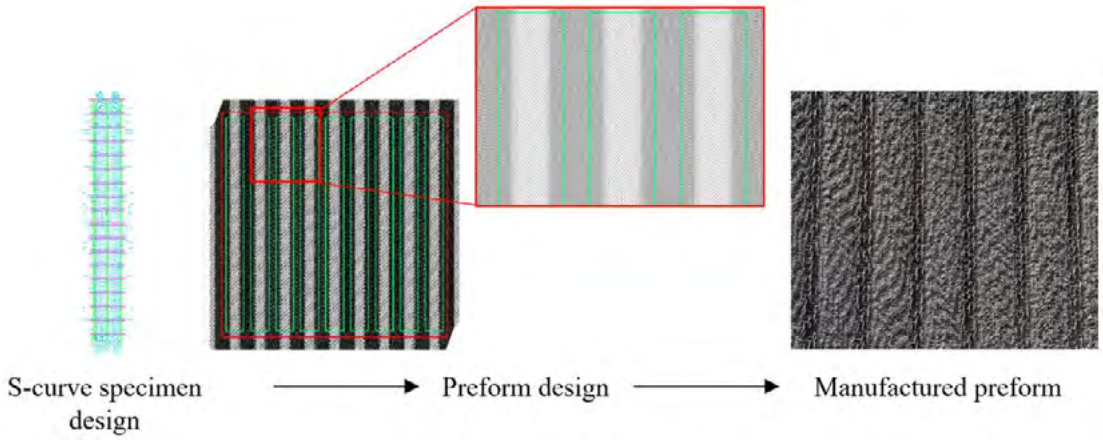


Figure 6. Process from specimen design to manufactured preform

While the input file for EDOstructure must be an Ansys .rst file, several export options for the fe-model export were available. Here, the fe-model was exported as a bulk data file (bdf) and imported into Siemens NX.

4. Conclusions and outlook

This paper successfully introduced a virtual-physical testing methodology for determining the material properties of variable-axial structural vanes for jet engines, integrating both TFP technology and a multi-level validation strategy. By effectively considering the influence of TFP parameters on material properties through both theoretical and experimental approaches, this research provides insights for optimising the design and manufacturing of lightweight, efficient aerospace components, supporting the broader goal of reducing environmental impact in the aviation industry. The presented numerical methods enable an efficient modelling of the tailored structures by plotting the fibre patterns (as DXF files) from the manufacturing process directly on the model as initially explained in [13]. This paper also shows the needed interacting process steps as well as the data flow between the different software

tools used. The proposed method facilitates an effective and efficient design and dimensioning of variable-axial engine structures based on reliable data for future applications.
Further work should focus on comparing physical and virtual test results within the developed framework. Moreover, analysing the higher levels in the validation pyramid will allow for the capture of additional effects of the developed material model on those levels. Through this analysis, the required structural behaviour at the component, sub-system, and system level could be investigated by appropriately setting the TFP process parameters.

5. Acknowledgments

The work took place as part of the projects "Development of a highly efficient linked product engineering process (PEP) for hybrid lightweight structures in the context of Industry 4.0" (PEP4.0, funding code 20X1717B) and “Load-appropriate fiber paths on curved structures using the example of a design space-conforming and aerodynamic Type-V hydrogen pressure tank and an engine ring structure with a development process-accompanying validation strategy” (LaSt, 20M2118F). The projects are funded as part of the fifth and sixth Luftfahrforschungsprogramm of the Bundesministerium für Wirtschaft und Klimaschutz BMWK.

6. References

[1] Europäische Kommission. 2011. *Flightpath 2050. Europe's vision for aviation; maintaining global leadership and serving society's needs; report of the High-Level Group on Aviation Research*. Policy / European Commission. Publ. Off. of the Europ. Union, Luxembourg.
[2] C.Klaus, R.N.Rao, S.Spitzer and M.Gude. Part of a gas turbine engine and method for the manufacturing the part. (Patent Nr. *US 2023/0193770*). https://depatisnet.dpma.de/DepatisNet/depatisnet?action=pdf&docid=US020230193770A1&xxxfull=1, 2023.
[3] J.Kluger et al. A digital process-data-assessment method for tailored fiber placement preforms in the manufacturing process of the structural composite guide vanes of a jet engine. In Sampe Europe Conference 2022 Hamburg, 2022.
[4] F.Töpfer et al. Integration and Interaction of Variable-Axial Fibre Reinforced Composite Components in the whole Engine Model for Future Jet Engines. Deutsche Gesellschaft für Luft- und Raumfahrt - Lilienthal-Oberth e.V., 2023.
[5] A.Dargel et al. Design, modelling and manufacturing of variable-axial composite structural guide vane for a jet engine. SAMPE Europe Conference 2021 Baden / Zürich, 2021.
[6] P.Mattheij, K.Gliesche, D.Feltin. Tailored fiber placement-mechanical properties and applications. J Reinf Plast Compos 1998;17(9):774–86, 1998.
[7] A.Spickenheuer. Zur fertigungsgerechten auslegung von faser-kunststoff-verbundbauteilen für den extremen leichtbau auf basis des variabelaxialen fadenablageverfahrens tailored fiber placement [Ph.D. thesis]. Technische Universität Dresden; 2014.
[8] K.Uhlig, L.Bittrich, A.Spickenheuer und J.H.Almeida Jr. Waviness and fiber volume content analysis in continuous carbon fiber reinforced plastics made by tailored fiber placement, Composite Structures, 2019.
[9] K.Uhlig et al. Meso-scaled finite element analysis of fiber reinforced plastics made by Tailored Fiber Placement, Composite Structures, 2016.
[10] The Composite Materials Handbook—MIL 17, Vol. 3, Rev. F, ASTM International, West Conshohocken, PA, 2002, Chaps. 4–7.
[11] Complex Fiber Structures GmbH. (n.d.). Homepage. Retrieved April 25, 2024, from https://www.cfs-dresden.de/.
[12] Hightex Verstärkungsstrukturen GmbH. (n.d.). Homepage. Retrieved April 25, 2024, from https://www.hightex-dresden.de/#.
[13] L.Bittrich et al. Optimizing Variable-Axial Fiber-Reinforced Composite Laminates: The Direct Fiber Path Optimization Concept", Mathematical Problems in Engineering, vol. 2019, Article ID 8260563, 11 pages, 2019.

Topology optimization method based on minimal surface lattice structure for the lightweight design

Hailun Zhou[a], David Zhang[a,*]

[a]*Faculty of Environment, Science and Economy, University of Exeter, North Park Road, Exeter, EX4 4QF, , UK*

Abstract

The lattice structure is regarded as the ideal structure in various applications such as energy absorption, bone implants, and lightweight design for aerospace. Compared to traditional lattice structures, novel lattice structures designed by triply periodic minimal surfaces (TPMS) based on mathematical methods exhibit a high stiffness-to-weight ratio. In my research, the design method of the I-graph-wrapped package (IWP) TPMS-based lattice structure will be proposed, especially the continuous change in the volume of the graded IWP structure. To investigate the relationship between its mechanical properties and structural relative density, the elastic matrix constants of the IWP lattice are calculated via the homogenization method. The homogenization method will be applied to obtain the relationship between elastic properties and the design parameter of IWP lattice. Furthermore, the topology optimization based on Simple Isotropic Material with Penalization (SIMP) algorithm was investigated to solve the optimal density distribution of IWP lattice filling structure. The results show that the overall stiffness of IWP lattice filling structure is higher than that of traditional BCC lattice filling structure with equivalent total volume. This research will guide the designers in choosing the appropriate structures with predictable mechanical properties during the process of structural optimization.

Keywords: lattice structure, topology optimization, Triply periodic minimal surfaces (TPMS), homogenization method

1. Introduction

Lattice structure is widely employed in structural optimization due to its high strength-to-weight ratio. The design method based on triply periodic minimal surfaces (TPMS) allows the lattice structure to be defined by a mathematical equation, free to select different types of unit cells and architectural details including cell repetitions and relative density. The minimal surfaces, which have a mean curvature of zero that resembles the surface curvature of the trabecular bone [1], are frequently regarded as excellent structures of biometric tissues. The TPMS-based lattice structures have a high surface-to-volume ratio [2] and pore connectivity [3]. The biocompatibility of bone implants can be enhanced by the smooth convergence of TPMS-based structures that can minimize the effect of stress shielding [4]. Furthermore, this design approach has received much attention in the application of designing continuous functionally graded materials by altering the relative density parameters [5] and even connecting several different types of TPMS structures smoothly [6]. Dawei Li et al. [7] presented a novel optimization strategy for designing functionally graded TPMS-based cellular structures with desired mechanical properties, which was used in lightweight design for aerospace applications.

Compared to the traditional body-centred cubic (BCC) lattice structure, the I-graph-wrapped package (IWP) lattice, one of the TPMS lattice structures, exhibits superior mechanical properties such as elastic modulus, yield strength, and energy absorption ability. The IWP lattice structure has a smoother external structure compared to the BCC structure. The lattice structure topology optimization (LSTO) method is to design lattices in-fill components with exceptional directional tensile or shear properties, considering various relative density limits. The optimized lattices

*Corresponding author
Email address: (hz376@exeter.ac.uk),(d.z.zhang@exeter.ac.uk) (David Zhang)

©2024 | 3_HAILUN ZHOU_Hailun_3776J.pdf

are then filled into the design space based on optimization results. The Simple Isotropic Material with Penalization (SIMP) algorithm is one of the most widely implemented methods. It interpolates Young's modulus of the material to the scalar selection field to solve the topology optimization (TO) problem with continuous variables. The intermediate densities are penalized due to the high cost of realizing these results. However, this artificial penalization implies that the topology is less optimal than if the intermediate densities had not been penalized. If there were a method to replace these intermediate regions, there would be no need to penalize them. Several previous studies attempt to tackle the TO problem by using multiple materials, including composites [8] and discrete regions of different materials [9, 10]. Additive manufacturing has been considered a manufacturing route for the intermediate density results by using a multi-material 3D printing technology, but there are a lot of constraints in the technology of multiple metal materials. Another approach that changes the architectural features of structures made of the same material was investigated. Since the relative density of the lattice unit cell is a variable, it can be used to replace the intermediate regions according to a relationship between the variable density of TO results and the variable relative density of the lattice. To get a continuous merging of structure, the relative density of these lattice unit cells should vary continuously.

The intermediate densities can be considered as materials with varying relative densitys of TPMS lattice structure. Thanks to the mathematical parametric design approach, lattice structures with different relative densitys can be smoothly interconnected through a functional equation. This research proposes an LSTO method based on the IWP lattice structure and improves the global stiffness under the requirement of total relative density. The finite element analysis was implemented to compare the stiffness of proposed IWP lattice filling structure with traditional BCC lattice filling structure. The research in mechanical properties of the continuously functionally graded lattice will lay a foundation for potential applications.

2. Design method of IWP lattice structure

The boundary between solid and void of the IWP lattice structure is described as implicit equation. Therefore, the solid IWP lattice region can be expressed as follows [11]:

$$\begin{aligned}\varphi_{IWP} = 2[&cos(\omega x)cos(\omega y) + cos(\omega y)cos(\omega z) + cos(\omega z)cos(\omega x)] \\ &- [cos(2\omega x) + cos(2\omega y) + cos(2\omega z)] - t \leq 0\end{aligned} \tag{1}$$

where ω is the parameter to control the unit size of lattice structure, t is the design variable used to adjust the relative density ρ of the IWP structure, which can be calculated by the following equation:

$$\rho = \frac{\iiint_{(\varphi_{IWP}\leq 0)\cap(|x|\leq \frac{L}{2})\cap(|y|\leq \frac{W}{2})\cap(|z|\leq \frac{H}{2})} dxdy}{LWH} \tag{2}$$

where L, W, and H are the length, width, and height of the lattice structure, respectively. In order to investigate the relationship between the offset parameter t and relative density, a polynomial fitted equation and the curve were shown in Fig.1. This would provide an approach allows that designer to obtain desired lattice structures rapidly by modifying the parameter t.

©2024 | 3_HAILUN ZHOU_Hailun_3776J.pdf:2

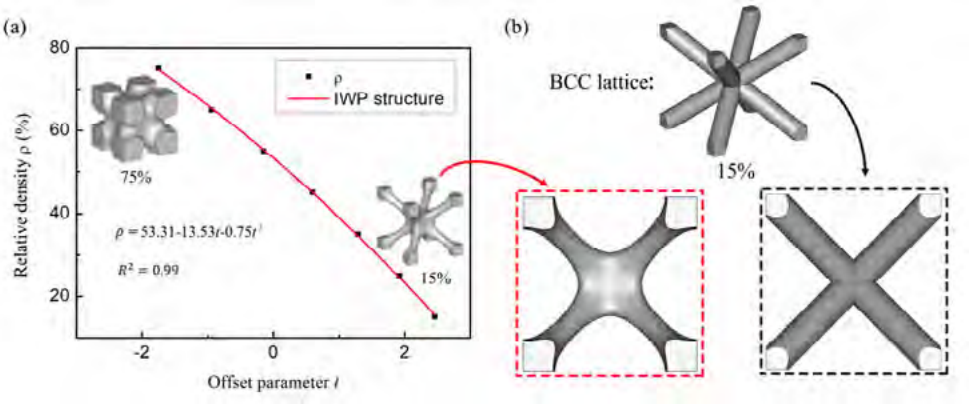


Fig. 1. (a) The fitting relationship between relative density ρ and parameter t of IWP lattice structure. (b) Traditional BCC lattice structure with 15% relative density.

3. Topology optimization of lattice filling structure

3.1. Homogenization method

The finite element analysis is used to investigate the mechanical properties of IWP lattice structure with different relative densitys. Given the periodic arrangement of lattice structures, a single lattice unit cell was chosen as the representative volume element (RVE) for simulating their mechanical properties [12]. Subsequently, periodic boundary conditions (PBCs) were implemented on the RVE to account for the influence of surrounding unit cells. To apply the PBCs, it was essential to ensure an equal number of nodes with corresponding coordinates on opposite surfaces. Consequently, a finite element model with a symmetric mesh (C3D10 element) was created by mirroring the 1/8 subdivision. EasyPBC, which is an Abaqus plugin developed to estimate the homogenized effective elastic properties of RVE, is applied in this work to calculate the equivalent mechanical properties of the IWP lattice structure. The equivalent mechanical properties were determined using the homogenization method with the imposition of PBCs. The material model for simulation employed a linear elastic model, where the elastic modulus was determined as 2200 MPa and Poisson's ratio was set at 0.35. Considering the cubic symmetry of the RVE, the constitutive properties of interpenetrating lattice structures were assumed to be linearly elastic and orthotropic. Therefore, the homogenized equation of Hooke's law can be simplified as:

$$\begin{bmatrix}\sigma_{11}\\ \sigma_{22}\\ \sigma_{33}\\ \sigma_{23}\\ \sigma_{12}\\ \sigma_{13}\end{bmatrix} = \begin{bmatrix}C_{11} & C_{12} & C_{12} & 0 & 0 & 0\\ C_{12} & C_{11} & C_{12} & 0 & 0 & 0\\ 0 & 0 & 0 & C_{44} & 0 & 0\\ 0 & 0 & 0 & 0 & C_{44} & 0\\ 0 & 0 & 0 & 0 & 0 & C_{44}\end{bmatrix} = \begin{bmatrix}\varepsilon_{11}\\ \varepsilon_{22}\\ \varepsilon_{33}\\ 2\varepsilon_{23}\\ 2\varepsilon_{12}\\ 2\varepsilon_{13}\end{bmatrix} \tag{3}$$

where σ_{ij}, $varepsilon_{ij}$ are the equivalent stress and equivalent strain, respectively. C_{11}, C_{12}, and C_{44} are the independent elastic constants which can be calculated by FEA analysis under PBCs [13]. The elastic modulus E can be calculated as:

$$E = \frac{C_{11}^2 + C_{11}C_{12} - 2C_{12}^2}{C_{11} + C_{12}} \tag{4}$$

The relationship between elastic constants and offset parameter t are plotted in Fig.2. The regression model employs a first-order exponential function, and the fitting results align well with the data values. The fitting equations are shown in Eq.5, which are then utilized in the following optimization model to capture the mechanical properties

©2024 | 3_HAILUN ZHOU_Hailun_3776J.pdf:3

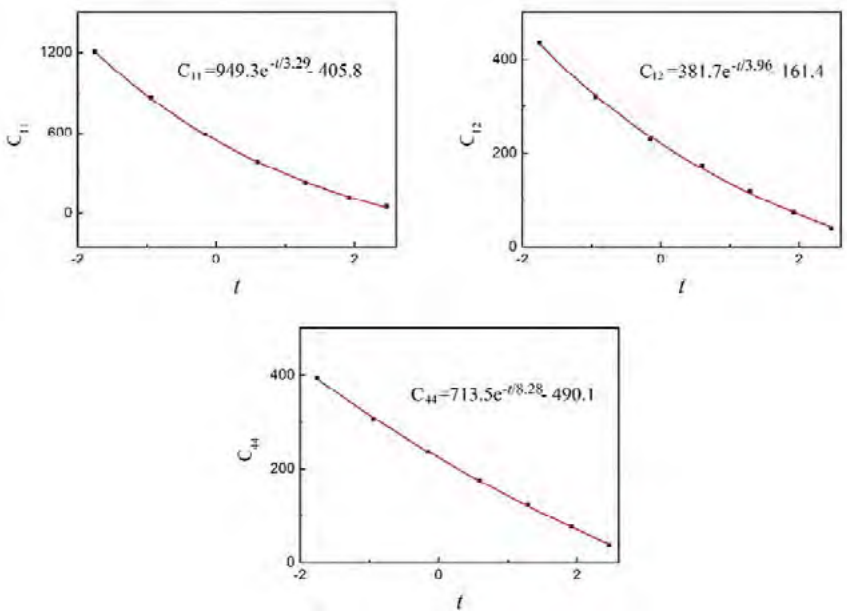


Fig. 2. The elastic constants C_{ij} versus offset parameter t for IWP lattice structure and the exponential fitting curves.

Table 1: Elastic properties of lattice structures.

Lattice type	Relative density	Elastic modulus E (MPa)
BCC	15%	9.88
BCC	25%	41.24
BCC	35%	84.13
IWP	15%	15.85
IWP	25%	63.84
IWP	35%	150.28

of IWP lattice structures with distinct relative densitys. The fitted data intersected with the simulated results, and all the R^2 values were greater than 0.99, indicating the high accuracy of the regression results.

$$\begin{aligned} C_{11} &= 949.3e^{\frac{t}{3.29}} - 405.8 \\ C_{12} &= 381.7e^{\frac{t}{3.96}} - 161.4 \\ C_{44} &= 713.5e^{\frac{t}{8.28}} - 490.1 \end{aligned} \tag{5}$$

As indicated in Table 1, it can be observed that at the same 15% relative density, the elastic modulus of the IWP lattice structure is 60% higher than that of the BCC structure, indicating superior load-bearing capacity. As the relative density of the IWP lattice structure increases, both the elastic modulus and shear modulus significantly rise, while the Poisson's ratio experiences a slight decrease.

3.2. LSTO model

The mechanical properties and deformation behaviour of the IWP lattice structure are influenced by the relative density ρ. To investigate the application of this lattice structure in structural design, a topology optimization method based on this lattice structure is studied to address the optimization problem of compliance. In this section, the optimization mathematical model can be represented by the following equations:

©2024 | 3_HAILUN ZHOU_Hailun_3776J.pdf:4

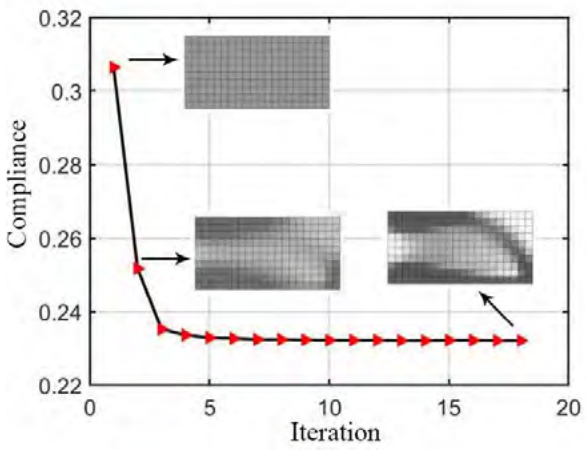


Fig. 3. The iterative curve of topology optimization based on IWP lattice without penalty.

$$\begin{aligned} Find \quad & :\rho = (\rho_1, \rho_2, ..., \rho_n) \\ Minimize \quad & :f(\rho) = U^T K(\rho) U \\ Subject\ to \quad & :F = K(\rho) U \\ & V = \sum_{i=1}^{N} \rho_i v - V_{max} \leq 0 \end{aligned} \tag{6}$$

where ρ represents the spatial distribution of the design variables, f is the compliance of the lattice in-fill structure, $K(\rho)$ is the global stiffness matrix, V and V_{max} denote the volume of optimized structure and the permissible maximum relative density (50%) of the entity structure, respectively. The flowchart of the topology optimization process based on the IWP lattice structure is depicted in Fig. 3. Firstly, the IWP lattice structures with varying design parameter, relative density ρ, is generated using the mathematical TPMS-based design method. Subsequently, the effective elastic constants C_{ij} of the IWP lattice are calculated via the homogenization method as mentioned in the previous section. Then, the design space for topology optimization is meshed by the hexahedral element type. The homogenized material model based on the elastic constants is implemented into the simulation analysis. In the next step, the objective function and constraints as indicated in Eq.6 are established and the final distribution of the design variable was optimized using the Solid Isotropic Material with Penalisation (SIMP) algorithm. The IWP lattice structure can be parametrically controlled for relative density, which can be applied to SIMP optimization processes to replace intermediate density results. Lastly, the 3D model of the IWP lattice filling structure will be generated based on the solved optimal distribution of relative density. The stiffness of a non-optimized traditional BCC lattice filling structure with the same total volume will be compared to that of the optimized IWP lattice structure. All optimization processes were implemented using MATLAB code.

3.3. Optimization results

The iteration curve of SIMP's topology optimization is shown in Fig.3. The design domain is discretized into finite element grids corresponding to unit cells of the lattice structure, and its grayscale value representing its relative density. It can be observed that the convergence shows a great outcome after more than 5 iterations, and the grayscale image of the optimized lattice filling structure can be obtained. The IWP lattice structure can change its relative density by controlling parameters. As shown in Fig.5, the controlling points were defined in the grayscale image grid, setting the control parameters t as functions that vary with these points enables the design of variable-density lattice filling structures. As shown in Fig.6, the IWP lattice filling structure obtained through the proposed optimization method is compared with the BCC lattice filling structure. In terms of stress distribution, high stress is mainly concentrated at the intersections of the support rods in the BCC structure, while in the IWP structure, the stress concentration phenomenon

©2024 | 3_HAILUN ZHOU_Hailun_3776J.pdf:5

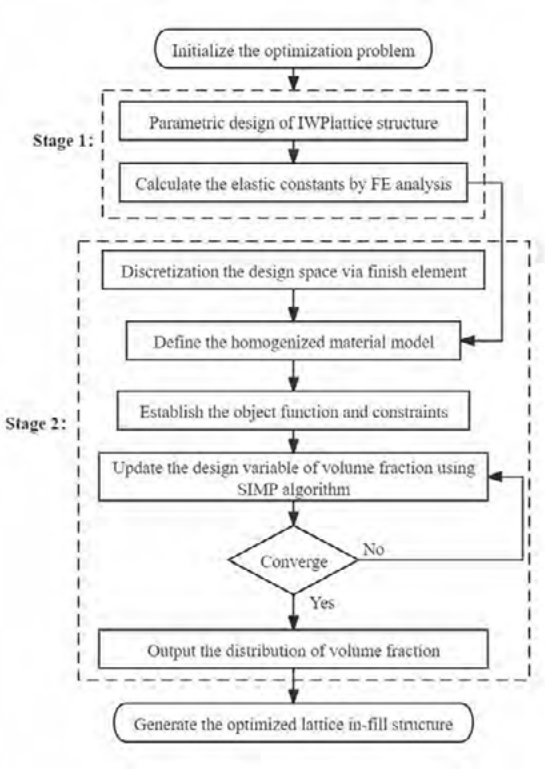


Fig. 4. The flowchart of the topology optimization process based on the IWP lattice structure.

Table 2: Mechanical properties of lattice filling structures.

Lattice type	Volume mm^3	Loading force N	Maximum displacement mm
BCC	3563.33	10	0.604
IWP	3204.57	10	0.147

is mitigated due to the transitional structure being arc-shaped. The stiffness of the IWP lattice filling structure has also been enhanced. Under the same constraints and external loads, the maximum displacement is reduced by 76% compared to the BCC lattice filling structure, as shown in Table 2.

©2024 | 3_HAILUN ZHOU_Hailun_3776J.pdf:6

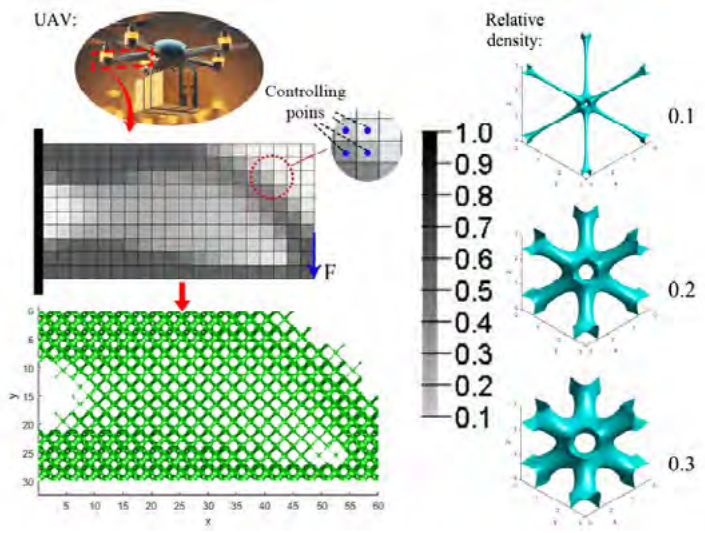


Fig. 5. The topology optimization of cantilever beam and lattice structure filling.

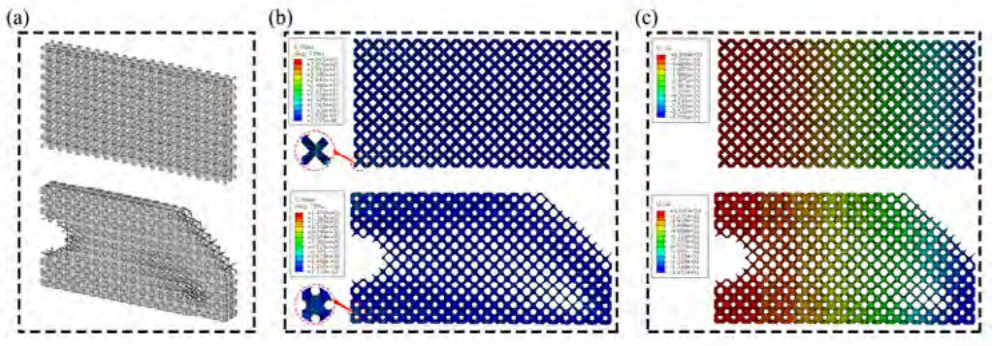


Fig. 6. The simulation results of lattice filling structures:(a) STL models of lattice filling structures, (b) stress distribution, (b) displacement under loading direction.

©2024 | 3_HAILUN ZHOU_Hailun_3776J.pdf:7

4. Conclusion

This study achieves parametrical design of lattice structure through mathematical equations, allowing for the adjustment of the structure's relative density by changing parameters. Additionally, a function relationship between the design parameter of the IWP structure and its mechanical properties is obtained through the homogenization method and applied to topology optimization. Subsequently, an optimization filling method for IWP lattice structures based on the SIMP algorithm is established using a case study of cantilever beam, optimizing the structural stiffness under total volume constraints. The results show that the optimized IWP lattice filling structure reduces the maximum displacement by 76% compared to the traditional BCC lattice filling structure under the same load condition, which indicates the stiffness performance is significantly improved.

Acknowledgement

This research was financially supported by the China Scholarship Council (CSC) under Grant No. 202006050041.

References

[1] H. Jinnai, Y. Nishikawa, M. Ito, S. D. Smith, D. A. Agard, R. J. Spontak, Topological similarity of sponge-like bicontinuous morphologies differing in length scale, Advanced Materials 14 (22) (2002) 1615–1618.
[2] D.-J. Yoo, Advanced porous scaffold design using multi-void triply periodic minimal surface models with high surface area to volume ratios, International journal of precision engineering and manufacturing 15 (2014) 1657–1666.
[3] A. O. Aremu, J. Brennan-Craddock, A. Panesar, I. Ashcroft, R. J. Hague, R. D. Wildman, C. Tuck, A voxel-based method of constructing and skinning conformal and functionally graded lattice structures suitable for additive manufacturing, Additive Manufacturing 13 (2017) 1–13.
[4] M. Zhao, F. Liu, G. Fu, D. Z. Zhang, T. Zhang, H. Zhou, Improved mechanical properties and energy absorption of bcc lattice structures with triply periodic minimal surfaces fabricated by slm, Materials 11 (12) (2018) 2411.
[5] A. Panesar, M. Abdi, D. Hickman, I. Ashcroft, Strategies for functionally graded lattice structures derived using topology optimisation for additive manufacturing, Additive manufacturing 19 (2018) 81–94.
[6] N. Yang, K. Zhou, Effective method for multi-scale gradient porous scaffold design and fabrication, Materials Science and Engineering: C 43 (2014) 502–505.
[7] D. Li, W. Liao, N. Dai, G. Dong, Y. Tang, Y. M. Xie, Optimal design and modeling of gyroid-based functionally graded cellular structures for additive manufacturing, Computer-Aided Design 104 (2018) 87–99.
[8] M. P. Bendsøe, O. Sigmund, Material interpolation schemes in topology optimization, Archive of applied mechanics 69 (1999) 635–654.
[9] L. Yin, G. Ananthasuresh, Topology optimization of compliant mechanisms with multiple materials using a peak function material interpolation scheme, Structural and Multidisciplinary Optimization 23 (2001) 49–62.
[10] X. Huang, Y. M. Xie, Bi-directional evolutionary topology optimization of continuum structures with one or multiple materials, Computational Mechanics 43 (2009) 393–401.
[11] O. Al-Ketan, R. K. Abu Al-Rub, Multifunctional mechanical metamaterials based on triply periodic minimal surface lattices, Advanced Engineering Materials 21 (10) (2019) 1900524.
[12] M. Zhao, X. Li, D. Z. Zhang, W. Zhai, Tpms-based interpenetrating lattice structures: design, mechanical properties and multiscale optimization, International Journal of Mechanical Sciences 244 (2023) 108092.

©2024 | 3_HAILUN ZHOU_Hailun_3776J.pdf:8

Hot-pressing of uncured metal-composite laminates: A numerical study on simultaneous deformation

Shichen Liu[1*], Jos Sinke[1], Clemens Dransfeld[1]

[1]Aerospace Manufacturing Technologies Group, Faculty of Aerospace Engineering, Delft University of Technology, Kluyverweg 1, 2629 HS Delft, The Netherlands

*Presenting Author: S.Liu-7@tudelft.nl

Keywords: Metal-composite laminates, Simultaneous deformation, Metal cracking, Prepreg buckling, Finite element modelling

Abstract

The research focuses on the simultaneous deformation of uncured metal-composite laminates under the press forming process of a double-curved dome part. The study is designed to evaluate the influence of material type, inter-ply friction and clamping force by the use of a finite element modelling method. The result shows that the main failure mode for aluminium-based hybrid materials is metal cracking while prepreg buckling dominates the failure of stainless steel-based hybrid materials. The increase of clamping force contributes to the deformation of fibre reinforced prepreg layer and decrease the risk of prepreg buckling, but the simultaneous increase of plastic deformation tends to induce the failure of metal cracking. The variation of friction coefficient at the metal-prepreg interface affects the inter-ply sliding displacement during the forming process. This work provides a numerical method on the material selection and process parameter optimisation where compatible deformation of the individual layers can be achieved through its own mechanisms.

1. Introduction

The Metal-composite laminates, which are also known as fibre metal laminates (FMLs), are one of those lightweight composite materials made by alternating thin sheets of metal alloys and layers of fibre reinforced polymers [1,2]. This hybrid combination creates a material which has excellent specific strength, higher stiffness, and superior fatigue resistance than the monolithic metal sheets as well as better impact strength and damage tolerance compared with full composites [3,4]. Traditional method for the manufacturing of metal-composite laminates is through layup techniques followed by autoclave curing, which is applicable for the product with a relatively simple shape, having large radiuses like aircraft fuselages [5]. As for the forming of small and medium sized part with relatively small radii and complex shapes, the concept of press forming is proposed where the hybrid laminates are pressed using a die and shaped by the deforming force [6]. However, there are some limitations for the press forming of hybrid laminates especially for the epoxy-based hybrid materials because of the needs for various forming and curing stages as well as for the complex deformation mechanisms. Therefore, this study puts forward a hot-pressing cycle involving a laminate preparing and preheating stage, forming of uncured laminate, consolidation or (partial) curing in a same mould as well as the cooling and removal of the component as shown in **Fig.1**. This approach contributes to a better formability of metal-composite laminates based on the understanding of different deformation mechanisms for both layers as well as the optimisation of processing parameters in the hot-pressing cycle.

The forming of metal sheet into the desired shape involves the elastic-plastic deformation of the material by bending, stretching and drawing. Typically, the deformation induces in-plane strain ratios from pure shear to biaxial stretch and the failure strain for the metal alloy materials is in the range of 10% to 50% [7,8]. Therefore, the deformability of the metal sheet is mainly determined by the metal

constituent and the failure mode is dominated by the metal cracking in the forming process [9]. The wrinkling may occur for metal sheet which caused by the increase of compressive stress, but the increasing thickness and clamping force contribute to the delay of such phenomenon [10]. For the deformability of composites, fibre reinforcements and prepregs are particularly prone to wrinkling due to the fibre composition and the possible slippage in-between the fibre tows [11,12]. The wrinkling of woven fabrics is related to intra-ply shear in studies based on the "shear locking angle", which is the maximum angle between warp and weft yarns [13]. Besides, the wrinkling of unidirectional (UD) fibres occurs due to the large differences in rigidity between the fibre orientation and its transverse direction. Therefore, the wrinkles are related to the bridging of the rigid ply and the ply-ply friction during forming [14]. Larberg [15] found that the stacking sequence of UD-prepreg laminates have a significant effect on wrinkle development when forming a spar geometry. He explained this effect as that the combination of 0° and 45° layers may reduce the material deformability through shearing. Akermo et.al [16] further discovered that the inter-ply friction improves the forming behaviour of cross-plied UD prepregs by serving as a connection between the plies, but also introduce wrinkles if not properly controlled.

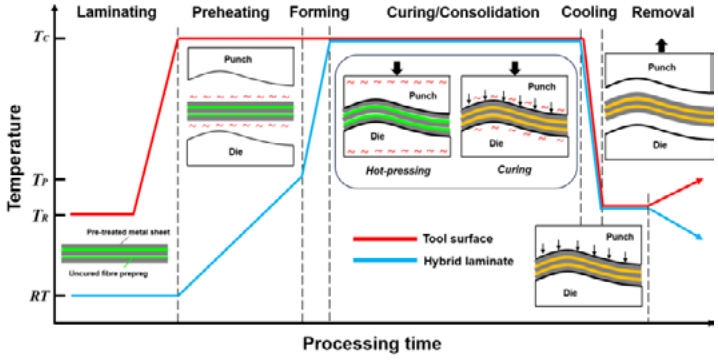


Fig.1: Processing temperature-time profile of the tool surface and hybrid laminates

The numerical modelling of metal-composite laminates can be approached mainly in three ways: micro-level, meso-level and macro-level. As for the micro-level approach, individual materials are differentiated in the model consisting of fibres and matrix. This is the most complex but realistic approach as it requires partitioning the model into different pieces [17]. The meso-level method regards the laminate as a system of independent layers with specific homogenized mechanical properties. This approach results in an effective modelling for all type of hybrid laminates as it requires relatively limited number of elements. Although there are some simplifications which skips the issue of layer boundary conditions, it would not affect the laminate performance unless delamination or other failure phenomena occur [18,19]. The macro-level approach describes the entire hybrid laminate as a homogenized material with anisotropic properties. This approach can be described as a simple generalization since only a few engineering constants are needed. The biggest problem for this method is to obtain the data of the homogenized material as the replacement for the hybrid laminate. One of the possible solutions is the application of Classical Laminate Theory which enables the description of their behaviour under external loads according to the engineering constants, representing membrane, bending and coupling behaviour, or by the uniaxial tensile test of the specimen in order to obtain the constant data in the theory [20,21]. Moreover, process simulation of the hot-pressing of fibre metal laminates requires an accurate mathematical description of the main deformation mechanisms like intra-ply shear, inter-ply sliding as well as bending [22]. None of these mechanisms is negligible or dominant, as the laminate deformability is supposed to be a result of a delicate balance among them [23,24]. Therefore, more advanced material constitutive models and boundary conditions of each deformation mechanisms are required to improve the predictive quality for manufacturing.

This paper aims to develop a homogenised meso-level model for simultaneous deformation in a hot-pressing process and implement it into numerical software Abaqus for analysis. A set of forming tools for the forming of double-curved hemisphere part are designed and the meso-level approach coupled

with the friction contact model for finite element simulation is established. The novelty of the research is to study the "harmony" deform of the individual layers with its own deformation mechanisms when applying the initial circle and square shapes for metal sheet and uncured fibre prepreg, respectively. The simulations are conducted with various material constituents, as well as the clamping forces and inter-ply friction coefficients to evaluate what combinations would be good for a maximum deformability. Then, the numerical model is capable of predicting the local strain distributions and the maximum draw depths for the uncured hybrid materials.

2. Materials and methods

2.1. Materials

The hybrid laminates involved in the research are the metal sheets of aluminium alloy 2024-T3 (Al) and stainless steel 304L (Ss), as well as the fibre reinforced prepregs of S2-glass/FM-94 (GFRP) and T300-carbon/MTC510 (CFRP). The metal-composite materials consist of two layers of 0.5-mm thick metal sheet and one layer of fibre prepregs which are known as a 2/1 layup. Each fibre layer includes two cross-plied unidirectional (UD) prepregs with a total thickness of 0.3mm. The UD fibre ply oriented at 0° corresponds with the rolling direction of metal sheet. The mechanical properties of the material constituents in hybrid laminates are shown in **Table 1** and the behaviour of the metal sheet cannot be affected under the studied temperature ranges. Two parameters of elastic modulus and ultimate strength for the UD reinforced fibre prepregs represent the properties in the fibre orientation of 0° and 90°, respectively.

Table 1 Mechanical properties of the material constituents in hybrid laminates [25,26]

	Density (g/cm^3)	Elastic modulus (GPa)	Poisson's ratio	Shear modulus (GPa)	Yield strength (MPa)	Ultimate strength (MPa)	Shear strength (MPa)	Elongation at break (%)
Aluminium alloy 2023-T3	2.7	71	0.33	28	320	480	283	16.2
Stainless steel 304L	8.0	200	0.30	77	210	574	378	45.6
UD glass fibre prepreg-FM94	2.6	54.0/9.4	0.33	5.5/2.6	-	1870/50	38.5	3.8
UD carbon fibre prepreg-MTC510	1.5	119.3/8.2	0.34	3.6/2.0	-	2282/54	99	1.3

2.2. Concept design

The concept of simultaneous deformation of uncured metal-composite laminates came from the design of an integral forming and curing cycle in the proposed hot-pressing process as exhibited in **Fig.1**. In order to investigate the three-dimensional (3D) deformations of the individual layers and the metal-prepreg interfaces, a double-curved hemisphere forming tool concept with draw bead is designed as the schematic graph shown in **Fig.2(a)**. The hybrid laminate with a circle shape of 70mm radius for metal sheet layer and a square shape of 100×100mm for fibre prepreg layer is placed symmetrically on the die surface and clamped by blank holder. As the schematic graph presented in **Fig.2(b)**, the metal sheet and fibre prepreg deforms independently through bias-stretch and intra-ply shear, and the different shape design contribute to the study of "harmony" deform for the individual layers. Furthermore, the concept of draw bead with the depth of 1mm and length of 5mm is proposed to constrain the material flow as well as to achieve a part without cracks and wrinkles. The hemisphere punch with a radius of 42.5mm moves vertically down the centreline of the laminate to a special displacement. In addition to the different material constituents studied in the research, the effects of clamping force and intra-ply friction are compared as well. **Table 2** presents the test parameters used for the forming simulation and the model is conducted varying one parameter at a time while keeping the other parameters at the baseline value. To simplify the hot-pressing temperature condition, the friction coefficient (μ) of 1 is regarded as

the forming condition of room temperature (RT). Then, the frictional contacts where μ= ∞(Tie), 0.5, 0.2 are created as the state of full-cured, medium-friction as well as low-friction, respectively.

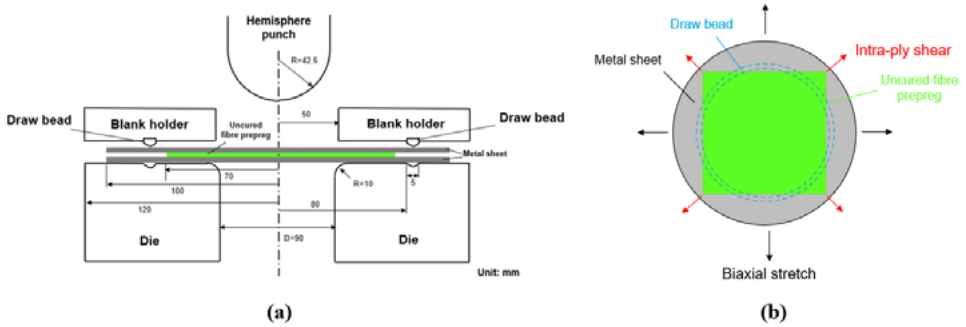


Fig.2: (a) Schematic graph of the double-curved dome forming tool design and dimension; (b) Deformation mechanisms and initial shapes of the individual metal sheet and fibre prepreg

Table 2 Test parameters used for the hybrid laminate hot-pressing concept

Test parameter	Baseline value	Additional values investigated
Clamping force (kN)	0	0.1, 1, 2
Inter-ply friction (μ)	1 (RT)	∞(Tie), 0.5, 0.2

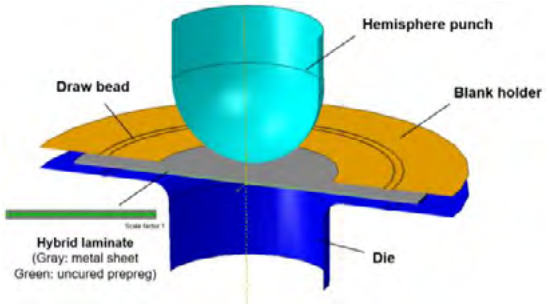


Fig.3: Finite element model of the hot-pressing process for uncured hybrid laminates

2.3. Finite element model

The application of finite element model (FEM) made it efficient to analyse the simultaneous deformation of uncured hybrid laminates and provide guidance for actual experimental testing. In the research, finite element analysis software Abaqus is used to simulate the forming process of the uncured laminates by using the stress-strain distributions of the metal sheet and the unique anisotropic properties of the fibre reinforced prepreg. **Fig.3** exhibits the simulation model established for the study and all the materials as well as tool geometries followed by the concept design. The elastic-plastic properties of the metal sheets and the elastic constants for the uncured prepreg lamina as shown in **Table 1** are imported into the material property module in Abaqus. In the finite element model, all tools including the hemisphere punch, die and blank holder are modelled as discrete rigid shell elements with a mesh size of 2 mm. Metal sheets and the uncured fibre prepreg are created as four-node doubly curved conventional shell element with reduced integration (S4R) in the same mesh size. The laminate structure in the simulation model is represented in the composite layup module where all layers and their parameters such as orientation, thickness, property and relative location are defined and assembled into the forming simulation. As for the interactions and boundary conditions in the model, the value of clamping force and punch displacement can be set, and the contacts between the fixed tools and the uncured laminates are set as penalty friction in a constant value of 0.15. The interaction at the metal-prepreg interfaces is also defined as friction contact as shown in **Table 2**.

3. Results and discussion

3.1. Effect of material composition

During the laminate press forming process, the metal and composite type both play a significant role in the deformability and failure modes of the hybrid materials. **Fig.4** shows the numerical results of the vertical displacement (U3) before failure for Al/GFRP laminate at room temperature and zero clamping force. The metal cracking which dealt by element deletion when the element exceeds the forming limits is the main failure mode as shown in the figure. It is observed that the lower aluminium sheet cracks first at the displacement of 25.08mm and the failure occurs at the centre regions of the metal material. The GFRP material, which is not shown in the figure, stays in contact with the outer metal layers and has no failure at such displacement. Also, the type of fibre prepreg has limited effect on the metal cracking and maximum depth for the aluminium-based hybrid laminates as the prepreg changes from GFRP to CFRP. The reason is due to the fact that the aluminium alloy has lower failure strain than the stainless steel while the fibre prepreg in the middle has not experienced large intra-ply shear strains nor failure at the same depth. When replacing the metal type from aluminium alloy to stainless steel, the failure mode for hybrid materials is totally different. The CFRP and GFRP material in the stainless steel-based hybrid laminate undergo prepreg buckling while the outer metal layers have no failure of metal cracking as exhibited in **Fig.5**. In this case, the numerical result on the vertical displacement (U3) before failure under room temperature and zero clamping force condition for the Ss/CFRP and Ss/GFRP laminates are 39.81mm and 44.64mm, respectively. The prepreg buckling is caused by the layer overlaps due to the increase of intra-ply shear strain which exceeds the locking angle. The locking strain for the GFRP is higher than the CFRP under the same condition which results in a larger failure depth during the forming process.

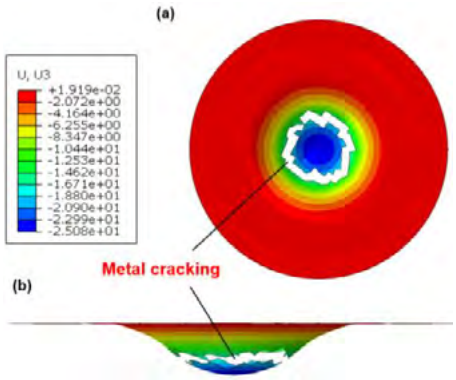


Fig.4: Numerical simulation on vertical displacement (U3) at the maximum value at room temperature and zero clamping force for Al/GFRP laminates: (a) XY plane-Al; (b) XZ plane-Al

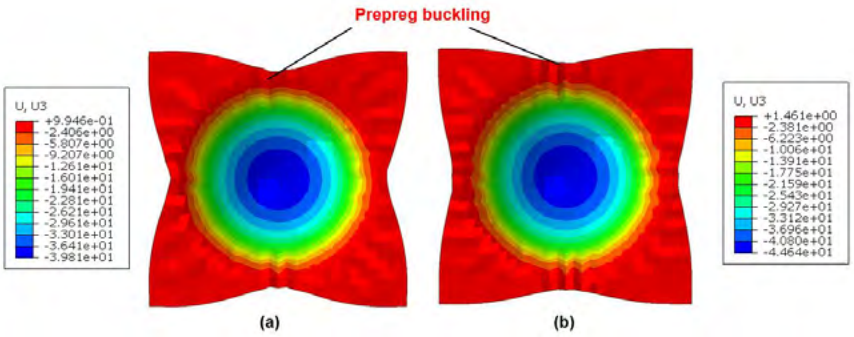


Fig.5: Numerical simulation on vertical displacement (U3) at the maximum value at room temperature and zero clamping force for stainless steel based hybrid materials: (a) CFRP; (b) GFRP

3.2. Effect of clamping force

Fig.6 shows the simulation results on maximum draw depth and its corresponding failure mode under four clamping force conditions at room temperature. For the aluminium-based hybrid laminates with both CFRP and GFRP materials, the increase of clamping force tends to decrease the maximum draw depths even though the influence is limited. The reason is mainly due to the increase in biaxial stress which induces earlier cracking of the aluminium sheet. Besides, the main failure mode for such laminates is metal cracking and the prepreg layer witnesses no prepreg buckling. However, the larger draw depth with less clamping force does not mean a better formability for Al/CFRP and Al/GFRP laminates as the metal wrinkling may occurs at the flange regions. For the stainless steel-based hybrid laminates, the failure mode is complex under various clamping forces. The increase of clamping force from 0kN to 1kN increases the maximum draw depth and the failure of metal cracking occurs coupled with prepreg buckling. As the clamping force reaches 2kN, the metal cracking is dominated with lower failure depth while the phenomenon of prepreg buckling does not exist anymore. This indicates that the increase of clamping force delays the prepreg buckling. A more detailed graph on the different failure modes for Ss/CFRP laminates under 1kN and 2kN is exhibited in **Fig.7**. It is obvious to see that higher clamping force lowers the maximum failure depth and metal cracking occurs at the inner radius regions. The firm clamping on the four-square corners for CFRP reduces the occurrence of prepreg buckling by inducing tension forces in the prepreg layers through friction between draw bead-metal and blank holder-metal interfaces. In order to investigate the friction effects, the comparison between two clamping forces against the initial and final prepreg shapes for Ss/CFRP laminates at room temperature and draw depth of 40mm is presented in **Fig.8**. When the clamping force is 0 kN, the CFRP is easier to flow into the central region which increase the possibility of prepreg buckling. However, the four-square corners of CFRP have nearly no movement when the clamping force is 2kN. Since the clamping force only applies on the four-square corners of the CFRP layer, the effect on the deformability of the 0°/90° CFRP at four central edge regions is limited as the relative displacement is measured to be almost the same. Therefore, the clamping force at 1kN can be seen as an optimised value for a better deformability.

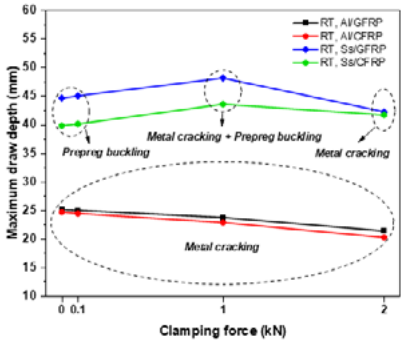


Fig.6: Numerical simulation on maximum draw depths and failure modes at room temperature under different clamping force for metal-composite laminates

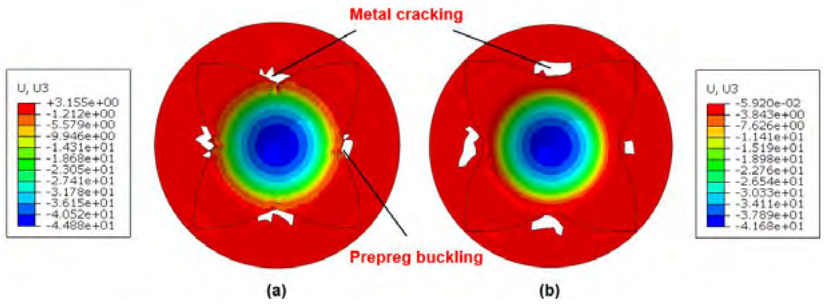


Fig.7: Numerical simulation on vertical displacement (U3) at the maximum value at room temperature for Ss/CFRP laminates under two clamping forces: (a) 1kN; (b) 2kN

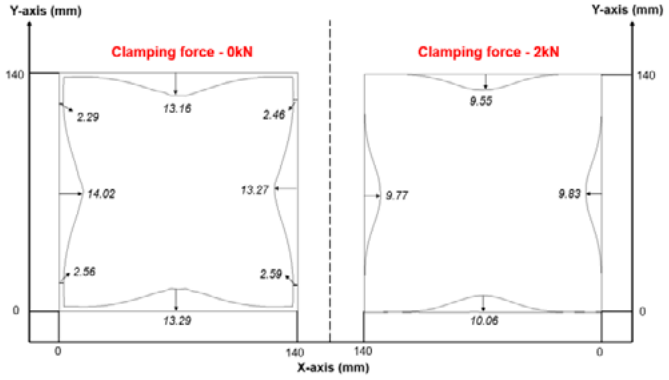


Fig.8: Comparison between two clamping forces against the initial and final prepreg shapes from the numerical simulation for Ss/CFRP laminates (Draw depth=40mm)

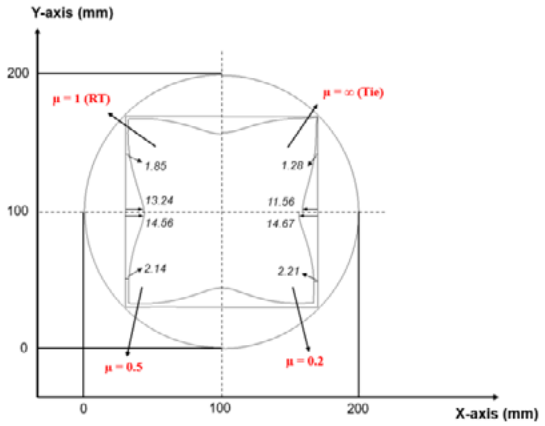


Fig.9: Comparison between inter-ply frictions against the initial and final laminate shapes from the numerical simulation for Ss/CFRP laminates under the clamping force of 1kN (Draw depth=40mm)

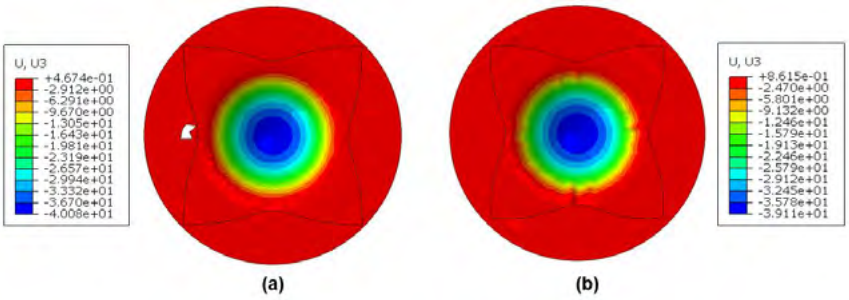


Fig.10: Numerical simulation on vertical displacement (U3,mm) before failure for Ss/CFRP laminates under the clamping force of 1kN and two inter-ply friction coefficients: (a) μ =∞; (b) μ =0.2

3.2. Effect of inter-ply friction

The importance of inter-ply friction can be underlined by conducting a "tie" constraint and simulations with different frictional coefficients. **Fig.9** shows the laminate shapes before and after forming at the draw depth of 40mm from the numerical simulation for Ss/CFRP laminates. The effect of friction on the inter-ply sliding is analysed by looking at the position of the edge of the prepreg layer. When the metal-prepreg interface is constrained which denotes a cured laminate, the maximum horizontal displacement for CFRP is 11.56mm and the horizontal gap at the centre location is small. With the decrease of inter-ply friction, the corresponding horizontal displacement and gap increases. This means that higher friction induces a limited sliding which constrain the deformation and delay the buckling of the CFRP

material. However, the high friction and low friction condition seems to have distinct influence on the failure mode. **Fig.10** presents the numerical results at the maximum vertical displacement for Ss/CFRP laminates under the clamping force of 1kN. It is seen that the metal-prepreg interfaces with a "tie" constraint witness a higher failure depth with metal cracking, while the failure of prepreg buckling is dominated when the inter-ply friction coefficient is 0.2. Therefore, the result demonstrates that a proper selection of inter-ply friction coefficient may help to increase the uncured laminate formability without the failure of either metal cracking or prepreg buckling.

4. Conclusions

The simultaneous deformation of uncured metal-composite laminates is numerically investigated under different material composition, inter-ply friction and clamping force conditions. The proposed method applies a initial circle and square shape for the metal sheet and uncured fibre prepreg, respectively. The main conclusions are:

(1) The failure mode of the uncured hybrid laminates depends on the type of metal composition. The aluminium-based materials with a lower fracture strain exhibit a lower maximum forming depth with aluminium cracking. While for the stainless steel-based materials, the prepreg buckling dominates the laminate failure with a higher maximum forming depth. In addition, the Ss/GFRP undergoes a higher forming depth than the Ss/CFRP under the same condition, but the effect of fibre reinforced prepreg layer on aluminium-based materials is limited.

(2) The increase of clamping force contributes to the deformation of fibre reinforced prepreg and decrease the risk of prepreg buckling, while the increase of baixial stress as well as the hinder of sliding and material flow tend to induce metal cracking for the stainless steel-based materials. A medium clamping force of 1kN is regarded as a compromise forming parameter since the effect of clamping on metal sheet and fibre prepreg is opposite.

(3) A proper heating of the uncured hybrid laminates under a medium temperature and friction condition increase the laminate deformability without the failure of either metal cracking or prepreg buckling.

Acknowledgments

The presenting author would like to thank the financial supports of China Scholarship Council ((No.201906040174).

References

[1] Asundi A, Choi AYN. Fiber metal laminates: An advanced material for future aircraft. *J Mater Process Technol*. 1997;63(1-3):384-394.

[2] Vogelesang LB, Vlot A. Development of fibre metal laminates for advanced aerospace structures. *J Mater Process Technol*. 2000;103(1):1-5.

[3] Botelho EC, Silva RA, Pardini LC, Rezende MC. A review on the development and properties of continuous fiber/epoxy/aluminum hybrid composites for aircraft structures. *Mater Res*. 2006;9(3):247-256.

[4] Sinmazçelik T, Avcu E, Bora MÖ, Çoban O. A review: Fibre metal laminates, background, bonding types and applied test methods. *Mater Des*. 2011;32(7):3671-3685.

[5] Sinke J. Manufacturing of GLARE Parts and Structures. *Appl Compos Mater*. 2003;10(4-5):293-305.

[6] Osakada K, Mori K, Altan T, Groche P. Mechanical servo press technology for metal forming. *CIRP Ann - Manuf Technol*. 2011;60(2):651-672.

[7] Wang X, Cao J. On the prediction of side-wall wrinkling in sheet metal forming processes. *Int J Mech Sci*. 2000;42(12):2369-2394.

[8] Suttner S, Merklein M. A new approach for the determination of the linear elastic modulus from uniaxial tensile tests of sheet metals. *J Mater Process Technol*. 2017;241:64-72.

[9] Blala H, Lang L, Khan S, et al. Forming Challenges of Small and Complex Fiber Metal Laminate Parts in Aerospace Applications—a Review. *Int J Adv Manuf Technol*. 2023; 126: 2509-2543.

[10] Chen Y, Yang Y, Wang Z, Wang H, Li J, Hua L. Accurate simulation on the forming and failure processes of fiber metal laminates: A review. *Int J Light Mater Manuf*. 2023;6(3):344-356.
[11] Chen Q, Boisse P, Park CH, Saouab A, Bréard J. Intra/inter-ply shear behaviors of continuous fiber reinforced thermoplastic composites in thermoforming processes. *Compos Struct*. 2011;93(7):1692-1703.
[12] Hallander P, Sjölander J, Åkermo M. Forming induced wrinkling of composite laminates with mixed ply material properties; an experimental study. *Compos Part A Appl Sci Manuf*. 2015;78:234-245.
[13] Guzman-Maldonado E, Wang P, Hamila N, Boisse P. Experimental and numerical analysis of wrinkling during forming of multi-layered textile composites. *Compos Struct*. 2019;208:213-223.
[14] Irani M, Kuhtz M, Zapf M. Investigation of the deformation behaviour and resulting ply thicknesses of multilayered fibre–metal laminates. *J Compos Sci*. 2021;5(7).
[15] Larberg Y, Åkermo M. In-plane deformation of multi-layered unidirectional thermoset prepreg - Modelling and experimental verification. *Compos Part A Appl Sci Manuf*. 2014;56:203-212.
[16] Åkermo M, Larberg YR, Sjölander J, Hallander P. Influence of interply friction on the forming of stacked UD prepreg. *ICCM Int Conf Compos Mater*. 2013;2013-July:919-928.
[17] Peter L, Jurgen P, Henk B, Clarice C. Modelling and Simulation of Fibre Metal Laminates. *ABAQUS Users Conf*, 2004: 421–439.
[18] Soltani P, Keikhosravy M, Oskouei RH, Soutis C. Studying the tensile behaviour of GLARE laminates: A finite element modelling approach. *Appl Compos Mater*. 2011;18(4):271-282.
[19] Zal V, Moslemi Naeini H, Sinke J, Abouhamzeh M, Benedictus R. A new procedure for Finite Element simulation of forming process of non-homogeneous composite laminates and FMLs. *Compos Struct.* 2017;163:444-453.
[20] Boisse P, Buet K, Gasser A, Launay J. Meso/macro-mechanical behaviour of textile reinforcements for thin composites. *Compos Sci Technol.* 2001;61(3):395-401.
[21] Smolnicki M, Stabla P. Finite element method analysis of fibre-metal laminates considering different approaches to material model. *SN Appl Sci*. 2019;1(5):1-7.
[22] Haanappel SP. Forming of UD Fibre Reinforced Thermoplastics. Univeristy of Twente, 2013.
[23] Sachs U, Akkerman R, Fetfatsidis K. Characterization of the dynamic friction of woven fabrics: Experimental methods and benchmark results. *Compos Part A Appl Sci Manuf.* 2014;67:289-298.
[24] Liu S, Sinke J, Dransfeld C. An inter-ply friction model for thermoset based fibre metal laminate in a hot-pressing process. *Compos Part B Eng*. 2021;227:109400.
[25] Solvay Adhesive Materials. Technical Data Sheet FM- 94 Film Adhesive. Technical Data Sheet FM- 94 Film Adhesive. https://www.solvay.com/en/product/fm-94#product-documents.
[26] SHD Composites. MTC510-UD epoxy prepreg datasheet. 2018;01:1-3. https://shdcomposites.com/admin/resources /mtc510-tds.pdf.

INVESTIGATING THE TRADE-OFF EFFECTS OF INORGANIC PHOSPHATE/SILICATE FLAME RETARDANT CONTENT ON THE FIRE PERFORMANCE AND POST-FIRE FLEXURAL MECHANICS OF EPOXY/GLASS FIBER COMPOSITES

S. Sunder[1], M. Jauregui Rozo[2], S. Inasu[1], B. Schartel[2], H. Ruckdäschel[1]

[1]Department of Polymer Engineering, University of Bayreuth, Bayreuth, Germany
sruthi.sunder@uni-bayreuth.de, www.polymer-engineering.de
sneha.inasu@uni-bayreuth.de, www.polymer-engineering.de
holger.ruckdaeschel@uni-bayreuth.de, www.polymer-engineering.de
[2]Bundesanstalt für Materialforschung und -prüfung (BAM), Berlin, Germany
maria.jauregui@bam.de, www.bam.de
bernhard.schartel@bam.de, www.bam.de

Keywords: flame retardants, post-fire, epoxy, glass fiber composites, prepregs

Abstract

Considering the existing challenges involved in the transfer of flame retardant (FR) formulations from epoxy (EP) resins to glass fiber reinforced composites (GFRCs), obtaining data on the post-fire flexural properties of such composites is even more challenging as this involves balancing test parameters with potential composite delamination. In this study, solvent-free FR additives: ammonium polyphosphate (APP), and inorganic silicate (InSi) were added at 10, 30% and 50% w/w loading to a Bisphenol A diglycidyl ether (DGEBA)-dicyandiamide (DICY)-Urone resin matrix. These resin formulations were transferred to bidirectional (BD) glass fiber composites via prepregs. A novel, but facile approach was developed to prepare the composite samples for furnace tests at 400 ºC. The composites were also subjected to fire exposure at different heat fluxes and times via a bench-scale test and subsequently tested via three-point bending. At approximately 3.5% P content, the FRs significantly improve the fire performance of both the resins and composites. However, they also degrade the systems' pre- and post-fire flexural modulus and strength. Therefore, improving the flame-retardant mode of action of the FRs in the composites, contrastingly reduces their structural integrity post-fire leading to a trade-off effect.

1. Introduction

Epoxy (EP)/glass fiber reinforced composites (GFRCs) are vital for lightweight structural applications in the construction and transport sector [1]. However, many epoxy resins, such as diglycidyl ether of bisphenol A resin (DGEBA), are not inherently flame retardant [2]. Data on the transferability of flame-retardant mode of actions from neat resins into fiber-reinforced composites prepared via prepregs is less available than adapting additive-based FRs for improving the flame retardancy of the resin alone. The use of intumescent FRs such as ammonium polyphosphate (APP) to improve char formation [3] can be further enhanced with the use of barrier formers such as inorganic silicates (InSi) [4] [5]. However, when such combinations are transferred to composites the modes of action of the FRs may be maintained [6] or hindered [3]. The presence of the thermally inactive glass fibers in the composite structure can eclipse the activity of the FRs, notably in intumescent systems [7]. Studying the post-fire flexural properties of such composites is also difficult as it involves balancing test parameters while preventing potential composite delamination due to resin burn-off effects that can make testing unviable. Of the existing studies on the post-fire flexural mechanics of epoxy-fiber-reinforced composites, only a limited few [8] [9] [10] involve mechanical characterization post-ignition, in a heat flux range of 30-50 kW/m^2

normally used in cone calorimeter tests. The reproducibility of the post-fire mechanical analysis used in these investigations is low, since the resin matrix burn-off and subsequent fiber delamination effects occur in a narrow test parameter range with a fire exposure time of less than 5 minutes. To the best of the authors' knowledge limited data is available on correlating flame retardancy with post-fire flexural behavior of the composites and investigating the potential tradeoffs therein. Here, the improvement in the fire performance using three loading levels of APP + InSi FRs in a DGEBA-dicyandiamide (DICY)-urone resin matrix is studied using their corresponding glass fiber composites. Thereafter, using a novel but facile method to ensure a universal sample preparation and testing method following fire exposure of reinforced composites, the post-furnace and post-fire properties of these composites are correlated with their fire performance.

2. Materials and Methods

A schematic summary of the materials and methods used in this investigation is given in Figure 1. DGEBA with an epoxy equivalent weight of 182-192 g/eq, was combined with a DICY hardener and a urone accelerator in the stochiometric ratio 100:6.5:1. APP and InSi were added in the ratio 8:2 at 10%, 30% and 50% w/w loading in the resin matrix. These formulations were then transferred to BD GFRCs with a fiber volume content of ~ 55% and a glass fiber aerial weight of ~ 600 g/m^2 via prepregs. The BD GF prepregs, containing equal densities of glass fibers in the 0 and 90^o orientations, were stacked and cured in an autoclave with a constant ramp rate of + 5 ^{o}C/min to 100 °C for 2 hours, followed by a second ramp to 140 °C with a ramp rate of + 5 ^{o}C/min for an additional 2 hours, and finally, a cooldown ramp of - 5 ^{o}C/min to room temperature over a minimum of 4 hours.

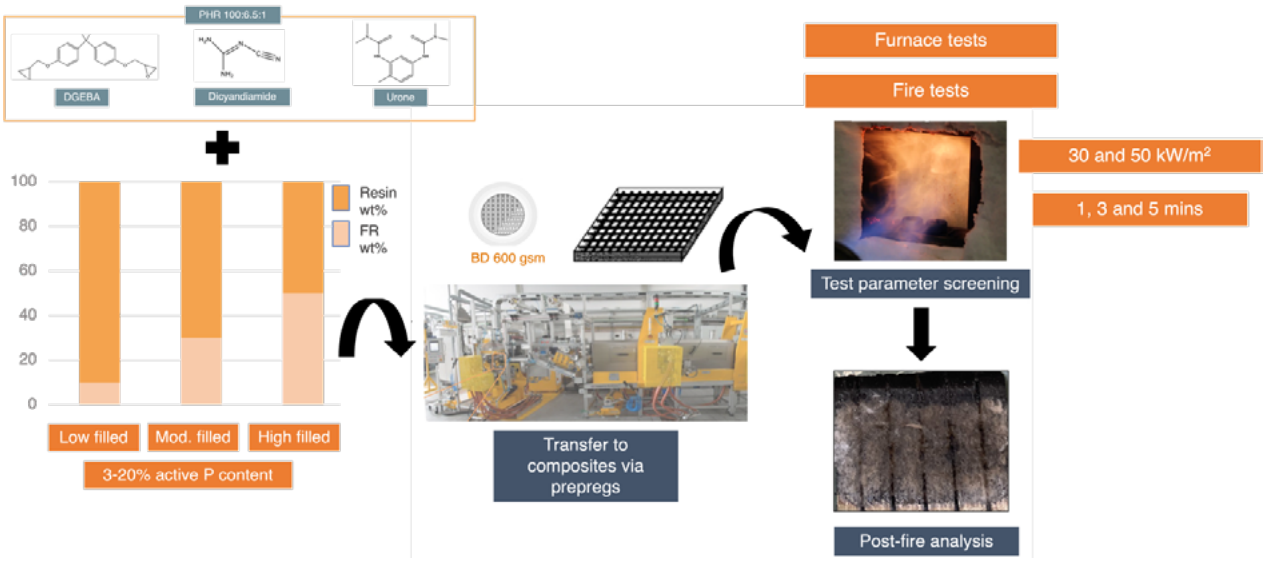


Figure 1. Summary of the materials and methods

A summary of the sample naming convention is given in Table 1. The overall GF content is maintained at ~ 70 wt.% to ensure high thermal inertness of the composite. The peak heat release rate (pHRR) composites are obtained via cone calorimetry measurements performed on specimens sized at 100 mm x 100 mm x 4 mm under an external heat flux of 50 kW/m^2 following ISO 5660-1 guidelines.

Table 1. Summary of composite formulations prepared via prepregs

Specimen name	*APP content in resin (%wt)*	*InSi content in resin (%wt)*	*BD GF content in composite*
E100:GF-BD	0	0	73
E90InSi2APP8:GF-BD	8	2	71
E70InSi6APP24:GF-BD	24	6	70
E50InSi10APP40:GF-BD	40	10	70

2.1 Sample preparation configuration for furnace, bench-scale tests and flexural testing

This study introduces an adapted sample preparation method for composite laminate specimens, which is analogous to the segmental division found in several commercial chocolate bars. A laminate with a uniform thickness of 4 mm was initially dimensioned into a square shape measuring 100 mm x 100 mm on each side. Before mechanical testing, each specimen was subjected to a partial cutting process. The cutting was executed so that approximately 0.1-0.3 mm of the laminate remained intact on one face, effectively leaving a thin, uncut layer that connects the sections. The rationale behind this technique is to significantly reduce the influence of edge effects, which are known to impact the mechanical performance during bending tests. Post-cutting, the specimen's partially cut side was exposed to a controlled fire to simulate realistic conditions of flame spread as described in Section 2.1.6. One set of samples was directly exposed to the fire at heat fluxes of 30 kW/m^2 for 3 mins and 50 kW/m^2 for 5 mins as shown in Figure 2. A bench-scale testing apparatus described in [11] was used to expose the composites to a controlled flame following the 14 CFR 25.856 Appendix F Part VII; 2003 guidelines. A second set was exposed to radiation in a muffler furnace at 400 ^{o}C for 1, 2 and 3 minutes.



Figure 2. Partially cut samples before exposure to the flame (left) in the bench-scale test and post fire exposure at 50 kW/m^2 for 5 mins (right). The lower half of the composite is left unburnt due to coverage by the clamps in the bench-scale apparatus to prevent complete edge delamination

After the fire or radiation exposures, the specimens were entirely separated from the main body of the composite plates using a diamond saw. Each separated specimen was subjected to three-point bending tests with the load applied on the burnt face of the material. For the analysis of the flexural behaviour of the composites pre-exposure and post-radiation/fire exposure, the machine was set up according to the DIN EN ISO 14125 standard using a crosshead speed of 2 mm/min on a Zwick Roell Z020 originally from Zwick Roell GmbH & Co. KG. The capacity of the load cell used was 20 kN. The dimensions of the composite samples used were 100 mm x 15 mm x 4 mm. For all the burnt/radiated samples the load was applied to the burnt side during testing.

3. Results and Discussion

3.1 Trade-offs in fire performance and pre-fire flexural modulus

From Figure 3, it is evident that the increased loading of the FRs results in improved fire performance via a decline in the pHRR obtained from cone calorimetry data. However, they simultaneously also cause a decrease in the pre-fire flexural moduli of the composites with an increase in the FR content. This implies that the flame retardants are effective in their primary role. They likely promote char formation, which acts as a barrier to heat and mass transfer, thus slowing down the combustion process. Here, APP catalyzes charring in the presence of heat and releases non-flammable gases that dilute the flammable gases near the combustion zone, contributing to lower pHRR values. Additionally, InSi can act as a heat sink, absorbing some of the heat generated during combustion, contributing to lower pHRR values. The high FR content can disrupt the continuity of the resin matrix and introduce defects or stress concentrators, particularly if the distribution of the flame retardants is not uniform [12] or due to a high P content [13]. These results will be verified in a future in-depth study using scanning electron microscopy (SEM) imaging. Thus, adding the FRs, specifically InSi increases the brittleness of the composite which decreases its ability to deform elastically under stress.

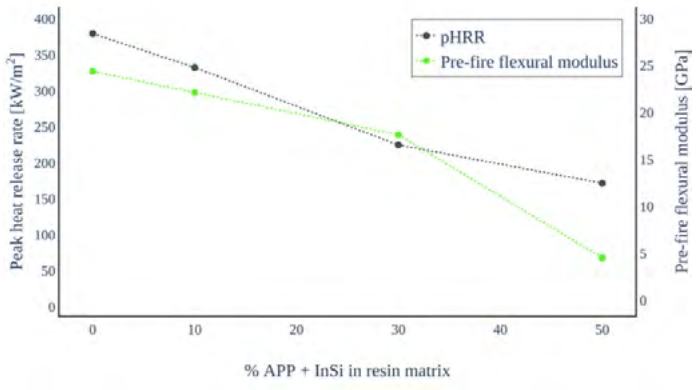


Figure 3. Simultaneous decline in the pHRR and the pre-fire flexural moduli of the composites with increasing FR content in the resin matrix

3.1 Comparison of pre- and post-furnace flexural properties

The flexural strength, strain and modulus of the BD GF composites with varying amounts of FRs are depicted in Figure 4 (a), (b) and (c) respectively. It is clear that the flexural strengths of the composite decrease not only with an increase in the furnace exposure time, but also with an increase in the FR content. A similar trend is observed in the case of the flexural strain of the composites. Thus, the exposure to radiation at 400 ^{o}C for 1 and 2 minutes causes a decline in the flexural strength, presumably via increasing degradation of the matrix-fiber interface. The increase in the FR content, especially at 50% loading, can lead to agglomeration or poor interfacial bonding causing stress concentration sites to form. The formation of char was also observed on the surface of the composites post-furnace exposure, which results in a brittle structure leading to a decrease in the flexural strain with exposure time and This is mirrored in the flexural moduli for E100:GF-BD and E90InSi2APP8:GF-BD, but not for E70InSi6APP24:GF-BD and E50InSi10APP40:GF-BD. In the latter two composites, a sudden recovery of the flexural modulus occurs after furnace exposure. This result can be explained by a potential barrier formation due to the InSi content in these composites, similar to the consolidation of fire residues via melting and sintering of nano-silica particles incorporated into novolac-based glass fiber composites [14].

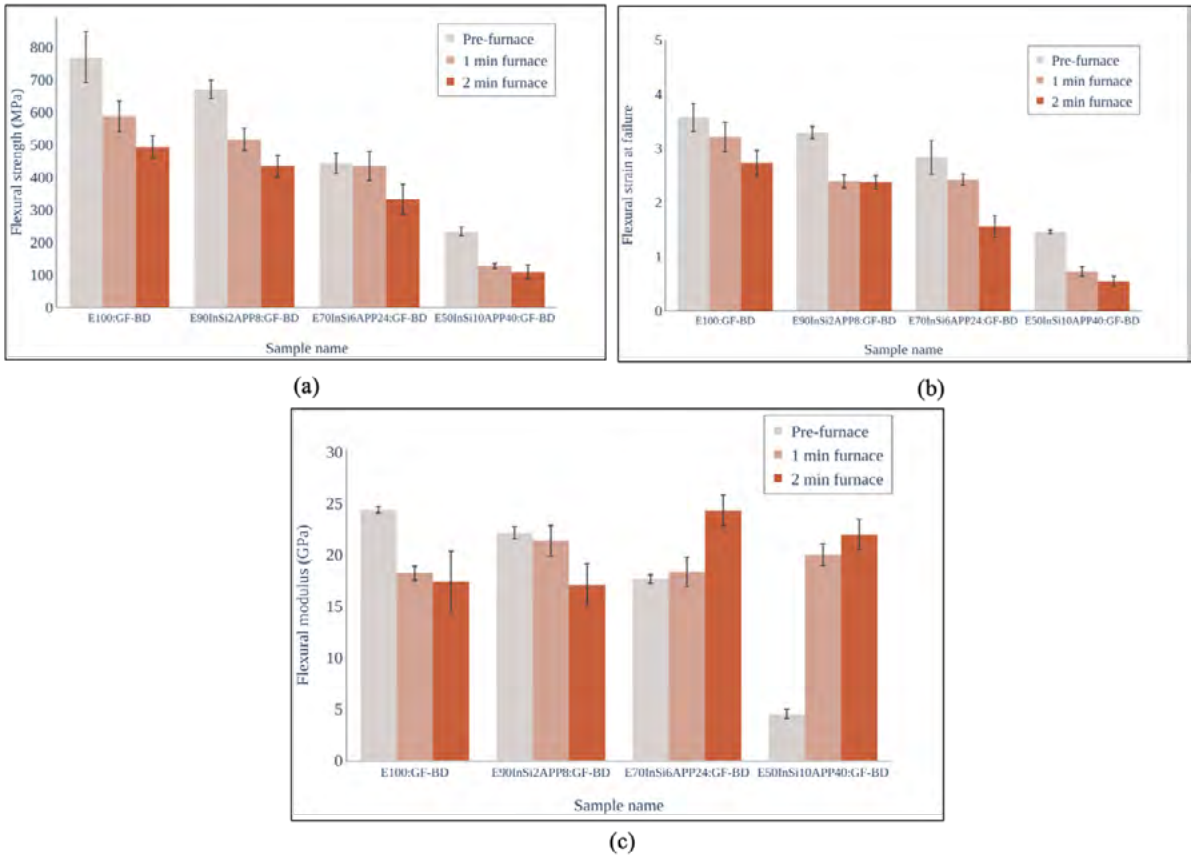


Figure 4. Pre- and post-furnace flexural strength (a) strain (b) and moduli (c) of the BD GF composites with increasing FR content

3.1 Comparison of pre- and post-fire flexural properties

Figure 5 depicts a three-dimensional image of the decline in the flexural strength and moduli of the BD GFRCs with increasing FR content and with increasing heat flux and time of exposure. The standard deviation for the data of the samples with 30 kW/m^2, 3 mins exposure is high due to the inhomogeneity of the burnt surfaces; the flame causes more concentrated burning towards the center of the composite compared to the edges. The residual flexural moduli after 50 kW/m^2 for 5 mins for the composites with 0%, 10%, 30% and 50% FR content are 13%, 9%, 6% and 1% respectively.

This result implies that the post-fire residues are not further stabilized by the addition of the FRs as in the case of the furnace-exposed samples. This result is potentially due to the char and pore formation overpowering the barrier formation effects contributed by InSi that caused a recovery of the post-furnace flexural modulus. Similar effects have been shown in past studies in literature with heat fluxes up to 10 kW/m^2 causing interlaminar damage, followed by decreases in mechanical strength already beginning at fluxes of 20 kW/m^2. With a further increase in the heat flux at 30 and 50 kW/m^2, matrix cracking increases, followed by complete resin burn-off and delamination [15] [16] [17]. However, in comparison to the literature, the residual post-fire flexural moduli for the composites are comparable to vinyl ester composites of similar compositions and higher than that of epoxy-glass fiber composites, potentially due to the higher GF content at 70% [18].

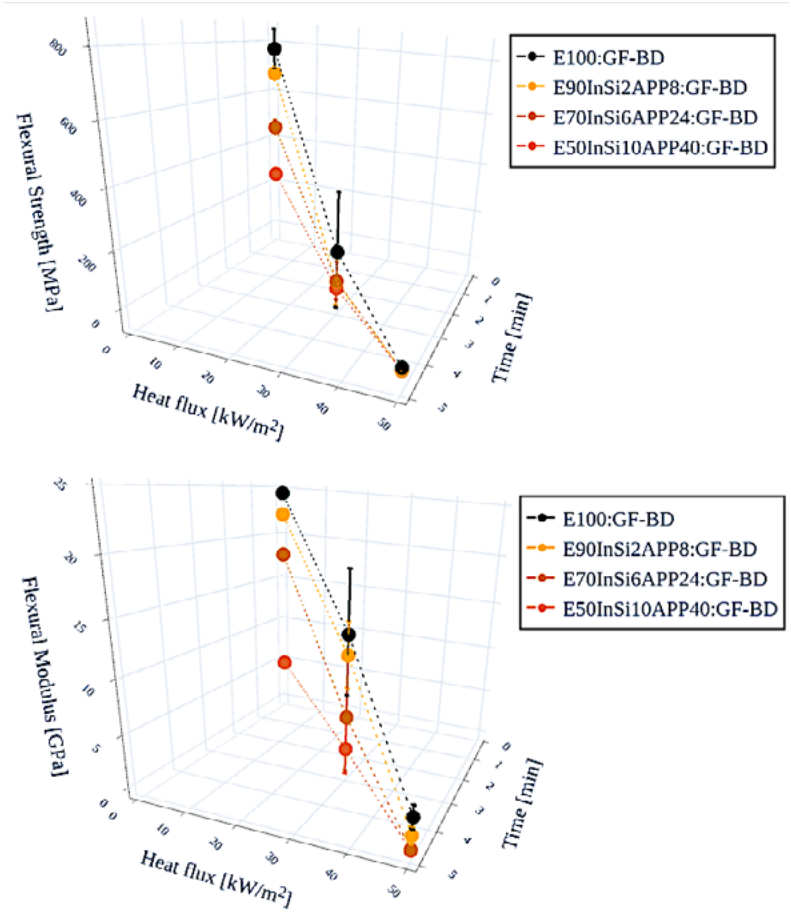


Figure 5. Comparison of the pre- and post-fire flexural strength (left) and moduli (right) after a fire exposure at 30 kW/m^2 for 3 mins and 50 kW/m^2 for 5 mins

3. Conclusions

In this investigation, a novel but facile approach was implemented to prepare and test the post-furnace and post-fire epoxy glass fiber composites (EP GFRCs) based on a Bisphenol A diglycidyl ether (DGEBA)-dicyandiamide (DICY)-Urone resin matrix and bidirectional glass fiber composites with a fiber weight content of 70%. The suggested method prevents undesirable edge effects and enables testing of the composites at a heat flux of up to 50 kW/m^2 and an exposure time of 5 minutes. These results show a significant improvement to the current state of the art where there are limited reproducible experimental studies on the post-fire flexural properties of EP GFRCs that involve actual ignition of the composites. The exposure to radiation at 400 °C for 1 and 2 minutes causes a decline in the flexural strength, presumably via increasing degradation of the matrix-fiber interface. In comparison to the literature, the residual post-fire flexural moduli for the composites are comparable to vinyl ester composites of similar compositions and higher than that of epoxy-glass fiber composites, potentially due to the higher GF content at 70%.

Acknowledgments
The authors would like to thank the German Research Foundation (DFG) with the grant number AL 474/53-1 and DFG SCHA730/26-1 for funding the project and Prof. Dr.-Ing. Volker Altstädt for his contribution to the project. The authors thank Keylab of the Bavarian Polymer Institute (BPI) and Annika Pfaffenberger for their contribution to the SEM measurements.

References

[1] J. Parameswaranpillai, H. Pulikkalparambil, S. M. Rangappa, and S. Siengchin, *Epoxy Composites: Fabrication, Characterization and Applications*. John Wiley & Sons, 2021.
[2] Y. Hu and X. Wang, *Flame Retardant Polymeric Materials: A Handbook*. CRC Press, 2019.
[3] W. P. Lim, M. Mariatti, W. S. Chow, and K. T. Mar, 'Effect of intumescent ammonium polyphosphate (APP) and melamine cyanurate (MC) on the properties of epoxy/glass fiber composites', *Compos. B Eng.*, 43(2):124–128, 2012.
[4] W. Liu *et al.*, 'Low-melting phosphate glasses as flame-retardant synergists to epoxy: Barrier effects vs flame retardancy', *Polym. Degrad. Stab.*, 185:109495, 2021.
[5] G. M. Wu, B. Schartel, M. Kleemeier, and A. Hartwig, 'Flammability of layered silicate epoxy nanocomposites combined with low-melting inorganic ceepree glass', *Polym. Eng. Sci.*,52(3):507–517, 2012.
[6] M. Rajaei, D.-Y. Wang, and D. Bhattacharyya, 'Combined effects of ammonium polyphosphate and talc on the fire and mechanical properties of epoxy/glass fabric composites', *Composites Part B: Engineering*, 113:381–390, 2017.
[7] B. Schartel, A. Weiß, F. Mohr, M. Kleemeier, A. Hartwig, and U. Braun, 'Flame retarded epoxy resins by adding layered silicate in combination with the conventional protection-layer-building flame retardants melamine borate and ammonium polyphosphate', *J of Applied Polymer Sci*, 118(2):1134–1143, 2010.
[8] A. P. Mouritz, 'Post-fire flexural properties of fibre-reinforced polyester, epoxy and phenolic composites', *J. Mater. Sci.*, 37(7):1377–1386, 2002.
[9] C. Katsoulis, B. K. Kandola, P. Myler, and E. Kandare, 'Post-fire flexural performance of epoxy-nanocomposite matrix glass fibre composites containing conventional flame retardants', *Compos. Part A Appl. Sci. Manuf.*, 43(8):1389–1399, 2012.
[10] C. P. Gardiner, Z. Mathys, and A. P. Mouritz, 'Post-fire structural properties of burnt GRP plates', *Mar. Struct.*, 17(1):53–73, 2004.
[11] B. Schartel, J. K. Humphrey, A. G. Gibson, A. Hörold, V. Trappe, and V. Gettwert, 'Assessing the structural integrity of carbon-fibre sandwich panels in fire: Bench-scale approach', *Composites Part B: Engineering*, 164:82–89, 2019.
[12] C. Thiyagu and U. NarendraKumar, 'Effect of ammonium polyphosphate on fire-retardant, mechanical, and vibrational analysis of epoxy/glass/ramie hybrid composite', *Polymer Composites*, 44(1):621–631, 2023.
[13] P. Li, J. Wang, C. Wang, C. Xu, and A. Ni, 'The Flame Retardant and Mechanical Properties of the Epoxy Modified by an Efficient DOPO-Based Flame Retardant', *Polymers*, 16(5):5, 2024.
[14] M. Häublein, K. Peter, G. Bakis, R. Mäkimieni, V. Altstädt, and M. Möller, 'Investigation on the flame retardant properties and fracture toughness of DOPO and nano-SiO2 modified epoxy novolac resin and evaluation of its combinational effects', *Materials*, 12(9):1528, 2019.
[15] E. Toubia, A. Morgan, and A. Elmushyakhi, 'Post-fire residual mechanical properties of a composite laminate—experimental study', *FL, December*, 11–14, 2017.
[16] A. P. Mouritz *et al.*, 'Review of fire structural modelling of polymer composites', *Composites Part A: Applied Science and Manufacturing*, 40(12):1800–1814, 2009.
[17] E. Kandare, B. K. Kandola, and P. Myler, 'Evaluating the influence of varied fire-retardant surface coatings on post-heat flexural properties of glass/epoxy composites', *Fire Safety Journal*, 58:112–120, 2013.
[18] A. P. Mouritz, 'Simple models for determining the mechanical properties of burnt FRP composites', *Materials Science and Engineering: A*, 359(1-2):237–246, 2003.

NUMERICAL INVESTIGATION OF THE EFFECT OF PRE-EXISTING SURFACE CRATERS ON FAILURE OF LEADING EDGE PROTECTION COATINGS FOR WIND TURBINE BLADES

A. Tempelis[1], L. Mishnaevsky Jr.[1], K. M. Jespersen[1]

[1]Department of Wind and Energy Systems, Technical University of Denmark, Risø Campus, Roskilde, Denmark - atem@dtu.dk

Keywords: leading edge erosion, wind energy, coatings, finite elements, roughness

Abstract
This study investigates how pre-existing surface craters of leading edge protection coating used against rain erosion of wind turbine blades affect the maximum strains during impacts of rain droplets. Surface craters in the form of pinholes can form during the coating application process. The investigation is carried out by using finite element models of droplet impacts on surfaces with craters, where the impact velocity, droplet size, and crater position and size are varied. The simulations predict that the maximum strain is located at the crater walls and increases as the impact velocity and droplet size increase, and that craters closer to the central impact axis experience larger strains than craters placed farther away. The size of the crater was not predicted to have an influence on strains. The position of the maximum strain value was at the crater walls for all cases, and it was larger than for an impact on a flat surface. Observations from rain erosion tests suggest that some fractures initiate from pre-existing craters which act as weak points of otherwise highly resistant coatings.

1. Introduction

A reduction in the annual energy production (AEP) of wind turbines has been observed due to leading edge erosion (LEE) of rotor blades [1, 2]. One of the main drivers of LEE is repeated impacts of rain droplets near the tip of the blade, which occur at high impact speeds (80 – 120 m/s) [3]. The water inside the impacting droplets enters its compressible region at such impact speeds and may exert large contact pressures on the protective coating materials, in the order of hundreds of MPa. The impact load causes stress waves to propagate through the coating material which results in the initiation and propagation of cracks. Eventually, the cracks lead to the gradual erosion of the surface of the leading edge, and to a reduction of the aerodynamic efficiency of blades (Figure 1). Apart from AEP losses, LEE increases maintenance costs as repairs are required once erosion breaks through the protective coating layer and propagates into the composite substrates. The composite substrates have a much lower erosion resistance than the polyurethane-based protective coatings and thus damage may propagate unpredictably fast after breakthrough of the coating layer. If erosion of the composite layers becomes severe, even the entire blade may have to be replaced. It is thus important to have predictive models [4] for the erosion of the coating layer to be able to predict how much time is needed until erosion propagates into the composite substrate. To make accurate predictions, it is necessary to understand how erosion damage initiates. Observations from rain erosion tests suggest that damage initiates from areas with surface anomalies or defects and recent numerical studies have predicted elevated impact stresses in such areas [5, 6]. This study investigates the effect of pre-existing surface craters of the coating layer on maximum strains during rain droplet impacts, by using finite element simulations. The effects of impact velocity, droplet size, surface crater size and positions on the maximum principal strain values and their location are explored and then compared with observations from tests. The maximum strain values for impacts on

flat surfaces are also calculated and are predicted to be much smaller than those for surfaces with craters, suggesting that erosion damage initiates from areas with surface irregularities.

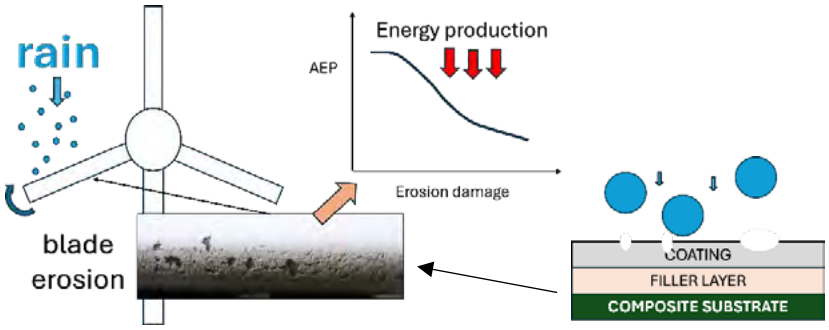


Figure 1. Rain erosion of wind turbine blades schematic.

2. Methods

2.1. Impact finite element model

A finite element (FE) model that simulates the impact of a single water droplet on the coating layer of the leading edge is used to study the effect of pre-existing surface craters. The simulation is performed with the commercial code ABAQUS. A time-dependent explicit analysis that uses the coupled Eulerian-Lagrangian approach for the fluid-solid interaction is used and more details about the model can be found in references [7, 8]. Figures 2A and 2B present the element mesh of the model and how surface craters are included. The polyurethane-based coating is modelled with a combined hyperelastic and viscoelastic model to consider the loading rate effect. The coating's density is 1200 kg/m^3 and the parameters of the Yeoh model for the hyperelastic behavior are C_{10} = 292.271·10^6 Pa and D_1 = 2.0498·10^{10} Pa. The viscoelastic behavior is modelled with time domain Prony series with parameters that are given in Table 1. This material model is obtained by fitting the master curve from a dynamic mechanical analysis (DMA) test using the MCalibration software by PolymerFEM. For the water inside the droplet, a Us-Up equation of state with constants c_0 = 1483 m/s, s = 0 and Γ_0 = 0 is used. The thickness of the coating layer was 0.5 mm for all simulations. Quarter symmetry is used to reduce the computational cost.

Table 1. Time domain Prony series parameters for the viscoelastic model of the coating.

#	1	2	3	4	5	6	7	8
gi [-]	6.79E-05	0.000111	0.000622	0.001217	0.006291	0.022798	0.069094	0.108979
τi [s]	1.00E+09	1.00E+08	1.00E+07	1.00E+06	100000	10000	1000	100
#	**9**	**10**	**11**	**12**	**13**	**14**	**15**	**16**
gi [-]	0.137753	0.168926	0.111678	0.102358	0.083703	0.062717	0.050124	0.072593
τi [s]	10	1	0.1	0.01	0.001	0.0001	1.00E-05	1.00E-06

The maximum tensile principal strains are used to study areas which are loaded more than others, since this quantity has been used in literature to predict lifetimes of rubber-like components [9], which behave similarly to polyurethane coatings. Impacts on flat surfaces are also studied to see how strain values change when including surface craters. Figure 2C presents a contour plot of the maximum tensile strain at every location of a cross section of the coating layer, for a flat impact surface.

2.2. Mesh sensitivity study

The sensitivity on mesh size is checked for two cases. For the first case, the impact surface is flat and for the second case, a surface pit is included in the model. The surface pit has a half-spherical shape of radius 0.1 mm, and its center is placed 0.2 mm away from the central impact axis. The impact velocity was 100 m/s and the droplet diameter was 2 mm for both cases. The element size is expressed as the number of elements per drop diameter (EPD). The results of the mesh sensitivity study are presented in Figure 3, where the time history of the maximum principal strain is plotted at the coating location where the maximum value is experienced. For both cases, a mesh size of 200 EPD provided sufficiently converged results and at the same time led to an affordable computational cost. This value was used to produce all the following results of this study.

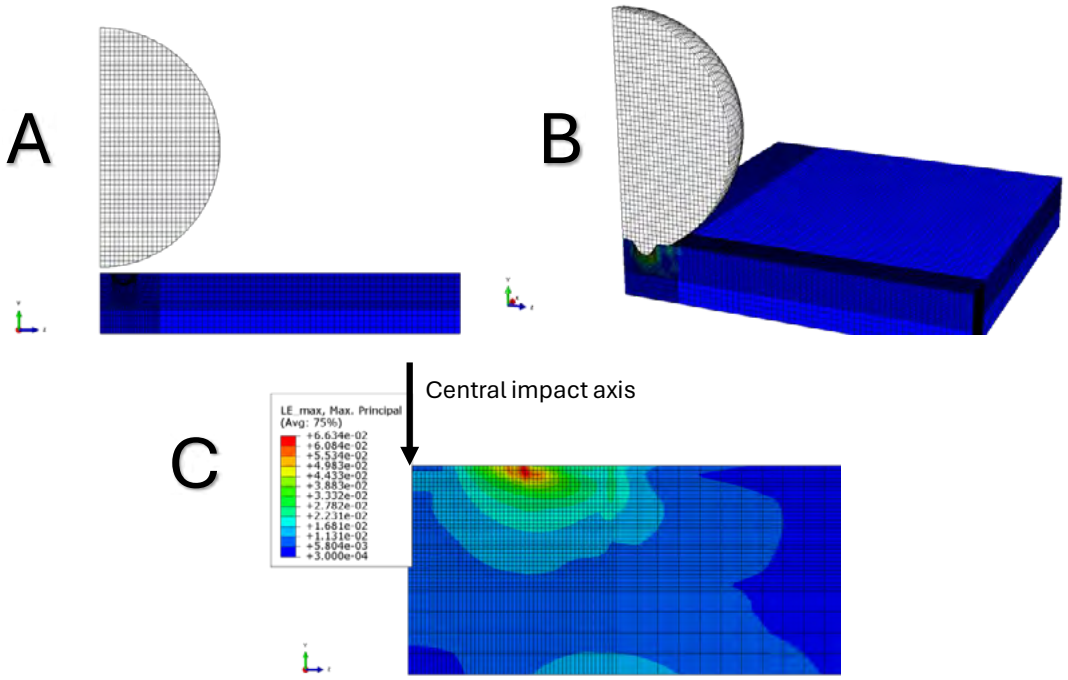


Figure 2. Finite element model of droplet impact on the protective coating layer (A), image during simulation as the water flows into a pre-existing surface defect (B) and the maximum tensile principal strains contour plot for an impact on a flat surface with a 2 mm droplet diameter and 100 m/s impact velocity (C).

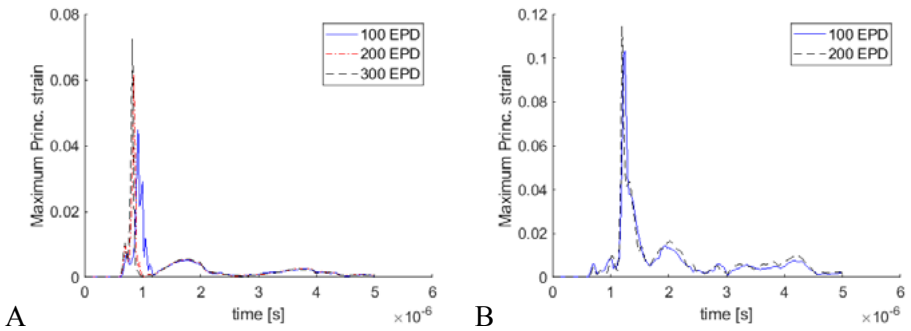


Figure 3. Mesh sensitivity study for impacts on a flat surface (A) and a surface with a pit (B). The impact velocity was 100 m/s, and the droplet diameter was 2 mm for both cases.

3. Results

3.1. Effect of impact velocity and droplet size

A half-spherical surface pit with a radius of 0.1 mm was used to check how the impact velocity affects the maximum principal strain (MPS) values. The pit center was placed 0.2 mm away from the impact axis and a droplet diameter of 2 mm was used for all impact velocity cases. The contours of the maximum MPS value at each point on a cross section of the coating layer that contains the surface pit are presented in Figure 4, for four impact velocities. The same contour plot is used in Figure 5, where now the droplet size varies, and the impact speed is 100 m/s for the four examined cases. The main observation for all of the cases is that the largest MPS values are located at approximately the same location at the wall of the surface pit. The maximum MPS values are examined in more detail in section 3.3.

3.2. Effect of pit location and size

Now the distance between the center of surface pit from the central impact axis is varied. The radius of the pit is again 0.1 mm while the impact velocity and droplet diameter are 100 m/s and 2 mm, respectively. The contour plots of the maximum MPS for four different locations of the pit are presented in Figure 6. The location of the largest MPS values now changes with the distance of the pit. When the pit is directly below the impacting droplet, the maximum MPS value is found at the base of the tip. The location of the maximum MPS rotates to the side of the wall of the pit as the distance from the impact axis increases. The effect of the pit size is also examined by varying the radius of the pit. The distance from the impact axis is 0.2 mm for all cases and the impact velocity and drop size are the same as the for Figure 5. The contours for this case are presented in Figure 7. Again, the maximum MPS values are found at the right side of the pit walls, and their location with respect to the parametric circumferential position seem to be independent of the pit radius.

3.3. Graphs of maximum tensile strain values versus the examined parameters

To check how each of the examined parameters influence the maximum MPS, the maximum MPS value is plotted against each parameter value in Figure 8. The maximum MPS value for the flat impact surface is also plotted in Figure 8A and 8B, for comparison. The simulations predict that the maximum tensile principal strain inside the pit increases as the impact velocity increases. The same trend is predicted for increases in droplet diameter values. The maximum strains for the surfaces with pits are larger than those of the flat impact surface, by a factor of approximately 1.5 for the same impact speed and droplet size. The distance of the surface pits is also predicted to be important as smaller distances led to larger strains in Figure 8C. The simulations do not predict a dependence on the size of the pit for the examined geometry, as observed in Figure 8D.

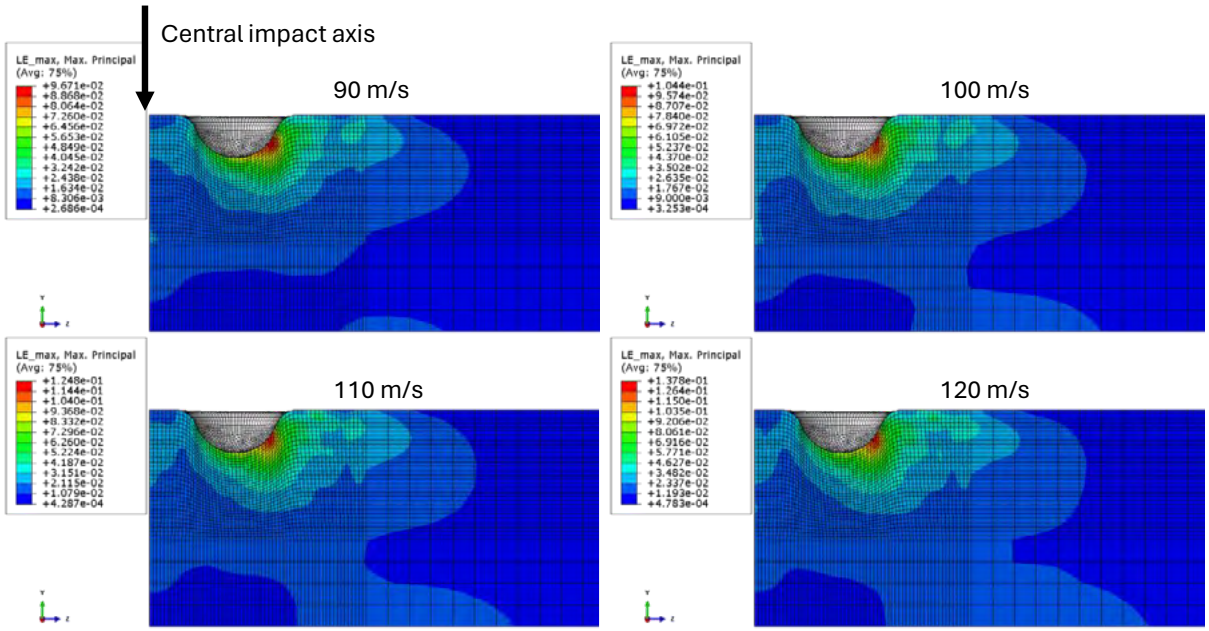


Figure 4. Contour plots of the maximum tensile principal strain value on a cross section of the coating layer which contains a surface pit. Four impact velocity cases: 90 m/s, 100 m/s, 110 m/s and 120 m/s. Droplet diameter 2 mm.

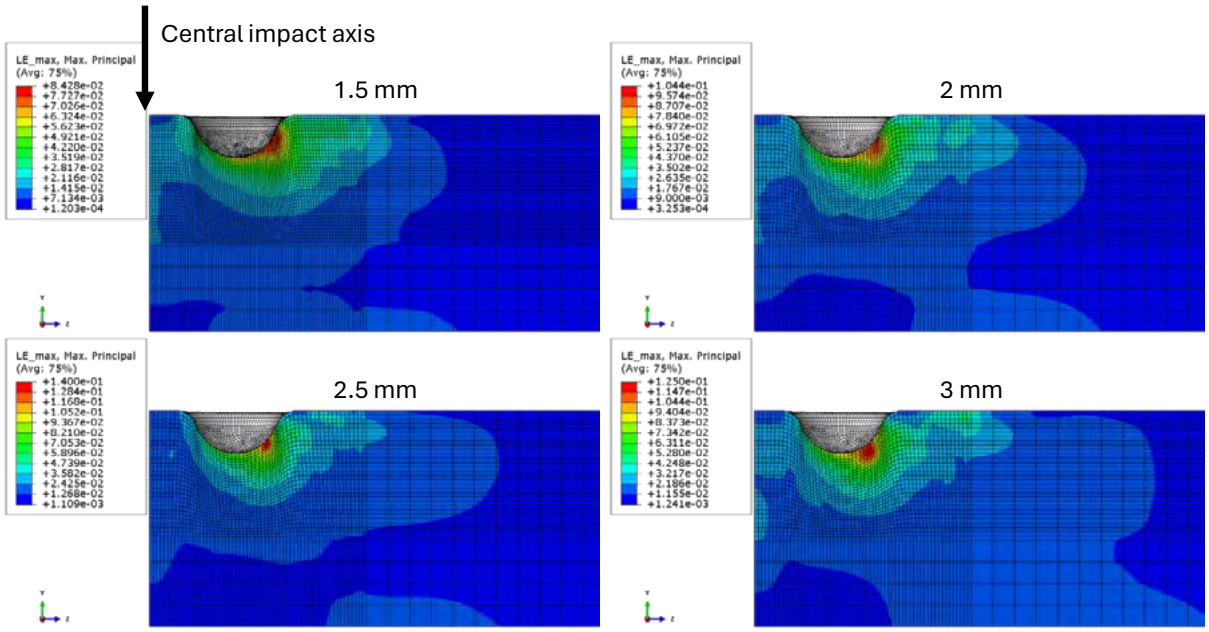


Figure 5. Contour plots of the maximum tensile principal strain value on a cross section of the coating layer which contains a surface pit. Four droplet diameter cases: 1.5 mm, 2 mm, 2.5 mm, and 3 mm. Impact velocity 100 m/s.

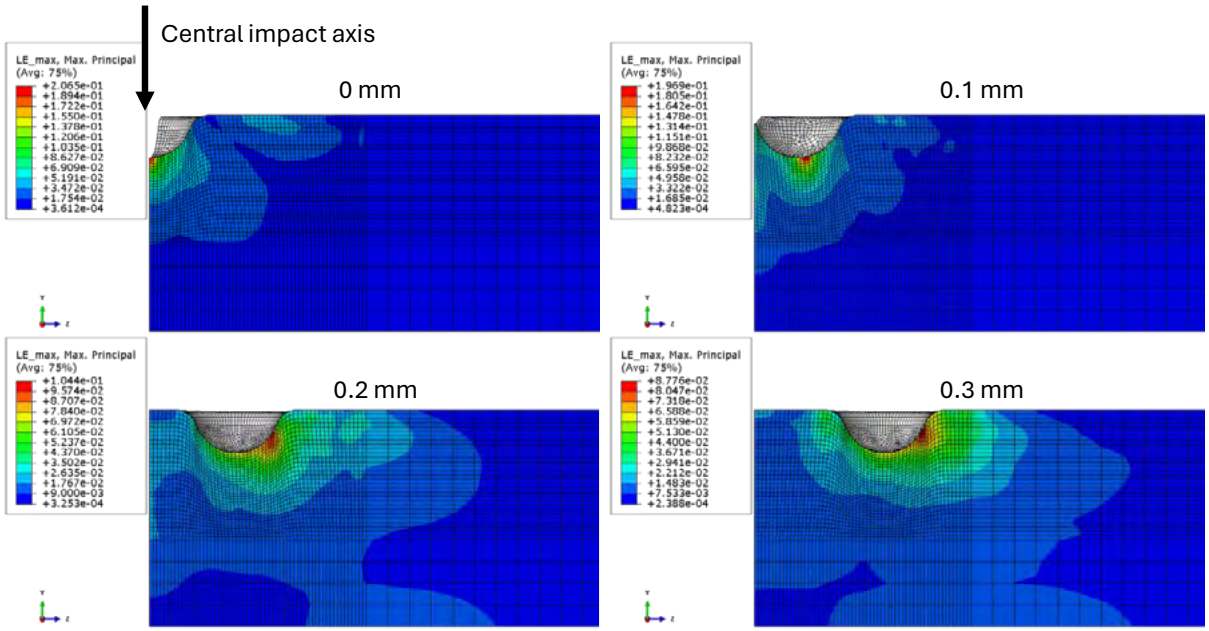


Figure 6. Contour plots of the maximum tensile principal strain value on a cross section of the coating layer which contains a surface pit. Four distance values between the pit and the impact axis: 0 mm, 0.1 mm, 0.2 mm, and 0.3 mm. Impact velocity 100 m/s and droplet diameter 2 mm.

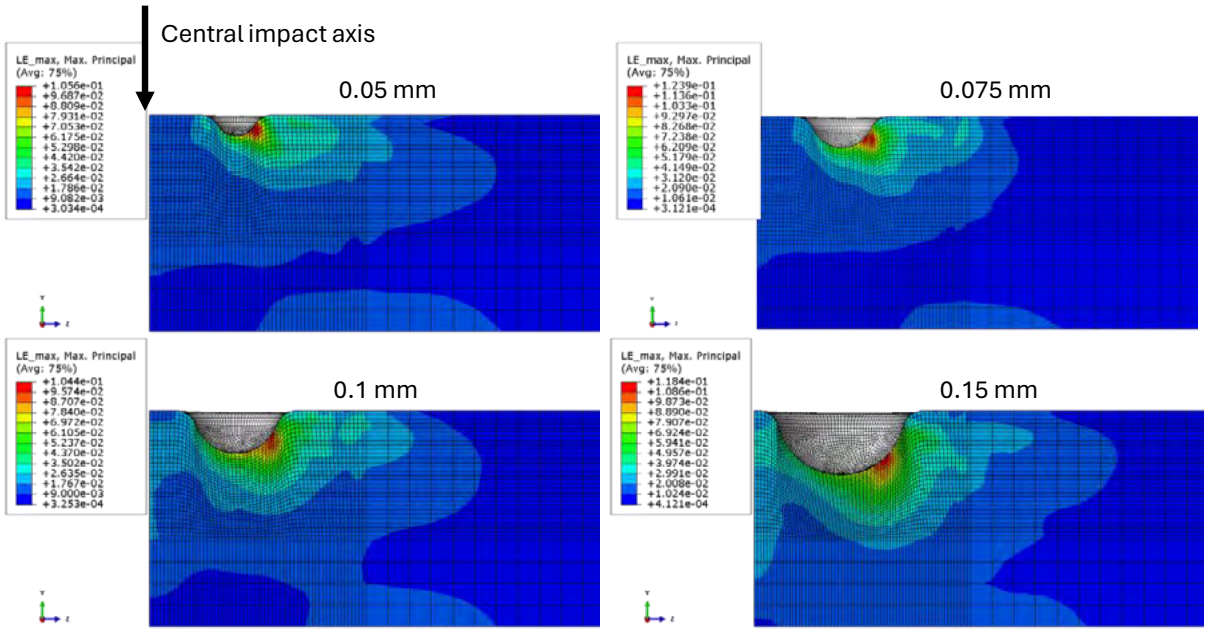


Figure 7. Contour plots of the maximum tensile principal strain value on a cross section of the coating layer which contains a surface pit. Four pit radius values: 0.05 mm, 0.075 mm, 0.1 mm, and 0.15 mm. Impact velocity 100 m/s and droplet diameter 2 mm.

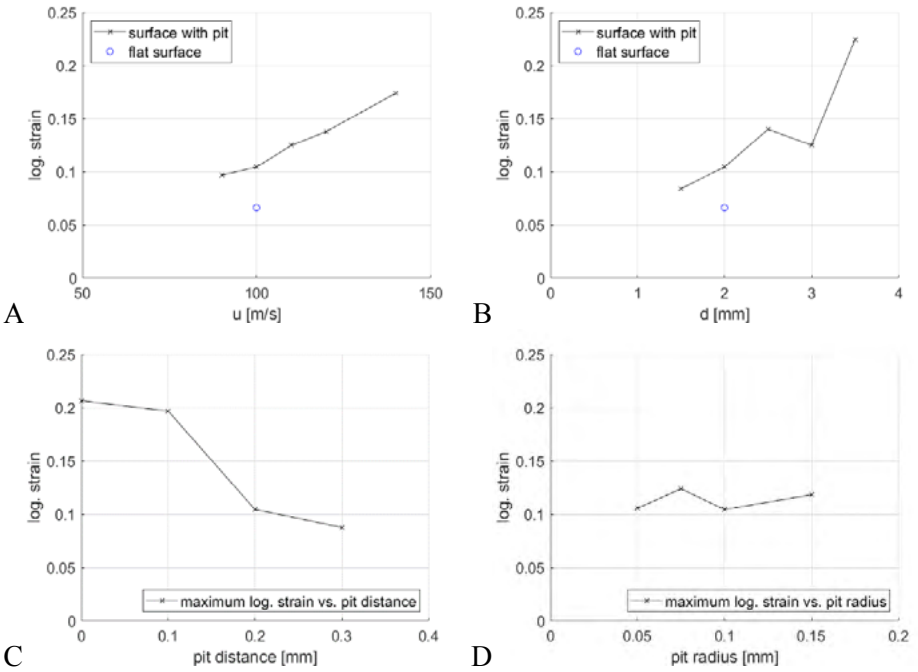


Figure 8. Maximum tensile principal strain versus impact velocity for drop diameter 2 mm (A), droplet diameter for impact velocity 100 m/s (B), pit distance for impact velocity 100 m/s and drop size 2 mm (C), pit radius for impact velocity 100 m/s and drop size 2 mm (D).

4. Experimental observations

Experimental images from rain erosion tests where failure seems to have initiated from pre-existing surface craters are presented in Figure 9. The locations of the pre-existing craters are indicated by arrows and the location where failure seems to initiate is at the walls of craters, similar to the observations from the simulations. Once failure initiates, the propagation direction seems to cause craters to grow in width and in some cases, cracks propagate deep into the coating layer and reach all the way down to the substrates.

5. Conclusions

In this study, the effect of pre-existing surface defects during rain droplet impacts on leading edge protection polyurethane coatings was investigated. A coupled Eulerian-Lagrangian approach was used to account for the large deformations of the droplet and study the fluid-solid interaction. The simulations predicted that the walls of surface craters experience the largest tensile strains during the impact, possibly due to the outward flow of water during the droplet splash. The effects of impact velocity, droplet size, crater position and size on the maximum principal strains at the walls of pre-existing surface craters were investigated. It was predicted that strain values at those locations increase with the impact velocity and droplet size. The location of the craters relative to the central impact axis was also predicted to influence strain values and the location of the maximum. More specifically, craters closer to the impact axis experienced larger strains than craters placed further away, and the position of the maximum value rotated from the base of the crater to the side of the crater walls as the crater moved away from the impact axis. The size of the crater was not predicted to have a strong influence on the maximum strain. Images of failed coating locations from rain erosion tests suggest that fracture initiates from pre-existing surface craters, and this could be justified by the results of the simulations. Coating surfaces with craters experienced larger strains than flat surfaces in the simulations, and this suggests that the state of the surface when performing lifetime calculations or tests should be considered.

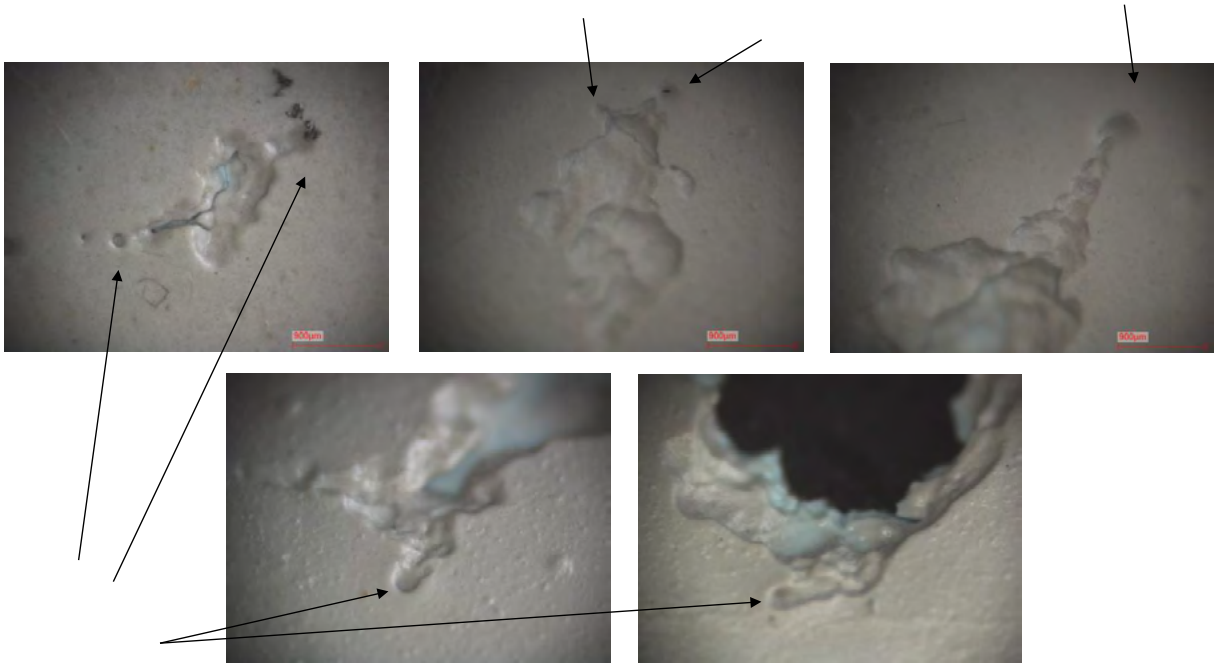


Figure 9. Images of failed locations from rain erosion tests. Failure seems to have initiated from pre-existing surface pits. The location of the pre-existing pits is shown by arrows.

Acknowledgments
The authors would like to acknowledge the project DURALEDGE for providing the rain erosion test samples from which the failure images in this work were extracted.

References

[1] R. Herring, K. Dyer, F. Martin and C. Ward. The increasing importance of leading edge erosion and a review of existing protection solutions. *Renewable and Sustainable Energy Reviews*, volume 115: 109382, 2019.
[2] A. Sareen, C.A. Sapre, M.S. Selig. Effects of Leading-Edge Protection Tape on Wind Turbine Blade Performance. *Wind Engineering*, volume 36(5): 525-534, 2012.
[3] SC Pryor, RJ Barthelmie, J Cadence, E Dellwik, CB Hasager, ST Kral, J Reuder, M Rodgers, M Veraart. Atmospheric drivers of wind turbine blade leading edge erosion: review and recommendations for future research. *Energies*, volume 15(22): 8553, 2022.
[4] G.S. Springer. *Erosion by liquid impact*, John Wiley and Sons, New York, 1976.
[5] A.N. Kaore, U.B. Kale, C.S. Yerramalli & H.K. Raval. Turbine specific fatigue life prediction model for wind turbine blade coatings subjected to rain erosion. *Materials Today Communications*, volume 31: 103487, 2022.
[6] A Tempelis and L Mishnaevsky Jr. Erosion modelling on reconstructed rough surfaces of wind turbine blades. *Wind Energy*, volume 26(10): 1017-1026, 2023.
[7] A Tempelis and L Mishnaevsky Jr. Surface roughness evolution of wind turbine blade subject to rain erosion. *Materials & Design*, volume 231: 112011, 2023.
[8] S. Doagou-Rad, L. Mishnaevsky Jr. Rain erosion of wind turbine blades: computational analysis of parameters controlling the surface degradation. *Meccanica*, volume 55(4):725-43, 2020.
[9] W.V. Mars, A. Fatemi. A literature survey on fatigue analysis approaches for rubber. *International Journal of fatigue*, volume 24(9): 949-961, 2002.

HETEROGENEOUSLY DISTRIBUTED FLAME RETARDANTS IN FIBRE-REINFORCED EPOXIES: NOVEL MANUFACTURING PROCESS AND TAILORED FLAME TESTS

Melissa Walter[1], Antonia Jarchow[1] and Bodo Fiedler[1]

[1]Hamburg University of Technology, Institute of Polymers and Composites,
Denickestraße 15, 21073 Hamburg, Germany
Email: melissa.walter@tuhh.de, antonia.jarchow@tuhh.de, fiedler@tuhh.de
Web Page: https://www.tuhh.de/kvweb

Keywords: Red Phosphorus, Fire Behaviour, Thermokinetic Methods, Co-Curing, Material Savings

Abstract
Fibre-reinforced polymers (FRPs) are increasingly used for mobility applications due to their excellent properties in lightweight design. In addition to adequate mechanical properties, flame retardancy is often a critical requirement. Because FRPs are usually combustible, flame retardants (FRs) are required. However, they can impair the properties of composites and should be used as little as possible. Typically, the surfaces of structural components are exposed to flames, therefore this work focuses on the protection of the outer layers with red phosphorus (RP). This study introduces a process containing a pre-curing of modified layers based on thermokinetic models. Thereby, the RP remains in the desired layers and its content can be kept minimal. In addition, three-point bending tests showed an adequate bonding of the pre-cured and non-pre-cured plies. There are several standardised fire tests for FRPs, but these usually require large test specimens and special devices. As part of this study, flame tests were developed to enable a qualitative comparison of different laminates using as little material and equipment as possible. Within those, it was found among other things that despite a saving of up to 82.5 wt.% RP related to homogeneously flame-retardant FRPs, significant improvements were achieved compared to unmodified configurations.

1. Introduction

Particularly in mobility applications, the protection of people is the priority. Fires must be delayed long enough to allow people to evacuate out of the danger zone. FRPs are now increasingly used to save resources and fuel, as their high specific strength and stiffness offer great potential for lightweight construction. However, compared to metal materials, most FRPs are not intrinsically flame-retardant, which means that flame retardants have to be added. Epoxy resins are widely used as matrix materials for FRPs. Without the use of FRs, epoxies ignite at approx. 375-425 °C [1].

The required factors for the development and maintenance of a fire can be visualised in a fire tetrahedron (Figure 1, left). A fire is caused by an external HEAT source, which decomposes the polymer in the pyrolysis zone. In the polymer, chemical bonds are decomposed and short-chain pyrolysis gases are produced, which serve as FUEL. The volatile component then forms a highly flammable air-gas mixture with atmospheric OXYGEN. Heat is released in the process and partially fed back into the polymer material. The process produces highly reactive OH and H radicals, which again generate new radicals (CHAIN REACTION). By reaching the auto-ignition temperature, the polymer ignites itself, which results in new heat and the process progresses. This thermal feedback is shown in Figure 1 (right). Over time, the pyrolysis zone moves continuously through the polymer material. The combustion produces carbon monoxide, carbon dioxide, carbon and water. If there is a lack of fuel or oxygen or if heat is

removed from the system, one of the necessary factors is no longer present and the fire extinguishes itself. Flame retardants can also interrupt the combustion process by suppressing at least one of the necessary parameters.

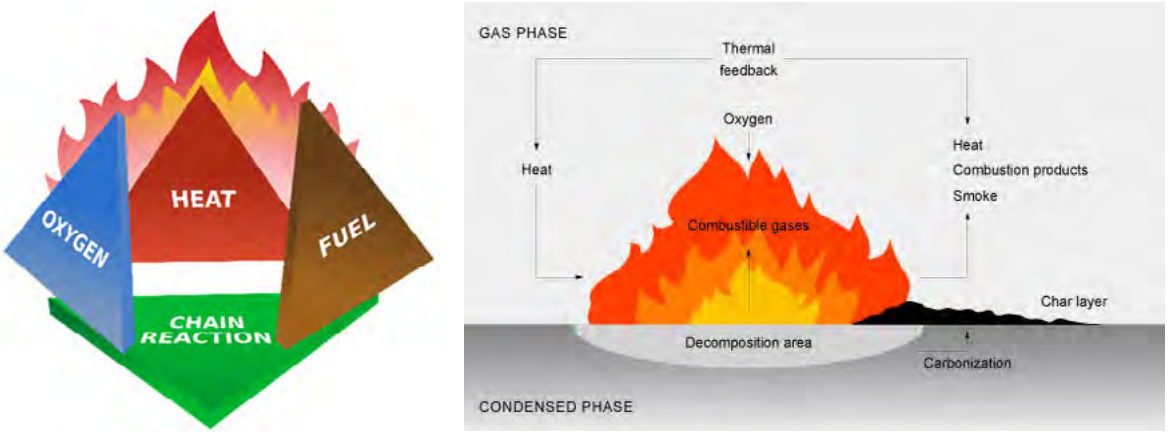


Figure 1. Left: Fire tetrahedron [2]. Right: Combustion process [3].

The mechanisms of FR are based on chemical and/or physical processes which occur in the gas and/or solid phase [4]. For example, the thermal decomposition of additivated red phosphorus above approx. 300 °C leads to a conversion to phosphoric acid, which extracts water from the pyrolysing substrate. In the solid phase, the phosphoric acid and the polymer substrate esterify to form a char (carbonisation), shielding heat and oxygen transport [5].

Various tests can be carried out to assess the fire behaviour. However, the real fire behaviour of materials depends on many other factors, such as ventilation, heat transport, the component itself or storage conditions. However, real room fire tests are very time-consuming and expensive. The fire behaviour of small test specimens can be tested on lab scale under ideal conditions. The influencing parameters of specimen geometry, ignition source, oxygen supply and heat yield can be controlled. UL 94 flame tests are frequently used, in which samples of the matrix material are flamed twice for 10 seconds with a defined Bunsen burner flame e.g. in a vertical flame test. After each flame treatment, the afterflame time is noted and the dripping of the material is analysed, allowing different classifications of the material as a result. In cone calorimetry, a sample is exposed horizontally to a constant heat flow for the duration of the test. In addition, a spark igniter is used, which ignites the material as soon as an ignitable mixture is created in the gas phase. The aim is to determine the heat release rate through oxygen consumption. In addition, the time-to-ignition (tti) and the mass loss of the sample, as well as the total amount of heat released and the maximum heat release rate are determined. In contrast to the UL 94 test, in which flammability and burning behaviour are examined, the fire process is determined energetically. In aircraft construction, test specimens are tested for their flame resistance following the "aircraft materials fire test handbook". The sample is clamped horizontally over a Bunsen burner and flamed for 15 seconds. The burn rate is determined. A metal mould with specified internal dimensions is used as a holder, which itself is non-combustible and corrosion-resistant. When positioning the mould, the side that is exposed to the flames in the real application must be placed towards the flame. Other standards, such as ASTM F776 according to DOT/FAA/AR-00/12 and DIN EN 60695-11-10, also provide methods for analysing horizontally tested test specimens, whereby different fire lengths are examined.

For mobility applications, these horizontal tests are more realistic, as FRPs are usually only exposed to potential flames on the surface and not over their cross-section. This study deals with the realisation and evaluation of FRs only at the surface and not over the entire cross-section of the FRP, thus reducing the overall amount of flame retardants. For instance, most flame retardants generally have a negative

influence on mechanical properties [6], which is why a reduction in the FR content is accompanied by a less pronounced influence on mechanical performance. In industrial practice, surface flame retardancy is sometimes achieved using gel coats or coatings [4]. Due to the additional material, this minimises the lightweight construction potential. The method investigated in this study examines the direct FR modification of individual layers of the FRP.

2. Materials and Methods

In the present study, the DGEBA resin 827 (*Epikote™ 827*, Westlake, Houston, USA) is cured with the amine curing agent 137H (*EPIKURE™ MGS™ RIMH 137*, Westlake, Houston, USA). RP (Red Phosphorus, Exolit RP 607, Clariant, Muttenz, Suisse) is added as a flame retardant. Composites were manufactured using 600 g/m² unidirectional glass fibre fabrics with 10 % backing fibres (R&G Faserverbundwerkstoffe GmbH, Waldenbuch, Germany). A 30 g/m² non-woven (R&G Faserverbundwerkstoffe GmbH, Waldenbuch, Germany) was partly added to the surfaces. As a release agent, Mikon® W64+ (Münch Chemie International GmbH, Weinheim, Germany) was used.

Stochiometric mixtures of 827 and 137H (weight shares: 100:28.57) are mixed and degassed in a Thinky Mixer ARE-250 (THINKY U.S.A., INC., Laguna Hills, USA) and a vacuum stirrer at 200 min^{-1} for at least 30 min. For the modified epoxies, RP was mixed into the epoxy system before. In the following, given percentages of RP refer to the relative mass of RP related to the total mass of resin and curing agent. To manufacture 4 mm thick plates, handlaminates were manufactured and cured vacuum-assisted for 8 h at 50 °C with a heating mat (msquare GmbH, Stuttgart, Germany) and post-cured for 16 h at 80 °C in a convection oven. Commercial prepregs are pre-cured to approx. 25 – 35 % which is described in the literature as *B-stage* [7; 8]. Various temperatures can be selected to realise the desired degree of curing. In this work, pre-curing is carried out at 50 °C, analogous to the complete curing, introduced before. Thermokinetic methods were conducted and validated via FTIR and DSC as described in [9] to determine the required time for pre-curing. After an initial study, 90 min at 50 °C (≈ 40 % pre-curing) is necessary to achieve a prepreg that is easy to process. Fibre-volume contents are approx. 40%, determined on four specimens for each configuration via calzination at 600 °C for 4 h. Table 1 gives an overview of the manufactured plates and their nomenclature.

Table 1. Manufactured Configurations with their amount of RP per plate (250 mm x 250 mm). NW: Non-woven fabric, *: pre-cured, x%: mass-related amount of RP.

Configuration	*Scheme*	*Absolut RP content (g)*	*Global RP fraction (wt%)*
$[0]_8$		0	0
$[NW,0_8,NW]$/ $[NW^*,0^*,0_7,NW]$		0	0
$[NW,0_8,NW]^{3\%}$		4	3
$[NW,0_8,NW]^{12\%}$		16	12
$[NW^{12\%*},0^{12\%*},0_7,NW]$		2.8	2.1

Specimens were cut with an ATM Brillant 265 saw (ATM Qness GmbH, Germany) and all specimens were conditioned in a vacuum oven at 40 °C for 48 h before testing. Three-point bending tests were performed based on DIN EN ISO 14125. Unmodified hand laminates with pre-curing [NW*,0*,0_7,NW] were tested to eliminate the influence of RP on mechanical properties. Five specimens were tested with the pre-cured part on the tensile side as well as on the compression side with a universal testing machine *Allroundline Z10* (Zwick Roell, Ulm, Germany).

The conducted flame tests were tailored to the flame-retardant surface modifications of the laminates considering methodical approaches of conventional test methods (see introduction). The 40 mm flame of a bunsen burner (0,7 kW, methane gas, technical grade) was applied centred at a distance of 25 mm to the surface of 100 mm x 100 mm specimens. Considering various flame tests, described in the introduction, *Test A* used ten flame applications of 60 s. A 180 s flame treatment was added afterwards. Between every flame treatment, the mass loss and the burning and afterflame times were evaluated via postprocessing of video recordings during the tests. The more, as a second test (*Test B*), a single flame treatment over 180 s was conducted. To prevent the flame from spreading over the edges, a steel frame was utilised. In addition, three temperature sensors (type K, Figure 2, left, 1-3) were installed to continuously measure the temperature development during flame treatment on the top (centred) and bottom (edge area) of the test specimen and on the frame. The tests are conducted in a *HVFAA Horizontal Vertical Flame Chamber* (Atlas Material Testing Technology, Mount Prospect, Illinois, USA).

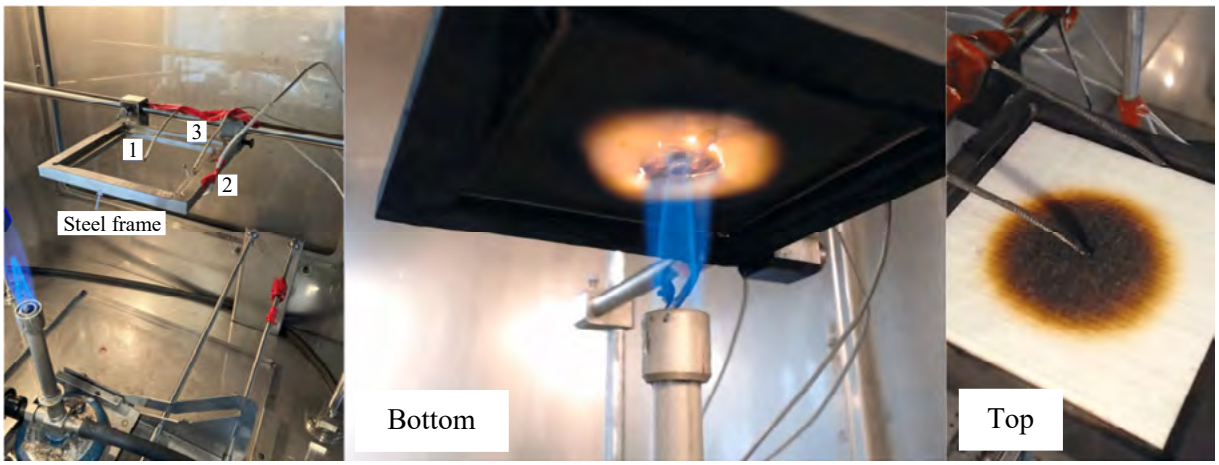


Figure 2. Set-up of the flame tests.

3. Results and Discussion

3.1 Pre-curing of the modified layers

Vacuum-assisted hand lamination is a simple process to manufacture composites with changing matrices. One typical problem while curing plies with and without flame retardants is the convey of particles into unmodified layers (Figure 3, left). As a result, the desired particle content on the surface is lower than intended. By pre-curing the modified plies, it was possible to ensure that the RP remained in the desired layers so that the filler content could be kept as low as necessary (Figure 3, right).

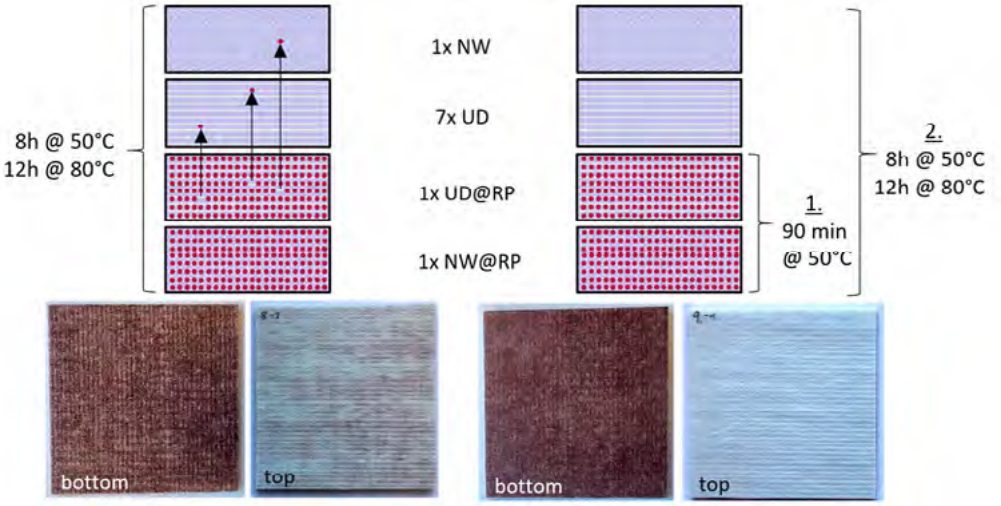


Figure 3. GFRPs containing partially modified layers without pre-curing (left) and pre-cured (right). NW: Non-woven fabric, UD: Unidirectional glass-fibre fabric; RP: Red Phosphorus.

3.2. Three-point bending tests

To verify an adequate bonding between the pre-cured and non-pre-cured layers, three-point bending tests were conducted. The configuration [NW*,0*,0_7,NW], tested with the pre-cured plies under compression load on the top of the test setup achieved bending strengths of 650.32 ± 39.10 MPa. With the pre-cured layers under tensile load, bending strengths of 641.66 ± 30.23 MPa were reached which means that no difference exceeding the standard deviation could be found. Furthermore, the specimens delaminated at other interfaces than between the pre-cured and non-pre-cured plies. This is shown in Figure 4 exemplary for the configuration [$NW^{12\%}$*,$0^{12\%}$*,0_7,NW], because the pre-cured layers are visually distinguishable in this case. Therefore, it can be stated, that the bonding is adequate and the pre-curing has no significant negative influence on the mechanical properties. For the flame tests performed in this study, it is sufficient that the adhesion is not so poor as to result in significant mechanical weakening. Therefore, additional tests to vary the stress ratios in the target interface (e.g., interlaminar shear strength, short beam shear) or cost-intensive double cantilever tests are not performed.

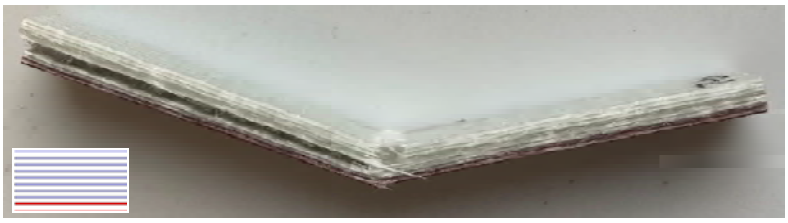


Figure 4. Specimen of configuration [$NW^{12\%*}$,$0^{12\%*}$,0_7,NW] after three-point bending test.

3.3. Tailored flame tests

Figure 5 (left) shows the results of the eleven flame treatments of *Test A*, while Figure 5 (right) displays the single 180 s flame treatment of *Test B*. The dots demonstrate the time-to-ignition (tti) within the flaming time (60 s or 180 s, grey column). On top of this column, the afterflame time is shown.

Firstly, the influence of the NW is analysed by comparing [0_8] with [NW,0_8,NW]. In addition to the positive influence on the surface quality, the non-woven fabric is beneficial for the GFRPs behaviour against fire, because it prevents the afterflame time after A3 while without NW six flame treatments

lead to an afterflame time. Considering the images of the flame-treated surface of the specimens (Table 2), it is noticeable that the fibres without the NW are already exposed after the first flame treatment, so that the matrix of the lower layers is more freely accessible, while the NW forms a closed layer above the load-bearing fibre layers. The matrix content is comparatively high in the NW, so more carbon is present, which can carbonise and form a char. If the number of flame treatments increases, the glass fibre non-woven cannot withstand any more, which is additionally noticeable in an afterflame time of 13 s after *A11*. It is also noticeable that the ttis with NW are significantly lower than without, however this does not have a negative influence on the afterflame times.

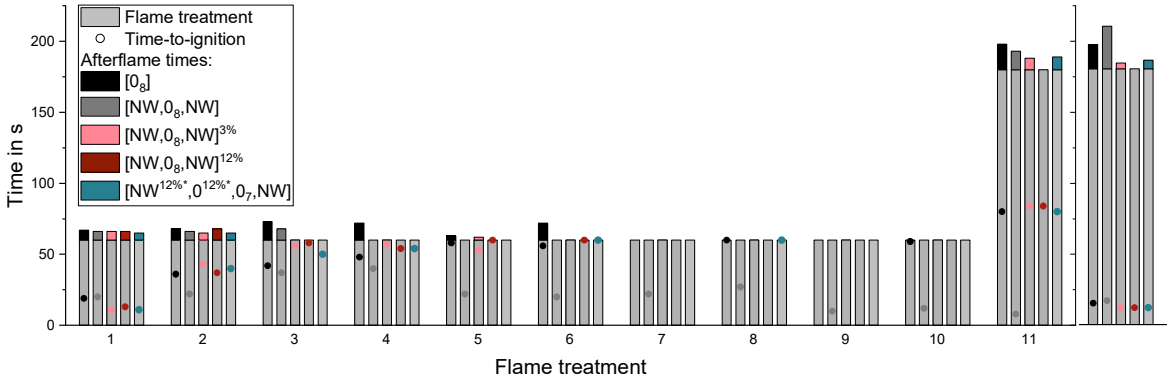
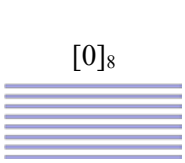


Figure 5. Afterflame times and tti in *Test A* with several flame treatments (left) and *Test B (right)*.

When using RP, no afterflame times can be observed for any of the configurations analysed from the third flame treatment onwards. The configurations only differ in the three-minute flame treatments. While no afterflame times can be determined for the 12 % modified configuration in *Test A11* and *B*, the configuration modified with 3 % RP throughout burns for eight seconds (*A11*) resp. four seconds in *Test B*. The only locally modified configuration is in a comparable range in terms of afterflame times. However, Table 2 shows that fewer fibres are exposed after *A11* than with [NW,0$_8$,NW]$^{3\%}$. On the other hand, *Test B* leads to comparable surfaces. Table 2 also shows that the modified configurations have a different char structure to the unmodified configurations due to the reaction of the RP described in the introduction. In general, *Test B* leads to a different visual impression. The load-bearing fibres are less exposed without prior flame treatment for all configurations with NW.

Table 2. Flamed surfaces after first, fifth and last flame treatment of *Test A* and after *Test B*.

Configuration	*A1*	*A5*	*A11*	*B*
[0]$_8$				
[NW,0$_8$,NW]				

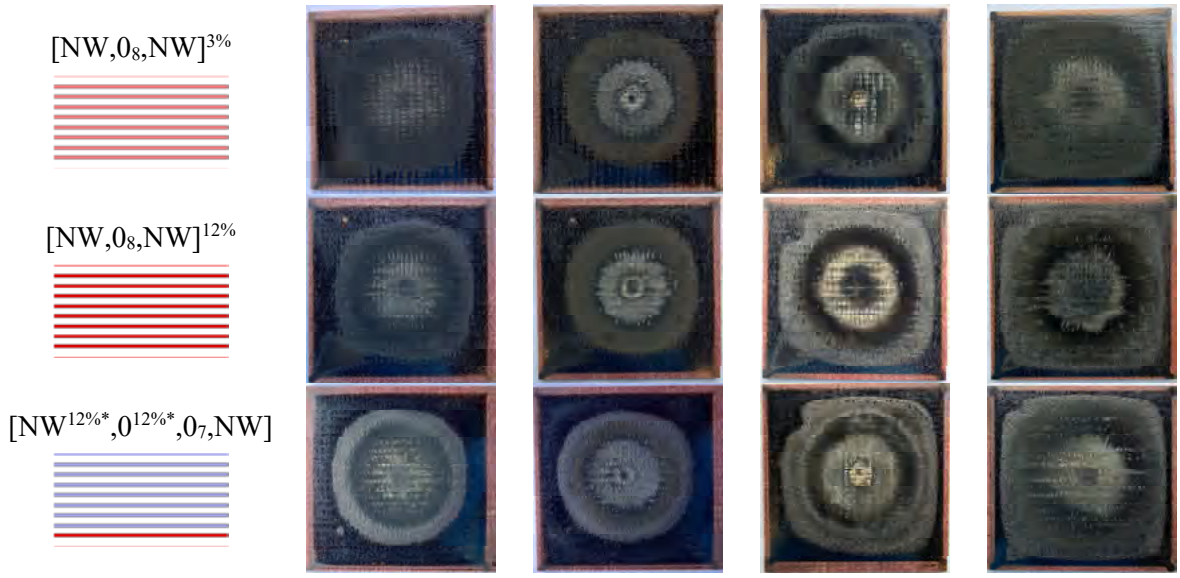


Figure 6 shows the temperature development over three minutes (*A11* and *B*) exemplary for the configuration [NW,0$_8$,NW]. However, in qualitative terms, the curve can be observed in the same way for all configurations. The temperature on the upper side initially rises more slowly, but the maximum measured value then exceeds that of test B as the flame exposure time increases. As described in the introduction, the shielding due to the formation of a char by the individual flame treatments therefore leads to a change in heat conduction. As the duration of the flame treatment increases, the heat conduction across the cross-section appears to increase proportionately more. The reason for this may be the 'failure' of the NW and thus the loss of the char built up on it. On the bottom side, the temperature is measured at the edge as described. In contrast to *Test B*, in *Test A11* a plateau at a comparatively lower temperature level is formed. In this case, the temperature also rises to a higher maximum value with further flame treatment.

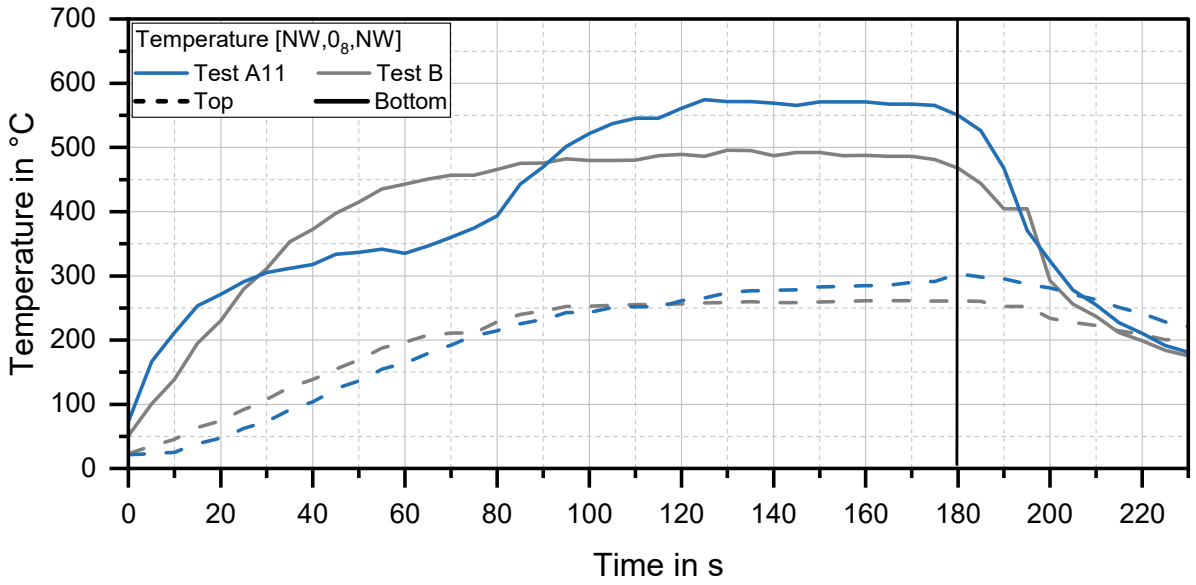


Figure 6. Temperatures on the flamed surface (bottom) and the top of the specimen [NW,0$_8$,NW]. 180 s flame treatment after 10 x 60 s (*Test A11*) and *Test B*.

4. Conclusions

With the methodology used, it was possible to show that the pre-curing determined from thermokinetic methods ensures that the modification remains in the desired plies and that the FR content can be kept as low as necessary. In addition, mechanical properties were not changed beyond the standard deviation. The test scenarios developed from various existing flame tests provide a screening method for making qualitative comparisons between different flame retardants or flame retardant proportions and their distribution in the laminate. It could be shown that the modification of individual layers with a small amount of FR already shows great improvements in fire behaviour compared to unmodified configurations. In a direct comparison of the heterogeneously modified configuration $[NW^{12\%*},0^{12\%*},0_7,NW]$ with the configuration $[NW,0_8,NW]^{3\%}$, approx. one third of FR can already be saved and similar results can be achieved concerning afterflame times. According to optical analyses, the heterogeneously modified specimen is even less affected. Compared to the configuration modified with 12 % throughout, 82.5 wt.% RP can be saved. Only with increasing fire load (180 s flame exposure), differences are recognisable. In addition, the use of a NW is not only useful for uniform surface qualities but also for fire protection applications, as the high matrix content leads to a more pronounced char.

It should be noted that the results are comparable within the study, but a quantified comparison, for example when using other burners, is not possible. As flame retardancy is highly component-dependent, it is necessary to examine the required amount of modificated plies by using suitable large-scale tests for the desired application.

Acknowledgments

The authors would like to thank the Ingeborg Gross Foundation for financial support and Westlake Epoxy as well as Clariant for the supply of material.

References

[1] D. Quang Dao, J. Luche, F. Richard, T. Rogaume, C. Bourhy-Weber and S. Ruban. Determination of characteristic parameters for the thermal decomposition of epoxy resin/carbon fibre composites in cone calorimeter. International Journal of Hydrogen Energy, 38, 8167–8178, 2013.

[2] Wikimedia Commons User: Gustavb / CC-BY-SA-3.0.

[3] Clariant Plastics & Coatings GmbH. Fire initiation and combustion process. Available at: https://www.flameretardants-online.com/fires/fire-initiation. Access: 26. April 2024.

[4] X.-H. Shi, X.-L. Li, Y.-M. Li, Z. Li and D.-Y. Wang. Flame-retardant strategy and mechanism of fiber reinforced polymeric composite: A review. Composites Part B: Engineering, 233, 109663, 2022.

[5] J. Sag. Phosphorhaltige Flammschutzmittel aus biobasierten Plattformchemikalien. Doctoral Thesis, Technische Universität Darmstadt, 2022.

[6] M. Shekarchi, E. M. Farahani, M. Yekrangnia and T. Ozbakkaloglu. Mechanical strength of CFRP and GFRP composites filled with APP fire retardant powder exposed to elevated temperature. Fire Safety Journal, 115, 2020.

[7] D. Budelmann, C. Schmidt and D. Meiners. Prepreg tack: A review of mechanisms, measurement, and manufacturing implication. Polymer Composites, 41:3440–3458, 2020.

[8] O. d. A. Raponi, R. d. A. Raponi, G. B. Barban, R. M. Di Benedetto and A. C. Ancelotti Junior. Development of a Simple Dielectric Analysis Module for Online Cure Monitoring of a Commercial Epoxy Resin Formulation. Materials Research, 20:291–297, 2017.

[9] M. Walter, M. Neubacher and B. Fiedler. Using thermokinetic methods to enhance properties of epoxy resins with amino acids as biobased curing agents by achieving full crosslinking. Scientific reports, 14, 4367, 2024.

DELAMINATION CLASSIFICATION IN COMPOSITE PLATES USING GUIDED WAVES AND 1D-CNN

Shain Azadi[1,2], Weikun Chen[2], Yoji Okabe[2], Valter Carvelli[1]

[1] Department A.B.C., Politecnico di Milano, Milan, Italy
Email: shain.azadi@polimi.it, valter.carvelli@polimi.it
[2] Institute of Industrial Science, The University of Tokyo, Tokyo, Japan
Email: chenwk@iis.u-tokyo.ac.jp, okabey@iis.u-tokyo.ac.jp

Keywords: guided waves, delamination, CFRP, 1D-CNN, damage detection

Abstract
This study assesses the effectiveness of Ultrasonic Guided Waves (UGWs) combined with a 1D Convolutional Neural Network (1D-CNN) for detecting and classifying delamination in carbon fiber reinforced polymer (CFRP) laminates. A dataset of 912000 waveforms from undamaged and damaged CFRP plates was analyzed using a shallow 1D-CNN with two convolutional blocks and a fully connected layer, designed for computational efficiency and robust generalization. The model processed data with a 70-30-10 split for training, validation, and testing, achieving an average accuracy of 90.27%. The analysis showed high recall and precision rates - over 90% in about 75% of classes and over 95% in about 40% of the classes. These metrics were particularly significant when the waveforms propagated parallel to the fiber direction: averaging Precision, Recall, and F1-Score at 96.2%. They highlighted the effectiveness of the model over a range of delamination depths and orientations. However, performance differences were observed in cases with deeper delamination and perpendicular wave propagation due to suboptimal wave excitation. These results highlight the potential of 1D-CNNs to effectively classify complex UGW signals for real-time health monitoring of structural composite components.

1. Introduction

Lightweight and resilient, Carbon-Fiber Reinforced Polymer (CFRP) laminates are essential in aerospace, energy, and automotive industries due to their superior mechanical properties [1]. However, these composites are susceptible to impacts, fatigue, and latent defects over their service life [2], requiring real-time monitoring and rapid damage detection.

Ultrasonic Guided Waves (UGWs) have emerged as a leading method for detecting, localizing, and classifying such damages, providing reliable identification of invisible flaws and critical insights into material integrity [3, 4]. However, traditional damage assessment using UGWs relies heavily on expert analysis, which can be slow, costly, and error-prone. These are problematic in safety-critical environments where fast and accurate assessments are critical.

To overcome these challenges, Convolutional Neural Networks (CNNs) have been used for their data analysis capabilities, although they require significant computational resources and large training datasets. In contrast, recently developed 1D Convolutional Neural Networks (1D-CNNs) offer a more efficient alternative to 2D-CNNs for analyzing one-dimensional signals, such as patient ECGs, bearing vibrations and waveforms. With simpler kernel structures, 1D-CNNs are less computationally demanding, facilitating deployment on consumer-level hardware, and enabling real-time applications in structural health monitoring and anomaly detection [5].

UGW-based 1D-CNNs have recently been applied to damage detection in aluminum [6] and metal [7] plates. However, their use in composite laminates, which exhibit more complex multimodal and dispersive behavior, has not yet been reported.

In this research, a 1D-CNN is used to detect and classify 20 mm x 20 mm square delamination in eight-layer CFRP cross-ply laminates with a $[90_2/0_2]_S$ stacking sequence. One intact and three artificially flawed specimens were prepared with delamination located at different depths (0.28 mm, 0.56 mm, and 0.84 mm). The CFRP plates were examined using a laser ultrasonic visualization inspector. One-dimensional waveforms were recorded using a wideband piezoelectric transducer. The resulting dataset, after Z-Score normalization, contained 228000 waveforms per plate, totaling 912000 signals.
The designed 1D-CNN architecture, with two convolutional blocks and one fully connected layer, inputs normalized data directly from the sensors to closely mimic real-time monitoring. The output layer categorizes twelve classes, assigning three classes per plate based on the direction of waveform propagation.
The organization of this paper is as follows: Chapter 2 provides a comprehensive overview of the materials used and the experimental setup. Chapter 3 describes the 1D-CNN architecture developed for this study. Chapter 4 examines and discusses the classification results achieved by the model. Finally, Chapter 5 outlines the conclusions derived from this research.

2. Materials and experimental setup

This study utilizes a UGW-based 1D-CNN to detect and classify delamination in eight-layer CFRP cross-ply laminates with a $[90_2/0_2]_S$ stacking sequence, as shown in Figure 1a. The anisotropic stiffness matrix components and thermal properties of the 0° ply, assuming 60% fiber volume fraction, are detailed in Table 1 [8].
Laminate plates, measuring 200 mm x 200 mm with a total thickness of 1.12 mm and individual plies 0.14 mm thick, were produced in four variants. The undamaged specimen is labeled "IO", while the other three contain a central 20 mm x 20 mm delamination at varying depths: "R1" between the 4th and 5th ply (z=0.54 mm), "R2" between the 6th and 7th ply (z=0.84 mm), and "R3" between the 2nd and 3rd ply (z=0.28 mm), as shown in Figure 1b.
A piezoelectric sensor (AE-900S-WB, NF CO., LTD.) with a bandwidth from 0.3 MHz to 1.5 MHz was attached to the top surface of the specimen outside the scanned area to detect the temporal waveforms generated by the laser ultrasonics (Figure 1c). The sensor positions were adjusted to vary the wave propagation directions relative to the fiber direction of the top ply, allowing for the collection of UGW waveforms in three orientations: perpendicular (0°, "PA"), diagonal (45°, "PB"), and parallel (90°, "PC") to the top ply fiber orientation, detailed in Figure 1d.

Table 1. Thermo-mechanical properties of the homogenized CFRP unidirectional ply with 0° fiber orientation (T700SC/2500 Toray)

Elastic Stiffness Coefficient		Specific Heat	Heat Conduction Coefficient		Thermal Expansion Coefficient	
C_{ij} (i,j=1...6) [GPa]		C [J/kg/K]	K_i (i=1...3) [W/m/k]		α_i (i=1...3) [W/m/k]	
C_{11}	133.0	923	K_1	60	α_1	4.8x10-7
$C_{12}=C_{13}$	4.978		$K_2=K_3$	0.59	$\alpha_2=\alpha_3$	4.0x10-5
C_{23}	5.345					
$C_{22}=C_{33}$	10.71					
C_{44}	2.700					
$C_{55}=C_{66}$	4.800					

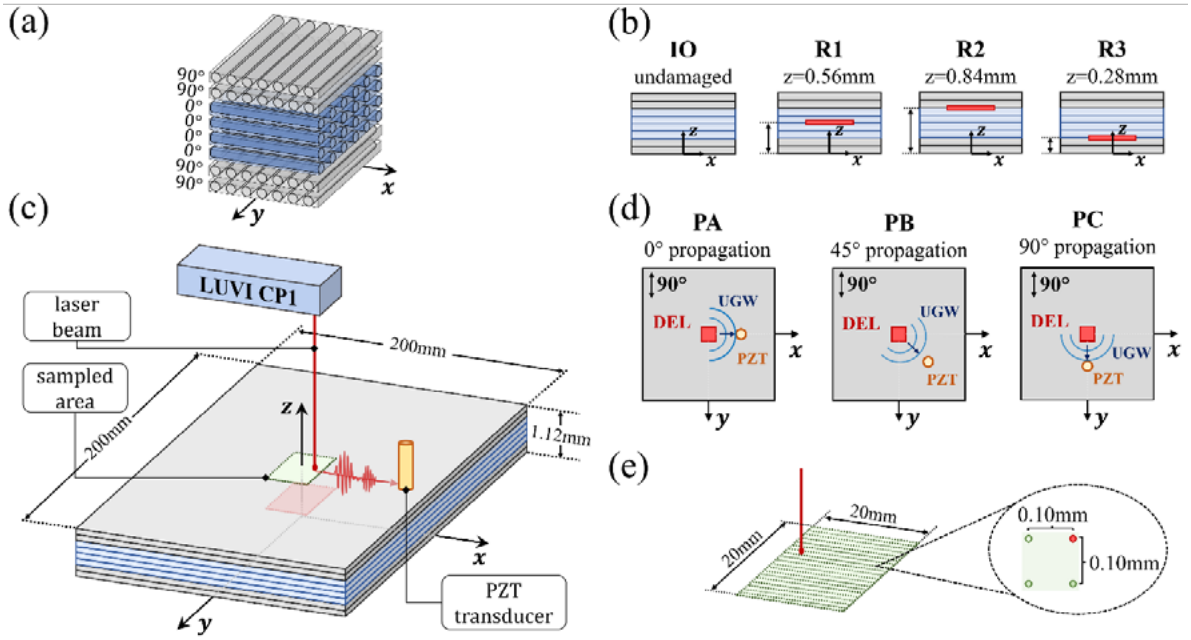


Figure 1. Experimental setup and configurations for UGW testing in CFRP Laminates. (a) cross-ply stacking sequence of the CFRP plate; (b) cross-sectional views of the laminate variants, illustrating intact and delaminated conditions at varying depths; (c) overview of the LUVI-CP1 system scanning a CFRP plate via laser-induced UGW excitation; (d) UGW propagation directions with respect to the fiber orientation in the laminate: 0° (PA), 45° (PB), and 90° (PC); (e) scanning area and grid details.

Surface vertical displacement is measured using a laser ultrasonic visualizing inspector (LUVI-CP1, Tsukuba Technology Co., Ltd). The LUVI system uses an Nd:YAG laser to induce rapid thermal expansion and contraction in the target area, creating broadband UGWs that propagate through the material. This system scans a 20 mm x 20 mm high-resolution area centered on the specimen with a 195x195 scan grid, spacing of d=0.103 mm between illumination points, and produces approximately 38000 waveforms per scan with a scan density of 100 points per mm². The laser parameters include an absorbed pulse energy (E_p) of 1e-4J, a pulse duration of 1e-8s and a beam radius of 5e-4m, with no gain applied to the recorded data.
Once collected, the data is normalized using Z-Score normalization [9], a statistical method that standardizes the scale of different variables by transforming the data to be normally distributed, which often leads to improved performance in machine learning algorithms. Each waveform in the dataset is transformed using the formula:

$$z = \frac{(x - \mu)}{\sigma} \tag{1}$$

where x is the original value, μ the mean of the waveform and σ its standard deviation.
Once normalized, the waveforms are associated with a categorical vector (*label*), randomly shuffled, and placed in indexed data containers. This process is repeated for each combination of plate type and UGW propagation direction, after which all sub-datasets are merged into the final dataset and then randomly shuffled.

3. Description of the 1D Convolutional Neural Network

CNNs typically consist of input, hidden, and output layers. The hidden layers, where learning takes place, include a series of convolutional layers, activation layers, normalization layers, and pooling layers, culminating in a fully connected layer and a classification function that outputs probabilistic values between 0 and 1 for object classification.

A convolution layer is defined by several key parameters: i) the filter (or kernel) size, which refers to the dimensions of the filter that passes over the input to compute dot products and extract features to produce a feature map; ii) the number of filters that pass over the input; iii) the stride, or the number of positions the filter moves as it passes over the input; and iv) the padding, which involves adding zeros (or using other techniques) to adjust the spatial dimensions of the output feature map produced by the convolution. The activation layer introduces non-linearities, enabling the network to learn complex patterns. The normalization layer standardizes network inputs or normalizes previous layer activations, enhancing training efficiency and stability. The pooling layer reduces computational demands by down-sampling, thus reducing the number of parameters. A fully connected layer learns non-linear combinations of high-level features, with each neuron connected to those in the previous layer to effectively integrate learned features for the final output. Finally, the classification function maps the processed inputs to predicted class labels, completing the model's learning process.

The model for this study is implemented in MATLAB® (R2024a). It features a 1D-CNN architecture consisting of two convolution blocks, each containing a 1D convolutional layer, an activation layer, and normalization layers. These are followed by a Global Average Pooling layer and a Fully Connected layer linked to a Classification Function. This architecture, which was refined after experimenting with different layer configurations, uses a shallow design. While this design minimizes computational demands and reduces the risk of overfitting, it may slightly compromise accuracy compared to deeper models.

The model processes time-series data from the Training Dataset, which includes 638820 waveforms, each with 1000 data points across a single channel. The first 1D-Convolution layer employs 32 size-5 filters that passes over the input with a stride of 1 and 'causal' padding, transforming the input into a 1000x32 feature map. This layer is followed by ReLU activation and layer normalization, chosen for its efficiency in handling non-linearities and its suitability for small batch sizes. A subsequent convolution block applies 64 filters of the same size and stride, enhancing the data into a 1000x64 feature map, also followed by ReLU activation and layer normalization. Following the convolutional blocks, a global average pooling layer reduces each feature dimension from 1000 to 1, condensing the feature map to a 1x64 representation. This condensed feature representation is then fed into a fully connected layer, which reduces the dimensionality to 12. The final output layer uses a Softmax activation function in the fully connected layer to classify the outputs into different classes, ensuring that the sum of the output probabilities is equal to 1. Figure 2 shows a schematic of the implemented 1-D CNN architecture.

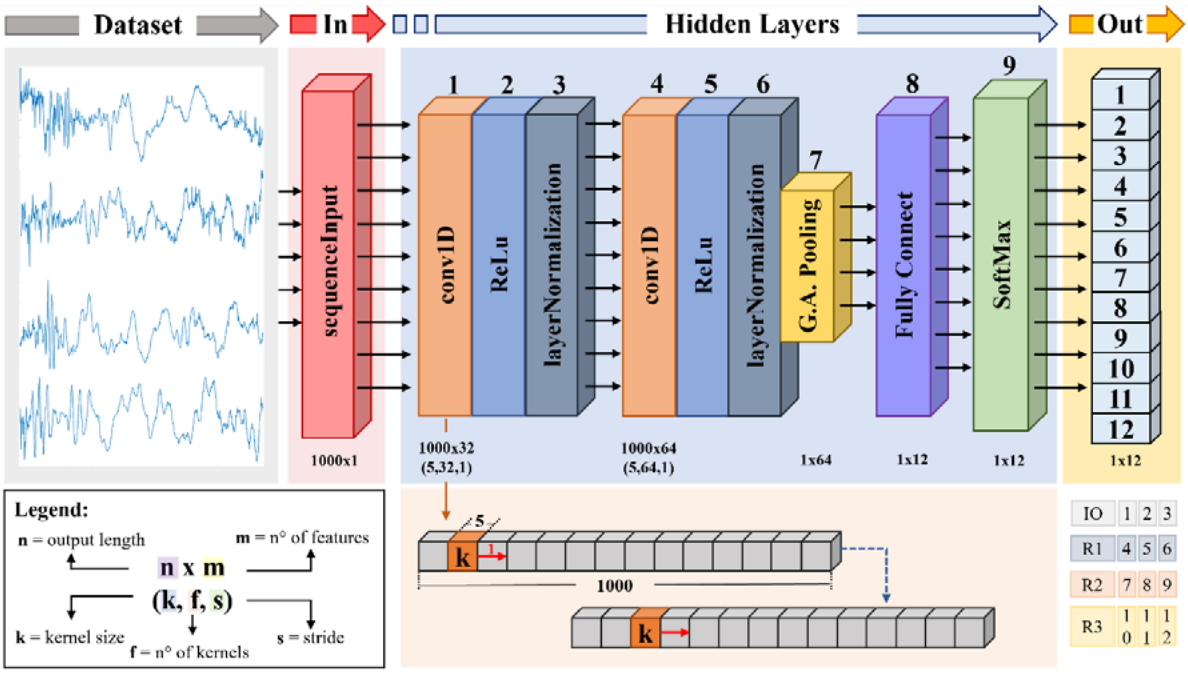


Figure 2. Architecture of the implemented 1D-CNN.

The model underwent training on an Intel(R) Xeon(R) W-2265 CPU with a dataset split of 70% training, 20% validation, and 10% testing. The training configuration for this study uses the Adam (Adaptive Moment Estimation) optimizer, which is known for its efficient handling of sparse gradients and adaptive learning rate capabilities that enhance convergence speed. The training is designed to run for a maximum of 10 epochs to balance computational efficiency with adequate exposure to the training data. The initial learning rate is set at 0.01 to foster rapid convergence without the risk of early overshooting of minima. 'Accuracy' is the primary metric monitored during training and serves as a quantitative measure of the model's performance in correctly predicting labels. Figure 3 illustrates the statistical variation in training accuracy over the 10 epochs.

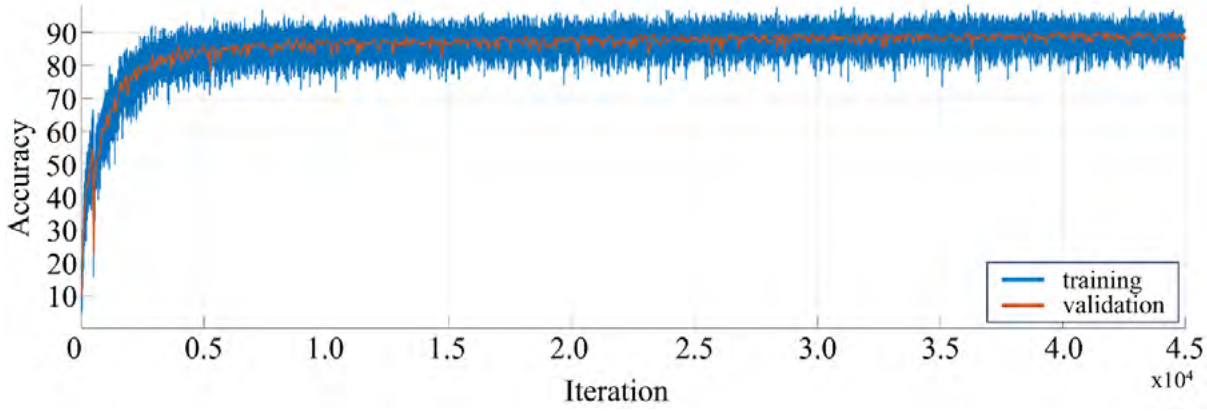


Figure 3. Accuracy evolution during training for a total of 10 epochs and 45000 iterations.

4 Results and discussion

After training is completed using the Training Dataset (70% of the total) and the Validation Dataset (20% of the total), the model's effectiveness is evaluated using the Test Dataset, which comprises the remaining 10% of the collected data. This testing phase is crucial as it assesses the general ability of the model to ensure a high level of performance on new, unseen data, thus confirming its robustness and applicability to real-world scenarios.

4.1. Confusion Matrix

The Confusion Matrix (CM) is a key tool used in predictive analytics to visualize and assess the performance of classification models, such as the 1D-CNN developed in this study.

Presented in a tabular format, the CM contrasts true class labels with predicted ones, clearly distinguishing correct from incorrect predictions. Each row of the matrix corresponds to instances of a True Class, and each column to instances of a Predicted Class. Correct predictions are shown along the diagonal, where the predicted classes match with the true classes. Conversely, off-diagonal elements highlight errors, indicating where the model confuses one class with another.

To effectively interpret a CM, the concepts of True Positive (TP), where the model correctly predicts the positive class; True Negative (TN), where it correctly identifies the negative class; False Positive (FP), where it incorrectly predicts the positive class; and False Negative (FN), where it fails to identify the positive class, are introduced.

Figure 4 displays the CM for the model predictions. The left vertical axis lists the True Classes from IO to R3, while the bottom horizontal axis shows the Predicted Classes. Errors (FN) are shown in off-diagonal row elements, with the Recall, ratio of TP to total elements per class (TP+FN), noted at the end of the row. Similarly, off-diagonal column elements show errors (FP), with the Precision, ratio of TP to total column elements (TP+FP), indicated at the bottom of each column.

Significantly, plates R1 and R3 in the PA direction were frequently misclassified, resulting in Recall and Precision rates of 73.5% and 70.5% for R1, and 68.0% and 71.2% for R3, respectively. Conversely, for the same plates in the PC direction, both Recall and Precision were consistently high, with R1

achieving 97.0% and 93.6%, and R3 scoring 95.3% and 97.2%, respectively.

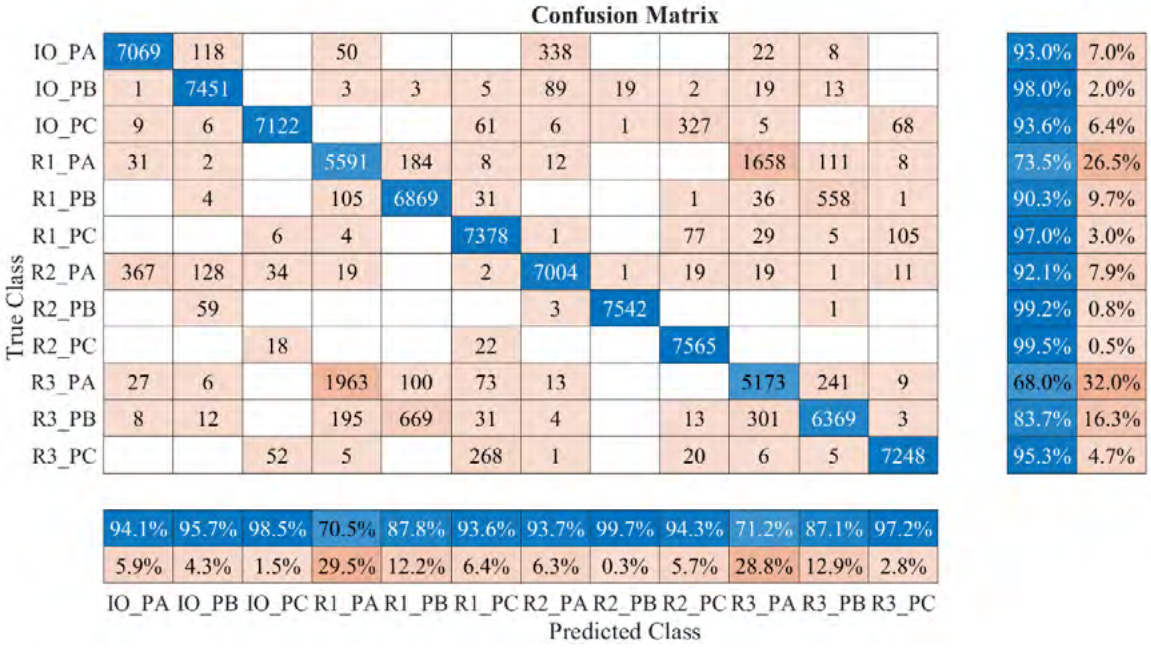


Figure 4. Confusion Matrix displaying the classification results for each class under UGW-based 1D-CNN analysis. The matrix illustrates the true class labels (rows) vs. the predicted class labels (columns). Each cell shows the count of predictions, with diagonal cells indicating correct classifications. The right and bottom margins show the Recall and Precision percentages for each class, respectively.

4.2. Evaluation Metrics

Having defined the key concepts of True Positive (TP), True Negative (TN), False Positive (FP), and False Negative (FN), the performance of the 1D-CNN architecture was evaluated using the following metrics:

i. Precision (P) is the ratio of correct positive predictions to the total predicted positives, calculated as:

$$P = \frac{TP}{TP + FP} \tag{2}$$

ii. Recall (R) measures the proportion of actual positives correctly identified by the model, given by:

$$R = \frac{TP}{TP + FN} \tag{3}$$

iii. F1-Score (F) is a statistical measure used to evaluate the accuracy of a test by calculating the harmonic mean of precision and recall.

$$F = \frac{2 \cdot P \cdot R}{P + R} \tag{4}$$

Precision (P), Recall (R), and F1-Score (F) metrics, estimated for each class in the confusion matrix, are analyzed by grouping the average results per plate type (Figure 5a) and UGW propagation direction (Figure 5b) to gain deeper insights. The performance analysis reveals that the intact IO plate and the R2 plate, with delamination close to the inspected surface at z=0.84 mm, give superior results with average scores of 96.1% and 96.4%, respectively. Conversely, the R1 and R3 plates, which have deeper

delamination at z=0.56 mm and z=0.28 mm, respectively, have lower scores of 85.4% and 83.7%. These results suggest that the absorbed pulse energy (Ep) of the laser used in the study results in reduced UGW excitation effectiveness for deeper delamination. Frequent misclassifications between R1 and R3, as observed in Figure 4, are likely due to their similar waveform characteristics resulting from the greater delamination depth.

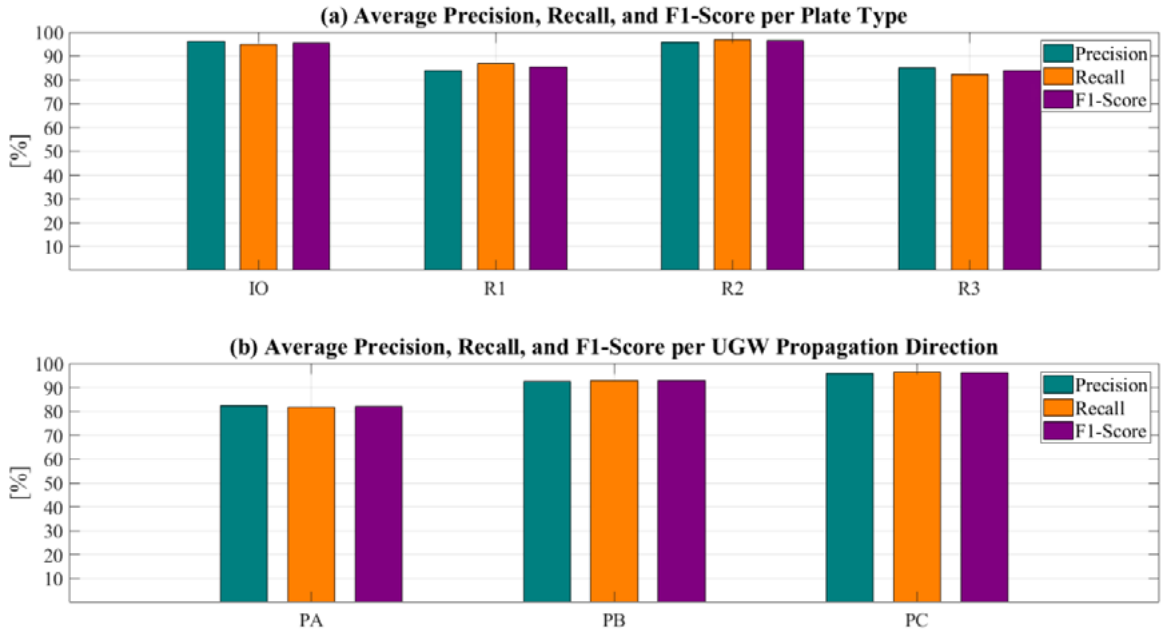


Figure 5. Comparative analysis of 1D-CNN metrics: Average Precision (teal), Recall (orange), and F1-Score (purple) (a) for four types of CFRP laminate plates: IO, R1, R2, and R3; (b) for three UGW propagation directions: PA (0°), PB (45°), and PC (90°). Each bar represents the average percentage of these metrics computed across all tests.

When analyzing model performance in relation to the direction of UGW propagation (Figure 5b), the scores show a significant dependence on the direction of wave propagation. For PA, where the waves propagate at 0° and perpendicular to the fiber direction of the top ply, the average score for all metrics is 82%. For PB, at 45°, this rises to 92.7%. It is noteworthy that for PC, where the wave propagation is 90°, parallel to the fiber orientation, the score peaks at 96.12%. This result indicates that the UGW is highly effective when the wave propagation direction is parallel to the fiber direction of the top ply illuminated by the laser, irrespective of the delamination depth.

5. Conclusions

This study demonstrates the effectiveness of a UGW-based 1D-CNN as a diagnostic tool for the detection and classification of delamination in cross-ply CFRP laminates. The research involved an extensive experimental campaign using an undamaged specimen and three damaged laminates, representing 12 classification classes. UGW waveforms for different damage scenarios and propagation directions were collected using a laser ultrasonic visualization inspector (LUVI-CP1) and a broadband piezoelectric transducer, resulting in a dataset of over 900000 waveforms. This dataset was pre-processed using Z-Score Normalization.

The dataset was then divided using a 70-20-10 split to ensure an equal representation of each class in each segment. A shallow 1D-CNN, consisting of two one-dimensional convolutional blocks and one fully connected layer, was designed to minimize computational effort while maintaining good model generalization. The model, which used “accuracy” as a training metric, was trained over 10 epochs and achieved an overall average accuracy of 90.27%.

Detailed performance analysis showed that the Recall for 9 out of 12 classes exceeded 90%, with 5 classes above 95%. Similarly, the Precision for 8 out of 12 classes was over 90%, with 5 classes above

95%. Data analysis by plate type revealed frequent misclassification between plates with deeper delamination (R1 and R3), probably due to insufficient laser energy to effectively excite deeper delamination. However, when considering the direction of wave propagation, it was observed that misclassifications occurred mainly when waves propagated perpendicular to the fiber direction of the top ply (PA). In contrast, for directions parallel to the fiber orientation (PC), both Recall and Precision were significantly high, reaching 97.0% and 93.6% for R1, and 95.3% and 97.2% for R3 respectively. In conclusion, the proposed 1D-CNN model accurately classifies UGW signals from damaged CFRP laminates using a shallow, efficiently implemented architecture.

References

[1] D. D. L. Chung, Introduction to Carbon Composites, in *Carbon Composites*, Elsevier, pp. 88–160, 2017 (doi: 10.1016/B978-0-12-804459-9.00002-6).

[2] R. Talreja, Manufacturing defects in composites and their effects on performance, in *Polymer Composites in the Aerospace Industry*, Elsevier, pp. 99–113, 2015 (doi: 10.1016/B978-0-85709-523-7.00005-0).

[3] G. Zhao, B. Wang, T. Wang, W. Hao, and Y. Luo, Detection and monitoring of delamination in composite laminates using ultrasonic guided wave, *Composite Structures*, 225, p. 111161, 2019 (doi: 10.1016/j.compstruct.2019.111161).

[4] F. Ricci, E. Monaco, N. D. Boffa, L. Maio, and V. Memmolo, Guided waves for structural health monitoring in composites: A review and implementation strategies, *Progress in Aerospace Sciences*, 129, p. 100790, 2022 (doi: 10.1016/j.paerosci.2021.100790).

[5] S. Kiranyaz, O. Avci, O. Abdeljaber, T. Ince, M. Gabbouj, and D. J. Inman, 1D convolutional neural networks and applications: A survey, *Mechanical Systems and Signal Processing*, 151, p. 107398, 2021 (doi: 10.1016/j.ymssp.2020.107398).

[6] P. Pandey, A. Rai, and M. Mitra, Explainable 1-D convolutional neural network for damage detection using Lamb wave, *Mechanical Systems and Signal Processing*, 164, p. 108220, 2022 (doi: 10.1016/j.ymssp.2021.108220).

[7] A. Rai and M. Mitra, Lamb wave based damage detection in metallic plates using multi-headed 1-dimensional convolutional neural network, *Smart Materials and Structures*, 30(3), p. 035010, 2021 (doi: 10.1088/1361-665X/abdd00).

[8] Inc. Toray Industries, Toray T700SC/2500 Technical Data Sheet, Aug. 03, 2021. https://www.cf-composites.toray/resources/data_sheets/pdf/datasheets_2500.pdf (accessed Oct. 30, 2023).

[9] N. Fei, Y. Gao, Z. Lu, and T. Xiang, Z-Score Normalization, Hubness, and Few-Shot Learning, in *2021 IEEE/CVF International Conference on Computer Vision (ICCV)*, IEEE, pp. 142–151, 2021 (doi: 10.1109/ICCV48922.2021.00021).

MODELLING COUPONS AT DOME AREA OF COMPOSITE PRESSURE VESSELS: FROM A 2D-SHELL TO A 3D-SOLID FORMULATION, WITH COMPARISON TO TEST RESULTS

M. Bruyneel[*,$], A. Rajaneesh[*], T. Watanabe[#], Y. Urushiyama[#], Y. Tsuchiyama[#]

*GDTech, Avenenue de l'Expansion 7, B-4431 Alleur, Belgium
$ University of Liège, Belgium
e-mail: michael.bruyneel@gdtech.eu, web page: www.gdtech.eu
Honda R&D Co., Ltd. Innovative Research Excellence
4630 Shimotakanezawa, Haga-machi, Haga-gun, Tochigi, 321-3393 Japan
web page: https://www.honda.co.jp/RandD/hgrx/

Keywords: pressure vessel, hydrogen, modeling, failure analysis

Abstract
This paper describes a methodology developed to accurately model the material properties in the dome area of composite overwrapped pressure vessels (COPV). First, a COPV is produced on a hexagonal-shaped so-called "soccer ball" mandrel, which has cleverly-designed flat faces in the dome and in the cylindrical regions. Coupons with specific dimensions and stacking sequences are extracted from the cylindrical region of the COPV and are tested, in order to identify the parameters of an advanced intra-laminar damage model for orthotropic plies. Coupons in the dome area are then extracted in longitudinal and circumferential directions. These coupons are flat on one side (the one in contact with the mandrel), and non-flat on the other side. They present a (complex) variable thickness pattern. Starting from a shell model of the coupons developed in a previous paper, a 3D solid-elements model is here developed, in which each layer is represented with its geometrical thickness. We then come up with a 3D model with variable thickness that represents the interlacements of the tapes resulting from the filament winding process. Four-point bending physical tests are conducted on the coupons, and the corresponding FEM simulations are performed. A good agreement is obtained between simulations and tests in terms of stiffness and strength.

1. Introduction

We are in the context of the analysis of carbon fiber reinforced plastics (CFRP) high-pressure vessel (COPV - Composite Overwrapped Pressure Vessel) of type 4, manufactured by filament winding (FW).

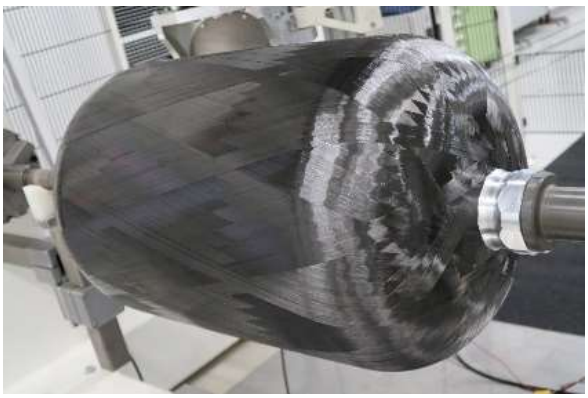


Figure 1. COPV produced by filament winding.

As it is the case for aerospace and automotive applications, efficient design and sizing of COPV must rely on advanced FEM modeling and simulation, on top of physical testing. There is therefore a need for accurate failure analysis in the context of COPV. Classically, the parameters of material models are identified based on flat UD-laminate coupons with specific predetermined fiber orientations (e.g. 0°, 90°, +45°), and based on standards like the ones of ASTM relevant for flat coupons made of UD plies. CFRP manufactured by FW has a unique and complex laminate structure, which presents curvatures, ply interlacements and variable thickness, that make testing and modeling difficult tasks. However, in practice, it is important to use coupons produced with the final manufacturing process for the parameter identification of the material models; if classical coupons produced by e.g. ply lamination are used, the effect of FW structure cannot be accounted for, and cannot be introduced in the material models. In [1], an efficient approach to create representative flat coupons based on the FW process is developed and explained. Flat coupons are created in the cylindrical part of the COPV, as well as in the dome area.



Figure 2. Specific mandrel with flat faces: detail of the filament winding process and tape interlacement at the dome area

In the philosophy of the pyramid of tests, coupons extracted from the cylindrical part are used to characterize the composite material and to determine the parameters of the material model, while coupons coming from the dome area are useful to validate the model and to better understand the damage mechanisms and strength of the material in the dome area, where variable thickness and complex interlacements of the tapes resulting from the filament winding process are present.

2. Material characterization and calibration of the intra-laminar material model

The flat coupons extracted fom the cylindrical part are used to determine the parameters of an advanced material model including non linear behavior and damage propagation [2]. That material model, which is an extension of the Ladeveze CDM model for UD plies [3], is implemented in LS-Dyna via user routines. Standard (ASTM-like) testing (tension, compression, …) is conducted, with cyclic loading when necessary. Next Figure illustrates some results of the parameter identification process (calibration of the material model).

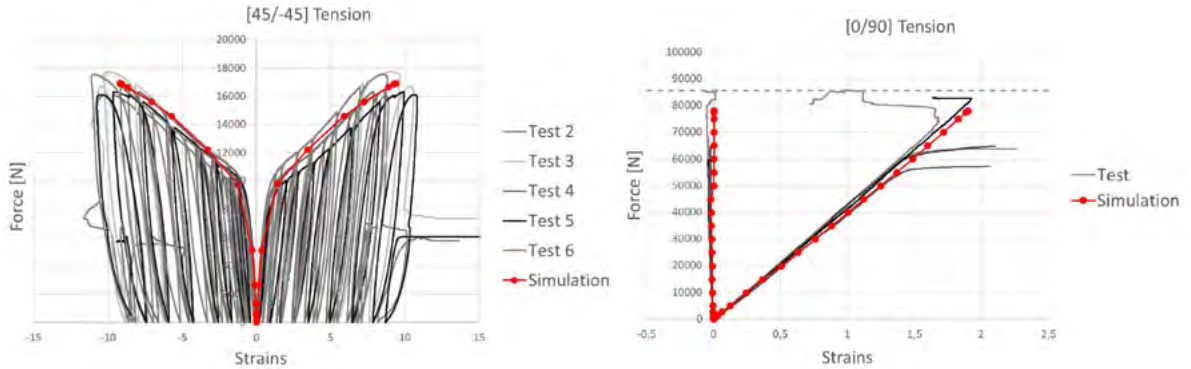


Figure 3. Comparison between test and simulation for the material model parameters identification

3. Modeling methodology of coupons at dome area

3.1. 2D-shell models

In [4], a specific numerical procedure is set up in order to model coupons in the dome area of a COPV. Coupons in the longitudinal and circumferential directions are considered. For modeling, first the tape pattern from the filament winding process is reproduced, and groups of finite elements are defined. The local fiber orientations are then assigned to each group of elements. 2D-multi-layer shell elements are used.

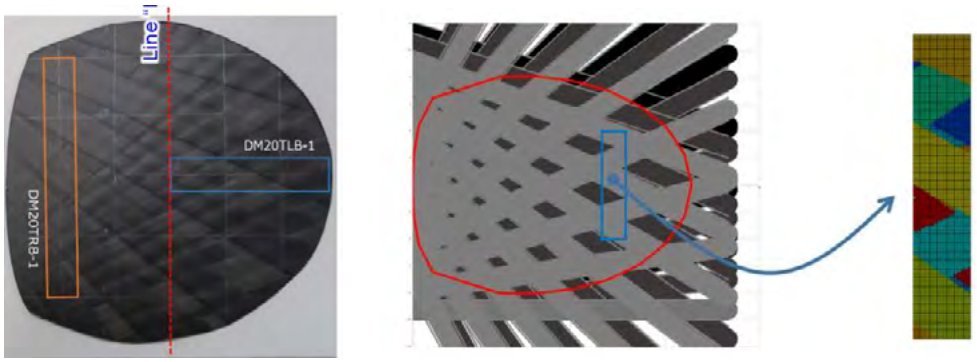


Figure 4. Flat part at the dome area, with indication of locations of longitudinal and circumferential coupons ; complex interlacement of tapes at the dome area of a COPV, and creation of a 2D-shell elements model of a circumferential coupon

3.2. Extension to 3D-solid elements models

Shell models of the previous section are now inflated, in order to create full 3D models built with solid elements. The geometric thickness can now be observed in the finite element model. A typical mesh is illustrated in the Figure below. The material model with parameters identified in Section 2 is assigned to each element, with local fiber orientations coherent with what was defined in the 2D-shell model.



Figure 5. 3D – solid elements FEM model of a coupon at the dome area of a COPV

3.3. Extension to 3D-solid elements models: comparison between tests and simulation

Four-points bending tests are conducted on coupons extracted in the longitudinal and circumferential directions (see Figures 4 and 6). It can be seen in the Figures below that depending on the orientation mechanical responses are very different, bending for circumferential coupons leading to very large dispalcements. We note a good agreement between tests and simulation, as shown in Figure 7 where force-displacement curves are compared.



Figure 6. Physical testing on coupons extracted from the dome area (left: longitudinal direction; right: circumferential direction)

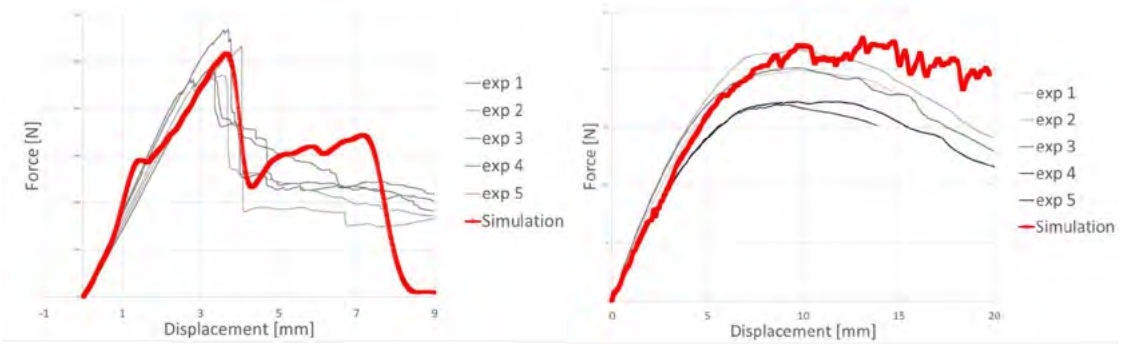


Figure 7. Comparison between test and simulation for 3D – solid elements FEM model of a coupon at the dome area of a COPV (left: longitudinal direction; right: circumferential direction)

4. Conclusions

In this paper, we derived an efficient modeling methodology for coupons extracted from the dome area of a composite pressure vessel. The models are based on 3D-solid elements meshes. Experimental and numerical results are compared for four-points bending ; a good agreement is observed in terms of stiffness and strength.

Acknowledgments

The material model used in this paper was developed during the research projects BEWARE CIS-IN (convention n°1510644) and WINGS (convention n°8441). Marie Curie program, SPW and Skywin are gratefully acknowledged

References

[1] Watanabe T., Urushiyama Y., Tsuchiyama Y., Bruyneel M. (2024). New solution for material damage characterization of CFRP laminate with filament winding structure using a hexagonal-shaped mandrel, SAE World Congress, Detroit, MI, April 2024

[2] Rajaneesh A., Bruyneel M. (2023). Low-velocity impact and compression after impact modeling of composites using modified mesoscale model. Composite Structures, 311, 116821.

[3] Ladeveze P., Le Dantec S. (1992). Damage modeling of the elementary ply for laminated composites, Composites Science and Technology, 43: 123-134, 1992.

[4] Bruyneel M., Rajaneesh A., Watanabe T., Urushiyama Y., Tsuchiyama Y. (2023). Validation of composite pressure vessels modelling methodology using 2D-shell elements at coupon level. ECCOMAS Thematic Conference on Mechanical response of Composites, September 12-14, Trapani, Sicily, Italy.

MECHANISM-BASED MODELLING OF THE VISCOELASTIC RESPONSE OF A UNIDIRECTIONAL COMPOSITE PLY: VALIDATION OF A NEW TRANSVERSELY ISOTROPIC MODEL THROUGH ANALYTICAL AND NUMERICAL HOMOGENISATION

Federica Daghia[1], Alexandre Lagache[2] and Livio Di Gennaro[3]

[1]Université Paris-Saclay, CentraleSupélec, ENS Paris-Saclay, CNRS, LMPS – Laboratoire de Mécanique Paris-Saclay, 4 avenue des Sciences, 91190 Gif-sur-Yvette, France
Email: federica.daghia@ens-paris-saclay.fr, Web Page: https://lmps.ens-paris-saclay.fr
[2]Arts et Métiers, Institut de Biomécanique Humaine Georges Charpak,
151 boulevard de l'Hôpital, 75013 Paris, France
Email: alexandrelagache@ensam.eu, Web Page: https://biomecanique.ensam.eu/
[3]DES Composites Ltd, United Kingdom
Email: livio.digennaro@descomposites.co.uk, Web Page: https://www.descomposites.com/

Keywords: viscoelasticity, transverse isotropy, homogenisation

Abstract
The viscoelastic response of long fibres, polymer matrix composites is mainly due to the deviatoric response of the matrix. This single microscale mechanism, however, results in different amount of viscous relaxation for the elastic constants defining the transversely isotropic behaviour at the scale of the composite ply. In a recent work, some of the authors proposed a reformulation of transverse isotropy based on the Cartan decomposition. This geometrical formulation of the constitutive law leads to a set of five elastic parameters which is different from those commonly used in the formulation of constitutive laws, but which is easier to relate to the underlying constituents. In particular, only two of the parameters are significanly affected by the deviatoric response of the matrix, thus largely simplifying the formulation of the viscoelastic constitutive behaviour at the composite scale. Analytical and numerical homogenisation procedures are used to evaluate the pertinence of the proposed model.

1. Introduction

The constitutive behaviour of a composite depends on the behaviours and on the arrangement of its elementary constituents. For long fibres, polymer matric composites, the fibres response can be considered elastic in a large range of temperatures, while the matrix has a viscoelastic response, especially involving its deviatoric part [1]. At the scale of the composite ply, on the other hand, the constitutive response can be considered as transversely isotropic, defined by five independent elastic parameters. The single relaxation mechanism at the microscale can potentially affect all of these elastic parameters, thus leading to the demultiplication of the viscous relaxation functions which need to be identified at the composite scale (see for example [2]).

In a recent work [3], some of the authors proposed a reformulation of transverse isotropy based on group representation theory, and in particular on an irreducible decomposition of the stress (resp. strain) tensors, also known as the Cartan decomposition. Such reformulation gives rise to a set of five elastic constants which is different from those commonly used in transverse isotropy, but it is easier to relate to the behaviour of the underlying constituents. In particular, the viscoelastic response was assumed to

affect only the longitudinal and transverse shear moduli, thus simplifying its description. The key points of the proposed formulation are recalled in Section 2 of the paper.

The assumptions introduced in [3] were challenged through analytical and numerical homogenisation in a follow-up work [4]. In particular, analytical results derived by Hashin [5] with a cylindrical model enabled us to formulate the five elastic constants of the composite as a function of the constituents' properties and volume fraction. Based on these formulas, presented in Section 3, the matrix shear modulus affects all of the five parameters for transverse isotropy, but only two of them go to zero when the matrix shear modulus goes to zero. This shows that the assumptions made in [3] are indeed an approximation of the viscoelastic behaviour of the composite, but that only a small error is introduced when typical behaviours for carbon fibres and polymer matrix are assumed. Finally, Section 4 shows some numerical homogenisation results, using periodic boundary conditions on a Representative Volume Element (RVE). In particular, relaxation tests are used for identification of the elastic and viscoelastic parts of the homogenised composite behaviour, while creep tests are used to compare the RVE response to the one of the homogenised model. The presented work confirms that the key features of the RVE response can be captured by the new transversely isotropic model based on Cartan decomposition.

2. Tranversely isotropic model based on Cartan decomposition

The new transversely isotropic model is recalled below. For details on its derivation, see [3].

The Cartan decomposition of the stress (resp. strain) tensor is given as

$$\boldsymbol{\sigma} = s_f \boldsymbol{M}_f + s_h \boldsymbol{M}_h + \boldsymbol{s}_{fs} + \boldsymbol{s}_d, \tag{1}$$

where $s_f \boldsymbol{M}_f$ is the stress in the fibres' direction, $\boldsymbol{s}_{fs}$ are the shear components involving the fibres' direction, $s_h \boldsymbol{M}_h$ and $\boldsymbol{s}_d$ are the hydrostatic and deviatoric components in the transverse isotropy plane, and $\boldsymbol{M}.$ are unit second order tensors. Based on this decomposition, a minimal integrity basis is constructed and used to formulate a Gibbs free energy for linear elasticity. This yields the following constitutive laws

$$\begin{bmatrix} e_f \\ e_h \end{bmatrix} = \begin{bmatrix} S_F & S_{FH} \\ S_{FH} & S_H \end{bmatrix} \begin{bmatrix} s_f \\ s_h \end{bmatrix}, \qquad \boldsymbol{e}_{fs} = S_{FS} \boldsymbol{s}_{fs}, \qquad \boldsymbol{e}_d = S_D \boldsymbol{s}_d, \tag{2}$$

where the new set of elastic constants $(S_F, S_{FH}, S_H, S_{FS}, S_D)$ can be related to the longitudinal and transverse Young's moduli E_L and E_T, the in plane Poisson's coefficient υ_{LT} and the longitudinal and transverse shear moduli μ_L and μ_T as follows

$$S_F = \frac{1}{E_L}, \qquad S_{FH} = -\frac{\sqrt{2}\upsilon_{LT}}{E_L}, \qquad S_H = \frac{2}{E_T} - \frac{1}{2\mu_T}, \qquad S_{FS} = \frac{1}{2\mu_L}, \qquad S_D = \frac{1}{2\mu_T}. \tag{3}$$

In [3], the terms (S_F, S_{FH}, S_H) are considered to be controlled essentially by the fibres' behaviour, as well as by the matrix's bulk response, thus they are considered elastic, while (S_{FS}, S_D) are considered to be affected by the matrix's deviatoric response, and thus they are considered as viscoelastic. This assumption is obviously an approximation of the real composite response. The quality of the approximation is evaluated through analytical and numerical homogenisation techniques.

3. Analytical homogenisation results

Analytical homogenisation results enabling to relate the constituents' properties and volume fractions to the elastic and viscoelastic response of transversely isotropic composites were derived by Hashin through a cylindrical model [5]. These results enable us to obtain a first evaluation of the pertinent of the assumption introduced in [3].

The results, discussed in more details in [4], show that the new elastic constants defined in [3] can be separated into two groups, depending on their behaviour as the matrix's shear modulus $\mu_m \to 0$:

- $(S_{FS}, S_D) \to \infty$, no stiffness remains;
- (S_F, S_{FH}, S_H) retain a finite value, and thus a finite stiffness remains.

This shows that the two sets of elastic parameters distinguished in [3] have fundamentally different dependence on the matrix shear modulus, and they are thus differently affected by its viscoelastic response.

A more quantitative evaluation can be obtained by computing the values of the different elastic constants as μ_m varies, for typical carbon fibres, polymer matrix composites properties. The results are depicted in Figure 1. Due to the significant stiffness gap (around 2 orders of magnitude) between the fibres and the matrix, the longitudinal response S_F is essentially unaffected by the matrix shear modulus. The terms S_{FH} and S_H, related respectively to the Poisson's effect coupling the fibres to the isotropy plane and to the hydrostatic response in the isotropy plane, are affected to some extent, but they retain 80-90% of their original stiffness when $\mu_m \to 0$. Therefore, neglecting this effect seems to give a reasonable approximation of the transversely isotropic composite response.

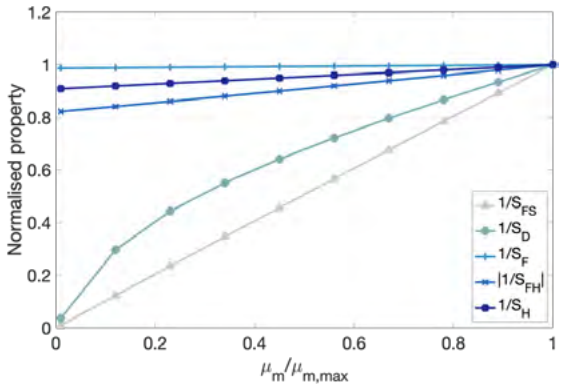


Figure 1. Normalised composite parameters for decreasing normalized matrix shear modulus (initial set of parameters from [6]: $E_f = 248$ GPa, $\upsilon_f = 0.2, E_m = 3.24$ GPa, $\upsilon_m = 0.4$, $\upsilon_f = 0.5$) – from [4]

4. Numerical homogenisation results

Numerical homogenisation can also be used to obtain the composite's properties based on its constituents' properties and microstructure. Here, a periodic homogenisation approach was used, enabling us to impose, for each component, the macroscopic stress Σ_{ij} or strain E_{ij} as a function of time. More specifically, three types of tests were simulated:

- relaxation tests ($E_{ij}(t) = 0.01$, other components = 0) to obtain the full relaxation response of the composite and identify the new composite model parameters;
- uniaxial creep tests at different loading angles ($\boldsymbol{\Sigma}(t) = 100\boldsymbol{e}_x \otimes \boldsymbol{e}_x$ MPa, with $\boldsymbol{e}_x \cdot \boldsymbol{e}_f = cos\theta$) to compare the response of the RVE to the one of the new composite model;
- a constrained creep test, where the stress is imposed in the transverse direction of the composite ($\Sigma_{xx}(t) = 100$ MPa with $\boldsymbol{e}_x \cdot \boldsymbol{e}_f = 0$), but the other normal strain components are blocked ($E_{yy}(t) = E_{zz}(t) = 0$); this last test is designed to test the limits of the proposed model by

highlighting the role of the terms S_{FH} and S_H, which are the ones for which the retained approximation is the least valid.

A periodic RVE extracted from a hexagonal fibres arrangement was used for the simulations. The finite element computations were carried out in Abaqus, using a in-house Python script to couple the corresponding nodes and introduce the additional constraint equations associated to periodic boundary conditions. The elastic properties of the constituents are the same as those used for analytical homogenisation (see caption of Figure 1), while a generalised Maxwell model is used to describe the matrix viscoelastic deviatoric behaviour, with three Maxwell elements having the following values of (τ_i, μ_i): (1 s,$0.1\mu_{inst}$), (10 s,$0.2\mu_{inst}$), (100 s,$0.2\mu_{inst}$). More details can be found in [4].

The results of the relaxation tests are depicted in Figure 2. The initial values of the RVE response are used to identify the elastic parameters for the new composite model. Furthermore, the curves for (S_{FS}, S_D) are used to identify the associated viscoelastic relaxation parameters, supposing also a three elements generalised Maxwell model for the composite. A more general viscoelastic relaxation model could be assumed for the composite, but this was beyond the scope of this work. The list of identified parameters is reported in [4].

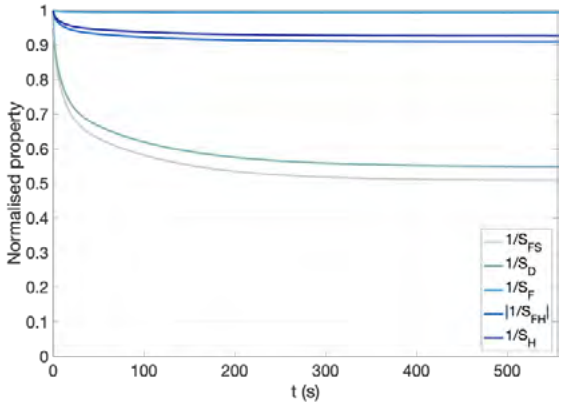


Figure 2. Normalised composite parameters as a function of time, obtained through numerical relaxation tests on the RVE – from [4]

The results of the creep tests are depicted in Figure 3. As it can be seen, the responses of the RVE and of the new composite model are nearly identical, which confirms the pertinence of the model proposed in [3].

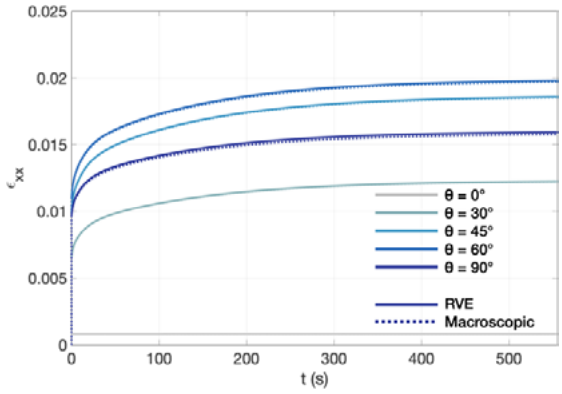


Figure 3. Strain as a function of time in the loading direction, obtained through numerical uniaxial creep tests on the RVE and on the new composite model – from [4]

Finally, the results of the constrained creep test are depicted in Figure 4. A discrepancy is observed between the RVE and the macroscopic model results, since this test is designed to excite particularly the terms S_{FH} and S_H, whose viscoelastic behaviour was neglected. Even in this unfavourable case, the maximum discrepancy between the two models amounts to 6% of the total strain in the loading direction. If this approximation is not acceptable for a given application, the composite model can be enriched by including viscoelastic relaxation for these terms, resulting in a more complex composite model.

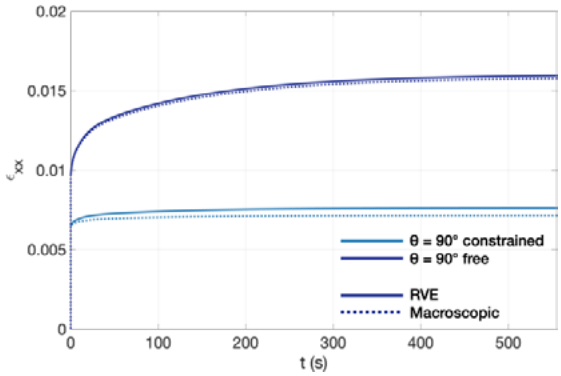


Figure 4. Strain as a function of time in the loading direction, obtained through free and constrained numerical creep tests on the RVE and on the new composite model – from [4]

5. Conclusions and perspectives

This work summarised the results presented in [3,4] on the viscoelastic modelling of transversely isotropic composites based on a Cartan decomposition. The new elastic parameters defined in [3] are easier to relate to the underlying constituents, and supposing a viscoelastic relaxation for only two of them leads to a limited error in the overall composite response, as assessed through analytical and numerical homogenisation approaches in [4]. Perspectives of this work include the implementation of a complete identification procedure for the viscoelastic response of the composite, as well as the exploration of the Cartan decomposition interest for the modelling of other aspects of the transversely isotropic response, as other nonlinear material and geometric behaviours.

Acknowledgments
The authors would like to acknowledge Dr. Marc Olive for his key role in the geometrical formulation of the macroscopic transversely isotropic model. This work was motivated and partly funded by Cetim within the framework of the Laboratoire Commun Comp'Innov.

References

[1] R. Lakes. *Viscoelastic materials*. Cambridge University Press. 2021.
[2] M. Kaliske. A formulation of elasticity and viscoelasticity for fibre reinforced material at small and finite strains. *Computational Methods in Applied Mechanics and Engineering*, 185:225-243, 2000.
[3] L. Di Gennaro, F. Daghia, M. Olive, F. Jacquemin, D. Espinassou. A new mechanism-based temperature-dependent viscoelastic model for unidirectional polymer matrix composites based on Cartan decomposition. *European Journal of Mechanics A/Solids*, 90:104364, 2021.
[4] F. Daghia, A. Lagache, L. Di Gennaro. Validation of a new viscoelastic model for unidirectional polymer matrix composites by analytical and numerical homogenization. *European Journal of Mechanics A/Solids*, 100:104975, 2023.
[5] Z. Hashin. Complex moduli of viscoelastic composites – II. Fiber reinforced materials. *International Journal of Solids and Structures*, 6:797-807, 1970.
[6] P. K. Mallick. *Fiber-Reinforced Composites – Materials, Manufacturing and Design*. CRC Press, 2007.

SIMULATION OF TRANSVERSE CRACKING AND SUBSEQUENT ACOUSTIC EMISSION IN LAMINATES

Aurélien. Doitrand[1], Zeina. Hamam[1], Nathalie. Godin[1], Pascal. Reynaud[1], Claudio. Fusco[1], Nicolas. Carrère[2]

[1]INSA-Lyon, Universite Claude Bernard Lyon 1, CNRS, MATEIS, UMR5510, 69621 Villeurbanne, France;
Email: aurelien.doitrand@insa-lyon.fr, web page: https://cv.hal.science/aurelien-doitrand

[2] IRDL, CNRS UMR6027, 29200 Brest, France

Keywords: Acoustic emission, Numerical simulation, Carbon fiber/epoxy matrix laminates

Abstract

Transverse cracking induced acoustic emission in carbon fiber/epoxy matrix composite laminates is studied both experimentally and numerically. The influence of the type of sensor, specimen thickness and ply stacking sequence is investigated. The frequency content corresponding to the same damage mechanism differs significantly depending on the sensor and the stacking sequence. However, the frequency centroid does not depend on the ply thickness except for the inner ply crack and a sensor located close enough to the crack. Outer ply cracking exhibits signals with a low-frequency content, not depending much on the ply thickness, contrary to inner ply cracking, for which the frequency content is higher and more dependent on the ply thickness. Frequency peaks and frequency centroids obtained experimentally are well captured by numerical simulations of the transverse cracking induced acoustic emission for different ply thicknesses

1. Introduction

A main challenge in acoustic emission (AE) monitoring of damage in composite materials consists in determining a link between the AE sources (*i.e.*, the damage mechanisms) and the acquired signals. This is essential in order to set-up robust damage mechanism classification approaches [1-3]. Establishing such a correspondence is not straightforward since the AE signals acquired by the sensors are actually the result of the initial source signal that propagated within a medium and that was transformed by a sensor. The AE signals depend not only on the damage source but also on the specimen geometry, the material properties and the type of sensor and acquisition chain [4].

This work focuses on the numerical simulation of the AE due to transverse cracking in laminate composites. The objective of the work is the experimental characterization and numerical simulation of the influence of the ply thickness and stacking sequence on transverse matrix cracking induced acoustic emission. The experimental setup and the numerical models are presented in Section 2. The influence of the ply sequence and thickness on the AE is studied in Section 3.

2. Experiments and simulation setup

Transverse cracking induced acoustic emission in carbon fiber/epoxy matrix composite laminates is studied both experimentally and numerically. Monotonic tensile tests are performed on AS4 carbon fiber (60 vol.%) embedded in epoxy resin [$0_n/90_n/0_n$] or [$90_n/0_n/90_n$] laminates (n=1 or 3, one ply thickness being 0.3 mm). Four AE sensors (two sensors of two different types, namely [micro80, Mistras Group, Princeton, NJ, USA] and [picoHF, Mistras Group,Princeton, NJ, USA are fixed on the specimens to detect signals originating from damage mechanisms occurring within the composites. Each couple of sensors are placed on both sides of the specimen. For each acquired signal, both temporal and frequency descriptors are extracted from the signal and its fast Fourier transform (FFT). Floating amplitude thresholds (0.1% for the beginning and 5% for the end of the signal) are used for the signal time windowing. In addition to the experiments, finite element (FE) simulations of matrix transverse cracking in 90 deg. plies are set-up. Boundary conditions consist of prescribed displacements at the end of the specimen. The symmetry of the studied configuration enables modelling only 1/8 ([$0_n/90_n/0_n$]) or 1/4 ([$90_n/0_n/90_n$]) of the specimen (Figure 1a) and compare the AE signal characteristic to the ones measured experimentally (Figure 1b).

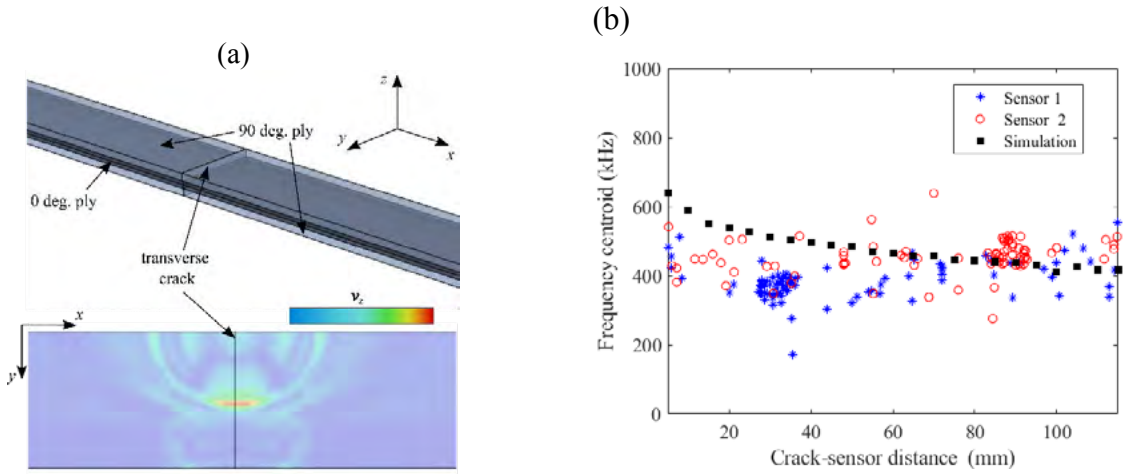


Figure 1. a) FE model of [$90_n/0_n/90_n$] laminates. Example of velocity field on the specimen surface. b) Frequency centroid variation as a function of the distance obtained numerically and experimentally.

A dynamic implicit solution is adopted in order to simulate first, transverse cracking nucleation dynamics and then acoustic wave propagation in the composite due to transverse cracking (Figure 1a). The mesh is refined in the vicinity of the transverse cracking location with at least 10 elements in one ply thickness, resulting in models containing approximately 500,000 degrees of freedom. Transverse cracking is modeled by progressively unbuttoning all the nodes along the crack surface during a given time at a loading level equal to the critical strain at first transverse cracking determined using finite fracture mechanics [5]. The maximum time step during the subsequent wave propagation is set to 10^{-7} s in order to consider a frequency range up to 1 MHz. AE signals are collected on a perfect punctual sensor at several distances from the transverse crack, from which temporal and frequency descriptors are calculated.

3. Results

We now analyze the transverse cracking induced acoustic emission with varying stacking sequence and ply thickness considering a perfect contact sensor. We study the influence of transverse cracking occurring either in inner [0n/90n/0n] (n = 1 or 3) or outer [90n/0n/90n] (n = 1 or 3) ply. Figure 2 shows the signals recorded by the sensor on the specimen surface at the transverse crack epicenter.

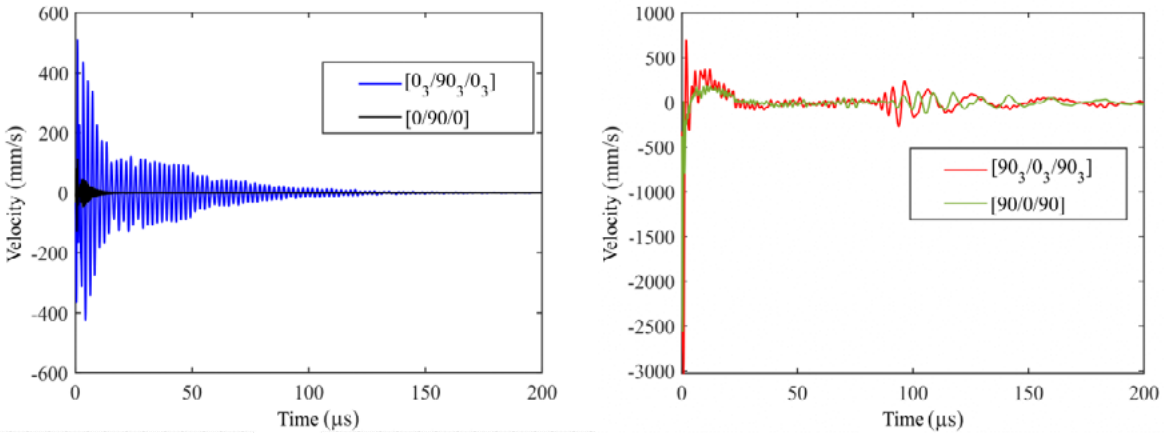


Figure 2. Acoustic emission signal obtained by a point-sensor at the crack epicenter for two ply thicknesses for a) $[0_n/90_n/0_n]$ or b) $[90_n/0_n/90_n]$ laminate.

Noticeable differences are evidenced depending on the ply thickness and transverse cracking location. This is due to the size of the initiated crack and also to the signal attenuation with propagation. Outer ply transverse cracking results in signals with a larger amplitude than inner ply transverse cracking at the crack epicenter. This is evidenced by inner ply cracking induced signals having larger amplitudes for larger plies and outer ply cracking induced signals having larger amplitudes than inner ply cracking signals. Outer ply transverse cracking induces similar signals at the crack epicenter, whatever the ply thickness (Figure 2a), whereas significantly different signals are induced by transverse cracking depending on the inner ply thickness (Figure 2b). This phenomenon may be explained by the difference in the acoustic wave propagation distance in the specimen thickness for inner ply cracking. Therefore, it is expected that the descriptors of the signals near the crack epicenter are close for outer ply cracking and different for inner ply cracking.

The same damage mechanism may result in signals exhibiting different descriptors depending on their location in the composite and on the composite stacking sequence. Frequency centroid of transverse cracking signals for the different stacking sequences and ply thicknesses are analyzed as a function of the distance between the sensor and the crack in Figure 3. Near the crack epicenter, the dependency of the frequency centroid on the ply thickness is marked for inner ply cracking and much less pronounced for outer ply cracking (Figure 3). However, far enough from the crack (distance larger than 60 mm), the same frequency centroid is retrieved whatever the ply thickness for a given stacking sequence. For any distances between the sensor and the crack, the frequency centroid magnitude is significantly different.

3. Conclusions

Experimental characterization of transverse cracking induced acoustic emission in composite laminates highlights the dependency of the AE results to the sensor type and the specimen thickness.

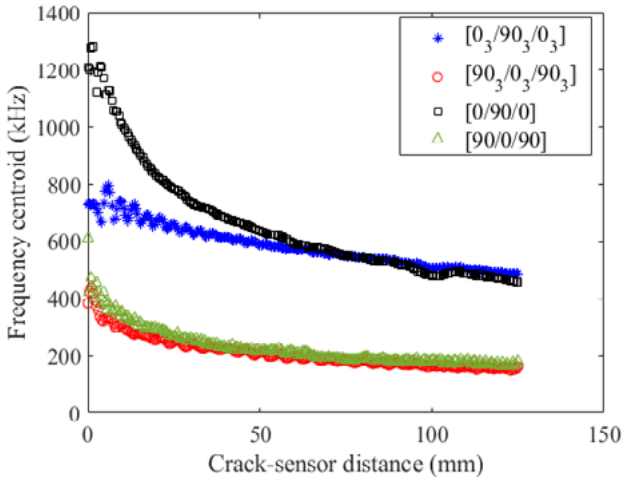


Figure 3. Frequency centroid variation as a function of the crack to sensor distance obtained for two different stacking sequences and two different ply thicknesses.

Frequency peak and frequency centroid obtained experimentally are well captured by numerical simulations of transverse cracking for different ply thicknesses. The influence of the ply thickness on acoustic emission signals recorded at the crack epicenter is significant only for inner ply transverse cracking, whereas similar signals are obtained for outer ply cracking. It thus raises the following question: should inner ply and outer ply transverse cracking should be considered as two different damage mechanisms in a classification approach? The influence of the ply thickness on AE signals (on the frequency centroid, for instance) decreases as the sensor is far from the crack; however, the influence of the stacking sequence remains, regardless of the sensor location. The frequency content of signals induced by outer ply transverse cracking does not depend on the ply thickness.

References

[1] Anastassopoulos, A.A. et al. Failure mechanism identification in composite materials by means of acoustic emission: is it possible? Non-Destructive Testing. Rotterdam : Balkema. 1996, doi: 10.1007/s10921-012-0132-1.

[2] Momon, S. et al. Unsupervised and supervised classification of AE data collected during fatigue test on CMC at high temperature. Composites part A 2012, doi : 10.1016/j.compositesa.2011.10.016.

[3] Morizet N. et al. Classification of acoustic emission signals using wavelets and Random Forests: Application to localized corrosion. Mechanical Systems and Signal Processing 2016, doi: 10.1016/j.ymssp.2015.09.025.

[4] Godin, N. et al. Challenges and Limitations in the Identification of Acoustic Emission Signature of Damage Mechanisms in Composites Materials. Applied Sciences 2018, doi:10.3390/app8081267.

[5] García, I. et al. Experimental study of the size effect on transverse cracking in cross-ply laminates and comparison with the main theoretical models. Mech. Mater. 2019, doi : 10.1016/j.mechmat.2018.09.006

THERMOMECHANICAL COUPLING DURING TENSILE TESTING OF PA6 AND SHORT FIBRE GLASS/PA6

D. Finazzi[1,2], G. Robert[3], L. Daelemans[1], K. De Clerck[1] and W. Van Paepegem[1]

[1] Department of Materials, Textiles and Chemical Engineering, Ghent University, Technologiepark 46, 9052 Zwijnaarde, Belgium
Email: daniele.finazzi@ugent.be, Web Page: https://composites.ugent.be/
[2] SIM M3 Program, Technologiepark 48, 9052 Zwijnaarde, Belgium
[3] DOMO Chemicals – PolyTechnyl SAS, Avenue Albert Ramboz, 69190 Saint Fons, France

Keywords: polyamide-6 (PA6), short fibre-reinforced composites (SFRPs), tensile tests, digital image correlation (DIC), thermomechanical coupling

Abstract
This paper studies thermomechanical coupling during room-temperature tensile testing of polyamide-6 (PA6) and short glass fibre/PA6 (50 wt%). The tests were performed for different dominant angles of the short fibres (0°, 45°, 90°), moisture contents (dry, 50%RH), and strain rates (10^{-4}, 10^{-2}, 10^{-1} s^{-1}). Digital image correlation (DIC) was coupled with infrared thermography. The contribution of the local strains, strain rates and temperatures to the global mechanical behaviour was investigated throughout deformation. The initial thermoelastic response was used to estimate the coefficient of thermal expansion. In PA6, neck development caused significant self-heating at high strain rates, differently between dry and 50%RH. In glass/PA6, however, temperature rises were always small (< +3 °C) despite local strain rate peaks in the fracture zone. This was ascribed to limited plastic deformation, as confirmed by post-mortem microscopy. The full-field data can be highly valuable for the development of advanced constitutive models for both pure polymer and short fibre composite.

1. Introduction

Short fibre-reinforced thermoplastic composites are increasingly popular in the automotive industry. Lightweight, low cost, easy processing and recyclability make them appealing as replacement for metal and thermoset-based parts. However, higher sensitivity to loading rate and environmental conditions may limit the range of applications. The material response needs to be thoroughly characterised keeping all those effects into account.

Among other thermoplastic composites, injection-moulded glass/polyamide-6 (GPA6) has found many applications in functional and structural car components. Like all polyamides, PA6 is hygroscopic: water molecules from the surroundings enter the material and break the hydrogen bonds between the chains in the amorphous phase, increasing their mobility and thus lowering the glass transition temperature (T_g). PA6 is also sensitive to the strain rate, and the rate sensitivity is temperature-dependent. All these effects are to some extent retained in the composite. The effect of moisture, temperature and strain rate on PA6 and GPA6 has been studied extensively [1–5].

Besides, the strain rate can also be related to self-heating. In polymers, work from plastic deformation is converted to heat. If heat is generated faster than can be evacuated to the surroundings, the material heats up. Due to low thermal conductivity, polymers may experience self-heating even under quasi-static loading [6,7]. In polymer composites, global failure strains are generally low, but the matrix may undergo local plastic deformation while interacting with the fibres, possibly leading to significant local

temperature rises as shown by simulations [8,9]. These effects have never been addressed in monotonic tensile testing of PA6 and GPA6.

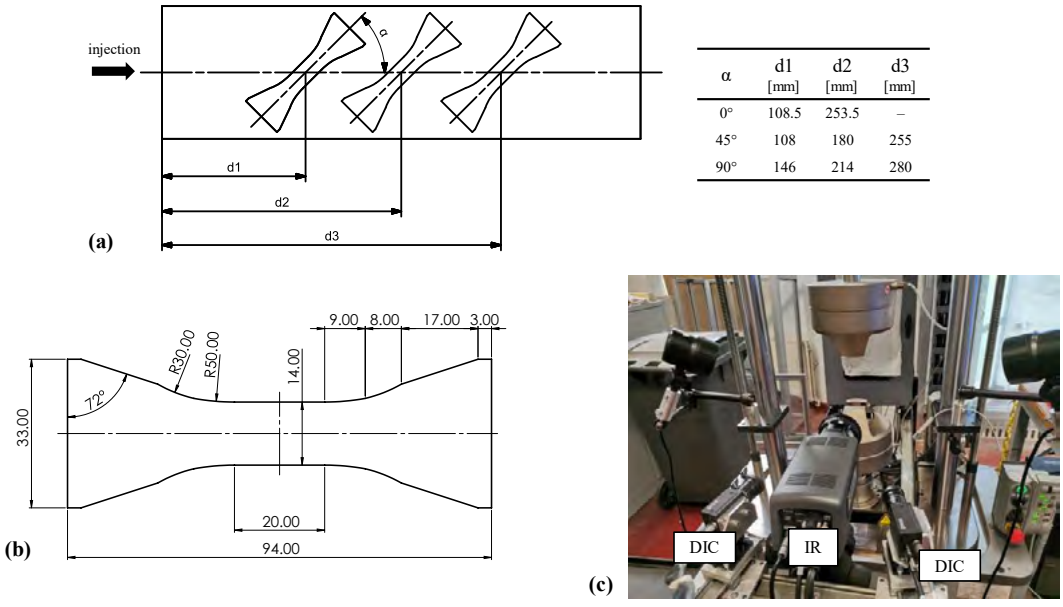
The aim of this work is to look into thermomechanical coupling and self-heating during monotonic tensile testing at room temperature of PA6 and GPA6. The influence of fibre orientation and moisture content was investigated at different strain rates. A dedicated setup with digital image correlation (DIC) and infrared (IR) thermography was used for synchronised, full-field measurement of strains and temperatures, to gain insight into thermomechanical coupling on both a local and global level. The results presented in this paper are included in [10].

2. Material and methods

The PA6 and GPA6 in this work were supplied by DOMO Chemicals – PolyTechnyl SAS (France) as injection-moulded plates with size 360 x 100 x 3 mm^3. The GPA6 grade had a high glass fibre content of 50 wt%. Dogbone specimens for tensile tests were machined from the plates, at different angles (0°, 45°, 90°) to the injection direction and at specific locations (Figure 1a). The PA6 specimens were only cut at 90°. The shape and dimensions of the tensile specimens are shown in Figure 1b.

Monotonic tensile tests were performed at room temperature. Prior to testing, the specimens were conditioned either dry (T_g = 70 °C) or 50%RH (T_g = 23 °C). The tests were performed in displacement control at 0.36, 36 and 360 mm/min, roughly corresponding to nominal strain rates of 1×10^{-4}, 1×10^{-2} and 1×10^{-1} s^{-1}. The strain rates were chosen to range from isothermal to adiabatic conditions, as will be clarified in Section 3.2.1.

Strains were measured full-field on the specimen surface via stereo DIC. The temperature field was also mapped with a FLIR A6750sc IR camera, calibrated and synchronised with the DIC cameras. The setup is shown in Figure 1c.



α	d1 [mm]	d2 [mm]	d3 [mm]
0°	108.5	253.5	–
45°	108	180	255
90°	146	214	280

Figure 1. (a) Specimen cutting layout. (b) Geometry of the tensile specimens of GPA6 and PA6 (all dimensions in mm). (c) Tensile test setup with DIC and IR cameras.

3. Results and discussion

3.1. Mechanical response

Figure 2 shows the true stress-true strain curves. For PA6, after yield the curves at 10^{-2} and 10^{-1} s^{-1} intersect with those at 10^{-4} s^{-1}, suggesting thermal softening as will be discussed in Section 3.2.3.

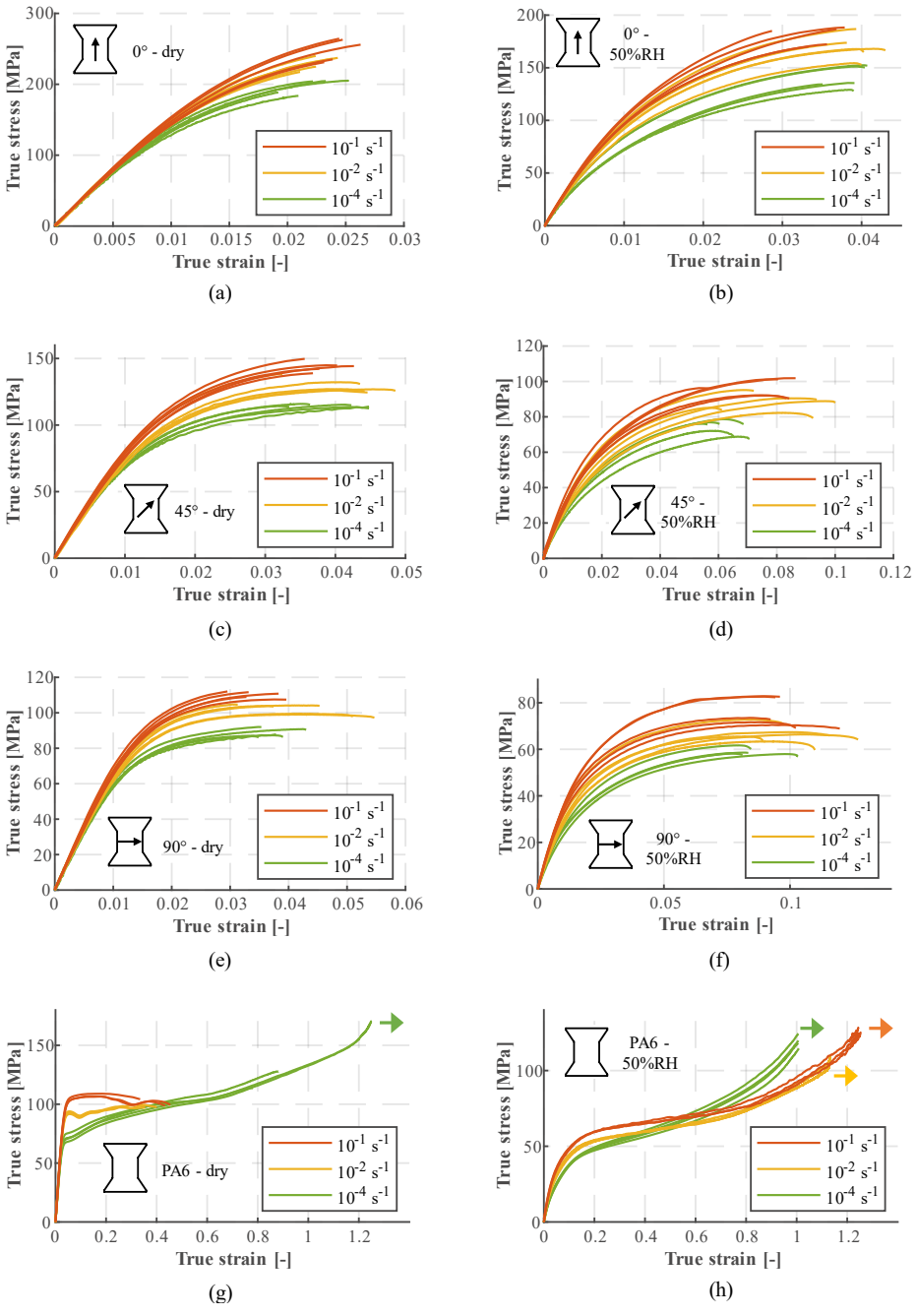


Figure 2. Stress-strain curves of GPA6 and PA6 at different (nominal) strain rates. *Left*: dry; *right*: 50%RH.

3.2. Thermomechanical coupling

3.2.1. Critical strain rate

As mentioned in the Introduction, plastic deformation in polymers is accompanied by heat generation. If the rate of deformation is higher than a critical value, heat is generated by plastic work faster than it

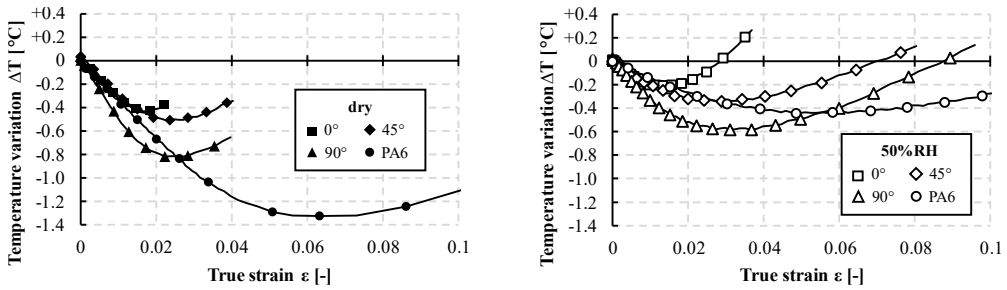
can be dissipated and the material heats up (adiabatic conditions). An approximate formulation for the critical strain rate $\dot{\varepsilon}_c$ can be derived from the characteristic thermal diffusion time Δt_d of the one-dimensional heat diffusion equation [6,8,11]:

$$\dot{\varepsilon}_c = \frac{1}{\Delta t_d} \approx \frac{(k/\rho c_p)}{L^2} \tag{1}$$

where: k is the thermal conductivity, ρ is the density, c_p is the specific heat capacity, and L is a characteristic length of the specimen. For PA6, this results in $1.62 \times 10^{-2}\ \mathrm{s}^{-1}$. Therefore, the following conditions are realised in this experimental campaign: $10^{-4}\ \mathrm{s}^{-1}$ isothermal; $10^{-2}\ \mathrm{s}^{-1}$ transition; $10^{-1}\ \mathrm{s}^{-1}$ adiabatic.

3.2.2. Thermoelasticity and coefficient of thermal expansion

In adiabatic conditions ($10^{-1}\ \mathrm{s}^{-1}$), the thermal response of the material is purely due to the mechanical deformation, while heat transfer can be neglected. This makes it possible to study thermomechanical coupling. Figure 3 gives the average temperature variation as a function of strain for the adiabatic case. The initial linear part reflects the thermoelastic effect, i.e. cooling associated with stretching. The temperature variations are in the order of fractions of a degree, so the impact on the mechanical response is minimal. Afterwards, the temperature starts increasing due to plastic dissipation, which will be addressed in Section 3.2.3.



(a) (b)

Figure 3. Average temperature variation vs. strain at a nominal strain rate of $10^{-1}\ \mathrm{s}^{-1}$ for PA6 and the different orientations of GPA6: (a) dry, (b) 50%RH. For PA6, the strain range is truncated to 0.1.

For a thermoelastic material under adiabatic deformation, the temperature variation ΔT is related linearly to the applied stress $\Delta\sigma$ by the equation:

$$\Delta T = -\frac{\alpha_T T}{\rho c_p}\Delta\sigma \tag{2}$$

where: α_T is the coefficient of linear thermal expansion, T the absolute temperature, ρ the density, and c_p the specific heat capacity at constant pressure [12,13]. Having access to mechanical and thermal data, it is possible to obtain the coefficient of thermal expansion. This approach was applied to PA6 and GPA6 for the different orientations and moisture contents, using literature values for c_p. Table 1 lists the calculated coefficient of thermal expansion for PA6 and GPA6. The values obtained in this study appear to be excellent estimates when compared to datasheet values for GPA6 [14].

Table 1. Coefficient of linear thermal expansion (α_T) estimated with Eq. (2). When available, literature values are provided within brackets for comparison.

Orientation	α_T dry [10^{-6}/K]	α_T 50%RH [10^{-6}/K]
PA6	80 (50–100)	102, 117
GPA6-0°	16 (13)	15, 16
GPA6-45°	30	39, 40
GPA6-90°	54 (55)	70

3.2.3. Self-heating

Figure 4 compares the temperature field of 50%RH PA6 for the different strain rates, at the same applied displacement of 52.4 mm. The strain rates of 10^{-2} and 10^{-1} s^{-1} show prominent self-heating, as opposed to 10^{-4} s^{-1}, thus confirming the theoretical calculations about the critical strain rate. It can be noted that the hot spots tend to move towards the shoulders of the neck. As can be seen in Figure 5, the strain rate concentrates there, while it is virtually zero in the middle. In fact, heat build-up is dependent on the local plastic work rate, in turn related to the local (true) strain rate. The full-field data allows to capture this interdependency.

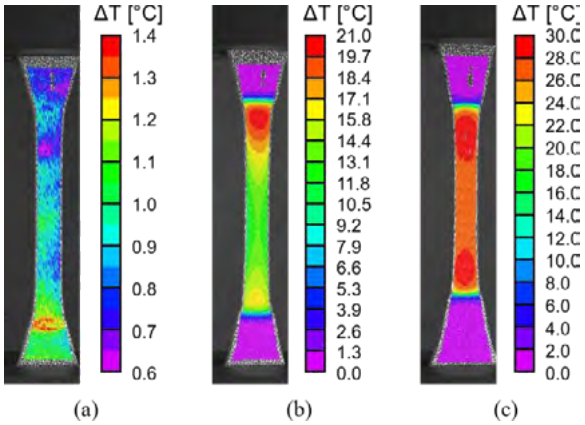


Figure 4. Temperature variation field of 50%RH PA6 for the different (theoretical) strain rates, at the same applied displacement of 52.4 mm: (a) 10^{-4} s^{-1}, (b) 10^{-2} s^{-1}, (c) 10^{-1} s^{-1}.

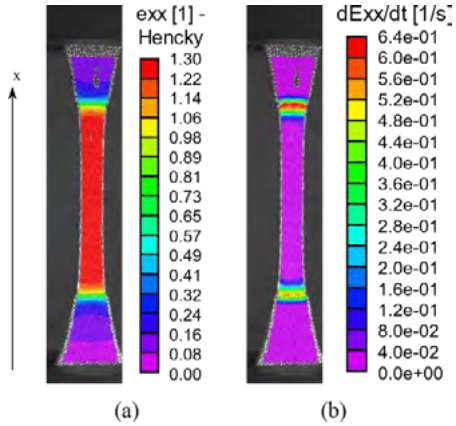


Figure 5. (a) Strain and (b) strain rate fields of 50%RH PA6 at 10^{-1} s^{-1}, at an applied displacement of 52.4 mm.

While the same general observations apply to dry PA6, necking is much more localised, leading to steeper temperature rises compared to 50%RH. In Figure 6, PA6 dry and 50%RH (10^{-1} s^{-1}) are compared at the same average strain of 0.41. Dry PA6 (Figure 6a) has a sharper strain gradient in the neck, such that the applied displacement at this stage is 6.5 mm as compared to 14.6 mm of 50%RH (Figure 6b). It also features a much higher temperature increase. In the next acquired frame, the local temperature increase of dry PA6 in the neck hits almost +70 °C, reaching about 92 °C which is well above the T_g.

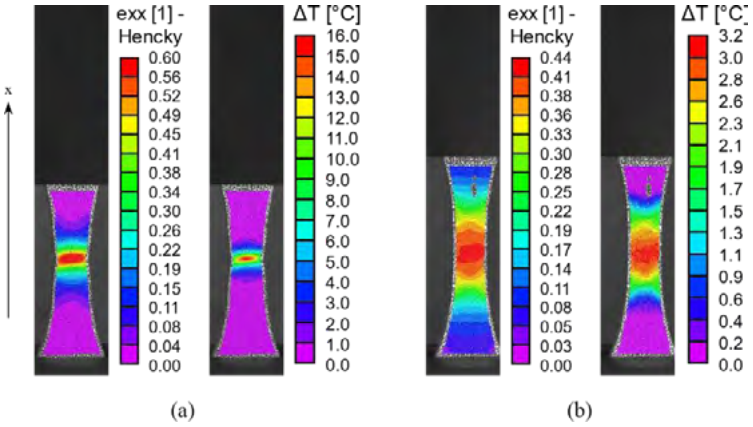


Fig. 6. Strain field and temperature variation field during a test at 10^{-1} s^{-1}, at an average strain level of 0.41: (a) dry PA6 (displacement = 6.5 mm), (b) 50%RH PA6 (displacement = 14.6 mm).

As for GPA6, Figure 7 depicts the strain, strain rate and temperature fields immediately before breakage of the specimen for which the most extreme strain rate concentration was observed (GPA6-90°, 50%RH, 10^{-2} s^{-1}). Even though the strain rate increased 80x in the fracture area compared to the nominal applied rate, the temperature increase was limited to +3 °C. This was the maximum temperature increase recorded among all the specimens. A possible explanation is that failure occurs too early in GPA6, the strain reaching at most 0.2 in 50%RH specimens in a very localised spot, while self-heating becomes prominent in PA6 starting from $0.3 - 0.4$ strain.

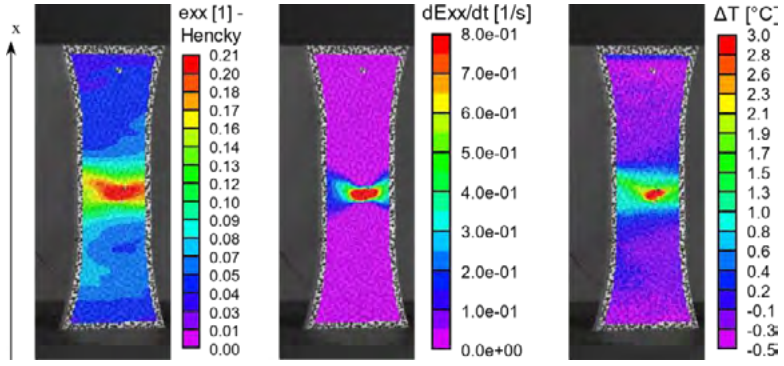


Figure 7. Strain, strain rate and temperature variation fields of 50%RH GPA6-90° at 10^{-2} s^{-1}, last frame before failure. Although the local strain rate peaks at 80x the theoretical nominal strain rate, the temperature rise is quite limited (~3 °C).

4. Conclusions

Thanks to synchronised DIC-IR measurements, full-field strain and temperature data were used to investigate thermomechanical coupling in PA6 and GPA6.

The coefficient of linear thermal expansion could be estimated from the linear thermoelastic response under adiabatic conditions (10^{-1} s^{-1}) for PA6 and GPA6 for all orientations and moisture contents, yielding excellent results.

Significant self-heating was recored in PA6 at 10^{-2} and 10^{-1} s^{-1} after yield. The necking phenomenon was different between dry and 50%RH specimens. In particular, the neck tended to localise in dry PA6 with very sharp gradients (temperatures exceeding the T_g in the neck), while in 50%RH PA6 it spread out more evenly across the gauge length. In both cases, heat accumulation could be linked to the true local strain rate field during plastic deformation measured by DIC. At any given instant, the local strain rate may be order of magnitudes higher or lower than the nominal strain rate estimated from the test speed.

Local surges in strain rate were also observed in GPA6 when approaching failure, yet self-heating was found to be insignificant there (max. local temperature rise +3 °C), likely because of early failure and limited matrix plasticity.

The results of this research can be valuable input for advanced material models for both pure polymers and SFRPs. The full-field data can be used to incorporate thermo-mechanical coupling in the rate-dependent response. The local strain rate information can lead to a more accurate interpretation of the global stress-strain behaviour.

Acknowledgments
The work leading to this publication has been funded by the ICON project “ProPeL”, which fits in the MacroModelMat (M3) research program, coordinated by Siemens (Siemens Digital Industries Software, Belgium) and funded by SIM (Strategic Initiative Materials in Flanders) and VLAIO (Flemish government agency Flanders Innovation & Entrepreneurship).
The authors gratefully acknowledge DOMO Chemicals for providing the materials.

References
[1] V. Miri, O. Persyn, J.-M. Lefebvre and R. Seguela. Effect of water absorption on the plastic deformation behavior of nylon 6. *European Polymer Journal*, 45(3):757–762, 2009.
[2] E. Parodi, G.W.M. Peters and L.E. Govaert. Prediction of plasticity-controlled failure in polyamide 6: Influence of temperature and relative humidity. *Journal of Applied Polymer Science*, 135(11):45942, 2018.
[3] G.-F. Shan, W. Yang, M.-B. Yang, B.-H. Xie, J.-M. Feng and Q. Fu. Effect of temperature and strain rate on the tensile deformation of polyamide 6. *Polymer*, 48(10):2958–2968, 2007.
[4] Z. Wang, Y. Zhou and P.K. Mallick. Effects of temperature and strain rate on the tensile behavior of short fiber reinforced polyamide-6. *Polymer Composites*, 23(5):858–871, 2002.
[5] L. V. Pastukhov, M.J.W. Kanters, T.A.P. Engels and L.E. Govaert. Influence of fiber orientation, temperature and relative humidity on the long-term performance of short glass fiber reinforced polyamide 6. *Journal of Applied Polymer Science*, 138(19):1–19, 2021.
[6] E.M. Arruda, M.C. Boyce and R. Jayachandran. Effects of strain rate, temperature and thermomechanical coupling on the finite strain deformation of glassy polymers. *Mechanics of Materials*, 19:193–212, 1995.
[7] M.C. Boyce and R.N. Haward. The post-yield deformation of glassy polymers. In: R.N. Haward, R.J. Young (Eds.), *The Physics of Glassy Polymers*, Springer Netherlands, Dordrecht, 1997, pages 213–293.
[8] C. Sorini, A. Chattopadhyay and R.K. Goldberg. Micromechanical modeling of the effects of adiabatic heating on the high strain rate deformation of polymer matrix composites. *Composite Structures*, 215:377–384, 2019.

[9] R.D.B. Sevenois, P. Hao, W. Van Paepegem and F.A. Gilabert. Numerical Study on the Effect of Matrix Self-Heating on the Thermo-Visco-Plastic Response of Continuous Fiber-Reinforced Polymers under Transverse Tensile Loading. *Polymers*, 14(10):1941, 2022.

[10] D. Finazzi, Y. Sinchuk, R.D.B. Sevenois, L. Daelemans, K. De Clerck, G. Robert and W. Van Paepegem. Study of self-heating and local strain rate in polyamide-6 and short fibre glass/polyamide-6 under tension through synchronised full-field strain and temperature measurements. *Polymer Testing*, 132:108361, 2024.

[11] M.J. Kendall and C.R. Siviour. Experimentally simulating adiabatic conditions: Approximating high rate polymer behavior using low rate experiments with temperature profiles. *Polymer*, 54(18):5058–5063, 2013.

[12] Y.K. Godovsky. *Thermophysical Properties of Polymers*. Springer Berlin, Heidelberg, 1992.

[13] R.N. Haward. Heating effects in the deformation of thermoplastics. *Thermochimica Acta*, 247(1):87–109, 1994.

[14] Kern GmbH. Polyamide 6 with 50 % glass fibre (PA 6 GF50), datasheet [online]. n.d. https://www.kern.de/de/technical-datasheet/polyamide-pa-6-gf50?n=1115_2 (accessed December 14, 2023).

Investigating Homogenisation, Mechanical Performance and Compression After Impact of Double-Double Laminates

Aidan Hawkins[1*], Scott L.J. Millen[1], Andrew McConnell[1], Fintan Cook[1], and M. Ali Aravand[1]

[1]Queen's University Belfast, School of Mechanical and Aerospace Engineering, Ashby Building, Belfast, BT9 5AH, Northern Ireland, UK
*Email: ahawkins05@qub.ac.uk

Keywords: Double-Double, Homogenisation, Mechanical Testing, Low-Velocity Impact, Compression After Impact

Abstract
An investigation of the homogenisation, mechanical performance and compression after impact strength of Double-Double (DD) laminates is presented. DD laminates are a new layup design approach composed of repeated sub-laminates, comprising two sets of bi-angled plies, ±Φ° and ±Ψ°. The DD laminate approach simplifies the design of composite structures, reduces manufacturing complexity, and allows for rapid thickness tapering, presenting substantial prospects for reducing structural mass. Updated homogenisation criteria are proposed, aimed at mitigating warpage in DD laminates. These criteria were experimentally validated through laminate manufacture using Carbon Fibre Reinforced Polymer (CFRP) prepreg material. A framework to convert any CFRP laminate to a DD sub-laminate, based on equivalent stiffness, has been developed. Physical testing of both in-plane tensile and flexural specimens, for quad and DD laminates, was carried out to validate the framework. Additionally, low-velocity impact and subsequent compression after impact testing were conducted on quad and DD laminates. Initial findings indicate the potential for a reduced delamination area and increased CAI strength.

1 Introduction

When the orientation of plies in a laminate is limited to a collection of 0°, ±45° and 90° angles, they are considered to be quad laminates or Legacy Quad Laminates (LQL). Designing with conventional quad laminates entails adhering to numerous design rules and guidelines. There are some 39 legacy guidelines for designing composite structures, summarised by Bailie *et al.* [1]. These guidelines have introduced vast complexity into the design process, limiting innovation and causing severe difficulties regarding layup optimisation.

DD laminates are a new layup design approach which seeks to address the limitations of quad laminates. First proposed by Tsai *et al.* in 2017 [2], DD simplifies the design of composite structures and allows for simplistic and rapid thickness tapering with the potential for structural mass reduction and increased manufacturing speeds. DD laminates are typically made up of repeated building blocks or sub-laminates, composed of two sets of bi-angled plies, as shown in Figure 1. LQLs limit the design space by restricting the angle increments to four discrete values. DD eliminates these restrictions, ensuring the presence of each ply angle in the laminate is optimised and justified, while simultaneously simplifying the design process.

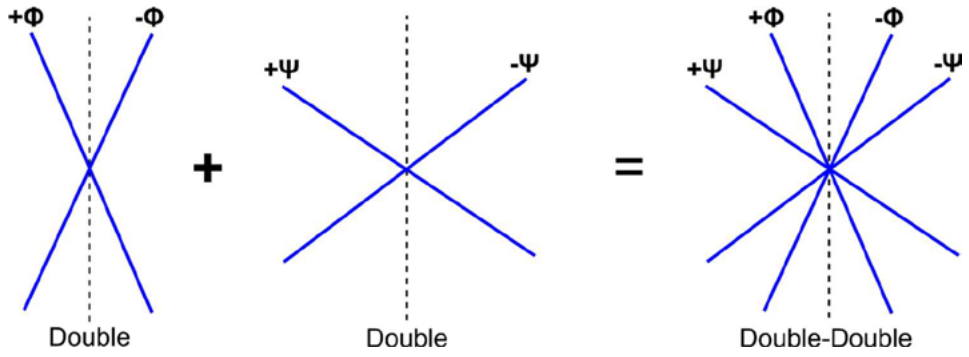


Figure 1 - Sub-laminate building block for DD Laminates.

Through-thickness homogenisation of the laminate is a fundamental characteristic of the DD layup methodology. It is achieved through a minimum number of repetitions of the asymmetric DD sub-laminate, sufficiently suppressing coupling terms in the laminate [ABD] matrix. Asymmetric laminates tend to warp when cooled from an elevated temperature cure cycle, due to unbalanced thermal residual stresses. Sufficient homogenisation ensures the DD laminate will be free from warpage, even when cured at an elevated temperature. Homogenisation criteria have been proposed for this purpose [3], [4, Ch. 4]. However, little experimental validation has been carried out to test and validate these criteria. The first part of this work assesses the existing homogenisation criteria through DD laminate manufacture. Following this, an updated homogenisation criteria was proposed and subsequently validated.

Given a quad or unconventional laminate, it is possible to convert to a DD layup, resulting in a DD laminate of equivalent stiffness. Exact in-plane stiffness matches are possible using the standard 4-ply DD sub-laminate when the quad laminate contains less than 50% 0° or 90° plies. A closed-form solution for converting to a standard DD layup was derived using lamination parameters by Tsai [4, pp. 26–28]. The work presented here builds on the Tsai's theory, establishing a novel framework for converting any laminate to a standard or extended DD sub-laminate. The efficacy of the framework was then validated through tensile and flexural mechanical testing of both quad and equivalent DD laminates.

Low-velocity impact (LVI) and compression after impact (CAI) are standard procedures in assessing the structural integrity of composite materials, particularly in aerospace applications. LVI involves subjecting a structure to a relatively low-energy impact, typically resulting in localised damage such as delamination, fibre breakage, and matrix cracking. Subsequently, CAI refers to the residual strength of the composite laminate, following an impact event, i.e. its ability to withstand further loading conditions. Understanding the mechanical response of a composite laminate to LVI and CAI is fundamental for predicting their damage tolerance and long-term performance, especially for aerospace applications. Little work has been done to assess the LVI and CAI performance of DD laminates [5], [4, Ch. 6]. The final section of this study compares the LVI and CAI performance of quad and in-plane/flexural stiffness equivalent DD laminates.

2 Methodology

Computations for homogenisation in Section 2.1 and stiffness matching framework in Section 2.2 are independent of CFRP material. This was achieved through the use of Master Ply values which represent the average proportions of stiffness in each direction for any CFRP material [6], [7], [8]. The Master Ply values used in this study were calculated by Tsai *et al.* [9] to be $Q_{11}^{*} = 0.8849$, $Q_{22}^{*} = 0.0525$, $Q_{66}^{*} = 0.0313$ and $\nu_{12}^{*} = 0.3$. Terms denoted with the superscript "n*", indicate thickness normalisation and computation using Master Ply values.

In each of the three studies, laminates were manufactured from a 145gsm carbon-epoxy prepreg, IM7 977-2. During layup, plies were tacked together using a heat gun, and the laminate underwent debulking

approximately every five plies to enhance stack consolidation. Subsequently, laminates were cured at 180°C under 6 bar pressure for 3 hours with ramp and cool down rates set to 2°C/min.

2.1 Homogenisation of Double-Double Laminates

2.1.1 Homogenisation Framework

A simplified homogenisation framework is shown in Figure 2. Initially, unique permutations are obtained by eliminating those that are effectively the same in terms of a DD sub-laminate. These unique permutations are then evaluated at specified increments between 0° and 90° to determine the minimum number of sub-laminate repetitions to meet the homogenisation criteria. For each angle combination the $[ABD]^{n*}$ matrix is calculated for both arrangements, or orders, of angles with the sub-laminate i.e. DD angle 1 = Φ, DD angle 2 = Ψ and vice versa. The angle order that that minimises the required repeats or minimises the highest value in the B^{n*} coupling matrix is selected. If both metrics are equal, no preferential order is specified.

Once all permutations for a particular sub-laminate have been evaluated, those requiring the minimum number of repeats to meet the criteria are identified. In the scenario where more than one permutation remains, the permutation that minimises the highest value in the B^{n*} coupling matrix is selected. Subsequently, the resultant grid recommends only one stacking sequence permutation per cell. The following sections will cover the use of this framework and present homogenisation grids for use as a design tool.

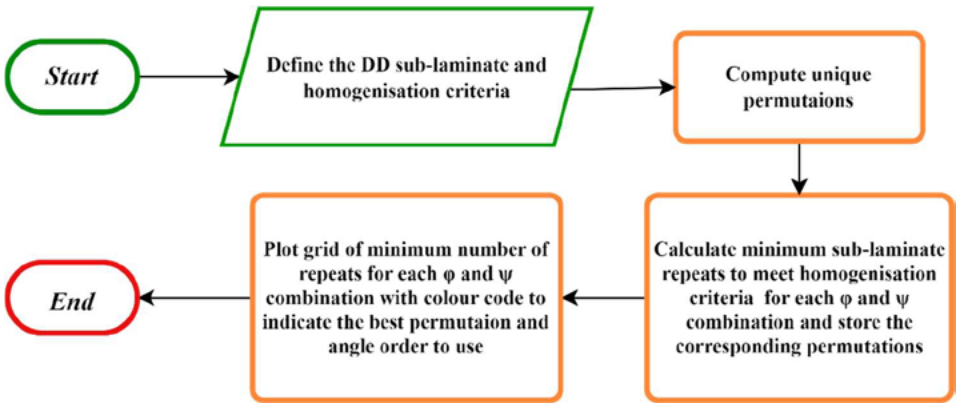


Figure 2 – Simplified illustration of homogenisation workflow.

2.1.2 Assessment of Homogenisation Criteria

The homogenisation criteria proposed previously in literature [4, Ch. 4] are summarised in Equation (1). Based on these criteria, four laminates were manufactured. The stacking sequences for these laminates are given in Table 1. It is noteworthy that not all of these stacking sequences are necessarily optimal for the specified angle combinations to achieve homogenisation. However, all fabricated laminates adhered to the homogenisation criteria outlined in Equation (1).

$$[\mathrm{D}^{n*}] - [\mathrm{A}^{n*}] < 2\% \quad \text{and} \quad [B^{n*}] < 2\% \tag{1}$$

Following the outcomes of the laminate manufacture based on the original homogenisation criteria, shown in Section 3.1.1, updated homogenisation criteria were proposed. These criteria further constrain the $[B^{n*}]$ coupling terms and are shown in Equation (2). Based on these updated criteria and framework outlined in Section 2.1.1, an additional four laminates were manufactured to assess the efficacy of this revised criteria. The stacking sequences are given in Table 1.

$$[\mathrm{D}^{n*}] - [\mathrm{A}^{n*}] < 2\% \quad \text{and} \quad [B^{n*}] < 1\% \tag{2}$$

Table 1 – Stacking sequences for assessment of homogenisation criteria.

Original Criteria	Updated Criteria
$[+22.5/-67.5/-22.5/+67.5]_4$	$[+22.5/-67.5/-22.5/+67.5]_8$
$[+22.5/-67.5/+67.5/-22.5]_5$	$[+17/-64.5/-64.5/-17]_8$
$[+61.5/-9/-61.5/+9]_5$	$[+9/-61.5/+61.5/-9]_5$
$[+47/-9/-47/+9]_5$	$[+9/-47/+47/-9]_5$

2.2 Mechanical Performance of Double-Double Laminates

An automated workflow has been developed to transform any CFRP laminate to a DD sub-laminate of equivalent thickness. Should a solution to the closed-form equations exist, it will be employed. In instances where there is no solution to the closed-form equations, an optimisation procedure will be executed utilising the Particle Swarm Optimisation Algorithm (PSOA) across all DD sub-laminates, with the optimal solution subsequently chosen. Notably, DD laminates with ID DD-An are tailored to match the in-plane properties of the candidate laminate, while the ID DD-Dn corresponds to a match of the out-of-plane flexural properties.

Readers are referred to [10] for a more detailed explanation of the automated conversion workflow, DD sub-laminate stiffness domain and closed-form solutions. The domain for which an exact stiffness match is possible can be expanded through the use of five and six ply DD sub-laminates. The authors previously derived closed-form equations for extended DD sub-laminates [10].

2.2.1 Mechanical Testing for Validation

In order to validate the aforementioned conversion workflow, tensile and flexural tests were performed in accordance with ASTM D3039 and ASTM D7264, respectively. Composite laminates were laid up with 16 or 20 plies of IM7 977-2. Table 2 shows the specimen details used in this study.

Table 2 – Stacking sequences for validation of framework.

Layup ID	Stacking Sequence	Test Type	No. of Specimens
Quad-TF	$[0/45/90/-45]_{2s}$	Tensile / Flexural	5 / 8
DD-An-T	$[22.5/-67.5/-22.5/67.5]_4$	Tensile	5
DD-Dn-F	$[9/-61/61/-9]_5$	Flexural	8

Tests were performed using a Zwick Z100 Proline. 100 kN and 10 kN load cells were used for the tensile and flexural specimens respectively. 350 Ω strain gauges were bonded to each tensile specimen and a System 8000 StrainSmart data acquisition system was used to record synchronised force-strain data.

2.3 LVI and CAI Performance of DD laminates

A quasi-isotropic quad laminate was chosen as the starting laminate for this study. Using the framework outlined in Section 2.2, DD sub-laminates were matched to the in-plane and flexural properties of the quad laminate. Table 3 shows the specimen details used in this study.

Table 3 – Stacking sequences for LVI/CAI Study.

Layup ID	Stacking Sequence	No. of Specimens
Quad-LC	$[0/45/90/-45]_{4s}$	3
DD-An-LC	$[22.5/-67.5/-22.5/67.5]_8$	2*
DD-Dn-LC	$[17/-64.5/64.5/-17]_8$	3

*One specimen emitted from results due to double impact during LVI testing

2.3.1 LVI Setup

LVI of the CFRP specimens was carried out in accordance with ASTM D7136. Based on a nominal laminate thickness of 4.64 mm, an impact energy of 31 J was used. The impact was administered using an ERN 45 Rosand Falling Weight Impact Tester. A steel hemispherical impactor with diameter 16 mm and total weight of 5.63 kg was released from a height of 561.5 mm. Post-impact, the panels were subjected to ultrasonic inspection where C-scan images were produced to assess internal delamination.

2.3.2 CAI Setup

CAI testing was performed in accordance with ASTM D7137. A Zwick-Roell Z100 Proline with 100 kN load cell and an Instron 2580 Series with 150 kN loadcell were used for the compression testing. The side of specimens subjected to the impact was painted white and speckled black. Two synchronised cameras were used to record the test. Digital Image Correlation (DIC) was subsequently performed using VIC3D from Correlated Solutions.

3 Results and Discussion

3.1 Homogenisation of Double-Double Laminates

Homogenisation grids in the subsequent sections were created using the framework set out in section 2.1.1. A 5° resolution between DD angles was chosen for visualisation purposes, with the framework capable of producing grids to any desired resolution.

3.1.1 Laminate Manufacture – Original Homogenisation Criteria

The homogenisation grid depicted in Figure 3 was based on the original homogenisation criteria, Equation (1). Figure 4 shows the resulting manufactured laminates. Significant warpage was observed in all laminates due to unbalanced thermal residual stresses induced during the cure cooldown cycle. This observation suggests that the original homogenisation criteria are insufficient in preventing warpage of DD laminates cured at elevated temperatures.

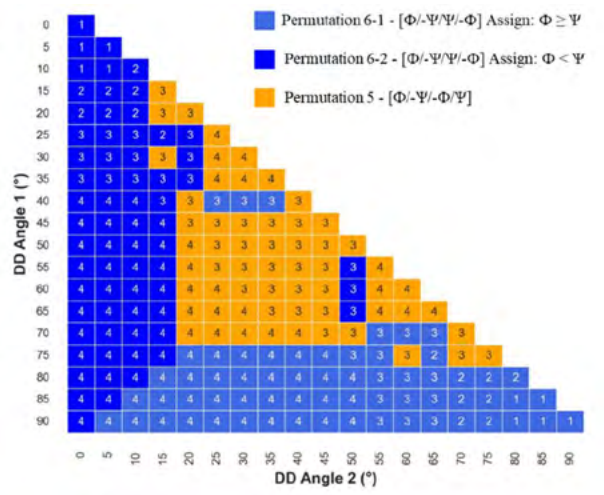


Figure 3 – Homogenisation grid based on original homogenisation criteria.

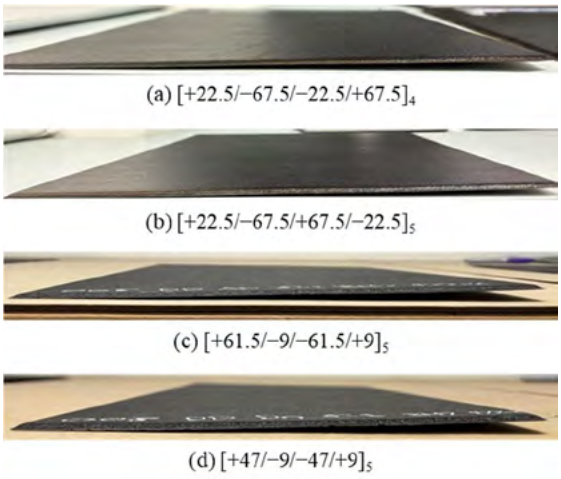


Figure 4 – Laminates manufactured based on original homogenisation criteria.

3.1.2 Laminate Manufacture – Updated Homogenisation Criteria

Figure 5 shows the resulting homogenisation grid based on the updated homogenisation criteria, Equation (2). A range of DD angle combinations were chosen for manufacture as previously set out in Table 1. The resulting laminates are shown in Figure 6. In all cases, zero or insignificant warpage was observed, suggesting the updated homogenisation criteria is sufficient to prevent warpage. Further validation, through laminate manufacture with additional DD angle combinations and material variations, is required.

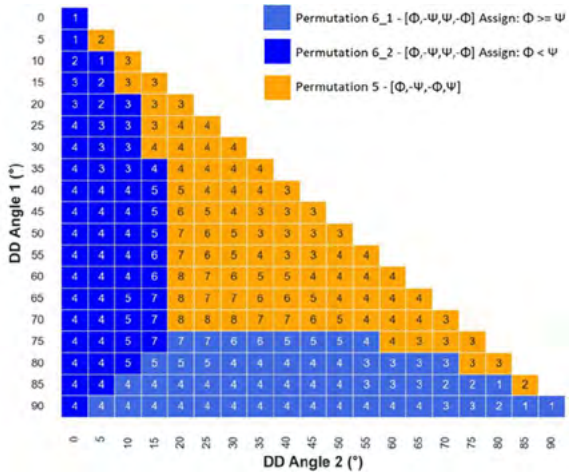


Figure 5 - Homogenisation grid based on updated homogenisation criteria.

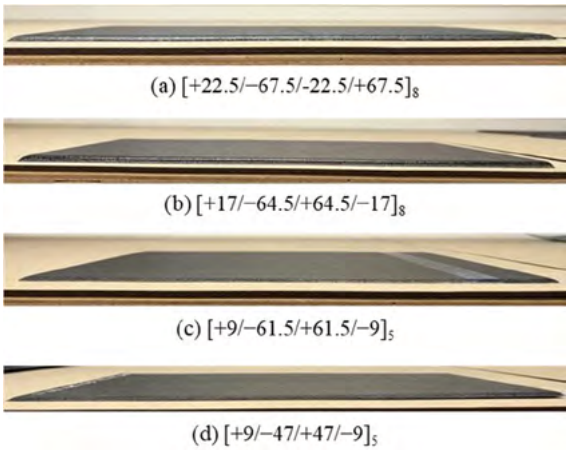


Figure 6 - Laminates manufactured based on original homogenisation criteria.

3.2 Mechanical Performance of Double-Double Laminates

The mechanical properties of quad and corresponding DD laminates are shown in Table 4. Tensile and flexural modulus values between quad and DD laminates correlate closely, with differences of 0.06 % and 2.05 % respectively. These preliminary tests establish a solid foundation in validating the framework in Section 2.1.1, which will be explored further in future studies.

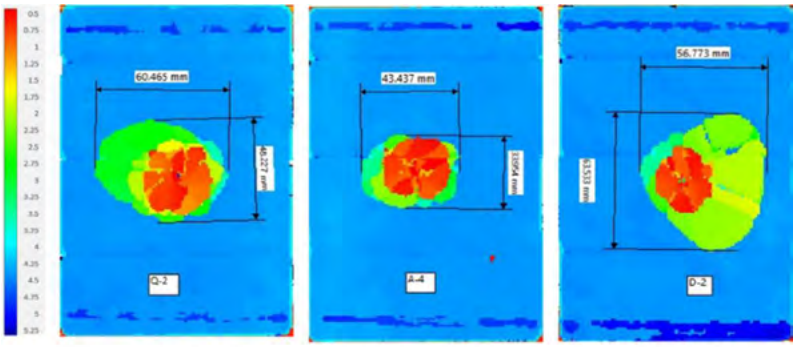
Table 4 –Mechanical properties of quad and DD laminates.

	Tensile Modulus		Flexural Modulus	
Layup ID	Quad-TF	DD-An-T	Quad-TF	DD-Dn-F
Mean (GPa)	52.31	52.28	60.99	62.24
SD (GPa)	0.95	1.98	0.70	1.18
CoV (%)	1.81	3.80	1.15	1.90

3.3 LVI and CAI Performance of DD laminates

3.3.1 Delamination of Specimens Subjected to LVI

C-scan images of one impacted specimen per laminate are shown in Figure 7. The DD-An-LC laminate, matched to the in-plane stiffness of the quad laminate, displayed the smallest delamination area. The largest delamination area was observed in the DD-Dn-LC laminate, matched to the flexural stiffness of the quad laminate. Since only one impacted specimen from each laminate was scanned, no definitive conclusions should be drawn. However, further study is planned with repeated specimens.



(a) Quad-LC (b) DD-An-LC (c) DD-Dn-LC

Figure 7 – C-scan images from ultrasonic inspection of impacted panels.

3.3.2 CAI Strength

The residual compressive strength results are given in Table 5. An increased in residual strength was observed in both DD laminates compared to the equivalent quad laminate. The increase in strength of 3.95 % in DD-An-LC is likely due to the decrease in delamination area compared to Quad-LC. DD-Dn-LC matched the out-of-plane flexural stiffness of Quad-LC. Despite having the largest delamination area, DD-Dn-LC had a 10.38 % higher residual strength compared to Quad-LC. This can be attributed to the 15.65 % higher pristine compressive strength of DD-Dn-LC when compared to Quad-LC. An ANOVA test, comparing DD-An-LC, DD-Dn-LC and Quad-LC, indicated a large effect size (factor = 2.13) but with no statistically significant difference between the means of the datasets at the 5% significance level ($p = 0.2137$). This result warrants further investigation of the CAI performance, with a larger number of specimens.

Table 5 – CAI residual strength of Quad and DD laminates.

Layup ID	Quad-LC	DD-An-LC	DD-Dn-LC
Mean (MPa)	218.26	226.89	240.91
SD (MPa)	12.62	8.50	16.18
CoV (%)	5.78	3.74	6.72

Conclusions

A framework for determining the best DD stacking sequencing and minimum sub-laminate repetitions to satisfy specified homogenisation criteria is presented. Through fabrication of numerous CFRP laminates, it was demonstrated that the previously proposed homogenisation criteria were inadequate in mitigating warpage in DD laminates subjected to elevated temperature curing. An updated homogenisation criteria is proposed and subsequently validated, producing warpage-free laminates. To further build confidence in these criteria, additional laminates in a variety of prepreg materials should be manufactured and examined.

The conversion framework outlined facilitates the transformation of any CFRP laminate into a stiffness equivalent standard or extended DD sub-laminate. An assessment of the tensile and flexural properties of DD laminates in comparison to their stiffness equivalent quad laminate was conducted. These initial tests form a solid foundation for validating the conversion framework.

LVI and CAI testing was conducted on quad and corresponding in-plane and flexural stiffness equivalent DD laminates. C-scan images show DD laminates have the potential to reduce delamination area. Improvements in residual strength were observed for both DD laminates when compared to the original quad laminate. Due to testing on a limited number of laminates and specimens, general conclusions on the performance of quad vs DD laminates for LVI and CAI cannot yet be drawn. Results obtained from this physical testing will be used to validate ongoing numerical simulation of LVI and CAI events for DD laminates.

References

[1] J. A. Bailie, R. P. Ley, and A. Pasricha, ‘A Summary of Composite Laminate Guidelines’. 1997. Accessed: Apr. 05, 2023. [Online]. Available: https://docplayer.net/41811348-A-summary-and-review-of-composite-laminate-design-guidelines.html

[2] S. W. Tsai, J. D. D. Melo, S. Sihn, A. Arteiro, and R. Rainsberger, *Composite Laminates: Theory and Practice of Analysis, Design and Automated Layup*. Stanford Aeronautics & Astronautics, 2017.

[3] S. W. Tsai, ‘Double–Double: New Family of Composite Laminates’, *AIAA J.*, vol. 59, no. 11, pp. 4293–4305, Nov. 2021, doi: 10.2514/1.J060659.

[4] S. W. Tsai, Ed., *Double-double: a new perspective in the manufacture and design of composites*, First edition. Honolulu: Composites Design Group, Department of Aeronautics & Astronautics, Stanford Univeristy, 2022.

[5] R. Dantas da Cunha, T. G. Targino, C. Cardoso, E. Paiva da Costa Ferreira, R. C. S. Freire Júnior, and J. Daniel Diniz Melo, 'Low velocity impact response of non-traditional double-double laminates', *J. Compos. Mater.*, p. 00219983231163513, Mar. 2023, doi: 10.1177/00219983231163513.
[6] S. W. Tsai and J. D. D. Melo, 'An invariant-based theory of composites', *Compos. Sci. Technol.*, vol. 100, pp. 237–243, Aug. 2014, doi: 10.1016/j.compscitech.2014.06.017.
[7] L. Jia, C. Zhang, J. Li, L. Yao, and C. Tang, 'Validation and development of trace-based approach for composite laminates', *Compos. Sci. Technol.*, vol. 221, p. 109348, Apr. 2022, doi: 10.1016/j.compscitech.2022.109348.
[8] S. K. Ha and C. A. Cimini, 'Theory and validation of the master ply concept for invariant-based stiffness of composites', *J. Compos. Mater.*, vol. 52, no. 12, pp. 1699–1708, May 2018, doi: 10.1177/0021998317728782.
[9] S. W. Tsai, S. Sihn, and J. D. D. Melo, 'Trace-based stiffness for a universal design of carbon-fiber reinforced composite structures', *Compos. Sci. Technol.*, vol. 118, pp. 23–30, Oct. 2015, doi: 10.1016/j.compscitech.2015.08.003.
[10] A. Hawkins, S. L. J. Millen, and M. A. Aravand, 'Investigating Stiffness Property Matching and Homogenization of the Double-Double Family of Laminates', presented at the American Society for Composites, 2023. doi: 10.12783/asc38/36673.

STRUCTURAL HEALTH MONITORING OF CFRTP UNDER THERMO-OXIDATIVE AGING BY NON-DESTRUCTIVE VIBRATIONAL METHOD

Weizhao Huang[1], Yi Wan[1] and Jun Takahashi[1]

[1]Department of Systems Innovation, The University of Tokyo, Tokyo, Japan
Email: huang-weizhao@cfrtp.t.u-tokyo.ac.jp (W. Huang), wan-yi@cfrtp.t.u-tokyo.ac.jp (Y. Wan), takahashi-jun@cfrtp.t.u-tokyo.ac.jp (J. Takahashi)

Keywords: CFRTP, structural health monitoring, thermo-oxidative aging, vibration

Abstract
Reducing vehicle weight through carbon fiber reinforced thermoplastic composites (CFRTP) is critical for improving automotive fuel efficiency and combating climate change impacts. However, these components, for example those used in under-the-hood automotive applications, might degrade under severe thermo-oxidative environments. Therefore, it is important to study aging processes and non-destructively assess the structural integrity. In this study, a sandwich-structured CFRTP with a sheet molding compound skin and carbon fiber paper reinforced thermoplastic core was investigated. Composites were fabricated with varying springback ratios (SBRs) to introduce a controlled porous structure and reduce weight. Thermo-oxidative aging at 90-170 °C for up to 100 hours simulated severe service environments. Aged composites were characterized using mechanical testing, vibration analysis, and microstructural evaluations, and an inverse finite element modeling approach was conducted to quantify residual modulus distribution. The results revealed that higher SBRs and aging temperatures/durations degraded flexural properties and induced fracture mode transitions from brittle failure to delamination. The detailed spatial modulus distribution was inversed by the natural frequencies of the specimen after aging, with a satisfying average absolute error as low as 4-6%. The proposed vibrational method provides with a perspective of non-destructively assessing the structural integrity.

1. Introduction

Climate change is among the most focused issues of global concern. Addressing climate change requires strict restrictions on CO_2 emissions [1][2]. Strict restrictions necessitate a reduction in the body weight of automobiles to improve their fuel efficiency and minimize their environmental impact [3]-[5]. In this regard, carbon-fiber-reinforced thermoplastic (CFRTP) has significant advantages in terms of its short molding time, low processing cost, and excellent recyclability. CFRTP has undergone extensive study for structures requiring low weight and high impact resistance, making it particularly suitable for mass-produced automotive components [6][7].

Polyamide 6 (PA6) with excellent performance and heat resistance has been largely applied in the automotive industry such as semi-structural components and some interior accessories [8]-[10]. Especially, there has recently been a strong demand for the use of molded composites that serve as divided manifolds, front-end modules, and other under-the-hood applications [11][12]. These applications place stringent requirements on CFRTP composites in terms of dimensional stability, mechanical properties, and chemical resistance. Once these composites are exposed to high temperatures for a prolonged period, they become sensitive and vulnerable to factors including radiation, moisture, heat, or light [13][14]. Hence, investigations into the mechanical properties under severe serving

environments and monitoring the structural health condition under temperatures as high as 150 °C, or even 200 °C are significant for long-term service of PA6-based CFRTP composites [15].

The imperative to address climate change and the demand for eco-friendly automotive materials underscore the need for innovative testing methods. The ultrahigh cost of static mechanical tests and the increasing need for real-time monitoring make destructive tests infeasible [16]. In contrast, nondestructive evaluation is an analytical and measurement technique for quantitatively characterizing materials, components, and structures in real-time and without causing any damage to material properties [17]. In particular, for the vibration method, with advantages of relatively simple equipment and low testing costs, it is necessary to apply an external excitation to the specimen and extract the modal parameters, such as natural frequencies (NFs) and vibration mode shapes, which are considered the main parameters for determining the elastic properties of a composite [18]. The vibrational method has shown satisfying accuracy when inversing the modulus distribution matrix [19].

In this study, sandwich structured composites were fabricated utilizing CFRTP sheet moulding compound (SMC) as skin and carbon fiber paper reinforced thermoplastics (CPT) as core and were reheated to achieve the springback phenomenon with different ratios. The specimens were aged under thermos-oxidative environments for various periods to simulate complex aging situations. The mechanical property decline was tested, and the vibrational signals of natural frequencies were conducted to reflect the changes. Finally, the aging mechanism was proposed to help understand the aging process of sandwich-structured CFRTP composites.

2. Experiments

2.1. Fabrication and aging

The sandwich composite was fabricated with 6 pieces of SMC as skin and 12 pieces of CPT as core. Both two kinds of prepregs were cut into the size of 125 * 250 mm and then were fabricated into plate composite under 280 ºC and 5 MPa, and the detailed temperature and pressure curves were shown in Fig. 1a. Then the margin parts (10 mm) of as-fabricated plate were cut off and the remained part was re-heated to specific thickness by two stoppers, as shown in Fig. 1b. The ratio of thickness before and after re-heating was named as springback ratio (SBR).

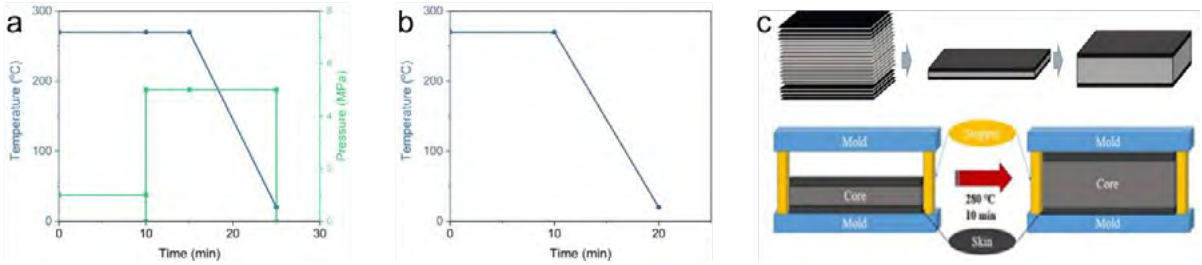


Fig. 1 Temperature and stress data for fabricating (a) sandwich and (b) springbacked plate and (c) scheme diagram of the two-step method for springbacked structure.

The thermo-oxidative aging test was carried out on a box-type electric furnace (Elepot SH, Hata Electric Co., Ltd.) in the air for a total of 100 hours. The test temperatures were chosen as 90 ºC, 130 ºC, and 170 ºC, respectively. Specimens with different SBRs (1.0, 1.2, and 1.6) were aged at a certain temperature for 20 hours and then naturally cooled in the furnace, which is defined as one cycle. The test lasted typically for 5 cycles.

2.2. Mechanical and vibrational properties

The sandwich composites with different SBRs were cut into sticks for a 3-point bending test using a 5 kN universal testing machine (AGS-X, Shimadzu, Japan). The specimens were manufactured to meet the span-thickness ratio standard of 16:1 and an additional 10 mm were maintained on each side and the speed of bending is 1 mm min^{-1}. A high-speed camera (FASTCAM SA-X) was applied to record the

fracture procedure during the flexural test. The micromorphy was observed by the digital microscope (VHX-8000, Keyence) and the X-ray scanning system of TDM1000-II 3D (Yamato Scientific Co., Ltd. Japan) was applied to analyze the inner structures. The natural frequency and mode shapes were tested using modal tests. The electrical signal was converted into visual vibrational data using a signal analyzer (OROS 34, TOYO, Japan). A dynamic mechanical analyzer (DMA, RSA-G2, TA Instruments, USA) was used to perform the tensile test to detect the tensile modulus, where temperature was set at 25 °C.

2.3. Modulus inversing based on NFs

This inverse analysis is based on FE simulation using the genetic algorithm, as shown in Fig. 2. The natural frequencies and modal shapes can be easily and accurately measured by modal tests. With the geometry information of the structure, the natural frequencies of the structure can also be predicted by FE simulation. However, the simulated natural frequencies may not agree with the natural frequencies of the real structure due to inaccurate material parameter settings in the FE model. So the inverse analysis is to update the material parameter setting in the FE simulation by optimization algorithm to make the simulated results agree with real results. The final material parameter setting in the FE model is the identified modulus of the structure, which is the residual modulus after aging.

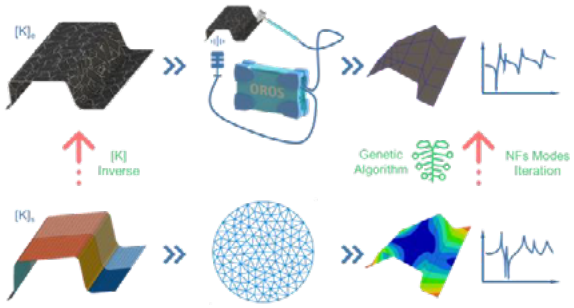


Fig. 2 Schemtic of inversing the residual modulus based on the non-destructive vibrational method.

3. Results and discussions

3.1. Microstructures of sandwich with various SBRs

The micromorphy apparently revealed the sandwich structure, as shown in Fig. 3. The different layers of SMC skin are easily observed. For the SBR1.0 specimen, few pores could be observed and the bond between skin and core is tight. The distribution of fiber and resin is not even, and the resin-rich may serve as failure initiation zones. The fiber in the CPT core shows a random orientation, from the isotropy of mat. After springback, the thickness of the two skins changed, mainly coming from the flowing during the second step of springback, showing the excellent molding property of SMC. And porous structure was generated while the porosity increased with the SBRs. Besides the expansion of the CPT core, the delamination occurred within the skin and was even more severe in the SBR1.6 specimen. Also, the interface gets weak, and more voids appear in the link area, making it easier to fail.

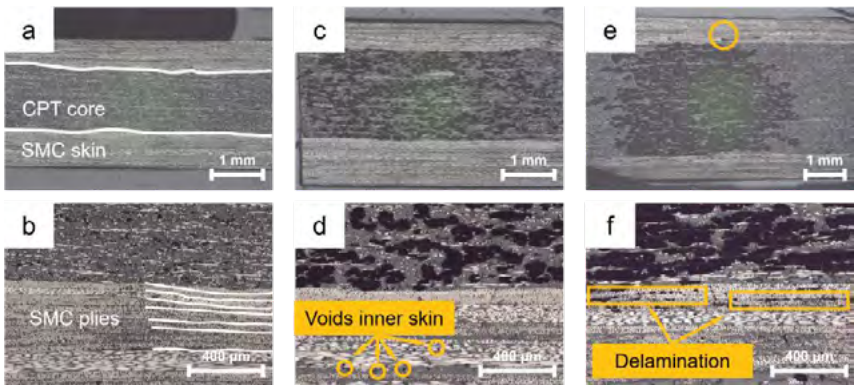


Fig. 3 Microstructure of specimens of (a-b) SBR1.0, (c-d) SBR1.2 and (e-f) SBR1.6.

Fig. 4 prensents the X-ray scanning results. For both the skin and core, the out-plane angle of θ highly concentrated at 90 °, resulting from the lamination of plies. The change of peak values after springback is not large because the SBR is limited. For the φ of SMC skin, the distribution is generally homogeneous, except for the abnormal peak at 90 °, which is similar to CPT. Also, For the core, the apparent peak at 0 ° is the machine direction of the raw CPT plies, showing an aligning performance. After aging at 170 °C for 100 hours, the trend shows good consistency with the specimen without aging. The springback ratio is smaller, resulting in a weak deformation.

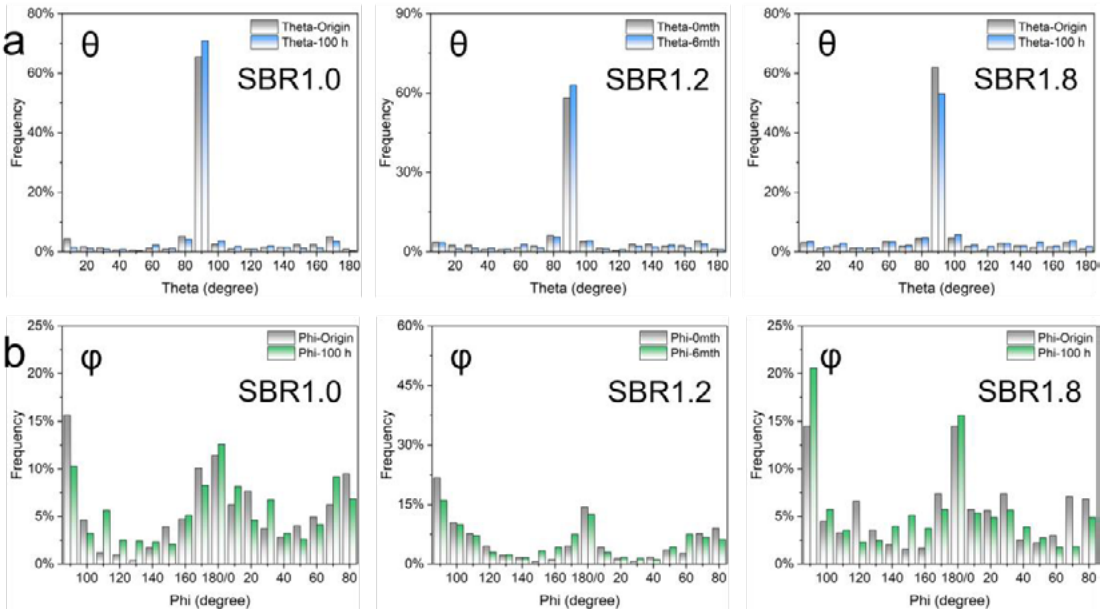


Fig. 4 Fiber orientation distributions of (a) θ and (b) φ of SMC skin.

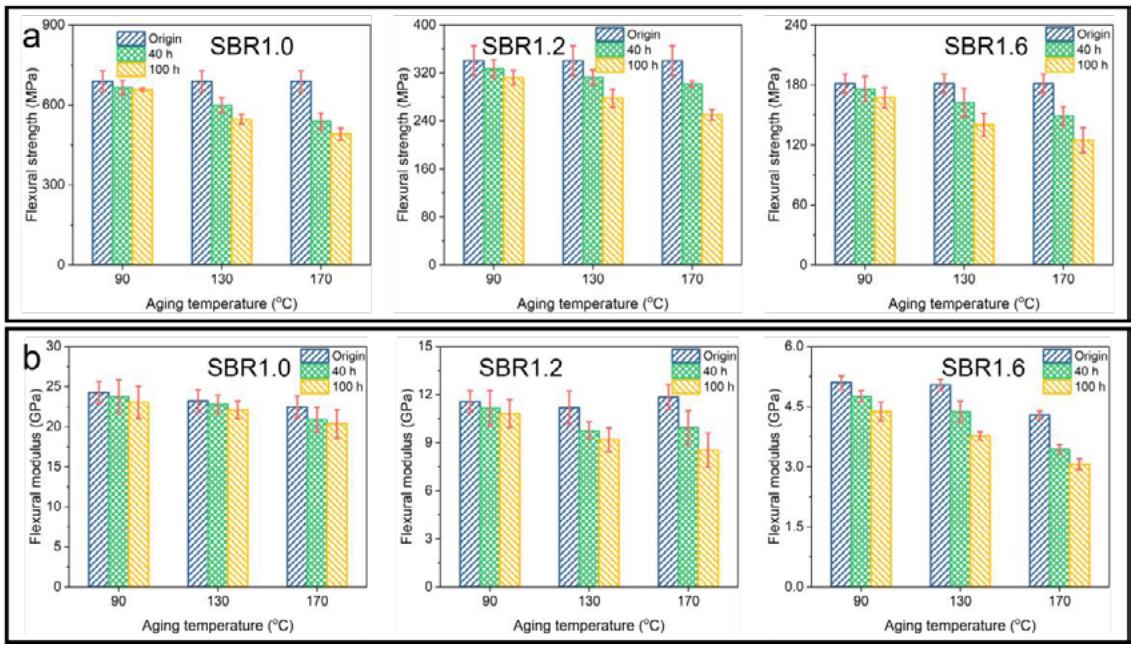


Fig. 5 Reduction of (a) flexural strength and (b) modulus after aging.

3.2. Mechanical properties

Both the flexural strength and modulus decreased with aging duration and SBR increasing, as shown in Fig. 5. The springback caused a giant reduction of the mechanical properties, and the porous structure does not benefit the bearing and easily generates cracks. The error of sandwich with SMC skin is large, mainly comes from the scatter of SMC. The reduction after the first 40 hours is apparent, proving the aging is effective. But the reduction ratio of modulus is relatively low because it is mainly determined by the skin of SMC. The thermo-oxidative aging caused enormous damage to the mechanical properties, so the assessment of structural integrity is necessary for the automobile application.

In Fig. 6a, for the original specimens of SBR1.0, the brittle failure occurred soon but a bearing period can be found for springbacked specimens before the failure. The displacement before fracture increased with SBRs, proved the advantage of energy absorption from the porous structure. But for aged specimens, the bonding between fiber and resin is destroyed and the transfer of stress gets weak. And delamination occurred in the springbacked specimens. And this kind of failure mode change is more obvious when aged at higher temperatures. The bearing force by the bottom skin after the first drop also reduced, from the aging damage to the resin.

The curves are divided into 4 parts for SBR1.0. point A belongs to the elastic period, and cracks were generated on the top surface because of the stress at Point B. For not springbacked specimens, the crack rapidly grows and penetrates through the bottom skin, causing brittle failure. But for aged specimens, the crack slowly propagates inner the core and finally reaches the bottom skin, and then causes the fracture. Partial delamination could be observed in the top skin, driven by the stress concentration during the start period. For SBR1.6 specimens, a gradual failure mode change occurred. The blue curve of the not-aged specimen shows a longer linear period before the first drop, which comes from the fracture on the top skin. Then the core is gradually compressed finally the bottom skin is fractured, leading to complete failure. For the aged specimens, two situations exist. The green curve shows a similar trend, with the first drop of crack on the top skin, but the second drop comes from the delamination at the interface. For the yellow curve, the delamination directly occurred before any crack was generated, showing a more severe aging effect.

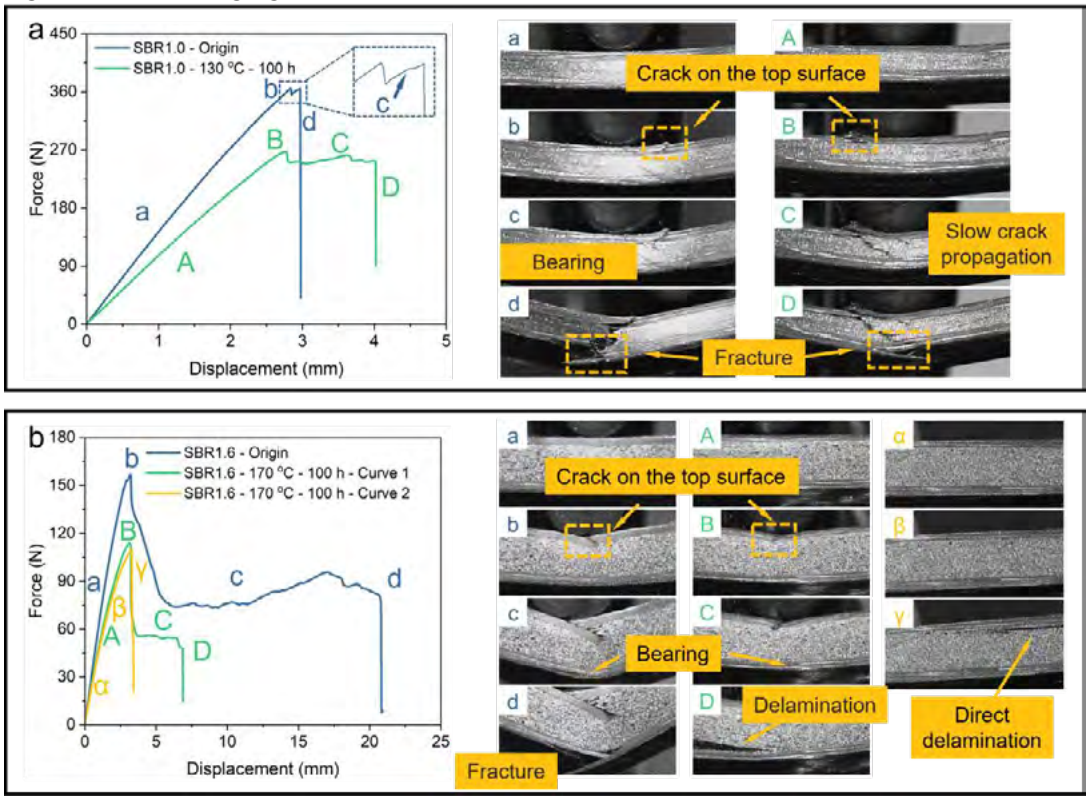


Fig. 6 Reduction of (a) flexural strength and (b) modulus after aging.

Acoustic emission (AE) testing was applied to monitor the fracture process, as shown in Fig. 7. The peak of the AE count is highly consistent with the fracture of the specimen. For the left figure, the fracture of two skin is reflected on the AE, while the middle signal proves the growth of cracks. For the middle figure, the count of delamination is much higher than the first drop of crack emerging, because delamination absorbs more energy by generating new surface. For the right figure, lower peaks of AE signals proved the process that the delamination first generated in the local position and then extended to the whole interface.

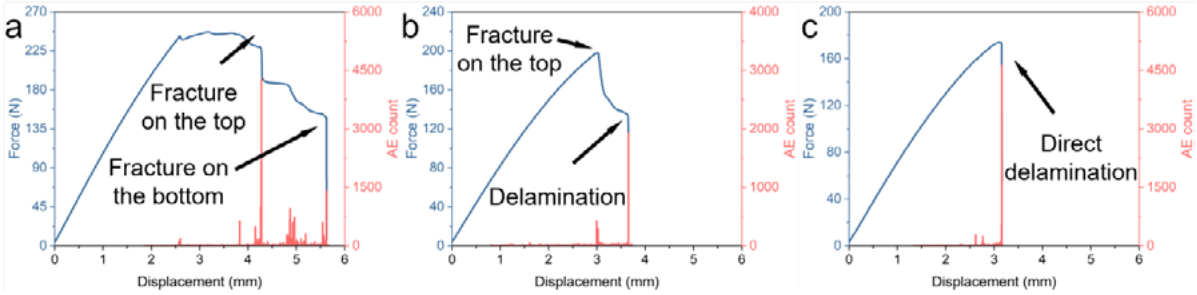


Fig. 7 AE counts of SBR1.2 (a) without aging and aged at 170 °C for (b) 40 hours and (c) 100 hours.

3.3. Structural strength assessing by vibration

It has been verified that the non-destructive vibrational method could be applied to inverse the detailed modulus distribution from easily tested natural frequency singles with satisfying accuracy [19]. In this case, the thermos-oxidative aging inflicted continuous damage on the specimens, and the gradual decrease in modulus is also reflected in the natural frequencies of the aged specimens, as shown in Fig. 8. Natural frequencies refer to the frequencies at which a system tends to oscillate or vibrate naturally, without any external forces acting on it. In a mechanical system with multiple degrees of freedom, there will be multiple natural frequencies, each corresponding to a specific mode of vibration. The order of natural frequencies is typically arranged from the lowest frequency to the highest. The value of the Y axis refers to the change of the first 40 hours and the additional 60 hours. The aging under the temperature of 90 °C is relatively weak, so the aging effect on natural frequencies is not strong. The reduction of all SBRs is small. When the temperature increased, the reduction immediately increased. The springback process brings porous structure to the specimens, so the aging is generally homogeneous occurred inner the core, causing a regular reduction of natural frequencies without abnormal values. Also, longer aging duration caused a larger reduction.

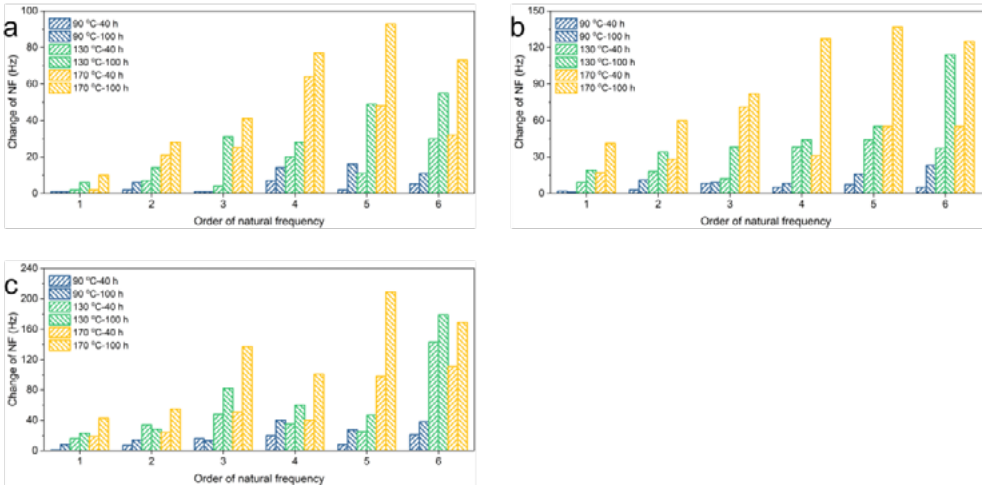


Fig. 8 Reduction of first 6 order NFs of (a) SBR1.0, (b) SBR1.2 and (c) SBR1.6.

The FE model and real sandwich plate after aging in freshwater for 6 months were as shown in Fig. 9(a-b), with geometry size of 100 * 100 mm. Both the virtual and real square plate were divided into 4 parts, and A1 and B1 are for modulus along the X direction, namely E_x, while A2 and B2 are for modulus vertical to the direction, namely E_y. The integration method of linking 3 models presents the best inversing accuracy. Beside the original plate without extra mass blocks, two kinds of mass distributions were achieved with the model shown in Fig. 9(d-e). The mass distribution affected the vibration, although the shapes of the same order are similar, the position relation is apparently different. The thickness was tested. And the inverse process is to calculated the modulus distribution and compare the calculated values with the tested values, which is referred to errors. And the everage absolute error refers to the average of error of all the four parts. For the sandwich and springback, the average absolute errors are around 4% and 6%, respectively. And the terms of P_x means the different plate models with various mass distributions, which is revealed in Fig. 9(d-e). The major factor of reduced accuracy is the thickness of the springbacked specimen is larger compared to the edge of the square, which cannot be regarded as a pure 2D stress state. However this accuracy still could be used to assess the structure integrity after long-time thermo-oxidativel aging.

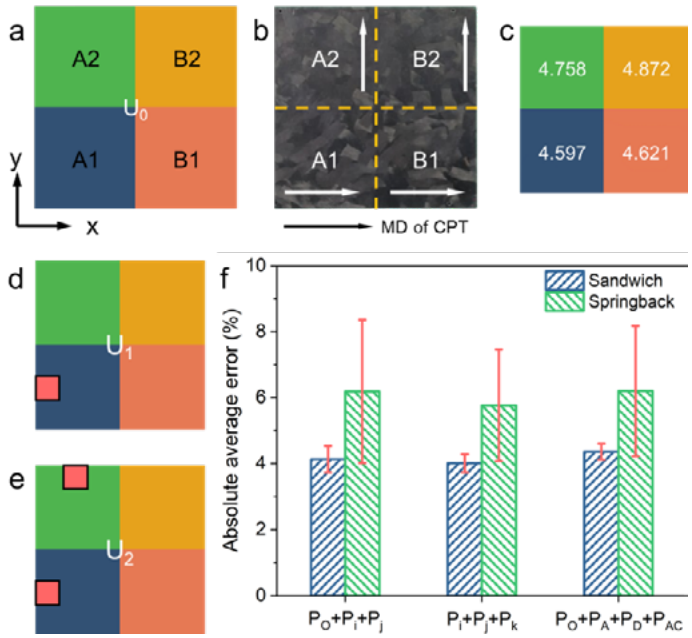


Fig. 9 (a) FE model and (b) real sandwich structures used for inversing residual modulus, (c) thickness distribution, (d-e) mass blocks distribution, and (f) inversed average absolute errors.

4. Conclusions

A sandwich structure with SMC skin and CPT core is prepared for use in automobile components and is lightweight through the springback effect with different SBRs; The springback phenomenon introduced porous structure and low density to the core material, which apparently reduced the mechanical properties. The thermo-oxidative aging simulating the automobile serving environment caused an apparent reduction of flexural strength and modulus, and the fracture mode also shifted to delamination at the interface. The application of the as-proposed inversing method was applied to the sandwich structure with various thicknesses, showing satisfying accuracy. For practical usage, concerning the influence of environmental factors, the effect of humidity and heat on the mechanical properties was investigated. In conclusion, this chapter provides valuable insights into the effects of thermos-oxidative aging on the mechanical properties, microstructure, and failure mechanisms of sandwich CFRTP composites. The non-destructive vibrational method proves to be a promising tool for assessing the structural integrity of aged composites.

Acknowledgments
The authors would like to thank the Industrial Technology Center of Fukui Prefecture for providing the SMC material used in this research, the WINGS-CFS of The University of Tokyo, and Designing Future Society Fellowship (030401SP52) for the support.

References
[1] S. Adams, F. Adedoyin, E. Olaniran, F. Bekun, *Econ. Anal. Policy* 2020, 68, 179-190.
[2] M. Honegger, A. Michaelowa, *J. Roy, Clim. Policy* 2021, 21, 678-698.
[3] K. Tanaka, R. Habe, M. Tanaka, T. Katayama, *J. Compos. Sci.* 2019, 3, 14.
[4] E. Gardie, V. Paramasivam, H. Dubale, E. Chekol, S. Selvaraj, *Mater. Today Proc.* 2021, 46, 7369-7374.
[5] S. Yao, F. Jin, K. Rhee, D. Hui, S. Park, *Compos. Part B* 2018, 142, 241-250.
[6] Y. Wan, S. Yamashita, J. Takahashi, *Mech. Compos. Mater.* 2022, 58, 395-408.
[7] G. Cai, T. Shirai, Y. Wan, K. Uzawa, J. Takahashi, *Appl. Compos. Mater.* 2021, 28, 573-586.
[8] W. Dong, P. Gijsman, *Polym. Degrad. Stab.* 2010, 95, 1054-1062.
[9] M. Clifford, T. Wan, *Polymer* 2010, 51, 535-539.
[10] A. Bernasconi, P. Davoli, A. Basile, A. Filippi, *Int. J. Fatigue* 2007, 29, 199-208.
[11] M. Akkapeddi, *Polym. Compos.* 2000, 21, 576-585.
[12] R. Li, X. Hu, Polym. *Degrad. Stab.* 1998, 62, 523-528.
[13] T. Mazan, R. Berggren, J. Jorgensen, A. Echtermeyer, *J. Appl. Polym. Sci.* 2015, 132, 6249-6260.
[14] J. Thomason, J. Ali, J. Anderson, *Compos. Part A* 2010, 41, 820-826.
[15] L. Sang, C. Wang, Y. Wang, Z. Wei, *RSC Adv*. 2017, 7, 43334-43344.
[16] W. Wang, T. Kam, *Compos. Struct.* 2000, 50, 347-352.
[17] D. Dorsey, R. Hebner, W. Charlton, *J. Compos. Mater.* 2004, 38, 1505-1519.
[18] J. Tam, Z. Ong, Z. Ismail, B. Ang, S. Khoo, *Mech. Adv. Mater. Struc.* 2017, 24, 971-986.
[19] Y. Zhang, B. Xiao, Y. Wan, W. Huang, J. Takahashi, *Appl. Compos. Mate.* 2023, 30, 1785-1818.

WEAR ANALYSIS OF MICROSTRUCTURE IMAGE-BASED 3D MODELS TO HELP DESIGN THE BEST ABRADABLE COATING COMPOSITION

Prakash Jadhav and Anitha Azmeera

Email: Prakash.j@srmap.edu.in

SRM University AP- Andhra Pradesh, India 522240

Keywords: Finite element analysis, Microstructure-image based modeling, Abradability

Abstract: Enhancing abradable or wear-resistant coatings within the high-temperature zones of aero engines is recommended to boost efficiency and power density in gas turbine engines for both military and commercial aircraft. The development of these coatings is driven by the aim of reducing blade failures and enhancing resistance to wear and erosion. Abradable coatings or seals are suggested to achieve these objectives, minimizing the space between the rotor and the shroud with an abradable seal at the blade's tip. Coatings typically consist of multiphase materials applied via thermal spray methods, comprising a metal matrix, oxide particles, and void space. Maintaining an optimal blend of qualities, such as erosion resistance and hardness, during production is crucial. The research objective is to devise a microstructure-based modeling methodology to mimic the coating wear process and aid in designing the composition of abradable coatings. This involves microstructure modeling, meshing, and wear analysis using tools such as Fusion360, Hyper Mesh, and LS-Dyna. An abradable coating model is developed and wear analysis is conducted using simulated rub rig tests. The relationship between percentage composition and morphological variations of metal, oxide, and voids with output parameters such as abradability over time is explored.

Introduction

Indeed, advancements in air transportation necessitate continuous improvements in jet engine performance, particularly in terms of efficiency and power output. Closing the gap between the blade tip and shroud is a critical area of focus to reduce parasitic leakage flows through seals. This is crucial for enhancing engine efficiency, reducing fuel consumption, and ultimately improving overall performance. Engineers and researchers are constantly working on innovative designs and materials to achieve tighter clearances and minimize leakage, thereby maximizing the efficiency and power output of industrial turbines for jet engines [1-3] Abradable seals are indeed a significant advancement in turbine technology, allowing for tighter clearances between the blade tip and shroud. In these systems, the blade tip intentionally incurs into the shroud, minimizing the tip gap. The various types of abradable materials are being developed for this purpose, and they can be manufactured using different methods. Among these methods, thermal spraying stands out as the most popular choice for processing abradable seal materials [4-5]. During the service, abradable materials undergo complex wear mechanisms due to interaction with blade tips. These mechanisms include cutting, smearing, adhesive transfer, crushing, melting, erosion, and oxidation. By employing high-quality abradable seal coatings, gas turbine blades become more reliable, as they are better protected against various types of failures, including high-temperature damage, creep failures, fatigue failures, corrosion failures, and thermal exposure [6-7]. Abradable materials typically comprise composite mixtures of two or three structural components to achieve the desired properties, including a metallic matrix and a second phase acting as a solid lubricant, often with controlled porosity. The testing of abradable coatings involves using a test rig that simulates the conditions experienced by turbine blades in a gas turbine engine. The ratio of volume loss due to shroud wear to blade wear is known as abradability and is a key parameter in assessing the performance of abradable coatings. Rub tests are conducted at various feed and exit speeds to measure the force and wear on the blade tip. Overall, the testing of abradable coatings is crucial for ensuring their effectiveness

©2024 | 3_Jadhav_Prakash_61QOA.pdf

in real-world applications [11-12]. Scanning Electron Microscopy (SEM) is an invaluable tool for studying the microstructures of coatings. Furthermore, Finite Element (FE) models are employed in simulation software to complement experimental observations and provide a deeper understanding of coating behavior. These models simulate the thermal and mechanical responses of coatings under various conditions, allowing researchers to ascertain the Residual Stress Distribution, Fracture Mode of Thermal Barrier Coating (TBC), Fretting Wear in Composite Cermet Coating, Effective Material Properties, Thermo-Mechanical Behavior [13-15]. Bolelli [16] work highlights the importance of incorporating microstructural details into finite element modeling to understand and predict the thermo-mechanical behavior of thermal spray coatings accurately. B.Klusemann [18] developed a comprehensive FE model of the microstructure of abradable coatings using SEM images. By incorporating detailed microstructural features such as porosity, phase distribution, and grain structure into the model, also simulate the mechanical behavior of the coating under various loading conditions. D. Aussavy [21] study likely involved comprehensive characterization of the thermo mechanical properties of various coatings, such as hardness, toughness, thermal conductivity, coefficient of thermal expansion, and elastic modulus. Prakash Jadhav [22] research focuses on utilizing microstructure-based image models of coatings to study abradability through simulations. This approach is highly valuable for gaining insights into the behavior of abradable coatings at the microstructural level and understanding their performance under different conditions. Azmeera.A.k [23] developed microstructure-based modelling methodology which mimics the coating wear process and subsequently help in designing the abradable coating composition. Microstructure modelling, meshing, and wear analysis using many tools such as Fusion360, Hyper Mesh, and LS-Dyna were used to develop an abradable coating model and perform wear analysis using a simulated rub rig test. The relation between percentage composition and morphology variations of metal, oxide, and voids to the output parameters such as hardness, abradability, and other mechanical properties is explored using simulated finite analysis models of real micrographic images of abradable coatings. The primary objective of current study is to establish and further validate a simulation approach aimed at comprehending and forecasting the abradability of coatings through microstructure-based image models. To validate the proposed methodology, experimental data from the paper referenced as [24] were utilized.

2. Methodology

2.1 Critical Design Factors for Turbomachinery Sealing Employing Systems Featuring Abradable Seal Coatings

The Coatings are resistant to attacks from corrosive substances at high temperatures, such as sulphides, chlorides, and silicates (CMAS), to sintering at high temperatures, and to thermal shock or cycle-induced degradation of solid particles. The primary purposes of abradable coatings are their compatibility with labyrinth seals, shrouded versions of turbine, compressor, or fan blades, or their unshrouded counterparts. This is because abrasive wear and/or friction-induced overheating of the dynamic component may be mitigated if the coating of the abradable counterpart is softer than the material of the dynamic rubbing component. Abradable seal systems are utilized on the surface of the stator to facilitate the blade tip's free incursion into the shroud. These coatings can be several millimeters thick and serve as sacrificial layers, minimizing the tip gap. Ideally, abradable coatings should not damage the blade as it incurs into the shroud and must maintain a perfectly smooth surface to achieve this objective. In particular, the coatings are designed to improve the clearance control between the turbine blades and the casing. Overall, the application of coatings like NiCrAl-Bentonite and CoNiCrAlY-BN-Polyester etc. plays a critical role in ensuring the safe and efficient operation of high-temperature turbine stages.

2.2 The Methodology for Rub Rig Event-Modelling

The rub experiments were conducted using the abradable test gear shown in fig, which employs an abradable seal to simulate the wear experienced by gas turbines during operation. In this test setup, a

©2024 | 3_Jadhav_Prakash_61QOA.pdf:2

wheel spins at high speeds, resulting in the removal of the coating and wear on the wheel itself. After each experiment, data is collected on the wear of the coating on coupons and the wear of the blade tip. The performance of the coating is typically evaluated in terms of its abradability, which is a measure of how effectively the coating wears compared to the blade. To assess abradability, simulations are used to replicate the dynamic processes occurring within the coating microstructure as it interacts with the blade. Abradability is quantified as the ratio of coating wear to wheel wear, determined by measuring wear on both the wheel surface and the coating surface. A desirable abradability ratio for a good abradable seal falls within the range of 10 to 20. This indicates that the coating wears at a rate that is 10 to 20 times greater than the wheel, ensuring sufficient clearance control while minimizing wear on the blade. By evaluating the abradability of coatings through rub experiments and simulations, researchers can assess their suitability for use in gas turbine applications. Achieving the optimal abradability ratio ensures effective sealing performance while mitigating wear on critical turbine components.

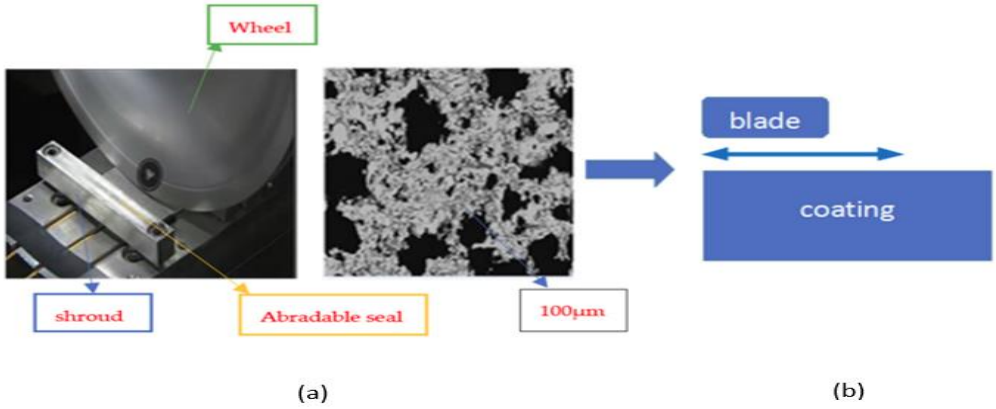


Figure 1 (a) Rub ring test apparatus. (b)Planning set up of rub rig test method

Figure 1 shows the modeling process involves creating 3D finite element analysis (FEA) models of the rub rig setup, incorporating a microstructure-based foundation to accurately represent the coating's behavior. The coating is initially prepared using air plasma spraying (APS) on coupons. The microstructure of the coating is then examined using micrograph to understand its structural characteristics. A proprietary technique is utilized to create the FEA model and mesh based on the microstructure image of the coating. Software tools such as Autodesk Fusion 360 2021 and Hyper Mesh 2021 are employed for this purpose. These tools allow for the creation of detailed and refined mesh structures that accurately represent the coating's microstructure. The generated mesh file is imported into LS-DYNA 13.1 for additional processing and simulation. The LS-DYNA program is used to simulate the behavior of the coating under dynamic wear conditions, replicating the rubbing action experienced in the rub rig test setup. The simulation accounts for the motion of the blade, which moves forward and backward repeatedly to mimic its motion in the actual test setup. After the simulation is complete, the abradability of the coating is evaluated by examining the volume loss of both the blade and the coating microstructure. This assessment allows researchers to determine how effectively the coating wears compared to the blade and assess its suitability for use in the intended application.

2.3 Representation of microstructure and its three-dimensional geometric modeling.

The microstructures of abradable coatings used in this study are derived from [24] in this paper, the focus is on abradable seals classified based on their temperature capabilities, specifically on NiCrAl-Bentonite coating. This coating is a metal matrix-dislocator designed to withstand temperatures up to 850 °C. The coating was applied using the combustion spray process with a Metco 6PII gun. Microstructures of coatings were obtained using Scanning Electron Microscopy (SEM) Phillips XL-30 and a ZEISS DSM 982 Gemini apparatus. After mounting the samples in low viscosity resin, conventional mechanical polishing metallographic techniques were employed. The coating images were

©2024 | 3_Jadhav_Prakash_61QOA.pdf:3

primarily captured under backscattering electron imaging conditions. This methodology allows for detailed examination and characterization of the coating microstructure, essential for understanding its properties and behaviour in high-temperature environments. In this study, NiCrAl-Bentonite -polyester was used as the material of interest to model and simulate the abrasion resistance of thermal barrier coatings. The following methodology was employed: Autodesk Fusion 360 2021 software was utilized for microstructure modeling. This software allows for the creation of detailed representations of microstructures, essential for accurately simulating material behavior. The Image J program was used to create separate DFX file formats for each of the three phases: metal, oxide, and porosity. These files serve as inputs for the modeling process and ensure consistency and accuracy in the representation of the coating microstructure. The DFX files for each phase were used to construct and assemble the three-phase models, incorporating the metal, oxide, and porosity components. Hyper Mesh 2021 software was employed to generate refined meshes with consistent element sizes and densities. Meshing is a crucial step in finite element analysis, as it determines the accuracy and reliability of the simulation results. Mesh style was utilized to create fine meshes, ensuring that the simulation captures detailed features of the microstructure accurately. The generated mesh file was imported into the LS-DYNA program for further processing. It was used to produce a 3D model of the coating and simulate the micrograph model, allowing for the analysis of abrasion resistance. This 3D representation was created using Fusion 360 software, where the porosity level was specified, and the metal and oxide phases were represented by distinct colors. Each phase exhibits unique sizes and shapes, contributing to the overall complexity of the microstructure. Despite the variations in the ingredients' sizes and shapes, the overall dimensions of the micrograph remain consistent, measuring 0.219 mm by 0.16 mm. This detailed visualization allows for a comprehensive understanding of the microstructure's porosity and its impact on the material's properties and behavior.

2.4 3D Mesh Modal for Microstructure

Just the 2D surface depiction is seen in Figure 2a, which displays the microstructures mesh. Different colors are used to identify the metal and oxide phases. A mesh was created for the metal oxide and porosity structure in this situation, using a first-area-phase (porosity) element size of 5. In the blade model, there were 64425 elements on average, compared to 614415 elements in the coating. Hex 8-node solid element with continuous stress was the element formulation applied to the coating and the blade model. Crucially, all of the ingredient’s metal, oxide, and porosity were formulated with the same elements.

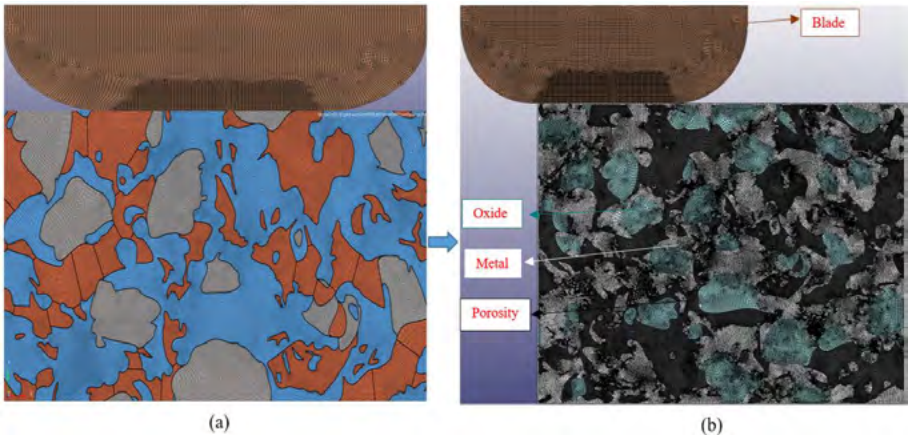


Figure 2 (a) two dimenstional microstructure mesh modal in Hper mesh tool (b) three dimenstional microstructure mesh modal in LS -Dyna tool.

The coating's 3D model in LS Dyna software, which is 0.219 mm by 0.16 mm in the planar direction and only a few elements thick in the thickness direction. Different hues correspond to the coating's metal, oxide, and porosity phases. Porosity is represented as modular components to avoid the model collapsing. The porosity is built as separate entities in the 3D modal and using a semicircular bottom

©2024 | 3_Jadhav_Prakash_61QOA.pdf:4

form and a thickness of a few elements, Figure shows a 0.17 mm × 0.06 mm 3D blade model was created. Importing the coating and blade models into the LS-Dyna 13.1 program completes the simulation setup. During post-processing, the blade moves back and forth to guarantee consistency after initially resting still on the coated material. By taking into account the existence of porosity and how it affects the behavior of the coating under dynamic loading conditions, this method enables the realistic modeling of the interaction between the blade and the coated material.

2.5 Microstructure FEM Modal in LS-DYNA 13.1 Software

The experimental rub rig emulates the challenges faced by blade tips interacting with a high-speed spinning wheel by placing a wheel onto a coupon at a predetermined feed rate. A coupon is coated and affixed to the mount, whereupon the blade tip scrapes the coating upon contact. Following the experiment, data on the coating wear on coupons and the tip wear on blades are collected. Abradability serves as a metric to assess coating performance, comparing coating wear to blade wear. Instead of simply replacing the revolving wheel with a rotating blade, the blade was programmed to move forward and backward repeatedly, replicating the wheel's motion. Furthermore, to closely emulate the rubbing action, the blade's movement matched the tangential speed of the revolving wheel, approximately 400 m/s. To prevent dynamic wave reflections from the bottom surface, appropriate boundary conditions for the coating model involve treating the bottom surface as non-reflective. Constraining the left and bottom sides along their edges aids in containing the coating. In the case of plain strain, longer vertical surfaces are constrained to a perpendicular or out-of-plane orientation. Additionally, the blade was assigned suitable boundary conditions, including forward and backward displacements, alongside velocity. Normal strain limitations also apply to surfaces of blade length. For material representation, the piecewise linear plasticity (Ti64) model was utilized for the blade, while the kinematic plasticity (AP) model was employed to simulate the alloy coating in LS-Dyna. Notably, a relatively small modulus was assigned to the porosity components. Strain-based failure assumptions were applied to all coating components, with estimates of failure strains provided for metal, oxide, and porosity. Through trial simulations, the optimal value of the porosity failure strain was determined to be between 1% and 2%.A piecewise linear plasticity model, accounting for temperature at 600 degrees Celsius, was employed alongside stress–strain data for the blade material. Modulus and Poisson’s ratio were additional inputs for the blade. The MAT ADD EROSION command was employed within the material model to define stress limits for blade failure under load. To mitigate hourglass errors, the hourglass command was universally implemented. Motion of blade represented as two sets of data indicating vertical and horizontal motion along the y-axis and x-axis, respectively. These data are expressed as velocity as distance versus time, divided into 60 intervals. The specified times ensure correct horizontal and vertical positions of the blade. The instruction specifying contact between the blade and the coating materials utilizes a contact eroding surface-to-surface approach. When elements near the failure limits defined in the material models, this contact enables the elements to fail. Similar to the gradual wearing away of particles over time, failed elements are eliminated from the simulation. The simulation calculates the overall volume loss percentage of coating material and blade elements. By comparing the volume of coating (metal and oxide) removed to the volume of the blade, the abradability parameter is determined. Optimal shrouds and coatings exhibit an abradability of 20 or more, indicating their capability to remove a volume of coating at least 20 times greater than that of the blade.

2.6 Material properties for both the coating and blade, as well as input parameters for the blade

The primary focus of this investigation was to assess how variations in the material properties of both the coating and blade components impact abradability. By understanding the influence of each individual parameter, optimal settings can be identified to enhance abradability effectively. As previously stated, a representative microstructure-based finite element analysis (FEA) mesh model is employed across all scenarios examined. Table 1 provides detailed attributes of the blade and shroud materials, emphasizing that all material inputs remain constant throughout the analysis. Notably,

©2024 | 3_Jadhav_Prakash_61QOA.pdf:5

porosity components are assigned a very small modulus value. Strain-based failure assumptions are applied uniformly across all coating components, with estimated failure strain limits provided for metal (1.5%), oxide (1%), and porosity (2%).

Table: 1 Characteristics of metal, porosity, oxide, and blade materials [21].

s.no	Material	Density (kg/mm³)	Young's modulus (Gpa)	Poisson's ratio	Yield strength (Gpa)	Tangent modulus (gpa)	Failure strain
1	Metal(NiCrAl-Bentonite)	2.7e-6	142	0.3	0.4	130	0.015
2	Porosity	1e-6	1	0.33	0.025	0.1	0.02
3	Oxide+Bentonite	3.8e-6	190	0.34	0.375	180	0.01
4	Titanium64	4.4e-6	159	0.342			

Blade material stress strain behavior data was used as input, with consideration given to its behavior at 600°C. Additionally, a value of 0.9 GPa is assumed for blade erosion in the event of stress-based failure.

3. Results

3.1 abradable seal after erosion results

The velocity depicted in Figure 5 dictates the motion of the blade. In Figure 7a, it can be observed that the blade ceases its movement after a predefined duration, with various colors denoting diverse pore sizes and shapes within three phases in microstructures corresponding to distinct metallurgical stages.

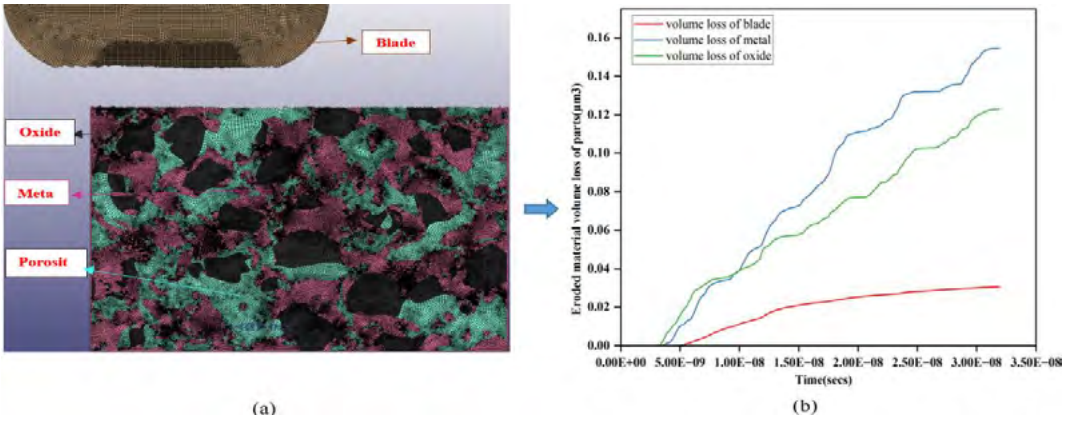


Fig 7: (a) Appearance of NiCrAl-Bentonite-polyester coating post-erosion. (b) Time-dependent erosion of metal and oxides and blade volume loss.

However, during this process, the coated material experiences some loss of its constituents, particularly metal and oxide. While the reduction in blade material is evident, it's crucial to acknowledge that losses in metal and oxide, as well as the blade itself,Occur concurrently. Eventually, a small gap emerges between the blade and the coated material. After completing the simulation, the volume of material loss for metal, oxide, and the blade was calculated using the volume fail command, as depicted in the D3 plot and the time history graph.

Figure 7b illustrates the increase in the rate of metal erosion as the blade penetrates deeper, with the volume loss of metal surpassing that of oxide, albeit marginally. Notably, the volume loss of the blade is observed to be lower than that of both metal and oxide. As the blade delves further into the coated substance, the graph demonstrates a corresponding increase in the volume loss of the blade. Throughout the entire duration, the volume loss of the blade, along with metal and oxide, was monitored. However,

©2024 | 3_Jadhav_Prakash_61QOA.pdf:6

it's worth noting that the abrasion-resistant seal incurred loss of metal and oxide compared to the abradable seal, which was expected to exhibit the highest volume loss at a given porosity and hardness. Consequently, the predicted volume loss of the blade over the entire time span was anticipated to be less than that of the abradable seal.

3.2 Variation of abradability with respect to time

The blade undergoes vertical downward motion from left to right and from right to left, adhering to the prescribed boundary conditions. With each cycle, it systematically removes metal fragments, thereby experiencing material loss. Over the entire sequence, spanning 50 rotations, the blade steadily eliminates material. However, Figure 7b provides an opportunity to compute individual metal volume loss, oxide volume loss, and blade volume loss based on data accumulated over the last 50 rotations.

Subsequently, the abradability is calculated using the following formula:

Abradability = (Volume fraction of coating removed or shroud wear) / (Volume fraction of blade removed).

Table: 2 Erosion properties and abradability evolution of the abradable seal over time.

s.no	Time (secs)	Metal wear (µm3)	Oxide wear (µm3)	Shrude wear (metal+oxide) (µm3)	Blade wear (µm3)	Abradability
1	5.82E-09	1.19E-02	2.11E-02	3.30E-02	1.40E-03	2.36
2	8.72E-09	2.99E-02	3.29E-02	6.28E-02	8.58E-03	7.32
3	1.17E-08	4.85E-02	4.35E-02	9.20E-02	1.40E-02	6.57
4	1.46E-08	6.95E-02	5.64E-02	1.26E-01	2.04E-02	6.17
5	1.74E-08	8.74E-02	6.68E-02	1.54E-01	2.28E-02	6.76
6	2.03E-08	1.11E-01	7.71E-02	1.88E-01	2.55E-02	7.37
7	2.32E-08	1.23E-01	8.95E-02	2.13E-01	2.69E-02	7.90
8	2.61E-08	1.32E-01	1.03E-01	2.35E-01	2.85E-02	8.23
9	2.92E-08	1.42E-01	1.13E-01	2.55E-01	2.97E-02	8.58
10	3.19E-08	1.54E-01	1.23E-01	2.77E-01	3.05E-02	9.08

The formula (1) allows for the determination of abradability, which exhibits a consistent increase from the initial time to the final interval of time, as depicted in Figure 8b. And the increasing and decreasing value of the abradable coating, blade, and abradability number is shown in Table 2. The loss of both the titanium blade and the abradable seal can be illustrated. Here, we can assume that the loss of the blade and the abradable seal increases linearly with time. The only difference is that the titanium blade has a much smaller volume loss than the abradable seal, and the abradable seal's volume loss is calculated as the sum of metal and oxide. The abradability increases gradually from the first interval of time to the last period of time. Until the gap created between the blade and seal, the abradability changes linearly with respect to time.

4. Conclusion

This study presents a microstructure-based modeling methodology designed to replicate the coating wear process and aid in formulating the composition of abradable coatings. Simulation techniques were employed to develop an abradable coating model and simulate wear using rub rig tests. The relationship between percentage composition and morphological variations of metal, oxide, and voids with output parameters such as hardness, abradability, and other mechanical properties was investigated using simulated finite analysis models based on real micrographic images NiCrAl-Bentonite polyester coatings. Based on these images, 3D finite element models of the coatings were constructed, meshed,

©2024 | 3_Jadhav_Prakash_61QOA.pdf:7

and refined by incorporating the blade using various tools. Subsequently, simulated rub rig tests were conducted on the coating models using LS-Dyna. The study concludes that the Abradability number increases as the level of coating wear rises or blade wear decreases over time.

5. Reference

[1] A.M. Wallis, J.D. Denton, A.A.J. Demargne. Journal of Turbomachinery, 123, 334.
[2] K.J. Melcher, J. Kypuros, Proceedings of the XVI International Symposium on Air Breathing Engines, Cleveland, OH, Aug. 31–Sep. 5, 2003, ISABE 2003-1102 (NASA/TM-2003-212627), 2003.
[3] B.M. Steinetz, R.C. Hendricks, J. Munson. NASA-TM 1998-206961.
[4] R.K. Schmid, F. Ghasripoor, M. Dorfman, X. Wei, ITSC 2000, Montreal, Canada. Ed. C.C. Berndt, Pub. ASM International, Materials Park, OH, USA, 1087.
[5] E.R. Novinski. ITSC 1991, Pittsburg, PA, USA. Ed. T.F. Bernecki, Pub. ASM International, Materials Parck, OH, USA. 451.
[6] M.O. Borel, A.R. Nicoll, H.W. Schäpfer, R.K. Schmid, Surf. Coat. Technol. 39/40 (1989) 117.
[7]. Carter, T.J. Common failures in gas turbine blades. Eng. Fail. Anal. 2005, 12, 237–247. [CrossRef]
[11]. Liu, J.; Yu, Y.; Liu, T.; Cheng, X.; Shen, J.; Li, C. The influence of composition and microstructure on the abradability of aluminum-based abradable coatings. J. Therm. Spray Technol. 2017, 26, 1095–1103.
[12]. Xiao, J.; Chen, Y.; Chen, D.; Tian, J.; Ouyang, H.; Wang, A. Interactions between blades and abradable coatings: A numerical approach considering geometrical nonlinearity. Int. J. Mech. Sci. 2021, 191, 106052.
[13]. Faraoun, H.I.; Grosdidier, T.; Seichepine, J.L.; Goran, D.; Aourag, H.; Coddet, C.; Zwick, J.; Hopkins, N. Improvement of thermally sprayed abradable coating by microstructure control. Surf. Coat. Technol. 2006, 201, 2303–2312.
[14]. Faraoun, H.I.; Seichepine, J.L.; Coddet, C.; Aourag, H.; Zwick, J.; Hopkins, N.; Sporer, D.; Hertter, M. Modelling route for abradable coatings. Surf. Coat. Technol. 2006, 200, 6578–6582. 13. Klusemann,
[15]. Klusemann, B.; Hortig, C.; Svendsen, B. Modeling and simulation of the microstructural behaviour in thermal sprayed coatings. In PAMM: Proceedings in Applied Mathematics and Mechanics; Wiley Online Library: Hoboken, NJ, USA, 2009; pp. 421–422.
[16]. Bolelli, G.; Candeli, A.; Koivuluoto, H.; Lusvarghi, L.; Manfredini, T.; Vuoristo, P. Microstructure-based thermo-mechanical modelling of thermal spray coatings. Mater. Des. 2015, 73, 20–34.
[18]. Klusemann, B.; Denzer, R.; Svendsen, B. Microstructure-based modeling of residual stresses in WC-12Co-sprayed coatings. J. Therm. Spray Technol. 2012, 21, 96–107
[21]. Aussavy, D. Processing Characterization and Modeling of Thermomechanical Properties of Threee Abradable Coatings: NiCrAlBentonite, CoNiCrAlY-BN-Polyester, and YSZ-Polyester. Ph.D. Dissertation, Université de Technologie de Belfort-Montbeliard, Belfort, France, 2016.
[22]. Jadhav, P. Abradable coatings: Design through microstructure-based models. Mater. Today Proc. 2022, 62, 7353–7357
[23] Azmeera, A. K., Jadhav, P., & Lande, C. (2023). Microstructure Image-Based Finite Element Methodology to Design Abradable Coatings for Aero Engines. Aerospace, 10(10), 873.
[24] Faraoun, Houda-Imane, et al. "Modelling route for abradable coatings." Surface and Coatings Technology 200.22-23 (2006): 6578-6582.

©2024 | 3_Jadhav_Prakash_61QOA.pdf:8

BENDING RESPONSE OF HYBRID ALUMINUM/THERMOPLASTIC COMPOSITE TUBE USING FOUR-POINT BENDING TEST

M. Rastak[1], S. V. Hoa[2], Daniel. Rosca[3]

[1]Concordia Center for Composites, Department of Mechanical, Industrial and Aerospace Engineering, Concordia University, Montreal, Canada
Email : mohammadali.rastak@mail.concordia.ca
[2]Concordia Center for Composites, Department of Mechanical, Industrial and Aerospace Engineering, Concordia University, Montreal, Canada
Email : hoasuon@encs.concordia.ca
[3]Concordia Center for Composites, Department of Mechanical, Industrial and Aerospace Engineering, Concordia University, Montreal, Canada
Email : daniel.rosca@concordia.ca

Keywords: Composite Materials, Hybrid Tube, Energy Absorption, Automated Fiber Placement, Four-Point Bending

Abstract

Composite materials are increasingly favored for their exceptional mechanical properties and lightweight nature, although their inherent brittleness poses challenges. Metals like aluminum offer ductility but lack lightweight properties. Hybrid materials, combining aluminum's ductility with composite materials' stiffness, offer enhanced energy absorption and performance. Understanding the bending response of these hybrid structures is crucial for optimal performance. Automated Fiber Placement (AFP) technology can wrap thermoplastic composite material around an aluminum tube precisely, as demonstrated in this paper. The four-point bending test conducted on a hybrid tube showed improved strength and stiffness compared to solely an aluminum tube. Additionally, the hybrid tube exhibits secondary resistance after failure. This research underscores the feasibility and advantages of integrating composite materials into aluminum structures, in a form of hybrid aluminum/thermoplastic composite tube, providing insights for enhancing performance in many applications such as energy absorber structures like bumpers and rocker panels in automobiles, or landing gear in helicopters. By combining the properties of both materials, engineers can achieve superior performance while maintaining overall lightweight.

1. Introduction

In engineering applications, lightweight structures offer numerous advantages. Lightweight structures find applications in industries such as aerospace, transportation, and pipelines [1-3]. In transportation, they contribute to improved fuel efficiency, reduced fuel costs, and lowered exhaust gas emissions. Additionally, lightweight structures decrease the quantity of materials needed for manufacturing. In this case, hybrid aluminum/composite structures prove highly beneficial, as both materials are lightweight and, when combined, they can attain the required properties for various engineering applications.

In simpler terms, hybrid aluminum/composite tubes enhance structural performance through their synergistic interaction. For instance, when exposed to transverse impact, these hybrid tubes exhibit superior impact resistance compared to singular composite tubes [4]. Regarding material selection for composite components, both glass and carbon fibers can be viable options depending on factors such as

the application, environment, and required specifications. However, for fatigue resistance, carbon fiber proves more durable than glass due to its superior strength-to-weight ratio and stiffness [5].

In most prior studies, thermoset resin was the prevalent choice for the composite part. However, considering thermoplastic composites could be a superior alternative, especially for applications where energy absorption is crucial. Therefore, manufacturing hybrid tubes using thermoplastic resin for the composite component is a worthwhile approach.

This study investigates the force-displacement characteristics of hybrid Aluminum/Carbon-PEEK tube during bending test and compared it with sole aluminum tube as well as analytical solution.

2. Experiment

2.1. Manufacturing procedure using Automated Fiber Placement (AFP)

To make a hybrid aluminum/composite tube, AFP can be used as it involves applying composite tape onto an aluminum tube, with layers gradually building upon each other over time as illustrated in Figure 1. This technique proves highly advantageous for hybrid tube production. The first reason is that certain applications require complex shapes that may not be easily fabricated using methods like hand lay-up or filament winding. AFP, on the other hand, is capable of generating various geometries across a wide size range rapidly and with minimal human involvement, ensuring greater consistency compared to hand lay-up, which is susceptible to human errors. Additionally, AFP is well-suited for thermoplastic composites, which offer superior performance in mentioned applications where energy absorption is a critical parameter. Unfortunately, previous research often had to resort to thermoset composites due to limitations in their chosen manufacturing techniques.

It's worth noting that using AFP positions the composite layer on the outer surface of the aluminum, making it impossible to have the composite on the inner side using AFP. However, a hybrid tube with aluminum inside the composite for transverse loading scenarios is likely to exhibit enhanced crashworthiness [6].

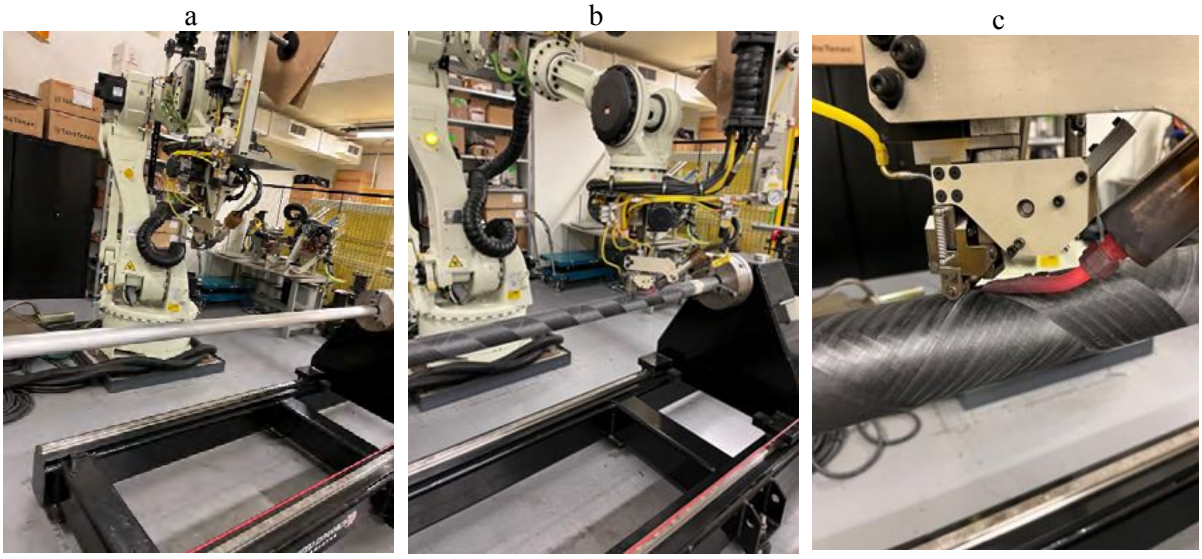


Figure 1. Using AFP for manufacturing of hybrid aluminum/Carbon-PEEK (a) An aluminum tube (b) Hybrid aluminum/Carbon-PEEK during manufacturing process (c) A closer view of the feeding tape on the surface of hybrid tube.

An aluminum mandrel made of T6061-T6 alloy, featuring an outer diameter of 63.5 mm, a thickness of 3.175 mm, and a length of 2438 mm, served as the pivotal component for depositing thermoplastic composites. For the composite layers, thermoplastic composite materials, specifically a carbon/PEEK composite, has been used.

A challenge emerged due to the substantial discrepancy in thermal expansion coefficients between aluminum and the thermoplastic composites. When subjected to the heat from the torch, the aluminum mandrel expanded more than the composite material. This creates good contact between the aluminum mandrel and the first layer of the composite. However, when things cool down, the aluminum mandrel contracts more than the composite, particularly in the initial layers at a 90-degree orientation. This resulted in the undesirable outcome of the aluminum mandrel loosely rotating within the initial layers of the composites.

To address this issue, a modified deposition schedule was employed, characterized by lower temperatures, and reduced compaction forces for the initial layers, as detailed below:

• Layer 1: Orientation - 90 degrees, Temperature (T) - 650°C, Compaction Force (F) - 30 lbs, Nitrogen Flow (N) - 60 Standard Liters per Minute (SLPM)
• Layer 2: Orientation - 90 degrees, Temperature (T) - 800°C, Compaction Force (F) - 30 lbs, Nitrogen Flow (N) - 60 SLPM
• Layer 3: Orientation - 90 degrees, Temperature (T) - 875°C, Compaction Force (F) - 40 lbs, Nitrogen Flow (N) - 60 SLPM
• Layers 4 to 40: Temperature (T) - 875°C, Compaction Force (F) - 60 lbs, Nitrogen Flow (N) - 80 SLPM

These adjustments effectively mitigated the issue of mandrel rotation and ensured the proper deposition of subsequent layers of thermoplastic composites.

During the initial deposition of the first four layers, a strategic cooling method was employed to maintain the mandrel's temperature. Compressed air was directed ahead of the torch, effectively reducing the heat transfer to the mandrel, and thereby minimizing its expansion. This approach was instrumental in ensuring that the initial composite layers adhered securely to the aluminum mandrel.

In this study, hybrid aluminum/carbon-PEEK composite tubes have been tested with a lay-up sequence as [Aluminum/90^{Glass}/90^{Carbon}/$(\pm 20)_5$/90_2/$(\pm 30)_4$/90_2/$(\pm 45)_4$]). It should be notable to mention that we introduced a layer of glass between aluminum and carbon as the first composite layer. This choice was driven by the imperative to avoid galvanic corrosion. Therefore, lay-up sequence comprises a total of 32 layers. The overall thickness was calculated as follows: aluminum (3.175 mm) + glass-PEEK (0.168 mm) + Carbon-PEEK (4.332 mm) = 7.675 mm. Figure 2 provides dimensions of the hybrid tube.

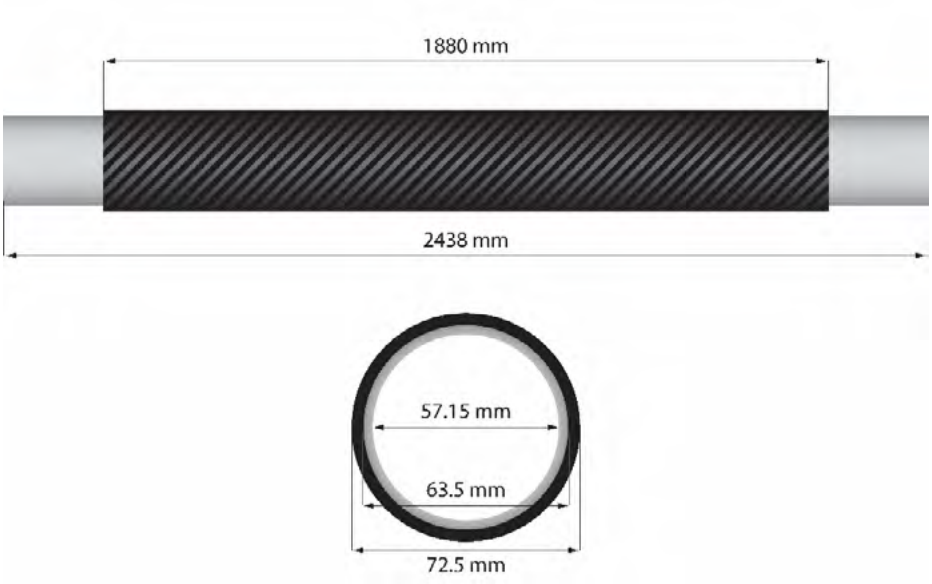


Figure 2. Dimensions of the hybrid tube.

2.2. Four-point bending test

The tube underwent a four-point bending test, where fiber glass/epoxy reinforcing pads were strategically affixed onto the tube's support and loading regions to mitigate stress concentrations. The locations of these supporting pads on the tube are illustrated in Figure 3.

Four-point bending tests were conducted at the Concordia Center for Composites using a specialized four-point bending fixture shown in Figure 4. This fixture utilizes servo hydraulic technology to operate a load cell. The load cell employed in this setup has a capacity of 50 KN.

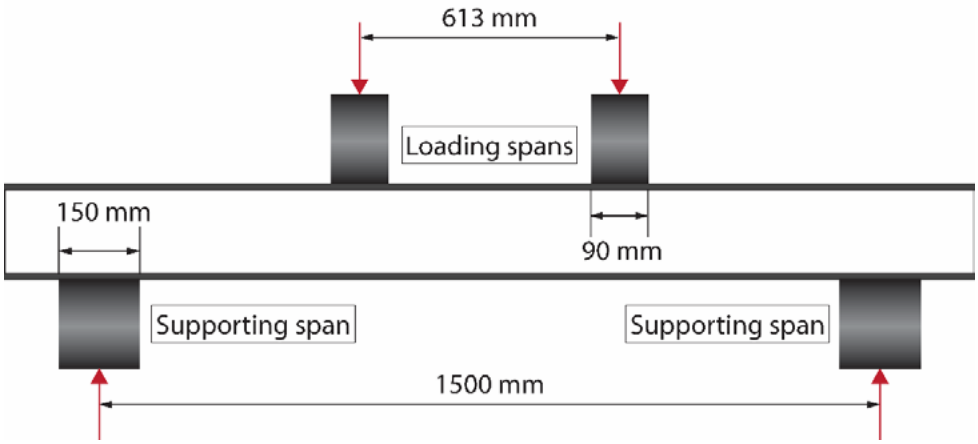


Figure 3. Locations of the reinforcing pads.



Figure 4. A hybrid aluminum/thermoplastic composite tube in the four-point bending test set-up.

3. Analytical solution

From the mechanics of materials, it is viable to calculate the flexural stiffness (or bending stiffness) of both tubes and plot the force-displacement diagram for the linear part. This provides insight into how closely the behavior of tubes in experiments aligns with or deviates from the analytical solution. To accomplish this, we assume there is a beam illustrated in Figure 5. The displacement can be expressed as a function of x [7].

$$\delta = \frac{Pa(3La - 3x^2 - a^2)}{12EI} \tag{1}$$

At the loading point where x=a, equation (1) can be rewritten as:

$$\delta = \frac{Pa^2(3L - 4a)}{12EI} \tag{2}$$

To plot the force-displacement diagram, we can rewrite equation (2) as:

$$\frac{P}{\delta} = \frac{12EI}{a^2(3L - 4a)} \tag{3}$$

In equation (3), EI represents bending stiffness. In order to calculate the bending stiffness, one way is using summation of bending stiffness of individual layers. In other words, we can utilize equation (4) as follows [8]:

$$(EI)_T = \sum_{i=1}^{n} E_i I_i \tag{4}$$

Equation (4) does not account for inter-layer interactions and cannot be useful for a case of composite tube or hybrid tubes. Thereby, we can use simple case of equation (4) for sole aluminum. Another equation, developed by Jolicoeur and Cardou [9], addresses this aspect:

$$(EI)_T = \sum_{n=1}^{N} \frac{\pi}{C_{33},n} \left\{ \begin{array}{c} \sum_{i=1}^{4} K_{i,n} \left(C_{34,n} \times g_{i,n} \times m_{i,n} - C_{13,n} - C_{23,n}(m_{i,n}+1) \right) \times \\ \left(\frac{b_n^{(m_{i,n}+2)} - a_n^{(m_{i,n}+2)}}{(m_{i,n}+2)} \right) + \\ (1 - \mu_{1,n}(C_{13,n} + 3C_{23,n}) + 2\mu_{2,n}C_{34,n}) \times (\frac{b_n^4 - a_n^4}{4}) \end{array} \right\} \quad (5)$$

All parameters in equation (5) are elucidated in [8,9] references. For a hybrid tube, we employ equation (5) to evaluate the difference in bending stiffness compared to experimental results. By computing the total bending stiffness using equations (4) and (5), and incorporating Equation (3), it becomes feasible to generate linear behavior plots for comparison with experimental results.

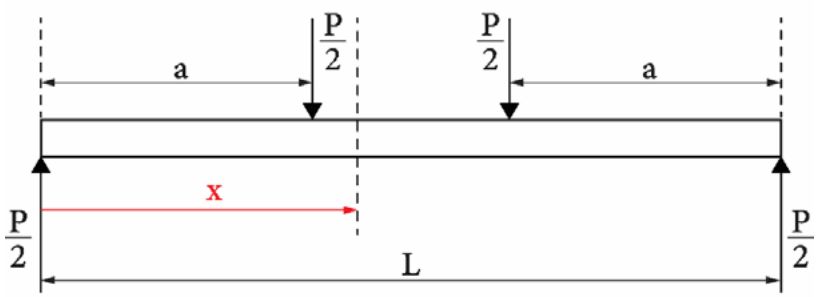


Figure 5. A beam under a four-point bending test with corresponding parameters.

4. Results and discussion

Figure 6 presents experimental data as well as analytical solutions. By studying Figure 6, it becomes evident that in terms of energy absorption, the hybrid tubes surpass those of the sole aluminum tube. The hybrid tube demonstrates notably stiffer and stronger resistance compared to the sole aluminum tube. Specifically, the load steadily increases until reaching 37,600 N at a displacement of 57.5 mm. At this juncture, there is a sudden drop in load to 22,400 N. Following this drop, there is additional resistance of the hybrid tube as the load increases again to 24,200 N and then decreases gradually. This observation holds significance because if failures occur in the hybrid tube, there exists secondary resistance after composite failure.

Secondary resistance helps mitigate sharp drops in force-displacement compared to a structure made solely of composite material. Combining aluminum and composite materials offers advantages over using a solely composite tube, where sharp drops in force-displacement occur after a certain point with no additional resistance. However, compared to using solely aluminum, the drop can be a disadvantage of using a hybrid tube. Therefore, addressing and minimizing this issue is vital to enhancing design quality. It's evident that achieving optimal stiffness and excellent load capacity isn't exclusive to metals such as aluminum; rather, one aspect cannot be achieved without the other.

Regarding the analytical solutions in Figure 6, the results for aluminum exhibit good agreement, as it is a single aluminum layer. For the hybrid tube, equation (5) overestimates the bending stiffness due to the consideration of interaction effects between all layers. In a real hybrid tube, slips may occur between

aluminum and composite parts, and perfect bonding cannot be achieved. Furthermore, defects occurring in the manufacturing process can diminish stiffness. Consequently, this disparity can be attributed to two factors: 1. Potential slippage between layers. 2. Presence of voids and other imperfections within composite layers. While it's inevitable to completely eliminate these issues, mitigating their impact is indeed possible.

In Figure (6), there is also a diagram illustrating the pure composite, which corresponds to the composite layers depicted in Figure (2). The diagram suggests that both the aluminum and composite layers contribute to the overall stiffness, as well as other parameters such as the maximum energy absorption of the hybrid tube.

Overall, it's important to compare important parameters associated with the hybrid tube. These parameters illustrate the advantages of the hybrid tube, including slope, maximum load, the degree of smoothness of the force-displacement diagram, energy absorption (EA), and specific energy absorption (SEA). Table 1 provides these parameters for both tubes. Based on the parameters mentioned in this table, four indicators for the hybrid tube can justify its advantages over the hybrid aluminum/composite tube. For instance, even creating a very thick aluminum tube to achieve the same maximum load and energy absorption results in a significant decrease in specific energy absorption as the total weight of the tube increases too much. Moreover, a purely composite tube can offer excellent maximum load capacity. However, due to the brittleness of the composite material, there is no secondary resistance, resulting in decreased energy absorption.

It stands to reason that optimizing these parameters cannot be achieved by using solely aluminum or solely composite materials. Instead, a hybrid aluminum/composite material can mitigate the limitations of each material and provide better overall performance.

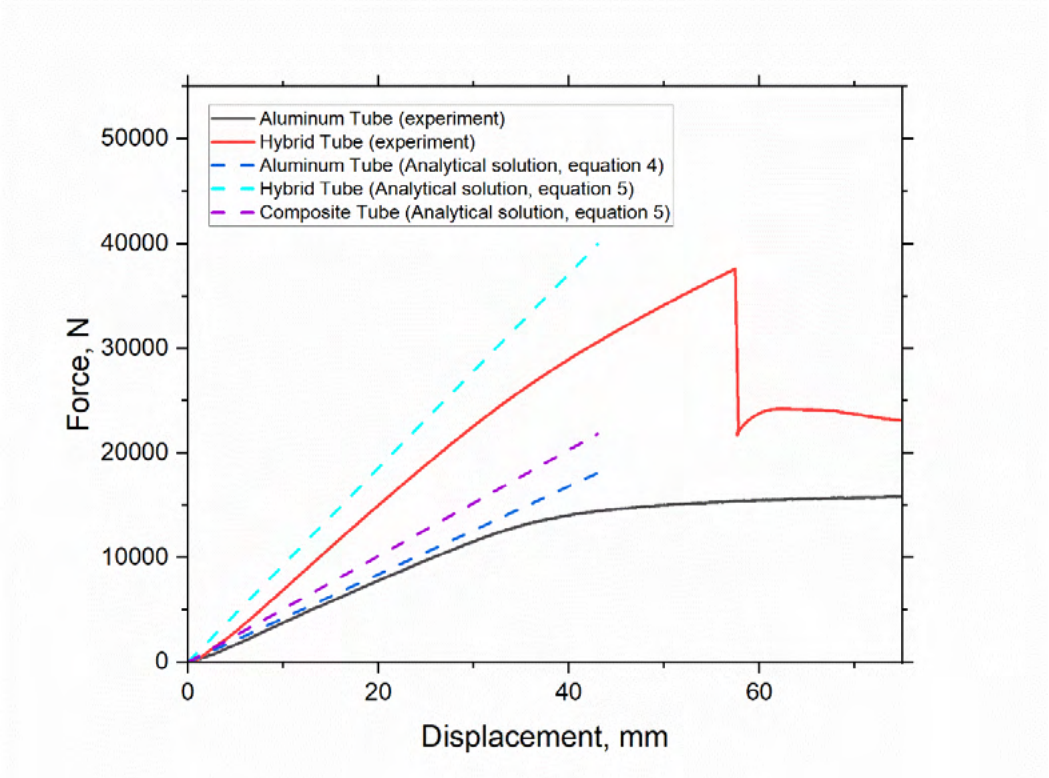


Figure 6. Load-displacement curves for three hybrid aluminum/thermoplastic composite tube tubes and a pure aluminum tube.

Table 1. Comparison of some parameters for both tubes.

Specimen	Slope (N/mm)	Maximum Force (KN)	Smoothness	EA (J)	SEA (j/g)
Aluminum Tube	384.7	15.85	Excellent	836.5	0.07967
Hybrid Tube	755.1	37.60	Moderate	1558.3	0.1113

5. Conclusions

The hybrid aluminum/thermoplastic composite tube presents a desirable characteristic vital for the functionality of bumpers and rocker panels in automobiles, as well as landing gear in helicopters. An examination of the important indicators or parameters reveals that to enhance overall performance, employing a hybrid aluminum/composite material can effectively address the limitations associated with using solely aluminum or composite materials. While achieving a flawless balance between a smooth diagram, excellent stiffness, maximum load capacity, and energy absorption might not be feasible, it's crucial to recognize that these parameters work together. One cannot be achieved without considering the others.

Acknowledgments

Financial support from the Natural Sciences and Engineering Research Council of Canada and Bell Flight are appreciated.

References

[1] D. Nestler et al., Continuous Film Stacking and Thermoforming Process for Hybrid CFRP/aluminum Laminates, *Procedia CIRP*, volume 66, pp. 107–112., 2017.

[2] C. J. Lissenden, Experimental investigation of initial and subsequent yield surfaces for laminated metal matrix composites, *International Journal of Plasticity*, volume 26, no. 11, pp. 1606–1628, 2010.

[3] Y. Chen, Y. Wang, and H. Wang, Research Progress on Interlaminar Failure Behavior of Fiber Metal Laminates, *Advances in Polymer Technology*, volume 2020. Article ID 3097839, 2020.

[4] Z. Pan, F. Qiao, M. Wang, Z. Wu, and Z. Ying, A novel damage mechanism analysis of integrally braided CFRP and CFRP/Aluminum hybrid composite tube subjected to transverse impact, *Materials & Design*, volume 206, 2021.

[5] H. Yadegari, R. Taherian, and S. Dariushi, Investigation on mechanical properties of hybrid aluminum/composite tubes manufactured by filament winding and hand lay-up, *Polymers and Polymer Composites*, volume 29, no. 9, pp. S1486–S1497, 2021.

[6] G. Sun, H. Yu, Z. Wang, Z. Xiao, and Q. Li, Energy absorption mechanics and design optimization of CFRP/aluminium hybrid structures for transverse loading, *International Journal of Mechanical Sciences*, volume 150, pp. 767–783, 2019.

[7] J.A. Gere, and B.J. Goodno, Mechanics of materials, *Cengage Learning*, p. 895, 2002.

[8] M.I. Geuchy Ahmad, S.V. Hoa, Flexural stiffness of thick walled composite tubes, *Composite Structures*, volume 149, pp.125–33, 2016.

[9] C . Jolicoeur, A. Cardou, Analytical solution for bending of coaxial orthotropic cylinders, *Journal of Engineering Mechanics*, volume 120, no. 12, 1994.

TENSION-COMPRESSION CYCLIC BEHAVIOUR OF ULTRA-THIN 90º PLY BLOCKS IN CFRP LAMINATES

S. Sánchez-Carmona[1], M.L. Velasco[2], C. Sandino[3] and E. Correa[4]

[1,2,3,4] Grupo de Elasticidad y Resistencia de Materiales, Departamento de Mecánica de Medios Continuos y Teoría de Estructuras, Escuela Técnica Superior de Ingeniería, Universidad de Sevilla, Camino de los Descubrimientos, 41092, Sevilla, España
[1] Email: sscarmona@us.es, Web Page: https://prisma.us.es/investigador/7003
[2] Email: mvelasco7@us.es, Web Page: https://prisma.us.es/investigador/4308
[3] Email: csandino@us.es, Web Page: https://prisma.us.es/investigador/5831
[4] Email: ecorrea@us.es, Web Page: https://prisma.us.es/investigador/931

Keywords: T-C fatigue, anti-buckling, ultra-thin plies, cross-ply laminates, microscopical inspection

Abstract
Tension-compression (T-C) cyclic loading is an open research topic nowadays in the composite field. There are different studies dealing with the appearance and growth of damages under T-C fatigue, its understanding at the microscopic level being relevant to insight into the physics of the microscopic damage processes. In this way, the comprehension of these damage mechanisms is studied hereby involving ultra-thin plies.
As the damage appearance is due to the tensile part of the load cycles, the specimen design is the same as the one used in tension-tension fatigue. To prevent buckling in the compressive part of the load cycles, a tailor-made anti-buckling device is used. Carbon/epoxy cross-ply laminates made of conventional (150 g/m^2) and ultra-thin (30 g/m^2) plies are cyclically tested.
A comparison of the damage onset observed in both conventional and ultra-thin 90º ply blocks is carried out. As expected, there is an advance in the appearance of the first transverse damage in the 90º ply block of a cross-ply laminate under T-C cyclic loading compared to the tension-tension case. The onset seems to be more pronounced when ultra-thin plies are used in the 90º ply block of a cross-ply laminate.

1. Introduction

Most composite structural components are subjected to fatigue during their life cycles. For instance, aircraft wing skins are constantly subjected to either tension or compression. Hence, it is a challenging task to broaden the scientific community's horizons about tension-compression (T-C) cyclic loading, which is an open research topic in the composite field. There are different works related to this matter from the late 90s up to nowadays, such as Gamstedt and Sjögren [1] and Carraro et al [2], respectively. Most of these studies use an anti-buckling device to prevent buckling phenomena in the compressive part of the load cycles because tension-like specimens are used as the damage onset is expected at the tensile part of the load cycles. Jeon et al [3] designed their own anti-buckling jig to obtain the S-N curves, thus the Goodman diagrams. Just et al [4] also performed their anti-buckling device, focused on the transverse cracking growth under fatigue, observing them microscopically. Liu et al [5] developed a simpler anti-buckling device comparing rectangular and dog-bone samples to obtain constant life diagrams and observe the fatigue fracture surfaces at the same time. Huang et al [6] designed their own anti-buckling device with openings to be able to use infrared thermography during fatigue, combining it with the use of synchrotron radiation computed tomography to observe damage in the post-mortem specimens.
There is an alternative study, Carraro et al [2], which uses shorter specimens under different stress ratios to observe the appearance and growth of the damage mechanisms, comparing the results with the

numerical predictions based on their damaged-based model for the simulation of fatigue damage in multidirectional laminates.
Although each research group has its study perspective, focusing on fatigue life (or S-N) models, phenomenological models, progressive damage models, or even a mix of them, the comprehension of the damage mechanisms affecting composite materials under T-C cyclic loading is essential to insight into the physics of the microscopic damage processes.
The comprehension of the appearance and growth of the different types of damages associated with the failure of composite materials at the microscopic level under fatigue motivates this study when ultra-thin plies are involved.

2. Experimental Methodology

2.1. Materials

Carbon/epoxy cross-ply laminates are made of TP402/T700S prepreg from North Thin Ply Technology. The stacking sequences selected are the same ones used in Sánchez-Carmona et al [7], which follow the configuration $[0_4/(90_n)/0_4]$, where all 0º plies are made of 150g/m^2 prepreg. Two different laminates are handly-layed-up manufactured, CP-30 means one ply (n=1) of 30g/m^2 prepreg and CP-450 means 3 plies (n=3) of 150g/m^2.
The samples are prepared following recommendations from the tension-tension (T-T) technical standard ASTM D3479 due to the fact that there are no standards for T-C testing. All samples are sanded and polished on their lateral free edges to be able to observe the onset of damages using an optical microscope.
The pattern of damages in the 90º ply under T-T cyclic loading is shown in Sánchez Carmona et al [8], an example being shown in Figure 1. Not all damages are transverse. As can be seen in Figure 1, longitudinal damages are also predominant when an ultra-thin ply is used due to the edge effect phenomenon.

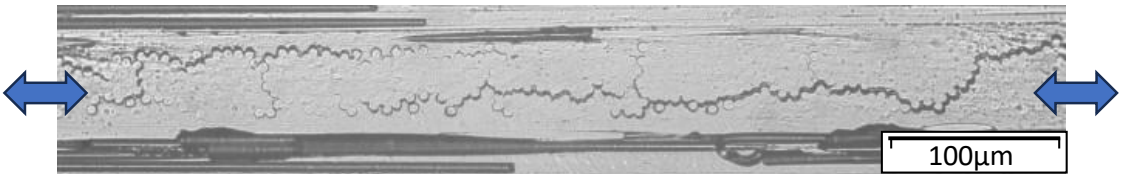


Figure 1. Damage mechanisms that occur in an ultra-thin 90º ply.

The same type of damage is expected to appear under T-C cyclic loading as T-T fatigue, although earlier regarding the number of cycles.

2.2. Experimental set-up

A tailor-made anti-buckling device is designed and manufactured for this experimental programme, Figure 2.(a), similar to the one used in Liu et al.[5]. As can be noticed, the separation between the device and the grips is the minimum possible to prevent local buckling along the free lengths.
To ensure that the set is not buckling two dial gauges are placed, one on each side of the assembly, to measure its lateral displacement, if present. Figure 2.(b) shows that the lateral displacement that the assembly is suffering is 15µm, which is completely negligible compared to the displacement during fatigue loading.
Once the set-up is ready, a cycling test is carried out in an Instron 8802 hydraulic testing machine, controlling the load by means of a sinusoidal function with a stress ratio R (being defined as the minimum applied stress divided by the maximum applied stress) which depends on the cross-ply laminate that is going to be tested. This stress ratio is selected as -0.84 for CP-450 and -0.71 for CP-30 since the biaxial stress state in the 90º ply block is intended to be the same for both laminates.



Figure 2. Anti-buckling device for T-C testing: (a) set-up installation, and (b) corroboration of its usefulness.

3. Results and discussions

The microscopic observation of damages in each 90º ply block along the free edges is carried out using a replica, taken from each sample free edge after stopping the cycling test as can be seen in Figure 3. Once the replica is cured, it can be taken away from the sample to continue cycling up to the next stop defined. The micrograph shown in Figure 1 is performed from a replica taken with this technique.

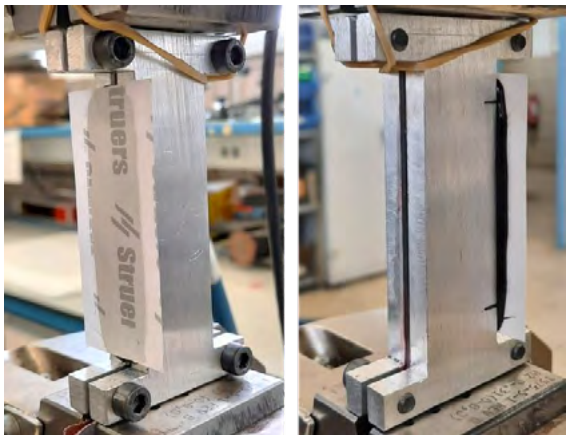


Figure 3. Performance of a replica at each stop defined.

Due to the novelty of these results, only the results for one specimen are shown in this paper. The onset of the first transverse damage that appears for each case is shown in Figure 4. The first transverse crack appears between $2 \cdot 10^4$ and $2{,}5 \cdot 10^4$ cycles for CP-450 whereas the first transverse damage for CP-30 occurs between 500 and 1000 cycles. Although it can be noticed that the first transverse damage appears before in the ultra-thin 90º ply, the overall relevance of the transverse damage is much lower than in the thicker case (CP-450). Whereas the transverse damage is a full transverse crack in CP-450, only a path of debonds that are not completely connected from one 0/90 interface to the other appears in CP-30.

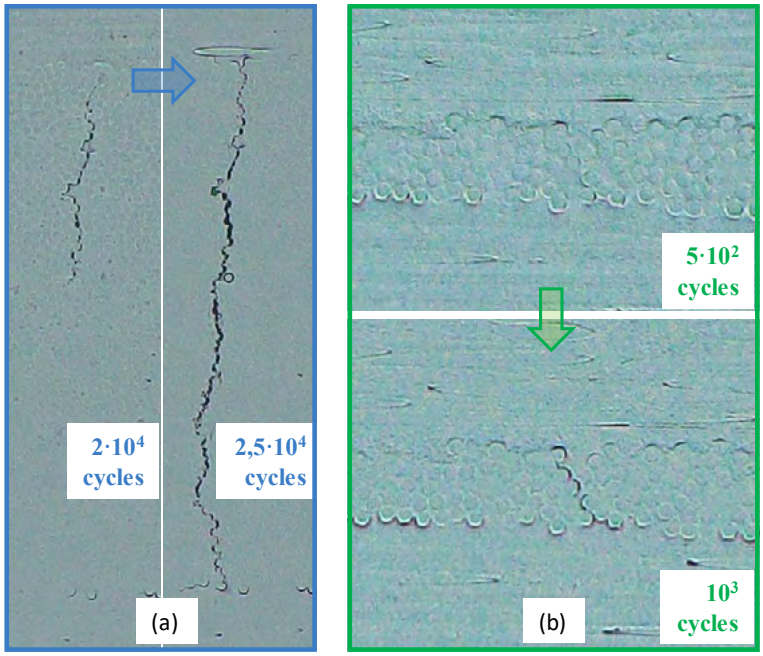


Figure 4. Appearance of the first transverse damage for: (a) CP-450 and (b) CP-30.

Comparing these T-C results to those from the T-T cyclic study of Sánchez-Carmona et al [7], the first transverse damage appears $2{,}5 \cdot 10^4$ cycles before in CP-450 whereas $9{,}9 \cdot 10^4$ cycles before in CP-30. As expected, T-C cyclic loading leads to an advance in the appearance of the first transverse damages in composites, being more accused in the ultra-thin case. Nevertheless, it is worth highlighting that the relevance of the first damage is much more damaging for the thicker case, as shown in Figure 4.

4. Conclusions

The experimental observation of the damage mechanism of ultra-thin plies under cyclic loading has been studied in this work. Two different cross-ply laminates, one made of conventional and another of ultra-thin plies, have been investigated. A preliminary result shows that there is an advance in the onset of transverse damage in the 90º ply block of a cross-ply laminate under T-C cyclic loading compared to the T-T case, being more pronounced when ultra-thin plies are used in the 90º ply block. However, the transverse crack in the thicker 90º ply block is much more damaging than the transverse damage, a path of debonds not completely connected to both 0/90 interfaces, that appears in the ultra-thin 90º ply block. More samples need to be tested to corroborate the advance of the onset of the transverse damages that appears in the 90º ply block of a cross-ply laminate under T-C cyclic loading compared to the T-T case.

Acknowledgments

The authors acknowledge the help of Antonio Cañas for manufacturing the anti-buckling device, and our students F. Javier Alférez and Jorge Marín for their help during the experimental programme.

References

[1] E. K. Gamstedt and B. A. Sjögren, “Micromechanisms in tension-compression fatigue of composite laminates containing transverse plies,” *Compos Sci Technol*, vol. 59, no. 2, pp. 167–178, 1999, doi: 10.1016/S0266-3538(98)00061-X.

[2] P. A. Carraro, L. Maragoni, and M. Quaresimin, “Damage evolution in cross-ply laminates under tension–compression and compression-compression cyclic loads,” *Compos Part A Appl Sci Manuf*, vol. 156, May 2022, doi: 10.1016/j.compositesa.2022.106888.

[3] K. W. Jeon, K. B. Shin, and J. S. Kim, "Evaluation of tension-compression and tension-tension fatigue life of woven fabric glass/epoxy laminate composites used in railway vehicle," *International Journal of Precision Engineering and Manufacturing*, vol. 12, no. 5, pp. 813–820, 2011, doi: 10.1007/s12541-011-0108-6.

[4] G. Just, I. Koch, M. Brod, E. Jansen, M. Gude, and R. Rolfes, "Influence of reversed fatigue loading on damage evolution of cross-ply carbon fibre composites," *Materials*, vol. 12, no. 7, pp. 1–21, 2019, doi: 10.3390/ma12071153.

[5] H. Liu *et al.*, "Fatigue modeling for carbon/epoxy unidirectional composites under various stress ratios considering size effects," *Int J Fatigue*, vol. 120, no. October 2018, pp. 184–200, 2019, doi: 10.1016/j.ijfatigue.2018.11.009.

[6] J. Huang, L. Guo, L. Chen, Z. X. Wang, and J. Li, "Damage evolution of 3D woven carbon/epoxy composites under the tension–compression fatigue loading based on multi damage information," *Int J Fatigue*, vol. 154, no. June 2021, p. 106566, 2022, doi: 10.1016/j.ijfatigue.2021.106566.

[7] S. Sánchez-Carmona, E. Correa, A. Barroso, and F. París, "Experimental observations of fatigue damage in cross-ply laminates using carbon/epoxy ultra-thin plies," *Compos Struct*, vol. 306, no. 116564, 2023, doi: 10.1016/j.compstruct.2022.116564.

[8] S. Sánchez-Carmona, A. Barroso, E. Correa, and M. L. Velasco, "Numerical and experimental analysis of ultra-thin plies in carbon/epoxy cross-ply laminates subjected to bending after tensile cyclic loading," *Theoretical and Applied Fracture Mechanics*, vol. 128, Dec. 2023, doi: 10.1016/j.tafmec.2023.104108.

GUIDELINE DEVELOPMENT FOR STRUCTURAL MODELING OF TEXTILE-BASED COMPOSITES FOR THE NUMERICAL PERMEABILITY PREDICTION

T. Schmidt and D. May

Leibniz-Institut für Verbundwerkstoffe GmbH,
Erwin-Schrödinger-Str. 58, 67663 Kaiserslautern, Germany
Email: tim.schmidt@ivw.uni-kl.de, Web Page: http://www.ivw.uni-kl.de

Keywords: permeability, model, statistical representative volume element, Liquid Composite Molding

Abstract
Permeability quantifies the ability of fluid to flow through a porous media such as composite fiber reinforcment structures. The multiscale structure of textile-based composites must be taken into account for numerical permeability prediction (NPP). Due to limited computing power, multiscale approaches are used for NPP by first calculating the microscale and then considering these results on the mesoscale. This requires models that accurately represent the structure. Also, suitable model size and resolution must be identified. Appropriate models can be described as statistical representative volume elements (SVEs). If several simulations are performed with randomised SVEs, a distribution of the permeability based on structural variations in textiles can be obtained analogous to experimental permeability determination.
The aim of this work is to develop guidelines for the creation of micro and meso-level SVEs for NPP. Experimental and numerical benchmark studies have shown that the results can be subject to a spread of over 20 % [1-3]. Therefore, the target is a maximum deviation of 20 % from experimental reference values. However, the best results in this study, considering randomized fiber and textile structrues with complex roving deformation due to a virtual compation, still show a deviation of 17 to 62 %.

1. Introduction

Textiles in fiber-reinforced polymers (FRP) exhibit multi-scale porosity with microscopic pore spaces within fiber bundles and mesoscopic pore spaces between the fiber bundles. Typical FRP components consist of multiple textile layers, formed into a preform and impregnated using e.g. liquid composite molding (LCM). The robustness and efficiency of the impregnation in LCM processes can be improved by filling simulations. For the filling simulations, a homogenized component model is used, which omits the fiber structure and therefore the physical effects at lower scale levels. The physical properties are directly assigned to the finite elements of the homogenized component model [4]. The permeability is one of these properties and a crucial input parameter for the simulation. It relies strictly on the geometric structure of the material. In order to determine the permeability numerically, multi-scale approaches can be used to maintain computational manageability. For this, seperate simulations are performed on each scale and the results are transferred to the respective upper scale [5-7]. The three scales typically considered for flow in LCM are microscale and mesoscale for the permeability determination and the macroscale for the filling simulation (Figure 1). At the microscale, numerical permeability prediction is based on the creation of structural models that statistically reproduce the fiber structure inside fiber bundles. For each material configuration, several randomized models must be created and calculated for statistical validation [8-10]. At the mesoscale, on the other hand, structural models are generated that are statistically representative for textile stacks as they can be found within the component. In these models, the rovings are created as continuum elements, to which the previously determined anisotropic microscopic permeability is then assigned. With this upscaling, the micro permeability is taken into account on the mesoscale. To perform a numerical simulation, three sets of input parameters have to be

defined: 1) the incompressible fluid viscosity, 2) the experimental process parameters including flow direction, boundary conditions and pressure difference and 3) the structural model [11].

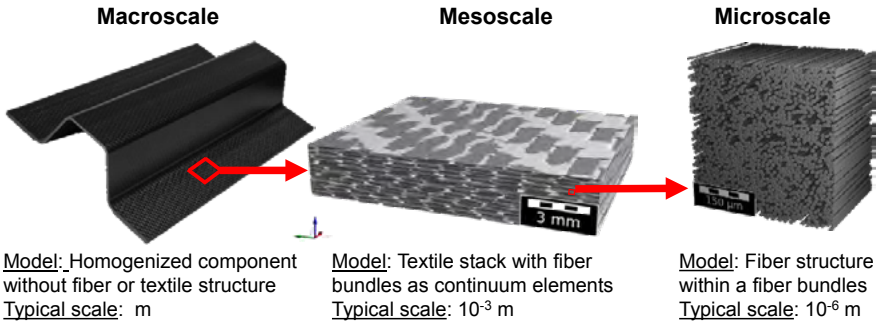


Figure 1: Relevant scales for the simulation of a LCM process

Creating sufficient structural models that take into account all relevant structural details is particularly critical and at the same time costly in terms of computational effort. The structural models can be generated artificially or derived from 3D images of a real structure [1, 6]. The latter requires a lot of effort and is limited to relatively small samples, which means that statistical variance of the structure, as given in real structures, can hardly be reproduced. The artificially created models, on the other hand, allow a systematic investigation of the influence of structural features, such as fiber diameter or fiber volume content (FVC). When considering the state of the art for modeling microscopic and mesoscopic models, one notes a considerable range from regularly distributed 2D cross sections [12] up to 3D models with randomly distributed, undulated fibers or fiber bundles [13]. Representative volume elements (RVEs) should be representative for the whole material with one simulation result as shown in Figure 2 [14]. This means that local variations are not considered and the models must be very large. This can lead to problems in terms of limited computing power. Further developed models show statistically distributed fibers and properties according to given boundary conditions. They are thus referred to as statistically representative volume elements (SVEs) [15-17]. Many studies exist on microscopic and mesoscopic structural models, but most of them do not validate the model size, resolution and number of individual models for statistical validation, as performed e.g. by Rimmel et al. [18] for 2D micro models.

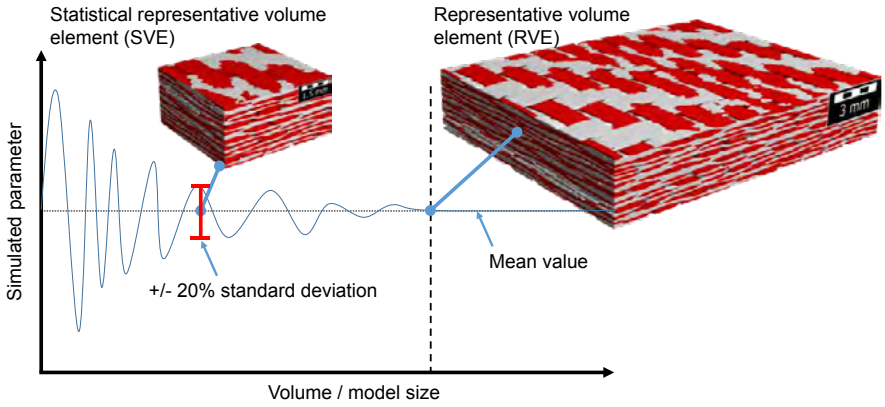


Figure 2: Difference between SVE and RVE adapted from Bear [19]

Based on the statistical representative volume elements (SVEs), the flow fields are solved numerically using the Stokes equation (2) and the permeability is calculated using Darcy's law [20]. Numerical permeability prediction in addition with artificial structure model generation allows for automated parameter studies to be carried out over a wide range. This allows an efficient screening of different model settings to identify suitable SVE settings. The objective for the SVE is to achieve an accuracy of +/- 20 %, as is also achieved in numerical and experimental benchmark studies [1-3].

2. Methods for SVE Development

Target accuracy is the most important factor in SVE development, which then also influences the range of settings to be analysed. The first step is to develop an SVE for the microscale that basically represents a structure as it could be present at a randomly selected position within a fiber bundle. Due to the statistical nature, the permeability of two randomly generated SVEs can strongly differ, just like in a real fiber bundle. For meaningful averaging procedures, the combination of model size and number of models simulated per randomization setting must reach a certain level, which is to be determined via a convergence analysis. Furthermore, a coarse resolution might cause numerical inaccuracies influencing the result but is of course beneficial in terms of computational effort. Therefore, the minimum model size and resolution without negative influence on the results must be identified. The voxel-based structure modeling is performed in GeoDict using FiberGeo [21]. This is a tool for generating fiber structures in which individual fibers are randomly placed in the domain until the defined FVC is reached. FlowDict (GeoDict) can then be used to determine the steady state saturated permeability using Darcy`s law. One flow simulation is performed for each direction along the coordinate axis with each structure model. Periodic boundary conditions (BCs) are defined in the flow direction and in tangential direction. In- and outflow regions of 10 voxels are added to the model, which do not contain any fibers and avoid the possibility of closed flow channels when using periodic BCs. A resin viscosity of 50 mPas is defined and the flow is induced by a differential pressure of 1 Pa from inlet to outlet. These settings are in accordance with the recommendations of the virtual permeability benchmark [1]. The LIR solver with the LIR-Tree-approach is used, that enables grid refinement during the flow simulation [22]. An error bound of 0.03 for in-flow and tangential permeabilities is defined as the stopping criterion [11]. To determine suitable SVEs for the microscale, ten randomized models for three model resolutions (0.4^3, 0.5^3, 0.6^3 µm^3/voxel) and five model sizes (120^3, 220^3, 320^3, 420^3, 520^3 voxels) were evaluated for three FVCs of 56 %, 60 %, 64% and two fiber diameters of 7 µm and 10 µm as shown in Figure 3.

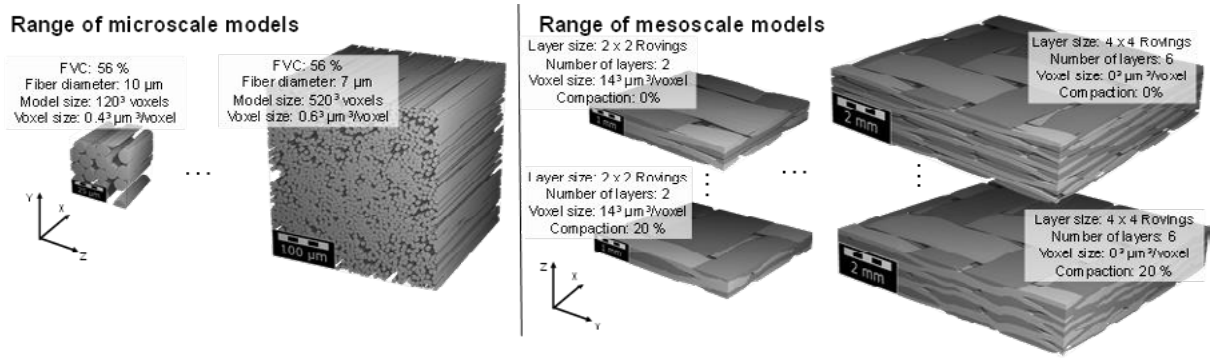


Figure 3: Range of the micro- and mesoscale models for the SVE development

For the SVE development on the mesoscale, the resolution is also considered again, but instead of the model size in voxels as on the microscale, the number of rovings per layer and the number of layers are considered. The number of rovings per layer is specified as 3x3, for example, which means that three weft and three warp rovings per layer are included in the model. The GeoDict modules WeaveGeo, LayerGeo and ProcessGeo are used for modelling. The model is created as follows: 30 individual textile layers are generated and then stacked with a randomised in the plane displacement. This stack is then cut to the appropriate size according to the number of rovings per layer. This is followed by four consecutive compaction steps, where the FVC of the textile stack is increased by 5 % during each step. The flow simulation is then carried out in FlowDict (GeoDict) using the SimpleFFT solver. In contrast to the LIR solver, the SimpleFFT solver enables the assignment of anisotropic micropermeabilities to the rovings. This means that customised anisotropic microscopic permeability values are assigned to all weft and warp rovings before the simulation. All other settings were selected analogue to the microscale. To determine suitable SVE settings, four layer sizes (2x2, 2.5x2.5, 3x3, 4x4 rovings per layer), four numbers of layers (3, 4, 5, 6 layers) and four different resolutions of (8^3, 10^3, 12^3, 14^3 µm^3/voxel) were investigated. The permeability of these setting combinations was determined for each compaction stage.

3. Statistical Representative Volume Element for the Microscale

The results of the SVE study for the microscale are presented in Figure 4, 5 and 6**Fehler! Verweisquelle konnte nicht gefunden werden.**. The standard deviation (SD) of the permeability for 10 randomized models per parameter set is displayed in the form of error bars in the diagrams. Configurations are sought that provide sufficiently accurate permeabilities for all directions and FVCs. It is assumed that large models with many fibers and the highest possible resolution achieve the most accurate results. Models with a higher resolution of 0.4^3 µm³/voxel contain fewer fibers compared to a lower resolution (e.g. 0.6^3 µm³/voxel) with the same number of voxels, but these are resolved over more voxels per diameter. Similarly, models with a higher FVC contain more fibers. The fact that the voxel sizes 0.4^3 and 0.6^3 µm³/voxel cannot exactly map the fiber diameter of 7 µm is solved in such a way that some of the fibers, e.g. at 0.4^3 µm³/voxel resolution, are modelled with 6.8 µm (17 voxels) and 7.2 µm (18 voxels), so that the average fiber diameter is 7.0 µm. The same applies to the combination of 0.6^3 µm³/voxel resolution and 10 µm fiber diameter.

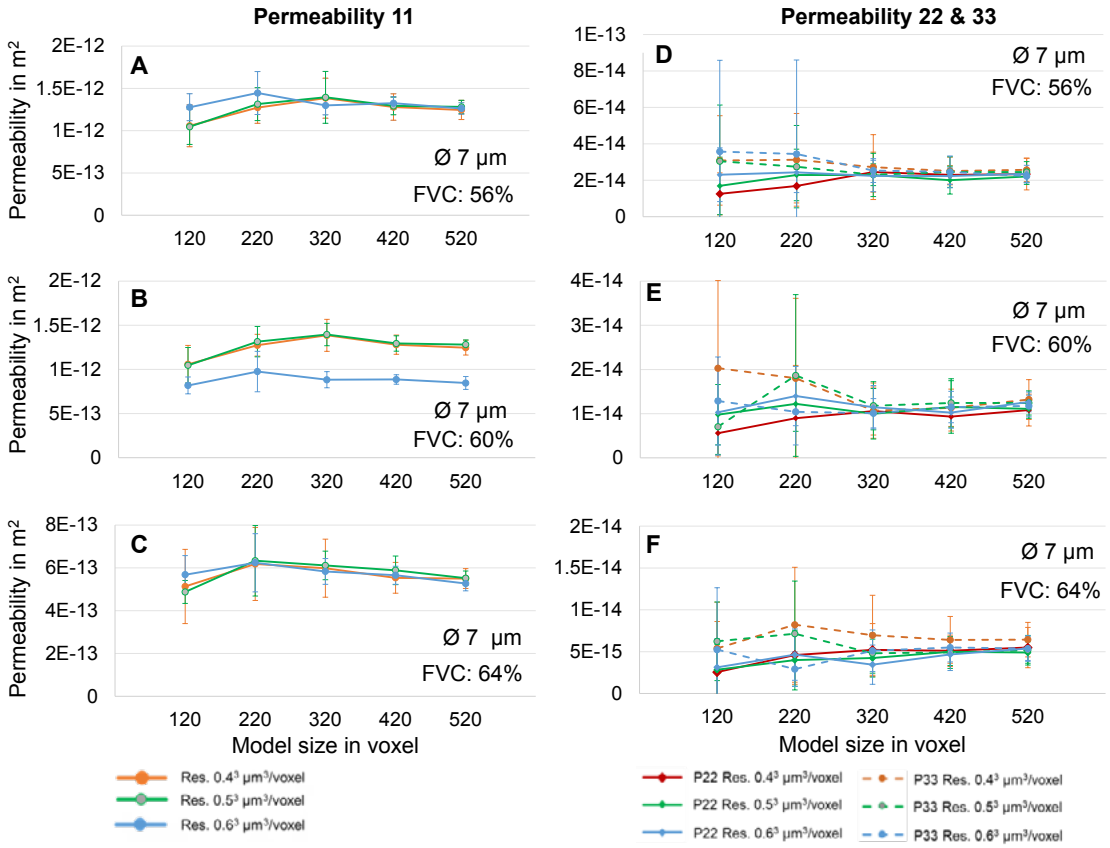


Figure 4: Permeability results of SVE development for models with 7 µm fiber diameter

Diagram B in Figure 4 and 5 show that the resolution of 0.6^3 µm³/voxel differs considerably from the results with a resolution of 0.4^3 and 0.5^3 µm³/voxel. In addition, there is a clear trend in all diagrams that the SD decreases with increasing model size. Diagrams D and E in particular show a significant difference between model sizes 220^3 and 320^3 voxels according to the SD. In Figure 5**Fehler! Verweisquelle konnte nicht gefunden werden.** (diagram D, E, F) the mean values for the models with a resolution of 0.4^3 µm³/voxel and a model size of 320^3 voxels also deviate significantly from the defined reference values. Based on these observations, the voxel size of 0.4^3 and 0.6^3 µm³/voxel and model sizes smaller than 320^3 voxels are excluded. Models with a resolution of 0.5^3 µm³/voxel and model sizes of 320^3, 420^3 and 520^3 voxels achieve comparable results and SD. In view of the strongly increasing computation time in Figure 6, a model size of 320^3 voxels was defined for the following studies as a

compromise between accuracy and computational effort. This corresponds to at least 14 voxels per fiber diameter at 7 µm fiber diameter and thus with a model size of 320^3 voxels about 450 fibers at 60% FVC. This is slightly less than the 785 fibers Rimmel and May [32] defined as minimum. However, they considered 2D models and taking into account that 3D models basically include multiple 2D slices this is a reasonable result. The voxel size of $1/14^{th}$ of a fiber diameter used in this study is significantly smaller compared to Rimmel and May's requirement of $1/10^{th}$ of a fiber diameter for 2D models.

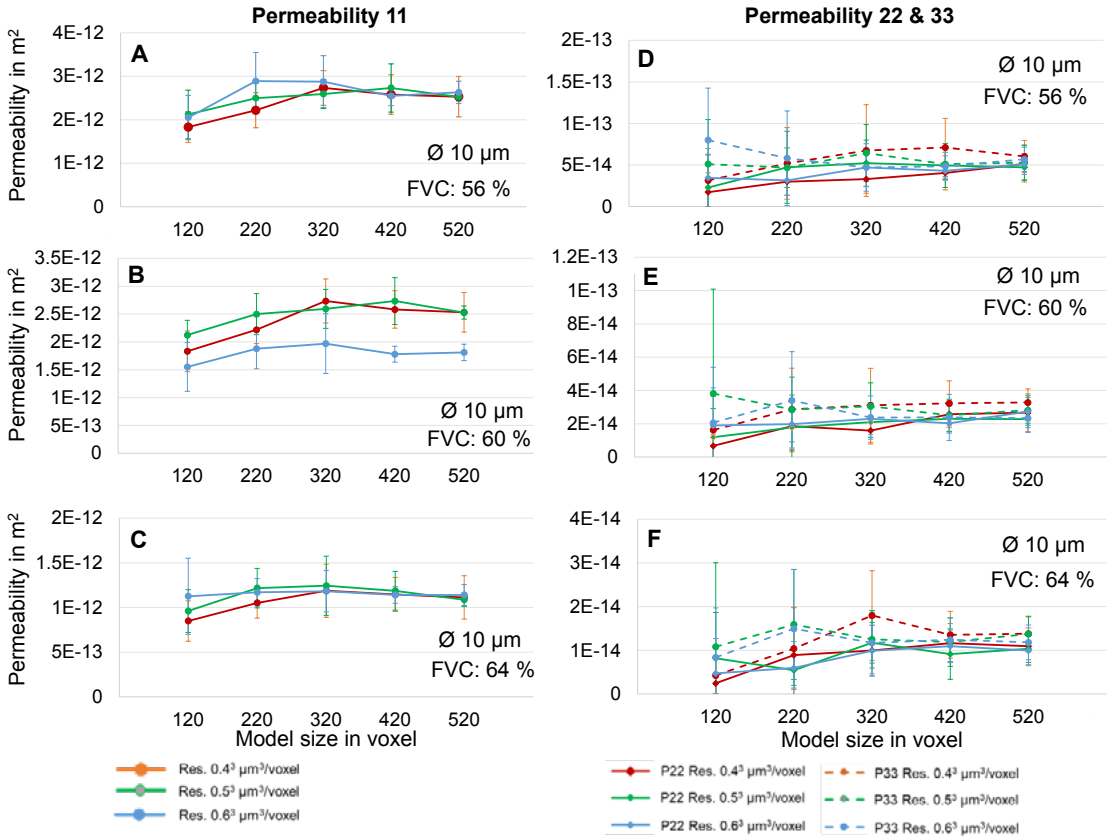


Figure 5: Permeability results of SVE development for models with 10 µm fiber diameter

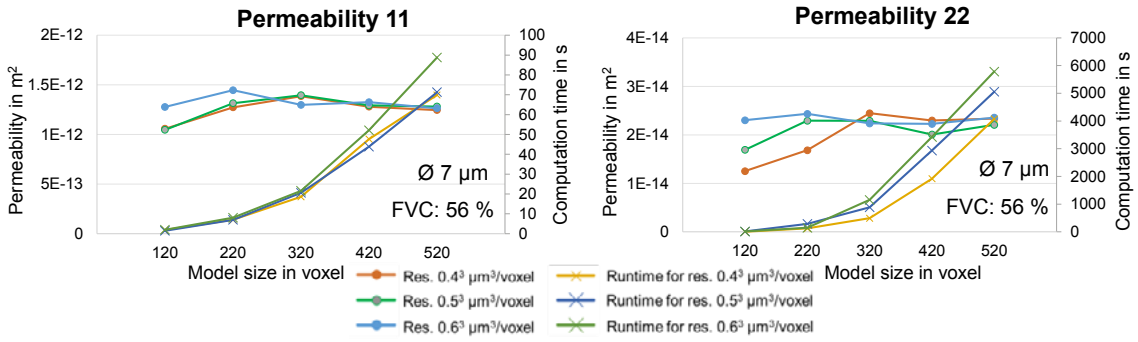


Figure 6: Permeability results and the corresponding computational times on the secondary axis

4. Statistical Representative Volume Element for the Mesoscale

The results of the first parameter screening are shown in Figure 7. Coefficients of variation (CV) of less than 20% were achieved in some cases, but only for low degrees of compaction and for K11 and K22. In all cases, the CV was highest for K33. One reason for this could be the significantly shorter flow paths. In addition, there was a clear trend that with increasing compaction, the results were subject to

greater scatter. Looking at the graphs in Figure 7, there is a clear trend that finer resolution produces better results than the coarser resolutions. The standard deviations are also lower with a number of layers of four or more than with two or three layers. The evaluation of the results for varying layer sizes showed that models with 3x3 rovings per layer had the lowest scatter, even compared to 4x4 rovings per layer. The mean CV for 3x3 rovings per layer and 8^3 µm³/voxel for all compaction levels was 29 % for K11, 15 % for K22 and 38 % for K33. If we only look at the compaction levels 0, 5 % and 10 %, the CV is reduced to 16 %, 12 % and 33 % for K11, K22 and K33.

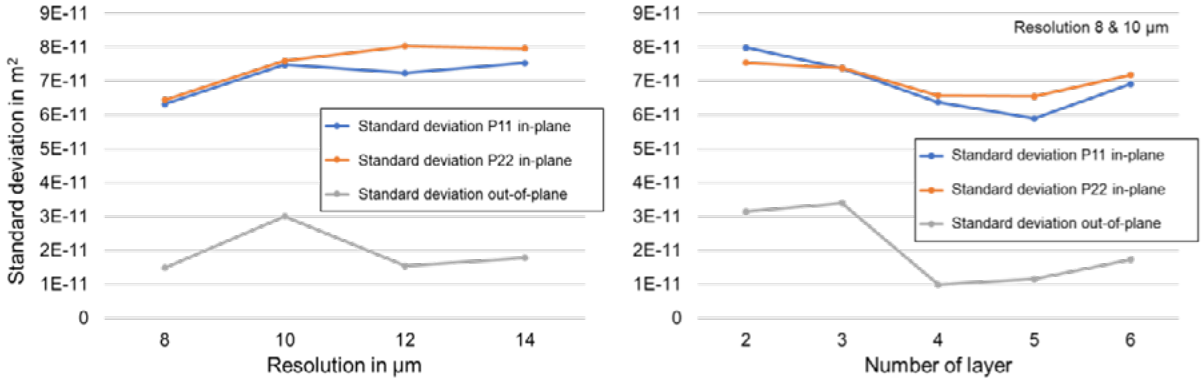


Figure 7: Results of the meoscale SVE development for different resolutions (left) and number of layers (right)

In order to achieve the objective of less than 20 % scattering for all values, additional simulations were carried out. The error bound was reduced from 0.03 to 0.01 in order to achieve more accurate results. Furthermore, a resolution of 8^3 µm³/voxel and 3x3 rovings per textile layer were defined and ten as opposed to five randomized models per parameter set were simulated. The number of textile layers was varied with 4, 5, 6 and 8. Even with these results (see Table 1), the required scatter of less than 20 % could not be achieved for all models. It has been shown here that K33 is still the critical value and that the scatter increases with increasing compaction. Furthermore, it can be seen that a number of layers greater than six does not provide better results. From this it can be interpreted that the resolution of 8^3 µm³/voxel may not be sufficient and higher resolutions of e.g. 6^3 µm³/voxel must be investigated.

Table 1: Results of the additional simulations for the SVE development

Number of layers	Compaction	Mean value in 10^{-12} m²			Standard deviation in 10^{-12} m²			Coefficient of Variation			Mean value of Solid volume percentage
		K11	K22	K33	K11	K22	K33	K11	K22	K33	
4	0 %	174.2	214.7	23.1	21.1	45.9	9.4	12 %	21 %	41 %	70.09 %
4	5 %	120.5	155.6	17.4	16.8	41.2	8.0	14 %	26 %	46 %	74.38 %
4	10 %	77.1	106.4	12.6	14.3	37.3	6.8	19 %	35 %	54 %	78.22 %
4	15 %	47.0	70.3	8.6	12.8	32.9	5.6	27 %	47 %	66 %	82.03 %
4	20 %	25.0	42.3	5.5	11.1	28.1	4.4	44 %	67 %	80 %	85.72 %
5	0 %	151.1	159.9	18.7	28.6	19.8	6.1	19 %	12 %	33 %	71.57 %
5	5 %	101.2	108.8	14.5	23.7	15.2	5.9	23 %	14 %	41 %	75.53 %
5	10 %	63.9	70.7	10.9	18.0	12.3	5.5	28 %	17 %	51 %	79.58 %
5	15 %	36.2	41.8	7.7	13.7	9.7	5.2	38 %	23 %	68 %	83.45 %
5	20 %	17.3	20.7	5.3	9.6	7.6	4.7	55 %	37 %	89 %	87.16 %
6	0 %	182.0	240.1	25.0	31.4	42.1	7.2	17 %	18 %	29 %	69.15 %
6	5 %	180.8	235.2	24.5	30.3	43.4	7.0	17 %	18 %	29 %	72.98 %
6	10 %	124.9	172.3	18.7	23.1	37.0	6.2	19 %	21 %	33 %	76.81 %
6	15 %	82.6	123.6	13.7	17.7	31.8	5.3	21 %	26 %	38 %	80.88 %
6	20 %	35.5	66.5	7.7	18.8	35.0	4.8	53 %	53 %	62 %	84.64 %
8	0 %	181.8	189.1	19.5	39.3	34.4	6.7	22 %	18 %	34 %	70.25 %
8	5 %	127.0	132.8	14.9	32.2	27.9	5.9	25 %	21 %	40 %	74.14 %
8	10 %	89.8	93.3	11.4	24.9	20.4	5.9	28 %	22 %	51 %	77.99 %
8	15 %	50.9	55.7	7.5	18.2	16.7	4.6	36 %	30 %	61 %	82.44 %
8	20 %	24.7	30.0	4.9	12.8	13.2	3.8	52 %	44 %	77 %	85.62 %

5. Discussions and Guidelines for the Generation of SVE for Microscale and Mesoscale

In this work, the focus is on an often unjustly neglected topic, the creation of suitable models for the numerical determination of characteristic values. In the SVE, not only the suitable structural characteristics, such as the fiber diameter or the FVC, must be correctly modeled, but also suitable modeling parameters, such as resolution, model size and a suitable number of models for statistical validation. The guidelines derived from this work are intended to provide assistance in developing suitable SVEs for the numerical determination of permeability.

The first step is to define a suitable scatter that is to be achieved. In this work, a dispersion of 20 % was defined, which is derived from the benchmark studies mentioned. For the creation of the micro- and mesoscale models, essential structural parameters must be known, such as fiber diameter, relevant FVC range, roving width, textile architecture, etc. This is the only way to generate meaningful models that can be used to develop SVEs. It is important to note that the SVEs are only valid within a limited spectrum. To ensure this, SVE development should ideally be carried out with combinations of characteristic values that cover this range.

For the microscale, a suitable model size and resolution for statistical representative volume elements (SVE) for fiber level permeability prediction was determined. A model size of 320^3 voxels and a voxel size 0.5^3 µm³/voxel were determined, which represents a voxel size of 1/14th of a fiber diameter and corresponds to 200 to 500 fibers per model, depending on fiber diameter and FVC. These values are to be seen as guidelines for comparable material structures, but must be checked for different materials or areas of application.

The target of 20 % could not be fully achieved for the mesoscale. However, these results prove all the more the necessity of SVE model development in order to be able to predict numerically reliable permeability values. In plane, the target values are achieved for lower compactions with a resolution of 8^3 µm³/voxel, 3x3 rovings per layer and 6 textile layers, but not for the entire targeted application area. In future studies, the causes of the increased scattering will be investigated and the guidelines will be successively expanded and specified.

Acknowledgments

The project „ML4ProcessSimulation - Machine Learning for Simulation Intelligence in Composite Process Design” is funded by the Leibniz Association within the Leibniz Collaborative Excellence funding program (funding reference: K377/2021).

References

[1] E. Syerko, Tim Schmidt et al., „Benchmark exercise on image-based permeability determination of engineering textiles: Microscale predictions“, Composites Part A: Applied Science and Manufacturing, no. 167, 107397, Apr. 2023, doi: 10.1016/j.compositesa.2022.107397.

[2] D. May et al., „In-plane permeability characterization of engineering textiles based on radial flow experiments: A benchmark exercise“, Composites Part A: Applied Science and Manufacturing, no. 121, p 100–114, June 2019, doi: 10.1016/j.compositesa.2019.03.006.

[3] A. X. H. Yong et al., „Out-of-plane permeability measurement for reinforcement textiles: A benchmark exercise“, Composites Part A: Applied Science and Manufacturing, no. 148, p 106480, Sep. 2021, doi: 10.1016/j.compositesa.2021.106480.

[4] R. Masoodi, K. M. Pillai, N. Grahl, und H. Tan, „Numerical simulation of LCM mold-filling during the manufacture of natural fiber composites“, Journal of Reinforced Plastics and Composites, no. 31, 6, p 363–378, March 2012, doi: 10.1177/0731684412438629.

[5] T. Schmidt, F. Schimmer, A. Widera, D. May, N. Motsch and C. Bauer, „A Novel Simulative-Experimental Approach to Determine the Permeability of Technical Textiles“, KEM, no. 809, p. 487–492, June 2019, doi: 10.4028/www.scientific.net/KEM.809.487.

[6] T. Schmidt, D. May, M. Duhovic, A. Widera, M. Hümbert and P. Mitschang, „A combined experimental–numerical approach for permeability characterization of engineering textiles“, Polymer Composites, no. 42, p. 3363–3379, July 2021, doi: 10.1002/pc.26064.

[7] S. V. Lomov et al., „Textile composites: modelling strategies“, Composites Part A: Applied Science and Manufacturing, no. 32, p. 1379–1394, Oct. 2001, doi: 10.1016/S1359-835X(01)00038-0.

[8] M. Bodaghi, A. Vanaerschot, S. V. Lomov and N. C. Correia, „On the variability of mesoscale permeability of a 2/2 twill carbon fabric induced by variability of the internal geometry“, Composites Part A: Applied Science and Manufacturing, no. 101, p. 394–407, Jan. 2017, doi: 10.1016/j.compositesa.2017.05.030.

[9] M. Bodaghi, G. Catalanotti and N. Correia, „On the statistics of transverse permeability of randomly distributed fibers“, Composite Structures, no. 158, p. 323–332, Jan. 2016, doi: 10.1016/j.compstruct.2016.09.045.

[10] A. Trofimov, C. Ravey, N. Droz, D. Therriault and M. Lévesque, „A review on the Representative Volume Element-based multi-scale simulation of 3D woven high performance thermoset composites manufactured using resin transfer molding process“, Composites Part A: Applied Science and Manufacturing, no. 169, p. 107499, June 2023, doi: 10.1016/j.compositesa.2023.107499.

[11] J. Hilden, S. Linden and B. Planas, „GeoDict 2023 User Guide. FlowDict handbook“. Math2Market GmbH, 2023. last: 31th July 2023. [Online]. Available under: https://doi.org/10.30423/userguide.geodict

[12] Z. Cai and A. L. Berdichevsky, „Numerical simulation on the permeability variations of a fiber assembly“, Polym. Compos., no. 14, p. 529–539, Jan. 1993, doi: 10.1002/pc.750140611.

[13] M. Engelfried, L. A. Mavoungou, I. Verspohl, P. Böhler, and P. Middendorf, „Generating Representative Volume Elements of Yarns with Non-circular Filaments Cross-sections“,International Conference on Flow Processes in Composite Materials 14, Lulea, Sweden, June 2018.

[14] R. Hill, „Elastic properties of reinforced solids: Some theoretical principles“, Journal of the Mechanics and Physics of Solids, no. 11, p. 357–372, Jan. 1963, doi: 10.1016/0022-5096(63)90036-X.

[15] M. Ostoja-Starzewski, „Material spatial randomness: From statistical to representative volume element“, Probabilistic Engineering Mechanics, no. 21, p. 112–132, Apr. 2006, doi: 10.1016/j.probengmech.2005.07.007.

[16] X. Du and M. Ostoja-Starzewski, „On the size of representative volume element for Darcy law in random media“, Proc. R. Soc. A., no. 462, p. 2949–2963, Oct. 2006, doi: 10.1098/rspa.2006.1704.

[17] X. Yin, W. Chen, A. To, C. McVeigh and W. K. Liu, „Statistical volume element method for predicting microstructure–constitutive property relations“, Computer Methods in Applied Mechanics and Engineering, no. 197, p. 3516–3529, Aug. 2008, doi: 10.1016/j.cma.2008.01.008.

[18] O. Rimmel and D. May, „Modeling transverse micro flow in dry fiber placement preforms“, Journal of Composite Materials, no. 54, p. 1691–1703, June 2020, doi: 10.1177/0021998319884612.

[19] J. Bear, Dynamics of Fluids in Porous Media. Dover Publications, 2013.

[20] Darcy H., „Les Fontaines Publiques de la ville de Dijon“, Paris: Libraire des Corps Imperiaux des Ponts et Chausses et des Mines, Jan. 1856.

[21] J. Hilden, S. Rief, und B. Planas, GeoDict 2023 User Guide. FiberGeo handbook. DE: Math2Market GmbH, 2023. last: 26th October 2023. [Online]. Available under: https://doi.org/10.30423/userguide.geodict

[22] S. Linden, A. Wiegmann and H. Hagen, „The LIR space partitioning system applied to the Stokes equations“, Graphical Models.

MECHANICAL BEHAVIOR OF CARBON FIBERS REINFORCED PEEK LAMINATES UNDER FIRE CONDITIONS

Julie Vacandare[1], Benoît Vieille[1], Fabrice Barbe[1] and Tanguy Davin[1]

[1] INSA Rouen Normandie, Univ Rouen Normandie, CNRS, GPM UMR 6634, F-76000 Rouen, France
Email: julie.vacandare@insa-rouen.fr
Email: benoit.vieille@insa-rouen.fr
Email: fabrice.barbe@insa-rouen.fr
Email: tanguy.davin@insa-rouen.fr

Keywords: Thermoplastic laminates, Kerosene flame, Mechanical testing, X-ray tomography

Abstract
As thermoplastic based composites are increasingly used in aeronautical applications, it is a major concern to understand their mechanical behavior in the critical conditions of an engine fire. The aim of this work is to investigate the tensile behavior of carbon reinforced PEEK laminates exposed to a kerosene flame. An experimental kerosene burner is employed to mimic the fire certification conditions (flame temperature of 1100°C and heat flux of 116kW/m²). The thermal decomposition during the first minute is characterized by calculating the porosity content. X-ray tomography analyses were performed and show that all stages of the porosity formation process occur during the first 15 seconds. The tensile behavior is then studied using two kinds of tests: (i) residual tensile tests at room temperature after fire exposure and cooling and (ii) in situ tensile tests during fire exposure and for different times of exposure. Compared to the virgin specimens, the in situ axial strength (-85% after 900s) decreases more significantly and faster than the residual axial strength (-80% after 900s).

1. Introduction

The current environmental concerns (CO_2 emissions and energy demand) shows that one of the key issues in aeronautics is the design of lightweight structures [1]. Therefore, the integration of polymer matrix composites in structural parts is increasing [2]. However, due to their polymer matrix, their behavior is highly dependent on their thermal working conditions, which can be an issue in the case of an exposure to a flame. In fact, polymers decompose at high temperatures (400-600°C), which results in the formation of cavities filled with pyrolysis gas inside the plies. As the solid matrix is replaced by gas, there is less matrix available to ensure the load transfer. Thus, the mechanical behavior of the composite is altered [3]. For this reason, fire issue is of primary concern for aircraft manufacturers [4]. Understanding the thermomechanical behavior of composites under critical conditions (fire) is therefore essential. The literature on the fire behavior of composites has mainly focused on thermoset (TS) matrix composites [3] and much less on thermoplastic (TP) based composites [5,6].

In a previous work [7], an experimental bench was instrumented to study the thermo-mechanical properties of CG/PEEK laminates with a quasi-isotropic lay-up. A kerosene burner was used to reproduce the conditions of certification fire tests of aeronautical structural parts: flame temperature of 1100°C and heat flux of 116kW/m² [4]. At the same time, a tensile load was applied to the sample. This study [7] has shown the dependence of the residual tensile properties (axial strength and axial stiffness) to the exposure time.

To understand the relationship between the thermal aggression and the mechanical loading, it is important to dissociate the different phenomena that occur within laminates. This study focuses on a

C/PEEK laminates with a QI stacking sequence. Several tests have been carried out. The thermal decomposition process in the first seconds of the fire exposure is first analysed in terms of porosity content; it correlates well with the evolution of the mechanical properties and thereby constitutes a good indicator of damage level. Then, the residual tensile properties at room temperature after exposure to the flame were determined. Finally, the tensile behavior during the exposure was investigated.

2. Materials and experimental set-up

2.1. Materials and specimens

The laminate used in this study consists of a polyetheretherketone (PEEK) thermoplastic matrix reinforced with a 5-harness satin weave carbon faber fabric (Tenax® -E HTA40 3K). The laminate consists of 7 plies following a quasi-isotropic (QI) lay-up [(0/90),(±45),(0/90),(±45),(0/90),(±45),(0/90)]. The fiber volume fraction is 50%. The average thickness of C/PEEK is approximately 2.17mm. The characteristic temperatures for C/PEEK are given in Table 1. Tensile specimens with dog-bone geometry were cut by water jet from 500x500mm² plates. Several thermogravimetric analyses were performed under N_2 at different heating rates to estimate the decomposition onset temperature.

Table 1. Characteristic temperatures of C/PEEK

Glass transition temperature (T_g)	Melting temperature (T_m)	Decomposition onset temperature (T_{onset})
145°C [8]	342°C [8]	600°C

2.2. Kerosene flame exposure

The burner is a domestic device supplied by Cuenod. A kerosene nozzle produces a hollow cone spray with an angle of 80°. The flow rate of 0.3g/s is controlled by a mass flow meter (MINI CORI-FLOW™ – Bronkhorst). Another mass flow meter (EL-FLOW® Prestige – Bronkhorst) controls the air flow. An air/fuel ratio of 0.85 of the stoichiometric value has been chosen to meet the aeronautical fire certification requirements, i.e. a flame temperature of 1100°C and a heat flux of 116kW/m². A protective shield is placed between the 50mm diameter steel tube and the sample. The function of this shield is to limit the area affected by fire to an area of a given size (e.g. 20x20mm² for samples used to determine porosity content and 40x20mm² for tensile specimens) and to ease the comparison between the different testing conditions.

2.3. Porosity content determination

First, the porosity content, i.e. the porosity volume fraction, is evaluated for 25x25mm² samples after a 15s, 30s, 45s and 60s exposure to the flame (20x20mm² area affected by fire). The purpose of these analyses is to understand the process of porosity formation from the first seconds of a fire. Different experimental techniques are used to determine the porosity content: (i) mass loss, (ii) geometry and (iii) X-ray tomography. The mass loss method involves measuring the mass of a sample before and after exposure to fire. The porosity content computed by mass loss is the ratio between the volume corresponding to the mass loss and the volume corresponding to the virgin mass. The geometry method consists in measuring the outer dimensions of a sample with a caliper before and after exposure and in computing the porosity volume from the dimensions changes. The X-ray tomography method is based on tomography analyses using an EasyTom150 device from RX Solutions. After segmentation and 3D reconstruction from the CT scans,the volume of each constituent can be determined. Two different volumes of analysis are considered (Figure 4): (i) a restricted central volume with a section of 3.7x3.7mm² and the specimen thickness and (ii) the whole sample, i.e. a section of 25x25mm². These methods have advantages and drawbacks, as summarized in Table 2.

Table 2. Experimental methods to determine porosity content

Method	Advantages	Disadvantages
Mass loss	Easy and rapid to implement	The mass of carbonaceous residue (char) on the sample after fire exposure could counterbalance the mass loss due to matrix decomposition Does not account for swelling of the material
Geometry	Take account of swelling Easy and rapid to implement	Dependent on where thickness is measured (due to swelling)
X-Ray Tomography	Possibility to analyze porosities (shape, repartition, localization)	Time consuming Dependent on the considered volume

2.4. Mechanical characterization of residual tensile properties

Monotonic mechanical tests allow the residual tensile properties of C/PEEK to be evaluated at room temperature (RT) after a 300s, 600s and 900s exposure to the flame. A 100kN capacity load cell of a MTS servo-hydraulic testing machine is used in displacement-controlled mode (1mm/min) to apply the tension. Axial strains were obtained from a blade extensometer. Three specimens were tested in each configuration and the mechanical properties were determined according to the European Standard EN 6035 [9].

2.5. Combined mechanical-thermal loadings

These tests (Figure 1) consist of two stages:

- A creep loading of 0.5kN during the flame exposure (300s, 600s and 900s) to prevent specimen buckling,
- A force-controlled tensile loading (0.5kN/s) until failure of the specimen.

During the test, mechanical load is measured by a 100kN load cell and the displacement is measured by means of a Linear Variable Differential Transformer sensor. In addition, a 7.5-14µm FLIR A655sc infrared (IR) camera, assuming a 0.9 sample emissivity and a 97% mirror transmission, measures the back surface temperature of the specimen during flame exposure. The average temperature is then calculated within two areas: (i) a centered 18x38mm² rectangle and (ii) a centered 10mm diameter circle (Figure 2). These measurements show a relatively homogeneous temperature field within the exposed area, denoting a relatively low in-plane conductive heat transfer.

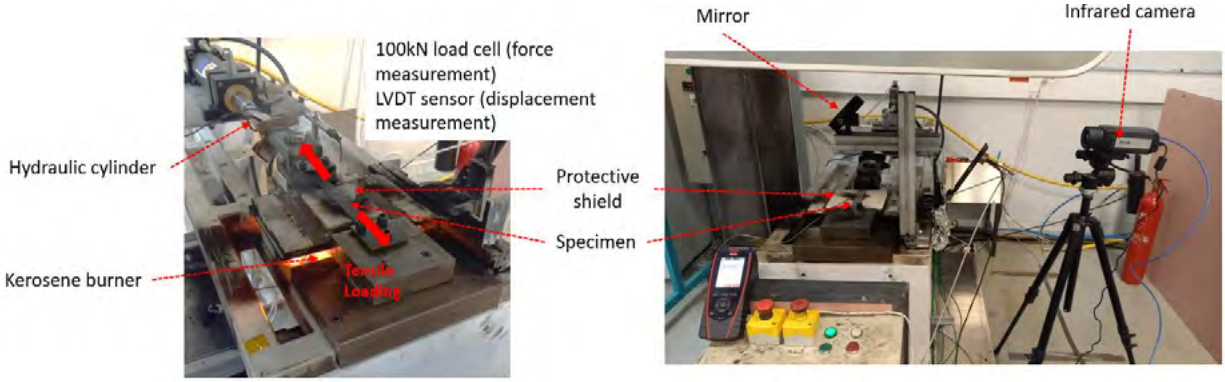


Figure 1. In situ tensile experimental bench: C/PEEK laminates subjected to a kerosene flame during mechanical loading

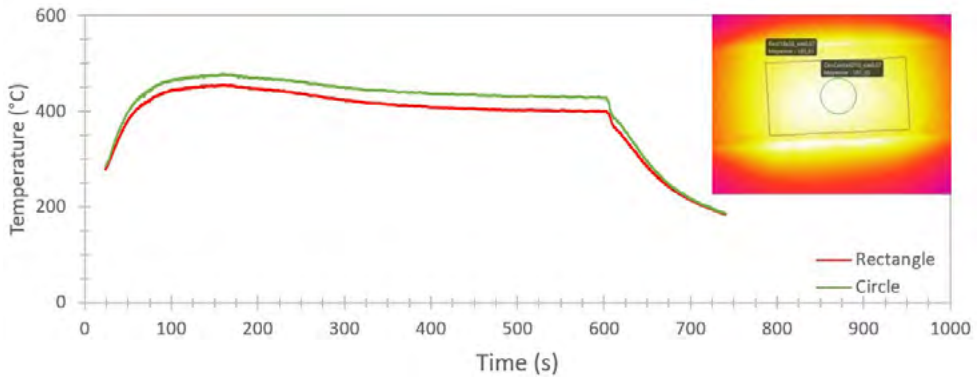


Figure 2. Back surface temperature evolution during 600s exposure on C/PEEK laminates, as measured by IR camera

3. Results and discussion

3.1. Mass loss and porosity content

During fire exposure, the PEEK matrix undergoes a thermal decomposition leading to mass loss and to swelling, resulting from the formation of porosities. Microscopic observations (Figure 4) show that two areas can be identified through the thickness of the sample: (i) a thermally degraded area and (ii) a relatively preserved area [10]. Thermal degradation starts within the first few seconds of exposure. Figure 3 shows the porosity content calculated by the different methods. Not surprisingly, a prolonged exposure results in an increase of the porosity content. However, there are a few differences between these methods. The porosity content obtained from the mass loss is lower than the one obtained from other methods. This can be explained by the fact that the mass loss method does not consider the swelling of the sample. The overall trend for porosity content calculated from geometry changes is similar to the one obtained from X-ray tomography observations on different volumes. The porosity content computed from CT-scans seems to depend on the considered volume. Indeed, for 15 and 30s exposure times, the restricted central volume provides the highest porosity content; at this place damage is more important than along the edges of the sample (Figure 4); and for 45 and 60s of exposure, then the full size sample provides the highest porosity content.

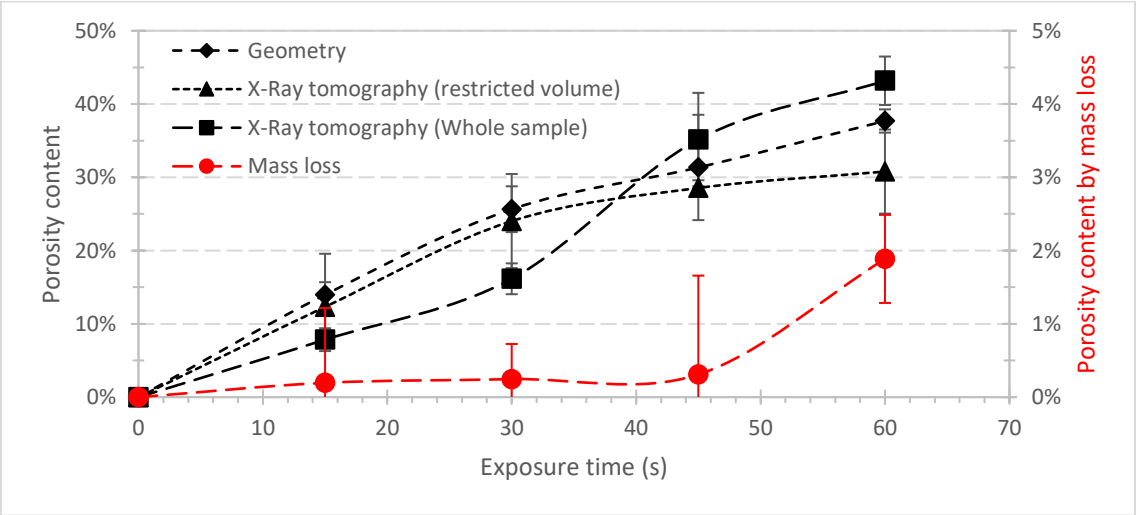


Figure 3. Comparison of porosity content obtained from different methods in C/PEEK laminates exposed to the flame for different lengths of time

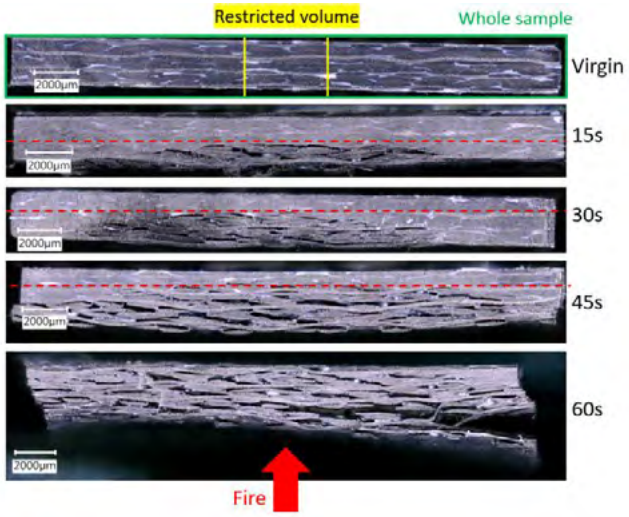


Figure 4. Through-thickness microscopic observations of C/PEEK laminates subjected to the flame for different lengths of time

X-ray tomography allows not only the porosity content to be obtained but also to visualize the porosity network. Different types of cavities, corresponding to different steps in the porosity formation process, can be identified in Figure 5: (i) small spherical cavities that have just nucleated, (ii) larger spherical ones that have grown due to the internal pressure of pyrolysis gases, (iii) those with disturbed shapes resulting from the coalescence of several spherical cavities, (iv) large ones leading to inter-ply delamination and (v) intra-fiber bundle longitudinal cavities along the fiber direction, resulting from the decomposition of the PEEK matrix used to impregnate fibers.

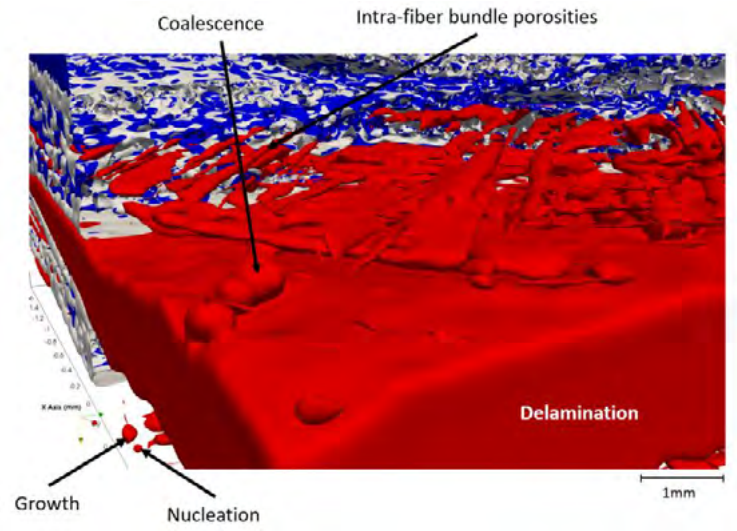


Figure 5. X-Ray tomography observation of C/PEEK after a 15s exposure to the flame

3.2. Residual tensile properties after fire exposure

To quantify the residual tensile properties of C/PEEK after flame exposure, monotonic tensile tests were performed on specimens after cooling. The macroscopic responses (Figure 6 (a)) show that the tensile behavior of both virgin and thermally degraded material is virtually elastic-brittle. The responses of thermally degraded specimens show several drops in the axial stress which could correspond to the failure of a ply. The response of the 600s exposed specimen is similar to that of the 900s specimen.

Figure 6 (b) shows that both axial strength and stiffness decrease with increasing exposure time. This can be correlated to the porosity content which becomes higher as the exposure time increases, also meaning that there is less matrix to ensure the load transfer. After 600s exposure, both axial stiffness and strength seem to reach a plateau at about 20% and 30% of the virgin properties respectively. As shown in Figure 7, the ultimate failure of the specimen is caused by the breakage of 0° fibers, i.e. in the direction of mechanical loading. Under fire conditions, the 0° oriented fibers bearing about 73% of the axial load (according to the classical laminates theory) are the ones contributing most to the axial strength in QI laminates.

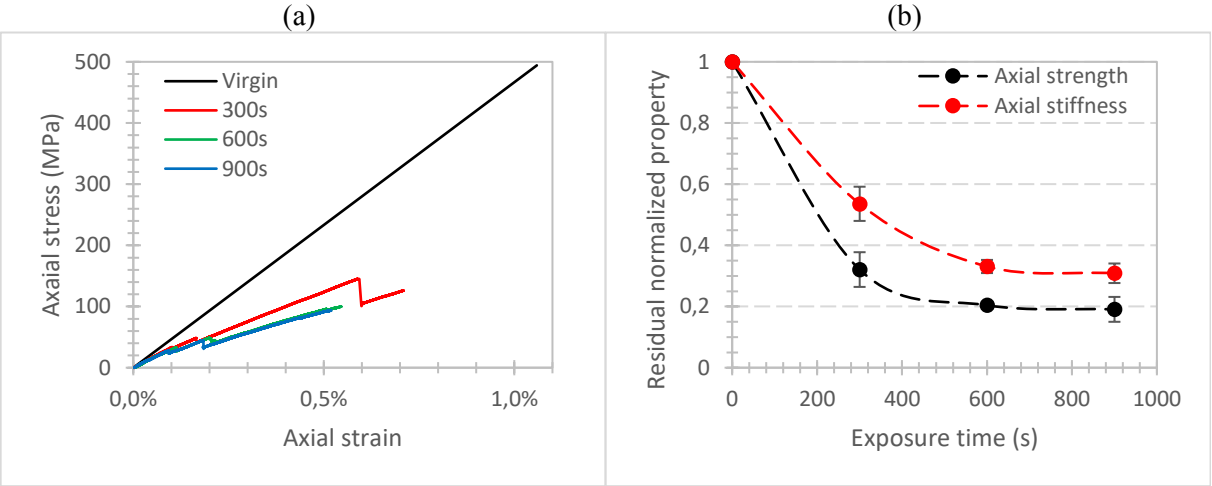


Figure 6. Tensile behavior of C/PEEK laminates subjected to the flame (a) Stress-strain response (b) Changes in tensile properties VS exposure time

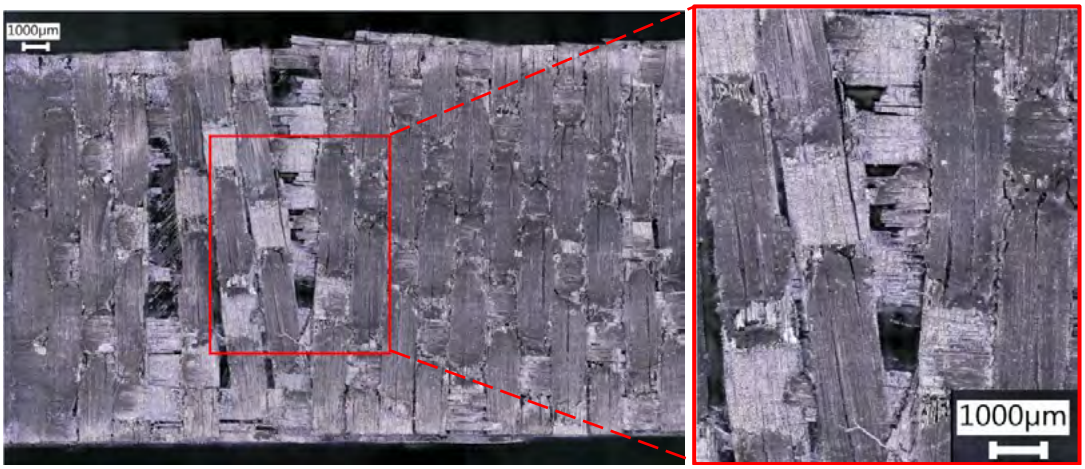


Figure 7. Microscopic observations of the exposed surface of the laminates after a 300s exposure to the flame and a residual tensile test

3.3. In situ tensile properties

The previous section allows the characterization of the tensile properties of QI C/PEEK laminates after a fire event and a cooling at RT. It is now interesting to compare the residual axial strength with the axial strength during fire exposure. Tensile tests under fire were then carried out. First, a specimen is exposed to the kerosene flame for a given time (300s, 600s or 900s) while maintaining a tensile load of 0.5kN to avoid specimen buckling. Then, still under fire exposure, a tensile load is applied in load-

controlled mode (0.5kN/s). At the same time, the back surface temperature is measured with an IR camera. Figure 8 shows that the axial strength remains stable at about 15% after a 300s exposure to fire. The axial strength is lower than the one determined after flame exposure. This difference could be explained by the back surface temperature. It reaches 450°C, which is higher than the melting temperature. Therefore, under the flame, the whole PEEK matrix is at best melted and at worst decomposed. As a result, the matrix does not ensure the load transfer between the fibers. In the case of residual tensile testing at RT, matrix that has not decomposed on the back surface, has resolidified and can therefore ensure the bond between fiber bundles and thus the load transfer. As for the back surface temperature, it increases up to 200s of exposure and then it slightly decreases to remain stable. This decrease could be explained by the delamination of the laminates contributing to form an insulating gas layer. X-ray tomography analyses show significant swelling and failure of the 0° oriented fibers on the exposed surface (Figure 9).

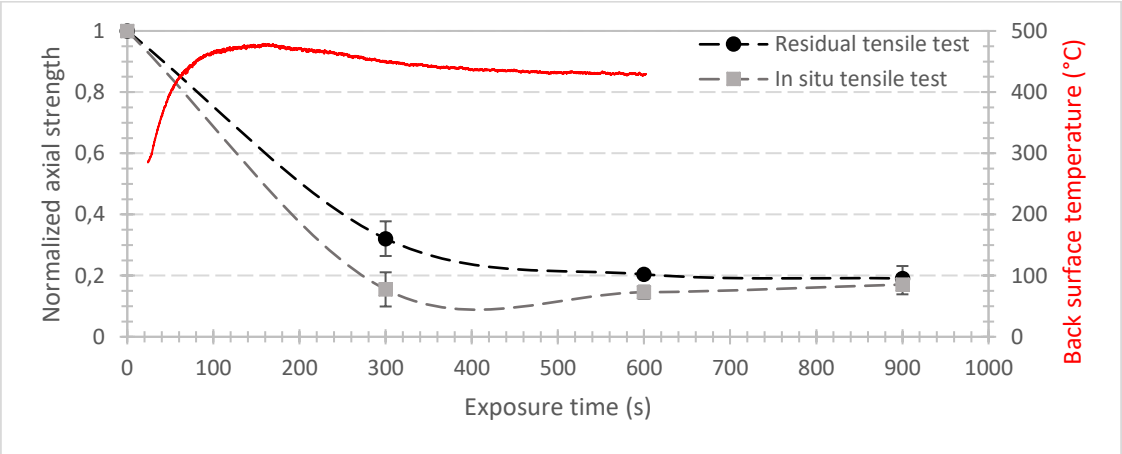


Figure 8. Changes in the axial strength of C/PEEK laminates subjected to a tensile loading after fire exposure (residual) and under (in situ) fire conditions

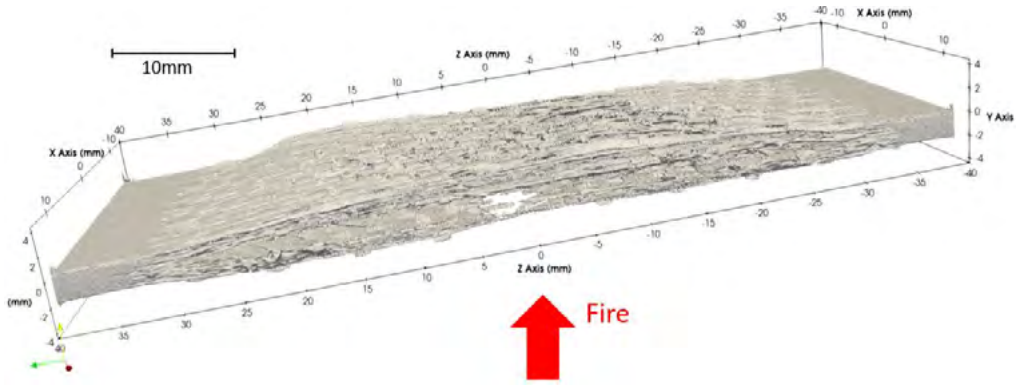


Figure 9. X-ray tomography observations of C/PEEK laminates after a 900s exposure to fire followed by an in situ tensile loading

4. Conclusion

The main objective of this work was to investigate both thermal and mechanical phenomena at play in quasi-isotropic carbon reinforced PEEK laminates. A fire test bench was used to mimic the aeronautical fire certification conditions (a 1100°C kerosene flame and 116kW/m² heat flux). To understand the thermal decomposition during the first minute of fire, the porosity content and morphological distribution were characterised. To study the relationship between thermal aggression and mechanical

loading, two types of tensile tests were carried out: residual tensile test at RT and in situ tensile test under the flame.

From the obtained results, the following conclusions can be drawn: (i) all the stages of the porosity formation process appear in the first few seconds of exposure and the porosity content reaches 40% after one minute of exposure, (ii) the residual axial strength is higher than the in situ axial strength because of the cooling of specimens leading to the resolidification of the PEEK matrix, (iii) the contribution of plies to axial strength depends on the orientation of fibers within each ply, (iv) porosities have a detrimental effect on the tensile properties but may contribute to the reduction of back surface temperature.

The temperature within the laminate needs to be further investigated in order to quantify the degradation of each ply and thus estimate the contribution of each ply to the load carrying capabilities. It is also necessary to develop a numerical model to estimate the temperature in-plane and through the thickness of the laminates.

Acknowledgments
This study has benefited from the financial support of Region Normandie and the European Funds for regional development (FEDER) through the ACERIN project 2023 for the equipment in X-Ray tomography.

References

[1] L. Zhu, N. Li, and P. R. N. Childs. Light-weighting in aerospace component and system design. Propulsion and Power Research, 7(2):103-119, 2018. doi: 10.1016/j.jppr.2018.04.001.
[2] T. Dursun and C. Soutis. Recent developments in advanced aircraft aluminium alloys. Materials & Design, 56:862–871, 2014. doi: 10.1016/j.matdes.2013.12.002.
[3] A. P. Mouritz and A. G. Gibson. Fire Properties of Polymer Composite Materials. Springer, Dordrecht, 2006.
[4] ISO 2685:1998. Environmental test procedure for airborne equipment — Resistance to fire in designated fire zones, 1998.
[5] A. G. Gibson, M. E. Otheguy Torres, T. N. A. Browne, S. Feih, and A. P. Mouritz. High temperature and fire behaviour of continuous glass fibre/polypropylene laminates. Composites Part A, 41(9):1219-1231, 2010. doi: 10.1016/j.compositesa.2010.05.004.
[6] B. Vieille, A. Coppalle, E. Schuhler, A. Chaudhary, A. Alia, N. Delpouve and A. Bourdet. Influence of kerosene flame on fire-behaviour and mechanical properties of hybrid Carbon Glass fibers reinforced PEEK composite laminates. Composite Structures, 279:114786, 2022. doi: 10.1016/j.compstruct.2021.114786.
[7] B. Vieille, A. Coppalle, A. Alia, E. Schuhler, A. Chaudhary, D. Bouscarrat and N. Delpouve. Influence of kerosene flame on in situ mechanical properties of hybrid fibers reinforced PEEK composite laminates. In Composites Meet Sustainability – Proceedings of the 20th European Conference on Composite Materials ECCM20, volume 3, pages 1061-1211, 2022.
[8] B. Vieille, J. Aucher, and L. Taleb. Comparative study on the behavior of woven-ply reinforced thermoplastic or thermosetting laminates under severe environmental conditions. Materials & Design, 35:707–719, 2012. doi: 10.1016/j.matdes.2011.10.037.
[9] Test standard EN 6035 : aerospace series - fiber-reinforced plastics - test method - determination of notched and unnotched tensile strength. European association of aerospace industries (AECMA), 1996.
[10] L. Lin, B. Vieille, and C. Bouvet. About the influence of a thermal aggression on the tensile behaviour of hybrid PEEK thermoplastic laminates. Composite Structures, 333: 117945, 2024. doi: 10.1016/j.compstruct.2024.117945.5.

BASIC STRUCTURAL DESIGN OF FIBER REINFORCED COMPONENTS BASED ON OPEN SOURCE SOFTWARE

U. Zimmermann[1], V. Urundolil[2] , M. Zogg[3] and G. A. Barandun[4]

[1]OST – Eastern Switzerland University of Applied Sciences, Rapperswil SG, Switzerland
Email: urs.zimmermann1@ost.ch , Web Page: https://www.ost.ch
[2]inspire AG, Zurich, Switzerland
Email: varun.urundolil@inspire.ch , Web Page: https://www.inspire.ch
[3]inspire AG, Zurich, Switzerland
Email: markus.zogg@inspire.ch , Web Page: https://www.inspire.ch
[4] OST – Eastern Switzerland University of Applied Sciences, Rapperswil SG, Switzerland
Email: gion.barandun@ost.ch , Web Page: https://www.ost.ch

Keywords: open-source, layered model, FEM, structural simulation, validation

Abstract
FEA simulations are state-of-the-art today in the industry. Due to the anisotropic properties of fibre-reinforced composites, FEA is a crucial tool when designing such parts and helps to reduce prototype iterations, money, and resources.

However, due to the high prices of commercial FEA software, SMEs are often choosing not to use these tools, despite the potential long-term economic gains. The commercial software available on the market is usually too feature-rich and complex for most applications, especially to validate a few layup ideas. Therefore, open-source software could provide a solution for SMEs.

Based on requirements as stated by SMEs for the basic dimensioning of FRP structures, Salome_Meca was identified as a potential open-source FEA software. In this work, the abilities of the software were validated by comparison to an analytical solution for a three-point-bending test of a carbon fibre-reinforced polymer sample. The comparison shows good agreement and hence validates the use of Salome_Meca for FRP structure dimensioning. Using Python, additional features can be added according to the use case of the SMEs, such as various failure criteria, visualization, and reporting.

1. Introduction

Today, the rough dimensioning of fibre-reinforced polymer (FRP) composite structures is usually performed with the experience of a skilled engineer. Pragmatic analytical formulas and a trial and error approach are common in SMEs to find a proper layup for their parts. FEM software is available and engineers at universities usually are trained on how to use and apply it to calculate different layups or even optimize the layup automatically, improving the material usage and reducing waste. Despite this fact, SMEs often stick to their approach as commercial FEM software exceeds their funds. The high acquisition, training, and operation costs won't lead to a sufficient turnaround.
Finding, evaluating and improving an open-source FEM software for the basic dimensioning of FRP structures for Swiss SMEs is part of an ongoing project. In the scope of the project, Code_Aster [1] was identified as a promising FE solver. The Salome (Simulation numérique par Architecture Logicielle en Open source et à Méthodologie d'Évolution) software package includes a CAD-geometry editor , a mesher and a visualisation tool. It supports industry-standard import formats for 3D files (IGES, STEP, BREP). The variation where the Code_Aster FE solver and FEM study creator are combined is called Salome_Meca .

In this work, the validation of Salome_Meca for use in dimensioning FRP structures is presented for simulations using 2d shell elements. These are valid for monolithic, shell-like FRP structures [2]. A three-point-bending test is implemented in FEA, and the resulting deflection is compared to the analytical solution. Additionally, the results are compared to commercially available FEM-Software.

2. Methods

The principle workflow of calculating the structural response of a 2D FRP part is shown in (Figure 1).

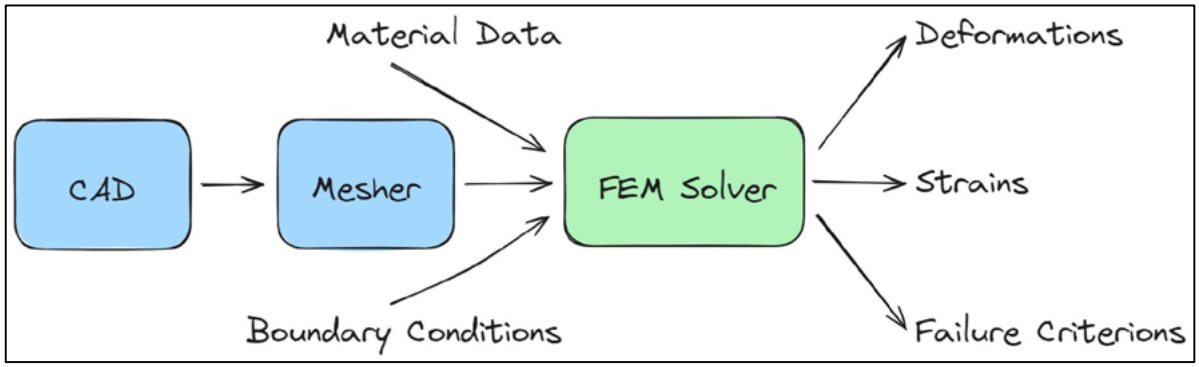


Figure 1. General Workflow for FEM Analysis of a FRP Structure in Salome_Meca

The shell geometry of the structure is either drawn in the geometry module or imported from CAD software. The geometry is subsequently meshed in the mesh module and finally the material properties, composite layup and boundary conditions are defined and the model is solved in the code-aster FE solver. The results can then be visualised using the Paravis [3] module, where deformation, strains and possible failure criteria can be shown.

In the scope of the project, SMEs filled out an extensive survey concerning their research needs and current technologies. The material they use most often is carbon fibre-reinforced composite (CFRP) with an epoxy matrix. The mechanical properties of such laminates with 40% fibre volume content were measured experimentally, using vacuum bagging as the manufacturing method. The measured properties for a unidirectional CFRP ply are summarised in (Table 1).

Table 1. Mechanical Properties of a single layer (CF UD 200g/m2; epoxy matrix, wet laminate, 40% FVC), experimentally measured values

Property	**Abbreviation**	**Unit**	**Value**
E-Module longitudinal (0°)	E_{11}	MPa	92500
E-Module transverse (90°)	E_{22}	MPa	6300
Shear modulus - planar	G_{12}	MPa	5700
Transverse contraction	ν_{12}	-	0.33
Layer thickness	t_i	mm	0.28

The validation of Salome_meca is conducted by considering a three-point bending test according to the ISO 14125 standard. The test is implemented in Salome_Meca and compared to the analytical solution (2.1). The geometry of the test setup is shown in (Figure 2). The test specimen is a plate of rectangular cross-section with a width w of 25 mm and a span length L of 300 mm. The thickness of the specimen is governed by the CFRP layup.

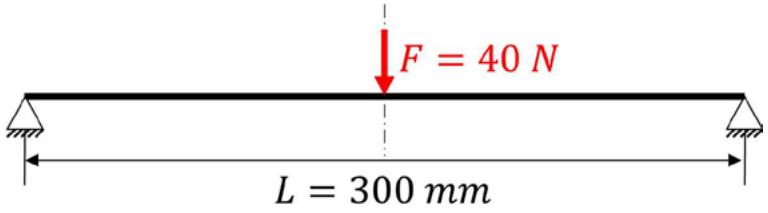


Figure 2. Three point bending experiment according to ISO 14125

As the homogenisation of the FRP layup in Salome_Meca is crucial for FEM analysis, specifically for loading under bending because of the stiffness distribution in the cross-section of the beam, two different layups of equal thickness were implemented. The primary direction, i.e. 0° orientation is along the span axis. In layup L1 the stiff 0° plys are at the exterior of the laminate, while in layup L2, the stiff plys are positioned in the center near the bending neutral plane. The resulting layups are summarized in (Table 2).

Table 2. Two different CFRP layups considered in this work.

Designation	Layup	Layer material	Bending Modulus [MPa]
L1	$[0°,0°,+45°,-45°]_S$	CF UD	83334
L2	$[+45°,-45°,0°,0°]_S$	CF UD	27741

The validation of the FEM model is conducted by comparing the maximal deflection under a known bending force F of 40 N.

2.1. FEM Analysis

For the FEM analysis of the bending test, the symmetry of the setup was exploited. In (Figure 3) the side view of the simulated test is shown including the symmetry plane in the center.

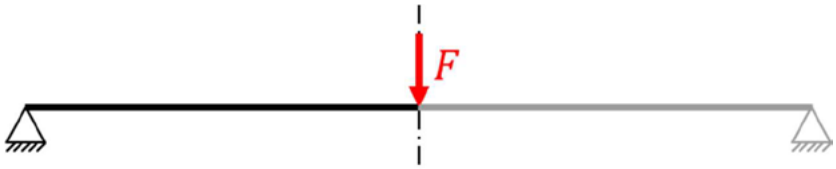


Figure 3. Simulated three-point bending test, including the symmetry plane in the center.

The specimen was modelled as a 2D rectangle of width w and length $L/2$ as seen in (Figure 4). The boundary conditions are also shown.

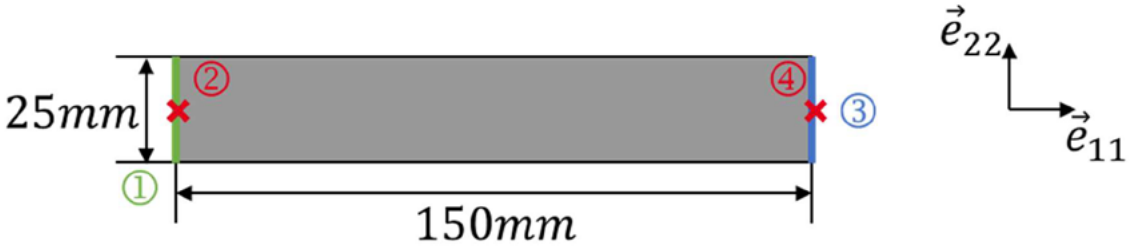


Figure 4. Top view of the simulated speciment with the numbered boundary condition location. The local coordinate system is also shown.

The edge on the fixed support (1) is fixed for rotary and translatory degrees of freedom (DoF) in two directions. The center point (2) is fixed in all 6 Dof. For the symmetry constraint, the edge on the right (3) is partially fixed as well as the point (4), which has to fulfil the symmetry constraint. The load was introduced as half the load F as a line load. Due to the symmetry, only half the load was applied in the simulation. The boundary conditions (2) and (4) are added, to ensure that sufficient DoFs are restricted for the simulation to converge. The load and boundary conditions are summarized in (Table 3).

Table 3. Summary of the boundary conditions applied in the FEM analysis.

Constraint Nr.	Constraint
(1)	$u_{33} = 0$
(2)	$u_{22} = u_{33} = 0$
(3)	$u_{11} = \omega_{11} = \omega_{22} = \omega_{33} = 0$
(4)	$u_{11} = u_{22} = \omega_{11} = \omega_{22} = \omega_{33} = 0$
F	$q_{33} = \frac{-F}{2 \cdot 25mm} = \frac{-40N}{2 \cdot 25mm} = -0.8\,{}^{N}/_{mm}$

2.2. Analytical Analysis

To validate the results the three-point bending specimen was approximated as a Euler-Bernoulli bending beam. This first-order theory is valid, as the length-to-thickness ratio is an order of magnitude over 10. For a three-point bending beam the maximal deflection u is calculated as shown in the following equations (Eq. 1, Eq. 2).

$$u = \frac{FL^3}{48 \cdot E \cdot I} \tag{1}$$

$$I = \frac{w \cdot h^3}{12} \tag{2}$$

As the specimen is made of CFRP, the bending stiffness of the specimen is calculated based on the homogenization of the layup using the Classical Laminate Theory [4]. To homogenize the properties the open-source program ElamX from TU Dresten [5] was used.

The resulting bending stiffness in the longitudinal direction (11-direction) is given for the two layups as in (Table 2)

3. Results and Discussion

The simulated specimen was made of 3900 2D DKT elements with a mean edge length of 1 mm. The undeformed and the two deformed results are shown in (Figure 5).

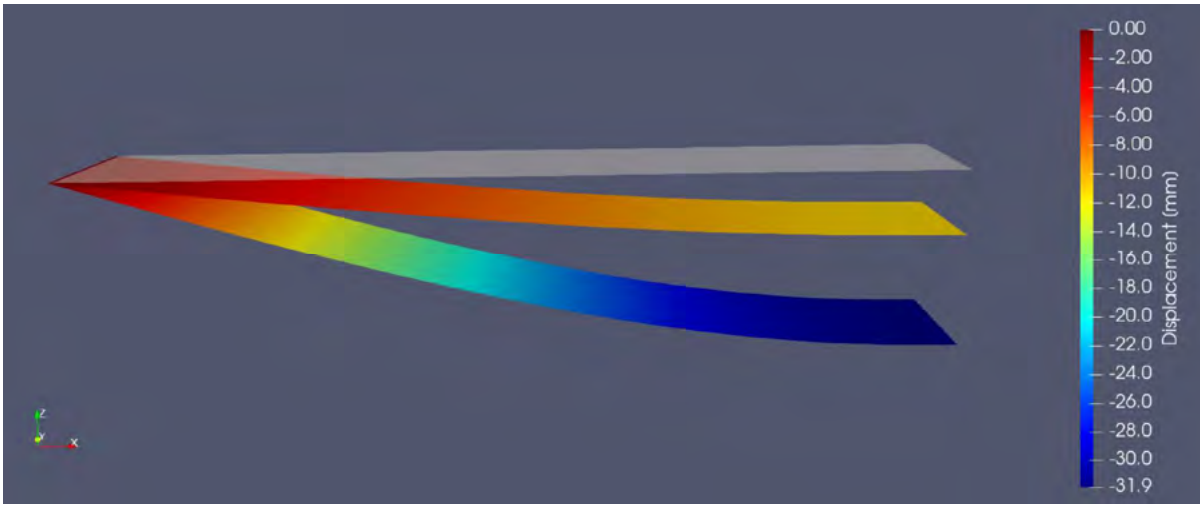


Figure 5. The undeformed and two deformed specimen shapes for the two layups shown in the Paravis module of Salome_Meca.

The displacement of the nodes can be extracted, and the maximal value is used for the validation for either layup. Obviously, the bending stiffness difference between L1 and L2 is visible by the different levels of deformation as seen in the figure above.

The maximal deflextion based on the FEM analysis and analyitical solution are summarised in (Table 4). Additionally, the maximal deflection is compared to a commercially available FEM programme in (Table 5).

Table 4. Summary of resulting maximal deflection of the FEM analysis and Analytical analyis. The difference is shown in percentage.

Result	Salome_Meca	Analytic	Deviation [%]
Bending test L1 [mm]	11.45	11.53	-0.70
Bending test L2 [mm]	31.91	34.64	-7.88

Table 5. Summary of resulting maximal deflection of the FEM (Salome_Meca) and a commercially available FEM software. The difference is shown in percentage

Result	Salome_Meca	Commercial FEA	Deviation [%]
Bending test L1 [mm]	11.45	11.43	0.18
Bending test L2 [mm]	31.91	31.25	2.11

All three results, the FEA by Salome_Meca, the FEM programme and the analytical results agree on the deflection order of magnitude. Furthermore, the increased deflection due to the lower bending stiffness of L2 is also well captured. The difference is below 1% for the stiffer specimen, whereas for L2 the difference is as large as 7.88%. Obviously, the error of the FEM analysis increases with lower bending stiffness. This is a consequence of the boundary conditions used. Idealised in a three-point bending loading scenario, the average tensile strain of the sample is 0. Experimentally this is seen as the sample moves on the simply supported supports. The way the FEM analysis is implemented, the boundary condition (1) does not allow any movement, only rotation. Hence for large deflections, the slipping of the specimen is prohibited, which introduces a tensile loading of the specimen superimposed to the bending load. Hence, the expected deflection is smaller, which is the case as seen in the results. Hence, the FEM analysis is validated.

4. Conclusion

As a validation to see if the model and the strategy used were correct, the three-point bending test was a good approach. Further tests will be done on the specimen to compare with the simulations.

As the next steps, other functions will be implemented, such as damage according to Hashin. A buckling analysis has already been performed but not validated.

To make it suitable for industrial applications, other geometries and load cases need to be implemented and tested to verify the usability for SMEs.

Acknowledgements

The authors greatfully acknowledge the support of Innosuisse with the grant 104.135 IP-ENG.

References

[1] EDF-CEA. *SALOME PLATFORM – The open-source platform for numerical simulation*. https://www.salome-platform.org
[2] L. T. Tenek and J. Argyris. *Finite Element Analysis for Composite Structures.* Springer Dordrecht. 1997
[3] Kitware inc. *ParaView – Open-source, multi Platform data analysis and visualization application.* https://www.paraview.org
[4] A. T. Nettles. *Basic mechanics of laminated composite plates.* Legacy CDMS. 1994
[5] TU Dresden. *eLamX – Chair of Aircraft Engineering – TU Dresden*. https://tu-dresden.de/ing/maschinenwesen/ilr/lft/elamx2/elamx

PREDICTION OF MECHANICAL BEHAVIOR OF CARBON FIBER BRAIDED COMPOSITES: A MULTI-SCALE SIMULATION-BASED PROGRESSIVE FAILURE MODEL

Jeong-Hyeon Baek[1], Se-Min Lee[1] and Hak-Sung Kim[1,2]

[1] Department of Mechanical Convergence Engineering, Hanyang University, 222, Wangsimni-ro, Seongdong-gu, Seoul, Republic of Korea
Email: jhbaek9489@gmail.com, Web Page: https://me.hanyang.ac.kr/
[2] Hanyang Research Center for Advanced Semiconductor Packaging, Hanyang University, 222, Wangsimni-ro, Seongdong-gu, Seoul, Republic of Korea
Email: kima@hanyang.ac.kr, Web Page: https://iss.hanyang.ac.kr/

Keywords: Braided composite, Multi-scale simulation, Micromechanics, Stress amplification, Progressive failure model

Abstract

In this study, a simulation model was developed to predict the nonlinear mechanical behavior of braided carbon fiber-reinforced pipes, incorporating multi-scale simulation and progressive failure analysis. The multi-scale modeling was employed by setting Periodic Boundary Conditions (PBC) for Representative Volume Elements (RVE) at the micro- and meso-scale levels. Then, the effective equivalent properties and Stress Amplification Factors (SAF) to predict and damage states at each scale were derived. From these results, the failure criteria of each material were applied to determine the stress states of fibers and matrix. As a result, the mechanical behavior of macro-scale pipe was predicted. To verify the simulation results, compression, bending, and torsion tests were conducted on carbon fiber-reinforced circular pipes with a 45-degree plain braid angle and a 70-degree twill braid angle. In summary, a multi-scale-based simulation model incorporating micro-scale damage mechanics for braided carbon fiber-reinforced composites was developed, showing a high accuracy through experimental validation.

1. Introduction

Owing to superior mechanical properties such as high stiffness and strength with low weight, carbon fiber-reinforced composites have received tremendous attention recently as essential materials for enabling innovative performance improvements in various industries. Particularly, woven carbon fiber-reinforced composites exhibit excellent impact resistance with their enhanced out-of-plane properties, and formability with balanced in-plane properties compared to unidirectional composites, making them widely utilized. Among various weaving techniques, braiding offers advantages in three-dimensional structure fabrication, localized direction and density control, and production automation, leading to increased applications in industries such as aerospace, automotive, and energy [1]. Therefore, there is a growing demand for understanding the properties of braided composites considering different braiding patterns and angles as shown in Figure 1.

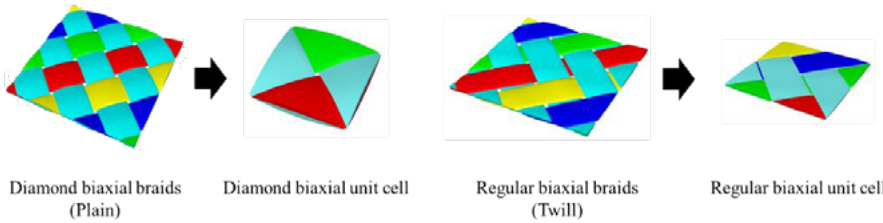


Figure 1. The schematic of braiding type

To simulate real braided composites and predict their mechanical properties, it is necessary to develop reliable models that realize complex braided composite structures. In this study, micro-mechanics based multi-scale modeling and finite element analysis were conducted to predict the non-linear behavior of braided composites [2]. Micro-scale and meso-scale representative volume element (RVE) models were developed, and the meso-scale stress of fiber yarn was transferred to the micro-scale stress of fiber and matrix using a stress amplification factor (SAF) [3]. A progressive damage model based on the multi-scale method was applied to the meso-scale RVE model consisting of fiber yarn and the matrix pocket, from which the non-linear behavior of a braided composite could be predicted [4]. Using the developed damage model, simulations for various braiding types and mechanical tests were conducted. The results of predicted damage model was compared with experimental results, and failure analysis was performed for the meso-scale braided material and macro-scale braided composite pipe.

2. Finite element analysis & Experimental verification

2.1. Multi-scale simulation to derive effective equivalent properties and the stress amplification factor

The multi-scale simulation of braided composites is presented in Figure 2. It was demonstrated that the braided composite damage of the macro-scale homogenous part can be indicated by meso-scale damage to either the fiber yarn or matrix pocket. Failure in the matrix pocket is regarded as damage in the isotropic matrix. Meanwhile, the damage mechanisms within the fiber yarn are represented by failure modes identified for a UD composite. Two micro-scale failure modes (fiber failure and matrix failure) were identified within the yarn. The local stress distributions in the braided composite could be obtained by linking an arbitrary global stress to the local stress.

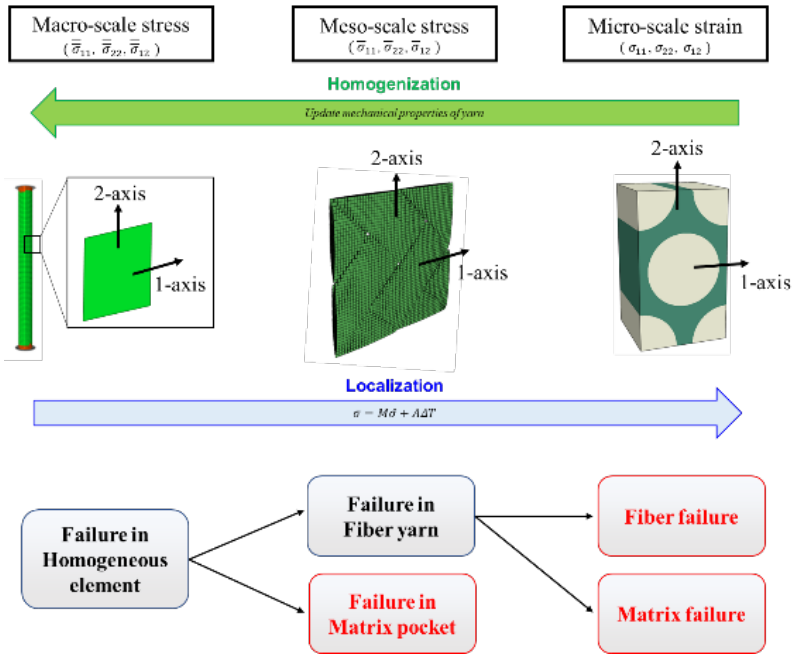


Figure 2. The schematic of multi-scale simulation process

To apply micro-mechanics based multi-scale analysis to yarn composed of fibers and matrix, a process of stress calculation meso-units to micro-units is necessary. A correlation between meso-scale stresses and micro-scale model stresses was established with the stress amplification factor as expressed by the following equation (1): [5]

$$\sigma_i = M_i \bar{\sigma} + A_i \Delta T \tag{1}$$

where σ_i and σ_i are the micro-scale stress and meso-scale stress. M_i is the stress amplification factor to calculate meso-scale stress with micro-scale stress, and A_i indicates the thermal stress amplification factor for the temperature increment. In this work, thermal stress caused by temperature changes was not considered. The SAF was determined through finite element simulation of the micro-scale RVE model with each corresponding periodic boundary condition as shown in Figure 3 (The mechanical properties of fiber and matrix are shown in Table 1) [6]. The relationship between meso-scale stress and micro-scale stress is expressed as follows:

$$\begin{pmatrix}\sigma_1\\ \sigma_2\\ \sigma_3\\ \sigma_4\\ \sigma_5\\ \sigma_6\end{pmatrix} = \begin{bmatrix}M_{11} & M_{12} & M_{13} & M_{14} & 0 & 0\\ M_{21} & M_{22} & M_{23} & M_{24} & 0 & 0\\ M_{31} & M_{32} & M_{33} & M_{34} & 0 & 0\\ M_{41} & M_{42} & M_{43} & M_{44} & 0 & 0\\ 0 & 0 & 0 & 0 & M_{55} & M_{56}\\ 0 & 0 & 0 & 0 & M_{65} & M_{66}\end{bmatrix}\begin{pmatrix}\bar{\sigma}_1\\ \bar{\sigma}_2\\ \bar{\sigma}_3\\ \bar{\sigma}_4\\ \bar{\sigma}_5\\ \bar{\sigma}_6\end{pmatrix} \quad (2)$$

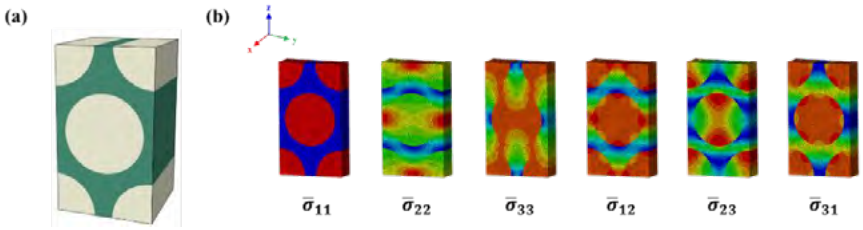


Figure 3. (a) Micro-scale RVE model and (b) stress distribution of micro RVE model according to each stress direction.

Table 1. The mechanical properties of carbon fiber and matrix.

Constituent	Properties	Value
Fiber	E_{f1} [GPa]	230
	E_{f2} [GPa]	15
	G_{f12} [GPa]	27
	G_{f23} [GPa]	7
	ν_{12}	0.2
	ν_{23}	0.2
	T_f [MPa]	4800
Matrix	E_m [GPa]	3.1
	ν_m	0.35
	T_m [MPa]	50
	C_m [MPa]	100
Yarn volume fraction	V_f	0.55

The stress calculation macro-scale to meso-scale was conducted by a similar process. The meso-scale RVE model was modeled using the textile geometric modeling software TexGen with various braiding

conditions. In this analysis, shell elements were used at the macro-scale model. Therefore, the relationship between macro-scale stress and meso-scale stress is expressed as follows:

$$\begin{pmatrix} \bar{\sigma}_{11} \\ \bar{\sigma}_{22} \\ \bar{\sigma}_{12} \end{pmatrix} = \begin{bmatrix} M_{11} & M_{12} & M_{13} \\ M_{21} & M_{22} & M_{23} \\ M_{31} & M_{32} & M_{33} \end{bmatrix} \begin{pmatrix} \bar{\bar{\sigma}}_{11} \\ \bar{\bar{\sigma}}_{22} \\ \bar{\bar{\sigma}}_{12} \end{pmatrix} \tag{3}$$

where $\bar{\bar{\sigma}}$ and $\bar{\sigma}$ are the macro-scale stress and meso-scale stress, respectively, and M is the stress amplification factor.

2.2. Progressive failure analysis

To accurately predict the non-linear behavior of a braided composite with finite element simulation, a distinguished failure criterion for the progressive damage model should be used (see Figure 4).

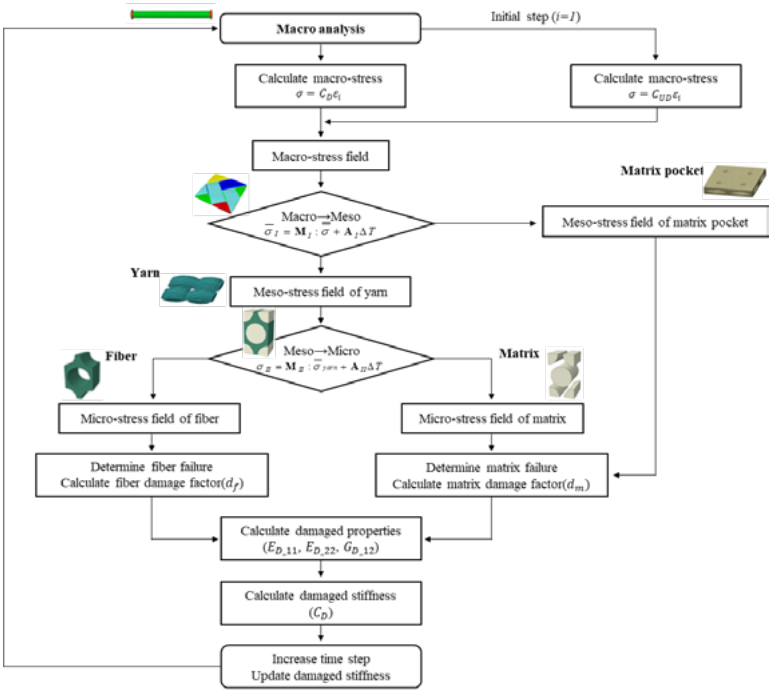


Figure 4. The schematic of multi-scale simulation

In the matrix, von Mises failure criterion was used as follows: [7]

$$\frac{\sigma_{VM}^2}{C_m T_m} + \left(\frac{1}{T_m} - \frac{1}{C_m}\right) I_1 = 1 \tag{4}$$

where C_m and T_m are the compressive and tensile strength of the matrix, and σ_{VM} and I_1 are the von Mises equivalent stress and the first stress invariant [8]. The matrix failure criterion is defined as a function of equivalent stress as follows: [9]

$$\sigma_{ep} = \frac{(\beta - 1) I_1 + \sqrt{(\beta - 1)^2 I_1^2 + 4\beta\sigma_{VM}^2}}{2\beta} \tag{5}$$

where β is defined as the ratio of the matrix compressive strength to the tensile strength. This equivalent stress is also termed Stassi's equivalent stress [10]. From this equation, failure criterion comparable to

the condition of equivalent stress, σ_{ep}, was calculated by the matrix failure index (k_m) according to the following equation:

$$k_m = \frac{\sigma_{eq}}{T_m} \tag{6}$$

where T_m is the tensile strength of the matrix. After matrix failure was generated, damage accumulated, and the stiffness of the matrix progressively decreased. The damage model was used as follows:

$$D_m = \begin{cases} 1 - exp[\gamma(1 - k_m)] & (1 < k_m < \alpha) \\ 0.99 & (\alpha < k_m) \end{cases} \tag{7}$$

where γ is a matrix damage factor. For gamma, the larger the braiding angle, the larger the gamma value used (for braiding angles of 70°, γ = 3 / 45°, γ = 1.5 / 20°, γ = 1). α is set to 1.5 [11]. When σ_{eq} is larger than the strength of the matrix, D_m is set to .99 to give complete fracture of the matrix. In the fiber, a maximum longitudinal stress failure criterion was used as following equation:

$$k_f = \frac{T_f}{\sigma_{f11}} \tag{8}$$

where k_f is the fiber failure index and T_f and σ_{f11} are the tensile strength and micro stress of the fiber in the longitudinal direction, respectively. When k_f was larger than 1, the fiber failed and its stiffness rapidly decreased. This fiber damage factor is expressed as follows:

$$D_f = \begin{cases} 0 & (k_f \leq 1) \\ 0.99 & (1 < k_f) \end{cases} \tag{9}$$

2.3. Mechanical tests of the braided composites

The tests for mechanical properties of the meso-scale braided composite were performed with carbon fiber/epoxy material with two braiding types (plain and twill) at angles of 20-degree, 45-degree, and 70-degree respectively. Meso-scale specimens were fabricated through a vacuum assisted resin transfer molding (VARTM) process, based on the ASTM standard method (see Figure 5(a)). In addition, macro-scale tests were conducted for circular composite pipe of two braiding type(plain 45-degree and twill 70-degree). The braided composite pipes were also fabricated through the VARTM process. In accordance with Figure 5, mechanical properties of meso-scale and macro-scale specimens were evaluated and compared with the results of the progressive failure model based on the multi-scale method.

(a)

	Tensile test	Compression test	Shear test
Schematic			
Test method	ASTM D 3039	ASTM D 6641	ASTM D 5379
Specimen	- Length : 200 mm - Width : 20 mm - Thickness : 1.5 mm	- Length : 140 mm - Width : 20 mm - Thickness : 2.5 mm	- Length : 76 mm - Width : 15 mm - Thickness : 2.5 mm

(b)

	Compression test	Torsion test	Bending test
Schematic			
Test method	ASTM D 695	ASTM A 938	ASTM D 790
Specimen	- Length : 240 mm - D_o : 24 mm - D_i : 16 mm 		

Figure 5. The schematic of mechanical properties measurement for (a) meso-scale specimen and (b) macro-scale specimen

3. Results and discussion

To verify the micro-meso multi-scale simulation, comparisons between the results of material property tests and simulations were conducted. The multi-scale simulation considered the failures of the matrix pocket and yarn component in meso-scale as well as the failures of fiber and matrix in micro-scale yarn. The micro-scale failures in the yarn were realized by the progressive failure model based on multi-scale simulation. The equivalent material properties of yarn were obtained through micro-scale RVE model simulation (Table 2).

Table 2. The equivalent mechanical material properties of yarn.

Properties	E_1 (GPa)	E_2 (GPa)	E_3 (GPa)	G_{12} (GPa)	G_{23} (GPa)	G_{31} (GPa)	v_{12}	v_{23}	v_{31}
Value	139	7	7	4	2.8	4	0.24	0.33	0.24

Figure 6 shows comparisons between tensile test results and simulation of the braided composite. A stress-strain curve of the meso-scale RVE model was effectively predicted by the progressive failure model based on multi-scale simulation. The elastic modulus and failure strength decreased as the braiding angle increased. The compressive tests results (Figure 7) and shear tests results (Figure 8) were also compared with compressive test simulations and shear test simulations, respectively. Similarly, stress-strain curves of the compressive test and shear test were closely predicted by the progressive failure multi-scale simulation. As a result, the non-linear mechanical behavior and mechanical properties of the braided composites were successfully predicted by the progressive failure model based on multi-scale simulation with high accuracy.

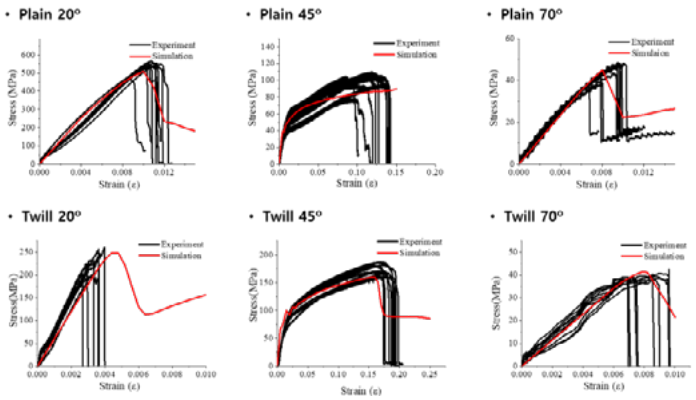


Figure 6. The tensile test results of braided composite with various braiding condition

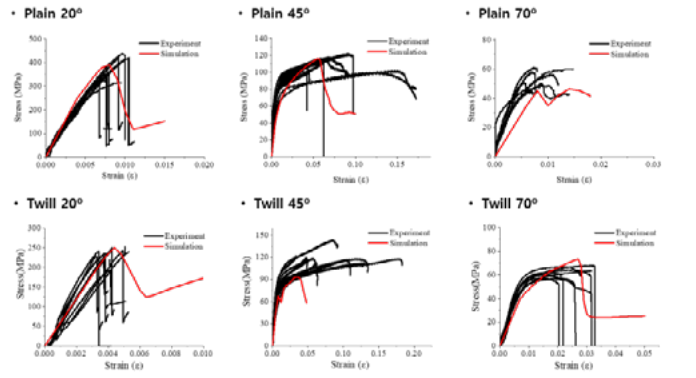


Figure 7. The compressive test results of braided composite with various braiding condition

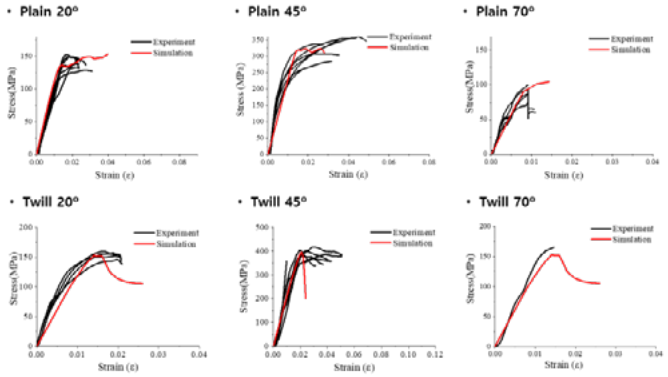


Figure 8. The shear test results of braided composite with various braiding condition

The macro-scale experiments and simulations were conducted using a braided composite pipe. Figure 9 shows comparison results between the experiment and simulations. Results for the compressive test, 3-point bending test, and torsion test confirmed that the mechanical behavior between the experiments and simulations were similar, and the load-displacement curves showed similar values. In addition, it was identified that the progressive failure behavior was realized through a decrease in load after matrix failure. Moreover, the failure pattern from the simulation results was similar to the failure pattern observed in actual experiments, as shown in Figure 10. It was confirmed that the progressive failure model based on multi-scale simulation accurately simulated actual experiments.

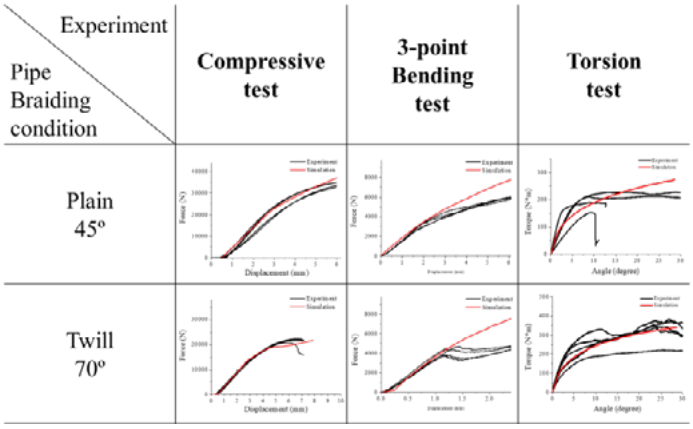


Figure 9. The compressive test, 3-point bending test and torsion test results of braided composite pipe with various braiding condition

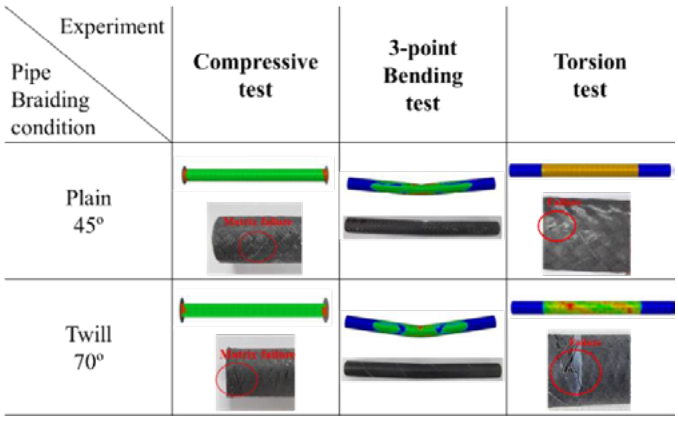


Figure 10. The comparision of failure pattern between experiment and simulation

4. Conclusion

In this study, a multi-scale approach to model the progressive failure in braided composites was proposed. Multi-scale modeling of three different scale units (micro, meso, and macro) was simulated to define the non-linear mechanical behavior of braided composites. The equivalent material properties were obtained from material property homogenizations based on RVE modeling with periodic boundary conditions. On the other hand, the stress amplification factor was employed to calculate local stress from the global stress. Additionally, the progressive failure model based on multi-scale simulation was used to evaluate fiber and matrix failures in micro-mechanical analysis. To verify the proposed progressive failure model based on multi-scale simulation, experiments using braided composite pipes were conducted and compared with simulations. As a result, the proposed model accurately predicted the actual experiments. This simulation model is expected to be utilized for predicting the nonlinear mechanical behavior of various braided composites considering fiber types, fiber dimensions, fiber volume fractions, and weaving patterns.

Acknowledgments

This work was supported by Korea Institute of Energy Technology Evaluation and Planning(KETEP) grant funded by the Korea government(MOTIE)(20212020800090, Development and Demonstration of Energy-Efficiency Enhanced Technology for Temperature-Controlled Transportation and Logistics Center). Also, this work was supported by Korea Institute of Energy Technology Evaluation and Planning(KETEP) grant funded by the Korea government(MOTIE)(20202020800360, Innovative Energy Remodeling Total Technologies(M&V, Design, Package Solutions, and Testing & Verifications Technologies) for the Aging Public Buildings)

References

[1] Sun, Xuekun, and Changjie Sun. "Mechanical properties of three-dimensional braided composites." Composite structures 65.3-4 (2004): 485-492.
[2] Huang Y, Jin C and Ha SK. Strength prediction of triaxially loaded composites using a progressive damage model based on micromechanics of failure. Journal of composite materials. 2013; 47: 777-792.
[3] Jin K-K, Huang Y, Lee Y-H and Ha SK. Distribution of micro stresses and interfacial tractions in unidirectional composites. Journal of Composite Materials. 2008; 42: 1825-1849.
[4] Singh A, Reynolds N, Keating EM, Barnett AE, Barbour SK and Hughes DJ. The effect of braid angle on the flexural performance of structural braided thermoplastic composite beams. Composite Structures. 2021; 261: 113314.
[5] Wu Z, Wu C, Liu Y, Cheng X and Hu X. Experimental study on the low-velocity impact response of braided composite panel: Effect of stacking sequence. Composite Structures. 2020; 252: 112691.
[6] Xia Z, Zhang Y and Ellyin F. A unified periodical boundary conditions for representative volume elements of composites and applications. International journal of solids and structures. 2003; 40: 1907-1921.
[7] Xu L, Jin CZ and Ha SK. Ultimate strength prediction of braided textile composites using a multi-scale approach. Journal of Composite Materials. 2015; 49: 477-494.
[8] Zhai J, Zeng T, Xu G-d, Wang Z-h, Cheng S and Fang D-n. A multi-scale finite element method for failure analysis of three-dimensional braided composite structures. Composites Part B: Engineering. 2017; 110: 476-486.
[9] Zhang D, Zheng X, Wang Z, Wu T and Sohail A. Effects of braiding architectures on damage resistance and damage tolerance behaviors of 3D braided composites. Composite Structures. 2020; 232: 111565.
[10] Zhang S, Jiang H, Ren Y, Qian Z and Lin Z. Multi-scale progressive damage model for analyzing the failure mechanisms of 2D triaxially braided composite under uniaxial compression loads. Applied Composite Materials. 2018; 25: 921-938.
[11] Zhang Y, Li H, Gao Y, Lou R, Ge L and Fang D. Multi-scale modeling and elastic properties prediction of 3D four-directional tubular braided composites. Composite Structures. 2022; 292: 115632.

STOCHASTIC THERMAL BUCKLING INVESTIGATION OF OPTIMIZED VARIABLE STIFFNESS COMPOSITE LAMINATES INCURRED INTERNAL FLAWS

Prateek Chandrakar[1], Narayan Sharma[2] and Dipak Kumar Maiti[3]

[1]Department of Aerospace Engineering, Indian Institute of Technology, Kharagpur, West Bengal, India
Email: pch.prateek@gmail.com
[2]Amity Institute of Defence Technology, Amity University, Noida, Uttar Pradesh, India
Email: narayan.sharma43450@gmail.com
[3]Department of Aerospace Engineering, Indian Institute of Technology, Kharagpur, West Bengal, India
Email: dkmaiti@aero.iitkgp.ac.in

Keywords: variable stiffness composite laminates, composite damage, thermal buckling, stochastic analysis

Abstract

The present investigation centers on examining the impact of composite uncertainty on the thermal buckling behavior of optimized variable stiffness composite laminates (VSCL) plates that incurred damage. The study involves the analysis of VSCL plates consisting of eight discrete composite materials that are subjected to SSSS boundary conditions. The damages have been observed to occur across two discrete locations (corner and mid), exhibiting three distinct levels of severity ($\Lambda = 3, 4, 5$). The impact of internal defects is evaluated through an improved first-order shear deformation theory (IFSDT) based finite element (FE) model. Further, the influence of uncertain composite properties of optimized VSCL plates on thermal buckling response is evaluated. In order to address the significant computational expenses involved with Monte-Carlo simulations (MCS), an RBFN-based surrogate model has been utilized. Moreover, the application of the RBFN-based surrogate model is expanded to the estimation of failure probability.

Nomenclature

u^*, v^*	=	in-plane displacements of mid-surface in x and y axes, respectively
w^*	=	transverse displacement of mid-surface
Ψ_x, Ψ_y	=	cross-sectional rotations around the y and x axes, respectively
h, χ	=	plate thickness and laoding parameter
$[K], [K_G]$	=	elastic and geometric stiffness matrix, respectively
$\{F\}, \{\delta\}$	=	force and displacement vector, respectively
Φ_1, Φ_2	=	damage parameters along and orthogonal to fiber direction, respectively
Λ	=	damage ratio
$\aleph$	=	approach to estimate uncertain composite properties effect
Θ, ϕ	=	MCS operator and stochasticity level
ω, r	=	weight coefficient and radial basis function
$\|\iota - \iota_p\|$	=	Euclidean distance of the point from the center ι_p
M, t	=	number and observation of uncertain samples

1. Introduction

Modern processing techniques enable the conception and production of complicated composite structures, even if numerous approaches for optimizing conventional constant stiffness composite laminates (CSCL) have been established. Akhavan and Ribeiro [1] studied the natural frequencies and mode shapes of VSCL, consisting of curvilinear fibers with fiber angle variation in the horizontal direction. Ribeiro and Akhavan [2] performed numerical experiments employing non-linearity in a p-version finite element technique to investigate oscillation discrepancies between VSCL and CSCL plates. Uncertain free vibration response of VSCL plates caused by various composite properties randomness is analyzed by Sharma et al. [3]. Punera and Mukherjee [4] presented the utility of VSCL plates towards flexibility in various composite measures such as design, stress distribution, and buckling load capacity. Despite having many benefits, composite materials are prone to internal defects. This can significantly reduce the stiffness of the structures, which in turn affects their various static and dynamic abilities. Valliappan et al. [5] modeled an anisotropic damage-based FE model and performed validation for the developed elastic constitutive relationship influenced by damage. Chandrakar et al. [6–10] have conducted various studies on composite laminates that have incurred internal defects while also considering the presence of uncertainties. Launch and reentry vehicles that operate at high speeds are exposed to extreme conditions, including aerodynamic heating, during routine operations. The structural integrity of supersonic and hypersonic vehicles may be compromised by material degradation at high temperatures and thermal stresses resulting from restrained thermal expansions at elevated temperatures, leading to reduced safety and longevity. Devarajan and Kapania [11] developed an efficient isogeometric analysis utilizing level sets to simulate the thermal buckling of stiffened laminated composite plates with cutouts. The study of Yang and Xie [12] showcases that the thermal buckling potential of Carbon Fiber Reinforced Plastics may be influenced by emulating bio-inspired Bouligand architectures.

Earlier researchers have investigated the enhancement of thermal buckling performance by optimizing VSCL plates composed of diverse composite materials [13]. Composite manufacturing is an intricate task, and this complexity may lead to variability in the composite properties; sometimes, this causes defects in the composite structures. The operating circumstances of composites may also be responsible for defect formation, and this defect potentially leads to the undesired mechanical performance of composite structures. Hence this study undertakes the possibility of damage formation and investigates the effect of uncertain damage composite characteristics in eight optimized VSCL plates. Furthermore, the potential of the IFSDT-based FE formulation has not been investigated for the impact of defects on thermal buckling characteristics, in conjunction with the use of optimized VSCL, for the estimation of buckling strength. The present investigation encompasses damages of varying severity and occurring in two distinct locations. The composite properties are subsequently exposed to variability to examine the impact on buckling performance. The Latin hypercube sampling method is utilized to generate random samples. The surrogate model based on RBFN serves as a substitute for the computationally expensive MCS. Subsequently, the RBFN-based surrogate model is utilized to approximate the likelihood of failure.

2. IFSDT based FE formulations

2.1. VSCL formulation

Single fiber orientation can not adequately characterize the angled fibers used in VSCL plates. Instead, the fiber orientation in VSCL laminates may vary across the plane based on the x and y coordinates. The fiber orientation that is being employed in the current study varies linearly with x, from θ_1 at the center of the plate to the other value, θ_2, at $a/2$ from the origin (Fig. 1). The designation of VSCL is done by $< \theta_1|\theta_2 >$. The fiber orientation (θ) at x units from the fiber's origin is represented as follows:

$$\theta(x) = \left\{ \begin{array}{c} \frac{-2}{a}(\theta_2 - \theta_1)\, x + \theta_1 \;\; for \; \frac{-a}{2} \leq x \leq 0 \\ \frac{2}{a}(\theta_2 - \theta_1)\, x + \theta_1 \;\; for \; 0 \leq x \leq \frac{a}{2} \end{array} \right\} \tag{1}$$

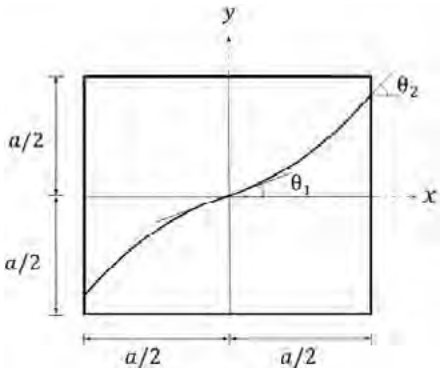


Figure 1. VSCL reference path

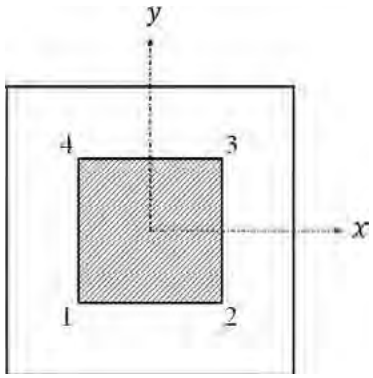


Figure 2. Damage zone location

2.2. Thermal buckling

The displacement field approximation considered in the present work is given as,

$$\left\{ \begin{array}{c} u\left(x,y,z\right) \\ v\left(x,y,z\right) \\ w\left(x,y,z\right) \end{array} \right\} = \left\{ \begin{array}{c} u^{*}\left(x,y\right) \\ v^{*}\left(x,y\right) \\ w^{*}\left(x,y\right) \end{array} \right\} - z \left\{ \begin{array}{c} \Psi_{x}\left(x,y\right) \\ \Psi_{y}\left(x,y\right) \\ 0 \end{array} \right\} \tag{2}$$

The shear stress estimation in FSDT does not follow the physical requirement, as it produces uniform shear stress throughout the thickness, thus to provide the actual parabolic shear stress variation the IFSDT incorporated in the present work. The IFSDT utilizes improved shear correction factor ($\kappa\left(z\right) = 5/4 - 5z^{2}/h^{2}$) to distribute shear stress accordingly [14]. The equation for the state of minimum potential energy equation provided by the equilibrium requirement is given below [15],

$$\Pi = \{\delta\}^{T}\left\{\left[\left[K\right] - \left[K_{G}\right]\right]\{\delta\} - \{F\}\right\} \tag{3}$$

The first derivative of the above equation leads to the estimation of $\{F\}$, which is further utilized to solve the generalized eigenvalue problem formed by the second minimization of energy functional, given as,

$$\left|\left[K\right] + \chi\left[K_{G}\right]\right| = 0 \tag{4}$$

The estimation of critical buckling temperature is then followed as,

$$T_{cr} = \chi \Delta T \tag{5}$$

2.3. Continuum damage modeling

The anisotropic damage modeled in the present work is considered to be non-progressive with the applied load as suggested by Valliappan et al. [5]. This formulation is based on the concept of stiffness change. The damage parameters are given by the equation,

$$\left.\Phi_{q} = 1 - \frac{A_{q}^{dam}}{A_{q}}\right\} q = 1,2 \qquad \Lambda = \Phi_{1}/\Phi_{2} \tag{6}$$

2.4. RBFN-based surrogate modeling

The undesired randomness in various composite properties is responsible for the structural uncertainties. Thus, the sources of randomness in the present study are given as,

$$\aleph\left(\phi\right) = \Theta\left\{ \begin{array}{l} E_{11}\left(\phi\right), E_{22}\left(\phi\right), G_{12}\left(\phi\right), G_{23}\left(\phi\right), G_{13}\left(\phi\right), \upsilon_{12}\left(\phi\right), \\ \alpha_{11}\left(\phi\right), \alpha_{22}\left(\phi\right), \theta_{1}\left(\phi\right), \theta_{2}\left(\phi\right), \Lambda\left(\phi\right) \end{array} \right\} \tag{7}$$

The RBFN model employed in the current work is one of the surrogate models used by modern engineering tools to find optimal solutions faster. The RBFN-built model is,

$$R(\iota) = \sum_{p=1}^{m} \omega_p r\left(\left\|\iota - \iota_p\right\|\right) \tag{8}$$

The algorithm produces a surrogate model and forecasts the results based on several predetermined radial basis functions [3]. The equation estimates the likelihood of failure as,

$$P_f = \frac{1}{M} \sum_{s=1}^{M} f\left(g\left(t^s\right) < 0\right) \tag{9}$$

Table 1. Thermal buckling verification table with ref.[13]

Materials	$< \theta_1 \mid \theta_2 >$	Present IFSDT (°C)	Zhao (°C)	NASTRAN (°C)
Graphite/Epoxy (Gr/Ep)	<60.7|32.19>	32.098	31.990	32.660
E-Glass/Epoxy (Eg/Ep)	<6.71|58.04>	5.482	5.480	5.540
S-Glass/Epoxy (Sg/Ep)	<16.12|54.74>	4.970	4.960	5.030
Kevlar/Epoxy (Ke/Ep)	<66.05|11.73>	15.976	16.090	16.270
Carbon/Epoxy (Ca/Ep)	<69|-5.705>	33.441	33.800	35.320
Carbon/Peek (Ca/Pe)	<63.07|29.5>	34.988	34.930	35.540
Carbon/Polyimide (Ca/Po)	<56.3|36.68>	75.338	74.890	76.890
Boron/Epoxy (Bo/Ep)	<6.57|63.28>	7.359	7.350	7.530

Table 2. Damage zone coordinates

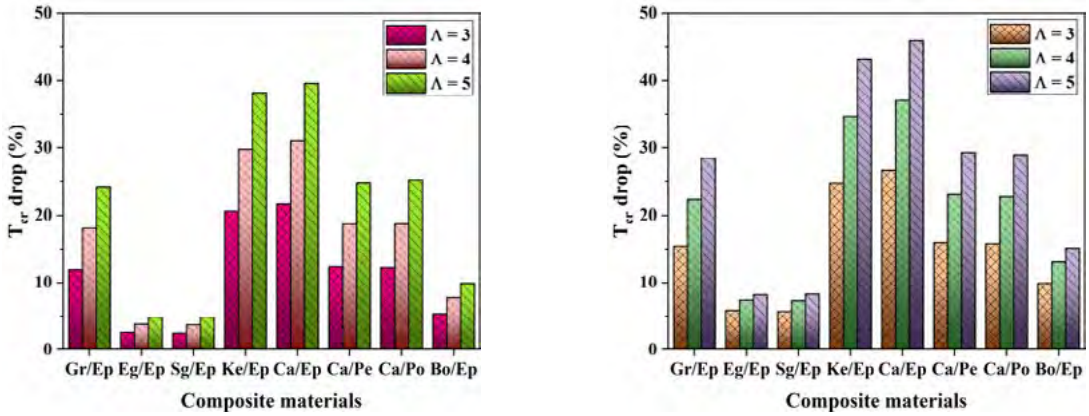
Damage zone	Vertices of damage zone			
	1	2	3	4
Corner	(-0.0625,-0.0625)	(0.0125,-0.0625)	(0.0125,0.0125)	(-0.0625,0.0125)
Mid	(-0.0375,-0.0375)	(0.0375,-0.0375)	(0.0375,0.0375)	(-0.0375,0.0375)

3. Results and Discussion

3.1. Thermal buckling analysis

The current study employed IFSDT-based FE MATLAB code to investigate the buckling performance of eight optimized VSCL plates (Figure 1) constrained to SSSS boundary conditions. The plates considered are the square ones with a uniform rise in temperature ($\Delta T = 1$). Three stages of damage severity are considered in the VSCL plates at the two most affected damage locations (corner and mid). The accuracy of the developed IFSDT-based FE model is established with ref.[13] (Table 1). The damage location is depicted in Table 2, and Figure 2. The suitable mesh size is found to be 12x12.

The buckling performance of VSCL plates is subject to variation due to damage, as it may impact the load-bearing capacity of the structure. Figure 3 displays the percentage decrease in critical buckling temperature resulting from the presence of damages located at the corner and mid of VSCL plates. The



(a) Corner damage **(b)** Mid damage

Figure 3. Critical buckling temperature drop (%) of damaged VSCL plates concerning healthy VSCL plates with multiple damage levels and damage locations

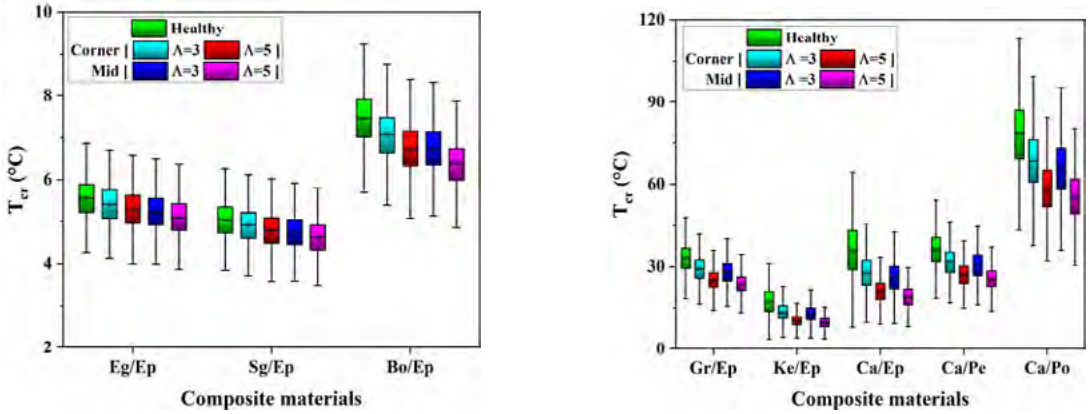


Figure 4. Composite properies randomness effect over multiple composite materials of VSCL plates

initial discernible finding suggests that the decline in performance is more conspicuous in the VSCL plates with mid damage. Nevertheless, the trajectory of the decrease adhered to similar trends for both the damage locations. The escalation in the severity of damage results in premature failure of the VCSL plates, regardless of the location of the damage. The present study pertains to the investigation of the impact of damage on the buckling strength reduction of eight distinct composite materials. The findings reveal that Ca/Ep exhibits the highest degree of sensitivity towards internal defects. However, the Eg/Ep and Sg/Ep plates exhibit superior resistance to composite damage.

3.2. Stochastic study

Further, the variability ($\phi = \pm 10\%$) in the various composite properties is introduced to observe the effect on the buckling behavior of various damaged (with minimum and maximum severity considered, i.e. $\Lambda = 3, 5$) composite materials (Figure 4). There is a very minimal difference in the scattering range of healthy and damaged Eg/Ep, Sg/Ep, and Bo/Ep VSCL plates; however, the incorporated damage proves its existence, as it reduces the mean critical buckling temperature. The highest-performing VSCL plate (Ca/Po) showcased the maximum dispersion of critical buckling temperature with the same input variability.

The composite material Ca/Po exhibited the highest critical buckling temperature. However, it is noteworthy that the maximum reduction in performance resulting from damage was observed in the case of Ca/Ep. The Ca/Po recorded maximized dispersion of output response. Nonetheless, the aforementioned

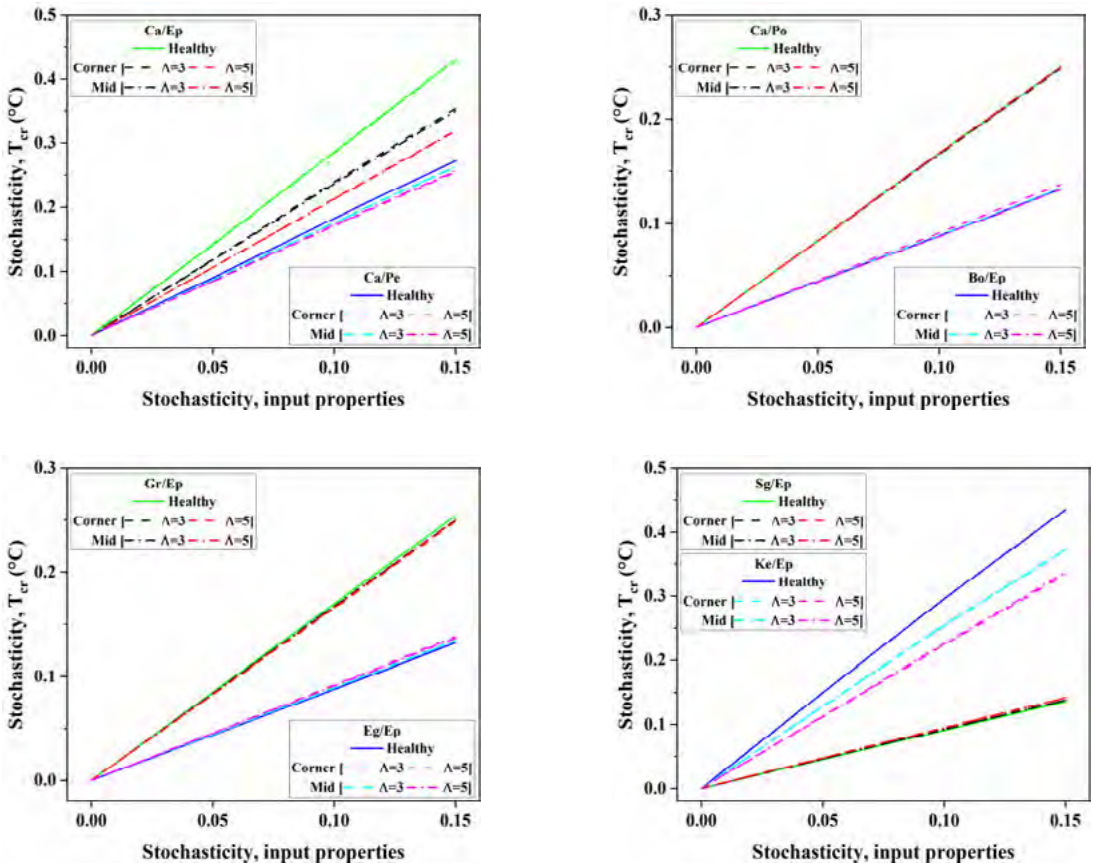


Figure 5. Output Stochasticity with respect to composite properties randomness

performance criteria are inadequate in offering a comprehensive understanding of output randomness. Figure 5 illustrates input-to-output stochasticity relation, with the response exhibiting a linear trajectory. The variability in the composite properties produced the highest critical buckling temperature randomness with Ca/Ep and Ke/Ep VSCL plates, indicating that the sensitivity of input randomness is maximum with Ca/Ep and Ke/Ep VSCL plates. Additionally, it has been observed that the Eg/Ep and Bo/Ep VSCL plates exhibit the lowest level of output stochasticity; this finding suggests that despite the introduction of equivalent levels of randomness in composite properties, the influence of input variability on buckling strength is notably reduced. Although the damage in the VSCL plates degraded the buckling strength, the output variability is also reduced with damage in the case of Ca/Ep, Ca/Pe, and Ke/Ep composite materials; this facilitates the fact that the correlation between input variability and buckling strength exhibits a considerably lower degree of dependence with damage. The reduction in percentage is notably substantial for plates that have sustained mid damage, although the stochastic response remains comparable across various damage locations. As the level of damage severity increases, a decrease in the degree of variance in buckling strength is noted. Furthermore, similar variations in response are observed between healthy and damaged (i.e., corner and mid) plates for the remaining composite materials.

The construction of a cumulative distribution function plot is a crucial aspect of stochastic analysis, particularly in the context of failure prediction (Figure 6). The initial instance of failure has been documented concerning Ca/Ep VSCL plates, whereas the Ca/Po VSCL plates have demonstrated the highest degree of resistance to such failure. The Bo/Ep composite material exhibits the lowest range of failure probability, implying that the Bo/Ep VSCL plates experience failure in significantly shorter durations than other composite materials. For all the studied composite materials, the damage may cause premature failure of VSCL plates. Nevertheless, empirical evidence suggests that the mid position of the

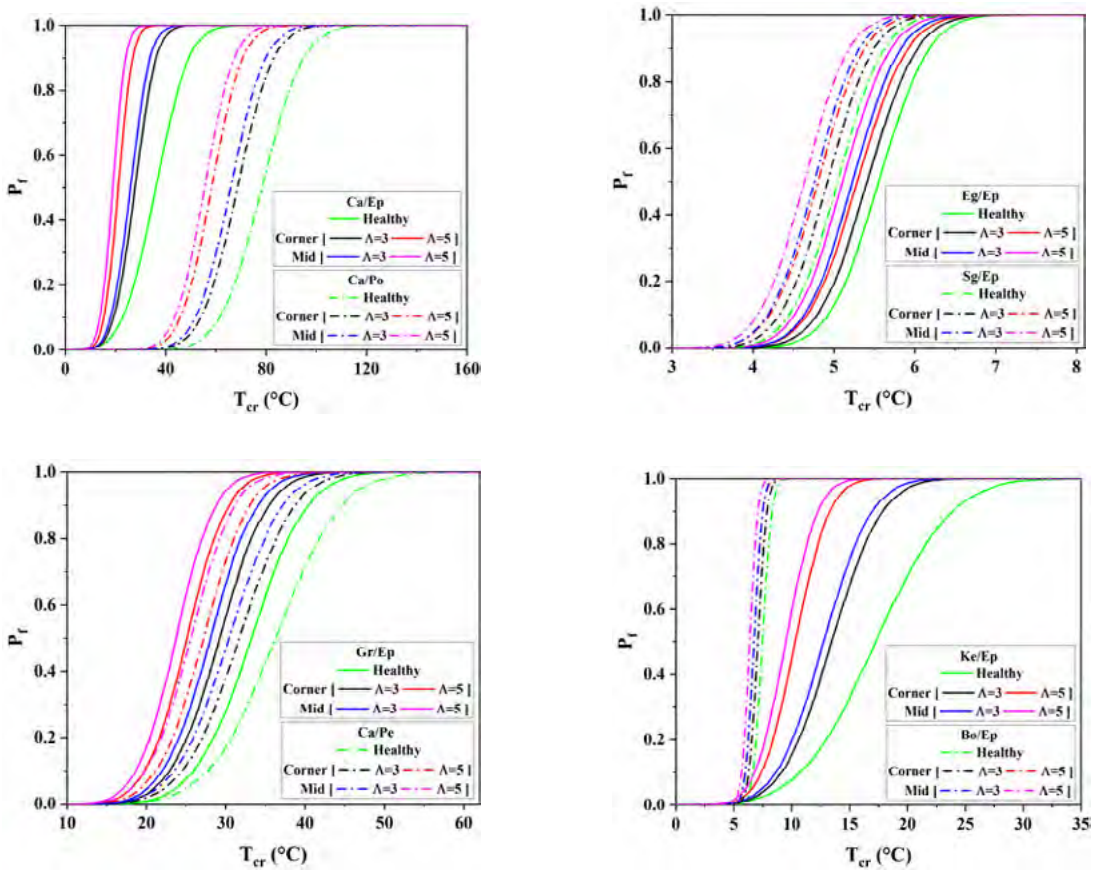


Figure 6. Failure probability estimation

damage is more prone to inducing the collapse of all VSCL plates.

4. Conclusions

The present research examines the impact of stochasticity ($\phi = \pm 10\%$) on the optimized VSCL comprising eight distinct composite materials under the influence of internal defects. The plates are subject to three degrees of damages ($\Lambda = 3, 4, 5$) at the corner and mid locations constrained to SSSS boundary conditions along their edges. The study reveals that the severity of damage is more pronounced in the mid location. Additionally, the Ca/Ep VSCL plates demonstrated heightened sensitivity to damage, while Eg/Ep and Sg/Ep VSCL exhibited superior resistance to composite damages. The introduction of variability in diverse composite materials results in the manifestation of linear input-to-output stochasticity. The study found that the Ca/Ep and Ke/Ep VSCL plates exhibited the greatest sensitivity to randomness in composite properties. Furthermore, the observation implies that despite the incorporation of comparable degrees of randomness in composite characteristics, the impact of input variability on buckling strength is significantly mitigated with Eg/Ep and Bo/Ep composite materials. The buckling strength of all damaged VSCL exhibits similar levels of randomness concerning damage location, suggesting that the location of the damage does not contribute much to variability response. The Ca/Ep VSCL plates have been observed to demonstrate the first occurrence of failure. In contrast, the Ca/Po VSCL plates have exhibited the most significant resilience against such failure. The Bo/Ep composite material exemplifies a comparatively lower probability of failure range, indicating that the Bo/Ep VSCL plates have a shorter duration of failure in comparison to other composite materials.

References

[1] H. Akhavan and P. Ribeiro. Natural modes of vibration of variable stiffness composite laminates with curvilinear fibers. *Composite Structures*. vol. 93. no. 11. pp. 3040–3047. 2011.

[2] P. Ribeiro and H. Akhavan. Non-linear vibrations of variable stiffness composite laminated plates. *Composite Structures*. vol. 94. no. 8. pp. 2424–2432. 2012.

[3] N. Sharma, P. K. Swain, D. Maiti, and B. Singh. Stochastic frequency analysis of laminated composite plate with curvilinear fiber. *Mechanics of Advanced Materials and Structures*. vol. 29. no. 6. pp. 933–948. 2022.

[4] D. Punera and P. Mukherjee. Recent developments in manufacturing, mechanics, and design optimization of variable stiffness composites. *Journal of Reinforced Plastics and Composites*. vol. 41. no. 23-24. pp. 917–945. 2022.

[5] S. Valliappan, V. Murti, and Z. Wohua. Finite element analysis of anisotropic damage mechanics problems. *Engineering Fracture Mechanics*. vol. 35. no. 6. pp. 1061–1071. 1990.

[6] P. Chandrakar, N. Sharma, and D. K. Maiti. Stochastic buckling response of variable fiber spacing composite plate under thermal environment. *Journal of Composite Materials*. vol. 57. no. 24. pp. 3821–3839. 2023.

[7] P. Chandrakar, N. Sharma, and D. K. Maiti. Stochastic rbfn-based reliability estimation of variable fiber spacing composite plates under thermal loading. *International Journal of Advances in Engineering Sciences and Applied Mathematics*. pp. 1–9. 2023.

[8] P. Chandrakar, N. Sharma, and D. K. Maiti. Buckling variability analysis in damaged composite laminates subjected to thermally varying environment. *Journal of Thermal Stresses*. pp. 1–23. 2024.

[9] P. Chandrakar, N. Sharma, and D. K. Maiti. Damage-induced buckling characteristics of thermally loaded variable angle tow laminated plates under uncertain environment. *European Journal of Mechanics-A/Solids*. vol. 103. p. 105188. 2024.

[10] P. Chandrakar, N. Sharma, and D. K. Maiti. Uncertain buckling characteristics of thermally loaded and internally defected variable fiber spacing composite laminates. *Journal of Composite Materials*. p. 00219983241230382. 2024.

[11] B. Devarajan and R. K. Kapania. Analyzing thermal buckling in curvilinearly stiffened composite plates with arbitrary shaped cutouts using isogeometric level set method. *Aerospace Science and Technology*. vol. 121. p. 107350. 2022.

[12] F. Yang and W. Xie. Thermal buckling behavior of bouligand inspired laminated composite plates. *Journal of Composite Materials*. vol. 56. no. 26. pp. 3939–3947. 2022.

[13] W. Zhao, K. Singh, and R. K. Kapania. Thermal buckling analysis and optimization of curvilinearly stiffened plates with variable angle tow laminates. *Journal of Spacecraft and Rockets*. vol. 56. no. 4. pp. 1189–1204. 2019.

[14] P. Van Vinh, N. Van Chinh, and A. Tounsi. Static bending and buckling analysis of bi-directional functionally graded porous plates using an improved first-order shear deformation theory and fem. *European Journal of Mechanics-A/Solids*. vol. 96. p. 104743. 2022.

[15] A. Y. Tamijani and R. K. Kapania. Buckling and static analysis of curvilinearly stiffened plates using mesh-free method. *AIAA journal*. vol. 48. no. 12. pp. 2739–2751. 2010.

A STRIP METHOD TO PREDICT SKIN-STIFFENER DEBONDING IN POST-BUCKLED PANELS

Richard Butler[1] and Thomas Maierhofer[1]

[1]Centre for Integrated Materials, Processes and Structures, University of Bath, Bath , UK
R.Butler@bath.ac.uk, http://www.bath.ac.uk/mech-eng/people/butler

Keywords: Strip method, Post-buckling, Debonding, Delamination, Thermoplastic, Welding

Abstract
A new semi-analytical method which calculates the strain energy released as a skin buckle relaxes during damage propagation by delamination or debonding of a stiffened panel is presented. Propagation can either occur in the bond or within the attached stiffener foot. An existing Strip method calculates skin buckling loads, and finite differences provide the sensitivity of these loads to perturbation of delamination or debonding variables. These are combined with post-buckled panel stiffness to obtain the strain energy release rate which, when equated to the critical strain energy release rate of the respective damage surface, determines the damage initiation load.

Strip results for stiffener debonding of an idealised panel are within 1% of converged FE results for a thermoplastic weld but differ by 9% for a co-cured thermoset joint. Depending on the relative toughness of the bulk and joint materials, damage may occur in the bond or in the stiffener. The new Strip based method creates opportunities for the design and analysis of bonded composite structures, with results that are (i) obtained in seconds of CPU, compared with hours using cohesive zone methods, and (ii) independent of mesh refinement and additional interface properties required by other commonly used FE methods.

1. Introduction

Bonding of composite parts is significantly more structurally efficient than the traditional use of mechanical fasteners, provided concerns about repeatable and certifiable strength can be overcome via testing and analysis [1]. Analysis of bond-line delamination using cohesive zone model (CZM) methods requires computationally expensive FE models which may be prohibitive for design and certification. Added to this, there is a need to consider the uncertainty of such joints, both in production and in service.

Analytical strain energy release rate has previously been calculated using the localised stress-strain distributions in the vicinity of delaminations [2-4]. This requires a detailed analysis of specific features or numerical FEA with sufficiently small elements to accurately capture the local energy.

Here we formulate the axial strain energy in terms of the applied load versus strain relationship with linear stiffness both before and after stable post buckling. We evaluate the Strain Energy Release Rate (SERR) in terms of the sensitivity of buckling load to perturbations in the damage variable, expressed as the width of a strip with thickness defined by the delamination interface. This new non-local approach does not require a detailed mesh, provided that the buckling mode is stable and can be modelled as periodic. We use a very efficient Strip method [5] to calculate the buckling load and the buckling sensitivity. Results are obtained for a post-buckled panel and compared with FEA results using a cohesive zone modelling approach.

2. Analytical Strip model

In the case of a stiffened panel with linear post-buckled stiffness, we can expand the strain energy release rate G, defined as the derivative of strain energy with respect to delamination area A_d, using

$$G = \frac{\partial U}{\partial A_d} = \left(\frac{\partial U}{\partial \varepsilon^C}\right)\left(\frac{\partial \varepsilon^C}{f(x)\,\partial b}\right)\left(\frac{f(x)\,\partial b}{\partial A_d}\right) = \left(\frac{\partial U}{\partial \varepsilon^C}\right)\left(\frac{\partial \varepsilon^C}{\partial b}\right)\left(\frac{\partial b}{\partial A_d}\right) \tag{1}$$

where ε^C is the buckling strain of the panel and ∂b is a perturbation of a strip width representing delamination. Note that $f(x)$, an unknown function in the axial x direction defining the shape of propagation, cancels enabling us to simplify the growth of delamination using a prismatic strip of width b.

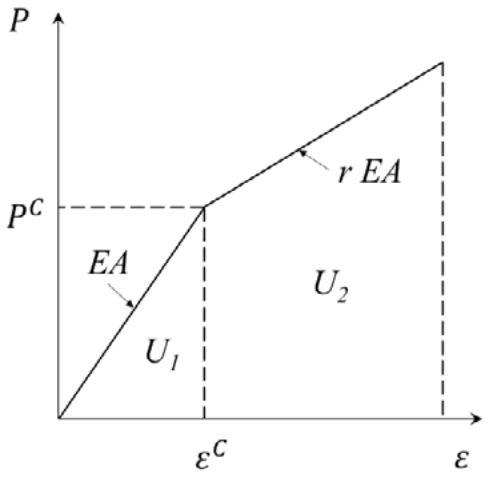


Figure 1. Axial load-strain plot for post-buckled panel. P^C and ε^C define the axial load and strain for panel buckling buckling, EA and $r\,EA$ are the pre-buckled and post-buckled axial stiffnesses of the panel, respectively.

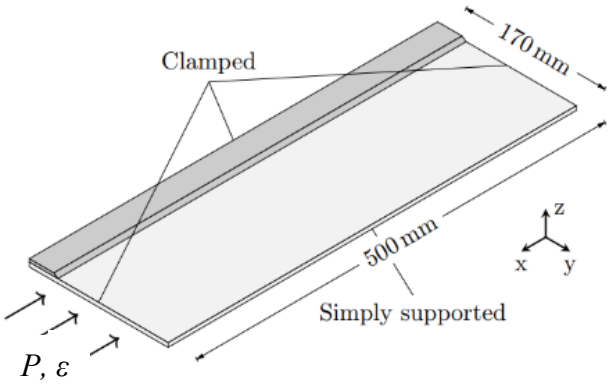


Figure 2. Schematic of the simplified stiffened panel with assumed boundary conditions.

From Fig. 1, the axial strain energy of the skin panel over one full buckling wavelength (2λ) at some strain ε above buckling is

$$U = U_1 + U_2 = \int_0^{2\lambda} EA\left[\left(\frac{\varepsilon^C}{2}\right)^2 + \varepsilon^C(\varepsilon - \varepsilon^C) + \frac{r}{2}(\varepsilon - \varepsilon^C)^2\right] dx$$

$$= 2EA\lambda\left[\left(\frac{\varepsilon^C}{2}\right)^2 + \varepsilon^C(\varepsilon - \varepsilon^C) + \frac{r}{2}(\varepsilon - \varepsilon^C)^2\right] \tag{2}$$

And therefore,

$$\frac{\partial U}{\partial \varepsilon^C} = 2EA\lambda(1-r)(\varepsilon - \varepsilon^C) \tag{3}$$

Assuming that delamination only occurs over the half wavelength causing opening, the area of delamination or debonding is given by

$$\partial A_d = \lambda \, \partial b$$

Hence

$$\frac{\partial b}{\partial A_d} = \frac{1}{\lambda} \tag{4}$$

Substituting Eqs. (3) and (4) into Eq. (1)

$$G = 2EA\,(1-r)(\varepsilon - \varepsilon^C)\frac{\partial \varepsilon^C}{\partial b} \tag{5}$$

Or, in terms of applied loading, noting that

$$\frac{\partial \varepsilon^C}{\partial b} = \frac{1}{EA}\frac{\partial P^C}{\partial b}$$

$$G = \frac{2}{EA}\,(1-r)(P - P^C)\frac{\partial P^C}{\partial b} \tag{6}$$

Since this strain energy release rate is (i) non-local because it is derived in terms of propagating a strip of width b and (ii) derived in terms of axial strain energy which is orthogonal to the direction of propagation (i.e. there is no crack driving force) we assume it gives a lower bound value, initiating as Mode I fracture. Hence, we can rearrange Eq. (6) to give the load at which delamination or debonding initiates

$$P_{init} = P^c + \frac{G_{1C}EA}{2(1-r)\frac{\partial P^C}{\partial b}} \tag{7}$$

Here we use the Strip software VICONOPT [5] to calculate both P^C the buckling load and $\partial P^C / \partial b$ the sensitivity of this load to perturbation of any strip width b. For the results that follow, the value for post buckling stiffness reduction r is determined using nonlinear FEA.

3. Results for an idealized skin-stiffened panel

Damage propagation of a fusion bonded joint between two thermoset composite components [6] is studied using the proposed new analytical Strip method and results are compared with FEA. Furthermore, the likelihood of damage propagation within the thermoset laminate of the adherend is studied and the potential mechanical performance gain between a fusion bonded joint and a co-cured thermoset joint is demonstrated.

To illustrate the new method, it is assumed that a bonded skin-stiffener joint within a stiffened panel can be represented by modelling a single skin-stiffener bay, as shown in Fig. 2 and by applying idealised boundary conditions. Thus, only the stiffener flange and the unsupported skin section are modelled. To account for the respective boundary conditions, the transverse ends (y-axis direction) are clamped. Along one longitudinal edge of the panel, where the stiffener flange is attached to the skin, it is assumed that the stiffener effectively prevents bending and torsion, which is simulated by a clamped boundary. The opposite longitudinal edge of the panel is assumed to be simply supported.

To account for the thermoplastic surface layer required to make the thermoset composite components weldable, a 250 µm thick polyetherimide (PEI) film is modelled on the respective weld interfaces of both the skin and the stiffener flange. The skin and stiffener laminates are HexPly® IM7/8552 (CF/epoxy), with a ply thickness of 0.125 mm. The ply properties are E_{11} = 150.0 GPa, E_{22} = 9.08 GPa, $G_{12} = G_{13}$ = 5.29 GPa, $\nu_{12} = \nu_{13}$ = 0.32, ν_{23} = 0.52, G_{IC} = 277 J/m^2 and G_{IIC} = 788 J/m^2. The properties of the PEI are E = 32 GPa, ν = 0.36, G_{IC} = 1,083 J/m^2 and G_{IIC} = 3,327 J/m^2. The skin has stacking sequence $[\pm 45/0/90/0_3/\pm 45/0_2/\overline{90}]_S$ and the stacking sequence of the stiffener flange is $[\pm 45/0/90/0_3/\pm 45/0_2/\overline{90}]_S$.

3.1 Finite Element results

FE results are obtained using the ABAQUS Explicit solver [7] with 8-node continuum shell (SC8R) elements for skin and stiffener, and zero-thickness surface-based cohesive zone model (CZM) interactions at the delamination interfaces. A ply-by-ply modelling approach with CZM surface interactions between individual plies is considered to study the likely location of damage initiation. Three separate delamination cases are considered: (i) along the welded joint between the skin and the stiffener; (ii) at the interface of the first and second plies in the stiffener flange and (iii) along the 8552-resin interface between a co-cured skin and stiffener. To study the crack growth behaviour of a weld at the joint interface, interlaminar CZM surface interactions within the flange were disabled and replaced with tie-constraints. The cohesive properties for a fusion bonded joint are s_{33} = 56.0 MPa, s_{13} = 107.0 MPa and η_{BK} = 2.90 and for a co-cured joint s_{33} = 62.3 MPa, s_{13} = 92.3 MPa and η_{BK} = 1.634 for 8552-resin. A penalty stiffness $K = 10^6$ N/mm^3 is used for all cohesive zone interfaces. For accuracy, multiple elements are required within the length of the cohesive zone. Using Hillerborg's approach [8], the length of the cohesive zone for PEI and 8552 is approximately 2.64 and 0.65 mm, respectively. Since the latter is prohibitively small, requiring element sizes of less than 0.3mm, the interface strengths are reduced, based on a method proposed by Turon et al. [9], to s_{33} = 29.8 MPa and s_{13} = 50.3 MPa, allowing for a mesh size of 0.5 mm in the region of delamination, see Fig. 3.

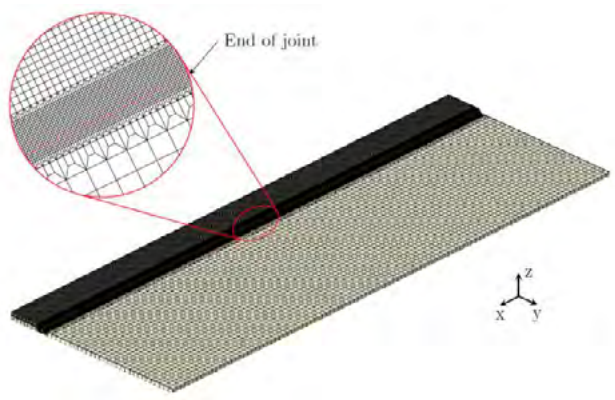


Fig. 3 FEA mesh of panel showing refinimenet near edge of skin-flange joint.

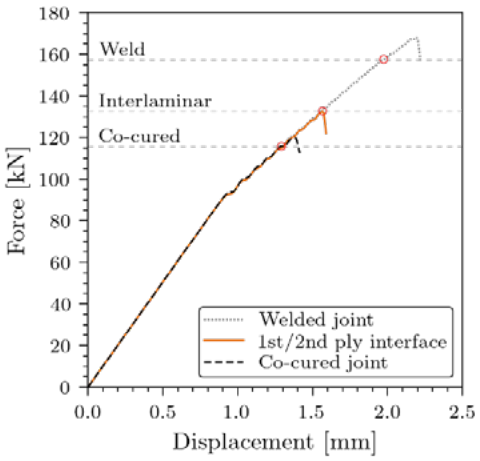


Fig. 4 FE results for delamination of welded and co-cured skin-flange joints. Circles indicate damage initiation.

Load-end shortening plots for delamination at the interfaces (i), (ii) and (iii) described above are given in Fig. 4 and the numerical values of loads at which buckling and delamination first occur are in Table 1. Note that the panel with a fusion bonded joint is predicted to delaminate between the first two plies in the flange before joint failure, since this occurs at lower load. The critical buckling mode is shown in Fig. 5.

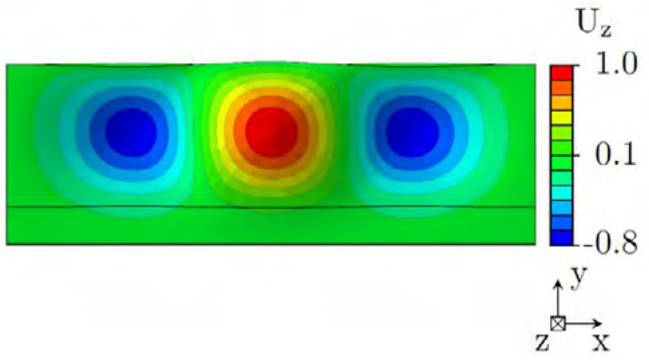


Fig. 5 FEA buckling mode for panel of Fig. 2

3.2 Strip results

The panel of Fig. 2 is also modelled using three strips, one each for the skin, stiffener flange and the skin beneath the flange. The sensitivity of buckling load to strip width $\partial P^C/\partial b$ is obtained for (i) a skin strip with a thickness representative of delamination along the bondline (PEI or 8552) interface; (ii) a flange strip of thickness representing delamination between the first and second flange plies nearest the weld. It is noted that buckling sensitivity along the bondline is independent of bonding material. The Strip analysis is executed for a range of buckling modes with half-wavelengths $\lambda = 500/n$ with n = 2, 3, …, 10, in order to capture the critical (lowest) buckling load. The post-buckling stiffness reduction r = 0.654, which is obtained from the FEA and the axial stiffness of the panel EA = 49,620 kN. Table 1 shows that the critical buckling mode has a half-wavelength λ = 125 mm and presents the buckling load, buckling sensitivities and delamination initiation loads for delamination in the fusion bonded and co-cured joint, and within the bulk material of the stiffener flange

Table 1. Comparison of axial loads for skin buckling and initiation of delamination using Strip and FEA models. Strip buckling sensitivities are also given. The critical buckling mode for the Strip results has half-wavelength λ = 125 mm.

P^C (kN)		Delamination Interface	$\partial P^C/\partial b$ (kN/mm)	P_{init} (kN)	
Strip	FEA		Strip	Strip	FEA
88.03	86.7 (+1.5%)	PEI weld	1.130	156.8	157.6 (+0.5%)
		Flange – above 1st ply	0.438	133.3	132.7 (-0.5%)
		Co-cured skin/flange	1.130	105.6	115.8 (+8.8%)

4. Discussion

Table 1 shows that the buckling loads produced by the Strip and FE models are within 2%. The Strip model assumes a periodic buckling mode, indicating that the mode shape evident in Fig. 5 can be represented by a sinusoidal mode with four half-waves over the panel length.

Table 1 also shows that the new Strip method to predict debonding and delamination is within 1% of FEA results for both (i) debonding of the fusion bonded joint and (ii) delamination at the first ply interface within the stiffener. The FEA prediction of the debonding load in the co-cured case is 9% above the Strip initiation load. It appears unlikely that the inaccuracy of this case is in the Strip result since the buckling load and sensitivity values are the same for debonding of both types of joint and the different delamination loads arise entirely from the difference in G_{IC} of the thermoplastic and thermoset materials present at the bondline. However, there will be a greater stress concentration in the FEA at the bondline than at the first ply interface within the flange. The mesh size and required alteration of the interface properties, may not be fully representative of the true localised stresses at the joint interface for 8552 matrix properties. Thus the initiation and propagation for the low toughness thermoset material may not be accurately captured.

In terms of structural performance, as suggested by the authors previous work [6], fusion bonding of thermoset composites improves the mechanical joint performance. It is observed that on a structural level, the tougher thermoplastic joint interface shifts the site of damage initiation from the bondline into the bulk material of the stiffener. Experimental testing would be required to confirm this behaviour, and to validate the accuracy of the Strip method. Nevertheless, the shift of damage away from the bondline is potentially an extremely attractive feature for the certification of fusion bonded joints for primary aerospace structural applications.

The proposed novel Strip method requires at least five orders of magnitude fewer elements than FEA using the traditional CZM approach showing significantly better computational efficiency, eliminating the need for small element sizes, being mesh-independent. This makes the method suitable for use in statistical analysis to explore uncertainty in material properties and as-manufactured geometry, as well as providing a fast toolset to assess joint performance during the design phase. However, it is important to note that (i) the post-buckled stiffness *rEA* requires nonlinear FEA, albeit with a coarse mesh, and (ii) such FEA needs to ensure that transition to another potentially unstable mode of buckling does not occur before debonding or delamination.

5. Conclusions

The new Strip method evaluates the Strain Energy Release Rate (SERR) in terms of the sensitivity of buckling load to perturbations in the damage variable, expressed as the width of a strip with thickness defined by the location of the delamination interface. This non-local approach does not require a detailed mesh, provided that the buckling mode is stable and can be modelled as periodic. Results are obtained for a post-buckled panel and compared with FEA using a cohesive zone modelling approach to predict bondline failure.

The new method predicts debonding or delamination to within 1% of FEA results for both (i) debonding of a fusion bonded joint and (ii) delamination at the first ply interface within the bulk material of the stiffener. The FEA prediction of the debonding load in the co-bonded case is 9% above the equivalent load predicted by the Strip model. The new method is solely based upon the strain energy released unlike FEA, which requires accurate resolution of localised stresses using a very fine mesh, rendering the analysis of larger structures impractical. This further raises a question about the reliability and applicability of the CZM approach for larger structures.

Results show that a tough thermoplastic joint interface as a result of fusion bonding of two thermoset components shifts the site of damage initiation from the bondline to interlaminar failure within the component. The shift of damage away from the bondline is potentially an extremely attractive feature for the certification of fusion bonded joints in primary structures. Experimental testing would be required to confirm this behaviour, and to validate the accuracy of the Strip method. Furthermore, a study on different joint geometries and the applicability of the Strip method to other structures needs to be investigated. Nevertheless, it is demonstrated that the new method may offer a vastly more efficient approach to analyse the onset of interlaminar damage propagation and disbonds.

Acknowledgements
Thomas Maierhofer has a PhD studentship (2020-2024) supported by GKN Aerospace.

References

[1] Löbel, T., Holzhüter, D., Sinapius, M. & Hühne, C., "A hybrid bondline concept for bonded composite joints," International Journal of Adhesion and Adhesives, vol. 68, pp. 229–238, Jul. 2016.

[2] Hutchinson, J.W, Suo, Z., Mixed Mode Cracking in Layered Materials, Advances in Applied Mechanics, Volume 29, pp. 63-191, 1991.

[3] Chai H., Babcock C.D., Two-dimensional modelling of compressive failure in delaminated laminates, J. Compos. Mater., 19, pp. 67-98, 1985.

[4] Köllner, A., Nielsen, M. W. D., Srisuriyachot, J., Rhead, A. T. & Butler, R., Buckle-driven delamination models for laminate strength prediction and damage tolerant design, Thin-Walled Structures. 161, 107468, 2021.

[5] Butler R., Williams, F.W., Optimum design using VICONOPT, a buckling and strength constraint program for prismatic assemblies of anisotropic plates, Computers & Structures, 43 (4), 699-708, 1992.

[6] Maierhofer, T., Loukaides, E., Carr, C., Bisagni, C. & Butler, R., Resistance-welded thermoset composites: A Bayesian approach to process optimisation for improved fracture toughness, Composites Part A: Applied Science and Manufacturing. 177, 12 p., 107894, 2024.

[7] SIMULIA Dassault Systemes, ABAQUS User Manual, 2020.

[8] Hillerborg, A., Modéer, M., Petersson, P-E., "Analysis of crack formation and crack growth in concrete by means of fracture mechanics and finite elements", Cement and Concrete Research, vol. 6, no. 6, pp. 773–781, Nov. 1976.

[9] Turon, A., Dávila, C. G., Camanho, P. P., & Costa, J., "An engineering solution for mesh size effects in the simulation of delamination using cohesive zone models," Engineering Fracture Mechanics, vol. 74, no. 10, pp. 1665–1682, Jul. 2007.

MULTISCALE STUDY ON NONLINEAR PROPERTIES OF CELLULOSE NANOFIBER-REINFORCED THERMOPLASTIC POLYMER COMPOSITE FILAMENTS

Chao Luo[1], Kanji Yano[2], Yoshinori Takashima[3], Yasutomo Uetsuji[1*]

1. Department of Mechanical Engineering, Osaka Institute of Technology, Osaka, Japan
2. Graduate school of engineering, Osaka Institute of Technology, Osaka, Japan
3. Department of Macromolecular Science, Graduate School of Science, Osaka University, Osaka , Japan
*yasutomo.uetsuji@oit.ac.jp

Keywords: cellulose nanofiber, thermoplastic polymer composite filaments, nonlinear properties, multiscale homogenization analysis

Abstract
This study investigated the reinforcing effect of cellulose nanofibers through multiscale nonlinear finite element analysis, aiming to enhance the mechanical properties of composite materials for improved stability and reliability in industrial applications. The research focused on characterizing the interfacial interactions between the fiber and the polymer, and further analyzed the impact of fiber morphology on material performance. The results show that the elastic modulus and maximum stress value in the longitudinal direction of the fiber in the model are both greater than those in the transverse direction. The randomization leads to an increase in the elastic modulus of the material and an increase in the maximum tensile stress compared to a uniform fiber arrangement. This study aimed to provide new guidelines for designing more efficient composite materials.

1. Introduction

Cellulose fiber-reinforced thermoplastic composites are renowned for their high stiffness, strength, moldability, and corrosion resistance. These properties position them as promising candidates for diverse applications in sectors such as transportation, information technology, healthcare, electronics, and architecture [1-3]. To achieve this potential, there is a surge in research and development activities focused on these composites, encompassing aspects from surface treatment of cellulose fibers to modifications in base polymers, interface interactions between fibers and polymer materials, blending of fibers with the polymer, as well as molding and recycling processes [4-6].

There are many factors influencing the performance of materials, and here, we will focus on fiber distribution. Based on the spatial dimensions of fiber arrangement, fiber distribution can be categorized into 1D, 2D, and 3D distributions. 1D distribution includes dry spinning [7], wet spinning [8], and 3D printing [9], among others, which have already been widely developed. 2D distributed materials are often sheets or films prepared by extrusion or hot pressing [10]. A classic example of 3D distribution is the random distribution of fibers during the injection molding process. This paper will focus on the performance changes and mechanism studies of materials under the fiber arrangements. In practical applications, the distribution of fibers directly affects the mechanical properties of composite materials. However, when it comes to analyzing the mechanism, it is difficult to design it at an experimental level. In this case, a common approach among researchers is to introduce simulation analysis methods. For example, finite element analysis (FEA) can help researchers better understand the impact of fiber

distribution on material properties. In addition, these simulation methods enable the optimization of fiber arrangement designs to achieve optimal performance in actual production.

In this study, we focused on fiber distribution to analyze mechanical properties. Employing multiscale nonlinear finite element analysis based on homogenization theory [11], we elucidated the mechanical behavior of cellulose composites under ideal conditions, considering one-dimensional orientation as the limit for performance improvement through controlled fiber orientation in fused filament fabrication and other applications. The impact of the fiber-polymer interface on the composite material's performance was assessed through a two-step homogenization process. This study aimed to provide new guidelines for designing more efficient composite materials.

2. Multiscale simulation

In our microstructural modeling, a representative volume element (RVE) model is utilized, where cellulose discontinuous fibers are oriented in one direction and randomly dispersed within the polymer. The generation of the fiber dispersed RVE model employs the Random Sequential Adsorption (RSA) algorithm. In the RSA process, fibers are added individually to the RVE domain until a predetermined fiber volume fraction is achieved. Interferences, where a newly added fiber intersects with previously inserted fibers, are resolved by either removing interfering fibers or reconfiguring and repositioning the newly added fiber. This methodology has been applied to various short fiber-reinforced composites, including glass, carbon, and cellulose fibers, and even Carbon Nanotubes [12], demonstrating its practicality.

Figure 1 presented the multiscale modeling of CNC-dispersed composite materials, considering the interface phase. In the microstructure, a cubic region is defined where CNC with the interface phase is adjacent. For the meso-structure, we assumed a dispersed state of fiber composites, reflecting the uniform characteristics derived from the microstructure. The nonlinear response to external loads in the macrostructure was analyzed. Treating high-stiffness, high-strength cellulose fibers as elastic materials, we incorporated the experimentally obtained nonlinear stress-strain relationship into the polymer for the nonlinear analysis of the composite. Material damage was not considered, with a focus on mechanical properties prior to damage occurrence. A multi-scale, scale-coupling analysis based on homogenization theory was employed. Simulations were conducted using Sim, and ANSYS was utilized as the FEM solver.

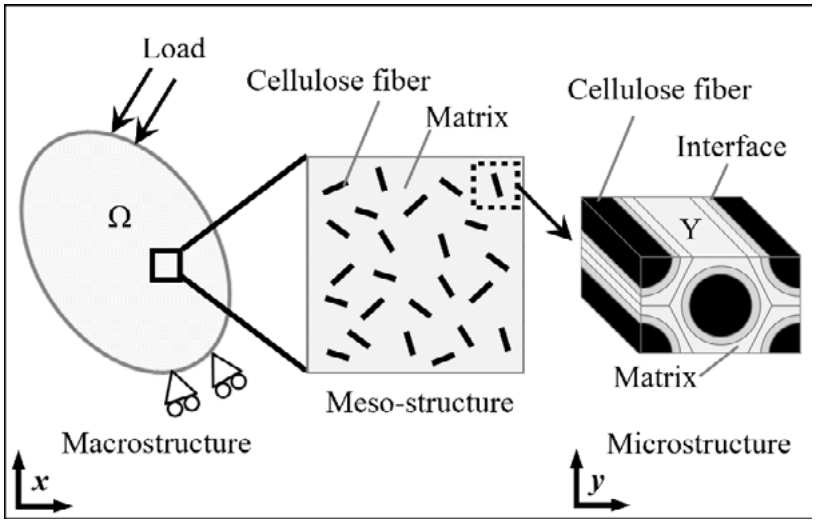


Figure 1. Multiscale modelling of cellulose nanofiber-reinforced polymer composite filaments

3. Results and discussion

To streamline the analysis, all fibers were aligned in a single direction. We then introduced two distinct fiber distribution models, depicted in Figure 2. These models consist of a random short fiber arrangement and a uniform short fiber arrangement. To thoroughly examine the impact of fiber distribution on performance, we maintained consistent fiber volume fractions across both models.

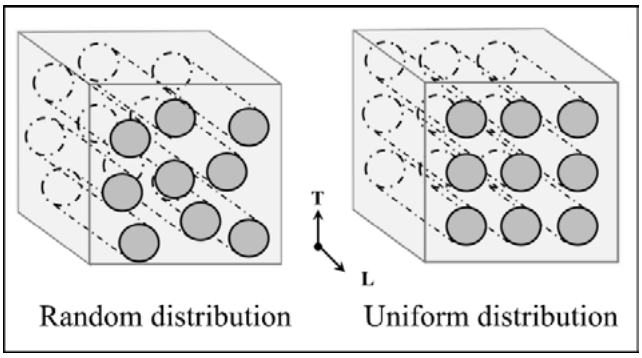


Figure 2. The models of random distribution and uniform distribution

Comparative analyses were carried out with the fiber length direction denoted as the "L direction" and the fiber diameter direction as the "T direction." The analysis of stress-strain results for the two models is illustrated in Figure 3. Based on the stress-strain curves, we analyzed the performance in both the L direction and the T direction for each model. Starting with the elastic modulus, the elastic modulus for both the L direction and the T direction are discussed. In both models, the elastic modulus in the L direction exceeds that in the T direction. It is well-established that fibers are inherently anisotropic materials, exhibiting optimal performance along the fiber's length direction and suboptimal performance along the fiber's diameter direction. In this simulation, since the fibers are oriented in a single direction, the elastic modulus in the L direction surpasses that in the T direction.

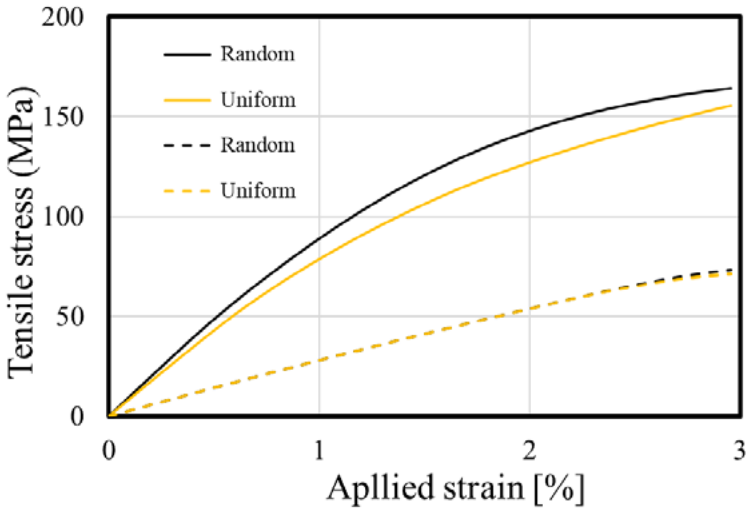


Figure 3. The stress-strain results of random distribution and uniform distribution

In the L direction, the random model exhibits the highest modulus. In the T direction, the modulus for both models are approximately similar. For the uniform model, its uniform arrangement results in more concentrated areas of the resin matrix, leading to a lower elastic modulus under external forces compared to the random arrangement model. Subsequently, we compared the maximum stress values, as shown in Figures 3, for both the L direction and the T direction. Similar to the elastic modulus, the maximum stress values in the L direction are higher than those in the T direction across all models. In the L

direction, the random model demonstrates the highest maximum stress value. In the T direction, the maximum stress values are approximately similar across all models.

4. Results and discussion

In this research, we utilized a multiscale nonlinear analytical method grounded in homogenization theory to examine the influencing elements and mechanisms on uni-directionally aligned nanocellulose composites under optimal conditions.

From the perspective of fiber distribution, compared to a uniform arrangement, the randomization of fiber alignment in short fiber-reinforced composite materials increases the elastic modulus in the L-direction by 11% and the maximum tensile stress by 5.5%. Additionally, the mechanical properties in the L-direction of composite long filaments are significantly greater than those in the T-direction. The insights gained from these results hold significant implications for the development and practical deployment of nanocellulose composites, offering crucial guidance for future exploration and advancements in this field.

5. Acknowledgement

This research was supported in part by JST, the Core Research for Evolutional Science and Technology (CREST) program JPMJCR22L4.

References

[1] Amita Sharma, Manisha Thakur, Munna Bhattacharya, Tamal Mandal, Saswata Goswami, Commercial application of cellulose nano-composites – A review, Biotechnology Reports, 21 (2019) e00316.
[2] Alain Dufresne, Nanocellulose: a new ageless bionanomaterial, Materials Today, 16 (2013), pp.220-227.
[3] Georgios Koronis, Arlindo Silva, Mihail Fontul, Green composites: A review of adequate materials for automotive applications, Composites Part B: Engineering Volume 44, Issue 1, 2013, Pages 120-127
[4] Yasutomo Uetsuji, Souta Higuchi, Kazushige Murayama, Kenji Aoki, Interfacial Adhesion of a Grafted Polymer on a Cellulose Surface: A First-Principles Study, Journal of Materials Science, 56, (2020), 3589-3599.
[5] A. Alhuthali, I.M.Low, C.Dong, Characterisation of the water absorption, mechanical and thermal properties of recycled cellulose fibre reinforced vinyl-ester eco-nanocomposites, Composites Part B: Engineering, Volume 43, 2012, Pages 2772-2781.
[6] Alessandro Pegoretti, Recycling concepts for short-fiber-reinforced and particle-filled thermoplastic composites: A review, Advanced Industrial and Engineering Polymer Research, 4, 2021, Pages 93-104
[7] Si Chen, Greg Schueneman, R. Byron Pipes, Jeffrey Youngblood, Robert J. Moon, Effects of Crystal Orientation on Cellulose Nanocrystals−Cellulose Acetate Nanocomposite Fibers Prepared by Dry Spinning, Biomacromolecules 15 (2014) 3827−3835.
[8] Pezhman Mohammadi, Matti S. Toivonen, Olli Ikkala, Wolfgang Wagermaier & Markus B. Linder, Aligning cellulose nanofibril dispersions for tougher fibers. Scientific Reports 7 (2017) 11860
[9] Qianqian Wang, Chencheng Ji, Lushan Sun , Jianzhong Sun, Jun Liu, Cellulose nanofibrils filled poly(lactic acid) biocomposite filament for FDM 3D printing, Molecules 25 (2020) 2319.
[10] Shiyu Geng, Daniela Wloch, Natalia Herrera, Kristiina Oksman, Large-scale manufacturing of ultra-strong, strain-responsive poly(lactic acid)-based nanocomposites reinforced with cellulose nanocrystals. Composites Science and Technology, 194 (2020) 108144
[11] Tsuboi, Tomoya, Yoshino, Taiki, Mori, Masahiro, Improvement of Physical Properties of Poly（lactic acid）by Adding Amorphous Cellulose, Seikei-Kakou, 24 (2012) 612-617 (in Japanese).
[12] Ji Su Lee, Yeon Sung Ryu, Ick-Soo Kim, Seong Hun Kim, Effect of interface affinity on the performance of a composite of microcrystalline cellulose and polypropylene/polylactide blends, Polymer International, 68, (2019), 1402-1410

MODELLING FATIGUE DAMAGE GROWTH OF T700/M21 COMPOSITES UNDER HIGH FREQUENCY TESTING

M. Lasen, J.Schönthaler and D. Di Maio

Abstract

Experimental laws used to characterise fatigue in composites materials, such as Paris-Erdogan Laws or S-N curves, require time consuming testing campaigns because of their low excitation frequencies [1]. To reduce this long-lasting testing time and to improve the tracking of damage by a more sensitive characteristic physical parameter, a High Frequency Fatigue Testing (HFFT) approach [2] is proposed as an alternative. HFFT can be used at excitation frequencies which can easily be two orders of magnitude higher than low frequency testing. Low frequency fatigue testing has been the benchmark in academia and industry and its extensive use has evolved to the level of a standardised method [3]. These standards allow to obtain experimental laws and hence easily derive, for example, Energy Release Rate (ERR) and crack progression during fatigue testing. However, to build a Paris-Erdogan Law with HFFT a hybrid approach is required to estimate the ERR as the crack progresses.

A Finite Element (FE) simulation routine, written in Python and Abaqus, is designed to reproduce the experimental conditions of the HFFT as accurately as possible. This work presents the first steps to the hybrid simulation-experiment fatigue laws, by introducing the framework of the Python-Abaqus routine.

Keywords: High Frequency Fatigue Testing, Abaqus, Python, Crack growth.

1. Introduction

HFFT is a testing approach to study fatigue at high frequencies by tracking the frequency response phase of the samples measured at constant excitation frequency [2,5,6]. Its main characteristics are that the samples are run at constant excitation frequency (near the resonance), constant amplitude severity and have time-dependent varying properties. Commercially available FE fatigue software are limited in this sense, not allowing to continuously modify these properties.

To overcome these limitations, a Python routine has been designed to iteratively adapt the input conditions to the simulations, such that at every single step of crack progression the excitation resonant frequency and time-dependent damping are modified, while maintaining the FE model samples at a constant severity level.

2. The FE model.

The Abaqus FE model, in Fig. 1 has a dimension of 270x25x2.5 mm. The model is clamped in the 3 middle columns of nodes at the nodal line of the first bending vibration mode. Fig. 1 shows the Concentrated Force Loading Nodes, attached with a Kinematic Constraint. At these Loading Nodes, the forces are applied to reach the desired displacement severity level, which is measured at the indicated Measuring Reference Point, 35 mm from the Clamped Nodes at the mid-width of the sample. Three parts are defined in the model which facilitate the definition of the interfacial properties between them. The continuous orthotropic material properties used in the FE-model are summarised in 1 [4].

The elements used in the model mesh are continuum solid shell elements (CSS8, Abaqus). The thickness of the model consists of 10 plies, with a single element per layer. Each layer has a thickness of 0.25 mm. The different plies that make up the laminate are unidirectional and are stacked with the following layup: $[90_{cut}/0_{cut}/90_{cut}/0/90/90/0/90/0/90]$, where 'cut' indicates the pre-crack separating the Top Part into Left and Right. The cut-ply is offset 10 mm from the clamped centre of the

sample, represented by the Transverse Crack Nodes in Fig. 1. From there, the horizontal crack is expected to grow, horizontally between the 3rd and 4th layers, to the left and right sides of the cut-ply.

The horizontal crack progression uses a VCCT fracture model, which allows to obtain the ERR at the left and right side of the transverse crack. In the Abaqus-Python routine the fracture criterion of the VCCT formulation does not determine to which side the crack is opened, the criterion is imposed after the VCCT simulation, by determining the highest ERR between the left and right sides.

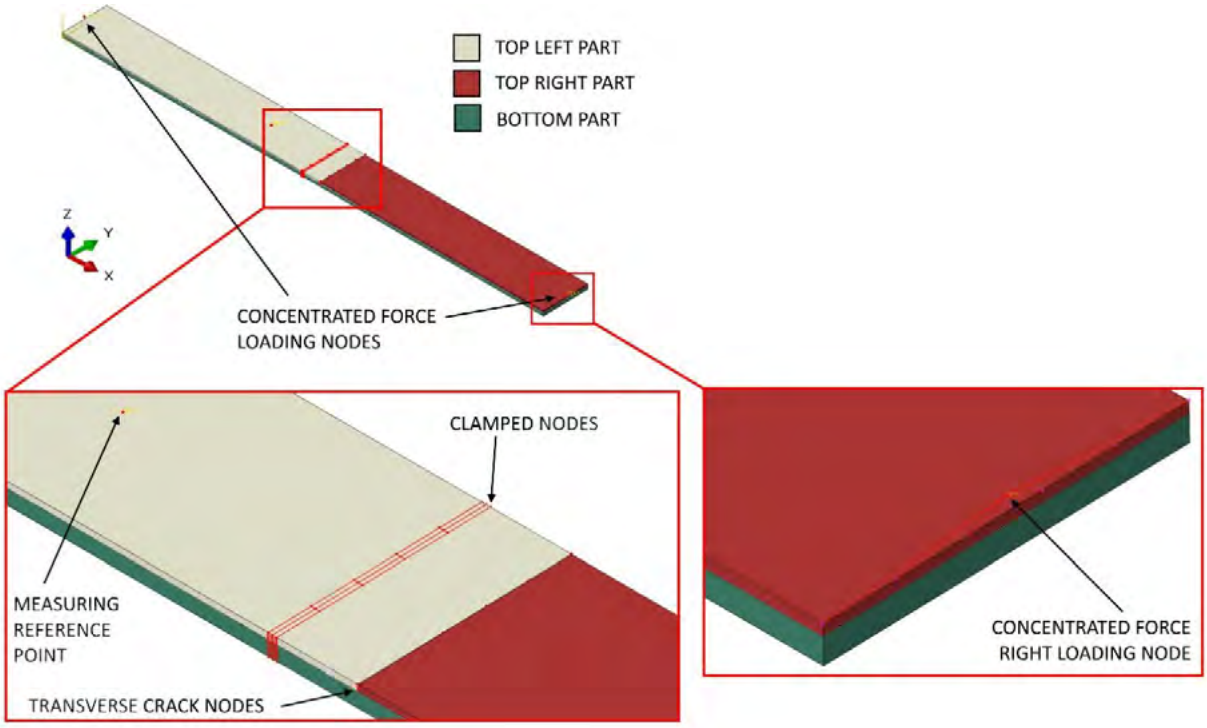


Figure 1 FE model overview and key node sets.

Table 1. T700/M21 material properties in the FE-model.

Properties	*Value*	*Unit*
Longitudinal Young's modulus E_1	124,250	MPa
Transverse Young's modulus E_2	7,660	MPa
Through-thickness Young's modulus E_3	7,660	MPa
Poisson's ratio 1-2 plane ν_{12}	0.36	-
Poisson's ratio 1-3 plane ν_{13}	0.36	-
Poisson's ratio 2-3 plane ν_{23}	0.5	-
Shear modulus 1-2 plane G_{12}	4,347.5	MPa
Shear modulus 1-3 plane G_{13}	4,347.5	MPa
Shear modulus 2-3 plane G_{23}	2,553.33	MPa
Density ρ	$1.58e^{-9}$	tonne/mm3
Structural damping s	0.004	-

A surface-to-surface contact is defined in the transverse and horizontal cracks, with a normal hard contact and a frictional tangential behaviour with a friction coefficient mu= 0.35.

3. The Python and Abaqus routine.

An overview of the Python-Abaqus is depicted in Fig. 2. The framework has 3 steps: '0: Base Case', '1: Steady State Dynamics' and '2: Static - VCCT', each of them is described in terms of the specific FE model used in each framework step, the corresponding Abaqus steps of each simulation and their key outputs.

The following subsections describe each framework step, the reasons behind them and the crack opening criterion used for the iteration of the routine.

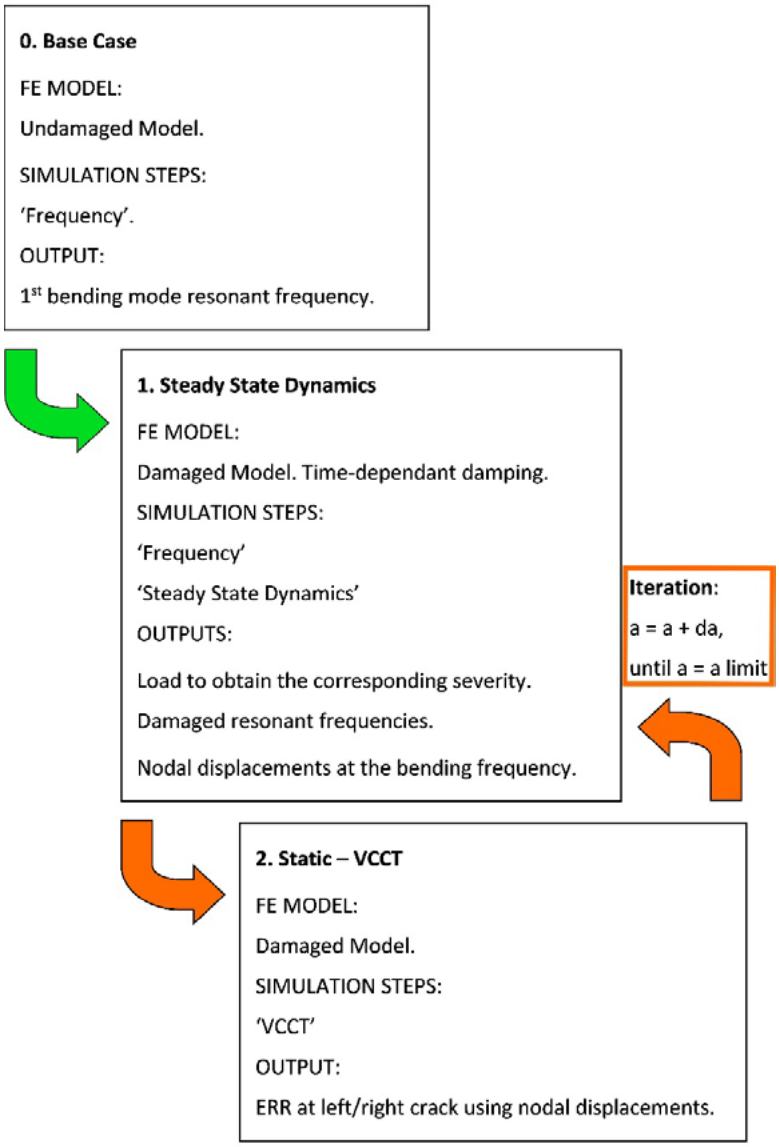


Figure 2 Python-Abaqus framework.

3.1 Framework Step 0: 'Base Case'

In Framework Step 0 (FW-step 0) an undamaged version of the FE model described in Section 1 is used, without cracks. This FW-step allows to obtain a base case of the 1st bending resonant frequency, which is used in the next FW-step.

3.2 Framework Step 1: 'Steady State Dynamics'

FW-step 1 makes use of the FE model described in Section 1. The first time the routine invokes FW-step 1, the crack opening consists of simply one element, 0.1 mm, to each side of the transverse crack. As the crack grows, the crack edge is opened uniformly across the width of the model such that the crack front is always a straight line.

To determine the right input load to match the desired severity level, the damaged FE model is run three times. The first two are run at arbitrary loading forces and the displacement severity is measured at the measuring point displayed in Fig. 1. From these two auxiliary simulations an interpolation is run to find the best representation of the loading conditions for the Steady State Dynamics, in the third simulation.

The damage accumulation needs to be reflected not only in the crack growth but also in the decay of the material properties, i.e. damping. Damping is hard to monitor during a real fatigue experiment, however, it can be studied before and after the fatigue test is done. The damping level used at each crack opening is simply an interpolation between the damping measured before and after a representative fatigue experiment.

The simulations have two Abaqus steps. (i) A 'Frequency' step is used within an arbitrary range with an upper frequency limit set by the undamaged resonant frequency from FW-step 0, from there the frequency only drops. (ii) A Steady State Dynamics (SSD) step is used to obtain the dynamic response of the damaged cases analysing two critical frequencies, the first is the current resonant frequency, obtained in (i) and the second is the previous damaged resonant frequency, at the previous crack opening.

The most important outputs of FW-Step 1 are twofold, (a) the nodal displacement at the damaged resonant frequency and (b) the dynamic response phase, phase lag between the input Concentrated Loading Force and the response of the system at the Measuring Reference Point. Studying the response allows to compare how the phase decays when damage accumulates as the crack and damping grow.

3.3 Framework Step 2: 'Static - VCCT'

FW-step 2 uses the same damaged FE model from FW-step 1. The purpose of this step is to quantify the ERR in a representative simplified loading cycle. The simplification is necessary because running iteratively a VCCT simulation to account for the ERR evolution with number of cycles, at each adjusted excitation frequency, is computationally too expensive.

To capture the behaviour of a simplified loading cycle, two Abaqus simulation are run within this step. (i) A positive bending static simulation, where the specimen is bent in a U-shape (upwards in the z-axis), and (ii) a negative bending static simulation, where the specimen is bent in an inverted U-shape. The load paths for both simulations (i, ii), are linear ('Ramp' Amplitude in Abaqus). This means that the load starts from a resting position until the prescribed nodal displacements, found in FW-step 1, are reached.

The boundary conditions holding the prescribed nodal displacements, extracted from the SSD simulations in FW-step 1 are applied sufficiently afar from the crack, otherwise it can affect the results of the total ERR. A safe window of 10.2 mm in the X-axis is used. This is considered a safe window volume since the total maximum crack length, imposed in the iteration of the Python-Abaqus routine is 5.1 mm and both left and right cracks develop sufficiently far from any of the edge's planes of this window volume. Several convergence simulations were tried against the crack opening tendency (which crack opens more left or right) to determine a safe window that does not affect this tendency.

The outputs of this step are the following, for each simulation positive and negative: the ERR of the individual modes (crack opening Mode -I, -II and III) and total ERR at each crack front, left and right. These outputs are key to determine in which direction the crack is opened in the next iteration.

3.4 Crack opening criterion in the Python-Abaqus framework.

After the last Abaqus simulation is finished, the total ERR from both positive and negative bending simulations are added at each crack front, in Python. Then the added total ERR (positive and negative) is compared between the left and right cracks, and the crack with the higher ERR is opened in the next iteration. The next iteration opens the crack front by da = 0.1 mm, either at the left or right crack, and the Python routine comes back to FW-step 1, with a modified FE model (larger crack, new damping level). The routine is iterated until an arbitrary total limit of 5 mm is reached, adding both left and right cracks.

4. Results

4.1 Crack progression

Fig. 3 shows the progression of the crack length to the left (blue) and right (red) of the transverse crack. The progression starts at the base of the vertical axis with the initial crack of 0.1mm at each side of the transverse crack, it then grows to the left towards the clamped nodes until it reaches a length of 2.4 mm without any growth to the right, only at this point the crack starts growing to the right.

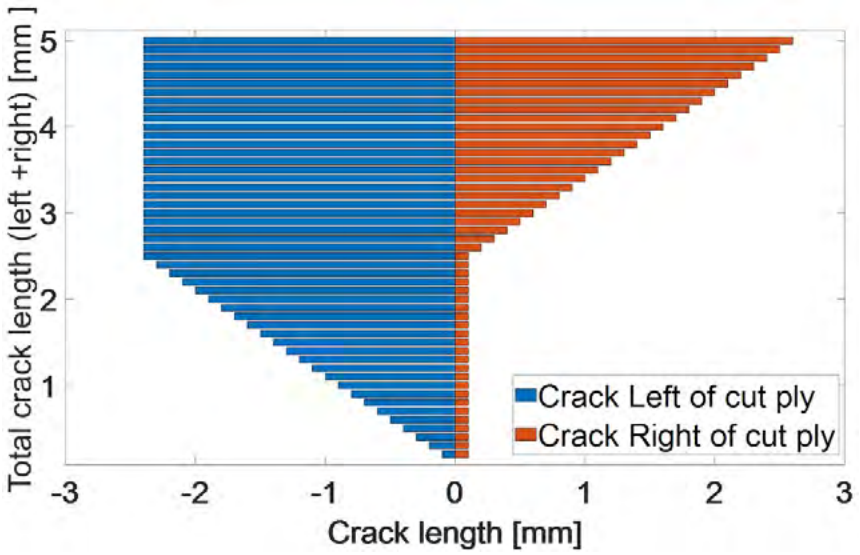


Figure 3 Simulation crack opening up to 5mm.

4.2 Phase decay

The concept of phase decay reflects on the fact that the structural strength of a component deteriorates with fatigue, this deterioration is captured in the dynamic phase response. It has previously been shown that the phase response which is the lag between the input-output (Measuring Point-Loading Point) grows as the material fatigues [5,6].

The Steady State Dynamics analysis, in FW-step 1, is performed at two key frequencies for each crack length, one is the frequency at the current damaged state, 'f_i', and the second is the frequency of the previous damaged state, 'f_{i-1}', see Fig. 4. This allows to determine the Instantaneous Phase decay, ϕ_I, which is the phase decay between the response vibration phase of, ϕ, at one damage case, c_I, at its resonance, f_i, and the resonance of the previous damaged case, f_{i-1}. Fig. 4 describes this concept by using simulated FRFs from the same damaged models (crack opening and evolving damping) used in the Python-Abaqus routine, it is worth noting that the Python-Abaqus routine only performs the SSD at $f_i$and f_{i-1} and that the FRFs shown here, with a frequency range between 116 - 122 Hz, are only used as a tool to explain the concept of phase decay. It can be seen in the close up view on the initial few damage cases

In reality, a good measurement system would compute the phase decay continuously, hence the Instantaneous Phase Decay need to be accumulated and gathered in a single curve to represent a total phase decay, as the crack grows. Fig. 5 displays the instantaneous phase decay at each crack length for a strategy considering a constant damping level equal to the initial damping state and a second strategy where the damping is continuously increased, as explained in Section 3.1.

The initial crack opening is 0.2 mm and the next opened case is 0.3 mm, therefore the first instantaneous phase decay is evaluated at c_I = 0.3 mm, as it is a differential with respect to the previous case. The total phase decay, $\Delta\Phi(c_I)$, is simply the sum of the instantaneous phase decay jumps from the initial case up to the current level of damage, that is, $\Delta\Phi(c_I) = -1 * [\phi_{I_i}(c_I) + \phi_{I_{i-1}}(c_I - 0.1mm) + \phi_{I_{i-2}}(c_I - 0.2mm) + \cdots + \phi_I(c = 0.3mm)]$. In other words, the total phase decay is the cumulative sum of previous phase jumps. Since $\Delta\Phi$ is an arbitrary function it has been adjusted to start from 0, such that $\Delta\Phi(c = c_I)$ is the total Phase decay jump for any c_I, its sign is negative to denote the loss of strength. Fig. 5(b) shows the total Phase decay with the definition explained above.

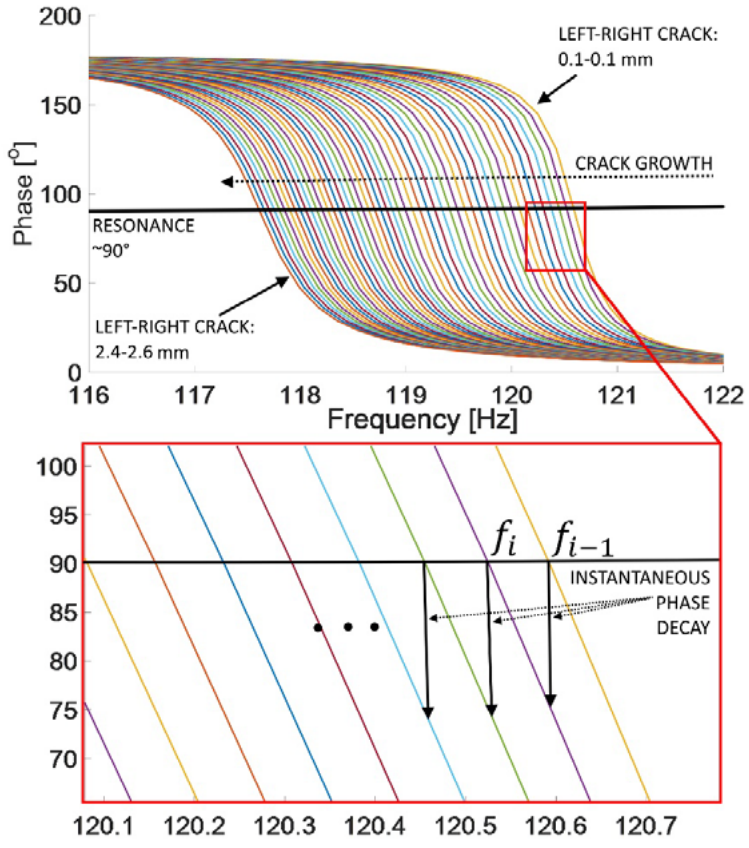


Figure 4 Concept of Phase decay explained with auxiliary FE model FRFs

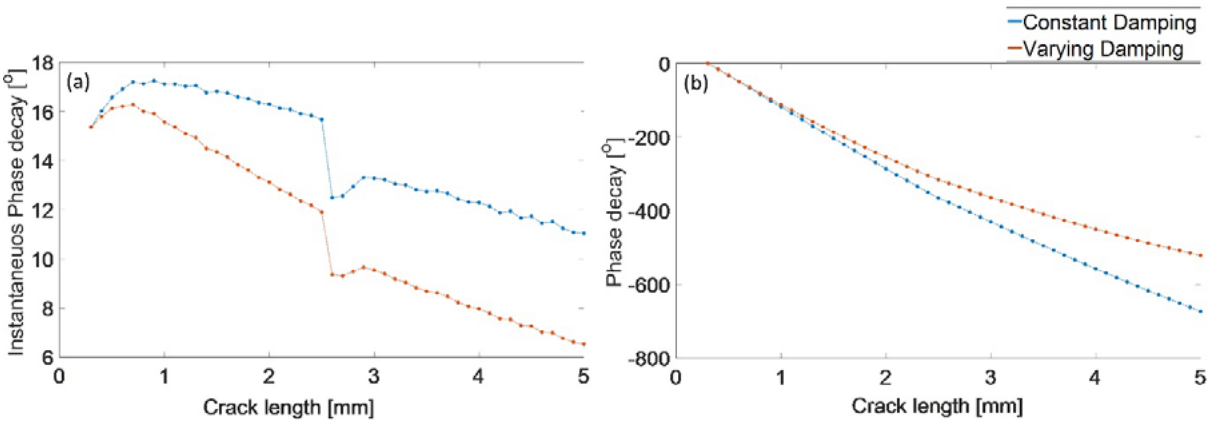


Figure 5 FE model Phase Decay. (a) Instantaneous. (b) Cumulative Total.

5. Discussion

It can be seen from Fig. 5(a) that at 2.5 mm crack length there is a sudden instantaneous phase jump. This is due to the start of the development of the right-side crack, as it can be seen from Fig 3. After that, the instantaneous phase decay of the right-side crack is the same as for the left side crack, a small increment, probably due to small or no sliding frictional behaviour at that interface, followed by a steady decrease.

In Fig. 5(b) the total accumulated Phase decay shows the effect of progressively decreasing magnitude of instantaneous phase jumps, by displaying a slight curvature.

The results in Fig. 5(a), also show the effect of a linear increasing varying damping, where the instantaneous jumps are smaller than the constant damping curve. The larger jumps in phase in the constant damping curve are reflected in the accumulated total phase decay, in Fig. 5(b), by displaying a steeper curve. The reason for this is that larger damping provides a softer response, which can be seen in Fig. 4, where the initial crack phase response is steeper around resonance than the last case of a total crack length of 5 mm.

6. Conclusions

This work shows the overview of a Python-Abaqus framework capable of representing the crack opening condition of a real HFFT experiment. Its main modelling capabilities are: (i) frequency variation due to damage, (ii) varying damping from material fatigue and (iii) constant severity level displacement throughout the entire routine.

These features provides insight into: (a) understanding of the crack growth at small scales, starting from 0.1 mm to arbitrary limits values, as well as (b) providing estimations of the ERR magnitudes for mixed modes and for two cracks, left and right, type of defects, and finally (c) a prediction of the total Phase Decay, which is an experimental signature characterising the material loss of strength from the HFFT experiments.

7. References

[1] Silvain A. Michel, Rolf Kieselbach, Hans Jörg Martens, Fatigue strength of carbon fibre composites up to the gigacycle regime (gigacycle-composites), International Journal of Fatigue, Volume 28, Issue 3, 2006, Pages 261-270, ISSN 0142-1123, https://doi.org/10.1016/j.ijfatigue.2005.05.005.

[2] Di Maio D, Magi F. Development of testing methods for endurance trials of composites components. Journal of Composite Materials. 2015; 49(24):2977-2991. doi:10.1177/0021998314558497

[3] Fatigue standards and fracture standards - standards products - standards & publications - products & services (no date) ASTM International - Standards Worldwide. Available at: https://www.astm.org/products-services/standards-and-publications/standards/fatigue-standards-and-fracture-standards.html (Accessed: 29 November 2023).

[4] Hongkarnjanakul, N., Rivallant, S., Bouvet, C., & Miranda, A. (2014). Permanent indentation characterization for low-velocity impact modelling using three-point bending test. Journal of Composite Materials, 48(20), 2441–2454. https://doi.org/10.1177/0021998313499197.

[5] G. Voudouris *et al.*, "Experimental fatigue behaviour of CFRP composites under vibration and thermal loading," *Int. J. Fatigue*, vol. 140, no. May, p. 105791, 2020, doi: 10.1016/j.engfracmech.2019.106626.

[6] M. Peluzzo, D. Di Maio, A. Cammarano, and P. Castellini, "Measurement and analysis of the nonlinear stiffness of cfrp components during vibration fatigue testing," in *Conference Proceedings of the Society for Experimental Mechanics Series*, 2020, doi: 10.1007/978-3-030-47721-9_7

NUMERICAL METHOD FOR FRACTURE MODELLING OF LATTICE INTERFACE MATERIALS IN COMPOSITE STRUCTURES

Michelle Hedvard, Philipp Weißgraeber

Chair of Lightweight Design, University of Rostock, Germany
Email : michelle.hedvard@uni-rostock.de, Web Page: https://www.cld.uni-rostock.de/

Keywords: Mechanical metamaterials, Architected interfaces, Thick bond lines, Failure, DCB test

Abstract
Mechanical metamaterials are known for superior material properties such as high strength-to-weight and stiffness-to-weight ratios. Introducing those mechanical metamaterials as an interface in thick bond lines allows for case-specific bond line design also referred to as architected interfaces. The wide range of geometries used for the cellular structures on the meso scale level requires a good modelling approach to understand the material and failure properties of those architected interfaces. This work presents a numerical model that considers a double cantilever beam configuration with a lattice interface material. Due to the loading configuration, the interface material is locally subjected to tensile and compression loading. The interface is described by beam elements allowing for a discontinuous representation of the highly-porous lattice structure. Failure of the individual struts is modelled by a complete softening of the base material taking the fracture toughness of the local structural element into account. Examples of different interface geometries are presented showing some of the advantages of using architected interfaces e.g. tunable material properties and toughening effect. The proposed method contributes to a better understanding of the behaviour and damage of architected interfaces.

1. Introduction

The geometrical cellular structure on the mesoscale level of mechanical metamaterials enables the possibility of achieving superior material properties such as high strength-to-weight and stiffness-to-weight ratios [1,2], high energy absorption [3], improved fracture toughness [4,5] etc. With the rapid development of additive manufacturing, we can today produce many of those complex structures from different base materials ranging from the nano to meter-scale [6,7].

Focusing the topic of mechanical metamaterials on lattice structures the materials can in general be divided into two groups, stretching and bending-dominated depending on their node connectivity [8]. Considering first the stretching-dominated structures, here the individual struts are loaded in tension whereas in the bending-dominated structures, the individual struts are bending loaded. This has a direct effect on the mechanical behaviour which is reflected in the material properties. Take as an example the Young's modulus for low strut thickness-to-length ratios (t/l) in the linear elastic regime, the dependence of the Young's modulus on this ratio can described by a power-law [8]:

$$E \propto \left(\frac{t}{l}\right)^n E_s \tag{1}$$

where E_s is the modulus of the base material and n is a scaling factor depending on the behaviour (stretching or bending dominated). For high thickness-to-length ratios, Zhong et al. [9] have proposed a model taking shear effects into account. The failure strength and fracture toughness are also directly related to the topology of the metamaterial [10]. Besides material failure of the base material, buckling failure must also be considered for stretching dominated structures [11]. Over the reason years multiple

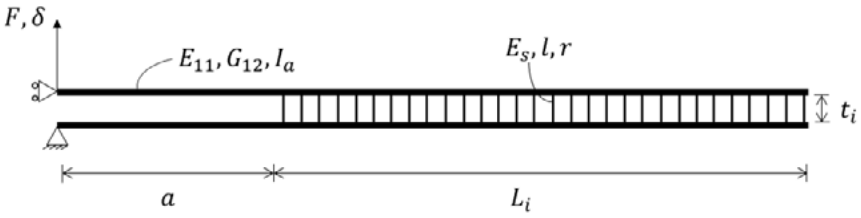


Figure 1. DCB with a pillar interface.

studies have been performed to improve the method to describe the failure mechanisms and fracture toughness of mechanical metamaterials [1,10,11,12].

Athanasiadis et al. [13] have proposed the use of mechanical metamaterials as a replacement for adhesives in thick bond lines utilising their significant material properties and the possibility of toughening mechanisms [14]. Today mechanical metamaterials are typically studied under the assumption of an infinity length scale neglecting boundary effects. To replace adhesives in thick bond lines or use mechanical metamaterials in other confined settings a better understanding of the behaviour and failure of confined metamaterials is needed. In this paper, we present a numerical model to study confined lattice materials. Failure is implemented by a complete softening of the base material allowing for the failure of individual struts without remeshing.

2. Modeling

We consider a double cantilever beam (DCB) with a thick interface of a stretching dominated lattice material loaded in mode I. An example is shown in Figure 1 where a simple pillar interface is represented. A CFRP UD laminate is considered for the adherend of the DCB with the modulus of $E_{11} = 150$ GPa and a shear modulus $G_{12} = 6$ GPa [15]. The thickness and width of the adherend $t_a = w = 5$ mm resulting in a second moment of area of $I_a = 1/12\, w t_a^3$. The initial crack length $a = 10 t_a$. The interface thickness $t_i = 10$ mm and the interface length L_i is varied from 400-800 mm so the full tension and compression zone occurring under loading is captured. The length of a single strut is denoted by l and it has a circular cross-section with a radius r. The interface is modelled using the elastic-brittle trimethylolpropane triacrylate (TMPTA) with the Youngs modulus $E_s = 430$ MPa, failure strength $\sigma_f = 11$ MPa, Poisons ratio $\nu = 0.3$ and fracture toughness $\mathcal{G}_0 = 840$ J/m^2 [11]. In the setup with the pillar interface the strut length $l = t_i$ and the pillars are placed at a distance of $s = t_i/2$. Comsol multiphysics is used for a finite element simulation using Timoshenko beam elements. The simulation is made displacement controlled by δ applied on the left end of the adherend as shown in Figure 1, and the resulting force is denoted F.

2.1. Material model for interface material

The material of the interface is assumed to be linear elastic up to failure occuring when the critical strain $\epsilon_f = \sigma_f / E_s$ is reached. The damage process is modelled based on the traction-separation law:

$$\sigma = \sigma_f \left(1 - \frac{u_f \sigma_f}{2\mathcal{G}_0}\right) \tag{2}$$

During the damage process, the modulus of the damaged lattice element is given by [16]:

$$E_D = -\frac{\sigma_f^2 l_{\text{elm}}}{2\mathcal{G}_0} \tag{3}$$

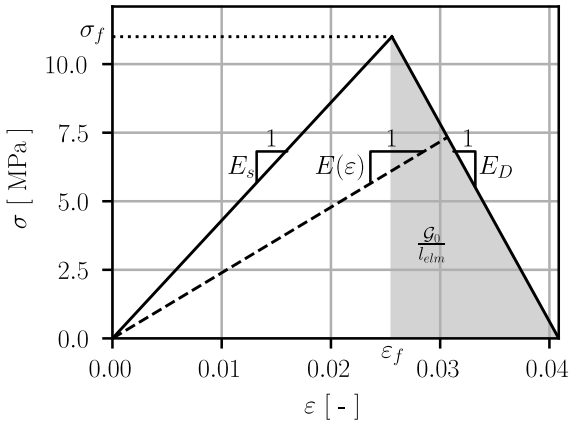


Figure 2. Representation of the material model for the base material of the interface.

where l_{elm} is the element length. The area under the stress-strain curve of the material model is shown in Figure 2 where $\mathcal{G}_0/l$ represents the area under the curve of the damage process [10]. The Young's modulus of the interface material implemented in the finite element model is given by:

$$E(\varepsilon) = \begin{cases} E_s & if\ \varepsilon < \varepsilon_f \\ \frac{\sigma_f - \varepsilon_f E_D}{\varepsilon} + E_D & if\ \varepsilon_f < \varepsilon < \varepsilon_u \\ \frac{E_s}{k} \approx 0 & if\ \varepsilon > \varepsilon_{max} \end{cases} \quad (4)$$

where E_s/k represents a minimum modulus of the interface material to ensure the modulus is strictly positive avoiding the need for remeshing [14]. In this study a value of $k = 10^9$ is used. Due to the brittle behaviour of the material, the modulus is evaluated from the maximum tensile strain over the cross-section thereby taking both tension loading and bending into account [4]. This will result in a reduction of the released energy from the fracture process since bending stresses lead to a variating stress level over the cross-section. Considering the assumption of a stretching-dominated interface only limited bending will be introduced, e.g. the strut in the pillar interface will experience small rotations at the boundaries from the bending of the adherends, thereby it can be assumed this reduction of the released energy will be small. Additionally, the assumption of limited bending allows the representation of a strut by a single element [17]. Representing a strut by only one element ensures that the strut can only fracture once along the length, which is expected in reality. Considering the slender structure of the struts loaded in compression loading failure can occur due to buckling. This is taken into account by comparing the axial strain of the centre line to the buckling strain determined from the Euler buckling load of a column with fixed boundaries. If this buckling load is exceeded the modulus is set to a very low value of E_s/k.

3. Results and discussion

3.1. Failure of confined lattice interface

The force-displacement of a pillar interface for a strut radius of 1 mm and 0.15 mm are depicted in Figure 3. For both strut radiuses, the force is first increased linearly where a tensile zone (area with red struts) and compression zone (area with blue struts) are introduced in the interface (A). As the strut radius decreases the interface modulus decreases (see eq. 1) so the size of the tension and compression zone increases. Considering the interface with a radius of 1 mm, when damage is introduced a softening of the materials occurs in the area next to the crack front, and the struts will fail one by one starting from the crack front (B). The force-displacement doing the crack growth follows the power-law relation of $F \propto \delta^{-0.5}$ also seen in homogenous interfaces [18]. For the interface radius of 0.15 mm failure is occurring in the compression zone due to buckling (C). Here, we see a sudden failure of a large area of the interface. It is important to note that no contact is incorporated in the model, so the model becomes invalid after the failure in such a large area of the interface in compression since it can not capture the

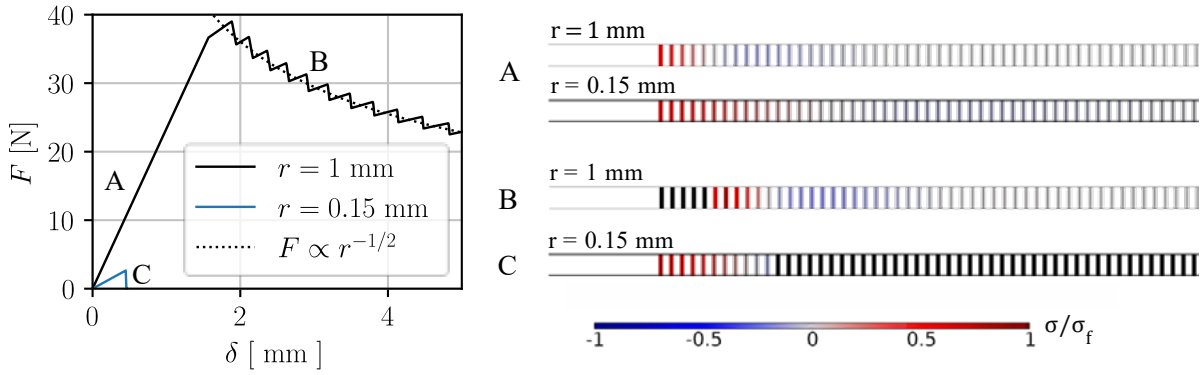


Figure 3. Force displacement plot a DCB with pillar interface. The failed interface is marked in black. For both interface radiuses, the interface length is longer than shown here so the entire tension and compression zone are fully captured at all times.

touching of the two adherends and the interface material in between. Similar results for both the tension and compression failure were reported by Hedvard et al. [14]. As mentioned in section 2 the material model is based on the assumption of the interface being stretching-dominated with only limited bending introduced. Considering the strain in the interface with a strut radius of 1 mm just before the first damage, the tensile strain contributes with 94% of the total maximum axial strain over the cross section so the assumption that the interface being stretching dominated holds.

The force can be normalized using [13]:

$$\tilde{F} = \frac{F\lambda^3}{E_{11} I_a h_i} \tag{5}$$

where λ is the characteristic wavelength given by $\lambda = \left(\frac{2h_i E_a I_a}{E_i w}\right)^{\frac{1}{4}}$. Here E_i is the homogenized modulus of the interface there for a pillar interface is given by $E_i = \pi(r/s)^2 E_s$. The maximal normalized force over the slenderness ratio (r/l) for different strut radiuses are plotted in Figure 4. The failure types can be separated in two: tension (material failure) and compression (buckling) related to the slenderness ratio. For each failure type regression is used to determine a power law [13]. The power law relation follows the maximal force well and can be used to determine the critical force and failure mechanism for a specific value of the slenderness ratio of the interface.

3.2. Toghening effects of lattice structures

An interface is created by four rows of equilateral triangles. The interface height is kept constant which results in a strut length of $l = 2.9$ mm. The slenderness ratio is set to $r/l = 0.1$. To break the symmetry of the setup and thereby avoid the unrealistic case of two symmetric cracks growing in the interface the strut radius of the first triangle in the top two rows is increased by 1%. The force-displacement plot for the triangular interface is shown in Figure 5. First (A) a linear relationship shown into damage of the interface is introduced. As for the pillar interface, a tension and compression zone of the interface is detected, however, horizontal struts in the tension zone experience compression due to the interface topology. After the damage onset, a toughening zone is detected (B) where the force is increased further. Here only a part of the struts are failing creating a bridging-like behaviour. The partly fractured material seen in the bridging zone is also detected in triangular mechanical materials by Hedvad et al. [14] or Gu et al. [19]. After the maximum force is reached a sudden large decrease of the force is detected and the crack starts to grow (C). As shown here by a simple change of the interface topology, the interface's failure process is changed significantly. Thereby with a good understanding of different interfaces, we can design case-specific interfaces controlling the damage process where toughening zones can be used for safe design.

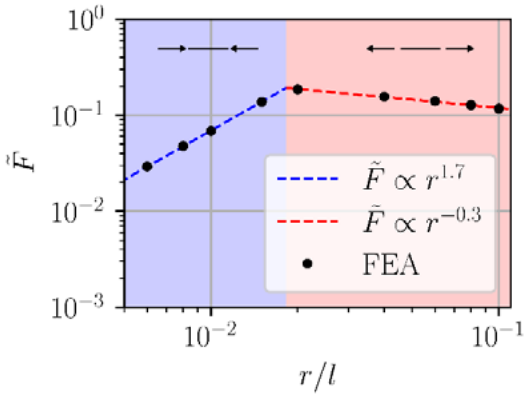


Figure 4. Failure map of DCB with pillar interface. The compression failure is marked in blue, while tension failure is marked in red.

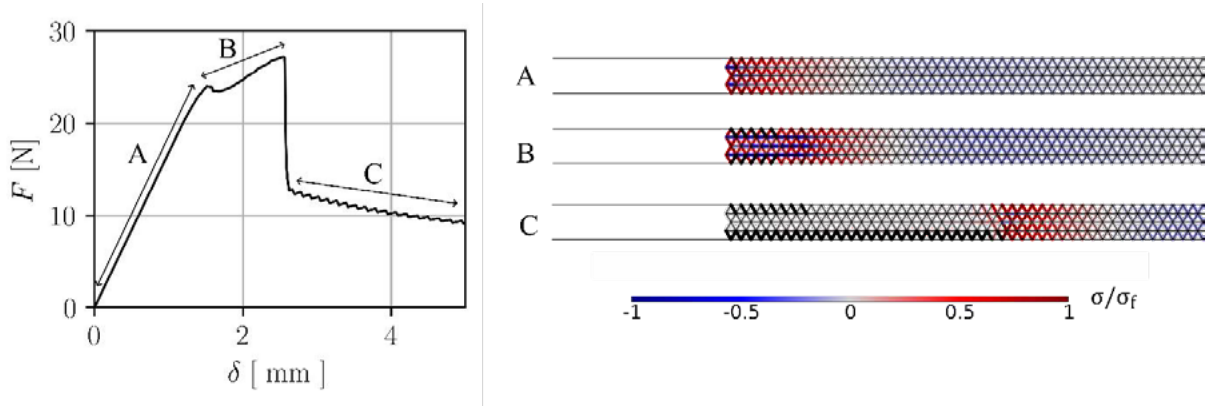


Figure 5. Force displacement plot a DCB with a triangular interface for $r/l = 0.1$. The failed interface is marked in black. For both interface radiuses, the interface length is longer than shown here so the entire tension and compression zone are fully captured at all times.

4. Conclusion

A numerical model has been implemented for investigating confined metamaterials in a double cantilever beam setup. The model allows for both material failure where the fracture toughness is taken into account and buckling failure. A failure map has been created for a simple pillar showing a power law relation for each of the two failure types. Additionally, a triangular interface is studied showing toughening effects under failure. Considering different topologies and slenderness ratios of the interface material, we can alter material properties and failure behaviour. This indicates the potential for the use of mechanical metamaterial as interface materials allowing us to create architected interfaces tuning the material and failure properties wanted for the specific design case.

References

[1] X. Zheng, H. Lee et al., Ultralight, ultrastiff mechanical metamaterials, *Science*, 344:1373-1377, 2014.
[2] J. B. Berger, H. N. G. Wadley and R. M. McMeeking, Mechanical metamaterials at the theoretical limit of isotropic elastic stiffness. *Nature* 543:533–537, 2017.
[3] X. Chen, Q. Ji, et al., Light-weight shell-lattice metamaterials for mechanical shock absorption, *International Journal of Mechanical Sciences*, 169:105288, 2020.
[4] H. C. Tankasala, V. S. Deshpande and N. A. Fleck, 2013 Koiter Medal Paper: Crack-Tip Fields and Toughness of Two-Dimensional Elastoplastic Lattices, *Journal of Applied Mechanic*, 82:091004, 2015.

[5] Z. Jia, L. Wang, 3D printing of biomimetic composites with improved fracture toughness, *Acta Materialia*, 173:61-73, 2019.

[6] S. M. Montgomery, X. Kuang et al., Recent advances in additive manufacturing of active mechanical metamaterials, *Current Opinion in Solid State and Materials Science*, 24:100869, 2020.

[7] J. Fan, L. Zhang, et al., A review of additive manufacturing of metamaterials and developing trends, *Materials Today*, 50: 303-328, 2021.

[8] L. J. Gibson, M. F. Ashby, *Cellular Solids: Structure and Properties*, Cambridge University Press, Cambridge, 1997.

[9] H. Zhong, R. Das, et al., Low-density, high-strength metal mechanical metamaterials beyond the Gibson-Ashby model, *Materials Today*, 68: 96-107, 2023.

[10] M. Omidi, L. St-Pierre, Fracture toughness of semi-regular lattices, *International Journal of Solids and Structures*, 270:112233, 2022.

[11] A. J. D. Shaikeea, H. Cui, et al. The toughness of mechanical metamaterials. *Nat. Mater.* 21:297–304, 2022.

[12] H. Gu, M. Pavier and A. Shterenlikht, Experimental study of modulus, strength and toughness of 2D triangular lattices, *International Journal of Solids and Structures*, 152–153: 0020-7683, 2018.

[13] A. E.F. Athanasiadis, M. A. Dias and M. K. Budzik, Can confined mechanical metamaterials replace adhesives?, *Extreme Mechanics Letters*, 48: 101411, 2021.

[14] M. L. S. Hedvard, M. A. Dias and M. K. Budzik, Toughening mechanisms and damage propagation in Architected-Interfaces, *International Journal of Solids and Structures*, 288:112600, 2024.

[15] A. de Morais, M. de Moura, et el., Mode-I interlaminar fracture of carbon/epoxy cross-ply composites, *Composites Science and Technology*, 62: 679-686, 2002.

[16] K. R. Mangipudi, P. R. Onck, Multiscale modelling of damage and failure in two-dimensional metallic foams, *Journal of the Mechanics and Physics of Solids*, 59: 1437-1461, 2011.

[17] H. C. Tankasala, N. A. Fleck, The crack growth resistance of an elastoplastic lattice, *International Journal of Solids and Structures*, 188–189: 233-243, 2020.

[18] M. K. Budzik, J. Jumel and M. E. R. Shanahan, Impact of Interface Heterogeneity on Joint Fracture, *The Journal of Adhesion*, 88: 885–902, 2012.

[19] H. Gu, M. Pavier and A. Shterenlikht, Experimental study of modulus, strength and toughness of 2D triangular lattices, *International Journal of Solids and Structures*, 152-153:207-216, 2018.

MULTI-SCALE MODELING OF TIME-DEPENDENT THERMAL EXPANSION AND CHEMICAL SHRINKAGE DURING THE CURING PROCESS OF POLYMER MATRIX COMPOSITES

Martin Hirsekorn[1], Lionel Marcin[2] and Thierry Godon[2]

[1]DMAS, ONERA, Université Paris-Saclay, 29 avenue de la Division Leclerc, 92320 Châtillon, France
Email: martin.hirsekorn@onera.fr
[2]Safran Aircraft Engines, Rond point René Ravaud, 77550 Moissy Cramayel, France
Email: lionel.marcin2@safrangroup.com, thierry.godon@safrangroup.com

Keywords: viscoelasticity, thermal expansion, chemical shrinkage, injection pressure, residual stress

Abstract
A multi-scale modeling strategy for the simulation of the stress evolution in a composite material during the curing process is presented. It consists of a coupled thermo-kinetic simulation of the evolution of temperature and degree of cure taking into account heat transfer and the exothermal reaction enthalpy, and a thermo-mechanical simulation taking into account the thermal expansion of the material, the volume loss of the resin due to chemical shrinkage and the resin added during the curing process to maintain the consolidation pressure. The temperature and cure dependent viscoelastic properties and expansion coefficients are obtained from the constituent properties by homogenization. Due to the viscoelastic behavior of the resin, the resulting expansion coefficients are time-dependent. The effect of the resin injection is modeled by an additional parametric strain accounting for the volume change of the resin in the same way as the volume loss due to chemical shrinkage. The added resin quantity is an additional degree of freedom that evolves with the aim of reaching equilibrium between the injection pressure and the pressure in the mold. With increasing resin viscosity, the change of resin quantity is slowed down, leading to a pressure drop when the resin passes the gel point.

1. Introduction

The generation of residual stresses in polymer matrix composites is a complex multi-physics and multi-scale process. The polymerization kinetics of the resin during the curing process can, in general, phenomenologically well be described by an autocatalytic model [1] for the evolution of the degree of cure, which depends on temperature and the current state of cure. The polymerization reaction is exothermal, thus influencing the temperature evolution in the composite part. Residual stresses are generated due to a volume loss of the resin during the polymerization (chemical shrinkage) and the different coefficients of thermal expansion (CTE) of the fibers and the matrix. The amount of residual stresses and their impact on the part shape and damage onset and evolution is influenced by the mechanical behavior of the constituent materials, which in the case of the resin strongly depends on temperature and degree of cure [2]-[4]. Residual stresses are present at each characteristic scale of the composite, starting from the micro-scale due to the mismatch between the expansion coefficients of the fibers and the matrix, over the meso-scale where the architecture of the fibrous reinforcement is defined, up to the macro-scale of the structure where residual stresses have an impact on the final shape of the composite part.

Numerical simulation of the generation of residual stresses thus requires constitutive models that take into account the different physics involved and appropriate scale change methods. In this contribution,

we present a multi-scale modeling strategy that consists of a thermo-kinetic simulation of the evolution of temperature and degree of cure and a thermo-mechanical simulation of the evolution of the internal stresses. The thermo-kinetic simulation takes into account the exothermal reaction enthalpy of the polymerization and the heat transfer within the composite and between the composite and the mold. The evolutions of temperature and cure in time at each integration point are taken as locally varying input parameters to the thermo-mechanical simulation. They drive the chemical shrinkage and the thermal expansion and influence the mechanical behavior of the material. The influence of the resin injection pressure is modeled phenomenologically by means of an additional parametric strain that accounts for the increase of the resin volume in the composite during the curing cycle, which compensates partially the volume loss due to chemical shrinkage. If the consolidation pressure decreases significantly before the degree of cure of the resin reaches a critical value, gas bubbles may nucleate leading to porosity in the composite part [5]-[6]. With the proposed approach, the pressure drop caused by the chemical shrinkage of the resin can be estimated and the risk of porosity formation can be evaluated.

For the mechanical behavior of the composite, a viscoelastic constitutive behavior with time-dependent expansion coefficients is used [8], which is obtained by homogenization [7]-[8] from the behavior of its constituents [4]. The formulation of the model and the homogenization method are briefly described in section 2. In section 3, the thermo-kinetic simulation of the curing process is presented. The thermo-mechanical simulation with the approach to take into account the influence of the resin injection pressure is described in section 4. Some results of the stress evolution in a composite plate obtained with the presented modeling strategy are shown in section 5.

2. Viscoelastic homogenization with time-dependent expansion coefficients

2.1. Viscoelastic behavior

The viscoelastic behavior of the resin and the composite is modeled by a 3D anisotropic version of a generalized Maxwell model [7]. The stress evolution is given by

$$\underline{\sigma}(\xi) = \left(\underline{\underline{E}}_\infty + \sum_{k=1}^{N} \underline{\underline{E}}_k\right) : \underline{\varepsilon}^{ve}(\xi) - \sum_{k=1}^{N} \underline{\underline{E}}_k : \underline{\varepsilon}_k^{ve}(\xi) \tag{1}$$

where $\underline{\underline{E}}_\infty$ is the asymptotic relaxed stiffness tensor of the material and $\underline{\underline{E}}_k$ are the coefficients of the Prony series expansion of the relaxation master curves. $\underline{\varepsilon}^{ve}$ is the viscoelastic part of strain (see section 2.2) and $\underline{\varepsilon}_k^{ve}$ are internal variables accounting for the strain history. Their evolution is given by

$$\frac{d\underline{\varepsilon}_k^{ve}(\xi)}{d\xi} = \frac{1}{\tau_k}\left(\underline{\varepsilon}^{ve}(\xi) - \underline{\varepsilon}_k^{ve}(\xi)\right) \tag{2}$$

ξ is a reduced time that describes the horizontal shifts of the relaxation curves along the logarithmic time scale upon change of temperature and degree of cure under the assumption of time-cure-temperature superposition [9]:

$$\xi(t) = \int_{-\infty}^{t} \frac{1}{a_T(t')} dt' \tag{3}$$

For the polymer matrix, the tensors $\underline{\underline{E}}_k$ and $\underline{\underline{E}}_\infty$ take an isotropic form. Creep is supposed to be isovolumetric, hence the $\underline{\underline{E}}_k$ are purely deviatoric. The experimentally observed shear relaxation master

curves are well reproduced by Prony series whose coefficients follow a continuous function of the form [4]

$$G(\tau) = A \exp\left(-\left(\frac{\log_{10}\tau - \log_{10}\tau_{peak}}{l_{peak}}\right)^2\right) + \frac{B}{2}\left(1 - \mathrm{erf}\left(\frac{\log_{10}\tau - \log_{10}\tau_{peak}}{l_{peak}}\right)\right) \tag{4}$$

Taking one relaxation time per decade provides a sufficiently smooth relaxation curve in good agreement with the experimental data [4]. For the viscoelastic behavior of the consolidated tows at the meso-scale and for the average behavior of the composite over a representative volume element (RVE), the tensors $\underline{\underline{E}}_k$ and $\underline{\underline{E}}_\infty$ are anisotropic and obtained from the homogenization procedure described in section 2.3. Besides the anisotropy of these tensors, the formulation of the model is the same.

2.2. Time-dependent expansion coefficients

In a small-strain framework, we use an additive decomposition of the strain tensor into a mechanical (viscoelastic) part $\underline{\varepsilon}^{ve}$ that is used in the constitutive behavior presented before, a thermal part $\underline{\varepsilon}^{th}$ that is caused by a temperature change, and a chemical part $\underline{\varepsilon}^{ch}$ that is caused by the volume loss of the resin during polymerization.

$$\underline{\varepsilon} = \underline{\varepsilon}^{ve} + \underline{\varepsilon}^{th} + \underline{\varepsilon}^{ch} \tag{5}$$

The mismatch in the CTE between the fibers and the matrix causes internal stresses in the composite if the temperature changes. Due to viscoelastic phenomena, such as creep and relaxation, these stresses evolve in time after a temperature change even if the temperature is kept constant. As a result, the average strain of the composite also evolves in time after a temperature change. This effect is modeled following a formulation proposed in [10] with a time-dependent CTE, which if written in terms of a Prony series, leads to a formulation similar to the generalized Maxwell model described in the previous section. The evolution of the thermal strain as a function of the reduced time (Eq. 3) is then given by [8]

$$\frac{d\underline{\varepsilon}^{th}(\xi)}{d\xi} = \left(\underline{\alpha}_\infty^{th}\big(T(\xi), c(\xi)\big) - \sum_{k=1}^{N} \underline{\alpha}_k^{th}\big(T(\xi), c(\xi)\big)\right)\frac{dT(\xi)}{d\xi} - \sum_{k=1}^{N} \frac{1}{\tau_k}\underline{\varepsilon}_k^{th}(\xi) \tag{6}$$

with internal variables $\underline{\varepsilon}_k^{th}$ accounting for the history of temperature and the CTE. Their evolution is given by

$$\frac{d\underline{\varepsilon}_k^{th}(\xi)}{d\xi} = \underline{\alpha}_k^{th}\big(T(\xi), c(\xi)\big)\frac{dT(\xi)}{d\xi} - \frac{1}{\tau_k}\underline{\varepsilon}_k^{th}(\xi) \tag{7}$$

The tensorial coefficients $\underline{\alpha}_\infty^{th}$ and $\underline{\alpha}_k^{th}$ of the Prony series expansion may depend on temperature and degree of cure, hence the slightly different formulation compared to the viscoelastic model presented in section 2.1. An exactly equivalent formulation can be used for the coefficients of chemical shrinkage (CCS), setting the CCS of the fibers to zero.

2.3. Homogenization

As shown in various works ([11] cited here only as an example), the generalized Maxwell model is obtained from the integral form of viscoelasticity if the time-dependent relaxation function is written in

terms of a Prony series. If the Laplace-Carson (LC) transform is applied to the integral form of a linear viscoelastic behavior, a relation equivalent to a linear elastic behavior is obtained, with a stiffness tensor that depends on the LC transform parameter. This well-known formalism was extended in [8] to time-dependent CTE written in the formulation of [10], leading to a thermo-elastic relation in the LC space. If Prony series are used for the relaxation function and the time-dependent CTE, the LC-transform can be written by a system of equations [7] for the relaxation function

$$\hat{\underline{\underline{E}}}(p_i) = \underline{\underline{E}}_\infty + \sum_{k=1}^{N} \mathcal{L}_{ik} \underline{\underline{E}}_k \tag{8}$$

where $\hat{\underline{\underline{E}}}(p_i)$ is the LC transform of the relaxation function evaluated at a LC-transform parameter p_i and $\mathcal{L}_{ik}$ are given by

$$\mathcal{L}_{ik} = \frac{p_i}{p_i + \frac{1}{\tau_k}} \tag{9}$$

The LC transform of the time-dependent CTE for a given temperature T and degree of cure c is given by

$$\hat{\underline{\alpha}}^{th}(p_i, T, c) = \underline{\alpha}_\infty^{th}(T, c) - \sum_{k=1}^{N} \mathcal{L}_{ik} \underline{\alpha}_k^{th}(T, c) \tag{10}$$

The same formulation is used for the CCS.

The LC transform of the relaxation function and the time-dependent expansion coefficients is then obtained with classical thermo-elastic homogenization methods. If we assume that the relaxation function and the expansion coefficients of the homogenized material can also be well fitted by a Prony series with weights that follow continuous functions if plotted against the logarithm of the relaxation times, we can choose the same relaxation times as for the matrix behavior to discretize these continuous spectra. Then, if we determine the LC transform of the homogenized behavior for at least $M \geq N$ different p_i, the homogenized behavior in the time-domain is obtained by solving the least squares problems given in Eqs. (8) and (10) to obtain the coefficients $\underline{\underline{E}}_k$ and $\underline{\alpha}_k^{th}$ of the homogenized material. Since this problem is often ill-conditioned, the proper choice of the p_i is important [7] and sometimes a Tikhonov regularization may be necessary [8]. In the case of a composite with a woven reinforcement, two homogenization steps are needed: the first one to determine the homogenized behavior of the consolidated tows from the constituent (fiber and matrix) behaviors, and the second one to determine the homogenized behavior of the composite.

3. Thermo-kinetic simulation of the curing process

The curing process of a flat plate of composite with a 3D woven reinforcement as the one used in [7]-[8] is simulated. The dimensions of the plate and the curing cycle correspond to those used in [13]-[14]. In the first step of the curing process simulation, the heat transfer equation is solved using the Finite Element (EF) software Z-set [12]. The heat generated by the exothermal polymerization reactions is taken into account by a heat source term that is added to the heat transfer equation:

$$\vec{\nabla} \cdot \left(\underline{\kappa} \cdot \vec{\nabla} T \right) = -\rho C_p \dot{T} + \rho H_R \dot{c} \tag{10}$$

where $\underline{\kappa}$ is the anisotropic 2nd order tensor of thermal conductivity of the composite, ρ is its mass density, C_p the heat capacity per unit mass and H_R the reaction enthalpy per unit mass. The evolution of the degree of cure c is simulated using the autocatalytic model proposed in [1]

$$\dot{c} = (k_1(T) + k_2(T)c^m)(1-c)^n \tag{10}$$

with reaction velocity coefficients $k_{1,2}$ that follow a classical Arrhenius dependence on temperature. The heat source term accounts for the overheating that may occur in thick composite parts. However, as the simulated plate is relatively thin (6.7mm), the temperature remains quite homogeneous during the curing process (not more than 0.5°C between the surfaces and the center of the plates). Therefore, the curing temperature is applied directly to the surfaces of the plate. Heat transfer boundary conditions can alternatively be applied, but this does not influence the result if the overheating due to the exothermal reaction is insignificant. The evolution of temperature and degree of cure are shown in Figure 1.

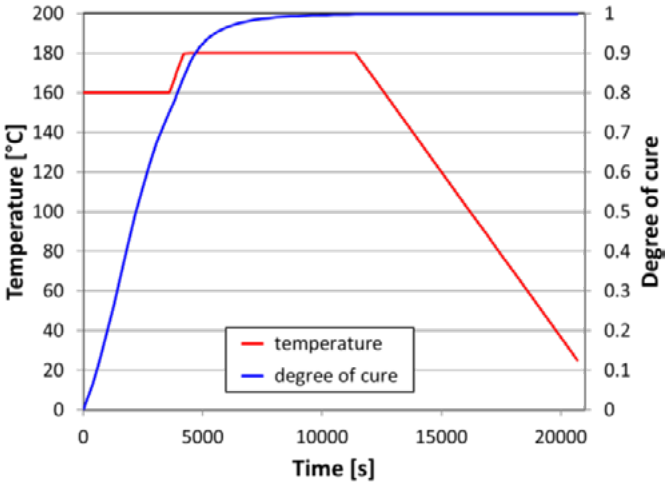


Figure 1. Evolution of temperature and degree of cure during the simulated curing cycle.

4. Thermo-mechanical simulation of the curing process

4.1. Boundary conditions and input parameters

Temperature and degree of cure obtained with the thermo-kinetic simulation are taken as input parameters to the thermo-mechanical simulation. They drive thermal expansion and chemical shrinkage and influence the viscoelastic behavior as described in section 2. The same FE mesh is used as in the thermo-kinetic simulation, so the data is directly transferred at each integration point. The presence of the mold is simulated by a frictionless contact at the top and bottom surface that allows the plate to contract through the thickness but not to expand with respect to its initial state. On the lateral surfaces of the plate, no contact conditions are applied, as there is a small space between the composite and the mold frame. During the curing process, this space is filled with resin at the injection pressure. Therefore, this pressure is applied to the sides of the plate.

4.2. Modeling the influence of the resin injection pressure

During the curing phase, the resin injection continues at a high pressure in order to compensate a part of the volume loss due to chemical shrinkage and maintain the consolidation pressure in the mold to ensure desorption of gas bubbles until the resin is sufficiently polymerized. The effect of this ongoing injection is modeled in the same way as the chemical shrinkage, as it leads to an increase of the resin

volume in the composite, while chemical shrinkage leads to a volume loss. An additional strain $\underline{\varepsilon}^{pr}$ is therefore added to Eq. (5) accounting for this volume increase. It follows the evolution given in Eq. (6) and (7) but is driven by the injected resin quantity instead of temperature for $\underline{\varepsilon}^{th}$ or degree of cure for $\underline{\varepsilon}^{ch}$. The expansion coefficient that translates its effect on the composite level is obtained by homogenization in the same way as the CCS of the composite, taking zero expansion for the fibers and the relative volume change for the resin.

The injected resin quantity is unknown and driven by the injection pressure. Therefore, this quantity is added as an additional degree of freedom to the FE problem. The associated residual for the global Newton-Raphson algorithm is the difference between the internal pressure in the mold (the volume average of the trace of the stress tensor) and the applied injection pressure. If the resin is liquid with negligible viscosity, it can flow everywhere in the composite and the equilibrium between pressure in the mold and injection pressure is reached immediately. However, the viscosity of the resin increases with degree of cure, which after the gel point becomes a viscoelastic solid. This transition is taken into account in the viscoelastic model by a Maxwell element with a relaxation τ_{gel} that increases exponentially with the degree of cure:

$$\tau_{gel} = t_{load} \exp(a + bc) \tag{10}$$

This leads to an apparent relaxed shear modulus that increases with the degree of cure as shown in Figure 2. This evolution is close to the one observed experimentally by [2] on a different epoxy resin. t_{load} corresponds to the loading time at which the apparent relaxed shear modulus is measured.

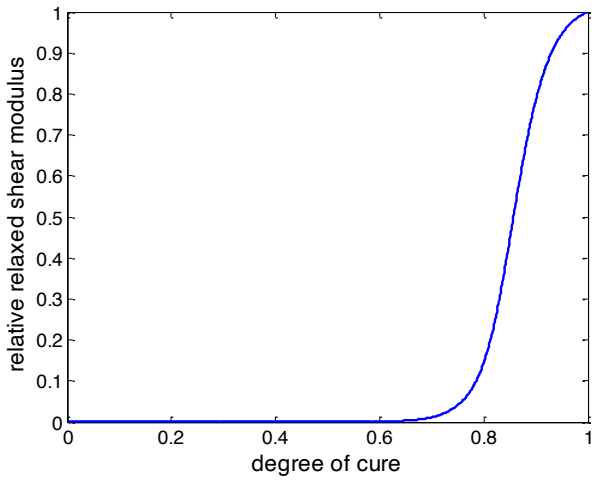


Figure 2. Evolution of the ratio between the relaxed shear modulus as a function of cure and its value for the fully cured resin.

The influence of the resin viscosity on the injection pressure transmission is taken into account by a residual that ensures that relative volume change of the resin in the mold is given by

$$\frac{\dot{V}}{V} = \frac{1}{\eta}\left(P^{ext} - P^{int}\right) \tag{10}$$

where η is the viscosity of the resin, P^{ext} the applied resin injection pressure and P^{int} the pressure in the mold. The resin viscosity is taken from the viscoelastic model, using for each Maxwell element the product of its shear modulus with the temperature and cure dependent relaxation time.

5. Results

The evolution of the out-of-plane stress in the composite plate throughout the curing process obtained with the presented simulation strategy is shown in Figure 3a. In Figure 3b, the out-of-plane stress is plotted against the degree of cure. Comparison with the temperature cycle presented in Figure 1 shows that during the first dwell at 160°C when the resin viscosity is still very low, the out-of-plane stress corresponds to the imposed injection pressure. Towards the end of the 160°C dwell, when the degree of cure exceeds about 60%, the relaxed stiffness of the resin starts to increase (see Figure 2) and thus the chemical shrinkage is no longer immediately compensated. This leads to a small decrease in pressure towards the end of the first dwell (between 60% and 70% of cure, see Figure 3b). During the heating phase up to 180°C, the out-of-plane stress increases due to the thermal expansion of the resin. When the 2nd dwell temperature is reached, the pressure starts to decrease immediately, as at this point the resin viscosity is already significant (about 84%, see Figure 3b), and the chemical shrinkage can no longer be compensated by the resin injection. With the present model for the resin viscosity, the out-of-plane stress drops to zero at a degree of cure of about 91%.

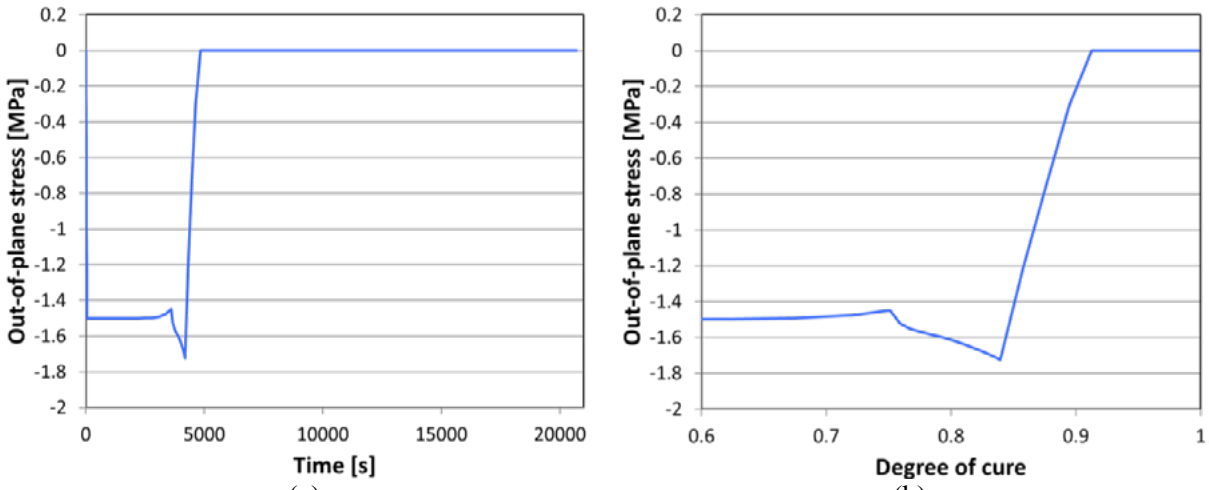


Figure 3. Evolution of the out of plane stress during the curing process of a composite plate as a function of time (a) and plotted against the degree of cure (b).

6. Conclusions

The presented multi-scale modeling strategy takes into account the couplings between the different physical phenomena involved in the generation of residual stresses in polymer matrix composites. With the presented homogenization strategies, the temperature- and cure-dependent material properties can be determined from the constituent behaviors. Due to the viscoelastic nature of the matrix, time-dependent expansion coefficients have to be used for the homogenized behavior of the composite. The ongoing resin injection during the curing phase that compensates part of the chemical shrinkage in order to avoid an early pressure drop is modeled by an expansion coefficient in the same way as the volume loss due to chemical shrinkage, but with an opposite sign. In the present model, this method supposes that the injected resin is distributed homogeneously through the whole composite. Especially in bigger parts, this assumption is in general not true. In these cases, the resin flow during injection has to be modeled beforehand, taking into account the increasing viscosity during the curing process and the permeability of the fibrous reinforcement. The resulting distribution of resin in the reinforcement can be used as heterogeneous input parameter with the presented model in the same way as the temperature and degree of cure obtained with the thermo-kinetic simulation are used for the thermal expansion and the chemical shrinkage in the thermo-mechanical simulation.

The presented test case of a thin flat plate is very simple and avoids most of the heterogeneities. Future work will consist in application of the presented modeling chain to more complex structures, with heterogeneous temperatures (either due to an inhomogeneous heating or overheating caused by the exothermal polymerization), heterogeneous material properties (various reinforcement architectures in one part) and more realistic boundary conditions. In particular, the thermal and mechanical deformation of the mold and the friction and adhesion between part and mold must be taken into account. Furthermore, the small space between the reinforcement and the mold frame is filled with resin and thus more realistically modeled by a thin resin layer around the composite. If these different aspects are correctly taken into account, the proposed modeling chain is able to predict both the evolution of the pressure in the composite during the curing process and the generation of residual stresses and their impact on the final part shape.

Acknowledgments
The research presented in this paper was funded by the Safran Group, France.

References

[1] M.R. Kamal, S. Sourour. Differential scanning calorimetry of epoxy cure: Isothermal cure kinetics. *Thermichimica Acta*, 14:41-59, 1976.
[2] D.J. O'Brien, P.T. Mather, S.R. White. Viscoelastic properties of an epoxy resin during cure. *Journal of Composite Materials*, 35(10):883-904, 2001.
[3] M. Zarrelli, A.A. Skordos, I.K. Patridge. Toward a constitutive model for cure-dependent modulus of a high temperature epoxy during cure. *European Polymer Journal*, 46:1705-1712, 2010.
[4] A. Courtois, M. Hirsekorn, M. Benavente, A. Jaillon, L. Marcin, E. Ruiz, M. Lévesque. Viscoelastic behavior of an epoxy resin during cure below the glass transition temperature: Characterization and modeling. *Journal of Composite Materials*, 53(2): 155-171, 2018.
[5] C. Pupin, A. Ross, C. Dubois, J.-C. Rietsch, N. Vernet, E. Ruiz. Formation and suppression of volatile-induced porosities in an RTM epoxy resin. *Composites: Part A*, 94:146-157, 2017.
[6] A. Trofimov, C. Tuloup, J. Le Pavic, C. Ravey, D. Therriault, M. Lévesque. Multi-scale modeling of process-induced pressure distribution inside 3D woven composites manufactured using Resin Transfer Molding. *Composites: Part A*, 165:107307, 2023.
[7] M. Hirsekorn, L. Marcin, T. Godon. Multi-scale modeling of the viscoelastic behavior of 3D woven composites. *Composites Part A*, 112:539-548, 2018.
[8] M. Hirsekorn; L. Marcin, T. Godon. Thermo-viscoelastic homogenization of 3D woven composites with time-dependent expansion coefficients. *International Journal of Solids and Structures*, 244-245:111569, 2022.
[9] Y. Eom, L. Boogh, V. Michaud, P. Sunderland, J.-A. Månson. Time-cure-temperature superposition for the prediction of instantaneous viscoelastic properties during cure. *Polymer Engineering and Science*, 40:1281-1292, 2000.
[10] H. Pettermann, A. DeSimone. An anisotropic linear thermo-viscoelastic constitutive law: Elastic relaxation and thermal expansion creep in the time domain. *Mechanics of Time-Dependent Materials*, 22:421-433, 2018.
[11] S.W. Park, R.A. Schapery. Methods of interconverion between linear viscoelastic material functions. Part I – a numerical method based on Prony series. *International Journal of Solids and Structures*, 36:1653-1675, 1999.
[12] Z-set – Non-linear material & structure analysis suite. http://www.zset-software.com/
[13] M. Benavente, L. Marcin, A. Courtois, M. Lévesque, E. Ruiz. Viscoelastic distortion in asymmetric plates during post curing. *Composites Part A*, 103:122-130, 2017.
[14] M. Benavente, L. Marcin, A. Courtois, M. Lévesque, E. Ruiz. Numerical analysis of viscoelastic process-induced residual distortions during manufacturing and post-curing. *Composites Part A*, 107:205-216, 2018.

The investigation of double impact positions on impact behavior of composite sandwich structure

Keyu Zhu, Xitao Zheng and Leilei Yan*

School of Aeronautics, Northwestern Polytechnical University, Xi'an 710072, China
*Email: yanleilei@nwpu.edu.cn https://www.nwpu.edu.cn/

Keywords: Composite sandwich, impact damage, double impact position, damage mechanism

Abstract
Composite structure sandwich are widely used in the aerospace industry due to their excellent in-plane mechanical properties. However, its face sheet exhibit poor delamination resistance subjected to impact, due to the lack of reinforcement in the through thickness. Besides, composite sandwich structure are often subjected to multiple impacts, and such impacts generally occur at certain distance from each other. Therefore, the impact behavior and CAI strength of composite sandwich structure considering different impact positions were investigated and studied. After each impact, non-destruction inspection (NDI) C-scans and scanning electron microscope (SEM) were performed to assess damage status and internal defects. The comparisons between repeated impact events in terms of impact history, absorbed energy history, contact duration and the delamination damage projected area (DDPA) were studied. The results show that there existed a obvious interference relationship between the first and second impact events. Moreover, the impact energy and bending stiffness at different impact position will also affect impact performance

1. Introduction

Composite sandwich structure attracted an increasing attention in automotive industry, aeronautics and astronautics due to excellent mechanical properties [1][2], such as lightweight, high specific stiffness and strength. However, its composite face sheet exhibited weak transverse load-bearing capacity, which was sensitive to low velocity impact [3]. The impact damage might cause internal damage without visible sign, resulting in the reduction of mechanical properties. Therefore, the dynamic mechanical responses of composite sandwich structure were wisely studied and discussed [4]. It was deserved to be noted that the composite structures usually experienced complex loading conditions such as being subjected to various impact events [5][6]. Some evidences exhibited that there was an overlapping state in damage regions on the double impact positions [7]. Moreover, the accumulation of repeated impact event with low impact energy might erode the mechanical properties, but a single impact did not [8]. Therefore, assessing the dynamic responses of composite laminate with double impact positions was very important and meaningful.

In recent years, some research had been conducted for composite laminate after being subjected to different impact events [9][10]. For instance, Atas et al. [11] conducted an experimental study the effect of various thickness on the repeated impact response of woven E-glass/epoxy composites. Kashani et al. [12] compared the impact responses of fiber metal laminates under the single impact and two divided impacts. It indicated that different impact energy and impact sequence have great influence on impact response. Li et al. [13] revealed the dynamic behavior of aluminium and composite layers as well as their interfaces considering four different impact angles. In fact, multi-impacts always occurred at the different position and had a certain distance from each other. Zhou et al. [14] investigated the mechanical responses of composite at double position subjected to low velocity impact. The results shown that the critical separation distance between the two impacts had different characteristic under different impact energy levels. Besides, Liao et al. [15] discussed the effect of Z-pinning technology on the impact

behaviors of composite laminates under double impact positions. It indicated that such technology could suppress the internal defects and delamination damage by weakening the damage interference at high impact energy. However, those studies on double-position impact behavior [16], but the effect of multiple impact damage on the compression after impact (CAI) strength was still lack of studies. Besides, the mechanism of influence between the multiple-impact is not clear.

Therefore, the impact responses and damage mechanism of the composite sandwich structure considering different impact positions were investigated. Besides, the delamination damage projected area (DDPA) and failure modes were measured and observed after each impact. Typical mechanical characteristic such as maximum impact force and displacement was compared to reveal the interference level between multiple impacts.

2. Material and preparation

Composite sandwich structure considering corrugated core and polymethacryimide (PMI) foam core were considered, and the schematic diagram was shown in Figure 1. The composite face sheet and corrugated core were fabricated using T700/9A16 unidirectional prepreg, and the face sheet and core were assembled using an adhesive film GXA120.

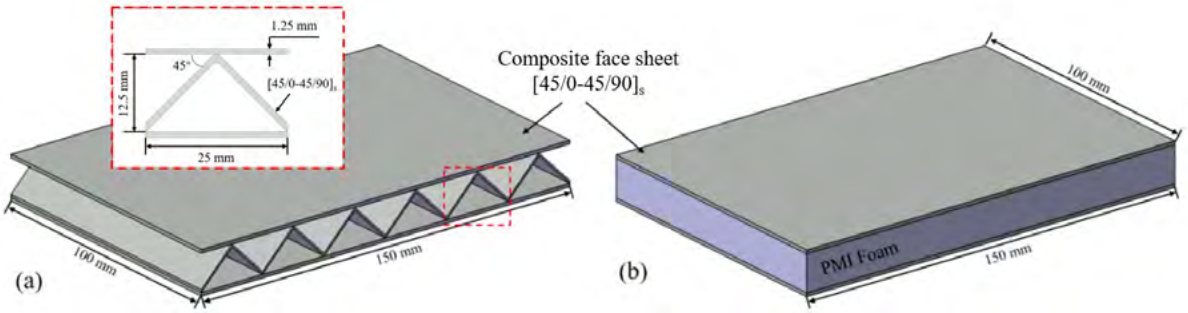


Figure 1. The schematic diagram of specimens. (a) Composite corrugated sandwich structure; (b) Composite PMI foam sandwich structure.

The double impact test of composite sandwich structure was conducted according to ASTM D7136 using Instron Dynatup 9350 HV Impact Testing Machine. The double impact test strategy for specimens was shown in Figure 2. The drop-point of impactor in machine is fixed, a modified fixture was designed as shown in Figure 3(a). Besides, after double impact, the CAI tests were carried out te assess the residual compressive properties of composite sandwich structure based on ASTM D7137, as shown in Figure 3(b). The impact test matrix was summarized in Table 1.

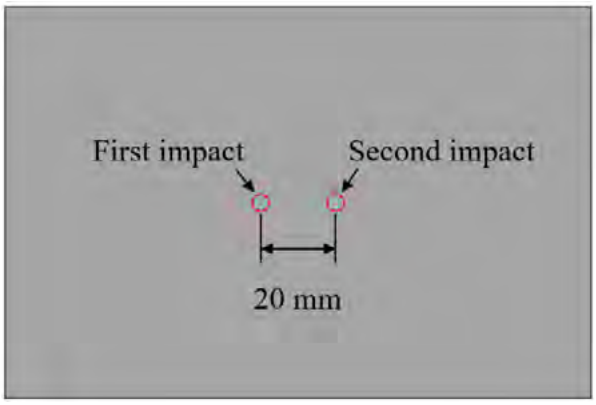


Figure 2. The double impact test strategy for specimens.

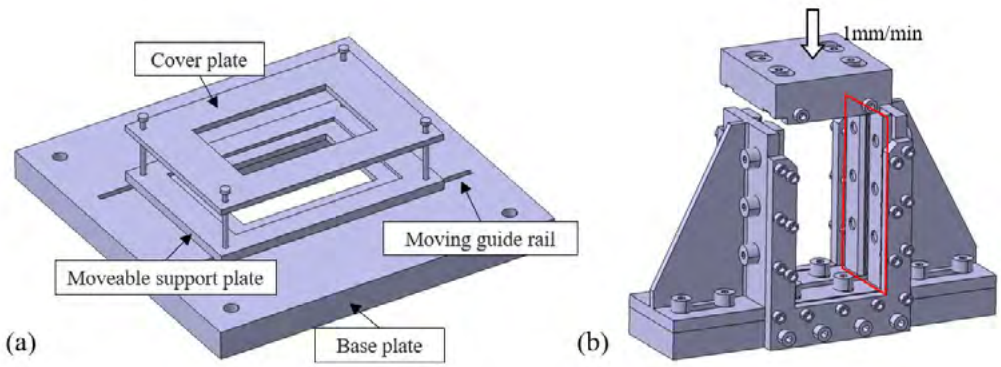


Figure 3. The experimental fixture. (a)Modified fixture suitable for double impact test; (b) The CAI fixture.

Table 1. The impact test matrix.

Specimen ID	Core material	Impact sequcen	Impact energy (J)
C-5J	Corrugated core	First	5
CS-5J	Corrugated core	Second	5
F-5J	Foam core	First	5
FS-5J	Foam core	Second	5
C-5J	Corrugated core	First	10
CS-5J	Corrugated core	Second	10
F-5J	Foam core	First	10
FS-5J	Foam core	Second	10

3. Results and discussion

3.1. Impact response

Figure 4 illustrated the impact responses of the composite corregated sandwich structure and composite foam sandwich structure at impact energies of 5 J and 10 J. It can be found that the impact responses of the first and second impact events for composite foam sandwich structure are in good agreement when impact energy is 5 J. For high impact energy case (10 J), then there is a slight deviation, but the maximum impact load, maximum impact displacement and absorbed energy are basically the same. Therefore, it can be considered as two separate impact event, and the first impact event has basically no influence on the second impact event.

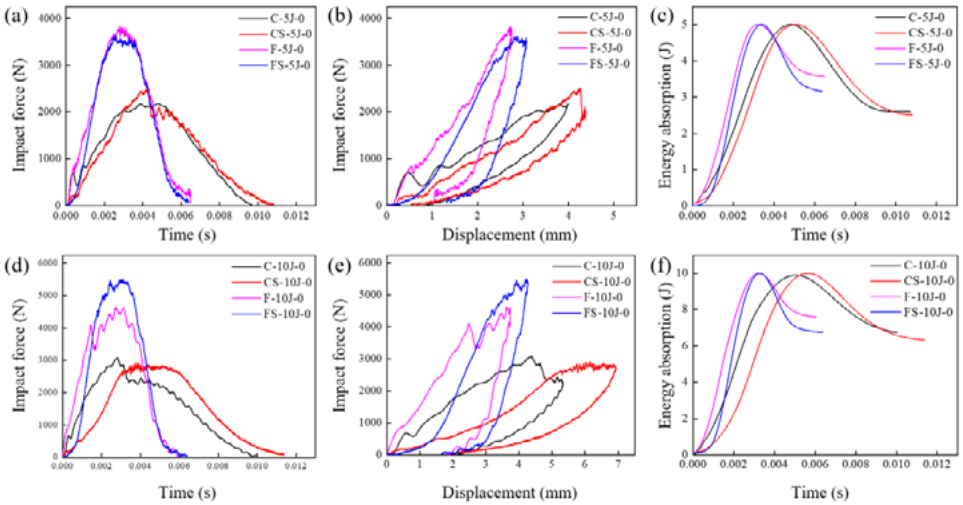


Figure 4. impact responses of the composite corregated sandwich structure and composite foam sandwich structure.

For composite corrugated sandwich structure, the impact response curve of second impact event starts smooth, and its maximum displacement is larger than that of the first impact event. The reason is that impact of the first impact event influenced the second impact event due to the reduction of bending stiffness. Besidesm the impact response curve of the first impact event at 5 J and 10 J did not decrease at the beginning of the curve, i.e., there is no fiber breakage. For second impact event at 10 J, the moment of impact load drop is slightly later than the first impact point. In a word, the first impact event could influence the impact response of the second impact event for composite sandwich structure when distance between impact position is 20 mm, and similar conclusion is not suitable for composite foam sandwich structure.

DDPA was normally regarded as an influential factor for evaluating resistance to impact damage, as shown in Figure 5. It could be observed that larger DDPA appeared for higher impact energy. The delaminate area of C-10J was 298.72 mm^2, and the two impact damage regions of CS-5J were still separate (i.e., non-interfering state). Then, for higher impact energy case, the two impact damage regions of CS-10J increased and overlapped (i.e., interfering state). Figure 6 illustrated the scanning electron microscope (SEM) results of C-10J and CS-10J at the impact point. It can be seen that fiber breakage and matrix cracking existed around the impact point.

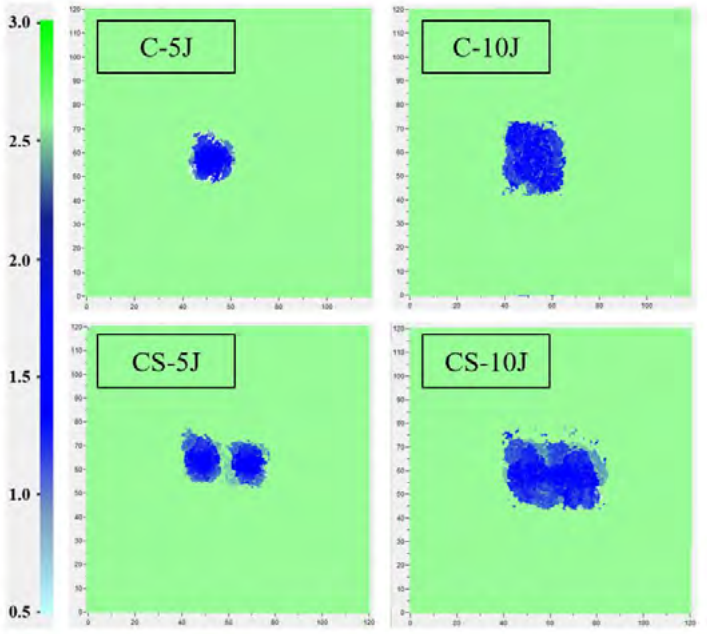


Figure 5. Ultrasonic C-scan damage of damaged laminates.

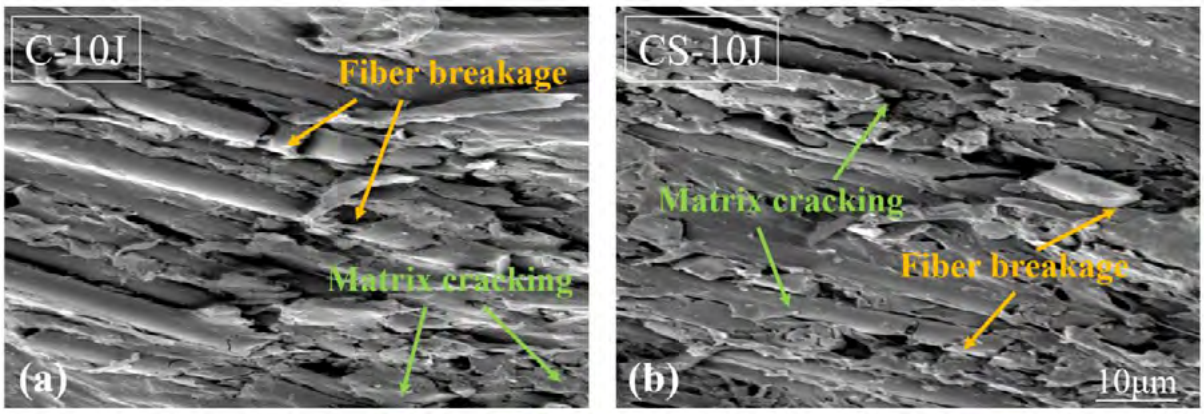


Figure 6. Scanning electron microscope (SEM) results of C-10J and CS-10J at the impact point.

3.2. Discussion of CAI strength

The CAI strength of composite corrugated sandwich structure and composite foam sandwich structure was shown in Figure 7. It can be seen that higher impact energy result in lower CAI strength, and the CAI strength of composite foam sandwich structure was larger than that of composite corrugated sandwich structure. The reason was that foam core provided stronger interface properties.

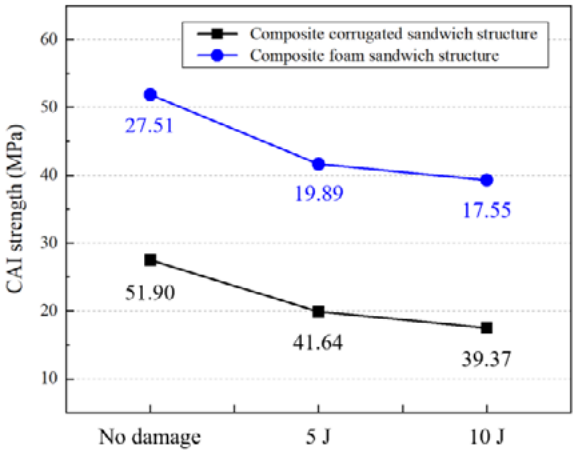


Figure 7. The CAI strength of composite corrugated sandwich structure and composite foam sandwich structure.

4. Conclusions

In this paper, the impact responses and damage mechanism of the composite sandwich structure considering different impact positions were investigated. The conclusions are shown as follows:

(1) For composite foam sandwich structure, it can be considered as two separate impact event, and the first impact event has basically no influence on the second impact event for all impact energy cases.

(2) Two impact damage regions composite corrugated sandwich structure of at 10 J impact energy increased and overlapped (i.e., interfering state), compared with 5 J impact case.

(3) The higher impact energy result in lower CAI strength, and the CAI strength of composite foam sandwich structure was larger than that of composite corrugated sandwich structure. The reason was that foam core provided stronger interface properties.

Acknowledgments

This work was supported by the National Key R&D Program of China (2023YFB3709603, 2023YFB3709602), National Natural Science Foundation of China (12372141), the Key R&D Program in Shaanxi Province (2024GH-ZDXM-27).

References

[1] J. Peng, Y. Qian, C. Liu. Low-velocity impact and compression after impact behavior of 3D integrated woven spacer composites. Thin-Walled Structures, 2022, 177: 109450.
[2] S. Ahmed, X.T. Zheng, L.L. Yan, et al. Influence of asymmetric hybridization on impact response of 3D orthogonal woven composites. Composites Science and Technology, 2020, 199: 108326.
[3] K.Y. Zhu, X.T. Zheng, C. Zhang, et al. Compressive response and energy absorption of all-composite sandwich panels with channel cores. Composite Structures, 2022, 289: 115461.
[4] B.L. Sy, Z. Fawaz, H. Bougherara. Damage evolution in unidirectional and cross-ply flax/epoxy laminates subjected to low velocity impact loading. Composites Part A: Applied Science and Manufacturing, 2018, 112: 452-467.
[5] M. Rezasefat, A. Gonzalez-Jimenez, M. Giglio, et al. Numerical study on the dynamic progressive failure due to low-velocity repeated impacts in thin CFRP laminated composite plates. Thin-Walled Structures, 2021, 167: 108220.
[6] W.B. Xie, W. Zhang, H.B. Yang, et al. Experimental investigation of high velocity impact response of CFRP laminates subjected to flyer plate impact. Thin-Walled Structures, 2022, 178: 109521.

[7] B.B. Liao, J.W. Zhou, Y. Li, et al. Damage accumulation mechanism of composite laminates subjected to repeated low velocity impacts. International Journal of Mechanical Sciences, 2020, 182: 105783.
[8] S. Tian, Z.G. Zhou. New criteria for simulating failure under multiple impacts of the same total energy on glass fiber reinforced aluminum alloy laminates. Materials & Design, 2016, 102: 142-150.
[9] S.H. Abo Sabah, A.B.H. Kueh, N.M. Bunnori. Failure mode maps of bio-inspired sandwich beams under repeated low-velocity impact. Composites Science and Technology, 2019, 182: 107785.
[10] X.Y. Zhu, X.Q. Fu, L.L. Liu, et al. Damage mechanism of composite laminates under multiple ice impacts at high velocity. International Journal of Impact Engineering, 2020, 168: 104296.
[11] C. Atas, B.M. Icten, M. Küçük. Thickness effect on repeated impact response of woven fabric composite plates. Composites Part B: Engineering, 2013, 49: 80-85.
[12] M.H. Kashani, M. Sadighi, A. Lalehpour, et al. The effect of impact energy division over repeated low-velocity impact on fiber metal laminates. Journal of Composite Materials, 2015, 49(6): 635-646.
[13] L.J. Li, L.Y. Sun, T.K. Wang, et al. Repeated low-velocity impact response and damage mechanism of glass fiber aluminium laminates. Aerospace Science and Technology, 2019, 84: 995-1010.
[14] J.W. Zhou, B.B Liao, Y.Y. Shi, et al. Experimental investigation of the double impact position effect on the mechanical behavior of low-velocity impact in CFRP laminates. Composites Part B: Engineering, 2020, 193: 108020.
[15] B.B. Liao, Z.W. Zhang, L.P. Sun, et al. Experimental investigation on the double-position impact responses and damage mechanism for Z-pinned composite laminates. Composite Structures, 2021, 259: 113463.
[16] R.S. Dhari. A numerical study on cross ply laminates subjected to stray fragments impact loading. Composite Structures, 2021, 261: 113563.

FLEXURAL RESPONSE OF REAL WOVEN COMPOSITE ENABLED VIA XCT-DRIVEN FINITE ELEMENT MODELING

Kamran A. Khan[1,2]*, Adnan Ahmed[3], Israr Ud Din[4]

[1]Department of Aerospace Engineering, Khalifa University of Science and Technology, Abu Dhabi, PO Box 127788, United, Arab Emirates
[2]Advanced Research and Innovation Center (ARIC), Khalifa University of Science and Technology, Abu Dhabi, 127788, United Arab Emirates
Email: *kamran.khan@ku.ac.ae
[3]Department of Aerospace Engineering, Khalifa University of Science and Technology, Abu Dhabi, PO Box 127788, United, Arab Emirates
Email: adnan.ahmed@ku.ac.ae
[4]Department of Aerospace Engineering, Khalifa University of Science and Technology, Abu Dhabi, PO Box 127788, United, Arab Emirates
Email: israr.uddin@ku.ac.ae

Keywords: Deployable folding structures, X-ray micro computed tomography (XCT), real representative volume element (RVE), FE modeling, flexure.

Abstract
In this work, X-ray micro computed tomography (XCT) based 3D model of the flexible region is developed which is composed of a single-layer plain-weave glass fiber reinforced elastomer. A representative unit cell called as representative volume element (RVE) of the flexible region was modelled by supervised segmentation of the XCT image stacks into 3D voxels associated to fibers having anisotropy and local orientation and isotropic matrix i.e. elastomer. Owing to the fact that there exist fibers' undulating patterns and also the material properties of both the fibers and the matrix are substantially different, therefore, it is expected that the bending response utilizing the real RVE will provide a more reliable bending-curvature response. The bending stiffness of the real RVE was determined and compared with the bending response of homogenized elastomer laminate using ABAQUS®. Quasi-static bending analysis for small strains was conducted in ABAQUS®, utilizing the linear elastic properties of constituent materials. It is concluded that a significant contrast was found in the bending stiffness obtained with the two approaches using real RVE and homogenized RVE during bending of the flexible region in the deployable folding structure.

1. Introduction

Foldable structures are increasingly utilized across industries such as space exploration, civil architecture, robotics, biomedical engineering, and biomimetic engineering [1–3]. Traditional metallic joints in foldable structures are susceptible to plastic deformation, prompting the exploration of jointless folding structures using rigid parts and elastic hinges. Fiber-reinforced polymer composites (FRPCs) offer a promising alternative, with several proposed composite folding structures showcasing novel materials, architectures, and fabrication techniques [4,5].

Designing these structures requires optimization in the design phase, which is challenging due to the difficulty in experimentally determining structural-level elastic constants. Morever, for thin laminates made of single layer of woven fabric, due to the complex undulating patterns of the fibers and substantial differences in material properties between the fibers and the matrix, the real micro-model of the laminate is expected to provide a more accurate bending-curvature response. Non-destructive techniques such as micro-CT (μCT) offer detailed examination capabilities for a wide range of engineering materials,

facilitating the development of voxel-based models for mesh generation and material property assignment since mechanical characterization and determination of elastic constants are time-consuming and challenging. A real 3D voxel based model of thin FRPCs laminates can be used to compute the bending stiffness for the finite element (FE) modeling. Recently, a generic XCT-driven virtual characterization framework was proposed by Ahmed et al. [6] capable to perform homogenization and predict the elastic properties of all the multi-material regions of a FRPC laminate to define the complete stiffness matrix required for the structure-level linear elastic FE modeling.

In this study, a 3D model of the flexible region is developed using X-ray micro computed tomography (XCT). This region comprises a single-layer plain-weave glass fiber reinforced elastomer laminate. The XCT image stacks are segmented into 3D voxels to distinguish fibers, which exhibit anisotropy and local orientation, from the isotropic matrix, which is the elastomer. This segmentation process facilitates the creation of a representative unit cell, known as the representative volume element (RVE). The Voxel model RVE for the elastomer laminate is developed using VoxTex®. The bending stiffness of the real RVE is determined by applying a moment on one side while imposing periodic boundary conditions (PBCs) and symmetry boundary conditions (BCs) on the remaining three sides of the 3D RVE model in the finite element (FE) software ABAQUS®. For comparison, RVE models of homogenized elastomer laminate, meshed with 3D solid FE element C3D8R in ABAQUS®, are also subjected to bending under the same curvature values. A quasi-static bending analysis for small strains is conducted in ABAQUS®, utilizing the linear elastic properties of the constituent materials.

2. Fabrication and Micro-CT

2.1. Fabrication of flexure member and its constituent laminates

To fabricate the elastomer laminate (flexible region), a dry woven glass fabric (GURIT® RE210D) has been infused with a silicone-based elastomer (Smooth SIL™ 936). Smooth SIL™ 936 is a two-part elastomer so appropriate quantitites (10A:1B) as recommended by the manufacturere of both the parts were mixed and poured into the mold followed by degassing for 10 min to remove any trapped bubbles (see **Figure 1**). For manufacturing of the stiff region made-up of the hybrid laminate, a 2×2 balanced twill weave glass/epoxy prepreg known as Hexply® M26 patches was stacked on the dry fabric and cured in hot press as illustrated in **Figure 1.** During the compression molding, a pressure of 2 bar was applied for a duration of 1.5 h at 124ºC . The elastomer mixture was poured on the dry fabric and then left to cure at room temperature for 24 h. The samples were cut in sizes of 200 mm × 20 mm, and 30 mm × 20 mm for µCT imaging. For the fold member, a large sized fabric is taken where the prepregs are placed with a gap which is filled with the elastomer achieving uniform thickness of 0.4 mm following the same technique as for the constituent laminates resulting in a complete flexure member ready for testing (**Figure 1)**.

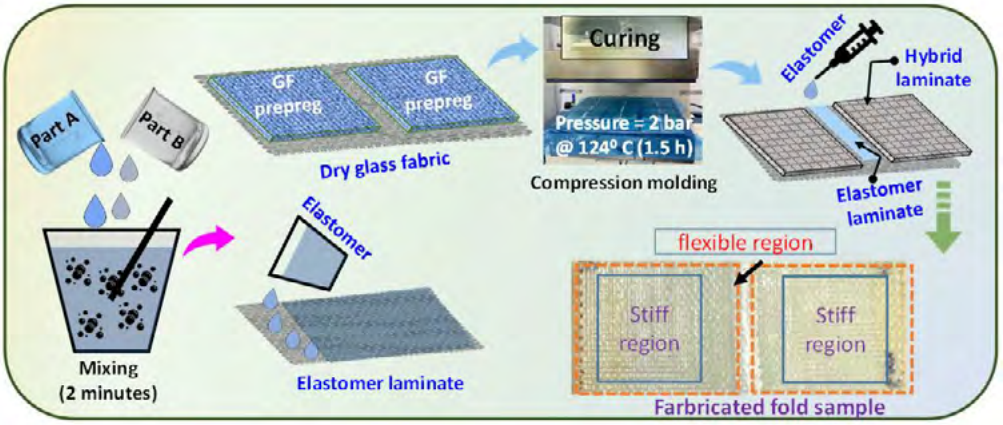


Figure 1 Preperation of elastomer, elastomer laminate and hybrid laminate for XCT and folding experiment.

2.2. Micro-CT assisted virtual characterization

A General Electric (GE) Phoenix Nantom® M X-ray computed tomography (XCT) machine (high-power nano-focus tube with a tungsten target, max capacity 180kV/15W) was used to scan the fabricated thin laminated samples. All the radiographic projections of the two different materials systems were performed with a tube voltage of 120 kV and current of 230 µA. A rotation angle step of $0.36^0/step$ was also provided as a user input to the XCT equipment which was used for the complete 360º radiographic projections of the samples mounted on the rotating platform. For glass fiber reinforced polymers (GFRPs), the recommended resolution is 4 µm [7] which was used to scan all of the samples.

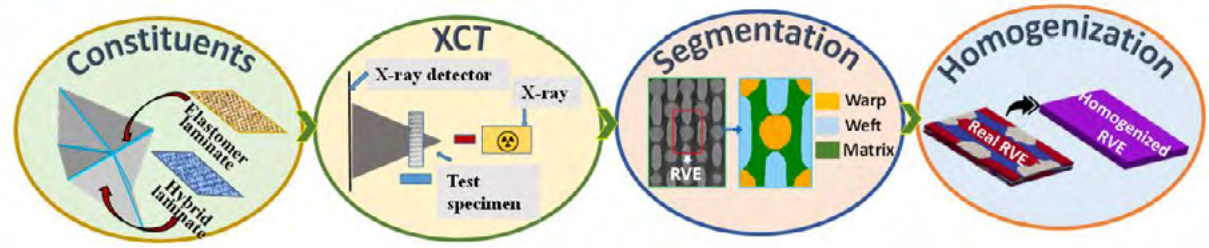


Figure 2 Micro-CT driven virtual characterization for computing homogenized properties of thin laminates

The 3D model and scanned images acquired from the XCT machines provide a digital representation of the actual geometry of the laminate. VoxTex is used for segmentation where a supervised learning technique (a class of machine learning technique) is employed to segment the FRPC laminate into the warp, weft and matrix. It starts with a manual selection of 3D sub-domains from the images provided serving as training sets for the matrix, warp, and weft. The voxel size was set to 16 µm or 4 pixels of 4 µm each as recommended. Segmentation of RVE into different constituents was performed based on a feature vector denoted by f (AGV, β, Phi), where AGV represents average gray value (or density), β signifies anisotropy, and Phi denotes fiber orientation angle. Anisotropy (β) is computed from the eigenvalues of the structure tensor (S), calculated from gradients of the image intensity in a 3D space.

The tensor $\boldsymbol{S}$ is computed from the gradients of the image intensity i.e. $\partial I/\partial x_i$ in a 3D image, $I = (x_1, x_2, x_3)$[7].

$$S_{ij} = \int_W \frac{\partial I}{\partial x_i}\frac{\partial I}{\partial x_j} dv \tag{1}$$

Where (W) is the window size of integration in a 3-dimensional (3D) space. The anisotropy (β) is calculated from the eigenvalues $\lambda_1 \leq \lambda_2 \leq \lambda_3$ of the tensor $\boldsymbol{S}$ and represented as:

$$\beta = \begin{cases} 1 - \dfrac{\lambda_1}{\lambda_3}, \lambda_3 > 0 \\ 0, \lambda_3 = 0 \end{cases} \tag{2}$$

The effective stiffness tensor $[C_{eff}]$ is calculated as:

$$C_{eff} = \sum_{i=1}^{N} w_i [T_i]^T [C_i][T_i] \tag{3}$$

Where w_i is the volume fraction of the i^{th} voxel in the RVE, N is the total number of voxels whereas C_i stands for the stiffness matrix of i^{th} voxel. $[T_i]$ is the transformation matrix used for transforming the local material coordinate system to the global RVE coordinate system. **Figure 2** shows the process of virtual characterization staring from X-ray scanning of constituent laminates to obtain the real and

homogenized RVE. The real RVE model can be imported in any commercial FEA software for futher analysis. In addition, Voxtex® also provides the homogenized elastic constants obtained through orientational averaging of properties of all the voxels in the model. The Chamis model is used for finding the elastic constants of each voxel pertaining to the yarns for which the elastic constants of each constituents are needed. The elastic constants of the glass fiber, epoxy and elastomer used to compute the homogenized elastic constants are given in **Table 1.**

Table 1 Material properties for the constituent materials

Material	**Young's modulus *(E)***	**Poisson's ratio (ν)**
E-glass fiber	72.45 (GPa)	0.22
Epoxy	3.50 (GPa)	0.35
Smooth SIL936	0.80 (MPa)	0.49

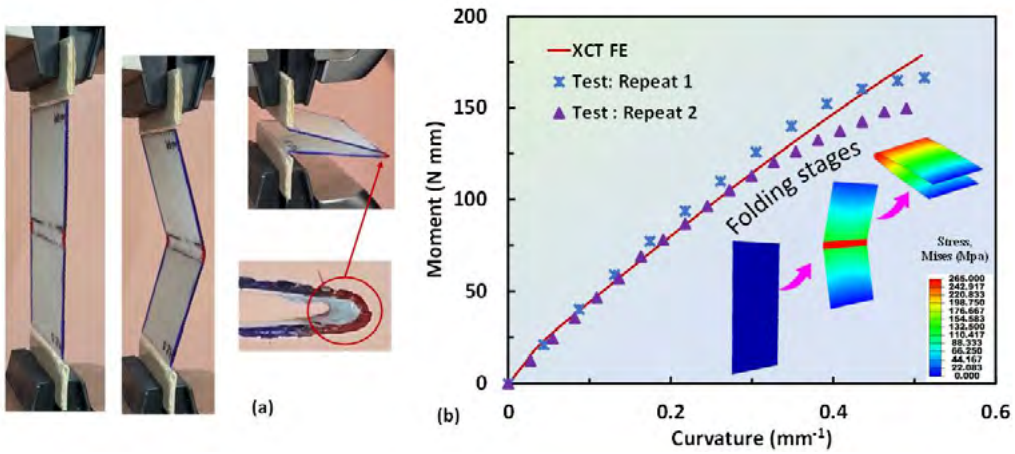


Figure 3 (a) Experimental setup and testing of a fold, (b) Comparsion of test and simulation results for moment vs. curvature of the fold

The bending stiffness matrices computed using the homogenized properties [6] and laminate thickness of the hybrid laminate (stiff laminate) and the elastomer laminate (flexible region) based on the classical laminate theory (CLT) are as follows:

$$D^{hy} = \begin{bmatrix} 129.721 & 20.211 & 0 \\ 20.211 & 155.469 & 0 \\ 0 & 0 & 27.306 \end{bmatrix} \text{N mm and } D^{el} = \begin{bmatrix} 8.689 & 1.273 & 0 \\ 1.273 & 9.786 & 0 \\ 0 & 0 & 0.131 \end{bmatrix} \text{N mm}$$

Where D_{ij}^{hy} is the the bending stiffness of the hybrid laminate and D_{ij}^{el} is the bending stiffness of the elastomer laminte in the flexible region. The bending test and a FE simulation has been perfomed for the fold using the the homogenized elastic constans of the contituents laminates as inputs and the moment vs. curvature results are compared as shown in **Figure 3 (b)** [8]. It can be seen that the FE results obtained using the homogenized properties of the thin laminates are in good agreement with the experimental results.

3. Real RVE

In the previous section, we demonstrated how XCT can be used to develop a voxel based real RVE of any FRPC laminate and to compute the homogenized elastic constants. The bending stiffness of the thin elastomer laminate presented in the previous section is computed from the homogenized inplane elastic constants which may be different from the real bending response due to the intricate undulating patterns of the fibers and the significant material property variations within both the fibers and the matrix. In this section, the real RVE model is used for computing the bending stiffness of the present single-layer

elastomer laminate. To compare bending stiffness obtained through different approaches, RVE models, i.e. homogenized elastomer laminate (HEL) and real RVE-based elastomer laminate (REL) were modeled in ABAQUS and subjected to bending up to the same curvature, achieved by applying an appropriate moment.

Periodic boundary conditions (PBCs) and symmetry BCs were applied to the three sides of the model, while a moment was applied to the fourth side [9] . The FE models displayed in **Figure 4**, measuring 2.128 mm × 1.6 mm × 0.4 mm, were meshed with C3D8R solid elements, with each side measuring 0.016 mm for REL and 0.32 mm for ELP models. Quasi-static bending analysis for small strains was conducted in ABAQUS®, utilizing the linear elastic properties of constituent materials.

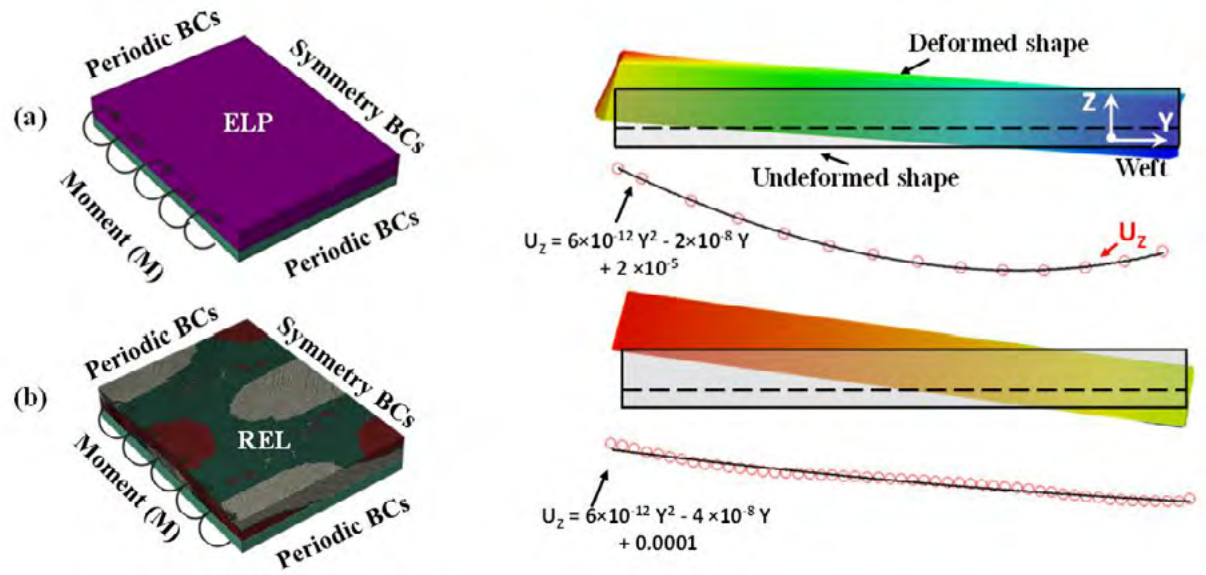


Figure 4: RVE models and the curvatures, (a) homogenized elastomer laminate plus elastomer (HEL) and (b) real RVE based elastomer laminate (REL).

Notably, when HEL is used within the flexible region, the viscoelastic effects from the pure elastomer layer become inconsequential due to the overwhelming dominance of the fabric laminate layer and therefore not discussed here in detail.

Table 2 compares the bending stiffness computed based on the three approaches. It was anticipated that the real RVE model would offer more accurate bending stiffness compared to the other two FE models. However, due to non-uniform curvature associated with local fiber undulation in the plain-weave fabric, the curvature was found to be non-uniform, leading to a highly underestimated bending stiffness. As a result, employing homogenized properties of the elastomer laminate provides a better option for modeling woven fabric thin laminates established through previous studies on XCT-assisted virtual characterization and FE modeling of thin laminates [6,8].

Table 2 Calculation of bending stifness of elastomer lamiante using various methods.

Bending stiffness (N mm)	CLT	Homogenous FE Model	Real RVE FE Model
D_{11}	8.689	8.621	0.392

4. Conclusions

An XCT driven FE model of a real RVE of an elastomer laminate is developed and analysed for its flexural response. The FE model incorporates the material properties of each constituent to be used for obtaining the effective bending stiffness of the thin laminate which is thought to be more accurate than obtained through homogenized elastic constants. However, when moment is applied on the real RVE model a non-uniform curvature is observed owing to the local fiber undulation in the plain-weave fabric leading to a vastly different bending stiffness than that obtained through homogenized RVE model. The strain energies were also found to be in great contrast amomg each other when FE models of pure elastomer , homogenized elastomer laminate plus elastomer (ELP) and real RVE based elastomer laminate (REL) were analysed. The study concludes that there is a significant difference in bending stiffness obtained with the two approaches i.e. using the real RVE and the homogenized RVE for the flexible region. In conclusion, it can be summarized that using the homogenized elastic constants is a better option for modeling woven fabric thin laminates.

Acknowledgments

This publication is based on work supported by the ASPIRE Abu Dhabi Award for Research Excellence (AARE-2020) under project number 8434000424/AARE20-124.

References

[1] T.-Y. Park, B.-G. Chae, H.-U. Oh, Development of 6 U CubeSat's Deployable Solar Panel with Burn Wire Triggering Holding and Release Mechanism, Int. J. Aerosp. Eng. 2019 (2019) e7346436. https://doi.org/10.1155/2019/7346436.
[2] F. Santoni, F. Piergentili, S. Donati, M. Perelli, A. Negri, M. Marino, An innovative deployable solar panel system for Cubesats, Acta Astronaut. 95 (2014) 210–217. https://doi.org/10.1016/j.actaastro.2013.11.011.
[3] M. Johnson, Y. Chen, S. Hovet, S. Xu, B. Wood, H. Ren, J. Tokuda, Z.T.H. Tse, Fabricating biomedical origami: a state-of-the-art review, Int. J. Comput. Assist. Radiol. Surg. 12 (2017) 2023–2032. https://doi.org/10.1007/s11548-017-1545-1.
[4] A.A. Deleo, J. O'Neil, H. Yasuda, M. Salviato, J. Yang, Origami-based deployable structures made of carbon fiber reinforced polymer composites, Compos. Sci. Technol. 191 (2020) 108060. https://doi.org/10.1016/j.compscitech.2020.108060.
[5] M. Sakovsky, S. Pellegrino, Closed cross-section dual-matrix composite hinge for deployable structures, Compos. Struct. 208 (2019) 784–795. https://doi.org/10.1016/j.compstruct.2018.10.040.
[6] A. Ahmed, I. Ud Din, R. Ramachandran, M.S. Sikandar Bathusha, W. Cantwell, K.A. Khan, Micro-CT driven characterization and validation of constituents' properties used in origami-inspired foldable composites fabricated via different manufacturing processes, Compos. Struct. 322 (2023) 117382. https://doi.org/10.1016/j.compstruct.2023.117382.
[7] I. Straumit, S.V. Lomov, M. Wevers, Quantification of the internal structure and automatic generation of voxel models of textile composites from X-ray computed tomography data, Compos. Part Appl. Sci. Manuf. 69 (2015) 150–158. https://doi.org/10.1016/j.compositesa.2014.11.016.
[8] I.U. Din, A. Ahmed, F. Tarek, W. Cantwell, K.A. Khan, Ultra-thin composites membrane for deployable structures: XCT driven characterization and FE modeling of folding structure, Compos. Sci. Technol. 245 (2024) 110341. https://doi.org/10.1016/j.compscitech.2023.110341.
[9] N. Nourmohammadi, N.P. O'Dowd, P.M. Weaver, Effective bending modulus of thin ply fibre composites with uniform fibre spacing, Int. J. Solids Struct. 196–197 (2020) 26–40. https://doi.org/10.1016/j.ijsolstr.2020.04.004.

NUMERICAL SIMULATION FOR FATIGUE FAILURE BY RANDOMLY VARIABLE LOADINGS FOR A VISCOELASTIC MATERIAL BASED ON ENTROPY DAMAGE CRITERION

Li Yutong[1], Natsuko Kudo[2], Minori Isozaki[2] and Jun Koyanagi[1]

[1]Department of Materials Science and Technology, Tokyo University of Science, 6-3-1 Niijuku, Katsushika, Tokyo, Japan
Email: liyutong@rs.tus.ac.jp, koyanagi@rs.tus.ac.jp, Web Page: https://www.rs.tus.ac.jp/koyanagi/home.html
[2] Department of Materials Science and Technology, Graduate School of Tokyo University of Science, 6-3-1 Niijuku, Katsushika, Tokyo, Japan
Email: 8219B01@alumni.tus.ac.jp, 8219012@alumni.tus.ac.jp

Keywords: Variable loading fatigue, Viscoelastic media, Entropy, Numerical simulation, Durability

Abstract
This study numerically predicts fatigue failures in viscoelastic materials caused by variable loadings, employing an entropy damage criterion for analysis. Understanding the durability of polymer matrix resin is crucial for ensuring the long-term reliability of composite materials, as it is a primary factor influencing their overall durability. This dependency on matrix resin, which is time-sensitive, is a critical aspect of our research.
Initially, a general S-N curve is derived from numerical simulations with constant amplitude fatigue loadings. The simulations use a single finite element, incorporating a constitutive relationship based on the entropy failure criterion. The load frequency in this study is a constant 2Hz, with a stress ratio consistently at zero. The material's viscoelastic characteristics are considered, and the dissipated energy related to viscosity work is linked to material damage through entropy value.
In authors' previous work, the authors integrated a constitutive relationship comprising 15 Maxwell models involving entropy damage into the commercial finite element method software ABAQUS, using the user subroutine UMAT. According to the linear cumulative damage (LCD) law, famously known as Miner's law, we determine a random variable loading set for fatigue failure based on the numerically obtained S-N curve. We vary the load sequence of this variable set and predict fatigue failures.
When the load sequence begins with the lowest amplitude, increases in order, and concludes with the highest amplitude, the total lifetime is as long as predicted by LCD, marking this as the longest case for fatigue failures due to variable loadings. Conversely, with a random sequence, the total lifetime is significantly shorter than that predicted by LCD. This shortening is even more pronounced in intermittent fatigue scenarios. In real-world fatigue conditions, such intermittent and random sequence loadings are common, suggesting that actual fatigue lifetimes may be considerably shorter than those predicted by conventional S-N curves and Miner's law. This discrepancy highlights the potential risk in conventional durability evaluation methods.
Furthermore, the study extends to explore the implications of these findings for the evaluation of composite material durability. The research underscores the necessity for more comprehensive and realistic testing methods to accurately predict the lifespan of composite materials in variable loading conditions. Our findings prompt a re-evaluation of standard durability assessment practices, advocating for a more cautious and nuanced approach to ensure safety and reliability in practical applications.

1. Introduction

The durability of Carbon fiber reinforced plastics (CFRPs) is still very important. There are several issues in the study of CFRP fatigue, including underdeveloped numerical simulation techniques, unclear dependence on stress ratio and frequency, unknown residual strength during fatigue, reliance on Miner's rule when the load level changes mid-cycle, unclear temperature dependence, and difficulty in conducting accelerated testing. To address these problems, the Koyanagi Laboratory is focusing its efforts on the study of CFRP fatigue, primarily through numerical simulations, even if this field may seem less prominent now.

When researchers want to quickly assess the durability of a material, they might increase the frequency of cyclic loading, which speeds up the testing process. However, this approach can cause problems when dealing with polymer materials or FRP. Since the durability of FRP is significantly influenced by the plastic matrix, we will consider only the durability of polymer materials. Polymers, being viscoelastic, are highly dependent on frequency. Specifically, different frequencies result in different numbers of cycles to failure. At low frequencies, the material is more affected by the viscous characteristics of viscoelasticity, leading to greater damage accumulation per cycle and a reduced number of cycles to failure. Conversely, at high frequencies, the heat generated due to viscoelasticity surpasses the heat dissipation from the material's surface, causing the temperature of the specimen to rise. As the temperature increases, the rate of heat dissipation from the surface also increases, eventually stabilizing at a temperature where heat generation and dissipation are balanced. Regardless, as the temperature rises, the time-dependent behavior is significantly accelerated according to the time-temperature superposition principle, resulting in greater damage accumulation per cycle and a reduced number of cycles to failure. Consequently, when plotting frequency on the horizontal axis and the number of cycles to failure on the vertical axis, the curve is convex, indicating different results depending on the frequency. The issue is that the peak of this convex curve, where temperature does not rise and the influence of viscosity is minimal, often corresponds to the cyclic loading conditions typically set by researchers aiming to evaluate durability. This means that the durability assessment in fatigue tests tends to overestimate the actual durability of the material.

Next, I would like to discuss cases where the load level fluctuates during cyclic loading. It is important to note that research on this topic is extremely challenging. Even when creating a simple S-N diagram for fatigue, the number of cycles to failure exhibits significant variability. Typically, the horizontal axis is logarithmic, so the order of variability is not in percentage terms but can be several times higher or lower, resulting in considerable spread when considering the actual experimental time. For instance, conducting fatigue tests with only two stress levels, changing from high to low and vice versa, and determining which condition results in a shorter fatigue life is highly complex. Previous results from the Koyanagi Laboratory have shown through numerical simulations that stress variation from high to low results in a shorter lifespan compared to low to high stress variation. When considering the initial loading condition, it was found that a zero-high-low sequence results in a shorter lifespan than a zero-low-high sequence, suggesting that significant stress variations shorten the fatigue life. Moreover, based on Miner's rule, the fatigue life under variable loading is consistently lower compared to constant stress fatigue life. Thus, considering that cyclic loads in real environments are not constant, fatigue tests under constant loads tend to overestimate the material's durability.

To address these challenges, the Koyanagi Laboratory has developed a viscoelastic/elastoplastic entropy damage model to summarize fatigue research encompassing the complex phenomena mentioned above. Additionally, they have developed a mesoscale model based on entropy to simulate strength degradation[1-13]. This work has enabled the creation of a numerical simulation environment for assessing the durability of polymer materials and FRP in general, facilitating a wide range of analyses. In the present study, we focus on durability of viscoelastic media subjected to variable loading fatigue because that of CFRP is dominated by the durability of viscoelastic media itself.

2. Numerical

2.1. Viscoelastic constitutive equation

In this study, parallel maxwell models shown in Fig. 1 is used.

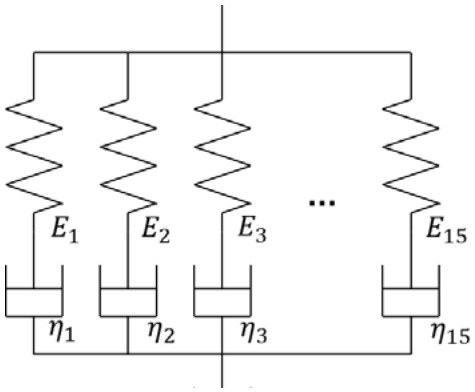


Fig.1 Maxwell model

Creep tests were conducted on epoxy resin over the temperature range of 40°C to 80°C, in 10°C increments, and at stress levels ranging from 10 MPa to 40 MPa, in 10 MPa increments. The obtained results were shifted using the time-temperature superposition principle, and the constants for C(t) were determined by comparing the results with the strain function (Eq.1).

$$\varepsilon(t) = C(t) \times \sigma \qquad Eq.1$$

$$C(t) = \frac{1 + \left(\frac{t}{T_c}\right)^n}{E_0} \qquad Eq.2$$

The inverse of C(t), denoted as the relaxation modulus E(t), was determined with the following parameters: E0 = 3300 MPa, Tc = 1000000, and n = 0.2. This E(t) was considered as the master curve for determining the material constants. While the standard transformation would require a Laplace transform, numerical calculations in this study showed close agreement, and thus, it was considered equivalent. Using the created master curve, the elastic modulus and viscosity coefficients for 15 Maxwell elements were determined. The determined material constants are presented in Table 1.

Table 1 Elastic Modulus and Viscosity Coefficient

No.	Elastic Modulus /MPa	No.	Viscosity Coefficient /MPa・s
E_1	220	η_1	7.94×10
E_2	220	η_2	5.01×10^{3}
E_3	220	η_3	1.00×10^{5}
E_4	220	η_4	6.31×10^{5}
E_5	220	η_5	2.51×10^{6}
E_6	220	η_6	2.00×10^{7}
E_7	220	η_7	3.98×10^{7}
E_8	220	η_8	2.51×10^{8}
E_9	220	η_9	5.01×10^{8}
E_{10}	220	η_{10}	3.16×10^{9}
E_{11}	220	η_{11}	1.58×10^{10}
E_{12}	220	η_{12}	3.98×10^{10}
E_{13}	220	η_{13}	5.01×10^{11}
E_{14}	220	η_{14}	6.31×10^{12}
E_{15}	220	η_{15}	1.00×10^{16}

Also, damage is related to dissipated energy and entropy. The detailed description is shown in some of authors previous works[10, 11].

2.2. S-N curve for constant amplitude fatigue failure and load set for variable loading fatigue

The numerical results for constant amplitude fatigue failure simulations are shown in Fig.2. Based on this result, we determine variable loading set as shown in Table 2, which is based on well-known Miner's law. The simulation is done by one element with commercial finite element analysis software ABAQUS. The entropy damage criterion is implemented using UMAT subroutine in ABAQUS.

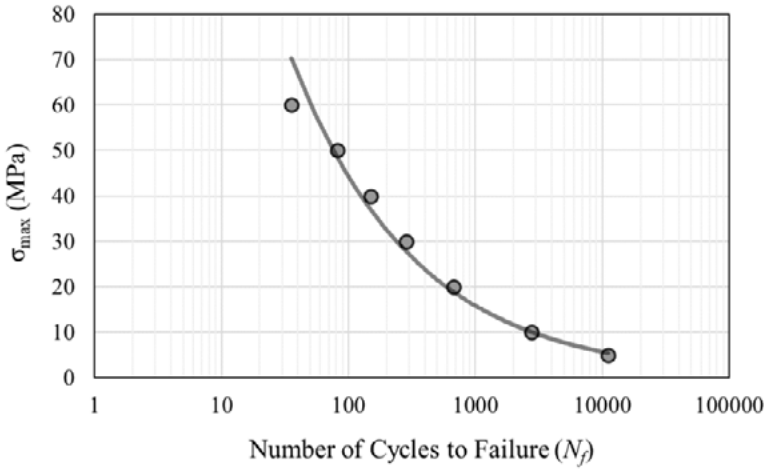


Fig. 2 Numerical results fatigue lifetime for constant amplitude

Table 2 Loading sequence from low to high based on the Miner's law

σ_{max} (MPa)	Number of cycles
5 MPa	371
10 MPa	189
20 MPa	98
30 MPa	56
40 MPa	28
50 MPa	14
60MPa	7

2.3. Results and conclusion

We simulate various patterns using the load set shown in Table 2 in which orders of variable loadings are varied. The results are not what we expected. Almost all cases result in the lifetime subjected to variable loading fatigue are shorter than that estimated by Miner's law. The important thing is that there is an interesting report of experimental work in which the lifetime of a FRP subjected to variable loading fatigue is much shorter than that estimated by Miner's law [14]. In other words, the result in this article is consistent with the numerical result presented in this study.

References

[1] N. Yamada, Y. Oya, N. Kato, K. Mori, J. Koyanagi, A Molecular Dynamics Simulation for Thermal Activation Process in Covalent Bond Dissociation of a Crosslinked Thermosetting Polymer, Molecules 28(6) (2023).

[2] H. Kagawa, Y. Umezu, K. Sakaue, J. Koyanagi, Numerical simulation for the tensile failure of randomly oriented short fiber reinforced plastics based on a viscoelastic entropy damage criterion, Composites Part C: Open Access 10 (2023).
[3] H. Deng, A. Mochizuki, M. Fikry, S. Abe, S. Ogihara, J. Koyanagi, Numerical and Experimental Studies for Fatigue Damage Accumulation of CFRP Cross-Ply Laminates Based on Entropy Failure Criterion, Materials 16(1) (2023).
[4] T. Sakai, N. Takase, Y. Oya, J. Koyanagi, A Possibility for Quantitative Detection of Mechanically-Induced Invisible Damage by Thermal Property Measurement via Entropy Generation for a Polymer Material, Materials 15(3) (2022).
[5] M. Morita, Y. Oya, N. Kato, K. Mori, J. Koyanagi, Effect of Electrostatic Interactions on the Interfacial Energy between Thermoplastic Polymers and Graphene Oxide: A Molecular Dynamics Study, Polymers 14(13) (2022).
[6] J. Koyanagi, A. Mochizuki, R. Higuchi, V.B.C. Tan, T.E. Tay, Finite element model for simulating entropy-based strength-degradation of carbon-fiber-reinforced plastics subjected to cyclic loadings, International Journal of Fatigue 165 (2022).
[7] H. Yoshida, H. Deng, J. Koyanagi, Enhanced Estimation of Axial Compressive Strength for CFRP Based on Microscale Numerical Simulation and the Response Surface Method, Materials 17(2) (2024).
[8] M. Takamura, M. Isozaki, S. Takeda, Y. Oya, J. Koyanagi, Evaluation of True Bonding Strength for Adhesive Bonded Carbon Fiber-Reinforced Plastics, Materials 17(2) (2024).
[9] T. Sakai, Y. Oya, J. Koyanagi, Evaluation of Volumetric Strain on Polyamide 6 by Thermodynamic Entropy Generation, Experimental Mechanics 64(1) (2024) 105-111.
[10] Y. Li, H. Deng, M. Takamura, J. Koyanagi, Durability Analysis of CFRP Adhesive Joints: A Study Based on Entropy Damage Modeling Using FEM, Materials 16(20) (2023).
[11] H. Deng, K. Toda, M. Sato, J. Koyanagi, Micro-Scale Numerical Simulation of Fatigue Failure for CFRP Subjected to Multiple-Amplitude Cyclic Loadings Based on Entropy Damage Criterion, Materials 16(18) (2023).
[12] N. Takase, J. Koyanagi, K. Mori, T. Sakai, Molecular dynamics simulation for evaluating fracture entropy of a polymer material under various combined stress states, Materials 14(8) (2021).
[13] M. Sato, K. Hasegawa, J. Koyanagi, R. Higuchi, Y. Ishida, Residual strength prediction for unidirectional CFRP using a nonlinear viscoelastic constitutive equation considering entropy damage, Composites Part A: Applied Science and Manufacturing 141 (2021).
[14] N.L. Post, J. Cain, K.J. McDonald, S.W. Case, J.J. Lesko, Residual strength prediction of composite materials: Random spectrum loading, Engineering Fracture Mechanics 75(9) (2008) 2707-2724.

PHYSICS-INFORMED NEURAL NETWORK FOR EFFICIENT PREDICTION OF THE MECHANICAL BEHAVIOUR OF SHORT FIBER-REINFORCED COMPOSITES

Minjun Kwak, Hyon-woo Pang, Wonjun Lee, and Woong-Ryeol Yu*

Department of Materials Science and Engineering, Seoul National University, 599 Gwanak-ro, Gwanak-gu, Seoul 151-742, Republic of Korea
*E-mail: woongryu@snu.ac.kr

Keywords: : Data-driven, Physic-informed learning, Constitutive model, Short-fiber reinforced composites, Finite element analysis

Abstract
In this paper, we developed an artificial neural network-based viscoplastic model to predict the properties of polymer matrix and combined fiber composite materials. The viscoplastic constitutive model chosen for the neural network features a 3-dimensional J2 yield function and isotropic hardening with power law. The ANN was used to calculate the corrected stress using the trial stress as input in the return mapping algorithm. The flow stress was also considered as an input to account for hardening, and the viscoplastic function was included to address strain rate effects. The training data for the neural network model was numerically generated using conventional return mapping . To optimize data collection and network training , dimensionality reduction techniques were implemented in the data space, including principal stress, deviatoric stress. During training , physics -based constraints were enforced using physics in the return mapping to prevent physically inconsistent predictions . We integrated our trained neural network into an ABAQUS user material subroutine originally designed for simulating the mechanical behavior of short-fiber reinforced plastics. The test involved single- element tests for tensile, shear, and biaxial tensile properties followed by multi-element tests at the part level. Our neural network -based model simulation results closely match those predicted by the return mapping constitutive model.

1. Introduction

Modeling the complex viscoplastic behavior of polymers is essential for accurately predicting the performance of polymers, either independently or as component of fiber composite materials. Numerous constitutive equations have been developed using return mapping based on Newton-Raphson iterations to simulate these viscoplastic properties. [1]

While these methods achieve satisfactory accuracy, their reliance on Newton-Raphson iterations results in significant computational costs and time limitations for practical applications such as pseudo-grain modeling of short fiber-reinforced plastics. Each pseudo-grain represents a set of aligned short fibers embedded within the plastic matrix, and its mechanical behavior can be simulated using Newton-Raphson iterations for every pseudo-grain calculation. [2] This substantial computational burden can be alleviated by employing a data-driven approach in viscoplasticity modeling.

The field of artificial neural networks has been rapidly growing recently, and there is a growing trend to apply artificial neural networks to describe the mechanical behavior of materials. Several studies have shown attempts at using ANN-based constitutive models, with examples seen in applications under plane stress conditions, elastoplasticity or hyperelasticity. [3,4,5] In applying artificial neural networks, it is essential to consider the appropriate reduction of noise for ensuring accuracy and interpretational stability, as well as obtaining an adequate dataset which greatly impacts the final performance.

In this study, we propose a viscoplastic model based on physics-informed artificial neural network that can replace Newton-Raphson iterations. To enhance data collection efficiency and improve overall performance by reducing output noise, we reduced the data space using deviatoric stress and principal stress transformation. We also incorporated physics related to return mapping into the training loss function to reduce noise of output. After the completion of training, the ANN model was implemented to ABAQUS User Subroutine (UMAT) and verified its performance. Single and multi-element simulations were conducted under typical loading paths such as uniaxial tension.

2. An artificial neural network-based constitutive model

2.1 Systems that introduce artificial neural network

With time-discrete stress integration scheme, the target system that introduce artificial neural network follows a J2 effective stress and power law-based isotropic hardening law as,

$$\varepsilon_{ij} = \varepsilon_{ij}^{e} + \varepsilon_{ij}^{vp} \rightarrow \Delta\varepsilon_{ij} = \Delta\varepsilon_{ij}^{e} + \Delta\varepsilon_{ij}^{vp} \tag{1}$$

$$\bar{\sigma} = \sqrt{J_2}, \quad J_2 = \frac{3}{2}(s : s) \tag{2}$$

$$\sigma_y^0 + \kappa(\varepsilon_e^{vP}) = \sigma_y^0 + C(\varepsilon_e^{VP})^B \tag{3}$$

where s is deviatoric stress and $\boldsymbol{\varepsilon_e^{VP}}$ is effective viscoplastic strain. The viscoplastic flow rule representing plasticity uses the Norton's power law as,

$$\dot{\varepsilon}^p = g_v(f)\frac{\partial f}{\partial \sigma}, \quad g_v(f) = \frac{\sigma_y}{\eta}\left(\frac{f}{\boldsymbol{\sigma_y^0}}\right)^m \tag{4}$$

where $\boldsymbol{g_v(f)}$ is viscoplastic function. Accordingly, the yield function f can be expressed as follows:

$$f = |\bar{\sigma}| - \sigma_y^0 - \kappa(\varepsilon_e^{vp}) \tag{5}$$

In the artificial neural network approach, the plastic corrector step in return mapping algorithm is replaced with ANN, while the elastic prediction step remains consistent with the conventional approach. After elastic prediction, consistency condition checks if given loading path induces plastic deformation using trial stress $\left(\boldsymbol{\sigma^{TR}}\right)$ and viscoplastic effective strain with following equation:

$$R = \bar{\sigma}(\sigma^{TR}) - \kappa(\varepsilon_e^{vp}) \tag{6}$$

If the computed value by the equation (6) is less than or equal to 0, it indicates elastic loading; updated stress equals trial stress and there is no accumulation of plastic strain. However, if it is above 0 then a plastic correction is necessary which occurs through return mapping. In a conventional return mapping scheme for viscoplasticity, iterative calculations are carried out based on Newton-Raphson algorithm applied to two equations iteratively.

$$k_\sigma\left(\varepsilon_e^{vp}, \bar{\sigma}\right) \equiv |\bar{\sigma}| + 3\mu_e \Delta\varepsilon_e^{vp} - |\bar{\sigma}|^{trial} = 0 \tag{7}$$

$$k_p\left(\varepsilon_e^{vp}, \bar{\sigma}\right) \equiv \Delta\varepsilon_e^{vp} - g_v(f)\Delta t = 0 \tag{8}$$

Meanwhile when a proposed ANN-assisted method is used, corrected stress can be directly determined without iterative return mapping process.

2.2 Selection of neural network inputs and outputs

To replace plastic correction using ANN, the trial stress obtained from elastic prediction is used as input to obtain corrected stress as output. In general, a 3D stress undergoing return mapping consists of six components, including 3 normal and 3 shear elements. Therefore, to set up stress as input and output, six components need to be added for both input and output, which is very inefficient for ANN construction. On the other hand, when stress is transformed into principal stresses through the principle of stress transformation, the stress can be represented in three principal components without any shear component.

Then, the transformed three-dimensional principal stresses can be decomposed into hydrostatic and deviatoric stresses. Hydrostatic stress does not affect plastic deformation and its value remains unchanged even after plastic correction. Plastic deformation is only affected by deviatoric stress, specifically for the J2 effective stress, stress changes on a 2D plane called deviatoric plane during plastic correction. When transforming the stress to a cylindrical coordinate system with the z-axis perpendicular to the deviatoric plane, only two components are needed because of the zero value for z axis. Since the plastic correction occurs perpendicular to the yield surface, the direction of correction for J2 effective stress always points towards the hydrostatic axis. As a result, when expressing coordinates in terms of radius and azimuthal angle on the deviatoric plane, there is no change in azimuthal angle during correction processes. Ultimately, stress changes due to plastic correction can be represented solely by the radial value ($\mathbf{S_R}$) on the deviatoric plane.

Therefore, the input and output stress of the artificial neural network are represented using $\boldsymbol{S_R}$ on deviatoric plane. Prior to applying the artificial neural network, a transformation of principal stresses, extraction of deviatoric stress, and coordinate system conversion take place. Following application of the artificial neural network, an inverse transformation process is carried out for the calculated output values. After converting output stress to deviatoric stress in the global coordinate system, add the saved hydrostatic component, then transform it to global stress using the stored eigen vector for principal stress calculation. In addition to stress, the flow stress from the previous step is used as an input to reflect the yield function affected by hardening. Lastly, the viscoplastic function value is used as input to account for the influence of strain rate in viscoplasticity. In the case of output, $\mathbf{S_R^{n+1}}$ is used to calculate the corrected stress and flow stress is used to determine the effective viscoplastic strain increment.

$$ANN : \left\{ \begin{array}{l} \mathrm{S}_R^{TR} \\ \rho(\bar{\varepsilon}^{p,n}) \\ g_v(f)\Delta t \end{array} \right\} \rightarrow \left\{ \begin{array}{l} \mathrm{S}_R^{n+1} \\ \rho(\bar{\varepsilon}^{p,n+1}) \end{array} \right\}$$

Figure 1. Proposed artificial neural network

3. Training the ANN model

3.1 construct database for ANN

The training data were generated numerically using a conventional return mapping scheme from an ABAQUS single-element simulation. As explained in the previous section, there are three main values

used as input and output in the artificial neural network: deviatoric stress, flow stress, and viscoplastic function. These three values were extracted by modifying the simulation conditions at each step of the simulation. The modified simulation conditions included final strain for 1 element simulation, time increment size, and strain rate and the established dataspace is shown in fig. 2. Due to significant scale differences between deviatoric stress, flow stress, and viscoplastic function, a regularization process was required.

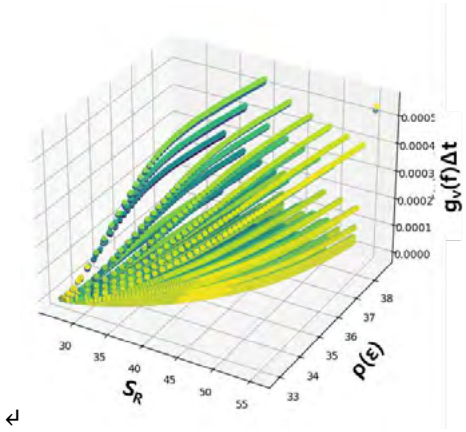


Figure 2. constructed dataspace

3.2 Physics-induced neural network (PINN)

When using an artificial neural network trained only on data, there could be some cases where physically impossible predictions are produced. For example, it is physically impossible for the effective plastic strain to decrease after a plastic correction. However, due to noise in the artificial neural network, such physically unrealistic predictions can be produced and it can lead to instability in finite element analysis when applied. To prevent these physically implausible predictions beforehand, it is possible to incorporate physics into the training of artificial neural networks and construct a Physics-induced Neural Network (PINN). By introducing physics, it is possible to more effectively learn patterns present in the data and aid in building a more stable network. Physics is incorporated into the loss during artificial neural network training by calculating physics loss based on the patterns found between input and output values; this physics loss is then added to the data-driven loss for use in training Two conditions have been added based on incorporated physics used during learning of constructed artificial neural networks: corrected deviatoric stress must be smaller than trial deviatoric stress and flow stress must increase after correction.

3.3 Selecting a neural network structure

To train a neural network, the database was divided into three parts: 90% for training, 9% for testing the final artificial neural network, and 1% for preventing overfitting during training by using it as a validation set. The data split was further refined by employing 5-fold cross-validation to ensure that all data points were utilized at least once for model training and validation. In order to build an artificial neural network that effectively captures the patterns in the data, it is crucial to appropriately configure the number of neurons and hidden layers in the neural network as these parameters directly impact the performance of neural network. In order to find the appropriate combination of neurons and hidden layers, we chose the grid search method. After training each structure for more than 10 epochs, we selected the simplest structure where overfitting did not occur based on the loss from the validation set. The final chosen structure consists of three hidden layers with 24 neurons in each hidden layer. Additionally, for nodes other than the output node, Rectified Linear Unit was used as the activation function.

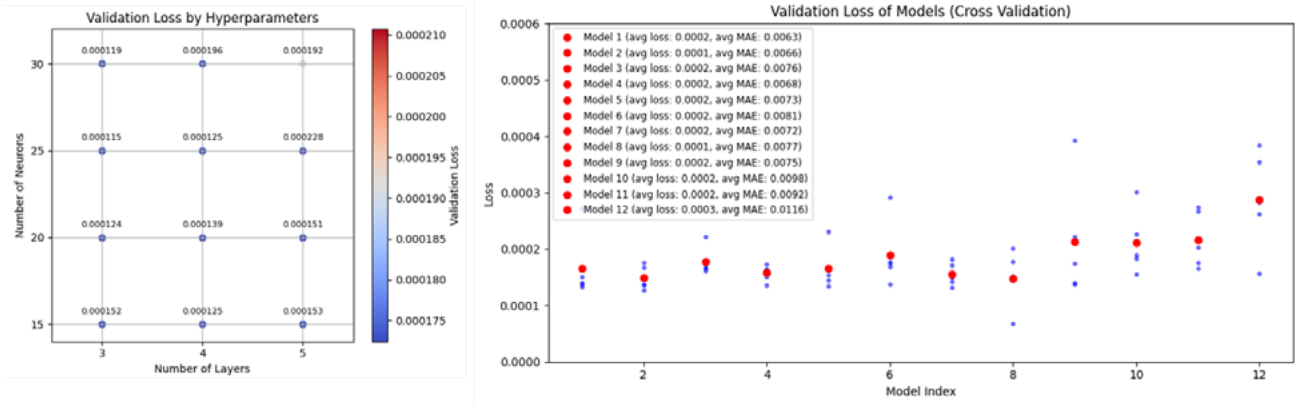


Figure 3. Grid search method and cross validation results

4. Neural network training results and UMAT application results

After completing the training, the artificial neural network was evaluated using test sets. When plotted for both predicted and actual values of two output variables, it showed remarkably high accuracy with an R-squared value of over 0.9999 in both cases as shown in fig. 4. The weights and biases of the trained artificial neural network were extracted and combined with ABAQUS UMAT for short fiber reinforced plastic with viscoplastic matrix homogenized with elastic fibers. Initially, tests were conducted on uniaxial tensile, biaxial tensile with ratio of 3:10, and shear cases for one element each; as shown in fig. 5, all three results closely matched those obtained from conventional return mapping analysis methods. To evaluate analysis stability and computation time, analyses were performed for 1000 elements under tensile and shear loading conditions. In both cases, the analyses completed stably without any aborts occurring and fig. 6 shows that its accuracy is moderate. The time taken for these analyses decreased by approximately 3%, demonstrating improved computational efficiency. When dealing with highly nonlinear paths during analysis, greater reductions in computation time can be expected.

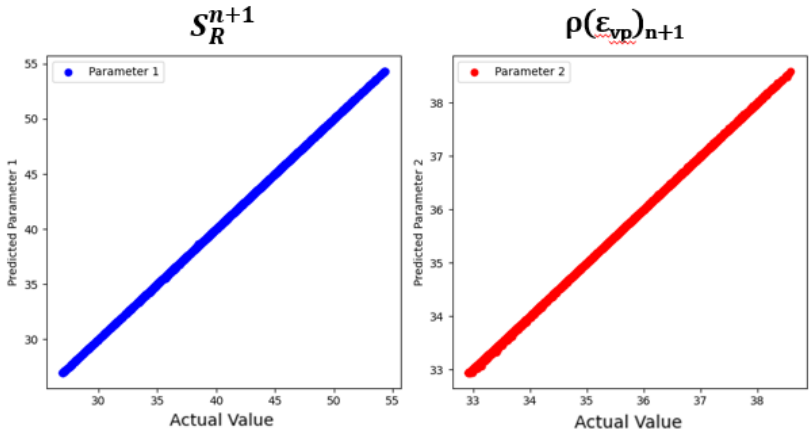


Figure 4. Training accuracy for each output parameter

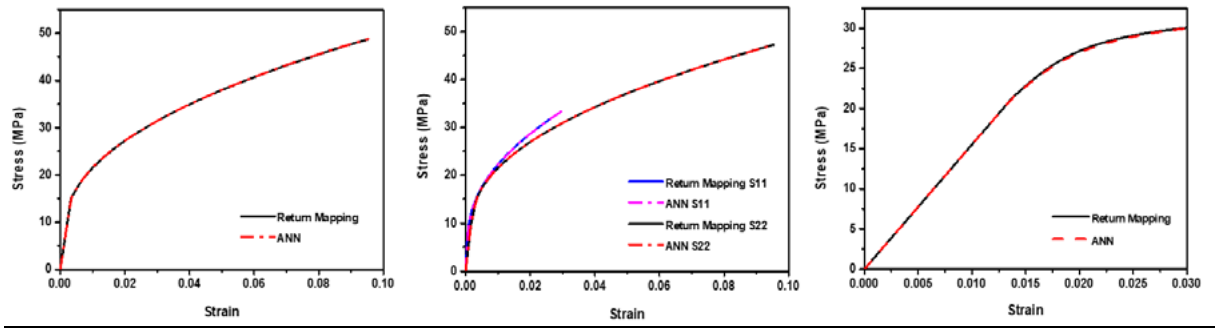


Figure 5. UMAT single element test results: (a) uniaxial tensile; (b) biaxial tensile; (c) shear test

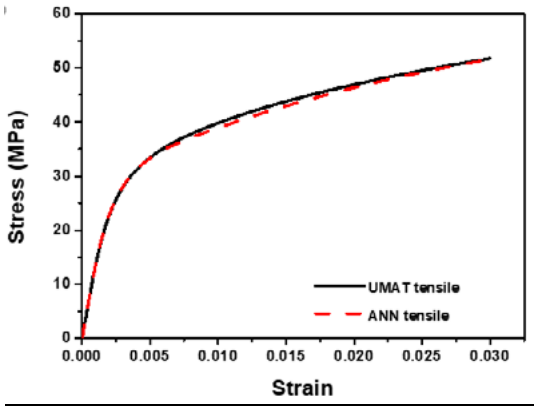


Figure 6. UMAT 1000 element uniaxial tensile test results

Acknowledgments

This work was supported by Hyundai Motor Group (0417-20230108) in Republic of Korea.

References

[1] Simo, J. C., & Taylor, R. A return mapping algorithm for plane stress elastoplasticity. *International Journal for numerical methods in engineering*, 22(3): 649-670, 1986.

[2] Choi, J. H., Yang, J., Jang, J., Pang, H., Cho, J. M., & Yu, W. R. Pseudo-grain decomposition of short fiber-reinforced plastics for two-step homogenization using machine learning approach. *Composite Structures*, 338: 118022, 2024.

[3] Jang, D. P., Fazily, P., & Yoon, J. W. Machine learning-based constitutive model for J2-plasticity. *International Journal of Plasticity*, 138: 102919, 2021.

[4] Kalina, K. A., Linden, L., Brummund, J., Metsch, P., & Kästner, M. Automated constitutive modeling of isotropic hyperelasticity based on artificial neural networks. *Computational Mechanics*, 69(1), 213-232, 2022.

[5] Zhang, A., & Mohr, D. Using neural networks to represent von Mises plasticity with isotropic hardening. *International Journal of Plasticity*, 132: 102732, 2020.

Revolutionizing Airbag Deployment Predictions: Study of TPO and PP's Dynamic Properties in Automotive Safety Modeling

Se-Min Lee[1], Gyu-Won Kim[1], Jae-Hyun Ahn[2], In-Soo Han[2] and Hak-Sung Kim[1, 3]

[1]Department of Mechanical Convergence Engineering, Hanyang University, 222 Wangsimni-ro, Seongdong-gu, Seoul, Republic of Korea
Email: minhappy96@hanyang.ac.kr, Web Page: http://mcdm.hanyang.ac.kr/
Email: kyuwon0817@gmail.com, Web Page: http://mcdm.hanyang.ac.kr/
[2] Hyundai Motor Group R & D Division, Gyeonggi-do, 18280, Republic of Korea
Email: nanmario@hyundai.com, Web Page: http://www.hyundai.com
Email: 94hans@hyundai.com, Web Page: http://www.hyundai.com
[3]Hanyang Research Center for Advanced Semiconductor Packaging, Hanyang University, 222 Wangsimni-ro, Seongdong-gu, Seoul, Republic of Korea
Email: kima@hanyang.ac.kr, Web Page: http://mcdm.hanyang.ac.kr/

Keywords: Split-Hopkinson pressure bar, Passenger airbag, Strain rate effect, Thermoplastic olefin, polypropylene

Abstract
Airbag covers made of thermoplastic olefin (TPO) material should be deployed quickly without debris under various environments. To accurately predict airbag deployment during a collision, the mechanical properties of polymer materials at high strain rates according to temperature should be considered. In this study, the mechanical properties of TPO and polypropylene were measured at high strain rates via split-Hopkinson pressure bar tests under various environmental temperatures ranging from -35 to 85 °C. Through this, tensile strength and failure strain were derived for each strain rate. As the polymer phase moves toward the high strain rate region, the β-transition becomes dominant, resulting in a non-linear increase in tensile strength in the Eyring plot. Additionally, an airbag module impact simulation was conducted to verify the effects of strain rate on airbag deployment using the LS-DYNA software. It was found that the TPO and polypropylene airbag deployment could be accurately predicted using the strain-rate-dependent mechanical behavior rather than quasi-static properties alone.

1. Introduction

Airbags serve as crucial components within vehicles, offering vital protection to occupants during collisions. According to the US National Highway Traffic Safety Administration (NHTSA), between 1987 and 2010, approximately 32,500 individuals were saved by frontal airbags. These airbags notably diminish driver fatalities by 29% in frontal crashes and reduce fatalities among front-seat passengers aged 13 and above by 32% [1]. Given their pivotal role in safeguarding human life within automobiles, it is imperative that airbags function effectively in the event of an accident.

Under normal circumstances, the airbag cover must withstand impact forces to accommodate the airbag cushion. In the event of a collision, the airbag cover should swiftly open to trigger the airbag module, facilitating the rapid deployment of the airbag cushion within milliseconds. Furthermore, it is crucial that airbags deploy securely, devoid of any fragments that could potentially harm occupants. Airbag covers must endure a range of temperature conditions and demonstrate appropriate opening behavior even under extreme temperatures.

Typically, during deployment in low-temperature environments (e.g., -35 °C), the airbag module should open within a designated cover area without fragmentation. Similarly, in high-temperature conditions (e.g., 85 °C), the cover should not deform or peel upon deployment.

To meet these criteria, thermoplastic olefin (TPO) materials have gained widespread use for airbag covers due to their combination of rubber-like hyperelasticity and the high modulus and strength of plastic. Achieving enhanced reliability in airbag components requires accurate prediction of airbag deployment in car crash simulations. Consequently, it is crucial to thoroughly investigate the effects of strain rates on the mechanical behavior of TPO, given the significant strain rates (ranging from 100 to over 1000 /s) induced during automobile crash events.

During airbag deployment, the airbag chute experiences extremely high strain rates, typically occurring within milliseconds. This underscores the importance for airbag manufacturers to meticulously design their systems, taking into account the strain-rate-dependent material properties.

This study involved measuring the mechanical properties of TPO and polypropylene (PP) at high strain rates using a split-Hopkinson pressure bar (SHPB), a widely employed apparatus for characterizing dynamic mechanical behavior at strain rates ranging from 100 to 10,000 s^{-1} [2,3]. Dynamic stress-strain curves of TPO and PP were recorded at various temperatures and strain rates. Subsequently, an airbag deployment simulation was conducted for passenger airbag (PAB) modules made of TPO and PP materials, incorporating strain-rate-dependent mechanical behavior, utilizing LS-DYNA, an impact finite element analysis (FEA) software. Additionally, a PAB deployment simulation was performed using only static properties of TPO and PP for comparison with results obtained considering strain-rate-dependent mechanical properties.

2. Experimental procedure and simulations

2.1. High strain rate test

Dynamic tensile tests were conducted using a modified tensile Split-Hopkinson Pressure Bar (SHPB), as illustrated in Fig. 1. In the SHPB setup, it is imperative that both the incident and transmission bars remain elastic to adhere to the one-dimensional elastic wave propagation theory [4]. Moreover, the length-to-diameter ratio of the bars must exceed 20 to ensure that the incident and reflected waves, measured by the strain gauge of the incident bar, do not overlap, thus maintaining the principles of one-dimensional elastic wave propagation [5].

For this experiment, the SHPB equipment consisted of two aluminum bars, each with a diameter of 20 mm and a length of 2 m (as specified in Table 1). Strain gauges were affixed to both bars, allowing for real-time measurement of incident, reflected, and transmitted wave signals, as depicted in Fig. 3. Strain gauges with a resistance of 350 ohms (manufactured by TML, Japan) were employed, featuring a gage length of 3 mm and a gauge factor of 2.11 ± 1.0%. To prevent overlap between the reflected and incident waves, strain gauges were symmetrically positioned 420 mm from the ends of the bars, ensuring a distance longer than one wavelength from the specimen.

The strain gauge signals were amplified using an ST-AM1000 amplifier (manufactured by SENSTECH, Korea), providing a 500-fold amplification of the output voltage. The amplified signals were then recorded using a data acquisition system consisting of a PXIe-1082 chassis equipped with a PXIe-5105 digitizer card, manufactured by National Instruments (USA).

Dynamic tensile tests were conducted at strain rates of 1000, 1500, and 2000 s^{-1} by adjusting the pneumatic pressure within the SHPB setup.

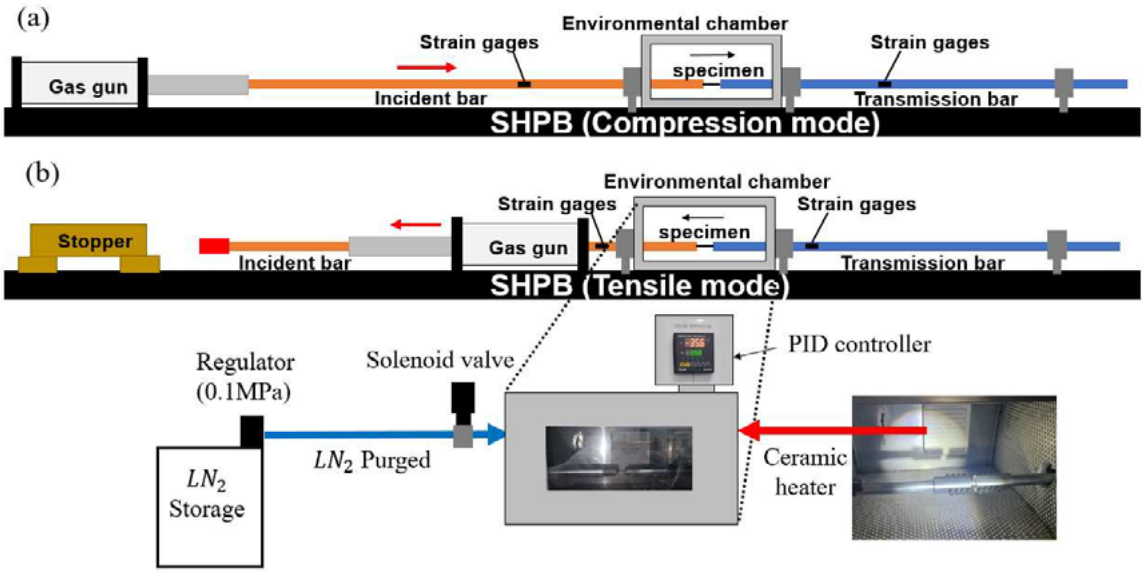


Figure 1. Schematic of Split Hopkinson Pressure Bar a)Compression mode b)Tensile mode

Table 1. Physical properties of incident and transmission bars.

Property	Unit	6061 aluminum alloy
Density	g/cm^3	2.70
Young's modulus	GPa	68
Tensile strength	MPa	310
Length	m	2
Bar diameter	mm	20

2.2. Quasi-static and medium strain rate tests

TPO and PP were evaluated as potential materials for airbag covers. Tensile test specimens were prepared in accordance with the ASTM D3039 standard. In designing the specimen shape, it was essential to ensure that the gauge length was sufficiently short to allow stress equilibrium during dynamic tests and to achieve high strain rates. Thus, a dog bone specimen shape was selected, as depicted in Fig. 4, with dimensions tailored accordingly. The width of the specimen was carefully chosen to minimize stress concentration at its ends, achieved by incorporating a smooth radius of curvature in the transition region. Aluminum grips were utilized to clamp the specimen securely, which were affixed to a cylindrical jig connecting each bar and fastened in place using screws.

2.3. Materials and specimen preparation

TPO and PP were evaluated as potential materials for airbag covers. Tensile test specimens were prepared in accordance with the ASTM D3039 standard. In designing the specimen shape, it was essential to ensure that the gauge length was sufficiently short to allow stress equilibrium during dynamic tests and to achieve high strain rates. Thus, a dog bone specimen shape was selected with dimensions tailored accordingly. The width of the specimen was carefully chosen to minimize stress concentration at its ends, achieved by incorporating a smooth radius of curvature in the transition region. Aluminum grips were utilized to clamp the specimen securely, which were affixed to a cylindrical jig connecting each bar and fastened in place using screws.

2.4. Airbag deployment simulations

Airbag deployment simulations were performed to verify the mechanical properties by considering the strain-rate effect. The simulations were conducted using the commercial FEA software LS-DYNA (Livermore, USA), which is often used for collision analysis. Fig. 2 (a) shows a FEA model of the cockpit of a DN8 vehicle (Hyundai Motors, Korea), while Fig. 2 (b) shows the PAB and airbag deployment. As shown in Fig. 2(c), the PAB deployment system consists of a crash pad, a PAB chute, and airbag housing. A crash pad is fabricated by injecting a PP material, and its function is to protect the driver and passengers by absorbing shock during a collision. The PAB chute, made from Thermoplastic Olefin (TPO) material, is integrated with the crash pad. During an accident, the PAB chute door opens, initiating the deployment of the airbag towards the passenger. The airbag housing, constructed from steel, contains the folded airbags. Upon collision, the inflator explosively deploys the airbag at high speed (refer to Fig. 2(b)).

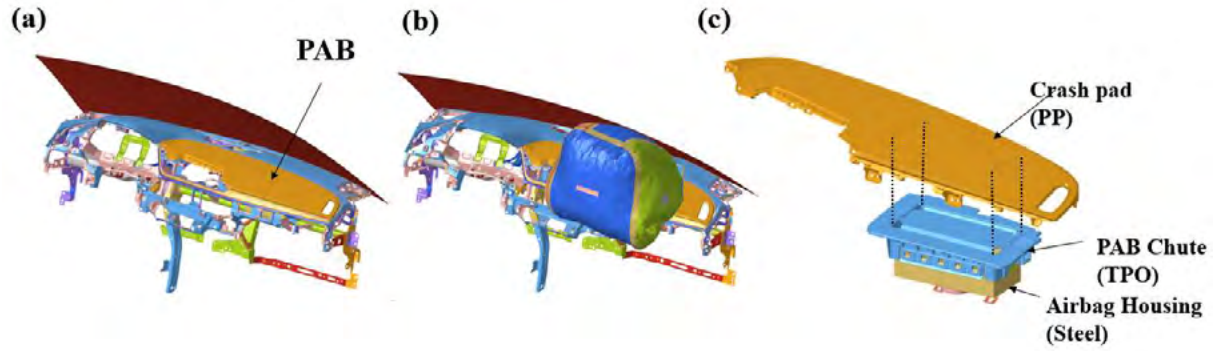


Figure 2. Passenger Airbag module (PAB) deploy FEM simulation ; a)before deploy (b)after deploy c) structure of PAB module

3. Results and discussion

Fig. 3 illustrates the tensile strength of TPO and PP at various temperatures as a function of strain rate, presented in an Eyring plot. Both TPO and PP exhibit significant dependence on tensile strength with respect to strain rate. At quasi-static rates, the Eyring plot shows a relatively gentle slope, indicating a minor increase in tensile strength with rising strain rate. However, at strain rates surpassing 1000 s^{-1}, both TPO and PP demonstrate a notable augmentation in tensile strength, with the rate of increase surpassing that observed at quasi-static rates.

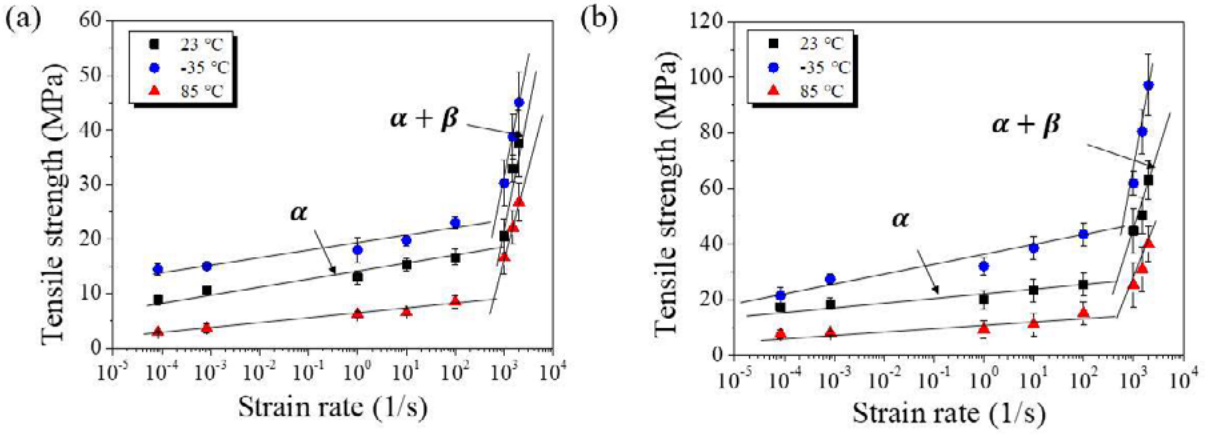


Figure 3. Passenger Airbag module (PAB) deploy FEM simulation ; a)before deploy (b)after deploy c) structure of PAB module

The slope of the Eyring plots for TPO and PP is determined through linear fitting, expressed by Equation (1):

$$\sigma_y = m * \left(\log \frac{d\sigma}{dt}\right) + c \quad (1)$$

The slope was calculated by dividing the tensile strength at each strain rate under each temperature condition into data of less than 100 s^{-1} and data of more than 1000 s^{-1}, and the results are summarized in Table 2. The relationship between tensile strength and strain rate in TPO and PP materials displays a bilinear dependency on strain rate. PP, being a semi-crystalline polymer, exists in two distinct crystalline forms known as the α- and β-phases. The transition between these phases is influenced by both temperature and strain rate.

Table 2. Linear fitting parameters in static and dynamic strain rates of TPO and PP

	Temperature	~100 s^{-1} (α)		1000~2000 s^{-1} ($\alpha + \beta$)	
		m	*c*	*m*	*c*
TPO	- 35 ℃	1.27	19.14	49.11	-117.08
	23 ℃	1.15	13.83	42.62	-102.73
	85 ℃	0.85	6.31	33.58	-84.22
PP	- 35 ℃	2.89	35.32	117.05	-289.82
	23 ℃	1.21	21.97	58.85	-133.22
	85 ℃	1.02	11.09	48.01	-119.58

At low strain rates, PP predominantly undergoes deformation governed by the α-transition, also known as segmental relaxation. This phase transition entails a high activation energy for deformation, resulting in a limited sensitivity of tensile strength to changes in strain rate. However, as the strain rate escalates, the polymer shifts towards the less stable β-phase. In this phase, deformation requires a lower activation energy, leading to a sharp increase in tensile strength with rising strain rate. This transition is known as the β-transition.

At high strain rates, both α- and β-transitions contribute to an elevated slope in the Eyring plot, thereby causing a more pronounced increase in tensile strength with increasing strain rate [6,7,8]. This phenomenon may be attributed to the glass transition moving towards room temperature under high strain rates [9].

The effect of the strain-rate-dependent mechanical properties on the door deployment angle in the PAB module deployment was analyzed and compared with the experimentally obtained deployment angle. As shown in Fig. 4(a), the deployment angle was measured at the center of the airbag door. The angle was measured by tracking three nodes on the crash pad, namely, the door opening point, the rotation center point, and a point on the pad. The angle was measured at two positions: the front door on the passenger side and the back door on the windshield side (see Fig. 4(a)). When the strain-rate-dependent material properties were used in the FEA model, the door angle changed faster than when only quasi-static mechanical properties were used in the FEA model. It is noteworthy that the strain-rate-dependent

behavior could make the FEA results more accurate, similar to the actual experimental results (see Figs. 4b–d).

This observation underscores the significance of strain-rate-dependent mechanical properties in enhancing the accuracy of FEA predictions. When solely quasi-static mechanical properties are utilized, the FEA model tends to reflect relatively low tensile modulus, tensile strength, and larger failure strains. Conversely, accounting for strain-rate-dependent mechanical properties leads to rapid airbag deployment, driven by the tendency for higher strain rates to correlate with increased tensile strength and reduced failure strains.

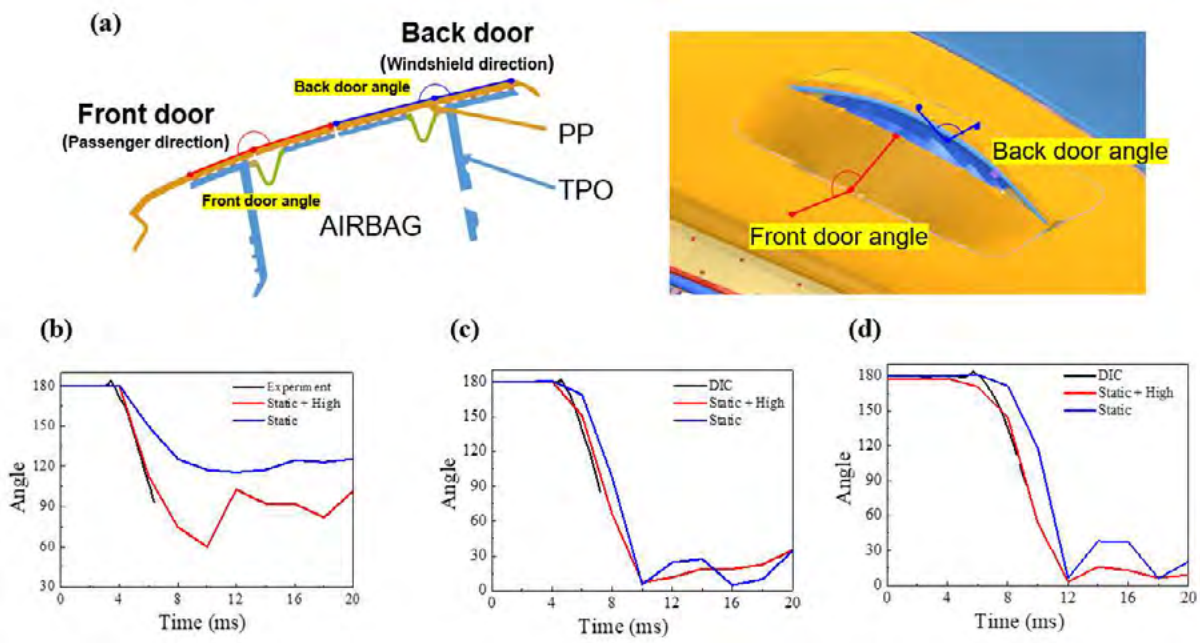


Figure 4. Passenger Airbag module (PAB) deploy FEM simulation ; a)before deploy (b)after deploy c) structure of PAB module

4. Conclusions

In this study, the strain-rate-dependent mechanical behavior of thermoplastic olefin (TPO) and polypropylene (PP) was measured under high strain rates and various temperature conditions using split-Hopkinson pressure bar equipment. The measurements were verified via high-speed camera imaging and digital image correlation analysis. Using the strain-rate-dependent properties of TPO and PP, an FEA simulation of passenger airbag (PAB) deployment was carried out and compared with the airbag deployment experimental results. It was found that the deployment angle and PAB deployment behavior could be accurately predicted using the strain-rate-dependent mechanical properties. Based on the results and findings of this study, it is suggested that the strain-rate-dependent mechanical properties should be measured and used in PAB chute simulation and design, because plastic materials show a much stiffer modulus and higher strength as the strain rate increases.

Acknowledgments

This work was supported by Korea Institute of Energy Technology Evaluation and Planning(KETEP) grant funded by the Korea government(MOTIE)(20212020800090, Development and Demonstration of Energy-Efficiency Enhanced Technology for Temperature-Controlled Transportation and Logistics Center). This work was also supported by a Collaborative Project between Hanyang University and Hyundai Motors Co. Ltd.

References

[1] Kahane CJ. Lives saved by vehicle safety technologies and associated Federal Motor Vehicle Safety Standards, 1960 to 2012–Passenger cars and LTVs–With reviews of 26 FMVSS and the effectiveness of their associated safety technologies in reducing fatalities, injuries, and crashes. Report No. DOT HS 812 (2015): 069.
[2] Chen WW, Bo S. Split Hopkinson (Kolsky) bar: design, testing and applications. Springer Science & Business Media, 2010.
[3] Kim DH, Kang SY, Kim HJ, Kim HS. Strain rate dependent mechanical behavior of glass fiber reinforced polypropylene composites and its effect on the performance of automotive bumper beam structure. Composites, Part B 2019;166:483-496.
[4] Abrate S. Impact on laminated composite materials. Appl Mech Rev 1991;44(4):155-90.
[5] Abrate S. Behavior of composite materials under impact: strain rate effects, damage, and plasticity. ASME Appl Mech Div-Publ-AMD 2001;250:41-50.
[6] Siviour CR, Walley SM, Proud WG, Field JE. The high strain rate compressive behaviour of polycarbonate and polyvinylidene difluoride. Polymer 2005;46(26):12546-12555.
[7] Okereke MI, Buckley CP, Siviour CR. Compression of polypropylene across a wide range of strain rates. Mech Time-Depend Mater 2012;16:361-379.
[8] Mulliken AD, Boyce MC. Mechanics of the rate-dependent elastic–plastic deformation of glassy polymers from low to high strain rates. Int J Solids Struct 2006;43(5):1331-1356
[9] Siviour CR, Jordan JL. High strain rate mechanics of polymers: a review. J Dyn Behav Mater 2016;2:15-32.

A TWO-LEVEL MACHINE LEARNING MODEL FOR FAILURE PREDICTION OF AN ORIGINAL Z-BEAM WING BOX CONCEPT

Runze Li[1], Mario Miranda[2] and Silvestre Pinho[3]

[1]Department of Aeronautics, Imperial College London, London, UK
Email: runze.li@imperial.ac.uk
[2] Department of Aeronautics, Imperial College London, London, UK
Email: m.miranda23@imperial.ac.uk
[3]Department of Aeronautics, Imperial College London, London, UK
Email: silvestre.pinho@imperial.ac.uk

Keywords: failure prediction, z-beam, composite, aeroelastic tailoring, machine learning

Abstract
Aeroelastic tailoring is a promising passive aeroelastic control method that can benefit the aerodynamic and structural performance of aircraft. To achieve the maximum performance of aircraft, original wing concepts need to be optimized in early design stages. For this purpose, it is necessary to enable fast prediction of the properties and performances for the wing box. Using an original Z-beam wing box concept as an application example, a two-level multi-scale machine learning model is proposed for the preliminary design of high aspect ratio wings with Z-beam structures applied in the wing tip region. The proposed model consists of two parts: 1) at the level of global Z-beam wings, a model is trained to predict the weight, homogenized stiffness, and potential failure hotspots of a Z-beam unit cell; 2) in the level of local hotspots, a model is trained to predict the failure indices from LaRC05 failure model. Unit cells of wing box with different geometric parameters and composite layups are sampled and simulated to build a database for training. Results show that the proposed model achieves high prediction accuracy for the novel wing structure.

1. Introduction

Europe's aviation industry has announced its initiative, Destination 2050, towards the net zero European aviation [1]. Increasing the wing aspect ratio to reduce induced drag is one of the main approaches [2]. For example, Boeing's 777-X utilizes a folding wingtip to increase its wingspan [3]. Airbus' zero emission (ZEROe) program [4], University of Bristol's Ultra-Green wing (BUG)[5], among others, are exploring the benefits and challenges of high aspect ratio wings in all aspects [2]. One of the major challenges is that the high aspect ratio significantly contributes to the wing structural weight [6].

Aeroelastic tailoring is a promising passive approach to affect the aerodynamic and structural performance in a beneficial way [7]. Stodieck and Airbus proposed a Z-beam structural concept to achieve more efficient aeroelastic tailoring, especially to reduce the manoeuvring and gust loads [8][9]. This can serve as an enabler to address the aeroelastic challenges of HARW, as shown in Figure 1. The black lines represent the spar and rib of the wing box, the grey lines represent the stringers, the red lines represent the Z-beam.

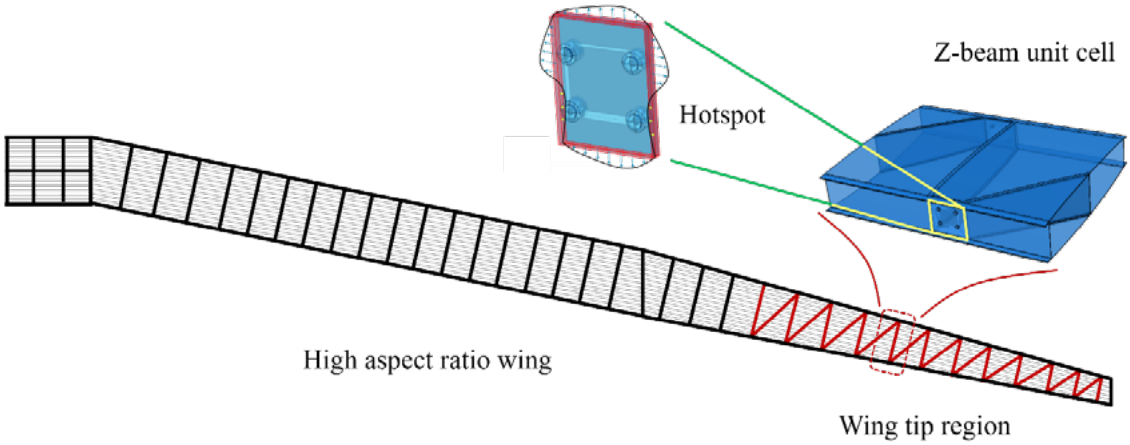


Figure 1. Z-beam structures in the wing tip region, and the hotspot for failure

In this paper, a two-level multi-scale machine learning model is proposed for the fast prediction of novel wing structures. The Z-beam structure is selected as an example. The behaviour of the Z-beam wing box of wing tip is represented by segmenting the Z-beam into several unit cells, as shown in Figure 1. The unit cell model is simulated under periodic boundary conditions including tension, bending and torsion. After identifying the hotspot of composite failure in the unit cell model, a refined local model for the hotspot is built for failure analysis.

2. Parametric Modelling and Computational Methods

2.1. Parameters of the Z-beam Unit Cell

The Z-beam unit cell consists of the upper and lower cover skins, the front and rear C-shape spars, the zigzag I-shape beam, and bolts. The bolts are made from Ti-6Al-4V aerospace grade titanium, the material for other parts is IM7/8551-7 carbon/epoxy. For simplicity, only three independent geometric parameters are chosen, as shown in Figure 2. Their meaning and range are listed in Table 1. It should be noted that the span-wise length (L_z, mm) is dependent on α_{beam}. The laminate layup is the same when the thickness is the same, and it is not changed during sampling or machine learning.

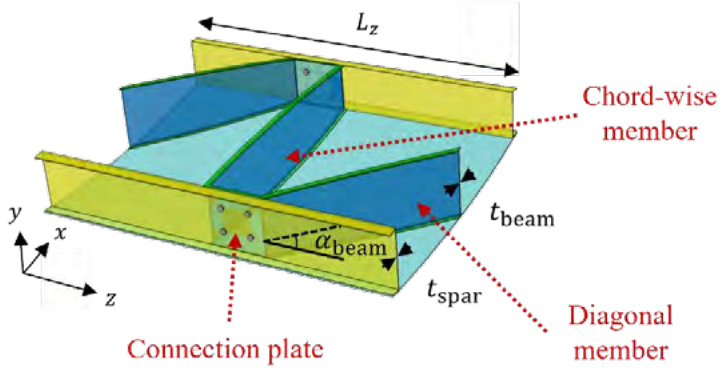


Figure 2. Geometric parameters of the Z-beam unit cell model

Table 1 Independent geometric parameters

Variable	Meaning	Range
t_{spar} (mm)	thickness of spar	[5, 25]
t_{beam} (mm)	thickness of beam	[10, 22]
α_{beam} (°)	angle between diagonal member of the beam and the spar	[20, 60]

2.2. Periodic Boundary Conditions

The behaviour of the complete zigzag beam in the wing tip region of BUG wing, as shown in Figure 1, is approximated by Z-beam unit cells arranged in a one-dimensional series. The aeroelastic deformation of the full wing box can be simulated by reduced order models [10], which only requires the homogenized stiffness matrix of each unit cell (Eq. 1).

$$\begin{bmatrix} F_z \\ M_z \\ M_x \\ M_y \end{bmatrix} = \begin{bmatrix} C_{11} & C_{12} & C_{11} & C_{14} \\ C_{21} & C_{22} & C_{23} & C_{24} \\ C_{31} & C_{32} & C_{33} & C_{34} \\ C_{41} & C_{42} & C_{43} & C_{44} \end{bmatrix} \begin{bmatrix} \epsilon_z \\ \kappa_z \\ \kappa_x \\ \kappa_y \end{bmatrix} \tag{1}$$

The loads applied on the unit cell model include the axial strain in z-axis (ϵ_z), twist rate about z-axis (κ_z, rad/mm), and the curvature about x/y-axis (κ_x, κ_y, 1/mm). The loads are employed using periodic boundary conditions (PBCs).

2.3. Finite Element Models

Abaqus is used as the numerical solver in this work. The failure criterion is the LaRC05 failure criteria [12]. A global-local modelling approach is employed to use a more refined mesh for the hotspot, so that more accurate failure predictions can be obtained. The details can be found in [13] and are therefore not repeated here.

3. Machine Learning for Z-beam wing boxes

3.1. Database

The database is built by evenly spaced sampling in the range listed in Table 1. There are 470 valid unit cell samples in the database. The homogenized stiffness matrix [C] and mass matrix ([M]) are extracted. Figure 3 shows the relationship between the stiffness components with geometry parameters. It shows that t_{spar} dominates C_{11}, C_{33}, C_{13}; t_{beam} dominates C_{23}; t_{spar} and t_{beam} have same level of influence on C_{22}.

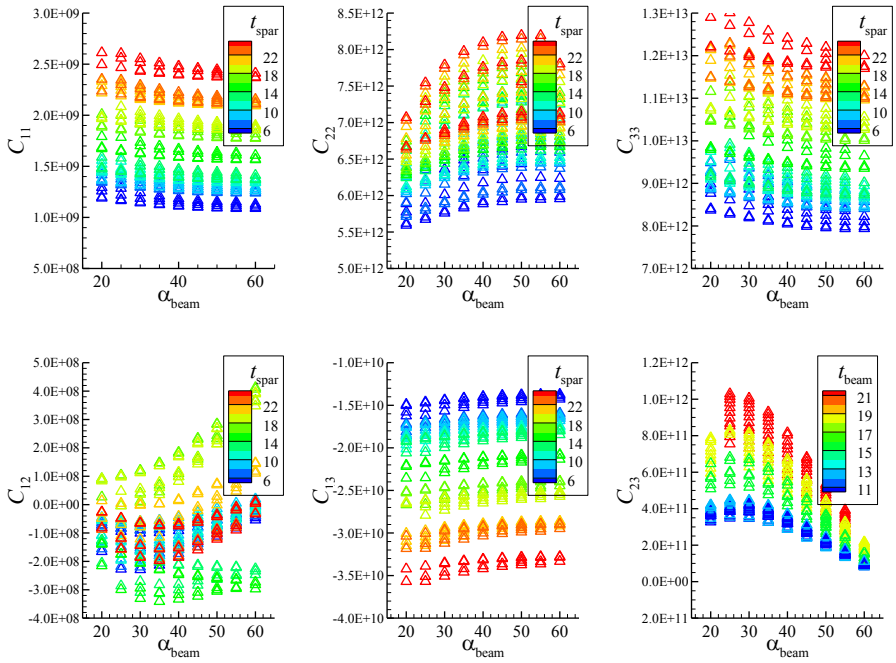


Figure 3. Distribution of stiffness components in the database

3.2. A Machine Learning Model for Z-beam Unit Cell's properties

A machine learning model is used to predict the properties of Z-beam unit cell that are independent of the loads, i.e., the weight and homogenized stiffness matrix. The model input is the geometric parameters,

the output is the weight (w) and components of the stiffness matrix, as shown in Figure 4. Denote the geometry parameters as $\boldsymbol{\theta} = [t_{\text{spar}}, t_{\text{beam}}, \alpha_{\text{beam}}]^T$. A simple artificial neural network (ANN) is employed, which contains three hidden layers with 512 neurons. The loss function is the mean square error (MSE) between the predicted values and the real values. The initial learning rate is 0.001 for 500 epochs. Adam optimizer[14] is used for training. 20 samples are randomly selected for testing. Figure 5 shows the prediction error on the training set and testing set during training. It shows that the model can achieve a good prediction accuracy.

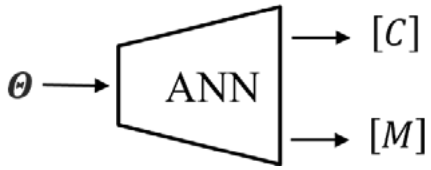


Figure 4. ANN for the prediction of weight and stiffness

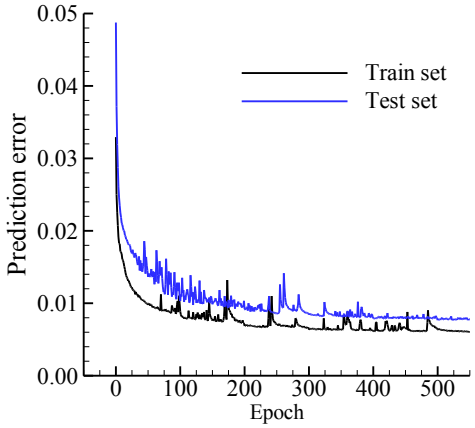


Figure 5. Prediction error on the training set and testing set during training.

3.3. A Two-level Machine Learning Model for Failure Prediction

As the results in [13] showed, the failure always happens around bolt holes. Since the geometry of the hotspot model is the same for unit cells with different beam angles, splitting the failure prediction into two levels can reduce the need for training samples. Figure 6 shows the architecture of the two-level machine learning model. The unit cell level model predicts the displacement boundary of the hotspot ($\boldsymbol{u}$) under specific geometry ($\boldsymbol{\theta}$) and loads $\boldsymbol{\Delta} = [\epsilon_z, \kappa_z, \kappa_x, \kappa_y]^T$. The hotspot level model predicts the stress field around bolt holes based on the geometry ($\boldsymbol{\theta} = [t_{\text{spar}}, t_{\text{beam}}]^T$) and boundary condition ($\boldsymbol{u}$). Then, the failure index field is calculated with the LaRC05 model, the maximum failure index is extracted, and the failure mode is determined. The two models, one of each level, are trained separately with their corresponding database. The loss function is the mean square error (MSE) between the predicted values and the real values. The initial learning rate is 0.001 for 2,000 epochs. Adam optimizer is again used for training. The database of the hotspot model is still in progress. The results will be presented in the conference.

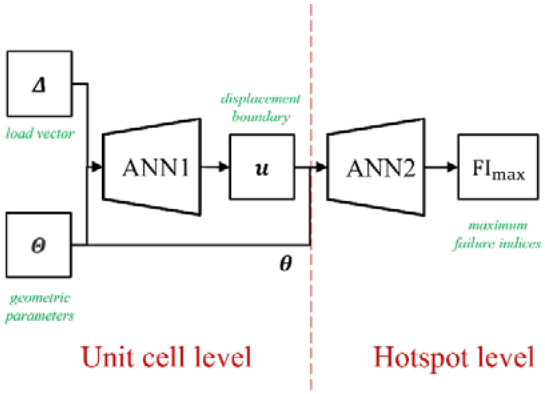


Figure 6. Two-level model for the failure prediction

4. Conclusions

The Z-beam structure can provide custom bending-torsion couplings by changing its geometry. A simple neural network is trained to predict the homogenized stiffness of the Z-beam unit cell, which provides fast and accurate predictions for preliminary design of high aspect ratio wings. A two-level machine learning model is proposed and trained for its failure prediction. The model takes advantage of the linear characteristics of the physical nature in its failure behaviour. Therefore, the proposed machine learning model achieves good prediction accuracy and generalization ability with fewer training samples. This approach is therefore shown to be usable for early-stage design of generic original composite concepts.

Acknowledgments

The authors would like to gratefully acknowledge the funding from Innovate UK under the Next Wing project No. 10002372 (https://gtr.ukri.org/projects?ref=10002372). The authors also thank Nicolae Lucian Iorga from Airbus UK for the support and helpful discussions.

References

[1] A route to net zero European aviation, Destination 2050, https://www.destination2050.eu/, last accessed on 02/05/2024.
[2] Y. Ma, A. Elham, Designing high aspect ratio wings: A review of concepts and approaches, *Progress in Aerospace Sciences*, 145: 100983, 2024.
[3] A. Kretov, D. Tiniakov, Evaluation of the Mass and Aerodynamic Efficiency of a High Aspect Ratio Wing for Prospective Passenger Aircraft, *Aerospace*, 9: 497, 2022
[4] ZEROe, towards the world's first hydrogen-powered commercial aircraft, Airbus. https://www.airbus.com/en/innovation/low-carbon-aviation/hydrogen/zeroe, last accessed on 02/05/2024.
[5] O. Stodieck, J. E. Cooper, S. A. Neild, and M. H. Lowenberg, Slender-Wing Beam Reduction Method for Gradient-Based Aeroelastic Design Optimization, *AIAA Journal*, 56(11): 4529-4545, 2018
[6] F. Afonso, J. Vale, E. Oliveira, et al., A review on non-linear aeroelasticity of high aspect-ratio wings, *Progress in Aerospace Sciences*, 89: 40-57, 2017
[7] M. Shirk, T. Hertz and T. Weisshaar, Aeroelastic tailoring - Theory, practice, and promise, *AIAA/ASME/ASCE/AHS 25th Structures, Structral Dynamics and Materials Conference,* Palm Springs, CA, May 14-16, 1984
[8] O. Stodieck, Tech-insight: Aeroelastic tailoring of wings using a z-beam concept, University of Bristal, 2019
[9] L. Iorga. Aerofoil structures with stiffness properties adjustment component. U.S. Patent No. 11,772,780 B2. United States Patent and Trademark Office. 3 Oct. 2023
[10] H. Hesse, R. Palacios, Reduced-Order Aeroelastic Models for Dynamics of Maneuvering Flexible Aircraft, *AIAA Journal*, 52(8): 1717-1732, 2014

[11] J. Dizy, R. Palacios, S. Pinho, Homogenisation of slender periodic composite structures, International Journal of Solids and Structures, 50: 1473-1481, 2013
[12] S. Pinho, R. Darvizeh, P. Robinson, et al., Material and structural response of polymer-matrix fibre-reinforced composites, *Journal of Composite Materials*, 46(20):2313–2341, 2012.
[13] M. Miranda, R. Li, S. Pinho, Multiscale modelling of a novel wing box structure with increased bend-twist coupling, 21st European Conference on Composite Materials, Nantes, France, July 2024.
[14] D. Kingma, J. Ba, Adam: A method for stochastic optimization, *arXiv preprint*, 2014, arXiv:1412.6980.

MULTISCALE MODELLING OF A NOVEL WINGBOX STRUCTURE WITH INCREASED BEND-TWIST COUPLING

Mário Miranda[1], Runze Li[1] and Silvestre T. Pinho[1]

[1]Department of Aeronautics, Imperial College London, Exhibition Rd, South Kensington, London SW7 2AZ, UK
Email: m.miranda23@imperial.ac.uk

Keywords: multiscale, composites, wing, machine learning, failure prediction

Abstract
A multiscale modelling approach is introduced to accurately predict the failure mode of a non-conventional wingbox structure with increased bend-twist coupling. The proposed methodology consists in employing both global-local analysis and machine learning to estimate the failure indexes of a bolted joint in a new structural concept. Applying strain based global loads, the failure indices of the local model are calculated and used to train a machine learning model, currently being trained. The expected outcome is a fast failure prediction tool for the analysis of novel structural features.

1. Introduction

As the aeronautical industry aims to reduce its impact on the environment, different designs and solutions have been proposed such as the change from metal to composite airframes. Another promising solution is the use of High Aspect Ratio Wings (HARW), which are able to offer higher aerodynamic efficiency and therefore less fuel consumption. However, some challenges arise due to their increased span, such as higher root bending moments and non-linear aeroelastics. A new concept, the Z-beam concept (Figure 1), was introduced by Stodieck [1] as a potential structural concept able to provide custom tailored bend-twist coupling of wings. This can serve as an enabler to address the aeroelastic challenges of HARW [2].

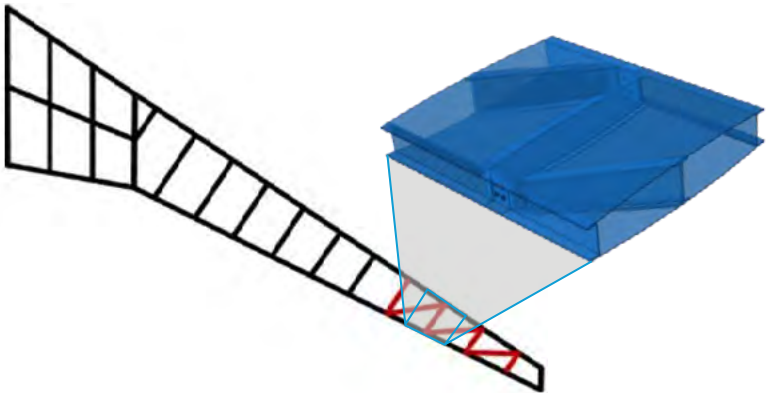


Figure 1. Z-beam concept.

However, moving away from conventional design brings significant challenges in the structural analyses of such novel configurations. Therefore, detailed analysis and simulations are required to evaluate these new concepts to ensure the structure satisfies the strength requirements (or a multitude of potential failure modes). Still, detailed numerical analysis of such components can also be time consuming, specially when large models are involved and sufficient accurate stress states need to be captured. This prevents its usage in the design stage, when multiple rapid iterations are required. In this work, a multiscale modelling strategy, including composite failure and machine learning, is introduced as a way of reducing costs and time in the design of novel components.

2. Methodology

The proposed methodology consists in a two-level multiscale analysis strategy, at the global and local levels, followed by machine-learning models. The workflow (Figure 2) starts by determining the strain-based loads which are to be applied on the global structure. This is a representative structural element of the wing, assumed to be subject to Periodic Boundary Conditions (PBCs). The analysis yields the displacement field, which is used to extract the boundary conditions of the local model. This is a more detailed model of a structural feature, in this case, the bolted joints of the spars, which can be used for failure indices estimation. The global-local analyses can be performed for a multitude of structural dimensions and applied loads. Generating sufficient data, it is then possible to train a machine learning model, which aim is to predict both the local model boundary displacements and maximum failure index based on the applied strains.

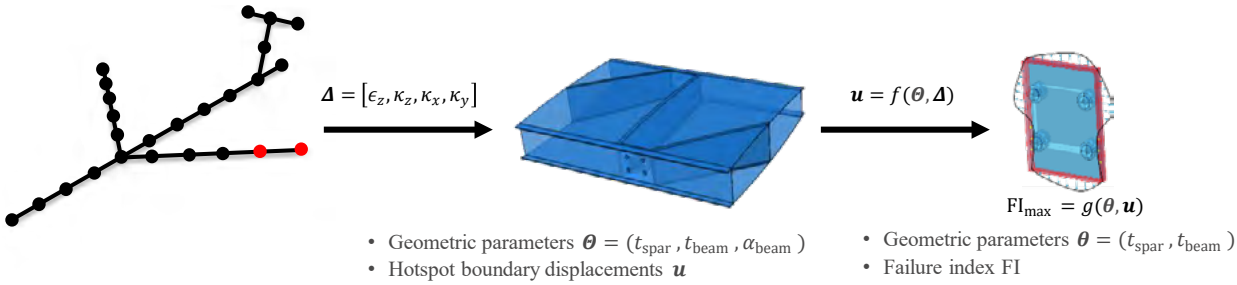


Figure 2. Multiscale model strategy workflow.

2.1. Global-Local

The global-local simulation strategy is a useful approach to be followed when a higher level of detail is needed to analyse a specific region, in this case, the bolted joints (Figure 3) of a larger parent structure [3]. There are different ways of employing this strategy. The one used in this work is referred to as series method [3]. In this method, after the displacement field of the global model is known, the values of the relevant nodes at the boundary of the zone of interest are used as interpolation points for the local model boundary displacement reconstruction.

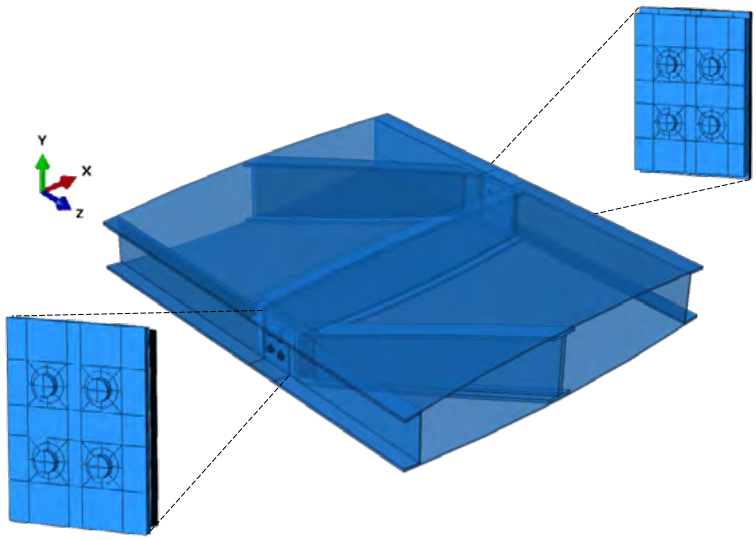


Figure 3. Global and local finite element models.

2.2. Machine learning

A physics guided artificial neural network model is proposed, the details of which can be seen in Ref. [4].

3. Finite element models

3.1. Geometry

The geometry of the Z-beam wing box was generated so it is fully parametrised, having 30 different parameters such as the angle of the diagonal members, airfoil shape and component thicknesses. The local model mimics the geometry of the bolt connection of the global counterpart.

3.2. Materials

The materials used for the composite parts are IM7/8551-7 carbon/epoxy and Ti-6Al-4V for the bolts. A model [5,6] evolved from LaRC05 [7] failure criteria was employed using an UVARM sub-routine to determine the failure indexes for different failure modes.

3.3. Mesh

Continuum shell elements with reduced integration (SC8R) were used to model the laminates of the global model, meaning 1 element per laminate with an attributed composite section. 8-noded linear brick elements (C3D8R) with enhanced hourglass control were employed in the local model and in the bolts of both models, having a 1 element per ply strategy been followed. The size of the mesh was sufficiently refined so that the convergence was attained. The final element ratio is approximately 15, i.e., the smallest element edge length in the radial direction in the local model is 15 times smaller than in the global one. Both meshes are displayed in Figure 4.

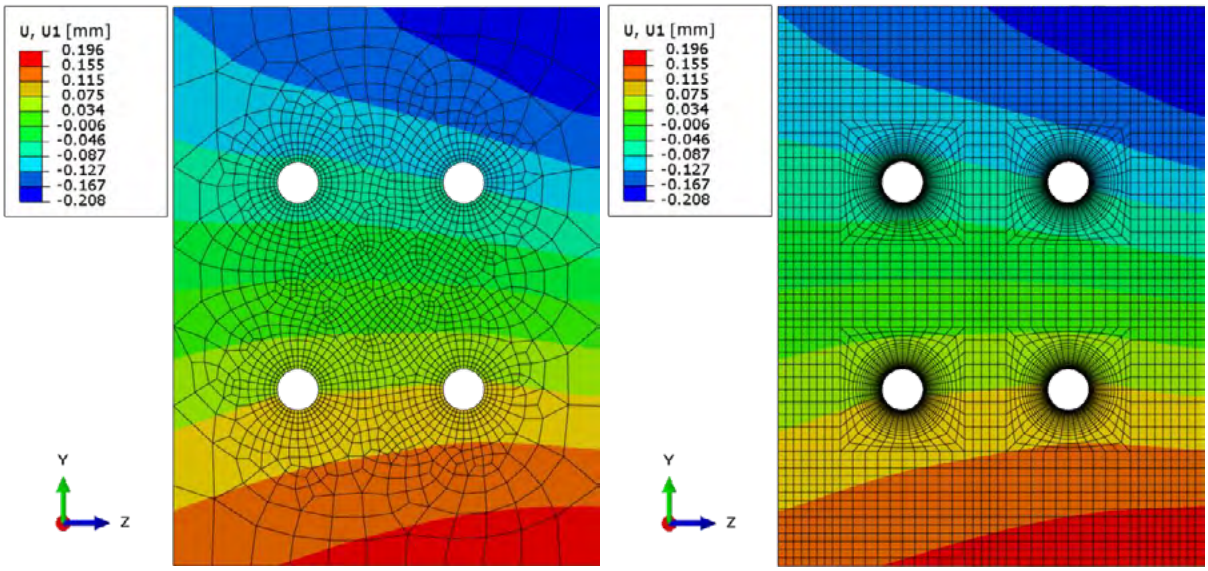


Figure 4. Global (left) and local (right) meshes and comparison of the U_1 displacement field.

3.4. Loads

Four different loading scenarios: tensile, bending due to drag and lift forces, and torsion, are applied using periodic boundary conditions which ultimately allows to determine the homogenised stiffness matrix of the Z-beam representative structural element.

4. Results

Regarding the local model, results have shown that its implementation is necessary once the registered strains to failure suffer a significant reduction for every load case (50-60%). This is due to the use of a more refined mesh, which is able to better capture the high stress gradients that arise near the hole boundaries, as seen in Figure 5.

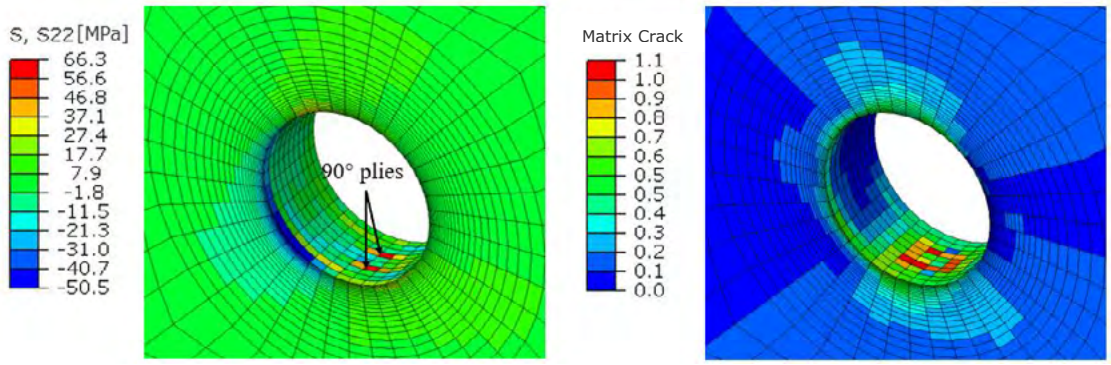


Figure 5. In-plane transverse stress (left) and matrix cracking failure index (right) fields at a spar bolt hole.

Relatively to the critical spots and failure mechanisms it was observed that the critical bolt holes were tendentially the same, having the failure mechanism transitioned from compressive nature failure modes to tensile ones, due to the high stress concentrations. The physics based neural network is currently under training, and the respective results will be shown at the conference.

5. Conclusions

A multiscale strategy is introduced as a fast and accurate composite failure prediction model, which is applied to a non-conventional wing box structure. For a strain based load applied to a representative structural element model of the new concept, the displacements are retrieved and enforced in a bolted joint local model, after which, the failure indices are calculated using LaRC05 failure criteria. A machine learning model is being trained with the available data generated for different cases. This methodology is promising for the design of novel components and features, reducing computational costs while maintaining a suitable degree of accuracy.

Acknowledgments

The authors would like to gratefully acknowledge the funding from Innovate UK under the Next Wing project No. 10002372 (https://gtr.ukri.org/projects?ref=10002372). The authors also thank Nicolae Lucian Iorga from Airbus UK for the support and helpful discussions.

References

[1] O. Stodieck. Tech-insight: Aeroelastic tailoring of wings using a z-beam concept. 2019
[2] L. Iorga. Aerofoil structures with stiffness properties adjustment component. U.S. Patent No. 11,772,780 B2. United States Patent and Trademark Office. 3 Oct. 2023
[3] M. A. McCartney. BOJCAS: Bolted joints in composite aircraft structures. 2023
[4] R. Li, M. Miranda, S.T. Pinho. A two-level machine learning model for failure prediction of an original z-beam wing box concept. ECCM21. 2024
[5] S. T. Pinho, M. Matos, R.O.S.S. Costa, A. Ibbotson, M. Ostergaard. Enabling multiscale analysis of very large composite structures. COMPOSITES 2021, 22-24, 2021
[6] S. T. Pinho, R.O.S.S. Costa, M. Matos, A. Ibbotson, M. Ostergaard. Multiscale analysis of an aircraft wingbox. ECCM20. 26-30, 2022
[7] S. T. Pinho, R. Darvizeh, P. Robinson, C. Schuecker, and P.P. Camanho. Material and structural response of polymer-matrix fibre-reinforced composites. Journal of Composite Materials, 46(19-20):2313–2341, 2012.

COMPUTATIONAL FLUID DYNAMICS MODELLING OF VACUUM-ASSISTED RESIN INFUSION IN COMPOSITE SANDWICH PANELS DURING WIND TURBINE BLADE MANUFACTURING

Md Tusher Mollah[1,*], Maksim Larionov[2], Robert S. Pierce[2] and Jon Spangenberg[1]

[1]Department of Civil and Mechanical Engineering, Technical University of Denmark, 2800 Kgs. Lyngby, Denmark
[2]Department of Wind and Energy Systems, Technical University of Denmark, 4000 Roskilde, Denmark
[*]Email: mtumo@dtu.dk

Keywords: Vacuum-Assisted Resin Infusion (VARI), Composite Sandwich Panels, Computational Fluid Dynamics (CFD), Experimental Validation, Infusion Time, Flow Front

Abstract
The manufacturing of wind turbine blades predominantly features composite sandwich panels made through the Vacuum-Assisted Resin Infusion (VARI) process. These sandwich regions involve multiple components, which include a lightweight balsa or foam core with grooves and channels encased in non-crimp glass-fibre fabric skins. Understanding resin flow behaviour and infusion time through these materials is difficult as there are a large number of parameters to consider. Therefore, this study focuses on developing a Computational Fluid Dynamics (CFD) model to provide a more accurate prediction of resin flow for the investigation of a wide range of parametric changes. The CFD model is initially developed to simulate resin flow through the lower reinforcement layers and shallow grooves of composite sandwich panels. The simulated flow front has been compared with the experimental ones captured at the top and bottom of the fabric at different infusion times. The experimental and simulated results agree relatively well; providing a new venue for investigating resin infusion performance through complex features of the layup. Furthermore, the model has been exploited to investigate the influence of groove spacing on the flow front, resin-filled volume, and infusion time.

1. Introduction

Vacuum-Assisted Resin Infusion (VARI) is an essential process in the modern composite manufacturing industry, particularly in wind turbine blade manufacturing, which requires large-scale production of lightweight and efficient components. Understanding resin flow plays a crucial role in this process [1]. Significant areas of wind turbine blades comprise composite sandwich panels, which provide the twofold benefit of high strength and lightweight regions. The representative layup of these panels consists of two configurations of glass NCF, including unidirectional and biaxial layers, serving as composite skins [2]. These layers are positioned on both sides of a lightweight foam core with specific grooves and channels to improve formability and resin flow. Additional layers of resin distribution media, perforated release films, and peel plies are also used underneath the vacuum bags to support resin flow and demoulding during manufacture. Understanding the resin flow and filling of these sandwich regions is critical as it directly relates to the performance and quality of the wind turbine blade.

Computational Fluid Dynamics (CFD) models have shown considerable success in predicting resin flow for different infusion techniques, including VARI, resin injection pultrusion, resin film infusion, resin transfer moulding, etc. [3–8]. The majority of the CFD models employed for the modelling of resin transport in porous media rely on Darcy's Law, linking fluid velocity to pressure drop within the

medium, resulting in a single differential equation [9–11]. A detailed summary of the simulation studies within the scope of the VARI process has been outlined by Pierce [2]. Such modelling approaches are sufficiently helpful in predicting the resin flow and approximate infusion time within the porous media; however, they neglect some considerable features [12]. For example, the interplay of the groove channel flow with the fabric-reinforced layers or the through-thickness flow behavior is commonly overlooked.

In this study, a CFD model has been developed to simulate resin flow through shallow grooves and the lower reinforcement layer of non-crimp glass-fiber fabric skin. The simulated results are compared with experiments to analyze the flow fronts at the bottom and top of the reinforcement layer. Furthermore, the effect of the cut-to-cut distances of shallow grooves on the flow fronts, resin-filled volume, and infusion time has been investigated. Section 2 outlines the methodology of the study, providing details of the experiments conducted and the CFD model. Section 3 presents the results of the study. Finally, the conclusions drawn from the results are summarized in Section 4.

2. Methodologies

2.1. Single channel flow experiments

In order to validate the CFD models, a series of single channel flow experiments were conducted. Four layers of 250×900 mm^2 biaxial glass fabric were sandwiched between an acrylic plate with a single machined channel and a tempered glass mold. The average thickness of the fiber preform was 2.2 mm. Permeability values for the fabric in three principal directions were determined from an independent set of experiments consistent with previous studies [13,14]: K_1 = 1.89e-10 m^2; K_2 = 6.14e-11 m^2; K_3 = 1.093e-11 m^2; with a K_1 orientation of 45.19 ± 1.38° relative to the roll direction. The 900×250×14.7 mm^3 transparent polymethyl methacrylate (PMMA) plate was used instead of real core material for two reasons: firstly, to simplify the validation case for modelling (avoiding resin absorption into the core) and secondly, to allow for video observation from both sides of the experiments.

The machined channel was produced with dimensions 1×3 mm^2 and a pressure sensor was placed as close to the channel inlet as possible as shown in Figure 1-a, to help establish the inlet pressure boundary conditions over time for modelling. The whole configuration was covered by a vacuum bag, representative of a typical VARI process, and a 200 mm peel-ply breaking zone was used to arrest the flow between the end of the channel and the vacuum outlet.

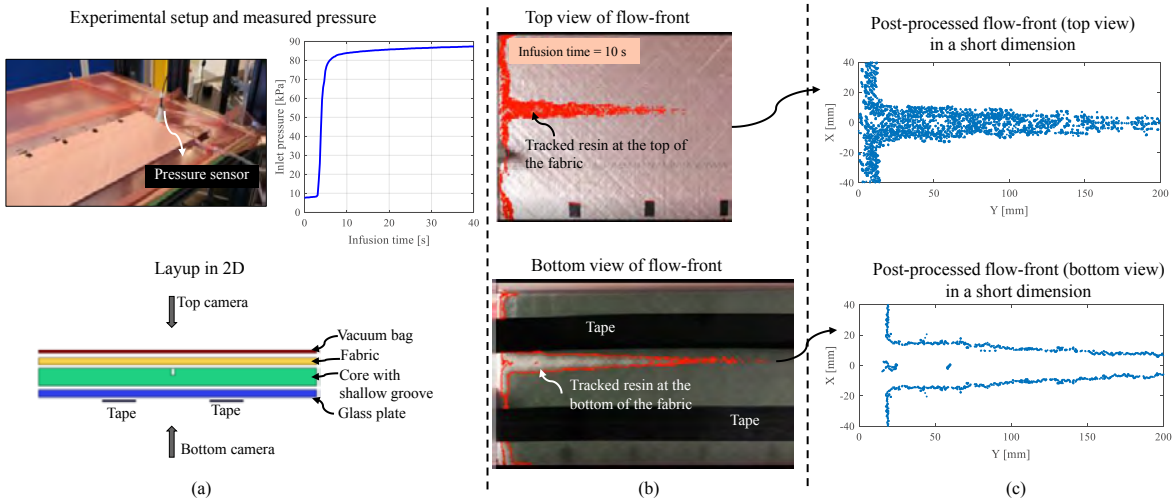


Figure 1. In-plane experiments and data post-processing. (a) Experimental setup, layup details, and the measured pressure profile over time; (b) Flow-front captured by the top and bottom camera after the tracking of the resin at the top and bottom of the fabric, respectively; (c) Post-processed flow-front in a short dimension to compare with the simulation results.

An 85% glycerol-water solution with density 1222 kgm^{-3} was used as the test fluid, with a viscosity of 0.0963 Pa.s at 20 °C, which is representative of a typical low-viscosity resin for infusion. The pressure difference between the fluid reservoir at the inlet (open to ambient conditions) and the vacuum outlet (set with a constant 7500 Pa pressure) was used to drive the flow in the experiments. Videos recorded from both the top and bottom of the experiments were processed with a Python image-processing script based on the OpenCV library in order to track and visualize the flow front position over time as seen in Figure 1-b. The flow front propagation has been investigated for a reduced area of interest (80×200 mm^2), cf. Figure 1-c, in order to assist the CFD analysis described in the later section.

2.2. CFD model

The CFD model has been developed in FLOW-3D® [15] to simulate resin flow through the lower reinforcement layers and shallow grooves of composite sandwich panels. The model comprises a non-porous shallow groove in the core material and a porous channel at the top replicating the lower reinforcement layers of non-crimp glass fiber fabric skins, cf. Figure 2-a. The figure 2-a also shows the computational domain and implemented boundary conditions. The porous channel and the shallow grove are assigned pressure inlet boundary conditions at one end and pressure outlet at the other end. Time-dependent pressure boundary conditions have been implemented at the inlet according to the measured values in the experiment (cf. previous subsection) to better replicate experimental conditions. A constant pressure of 7500 Pa is applied at the outlet to mimic the vacuum outlet pressure during experiments. The top plane of the domain is a stationary wall representative of a rigid mold surface. The bottom plane (i.e., bottom of the porous channel and shallow groove) is also assigned to wall boundary conditions, reflective of the PMMA experiments. Although it should be acknowledged that this configuration neglects any fluid absorbance into the real core material. The rest of the planes are assigned to continuative boundary conditions having a zero velocity gradient while exiting the boundary.

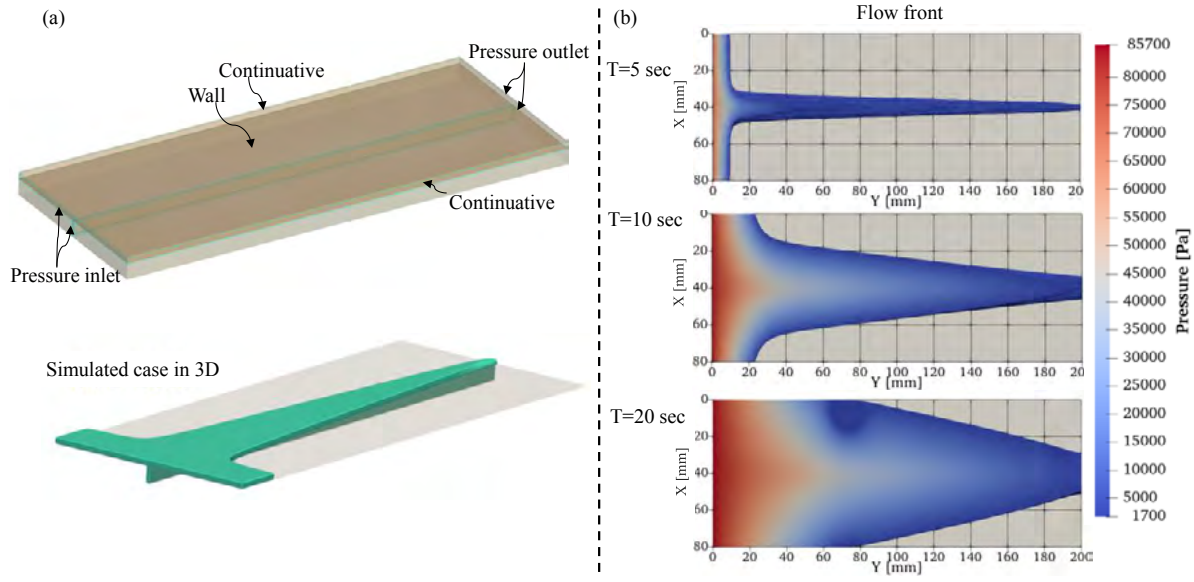


Figure 2. (a) CFD model geometry and the boundary conditions (top) and simulated sample in 3-dimension (bottom); (b) Flow front and pressure profile of the simulated cases at different infusion times.

The fluid flow is assumed to be transient, isothermal, and incompressible with a constant density ρ. The flow within the porous medium is solved based on the Darcian saturated drag model that adds a drag term to the momentum equations. Therefore, the flow dynamics are governed by the following mass and momentum conservation equations:

$$\nabla . \boldsymbol{u} = 0 \qquad (1)$$

$$\frac{\partial \boldsymbol{u}}{\partial t} + \boldsymbol{u}.\nabla \boldsymbol{u} = -\frac{1}{\rho}\nabla p + \boldsymbol{g} + \frac{\mu}{\rho}\nabla^2 \boldsymbol{u} - \boldsymbol{F} \quad (2)$$

where $\boldsymbol{u}$ is the velocity vector, p is the pressure, t is the time, $\boldsymbol{g}$ is the gravitational acceleration vector with components $(0,0,-g)$; $g = 9.81$ ms^{-2} is the gravitational acceleration, and $\boldsymbol{F}$ is the resistance to flow in the porous medium, i.e., the drag term, and is given as follows:

$$\boldsymbol{F} = \boldsymbol{F_d}\boldsymbol{u} \quad (3)$$

where $\boldsymbol{F_d}$ is the drag coefficient vector of the porous media and is given as follows:

$$\boldsymbol{F_d} = \frac{\boldsymbol{\epsilon}\mu}{\rho K} \quad (4)$$

where $\boldsymbol{\epsilon} = (\epsilon_x,\ \epsilon_y,\ \epsilon_z)$ is the porosity vector equivalent to the volume fraction of the porous media, and K is the permeability of the porous media.

The permeability values found in experiments are different in x, y, and z directions (three principal directions) with a constant porosity (0.506 = volume fraction) in all directions, and they are implemented in the CFD model as directional porosity found by the equation of the drag coefficient, i.e., by Equation 4, where the permeability K is constant. Initially, the drag coefficient is calculated by $F_d = \epsilon\mu/\ \rho K$; where $\epsilon = 0.506$, and $K = 1.25$e-10 (derived from the sinusoidal transformation of the permeability along the principal direction, i.e., averaging K_1 and K_2, as the angle of orientation is 45°). Finally, three porosity values are obtained by $\epsilon_i = F_d \rho K_i/\mu;$ using the calculated F_d and the princpal permeabilities (K_1, K_2, K_3). The porosity values corresponding to the permeability in principal directions are summarized in Table 1, which also includes specific details regarding the shallow cut and fabric dimensions.

The developed one fluid and void model uses the Volume of the Fluid method to track the free surface of the fluid through the low-pressure void domain, and the Finite Volume Method is used to discretize and solve the continuity and momentum equations. Figure 1-b showcases the simulated flow front for different infusion times, where the color represents the fluid pressure profile that changes over time.

Table 1. Properties of the fabric and details of the porous channel and shallow cut.

Case ID	Fabric thickness (mm)	Fabric volume fraction (-)	Fabric permeability (m^2)/porosity (-)			Dimension of the fabric or porous channel (mm^3)	Shallow cuts (-)	CtC spacing (mm)
			along x-direction	along y-direction	along z-direction			
1	2.22	0.506	1.89e-10/ 0.763	6.14e-11/ 0.248	1.093e-11/ 0.0668	80×200×2.22	1	N/A
2							2	10
3							2	20
4							2	40

3. Results and discussions

The flow fronts and the fluid filling between grooves over infusion time are investigated for two different configurations of the shallow grooves, i.e., single and double grooves, and are presented in Figures 3 to 7. Figures 3 to 5 present the flow fronts at different infusion times, specifically 5, 10, and 20 seconds, representing distinct stages of inlet pressure: sudden pressure buildup, the end of the buildup, and stabilized pressure, respectively. Figure 3 showcases experimental and simulated flow fronts at the bottom and top of the fabric at the infusion time of 5 seconds. The experiment shows that the flow fronts at the bottom and top of the fabric have significant differences, as expected, attributed to the more prominent flow along the groove and the slower flow along the z-direction within the fabric due to its lower permeability, cf. Figure 3-a. The simulated flow fronts at the bottom and top of the fabric

presented in Figure 3-b effectively capture the above phenomena. Figure 3-c provides the qualitative comparison between the experimental and simulated flow fronts. While simulations exhibit relatively good agreement, small discrepancies are observed. Specifically, the simulation slightly under-predicts the flow front length and width in both views; nevertheless, the resin flow within the fabric is more accurately predicted in the top view compared to the bottom view.

Figure 4 presents the flow fronts at the bottom and top of the fabric obtained from both experiment and simulation at an infusion time of 10 seconds, corresponding to the phase when the inlet pressure begins to stabilize. The experimental and simulated results, as illustrated in Figures 4-a and 4-b, respectively, exhibit similar patterns as observed in Figures 3-a and 3-b, apart from the fact that the flow front is more developed at this stage due to longer infusion time and the inlet pressure buildup. The qualitative comparison between the experimental and simulated flow fronts is presented in Figure 4-c. It is seen that the simulations tend to over-predict the flow compared to the experimental observations, regardless of the viewing perspective (i.e., top or bottom views).

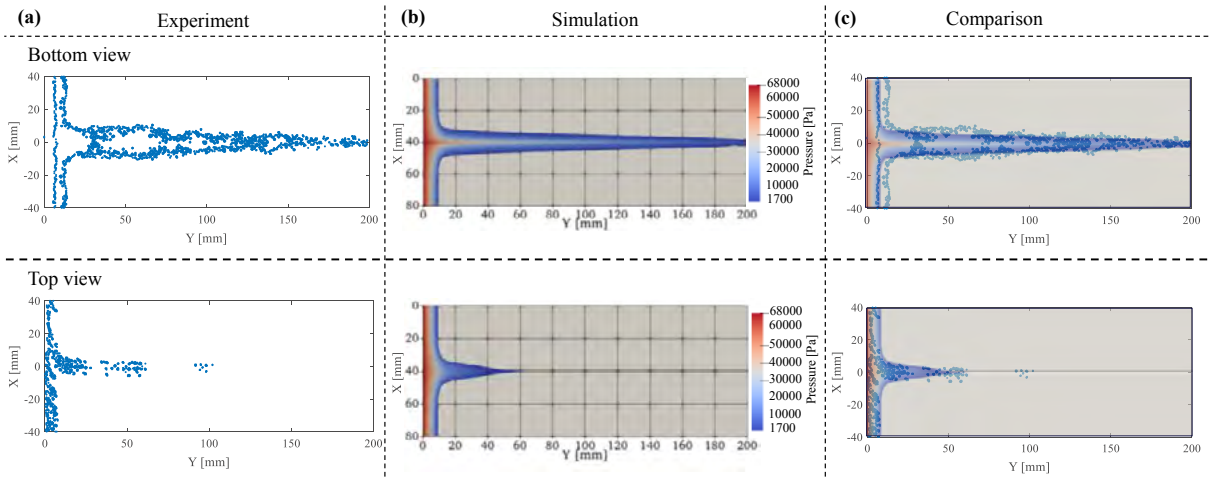


Figure 3. Flow fronts at the bottom and top of the fabric at an infusion time of 5 seconds. (a) Flow front captured during the experiment; (b) simulated flow fronts; and (c) qualitative comparison between experimental and simulated flow front.

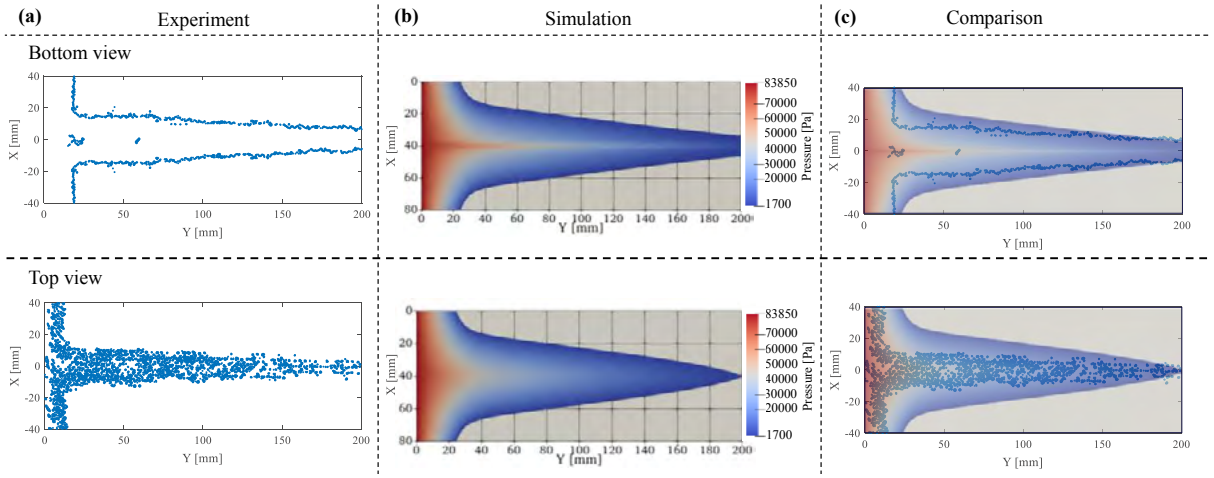


Figure 4. Flow fronts at the bottom and top of the fabric at an infusion time of 10 seconds. (a) Flow front captured during the experiment; (b) simulated flow fronts; and (c) qualitative comparison between experimental and simulated flow front.

Furthermore, the flow fronts are investigated at an infusion time of 20 seconds, corresponding to stable inlet pressure, and presented in Figure 5. Unlike previous observations, both experimental and simulated flow fronts at the bottom and top of the fabric are nearly identical, cf. Figures 5-a and 5-b. This similarity primarily arises from the dominance of flow through the fabric by high inlet- and groove-pressure, especially when looking into a smaller dimension. However, this phenomenon is required to be investigated to better understand this behaviour for different thicknesses, permeability of the fabric, and inlet pressure. The qualitative comparison between the experimental and simulated flow fronts in Figure 5-c gives similar information as seen in Figure 4-c that simulation tends to over-predict the flow in the fabric.

Overall, the simulations well predicted the nature of the flow fronts and their differences at both the top and bottom of the fabric. The simulations show the flow fronts and the resin flow in the fabric give the closest experiments when the infusion time is shorter. For larger times, the discrepancies become strong due to the dominating nature of the flow in the fabric from the channel in the investigated cases. These discrepancies can partially be due to issues of variability in permeability characterization and the difficulty in non-destructively assessing experimental fibre volume fractions. The predicted details are, however, sufficiently in agreement with the experiments, so the CFD model is used to investigate the flow fronts and filling between two grooves for different cut-to-cut (CtC) spacing of shallow grooves and are presented in Figures 6 and 7.

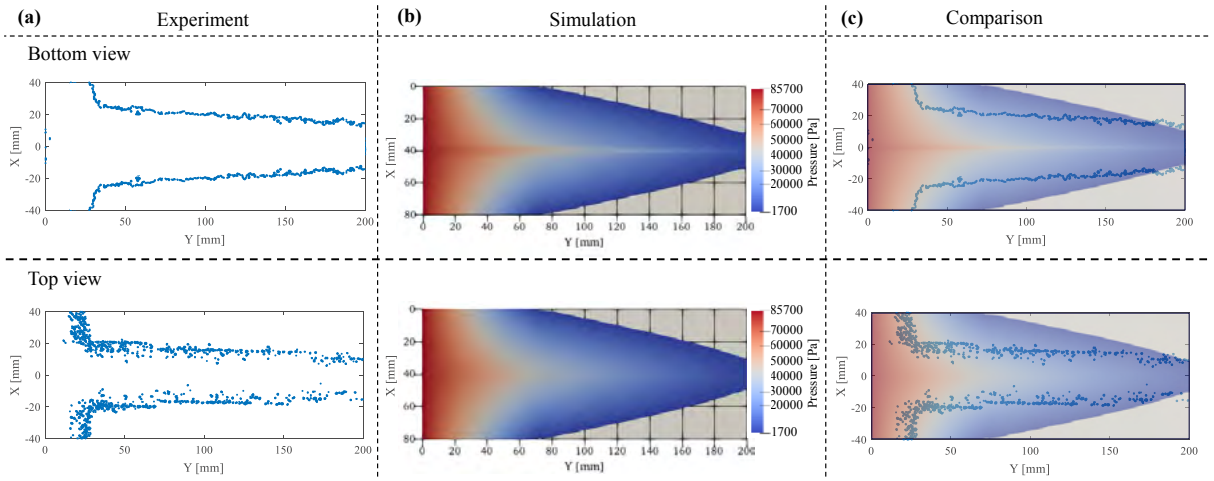


Figure 5. Flow fronts at the bottom and top of the fabric at an infusion time of 20 seconds. (a) Flow front captured during the experiment; (b) simulated flow fronts; and (c) qualitative comparison between experimental and simulated flow front.

Figure 6 illustrates the flow fronts at various infusion times for two grooves with different cut-to-cut (CtC) spacings: 10 mm, 20 mm, and 40 mm. The computational domain remains constant, as in the previous simulated case, at 80×200×2.22 mm³, with the number of grooves limited to two. Realistically, a repeated pattern of grooves would be used in the true core materials. Therefore, while keeping computational complexity down, the presented results focus only on the filling between channels. Figure 6 shows that increasing CtC spacing increases the filling time between the channels, as expected. It can also be noticed that the minimum flow distance between channels (FD_{min}) changes for different CtC spacing, cf. Figure 6. Figure 7 quantifies the FD_{min} and presents it as a function of infusion time for both the top and bottom fabric surfaces. The FD_{min} reaches the length of the domain (200 mm) faster when the CtC is smaller, while it takes longer for the larger CtC spacing. Furthermore, it can seen that the FD_{min} at the top and bottom of the fabric varies. For CtC 10 mm, the largest differences between the top and bottom FD_{min} are observed (blue curves), while the differences reduce when CtC spacing increases. For the largest investigated CtC 40 mm, the FD_{min} is identical at the top and bottom of the fabric throughout the filling (purple curves).

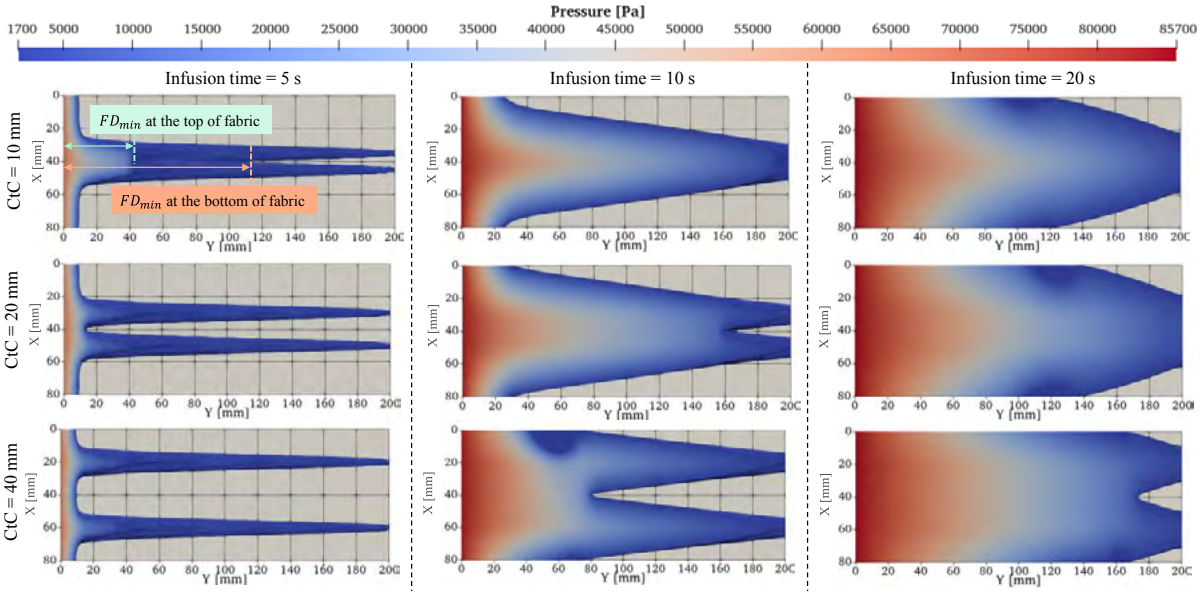


Figure 6. Flow fronts for different cut-to-cut (CtC) spacing of 10, 20, and 40 mm at different infusion times of 5, 10, and 20 seconds.

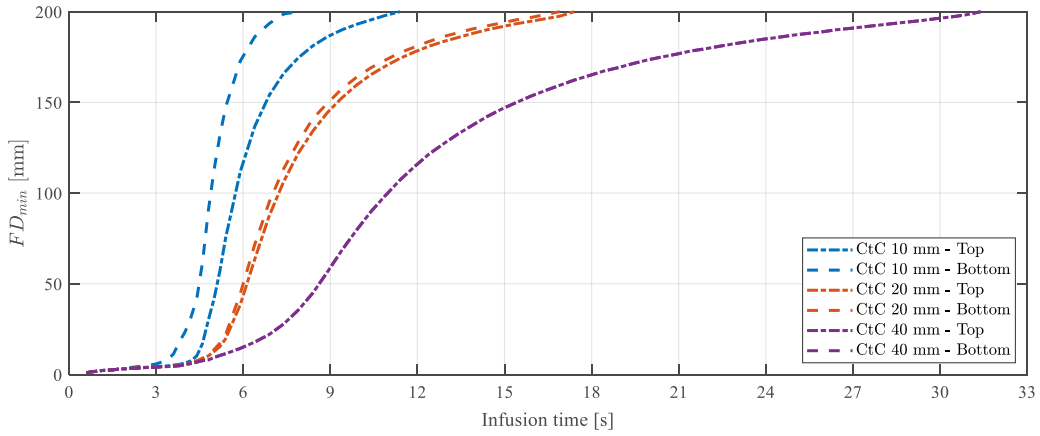


Figure 7. Minimum flow distance between channels (FD_{min}) at the top and bottom of the fabric as a function of infusion time for different cut-to-cut (CtC) spacing.

3. Conclusions

This paper investigates the Vacuum-Assisted Resin Infusion (VARI) process for manufacturing composite sandwich panels using experiments and simulations. The study focuses on the lower reinforcement layers and shallow grooves of the composite sandwich panels to analyze flow front profiles and infusion time. The simulated results accurately capture flow front profiles and patterns at both the bottom and top of the fabric, showing reasonable agreement with experimental data. Discrepancies are observed primarily for larger infusion times. Both experiments and simulations demonstrate that flow fronts at the bottom of the fabric are more pronounced than those at the top for smaller infusion times. However, as infusion time increases, flow fronts become more identical due to the dominance of flow through the fabric driven by high inlet and groove pressure. Furthermore, the model is utilized to simulate infusion with the presence of two shallow cuts, and the filling of fluid between two grooves is investigated for different cut-to-cut (CtC) spacings. As expected, the filling of fluid between two grooves takes less time for smaller CtC spacing. Additionally, it is noted that the minimum flow distance between the grooves varies at the top and bottom of the fabric. The differences are more pronounced when the CtC spacing is smaller, and they decrease when the CtC spacing is increased.

In future work, the simulated results can be compared with experiments involving various configurations of the channel, through-thickness experiments, and different fabric properties. This comparative analysis will provide deeper insights into the accuracy and applicability of the simulation model across diverse scenarios. Subsequently, a parametric study can be performed to better understand the process.

Acknowledgements
The authors would like to acknowledge the financial support of the Energy Technology Development and Demonstration Program (EUDP) for the "Opticore Platform" Udvikling Demonstration Project, Grant No. 64022-1041. The authors, MTM and JS, would like to thank FLOW-3D® for their support regarding licenses. Moreover, the author, MTM, would like to acknowledge Dr. Berin Šeta for the scientific discussion on CFD modelling.

References
[1] Zhao C, Zhang G, Wu Y. Resin Flow Behavior Simulation of Grooved Foam Sandwich Composites with the Vacuum Assisted Resin Infusion (VARI) Molding Process. Materials 2012;5:1285–96. https://doi.org/10.3390/ma5071285.
[2] Pierce RS. Challenges in permeability characterisation for modelling the manufacture of wind turbine blades. IOP Conf Ser: Mater Sci Eng 2023;1293:012009. https://doi.org/10.1088/1757-899X/1293/1/012009.
[3] Sandberg M, Hattel JH, Spangenberg J. Flow-Induced Fibre Compaction in Resin-Injection Pultrusion. Transp Porous Med 2023;147:541–71. https://doi.org/10.1007/s11242-023-01911-x.
[4] Spangenberg J, Larsen M, Rodríguez RR, Sánchez PMM, Rasmussen FS, Sonne MR, et al. THE EFFECT OF SATURATION ON RESIN FLOW IN INJECTION PULTRUSION: A PRELIMINARY NUMERICAL STUDY 2017.
[5] Koefoed MS. Modeling and Simulation of the VARTM Process for Wind Turbine Blades n.d.
[6] Han K, Jiang S, Zhang C, Wang B. Flow modeling and simulation of SCRIMP for composites manufacturing. Composites Part A: Applied Science and Manufacturing 2000;31:79–86. https://doi.org/10.1016/S1359-835X(99)00053-6.
[7] Celle P, Luca P, Drapier S, Bergheau J-M. Numerical modeling of infusion processes (LRI and RFI). vol. 52. 2007.
[8] Bickerton S, Advani SG, Mohan RV, Shires DR. Experimental analysis and numerical modeling of flow channel effects in resin transfer molding. Polym Compos 2000;21:134–53. https://doi.org/10.1002/pc.10172.
[9] Deléglise M, Binétruy C, Krawczak P. Solution to filling time prediction issues for constant pressure driven injection in RTM. Composites Part A: Applied Science and Manufacturing 2005;36:339–44. https://doi.org/10.1016/j.compositesa.2004.07.001.
[10] Sandberg M, Yuksel O, Comminal RB, Sonne MR, Jabbari M, Larsen M, et al. 6 - Numerical modeling of the mechanics of pultrusion. In: Silberschmidt VV, editor. Mechanics of Materials in Modern Manufacturing Methods and Processing Techniques, Elsevier; 2020, p. 173–95. https://doi.org/10.1016/B978-0-12-818232-1.00006-0.
[11] Sandberg M, Hattel JH, Spangenberg J. Simulation of liquid composite moulding using a finite volume scheme and the level-set method. International Journal of Multiphase Flow 2019;118:183–92. https://doi.org/10.1016/j.ijmultiphaseflow.2019.06.014.
[12] Isoldi LA, Oliveira CP, Rocha LAO, Souza JA, Amico SC. Three-dimensional numerical modeling of RTM and LRTM processes. J Braz Soc Mech Sci & Eng 2012;34:105–11. https://doi.org/10.1590/S1678-58782012000200001.
[13] Nedanov PB, Advani SG. A Method to Determine 3D Permeability of Fibrous Reinforcements. Journal of Composite Materials 2002;36:241–54. https://doi.org/10.1177/0021998302036002462.
[14] Weitzenböck JR, Shenoi RA, Wilson PA. Measurement of three-dimensional permeability. Composites Part A: Applied Science and Manufacturing 1998;29:159–69. https://doi.org/10.1016/S1359-835X(97)00049-3.
[15] FLOW-3D. FLOW-3D n.d. https://www.flow3d.com/products/flow-3d/ (accessed May 7, 2024).

EFFECT OF TEMPERATURE ON THE MODE II FATIGUE DELAMINATION OF A GLASS FIBER REINFORCED POLYMER (GFRP)

Marcio Moreira Arouche[1], Sigurdur Egilsson[1] , Weikang Feng[1] and Marko Pavlović[1]

[1]Department of Engineering Structures, Faculty of Civil Engineering and Geosciences, Delft University of Technology, Stevinweg 1 - 2628 CN Delft, Netherlands
Email: marcio.m.arouche@gmail.com

Keywords: Delamination, Fatigue, ENF test, Temperature, GFRP

Abstract
A new technology of composite wrapped joints emerges as a promising solution for improving the long-term performance of connections between circular hollow sections (CHS). The use of composite materials is shown to improve the fatigue life of structures. However, a major challenge to the implementation of this technology is to ensure the long-term performance of the composite materials subjected to the operational conditions. This work aims to evaluate the effects of temperature changes on the fatigue delamination of a glass fiber reinforced polymer (GFRP) for application in offshore structures. Specimens were manufactured by hand lay-up and series of experiments are performed to access delamination fatigue crack growth behavior in a range of operational temperatures: -10, 21 and 70 °C. Displacement controlled end-notched flexure (ENF) tests were applied to measure the fatigue behavior together with a digital image correlation (DIC) system to monitor the displacements during the tests. Results show that the delamination fatigue performance of the composite material is not significantly affected by the range of tested temperatures. The fracture behavior also remained unchanged. Standard ENF test method has limited range of crack growth to evaluate the fatigue behavior of composite laminates.

1. Introduction

Composite materials, e.g. fiber-reinforced polymers (FRPs), are increasingly popular in structural applications due to their high strength-to-weight ratio, design flexibility, and fatigue resistance. In the construction sector, an innovative joining technique for steel hollow sections has been introduced using wrapped composite joints instead of traditional welded joints [1]. The loadings in jacket structures are transmitted through a wrapped glass fibre reinforced polymer (GFRP) with a large bonded area. The stress concentration can be significantly relieved, improving fatigue resistance. The elastic stiffness, static resistance, and fatigue behaviour are equivalent to or larger than those of their welded alternative for the properly designed composite wrap. However, the mechanical behavior of the composite material under operational conditions still needs to be clarified for the implementation of the technology.

The performance of composite structures is significantly influenced by environmental factors [2]. Short-term changes of temperature can have a significant impact on the mechanical properties of the material. In particular, the mode II delamination crack growth is the most relevant for the design of composite wrapped joints. Understanding the effects of temperature on the mode II delamination fracture and fatigue of the material is crucial for the design and structural integrity of the joints during operational life.

©2024 | 3_MOREIRA AROUCHE_Marcio_14XKZ.pdf

In this work, the effects of temperature changes on the fatigue delamination of a glass fiber reinforced polymer (GFRP) is investigated. Specimens were manufactured by hand lay-up and series of experiments are performed to access delamination fatigue crack growth behavior in a range of operational temperatures. The reference temperature of 21 °C, a low temperature of -10 °C and a high temperature condition of 70 °C are tested.

2. Materials and Manufacturing

Glass fiber reinforced polymer (GFRP) plates were manufactured. A vinyl ester resin was applied to the hand lay-up lamination of glass fiber bi-directional woven interleaved to layers of glass fiber chopped strand mat (CSM), as shown in Figure 1. A non-adhesive insert of 32 µm thickness was placed at the mid-plane to create an artificial pre-crack. The laminated plate cured in air conditions of 18±1 °C and 50±5% humidity. Then, the composite plate was cut to 0/90 coupon specimens using water jet. Finally, part of the specimens was post cured in an oven at 120 °C for 7 h. The testing specimens have a nominal length of 230 mm, and an average width (w) and thickness (2h) of 19.68±0.14 mm and 7.68±0.21 mm, respectively, measured from the average of 3 different sections using a digital caliper.

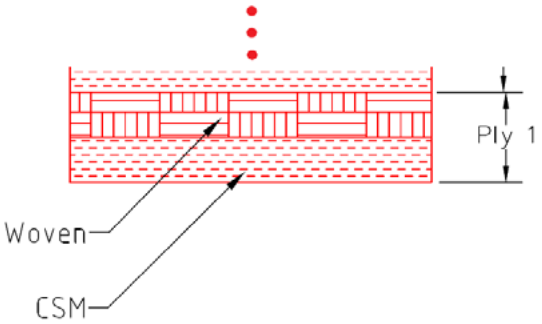


Figure 1. Scheme of the composite lay-up.

3. Experimental procedures

3.1. Test Set Up

A thin layer of white matt paint was coated and a random black speckle pattern was applied to the measurement surface of the specimen. A high resolution camera (50.6 MPx) and a blue LED light source were positioned to the measurement surface to acquire the full field displacements by DIC. Photos were taken every 200 cycles at the minimum and maximum displacements, synchronized with load measurements from the testing machine. For the image processing, surface points were recognized by a small neighborhood of a square with a side length of 19 pixels and a step size of 11 pixels set in the DIC software.

Displacement controlled fatigue ENF tests were performed. Table 1 shows the test matrix. The first test (01-RT) was used to verify the most appropriate displacement level. Then, the maximum displacement, δ_{max}, was set to have an initial force of 70% of the critical force obtained from quasi-static tests. The minimum displacement, δ_{min}, was set to have $\delta_{max}/\delta_{min}$ equals 0.1. Table 1 also includes the mode II critical SERR, G_{IIc}, and the flexural modulus of the material, E_f, obtained from static tests of specimens cut from the same plate and tested in different temperatures.

Specimens were tested at the room temperature (RT) of 21±1 °C, and a climate chamber was used with the test set up for conditioning specimens in the low temperature (LT) of -10±1 °C and the high temperature (HT) of 70±1 °C. Two air mixing fans improved stability of air conditions over time and

the specimens were maintained in a constant condition for 7 hours prior to the tests to ensure a homogeneous temperature field in the material. Series of 3 specimens were tested in each configuration.

Table 1. Test matrix.

Specimen	Temperature (°C)	Maximum Displacement (mm)	G_{IIc} (N/mm²)	E_f (GPa)
01-RT	21	1.48 - 2.20 - 2.64	3.833	9.09
02-RT	21	2.05		
03- RT	21	2.31		
04-HT	70	3.28	7.664	7.92
05-HT	70	3.13		
06-HT	70	3.09		
07-LT	-10	2.70	3.837	12.50
08-LT	-10	2.67		
09-LT	-10	3.01		

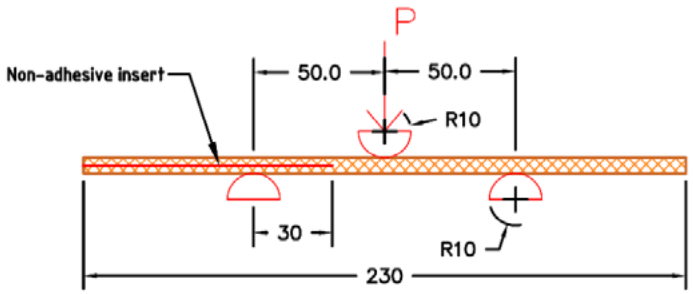


Figure 2. ENF test set up.

3.2. Calculation of the strain energy release rate

The delamination fracture toughness is described by the Resistance curves, or R-curves, that relates the strain energy release rate (SERR) with the crack length. The SERR, or *G*, from the crack growth of a tested specimen can be analytically derived from Irwin-Kies Equation (1):

$$G = \frac{P^2}{2B}\frac{dC}{da} \tag{1}$$

where *P* is the applied load, *B* is the specimen width, *C* is the specimen compliance, or the ratio of the load point displacement to the applied load ($C = \delta/P$), and a is the crack length. The compliance based beam method (CBBM) [3] relates Timoshenko beam theory and the specimen compliance to obtain the fracture energy.

For a ENF test set up, the specimen compliance becomes Equation (2):

$$C = \frac{3a^3 + 2L^3}{8E_f Bh^3} + \frac{3L}{10G_{13}Bh} \tag{2}$$

where L is the half span of the ENF test. Combining Equations (1) and (2), the mode II fracture toughness, G_{II}, can be obtained:

$$G_{II} = \frac{9P^2a^2}{16B^2h^3E_f} \tag{3}$$

The flexural modulus, E_f, can be estimated experimentally, for each ENF test specimen, using the initial compliance C_0 and the initial crack length a_0, as shown in Equations (4) and (5):

$$E_{f(ENF)} = \frac{3a_0^3 + 2L^3}{8Bh^3C_{0\text{corr}}} \tag{4}$$

Where:

$$C_{0\text{corr}} = C_0 - \frac{3L}{10G_{13}Bh} \tag{5}$$

Finally, the CBBM suggests that the crack length, a, can be estimated from the specimen compliance as an equivalent crack length, a_e, obtained directly from Equation (6):

$$a_e = \left[\frac{1}{3}\left(\left(C - \frac{3L}{10G_{13}Bh}\right)8E_fBh^3 - 2L^3\right)\right]^{1/3} \tag{6}$$

This method allows accounting for the variation in the bending modulus of the material of each specimen and due to the effect of temperature.

4. Results and Discussion

The mode II SERR was calculated by the CBBM using Equation (4). In the case of the fatigue ENF tests performed in this work, the displacements were measured with DIC as the difference between the vertical displacement of the load point and the average vertical displacement of the support points. The initial compliance was the measured minimum compliance in the points of maximum displacement. A nominal value of 3.5 GPa was used for G_{13}.

The variation of the SERR with the mode II fatigue cycles is presented in Figure 3 for the different temperautres. The range of SERR in fatigue over the critical SERR ($\Delta G_{II}/G_{IIc}$) remained below 0.4, which is typical of the ENF test set up [4]. Tests in room and low temperatures showed similar results, such as in the G_{IIc} from static tests (see Table 1). A more significant decrease of ΔG_{II} is noticed in high temperatures.

Figure 4 shows the Paris curves of ENF tests in different temperatures. It is observed that high temperature conditions resulted in a slightly better performance of the mode II interlaminar fracture under cyclic loadings. This can be measured by the slope of the Paris curves, represented by the m-parameter in Table 2 where results of high temperature shows relatively smaller m parameter than others.

The experimental flexural modulus (E_f) was obtained from the fatigue tests using the initial compliance at the maximum force. Differently from the results of static tests (see Table 1), the fatigue tests was not able to measure a clear change of the E_f with temperature.

Representative fracture surfaces are shown in Figure 5. All tests resulted in the same failure mode. The crack growth occurred between the woven, on the upper side, and the chopped strand mat, on the lower side of the specimens.

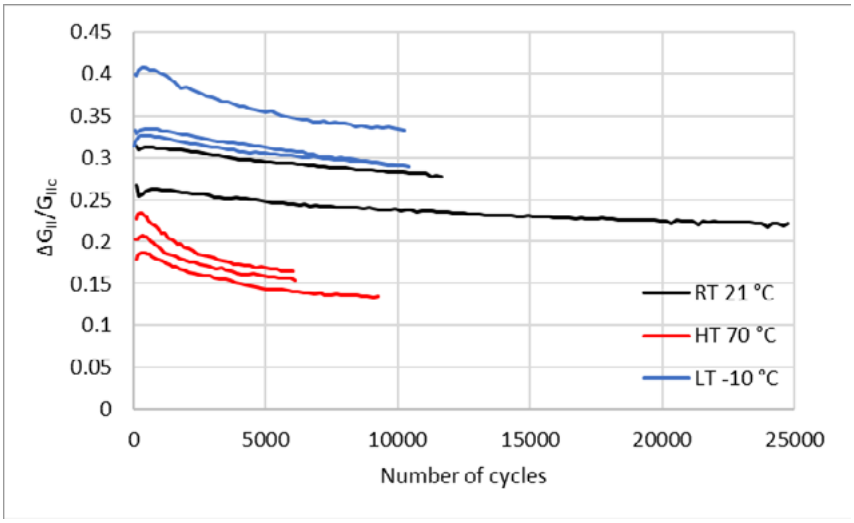


Figure 3. Variation of the SERR with the mode II fatigue cycles in different temperatures.

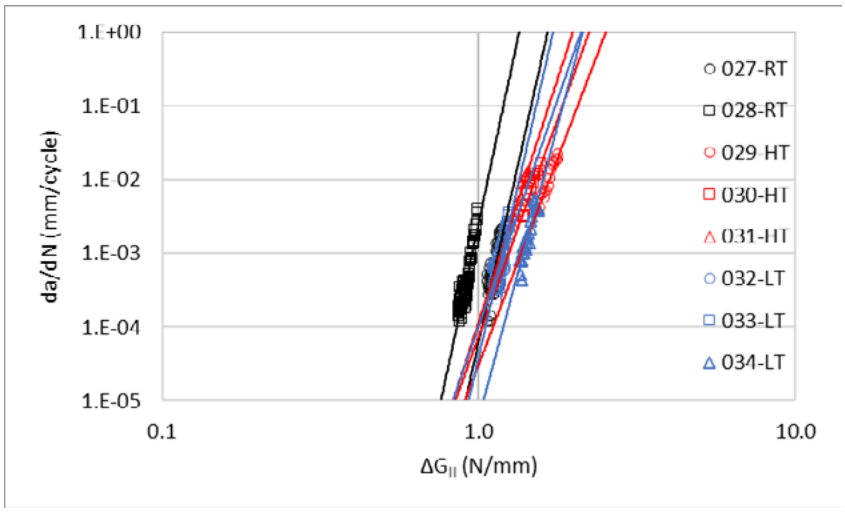


Figure 4. Paris curves from fatigue ENF tests in terms of (a) ΔG_{II} and (b) $\Delta G_{II}/G_{IIc}$.

Table 2. Experimental parameters from fatigue Paris curves.

Specimen	Temperature (°C)	E_f (GPa)	C	m	R
026-RT	21	12.2	-	-	-
027-RT	21	11.9	6.0E-05	19.297	0.845
028- RT	21	10.8	2.6E-03	20.295	0.927
029-HT	70	10.4	3.0E-05	11.227	0.933
030-HT	70	10.3	8.0E-05	11.832	0.942

031-HT	70	9.6	1.0E-04	13.228	0.928
032-LT	-10	10.7	1.0E-04	12.353	0.701
033-LT	-10	11.7	4.0E-05	18.747	0.910
034-LT	-10	10.6	6.0E-06	15.964	0.675

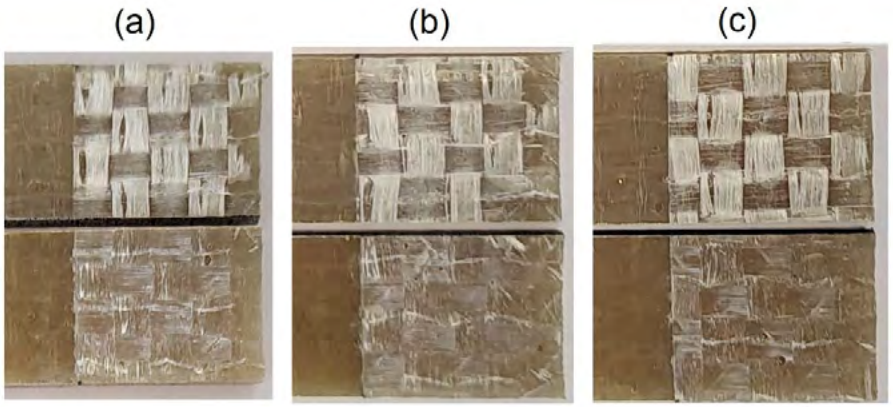


Figure 5. representative fracture surfaces of specimens tested in different temperatures.

5. Conclusions

The effects of temperature changes on the fatigue delamination of a GFRP was investigated. Displacement controlled ENF tests were applied to measure the fatigue performance in room conditions (21 °C), and using a chamber at -10 and 70 °C. A DIC system to monitor the displacements during the tests.

Changes of temperature did not significantly affect the delamination fatigue performance of the composite material. In addition, no change in the fracture surfaces was observed with temperature.

The standard ENF test method has limited range of crack growth to evaluate the fatigue behavior of composite laminates.

Acknowledgments

The authors would like to express their gratitude to RVO for the financial support with Topsector Energiesubsidie van het Ministerie van Economische Zaken through WrapNode-II project, and Tree Composites B.V. for the production of specimens.

References

[1] W. Feng and M. Pavlovic. Fatigue behaviour of non-welded wrapped composite joints for steel hollow sections in axial load experiments, Eng. Struct., 249:113369, 2021.
[2] M. M. Arouche and M. Pavlovic. Effect of offshore environmental conditions on the mechanical behavior of glass fiber reinforced polymers (GFRPs). In: 11th International Conference on Fiber-Reinforced Polymer (FRP) Composites in Civil Engineering (CICE), Rio de Janeiro, Brazil, 2023.
[3] M. F. S. F. de Moura, R. D. S. G. Campilho and J. P. M. Gonçalves. Pure mode II fracture characterization of composite bonded joints. Int. J. Solids Struct., 46(6):1589-1595, 2009.
[4] W. Feng, M. M. Arouche and M. Pavlovic. Fatigue crack growth characterization of composite-to-steel bonded interface using ENF and 4ENF tests, Compos. Struct., 334:117963, 2024.

BICOMPONENT MELT-SPINNING OF FILAMENTS FOR MATERIAL EXTRUSION 3D PRINTING

Sithiprumnea Dul[1], Edith Perret[1,2] and Rudolf Hufenus[1]

[1]Laboratory for Advanced Fibers, Empa, Swiss Federal Laboratories for Materials Science and Technology, Lerchenfeldstrasse 5, 9014 St. Gallen, Switzerland
Email: sithiprumnea.dul@empa.ch, Web Page: https://www.empa.ch/web/s402
[2]Center for X-ray Analytics, Empa, Swiss Federal Laboratories for Materials Science and Technology, Überlandstrasse 129, 8600 Dübendorf, Switzerland

Keywords: Bicomponent melt-spinning, filament, 3D printing, co-extrusion, overcoating extrusion.

Abstract
This study explores the use of bicomponent core-sheath filaments, featuring a hard core and a soft sheath, as a potential solution to common issues such as poor adhesion, voids, and rough surfaces, which are often encountered with conventional monofilaments. Through co-extrusion and overcoating techniques, various filaments were produced and evaluated. The tensile properties of 3D-printed parts from bicomponent filaments, at different raster angles (0° and 45°), were compared to those of standard monofilaments. Results indicated that while bicomponent filaments made of polylactic acid (PLA) performed comparably to monofilaments, those with polyamide (PA) cores showed significant improvements, particularly at the 45° raster angle. Notably, filaments with a carbon fiber reinforced PA core and a PA sheath enhanced both processability and structural integrity. Additionally, two overcoated filaments, featuring polyethylene terephthalate (PET) and polyphenylene sulfide (PPS) monofilament cores with a copolyester (CoPES) sheath, were developed for 3D printing. Parts printed from PET/CoPES overcoated filaments exhibited good consolidation when printed at temperatures above the melting point of PET.

1. Introduction

In the field of additive manufacturing (AM), material extrusion (MEX), commonly known as fused deposition modeling (FDM) or fused filament fabrication (FFF), is notable for its simplicity, cost-effectiveness, and versatility in materials. However, the layering structure often results in limited adhesion and the formation of voids between layers, which adversely affects the mechanical properties of the printed parts, leading to reduced strength and durability [1, 2]. Additionally, the rough surfaces produced by the FDM process and abrasive surface materials, such as short fiber-reinforced composites, can pose challenges for post-processing tasks such as painting, chrome-plating, or milling. To address these challenges, employing a bicomponent core-sheath approach offers a promising solution [3, 4]. This technique uses a high-viscosity polymer core for structural integrity, paired with a low-viscosity sheath material, ideally compensating for irregularities resulting from the layered production.

Bicomponent melt-spinning technology, dating back to the 1960s, combines two polymers to enhance functionality [5, 6]. However, incorporating different polymers in products complicates recycling due to sorting and separation challenges. Identifying and separating polymers becomes costly and complex, diminishing recycling feasibility. Therefore, careful polymer selection in product design is crucial, ensuring products composed of different polymers are designed for recyclability to promote sustainable recycling practices.

In this work, we prioritized recycling strategies. Using co-extrusion melt-spinning technology [5] or overcoating extrusion [7], we produced various bicomponent feedstock filaments compatible with filament forming techniques. To ensure miscibility, recyclability, and polymer-polymer adhesion through chain interdiffusion, we selected the same generic polymers as core and sheath materials for specific co-extruded filaments. We chose two different polylactic acid (PLA) grades with varying melt flow indexes (MFI): PDLLA (a mixture of both L-lactic acid and D-lactic acid) specifically formulated for materials extrusion 3D printing, and a low-viscosity PDLA homopolymer. Polyamides (PA), another commonly used polymer group in 3D printing, offer a large choice of miscible materials with various properties such as melt temperature, viscosity, softness, and short fiber reinforcement. To tackle the challenge of 3D printing soft materials, we pursued two approaches: (i) utilizing bicomponent melt-spinning with a soft co-polyamide (CoPA) in the core of a PA filament, and (ii) employing overcoating of a tensile polyester monofilament with a soft co-polyester (CoPES) hot melt adhesive. An added advantage of the overcoating technique is the ability to co-extrude two materials with significant differences in melting temperatures, allowing for a sheath material with high melt flowability (high MFI) compared to the core. This high flowability of the adhesive, combined with the solidification and stabilization of the base polymer during 3D printing, enhances adhesion by maximizing contact area between the two materials.

Our objective was to assess the printability of bicomponent filaments and compare the properties of resulting 3D-printed parts to those made from monocomponent filaments. The study involved analyzing the effect of different filament types on the printability of infilled 3D structures with two raster angles (0° and 45°), and evaluating the corresponding mechanical properties of the printed parts.

2. Materials and methods

2.1. Materials processing and sample preparation

For the co-extrusion process, various polymer combinations were utilized. Two grades of PLA were employed: PDLA LUMINY® D120 from TotalEnergies Corbion (Gorinchem, The Netherlands), and PLA Ingeo 3D850 from Natureworks LLC (Minnesota, USA), serving as the reference material. EMS-Chemie AG (Domat/Ems, Switzerland) supplied four grades of PA: PA6 Grilon A26, Grilon F34 (a PA6 variant), Grilon CF6S (a low viscosity Co-PA), and PA12 Grilamid L16. Spectrum PA6 CF15S, a filament reinforced with 15% carbon fiber (CF), was provided by Spectrum Group Sp. z o.o (Warsaw, Poland), pelletized for extrusion in this study. Griltex® D 1619E, a CoPES hotmelt adhesive, was also supplied by EMS-Chemie AG. Two types of monofilaments were used for overcoating: polyethylene terephthalate (PET) monofilament Rhodia Y114 from Nexis Fibres a.s. (Humenné, Slovakia), and polyphenylene sulfide (PPS) monofilament 50–46 E from Monosuisse AG (Emmenbrücke, Switzerland).

Co-extruded bicomponent filaments were fabricated using an extrusion line comprising two extruders, a spin pack, and a filament take-up unit, as depicted. The extrusion unit, custom-manufactured by Collin Lab & Pilot Solutions GmbH (Maitenbeth, Germany), consisted of a 16 mm and a 20 mm, 30 L/D single-screw extruder, each equipped with a gear pump (Mahr Metering Systems GmbH, Göttingen, Germany) respectively. These gear pumps were controlled to regulate the polymer output rates, ensuring consistent filament diameter and core/sheath volume ratio. The core and sheath polymers were joined in the spin pack using a specially designed "single" die [5] with a 3.5 mm diameter die capillary and a 3.0 mm diameter core capillary, developed by our laboratory. Extrusion temperatures were adjusted to equalize the viscosities of both polymer melts within the die, guaranteeing steady melt flow during filament production.

For the overcoated filaments, a custom pilot line was employed, featuring a 16 mm, 30 L/D single-screw extruder (Collin Lab & Pilot Solutions GmbH, Maitenbeth, Germany) equipped with a 1.2 cm³ gear pump (Mahr Metering Systems GmbH, Göttingen, Germany). The overcoating of the monofilaments (or yarns) with pressurized molten polymer was performed within a custom-made wire coating spin pack, as depicted in reference [7]. To accommodate the lack of rigidity in PET and PPS monofilaments,

a metallic capillary tube was used as a guide within the coating die, which had a diameter of 3.5 mm. CoPES, dried and fed into the extruder, was melted and pressurized to 40 bar, then conveyed by the melt pump to the overcoating die operating at 150°C.

All extruded filaments were then cooled in water and collected using a customized take-up unit, maintaining a controlled speed of 10-11 m/min to achieve the desired filament diameter, measured by the X/Y laser controller Zumbach ODAC 18XY (Zumbach Electronic AG, Orpund, Switzerland). Each filament, with a diameter of 1.75 ± 0.04 mm, was wound onto a standard spool for 3D printing. **Table 1** summarizes all received filaments and co-extruded and overcoated bicomponent filaments, along with the materials employed for the core and sheath, including their respective volume ratios.

Table 1. List of as-received filaments and co-extruded and overcoated bicomponent filaments with calculated and measured core diameter and sheath thickness.

Reference and co-extruded filaments	Core material	Sheath material	Core diameter (mm)	Sheath thickness (mm)
PLA*	PLA 3D850		NA	NA
PLA/PDLA	PLA 3D850	PDLA D120	1.43[a]	0.16[a]
PDLA/PLA	PDLA D120	PLA 3D850	1.01[a]	0.37[a]
PA6	PA6 A26		NA	NA
CoPA/PA6	CoPA CF6S	PA6 A26	(1.04 ± 0.01)[b]/1.01[a]	(0.40 ± 0.03)[b]/0.37[a]
PA12/PA6	PA12 L16	PA6 A26	(1.04 ± 0.03)[b]/1.01[a]	(0.38 ± 0.02)[b]/0.37[a]
PA6/PA12	PA6 A26	PA12 L16	(1.47 ± 0.01)[b]/1.43[a]	(0.16 ± 0.01)[b]/0.16[a]
HD-PA6/PA6	PA6 F34	PA6 A26	(1.50 ± 0.01)[b]/1.43[a]	(0.17 ± 0.01)[b]/0.16[a]
PACF/PA6	PA6 CF15	PA6 A26	(1.45 ± 0.03)[b]/1.43[a]	(0.16 ± 0.01)[b]/0.16[a]
PACF*	PA6 CF15		NA	NA
Overcoated filaments	**Core material**	**Sheath material**	**Core (inner filament) diameter (mm)**	**Sheath thickness (mm)**
PET/CoPES	PET Monofil Type Y114	CoPES D 1619E	(0.52 ± 0.01)[b]/0.5 [a]	(0.64 ± 0.04)[b]/0.625[a]
PPS/CoPES	PPS Monofilament 50-46 E	CoPES D 1619E	(0.72 ± 0.01)[b]/0.7[a]	(0.54 ± 0.05)[b]/0.525[a]

* As-received commercial filaments.
[a] Calculated values, [b] Measured values.

3D-printed samples were manufactured using the Flashforge Guider IIS 3D-printer (Flashforge, Zhejiang Province, China) in high-temperature processing mode, fed with monofilaments and co-extruded or overcoated bicomponent filaments. 3D-printed specimens from monofilaments PLA, PA6 and PACF served as reference samples. For tensile testing, dumbbell-shaped specimens of ISO 527 type 1BA (width 5 mm, thickness 2 mm) [8] were printed using monofilaments and co-extruded bicomponent filaments. For each filament type, several specimens were printed with raster angles, [0°/0°] and [+45°/−45°], respectively. Other dumbbell-shaped specimens of different size (width 12 mm, thickness 2 mm, Figure 3b) were printed using overcoated filaments, because a larger diameter of nozzle was used, resulting in larger deposited strands.

2.2. Characterzations

Dumbbell-shaped specimens underwent uniaxial tensile tests at 23°C and 50% relative humidity by using a Zwick Z100 testing machine (Zwick-Roell AG, Ulm, Germany), equipped with a 5 kN load cell. Strain was recorded using videoXtens. The elastic modulus of 3D-printed dumbbell-shaped specimens, following ISO 527 type 1BA standards, was determined employing a crosshead speed of 1 mm/min and

a gauge length of 30 mm. As per ISO 527, the elastic modulus was calculated as the average secant values between strain levels of 0.05% and 0.25%. Fracture properties were assessed for dumbbell-shaped specimens of ISO 527 type 1BA from co-extruded filaments at a crosshead speed of 10 mm/min.

3. Results and discussion

The tensile properties of dumbbell-shaped samples made from co-extruded bicomponent filaments were evaluated and compared with those of reference samples produced from monofilaments. The samples were divided into three groups: PLA, PA, and PA reinforced with carbon fibers, as depicted in **Figure 1**. The PLA, PDLA/PLA, and PLA/PDLA samples demonstrated similar elastic moduli, approximately 3.3 GPa, peak maximum tensile stress around 54 MPa, and strains at break about 2%. This analysis reveals that the mechanical properties of the bicomponent and monofilament samples are similar, due to the similar material characteristics of PLA and PDLA, which did not significantly enhance the tensile properties of 3D-printed components using a bicomponent approach.

PA-based specimens fabricated with a 0° raster angle showed average elastic moduli between 1.0 and 1.5 GPa, with maximum tensile stresses ranging from 32.5 to 40.5 MPa, which are typical for conditioned polyamide [9]. The elastic moduli of PA6 and HD-PA/PA6 specimens are comparable due to the similar properties of these materials. However, specimens combining PA6 with PA12 (PA6/PA12 and PA12/PA6) exhibited superior performance. This enhanced performance is attributed to two factors: (i) water acts as a plasticizer in PA, diminishing its strength and stiffness, and (ii) PA12 has a lower equilibrium moisture content than PA6, which contributes to higher tensile strength and stiffness. Technical datasheets from manufacturers confirm that conditioned PA12 is superior to PA6. Additionally, the thermal properties, such as viscosity and melting points, of PA12 differ significantly from those of PA6. Despite this, the effectiveness of the reinforcement might be compromised in the PA6/PA12 configuration due to the thinness of the PA6/PA12 filament sheath, which measures only 0.16 mm, compared to a thicker 1.0 mm core in the PA12/PA6 configuration, (see **Table 1**).

When assessing the mechanical properties of 3D-printed specimens with a 45° raster angle against those with a 0° raster angle, notable differences emerge. For PA6 and HD-PA/PA6 materials, both the elastic modulus and maximum stress increase at a 45° raster angle, likely due to enhanced contact between the extruded non-oriented microfilaments and a reduced presence of voids at this angle. On the other hand, samples made from PA12 and PA6, co-extruded into bicomponent filaments and printed at the 45° raster angle, showed decreased maximum stress compared to those without PA12, shown **Figure 1b**. The lower performance in PA6/PA12 and PA12/PA6 at the raster angle 45° samples is most likely due to fractures at the PA6-PA12 interface, caused by insufficient adhesion between the two polymers. This type of failure was not observed in samples with a 0° raster angle, where the PA6-PA12 interfaces align parallel to the stress direction. Additionally, the CoPA/PA6_45° samples performed well, likely because CoPA is specifically designed as an adhesive polymer that effectively bonds to PA6.

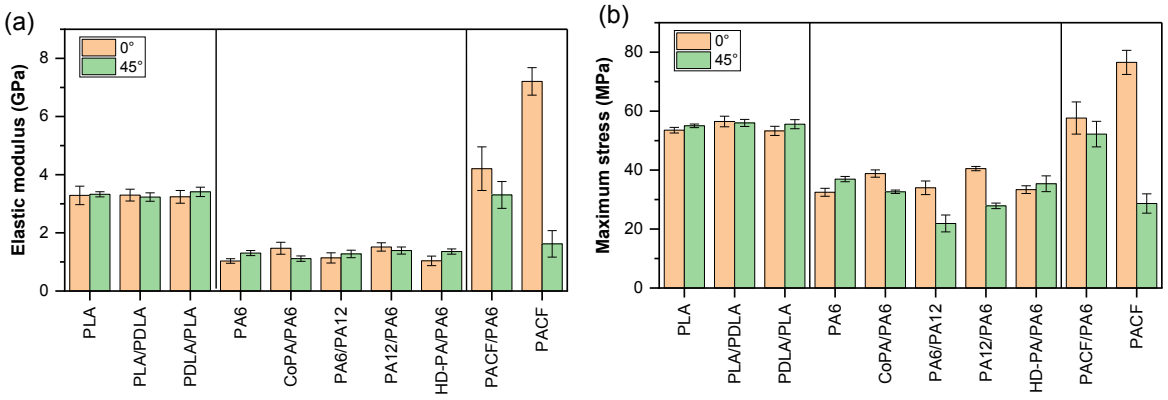


Figure 1. Tensile properties of PLA and PA specimens 3D-printed with a 0° and 45° raster angle: Elastic modulus (a) and maximum stress (b).

The third set of specimens included those reinforced with carbon fiber in a PA matrix. 3D-printed specimens composed of PACF/PA6 and PACF alone, with a 0° raster angle, showed superior elastic moduli and tensile strengths relative to PA6 alone. This enhancement is attributed to the reinforcing effects of the carbon fibers, which are highly oriented within the strands. Notably, **Figure 1** illustrates that due to a lower carbon fiber content of about 9.9 wt% in the PACF/PA6 filament, both the elastic modulus and tensile strength of the bicomponent PACF/PA6_0° are less than those of the PACF 0° alone. The PACF/PA6_45° sample displayed improved mechanical performance compared to the pure PACF_45° specimens.

To overcome the challenges associated with 3D printing soft materials, we implemented a method by overcoating two commercially available PET and PPS yarns and producing 3D prints from them. We utilized a CoPES sheath as an adhesive layer to effectively minimize voids in the 3D-printed objects. Additionally, the yarn within the filament acted as a structural support, enhancing the printability of these materials. This combination of yarn with a CoPES sheath could be a promising technique for optimizing quality and performance of 3D-printed parts.

Figure 2 shows the actual 3D-printed specimens at a 45° raster angle and cryo-fracture cross-sections of these printed specimens. Initially, it was intended to print below the melting point of the core yarn, however, nozzle clogging issues prohibited a successful printing using this approach. To maintain a steady flow of the yarn core between layers, it was necessary to increase the working temperature above the core material's melting point. For instance, PET/CoPES was successfully printed at 280°C, achieving a smooth surface finish as shown in **Figure 2**. On the other hand, PPS/CoPES required a higher temperature of 300°C and utilized a larger 0.8mm nozzle. Attempts to print with nozzles sized 0.4mm and 0.6mm were unsuccessful due to clogging. Using the 0.8mm nozzle resulted in a rough and irregular surface on the specimens, as evidenced in **Figure 2**, likely due to irregular flow.

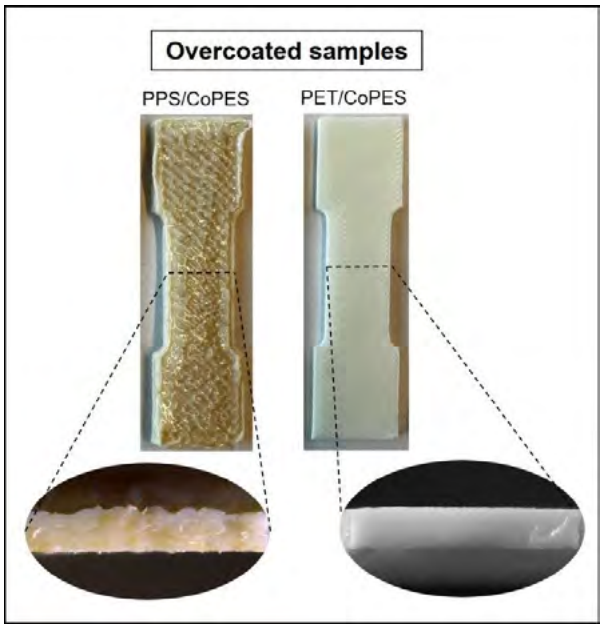


Figure 2. Specimens 3D-printed from overcoated filaments with 45° raster angles.

4. Conclusions

This study explores the impact of bicomponent feedstock filaments, produced through co-extrusion melt-spinning and overcoating extrusion technology, on both the 3D printing process and the tensile

properties of resulting printed parts. These filaments with a core-sheath structure, comprising two polymers of the same generic type but with distinct viscosities, promoting miscibility to enhance polymer-polymer adhesion and recycling strategies. This enhances the utility of these bicomponent filaments compared to traditional monocomponent ones.

When utilizing PLA-based bicomponent filaments for 3D printing, no significant differences were noted compared to monocomponent filaments, owing to their similar properties. PA-based bicomponent filaments showcased notable improvements. In particular, when printing infilled structures at a 45° angle, the combination of different PA types distinctly influenced the properties of 3D-printed parts, unlike printing at a 0° angle, where no significant differences were observed. The bicomponent PACF/PA6 filament particularly demonstrated enhanced processability and increased stiffness and tensile strength of infilled structures printed at a 45° angle.

Two overcoated filaments, consisting of PET and PPS monofilaments coated with a CoPES sheath, were assessed for their 3D printability. PET/CoPES exhibited good consolidation and satisfactory results when printed at a 45° angle above the melting point of the PET monofilament, whereas the filament with the PPS core did not show improvement.

Funding sources
This research was partially funded by Innosuisse (Switzerland), grant number 58114.1 INNO-ENG.

References

[1] H. Zhou, X. Cheng, X. Jiang, G. Zheng, J. Zhang, Y. Li, and M. Tang. Study of the interlayer bonding strength for combined 3D printing and milling of polyetheretherketone. *Journal of Applied Polymer Science*, 140(17): e53773, 2023.
[2] G. Barera, S. Dul, and A. Pegoretti. Screw Extrusion Additive Manufacturing of Carbon Fiber Reinforced PA6 Tools. *Journal of Materials Engineering and Performance*, 2023.
[3] F. Peng, Z. Zhao, X. Xia, M. Cakmak, and B.D. Vogt. Enhanced Impact Resistance of Three-Dimensional-Printed Parts with Structured Filaments. *ACS Applied Materials & Interfaces*, 10(18): 16087, 2018.
[4] A. Naqi, Z. Swain, and M.E. Mackay. Dual Material Fused Filament Fabrication via Core–Shell Die Design. *ACS Applied Polymer Materials*, 5(4): 2481, 2023.
[5] R. Hufenus, Y. Yan, M. Dauner, D. Yao, and T. Kikutani, Bicomponent Fibers. In *Handbook of Fibrous Materials,* Wiley Online Library: Hoboken, NJ, 2020.
[6] R. Hufenus, Y. Yan, M. Dauner, T. Kikutani. Melt-Spun Fibers for Textile Applications. Materials, 13(19): 4298, 2020.
[7] A.A. Leal, J.C. Veeramachaneni, F.A. Reifler, M. Amberg, D. Stapf, G.A. Barandun, D. Hegemann, and R. Hufenus. Novel approach for the development of ultra-light, fully-thermoplastic composites. *Materials & Design*, 93(1): 334, 2016.
[8] S. Dul, B.J.A. Gutierrez, A. Pegoretti, J. Alvarez-Quintana, L. Fambri. 3D printing of ABS Nanocomposites. Comparison of processing and effects of multi-wall and single-wall carbon nanotubes on thermal, mechanical and electrical properties. *Journal of Materials Science & Technology*, 121(1): 52, 2022.
[9] PA6 Grilon F34 Material Data. Available online: https://ems.materialdatacenter.com/eg/material/pdf/0/datasheet?rnd=1711441596931 (accessed on 25 March 2024).

THE SCALE EFFECT OF CRASHWORTHINESS OF COMPOSITE TUBE: EXPERIMENTAL AND SIMULATION STUDY

Jiangwei Qi[1], Wenxin Zhang[1], Xin Liu[1], Di Zhang[1], Jun Wang[2], Jie Xue[2], Jin Zhou[1] and Yugang Duan[1]

[1] School of Mechanical Engineering, Xi'an Jiaotong University, Xi'an, 710049, China
Email: jiangweiqi@stu.xjtu.edu.cn
Email: wenxiaoxin@stu.xjtu.edu.cn
Email: liuxin1998@stu.xjtu.edu.cn
Email: zhangdi0719@xjtu.edu.cn
Email: jin.zhou@mail.xjtu.edu.cn, Web Page: https://gr.xjtu.edu.cn/en/web/jin.zhou/home
Email: ygduan@mail.xjtu.edu.cn, Web Page: https://gr.xjtu.edu.cn/en/web/ygduan
[2] Key Laboratory of liquid rocket Engine Technology, Xi'an Aerospace Propulsion Institute, Xi'an, China
Email: junw83@163.com
Email: xuejie_zg_1983@163.com

Keywords: Crashworthiness, Scale effect, Crush behaviour, Failure modes, Energy absorption

Abstract
With an increasing demand for lightweight solutions, there is a growing focus on delving deeper into the energy absorption characteristics of thin-walled structures. This study employs a combined approach of numerical simulation and experimentation to investigate the size effect of energy absorption properties in carbon fiber resin matrix composite tubes. Four sets of proportionally sized 3D-scaled composite tubes were designed, and quasi-static axial crushing tests were conducted, concurrently establishing finite element models. Normalized analysis of the experimental results reveals that the load-displacement curves for the three different-sized composite tubes almost overlap, but the load for the 1/4 scale is slightly higher than the other sizes. Analyzing the failure modes of composite tubes of different sizes also shows highly similar post-crushing damage morphologies for size ratios of 1/2, 3/4, and 1, all exhibiting a 'flower-like' failure pattern, while the 1/4 size ratio displays a 'water ripple' pattern formed by the fracture of 90° fibers. Additionally, the finite element results exhibit high consistency with the experimental results, effectively replicating the experimental failure processes.

1. Introduction

The composite material has excellent mechanical properties, corrosion resistance, light weight and high strength. In recent years, composite materials have been widely used in various fields, especially in the design and manufacture of thin-walled structures [1-3]. With an increasing demand for lightweight solutions, there is a growing focus on delving deeper into the energy absorption characteristics of thin-walled structures. The energy absorption properties of composite materials are influenced by numerous factors, encompassing ply stacking sequence [4, 5], geometry, and trigger shape [6, 7]. The design of the ply stacking sequence structure can modulate the strength, toughness, and energy absorption capacity of the composite material, while geometry directly impacts the efficiency and mode of energy absorption. Trigger shape plays a pivotal role in the initiation and regulation of the process. Additionally, considering the size effect of composite material properties holds significant implications for broadening its engineering applications and minimizing testing costs.

The size effect, characterized by a change in strength with specimen dimensions, is a recognized phenomenon in composites [8]. Numerous scholars have extensively investigated this size effect. For instance, Swanson et al. [8] explored the scaling laws associated with impact damage in composite materials and structural size. Through fracture mechanics predictions, they observed that the phenomenon of stratification is contingent on the absolute specimen size. Carrillo et al. [9, 10] conducted a study on the size effects of fibra-metal laminate using a scale model. They analyzed the geometric impacts on stiffness, strength, failure strain, and stress/strain response under three scaling methods (1D: scaling thickness dimensions, 2D: scaling plane dimensions, and 3D: scaling all dimensions). In a separate study, Farley et al. [11] investigated the effect of the internal diameter/wall thickness (D/t) ratio on the energy absorption characteristics of graphite and Kevlar reinforced epoxy resin tubes. The results indicated a nonlinear increase in energy absorption capacity with a decrease in the D/t ratio. Green et al. [12] examined the impact of size on the tensile strength of notched composites, maintaining a constant ratio of the hole diameter to the specimen's width and length. Their findings revealed that as the sample size increases, the tensile strength decreases, with a maximum reduction of 64%. In a separate study, Wisnom [13] et al. explored the size effect on the tensile strength of unidirectional and quasi-isotropic epoxy carbon fiber composites. They found that the tensile strength of unidirectional specimens decreases as the size of the specimen increases, with a linear size change coefficient exceeding 14% of 8. Meanwhile, the strength of quasi-isotropic specimens increases with the growth in thickness - a strength increment of 10% was observed when moving from a single layer to four layers. However, the trend reversed when the thickness was further increased by altering the thickness of the blocks, with strength decreasing by 62% when moving from one to eight layers. In all scenarios, none of the laminates achieved the equivalent strength of a unidirectional material. This suggests that in all cases, lateral cracking and edge delamination were the primary causes of early failure.

With the rapid advancement of computing power, numerical calculation methods prove effective in analyzing the impact on the performance of energy-absorbing structures. Utilizing advanced analytical or numerical models for predicting the mechanical behavior of composite structures can serve as a substitute for some mechanical tests, significantly reducing the cost of composite design while providing engineers with essential information for optimized designs. For instance, Luo et al. [14], considering the anisotropic constitutive relationship of composite materials, established a stiffness degradation model based on the extended Hashin failure criterion and the damage evolution law of continuous damage mechanics. They analyzed the progressive failure of G803/5224 composite pipes. Compared with experimental results, the relative error between specific energy absorption and average load was less than 6%. This method demonstrated its utility in estimating the energy absorption characteristics of composite tubes. Sokolinsky et al. [15] proposed a physics-based finite element model for quasi-static crushing of corrugated carbon-epoxy fabric composite plates, considering both intralayer (in-plane) and interlayer (layered) failure mechanisms. The in-plane response of the fabric layer was modeled using a constitutive model implemented in the commercial finite element software Abaqus/Explicit. The layered response of composite plates was simulated using the cohesive surface capability in Abaqus software. Results from Abaqus/Explicit simulation aligned well with experimental data both quantitatively and qualitatively, indicating the applicability of the proposed method and tool for simulating the real extrusion of composite structures. Building on this foundation, Qi et al. [16] and Zhao et al. [17] applied this method to study the energy absorption characteristics of bionic polycysts and tubes with different sections, respectively. Zhang et al. [18] utilized commercial finite element software LS-DYNA to establish a finite element model for the axial crushing energy absorption of composite tubes. Tan et al.'s work leveraged improvements made by Falzon et al. [19-22] to the composite damage model, including enhanced nonlinear shear response and a unified matrix-led damage initiation and mixed model inner damage progression, to simulate post-impact effects and compression.

In this study, the size effect of energy absorption in a carbon fiber resin matrix composite tube is investigated through a combination of numerical simulation and experimentation. The paper analyzes the impact of the layering structure on the size effect of energy absorption, as well as the influence of the diameter-to-thickness ratio of the composite tube on this size effect. These findings offer valuable insights for guiding the design of large-scale energy absorption structures in engineering.

2. Experimental procedures

To investigate the size effect on the energy absorption properties of composite structures, four types of proportionally sized composite tubes were designed and fabricated. Figure 1 illustrates the composite energy absorption tube samples used in this study, while Table 1 provides additional details regarding their sizes. To minimize the impact of irrelevant variables on the size effect of energy absorption properties, the stacking sequence of the composite tube was designed as $[0/90]_{2n}$. By calculating the stiffness of the stacking sequence for different sizes, the stacking sequence structural matrices were set to be proportionally related. Table 2 provides the ABD stiffness matrices for composite tubes at different proportions.

Table 1. The geometric parameters of scaled samples

n	Diameter (mm)	Height (mm)	Thickness (mm)	Lay up
1/4	20	20	0.6	$[0/90]_2$
2/4	40	40	1.2	$[0/90]_4$
3/4	60	60	1.8	$[0/90]_6$
4/4	80	80	2.4	$[0/90]_8$

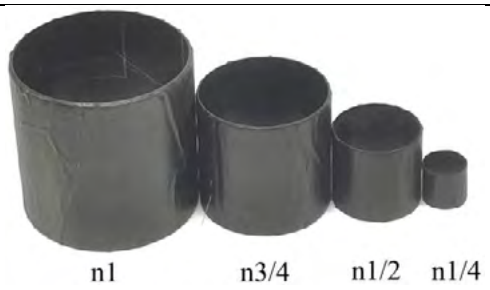


Figure 1. Testing specimens of different scales.

Table 2. The ABD stiffness matrices of scaled samples.

n	The extensional stiffnesses **A** (MPa)	The coupling stiffnesses **B** (MPa)	The bending stiffnesses **D** (MPa)
1/4	$A_{n1/4}=\begin{bmatrix}41961 & 1630 & 0\\ 1630 & 41961 & 0\\ 0 & 0 & 3000\end{bmatrix}$	$B_{n1/4}=\begin{bmatrix}2739 & 0 & 0\\ 0 & -2739 & 0\\ 0 & 0 & 0\end{bmatrix}$	$D_{n1/4}=\begin{bmatrix}1258.8 & 48.9 & 0\\ 48.9 & 1258.8 & 0\\ 0 & 0 & 90\end{bmatrix}$
2/4	$A_{n2/4}=\begin{bmatrix}83922 & 3260 & 0\\ 3260 & 83922 & 0\\ 0 & 0 & 6000\end{bmatrix}$	$B_{n2/4}=\begin{bmatrix}5479 & 0 & 0\\ 0 & -5479 & 0\\ 0 & 0 & 0\end{bmatrix}$	$D_{n2/4}=\begin{bmatrix}10070 & 391 & 0\\ 391 & 10070 & 0\\ 0 & 0 & 720\end{bmatrix}$
3/4	$A_{n3/4}=\begin{bmatrix}125884 & 4890 & 0\\ 4890 & 125884 & 0\\ 0 & 0 & 9000\end{bmatrix}$	$B_{n3/4}=\begin{bmatrix}8218 & 0 & 0\\ 0 & -8218 & 0\\ 0 & 0 & 0\end{bmatrix}$	$D_{n3/4}=\begin{bmatrix}33988 & 1320 & 0\\ 1320 & 33988 & 0\\ 0 & 0 & 2430\end{bmatrix}$
4/4	$A_{n4/4}=\begin{bmatrix}167845 & 6520 & 0\\ 6520 & 167845 & 0\\ 0 & 0 & 12000\end{bmatrix}$	$B_{n4/4}=\begin{bmatrix}10958 & 0 & 0\\ 0 & -10958 & 0\\ 0 & 0 & 0\end{bmatrix}$	$D_{n4/4}=\begin{bmatrix}80565 & 3129 & 0\\ 3129 & 80565 & 0\\ 0 & 0 & 5760\end{bmatrix}$

This study employed unidirectional T300/BR909 carbon/epoxy prepregs with a cured ply thickness of 0.15 mm, supplied by Shanghai Hanhe Ltd. Quasi-static axial crushing tests were performed using a standard testing machine with a maximum load capacity of 200 kN. The tests were conducted at a loading rate of $2\times n$ mm/min, and the final crushing displacement was set at 70% of the sample's total length.

To assess the energy absorption characteristics of the composite energy absorption tube, the following criteria were employed for evaluation: total energy absorption (EA) and specific energy absorption (SEA). The formulas are expressed as follows:
Fp represents the maximum force observed during the crushing process. In most cases, the peak force occurs at the outset of the crushing process, signifying failure initiation following an elastic stage [5].
The EA can be obtained by integrating the force-displacement curve shown in Eq. (1):

$$EA = \int_0^l F(x)dx \tag{1}$$

where 'l' represents the effective crushing distance and F(x) is the reactive load recorded by the drop-weight impact system.
The SEA is used to evaluate the energy absorbing efficiency, accounting for the lightweight requirement for the design of a good energy absorber. This can be calculated by dividing EA by the mass of the damaged part (m) according to Eqs. (2) and (3):

$$SEA = \frac{\int_0^l F(x)dx}{m} \tag{2}$$

$$m = M \times \frac{l}{H} \tag{3}$$

where 'M' and 'H', as indicated before, correspond to the total mass and height of each specimen before impact, respectively.

3. Numerical simulation

A 3D finite element model was created using ABAQUS/Explicit to simulate the crushing behavior of scaled tubes. Figure 2 illustrates the applied boundary conditions, loading direction, and discretized model for the scaled tubes. To represent the load and base platens, discrete rigid elements (R3D4) were utilized. The modeling of the scaled tubes employed 8-noded continuum shell elements (SC8R) with reduced integration and hourglass control.

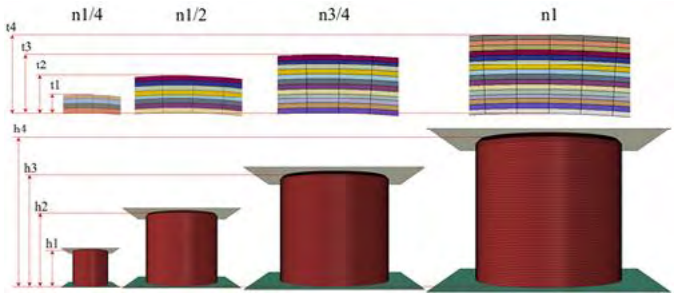
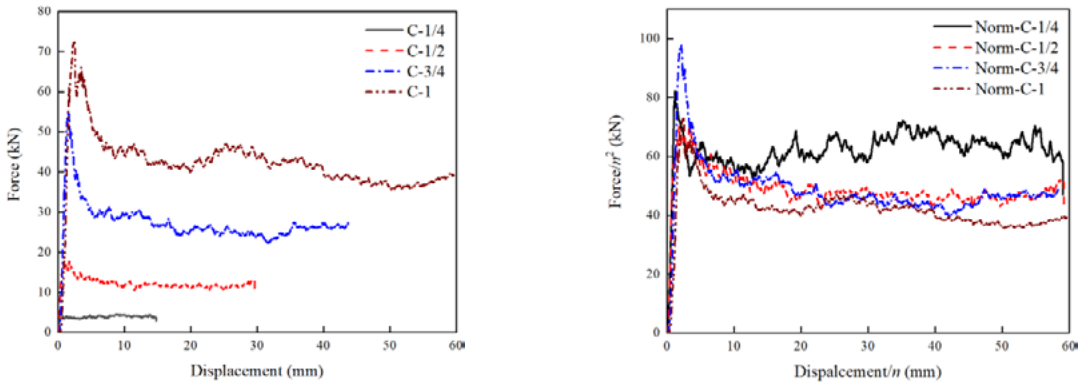


Figure 2. The finite element (FE) model for scaled samples.

4. Results and discussion

4.1. Experimental results

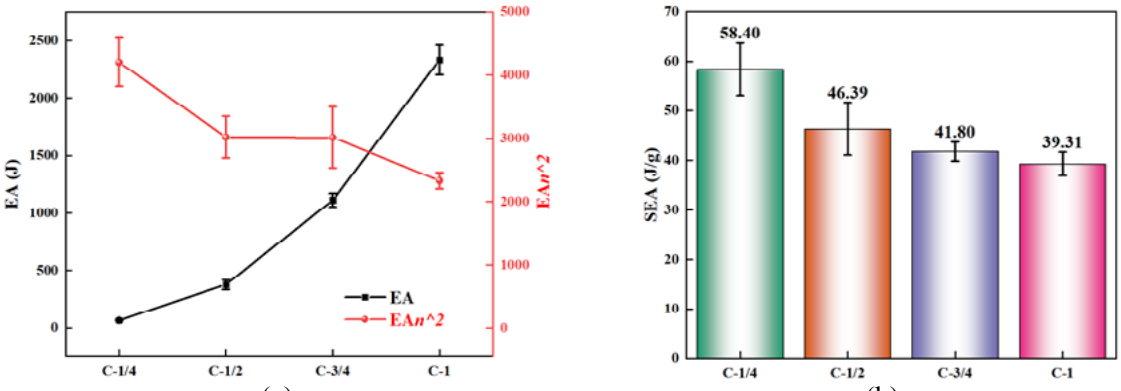
The displacement and load curves of composite tubes with different sizes were obtained using a testing machine, as depicted in Figure 3(a). The energy absorption tubes of various sizes exhibited distinct four-level in their displacement and load curves. Figure 3(b) illustrates the resulting normalized force-displacement curves for the previously mentioned scaled samples in Figure 3(a). It can be observed that all the normalized curves share a striking resemblance, converging into a single trace. This suggests that the axial energy absorption characteristics of composite tubes follow a simple scaling law.



(a) (b)

Figure 3. The comparison of scaled samples: (a) the absorbed energy(EA) for and (b) the specific energy absorbing (SEA).

Figure 4 compares the total absorbed energy and specific absorbed energy of energy absorbers with different scales. It is observed that the total absorbed energy exhibits a nonlinear increase as the scale proportion increases. Furthermore, after normalization, it is evident that smaller sizes tend to absorb more energy, which is also reflected in the specific absorbed energy (Figure 4(b)).



(a) (b)

Figure 4. (a) Crushing force vs. displacement traces for scaled samples and (b) normalized crushing force vs. displacement traces.

Comparison of final failure modes of composite tubes with different scales is shown in Figure 5. It can be observed that the final failure modes of composite tubes with scales N=1/2, 3/4, and 1 are characterized as 'flower-like' failure pattern, whereas the failure mode of composite tubes with scale N=1/4 exhibits a 'water ripple' failure pattern. This may be attributed to the thinner wall thickness of the N=1/4 composite tubes, resulting in this specific failure mode which leads to greater material damage. Consequently, the normalized specific energy absorption is higher in this case.

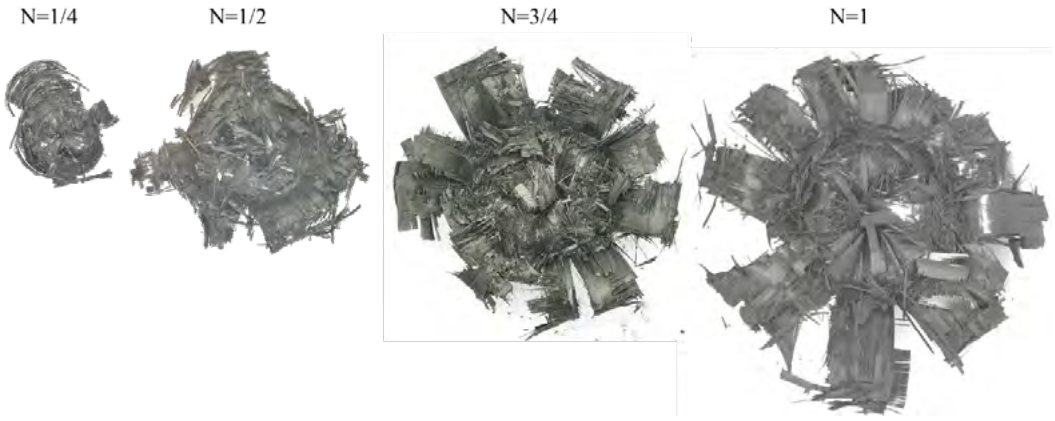


Figure 5. The failure mode of different scales.

4.2. Simulation results

To improve the accuracy of the finite element model, the influence of the verification mesh size on the computational accuracy of the finite element model was examined. Figure 6 presents the comparison of the calculated energy absorption results of the C-1 composite tube finite element model at three mesh sizes with experimental results, along with the corresponding error magnitudes. It can be observed from the figure that as the mesh size becomes finer, the computational accuracy continuously improves. When the mesh size is 1mm × 1mm × 0.15mm, the calculation error is only 1.09%. Therefore, the final mesh size for the C-1 composite tube was set to 1 × 1 × 0.15mm. To ensure consistency of irrelevant variables, the mesh sizes of finite element models for composite tubes of different proportional sizes were set proportionally. The mesh size for the C-3/4 composite tube was set to 0.75 × 0.75 × 0.15mm, the C-1/2 composite tube to 0.5 × 0.5 × 0.15mm, and the C-1/4 composite tube to 0.25 × 0.25 × 0.15mm.

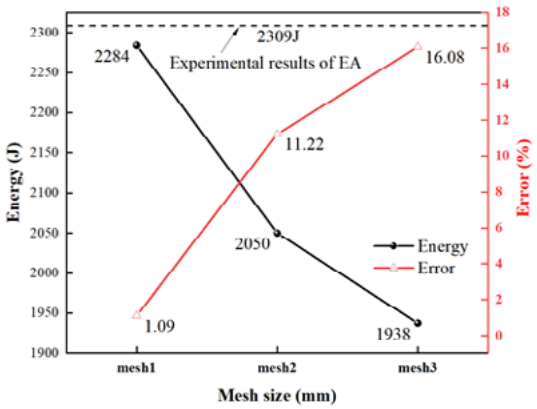
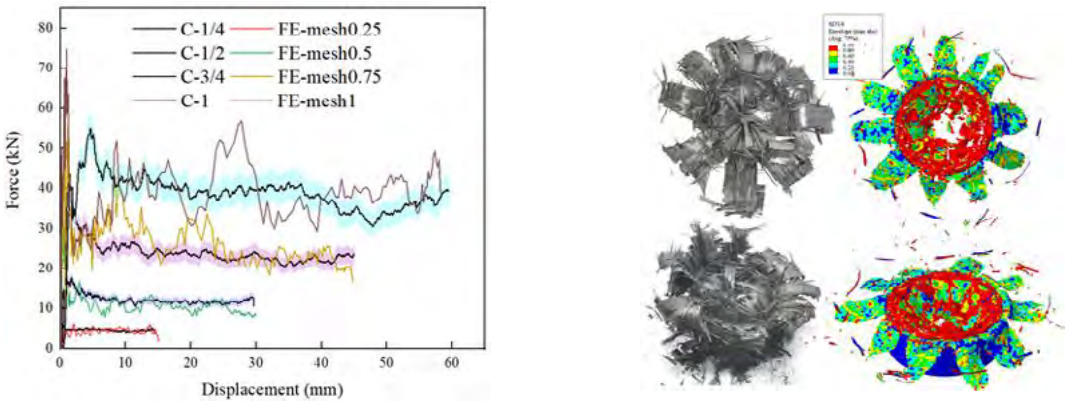


Figure 6. Grid sensitivity verification of finite element model.

Fig. 7 depicts the comparison between the force-displacement curve and the final crushing mode of sample C-1 obtained from the numerical model and the experimental results. The finite element simulation results effectively predict the displacement-load curve and the final failure mode observed in the experimental data.



(a) (b)

Figure 7. Comparison between the numerical and experimental results of C-1 sample: (a) Force-displacement curves; (b) Final crushed mode.

3. Conclusions

This paper investigates the scale effects on the axial energy absorption characteristics of composite tubes. The findings reveal that these characteristics can be accurately predicted using a simple scaling law and a finite element model for composite tubes of various sizes. The study's results provide evidence supporting the use of scaling laws to predict the crashworthiness of composite tubes. This has the potential to reduce costs associated with manufacturing and testing full-scale components.

References

[1] Clyne TW, Hull D. An introduction to composite materials: Cambridge university press; 2019.
[2] Feng J, Safaei B, Qin Z, Chu F. Nature-inspired energy dissipation sandwich composites reinforced with high-friction graphene. Composites Science and Technology. 2023;233:109925.
[3] Le VT, Jin T, Goo NS. Mechanical behaviors and fracture mechanisms of CFRP sandwich composite structures with bio-inspired thin-walled corrugated cores. Aerospace Science and Technology. 2022;126:107599.
[4] Duan Y, Zhang T, Zhou J, Xiao H, Chen X, Al Teneiji M, et al. Energy-absorbing characteristics of hollow-cylindrical hierarchical honeycomb composite tubes inspired a beetle forewing. Composite Structures. 2021;278:114637.
[5] Qi J, Zhou J, Wang J, Xi X, Liu X, Duan Y, et al. Energy-absorbing characteristics of hollow-cylindrical hierarchical honeycomb composite tubes under conditions of dynamic crushing. Composites Science and Technology. 2023;243:110254.
[6] Jimenez M, Miravete A, Larrode E, Revuelta D. Effect of trigger geometry on energy absorption in composite profiles. Composite Structures. 2000;48(1-3):107-11.
[7] Lv R, Ren Y. Improving the crashworthiness of carbon fiber-reinforced composite channel section structure through controllable failure mechanisms. Aerospace Science and Technology. 2023;141:108582.
[8] Swanson SR. Scaling of impact damage in fiber composites from laboratory specimens to structures. Composite Structures. 1993;25(1-4):249-55.
[9] Carrillo J, Cantwell W. Scaling effects in the tensile behavior of fiber-metal laminates. Composites Science and Technology. 2007;67(7-8):1684-93.
[10] Carrillo JG, Cantwell WJ. Scaling Effects in the Low Velocity Impact Response of Fiber-Metal Laminates. Journal of Reinforced Plastics and Composites. 2008;27(9):893-907.
[11] Farley GL. Effect of specimen geometry on the energy absorption capability of composite materials. Journal of Composite Materials. 1986;20(4):390-400.
[12] Green BG, Wisnom MR, Hallett SR. An experimental investigation into the tensile strength scaling of notched composites. Composites Part A: Applied Science and Manufacturing. 2007;38(3):867-78.

[13] Wisnom MR, Khan B, Hallett SR. Size effects in unnotched tensile strength of unidirectional and quasi-isotropic carbon/epoxy composites. Composite Structures. 2008;84(1):21-8.
[14] Luo H, Yan Y, Meng X, Jin C. Progressive failure analysis and energy-absorbing experiment of composite tubes under axial dynamic impact. Composites Part B: Engineering. 2016;87:1-11.
[15] Sokolinsky VS, Indermuehle KC, Hurtado JA. Numerical simulation of the crushing process of a corrugated composite plate. Composites Part A: Applied Science and Manufacturing. 2011;42(9):1119-26.
[16] Qi J, Zhou J, Wang J, Xi X, Liu X, Duan Y, et al. Energy-absorbing characteristics of hollow-cylindrical hierarchical honeycomb composite tubes under conditions of dynamic crushing. Composites Science and Technology. 2023;243.
[17] Zhao X, Zhu G, Zhou C, Yu Q. Crashworthiness analysis and design of composite tapered tubes under multiple load cases. Composite Structures. 2019;222.
[18] Zhang Z, Sun W, Zhao Y, Hou S. Crashworthiness of different composite tubes by experiments and simulations. Composites Part B: Engineering. 2018;143:86-95.
[19] Chiu LN, Falzon BG, Boman R. A Continuum Damage Mechanics Model for the Analysis of the Crashworthiness of Composite Structures: A work in progress. AIAC15: 15th Australian International Aerospace Congress: Australian International Aerospace Congress Melbourne, Vic.; 2013. p. 554-64.
[20] Faggiani A, Falzon B. Predicting low-velocity impact damage on a stiffened composite panel. Composites Part A: Applied Science and Manufacturing. 2010;41(6):737-49.
[21] Falzon B, Apruzzese P. Numerical analysis of intralaminar failure mechanisms in composite structures. Part I: FE implementation. Composite Structures. 2011;93(2):1039-46.
[22] Falzon B, Apruzzese P. Numerical analysis of intralaminar failure mechanisms in composite structures. Part II: Applications. Composite Structures. 2011;93(2):1047-53.

EFFECTS OF TEMPERATURE AND ELECTRO SPUN VEILS ON THE LOW VELOCITY IMPACT RESPONSE OF BASALT/EPOXY COMPOSITES TESTED WITH DIFFERENT IMPACTOR MASSES AND IMPACT ENERGIES

C. Sergi[1], J. Tirillò[2], L. Lampani[3] and F. Sarasini[4]

[1]Department of Chemical Engineering Materials Environment, Sapienza University of Rome & UdR INSTM, Via Eudossiana 18, 00184 Rome, Italy
Email: claudia.sergi@uniroma1.it
[2]Department of Chemical Engineering Materials Environment, Sapienza University of Rome & UdR INSTM, Via Eudossiana 18, 00184 Rome, Italy
Email: jacopo.tirillo@uniroma1.it
[3]Department of Mechanical and Aerospace Engineering, Sapienza University of Rome, Via Eudossiana 18, 00184 Rome, Italy
Email: luca.lampani@uniroma1.it
[4]Department of Chemical Engineering Materials Environment, Sapienza University of Rome & UdR INSTM, Via Eudossiana 18, 00184 Rome, Italy
Email: fabrizio.sarasini@uniroma1.it

Keywords: Basalt fibers, impact behavior, impact mass, temperature, electro spun veils

Abstract
The 2000/53/EC regulation promulgated by the European Union was specifically addressed to the transportation sector imposing greener policies and the identification of bio-based alteratives to traditional materials. Basalt fibers were selected as excellent substitute to glass ones in the manufacturing of polymer composites and many studies validated their feasibility both from the quasi-static and dynamic perspective. Despite this, none of them assessed the effect of impactor mass in equienergetic impacts and for this reason the present work focused on this aspect evaluating potential variation in laminates response also as a function of temperature, i.e., 80 °C, and as a consequence of the introduction of electro spun nanoveils as toughening elements. Impactor mass proved to significantly affect basalt/epoxy composites' impact response and damage mode especially at higher impact energies with a progressive decrease in peak force and a progressive increase in maximum displacement for increasing impactor masses, which also resulted in a higher concentration of the damage. The increase in impact temperature made the strain rate effect more visible even at lower impact energies due to the more compliant behavior of the structure while the introduction of electro spun nano veils did not seem to modify significantly the impact response of the laminate.

1. Introduction

The massive production of glass fibers started in 1893 [1] and encountered a steep growth during World War II when structures lightening was of primary importance and their integration with unsaturated polyester resin led to the progressive development of polymer composite materials [2,3]. Since that moment, glass fibers dominated the market of fibrous reinforcements accounting for more than 95 % of the global reinforcements used at an industrial scale [4] especially in the autmotive sector, where their lower cost compared to carbon fibers made them the preferred choice to reduce vehicles weight and the related fuel consumption while keeping low the cost of the final product.

Despite their dominance in the industrial landscape, the environmental decay observed in the last decades encouraged most countries to undertake greener and more restrictive policies in the field of environmental pollution. In particular, the 2008/1/EC directive in the field of Integrated Pollution Prevention and Control (IPPC) issued by the European Union aimed to foster the use of eco-friendlier materials from renewable resources. In this framework, many efforts were made to identify a suitable alternative to the widespread glass fibers and a compelling solution was found in basalt fibers.

Basalt is a bio-based material extracted from volcanic rocks [5] characterized by tensile properties higher than E-glass fibers [6] and by a greener manufacturing process. In particular, basalt fibers manufacturing process is similar to glass fibers one thus ensuring a good adaptability of the industrial plants already available with low investment costs and it is characterized by a lower energy consumption and no need of chemicals and additives addition during the manufacturing process [5,7,8].

Many studies already validated the feasibility of basalt fibers composites from a mechanical perspective [5] and many of them also focused on their impact behavior assessing the effect of different polymeric matrices [9,10], providing comparison with other fiber reinforcements, such as glass and carbon fibers [11–13], and disclosing the effect of low operating temperatures [14], but none of them focused on the effect of impactor mass being equal the impact energy, i.e., strain rate effect.

In light of this and considering that this aspect was deeply analyzed for carbon fiber reinforced composites [15–17], the present work aims to bridge this gap of knowledge providing a thorough characterization of the impact behavior of basalt/ epoxy composites and the related damage assessing the effect of impactor mass for equienergetic impact events using three different impact energies and three different impactor masses. Moreover, the effect of operating temperature was investigated performing the same experimental campaign not only at room temperature, but also at 80 °C. Furthermore, the effect of electrospun nano veils interleaving as toughening elements in basalt/epoxy composites was investigated in the same dynamic conditions.

2. Materials and methods

2.1. Materials and composite production

The basalt/epoxy composite laminates were manufacture by vacuum bagging and autoclave using a prepreg obtained from the plain woven fabric BAS 220 P by Basaltex impregnated with the toughened epoxy resin HEMT-3 by the Fibertechgroup. The laminates were produced by stacking 24 prepreg layers and were cured at 130 °C for 90 minutes applying a 70 mbar vacuum in the bag and a 5 bar in the autoclave for the whole curing according to the optimized procedure provided by the manufacturing company.

Moreover, the Xantu.Layr® electro spun nanoveils provided by Revolution fibers were interleaved in the basalt composite laminates to assess their effect on the overall impact response. This non-woven interlaminar reinforcement is obtained through electrospinning of tough thermoplastic nanofibers and thanks to its high porosity is able to ensure a good penetration of the thermosetting matrix and to ensure an increase in laminates resistance to delamination. Four electro spun nano veils with an areal density of 4.5 g/m^2 were interleaved in the laminate according to the stacking sequence shown in Figure 1.

2.2. Impact tests

The main goal of the present study is to investigate the effect of different strain rates on the impact behavior of basalt composites being equal the impact energy. To this aim, three different impactor masses of 5.055, 10.055 and 15.055 kg were selected and their effect on both reference and interleaved laminate configurations at three different impact energies, i.e., 15, 30 and 45 J, was evaluated. Impact tests were carried out in an Instron/ CEAST 9340 instrumented drop weight tower using a 12.7 mm diameter hemispherical impactor and a circular sample holder with a 40 mm unsupported area according to ATSM D3763 and ISO 6603.Moreover, the combined effect of temperature and impactor mass was also investigated performing the tests on reference basalt composites also at 80 °C. Specimens were pre-

©2024 | 3_SERGI_Claudia_5K3XU.pdf:2

conditioned for 1 hour at the desired temperature to ensure a uniform temperature profile throughout the whole thickness of the laminate.

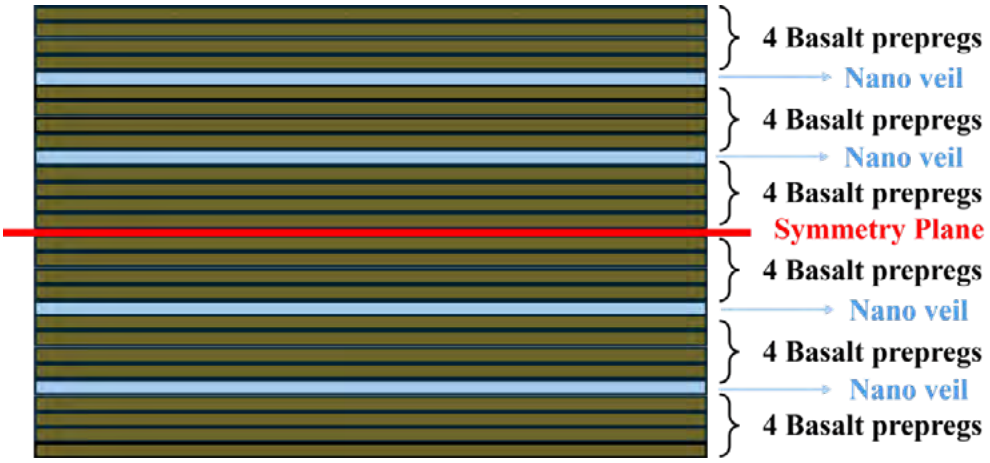


Figure 1. Stacking sequence of the basalt composites interleaved with the electro spun nanoveils

2.3. Post-impact damage analysis

A post-impact analysis through non-destructive techniques, i.e., C-scan and profilometry, was performed on the impacted samples to evaluate the damage extent, i.e., delaminated area and permanent indentation, respectively. The OmniScan MX2 ultrasonic system was used to perform the C-scan analysis using a phased array probe of 3.5 MHz, 64 elements, a 64 mm active aperture, a pitch of 1 mm, an elevation of 7 mm and a water immersion with 25 mm water wedge. The laser profilometer Talyscan 150 by Taylor-Hobson was used to carry out the profilometric analysis using a scanning speed of 8500 µm/s which allowed to obtain a 3D reconstruction of the permanent indentation of the impacted area.

3. Results and discussion

3.1. Impactor mass effect

The effect of impactor mass on basalt/epoxy laminates impact response at equienergetic impacts was investigated at 15, 30 and 45 J and the resulting force versus time and displacement versus time curves are reported in Figure 2.

For all impact energies, it appears evident that a decrease in impactor mass, i.e., an increase in impact velocity, being equal the impact energy, induces a faster response of the laminate with a shifting towards lower values of times of both peak force and maximum displacement. The effect of an increasing strain rate resulting from the decrease in impactor mass is particularly evident at 45 J, where a progressive increase in peak force and a progressive decrease in maximum displacement can be observed for decreasing impactor masses. This highlights a stiffer response of the laminate as also confirmed by the higher slope of the force and displacement versus times curves in the first linear elastic region.

This stiffer response is confirmed also at 30 J and 15 J where a difference in curves slope can be still recognized, but due to the progressive reduction in the impact velocity difference the effect on peak force and maximum displacement becomes progressively less evident. In particular, at 30 J the increase in peak force and the decrease in maximum displacement can be observed only moving from the 15 kg configuration to the 10 kg configuration, but no significant variations were observed with a further reduction of the mass at 5 kg. The effect appears even less pronounced at 15 J where no significant variations in peak force can be observed among the different configurations and just an increase in maximum displacement can be observed for the 10 and 15 kg impacted specimens compared to the 5kg.

No significant variations were observed in laminates damage degree, i.e., ratio between the absorbed and the impact energy, but some variations in composites damage mode were detected. In particular, for the 45 J impacted specimens, a higher localization of the damage resulting in a higher permanent indentation was observed for the 15 and 10 kg impacted specimens while the more impulsive stress resulting from the 5 kg impact induced mainly a diffused delamination in a higher number of plies. This effect is still detectable at 30 J where 5 kg impacted specimens still display a slightly higher delaminated area while no significant differences in the damage mode where observed for the 15 J impact.

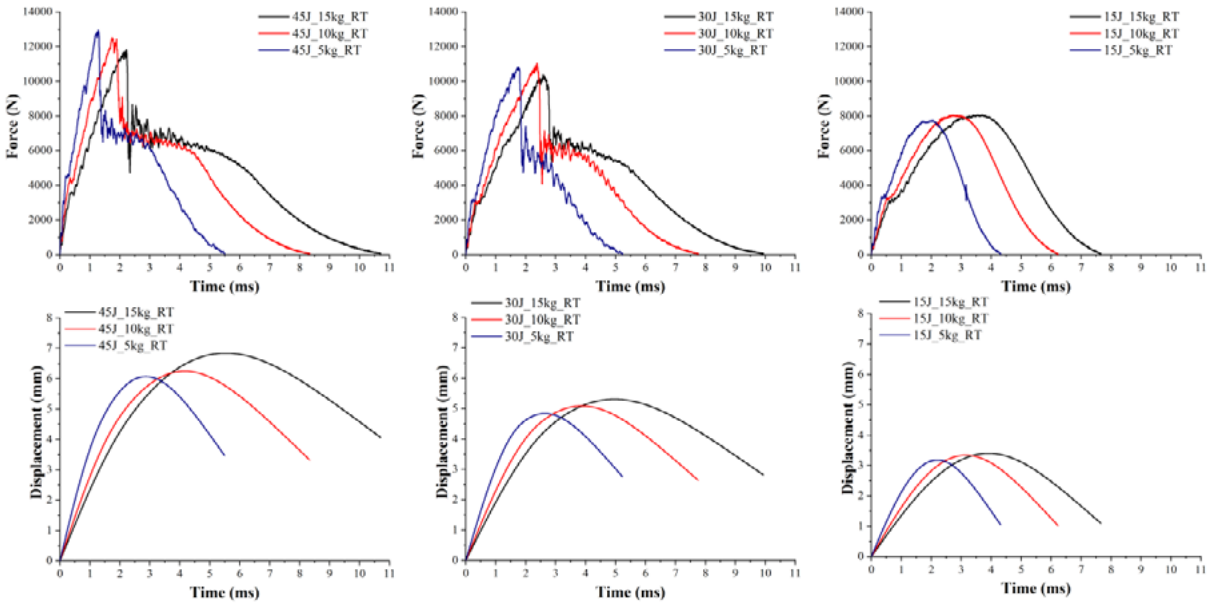


Figure 2. Force vs. time and displacement vs. time curves of basalt/epoxy composites impacted at 45, 30 and 15 J with the three different impactor masses

3.2. Temperature and electrospun nanoveils effects

Concerning the effect of temperature, the increase from room temperature to 80 °C determined a progressive decrease in laminate stiffness thus making it more compliant towards the impact with a decrease in peak force and an increase in maximum displacement. The trend observed as a function of impactor mass in peak force and maximum displacement at room temperature for the 45 J is confirmed also at 80 °C and it can be extended also to the 30 J impact events. Indeed, the reduced stiffness and brittleness of the laminate make the effect of lower strain rates differences more easily detectable. Concerning the 15 J impacts at 80 °C, a trend similar to the one observed at room temperature for the 30 J impact was detected with a progressive decrease in maximum displacement for decreasing impactor masses.

Even in this case no significant variations in the damage degree among the different configuration impacted with different masses were observed, but again a higher localization of the damage with a higher permanent indentation was observed at 45 and 30 J for the specimens impacted with a 15 kg and 10 kg impactor.

The introduction of the electrospun nanoveils does not modify significantly the overall impact response of basalt/epoxy laminates highlighting the same trend observed for the reference composites at 30 and 15 J impacts.

4. Conclusions

Basalt fibers were identified as suitable bio-based alternative to glass fibers for the production of structural epoxy composites applicable in different industrial fields such as the transportation one where the more restrictive regulations promulgated by the European Union impose ecofriendlier policies.

Many studies validated the feasibility of basalt fibers as structural reinforcement in composite laminates investigating both their quasi-static and dynamic performance, but none of them focused on the effect of impactor mass being equal the impact energy. In light of this, the present study aimed to bridge this gap of knowledge providing a characterization of the impact behavior of basalt/ epoxy composites and the related damage investigating the effect of impactor mass for equienergetic impact events evaluating also the effect of operating temperature and investigating the effect of potential toughening mechanisms such as electrospun nano veils interleaving.

The effect of impactor mass proved to be progressively more relevant for increasing impact energies determining a stiffer response of the laminate with an increase in peak force and a decrease in maximum displacement for decreasing impactor masses. This also resulted in a lower localization of the damage with a lower permanent indentation and a more widespread delamination.

The increase of impact temperature at 80 °C made laminate response more compliant toward the impact better highlighting the differences in peak force and maximum displacement also at lower impact energies while the introduction of electrospun nano veils does not modify significantly the overall impact response of the laminate with respect to the reference one.

Acknowledgments

This work was funded by the European Union - NextGenerationEU (National Sustainable Mobility Center CN00000023, Italian Ministry of University and Research Decree n. 1033 - 17/06/2022, Spoke 11 - Innovative Materials & Lightweighting).

References

[1] K.L. Loewenstein, The manufacturing technology of continuous glass fibres, 3rd ed., Elsevier, Amsterdam, 1993.

[2] R.R. Nagavally, Composite Materials - History, Types, Fabrication Techniques, Advantages, and Applications, in: Proc. 29th IRF Int. Conf., 2016: pp. 25–30.

[3] A. Cevahir, Glass fibers, in: M. Özgür Seydibeyoğlu, A.K. Mohanty, M. Misra (Eds.), Fiber Technol. Fiber-Reinforced Compos., Elsevier Ltd., Sawston, Cambridge, 2017: pp. 99–121. https://doi.org/10.1016/B978-0-08-101871-2.00005-9.

[4] E. Witten, V. Mathes, The European Market for Fibre-Reinforced Plastics and Composites 2022, Frankfurt, Deutschland, 2023. https://www.avk-tv.de/files/publications/files/2023_avk_market_report_final.pdf.

[5] V. Fiore, T. Scalici, G. Di Bella, A. Valenza, A review on basalt fibre and its composites, Compos. Part B Eng. 74 (2015) 74–94. https://doi.org/10.1016/j.compositesb.2014.12.034.

[6] J. Liu, M. Chen, J. Yang, Z. Wu, Study on Mechanical Properties of Basalt Fibers Superior to E-glass Fibers, J. Nat. Fibers. 19 (2022) 882–894. https://doi.org/10.1080/15440478.2020.1764438.

[7] J. Militký, R. Mishra, H. Jamshaid, Basalt Fibers, in: A.R. Bunsell (Ed.), Handb. Prop. Text. Tech. Fibres, Woodhead Publishing, Sawston, Cambridge, 2018: pp. 805–840. https://doi.org/10.1016/B978-0-08-101272-7.00020-1.

[8] A.E. Al Ghali, N.E. El Ezz, B. Hamad, J. Assaad, A. Yehya, Comparative study on shear strength and life cycle assessment of reinforced concrete beams containing different types of fibers, Case Stud. Constr. Mater. 19 (2023) e02497. https://doi.org/10.1016/j.cscm.2023.e02497.

[9] P. Russo, G. Simeoli, F. Cimino, I. Papa, M.R. Ricciardi, V. Lopresto, Impact Damage Behavior of Vinyl Ester-, Epoxy-, and Nylon 6-Based Basalt Fiber Composites, J. Mater. Eng. Perform. 28 (2019) 3256–3266. https://doi.org/10.1007/s11665-019-04037-8.

[10] J.J. Llanos, K. Wang, F. Taheri, Characterization of Low- and High-Velocity Responses of Basalt–Epoxy and Basalt–Elium Composites, (2024).

[11] F. Sarasini, J. Tirillò, M. Valente, T. Valente, S. Cioffi, S. Iannace, L. Sorrentino, Effect of basalt fiber hybridization on the impact behavior under low impact velocity of glass / basalt woven fabric / epoxy resin composites, Compos. Part A. 47 (2013) 109–123. https://doi.org/10.1016/j.compositesa.2012.11.021.

[12] V. Lopresto, C. Leone, I. De Iorio, Mechanical characterisation of basalt fibre reinforced plastic, Compos. Part B. 42 (2011) 717–723. https://doi.org/10.1016/j.compositesb.2011.01.030.

[13] F.A. Shishevan, H. Akbulut, M.A. Mohtadi-Bonab, Low Velocity Impact Behavior of Basalt Fiber-Reinforced Polymer Composites, J. Mater. Eng. Perform. 26 (2017) 2890–2900. https://doi.org/10.1007/s11665-017-2728-1.

[14] M.R. Ricciardi, I. Papa, F. Impero, A. Langella, V. Lopresto, V. Antonucci, Low-temperature effect on the impact and flexural behaviour of basalt composite laminates, Compos. Struct. 249 (2020) 112607. https://doi.org/10.1016/j.compstruct.2020.112607.

[15] H. Zabala, L. Aretxabaleta, G. Castillo, J. Urien, J. Aurrekoetxea, Impact velocity effect on the delamination of woven carbon-epoxy plates subjected to low-velocity equienergetic impact loads, Compos. Sci. Technol. 94 (2014) 48–53. https://doi.org/10.1016/j.compscitech.2014.01.016.

[16] J.A. Artero-Guerrero, J. Pernas-Sánchez, J. López-Puente, D. Varas, Experimental study of the impactor mass effect on the low velocity impact of carbon/epoxy woven laminates, Compos. Struct. 133 (2015) 774–781. https://doi.org/10.1016/j.compstruct.2015.08.027.

[17] B. Aryal, E. V. Morozov, H. Wang, K. Shankar, P.J. Hazell, J.P. Escobedo-Diaz, Effects of impact energy, velocity, and impactor mass on the damage induced in composite laminates and sandwich panels, Compos. Struct. 226 (2019) 111284. https://doi.org/10.1016/j.compstruct.2019.111284.

BUCKLING OF A $[\mp 45]_S$ LAMINATE IN A COMPRESSION-COMPRESSION BIAXIAL TEST WITH A CRUCIFORM SPECIMEN

MC Serna Moreno and S Horta Muñoz

Universidad de Castilla-La Mancha, Escuela de Ingeniería Industrial y Aeroespacial de Toledo, Instituto de Investigación Aplicada a la Industria Aeronáutica, Av. Carlos III, Real Fábrica de Armas, 45004 Toledo, Spain
Email: mariacarmen.serna@uclm.es

Keywords: carbon fibres, geometrical instability, laminate mechanics, biaxial testing, DIC

Abstract
Traditionally, the study of the biaxial stress states with cruciform specimens has been focused on positive load ratios. However, more recently there has been a shift towards their application in load cases involving at least one compressed direction. This work proposes the compression-compression test with cruciform specimens (CC test) as a reasonable option to analyse the geometrical instability of a carbon fibre-reinforced polymer. The region of interest (ROI) is tested under equal applied stresses, and is composed of a $[\mp 45]_S$ laminate that exhibits significant flexural-torsional coupling. The ROI possesses a shape and boundary conditions akin to a clamped square plate. Full-field displacements and strains are registered by Digital Image Correlation, determining the bifurcation onset by comparing the strain evolution in both sides of the ROI with the help of strain gages. The bifurcation stress is found to be close to the critical stress obtained according to actual regulations for metallic structures. However, due to the complex response of laminated composites, further work is needed to estimate the relation of the global instability with apparent material non-linearities. In addition, this research explores whether the experimental deflection surface can provide valuable information for quantifying the bending and twist moments at the onset of bifurcation.

1. Introduction

The use of carbon fibre-reinforced polymer-matrix (CFRP) laminates in the primary structure of light vehicles is increasing. These laminates usually have small thickness compared to their other two dimensions. Then, under workloads the problem can be addressed assuming that the stress components outside the plane that defines the laminate are negligible compared to those contained in the plane (plane stress state). There are cases in which the predominant components are normal stresses, as in the pressure hull of submarines that can withstand in-plane bidirectional compression that could lead to geometrical instabilities. While analytical closed-form solutions exist for laminates free of couplings [1-2], most of the results proposed in the literature rely on semi-analytical or semi-numerical approaches [3-5]. A particularly intricate scenario arises when analyzing buckling behavior in ±45º symmetric laminates with a limited number of alternating layers, which exhibit significant flexural-torsional coupling. However, the high sensitivity of compressive tests to boundary conditions and initial geometrical defects presents challenges when comparing the experimental data with the results of theoretical models. This issue becomes more noticeable at the coupon scale with small sizes of the tested region. Consequently, this research investigates the capacity of biaxially loaded cruciform specimens (at the coupon scale) to assess the stability of bi-compressed laminates, even in the presence of pronounced coupling effects.

Cruciform specimens, developed over the past few decades, serve as valuable tools for monitoring material behavior when subjected to biaxial loading. Traditionally, these caharacterizations have

focused on positive load ratios. However, more recently, researchers have proposed their use for analyzing scenarios where at least one direction experiences compression. The literature has primarily explored the tension-compression behavior [6-9], but the experimental works of Horta Muñoz and Serna Moreno [7,9,10] and Zumaquero [8] stand out for the use of cruciform specimens in compression-compression tests (CC tests). Zumaquero investigated the transverse biaxial response of a unidirectional CFRP, revealing that global buckling can significantly impact the cruciform specimen's performance. Meanwhile, Horta Muñoz and Serna Moreno [7,10] specifically examined an equally bi-compressed $[\mp 45]_S$ CFRP laminate using a fixture to mitigate the risk of buckling in the arms of the sample.

The present work is of scientific interest because it introduces the CC test with cruciform specimens as a suitable technique for providing fundamental insights into the bifurcation phenomenon. In particular, the proposal is to evaluate experimentally the geometrical instability of a $[\mp 45]_S$ CFRP laminate, with shape and boundary conditions close to a clamped square plate submitted to equal bi-compression [10]. The test is performed on carbon-fiber/epoxy ∓45º symmetric laminates which exhibit a significant flexural-torsional coupling, adding complexity to the buckling analysis. The use of the Digital Image Correlation (DIC) technique allows to observe the experimental deflection surface, which validates the numerical predictions with the finite element method [11]. This experimental outcome is utilized for analytically estimating the relation between the bending and torsional moments at the instability onset, which could provide valuable information about the post-buckling behavior of the laminate. As well, the method of the strength reduction, usual in the current European regulations for evaluating the buckling capacity of metallic members, is here adapted to estimate the critical stress of a bi-compressed laminate. Considering apparent elastic properties of the laminate in the loading directions, the proposed estimation is found to be close to the experimental bifurcation stress.

2. Materials and methods

2.1. Material, specimen and equipment

A symmetrical ∓45º angle-ply laminate made of pre-impregnated CFRP (M21E/34%/UD268/IMA-12K) [12] is analyzed. Each cured layer has 0.25 mm thickness and consists of an epoxy matrix reinforced with unidirectional carbon fibers (UD). Elastic moduli E_1 and E_2, Poisson ratios ν_1 and ν_2, and failure strengths σ_1^u and σ_2^u were estimated from uniaxial tests on UD specimens [7]. In-plane shear modulus G_{12} was obtained from tension-compression biaxial tests with cruciform specimens following UNE 0074:2023 recommendations [7,9,13]. Meanwhile, the apparent elastic response (elastic modulus E_a and Poisson ratio ν_a) of the proposed symmetrical ∓45º angle-ply configuration under uniaxial compression is defined in Table 2 [14]. Please notice that the non-conventional response of laminates is reflected in an apparent Poisson coefficient higher than 0.5.

Table 1. Average elastic properties and strengths in the in-plane principal material directions [7,9].

E_1 (GPa)	E_2 (GPa)	ν_{12}	ν_{21}	G_{12} (GPa)	σ_1^u (MPa)	σ_2^u (MPa)
132.99	9.14	0.19	0.01	5.35	628.5	172.3

Table 2. Apparent elastic response under uniaxial compression of a symmetrical ∓45º angle-ply laminate [14].

E_a (GPa)	ν_a
18.20	0.74

The hand lay-up technique is used to create 300 mm x 300 mm square plates with a $[\mp 45]_{4S}$ stacking sequence. These plates undergo a curing cycle of 7 bars at 180 ºC for 120 minutes using a hydraulic heated platen press LabEcon 300 from Fontijne Grotnes Group. The final geometry and dimensions of

the specimen are achieved through computer numerical control milling (Fig. 1). The cruciform specimen comprises $[\mp 45]_{4S}$ laminate arms, of width l = 30 mm and a thickness H = 4 mm (Fig. 1), uniaxially loaded. Then, a stepped thickness reduction up to h = 1 mm is performed in the biaxially loaded region, transitioning to a $[\mp 45]_S$ stacking sequence. The central region is assumed to be a nearly squared plate clamped at all edges. The CC test is conducted using an electromechanical multiaxial machine from the company Microtest. This installation features four closed-loop synchronized actuators driven by an electric motor, precisely controlled via encoders. Additionally, four force transducers with a capacity of 50 kN are employed using a force control. To enhance stability and minimize issues from sample imperfections, a biaxial anti-buckling fixture is employed [15]. Both the DIC technique and a strain rosette are employed simultaneously on both sides of the central region biaxially loaded. A speckle pattern is applied on the frontal surface for obtaining the full-field displacements and strains by a LaVision Strain-Master stereo-DIC system with two cameras. Meanwhile, in the rear surface a strain rosette, connected to a Kyowa PCD-300B sensor interface, measures the ε_{xx} and ε_{yy} strains in the horizontal and vertical load directions. Each strain gage has a range of acquisition up to 20 millistrains and averages the deformation over a 5 mm length.

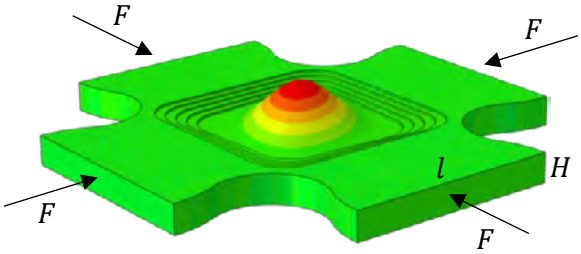


Figure 1. Representation of the buckled cruciform specimen numerically estimated [7,11], indicating the equal bi-compression and the dimensions of the arms' cross-section.

2.2. Analytical approaches

A multiaxial machine applies equal compressive forces F to the arms of the cruciform specimen (Fig. 1). During the linear response of an ideal CC test, the normal stress components of the central region in both load directions are assumed to be equal and denoted as σ. In parallel, longitudinal strains in both load directions are expected to be similar due to the analogous apparent material's behavior. Then, the response of the central region is analyzed using the global biaxial stress (σ) and averaged strain (ε), even when non-linearities occur in the stress-strain relationship after trespassing the critical stress σ_c.

$$\sigma = f\frac{|F|}{lH} \tag{1}$$

$$\varepsilon = \frac{\varepsilon_{xx} + \varepsilon_{yy}}{2} \tag{2}$$

The central stress (Eq. 1) is calculated from the applied force F and the averaged dimensions of the width l and thickness H of the arms' cross-section (Fig. 1). As well, a numerically estimated conversion factor f = 1.496, equal in both loading directions, is taken into consideration. This is obtained from a linear simulation with the finite element method using the software Abaqus/Standard 2021, evaluating the amount of the applied load that is transferred to a central squared zone of 5 mm x 5 mm [7]. An engineering approach is considered, referring the conversion factor to the undeformed geometry.

During the linear stage, the apparent elastic modulus is estimated in both loading directions using Classical Laminate Plate Theory (CLPT) for ∓45º symmetric configurations. The studied $[\mp 45]_S$

laminate exhibits no coupling between in-plane axial terms and in-plane shear, and the membrane-moment coupling components are negligible. Consequently, the apparent biaxial stiffness in the x- and y-directions can be calculated. This serves as a reference for evaluating experimental observations obtained from the CC test with cruciform specimens.

$$E_{\mp 45^\circ}^{CC} = \frac{E_1(1 + 2\nu_{21} + \nu_{21}/\nu_{12})}{2(1 - \nu_{12}\nu_{21})} \tag{3}$$

The buckling stress σ_c accounts for material limitations (finite stress capacity σ^u) and non-ideal conditions (initial imperfections and loading asymmetry). If the strength reduction method is used, a reduction factor $\chi = \sigma_c/\sigma^u$ is typically proposed to estimate the buckling capacity for different modified slimness values $\bar{\lambda}$. Considering a square plate with a side l and a thickness h, clamped in all its edges, that presents a linear elastic material behavior with similar responses in both loading directions and is subjected to equal biaxial compression, the modified slimness that is taken into account is given in Eq. 4 [16,17].

$$\bar{\lambda} = \frac{l}{h}\sqrt{\frac{\sigma^u(1 - \nu_a^2)}{4.4E_a}} \tag{4}$$

Following the recommendation in Annex B of EN 1993-1-5 [18], the real buckling curve could be approximated following an Ayrton-Perry type function which is represented in Fig. 2, assuming that at modified slimness $\bar{\lambda} < 0.7$ the material fails before the plate would buckle.

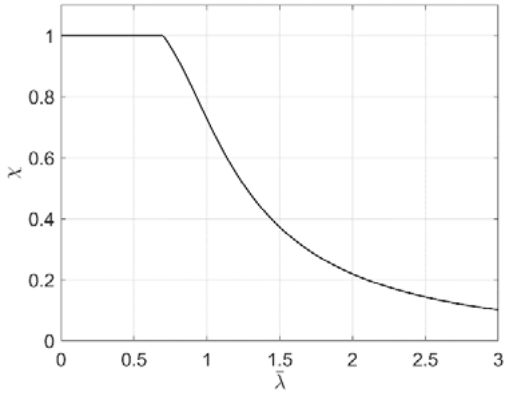


Figure 2. Estimation of the real buckling capacity [18].

3. Results and discussion

In a cruciform specimen subjected to a CC test, the stress-strain evolution of the biaxially loaded region is analysed. Fig. 3 (centre) illustrates this response using the global stress σ (Eq. 1) versus the global strain ε (Eq. 2) and the strain components in each loading direction (ε_{xx} and ε_{yy}) measured by the strain rosette. Fig. 3 (centre) reveals distinct strain states at the ply level because the presence of local shear strains introduces discrepancies between the ε_{xx} and ε_{yy} strains. However, the local shear effects are expected to be mitigated by neighbouring plies. This should result in a null global shear strain ε_{xy} and, therefore, at the global level no significant deviations from the average strain value ε (Eq. 2) are assumed. Therefore, the apparent σ-ε evolution is compared to the CLPT linear estimation (dashed red line). By substituting the compressive properties from Table 1, the biaxial elastic modulus is estimated to be $E_{\mp 45^\circ}^{CC} = 72.98$ GPa (Eq. 3), which agrees with the experimental σ-ε slope at the linear stage. The

onset of instability is assumed to occur when apparent biaxial strain ε deviates from the linear evolution, which is here produced nearby $\sigma_c = 120$ MPa. Prior to this threshold, a biaxial-driven response is assumed, transitioning to a moment-driven response afterwards.

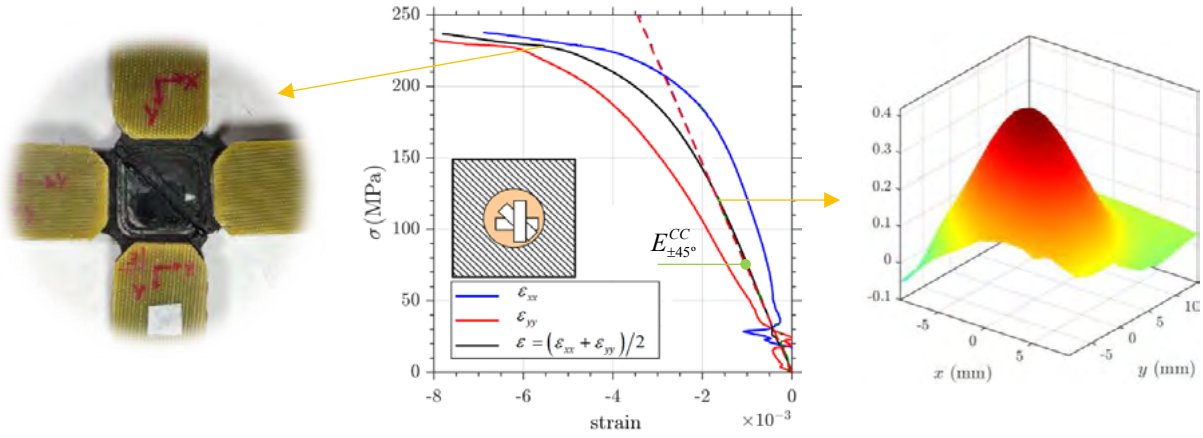


Figure 3. Stress-strain evolutions σ-ε_{xx}, σ-ε_{yy} and σ-ε, detailing: the slope at linear stage including the dashed linear tendency (centre), the out-of-plane displacement at the onset of buckling (right) and the final failure pattern (left).

Despite the visual limitations posed by the opening of the anti-buckling fixture, Fig. 3 (right) displays the deflection surface captured by the 3D DIC system at the point of bifurcation onset. The experimental deflection surface presents strong evidence in the elliptical plane projections of the flexural-torsional coupling, what agrees with the numerical predictions [11]. The final failure of a representative specimen given in Fig. 3 (left) is in concordance with the observed buckling mode, presenting matrix cracking in parallel to the outer fibres and typical kink bands.

As a verification tool of the experimental outcome, it is checked if the experimental bifurcation stress is in concordance with the approximation represented in Fig. 2. The reduction factor is estimated taking into account that its value relies heavily on limit stress determination. As a conservative assumption, the limit value is considered to be equal to the matrix strength under uniaxial compression, i.e. $\sigma^u = \sigma_2^u$ (Table 1). Then, the experimental reduction factor is calculated as $\chi = 0.7$, while the modified slimness factor is $\bar{\lambda} = 0.94$. Please, note that these values are in concordance with the approximation of the real buckling curve given in Fig. 2.

4. Conclusions

In the context of CC tests using cruciform specimens, the buckling features of a clamped square plate made of a $[\mp 45]_S$ CFRP laminate are reviewed. To prevent instability in the specimen's arms, an anti-buckling fixture is employed. Analysing the multiaxial response in an anisotropic material presents complexities, difficulties that are increased by strain variations at the ply level. Considering the global biaxial stress-strain behaviour, prior to strain bifurcation the stiffness agrees with the CLPT prediction. As well, the bifurcation stress is aligned with the critical stress predicted using an adaptation of the reduced strength method. Nevertheless, given the intricate nature of laminated composites, further investigation is needed to understand the relationship between global instability and apparent material non-linearities. After the bifurcation onset, the influence of high flexural-torsional coupling becomes evident in the buckling mode captured by DIC technique, observing an experimental deflection surface which agrees with the numerical predictions. These findings could imply that employing the CC test with cruciform specimens, along with an anti-buckling fixture, offers a suitable approach for observing the buckling modes in bi-compressed laminates. Finally, the variation in the relationship between central thickness and the arms' thickness could provide an opportunity to analyse the instability of the biaxially tested region considering diverse boundary conditions.

Acknowledgments
This work has been financially supported within the Grants DPI2016-77715-R, PDC2021-121154-I00 and PID2022-137387OB-I00 funded by MICIU/AEI /10.13039/501100011033, "ERDF UE A way of making Europe" and "European Union NextGenerationEU/PRTR". These authors would like to thank the company Airbus for providing the material used in the preparation of the specimens.

References

[1] J.M. Whitney. *Structural analysis of laminated anisotropic plates*. CRC Press, New York, 1987.
[2] R.M. Jones. *Mechanics of composite materials*. Taylor and Francis, 1975.
[3] M. Kazemi. A new exact semi-analytical solution for buckling analysis of laminated plates under biaxial compression. *Archive of Applied Mechanics*, 85:1667-1677, 2015.
[4] A. Teter and Z. Kolakowski. Influence of mechanical couplings on the buckling behaviour of thin-walled plates made of general laminates under compression. *Composites Structures*, 166:68-76, 2017.
[5] J. Loughlan. The influence of mechanical couplings on the compressive stability of anti-symmetric angle-ply laminates. *Composites Structures*, 57:473-482, 2002.
[6] H.F. Nguyen. Bi-axial testing of composite laminates and adhesive bonded joints. PhD Thesis, Nanyang Technological University (Singapore), 2018.
[7] S. Horta Muñoz. Complexity of the structural response of fibre reinforced polymer matrix composites, PhD Thesis, Universidad de Castilla-La Mancha (Spain), 2020.
[8] P.L. Zumaquero, E. Correa, J. Justo, F. París. Transverse biaxial tests on long fibre reinforced composites, *Composites Structures*, 297:115868, 2022.
[9] S. Horta Muñoz and M.C. Serna Moreno. Tension–compression biaxial test with ±45◦ symmetric angle-ply laminates for determining the pure shear response in principal material directions of a lamina. *Composites Part B*, 261:110792, 2023.
[10] M.C. Serna Moreno and S. Horta Muñoz. Experimental evaluation of the use of cruciform specimens for biaxial stability analysis. Under review.
[11] M.C. Serna Moreno and S. Horta Muñoz. Elastic stability in biaxial testing with cruciform specimens subjected to compressive loading. *Composites Structures*, 234:111697, 2020.
[12] HexPly® M21 datasheet. Specifications sheet. Available online: https://www.hexcel.com/user_area/content_media/raw/HexPly_M21_global_DataSheet.pdf. [Accessed 14 December 2023].
[13] UNE 0074:2023. Plastic materials. Shear test method by means of tension-compression on cruciform specimen. 2023, Specification. Asociación Española de Normalización.
[14] M.C. Serna Moreno and S. Horta Muñoz. Pseudo-ductile effects in angle-ply CFRP laminates under uniaxial loading: Compression and cyclic tensile test. *Composites Part B*, 233:109631, 2022.
[15] M.C. Serna Moreno and S. Horta Muñoz. Dispositivo para evitar pandeo en ensayos biaxiales de probetas cruciformes. 2022, Spanish Utility Model 2022/20461.
[16] S.P. Timoshenko, J.M Gere. Theory of Elastic Stability, 2nd ed., McGraw-Hill, 1961.
[17] C.Y. Warren, R.G. Budynas. Roark's formulas for stress and strain, seventh edition, McGraw-Hill, 2002.
[18] EN1993-1-5:2005, Eurocode3: Design of Steel Structures, Part 1-5, Plated Structural elements, 2006.

INVESTIGATING THE PERMEABILITY OF CFRP FOR LIQUID HYDROGEN STORAGE

Jean Vereecke[1,2,3], Christophe Bois[2,3,*], Jean-Christophe Wahl[2,3] , Florian Lavelle[4], Bruno Desmars[1]

[1] ArianeGroup SA, Saint-Médard-en-Jalles, France
[2] Univ. Bordeaux, CNRS, Bordeaux INP, I2M, UMR 5295, F-33400, Talence, France
[3] Arts et Metiers Institute of Technology, CNRS, Bordeaux INP, Hesam Universite, I2M, UMR 5295, F-33400 Talence, France
[4] Direction des Lanceurs, Centre National d'Études Spatiales (CNES), Paris, France

Keywords: Permeability, Damage, Hydrogen, Spectrometry, Leak

Abstract

In a context of massive investments in cryogenic propellant storage, full composite tanks consitute a technological challenge. Their mass-to-performance ratio justifies their potential in aerospace industry, but their permeability is a limiting factor. Indeed, the pressurization of the tank and cryogenic temperatures generate matrix damages that coalesce and generate leakage paths. In order to master the permeability of the structure, composites tubes undamaged and damaged are studied. A methodology is proposed to measure the permeability using mass spectrometry. Tubular specimens are pressurized using helium gas and leak rates are measured. The bench test is then extended to low temperature. Finally, the evolution of the number of leak points is studied since they significantly rise the permeability of the structure.

1. Introduction

The application of CFRP laminates to the structures of cryogenic propellant tanks has been widely attempted in order to drastically reduce the weight of space launch vehicles. However, recent studies suggest that the conventional thermoset composites used in these tanks are prone to matrix cracking when exposed to extreme thermomechanical loads [1], [2]. These damage mechanisms are critical regarding the permeability since this can lead to propellant leakage. These leaks can be tolerated if mastered, therefore it is necessary to evaluate the accumulation of leak points and the leakage rate of the composite as a function of the internal pressure and the temperature.

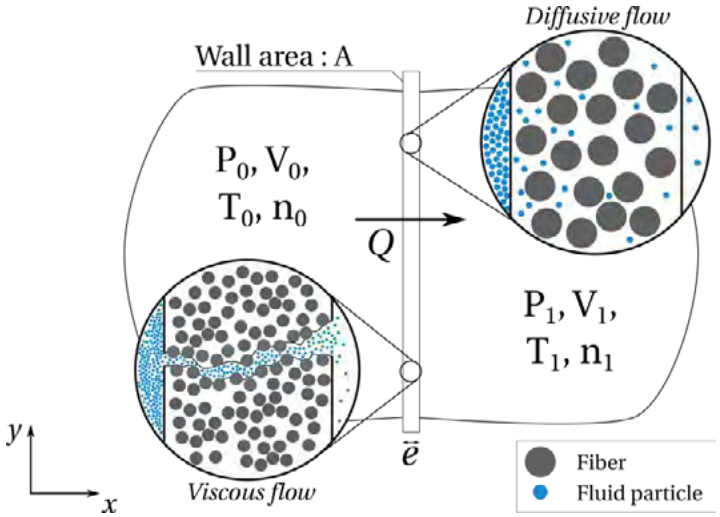


Figure 1. Two types of flow through a wall

Two principle types of flow can go through a composite wall : diffusive flow and viscous flow. The phenomena which govern them are substantially different and imply a definition of the coefficient of permeability which is peculiar to them and which we will try to define on the basis of the case study presented in Figure 1. On the latter, the index 0 and 1 parameters refer respectively to the physical quantities on either side of the wall. We will consider that the test conditions favour a flow from state 0 to state 1.
Diffuse flow can be a dimensioning criterion during long-term storage. These operating conditions involve relatively low flow rates, but can become critical beyond a certain time as for hydrogen storage. In this case, the permeability coefficient is, by definition, the product of the solubility coefficient by that of diffusion [3, 4], it is proportional to the flow rate Q_n through the wall.

$$Pe = \frac{Q_n e}{\Delta P A} \tag{1}$$

With :

- Q_n : the flow rate in $mol.s^{-1}$
- A : the observed area in m^2
- e : the wall thickness in m

When the wall reaches a certain damage level, leak points start accumulating. The opening of the cracks is such that the flow through them is viscous and called Darcy's flow. In the case of the laminar flow of a perfect gas incompressible in steady state, Darcy's law expresses the proportionality between the passing flow and the pressure gradient [5]:

$$k = Q_n \frac{RT\mu e}{\Delta P A P_1} \tag{2}$$

With :

- R : the perfect gas constant in $J.mol^{-1}.K^{-1}$
- μ : the dynamic viscosity in $Pa.s$
- k : the composite permeability in m^2

This expression can be generalized in the case of a compressible fluid. Assuming that the temperature is constant in the system, the permeability k of the wall is written [6]:

$$k = Q_n \frac{2RT\mu e}{\Delta P (P_0 + P_1) A} \tag{3}$$

Permeabilities k or Pe are independent from the test environment (fluid property, pressure, wall thickness…). The physical meaning attributed to the permeability of a material thus depends on the type of flow that passes through it. In the following, we shall distinguish the coefficient Pe from the permeability k according to the type of flow considered. These two parameters are however calculated from the same experimentally measured quantity: the material flow rate Q_n. In practice, the measured quantity is the leakage rate Q expressed in $Pa.m^3.s^{-1}$.

2. Experimental setup

2.1. Specimen design and manufacturing

In order to measure the leakage rate, tubular specimens are manufactured in automated fiber placement (AFP). This type of specimen allows a biaxial loading that is far more representative of the industrial application than place specimen. Il can also reduce significantly the edge effects and it can be pressurized. The stratification is [-50/15/35_2/-35_2/-15/50] with 140 µm plies. It has been developed in order to master the damage scenario. Indeed, the $\pm 35°$ plies damage at first and interact with the adjacent $\pm 15°$ plies, then the $\pm 50°$ ply, that have a slightly higher crack threshold, damage independently from the other plies and drive the accumulation of leak points. To generate a biaxial load, the tube are closed with two INVAR machined flanges. The INVAR is a stainless steel alloy with a very low coefficient of thermal expansion which allows to limit the clearance between the tube and the flanges during tests at low temperatures. The assembly is sealed with PTFE lip seal. In order to transmit the axial loading to the tube, [7] proposes to use a pinned joint as shown in Figure 2.

We chose to integrate the heels directly into the composite tube by drapeing extra prepreg composite. The heel are made of 8 plies with the stacking sequence $[(0/90)/\pm 45]_4$ giving 25% reinforcement at 0°, 90°, 45° and -45°. Their thickness gradually decreases at an angle of around 15° to prevent brutal variation of stiffness. They are also used to reduce the circumferential deformation at the ends, in order to maintain the tightness of the assembly, and to reduce the edge effects by deflecting the flow of forces.

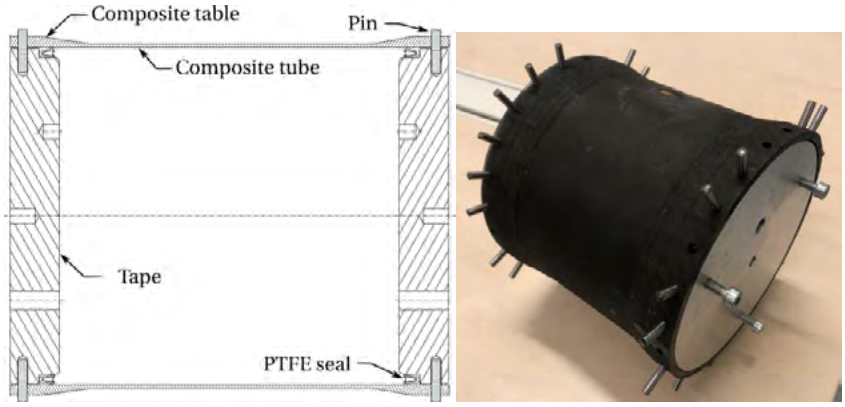


Figure 2. Biaxial loading device on tubular specimen

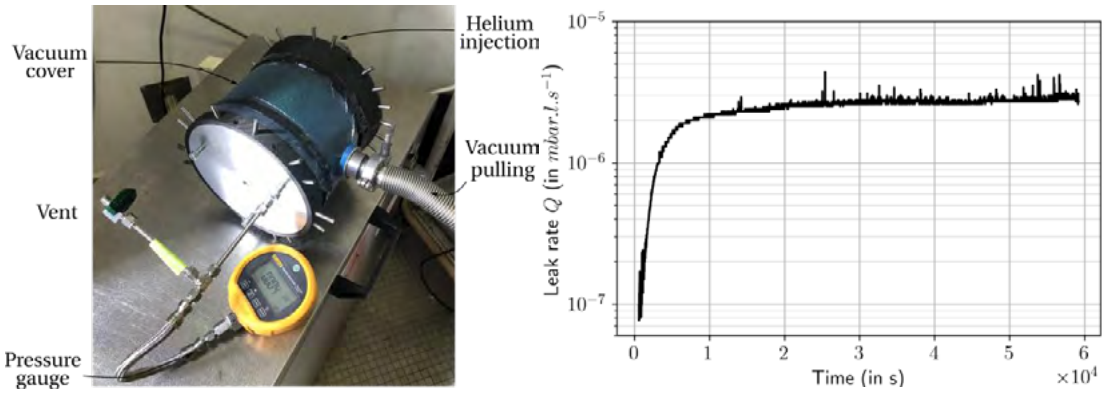
2.2. Permeability measurement on undamaged composite

2.2.1. Permeability at room temperature

The permeability measurement is performed with the vacuum detection method as in [8] work. The useful surface of the tube is covered with a vacuum bag, the sealing of which is provided by a pre-formed butyl mastic as shown in Figure 3a. The vacuum bag is directly connected to the Pfeiffer Vacuum ASM 340 mass spectrometer by means of a steel vacuum socket. The vacuum is pulled to a pressure of less than $5 \times 10^{-3}\ mbar$ between the bag and the composite. The tube is then pressurized with helium and the leakage rate is measured. Figure 3b shows the evolution of the leakage rate Q over time on an undamaged tube for a pressure difference of 3 bars (2 bar of relative pressure in the tube and the vacuum in the bag). It first passes through a transient regime during which the helium concentration gradually increases in the wall before reaching a plateau value. The established regime reflects the constant flow of helium through the wall.

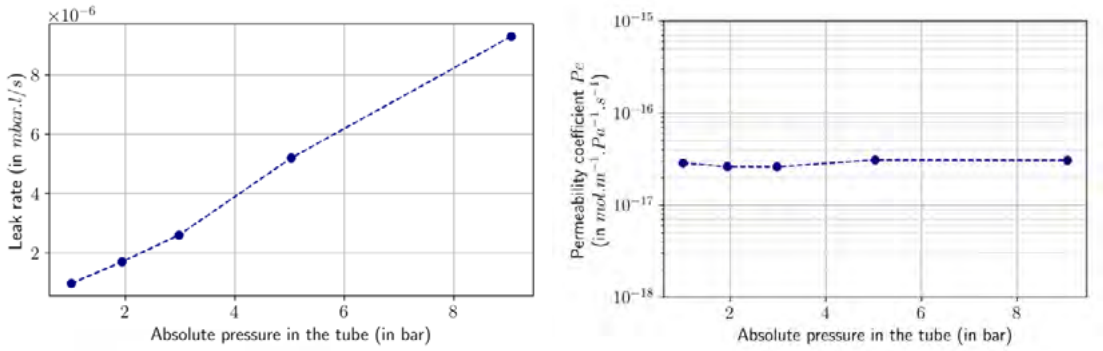
Several leakage rate measurements were made by pressurizing the tube to 1, 2, 3, 5 and 9 bar. At these pressures, no cracks are created *a priori*. The results are plotted in Figure 4a and show the linear relationship between the internal pressure of the tube and the leakage rate measured, which

reflects a diffusive flow. The permeability coefficient Pe of the composite tube is thus independent of the test conditions and $Pe = 2.1 \times 10^{-17}\ mol.m^{-1}.Pa^{-1}.s^{-1}$.



(a) (b)

Figure 3. Leak rate measurement device (a) and leak rate evolution for a pressure difference of 3 bar (b)

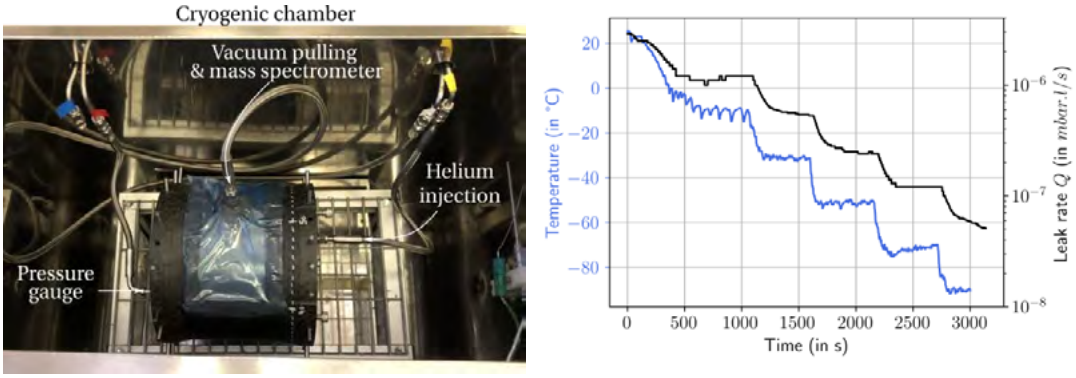


(a) (b)

Figure 4. Leak rate (a) and permeability coefficient $\boldsymbol{Pe}$ (b) measured against the pressure

2.2.2. Permeability under cryogenic conditions

In cryogenic storage, the temperature of the wall strongly influences its permeability by reducing the molecular agitation. In order to assess the temperature dependency, a leak rate measurement is first performed at the room temperature and then, once the plateau value is reached, the tube is placed in the cryogenic chamber as shown in Figure 5a. Pressurization at room temperature allows the helium wall to be saturated to reduce the duration of the test. The temperature is then gradually reduced in 30°C increments as shown in Figure 5b. The transition to the next temperature step is made when the leakage rate reaches a plateau value. The measurement was stopped at -90°C, the temperature at which the butyl seal no longer seals the vacuum bag.



(a) (b)

Figure 5. Bench test for the leak measurement at low temperature (a) and evolution of leakage rate and temperature during the test (b)

The permeability coefficients Pe measured at different temperatures are plotted in Figure 6. The Arrhenius law (Eq. 4) was identified from these results with an activation energy $E_p = 14.61\ kJ.mol^{-1}$, which is consistent with the results of [8] and [9], respectively of 25 $kJ.mol^{-1}$ and between 14,6 $kJ.mol^{-1}$ and 19.7 $kJ.mol^{-1}$.

$$Pe(T) = Pe_0 \exp\left(-\frac{Ep}{RT}\right) \tag{4}$$

The quality of the interpolation makes it possible to extrapolate the permeability coefficient of the undamaged material to very low temperatures. Besides, the quality of the results on undamaged material, and thus low permeability, allows to apply the measurement procedure on damaged material with confidence.

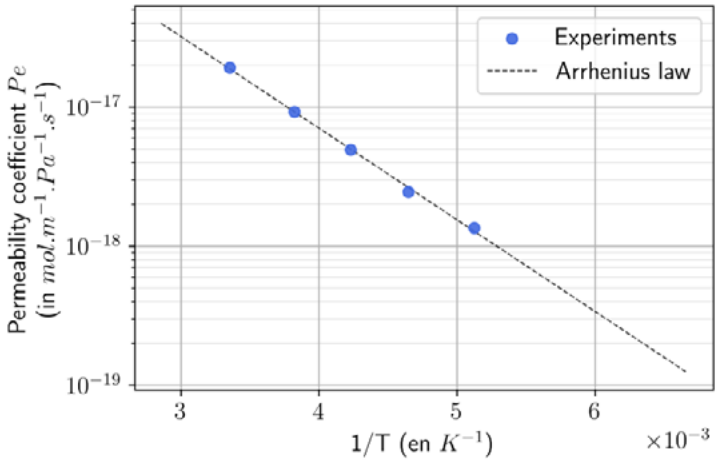


Figure 6. Identification of Arrhenius law from permeability coefficients measured at low temperatures for a pressure difference of 3 bar

3. Permeability of damaged composite

3.1. Leak kinetics measurement

During loading, the accumulation of transverse cracks in the various plies can generate leakage points. In this section we study the evolution of permeability and the number of leakage points during loading. The test bench is shown in Figure 7. Axial and circumferential strains as well as temperature are

measured, and six sensors for Acoustics Emission (AE) monitoring are distributed over the surface of interest.

After each loading step, the leakage rate is measured with a pressure difference of 3 bar. The tube gradually damages, and beyond a loading threshold, it generates leakage points and the flow becomes viscous. This involves studying permeability k rather than permeability coefficients Pe. Figure 8 shows the evolution of permeability k measured at room temperature between each pressure level as well as the cumulative energy of acoustic events. The measured permeability k does not change up to 25 bar, then beyond 27.5 bar, it goes from $1.3 \times 10^{-23}\ m^2$ to $5.1 \times 10^{-23}\ m^2$. Sound activity intensifies at this loading level, which shows that the damage threshold estimated by acoustic emission is the same as the permeability threshold. At 32.5 bar, 120 leakage points were counted manually using a gas revealing spray.

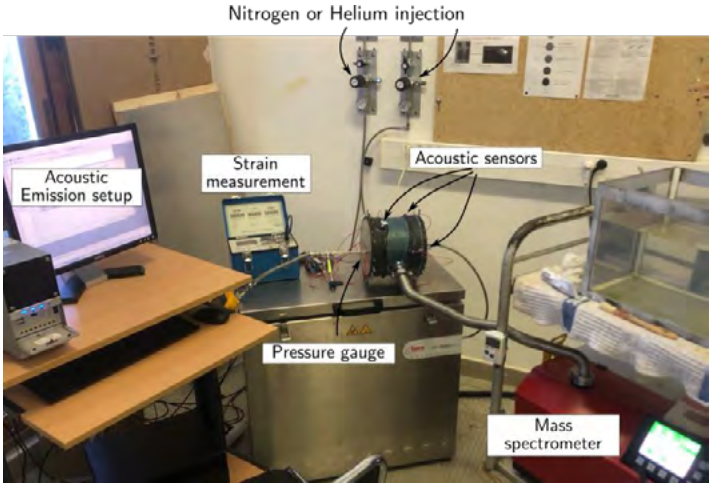


Figure 7. Test bench for the study of tubes subjected to biaxial loading

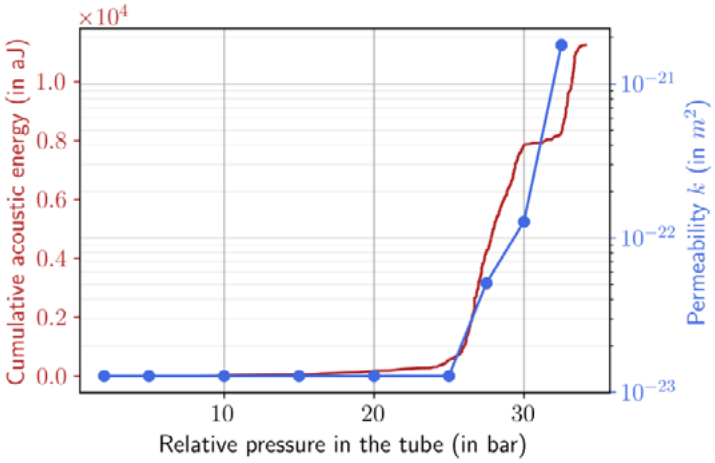
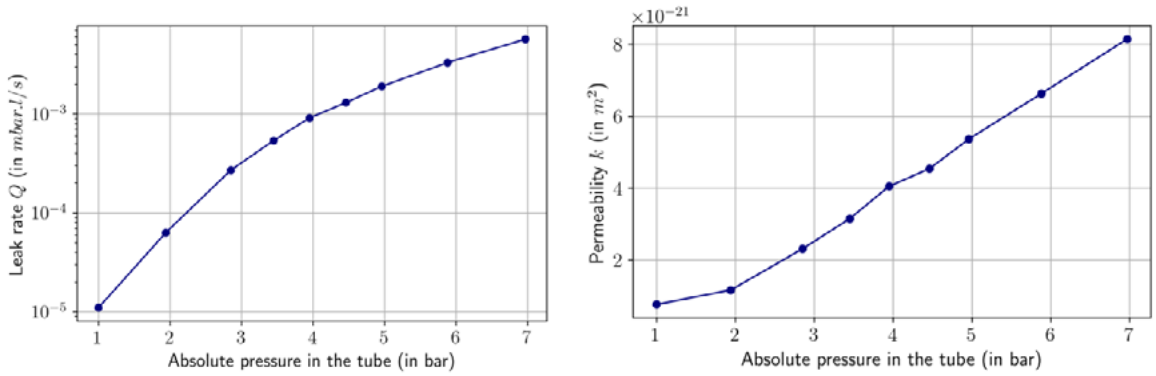


Figure 8. Evolution of permeability and acoustic activity as a function of internal tube pressure at room temperature

3.2. Leak rate evolution

The overall leakage rate Q was measured at different pressure levels below the maximal pressure applied to the tube to determine the influence of pressure on permeability k for a given damage state. These values are plotted on Figure 9 as a function of absolute pressure, since the vacuum is drawn into the bag, this pressure also corresponds to the pressure difference across the wall. As expected, the leakage rate increases with pressure, but the Darcy permeability also increases. This behaviour reflects the effect of

pressure on the opening of cracks in the leakage network, this opening being directly related to the crossing section and therefore to the overall flow rate. This observation has already be made by [10, 11].



(a) **(b)**

Figure 9. Evolution of the overall leakage rate and permeability as a function of the internal pressure after a maximal pressurization of 32.5 bar

3.3. Leak rate under cryogenic conditions

We chose to measure the flow rate of a leakage point using a smaller vacuum bag to identify the influence of the temperature on the leak rate of each leak point. The pressure difference taken is 3 bar. The leakage rate as a function of temperature is plotted in Figure 10. It is noted that, unlike the permeability measurement on a healthy wall, the temperature drop is accompanied by an increase in flow rate from the leakage point. In fact, the increase in cold thermal induced stresses tends to open the cracks, which increases the cross-section and thus the flow rate.

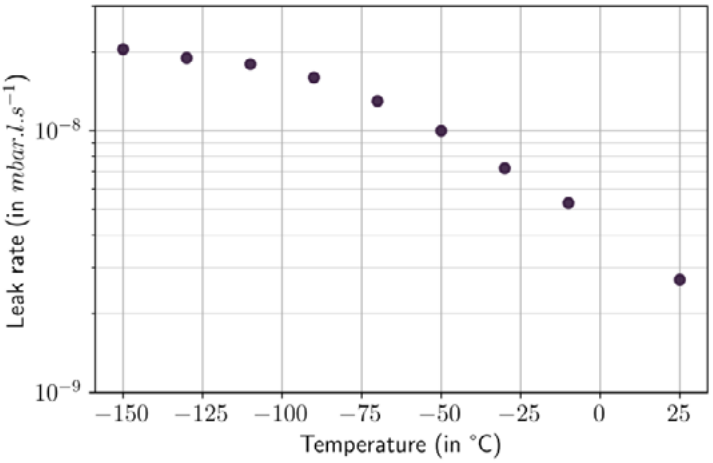


Figure 10. Local leakage rate as a function of temperature

Thermomechanical loading was applied to a second tube. Figure 11 shows the change in the number of leak points counted at -150°C compared to the results at 20°C. At -150°C, the first 77 leak points are observed at 26.5 bar. At this pressure level, the circumferential strain $\epsilon_{\theta\theta}$ is 0.87% against 1.01% at room temperature. Despite the lower strain state of the composite at -150°C, leak points are observed at a lower pressure level than at room temperature. The leakage kinetics is then faster and at 32 bar, 541 leakage points are observed.

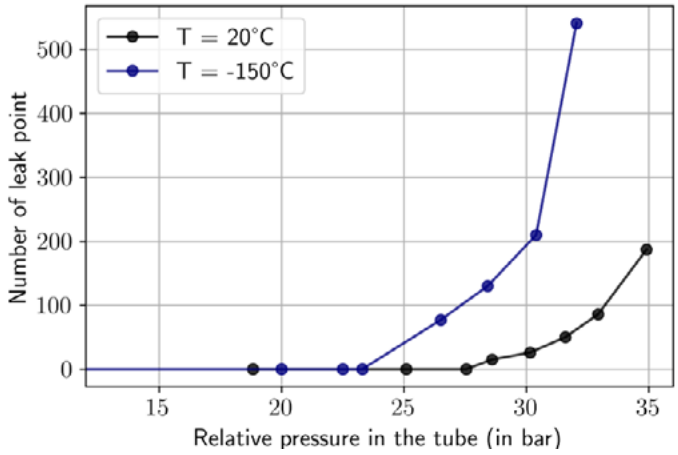


Figure 11. Evolution of the number of leak points as a function of pressure at 20°C and -150°C

4. Conclusion

In this paper, we proposed experimental methods to measure the permeability of a composite laminate using mass spectrometry. Tubular specimens allow applying biaxial stress state representative of a propellant tank. The two types of flow imply the use of two different permeability parameters, able to characterize the permeable behavior of the wall independently from the test conditions. These parameters have been measured on undamaged and damaged composite walls at room temperature and at low temperature. The permeability of the healthy material decreases with temperature but leak points appears at a lower pressure level.

Acknowledgments

The authors would like to thank the CNES, the French space agency, and ArianeGroup for their financial support.

References

[1] Kumazawa, H., Aoki, T., and Susuki, I. (2003). Analysis and Experiment of Gas Leakage Through Composite Laminates for Propellant Tanks. AIAA J, 41(10) :2037–2044.
[2] Kumazawa, H., Aoki, T., and Susuki, I. (2004). Analysis and Experiment on Gas Leakage through CFRP Cross-Ply Laminates under Biaxial Loadings. JAXA Research and Development Report, JAXA-RR-03-012E, 3.
[3] Graham, T. (1866). LV. On the absorption and dialytic separation of gases by colloid septa. The London, Edinburgh, and Dublin PhilosophicalMagazine and Journal of Science, 32(218) :401–420.
[4] Klopffer,M. H. and Flaconneche, B. (2001). Transport Properdines of Gases in Polymers : Bibliographic Review. Oil & Gas Science and Technology - Rev. IFP, 56(3) :223–244.
[5] Darcy, H. (1856) In: Dalmont, V., Ed., Les Fontaines Publiques de la Ville de Dijon: Exposition et Application des Principes a Suivre et des Formulesa Employer dans les Questions de Distribution d'Eau. Paris, 647 p.
[6] McPhee, C., Reed, J., and Zubizarreta, I. (2015). Chapter 5 – Routine Core Analysis. InMcPhee, C., Reed, J., and Zubizarreta, I., editors, Developments in Petroleum Science, volume 64 of Core Analysis, pages 181–268. Elsevier.
[7] Briand, T. (2021). Caractérisation et modélisation de la relation entre l'endommagement et la perméabilité dans un composite strati é en condition cryogénique. Thèse de doctorat, Université Bordeaux.
[8] Disdier, S., Rey, J. M., Pailler, P., and Bunsell, A. R. (1998). Helium permeation in composite materials for cryogenic application. Cryogenics, 38(1) :135–142.
[9] Schultheiß, D. (2007). Permeation Barrier for Lightweight Liquid Hydrogen Tanks. PhD thesis, Universität Augsburg.

[10] Bechel, V. T., Camping, J. D., and Kim, R. Y. (2005). Cryogenic/elevated temperature cycling induced leakage paths in PMCs. Composites Part B : Engineering, 36(2) :171–182.
[11] Yokozeki, T., Ogasawara, T., Aoki, T., and Ishikawa, T. (2009). Experimental evaluation of gas permeability through damaged composite laminates for cryogenic tank. Composites Science and Technology, 69(9) :1334–1340.

A DUAL-SCALE MODEL FOR TENSILE STIFFNESS AND STRENGTH PREDICTION OF CFRTP-SMC BASED ON MICROPOLAR PERIDYNAMIC METHOD

Zhiyu. Wang[1], Yi. Wan[1], and Jun. Takahashi[1]

[1]Department of Systems Innovation, The University of Tokyo, 7-3-1, Bunkyo-Ku, Tokyo, Japan
Email: wang-zhiyu@cfrtp.t.u-tokyo.ac.jp, Web Page: http://j-t.o.oo7.jp/index-e.html
Email: wan-yi@cfrtp.t.u-tokyo.ac.jp, Web Page: http://j-t.o.oo7.jp/index-e.html
Email: takahashi-jun@cfrtp.t.u-tokyo.ac.jp, Web Page: http://j-t.o.oo7.jp/index-e.html

Keywords: *CFRTP-SMC, Peridynamics, Multiscale modeling, Stiffness, Strength*

Abstract
The mechanical properties of carbon fiber reinforced thermoplastic sheet molding compounds (CFRTP-SMC) are closely related to the fiber orientation distribution and its microstructure. A dual scale model has been established to reconstruct the microstructure of SMC material based on probability distribution function and Voronoi diagram. Based on the micropolar peridynamics (MPPD) model considering Timoshenko beam theory, the PD formula was extended to SMC material with three kinds of bond describing the intralayer and interlayer deformation, and the dual-scale model was utilized as the input data for PD model. This model was employed to predict the tensile behavior of SMC material. The predicted tensile stiffness and strength values were found to increase with increasing tape length, which agrees well with literature data, and thus demonstrates the reliability of the proposed modelling framework.

1. Introduction

Mechanical properties of carbon fiber reinforced thermoplastic sheet molding compounds (CFRTP-SMC) are strongly influenced by the complex material flow patterns during the compression molding process [1], besides the randomly oriented strands in SMC induce a multi-scale structure and high heterogeneity [2] which results in the high scatter of its mechanical properties. A lot of research work has been done in establishing multiscale modeling methods for random fiber reinforced composite material [3][4][5]. The common approach is to use information from microscale to homogenize local properties and then the homogenized properties are used as input for subsequent macroscale finite element analyses (FEA) to predict macroscale elastic properties. However, the multiscale structure and high heterogeneity leads to difficulties in mechanical analysis of SMC with FEA. The micro cracks, that is, discontinuous areas in SMC are in natural conflict with the continuity assumption in Classical continuum mechanics (CCM) [6]. Silling [7] proposed a non-local theory of continuum mechanics called the bond-based peridynamic (PD) theory which attracts huge attention for its great advantages in dealing with discontinuous problems. The governing formulas of PD are in integral forms without spatial derivatives so cracks can spontaneously initialize, propagate, converge, and penetrate without prior knowledge of fracture criteria, making PD suitable for analyzing discontinuous problems and being widely utilized in damage and fracture prediction. Gerstle et al. [8] introduced a micropolar PD model (MPPD) by considering pairwise moments as well as forces in the bond-based PD model.

To accurately predict the tensile stiffness and strength of SMC, a dual-scale model has been proposed to reconstruct the mesoscopic structure of SMC. Based on the Timoshenko beam-based micropolar peridynamic method [9][10], the peridynamic model was extended to SMC materials, and the dual-scale model is utilized as the input data of the MPPD model to predict the stiffness and strength of SMC.

2. Dual-scale CFRTP-SMC Model

The SMC microstructure is featured by the random distribution of fiber bundles, not isolated fibers. Figure 1 (a) shows typical SMC microstructure viewed from the thickness direction. Two important features of SMC were observed: 1) The microstructure consists of randomly-oriented fiber tows; 2) Each fiber tow consists of aligned fibers. All fibers have the same orientation inside each fiber tow. Instead of tracing the orientation angle of each fiber, the fiber orientation distribution of the composite is represented by the statistical distribution of fiber tow orientations weighted by the fiber tow area.

Therefore, in this dual-scale CFRTP-SMC model, the probability distribution function (PDF) was recovered of fiber orientation from the fiber orientation tensor in micro-scale. And the Voronoi diagram-based reconstruction algorithm is proposed for constructing the substructure features in SMC composites in meso-scale.

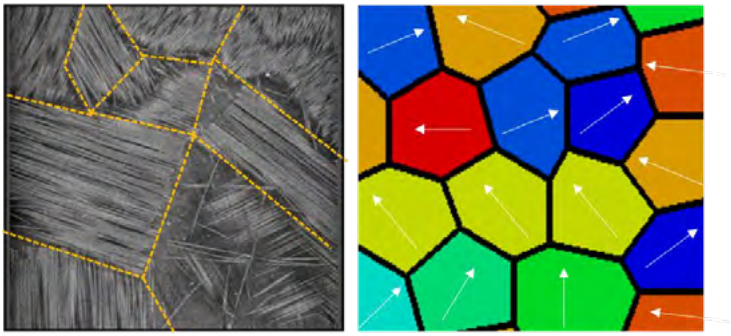


Figure 1. Microstructure image of SMC sample (a), representation of the fiber tows using Voronoi diagram (b)

2.1 Micro-scale

In the microscopic scale, fiber orientation tensor is utilized to reconstruct the probability density function (PDF) of fibers. Notating the fiber orientation tensor matrix by $\boldsymbol{A}$, the second order and fourth order fiber orientation tensors are defined as:

$$\boldsymbol{A}_{ij} = \oint_i^p p_j \psi(\mathbf{p}) \mathrm{d}\mathbf{p}, \tag{1}$$

$$\boldsymbol{A}_{ijkl} = \oint_i^p p_j p_k p_l \psi(\mathbf{p}) \mathrm{d}\mathbf{p}. \tag{2}$$

Where p_i are the components of the unit vector $\psi(\mathbf{p})$ describing the direction of a single fiber and $\psi(\mathbf{p})$ is the fiber orientation PDF. The PDF can be recovered once the fiber orientation tensors are written as:

$$\psi(\mathbf{P}) = \frac{1}{4\pi} + \frac{15}{8\pi} b_{ij} f_{ij}(\mathbf{p}) + \frac{315}{32\pi} b_{ijkl} f_{ijkl}(\mathbf{p}) + \cdots. \tag{3}$$

Where b_{ij} and b_{ijkl} are the deviatoric versions of the orientation tensors, and $f_{ij}(\mathbf{p})$, $f_{ijkl}(\mathbf{p})$ are tensor basis functions of $\mathbf{p}$.

2.2 Meso-scale

In the meso-scale, a random fiber tape reconstruction algorithm is developed to generate a mesostructured model with relative high fiber volume fraction. The number of fiber tapes representing each layer is estimated based on the information of the tape sizes and SMC laminate sizes. Total number of fiber tapes are represented by N_L and N_T respectively, which can be estimated as:

$$N_L = \left\lceil \frac{W_L \cdot L_L}{W_T \cdot L_T} \right\rceil, \tag{4}$$

$$N_T = N_L \cdot n_P. \tag{5}$$

Where W_L and L_L is the width and length of SMC laminate, and W_T and L_T is the width and length of tape respectively. All the parameters beforementioned are the input data of SMC reconstruction based on Voronoi diagram, which is showed in Figure 1 (b). Each Voronoi cell represent a fiber tow, which means that the fibers within each cell are oriented alone the same orientation, as shown by the white arrows.

Figure 2 shows the example of the SMC reconstruction. The fiber orientation tensor $\mathbf{A} = \begin{pmatrix} 0.5 & 0 \\ 0 & 0.5 \end{pmatrix}$, and tape size is 5mm*6mm, 5mm*18mm, 5mm*30mm.

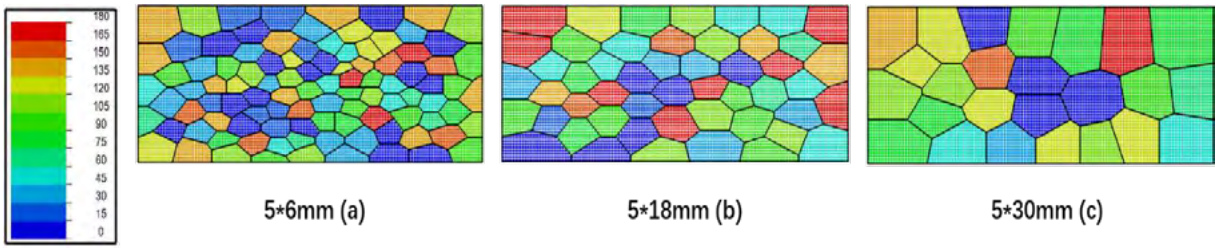


Figure 2. SMC microstructure reconstruction of different tape length

3. Briefly review of MP-PD model for orthotropic materials

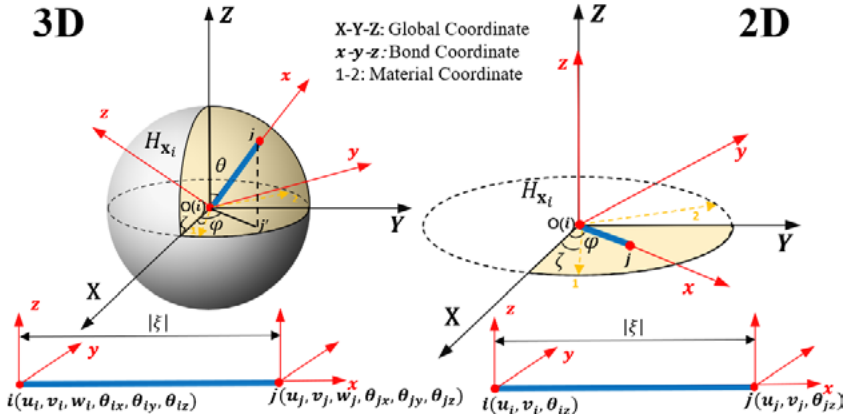


Figure 3. Displacement components in MP-PD model

In MP-PD model, the interaction of material points i and j can be regarded as a beam, which means it can both subject the axial and transverse forces. For 2D orthotropic materials, the displacement vector consisting of the bond endpoint ij, defining as $\mathbf{u}'_{ij}$, which possess six components can be written as:

$$\boldsymbol{u}'^{\mathrm{T}}_{ij} = \{u'_i\ v'_i\ \theta'_{iz}\ u'_j\ v'_j\ \theta'_{jz}\}. \tag{6}$$

The micropotential energy of bond ij, defining as ω_{ij} (J/m^6) includes bending micropotential energy and shear micropotential energy. The micropotential energy of bond ij can be obtained as [9]:

$$\omega_{ij} = \frac{1}{2}\int_{x'_i}^{x'_j} \frac{1}{2}\left(\mathbf{u}'_{ij}(\chi)\right)^{\mathrm{T}} \mathbf{D}\mathbf{u}'_{ij}(\chi)\mathrm{d}x. \tag{7}$$

ω_{ij} can also be rewritten as:

$$\omega_{ij} = \frac{1}{2}\mathbf{u}'^{\mathrm{T}}_{ij}\mathbf{K}^{local}_{ij}\mathbf{u}'_{ij}, \tag{8}$$

where $\mathbf{D}$ is the off-axis micromodule matrix and $\mathbf{K}^{local}_{ij}$ is the local micro stiffness matrix, and can be written as:

$$\mathbf{D} = \begin{bmatrix} C_{xx} & C_{xy} \\ C_{xy} & C_{yy} \end{bmatrix}. \tag{9}$$

$$\mathbf{K}^{local}_{ij} = C_{xx}\begin{bmatrix} 1/\xi & 0 & 0 & -1/\xi & 0 & 0 \\ 0 & 0 & 0 & 0 & 0 & 0 \\ 0 & 0 & I/(A\xi) & 0 & 0 & -I/(A\xi) \\ -1/\xi & 0 & 0 & 1/\xi & 0 & 0 \\ 0 & 0 & 0 & 0 & 0 & 0 \\ 0 & 0 & -I/(A\xi) & 0 & 0 & I/(A\xi) \end{bmatrix}$$
$$+C_{yy}\begin{bmatrix} 0 & 0 & 0 & 0 & 0 & 0 \\ 0 & 1/\xi & 1/2 & 0 & -1/\xi & 1/2 \\ 0 & 1/2 & \xi/4 & 0 & -1/2 & \xi/4 \\ 0 & 0 & 0 & 0 & 0 & 0 \\ 0 & -1/\xi & -1/2 & 0 & 1/\xi & -1/2 \\ 0 & 1/2 & \xi/4 & 0 & -1/2 & \xi/4 \end{bmatrix} + C_{xy}\begin{bmatrix} 0 & 1/\xi & 1/2 & 0 & -1/\xi & 1/2 \\ 1/\xi & 0 & 0 & -1/\xi & 0 & 0 \\ 1/2 & 0 & 0 & -1/2 & 0 & 0 \\ 0 & -1/\xi & -1/2 & 0 & 1/\xi & -1/2 \\ -1/\xi & 0 & 0 & 1/\xi & 0 & 0 \\ 1/2 & 0 & 0 & -1/2 & 0 & 0 \end{bmatrix}. \tag{10}$$

For orthotropic material, critical micropotential energy ω_c need to change continuously with the direction of bond. In order to fully address this anisotropic properties, spherical harmonic expansion was employed to approximate critical micropotentical energy function. The expression of ω_c can be written as:

$$\omega_c(\zeta - \varphi) = A_{00} + A_{20}P_2^0\big(cos(\zeta - \varphi)\big) + A_{40}P_4^0\big(cos(\zeta - \varphi)\big). \tag{11}$$

Where

$$\begin{aligned} P_2^0(cos(\zeta - \varphi)) &= \frac{1}{2}(3\cos^2(\zeta - \varphi) - 1), \\ P_4^0(cos(\zeta - \varphi)) &= \frac{1}{8}(35\cos^4(\zeta - \varphi) - 30\cos^2(\zeta - \varphi) + 3). \end{aligned} \tag{12}$$

For the 1 and 2 axes, assuming that $\omega_c(0°) = \omega_{c1}$ and $\omega_c(90°) = \omega_{c2}$. In order to achieve a smooth transition of $\omega_c(\zeta - \varphi)$ between 0° and 90°, in this study, it is assumed that $\omega_c(45°) = \frac{\omega_{c1}+7\omega_{c2}}{8}$. Substituting these three conditions ($\omega_c(0°) = \omega_{c1}, \omega_c(90°) = \omega_{c2}, \omega_c(45°) = \frac{\omega_{c1}+7\omega_{c2}}{8}$) into eq (11) and eq (12) respectively, and solve the system of four linear equations. The coefficients A_{n0} can be expressed as a linear combination of ω_{c1} and ω_{c2}:

$$\begin{aligned} A_{00} &= 0.1333\omega_{c1} + 0.8667\omega_{c2}, \\ A_{20} &= 0.5238(\omega_{c1} - \omega_{c2}), \\ A_{40} &= 0.3429(\omega_{c1} - \omega_{c2}). \end{aligned} \tag{13}$$

For brittle materials, the energy required for a crack to split a body into two halves equals the sum of the rupture energy of the bonds that initially crossed the crack surface [11]. The critical strain energy release rate is this energy divided by the area of the crack surface. Therefore, the strain energy release rate normal to 1 and 2 of material coordinate systems can be written as:

$$G_{\zeta=0} = 2t\int_0^{\delta}\int_z^{\delta}\int_0^{\cos^{-1}\left(\frac{z}{\xi}\right)} \omega_c(\varphi)\xi \mathrm{d}\varphi \mathrm{d}\xi \mathrm{d}z, \tag{14}$$

$$G_{\zeta=\frac{\pi}{2}} = 2t\int_0^{\delta}\int_z^{\delta}\int_{\cos^{-1}\left(\frac{z}{\xi}\right)}^{\frac{\pi}{2}} \omega_c(\varphi)\xi \mathrm{d}\varphi \mathrm{d}\xi \mathrm{d}z. \tag{15}$$

Therefore, by solving this linear equation group, ω_{c1} and ω_{c2} can be obtained:

$$\begin{aligned} \omega_{c1} &= \left(2.1207G_{\zeta=0} - 0.6205G_{\zeta=\frac{\pi}{2}}\right)\Big/_{t\delta^3} \\ \omega_{c2} &= \left(0.1471G_{\zeta=0} + 1.3528G_{\zeta=\frac{\pi}{2}}\right)\Big/_{t\delta^3} \end{aligned}. \tag{16}$$

Where t is the thickness of model and δ is the radius of PD horizon.

4. MP-PD model for SMC materials

The PD bond in SMC model is consists with three kinds of bond: intra-cell bond which is used to describe deformations within Voronoi cell and inter-cell bond, using to describe inter-cell deformations. Inter layer bond is employed to show the interlayer deformation.

4.1 Intra-cell bond

Each Voronoi cell can be considered as an orthotropic lamina since fibers have the same orientation, and it has independent elastic constants. If two material points are in the same Voronoi cell like bond ij in Figure 4 (a), they are connected by intra-cell bond. The MPPD model for orthotropic materials proposed in section 3 can be directly applied in this case.

4.2 Inter-cell bond

If the material points are in the same ply but belong to different Voronoi cells, like bond ik in Figure 4 (a), it can be considered as inter-cell bond. The peridynamic parameters of such kind bond are determined by averaging the peridynamic parameters of two material points connected. Therefore, MPPD model proposed in section 3 is also available.

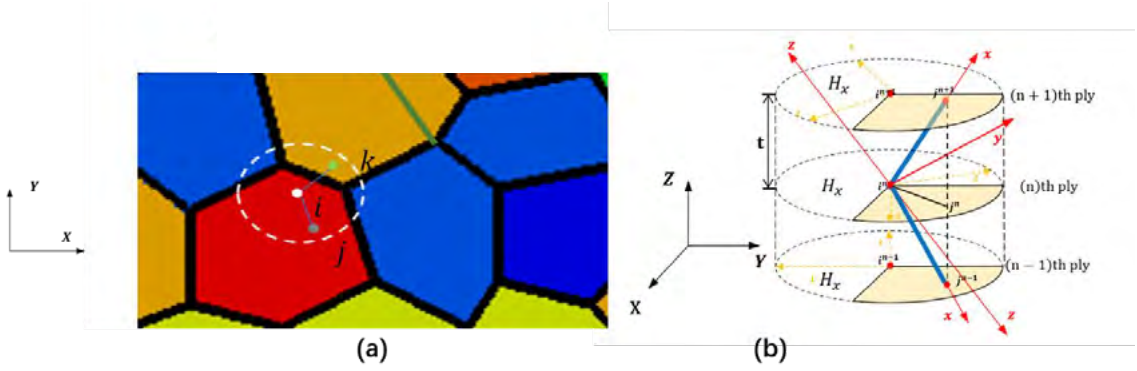


Figure 4. Intra-cell bond, inter-cell bond (a) and inter layer bond (b)

4.3 Interlayer bond

If the material points are in the different ply, it can be considered as interlayer inter-cell bond, which is showed in Figure 4 (b). PD theory assumes that when the stretch index, s_{kj}, exceeds its critical value, s_c, the onset of damage occurs. Damage is reflected by removing the force density vectors between the material points in an irreversible manner. The values of s_c was determined by the type one and type two critical energy release of matrix:

$$S_{\text{Normal}} = \sqrt{\frac{2G_{\text{IC}}}{tE_m}} S_{\text{Shear}} = \sqrt{\frac{G_{\text{IIC}}}{tG_m}}. \quad (11)$$

Where G_{IC} and G_{IIC} are the interface toughness of resin.

5 Numerical simulation and verification

In this section MPPD model was employed to predict the stiffness and strength of SMC within different tape length.

5.1 Determination of appropriate number of layers

The thickness of the tape is 44 μm, while the thickness of the SMC laminate after compression molding is about 2mm-3mm, meaning that there are about 40-50 layers of tape along the thickness direction, which is too much considering computation efficiency in numerical simulation.

Therefore, the tensile modulus of SMC laminate was calculated with layer numbers ranging from 5 to 25 layers, with a total of 6 models per layer, and the microstructure of each model was randomly generated. The results are showed in Figure 5 (a). As the number of layers increases, the fluctuations of calculated tensile modulus begin to decrease. It is determined to have 20 layers in the MPPD model in order to achieve a balance between the prediction accuracy and the computational costs. The mechanical properties of SMC can be referenced in [2][12].

The numerical results of stiffness and strength are compared with experiment results which shows in Figure 5 (b) and Figure 6. A total of six SMC microstructures of 20 layers were randomly generated for each tape length, and the average stiffness and strength of the six models were calculated, as shown in Figure 6. Figure 7 shows the predicted failure path. The microstructure shown in the Figure 7 is the microstructure of the first layer.

It can be seen that the stiffnesses of the six models in the same tape length within 20 layers are relatively close. As the tape length increases, the stiffness increases, which is consistent with the results obtained from the SMC tensile experiment [12]. In terms of strength, the strength of models with different microstructures under the same tape length fluctuated. Figure 5 (b) illustrates the average strength of the six models in each tape length and compared with the experimental results. The standard deviation of the SMC strength obtained from simulation and experiment is very large**,** which is related to the high heterogeneity of this material.

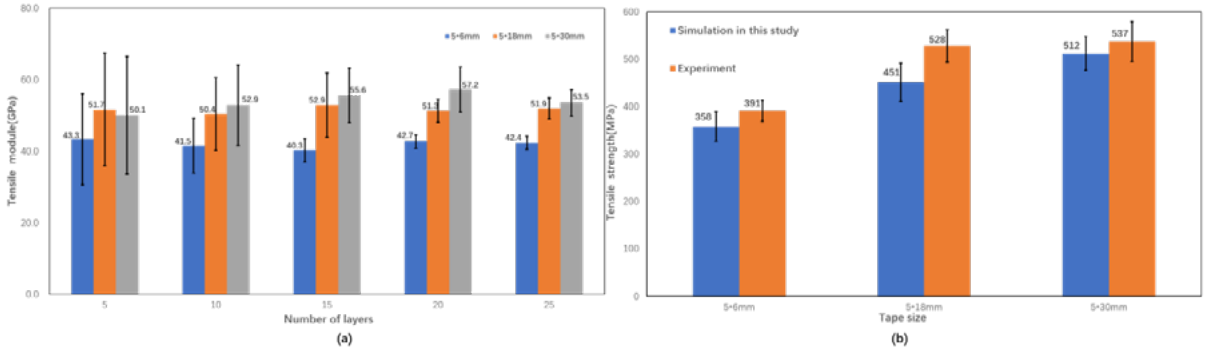


Figure 5 . Tensile module of different layer numbers (a), tensile strength of different tape length (b)

5. Conclusion

A dual-scale numerical model is propped in this study for the mechanical analysis of CFRTP-SMC. This model provides a new numerical modeling method for heterogeneous materials with randomly oriented reinforcements. The model is innovative in its approach, comprising two distinct components.

Firstly, it introduced a microstructure reconstruction method for SMC, leveraging fiber probability density functions and Voronoi diagram. This enables a detailed representation of the material's internal structure, crucial for accurate mechanical analysis. In the second part, the model incorporates a heterogeneous framework based on the MP-PD theory, and three types of PD bonds that characterize both intralayer and interlayer deformation in SMC. By applying this model to simulate tensile tests on SMC, the study quantitatively assesses the impact of tape length on stiffness, strength, and failure strain. Furthermore, the model is able to predict the failure path of SMC, enhancing its utility for predictive analysis and structural design. The actual toughness of SMC from experiments was employed in the damage analysis, making the failure and damage simulation closer to the real situations.

This study's dual-scale numerical model represents an innovative numerical model of CFRTP-SMC, offering a novel approach to understanding and optimizing the mechanical properties of heterogeneous materials, with wide-ranging implications for various engineering applications.

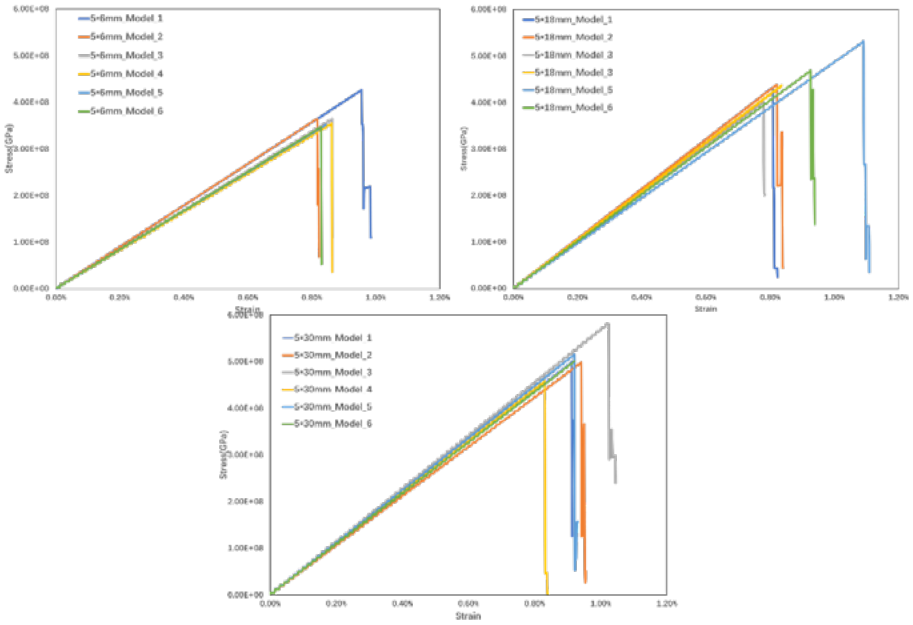


Figure 6. Stress-strain curve

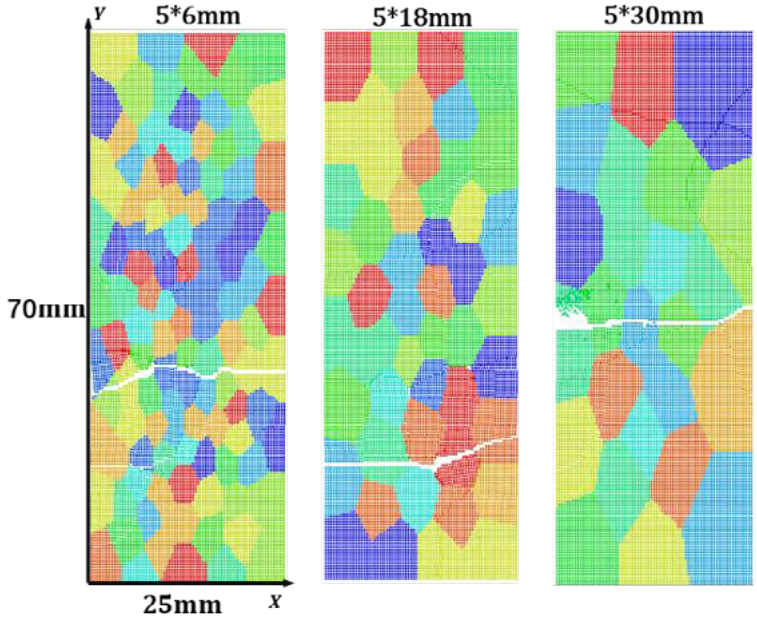


Figure 7. Failure path of SMC laminate

Acknowledgments
This work was supported by JST SPRING, Grant Number JPMJSP2108, and would like to express sincere thanks to Industrial Technology Center of Fukui Prefecture for supplying the specially developed CFRTP-SMC material.

References
[1] Z. Cheng, H. Huang, Y. Shen, et al. Multiscale finite element modeling of sheet molding compound (SMC) composite structure based on stochastic mesostructure reconstruction. *Compos Struct*, Vol 188:25-38, 2018.
[2] P. Qu, Y. Wan, J. Takahashi, et al. A new numerical method for the mechanical analysis of chopped carbon fiber tape-reinforced thermoplastics. *Compos Struct*, Vol 201:857-866, 2018.
[3] J. D. Eshelby. The determination of the elastic field of an ellipsoidal inclusion, and related problems. *Proc. R. Soc. London A: Math. Phys. Eng. Sci: R. Soc*, 376-396, 1957.
[4] T. Mori, K. Tanaka. Average stress in matrix and average elastic energy of materials with misfitting inclusions. *Acta Metall*, Vol 21:571-574, 1973.
[5] J. Guedes, N. Kikuchi. Preprocessing and postprocessing for materials based on the homogenization method with adaptive finite element methods. *Comput Methods Appl Mech Eng*, Vol 83(2):143-198, 1990.
[6] J. Madenci, E. Otekus. *Peridynamic Theory and Its Applications*. Shanghai Jiao Tong University Press, SHANGHAI, 2019.
[7] S. A. Silling. Reformulation of elasticity theory for discontinuities and long-range forces. *J Mech Phys Solids*, Vol 48(1):175-209, 2000.
[8] W. Gerstle, N. Sau, S. A. Silling. Peridynamic modeling of concrete structures. *Nucl Eng Des*, Vol 237:1250–1258, 2007.
[9] G. Zheng ,Y. Xia, H. Wang, et al. Discontinuous Galerkin isogeometric analysis with peridynamic model for crack simulation of shell structure. *Comput Methods Appl Mech Eng*, Vol 398:115-193, 2022.
[10] V. Diana, S. Caslo. A full orthotropic micropolar peridynamic formulation for linearly elastic solids. *Int J Mech Sci*, Vol 160:140-155, 2019.
[11] S. A. Silling, E. A. Askari. Meshfree method based on the peridynamic model of solid mechanics. *Comput Struct*, 83 (17-18):1526-1535, 2005.
[12] S. Yamashita, K. Hashimoto, H. Suganuma, et al. Experimental characterization of the tensile failure mode of ultra-thin chopped carbon fiber tape-reinforced thermoplastics. *J Reinfo Plast Compos*, Vol 35(18):1342–1352, 2016.

STOCHASTIC ANALYSIS OF SPATIAL INHOMOGENEITY OF CARBON FIBER PAPER REINFORCED THERMOPLASTICS USING MONTE CARLO METHOD

Peng Xue[1], Qian Gao[1], Yi Wan[1], and Jun Takahashi[1]

[1]Department of Systems Innovation, University of Tokyo, Tokyo, Japan
Email : xue-peng@g.ecc.u-tokyo.ac.jp, fionagaoqian@gmail.com, wan-yi@cfrtp.t.u-tokyo.ac.jp, takahashi-jun@cfrtp.t.u-tokyo.ac.jp

Keywords: CFRP, FEM, Reliability analysis, Monte Carlo method

Abstract
The increasing application of Carbon Fiber Reinforced Plastics (CFRP) across various industries has led to a shift from deterministic to stochastic methods in evaluating their inherent variability. This approach fully leverages the properties of composite materials, particularly in reliability-based design. Carbon Fiber Paper Reinforced Thermoplastics (CPT), a type of potential recycled CFRP, is recognized for its robust mechanical properties and cost-effectiveness, making it suitable for industries such as wind energy and automotive manufacturing. This study utilizes Monte Carlo (MC) methods to explore uncertainties in CPT, particularly focusing on the effects of spatial variability from mesoscopic to macroscopic scales. At the mesoscopic scale, the stochastic distribution of carbon fiber orientation is analyzed using X-ray CT techniques, and the Cox model is employed to calculate the tensile modulus distribution in the principal directions of the sample plane. The study addresses spatial inhomogeneity by generating specimens with varying moduli distributions using an MC approach, significantly impacting the ultimate failure path of CPT laminates. A three-point bending test case study further investigates this aspect, with finite element simulations calibrated against experimental data to ensure accuracy. This analysis examines the ultimate displacement and maximum load in relation to moduli distributions and evaluates the reliability and failure probability of the samples. The error of global strain's mean value is 4.0% while for the stress's is 1.7%, which demonstrate the good consistency between the simulation methods and experimental results.

1. Introduction

The recycling of carbon fibers (CFs) from carbon fiber-reinforced plastic (CFRP) waste is gaining significant attention due to environmental and economic considerations. Various studies have highlighted the importance of efficiently recycling carbon fibers (rCFs) from CFRP waste to be reused in high-value applications [1]. The circular economy approach, coupled with the ability to recover carbon fibers with properties similar to virgin fibers at a lower cost and energy consumption, has motivated research in CFRP recycling [2]. However, the heterogeneous properties of recycled CFRP play a significant role in various manufacturing processes and material applications. The heterogeneity of CFRP, characterized by differences in fiber orientation, distribution, and mechanical properties between the phases of the composite, poses challenges in machining, drilling, and other fabrication processes [3]. Understanding the influence of inhomogeneity in recycled CFRP is essential for optimizing recycling methods and ensuring the quality and performance of the recycled material. Studies on the micromechanical properties and reinforcement architecture of recycled composites have highlighted the impact of inhomogeneities on mechanical responses and failure initiation [4]. Moreover,

the inhomogeneity of recycled CFRP may differ from that of virgin CFRP, necessitating further research to assess differences in machinability and material behavior [5].

In the realm of methodology, the application of Monte Carlo(MC) and k-means methods has been explored in the context of composite materials. The application of the k-means method in composite materials, particularly in the context of inclusions, offers a valuable approach to understanding and analyzing the distribution and clustering of different components within the composite structure. Composite materials, which consist of a matrix and reinforcing inclusions, often exhibit complex microstructures that influence their overall properties and behavior. By applying the k-means method, researchers can effectively segment and classify inclusions based on their characteristics, such as size, shape, and distribution, enabling a deeper insight into the composite's structural organization [6]. On the other hand, the Monte Carlo method provides a powerful tool for considering the randomness and uncertainty inherent in composite materials. By utilizing random sampling techniques, Monte Carlo simulations can model the stochastic nature of material properties, manufacturing variations, and environmental factors that impact composite performance. In the context of composite materials, Monte Carlo simulations can be employed to analyze the probabilistic distribution of mechanical properties, predict failure modes under uncertain conditions, and optimize material design considering variability in constituent properties.

In our previous research, the properties of recycled CFRP composed of short fiber materials were investigated and a property prediction method based on the Monte Carlo method was developed [7]. To further quantify carbon fiber reinforced thermoplastics s uncertainty, this study developed a stochastic model through experimental and numerical methods. The process for constructing this stochastic model is depicted in Figure 1. The study investigates the stochastic distribution of carbon fiber orientation at the mesoscopic scale using X-ray techniques, which enables the fitting of probability distribution functions. Employing the Cox model [8], the distribution of local tensile modulus in the two principal directions of the sample's plane is calculated. Additionally, the experiments facilitate the collection of data on the local modulus distribution. To capture features of inhomogeneity, the k-means clustering method is utilized, allowing for the development of a global model that incorporates spatial inhomogeneity. A deterministic FEM model is formulated based on the experimental data. Integrated with Monte Carlo simulation, this approach allows for the collection of the sample responses' distribution, which is then validated and implemented in structural analysis.

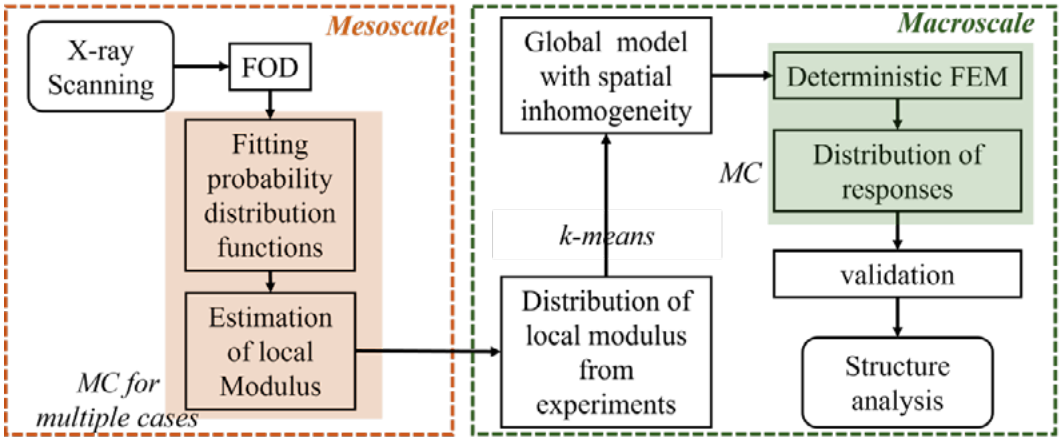


Figure 1. Construction of the stochastic model.

2. Material and method

2.1 Manufacturing of the materials

The material used in this study is manufactured using the wet laid nonwovens process, as shown in Figure 2. Initially, CFs and polyamide 6 (PA6) fibers are mixed in a water-based suspension to form a slurry. This slurry contains CFs and typically includes water or a combination of water and a binding agent, aiding in fiber cohesion during processing. The slurry is then poured onto a moving mesh conveyor or a forming machine, commonly known as a "Fourdrinier machine." As the slurry advances through the conveyor or machine, water drains through the mesh, causing the fibers to interlace and form a fibrous mat. The freshly formed wet mat undergoes pressing and rolling to remove excess water, promoting fiber consolidation and mat compaction. After partial dewatering, the mat is subjected to a drying process to eliminate any remaining moisture. Once dry and with any binding materials removed, the mat is ready for further processing or finishing as needed.

The control of fiber orientation in wet-laid nonwoven mats is influenced by various manufacturing parameters, including line speed, uptake angle, and headbox geometry. Consequently, the resultant wet-laid nonwoven mats typically do not exhibit uniform isotropic characteristics. Instead, the properties of composites depend on the specific orientation of the cut preform. In this study, the composite properties along the machine flow direction (MD) and cross direction (CD) within the manufacturing line are explored, as depicted in Figure 2(b). The MD and CD prepreg sheets were randomly distributed and stacked to produce cross-plied CF/PA6 composites. The stacking sequence of the cross-plied composites is shown in Figure 2(d). For CPT samples oriented in the CD and MD, the elastic modulus in the tensile direction and perpendicular to the tensile direction are significantly different. This variation complicates clustering because the DIC method can only measure the modulus distribution along the tensile direction. In contrast, for cross-plied specimens, the difference in elastic modulus between the two directions is smaller and displays more random characteristics. Consequently, this study will utilize the modulus distribution from cross-plied specimens as the reference for clustering.

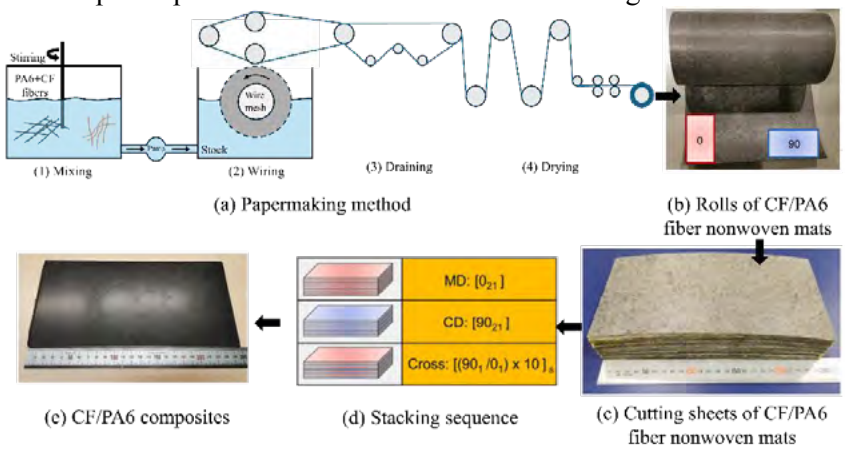


Figure 2. Schematic for the manufacturing of CPTs.

2.2 Detecting of mesoscale features

The internal structural details of the CPTs were captured using the TDM1000-II 3D X-ray scanning system provided by Yamato Scientific Co., Ltd, Japan. During the observation, specimens were secured on a rotating platform. To ensure clear resolution of embedded fibers, the distance between the rotation axis and the radiation source was maintained at 10 mm. The scanning process yielded a raw volume shaped as a right circular cylinder, measuring 0.88 mm in radius and 1.76 mm in height, due to the continuous rotation of the stage. The 3D micro-CT images were reconstructed with a uniform pixel size of 3.4 μm, comprising 512 stacked images in the out-of-plane direction. To enhance image resolution and contrast, air portions within the scanned raw images were excluded during CT acquisition. The CT procedures adhered to the Cartesian coordinate system, necessitating a cubic volume for scanning. Accordingly, the sample was strategically positioned within the scanner's field of view, constrained to a physical volume of 1×1×1 mm, air excluded. For this study, five samples (10 × 2 × 2 mm) were selected from various positions on each panel. Each sample was tested at four different heights. The X-

ray tube's voltage and current were consistently set at 40 kV and 100 μA for all specimens. X-ray projection images were acquired with a rotation step of 0.24 degrees over a total rotation time of 25 minutes. The 3D image reconstruction utilized the image processing unit of the X-ray system, stacking 325 images along the out-of-plane direction for subsequent image processing and CT analysis. A diagram of the scanning process is illustrated in Figure 3(a).

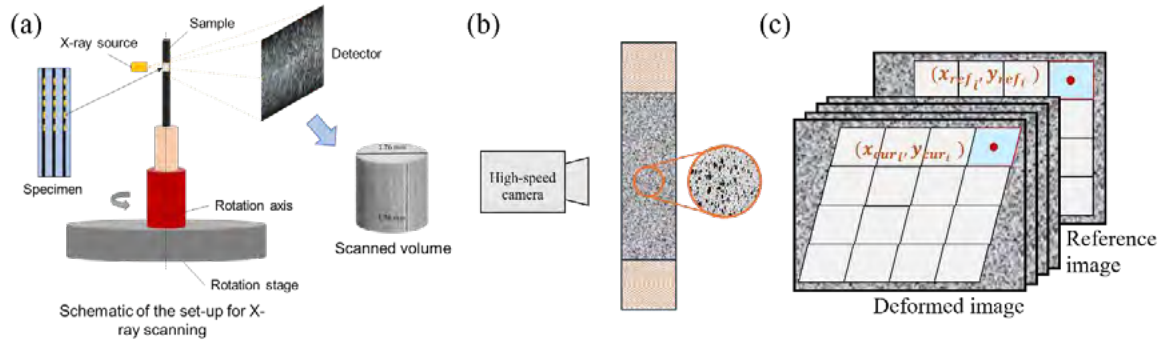


Figure 3. Schematic for (a) X-ray scanning system, (b) DIC method, (c) DIC post-processing

2.3 Calculation of the local modulus

The netting analysis was used to predict the tensile stiffness in this study. This method is useful for quick estimation and gives a simple result by ignoring the presence of the matrix and considering only the loading of the fibers. It assumes that a singe fiber can only transfer tension loading of fiber ends. It assumes that a single fiber can only transfer tension loading and neglects flexural stiffness. When a planar mat of fibers is subjected to tensile strains in two directions and a shear strain ($\varepsilon_x, \varepsilon_y, \gamma_{xy}$), the strain of the fiber at an angle ϕ can be expressed as $\varepsilon_\phi = \varepsilon_x \sin^2\phi + \varepsilon_y \cos^2\phi + \gamma_{xy} \sin\phi \cos\phi$.
The distribution function $f(\phi)$ represents the number of fibers at an angle ϕ and can be written as $\int_0^\pi f(\phi)d\phi = 1$. The elastic moduli along the longitudinal direction (E_L) can be calculated using Eq. 1 combined with the ROM:

$$E_L = E_f V_f \left(c_{11} - \frac{c_{22}^2}{c_{12}}\right) + E_m(1 - V_f) \tag{1}$$

where,

$$c_{11} = \int_0^\pi \cos^4\phi f(\phi)\phi, \quad c_{22} = \int_0^\pi \sin^4\phi f(\phi)\phi, \tag{2}$$

2.4 DIC technology

The local modulus of the CPTs will be investigated using Digital Image Correlation (DIC) technology. The layout and schematic of the DIC setup are illustrated in Figures 3(b) and 3(c). In this study, an open-source two-dimensional digital image correlation (2D-DIC) software package, Ncorr, will be utilized to process the DIC data. The distortions in the x, y, and xy directions will be calculated and visualized separately. Prior to testing, the sample surfaces were prepared by uniformly spraying white paint with an airbrush and then randomly applying black speckles to create contrast, as depicted in Figure 3(b). The mechanical testing was conducted using a set of six groups of axial tensile tests according to JIS K 7073 standards, employing a universal testing machine (AUTOGRAPH AGS-X plus 100KN, Shimadzu Co., Ltd., Japan). During the tests, a high-speed camera captured the deformation of the samples. The resulting images will be processed as shown in Figure 3(c), enabling the collection of detailed strain fields and displacement fields.

2.5 Deterministic FE model

A 2D shell element was constructed using the P11 sandwich property in Altair Radioss to simulate the properties of CPT laminates, as depicted in Figure 6(a). For the CPT sample layers, the material model LAW25 was applied, supplemented by /FAIL/HASHIN for failure analysis. In the bending test, both the cylindrical loading bar and support bars were assigned rigid body properties. The loading bar moved at a constant speed of Vz=120 mm/min vertically to measure the reactive force induced by the sample's deformation. The support bars remained stationary, and surface-to-surface contacts were established between the cylindrical bars and the sample. Element sizes in the contact areas were minimized to enhance the accuracy of stress distribution, while larger elements were used in other regions to reduce computational time. The material properties and failure parameters for this FE model are detailed in Table 1.

Table 1. Mechanical properties for FE model

Parameter			
	Elastic Modulus (GPa)	E_1	32.00
		E_2	11.00
		E_3	11.00
	Shear Modulus (GPa)	G_{12}	2.10
		G_{13}	1.08
		G_{23}	1.08
Strength	Tensile strength (MPa)	X_T,Y_T	360.00
	Tensile fracture strain (%)	ε_T	1.00
	Compressive strength (MPa)	X_C,Y_C	240.00
	Compressive fracture strain (%)	ε_C	0.80
	Shear strength (MPa)	X_S	170.00
	Shear fracture strain (%)	ε_S	1.31

3. Results and discussions

3.1 Modulus distribution of CPTs

An example of the tensile modulus E_{yy} distribution for cross-ply samples, calculated using the DIC method, is shown in Figure 4. The data obtained through DIC reveal a non-uniform distribution of strain across the surface, suggesting a non-uniform internal distribution within the CPTs. The modulus values derived from the DIC method were calculated based on the strain fields output, while the stress values were global and calculated based on the real-time loads. The approximate condition is generally considered acceptable, and the obtained modulus distribution results are viewed as reliable. The distribution of the sample modulus can serve as a reference for assessing the inhomogeneity of the material geometry.

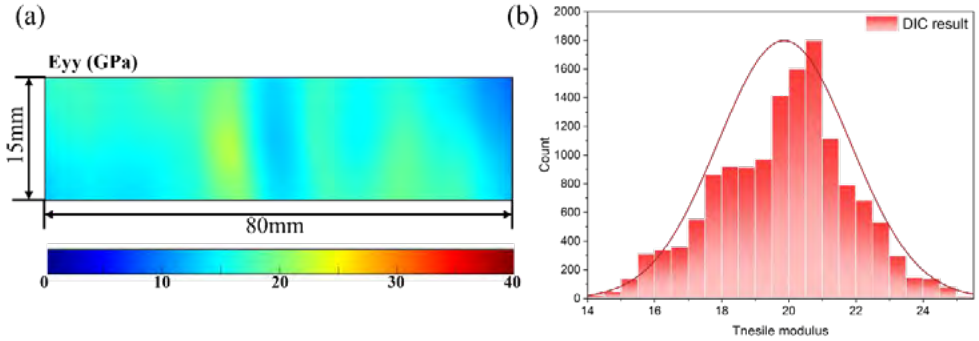


Figure 4. Elastic modulus distribution in Cross-Ply CPT (a) Contour, (b) Counts

3.2 Clustering results

In this study, the modulus data collected from the DIC method is a 3D array including x y coordinates and the modulus value. K-means clustering algorithm can process these data into K clusters which contains the information of modulus inhomogeneity for the samples, as shown in Figure 5 (a). Physically, the uneven modulus distribution in the sample stems from the non-uniform fiber orientation. Applying a clustering algorithm can discretize this continuous non-uniform distribution of fibers, which aids in developing models that incorporate uncertainty. However, determining the optimal number of clusters is a crucial aspect of the k-means clustering method. In this study, both the silhouette method and the elbow method were employed to determine the optimal cluster number. A higher average silhouette score indicates better-defined clusters, and the number of clusters corresponding to the peak silhouette score is considered optimal. On the other hand, the elbow method evaluates the variance within clusters relative to the number of clusters. This method involves plotting the variance explained as a function of the number of clusters and identifying the "elbow" point, which signifies where the addition of more clusters does not yield a significant improvement in the variance explained. The number of clusters at this elbow point is considered optimal for the dataset. By integrating the results from both methods, the optimal cluster number was determined to be 10 for each sample.

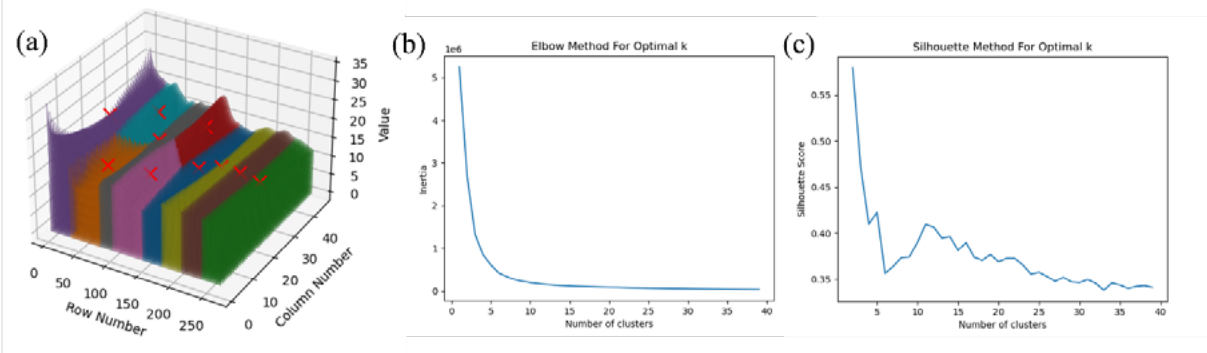


Figure 5. (a) Clustering result for DIC modulus distribution with 10 centroids, (b) Elbow result for a sample, (c) Silhouette result for a sample

3.3 Calibration of FE model

To validate the FE model, a set of 30 samples underwent a 3-point bending test. The results of both the experiment and the simulation are displayed in Figure 6 (b). To enhance the calculation efficiency in the FE solver, the loading speed was set higher than in the actual experiment. Concurrently, the update of the unit stiffness matrix occurred slower than the actual process. Additionally, due to computational time limitations, the element size was set larger. These adjustments resulted in some fluctuations in the calculated displacement-load curve of the simulation; however, these fluctuations did not impact the accuracy of the final maximum load and displacement results. The deterministic simulation results closely matched the experimental outcomes. The failure of the sample, as depicted in Figure 6 (c),

occurred due to tension at the bottom of the sample. In the simulation, elements meeting the failure criteria were dynamically removed after a specified time. Both the experiment and the FE results demonstrated the same failure pattern, characterized by a brittle tensile failure at the bottom of the sample.

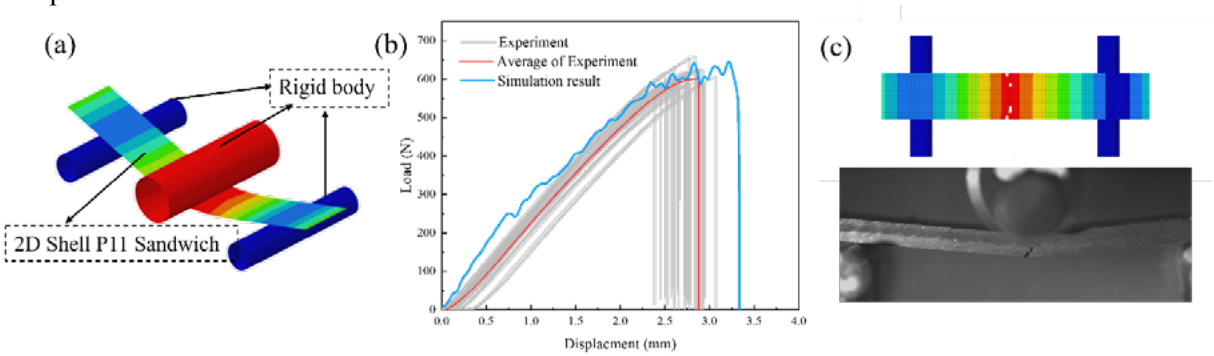


Figure 6. (a) FE model setting (b) Comparison of experiment and simulation results (c) failure status for FE and experiment

3.4 Stochastic results

Stochastic FE models were developed using the clustering results. Voronoi meshes were generated, with the location of centroids predefined. To maintain consistency across the models, the geometry of each model was kept constant, while the elastic moduli E_{11}, E_{22} and G_{12} were varied randomly based on values calculated through the previous netting analysis method. A total of 100 times FE models were computed, providing outputs for contact loads and displacements. Given the variability in specimen sizes, the global stress and strain from both simulations and experiments were quantified and compared.

The simulation and experimental results were analyzed using a Gaussian distribution, where μ is the mean or expectation of the distribution, and σ is the standard deviation. The 95% percentile intervals were also established. Despite the limited number of experimental trials, which contributed to discrepancies between the simulated and experimental strain results, the simulation displacements were also noted to be smaller than the experimental averages. Nevertheless, the 95% percentile intervals derived from the distribution correlated well with the experimental results, affirming the reliability of the stochastic models in capturing key trends and behaviors. The error of global strain's mean value is 4.0% while for the stress's is 1.7%. Standard error for the stress is 5.6%, but for the strain's error, standard error, the error reaches 37%. The main reason for it is that the strain data is relatively small than stress result, and the experimental results are few, which leads to a certain error between the fitting distribution function.

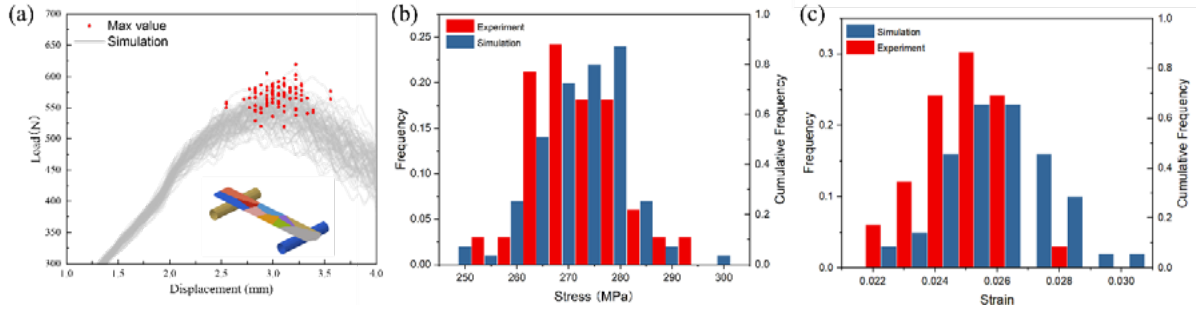


Figure 7. (a) Result of FE models, (b) distribution of global flexural stress, (c) distribution of global flexural strain

Table 2. Statistical results distribution

	Strain (Experiment)	Stress (Experiment)	Strain (Simulation)	Stress (Simulation)
95% percentile interval	[0.0196, 0.0290]	[239, 301]	[0.0195, 0.0325]	[242, 307]
$\boldsymbol{\mu}$ (MPa)	0.025	269.42	0.026	274.10
$\boldsymbol{\sigma}$	0.00236	15.43	0.00325	16.30

4. Conclusions

In the present study, the following conclusions have been drawn:

1. The primary source of inhomogeneity in CPT samples is the uneven fiber orientation, which were assessed using the X-ray scanning method in mesoscale.
2. The size and shape of the inhomogeneity in the CPT samples were evaluated using k-means clustering, and Voronoi meshes were effectively utilized to reconstruct the inhomogeneity geometry.
3. The MC method were applied for local elastic modulus prediction, allowing the mechanical performance distribution of the samples to be calculated based on FE models combined with Voronoi inhomogeneity geometry models.
4. Experiments were conducted to validate the performance distribution of CPT samples, demonstrating good consistency between the simulation and experimental results. The error of global strain's mean value is 4.0% while for the stress's is 1.7%.

However, the inhomogeneity of CPTs may also be influenced by other factors such as the manufacturing process and fiber length, which were not considered in this study. Additionally, only the modulus in a single direction was considered to ensure the consistency of the clustering results. Future researches will include and thoroughly investigate these factors.

Acknowledgments

This work was supported by JST SPRING, Grant Number JPMJSP2108.

References

[1] Wu, J., Gao, X., Wu, Y., Wang, Y., Nguyen, T. T., & Guo, M. Recycling carbon fiber from carbon fiber-reinforced polymer and its reuse in photocatalysis: a review. *Polymers*, 15(1), 170. 2022.

[2] Butenegro, J., Bahrami, M., Abenójar, J., & Martínez, M. Recent progress in carbon fiber reinforced polymers recycling: a review of recycling methods and reuse of carbon fibers. *Materials*, 14(21), 6401. 2021.

[3] Xu, Z. and Wang, Y. Study on milling force and surface quality during slot milling of plain-woven cfrp with pcd tools. *Materials*, 15(11), 3862. 2022.

[4] Pimenta, S. and Pinho, S. The influence of micromechanical properties and reinforcement architecture on the mechanical response of recycled composites. *Composites Part A: Applied Science and Manufacturing*, 56, 213-225. 2014.

[5] Geier, N., Poór, D. I., Pereszlai, C., & Tamás-Bényei, P. Drilling of recycled carbon fibre–reinforced polymer (rcfrp) composites: analysis of burrs and microstructure. *The International Journal of Advanced Manufacturing Technology*, 120(3-4), 1677-1693. 2022.

[6] Kanaun, S. K. and Levin, V. M. Self-consistent methods in the problem of axial elastic shear wave propagation through fiber composites. *Archive of Applied Mechanics (Ingenieur Archiv)*, 73(1-2), 105-130. 2003.

[7] Gao Q, Wan Y, Wei H, Takahashi J. Characterization and prediction of tensile properties of carbon fiber-reinforced thermoplastics composed of hybrid short carbon fiber/PA6 fiber nonwoven mats. *Composite Structure.* 334:117996. 2024.

[8] Cox, H. L. The elasticity and strength of paper and other fibrous materials. *British Journal of Applied Physics* 3(3): 72. 1952.

Residual Strength Monitoring of Ceramic Matrix Composites Based on Damage Self-Sensing Method

Guoqiang Yu[1,*], Chuyang Xie[1] , Wenbing Ma[1] , Xiguang Gao[1] and Yingdong Song[1,2]

[1] College of Energy and Power Engineering, Nanjing University of Aeronautics and Astronautics, Nanjing 210016, P.R. China
[2] Harbin Engineering University, Heilongjiang 150001, P.R. China

*Email: ygq@nuaa.edu.cn

Keywords: Residual strength, Oxidation, Acoustic emission, Electrical resistance, Ceramic matrix composites

Abstract
SiC/SiC mini-composites, the primary load-bearing unit of braided composites, are frequently utilized in studies of damage and failure mechanisms due to their straightforward structure. This paper commences with a theoretical and experimental investigation into the oxidation kinetics of the SiC matrix under stress-free environmental conditions. Subsequently, research was conducted on the stress-free oxidation and tensile residual strength testing of SiC/SiC mini-composites, leading to the establishment of a stress-free oxidation model for SiC/SiC mini-composites based on electrical resistance response. Ultimately, post-oxidation residual strength tests and model calculations were performed on the SiC/SiC mini-composites, achieving the prediction of residual strength after stress-free oxidation based on electrical resistance response for SiC/SiC mini-composites.

1. Introduction

Ceramic Matrix Composites (CMCs) have excellent properties such as low density, high strength, high temperature resistance, oxidation resistance, abrasion resistance, corrosion resistance, and small coefficient of thermal expansion. This is not available in many metal materials, polymer materials, and composite materials[1]. In addition, the reinforcement phase enables CMCs to overcome the high brittleness and defect sensitivity of ceramic materials, improving the reliability of CMCs. Therefore, CMCs have become the preferred material for hot end components of aero-engines[2]. Since the 1980s, CMCs have been used in hot-end components such as adjustment sheet, combustion chamber flame cartridges, and turbine blades, which have greatly improved engine efficiency and thrust-to-weight ratios [3].

CMCs structures are not only subjected to fatigue and impact loads during service, but also to high temperatures, water and oxygen, etc., which can easily result in changes in structural performance or damage. Therefore, timely detection of damage and destruction of CMCs structures is of great significance to avoid causing sudden damage to the structures. To ensure the safety and reliability of aero engine structures, traditional methods rely on regular maintenance to reduce the failure rate. This is not only inefficient, but also results in high costs[4]. Structural Health Monitoring (SHM) is the process of identifying and characterizing structural damage. It involves putting sensors into structural components to gather data and information about the health of the structure. This allows for monitoring and tracking of the extent and progression of damage within the structure, enabling prediction of structural damage and estimation of the remaining strength and life of the structure. The application of SHM technology to engine structures results in enhanced efficiency and a reduction in maintenance costs[5].

To achieve real-time "sensing" of damage, the monitoring technology for CMCs structural damage state requires a high level of automation and in-situ detection capability. Commonly used detection techniques of CMCs damage include ultrasound, Infrared Thermography (IRT), and X-ray Computed

Tomography (XCT)[6]. The ultrasonic method can detect materials very well, but it is difficult to detect thinner materials and small defects. It also requires a high level of expertise from the operator[7]. IRT is very effective. However, it can be affected by high temperatures and requires a certain distance from the object being inspected[8]. XCT can detect microscopic defects inside structures, but the equipment is complex and unsuitable for on-site inspections. It also has low detection efficiency and high costs[9].

In this paper, the damage self-sensing capability of ceramic matrix composites is used, combining electrical properties with acoustic emission. By analyzing electrical and AE signals, the relationship between these signals and mechanical properties of the composites is acquired. A residual strength prediction model based on acoustic emission and electrical impedance signals for SiC/SiC mini-composites is established. The prediction results are consistent with experiment.

2. Material and Experimental

2.1. Material and Specimen

In this paper, the material chosen is a SiC/SiC mini-composites with a BN interface, prepared using the PIP process. As shown in Figure 1(a), the graphite mould frames with grooves on the top and bottom sides were prepared, and as shown in Figure 1(b), the SiC fibers were wound onto the graphite mould. This was followed by the deposition of a BN interface on the fiber tows. Finally, the polycarbosilane solution was impregnated into the SiC fiber preform, dried and cured, and then cracked at high temperature under inert gas protection. The preparation of SiC/SiC mini-composites was completed after obtaining SiC matrix with high densities after several cycles of the above operations.

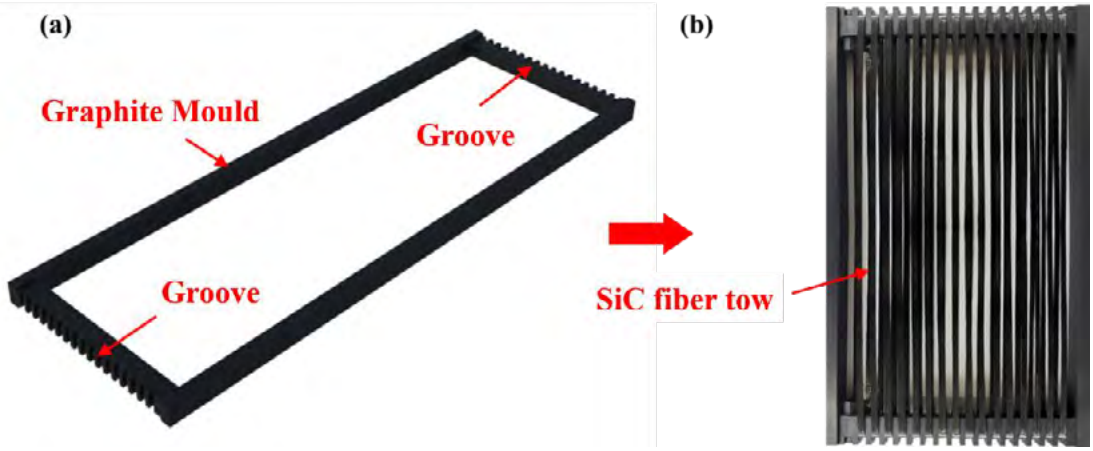


Figure 1. Graphite moulds prepared from SiC/SiC mini-composites

The SiC/SiC mini-composites used is shown in Figure 2, with an overall elongated cylindrical shape. A representative cross-section of the specimen is shown in Figure 2. It can be observed that there are several small pores within the specimen, which are attributed to the escape of numerous small molecules during the decomposition process of the SiC matrix precursor in the densification stage. This results in a large number of holes inside the specimen and causes the overall high porosity of the specimen. There are more microcracks between the matrix blocks and differences in crack sizes. This is due to the fact that the precursor undergoes several cycles of crystallisation and shrinkage during multiple cleavage cycles, resulting in a huge volume contraction of the matrix and hence many of microcracks[10].

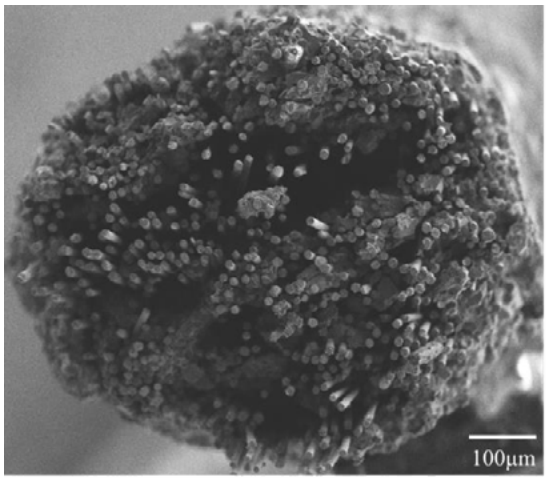


Figure 2. SiC/SiC mini-composites specimen

2.2. Experimental setup and Method

Initially, the electrical resistance of the SiC/SiC mini-composites is measured before and after oxidation. The some areas of specimens were oxidised in a homemade high-temperature furnace to avoid as much as possible the disturbance caused by the high-temperature oxidation process. Before oxidation, electrodes and wires were attached at both ends of the specimen, followed by attaching high temperature resistant ceramic tubes to both ends of the specimen. Figure 3 shows the SiC/SiC mini-composites specimen after preparation.

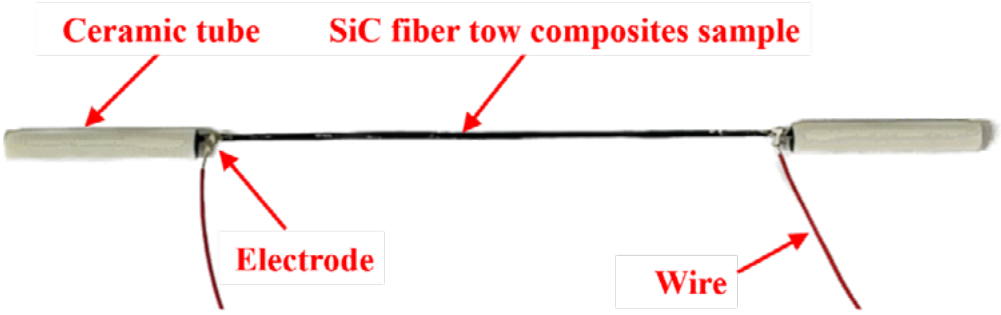
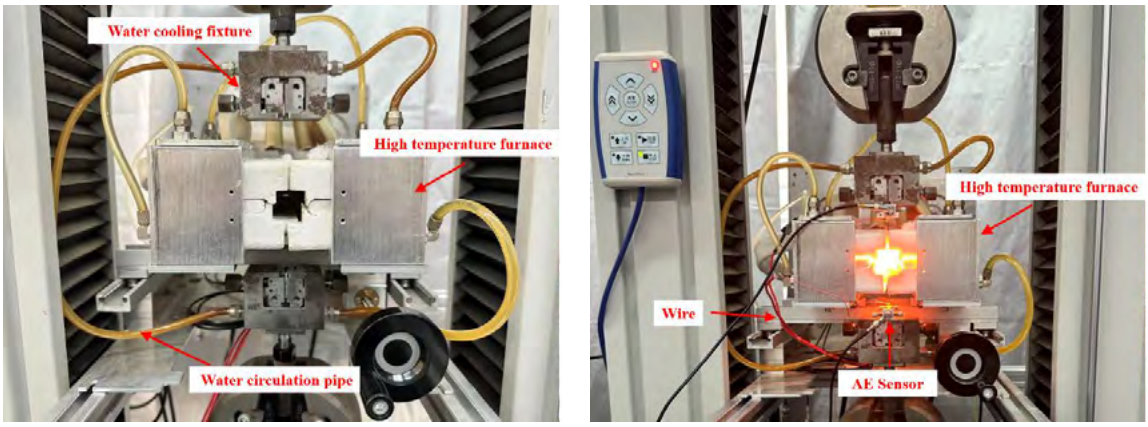


Figure 3. SiC/SiC mini-composites specimen with electrode

Figure 4(a) shows the high-temperature oxidation test system built on an electronic tensile testing machine. The whole device consists of a high-temperature furnace, a water-cooled fixture, a temperature control system and a water circulation cooling system. The high-temperature furnace is used with the temperature control system to create the entire high-temperature test environment. The high-temperature furnace is of the left-right folio type, with a silicon molybdenum rod serving as the heating element on the left and right sides. The water-cooled fixture has a water-circulation connection at the top of both sides of the fixture and two bolts at the bottom to control the displacement of the inner collet for specimen clamping. The water circulation cooling system keeps the high-temperature furnace and fixture cool by circulating water around them. This keeps the system stable for a long time. The system can achieve room temperature ~ 1400 ℃ oxidation environment under static tensile and creep loading.



（a）High temperature furnace （b）high temperature oxidation process

Figure 4. SiC/SiC mini-composites high temperature oxidation test

3. Post-oxidation residual strength model under stress-free conditions

3.1. Assumptions of the model

Figure 5 shows the microstructure of the SiC/SiC mini-composites after XCT scanning. The specimen approximates an elongated cylindrical structure with a small number of internal pores. The matrix enveloping the interior fiber surfaces demonstrates a relatively regular blocky configuration, featuring discernible intervals between each matrix block. In contrast, the matrix adjacent the specimen's surface and surrounding the internal pore surfaces varies in shape and size, showing significant differences in the inter-block gaps.

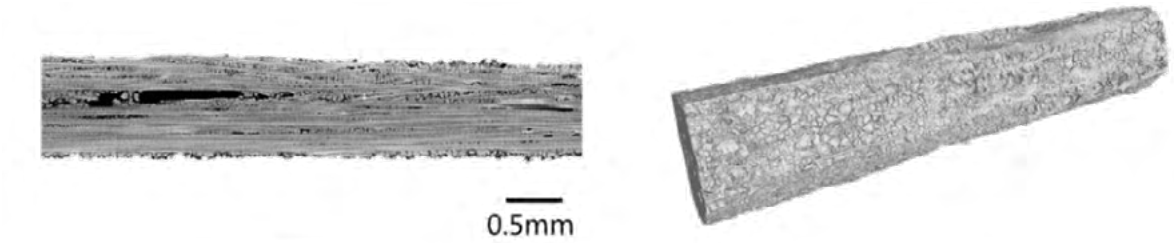
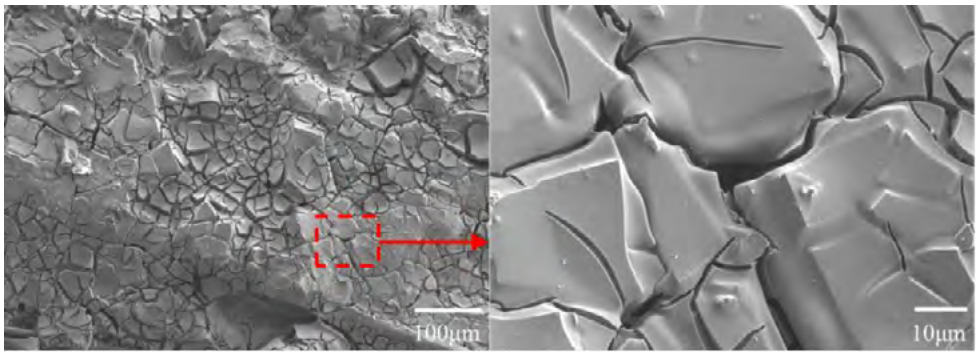


Figure 5. the microstructure of the SiC/SiC mini-composites

Unlike the microcracks formed in CVI processes due to the mismatch of thermal expansion coefficients between SiC fibers and the SiC matrix, the SiC/SiC mini-composites produced by PIP process have a significant volumetric shrinkage of the matrix due to multiple impregnations and pyrolysis during densification, resulting in a block-like distribution of the matrix and a vast number of matrix cracks. Therefore, for materials prepared by the PIP process, matrix cracks serve as the primary pathway for O_2 to penetrate into the material's interior during stress-free oxidation.

Figure 6 revealed that during the oxidation process, it is challenging for the oxidation products to completely block the oxygen diffusion pathway and prevent further oxidation in the PIP process materials due to the matrix crack opening distance.



（a）Surface after oxidation at 1100℃ for 0.5h （b）Local enlargement

Figure 6. Surface morphology of SiC/SiC mini-composites after oxidation at 1100°C

3.2. Establishment of model

Based on the tensile stress-strain curves of SiC/SiC mini-composites after stress-free oxidation and tensile fracture results[12]. The mechanical properties of SiC/SiC mini-composites fabricated through the PIP process are primarily dominated by the SiC fibers. The presence of numerous microcracks significantly diminishes the mechanical of the SiC matrix. The tensile fracture of the oxidized specimens exhibit distinct characteristics of brittle fracture. The morphology and failure characteristics of the materials mentioned above indicate that the oxidized SiC/SiC mini-composites are carried by fibers. The failure of SiC fibers occurs at the crack surface of the matrix, without interface slip or fiber pulling out.

It is thought that the initial cracks in the specimen have reached saturation, so no new cracks will form under stress. The cracks are evenly spaced and parallel to each other, as shown in Figure . The total length of the entire specimen is l_c, the width of the initial matrix crack is e_0, and the initial crack spacing is l_{r0}. The strength of SiC fibers obeys a Weibull distribution. The fracture of the fiber only needs to consider the probability of fracture at the crack surface. The tensile failure process can be simplified as a single-crack failure mode.

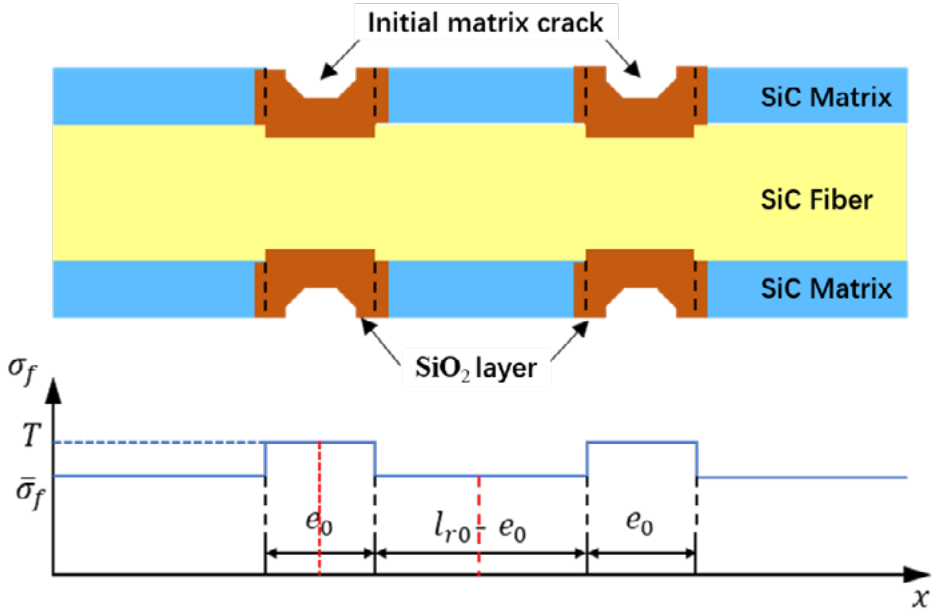


Figure 7. Oxide morphology and stress distribution of SiC fibers after stress-free oxidation

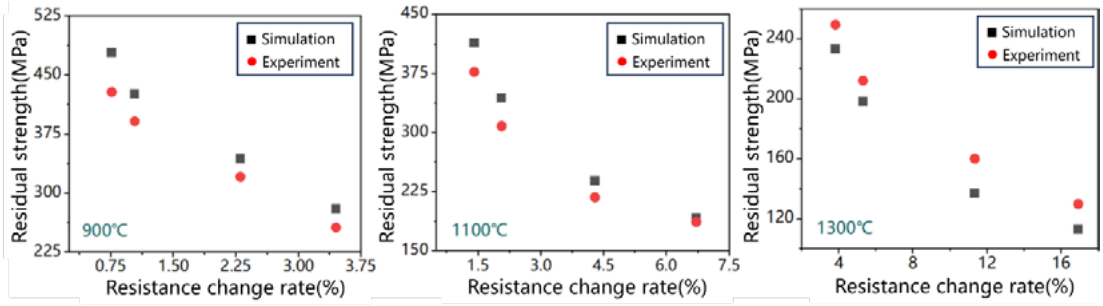
At this point, the stress distribution $\sigma_f(x)$ in the fiber can be express as:

$$\sigma_f(x) = \begin{cases} T & \left(0 \le x \le \frac{e_0}{2}\right) \\ \bar{\sigma}_f & (e_0/2 < x \le l_{r0}/2) \end{cases} \quad (1)$$

Where x is the direction of fiber length, T is the fiber stress on the cracked surface, and $\bar{\sigma}_f$ is the fiber stress on the unoxidised surface.

3.3. Experimental Verification

The residual strength of SiC/SiC mini-composites with different electrical resistance responses after oxidation at different temperatures was calculated using the above stress-free oxidation residual strength prediction model and compared with the experimental values. As illustrated in Figure 8, the discrepancy between the residual strength values calculated based on the resistance response and the test values following the oxidation of the specimens at 900°C, 1100°C and 1300°C is less than 11.60%, 10.28% and 14.48%, respectively. This verifies the reliability of the residual strength values calculated by the aforementioned model and also demonstrates the accuracy and validity of the oxidation morphology dimensions of the specimens calculated by the stress-free oxidation model based on the resistance response.



（a）900℃ （b）1100℃ （c）1300℃

Figure 8. Comparison of residual strength between calculated and tested results of SiC/SiC mini-composites after stress-free oxidation

4. Conclusions

This paper presents a stress-free oxidation residual strength prediction model for SiC/SiC mini-composites. The model is based on the microstructure characteristics of SiC/SiC fiber composites by PIP process, with brittle fracture after stress-free oxidation.The model makes a prediction of the residual strength of the specimen based on the thickness of the internal fiber SiO_2 layer obtained from the stress-free oxidation model. Results indicates that the calculated results agree well with the experimental results, with an error of the model not exceeding 14.48%.

Acknowledgments

This work was supported by National Natural Science Foundation of China (12202186), the Science Center for Gas Turbine Project (P2022-B-III-009-001), the Projects International Cooperation and Exchanges NSFC (12111530104), the Young Elite Scientists Sponsorship Program by CAST(2022QNRC001).

References

[1] Shengqiong Wen, Aijie He. Application of CMC on Thermal Parts of Aeroengine. Aerospace Manufacturing Technology, 2009(S1):4-7.

[2] Qiaomu Liu, Shunzhou Huang, Aijie He.Application requirements and challenges of CMC-SiC composites on aero-engine.Journal of Matericals Engineering, 2019,47(02):1-10.

[3] Chunhua Liang. Application of fiber-reinforced ceramic matrix composites on foreign aero-engines. Aerospace Manufacturing Technology, 2006(03):40-45.

[4] Zhang Shugang. Key Technologies of On-board Health Diagnosis for Civil Turbofan Engine. Northwestern Polytechnical Universtiy,2014.

[5] Xiasheng Sun, Yingchun Xiao, Shengbao Bai.et al. Research on Structural Health Monitoring Technology of Civil Aircraft Composites. Aeronautical Science and Technology, 2020,31(07):53-63.

[6] Sun J G, Verrilli M J, Stephan R R, et al. Nondestructive evaluation of ceramic matrix composite combustor components[J]. American Institute of Physics, 2003, 657(1): 1011-1018.

[7] Stoessel R, Krohn N, Pfleiderer K, et al. Air-coupled ultrasound inspection of various materials[J]. Ultrasonics, 2002,40(1-8):159-163.

[8] Maldague X. rechen[J]. Materials Evaluation, 2002,60(9):1060-1070:1071-1073.

[9] Kim J, Kwon S T, Kim W K. NDE Characterization and mechanical behavior in ceramic matrix composites[J]. Key Engineering Materials, 2006,321-323(Pt2):946-951.

[10] Xingui Zhou. Research Status of Creamic Matrix Composites via PIP Process. Aerospace Manufacturing Technology, 2014,450(006):30-34.

[11] Yang Wang, Lijuan He, Yuanyuan Liu, et al. Advances in SiC/SiC composites preparation technologies. Aerodynamic Missile Journal, 2019(6):92-97.

[12] Chuyang Xie. Research on Residual Strength Monitoring Technology of Ceramic Matrix Composites Based on Acoustic-electrical Information Fusion. Nanjing University of Aeronautics and Astronautics,2024.

AN INVESTIGATION ON THE IMPACT RESISTANCE OF COMPOSITES WITH NANOPARTICLES

Dayou Ma[1,*], Chiara Colombo[1], Sandro C. Amico[2], Marco Giglio[1], Andrea Manes[1]

[1]Politecnico di Milano, Department of Mechanical Engineering, via la Masa, 1, Milan 20156, Italy
Email: Dayou.ma@polimi.it; Chiara.colombo@polimi.it; Marco.giglio@polimi.it; Andrea.manes@polimi.it
[2]Federal University of Rio Grande do Sul, Av. Bento Gonçalves, 9500. Porto Alegre, 91501-970, Brazil
Email: Amico@ufrgs.br

Abstract
Adding nanoparticles to composite materials may enhance their material properties. Specific attention has been devoted to the mechanical properties. However, considering their complex mechanical response under impact loading, the effect of nanofillers is still unclear. Therefore, impact resistance of plain-weave aramid/epoxy composites with nanoparticles is investigated by means of experimental approaches. Carbon nanotubes and graphene nanoplatelets were simultaneously dispersed in epoxy prior to manufacturing the composite. Material tests of composites, including tensile, compressive and shear tests, were conducted to identify the mechanical properties, and improved modulus and strength were found with nanofillers. Similar results for composites with and without nanoparticles were obtained from low-velocity impact tests. However, thermography revealed a smaller delamination area for the specimens with nanoparticles compared to those without, indicating that investigations on nanofillers for high-performance composites should focus on the interface, where delamination can be regarded as focus for nanofiller-reinforced composites.

Keywords: low velocity impact; polyaramid; delamination; thermography

1. Introduction

Nanoparticles are regarded as an efficient solution for the improvement in mechanical properties of composite materials regarding fracture toughness [1,2] as well as impact resistance [3], considering their size effect and unique set of properties. However, as more works on composites with nanofillers are reported, the improvement on the strength and modulus reinforced by nanofillers is limited, especially compared to continuous fibers, which has motivated new focuses regarding their use in composites.

Low-velocity impacts are regarded as a critical threat which can produce invisible impact damage and significantly affect the mechanical performance of composites [4,5].The effect of hybrid nanofillers on the impact resistance of composites has been discussed under low velocity impact [6], where improved impact resistance was barely obtained with the random distribution of nanofillers. Furthermore, the defects introduced with the nanofillers are also an issue. As indicated in [2,7], voids and poor distribution were observed to have a significant effect on the impact and fracture resistance of composites. However, the interface fracture toughness was improved around 60% with nanofillers under both static and dynamic conditions [8], indicating that nanofillers may reinforce the interface, which may provide new insights into nanofiller-reinforced composites.

* Corresponding author

In this work, a comprehensive experimental investigation was conducted including both material characterization and low velocity impact tests for composites with hybrid nanofillers, and interface damage was monitored with thermography to support the findings.

2. Manufacture and specimen preparation

Plain-weave composites, with and without nanofillers, were produced. Kevlar™-29 plain-weave fabric (from Dupont) 0.5 mm thick was used along with Ampreg 26 (from Barracuda Composites), a DGEBA epoxy resin, and a hardener. Multi-walled carbon nanotubes (MWCNT, diameter: 10–30 nm, length: ~30 μm and 85% purity) and graphene nanoplatelets (GNP, thickness: 6-8 nm, width: 25 μm) were used in the current work as a hybrid nano-reinforcements.

The hybrid nanofillers were firstly dispersed in a solution of 60% acetone and 40% ethanol with the VibraCell VCX750 (frequency: 20 kHz) ultrasonic mixer at an amplitude of 250 W for 45 min, repeatedly vibrating for 25 s followed by a 10-s pause. The hybrid ratio for the two nanofillers was set to 1:1 (in weight). A mixture containing hybrid nanofillers was brushed onto both sides of the dried fabric to guarantee a random and homogeneous spread. Five layers of fabric were stacked and sealed for the vacuum infusion process. After infusion, the resin was left to cure for 24 h at room temperature and post-cured for 6 h at 80 °C as suggested by the resin manufacturer. The overall weight fraction of hybrid nanofillers was 1.0 wt.%. Specimens without nanofillers were also manufactured as reference. Specimens were then cut from the laminate using a waterjet cutter, and the edges of each panel were discarded.

3. Experiments

3.1 Material characterization

Composite characterization was performed to obtain their fundamental mechanical properties, with and without nanofillers. Tensile tests were carried out according to ASTM D3039 with a loading rate of 2 mm/min with deformation of the specimens monitored. Compression tests were conducted based on ASTM D6641 with a loading rate of 1.3 mm/min with a strain gauge in the middle of the gauge length. And V-notched-rail shear tests according to ASTM D7078 were carried out with a loading speed of 2 mm/min for in-plane shear properties.

3.2 Low velocity impact

Low-velocity impact tests using a drop tower were performed to assess the effect of nanofillers. The tests followed the standard ASTM D7136 with fully fixed gripping for specimens considering the fully fixed boundary conditions [9]. A hemispherical impactor with diameter of 16 mm was applied. Two different energy levels were considered in the current work, 30 J and 70 J. In the tests, the reaction of the impactor was recorded with an optical sensor for the velocity as well as displacement of the impactor, while the load cell was used to monitor the force between the impactor and the specimen. A pneumatic arm prevented multiple hits to the objectives.

3.3 Delamination detection for impacted specimens

In the current work, infrared thermography is applied for delamination characterization using a continuous heating source from a 1kW halogen lamp. The thermal transient is documented by the infrared camera FLIR Titanium to identify the damaged area. For accurate results on damage morphology, thermal imaging at a 30 Hz frame rate was captured for 40 s. All thermal images are then post-processed with a procedure to obtain the invisible damage morphology for composites with and without nanofillers. The normalized temperature $\hat{T}$ is calculated to enhance the thermal contrast and cancel reflections and non-uniform heat sources, following the equation [10]:

$$\hat{T}(t) = \frac{T(t) - T(t=0)}{T(t=2) - T(t=0)}$$

where $T(t{=}0)$ is the temperature at the beginning of the test, $T(t{=}2)$ is the temperature of the image acquired after 2 s, and $T(t)$ is the temperature of the processed pixel at the general time t. The result will focus on $\hat{T}$ at 10 s, when the thermal contrast is the most suitable to identify the impact damage.

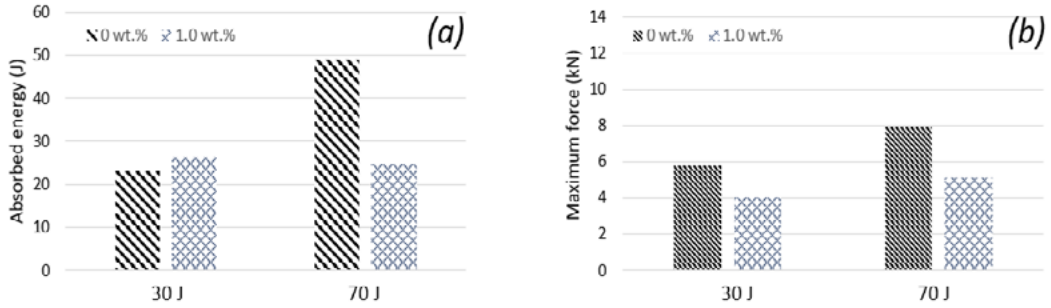
4. RESULTS AND DISCUSSIONS

The results of the composite material characterization with and without nanofillers are shown in Table 1. Some mechanical properties of the composite with nanofillers improved compared to that without nanofillers. The increase in modulus and strength is approximately 20% and 10%, respectively. However, properties such as shear and compressive strength remained constant. Those properties are more related to the matrix where the distribution of nanofillers may not be sufficiently concentrated. Additionally, the matrix includes both nanofillers and defects such as voids during curing, reducing the reinforcement of nanofillers [11]. Even so, the increase in both tensile strength and modulus may improve the impact resistance.

Table 1 Material properties for composite materials with and without nanofillers.

Parameter		Neat composite	Composite with 1.0 wt.% nanofillers
E_X	Elastic modulus along X direction (MPa)	19630 ± 720	20061 ± 1286
E_Y	Elastic modulus along Y direction (MPa)	15220 ± 1120	19240 ± 804
G_{XY}	In-plane shear modulus (MPa)	2123 ± 134	1651 ± 62
S_X^T	Tensile strength along X direction (MPa)	496.7 ± 5.9	513.7 ± 9.9
S_X^C	Compressive strength along X direction (MPa)	94.4 ± 4.2	106.1 ± 5.4
S_Y^T	Tensile strength along Y direction (MPa)	380.6 ± 14.1	486.8 ± 17.3
S_Y^C	Compressive strength along Y direction (MPa)	112.7 ± 5.5	116.1 ± 2.9
S_{XY}	In-plane shear strength (MPa)	38.8 ± 1.2	32.5 ± 1.9

However, the impact performance is not as expected based on Figure 1. Similar results of stiffness and absorbed energy were found at an impact energy of 30 J for composites with and without nanofillers. The composite with nanofillers has even lower performance regarding absorbed energy, being penetrated during impact, while the specimen without nanofillers rebounded the impactor. Considering the main impact, loading may be absorbed by the continuous fibers of the plain-weave composites and the effect of nanofillers can be limited in this case [11]. The difference between material tests and low velocity impact is perhaps due to the effect of defects. For material tests, the dimension of the specimen is limited while the impact specimens are larger and more dependent on the characteristics of the impact zone [7,12], which can amplify the effect of defects.



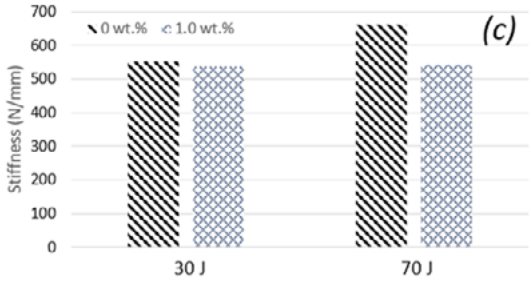


Figure 1 Results of absorbed energy (a), maximum force (b) and stiffness (c) of the composites.

For another perspective, the impact-induced damage was analyzed with thermography (see Figure 2). Thermal images present the rear face of the panels, where the damage is the most critical. The nanofilled composite warmed up much more than the unfilled one, reaching a temperature of about 50°C after the 40 s warming with respect to the unfilled that reached about 35°C. Besides, the thermal transient is different for the two cases; indeed, the nanofilled composite has a steeper warming. For this reason, the normalization procedure resulting in the thermal images of Figure 2 gives $\hat{T}$ values for the nanofilled lower than the unfilled. This is due to the nanofillers that change the thermal conductivity of the composite. However, focusing on the impact application, this is not a limitation, because the procedure allows identifying clearly the damaged region.
With the increase in impact energy, the damage area was larger for both composites (with and without nanofillers), as expected from general investigations [13]. However, the damage area was clearly reduced in the presence of nanofillers, indicating the increase in fracture toughness of the interface. Compared to the uncertain impact resistance of composites with nanofillers, the reinforced interface properties are more interesting.

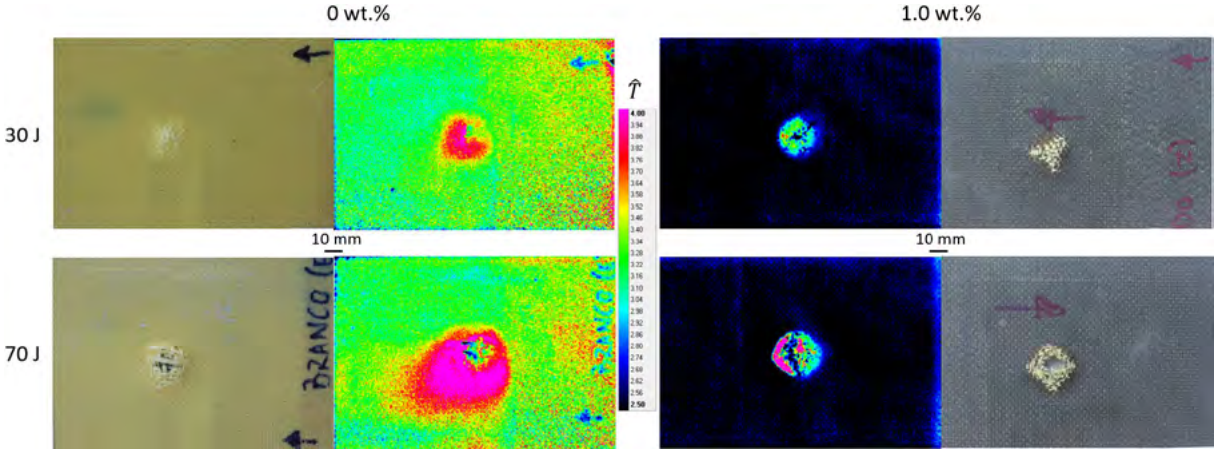


Figure 2 Thermographic results for the damaged composites at the rear face.

5. Conclusions

In this work, a comprehensive experimental activity was performed considering both material characterization and low velocity impact tests, and thermography was used for damage indication. Important material properties were improved, but the results from low velocity impacts were varied and showed limited reinforcement from the nanofillers attributed to the existence of defects. However, the delamination area was significantly reduced by the addition of nanofillers, indicating reinforcement of the interface fracture toughness under impact loading. Therefore, nanofillers were able to reinforce composites if the focus is on interface fracture toughness, which can benefit overall damage resistance and impact resistance, especially if the introduction of defects is limited.

References

[1] Ma D, Verleysen P, Chandran S, Giglio M, Manes A. A modified peridynamic method to model the fracture behaviour of nanocomposites. Eng Fract Mech 2021;247:107614. https://doi.org/10.1016/j.engfracmech.2021.107614.

[2] Esmaeili A, Ma D, Manes A, Oggioni T, Jiménez-Suárez A, Ureña A, et al. An experimental and numerical investigation of highly strong and tough epoxy based nanocomposite by addition of MWCNTs: Tensile and mode I fracture tests. Compos Struct 2020;252:112692. https://doi.org/10.1016/j.compstruct.2020.112692.

[3] Cheon J, Kim M. Impact resistance and interlaminar shear strength enhancement of carbon fiber reinforced thermoplastic composites by introducing MWCNT-anchored carbon fiber. Compos Part B Eng 2021;217:108872. https://doi.org/10.1016/j.compositesb.2021.108872.

[4] Nor AFM, Sultan MTH, Jawaid M, Azmi AMR, Shah AUM. Analysing impact properties of CNT filled bamboo/glass hybrid nanocomposites through drop-weight impact testing, UWPI and compression-after-impact behaviour. Compos Part B Eng 2018. https://doi.org/10.1016/J.COMPOSITESB.2018.12.061.

[5] Li X, Ma D, Liu H, Tan W, Gong X, Zhang C, et al. Assessment of failure criteria and damage evolution methods for composite laminates under low-velocity impact. Compos Struct 2019;207:727–39. https://doi.org/10.1016/J.COMPSTRUCT.2018.09.093.

[6] Rahman AS, Mathur V, Asmatulu R. Effect of nanoclay and graphene inclusions on the low-velocity impact resistance of Kevlar-epoxy laminated composites. Compos Struct 2018;187:481–8. https://doi.org/10.1016/j.compstruct.2017.12.054.

[7] Ma D, dos Santos Cougo CM, Amico SC, Giglio M, Manes A. A novel numerical method for stochastic study of fiber-reinforced composites with nanoparticles under impact loading. Int J Impact Eng 2023;180:104662. https://doi.org/10.1016/J.IJIMPENG.2023.104662.

[8] Li Z, Wang Z, Lu W, Zhou X, Suo T. Loading rate dependence of mode II fracture toughness in laminated composites reinforced by carbon nanotube films. Compos Sci Technol 2021;215:109005. https://doi.org/10.1016/J.COMPSCITECH.2021.109005.

[9] Ma D, Rezasefat M, Aparecido da Cruz J, Campos Amico S, Giglio M, Manes A. Effect of fixture boundary conditions for low-velocity impact: A focus on composites with different matrix and fibers. Mater Lett 2024;355:135370. https://doi.org/10.1016/J.MATLET.2023.135370.

[10] Heydari Astaraee A, Salerno A, Bagherifard S, Carlone P, Parmar H, Astarita A, et al. Thermographic Analysis of Composite Metallization through Cold Spray. Metals (Basel) 2021;11:1860. https://doi.org/10.3390/met11111860.

[11] Ma D, González-Jiménez Á, Giglio M, dos Santos Cougo CM, Amico SC, Manes A. Multiscale modelling approach for simulating low velocity impact tests of aramid-epoxy composite with nanofillers. Eur J Mech - A/Solids 2021:104286. https://doi.org/10.1016/j.euromechsol.2021.104286.

[12] Ma D, Campos Amico S, Giglio M, Manes A. Effect of fibre bundle uncertainty on the tensile and shear behaviour of plain-woven composites. Compos Struct 2021;259:113440. https://doi.org/10.1016/j.compstruct.2020.113440.

[13] Ma D, Scazzosi R, Manes A. Modeling approaches for ballistic simulations of composite materials: Analytical model vs. finite element method. Compos Sci Technol 2024;248:110461. https://doi.org/10.1016/J.COMPSCITECH.2024.110461.

EXPERIMENTAL AND NUMERICAL STUDY OF THE MECHANICAL BEHAVIOUR OF AN OXIDE/OXIDE CERAMIC-MATRIX-COMPOSITE AT HIGH TEMPERATURE

A. Débarre[1], J.-F. Maire[1], C. Przybyla[2] and F. Laurin[1]

[1]DMAS, ONERA, Université Paris-Saclay, F-92320 Châtillon, France – antoine.debarre@onera.fr
[2]Air Force Research Laboratory, Wright-Patterson Air Force Base, Ohio; USA

Keywords: Ceramic Matrix Composites; damage model; creep; viscoelasticity; viscoplasticity;

Abstract
Oxide/oxide composites are ceramic matrix composites (CMC) designed for thermomechanical applications. When used at high temperatures, the progressive appearance of creep has been observed. Damage models are therefore no longer sufficient for dimensioning parts. In this paper, the creep of the material is studied experimentally in order to propose a stationary creep law, and then a viscous constitutive equation to take into account variations in loading. This creep modelling is introduced in an elastic-damaging constitutive equation.

1. Introduction

Ceramic matrix composites are one of the most promising solutions for improving aero-engine performance. Compared with the metallic materials used today, they offer superior operating temperatures and lower densities. The development of these materials has accelerated in the last years. Recent examples include CFM's new LEAP engine, which uses SiC/SiC CMC shrouds [1] or an alumina oxide fibre reinforced alumina oxide mixer nozzle developped by GE Aviation in its Passport gas-turbine [2]. Despite these achievements, the demands for incorporating these materials into crucial applications like aerospace gas-turbine engines necessitate extensive testing for design, certification and sustainment. It is therefore necessary to work on design methods that take into account the complex non-linear behavior of these materials.

In the aeronautic industry oxide/oxide composites materials are candidates for exhaust parts, subjected to moderate mechanical loads and temperature of around 700 to 800 °C, for next generation engines. These materials generally consist of alumina fibres embedded in a porous alumina matrix. 3M, the leading manufacturer of oxide fibres, is marketing new products: fabrics to reduce material production costs [3], and tow-pregs for AFP processes [4]. However, the majority of manufacturing processes reported in the literature involve impregnating 2D fabrics and then stacking the plies, pressing them and sintering the whole stack for a short time [5–8]. These brief high-temperature treatments enable the matrix to retain a high porosity level (Figure 1). By introducing such a high porosity rate into the material, the gap between the stiffness of the fibres and that of the matrix is sufficiently large for cracking energy to dissipate within the matrix without breaking the fibres. In a way, this brings it somewhat comparable to polymer matrix composites. In the field of CMC, this is the concept of a weak matrix, as opposed to the principle of composites with a weak interphase [9].

Because of their intrinsically fragile matrix and the dependence on fibres to bear the main load, matrix damage typically initiates at relatively low load levels. Then, damage evolves through processes such as fibre-matrix debonding, fibre sliding, and ultimately delamination and fibre breaking at higher loads. The stress-strain response generally remains almost linear when the load is applied parallel to the fibre reinforcement direction [6,10–12]. Non-linear behaviour is more pronounced for loading off

the direction of the fibres [13,14]. At room temperature, damage mechanisms are the main source of non-linearity.

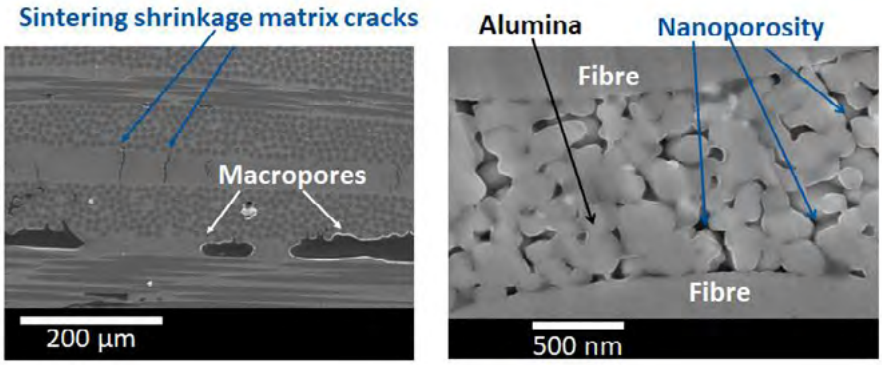


Figure 1. Oxide/Oxide composite microstructure

Fewer studies have been devoted to the oxide/oxide behaviour at high temperatures. Most of these have dealt with the behaviour of fibres or composites at temperatures above 1000°C. This highlighted the loss of stability of oxide fibres, which suffer from granular coarsening and creep. Our previous work focused on intermediate temperatures between 700 and 1000°C, which enabled us to demonstrate the progressive onset of creep [15]. A damage model dealing with in-plane behaviour has also been proposed for loading at temperatures where creep remains negligible [16]. One of the limitations of the work is the underestimation of the strain when the temperature becomes too high.

In this work, we propose a modification of the constitutive equation incorporating viscous behavior so that viscous deformation can be taken into account in part design. It focusses the behavior in tension in the fibre direction. Therefore, a simplified version of the damage law is first presented together with the associated identification. The second part is devoted to creep. First, stationary creep is identified on experimental data. Then, a viscous constitutive equation combining the stationary creep law and a viscoelastic term is proposed and identified in order to be applied to tests with load variations.

2. Damage modelling

A uniaxial version of the law developed in [16] is proposed. The constitutive equation is derived from the Helmholtz free energy (Ψ) as follows:

$$\sigma = \rho\frac{\partial\Psi}{\partial\varepsilon} = E^{eff}.\left(\varepsilon - \varepsilon^{th}\right) - E^{0}.\varepsilon^{r} \tag{1}$$

where ε, ε^{th} and ε^{r} are the total, thermal and residual strains, E^0 and E^{eff} are the intial and effective stifnesses and ρ is the material density.

The driving force for damage (y) is defined using the positive elastic strain (equal to the total strain in this simplified case) $< \varepsilon^{*} >_{+}$ and the initial stiffness E^0. It is written as:

$$y = \frac{1}{2}E^{0} < \varepsilon^{*} >_{+} < \varepsilon^{*} >_{+} \tag{2}$$

In line with ODM models dedicated to microstructure-driven damage [17–22], the driving force is defined in a non-standard thermodynamic framework, i.e. it no longer derives from the thermodynamic potential. However, this model is thermodynamically admissible because it is very easy to demonstrate the Clausius-Duhem's inequality. The use of positive strain alone only allows damage growth in tension.

The damage variable (d) is written as:

$$d = d_c(1 - \exp(-g(y_{max})^{p_c})) \quad \text{with} \quad g(y) = < \frac{\sqrt{y} - \sqrt{y_0}}{\sqrt{y_c}} >_+ \tag{3}$$

where y_c, p_c and d_c are three model parameters, y_0 the driving force at the damage threshold and y_{max} the maximum driving force y observed during loading. The form chosen for the damage variable allows the definition of a threshold below which the material's behavior remains elastic. One of the particularities of the damage variable defined in ODM models is that it can vary between 0 and $+\infty$, unlike most models for which the damage variable cannot exceed 1.
The damage activation index (η) is introduced to take account of whether cracks are open or closed, and is then worth 0 or 1 respectively. More details on its calculation are given in [16].

The effective compliance (S^{eff}) is expressed as:

$$S^{eff} = \frac{1}{E^{eff}} = S^0(1 + d\eta) \tag{4}$$

Finally the derivative of the residual strain with respect to time is expressed as:

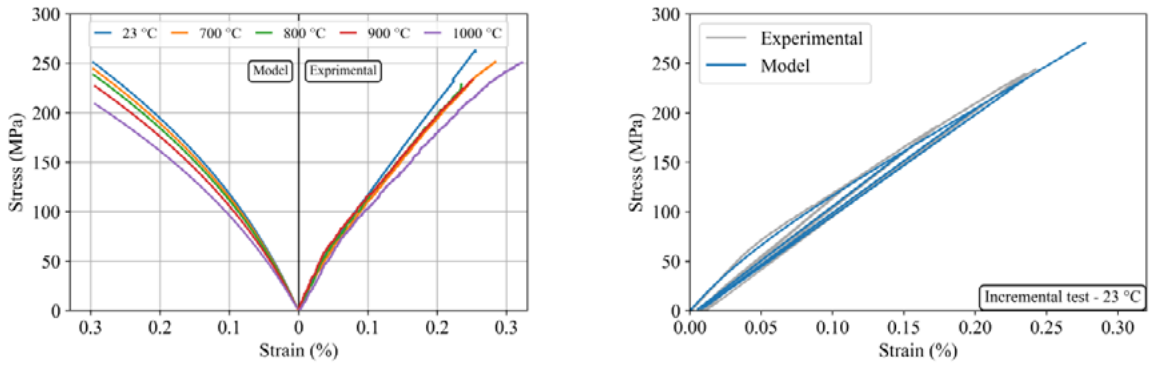
$$\dot{\varepsilon_r} = S^0 \chi \dot{d}. E^{eff}. \eta S^0. E^{eff}. (\varepsilon - \varepsilon^{th}) \tag{5}$$

where χ is a model parameter for adjusting the amplitude of residual strain.

The effect of temperature on the damage behaviour is introduced by the dependence of the initial stiffness (E^0) and the damage threshold (ε^{se}) on temperature using Eq (6).

$$\begin{cases} E^0(T) = E^0.\left(1 + \exp\left(\dfrac{T - T^{se}}{a}\right)\right)^{-1} \\ \varepsilon^{se}(T) = \varepsilon_0^{se}.\left(1 + \exp\left(\dfrac{T - T^{se}}{a}\right)\right) \end{cases} \tag{6}$$

The stiffness and damage threshold as a function of temperature are identified from tensile tests. The other four parameters (d_c, y_c, p_c and χ) are obtained from monotonic and incremental tests, i.e. cyclic tests with charges and discharges while increasing the maximum stress at each cycle. Figure 2 (a) illustrates the comparison between the experimental and the simulated response from monotonic tests.



(a) (b)

Figure 2. Monotonic tensile behaviour from room temperature up to 1000 °C: comparison between experimental data and model (a) and incremental tensile tests at room temperature (b)

With regard to the experimental dispersion, the identification carried out is considered satisfactory. Figure 2 (b) demonstrates how residual strain is taken into account after unloading once the damage threshold has been exceeded. At room temperature, the amplitude is well reproduced. However strain is underestimated beyond 900 °C. This can be explained by the gradual onset of creep. Tests at two loading rates (0.5 mm.min^{-1} and 5 µm.min^{-1}) have shown that creep becomes non-negligible over a period of around one hour before 900°C [15].

3. Introduction of creep in the constitutive equation

3.1. Experimental study of stationary creep

Creep tests were carried out in tension in the fibre direction at temperatures between 850 °C, where measurable creep deformations were observed, and 1050 °C with a fixed duration of 72 hours. Stresses of between 26 and 182 MPa were applied, i.e. 10 to 70% of the average stress at failure of the material at room temperature. Low creep rates are observed at temperatures below 900 °C, even for high stresses. Above 1000 °C, strains of several percent that can lead to failure can be obtained for relatively short periods of time. With the exception of the test carried out at 850 °C, for which the measured strain is very small, the primary creep stage is relatively short and only accounts for a small proportion of the total strain. Behaviour is therefore mainly governed by stationary creep, with strain increasing linearly with time.

It therefore seemed appropriate to use a classical creep law to model the effect of temperature and stress on creep rate. A simple Norton law, in which the creep rate is related to the stress via a stress exponent (n) is combined with an Arrhenius term for the effect of temperature (Eq. (7)).

$$\dot{\varepsilon}^{vp} = A\sigma^n \exp\left(-\frac{Q}{RT}\right) \tag{7}$$

An identification process was implemented by scanning the values of n and Q and calculating the value of $log(A)$ minimising the mean square error between the experimental and simulated values. The numerical values of the three coefficients of the law are then identified: n = 3.5, Q = 632 kJ.mol^{-1} and A = 36.10^{10}. It is then possible to compare the rates calculated by this law with the experimental data from which they are derived (Figure 3). The proposed law, one of the simplest in the literature [23], is an accurate representation of the stationary creep of the studied material.

In order to analyse these results, they were compared with results obtained on fibres alone [24]. Using the previous identification method, the following coefficient values were calculated: n = 3, Q = 632 kJ.mol^{-1} and A = 89.10^{10}. The stress exponent and activation energy are very close to those determined for the composite. Creep therefore appears to be essentially driven by the fibres.

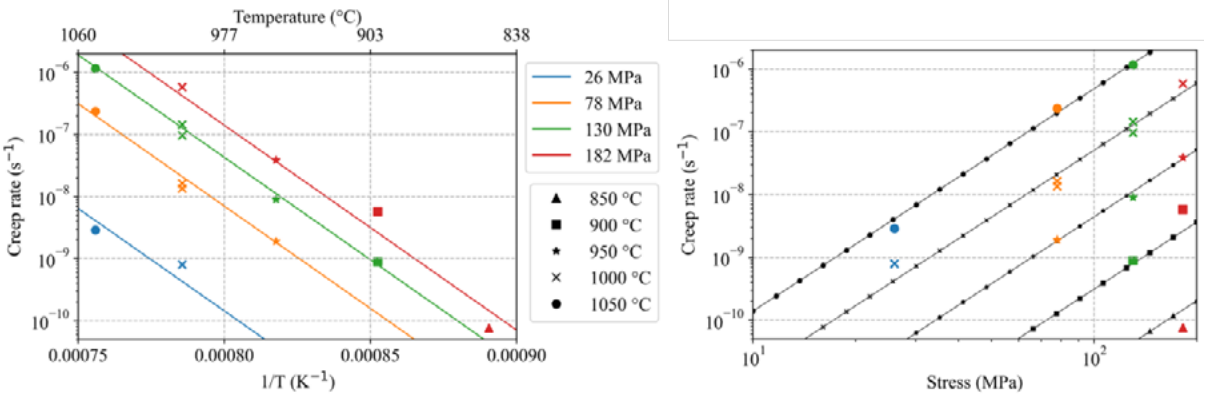


Figure 3. Creep rates as a function of applied stress and test temperature

3.2. Creep modelling

Once again, the formulation is based on the Helmholtz free energy to derive a thermodynamically consistent relationship for the material behaviour:

$$\Psi = \frac{1}{2\rho}\left[\left(\varepsilon - \varepsilon^{th} - \varepsilon^{v}\right).E^{eff}.\left(\varepsilon - \varepsilon^{th} - \varepsilon^{v}\right) - \varepsilon^{r}.E^{0}(T).\varepsilon^{r} + \xi.E^{R}.\xi\right] \tag{8}$$

where ρ is the density, ε, ε^{th} and ε^{r} are the total, thermal and residual strain, ε^{v} and ξ the internal variables representing the viscous strain and the strain-hardening mechanism respectively, E^{0} and E^{eff} are the initial and effective stiffness's and E^{R} the viscous modulus. The definition of the two stiffness's E^{0} and E^{R} makes it possible to define a different evolution of the elastic and viscous mechanisms. In particular, no temperature dependence of E^{R} is considered. In order to keep the model simple, viscoelasticity is assumed to be linear. The internal variables can therefore be written as follows:

$$\begin{aligned} \dot{\varepsilon}^{v} &= \dot{\xi} + a(T).(\xi.E^{R}.\xi)^{p_2}.S^{R}.\sigma \\ \dot{\xi} &= \frac{1}{\tau}(S^{R}.\sigma - \xi) \end{aligned} \tag{9}$$

where τ is the characteristic time of the viscous mechanism ξ and $S^{R} = 1/E^{R}$.

Noting that, in the linear viscoelastic steady-state case, ξ tends to $S^{R}.\sigma$, the viscous strain rate is expressed as:

$$\dot{\varepsilon}^{v} = a(T).(\sigma.S^{R}.\sigma)^{p_2}.S^{R}.\sigma \tag{10}$$

Finally, in order to preserve the stationary creep law identified above, the following conditions are also imposed:

$$p_2 = \frac{n-1}{2} \quad ; \quad a(T) = A\ E^{R\,p_2+1}\exp\left(-\frac{Q}{RT}\right) \tag{11}$$

The viscous strain rate ($\dot{\varepsilon}_v$) comes from two contributions. The first is linked to a viscoelastic phenomenon whose formalism was introduced by Maire [25] and Schieffer [26] to describe the viscous behaviour of PMC laminates or Marcin [20] in ODM models. The form adopted for this viscous term allows a deformation plateau to be reached for a time approximately equal to three times the characteristic time τ. The second term is the result of viscoplastic phenomena and, in our conditions, under uniaxial loading and steady state conditions, allows a strain at a constant rate equal to that predicted by Norton's law.

The law was identified using all the creep tests. Two validation tests called dip-tests were carried out. This involves letting the material creep and then suddenly reducing the applied load. In a first test carried out at 950 °C, a stress of 182 MPa was applied for 45 hours, and then quickly reduced to 72 MPa. Both creep rates measured in the stationary domains are in agreement with the previously identified law. The stiffness measured during discharge is also in agreement with that predicted by the damage model. The second dip-test (Figure 4) was carried out at 1000 °C at a stress of 130 MPa, which was suddenly reduced to 26 MPa. On the close-ups taken during loading and unloading, the stationary creep is well represented by the Norton model (in orange). In addition, the introduction of the viscoelasticity term (in green) helps to better capture the smoothing of the curves during load variations.

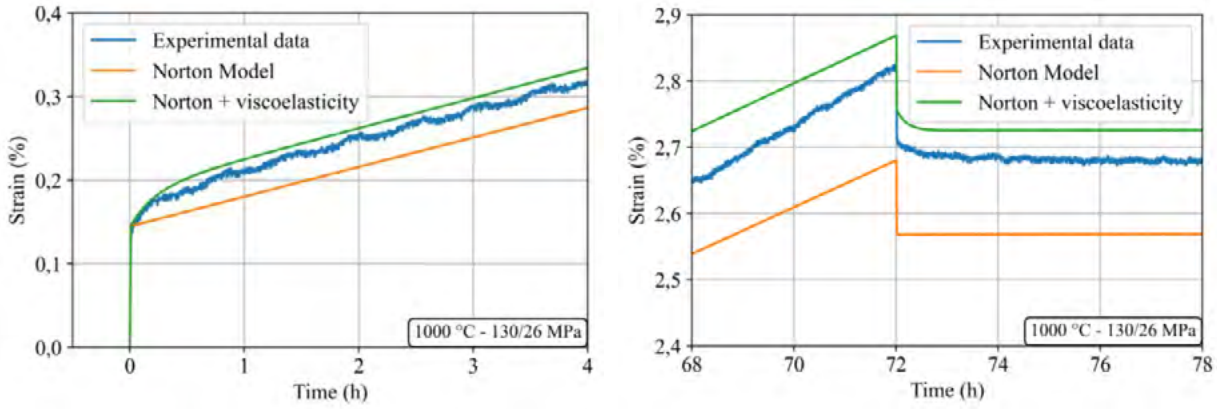


Figure 4. Comparison between a dip-test at 1000 °C (130 then 26 MPa) and simulation with and without viscoelasticity term

The model combining damage and viscous behaviour can then be used to simulate incremental tests, which suffered from underestimated strain during discharges. For this purpose, data on the force applied by the machine as a function of time is used as loading conditions for the model. This represents a test at 0.5 mm.min^{-1} with discharges at each maximum stress increment of 27 MPa. Figure 5 illustrates the simulation of the test with the damage model alone (left) and with the addition of creep (right). Adding the creep term allows the amplitude of the strains to be reproduced when the load returns to zero. Compared to the calculation with damage only, there is also a shift in strain when the load returns to the maximum of the previous increment. This is also observed experimentally and is explained by the material continuing to creep during discharges.

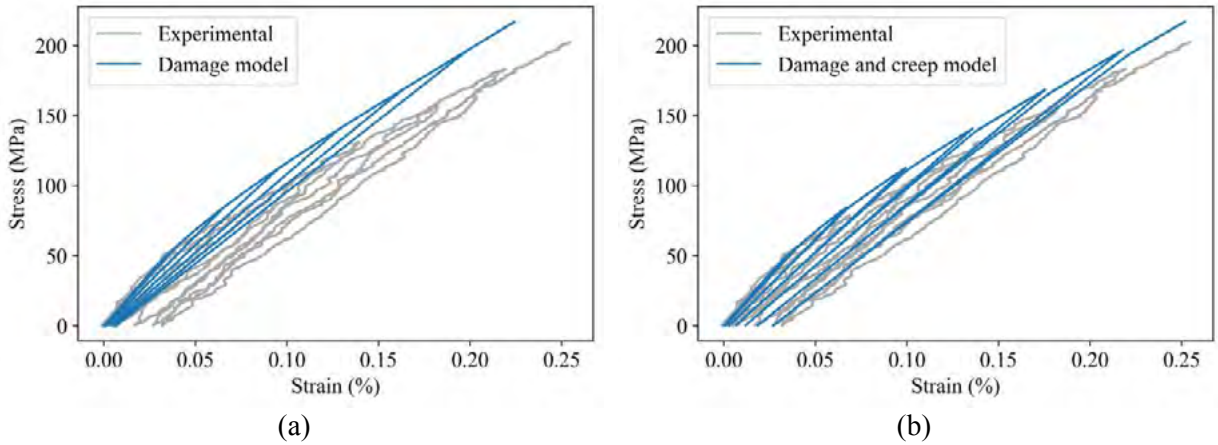


Figure 5. Comparison of the simulated stress-strain behavior during an incremental test at 1000 °C to the experimental data without (a) and with (b) taking creep into account

Finally, this model is intended to be used in a structural calculation code, in particular to help with design of parts. To optimise the use of this material, it seems appropriate to tolerate a certain amount of creep strain. In addition to stress and temperature, the time of use is also a factor to take into account. Figure 6 shows a possible use of the law, indicating the maximum time to reach 0.1% viscous strain as a function of load conditions. At low temperatures, the boundary between yellow and green corresponds to the time taken for viscoelasticity to set in. This graph should of course be combined with a design that takes into account the effect of temperature on stiffness and material damage.

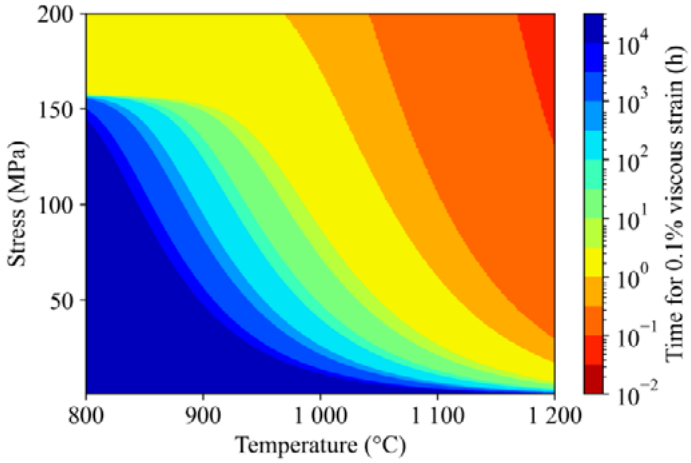


Figure 6. Stress-Temperature-Time diagram for a maximum of 0.1% viscous strain

4. Conclusions

Oxide/oxide composites are being considered for structural temperature applications. While damage does not appear to be affected by temperature, stiffness decreases significantly above 800°C. It is therefore important to have calculation codes that take into account the effect of temperature and material damage. However, creep is also gradually appearing. To use the full potential of these materials, it is therefore necessary to address creep and integrate it into the constitutive equation. In this paper, a creep model based on a Norton's law for the stationary part and a linear viscoelasticity term to better capture load variations was introduced in a damage model. The viscous law was identified on simple creep tests and validated on dip-tests. The value of this law was then demonstrated on an incremental tensile test at 1000 °C. To take this a step further, it is necessary to study creep outside the fibres direction to fully identify the in-plane behavior and thus complete the multiaxial damage model already identified. It also seems important to study the material's behaviour during fatigue tests with holding times that are more representative of aeronautical operating cycles.

Acknowledgments

The authors would like to thank Guillaume Pujol and Grégory Lacoste for conducting the mechanical tests presented in this work.

References

[1] Steibel J. Ceramic matrix composites taking flight at GE Aviation. American Ceramic Society Bulletin 2019;98.
[2] Gardiner G. Leveraging towpreg to reduce the cost of CMC. Composites World 2020. https://www.compositesworld.com/articles/leveraging-towpreg-to-reduce-the-cost-of-cmcs.
[3] Pritzkow WEC, Almeida RSM, Mateus LB, Tushtev K, Rezwan K. All-oxide ceramic matrix composites (OCMC) based on low cost 3M Nextel™ 610 fabrics. Journal of the European Ceramic Society 2020;41:3177–87. https://doi.org/10.1016/j.jeurceramsoc.2020.05.070.
[4] 3M™ Nextel™ 610 Towpreg n.d. https://multimedia.3m.com/mws/media/1791982O/3m-nextel-610-towpreg-flyer.pdf (accessed May 10, 2024).
[5] Simon RA. Progress in Processing and Performance of Porous-Matrix Oxide/Oxide Composites. International Journal of Applied Ceramic Technology 2005;2:141–9. https://doi.org/10.1111/j.1744-7402.2005.02016.x.
[6] Pritzkow WEC, Nöth A, Rüdinger A. Oxide Ceramic Matrix Composites – Manufacturing, Machining, Properties and Industrial Applications. Ceramic Applications 2015;3.
[7] Ben Ramdane C, Julian-Jankowiak A, Valle R, Renollet Y, Parlier M, Martin E, et al. Microstructure and mechanical behaviour of a Nextel™610/alumina weak matrix composite subjected to tensile and compressive loadings. Journal of the European Ceramic Society 2017;37:2919–32. https://doi.org/10.1016/j.jeurceramsoc.2017.02.042.

[8] Almeida RSM, Pereira TFS, Tushtev K, Rezwan K. Obtaining complex-shaped oxide ceramic composites via ionotropic gelation. Journal of the American Ceramic Society 2019;102:53–7. https://doi.org/10.1111/jace.15990.
[9] Zok FW. Developments in Oxide Fiber Composites. Journal of the American Ceramic Society 2006;89:3309–24. https://doi.org/10.1111/j.1551-2916.2006.01342.x.
[10] Zawada LP, Hay RS, Lee SS, Staehler J. Characterization and High-Temperature Mechanical Behavior of an Oxide/Oxide Composite. Journal of the American Ceramic Society 2003;86:981–90.
[11] Behrendt T, Hackemann S, Mechnich P, Shi Y, Hönig S, Hofmann S, et al. Development and Test of Oxide/Oxide Ceramic Matrix Composites Combustor Liner Demonstrators for Aero-engines. Journal of Engineering for Gas Turbines and Power 2017;139:031507. https://doi.org/10.1115/1.4034515.
[12] Ramachandran K, Leelavinodhan S, Antao C, Copti A, Mauricio C, Jyothi YL, et al. Analysis of failure mechanisms of Oxide - Oxide ceramic matrix composites. Journal of the European Ceramic Society 2022;42:1626–34. https://doi.org/10.1016/j.jeurceramsoc.2021.11.020.
[13] Ozer M, Ruggles-Wrenn MB. Effects of Environment on Creep Behavior of NextelTM 720/Alumina-Mullite Ceramic Composite with ±45° Fiber Orientation at 1200°C. In: Singh D, Salem J, Mathur S, Ohji T, editors. Ceramic Engineering and Science Proceedings, Hoboken, NJ, USA: John Wiley & Sons, Inc.; 2010, p. 245–60. https://doi.org/10.1002/9780470944127.ch24.
[14] Samuel AF, Christodoulou PG, Zok FW. Strain fields around strain-concentrating features in fiber-reinforced oxide composites. J Am Ceram Soc 2020;103:1942–55. https://doi.org/10.1111/jace.16840.
[15] Débarre A, Julian-Jankowiak A, Parlier M, Renollet Y, Pujol G, Boussuge M. Effect of temperature on the mechanical behaviour of an oxide/oxide composite. Journal of the European Ceramic Society 2022;42:7149–56. https://doi.org/10.1016/j.jeurceramsoc.2022.08.002.
[16] Débarre A, Przybyla C, Laurin F, Jackson T, Maire J-F. Characterisation and damage modelling of oxide/oxide composites considering temperature dependence. Journal of the European Ceramic Society 2024. https://doi.org/10.1016/j.jeurceramsoc.2024.05.015.
[17] Ben Ramdane C. Etude et modélisation du comportement mécanique de CMC oxyde/oxyde. Thèse de l'Université de Bordeaux, 2014.
[18] Sally O. Stratégies de calcul pour la prévision de la durée de vie de structures composites soumises à des chargements complexes : Application aux composites oxyde/oxyde. Thèse de l'Université Paris-Saclay, 2020.
[19] Maire J-F, Chaboche JL. A new formulation of continuum damage mechanics (CDM) for composite materials. Aerospace Science and Technology 1997;1:247–57. https://doi.org/10.1016/S1270-9638(97)90035-3.
[20] Marcin L. Modélisation du comportement, de l'endommagement et de la rupture des matériaux composites à renforts tissés pour le dimensionnement robuste de structures. Thèse de l'Université de Bordeaux 1, 2010.
[21] Rakotoarisoa C. Prévision de la durée de vie en fatigue des composites à matrice organique tisses interlock. Thèse de l'Université de Technologie de Compiègne, 2014.
[22] Hemon E. Modèles multi-niveaux de prévision des durées de vie en fatigue des structures composites à matrice céramique pour usage en turbomachines aéronautiques. Thèse de l'Université de Bordeaux 1, 2013.
[23] Naumenko K, Altenbach H. Modeling of Creep for Structural Analysis. Berlin, Heidelberg: Springer Berlin Heidelberg; 2007. https://doi.org/10.1007/978-3-540-70839-1.
[24] Hammond VH, Elzey DM. Comparing the creep response of alumina tows and single filaments. Scripta Materialia 2002;46:287–91. https://doi.org/10.1016/S1359-6462(01)01240-4.
[25] Maire J-F. Etudes théorique et expérimentale du comportement de matériaux composites en contraintes planes. Thèse de l'Université de Franche-Comté, 1992.
[26] Schieffer A. Modélisation multiéchelle du comportement mécanique des composites à matrice organique et effets du vieillissement thermique. Thèse de l'Université de Technologie de Troyes, 2003.

FIBER-MATRIX INTERFACE DEBONDING CHARACTERIZATION USING A DUAL-VISION SYSTEM

H. Girard[1], M. Tosti-Umemura[1], A. Doitrand[1], N. Godin[1], R.G. Rinaldi[1], B. Koohbor[2] and J. Bikard[3]

[1]INSA-Lyon, Universite Claude Bernard Lyon 1, CNRS, MATEIS,
UMR5510, 69621, Villeurbanne, France
Email: hugo.girard@insa-lyon.fr, milena.umemura@insa-lyon.fr aurelien.doitrand@insa-lyon.fr
nathalie.godin@insa-lyon.fr and renaud.rinaldi@insa-lyon.fr
[2]Axel'one (Solvay),
87 Avenue des Frères Perret, CS 70061, 69192 Saint Fons, France
Email: jerome.bikard@solvay.com
[3]Department of Mechanical Engineering,
Rowan University, 201 Mullica Hill Rd., Glassboro, NJ 08028, United States of America
Email: koohbor@rowan.edu

Keywords: Fiber-matrix, interface, debonding, characterization

Abstract
Fiber-matrix interface debonding is characterized experimentally using single transverse glass fiber within an epoxy matrix specimen tested under uniaxial tension. A dual-vision system, consisting of two synchronized cameras, is used to monitor the initiation and propagation of the fiber-matrix debonding as a function of the applied remote loading. Debonding was found to initiate at the free surface to tunnel at the fiber pole. Debonding topologies are characterized in terms of maximum opening and through thickness length and angle. The debonding angles are challenging to determine experimentally, so that a numerical model is established, which validated the accuracy of the experimental measurements.

1. Introduction

Fiber-matrix interface in composite materials is known to play a major role in the damage and associated ultimate properties. Indeed, stress concentration resulting from elastic mismatch, proximity to adjacent fibers, and low fracture properties can rapidly induce damage at the interface. Therefore, it is crucial to accurately characterize their fracture properties.

Fiber-matrix interface fracture characterization can be achieved using single-fiber tests such as, *e.g.*, multi-fragmentation or pull-out tests [1]. Fiber-matrix interface primarily undergoes shear loading using above-mentioned methods. However, tensile properties are as important and require other characterization methods to be used. Single-fiber sample loaded transversely can be used to assess opening fracture properties. Koyanagi *et al*. [2] used the debonding length and cohesive zone model to identified fracture properties. Authors reported the difficulty in identifying the debonding shape due to compression loading on the fiber equators. Debonding monitoring may thus require more in-depth characterization method to enable accurate inverse identification.

Livingston and Koohbor [3] performed experimental observations of macro-scale debonding. Single-fiber composite specimens were tested under uniaxial tension and full-field measurements at the fiber vicinity was performed to observe debonding stages. For this purpose, DIC was used to extract local strain fields and debonding angle at the free surfaces as a function of the applied loading [4]. However, debonding observations are limited to the front surface which provides limited information on the complete debonding process.

The present work thus improves the above-discussed experimental investigation of fiber-matrix interface by using a dual-vision approach to enable the simultaneous characterization of in-plane and through-thickness debonding process in single macro fiber model composites. Section 2 details the experimental set-up along with samples preparation. Results obtained from the debonding characterization are presented and confronted to numerical simulations to be further discussed in Section 3. Finally, conclusions on the proposed approach are drawn.

2. Experiments

2.1. Materials and sample preparation

Single fiber samples are made by embedding a 1 mm diameter quartz glass fiber in a translucid, room-curable epoxy. The epoxy resin (SD2505/SR1500, Sicomin, France) is cured at room temperature for one month to ensure that the resin is fully cured. Isotropic elastic properties of the fiber and the matrix are given in Table 1. Elastic properties of the epoxy matrix are determined in-house, using 5 tensile fiber-free samples prepared under the same curing conditions. The final sample, whose geometry is shown in Figure 1, has a 5 mm wide and 5 mm thick cross-section.

Table 1. Elastic properties of the matrix and fiber.

Property	Epoxy	Glass fiber
Young's modulus [GPa]	2.7 ± 0.2	72
Poisson's ratio	0.41 ± 0.04	0.3

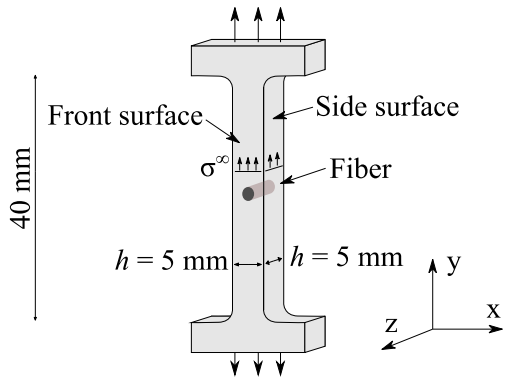


Figure 1. Single fiber specimen geometry and dimensions.

The single fiber is held in place using a 3D-printed jig. The surface of the fiber is cleaned with isopropanol to remove any unwanted substances from the surface. The matrix is poured into a silicone mold, where the latter is drilled at the location of the fiber to allow it to protrude from the final sample. This eliminates the need to polish the end of the fiber itself. The front surface of the sample is slightly polished with fine sandpaper with a grain size of approximately 8 µm. The side surfaces are also polished, first using similar fine sandpaper, then using a rotating cotton disc coupled with a polishing solution to obtain a perfectly transparent, flat side surface. The front surface is then spray painted for DIC. Samples are tested under tension at room temperature at a constant displacement rate of 0.18 mm/min. A dual-vision system consisting of two perpendicularly positioned cameras (FLIR Grasshopper GS3-U3-41C6M-C) is installed. This allows simultaneous observation of the front and side surfaces of the sample.

2.2 Mechanical test and image-based measurements

Figure 2 shows the parameters describing debonding geometry. Since straight-faced samples are used, debonding is likely to initiate at the free surface [5]. Debonding can be described by the debonding angle θ_{d} at the free face, measured by the angle between the two debonding tips. The quantity δ_{nn} corresponds to the maximum normal debonding opening. It is worth noting that considering the samples geometry and loading condition, maximum opening will occur at the pole of the fiber. The debonding opening actually reflects the distance separating the two lips of the crack. The length of debonding through the thickness is described by l_{d}, which corresponds to the length of debonding in the z-direction at the pole of the fiber.

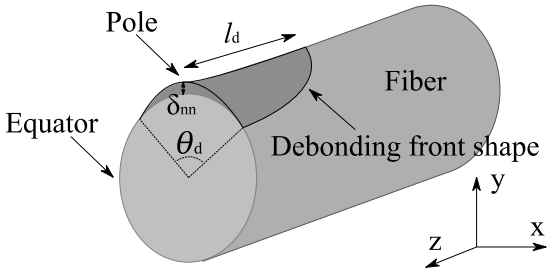


Figure 2. Fiber-matrix debonding geometrical parameters.

The debonding length determination consists in observing and monitoring the debonding propagation through the thickness of the sample, *i.e.*, in the z-direction. Since the debonding is likely to initiate and propagate at the fiber pole with respect to the loading direction due to the maximum stress attained at this location, the latter also corresponds to the maximum possible debonding length l_d. The method used to determine the debonding length makes use of the image processing free software, ImageJ. The side images are first imported into the software, then aligned to eliminate any motion induced by the tensile test, with the images shifted to match the previous one. In this way, the location of the fibers remains constant for several remote stresses, which facilitates identification of the debonding. The image preceding the onset of debonding is then selected, from which the gray level difference for each pixel is calculated with the subsequent images. As a result, the debonding area results in a large gray level difference compared to the initial image, while the other areas result in a difference close to 0. A threshold of 17% in gray level intensity is then applied to the difference between the two images and superimposed on the real image. The threshold value is set so that the results coincide with the visual observation of a large debonding surface. The new images highlight the debonded area, which length is determined as the maximum distance within the threshold area.

Maximum debonding opening is determined using the displacement fields deduced from DIC measurement. In details, a camera is positioned parallel to the sample front surface. The approach involves the use of Ufreckles software [6], from which displacement fields can be derived. A virtual gauge aligned with the loading direction and passing through the fiber and the matrix at the top pole is positioned. The U_y displacement is determined along the gauge as a function of the applied remote load within both the fiber and matrix. From a certain loading level, displacement discontinuously develops at the fiber-matrix interface, which can be associated with debonding initiation. From this loading level, the displacement remains almost constant within either the matrix or the fiber, allowing the debonding opening δ_{nn} to be assessed by computing the displacement jump.

The debonding angle remains difficult to observe because it is characterized by sub-pixel mechanisms that cannot be captured either by optical observation or by the DIC residuals. As a consequence, inverse calculation based on elastic calculations performed on a 3D numerical is used to determine the debonding angle.

3. Results and discussion

The following results are presented for one sample to illustrate the characterization approach. Since debonding is likely to initiate from the free surfaces of the sample at the pole of the fiber relative to the loading direction, 4 preferred initiation sites can be defined. For the sake of simplicity, only the first debonding site is considered in what follows.

Figure 3a shows multiple side images illustrating the debonding process, with both raw and thresholded images, left and right images, respectively, for different loading level σ^∞. The location of the crack tip is highlighted by a red triangle marker, enabling the debonding length to be determined as the distance

to the free surface. Notably, the fiber from the studied sample is slightly tilted, approximately 4 deg. relative to the loading direction, potentially influencing the debonding shape topology.

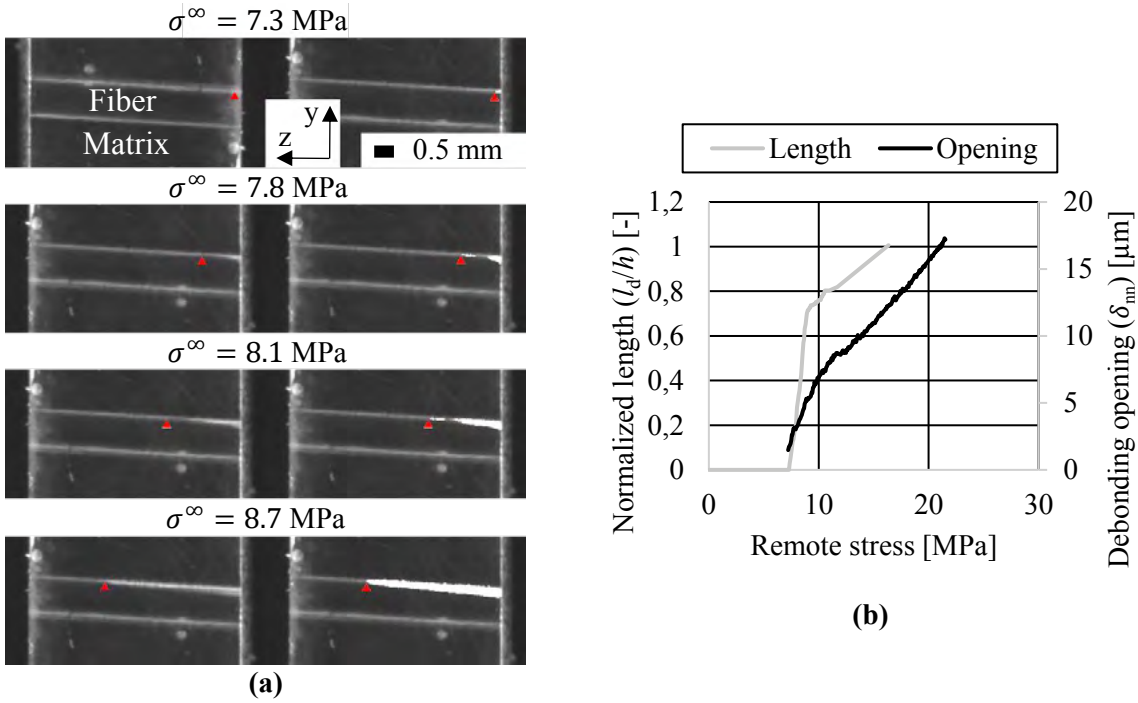


Figure 3. (a) Debonding propagation observed using the raw image, left column and using a threshold, right column. **(b)** Variation of both debonding length and opening as a function of the remote stress.

Figure 3b shows the variation in debonding opening and normalized length as a function of remote stress at the same debonding initiation site. The debonding length is normalized by the sample thickness h. Debonding initiation occurs at a remote stress of 7.2 MPa with both opening and length predictions being consistent. The maximum debonding opening at initiation are given in Table 2. Since debonding initiation occurs between two images, upper and lower bounds for debonding initiation opening can be determined.

Table 2. Debonding opening at initiation.

δ_{nn} [µm] lower bound	δ_{nn} [µm] upper bound
1.5 ± 1.0	1.7 ± 1.0

Difficulties in determining debonding angles are encountered experimentally. The pixel size obtained with the front camera varies between 10 and 12 µm, whereas the DIC provides debonding initiation opening with a sub-pixel size of 1 to 3 µm. Consequently, the resolution of the camera is not sufficient to capture the early stages of debonding at the free surface. Nevertheless, coupled experimental-numerical approach is established to retrieve the debonding angle and shape that best match the experimentally measured opening and debonding length. The approach consists of numerically comparing various debonding geometries approximated using a power-law of exponent 4. The appropriate geometry thus gives the debonding angle at the free surface and the shape of the debonding front. Identification can be performed at several debonding stages, providing debonding angles as a function of remote loading.

Debonding angles obtained from the coupled numerical-experimental approach are shown in Figure 4 by the white markers. The debonding angle can also be assessed using the side observation, using results from Figure 3a, shown by the solide line in Figure 4. The side observation method provides precise debonding angles for small angles only. For angles larger than 70 degrees, the difference in reflective index brought by the debonded zone is not sufficient to capture the actual debonding area. The mixed shear-compression loading causes the debonding area to be partially captured. Despite those differences, the proposed method offers an accurate description of the debonding angle for early stages of debonding.

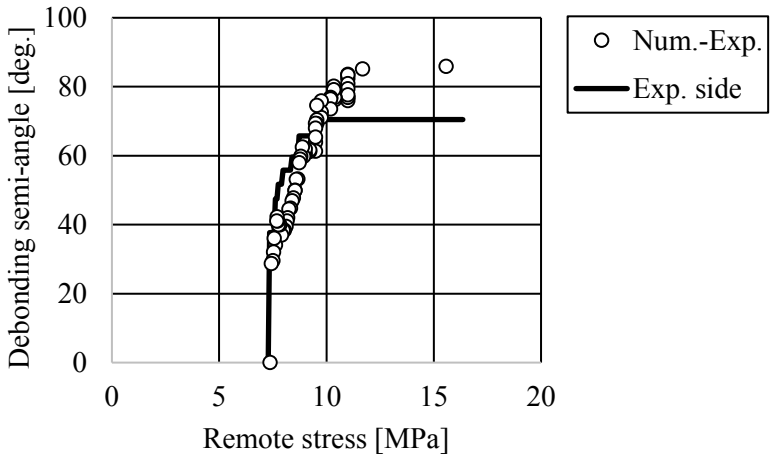


Figure 4. Variation of the debonding semi-angle as a function of the remote stress.

4. Conclusion

The proposed method enables the thorough description of the debonding process using different geometrical parameters. The extracted quantities provide key information such as the debonding initiation remote loading. Additionally, the debonding propagation can be monitored as a function of the remote stress. Experimental-numerical approach that couples experimental debonding opening and length to numerical results enables determining the debonding angle as a function of the remote loading. Debonding angle determined using the side observation is confirmed to be accurate except when the interface undergoes mixed shear-compression. Such experimental debonding observation can be used to calibrate an inverse identification approach that requires the debonding topology to be computed. Such inverse identification may enable the determination of the fiber-matrix interface fracture properties.

References

[1] Zhandarov, S., et E. Mäder. « Characterization of fiber/matrix interface strength: applicability of different tests, approaches and parameters ». Composites Science and Technology 65, nº 1 (2005): 149-60. https://doi.org/10.1016/j.compscitech.2004.07.003.

[2] Koyanagi, J., P. D. Shah, S. Kimura, S. K. Ha, et H. Kawada. « Mixed-mode interfacial debonding simulation in single-fiber composite under a transverse load ». Journal of Solid Mechanics and Materials Engineering 3, nº 5 (2009): 796-806. https://doi.org/10.1299/jmmp.3.796.

[3] Livingston, R., et B. Koohbor. « Characterizing fiber-matrix debond and fiber interaction mechanisms by full-field measurements ». Composites Part C: Open Access 7 (2022): 100229. https://doi.org/10.1016/j.jcomc.2022.100229.

[4] Girard, H., B. Koohbor, A. Doitrand, et R. Livingston. « Experimental characterization of in-plane debonding at fiber-matrix interface using single glass macro fiber samples ». Composites Part A: Applied Science and Manufacturing 171 (2023): 107573. https://doi.org/10.1016/j.compositesa.2023.107573.

[5] Ogihara, S., Y. Sakamoto, et J. Koyanagi. « Evaluation of Interfacial Tensile Strength in Glass Fiber/Epoxy Resin Interface using the Cruciform Specimen Method ». Journal of Solid Mechanics and Materials Engineering 3, nº 9 (2009): 1071-80. https://doi.org/10.1299/jmmp.3.1071.

[6] Julien, Rethoré. « UFreckles ». Zenodo, 1 octobre 2018. https://doi.org/10.5281/ZENODO.1433775.

INTERLAMINAR FRACTURE BEHAVIOUR OF EMERGING LAMINATED-PULTRUDED CFRP PLATES FOR WIND TURBINE BLADES UNDER DIFFERENT LOADING MODES

X. Li[1*], F. Monticeli[1], J.A. Pascoe[1] and Y. Mosleh[2]

[1]Department of Aerospace Structures and Materials, Faculty of Aerospace Engineering, Delft University of Technology, Kluyverweg 1, 2629 HS Delft, the Netherlands
Email: lixinwpu@foxmail.com, F.M.Monticeli@tudelft.nl, J.A.Pascoe@tudelft.nl
[2]Department of Engineering Structures, Faculty of Civil Engineering and Geosciences, Delft University of Technology, Stevinweg 1, 2628 CN Delft, The Netherlands
Email: Y.Mosleh@tudelft.nl

Keywords: Crack propagation, Fracture criteria, Mode I, II, and mixed mode I/II fracture toughness, Pultruded plates, CFRP

Abstract

Driven by the energy transition and the reduction of carbon emissions, pultruded CFRP plates have emerged as an affordable high performance material for designing wind turbines with larger rotors. To enable the creation of thicker laminates, pre-cured plates are bonded together using an epoxy resin. The present study focuses on characterizing the fracture behaviours of these laminated bonded plates under different modes, and to generate fracture criteria for numerical simulations establishing design allowables and service life. Double cantilever beam tests, end-loaded split tests, and mixed-mode bending tests were conducted under quasi static loading for such plates. Mode I crack propagation showed brittle failure while mode II fracture tests on the other hand, presented a more stable crack growth. Finally, power law and Benzeggagh-Kenane law criteria were established to numerically describe the fracture behaviours. Overall, the results show that the available standards for fracture toughness testing are also suitable for these laminated-pultruded composite plate structures, enabling the material characterization needed for design.

1. Introduction

Larger and larger rotors have been designed for wind turbine blades to enable more energy capture, resulting in ever increasing structural loading. Carbon fibre reinforced polymer (CFRP) composites, due to their outstanding mechanical performance, have been utilized in spar caps of wind turbine rotors to carry and transfer increased loads in the flap direction. Among them, pultruded CFRP plates have emerged as an affordable high performance material for wind turbine design [1, 2]. To enable the creation of thicker laminates, pre-cured plates are bonded together using an epoxy resin. Considering the dominant role of such CFRP composites in load-bearing structures of wind turbine blades, it is necessary to characterize the fracture behaviours of these novel laminates under different modes, and to further generate fracture criteria for numerical simulations establishing design allowables and service life.

One question which may rise first is should these laminated pultruded plates be treated as composite laminates or adhesive joints? Considering the standardized tests are mainly proposed for composite laminates with a thickness of 2 mm to 5 mm, it is not clear whether the characterization of fracture

behaviours of such bonded pultruded plates can follow these existing test standards or not. So far, some researches have been conducted to consider the modification of standard specimen dimensions for pultruded composites. Burda et al. [3] recommended that the length of double cantilever beam specimens should be at least 250 mm to characterise the pure mode I fracture behaviour of pultruded glass fibre-reinforced epoxy rods and to provide a suitable R-curve. Yan et al. [4] found that mode II crack propagation using the end-notched flexure test configuration becomes more stable when increasing pre-crack length for pultruded carbon fibre-epoxy composites. Zhang et al. [5] increased the length of specimens for end-loaded split tests to investigate the mode-II fracture properties for an adhesive layer of 2 mm thickness. However, a systematic inversitiagtion into the applicability of different test standards on the laminated pultruded composite plates is needed, covering different loading modes (i.e. mixed mode ratio). Besides, it will also be interesting to understand how the the development of the fracture pattern is affected by different loading modes for such plates, which is rarely reported in literature.

Therefore, the present study aims at provide a comprehensive insight on quasi-static behaviours of laminated pultruded composite plates under four types of loading modes. Both the applicability of the existing test standards and effect of loading modes on the fracture pattern of such plates will be explored further.

2. Experimental setups

2.1. Materials and specimens

Zoltek™ PX35 pultruded plate bonded with SWANCOR 2511-1AL/BL epoxy resin was studied in the present work, and the overall thickness of such laminated pultruded plates is about 6.1 mm. At the interfaces between the top and the bottom pultruded plate, a glass fibre veil (M524-ECR30A) with an areal weight of 30 g/m^2 was placed during the resin infusion process, to improve the fracture toughness. The curing process consists of 24-hour curing at room temperature, followed by 3-hour curing at 65°C and 4-hour curing at 80°C. According to ASTM D5528, ISO 15114 and ASTM D6671 [6,7,8], specimens were cut in different dimensions for each type of loading mode, as summarized in Table 1. The initial crack length is measured from the loading line to the crack front. Aluminum loading blocks were bonded on the specimens using LOCTITE EA 3430 and cured at room temperature for at least 24 hours.

Table 1. Geometry dimensions of different types of specimens.

Specimen Type	Loading mode	Length (mm)	Width (mm)	Initial crack length (mm)
DCB	Mode I	200	25	80
ELS	Mode II	180	20	66
MMB	Mixed mode I/II	170	25	32

2.2. Experimental procedures

For most of specimens, mode-I pre-cracking with a length of 2 mm to 10 mm was created. Afterwards, double cantilever beam tests (DCB), end-loaded split tests (ELS), and mixed-mode bending (MMB) tests were conducted under quasi static loading at a rate of 0.5 mm/min or 1 mm/min, as shown in Figure 1. For ELS specimens, the free delamination length is 110 mm and the clamping region is 60 mm. For MMB specimens, the distance from the loading line to the mid supporter is 70 mm. Eventually, four mixed-mode ratios (MMRs), calculated as the ratio of mode II strain energy release rate to the total strain energy release rate, were covered in the present study, i.e. 0, 0.33, 0.67, 1. During the tests, the crack propagation was monitored by an OPTOMOTIVE camera with a resolution of 2048 × 2048 pixels, and image acquisition was performed every 1-5 second(s). For DCB tests, the test was stopped when the crack propagated along the entire interface. For ELS tests, the test was

stopped when the crack propagated close to the clamping region where the force start to increase. For MMB tests, the test was stopped at either the crack propagating to the middle support or unstable crack propagation along with a sudden drop of force. Three to four tests were repeated for each mixed mode ratio. Regarding the data reduction methods for determining mode I and mode II crack intiation toughness, the Compliance Calibration method [6] and the Corrected Beam Theory using Effective crack length [7] were used for mode I and mode II, respectively.

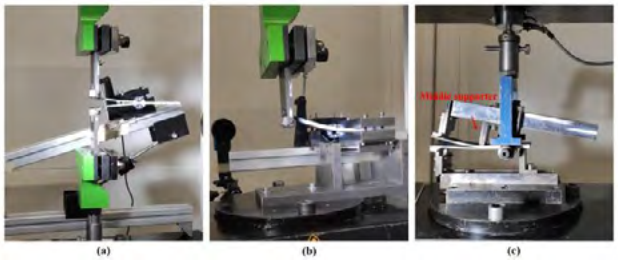


Figure 1. Test setups: (a) DCB tests, (b) ELS tests, (c) MMB tests.

3. Results and discussions

FigureFigure ***2*** shows the force-displacement curves and the crack length history under different loading modes. Overall, a sudden drop of force occurred more frequently for mode I dominant fracture tests (i.e. MMR = 0 and 0.33) accompanying unstable or fast crack propagation, while the post-peak section of force-displacement curves were smoother along with stable and slow crack propagation for mode II dominant fracture tests (i.e. MMR = 0.67 and 1). For the mode I dominant fracture tests, adhesive and substrate failure accompanied cohesive failure. In contrast, mode II dominated fracture tests only showed cohesive failure of the epoxy resin at the interfaces.

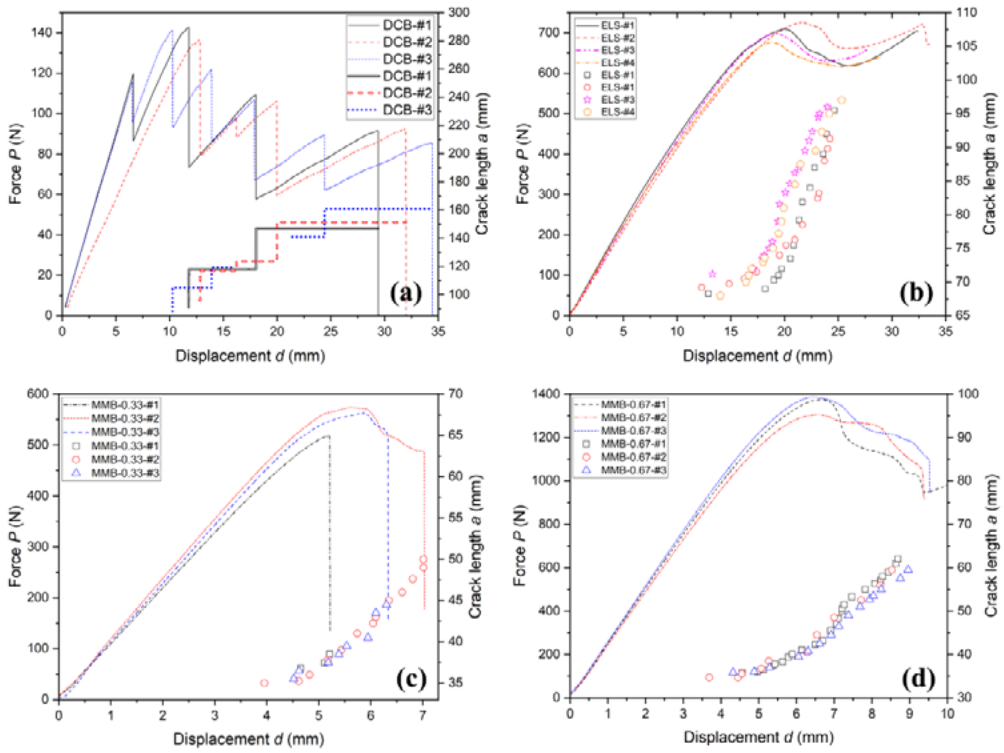


Figure 2. Force-displacement curves and crack length-displacement curves obtained from DCB tests (a), ELS tests (b), MMB tests at a mix-mode ratio of 0.33 (c) and MMB tests at a mix-mode ratio of 0.67 (d).

A plateau of the SERR-crack length curves was not clearly presented for all loading modes, as shown in FigureFigure ***3***. This phenomenon indicates either the crack propagation of such laminated-pultruded plates is relatively less stable in general or suggests a redesign of specimen dimensions to allow sufficient crack growth.

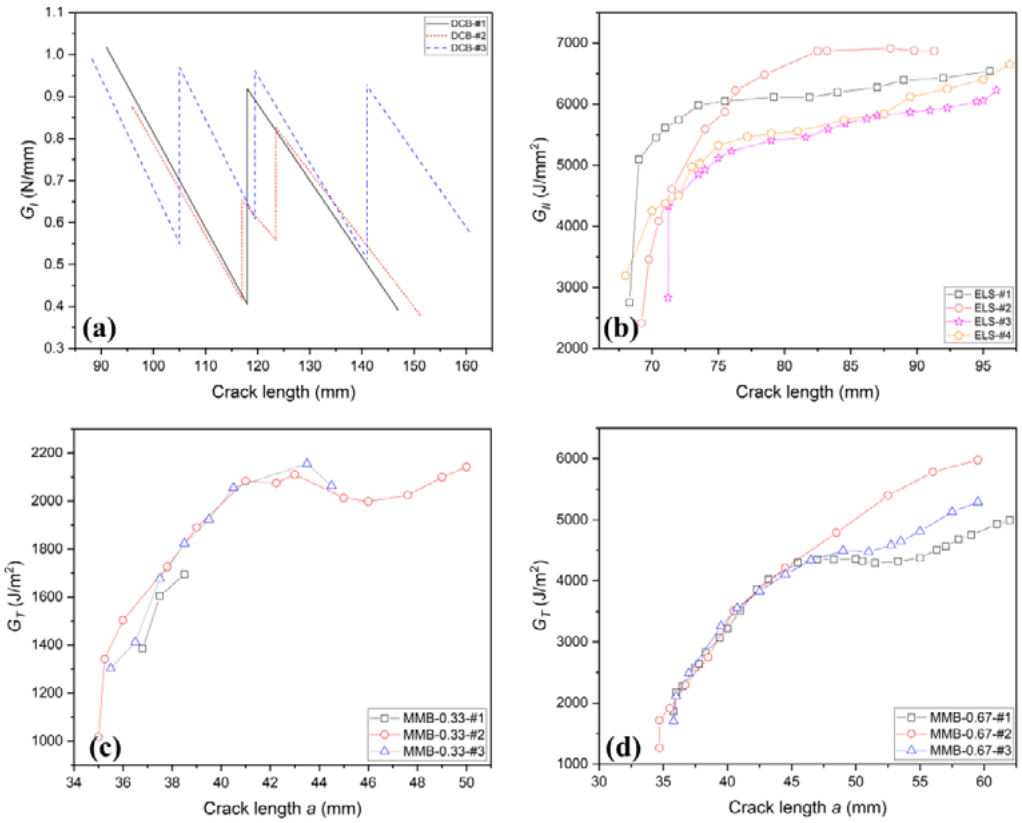


Figure 3. R-curves obtained from DCB tests (a), ELS tests (b), MMB tests at a mix-mode ratio of 0.33 (c) and MMB tests at a mix-mode ratio of 0.67 (d).

To establish the mixed mode I/II failure envelope, both power law and Benzeggagh-Kenane (B-K) law were selected. In the present study, the crack initiation toughness was considered for fitting the failure envelope while the crack propagation toughness could not be determined as no clear plateau of the SERR - crack length curves can be recognized from the DCB, ELS and MMB tests. The crack initiation was identified visually, rather than using the criteria based on the change of compliance of force-displacement curves which could produce over-conservative measurements. Although the determination of crack initiation using the visual observation is highly affected by the image resolution and may create manual deviations, it is less conservative. As shown in Figure Figure ***4***, a high coefficient of determination (R^2) is presented whether using the power law or B-K law. Among the three different fits by applying the power law, the one with fitting parameters equal to 1.0 (Fitted 3 in Figure Figure ***4*** (a)) indicates the possibility of a linear relation between the mixed mode I/II fracture toughness components.

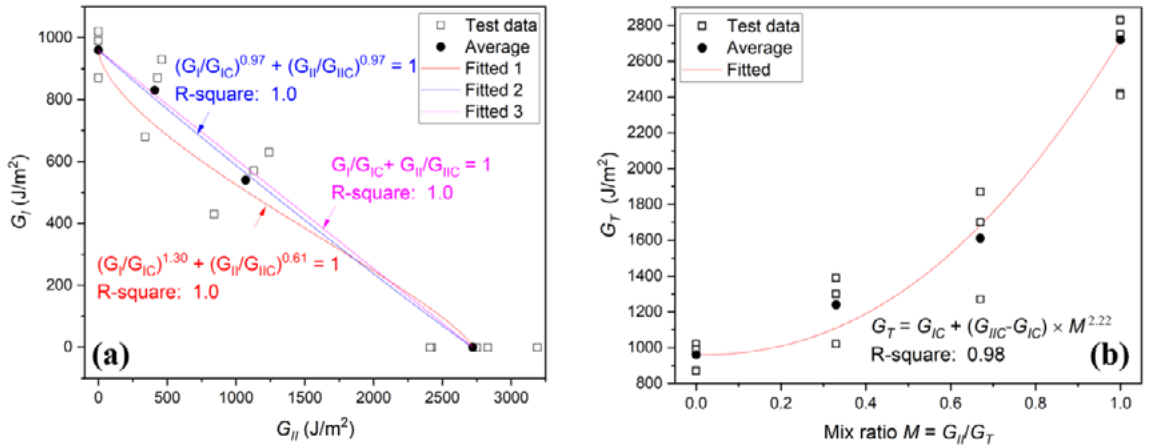


Figure 4. Mixed mode I/II failure envelope based on power law (a) and B-K law (b).

By following specimen design and test configurations introduced in the test standards [6,7,8] , the pure mode I mode I, pure mode II and mixed mode I/II interlaminar fracture behaviour of laminated pultruded composite plates can be obtained properly. However, considering the specimen thickness in the present work is close to the recommend values, whether these test standards are applicable for very thick laminated pultruded composite plates should be investigated further.

4. Conclusions

The interlaminar fracture behaviours of laminated pultruded CFRP plates was characterized at four mode mix ratios by conducting DCB, ELS and MMB tests. Then both power and B-K laws were selected to create the mixed mode I/II failure envelope. The main conclusions are listed hereafter:

1) Mode I dominant fracture tests presented frequent sudden drop of force accompanying unstable or fast crack propagation. As for mode II dominant fracture tests, the post-peak section of force-displacement curves were smoother along with stable and slow crack propagation.
2) Both the power law and B-K law are capable to describe the mixed mode I/II failure envelope. A linear relation between the mode I SERR component and the mode II SERR component may exist for such plates according to the fits using the power law.
3) The existing test standards are applicable for such laminated pultruded CFRP plates with a thickness slightly over the recommend limit. However, more investigations should be continued to verify their capabilities for very thick laminated pultruded composite plates.

Acknowledgments

The authors would like to acknowledge Dr. Jaykarna Bhangale for help in manufacturing the specimens. The research was funded by the European Union under GA No. 101091409 (D-STANDART). Views and opinions expressed are however those of the author(s) only and do not necessarily reflect those of the European Union. Neither the European Union nor the granting authority can be held responsible for them.

References

[1] B. Ennis, S. Das and R. Norris. Economic competitiveness of pultruded fiber composites for wind turbine applications. *Composites Part B: Engineering,* p. 110960, 2023.

[2] P. Mindermann, M.-U. Witt and G. T. Gresser. Pultrusion-winding: A novel fabrication method for coreless wound fiber-reinforced thermoset composites with distinct cross-section. *Composites Part A: Applied Science and Manufacturing*, 154: 106763, 2022.

[3] I. Burda, A. J. Brunner and M. Barbezat. Mode I fracture testing of pultruded glass fiber reinforced epoxy rods: Test development and influence of precracking method and manufacturing. *Engineering Fracture Mechanics*, 149: 287-297, 2015.

[4] X. Yan, X. Guo, Y. Gao, Y. Lin, N. Zhang and Q. Zhao. Mode-II fracture toughness and crack propagation of pultruded carbon Fiber-Epoxy composites. *Engineering Fracture Mechanics*, 279: 109042, 2023.

[5] Y. Zhang, A. P. Vassilopoulos and T. Keller. Mode I and II fracture behavior of adhesively-bonded pultruded composite joints. *Engineering Fracture Mechanics*, 77: 128-143, 2010.

[6] ASTM D5528. Standard test method for mode I interlaminar fracture toughness of unidirectional fiber-reinforced polymer matrix composites. ASTM International, 2014.

[7] ISO 15114. Fibre-reinforced plastic composites - Determination of the mode II fracture resistance for unidirectionally reinforced materials using the calibrated end-loaded split (C-ELS) test and an effective crack length approach. 2014.

[8] ASTM D7905. Standard test method for determination of the mode II interlaminar fracture toughness of unidirectional fiber-reinforced polymer matrix composites. ASTM International, 2014.

TRANSLAMINAR FRACTURE BEHAVIOR OF HYBRID WOVEN-PLY PEEK THERMOPLASTIC LAMINATES UNDER ISOTHERMAL AND KEROSENE FLAME EXPOSURE

Lanhui LIN[1], Benoit VIEILLE[1], Christophe BOUVET[2] and Tanguy DAVIN[1]

[1] Groupe de Physique des Matériaux (UMR CNRS 6634) INSA Rouen Normandie,
Univ Rouen Normandie, CNRS, Normandie Univ, F-76000 Rouen, France
Email: lanhui.lin@insa-rouen.fr, benoit.vieille@insa-rouen.fr and tanguy.davin@insa-rouen.fr
Web Page: http://www.insa-rouen.fr and http://gpm.univ-rouen.fr
[2] Institut Clément Ader (UMR CNRS 5312) Université de Toulouse,
ISAE-SUPAERO – UPS – IMT Mines Albi – INSA, F-31400 Toulouse, France
Email: christophe.bouvet@isae-supaero.fr, Web Page: https://ica.cnrs.fr

Keywords: Thermoplastic composite, Translaminar fracture, High temperature, Kerosene flame

Abstract
The present work aims at studying the influence of different thermal stress conditions on the fracture behavior of PolyEther Ether Ketone-reinforced carbon/glass fiber hybrid laminates (CG/PEEK), as a function of heating temperature and fire exposure time. Compact Tensile (CT) specimens are exposed to isothermal (from 350°C to 550°C in a high temperature furnace) and kerosene flame (characterized by a heat flux of 116 kW/m^2 and a temperature of 1150°C) exposure conditions. Tensile tests are then conducted to assess the mode I translaminar fracture toughness at room temperature. Crack propagation is measured during mechanical loading using a Digital Image Correlation (DIC) device combined with a binarization algorithm. Then, the G-R curves have been obtained from the compliance method. In the isothermal case, the residual mechanical properties degrade with increasing temperature, particularly once thermal decomposition is about to start, due to the formation of porosities and extensive delamination. Under the flame exposure, the microscopic and tomographic observations reveal thermally and mechanically induced damages with a heterogeneous distribution due to temperature gradients. Depending on the pyrolysis degree of each ply, the structural capacities of the plies gradually deteriorate from the exposed to the opposed side, resulting in a lower strain energy release rate and larger secondary cracks.

1. Introduction

Along with the development of manufacturing techniques and certification issues, there has been a growing demand to use high performance thermoplastic-based (TP) composites in aeronautics field over the last fifteen years [1]. However, regarding the flammability of composites and stringent fire safety regulations, the wide use of most TPs is limited by their mechanical properties under severe heat exposure with different environmental conditions [2]. After exposure to elevated temperatures up to the polymer matrix decomposition, it is a critical safety issue to determine the residual mechanical properties since the loss in creep resistance could cause the ultimately failure of composite structures [3]. Compared to isothermal conditions, the presence of high temperature gradients (resulting from a fire event) through the thickness could induce different physical and chemical transformations [4].

Compact Tension (CT) specimens are typically used to estimate the translaminar fracture toughness of laminates, which plays a fundamental role in the damage tolerance of composite structures [5]. To date, most of the studies dealing with translaminar mode I failure are based on unidirectional-ply (UD)

thermosetting (TS) matrix laminates. However, there are far less studies dealing with the fracture toughness of TP-based composites under critical service conditions met in aeronautics [5]. The question is still open when it comes to the assessment of the residual fracture behavior of severely thermally degraded woven-ply composites [8]. Indeed, it is therefore essential to understand the thermomechanical response and design properties of TP-based woven-ply composite subjected to severe temperature environments (for temperatures higher than melting and pyrolysis temperatures).

Thus, the present work was aimed at investigating the thermal decomposition and the residual translaminar fracture behavior of CG/PEEK laminates under different temperature conditions, including isothermal (from matrix melting temperature 350°C to pyrolysis temperature 550°C) and kerosene flame exposure (116 kW/m^2 and 1150°C) conditions. This involves the experimental measurement of the critical energy release rate at initiation and the fracture energy during propagation using CT specimens. The post-mortem examination by means of microscopic observations and micro-CT analyses makes it possible to understand the influence of severe thermal aggression on both the thermal degradation mechanisms and the translaminar fracture of TP based laminates.

2. Materials and experimental set-up

2.1. Materials and specimens

The laminates used in this study is CG/PEEK, which consist of a PolyEther Ether Ketone (PEEK) thermoplastic matrix reinforced with a continuous carbon fiber fabric, and the two outer plies of glass fabric are used to provide corrosion and electrical protection. The Compact Tension (CT) specimens (in accordance with ASTM test standard E399-12 [9]) have 16 plies (average thickness is about 4.5 mm) with a quasi-isotropic layup $[(0/90)_G,(0/90),(\pm45),(0/90),(\pm45),(0/90),(\pm45),(0/90)]_S$. The characteristic temperatures of PEEK matrix are given in Table 1.

Table 1. Characteristic temperatures of CG/PEEK laminates [2].

$T_{\text{glass transition}}$ (°C)	T_{melting} (°C)	$T_{\text{decomposition}}$ (°C)
143	350	583

2.2. Isothermal and fire exposure conditions

In this study, a high temperature furnace and kerosene burner bench [4] are used to provide isothermal and fire exposure, respectively, to reach temperature levels resulting in the phase transitions of the PEEK matrix (Figure 1). The specimens were placed on a grid platform in the furnace. Considering the characteristic temperature, the tests were carried out for 900 s at 350-450-500-550°C. In the case $T > T_d$, as the high temperature furnace has a relatively enclosed heating environment, it may lead to the ignition of the pyrolysis gases and damage the furnace. In agreement with certification requirements, a maximum 900 s exposure to a 1150°C flame was chosen to comply with fire exposure conditions. A protective shield is used to limit the thermal decomposition area of the specimen (Figure 1.b). Three CT specimens have been tested in each configuration: after a 300-600-900 s kerosene flame exposure.

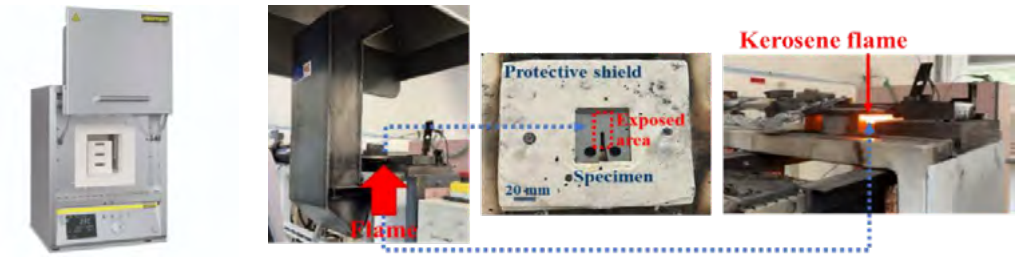


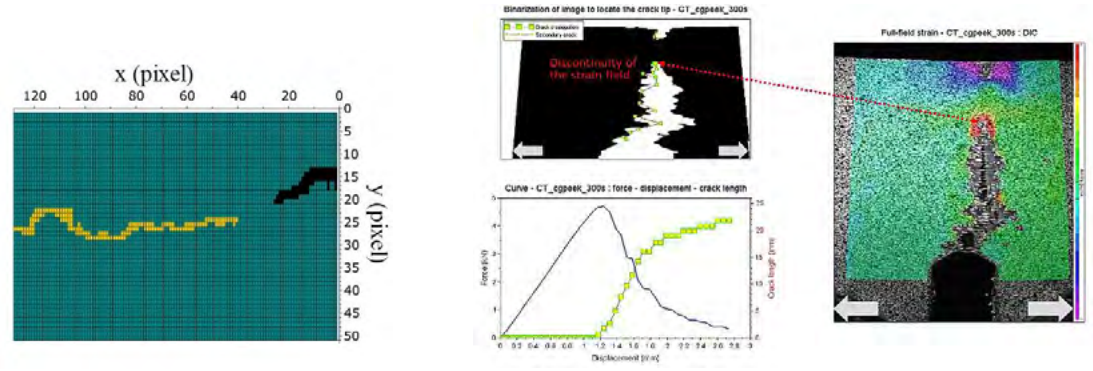
Figure 1. Experimental heating set-up: (a) High temperature furnace – (b) Kerosene burner bench [3].

2.3. Mechanical characterization of residual properties and fractographic analysis

After thermal degradation under isothermal and fire exposure conditions, mechanical tests were further performed in displacement-controlled mode (1 mm/min) at Room Temperature (RT) by means of a MTS 810 uniaxial servo-hydraulic tensile machine consisting of a 100 kN capacity load cell. The specimens are held in position by a standardized device in accordance with ASTM-399 [9], which is maintained by the hydraulic grips of the machine and transfers the mechanical load via pins inserted in the holes of the specimens [7]. Fractographic analyses have been carried out by means of microscopic (numerical optical microscope Keyence VHX-5000) and tomographic (RX Solutions EasyTOM-150) observations to visualize, classify and quantify the thermally and mechanically damaged areas.

2.4. Crack growth measurement and data reduction method

A DIC non-periodic pattern is painted on each CT specimen back surface, and VIC-Snap software is used to process the images correlation. Using an algorithm implemented in the Scilab code [8], the crack tip is located via the discontinuity of the strain field resulting from the crack propagation (Figure 2.a). The evolution of crack length when the load gradually decreases during propagation is then determined from the crack tip position in each pattern, as shown in Figure 2.b. The spatial resolution of the crack length is defined by the size of the subsets used in the DIC method [7].



(a) **(b)**

Figure 2. Binarization algorithm to locate the crack tip during mechanical loading [8]: (a) Algorithm illustration – (b) Example of specimen after 300 s flame exposure.

The compliance method is used to calculate the evolution of the strain energy release rate from the force-displacement curve at the initiation and propagation of the crack, and then to determine the evolution of compliance $C = \delta/P$, where δ is the displacement, P the force and e the thickness of CT specimen:

$$G_{\mathrm{I_c}} = \frac{P_c^2}{2e}\left(\frac{\mathrm{d}C}{\mathrm{d}a}\right) \tag{1}$$

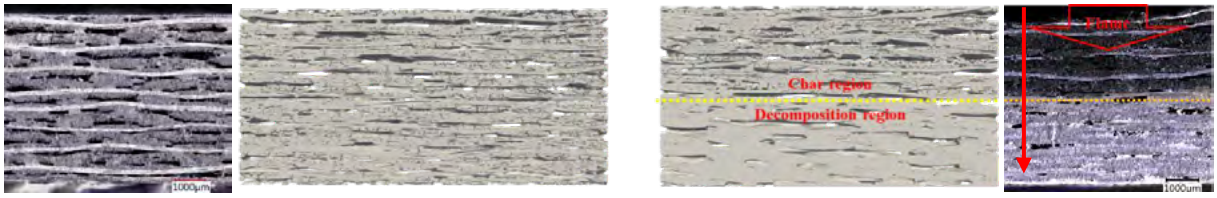
Classically a cubic function of the compliance versus the crack length has been fitted on the whole test for each experiment [10], then an analytical derivative was used to compute the fracture toughness value.

3. Results and discussion

3.1. Thermally induced degradation and fire behavior

As temperature increases, the PEEK matrix is gradually degraded and undergoes a gradual transformation from matrix melting, cracking and eventually into pyrolysis gases. The degradation of matrix caused by the increasing temperature results in the fibers becoming visible and further leads to the production of heat, smoke, and volatiles. When the temperature reaches T_d, the heat flux causes

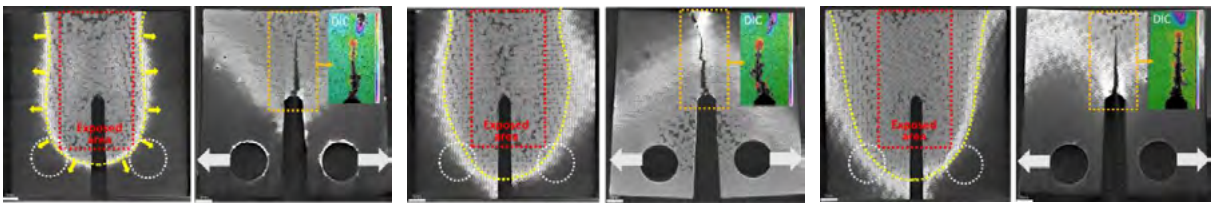
chemical bonds to break, which results in the thermal decomposition, leading to the formation of porosities and delamination, as shown in Figure 3.a. Compared to the isothermal conditions, the through-thickness and in-plane temperature gradients cause heterogeneous damages modes. Following the through-thickness direction, the laminates after flame exposure could be divided into two well-defined areas: the thermal degraded area and the relatively preserved area, as shown in Figure 3.b. In the first region of char, which is a carbon residue [1], the polymer content is negligible since the matrix has decomposed, then the matrix in the second region is partially decomposed (char and pyrolysis gases). Below it, the laminates observations show delamination cracks between the plies and small matrix cracks within the plies because of the combination of pressure build-up and matrix softening.



(a) (b)

Figure 3. Microscopic and tomographic observations of CG/PEEK laminates subjected to different conditions: (a) Isothermal heating for 900 s at 550°C – (b) Kerosene flame exposure for 500 s.

In addition, micro-CT observations of post exposure specimens (before and after tensile test) allow the thermal aggression and the crack propagation to be visualized in each ply. As shown in Figure 4, the exposed surface of laminates reveals that the magnitude of temperature and thermally-induced degradation gradients significantly depends on the flame exposure time. As expected, the degraded area becomes larger as the exposure times increases. Under one-sided kerosene flame exposure up to 900s, the carbonaceous char formed along with the matrix melting and pyrolysis on the exposed surface, whereas the back-surface experiences little matrix melting. The decomposition of PEEK matrix further results in both extensive delamination and ablation of Glass/PEEK outer ply after flame exposure. These thermal degradation within the laminates are expected to have a further influence on their post-fire mechanical performance.



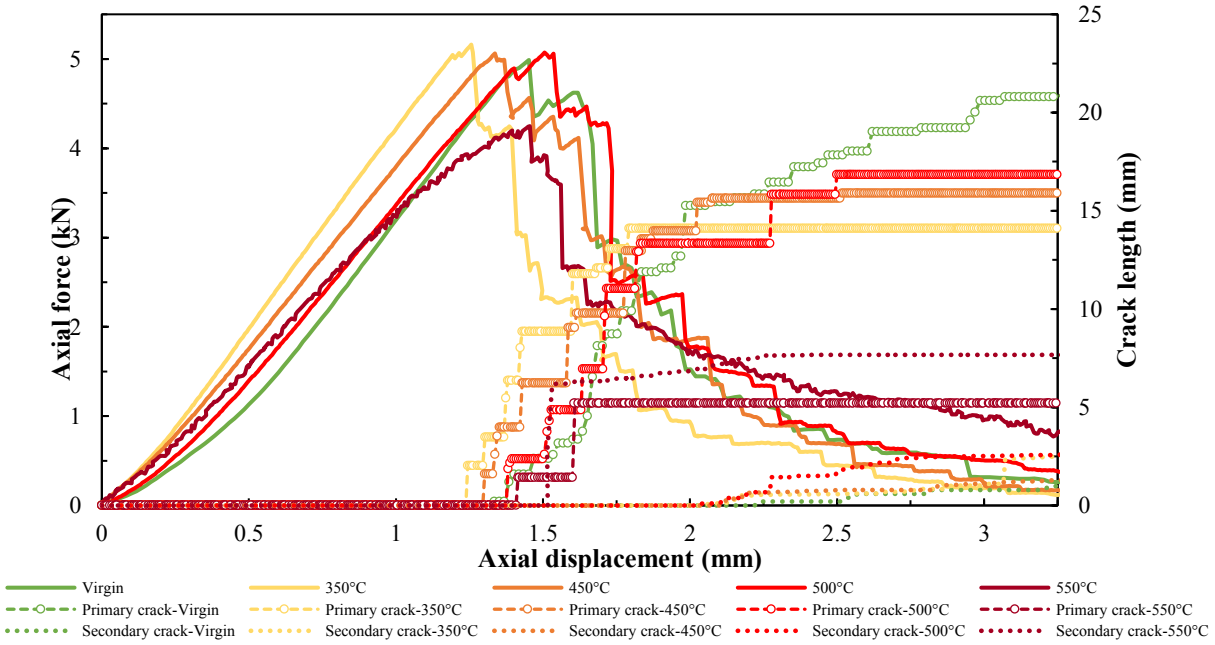
(a) (b) (c)

Figure 4. Tomographic observations of post fire CT specimens: (a) 300 s – (b) 600 s – (c) 900 s.

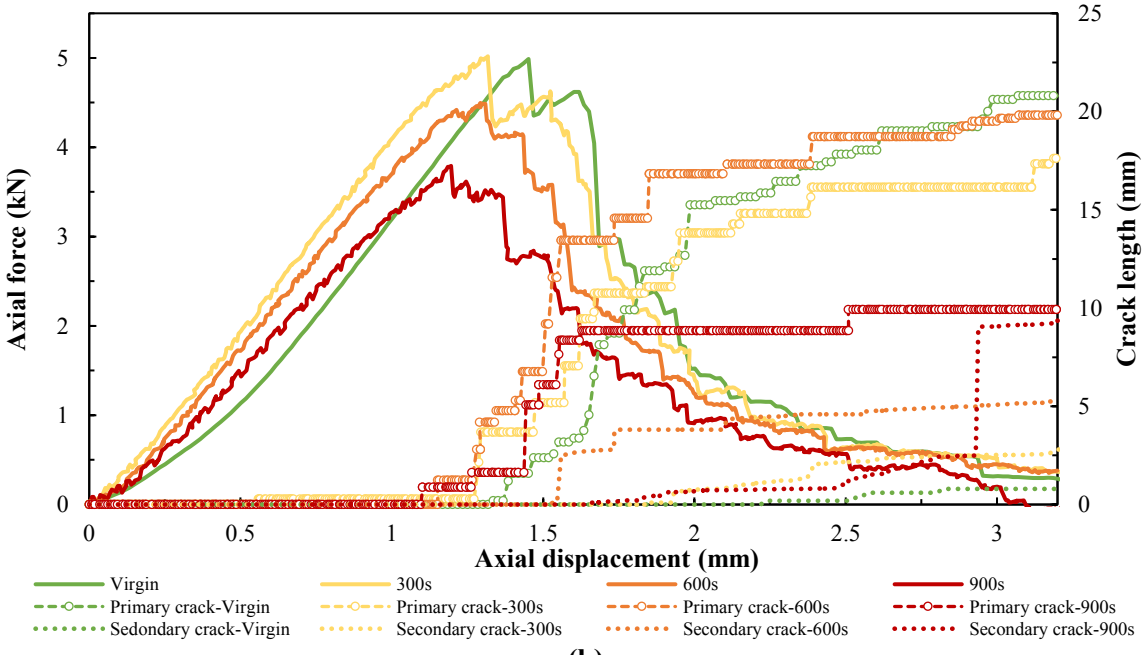
3.2. Residual fracture behavior

The propagation of the macroscopic crack is identified from the jumps observed on the force-displacement curves [8]. From the curves shown in Figure 5, it is observed that CG/PEEK quasi-isotropic laminates have similar macroscopic responses with a quasi-linear force-displacement curve before crack propagation. In the isothermal case, when the heating temperature below T_d, the overall response is similar to the one of as received specimens (referred to as virgin specimens unexposed to thermal aggression) with almost the same level of load before the first fiber breakage. At the end of the CT test, the primary crack (tensile crack) length increases as the environment temperature increases. Compared to virgin specimens, the final secondary crack length (compressive crack) grows larger, as the result of PEEK matrix melting and re-solidification.

Once the temperature reaches $T_{d,}$ the decomposition process of PEEK matrix has a major influence on the structural capabilities and contributes to a significant decrease in the residual properties of laminates compared to previous cases. The macroscopic observations of damaged areas suggest that an extensive delamination occurs during CT testing as well. The mechanical loading causes a significant increase in the secondary crack length, since the load bearing capabilities of the laminate is significantly affected, with a volume porosity ratio (defined by the percentage of porosities of matrix over the whole specimen) around 34% (estimated from tomographic analyses).



(a)



(b)

Figure 5. Mechanical responses and changes in the crack length for different testing conditions: (a) Isothermal conditions (different temperatures) – (b) Fire conditions (different exposure time).

When subjected to a one-sided kerosene flame exposure, longer fire exposure times lead to (i) lower initiation loads at failure and (ii) larger cracks with respect to the ones observed in as received specimens (Figure 5). The microstructure of charred layers (Figure 3.b) is characterized by a high void content and a small amount of solid char. Consequently, the mechanical properties of the charred layers are rather low for different loading conditions due to degraded load transfer capabilities. In the case of a 300 s exposure, the influence of thermal aggression remains moderate, despite the early appearance of fracture. After a 600 s fire exposure, the initiation of compressive failure by plastic buckling (Figure 6.b) on the edge opposite the notch was observed, which is mainly attributed to the decomposition of the matrix and the formation of porosities within the laminates. With a prolonged exposure time up to 900 s, the secondary crack tends to play a more important role than the one under isothermal conditions.

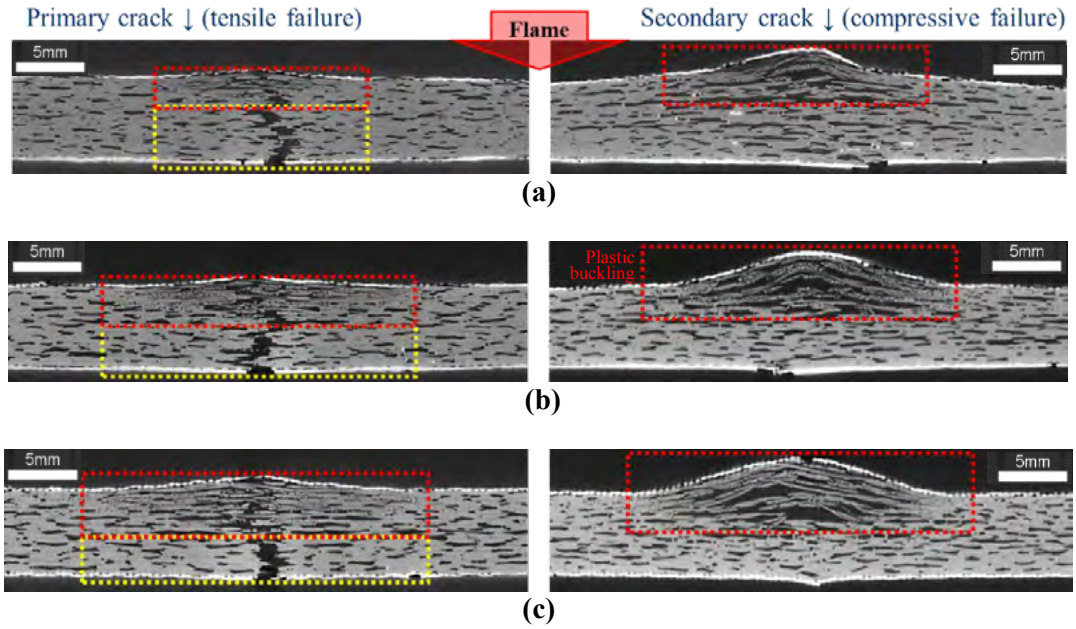


Figure 6. Tomographic observations of post-fire CT specimens' failure mechanisms as a function of flame exposure time: (a) 300 s – (b) 600 s – (c) 900 s.

Post-mortem damages are also analyzed by means of micro-CT observations (Figure 6). The mode I failure of quasi-isotropic laminates primarily results from the translaminar failure of the fibers in tension. The cross sections of primary and secondary crack clearly reveal that the two regions (char and decomposition region) with different thermally-induced damages do not contribute the same way to take up the tensile loading from mechanical behavior standpoint. Depending on the thermal decomposition of each ply (function of the exposure time), the bearing capabilities of the plies is gradually degraded along with delamination growth in the char region due to compressive failure. Thus, it is expected that the residual mechanical properties may reflect on the thermal degradation degree within different regions of the laminates, previously exposed to a kerosene flame for different exposure times.

3.3. Estimation of the strain energy release rate

Within the framework of Linear Elastic Fracture Mechanic (LEFM), the determination of R-curves is the key point to quantify fracture in terms of energy required to grow a crack in quasi-isotropic laminates [7]. The resistance of a laminate to translaminar crack initiation and propagation are characterized by a resistance curve, called the R-curve. The first point of the curve can be defined as the critical strain energy release rate related to crack initiation (G_{Ic}). Here, the compliance method is used to estimate the critical strain energy release rate (by Eq. 1) during the crack propagation [10], as shown in Figure 7.

Under isothermal conditions, when the temperature is lower than T_d (350°C), PEEK matrix melting and re-solidification seem to foster the intrinsic toughness [7] at the crack tip, whereas a decreasing evolution of the fracture energy is observed during crack propagation, with lower values compared to the virgin case. For higher temperatures (450°C and 500°C), the overall evolution of R-curves is similar: the initial value decreases with the increasing environment temperature, and tends to slightly increase during the crack propagation. Once temperature reaches T_d, the formation of porosities and delamination (Figure 3.a) induced by PEEK matrix pyrolysis has a major influence on the structural integrity of laminates, resulting in different R-curves compared with the previous cases. Secondary cracks appearing almost at the same time as the primary ones, the strain energy release rate at the crack initiation is more significant in this case. The curve tends to decrease dramatically once these two cracks propagate in the opposite direction, with much shorter primary cracks induced by the severe delamination.

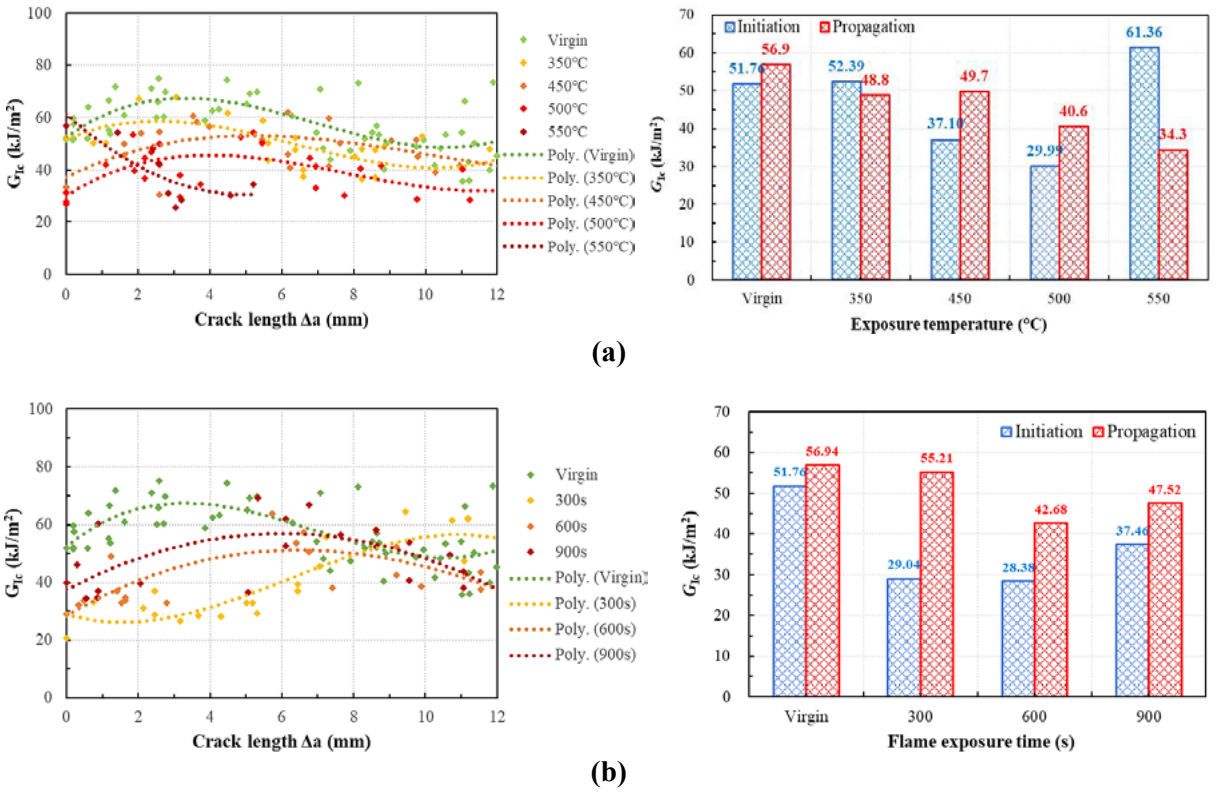


Figure 7. R-curves obtained with the compliance method from CT specimen tests: (a) Isothermal conditions (different exposure temperature) – (b) Fire conditions (different exposure time).

Regarding the influence of different flame exposure times, the structural capacities decrease as flame exposure time increases. In the 300 s and 600 s exposure cases, the same level of initial value is observed with respect to the case of 500°C, as the decomposition region has a porosity ratio close to the isothermal environment. During crack propagation, the R-curves tend to increase and then decrease slightly, which could be explained by the early appearance of secondary fracture induced by the char region. After a 900 s exposure, the char region representing almost 2/3 of the laminates thickness, the compressive failure plays a more important role (Figure 6.c), ultimately resulting in higher strain energy release rates compared to the 600 s case. Indeed, secondary cracks contribute to the dissipation of mechanical energy during fracture, which prevents an accurate assessment of the strain energy release rate from an overall computation using force-displacement curves.

4. Conclusions

The influence of different critical temperature conditions (isothermal and kerosene flame exposure) on the thermal degradation and the residual translaminar fracture behavior of CG/PEEK laminates was studied by means of CT specimens. The evolution of the strain energy release rate associated with mode I tensile failure from force-displacement curves during crack propagation is monitored using the compliance method combined with a digital image analysis technique.

From the obtained results, the following conclusions can be drawn: (i) the thermo-mechanical behavior clearly depends on the temperature conditions, the presence of a temperature gradient (fire exposure case) causes heterogeneous degradation mechanisms, compared to the isothermal case; (ii) under isothermal conditions, with the increasing temperature, the secondary crack becomes more important due to PEEK matrix melting and cracking, and the structural integrity of the laminate is significantly affected by the decomposition of PEEK matrix once temperature reaches T_d; (iii) under kerosene flame exposure, the bearing capabilities of the plies are gradually degraded as a function of the exposure time, and the two regions (char and decomposition region) characterized by different thermally-induced damages do not take up the mechanical loading the same way; (iv) regarding the critical strain energy release rate, the initial value decreases with more severe temperature conditions. The translaminar fracture toughness tends to slightly increase during crack propagation, whereas the structural capabilities of CG/PEEK laminates decrease with the increasing flame exposure time, as secondary cracks within the char region may prevent the compliance method to be applied.

Ultimately, the correlation between post-fire residual mechanical properties and thermally degraded regions needs to be further investigated. In a forthcoming work, an analytical model based on the porosity content ratio of each region will be implemented to better account for the coupling between thermomechanical behavior and different critical service conditions.

Acknowledgments

The financial support from China Scholarship Council is greatly appreciated (CSC 202208120011).

References

[1] A.P. Mouritz, A.G. Gibson. *Fire Properties of Polymer Composite Materials*. Solid Mechanics and its Applications, Springer, Dordrecht, 2006.
[2] B. Vieille, A. Coppalle, E. Schuhler, et al. Influence of kerosene flame on fire-behaviour and mechanical properties of hybrid Carbon Glass fibers reinforced PEEK composite laminates. *Composite Structures*, 279: 114786, 2022.
[3] L. Lin, B. Vieille, C. Bouvet. About the influence of a thermal aggression on the tensile behaviour of hybrid PEEK thermoplastic laminates. *Composite Structures*, 333: 117945, 2024.
[4] E. Schuhler, A. Chaudhary, A. Coppalle, B. Vieille. Fire behaviour of composite materials using kerosene burner tests at small-scales. *Fire Safety Journal*, 121: 103290, 2021.
[5] M. J. Laffan, S. T. Pinho, P. Robinson, A. J.McMillan. Translaminar fracture toughness testing of composites: A review. *Polymer testing*, 31(3): 481-489,2012.
[6] R. Rutar, J. Serra, Q. Bausiere, C. Bouvet. Experimental characterization of tensile and compressive translaminar fracture toughness coupling multi-physics measurements. *Engineering Fracture Mechanics*, 291: 109568, 2023.
[7] B. Vieille, J. D. Gonzalez, C. Bouvet. Fracture mechanics of hybrid composites with ductile matrix and brittle fibers: Influence of temperature and constraint effect. *Journal of Composite Materials*, 53(10): 1361-1376, 2019.
[8] J. D. Gonzalez, B. Vieille, C. Bouvet. High temperature translaminar fracture of woven-ply thermoplastic laminates in tension and in compression. *Eng. Fract. Mech.*, 246: 107616, 2021.
[9] Standard, A. S. T. M. E399-12. *Standard test method for linear-elastic plane-strain fracture toughness KIc of metallic materials*, American Society for Testing and Materials, 2012.
[10] M. J. Laffan, S. T. Pinho, P. Robinson, L. Iannucci. Measurement of the in situ ply fracture toughness associated with mode I fibre tensile failure in FRP. Part I: Data reduction. *Composites Science and Technology*, 70(4): 606-613, 2010.

HIGHLY ELECTRICALLY CONDUCTIVE NANOCOMPOSITES FOR STRAIN SENSING DEVICE IN STRUCTURAL HEALTH MONITORING

Fabrizia Cilento[1], Barbara Palmieri[1], Alfonso Martone[1], Leonardo Zappelli [2], Davide Mencarelli[2], Michele Giordano[1]

[1] Institute of Polymers, Composite and Biomaterials (IPCB), National Research Council of Italy, 80055 Portici, Italy
fabrizia.cilento@ipcb.cnr.it, barbara.palmieri@ipcb.cnr.it, alfonso.martone@ipcb.cnr.it, michele.giordano@ipcb.cnr.it
[2] Department of Information Engineering, Università Politecnica delle Marche, Ancona, Italy
d.mencarelli@staff.univpm.it, l.zappelli@staff.univpm.it

Keywords: Conductive nanocomposite, strain sensor, metasurface, spray deposition

Abstract
Chipless, passive and wireless sensors are one of the most important expected developments in wireless sensor technology for Structural Health Monitoring (SHM) because of their compactness and the absence of a battery or chip for the sensor operation. Strain sensitive resonant antenna reflectors based on the strain sensing metasurfaces (i.e. frequency-selective surfaces) are employed for this application. The variation of the spectral response of the metasurface with external perturbation results in an intrinsically effective sensing mechanism. Highly electrically conductive nanocomposites are required for this application. In this work, nanocomposites at high graphite nanoplatelets content (70 wt%) are fabricated by a spray deposition process on a polyetherimide (PEI) support. Experimental tests have been conducted to investigate the electromagnetic response of the material in the X band (8-12 GHz), showing an electrical conductivity of about 2.0 x 10^4 S/m. The design of the metasurface geometry and numerical simulations have been introduced that account for the electromagnetic properties of the material in the non-naturally frequency selectivity response under the mechanical strain in the X band.

1. Introduction

Chipless passive wireless sensors (CLPWs) are among the most important developments in wireless sensor technology. Their compactness combined with the unnecessity of battery or chip for their operation, make these sensors interesting in various fields, medical diagnostics, security, predictive maintenance, and environmental safety [1]–[3]. The recent progress in the materials field goes towards this development. Specifically, metamaterials and metasurfaces are very well-suited for telemetric sensing applications. They are collections of far-subwavelength resonating structures, typically aligned in a regular crystal lattice designed to interact with the free-space propagating electromagnetic waves. These resonators are designed to interact with the free-space propagating electromagnetic waves, rather than being excited directly by a waveguide or transmission line. Due to external perturbations, the spectral resonances can change, resulting in an intrinsic effective sensing mechanism.
Because the metamaterial properties typically depend on the shape, size, orientation, and proximity of the conducting elements, techniques that alter the geometry of the conducting elements can provide an excellent means for tuning or switching the metamaterial response [4]. Owing to their versatility, metasurfaces are currently proposed for several applications. In the recent literature, sensors for strain detection are found [5]–[8]. They are mostly based on shifting of frequency selective surfaces and are characterized by varied sizes and sensitivity. However, reversibility over cycling deformation is not

fully addressed in these preliminary works. For real applications strain sensing sensors based on metasurfaces would require elevated levels of stretchability other than high stretchability and should retain functionality even when being mechanically deformed.
The fabrication of metasurfaces can be complex especially when the periodic structure is not a simple pin or patch. Methods like drilling and milling are limited to simple structures [9]. Additive Manufacturing (AM) is a promising candidate to implement metasurfaces. The design flexibility combined with the possibility of employing a wide variety of materials makes this technique suitable for the rapid prototyping of strain sensors. 3D printed nanocomposite with metal nanofillers, such as silver nanowires (AgNWs) and nanoplatelets (AgNPs) are reported to exhibit the highest electrical conductivity of 10^5 S/m [10], [11], followed by carbon nanotubes (CNTs) (10^4 S/m) [12], [13] and graphene nanoplatelets (GNPs) (10^3-10^4 S/m) [14], [15]. However, this technique limits the electrical conductivity of nanocomposites due to the low content of conductive nanoparticles that can be added to the insulating polymer and produce samples with fraction-of-a-millimeter thicknesses. In this work, a spray deposition printing process is employed to produce thin GNPs/Epoxy nanocomposite coating with high electrical conductivity to be employed in the modelling and fabrication of strain-sensing metasurfaces.

2. Modeling sensor

The physical principle of the sensing mechanism is given by the shift of resonance frequencies due to strain. Design-level simulation provides metasurface geometries optimized for the specific mechanical strain detection, at the frequencies of interest, 10 GHz (X band). The proposed metasurface geometry can decouple surface strain components. Full-wave electromagnetic modelling is employed for optimization.

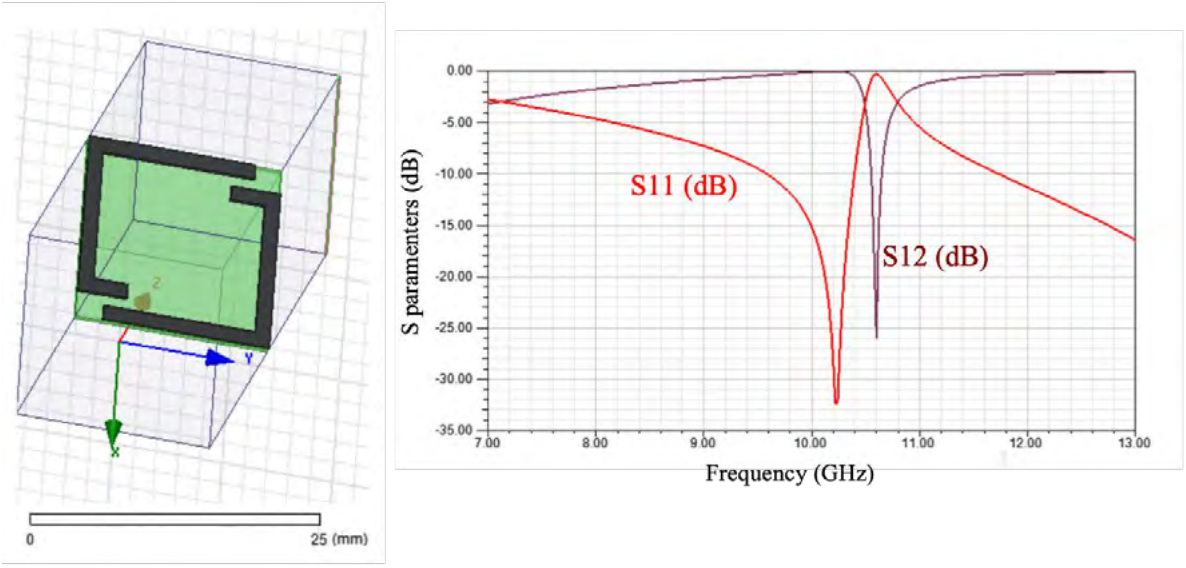


Figure 1. One quarter of metacell for the X band

The size of the unit cell, which is spatially repeated to form a metasurface, directly impacts the final size of the device. Figure 1shows an example of unit cell (only one quarter of metacell is shown for symmetry: metal and substrate are respectively 0.4 mm and 0.5 mm thick and have respectively conductivity 4*10^5 and permittivity 2.5) for the operation of the X band.
It is possible to verify, but it is not reported here for brevity, that a strain along x and y directions produces frequency shift of opposite signs. The above considerations assume metallic behavior of the nano-composite material used to define the resonant rings. It is noted that such assumption is well verified, at the considered frequency, for material conductivity exceeding 10^5 S/m. For a strain-detection able to simultaneously disentangle the x- and y-directed strain, the same principle physical mechanism as above can be used. A proper unit cell design allows adjusting their size to let them resonate at the desired frequency band and vice versa. Increasing the size of the unit cell design allows more than one

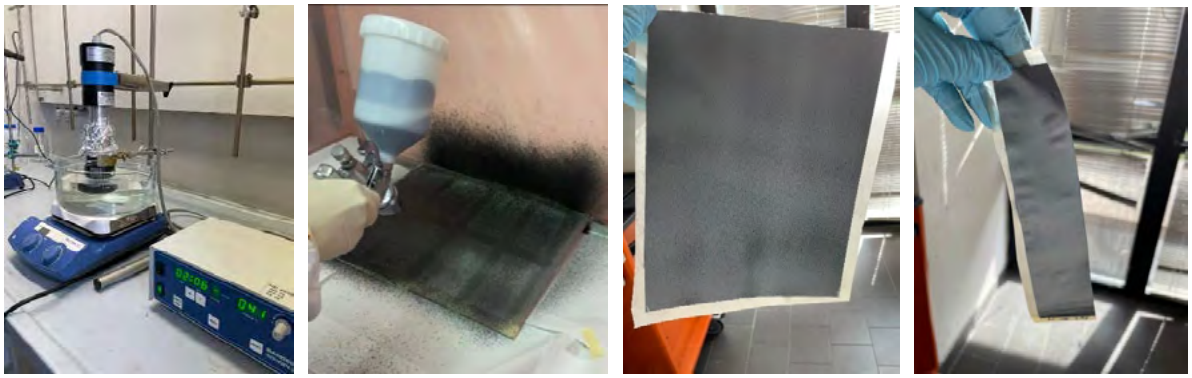
resonance to come into play, and places more than one zero and/or pole of the transfer function (reflection or transmission) close to each other, to achieve a specific frequency selectivity.

3. Materials production

Graphite nanoplatelets (GNP)/epoxy nanocomposite films have been fabricated with a top-down approach based on a spray deposition process. The GNPs used in this work have a large aspect ratio of 2143 with a lateral size of 30 μm and thickness of 14 nm (supplied by NANESA S.r.l). A three-component resin made of Bisphenol A diglycidyl ether (DGEBA) epoxy resin (ARALDITE® LY 3508), tetrahydro-methyl phthalic anhydride (THMPA) curing agent (ARADUR® 917-1) and 2,4,6-tris (dimethyl aminomethyl) phenol as the catalyst (Accelerator 960-1) was employed in this study, provided by Huntsman corporation. An epoxy mixture with a stoichiometric ratio between epoxy and acyls equal to 0.6 was employed. The substrate used is a polyetherimide film of 100 μm thickness (PEI, Toray Cetex TC1000).

The GNPs/Epoxy nanocomposite coating was deposited on the PEI support using a spray deposition process. Firstly, a dilute dispersion of GNPs in a volatile solvent (acetone) is prepared using a mass volume ratio of 1.4%. The nanoplatelets dispersion is performed using a high-power tip sonicator. Once the dispersion is homogeneous, the epoxy resin is added and further sonicated (Figure 2a). The obtained solution is deposited on the PEI film utilizing an airbrush mounted (Figure 2b). The deposited material is dried all night at room temperature to let the solvent evaporate (Figure 2c). Subsequently, the material is compacted with a calender to promote particle orientation and compactness, obtaining a coating with a metal finish (Figure 2d). Finally, the sample is cured according to the resin polymerization process for 1h30min at 120°C and post-cured for 1h at 140°C.

The thickness (t) of the samples is measured using a digital micrometer by subtracting the PEI substrate thickness of 100 μm. An average value of 13±3 μm is calculated based on several measure points over the area of the sample is considered.



(a) (b) (c) (d)

Figure 2 Steps of the fabrication process of GNPs/Epoxy nanocomposite supported on PEI support. (a) Dispersion of nanoplatelets by ultrasonication. (b) Spray deposition process by using an airbrush. Deposition on PEI substrate (c) prior calendering and (d) post calendering

The sheet resistance (R_{sheet}, Ω/sq) of the coating has been evaluated with a 4-probe system (Napson, Resistest-8A). An average value was obtained considering 5 measure points. The static electrical resistivity (ρ, Ωm) and conductivity (σ, S/m) are computed considering the thickness (t) of the sample, as follows:

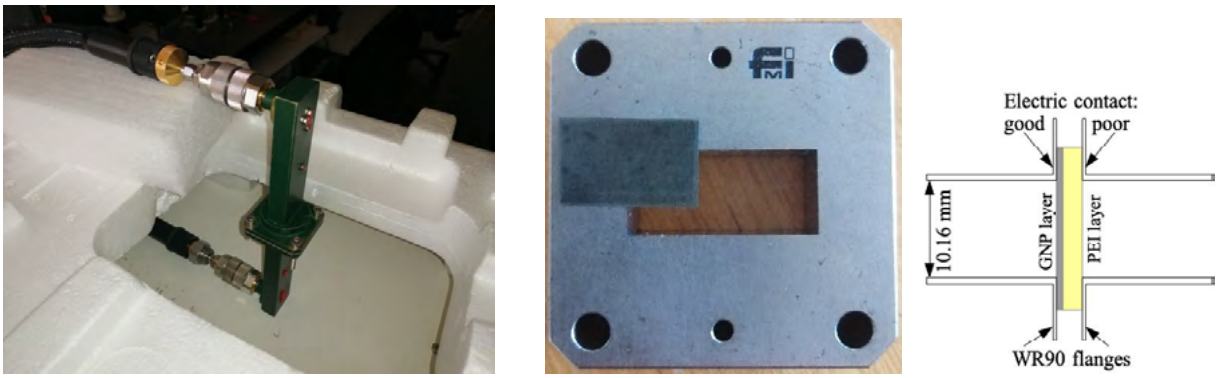
$$\rho = R_{sheet} \cdot t$$
$$\sigma = \frac{1}{\rho} \quad (1)$$

The conductivity (σ, S/m) as estimated by sheet resistance measurements is 2.05 x 10^4 S/m.

4. Electromagnetic Testing

The electromagnetic characterization of the GNPs/Epoxy nanocomposite in the X band (8-12 GHz) has been performed by putting a thin rectangular sample of the material in the cross section of a WR90 rectangular waveguide (22.86x10.16 mm^2) as shown in Figure 3. A Vector Network Analyzer (VNA) has been used to measure the scattering parameters of the sample. TLR calibration technique has been applied to define the reference planes for the scattering parameters at the connecting flanges in the center of Figure 3.

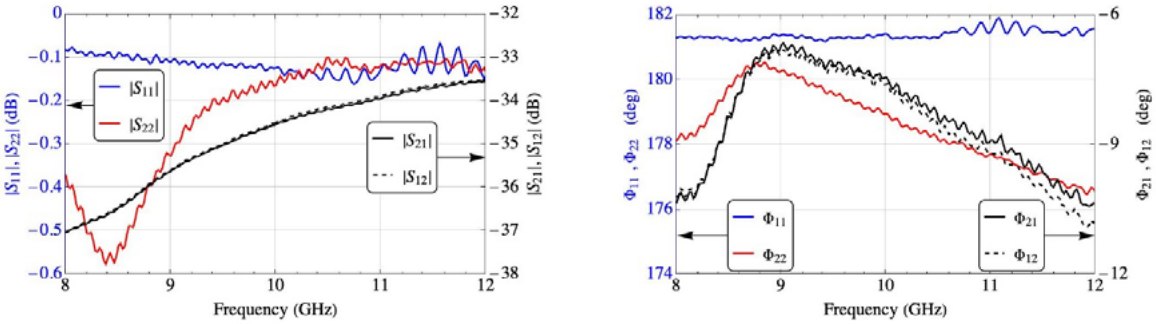
Hence, the scattering parameters S_{ij} shown in Figure 4 are exactly those measured to the left (port 1 of VNA) and to the right of the sample (port 2 of the VNA), in the empty waveguide.



(a) (b) (c)

Figure 3 (a) WR90 rectangular waveguides with the rectangular sample filling the cross section between the connecting flanges in the center of the image. (b) detail of the inner of the WR90 waveguide and a reduced piece of GNPs/Epoxy nanocomposite filling the cross section. (c) detail of the contact between the sample and the waveguide flanges (not in scale).

Amplitudes $|S_{11}|$ and $|S_{22}|$ and phases Φ_{11} Φ_{22} of the reflection coefficients at the two ports are slightly different because the sample is made by two different lossy material layers (the GNPs/Epoxy nanocomposite, d^{GNP}=13 µm thick, and the PEI support, d^{PEI}=100 µm thick) and the effect of the excitation from the two ports of the sample produce different reflections seen at the two ports. The measured amplitudes $|S_{12}|$, $|S_{21}|$ and phases Φ_{12}, Φ_{21} ensure a particularly good reciprocity of the composite medium both amplitude and phase. As a preliminary analysis, the amplitudes of the reflection coefficients are very close to 0 dB (less than –0.2 dB for $|S_{11}|$ and –0.6 dB for $|S_{22}|$) and their phases are close to 180° and these values imply that the composite material has high reflection property, similarly to an ideal conductor that is characterized by total reflection (0 dB amplitude and 180° phase). The differences between S_{11} and S_{22} in the lower part of the band are related to the fact that the wave impinging from the PEI port can flow also in the upper part of the metallic flange of the WR90 waveguide. In fact, the sample placed between the flanges is slightly larger than the cross section to ensure a flat placement between them when they are brought together and screwed. Unfortunately, this kind of placement and overlapping with the flange in the PEI port does not produce perfect electric contact between the PEI part of the sample (dielectric) and port that can cause the difference between S_{11} and S_{22}. On the contrary, electric contact between port 1 and sample is better because the GNP part of the sample is conductive.



(a) (b)

Figure 4 (a) Amplitude and (b) phase of the scattering parameters of the rectangular sample of the GNPs/Epoxy nanocomposite supported on PEI support**.**

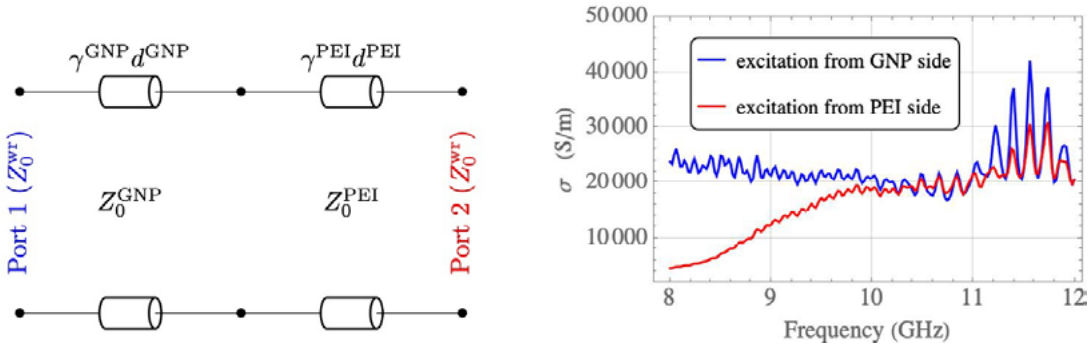
4.1. Electromagnetic properties estimation

The estimation of the conductivity of the GNPs/Epoxy nanocomposite can be obtained by the equivalent circuit shown in Figure 5(a). In fact, the two materials (GNPs/Epoxy nanocomposite and PEI) can be seen as two transmission lines characterized their modal impedance based on their conductivity σ and dielectric permittivity $\varepsilon=\varepsilon_0\varepsilon_r$ where ε_0 is the vacuum permittivity and ε_r the relative permittivity:

$$Z_0 = \frac{j\omega\mu}{\gamma} \tag{2}$$

$$\gamma = \sqrt{j\omega\mu_0(\sigma + j\omega\varepsilon_0\varepsilon_r) + \left(\frac{\pi}{a}\right)^2} \tag{3}$$

For the GNPs/Epoxy nanocomposite we can assume the hypothesis of good conductor which implies $\sigma \gg j\omega\varepsilon_0\varepsilon_r$. In Figure 4(a), $Z_0^{PEI}, Z_0^{GNP}, \gamma^{PEI}, \gamma^{GNP}$ refer to the modal impedance and propagation constant in the PEI or in the GNPs/Epoxy nanocomposite. Finally, Z_0^{wr} refers to the modal impedance of the empty WR90 waveguide, where the scattering parameters are measured and normalized. By the transmission line theory, we can calculate the theoretical value of the reflection coefficient seen at the two sides and by equating them to the experimental values we can extract an estimation of the conductivity of the GNPs/Epoxy nanocomposite, assuming ε_r=3.15 and $\frac{\sigma}{\omega\varepsilon_0\varepsilon_r} = 0.0013$ at 1 MHz for the PEI. The estimated values are shown in Figure 5(b) in the hypothesis of excitation from the GNP side (port 1, blue line) or the PEI side (port 2, red line).



(a) (b)

Figure 5 (a) Equivalent circuit of the GNPs/Epoxy nanocomposite supported on PEI. (b) Estimation of the conductivity of the GNPs/Epoxy nanocomposite.

The results in Figure 5(b), about the estimated conductivity of the GNPs/Epoxy nanocomposite, show a good agreement between the measurements made at the two ports of the sample. The differences in the lower part of the frequency band are related to the differences between S_{11} and S_{22}, as previously discussed.

4. Conclusions

This research serves as a significant starting step in the development of nanocomposite-based metasurfaces for structural health monitoring. The initial design of strain-sensitive resonant antenna reflectors has yielded important insights into the potential of this emerging technology to detect strain within the X-band frequency range (8-12 GHz) using chipless, passive, and wireless sensors. The modeling highlighted the importance of high conductivity for the successful operation of such metasurfaces as strain sensors.

A high electrical conductivity (approximately 20,000 S/m) was achieved using graphite nanoplatelets supported by a polyetherimide (PEI) dielectric film. The application of a spray deposition process to manufacture these nanocomposite layers proved to be an effective method for applying thin, uniformly conductive layers onto non-conductive substrates. This manufacturing technique is not only innovative but also scalable, making it suitable for widespread commercial use.

Acknowledgements

This research was supported by the PIANO NAZIONALE DI RIPRESA E RESILIENZA (PNRR) Missione 4 “Istruzione e Ricerca” - Componente C2 Investimento 1.1, “Fondo per il Programma Nazionale di Ricerca e Progetti di Rilevante Interesse Nazionale (PRIN)” Decreto Direttoriale n. 104 del 2 febbraio 2022 by Ministero dell’Università e della Ricerca, grant number PRIN2022M4LSK5_PE11, CUP B53D23008840006.

References

[1] V. V Kondalkar, X. Li, S. S. Yang, and K. Lee, "Towards a wireless chip less smart current sensor system based on giant magnetoresistance," in *2017 19th International Conference on Solid-State Sensors, Actuators and Microsystems* , IEEE, 2017, pp.1092–1095.

[2] G. Ponraj, W. L. Yeo, K. S. Kumar, M. S. Kalairaj, C. J. Cai, and H. Ren, "Chip-Less Wireless Sensing of Kirigami Structural Morphing Under Various Mechanical Stimuli Using Home-Based Ink-Jet Printable Materials," in *2021 IEEE International Conference on Robotics and Automation (ICRA)*, 2021, pp. 11400–11407. doi: 10.1109/ICRA48506.2021.9561945.

[3] G. Ponraj, C. Cai, and H. Ren, "Chip-Less Real-time Wireless Sensing of Endotracheal Intubation Tubes by Printing and Mounting Conformable Antenna Tag," *IEEE Robot. Autom. Lett.*, 2022.

[4] J. P. Turpin, J. A. Bossard, K. L. Morgan, D. H. Werner, and P. L. Werner, "Review Article Reconfigurable and Tunable Metamaterials: A Review of the Theory and Applications," 2014, doi: 10.1155/2014/429837.

[5] S.-D. Jang, B.-W. Kang, and J. Kim, "Frequency selective surface based passive wireless sensor for structural health monitoring," *Smart Mater. Struct.*, vol. 22, no. 2, p. 25002, 2012.

[6] E. C. Kinzel, K. M. Donnell, and K. Chandrashekhara, "Structural health monitoring and remote sensing of transportation infrastructure using embedded frequency selective surfaces.," Missouri University of Science and Technology. Center for Transportation …, 2014.

[7] Y. Yoo, H. Jeong, D. Lim, and S. Lim, "Stretchable screen-printed metasurfaces for wireless strain sensing applications," *Extrem. Mech. Lett.*, vol. 41, p. 100998, 2020.

[8] R. Melik, E. Unal, N. K. Perkgoz, C. Puttlitz, and H. V. Demir, "Metamaterial-based wireless strain sensors," *Appl. Phys. Lett.*, vol. 95, no. 1, p. 11106, 2009.

[9] P. Stuardo, F. Pizarro, and E. Rajo-Iglesias, "3D-Printed Sievenpiper Metasurface Using Conductive Filaments," *Mater. 2020, Vol. 13, Page 2614*, vol. 13, no. 11, p. 2614, Jun. 2020, doi: 10.3390/MA13112614.

[10] H. Wei *et al.*, "Direct 3D printing of hybrid nanofiber-based nanocomposites for highly conductive and shape memory applications," *ACS Appl. Mater. Interfaces*, vol. 11, no. 27, pp. 24523–24532, 2019.

[11] L. Rivière, A. Lonjon, E. Dantras, C. Lacabanne, P. Olivier, and N. R. Gleizes, "Silver fillers aspect ratio influence on electrical and thermal conductivity in PEEK/Ag nanocomposites," *Eur. Polym. J.*, vol. 85, pp. 115–125, 2016.

[12] V. Skákalová, U. Dettlaff-Weglikowska, and S. Roth, "Electrical and mechanical properties of nanocomposites of single wall carbon nanotubes with PMMA," *Synth. Met.*, vol. 152, no. 1, pp. 349–352, 2005, doi: https://doi.org/10.1016/j.synthmet.2005.07.291.

[13] R. Ramasubramaniam, J. Chen, and H. Liu, "Homogeneous carbon nanotube/polymer composites for electrical applications," *Appl. Phys. Lett.*, vol. 83, no. 14, pp. 2928–2930, 2003.

[14] V. B. Mohan, B. J. Krebs, and D. Bhattacharyya, "Development of novel highly conductive 3D printable hybrid polymer-graphene composites," *Mater. Today Commun.*, vol. 17, no. September, pp. 554–561, 2018, doi: 10.1016/j.mtcomm.2018.09.023.

[15] R. Taherian, "Experimental and analytical model for the electrical conductivity of polymer-based nanocomposites," *Compos. Sci. Technol.*, vol. 123, pp. 17–31, 2016, doi: 10.1016/j.compscitech.2015.11.029.

SUSTAINABLE GREEN COATING FOR NATURAL FIBERS: A FLAME RETARDANT APPROACH FOR PLA-BASED COMPOSITES

A. Pantaleoni[1], M.P. Bracciale[1], I. Bavasso[1], P. Russo[2], J. Passaro[2], L. Giorgini[3], G. Malucelli[4], A. Marrocchi[5], and F. Sarasini[1]

[1] Department of Chemical Engineering Materials Environment, Sapienza-Università di Roma, Via Eudossiana 18, 00184, Roma, Italy
alessia.pantaleoni@unieoma1.it ; mariapaola.bracciale@uniroma1.it ; irene.bavasso@uniroma1.it ; fabrizio.sarasini@uniroma1.it
[2] Institute for Polymers, Composites and Biomaterials, National Research Council, Via Campi Flegrei 34, 80078 Pozzuoli (Na) (Italy)
pietro.russo@ipcb.cnr.it ; jessica.passaro@ipcb.cnr.it
[3] Department of Industrial Chemistry "Toso Montanari", University of Bologna, Viale Risorgimento 4, 40136, Bologna, Italy
loris.giorgini@unibo.it
[4] Department of Applied Science and Technology, Politecnico di Torino, Viale Teresa Michel 5, 15121, Alessandria, Italy
giulio.malucelli@polito.it
[5] Department of Chemistry, Biology and Biotechnology, University of Perugia, Via Elce di Sotto 8, 06123, Perugia (Italy)
assunta.marrocchi@unipg.it

Keywords: biocomposites, phosphorous-based flame retardant, flax fiber, basalt fiber, fiber coatings

Abstract
This study presents a sustainable approach to enhance the fire resistance of natural fiber-reinforced poly(lactic acid) (PLA) composites. A bioinspired approach to functionalize the surface of flax (FF) and basalt (BF) fibers with an innovative organic-inorganic hybrid flame retardant (FR) is proposed. The fibers underwent a three-step coating method: first, ozone (O_3) pretreatment enhanced their surface reactivity by forming oxygen-containing functional groups that, in turn, enable the covalent immobilization of gallic acid (GA) units. Ultimately, inspired by the bacterial iron acquisition mechanism, iron phenylphosphonate was complexed with the phenolic groups of gallic acid units, resulting in FR-coated fibers. The coated flax and basalt fibers were used to produce PLA-based composite materials, named PLA/FF-FeP and PLA/BF-FeP, respectively. Thermogravimetric analysis (TGA) results revealed that, despite the low loading (0.1 wt% as assessed by Microwave Plasma Atomic Emission Spectroscopy - MP-AES) of the coating on the fiber surface, both composites exhibited improved thermal stability. The cone calorimetry test (CCT) highlighted an extended time to ignition (TTI), a reduced time to flame out, an 8% decrease in the peak of heat release rate (pHRR) and a 15% decrease in Fire Propagating Index (FPI) for PLA/BF-FeP. Further, the PLA/FF-FeP turned out to be smoke suppressant, showing a decrease in both total smoke release (TSR) and specific extinction area (SEA) of about 87 and, 68%, respectively.

1. Introduction

In recent years, increased awareness of environmental issues has prompted the implementation of various regulations, both locally and globally, aimed at directing industries toward reducing their environmental footprint and promoting the use of renewable materials [1,2]. In response, both industries and academic research are increasingly focusing on the development of high-performance

materials from renewable origin. In this context, natural fiber-reinforced biopolymers have emerged as a compelling sustainable alternative to traditional synthetic fiber reinforced polymer (FRP) composites [3]. Among the polymer matrices derived from renewable feedstock, poly(lactic acid) (PLA), a biodegradable aliphatic thermoplastic polyester, has received considerable attention [4]. Due to its unique characteristics such as high stiffness and transparency [5], PLA has found applications in various fields, from packaging to fiber production and composite manufacturing [6]. Numerous studies have focused on reinforcing PLA with plant fibers to obtain composites with a favorable combination of physical and mechanical properties [7]. The growing interest in these composites arises from their valuable properties, cost-effective production, and eco-friendly nature. Consequently, there is a growing demand for PLA composites reinforced with natural fibers in various industrial sectors such as construction and automotive. However, despite their merits, significant concern with biocomposite materials regards their limited fire resistance. Indeed, such biopolymers as PLA inherently exhibit high flammability, which intensifies fire propagation, notably through the generation of extended dripping [8]. Compared to synthetic reinforcing fibers, the incorporation of natural fibers significantly exacerbates their already poor fire resistance [9]. This shortcoming is an obstacle to the widespread commercial use of biocomposites, especially in the transportation sector, where fire safety regulations are stringent [10]. Therefore, the use of flame retardants (FRs) is essential to improve the flammability resistance of biocomposites. The predominant approach involves the direct incorporation of FRs into the polymer matrix [11,12]. However, this method frequently leads to compromised mechanical properties and leaching of the FR due to the inherent low compatibility between the two components [13]. An alternative strategy involves the direct grafting of the FR onto the surface of the reinforcing fiber. This approach avoids FR leaching and mitigates the "candlewick effect" induced by the higher thermal conductivity of the fibers as compared to the polymer matrix [14]. This method finds primary application in composites reinforced with plant fibers, exploiting their functional groups to facilitate the bonding of appropriate FRs [15].
The proposed study introduces a bioinspired protocol for the surface modification of flax fiber (FF) and basalt fiber (BF) with a halogen-free phosphorus-based hybrid FR specifically tailored for flame retardant applications in PLA-based biocomposites. FF and BF fibers were selectively chosen considering their different surface reactivity properties. Ozone (O_3) was selected as a safe oxidizing agent for fiber pretreatment to enhance surface chemical reactivity by forming hydroxyl and carboxyl groups for BF and FF, respectively. The new surface functional groups were exploited for the covalent immobilization of renewable gallic acid (GA) units. Subsequently, taking inspiration from the bacterial enterobactin-mediated iron acquisition mechanism [16], iron phenylphosphonate was complexed to the GA phenolic groups. The modified fibers were thoroughly characterized using Fourier transform infrared spectroscopy (FT-IR), thermogravimetric analysis (TGA), scanning electron microscopy coupled with energy-dispersive X-ray spectroscopy (SEM-EDS) and microwave plasma atomic emission spectroscopy (MP-AES). The FR-coated fibers were used as reinforcement in PLA-based composites, with fire resistance assessed through cone calorimetry tests (CCT); further, the mechanical properties were preliminarily evaluated.

2. Materials and Methods

2.1 Fiber coating

A Salinovo ozone generator, air-fed with a maximum diffusion rate of 0.5/h, was employed for fibers ozonization. 20g of fibers were placed in a 500 cm^3 ozonation chamber. The treatment lasted for a maximum of 7 hours. Gallic acid (GA) (34 g, 0.2 mol) and thionyl chloride (100 mL, 0.9 mol) were introduced into a dried single-necked flask. The reaction mixture was heated to 80 °C for 3 hours. After the reaction time, excess $SOCl_2$ was removed under vacuum. Crude galloyl chloride (36.9 g) obtained was dissolved in tert-Amyl methyl ether (TAME) (270.6 g, 2.6 mol) to yield a 12% (w/w) mixture. 30g of fibers were immersed in the mixture and stirred for 2 hours. The resulting sample was washed with H_2O and dried. 36 g of GA-functionalized fibers were mixed with 520 mL of deionized water in a beaker. 130 mL of $FeCl_3 \cdot 6H_2O$ (0.82 g, 3 mmol) aqueous solution was added. After stirring, PPA (0.96 g, 6 mmol), previously dissolved in 130 mL of H_2O, was added dropwise over 6 hours. The

reaction proceeded at room temperature for 12 hours. The resulting iron phosphonate-coated fibers were washed with H_2O and dried [17].

2.2 Composite Manufacturing

The composites were fabricated using Brabender-like equipment (Rheocord EC, Haake Inc.) and a lab hydraulic press (Collin model P400E) to create 100 mm × 100 mm × 4 mm plates. The fibers were mixed with PLA using a micro compounder set at 60 rpm and 180 °C for 5 minutes. Subsequently, the PLA composites were compression-molded at 180 °C with a pressure profile of 2 min at 0 bar, 1 min at 5 bar, 1 min at 10 bar, and 1 min at 20 bar. The cooling down to room temperature was performed while maintaining the material at the maximum pressure of 20 bar. The fiber content was set at 20 wt%. The composite specimens suitable for tensile tests were prepared via injection molding (Haake MiniJet II Pro, Thermo Fisher Scientific) with the loading cylinder at 190 °C and the temperature mold set at 45 °C.

2.3 Characterization techniques

Fourier Transform Infrared spectra were acquired with a Bruker VERTEX 70 spectrometer equipped with an attenuated total reflectance diamond (ATR) cell. The spectra were recorded in the mid-infrared region (400-4000 cm^{-1}) collecting 128 scans, with a resolution of 4 cm^{-1}. The morphology of the fiber surface was examined with a Field Emission Scanning Electron Microscope (FE-SEM) coupled with Energy Dispersive Spectroscopy (EDAX). Micrographs were acquired on a Tescan Mira3 system at 10 kV after having sputtered the samples with chromium. Thermogravimetric analysis was performed with an SDT-Q600 thermoanalyzer (TA Instruments) in a nitrogen atmosphere (100 mL/min) with a heating rate of 10 °C/min from room temperature to 800 °C. Differential scanning calorimetry (DSC) analysis was conducted using a DSC 250 calorimeter (TA Instruments) with high-purity nitrogen flowing at 40 mL/min and heating and cooling rates of 10 °C/min. Detection of iron content on FR-coated fibers was carried out with an MP-AES 4210 instrument. Tensile tests were carried out on a Zwick/Roell Z010 universal testing machine in accordance with ISO 527-2.
The fire behavior was evaluated utilizing an oxygen consumption cone calorimeter (CCT) (Fire Testing Technology Limited FFT Cone Calorimeter model and Noselab instrument (Nova Milanese, Italy) following the ISO 5660 standard.

3. Results

3.1 FR-coated fibers characterization

The effectiveness of O_3 pretreatment in the surface functionalization of flax fibers (FF) with carboxylic groups and basalt fibers (BF) with -OH groups was checked through FT-IR analysis. Pretreated FF showed a new signal at 1731 cm^{-1} associated to carboxylic C=O stretching [18], while BF exhibited new absorptions at 3365 cm^{-1} and 1637 cm^{-1}, attributed to adsorbed water and Si-OH stretching, respectively [19]. TGA analysis of the ozonated FF indicated a marginal decrease in the lignin degradation temperature, attributed to O_3 improved reactivity toward phenols and polyphenols [20]. Pretreated BF exhibited increased weight loss between 200 and 300 °C, likely due to the depletion of surface hydroxyl groups [21]. FT-IR analysis of the fibers, following functionalization with GA units, revealed signals corresponding to O-H stretching of the phenolic ring, C-C stretching of the aromatic ring, C-O stretching, and O-H bending. These signals confirm the presence of GA units bound to the surface of both fibers [22]. The successful functionalization is further corroborated by a noticeable morphological change observed on the fiber surface, as depicted in SEM micrographs (Figure 1). In Figures 1b and 1e, the previously clean and smooth surface of the untreated fibers (Figure 1a and 1d) is replaced by a new rough layer, attributed to the immobilization of GA units. The phenolic groups of GA units were then exploited for iron phenylphosphonate complexation. SEM analysis of the resulting coated fibers (Figures 1c and 1f) revealed the occurrence of a distinct globular coating on the fiber surface. EDS analysis confirmed the presence of phosphorus (P) and iron (Fe), validating that the material adhered to the fiber was indeed iron phenylphosphonate. MP-AES analysis revealed an iron loading of 0.1 wt% on both coated fibers, indicating a reduced amount but significant complexation of Fe^{III}-gallic acid units on their surfaces. TGA analysis of FR-coated BF showed two

distinct stages of weight loss occurring in temperature ranges of 170-270 °C and 270-400 °C, respectively. The 1.8 wt% decrease in the lower range is attributed to the decomposition of gallic acid units [23] and phenyl moiety of FR complex, while the 5.4 wt% reduction at higher temperatures is ascribed to the breakdown of C-C, C-H, and C-P bonds present in the structure of the phenylphosphonic units [24]. FR-coated FF exhibited a maximum decomposition rate temperature (T_{max}) of 309 °C, which is lower than that of untreated FF (354 °C), and a second degradation step in the temperature range from 400 °C to 520 °C. This can be attributed to the presence of the FR complex; the shift to lower T_{max} temperatures is ascribed to the degradation of gallic acid and phosphonate phenyl moieties, which degrade at about 250-260 °C. Subsequently, the iron phenylphosphonate undergoes a secondary stage of thermal degradation at temperatures above 420 °C, associated with the decomposition of the organic constituents of the coordination complex and/or dehydration of the H_2PO_4 and HPO_4 groups formed during the thermal degradation process [25].

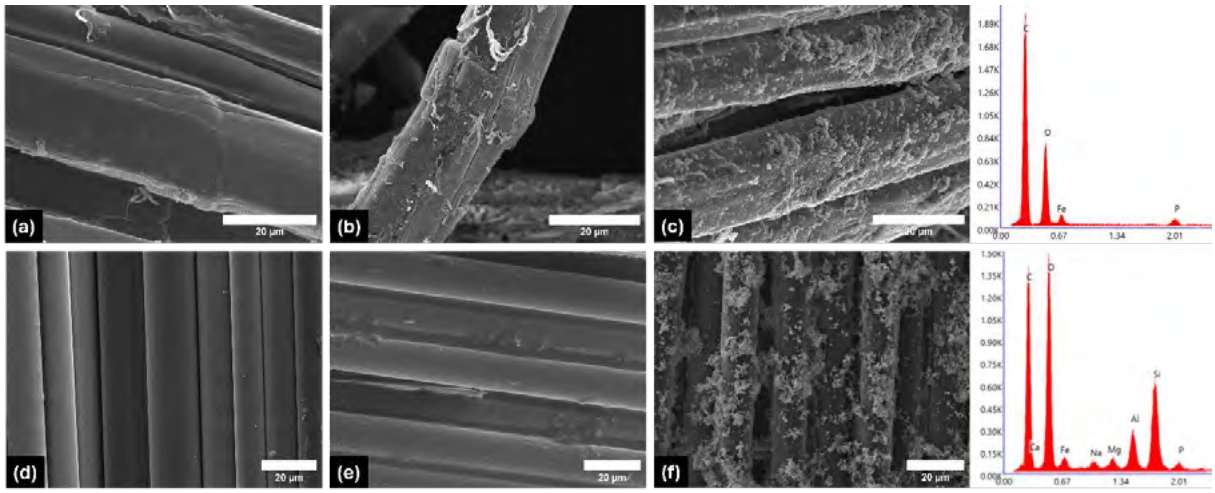


Figure 1. SEM-EDS analysis of (a) neat FF, (b) GA unit-functionalized FF, (c) FR-coated FF, (d) neat BF, (e) GA unit-functionalized BF and (f) FR-coated BF

3.2 PLA-based composites characterization

Fibers coated with the developed flame retardant (FR) complex were employed as reinforcement for fabricating PLA-based composites. Both composites reinforced with coated fibers (PLA/FF-FeP and PLA/BF-FeP) and those reinforced with uncoated fibers (PLA/FF and PLA/BF) were subjected to thermal characterization. The PLA/BF composite exhibited a temperature corresponding to 5% weight loss ($T_{5\%}$) at about 328.5 °C, a temperature for 10% weight loss ($T_{10\%}$) at approximately 338.7 °C, and a maximum decomposition temperature (T_{max}) of roughly 358.1 °C. Conversely, PLA/BF-FeP demonstrated slightly higher temperatures, with values of about 337.8 °C, 345.1 °C, and 365.6 °C for $T_{5\%}$, $T_{10\%}$, and T_{max}, respectively. A marginal increase in temperature was also observed for PLA/FF-FeP compared to PLA/FF. Specifically, PLA/FF recorded $T_{5\%}$, $T_{10\%}$, and T_{max} values at roughly 308.4 °C, 319.4 °C, and 350.9 °C, while PLA/FF-FeP showed slightly higher readings at approximately 318.8 °C, 331.3 °C, and 359.1 °C, respectively. Therefore, despite the low load on the fiber surface, the developed coating appears to be promising for improving the thermal stability of PLA composites.
DSC analysis revealed a peak of cold crystallization temperature (T_{cc}) at about 118.8 C for PLA/FF-FeP and approximately 119.8 °C for PLA/FF. Conversely, no significant differences were observed between PLA/BF and PLA/BF-FeP. To gain deeper insights into the impact of the flame retardant on the thermal properties of the composite, DSC analyses were performed by incorporating the as-synthesized iron phenylphosphonate into neat PLA at a concentration of 1 wt.% (PLA-FeP). The results revealed a reduction in T_{cc} for PLA-FeP (about 111.0 °C) compared to neat PLA (about 115.2 °C), as well as a

significant 65% increase in the degree of crystallinity. This suggests that the FR complex promotes the nucleation phase of the PLA crystallization process.

Cone calorimetry tests were conducted on the composites to evaluate the flame-retardant properties of the developed FR coating complex. PLA/FF-FeP compared to PLA/FF exhibited a slight increase in time to ignition (TTI), a 7% reduction in the peak heat release rate (pHRR), and, most significantly, a remarkable reduction in both specific extinction area (by about 68%) and total smoke released (87%), hence highlighting the high smoke suppressant activity exerted by the treated fiber. In addition, a reduction of 15% in the Fire Propagating Index (FPI = pHRR/TTI ratio) was recorded. When comparing PLA/BF-FeP to PLA/BF, a slight increase in TTI was observed, along with reductions of 13%, 8%, and 14% in the time to flame out, pHRR, and FPI, respectively. Despite its minimal presence on the fiber surface, the designed FR coatings acted as high efficient flame retardants. Finally, some preliminary tensile tests were conducted to assess the impact of FR coating on the mechanical properties of the composites. PLA/FF-FeP and PLA/BF-FeP exhibited a 5% and 17% reduction in tensile strength, respectively, compared to PLA reinforced with the corresponding untreated fibers. This decrease may be attributed to the presence of the organic-inorganic hybrid coating, potentially acting as a stress concentrator [26]. Furthermore, the non-uniform distribution of the coating on the fiber surface might have exacerbated this effect. Conversely, PLA/FF-FeP and PLA/BF-FeP exhibited an increase in stiffness by 15% and 8%, respectively. This finding is likely to be due to the enhancement of fiber stiffness resulting from the presence of the hybrid coating, thereby leading to an increased Young's modulus for the composite. Further characterizations are needed to validate these hypotheses.

4. Conclusion

A sustainable method of coating basalt and flax fibers with an organic-inorganic hybrid flame retardant has been successfully devised. This bioinspired coating process facilitates the immobilization of iron phenylphosphonate on the fiber surface, utilizing moderate reaction temperatures and eco-friendly solvents such as TAME and H_2O. Comprehensive characterization analyses including SEM-EDS, FT-IR, TGA, and MP-AES attest to the efficacy of the coating process, confirming the successful grafting f the flame retardant onto the fiber surface.

The incorporation of these coated fibers into PLA-based composites resulted in improvements in thermal stability and flame retardancy, despite the low loading of the FR coating on the fiber surface. Cone calorimetry tests revealed such improvements as a slight increase in Time to Ignition (TTI), a 5% reduction in Peak Heat Release Rate (pHRR), and substantial decreases of 87% in Total Heat Release (THR) and 68% in Smoke Evolution Area (SEA) for PLA/FF-FEP. Similarly, PLA/BF-FeP exhibited an extended TTI, reduced flame out time, an 8% decrease in pHRR, and a 15% decrease in Fire Propagation Index (FPI) compared with neat fiber-reinforced composite.

However, PLA reinforced with FR-coated fibers showed a decrease in tensile strength compared to the counterparts reinforced with unmodified fibers, likely due to the effect of the hybrid complex that could act as a stress concentrator. Nonetheless, an increase in Young's modulus suggests a potential influence of FR coating on fiber stiffness.

Acknowledgments

Financed by the European Union - NextGenerationEU (National Sustainable Mobility Center CN00000023, Italian Ministry of University and Research Decree n. 1033 - 17/06/2022, Spoke 11 - Innovative Materials & Lightweighting).

References

[1] A. Hejna, Renewable, Degradable, and Recyclable Polymer Composites. *Polymers*, 15(7): 1769, 2023.

[2] C. Böhringer. The Kyoto protocol: a review and perspectives. *Oxford Review of Economic Policy*, 19(3): 451-466, 2003.

[3] G. Rajeshkumar, S.A. Seshadri, G-L. Devnani, M.R. Sanjay, S. Siengchin, J.P. Maran, A.R. Anuf. (2021). Environment friendly, renewable and sustainable poly lactic acid (PLA) based natural

fiber reinforced composites–A comprehensive review. *Journal of Cleaner Production*, 310:127483, 2021.

[4] P. McKeown, M. D. Jones. The Chemical Recycling of PLA: A Review. *Sustainable Chemistry*, 1(1): 1–22, 2020.

[5] A. Sudamrao Getme, B. Patel. A Review: Bio-fiber's as reinforcement in composites of polylactic acid (PLA). *Materials Today: Proceedings*, 26:2116-2122, 2020.

[6] R. Siakeng, M. Jawaid, H. Ariffin, S. M. Sapuan, M. Asim, N. Saba. Natural fiber reinforced polylactic acid composites: A review. *Polymer Composites*, 40(2): 446-463, 2029

[7] M. N. M. Azlin, S. M. Sapuan, R. A. Ilyas, E. S. Zainudin, M. Y. M. Zuhri. Natural Polylactic Acid-Based Fiber Composites: A Review. *Advanced Processing, Properties, and Applications of Starch and Other Bio-based Polymers*, 21–34, 2020.

[8] W. S. Chow, E. L. Teoh, J. Karger-Kocsis. Flame retarded poly(lactic acid): A review. *Express Polymer Letters*, 12(5): 396-417, 2018.

[9] M. W. Chai, S. Bickerton, D. Bhattacharyya, R. Das. Influence of natural fibre reinforcements on the flammability of bio-derived composite materials. *Composites Part B: Engineering*, 43(7): 2867-2874, 2012.

[10] N. K. Kim, S. Dutta, D. Bhattacharyya. A review of flammability of natural fibre reinforced polymeric composites. *Composites Science and Technology*, 162: 64-78, 2018.

[11] F. Shukor, A. Hassan, M. Saiful Islam, M. Mokhtar, M. Hasan. Effect of ammonium polyphosphate on flame retardancy, thermal stability and mechanical properties of alkali treated kenaf fiber filled PLA biocomposites. *Materials and Design*, 54: 425-429, 2014.

[12] L. Shumao, R. Jie, Y. Hua, Y. Tao, Y. Weizhong. Influence of ammonium polyphosphate on the flame retardancy andmechanical properties of ramie fiber-reinforced poly(lactic acid) biocomposites. *Polymer International*, 59(2): 242-248, 2010.

[13] C. Yargici Kovanci, M. Nofar, A. Ghanbari. Synergistic Enhancement of Flame Retardancy Behavior of Glass-Fiber Reinforced Polylactide Composites through Using Phosphorus-Based Flame Retardants and Chain Modifiers. *Polymers (Basel)*, 14(23): 5324, 2022.

[14] K. E. Decsov, B. Ötvös, T. T. T. Nguyen, K. Bocz. The Effect of Cellulose Fibre Length on the Efficiency of an Intumescent Flame Retardant System in Poly(lactic acid). *Fire*, 6(3): 97, 2023.

[15] D. P. Ferreira, J. Cruz, R. Fangueiro. Surface modification of natural fibers in polymer composites. *Green Composites for Automotive Applications*, 3-41, 2018.

[16] K. N. Raymond, E. A. Dertz, S. S. Kim. Enterobactin: An archetype for microbial iron transport. *Proceedings of the national academy of sciences,* 100(7): 3584-3588, 2003.

[17] A. Pantaleoni, F. Sarasini, P. Russo, J. Passaro, L. Giorgini, I. Bavasso, M.L. Santarelli, E. Petrucci, F. Valentini, M.P. Bracciale, A. Marrocchi. Facile and Bioinspired Approach from Gallic Acid for the Synthesis of Biobased Flame Retardant Coatings of Basalt Fibers. *ACS omega*, 9(17): 19099–19107, 2024.

[18] B. Fathi, M. J. Harirforoush, Mr. R. Foruzanmehr, S. Elkoun, M. Robert. Effect of TEMPO oxidation of flax fibers on the grafting efficiency of silane coupling agents. *Journal of Materials Science*, 52(17): 10624-10636, 2017.

[19] S. H. Kim, S. M. Park, S. J. Park. Role of dry ozonization of basalt fibers on interfacial properties and fracture toughness of epoxy matrix composites. *Nanotechnology Reviews*, 10(1): 710-718, 2021.

[20] Y. Rosen, H. Mamane, Y. Gerchman. Short Ozonation of Lignocellulosic Waste as Energetically Favorable Pretreatment. *Bioenergy Research*, 12(2): 292-301, 2019.

[21] L. Zhang, V.U. Kiny, H. Peng, J. Zhu, R.F. Lobo, J.L. Margrave, V.N. Khabashesku. Sidewall functionalization of single-walled carbon nanotubes with hydroxyl group-terminated moieties. *Chemistry of Materials*, 16(11): 2055-2061, 2004.

[22] I. Mohammed-Ziegler, F. Billes. Vibrational spectroscopic calculations on pyrogallol and gallic acid. *Journal of Molecular Structure*, 618(3): 259-265, 2002.

[23] Z. Aytac, S. I. Kusku, E. Durgun, T. Uyar. Encapsulation of gallic acid/cyclodextrin inclusion complex in electrospun polylactic acid nanofibers: Release behavior and antioxidant activity of gallic acid. *Materials Science and Engineering C*, 63: 231- 239, 2016.

[24] P. Bhanja, K. Ghosh, S. S. Islam, A. K. Patra, S. M. Islam, A. Bhaumik. New Hybrid Iron Phosphonate Material as an Efficient Catalyst for the Synthesis of Adipic Acid in Air and Water. *ACS Sustainable Chemistry & Engineering,* 4(12): 7147-7157, 2016.

[25] B. Bujolv, P. Palvadeau, J. Rouxel. Synthesis of New Lamellar Iron(III) Phosphonates," *Chemistry of Materials*, 2: 582-589, 1990.

[26] Z. Cao, C. Ren, Z. Wang. Copper phenyl phosphonate for epoxy resin and cyanate ester copolymer with improved flame retardancy and thermal properties. *e-Polymers*, 23(1):20230004, 2023

CRASHWORTHINESS PERFORMANCES OF AN INNOVATIVE CYLINDRICAL TRI-AXIAL BRAIDED CARBON FIBER COMPOSITE

Riccardo Piani[1], Alessandro Polla[1], Fukun Xia[2], Dong Ruan[2], Giacomo Frulla[1], Enrico Cestino[1], Guoxing Lu[2], Pier Marzocca[3]

[1]Politecnico di Torino, c.so Duca degli Abruzzi 24, Turin, 10129, Italy
Email: riccardo.piani@studenti.polito.it, alessandro.polla@polito.it, giacomo.frulla@polito.it, enrico.cestino@polito.it
[2]School of Engineering, Swinburne University of Technology, Hawthorn, Victoria, 3122, Australia
Email: fxia@swin.edu.au, druan@swin.edu.au, glu@swin.edu.au
[3]RMIT University, Melbourne, Victoria, 3000, Australia
Email: pier.marzocca@rmit.edu.au

Keywords: Crashworthiness, Triaxial braided composites, Energy absorption, Dynamic crush testing, CFRC tubes

Abstract
The following article presents an experimental investigation into the crashworthiness performance of an innovative tri-axial braided carbon fiber reinforced composite (CFRC) cylinder under dynamic crush loading. Two different test methods were employed, a drop tower test and a very high-speed (VHS) machine test, using both flat and conical impactors. The specimens were manufactured via a novel resin infusion process directly onto the mandrel utilized for the braided process, avoiding any damages to the dry fibers. For each test configuration, the Specific Energy Absorption (SEA), peak load, steady-state crushing load, and Crushing Efficiency (CE) were evaluated and compared against literature data. The flat impactor resulted in higher energy absorption due to fiber fragmentation but lower CE from a high initial peak load. Conversely, the conical impactor exhibited higher CE from smoother load initiation but lower energy absorption dominated by friction and delamination mechanisms. Braided architecture has demonstrated SEA values consistent with the literature while providing higher CE than comparable unidirectional laminates, suggesting the suitability of this architecture for crashworthy applications. However, the contrasting impactor results highlight the need to carefully consider prioritizing either high energy absorption or low peak acceleration for the specific design scenario.

1. Introduction

Industrial interest in carbon fiber reinforced composites (CFRP) for energy-absorbing crashworthy structures is increasing rapidly [1]. Their excellent specific strength, and specific stiffness, among other mechanical properties, are essential for offsetting the structural weight of primary aircraft structures.
Design specifications and standards impose specific limits on the maximum allowable accelerations experienced by vehicle occupants during a crash [2][3]. The use of composite materials allows the designers to have a greater ability to tailor the specific reinforcement direction to control the high initial peak force, thus accelerations experienced during impact, and allow the structure to get into a steady-state crushing phase, through energy absorption [4].

The complex failure modes of composite materials during crushing allow for a much higher energy absorption; while plastic deformation is the main energy absorption mechanism in metallic specimens, multiple failure modes contribute significantly in composites, including transverse shearing (fiber kinking), lamina bending, local buckling, friction between plies, and delamination. Generally, the first two dominate during brittle fracture behaviors [4][5][6].

Crushing is defined as the material characteristic of continuously absorbing energy through fragmentation and destruction [7]. A series of parameters need to be introduced to evaluate the crushing performances of these structures. These include the Specific Energy Absorption (SEA), the Peak Force, the Steady-State Force, and the Crushing Efficiency (CE) just to name but a few.

This work utilizes a tubular specimen produced with a tri-axial braided architecture via Resin Infusion (RI) to assess the crushing behavior and capabilities of the selected geometry and novel fiber architecture.
It has been proven that closed-section geometries have beneficial effects on crushing performance, hence the specific specimen geometry chosen is in this fashion.
This is thanks to the stacking sequence of the hoop fibers that constrain the axial fibers preventing them from splaying, suppressing the propagation of the crush front, and increasing the energy absorption capabilities [8].

The choice of braided fiber architecture is due to its ascending interest inside the aerospace sector to realize primary structural components such as wing flaps, horizontal stabilizer, and fuselage [9]. This architecture resembles a combination of filament winding and weaving that shows a mechanical interlock between fiber yarns, suggesting higher energy absorption capabilities [9]. The ascent of this textile is mainly driven by the possible reduction in production costs due to the possibility of process automation in textile weaving and placing. The architecture is composed of two sets of yarns placed at +60° and -60° degrees and an axial fiber bundle placed at 0°. A specific repetitive unit cell (UC) is obtained [10]; the UC has to follow specific rules of ratios and dimensions, which will be presented later on.
Two different types of test scenarios have been considered. The first scenario simulates a crush with a drop tower where the initial velocity is known, energy is absorbed during the crush, and the drop weight decelerates until the mass reverses its motion. The second scenario analyzed aims to simulate the absence of inertia, maintaining a constant velocity throughout the crushing. The crushing stroke is fixed and given as an input parameter. Moreover, for each of the two testing machines, two different impactors are employed, the first being a flat plate and the second being a conical plug impactor.

For each test performed, a total of 4 samples have been evaluated, so that any variance in experimental data could be analyzed. To maintain statistical consistency, each sample has been produced following the same methodology and under the same environmental conditions. A set of control tests was implemented to strictly follow the manufacturing process, such as infusion time, amount of resin utilized, environmental temperature during infusion, vacuum bag drop tests before infusion, etc. Finally, all the samples were tested using a non-destructive, X-ray CT scan to ensure porosity control and avoid manufacturing defects.

2. Speciment design and manufacturing

The test specimen is a cylinder; its dimensions have been chosen to avoid buckling failure modes, namely, the inner diameter is 50 mm, and the height is 120 mm. The layup consisted of 3 braiding layers with an equivalent stratification of a weaved $[+60°/0°/-60°]_3$, resulting in an average wall thickness of 2.5 mm. An inner 45° chamfer has been machined and used as triggering geometry on one end of the samples. The material system utilized was a Grafil 34-700 12k and 24k carbon fiber tow and a KineTix R118-H103 epoxy resin system.

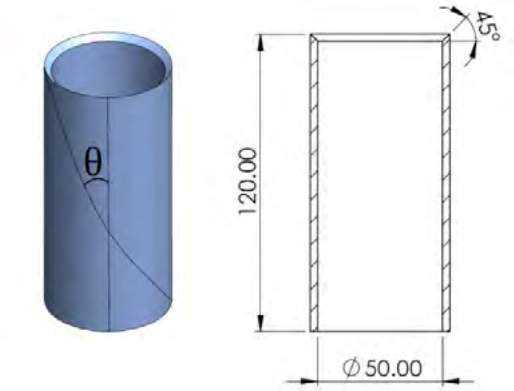


Figure 1. CAD model of the specimen design (dimensions in [mm])

A Herzog RF 1/48-100 radial machine and a Kuka 6-axis robotic arm were used to weave the specified material geometry. The machine has 48 radial bobbins, split into two groups, that spin in opposite directions while interweaving each other. A total of 24 axial bobbins are installed radially on the outer diameter of the specified machine. The radial bobbins are loaded with the 12k carbon fiber tow, while the axial ones with the 24k tow. During the braiding process, two main parameters were controlled: axial speed and rotational speed. The first one is the velocity at which the robotic arm pushes the mandrel into the machine; the second one is the rotational speed of the radial bobbins around the inner diameter of the Herzog. These parameters are strongly related to the diameter of the mandrel and lead to different wrapping angles of the angled tows, resulting in different levels of fiber compaction. In this specific case, the angle and the diameter were set as requirements, and different pairs of speeds were tested. The final speed parameters chosen were 0.0115 m/s for the axial speed and 100 rpm for the rotational speed.



Figure 2. Herzog RF 1/48-100

These two parameters enabled the definition of a repetitive unit cell (UC) [11] comparable to what can be found in the work of Littell et al [10], with similar proportion on both the height-to-width of the cell and the angle of +60° and -60° of the radial fibers.

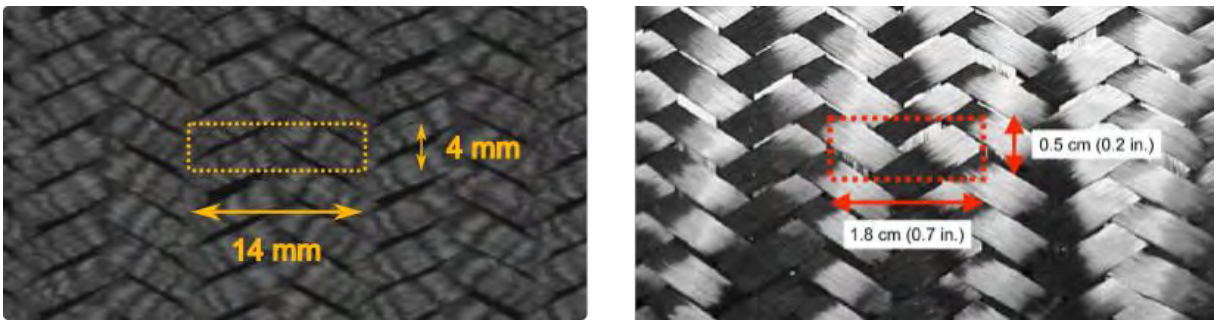


Figure 3. Comparison between the obtained UC (left) and Littell UC (right)

The braiding process described is commonly done by interwinding yarns onto a mandrel.
However, in the case of this study, the mandrel acted also as the mould to allow for a direct resin infusion of the dry fiber architecture. This innovative approach ensured superior mechanical characteristics because it avoided the need to move or cut the fibers from the mandrel to prepare the preform. Figure 4 shows the mould design realized for this scope. It is composed of 4 segments, called sectors, that create the circumferential shape of the cylinder. These segments are held in place by two rims, placed at each end of the mould.



Figure 4. Mould design - Exploded view

This design was then mounted onto the robotic arm and was pushed through the braiding machine. Since the braiding textile design has the 24k tows running in the axial direction, overlapping each braid on top of the other would create a nervature deposition of the fibers (as seen in Figure 5, on the left). To mitigate this phenomenology, every braid layer was deposed onto the previous one with a rotational offset to allow an even deposition of the 24k tows (in Figure 5, right picture).

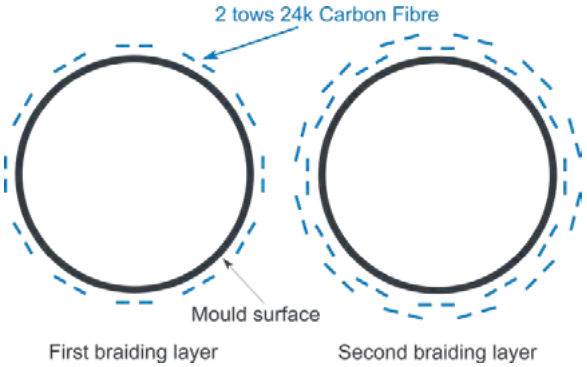


Figure 5. 24k tow deposition onto the mould

Once the preform was laid onto the mould, the consumables needed for the resin infusion process were applied and the component infused.
The resin infusion process employed is a modified SCRIMP. For this specific application, a self-adhesive PTFE-coated fabric sheet was applied onto the mould before braiding, to prevent excessive resin from filtering through the different mould sectors and to give a uniform finish on the inner diameter of the cylinders. The PTFE layer was also needed for an easier demoulding of the final component. After the deposition of the braid layers, peel-ply was added, and then the flow media was specifically cut to reduce resin front flow speed and allow for an even and slow infusion. The vacuum bag design was an envelope bag: one vacuum bag runs on the inner side of the mould and the second one runs on the outer part. The two bags are then sealed at each end with tacky tape. The cylinder was infused vertically, with the resin inlet on the bottom and the venting port on the top. The infusion process was about 40 minutes long, including a 10-minute stop after the tap opening. This allowed for the air contained in the inlet tube to be evacuated correctly, restoring the initial vacuum integrity. Before infusion, the vacuum bag

was inspected with a vacuum drop test for 1 hour; requirements prescribe a pressure drop lower than 0.05 bar to consider the test passed.
To have more vacuum integrity and control over the process, the component once ready to be infused was placed into an oven at 40° C to allow for air expansion and easier evacuation by the vacuum pump. This reduces even more the possibility of having porosity inside the final sample.



Figure 6. Vacuum bag setup

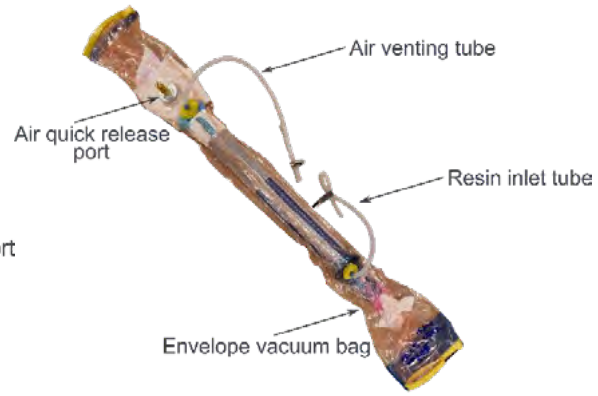


Figure 7. Process layout

Once the curing cycle was completed at ambient temperature, post-curing was necessary; this peaks at a temperature of 90°C for 8 hours. After that, the mould was disassembled and the carbon fiber cylinder was extracted. From each of the produced cylinders, it was possible to extract 3 samples. Each sample was cut to specification employing a water-cooled diamond disk saw. The trimmed sides were then lightly sanded to eliminate the trimming imperfections that occurred during the cut.

After production, each component was weighed and, before testing, specimen quality was assured by CT scanning each sample and checking for porosity, unwanted inclusions, and unexpected premature delamination. No observable defects have been found in the tested samples.
With the formulation found in [9], it was possible to calculate the mean volume fraction of the produced samples. This shows a mean fiber fraction volume of 0.55, compatible with a standard CFRP structure. Tables 1 and 2 show the weighted samples ready for testing. From every cylinder produced, the 3 samples obtained were progressively numbered to retrieve their characterization information. During tests, the specimens have been randomly selected amongst the aforementioned list, in order to avoid the possibility of false behavior due to potential production errors in specific batches.

Table 1. Sample weight for Drop tower

	Production cylinder #	Weight [g]		Production cylinder #	Weight [g]
BR_DF01	9	68,35	BR_DC01	16	67,46
BR_DF02	1	66,71	BR_DC02	13	68,83
BR_DF03	15	67,77	BR_DC03	8	67,74
BR_DF04	10	66,26	BR_DC04	3	66,78

Table 2. Sample weight for VHS

	Production cylinder #	Weight [g]		Production cylinder #	Weight [g]
BR_VF01	5	67,35	BR_VC01	14	68,13
BR_VF02	12	64,51	BR_VC02	7	68,25
BR_VF03	2	66,70	BR_VC03	11	66,67
BR_VF04	4	66,45	BR_VC04	6	64,69

3. Experimental method

The US Department of Defense (DoD) mandates precise criteria for crashworthy structures, as outlined in MIL-STD-1290A (Military Standards 1290A) [2]. This standard stipulates that airframes must be designed to withstand a minimum vertical impact speed of 8 m/s. Concurrently, other works on braided structures [12], performed impact tests with velocities ranging from 7.21 to 8.51 m/s using the same geometry specimen but in different sample sizes. Those tests were carried out using braided T700S 12K fiber tows and PR520 resin system.
In this particular study, the designated test speed was set at 6 m/s, determined by the maximum energy absorption capabilities of the tested samples. Establishing the permissible energy, allowed for the calculation of parameters crucial for energy determination, namely, the height and total mass of the impacting hammer. While maintaining constant energy, reducing the weight allows for a greater dropping height and, thus, higher initial crushing velocity. However, due to equipment limitations, the minimum weight that could be dropped was ≈ 50 kg. This restricts the drop height to around 1.8 m. The limitation to 6 m/s is then matched onto the Instron 8800 as testing speed, to obtain a comparable value of crushing speed in both test setups.
The crushing speed, coupled with the sample dimensions already provided, showcases a strain rate of 60 s^{-1} which can be considered a mid-high strain rate test and can be compared with other crushing strain rates as reported in the available literature [12][13].

In both test setups, a 3D High-speed DIC (Digital Image Correlation) system is implemented to capture the displacements during crushing. This system uses 2 Phantom cameras, one being a V2640 and the other being a V2512 model. Both cameras use a Nikon AF 24-85mm f/2.8-4 D IF, and are set to 85 mm and f/8 aperture with an exposure time set to 2.5 µs. The frame rate utilized is 35000 fps with frame resolution set to 768x768 pixels. DIC results are not presented in the context of this preliminary analysis.

3.1. Drop tower

A drop weight test rig was utilized to perform the impact, using two different impactors: a conventional flat plate and a conical impactor. For both scenarios, the total impactor mass was around 50 kg (see Table 3 for details), while the drop height was set equal to 1.83 m. With this data, an impact velocity of approximately 6 m/s and an impact energy of almost 900 J were measured. A laser gate system was used to check the correct height for each drop. A load cell with a range of 100 kN was used to capture the impact loads. A digital oscilloscope was used to acquire the displacement data during crush.
The samples were kept in position by a steel support that allowed the cylinders to be fit into position. Figure 8 shows the experimental setup designed for the drop tower.
To correctly capture the images of the crush, the exposure value seen on the camera must be close to 0 EV. As a result, the light needed was provided by 3 Godox SL200// lights at maximum power and two additional high-beam LED lights.



Figure 8. Steel support

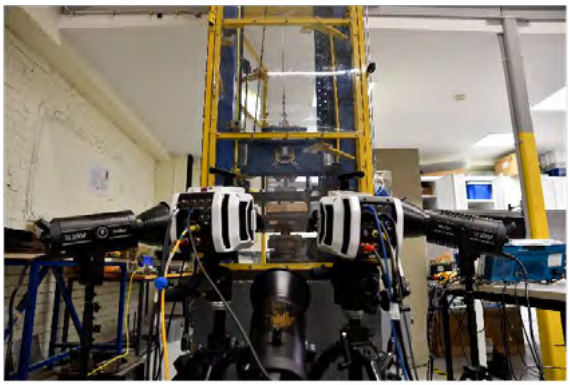


Figure 9. Drop Tower setup

3.2. Very-High speed machine (VHS)

The use of a drop tower will inevitably demonstrate the effect of the deceleration of the impacting mass, as it initially possesses a notable velocity that decreases as the cylinder collapses, absorbing energy. However, a test in which this inertial effect is removed can demonstrate different behaviors of the structure, and must, therefore, be investigated. In this scenario, depicted in Figure 10 and Figure 11, an Instron 8800 very high-speed (VHS) machine was programmed to maintain a constant speed of 6 m/s during the whole crushing stroke. A total crushing displacement of 50 mm was set as input into the machine with an additional displacement of ≈ 20 mm to allow the machine to come to a full stop after the crushing stroke. This experimental setup can reveal the effect that would occur during a crush if the tested component were mounted on an airframe or structure that needs to be protected during an accident. In such a scenario, the airframe (or structure) mass would be significant enough that an immediate deceleration during the collapse would not be observed, unlike in the drop tower tests.

In this setup, the specimen was held in place with a clamping mechanism in which the sample hung from the top, and the crushing head was pushed from the bottom up. All the needed crushing parameters have been provided by the program written into the machine (such as displacement function, crushing speed function, load function, etc).
Compared to the setup used in the drop tower, the camera layout for the high-speed recording in the VHS machine showed some differences: the illumination was provided by 3 high beam LED lights put inside the safety enclosure of the machine, mounted using 3 magic arms that ensure their fine-tuning positioning.

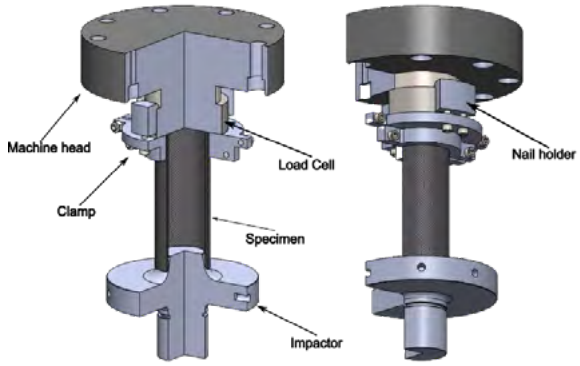


Figure 10. VHS Specimen support



Figure 11. VHS setup

Table 3. Testing setups and machine parameters

	Drop Tower		VHS	
	Conical impactor	Flat impactor	Conical impactor	Flat impactor
Active mass	49,96 kg	49,935 kg	∞	∞
Dropping height	1,83 m	1,83 m	N/A	N/A
Nominal speed	6 m/s	6 m/s	6 m/s	6 m/s
Nr of samples	4	4	4	4

4. Results and analysis

4.1. Crush performances results

Multiple values can be calculated to evaluate the performances of a specific sample geometry and textile architecture during a crush: peak crushing load, steady-state crushing load, specific energy absorption, and crushing efficiency, to name a few.
Among these, the most significant are the energy absorption (or the specific energy absorption), and the peak force, because they are directly correlated to the protective performances. Best practice design requires high energy absorption and low peak force to represent the ideal scenario in a crushing absorption system. Crushing efficiency is classically introduced to represent optimal design performances, it is the ratio between the peak force, which is the highest force measured during crush,

and the steady-state force, which is the mean force at which the crush continues unfolding after the initial trigger is consumed and the passing of the peak force[13].

$$CE = \frac{F_{SS}}{F_{Peak}} \tag{1}$$

The crushing efficiency is helpful to define whether the crush has been characterized by a catastrophic failure or if the crush itself was effective. The first situation is characterized by high peak force and little steady state force (low CE), while the second shows high energy absorbed and a CE close to the unity [14]. The latter is the optimal design scenario in the case of a crush-absorbing structure.
Another design parameter is the Specific Energy Absorption (SEA), which is defined as the energy absorption divided by the mass of the structure, namely the area under the force/displacement curve, divided by the mass of the collapsed structure. The resultant collapsed mass can be defined as the linear density of the structure, ρ_{lin}, multiplied by the crushed displacement, δ.

$$SEA = \frac{\text{Energy absorbed}}{\text{Mass of the collapsed structure}} = \frac{\int_{X_{start}}^{X_{end}} F\,dx}{\rho_{lin} \cdot \delta} \tag{2}$$

These data are presented in Table 4 for better clarity and organization.

Table 4. Testing results

	Drop Tower		VHS	
	Conical impactor	Flat impactor	Conical impactor	Flat impactor
Peak load [kN]	15.16	38.85	15.94	42.88
Steady-state load [kN]	5.33	20.29	12.68	31.49
SEA [J/g]	11.38	41.48	21.74	56.03
CE [-]	0.35*	0.53*	0.80	0.73
Displacement [mm]	79.69	42.07	48.27	57.85

**CE data regarding the Drop Tower have been calculated for completeness. Although, without a steady-state crushing force, the resulting test data do not hold any significance.*

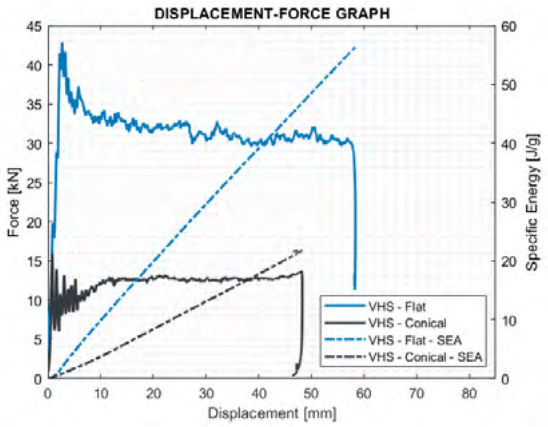


Figure 12. VHS Force - Displacement results

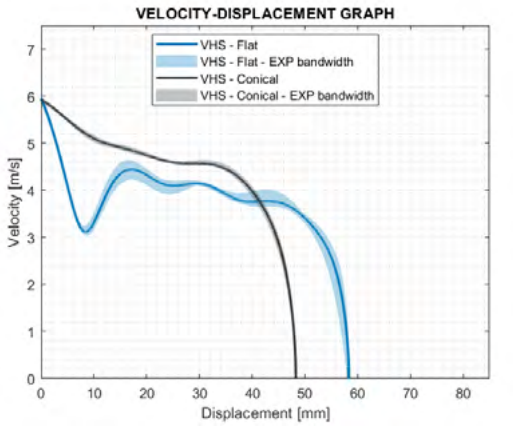


Figure 13. VHS Velocity - Displacement results

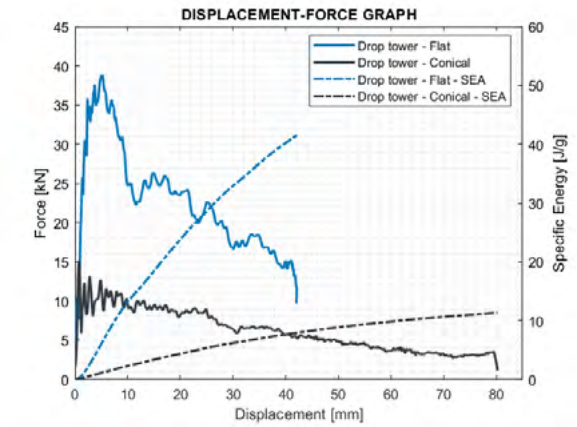


Figure 14. Drop tower Force - Displacement results

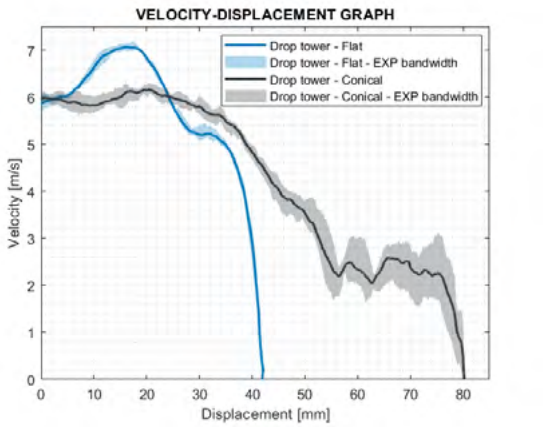


Figure 15. Drop tower Velocity - Displacement results

4.2. Crushing efficiency

The experimental crushing of cylinders using a flat impactor on the VHS reveals a Crush Efficiency (CE) of 0.73. This finding aligns with the literature data available from Pereira et al. [12], who conducted experimental testing on triaxial braided cylindrical samples, and shows higher CE in comparison to Reuter et al. work [7], who performed similar experimental testing using unidirectional $[90_2/(0_2/45_2/\text{-}45_2)_2]_s$ layup carbon-epoxy prepreg. The correspondence with Pereira et al. work suggests that the experimental crushing conducted has been successful, and the collapse of the cylinders has occurred in a manner consistent with an energy-absorbing structure, while it also shows better performances over unidirectional quasi-isotropic lamination of the braided architecture in reducing peak forces during impact scenarios.

If the obtained crushing efficiency of the conical plug and the flat plate impacts on the VHS is compared, the conical impactor has shown a higher CE, reaching a value of 0.80; this is because of the lower peak force at the beginning of the impact on the samples. The reduced peak force is strictly correlated with the easier breaking initiation given by the shape of the impactor. In this case, there is no need to crush an initial amount of material before the activation of the plies delamination of the cylinders, since this is immediately activated by the specific shape of the impactor.

4.3. Peak load and steady-state load

The peak load shows an interesting correlation between the drop tower and VHS test methods, suggesting that the initial crushing speed was, in fact, similar. After the erosion of the triggering geometry, the peak load should not differ under the same impactor geometry, given the same initial impact speed. Regarding the steady-state crushing force, the values differ quite significantly (more than twice the magnitude for the conical impactor and 50% for the flat impactor). This is expected, since in the drop tower scenario there is significant deceleration, while this does not occur for the VHS.

4.4. Specific energy absorption discussion

The Specific Energy Absorption (SEA) extracted from the VHS tests shows a good correlation with available literature data. Work by Pereira et al. [12] calculated a SEA of ≈ 59.5 J/g, with an uncertainty of ±2 J/g. Under similar testing conditions and impactor geometry, the present work found a SEA of 56.03 J/g, suggesting the two energy values are comparable.
Differences were found when the conical impactor was employed, with literature data finding ≈ 34.5 J/g, while this work extracted 21.74 J/g. However, in this scenario, the conical impactor geometry plays a major role in the crushing behavior of the specimen, and, without being able to define the differences between the two impactor geometries, further analysis is not possible.

Regarding the drop tower data, the calculated SEA values show a similar trend to that found for the VHS tests. Available literature data from McGregor et al. [15] shows a good correlation with the flat impactor,

although the test specimen geometry differs. With the use of the conical plug impactor, the literature data findings show the same trend of magnitude reduction but with different values.

4.5. Fracture morphology analysis

The data presented in Table 4 yield several noteworthy observations. When subjected to the flat impactor crush, the material experienced a crushing failure characterized by both internal and external material displacement within the tube. This resulted in the distortion of the fiber braid and failures across the bias, 60°, and -60° tows, as well as along the axial fibers, leading to fiber kinking as a principal failure mechanism (an inter-fiber rupture phenomenon characterized by a shear rupture[4][12][14]. Fiber kinking mechanism leads to the formation of fragmentation debris that are being compacted together, creating a debris wedge. Figure 16 shows the crushing continuation, with the debris wedge pushing the inner hoop layers internally, causing compressive microfractures while, at the same time, the outer hoop is pushed externally, with the continuous instauration of tensile forces that lead the outer hoop to fracture. This is necessary as the cylinder has to expand while the splaying mode is unfolding.

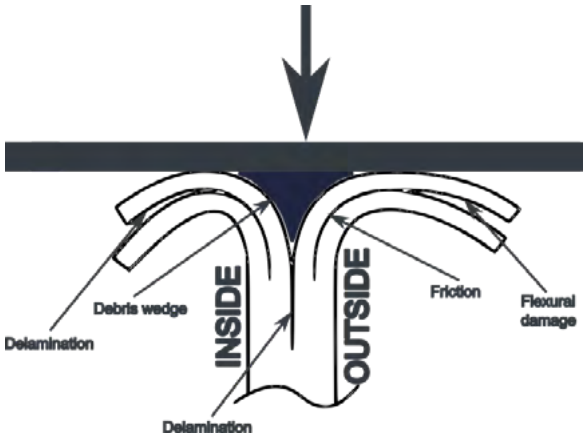


Figure 16. Flat impactor crushing morphology (source [15])

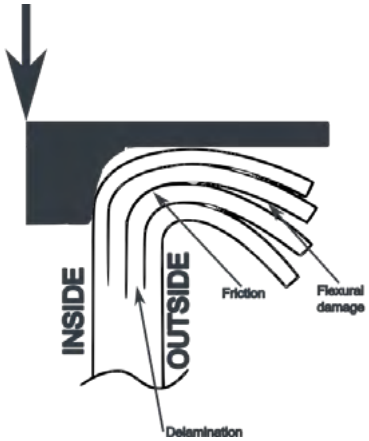


Figure 17. Conical impactor crushing morphology (source [15])

Fiber kinking phenomenon happens because of a reduced curvature radius at the front of the crushing platen where the biaxial fibers lock the axial ones from splaying. At some point, this curvature radius will be so small that the axial fibers have to undergo a shear fracture.

In Figure 17 the failure mechanism of a conical impactor crush is presented. This induces a failure mode wherein all crushed material is predominantly pushed radially outward, forming fronds of uniform width. Notably, this mode led to severe failures of the bias tows but with reduced fragmentation and fewer failures along the axial fibers. In the absence of a debris wedge, the axial fibers tend to be pushed outward with the biaxial hoop fibers that are constraining this splaying from happening. In this scenario, friction and delamination between laminae are the two principal fracture mechanisms that absorb energy, with the absence of the debris wedge compressive and friction forces[4][12][14].
Although this crush behavior is stable, a significantly lower overall force level was obtained when compared to the flat impactor. Conical impactor resulted in a reduction of the initial peak force values typically observed with this impactor in crush experiments. This lower force level also correlated with the reduced SEA threshold of the specimens, likely attributed to diminished fiber fragmentation during the crushing events.
Figures 18 illustrate two examples of crushed cylinders with the VHS, one with a flat impactor and the other with a conical impactor. The left image clearly shows how fragmentation has affected the sample impacted with the flat plate, with the material being pushed both inward and outward. The two detailed views allow for a clear understanding of the debris wedge created due to the material fragments being compacted while the crushing was happening. The sample crushed with the conical plug exhibits a predominantly outward push of the material, resulting in a radial-symmetrical fracture opening. In the

case of the conical impactor, the bias fiber breaking is much more severe (highlighted in the detailed view), with little to no rupture of the axial fibers, which leads them to a splaying mode outward.

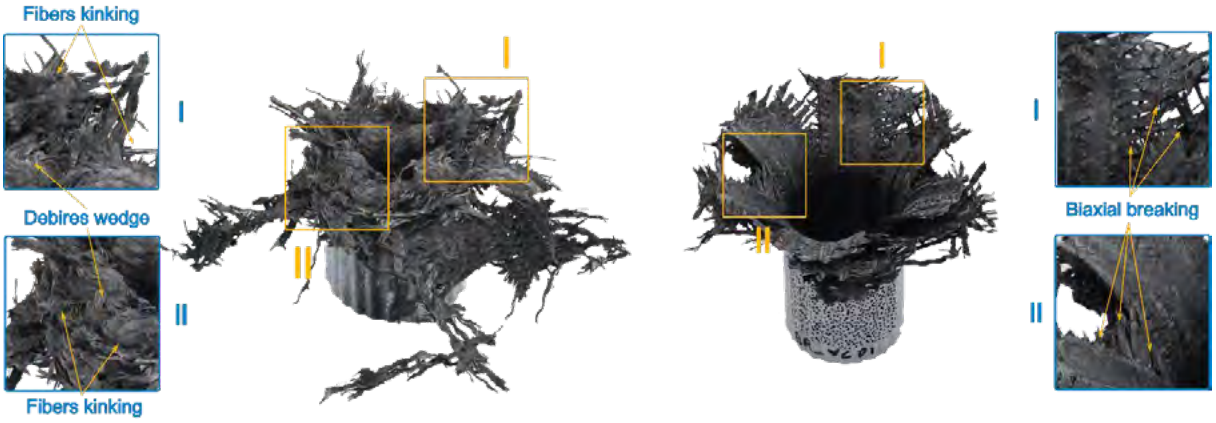


Figure 18. Flat (left) vs conical (right) impacted samples on the VHS

The drop tower test results, depicted in Figure 14, show the differences between using flat and conical plug impactors. Similar to the VHS tests, the flat impactor exhibits a much higher initial peak force compared to the conical impactor. However, in these drop tower tests, the force does not maintain a constant crushing value indicative of progressive crushing. Instead, it tends to reduce as the displacement increases. This is due to the deceleration of the impacting mass, as the energy absorption phase consumes the impactor's velocity during the crush event [15][16].
An important observation is the total displacement of the two different impactors. In these tests, the displacement indicates the portion needed to dissipate all the impactor's kinetic energy (which results almost identical for both impactors) before it comes to a stop or rebounds. A smaller displacement means the sample has a high energy absorption rate, which is desirable for an energy absorption structure. A larger displacement suggests the energy-dissipating mechanisms were less effective. This result suggests a similar energy-absorbing behavior to what was revealed in the VHS tests.

Figure 12 represents the VHS force-displacement diagram for the investigated braided cylinders impacted with a flat impactor and a conical impactor, in blue and black respectively; the dashed line represents the two different specific energy absorption lines vs the crushing displacement.
The velocity vs time diagram produced with the VHS depicted in Figure 13 shows that the speed had not been maintained constant as required by the experimental setup. The inability of the VHS machine to do so could be attributed to multiple reasons; the first could be attributed to the fact that the machine was working on the upper limit of its maximum load capacity, peaking at 45 kN over 60 kN load cell capacity; the second could be related to the data filtering set in place for the data cleanup.
Although the velocity was not constant to 6 m/s as expected, an interval of constant speed, to a lower value, has been established. This velocity value is ≈ 4 m/s for the flat impactor and ≈ 5 m/s for the conical impactor. This constant interval led to a constant crushing load onto the force-displacement graph, which is sufficient to make the necessary considerations regarding an impact at constant velocity.

5. Conclusions

Experimental testing on carbon fiber reinforced composite (CFRC) braided cylinders was conducted using two different test methods and impactor's design.
Experimental results with the flat impactor demonstrated high energy absorption compared to the conical impactor results. However, this setup resulted in lower crushing efficiency due to a higher initial peak force. Characteristic fracture mechanisms such as fiber kinking, fiber fragmentation, and interlaminar delamination surfaces have been observed in a post-impact analysis of crushed composite cylinders with the introduced flat impactor. Conversely, the conical impactor test results revealed lower peak forces and higher crushing efficiency, resulting in a reduced overall energy absorption compared with flat impactor tests. The observed reduction in energy absorption was primarily attributed to less

effective energy-absorbing mechanisms such as interlaminar delaminations and friction between adjacent composite plies compared to the main fracture mechanisms previously characterized.

As experimentally observed, VHS tests avoid the immediate deceleration and velocity reduction that is instead observed in the drop tower tests. This allows for the characterization of the material crushing performances undergoing a progressive crushing scenario.

The study also explored whether the braiding architecture could serve as a crashworthy structure capable of efficiently absorbing energy and maintaining a stable collapse phase during high-energy impacts. Findings showed that braided architectures' specific energy absorption and crushing efficiency are comparable with existing literature on similar crush absorbers and exhibit higher CE if compared to unidirectional structures, confirming their potential for impact scenarios. Nonetheless, the varied performance in SEA and CE with different impactors suggests that the specific requirements of the intended application should dictate the choice between optimizing for energy absorption or minimizing peak force.

References

[1] B. G. Falzon and W. Tan, “Virtual Testing of Composite Structures: Progress and Challenges in Predicting Damage, Residual Strength and Crashworthiness,” in *The Structural Integrity of Carbon Fiber Composites*, pp. 699–743.
[2] “MIL-STD-1290A, MILITARY STANDARD: LIGHT FIXED AND ROTARY WING AIRCRAFT CRASH RESISTANCE,” Sep. 1988.
[3] “JSSG-2010-7, Departement of Defence Joint Service specification guide - crew systems crash protection handbook. US Department of Defence,” 2002.
[4] D. Hull, “A unified approach to progressive crushing of fibre-reinforced composite tubes,” *Compos. Sci. Technol.*, vol. 40, no. 4, pp. 377–421, Jan. 1991, doi: 10.1016/0266-3538(91)90031-J.
[5] S. Mantovani, M. Cavazzuti, E. Torricelli, and P. Fabbri, “Lightweight crash energy absorber design using composite materials,” May 2011.
[6] C. Bisagni, G. Pietro, L. Fraschini, and D. Terletti, “Progressive crushing of fiber-reinforced composite structural components of a Formula One racing car,” *Compos. Struct.*, vol. 68, pp. 491–503, May 2005, doi: 10.1016/j.compstruct.2004.04.015.
[7] C. Reuter, K.-H. Sauerland, and T. Tröster, “Experimental and numerical crushing analysis of circular CFRP tubes under axial impact loading,” *Compos. Struct.*, vol. 174, pp. 33–44, Aug. 2017, doi: 10.1016/j.compstruct.2017.04.052.
[8] P. Feraboli, B. Wade, F. Deleo, and M. Rassaian, “Crush energy absorption of composite channel section specimens,” *Compos. Part Appl. Sci. Manuf.*, vol. 40, no. 8, pp. 1248–1256, Aug. 2009, doi: 10.1016/j.compositesa.2009.05.021.
[9] A. D. Kelkar and J. D. Whitcomb, “Characterization and Structural Behavior of Braided Composites,” Technical report DOT/FAA/AR-08/52, Jan. 2009.
[10] J. D. Littell, W. K. Binienda, G. D. Roberts, and R. K. Goldberg, “Characterization of Damage in Triaxial Braid Composites Under Tensile Loading,” NASA/TM-2009-215645, May 2009. Accessed: Jan. 19, 2024. [Online]. Available: https://ntrs.nasa.gov/citations/20090023169
[11] C. Sorini, A. Chattopadhyay, R. K. Goldberg, and L. W. Kohlman, “Development of a Subcell Based Modeling Approach for Modeling the Architecturally Dependent Impact Response of Triaxially Braided Polymer Matrix Composites,” NASA/TM-2016-219116, Jul. 2016. Accessed: Jan. 19, 2024. [Online]. Available: https://ntrs.nasa.gov/citations/20160009767

[12] J. M. Pereira, B. Strohminger, N. Pini, C. Ruggeri, and S. Miller, "Dynamic Crush Performance of Thermoplastic and Resin Infused Thermoset Triaxially Braided Composite Structures," *Am. Soc. Compos. ASC 38th Annu. Tech. Conf.*, Sep. 2023.
[13] L. N. S. Chiu *et al.*, "Crush responses of composite cylinder under quasi-static and dynamic loading," *Compos. Struct.*, vol. 131, pp. 90–98, Nov. 2015, doi: 10.1016/j.compstruct.2015.04.057.
[14] G. L. Farley and R. M. Jones, "Crushing Characteristics of Continuous Fiber-Reinforced Composite Tubes," *J. Compos. Mater.*, vol. 26, no. 1, pp. 37–50, Jan. 1992, doi: 10.1177/002199839202600103.
[15] C. McGregor, R. Vaziri, and X. Xiao, "Finite element modelling of the progressive crushing of braided composite tubes under axial impact," *Int. J. Impact Eng.*, vol. 37, no. 6, pp. 662–672, Jun. 2010, doi: 10.1016/j.ijimpeng.2009.09.005.
[16] D. E. Sommer, D. Thomson, O. Falcó, G. Quino, H. Cui, and N. Petrinic, "Damage modelling of carbon fibre composite crush tubes: Numerical simulation and experimental validation of drop weight impact," *Compos. Part Appl. Sci. Manuf.*, vol. 160, p. 107033, Sep. 2022, doi: 10.1016/j.compositesa.2022.107033.

INVESTIGATION OF BASALT FIBRE FIBRE-REINFORCED EPOXY COMPOSITES USING STAR-LIKE POLYMERS

Rochele Pinto[1]*, Tatjana Glaskova-Kuzmina[1], Vladimir Spacek[2], Marie Novakova[2], and Daiva Zeleniakiene[1]

[1]Department of Mechanical Engineering, Kaunas University of Technology, Kaunas, Lithuania
Email: rochele.pinto@ktu.edu, tatjana.glaskova-kuzmina@ktu.lt, daiva.zeleniakiene@ktu.lt
[2]SYNPO a.s., Pardubice, Czech Republic
Email: vladimir.spacek@synpo.cz, marie.novakova@synpo.cz
*Corresponding author (rochele.pinto@ktu.edu)

Keywords: basalt fibre, star-like polymer, mechanical properties

Abstract
The study investigates the effect of star-like polymers on basalt fibre-reinforced plastic (BFRP) composites. Basalt fibres are chosen for their lower emissions and cost-effectiveness compared to alternatives like glass or carbon fibres, but they lack good adhesion with the matrix, which affects mechanical performance. The research entails mixing different weight percentages of star-like poly(n-butyl methacrylate)-(glycidyl methacrylate) block copolymer into a biobased matrix and reinforced with basalt fibres. Mechanical tests such as dynamic mechanical analysis, tensile, impact, and fracture toughness, were conducted to evaluate the influence of the star-like polymers on the composite's performance. The study demonstrated that adding star-like polymers enhanced the mechanical properties of BFRP specimens, making them comparable to conventional composites. Scanning electron microscopy was performed to help visualise the interlaminar damage caused post mechanical testing.

1. Introduction

Basalt fibres and its properties have been increasingly researched as industries have now been focusing on the development of sustainable composites. Basalt fibres are produced with lower emissions and cheaper in cost in comparison to its counterparts. Furthermore, basalt fibre-reinforced plastic (BFRP) composites demonstrate remarkable resilience to acids, and other corrosive substances, thermal stability, prolonging the lifespan of fibre-reinforced plastics (FRPs) in outdoor settings in contrast to carbon and glass fibre-reinforced plastics (CFRP and GFRP) [1]. The bond between the matrix and fibre is crucial for enabling efficient stress transfer and achieving superior mechanical properties. Star-like polymers have shown to improve adhesion and impact energy absorbing capabilities within carbon fibre reinforced polymer laminate due to a bridging effect [2].

The aim of this study is to investigate the effect of star-like poly(n-butyl methacrylate)-(glycidyl methacrylate) block copolymer on the properties of BFRP. Different wt.% ranging between 0 and 7% are employed to check the influence on addition of the polymer. Dynamic mechanical analysis (DMA) and tensile tests on epoxy (neat and modified) specimens are performed to ascertain the ideal wt.% of star-like polymer that can then be reinforced with basalt fibres for further testing. Interlaminar fracture tests along with scanning electron microscopy post failure are performed to determine the adhesion within BFRP laminates and visualise the damage caused.

2. Materials and Methods

2.1. Materials

The star-like poly(n-butyl methacrylate)-(glycidyl methacrylate) block copolymer, was incorporated into a biobased epoxy matrix reinforced with basalt fibres to enhance the mechanical properties. SR Greenpoxy 33 (Sicomin, France) and LITE 2401 (Cardolite, Belgium) sourced from biobased carbons and cashew nutshell liquid respectively were mixed to create a matrix of bio content of approx. 33%. The star-like polymer was mixed with the resin over 24 hours at 80 °C to produce a masterbatch with a concentration of 10 wt. %. This masterbatch was then diluted to create samples with concentrations of 0.25, 0.5, and 1 wt.% for comparison with the neat matrix. Unidirectional and twill woven basalt fibre fabric (Basaltex, Belgium) was used to fabricate the laminate plates for interlaminar and tensile tests respectively, which were impregnated with the same content of star-like polymer as the epoxy.

2.2. Methods

Dynamic mechanical analysis (DMA) was implemented to study the effect of filler content on the epoxy viscoelastic properties. DMA tests were conducted in a tension mode at a force of 2 N using a Mettler Toledo (Columbus, OH, USA) DMA/SDTA861 instrument to estimate the thermomechanical properties of the investigated materials. All tests were conducted at a frequency of 1 Hz and temperature range between 30-180 °C at a heating rate 3 K/min to ensure slow heating, thus avoiding any temperature gradient. The maximum peak of the loss modulus vs. temperature graphs was used to identify the α-relaxation associated with the glass transition. Subsequently, the temperature corresponding to this point was adopted to determine the glass transition temperature across all examined samples.

Tensile tests were performed on modified epoxy specimens which were fabricated according to ISO-527-1B using H10 KT universal column testing machine (Tinius Olsen, UK), with a crosshead strain rate of 2 mm/min.

For the developed BFRP laminates, Mode I interlaminar fracture toughness tests were carried out according to ASTM D5528 to study the effect of star-like polymers on mechanical properties. The double cantilever beam (DCB) samples were cut from the BFRP plate to have dimensions of 125 × 25 × 3 mm, as shown in Figure 1. Finally, the BFRP samples were prepared for Mode I interlaminar fracture toughness tests by gluing loading blocks. The tests were performed using a Zwick 2.5 testing machine at a crosshead speed of 1 mm/min at room temperature and Canon EOS40D to capture photos every 3 s for the crack propagation analysis until failure occurred. ImageJ 1.38x software was used to estimate the delamination length in DCB samples.

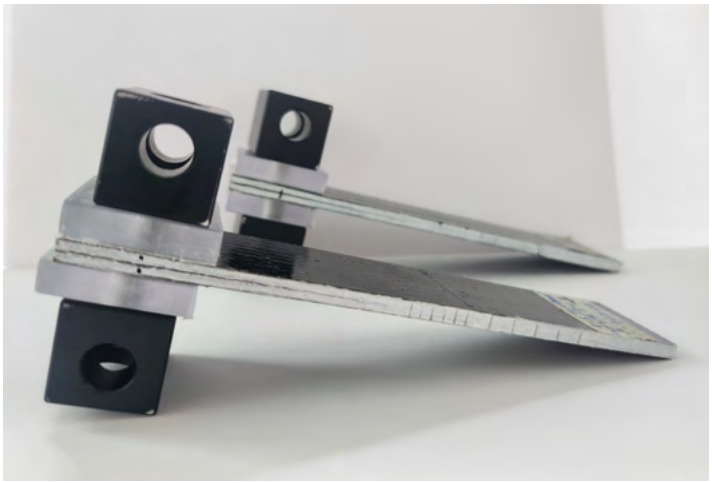


Figure 1. DCB samples of BFRP and epoxy with 0.5 wt.% of star-like polymers for Mode I interlaminar fracture toughness.

Scanning electron microscopy was performed to check the interlaminar damage created post-failure.

3. Results and Discussion

3.1. Tensile properties of BFRP

To investigate the effect of the star-like polymer on the biobased matrix, different wt.% epoxy specimens were fabricated. The tests (Figure 2) showed that with increase in the wt.% of star-like polymers, the properties degrade, owing to the fact that with increase in star-like polymer content, viscosity of the mixture increases. High viscosity causes trapping of bubbling and formation of voids and hence weaker tensile strength. Addition of 1 wt.% of star-like polymer showed the highest improvement in properties.

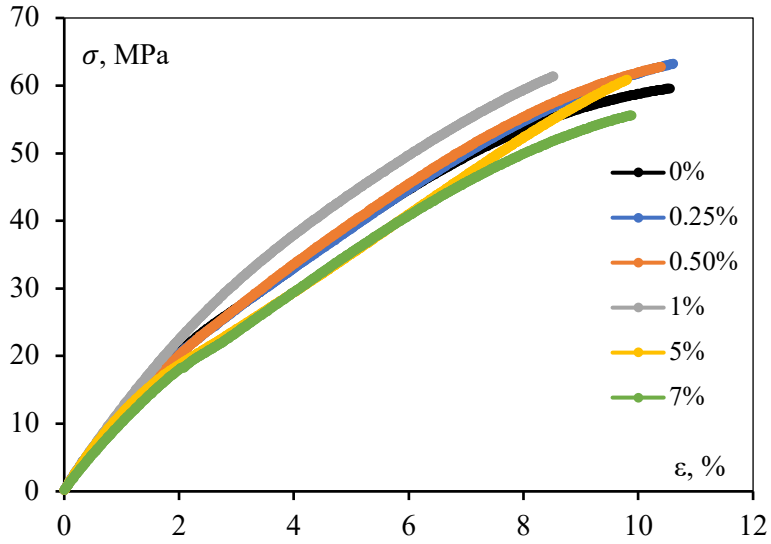


Figure 2. Stress vs strain curves for modified biobased matrix.

3.2.Thermomechanical properties of BFRP

DMA is a commonly employed technique for investigating the viscoelastic characteristics of polymers in response to oscillating forces. It aids in understanding the mobility of polymer chains and provides insights into their thermomechanical properties. DMA plays a crucial role in determining the glass transition temperature of polymers. Amorphous polymers exhibit distinct glass transition temperatures, beyond which they transition from a glassy state to a rubbery state, leading to a significant decrease in stiffness and viscosity.

The representative DMA curves for the storage modulus of the epoxy filled with different content of star-like polymers - 0, 0.25, 0.5 and 1 wt.%, is shown in Figure 3. The storage modulus increased with the increase of the star-polymer content except for 0.25 wt.%, revealing higher resistance to the dynamic loading at all temperatures. The highest storage modulus was registered for epoxy filled with 0.5 wt. % of the star-like polymers.

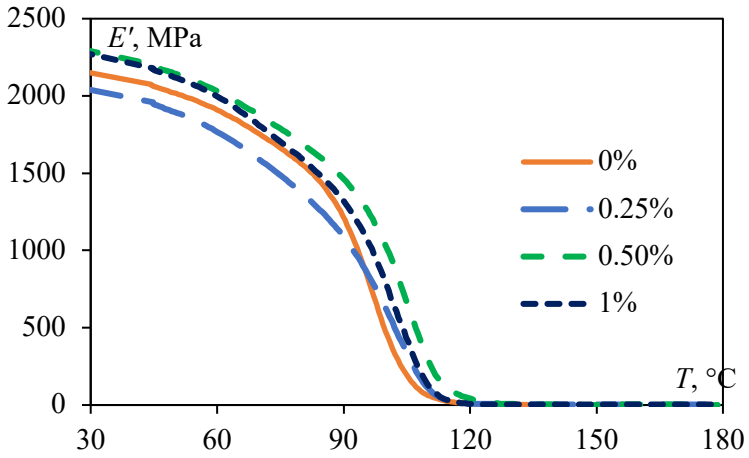


Figure 3. Storage modulus vs. temperature for the epoxy resin filled with the star-like polymers.

Figure 2 shows that the storage modulus decreased dramatically at the glass transition. Thus, evaluated at the maximal value of loss modulus, the glass transition temperature as a function of the star-like polymer content slightly increased by 7.6 °C, proving some reinforcement effect of the filler particles. Small data scattering was obtained for the identical material specimens, proving the repeatability of the results and sufficient quality of the test specimens.

3.3. Interlaminar fracture toughness of BFRP

In the DCB test, as the delamination grows from the insert, the resistance-type fracture behaviour typically develops where the calculated G_{Ic} increases monotonically and stabilizes with further delamination growth. The fracture toughness is assessed by the delamination resistance curve (G_{Ic} versus a) obtained from DCB tests, at the point where deviation from linearity occurs in the load-displacement curve.

To estimate Mode I interlaminar fracture toughness, the modified beam theory equation (Eq. 1) was used to correct the rotation at the delamination front by treating the DCB as if it contained slightly longer delamination, $a + \Delta$, where Δ is determined experimentally by generating a least-squares graph of the cube root of compliance, $C^{1/3}$, vs. delamination length:

$$G\,I\, = \, 3P\delta\,2b\,a + \,\Delta\,\,\,, \tag{1}$$

where P represents the load, δ denotes the displacement at the load point, b stands for the width of the specimen, and a indicates the delamination length of the specimen.

For the specimens incorporating loading blocks, two correction parameters are suggested [3]: a parameter F, which adjusts for the shortening of the moment arm and the tilting of the end blocks, and a parameter N, which compensates for the stiffening effect of the blocks on the specimen:

$$F = 1 - \,3\,10\, \,\delta\,a\,\,\,2\, - \,3\,2\, \,\delta t\, \,a\,2\,\,\,, \tag{2}$$

$$N = 1 - \quad L\,'\,\,a\,\,\,3\, - \,9\,8\, \,1 - \quad L\,'\,\,a\,\,\,2\,\,\, \,\delta t\, \,a\,2\,\,\,\, - \,9\,35\, \,\delta t\, \,, \tag{3}$$

where L' and t are the geometrical parameters of the blocks.

Then, the corrected formula for interlaminar fracture toughness by using the modified beam theory method takes the form:

$$G_I = \frac{3P\delta}{2b}\left(a + |\Delta|\right) \cdot F_N. \quad (4)$$

Representative load-crack opening displacement (COD) curves obtained for BFRP impregnated with the epoxy with different star-like polymer content are provided in Figure 4. A rather significant deviation among the data was observed, which is typical for such tests. The fracture toughness evaluated by Eq. (4) for BFRP impregnated with the epoxy is shown in Figure 5.

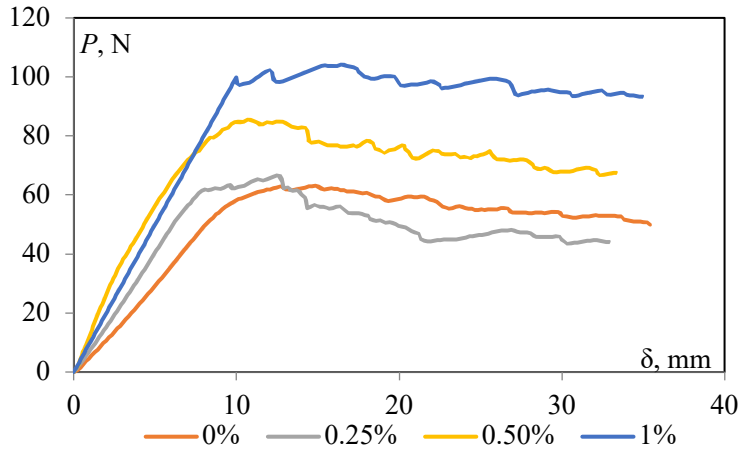
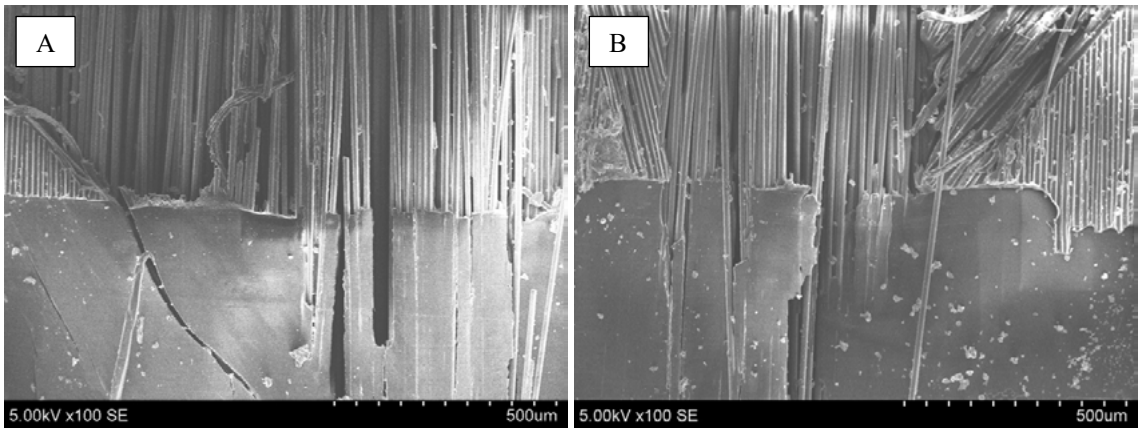


Figure 4. Representative load-COD curves from DCB tests for BFRP impregnated with the epoxy at different contents of star-like polymers as indicated on the graph.

3.4. Characterisation post failure

Scanning electron microscopy on the laminates post interlaminar fracture was conducted. It can be seen in Figure 6 that with increasing wt.% of star-like polymer, less matrix cracking around the edge of the specimen is visible. Neat matrix specimens appear to have larger and highly propagated cracks while modified specimens have smaller crack and a very intact matrix layer.



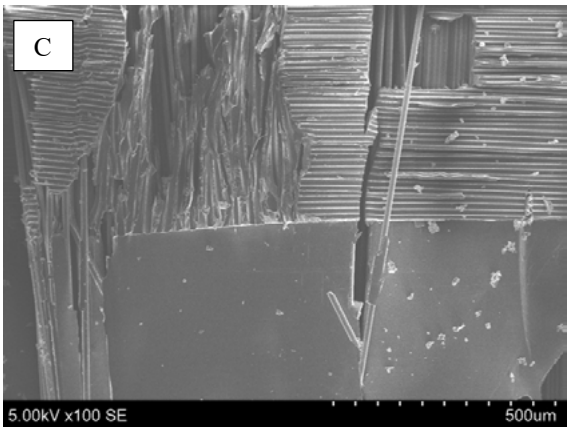


Figure 6. SEM images of damage post interlaminar fracture toughness tests on BFRP **A** - neat epoxy; **B** - 0.5wt.%; **C** - 1wt.%

4. Conclusions

The epoxy resin was modified by the addition of star-like polymers (poly(n-butyl methacrylate)-(glycidyl methacrylate) block copolymer) of different wt.% and used for the impregnation with basalt fibres. Tensile tests showed that smaller weight percentage of the star-like polymer presented better results. It was observed that the effect of star-like polymers on interlaminar fracture toughness properties of BFRP was substantial, leading to an improvement of 68%. Moreover, a slight increase of 7.6°C in the glass transition temperature was observed in the epoxy filled with star-like polymers. This could be ascribed to the heightened crosslink density and toughening impact of the star-like polymer, indicating their integration into the epoxy continuous phase and potentially enhancing adhesion between the epoxy matrix and basalt fibres. Scanning electron microscopy showed more damage in neat epoxy when compared to modified star-like polymer specimens.

Acknowledgements

This work has been funded by the Research Council of Lithuania (LMTLT), agreement No. S-MIP-23-134.

References

[1] T. Glaskova-Kuzmina, A. Zotti, A. Borriello, M. Zarrelli, A. Aniskevich. Basalt fibre composite with carbon nanomodified epoxy matrix under hydrothermal ageing. *Polymers*, 13 (4), 532, 2021.

[2] R. Pinto, G. Monastyreckis, H.M. Aboelanin, V. Spacek, D. Zeleniakiene. Mechanical properties of carbon fibre reinforced composites modified with star-shaped butyl methacrylate. *Journal of Composite Materials,* 56 (6), 951-959, 2022.

[3] ASTM Standard D 5528-01; Standard test method for Mode I interlaminar fracture toughness of unidirectional fiber-reinforced polymer matrix composites. ASTM International: West Conshohocken, PA, USA, 2004.

EFFECT OF IN-SITU CONSOLIDATION ON THE IN-PLANE ELASTIC MODULI OF CARBON/PEEK THERMOPLASTIC COMPOSITES MADE BY AUTOMATED FIBER PLACEMENT (AFP) PROCESS

E. Pourahmadi[1, 2], R. Ganesan[1, 2] and F. Shadmehri[1, 2]

[1]Concordia Center for Composites (CONCOM), Department of Mechanical, Industrial and Aerospace Engineering, Concordia University, Montreal, Quebec, Canada
[2]Research Center for High-Performance Polymer and Composite Systems (CREPEC), Montreal, Quebec, Canada
emad.pourahmadi@mail.concordia.ca
r.ganesan@concordia.ca
farjad.shadmehri@concordia.ca

Keywords: Carbon/PEEK thermoplastic composite, Automated Fiber Placement (AFP), In-situ consolidation, Representative Volume Element (RVE), Random microstructure.

Abstract
Despite facing certain challenges, the Automated Fiber Placement (AFP) process offers a feasible and cost-effective alternative to costly and time-consuming traditional manufacturing techniques, such as hand lay-up and autoclave processes. The present research focuses on predicting the effective in-plane elastic moduli, E_1 and E_2, of in-situ-consolidated Carbon/PEEK thermoplastic composite material by generating two-dimensional Representative Volume Elements (RVEs) at the micro-scale. In order to consider the influence of fiber volume fraction, void content, degree of crystallinity, and interlaminar resin pockets in the simulation, two sample groups were fabricated using the AFP in-situ consolidation and autoclave re-consolidation techniques. These specimens were evaluated through a micrographic study and thermoanalytical Differential Scanning Calorimetry (DSC) method to gather the necessary inputs for micromechanical analysis. It was shown that the AFP in-situ consolidation may cause decreases close to 7% and 10% in the elastic moduli of Carbon/PEEK thermoplastic composite material in fiber and transverse directions, respectively.

1. Introduction

To manufacture a composite laminate, a robotic arm and a fiber placement head, either thermoset or thermoplastic, work together in the robotic AFP machine that is capable of positioning narrow composite tows close to one another on a mandrel. In this process, heat and compressive force are simultaneously applied using a compaction roller and a heating system, such as a hot gas torch. The lengthy and expensive curing process associated with thermoset composites has prompted a more frequent adoption of their thermoplastic counterparts as substitutes. One notable advantage of manufacturing thermoplastic composites is the potential for in-situ consolidation during the AFP process. However, a significant discrepancy in quality exists between the in-situ-consolidated and the autoclave-treated thermoplastic composites due to crucial factors including fiber volume fraction, void content, interlaminar resin pocket and degree of crystallinity, arising from short AFP processing time [1–3].

While experimental methods are indispensable for evaluating material properties, mechanical testing of unidirectional thermoplastic composite specimens presents difficulties owing to the warpage occurring throughout the AFP in-situ consolidation process. Micromechanical computational models provide a valuable source to conduct virtual experiments and analyse different material systems in the design

phase. Although the utilization of the Representative Volume Element (RVE) technique allows researchers to simulate diverse microstructures along with their constituents, shapes, orientations and distribution, the generation of an RVE that can accurately capture the mechanical behaviour and response of long-fiber-reinforced composites with high fiber volume fraction poses significant modeling challenges [4]. To achieve this objective, various algorithms have been devised by different researchers, such as Random Sequential Adsorption (RSA) [5], Random Sequential Expansion (RSE) [6], Random Microstructure Generator (RAND_uSTRU_GEN) [7], etc., aiming to enhance the authenticity of the generated RVE model with non-uniform distribution of fibers.

While fiber volume fraction is the determining factor for material response in fiber direction, the existence of voids, interlaminar resin pockets and the variation in the degree of crystallinity have a significant impact on the material properties in the transverse direction. As a result, in the present research work, both longitudinal and transverse cross-sections of Carbon/PEEK thermoplastic composite material were investigated by generating the corresponding 2D Representative Volume Elements (RVEs) with randomly distributed fibers at a micro-scale. To incorporate sufficient details into the micromechanical simulation, micrographic study and thermoanalytical Differential Scanning Calorimetry (DSC) analysis were performed on two groups of Carbon/PEEK thermoplastic composite samples manufactured by in-situ consolidation and autoclave re-consolidation. The RVEs were exposed to Periodic Boundary Conditions (PBCs). The Asymptotic Homogenization Theory (AHT) was employed to predict the effective in-plane elastic moduli of the material resulting from the AFP in-situ consolidation manufacturing process. The modeling procedures were executed using an ABAQUS Scripting Interface (ASI) scripted in the Python programming language, supplemented by MATLAB, which defined the RVE geometry. The obtained results will be very useful in the finite element modeling, analyses, and design of thermoplastic composite laminates that are manufactured by the AFP process.

2. Manufacturing procedure

An HGT-assisted Automated Fiber Placement (AFP) machine comprising a 6-axis Kawasaki articulated robot arm boasting a 125 kg payload, outfitted with a thermoplastic head provided by the Trelleborg Group, is available to researchers at the Concordia Centre for Composites (CONCOM), as shown in Figure 1. Unidirectional AS4/APC-2 tape from the Solvay Group [8] with a weight ratio of 68:32, a fiber volume fraction of 60% and a thickness of 0.140 mm was used for manufacturing two laminates. During the AFP in-situ consolidation, processing parameters of hot gas torch temperature, Nitrogen flow rate, compaction force and deposition rate were set to 875° C, 80 SLPM, 266.9 N and 50.8 mm/s, respectively, which are in good agreement with optimum values suggested in the literature [9].

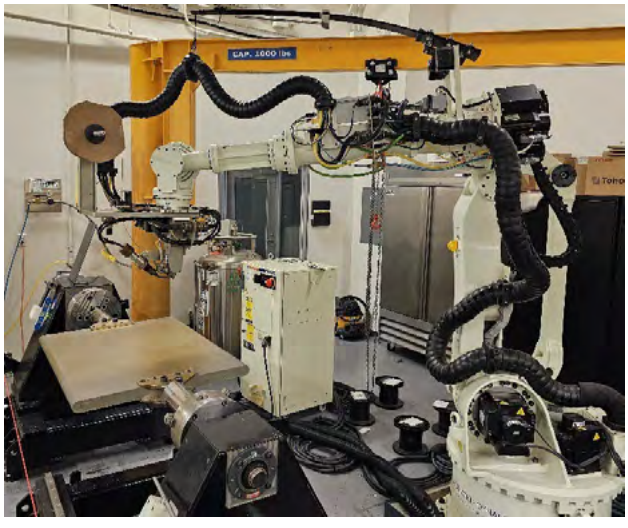
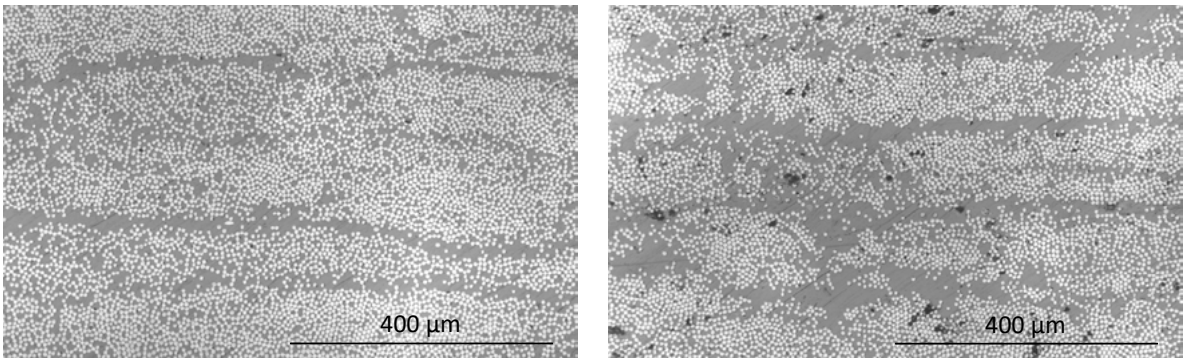


Figure 1. HGT-assisted Automated Fiber Placement (AFP) machine at CONCOM.

The second in-situ-consolidated Carbon/PEEK thermoplastic composite laminate was vacuum-bagged and then treated in an autoclave at temperature and pressure of 390° ± 10° C and 100 ± 5 psi, respectively, for 20 ± 5 minutes to serve as a baseline [8].

3. Micrographic study and DSC analysis

Understanding the microstructure of Carbon/PEEK thermoplastic composite samples fabricated through autoclave re-consolidation and AFP in-situ consolidation can help to identify the causes of distinctions in their mechanical properties. Samples from both types of laminates were cut and polished before being examined under a microscope. Micrographic study of the specimens highlights significant differences between thermoplastic composite laminates produced by AFP in-situ consolidation and autoclave re-consolidation processes in terms of fiber volume fraction, void content and interlaminar resin-rich areas, as depicted in Figure 2, leading the mechanical performance of the final product to be adversely affected. The color thresholding technique, implemented by *ImageJ* software, was employed to calculate void content and fiber volume fraction by differentiating between voids, fibers, and resin. For this purpose, thirty Representative Volume Elements (RVEs) were randomly chosen from diverse positions within the micrographs, each maintaining a consistent size equivalent to the thickness of each composite layer, which is 140 µm. These RVEs were employed to quantify key factors, including fiber volume fraction, void content, and the percentage of interlaminar resin pockets (for more information on how to measure each factor precisely, see Ref. [10]). The mean values of each factor caused by in-situ consolidation and autoclave re-consolidation manufacturing methods are listed in Table 1.



(a) Autoclave re-consolidation (b) AFP in-situ consolidation

Figure 2. Microstructure of Carbon/PEEK samples manufactured by (a) autoclave re-consolidation and (b) AFP in-situ consolidation at 20X magnification.

Table 1. Mean values of fiber volume fraction, void content and percentage of interlaminar resin pocket calculated from the micrographic study.

	Autoclave re-consolidation	AFP in-situ consolidation
Fiber volume fraction (%)	60	56
Void content (%)	0	1.5
Interlaminar resin pocket (%)	0	12

The other influential factor is the degree of crystallinity, quantifiable through Differential Scanning Calorimetry (DSC) analysis. To this end, 10 mg samples from each in-situ-consolidated and autoclave-reconsolidated Carbon/PEEK thermoplastic composite material underwent a heat-cool-heat cycle. The process involved heating at a rate of 10 °C/min, reaching a maximum temperature of 390 °C in a Nitrogen atmosphere, followed by a cooling rate of 5 °C/min. The following equation is used to calculate the degree of crystallinity, X, [1]:

$$X = \frac{\Delta H_m - \Delta H_c}{\Delta H_f (1 - \alpha)} \quad (1)$$

where α is the weight ratio of Carbon fibers in the Carbon/PEEK thermoplastic composite tape. ΔH_m, ΔH_c and ΔH_f denote the enthalpies of fusion at endothermic melting point, at exothermic crystallization peak and for fully crystalline PEEK, respectively. The outcomes of the DSC examination are displayed in Table 2, containing mean values of the degree of crystallinity and melting temperature derived from no fewer than five specimens manufactured by each technique.

Table 2. Mean values of the degree of crystallinity resulting from AFP in-situ consolidation and autoclave re-consolidation processes.

	Crystallinity (%)	SD*	Melting temperature (°C)	SD*
AFP In-situ consolidation	25.07	0.82	345.31	0.17
Autoclave re-consolidation	34.96	0.38	345.52	0.15

*SD = Standard Deviation

The effect of the degree of crystallinity on the elastic modulus of neat PEEK resin was examined in many research works, showing an approximately linear correlation between the degree of crystallinity and the elastic modulus. As a result, for every 5% drop in the degree of crystallinity from the baseline, that is 35%, a 4% decrease in the elastic modulus of neat PEEK resin was taken into consideration in the present study [11].

4. Finite element modeling

Creating randomly distributed fibers in a Representative Volume Element (RVE) with a fiber volume fraction surpassing 50% poses a significant difficulty because programming languages, including MATLAB and Python, have limitations in identifying appropriate locations solely through random generators for adding new fiber center points. The methodology applied in the present work adheres to the algorithm introduced by Melro *et al.* [7] and refined by Ghayoor *et al.* [12], which entails repositioning the most isolated fibers within the RVE to achieve an elevated fiber volume fraction, such as 60%.

To take into account the effect of interlaminar resin pockets on the prediction of in-plane elastic moduli, constraints were imposed on the top and bottom boundaries of the Representative Volume Element (RVE) to keep fibers closer together. This involved limiting the randomly generated center points of fibers within a certain percentage range of the RVE length in the y-direction, such as between 6% and 94% to create a 12% interlaminar resin pocket. While maintaining a constant fiber volume fraction, this process shifted fibers toward the center, resulting in the formation of resin-rich areas at the top and bottom edges of the RVE, resembling the observations from the micrographic study.

Regarding the generation of voids, the Random Sequential Adsorption (RSA) technique [5] was implemented to randomly assign locations for voids inside the RVEs. If the selected position coincides with the area already occupied by fibers, a new point is generated; otherwise, the void radius is randomly chosen within the range of 0 to the distance between the void and its closest fiber. This procedure is repeated until the void content reaches the predetermined threshold, that is 1.5% as listed in Table 1.

To predict the elastic moduli of Carbon/PEEK thermoplastic composite material in the fiber (E_1) and transverse (E_2) directions through two-dimensional micromechanical analysis, distinct Representative Volume Elements (RVEs) are required, generated based on the longitudinal and transverse cross-sections. The finite element analysis conducted for both types of RVEs in ABAQUS is identical, except for the method employed to generate the geometry using MATLAB programming code. For the longitudinal cross-section, fibers may exhibit full radii or be partially visible on the surface of the composite material, depending on their actual position within the structure. To this end, the simulation

approach for the longitudinal-cross-section RVE must involve generating random radii for fibers in addition to their random locations, whereas fibers' radii remain constant in the RVE depicting the transverse cross-section of the composite material. Thus, MATLAB code already written for RVE generation based on the transverse cross-section was developed, particularly in terms of the compatibility conditions to prevent any intersections between either fibers or fibers and voids, to create those inspired by longitudinal cross-section from the ground up. The final geometries of these RVEs, representing AFP in-situ consolidation and autoclave re-consolidation processes, are illustrated in Figure 3 based on their respective cross-sections. It should be noted that in the case of the longitudinal cross-section, the percentage of the fiber volume fraction might be either higher or lower than that calculated in the transverse cross-section, depending on the location of the cut. Therefore, the average values, listed in Table 1, were considered for the generation of longitudinal-cross-section RVEs representing each manufacturing process.

After determining the positions of fibers and voids within the Representative Volume Element (RVE) to meet the specified fiber volume fraction, void content and percentage of interlaminar resin pocket, a micro-scale numerical analysis of both random and periodic microstructures was conducted by considering ideal bonding between fibers and matrix. This analysis was executed using the ABAQUS Scripting Interface (ASI) written in the Python programming language. To this end, the Representative Volume Element (RVE) was defined with a length of 140 µm, aligning with the thickness of individual Carbon/PEEK layers. The Carbon fibers, with a diameter of 7 µm, were positioned at a minimum distance of 0.01 times the fiber radius. Triangular 3-node linear plane strain elements (CPE3) sized at one-fourth of the fiber radius were employed for the analysis [10]. Table 3 presents the material properties of the PEEK resin and Carbon fiber, constituents of the thermoplastic composite material, used in the numerical analysis.

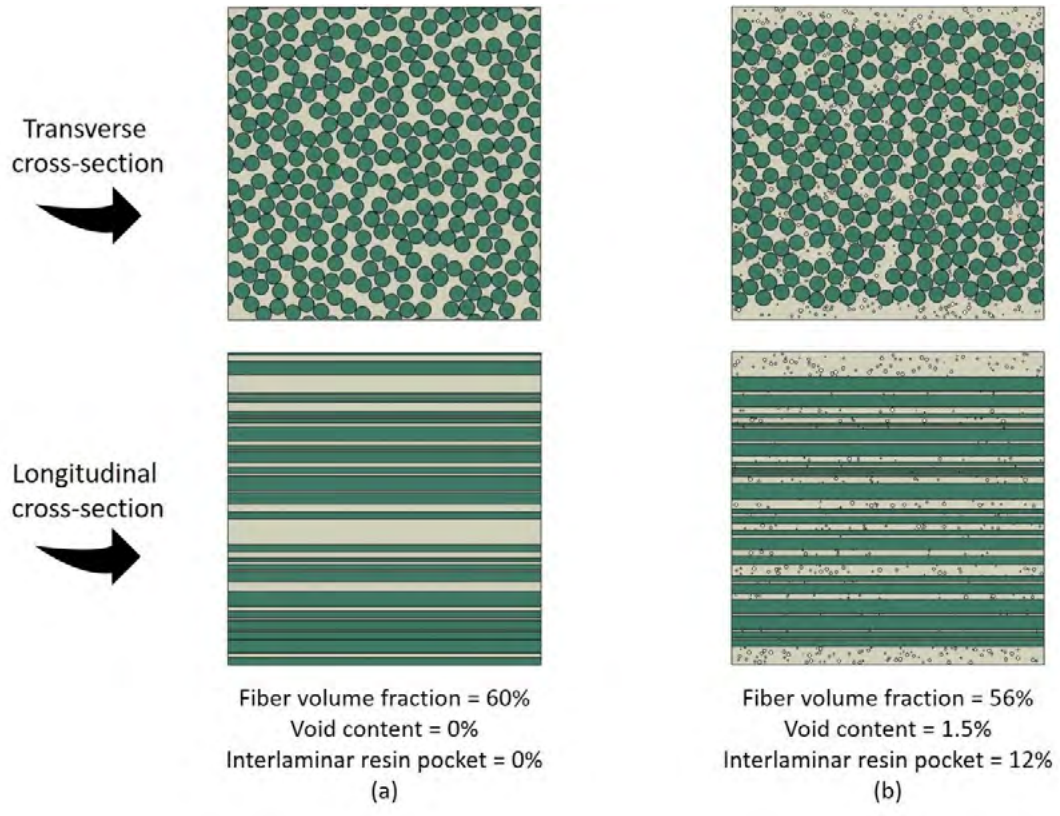


Figure 3. Typical geometry of RVEs by considering the variations of fiber volume fraction, void content and interlaminar resin pocket: (a) Autoclave re-consolidation and (b) AFP in-situ consolidation.

Table 3. Material properties of PEEK resin and Carbon fiber in principal directions [8].

	E_1 (GPa)	$E_2 = E_3$ (GPa)	$\nu_{12} = \nu_{13}$	ν_{23}
Carbon fiber (AS4)	228	22	0.20	0.25
PEEK resin (APC-2)	3.6	3.6	0.38	0.38

Composite materials are commonly modelled as an arrangement of periodic Representative Volume Elements (RVEs), requiring the imposition of Periodic Boundary Conditions (PBCs). These conditions guarantee compatible deformation across all RVEs, preventing overlap or separation between adjacent units. The utilization of Periodic Boundary Conditions (PBCs) in conjunction with the RVE approach proves to be an effective method for homogenization and microstructural analysis. The definition of periodic boundary conditions is as follows [13]:

$$u_i^{j+} - u_i^{j-} = \bar{\varepsilon}_{ik}\left(x_k^{j+} - x_k^{j-}\right) = \bar{\varepsilon}_{ik}\Delta x_k^j \tag{2}$$

where u_i and $\bar{\varepsilon}_{ik}$ denote the displacement and average strain of a point on the RVE boundary, respectively. x_k represents the cartesian coordinate of the point. Superscripts $j+$ and $j-$ are used to index the jth pair of parallel opposite edges in an RVE.

It is generally assumed that the mean mechanical characteristics of the RVE align with those demonstrated by the unidirectional composite lamina at the macrostructural level. Effective material properties of a Representative Volume Element (RVE) can be determined using the homogenization theory based on how it reacts to different loading conditions. The calculation of in-plane elastic moduli entails subjecting the RVE to horizontal displacement. Figure 4 shows the boundary conditions and tension loading case to which the RVEs are exposed. Subsequently, the equations provided below can be utilized to compute E_1 and E_2, depending on the chosen cross-section type in the simulation, whether it is longitudinal or transverse [7]:

$$E_1 = \frac{\bar{\sigma}_{11}}{\bar{\varepsilon}_{11}}, \qquad E_2 = \frac{\bar{\sigma}_{22}}{\bar{\varepsilon}_{22}} \tag{3}$$

where $\bar{\sigma}$ and $\bar{\varepsilon}$ are volume average stress and strain, respectively [13].

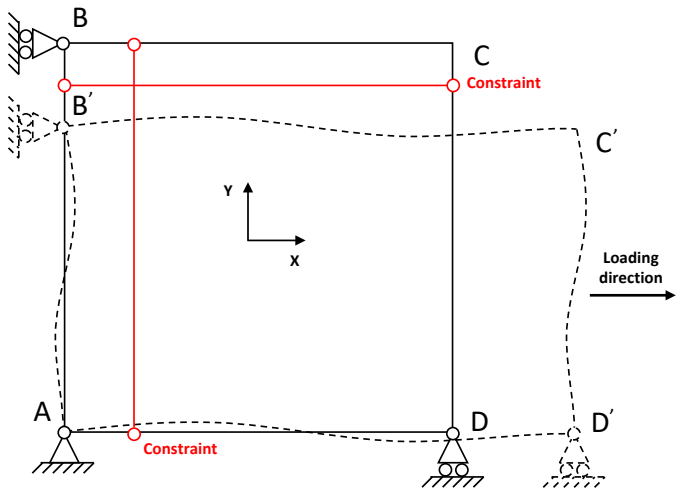


Figure 4. Schematic of an initial and deformed RVE subjected to PBCs under tension loading case.

5. Results

To verify the validity of the results of finite element analysis, Representative Volume Elements (RVEs) were generated with a fiber volume fraction of 60% and without void content and interlaminar resin pockets to simulate autoclave manufacturing conditions. The evaluation of numerical outcomes against the CYTEC technical data sheet [8], as listed in Table 4, demonstrated that the proposed finite element model exhibits proficiency in predicting the effective in-plane elastic moduli of Carbon/PEEK thermoplastic composite material, with an error margin of less than 5%.

Following the validation of the proposed Finite Element (FE) model, the influence of AFP in-situ consolidation manufacturing process can be explored by modifying the values of the four identified key factors. This modification is aimed at generating Representative Volume Elements (RVEs) that accurately simulate Carbon/PEEK thermoplastic composites undergoing in-situ consolidation. The predicted in-plane elastic moduli resulting from the different manufacturing techniques are presented in Table 4. Based on the findings, the application of AFP in-situ consolidation resulted in a reduction of the elastic moduli in the fiber and transverse directions by 6.83% and 10.43%, respectively, in comparison with autoclave re-consolidation.

Table 4. Prediction of in-plane elastic moduli of Carbon/PEEK thermoplastic composite material manufactured by AFP in-situ consolidation and autoclave treatment.

	Cytec Data [8]	Autoclave re-consolidation	AFP in-situ consolidation	Difference* (%)
$E_1\ (GPa)$	138	139.44	129.92	6.83
$E_2\ (GPa)$	10.3	10.45	9.36	10.43

*With reference to the values that correspond to the autoclave re-consolidation process.

It should be noted that although the effects of four factors were attempted to be considered during the simulation of RVEs representing the in-situ consolidation process, their relative significance is not the same in the prediction of E_1 and E_2 using the longitudinal and transverse cross-sections. Since void content, interlaminar resin pockets, and degree of crystallinity are associated with the matrix phase in composite materials, they significantly influence the prediction of the transverse elastic modulus (E_2). However, the primary factor impacting the behaviour of composite material in the fiber direction (E_1) is the fiber volume fraction. To demonstrate this, the fiber volume fraction was reduced to 56% while the remaining three factors were maintained unchanged (i.e., the values resulting from autoclave treatment conditions as detailed in Table 1).

Table 5. Influence of fiber volume fraction on the elastic moduli in fiber and transverse directions.

	60% fiber volume fraction	56% fiber volume fraction	Difference (%)
$E_1\ (GPa)$	139.44	131.36	5.79
$E_2\ (GPa)$	10.45	9.72	6.98

According to the results shown in Table 5, the decrease of (only) fiber volume fraction to 56% caused the elastic modulus in the fiber direction to be reduced by 5.79%, which is the majority part of the reduction presented in Table 4. In other words, the presence of voids and interlaminar resin pockets and the change in the degree of crystallinity have minimal effects on the elastic modulus in fiber direction. Nonetheless, these matrix phase-related factors exert a significant influence on the transverse elastic modulus and take up a good portion of the decline listed in Table 4.

6. Conclusion

The use of in-situ consolidation through Automated Fiber Placement (AFP) presents advantages in terms of time and cost efficiency when compared to the traditional autoclave method for the fabrication of thermoplastic composite materials. Nonetheless, challenges emerge due to the shorter AFP processing time in which heat and pressure are applied, along with a higher cooling rate, in contrast to the more

extended autoclave curing. This constrained exposure has adverse effects on fiber volume fraction, void content, fiber distribution, and degree of crystallinity, which determine the mechanical response of composite materials.

In the present research, two groups of Carbon/PEEK thermoplastic composite samples were manufactured by AFP in-situ consolidation and autoclave re-consolidation techniques. Specimens from both groups underwent micrographic study and DSC analysis to acquire input data required for the micromechanical simulation. Two-dimensional RVEs at the micro-scale were generated in accordance with the longitudinal and transverse cross-sections to predict the in-plane elastic moduli of Carbon/PEEK thermoplastic composite material. The results revealed that AFP in-situ consolidation can lead the elastic moduli in fiber and transverse directions to be reduced by 6.83% and 10.43%, respectively. These variations in material properties are of great importance and must be considered in further numerical analysis of Carbon/PEEK thermoplastic composites manufactured by AFP in-situ consolidation method.

Acknowledgment
The financial contributions from the Natural Sciences and Engineering Research Council of Canada (NSERC) and Research Center for High Performance Polymer and Composite System (CREPEC) are appreciated.

References
[1] F. Shadmehri, S. V. Hoa, J. Fortin-Simpson and H. Ghayoor. Effect of in situ treatment on the quality of flat thermoplastic composite plates made by automated fiber placement (AFP). *Advanced Manufacturing: Polymer & Composites Science*, 4(2):41-47, 2018.
[2] E. Oromiehie, U. Garbe and B. Gangadhara Prusty. Porosity analysis of carbon fibre-reinforced polymer laminates manufactured using automated fibre placement. *Journal of Composite Materials*, 54(9):1217-1231, 2020.
[3] E. Oromiehie, A. K. Gain, M. J. Donough and B. G. Prusty. Fracture toughness assessment of CF-PEEK composites consolidated using hot gas torch assisted automated fibre placement. *Composite Structures*, 279:114762, 2022.
[4] J. Aboudi. *Mechanics of composite materials: a unified micromechanical approach*. Elsevier, 2013.
[5] J. Ohser and F. Mücklich. Statistical Analysis of Microstructures in Materials Science. *Practical Metallography*, 38(9):538-539, 2001.
[6] L. Yang, Y. Yan, Z. Ran and Y. Liu. A new method for generating random fibre distributions for fibre reinforced composites. *Composites Science and Technology*, 76:14-20, 2013.
[7] Melro, P. Camanho and S. Pinho. Generation of random distribution of fibres in long-fibre reinforced composites. *Composites Science and Technology*, 68(9):2092-2102, 2008.
[8] CYTEC. *APC-2-PEEK Thermoplastic Polymer*. www.cytec.com, 2012.
[9] X. Cai, F. Shadmehri, M. Hojjati, J. Chen and S. V. Hoa. Determination of optimum process conditions for processing AS4/APC-2 thermoplastic composites by automated fiber placement. In *The Society for the Advancement of Material and Process Engineering (SAMPE) conference*, 2012.
[10] E. Pourahmadi, R. Ganesan and F. Shadmehri. Micromechanical characterization of Carbon/PEEK thermoplastic composite material in-situ consolidated by automated fiber placement: Stiffness prediction. *Composites Science and Technology*, 246:110390, 2024.
[11] M. F. Talbott, G. S. Springer and L. A. Berglund. The Effects of Crystallinity on the Mechanical Properties of PEEK Polymer and Graphite Fiber Reinforced PEEK. *Journal of Composite Materials*, 21(11):1056-1081, 1987.
[12] H. Ghayoor, S. V. Hoa and C. C. Marsden. A micromechanical study of stress concentrations in composites. *Composites Part B: Engineering*, 132:115-124, 2018.
[13] F. Taheri-Behrooz and E. Pourahmadi. A 3D RVE model with periodic boundary conditions to estimate mechanical properties of composites. *Structural Engineering and Mechanics*, 72(6):713-722, 2019.

CONTENTS

DEVELOPMENT OF DESIGN GUIDELINES FOR ADHESIVE BOND LINES IN SEGMENTED WIND ROTOR BLADES

D. Voigt[1], F. Wunderle[1], M. Opitz[1], M. Griese[2] and S. Hartwig[2]

[1]INVENT GmbH, Business Unit Industry & Innovation, Christian-Pommer-Str. 47, 38112 Braunschweig, Deutschland, E-Mail: fabian.wunderle@invent-gmbh.de
[2]Institut für Füge- und Schweißtechnik, Fakultät für Maschinenbau, TU Braunschweig, Langer Kamp 8, 38106 Braunschweig, Deutschland, E-Mail: m.griese@tu-braunschweig.de

Keywords: Modularity, Wind Rotor Blade, Adhesive T-Joint, Numerical Modeling, Design Guidelines

Abstract

The research compares two modular design concepts for T-joints in segmented wind rotor blades, focusing on sustainability and efficiency of the bonding in load-bearing applications. The study incorporates the use of End-of-Life (EoL) material to improve environmental sustainability through recycling and reuse of disassembled rotor blade parts. The first concept uses a high viscous epoxy adhesive with specific additives. Local stress concentrations are reduced by applying adhesive fillets and a machined radius surface to the EoL material. This joint design increases the load capacity of the T-joint. In contrast, concept II combines cleats with a thin layer of adhesive, which enables the use of low viscosity adhesives. The second concept significantly reduces adhesive consumption and improve repair- and reusability. A numerical simulation with volume and cohesive elements has shown that concept II not only reduces adhesive consumption, but also achieves a 50 % higher load capacity per joint weight compared to concept I under bending load. Experimental bending tests of T-Joints were used to validate these numerical results. Thus, concept II with an optimized cleat design and minimized adhesive consumption offers significant advantages for sustainable modularity in segmented rotor blade designs. As a result, global goals like reducing the environmental impact and improving the life cycle management of wind rotor blades can be achieved.

1. Introduction

In relation to the increasing importance of renewable energy resources, the continuous development of wind power turbines is essential. To strengthen the sustainability of wind turbines, the design of conventional wind rotor blades must be reworked. An approach describes the division of wind rotor blades into several manageable segments. This simplifies the transportation and assembly of wind rotor blades as well as the replacement of segments that have been damaged during operation [1]. Even after the product life cycle of a wind rotor blade, the segmentation allows the return of intact components to the life cycle of new wind rotor blades. The modular design thus offers a high recycling potential. Within a research project a modular design for an 8m rotor blade will be developed. The design differs from conventional rotor blades consisting of an outer skin and web components. Instead, the modular rotor blade design is inspired by an aircraft wing, in which the load-bearing structure is formed by a pultruded composite spar and attached ribs. To further increase the sustainability of the design, the rib structure shall be machined from decommissioned wind rotor blade shells.

Within a conventional rotor blade, the final assembly step always produces an undefined blind bonded joint. The final segment is applied to the load-bearing inner structure without ensuring a complete connection between the adherends. The blind bonded joint is assumed to lead to reduced bonding properties. Furthermore, this blind connection consumes more adhesive than a defined adhesive joint. The additional adhesive mass can lead to a break-off during the service life, resulting in a clump of adhesive damaging the inner structure of the rotor blade with every revolution [2].

Mendoza et al. [3] conducted a study on the segmentation of wind rotor blades in which the influence of added masses at different joint connections on the natural frequencies of the rotor blade was investigated. The results show that adhesive joints cause a smaller increase in the total mass compared to mechanical joints. Thus, the influence of adhesive joints on the natural frequencies of a wind rotor blade is less than that of mechanical joints. For an assembly of segments, adhesive bonds should be preferred. A drawback of adhesive joints is the missing option for a non-mechanical debonding. A mechanical debonding often leads to damages on adjacent components and thus prevents a reuse. Another solution is offered by thermal debonding-on-demand adhesives. These adhesives include thermally expandable particles (TEPs) that expand when heat is applied and cause a cohesive separation of the adhesive bond line. This technology allows for a debonding without damaging the individual rotor blade components. However, various studies of quasi-static tests have shown that TEPs can lead to a reduction in tensile and shear strength of up to 15 % [4, 5].
The described technologies and the segmented design results in a wide range of different bonded joints. An important adhesive joint describes the connection of the load-bearing inner structure to the aerodynamic outer skin, which results in a T-joint. This paper will discuss two different concepts of T-joints in terms of design and mechanical performance. For this purpose, numerical models with volume and cohesive elements are developed and the joints are subjected to a bending load. In addition, the influences of different joining materials, adhesives, thermally expanding particles, and adhesive fillet designs are discussed. To reach a final conclusion the two concepts are compared by the load capacity per joint weight.

2. Adhesive T-joint in Segmented Wind Rotor Blades

2.1. Design concepts

Figure 1 presents two potential concepts for the T-joint connection of the rib structure and the outer skin of a modular wind rotor blade. Both concepts show a cut through the rib geometry for better visualization.

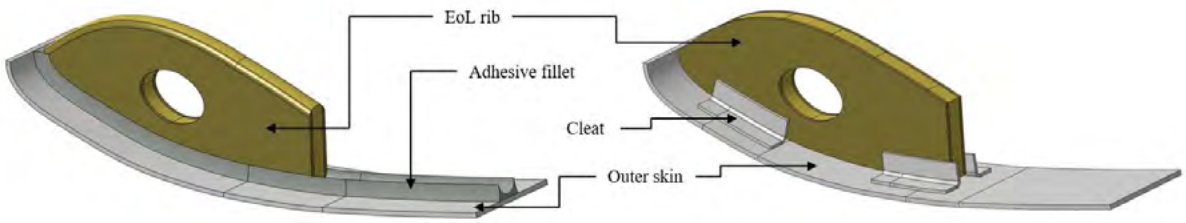


Figure 1. Design concept I (left) and II (right) for an adhesive T-joint in a rotor blade segment

Concept I is based on the vast adhesive joints of a conventional wind rotor blade (e.g. connection of the web structure to the outer shells). Within the rotor blade manufacturing industry there is a need for large bonding gaps between two components. The extensive bonding gaps are due to high safety factors and manufacturing tolerances. To reduce stress concentrations occurring at the corners of the T-joint, so-called adhesive fillets can be applied [6]. For the application of adhesive fillets, an adhesive with a sufficiently high viscosity is required. The range of adhesives is therefore limited. Stress concentrations can be further reduced by machining a radius surface on the bonding surface of the EoL rib [7]. Although this results in a higher production expenditure, it ensures complete and direct load transfer between the adherends. The design from concept I results in a T-joint with fully embedded ribs, see figure 1 left. This increases the likelihood of defects, such as air voids, which can significantly reduce the performance of an adhesive joint [8].
In concept II, the outer skin and the rib structure are not directly connected via an adhesive. The inner structure (EoL ribs) and the outer skin are joined together using cleat structures, to increase the modularity of the segmented wind rotor blades, see figure 1 right. Bhat et al [9] used shaped brackets to connect rotor blade segments, which connect web to web and outer skin to outer skin of conventional rotor blades. Based on cleats from the aviation industry, which connect the rib structure of frames and

stringers with the outer skin of the aircraft, the concept can be transferred to wind rotor blades. Concept II allows a load-optimized cleat design with free choice of material. To reduce the overall weight of the rotor blade, materials with low specific densities, such as aluminum or composites, can be selected. To increase the necessary load capacity, the contact surfaces of the cleats must be enlarged. In contrast to concept I, additional cleat structures allow the use of adhesives that are also suitable for low adhesive thicknesses. This reduces the amount of adhesive used within the rotor blade and therefore the likelihood of defects. Furthermore, the application of adhesive fillets and the machining of a radius surface to reduce stress concentrations is no longer necessary. To further reduce possible stress concentrations, the edges of the cleats can be chamfered [10]. A disadvantage for concept II is the non-planar and low quality surface of the EoL rib and the free-form surface of the aerodynamic skin. However, small deviations in the rib structure surface can be tolerated using a slightly bigger adhesive layer. Contrarily different rib geometries lead to a higher variety of cleat components with different surface dimensions. This increases the acquisition costs of tool molds and the production costs in general.

2.2. Materials

Both concepts use the same two materials for the outer skin and the rib structure to enable a comparison of the results. The rib geometry consists of an EoL glass fiber reinforced plastic (GFRP) sandwich laminate, which is obtained from a decommissioned rotor blade, see figure 2. In the previous product life cycle, the GFRP sandwich laminate formed the outer shell of the rotor blade, which was manufactured using vacuum resin infusion. Depending on the removal position, one of the two face sheets has a slightly bigger laminate thickness. After a pyro analysis of the laminates, a specific layup structure orientated in 0° and ±45° is obtained. The manufacturing process of the vacuum resin infusion also resulted in positions with an increased matrix content, which also influences the laminate thickness of the face sheets. In consequence, the exact laminate structure at every position of the outer skin is not known and can therefore only be assumed theoretically. An open-cell rigid foam with a core thickness of approximately 22 mm was used as the sandwich core. To determine the bending stiffness of the EoL sandwich laminate, three-point bending tests were carried out according to EN 310. This revealed a bending stiffness of approximately 7850 N/mm², see figure 2 right.



Figure 2. EoL rotor blade and bending test according EN 310 from Fraunhofer Wilhelm-Klauditz-Institut (Peter Meinlschmidt – E-Mail: peter.meinlschmidt@wki.fraunhofer.de)

The outer skin of the segmented rotor blade within this study is supposed to be made of a composite material. A carbon fibre reinforced plastic (CFRP) laminate made of pre-impregnated woven fabric is produced by INVENT. The laminate layup consists of a symmetrical, biaxial structure in 0/90°-direction with 24 laminate layers. For concept I the epoxy adhesive Adekit A170-1 was selected. This adhesive has a high viscosity which allows the manufacturing of thick adhesive gaps and geometric fillets. For the debonding case the adhesive is also combined with TEPs of the type Expancel 031 DU40 at 20 w.-%. For the lower bonding gap in concept II, the following adhesives from literature are selected. These include the adhesives Araldite AV138, Araldite A2015, Adekit A170-1 and SikaForce 7752.

3. Numerical Modeling of the Adhesive T-joints

Two numerical models are created to investigate the design concepts, including the various geometrical parameters for adhesive fillet (concept I) and cleat (concept II) (Figure 3). The models have a depth of 60 mm. The EoL rib specimen is perpendicular to the CFRP laminate specimen and is additionally loaded by a transverse load. This is a simplified representation of a load case resulting from the bending of the rotor blade due to the wind or inertial forces acting on it.

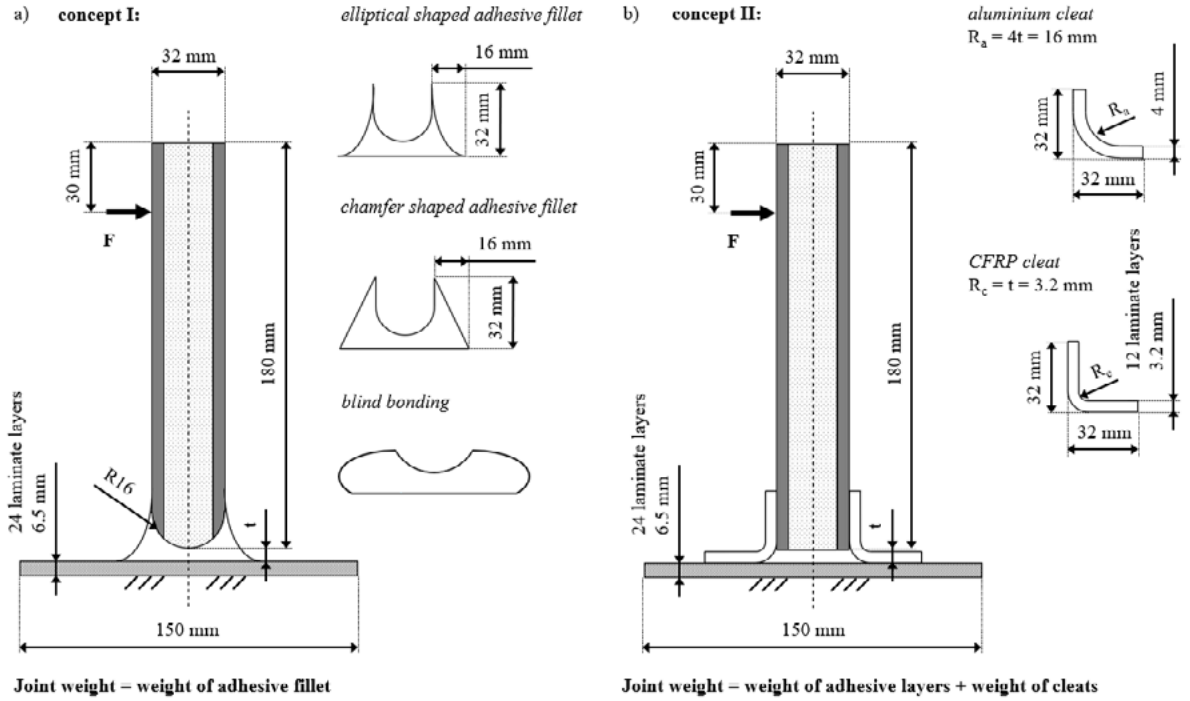


Figure 3. Cross section, dimensions and boundary conditions of the numerical model for design concept I (a) & II (b)

3.1 Material Parameters of the Adherends

To define the material parameters of the EoL material within the simulation software, a sandwich laminate is modeled whose face sheets consists of the layup $[(+45/-45/0)_3$ / core / $(+45/-45/0)_3]$. The bending load is applied to the face sheet with the outer layer of +45°. Each face-sheet has a total thickness of 5 mm. For the individual unidirectional layers of the face sheets, E-Glass fiber parameters from the Ansys database are assumed. An isotropic core body is placed between the face sheets. The shear stiffness of the core is adjusted iteratively until the bending stiffness of the EoL laminate matches the experimental bending tests according EN 310. This ensures a correct modeling of the bending stiffness of the EoL material for the bending load case. In the model, the nodal points of the face sheets and the foam core in contact are connected using a merge constraint type to increase convergence. The characteristic elastic values used for the semi-finished products can be seen in Table 1.

Table 1. Material parameters

Material	E_x [GPa]	E_y [GPa]	E_z [GPa]	ν_{xy}	ν_{yz}	ν_{xz}	G_{xy} [GPa]	G_{yz} [GPa]	G_{xz} [GPa]
GFRP UD	35	9	9	0,28	0,4	0,28	4,7	3,5	4,7
Foam Core	0,046	-	-	0,45	-	-	0,016	-	-
CFRP Woven	50,23	50,23	7,90	0,038	0,42	0,42	3,26	2,78	2,78
EN AW-7020	70	-	-	0,33	-	-	26,4	-	-

3.2 Model of Concept I

The adhesive fillet from concept I is numerically represented by a solid. To avoid inaccuracies in the stress or strain prediction, a mesh with a high meshing density and an element size of 1.2mm is defined [11]. The adhesive fillet is connected to the adherends via two joining surfaces by means of asymmetrical contacts. In addition, a material characteristic with multi-linear isotropic hardening is assigned to the adhesive joint. A maximum strain criterion of 2 % is defined for failure prediction according to the data sheet. Multiple numerical studies are carried out to determine an ideal fillet geometry. Additionally, to the influence of the thickness of the adhesive gap *t* between the adherends, the outer geometry of the fillet is investigated, see figure 4. Experimental tests of the different concept modifications are carried out to validate the simulations.

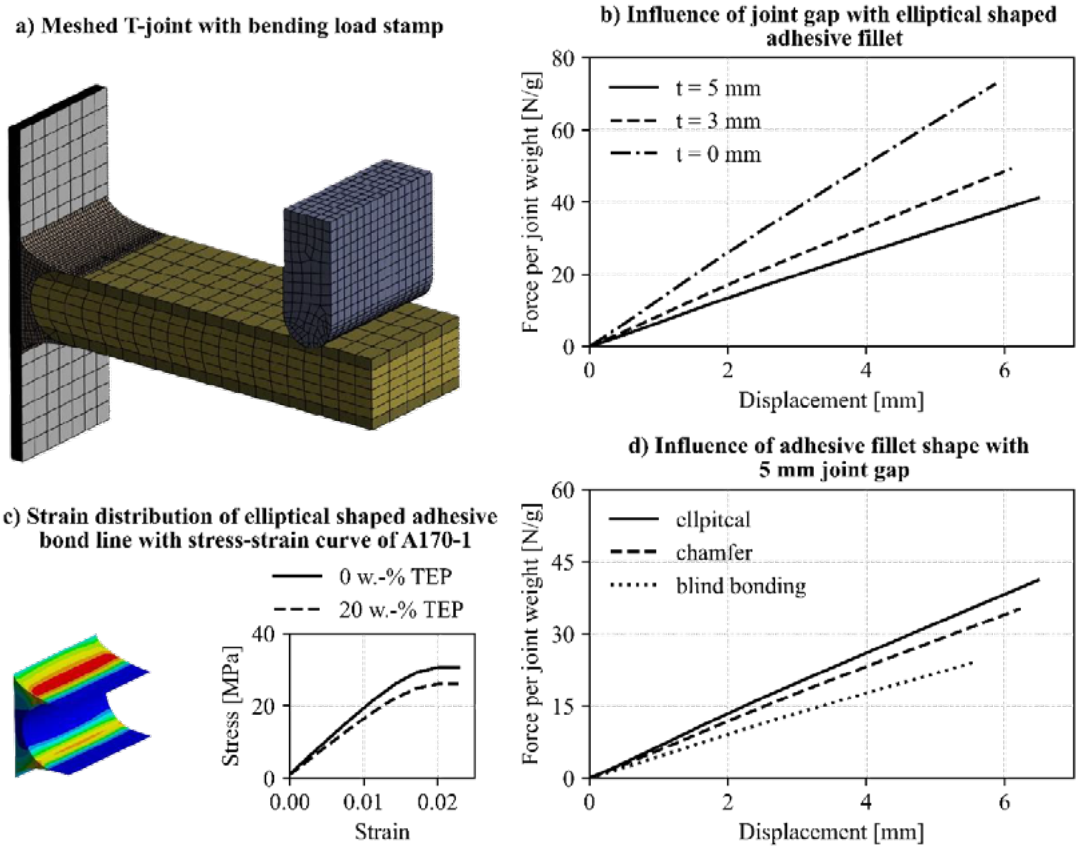


Figure 4. Results of numerical studies for concept I

The simulation demonstrates that for an elliptical shaped adhesive fillet an adhesive gap of 0 mm between the radius of the EoL rib and the outer skin achieves the highest load capacity per joint weight, see figure 4b. The fracture zone within the simulation is in line with the experimental results. A reduction of the adhesive gap with the same fillet geometry leads to an increase in the mass-related strength and stiffness of the T-joint, as there is less unstressed material between the adherends. Furthermore, the numerical simulations show that a fillet with an elliptical shape achieves the highest strength per joint weight and stiffness compared to the chamfer shaped adhesive fillet and the blind bonding, see figure 4d. The blind bonding in particular shows a significant drop in adhesive strength per joint weight by approximately 40 %. The experimental tests confirm this drop in strength. The main factor for the load capacity of the T-joint are the face-sheets of the EoL ribs. Thus, the reason for the decrease in strength is the reduced proportion of adhesive in contact with the face-sheets of the EoL rib. In addition, the test lot for the blind bonding tests show a standard deviation of over 60 %. To counteract this large standard deviation the safety factor should be increased. Blind bonding should therefore be avoided wherever possible.

Furthermore, the experiments exhibit that the use of TEPs results in a loss of strength. This must be considered within the model by scaling the material properties of the adhesive, see figure 4c. The reduction of mechanical properties due to the use of TEPs amounts to approximately 15 % in strength, which corresponds to previous studies from the literature [4, 5]. The corresponding downscaling of the modulus of elasticity is negligible within the simulation.

3.3 Model of Concept II

In the simulation model for concept II, the cleat is connected to the adherends via two contact definitions. These contacts are modeled with a contact modeling failure, which is defined by a bilinear traction separation law (TSL). The contacts represent the adhesive layers in the model using cohesive elements. The bonding gap is set to 0.2 mm and the contacts are assigned a corresponding contact stiffness K_n. The Mode I and Mode II behavior of the cohesive elements is coupled via a weighting parameter of two (default property of ansys). Within the material characteristics the damping factor is set to 0.01 s to increase the stability of the calculation. Finally, tangential sliding of the joining parts under normal pressure is blocked.
A literature review revealed various cohesive-zone model (CZM) material characteristics for structural epoxy adhesives, which are summarized in Table 2 [12]. These include the adhesives Araldite AV138 and Araldite A2015 from Huntsman and the Adekit A170-1 used in concept I. Numerous single lap shear tests were used to create the CZM material properties for the Adekit A170-1. The SF7752 adhesive from SikaForce is the only polyurethane (PU) based adhesive.

Table 2. Material parameters of adhesives for bilinear TSL characteristics [11]

Adhesive	E [GPa]	G [GPa]	t_n^0 [MPa]	t_s^0 [MPa]	G_{IC} [N/mm]	G_{IIC} [N/mm]	K_n [kN/mm^3]
AV138	4,89	1,56	39,45	30,20	0,20	0,38	24,45
A2015	1,85	0,56	21,63	17,90	0,43	4,70	9,25
A170-1	1,90	0,69	17,00	12,00	0,43	3,00	9,50
SF7752	0,49	0,19	11,48	10,17	2,36	5,41	2,45

Within concept II, numerical investigations with regard to the material of the cleats are also carried out. Aluminum EN AW-7020 and CFRP are applied, whereby the laminate structure of the CFRP is varied. Two biaxial laminate structures are chosen. The first is aligned at 0/90° and the second at ±45°.
The results of the numerical investigations in figure 5 show that under a bending load, the stiffness of the T-joint is mainly determined by the stiffness of the cleat. As a result, the CFRP cleats achieve a higher mass-related stiffness and strength compared to the aluminum cleat. A CFRP cleat with a more rigid 0/90°-laminate structure in bending attains the highest mass-related load capacity, see figure 5b. When using a CFRP cleat with a biaxial laminate structure of 0/90°-orientation, the structural epoxy adhesives AV138, A2015 and A170-1 are less effective than the more ductile PU adhesive SF7752 in terms of maximum joint weight-related force absorption, see figure 5c. This can be attributed to the increased fracture energy in Mode I, which delays the peeling of the upper cleat. In concept II it can therefore be assumed that a low strength in Mode I of a ductile adhesive can be compensated by a higher fracture toughness [13]. Furthermore, a PU adhesive should be preferred to a brittle epoxy adhesive for a T-joint under transverse loading.

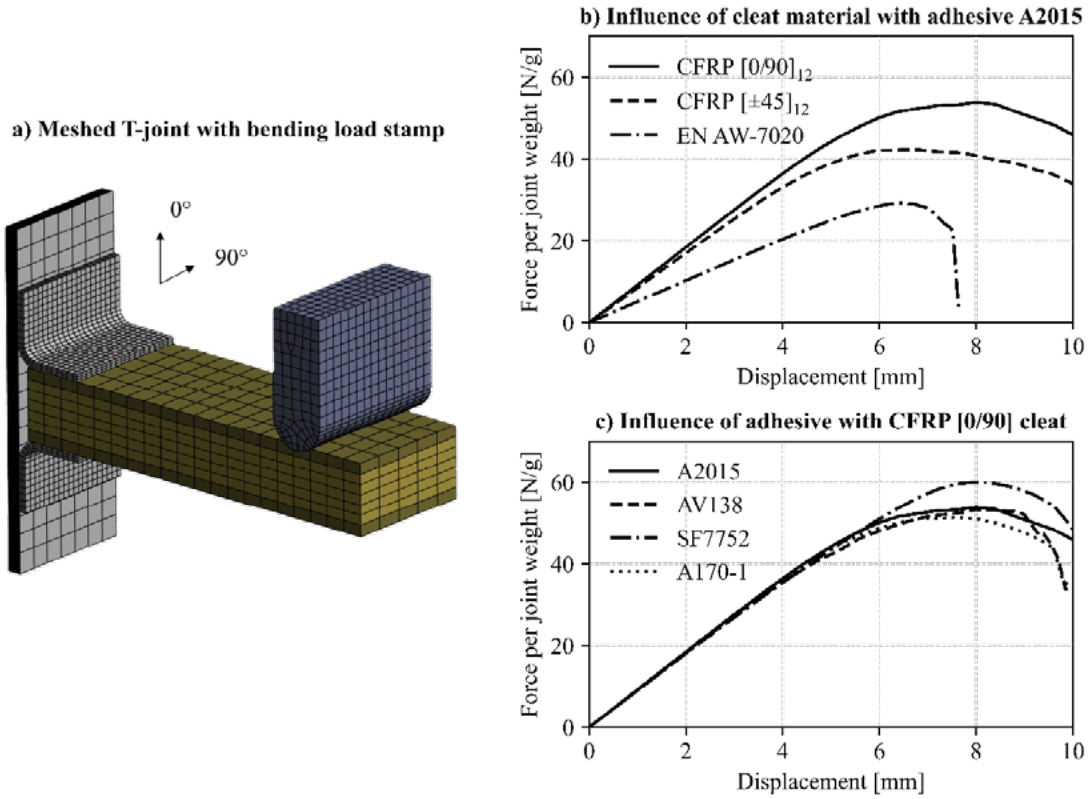


Figure 5. Results of numerical studies for concept II

4. Comparison of the Concepts

For the comparison of the concepts, the elliptical shaped adhesive fillet from concept I and the CFRP cleat with a 0/90°-layup from concept II are used. Both options are computed with regard to the highest maximum force per joint weight. The concepts are simulated with a 5 mm joint gap between the main adherends. The results from the numerical simulations are shown in figure 6 with respect to the force per joint weight, see figure 6a, and mass proportions, see figure 6b. In general, it should be stated that concept II surpasses the maximum strength by joint weight of concept I by approximately 50 %. Additionally, concept II achieves a higher maximum displacement with the more ductile PU adhesive.

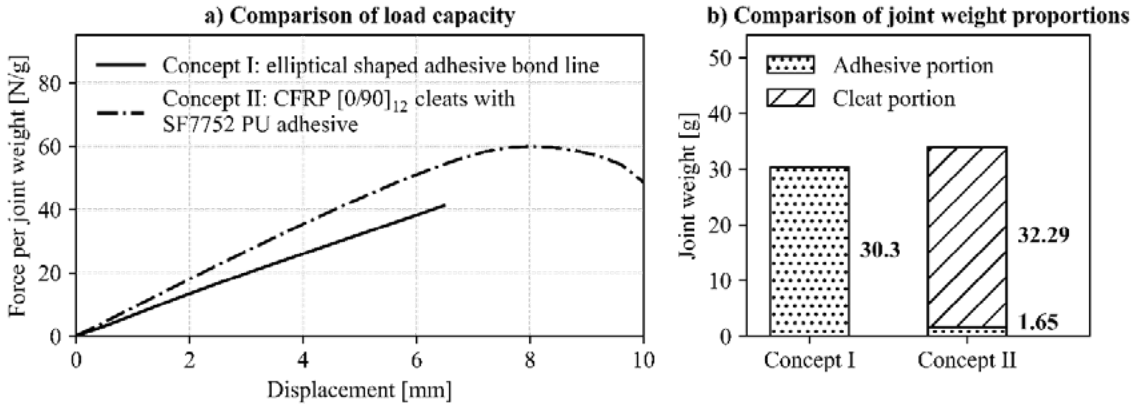


Figure 6. Comparison of configurations from concept I and II with a 5 mm joint gap

Considering the requirements of the industry, concept II is chosen for further development. The reason for this is the high adhesive consumption from concept I. In concept I the TEPs simplify the debonding

through the cohesive destruction of the adhesive bond line after a specific temperature application. The separation enables the reuse of the EoL rib and the FRP outer skin. However, for a new product life cycle, the adhesive fillet must be newly applied with a high adhesive consumption. In contrast, the adhesive consumption of concept II is significantly lower and reduces the amount of adhesive needed by approximately 95 %, see figure 6b. Despite the higher total mass for the joint of concept II, a higher level of sustainability can be fulfilled with less adhesive needed. In addition, both the EoL rib and the cleat can be returned to new product life cycles.

5. Conclusion

The present paper pursued the investigation of two different design concepts for T-joints in segmented rotor blades. Both concepts represent suitable adhesive T-joints for a modular design of a segmented rotor blade to safely absorb a bending load. The study enables the prediction of various parameter influences, which can be applied as design guidelines to specific use cases.
However, it is generally important to align the concept with the requirements and the application itself. Concept II with a CFRP cleat and a PU adhesive achieves the highest load capacity per joint weight. Consequently, concept II will be further explored. For this, the laminate structure, and the size of the adhesive surfaces to the adherends are designed based on a real rotor blade load case. Furthermore, the design of the cleat is extended by a double curvature, which enables a defined starting point for a peeling separation of the cleat from the EoL rib after the product life cycle. Since PU adhesives with increased ductility offer advantages in terms of load capacity under a peeling load, a possible application of adhesive films with higher fracture energy is being considered.

Acknowledgements

This paper is a result of the research project RECREATE and has received funding from the European Union's Horizon Europe research and innovation program under Grant Agreement No. 101058756.

References

[1] M. Peeters, G. Santo, J. Degroote and W. V. Paepegem, The Concept of Segmented Wind Turbine Blades: A Review, *Energies*, 10(8), 2017.
[2] P. Meinlschmidt, J. Peinke and G. Gülker, Rotorblatt und Rotorblattspitze, DE 102012015353, August 2012
[3] A. S. E. Mendoza, S. Yao, M. Chetan and D. T. Griffith, Design and Analysis of a Segmented Blade for a 50 MW Wind Turbine Rotor, *Wind Engineering*, 46(4), pp. 1146-1172, 2022.
[4] M. D. Banea, L. F. M. da Silva, R. J. C. Carbas and R. D. S. G. Campilho, Mechanical and thermal characterization of a structural polyurethane adhesive modified with thermally expandable particles, *International Journal of Adhesion & Adhesives*, 54, pp. 191-199, 2014.
[5] G. Piazza, M. Burczyk, M. Gerlini-Romagnoli, G. Belingardi and S. A. Nassar, Effect of thermally expandable particle additives on the mechanical and reversibility performance of adhesive joints, *Journal of Advanced Joining Processes*, 5, 2022.
[6] G. Di Bella, C. Borsellino, E. Pollicino and V. F. Ruisi, Experimental and numerical study of composite T-joints for marine application, *International Journal of Adhesion & Adhesives*, 30, pp. 347-358, 2010.
[7] G. Luo and C. Kuo, Application of Bionic Design to FRP T-Joints, *Applied Composite Materials*, 25, pp. 983-999, 2018.
[8] Y. Hua, A. R. M. Kasavajhala and L. Gu, Elastic-plastic analysis and strength evaluation of adhesive joints in wind turbine blades, *Composites Part B: Engineering*, 44(1), pp. 650-656, 2013.
[9] C. Bhat, D. J. Noronha and F. A. Saldanha, Structural Performance Evaluation of Segmented Wind Turbine Blade Through Finite Element Simulation, *International Journal of Mechanial & Mechatronics Engineering*, 9, pp. 996-1005, 2015.
[10] L. F. M. da Silva and R. D. Adams, Techniques to reduce the peel stresses in adhesive joints with composites, *International Journal of Adhesion & Adhesives*, 27, pp. 227-235, 2007.
[11] L. D. C. Ramalho, R. D. S. G. Campilho, J. Belinha and L. F. M. da Silva, Static strength prediction of adhesive joints: A review, *International Journal of Adhesion & Adhesives*, 96, 2020.
[12] U. T. F. Carvalho and R. D. S. G. Campilho, Validation of pure tensile and shear cohesive laws obtained by the direct method with single-lap joints, *International Journal of Adhesion & Adhesives*, 77, pp. 41-50, 2017.
[13] J. Pettersson, Analysis and Design of an Adhesive Joint in Wind Turbine Blades, *Master's Dissertation*, Lund University, Structural Mechanics, 2016.

PROMISES AND CHALLENGES OF USING ELECTRICAL RESISTANCE CHANGE TO DETECT DAMAGE IN CARBON FIBRE COMPOSITE LAMINATES

J. David. Acosta*, Andrew Hamilton and Meisam Jalalvand

Engineering Materials, School of Engineering, University of Southampton, England, UK
*Email: j.d.acosta-correa@soton.ac.uk

Keywords: Electrical resistance, CFRP, Finite element method (FEM), Structural health monitoring (SHM).

Abstract
Monitoring the structural health of composite materials, specifically carbon fibre composites (CFRP), can be effectively achieved by assessing damage via electrical resistance change. This work proposes a 4 X 4 electrode array to detect damage and determine the minimum detectable crack length for this electrode configuration. This research studies experimentally and numerically, using the finite element method (FEM), the electrical resistance changes due to the presence of a crack in different CFRP laminates. The results showed that the minimum detectable crack length would depend on the monitored area. It was found that the minimum detectable crack length for a central crack in multidirectional laminates, such as [0,90], [+45,-45], and $[0,90,45,-45]_s$ is 27 % of the monitored area, while for a unidirectional laminate is 93 %. Alternatively, the monitored area could be scaled to achieve a required detectable crack length using an array of 4 X 4 electrodes patterned over the area of interest. In conclusion, a small monitored area with four electrodes is able to detect a small crack, and this basic electrode arrangement can easily be scaled and patterned to achieve specific health monitoring requirements.

1. Introduction

One of the methods to monitor the health of composite materials, specifically carbon fibre composites (CFRP), is the electrical resistance change (ERC) method. It is a relatively straightforward and non-intrusive method that could detect damage on large structures such as aircraft, bridges, and ships. ERC faces some challenges, principally because the damage that could lead to failure is generally localised and may have an insignificant effect on the overall ERC [1]. As a result, several electrodes are required to detect small cracks, increasing the cost and possibly the structure's weight, which is relevant in aerospace structures.

Carbon fibre-reinforced polymer (CFRP) composites have been used as structural materials because they have several desirable properties, including a high tensile stiffness-to-weight ratio and chemical resistance. Besides, their electrical properties are measured to detect changes in the material, identifying variables such as stress, strain, damage or temperature [2]. CFRP is electrically orthotropic, and for unidirectional (UD) CFRPs, the longitudinal conductivity is much higher than that in transverse and trough-thickness directions [3].

Although the damage has been successfully detected, a high number of electrodes on a relatively small area to detect small cracks makes this approach very difficult to implement on a full-scale structure. Some studies have used multiple electrodes, establishing a minimum detectable damage size according to a sensing area where it is possible to detect damage. Idris et al. [4] found that the minimum detectable

damage area for a woven carbon plate of 113 mm X 84 mm was about 0.04% of the sensing area using fourteen electrodes and an electrode separation of 26 mm in the X-direction and 16 mm in the Y-direction, as shown in Figure 1(a). On the other hand, Cagáň [5] concluded that using nineteen electrodes on a 100 mm diameter circular plate, as shown in Figure 1(b), the minimum detectable damage area was 0.1% of the total sensing area. Additionally, the data to process and the wiring increase with the number of electrodes to sense damage, increasing the weight and cost of the SHM system and compromising its attractiveness.

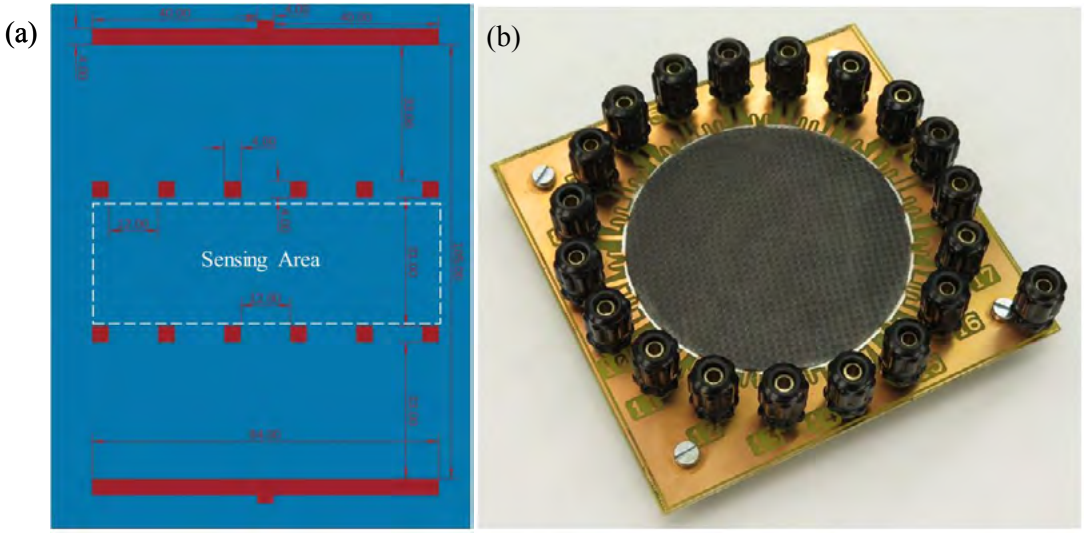


Figure 1. (a) Fourteen [4] and (b) nineteen electrode arrays [5].

Also, electrical resistance change depends on stacking sequence due to the electrical conductivity mechanisms of CFRP laminates, such as conductivity along the fibres and due to contact between fibres, also known as inter-fibre contacts [6]. Then, detecting damage in composite structures depends on the laminate, and different stacking sequences should be evaluated to know the electrical behaviour of each case.

This work proposes an electrode array with the minimum number of electrodes to monitor a rectangular area. Then, a 4 X 4 electrode array is proposed to detect damage and determine the minimum detectable crack length for this electrode configuration in different CFRP laminates, such as unidirectional (UD), cross-ply (CP) [0/90], 45-angle ply (45AP) [45/-45] and quasi-isotropic (QI) $[0/90/45/-45]_S$. The electrical resistance change is experimentally and numerically studied using the finite element method (FEM). Experimentally, the electrical resistance is measured using the two-probe method, minimising the wiring and the amount of data to process, compared to the four-probe method. This simple electrode configuration can be replicated in a structure as much is required to scale their application to achieve specific health monitoring requirements.

2. Concept

CFRPs have demonstrated their capacity to detect damage by changing their electrical resistance [7], [8]. However, reducing the number of electrodes would help to decrease the weight and complexity of the system. Therefore, we propose a simple electrode configuration on a sensing layer that can be replicated in a structure as much is required to be part of an SHM system. Figure 2 shows the schematic of an aeroplane wing to illustrate the concept and how it could be implemented in practice.

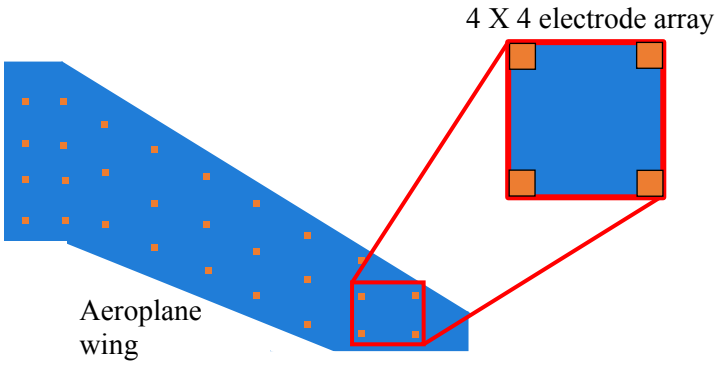


Figure 2. 4 X 4 electrode array concept.

Four electrodes are placed in each corner of the sensed area to maximise the monitoring area with the minimum number of electrodes. These sensing layers are made of carbon plies, and the electrodes are on the top corners. From the four electrodes, A, B, C and D, it is possible to measure the electrical resistance change in six different pairs of electrodes using the two-probe method, A-B, A-C, A-D, B-C, B-D and C-D, as it is illustrated in Figure 3**Error! Reference source not found.** in a cross-ply laminate. Notice that this method can be applied to any laminate, and a few options are explored in this work.

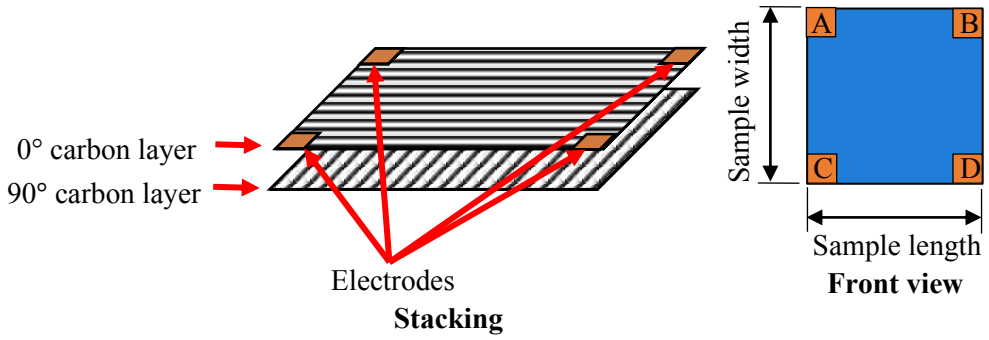


Figure 3. Schematic of (a) a cross-ply laminate with a 4 X 4 electrode array.

3. Method

Many stacking sequences can be studied as sensing laminates. However, fewer plies imply lower prices and weight in the monitored structure. Some of the most common laminates, such as UD, cross-ply (CP), ±45 angle ply (±45AP) and quasi-isotropic (QI) stacking sequences, are numerically evaluated using the Finite Element Method (FEM) to determine the laminate with fewer plies capable that allows detection of damage. Table 1 lists the laminates evaluated in this work.

Then, to validate the numerical model, experiments are performed on the laminate with the fewest plies capable of detecting damage.

Table 1. Evaluated sensing laminates.

Laminate	Layup	Laminate thickness [mm]
Unidirectional (UD)	[0]	0.029
Cross-ply (CP)	[0/90]	0.058
±45 angle ply (±45AP)	[45/−45]	0.058
Quasi-isotropic (QI)	$[0/90/45/-45]_s$	0.236

3.1. Numerical models

A 3D finite element analysis (FEA) is developed in Abaqus software to study the electrical resistance change under specific crack lengths for the proposed laminates. Numerical models of plates of 150 mm X 150 mm were numerically evaluated. First, an undamaged geometry is simulated to know the initial resistance without damage. Models with different crack lengths are created to calculate the resistance change with the new resistance. Then, two parts of the sample were modelled to create the crack, tying them at the edges except for the crack area and thus creating the crack. In this way, the tied areas act as part of a continuum material, and the untied areas act as a crack, as shown in Figure 4.

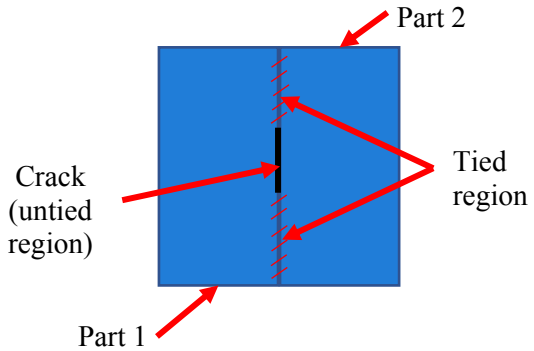


Figure 4. Schematic of the numerical model.

The finite element model was built using individual layers meshed with hexahedral elements type Q3D78 to simulate the electrical behaviour. The mesh size is 1.0 mm, which guarantees a good quality mesh.

CFRP material is modelled as a homogeneous material, which means that the electrical behaviour modelled is the one for a unidirectional ply and not the behaviour for fibre and matrix, separately. The different layers are tied to each other.

Laminates are modelled with four 5 mm X 5 mm X 0.02 mm thick electrodes on the top corners of the plate. An electrical potential difference of 0.6 V between each pair of electrodes is imposed because of the potential difference applied by the multimeter in the experimental tests. This way, the reaction current is obtained by calculating the electrical resistance through Ohm's law, $R = V/I$. Where R is resistance, V is the potential difference, and I is electrical current. The carbon composite chosen for these laminates is the M46JB/513 epoxy, whose electrical properties, like the properties of copper for electrodes, are listed in Table 2.

Table 2: Electrical properties

Material	Longitudinal resistivity [Ωmm]	Transverse resistivity [Ωmm]
M46JB carbon fibre [9]	0.09×10^{-3}	
M46JB/513 epoxy[a]	0.016	24.73
Copper	1.68E-5	

[a] *Found experimentally.*

3.2. Experiments

The material used for the experimentation is UD thin-ply carbon fibre prepreg from North thin-ply technology having M46JB carbon fibre and 513 epoxy resin system with a ply thickness of about 29 microns when cured. The areal weight is 29 gsm with a fibre volume fraction of 53%, as specified in the manufacturer's datasheet [9].

Conventional processes for curing standard prepregs were used. The M46JB/513 cross-ply laminate was stacked up with 20-micron thickness copper electrodes located accurately in the top corners and pressed firmly by hand onto the prepreg layup. Both resin systems have a similar cured cycle. Then, the prepregs were cured in an autoclave for the recommended temperature and pressure cycle for the Hexcel in the 913 epoxy resin, 90 minutes at 125 C and 7 bars.

Three specimens of 150 mm X 150 mm were manufactured. After cured, the electrical resistance was measured on the electrodes with an HMC 8012 digital multimeter with an accuracy of ±0.05-0.005% following the two-point probe method. A central crack was cut in the laminate using a Dremmel tool at 30000 RPM, avoiding extra damage such as delamination. Then, the resistance was measured, and the specimen was cut again, increasing the crack length and repeating the measurement process several times.

4. Results and discussion

Different central crack lengths were simulated to evaluate their effect on the electrical resistance change for UD, CP, ±45AP and QI sensing laminates. Figure 5 shows the increasing electrical resistance change with the crack length between the A-B, A-C and A-D electrodes. The electrical resistance change is defined as $\Delta R/R_i$, where ΔR is the difference between the initial resistance without the crack and the final resistance after the crack. R_i, is the initial resistance, where the sample does not have any crack. Due to the symmetric conditions, the resistance change for the pair of electrodes, C-D, B-D and B-C, is the same as that of A-B, A-C and A-D electrodes, respectively. Therefore, only three of the six pairs of electrodes have all the information required for the analysis.

Each of the evaluated laminates showed different resistance change values. The primary conductive path in UD laminates is along the fibre direction, as shown in Figure 6. For this reason, the resistance change is zero up to a crack length/sample width of 0.93, as shown in Figure 5 (a), where the crack started to interrupt the conductive path between electrodes A and B. CP and ±45AP laminates presented the exact electrical resistance change, then only a graph is presented for both laminates. On the other hand, multidirectional laminates present an increasing change of electrical resistance even at small crack lengths, as illustrated in Figure 5 (a), (b). This increasing electrical resistance change is due to the conductive path combining fibre and transverse direction for multidirectional laminates, as shown in Figure 6. Then, multidirectional laminates are more sensitive to detecting more minor cracks than UD laminates, as shown in Figure 5 (a), (b), and (c).

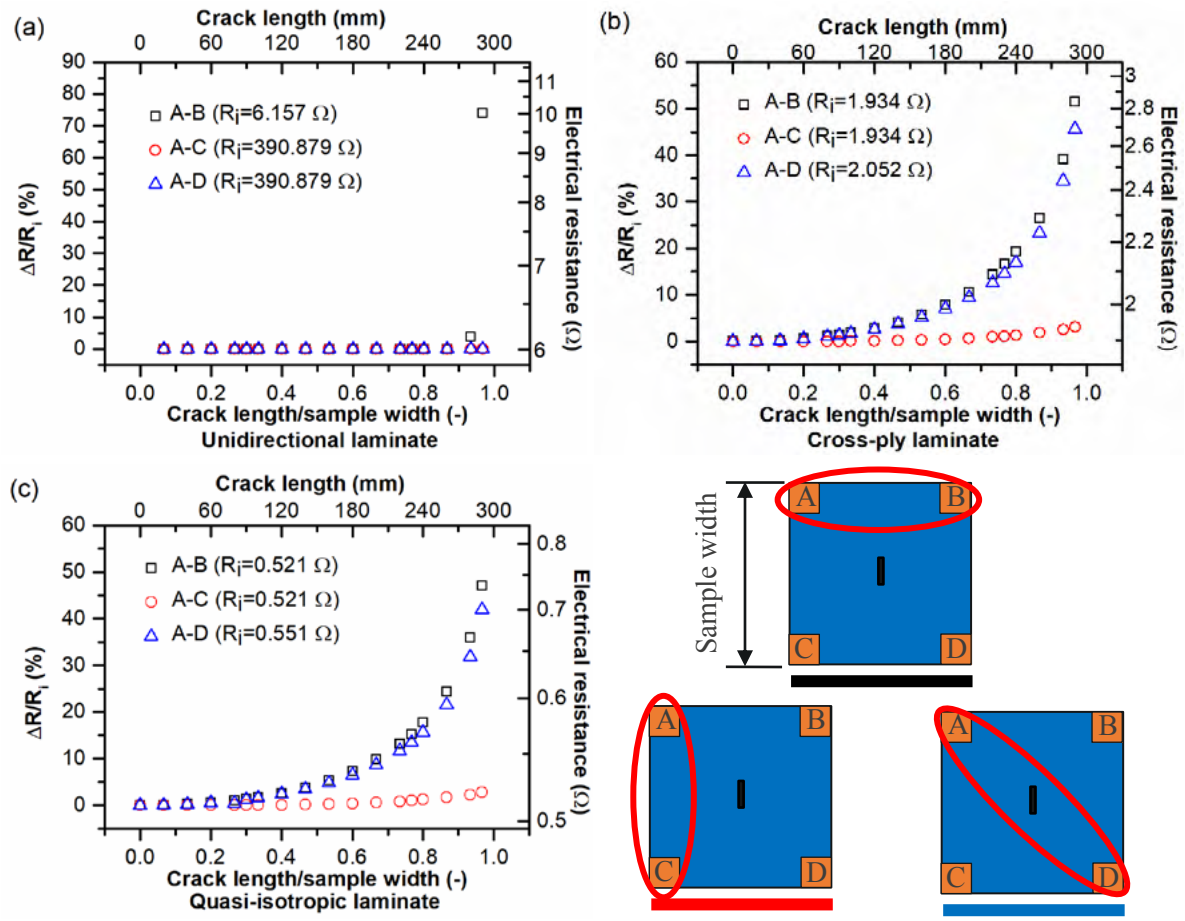


Figure 5. Numerical results for the effect of the crack length in the electrical resistance response in (a) unidirectional, (b) cross-ply, ±45 angle ply and (c) quasi-isotropic laminates.

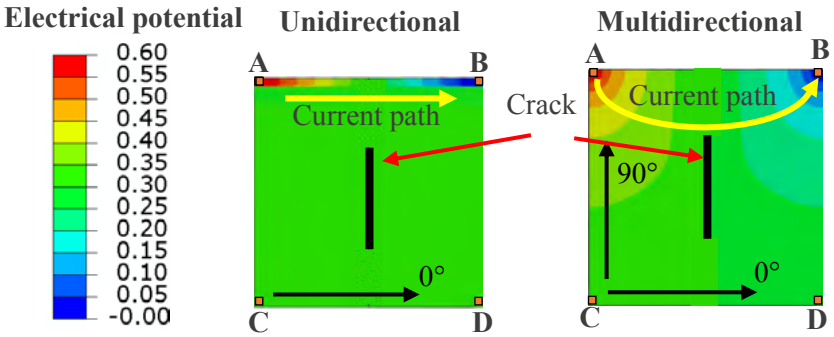


Figure 6. Electrical potential distribution for unidirectional and multidirectional laminates.

The experimental and numerical results for the electrical resistance change vs. crack length/sample width ratio are presented in Figure 7 for the CP laminate. Both results show a similar increment of the resistance change with the crack length. In this way, the FEM model was validated. Additionally, the resistance change increases non-linearly with the crack length. However, electrodes A-C are parallel to the crack orientation. Hence, the resistance change is lower than that of electrodes A-B and A-D because the conductive path is not interrupted directly, as with the other electrodes.

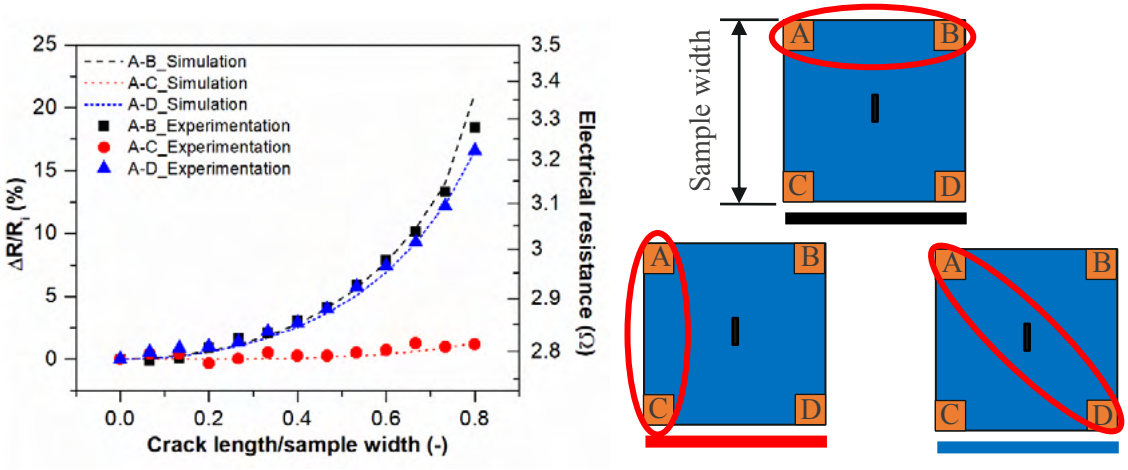


Figure 7. Experimental and simulation results for the effect of the crack length on the electrical resistance.

5. Conclusions

It was shown numerically and experimentally that the 4 X 4 electrode array proposed in this work detects damage. Besides, the minimum detectable crack length for a central crack in multidirectional laminates, such as CP, 45AP and QI, is 27 % of the monitored area, while for a unidirectional laminate is 93 %.

The crack should interrupt the conductive path between electrodes to be detected. Therefore, multidirectional laminates such as CP, 45AP and QI can detect more minor cracks than UD laminates. This response is because the conductive path for UD laminates is mainly along the fibres. In contrast, the conductive path combines electrical conduction along the fibres and transverse direction for multidirectional laminates.

The sensing area is directly related to the minimum detectable crack length. Then, it is possible to design a structural health system to monitor different structures according to their needs.

References

[1] C. R. Farrar and K. Worden, "An introduction to structural health monitoring," *Philosophical Transactions of the Royal Society A: Mathematical, Physical and Engineering Sciences*, vol. 365, no. 1851, pp. 303–315, 2007, doi: 10.1098/rsta.2006.1928.

[2] D. D. L. Chung, "A review of multifunctional polymer-matrix structural composites," *Compos B Eng*, vol. 160, no. November 2018, pp. 644–660, 2019, doi: 10.1016/j.compositesb.2018.12.117.

[3] J. C. Abry, Y. K. Choi, A. Chateauminois, B. Dalloz, G. Giraud, and M. Salvia, "In-situ monitoring of damage in CFRP laminates by means of AC and DC measurements," *Compos Sci Technol*, vol. 61, no. 6, pp. 855–864, 2001, doi: 10.1016/S0266-3538(00)00181-0.

[4] M. K. Idris, P. Naderi, G. W. Melenka, and G. Grau, "Damage location sensing in carbon fiber composites using extrusion printed electronics," *Functional Composites and Structures*, vol. 3, no. 4, p. 045001, Dec. 2021, doi: 10.1088/2631-6331/ac3731.

[5] J. Cagáň, "Hardware implementation of electrical resistance tomography for damage detection of carbon fibre–reinforced polymer composites," *Struct Health Monit*, vol. 16, no. 2, pp. 129–141, Mar. 2017, doi: 10.1177/1475921716666004.

[6] D. Wang and D. D. L. Chung, “Through-thickness piezoresistivity in a carbon fiber polymer-matrix structural composite for electrical-resistance-based through-thickness strain sensing,” *Carbon N Y*, vol. 60, pp. 129–138, 2013, doi: 10.1016/j.carbon.2013.04.005.

[7] H. D. Roh, S. Y. Oh, and Y. Bin Park, “Self-sensing impact damage in and non-destructive evaluation of carbon fiber-reinforced polymers using electrical resistance and the corresponding electrical route models,” *Sens Actuators A Phys*, vol. 332, p. 112762, 2021, doi: 10.1016/j.sna.2021.112762.

[8] A. Todoroki, Y. Mizutani, Y. Suzuki, and D. Haruyama, “Fatigue damage detection of CFRP using the electrical resistance change method,” *International Journal of Aeronautical and Space Sciences*, vol. 14, no. 4, pp. 350–355, Dec. 2013, doi: 10.5139/IJASS.2013.14.4.350.

[9] North thin ply technology, “M46JB carbon fibre datasheet.” Accessed: Apr. 28, 2023. [Online]. Available: https://www.thinplytechnology.com/datasheets

A NEW SEMI-DISCRETE CONTINUUM DAMAGE MODELLING FRAMEWORK FOR COMPOSITES WITH FOCUS ON OPEN-HOLE COMPRESSION FAILURE

Amit Chaudhary[1], Supratik Mukhopadhyay[1]

[1] Indian Institute of Technology Kanpur, Department of Mechanical Engineering, Kalyanpur, Kanpur, Uttar Pradesh 208016, India
Email: chamit@iitk.ac.in
Email: smukh@iitk.ac.in, Web Page: https://www.iitk.ac.in/new/supratik-mukhopadhyay

Keywords: Composites, Kink-band, Continuum damage mechanics, Open Hole Compression, Finite Element Analysis

Abstract

Fibre-reinforced composites are lightweight and possess many attractive mechanical properties such as high specific stiffness, specific strength, and improved fatigue endurance etc. Intriguingly, the compressive strength of unidirectional composites is approximately 30% lower than their tensile strength [1]. The main reason for this asymmetry is related to a unique instability-driven failure mechanism known as 'fibre kinking' under compression, which promotes early structural failure. Fibre kinking is triggered by local fibre misalignments, which, when subjected to compressive loading, promote further fibre rotation, resulting in the formation of a narrow kink band of very high localized shear strain. This eventually propagates, causing a sudden and unstable structural collapse. To simulate fibre kinking in a numerical framework, continuum damage mechanics models are typically employed. However, their smeared stiffness degradation methodology makes it impossible to capture the kinematics of kink formation and evolution accurately. In the current work, a novel three-dimensional semi-discrete continuum damage modelling framework, implemented in commercial software as a user-defined material package, is applied to predict failure in open-hole compression laminates. Several benchmark cases are demonstrated showing the effectiveness of the present kink-band modelling method.

1. Introduction

High demand for the reduction of weight in structures has led to the use of composite materials in the aerospace industry. High-performance structural components with lighter weight can be obtained by using composite materials. The pronounced anisotropy and heterogeneity observed in unidirectional fibre-reinforced composites give rise to distinct failure mechanisms, varying significantly based on the imposed load conditions. The primary mode of failure under longitudinal compression loading is fibre kinking [2]. Understanding, modelling and finally predicting the compressive response of CFRP material is a long-standing and unresolved issue. It is therefore important to develop a robust physically based failure model for progressive analysis of compressive damage. To estimate the compressive strength associated with kink band development, many theoretical models can be found in the literature.

Rosen [3] developed a model on fibre micro-buckling and the fibre's buckling stresses can be obtained by minimizing the internal energy. Rosen's model exhibited an overestimation in predicted outcomes when compared with experimental results [4]. Argon [5] considered kinking as a separate failure mode and proposed the kinking model by assuming initial misalignment angle is the only reason for kinking. Budiansky [6] improved Argon's model by considering the effect of matrix shear yield strain. Kinking is initiated by the formation of a close loop between fibre initial misalignment and shear stress between fibres. Budiansky and Fleck [7] developed fibre kinking theory (FKT) for kink band initiation and propagation. In a numerical framework, Pinho et al. [8,9] developed and implemented a 3D progressive

fibre kinking model. An embedded crack model within a continuum damage framework is usually employed to model fibre kinking. A set of three-dimensional failure criteria for laminated fibre-reinforced composites denoted LaRC04, is proposed [10]. Leone et al. [11] predict kinking using deformation gradient tensor decomposition (DGD) and Bergan et al. [12] created a semi-discrete mesoscale constitutive damage model by considering shear nonlinearity to represent the fibre kinking phenomenon accurately. Jansson and Fagerström [13] formulated the physical behaviour of kinking in a novel way. In contrast to the traditional model, which usually shows a constant plateau after initial softening, their better method provides a characteristic stiffening effect at higher strains.

This paper seeks to advance beyond the limitations of a smeared formulation by introducing a kinematically enriched formulation that implicitly identifies the kink band and the undamaged bulk within a single unified volume. Given the narrow width of the kink band, a smeared formulation fails to capture the strong variation in strain across this region. To address this limitation, our current study employs a two-scale mesoscale continuum damage mechanics model tailored for longitudinal compression. This model explicitly accounts for the strong strain variation within the localized kink band in comparison to the undamaged bulk region [14]. The model's compressive strength is predicted using Finite Element analysis, and then compared to experimental results from literature. Stress-strain curves show excellent agreement between predicted and experimental data.

2. Formulation of two-scale model

In engineering composites, the fibres typically aren't perfectly straight. We incorporate an initial misalignment to address this imperfection in our current model. When these misaligned fibres are subjected to compressive loading, they can trigger fibre kinking (see Figure 1).

2.1. Geometrical description

Kinking, we assume, occurs within a transversely isotropic ply, uni-directional lamina under compressive loading. We consider a volume of the whole continuum, Ω and the length in 1- direction is H. The localization kink band of the thickness (w_{KB}) and volume (Ω_{KB}) surrounded by a bulk material, Ω_B as shown in Figure 1. Assuming that the average cross-section area of localization kink band and

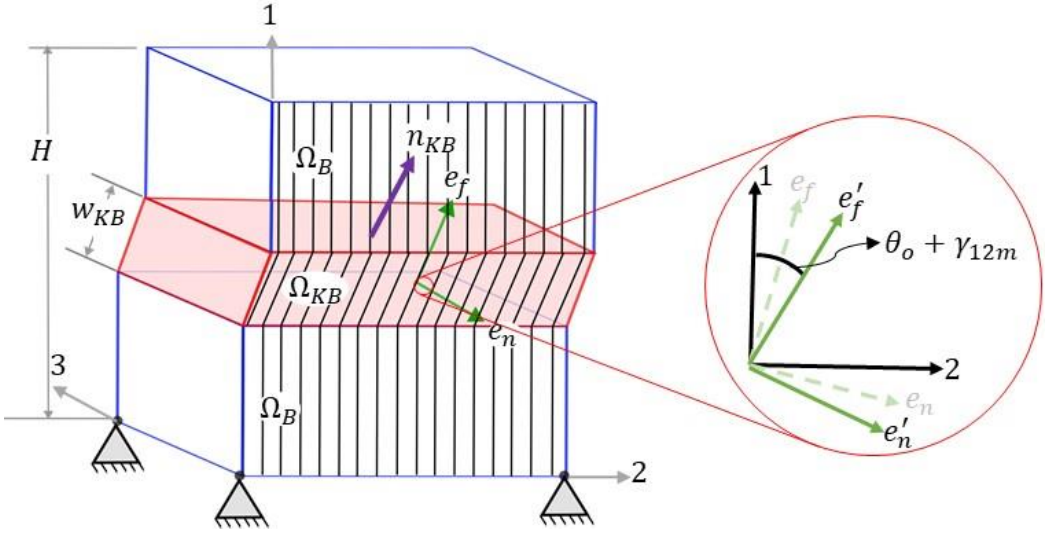


Figure 1. Schematic illustration of kink band formation in Deformed configuration.

outside bulk material is the same i.e. A and volume of the whole continuum is Ω. The volume fraction (η) of the localization zone is:

$$\eta = \frac{\Omega_{KB}}{\Omega} = \frac{w_{KB}A}{\Omega} \tag{1}$$

The characteristic length of considered volume, η is the ratio of considered volume to element length in 1- direction i.e. $H = \Omega/A$, then the volume fraction becomes:

$$\eta = \frac{w_{KB}}{H} \tag{2}$$

The volume fraction η in this configuration can be defined as the ratio length of the localized kink band and the length of the whole element.

2.2. Strain decomposition

Within the entire domain (Ω), the overall stress and strain are represented as $\boldsymbol{\sigma}$ and $\boldsymbol{\varepsilon}$ respectively, while the stress and strain components within and outside the localization band are denoted by $(\boldsymbol{\sigma}_{KB}, \boldsymbol{\varepsilon}_{KB})$ and $(\boldsymbol{\sigma}_{B}, \boldsymbol{\varepsilon}_{B})$ respectively.
The strain rate inside and outside of the localisation band can be expressed by following mixture theory:

$$\dot{\boldsymbol{\epsilon}} = \eta\dot{\boldsymbol{\epsilon}}_{KB} + (1-\eta)\dot{\boldsymbol{\epsilon}}_{B} \tag{3}$$

For a very thin localization kink band ($w_{kb} \ll H$), the rate of inelastic strain [15] within the band can be approximated as:

$$\dot{\boldsymbol{\epsilon}}_{KB} = \dot{\boldsymbol{\epsilon}}_{B} + \frac{1}{w_{kb}}(n_{KB} \otimes [\![\dot{\boldsymbol{u}}]\!])^{sym} \tag{4}$$

Where $[\![\dot{\boldsymbol{u}}]\!]$ is the velocity jump across the opposite sides of the localization band, n_{KB} denotes the localization band's unit normal vector and $\otimes$ is the dyadic product. Solving Eq. (3) and Eq. (4). Strain rate inside and outside of the localisation band can be obtained in terms of incremental macro strain ($\dot{\boldsymbol{\epsilon}}$) and velocity jump ($[\![\dot{\boldsymbol{u}}]\!]$).

$$\dot{\boldsymbol{\epsilon}}_{KB} = \dot{\boldsymbol{\epsilon}} + \frac{1-\eta}{w_{KB}}(n_{KB} \otimes [\![\dot{\boldsymbol{u}}]\!])^{sym} \tag{5}$$

and

$$\dot{\boldsymbol{\epsilon}}_{B} = \dot{\boldsymbol{\epsilon}} - \frac{\eta}{w_{KB}}(n_{KB} \otimes [\![\dot{\boldsymbol{u}}]\!])^{sym} \tag{6}$$

The incremental macro strain in the global frame is determined by solver. To derive the velocity jump, we start by integrating the constitutive equations for stress rate both inside and outside the localization band into the traction continuity equation in its rate form. This equation ensures that the traction rate inside the band ($\dot{t}_{KB}$) matches that outside the band ($\dot{t}_{B}$). The traction continuity equation simplifies to:

$$\dot{\sigma}_{KB} \cdot n_{KB} = \dot{\sigma}_{B} \cdot n_{B} \tag{7}$$

By substituting the stress rates inside and outside the localization band, we get:

$$\mathbb{D}_{KB} : \dot{\boldsymbol{\epsilon}}_{KB} \cdot n_{KB} = \mathbb{D}_{B} : \dot{\boldsymbol{\epsilon}}_{B} \cdot n_{B} \tag{8}$$

where $\mathbb{D}_{B}$ is typically a linear elastic stiffness matrix and $\mathbb{D}_{KB}$ is a non-linear elastic stiffness matrix. Note that the inplane shear response in the current model is assumed to be non-linear. In constitutive response all other components are linear, and only 12 local material direction relations are non-linear. This shear non-linearity can be idealised by using the Ramberg-Osgood [16] type model as follows:

$$\gamma_{ij} = \frac{1}{G_{ij}}\left[\tau_{ij} + \alpha_{pl}\,\mathrm{sign}(\tau_{ij})\left|\tau_{ij}\right|^{n_{pl}}\right] \tag{9}$$

where α_{pl} and n_{pl} are used to fit the experimental data.

2.3. Calculation of macro stress to return the solver

The macro stress behaviour, unlike macro strain behaviour, cannot be described by an averaged form following mixture theory. Instead, it is elucidated from the virtual work equation, which states that the work produced by macro stress and strain rate should equate to the volume-averaged work due to stresses and strain rates inside and outside the localization zone. The macroscopic behaviour inside the localization band and the remaining part can be expressed by the Hill-Mandel [17] equation as follows:

$$\boldsymbol{\sigma} : \dot{\boldsymbol{\varepsilon}} = \eta\, \boldsymbol{\sigma}_{KB} : \dot{\boldsymbol{\varepsilon}}_{KB} + (1-\eta)\, \boldsymbol{\sigma}_{B} : \dot{\boldsymbol{\varepsilon}}_{B} \tag{10}$$

Substituting the value of $\dot{\boldsymbol{\varepsilon}}_{KB}$ and $\dot{\boldsymbol{\varepsilon}}_{B}$ in terms $\dot{\boldsymbol{\varepsilon}}$ of from Eq. (5) and (6) into the Eq. (10) and rearranging the above equation in terms of primary variables (i.e. $\dot{\boldsymbol{\epsilon}}$ and $[\![\dot{\boldsymbol{u}}]\!]$) and applying traction continuity conditions. The macro stress behaviour with two different region's stress can get:

$$\boldsymbol{\sigma} = \eta\, \boldsymbol{\sigma}_{KB} + (1-\eta)\, \boldsymbol{\sigma}_{B} \tag{11}$$

As can be seen from the above Eq. the volume-averaged response forms of both macro stress and strain can co-exist while meeting the Hill-Mandel condition.

3. Single-element test model and material properties

The VUMAT model was implemented in Abaqus to examine various aspects of its behaviour through single-element analysis. This section focuses on highlighting several key features of the model. Specifically, we investigate the influence of kink bandwidth, and the behaviour of the localized region and the bulk region outside of it on the constitutive response of the model. The material used in this study is IM7/8552, and a summary of its properties can be found in Table 1. A single-element model (C3D8R) was employed, with uniform end shortening displacement applied along the longitudinal direction. The element size was set to 0.25 mm on all sides. To ensure compatibility, the applied displacement was supported by a simply supported boundary condition on the opposite face (see Figure 2).

Table 1: Mechanical properties of IM7/8552 [18]

Elastic Properties				
Modulus			Poisson's ratios	
E_{11} (MPa)	E_{22} (MPa)	G_{12} (MPa)	ϑ_{12} (-)	ϑ_{23} (-)
161000	11380	5481	0.32	0.436
Strength Properties				
Y_T (MPa)	S_L (MPa)	X_C (MPa)	Y_C (MPa)	
62.3	90	1690	250	
Non-linear shear properties				
α_{PL} (MPa$^{1-n_{PL}}$)			n_{PL} (-)	
4.41×10^{-10}			5.934	

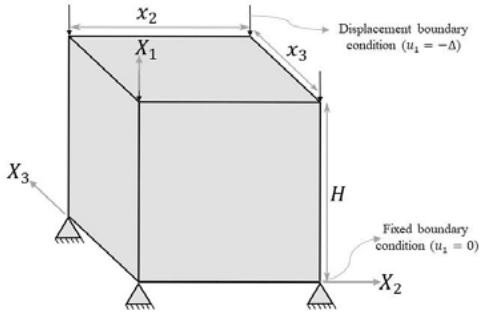
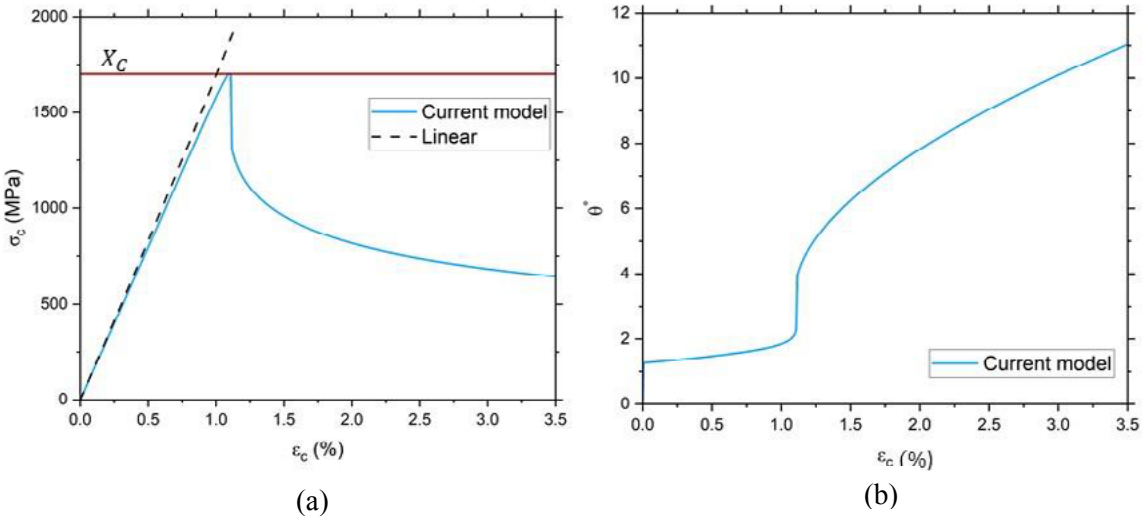


Figure 2. Single-element test model.

4. Results and Discussion

4.1 Constitutive response of single element model (Two scale model)

The constitutive response of the model under longitudinal compression of the single-element model is shown in Figure 3. In this response, the kinking happens to the whole element i.e. the kink bandwidth is 250 μm (same as element dimension). The initial misalignment angle ($\theta_i = 1.26^\circ$) is chosen in such a way that the load curve starts dropping when it reaches material longitudinal compressive strength i.e. $X_c = 1690$ MPa. The constitutive response includes several features like the linear response at small strain, pre-peak nonlinearity, sudden drop in load immediately reaching material strength (post-peak response) due to large fibre rotation (see Figure 3(b)), and plateau in stress at a residual stress level, σ_r, as shown in Figure 3(a).



(a) (b)

Figure 3. (a) Stress vs strain and (b) Fibre rotation vs. strain response.

The stress-strain behaviour of the current model is shown as a solid blue line. The linear stiffness, obtained by deactivating the nonlinear shear response, is represented by a black dotted line. The material's strength is indicated by a solid red horizontal line at X_c. Interestingly, the FKT results exhibit a snap-back phenomenon, showing a sudden load drop followed by an asymptotic residual stress level (σ_r). Remarkably, our current model predicts the same response as the FKT [6] results. The stress versus current fibre rotation response, as depicted in Figure 3(b), highlights that fibre rotation remains minimal until the strength limit is reached, after which there is a sudden increase in fibre rotation. This rotation continues to grow as the model approaches the residual stress state.

4.2 Constitutive response of two scale models with varying kink bandwidth

This selection of w_{KB} has a major impact on the post-peak behaviour, for a smaller w_{KB} there is a very large jump on the curve once stress reaches peak load because as we compress it and the instability happens, a large amount of stored elastic strain energy is released by the bulk that causes a large fall in load as shown in Figure 4 (a). Wider kink bands prevent fibres from rotating (see Figure 4(b)), which increases the residual stress that the material experiences during the softening process (see Figure 4(a)). Interestingly, most kink band rotation appeare suddenly after the load decrease that occurs when after peak stress is reached. The residual stresses are sensitive to kink bandwidth.

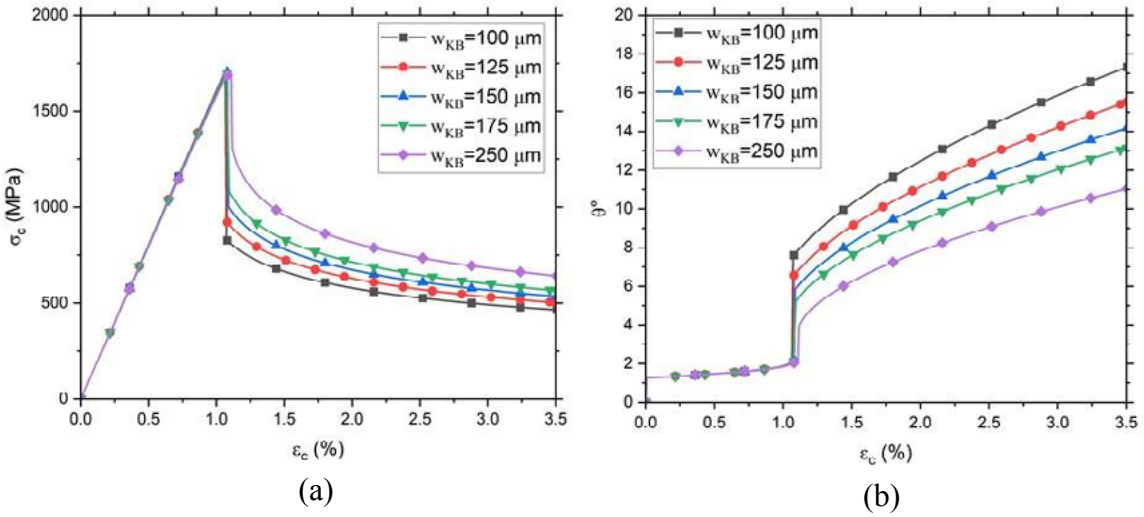


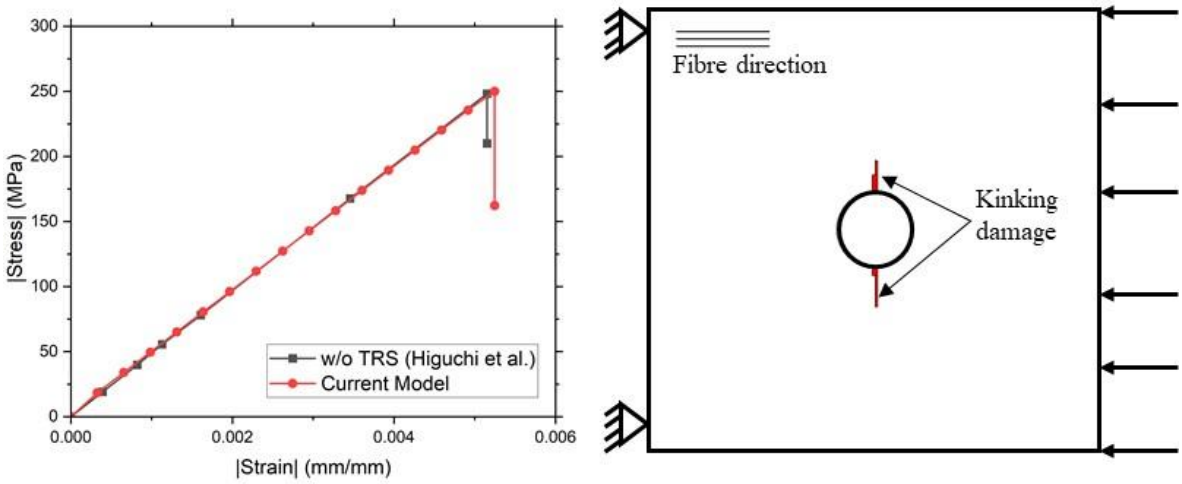
Figure 4. (a) Stress vs. strain and **(b)** Fibre rotation vs. strain response with varying w_KB.

4.3 Open-hole compression example

The geometric configuration of the model is based on Higuchi et al. [19]. It involves a laminate with a width and length of 38.1 and 305 mm, respectively, featuring a central hole of 6.35 mm diameter. The specimen's gauge length is 38.1 mm, but for finite element simulation, only the central portion is considered. The material properties of the T800S-3900-B [20,21,22] prepreg system are adopted. For the laminate stacking sequence, a quasi-isotropic arrangement $[45^{\circ}/90^{\circ}/-45^{\circ}/0^{\circ}]_{2s}$ is employed, with each ply having a thickness of 0.125 mm. A single element per ply is used in the thickness direction, and all plies are meshed with 8-node solid elements, employing reduced integration and hourglass control (C3D8R) to simulate matrix cracks and fibre kinking. Interfaces are modelled using 8-node cohesive elements (COH3D8) to represent delamination, with a resin-rich thickness of 0.01 mm[18]. A fine mesh is applied with an in-plane size of 0.25 mm × 0.25 mm around the hole, covering a sufficiently large rectangular area to capture ply matrix cracks and fibre kinking across all ply blocks. Two regions are defined outside this area: the Far-Field region (FFR) and the Transition region (TR), each with a coarser mesh. The TR employs a mesh size varying from 0.25 mm to 3 mm, while the FFR has an in-plane size of 3 mm × 3 mm. To apply compressive boundary conditions, displacement is imposed in the X-direction at one end of the laminate, while the other end is fixed, with an amplitude that varies smoothly. Additionally, out-of-plane displacements are constrained to zero in the FFR and TR to mimic anti-buckling guides in the OHC test fixture.

An improved fibre kinking model that uses a kinematically separated two-scale formulation is used to simulate compressive damage in the axial plies. Mesh-independent onset and propagation of discrete ply cracks are realized using the directed continuum damage mechanics method (D-CDM) recently proposed by Mukhopadhyay and Hallett [23]. This methodology is used to simulate failure under compression in OHC laminates across a varied range of lay-ups.

The laminate consists of an equal number of plies oriented at 45°, 90°, -45°, and 0° angles. Its load-displacement curve, excluding thermal residual stress, is depicted in Figure 5(a). Upon comparing the stress-strain curve of our current model with that of Higuchi et al. [19], we observe a high level of agreement. The laminate sustains a maximum load of approximately 32 kNAdditionally, at 91% of the peak load, Figure 5(b) illustrates the distribution of internal damage (kinking) within the 0° ply. It's noteworthy that fibre kinking begins near the hole's tip, and as compressive loading increases, kinking is triggered by unstable growth of the kink band in the 0° ply.



(a) (b)

Figure 5. (a) Load-displacement response of current model compared with Higuchi's model [19] without thermal residual stress (w/o TRS), and **(b)** Internal damage (kinking) distribution in 0° ply of quasi-isotropic laminate at 91% of peak load.

5. Conclusions

This work presents a two-scale continuum damage model for compressive failure in composites that captures the kinematics of kink band formation and evolution accurately. The biggest advantage of this model is its simplicity and compatibility with our existing numerical codes. The proposed model captures the kinematics of the strong variation in strain across the kink band in a more accurate way by using the coupled response between the kink band and the undamaged bulk region. The model can effectively capture various aspects of the material's response, such as its compressive stiffness, strength, susceptibility to instability at the onset of kink-band formation, and the stress plateau observed after reaching the peak.

Acknowledgements

The first author would like to acknowledge the financial support given by the Ministry of Education, India towards the completion of his PhD work. The second author gratefully acknowledges the support of the Science and Engineering Research Board (SERB), India via the Start-up Research Grant (Grant No. SRG/2019/000488).

References

[1] C. Soutis, "Measurement of the Static Compressive Strength of Carbon-Fibre Epoxy Laminates," vol. 42, pp. 373–392, 1991.
[2] C. Soutis, N. A. Fleck, and P. A. Smith, "Failure Prediction Technique for Compression Loaded Carbon Fibre-Epoxy Laminate with Open Holes," *J. Compos. Mater.*, vol. 25, no. 11, pp. 1476–1498, 1991.
[3] V. W. Rosen, Mechanics of composite strengthening, *Fiber Composite Materials American Society of Metals*, Metals Park, Ohio,37-75, 1965.
[4] A. M. Waas, C. R. Schultheisz, Compressive failure of composites, *part II: experimental studies, Progress in Aerospace Sciences*, 32, 43-78, 1996.
[5] S. Argon, Fracture of composites, in *Treatise on Materials Science and Technology, Academic Press, New York,* pp. 79–114, 1972.
[6] B. Budiansky, "Micromechanics.," *Proc. U.S. Natl. Congr. Appl. Mech.*, pp. 25–32, 1986.

[7] B. Budiansky, N. A. Fleck, and J. C. Amazigo, "On kink-band propagation in fibre composites," *J. Mech. Phys. Solids*, vol. 46, no. 9, pp. 1637–1653, 1998.
[8] S. T. Pinho, L. Iannucci, and P. Robinson, "Physically-based failure models and criteria for laminated fibre-reinforced composites with emphasis on fibre kinking : Part I : Development," vol. 37, pp. 63–73, 2006.
[9] S. T. Pinho, L. Iannucci, and P. Robinson, "Physically based failure models and criteria for laminated fibre-reinforced composites with emphasis on fibre kinking . Part II : FE implementation," vol. 37, pp. 766–777, 2006.
[10] S. T. Pinho, C. G. Dávila, P. P. Camanho, L. Iannucci, and P. Robinson, "Failure Models and Criteria for FRP Under In-Plane or Three-Dimensional Stress States Including Shear Non-Linearity," 2005.
[11] F. A. L. Jr, "A Continuum Damage Mechanics Model to Predict Kink-Band Propagation Using Deformation Gradient Tensor Decomposition," pp. 1–17, 2019.
[12] A. C. Bergan, M. Herráez, C. González, and C. S. Lopes, "A constitutive model for fi ber kinking : Formulation, fi nite element implementation, and veri fi cation," vol. 129, no. October 2019, 2020.
[13] N. Jansson and M. Fagerstr, "A kinking-based failure model for engineering simulation of compressive crushing of composite structures," vol. 329, no. December 2023, 2024.
[14] G. D. Nguyen, C. T. Nguyen, V. P. Nguyen, H. H. Bui, and L. Shen, "A size-dependent constitutive modelling framework for localised failure analysis," *Comput. Mech.*, vol. 58, no. 2, pp. 257–280, 2016.
[15] M. Jirásek, "Mathematical analysis of strain localization," *Rev. Eur. génie Civ.*, vol. 11, no. 7–8, pp. 977–991, 2007.
[16] W. Ramberg and W. R. Osgood, "Description of stress-strain curves by three parameters," *Natl. Advis. Comm. Aeronaut.*, p. Technical Note No. 902, 1943.
[17] R. Hill, "Elastic properties of reinforced solids: Some theoretical principles," *J. Mech. Phys. Solids*, vol. 11, no. 5, pp. 357–372, 1963.
[18] L. F. Kawashita and S. R. Hallett, "A crack tip tracking algorithm for cohesive interface element analysis of fatigue delamination propagation in composite materials," *Int. J. Solids Struct.*, vol. 49, no. 21, pp. 2898–2913, 2012.
[19] R. Higuchi, S. Warabi, A. Yoshimura, T. Nagashima, T. Yokozeki, and T. Okabe, "Experimental and numerical study on progressive damage and failure in composite laminates during open-hole compression tests," *Compos. Part A Appl. Sci. Manuf.*, vol. 145, Jun. 2021.
[20] D. Zhang, X. Zheng, and T. Wu, "Damage characteristics of open-hole laminated composites subjected to longitudinal loads," *Compos. Struct.*, vol. 230, no. September, p. 111474, 2019.
[21] P. P. Camanho, C. G. Dávila, S. T. Pinho, L. Iannucci, and P. Robinson, "Prediction of in situ strengths and matrix cracking in composites under transverse tension and in-plane shear," *Compos. Part A Appl. Sci. Manuf.*, vol. 37, no. 2, pp. 165–176, 2006.
[22] T. Yokozeki, T. Ogasawara, and T. Ishikawa, "Nonlinear behaviour and compressive strength of unidirectional and multidirectional carbon fibre composite laminates," *Compos. Part A Appl. Sci. Manuf.*, vol. 37, no. 11, pp. 2069–2079, 2006.
[23] S. Mukhopadhyay and S. R. Hallett, "A directed continuum damage mechanics method for modelling composite matrix cracks," *Compos. Sci. Technol.*, vol. 176, no. March, pp. 1–8, 2019.

IDENTIFICATION OF LOCAL TO GLOBAL MECHANICAL PROPERTIES OF CLEAR WOOD PEELED VENEERS FROM OFF-AXIS TENSILE TESTS USING FULL-FIELD LOCAL DISPLACEMENT MEASUREMENTS

L. Demoulin[1], G. Pot[2], L. Denaud[3], S. Girardon[4] and B. Marcon[5]

[1]Arts et metier Institute of technology, LABOMAP, Université Bourgogne Franche-Comté, F-71250 Cluny, France
Email: leyne.demoulin@ensam.eu, Web Page: https://labomap.ensam.eu/
[2]Arts et metier Institute of technology, LABOMAP, Université Bourgogne Franche-Comté, F-71250 Cluny, France
Email: guillaume.pot@ensam.eu, Web Page: https://labomap.ensam.eu/
[3]Arts et metier Institute of technology, LABOMAP, Université Bourgogne Franche-Comté, F-71250 Cluny, France
Email: louis.denaud@ensam.eu, Web Page: Web Page: https://labomap.ensam.eu/
[4]Arts et metier Institute of technology, LABOMAP, Université Bourgogne Franche-Comté, F-71250 Cluny, France
Email: stephane.girardon@ensam.eu, Web Page: Web Page: https://labomap.ensam.eu/
[5]Arts et metier Institute of technology, LABOMAP, Université Bourgogne Franche-Comté, F-71250 Cluny, France
Email: bertrand.marcon@ensam.eu, Web Page: Web Page: https://labomap.ensam.eu/

Keywords: Digital Image Correlation, Fibre orientation, Density, Young Modulus, Strength

Abstract
This study examines the influence of fiber orientation variability on the mechanical properties of wood, focusing on veneer clear wood specimens. The research is motivated by the need to develop high-performance composite materials for sustainable transportation applications, particularly in reducing greenhouse gas emissions. The experimental protocol involves manufacturing veneers from beech wood, followed by producing the manufacturing of veneers from beech wood, followed by the production of small specimens with deliberate variations in fiber orientation. Non-destructive measurements of local fiber orientations and global density are conducted, along with tensile tests to determine local mechanical properties, i.e., Young's modulus, strength, and the shear modulus Advanced imaging techniques (DIC) and models for isotropic materials are employed for analysis.
The results reveal that fiber orientation has a significant role in wood variability, with pronounced effects on Young's modulus and strength at low angles. Transversal and shear modulus appear lower than in the literature due to the cracks due to the manufacturing of veneer (peeling process).

1. Introduction

The transport industry is determined to reduce its carbon footprint in order to reduce the problems caused by greenhouse gases. To achieve this goal, high-performance materials made from wood could be used for structural applications. This is the rationale behind the WOOFHI (Wood/natural Fiber High homogeneity/performance composite) project, which aims to produce homogeneous, optimized composite materials made from heterogeneous, variable materials. This application requires the ability to sort wood material according to its mechanical properties, based on non-destructive and quantitative

measurement methods. Visual sorting is standardized but not very efficient, and mechanical properties after sorting are not optimal (Faydi 2017, Duriot 2021). Several studies attempt to predict the elastic modulus and mechanical strength of structural wood products accurately and reliably, as shown by Hakkarainen et al. (2019) using local fiber orientation and global density measured on wood (Viguier et al. 2018). The coefficient of determination obtained is less than 0.7 and few predictive studies concerning veneers and small flawless samples have been made (Pramreiter et al. 2021, Cha 2003).

The aim of this work is to understand the mechanical behavior of clear wood and how local disturbances influence the material's behavior.
An experimental protocol on small specimens made from visually "clear" veneers was set up. First, non-destructive measurements of fiber orientation and density were carried out, then the specimens were loaded to failure in a tensile test.

2. Material and methods

2.1. Experimental protocol

The first stage of the protocol concerns the manufacture of veneers from the peeling process. The species studied is beech (fagus sylvatica) from the Centre Val de Loire region. Secondly, test specimens measuring 350 mm long, 20 mm wide, and 2 mm thick were produced from these veneers using a laser cutting machine. The specimens were stored at a temperature of 24°C with a relative air humidity of 50% in order to stabilize them at a humidity of 10%. The specimens were cut at angles relative to a direction assumed to be 0° to deliberately create variability within the fiber orientation. This distribution is shown in Table. 1. Nearly 40 veneers were required to produce 129 specimens.

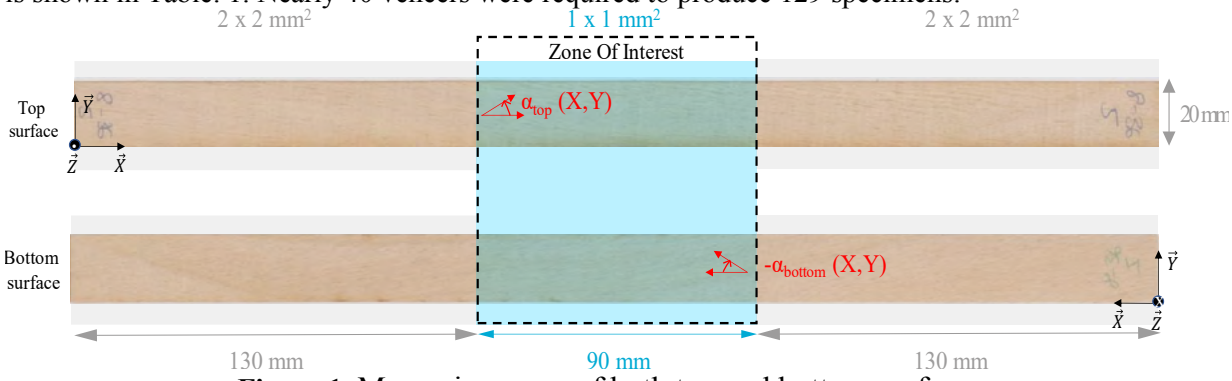


Figure 1. Measuring areas of both top and bottom surfaces

Table 1. Distribution of specimens according to their cutting angle, number of tested specimens, and cross-head speed during the tensile mechanical test

Cutting Angle θ (°)	**0**	**5**	**10**	**15**	**20**	**30**	**45**
Number	40	16	15	11	24	14	9
Cross-head speed (mm.min^{-1})	2	2	1	1	1	0.5	0.5

The samples were then scanned using a machine equipped with a camera and laser pointer, which scanned their entire surface. This technology uses the tracheid effect (Nyström (2003), Simonaho et al. (2002)). This involves projecting a circular laser onto a flat wooden surface. As light scattering is higher in the direction of the wood fiber, a luminous ellipse is formed whose major axis follows this orientation. The top and bottom surfaces of the sample were scanned at different resolutions (Figure. 1) to obtain angle maps (Figure. 2 (a), (c)). The central zone was more highly resolved than the extremities, as this is the zone of interest visible between the tensile jaws. The next step was to scan the specimens using a

conventional scanner to obtain an image with a resolution of 400 Dpi. Figure. 2 shows the overlay of the angle mapping obtained with the scan (Figure. 2(b), (d)).

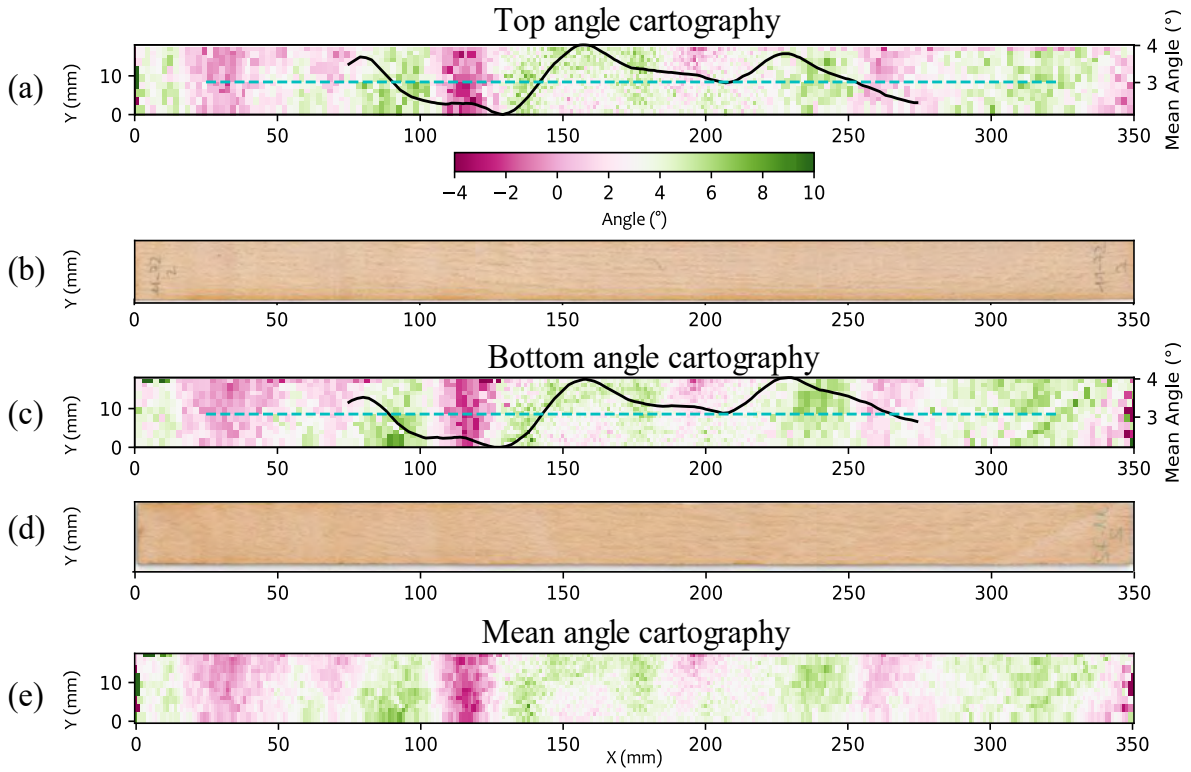


Figure 2. (a) The angle cartography in degrees of the top surface of the specimen. The black curve represents the average value of the grain angle along the Y direction for each X step in the ZOI (Zone Of Interest) with a length of 50 mm, the dashed blue line represents the average angle value within the ZOI (b) color image of the top surface, (c) The angle cartography in degrees of the bottom surface of the specimen, (d) color image of the bottom surface, (e) The average angle cartography in degrees of the top and bottom face angles of the specimen.

Width was measured with a caliper, and thickness with an external micrometer. The samples were then weighed using a balance. These measurements were used to calculate the average density. The tensile test was designed to determine local mechanical properties using a ZWICK-Roell, universal testing machine (250 kN). Displacements were measured by image stereo-correlation using technology developed by LaVision. A preload of 0.1 MPa was applied before testing. The displacement speeds imposed on the specimens are described in Tab.1. Speeds were set to give a test time of between 100 and 180 s to failure.

2.2. Young modulus determination

The equivalent local modulus of elasticity along the specimen can be calculated using a virtual extensometer of length δ (Figure. 3). This modulus was calculated based on the standard (EN 408 2012), i.e. a linear regression is calculated between 10 and 40% of the estimated maximum force.

In the $\vec{X}$ direction, the elastic modulus is calculated according to Eq. 1. Strain was calculated as a rate of increase in displacement as shown in Eq. 2. Displacement was calculated as the average of displacements over the width of the specimen (yellow bands (Figure. 3). Stress is the ratio of force divided by specimen cross-section (Eq. 3). Using this method, a local modulus can be calculated at each point along the length of the specimen. The central zone can be scanned over the 90 mm length of the zone of interest using the virtual extensometer with a length δ = 50 mm. The type of results obtained for one specimen is shown in Figure. 4.

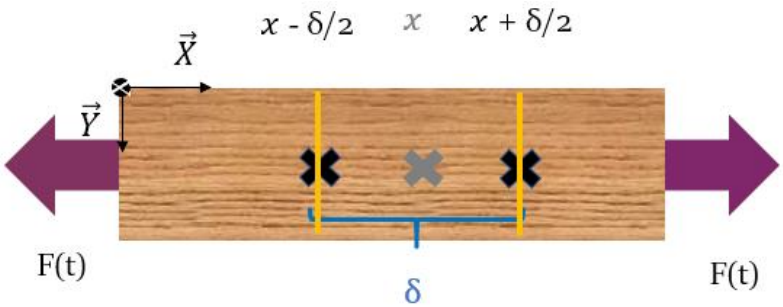


Figure 3. Tensile test with x the position along the length of the specimen at the center of the extensometer, δ the length of the extensometer and F(t) the force as a function of time.

$$E_{xx}(x) = \frac{\sigma}{\varepsilon_{xx}(x)} \quad (1)$$

$$\varepsilon_{xx}(x) = \frac{u(x+\delta/2) - u(x-\delta/2)}{\delta} \quad (2)$$

$$\sigma = \frac{Force}{Section} \quad (3)$$

$$u(x) = \frac{1}{19-1+1}\sum_{i=1}^{19} u(x, y_i) \quad (4)$$

Where $E_{xx}(x)$, $\varepsilon_{xx}(x)$ and σ are respectively the young modulus (in GPa), the strain in the $\vec{X}$ direction, and the stress (in MPa). The force is in N and the section in mm. $u(x)$ is the mean displacement in mm on the yellow band (Figure 3).

2.3 Strengh

Models of mechanical strength using grain angles can be used, such as the Hankinson (1921), Norris (1962), and Tsai-hill (1965) models as shown respectively by Eq. 5, Eq. 6, and Eq. 7.

$$\mathrm{MOR}_H = \frac{F_L \times F_T}{F_L \times \sin(\alpha)^2 + F_T \times cos(\alpha)^2} \quad (5)$$

$$\mathrm{MOR}_N = \frac{1}{\sqrt{\frac{1}{{F_T}^2} \times \sin(\alpha)^4 + \frac{1}{{F_L}^2} \times \cos(\alpha)^4 + (\frac{1}{{f_v}^2} - \frac{1}{F_L * F_T}) \times \sin(\alpha)^2 \cos(\alpha)^2}} \quad (6)$$

$$\mathrm{MOR}_{TH} = \frac{1}{\sqrt{\frac{1}{{F_T}^2} \times \sin(\alpha)^4 + \frac{1}{{F_L}^2} \times \cos(\alpha)^4 + (\frac{1}{{f_v}^2} - \frac{1}{{F_L}^2}) \times \sin(\alpha)^2 \cos(\alpha)^2}} \quad (7)$$

Where F_L and F_T are respectively the tensile strength in the longitudinal, transversal direction (in MPa) and f_v the ultimate shear strength in the plane LT (in MPa) and α is the angle (in degree).

3. Results

3.1 Young modulus

The results obtained for each specimen are shown in Figure. 4, which illustrates the strong correlation between the longitudinal modulus of elasticity and the angle at each point on the map. By superimposing all the specimens on the same graph, the mechanical properties have been determined by considering an orthotropic behavior law (Figure. 5). The longitudinal modulus of 16.14 GPa appears to agree with the literature (OŻYHAR et al. 2012, Ozyhar et al. 2013, Peter et al. 2015) despite a relatively low transverse

modulus and shear modulus, possibly indicating the considerable influence of cracks resulting from the veneer manufacturing process (Pot et al. 2015, Krüger et al. 2023). Moreover, a wide range of the MOE is observed (from 12 to 20 GPa). This variability may stem from density, microfibril angle, tension wood, or the presence of out-of-plane angles.

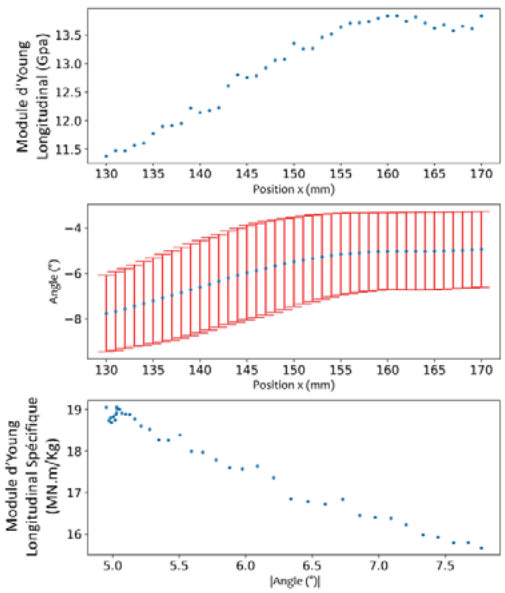


Figure 4 : Example of a specimen result: longitudinal modulus and angle measurement as a function of position along the length of the specimen, specific longitudinal modulus as a function of angle

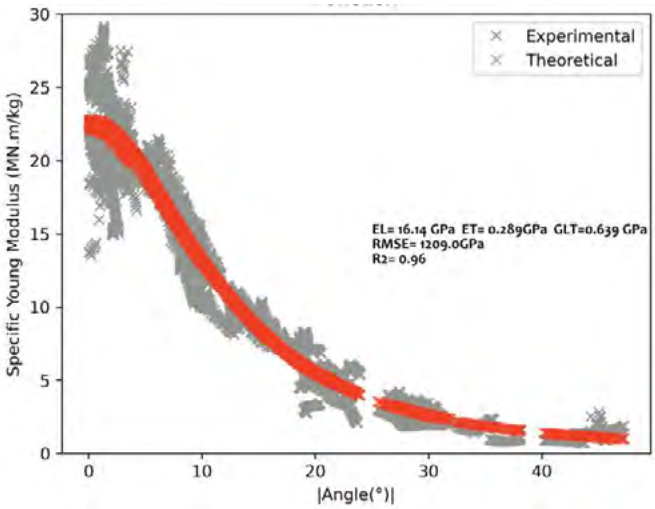


Figure 5 : Optimization and superposition of mechanical properties based on an orthotropic behavior law (RMSE = Root Mean Square Error, R2 = coefficient of determination, EL = longitudinal modulus and ET = transverse modulus, GLT = shear modulus)

3.2 Strength

The relationship between the mean absolute angle and the strength (MOR) within the length of the ZOI measured in step 4 is depicted in Figure 6. Hankinson, Norris, and Tsai-Hill failure criteria (respectively Eq. 5, 6, and 7) were fitted to the experimental data, giving the coefficients in Table 2.

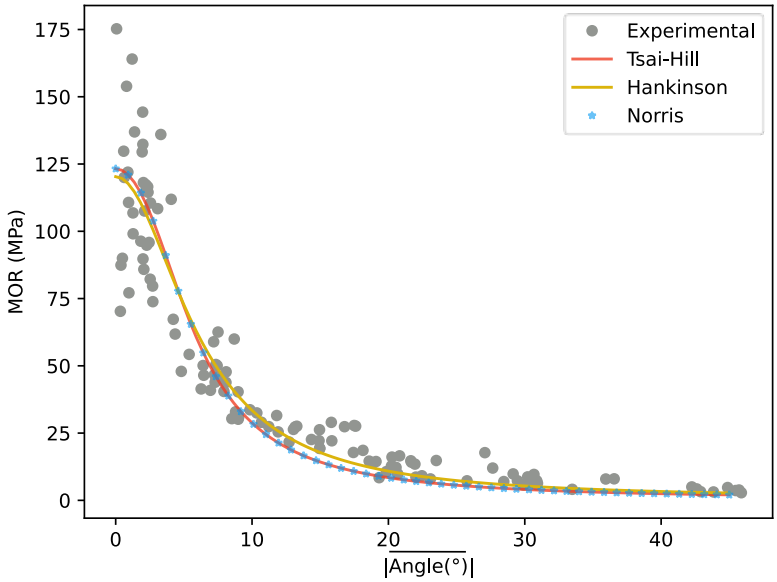


Figure 6: MOR VS $|\overline{Angle}|$

MOR correlates quite well with the measured angle in the ZOI with the three models (Figure 6 and Table 2). For angles close to 0°, there was a wide variation in MOR. The Hankinson (1921) model has a coefficient of determination which is the highest. However, this model only provides longitudinal and transverse mechanical strength, in contrast to the Tsai-Hill (1965) and Norris (1962) models, which also allow to evaluate a shear strenght.

Table 2. Coefficients of rupture models.

Model/Coefficient	F_L (MPa)	F_T (MPa)	f_v (MPa)	R^2	RMSE (MPa)
Hankinson	121	1.0	-	0.90	14.1
Norris	123	1.0	8.0	0.88	15.0
Tsai-Hill	125	1.0	14.0	0.89	15.0

4. Conclusion

Fiber orientation appeared to be an important parameter in wood variability for the young modulus and tensile strength. Large variations in young modulus and strength were more significant for small angles than for large angles. These variations could be due to the locale variation of the density, the out-of-plane angle, or the microfibril angle.
The approach of calculating elastic modulus is rather simplistic for understanding local behavior. Inverse identification of mechanical properties for each specimen using a finite element model incorporating fiber orientation seems essential to understanding strains and local properties.

Acknowledgments

This work is supported by the "Investissement d'Avenir" program, ISITE-BFC project (ANR-15-IDEX-003 contract).

References

[1] Azzi VD, Tsai SW (1965) Anisotropic strength of composites: Investigation aimed at developing a theory applicable to laminated as well as unidirectional composites, employing simple material properties derived from unidirectional specimens alone. *Experimental Mechanics* 5:283–288. https://doi.org/10.1007/BF02326292
[2] Cha J-K (2003) Tensile Strength of Clear Thin Wood Samples in Relation to the Slope of Grain. Journal of the Korean *Wood Science and Technology*. 2003. Vol. 31, n° 3, pp. 35-41.
[3] Duriot R (2021). *Développement de produits LVL de douglas aux propriétés mécaniques optimisées par l'exploitation de la mesure en ligne de l'orientation des fibres lors du déroulage* Thèse de doctorat. HESAM.
[4] EN 408 (2012). *Timber structures – Structural timber and glued laminated timber – Determination of some physical and mechanical properties*.
[5] Faydi Y (2017) *Classement pour la résistance mécanique du chêne par méthodes vibratoires et par mesure des orientations des fibres*. Thèse de doctorat. ENSAM.
[6] Hankinson (1921) Investigation of crushing strength of spruce at varying angles of grain. *Air service information circular* 3:16
[7] Krüger R, Buchelt B, Wagenführ A (2023) Method for determination of beech veneer behavior under compressive load using the short-span compression test. *Wood Science and Technology* 57:1125–1138. https://doi.org/10.1007/s00226-023-01489-z
[8] Nyström J (2003) Automatic measurement of fiber orientation in softwoods by using the tracheid effect. *Computers and Electronics in Agriculture* Vol. 41, n° 1-3, pp. 91-99. DOI 10.1016/S0168-1699(03)00045-0.
[9] Ozyhar T, Hering S, Niemz P (2012) Moisture-dependent elastic and strength anisotropy of European beech wood in tension. *Materials Science* 47:6141–6150. https://doi.org/10.1007/s10853-012-6534-8

[10] Peter N, Tomasz O, Stefan H, Walter S (2015) Moisture dependent physical-mechanical properties from beech wood in the main directions. *Pro ligno* https://doi.org/10.24451/ARBOR.5636

[11] Ozyhar T, Hering S, Niemz P (2013) Moisture-dependent orthotropic tension-compression asymmetry of wood. *Holzforschung* 67:395–404. https://doi.org/10.1515/hf-2012-0089

[12] Pot G, Denaud LE, Collet R (2015) Numerical study of the influence of veneer lathe checks on the elastic mechanical properties of laminated veneer lumber (LVL) made of beech. *Holzforschung* 69:247–316. https://doi.org/10.1515/hf-2014-0011

[13] Pramreiter M, Stadlmann A, Huber C, Konnerth J, Halbauber P, Baumann G, Mülher U (2021) The Influence of Thickness on the Tensile Strength of Finnish Birch Veneers under Varying Load Angles. *Forests*.Vol. 12, n° 1, pp. 87. DOI 10.3390/f12010087.

[14] Simonaho S-P, Silvennoinen R (2002) Determination of wood grain direction from laser light scattering pattern. *Optics and Lasers in Engineering*. 2002. Vol. 41, n° 1, pp. 95-103. DOI 10.1016/S0143-8166(02)00144-6.

[15] Viguier J, Bourgeay C, Rohumaa A, Pot G, Denaud L (2018) An innovative method based on grain angle measurement to sort veneer and predict mechanical properties of beech laminated veneer lumber. *Construction and Building Materials*. Vol. 181, pp. 146-155. DOI 10.1016/j.conbuildmat.2018.06.050. ACL

INVESTIGATING LOAD INTRODUCTION METHODS FOR AIRCRAFT FLOOR PANELS MADE OF FOAM CORE SANDWICH

A. Dimassi[1], J. Dietrich[2], R. Emmerich[3] and C. Klemm[4]

[1]Faserinstitut Bremen e.V., Am Biologischen Garten 28359 Bremen, Germany
Email: dimassi@faserinstitut.de, Web Page: http://www.faserinstitut.de
[2]Faserinstitut Bremen e.V., Am Biologischen Garten 28359 Bremen, Germany
Email: dietrich@faserinstitut.de, Web Page: http://www.faserinstitut.de
[3]Institut für Textiltechnik der RWTH Aachen University, Otto-Blumenthal-Str. 1 52074 Aachen, Germany
Email: rebecca.emmerich@ita.rwth-aachen.de, Web Page: http://www.ita.rwth-aachen.de
[4]Institut für Textiltechnik Augsburg gemeinnützige GmbH, Am Technologiezentrum 5 86159 Augsburg, Germany
Email: christoph.klemm@ita-augsburg.de, Web Page: http:// www.ita-augsburg.de

Keywords: Floor panels, Inserts, Sandwich structures, Cork, Foam core

Abstract

This study investigates alternative fastening methods for aircraft floor panels composed of foam core sandwich structures, aiming to enhance manufacturing efficiency and reduce costs without compromising mechanical performance. Traditional glass fibre-reinforced polymer (GFRP) plugs were compared with polyetherimide (PEI) plugs, EJOT TSSD® inserts, and Bossard MM-Welding® inserts. The research focused on pull-out and shear-out tests to evaluate the mechanical integrity of each fastening solution. Results demonstrated that all fasteners displayed similar performance in pull-out tests, which was predominantly influenced by the face sheet properties of the panels. Among the methods, the GFRP plugs showed marginally superior shear-out strength, but the performance of the Bossard and EJOT fasteners was sufficiently robust, suggesting their potential suitability for use in floor panel applications. Particularly, the EJOT and Bossard methods promise significant enhancements in production efficiency due to their ease of integration into existing manufacturing processes. Further refinements could involve optimizing the contact surface between inserts and the foam core, as well as exploring stiffer insert materials to improve load-bearing capacity. This study underlines the potential of these new fastening techniques to modernize the construction of aircraft floor panels while maintaining essential mechanical properties.

1. Introduction

Floor panels are an important component in the cabin of civil aircraft and they contribute strongly to the CO2 footprint of the aircraft [1]. State-of-the-art aircraft floor panels generally consist of a honeycomb core and prepreg (carbon fibre) face sheets [2]. To assemble the floor panels onto the aircraft's supporting frame structure, special load-introducing elements known as plugs are employed, ensuring a smooth load distribution. These cylindrical plugs, matching the core's thickness, are mostly made from fibre-reinforced prepreg material. Generally, glass fibre is used as reinforcement. The integration of these plugs during the panel layup preparation, before curing, may result in tolerance issues. In the project EcoFloor, we aim to develop a new floor panel with a novel concept that improves both the sustainability of the structure and the efficiency of the manufacturing process. For that purpose, polymeric foam material (Diab Divinycell F) with an additional cork layer is used as sandwich core material. The cork layer is used to improve the acoustic properties and the impact

performance of the panel. Additionally, there are plans to integrate fastening elements post-manufacture, allowing the use of off-the-shelf sandwich panels and increasing the manufacturing rate.

In this work, a screening of available fastening methods has been done. For the screening, pull-out tests and shear-out tests were performed to assess the mechanical performance. In addition to the reference GFRP plug, three fastening methods were investigated: A PEI-plug, an EJOT TSSD® insert, and a Bossard MM-Welding® insert. While the PEI-plug is integrated in a similar way to the reference plug, it is cheaper than the GFRP-plug. The EJOT TSSD® insert is made of PA6 plastic, does not require a pilot hole, and the joining takes place due to frictional heat caused by the rotation and an axial force. The Bossard MM-Welding® fastening method also uses ultrasonic energy to partially liquefy the thermoplastic material and create the connection to the sandwich core, but does so by axial movement, not radial like in the EJOT process. After testing, the results were analysed and a comparison to the reference GFRP-Plug was done in order to estimate the suitability of the new load introduction methods.

2. Experimental Investigations

2.1. Materials and Manufacturing

Sandwich panels with a total thickness of about 10 mm made of two thin carbon-epoxy skins (one layer of HexForce® G0926 D 1304 TCT INJECTEX E01 2F HS06K woven, bidirectional carbon fibre fabric for each side) separated by a closed cell Diab Divinycell F (F50 or F90) and a thin cork layer Amorim Corecork NL25. The panels were manufactured with the Modified Vacuum Infusion (MVI) system as described in [3]. Like previously mentioned, four insert types were investigated: A GFRP-plug and a PEI-plug with a diameter of 18 mm, and an EJOT TSSD® insert, and a Bossard MM-Welding® insert with a diameter of 16 mm. While the plugs were integrated during the manufacturing of the sandwich panel, the Ejot and the Bossard inserts were inserted after the curing of the panel. In order to be able to perform pull-out tests with the Ejot TSSD-insert a washer was used, as the geometry of the insert is not suited for the used screw joint. The tested insert are depicted in Figure 1.



Figure 1. Tested Inserts

In addition to the use of four different inserts, the foam core density and the cork layer thickness were variable. In total seven different specimen configurations were investigated during this test campaign. Table 1 gives an overview about the main characteristics of each configuration.

Table 1. Investigated specimen configurations.

Specimen Type	*Insert type*	*Foam Core*	*Cork thickness [mm]*	*Foam core thickness [mm]*
PEI-Plug	PEI-Plug	F50	1	9
GF-Plug	GFRP-Plug	F50	1	9
EJOT F50	EJOT TSSD	F50	1	9
EJOT F90	EJOT TSSD	F90	1	9
Bossard F50	Bossard MM-Welding	F50	1	9
Bossard F90	Bossard MM-Welding	F90	1	9
Bossard F90-2	Bossard MM-Welding	F90	2	8

2.2. Test setup

In real application, a floor panel is generally mounted on stiff metallic support structure by means of multiple screws with countersunk head and nuts. The Insert is subject to shear loads and pull loads in screw axial direction, where the support creates a kind of resistance against axial deformation (see Figure 2).

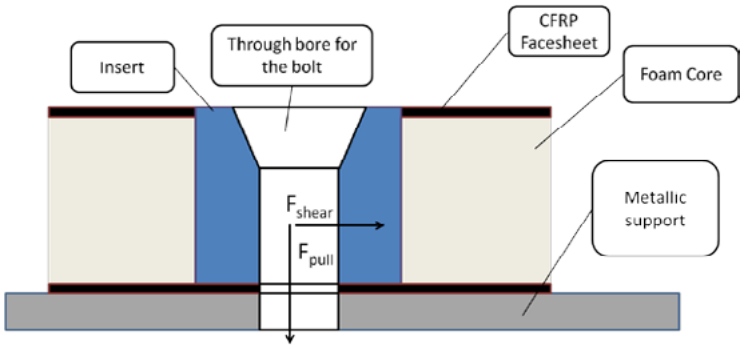


Figure 2. Schematic illustration of a floor panel insert under load

In order to evaluate the performance of the inserts two tests were conducted: pull-out test (see Figure 3 left) and shear-out test (see Figure 3 right). For the conducted tests, there is no specific norm that describes the test procedures. For that reason, the test setup was defined based on the work of Heimbs [4]. The specimen for the pull-out test has a flat surface of 100 x 100 mm². The rigid support structure has a hole with a diameter of 70 mm and it disables the translation of the test specimen in loading direction. The specimen is then loaded in out-of plane direction until rupture. The specimen for the shear-out test has a flat surface of 95 x 95 mm² and is fixed with a picture frame that blocks the translation in loading direction. The shear force is introduced until the first significant load drop appears. For the assessment of the insert performance, the load-displacements diagrams are recorded and the maximum loads at failure as well as the damage modes are analysed.

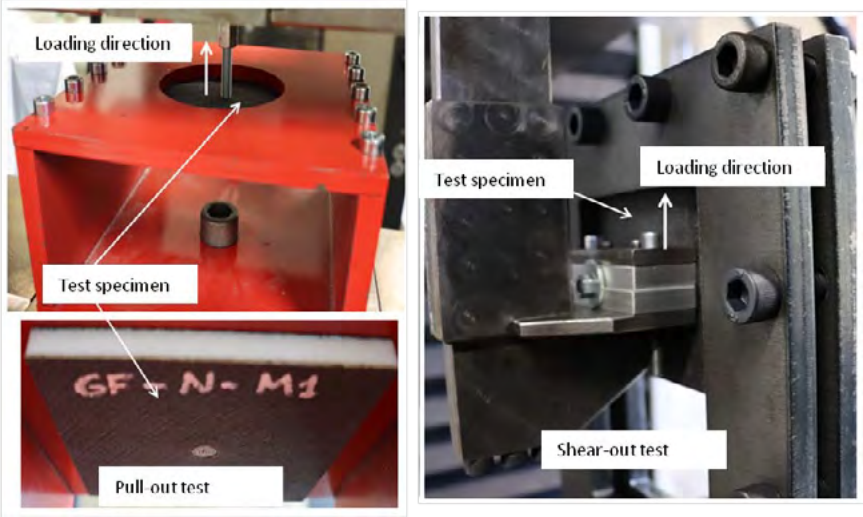


Figure 3. Test Setup of the pull-out test (left side) and the shear-out test (right side)

2.3. Test results

The load-displacement diagram of the specimens "Bossard F50" under pull-out loading is depicted in Figure 4-A. It can be seen that the response is linear until about 2000 N, at which the specimen reached their strength limits. At about 500 N a small kink in the curve is observed, which indicated the initiation of the first damage, which was the failure of the bonding connection between the insert and the core material. All specimen types showed similar load-displacement curves with minor differences and failed at a load of about 2000 N. The highest pull-out strength was measured with the GF-Plugs at about 2200 N and the lowest with the Bossard-Insert at about 1900 N. The EJOT insert has strength similar to the strength of the GF-Plugs, but it should be mentioned that a washer was used to be able to perform the test, which has improved the strength value slightly by increasing the contact surface. A comparison of the measured pull-out-strengths is illustrated in Figure 4-B.

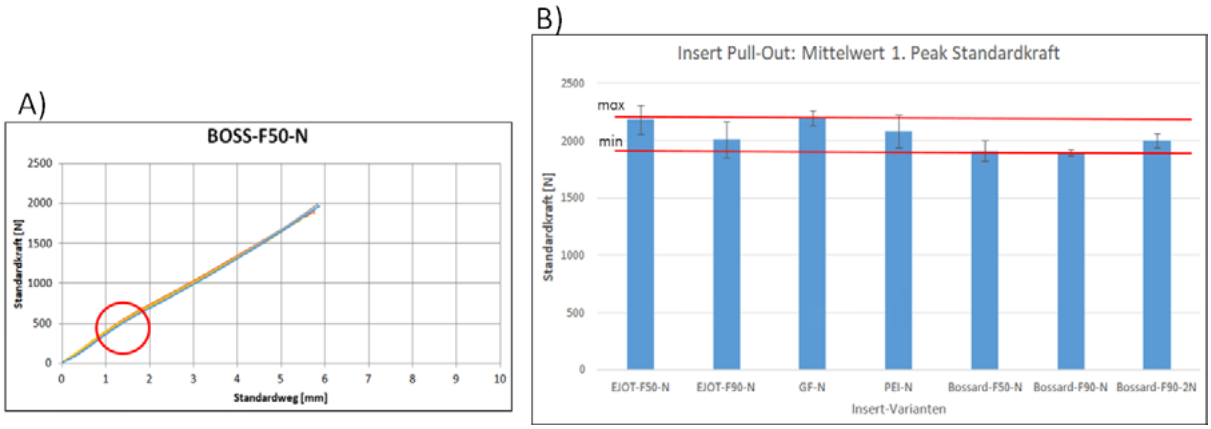


Figure 4. A) Load-displacement diagram with Bossard-insert under pull-out load; B) Measured Pull-out strengths of the tested configuration

Regarding the damage mode (see Figure 5), all tested insert showed similar behaviour. On the tension side, a dent with face sheet damage (fibre breakage) could be observed as the lower face sheet of the sandwich specimen creates a resistance against the insert deformation. On the opposite side, the pressure side (the side with the screw head) we can observe the debonding of the insert and how the insert disconnects from the upper face sheet. From these tests, it can be concluded that the dominant

influencing factors of the pull-out strength the strength of the face sheet and the contact surface between the insert and the lower face sheet.

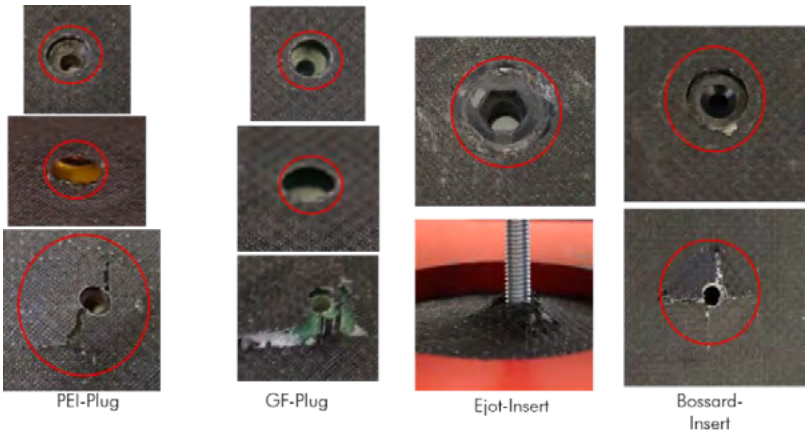


Figure 5. Observed damages due to pull-out loads

Under shear load the shape of the load-displacement diagram (Figure 6-A) looks quite different compared to the diagram of the pull-out test. Due to the complexity of the test setup, it takes between 1.5 mm and 2 mm until the load is correctly introduced and the linear elastic phase starts. The damage is not any more brittle und we can observe a kind of plastic deformation. Regarding the shear-out strength Figure 6-A shows that on the one hand the GF-plug has the highest strength, which reached about 2900 N. The performance of the PEI-plugs was slightly lower compared to the GF-plugs (about 2370 N). On the other hand, the Bossard and the EJOT inserts combined with Diab F50 foam and 1 mm cork have similar values of about 2230 N. Despite increasing the foam core density the strength under shear loads didn´t improve, as we observed a small strength reduction. It can be explained by a poorer bonding strength between the insert and the foam with higher density. Observing the standard deviations shows however that the plugs have large standard deviations, while the EJOT and Bossard insert showed better reproducibility as the standard deviation is much smaller.

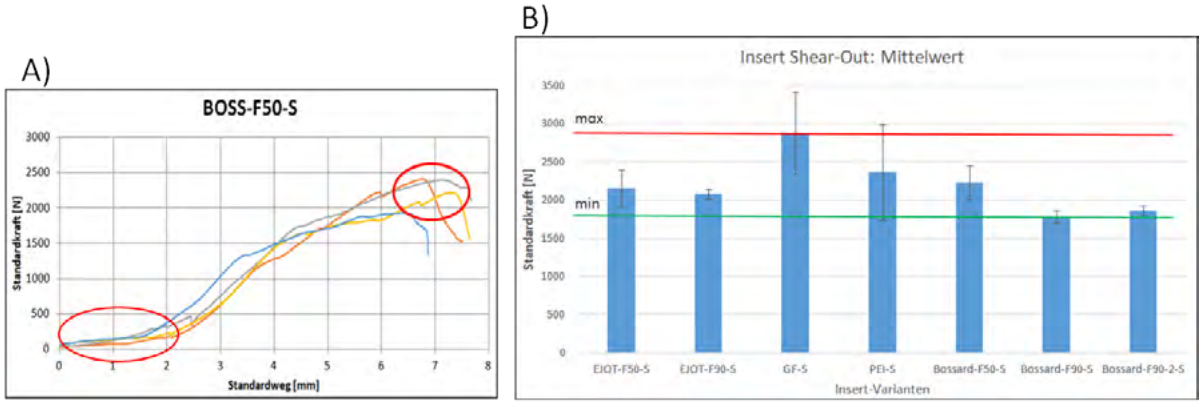


Figure 6. Load-displacement diagram with Bossard-insert under shear-out load; B) measured shear-out strengths of the tested configuration

Figure 7 shows typical insert shear damage consisting of debonding of the skin insert connection, core crushing in the compression side and a sliding of the insert under the skin. In addition, the stiffness of the insert material seems to have a dramatic influence on the plastic deformation of the insert as we

can observe a large widening of the EJOT hole, while no widening could be observed with the GF-plugs.



Figure 7. Observed damages due to shear-out loads

3. Conclusions

In this work, alternative methods for load introduction into floor panels have been investigated in order to find efficient inserts that enable the reduction of production costs and have similar mechanical performance compared to the widely used GFRP-plugs.

The tests demonstrated that all investigated fastening methods perform similarly in thickness direction (pull-out test), with face sheet properties being the dominant factor for pull-out strength. This lies on the loading direction of the specimen. Probably loading in the opposite direction would lead to different results. The shear-out tests show that the GFRP-plugs slightly outperform the other fastening methods. However, the shear-out strengths of the Bossard MM-Welding® and EJOT TSSD® fasteners are likely sufficient to enable their use in floor panels. Using one of these two fastening methods in foam core floor panels would dramatically increase the efficiency of the manufacturing process of aircraft floor panels. Further improvement of the shear-out strength could be reached by increasing the contact surface of the insert with the foam core and by using stiffer insert materials.

Acknowledgments

This work was funded by the German Federal Ministry for Economic Affairs and Climate Action through the Federal Aeronautical Research Program LuFo VI-2 within the project EcoFloor under the Grant No. 20E20101A. The authors wish to acknowledge this support. We thank both the KVT-Fastening GmbH (Multi-Material-Welding, a Bossard company) and EJOT SE & Co. KG for integrating their respective products into the EcoFloor Sandwich Panels, free of charge.

References

[1] https://www.grandviewresearch.com/industry-analysis/aerospace-floor-panels-market. Online, 2016.
[2] Euro-Composites Group. Document Nr. EC562-135e. Echternach-L, 2019.
[3] P. C. Zahlen, M. Rinker, C. Heim. Advanced manufacturing of large, complex foam core sandwich panel. In *International conference of sandwich structure,* 2008.
[4] S. Heimbs. Sandwichstrukturen mit Wabenkern: *Experimentelle und numerische Analyse des Schädigungsverhaltens unter statischer und kurzzeitdynamischer Belastung*. Institut für Verbundwerkstoffe GmbH, Kaiserslautern, 2008.

METHOD DEVELOPMENT OF COMPRESSION STATIC TEST THROUGH FINITE ELEMENT MODELLING OPTIMISATION

N. Dubary[1], A. Fraisse[2] and L.P. Mikkelsen[3]

[1,2,3]Department of Wind and Energy Systems, Technical University of Denmark,
DTU Risø Campus, Frederiksborgvej 399, DK-4000 Roskilde, Denmark
[1]Email: nicdu@dtu.dk, https://wind.dtu.dk/
[2]Email: antf@dtu.dk
[3]Email: lapm@dtu.dk

Keywords: Compression, Modelling, Pultruded Carbon, Mechanical Characterization, Testing

Abstract
Due to incorrect failure during experimental characterisation of high-performance composites, full potential is not measured or correctly obtained using standardised test methods. Structural effects, stress concentrations, experimental uncertainties, and several other parameters influence and interact with the material's performance. Investigations of the geometry, size, and test conditions are needed to obtain a representative and repeatable method. An entire experimental approach is not appropriate due to the complexity of the involved phenomena. For this matter, models are efficient tools to support the development of new methods and designs to tackle encountered experimental issues. This study exposes a dialogue approach between experimental observations and model feedback information to assist in developing a new testing specimen geometry. The steps presented for a 5 mm thick unidirectional pultruded carbon fibre profile led to a new specimen shape with a resulting improved measured compressive strength of 3 %.

1. Introduction

Used in wind turbine blades subjected to bending, pultruded carbon profiles are then loaded in tension or compression. Accurately determining the tensile and compressive properties is essential for designing these structures. The mechanical properties of materials are typically obtained by standardised test methods.
New materials and upcoming composites exhibit improved properties and performance that challenge these methods: following the available standards doesn't allow for measuring the correct potential strength, leading to overdesign [1].

Previous experimental testing campaigns, for instance, from Ferguson et al. [2] showed that constant-width compression specimens exhibit a wrong failure mode in the load introduction region. Specimen geometry has, therefore, been modified to waisted specimens (W6). Even if they are found to carry a higher load, the same conclusion is drawn: the final failure occurs out of the gauge section, in the waisted region, under the tabs, or in the junction with the grips (Figure 1). The failure mechanisms exhibit kink-band and splitting, leading to the final failure of the test specimen, typically observed during compression tests [2,3,4]. Thus, again, the material's full design potential is not captured.

A similar problem is faced during experimental tension strength determination [1,5], and some work has been done to analyse the gain in modifying the test geometries. Parameters linked to specimen geometry, tabs, and the material of the tabs have been explored. Iterations and studies are still ongoing. Regarding compressive tests, it is well known in the literature that the experimental strength measurements depend on experimental parameters, settings, and composite configuration [6]. The "structural effect" of

compressive tests is highlighted by Grandidier et al. [7], explaining that the compressive performance of composites is not an intrinsic material property: it depends on overall parameters such as laminate thickness, lay-up configuration or plies scale.

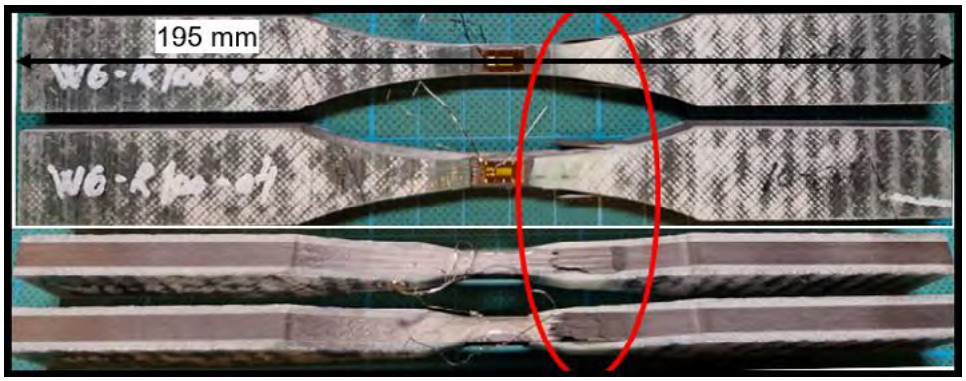


Figure 1. Out of gauge section failure during compressive tests on 5 mm thick pultruded carbon fibre profile specimen – waisted shape, front and side views

Fibre micro buckling and fibre kinking are two main scenarios for compressive failure modes. Several models have been developed to assess the compressive strength of UD composite under compressive loading along the fibre direction [4, 8, 9]. For instance, the Budiansky model [9] for compressive strength prediction is related to the in-plane shear characteristics of the composite and fibre waviness [10, 11]. These approaches mainly concern laminas. Special attention also addresses that the fibre misalignment and void content play a critical role in the compressive behaviour of the composite [2, 12]. Gutkin et al. [13] developed a micro-mechanical finite element model, showing that the failure mechanisms are defined by shear-driven fibre compressive failure with kink-band formation and splitting.

The presented investigation focuses on compression tests of 5 mm thick pultruded carbon fibre profiles and on using a modelling approach to support the development of new test geometries. The objective is to drive the failure into the gauge section by sizing and enhancing the specimen shape/geometry. A modelling-based approach is relevant to tackle this issue, as it constitutes an excellent alternative to long experimental campaigns and allows for a parametric study.

The first step of the study, with a linear model, is to capture the first information about the behaviour and stress repartition. A parametric study is performed, and the stress distribution is compared between different iterations. A dialogue between experimental and numerical is carried out.

2. Description of the model

2.1. Abaqus model – FEM presentation

In this context, a 3D Abaqus Implicit Finite Element (FE) model is built to study the specimen loading in compression and analyse the phenomenon contributing to the early failure. The model consists of modelling the different parts of the specimen (Figure 2), using 3D elements: the specimen, the tabs and the epoxy adhesive layer between the tabs and the specimen. Coinciding nodes link all these parts. 3D elements are also used for the grips. A Surface-to-Surface interaction defines the contact formulation between the grips and the tabs. The contact formulation in the Normal direction is defined as “Hard” contact and allows separation after contact, while the tangential behaviour is given through a penalty friction formulation with a friction coefficient of 0.4. Symmetry is considered in the middle of the specimen following the XZ plane. The boundary conditions reflect the experimental test conditions and are applied through Reference Points (RP). The compression is applied with a concentrated load

distributed over the specimen and grips surfaces through a kinematic coupling between the surfaces and the concentrated force applied on the RP. Grips pressure is applied similarly (representative load defined after measurement on a testing machine). A mesh sensitivity analysis has been performed, and the mesh is refined in the area under the end of the tabs.

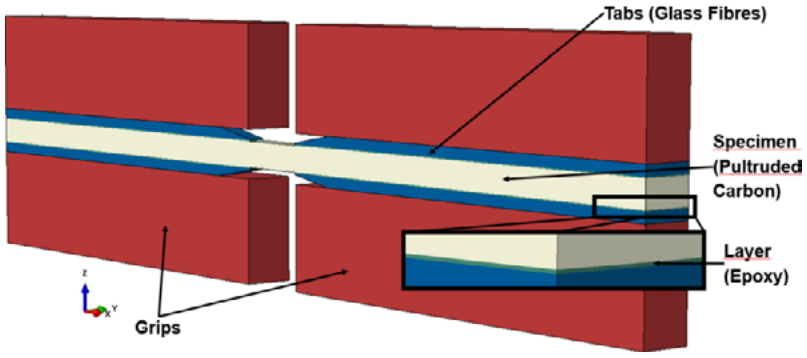


Figure 2. Modelling of Specimen, Epoxy Layers, Tabs and Grips

As a first approach, the 5 mm thick pultruded carbon specimen and the 2 mm biax Glass/Epoxy tabs are simulated using Elastic formulation and Engineering Constants **(**Table 1**)** and the epoxy layer as well as the steel grips with Isotropic elastic formulation **(**Table 2).

Table 1. Material parameters for Engineering constant for composites (1: loading direction, 2: transverse direction, 3: out-of-plan direction).

	E_1 (GPa)	E_2 (GPa)	E_3 (GPa)	G_{12} (GPa)	G_{13} (GPa)	G_{23} (GPa)	ν_{12}	ν_{13}	ν_{23}
Pultruded Carbon	132.000	8.900	8.900	4.975	4.975	4.975	0.30	0.30	0.30
Biax Glass/Epoxy 45°	11.160	3.000	3.000	5.000	4.000	4.000	0.27	0.27	0.27

Table 2. Material parameters for isotropic elastic materials.

	E (GPa)	ν
Steel	210.000	0.30
Layer Epoxy	3.121	0.30

2.2. Model of the reference geometry

The reference geometry is a waisted shape specimen, W6, as seen in Figure 1. The modelling conditions and loading represent experimental conditions (defined by the failure load obtained during compressive tests on the reference geometry). Experimentally, the compressive load is applied in the gripping part of the end-tabbed test specimen. It results in a combined compressive and shear load introduced through the tabs. A uniform unidirectional compression load is induced into the gauge section of the test specimen. As previously described for this geometry, the load measured at failure is close to -39 kN, representing a compressive strength of -1300 MPa and strain to failure of ~-0.98 %. With the linear assumption, this load is applied in the static model to screen the stress repartition at failure.
This first model is validated by observing the load introduction and the shear transition between the grips and the tabs. In addition, the compressive stress (S11) in the gauge area corresponds to the expected

stress level (-1300 MPa). Based on experimental observation and the first assumption, stresses of interest are longitudinal stress S11, out-of-plane stress S33, and, initially, shear stress S13, which is considered critical to trigger the failure (direction 3 is the normal pressure on the grips). These stresses are plotted along two paths, as defined in Figure 3.

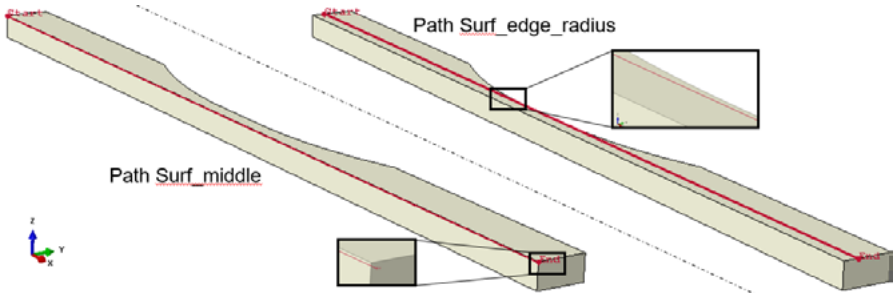


Figure 3. Paths for stress analysis

The specimen's maximum stresses, subjected to numerical singularities, are observed under a compressive load of -39 kN (Table 3).

Table 3. Maximum stresses in the specimen – Reference geometry model

Component	S11	S22	S33	S12	S13	S23
Stress (MPa)	-1588	-18,4	-33,8	-102,4	-42,6	-8,6

Figure 4 gathers the obtained plots. Stress S13 exhibits maximum stress values around the experimental failure's location, supporting the assumption that shear component acts on the fibre and resin leading to final failure.

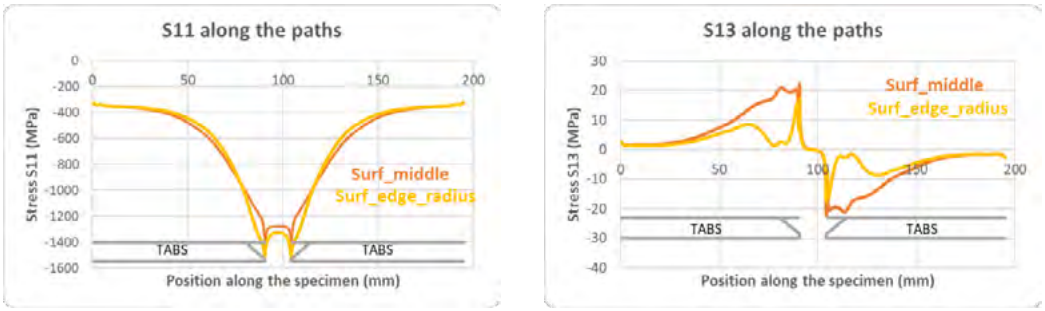


Figure 4. Numerical stresses S11 and S13 along the paths for the reference specimen.

3. Parametric Study: numerical and experimental

3.1. Set up of the study and first iteration

Under the same compressive load, a parametric study is conducted to monitor the influence of specimen geometrical parameters change and the effect on the stress repartition. The objective is to reduce shear stresses in the specimen by modifying parameters such as tab thickness, length of the chamfered area, tab fibre orientation, and radius of the waisted area. To automatise the generation of the model and lead a robust comparison, a Python script is established with all the parameters identified.

As the first results, thicker tabs lead to higher shear stress S13, a higher radius seems to distribute stress along the paths, the length of the tabs' chamfer doesn't really influence the stresses along the edge radius but lower the shear stress in the centre of the specimen. Buckling issues and manufacturing processes are also considered for the proposed solution. Combinations of different modifications are then investigated, and the proposed solution combines a 600 mm Radius and a 20 mm chamfer length. The maximum stresses in the Iteration 1 specimen (Table 4) are lower than in the reference specimen.

Table 4. Maximum stresses in the specimen – Iteration 1 geometry model.

Component	S11	S22	S33	S12	S13	S23
Stress (MPa)	-1487	-10,4	-24,8	-48,8	-23,6	-6,5

Compared to the reference specimen, Figure 5 below also shows a reduction of the S13 stress along the paths.

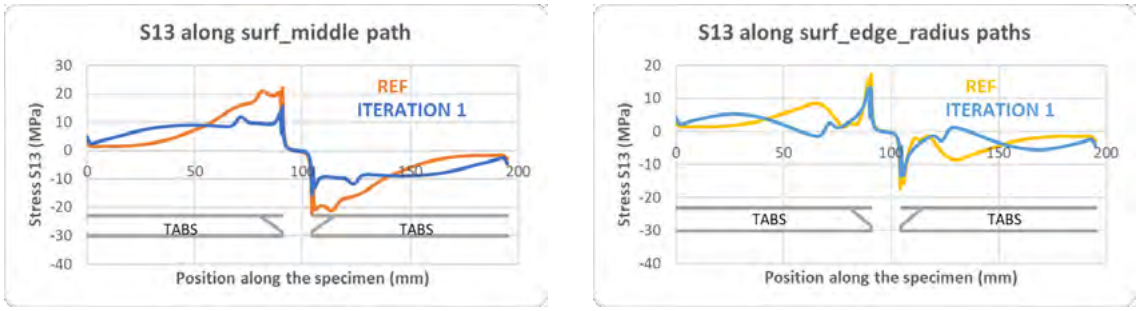


Figure 5. Numerical stress S13 along the paths: Iteration 1 is compared to the reference specimen.

Two specimens are then manufactured to be tested (Figure 6). With a load at failure of -38 kN (compressive strength of -1240 MPa), the results are slightly lower than the reference specimen. The failure generates in the radius of the specimen, as exposed in Figure 6-b), away from the gauge area.

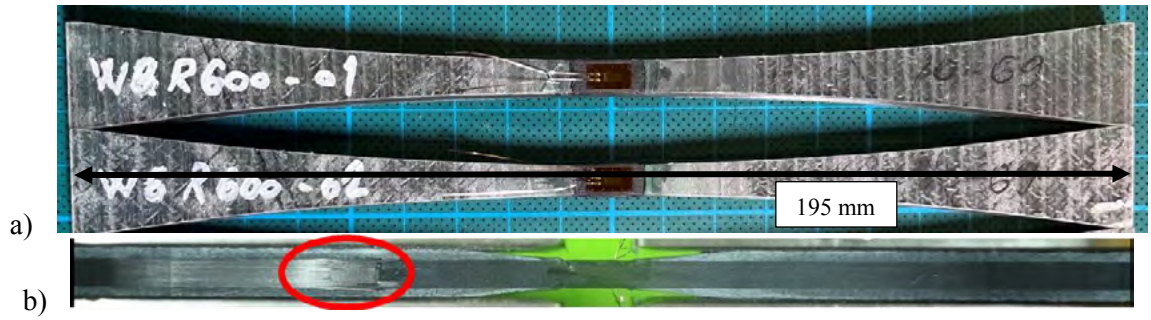


Figure 6. a) Proposed specimen geometry out of Iteration 1. b) Side view of the failure location after compression test on Iteration 1 geometry.

3.2. Second iteration

From these two configurations, the results obtained can be used to provide more information in the numerical/experimental dialogue. From Tables 3 and 4, maximum stress values obtained for S22 and S13 in the specimen enable us to "neglect" the effect of these components. However, from now on, all

numerical stresses are considered, and new analysis paths (surf_edge_circle) are defined (Figure 7). The locations of the failures are also known (in red in the graphs) and are essential information for observing the stresses in these areas.

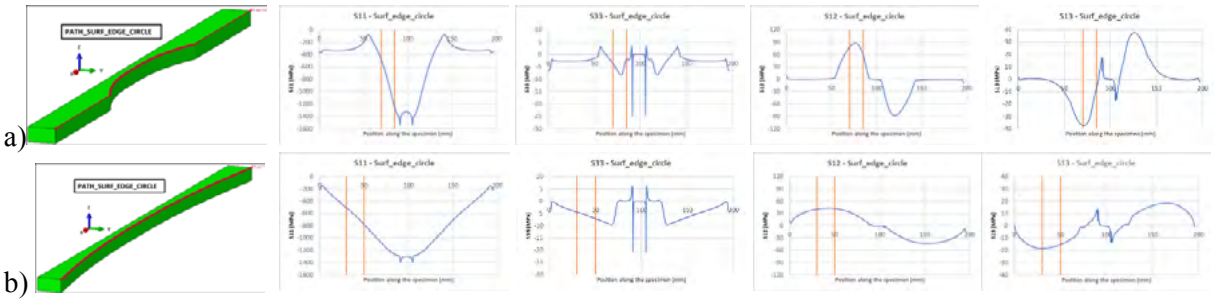


Figure 7. New path for stress analysis along the edge and the associated stress repartition S11, S33, S12 and S13: a) Reference geometry, b) Iteration 1 geometry.

After analysing the effect of different modifications and comparing the stress curves during Iteration 2, a new geometry is proposed with a 300 mm radius, a 20 mm chamfered length, 30 mm external width and 0° fibre-oriented tabs. Figure 8 shows the stresses in comparison with Reference and Iteration 1.

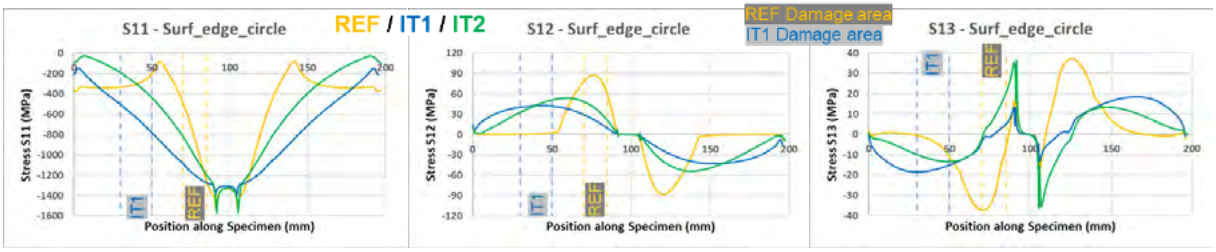


Figure 8. Comparison of the stresses S11, S12, and S13 along the path on edge for the reference (Yellow), Iteration 1 (Blue) and Iteration 2 (Green) configurations, with failure locations for reference and Iteration 1.

Considering the stress combination as a trigger for the failure, this stress repartition is more distributed and seems lower than the compared ones. However, the S13 stress concentration is higher at the tip of the tabs and the beginning of the gauge area. To provide the model with more information at this step, Iteration 2 geometry is then manufactured (specimen shown in Figure 9), and four specimens are tested.

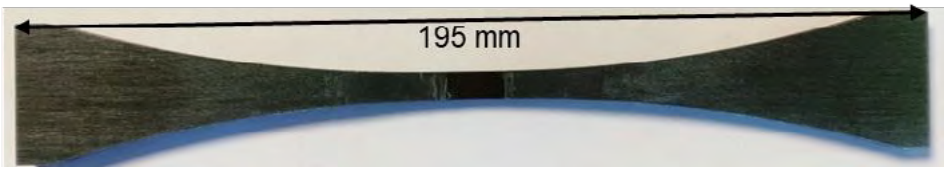


Figure 9. Iteration 2 specimen geometry.

The experimental results drive to a failure around -42 kN and compressive strength of -1345 MPa, corresponding to a 3 % improvement compared to the reference specimens' performance. However, the failure is still not located in the gauge section and occurs at the tip of the tabs for three specimens and in the radius for the fourth specimen.

4. Conclusions

This study presents the initial stages of a modelling approach for designing optimised compression specimens. Results underscore the complexity of compressive behaviour and the importance of shear stress consideration, emphasising the significance of numerical and experimental interactions for a deeper understanding.

At this stage, after iterations on parameters modification and comparison, a new geometry for compressive tests is proposed, leading to a 3% increase in compressive strength. New experimental results will bring extra information to continue the specimen optimisation using numerical study. To build a topology optimisation strategy, the specimen's failure criterion must be defined. The main objective to drive the failure in the gauge section is still to be achieved, leading to a repeatable and representative test method to measure compressive strength of pultruded profiles.

References

[1] B. Fazlali, S. Upadhyay, S.A. Ashodia, F. Mesquita, S.V. Lomov, V. Carvelli, Y. Swolfs. Specimen designs for accurate tensile testing of unidirectional composite laminates. *Composites Part A: Applied Science and Manufacturing*, 175, 2023.
[2] O.V. Ferguson, S.P.H Skovsgaard, H.M. Jensen, L.P. Mikkelsen. Compressive strength prediction of carbon fiber-reinforced pultruded profiles including realistic volumetric fiber orientations. *European Journal of Mechanics – A/Solids*, 104, 2024.
[3] H.M.Jensen. Residual stress effects on the compressive strength of uni-directional fibre composites. *Acta Materialia*, 50:2895-2904, 2002.
[4] N.K. Naik, R.S. Kumar. Compressive strength of unidirectional composites: evaluation and comparison of prediction models. *Composite Structures*, 46:299-308, 1999.
[5] R. Kumar, L. P. Mikkelsen, H. Lilholt, B. Madsen. Experimental Method for Tensile Testing of Unidirectional Carbon Fibre Composites Using Improved Specimen Type and Data Analysis. *Materials*, 14:3939, 2021.
[6] E.T. Camponeschi Jr. Compression of Composites Materials: A Review. *DTRC*, 87/050, 1987.
[7] J.-C. Grandidier, P. Casari, C. Jochum. A fibre direction compressive failure criterion for long fibre laminates at ply scale, including stacking sequence and laminate thickness effects. *Composite Structures*, 94:3799-3806, 2012.
[8] YL. Xu, KL Reifsnider. Micromechanical modeling of composite compressive strength. *J Composite Mater*, 27(6):572-588, 1993.
[9] B. Budiansky. Micromechanics. *Computers & Structures*, 16:3-12, 1983.
[10] J. Lee, C. Soutis. Thickness effect on the compressive strength of T800/924C carbon fibre-epoxy laminates. *Composites Part A: Applied Science and Manufacturing*, 36:213-227, 2005.
[11] A. Jumahat, C. Soutis, F.R. Jones, A. Hodzic. Fracture mechanisms and failure analysis of carbon fibre/toughened epoxy composites subjected to compressive loading. *Composite Structures*, 92:295-305, 2010.
[12] M.R. WISNOM. The effect of fibre misalignment on the compressive strength of unidirectional carbon fibre/epoxy. *Composites*, 21(5):403-407, 1990.
[13] R. Gutkin, S.T. Pinho, P. Robinson, P.T. Curtis. Micro-mechanical modelling of shear-driven fibre compressive failure and of fibre kinking for failure envelope generation in CFRP laminates. *Composites Science and Technology*, 70:1214-1222, 2010.

SUPPRESSION OF DELAMINATION IN CFRP LAMINATES WITH PLY DISCONTINUITIES USING POLYAMIDE MESH MATERIAL

M. J. Mohammad Fikry[1], Keisuke Iizuka[2], Hayato Nakatani[3],
Satoru Yoneyama[4], Vladimir Vinogradov[5] and Shinji Ogihara[6]

[1]Department of Mechanical and Aerospace Engineering, Tokyo University of Science, Chiba, Japan
Email: fikry@rs.tus.ac.jp
[2]Department of Mechanical Engineering, Aoyama Gakuin University, Kanagawa, Japan
Email: iizuka@me.aoyama.ac.jp
[3]Department of Mechanical Engineering, Osaka Metropolitan University, Osaka, Japan
Email: hayatonakatani@omu.ac.jp
[4]Department of Mechanical Engineering, Aoyama Gakuin University, Kanagawa, Japan
Email: yoneyama@me.aoyama.ac.jp
[5]School of Engineering, Newcastle University, Newcastle upon Tyne, United Kingdom
Email: vladimir.vinogradov@newcastle.ac.uk
[6]Department of Mechanical and Aerospace Engineering, Tokyo University of Science, Chiba, Japan
Email: ogihara@rs.tus.ac.jp

Keywords: delamination, fracture toughness, CFRP laminate, ply discontinuity, stress analysis

Abstract
Carbon fiber reinforced plastics (CFRP) laminates, known for their superior in-plane properties, often exhibit less robust interlaminar toughness, particularly vulnerable at structural complexities such as tapered sections and bolt hole regions. This study explores the use of polyamide (PA) mesh as an innovative method to enhance the interlaminar fracture toughness of CFRP laminates, aiming to improve overall durability by mitigating delamination. By integrating PA mesh between laminate layers, particularly around areas of ply discontinuity, the study evaluates the effectiveness of this approach in suppressing damage initiation and promoting energy absorption during fracture processes. Experimental investigations were conducted using End Notch Flexure (ENF) tests, which demonstrated a significant enhancement in fracture toughness—up to three times that of unmodified CFRP laminates. The microstructural configuration of the PA mesh was found to obstruct crack propagation effectively, thereby increasing the energy absorbed during fracture. Additionally, the study tested two configurations of PA mesh placement: a complete insertion between continuous and discontinuous plies and a localized insertion around the resin pockets. Both configurations prevented the onset of delamination typically initiated by matrix cracks, with a noticeable reduction in delamination propagation under tensile stress.

1. Introduction

Carbon fiber reinforced plastics (CFRP) laminates generally possess strong in-plane properties, while their out-of-plane characteristics, such as interlaminar toughness, are commonly seen as less robust. In the actual structure of CFRP, complex structural elements such as tapered sections for varying thickness and fiber-discontinuous regions due to bolt hole placements for joining become the primary locations for intralaminar damage initiation, which subsequently triggers interlaminar failure [1, 2]. Crack propagation in materials can be suppressed by incorporating features that absorb energy, preventing the initiation and growth of cracks [3, 4, 5]. One of the methods being attempted to improve the interlaminar fracture toughness of CFRP laminates is the placement of high-toughness materials between the layers [6].

©2024 | 3_FIKRY_M. J. Mohammad_TO39P.pdf

In this study, we consider the utilization of polyamide (PA) mesh material as one method to enhance the interlaminar fracture toughness of CFRP. Specifically, to improve the interlaminar fracture toughness and suppress interlayer damage initiation i.e., delamination. This involves addressing the complex structures of laminates with ply-discontinuous regions, implementing localized PA mesh configurations, and verifying damage suppression. In the study, the mechanism of enhancing interlaminar fracture toughness through the incorporation of PA mesh material was examined via double cantilever beam (DCB) and end notch flexure (ENF) tests. The study further confirmed the effective placement of PA mesh within CFRP laminates through experiments involving laminates with ply discontinuity under tensile load conditions. Two distinct configurations were employed for this purpose: firstly, the insertion of PA mesh material as a whole, positioned between continuous and discontinuous plies, and secondly, the insertion of 20 mm cut PA mesh material around the resin pocket (the region of fiber discontinuity), again placed between continuous and discontinuous plies.

2. Fracture toughness evaluation

2.1. Materials and Methods

For the manufacture of test specimens for interlaminar fracture toughness evaluation, prepreg (T700SC/2592, manufactured by Toray Industries) with a thickness of 0.14 mm was used. As the specimens for the interlaminar fracture toughness test, a unidirectional (UD) $[0]_{20}$ laminate was manufactured. The prepregs, each with a thickness of 0.14 mm per ply, were cut into 20 pieces of 200 x 200 mm. These were then stacked up into two sets of 10 pieces each. As shown in Figure 1, a PA mesh, measuring 175 x 200 mm was sandwiched between these two sets of stacked prepregs. The PA mesh used in this study has a fiber diameter of 50 µm, a thickness of 87 µm, and an opening of 95 µm (N-NO175T, NBC Meshtec Inc.). To create an initial crack in the specimen, polyimide film, measuring 25 x 200 mm was also sandwiched in between the upper and lower plies. The polyimide film used was 25 µm thick. An autoclave (DANDELION 2010) was used to cure the laminate at 130°C and a pressure of 0.2 MPa. Laminates were then cut into specimens suitable for DCB and ENF tests.

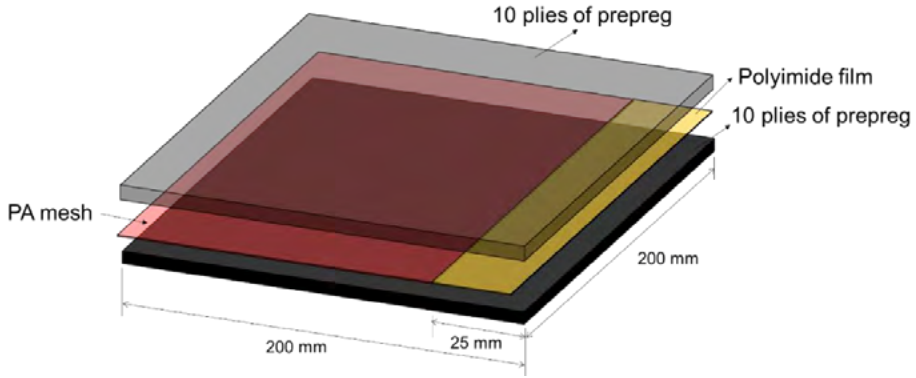


Figure 1. Illustration of the lay-up of a laminate for interlaminar fracture toughness evaluation.

For DCB test, measurements were taken of the load P, crack length a, and crack opening displacement (COD). Five specimens were tested. The first measurement was taken when the crack had propagated 3 mm from the initial crack, and subsequent measurements were made every 3 mm of crack propagation, with a total of five measurements per specimen. The loading speed was set at 0.5 mm/min up to 6 mm from the initial crack, and increased to 1.0 mm/min for crack propagation beyond 6 mm. Mode I interlaminar fracture toughness value G_I, was calculated using the following formula:

$$G_I = \frac{3}{2(2H)}\left(\frac{P_C}{B}\right)^2 \frac{(B\lambda)^{\frac{2}{3}}}{\alpha_1} \quad (1)$$

G_I was determined using the critical load P_C, the compliance of the COD in the elastic portion of the load-COD curve λ, and the slope of the linear approximation of the cube root of the compliance of the normalized crack length per unit width α_1.

For ENF test, measurements were taken of the load P and (maximum) deflection δ. Similar to DCB test, five specimens were tested. The load was applied at the midpoint of the support span with a distance of $2L = 70$ mm, as shown in Figure 2. The test speed was set at 0.5 mm/min. The mode II fracture toughness value G_{IIC} was calculated from Eq. (2). In the equation, a_1 represents an estimated value of crack length at a specific load. Additionally, P_1 represents a specified load, C_0 denotes the compliance of the initial elastic part and C_1 represents the compliance at a specified load, calculated from the load-COD curve. The maximum load $P_{\max}$ was used as P_1 in this study.

$$G_{IIC} = \frac{9a_0^2 P_1^2 C_1}{2B(2L^3 + 3a_1^3)}, \qquad a_1 = \left[\frac{C_1}{C_0}a_0^3 + \frac{2}{3}\left(\frac{C_1}{C_0} - 1\right)L^3\right]^{\frac{1}{3}} \tag{2}$$

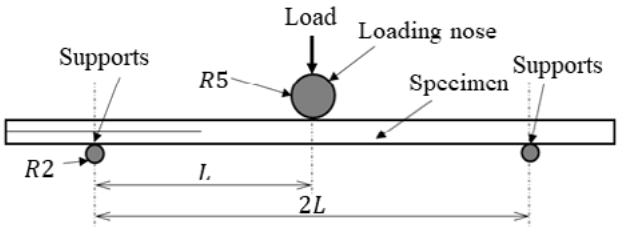


Figure 2. Schematic for ENF test set up.

2.2. Results and Discussion

Figure 3 shows the mode I fracture toughness G_I – crack length relationship for all specimens. Here, the dotted lines show the average G_I values. G_{IC} is the fracture toughness value calculated from the first loading and represents the critical strain energy release rate necessary for the initiation of delamination. It quantifies the energy per unit area required to initiate a delamination under mode I loading conditions. Conversely, G_{IR} represents the average fracture toughness value from the second to the fifth loading. This parameter is the propagation strain energy release rate, which measures the energy required to propagate an existing delamination. The average G_{IC} and G_{IR} for all five specimens are 519 J/m² and 336 J/m², respectively. Figure 4 displays bar charts comparing the G_{IC} and G_{IR} values of neat CFRP laminate (specimen without PA mesh insert) and CFRP laminate with PA mesh insert. The G_{IC} value for the CFRP with PA mesh insert is approximately three times higher than that of the neat CFRP, which has a G_{IC} value of 171 J/m². However, it should be noted that the G_{IR} value is slightly reduced compared to the neat CFRP (366 J/m²). The values of G_{IC} and G_{IR} of neat CFRP were taken from [6].This indicates that inserting PA mesh into the CFRP laminate requires higher strain energy to initiate delamination, but once initiated, the propagation becomes easier under mode I loading conditions. This indicates that the dimensions and configurations of the PA mesh used in this study are not optimal for enhancing the interlaminar fracture toughness performance of CFRP laminates under mode I loading.

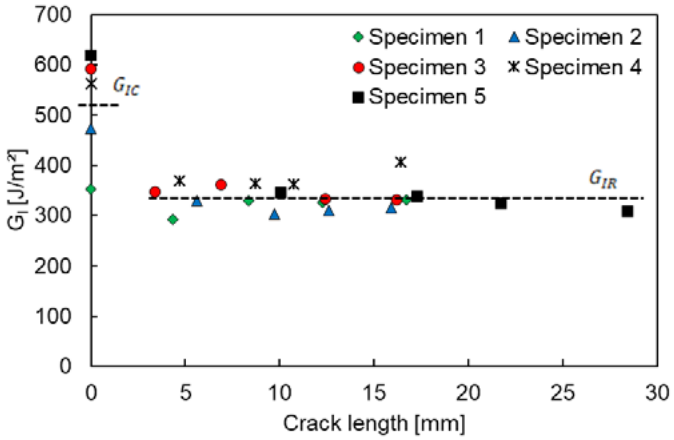


Figure 3. Mode I fracture toughness G_I– crack length relationship for all specimens. Dotted lines show the average G_I values.

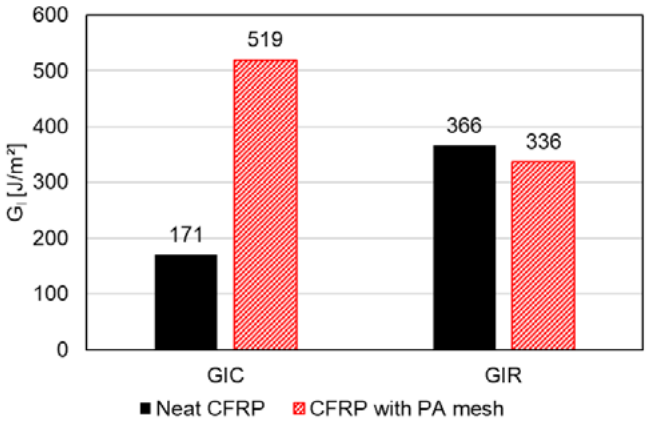


Figure 4. Comparison of mode I interlaminar fracture toughness between neat CFRP laminate and CFRP laminate with PA mesh insert.

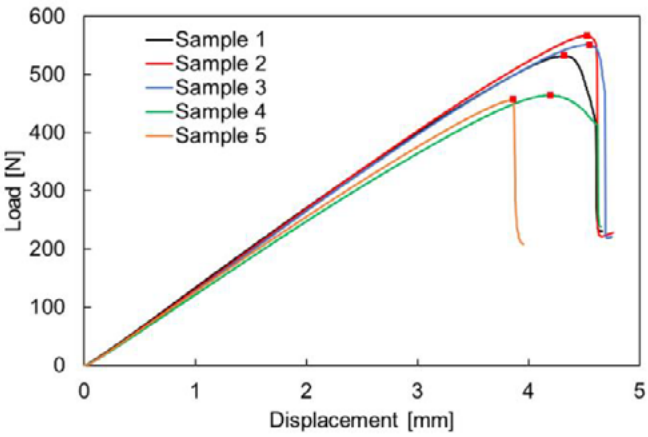


Figure 5. Load – deflection curves from ENF tests. The red dots represent the maximum load point of each test.

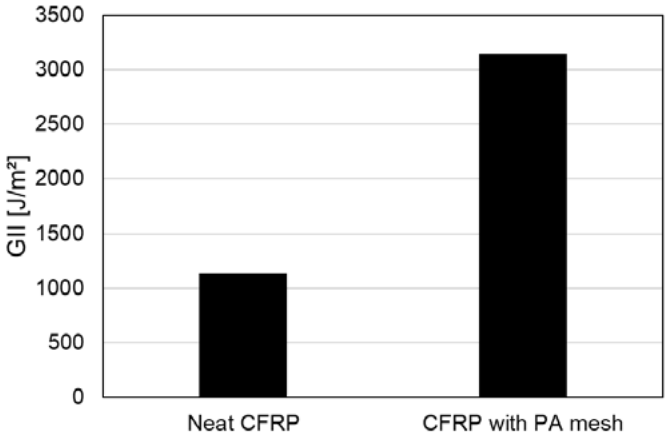


Figure 6. Comparison of mode II interlaminar fracture toughness between neat CFRP laminate and CFRP laminate with PA mesh insert.

Figure 5 presents the load-deflection curves from the ENF test conducted on five specimens. The peak loads for each specimen are highlighted with red dots on the curves. Figure 6 illustrates a comparison of the mode II fracture toughness G_{IIC}, values between CFRP laminates with and without PA mesh inserts. The displayed G_{IIC} values are averaged from five specimens tested. It is apparent that the CFRP laminates incorporating a PA mesh insert exhibit a mode II fracture toughness approximately three times greater than that of the neat laminates. This enhancement can be attributed to the integration of PA mesh

within the CFRP layers, which absorbs the energy and altering the crack trajectory due to its microstructure, under shear stresses (mode II loading).

The total of the G_{IC} and G_{IIC} values suggests that CFRP laminates with PA mesh inserts markedly outperform their neat counterparts in handling diverse loading conditions. Future research should continue to refine the mesh configurations to maximize these benefits across different modes of fracture, ensuring optimal performance and extended usability of CFRP structures.

3. Application of PA mesh in CFRP laminates with ply discontinuities

3.1. Materials and Methods

Laminate configuration of the specimens used in the uniaxial tensile test was $[0_2/PA/0_2]s$. Initially, as illustrated in Figure 7, a stack of four plies of carbon fiber/epoxy UD tape prepreg (Torayca, T700SC/2592), each with a thickness of 0.14 mm, was bisected perpendicularly to the fiber direction into two equal halves. These halves were then aligned with a predefined gap to form a symmetrical laminate structure, with two PA meshes and continuous $[0]_2$ UD laminates attached above and below the gap. The gap or resin pocket length L_0 was set to approximately 1 mm.

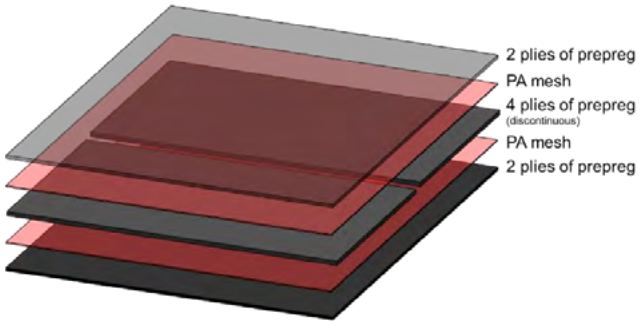


Figure 7. Illustration of laminate with discontinuous plies and PA mesh embedded.

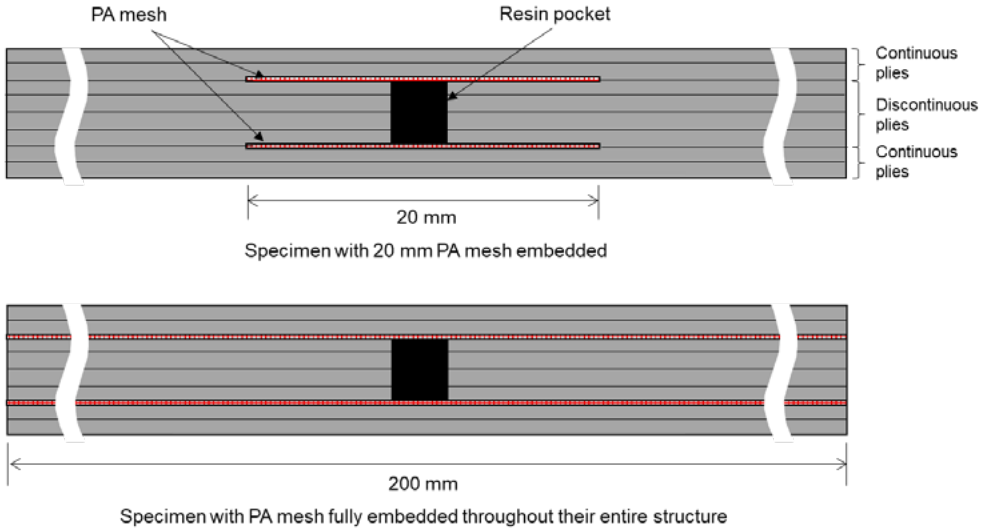


Figure 8. Placement of PA mesh in the specimen.

In this study, the specimens were manufactured with a 20 mm PA mesh embedded and with PA mesh fully embedded throughout their entire structure. A schematic diagram of the structures is shown in Figure 8. The laminate was then cured using autoclave molding at a temperature of 130°C and a pressure of 0.2 MPa. During the curing process, the elevated temperature caused the epoxy resin in its gel-phase condition from the adjacent UD plies to flow into the gap, forming a resin pocket. This resin pocket then cured simultaneously with the rest of the laminate. After cooling to room temperature, the laminates were sectioned into specimens as depicted in Figure 9.

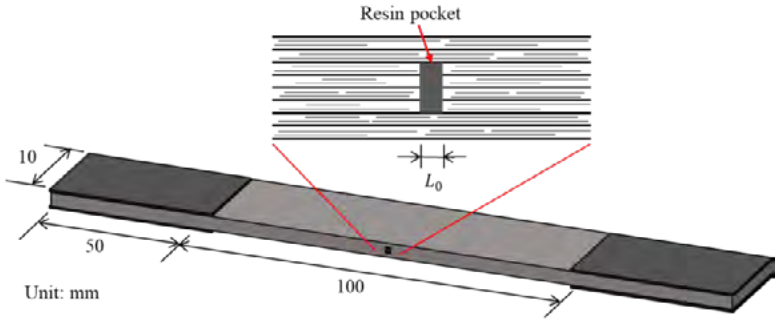


Figure 9. Specimen measurement.

3.2. Results and Discussion

To confirm the suppression of interlaminar delamination by embedding the PA mesh, a tensile test was also conducted on neat CFRP specimens (specimens without the insertion of PA mesh) for comparison purposes. The stress-strain curves and results of edge observations (around the resin pocket area) at specific applied stress levels for a neat CFRP specimen are shown in Figure 10. Results from neat CFRP specimens, referenced from our study [7], revealed an initial crack at 451 MPa. Subsequent matrix cracks were observed at 564 MPa and 679 MPa, with delamination initiating from the crack tip at 564 MPa, confirmed by changes in the stress-strain curve's gradient. Complete delamination between continuous and discontinuous plies was noted at approximately 725 MPa.

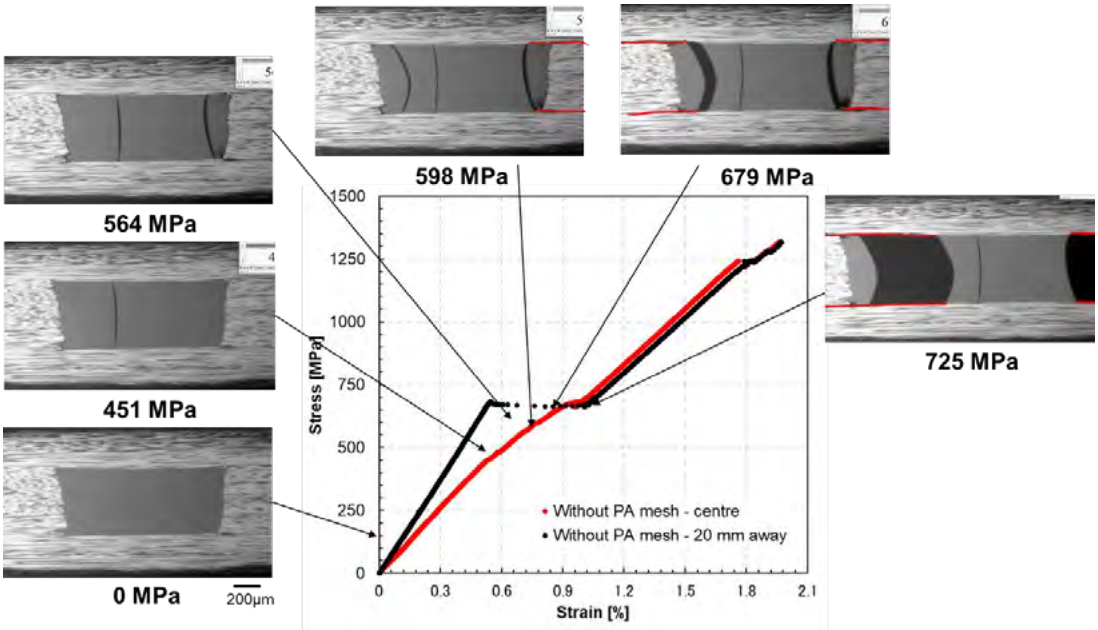


Figure 10. Stress-strain curves and results of edge observations (around the resin pocket area) at specific applied stress levels for a neat CFRP specimen [7].

The uniaxial tensile test results comparing specimens with 20 mm PA mesh inserts to neat CFRP specimens showed significant differences in stress-strain behavior, as presented in Figure 11. Edge observations detailed the progression of damage, particularly around the resin pocket area, with matrix cracks at 456 MPa and 520 MPa, and delaminations starting at 617 MPa. Even with PA mesh embedded locally, delamination was effectively suppressed, demonstrating the mesh's ability to stabilize the laminate structure. Unlike neat CFRP, which showed rapid delamination post-600 MPa, PA mesh specimens maintained a stable stress-strain curve up to higher stress levels. A significant strain jump at 720 MPa indicated sudden delamination, progressing slowly until reaching a critical stress level of 1121 MPa, far higher than the 725 MPa in neat specimens, resulting in complete delamination and fracture. This underscores PA mesh's role in increasing fracture toughness and suppressing delamination in CFRP laminates, even when applied locally.

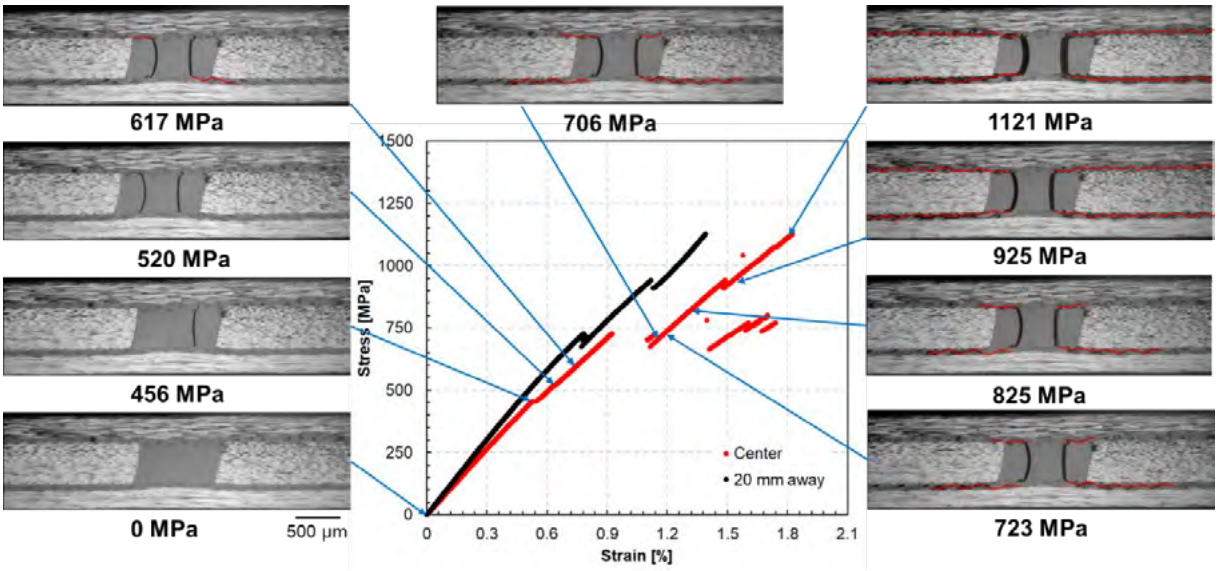


Figure 11. Stress-strain curves and results of edge observations (around the resin pocket area) at specific applied stress levels for a specimen with a 20 mm PA mesh embedded.

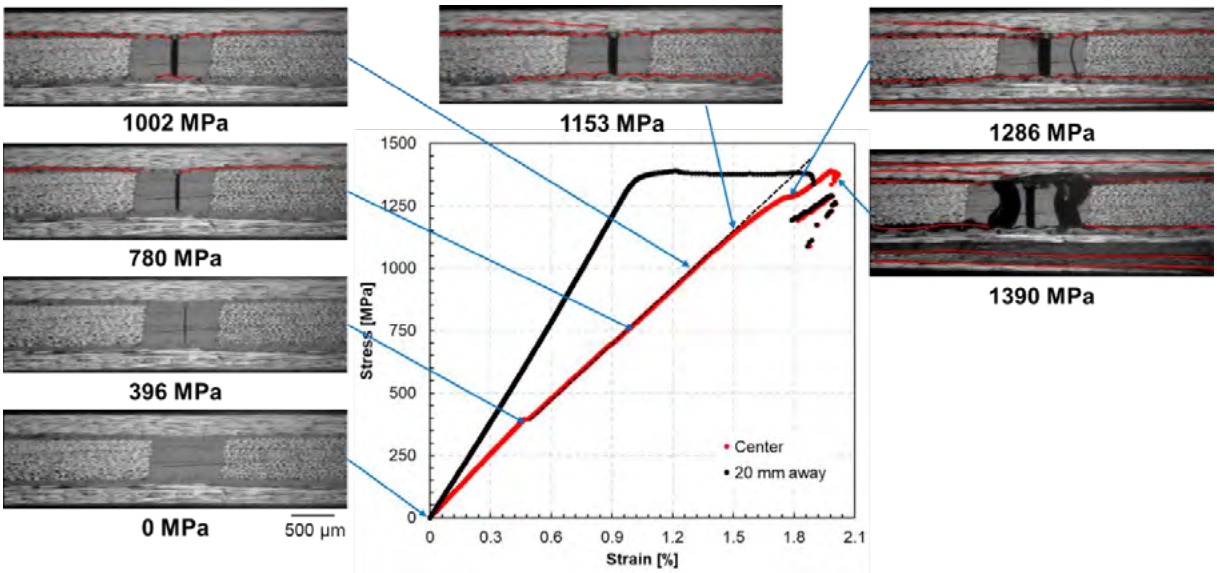


Figure 12. Stress-strain curves and results of edge observations at specific applied stress levels for a specimen with a PA mesh fully embedded throughout its entire structure.

The uniaxial tensile test results comparing laminates with fully embedded PA mesh to neat CFRP specimens showed significant differences in stress-strain behavior, as presented in Figure 12. Edge observations in the figure detailed damage progression around the resin pocket area. The first matrix crack in the resin pocket occurred at 396 MPa, slightly lower than in the neat CFRP specimen. However, the second matrix crack in the fully embedded PA mesh specimen occurred at 1286 MPa, significantly later than in other specimens. Unlike neat CFRP, where delamination progressed rapidly post-600 MPa, PA mesh specimens showed a stable, linear stress-strain curve up to high stress levels, with slow delamination progression. Additionally, compared to the specimen with a 20 mm PA mesh embedded, the specimen with a fully embedded PA mesh shows much later non-linearity in the stress-strain curve and significantly slower propagation of delamination. Delamination was observed at 780 MPa and propagated slowly, reaching 1153 MPa between continuous plies, indicating enhanced interlaminar toughness due to PA mesh. The specimen fractured at 1390 MPa following complete ply separation. As previously mentioned, this substantial enhancement in suppressing delamination is attributed to the PA mesh interrupting crack propagation. The PA mesh absorbs energy and alters the crack trajectory due to

its microstructure during crack propagation. Also, it should be noted that despite the mesh, the material strength remained unaffected, with similar fractured stress and strain compared to neat CFRP specimen.

3. Conclusions

Comparing neat CFRP laminates with those incorporating PA mesh inserts reveals clear differences in delamination behavior and stress-strain characteristics. Neat CFRP specimens show rapid delamination following an initial matrix crack, resulting in a steep decline in the stress-strain curve slope. In contrast, laminates with PA mesh, whether as a 20 mm section or fully embedded, maintain a more stable initial stress-strain curve and exhibit slower delamination, enhancing crack propagation resistance. The fully embedded PA mesh variant performs best, significantly delaying delamination even under higher stress levels while maintaining material strength equivalent to neat CFRP. This improvement can be attributed to the integration of PA mesh within the CFRP layers, which absorbs energy and alters the crack trajectory due to its microstructure. However, the study suggests that the current PA mesh configurations may not yet optimize delamination suppression under mode I loading, indicating a potential for further improvement in mesh dimensions and placement. Future research should focus on optimizing these factors through factorial design experiments to maximize the observed benefits of PA mesh in CFRP laminates.

Acknowledgments

This work was supported by JKA and its promotion funds from KEIRIN RACE.

References

[1] M. J. M. Fikry, V. Vinogradov and S. Ogihara. Mechanical properties and damage behavior of tapered unidirectional CFRP laminates. *Mechanical Engineering Journal,* 10(4):23-00079, 2023.

[2] M. J. M. Fikry, Q. Wang, M. Irita, S. Ri, N. Toyama, V. Vinogradov and S. Ogihara. Measurement of microscopic strain distributions of CFRP laminates with fiber discontinuities by sampling moiré method. *Advanced Composite Materials,* 31(3):273-288, 2022.

[3] M. Farshad and P. Flueler. Arrest of rapic crack propagation in polymer pipes. *Plastics Rubber and Composites Processing and Applications,* 25(6):291-293, 1996.

[4] H. Kobayashi, S. Yoshida, H. Kato, K. Fukui and K. Tarama. Theoretical studies of hydrogen molecule adsorption on flat and stepped platinum surfaces. *Surface Science,* 79(1):189-204, 1979.

[5] M. Yasaee, I. P. Bond, R. S. Trask and E. S. Greenhalgh. Mode I interfacial toughening through discontinuous interleaves for damage suppression and control. *Composites Part A: Applied Science and Manufacturing,* 43(1):198-207, 2012.

[6] N. Terashi, D. Isobe, K. Koizomi, T. Yamazaki, M. J. M. Fikry and S. Ogihara. Improvement of CFRP Interlaminar Fracture Toughness and Influence of Mechanical Properties by Inserting Non-Woven Carbon Tissue. *Journal of the Japan Society for Composite Materials,* 49(2):41-47, 2023.

[7] M. J. M. Fikry, V. Vinogradov and S. Ogihara. Experimental observation and modeling of resin pocket cracking in unidirectional laminates with ply discontinuity. *Composites Science and Technology,* 218:109175, 2022.

EFFECT OF ALTERNATING SALT FOG AND DRY CONDITIONS ON THE BEHAVIOR OF FLAX FIBER REINFORCED EPOXY COMPOSITES

V. Fiore[1], L. Calabrese[2], C. Sanfilippo[1], E. Proverbio[2] and A. Valenza[1]

[1]Department of Engineering, University of Palermo, Viale delle Scienze, 90128 Palermo, Italy
Email: vincenzo.fiore@unipa.it, carmelo.sanfilippo01@unipa.it, antonino.valenza@unipa.it
[2]Department of Engineering, University of Messina, Contrada Di Dio, 98166 Messina, Italy
Email: lcalabrese@unime.it, eproverbio@unime.it

Keywords: biocomposites, flax, durability, wet/dry cycles, salt-fog, aging

Abstract
This paper investigates the reversibility of FFRCs' performance under realistic environmental conditions, focusing on semi-structural applications. To achieve this, FFRCs were subjected to cycles mimicking real-world exposure, consisting of 10 days of humid (i.e., salt-fog spray) and 18 days of dry conditions (22°C, 50% RH), repeated three times. The mechanical properties of the composites were monitored throughout the dry phase of each cycle (at 0, 5, 10, and 18 days of drying) by means of quasi-static three-point bending tests. Furthermore, the water absorption and desorption were assessed by tracking the weight changes of composites during the entire aging campaign.

1. Introduction

In recent years, natural fiber reinforced composites (NFRCs) have gained significant attention due to their potential to combine good mechanical performance with environmental friendliness. However, their widespread use, particularly in wet or humid environments, is limited due to some drawbacks associated with natural fibers such as their inherent variability, their high moisture absorption tendency, and their weak adhesion with several polymer matrices.

In such a context, although a wide literature is available on how NFRCs perform in humid or wet conditions [1]-[2], a research gap exists in understanding their behavior in outdoor applications with fluctuating humidity levels. Additionally, there is a lack of knowledge regarding how they recover their performance after drying. In light of this, our recent research focused on the effects of humidity exposure and drying on the performance of composites made with glass, flax, or a combination of both fibers, in simulated marine environments [3]-[5]. Specifically, we investigated the ability of these composites to recover their physical and mechanical properties after a single cycle of exposure to salt fog (humid) followed by drying.

The experimental results showed that these composites experience both reversible and irreversible aging phenomena during the initial humid step. Additionally, they exhibit a noticeable recovery of their mechanical properties during the following dry step, especially for short humid cycles.

Motivated by these interesting findings, and recognizing that the reversibility of performance recovery in flax fiber-reinforced epoxy composites (FFRCs) after consecutive salt spray and dry cycles is not well understood, this work aims to evaluate how three repeated humid-dry aging cycles impact the

©2024 | 3_FIORE_Vincenzo_ODTTB.pdf

reversibility of physical and mechanical properties in FFRCs' manufactured through the vacuum-assisted resin infusion process.

2. Materials and methods

Epoxy composites reinforced with five layers of twill weave woven flax fabric with an areal weight of 318 g/m^2 (shown in Figure 1) were manufactured through vacuum assisted resin infusion process, underwent an initial curing step at 25 °C for 24 hours followed by a post-curing step at 50 °C for 15 hours. A commercial DEGBA epoxy resin (SX8 EVO) mixed with its amine-based hardener (100:30 by weight) was used as the matrix.



Figure 1. Wave architecture of flax woven fabric

The whole aging campaign lasted 3 months (i.e., 12 weeks), consisting of three wet/dry cycles, each lasting 4 weeks: 10 days of foggy environment (wet phase) followed by 18 days of drying (dry phase). In more detail, the wet phase was achieved by exposing composites to salt-spray fog conditions (5 wt% NaCl solution) at 35°C and 100% R.H. using a corrosion chamber (model CC1000IP by Ascott) in accordance with the ASTM B 117 standard. The dry phase was carried out by keeping them under controlled conditions (i.e., 22°C and 50% R.H).

To assess water absorption and desorption, the weight of composite samples was monitored at regular intervals throughout the aging campaign. In particular, three square samples (100 mm x 100 mm) were daily removed from the salt-fog chamber for 10 days, wiped with a dry cloth, and weighed using an analytical balance (model AX 224 by Sartorius). In accordance with ASTM D570 standard, the weight percentage change WC of FFRCs was calculated using the following equation (Eq. 1):

$$WC(\%) = 100(M_i + M_0)/M_0. \quad (1)$$

Where M_0 represents the weight of unaged samples and M_i is the weight of the sample at aging time t_i, which is the sum of the time intervals in the salt-fog chamber and drying.

Quasi-static three-point bending tests were performed after 0, 5, 10, and 18 days of drying, for each cycle, using a universal testing machine (UTM, model Z005 by Zwick-Roell equipped with a 5 kN load cell), according to the ASTM D790 standard. For each condition, five samples (13 mm x 64 mm) were tested by setting the crosshead speed and the support span at 1.4 mm/min and 54 mm, respectively.

The fractured surfaces' morphology was observed using a scanning electron microscope (SEM, model 450 by Quanta). To prevent electrostatic charging, all analyzed surfaces were pre-sputtered with a thin gold layer

3. Results and discussion

3.1. Absorption and desorption measurements

First, the composites were found to experience a progressive increase in weight during the humid step, followed by a decrease in weight during the subsequent dry step, regardless of the cycle number. More interestingly, it is possible to observe an increase in the maximum water uptake values shown at the end of the humid phase with increasing cycle number. On the other hand, the residual weight changes at the end of the dry phases decreased when comparing the first, second and third cycle. Therefore, an increase in the difference between the maximum and minimum weight values reached at the end of the humid and dry phases can be observed as a function of the aging cycle number, as reported in Table 1.

Table 1. Weight changes at varying aging cycles.

Cycle's number	*Maximum WC* (%)	*Residiual WC* (%)	*Difference WC* (%)
1	7.9	1.5	6.4
2	8.2	1.4	6.8
3	8.6	1.2	7.4

These experimental results can be attributed to degradation phenomena occurring during the humid phase of each cycle. Due to water adsorption and diffusion into the bulk material, the microstructure of composites alters as a result of the activation and propagation of microcracks and/or interfacial debonding. This modification becomes more significant with an increase in the number of aging cycles.

3.2. Mechanical characterization

Figure 2 shows the hystogram of flexural strength and modulus values after varying drying times for each imposed aging cycles. The composite progressively reduces in strength and stiffness during the humid phase (i.e., 0D samples), followed by a recovery during the next dry phase. The results acquired at different drying times show that the mechanical performances can be significantly recovered even after just a few days of exposure to a dry environment.

Regardless of the aging cycle, approximately 20-30% of the composite's strength is recovered after 5 drying days (i.e, 5D samples in Figure 2a). This indicates that the degradation mechanisms responsible for the decay of the composite's strength during the humid phase are mainly reversible. While evaluating Figure 2b, although the modulus of the FFRCs also shows a clear increase in its value as the drying time increases, it always remains significantly lower than that of the unaged specimen. At the end of the aging campaign, the average flexural modulus shown by FFRCs is 3.16 GPa, which is about 25% lower than the unaged material (i.e., 4.18 GPa).

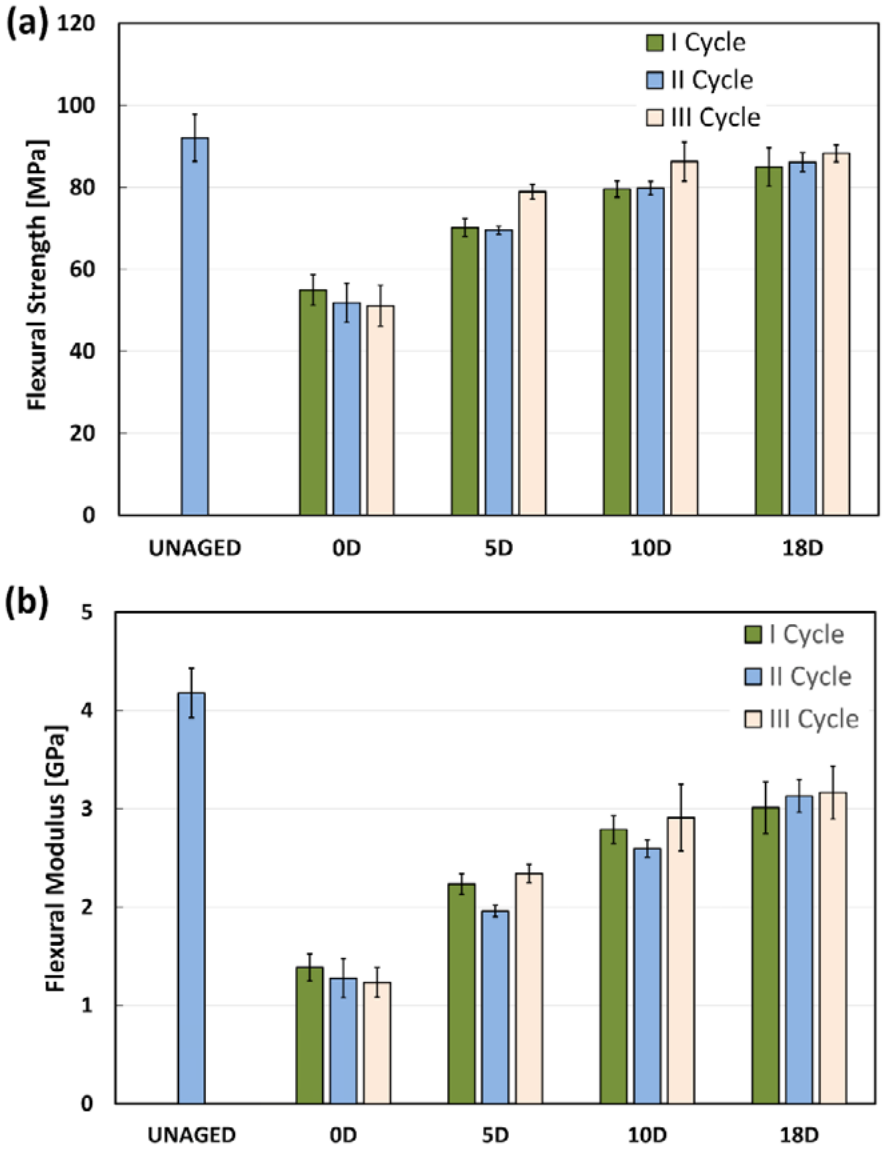


Figure 2. Flexural (a) strength and (b) modulus of FFRCs at increasing drying time for the 1st, 2nd, and 3rd aging cycle

This behavior can be ascribed to diverse degradative mechanisms that play a crucial role in worsening the composites' overall performances. The water absorption could induce swelling of the hydrophilic fibers, triggering the formation of matrix microcracks [6]. These favour local stresses mainly located on the fiber-matrix interface, which further promote crack initiation and propagation. However, limited exposure to salt fog (i.e., 10 days) might not be enough time for many cracks to form. As a result, the damage might be non-permanent. This means the material could recover once removed from the wet environment, thus explaining the observed flexural strength trend.

On the other hand, the decrease in stiffness can generally be related to softening and plasticization phenomena induced in wet NFRCs [7]. This stiffness drop is likely due to a combined effect of both matrix and fiber softening. Dry flax fibers have very stiff cellulose fibrils, where the cellulose molecules are tightly bound together. However, water can permeate the fibers and interact with the hydroxyl groups on the cellulose molecules. This interaction creates weak hydrogen bonds, which weaken the rigid structure of the flax fibers. In essence, the water acts like a lubricant, allowing the cellulose molecules to move more freely and making the fibers more flexible [8]. Furthermore, the epoxy matrix absorbs both free and bound water. Free water molecules have high mobility, diffusing easily through the gaps

and holes inside the thermoset's bulk, thus leading to a reversible sorption effect. Vice versa, bound water molecules are constrained by interaction to the polar groups inside the polymer network, leading to permanent sorption effects [9]. Figure 3 compares the SEM micrographs at high magnification of fractured specimens from flexural tests.

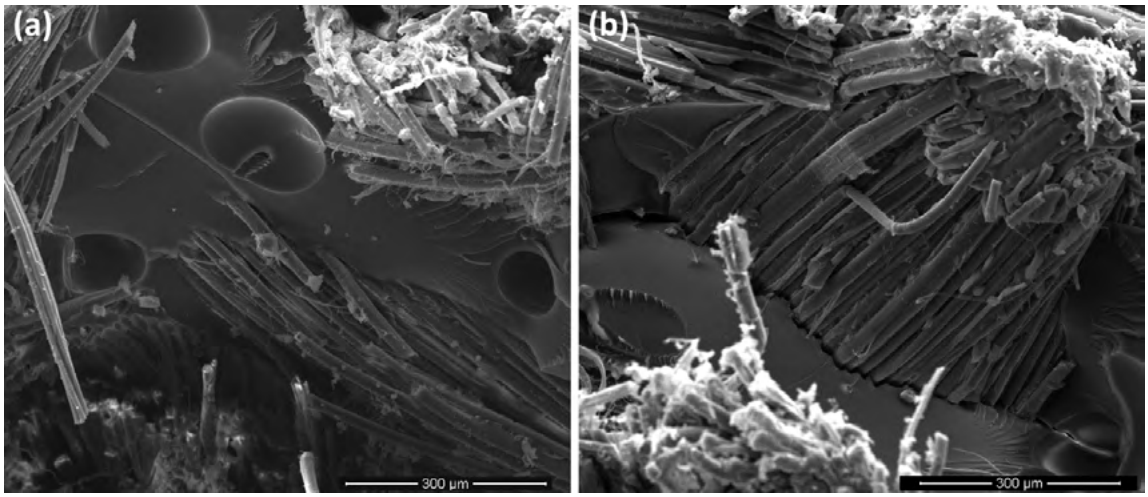


Figure 3. Close-up views of fractured surfaces:(a) unaged and (b) fully aged samples

Quite good compatibility between flax fibers and the surrounding polymer can be identified by observing the morphology of unaged samples shown in Figure 3a. In other words, the epoxy matrix fills the gaps between flax fibers, creating suitable interfacial adhesion and even stress distribution at the fiber/matrix interface, thus preventing cavity formation.

On the other hand, a loss of adhesion at the fiber-matrix interface is evident in the FFRCs after the aging cycle (i.e., after three aging cycles), as clearly shown in Figure 3b. This is likely due to absorbed water, which leads to debonding phenomena at the interface. Consequently, the formation of preferential water pathways at the fiber-matrix interface further weakens the adhesion. These structural discontinuities, formed during the humid phase of each cycle, endure also during the following dry phase, and their relevance increases with increasing cycle number. This limits interfacial stress transfer capability, resulting in the irreversible reduction of the FFRCs' stiffness.

3. Conclusions

The impact of repeated and consecutive humid-dry aging cycles on the mechanical stability and water absorption/desorption behavior of flax fiber-reinforced composites (FFRCs) was assessed in this research paper. To this aim, FFRCs, manufactured through vacuum infusion technique, were exposed for a total period of 12 weeks to three repeated cycles of humid (salt-fog) and dry environments.

The investigated composites showed weight gain during the humid phase of each cycle, followed by weight loss during each drying phase. More in detail, the maximum water uptake values increased at the end of each humid phase, while the residual weight values decreased at the end of each dry phase, with an increasing number of cycles. Therefore, a greater difference between the maximum and minimum weight change values was observed as a function of the aging cycle number. This results can be attributed to the degradation phenomena that occurred during the salt-fog exposure, which became more significant as the number of applied cycles increased.

From a mechanical standpoint, FFRCs weakened when exposed to the salt-fog environment. However, they were also able to recover some of their mechanical stability during the subsequent dry phase of

each cycle, regaining 20-30% of their strength after a few days. This indicates that the strength reduction is almost fully reversible. However, the flexural modulus of FFRCs at the end of the aging campaign (i.e., after three aging cycles) resulted about 25% lower than that of unaged composites.

References

[1] Q. Wang, T. Chen, X. Wang, Y. Zheng, J Zheng and G. Song. Recent Progress on Moisture Absorption Aging of Plant Fiber Reinforced Polymer Composites. *Polymers*, 15(20):4121, 2023.
[2] T.H. Mokhothu and M. J. John. Review on hygroscopic aging of cellulose fibres and their biocomposites. *Carbohydrate Polymers*, 131:337-354, 2015.
[3] V. Fiore, L.Calabrese, R. Miranda, D. Badagliacco, C. Sanfilippo, D. Palamara, A. Valenza and E. Proverbio. On the response of flax fiber reinforced composites under salt-fog/dry conditions: Reversible and irreversible performances degradation. *Composites Part B*, 230(1):109535, 2022.
[4] L.Calabrese, V. Fiore A. Valenza and E. Proverbio. A topological weakening and softening map as simplified tool to assess the performances recovery of hybridized natural fiber reinforced composites subjected to alternate salt-fog/dry cycle. *Polymer Testing*, 127: 108186, 2023.
[5] V. Fiore, L.Calabrese, R. Miranda, D. Badagliacco, C. Sanfilippo, D. Palamara, A. Valenza and E. Proverbio.. An experimental investigation on performances recovery of glass fiber reinforced composites exposed to a salt-fog/dry cycle. *Composites Part B*, 257: 110693, 2023.
[6] T. Cadu, L. Van Schoors, O. Sicot, S. Moscardelli, L. Divet and S. Fontaine. Cyclic hygrothermal ageing of flax fibers' bundles and unidirectional flax/epoxy composite. *Industrial Crops and Products*, 141:111730, 2019.
[7] H.J. Kim and D.W. Seo. Effect of water absorption fatigue on mechanical properties of sisal textile-reinforced composites. *International Journal of Fatigue*, 28(10): 1307-1314, 2006.
[8] T. Alomayri, H. Assaedi, F.U.A. Shaikh and I.M. Low. Effect of water absorption on the mechanical properties of cotton fabric-reinforced geopolymer composites. *Journal of Asian Ceramic Societies*, 2(3): 223-230, 2014.
[9] C. Maggana and P. Pissis. Water sorption and diffusion studies in an epoxy resin system. *Journal of Polymer Science, Part B: Polymer Physic*, 37(11): 1165-1182, 1999.

AGING MECHANISMS OF CERAMIC MATRIX COMPOSITES

Guillaume German[1,2], Émilie Perret[1], Francis Rebillat[2], Aurélien Debelle[3], Xavier Bourbon[3], Jérôme Roger[2]

[1]High Performance Multifunctional Materials Domain IRT Saint Exupéry
Email: guillaume.german@irt-saintexupery.com, Web Page: www.irt-saintexupery.com
Email: emilie.perret@irt-saintexupery.com, Web Page: www.irt-saintexupery.com

[2]Laboratoire des Composites Thermo Structuraux (LCTS), U. Bordeaux
Email: german@lcts.u-bordeaux.fr , Web Page: http://www.lcts.u-bordeaux.fr
Email: rebillat@lcts.u-bordeaux.fr, Web Page: http://www.lcts.u-bordeaux.fr
Email: roger@lcts.u-bordeaux.fr, Web Page: http://www.lcts.u-bordeaux.fr

[3]Agence nationale pour la gestion des déchets radioactifs (Andra)
Email: aurelien.debelle@andra.fr, Web Page: www.andra.fr
Email: Xavier.Bourbon@andra.fr, Web Page: www.andra.fr

Keywords: aging CMC, radioactive waste, geological disposal, mechanical study, thermodynamic calculations.

Abstract

This research examines the hydrothermal aging behavior of ceramic matrix composites (CMCs) in the field of deep geological disposal of high-level radioactive waste (HLW) The study focuses on alumina powder as a representative CMC matrix material. Accelerated aging experiments were conducted in aqueous environments (pH > 11.5, T = 70°C and P = 1.3 bar). The research used a cross-disciplinary approach integrating thermodynamic calculations and physicochemical analyses to determine the behavior of alumina with the aqueous aging solution. The characterization of the aged alumina powders revealed the presence of unaltered alumina, an amorphous phase, and calcium carbonate precipitates from the aqueous solution. Thermodynamic calculations indicate: (1) the hydrolysis of alumina to diaspore (2) the formation of an aluminosilicate phase and calcium carbonate. These calculations corroborate the experimental results. Furthermore, thermodynamic calculations demonstrate that variations in pressure and volume have a negligible effect on the evolution of equilibrium in this system at the temperature considered.

1. Introduction

Since 1999, the French national agency for radioactive waste disposal (Andra) has been working on the possibility of long-term deep geological disposal of high-level waste (HLW) and long-lived intermediate-level waste (ILW) [1–3]. The Cigéo project, which is aimed at accommodating HL and ILW waste, encompasses both existing stocks and future waste from current or authorized nuclear facilities. [3]. The proposed solution entails deep geological disposal, which aims to safeguard the environment from radioactive hazards by placing waste in micro-tunnels excavated 500 meters underground within a stable Callovo-Oxfordian (clay) layer, undisturbed for 160 million years [2]. Currently, the

preferred approach involves the use of a cell liner made of low-carbon steel liner, although Andra is investigating alternative materials to potentially further improve the disposal. The collaborative C3N (Composite ceramic nuclear lining) project has successfully overcome the technological challenges associated with ceramic matrix composites (CMC) for tunnel liners. Ceramic matrix composites were initially developed for applications in extreme conditions, including high temperatures, oxidizing environments, mechanical stress, and even irradiation. They combine a unique set of properties such as: mechanical properties, resistance to oxidation, and thermal stability [4]. The behavior of CMCs in geological disposal conditions remains largely unexplored. The objective of this work is to establish a scientific methodology to assess and understand the performance of CMCs in environments that are unusual for such materials, particularly when they are immersed in a highly alkaline aqueous solution. For these reasons, it was decided to initially work on composite made of alumina matrix reinforced with alumina fibers, and more precisely on the alumina powder precursor for this matrix. In this present work, the accelerated hydrothermal aging of alumina is explored. A combination of thermodynamic calculations and physicochemical analyses demonstrates the evolution of the nature of alumina-based matters in the system: aqueous solution and precipitation of additional solid phases.

2. Materials and Methods

2.1. Experiments and starting materials

The powdery precursor of the composite matrix was used to get accelerated conditions of aging through an extended surface exposed to reactions, and thus to determine the behavior of alumina during accelerated aging. The powder sourced from Baikowski was 99.99% pure α-alumina. The average diameter of the alumina grains was approximately 150 nm. The hydrothermal aging test was conducted in a 500 mL PTFE reactor containing an aqueous solution prepared with Milli-Q® water (resistivity = 18.2 $M\Omega.cm$). This latter was prepared in a controlled atmosphere within a glove box. The following salts were used: potassium chloride (KCl), potassium sulfate (K_2SO_4), aluminum sulfate octadecahydrate ($Al_2(SO_4)_3$,$18H_2O$), calcium sulfate dihydrate ($CaSO_4$,$2H_2O$), sodium silicate pentahydrate (Na_2SiO_3,$5H_2O$), sodium bicarbonate ($NaHCO_3$) and sodium hydroxide (NaOH) to achieve a final pH of 11.2. Reactors were placed in a oven at 70°C for seven months.

The prepared aqueous solution was also aged alone at different temperatures (25°C, 50°C and 70°C) to compare its evolution (aqueous part in regard to solid one) without alumina powder and to ensure the aqueous solution's stability for the remainder of the tests. To achieve this, the solution was placed in three different ovens for three months. Once removed from the oven, the reactors containing the solution were quickly transferred in a glove box in an insulated environment to limit the temperature drop. The liquid part was collected to analyze the species present in solution and compare them to the species initially introduced into the mixture. The precipitated species were recovered by evaporating the residual liquid. The soluble and dissolved component into the aged solutions at different temperatures were analyzed by inductively coupled plasma atomic emission spectroscopy (ICP-AES, iCAP PRO Duo – Thermo Scientific).

The search of precipitates formed into an aqueous solution was carried out by X-ray diffraction (XRD, Bruker D8 Advance diffractometers using a Cu Kα anticathode.).

Following the aging period, some of the powder samples were removed from the reactors for analysis, while the remainder was subjected to a longer aging period. The collected samples were divided into two groups: one was rinsed with Milli-Q water and the other was left unaltered. In both cases, the powder was dried. The hydrolyzed surfaces were observed by scanning electron microscopy SEM, FEI Quanta 400FEG) operated at 20 kV equipped with an energy-dispersive X-ray spectroscopy detector (EDX, Ultim Max, Oxford Instruments), and transmission electron microscopy (TEM, JEOL JEM 2200FS FEG HR 200 kV High resolution camera) equipped with an EDX detector. Subsequently, analysis via ICP-AES are done on the aqueous media employed in the post-test phase.

2.2. Thermodynamic calculations

Thermodynamic calculations were carried out to identify and determine the final equilibrium state of a chemical system. These calculations will give the species and phases present at equilibrium.
To get these, the first and second principles of thermodynamics are combined by the extensive state function: the minimization of the free enthalpy G_T of the system given by the Gibbs relation (Eq. 1):

$$G_T = \Delta H^0_{298.15K} + \int_{298.15K}^{T} C_p \, dT - T \left(S^0_{298.15K} + \int_{298.15K}^{T} \frac{C_p}{T} dT \right) \quad (1)$$

where $\Delta H^0_{298.15K}$ is the standard enthalpy of formation at 298.15 K, $S^0_{298.15K}$ is the standard entropy at 298.15K, C_p is the heat capacity as a function of temperature and T is the absolute temperature. The guidance in the evolution of a chemical system is a decrease of the state function G_T. Equilibrium is reached when G_T is minimal ($dG = 0$). The Thermo-Calc software was be used to perform these thermodynamic calculations. This software is based on the Calphad method (calculation of phase diagrams) [5–7]. This method, introduced by Larry Kaufman in the 1960's, is based on various types of experimental data and theoretical values to produce thermodynamic database giving the $G_{T,P}$ of each phase or species in a phase (liquid)(e.g. those derived from first-principles calculations). The calculated data are the states of present phases, solid, liquid and gas and their constituent species, the pH value and the potential value of an aqueous solution.This data can be used to make predictions for multi-component systems of industrial importance.
The chosen approach is to select from the literature the solid phases relevant to the system under consideration and extract the correlated thermodynamic data to compile them in a specific database that complements the following commercial Thermocalc databases: GCE, TCAQ and TCOX [5]. Thus, the development of a complete model is made possible on the evolution of alumina in the aqueous solution under consideration. More than 440 phases have been listed. The free enthalpies (G_T) of these phases are recalculated from data on standard enthalpy ($\Delta H^0_{298.15K}$), standard entropy ($S^0_{298.15K}$) and heat capacities (C_p). [8–19]. Once the database was built, the thermodynamic model was developed step by step from a Python code using the TC-Python library. In the first step, the calculations were completed by considering only the aqueous solution. In a second one, alumina could be introduced into the system, to progress in calculations. The methodology followed was to perform a series of thermodynamic calculation cycles for a temperature of 70°C (corresponding to the aging temperature in the PTFE reactors). The steps in the first simulated aging cycle correspond to: (1) the introduction of one mole of alumina (m = 101.961g) (2) the introduction of one liter of aqueous solutions (3) the start of the calculation to obtain the thermodynamic equilibrium and (4) the identification of the solid phases, aqueous species and gas species formed. For all other simulated cycles, steps become : (5) the conservation of the solid phases obtained in the previous cycle (6) the introduction of one liter of initial aqueous solution (7) the start of the calculation to obtain thermodynamic equilibrium and (8) the identification of solid phases, aqueous species ans gas species formed. Two types of calculations were carried out: the first based on a fixed pressure (to simulate the environment in which the composites would be stored) and the second based on a fixed volume (to represent the aging systems of this research). This verifies that the aging methods chosen are comparable to the real environment. Finally, in both cases a neutral gas (argon) is introduced, since the aging conditions are anoxic.

3. Results and discussion

3.1. Aqueous aging solution

The results of the XRD analysis of the precipitate formed after preparation of the aqueous solution show that it is mainly calcium carbonate. A phase containing sodium potassium aluminosilicate was also identified (Figure 1). ICP analysis of the aqueous solution and the precipitate formed (without alumina) at different temperatures shows that with the exception of aluminum, the amounts of present species do not change significantly, indicating that temperature does not affect the composition of the solution over this three months time interval (Figure 2). The main constituents into the precipitate are calcium, potassium and sulfur. The aluminum concentration in the aqueous solution increases with increasing temperature. These two analyses confirm that calcium carbonate is formed by precipitation from the aqueous solution. It is possible to deduce that a second phase was formed, corresponding to a sodium and potassium aluminosilicate.

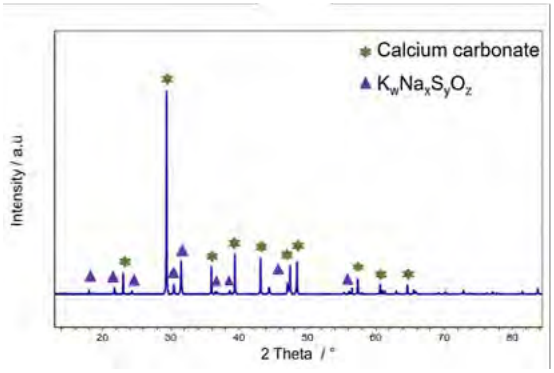


Figure 1. XRD of precipitate formed after preparation of the aqueous solution (K_α Cu)

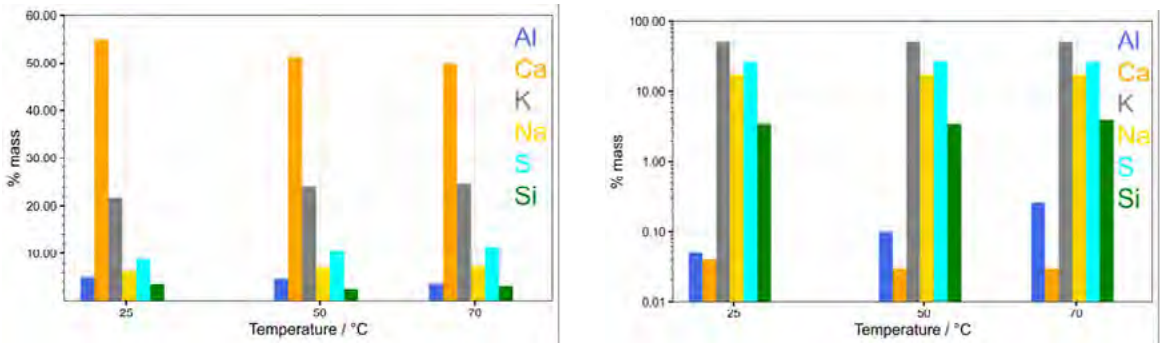
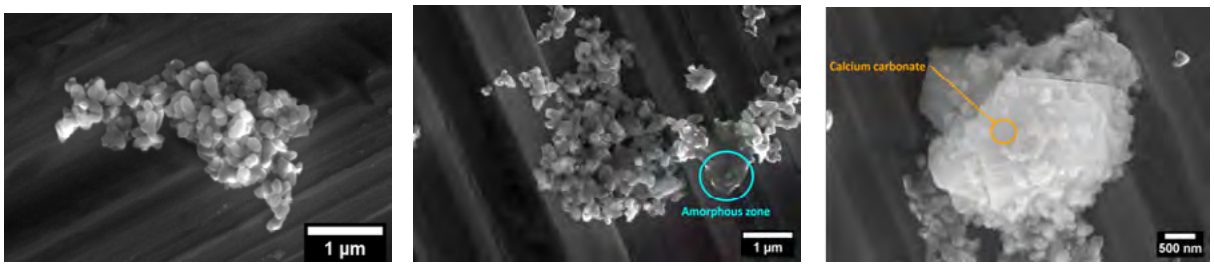


Figure 2. ICP of the aged aqueous solution at different temperatures without alumina. (a) formed precipitate and (b) liquid solution

3.2. Aged alumina powder

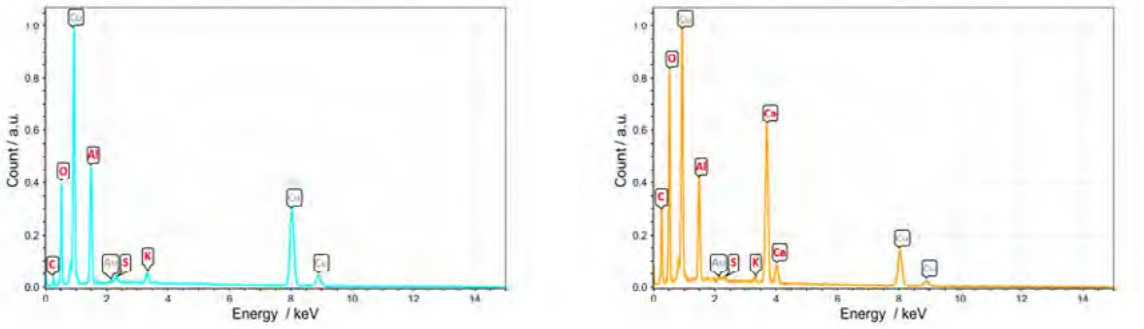
Observations by SEM (coupled with EDX) show the presence of three types of alumina powders areas. One appears to correspond to crystalline alumina, a second area shows an amorphous phase and finally a third one corresponds to calcium carbonate (Figure 3). This carbonate comes from the aqueous solution and is a precipitation product.



(a) **(b)** **(c)**

Figure 3. SEM of initial and aged alumina powder (a) and (b) respectively, (c) calcium carbonate precipitate from the aqueous solution

The EDX analyses corresponding to the circled zone on the Figure 3b show that the amorphous grains are composed of oxygen, aluminum and carbon, but also sulfur and potassium with the atomic proportions O:Al:C:S:K = 57:14:21:3:5. The zone noticed on the Figure 3c shows the presence of majority of calcium carbonate with the atomic proportions Ca:C:O = 20:26:54.



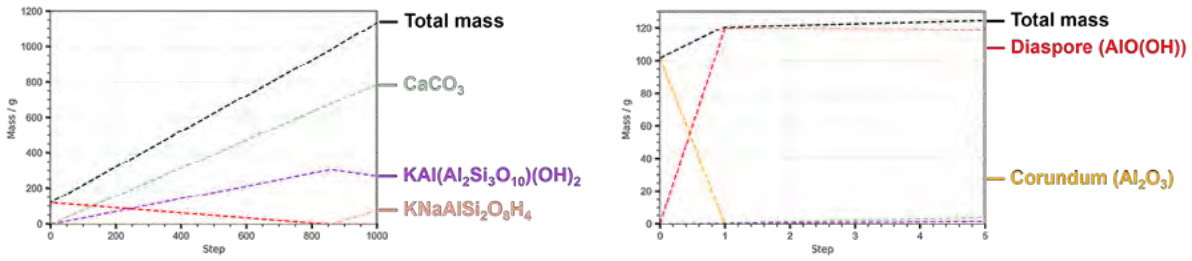
(a) **(b)**

Figure 4. EDX of aged alumina powder (a) amorphous zone and (b) calcium carbonate

3.3. Thermodynamic calculations

On Figure 5 the thermodynamic calculations show the alumina hydrated to diaspore during the first cycle. Over 1000 cycles, the amount of diaspore gradually decreases until it disappear by the 840th cycle, giving way to a solid sodium and potassium aluminosilicate phase. A potassium aluminosilicate phase appears in the second cycle, facilitated by the dissolution of the diaspore and the supply of species from the aqueous solution. This phase decreases after the disappearance of the diaspore. This indicates that the $KNaAlSi_2O_8H_4$ phase is thermodynamically more stable under these conditions. The result of the ICP analysis (Figure 2a) on the precipitated species in the aged solution alone confirms the presence of calcium, potassium and aluminum, in agreement with the thermodynamic calculations. Calcite precipitates during aging, as identified by XRD analysis on the precipitates into the aged solution. A silicate phase is also present, as shown by the XRD and EDS analyses. Finally, at temperatures considered in

the calculations, it can be concluded that volume and pressure do not appear to have any effect on the evolution of the system. These calculations are consistent with the initial results obtained experimentally.



(a) **(b)**

Figure 5. Solid phases formed during the cycles calculated by ThermoCalc. (a) all cycles and (b) focusing on the first 5-cycles

4. Conclusion

This work is part of a broad study aiming at determining the chemo-mechanical behaviour of CMCs under conditions encountered in a deep geological disposal facility, and more precisely in the high-level waste area. In this work, a methodology to assess this behaviour is proposed, and it is first implemented on alumina powders as the major constituent of the studied CMCs. Scanning electron microscopy and other analyses have revealed complex alteration mechanisms, including the formation of calcium carbonates and aluminosilicate phases. In addition, thermodynamic calculations revealed the transformation of alumina to diaspore with the precipitation of calcite and silicate phases from the solution. Under aging conditions, the hydratation of alumina appears to have no real influence on the nature of species into the solution. Perspectives could include studying the phase composition of corrosion products formed on exposed surfaces using advanced analytical techniques such as X-ray photoelectron spectroscopy (XPS) and time-of-flight secondary ion mass spectrometry (ToF-SIMS). Investigations will continue by measuring the evolution of mechanical properties of the CMC and its independent constituents, after accelerated aging, using tensile and bending tests.

References

[1] "LOI n° 2006-739 du 28 juin 2006 de programme relative à la gestion durable des matières et déchets radioactifs (1)," 2006.

[2] "Protéger des déchets radioactifs les plus dangereux," 2022.

[3] "Comment fonctionnera cigéo ? | sur cigéo - centre d'informations et de ressources sur CIGEO," 2022.

[4] G. Camus, C. Lorrette, R. Pailler, F. Rebillat, B. Reignier, and F. Teyssandier, *Matériaux composites à matrice céramique et à renfort par fibres longues*. Editions TI, 2016.

[5] J.-O. Andersson, T. Helander, L. Höglund, P. Shi, and B. Sundman, "Thermo-calc & dictra, computational tools for materials science," *Calphad*, vol. 26, no. 2, pp. 273–312, 2002.

[6] N. Saunders and A. P. Miodownik, *CALPHAD (calculation of phase diagrams): a comprehensive guide*. Elsevier, 1998.

[7] H. Lukas, S. G. Fries, and B. Sundman, *Computational thermodynamics: the Calphad method*. Cambridge university press, 2007.

[8] D.-G. Kim, B. Konar, and I.-H. Jung, "Thermodynamic optimization of the k2o-al2o3-sio2 system," *Ceramics International*, vol. 44, no. 14, pp. 16712–16724, 2018.

[9] B. Lothenbach, L. Pelletier-Chaignat, and F. Winnefeld, "Stability in the system cao–al2o3–h2o," *Cement and concrete research*, vol. 42, no. 12, pp. 1621–1634, 2012.

[10] S. A. Utlak and T. M. Besmann, "Thermodynamic assessment of the na2o-al2o3-sio2-b2o3 pseudo-binary and-ternary systems," *The Journal of Chemical Thermodynamics*, vol. 130, pp. 251–268, 2019.

[11] B. Hallstedl, "Assessment of the cao-al2o3 system," *Journal of the American ceramic society*, vol. 73, no. 1, pp. 15–23, 1990.

[12] M. Gottschalk, "Internally consistent thermodynamic data for rock-forming minerals in the system sio 2-tio 2-al 2 o 3-cao-mgo-feo-k 2 o-na 2 oh 2 o-co 2," *European Journal of Mineralogy*, vol. 9, no. 1, pp. 175–223, 1997.

[13] J. Yaokawa, K. Oikawa, and K. Anzai, "Thermodynamic assessment of the kcl–k2co3–nacl–na2co3 system," *Calphad*, vol. 31, no. 2, pp. 155–163, 2007.

[14] B. Lothenbach, T. Matschei, G. Möschner, and F. P. Glasser, "Thermodynamic modelling of the effect of temperature on the hydration and porosity of portland cement," *Cement and Concrete Research*, vol. 38, no. 1, pp. 1–18, 2008.

[15] T. Holland and R. Powell, "An improved and extended internally consistent thermodynamic dataset for phases of petrological interest, involving a new equation of state for solids," *Journal of metamorphic Geology*, vol. 29, no. 3, pp. 333–383, 2011.

[16] K. Matsuo, *Thermodynamic Modelling of the CaO-SiO2-H2O Cementitious System & the Production of Waste-Derived Cement*. McGill University (Canada), 2017.

[17] D. Kim, *Coupled experimental study and thermodynamic optimization of the K2O-Na2O-CaO-MgO-Al2O3-SiO2 system*. McGill University (Canada), 2017.

[18] E. Nekhoroshev, *Thermodynamic Optimization Of The Na2O-K2O-Al2O3-CaO-MgO-B2O3-SiO2 System*. PhD thesis, Ecole Polytechnique, Montreal (Canada), 2019.

[19] E. Yazhenskikh, T. Jantzen, D. Kobertz, K. Hack, and M. Mueller, "Critical thermodynamic evaluation of the binary sub-systems of the core sulphate system na2so4–k2so4–mgso4–caso4," *Calphad*, vol. 72, p. 102234, 2021.

DEVELOPMENT OF TRANSLUCENT EPOXY-BASED SHEET MOLDING COMPOUNDS WITH FLAME RETARDANT PROPERTIES FOR AIRCRAFT APPLICATIONS

Dr.-Ing. Florian Gortner[1], Prof. Dr.-Ing. Thomas Neumeyer[1]

[1]Leibniz-Institut für Verbundwerkstoffe GmbH, Processing Technologies, RPTU,
Erwin-Schrödinger-Straße 58, 67663 Kaiserslautern, Germany
Email: florian.gortner@leibniz-ivw.de, Web Page: http://www.leibniz-ivw.de
Email: thomas.neumeyer@leibniz-ivw.de, Web Page: http://www.leibniz-ivw.de

Keywords: Sheet Molding Compound (SMC), translucent, epoxy-based, flame retardant, aircraft interior

Abstract
Sheet Molding Compounds (SMC) conventionally consist of chopped reinforcement fibers with a length of 25.4 to 50.8 mm (1 to 2 inch) in combination with a thermoset-based resin paste. They offer high mechanical performance and lightweight potential compared with short processing times. Therefore, SMC materials are used for applications in large-scale serial production in compression molding processes for example in electronics and construction sector as well as in aircraft and automotive. Flame retardant SMC materials for public transport and aircraft interior applications are state of the art. Those materials show a good mechanical performance, but a lack in surface quality and freedom in color, due to their high amount of mineral fillers and flame retarding additives.

In the research project “TRANA”, a new and innovative SMC system, which fulfills flame retardancy requirements, shows a good surface quality and is also homogenously colorable, was developed.
Mechanical properties like Tensile strength and Young’s modulus are up to 25 % higher compared to conventional flame retarding SMC materials and at the same time, their density is about 20 % lower.

1. Introduction

Fiber reinforced polymer composites (FRPC) and their special abilities for high specific strength and stiffness enable a new freedom of design for structural and non-structural components. This class of materials allows a reduction of components weight while improving their mechanical properties. A further very important point regarding the safety of FRPC materials is their flame retardancy behavior. To fulfill specific flame retardant properties, different flame retarding additives can be used. All these options meet the current demands of the industry in terms of material efficiency and CO_2 savings. Sheet Molding Compound (SMC) provide the ability of producing near-net-shape components in parallel controlled compression molding processes in one process step at advantageous costs and short cycle times [1]. These advantages lead to a market share for SMC of almost 20 % in glass fiber reinforced polymer composites (GFRPC) in Europe [2]. A standard glass fiber reinforced SMC mainly consists of an unsaturated thermoset polyester resin, a variety of different processing additives, glass fibers (GF) with a length of 25.4 to 50.8 mm (1 to 2 inch) as reinforcement and different non-functional and functional filler materials, see Figure 1 [3, 4]. GF-SMC semi-finished products exhibit a density of 1.7 up to 2.0 g/cm³ based on the high content (up to 40 wt.-%) of mineral fillers with a density of 1.8 to 2.7 g/cm³ [5, 6].
SMC materials are mainly used for applications in large-scale serial production and are processed in compression molding processes. Main fields of use are for example in the electronics and the construction sector as well as in aircraft and automotive applications. Flame retardant SMC materials

for public transport and aircraft interior applications are state of the art, e.g. HUP63/15 RB-9010, supplied by Polynt Composites GmbH (Miehlen, Germany) [7].

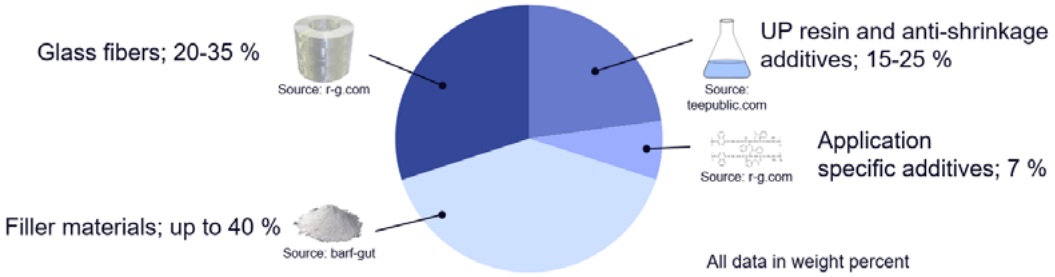


Figure 1: Abbreviated composition of a standard SMC [3]

A big disadvantage of flame-retardant SMC materials is the poor achievable surface quality of the final parts. As these semi-finished products contain very high filler contents of up to 350 phr flame retarding agent related to the resin system, the fillers often emerge at the surface of the parts. So the parts cannot be used for visible or even decorative applications. For this reason, many of those components require a costly and energy-intensive post-treatment. This involves several processing steps in which each component has to be sanded, filled and painted. This increases the component costs and the ecological impact, which severely limits the possible areas of potential applications.
In the research project "TraNa", a new translucent and flame-retardant SMC semi-finished product has been developed, which meets the FST requirements of the aviation sector, in particular FAR 25.853. This SMC material was developed in such a way that it either has translucent properties ("milk glass"-like), but can also homogeneously be colored. Furthermore the material shows very good surface quality and mechanical properties, which can be compared to standard SMC semi-finished products. This can open up new fields of application for SMC components. These could be for example passenger information or lighting applications.
In order to achieve a translucent or even transparent component quality, the scattering of the incident light must be reduced. Therefore the particle size of the (flame-retarding) powdery fillers has to be minimized. This leads to a significant decrease of the scattering of the light: a 10 nm particle scatters around 1 million times less light than a 100 nm particle [8]. Subsequently, the composition of the semi-finished product was adapted in order to obtain a perfect dispersion of the solid modifiers. As a part of the research project, the influence of both, liquid phosphorus-based and state of the art particulate flame retardant additive in combination with newly developed particulate nanoparticles acting as flame retardant additives were investigated. Those results were already published by Kayser, Gortner et al. [9, 10, 11].
This study investigates the effects of particular flame retardant additives in combination with liquid flame retardant additives on the colorability and the resulting mechanical properties of SMC materials.

2. Materials and methods

2.1 Materials

As part of the research project, several EP-based resin systems were investigated with regard to their transparency, thickening behavior and processing properties [9, 10]. In this paper a low viscosity styrene-monomer free epoxy resin (Epikote TRAC 06605, Westlake Epoxy GmbH, Duisburg, Germany) was used according to SMC process requirements. As hardener two catalyzed products (Epikure TRAC 06612 and Epikure TRAC 06624, Westlake Epoxy GmbH, Duisburg, Germany) were studied. Furthermore two air release additives (BYK A500 and BYK W969, BYK Chemie GmbH, Wesel, Germany) and an internal release agent (TRAC 06807, Westlake Epoxy GmbH, Duisburg, Germany) were used. As flame retardant additives a mixture of a powdery (ON904 Huber Advanced Materials Martinswerk GmbH, Bergheim, Germany) and liquid (HF P70, Lehmann & Voss, Hamburg, Germany) additive was utilized.

2.2. METHODS

2.2.1 Resin paste preparation

In a first step all liquid components of the resin paste formulation are mixed to a homogeneous paste with a circular disc stirrer at 600 rpm for 2 minutes. Subsequently, this mixture is evacuated for 1 minute at - 0.08 MPa. In a second step, all powdery components are incorporated to a homogeneous paste also with a circular disc stirrer at 1200 rpm. Afterwards, the resin paste was mixed until a temperature of 40 °C was reached. This temperature was measured contactless with an IR-thermometer. When reaching the predefined temperature, mixing was stopped and the whole mixture was evacuated again at - 0.08 MPa. After evacuation, the resin paste was stored at 40 °C in an oven till processing.

2.2.2 Coloring tests

To examine the colorability of the SMC resin pastes and color accuracy of SMC sample plates, color pastes EP2037 (Altropol Kunststoff GmbH, Stockelsdorf, corresponding to RAL 7035) - light grey and EP2043 (Altropol Kunststoff GmbH, Stockelsdorf, corresponding to RAL 3028) - pure red were mixed with the SMC resin paste with a dosage of 0.5 to 5 wt.-% in 0.5 wt-% steps. After mixing the color paste, the resin paste was evacuated and processed to SMC semi-finished products and sample plates in the same way as the uncolored resin paste.

The color accuracy measurements were carried out by Fraunhofer ISC (Würzburg, Germany) in a CIELab color space using the reflection method on a spectrophotometer (Color i, manufacturer X-Rite, 6 mm diaphragm). In this method, a three-dimensional color space is spanned, which is built up by the brightness (L*), which is on the color plane (a*, b*). The measurable brightness values range from 0 (black) to 100 (white) and from -90 to 90 for a* (red-green) and from -100 to 100 for b* (yellow-blue). The reflection spectrum is measured in the range from 360 to 750 nm, whereby this range is run through in 10 nm steps. Only the range from 400 to 700 nm, which is visible to humans, is considered. The measurement provides both the wavelength and the percentage of reflected light.

2.2.3 Preparation of SMC semi-finished material

The resin paste is transferred to the SMC line (SMCline600, Schmidt&Heinzmann, Bruchsal, Germany [12]). The doctor boxes and the transport belt of the SMC line were electrically pre-heated to 40 °C. The resin paste was filled into the doctor boxes of the SMC line, see Figure 2 left. Within this doctor boxes, a resin film of 1.4 mm was applied and the reinforcement fibers with a length of 25.4 mm were spread randomly and homogenously on this resin film. Afterwards, a second carrier film with a second resin film covered the reinforcement fibers and this stack was running through the compaction unit (Figure 2, middle). After impregnation, the SMC semi-finished product was stored on rolls (Figure 2, right) over night, to foster the thickening process.

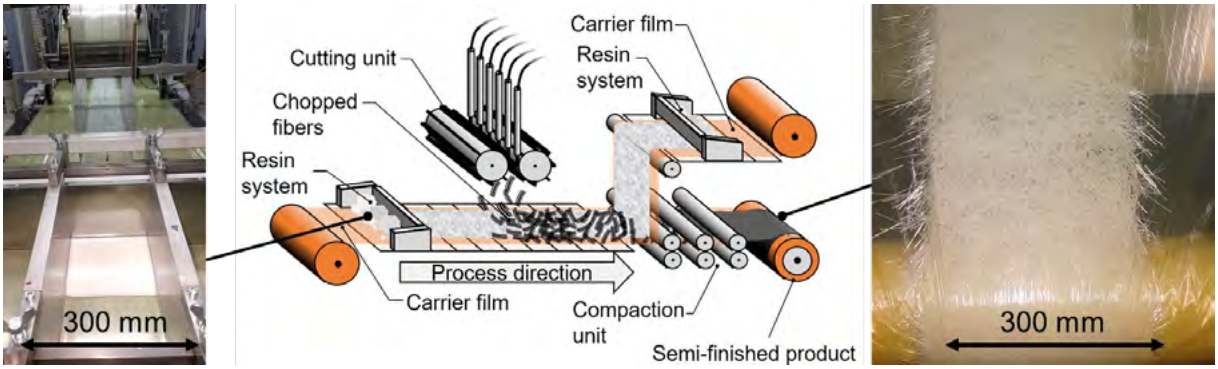


Figure 2: View into the doctor box (left), schematic drawing of SMC processing line (middle) and SMC semi-finished material at the end of the SMC line (right)

2.2.4 Processing of SMC to sample plates

After the thickening process, the SMC semi-finished materials were processed in a compression molding process on a parallel controlled press (Dieffenbacher PHP 800/650). A sealing edge mold with a size of

250 x 696 mm² was used. The SMC material was cut to sheets with a size of 180 x 580 mm², which corresponds to 60 % of the mold size. After cutting, the carrier film of each sheet is was withdrawn and stacks with defined weight were prepared, see Figure 3. These stacks were processed with the processing parameters, given in Table 1.



Figure 3: Stack of SMC semi-finished product in sealing edge mold before processing

Table 1: Compression molding process parameters

Parameter	Unit	Value
Mold temperature	[°C]	140-145
Cycle time	[min]	5
Mold pressure	[MPa]	12
Mold coverage	[%]	60
Closing speed	[mm/s]	1.5

While compression molding process, the viscosity of the SMC material decreases and enables the material to flow and fill-up the mold completely. After curing, the testing plate was removed from the mold. A standard cycle time for SMC-processing is between three and five minutes, depending on the thickness of the sample plates [13].

2.2.5 Mechanical testing

After the SMC semi-finished material was processed to sample plates with the dimensions 250 x 696 x 4 mm³, rectangular specimens for the mechanical characterization were cut out using a diamond-studded circular saw.

Tensile properties were determined according to DIN EN ISO 527-4 [14] in a conditioned laboratory at 23 °C on a Zwick universal testing machine, type 1485 with a 100 kN load cell. Specimen size was 250 x 25 x 4 mm³.

Bending properties were determined according to DIN EN 14125 [15] in a conditioned laboratory at 23 °C on a Zwick universal testing machine, type 1485 with a 100 kN load cell. Specimen size was 80 x 15 x 4 mm³.

2.2.6 Determination of fiber mass content according to DIN EN ISO 1172

For the determination of the fiber mass content, samples were extracted from the material insert position and near the end of the flow area The real fiber mass content in the component was determined using the calcination method in accordance to DIN EN ISO 1172. Method B according to [16] was used in this work. These results can be compared with gray value analyses from micrographs of the light

microscope. The calcination method offers a more precise method than the gray value analysis, as this method can be used based on bulk volume and not singular two-dimensional just cross-section.

3 Results

3.1 Results of coloring test

As the proportion of color additive increases, the brightness of light grey increases slightly and approaches the RAL color tone. The reference RAL color is black framed in Figure 4. Furthermore, as the proportion of color additive increases, the target color intensifies and the yellow component in particular decreases significantly. The measurement of the different color levels, see Figure 5, shows no difference in the reflected light above two weight percent of color additive. This means that the entire color component is reflected in the light visible to humans, making it appear grey. In addition, approx. 50 % of the light is reflected. The deviations at 600 nm are within the range of measurement accuracy.

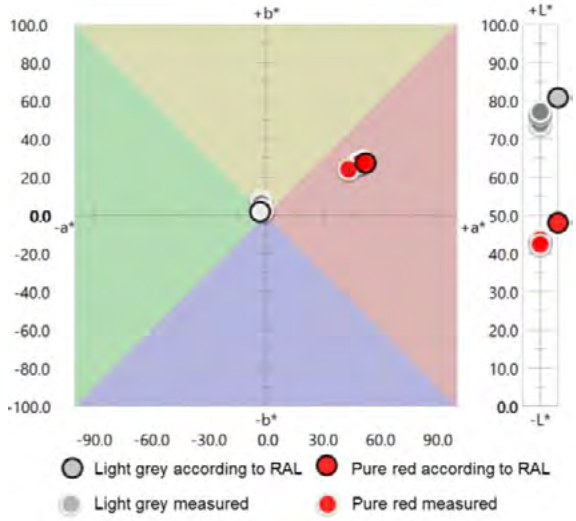


Figure 4: Results of color measurement according to CIELab color chart

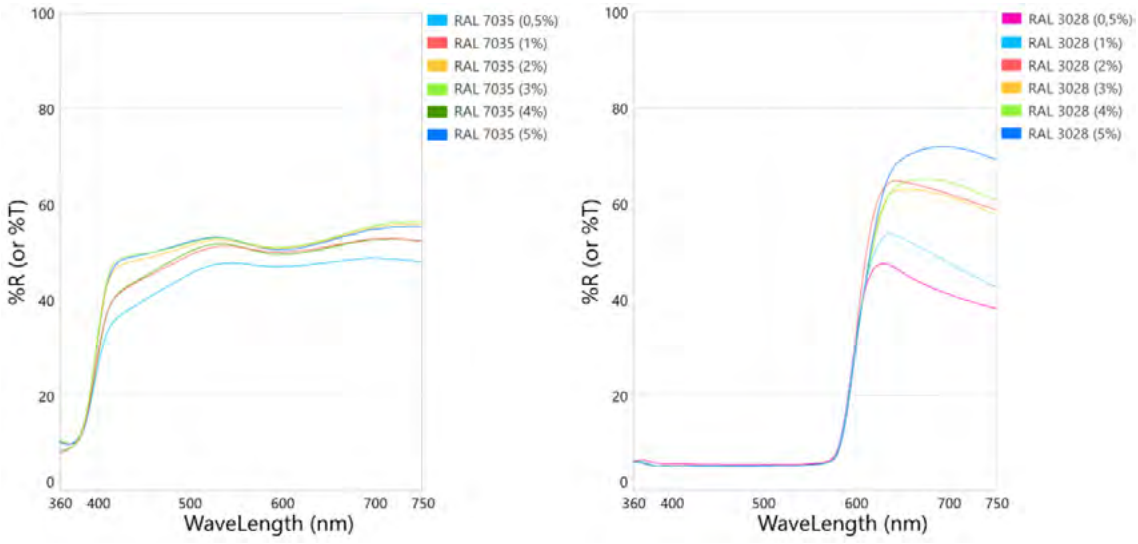


Figure 5: Colored SMC sample plates; left: 0,5 - 3 % grey, middle: 0,5 and 5 % red

The color pure red showed a low scattering in each of the three dimensions for all tested color components. While the brightness only deviates from the target value by 5%, the dimensions a* and b* are significantly further away from the target value. This is particularly evident in the samples with 0.5 and 1 % color additive content, which represents the lowest proportion of red. The measured colors

show only slight differences in the range up to 720 nm and the transmitted or scattered light only splits at a higher wavelength. To the trained eye, however, no significant difference in color fidelity is noticeable with pure red up to 5 wt.-% color content. Nevertheless, it can be seen that a higher proportion of color reflects more light (up to 70 % at 5 wt.-% color proportion).

3.2 Results of fiber mass content analysis

The real fiber mass content was determined using 3 samples taken from the insert area of the SMC stacks. The samples were first dried and then incinerated. Since the ATH fillers cannot be thermally degraded, they were dissolved out of the samples using hydrochloric acid. The target fiber mass content is 25% by weight. The measurements determined a real fiber mass content of 22 +/- 1 % by weight. This corresponds to a deviation from the target value of 3 to 4 %. Figure 6 shows a micrograph of a GF-SMC sample. Based on nine images (transverse and longitudinal), a fiber area content of 9.95 % (±1.66 %) was determined using gray scale analysis. This value can be calculated to a fiber mass content of 21 %. There is a very good accurence of the values of fiber mass content and fiber area content.

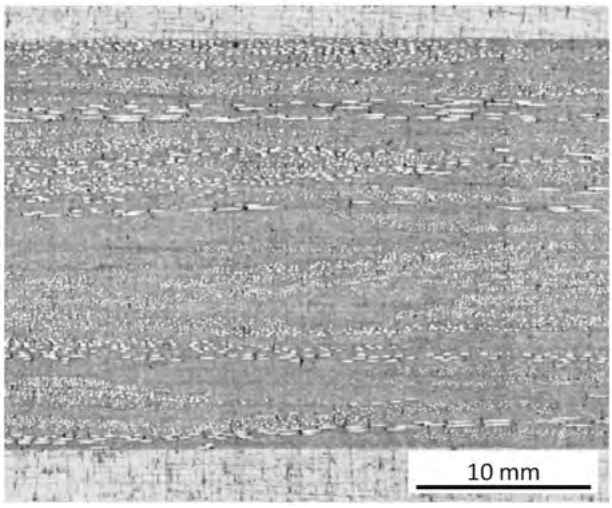


Figure 6: Micrograph of GF-SMC

3.3 Results of mechanical properties

The mechanical properties were determined on colored and non-colored samples. There was no influence in coloring to mechanical properties. The values given in this paper were determined on non-colored samples. In Figure 7 (left), the results for Young's modulus and tensile strength are given in longitudinal (L) and cross direction (Q) of the sample plates. While preparation of the resin paste, two different contents of 10 phr and 15 phr of liquid flame retarding additive HF P70 were used, while dosage of powdery flame retarding additive (ON 904) remained constant.

The mechanical characteristic values achieved for the Young's modulus are between 16.4 and 18.4 GPa in the longitudinal direction and 14.3 to 16.3 GPa in the transverse direction. A clear directional dependence can be seen. When determining the tensile strength, a tensile strength of 150 to 167 MPa in the longitudinal direction and 100 MPa in the transverse direction was detected. The mechanical properties of the SMC semi-finished products developed are significantly higher than the characteristic values of the reference fire protection SMC semi-finished products in terms of both Young's modulus and tensile strength [7]. Furthermore, a clear isotropy can be seen, which indicates an alignment of the fibers during the flow process.

The results of bending properties are given on the right side of Figure 7. In these samples, a distinction is also made between the longitudinal (L) and transverse (Q) directions and the content of the liquid fire retardant additive. A difference between the longitudinal and transverse directions can be seen in all samples. All longitudinally oriented samples have a higher flexural modulus and a higher flexural strength than the transverse samples. Depending on the content of liquid fire protection additive, flexural moduli of 17.3 to 18.8 GPa are achieved in the longitudinal direction and around 16.3 GPa in the

transverse direction. In terms of flexural strength, strengths of 280 to 339 MPa were achieved in the longitudinal direction and 242 MPa in the transverse direction.

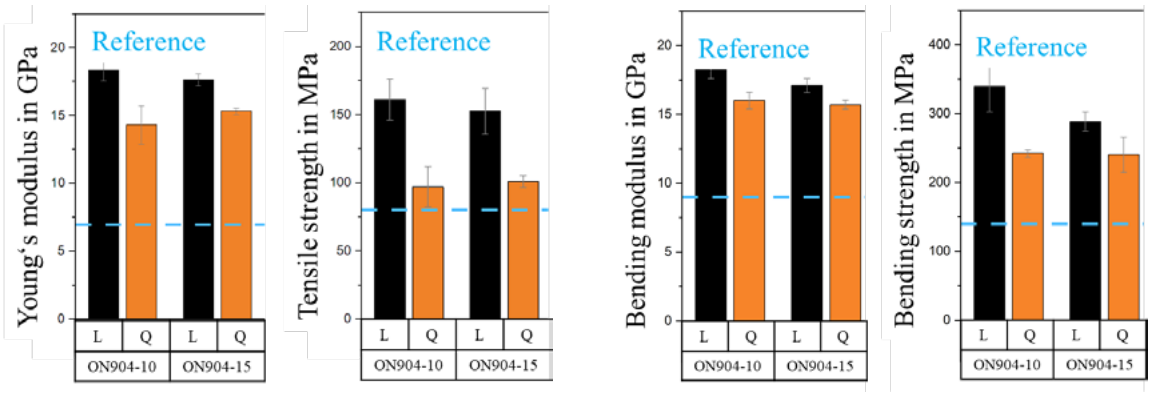


Figure 7: Results of mechanical testing; tensile properties (left), bending properties (right)

4 Discussion and conclusion

An SMC semi-finished product was developed on the basis of an epoxy resin system and glass fibers as reinforcing fibers, which has with 22 wt.-% fiber mass content almost the same fiber mass content as the reference flame retarding SMC system HUP63 (25 wt.-% GF). This semi-finished product achieves significantly higher mechanical properties than the reference material.
Within the new SMC material, a combination of combining liquid and powdery flame retardant additives were used. This enabled the use of a lower overall quantity of ATH, compared to reference material, and leads to a better surface quality of sample plates. The reduced amount of ATH enables a homogenous coloring of the SMC semi-finished materials and sample plates. Furthermore the reference material can be manufactured and processed reliably on a conventional SMC line.
The color fidelity was verified by using spectrophotometer measurements. The components show closed and homogeneous surfaces that do not require any reworking. Due to the homogeneous coloring and the very good surface qualities, no expensive and time-consuming reworking is required. Initial publications [9, 10, 11] have already presented results on translucency and the results of fire protection tests. If the semi-finished products are not colored, it is possible to achieve translucent component properties. The semi-finished products also pass fire tests in accordance with UL 94-V0 no matter whether they are colored or not.

In summary, the "TraNa" research project successfully developed a translucent and fire-protected SMC semi-finished product for aviation interior applications by skillfully combination of powdery and liquid flame retarding additives. Based to the translucent and fire-protected properties, the spectrum of applications for SMC semi-finished products can be expanded, e.g. in the mobility sector.

Acknowledgments
The project “TraNa – Translucent and dyeable flame retardant Sheet Molding Compounds based on novel nanoscale flame retardants for applications in the aerospace interiors” was funded by the Federal Ministry for Economic Affairs and Climate Action - program “LuFo VI-1” on the basis of a decision by the German Bundestag, funding reference: 20Q1902C

We would also like to acknowledge on all project partners of the project, which are CompriseTec, Fraunhofer IAP / ISC and Schmidt & Heinzmann for the target-orientated and exemplary cooperation.

References

[1] M. Neitzel, P. Mitschang und U. Breuer, Handbuch Verbundwerkstoffe - Werkstoffe, Verarbeitung, Anwendung [Composite materials handbook - materials, processing, application], München: Hanser Verlag, 2014.
[2] AVK | Industrievereinigung verstärkte Kunststoffe, „Der Markt für Glasfaserverstärkte Kunststoffe (GFK) 2019 [The market for glass fiber reinforced composite materials],“ September 2019. [Online]. Available: https://www.avk-tv.de/news.php?id=405. [Zugriff am 25 10 2019].
[3] AVK, Industrievereinigung Verstärkte Kunststoffe, Handbuch Faserverbundkunststoffe: Grundlagen, Verarbeitung, Anwendungen [Handbook of fiber reinforced materials: fundamentals, processing, applications], Wiesbaden: Springer Verlag, 2014.
[4] European Alliance for SMC/BMC - DESIGN FOR SUCCESS, „www.smcbmc-europe.org, “ 2016. [Online]. Available: www.smcbmc-europe.org. [Zugriff am 25 10 2017].
[5] Omya GmbH, Produktdatenblatt Millicarb®-OG, Köln: Omya GmbH, 2011.
[6] Martinswerk GmbH, Produktdatenblatt Martinal® ON-307, Bergheim: Martinswerk GmbH, 2011.
[7] Polynt Composites GmbH, „Technical Data Sheet "HUP 63/25 RB-9010",“ 2017. [Online].
[8] „Malvern Panalytical Ltd,“ [Online]. Available: https://www.malvernpanalytical.com/de/products/technology/light-scattering. [Zugriff am 03 05 2024].
[9] Simon T. Kaysser, Christian A. Keun, Maximilian Ritschel, Sebastian Steffen, Jens Kürsten, Benedikt Schug, Florian Gortner, „Development of translucent and flame retardant epoxy SMC for aircraft cabin applications,“ in SAMPE Deutschland, Hamburg, 2022.
[10] Simon T. Kaysser, Christian A. Keun, Maximilian Ritschel, Sebastian Steffen, Jens Kürsten, Benedikt Schug, Florian Gortner, „Innovative translucent epoxy SMC for applications with flame retardant properties,“ in SAMPE US , Seattle, 2023.
[11] Florian Gortner, Peter Mitschang , Translucent SMC with flame retarding additives, Kaiserslautern : Internationales IVW Kolloquium, 2023.
[12] „Duroplastimprägnier- und SMC-Anlage,“ [Online]. Available: https://www.ivw.uni-kl.de/de/forschung-entwicklung/apparative-ausstattung/duroplastimpraegnier-und-smc-anlage. [Zugriff am 03 05 2024].
[13] D. Schommer, M. Duhovic, F. Gortner and M. Maier, Advanced Simulation of Polymer Composite SMC Compression Molding using Fluid-Structure Interaction in LS-DYNA, Detroit: 13th International LS-DYNA User Conference, 2014.
[14] DIN EN ISO 527-4:1997-07, Kunststoffe - Bestimmung der Zugeigenschaften - Teil 4: Prüfbedingungen für isotrop und anisotrop faserverstärkte Kunststoffverbundwerkstoffe (ISO 527-4:1997), Berlin: Beuth Verlag, 1997.
[15] DIN EN ISO 14125:2011-05, Faserverstärkte Kunststoffe - Bestmmung der Biegeeigenschaften (ISO 14125:1998 + Cor.1:2001 + Amd.1:2011), Berlin: Beuth Verlag, 2011.
[16] Florian Gortner, Bio-basierte und nachwachsende Füllstoffe für dichtereduzierte Sheet Molding Compounds, Kaiserslautern : Institut für Verbundwerkstoffe GmbH, 2019.

AN EFFECTIVE SIMULATION METHOD FOR THE LAMINATED COMPOSITE FAN BLADE STRUCTURE WITH FIBER-DRAPING ANALYSIS

Thuan Ho-Nguyen-Tan[1], Minkook Kim[1] and Soon Ho Yoon[1]

[1]Composite Materials Applications Research Center, Institute of Advanced Composite Materials, Korea Institute of Science and Technology (KIST), 92 Chudong-ro, Bongdong-eup, Wanju-gun, Jeonbuk 55324, Republic of Korea
Emails: hntt77@kist.re.kr, minkook@kist.re.kr, soonho@kist.re.kr

Keywords: laminated composite, draping analysis, finite element simulation

Abstract
This paper introduces an effective simulation method for the laminated composite fan blade structure, which takes into account the change in fiber orientations during the manufacturing process. A numerical draping analysis is proposed to estimate the distortion of the fiber angle due to the curvature of the fan blade structure. The middle shell mesh of the fan blade is utilized for lamination modeling and simulation stages. To demonstrate the effectiveness of the proposed draping method, thermal deformation simulation of the laminated fan blade is conducted. A numerical comparison of structural performance, with and without considering draping analysis, is performed to show the efficacy of the present methodology.

1. Introduction

During the manufacturing process, the fiber orientations in a flat ply must be changed to conform with the tool surfaces, that significantly impact the mechanical performance of laminated composite structures. Specifically, for fan blade structures exhibiting double geometric curvatures, accurate prediction of fiber path distortion during the hand lay-up process necessitates a thorough fiber-draping analysis. To address this phenomenon, both finite element analysis (FEA)-based and kinematic methods have been widely utilized. In the FEA-based approach, 3D and shell FE models have been employed to simulate the draping behavior of composite reinforcements [1]. Additionally, hyper-elastic constitutive approaches have been developed to simulate the forming behavior of fibers during the draping process on double-curved surfaces [2]. Accordingly, an accurate correlation of material properties with experimental data is essential when developing the constitutive model for fiber reinforcement. By conceptualizing the textile reinforcement as a unit cell, it becomes possible to naturally account for changes in the direction of fiber-draped orientations [3]. However, these approaches often incur high computational costs.

On the other hand, the kinematic method predicts fiber-draped orientation by utilizing a pin-jointed and net cells approach, based on a provided geometry [4]. This method assumes infinite fiber extensional stiffness and zero shear stiffness. Recently, due to its cost-effectiveness, optimization techniques have been employed to enhance the solution of fiber-draping analysis within the kinematic model [5]. However, since the kinematic model cannot consider boundary and process conditions, it is crucial to validate the algorithm using experimental results. In this study, we develop a numerical method for fiber-draping analysis based on the shell mesh. Shell element curvatures are utilized to estimate changes in fiber-draped orientations during the draping process. These predicted orientations are then applied in thermal deformation simulations of the laminated fan blade. To validate our approach, we investigate numerical findings to underscore the effectiveness of the present method.

2. Simulation method

2.1. Finite element modelling

This study considers a fan blade structure, where the geometric shape and dimensions are described in **Figure 1**. The twisting angle between the tip and root sections is $\pi/4$. Structural thicknesses gradually vary from the root section to the top section of the fan blade, with the maximum thicknesses specified as 4.0 mm for the root section and 2.0 mm for the tip section. The minimum thickness of the fan blade is 0.4 mm. The composite material used in the design and fabrication of the fan blade structure is TC1200/PEEK [6]. It is a unidirectional (UD) tape prepreg incorporating AS4 carbon fibers and polyether ether ketone (PEEK) resin. The material has a volume fraction of 59% and the lamina ply thickness of 0.1 mm.

Cross-section profiles of the CAD solid model are extracted to create the shell mesh for the fan blade structure. In this study, the number of extracted sections is 40. Subsequently, these sections are imported into an in-house pre-processor MATLAB program for the mesh generation. For generating a high-quality shell mesh, a uniform discretization is applied to all sections, ensuring an equal number of nodes for each section. The upper and lower surfaces, along with their middle surface, of the fan blade structure are discretized into quadrilateral shell meshes, as shown in **Figure 1**. Each shell mesh depicted in this figure consists of 1521 quadrilateral shell elements and 1600 nodes. In this study, the middle shell mesh is selected to use for the modeling and analyzing the fan blade structure. To aim this, the thickness of the fan blade structure needs to be converted into nodal thickness represented on the middle shell mesh.

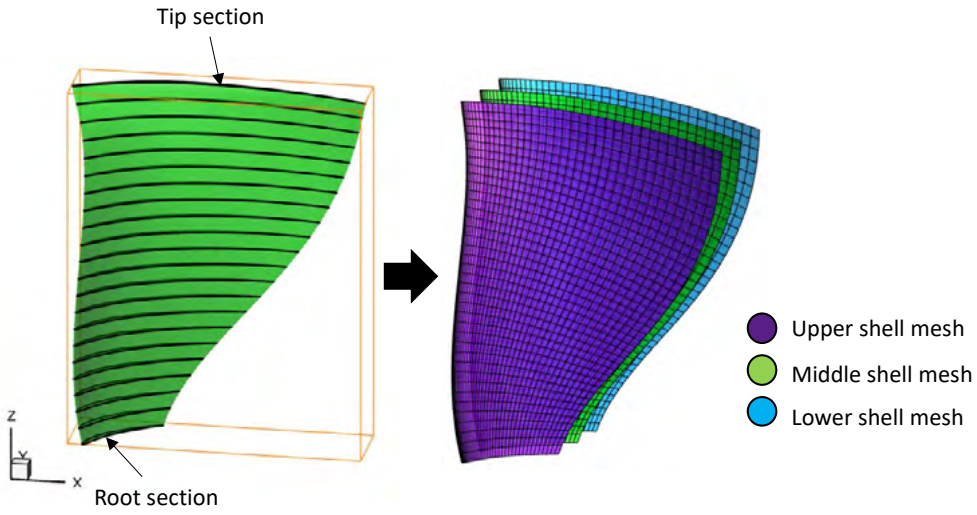


Figure 1. Finite element shell mesh generation.

Figure 2 illustrates the nodal thickness distribution on the middle shell mesh. Based on the thickness distribution of the fan blade structure and the lamina ply nominal thickness, the number of plies on the middle shell mesh can be determined. As a result, the minimum number of plies is 4, and the maximum number of plies is 40. Due to the varying thickness of the fan blade structure, the element groups are generated in descending order from the root section to the tip section, as shown in **Figure 2**. Finally, 10 element groups are genereated on the middle shell mesh.

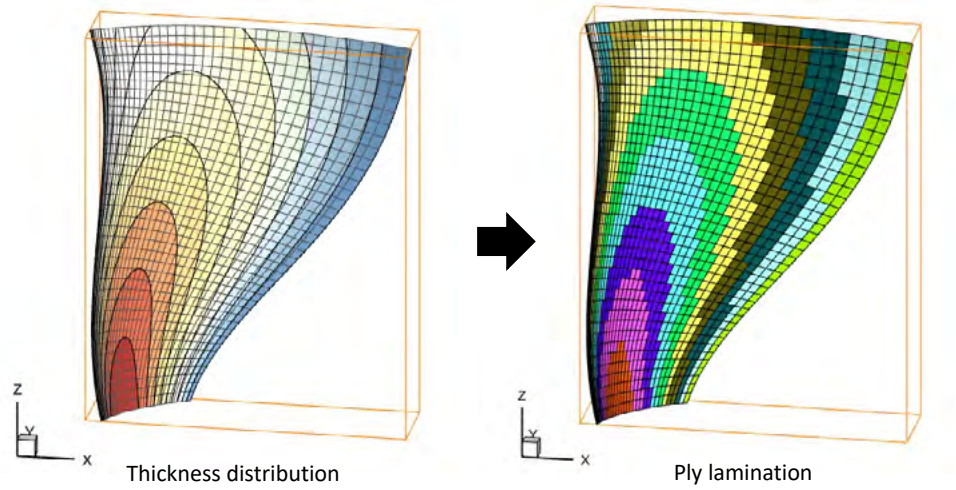


Figure 2. Ply lamination design of the fan blade structure.

2.2. Numerical draping analysis

Due to the double geometric curvature of the fan blade structure, a fiber-draping analysis is required to accurately predict the distortion of the fiber paths that occurs during the hand lay-up process. However, many existing fiber-draping simulation methods pose implementation challenges due to the complexity of their formulations. In this study, to overcome this challenge, we propose a numerical approach for the fiber-draping analysis. The middle shell mesh is used to perform the fiber-draping analysis of the fan blade structure. Based on the curvatures of shell elements, tangent covariant and normal vectors at the shell element center are obtained as

$$\boldsymbol{\varphi}_i(r_1, r_2, r_3) = \frac{\partial \boldsymbol{x}(r_1, r_2, r_3)}{\partial r_i}, \qquad i = 1,2,3 \tag{1}$$

where (r_1, r_2, r_3) is the natural coordinate system, $\boldsymbol{x}$ is the geometric vector. Next, the element draping coordinate system is defined based on the shell curvatures to compute the draped orientation angles of fibers, as illustrated in **Figure 3**. Based on a given global reference material coordinate system, in this figure, in-plane unit vectors of the shell element $\boldsymbol{V}_i^{(e)}$ with respect to the fiber-draping system are computed. The projection operator of an in-plane unit vector on the reference plane as

$$\boldsymbol{p}_i = \text{proj}_{Ox_m y_m}\left(\boldsymbol{V}_i^{(e)}\right) = \boldsymbol{V}_i^{(e)} - \text{proj}_{\boldsymbol{n}}\left(\boldsymbol{V}_i^{(e)}\right), \qquad k = 1,2 \tag{2}$$

where $\boldsymbol{n}$ is the shell element normal vector defined at its center. The prediction of the change in fiber orientation angles for typical directions of $0°$, $90°$, and $\pm 45°$ is expressed as follows

$$\begin{cases} \Delta\emptyset_{[0]} = \tan^{-1}\left(\dfrac{\left(\boldsymbol{e}_1 \times \boldsymbol{p}_1^{(e)}\right)\cdot \boldsymbol{n}}{\boldsymbol{e}_1 \cdot \boldsymbol{p}_1^{(e)}}\right), \\ \Delta\emptyset_{[90]} = \tan^{-1}\left(\dfrac{\left(\boldsymbol{e}_2 \times \boldsymbol{p}_2^{(e)}\right)\cdot \boldsymbol{n}}{\boldsymbol{e}_2 \cdot \boldsymbol{p}_2^{(e)}}\right), \\ \Delta\emptyset_{[\pm 45]} = \tan^{-1}\left(\dfrac{\left[(\boldsymbol{e}_1 \pm \boldsymbol{e}_2) \times \left(\boldsymbol{p}_1^{(e)} \pm \boldsymbol{p}_2^{(e)}\right)\right]\cdot \boldsymbol{n}}{(\boldsymbol{e}_1 \pm \boldsymbol{e}_2)\cdot\left(\boldsymbol{p}_1^{(e)} \pm \boldsymbol{p}_2^{(e)}\right)}\right), \end{cases} \tag{3}$$

where $\boldsymbol{e}_i$ are the unit vector of the reference coordinate system. It should be noted that the advantage of the present method lies in its robustness and ease of implementation, achieved by directly considering the element shell curvatures. In contrast, other existing fiber-draping simulation methods often require numerous steps and complex formulations.

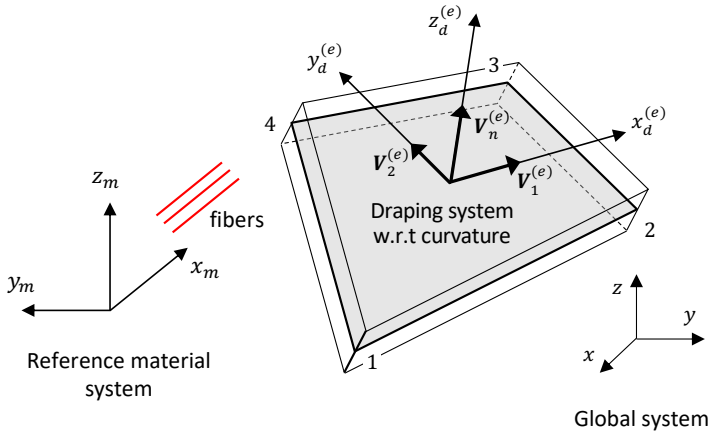


Figure 3. Coordinate systems for the draping analysis.

2.3. Simulation process

In this section, we present the generation of the finite element model used for ABAQUS software. The middle shell mesh is exported to the ABAQUS input format (.inp), including the material orientation system, nodal coordinates, element connectivity, material properties, and shell element sections. For the investigation purposes, two separate shell meshes are exported: one without incorporating fiber-draping analysis and another with fiber-draping analysis, as illustrated in **Figure 4**. Accordingly, in the absence of the fiber-draping analysis, the shell mesh consists of 10 element sets, as shown in **Figure 4**(a). In contrast, when the fiber-draping analysis is considered, each shell element is individually generated into one element set, as depicted in **Figure 4**(b). This export process is executed by an in-house MATLAB pre-processor program.

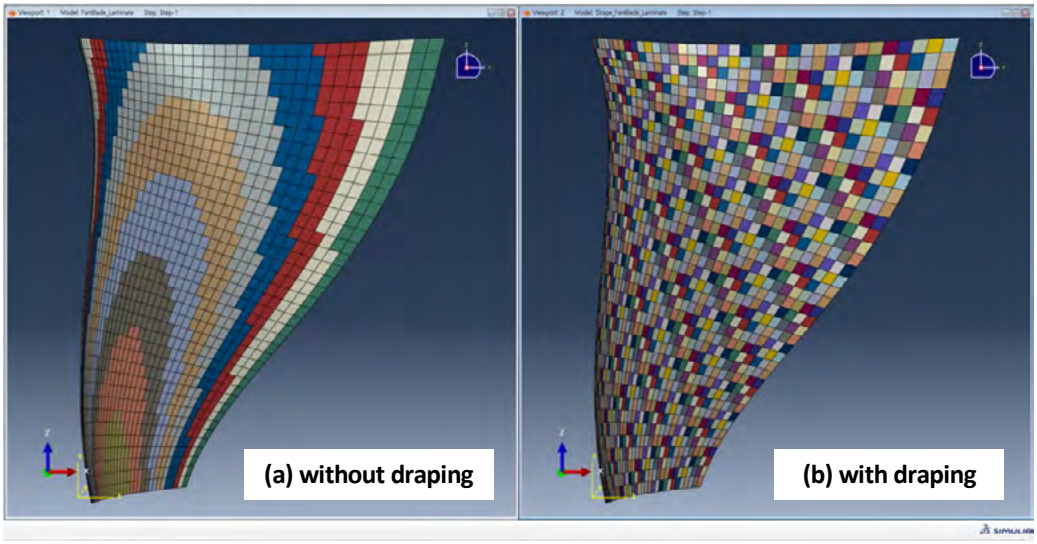


Figure 4. Visualization of finite element model imported from input file (.inp) (a) without draping analysis and (b) with draping analysis.

Thermal deformation of the laminated fan blade structure is conducted, assuming a cooling process for the simulation. Mechanical properties of composite materials, dependent on temperature [7], are utilized. To integrate the temperature profile of the cooling process into ABAQUS, predefined fields are employed to linearly distribute temperatures across the composite fan blade. Specific values are assigned at the maximum temperature of 350°C and the room temperature of 25°C. Additionally, the temperature gradient along the shell section option is chosen, featuring a thickness gradient of 0.1 mm. **Figure 5** illustrates the thermal deformation of the laminated fan blade, highlighting a significant effect of draping analysis on structural behavior.

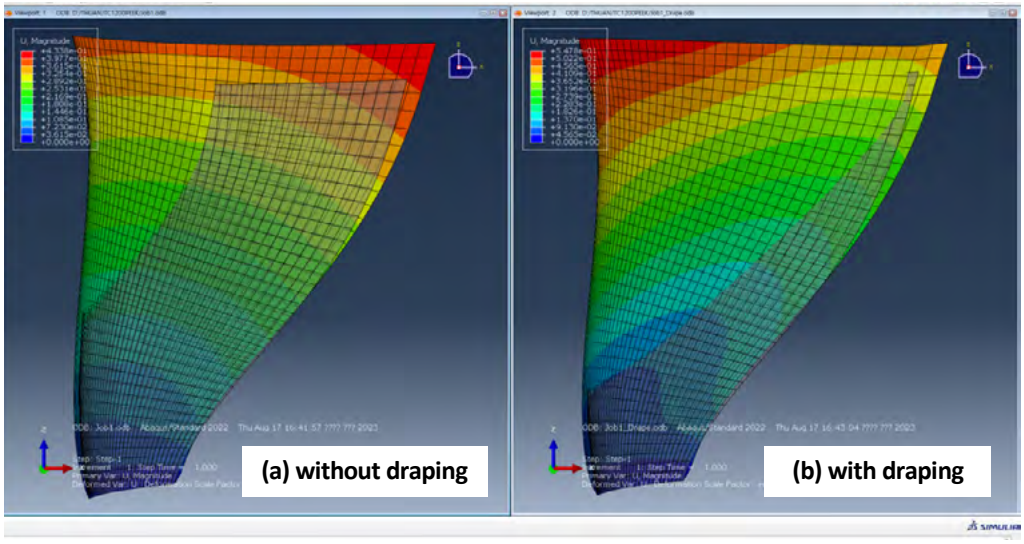


Figure 5. Thermal deformation of laminated fan blade (a) without draping analysis and (b) with draping analysis.

3. Conclusion and future work

In this paper, we presented a robust simulation method for the laminated fan blade structure. The middle shell mesh with nodal thicknesses was considered for structural modeling and simulation. To accurately estimate fiber-draped orientations resulting from the shell curvatures, we proposed a numerical

kinematic method for fiber-draping analysis. This approach allows for a direct estimation of the distortion of fiber orientations in each shell element based on its curvatures. Numerical results highlighted the substantial impact of fiber-draped orientations on thermal deformation.

In future work, to validate the numerical results, the laminated fan blade needs to be manufactured using the lamination autoclave curing process. Subsequently, a comparison between the numerical deformations and those observed in experimental outcomes will be thoroughly addressed.

Acknowledgments
This work was supported by the Commercialization Promotion Agency for R&D Outcomes (COMPA) grant funded by the Korean Government (Ministery of Science and ICT), (No. RS-2023-00304729).

References
[1] Bai, R., Colmars, J., Chen, B., Naouar, N., Boisse, P.. The fibrous shell approach for the simulation of composite draping with a relevant orientation of the normals. *Composite Structures*, 285:115202, 2022.
[2] Aimene, Y., Vidal-Salle, E., Hagege, B., Sidoroff, F., Boisse, P.. A hyperelastic approach for composite reinforcement large deformation analysis. *Journal of Composite Materials*, 44(1):5–26, 2010.
[3] Harrison, P.. Modelling the forming mechanics of engineering fabrics using a mutually constrained pantographic beam and membrane mesh. *Composites Part A: Applied Science and Manufacturing*, 81:145–157, 2016.
[4] Krogh, C., Bak, B.L., Lindgaard, E., Olesen, A.M., Hermansen, S.M., Broberg, P.H., et al. A simple MATLAB draping code for fiber-reinforced composites with application to optimization of manufacturing process parameters. *Structural and Multidisciplinary Optimization*, 64:457–471, 2021.
[5] Krogh C, Hermansen SM, Lund E, Kepler J, Jakobsen J. A matter of course: Generating optimal manufacturing instructions from a structural layup plan of a wind turbine blade. *Composites Part A: Applied Science and Manufacturing*, 172, 2023.
[6] Toray Cetex® TC1200 PEEK. *Product data sheet*, 2019.
[7] Sun, C., Yoon, K.. Characterization of elastic-plastic behavior of AS4/PEEK thermoplastic composite for temperature variation. *Journal of Composite Materials*, 25(10):1297–1313, 1991.

ENHANCEMENT OF INTERLAMINAR FRACTURE TOUGHNESS BY MICRO-BRIDGING AT CRACK TIP IN BONDED DISSIMILAR MATERIALS

Atsushi Hosoi[1,2] and Hiroyuki Kawada[1,2]

[1]Department of Applied Mechanics and Aerospace Engineering, Waseda University,
3-4-1 Okubo, Shinjuku-ku, Tokyo 169-8555, Japan
Email: hosoi@waseda.jp
[2]Kagami Memorial Research Institute for Materials Science and Technology,
2-8-26 Nishi-waseda, Shinjuku-ku, Tokyo 169-0051, Japan

Keywords: Dissimilar bonding, Delamination, Fracture toughness, Micro bridging

Abstract
Generally, there is a trade-off relationship between strength and toughness. Concerning adhesive structures, reducing the adhesive thickness improves joint strength, while increasing the adhesive thickness enhances fracture toughness. We proposed a technique to significantly improve both bonding strength and fracture toughness in the dissimilar bonding of thermoplastic carbon fiber reinforced plastic (CFRP) laminates and aluminum alloy. The mechanism behind this improvement is examined in this study. The mechanism by which the nanostructure at the interface leads to the formation of numerous plastic deformations in the resin, causing fuzzing, was investigated. A mechanical model was derived to consider the bridging of matrix resin behind the crack tip. It was found that the bridging near the crack tip occurs in a narrow area but has a significant effect on the crack propagation resistance.

1. Introduction

In order to reduce the structural weight of automobiles, aircraft, and other transportation equipment, the technological development for joining composite materials and metals is being promoted. In particular, applications of thermoplastic carbon fiber reinforced plastic (CFRP) are expanding because thermoplastic resins have excellent heat resistance and recycling properties. However, some thermoplastics lack adhesive properties due to their chemical stability. On the other hand, there have been many studies on adhesive thickness and bonding strength and fracture toughness. A thinner adhesive layer improves bond strength, while a thicker adhesive layer improves fracture toughness, and these are trade-offs [1]. The authors have shown that in bonding thermoplastic CFRP laminates to aluminum alloys, both bonding strength and fracture toughness are improved by fabricating nano-convex structures on the aluminum alloy surface and adding silane coupling agents to the surface to improve bonding to the matrix thermoplastic resin [2-4]. A number of resin fluffing was observed on the fracture surface, which is assumed to be a factor, but the mechanism by which the nanostructure at the interface improves fracture toughness is not well understood.

A theoretical analysis of fracture mechanics at the interface between dissimilar materials was performed by Williams [5]. He noted oscillatory stress singularity in the vicinity of the crack tip and unrealistic crack surface interpenetration. Based on his work, Rice and Sih [6,7] derived an exact solution using complex stress functions. Crack propagation characteristics at dissimilar interfaces were also studied intensively in the 1980s and 1990s [8-10]. Fracture of Mode I and Mode II cannot be separated in the evaluation by the stress intensity factor at the crack tip of the dissimilar material interface. Because of the inhomogeneous nature of composite materials, evaluation by total energy release rate or J-integral

is often used rather than by stress intensity factor [11-13]. Davidson et al. [14] proposed the crack tip element approach for mode separation at the interface of dissimilar materials by energy release rate. Wang and Qiao [15] incorporated the effects of transverse shear force and root rotation at crack tip into that approach. Yokozeki [16] extended the model proposed by Wang and Qiao to include the influence of thermal residual stress. In this study, the crack tip element method is extended to evaluate the effect of bridging on crack propagation at dissimilar material interfaces.

2. Experiments

2.1. Materials

Experiments were taken from previous our work [3]. Here is a brief description of the experiment. Plain woven thermoplastic CFRP laminates with polyamide 6 (PA6) matrix resin and aluminum alloy A5052 were used as test materials. For the thermoplastic CFRP laminates, the carbon fiber of Toray T300B-3K was used, and the fiber volume fraction was V_f = 50%. The stacking sequence of the laminate was $[(0/90)_9]$. The thickness of both thermoplastic CFRP and aluminum alloy was 2 mm, respectively.

2.2. Manufacturing procedure of the nanostructure on aluminum alloy surface

Nanostructures were fabricated on aluminum alloy surfaces with the aim of improving bonding strength. The nanostructures were fabricated by two-step processes of anodizing and etching. The conditions of the anodizing and etching processes are shown in Table 1. Removing alumina by etching after the first anodizing treatment allows the pores to grow uniformly in the second anodizing treatment. As a pretreatment, the aluminum alloy surface was degreased in acetone for 10 minutes using an ultrasonic bath. The anodizing treatment was performed in a low-temperature water bath maintained at 10°C and 400 V using a carbon rod as a cathode and an agitator. The etching process was performed in a high temperature water bath at 63°C. The fabricated nanostructure observed using scanning electron microscope (SEM) was shown in Figure 1.

2.3. Manufacturing procedure of the test specimen

To improve the bonding of aluminum alloy to the matrix resin of thermoplastic CFRP, a silane coupling agent was applied to the surface of an aluminum alloy. The thermoplastic CFRP laminate and aluminum alloy were then joined by hot pressing under atmospheric conditions. 12.5 μm thick polyimide film was inserted at the bonding interface at 45 mm from the tip of the specimen as a pre-crack starter notch to perform the DCB test. The hot press conditions were 0.4 MPa at 300°C, pressurized for 3 minutes, and then cooled for about 5 minutes until the temperature reached 50°C.

2.4. DCB test conditions

Double cantilever beam (DCB) tests were performed according to JIS K 7086. The dimensions of the specimen are shown in Figure 2. To apply tensile load, loading blocks were glued to the specimens with adhesive. A universal testing machine equipped with a 10 kN load cell was used for displacement control, and the test speed was 0.5 mm/min. The specimens were pre-cracked from the insert film by applying tensile load to the specimens under the same conditions as in the DCB test to propagate cracks. The length from the load line to the crack tip was defined, and displacement δ and load P were measured. The load point displacement δ measured during the test was assumed to correspond to the calculated crack opening displacement. The area near the crack tip was continuously monitored with a charge-coupled device camera during loading, and the increase in crack length was calculated by digital image correlation method. In this study, the specimen with the nanostructure fabricated on the aluminum alloy and silane coupling treatment applied to its surface is called Si-NS, and the specimen with silane coupling treatment on the aluminum alloy without fabricating nanostructures is called Si-AR.

Table 1. The conditions of the anodizing and etching processes.

Step	Solution	Temperature (°C)	Time (min)
1st anodizing	2 wt% citric acid + 2 wt% ethylene glycol (1:2)	10	540
1st etching	6 wt% H_3PO_4 + 1.5 wt% H_2CrO_4 (1:1)	63	60
2nd anodizing	2 wt% citric acid + 2 wt% ethylene glycol (1:2)	10	540
2nd etching	6 wt% H_3PO_4 + 1.5 wt% H_2CrO_4 (1:1)	63	20

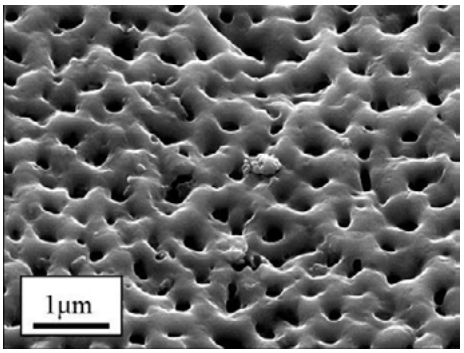


Figure 1. Fabricated nanostructure on aluminum alloy surface.

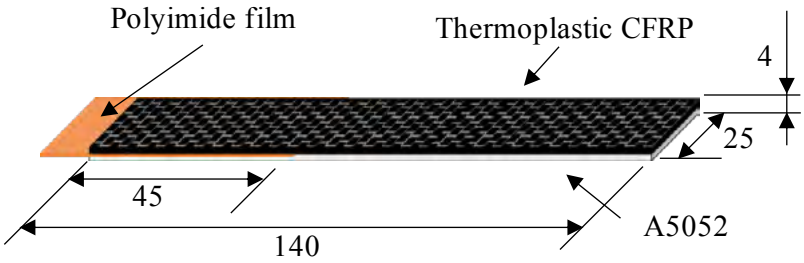


Figure 2. Dimensions of DCB specimen bonded with thermoplastic CFRP and aluminum alloy.

3. Energy release rate associated with delamination growth

The crack tip element method was used to derive the energy release rate associated with crack propagation at the interface of dissimilar materials [15-17]. In this study, the energy release rate associated with interfacial crack propagation was derived by considering the bridging that occurs behind the crack tip. Figure 3 shows the proposed model considered in this study, where N, Q, and M represent axial force, transverse shear force, and bending moment, respectively. The subscripts 1 and 2 indicate the different types of materials. (x) indicates the physical quantity at distance x from the crack tip. The subscript T indicates the sum of materials 1 and 2. Figure 4 (a) shows bridging behind a crack tip and Figure 4 (b) shows the free body diagram at the crack tip. The subscript c represents the interfacial force acting in front of the crack tip. The subscript $i0$ ($i = 1, 2$) indicates the posterior direction of the crack.

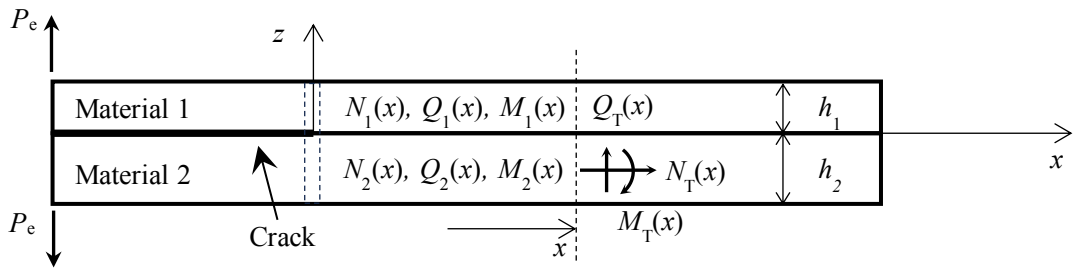


Figure 3. A bi-layer model with cracks under DCB test.

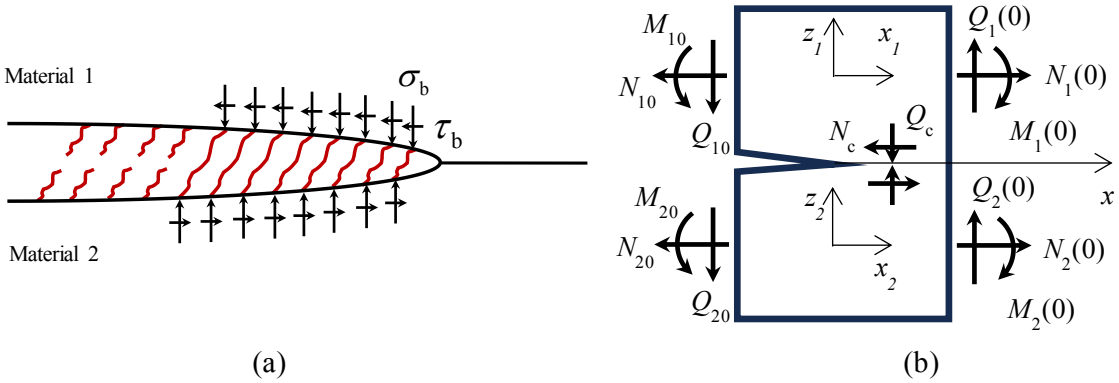


Figure 4. Mechanical state near crack tip: (a) Bridging behind a crack tip; (b) Free dody diarram at crack tip.

The energy release rates for modes I and II can be expressed as follows.

$$\begin{aligned} G_{\mathrm{I}} &= \frac{1}{2B}\left(\frac{1}{\kappa C_1}+\frac{1}{\kappa C_2}\right)Q_{\mathrm{c}}^2 \\ G_{II} &= \frac{1}{2B}\left(a_1+a_2+\frac{h_1^2}{4}d_1+\frac{h_2^2}{4}d_2\right)N_{\mathrm{c}}^2 \end{aligned}, \tag{1}$$

where, C_i is the shear stiffness, κ is the shear factor (=5/6). a_i and d_i are the compliance of each material, and h_i is the thickness of each material. B is specimen width. From Figure 4 (b), the force balance at the crack tip can be expressed by the following equation.

$$\begin{aligned} N_c &= N_1(0)-N_{10} \\ Q_c &= Q_1(0)-Q_{10} \end{aligned}. \tag{2}$$

The forces behind the crack tip considering bridging is expressed as follows.

$$\begin{aligned} N_{10} &= \int_0^b \tau_b(x')\,dx' \\ Q_{10} &= -P_{\mathrm{e}}+\int_0^b \sigma_b(x')\,dx' \end{aligned} \tag{3}$$

where P_e is the transverse load applied to the DCB specimen, b is the length of the bridging region, and x' is the coordinate system in the opposite direction of the x-axis with the crack tip at the origin.

4. Results and Discussions

The DCB test results of the specimens without and with nanostructures on the aluminum alloy surface were compared. The critical energy release rates of the specimens of Si-AR and Si-NS were $G_c = 0.38$ kJ/m^2 and $G_c = 0.98$ kJ/m^2 , respectively. The fracture surface of the Si-AR specimen was smooth and brittle, whereas the surface of the Si-NS specimen showed resin fluffing as shown in Figure 5. This fluffing is considered to have significantly improved the apparent fracture toughness.

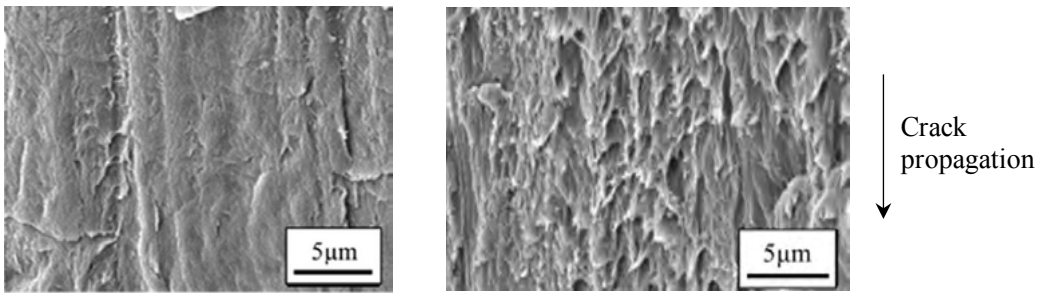


Figure 5. Fracture surfaces observed by SEM: (a) Si-AR; (b) Si-NS.

When the fracture toughness of the bonding interface is too high, the crack propagates into the matrix resin; when the fracture toughness of the interface is too low, the crack propagates along the interface. Therefore, it is considered necessary to have adequate interfacial toughness to produce bridging with fluffing as observed in the experiments. When the interface of the joint is kinked, there may be partially interfacial debonding ahead of the crack tip at angles where the Mode I value is higher. When these conditions are met, the crack may propagate with bridging near the crack tip as shown in Figure 6. The proposed model showed that bridging significantly improves crack propagation resistance.

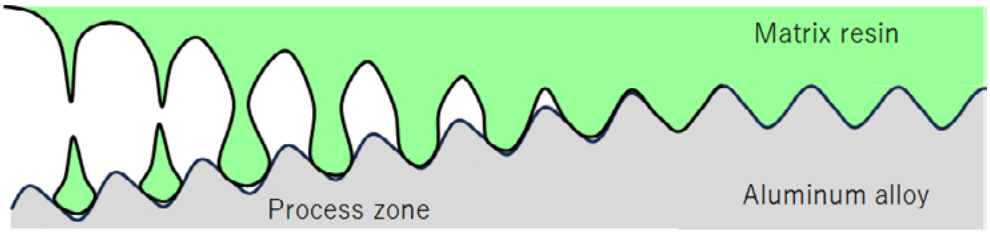


Figure 6. Schematic diagram of resin bridging caused by nanostructures at the bonding interface.

Conclusions

In this study, the influence of the interfacial nanostructure on the crack propagation resistance of thermoplastic CFRP and aluminum alloys was evaluated. Experiments showed that the nanostructure at the interface significantly increased the fracture toughness. This may be due to the large number of matrix resin fluffs at the interface. The micro-bridging caused by the interfacial nanostructure may be due to partially interfacial debonding occurring ahead of the crack tip at the location where the Mode I energy release rate is higher. The energy release rate associated with crack propagation considering the bridging behind the crack tip was derived. The bridging effect contributed significantly to the increase in the crack growth resistance.

Acknowledgments
This work was partially supported by a project of NEDO Leading Research Program/Unexplored Challenge (P14004) and JSPS KAKENHI Grant Number 21H01219.

References

[1] M. D. Banea, L. F. M. da Silva and R. D. S. G. Campilho. The effect of adhesive thickness on the mechanical behavior of a structural polyurethane adhesive. *The Journal of Adhesion*, 91: 331-346, 2015.
[2] K. Wada, H. Ota, K. Saito, K. M. Jespersen, A. Hosoi and H. Kawada. Effect of nanostructured surface on strength and fracture morphology in dissimilar bonding of aluminum alloy and carbon fiber reinforced thermoplastics laminate. *Journal of the Japan Society for Composite Materials*, 46(4): 162-169, 2020. (in Japanese)
[3] H. Ota, K. M. Jespersen, K. Saito, K. Wada, K. Okamoto, A. Hosoi, H. Kawada. Effect of the interfacial nanostructure on the interlaminar fracture toughness and damage mechanisms of directly bonded carbon fiber reinforced thermoplastics and aluminum. *Composites Part A: Applied Science and Manufacturing*, 139: 106101, 2020.
[4] K. Saito, K. M. Jespersen, H. Ota, K. Wada, A. Hosoi and H. Kawada. Fatigue delamination growth characterization of a directly bonded carbon-fiber-reinforced thermoplastic laminates and aluminum alloys with surface nanostructure using DCB test. *Journal of Composite Materials*, 55(22): 3131-3140, 2021.
[5] M. L. Williams. The stress around a fault or crack in dissimilar media. *Bulletin of the Seismological Society of America*, 49(2): 199-204, 1959.
[6] G. C. Sih and J. R. Rice. The bending of plates of dissimilar materials with cracks. Journal of Applied Mechanics. *Journal of Applied Mechanics.* 31(3): 477-482, 1964.
[7] J. R. Rice and G. C. Sih. Plane problems of cracks in dissimilar media. *Journal of Applied Mechanics*. 32(2): 418-423, 1965.
[8] A. G. Evans, B. J. Dalgleish, M. He and J. W. Hutchinson. On crack pathe selection and the interface fracture energy in bimaterial systems. *Acta Metallurgica*. 37(12): 3249-3254, 1989.
[9] J. W. Hutchinson and Z. Suo. Mixed mode cracking in layered materials. *Advanced in Applied Mechanics*. 29: 63-191, 1991.
[10] W. Wang, S. T. D. Freitas, J. A. Poulis and D. Zarouchas. A review of experimental and theoretical fracture characterization of bi-material bonded joints. *Composites Part B: Engineering.* 206: 108537, 2021.
[11] J. Nairn, On the calculation of energy release rates for cracked laminates with residual stresses. *International Journal of Fracture*. 139: 267–293, 2006.
[12] P. Fraisse and F. Schmit. Use of J-integral as fracture parameter in simplified analysis of bonded joints. *International Journal of Fracture*. 63: 59-73, 1993.
[13] H. L. Toftegaard and B. F. Sørensen. General J integral solution for specimens loaded by moments, axial forces and residual stresses – A unifying stiffness formulation. *Engineering Fracture Mechanics*. 217: 106500, 2019.
[14] B. D. Davidson, H. Hu and R. A. Schapery. An analytical crack-tip element for layered elastic structures. *Journal of Applied Mechanics*. 62(2): 294-305, 1995.
[15] J. Wang and P. Qiao. Mechanics of bimaterial interface: Shear deformable split bilayer beam theory and fracture. *Journal of Applied Mechanics*. 72(5): 674-682, 2005.
[16] T. Yokozeki. Energy release rates of bi-material interface crack including residual thermal stresses: Application of crack tip element method. *Engineering Fracture Mechanics*. 77: 84–93, 2010.
[17] K. Harada, K. M. Jespersen, M. Shima, A. Hosoi and H. Kawada. Experimental evaluation of mode I fracture toughness of dissimilar-material joints with thermal residual stresses. *Composites Science and Technology*. 224(16): 109459, 2022.

COMREHENSIVE EVALUATION FOR JOINT STRENGTH OF ULTRASONIC-WELDED CFRTP INVOLVING INTERFACE AND RESIN STRENGTH

Minori Isozaki[1], Maruri Takamura[2], Shinichi Takeda[3] and Jun Koyanagi[4]

[1]Department of Materials Science and Technology, Graduate School of Tokyo University of Science, 6-3-1 Niijuku, Katsushika-ku, Tokyo 125-8585, Japan,
Email: 8223507@ed.tus.ac.jp, Web Page: https://www.rs.tus.ac.jp/koyanagi/home.html
[2]Department of Materials Science and Technology, Graduate School of Tokyo University of Science, 6-3-1 Niijuku, Katsushika-ku, Tokyo 125-8585, Japan,
Email: 8217056@alumni.tus.ac.jp, Web Page: https://www.rs.tus.ac.jp/koyanagi/home.html
[3]Japan Aerospace Exploration Agency, 6-13-1 Osawa Mitaka-shi, Tokyo 181-0015, Japan,
Email: takeda.shinichi@jaxa.jp, Web Page: https://www.jaxa.jp/
[4]Department of Materials Science and Technology, Tokyo University of Science, 6-3-1 Niijuku, Katsushika-ku, Tokyo 125-8585, Japan,
Email: koyanagi@rs.tus.ac.jp, Web Page: https://www.rs.tus.ac.jp/koyanagi/home.html

Keywords: CFRTP, Ultrasonic Welding, Adhesive Joint, Numerical Simulations, Strength Test,

Abstract
In this study, we propose a comprehensive method for evaluating the joint strength of ultrasonic-welded carbon-fiber-reinforced-thermosetting-plastic (CFRTP). Ultrasonic welding is one of the promising joining methods for CFRTP, which is expected to be applied to joint large parts such as aircraft components, but this welding has not been generally applied. This is because a method to evaluate joint strength quantitatively and comprehensively has not yet been established. Current strength evaluations are based only on experiments such as single lap shear test (SLS) or double cantilever beam test (DCB), however, what is obtained here is only apparent strength that does not consider the stress state, failure mode, or failure initiation point of the joint. Therefore, we suggest a new strength evaluation method that can evaluate true strength not apparent strength. In this paper, we calculate the strength quantitatively and comprehensively by using stress analysis in Abaqus and the preceding failure theory, in addition to strength tests. In this process, the interface strength and the resin strength of the joint are determined separately to get a more accurate strength. Then, these strengths are combined on the same plane to develop a comprehensive failure envelope that enables the evaluation of true joint strength.

1. Introduction

Carbon-Fiber-Reinforced-Plastic (CFRP) is a material widely used in the aerospace industry because of its high specific strength, stiffness, and light weight. In the most cases, thermoset resin composites (FRTS) have been used in the past, but in recent years, thermoplastic resin composites (FRTP) have been used due to their high recyclability and processability. A notable feature of CFRTP is that it can be weld-joined. Today, mechanical joining with bolts or rivets is the main method of joining composite materials in large structures such as aircraft. If composite materials can be joined by welding or bonding, many advantages can be expected, such as weight reduction, improved mechanical properties, and recyclability. Thus, welding and bonding of CFRTP is a remarkable technology, and we aim to apply ultrasonic welding, which is one of the most efficient welding methods [1], to large structures.
Now, three reasons hinder the widespread adoption of ultrasonic welding for CFRTP: (1) welding mechanism is not known, (2) the joint strength is not clear, and (3) the durability is not clear. We have

studied the melting behavior of Energy Director (ED) [2,3], which is used to improve the welding efficiency of ultrasonic welding of CFRTP, to elucidate the welding mechanism. We are now working to clarify the joint strength in ultrasonic-welded CFRTP.
Previously, joint strength of ultrasonic-welded CFRTP has been evaluated by SLS and DCB [4,5]. However, it is known that joints have stress distribution, and that joint fails in a mixed mode of tensile and shear stresses [6]. The conventional evaluation based only on experiments is only an evaluation of apparent strength, because it does not consider the complex stress state and failure type of the joint. Therefore, we propose a new strength evaluation method that can evaluate joint strength quantitatively and comprehensively.
Thus far, we have proposed a new strength test that improved upon the conventional strength test [7] and discussed the most appropriate strength evaluation through numerical analysis [8]. In this paper, we focus on the failure mode at the origin of failure. There are two types of failure modes for adhesive and welded joints: interface failure or resin failure, and consideration of the failure mode is necessary for more accurate strength evaluation. We calculate the interfacial strength and the cohesive strength separately, and finally describe them on the same plane to develop a comprehensive failure envelope to clear true strength. Besides, in addition to experimental results, numerical analysis and failure theory are used to calculate each strength, considering the stress distribution and failure under combined stress conditions.

2. Ultrasonic Welding and Strength test

CF/PEEK prepreg (IMS/PEEK (TEIJIN LIMITED), 1.5 mm thick, 30 mm square (16-ply)) was used as the adherend, and welding tests were performed using an ultrasonic welder (Ultrasonic Welder JP80s, SEIDENSHA ELECTRONICS CO.,LTD., Fig. 1). As shown in fig. 1, three pieces of general-purpose Poly Ether Ether Ketone (PEEK) mesh (#25, (CLEVER CO.,LTD.), thickness 0.13 mm, 30 mm square) were inserted between the adherends as an ED. Four sets comprising two CFRTP laminates and three PEEK sheets were prepared, and ultrasonic-welded CFRTP were made which named specimen No. 1 to 4. CFRTP was successfully bonded to all two specimens.

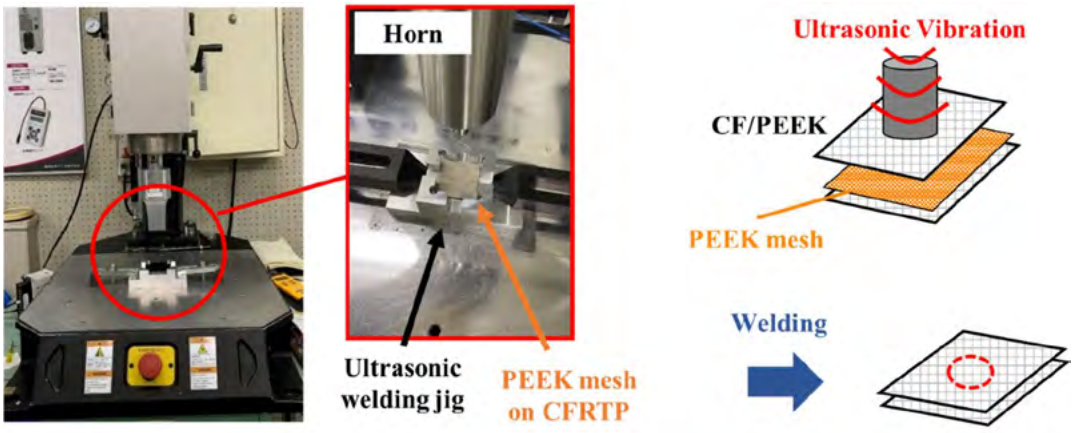


Figure 1. Picture of Ultrasonic welder (JP80s) and Schematic of Ultraconic welding in this study

We performed “Shear Test by Compression” on specimen No. 1 to 4. In this test, one side of the specimen was fixed by a jig and a load was applied to the other side, as shown in fig. 2. A universal testing machine (10 kN) was used for this test. A 20 mm displacement was applied to the load cell at 1 mm/min and the displacement-load was measured. fig. 3 displays images of the fracture surfaces. A summary of all experimental results is presented in table 1. As evident from fig. 3, specimen No. 1 showed only interface failure, No. 2 was dominated by interface failure, and No. 3 and No. 4 showed a mixture of interface and resin failure. This suggests that the failure modes, serving as the origins of failure, vary depending on the condition. Hence, it is important to derive interface strength and resin strength separately and then to evaluate the strength comprehensively. In the following chapter 3.1 and

3.2, the interface strength and resin strength are calculated respectively, and a comprehensive strength evaluation is given in chapter 3.3.

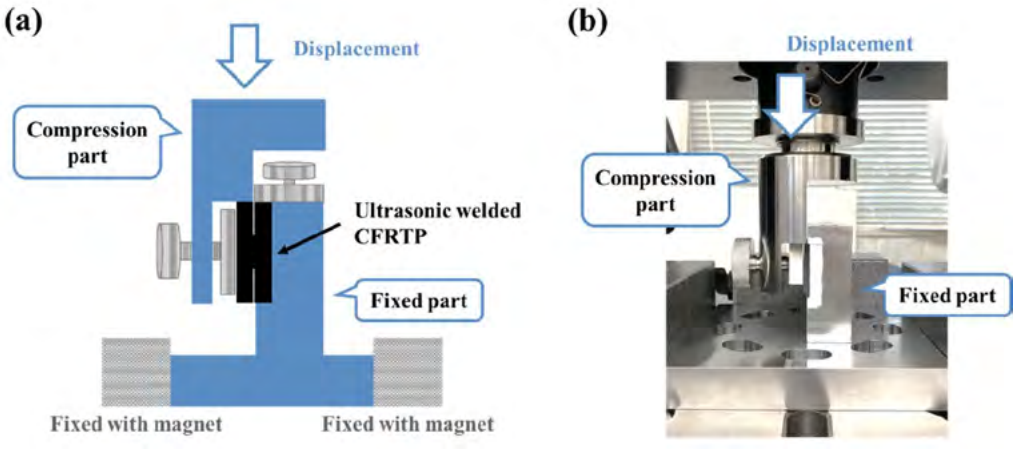


Figure 2. Shear Test by Compression ((a) Schematic diagram / (b) Picture)

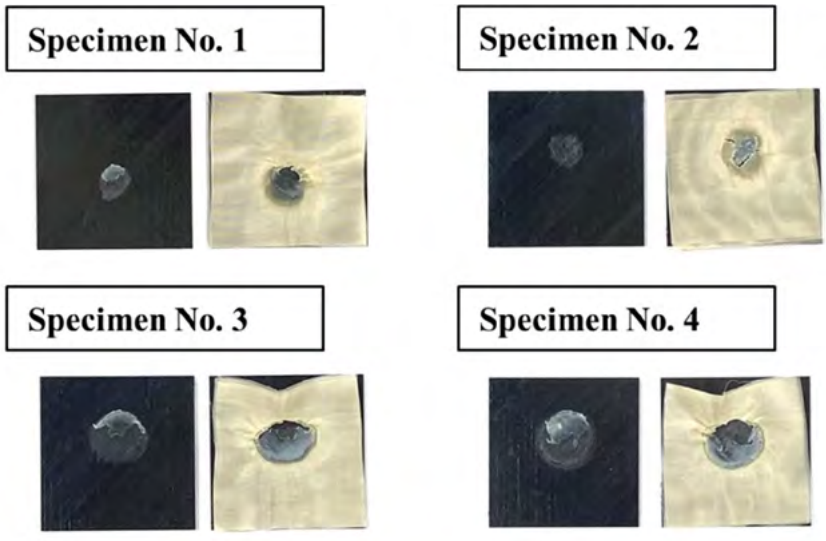


Figure 3. Picture of Fracture Surface after Shear Test by Compression. No. 1 was only interface failure, No. 2 was mainly interface failure, and No. 3-4 showed a mixture of interface and resin failure.

Table 1. Results of Shear Test by Compression. (welding time of each Ultrasonic-welded CFRTP / welded area calculated by using X-ray CT / Failure Load / Failure type (fig. 3))

Specimen No.	Welding time (s)	Diameter of welding area (mm)	Failure load (N)	Failure type
1	3	7.76	1340	interface
2	3	6.00	652	interface
3	5	10.7	4020	interface + resin
4	5	11.7	4780	interface + resin

3. Evaluation of Joint Strength

3.1. Interface Strength

The interface strength was determined by simulating the shear test using numerical analysis (Abaqus 2020). This was based on the experimental results of specimen No. 1 and 2 in which interfacial failure was dominant.

The model consists of two CFRTP laminates of 30 mm square and a circular bonded zone (PEEK) between them (fig. 4(a)), and we inserted a cohesive element between the CFRTP and the resin. The diameter of the joint (α mm) was changed based on the welding condition of the specimen observed by X-ray CT (table 1), assuming the shape of the weld to be a perfect circle. The material properties were shown in table 2-3 and plasticity property was assigned in resin (fig. 4(b)). The test was reproduced by applying boundary conditions in the y-direction to the top and bottom surfaces of the CFRTP on one side and in the z-direction to both sides of the CFRTP, and y-direction displacement to the top surface of the CFRTP on the other side, which was not fixed in the y-direction (fig. 4(a)). The interface strength was calculated by fitting the cohesive properties (table 3 [9]) so that the failure load in the analysis equals the experimental value.

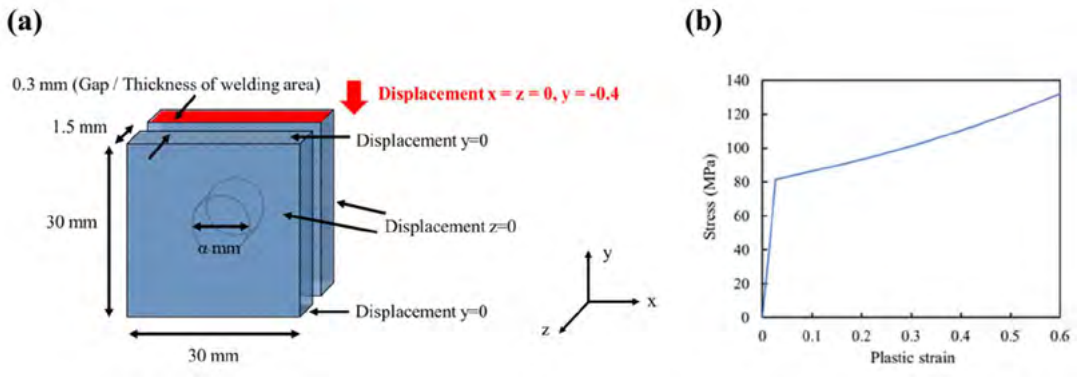


Figure 4. Analysis Conditions ((a) model size and boundary conditions (b) PEEK properties)

Table 2. Material properties (CFRTP / PEEK)

	Young modulus (MPa)	Poisson' ratio
CFRTP	9300	0.2
PEEK	3000	0.37

Table 3. Cohesive properties [9]

	Interface Strength (MPa)		
	Vertical	Shear1	Shear2
Cohesive	$\beta/\sqrt{2}$	β	β

Table 4 shows the strength from experiments and the strength calculated by the analysis. We calculated experimental strength from the X-ray CT (SHIMADZU Co.) images of area of the weld zone and the corresponding failure load ($\text{experimental strength} = \text{failure load}/\text{welded area}$). This apparent strength in experiment, which did not consider the stress distribution, was significantly different from the strength in analysis. Fig. 5 shows the stress state at the interface when the interface fails (specimen No. 1), indicating that stress was concentrated at the edge of the joint. We could also conclude that the failure occurs in a mixed mode of tensile and shear stresses. These results were also observed in the analysis for specimen No. 2.

Table 4. Interface Strength from experiment or FEM analysis

Specimen No.	Shear Strength (MPa)	
	Experiment	FEM
1	28.4	67.9
2	44.6	49.6
Average	36.5	58.8

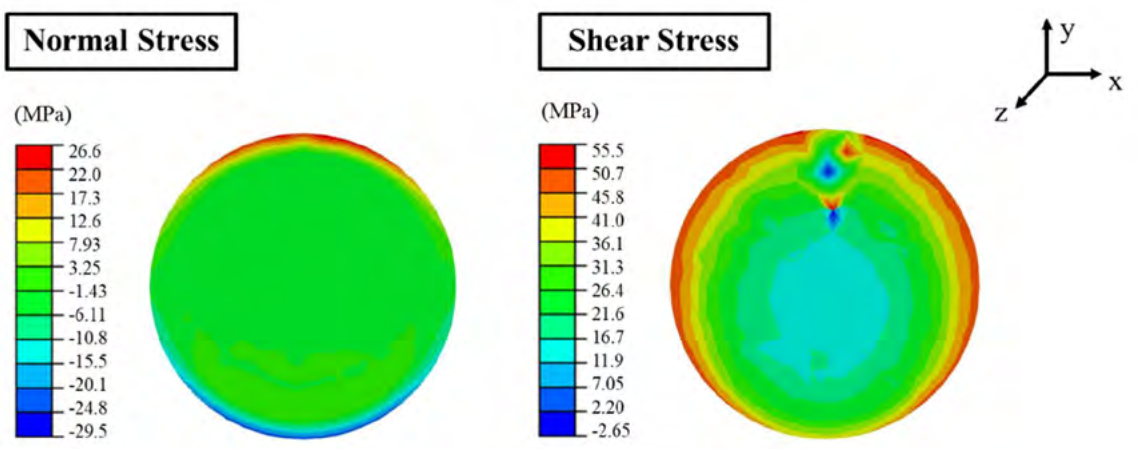


Figure 5. Distribution of Normal and Shear Stresses at the joint interface

Since the interface failure is based on the parabolic criterion [9,10] and the interface strength obtained in this experiment and analysis, the interface strength can be given by the following Eq. 1. According to the parabolic criterion, $c_1 = -7.4 \times 10^{-3}$ and $c_2 = 67.2$ can be calculated. Stress in Normal direction is t_n and Stress in Shear direction is t_s; and this parabola shows the interface strength under combined stress conditions (normal + shear stress).

$$t_n = c_1 {t_s}^2 + c_2 \tag{1}$$

3.2. Resin Strength

The resin strength was derived based on Christensen's failure criteria (Eq. 2 [11,12]). This criterion predicts ductile yielding and brittle failure of isotropic materials in the same equation. C and T are the uniaxial failure stresses in compression or tension and σ is the stress in each direction.

Applying Christensen's failure criterion to the Shear test by Compression in this paper, we can consider Eq. 3 and Eq. 4. This is because only S33 is the normal stress for the adhesive elements, whereas transverse shear stress S13 and longitudinal shear stress S23 are the output of the shear stress, in shear test. As before, t_n is Normal stress and t_s is Shear stress. From the above, $c_3 = 0.303$, $c_4 = 0.952$, $c_5 = 1.2$ can be derived in Eq. 5. We derived Eq. 4 by taking this assumption and the following material properties: $T = 100$ MPa [13], $C = 250$ MPa, $\nu = 0.37$. Eq. 5 shows the resin strength under combined stress conditions.

$$\left(\frac{1}{T} - \frac{1}{C}\right)(\sigma_{11} + \sigma_{22} + \sigma_{33}) + \frac{1}{TC}\left\{\frac{1}{2}[(\sigma_{11} - \sigma_{22})^2 + (\sigma_{22} - \sigma_{33})^2 + (\sigma_{33} - \sigma_{11})^2] + 3({\sigma_{12}}^2 + {\sigma_{23}}^2 + {\sigma_{31}}^2)\right\} \leq 1 \tag{2}$$

$$\sigma_{11} = \frac{\nu}{1-\nu}\sigma_{33}, \qquad \sigma_{22} = 0, \qquad \sigma_{12} = 0 \tag{3}$$

$$t_{\mathrm{n}} = \sigma_{33}, \qquad t_{\mathrm{s}} = \sqrt{{\sigma_{23}}^2 + {\sigma_{31}}^2} \tag{4}$$

$$\frac{1}{T^2}\{c_3 {t_{\mathrm{n}}}^2 + T c_4 t_{\mathrm{n}} + c_5 {t_{\mathrm{s}}}^2\} \leq 1 \tag{5}$$

3.3. Parabolic Criterion

We propose to evaluate strength using comprehensive failure envelope that includes both interface strength and resin strength. Using Eq. 1 and Eq. 5 derived so far, the interface strength and the resin strength were described on the same plane (fig. 6).

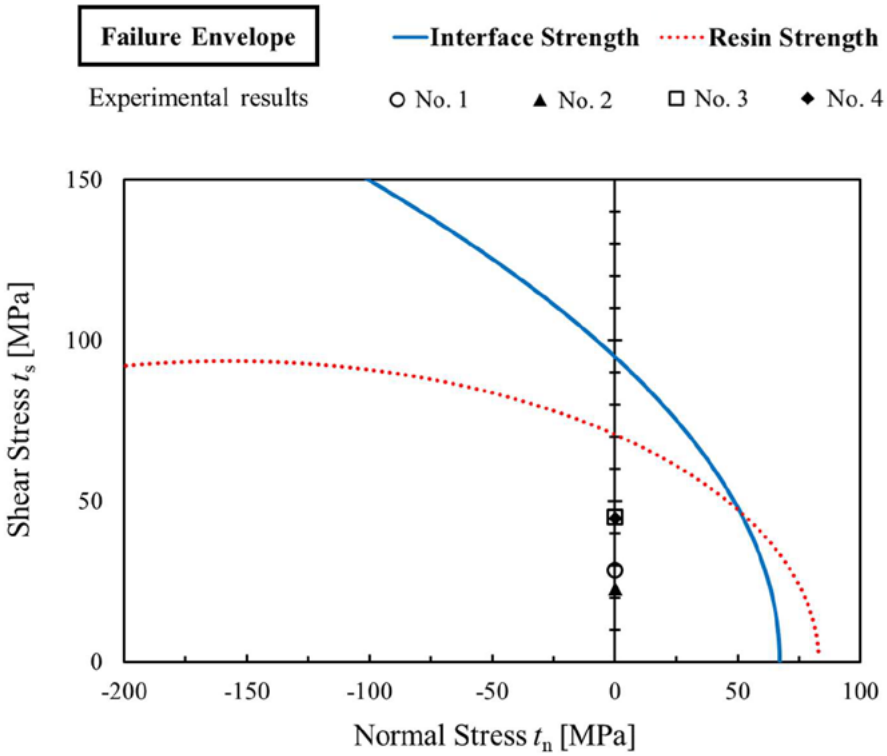


Figure 6. Comprehensive Failure Envelope including both Interface Strength and Resin Strength

Fig. 6 shows that the failure mode differs depending on the stress state of the joint. Using this comprehensive failure envelope, it is possible to evaluate the joint strength of ultrasonic-welded CFRTP considering the following points:

I. Stress distribution (each strength was calculated using numerical analysis and failure theory)
II. Strength under various stress conditions (tensile stress or shear stress)
III. Failure mode at the point of failure (interface failure or resin failure)

4. Conclusions

In this study, we calculated interface strength and resin strength separately, based on strength tests, numerical analysis, and failure theory. Then, a comprehensive failure envelope representing the joint strength of ultrasonic-welded CFRTP was constructed by combining each strength on the same plane. Using this envelope, we were able to quantitatively and comprehensively evaluate the strength of the joints, considering three factors: stress distribution in the joint, failure under combined tensile and shear stress conditions, and failure mode.

References

[1] Zhao, T,. Palardy, G., VillegasIrene, I, F., Rans, C., Martinez, M., Benedictus, R., Mechanical behavior of thermoplastic composites spot-welded and mechanically fastened joints: A preliminary comparison. Compos, *Composite Part B* Eng. 112, 224–234, 2017

[2] Takamura, M., Uehara, K., Koyanagi, J., Takeda, S., Multi-Timescale Simulation of Temperature Elevation for Ultrasonic Welding of CFRP with Energy Director, *Journal pf Multiscale Modeling*, Vol. 12, No. 04, 2021

[3] Koyanagi, J., Takamura, M., Wakayama, K., Uehara, K., Takeda, Shinichi., Numerical simulation of ultrasonic welding for CFRP using energy director, *Advanced Composite Materials*, Vol. 31, Issue 4, 428-441, 2022

[4] Villegas, I, F., Bersee HEN, C., Ultrasonic welding of advanced thermoplastic composites: An investigation on energy-directing surfaces, *Advances in Polymer Technology*, Vol. 29, Issue 2, 112-121, 2010

[5] Wang, Y., Rao, Z., Liao, S., Wang, F., Review Ultrasonic welding of fiber reinforced thermoplastic composites: Current understanding and challenges, *Composite Part A: Applied Science and manufacturing*, 149, 2021

[6] JP, Reis., M de Moura,., S, Samborski., Thermoplastic composites and their promising applications in joining and repair composites structures: A review, *Materials 2020*, 13(24), 2020

[7] Isozaki, M, Takamura, M , Takeda, S, Koyanagi, J, Comprehensive Evaluation method of Bond Strength in Ultrasonic Welding for CFRTP, *Procedia Structural Integrity*, 52, 176-186, 2024

[8] Takamura, M, Isozaki, M, Takeda, S, Oya, Y, Koyanagi, J, Evaluation of True Strength for Adhesive Bonded Carbon Fiber-Reinforced Plastics, *Materials*, 17-2, 394, 2024

[9] Koyanagi, J., Nakatani, H., Ogihara, S., Comparison of glass-epoxy interface strength examined by cruciform specimen and single-fiber pull-out tests under combined stress state, *Composites Part A: Applied Science and Manufacturing*, Vol. 43, Issue 11, 1819-1827, 2012

[10] Ogihara, S., Koyanagi, J., Investigation of combines stress state failure criterion for glass fiber/epoxy interface by the cruciform specimen method, *Composites Science and Technology*, Vol. 70, Issue 1, 143-150, 2010

[11] Richard M. Christensen, A comprehensive theory of yielding and failure for isotropic materials, *J. Eng. Mater. Technol*, 129(2): 173-181, 2007

[12] Y. Yamazaki, J. Koyanagi, Y. Sawamura, M. Ridha, S.Yoneyama, T.E. Tay, Numerical simulation of dynamic failure behavior for cylindrical carbon fiber reinforced polymer, *Composite Structures*, 203: 934-942, 2018

[13] P. J. Rae, E. N. Brown, E. B. Orler, The mechanical properties of poly(ether-ether-ketone) (PEEK) with emphasis on the large compressive strain response, *Polymer*, Vol. 48, Issue 2, 598-615, 2007,

CONTENTS

COMPRESSIVE ENERGY ABSORPTION OF 3D PRINTED CONTINUOUS FIBER REINFORCED COMPOSITE WITH DIFFERENT PRINTING PATH

M.-H. Jeon[1], G.-S. Shin[1], S.H. Yoon[1+], M. Kim[1], J. Hwang[1]

[1]InstituteKorea Institute of Science and Technology, Institute of Advanced Composite Materials, Wanju, Republic of Korea
[+]Email: soonho@kist.re.kr, Web Page: jb.kist.re.kr

Keywords: 3D printing, Continuous fiber, Printing path, Comrpession test, Strength

Abstract
Lattice or grid-stiffened structures are essential for lightweight designs. These structures consist of ribs that support external and internal loads, utilizing the high stiffness and strength of unidirectional fibers. 3D printing allows for diverse unit cell designs, each with unique stiffness, strength, and energy absorption properties. In this study, the compressive strength of 3D-printed composite lattice structures with three different printing paths was investigated. T300 carbon fiber tow and thermoplastic polylactic acid (PLA) filament were used. The specimens were prepared with printing paths with and without crossing continuous fiber filaments and were printed thick enough to prevent out-of-plane buckling. Compression tests were conducted using the ASTM D3410 fixture. Glass fabric tabs and aluminum blocks were used to extend the specimens to ensure stable and uniform compressive load. The compressive strength was compared for each specimen.

1. Introduction

Composite lattice structures are highly efficient structure for bearing high loads [1, 2]. The structure consists of ribs to endure external loads and enhance buckling performance. External and internal loads in the structure are supported by each rib utilizing the high stiffness and strength of unidirectional fibers. These structures are manufactured through filament winding, automated fiber placement, and hand lay-up. Furthermore, the technology of three-dimensional (3D) printing with continuous fiber is becoming a promising technique for manufacturing composite lattice structures.

Many studies have been conducted on 3D-printed energy absorption structures with different types of unit cells exhibiting different stiffness, strength, and energy absorption properties [3-6]. Wang et al. [3] performed tensile tests on 3D-printed continuous fiber reinforced composite grid structures. Ren et al. [4] performed tensile tests on continuous fiber reinforced grid unit cells to obtain tensile modulus. The measured modulus was used in a path-planning approach to find an efficient and performance-optimized fabrication process for grid-stiffened composite panel. The approach was mainly compared by buckling performance. Habib et al. [5] discussed the effect of 3D-printed honeycomb cell shape on the performance of energy absorption structures. Triangular, quadratic, diamond, hexagonal, octagonal, and circular shapes were compared for energy absorption efficiency. Bokharaie et al. [6] presented an approach to enhance the structural performance of 3D-printed composite materials with different geometries of hexagonal cells. Tensile tests were performed, and the fracture mechanisms weres examined by experimental and numerical procedures. A multiscale homogenization and the Hashin damage model were used.

In the studies above, the tensile properties were main research topic, and joint configuration was not primarily considered for compressive properties. Structures printed with continuous fiber must have joint points between each rib. The printing strategy for these joint points is important for enhancing the compressive energy absorption capacity. Understanding the properties of joint point with different printing paths is necessary before design and manufacturing; however, study on this aspect has not been sufficiently reported.

In this study, the compressive properties of a 3D printed composite lattice structure with three different types of printing paths was investigated. T300 carbon fiber tow and thermoplastic polylactic acid (PLA) filament were used in the fabrication process. The purpose of this test is to investigate the in-plane properties of the specimen, and the specimen was printed with a sufficiently thick thickness to prevent out-of-plane buckling and deformation. Compression tests on the printed specimens were conducted using the ASTM D3410 fixture. Glass fabric tabs were attached to the top and bottom areas of the specimen, and a stable and uniform compressive load was applied to specimen by shear force from the fixture. The compressive strength was compared for specimens with different joint shape.

2. Compression test

2.1. Specimen and test procedure

Specimens were fabricated using T300 carbon fiber tow and PLA filament. The carbon fiber tow and PLA filament were printed together from the nozzle of 3D printer. Three specimens with different printing path were prepared, as shown in Figure 1. In Pattern I as shown in Fig 1 (a), the filaments with carbon fiber tow are crossed at the joints on the same layer. The filament can pass through the previously printed filament because PLA was in a liquid state during printing. Pattern II is similar to Pattern I. The filament in one direction was printed first, and that in the other direction was printed at the upper layer. The number of layer of Pattern I is twice of Pattern II. There are empty spaces between the filaments and those were subsequently filled by the melted PLA. In Pattern III, the filaments were printed without crossing. At the joints, the printing path was set to turn around without crossing. The number of layer is 15 for Pattern I and III, and 8 for Pattern II. The width of printed filament is 3 mm, and total thickness is 6 mm to observe in-plane behavior without out-of-plane deformation. Total heith and width of the specimen is 35 mm. Joint area of left and right side at middle height was cut to obtain compressive property of single unit cell.

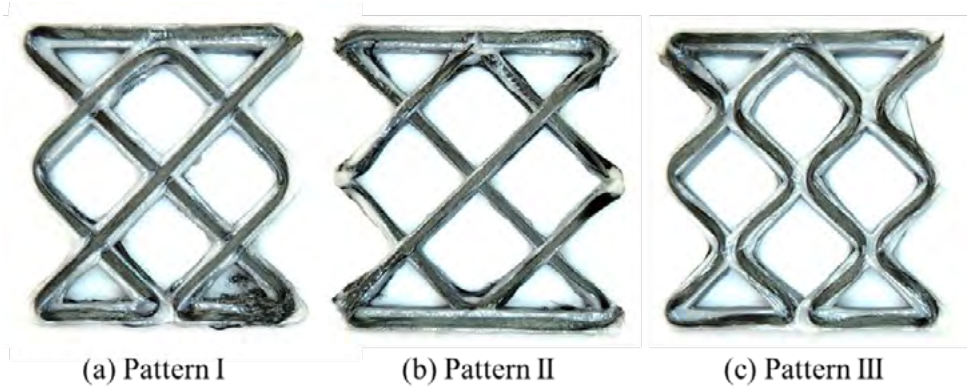


Figure 1. Specimens with different printing path.

To ensure uniform and stable compressive load for the specimen, the ASTM D3410 test fixture was used (Figure 2). The specimens were extanded by glass fabric tab and the empty space was filled with an aluminum block (Figure 3). The surface of glass fabric tab was contacted with the jaw surface of test fixture. Test was perfomed with displacement control and speed set to 1 mm/min. Universal testing machine with 30 kN capacity was used.

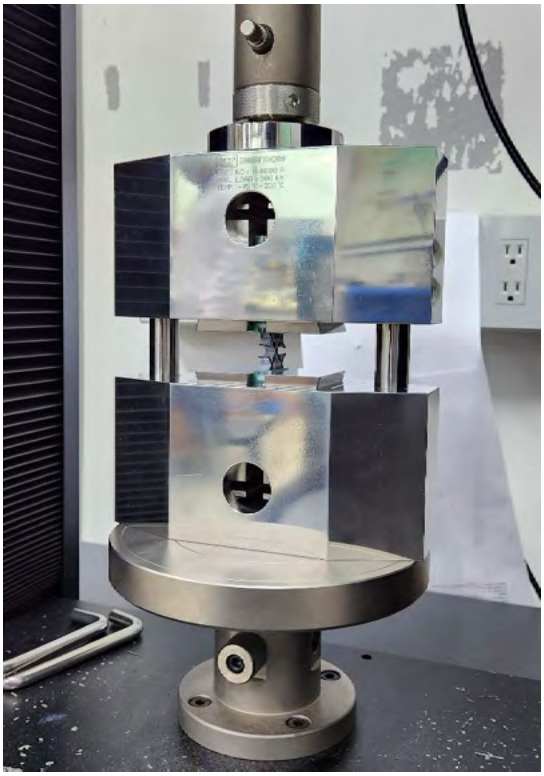


Figure 2. Compression test using ASTM D3410 test fixture.

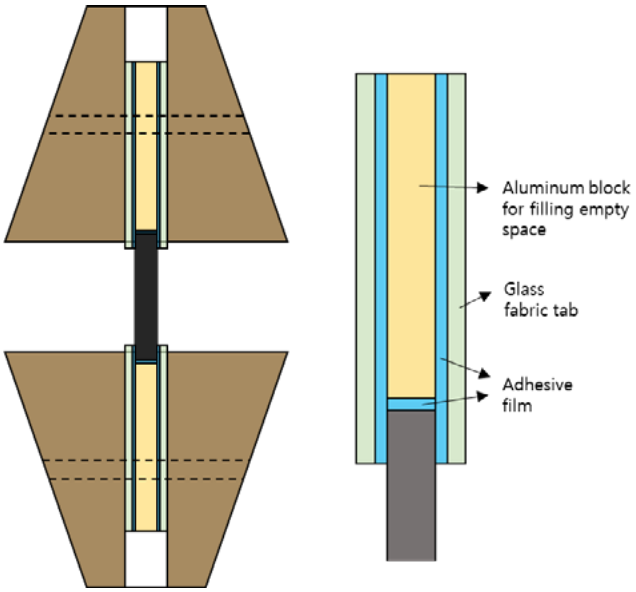


Figure 3. Extended specimen with glass tab and aluminum block.

2.2. Test results

Compression test results are shown in Figure 4, and the maximum loads of each specimen are listed in Table 1. It was confirmed that Pattern I had the highest compressive strength, while Pattern II had the lowest strength. The number of layers in Pattern II is half that of the other specimens, and the space between each layer is not sufficiently filled with resin. Consequently, the out-of-plane shear stiffness is too low, the compressive rigidity and strength are significantly reduced. The initial stiffness of Pattern III is slightly higher than that of Pattern I, but the bifurcation point due to fracture occurred at a lower load, resulting in a maximum strength lower than that of Pattern I.

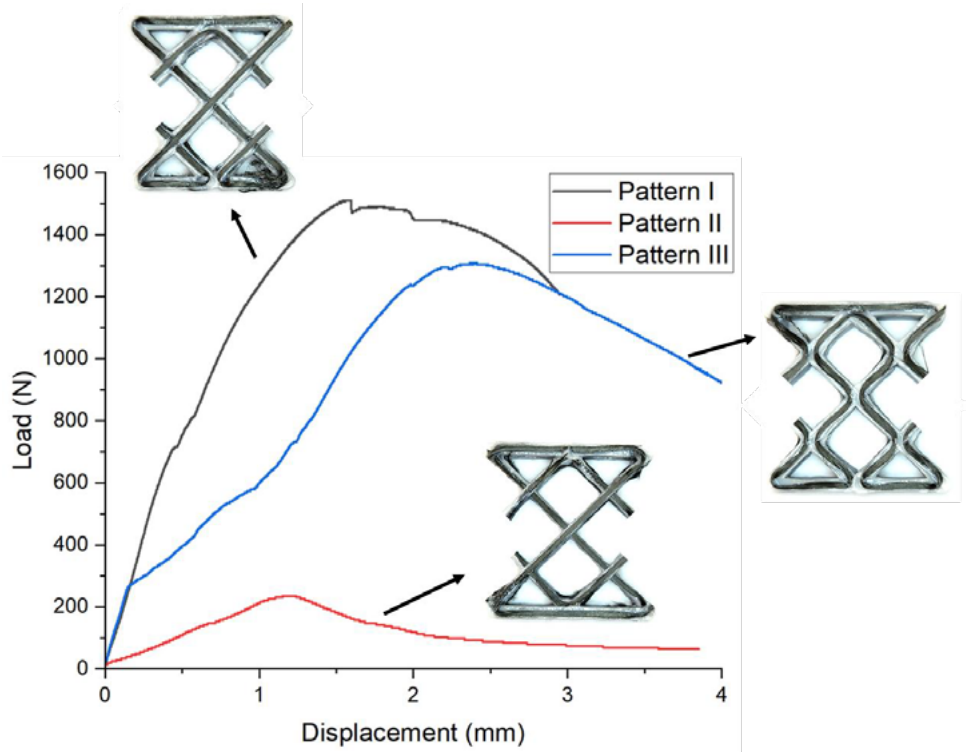


Figure 4. Measured load-shortening curve.

Table 1. Maximum load of each specimen.

Path-1	Path-2	Path-3
1510 N	235 N	1309 N

3. Conclusions

In this study, compression tests were performed on composite lattice unit structures fabricated using continuous fiber printing. Specimens were fabricated with three different printing paths, and their compressive strengths were compared. To apply a stable compressive load to the specimens, tabs were attached, and a jaw block type compression test fixture was used.

The compressive strength was highest in the pattern with intersecting fibers. The initial stiffness did not show a significant difference depending on whether the fibers crossed or not. The specimens printed to maintain a uniform shape of the laminated fibers with the crossing fiber filament exhibited the lowest performance due to insufficient lamination in the thickness direction.

Further work will involve fabricating specimens with various angles and conducting additional tests to compare and analyze the stiffness and strength according to the angles and printing paths. Additionally, finite element analysis will be utilized to propose criteria for defining buckling and bifurcation points.

References

[1] V.V. Vasiliev, V.A. Barynin, and A.F. Rasin. Anisogrid lattice structures-survey of development and application. *Composite Structures*, 54(2-3):361-370, 2001.
[2] V.V. Vasiliev, V.A. Barynin. and A.F. Rasin. Anisogrid composite lattice structures – Development and aerospace applications. *Composite Structures*, 94(3):1117-1127, 2012.

[3] Y. Wang, G. Zhang, H. Ren, G. Liu, and Y. Wiong. Fabrication strategy for joints in 3D printed continuous fiber reinforced composite lattce structures. Composites Communications, 30(101080), 2022.
[4] H. Ren, G. Zhang, Y. Wang, D. Wang, and Y. Xiong. Buckling performance-aware path planning for 3D printing of curved grid-stiffened fiber-reinforced polymer composite structures. *Journal of Manufacturing Processes*, 116:192-201, 2024.
[5] F.N. Habib, P. Lovenitti, S.H. Massod, and M. Nikzad. Cell geometry effect on in-plane energy absorption of periodic honeycomb structures. *The International Journal of Advanced Manufacturing Technology*, 94:2369-2380, 2018.
[6] B. Bokharaie, R. Aghababaei, M.A. Dias, and M.K. Budzik. Failure of 3D-printed composite continuous carbon fibre hexagonal frames. Composites Part B, 275(111307), 2024.

DESIGN AND FABRICATION OF VARIABLE STIFFNESS COMPOSITE LAMINATES WITH ENHANCED DYNAMIC BEHAVIOR

P. Khandar Shahabad[1], M. Rafiei Anamagh[2], G. Serhat[3], I. Basdogan[4] and B. Bediz[1,5]

[1] Faculty of Engineering and Natural Sciences, Sabanci University, Istanbul, Türkiye
Email: peiman@sabanciuniv.edu

[2] School of Mechanical Engineering, Technological University Dublin, Dublin, Ireland
Email: mirmeysam.rafieianamagh@tudublin.ie

[3] Department of Mechanical Engineering, KU Leuven, Bruges, Belgium
Email: gokhan.serhat@kuleuven.be

[4] Mechanical Engineering Department, Koc University, Istanbul, Türkiye
Email : ibasdogan@ku.com.tr

[5] Integrated Manufacturing Technologies Research and Application Center, Sabanci University, Istanbul, Turkey
Email : bbediz@sabanciuniv.edu

Keywords: Fiber-reinforced composites, variable stiffness laminates, fiber steering, lamination parameters, meshless methods, structural optimization.

Abstract

Design of variable stiffness (VS) laminates, featuring curvilinear fiber paths, requires efficient methodologies to attain structural performance levels beyond those of conventional constant stiffness (CS) composites. However, optimization and fabrication of VS laminates pose significant challenges. This problem is addressed in the present study, where lamination parameters (LPs) and spectral Chebyshev approaches are incorporated to obtain a multi-step design framework for symmetric and balanced composites. Initially, master points were defined to attain optimal LP distributions, which were subsequently used to retrieve the discrete fiber angles. Then, to obtain the continuous fiber paths, streamline and equidistant fiber path planning methods were implemented. For modal testing, laminate samples with the optimal fiber paths were fabricated via the automated fiber placement technique. The results show that the designed VS panels provide up to 8% performance improvement over optimal CS laminates. The experimental fundamental frequencies were found to be around 20% lower than the simulation results on average.

1. Introduction

The superior mechanical properties of laminated composites have been boosting their use across various industries. Traditional laminates reinforced with straight fibers result in constant (in-plane) stiffness (CS) [1]. Recently, advanced composite fabrication techniques, such as automated fiber placement (AFP), have enabled the fabrication of variable stiffness (VS) laminates having curvilinear fibers. This concept enhances the load distribution within the structure; however, it also significantly enlarges the design space, necessitating efficient optimization and path-planning approaches [2]. One prevalent method for defining fiber paths involves using predefined equations, which ensure smoothness while restricting design space [3]. Conversely, treating fiber angles as design variables at discrete points enables obtaining more diverse laminate configurations exhibiting greater performance [4]. However, this expansion of design space simultaneously brings significant challenges in terms of optimization complexity and computational cost.

VS laminates can also be designed using a multi-step design strategy based on lamination parameters (LPs) [5,6]. Using LPs as design variables provides a compact representation of the laminate stiffness

and convex responses for most mechanical responses such as the fundamental frequency [7,8]. However, this approach necessitates a post-processing (or an additional optimization) step to determine fiber angles. Furthermore, another process is typically required to obtain manufacturable fiber paths, for which different path-planning methods have been proposed in the literature [9–12].

Finite element analysis (FEA) is commonly used for designing composite structures due to its adaptability and precision [13,14]. However, accurate modeling of VS laminates requires finer meshes, leading to high computational costs. To overcome this problem, we implemented a meshless analysis method based on the Chebyshev polynomials. The LPs at sampling locations or selected master points are set as design variables. We used the design framework to maximize the fundamental frequencies of panels with different aspect ratios and boundary conditions. Discrete fiber angles were retrieved from optimal LPs via trigonometric formulations. Then, continuous fiber paths satisfying the manufacturing constraints were derived using the streamline and equidistant path planning techniques. Finally, symmetric and balanced VS laminates composing 8 and 24 layers were fabricated for modal testing, and the experimental eigenfrequencies were compared with the simulation results to validate the proposed methodology.

2. Model development

The geometry of the studied thin VS laminated composite plates is illustrated in Fig. 1a. The dimensions of the laminate along $\boldsymbol{x}$, $\boldsymbol{y}$, and $\boldsymbol{z}$ directions are $\boldsymbol{L_x}$, $\boldsymbol{L_y}$, and $\boldsymbol{h}$, respectively. Applying Hamilton's principle, the governing equations for free vibration can be obtained as

$$\int_{t_1}^{t_2}\left\{\int_{\mathbb{A}}\int_{-h/2}^{h/2}\left(\rho\,\ddot{\boldsymbol{q}}^{\mathrm{T}}\delta\boldsymbol{q}+\boldsymbol{q}^{\mathrm{T}}\boldsymbol{B}^{\mathrm{T}}\boldsymbol{C}\boldsymbol{B}\delta\boldsymbol{q}\right)\mathrm{d}z\mathrm{d}\mathbb{A}\right\}\mathrm{d}t=0 \tag{1}$$

where ρ is density, and $\boldsymbol{q}=\{u_0;v_0;w_0;\phi_x;\phi_y\}$ is the deflection vector based on the first-order shear deformation theory (FSDT). The variables u_0, v_0, and w_0 correspond to the displacements along x, y, and z axes, while ϕ_x and ϕ_y are the rotations in the xz and yz planes, respectively.

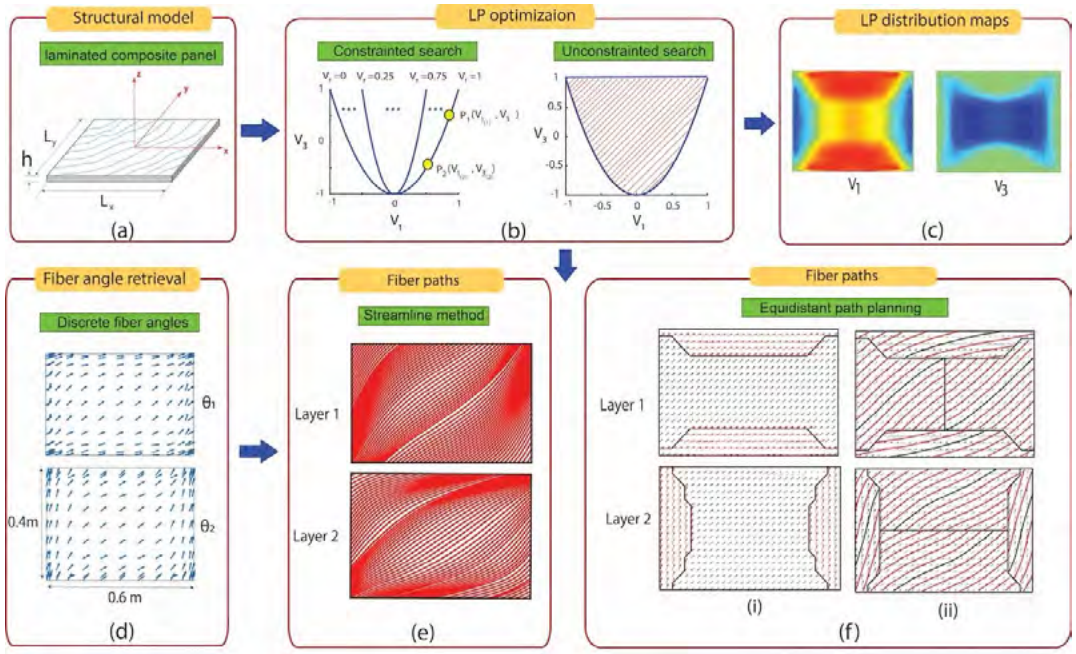


Figure 1. Flowchart of the developed multi-stage design framework for VS laminates.

The $\boldsymbol{B}$ ($\boldsymbol{\epsilon} = \boldsymbol{Bq}$) and $\boldsymbol{C}$ ($\boldsymbol{\sigma} = \boldsymbol{C\epsilon}$) matrices relate strains to the displacements and stresses, respectively. The constitutive matrix ($\boldsymbol{C}$) consists of material invariants and LPs. For symmetric and balanced laminate configurations that are homogeneous through the thickness, the constitutive matrix can be formulated using only two LPs, V_1 and V_3. The design domain is defined by the trigonometric relations between the LPs [15], and it is demonstrated by the Miki's diagram (see Fig. 1b).

2.1. Solution method

A meshless technique based on Chebyshev polynomials is employed to numerically solve Eq. (1). The deflection of the laminate is expressed through a double expansion of Chebyshev polynomials:

$$q(x,y) = \sum_{k=1}^{N_x} \sum_{l=1}^{N_y} a_{kl}\, \mathcal{T}_{k-1}(x)\, \mathcal{T}_{l-1}(y) \tag{2}$$

Here, a_{kl} and $\mathcal{T}$'s denote the expansion coefficients and Chebyshev polynomials, respectively. The variables N_x and N_y are the polynomial numbers used along x and y directions, respectively. The problem domain is discretized using the Gauss-Lobatto sampling points. To perform the derivative and the integral operations, differentiation matrices ($\boldsymbol{Q_x}$ and $\boldsymbol{Q_y}$) and inner product matrix ($\boldsymbol{\mathcal{V}}$) are calculated, respectively [11,15]. The equation of motion for shells with free boundary conditions can be expressed as $\boldsymbol{M\ddot{q} + Kq = 0}$. The $\boldsymbol{M}$ and $\boldsymbol{K}$ are the mass and stiffness matrices of the laminate, respectively:

$$\boldsymbol{M} = \rho \begin{bmatrix} h\boldsymbol{\mathcal{V}} & 0 & 0 & 0 & 0 \\ 0 & h\boldsymbol{\mathcal{V}} & 0 & 0 & 0 \\ 0 & 0 & h\boldsymbol{\mathcal{V}} & 0 & 0 \\ 0 & 0 & 0 & \frac{h^3}{12}\boldsymbol{\mathcal{V}} & 0 \\ 0 & 0 & 0 & 0 & \frac{h^3}{12}\boldsymbol{\mathcal{V}} \end{bmatrix} \quad \boldsymbol{K} = \boldsymbol{B}^T \begin{bmatrix} h\boldsymbol{\mathcal{V}_{11}} & h\boldsymbol{\mathcal{V}_{12}} & h\boldsymbol{\mathcal{V}_{13}} & 0 & 0 \\ h\boldsymbol{\mathcal{V}_{12}} & h\boldsymbol{\mathcal{V}_{22}} & h\boldsymbol{\mathcal{V}_{23}} & 0 & 0 \\ h\boldsymbol{\mathcal{V}_{13}} & h\boldsymbol{\mathcal{V}_{23}} & h\boldsymbol{\mathcal{V}_{33}} & 0 & 0 \\ 0 & 0 & 0 & \frac{h^3}{12}\boldsymbol{\mathcal{V}_{44}} & \frac{h^3}{12}\boldsymbol{\mathcal{V}_{45}} \\ 0 & 0 & 0 & \frac{h^3}{12}\boldsymbol{\mathcal{V}_{45}} & \frac{h^3}{12}\boldsymbol{\mathcal{V}_{55}} \end{bmatrix} \boldsymbol{B} \tag{3}$$

The essential boundary conditions for the clamped (C) and simply supported (S) edges are applied using the projection matrices. The system mass and stiffness matrices after imposing the boundary conditions can be obtained as $\mathbb{M} = \boldsymbol{P}^{\mathrm{T}}\, \boldsymbol{M}\, \boldsymbol{P}$ and $\mathbb{K} = \boldsymbol{P}^{\mathrm{T}}\, \boldsymbol{K}\, \boldsymbol{P}$, respectively. Here, $\boldsymbol{P}$ is the projection matrix. The laminate natural frequencies ω_n and the corresponding mode shapes ($\boldsymbol{u}$) can be calculated by solving the eigenvalue problem $(\mathbb{K} - {\omega_n}^2 \mathbb{M})\boldsymbol{u} = \boldsymbol{0}$.

2.2. Optimization of lamination parameters

We used two different approaches to optimize the laminate stiffness. First, LPs at each sampling point are treated as design variables. This approach, which is here named global lamination parameter optimization method (GLPM), results in a total number of design variables: $2 \times N_x \times N_y$. Second, to decrease the number of design variables, we introduced several master points on the structure to calculate the LP distribution based on the distance between any location and master points. Here, we used three sub-techniques: (i) LP interpolation method (LPIM), (ii) LP extrapolation method (LPEM), and (iii) relaxed LP interpolation method (RLPIM). The GLPM generally provides higher performance since LPs can be changed freely within Miki's diagram; however, it generates sharp LP variations. On the other hand, the distance-based methods achieve smoother LP distributions by constraining the domain by volumetric ratio (V_r) curves defined as follows:

$$V_1 = (2V_r - 1)\sqrt{\left((V_3 + 1)/2\right)} \tag{4}$$

Distance-based techniques involve defining design variables such as the coordinates of master points $(\boldsymbol{x_m}, \boldsymbol{y_m})$, associated LP values $(\boldsymbol{V_{3m}})$, and volumetric ratios $(\boldsymbol{V_r})$. The primary distinction between these methods stems from the constraints imposed on these design variables and the $\boldsymbol{V_r}$ curves [11]. The total number of design variables is $\boldsymbol{3m+1}$ for LPIM/LPEM and $\boldsymbol{4m}$ for RLPIM, where $\boldsymbol{m}$ represents the number of master points that is set to 2 in the present study.

2.3. Fiber path retrieval

Initially, fiber angles are determined at each sampling point using trigonometric relations between LPs. As a result of the Gauss-Lobatto sampling, a nonuniform distribution of fiber angles with a dense concentration at the boundaries is obtained. Thus, the optimal angle distribution is interpolated to create a uniform field over the domain. The angles are then transformed into smooth and manufacturable fiber paths. Two methodologies are employed for this purpose: the streamline and equidistant path planning. In the former approach, a manufacturing constraint (denoted as α) is applied to ensure the continuity and smoothness of the fiber paths [10,15]:

$$\left[\boldsymbol{\mathcal{V}} + \alpha\left(\boldsymbol{Q_x}^T \boldsymbol{\mathcal{V}}\, \boldsymbol{Q_x} + \boldsymbol{Q_x}^T \boldsymbol{\mathcal{V}}\, \boldsymbol{Q_x}\right)\right]\boldsymbol{\theta'} = \boldsymbol{\mathcal{V}\theta} \tag{5}$$

Here, θ and θ' represent the fiber angles obtained after the interpolation and application of the α constraint, respectively. In the latter approach, we use a clustering method to divide the in-plane domain into regions with similar fiber angles, and we subsequently apply a continuous path planning approach to obtain a VS laminate composed of CS or VS [16].

3. Fabrication and experimental setup

Symmetric and balanced VS laminates composed of 8 and 24 layers were fabricated using AFP based on the obtained fiber path distributions. In the AFP, we used OM12LT slit tape, and the fabricated panels were cured around 115-125 ℃ in autoclaving process. To validate the optimized fundamental frequencies, modal tests were performed on fabricated laminates using the experimental setup depicted in Fig. 2. As shown in the figure, the panel was excited using an impact hammer, and the response of the system was measured using an accelerometer. Finally, the identified fundamental frequencies from the measured frequency response functions were compared to the computational results.

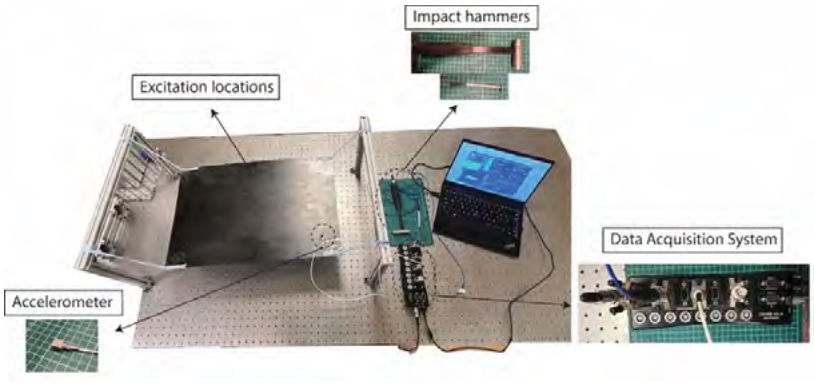


Figure 2. The experimental setup used for modal testing.

4. Results and discussion

We performed several case studies to compare different optimization approaches and validate the accuracy of the modeling technique. Prior to those investigations, a convergence analysis was performed, and the required polynomial numbers $(N_x \times N_y)$ were found as 13×13 and 13×11 for square and rectangular panels, respectively.

4.1. Validation of modeling framework

We investigated square $(L_x/L_y = 1.0)$ and rectangular $(L_x/L_y = 1.5)$ VS flat panels with fully clamped (CCCC) and fully simply supported (SSSS) boundary conditions, respectively. The thickness ratio is set as $h/L_y = 0.01$ for both panels. The material properties used in this section are $E_{11}/E_{22} = 25$, $G_{12}/E_{22} = 0.5$, $G_{23}/E_{22} = 0.2$, and $\nu_{12} = 0.25$ [17]. For each case, the laminates were optimized, and the corresponding first three non-dimensional natural frequencies were compared with the results from the FEA and literature (see Table 1). The optimal LP distributions are depicted in Fig. 3.

Table 1. The first three non-dimensional natural frequencies of fully clamped (CCCC) square $(L_x/L_y = 1.0)$ and simply supported (SSSS) rectangular $(L_x/L_y = 1.5)$ flat VS laminates with the thickness ratio of $h/L_y = 0.01$.

Method	CCCC, $L_x/L_y = 1$			SSSS, $L_x/L_y = 1.5$		
	$\overline{\omega_1}$	$\overline{\omega_2}$	$\overline{\omega_3}$	$\overline{\omega_1}$	$\overline{\omega_2}$	$\overline{\omega_3}$
LPIM	35.25	51.79	78.19	16.04	22.77	33.13
FEA	35.16	51.77	78.33	15.99	22.85	33.27
LPEM	37.13	64.45	74.09	16.46	20.86	30.53
FEA	36.97	64.22	74.55	16.43	21.25	30.94
RLPIM	40.08	74.57	75.73	16.44	21.08	30.78
FEA	39.82	74.65	75.93	16.42	21.46	31.20
GLPM	42.54	70.44	70.45	16.52	21.61	32.20
FEA	41.94	71.26	71.27	16.44	21.97	32.31
Ref. [18]	42.70	73.00	73.00	-	-	-

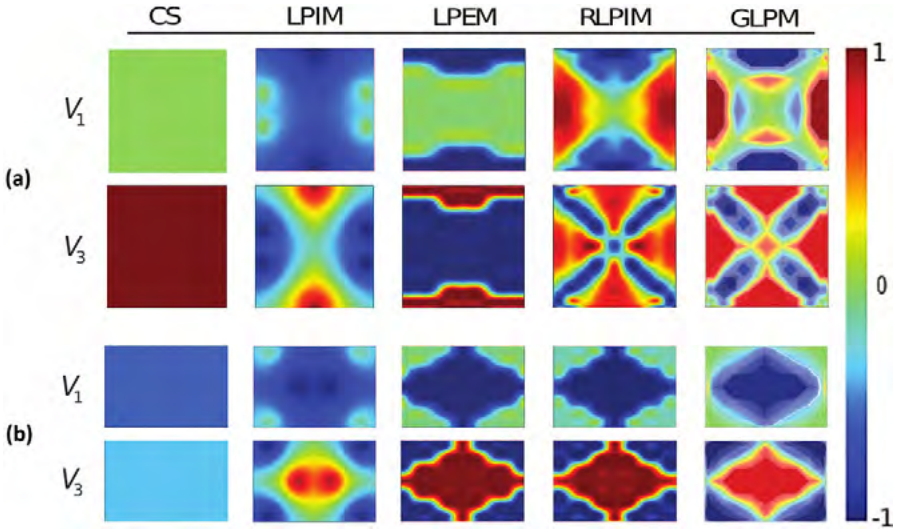


Figure 3. Optimal LP distributions for the (a) fully clamped square $(L_x/L_y = 1.0)$ and (b) simply supported rectangular $(L_x/L_y = 1.5)$ panels.

The analyses revealed a close agreement between the results calculated through the developed framework and FEA as well as those documented in the literature. The GLPM method enabled the highest improvements levels, which are 28.4% and 9.8% for square and rectangular panels, respectively. Although distance-based techniques yielded lower frequency values, the optimal solutions were found much faster due to the reduced design variables. Those methods also provide smoother LP distributions since they impose additional constraints on the design space.

4.2. Fabrication

For the fabrication of CS and VS flat panels, the panel geometry was set to $L_x = 0.6$ m, $L_y = 0.4$ m, and $h = 0.0013$ m (corresponds to 8 layers) or $h = 0.0038$ m (corresponds to 24 layers). Prior to design and experimental studies, material characterization tests on the composite material were conducted, and the material properties were obtained as $E_{11} = 131.34$ GPa, $E_{22} = 8.04$ GPa, $G_{12} = 3.66$ GPa, $G_{23} = 1.46$ GPa, $\nu = 0.265$, and $\rho = 1450$ kg/m^3. Then, optimal designs for the unconstrained panels were determined and compared to optimal CS laminates (see Table 2).

Table 2. Optimal fundamental frequencies (Hz) of unconstrained CS and VS flat laminates with dimensions of $L_x = 0.6$ m and $L_y = 0.4$ m.

Method	$h = 0.0013$ m		$h = 0.0039$ m	
	ω_1	Diff. (%)	ω_1	Diff. (%)
CS	23.10	-	65.35	-
LPIM	23.31	0.91	65.98	0.96
LPEM	23.29	0.82	65.86	0.93
RLPIM	23.56	1.99	67.09	2.66
GLPM	23.80	3.03	68.37	4.62

Although free (unconstrained) laminates lead to lower performance improvements compared to CCCC and SSSS panels, the main motivation behind selecting this boundary condition was its convenience for the modal testing. The computed optimal LP distributions (see Fig. 1c) were transformed into discrete fiber angles (see Fig. 1d). These angles were then converted into curvilinear fiber paths using streamline method and path planning technique based on clustering (see Figs. 1e and f, respectively). Note that the path planning approach involves segmentation of the panel into four clusters comprising either straight fibers (CS clusters) or curvilinear fibers (VS clusters) as depicted in Fig. 1f (i) and (ii), respectively.

Following the design procedure, multiple symmetric and balanced laminates were manufactured. Initially, 24-layered plates featuring two independent layers ($[(\pm\theta_1)_3, (\pm\theta_2)_3]_s$) were fabricated using a streamlined method. Figure 4 shows (a) a CS design together with the (b) first and (c) final layers of an equally thick VS laminate. For the CS case, the fiber angles were determined as $\pm 18^\circ$ and $\pm 48^\circ$. The first VS layer demonstrates gaps, overlaps, and wrinkling occurring due to the fiber curvatures; while the complete VS plate reveals accumulated overlaps that thicken the structure and affect its behavior.

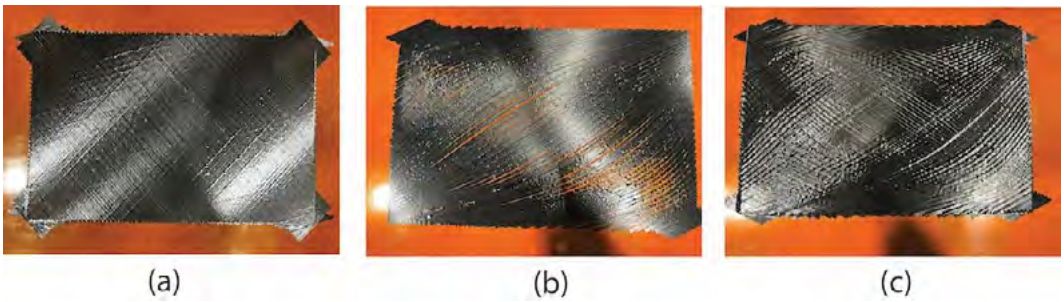


Figure 4. Fabricated 24-layered composite laminates with dimensions $L_x = 0.6$ m, $L_y = 0.4$ m and $h = 0.0039$ m: (a) CS, (b) VS-streamline - First layer, and (c) VS-streamline - Last layer.

To overcome the mentioned fabrication problems, the designs based on the clustering and equidistant path planning approach were used in the second case to manufacture an 8-layered VS laminate with the layup $[\pm\theta_1, \pm\theta_2]_s$ (see Fig. 5). Again, an equally thick CS laminate with the optimal fiber angles of $\pm 18^\circ$ and $\pm 48^\circ$ was also fabricated. As seen in the figure, this method eliminates the gaps and overlaps between fiber paths within the cluster domain and effectively addresses curvature constraints. Yet,

discontinuities at cluster boundaries potentially present other manufacturing challenges that need to be investigated.



Figure 5. Fabricated 8-layered composite laminates with dimensions $L_x = 0.6$ m, $L_y = 0.4$ m and $h = 0.0013$ m: (a) CS, (b) VS-streamline - First layer, and (c) VS-streamline - Last layer.

4.3. Modal tests

From the initial optimization step to experimental analysis, the results obtained throughout the entire process for the 8-layer laminate having two independent fiber angles ($[\pm\theta_1, \pm\theta_2]_s$) are summarized in Table 3. For each design, the fundamental frequency values obtained via five different approaches were calculated and compared with those of the initial design. The first column shows the optimization results obtained by optimizing LPs to maximize the fundamental frequency. In the second column, the values after retrieving fiber angles at sampling points are provided. In the third column, the frequencies obtained considering the full constitutive matrix (i.e., both in-plane ($V^A_{1,2,3,4}$) and bending ($V^D_{1,2,3,4}$) LPs) in stiffness formulation are given. The fourth column contains the FEA results obtained using COMSOL with the full constitutive matrix for validation purposes. The last column shows the fundamental frequencies obtained through modal testing.

Table 3. Comparison of fundamental frequencies (Hz) of simulated and fabricated laminates.

	2 LP		8 LP		
	Opt. ($V_{1,3}$)	Fiber retrieval	($V^A_{1,2,3,4}$, $V^D_{1,2,3,4}$)	FEA	Exp.
CS	23.10	22.78	18.07	18.06	16.00
VS - CS clusters	23.80	22.88	21.46	21.49	17.20
VS - VS clusters	23.80	22.78	21.53	21.51	16.80

The conversion of the obtained LPs into straight and curved fiber distributions evidently leads to a decrease in the maximum fundamental frequency for both CS and VS laminates. However, when 8 LPs are used, the CS plate exhibits a significant decrease in dynamic performance with respect to the VS case (comparing the results for 2 and 8 LPs in Table 3) because of the additional bending stiffness terms. The primary reason behind this drop is expressing the obtained optimum LP distribution with only two independent layers (using three independent layers for that CS case leads to a stacking sequence of $[\pm 41^\circ/\pm 2^\circ/\pm 48^\circ]$ and the fundamental frequency value of 21.73).

5. Conclusions

This study demonstrates a multi-step design framework for optimizing eigenfrequencies of variable stiffness laminates. The composite stiffness properties are expressed in terms of lamination parameters. The governing equations are solved using a meshless modeling approach based on Chebyshev polynomials and FSDT kinematic relations. Different design techniques are investigated to optimize lamination parameter distributions. Actual fiber paths are determined using streamline or continuous equidistant path planning methods.

The presented design approach was used to maximize the fundamental frequency of the variable stiffness laminates. The modeling accuracy was validated by comparing the results to those obtained via FEA and available in the literature. Furthermore, for a selected case, different laminates were fabricated using AFP for modal testing. The 8-layered VS laminates with constant and variable stiffness clusters yielded 7.5% and 5% performance improvements over CS designs, respectively. Experimental investigations also demonstrated that dynamic performance of CS plates is lower than VS plates.

Acknowledgements
This work was supported by the Scientific and Technological Research Council of Turkey (TUBITAK) under Grant No. 120M598 (PI: Bekir Bediz).

References
[1] Nikbakt S, Kamarian S, Shakeri M. A review on optimization of composite structures Part I : Laminated composites. Composite Structures 2018;195:158–85.
[2] Ghiasi H, Fayazbakhsh K, Pasini D, Lessard L. Optimum stacking sequence design of composite materials Part II: Variable stiffness design. Composite Structures 2010;93:1–13.
[3] Gürdal Z, Olmedo R. In-plane response of laminates with spatially varying fiber orientations: Variable stiffness concept. AIAA Journal 1993;31:751–8.
[4] Setoodeh S, Abdalla MM, IJsselmuiden ST, Gürdal Z. Design of variable-stiffness composite panels for maximum buckling load. Composite Structures 2009;87:109–17.
[5] Serhat G, Basdogan I. Lamination parameter interpolation method for design of manufacturable variable-stiffness composite panels. AIAA Journal 2019;57:3052–65.
[6] Serhat G, Bediz B, Basdogan I. Unifying lamination parameters with spectral-Tchebychev method for variable-stiffness composite plate design. Composite Structures 2020;242:112183.
[7] Serhat G, Anamagh MR, Bediz B, Basdogan I. Dynamic analysis of doubly curved composite panels using lamination parameters and spectral-Tchebychev method. Computers and Structures 2020;239:106294.
[8] Serhat G. Design of circular composite cylinders for optimal natural frequencies. Materials 2021;14:3203.
[9] Shirinzadeh B, Cassidy G, Oetomo D, Alici G, Ang MH. Trajectory generation for open-contoured structures in robotic fibre placement. Robotics and Computer-Integrated Manufacturing 2007;23:380–94.
[10] Demir E, Yousefi-louyeh P, Yildiz M. Design of variable stiffness composite structures using lamination parameters with fiber steering constraint. Composites Part B 2019;165:733–46.
[11] Khandar Shahabad P, Rafiei Anamagh M, Serhat G, Basdogan I, Bediz B. Advanced lamination parameter interpolation and extrapolation methods for designing manufacturable variable stiffness laminates. Composite Structures 2023;326:117608.
[12] Sheikhi M, Rafiei Anamagh M, Bediz B, Tunc LT. Design of manufacturable variable stiffness composite laminates using spectral Chebyshev and normalized cut segmentation methods. Composite Structures 2024;330:117836.
[13] Serhat G, Basdogan I. Multi-objective optimization of composite plates using lamination parameters. Materials and Design 2019;180:107904.
[14] Serhat G. Concurrent lamination and tapering optimization of cantilever composite plates under shear. Materials 2021;14:2285.
[15] Rafiei Anamagh M, Khandar Shahabad P, Serhat G, Basdogan I, Bediz B. Eigenfrequency optimization of variable stiffness manufacturable laminates using spectral Chebyshev approach and lamination parameters. Mechanics of Advanced Materials and Structures 2023.
[16] Tunc LT, Sheikhi M. AFP tool path planning for manufacture of variable stiffness composites. CIRP Annals 2023;72:381–4.
[17] Diaconu CG, Sato M, Sekine H. Buckling characteristics and layup optimization of long laminated composite cylindrical shells subjected to combined loads using lamination parameters. Composite Structures 2002;58:423–33.
[18] Rashed A, Demir E. Design of variable stiffness composites for maximum fundamental frequency considering manufacturing constraints of tow steering. Composite Structures 2022;284:115151.

CHALLENGES IN CHARACTERIZING AND MODELING 3D WOVEN COMPOSITES

Doyoung Kim[1], Hyun Joon Yang[2], Kyeong Mo Kang[3], and Woong-Ryeol Yu[*]

[1,2,3,*]Department of Materials Science and Engineering, Seoul National University, 599 Gwanak-ro, Gwanak-gu, Seoul 151-742, Republic of Korea
Email: rezimia@snu.ac.kr[1], hyunjoon92@snu.ac.kr[2], bbambirra@snu.ac.kr[3], woongryu@snu.ac.kr[*]

Keywords: 3D woven composite, 3D mechanical properties, finite element method, fiber-based continuum analysis, measurement method

Abstract
3D composites provide superior properties in the thickness direction, expanding their application potential across various industries. However, accurately characterizing their full 3D behavior presents several challenges. First, the absence of standardized testing methods for through-thickness properties complicates comprehensive evaluation. Additionally, complex weaving patterns, such as fixed and wrapping warp bundles, require tailored assessment approaches. These bundles enhance the composite along the x axis and z axis during weaving, forming proper layer boundaries and structure. Furthermore, producing test specimens to standard specifications and securing a sufficient number of samples for analysis are also challenging. To address these issues, we developed a detailed mechanical model using fiber based continuum analysis. This model defines the 3D woven structure at each material point within the composite and assigns material properties via a constitutive law. It successfully calculates key properties such as tensile modulus, shear, and delamination strength, and developed a new measurement method for accurately determining the tensile strength in the thickness direction.

1. Introduction

Composite materials have played a pivotal role in advancing material engineering, evolving from 2D laminates to sophisticated 3D composites. These advanced materials are known for their enhanced properties in the thickness direction, offering significant improvements over their 2D counterparts. The unique characteristics of 3D composites make them particularly suited for high-performance applications across a range of industries including aerospace, automotive, and construction.

One of the primary challenges in the deployment of 3D composites lies in the absence of standardized testing methods for accurately assessing through-thickness properties. Traditional testing methods are often inadequate, as they predominantly focus on 2D material characteristics and fail to address the complexities introduced by the third dimension. Additionally, the intricate 3D weaving patterns, exemplified by fixed and wrapping warp bundles, introduce an added layer of complexity. These patterns influence the mechanical behavior of the composite in ways that are not yet fully understood, thus complicating the prediction and analysis of their performance under real-world conditions.

Given these challenges, there is a critical need for tailored testing methodologies that can accurately measure important properties such as tensile modulus and strength in the thickness direction. This need is amplified by the growing demand for composites that can reliably perform under the rigorous conditions faced by the aerospace, automotive, and construction industries. Addressing this gap requires a fresh approach to both testing and modeling of 3D composites.

In recent years, various numerical analysis of 3D woven were performed. Because of their complex structures, research has progressed in various directions. Among these, computational analysis using homogenization methods have been extensively studied. Homogenization techniques have been successful for out-of-plane failure and damage[1]. Various studies have been conducted depending on which parts are homogenized and which are modeled. For modeling, the first part of 3D woven

composite modeling was their geometric modeling[2]. 3D modeling for 3D woven composites was examined[3]. The structure of 3D woven composites significantly influences their properties, and the closer the modeling is to reality, the more accurate the calculations can be. However, there is a need for research which focuses on less modeling when considering the simplicity of computation and cost reduction. so the mechanical properties of 3D composites were predicted with 3D unit cell approach[4]. And also failure analysis has been investigated with unit cell approach[5].

The objective of this research is to develop a detailed mechanical model using fiber-based continuum analysis. Ahn. [6] developed a new numerical model to analyze the mechanical properties of 3D textile composites based on continuum mechanics framework. He assumed that fiber structure can be defined at every point and its properties were evaluated using a layer method, Puck's criterion, and modified ply discount method. Our laboratory can manufacture 3D woven composites with various structures and we have adopted continuum analysis method to predict the elastic property and failure. The goal of our research is to establish measurement method for 3D woven composites through thickness direction and predict the mechanical behavior. User subroutine material code was implemented into ABAQUS software and used in this study.

2. Experimental and results

Carbon fiber yarns (A-38, A-42, DOWAKSA, Turkey) were used, and the tensile strength of each carbon fiber yarn was 3800 MPa and 4200 MPa. 3D woven structures were fabricated using warp, weft, and z-binder yarns of 6K (A-38), 12K (A-42), and 3K (A-38) carbon fibers, respectively.

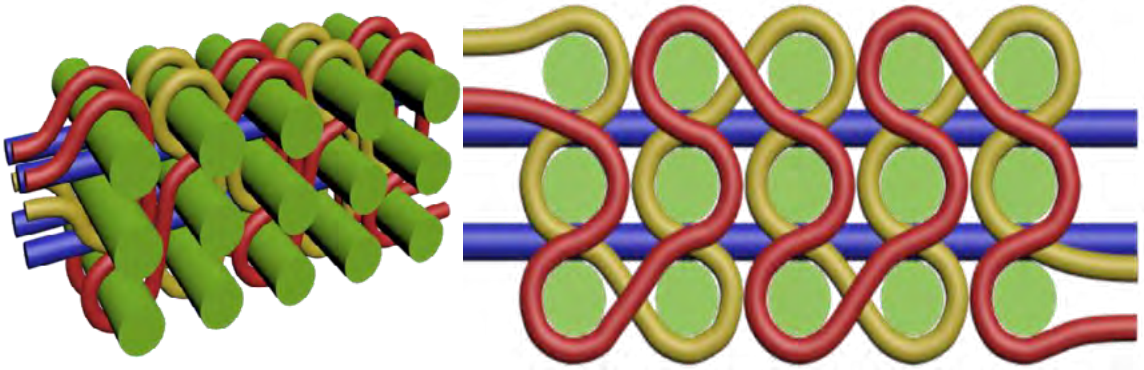


Figure 1. The image of 3D woven fibers and their structures

Figure 1 shows the weaving pattern of 3D woven structure. 2 different warps are weaved wrapping the weft yarns. 3D woven composites were manufactured with this structure using vacuum-assisted resin transfer molding. And the specimens were prepared according to the ASTM D3039 standard for tensile test. Specimen size was 100 X 15 X 2mm^3 and gauge length was 600mm. tensile test was performed at a loading speed of 2mm/min with a 100kN load cell.

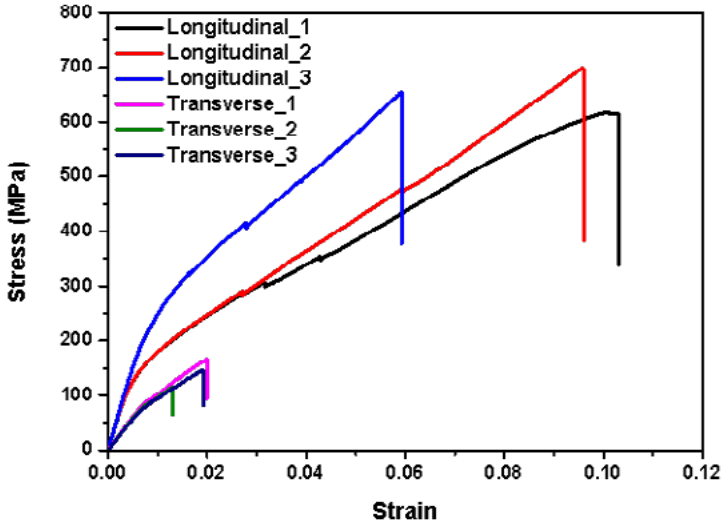


Figure 2. S-S curve of tensile test of 3D woven composite

Figure 2 shows the Stress-Strain curve of 3D woven composite tensile test through longitudinal and transverse directions. Longitudinal tensile strength is 650MPa and transverse tensile strength is 140MPa. Both tensile strength is lower than conventional 2D composites because the volume fraction for each direction is much lower than 2D laminate composites.

To simulate the S-S curve of transverse direction tensile test, UMAT code was implemented to ABAQUS program. In UMAT code, the combination of warp yarns, z-binder yarns, and weft yarns were expressed by the transformation of braiding angle and crimp. The periodic boundary condition was used for the simulation. Eight-node brick elements (C3D8) were used to model the composites. And the implicit solver was used for simulations. The result of simulation was showed in figure 3.

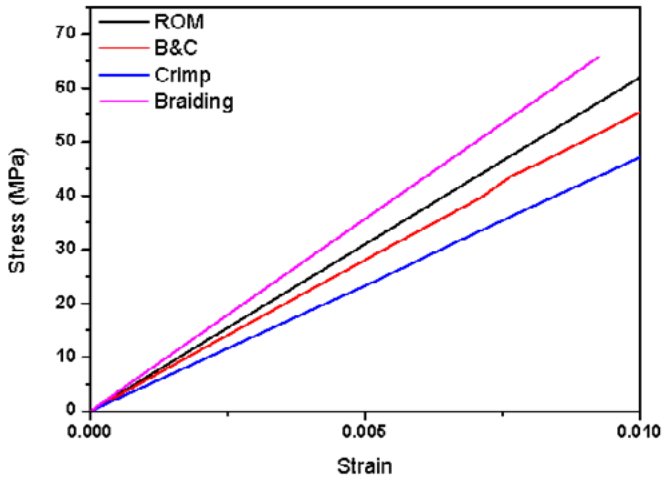


Figure 3. The simulation result of braiding and crimp transformation

The result compares the stress na dstrain curves of rule of mixture, braiding angle transformation, crimp transformation and both transformation. Both transformation works well and total transformation stiffness is lower than the stiffness of rule of mixture. Slight discrepancy between simulation and

experiments is observed. The reason is that model expressed z-binder yarns angle into simple wavelength function. We created a minimal model that contains information on one braiding angle and one crimp angle within a single unit cell. However, increasing the amount of information could lead to more accurate results.

3. Conclusion

A numerical analysis using fiber-based continuum model was developed to predict 3D woven composites mechanical properties. It is useful when the model is considered in macroscale level. The analysis and experiments were compared to achieve validity of developed method. As a result, the simulation and experimental values showed similar results. And through this, the properties in the thickness direction were studied.

4. Acknowledgements

5. References

[1] Hello G, Schneider J, Aboura Z. Numerical Simulations of Woven Composite Materials with Voxel-FE Models. *In: 16th European conference on composite materials*, p. 22–6, June, 2014.
[2] Ansar M, Xinwei W, Chouwei Z. Modeling strategies of 3D woven composites: a review. *Compos Struct,* 93, 1947–63, 2011.
[3] Adanur S, Liao T. 3D modeling of textile composite preforms. *Compos Part B: Eng,* 29, 787–93, 1998.
[4] Hage CE, Younès R, Aboura Z, Benzeggagh ML, Zoaeter M. Analytical and numerical modeling of mechanical properties of orthogonal 3D CFRP. *Compos Sci Technol,* 69,111–6, 2009.
[5] Ivanov DS, Baudry F, Van Den Broucke B, Lomov SV, Xie H, Verpoest I. Failure analysis of triaxial braided composite. *Compos Sci Technol,* 69,1372–80, 2009.
[6] H.C. Ahn, Mechanical analysis of 3D braided and woven composites using fiber-based continuum analysis. *Composite Structures.* 160, 1105-18, 2017.

VIBRATION ANALYSIS OF SYNTACTIC FOAM CORE SANDWICH COMPOSITES USING AN EXACT STATE-VECTOR FORMULATION

Nagendra Gopal Kondagunta[1], R. Sohan[2]

[1]Department of Aerospace Engineering, Indian Institute of Technology Madras, Chennai, India
Email: gopal@smail.iitm.ac.in,
[2]Department of Aerospace Engineering, Indian Institute of Technology Madras, Chennai, India
Email: ae22m016@smail.iitm.ac.in

Keywords: syntactic foam, sandwich composites, state-vector formulation, differential quadrature method

Abstract
Syntactic foams are particulate composites that have hollow glass or ceramic microspheres embedded in a matrix usually thermoset polymers. These closed cell structural foams possess significantly higher specific mechanical properties than traditional foams used in sandwich structures. Sandwich structures with syntactic foam core demonstrate excellent damage tolerance, residual strength and dynamic performance. In this paper, an exact state vector based elasticity formulation is developed for the free vibration response of sandwich panels with syntactic foam core. In this formulation, a state vector is defined to include both displacements and transverse stresses. The state vector can be augmented with other field variables such as temperature and heat flux for modelling multiphysics response. A parametric study of the free vibration response of these panels is presented for two different boundary conditions. The solutions are obtained using a combination of closed-form analytical solutions (SSM) and meshless differential quadrature method (SSDQM). The effect of volume fraction and geometry of the microspheres on the natural frequencies is examined. The combined approach provides exact or highly accurate results for the natural frequencies.

1. Introduction

Sandwich composite plates and shells are extensively used to meet the high performance demands in aerospace, marine and general transport vehicle structures due to their high specific stiffness and strength ratios, ease of manufacturing, and flexibility in design [1]. In recent years, syntactic foams have gained considerable attention as core materials in sandwich structures. Syntactic foams are essentially closed-cell foams and particulate composites obtained by filling a matrix (commonly polymers) with hollow spherical inclusions [2]. These closed-cell structured foams have an excellent combination of mechanical and non-mechanical properties that make them very attractive as core materials for both structural [3, 4]and multifunctional sandwich structures [5]. On a macro scale, syntactic foams behave nearly like isotropic material. Graded foam cores can be also be fabricated by varying the diameter or wall thickness of the dispersed inclusions.

The static and dynamic response of sandwich composites are commonly modelled using equivalent single layer (ESL) plate and shell models that assume apriori displacement field and aim to include the transverse shear effects in different ways. These theories usually underestimate transverse deflections while overestimating the critical buckling loads and natural frequencies, particularly for thick laminates. There are also layer-wise (LW) theories in which the laminate is treated as an assembly of individual layers with an assumed displacement field, and these individual layers are combined by the interlaminar relationships to keep the displacement continuity and stress equilibrium. Special sandwich panel theories (HSAPT, EHSAPT) have also been developed [6, 7] to improve upon the inaccuracies of the conventional ESL theories and capture the localized effects particularly in a flexible core. However,

these theories usually demand a large number of variables in direct proportion to the number of plies, and increase the computing cost [8].

In such a scenario, the three-dimensional elasticity formulation, which doesn't include any apriori assumption on the field variables, plays a crucial role in the accurate modelling and analysis of these structures. They not only serve as benchmark solutions but become necessary in the case of sandwich panels with considerable variation in elastic modulus among the layers, high thickness-to-span ratio, functional gradation in material properties, presence of localized loads, etc.

The state space method (SSM) involves grouping displacements and out-of-plane stresses to create a state vector [9]. In-plane stresses become derived variables that are dependent on the state vector. The key idea is to transform the boundary value problem into an analogous initial value problem in thickness coordinates by using the initial and final values of the state vector obtained from the lateral boundary conditions. While analytical solutions of this exact formulation are restricted to simple boundary conditions, SSM can be easily combined with finite element method (FEM) or differential quadrature method (DQM), etc. to provide highly accurate numerical solutions to various edge boundary conditions.

This paper presents an exact state-space formulation (SSM) for the dynamics of rectangular sandwich composites plates with syntactic foam core and a study of the free vibration for different edge boundary conditions using the hybrid state space differential quadrature method (SSDQM).

2. Exact state space formulation and solution methodology

2.1. State space approach (SSA)

For an orthotropic material, the three-dimensional linear elastic stress-strain relations, in matrix-vector form in the principal cartesian axes is given by the generalized Hooke's law below.

$$\begin{aligned}
&\sigma_i = C_{ij}\varepsilon_j \quad i,j = 1,6 \\
&\sigma_1 = \sigma_{11}, \sigma_2 = \sigma_{22}, \sigma_3 = \sigma_{33}, \sigma_4 = \tau_{23}, \sigma_5 = \tau_{31}, \sigma_6 = \tau_{12} \\
&\varepsilon_1 = \varepsilon_{11}, \varepsilon_2 = \varepsilon_{22}, \varepsilon_3 = \varepsilon_{33}, \varepsilon_4 = \gamma_{23}, \varepsilon_5 = \gamma_{31}, \varepsilon_6 = \gamma_{12}
\end{aligned} \tag{1}$$

The elastic stiffness matrix and the linear strain-displacement relations are given by

$$[C] = \begin{bmatrix} C_{11} & C_{12} & C_{13} & 0 & 0 & 0 \\ C_{12} & C_{22} & C_{23} & 0 & 0 & 0 \\ C_{13} & C_{23} & C_{33} & 0 & 0 & 0 \\ 0 & 0 & 0 & C_{44} & 0 & 0 \\ 0 & 0 & 0 & 0 & C_{55} & 0 \\ 0 & 0 & 0 & 0 & 0 & C_{66} \end{bmatrix} \text{ and } \begin{Bmatrix} \varepsilon_1 = \varepsilon_{11} \\ \varepsilon_2 = \varepsilon_{22} \\ \varepsilon_3 = \varepsilon_{33} \\ \varepsilon_4 = \gamma_{23} \\ \varepsilon_5 = \gamma_{13} \\ \varepsilon_6 = \gamma_{12} \end{Bmatrix} = \begin{Bmatrix} u_{1,1} \\ u_{2,2} \\ u_{3,3} \\ u_{3,2} + u_{2,3} \\ u_{1,3} + u_{3,1} \\ u_{1,2} + u_{2,1} \end{Bmatrix} \tag{2}$$

$$\frac{\partial \sigma_{ji}}{\partial x_j} = \rho \frac{\partial^2 u_i}{\partial t^2} \quad i,j = 1,3. \tag{3}$$

The displacements (u_1, u_2, u_3) and transverse stresses $(\sigma_{33}, \sigma_{13}, \sigma_{23})$ are combined to form a state vector $\boldsymbol{\delta}$. Combining and rearranging the set of Eq. (1) – (3), the state equations are derived in the matrix form as given below.

$$\frac{\partial}{\partial x_3}\{\delta\} = [G]\{\delta\}$$

where the state vector δ and the coefficient matrix G are defined as (4)

$$\delta = \{\sigma_{33} \quad u_1 \quad u_2 \quad u_3 \quad \sigma_{13} \quad \sigma_{23}\}^T \text{ coefficient matrix } [G] = \begin{bmatrix} 0 & A \\ B & 0 \end{bmatrix}$$

$$[A] = \begin{bmatrix} \rho\partial_t^2 & -\partial_{x_1} & -\partial_{x_2} \\ -\partial_{x_1} & \frac{1}{C_{55}} & 0 \\ -\partial_{x_2} & 0 & \frac{1}{C_{44}} \end{bmatrix}, \quad [B] = \begin{bmatrix} \frac{1}{C_{33}} & -\frac{C_{13}}{C_{33}}\partial_{x_1} & -\frac{C_{23}}{C_{33}}\partial_{x_2} \\ -\frac{C_{13}}{C_{33}}\partial_{x_1} & B_{22} & B_{23} \\ -\frac{C_{23}}{C_{33}}\partial_{x_2} & B_{23} & B_{33} \end{bmatrix} \tag{5}$$

where

$$B_{22} = \rho\partial_t^2 - \left(C_{11} - \frac{C_{13}^2}{C_{33}}\right)\partial_{x_1}^2 - C_{66}\partial_{x_2}^2 \quad B_{23} = \left(-C_{66} - C_{12} + \frac{C_{13}C_{23}}{C_{23}}\right)\partial_{x_1 x_2}^2$$
$$B_{33} = \rho\partial_t^2 - C_{66}\partial_{x_1}^2 - \left(C_{22} - \frac{C_{23}^2}{C_{33}}\right)\partial_{x_2}^2 \tag{6}$$

2.2. Analytical solutions for SSM

The above formulation is a system of first order differential equation in the state vector with constant variables. The solution can be written for the state vector as a function of the 'z' coordinate as in Eq. (7)

$$\{\delta(z)\} = e^{[G]z}\{\delta(0)\} = \mathbf{T}(z)\{\delta(0)\}$$
$$\{\delta(0)\} \text{ is initial value of state vector at } z = 0. \tag{7}$$
$$\mathbf{T}(z) \text{ is called the transfer matrix.}$$

For given boundary conditions on the lateral surfaces of a plate [0, h] , state vector can be solved for any location z through the thickness. The in-plane field variables can be computed from the other relations. The formulation can be applied for any type of plate construction, including homogeneous single layer or multilayered and sandwich plates, isotropic, anisotropic and heterogeneous plates. For multilauyered plates, a local transfer matrix is obtained for each layer and need to combined to apply the global surface boundary conditions on the plate. But, analytical solutions of the formulation are limited to few boundary conditions such as simply supported edges.

Consider the free vibrations response of a rectangular plate with in-plane dimensions a, b and thickness h, in the reference coordinate system (x,y,z) simply supported on all four edges. A double series expansion of the state variables can be assumed for the state vector as given below with the coefficients being unknown functions of the thickness coordinate.

$$\begin{Bmatrix} \sigma_z \\ u \\ v \\ w \\ \tau_{xz} \\ \tau_{yz} \end{Bmatrix} = \sum_{m=0}^{\infty}\sum_{n=0}^{\infty} \begin{Bmatrix} Z_{mn}(z)\sin\left(\frac{m\pi x}{a}\right)\sin\left(\frac{n\pi y}{b}\right) \\ U_{mn}(z)\cos\left(\frac{m\pi x}{a}\right)\sin\left(\frac{n\pi y}{b}\right) \\ V_{mn}(z)\sin\left(\frac{m\pi x}{a}\right)\cos\left(\frac{n\pi y}{b}\right) \\ W_{mn}(z)\sin\left(\frac{m\pi x}{a}\right)\sin\left(\frac{n\pi y}{b}\right) \\ X_{mn}(z)\cos\left(\frac{m\pi x}{a}\right)\sin\left(\frac{n\pi y}{b}\right) \\ Y_{mn}(z)\sin\left(\frac{m\pi x}{a}\right)\cos\left(\frac{n\pi y}{b}\right) \end{Bmatrix} e^{i\omega_{mn}t} \tag{8}$$

The above expansion can be substituted in Eq. 4 to get the matrix equation

$$\frac{\partial}{\partial z}M = \bar{\mathbf{T}}(z)M,\ \bar{\mathbf{T}}(z) = \begin{bmatrix} 0 & \bar{A} \\ \bar{B} & 0 \end{bmatrix}$$
$$M(z) = \{Z_{mn} \quad U_{mn} \quad V_{mn} \quad W_{mn} \quad X_{mn} \quad Y_{mn}\}^T \tag{9}$$

$$\left[\bar{A}\right] = \begin{bmatrix} -\rho\omega_{mn}^2 & \left(\frac{m\pi}{a}\right) & \left(\frac{n\pi}{b}\right) \\ -\left(\frac{m\pi}{a}\right) & \frac{1}{C_{55}} & 0 \\ -\left(\frac{n\pi}{b}\right) & 0 & \frac{1}{C_{44}} \end{bmatrix}, \left[\bar{B}\right] = \begin{bmatrix} \frac{1}{C_{33}} & \frac{C_{13}}{C_{33}}\left(\frac{m\pi}{a}\right) & \frac{C_{23}}{C_{33}}\left(\frac{n\pi}{b}\right) \\ \frac{C_{13}}{C_{33}}\left(\frac{m\pi}{a}\right) & \bar{B}_{22} & \bar{B}_{23} \\ \frac{C_{23}}{C_{33}}\left(\frac{n\pi}{b}\right) & \bar{B}_{23} & \bar{B}_{33} \end{bmatrix} \tag{10}$$

$$\bar{B}_{22} = \rho\omega_{mn}^2 + \left(C_{11} - \frac{C_{13}^2}{C_{33}}\right)\left(\frac{m\pi}{a}\right)^2 + C_{66}\left(\frac{n\pi}{b}\right)^2$$
$$\bar{B}_{23} = -\left(-C_{66} - C_{12} + \frac{C_{13}C_{23}}{C_{23}}\right)\left(\frac{m\pi}{a}\right)\left(\frac{n\pi}{b}\right) \tag{11}$$
$$\bar{B}_{33} = \rho\omega_{mn}^2 + C_{66}\left(\frac{m\pi}{a}\right)^2 + \left(C_{22} - \frac{C_{23}^2}{C_{33}}\right)\left(\frac{n\pi}{b}\right)^2$$

The above equation can be used to get the global equation relating the top and bottom surfaces of a single layer plate. For multilayered plates, the conventional transfer matrix method, (CTMM) [10] uses the interlayer continuity and equilibrium conditions on the state vector elements to obtain the global transfer matrix relating the state vector at the top and bottom faces through multiplication of the transfer matrices for the individual layers. Enforcing the traction free load conditions on the plate lateral faces gives the non-trivial solution for the free vibration problem. For a plate comprised of p layers, through matrix multiplication of local transfer matrices, we get as in Eq. 12

$$\delta_1^{(p)} = \mathbf{T}\delta_0^{(1)}, \quad \mathbf{T} = \mathbf{T}_p \mathbf{T}_{p-1} \ldots \mathbf{T}_2 \mathbf{T}_1$$
$$\det \mathbf{T} = 0 \tag{12}$$

An alternative has been used in this work to overcome the numerical instabilities that may be encountered with CTTM for certain configurations and also in SSDQM. In this approach, all transfer relations between the state vectors at the upper and lower surfaces of the individual layers are assembled rather than translated into a global relation in equation through matrix multiplications.

2. 3 Semi-analytical solutions using SSDQM

The DQM transforms a differential equation defined at all points in a domain into an analogous set of algebraic equation by expressing at each grid point the operator value of a function with respect to a coordinate direction at any discrete point as the weighted linear sum of the function's values at all discrete points chosen in that direction.

Consider a two-dimensional rectangular domain, where a solution to a differential equation is needed in terms of the function $f(x,y)$. Any arbitrary order partial derivative of $f(x,y)$ with respect to coordinates x and y at any grid point (x_i, y_i) is given as:

$$\frac{\partial^p}{\partial x^p} f(x_i, y_j) = \sum_{k=1}^{N_x} X_{ik}^{(p)} f(x_k, y_j), \quad \frac{\partial^q}{\partial y^q} f(x_i, y_j) = \sum_{k=1}^{N_y} Y_{jk}^{(q)} f(x_i, y_k)$$
$$\frac{\partial^{p+q}}{\partial x^p \partial y^q} f(x_i, y_j) = \sum_{k=1}^{N_x} X_{ik}^{(p)} \sum_{r=1}^{N_y} Y_{jr}^{(q)} f(x_k, y_r) \tag{13}$$

N_x and N_y are the total number of sampling points in the grid along the x- and y- directions respectively.

The accuracy of the DQM is sensitive to the distribution of the grid points amd the weighting coefficients. A non-uniform grid distribution is found to give more accurate results when compared to uniform grids with the same number of grid points The most commonly used are the Chebyshev–Gauss–Lobatto grid points. The procedure to obtain the weight coefficients for first-order derivatives and the recurrence relations for higher order derivatives are outlined in Shu [10]. The use of DQM in the original state space equations yields different state equations for each type of edge boundary conditions [11].

To apply the SSDQM for the sandwich plates, while the SSM is applied in the thickness direction, at each thickness location the DQM is applied in the corresponding lateral surface. Depending on specific plate edge boundary conditions a complete 2D dimensional (x,y) grid or only a 1-D grid along the x- or y- directions may be required for the DQM with a series solution assumed in the other direction. Hence each comnbination of plate boundary conditions yields a different form of the state equation and corresponding transfer matrix.

3. Results and discussion

The formulation was applied for the analysis of the dynamic behaviour of a [0°/90°/core/90°/0°] sandwich plate with syntactic foam core [12]. The face sheets are woven glass-epoxy laminates with elastic properties: $E_1 = E_2 = 21.7$ GPa, $E_3 = 8.5$ GPa, $G_{12} = 3.91$ GPa, $G_{13} = G_{23} = 4.1$ GPa, $\nu_{12} = 0.169$, $\nu_{13} = \nu_{23} = 0.28$, $\boldsymbol{\rho_f} = 1720$ kg/m^3. The syntactic foam core is made of hollow glass inclusions and epoxy resin with $E_m = 2.8$ GPa, $\nu_m = 0.41$, $\rho_m = 1180$ kg/m^3, $E_g = 70.11$ GPa, $\nu_g = 0.23$, $\rho_g = 2600$ kg/m^3. The inclusion radius $R_p = 25$ µm, inclusion wall thickness $t_p = 1$µm, and filler volume percentage $V_f = 60\%$. All the inclusions are of the same size and shape, randomly distributed in the matrix and free of voids. The effective properties of the syntactic foam core were obtained using a homogenization method [2].

3.1 Validation Study

The formulation was implemented in MATLAB™ and validated initially on a syntactic foam core sandwich plate with cross-ply graphite/epoxy laminate facesheet simply supported on all its four edges [12]. The results were compared with those obtained from FEA and the analytical multiple-scale asymptotic expansion method. The fundamental frequency parameter is non-dimensionalized as

$$\bar{\omega} = \omega \frac{a^2}{h} \sqrt{\frac{\rho_f}{E_f}} \tag{14}$$

Table 1. Non-dimensional fundamental frequency with varying (a/h) for $t_c/t_f = 10$

a/h	Present (SSM)	Asym. Method [12]	FEM
10	8.779	8.841	8.780
5	6.780	7.914	6.780

Table 2. Non-dimensional fundamental frequency with varying (t_c/t_f) for $a/h = 10$

t_c/t_f	Present (SSM)	Asym. Method [12]	FEM
5	9.340	10.051	9.341
2	9.397	10.941	9.397

3.2 Effect of volume fraction and wall thickness of microspheres on the natural frequency

The free vibration response of the symmetric square syntactic foam sandwich plate with glass/epoxy cross-ply laminate subjected to two different edge boundary conditions is investigated for $a/h = 20,\ t_c/t_f = 20,\ a = 1.0\ m$. The effect of volume fraction and wall thickness of the microspheres on the fundamental natural frequency of the sandwich plate was obtained for different plate boundary conditions. The SSDQM results obtained with 15 grid points are presented alongside the exact SSM result for the SSSS condition and shown in Tables 3 and 4 respectively.

Table 3. Variation of fundamental frequency (Hz) with V_f

Boundary conditon	Volume fraction of the microspheres (V_f)						
	0.1	0.2	0.3	0.4	0.5	0.6	0.7
SSSS (exact)	122.473	126.473	130.879	135.768	141.242	147.432	154.518
SSSS	122.473	126.473	130.879	135.768	141.242	147.432	154.518
SCSC	182.122	188.160	194.808	202.184	210.440	219.778	230.469

Table 4. Variation of fundamental frequency (Hz) for different values of t_p

Boundary conditon	Wall thickness of the microsphere (V_f)					
	0.5	1	1.5	2	2.5	3
SSSS (Exact)	147.983	147.432	145.979	144.354	142.765	141.280
SSSS	147.983	147.432	145.979	144.354	142.765	141.280
SCSC	218.944	219.778	218.164	215.970	213.697	211.518

It is observed from Table 3 that the natural frequency of the panel increases with the increase in the volume fraction of the inclusions of the syntactic foam as expected. Also, the SCSC panel is the most stiff, while the SSSS panel is the least stiff.

From Table 4, it can be inferred that the natural frequency decreases as the inclusion wall thickness increases. Both the effective stiffness and density of the syntactic foam increase with the wall thickness of the microsphere. However, the density increment dominates the stiffness increment resulting in a drop of fundamental natural frequencies.

3.3 Effect of plate aspect ratio and ratio of core to facesheet thickness on the natural frequency

The effect of varying the aspect ratio of the plate aspect for a given core-to-facesheet thickness ratio on the natural frequency is given in Table 5 below.

Table 5. Variation of fundamental frequency (Hz) with aspect ratio *a*/*h*

Boundary conditon	Thickness ratio (a/h)				
	100	50	25	20	10
SSSS (Exact)	30.046	59.948	74.801	147.432	279.447
SSSS	30.046	59.948	74.801	147.432	279.447
SCSC	46.334	92.019	114.433	219.778	385.770

For a fixed core-facesheet thickness ratio, the fundamental frequency decreases with increasing aspect ratio. The effective stiffness and mass of the panel decrease as the thickness ratio increases. However, the drop in the effective stiffness of the panel outweighs the mass decrement, resulting in a lower fundamental frequency. The SSSS panel has a lower stiffness and thus lower fundamental frequency. On the contrary, the stiffer SCSC panel has a fundamental frequency of almost 1.5 times that of the SSSS panel for a thickness ratio of 100. The same factor is observed even for the thickness ratio of 10.

Table 6. Variation of fundamental frequency (Hz) with h_c/h_h

Boundary conditon	Ratio of the thickness of core and facesheet (h_c/h_f)					
	50	25	20	10	5	2
SSSS (Exact)	119.091	130.118	134.286	147.432	156.913	158.321
SSSS	119.091	130.118	134.286	147.432	156.913	158.321
SCSC	176.163	193.633	200.081	219.778	233.110	234.768

The variation of the natural frequency with $\frac{h_c}{h_f}$ is given in Table 6. The natural frequency decreases with the increase of $\boldsymbol{h_c/h_f}$. As the $\boldsymbol{h_c/h_f}$ ratio increases for a certain plate thickness, the effective stiffness and density of the panel decrease due to the softer material used for the core. A reduction in effective stiffness prevails over the reduction in density, leading to lower frequency. For larger $\boldsymbol{h_c/h_f}$, the facesheets are too thin relative to the core to contribute to the plate's stiffness. Furthermore, the SSSS plate has the lower stiffness when compared to SCSC conditions. The SCSC panel's fundamental frequency is nearly 1.5 times that of the SSSS panel for all $\boldsymbol{h_c/h_f}$ ratios.

4. Conclusions

In the present study, the state space differential quadrature technique formulated from the exact theory of 3D elasticity was successfully applied to model the free vibration analysis of a syntactic foam core sandwich plate with arbitrary edge boundary conditions. The accuracy of the model was demonstrated

by comparing the results of the present method with those obtained with the finite element method and multiple-scale asymptotic method. The method demonstrated a fast convergence using only a few grid points. The influence of varying plate aspect ratio and core-facesheet thickness on the natural frequency is evaluated. More significantly, the effects of the volume fractions and geometry of the microspheres on free vibration analysis were investigated.

References

[1] Birman, V. and Kardomateas, G.A., 2018. Review of current trends in research and applications of sandwich structures. *Composites Part B: Engineering*, *142*, pp.221-240.
[2] Bardella, L. and Genna, F., 2001. On the elastic behavior of syntactic foams. *International Journal of Solids and Structures*, *38*(40-41), pp.7235-7260.
[3] Gupta, N., Zeltmann, S.E., Shunmugasamy, V.C. and Pinisetty, D., 2014. Applications of polymer matrix syntactic foams. *JOM*, 66, pp.245-254.
[4] Antunes, F.V., Ferreira, J.A.M. and Capela, C., 2011. Numerical modelling of the Young's modulus of syntactic foams. *Finite Elements in Analysis and Design*, *47*(2), pp.78-84.
[5] Galvagninin, F., Dongato, A., Fambri, L., Fredi, G., and Pegoretti, A., 2021. Thermophysical properties of multifunctional syntactic foams containing phase change microcapsules for thermal energy storage. *Polymers*, 13(11), 1790.
[6] Frostig, Y., Thomsen, OT., 2004. Higher-order free vibration of sandwich panels with a flexible core. *International Journal of Solids and Structures*, 41(5), pp. 1697-1724.
[7] Phan CN, Frostig, Y. and Kardomateas, G.A., 2012. Analysis of sandwich beams with a compliant core and with in-plane rigidity- extended high-order sandwich panel theory versus elasticity. *Journal of Applied Mechanics*, 79(4): pp. 041001-1-12.
[8] Lü, C.F., Chen, W.Q. and Shao, J., 2008. Semi-analytical three-dimensional elasticity solutions for generally laminated composite plates. *European Journal of Mechanics-A/Solids*, *27*(5), pp.899-917.
[9] Ye, J., 2002. *Laminated composite plates and shells: 3D modelling*. Springer.
[10] Shu 2000 *Differential Quadrature and Its Application in Engineering,* Springer.
[11] Udayakumar, B., Gopal, K., 2019. A modified state space differential quadrature method for free vibration analysis of soft core sandwich panels. *Journal of Sandwich Structures and Materials*, 21(6), pp. 1843-1879
[12] Gopal, K. N. and Asdev, J., 2014. Dynamic response of syntactic foam core sandwich using a multiple scales based asymptotic method, *ECCM16, 16th European Conference on Composite Materials, Seville, Spain*, 22-26 June 2014.

INTEGRATION CONCEPT FOR RECYCLED CARBON FIBER NONWOVENS IN CFRP BOSS STRUCTURES OF PRESSURE VESSELS

Maximilian Korff[1*], Eduardo Szpoganicz[2], Georg Stegschuster[3], Fabian Hübner[4], Holger Ruckdäschel[2] and Tobias Dickhut[1]

[1]Chair of Composite Materials and Engineering Mechanic, Aeronautical Engineering, University of the Bundeswehr Munich, Werner-Heisenberg-Weg 39, 85579 Neubiberg, Germany,
*Corresponding author email: maximilian.korff@unibw.de
[2]Department of Polymer Engineering, University of Bayreuth,
Universitätsstraße 30, 95447 Bayreuth, Germany
[3] Institut für Textiltechnik Augsburg gGmbH, Am Technologiezentrum 5, 86159 Augsburg, Germany
[4] Airbus Central Research and Technology, Willy-Messerschmitt-Str. 1, 82024 Taufkirchen Munich

Abstract
In this study, recycled non-woven carbon fibers were successfully implemented as reinforcing filler material for reinforced material for functional parts in pressure vessels. Using recycled carbon fiber nonwoven efficiently and sustainably allows the reduction of the amount of new fibers used to the necessary minimum per component. Despite the high requirements on the material in carbon fiber reinforced pressure vessels, the fittings (endcaps/bosses) enable possibilities to integrate a significant amount of recycled material without reducing the design or performance capability. The integration of both, recycled and UD materials will be realized through a sandwich-like structure, wherein the recycled material fills the core while the load-bearing fabric layer serves as the outer shell. For this study, a tensile strength of 12.8 MPa in the machine direction and 17.4 MPa in the transverse direction was achieved using the resin transfer moulding (RTM) process for the finite element modelling and compared with the material properties from the vacuum assisted resin infusion (VARI) process.

Keywords: Pressure vessel, CFRP boss, recycling, nonwoven

1. Introduction

Due to the growing use for carbon fibers, the need for possibilities for recycling carbon fibers is increasing [1]. There are various ways of processing recycled carbon fibers into semi-finished products, including the production of nonwovens from carbon fibers using the carding process [2] [3]. In this process, dry offcuts and pyrolyzed carbon fibres are chopped up, combed and laid down to form a thin fibre pile. Afterwards, the pile is duplicated and needled to increase compatibility and stability. One of the challenges associated with recycled carbon fibres is the anisotropic and fluctuating mechanical properties of nonwoven composites [4]. In addition to technical feasibility, finding areas of application for recyclates is also a major challenge for carbon fiber recycling. Because of the rising influence of hydrogen for energy storage, pressure vessels made of CFRP for lightweight transport are becoming more widespread and the demand is increasing.
In the production of CFRP tanks via filament winding [5], bosses made of aluminum are used in state of the art [6]. Considering the lower density of CFRP compared to aluminum [7], transitioning the boss material to CFRP is generally preferred. Moreover it has to be stated that another huge benefit comes from the lower CTE mismatch between CFRP-CFRP over CFRP-aluminum [8].

The tank wall consists mainly of highly stressed CFRP rovings [9], the layer structure of which is adapted to the load for the design.
Due to the fluctuations in the material properties and missing unidirectional alignment of the fibers [10], recycled nonwoven is not usable in the highly stressed tank wall. However, since bosses made of CFRP are feasible [11] and there is the possibility of using recycled fibers in the bosses, as there are areas in the center of the boss with a high volume but decreased load conditions. This paper presents a possible method for integrating recycled carbon fiber nonwoven into pressure vessels, which replaces a portion of the carbon fiber material with nonwoven and allows adjustment of the mechanical properties of the component via wrapped fabric layers.

2. Material and Method

2.1 Material Characterization

For the integration of carbon fiber nonwoven into CFRP boss structure, it is crucial to determine the mechanical properties of the recycled nonwoven material. It must also be determined whether the material properties differ in the machine direction (MD), the production direction during nonwoven production, compared to the cross direction (CD), 90° to the production direction. Therefore, sample plates were produced in vacuum assisted resin transfer molding (RTM) process. After stacking six layers of nonwoven with 100 gsm and similar production direction, the textile preform is infused with resin in in a mould with a pressure of 6 bar.
Then samples are produced according to DIN EN 2561 standard and the sample geometry A, which has a width of 10 ± 0,5 mm and a height of 2 ± 0,2 mm. The GFRP end tabs have a length of 60 mm each.
To also evaluate the potential of non-pressure assisted manufacturing, VARI was used to prepare alternative samples. A comparison of the RTM plate with the sample plate from the VARI process shows a significantly more uneven surface. In addition, vacuum infusion results in an irregular increase in sample thickness, which can be attributed to the expansion of the nonwoven due to internal stresses caused by the production process. This results in the need for external space limitation, particularly regarding the shape quality. These results are also reflected in the fiber volume contents (FVC), which are determined using loss on ignition method. The results of the mechanical tests and the determination of the FVC are shown in Table 1. Due to the thickness ondulations of the infused sample plate, the minimum thickness is used for the calculation of the Young's modulus (E) and the tensile strength (σ), since the samples fail at these points.

Table 1. Results of the tensile and loss ignition tests of CFRP-nonwoven

Specimen Type		E_1 (GPa)	σ_1 (MPa)	FVC (%)
RTM	Machine Direction (MD)	12.8	183	42
	Cross Direction (CD)	17.4	239	
VARI	Machine Direction (MD)	7.6	98	22
	Cross Direction (CD)	13.2	163	

2.2 Boss Concept

In order to integrate recycled carbon fiber nonwoven into CFRP bosses, the boss is divided into two different material areas. on the inside of the boss, carbon fiber nonwoven is placed as the core material (Figure 2). The nonwoven provides a volume filling function, compared to a sandwich structure. Fabric layers are placed around the nonwoven core, which define the desired mechanical properties of the boss by changing the number of layers. The sandwich structure of high-performance continuous fiber-reinforced layers and the recycled, lower-performance layers in between means that fabric layers can be saved and loaded more efficiently compared to a CFRP boss made exclusively from fabric layers.

To validate the concept, a finite element method (FEM) model of the component cross-section is created based on these requirements. Regarding a production in an RTM mold, the fabric layers are placed horizontally to the component boundaries and enclose the nonwoven core. To make the mechanical characteristics of the nonwoven as isotropic as possible for the rotationally symmetrical component, a quasi-isotropic layer structure is selected. Therefore, it is placed in the mold with a layer-structure of (0/90/±45) horizontal to the orientation shown in Figure 1. For the fabric, E_1, E_3 is assumed as 28000 MPa and E_2 = 6000 MPa. A load is applied on the boss analog to the load situation described in [12] by applying inner pressure on the laminate and the boss.

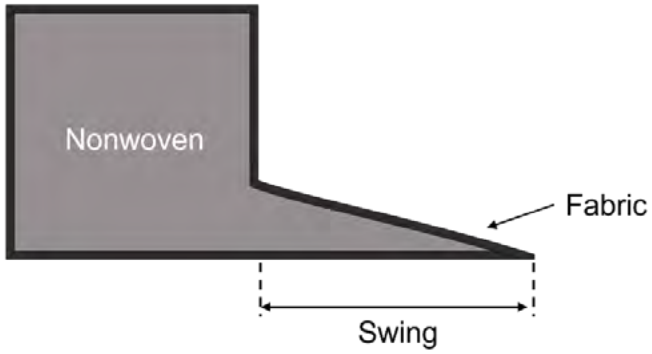


Figure 1. Concept and qualitative calculation of sandwich structure consisting of internal nonwoven with external fabric.

3. Results and Discussion

The qualitative analysis of the FEM model as depicted in Figure 2, reveals that the lower modulus of the fabric results in a greater load bearing capacity of the outer fabric as compared to the inner core of the nonwoven. This is illustrated by the jump between the tensions in the fabric layer and the nonwoven in the core. By changing the layer thickness of the fabric, the mechanical behavior of the boss part can be adjusted to minimize the proportion of fabric to increase the amount of recycled material as much as possible. This is shown by the concentration of high maximum principal stresses in the area of the fabric layers, which generally result from the load situation due to internal pressure on the boss and the CFRP laminate (Figure 2). A clear stress peak can be seen on the upper side of the boss wing. In contrast, the remaining fabric layers apart from the one on the swing arm exhibit moderate to low stresses. The core material exhibits the lowest stresses.

Based on the calculation, it can be concluded to place the fabric exclusively in the area of the boss wing, as this is subject to particularly high loads and, in contrast, the loads are low, especially in the direction of the boss opening. Table 2 shows the layer heights and areal weight of the nonwoven in relation to the different processing forms of the dry fiber layer, the layer in the RTM process and in the infusion process as well as in relation to the fiber volume content from Table 1.

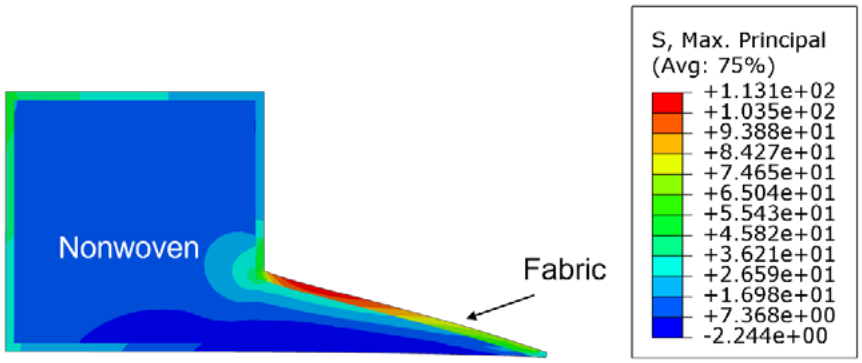


Figure 2. Concept and qualitative calculation of internal nonwoven with external fabric with a load situation as in [12] by applying inner pressure on the laminate and the boss

Due to the elastic behaviour of the dry nonwoven, the number of layers required for a CFRP bump is quite large, which leads to a high degree of compaction of the dry fibres that have to be applied during an infusion process through the RTM mould or a vacuum setup. This leads to a susceptibility to possible displacements of the fibres within the structure, which are not visible before infusion. This results in the risk of fiber-free areas in the component or unevenness in the deposition of overlying fabric layers.

Table 2. Manufacturing data of the nonwoven

Areal weight	100 g/m^2
Layer hight dry	2.8 mm
Layer hight infused	0.72 mm
Layer hight RTM	0.25 mm

Based on these investigations, the CFRP boss with fabric covering is manufactured in an RTM mold and cutted in cross-section and polished for examination (Figure 4). The fine white line in the laminate in the lower area of the boss shows that the interlaminar unevenness of the nonwoven during the process leads to the formation of undulations in the component. However, when looking at the outer contour on which the fabric is placed, there are no significant deviations, so that the main load-bearing fabric layer can be assessed as intact and even. Inserts can be fitted in this area to enable a transition to the piping of the tank. Pull-out tests can be used to design this interface area, which would leads to a determination of the number, size and type of thread inserts.



Figure 4. CFRP bosspart with a nonwoven inner core.

4. Conclusion

This paper demonstrates the feasibility of integrating recycled carbon fibers in the form of nonwovens into pressure tanks without sacrificing structural integrity. This is achieved by incorporating the nonwoven material as a core within the boss and overlaying it with fabric layers of adjustable thickness. These covering layers are mainly relevant for the mechanical strength due to their significantly higher mechanical properties. This means that high-quality semi-finished products made from continuous fibers can be saved efficiently and existing fibers can be used effectively. This contributes to a more ecologically valuable production without hindering design-relevant sizes.
This approach supports environmentally conscious production while maintaining the essential design parameters.
This study has presented first investigation on application of recycled fibres for a major pressure tank component manufactured in RTM and VARI. Regarding production, the significant differences in volume and fiber volume content between the dry single layer and the resin-impregnated layers of the infusion and RTM process present challenges in terms of tool construction and scalability for automation processes, which require further investigation. Overall, the construction of sandwich structures from recycled and continuous fibre-reinforced plastic composites offers great potential for further investigations into the use of recycled carbon fibre nonwoven as a core material for sandwich-like structures for applications such as CFRP bosses.

Acknowledgments

The research is done within the framework of project INTAKT (BLU-2109-0023) [13]. INTAKT is funded by the Bavarian Ministry of Economic Affairs, Regional Development and Energy and guided by Industrieanlagen-Betriebsgesellschaft mbH.

References

[1] Z. Jin, L. Gang, V. Uday and W. Hao, "Past, present and future prospective of global carbon fibre composite developments and applications," *Composites Part B: Engineering,* vol. 250, p. 110463, 2023.

[2] F. Manis, G. Stegschuster, J. Wölling and S. Schlichter, "Influences on Textile and Mechanical Properties of Recycled," *Journal of Conposite Science,* vol. 5, no. 8, p. 209, 2021.

[3] S. Pickering, Z. Liu, T. Turner and K. Wong, "Applications for carbon fibre recovered from composites," in *IOP Conference Series: Materials Science and Engineering*, 2016.

[4] Y. Shao, M. Matsushita, Y. Yang, A. Ohtani, D. Zhao, R. Liu and Y. Yang, "Effect of the carding process and reinforcement method of carbon fiber/polypropylene fiber nonwoven fabrics on the anisotropic mechanical properties of hot-pressed composites," *Fibers and Polymers,* vol. 21, pp. 1115-125, 2020.

[5] A. Blachut, T. Wollmann, M. Panek, M. Vater, J. Kaleta, J. Detyna, S. Hoschützky and M. Gude, "Influence of fiber tension during filament winding on the mechanical properties of composite pressure vessels," *Composite Structures,* vol. 304, p. 116337, 2023.

[6] J. Zhu, Y. Li, W. Cao, Y. Li and Z. Gao, "Failure Analysis of Novel BOSS Structures for Type IV Hydrogen Storage Vessels," *Energies,* vol. 16, no. 10, p. 4005, 2023.

[7] J. Kählert, "Hochbelastete CFK-Bauteile im Maschinenbau—Anforderungen, Lösungen, Mehrwert," *Lightweight Design,* vol. 2, no. 4, pp. 67 - 70, 2009.

[8] S. Andreas, R. Christopf, M. Groß, F. Hübner and T. Dickhut, "Feasibility study of a CFRP boss for application in linerless composite Type V tanks," *ICCM 23 Belfast,* 2023.

[9] J. Ramirez, B. Pedro, D. Halm, J.-C. Grandidier, S. Villalonga and F. Nony, "700 bar type IV high pressure hydrogen storage vessel burst--Simulation and experimental validation," *International Journal of Hydrogen Energy,* vol. 40, no. 38, pp. 13183-13192, 2015.

[10] J. Bachmann, M. Wiedemann and P. Wierach, "Flexural mechanical properties of hybrid epoxy composites reinforced with nonwoven made of flax fibres and recycled carbon fibres," *Aerospace,* vol. 5, no. 4, p. 107, 2018.

[11] D. Whitehead and B. Wilson, "Composite Boss Technology," *NASA,* no. 19980227808, 1998.

[12] G. Park, H. Jang and C. Kim, "Design of composite layer and liner for structure safety of hydrogen pressure vessel (type 4)," *Journal of Mechanical Science and Technology,* vol. 35, no. 8, pp. 3507 - 3517, 2021.

[13] "Project Overview of INTAKT project," [Online]. Available: https://www.unibw.de/mb/forschung/2022/intakt-fluessigwasserstofftankkonzept.

A KINEMATICALLY ENRICHED DIRECTED CONTINUUM DAMAGE MECHANICS APPROACH TO MODEL LOW-VELOCITY IMPACT DAMAGE IN COMPOSITES

Manish Kumar[1], Supratik Mukhopadhyay[1]

[1]Indian Institute of Technology Kanpur, Department of Mechanical Engineering, Kanpur, Uttar Pradesh-208016, India

Email: kumanish@iitk.ac.in

Email: smukh@iitk.ac.in, Web Page: https://sites.google.com/view/supratikmukhopadhyay

Keywords: Composites, Low-velocity impact, Damage analysis, Directed continuum damage mechanics, Finite element analysis

Abstract

This study presents an advanced modelling technique to precisely simulate various damage modes caused by low-velocity impacts on fibre-reinforced composite structures. This method utilises a novel kinematically enriched continuum damage mechanics approach to model semi-discrete intralaminar cracks with solid elements, enabling cracks to grow independently of fibre-oriented ply mesh pattern. That greatly simplifies the meshing effort and eliminates the necessity of tie constraints due to mesh mismatch at ply interfaces. The approach incorporates crack kinematics by distinguishing cracked and uncracked domains at the constitutive level. Inter-ply delamination is modelled using cohesive elements. The methodology is applied to quasi-isotropic laminate. The results demonstrate the capability of the proposed method to simulate solution-dependent multiple discrete cracks and crack-delamination interactions with reduced computational time and complexity, compared to a reference model employing ply-oriented mesh and pre-seeded cracks at predetermined locations.

1. Introduction

Fibre-reinforced polymer (FRP) composites are highly used in aviation and automobile industries due to their combination of lightweight and impressive strength. Despite numerous advantages, composite structures are prone to catastrophic failure due to their innate brittleness, which is a significant concern for aviation and transportation sector where passenger safety is paramount. One common damage event for composite structures is low-velocity impact (LVI). External aircraft components may experience unforeseen impact loads in diverse scenarios, ranging from ground operations to encounters with birds. This type of impact typically affects the interior of the laminate, leaving the exterior seemingly undamaged upon visual inspection. Therefore, it is also referred to as Barely Visible Impact Damage (BVID). Advanced structural health monitoring techniques are commonly required to identify the location and extent of this type of damage experimentally, which increases inspection cost and time. Computational realization of LVI events incorporating accurate damage models provides an alternate route to understand better this type of damage in a quick and inexpensive way.

In a Finite Element (FE) framework, modelling of damage under LVI commonly involves the utilization of continuum damage mechanics (CDM) framework at ply-level and cohesive zone models (CZM) for interface damage. However, the conventional CDM method degrades material stiffness over the entire element volume. This smeared damage approach results in an overall softening response but fails to represent the 'discrete' nature of ply cracks and crack-delamination interaction. Another drawback of the classical CDM is the mesh direction bias [1]. To circumvent these problems, a local fibre direction-oriented mesh is often employed for each ply [2,3,4], which increases meshing efforts significantly and

causes mesh mismatch at ply interfaces. This necessitates the imposition of tie constraints to maintain assembly integrity which significantly increases computational time.

The present work employs a kinematically enriched directed CDM (D-CDM) approach [5,6], to numerically simulate the onset and growth of damage under LVI in a multidirectional laminate. The D-CDM enhances traditional CDM by incorporating an accurate kinematic representation of the sharp crack topology of ply matrix cracks at the constitutive level. Additionally, a crack tracking algorithm is applied to eliminate mesh orientation bias in ply crack growth, reducing meshing efforts. The removal of tie constraints further contributes to a reduction in analysis time. This technique is implemented as a 3D user-defined material in Abaqus/Explicit [7]. The numerical results obtained through this novel method are compared with experimentally obtained damage patterns reported in the literature [2].

The architecture of the paper is organised as follows: Section 2 dictates the material models of intra-ply cracking and interface delamination. In this work, fibre damage is not considered because, under LVI test case matrix crack, delamination and their interaction are reported to be the most dominant failure modes [2]. In Section 3, modelling details of multidirectional laminate are described. Results are discussed in Section 4. Finally, conclusions of this work are presented in Section 5.

2. Constitutive damage law and methodology

In this analysis, accurate modelling of matrix cracks is achieved by considering embedded discontinuity within a continuum medium, drawing inspiration from the work of Nguyen et al. [8] as shown in Figure 1. Interface damage, on the other hand, is captured using a linear traction-separation cohesive formulation outlined by Jiang et al. [9] considering the effect of compression enhancement [2,3]. Comprehensive details regarding these formulations and overall methodology are extensively covered in a recent publication authored by Kumar and Mukhopadhyay [6]. This paper extensively utilizes the present formulation to simulate damage during a quasi-static indentation test. Interested readers are encouraged to consult the referenced article for a more comprehensive understanding of the concepts elucidated herein.

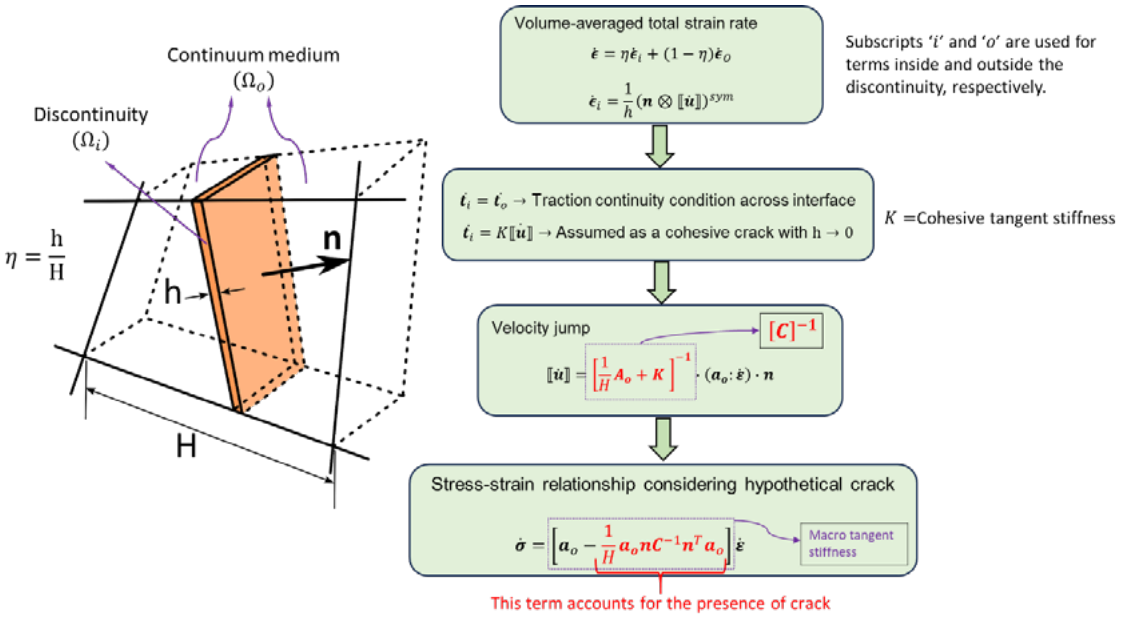


Figure 1. Kinematically enriched CDM formulation.

3. Finite element model

To investigate damage during LVI, the experimental work reported in [2] on the ply-blocked scaled specimen is numerically reproduced here. This particular case is selected for its representative nature, showcasing damage patterns in a multidirectional laminate and highlighting the strong interaction between ply cracks and delamination. The modelling specifics are outlined in Figure 2, with the laminate featuring a stacking sequence of $\left[45_2^\circ/0_2^\circ/90_2^\circ/-45_2^\circ\right]_{2S}$, and material properties are detailed in Table 1. For comparison purposes, two distinct modelling approaches are considered. The first approach employs the presently developed method as discussed in Section 3.1. The second approach follows the methodology presented in [2,3], where ply cracks are explicitly represented by strategically inserting cohesive 'split' elements at predetermined locations within a fiber-oriented mesh.

3.1 D-CDM-based model with uniform ply mesh

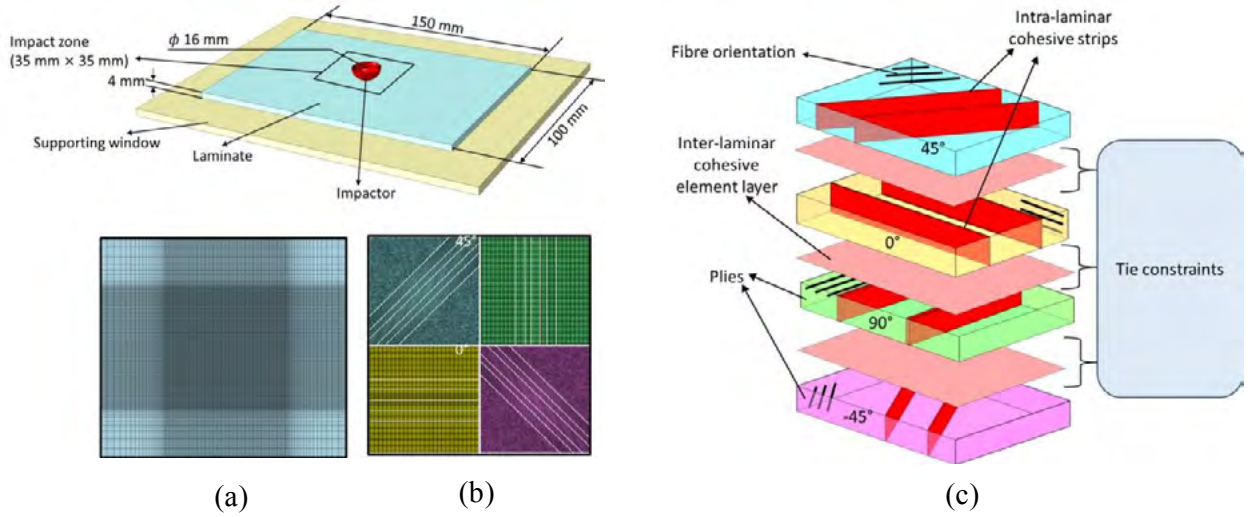
The modelling intricacies of the laminate, depicted in Figure 2(a), are outlined as follows: each doubled-up ply block, with a thickness of 0.25 mm, is represented by a single layer of solid C3D8R finite elements with hourglass control. The interfaces between ply blocks are modelled using cohesive COH3D8 elements, each with a thickness of 0.01 mm. To account for localized deformation, a fine mesh with an in-plane element size of 0.2 mm is implemented within the central region of the laminate where impact is anticipated. Beyond this region, mesh density is relaxed to optimize computation, with maximum element sizes extending up to 3 mm near the laminate periphery. This mesh pattern is kept the same for all the plies and interfaces in the laminate. The total number of elements in the model approximates 1.5 million.

Numerical simulation of LVI adheres to the ASTM drop weight impact standard [10]. The laminate, with in-plane dimensions of 100 mm × 150 mm, is supported by a rigid rectangular plate that has a rectangular opening of in-plane dimensions of 75 mm × 125 mm. A rigid hemispherical impactor of mass 6.35 kg with 16 mm diameter is impacted on laminate. For the low-velocity impact, a low-impact energy of 10 J is provided to the impactor by prescribing the initial velocity of 1.75 m/s. Surface-to-surface contact formulation [7] governs the interaction between the impactor and laminate, employing a penalty contact stiffness of 10^5 N/mm in the normal direction and a sliding contact in the tangential direction, characterized by a friction coefficient of 0.3. The same contact formulation is applied between the supporting window and the laminate, with the window held fixed in all directions.

Preceding impact, a thermal load step is introduced to simulate the laminate's cool-down from the cure temperature (180°C) to room temperature (20°C) and to simulate the generation of residual stresses. This step is crucial as incorporating cure-induced residual stresses enhances solution accuracy. Notably, the impactor is positioned at a distance of 1.88 mm from the upper surface of the laminate, facilitating simultaneous movement of the impactor and cooldown of the laminate.

3.2. Fibre-oriented cohesive split model

In this instance, while the model geometry remains the same, adjustments are made to the meshing to align with conventional practices. Each ply mesh pattern is oriented along the local fibre direction, as illustrated in Figure 2(b). This adaptation inevitably introduces mesh mismatches at ply interfaces which is handled by implementing kinematic tie constraints between solid and cohesive element layers at these interfaces, as depicted in Figure 2(c). Within this model, cohesive elements serve the dual purpose of simulating both delamination and ply matrix cracks. Following the methodology outlined in [2,3], six cohesive strip layers are strategically pre-seeded between solid ply elements at predefined locations within each ply. The cohesive damage formulation, incorporating compression enhancement with a factor of 0.58 as detailed in [2,3,9], is applied to both delamination and matrix cracking. To ensure a fair comparison of computational costs, the total number of elements in this model remains consistent with the D-CDM model. All other modelling parameters remain unchanged from those specified in Section 3.1.



(a) (b) (c)

Figure 2. Finite element model of LVI set-up (above). Mesh details of the impact zone (below): (a) Uniform grid mesh for all plies in the D-CDM model, (b) Fibre-oriented cohesive split model (Splits are shown by white lines) and (c) Exploded view of laminate showing mesh details in the cohesive split model.

Table 1. Elastic material properties of unidirectional IM7/8552 ply material [11,12].

Ply material properties	E_{11} = 161 GPa, E_{22} = E_{33} = 11.4 GPa ν_{12} = ν_{13} = 0.3, ν_{23} = 0.436 G_{12} = G_{13} =5.17 GPa, G_{23} =3.98 GPa Thermal expansion coefficients $\alpha_{11} \approx 0$, $\alpha_{22} = \alpha_{33} = 3\times10^{-5}$ mm/°C Density = 1.6 g/cm^3
Interface material properties	σ_{IMAX} = 60 MPa, σ_{IIMAX} = 90 MPa, G_{IC} = 0.2 N/mm, G_{IIC} = 1.0 N/mm, $K_I = K_{II} = 10^5$ N/mm^3, Power law exponent = 1.0, Compression enhancement factor = 0.58 Density = 1.0 g/cm^3

4. Results

In this section, numerical results of D-CDM models are compared with cohesive split model and experimental [2] results by force-time curve, and damage response of laminate.

4.1. Overall laminate response

Figure 3 presents a comparative analysis of the force-time curves generated by two distinct models alongside experimental data. Evidently, both models closely follow the experimental curve. The critical load value projected by both the D-CDM and cohesive split models is consistent, approximately 4.87 kN, which is marginally lower by 3% compared to experimental value. Notably, both models adeptly capture the magnitude of load drop and each force oscillation. The reason for load drop is discussed in section 4.2. However, there is a slightly prolonged impact duration in the finite element (FE) simulations compared to the experimental setup. Furthermore, it's elucidated that the peak force prediction in FE simulations is higher than the experimental results due to the predicted delamination area being smaller than observed in experiment, as depicted in Figure 4 for both FE simulations. In this context, the cohesive split model gives better results owing to its explicit modelling of matrix cracks. Nonetheless, it's acknowledged that explicit modelling of matrix cracks may not always be feasible.

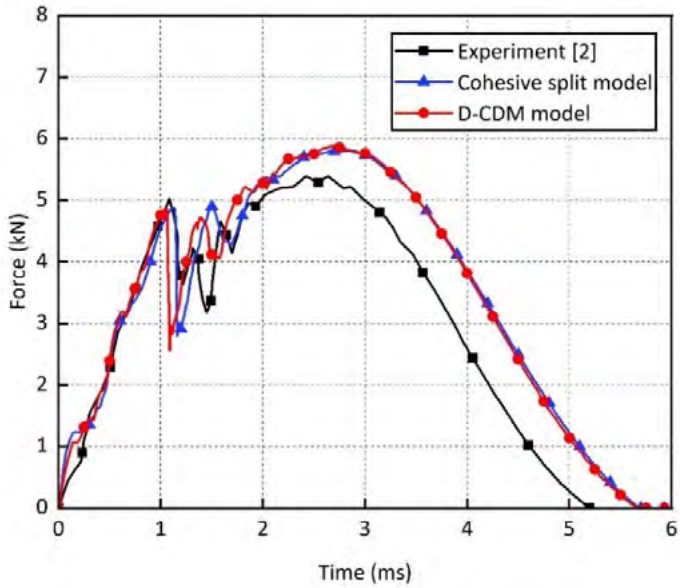


Figure 3. Comparison of force-time curve between experimental and finite element results.

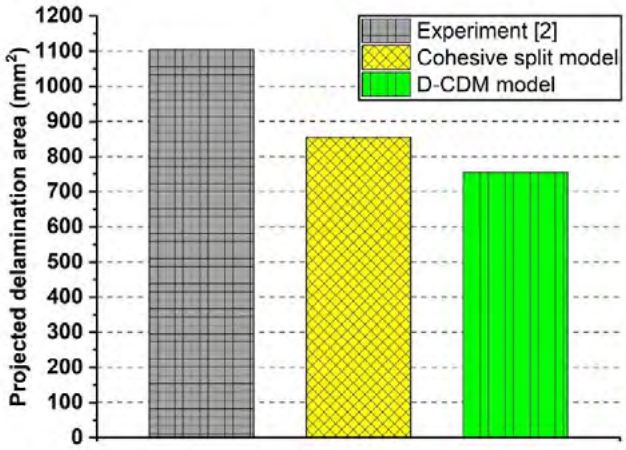


Figure 4. Comparison of projected delamination area between experimental and finite element results.

4.2. Damage response

A comparison of the delamination pattern interface-by-interface comparison throughout the entire thickness of the laminate is undertaken between experiment and two models as illustrated in Figure 5. Figure 5(a), sourced from [2], displays a CT scan where colour-coded interfaces highlight the impact zone with isolated delamination pattern. Notably, beneath the impactor, a region exhibits suppressed delamination due to compressive normal stresses [2,3], effectively inhibiting delamination initiation. Both the D-CDM and cohesive split models successfully capture this 'delamination-free' region, courtesy of the compression enhancement effect integrated into the cohesive law. Additionally, the overall size and shape of the delaminated area closely align between the two models (Figure 5(b) and (c)) and with the experiment. It's elucidated by Sun et al. [2] and Figure 5 that within this laminate, the major load drop results from complex interaction between ply matrix cracks and delamination, as well as large delamination area in 90° ply interface.

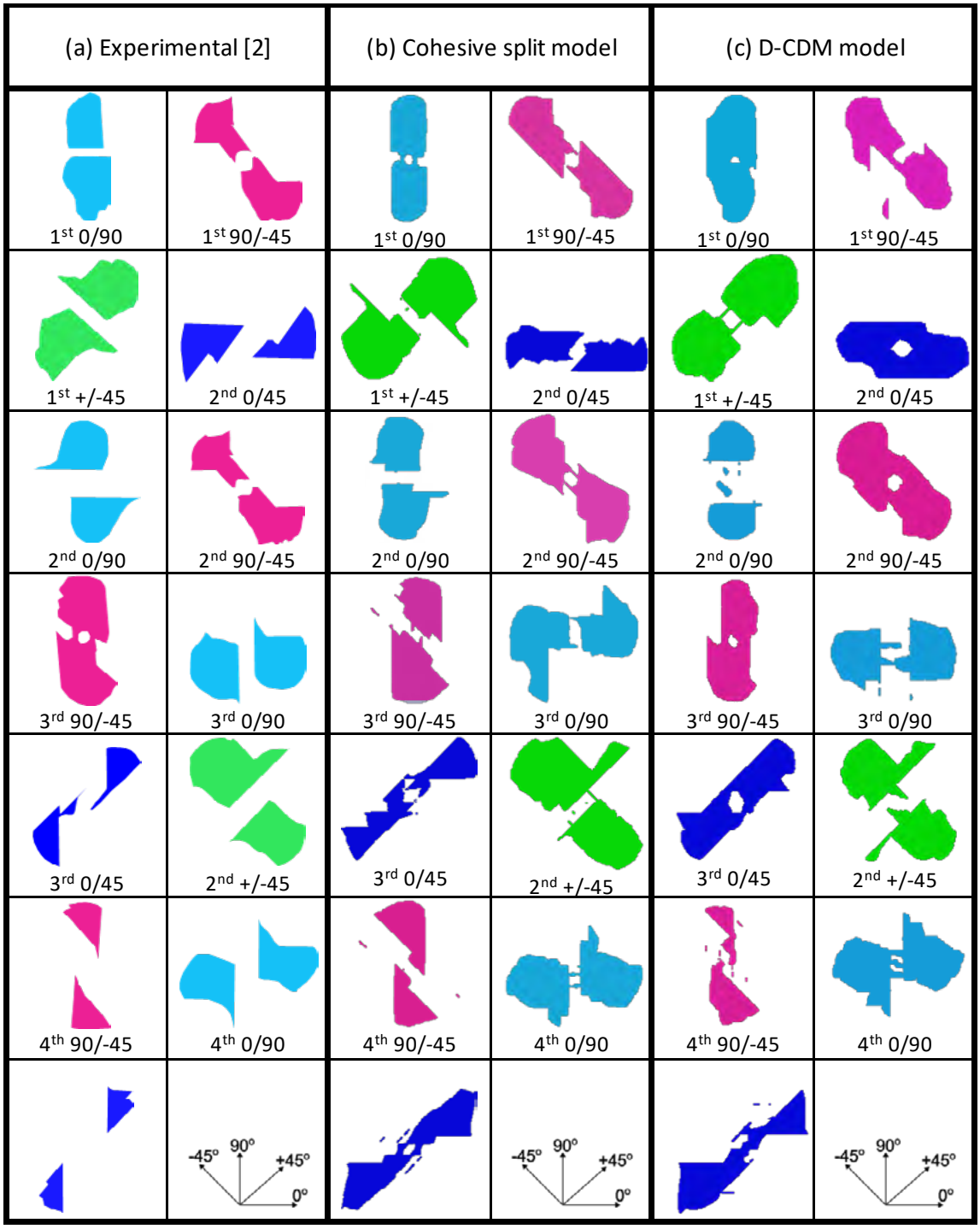


Figure 5. Comparison of individual interface delamination pattern.

In Figure 6, formation of matrix cracks is depicted across all ply interfaces within the laminate. The crack spacing is 3 mm, with a maximum allowance of 6 cracks. A dedicated investigation, detailed in a recent publication [6], utilized a D-CDM-based model. This study aimed to explore the effect of varying parameters such as ply crack spacing and maximum cracks per ply on the overall load-displacement behaviour. Surprisingly, no significant disparities were noted in the global response. Nevertheless, the research highlights the D-CDM method's capacity to accurately simulate densely distributed, parallel 'sharp' crack networks with numerous cracks across a large-scale model, all while maintaining numerical stability which is difficult to achieve with eXtended finite element method (XFEM) type discrete crack models.

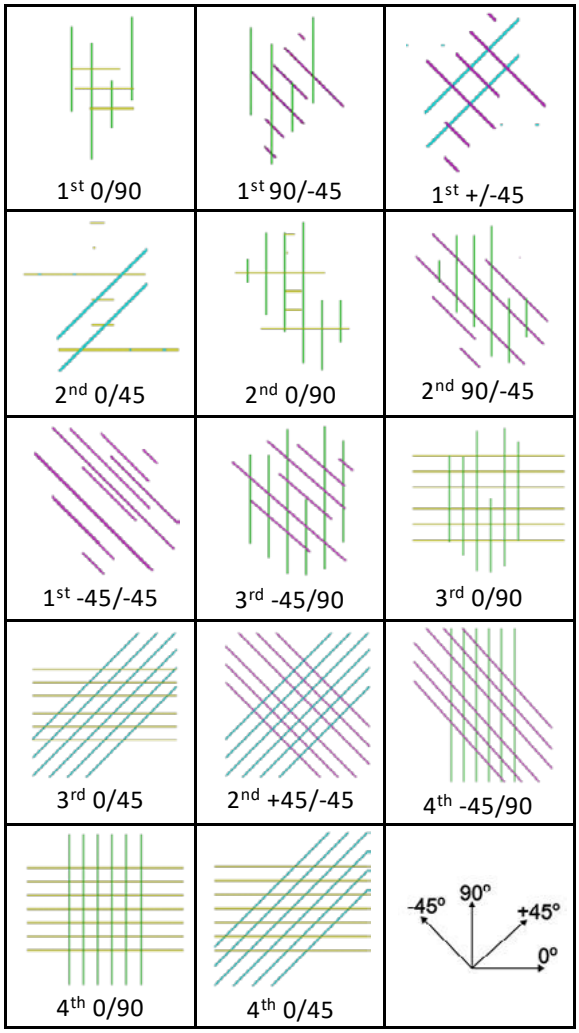


Figure 6. Ply matrix cracks captured by D-CDM model.

4.3. Numerical efficiency

The utilization of D-CDM presents a notable advantage in simplifying the meshing process for the entire laminate, thereby saving time during model construction. Further, D-CDM obviates the need for seeding cohesive elements within the ply mesh at predetermined locations to simulate ply cracks, thus further simplifying meshing procedures and enhancing the versatility of the model. Moreover, the D-CDM approach significantly accelerates the analysis process. All simulations are carried out in a cluster computer running parallelly with 40 cores of Intel® Xeon 5218R CPU with 2.10 GHz base frequency. D-CDM model demonstrates a runtime of approximately 67 hours. In contrast, the reference model, utilizing fiber-oriented mesh and pre-inserted cohesive splits, requires roughly 108 hours under identical conditions. This substantial 38% reduction in computational time with D-CDM model is primarily attributed to the elimination of tie constraints at every ply interface with mismatched ply mesh patterns.

5. Conclusions

In this study, an enhanced modelling approach is introduced aimed at accurately simulating the progressive damage occurring in composites under LVI. D-CDM-based semi-discrete ply crack model can generate and propagate multiple sharp cracks within multidirectional laminates similar to XFEM. This approach maintains the simplicity and reliability of continuum damage mechanics while allowing for the initiation and growth of solution-dependent cracks. One notable advantage of the approach is its "mesh-independent" characteristic. This feature offers two significant benefits to analysts: simplification

of mesh design and elimination of the need for tie constraints or tie-based cohesive contact at mismatched mesh interfaces. This not only simplifies the modelling process but also reduces computational time by approximately 38%, as demonstrated in the case study. Furthermore, this method effectively captures the interaction between intra and interlaminar damage by virtue of the discrete nature of D-CDM matrix cracks. This capability results in a highly accurate prediction of the load history behaviour, enhancing the overall fidelity of the simulation.

Acknowledgements

The first author would like to acknowledge the financial support given by the Ministry of Education, India towards the completion of his PhD work. The second author gratefully acknowledges the support of the Science and Engineering Research Board (SERB), India via the Start-up Research Grant (Grant No. SRG/2019/000488).

References

[1] K. Song, F. A. Leone, and C. A. Rose, "Analysis of progressive damage in cross-ply and quasi-isotropic panels subjected to quasi-static indentation," in *AIAA/ASCE/AHS/ASC Structures, Structural Dynamics, and Materials Conference, 2018*, American Institute of Aeronautics and Astronautics Inc, AIAA, 2018.

[2] X. C. Sun and S. R. Hallett, "Barely visible impact damage in scaled composite laminates: Experiments and numerical simulations," *Int J Impact Eng*, vol. 109, pp. 178–195, Nov. 2017.

[3] X. C. Sun, M. R. Wisnom, and S. R. Hallett, "Interaction of inter- and intralaminar damage in scaled quasi-static indentation tests: Part 2 – Numerical simulation," *Compos Struct*, vol. 136, pp. 727–742, Feb. 2016.

[4] C. S. Lopes, S. Sádaba, C. González, J. Llorca, and P. P. Camanho, "Physically-sound simulation of low-velocity impact on fiber reinforced laminates," *Int J Impact Eng*, vol. 92, pp. 3–17, Jun. 2016.

[5] S. Mukhopadhyay and S. R. Hallett, "A directed continuum damage mechanics method for modelling composite matrix cracks," *Compos Sci Technol*, vol. 176, pp. 1–8, May 2019.

[6] M. Kumar and S. Mukhopadhyay, "Efficient modelling of progressive damage due to quasi-static indentation on multidirectional laminates by a mesh orientation independent kinematically enriched continuum damage model," *Compos Part A Appl Sci Manuf*, vol. 178, p. 108002, Mar. 2024.

[7] Dassault Systèmes Simulia Corp. Abaqus 2016 Documentation. Providence,RI,USA: 2016.

[8] V. P. Nguyen *et al.*, "Modelling complex cracks with finite elements: a kinematically enriched constitutive model," *Int J Fract*, vol. 203, no. 1, pp. 21–39, 2017.

[9] W. G. Jiang, S. R. Hallett, B. G. Green, and M. R. Wisnom, "A concise interface constitutive law for analysis of delamination and splitting in composite materials and its application to scaled notched tensile specimens," *Int J Numer Methods Eng*, vol. 69, no. 9, pp. 1982–1995, Feb. 2007.

[10] ASTM D 7136/D 7136M-05, Standard test method for measuring the damage resistance of a fiber-reinforced polymer matrix composite to a drop-weight impact event. In: Annual book of ASTM standards. West Conshohocken, PA: ASTM International, 2005.

[11] S. R. Hallett, B. G. Green, W. G. Jiang, and M. R. Wisnom, "An experimental and numerical investigation into the damage mechanisms in notched composites," *Compos Part A Appl Sci Manuf*, vol. 40, no. 5, pp. 613–624, May 2009.

[12] G. A. Schoeppner and S. Abrate, "Delamination threshold loads for low velocity impact on composite laminates," *Compos Part A Appl Sci Manuf*, vol. 31, no. 9, pp. 903–915, Sep. 2000.

INVESTIGATION HOW THE FLAME-RETARDANT CONTENT AFFECTS THE MECHANICAL PROPERTIES OF GFRP FOR LIGHTWEIGHT SHIP CONSTRUCTIONS

A. F. Liebau[1], S. Schmidt[1] and W. Flügge[1]

[1]Fraunhofer Institute for Large Structures in Production Engineering, Rostock, Germany
Email: alex.frederick.liebau@igp.fraunhofer.de, Web Page: https://www.igp.fraunhofer.de/en.html

Keywords: composites, GFRP, flame-retardant, mechanical properties, shipbuilding, fire safety

Abstract
The flammability of the organic polymer matrix of fiber-reinforced plastics is currently a major obstacle for their use as lightweight construction materials. Additive fire retardants improve the fire resistance, but also influence the mechanical behavior. The influence on the mechanical properties is currently difficult to quantify, which often leads to the oversising of fire protection-relevant components.
The aim of this work is to quantify the influence of a flame retardant on the mechanical properties of a glass fiber reinforced plastic. In order to evaluate the influence of fire retardants, quasi-static tensile, compression and flexual tests are carried out on quasi-isotropic laminates with and without fire retardants. In addition, shear tests on biaxial laminates are performed.
The test results are quantified for various parameter and load combinations and given in the form of reduction factors. For example, while the strength and stiffness of flame retardant specimens under tensile load decrease compared to the reference series without fire retardants, the mechanical properties under shear load are less or even positively affected. Furthermore, the results show that the manufacturing process in combination with the flame retardant influences the degree of consolidation, the fiber volume content and thus the mechanical properties. The derived reduction factors can be used for the material-specific design of components, taking into account the adapted mechanical properties.

1. Introduction

Due to their high lightweight construction potential, fiber-reinforced plastics (FRP) can help to reduce fuel consumption and emissions in the mobility sector [1]. In shipbuilding, the use of FRP instead of the commonly used steel can reduce the mass, which saves fuel and thus either reduces CO_2-emissions or enables a higher cargo load with the same fuel requirement. Furthermore, FRP has advantages over steel in terms of corrosion resistance and freedom of design. In commercial shipping, however, the strict fire safety regulations of the International Maritime Organisation (IMO) in SOLAS (International Convention for the Safety of Life at Sea) apply [2]. According to these regulations, only materials that are classified as non-combustible can be used in safety- and structurally relevant areas. Consequently, the low thermal resistance of the organic polymer matrix is a major obstacle to the use of FRP in shipbuilding [3, 4]. Under the influence of temperature, the strength and stiffness of the matrix decrease, whereby its protective and supporting properties are lost, leading to failure of the composite [5]. In addition, the organic plastic matrix can burn at temperatures as low as approx. 300-400 °C with a strong release of heat [5, 6], producing toxic fumes such as carbon monoxide [3].
In order to meet the safety requirements of the IMO and to use FRP in shipbuilding, an equivalent level of safety to that of steel structures must be demonstrated (Chapter II-2/17 of SOLAS [2]). To increase the fire resistance of a FRP, either external insulation is used, flame-retardant coatings are applied or reactive or additive fire retardants are added to the resin of the FRP [6–8]. Flame retardant additives are a particularly popular variant to improve the fire resistance of an FRP, as no additional design measures are required. However, in order for additives to improve the fire resistance of a FRP large quantities must be added [9–12]. For example, tests by Shekarchi et al. [10] show that substituting 20 % or 40 % of the matrix component with the flame retardant additive ammonium polyphosphate reduces the flexural and tensile strength of the composite, which the authors attribute to reduced fiber-matrix

adhesion. The decrease in strength and stiffness increases with the test temperature. Studies by Petersen et al. [11] confirm the decrease in tensile, compressive and shear strength and stiffness due to the addition of the flame retardant alumina tri-hydrate.
However, it is not only the reduction in mechanical properties that currently inhibits the use of flame-retardant FRP in shipbuilding. Another problem is the complex production of FRP with flame retardant additives. Tests on the process-optimised production of FRP components with a combination of aluminium-trihydroxide and ammonium-polyphosphate demonstrate the difficulty to ensure the homogeneous distribution of the flame retardant in the laminate [13]. While the flame retardant only settles between the individual layers of the semi-finished fiber product during manual application (hand lay-up), the flame retardant concentration decreases along the flow front during vacuum infusion, as the fibers filter out the mineral components from the FRP matrix mixture.
As shown above, the production and use of fiber composites with uniform flame retardancy in shipbuilding is still associated with great challenges. In addition to the reduced mechanical properties, uniform distribution of the flame retardant in the FRP is particularly problematic, as this not only results in uneven fire protection properties but also high standard deviations in the mechanical parameters [10, 12]. The latter complicates the design of fiber composite constructions with flame retardant additives. Fire protection-relevant components are therefore often oversised, which contradicts the concept of lightweight construction and is associated with increased resource consumption.
In the present work, the problems are countered by using a pre-impregnated semi-finished product (prepreg) with a flame retardant additive already mixed into the resin. The mechanical production of flame-retardant prepregs improves the uniformity of the subsequent laminates and thus the resulting mechanical and fire protection properties. At the same time, the use of prepregs improves occupational safety and enables large-scale production of fiber composite components. The different manufacturing processes used in the work (vacuum bag moulding and hot pressing) for processing the prepregs have a direct influence on the resulting mechanical properties of the test specimens. By referencing the results to a comparative series without flame retardant, not only the influences of the manufacturing process but also those of the flame retardant are revealed.

2. Material and methods

2.1. Test methods and standards

The experimental test program consists of a series of quasi-static tests on quasi-isotropic and biaxial laminates with and without fire retardants (Chapter 2.2). In each case, one laminate was produced using hot pressing technology (Chapter 2.3) and one laminate using vacuum bag moulding (Chapter 2.3). Table 1 provides an overview of the mechanical tests carried out, including the standards applied. All quasi-static tests were carried out on the Zwick/Roell universal testing machine (Z50). For the displacement measurement, a videoextensometer with a measurement pattern on the specimen was used. For the flexual tests at 90 °C, the testing area of the testing machine was enclosed using a temperature chamber (Zwick/Roell TE-TC12.00).

Table 1. Test type, conditions, standards and determined values for mechanical tests

Test type (temperature)	Test standard	Determined values
Tensile (23 ± 3 °C)	DIN EN ISO 527-4	Stress/Strain, Strength, Modulus
Compression (23 ± 3 °C)	DIN EN ISO 14126	Stress/Strain, Strength
Shear (23 ± 3 °C)	DIN EN ISO 14129	In-plane Stress/Strain, Strength, Modulus
Flexual (23 ± 3 °C)	DIN EN ISO 14125 Three-point flexure	Stress/Strain, Strength, Modulus (large deflections)
Flexual (90 ± 3 °C)	DIN EN ISO 14125 Three-point flexure	Stress/Strain, Strength, Modulus (large deflections)

In addition, microscopic and energy dispersive X-ray spectroscopy (EDX) analyses were carried out on certain laminates in order to enable a correlation between the mechanical properties and the microstructural composition of the material. Therefore a scanning electron microscope (SEM) JSM-IT100 from the manufacturer JEOL Ltd. was used.

2.2. Material and laminate structure

A glass fiber-reinforced prepreg with a ±45°-biaxial non-crimp fabric (areal weight 810 g/m^2) and with 40 % resin content (535 g/m^2) was used to manufacture the laminates. For the series with flame retardant, a powdered flame retardant with aluminum-trihydroxide and ammonium-polyphosphate was added to epoxy resin *CP003* (*c-m-p GmbH*) by 33 wt.-% of the resin (177 g/m^2) before the impregnation of the semi-finished fiber product. For the reference series without flame retardant, the same biaxial glass fiber reinforced prepreg was used but without additive. A quasi-isotropic laminate structure $[0°/90°/+45°/-45°]_s$ was used for the quasi-static tensile, compression and flexual tests. The specimens for the in-plane shear tests were taken from biaxial laminates $[+45°/-45°/+45°/-45°]_s$.

Fiber volume content: During the production of the laminates, the fiber volume content (FVC) should be kept as constant as possible within the series with and without fire retardants in order to eliminate one of the main factors influencing strength and stiffness. The degree of consolidation and thus the FVC of the laminates depends on the selected manufacturing process. In the vacuum bag moulding, consolidation is achieved by the vacuum pressure. Thereby, the resulting FVC of the laminates is influenced by various parameters, including the number of fleece-layers in the vacuum bag (Chapter 2.3), the viscosity profile of the epoxy resin and the quantity and distribution of the flame retardant [12, 13].
While the FVC of laminates without fire retardants can be determined by means of thermal calcination in accordance with DIN EN ISO 1172, the flame retardant in the series with fire retardants prevents the residue-free ashing of the matrix. The fiber volume content of series with fire retardants are therefore determined by calculation and on the basis of the measured thickness of the cured vacuum bag moulding laminates. As the thickness of the laminates can be adjusted much more flexibly in the hot pressing process using the compression force, the thicknesses of the vacuum bag laminates are crucial. The FVC φ is calculated using Formula (1):

$$\varphi = \frac{n * G}{\rho * d * 1000} \tag{1}$$

where n is the number of prepreg-layers, G is the fiber areal weight (810 g/m^2), ρ is the fiber-density (2.6 g/cm^3) and d is the laminate thickness in mm.
In pre-tests, a thickness of approx. 2.5-3.0 mm was measured for vacuum bag moulding laminates without flame retardant and a thickness of approx. 3.0-3.5 mm for laminates with fire retardants. In the hot pressing process, the thickness of the laminates can be adjusted by using spacers. In order to achieve the thickness of the series without fire retardants from the vacuum bag moulding process, a spacer of 2.75 mm was chosen. For the series with fire retardants, spacers with a thickness of 3.3 mm were used.

2.3. Manufacturing and curing

Before the laminates are produced, the prepreg was removed from the freezer (-20 °C) and cut into size. The prepreg-blank was conditioned for 24 h in a normal climate (23 °C, 50 % RH). The biaxial layers of the prepreg were laid down and pressed down with a squeegee. An peel ply (PA6, 85 g/m^2) was applied on both sides of the laminate. The laminates were initially tempered for 8 h at 85 °C, with a heating rate of 1 K/min (cooling uncontrolled). For final curing, the laminates were tempered once again at 110 °C for 12 h (1 K/min, cooling uncontrolled) in an universal tempering oven (*Memmert UF750plus*).

Vacuum bag moulding: The laminates in the “vacuumpressing” series were produced on a heatable laminating plate coated with a release agent (*PARTALL® Hi-Temp Wax*). The vacuum structure was

created using a perforated film made of fluoropolymer, a vacuum foil (*VACF 465B*), a vacuum sealing tape (*Airseal 3WT*) and a non-woven fleece (*Breatex*™, 150 g/m²). The non-woven fleece served simultaneously as a breather and bleeder and made a significant contribution to resin flow and consolidation. After initial curing, the laminates were demoulded and post-cured.

Hot pressing: The laminates in the "hotpressing" series were produced in a hot press with an aluminum tool heated on both sides. Release agent (PARTALL® Hi-Temp Wax) and peel ply (PA6, 85 g/m²) were used on both sides for easier demoulding. Initially, the biaxial layers of the prepreg were applied and pressed down with a squeegee. Spacers were placed between the aluminum plates of the forming tool to adjust the laminate thickness (Chapter 2.2). With the help of a bolted frame and a pressure pad press, a sufficiently high pressing pressure was applied so that the moulds rested on the spacer. After initial curing, the laminates were demoulded and post-cured.

3. Results and Discussion

The quasi-static properties are determined in accordance with the test standards (Chapter 2.1). For each series and load type (tension, compression, flexual, shear) force-displacement-curves are recorded and stress-strain-curves are derived.
As an example, the stress-strain-curves from the tensile test according to DIN EN ISO 527-4 are presented in Figure 1. The curves of each series are linear up to around 50 N/mm² or 0.25 % strain. Thereafter, all curves show a bend that extends to around 100 N/mm², which indicates a partial failure of the 90°-fiber layers of the composite running transverse to the direction of loading. Subsequently, the curves are linear again and have different slopes and different maximum stresses depending on the series. These differences show the influence of the flame retardant content and the manufacturing process on the mechanical behavior of the FRP under quasi-static tensile load. In concrete terms, the two series with fire retardants run below the series without fire retardants. Furthermore, it can be seen that the vacuum bag moulding process has a positive impact on the strength and stiffness of the laminates without fire retardants while hot pressing leads to higher strengths in laminates with fire retardants.

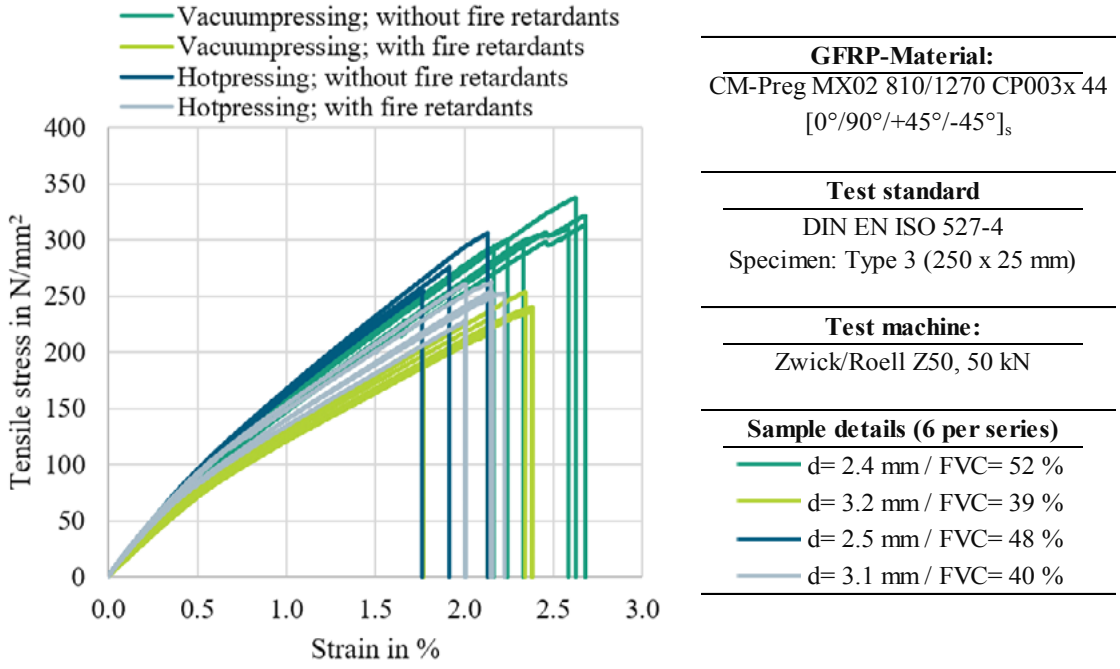


Figure 1: Tensile stress-strain-curves to investigate the tensile behaviour depending on the manufacturing process and flame retardant content

Figure 2 shows the tensile strength and Young's modulus of the four series as bar chart with specification of the corresponding reduction factors. The lower gradient of the curves without flame retardant in the initial range <50 N/mm² (Figure 1) is due to a lower stiffness of the test specimens. The Young's modulus (Figure 2) decreases by 6.5 % for the vacuum-pressed test specimens and by 11.5 % for the hot-pressed test specimens. This decrease appears to be directly related to the flame retardant, which reduces the stiffness of the matrix component and thus the modulus of the composite material. In addition, it becomes clear that the tensile strength and the Young's modulus of the vacuum-pressed laminates decrease more than those of the hot-pressed laminates due to the fire retardant content.

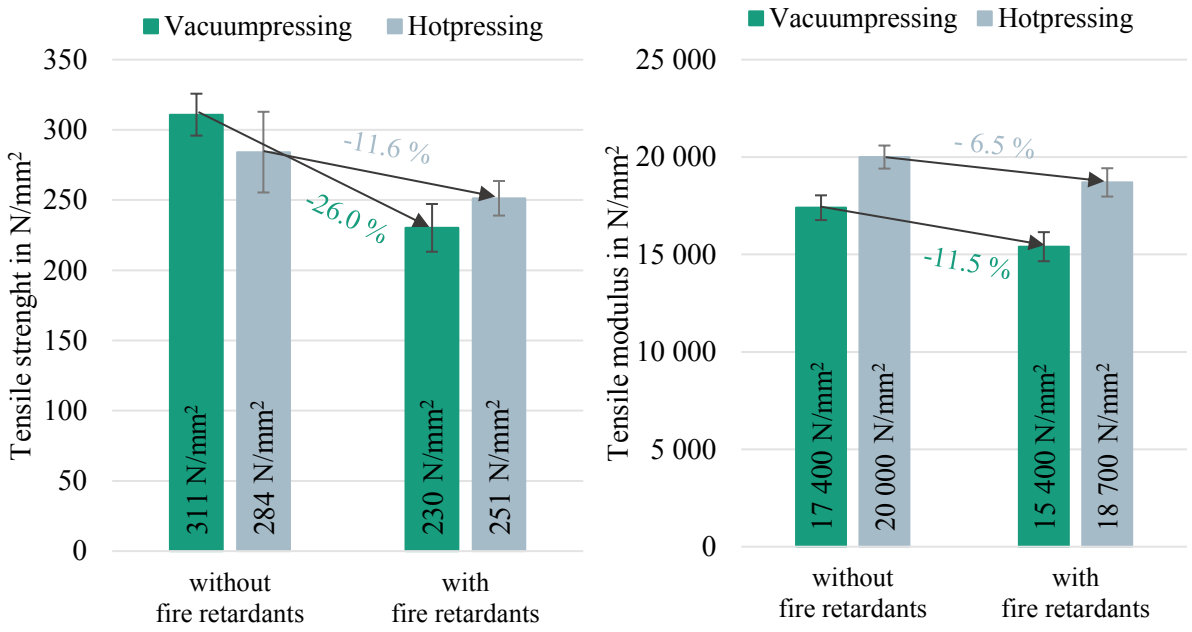


Figure 2: Comparison of tensile strength (left) and tensile modulus (right) with and without flame retardant differentiated according to the manufacturing process

Table 2 shows the strength and Table 3 the stiffness of the four series under tensile, compressive, shear and flexual loads as well as the reduction factors in strength and stiffness due to the addition of the flame retardant. The compressive strength of the four series decreases with the addition of fire retardants in the same way as the tensile strength. Under compression, the negative influence of the flame retardant on the strength is almost similar between the two manufacturing processes (-16.1 % and -16.5 %).
The results of the flexural tests at room temperature and at 90 °C also show a decrease in the characteristic values with the addition of the flame retardant additive. The percentage decrease is slightly greater for the hot-pressed laminates than for the vacuum-pressed ones. In principle, the outer layer of the test specimens is decisive for the mechanical integrity under flexual loading, as this is where the maximum elongation of the matrix and fibers occurs. Due to the flame retardant, the fiber volume content in the load-bearing unidirectional outer layers is lower than in the laminates without flame retardant. This could lead to the strong decrease in mechanical properties. The significant decrease in mechanical integrity in the flexual specimens is also confirmed by the decrease in flexural modulus (Table 3).
For all characteristic values dominated by fibers (tension, compression, flexual), the compression in the manufacturing process, the resulting specimen thickness and the difference in the FVC associated with the specimen thickness have a significant influence on the mechanical strength and stiffness. Therefore, it should be noted that the FVC of the series with flame retardant is almost 10 % lower than that of the reference series without flame retardant (Figure 1).

Table 2: Strength properties of the series vacuumpressing (VP) and hotpressing (HP) with and without fire retardants (fr)

Strength in N/mm²					
	VP without fr		**VP with fr**		**Reduction Factor**
	Mean	SD*	Mean	SD*	(%)
Tensile	311	15	230	17	-26.0
Compression	304	35	255	21	-16.1
Shear (in-plane)	50	0.6	48	0.7	-4.0
Flexural (23 °C)	651	64	549	65	-15.7
Flexural (90 °C)	392	36	222	42	-43.4
	HP without fr		**HP with fr**		**Reduction Factor**
	Mean	SD*	Mean	SD*	(%)
Tensile	284	29	251	12	-11.6
Compression	339	18	283	26	-16.5
Shear (in-plane)	48	1	47	1	-2.1
Flexural (23 °C)	725	76	572	18	-21.1
Flexural (90 °C)	497	58	223	7	-55.1

*SD= standard deviation

The shear strength (Table 2) and the shear modulus (Table 3), on the other hand, are matrix-dominated. These characteristic values are less influenced by the FVC. Instead, the mechanical properties of the matrix have a significant influence on these properties. Interestingly, the shear strength (-9.0 %) and the shear stiffness (+0.6 %) are only slightly or even positively influenced by the fire retardant. On the one hand, the larger cross-sectional area of the specimens with fire retardants should decrease the shear properties. On the other hand, the fire retardants seem to cause a stiffening effect.

Table 3: Modules of the series vacuumpressing (VP) and hotpressing (HP) with and without fire retardants (fr)

Modulus in N/mm²					
	VP without fr		**VP with fr**		**Reduction Factor**
	Mean	SD*	Mean	SD*	(%)
Tensile	17 400	636	15 400	745	-11.5
Compression	-	-	-	-	-
Shear (in-plane)	3 440	41	3 130	79	-9.0
Flexural (23 °C)	22 900	1 742	19 600	1 654	-14.4
Flexural (90 °C)	19 300	656	14 100	331	-26.9
	HP without fr		**HP with fr**		**Reduction Factor**
	Mean	SD*	Mean	SD*	(%)
Tensile	20 000	592	18 700	727	-6.5
Compression	-	-	-	-	-
Shear (in-plane)	3 180	77	3 200	54	0.6
Flexural (23 °C)	23 100	987	20 200	894	-12.6
Flexural (90 °C)	21 100	985	15 700	252	-25.2

*SD= standard deviation

The results show that the mechanical properties are strongly influenced by the manufacturing process. The compression of the prepreg layers and the evacuation of the air pockets in the early stages of curing are crucial. The compression force during vacuum processing is low compared to the hot pressing process. As a result of the low pressure, the flame retardant agglomerates between the reinforcing fibers inhibiting the resin flow in the direction of the laminate thickness (Figure 3).

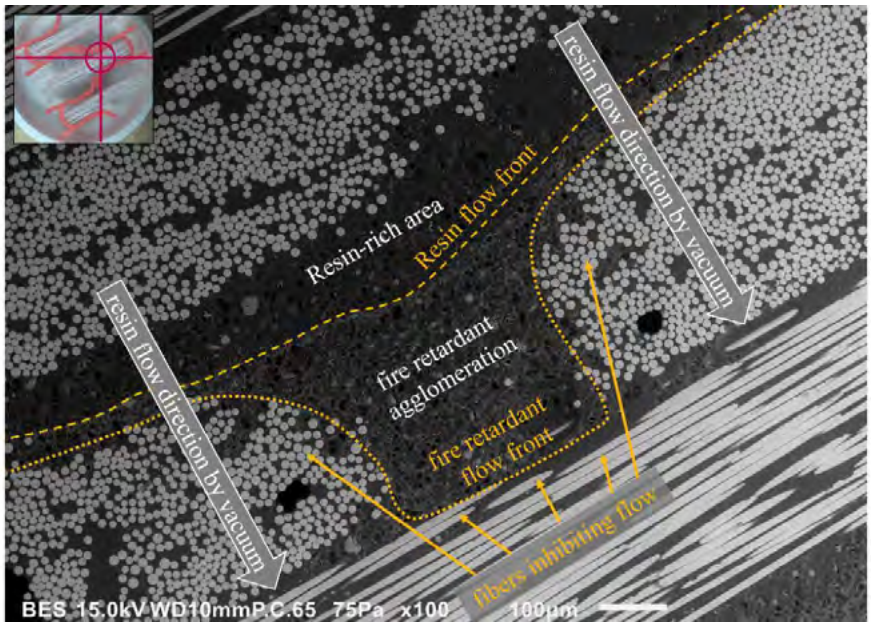


Figure 3: SEM image for the analysis of resin and flame retardant accumulations

In vacuum bag moulding, the presence of the flame retardant therefore leads to thicker laminates with lower FVC and lower cross-sectional properties. As a result, fiber-dominated properties such as tensile, compression and flexural properties are strongly influenced by the laminate thickness variations. In the hot pressing process, a strong resin flow in the laminate thickness direction is inherently excluded due to the mould. Instead, the resin flows out of the material along the prepreg layers, taking some flame retardant with it. The pressure is high enough that the laminate is compressed to the thickness of the spacers. As a result, the difference between the thickness and the FVC of the laminates with and without flame retardant is smaller impairing fiber-dominated characteristic values such as tensile strength and Young's modulus to a lesser extent.

4. Conclusion

The results of the quasi-static tests show that the mechanical properties are strongly influenced by the manufacturing process (Vacuum bag moulding / hot pressing technology) and the presence of the flame retardant. Based on a SEM image, it is shown that the combination of flame retardant and semi-finished fiber product restricts the resin flow if the compression force is too low. The fiber-dominated properties such as tensile, compression and flexural properties are negatively influenced by the variations in the restricted resin flow, the remaining laminate thickness and the fiber volume content. The situation is quite different for matrix-dominated characteristic values such as shear strength and shear modulus. The low decrease in strength and the slight increase in shear modulus indicate that the presence of the flame retardant could have a stiffening effect.
It can be concluded that the influence of the flame retardant cannot be generalised. Even though fire retardants lead to an increase in sample thickness and a decrease in fiber volume content not all strength and stiffness properties are impaired. Instead, the type of loading must always be taken into account. The negative influence of the flame retardant is greater for fiber-dominated characteristic values (tension, compression and felxual) than for matrix-dominated ones (shear). Accordingly, the reduction factor must be selected depending on the type of load.

References

[1] G. Gardiner; Removing the barriers to lightweighting ships with composites, *CompositesWorld*, S. 26-33, 2019.
[2] International Maritime Organization; SOLAS - International Convention for the Safety of Life at Sea, 1974.
[3] S. Backens; J. Unseld; N. Glück et al.; Nichtbrennbare, anorganische Faserverbundwerkstoffe für den Schiffbau, *Lightweight Design*, Nr. 6, S. 38-43, 2019.
[4] A. de Bruijn, S. Paboeuf, M. Krause, et al.; Ramsses - Final Recommendations to Rule and Policy makers, S. 7-103, 2021.
[5] Timme, S.; Feuerwiderstand von unversteiften und versteiften CFK Schalenstrukturen und der Einfluss von integrierten Flammschutzlagen, S. 1-202, 2019
[6] Hörold, A.; Schartel, B.; Trappe, V. et al.; Protecting the structural integrity of composites in fire: Intumescent coatings in the intermediate scale, *Journal of Reinforced Plastics and Composites*, Nr. 24, S. 2029-2044, 2015.
[7] F. Evegren, M. Rahm, T. Hertzberg; Fire Tests of FRP Composite Ship Structures, S. 7-426, 2016.
[8] AVK - Industrievereinigung Verstärkte Kunststoffe e.V.; *Handbuch Faserverbundkunststoffe / Composites, Grundlagen, Verarbeitung, Anwendungen*. Wiesbaden: Springer Vieweg, 2013.
[9] L. Carsten; Glasfaserverstärkte Kunststoffe unter hoher thermischer und mechanischer Belastung, S. 1-282, 2009.
[10] Shekarchi, M.; Farahani, E. M.; Yekrangnia, M. et al.; Mechanical strength of CFRP and GFRP composites filled with APP fire retardant powder exposed to elevated temperature, *Fire Safety Journal*, S. 1-15, 2020.
[11] Petersen, M. R.; an Chen; Roll, M. et al.; Mechanical properties of fire-retardant glass fiber-reinforced polymer materials with alumina tri-hydrate filler, *Composites Part B: Engineering*, S. 109-121, 2015.
[12] S. Wachtmann; Experimentelle Untersuchungen an einem brandgeschützten Glasfaser-Prepreg für E-Schiffe in Leichtbauweise, S. 1-144, 2023.
[13] Backens, S.; Schmidt, S.; Schlusssachbericht Feuerfest, S. 1-26, 2019.

THE RESEARCH OF THE RESIDUAL STRESS INFLUENCE ON UNIDIRECTIONAL COMPOSITE MATERIALS MECHANICAL PROPERTIES THROUGH MICROMECHANICAL ANALYSIS.

First Qingchuan. Liu[1], Second Xiaodong. Wang[2] , Third Zhidong. Guan[3] and Fourth Zengshan. Li[4]

[1]School of Aeronautic Science and Engineering, Beihang University, 100191, China
Email: liuqingchuan1215@163.com
[2]School of Aeronautic Science and Engineering, Beihang University, 100191, China
Email: wangxd819@163.com
[3]School of Aeronautic Science and Engineering, Beihang University, 100191, China
Email: zdguan@buaa.edu.cn
[4]School of Aeronautic Science and Engineering, Beihang University, 100191, China
Email: lizengshan@buaa.edu.cn

Keywords: Polymer matrix composites (PMCs), Micro-scale simulation, Residual stress, Failure mechanism, Finite element analysis (FEA)

Abstract
The structure of carbon fiber resin matrix composites (CFRP) introduces residual stress (RS) due to the differences in the performance evolution of the constituent materials during the manufacturing process, which in turn affects their failure strength and mechanisms. In this study, the viscoelastic constitutive parameters of the resin curing process were obtained through experimental methods. Using micromechanical computational methods, this paper establishes a finite element (FE) model that combines RS with the representative volume element (RVE) at the microscale. The model simulates the distribution pattern of RS and the form of matrix crack propagation in 90° unidirectional laminates (UD), and calculates the failure results of the UD under typical loading conditions. The findings reveal that under the influence of RS, debonding between the fiber and the matrix occurs after the curing process is completed. Additionally, it was observed that the transverse tensile ultimate strength increased, the failure strain and ultimate strength in transverse compression slightly decreased, and the failure strain in longitudinal shear slightly increased while the ultimate strength remained almost unchanged. Hence, it is both significant and imperative to account for the effects of RS in the strength design of composite materials.

1. Introduction

The manufacturing of composite structures introduces residual stress (RS) that are not visible to the naked eye, and the presence of these RS can affect the mechanical properties of composite structures[1]. Excessive RS can cause initial delamination and matrix cracks, leading to damage before the structure is subjected to loading[2, 3]. RS typically impacts the failure strength of composites, and using micromechanical models can reveal the mechanisms by which RS causes structural damage[4]. Establishing micromechanical models for composites involves not only finite element geometric modeling but also the accurate characterization of the mechanical properties of each constituent material, including stiffness, strength, and failure processes.
Many researchers have achieved significant results in the field of micromechanical analysis of composites. For fibers, brittle failure is typically considered; for resin matrices, the Drucker-Prager (D-P) criterion is often used to describe the plasticity of pressure-sensitive materials[5–7], and the ductile

criterion is used to describe the damage process[8]. For the interface between the matrix and fibers, the traction-separation law is commonly used to describe the damage process[8,9]. These models can effectively describe the failure behavior at the microscale of composites.
Some researchers have also studied the impact of RS on the mechanical properties of composites. For example, Hui[8] used a linear elastic constitutive model to characterize the resin matrix, introduced RS, and investigated its effect on transverse tensile strength, finding that RS increases the transverse tensile strength of unidirectional laminates. Xu *et al.*[10] examined the mechanical response of unidirectional laminates under transverse compression with and without considering RS and discussed the effect of random fiber distribution on the results.
While these studies have explored the impact of RS, they lack precise introduction of RS and detailed discussion under various loading conditions. Therefore, this paper aims to address these aspects.

2. Methods

Considering that the longitudinal performance of unidirectional laminates is primarily governed by the fibers and that the magnitude of RS is relatively small, this paper focuses on discussing the impact of RS on the transverse mechanical properties of unidirectional laminates.

2.1. Experiment analysis

The subject of this study is the M40J/HT-280 high-modulus CFRP. To investigate the impact of RS on the transverse mechanical properties of unidirectional laminates, it is essential to first obtain an accurate distribution of RS in the micromechanical model. The fibers are assumed to undergo no chemical changes during the curing process, maintaining constant mechanical properties. The resin is modeled using a simplified viscoelastic constitutive model that accounts for stress relaxation, with specific parameters obtained through experimental methods.
The experiment conducted was Dynamic Mechanical Analysis (DMA) using the NETZSCH DMA 242 E dynamic mechanical analyzer, as shown in Figure 1.



Figure 1. NETZSCH DMA 242 E Dynamic mechanical analyzer

The coefficient of thermal expansion (CTE) of the resin varies slightly in different states during curing. However, studies indicate that the thermal expansion and contraction of uncured resin contribute minimally to RS. Therefore, only the CTE of the fully cured resin at different temperatures is tested, assuming that the CTE of the resin remains the same in different curing states. The experimental equipment used is the NETZSCH DIL 402C dilatometer.

2.2 Constitutive Model of the Material

To accurately simulate the impact of RS on the transverse performance of composite materials, it is essential to first determine the load-bearing and failure behaviors of the constituent materials, including the fibers, matrix, and fiber-matrix interface. Under transverse loading, the mechanical behavior of the fibers remains linear-elastic until overall failure. Therefore, the fibers are modeled as transversely isotropic linear elastic solids, characterized solely by their elastic parameters. The specific parameters for the fibers are listed in Table 1.

Table 1. M40J fiber paremeters[11]

E_{1f}/GPa	$E_{2f}=E_{3f}/GPa$	$\nu_{12f}=\nu_{13f}$	ν_{23f}	$G_{12f}=G_{13f}/GPa$	G_{23f}/GPa
356	16.2	0.212	0.266	10.2	6.4

The matrix constitutive model is defined as an isotropic elasto-plastic model, with the plastic behavior governed by the Drucker-Prager yield criterion.

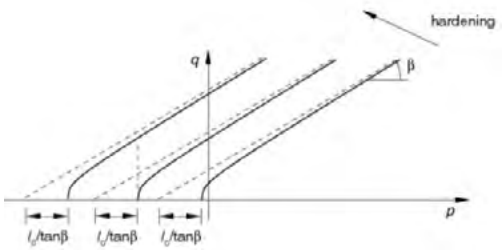


Figure 2. Hyperbolic Drucker-Prager yield criterion[12]

The initiation of damage in the resin matrix is determined using the Ductile criterion. The mechanical properties of the resin are presented in Table 2.

Table 2. Mechanical parameters of resin HT280[11]

E_m(GPa)	ν_m	σ_{mt}(MPa)	σ_{mc} (MPa)	$\beta(°)$	$p_t\|_0$ (MPa)	G_C $(\frac{J}{m^2})$
4.283	0.35	56	360	42.36	13.8	3

The interfacial mechanical behavior is characterized by the Cohesive model, which is effective in representing crack behavior, especially the mechanical behavior at the interface between two different materials. In this study, a bilinear traction-separation criterion, as illustrated in Figure 3, is employed. Prior to damage initiation, the mechanical behavior is linear elastic, with an initial stiffness denoted by K. In the post-damage stage, the evolution of damage is represented by stiffness degradation. The mechanical behavior in the pre-damage initiation stage is defined by the following equation:

$$\begin{Bmatrix} t_n \\ t_s \\ t_t \end{Bmatrix} = \begin{bmatrix} K_{nn} & & \\ & K_{ss} & \\ & & K_{tt} \end{bmatrix} \begin{Bmatrix} \delta_n \\ \delta_s \\ \delta_t \end{Bmatrix} \quad (1)$$

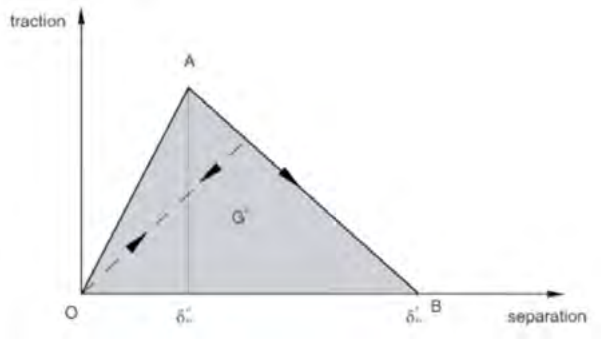
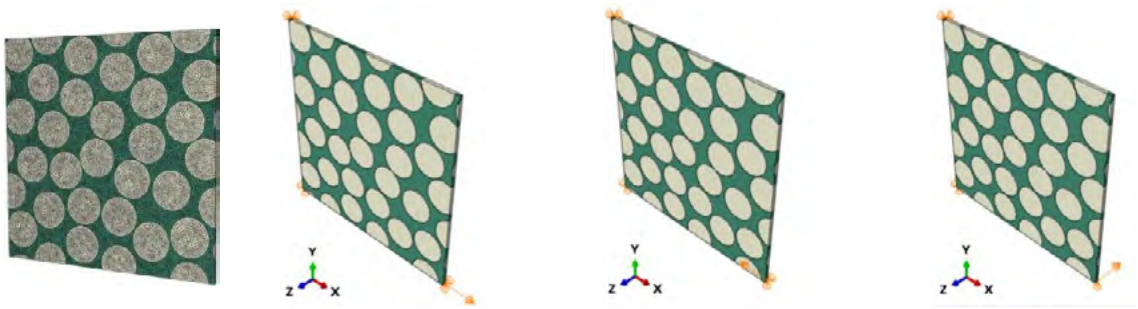


Figure 3. Law of traction-separation

2.3 Micro-scale FE simulation

The geometric model is consistent with the literature[11], as shown in Figure 4, and can be considered a representative volume element of a unidirectional plate. It contains a total of 30 fibers, with a fiber radius of 2.57 μm and a fiber volume fraction of 65%. Considering that the geometric shape along the fiber direction is generally consistent and has minimal impact on the results, the model's dimension along the fiber axis is set to one-tenth of the fiber diameter. The model consists of three parts: fibers, matrix, and fiber-matrix interface, where the fiber-matrix interface is represented by zero-thickness Cohesive elements. These parts are connected through Tie constraints to form a complete finite element model. Convergence analysis indicates that a mesh size of 0.3 μm yields accurate results while maintaining computational efficiency. Periodic boundary conditions are employed to ensure the continuity of stress at the boundaries of the representative volume element.
The loading conditions include three common forms: transverse tension, transverse compression, and longitudinal Shear. Due to the periodic boundary conditions, applying displacement loads at the master control point achieves uniform loading across the model. The boundary conditions are depicted in Figure 4. The mesh types for the fibers and matrix are C3D8R and C3D6R, respectively, while the mesh type for the fiber-matrix interface is COH3D8.

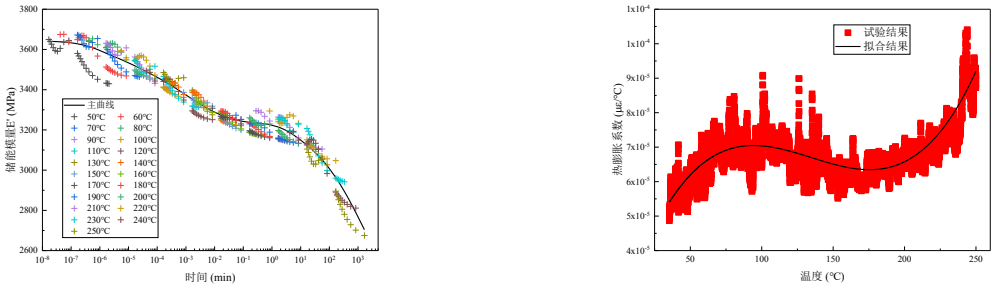


(a) RS Simulation (b) Transverse Tension (c) Transverse Compression (d) Longitudinal Shear

Figure 4. Micro-scale FE model and loading boundary conditions

3. Result and Discussion

3.1 Experimental result



(a) DMA test main curve (b) Results of thermal expansion coefficient test

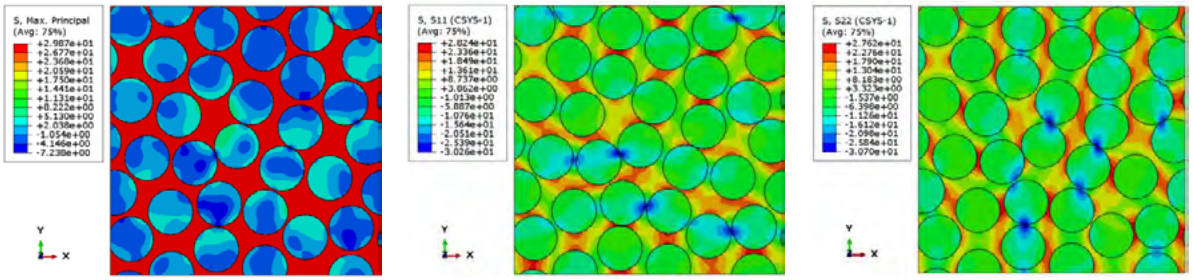
Figure 5. Experimental result

Based on the analysis and fitting of the DMA master curve results shown in Figure 5(a), the characteristic temperature T_c in the simplified constitutive model considering stress relaxation is determined to be 106°C. The test specimens are fully cured resin blocks, with the testing temperature range from room temperature to 250°C and a heating rate of 2°C/min. After processing the data, the results for the thermal expansion coefficient are shown in Figure 5(b).
It can be observed that the data exhibit some scatter but generally follow a nonlinear trend with temperature. A third-order polynomial function is used to fit the experimental results, and the resulting formula is:

$$\alpha_m = 2.62 \times 10^{-11} T^3 - 1.06 \times 10^{-8} T^2 + 1.30 \times 10^{-6} T^2 + 2.02 \times 10^{-5} \quad (2)$$

3.2 RS analysis and distribution results

The RS calculation results are shown in Figure 6. The maximum principal stress results are depicted in Figure 6(a). Due to the transverse thermal expansion coefficient of the fibers being smaller than that of the matrix, the matrix is generally in a tensile state, while the fibers are in a compressive state. The maximum residual principal stress in the matrix is approximately 29.9 MPa, while the maximum residual principal stress in the fibers is about 7.24 MPa.As shown in Figures 6(a), (b), and (c), within the in-plane transverse RS distribution of the laminate, significant tensile stress appears in the matrix near the top and bottom vertices of the fibers, and considerable compressive stress appears in the matrix near the left and right vertices of the fibers. Furthermore, smaller tensile stress is observed at locations farther from the left and right vertices.



(a) (b) (c)

Figure 6. Calculation results of RS in the microscopic model

3.3 Influence of RS on mechanical properties

The stress-strain curves for transverse tension, transverse compression, and longitudinal shear of the unidirectional plate, considering and not considering RS, are shown in Figure 7. It can be observed that

for tensile loading, the overall stiffness before damage is nearly identical in both cases. In the stage approaching the stress peak and near failure, overall nonlinear behavior appears. When considering RS, the overall failure strain significantly increases from 0.46% to 0.50%, and the strength also increases notably from 37.0 MPa to 39.7 MPa. For compression loading, nonlinearity occurs earlier. With RS taken into account, the overall failure strain markedly increases from 2.06% to 2.34%, and the strength also rises significantly from 182 MPa to 201 MPa. For shear loading considering RS, the overall failure strain increases significantly from 2.34% to 2.50%, and the strength slightly increases from 70.1 MPa to 72.0 MPa.

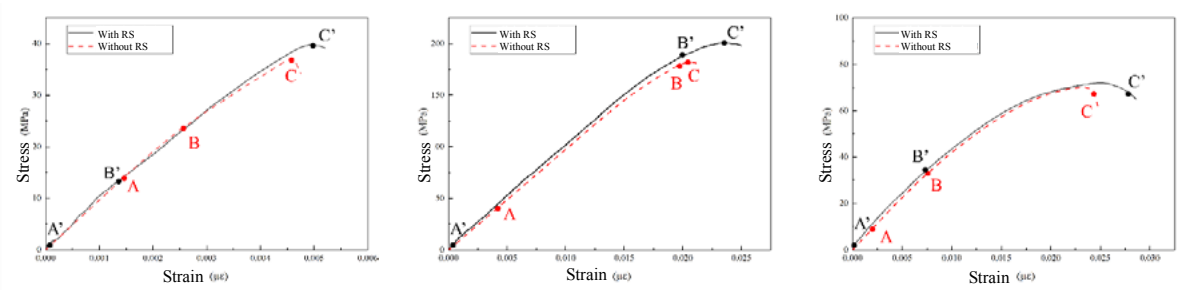


Figure 7. Stress-strain curve for unidirectional plate under typical loading

When RS is not considered, it is assumed that there is no RS distribution in the model at the beginning of loading. The progressive damage process is shown in Figure 8, with corresponding curve positions marked in Figure 7. The matrix damage locations are uniformly distributed near the equator of adjacent fibers, thus the initial location of interface damage determines the position of the overall fracture plane, propagating along the shortest path of matrix damage from the interface damage location. The initial location of interface damage also corresponds to the stress concentration positions at times A and B.

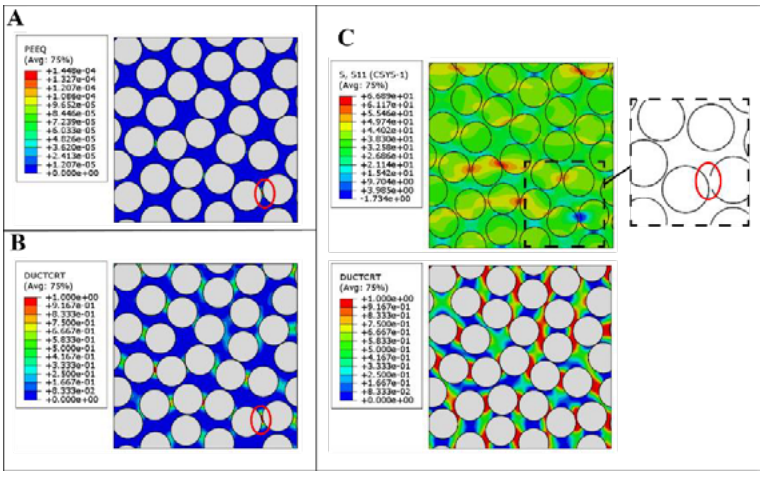


Figure 8. The progressive damage process without RS under tension load

When RS is considered, it is assumed that there is a RS distribution in the model at the beginning of loading. The progressive damage process is shown in Figure 9, with corresponding curve positions marked in Figure 7. At time A' (strain 0%, stress 0% σ_{max}), plastic deformation of the matrix occurs even before loading, indicating that RS itself induces plastic deformation in the matrix, causing it to

appear earlier. With further loading, at time B' (strain 0.14%, stress 4.44% σ_{max}), matrix damage occurs earlier compared to the case without RS. As loading continues, at time C' (strain 0.50%, stress 100% σ_{max}), interface damage appears and rapidly connects with matrix damage, forming a fracture crack perpendicular to the loading direction. Due to the presence of RS, most of the matrix is under tensile stress in the loading direction even before loading, causing significant nonlinear behavior in the overall mechanical response before time C'. Additionally, interface damage is delayed due to compressive RS, resulting in a larger strain at time C', increased overall strength, and a different location of interface damage, altering the final fracture plane position as shown in Figure 10.

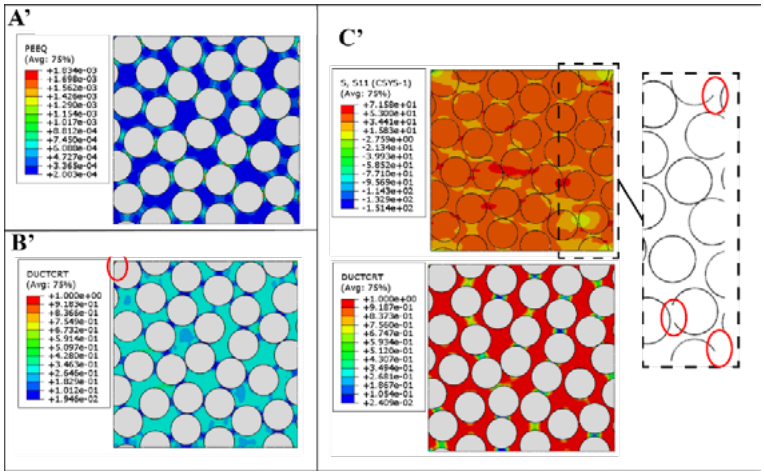


Figure 9. The progressive damage process with RS

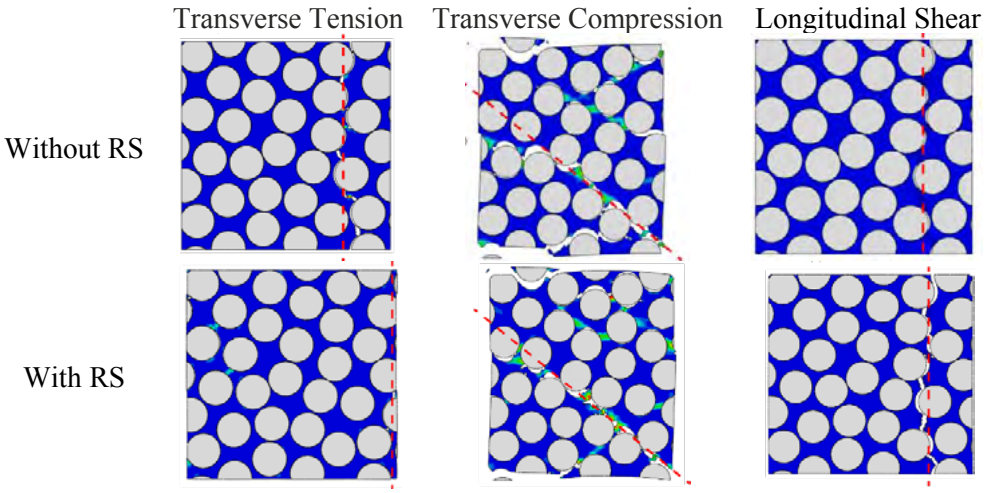


Figure 10. The progressive damage process with RS

In summary, for the transverse tensile performance of the unidirectional plate, the presence of RS leads to earlier plastic deformation and initial damage in the matrix, with changes in their locations. However, RS causes most of the matrix to enter a damaged state before overall fracture, resulting in nonlinear behavior and delaying the occurrence of interface damage. This increases the overall failure strain and ultimate strength. For compressive performance, the presence of RS essentially does not affect the occurrence of interface damage but delays the initial damage in the matrix. Consequently, this increases the overall failure strain and ultimate strength. For shear performance, RS delays the widespread occurrence of interface damage, which in turn delays the stress redistribution caused by interface

damage. This results in later matrix damage and increases the overall failure strain. However, since the overall unloading and fracture are primarily determined by the matrix, and RS does not have a shear component, the ultimate strength and the load level at the onset of fracture are not significantly affected.

4. Conclusions

This study discussed the viscoelastic constitutive parameters for simulating curing-induced RS in composite materials. By calculating microscale RS, the distribution pattern in 90° unidirectional plates is determined, and RS are integrated into the microscale model. The analysis under transverse tension, compression, and longitudinal shear loads reveals that RS increases the ultimate strength in transverse tension; slightly decreases the ultimate strain and strength in transverse compression; and slightly increases the ultimate strain in longitudinal shear, but has minimal impact on ultimate strength.

5. Acknowledgments

This work was supported by Z. Guan and X. Wang, from Beihang University.

6. References

[1] P. Czapski. Influence of laminate code and curing process on the stability of square cross-section, composite columns – Experimental and FEM studies, *Composite Structures*, vol. 250, p. 112564, 2020.
[2] M. M. Shokrieh and M. Safarabadi. Three-dimensional analysis of micro-residual stresses in fibrous composites based on the energy method: a study including interphase effects, *Journal of Composite Materials*, vol. 46, no. 6, pp. 727–735, 2012.
[3] H.-L. Ma, K. Lau, D. Hui, S. Shi, and C. Poon. Theoretical analysis on the pullout behavior of carbon nanotube at cryogenic environment with the consideration of thermal residual stress, *Composites Part B: Engineering*, vol. 128, pp. 67–75, 2017.
[4] M. Hardiman, T. J. Vaughan, and C. T. McCarthy. The effect of microscale residual stress from thermal cooldown on the nanoindentation properties of fibre-reinforced composites, *Journal of Composite Materials*, vol. 50, no. 29, pp. 4147–4158, 2016.
[5] L. Yang, Y. Yan, Y. Liu, and Z. Ran. Microscopic failure mechanisms of fiber-reinforced polymer composites under transverse tension and compression, *Composites Science and Technology*, vol. 72, no. 15, pp. 1818–1825, 2012.
[6] D. Pulungan, G. Lubineau, A. Yudhanto, R. Yaldiz, and W. Schijve. Identifying design parameters controlling damage behaviors of continuous fiber-reinforced thermoplastic composites using micromechanics as a virtual testing tool, *International Journal of Solids and Structures*, vol. 117, pp. 177–190, 2017.
[7] C. Fu and X. Wang. Micro-mechanical analysis of matrix crack-induced delamination in cross-ply laminates in tension, *Composite Structures*, vol. 243, p. 112202, 2020.
[8] X. Hui, Y. Xu, and W. Zhang. An integrated modeling of the curing process and transverse tensile damage of unidirectional CFRP composites, *Composite Structures*, vol. 263, no. February, p. 113681, 2021.
[9] Q. Sun *et al.* In-situ effect in cross-ply laminates under various loading conditions analyzed with hybrid macro/micro-scale computational models, *Composite Structures*, vol. 261, p. 113592, 2021.
[10] X. Hui, Y. Xu, J. Wang, and W. Zhang. Microscale viscoplastic analysis of unidirectional CFRP composites under the influence of curing process, *Composite Structures*, vol. 266, p. 113786, 2021.
[11] X. Wang *et al.* Prediction of the inter-fiber mechanical properties of composites: Part I standardization micro-scale modelling method and damage analysis, *Composite Structures*, vol. 271, p. 114127, 2021.
[12] Simulia DS. Abaqus 6.13 User's Guide. France: Dassault Systems, Providence, RI, 2013.

DESIGN AND ANALYSIS OF CFRP CRASH TUBES FOR ENERGY ABSORPTION IN eVTOLS

M. Adli Dimassi[1], Roland A. Marciniak[2], Harald K. Bachem[3] and Jan Y. Dietrich[4]

[1]Faserinstitut Bremen e.V, Am Biologischen Garten 28359 Bremen, Germany
Email: dimassi@faserinstitut.de, Web Page: http://www.faserinstitut.de
[2]Ostfalia University of Applied Sciences, Kleiststraße 26, 38440 Wolfsburg, Germany
Email: ro.marciniak@ostfalia.de, Web Page: https://www.ostfalia.de/cms/de/f/lff/
[3]Ostfalia University of Applied Sciences, Kleiststraße 26, 38440 Wolfsburg, Germany
Email: h.bachem@ostfalia.de, Web Page: https://www.ostfalia.de/cms/de/f/lff/
[4]Faserinstitut Bremen e.V, Am Biologischen Garten 28359 Bremen, Germany
Email: dietrich@faserinstitut.de, Web Page: http://www.faserinstitut.de

Keywords: eVTOL, Crashworthiness, CFRP Crash tubes, FEM, Testing

Abstract
This study examines the design, analysis, and validation of carbon fibre-reinforced polymer (CFRP) crash tubes for energy absorption in electric vertical take-off and landing (eVTOL) aircraft seats, aiming to optimize configurations for enhanced passenger safety. It incorporates static and dynamic testing of various CFRP tubes with differing diameters and layer orientations. Static tests focused on force-displacement characteristics, deriving crucial design parameters such as peak and plateau loads, and energy absorption. Dynamic tests, performed with a drop tower, mimicked eVTOL crash scenarios to observe tube behavior under realistic conditions. Results indicated that increasing unidirectional layers and tube diameter improves load capacity and energy absorption. Conversely, changing weave orientation from 0°/90° to ±45° reduces energy absorption, underscoring the significance of layup configuration. These insights facilitated the refinement of tube specifications to meet safety goals. Additionally, a finite element model (FEM) developed using the Altair Radioss solver validated the experimental findings, accurately capturing crash behavior and supporting design iterations with reduced physical testing needs. This study confirms that tailored CFRP crash tubes can significantly enhance eVTOL crashworthiness, with combined experimental and simulation approaches offering a robust iterative methodology for optimizing aviation safety systems and reducing the need for extensive material characterization.

1. Introduction

New urban air mobility (UAM) systems could be able to emerge the aviation market in the next three decades, as the needs to shorten travel times and to avoid traffic jams in mega cities are increasing. Based on a Roland Berger´s study [1], it is estimated that more than 160.000 flying vehicles will be part of our air transport ecosystem. Most of these aircrafts will use electric motors for propulsion to avoid CO2-emissions and will have vertical take-off and landing capabilities to enable point-to-point transportation. This creates a new aircraft class called electric vertical take-off and landing vehicles (eVTOL). The rapid increase of air traffic participants in an urban area would increase the risk of air accidents and adds new challenges regarding the crashworthiness of the aircraft and the safety of the passengers.

In order to protect the passengers, the kinetic energy of the aircraft during an accident should be absorbed. Part of the kinetic energy could be absorbed by the collapse of specific parts in the aircraft that are specially designed to absorb energy at constant load level, which would reduce the load

experienced by the aircraft occupants [2]. Examples of typical energy absorbing elements are sandwich components with aluminium honeycomb core or crash tubes made of aluminium or carbon composites (CFRP) [3]. In addition to the high specific strength and specific stiffness of carbon composite materials, CFRP crash tubes offer the flexibility to shape the crushing properties following the defined requirements, such as the absorbed energy, the peak load and the average crushing load, which could be adjusted by simply modifying the laminate layup and the diameter of the crash tube [4].

Energy absorbing systems (E/A) for passenger-seats are designed to absorb a part of the kinetic energy and to reduce the acceleration transmitted to the passengers. Different concepts for E/A-systems are possible. In this study, the results of an approach to design CFRP crash tubes for eVTOL-seats are presented. The design specifications were obtained from the CS-27 certification document for small VTOL aircrafts. CFRP crash tubes with different layups and diameters were manufactured. Afterwards they were crushed statically and impacted dynamically, in order to obtain the energy absorbing characteristics. A finite element model is then developed using the explicit dynamic solver in Radioss. The experimental dynamic results were used to validate the numerical model. The model can capture the damage occurrence and the load displacement reaction with high accuracy and small simulation effort. Finally, a suited crash tube design was obtained.

2. Materials und manufacturing

For the investigation of the energy absorbing properties of CFRP tubes ten different tube setups were manufactured. The first and the last layers of the tubes consist of carbon twill weave with areal weight of 200 g/m² (ECC Style 452). The layers in the middle are unidirectional carbon layers with an aerial weight of 329 g/m² (ECC eUD320CHT-A) oriented in the same direction as the tube main axis (loading direction). Both materials are obtained from C. Cramer & Co GmbH Germany. The epoxy resin Sika Biresin CR122 with the hardener Sika Biresin CR122-5 was used for the manufacturing. The impregnated carbon layers were manually winded over an aluminum tool with the desired diameter and then compacted with a shrinkable peel ply tape to improve the compaction of the CFRP tubes. The following features were modified: the tube diameter, the number of the UD-layers and the orientation of the inner and outer weave layers. The length of the tubes is the same (150 mm). In order to enable a proper damage initiation a 2x45° chamfer on one side of the tube (the side for load introduction) was created. A detailed overview of the investigated CFRP tubes is listed in Table 1.

Table 1. Manufactured CFRP-tubes for the static and dynamic tests

Specimen	Diameter (mm)	Number of UD-layers	Weave orientation (°)
01	20	2	0/90
02	20	3	0/90
03	20	4	0/90
04	25	2	0/90
05	25	3	0/90
06	25	4	0/90
07	25	3	+/-45
08	30	2	0/90
09	30	3	0/90
10	30	4	0/90

3. Static component testing

The crash tubes were simply supported in a test fixture that eliminate the transition of the supported edge in x- and y-direction. The loading in the cylinder axial direction was introduced at a deformation rate of 25 mm/min. The force-displacement diagrams were recorded and two specimens were tested for every crash tube configuration (see Figure 1). From the force-displacement diagrams three key parameters could be extracted that are relevant for the design of the E/A-system: the pick load, which is important for the damage initiation of the E/A-system, the plateau load that has a huge influence on the estimation of passenger injury and the absorbed energy, which gives an estimation about the required tube length.

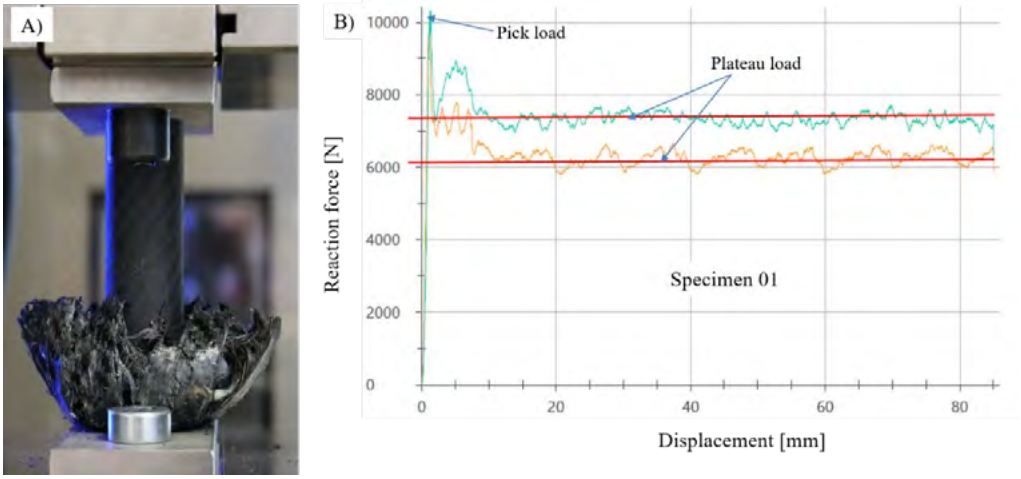


Figure 1. A) A CFRP-tube under static load; B) Force-displacement of CFRP-Tube Nr. 01

The assessment of the results depicted in Figure 2 shows that the increase of the UD-layers and the tube diameter would increase the plateau load, the pick load and the amount of absorbed energy. Changing the orientation of the weave layers from 0°/90° to ±45° led however to the reduction of the energy absorption and the load level. In order to choose the right crash tube, the CFRP tube should absorb the defined kinetic energy within the available length and the load levels should not exceed or deceed the specified values to avoid injuries or early activation of the E/A system. With the static test, a predesign could be defined. However, dynamic impact tests are mandatory for the final design as the structure response may change under dynamic loads.

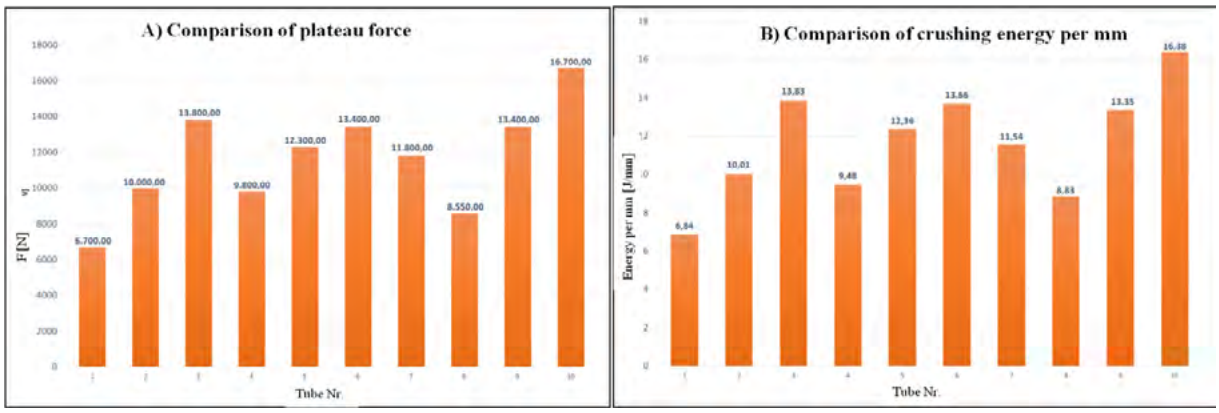


Figure 2. A) Comparison of plateau force; B) Comparison of crushing energy per crushed mm

4. Dynamic component testing

The tests under dynamic loads were carried out using a drop tower test bench with a guided sled. Figure 3 shows the test setup with all its components.

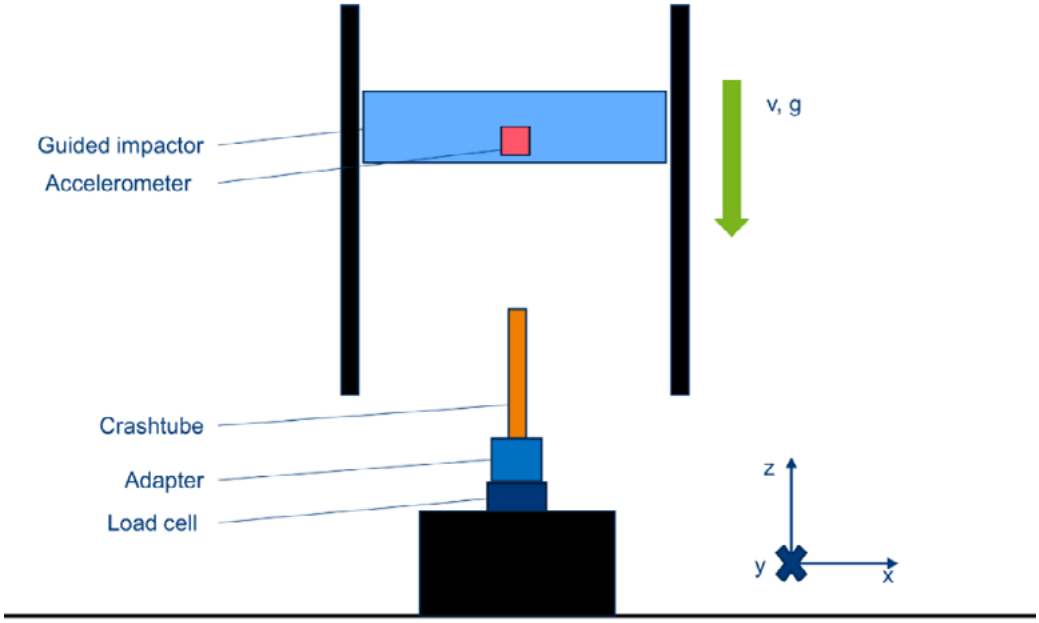


Figure 3. Drop tower setup for dynamic tests.

During each test three measurement data sets with frequency of 10,000 1/s were taken. First of all, the force under the crash tube was measured using a uniaxial load cell. To achieve certain redundancy and to check the plausibility of the measured force. The acceleration of the impactor was also documented. Furthermore, a laser distance sensor was used to measure the deformation of the specimens. To document and analyse optically the crash behaviour of the tested crash tubes, high-speed videos of each experiment were also taken with frequency of 2000 frames per second (fps).

The boundary conditions of the performed tests were established based on requirements defined in the document CS-27 regarding the emergency landing scenarios and the E/A systems. In the considered test constellation, the generated kinetic energy should be set to approximately 1200 J for a single crash tube. This assumption was formulated based on the considered seat design in the project and is not necessarily valid for other scenarios.

In order to achieve the required amount of kinetic energy, an adjustment of two parameters, which are offered by the drop tower test bench, can be made. Consequently, the impactor's velocity was set to 7.9 m/s and its weight was determined to be 40 kg. That corresponds with the calculated vertical velocity vector regarding the specifics of the dynamic landing conditions and with 50% of the mass of a 77 kg passenger with a 3 kg seat structure. The mass of the impactor was reduced by 50% intentionally because of the application of two energy absorbing crash tubes in the seat structure.

Table 2 shows all the results that have been obtained in this test series. Specimen 01 was not able to absorb the generated kinetic energy, which led to a total damage of the crash tube. Therefore, the results of specimen 01 are not conclusive and not shown in the following table.

Table 2. Results of dynamic tests on CFRP-tubes

Specimen	Peak Force [kN]	Plateau Force [kN]	Deformation [mm]
01	-	-	-
02	17.96	13.00	99
03	19.30	17.00	96
04	17.98	12.50	101
05	17.90	14.50	98
06	21.97	19.70	71
07	20.71	17.00	87
08	17.44	14.50	96
09	22.22	17.90	73
10	26.19	22.50	68

The results show that the flexibility of the layup has an extensive advantage regarding the design of the E/A-system. Adjustment of its properties can lead to an optimal solution for various use cases. The influence of the orientation of the weave has also proved a usable potential in terms of increasing forces and decreasing deformations if needed.

In two additional tests that are not listed in Table 2, the weight of the impactor was reduced from 40 kg to 25 kg to simulate the interaction of a smaller passenger (e.g., 5% female ATD) with the E/A-system. Figure 4 shows a comparison of force-displacement-curves between two tests. Both tests were carried out on the specimens with the same geometry and laminate layup and the same boundary conditions except for the impactor mass. Diagram a) correlates with the impactor mass of 40 kg, while diagram b) refers to the impactor mass of 25 kg. The speed of impact was set in both cases to 7.9 m/s.

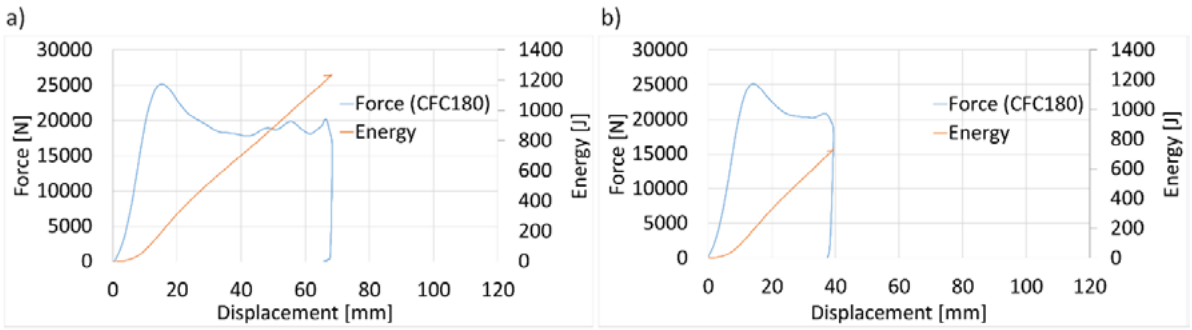


Figure 4. Test results of specimen 10 (force, displacement and energy) with impact velocity of 7.9 m/s and a) 40 kg and b) 25 kg fall weight.

The reduction of the impactor mass has no influence on the characteristics of the initial energy absorption. The peak force and the plateau force stay on the same level. Only the deformation was proved to vary due to the lower kinetic energy generated by the lighter impactor and absorbed by the crash tube.

5. FE Models of CFRP Crash Tubes

This study uses the finite element method (FEM) to analyse the process of energy absorption of CFRP crash tubes with the purpose of determining their optimal geometry while taking into consideration parameters as material, laminate layup, available space in the seat for installation and all restrictions and requirements defined by European Union Aviation Safety Agency (EASA) in CS-27 regulation

regarding velocity and weight of occupant. The explicit solver that was used for this study is Altair Radioss.

Because of complexity of the seat structure, the energy and the loads that occur in the case of a crash spread over many of its parts. It is an important fact regarding the initial load that causes the activation of the E/A-system. It must not be extensively high in order to avoid injuries of occupants but on the other hand, it must not be too low in order to avoid random activation without a crash. Furthermore, the desired energy absorption depends on the loads that affect the E/A-system. A FE model of the whole seat system with a seatbelt and an 50% anthropomorphic test device (ATD) with its weight of 77 kg was created in order to establish the actual initial load and the further loads that occur in the E/A-system under the dynamic landing conditions described in CS-27. Furthermore, using those loads and the maximum available space for the E/A-system in the seat structure, the desired energy absorption by the E/A-system was determined. Based on this data, a FEM model of a crash tube was developed to determine the best geometry and laminate layup.

The length and the diameter of the tube must not exceed 150 mm and 30 mm respectively, because the available space in the seat structure is limited. To determine the optimal constellation of tube diameter and number of unidirectional layers, those two parameters were successively adjusted in the simulation. Furthermore, the weave orientation was examined using values of +/-45° and 0°/90°. As a result, after performing sufficient number of simulations, the most promising variants of crash tube geometry and its laminate layup were defined with regard to the requirements and the specification of the considered seat system. The weave orientation in nine of ten variants is +/-45°, which led to promising results. In spite of that, one variant with diameter of 25 mm and 3 unidirectional layers has weave with orientation of 0°/90°, which also delivered acceptable results and was pursued to examine the influence of this parameter more closely using results from real tests.

Figure 5 shows the FE model of a crash tube, its boundary conditions, and its dimensions. In this example, the diameter is 30 mm and the following laminate layup is shown: 0°/90° weave – three unidirectional layers – 0°/90° weave.

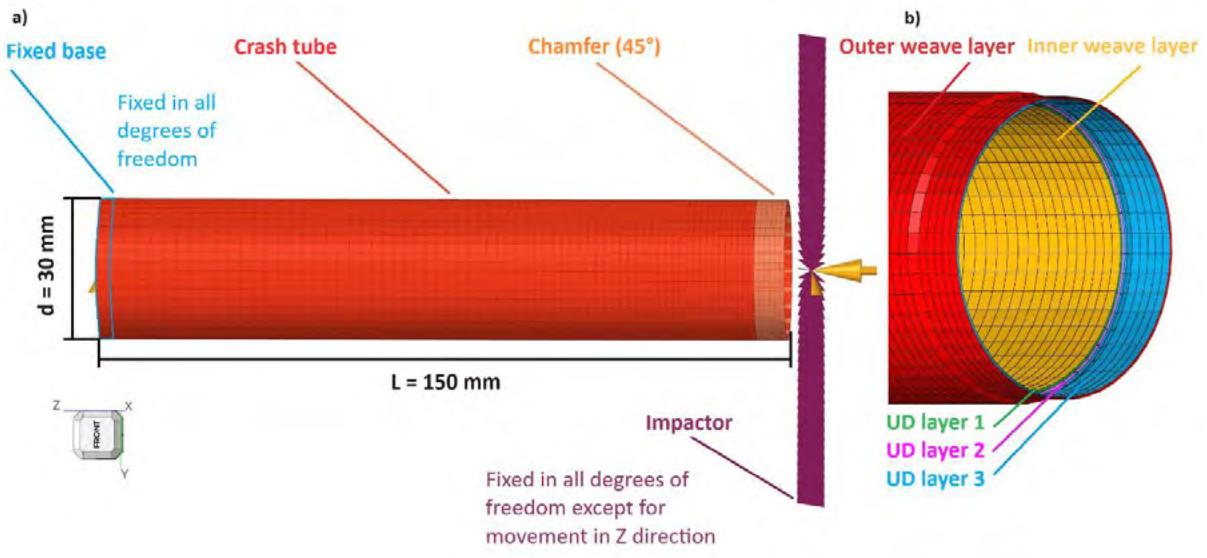


Figure 5. a) FE model of a crash tube with applied boundary conditions and its dimensions displayed; b) Stacking of the laminate

In Figure 5 b) a 45° chamfer of the crash tube on its top is also displayed. The purpose of this chamfer is to reduce the initial load that occurs to initiate the first stage of the desired damage process. This

feature was also taken into account in the manufacturing process of the crash tubes. All ten variants that were considered in the FE analysis are presented in Table 1.

Figure 6 shows an optical comparison between the FE simulation and the dynamic drop tower test regarding the specimen Nr. 10 with four UD layers and 30 mm of diameter.

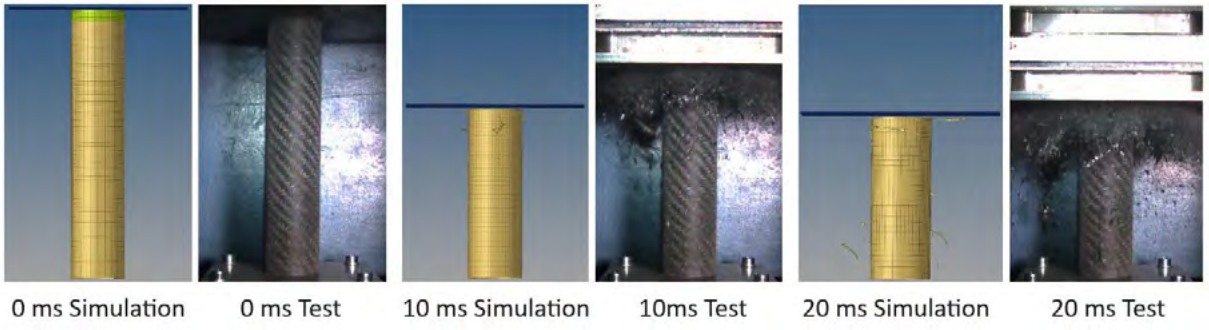


Figure 6. Optical comparison between the results of a dynamic test and the simulation (specimen 10)

The simulation based exclusively on material parameters obtained from material tests delivered satisfying results compared to the real tests. That can be also seen in Figure 7 that presents a comparison regarding the force and the kinetic energy absorbed by the specimen 10. After a validation process a very realistic FE model of the energy absorbing structure in form of a crash tube was created, which will be used for further analysis in order to establish an optimal geometry and composite layup using a model of the whole seat-dummy-system, which addresses all relevant injury criteria e.g., the lumbar load and the energy absorption potential of the other components of the seat.

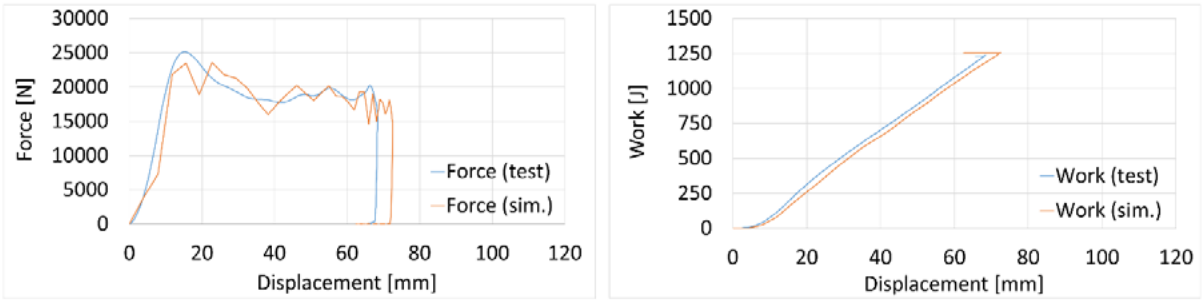


Figure 7. Comparison of force-displacement and work: dynamic test vs. simulation

6. Conclusions

In this work, it was possible to compare the dynamic tests results with the static ones and identify how we can use the static results to define a first layout of the crash tube. This would reduce the number of dynamic tests and the simulation effort. The results shows that the energy absorption and the load levels under dynamic loads are slightly higher compared to the static result. That means using the static results would lead to a conservative design of the E/A system.

The numerical simulation could be used to increase the efficiency of the crash tube design and reduce the number of dynamic tests, as they are more expensive. It is important to note, that when designing an E/A system for an aircraft seat, a huge amount of the kinetic energy will be absorbed by the seat structure and the occupant, so that design should be verified with the simulation of the whole system.

An FE analysis with the whole seat-dummy-system was done in this study and showed that in the crash scenario defined by EASA only 30 % of the kinetic energy that is generated with the whole system

including ATD under dynamic landing conditions can be absorbed by the E/A-system. The rest is absorbed by the other system components. Simulating only the crash tube would not be enough to achieve a robust design. Therefor the design of the E/A crash tubes must be adjusted by verification loops with the system (seat + ATD) model.

Acknowledgments
This work was funded by the German Federal Ministry for Economic Affairs and Climate Action through the Federal SME Research Program ZIM within the project Safe(F)light under the Grant No. 16KN078757. The authors wish to acknowledge this support.

References

[1] S. Hader and M. Baur. Die Senkrechtstarter-Branche: Wie Urban Air Mobility abhebt. *https://www.rolandberger.com/de/Insights/Publications/Die-Senkrechtstarter-Branche-Wie-Urban-Air-Mobility-abhebt.html*, 08.05.2024.
[2] S. Heimbs. Energy absorption in aircraft structures. In *International Workshop on Hydraulic Equipment and Support Systems for Mining (IWHEM 2012)*, Huludao, China, 2012.
[3] Verein Deutscher Ingenieure VDI e.V. *VDI 5911: Occupant protection for small aircraft.* Beuth Verlag GmbH, Berlin, 2022.
[4] M. Abbasi, A. Khalkhali and J. Sackmann, A probabilistic study into the influences of fiber angle orientations on energy absorption performance of carbon fiber-reinforced polymer composite tubes. Journal of Composite Materials: 35-47, 2023.

OPTIMIZATION OF ANODIZING PROCESS PARAMETERS TO IMPROVE ADHESION BETWEEN FIBER REINFORCED POLYMERS AND 3D-PRINTED METAL SUBSTRATES WITH MACROSCOPIC PINS

Riccardo Miranda[1], Vincenzo Fiore[1], Francesca Mazzara[1], Francesco Di Franco[1], Alberta Aversa[2], Sara Biamino[2], Eleonora Atzeni[3], and Fabrizio Sarasini[4]

[1]Department of Engineering, Università degli Studi di Palermo, Viale Delle Scienze, 90128 Palermo, Italy
Email: riccardo.miranda@unipa.it, vincenzo.fiore@unipa.it, francesca.mazzara04@unipa.it, francesco.difranco@unipa.it
[2]Department of Applied Science and Technology (DISAT), Politecnico di Torino, Corso Duca degli Abruzzi 24, 10129 Torino, Italy
Email: alberta.aversa@polito.it, sara.biamino@polito.it
[3] Department of Management and Production Engineering (DIGEP), Politecnico di Torino, Corso Duca degli Abruzzi 24, 10129 Torino, Italy
Email: eleonora.atzeni@polito.it
[4] Department of Chemical Engineering Materials Environment, Sapienza-Università di Roma, Via Eudossiana 18, 00184 Roma, Italy
Email: fabrizio.sarasini@uniroma1.it

Keywords: Anodizing, Additive Manufacturing (AM), AlSi10Mg, Adhesive joint, Fiber reinforced composite

Abstract
In this work, an innovative joint between the aluminium alloy (AlSi10Mg) manufactured trough Additive Manufacturing (AM) and basalt fabric-reinforced epoxy composite substrates was evaluated through modifications of the surface morphology. Macroscopic arrow-shaped pins were printed on the AM surface. Then, a sulfuric acid anodizing (SAA) technique was applied to enhance the metal to composite adhesion and corrosion resistance of the metallic substrate. Scanning electron microscopy (SEM) and electrochemical impedance spectroscopy (EIS) were evaluated to study the nanoscopic morphology on the treated surface of the pins and to assess how the corrosion resistance changes with anodising. A single-lap shear test was performed to investigate the influence of anodising on the macroscopic mechanical performance of the joint. SEM images and EIS measurements show that anodising in SAA generates a porous layer of aluminium oxide that increases corrosion resistance. Single-lap shear tests revealed no change in mechanical performance after anodizing. This is likely due to the pin's shape, which promotes failure within the composite substrate's interlayer instead of at the metal-composite interface.

1. Introduction

Nowadays, the demand for more efficient materials in terms of sustainability leads the industry to confront new challenges. Lightness is a key point in terms of fuel consumption in a moving structure. In this context, composite materials have played an important role in the last decades, ensuring high mechanical performance with low weight. However, it is difficult to create a complex object with a single material. For this reason, it is necessary to couple materials of different nature. Historically,

metals rule in every industrial sector as useful material, but their processing presents certain difficulties when the geometry is very complex. Today, thanks to the additive manufacturing (AM) this problem has been overcome. Indeed, the shape is no longer an issue as the material is created layer by layer [1–4]. Currently, different metal AM processes are available on the market and Powder Bed Fusion-Laser Beam (PBF-LB) is certainly among the most used ones. In the latter, metal is deposited in powder form and melted by a laser, layer by layer, creating the shape designed before printing. Through this technique, it is possible to create several metallic parts having mechanical properties close to those obtained with the conventional processes. AlSi10Mg is a common aluminium alloy powder for AM. Many papers on its application can be found in the literature [5–7]. Compared to the conventional process PBF-LB is the most used thanks to its potentialities and flexibility that allow parts to be produced sustainably and with enhanced properties. However, anisotropy, porosity, residual stress, and other defects are some of the disadvantages of the applications of this material [8]. These defects could be overcome by means of post-processing technique. A challenge that has not been answered yet is the possibility of reducing the high surface roughness after processing when the geometry is very complex. For example, Scherillo [9] developed a two-step chemical etching, consisting of so-called chemical machining (CM) and chemical brightening (CB). In this work, CM step is useful for removing irregularities from the surface of the component, while the CB process smooth the surface, without any change in chemical composition of the AlSi10Mg alloy.

Surface roughness is crucial in the context of the coupling of different materials through adhesive joints. Nowadays, the ability to combine polymeric-reinforced composites to additively manufactured metals, opens up a new way of realising structures, creating new possibilities for complex shape with high performance and lightness. Based on this, process engineering can be considered as the fine-tuning of the metal surface so that it best fits at the interface with the composite. Traditionally, there are different ways to improve the surface between two different materials. From the metals point of view, mechanical treatment with sandblasting or sandpaper is the simplest one but it is not so effective to increase the mechanical properties and, at the same time, to protect the joined component from the surrounding aggressive environments during its service life. In the latter case, chemical treatment by using coupling agents or anodizing can be considered more suitable approaches [10,11].

Anodizing technique on AM AlSi10Mg is a challenge today due to the non-uniformity of the chemical composition with the presence of silicon. Revilla et al. [12,13] examined how Al-Si alloys, manufactured through the PBF-LB method, behave during anodization. They found that the silicon particles underwent complete oxidation because of their exceptionally small size in comparison to those in cast alloys of identical chemical makeup. Consequently, a substantial portion of the anodic charge was utilized during anodization, leading to a notably slower growth rate of the anodic layer in the PBF-LB samples compared to the cast alloy.

In addition to chemical or electrochemical technique, with AM, the fine-tuning of the surface could take place through the creation of a complex macroscopic texture to increase the bond with the adhesive. For example, Zou et al. [14] create a surface structure printed on a titanium alloy. They demonstrated that the AM structure with diamond or honeycomb shapes increase the mechanical interlock with ultra-high molecular weight polyethylene (UHMWPE). Furthermore, they pointed out that the structure complexity and the defects in additive manufacturing should be considered when designing the surface structure. In fact, a simpler structure such as honeycomb instead of diamond, generated better filling efficiency and stability.

The aim of this work is to create a joint between epoxy reinforced composite with basalt fabrics and AM AlSi10Mg substrates. A fine-tuning of the surface of the metal substrate was carried out through the creation of macroscopic arrow-shaped pins to evaluate their influence on the performance of the joint. In addition, the aluminium surface was electrochemically treated to improve adhesion and corrosion resistance of the AM substrate. The anodising technique was evaluated by studying its feasibility due to the high surface roughness of the AM metal and its composition.

2. Experimental

2.1. Materials

Commercially available AlSi10Mg spherical powder, with particle sizes ranging from 25 µm to 65 µm, supplied by EOS GmbH (Krailing, Germany), was used to create the metal substrates of the joints. The powder was processed by EOS GmbH system with the following process parameters:

- Layer thickness: 30 µm
- Laser spot size: 100 µm
- Scanning speed: 800 mm/s
- Laser power: 195 W
- Hatch distance: 0.17 mm
- Scanning strategy: Stripes 67°
- Platform temperature: 100 °C

The AlSi10Mg substrates were then subjected to a stress relieving heat treatment at 310 °C for 1 hour followed by furnace cooling. The substrates were then removed from the build plate using Electrical Discharge Machining.
Geometrical dimension of the final substrate was 80 mm long, 25 mm wide and 3 mm thick.
Furthermore, samples had macroscopic pins in an area of 25x25 mm, with 15 pins for each edge, i.e., a total amount of 225 pins in the area. The geometry of the pin is showed in Figure 1.

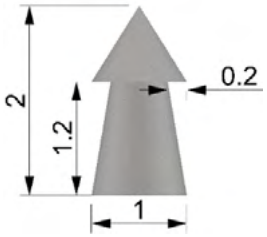


Figure 1. Geometry detail in mm of a single pin printed on the surface of AlSi10Mg substrate.

On the other hand, the polymeric composite was produced with a lay-up of 18 layer of silanized basalt fabric 220 g/m^2 with (3-Aminopropyl)trimethoxysilane and an epoxy matrix supplied by R*Concept with a commercial name of Polar. This resin is a bio-based epoxy with a bio-content higher than 28% and recyclable. The chemical recyclability works thanks to the nature of the curing agent which is a “cleavable” amine, that can open the cross-link if the composite is immersed in a mild acid solution. After the recycling process, it is possible to recover entirely the reinforcement because the epoxy matrix became a thermoplastic material that precipitate in the solution.

2.2. Surface treatments on AlSi10Mg substrate

Electrochemical technique of anodising was used in this work to enhance the interlocking between aluminium alloy surface and polymeric composite and its corrosion resistance. An aqueous stirred solution of sulfuric acid (H_2SO_4) 3M was employed as electrolyte in a cell composed by a galvanostat, an aluminium counter electrode and the sample dipped in the solution. Current density of 10 mA/cm^2 was imposed for 20 minutes, hence the process was carried out galvanostatically. The growth curve of the porous oxide layer, V vs time, is plotted in Figure 2. In the following, this treatment is named SAA.

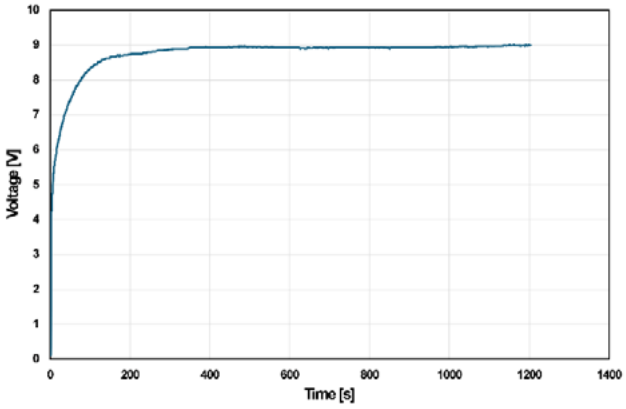


Figure 2. Growth curve of SAA samples with pins.

2.3. Manufacturing of the joint

Single lap co-cured joints were manufactured by vacuum infusion process. Five metallic substrates were placed in a plain mould and the dry basalt fabrics were then laid out over them in the overlapping area (25x25 mm) and in a vacuum bag. Subsequently, the epoxy resin was infused due to the pressure difference between the vacuum bag and the exterior. The curing process proceeded for 24 hours at room temperature and under vacuum. Then, the samples were post-cured in oven at 100 °C for 3 hours. Finally, single lap samples were cut with a rotative blade Bosch GCM 800 SJ. The final geometry of the samples is showed in Figure 3.

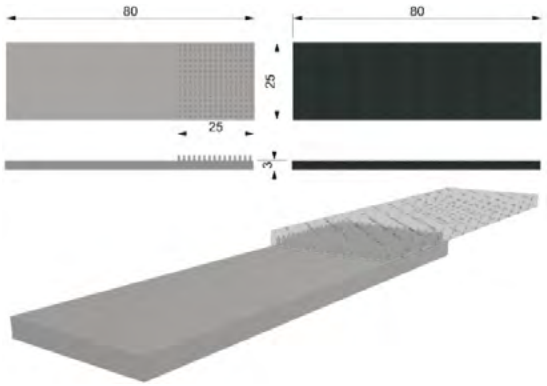


Figure 3. Geometry detail of the single lap configuration in mm. The transparency of the composite substrate in the draw is simply used to highlight interlocking with Pins.

The following nomenclature was used to identify the specimens: PIN-AP, PIN-AN. The acronym AP is referred to “As Printed”, meaning the samples have not received any treatment. AN refers to “ANodized”, i.e., the AP specimens that undergo the anodizing process in SAA.

2.4. Morphological characterization and corrosion resistance measurements

The structure of the porous layer formed through the anodization process was examined using a scanning electron microscope (SEM) model Tescan S900G. Microstructural differences between PIN-AP and PIN-AN samples were investigated by comparing their morphologies after the electrochemical process. The corrosion resistance of the samples was measured by electrochemical impedance spectroscopy (EIS). The samples were immersed in a 3.5% NaCl solution and connected to a Parstat 2273 potentiostat in a three-electrode configuration consisting of the sample, a platinum counter and an Ag/AgCl reference. The open circuit potential (OCP) was measured in the cell for 30 minutes. Subsequently, the

EIS measurement was performed by imposing a sinusoidal potential with an amplitude of ±10 mV referred to the OCP value, varying the frequency from 100 kHz to 100 mHz.

2.5. Lap-shear test

Five single lap samples for each type were tested with the geometry exposed in Figure 3. Universal testing machine Wance ETM-C equipped with a 50kN load cell was employed. The crosshead speed was set as 1.27 mm/min. The maximus force in kN was compared between the samples. The lap-shear strength in MPa was not evaluated due to the 3D shape of the joint surface.

3. Results and discussions

3.1. Comparison of AM surfaces

SEM images were useful to evaluate the morphology of the AM surface with the pins and how the anodization process change it during the process. In Figure 4 are exposed all the detailed shape of the metal surface.

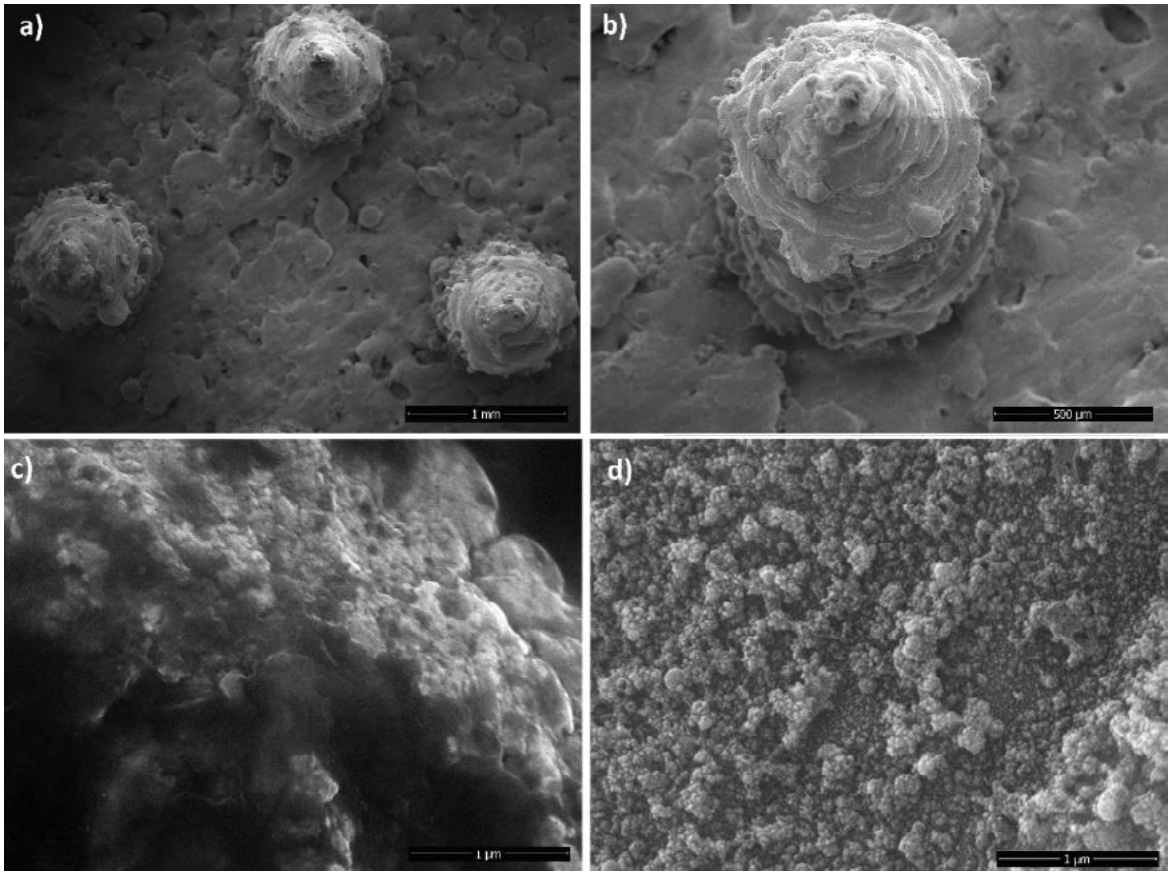


Figure 4. a) PIN-AP at low magnification; b) PIN-AP details of the single pin; c) surface morphology of the pin edge of PIN-AP at 100kX magnification; d) surface morphology of the pin edge of PIN-AN at 100kX magnification.

In Figure 4a and b it can be seen that the macroscopic morphology of the samples is very discontinuous and rough, especially the surface of the individual pin, due to the difficulty of stacking the powder layer by layer in such small parts. Moving to high magnification, in Figure 4c, it can be noted that the surface of the pin edge is rough but uniform, with no differences between the silicon and aluminium parts, due to the very fine silicon powders in the mixture. In contrast, after anodising (Figure 4d) it is possible to

observe the brighter part that is the silicon structure and the darker part that is the porous alumina layer. In this case, unlike cast aluminium structures, anodising, through the oxidation of silicon, which requires a lot of current generating a thinner layer of alumina, creates this porous layer surrounded by silicon.

3.2. Corrosion resistance of the AM samples

EIS measurements are useful to generate the Nyquist diagram where the impedance of the system was plotted with its imaginary and real part normalized by the area immersed in the solution. The curves in the graph are semi-circle where the diameter is the polarization resistance. This value is strictly correlated to the resistance against the corrosion current. The greater the polarisation resistance, the larger the semicircle size, the greater the corrosion resistance of the samples. In Figure 5 PIN-AP and PIN AN are exposed in the Nyquist diagram.

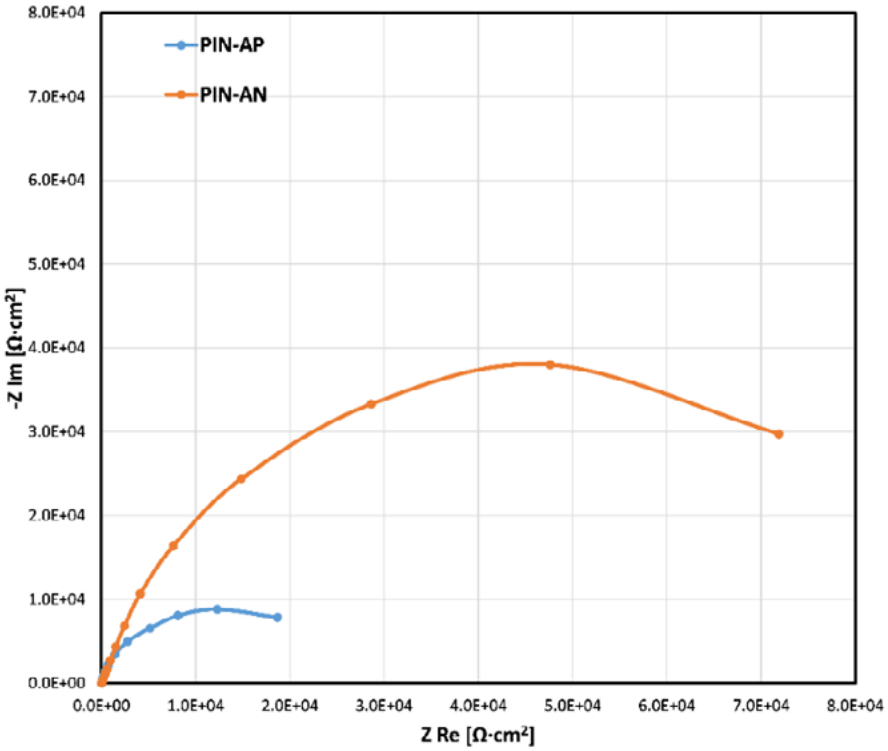


Figure 5. Nyquist diagram for PIN-AP and PIN-AN evaluating the corrosion resistance.

As can be seen in Figure 5, the PIN-AN curve is four times larger than that of PIN-AP. This is related to the effective growth of the anodic porous layer on the metal surface after the anodising process. The difference is not very large due to the presence of silicon structures, as mentioned in the previous paragraph. The anodising current is partly consumed by the anodising of the silicon rather than the formation of the porous alumina layer, resulting in a thinner and therefore less protective porous layer against corrosion. However, although thin, the porous alumina layer exists and because of it, the corrosion resistance of PIN-AN is greater than that of PIN-AN.

3.3. Single lap shear results

The results of the single lap shear test are shown in Figure 6.

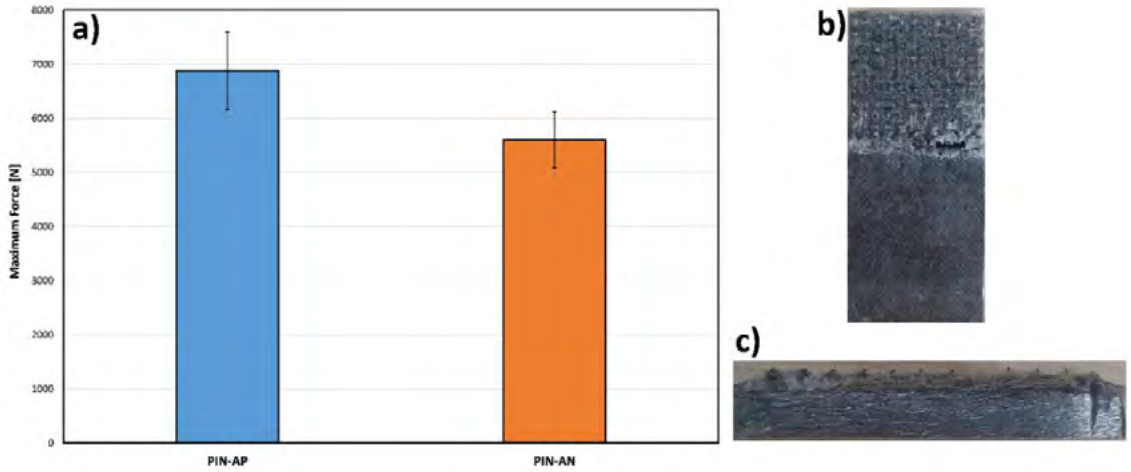


Figure 6. a) Maximus force in the single lap tests for the samples; b) top view of the fracture surface of PIN-AN; c) lateral view of the fracture surface of PIN-AN.

By means of single lap shear tests, it is not possible to highlight the influence of anodising on the mechanical performance of joints. This is due to the failure mode visible in Figure 6b and c. The presence of 2 mm high pins within a 3 mm thick composite generates a fracture between the composite layers. This phenomenon is clearly visible by observing the section of the fracture surface (Figure 6c). Here, the top of the pins is visible, indicating that the layer that has collapsed is the one between the top of the pins. For this reason, the achieved value of the maximum force represents the mechanical resistance of the composite layer against the crack propagation within the layer generated by the presence of the pins. In this case, the effect of the nano-porous layer is not macroscopically observable and the decrease shown in Figure 6a cannot be related to the anodizing process, but rather to the variability of the resistance in the inter-layer of the composite substrate.

4. Conclusions

In this work, the effect of the anodising technique on an aluminium AM (AlSi10Mg) substrate with macroscopic pins was evaluated by bonding it to an epoxy matrix reinforced with basalt fabrics in a co-cured single-lap joint configuration. The surface morphological structures were evaluated through SEM observations. In addition, the corrosion resistance of the specimens was estimated with EIS measurements. Finally, single-lap tests were conducted to highlight the influence of anodising on the AM metallic surface. The results showed that the presence of the porous anodic layer is confirmed by SEM images through the change in morphology. In addition, a silicon structure is visible that generates a negative interference in the formation of the anodic porous layer. However, the EIS results with the Nyquist diagram showed that the corrosion resistance of the PIN-AN sample is four times higher than that of PIN-AP, meaning that the porous layer exists and is efficient against the corrosion current. Due to the size of the pins, the mechanical testing couldn't detect any influence of the presence of the anodic layer. In conclusion, despite the irregularity and roughness of the AM substrate, anodising in SAA creates a porous alumina layer that can increase the corrosion resistance of AM samples. Probably by changing the size of the pins, avoiding the interlayer failure, the effect of the presence of the pins could also be assessed in the mechanical strength, since the porous layer was formed correctly.

Acknowledgments

This work was supported by Project ‘‘TARGET - addiTive mAnufactuRing for liGhtwEight joinTs”. (PRIN-2020) CUP: B73C22000130001. Furthermore, the authors thank Prof. Elpida Piperopoulos for the support in the morphology experimental analysis.

References

[1] Tuli NT, Khatun S, Rashid A Bin. Unlocking the future of precision manufacturing: A comprehensive exploration of 3D printing with fiber-reinforced composites in aerospace, automotive, medical, and consumer industries. Heliyon 2024;10:e27328. https://doi.org/https://doi.org/10.1016/j.heliyon.2024.e27328.

[2] Song Y, Ghafari Y, Asefnejad A, Toghraie D. An overview of selective laser sintering 3D printing technology for biomedical and sports device applications: Processes, materials, and applications. Opt Laser Technol 2024;171:110459. https://doi.org/https://doi.org/10.1016/j.optlastec.2023.110459.

[3] Buchanan C, Gardner L. Metal 3D printing in construction: A review of methods, research, applications, opportunities and challenges. Eng Struct 2019;180:332–48. https://doi.org/https://doi.org/10.1016/j.engstruct.2018.11.045.

[4] Elhadad AA, Rosa-Sainz A, Cañete R, Peralta E, Begines B, Balbuena M, et al. Applications and multidisciplinary perspective on 3D printing techniques: Recent developments and future trends. Materials Science and Engineering: R: Reports 2023;156:100760. https://doi.org/https://doi.org/10.1016/j.mser.2023.100760.

[5] CHEN J, HOU W, WANG X, CHU S, YANG Z. Microstructure, porosity and mechanical properties of selective laser melted AlSi10Mg. Chinese Journal of Aeronautics 2020;33:2043–54. https://doi.org/https://doi.org/10.1016/j.cja.2019.08.017.

[6] Ishfaq K, Abdullah M, Mahmood MA. A state-of-the-art direct metal laser sintering of Ti6Al4V and AlSi10Mg alloys: Surface roughness, tensile strength, fatigue strength and microstructure. Opt Laser Technol 2021;143:107366. https://doi.org/https://doi.org/10.1016/j.optlastec.2021.107366.

[7] Zhao L, Song L, Santos Macías JG, Zhu Y, Huang M, Simar A, et al. Review on the correlation between microstructure and mechanical performance for laser powder bed fusion AlSi10Mg. Addit Manuf 2022;56:102914. https://doi.org/https://doi.org/10.1016/j.addma.2022.102914.

[8] Piscopo G, Atzeni E, Salmi A. Mitigation of Residual Stress and Distortion of AlSi10Mg Parts Produced by Laser Powder Bed Fusion through a Proper Selection of Support Geometry. J Mater Eng Perform 2024. https://doi.org/10.1007/s11665-023-09108-5.

[9] Scherillo F. Chemical surface finishing of AlSi10Mg components made by additive manufacturing. Manuf Lett 2019;19:5–9. https://doi.org/10.1016/j.mfglet.2018.12.002.

[10] Fiore V, Di Franco F, Miranda R, Santamaria M, Badagliacco D, Valenza A. Effects of anodizing surface treatment on the mechanical strength of aluminum alloy 5083 to fibre reinforced composites adhesive joints. Int J Adhes Adhes 2021;108. https://doi.org/10.1016/j.ijadhadh.2021.102868.

[11] Di Franco F, Fiore V, Miranda R, Badagliacco D, Santamaria M, Valenza A. Influence of anodizing surface treatment on the aging behavior in salt-fog environment of aluminum alloy 5083 to fiber reinforced composites adhesive joints. Journal of Adhesion 2023;99:277–96. https://doi.org/10.1080/00218464.2021.2011240.

[12] Revilla RI, Terryn H, De Graeve I. Role of Si in the Anodizing Behavior of Al-Si Alloys: Additive Manufactured and Cast Al-Si10-Mg. J Electrochem Soc 2018;165:C532–41. https://doi.org/10.1149/2.1301809jes.

[13] Revilla RI, Verkens D, Couturiaux G, Malet L, Thijs L, Godet S, et al. Galvanostatic Anodizing of Additive Manufactured Al-Si10-Mg Alloy. J Electrochem Soc 2017;164:C1027–34. https://doi.org/10.1149/2.1121714jes.

[14] Zou X, Huang L, Chen K, Jiang M, Zhang S, Wang M, et al. Surface structuring via additive manufacturing to improve the performance of metal and polymer joints. Metals (Basel) 2021;11. https://doi.org/10.3390/met11040567.

IMPROVEMENT OF IMPACT ENERGY OF CELLULOSE NANOFIBER-ADDED CFRP BY WATER ABSORPTION UNDER HIGH TEMPERATURE AND PRESSURE CONDITIONS

Seiji Mitsubayashi[1] and Kenichi Takemura[2]

[1]Department of Mechanical Engineering, Kanagawa University, 3-27-1, Rokkakubashi, Kanagawa-ku, Yokohama, Japan
Email: mitsubayashi@kanagawa-u.ac.jp
[2]Department of Mechanical Engineering, Kanagawa University, 3-27-1, Rokkakubashi, Kanagawa-ku, Yokohama, Japan
Email: takemuta@kanagawa-u.ac.jp

Keywords: CFRP, Water absorption, Cellulose Nanofibers, Impact Energy

Abstract
The objective of this study was to clarify the effect of water absorption under high temperature and pressure conditions on the impact energy of cellulose nanofiber (CNF)-added CFRP. In this study, the water absorption rate was measured by adjusting the pressure, CNF additive rate, and water absorption time, and the changes in water absorption were compared. Izod impact tests were also conducted to evaluate the effect of water absorption under high temperature and pressure conditions on the impact properties of CNF-added CFRP. The results showed that the water absorption rate of CFRP without CNF and CFRP with CNF tended to increase with the water absorption time and then saturated at a certain value. The water absorption rate and impact energy tended to increase as the pressure during water absorption increased, and as the CNF addition rate increased, the water absorption and impact energy increased compared to the condition without CNF. It is suggested that in contrast to hydrophobic CFRP, water absorption in CFRP may be enhanced by the addition of hydrophilic CNF. The results indicate that the addition of CNF to CFRP, under high-temperature and high-pressure conditions, improves impact energy compared to CFRP without CNF.

1. Introduction

Carbon fiber reinforced plastics (CFRP) are used in a wide range of fields such as automotive and aerospace industries due to their high specific strength. However, it is known that polymeric materials are easily affected by water when used in harsh environments such as high temperature and high humidity, and the mechanical properties of CFRP are also significantly affected by these environmental factors. Katougi et al. investigated the flexural strength of CFRP that had absorbed water in a high-temperature environment and reported that water absorption reduced the flexural strength of CFRP by 2.3% [1]. On the other hand, since CFRP used in these fields requires high impact resistance, studies on water absorption of CFRP have been conducted to improve impact resistance. Hironaka et al. reported that long-term water absorption of CFRP improved the impact value by up to 8% compared to the value before water absorption [2]. Therefore, it is expected that the impact resistance of CFRP can be improved by increasing its water absorption. Therefore, in this study, we focused on water absorption under high temperature and pressure conditions.

In recent years, research has been conducted to improve the mechanical properties of CFRP by adding nano-sized or micro-sized fibers to the base material of CFRP [3]. Various fibers such as sub-micron glass fibers [4] and carbon nanotubes [5] have been used as additives. Among them, cellulose nanofibers (CNFs) derived from plants have attracted much attention because of their low environmental impact. Hayashi et al. reported that the addition of CNF to CFRP improved the flexural properties and interfacial

bond strength [6]. Nomura et al. also showed that the addition of CNF improved the vibration damping properties of CFRP. Therefore, the addition of CNF is expected to improve the impact strength of CFRP [7]. However, the effect of water absorption under high temperature and pressure conditions on the impact properties of CNF-added CFRP has not been clarified. Therefore, the objective of this study was to clarify the effect of water absorption under high temperature and pressure conditions on the impact energy of CNF-added CFRP.
In this study, the water absorption rate was measured by adjusting the pressure, CNF addition rate, and water absorption time, and the changes in water absorption were compared. Izod impact tests were also conducted to evaluate the effect of water absorption under high temperature and pressure conditions on the impact properties of CNF-added CFRP.

2. Experimental method

2.1. Test specimens

The test specimens were composed of plain weave PAN-based carbon fiber Torayca Cloth (CO6343, Toray Industries, Inc.) as the reinforcement material, epoxy resin (jER828, Mitsubishi Chemical Corporation) and epoxy resin curing agent (jER Cure Lv11, Mitsubishi Chemical Corporation) as the matrix material. In this study, an aqueous solution containing 2 wt.% CNF (BinFi-s WFo-10002, Sugino Machine Co., Ltd.) was used to mix with the epoxy resin. CNF aqueous solutions were prepared by diluting this solution to 0.03 wt.%, 0.05 wt.% and 0.1 wt.%. Here, the ethanol displacement method [2] was used to remove the water contained in the CNF, as it is very difficult to add CNF aqueous solution to the epoxy resin. The CFRP was fabricated using the hand lay-up method. The fabricated CFRP was made into test specimens with a length of 80 ± 2.0 mm, a width of 10 ± 0.2 mm and a thickness of 4.0 ± 0.2 mm according to JIS K 7110.

2.2. Method of water absorption

In this study, the CFRP specimens were placed in a 5.5 L pressure cooker with purified water for research purposes and the specimens were allowed to absorb water. The test conditions are shown in Table 1. The specimens were allowed to absorb water under four different pressure conditions (101 kPa, 161 kPa, 201 kPa, and 247 kPa). The water absorption temperatures were 100 °C, 114 °C, 120 °C, and 127 °C, respectively, in order of decreasing pressure. The water absorption time was 6, 12, 24, and 48 hours at each pressure condition, and the number of tests was five. After the specimens absorbed water, the water absorption was calculated using the following equation (1) according to JIS K 7290.

$$C = \frac{m_1 - m_0}{m_0} \times 100. \quad (1)$$

Table 1 Conditions of water absorption.

Specimen Type	Pressure p (kPa)	Temperature T (°C)	Absorption time (hrs)
A	101	100	6, 12, 24, 48
B	161	114	6, 12, 24, 48
C	201	120	6, 12, 24, 48
D	247	127	6, 12, 24, 48

2.3. Izod impact test

The impact energy of the water-absorbed specimens was measured using a DG-IB digital impact tester (Toyo Seiki Mfg. Co., Ltd.) in accordance with JIS K 7110. Here, an I5.5J hammer was used and the direction of impact was flatwise. The ambient temperature was room temperature, and the samples were used within one hour of removal from the pressure cooker.

3. Results and discussion

3.1 Change of water absorption rate with respect to CNF additive rate

Figure 1 show the relationship between water absorption and water absorption time for CFRP without CNF and CFRP with CNF in the Izod impact test. Here, (a), (b), (c), and (d) in Figure 1 represent the results at pressures of 101 kPa, 161 kPa, 201 kPa, and 247 kPa, respectively, during water absorption. With increasing water absorption time and pressure, the water absorption of CFRP without CNF and CFRP with CNF increased. For water absorption times other than 48 hours, the water absorption rate tended to increase with increasing CNF additive rate. It was found that water absorption of CFRP without CNF and CFRP with CNF both tended to increase with increasing water absorption time and pressure.

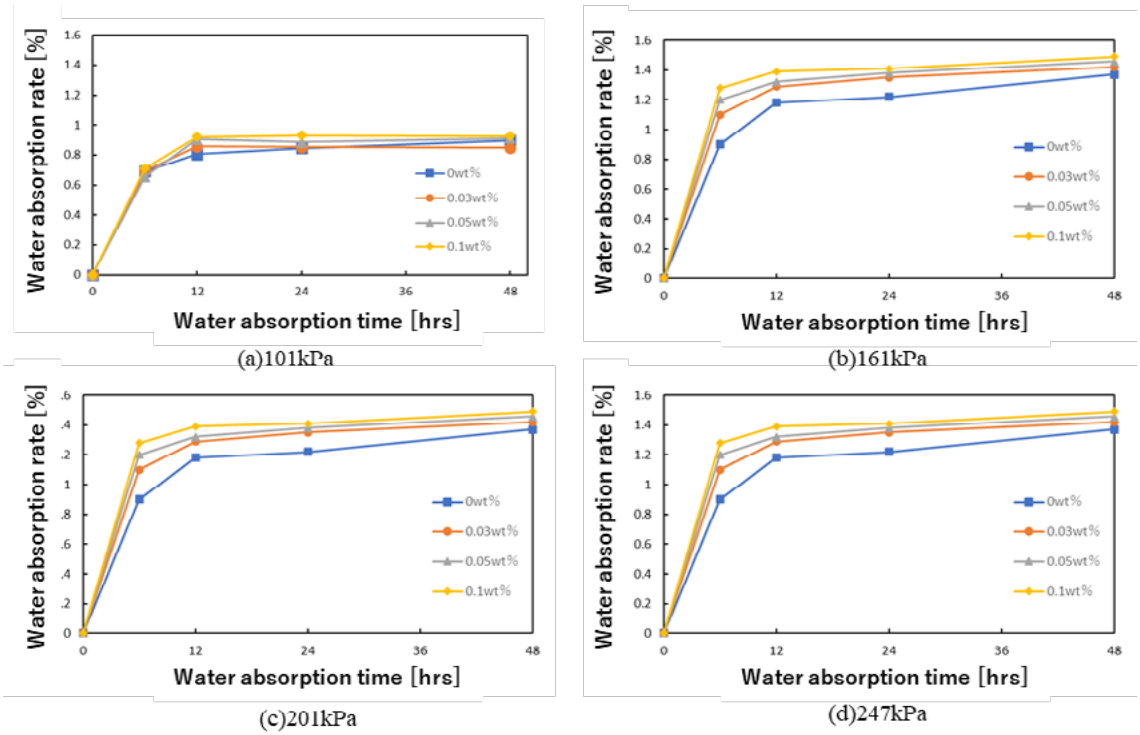


Figure 1 Changes of relationship between water absorption rate and immersion time with respect to pressure during water absorption.

3.2 Change of water absorption rate with respect to CNF additive rate

Figure 2 show the relationship between water absorption and impact values of CFRP without CNF and CFRP with CNF after water absorption and without water absorption. Here, (a), (b), (c), and (d) in Figure 1 represent the results at pressures of 101 kPa, 161 kPa, 201 kPa, and 247 kPa, respectively, during water absorption. While water absorption at a pressure of 247 kPa increased the impact value of CFRP without CNF by 59.7%, the addition of CNF increased the impact value by a maximum of 102% when water was absorbed at a pressure of 247 kPa. In addition, the results of the comparison of impact values for different additive rate of CNF showed that the impact energy tended to improve as the additive rate of CNF increased, as shown in Figure 2.Since the water absorption rate also increases with an increase in the addition rate of CNF according to Section 3.1, it was found that both the water absorption rate and impact energy can be improved by adding CNF and increasing the pressure during the water absorption process.

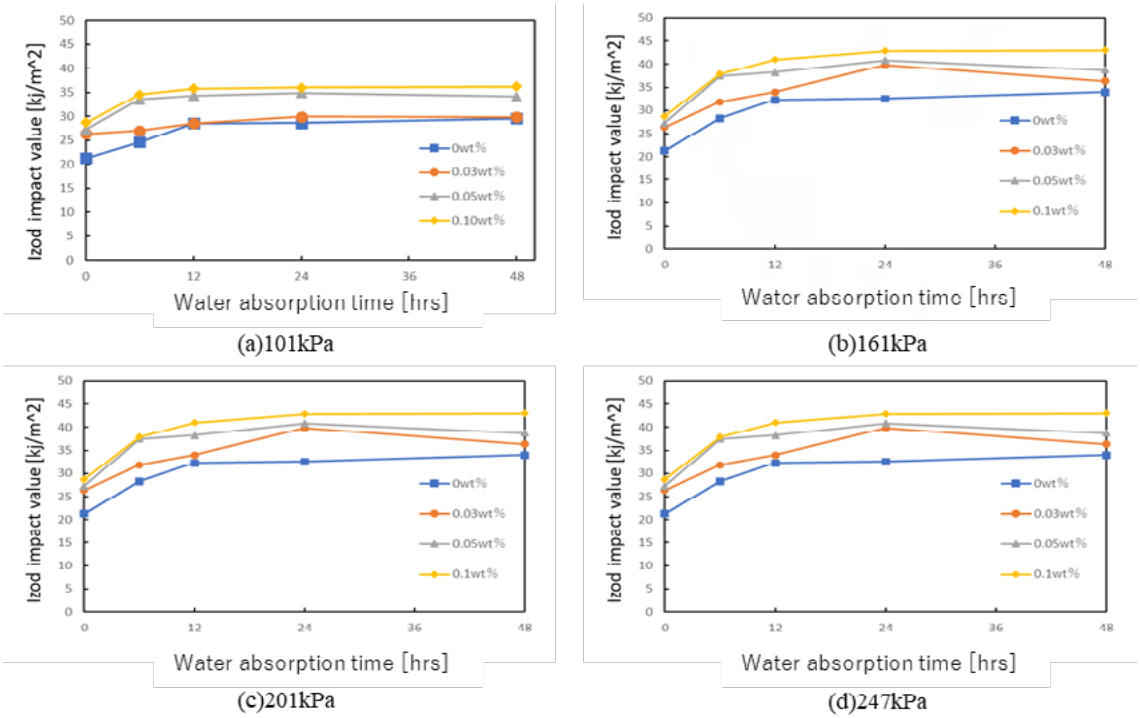


Figure 2 Changes of relationship between Izod impact value and immersion time with respect to pressure during water absorption.

3.3 Fracture surface of water-absorbed CFRP

Figure 3 show the SEM observation of CFRP after impact test. Here, (a), (b), (c), and (d) in Figure 3 represent the results at pressures of 101 kPa, 161 kPa, 201 kPa, and 247 kPa, respectively, during water absorption. Observation results showed that the amount of epoxy resin remaining on the fiber surface tended to decrease as the pressure increased. This indicated that the adhesive strength between the fiber and the resin was decreased as the water absorption rate became higher, and that interfacial fracture was more likely to occur.

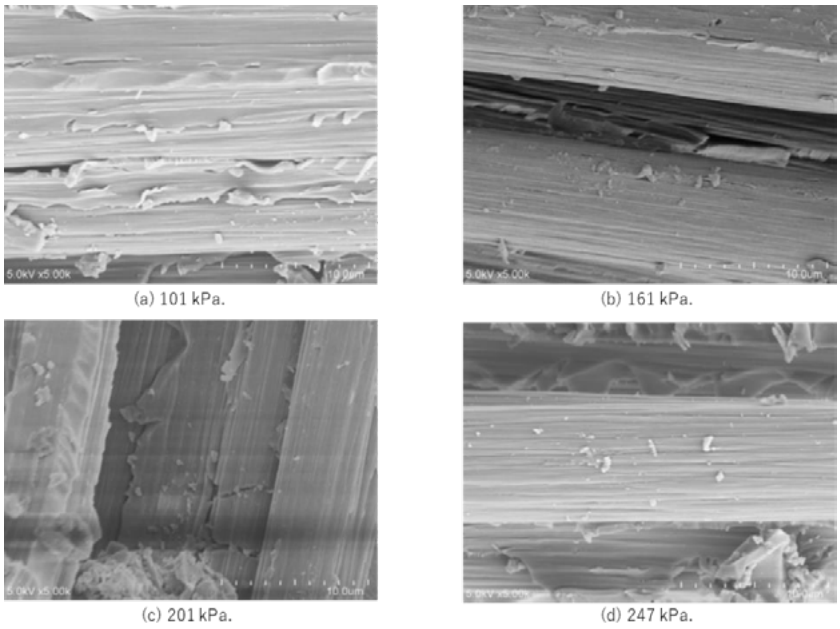


Figure 3 Change of impact fracture surface of CFRP with respect to pressure during water absorption at 0.1 wt.% of CNF additive rate.

Figure 4 also show the SEM observation of CFRP after impact test. Here, (a), (b), (c), and (d) in Figure 4 represent the results at CNF additive rate of 0 wt.%, 0.03 wt.%, 0.05 wt. %, and 0.10 wt.%, respectively, during water absorption. Observation results showed that the amount of epoxy resin remaining on the fiber surface tended to decrease as the pressure increased. It was considered that as the amount of hydrophilic CNF increased, the adhesive strength between the fiber and the resin decreased, which affected the impact energy of the CFRP.

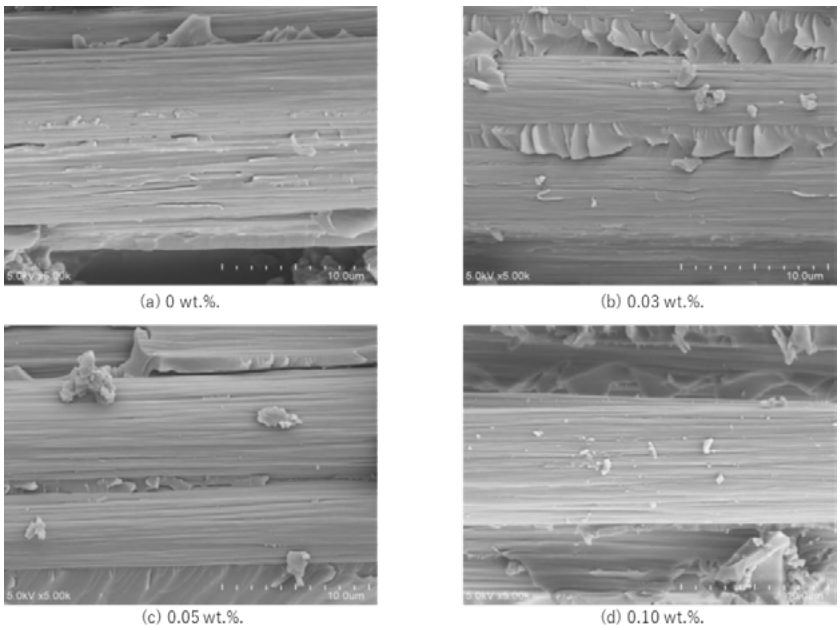


Figure 4 Change of impact fracture surface of CFRP due to the addition of CNF under the condition of water absorption at 247 kPa.

4. Conclusions

The following conclusions are obtained from this study.

[1] The results indicate that the addition of CNF to CFRP, under high-temperature and high-pressure conditions, improves impact energy compared to CFRP without CNF.

[2] The improvement in the impact characteristics of water-absorbed CFRP due to the addition of CNF can be attributed to the hydrophilic property of CNF.

Acknowledgement

We would like to thank the Research Institute for Engineering at Kanagawa University for the use of their facilities. We gratefully thank Mr. Miyashita at Kanagawa University for support in the data acquisition.

References

[1] H. Katougi and K. Takemura, "Effect of Water Absorption on Flexural Strength and Creep Property of Carbon Fiber Reinforced Composite", Journal of the Japan Society for Composite Materials, Vol.35, No.6, pp.233-240, (2008)

[2] N. Hironaka, K. Inoue, M. Kanda and Y. Nishi, "Change in Mechanical Properties by Water Absorption of CFRP", J. Japan Inst. Met. Mater., Vol.71, No.12, pp.1102-1106, (2007)

[3] K. Obunai, K. Okubo and K. Hayashi, “Improvement of Fatigue Life of Plain Woven CFRP Plate by Adding Cellulose Nano Fibers and Investigation on Its Mechanism”, Journal of the Society of Materials Science, Japan, Vol.69, No.5, pp.351-357, (2020)

[4] R. Murayama, K. Obunai, K. Okubo and L. Bao, “Improvement in Impact Energy Absorption of UD-CFRP by Sub-Micron Glass Fiber into Its Matrix”, Open Journal of Composite Materials, Vol.11, No.4, pp.82-93, (2021)

[5] G. Tefera, G. Bright and S. Adali, “Flexural and shear properties of CFRP laminates reinforced with functionalized multiwalled CNTs”, Nanocomposites, Vol.7, No.1, pp.141-153, (2021)
[6] K. Hayashi, K. Okubo and K. Obunai, "Improvement of Interfacial Adhesion Strength and Mechanical Properties of CFRP by Fabricated with Modified Matrix by Adding Nano Fibers", Journal of the Adhesion Society of Japan, Vol. 54, No.11, pp.402-409, (2018)
[7] T. Nomura, K. Obunai and K. Okubo, "Improving Damping Properties of Carbon Fiber Reinforced Plastic Fabricated with Modified Matrix by Adding Cellulose Nanofibers -Influence of Aspect Ratio of Cellulose Nanofibers Added to Matrix on Damping Properties-", Journal of the Japan Society for Composite Materials, Vol.47, No.4, pp.131-136, (2021)

©2024 | 3_MITSUBAYASHI_Seiji_KNJKB.pdf:6

NON-STRUCTURALLY DAMAGING FILM-BASED SENSORS FOR IN-SITU MANUFACTURING PROCESS AND CURING MONITORING OF FIBRE-REINFORCED COMPOSITES

Imke Möllmann[1], Christian Lauter[1]

[1]PHWT Institute, Department Design, Lightweight and Fibre-reinforced plastics, PHWT, Am Campus 2, 49356 Diepholz, Germany
Email: moellmann@phwt.de, lauter@phwt.de, Web Page: http://www.phwt.de/

Keywords: Composite lightweight design, manufacturing of composites, carbon fibre prepreg, epoxy resin, curing of fibre-reinforced plastics, film-based sensor

Abstract

Fibre-reinforced plastics are commonly used as lightweight design materials due to their high specific mechanical properties. However, manufacturing methods such as autoclave methods require significant amounts of energy and time to produce these structures. The aim of this research is to develop a film-based sensor that can realise an in situ measurement of the curing processes of epoxy resins. The sensor measures physically variable parameters, such as the electrical capacity of the epoxy matrix during curing. The measured values are correlated with the degree of curing or other process parameters. For this purpose, the sensor remains in the material and should not be structurally damaging. Therefore various films are being investigated as sensor carrier materials as part of the research.

1. Introduction

Fibre-reinforced plastics are versatile lightweight design materials that are commonly used in different applications and branches of industries. The autoclave process is a common method for manufacturing structures from these composites, but it is associated with long cycle times, and high production costs. For the manufacturing of these lightweight structures, prepregs are often used as semi-finished products. Prepregs consists of fibres that are pre-impregnated with matrix materials like epoxy resins. During the autoclave process the prepregs are laid into molds and cured under pressure and elevated temperature. Proper adjustment of process parameters is crucial. If the resin curing reaction occurs too quickly or at too high a temperature, voids and pores can be formed in the final product. That results in a significant decrease in quality. [1, 2] Conversely, if the curing reaction occurs too slowly, it results in significantly higher costs, including energy costs for providing pressure and temperature, machine costs as the autoclave is occupied for a longer period, and overall production costs, e.g., due to waiting and delivery times. [3, 4]

Currently, the industry often relies on empirical values or guidelines for designing an autoclave process. This research aims to develop a film-based sensor to adjust process parameters in real-time using in situ measuring during the curing of the prepreg-material. It is based on environmental conditions, such as resin reactivity, local tool temperature, ambient temperature, and other process parameters. The aim is to incorporate small film-based sensors into fibre-reinforced laminates to measure physical quantities like temperature and capacitance during curing (Figure 1). This enables precise adjustments to achieve the desired properties. The current state of the art uses sensors to measure ion viscosity. This measured value is based on an electrical resistance which depends on changing viscosity due to the chemical reaction during the curing reaction. [5, 6, 7, 8]

The study evaluates different film materials based on their properties to determine their suitability for the application. Common used materials for film-based sensors are actual polyimide (PI) films. [9, 10] A major challenge is to develop sensors, that can be applied to structurally loaded composite structures and remain inside the laminate during the use of the component. This means that the sensor and the film material must not be structurally damaging. [11]

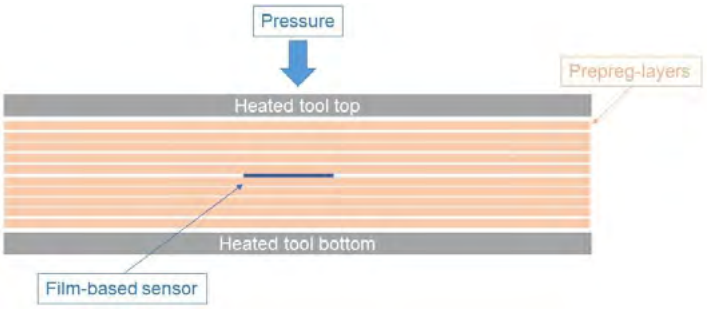


Figure 1. Non-structurally damaging film-based sensor between prepreg layers

2. Requirements for the film material and test methods

In order to facilitate the development of the sensor, it is essential to define the requirements for the film material, as this material exerts the greatest influence on the damaging process in the subsequent component, as outlined in chapter one. Consequently, the initial step in the process is to define the boundary conditions for the film material. This is followed by the selection of appropriate test methods to assess the various plastics for the desired properties. [12]

The main objective of the investigations was to find and characterize a film material for the further sensor that meets several requirements. These requirements include a mandatory temperature resistance of up to 200 °C, which corresponds to the temperature cycles in the autoclave process e.g. in the aerospace industry. Additionally, the film should have a rough surface to maximise adhesion between the prepreg resin and the film. Furthermore, a high surface roughness enables good printability of the film material using silver conductive paste in order to precisely realize a sensor structure. The sensor pattern or meander structures will be applied afterwards using this method. [2]

Different film materials were selected for the investigations and evaluated based on the above-mentioned requirements. The materials for the analyses were polyethylene (PET) with acrylic resin, PET, PET with PI coating, polyetherimide (PEI), PI, polycarbonate (PC) and polyethylene naphthalene (PEN) as shown in Figure 2.

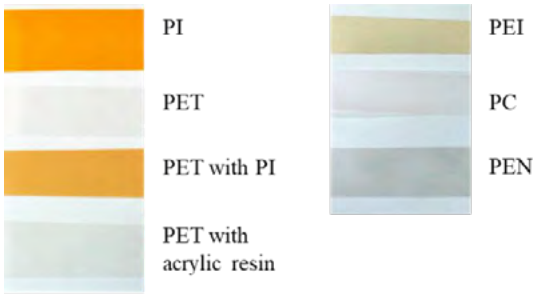


Figure 2. film materials

To ensure high measurement accuracy, the humidity absorption of the film materials is tested in accordance with ISO 62, as the accuracy of the electrical resistance measurement depends heavily on it. Therefore it is important to keep the humidity absorption of the films as low as possible. [13]

A further criterion is the material thickness of the film, which should be as low as possible to minimise the defect introduced by the subsequent sensor in the composite. As the material thickness can be influenced by the film manufacturers, it should also be analysed when checking the data sheet characteristics, but should not be selected as the decisive criterion for the film material. It can be measured with a micrometer screw. As an adhesion promoter (HV) is often used to apply the silver conductive paste, the film properties should be investigated with regard to the influence of the adhesion promoter. The material is a single-component material for processing in the printing, injection moulding and forming process up to 240 °C according to the data sheet. It is expected that the adhesion promoter will have an effect on the surface roughness of the films.

Thermal analyses are conducted to evaluate the temperature resistance of the materials. Differential scanning calorimetry (DSC) is suitable for determining the melting and glass transition temperatures of materials. As not all materials to be analysed exhibit a melting or glass transition temperature, a thermogravimetric analysis (TGA) is also performed. In this use case, the DSC is employed for the thermoplastic materials in the tests. The TGA is primarily utilized for the thermoset materials. The DSC analyses were carried out in accordance with DIN EN ISO 11357-1 and the TGA analyses in accordance with DIN EN ISO 11358-1. [14, 15]

3. Results

The purpose of this study was to analyse typical film materials with regard to their application in structurally non-damaging film sensors. Consequently, the requisite specifications for the film material were delineated, followed by the selection of distinct analytical methodologies to assess the diverse materials as in the previous chapter described. Based on this, a carrier material for the silver conductive paste of the sensor can be selected.

In addition, the influence of an adhesion promoter will be analysed. This will be used to apply the conductive silver paste on the film-material. It is expected that the adhesion promoter will not affect the properties of the film material in terms of surface roughness. The aim is to determine whether the applied adhesion promoter has a positive or negative effect on the adhesion between the prepreg material and the sensor.

3.1 Differential scanning calorimetry (DSC)

The DSC measurements were performed with a Netzsch DSC 204 F1 Phoenix. The DSC is comprised of a preciously defined measuring cell, which contains a reference pan and a sample pan. The system employs the heat flow principle in order to determine specific temperatures. All experiments were carried out in accordance to DIN EN ISO 11357-1 with a constant nitrogen flow of 20 l/min and the sample weight was between 4 – 8 mg. A concave pan was used and the DSC cell was pre-cooled to 0 °C. The measurement cell was heated to 450 °C following a cooling at 0 °C and a second heat and cooling phase at 450 °C and 0 °C. The heat rate was every time 10 °C/min. [14]

Figure 3 displays the results of the DSC analyses. The temperature ranges indicating a change in the plastic are important for material selection. This can be either the melting temperature or the glass transition temperature, depending on the material. The diagram specifies the melting temperature for all film materials except PEN, for which the glass transition temperature is more pronounced and shown in the diagram. The measurement evaluation indicates that the adhesion promoter has no significant effect on the melting temperature of any sample. The PEN film has a glass transition temperature of approximately 120 °C, while the PC film has the lowest melting temperature of approximately 152 °C. The PET films have the highest melting temperatures at approximately 255 °C. The melting temperature

of the PEI film was approximately 220 °C, and the different coatings of the PET film had no effect on its melting temperature. The PI film was not analysed because it is a thermoset material that does not have a melting temperature, but rather a decomposition temperature.

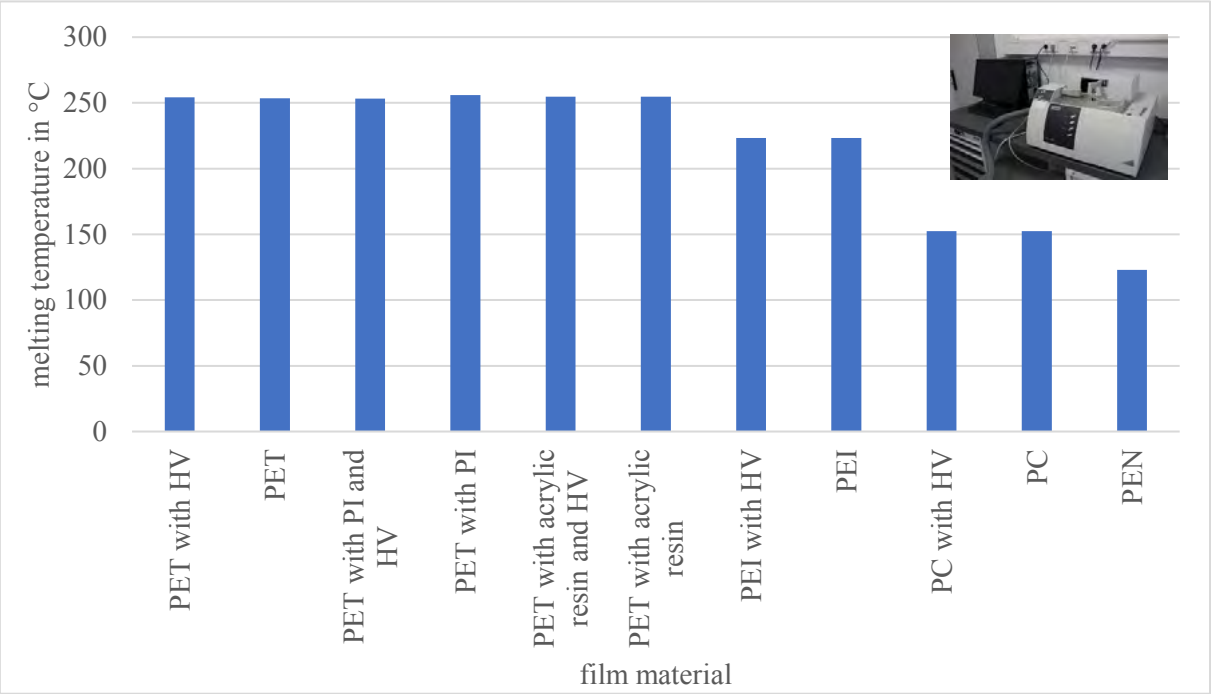


Figure 3. DSC-analysis

The results of the DSC analyses indicate that the adhesion promoter does not affect the melting or glass transition temperature of the film materials, as expected. Therefore, the adhesion promoter was not extensively analysed during the TGA (Figure 4). The DSC analyses also revealed that the film materials PC and PEN are not temperature-resistant up to 200 °C, while all other film materials meet the requirements. No difference in melting temperatures was observed between PET films with and without coatings. This can be explained by the fact that the base material, PET, has a lower melting temperature compared to the two coating materials, and therefore, the influence of the base material is predominant.

3.2 Thermogravimetric analysis (TGA)

The TGA measurements were performed with a Netzsch TG 209 F1 Libra. In the TGA the mass of a small sample is measured during temperature change. All experiments were carried out in accordance to DIN EN ISO 11358-1 with a constant nitrogen and oxygen flow of 20 l/min and the smple weight was between 4 – 8 mg. The sample was heated up to 950 °C. [15]

The TGA analyses indicate that the PI film has the highest decomposition temperature at 585 °C. The PET and PEN films show the lowest decomposition temperature at approximately 410 °C due to the covalent bonds between the molecular chains and the pronounced intermolecular cross-linking structure. The DSC analyses do not reveal any influence of the coatings on the PET films, which can be attributed to the lower decomposition temperature of the PET compared to the coating materials. The results of both analysis are therefore logically comprehensible and reflect expectations. According to the first analyses carried out, the PI film has the best properties as a carrier material for the sensor. PET films and PEI films are also well suited.

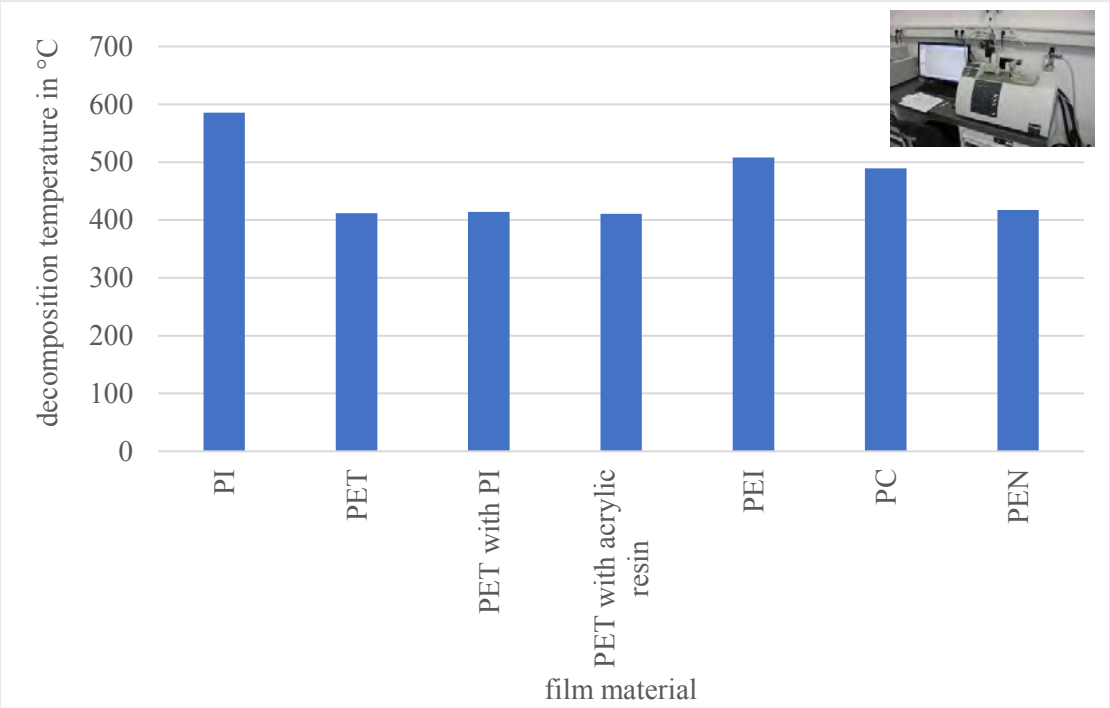


Figure 4. TGA-analysis

3.3 Surface roughness

The measurement of the surface roughness were performed with a Mitutoyo Surftest SJ-310. A diamond tip is drawn over a surface at 0.75 mN at an angle of 60°. The centre roughness value can be determined using the induction method.

The analyses of the surface roughness of the film materials produced varying results (Figure 5). It was anticipated that differences between the coatings of the PET film would be measurable when analysing the roughness. Additionally, an influence of the adhesion promoter is assumed, as it acts like a coating on the films. The PC films exhibited the greatest roughness at approximately 0.52 µm, followed by the PI films at approximately 0.32 µm and the PEI films at approximately 0.19 µm. The roughness of the PET film was lowest when it was not coated. The measurements showed that coating the PET films has an impact on their roughness. Specifically, the PET film coated with acrylic resin had a surface roughness around 15% greater than the base material, while the PET film coated with PI had a surface roughness around 25% higher than the base material.

In almost all cases, the adhesion promoter reduced surface roughness. When inserting films wetted with adhesion promoter into the prepreg material for sensor development, it is important to consider the overall objective.

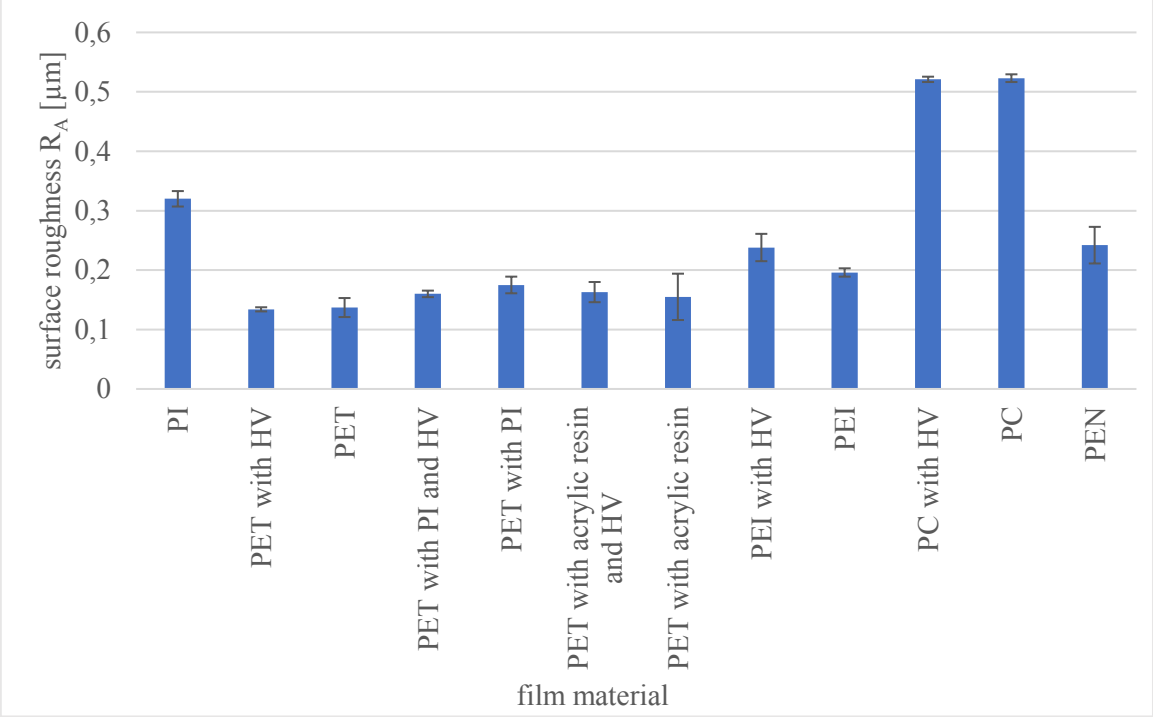


Figure 5. Average surface roughness R_A

3.4 Humidity absorption

The measurement of the humidity absorption (Figure 6) were performed in a climate cabinet CTS C-40/200 in accordance with ISO 62. First all samples were dired for 8 h at 70 °C. The weight of the samples were mearued before and after drying. Following the drying the samples were in a humid environment for 24 h. After that the samples were weighed again and the humidiy absorption could be calculated. [13]

When analysing humidity absorption (Figure 6), it was assumed that the coatings on the PET films could have an influence on the measurement. The PI film exhibits the highest humidity absorption. This observation is confirmed when comparing the PET films with coating, where the PI-coated film also shows increased humidity absorption. In comparison, the PET film with acrylic resin coating exhibits slightly lower humidity absorption than the pure base material, while the PC film exhibits the lowest humidity absorption. The PEN film falls within a similar range to the PET films. The PEI film exhibits the highest water absorption after the PI film.

Therefore, it can be concluded that the use of PET, PEN or PC films best meets the requirements. The measured results could be validated using the data sheets of the film manufacturers.

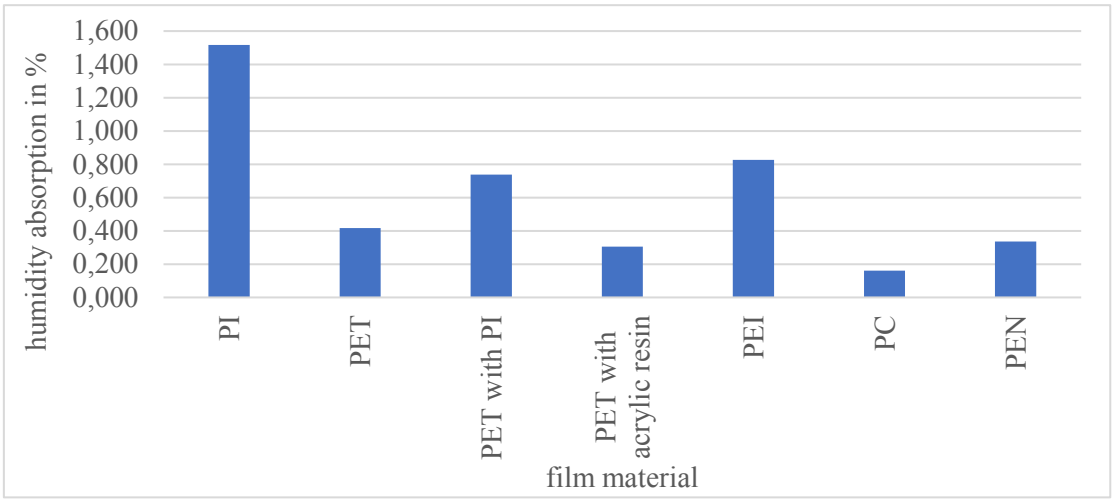


Figure 6. Humidity absorption

3.5 Material thickness

Figure 7 shows the results of determining the material thickness of the films produced. It was measured with a micrometer screw. The PI film has the lowest material thickness at approximately 0.064 µm, while the PC film has the greatest material thickness at approximately 0.25 µm. There is no difference found between coated and uncoated PET films, and the application of the adhesion promoter also has no measurable effect on the material thickness. These measurement results are confirmed by comparing them with the data sheets for the film materials.

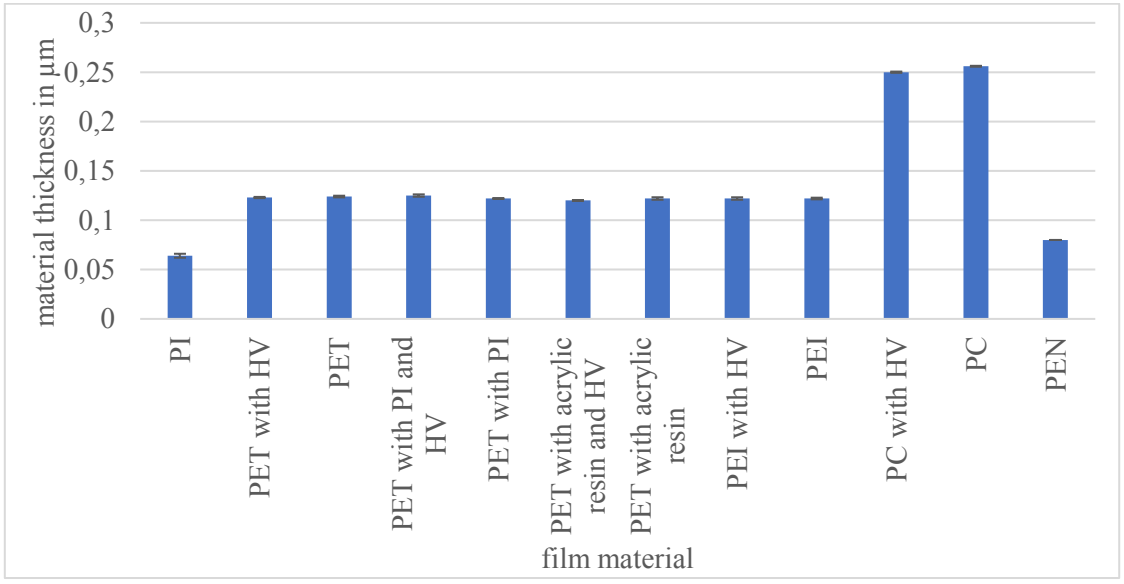


Figure 7. Averaged material thickness

4. Discussion and Conclusion

The tests conducted helped to limit the selection of film materials suitable for use in film sensors, that can be integrated into composite laminate structures. A PI film is highly recommended due to its high

decomposition temperature, temperature resistance, high roughness, and low material thickness. However, it should be noted that this film material has increased humidity absorption, which must be taken into account. PET-based films can be used as an alternative to this film as they performed well in all tests. In a direct comparison of the base material with the two coatings, the acrylic resin coating is a good carrier material. PEI films are also suitable as a carrier material, according to the tests carried out. However, it is important to consider the exact area of application when using PEI film as a sensor due to its melting temperature being close to the specified 200 °C. Additionally, it has a tendency to absorb more humidity. Further tests are planned to finalise the definition of the film, including delamination properties in the prepreg material, printability with silver conductive paste, and measuring accuracy in the prepreg.

Acknowledgments

This Project is supported by the Federal Ministry for Economic Affairs and Climate Action (BMWK) on the basis of a decision by the German Bundestag.The authors would like to thank the BMWK for the funding and Roos GmbH and 3D ICOM GmbH for supporting this research.

References

[1] P. Hubert, G. Fernlund, und A. Poursartip. Autoclave processing for composites. in *Manufacturing Techniques for Polymer Matrix Composites (PMCs)*, S. 414–434, 2012.
[2] P. Hubert. Autoclave and out-of-autoclave processing of prepregs. in *Design and Manufacture of Structural Composites*, S. 209–236, 2023.
[3] N. Poyyamozhi *u. a.* Ecosystem sustainability and conservation of waste natural fiber strengthen epoxy composites for lightweight applications. in *Environmental Quality Management*, Juni 2023.
[4] M. A. Hubbe. Sustainable Composites: A Review with Critical Questions to Guide Future Initiative. in *Sustainability*, Bd. 15, Nr. 14, S. 11088, Juli 2023.
[5] H. Li und B. Zhang. Improved models of viscosity and relaxation modulus for epoxy resin during cure. in *Polymer Engineering and Science*, Bd. 56, Nr. 6, S. 617–621, Juni 2016.
[6] C. Garschke, C. Weimer, P. P. Parlevliet, und B. L. Fox. Out-of-autoclave cure cycle study of a resin film infusion process using in situ process monitoring. in *Composites Part A: Application Science and Manufacturing*, Bd. 43, Nr. 6, S. 935–944, Juni 2012.
[7] J. O. Simpson und S. A. Bidstrup. Rheological and dielectric changes during isothermal epoxy-amine cure. in *Journal of Polymer Science Part B: Polymer Physics*, Bd. 33, Nr. 1, S. 55–62, Jan. 1995.
[8] H. Park. Dielectric cure determination of a thermosetting epoxy composite prepreg. in *Journal of Applied Polymer Science*, Bd. 134, Nr. 15, Apr. 2017.
[9] Y. Zhu, P. Xia, J. Liu, Z. Fang, L. Du, und Z. Zhao. Polyimide-Based High-Performance Film Bulk Acoustic Resonator Humidity Sensor and Its Application in Real-Time Human Respiration Monitoring. in *Micromachines*, Bd. 13, Nr. 5, S. 758, Mai 2022.
[10] M. Tomikawa. Polyimides for Micro-electronics Applications. in *Polyimides*, 2022.
[11] A. Kyriazis, R. Kilian, M. Sinapius, K. Rager, und A. Dietzel. Tensile Strength and Structure of the Interface between a Room-Curing Epoxy Resin and Thermoplastic Films for the Purpose of Sensor Integration. in *Polymers*, Bd. 13, Nr. 3, S. 330, Jan. 2021.
[12] H. M. Pathan. *u. a.*. Thin Film Materials and Devices. *ES Material Manufacturing*, 2020.
[13] SO 62:2008. Plastics - Determination of water absorption.
[14] ISO 11357-1:2023. Plastics - Differential scanning calorimetry (DSC) - Part 1: General principles.
[15] ISO 11358-1:2022. Plastics - Thermogravimetry (TG) of polymers - Part 1: General principles.

VIBRATION-BASED PROGRESSIVE FATIGUE DAMAGE DETECTION AND CLASSIFICATION FOR THERMOPLASTIC COUPONS UNDER POPULATION AND OPERATIONAL UNCERTAINTY

Niki Tsivouraki[1,2], Konstantinos Tserpes[1] and Spillios Fassois[2]

[1]Laboratory of Technology & Strength of Materials, Department of Mechanical Engineering & Aeronautics, University of Patras, Patras 26500, Greece
Emails: niki.tsivouraki@upnet.gr, kitserpes@upatras.gr, Web Page: http://ltsm.mead.upatras.gr
[2]Stochastic Mechanical Systems and Automation Laboratory, Department of Mechanical Engineering & Aeronautics, University of Patras, Patras 26500, Greece
Email: fassois@upatras.gr, Web Page: http://www.smsa.upatras.gr

Keywords: Thermoplastics, SHM, Vibration-based methods, Fatigue damage detection, Fatigue damage classification

Abstract
The problem of vibration-based progressive fatigue damage detection and classification for thermoplastic coupons is addressed under population and experimental uncertainty. The study is based on a population of 6 thermoplastic coupons subjected to tension-tension fatigue which is interrupted at 10 000 cycles long intervals. The methodology employs Multiple Model Representations of the uncertain dynamics using parametric ARMA random vibration modeling. The results of the study provide: (a) A clear demonstration of the effects of fatigue on the coupon structural dynamics, with almost monotonic dependence on the number of fatigue cycles, (b) excellent fatigue damage detection performance characterized by 100% correct detection for all coupons under any fatigue state, and (c) a very good fatigue state classification performance reaching an aggregate (over all coupons) correct determination rate up to 90%. The outcomes of the study demonstrate the potential of the method for automated detection and classification of fatigue damage in thermoplastic aerostructures under population and experimental uncertainty.

1. Introduction

Composite materials, particularly thermoplastics, have emerged as dominant materials in the aerospace industry, overcoming thermosets due to their distinct advantages such as advanced impact performance, recyclability, and weldability [1]. Despite composite materials' expected superior fatigue lifetimes, fatigue remains a critical issue in the design process, especially for structures subjected to dynamic loads [2]. The anisotropic nature of fiber-reinforced polymers introduces complexity to fatigue damage characterization, encompassing various damage modes like matrix cracks, delamination, and fiber breakage [3]. Structural Health Monitoring (SHM) methods, including vibration-based techniques, have witnessed significant advancements, offering alternatives to traditional non-destructive testing (NDT) methods [4]. These facilitate continuous, online, monitoring, presenting a departure from offline approaches such as X-rays. Vibration-based methodologies, including global modal parameter based analysis, methods based on the wavelet transform and on AutoRegressive (AR) modeling, enable comprehensive fatigue damage assessment for composite structures [5,6]. Each methodology offers unique advantages and limitations, ranging from macroscopic insights provided by global modal parameters to the nuanced detection facilitated by wavelet transform and AR modeling.

Key studies in the field have demonstrated the efficacy of vibration-based methods in fatigue damage assessment within composite structures. These studies, utilizing techniques such as global modal properties [7,8], frequency response functions (FRFs) [9,10], wavelet transform [11,12], and AR models [13,14], have significantly contributed to the understanding and characterization of fatigue damage initiation, propagation, and accumulation.

Although the significant contribution of the aforementioned studies, lack is located to a complete and comprehensive study of progressive fatigue damage initiation and evolution using exclusively on-line methods, which part of this, is covered by the present study. This study presents an extensive experimental process for investigating progressive fatigue damage in quasi-isotropic thermoplastic coupons subjected to tension-tension fatigue. Utilizing non-contact vibration tests, the study presents a comprehensive detection and classification of fatigue damage, highlighting the potential of vibration-based methods for monitoring progressive fatigue damage in thermoplastics.

2. Experimental set-up

2.1. Material and coupons

The coupons are of dimensions $250\,mm \times 25\,mm \times 2.24\,mm$, and the bonded tables are $50\,mm\ x\ 25\,mm\ x\ 2.24\,mm$. The coupons and the tabs are made of thermoplastic TC 1225 LM PAEK prepreg plies with a fiber volume fraction of 66%. The 0.14 mm-thick plies are stacked in a quasi-isotropic stacking sequence with a lay-up of $[-45/0/45/90]_{2s}$.

2.2. Experimental procedure

Three types of mechanical tests were conducted: Quasi-static tension tests (Coupons #1-5) on virgin coupons based on the ASTM D3039 standard [15], non-interrupted tension-tension (T-T) fatigue tests (Coupons #6-10), and interrupted tension-tension (T-T) fatigue tests (Coupons #11-16), both based on the ASTM D3479 standard [16]. For all mechanical tests, an MTS Landmark machine with a 100 kN load cell was used. Initial tensile tests were conducted for material characterization. In the interrupted T-T fatigue tests, every 10,000 cycles the coupons were subjected to random vibration tests. This procedure was repeated until fatigue failure of each coupon. The equipment for the vibration test comprised a laser vibrometer (OFV-505), its controller (OFV-5000), a NI-9230 acquisition card, speakers, and a PC. The excitation is acoustic, MATLAB-generated, white noise, while the coupons were supported by elastic chords (free-free boundary conditions). Fig. 1 illustrates the experimental setup for the random vibration test. Six coupons were used for the vibration tests, which thus accounted for population (mass, geometry), operational (set-up, excitation), and environmental (temperature) uncertainty. Fatigue and random vibration test parameters are outlined in Table 1.

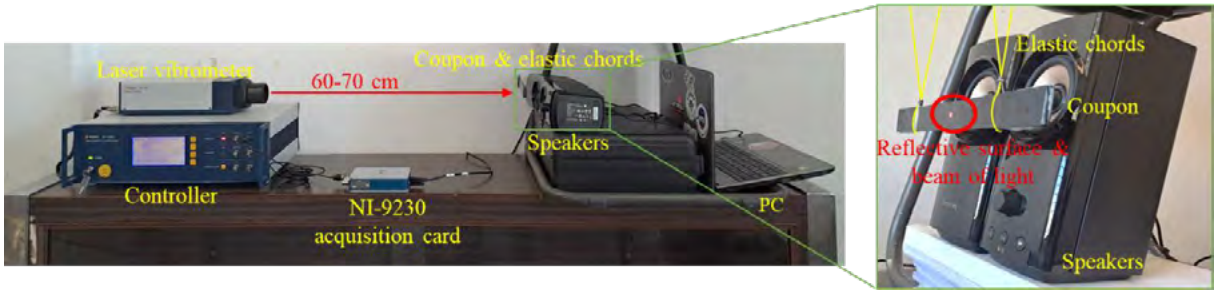


Figure 1. Experimental set-up for the random vibration test.

3. Fatigue damage detection and classification methodology

Fatigue damage detection and classification are realized through a vibration-data and Multiple Model Representation (MMR) based methodology. This is a data-based methodology encompassing a *Training or Baseline Phase,* performed once and initially in order to make proper selections, and an *Operational or Inspection Phase* during which diagnostic decisions are made. While the Baseline Phase requires

vibration response signals obtained from experiments with various coupons, the Inspection Phase is based on a single signal obtained from any specific coupon, potentially under normal structural operation. In this context it should be clarified that the term *detection* refers to the confirmation of the presence of damage in a coupon, while the term *classification* refers to inferring the precise *Fatigue State (FS)* for any coupon based on the measured vibration signal.

Table 1. Fatigue test parameters and random vibration signal characteristics.

Fatigue test		Random vibration test (Signal Characteristics)	
Parameter	Value	Parameter	Value
f	5 Hz	Sampling frequency f_s	12,800 Hz
σ	$0.6\sigma_{max}$	Signal duration	60 s
R	0.1	Signal bandwidth	0-6,400 Hz

3.1. Damage detection

The dynamics of the healthy population of specimens are modeled via an MMR consisting of a number of ARMA models of a properly selected order. In the *Baseline Phase* a number, say p, of vibration response signals are obtained from various healthy coupons. Let each one of them be designated as $m_{0,i}$ $(i = 1, \dots, p)$, with the estimated AR/MA parameter vector following a Gaussian probability density function with mean the obtained point estimate $\boldsymbol{a}_{0,i}$ and covariance matrix $\boldsymbol{\Sigma}_{0,i}$. In the *Inspection Phase*, given a new vibration response signal from any coupon, the objective is to detect the presence of damage by examining whether or not the underlying coupon dynamics is represented well by the MMR m_0, in which case the current coupon is declared as healthy; else, as damaged. For this purpose a new ARMA model (of the exact same orders), say m_u, is estimated, and then its proper pseudo-distance from m_0, say $D(m_0, m_u)$, is determined. Decision making is then based on a test of the form:

$$\begin{aligned} D(m_0, m_u) \leq l_{lim} &\Longrightarrow Healthy\ Coupon \\ D(m_0, m_u) > l_{lim} &\Longrightarrow Damaged\ Coupon \end{aligned} \tag{1}$$

The pseudo-distance $D(m_0, m_u)$ is presently defined as the minimum of the individual distances of m_u from all elements of m_0, that is:

$$D(m_0, m_u) := \min_k \left[d(m_{0,k}, m_u) \right] \tag{2}$$

with $d(m_{0,k}, m_u)$ designating the distance between two individual models. Two types of such distances are employed, as discussed below.

3.1.1. The Mahalanobis distance

The Mahalanobis distance is defined as:

$$d(m_{0,k}, m_u) := \sqrt{(\boldsymbol{a}_{0,k} - \boldsymbol{a}_u)^T \boldsymbol{\Sigma}^{-1} (\boldsymbol{a}_{0,k} - \boldsymbol{a}_u)} \tag{3}$$

in which the superscript T designates transposition and $\boldsymbol{\Sigma}$ the sample covariance of the AR/MA parameter vectors within the MMR m_0, with the individual covariances $\boldsymbol{\Sigma}_{0,k}$ $(k = 1, \dots, p)$ and $\boldsymbol{\Sigma}_{\boldsymbol{u}}$ considered negligible compared to $\boldsymbol{\Sigma}$.

3.1.2. The cosine similarity distance

The cosine similarity distance is defined as:

$$d(m_{0,k}, m_u) := cos(\boldsymbol{a}_{0,k}, \boldsymbol{a}_u) = \frac{\boldsymbol{a}_{0,k} \cdot \boldsymbol{a}_u}{\|\boldsymbol{a}_{0,k}\| \cdot \|\boldsymbol{a}_u\|} \quad (4)$$

in which the dot designates inner product and $\|\cdot\|$ the Euclidean norm of the indicated vector.

3.2. Damage classification

Following fatigue damage detection, Fatigue State (FS) classification follows. This is performed in a similar manner, with the exception that now each FS is modeled in the *Baseline Phase* and then a number of tests of the form (1) (each for each FS) are included in the *Inspection Phase*. Two bounds, at 5% and 10%, are included in the limits corresponding to each FS.

The first 20 parameters are included in each parameter vector for detection and classification using both metrics. Concerning fatigue damage detection, a set of 4 among 6 healthy coupons is selected, referred to as baseline coupons, for use in the method's Baseline (Training) phase. The remaining 2 healthy coupons and the 6 damaged coupons are referred to as inspection coupons – considered as 'unknown' structural state – and are reserved for the method's assessment in the Inspection (Diagnosis) phase. The employed combinations are designated as employed sets of baseline coupons and lead to different sets of baseline coupons.

4. Results

4.1. Preliminaries

A set of 4, among a total of 6, healthy coupons are selected for use within the *Baseline Phase*; these are also referred to as *Baseline Coupons*. The remaining 2 healthy coupons, along with 6 progressively damaged coupons, are used for testing the method in the *Inspection Phase* and are referred to as *Inspection Coupons*. By exchanging healthy Baseline Coupons with healthy Inspection Coupons, a number of rotations are implemented, leading to a total number of 280 healthy baseline coupons and 140 baseline coupons per FS.

The ARMA modeling of the vibration response signals for the healthy coupons leads to models of selected orders (80,50), that is ARMA(80,50) models. Models of the same orders are employed for all Fatigue States as well. Based on these a preliminary analysis of the influence of the FS on the coupon dynamics, as captured by the ARMA models, is undertaken. In this context, the decreasing value of the natural frequency at around $3500\ Hz$ (for the healthy state), the increasing value of the corresponding damping ratio, and the increasing spectral distance - the log-spectral distance involves the transformation of time-series signals into the spectral domain, and the distance of ARMA estimated Power Spectral Density (PSD) Welch spectrums of each damaged state from the healthy one is calculated - (from the healthy state) with increasing Fatigue State for Coupon #1 (based on all 70 Healthy and 35 per Fatigue State cases), are, along with their uncertainties, presented in Fig. 2. The high uncertainty associated with Fatigue States 1 and 2 is due to the uncertain nature (among the coupons) of fatigue damage evolution in the initial stages. This behavior is also reflected in PSD Welch estimates obtained in our preliminary work [17]. The main conclusion from this analysis is that the progression of fatigue damage significantly influences the coupon structural dynamics as captured by the ARMA models; while, furthermore, this influence is almost monotonically dependent on the Fatigue State. The implication of this is that both damage detection and FS classification should be possible by the method; this is to be formally discussed in the sequel.

Finaly note that only the first 20 parameters of the AR/MA parameter vector are subsequently used for damage detection and classification.

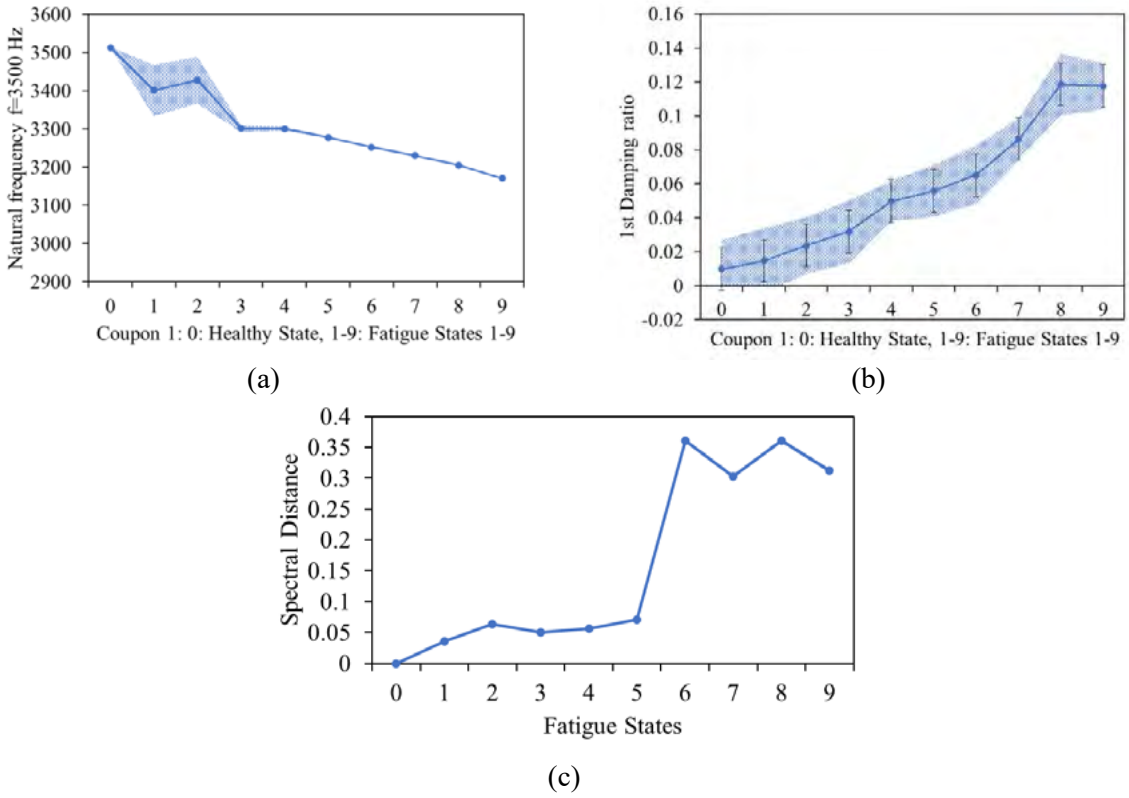


Figure 2. Evolution of the natural frequency at around 3500 Hz (a), the damping ratio (b), and spectral distance (c) with Fatigue State for Coupon #1 (0 corresponds to the Healthy state and i=1,…,9 to the corresponding Fatigue States).

4.2. Fatigue damage detection results

Fatigue damage detection results, using the Mahalanobis and the cosine similarity distances are presented in Figs. 3 and 4 for hundreds of Inspection Experiments. The results are excellent as the Distance metric *D* is, for all damaged cases, much higher than that of the healthy cases.

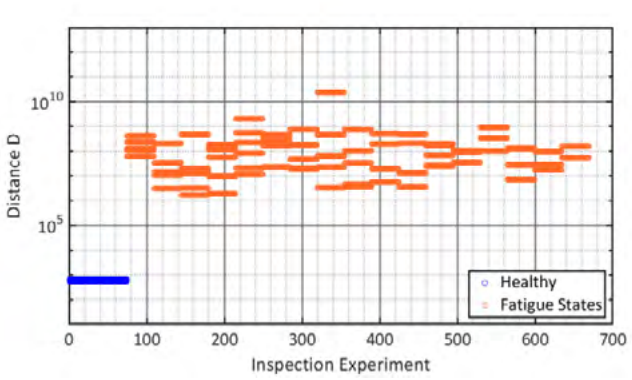


Figure 3. Random vibration-based progressive fatigue damage *detection* in the Inspection Phase using the *Minimum Mahalanobis Distance*: The Distance *D* for all Inspection Experiments for Coupons # 11 – 16 starting from the Healthy State and progressing towards Fatigue State 17 (70 Detection Test Cases per Coupon under the Healthy State and 35 under each Fatigue State).

4.3. Fatigue damage state classification results

Correct and incorrect classification rates for each coupon across all fatigue damage states (FSi,

i=1,…,17) using the Mahalanobis distance and the cosine similarity distance metrics are depicted in Fig. 5 and Fig. 6, respectively, while correct and incorrect classification rates are reported in Table 2. As observed, using the 5% limits provides higher performance.

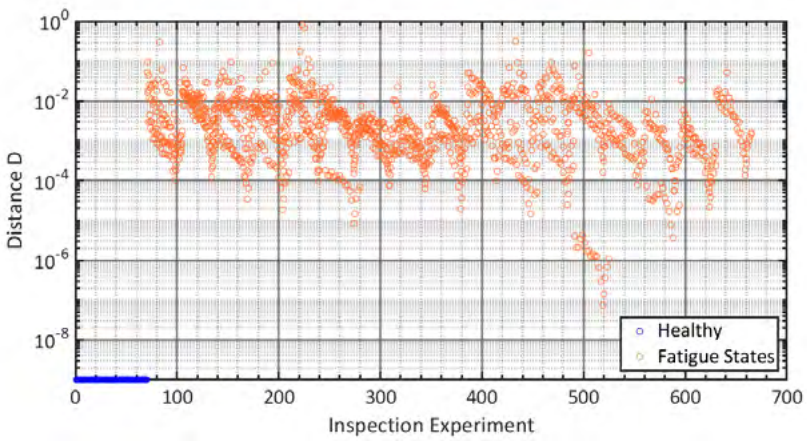


Figure 4. Random vibration-based progressive fatigue damage *detection* in the Inspection Phase using the *Minimum Cosine Similarity*: The Distance D for all Inspection Experiments for Coupons # 11 – 16 starting from the Healthy State and progressing towards Fatigue State 17 (70 Detection Test Cases per Coupon under the Healthy State and 35 under each Fatigue State).

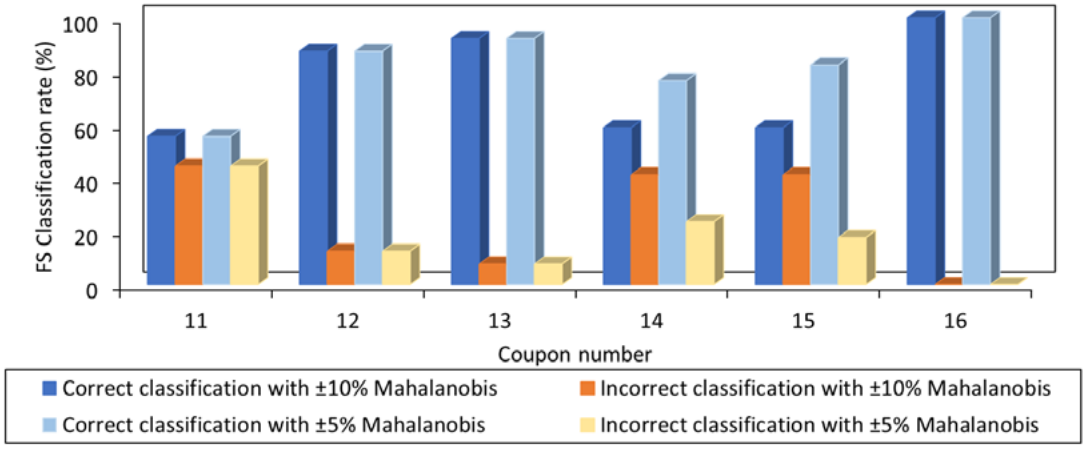


Figure 5. Random vibration-based Fatigue State *determination* results in the Inspection Phase using the *Minimum Mahalanobis Distance*: Correct (blue) and incorrect (orange) classification rates for Coupons # 11 – 16 for all Fatigue States ($FS_i, i = 1, \dots, 17$). Aggregate results in the rightmost part. (35 Test Cases per Coupon and Fatigue State; results based on $\pm 5\%$ and $\pm 10\%$ limits are shown.)

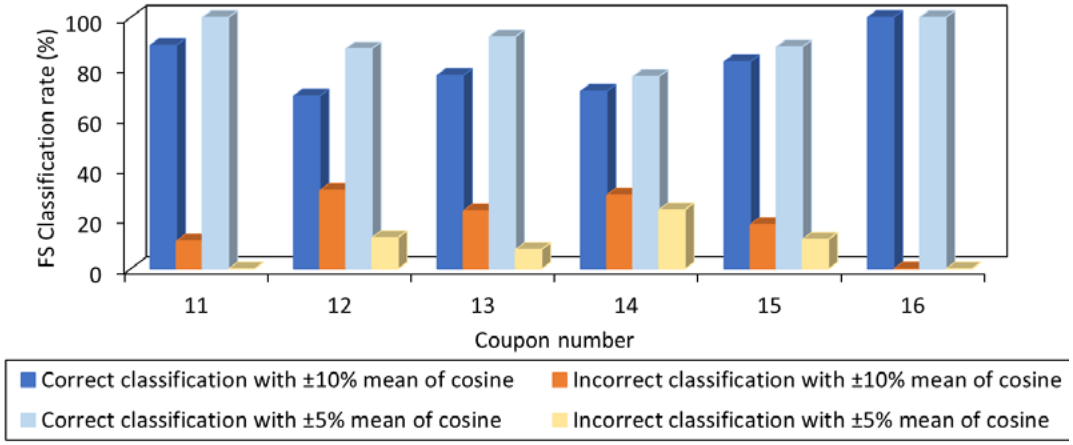


Figure 6. Random vibration-based Fatigue State *determination* results in the Inspection Phase using the *Minimum Cosine Similarity Distance*: Correct (blue) and incorrect (orange) classification rates for Coupons # 11 – 16 for all Fatigue States ($FS_i, i = 1, \dots, 17$). Aggregate results in the rightmost part. (35 Test Cases per Coupon and Fatigue State; results based on $\pm 5\%$ and $\pm 10\%$ limits are shown.)

Table 2. Summary vibration-based Fatigue State *determination* results in the Inspection Phase in terms of correct and incorrect classification rates for Coupons # 11 – 16 for all Fatigue States ($FS_i, i = 1, \dots, 17$) using either the Minimum Mahalanobis or Cosine Similarity Distance (35 Test Cases per Coupon and Fatigue State; results based on $\pm 5\%$ and $\pm 10\%$ limits are shown).

Fatigue State Classification Method	Correct Classification Rate (%)
Minimum Mahalanobis Distance ($\pm 5\%$ / $\pm 10\%$ limits)	82.36 / 75.50
Minimum Cosine Similarity Distance Metric ($\pm 5\%$ /$\pm 10\%$ limits)	90.75 / 81.25

5. Conclusions

An investigation on random vibration-based progressive fatigue damage monitoring for thermoplastic coupons has been carried out. The work has been based on 6 nominally identical coupons subjected to interrupted (every 10 000 cycles) fatigue and random vibration tests. The main conclusions of the study may be summarized as follows: (i) The effects of fatigue damage on the coupon structural dynamics, with almost monotonic dependence on the number of fatigue cycles, have been demonstrated; (ii) fatigue damage detection has been flawless; (iii) fatigue damage classification has been very good, characterized by an aggregate (over all coupons) correct classification rate up to 90%. Overall, the results of the study are indicative of the method's high potential for fully automated, in-operation, fatigue damage monitoring for thermoplastic structures, without the need for interrupting regular service and in the presence of population and operational uncertainty.

References

[1] Barile M, Lecce L, Iannone M, Pappadà S and Roberti P 2020 Thermoplastic Composites for Aerospace Applications *Revolutionizing Aircraft Materials and Processes* ed S Pantelakis and K Tserpes (Cham: Springer International Publishing) pp 87–114.
[2] Pantelakis S and Tserpes K 2020 *Revolutionizing Aircraft Materials and Processes* (Cham: Springer International Publishing).
[3] Tserpes K I, Papanikos P, Labeas G and Pantelakis S 2004 Fatigue damage accumulation and residual strength assessment of CFRP laminates *Composite Structures* **63** 219–30.
[4] Fassois S D and Kopsaftopoulos F P 2013 Statistical Time Series Methods for Vibration Based Structural Health Monitoring *New Trends in Structural Health Monitoring* CISM International

Centre for Mechanical Sciences vol 542, ed W Ostachowicz and J A Güemes (Vienna: Springer Vienna) pp 209–64.
[5] Chaupal P and Rajendran P 2023 A review on recent developments in vibration-based damage identification methods for laminated composite structures: 2010–2022 *Composite Structures* 116809.
[6] García-Fernández N, Aenlle M, Álvarez-Vázquez A, Muniz-Calvente M and Fernández P 2023 A review on fatigue monitoring of structures *International Journal of Structural Integrity* **14** 133–65.
[7] Bedewi N E and Kung D N 1997 Effect of fatigue loading on the modal properties of composite structures and its utilization for prediction of residual life *Composite Structures* **37** 357–71.
[8] de Medeiros R, Sartorato M, Marques F D, Tita V and Vandepitte D 2013 Vibration-based damage identification applied for composite plate: xperimental analyses *22nd International Congress of Mechanical Engineering* COBEM 2013 p 13.
[9] Aidi B, Philen M K and Case S W 2015 Progressive damage assessment of centrally notched composite specimens in fatigue *Composites Part A: Applied Science and Manufacturing* **74** 47–59.
[10] Patil S and Mallikarjuna Reddy D 2020 Impact damage assessment in carbon fiber reinforced composite using vibration-based new damage index and ultrasonic C-scanning method *Structures* **28** 638–50.
[11] Bayissa W L, Haritos N and Thelandersson S 2008 Vibration-based structural damage identification using wavelet transform *Mechanical Systems and Signal Processing* **22** 1194–215.
[12] Silik A, Noori M, A. Altabey W, Ghiasi R and Wu Z 2021 Comparative Analysis of Wavelet Transform for Time-Frequency Analysis and Transient Localization in Structural Health Monitoring *Structural Durability & Health Monitoring* **15** 1–22.
[13] Varouxis T., Tserpes K. and Fassois S D 2022 Progressive fatigue damage detection and assessment in composite specimens using random vibration response signals *Composites Meet Sustainability – Proceedings of the 20th European Conference on Composite Materials, ECCM20. 26-30 June, 2022, Lausanne, Switzerland* ECCM20 (Lausanne, Switzerland) p 8.
[14] Saxena A, Goebel K, Larrosa C C and Chang F-K 2011 Accelerated Aging Experiments for Prognostics of Damage Growth in Composite Materials The 8th International Workshop on Structural Health Monitoring vol 15 (Stanford, CA: F.-K. Chang) p 9.
[15] D30 Committee. Test Method for Tensile Properties of Polymer Matrix Composite Materials. *ASTM International.*
[16] D30 Committee. Test Method for Tension-Tension Fatigue of Polymer Matrix Composite Materials. *ASTM International.*
[17] Tsivouraki N, Tserpes K and Fassois S 2024 Random vibration-based progressive fatigue damage monitoring in thermoplastic coupons: a preliminary investigation *J. Phys.: Conf. Ser.* **2692** 012033.

ANALYTICAL AND NUMERICAL MODELING OF THERMAL STRAINS OF COMPOSITES

C. Nikolaou[1], E. Polyzos[2], L. Pyl[3]

[1,2,3]Department of Mechanics of Materials and Constructions, Vrije Universiteit Brussel (VUB), 1050 Brussels, Belgium

[1]Email: christos.nikolaou@vub.be, Web Page: https://researchportal.vub.be/en/persons/christos-nikolaou

[2]Email: efstratios.polyzos@vub.be, Web Page: https://researchportal.vub.be/en/persons/efstratios-polyzos

[3]Email: lincy.pyl@vub.be, Web Page: https://researchportal.vub.be/en/persons/lincy-pyl

Keywords: Thermal expansion coefficient, Thermal strains, Effective field methods, Composites, Modeling

Abstract

In the present study a novel methodology for modeling thermal strains in composite materials is introduced. Initially, a new formulation for calculating the thermal strains from the effective coefficient of thermal expansion (CTE) is presented. This formulation is then implemented both analytically and numerically. Subsequently, the analytical formulation based on effective field methods (EFMs) is introduced followed by the numerical models developed using the finite element (FE) method. Finally, two case studies for particulate and fibrous composites are discussed, and comparisons between analytical and numerical results are provided, demonstrating great agreement.

1. Introduction

Fibrous composites are widely used in many sectors of the industry due to their remarkable specific properties. However, their distinct constituents have varying coefficients of thermal expansion (CTEs), causing them to expand or contract differently when exposed to temperature changes. This creates internal stresses, leading to structural damage, compromised performance, and compromised safety [1].

Modeling thermal strains allows predicting the manner that composites respond to temperature variations. Analytical and computational models can be employed to simulate the behavior of composites under thermal stress by the prediction of the CTE. This predictive ability is important during the design phase, enabling optimization of material selection, layup configurations, and manufacturing processes to mitigate thermal effects [1].

Various models have been proposed over the years to predict the effective CTEs of composite materials.

Turner's model [2] assumes negligible shear deformation and uniformity of strain across components, providing a heuristic relation based on volume fractions of phases, bulk moduli, and CTEs. Thomas' model [3] offers a phenomenological equation with an adjustable parameter allowing for the extraction of volume averages of CTEs or their inverses. Arthur and Coulson's model [4], later corrected in [5], interrelates Young's modulus and Poisson's ratio based on an empirical relationship, contributing to an understanding of their role in determining the CTE. Levin's model [6] establishes a link between effective bulk modulus and CTE for isotropic composites. Schapery's model [7] derives bounds on effective CTEs using extremum principles of thermoelasticity, providing insights into composite behavior under thermal stresses. Tummala and Friedberg's model [8] considers spherical inclusions without interaction between inhomogeneities, offering insights into simple composite microstructures. The aforementioned models utilize either empirical relations or are derived for simple composite microstructures. The most accurate model built on a solid physics background and able to consider composites with arbitrary microstructures is the model of Sevostianov [9]. This model is based on property contribution tensors which define the proper microstructural parameter in terms of which an effective property (e.g., the CTE) is derived. For these reasons, this model is utilized in the present study.

Modeling thermal strains in composite structures presents inherent challenges due to the complexities arising from the shape, orientation, and properties of the matrix and inhomogeneities. The aim of this work is to address these challenges by presenting a novel methodology for modeling thermal strains in composite parts. In Section 2., the formulation for calculating the thermal strains from the effective CTE is presented. This formulation is general and can be implemented both analytically and numerically. In Section 3.1.1, the analytical formulation based on effective field methods (EFMs) is presented accounting for the general case of anisotropic inhomogeneities of arbitrary shape and orientation within an anisotropic matrix. In Section 3.1.2, numerical models developed using the finite element (FE) method are presented. Finally, two case studies for particulate and fibrous composites are discussed and comparisons between analytical and numerical results are provided.

2. Analytical formulation

Consider the case of an infinite three-dimensional medium, of volume V containing an inhomogeneity with a volume V^*. The properties utilized for the inhomogeneities and the matrix are denoted by '*' and '0' respectively. The angle brackets $\langle ... \rangle_V$ express average over the indicated volume V. The volume V is subjected to a uniform temperature change T, and its boundary remains free of traction. According to Sevostianov [9], the thermal expansion contribution tensor H_T of the inhomogeneity in relation to the volume average thermal strain $\langle \varepsilon_{ij} \rangle_V$ and the thermal expansion tensors of the matrix α_{ij}^0 and the composite α_{ij}^{eff} is expressed as:

$$\langle \varepsilon_{ij} \rangle_V = \alpha_{ij}^0 T + H_{ij}^T T = \alpha_{ij}^{eff} T. \tag{1}$$

$H_{ij}^T T$ represents the induced strain perturbation $\Delta\varepsilon_{ij}$ due to the presence of the inhomogeneity in the matrix. Additionally, the volume average stress of the composite can be expressed as:

$$\frac{V^*}{V}\langle\sigma_{ij}\rangle_{V^*} + \frac{V-V^*}{V}\langle\sigma_{ij}\rangle_{V-V^*} = 0, \tag{2}$$

where $\langle\sigma_{ij}\rangle_{V^*}$, $\langle\sigma_{ij}\rangle_{V-V^*}$ denote the volume average stress of the inhomogeneities and the matrix, respectively. The volume average strain (eq. (1)) can also be expressed using Hooke's law for the constituents as:

$$\langle\varepsilon_{ij}\rangle_V = \frac{V^*}{V}(S^*_{ijkl}\langle\sigma_{kl}\rangle_{V^*} + \alpha^*_{ij}T) + \frac{V-V^*}{V}(S^0_{ijkl}\langle\sigma_{kl}\rangle_{V-V^*} + \alpha^0_{ij}T), \tag{3}$$

where S^*_{ijkl} and S^0_{ijkl} denote the compliance tensor of the inhomogeneity and the matrix, and α^*_{ij} denotes the CTE of the inhomogeneity.

Solving eq. (2) for $\langle\sigma_{ij}\rangle_{V-V^*}$ and substituting in eq. (3) leads to:

$$\langle\varepsilon_{ij}\rangle_V = \frac{V^*}{V}((S^*_{ijkl} - S^0_{ijkl})\langle\sigma_{kl}\rangle_{V^*} + (\alpha^*_{ij} - \alpha^0_{ij})T) + \alpha^0_{ij}T. \tag{4}$$

Using eq. (4) and eq. (1), $\langle\sigma_{kl}\rangle_{V^*}$ can be obtained as:

$$\langle\sigma_{kl}\rangle_{V^*} = (S^*_{ijkl} - S^0_{ijkl})^{-1}\left(\frac{V}{V^*}(\alpha^{eff}_{ij} - \alpha^0_{ij}) - (\alpha^*_{ij} - \alpha^0_{ij})\right)T. \tag{5}$$

$\langle\sigma_{ij}\rangle_{V-V^*}$ can be obtained using eq. (2) and eq. (5). $\langle\varepsilon_{ij}\rangle_{V-V^*}$, $\langle\varepsilon_{ij}\rangle_{V^*}$ can be calculated using:

$$\langle\varepsilon_{ij}\rangle_{V-V^*} = S^0_{ijkl}\langle\sigma_{kl}\rangle_{V-V^*}, \quad \langle\varepsilon_{ij}\rangle_{V^*} = S^*_{ijkl}\langle\sigma_{kl}\rangle_{V^*}. \tag{6}$$

Utilizing eqs. (2), (5), and (6) one can use α^{eff}_{ij} to calculate $\langle\varepsilon_{ij}\rangle_{V-V^*}$ and $\langle\varepsilon_{ij}\rangle_{V^*}$. The evaluation of α^{eff}_{ij} can be done either analytically or numerically as elaborated below.

3. Case Studies

One particulate and one fibrous composite are used as case studies. The particulate composite is comprised of a copper matrix with diamond spherical inclusions (SP) [9] and the fibrous composite is comprised of an epoxy-resin matrix with unidirectional glass fibers (UD) [10] and their properties are given in Table 1. The thermal strains are calculated using analytical and numerical means for both cases based on the formulation of Section 2.

Table 1. Young's modulus E, shear modulus G, Poisson's ratio v, and CTE of copper, diamond, epoxy-resin and glass.

Material Type	E (GPa)	G (GPa)	v (-)	α ($^{\circ}C^{-1}$)
Copper	134.4	50.2	0.34	16.6×10^{-6}
Diamond	904.8	364.8	0.24	1.1×10^{-6}
Epoxy-Resin	3.1	1.1	0.40	66.0×10^{-6}
Glass	71.6	28.6	0.25	4.8×10^{-6}

3.1 Evaluation of effective thermal expansion coefficient

3.1.1 Effective field methods

EFMs are utilized to analytically evaluate the α_{ij}^{eff} of the two composites. The EFMs used are the Mori-Tanaka method and the Maxwell method. The Mori-Tanaka method [11] assumes that each inhomogeneity experiences an effective field equal to the average over the matrix thus capturing interactions between inhomogeneities. The Maxwell method [12] considers that a domain of shape Ω containing inhomogeneities is embedded within the matrix material to model interactions among the inhomogeneities [13]. The effective CTE within the framework of the Mori-Tanaka method and the Maxwell method can be expressed as [9]:

$$\alpha_{ij}^{eff} = \alpha_0 \delta_{ij} + H_{ijkl}^{A} (S_{klmn}^{*} - S_{klmn}^{0})^{-1} (\alpha_{mn}^{*} - \alpha_{mn}^{0}), \tag{7}$$

where δ_{ij} denotes the Kronecker delta and H_{ijkl}^{A} is the compliance contribution tensor evaluated for each EFM A (i.e., Mori-Tanaka (MT), Maxwell (MX)) as:

$$H_{ijkl}^{MT} = \left((1 - \frac{V^*}{V})(H_{ijkl}^{NI})^{-1} + (S_{ijkl}^{*} - S_{ijkl}^{0})^{-1} \right)^{-1}, \quad H_{ijkl}^{MX} = \left((H_{ijkl}^{NI})^{-1} - Q_{ijkl}^{\Omega} \right)^{-1}, \tag{8}$$

with:

$$H_{ijkl}^{NI} = \frac{V^*}{V} \left((S_{ijkl}^{*} - S_{ijkl}^{0})^{-1} + Q_{ijkl}^{*} \right)^{-1}, \quad Q_{ijkl}^{*} = (S_{ijmn}^{0})^{-1} (I_{mnkl} - s_{mnkl}^{*}), \tag{9}$$

where H_{ijkl}^{NI} is the compliance contribution tensor evaluated using the Non-Interaction EFM [14], I_{ijkl} is the fourth-rank identity tensor, s_{ijkl}^{*} represents Eshelby's tensor [15], and Q_{ijkl}^{Ω} can be calculated by following the methodology in [16].

For this study, the Mori-Tanaka method and Maxwell method are employed to determine the effective CTE for both the UD and the SP composites. Volume fractions ranging from 0.01 to 0.7 are considered for both methods. Then, the formulation of Section 2. is utilized to extract the volume average strain for the inhomogeneities $\langle \varepsilon_{ij} \rangle_{V^*}$ and the matrix $\langle \varepsilon_{ij} \rangle_{V-V^*}$.

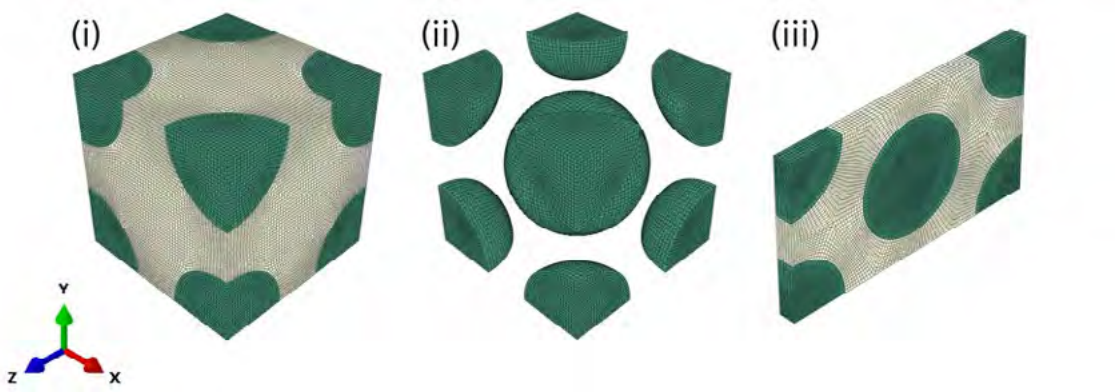


Figure 1. (i) FE model after the meshing process generated for the SP composite with a volume fraction 0.4. (ii) Visualization of the inclusions in the SP model with the matrix elements excluded. (iii) FE model after the meshing process generated for the UD composite with volume fraction of 0.4. Green and beige regions denote the inhomogeneities and matrix, respectively.

3.1.2 Finite element modeling

Two different composite geometries (SP, UD) are created in ABAQUS [17] FE software. The concept of the representative volume element (RVE) is employed to define a unit cell representing the microstructure. In this case, the inhomogeneities are defined based on the type of composite being modeled; spherical inhomogeneities for the SP composite and cylindrical for the UD composite. Five inhomogeneities are periodically positioned in each model. Subsequently, periodic boundary conditions are imposed using the methodology in [18]. The simulations are conducted for volume fractions of 0.1, 0.2, 0.3, 0.4, and 0.5. The analysis utilizes 20-node reduced integration brick elements (referred to as C3D20R elements in ABAQUS). A uniform temperature field of 1 degree is applied to the RVE to simulate expansion. An example of the meshed geometry for both composites is illustrated in Figure 1.

Once the simulations are completed, α_{ij}^{eff} is evaluated as:

$$\alpha_{ij}^{eff} = \langle \varepsilon_{ij} \rangle_{V^*} = \frac{1}{V^e} \sum_e \varepsilon_{ij}^{(e)} V^{(e)}, \tag{10}$$

where e refers to each FE.

Substituting the numerically evaluated α_{ij}^{eff} from eq. (10) to the formulation of Section 2., one can evaluate the strains of the inhomogeneities and the matrix.

As a verification, the volume average strain for the inhomogeneities $\langle \varepsilon_{ij} \rangle_{V^*}$ and for the matrix $\langle \varepsilon_{ij} \rangle_{V-V^*}$ can be calculated as:

$$\langle \varepsilon_{ij} \rangle_{V^*} = \frac{1}{V^*} \sum_{*e} \varepsilon_{ij}^{(*e)} V^{(*e)}, \quad \langle \varepsilon_{ij} \rangle_{V-V^*} = \frac{1}{V-V^*} \sum_{0e} \varepsilon_{ij}^{(0e)} V^{(0e)}, \tag{11}$$

where $(*e), (0e)$ refer to the elements of the inhomogeneities and the matrix, respectively.

4. Results

The results of the formulation using the EFMs and the FE models are presented in Figure 2 for the SP and the UD composites. Mori-Tanaka method, Maxwell method, FE, and verification denote the results achieved using eqs. (7), (10), and (11). Note that the SP composite demonstrates an isotropic behavior whereas the UD composite a transversely isotropic behavior. Hence, the respective parts of the thermal strain tensors are presented. The direction $1,2,3$ refer to x,y,z of the coordinate system illustrated in Figure 1.

In general, a great agreement is presented between the analytical and the numerical results. This demonstrates that the formulation presented in Section 2. can be used with high accuracy in estimating the thermal strains of composites.

Interestingly, the thermal strains of the SP composite present an almost linear drop with increasing volume fraction both for the inhomogeneities and the matrix. However, for the UD composite, ε_{11} of the inhomogeneities shows an exponential drop while ε_{22} increases. ε_{11} of the matrix shows also an exponential drop but ε_{22} first increases until a volume fraction of 0.2 and then drops almost linearly.

Finally, an interesting note can be given regarding the comparison between the EFMs that shows perfect agreement. This is attributed to the fact that the inhomogeneities in each case study are of the same shape as the domain Ω used in the Maxwell method. Under this condition the results of the Mori-Tanaka method and the Maxwell method coincide.

5. Conclusion

The aim of this study was to present a novel methodology for modeling thermal strains in composite materials. A new formulation was provided for computing thermal strains from the effective CTE and was implemented both analytically, by utilizing EFMs, and numerically, by utilizing the FE method. Two case studies were presented, one with particulate and one with fibrous composites. The results for both composites demonstrated great agreement validating the accuracy of the methodology provided.

References

[1] I. M. Daniel. “Thermal Deformations and Stresses in Composite Materials”. *Thermal Stresses in Severe Environments*. Ed. by D. P. H. Hasselman and R. A. Heller. Boston, MA: Springer US, 1980, 607–628.

[2] P. S. Turner. Thermal-expansion stresses in reinforced plastics. *Journal of research of the National Bureau of Standards* 37 (1946), 239.

[3] J. P. Thomas. Effect of inorganic fillers on coefficient of thermal expansion of polymeric materials (1960).

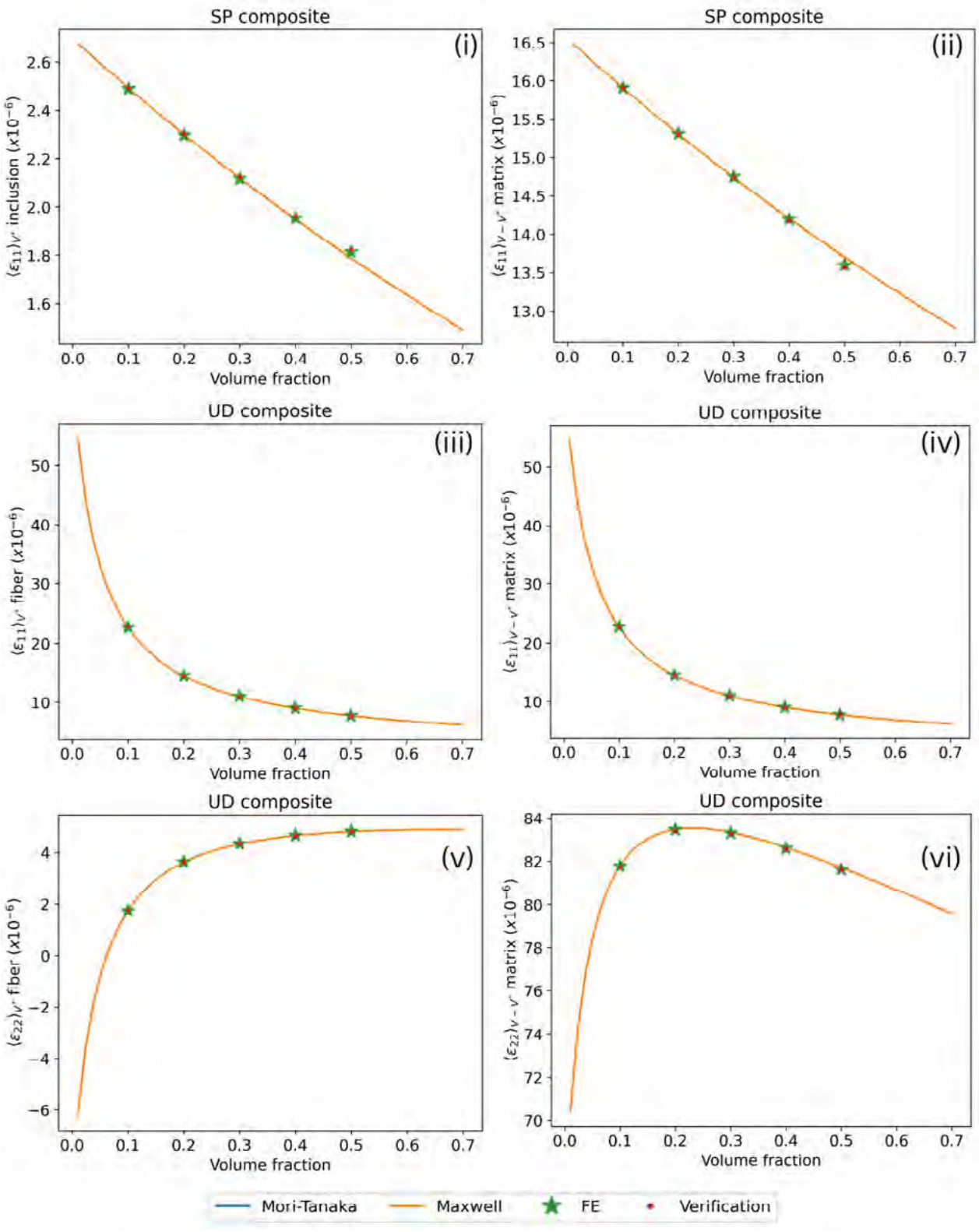


Figure 2. Volume average strain of the inhomogeneities and the matrix for the SP ((i) and (ii)) and the UD ((iii) - (vi)) composites.

[4] G. Arthur and J. Coulson. Physical properties of uranium dioxide-stainless steel cermets. *Journal of Nuclear Materials* 132 (1964), 242–253.

[5] L. Holliday and J. Robinson. Review: The thermal expansion of composites based on polymers. *Journal of Materials Science* 8 (1973), 301–311.

[6] V. Levin. On the Coefficients of Thermal Expansion of Heterogeneous Materials. *Mekhanika Tverdogo Tela* (1967), 88.

[7] R. Schapery. Thermal Expansion Coefficients of Composite Materials Based on Energy Principles. *Journal of Composite Materials* 2 (1968), 380 –404.

[8] R. R. Tummala and A. L. Friedberg. Thermal Expansion of Composite Materials. *Journal of Applied Physics* 41 (1970), 5104–5107.

[9] I. Sevostianov. On the thermal expansion of composite materials and cross-property connection between thermal expansion and thermal conductivity. *Mechanics of Materials* 45 (2012), 20–33.

[10] C.-H. Hsueh and P. F. Becher. Thermal Expansion Coefficients of Unidirectional Fiber-Reinforced Ceramics. *Journal of the American Ceramic Society* 71 (1988).

[11] T. A. Mori and K. Tanaka. Average stress in matrix and average elastic energy of materials with misfitting inclusions. *Acta Metallurgica* 21 (1973), 571–574.

[12] I. Sevostianov and A. Giraud. Generalization of Maxwell homogenization scheme for elastic material containing inhomogeneities of diverse shape. *International Journal of Engineering Science* 64 (2013), 23–36.

[13] I. Sevostianov, S. Mogilevskaya, and V. Kushch. Maxwell's methodology of estimating effective properties: Alive and well. *International Journal of Engineering Science* 140 (2019), 35–88.

[14] I. Sevostianov and M. Kachanov. Explicit cross-property correlations for anisotropic two-phase composite materials. *Journal of the Mechanics and Physics of Solids* 502 (2002), 253–282.

[15] I. Sevostianov et al. Effective elastic properties of matrix composites with transversely-isotropic phases. *International Journal of Solids and Structures* 422 (2005). Micromechanics of Materials, 455–476.

[16] I. Sevostianov. On the shape of effective inclusion in the Maxwell homogenization scheme for anisotropic elastic composites. *Mechanics of Materials* 75 (2014), 45–59.

[17] M. Smith. *ABAQUS/Standard User's Manual, Version 6.9*. English. United States: Dassault Systèmes Simulia Corp, 2009.

[18] E. Polyzos, D. Van Hemelrijck, and L. Pyl. Modeling elastic properties of 3D printed composites using real fibers. *International Journal of Mechanical Sciences* 232 (2022), 107581.

EFFECTIVE SPECIFIC HEAT OF MULTI-PHASE COMPOSITES USING EFFECTIVE FIELD METHODS

E. Polyzos[1], L. Pyl[2]

[1,2]Department of Mechanics of Materials and Constructions, Vrije Universiteit Brussel (VUB), 1050 Brussels, Belgium

[1]Email: Efstratios.Polyzos@vub.be, Web Page: https://researchportal.vub.be/en/persons/efstratios-polyzos

[2]Email: Lincy.Pyl@vub.be, Web Page: https://researchportal.vub.be/en/persons/lincy-pyl

Keywords: Effective field methods, Property contribution tensors, Thermoelastic materials, Specific heat, Homogenization

Abstract

The present work investigates the influence of local stress and strain effects on the homogenized (effective) specific heat of multi-phase composites. A new formulation is developed using property contribution tensors and the specific heat contribution tensor (scalar) is derived in the framework of the Non-Interaction, the Mori-Tanaka, and the Maxwell, effective field methods (EFMs). The novel formulas are presented for the general case of an anisotropic matrix with anisotropic inhomogeneities of diverse shapes and orientations. Two limited cases of particulate and fibrous two-phase composites are discussed and the results of the novel formulation are compared to results of experiments and finite element models, and exhibit a great agreement.

1 Introduction

Effective properties can be obtained via analytical, numerical, and semi-analytical methodologies [1]. Commonly, these methodologies are used for the evaluation of the effective stiffness (or compliance) tensor [2] and coefficient of thermal expansion [3], the thermal conductivity (or thermal resistivity) tensors [2], and the magnetic permeability (or electrical conductivity) tensors [4].

The specific heat is another property that is important to be evaluated [5]. The specific heat is the amount of heat that is needed in order to increase the temperature of one mass unit of a material by one degree and it appears in heat flow problems. In composite materials, effective specific heat is regularly evaluated by volume [6] or mass [7] averaging. This is mentioned as the rule-of-mixture (ROM) model [8] and it is indeed a logical assumption for applications to composites whose properties exhibit a linear dependency on the volume (or mass) of their constituents.

Despite this fact, Rosen and Hashin [5] argue that this can result in inaccuracies. The authors state that the imposition of a uniform temperature rise in a composite for the evaluation of the effective specific heat results in zero average (over the volume of the composite) stresses or strains under conditions of constant surface tractions or displacements, respectively. Nevertheless, the values of stresses and strains locally are, in general, non-zero and depend on the material and geometric parameters of the constituents. The material parameters are the elastic properties and the thermal expansion of the matrix and the inhomogeneities whereas the geometric parameters are the orientation and shape of the inhomogeneities.

This work aims to investigate the initial assumption of Hashin and Rosen regarding the influence of local stresses and strains on the effective specific heat. To this end, a novel formulation based on effective field methods (EFMs) is developed for multi-phase composites as elaborated below.

2 Analytical modeling

Consider first the coupled constitutive equations of thermoelasticity [2]:

$$\varepsilon_{ij} = S_{ijkl}\sigma_{kl} + \alpha_{ij}T \quad s = \alpha_{ij}\sigma_{kl} + \chi T, \tag{1}$$

where ε_{ij}, σ_{ij}, S_{ijkl}, α_{ij} denote the strain, the stress, the compliance, and the coefficient of thermal expansion tensors and T the uniform temperature. s and χ denote the entropy and the specific heat, which are scalar quantities. Eq. (1) is applicable to any solid or system of solids, such as a composite material.

Consider now the single inhomogeneity (particle, fiber, etc.) problem where an inhomogeneity of volume $V^{(p)}$ is embedded in an infinite and homogeneous matrix of volume $V^{(0)} = V - V^{(p)}$, with V the total volume of the composite. Note that the superscripts (p) and (0) denote properties of the inhomogeneity and the matrix, respectively.

For an imposed constant and uniform temperature field T, the volume average entropy $\langle s \rangle_V$ can be written as:

$$\langle s \rangle_V = \frac{V^{(p)}}{V}\langle s^{(p)} \rangle_{V^{(p)}} + \frac{V - V^{(p)}}{V}\langle s \rangle_{V-V^{(p)}} = \bar{\chi}T. \tag{2}$$

Note that the notation $\langle \cdot \rangle_V$ is the volume average operator with respect to volume V and that $\bar{\cdot}$ denotes an effective property. Therefore, $\bar{\chi}$ denotes the effective specific heat. Furthermore, note that the classical expansion problem that is assumed here considers a traction-free boundary, i.e., the average traction on the surface of the composite and, by extent, the volume average stress of the composite $\langle \sigma_{ij} \rangle_V$ are zero, i.e.:

$$\langle \sigma_{ij} \rangle_V = \frac{V^{(p)}}{V} \langle \sigma_{ij} \rangle_{V^{(p)}} + \frac{V - V^{(p)}}{V} \langle \sigma_{ij} \rangle_{V - V^{(p)}} = 0, \tag{3}$$

Using eq. (1) and (2), the volume average entropy $\langle s \rangle_V$ can be written as:

$$\langle s \rangle_V = \frac{V^{(p)}}{V} \left[\alpha_{ij}^{(p)} \langle \sigma_{ij} \rangle_{V^{(p)}} + \chi^{(p)} T \right] + \frac{V - V^{(p)}}{V} \left[\alpha_{ij}^{(0)} \langle \sigma_{ij} \rangle_{V - V^{(p)}} + \chi^{(0)} T \right]. \tag{4}$$

The volume average entropy can be written as a sum of the entropy of the matrix $\langle s \rangle_{V - V^{(p)}} = \alpha_{ij}^{(0)} \langle \sigma_{ij} \rangle_{V - V^{(p)}} + \chi^{(0)} T$ and a perturbation $\Delta s = \frac{V^{(p)}}{V} H^{(Sp)} T$ due to the presence of the inhomogeneity p as:

$$\langle s \rangle_V = \langle s \rangle_{V - V^{(p)}} + \Delta s = \alpha_{ij}^{(0)} \langle \sigma_{ij} \rangle_{V - V^{(p)}} + \chi^{(0)} T + \frac{V^{(p)}}{V} H^{(Sp)} T. \tag{5}$$

with $H^{(Sp)}$ being the specific heat contribution tensor. Solving eq. (5) for $H^{(Sp)}$ and substituting eqs. (3) and (4), $H^{(Sp)}$ can be evaluated as:

$$H^{(Sp)} T = \frac{V^{(p)}}{V} \left[\left(\alpha_{ij}^{(p)} - \alpha_{ij}^{(0)} \right) \langle \sigma_{ij} \rangle_{V^{(p)}} + \left(\chi^{(p)} - \chi^{(0)} \right) T \right]. \tag{6}$$

Note that the specific heat contribution tensor is a rank 0 tensor, i.e., a scalar value.

Finally, using eqs. (2) and (6), the effective specific heat is given as:

$$\bar{\chi} = \chi^{(0)} + \frac{V^{(p)}}{V} H^{(Sp)}. \tag{7}$$

Due to eq. (6) and (7), the effective specific heat depends on the local effects of stresses of the inhomogeneities due to $\langle \sigma_{ij} \rangle_{V^{(p)}}$.

Eq. (6) can also be used to express $H^{(Sp)}$ in terms of the thermal expansion contribution tensor $H_{ij}^{(Tp)} = \frac{V^{(p)}}{V} \left[\left(S_{ijkl}^{(p)} - S_{ijkl}^{(0)} \right) \langle \sigma_{kl} \rangle_{V^{(p)}} + \left(\alpha_{ij}^{(p)} - \alpha_{ij}^{(0)} \right) T \right]$ derived in [3]. After some tensor algebra $H^{(Sp)}$ is written as :

$$H^{(Sp)} = H_{ij}^{(Tp)} Q_{ijkl}^{(p)} \left(\alpha_{kl}^{(0)} - \alpha_{kl}^{(p)} \right) + \left(\chi^{(p)} - \chi^{(0)} \right), \tag{8}$$

with $Q_{ijkl}^{(p)} = C_{ijmn}^{(0)} \left(I_{mnkl} - \mathsf{S}_{mnkl}^{(p)} \right)$ and $\mathsf{S}_{mnkl}^{(p)}$ being Eshelby's tensor [9]. $H^{(Sp)}$ is directly linked to the compliance contribution tensor $H^{(p)}$. Using:

$$H_{ij}^{(Tp)} T = H_{ijkl}^{(p)} \left(S_{klmn}^{(p)} - S_{klmn}^{(0)} \right)^{-1} \left(\alpha_{mn}^{(p)} - \alpha_{mn}^{(0)} \right), \tag{9}$$

$H^{(Sp)}$ becomes:

$$H^{(Sp)} = H^{(p)}_{ijkl}\left(S^{(p)}_{klmn} - S^{(0)}_{klmn}\right)^{-1}\left(\alpha^{(p)}_{mn} - \alpha^{(0)}_{mn}\right)Q^{(p)}_{ijrs}\left(\alpha^{(0)}_{rs} - \alpha^{(p)}_{rs}\right) + \left(\chi^{(p)} - \chi^{(0)}\right). \tag{10}$$

Eq. (10) can be used to evaluate the effective specific heat using the Non-Interaction (NI), the Mori-Tanaka (MT), and the Maxwell (MX) methods. As explained in [3], the form of (10) allows to simply substitute the compliance contribution tensors of the three EFMs. These are given as [3]:

$$\begin{aligned} H^{(NIp)}_{ijkl} &= \left[\left(S^{(p)}_{ijkl} - S^{(0)}_{ijkl}\right)^{-1} + Q^{(p)}_{ijkl}\right]^{-1}, \; H^{(MTp)}_{ijkl} = H^{(NIp)}_{ijmn}\left[I_{mnkl} - \sum_p \frac{V^{(p)}}{V} Q^{(p)}_{mnrs} H^{(NIp)}_{rskl}\right]^{-1}, \\ H^{(MXp)}_{ijkl} &= H^{(NIp)}_{ijmn}\left[I_{mnkl} - Q^{(\Omega)}_{mnrs}\sum_p \frac{V^{(p)}}{V} H^{(NIp)}_{rskl}\right]^{-1}, \end{aligned} \tag{11}$$

where tensor $Q^{(\Omega)}_{ijkl}$ can be obtained via the methodology presented in [4].

3 Case studies

Two case studies are presented in this article to further investigate the applicability of the formulas derived in section 2. The first case study considers the case of overall isotropy of a particulate composite of polypropylene with copper particles. The second case considers two fibrous composites, a glass and a carbon fiber-reinforced epoxy composite.

This section presents first the development of the FE models (section 3.1) for the particulate and the fibrous composites and then the results (section 3.2) of the analytical formulas, the experiments, and the FE models.

3.1 Finite element modeling

Two geometries, one representing a particulate composite and one a fibrous composite, were created in the ABAQUS FE software [10]. For the particulate composite, the geometry of the inhomogeneities is spherical, whereas for the fibrous composite, it is cylindrical. Periodic boundary conditions (PBCs) were imposed using the methodology presented in [11]. The volume fraction of the inhomogeneities in each geometry was taken as 0.1, 0.2, 0.3, 0.4, and 0.5. The 20 node reduced integration brick elements (C3D20R elements by the terminology of ABAQUS) were used for the analysis. An example of the geometry of the particulate and the fibrous composite is given in Figure 1. The mesh was determined by mesh convergence studies.

A uniform temperature field of 1 degree was imposed on each geometry so as to simulate expansion. After the solution of the problem, the volume average stress of the inhomogeneities $\langle\sigma_{ij}\rangle^{(p)}_V$ and the matrix $\langle\sigma_{ij}\rangle^{(0)}_V$ were calculated by:

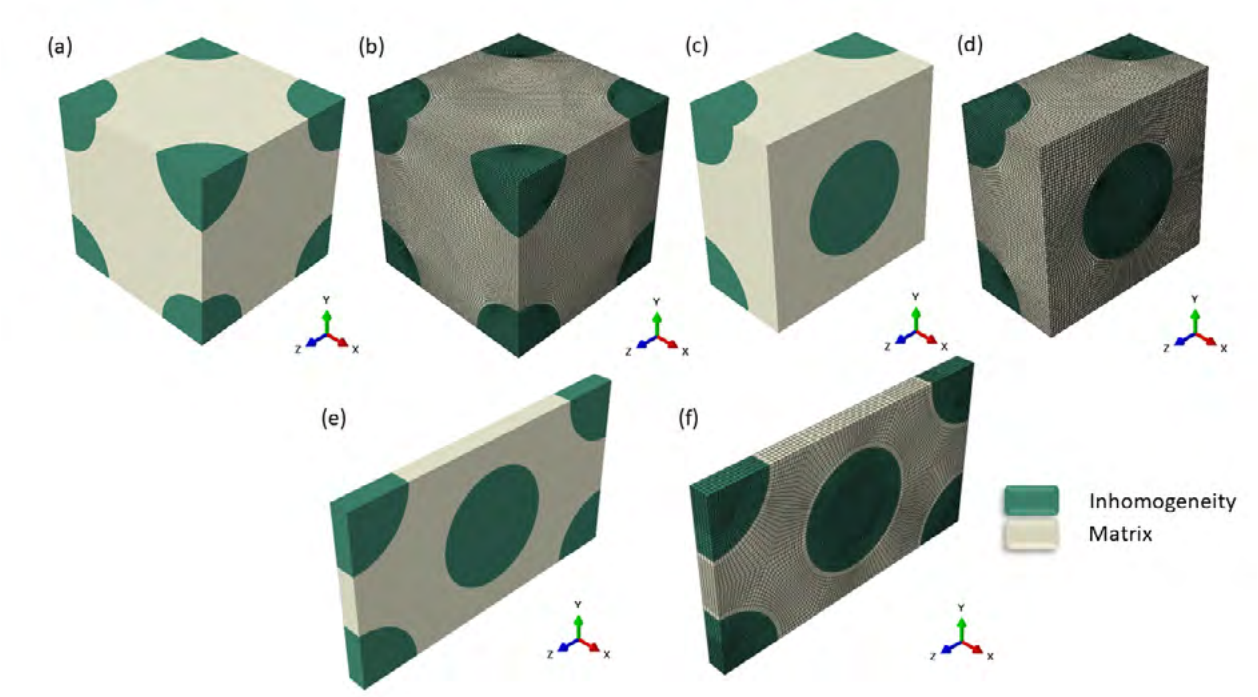


Figure 1. Example of the FE models generated for the particulate ((a)-(d)) composite with volume fraction 0.2 and the fibrous ((e) and (f)) composite with volume fraction of 0.4. (a), (c), and (e) present the geometry before and (b), (d), and (f) after meshing. (c) and (d) show a cross-section of the model.

$$\langle \sigma_{ij} \rangle_{V^{(p)}} = \frac{1}{V^{(p)}} \sum_e \sigma_{ij}^{(pe)} V^{(pe)}, \quad \langle \sigma_{ij} \rangle_{V^{(0)}} = \frac{1}{V^{(0)}} \sum_e \sigma_{ij}^{(0e)} V^{(0e)} \tag{12}$$

where $\sigma_{ij}^{(pe)}$ and $\sigma_{ij}^{(0e)}$ are the stress of element e of inhomogeneity p and of the matrix 0 and $V^{(pe)}$ and $V^{(0e)}$ their volume. The solutions of $\langle \sigma_{ij} \rangle_{V^{(p)}}$ and $\langle \sigma_{ij} \rangle_{V^{(0)}}$ were then substituted in eq. (4) in order to obtain the volume average specific heat of the composite as $\bar{\chi} = \langle s \rangle_V / T$.

The properties (elastic, thermal expansion, and specific heat) of the polypropylene [6], the copper particles [6], the glass fibers [12, 13], the carbon fibers [12, 14], and the epoxy resin [12] are taken from the literature and are given in Table 1.

3.2 Results

3.2.1 Particulate composites

Data from [6] is used for the polypropylene with copper particles (PP/Cu) composite. The authors prepared two types of samples with different sizes of copper fillers (PP/Cu_a and PP/Cu_b) and determined the effective specific heat of the composite using differential scanning calorimetry (DSC). Since the size of the particles is not considered in the presented formulation of section 2 or the FE models of section 3.1, the analytical

Table 1. Properties (elastic, thermal expansion, and specific heat) of polypropylene, copper particles, glass fibers, carbon fibers, and epoxy resin. E_{11}, E_{22}, G_{12}, and G_{23} in GPa, ν_{12} in -, α_{11} and α_{22} in $10^{-6}/K$, χ in $J/(kg.K)$.

	E_{11}	E_{22}	G_{12}	G_{23}	ν_{12}	α_{11}	α_{22}	χ
Polypropylene	1.35	1.35	0.52	0.52	0.30	166.00	166.00	1731
Copper	110.00	110.00	42.30	42.30	0.30	17.00	17.00	381
Glass fibers	68.00	68.00	27.20	27.20	0.25	9.00	9.00	803
Carbon fibers	234.00	15.00	15.00	7.00	0.20	-1.35	6.84	600
Epoxy	3.00	3.00	1.15	1.15	0.30	57.50	57.50	1400

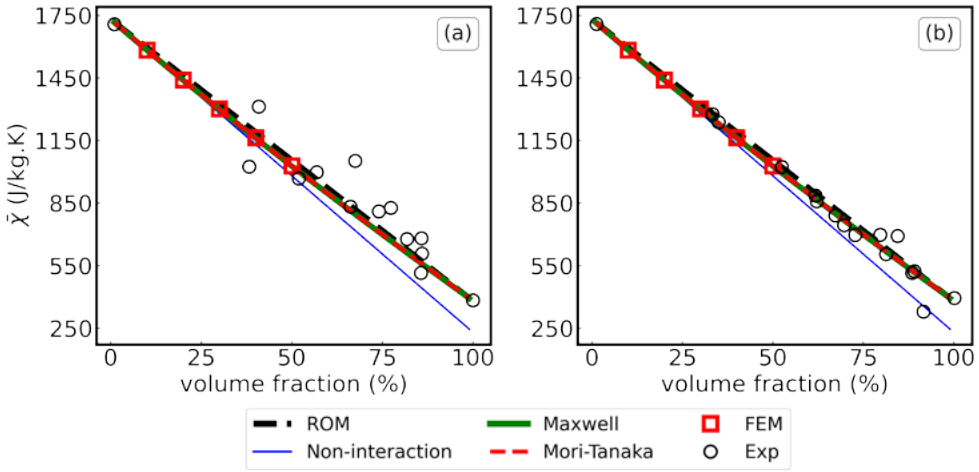


Figure 2. Comparison of the effective specific heat (in J/kg.K) from experiments [6] (with permission from Elsevier) with the predictions of the Non-Interaction, the Mori-Tanaka, and the Maxwell EFMs and the results of the ROM and FE models. PP/Cu$_a$ specimens are presented in (a) and PP/Cu$_b$ specimens in (b).

formulas and the FE models are applicable to both types of samples. For specifics regarding the experimental process, the reader is referred to their work [6].

The results of the three EFMs, the Non-Interaction, the Mori-Tanaka, and the Maxwell, and the FE models compared to the experimental data (average values) of [6] for the effective specific heat of the two types of specimens PP/Cu$_a$ and PP/Cu$_b$ are presented in Figure 2 for increasing values of the volume fraction of copper particles. The figure also contains the estimates of the ROM model, so that it can be compared to the newly derived analytical formulas and the FE models.

The comparison reveals a great agreement of the analytical and the numerical models with the experimental data. For volume fractions below 0.5 the Non-Interaction method gives also good predictions and does not deviate drastically from the Mori-Tanaka and the Maxwell methods and the ROM and FE models. However, it is evident that the Non-Interaction method provides physically inaccurate estimates for high volume fractions since the upper limit of volume fraction 1.0 must coincide with the specific heat of the inhomogeneities. This can be explained by the inability of the method to capture interactions between inhomogeneities. The predictions of the Mori-Tanaka and the Maxwell methods are also in good agreement with the ROM model.

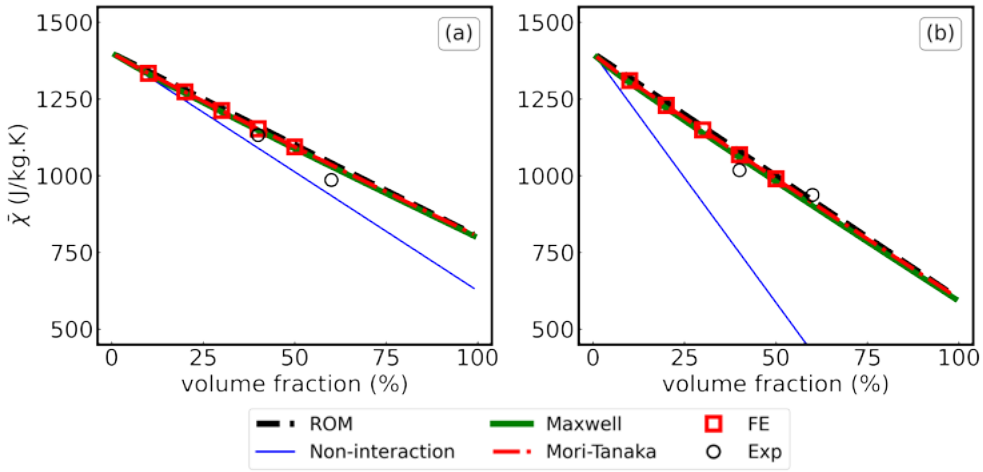


Figure 3. Comparison of the effective specific heat (in J/kg.K) from experiments [12] with the predictions of the Non-Interaction, the Mori-Tanaka, and the Maxwell EFMs and the results of the ROM and FE models. GFRP specimens are presented in (a) and CFRP specimens in (b).

A small deviation is demonstrated with slightly lower values of effective specific heat being predicted by the two EFMs. The results of the FE model are in perfect agreement with the Mori-Tanaka and the Maxwell methods.

3.2.2 Fibrous composites

Two types of (unidirectional) fibrous composites, one of epoxy reinforced with glass (GFRP) and one reinforced with carbon (CFRP) fibers, are examined in this section. The results of laser flash diffusivity tests from [12] are presented in Figure 3 for fiber volume fractions of 0.4 and 0.6 and compared to the analytical and numerical models.

The majority of the analytical methods (apart from the Non-Interaction method) follow well the experimental data. The Non-Interaction method presents differences due to its inaccuracy in estimating the compliance contribution tensor which is used in eq. (10). The Mori-Tanaka and the Maxwell methods are in good agreement with the ROM model. The two methods demonstrate also a perfect agreement with the results of the FE models.

4 Conclusions

The aim of the work was to investigate the influence of local stresses and strains on the effective specific heat. This was achieved by a novel formulation of EFMs and comparison with numerical and experimental results. The main conclusions of this work can be summarized as follows. The formulation shows that the effective specific heat depends not only on the volume fractions and the specific heats of the constituents but also on local effects of stresses. However, these local effects are negligible.

5 Acknowledgements

The financial contribution of the FWO Research Foundation–Flanders (file number 1102822N) is gratefully acknowledged.

References

[1] E. Polyzos, D. Van Hemelrijck, and L. Pyl. Stochastic modeling of the elastic response of parts produced by material extrusion using ideal voids. *International Journal of Solids and Structures* (2023), 112346.

[2] I. Sevostianov and M. Kachanov. Connections between elastic and conductive properties of heterogeneous materials. *Advances in applied mechanics* 42 (2009), 69–252.

[3] I. Sevostianov. On the thermal expansion of composite materials and cross-property connection between thermal expansion and thermal conductivity. *Mechanics of Materials* 45 (2012), 20–33.

[4] I. Sevostianov. On the shape of effective inclusion in the Maxwell homogenization scheme for anisotropic elastic composites. *Mechanics of Materials* 75 (2014), 45–59.

[5] B. W. Rosen and Z. Hashin. Effective thermal expansion coefficients and specific heats of composite materials. *International Journal of Engineering Science* 82 (1970), 157–173.

[6] A. Boudenne et al. Electrical and thermal behavior of polypropylene filled with copper particles. *Composites Part A: Applied Science and Manufacturing* 3611 (2005), 1545–1554.

[7] L. Rivière et al. Specific heat capacity and thermal conductivity of PEEK/Ag nanoparticles composites determined by Modulated-Temperature Differential Scanning Calorimetry. *Polymer Degradation and Stability* 127 (2016), 98–104.

[8] W. Voigt. Ueber die Beziehung zwischen den beiden Elasticitätsconstanten isotroper Körper. *Annalen der Physik* 27412 (1889), 573–587.

[9] I. Sevostianov et al. Effective elastic properties of matrix composites with transversely-isotropic phases. *International journal of solids and structures* 422 (2005), 455–476.

[10] M. Smith. *ABAQUS/Standard User's Manual, Version 6.9*. English. United States: Dassault Systèmes Simulia Corp, 2009.

[11] E. Polyzos, D. Van Hemelrijck, and L. Pyl. Modeling elastic properties of 3D printed composites using real fibers. *International Journal of Mechanical Sciences* 232 (2022), 107581.

[12] A. Saripally. "A Micromechanical Approach to Evaluate the Effective Thermal Properties of Unidirectional Composites". PhD thesis. Birla Institute of Technology and Science, 2015.

[13] F. Desrumaux, F. Meraghni, and M. L. Benzeggagh. Generalised Mori-Tanaka scheme to model anisotropic damage using numerical Eshelby tensor. *Journal of Composite Materials* 357 (2001), 603–624.

[14] R. P. Tavares et al. Mechanics of hybrid polymer composites: analytical and computational study. *Computational Mechanics* 57 (2016), 405–421.

ELECTRICAL MONITORING OF BONDED JOINTS

Alessandro Pontefisso[1], Paolo A. Carraro[1], Marino Quaresimin[1], Michele Zappalorto[1], Massimo Dalla Benetta[1]

[1]Department of Management and Engineering, University of Padova, stradella S. Nicola 3 – 36100 Vicenza, Italy
Email: alessandro.pontefisso@unipd.it

Keywords: Structural Health Monitoring, Single-lap Bonded Joints, Electrical Monitoring, Analytical Model, Experimental Validation

Abstract
The research aims to explore the feasibility of using electrical measurements to monitor damage in single-lap bonded joints. To begin with, an analytical model is developed to estimate the increase in electric resistance across the joint bond surface due to damage. The model's accuracy is validated numerically using Finite Element Analysis and experimental fatigue tests are conducted on single lap joints with Aluminium adherends and a conductive epoxy adhesive. Following tests on Carbon-epoxy composite laminates highlight the importance of considering actual damage mechanisms. To this end, a procedure is presented, where crack-surface electrical conductivity evolves with crack length. A final test case demonstrates the model's effectiveness in continuously monitoring damage presence in bonded joints through electrical measurements.

1. Introduction

In recent years, the adoption of fibre-reinforced polymer composites for structural purposes has seen significant growth, driven by industries such as aerospace and automotive. When using composite materials in structural applications, the need arises to join various components together. Among the available joining methods, adhesive bonding stands out as an excellent choice due to its lightweight and cost-effective connections, and unlike other techniques, adhesive bonding avoids the need for drilling holes in composite parts. However, designing bonded connections to withstand static and, primarily, fatigue failure is a challenging task.

A significant challenge lies in dealing with defects of purely bonded connections: some defects (such as voids, pre-cracks, or cracks formed during service life) can be detected through periodic inspections and managed with appropriate design tools, yet defects related to poor bonds (due to contaminating agents) remain undetectable. Consequently, proving the integrity of purely bonded connections before putting them in service becomes impossible, leading to uncertified applications in critical industrial sectors. To mitigate uncertainties, companies often resort to combined bonded/bolted joints, sacrificing the economic, weight, and performance advantages of adhesive bonding. As a result, there is a growing focus on simulating fatigue damage initiation and evolution accurately in bonded connections and developing effective crack-stopping mechanisms and health monitoring methods [1-4].

In the context of this study, the objective of the paper is to develop models and methods for continuous Structural Health Monitoring (SHM) of bonded connections. The electrical method was the chosen SHM strategy, since it has shown promising results for monolithic composite parts [5-11]. This approach, that requires only properly positioned electrodes connected via cables to the component, leverages the irreversible increase in electrical resistance caused by damage formation, specifically bondline cracks in bonded joints. Naturally, this method relies on the use of electrically conductive materials for both adherends and adhesive. Carbon fibre-based composites inherently exhibit conductivity, while for glass fibres, a matrix nano-modification using conductive fillers can be employed.

2. Methodology overview

As a first step, an analytical model of the damage-induced increase of the electric resistance across the single-lap joint bond surface is developed for inferring the crack length. The model analytically depicts the electric field within the joint and it is able to estimate the resistance increase due to damaging following adherend/adhesive debonding in the configuration shown in Figure 1. To this end the model assumes that the crack faces are perfect insulators. After a numerical validation by means of Finite Element Analysis, further proof of the model accuracy is provided by experimental tests on single lap joints, where the adherends are made of Aluminium and the adhesive is a conductive epoxy. In more detail, the joint stiffness reduction is periodically evaluated during fatigue cycles, at fatigue ratio 0.1, by means of digital image correlation, and it is compared with the prediction of a Finite Element model of the joint created accounting for the damage information determined by the analytical model. In order to account for residual electrical conductivity across crack faces, the model is modified, and its predictions are compared with the results of tests on bonded joints obtained with adherends made of Carbon-epoxy composite laminates where, due to fibre-bridging and damaging running inside the adherend, the crack faces exhibit a residual electrical conductivity. Eventually, a comprehensive procedure is presented, where the evolution of the crack-surface electrical conductivity as a function of crack length is represented by a parameter evaluated by best-fit of a preliminary sub-set of joints. A final test case proves the model efficacy in continuously monitoring the presence of damage in bonded joints through electrical measurements.

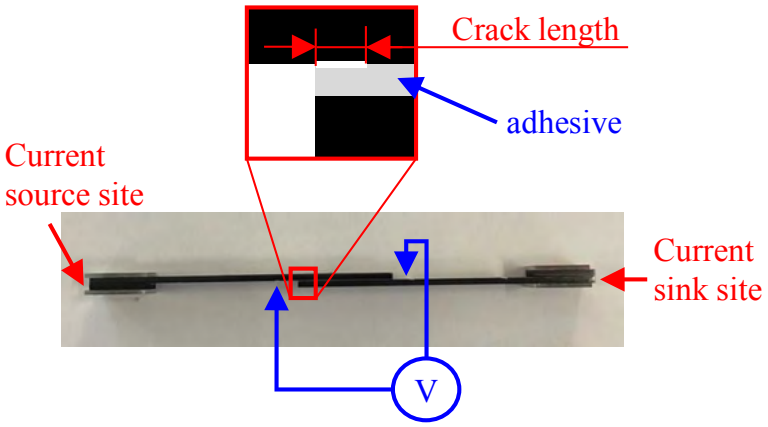


Figure 1. Investigated bonded joint configuration. The image highlights the position of current sink and source sites, as well as the position of the voltage measurement probes.

3. Analytical model

The model relies on the electrical scheme reported in Figure 2. The upper adherend is considered as constituted by a fixed resistance, Ra^{U}, and a variable resistance, Ra^{U*}, and the same applies to the lower adherend, with Ra^{L} and Ra^{L*} respectively. The adhesive is represented by another variable resistance, Rad. In the undamaged configuration, Ra^{U*} and Ra^{L*} are zero. As soon as damage takes place, the current is supposed to be unable to cross the crack faces, and the adherends behaves as if they elongated by an amount equal to crack length: the associated increase in the electrical resistance is represented by Ra^{U*} and Ra^{L*}. At the same time the contact surface between the adherends and the adhesive is reduced, thus resulting in an increase of Rad.

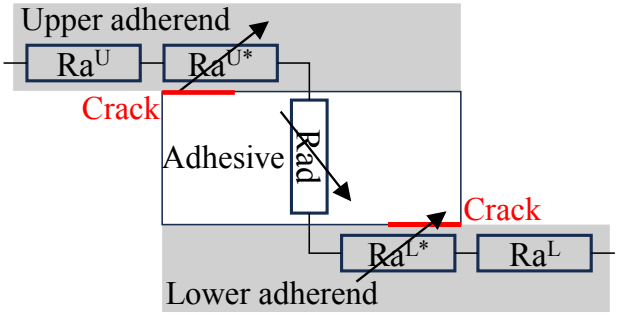


Figure 2. Simplified electrical scheme of the joint.

Upon a closer analysis, to properly model the electrical field between crack tips it appears that the abovementioned model is not accurate enough. In fact, the electricity is not instantly transferred from the adherend to the adhesive, but there is an electrical field along the joint length also within the adherend portion that is still attached to the adhesive.
Following these considerations, it is possible to build a system of differential equations that represents the electrical current density variation along the joint length, redefining Rad as the electrical resistance of the joint between crack tips, thus considering both the adhesive and the adherends (see Figure 3).

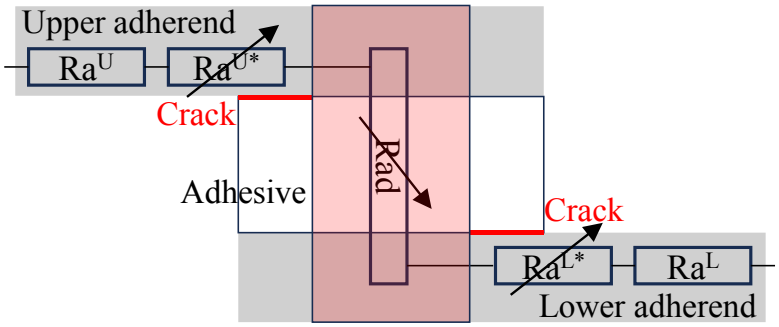


Figure 3. Electrical scheme of the joint considered in the analytical model. A red overlay highlights the material considered for the analytical model.

The differential equation of the current density through-the-thickness (z direction) j_z is represented by the following equation (Eq. 1), valid for both adherends and adhesive:

$$j_z = -\frac{1}{\eta_z}\frac{\partial V(z)}{\partial z} \tag{1}$$

where η_z represents the material out-of-plane resistivity. It is then possible to evaluate through-the-thickness average values of the electric potential in each layer $\overline{V}$ by means of (Eq. 2):

$$\overline{V} = \frac{1}{t}\int_0^t V(z)\,dz \tag{2}$$

with t the layer thickness (both for adherend and adhesive).
It is then possible to describe the current flow along the joint length (x direction), leveraging on the charge conservation principle, as (Eq. 3):

$$\begin{cases} \dfrac{\partial j_x^{(1)}}{\partial x} - \dfrac{1}{t_1} j_c^{(1-2)} = 0 \\ \dfrac{\partial j_x^{(2)}}{\partial x} - \dfrac{1}{t_2}\left(j_c^{(2-3)} - j_c^{(1-2)} \right) = 0 \\ \dfrac{\partial j_x^{(3)}}{\partial x} + \dfrac{1}{t_3} j_c^{(2-3)} = 0 \end{cases} \tag{3}$$

where superscript (1) refers to the upper adherend, (2) refers to the adhesive, and (3) refers to the lower adherend. j_c is the current density moving in z direction at the interface of the layers.

Following these assumptions, it is possible to derive an analytical expression of the current field. The complete framework is under publication in Structural Health Monitoring journal, published by Sage.

It is worth noting that if the adhesive electrical resistance is significantly higher than that of the adherends, the expression of the joint electrical resistance following damage, R, simplifies to (Eq. 4):

$$R = R_0 \frac{w}{w - \left(a^U + a^L \right)} \tag{4}$$

where R_0 is the electrical resistance in the undamaged configuration, a^U and a^L are the crack lengths at adhesive/upper-adherend interface and adhesive/lower-adherend interface respectively, and w is the initial adhesive ligament length along the joint-length direction.

4. Numerical validation

The model was initially validated by means of Finite Element Analysis, using Ansys Mechanical APDL. The material properties used in the analysis are reported in Table 1.

Table 1. Electrical material properties used for numerical validation.

Material	in-plane resistivity, η_x [Ω mm]	through-the-thickness resistivity, η_z [Ω mm]
Aluminium	2.82E-11	2.82E-11
CNT-modified GFR laminates	6.15E+04	7.08E+04
Araldite ® adhesive	1.37E+07	1.37E+07
CNT-modified epoxy adhesive	2.42E+04	2.42E+04

In Figure 4 a comparison between the FEA and the analytical results is shown. Two different material pairs were considered: Aluminium adherends and Araldite adhesive, case I, and CNT modified GFR laminates with CNT modified epoxy adhesive, case II. For case I Eq. 4 is enough to describe the joint behaviour, given that the lines of the prediction of the full analytical model and of the simplified model overlap. It appears that the proposed model is effective in predicting the electrical resistance variation due to damaging in both configurations. Moreover, the FEA analyses prove that the relative length of a^U and a^L do not influence the resistance variation, which is affected only by their sum: i.e. the overall damage extent.

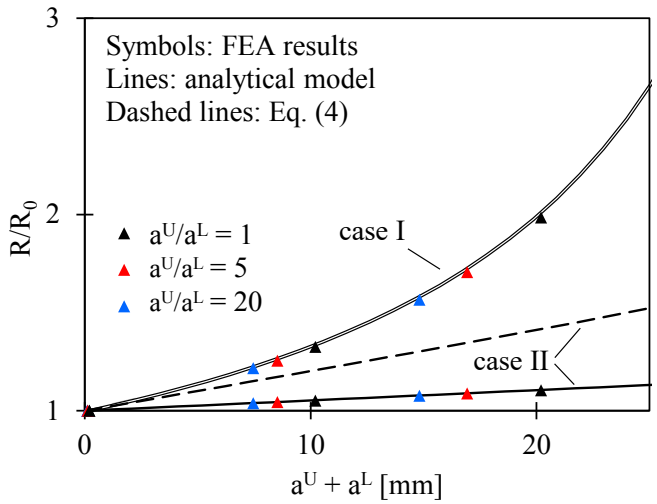


Figure 4. Comparison between FEA results and analytical model for different joint geometrical configurations and materials.

5. Experimental validation

Two material pairs for the joint adherends and adhesive were evaluated: the first one considers adherends made of Aluminium with Huntsman Araldite® 40300 adhesive, whilst the second one makes use of CFR UD laminated adherends with the same adhesive. Araldite® is a conductive epoxy adhesive that contains Miralon® particles. The assessment of the damage evolution was done measuring the joint stiffness reduction during cyclic loadings.
The Aluminium adherends have a thickness of 1.85 mm and have been obtained from a flat panel, while the CFR UD laminate is obtained stacking 4 layers of a UD HS600 – ET445 – 35% prepreg and processing them in autoclave.
Tabs made of the same material of the adherends were then applied to the specimen ends, followed by additional Glass/Epoxy tabs to ensure electrical insultation between the sample and the grips of the testing machine.

In Figure 5 the procedure used for validating the model is depicted. The samples have been loaded with fatigue ratio 0.1 by a servo-hydraulic machine and data was collected in terms of force, displacement field of the joint, and electrical conductivity. Conductivity measurements allow the use of the analytical model for estimating the total crack length. Then, the estimated crack length can be used in a Finite Element virtual twin of the joint to assess its loss of stiffness, here represented as the stiffness of the damaged configuration, K, divided by the stiffness of the undamaged configuration, K_0. The value of K/K_0 so predicted can then be compared to the experimental joint stiffness reduction.

The electrical properties of the materials used for manufacturing the joints are reported in Table 2.

Table 2. Electrical material properties used for experimental validation.

Material	in-plane resistivity, η_x [Ω mm]	through-the-thickness resistivity, η_z [Ω mm]
Aluminium	2.82E-11	2.82E-11
CFR UD laminate	2.00E-01	2.70E+04
Araldite ® adhesive	1.37E+07	1.37E+07

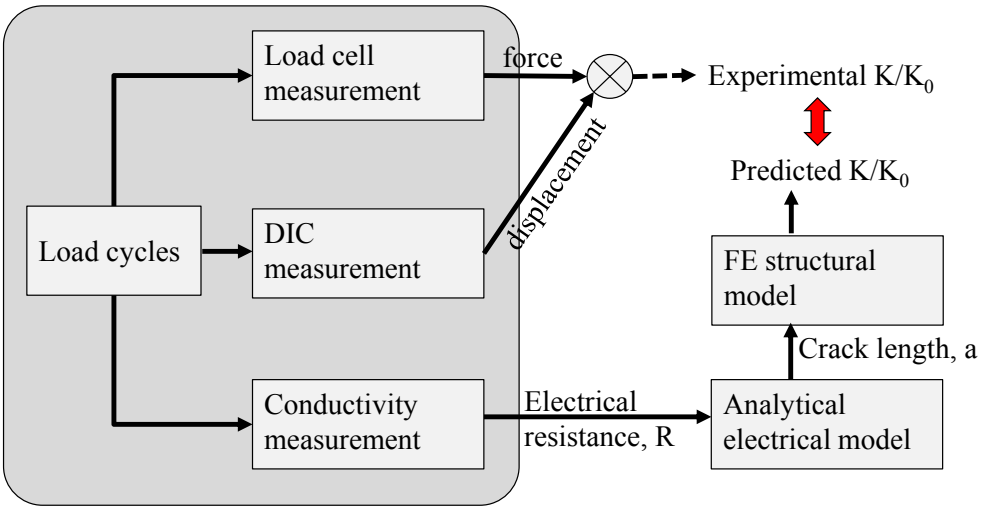


Figure 5. Scheme of the dataflow used for validating the model.

The proposed comparison for a sample joint made of Aluminium adherend is reported in Figure 6. It appears that the model is fully capable of predicting the stiffness reduction by means of electrical measurements.

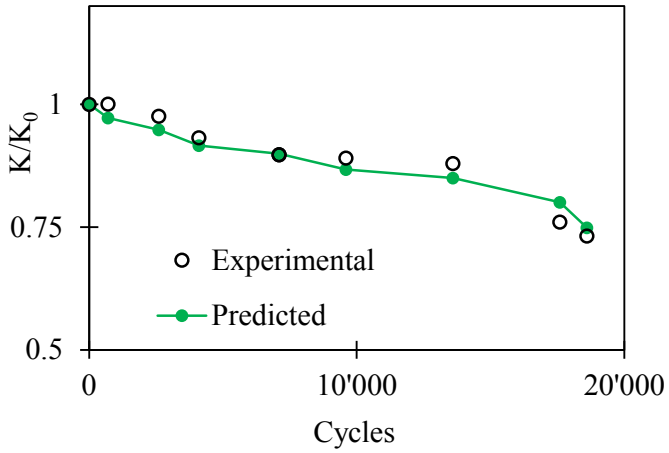


Figure 6. Comparison of experimental and predicted results for a specimen made of Aluminium adherends.

5. Model modification and validation

The methodology presented so far relies on the hypothesis that crack faces are fully insulating, thus there is a direct relationship between the load-carrying surface and the electricity-conducting one. However, it is well known that in the case of fibre-reinforced laminates fibre bridging takes place, and its direct consequence is that electricity can flow across the crack surfaces. Another common damage mode that can take place is that crack tilts from the adherend-adhesive interface to the inside of the adherend, thus resulting, again, in a reduced electrical insulation.

To account for these behaviours, Eq. 4 can be modified into (Eq. 5):

$$\frac{R}{R_0} = \frac{w}{w - a_{TOT}(1-\varphi)} \tag{5}$$

where φ is a parameter that quantifies the residual electrical conductivity across crack faces. In more details, φ can be expressed as (Eq. 6):

$$\varphi = \frac{1}{\left(1 + \frac{r_i}{\eta_a \cdot t_a}\right)} \tag{6}$$

where r_i is the interface resistance, η_a is the adhesive electrical resistivity, and t_a is the adhesive thickness. The same hypotheses standing for Eq. 4 apply.

It is important to consider that φ actually depends on the crack length, since fibre bridging mechanism requires some crack extension to develop. As such, in order to apply the method, it is necessary to calibrate φ with an experimental campaign on the target joint, so that its value is known for each crack length. In the following, the calibration was performed by testing 3 specimens and evaluating φ average value and standard deviation.

Finally, to use the proposed model to estimate a joint stiffness reduction, Eq. 5 can be applied. Since the crack extension influences the value of φ, an iterative numerical procedure is required. The results for a test specimen are reported in Figure 7, where the band represents the predictions associated to φ values at 10% and 90% probability, according to standard distribution.

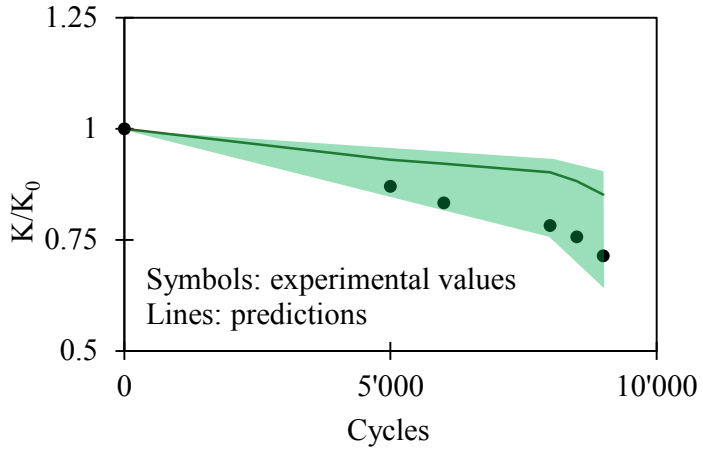


Figure 7. Comparison of experimental and predicted results for a specimen made of CFR UD adherends.

Even though the scatter of the forecasts is not irrelevant, it appears that the model is able to follow the experimental data trend. Such scatter is the result of unpredictability in the damage mode in the considered joints. In more details, the event of the crack tilting inside the adherend affects relevantly the experimental trend, but the occurrence of that event is not predictable, thus requiring a probabilistic approach.

6. Conclusions

The current manuscript explored the feasibility of using electrical measurements to monitor damage in single-lap bonded joints. An analytical model was presented to estimate the increase in electric resistance across the joint bond surface due to damage, accounting for the differential equations describing electrical fields in the joint. The model's accuracy was proved numerically using Finite Element Analysis, considering both high-conductivity and low-conductivity adherends with different crack length. Later on, experimental fatigue tests were conducted on single lap joints with Aluminium adherends and a conductive epoxy adhesive, showing that the ability of the model in inferring the damage extent using data from electrical monitoring can be put in use in a FE structural model to predict

the joint stiffness reduction. To account for residual electrical conductivity across crack faces in fibre reinforced adherends, the model was modified, and following tests on Carbon-epoxy composite adherends showed the model was still able to assess the joint stiffness reduction. At the same time the tests highlighted the importance of employing a probabilistic approach to account for the actual damage mechanisms.

Acknowledgments
Financed by the European Union - NextGenerationEU (National Sustainable Mobility Center CN00000023, Italian Ministry of University and Research Decree n. 1033 - 17/06/2022, Spoke 11 - Innovative Materials & Lightweighting). The opinions expressed are those of the authors only, and should not be considered as representative of the European Union or the European Commission's official position. Neither the European Union nor the European Commission can be held responsible for them.

References

[1] K.I. Tserpes, G. Peikert, I.S. Floros. The Effectiveness of Corrugation as a Crack Stopper in Composite Bonded Joints. In *4th International Conference of Engineering Against Failure (ICEAF IV), 24-26 June 2015, Skiathos, Greece*.
[2] I. Floros, K.I. Tserpes. Numerical simulation of quasistatic and fatigue debonding growth in adhesively bonded composite joints containing bolts as crack stoppers. *The Journal of Adhesion*, 97(7):1-23, 2019.
[3] S. Yashiro, J. Wada, Y. Sakaida. A monitoring technique for disbond area in carbon fiber–reinforced polymer bonded joints using embedded fiber Bragg grating sensors: Development and experimental validation. *Structural Health Monitoring*, 16(2):185–201, 2017.
[4] X.F. Sánchez-Romate, C. Sbarufatti, M. Sánchez, A. Bernasconi, D. Scaccabarozzi, F. Libonati, S. Cinquemani, A. Güemes, A. Ureña. Fatigue crack growth identification in bonded joints by using carbon nanotube doped adhesive films. *Smart Mater Struct*, 29(3):1-14, 2020.
[5] K. Schulte, C. Baron. Load and failure analyses of CFRP laminates by means of electrical resistivity measurements. *Compos Sci Technol*, 36:349–356, 1989.
[6] L. Böger, M.H. Wichmann, L.O. Meyer, K. Schulte. Load and health monitoring in glass fibre reinforced composites with an electrically conductive nanocomposite epoxy matrix. *Compos Sci Technol*, 68:1886-1894, 2008.
[7] S.P. Fernberg, R. Joffe. Damage detection in carbon fibre cross-ply laminates by aid of carbon nanotube doped resin. In: *Proceedings of the 13th European Conference on Composite Materials ECCM13, Stockholm, Sweden, June 2-5, 2008*.
[8] L. Gao, E.T. Thostenson, Z. Zhang, T.W. Chou. Sensing of damage mechanisms in fiber-reinforced composites under cyclic loading using carbon nanotubes. *Adv Funct Mater*,19: 123–130, 2009.
[9] M. Zappalorto, F. Panozzo, P.A. Carraro, M. Quaresimin. Electrical response of a laminate with a delamination: modelling and experiments. *Compos Sci Technol*, 143:31-45, 2017.
[10] P.A. Carraro, M. Zappalorto, M. Quaresimin. Health monitoring of cross-ply laminates: Modelling the correlation between damage evolution and electrical resistance change. *Compos Part A*, 82:151-158, 2016.
[11] T. Takeda, F. Narita. Fracture behavior and crack sensing capability of bonded carbon fiber composite joints with carbon nanotube-based polymer adhesive layer under Mode I loading. *Compos Sci Technol*, 146: 26–33, 2007.
[12] P.A. Carraro, F. Panozzo, A. Pontefisso, M. Quaresimin, M. Zappalorto. Damage monitoring of composite bonded joints using the electrical method: modelling and experiments. In *Proceedings of the 20th European Conference on Composite Materials, Lausanne, Swizterland, June 26-30, 2022*.

NONDESTRUCTIVE INSPECTION OF THICK MULTI-LAYERED THERMOPLASTIC COMPOSITE PIPES

Mohd Fadzil Mohd Tahir[1], Guillaume Pors[2], Andreas T. Echtermeyer[3]

[1]Department of Mechanical and Industrial Engineering, Norwegian University of Science and Technology (NTNU), Richard Birkelands vei 2B, 7491, Trondheim, Norway
Email: mohd.f.b.m.tahir@ntnu.no, Web Page: https://www.ntnu.no
[2]Technical Center of Mechanical Industries (CETIM), 74 Route de la Jonelière, C50814, 44308 Nantes , France
Email: guillaume.pors@cetim.fr, Web Page: https://www.cetim.fr
[3]Department of Mechanical and Industrial Engineering, Norges Teknisk-Naturvitenskapelige Universitet (NTNU), Richard Birkelands vei 2B, 7491, Trondheim, Norway
Email: andreas.echtermeyer@ntnu.no, Web Page: https://www.ntnu.no

Keywords: Thermoplastic Composite Pipe, Phased Array Ultrasonic Testing, Computed Tomography

Abstract
A collaborative effort is underway to establish standardized methods for ensuring the structural integrity of composite pipes, focusing on thick fiber-reinforced composite pipes like thermoplastic composite pipe (TCP) and reinforced thermoplastic pipe (RTP). These flexible pipes offer advantages over metal counterparts, including high strength-to-weight ratios and corrosion resistance, making them ideal for various industries, including oil and gas and renewable energy. However, non-destructive testing (NDT) of thick composites utilizing the widely used ultrasonic testing (UT) technique presents challenges. Current technologies, developed primarily for metal and thinner composites, struggle to effectively detect defects in multi-layered materials. This project addresses this limitation by utilizing phased array ultrasonic testing (PAUT) with the implementation of the classical time-corrected gain (TCG) method. The proposed technique demonstrated reliable detectable signals with good signal-to-noise ratios (SNR). Subsequently, it successfully detected and characterized delamination and impact damage. The defect morphology reported by the proposed method was further validated using X-ray computed tomography (CT). Although this imaging-based technique faces practical limitations for field use due to size, portability, and cost constraints, it offers more detailed, three-dimensional visualizations of the internal structures of the tested materials. Overall, the UT technique shows promise for immediate practical applications, while X-ray CT remains more suitable for laboratory or controlled environments.

1. Introduction

TCP and RTP gradually replace traditional metal pipes due to their non-corrosive nature, flexibility, and high strength-to-weight ratio. These qualities make them ideal for reducing maintenance and overall installation costs while extending service life. However, despite these advantages, both materials are susceptible to various defects, including delamination within composite laminate layers, debonding at interfaces between different layers, fiber breakage, matrix deformation, matrix degradation, and thinning of protective layers due to external forces. Thus, the need for NDT techniques to reliably detect these anomalies remains crucial. NDT techniques that can be applied directly onsite are essential. While ultrasonic wave-based methods are widely used in the market, they were primarily developed for isotropic and homogeneous materials like metals. The main challenge faced when applying UT to polymer and polymer composite materials is severe attenuation due to absorption in polymer materials, which is four orders of magnitude greater than that of metals [1], and the scattering at fiber-matrix interfaces in random directions [2].

As composite materials gain prominence in industries such as aerospace and automotive, the demand for reliable NDT techniques for structural integrity assessment has surged. UT has been extensively studied and proven effective in identifying defects such as delamination [3][4][5] and impact damage [6][7][8] in thin composite structures. The relatively short propagating distance in thin structures compensates for the severe attenuation of ultrasonic waves. However, thick TCP and RTP pose additional challenges due to their increased thickness and the presence of thick thermoplastic covers and inner liners. Limited research was performed to study the UT capability related to this specific application, particularly concerning thick multi-layered composite structures [9][10]. Using standard procedures employed for metals or thin composites is insufficient, as increasing instrument gain not only amplifies the signal of interest but also amplifies noise from multiple layers of composite laminate. This study focuses on overcoming the limitations of current PAUT technology in inspecting such materials by incorporating the classical TCG method to compensate for spatial signal attenuation and a focusing technique for improved defect characterization. Additionally, X-ray CT scans are conducted to obtain a three-dimensional representation of delamination and impact damage for comparison with UT results.

2. Materials

2.1 TCP and RTP

This study investigated two types of composite pipes, which are TCP and RTP, each comprising three distinct layers. These layers include a thermoplastic outer cover, multiple fiber-reinforced composite laminate layers, and a thermoplastic inner liner. In the production of TCP, prepreg tapes are wound around a thermoplastic pipe at a typical winding angle of ±55°, forming multiple composite laminate layers. These prepreg tapes are made of continuous glass or carbon fiber reinforcement with a similar thermoplastic material as in the cover and liner as matrix materials. Subsequently, a thermoplastic outer cover is applied around these composite layers, and they are melt-fused to establish strong bonding between each layer, creating the cover-laminate and liner-laminate interface layers. Despite the matching acoustic impedance between these layers due to the presence of similar thermoplastic materials, which theoretically facilitates the transmission of ultrasonic energy through the boundary, severe attenuation occurs due to absorption in the polymer material and multiple reflections within the fiber-reinforced composite laminate layers, posing significant challenges to the UT technique. Meanwhile, RTP is produced by helically wrapping two layers of continuous and twisted aramid yarns, over the thermoplastic liner at ±55° angles. Subsequently, a thermoplastic cover layer is extruded over these layers after heat bonding. Unlike TCP, there is no bonding between the aramid yarns and thermoplastic matrix material because the fibers are not impregnated, posing an additional challenge to the UT technique.



Figure 1. (a) Glass fiber reinforced TCP with FBH (measurements are in millimeters), (b) carbon fiber reinforced TCP with delamination, and (c) aramid fiber reinforced RTP with impact damage.

2.2 Anomalies

In the first scenario, a glass fiber reinforced TCP sample was cut longitudinally along its axial centerline. Then, a flat bottom hole (FBH) was bored from the internal side of the sample until within the composite laminate layer, as illustrated in **Figure 1**(a). The FBH represents a one-sided delamination with a

perfectly flat base perpendicular to the ultrasonic wave propagation. At the material-air interface, total reflection of ultrasonic energy occurs due to a significant acoustic impedance mismatch [2]. In the second case, a carbon fiber reinforced TCP sample was subjected to axial compression using a hydraulic testing machine, inducing delamination within the composite laminate layer, as depicted in **Figure 1**(b). For the third scenario, impact damage was inflicted on two aramid fiber reinforced RTP samples by dropping a sharp impactor aligned perpendicularly to the axial length of the pipe. The weight and drop height of the impactor were carefully selected to ensure that the impact energy was sufficient to damage the highly ductile thermoplastic material. This damage extended to the fiber reinforcement layer in one sample when subjected to an impact energy of 0.97 kJ, whereas it penetrated through the entire thickness in the other sample when impacted with 1.88 kJ of energy, as shown in **Figure 1**(c).

3. NDT Methods

This study aimed to compare the capabilities of radiographic imaging and ultrasonic wave-based NDT techniques, utilizing X-ray CT and PAUT. The former was selected for its ability to provide detailed three-dimensional and cross-sectional radiographic images that closely resemble actual anomalies in size and shape. Conversely, PAUT was chosen due to its accessibility and widespread use in the field.

3.1 X-Ray CT

X-ray CT scan was conducted on the carbon fiber reinforced TCP and aramid fiber reinforced RTP samples using the Nikon XT h 225 ST scanner. The sample was positioned between the X-ray source and a flat panel detector during the scan. To ensure consistent imaging along the pipe's length, the sample's longitudinal axis was aligned perpendicular to the X-ray beam. Multiple two-dimensional projection images were captured at various angles around the pipe, encompassing a complete 360° sample rotation. These images were then processed to reconstruct a detailed three-dimensional image of the sample, enabling cross-sectional views on three-perpendicular planes within the internal structure. This reconstruction facilitated a comprehensive analysis of any damages present. The reconstructed datasets were visualized and analyzed using the open-source myVGL software.

3.2 PAUT

PAUT was conducted using multiple transducers with varying numbers of elements and frequencies, ranging from 1.0 MHz to 5.0 MHz, supplied by Olympus. The raw data was captured using the Olympus OmniScan SX flaw detector and analyzed using the OmniPC 5 software, a complimentary companion software for the Olympus OmniScan series [11]. A notable challenge in inspecting multi-layered composite materials with PAUT is the significant signal attenuation beyond the first interface layer. Consequently, standard inspection methods typically used for metals are not directly applicable to TCP and RTP. Therefore, this study proposed implementing the classical TCG method to compensate for the severe spatial attenuation. The TCG method gradually increases system gain over time so that successive signal amplitudes are at the same height as the initial signal amplitude, irrespective of their distance from the transducer. However, this inherent limitation proves beneficial for implementing the TCG method, as the repeated signal from the first interface layer, which could superimpose with defect signals located beyond it, is minimal and negligible. This method is not applicable for inspecting multi-layered structures made of metals due to challenges in data interpretation. There will be a mixing of received signals beyond the first interface layer, comprising multiple consecutive echoes of the first interface layer, discontinuities, the second interface layer, and signals from the back wall, which could cause y lead to erroneous data interpretation.

In addition to the TCG method, this study incorporated the focusing technique to enhance the characterization of impact damage in RTP. Focusing the ultrasonic beam at a specific focal point within the inspected object intensifies the sound energy per unit area, thereby enhancing sensitivity to small reflectors within the area. Consequently, this approach provides a better characterization of damage dimensions and morphology. To ensure accurate measurements, sound velocity calibration was conducted individually on each sample using a two-point calibration method. The thickness of the outer cover or the inner liner, as well as the total sample thickness, served as the lowest and highest thickness references, respectively. Since ultrasonic waves propagates through multiple dissimilar materials with

varying velocities due to differences in density and elasticity, the calibrated velocity utilized in this study represents an average velocity value. It is important to note that this calibrated velocity is applicable only to samples with similar constructions [10].

4. Results and Discussions

4.1 PAUT Results After Implementing TCG Method at Defect-Free Region

Figure 2 illustrates the typical PAUT signal when the transducer is placed at the defect-free area of the glass fiber reinforced TCP (upper row) and carbon fiber reinforced TCP (lower row), comprising two types of signal representation. The left side displays an A-scan view, while the right side presents an E-scan view, depicting the real-time cross-sectional image of the inspected object. This real-time imaging is captured by the phased array electronically scanning the area under the active aperture without moving the transducer. Before implementing the TCG method, only the signal from the first interface layer is discernible, as shown in **Figure 2**(left column). In contrast, the signal from the second interface layer and the back wall are severely attenuated. Additionally, the repeated signal from the first interface layer is considered to fully dissappear due to severe attenuation. This phenomenon is advantageous because the unwanted repeated signal can be suppressed when the gain is partially increased at specific TCG points corresponding to the signals of interest beyond the first interface layer, marked with red points in the A-scan view. Consequently, a defect can be detected if it is located in that position. Following the TCG implementation, the signals from the second interface layer and the back wall increase to the same level as the first interface layer, as shown in **Figure 2**(right column). At the same time, the background noise exhibited a linear increase between two TCG points.

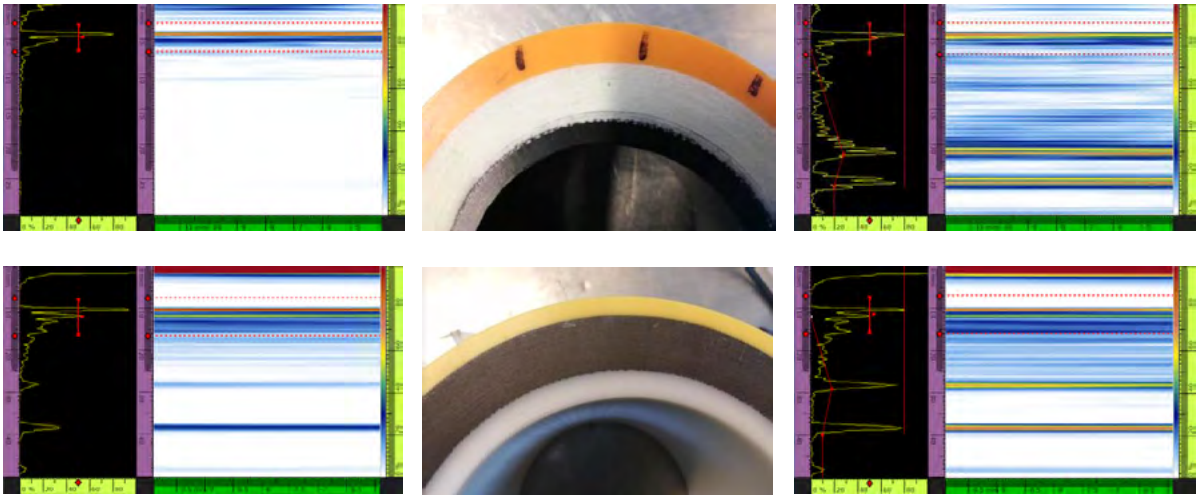


Figure 2. Typical PAUT signal on glass fiber reinforced TCP (upper row) and carbon fiber reinforced TCP (lower row), before (left column) and after (right column) implementing the TCG method.

4.2 FBH on Glass Fiber Reinforced TCP

The proposed technique, while positioning the transducer on the outer surface of the sample using a direct contact method, demonstrates its capability to detect the FBH on the glass fiber reinfoced TCP. The transducer is positioned in such a way that one half of the active aperture lies above the FBH position, while the other half covers the defect-free region, ensuring accurate detection. **Figure 3** shows the PAUT result. The left side of the E-scan view displays the signal from the FBH measured at 15.0 mm compared to the actual position of 15.2 mm. Meanwhile, the right side of the E-scan view represents the defect-free region. The A-scan view corresponds to the aperture selected by the user-controlled blue vertical cursor on the E-scan view, indicating the center aperture at approximately the FBH's edge. Additionally, the result clearly indicates that the FBH is located within the composite laminate layers, as its measured distance is between the signal of both interface layers. Despite the linearly increased background noise after implementing the TCG method, the FBH is reliably detected with a good SNR,

exceeding the practical standard minimum of 3 required for a signal to be considered an indication [12]. The comprehensive details of the study on FBH detection will be outlined in [13].

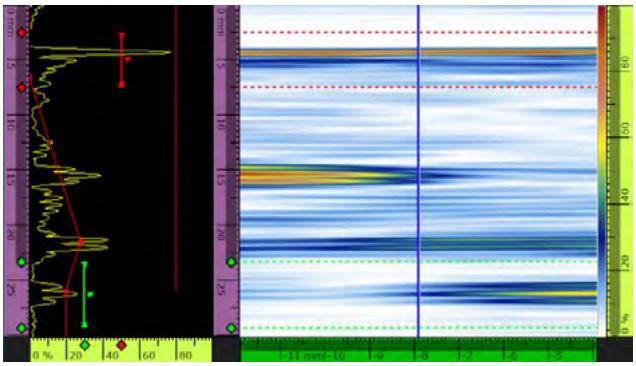


Figure 3. PAUT result of the FBH on glass fiber reinforced TCP.

4.3 Delamination on Carbon Fiber Reinforced TCP

The proposed technique was further employed to detect delamination on carbon fiber reinforced TCP. A mechanical encoder recorded the measured distance and provided information about the damage dimension. In **Figure 4**(a), a representative B-scan view of a defect-free region without the TCG method reveals only the signal from the first interface layer, with signals from the second interface layer and the back wall significantly attenuated. This cross-sectional view provides a two-dimensional illustration of variations in the thickness of each layer across different positions. After implementing the TCG method, signals from the second interface layer and back wall are increased, and the signal from the delamination, denoted as Delam01, appears as well, as represented by **Figure 4**(b). Multiple B-scan views can be stacked together generating a three-dimensional C-scan that illustrates a plan view of the sample with information about the thickness of each layer plotted over position both horizontally and vertically. A corresponding C-scan is generated by placing an electronic gate over the pulse width of the delamination, as shown in **Figure 4**(c). In addition to Delam01, another smaller delamination, oriented parallel to the fiber direction, is detected and denoted as Delam02.

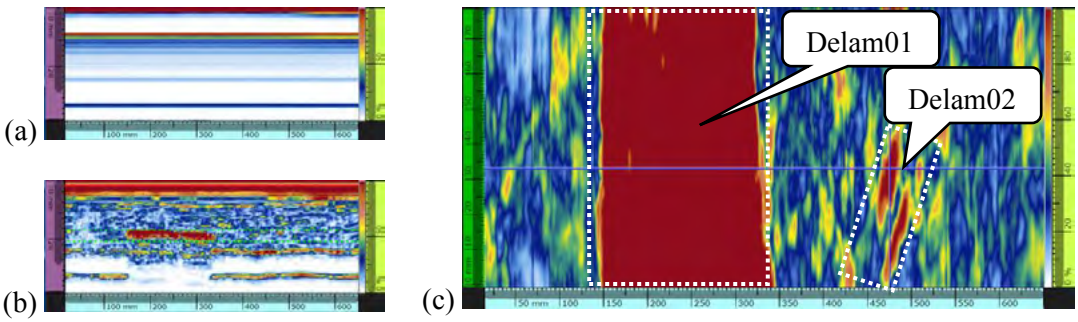


Figure 4. PAUT results of the delamination on carbon fiber reinforced TCP.

The reconstructed radiographic image obtained from the X-ray CT scan clearly displays both delaminations, as depicted in **Figure 5**. This image represents a cross-sectional view of the sample within a single plane perpendicular to the axial direction, positioned approximately at the midpoint of the sample to capture both delaminations. Multiple additional planes are adjacent to this plane in both directions, and their space between each other depends on the scanning resolution. Further investigation reveals that by selecting planes towards one end of the sample, the relative position of Delam02 to Delam01 reduces, implying that Delam02 runs parallel to the fiber direction and progressively closer toward Delam01. The comprehensive details of the study on the detectability of the delamination will be outlined in [14].

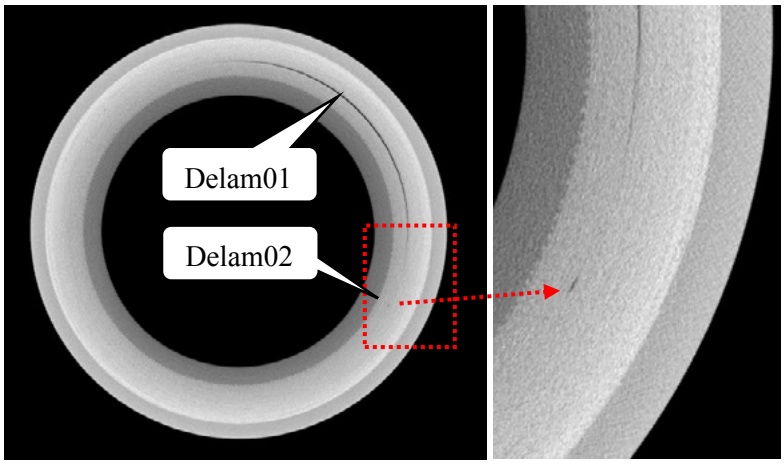


Figure 5. X-ray CT results of the delamination on carbon fiber reinforced TCP.

4.4 Impact Damages on Aramid Fiber Reinforced RTP

PAUT was conducted from the internal side of the RTP sample in an attempt to detect external impact damage. The immersion technique was implemented in away that the sample was partially submerged in water, and the transducer was not fully immersed and fixed in a stable position while the sample was rotated for scanning. This approach allowed for clear detection of the water-sample interface and the fiber reinforcement, while the TCG method was applied to enhance the severely attenuated back wall signal. Additionally, the ultrasonic beam was focused at the back wall and reinforcement layer to increase the amount of energy interacting with the impact damages oriented not perpendicularly to the wave propagation like FBH or delamination. **Figure 6** presents a comparison between the cross-sectional radiographic images from the X-ray CT scan on the left column and the ultrasonic B-scan view with unfocused and focused ultrasonic beams on the middle and right columns, respectively.

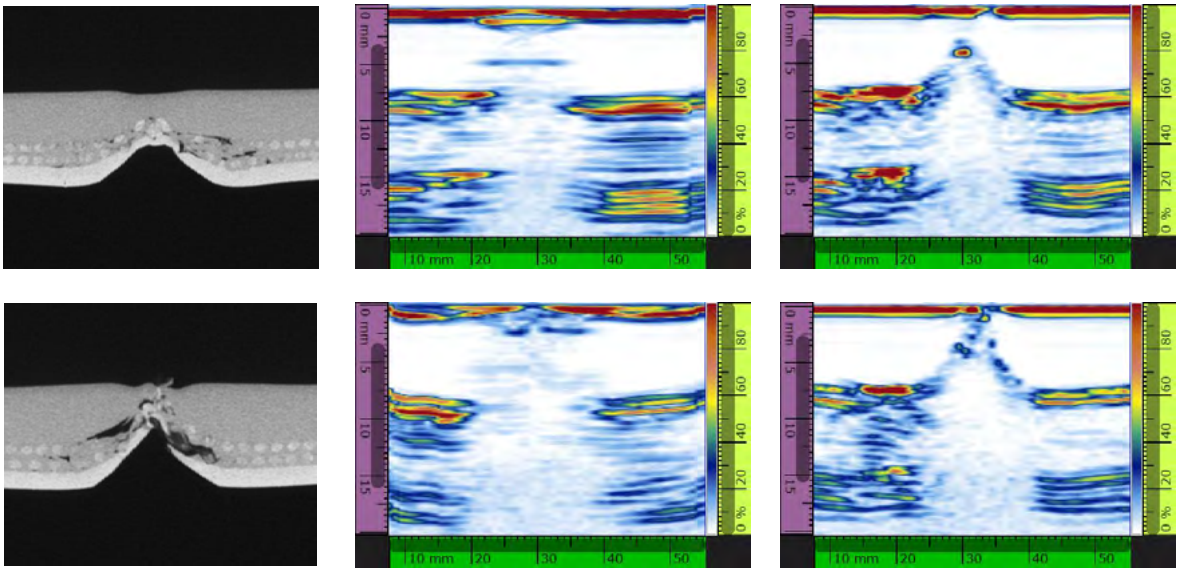


Figure 6. NDT results of impact damages on aramid fiber reinforced RTP under 0.97 kJ (upper row) and 1.88 kJ impact energies (lower row); cross-sectional radiographic images (left column), B-scan images using unfocused (middle column), and focused ultrasonic beams (right column).

A 0.94 kJ impact energy penetrates the RTP up to a few millimeters (upper row), while a 1.88 kJ impact energy penetrates all through (lower row). Reflectors perfectly perpendicular to wave propagation reflect off energy efficiently when the ultrasonic beam is not focused. In contrast, reflectors not oriented favorably to wave propagation cause ultrasonic signal attenuation because they reflect this propagating

in random directions. However, this study found that even reflectors oriented unfavorably to the propagation of the wave can reflect some amount of energy with a focused ultrasonic beam, which leads to generation of cross-sectional ultrasonic B-scan images similar to the radiographic images captured by the X-ray CT scan. There is good agreement between the B-scan data generated by the focused ultrasonic beam and the cross-sectional radiographic images. The comprehensive details of the study on the detectability of the impact damages will be outlined in [15].

The outcomes derived from a comprehensive series of studies examining the detection capabilities of PAUT with the implementation of the TCG method indicate its immediate applicability in either manufacturing or field operations for identifying fabricated and in-field damages. While an X-ray CT scan offers a better representation of defects than PAUT, its practical field application presents formidable challenges. This limitation is primarily due to the need to rotate either the entire testing apparatus or the kilometer-long pipe to capture multiple two-dimensional radiographic images, subsequently reconstructed into virtual slice images for generating three-dimensional data.

5. Conclusion

This paper summarizes a series of ongoing studies on detecting various damage types in two types of composite pipes, thermoplastic composite pipes (TCP) and reinforced thermoplastic composite pipe (RTP). Each pipe comprises a thermoplastic outer cover, fiber reinforcement layers, and a thermoplastic inner liner.

The study leverages the radiographic imaging and ultrasonic wave-based NDT techniques, specifically comparing X-ray computed tomography (CT) and phased array ultrasonic testing (PAUT). While X-ray CT provides detailed three-dimensional images, PAUT was selected for its accessibility and widespread use in the field. This study proposed implementing the classical time-corrected gain (TCG) method to compensate for the severe attenuation of ultrasonic energy propagating in multi-layered polymer and polymer composite materials. It is worth noting that the TCG method is not applicable to similar multi-layered structures made of metals due to mixing of multiple repeated signals beyond the first interface layer.

The study evaluated the capability of PAUT with the TCG method to detect defects in composite pipes, including flat bottom hole (FBH), delamination, and impact damages. The results showed that PAUT with TCG method not only enhanced defect detection but also allowed for accurate localization and characterization. FBH detection in glass fiber reinforced TCP demonstrated the method's precision, detecting FBHs within composite laminate layers with a good signal-to-noise ratio (SNR). Delamination detection in carbon fiber reinforced TCP indicated the method's ability to identify small and large delamination within the composite laminate layers. Additionally, X-ray CT scans corroborated these findings, giving information about multiple cross-sectional radiographic views of the sample parallel to the axial direction.

Furthermore, the proposed technique successfully detected impact damages in aramid fiber reinforced RTP, a scenario where the damages are not favorably oriented to wave propagation. The use of focused ultrasonic beams improved detection sensitivity, generating cross-sectional B-scan images comparable to X-ray CT scans. This highlights the immediate applicability of PAUT technique in identifying various damages and overcoming challenges associated with X-ray CT's practical field application, despite its superior detection capability.

Acknowledgments

This work is part of the DNV-led Joint Industry Project “C-PIMS” with 12 industrial partners and the Norwegian University of Science and Technology (NTNU). The authors would like to express their gratitude for the financial support from the Research Council of Norway (Project No. 309238 in the PETROMAKS programme).

References

[1] Mark HF (2003) Encyclopedia of polymer science and technology, volume 5, 3rd edn. John Wiley & Sons Inc, New Jersey, pp 1-47
[2] Hellier CJ (2013) Handbook of nondestructive evaluation, 2nd edn. McGraw-Hill Education, New York, pp 7.1-7.116, pp 12.1-12.66
[3] Hassen AA (2016) Taheri H, Vaidya UK. Non-destructive investigation of thermoplastic reinforced composites. Compos Part B 97:244-254. https://doi.org/10.1016/j.compositesb.2016.05.006
[4] Hasiotis T, Badogiannis E, Tsouvalis NG (2011) Application of ultrasonic C-scan techniques for tracing defects in laminated composite materials. J Mech Eng 57(3):192-203. https://doi.org/10.5545/sv-jme.2010.170
[5] Szymański R (2020) Non-destructive testing of thermoplastic carbon composite structures. Trans Aerosp Res 1(258):34-52. https://doi.org/10.2478/tar-2020-0003
[6] Santos MJ, Santos JB, Reis P, Amaro A (2019) Ultrasonic C-scan techniques for Damage evaluation of carbon fiber reinforced polymers submitted to low energy impacts. Proc Meet Acoust (POMA) 2019, Bruges, Belgium (Volume 38). https://doi.org/10.1121/2.0001062
[7] Papa I, Lopresto V, Langella A (2021) Ultrasonic inspection of composite materials: Application to detect impact damage. Int J Lightweight Mater Manuf 4(1):37-42. https://doi.org/10.1016/j.ijlmm.2020.04.002
[8] Pagliarulo V, Papa I, Lopresto V, Langella A, Ferraro P (2019) Impact damage investigation on glass fiber-reinforced plate laminates at room and lower temperatures through ultrasound testing and electronic speckle pattern interferometry. J Mater Eng Perform 28(6):3301-3308. https://doi.org/10.1007/s11665-019-04134-8
[9] Hassen AA, Vaidya UK, Britt F (2015) Structural integrity of fiber reinforced plastic piping. Mater Eval 73(7):918-929. https://www.researchgate.net/publication/281068198
[10] Ibrahim ME (2021) Ultrasonic inspection of hybrid polymer matrix composites. Compos Sci and Technol 208:108755. https://doi.org/10.1016/j.compscitech.2021.108755
[11] Blanchette D. Are you aware that OmniPCTM 5 software is actually freeware? https://www.olympus-ims.com/en/insight/omnipc-freeware/ [accessed 1 April 2024]
[12] Olympus (2017) Introduction to phased array ultrasonic technology applications, 1st ed, 4th print. Olympus, Waltham
[13] Tahir MFM, Echtermeyer AT. Phased array ultrasonic testing on thick glass fiber reinforced thermoplastic composite pipe implementing the classical time-corrected gain method (to be published)
[14] Tahir MFM, Pors G, Echtermeyer AT. Detection capability of delamination within the thick carbon fiber reinforced polyamide composite laminate with the presence of thermoplastic lining by means of ultrasonic testing and X-ray computed tomography techniques (to be published)
[15] Tahir MFM, Echtermeyer AT. Impact damage detection on thick reinforced thermoplastic pipe utilizing ultrasonic testing and X-ray computed tomography techniques (to be published)

INTEGRATION OF JOHNSON-COOK RATE-DEPENDENT CONSTITUTIVE MODEL FOR IMPROVED PREDICTION OF UNIDIRECTIONAL GLASS-EPOXY COMPOSITES BALLISTIC RESPONSE

Shubham[1] and Chandra Sekher Yerramalli[2]

[1]Department of Aerospace Engineering, Indian Institute of Technology Bombay, Mumbai, 400076, India
Email: 30005127@iitb.ac.in
[2]Department of Aerospace Engineering, Indian Institute of Technology Bombay, Mumbai, 400076, India
Email: chandra@aero.iitb.ac.in

Keywords: Johnson-Cook, Constitutive Model, Ballistic Impact, Unidirectional Composites, Finite Element Analysis

Abstract
In this study, the ballistic characteristics of unidirectional glass-epoxy (UD-GE) composites, employing both experimental and numerical approaches underpinned by the rate-dependent Johnson-Cook (J-C) constitutive model, are examined. Finite element analysis (FEA) integrates the J-C plasticity and damage model to forecast stress-strain behavior and failure mechanisms during high-velocity impacts. Utilizing a UD-GE laminate prepared using a hand layup technique with a thickness of 3.6±0.1 mm and $[0]_6$ stacking sequence, reference velocities for numerical simulations were established at the ballistic limits, namely V_0, V_{50}, and V_{100}. Experimentally, mean velocities of 88 m/s, 108 m/s, and 124 m/s respectively were determined for V_0, V_{50}, and V_{100}. The observed damage patterns in the optical images of the experimented samples closely mirror those predicted by numerical simulation outputs. Building upon prior research, this study underscores the efficacy of rate-dependent constitutive models in accurately anticipating the response and damage evolution of fiber-reinforced polymer (FRP) composites under high-velocity impact conditions.

1. Introduction

Due to the relevance in various fields such as space sciences and military technologies for personal and structural protection, as well as in high-speed impact dynamics, the study of ballistic impact behavior of materials is of considerable interest across experimental [1], theoretical [2, 3], and numerical [4] research domains. Armors made with traditional materials like steel were commonly utilized due to their cost-effectiveness, but they suffered from high weight. Polymer matrix composite armors, particularly laminated composites, present a promising alternative owing to their superior weight-normalized mechanical properties, including stiffness and strength [5–8]. Consequently, much of the research in ballistic studies has focused on understanding the behavior of laminated composite structures when subjected to impact, which is a crucial yet intricate challenge. This complexity arises from the interplay of various factors, such as material behavior, failure mechanisms, and load transfer mechanisms, all of which entail numerous uncertainties [9–11]. Consequently, accurately predicting impact behavior remains a quest, prompting investigations employing diverse methodologies, from simplistic empirical models to highly intricate numerical techniques. Proposing a method that utilizes fewer data inputs is necessary to streamline computation.

Numerous researchers [12–14] have devised analytical models reliant on experimental data. Several studies have addressed different aspects of ballistic impact and armor performance. Porwal and Phoenix [15] investigated the effects of system dynamics due to ballistic impact on flexible, multilayered targets without inter-layer bonding with a cylindrical projectile. They discovered that V_{50} and residual velocity are influenced by the arrangement of layers with varying mechanical properties, and the V_{50} velocity upsurges with the layers strain-failure ratio. Cuniff [16] advanced a parametric model to predict the performance of body armor systems against steel projectiles, utilizing nonlinear regression analysis of Kevlar 29 test data. Roylance et al. [17] utilized a finite difference method (FDM) to simulate ballistic impact on fabric, modeling the fabric as an interconnected mesh assembly with artificial buckup springs playing a role in ballistic limit determination. Landa et al. [18] formulated an analytical model for predicting the impact behavior of soft armors against rigid projectiles, making basic assumptions about projectile movement and material behavior. Billon and Robinson [19] proposed a model (analytical) for ballistic impact on fabric armor, neglecting inter-layer interaction and maximizing ballistic limit velocity by using layers made from materials with the ballistic limit velocity highest for single-layer.

The epoxy material properties being influenced by strain rate are well known in the research community, but information on how yarn properties are affected by strain rate is scarce. In our previous study [20], Abaqus software was used to numerically assess the impact of yarn's strain-rate dependency. A finite element composite model was employed featuring square prismatic-shaped split Hopkinson pressure bar (SHPB) samples. The yarn properties were homogenized to mimic those of a high fiber volume fraction composite. Both the bulk epoxy and yarn material properties were described using the Johnson-Cook (JC) constitutive model, while the failure mechanism was characterized using the JC damage model. This model was chosen because of its widespread availability and ease of implementation in various finite element analysis (FEA) simulation software. Three scenarios were examined: one where both yarn and bulk matrix properties were strain-rate dependent, another where only the bulk matrix showed strain-rate dependency and a third where both yarn and matrix were strain-rate independent. It was observed that the model incorporating complete strain-rate dependency exhibited peak stress and strain values comparable to experimental results, outperforming the other models in this aspect.

In this study, the JC material and damage model will be used for estimating the ballistic response of the UD glass epoxy composite laminate. The ballistic limit velocities are the prime focus. The three important Ballistic limit velocities are V_0, V_{50} and V_{100}. The greatest velocity at which no full penetration will take place is V_0. The velocity at which both full and incomplete penetration have an equal chance of happening is known as V_{50} and the lowest velocity at which there is a complete chance of full penetration is regarded as V_{100}. Experimental iterations were done to find out these velocities, and numerical analysis were done for the same values for comparison. The applicability of the JC model with the used parameters will be discussed properly in this article.

2. Experimental Procedure

2.1. Material Selection and Sample Preparation

The epoxy (diglycidyl ether bisphenol A type) resin, commercially known as Lapox (L12), and the hardener (triethylenetetramine), commercially known as K-6, were sourced from Atul Industries Ltd in India. The epoxy resin exhibits a density of 1.15 g/cc, a tensile elastic modulus ranging between 3.25 and 4.0 GPa, and a tensile strength ranging from 55 to 70 MPa. An E-Glass fiber UD mat was utilized in this study as reinforcement.

Six layers of UD-GE fabric mat were utilized to fabricate a GE laminate using the hand lay-up method. The ratio of epoxy resin to hardener was maintained at 10:1 (by weight) in accordance with the manufacturer's guidelines. Subsequent to laminate preparation, compression was applied, and the laminate was left for curing in a similar state at room temperature (RT) for twenty-four hours. Afterward, the samples underwent precise cutting and polishing to attain the specified dimensions and square geometry, ensuring precision within a tolerance of ±0.1 mm. Furthermore, a post-curing process was

carried out in an oven set at 140°C for 6 hours, followed by gradual cooling to room temperature inside the oven [21]. The fiber volume fraction of the resultant samples was assessed using the resin burn-off test, yielding a value of 0.56 ± 0.01.

2.2. Ballistic Setup

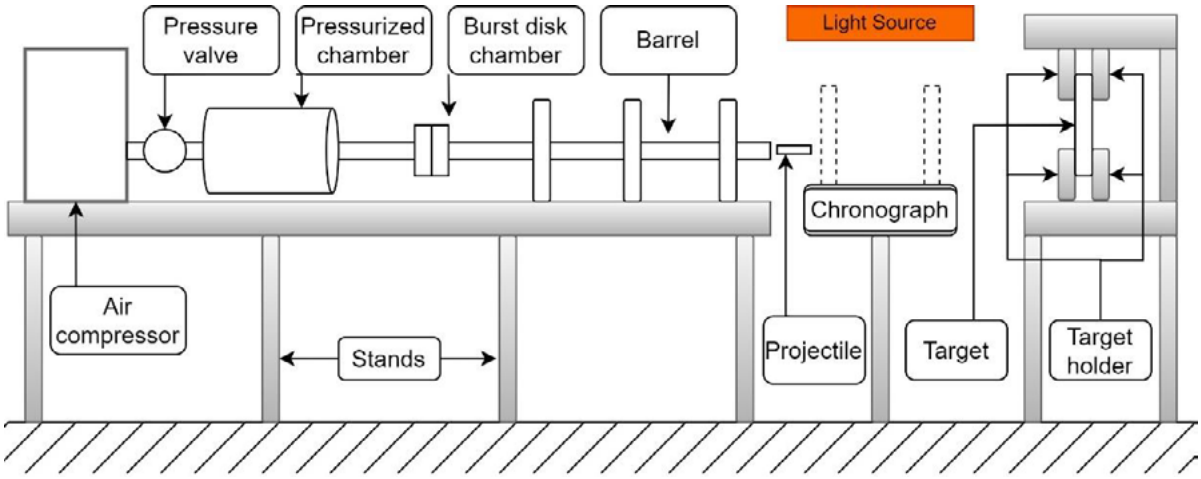


Figure 1. Schematic representation of the ballistic testing apparatus used in this study.

The impact behavior of targets was assessed utilizing a single-stage gas gun setup, employing 6.3 mm flat-end cylindrical steel projectiles of length 30 mm. Figure 1 is the schematic representation of the ballistic setup used. The setup featured a burst disk mechanism. Pressure regulation was achieved using an air compressor supplied by BAUER KOMPRESSOREN. Burst disks of varying thicknesses were utilized to control pressures and velocities. Projectile velocities were recorded using a chronograph. Composite targets were securely clamped between steel plates and the ballistic responses were examined. Prior to conducting the experimental test, the alignment of the barrel and target was verified.

3. Numerical Details

The laminated UD-GE composite was initially modeled at the yarn-level homogenization using ANSYS DesignModeler. Following this, the model underwent meshing, application of boundary conditions and analysis within the ANSYS Workbench environment. Additionally, the material behavior of the matrix-impregnated yarn and bulk matrix was characterized by incorporating strain-rate dependency, utilizing the J-C constitutive and damage model. The subsections below discuss this approach in detail.

3.1. Yarn-Level Finite Element Modeling

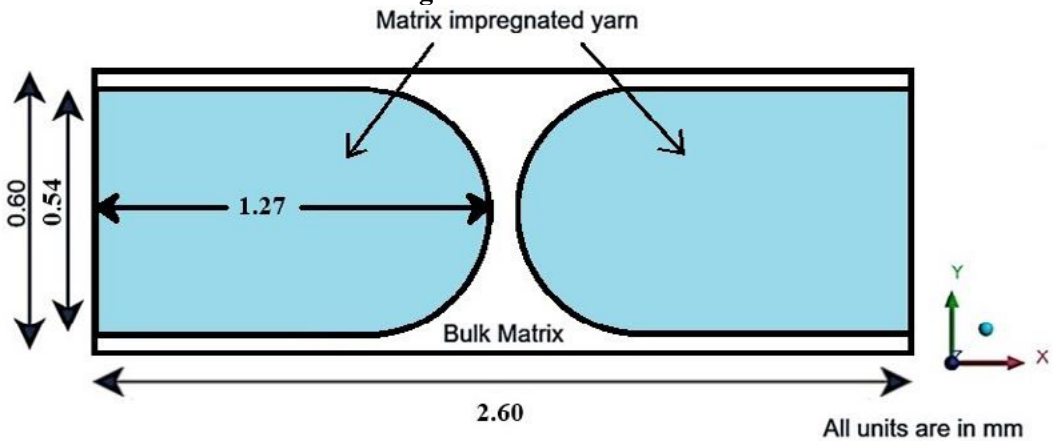


Figure 2. RUC schematic representation of the composite laminate at yarn level modeled for FEA

To define the yarn's cross-section, a 2-dimensional (2D) near representation was obtained by sectioning it with a perpendicular plane to its length. This cross-section, typically exhibiting a buldging shape towards ends, encapsulates the smallest segment of the yarn containing all fibers and is assumed to be uniform along its length. Figure 2 presents a schematic depiction of the representative unit cell (RUC) illustrating the cross-section of the yarn that was used for the modeling of the composite plate. The cross-sectional profile of the yarn was modeled in Ansys design modeler using the oval (four edges) tool. The material properties of the matrix-impregnated yarn and bulk epoxy utilized the J-C constitutive and damage model, the parameters of which were kept the same as estimated in our previous research work [20]. The details of the material behavior model and parameter fitting can be found there.

3.2. Simulation Details

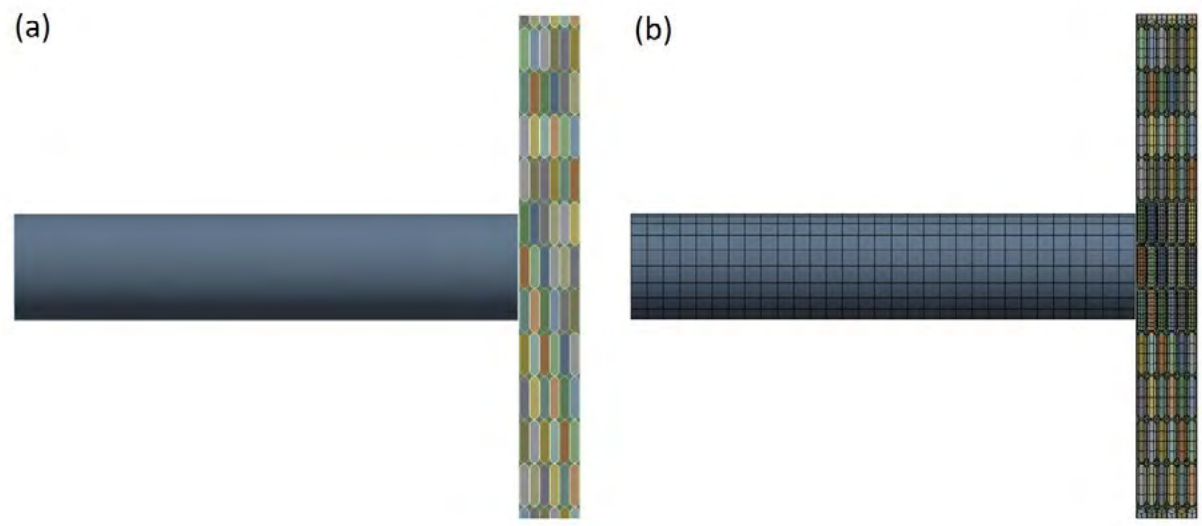


Figure 3. Numerical UD-GE target plate and projectile (a) geometrical model (b) meshed model.

In the FEA performed, the target exhibits identical geometrical characteristics to those employed in the experiment, ensuring a direct and accurate comparison. Figure 3a illustrates the geometrical model analyzed. In the experiment, the open square window for the target measured approximately 30 mm along the edge, which was replicated in the numerical modeling by providing appropriate boundary conditions. Fixed support were provided along the edges. The projectile material and dimesion were also kept identical to the experiment, and a coefficient of friction of 0.42 was provided between the projectile and the target. In Figure 3b, the mesh size and pattern at the cross-section of the UD-GE laminate are depicted. In order to make this study computationally efficient, the yarns coming under direct impact of the projectile under all the layers were meshed finer compared to the rest of the yarns. The numerical model comprised a total of 381,297 nodes and 252,481 elements. There was an initial 0.1 mm distance between the target plate and the projectile geometry. The projectile was imparted with an initial velocity of 88 m/s, 108 m/s and 124 m/s and directed to strike the target (UD-GE laminate) in line with the axis of the setup.

4. Result and Discussions

After a number of ballistic impact iterations on the UD-GE samples, the ballistic limits were determined, as shown in Figure 4. The average values observed for V_0, V_{50} and V_{100} were 88 m/s, 108 m/s and 124 m/s with a decent standard deviation as shown in the bar graph. The same velocities were taken as a reference for the ballistic simulation in the Ansys explicit dynamics software and the projectile fired were given initial velocities accordingly.

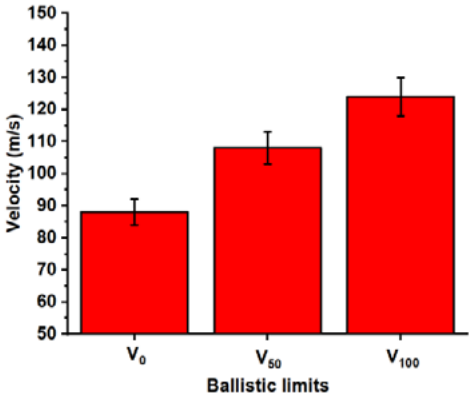


Figure 4. Ballistic limits obtained using experimental investigation

Figure 5 shows the deformation pattern observed at different ballistic limits. It is quite clear from the image that when a projectile impacts a UD-GE laminate, the deformation pattern varies depending on the velocity of the projectile and the ballistic limits. When we talk about the V_0 ballistic limit, it indicates a 0% risk of penetration or the limit velocity at which the laminate can stop the projectile without penetration. At V_0, the laminate experienced some deformation, but it was able to withstand the impact without allowing the projectile to pass through. The deformation pattern included localized delamination, fiber breakage, and some bulging or denting of the back side of the laminate. The V_{50} ballistic limit represents a higher velocity at which the laminate can still stop the projectile sometimes without penetration, but in half of the cases, the projectile is able to get through. At V_{50}, the deformation pattern became more severe compared to V_0. There was more extensive fiber breakage, significant bulging and denting of the laminate. However, in a few cases, the laminate could still be able to prevent penetration by the projectile. Finally, the V_{100} ballistic limit indicates a 100% risk of penetration or the limit velocity at which the laminate cannot stop the projectile and there will be a complete penetration. At V_{100}, the deformation pattern was the most extreme. The laminate experienced severe delamination, extensive fiber breakage, and significant deformation, including large-scale tearing of the material. At this velocity the laminate could not prevent the projectile from penetrating through.

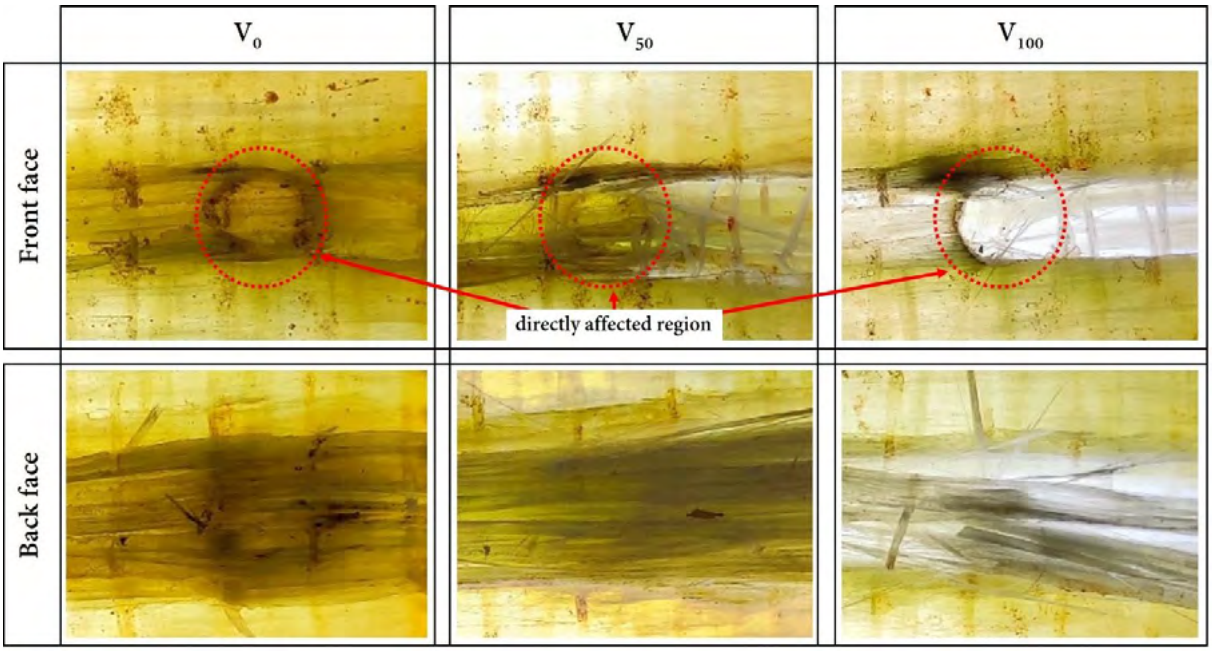


Figure 5. Photographs near the impacted area of UD-GE samples tested at the ballistic limits.

The simulation results shown in Figure 6 obtained using Ansys closely mirror the observed damage patterns depicted in Figure 5. Through numerical simulations, we effectively captured the deformation

behavior of UD-GE laminates under varying ballistic limits, reflecting the impact of projectile velocity on material response. At the V_0 ballistic limit, the simulations demonstrated localized delamination, fiber breakage, and minor bulging or denting on the back side of the laminate, consistent with the experimental findings. Moving to the V_{50} ballistic limit, numerical simulations depicted a progression towards more severe damage, with extensive fiber yarn breakage, significant bulging and even penetration, and denting evident. The simulations aligned with the observed trend of increased damage severity compared to V_0 & showed complete projectile penetration. Finally, at the V_{100} ballistic limit, numerical simulations showcased the most extreme deformation patterns, echoing the experimental results of severe delamination, extensive fiber yarn breakage, and significant material tearing. Consistently, the simulations highlighted the inability of the laminate to prevent projectile penetration at this velocity, in line with the experimental observations. Overall, the numerical simulations effectively replicated the deformation patterns observed in the experimental data, providing valuable insights into the ballistic performance of UD-GE laminates under different impact velocities.

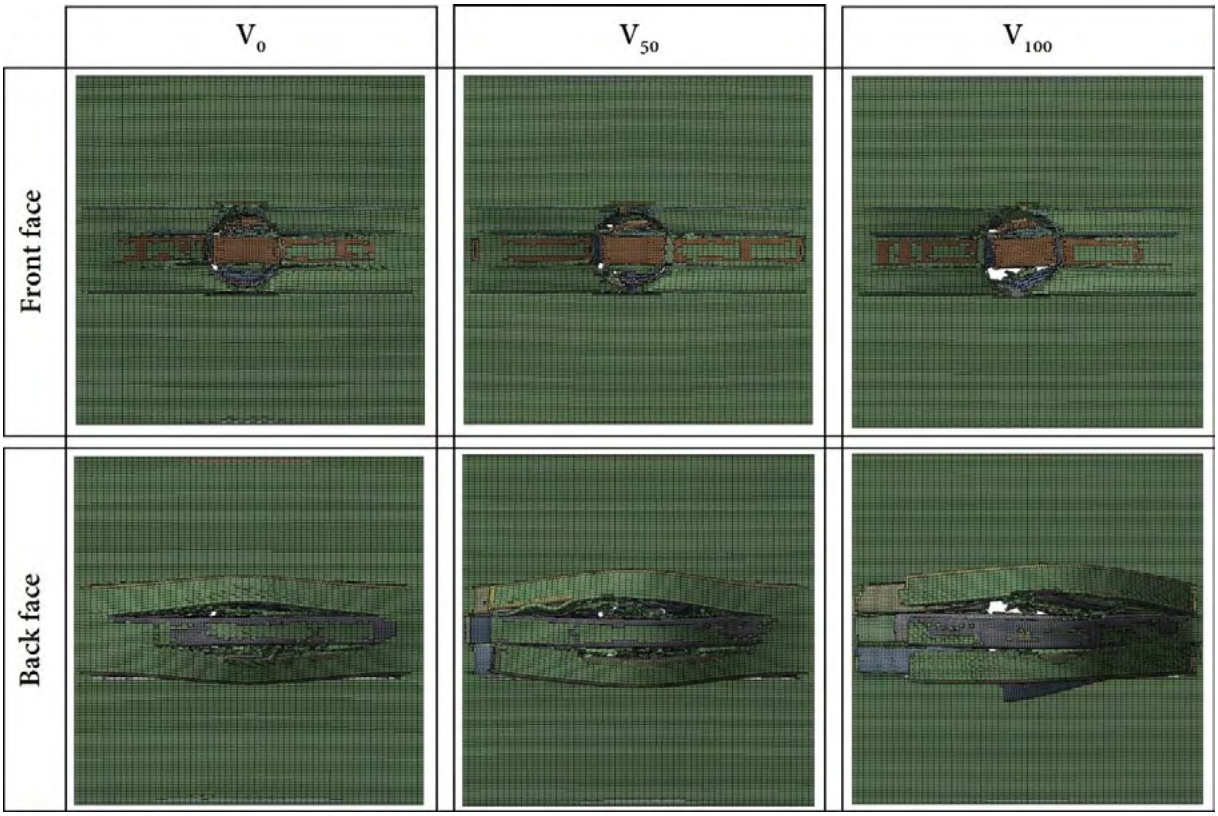


Figure 6. Simulation results of UD-GE samples tested at the ballistic limits.

5. Conclusions

This study concerns the ballistic response of UD-GE composites, employing a combination of experimental analysis and numerical simulations utilizing the rate-dependent Johnson-Cook (J-C) constitutive and damage model. Through a series of ballistic impact iterations and subsequent experimental investigations, the ballistic limits of the laminates were determined. These limits, characterized by V_0, V_{50}, and V_{100} velocities, represent crucial thresholds delineating the ability of the laminate to withstand projectile impact without penetration. Our experimental findings showcased distinct deformation patterns at these ballistic limits, ranging from localized delamination and fiber breakage at V_0 to severe delamination and extensive fiber breakage at V_{100}. Furthermore, our numerical simulations using Ansys explicit dynamics software closely mirrored these observed damage patterns. The simulations effectively captured the progressive deterioration of the laminates integrity with increasing projectile velocity, aligning with the experimental observations. Specifically, at the V_0 ballistic limit, simulations demonstrated minor damage consistent with experimental findings, while at

V_{50} and V_{100} limits, simulations depicted increasingly severe damage patterns, culminating in complete projectile penetration. Drawing from prior research, this study underscores the efficacy of rate-dependent constitutive models in accurately predicting the response and damage incurred by fiber-reinforced polymer composites under high-velocity impacts. Validation against experimental data bolsters the credibility of the findings and ensures alignment between simulation results and real-world observations. Further advances in this approach may be applied to make it even more close to real scenario.

References

1. Shubham, Ray, B.C.: Characterization Techniques in Different Strain-Rate Spectra. In: Shubham and Ray, B.C. (eds.) Fiber Reinforced Polymer (FRP) Composites in Ballistic Protection: Microstructural and Micromechanical Perspectives. pp. 51–62. Springer Nature, Singapore (2024)
2. Pol, M.H., Liaghat, G., Zamani, E., Ordys, A.: Investigation of the ballistic impact behavior of 2D woven glass/epoxy/nanoclay nanocomposites. Journal of Composite Materials. 49, 1449–1460 (2015).
3. Shubham, Ray, B.C.: Recent Development of Constitutive Models for Strain-Rate Sensitive FRP Composite Materials. In: Shubham and Ray, B.C. (eds.) Fiber Reinforced Polymer (FRP) Composites in Ballistic Protection: Microstructural and Micromechanical Perspectives. pp. 97–107. Springer Nature, Singapore (2024)
4. Shubham, Ray, B.C.: High-Velocity Impact Modeling in Materials Science: A Multiscale Perspective. In: Shubham and Ray, B.C. (eds.) Fiber Reinforced Polymer (FRP) Composites in Ballistic Protection: Microstructural and Micromechanical Perspectives. pp. 109–125. Springer Nature, Singapore (2024)
5. Nascimento, L.F.C., Louro, L.H.L., Monteiro, S.N., Lima, É.P., da Luz, F.S.: Mallow Fiber-Reinforced Epoxy Composites in Multilayered Armor for Personal Ballistic Protection. JOM. 69, 2052–2056 (2017).
6. Shubham, Prusty, R.K., Ray, B.C.: High Strain-Rate Through-Thickness Compression Testing of Symmetrical Inter-ply Hybrid Polymer Composites Reinforced with Carbon/Glass and Carbon/Kevlar Fibers. Trans Indian Inst Met. (2022).
7. Shubham, Yerramalli, C.S., Prusty, R.K., Ray, B.C.: Through-Thickness High Strain Rate Compressive Response of Glass/Epoxy-Laminated Composites Embedded with Randomly Oriented Discontinuous Carbon Fibers. In: Jonnalagadda, K., Alankar, A., Balila, N.J., and Bhandakkar, T. (eds.) Advances in Structural Integrity. pp. 103–111. Springer, Singapore (2022)
8. Shubham, Ray, B.C.: Introduction to Composite Materials. In: Shubham and Ray, B.C. (eds.) Fiber Reinforced Polymer (FRP) Composites in Ballistic Protection: Microstructural and Micromechanical Perspectives. pp. 1–20. Springer Nature, Singapore (2024)
9. Mohan, S., Velu, S.: Ballistic impact behaviour of unidirectional fibre reinforced composites. International Journal of Impact Engineering. 63, 164–176 (2014).
10. Shubham, Ray, B.C.: Microstructural Failure Mechanisms Analysis. In: Shubham and Ray, B.C. (eds.) Fiber Reinforced Polymer (FRP) Composites in Ballistic Protection: Microstructural and Micromechanical Perspectives. pp. 63–77. Springer Nature, Singapore (2024)
11. Kulkarni, S.G., Gao, X.-L., Horner, S.E., Zheng, J.Q., David, N.V.: Ballistic helmets – Their design, materials, and performance against traumatic brain injury. Composite Structures. 101, 313–331 (2013).
12. Sudheer, M., Pradyoth, K.R., Somayaji, S.: Analytical and numerical validation of epoxy/glass structural composites for elastic models. American Journal of Materials Science. 5, 162–168 (2015)
13. Naik, N.K., Shrirao, P., Reddy, B.C.K.: Ballistic impact behaviour of woven fabric composites: Formulation. International Journal of Impact Engineering. 32, 1521–1552 (2006).
14. Leigh Phoenix, S., Porwal, P.K.: A new membrane model for the ballistic impact response and *V*50 performance of multi-ply fibrous systems. International Journal of Solids and Structures. 40, 6723–6765 (2003).

15. Porwal, P.K., Phoenix, S.L.: Modeling System Effects in Ballistic Impact into Multi-layered Fibrous Materials for Soft Body Armor. Int J Fract. 135, 217–249 (2005).
16. Cunniff, P.M.: An Analysis of the System Effects in Woven Fabrics under Ballistic Impact. Textile Research Journal. 62, 495–509 (1992).
17. Roylance, David, Paula Hammas, Joe Ting, Hank Chi, and Brian Scott. "Numerical modeling of fabric impact. ASME-PUBLICATIONS-AD 48, 155-160 (1995).
18. Parga-Landa, B., Hernández-Olivares, F.: An analytical model to predict impact behaviour of soft armours. International Journal of Impact Engineering. 16, 455–466 (1995).
19. Billon, H.H., Robinson, D.J.: Models for the ballistic impact of fabric armour. International Journal of Impact Engineering. 25, 411–422 (2001).
20. Shubham, Yerramalli, C.S., Sumant, C., Prusty, R.K., Ray, B.C.: Finite element modelling and experimentation of plain weave glass/epoxy composites under high strain-rate compression loading for estimation of Johnson-Cook model parameters. International Journal of Impact Engineering. 104262 (2022).
21. Shubham, Prusty, R.K., Ray, B.C.: In-Situ Elevated Temperature Interlaminar Shear Response and Thermal Behavior of Graphene Nanoplatelet Reinforced Kevlar/Epoxy Laminated Composites. Polym. Sci. Ser. B. (2022).

DAMAGE TOLERANCE OF 3D WOVEN COMPOSITES

Christian Stewart[1*], Bassam El Said[1] and Stephen Hallett[1]

[1]Bristol Composites Institute, University of Bristol, BS8 1TR, Bristol, United Kingdom
*Email: christian.stewart@bristol.ac.uk, Web Page: https://www.linkedin.com/in/christianstewart95/

Keywords: Woven composite, Damage tolerance, BVID, CT scanning

Abstract
3D woven composite materials provide key mechanical performance advantages over their laminated counterparts, such as higher resistance to out-of-plane loading, as well as higher damage tolerance. Consequently, it is important to investigate the effect of barely visible impact damage (BVID) on their mechanical behaviour. In this study, experimental investigations are carried out to study how BVID affects the tensile performance of 3D woven composites. Interrupted quasi-static indentation tests are first carried out, and the damage at each level is characterised. The damage level, most representative of BVID, is identified and used for subsequent static tensile testing. It is found that the presence of BVID causes a reduction in tensile stiffness, but does not have a significant influence on the failure tensile strength and strain. The experimental results presented in this work give further insight on the damage tolerance of 3D woven composites.

1. Introduction

3D woven composite materials are seeing increasingly wider use in engineering applications such as automotive, renewable energy, and aerospace structures. This category of composites provides several economic and performance advantages over their laminated counterparts and metal alloys. 3D woven composites are usually prepared in near net-shape preforms before being infused by resin and cured to form the final structure, eliminating the costs associated with the layup of laminated composites or with the use of expensive prepreg materials. Additionally, 3D woven composites provide some key mechanical performance advantages, such as higher resistance to out-of-plane loading, as well as higher damage tolerance [1]. Consequently, the main area of application for these composites involves impact. The presence of barely visible impact damage (BVID) can be detrimental when structures are subjected to subsequent static and fatigue loading. It is therefore necessary to investigate the effect of BVID on the mechanical performance of these composites. In the present work, experimental investigations were carried out to determine how the presence of BVID affects the tensile performance of carbon/epoxy with a layer-to-layer 3D weave.

2. Materials and Methods

2.1. Materials Description

The considered 3D woven composite has a layer-to-layer reinforcement, characteristed by the interlacing of warp, weft, and binder yarns in 3D space. The weave architecture is shown in Figure 1. The woven yarns are made from HexTow IM7 24k tows, and the nominal dimensions of the representative volume element (RVE) are 9.1 mm, 14.5 mm, and 4 mm, in the warp, weft and through-thickness directions, respectively. Dry woven preforms of size 490 x 220 mm were infused with RTM6 epoxy resin through resin transfer moulding (RTM), and cured to produce flat composite panels. The specimens used for mechanical testing were cut from these panels using a diamond saw blade.

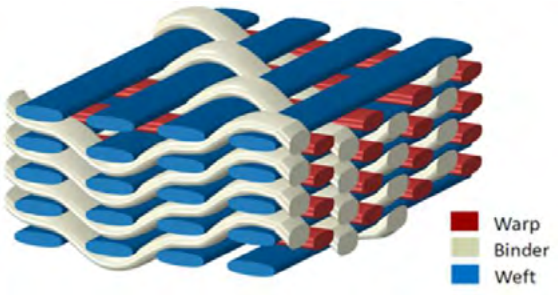


Figure 1. 3D layer-to-layer weave architecture.

2.2. Quasi-Static Indentation

The aim of this study is to investigate the effect of the presence of BVID on the mechanical behaviour of 3D woven composites. Therefore, a level of damage, which is representative of BVID, had to first be identified and introduced into the specimen before subsequent testing. In this study, BVID was imparted using quasi-static indentation (QSI) tests. The specimen dimensions used were 50 x 75 mm, with a 37.5 x 62.5 mm support window, a hemispherical indenter of 8 mm diameter, and a displacement-controlled loading at a rate of 1 mm/min. With these dimensions, several RVEs are present across the width and length of the specimen, promoting the representative behaviour of the woven material.

The level of damage at different indentation levels were characterised. First, the extent of damage was characterised by Ultrasonic C-scanning in pulse echo mode. X-ray Computed Tomography (CT) scanning was then performed, to better investigate the damage mechanisms present. A Nikon XTH320 was used for this purpose, obtaining a voxel size of around 24 μm.

2.3. Static Tension Tests

To assess the influence of BVID on the static performance, tensile tests were performed on both undamaged and post-BVID specimen. Uniaxial tensile tests were performed on a servo-hydraulic test machine (Instron 1342) with a 250 kN load cell. The specimen were loaded at a constant crosshead speed of 1 mm/min, up to failure. Stereo digital image correlation (DIC) was employed to obtain extension and strain data during the test.

3. Results and Discussion

3.1. Quasi-Static Indentation Tests

The typical load-displacement behaviour of 3D woven composites under QSI is illustrated in Figure 2a, where three distinct stages are identified: (A to B) a linear elastic stage up to damage onset, (B to C) knee point followed by damage propagation, and (after C) load drop due to yarn failure on the tension side [2]. Several QSI tests were interrupted along the damage propagation region, as shown in Figure 2b, and the damage at each level was characterised by non-destructive testing (NDT) methods.

The ultrasonic C-scanning of the interrupted QSI specimen illustrated the extent of damage at each indentation level. However, it did not provide information about the actual damage mechanisms present. Therefore, X-ray CT-scanning was carried out to better understand the development of damage mechanisms. Figure 3 illustrates examples of CT scan slices taken through the damaged region. Different damage mechanisms can be identified, namely matrix cracks, intra-yarn transverse cracks, and yarn debonding. The figure shows that as the indentation level increases, there is an increase of transverse cracks in the weft yarns and the resin-rich regions, as expected. There is no evidence of yarn debonding at indentation level 1. However, yarn debonding initiated before indentation level 2, and

became significant at indentation level 3. Since indentation level 2 exhibited diffused damage, it was deemed as the most representative of BVID. Therefore, it was selected as the damage level to be used in subsequent static testing.

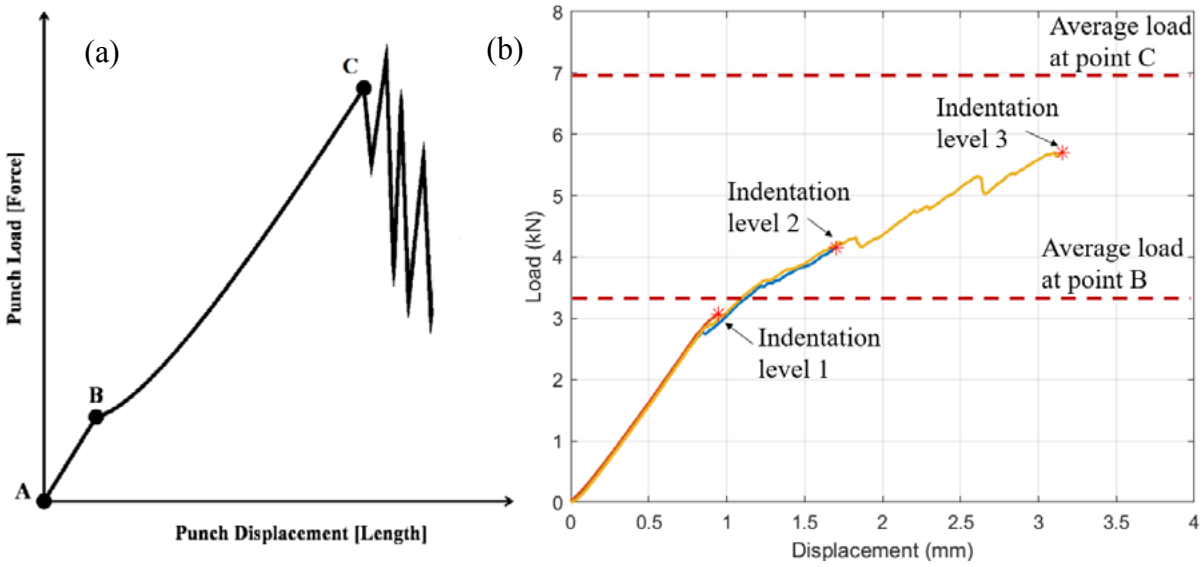


Figure 2. (a) Typical load-displacement response of 3D woven composites (Adapted from [3]); (b) Load-displacement results for interrupted QSI tests.

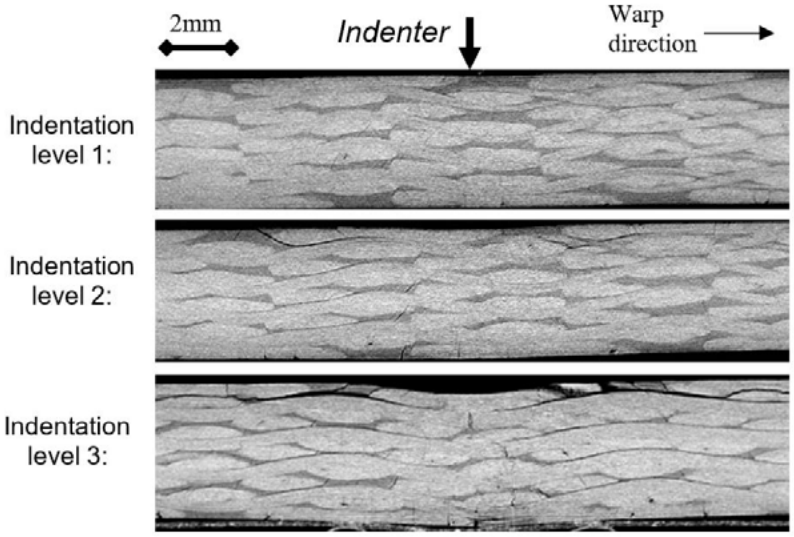


Figure 3. CT-scan 2D slices showing damage at different indentation levels.

3.2. Static Tensile Tests

Several undamaged and damaged specimen were subjected to uniaxial tensile testing up to failure. The weft direction was oriented with the loading axis. Table 1 illustrates the effect of the presence of BVID on the mechanical properties of the tested 3D woven composites. It can be noted that the presence of BVID has no significant effect on the tensile strength and strain-to-failure. This highlights the

insensitivity of these woven materials to the presence of BVID, which is one of the main benefits of such materials. The stiffness was reduced by around 5% with the presence of BVID. This is because the open cracks present within the BVID region increase the compliance of the specimen when subjected to tension.

Table 1. Static mechanical properties of specimen with and without BVID.

Specimen Type	Youngs Modulus (GPa)	Tensile Strength (MPa)	Strain-to-Failure (%)
Undamaged	53.60 ± 0.63	474.6 ± 12.3	1.35 ± 0.06
With BVID	51.00 ± 0.82	482.7 ± 8.3	1.37 ± 0.04

4. Conclusions

In this study, experimental investigations were carried out to study how the presence of BVID affects the tensile performance of carbon/epoxy with a layer-to-layer 3D weave. Woven composite specimens were first subjected to interrupted QSI tests, and the level of damage was characterised by NDT techniques. The damage level, most representative of BVID, was identified and used in subsequent static tests. The damaged specimen were then subjected to static tensile tests, and compared to the performance of undamaged specimen. It was shown that the BVID caused a reduction in stiffness, but did not have a significant influence on the failure strength and strain. The experimental results presented in this work give further insight on the damage tolerance of 3D woven composites.

Acknowledgments
The authors wish to acknowledge the support of Rolls-Royce plc through the Composites University Technology Centre (UTC) at the University of Bristol and the EPSRC through the CoSEM Centre for Doctoral Training grant, no. EP/S021728/1.

References
[1] M. N. Saleh and C. Soutis. Recent advancements in mechanical characterisation of 3D woven composites. *Mechanics of Advanced Materials and Modern Processes*, 3(12):1-17, 2017.
[2] R. Gerlach, C. R. Siviour, J. Wiegand, and N. Petrinic. In-plane and through-thickness properties, failure modes, damage and delamination in 3D woven carbon fibre composites subjected to impact loading. *Composites Science and Technology*, 72(3):397-411, 2012.
[3] J. N. Baucom and M. A. Zikry. Evolution of Failure Mechanisms in 2D and 3D Woven Composite Systems Under Quasi-static Perforation. *Journal of Composite Materials*, 37(18):1651-1674, 2003.

DETERMINATION OF TENSILE PROPERTIES AND DAMAGE ONSET OF THIN-PLY CFRP LAMINATES IN CRYOGENIC ENVIRONMENTS

Eduardo Szpoganicz [1], Fabian Hübner [2], Uwe Beier [2], Matthias Geistbeck [2], Holger Ruckdäschel [1*]

[1] Polymer Engineering Department, University of Bayreuth, Bayreuth, Germany
[2] Airbus Central Research and Technology, Munich, Germany
* Corresponding author (ruckdaeschel@uni-bayreuth.de)

Keywords: *Carbon-fiber-reinforced plastics, Cryogenics, Damage onset, Mechanical properties*

Abstract

Transitioning from standard jet-fuel to liquid hydrogen holds promise for zero-emission aviation, eventually requiring lightweight storage solutions. Carbon-fiber reinforced polymer (CFRP) composites offer an attractive alternative to heavy metallic tanks, but their susceptibility to damage and leakage in cryogenic environments (CT) presents challenges. Existing literature often overlooks the critical aspect of damage onset in CFRP materials for liquid hydrogen tanks, focusing predominantly on failure properties of unidirectional and birectional standard lamiantes. To address this gap, a study conducted *in-situ* cryogenic tensile testing on cryogenic-design unidirectional and quasi-isotropic thin-ply CFRP laminates to assess properties and damage onset behavior. Using an extensometer sensitive to damage, it was observed that the CFRP material sustained major delamination damage up to 0.8% strain-load and 650-750 MPa stress-load at 77 K, indicated initial delamination damage. Microscopy analysis validated these findings, revealing critical views of delamination between 90° and 45° plies once 0.8% strain-load in 77 K is applied to the laminate. No major damage was detected prior to 0.8% of strain-load. This study contributes to designing and characterizing CFRP materials tailored for cryogenic storage tanks, enhancing their viability for emerging aviation technologies.

1. Introduction

The International Energy Agency (IEA) highlighted recently the CO2 emission of the aviation section in approximately 2-3% on a global level, which are likely to increase with increasing demands of commercial passenger and freight flights. [1] It is therefore a current critical matter to find alternative solutions for reducing the overall emission, such as transitioning from standard jet-fuel to hydrogen. Carbon-fiber reinforced polymer (CFRP) composites are increasingly favored for lightweight materials in cryogenic storage tanks for commercial aircraft due to their exceptional strength-to-weight ratio [2,3]. The ability of CFRP vessels to withstand the extreme conditions of storing liquid hydrogen (LH2), as low as 20 K, is crucial for their successful use. However, exposure to ultra-low temperatures presents challenges such as thermal fatigue and embrittlement, leading to microcracking and material damage [2]. Reliable CFRP materials for cryogenic temperature (CT) applications require thorough *in-situ* testing to understand their behavior under operational conditions. Immersion testing (*in-situ*), which simulates the storage environment, is essential to assess how CFRP composites will perform in CT.
Current studies in the literature focus on failure criteria and mechanical performance of CFRP composites in CT. [4-6] Gong M. et al. [4] reported a 20% increase in CFRP strength when tested at 77 K, attributing this to increased stiffness of the matrix material. They described the failure as brittle, emphasizing embrittlement due to ultra-low temperatures. Wang W. et al. [5] studied the static tensile stress-failure of T700 and T800 carbon-fiber based CFRP, observing increased strength in both 0° and

90° unidirectional laminates in a 77 K environment, likely due to overall stiffening effects. Aerospace studies have explored thermal fatigue effects on reinforced composites in CT environments [7-9]. These studies, using high-temperature epoxy matrix systems like BMI, show that increasing thermal cycles and temperature range leads to higher microcrack density and clearer damage visibility. However, most research focuses on 0°/90° bidirectional laminates, which differs from the typical quasi-isotropic (QI) laminates used in LH2 tank manufacturing, limiting practical applicability of these results.
Understanding the practical use of QI CFRP laminates for actual LH2 tanks are typically uncovered, as focus is given to unidirectional and bidirectional stacking configurations. Thermal residual stresses (arising from curing to cryogenic temperatures) significantly influence damage progression and failure criteria, which is a consequence from the crossply stacking configuration, making this analysis important. In QI CFRP composites, damage often starts with 90° ply failure, progressing through other orientations until 0° ply failure occurs, identifiable by signals like acoustic emissions or structural deformations known as "Puck's knee," marking the onset of damage. Hohe et al. [10] investigated static stiffness and strength tests in helium (LHe), 4 K, finding microscopic residual stresses at the single-ply level influenced by thermally induced residual stresses in multidirectional laminates. However, no overall loss of stiffness was found through the tensile testing, indicating no structural implication of the local damage event. Yuanchen et al. [11] examined mechanical behavior of QI CFRP laminates at low temperatures, highlighting embrittlement and delamination characteristics. A macroscale model was created based on the results. Regardless, research still mainly focuses on ultimate stress-strain failure and matrix improvements against embrittlement, often using standard materials and uni- or bi-directional laminates, lacking of LH2 tank representation.
This study aims to investigate tensile properties of cryogenic-designed thin-ply CFRP laminates in unidirectional and QI configurations for CT tensile testing. Tensile properties are particularly crucial for materials used in storage tanks, as their membrane condition state is constantly under tensile stress. Furthermore, to evaluate and discuss the process of damage onset for QI laminates *in-situ* (immersed in liquid nitrogen) and use microscopy methods to correlate damage signals with the laminate microstructure. The results should provide insights for methodology with CFRP cryogenic testing and damage onset observation for specific LH2 storage tank material design.

2. Materials and Methods

2.1 Prepreg tape and laminate

In this study, aerospace-grade unidirectional carbon fibers (HexTow® IM7) from Hexcel Corporation were impregnated with a low-tackiness epoxy resin designed for CT operation (EPCr), thin-ply manufacturing and AFP process. Further information on the cryogenic-designed epoxy resin can be found in Hübner et al. [12,13]. The prepreg tape manufacturing process was conducted using a hot-melt prepreg impregnation unit by Roth Composite Machinery GmbH (Steffenberg, Germany). The prepreg tape was produced with a fiber area weight of 70 g/m^2 (gsm) as continuous tapes. The target carbon fiber volume content (FVC) in the prepregs was set at 60%. The laminate CFRP material is then named as EPCr-IM7 throughout this work. Subsequently unidirectional longitudinal ([0°]), transversal ([90°]), and symmetric quasi-isotropic laminates ([0°,+45°,90°,-45°]$_s$) from these prepreg tapes were manufactured using hand layup and autoclave curing at 130 °C. Laminates were cut into tensile specimens using an oscillating cutting machine Servocut 602 from Metkom Instruments Inc. (Bursa, Turkey).

2.2 Tensile testing and damage onset in cryogenic

The tensile testing procedure was conducted using a 100 kN universal testing machine, customized with polytetrafluoroethylene (PTFE) molds to create a controlled 77 K environment within liquid nitrogen (LN2). Before each specimen test, the mold was carefully sealed with silicone to prevent LN2 leakage from the specimen's cavity. An illustrative schematic of the adapted testing can be found in **Figure 1**. Testing procedures and specimen characteristics followed D3039 guidelines. To accurately capture local strain up to ultimate failure, an cryogenic-resistant axial extensometer from Sandner messtechnik GmbH

(Biebesheim am Rhein, Germany) was employed. This sensitive extensometer not only measures the laminate strain but also detects strong vibrations emitted by the specimens during testing, which have been linked to the onset of damage. In a different approach to validate the onset of damage, incremental levels of tensile load were applied to the specimens in CT, following 0.2%, 0.5%, and 0.8% strain-load. These systems were subsequently evaluated in optical and scanning microscopy, to observe a correlation between damage detected *in-situ* testing and after the incremental loads.



Figure 1 – Illustrative and schematic view of the *in-situ* tensile testing with LN2 incorporating the cryogenic-resistant extensometer.

3. Results

3.1 Static tensile testing

For the tensile stress-strain behavior of EPCr-IM7 laminates in 0° and 90° orientation, a representative curve of each laminate is shown in **Figure 2** for RT and CT environments is shown, respectively. At RT, the behavior of 0° CFRP specimens primarily reflects the influence of the carbon fibers. Due to the already optimized state of the fibers, exposing these specimens to cryogenic temperatures does not significantly increase their stiffness. However, the compression of the resin surrounding the fibers still elevates significantly the Young's modulus and tensile strength of the material. The strain behavior of a laminate in CT is believed to be reduced due to the embrittlement of the matrix. However, in 0° laminates, the failure mode remains controlled by the fibers rather than the matrix. This results in the same elongation level of CT and RT. A study [14] experienced increase elongation at break, claiming that cracks accumulate in CT but cannot reach to the complete material failure. This would result in multiple cracks spread throughout the structure and a brittle fracture behavior.
The 90° unidirectional specimens have a stronger influence from the testing temperature, as the behavior is led by the matrix and matrix-interface. As a consequence of the matrix stiffening, the Young's modulus here increases by more than 50%, rising the stress response of the material at 77 K. The strain however, is reduced due to the matrix embrittlement and heightened sensitivity to irregularities within the laminate (residual strain, waviness, porosity, fiber-rich zone). This sensitivity is exemplified by the stress concentration at the tabs, which was a predominant factor in failure at 77 K. Accordingly, as the tensile failure of the 90° specimens where similarly found in the range of 70-80 MPa in both tensting conditions, the strain at 77 K was significantly reduced from 1.20% to 0.70%.

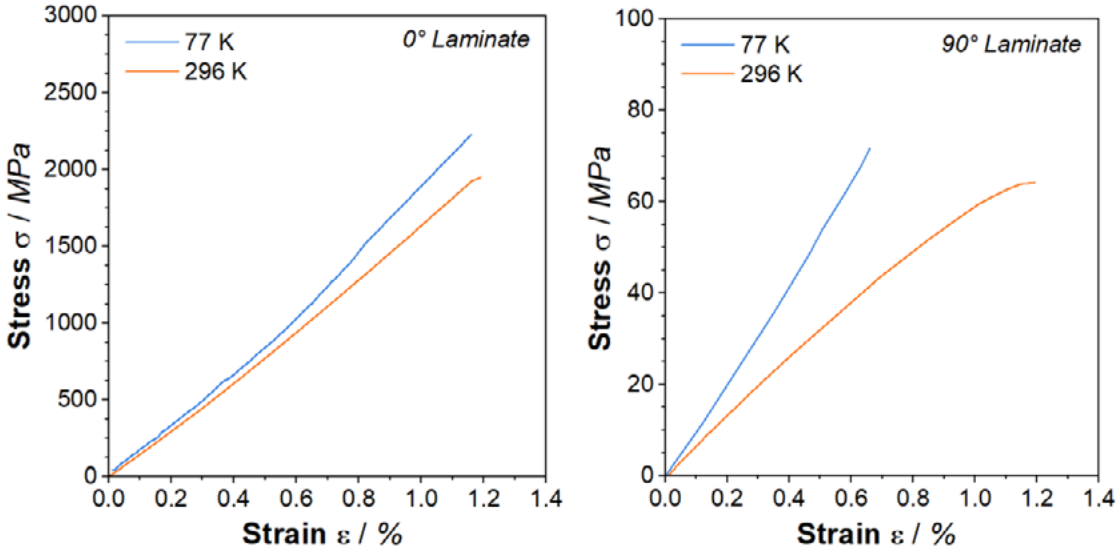


Figure 2 – Stress-strain representative curves of the EPCr-IM7 laminate as 0° configuration (left) and 90° configuration (right) in RT and CT tensile testing.

The representation of the QI laminates tested in RT and CT environments are shown in **Figure 3**, alongside a representative image of their macroscopic failure. The mechanical behavior of QI laminates at low temperatures, specifically at 77 K reveals complex failure mechanisms influenced by thermal stresses and material properties. A macroscale model analysis was carried out by [11] for QI at 93 K testing, suggesting that the concentration of thermal stresses leads to significant transversal damage on the material. This would cause a matrix tensile damage due to their lower strength. When observing **Figure 3**, the tensile strength of the QI laminate slightly decreases as temperature drops, primarily attributed to significant residual stress among the different orientation plies. Given the significant temperature differential (326 K) between the curing process and subsequent CT testing, ply shrinkage contributes substantially to the generation of strain within the laminate prior to testing. This pre-existing strain significantly influences the material's behavior during testing, partially predisposing it to failure. As a result, despite exhibiting a higher modulus in cryogenic conditions, specimens ultimately demonstrate a lower stress-strain response.

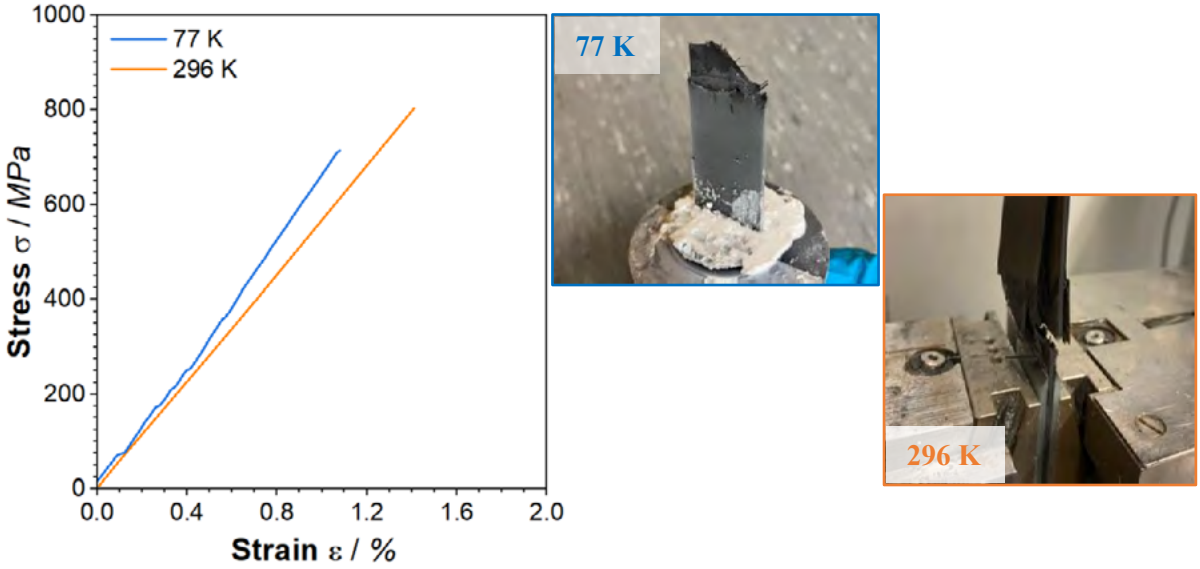


Figure 3 – Stress-strain representative curves of the EPCr-IM7 laminate as quasi-isotropic configuration (left) and observed failure modes (right) in RT and CT tensile testing.

At RT, laminates exhibit progressive failure with extended delamination, allowing for a longer stress-strain response before ultimate failure. In contrast, CT conditions result in brittle failure due to matrix embrittlement, where cracks propagate rapidly without significant delamination. The low temperatures induce significant residual stresses, contributing to reduced stress-strain behavior. The fracture behavior further reflects temperature dependence, with CT specimens showing clear perpendicular fracture planes indicative of brittle failure, while RT specimens exhibit ductile behavior with extensive signs of delamination. The Young's modulus is slightly effected by the temperature within the QI laminates. A summary of the measured tensile properties is shown in **Table 1**.

Table 1 – Summary of tensile properties of 0°, 90° and QI EPCr-IM7 laminates in RT and CT.

Laminates	Elastic modulus (GPa)		Failure stress (MPa)		Failure strain (%)	
	296 K	77 K	296 K	77 K	296 K	77 K
0°	158 ± 4	164 ± 2	2130 ± 157	2407 ± 35	1.19 ± 0.01	1.16 ± 0.03
90°	7 ± 1	11 ± 2	71 ± 2	75 ± 5	1.20 ± 0.07	0.70 ± 0.10
QI	55 ± 3	68 ± 6	830 ± 14	774 ± 64	1.48 ± 0.06	1.07 ± 0.05

3.2 Damage onset

In **Figure 4**, two representative curves of the EPCr-IM7 laminate measured in CT exhibit how the damage onset was obtained. The original curve, incorporating the signal shift due to damage, and the normalized curve (which corrects the damage shift) are presented. The normalized curve is derived from a baseline projection of the original curve using linear regression, precluding the damage-induced signal shift. This methodology does not conflit with Puck's failure criterion, as Höhe et al [3] shown that no significant loss of stiffness is found for CFRP testing in CT. Notably, laminate damage does not substantially reduce material stiffness, as evidenced by the maintained slope of the curve post-damage occurrence, consistent with the results in **Figure 3**.

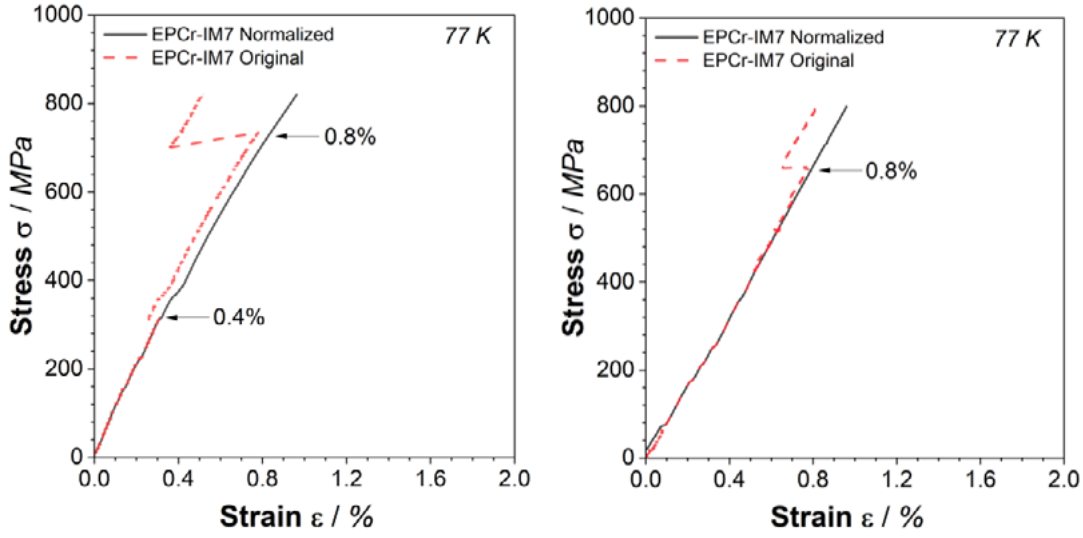


Figure 4 – Stress-strain representative curves of EPCr-IM7 QI laminate measured in CT with original and normalized curves.

The mechanisms of tensile failure in QI laminates involve multiple interactions between plies. Typically, these laminates exhibit progressive damage mechanisms such as transverse cracking and delamination when subjected to tensile loading. Transverse cracking often initiates due to high tensile stress in the 90° ply, which can stem from matrix cracking or fiber/matrix interfacial debonding. This type of damage however is apparently not causing vibration enough so signal-shift is detected during the test. The transverse cracking is espected to happen rapidly in CT environments due to the embrittlement. Standard

epoxy CFRP systems (such as BMI) can exhibit transverse cracks within the 90° plies immediately as immersed in CT, where the thermal strain proves to be enough. Cryogenic designed matrix (such as EPCr) should be able to withstand further. Delamination, on the other hand, is triggered by shear stress concentration between adjacent plies, moving the whole testing setup enough to cause a signal shift differ. The first sign of delamination under low-temperature conditions often occurs at this interface. All the EPCr-IM7 QI specimens exhibit a signal shift in the range between 0.7-0.8% strain and 650-750 MPa stress. This indicates that the failure of the 90° plies (seen in the range of 0.7% in **Figure 2**) is acting on the adjacent 45° plies. Noticebly, not long after the first signal of damage is detected, the 0° plies seem to fail in similar range (1.0-1.1% strain, 750-850 MPa stress). Another feature detected in some cases was a small signal shift within 0.4% strain. As no signs of damage were found in this range in the microscopy analysis, it is likely that this damage signal was a failure within the taps of the specimen.
Overall, it is important to highlight that there was only a slight difference observed in the initiation of damage and ultimate strength of the EPCr-IM7 thin-ply QI laminate. These findings indicate that when employing a cryogenic-design QI laminate into 77 K, the composite's damage response resembles that of a homogeneous and brittle solid. This behavior contrasts with the traditional patterns seen in standard ply-thickness composites tested in RT, where early first ply failures and delamination propagation are typically observed.

3.3 Damage under progressive load

A progressive tensile load at 77 K testing was applied to different EPCr-IM7 QI specimens, which were subsequently analyzed by scanning electron microscopy (SEM). The microscopy evolution of 0.2%, 0.5%, and 0.8% of tensile-load strain can be seen in **Figure 5**.

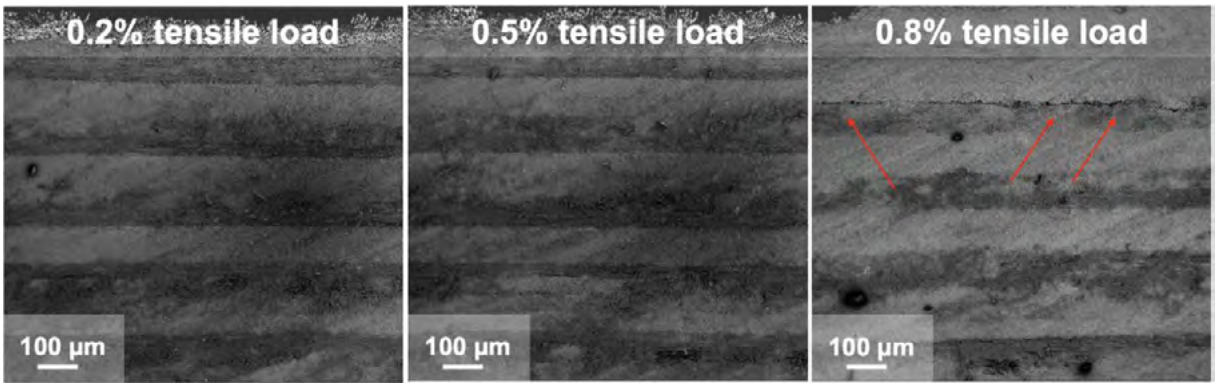


Figure 5 – SEM images of incremental levels of tensile strain-load in CT testing within the transversal view of the QI specimen.

At 0.2% strain, no visible signs of damage were detected in the microscopy specimens. This outcome was anticipated, as previous tensile measurements did not indicate any damage, suggesting that the material's microstructure remained intact under this level of strain.
Upon increasing the strain to 0.5%, some specimens exhibited signs of damage during tensile testing (see **Figure 4**), although microscopy images did not reveal any discernible structural changes. Overall, no damaged area could be found in the laminate structure. This matched the hypothesize that the detected damage from the testing was likely due to the failure of the adhesive used to attach the specimen tabs, which eventually delaminated under increased stress.
As the strain was further increased to 0.8%, clear evidence of delamination damage was observed in the microscopy images, aligning with the evaluated damage signals in the tensile testing. The damage was always located at the interface between 90° and 45° plies. These finding confirmed that at the 0.8% strain level, the material experienced its initial delamination failure, marking a critical point in the material's response to mechanical stress. At this stage, the 0° plies have a short range of functionally until the material fails completely.

As a final observation, microscopy images of the 0.8% loaded specimen were studied to identify the extent of transversal cracks within the plies, particularly focusing on the 90° plies. **Figure 6** show the images in a 500× magnification, as a broad overview (left) and as localized representation (right). Remarkably, the toughened material design for cryogenic environments did not exhibit any sign of transversal cracks, even at the interlaminar delamination stage. This suggests that the EPCr matrix is suitable for cryogenic environments and that the QI stacking configuration of the thin-ply CFRP laminate provides an efficient stress distribution. According to G. Guillamet [15], the occurrence of transverse cracks and free-edge delamination can be postponed or suppressed in regions without ply clustering, with a significant influence from the direction of the off-axis stress. This effect is expected to be more noticeable in 77 K environment, where sensitivity and residual stress levels are notably heightened before load is even applied.

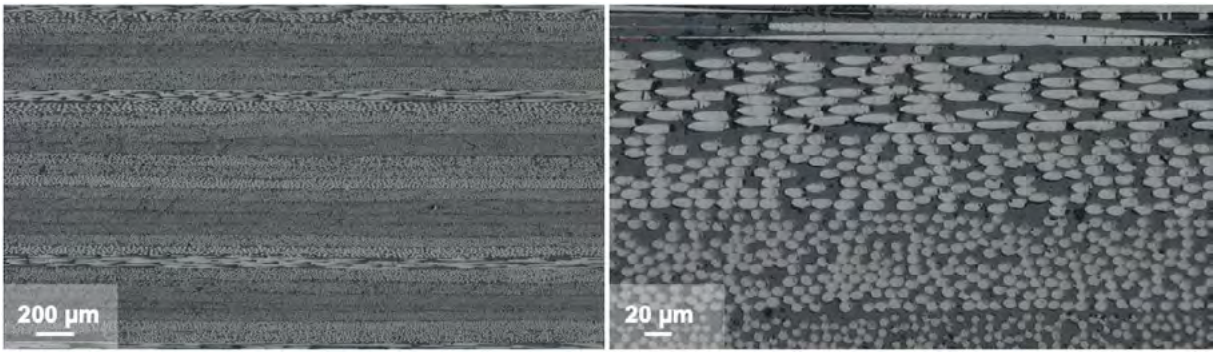


Figure 6 – Optical microscopy images of the 0.8% strain-loaded specimen in 77 K as 500×.

3. Conclusions

In this study, the investigation of a cryogenic-design CFRP material within a QI representative configuration of a CFRP storage tank was carried out. The aim was to explore its performance in cryogenic environments and to establish an alternative method for determining the damage onset of the material at 77 K, which represents a possible limit for its use as a LH2 storage tank.

The properties of the material exhibited significant differences between RT and CT environments, clearly showing stiffening and embrittlement effects caused by ultra-low temperatures. Surprisingly, the 0° configuration laminates demonstrated comparable strain-failure behavior in both CT and RT conditions, likely attributed to the excellent crack distribution capability of the thin-ply cryogenic-composite laminate. The modulus increased from 158 GPa at RT to 164 GPa in CT, rising the strength from 2130 to 2400 MPa in stress as strain was maintained in the range of 1.2%. On the other hand, the 90° oriented laminates exhibited extreme sensitivity to defects and stress concentration at the tabs, leading to anticipated failures. Additional to the material embrittlement, all 90° specimens failed at the tabs when tested in 77 K, suggesting that values can be even higher than the former 0.70% evaluated. QI laminates exhibited similar values of stress failure, with significant reduced responses in CT testing (774 MPa stress and 1.07% strain) compared to RT (830 MPa stress and 1.48% strain), likely due to embrittlement effects and increased sensitivity. The failure modes observed in CT and RT differed significantly. In RT QI samples, extensive delamination was observed, maximizing energy transfer between plies. In contrast, CT samples exhibited a more brittle, monolithic failure mode with less delamination, characteristic of less ductile environments. The *in-situ* damage onset method provided valuable insights into material functionality, detecting major signs of damage such as ply failure and delamination that correlated with the damage onset of QI laminates at 77 K. Evidently, no failure occurred until 0.8% strain-load was applied, indicating this a critical threshold where the 90°/45° crossply structure could no longer withstand the tensile load without partial delamination.

Overall, this study offers comprehensive insights into a material specifically designed for LH2 tanks, covering tensile properties and failure behavior. Importantly, it introduces a reliable method for understanding damage onset mechanics in QI laminates, essential for optimizing CFRP materials for LH2 tank applications, and providing valuable tools to the design process.

Acknowledgments
This project was carried out under the guidance of *Industrieanlagen-Betriebsgesellschaft mbH* (iABG) and financed by the Bavarian Ministry of Economic Affairs, Regional Development and Energy (STmWi) according to the registration number BLU-2109-0024.

References

[1] International Energy Agency. Transport. Paris: IEA; 2024.

[2] Z. Sàpi, and R. Butler. Properties of Cryogenic and Low Temperature Composite Materials – A Review. *Cryogenics* v111, p-p, 2020.

[3] J. Hohe, et al. Performance of Fiber Reinforced Materials under Cryogenic Conditions — A Review. *Composites Part A: Applied Science and Manufacturing,* v141, p-p, 2021

[4] M. Gong, X.F. Wang, and J.H. Zhao. Experimental Study on Mechanical Behavior of Laminates at Low Temperature. *Cryogenics* v47, 1-7, 2007.

[5] W. Wang, et al. Cryogenic Performances of T700 and T800 Carbon Fibre- Epoxy Laminates. *IOP Conference Series: Materials Science and Engineering*, v102, 2015.

[6] J. Hohe, et al. Effect of Cryogenic Environments on Failure of Carbon Fiber Reinforced Composites. *Composites Science and Technology,* v212, 2021.

[7] J. Jaehyung, and Roger J. Morgan. Characterization of Microcrack Development in BMI-Carbon Fiber Composite under Stress and Thermal Cycling. *Journal of Composite Materials,* v38, 2007.

[8] S. K. Gupta, M. Hojjati. Moisture/Freeze/Dry Cycle, Thermal Cycling, Composites, Micro-Crack Initiation. *International Journal of Composite Materials*, v9, 2019.

[9] J. Timmerman, B. S. Hayes, and J. C. Seferis. Cryogenic Microcracking of Carbon Fiber/Epoxy Composites: Influences of Fiber-Matrix Adhesion. *Journal of Composite Materials,* v37, 2003.

[10] J. Hohe, et al. Validation of Puck's Failure Criterion for CFRP Composites in the Cryogenic Regime. *CEAS Space Journal,* v13, 2021.

[11] L. Yuanchen, et al. Cryogenic Mechanics and Damage Behaviors of Carbon Fiber Reinforced Polymer Composites. *Composites Part A,* v169, 2023.

[12] F. Hübner, et al. Low Temperature Fatigue Crack Propagation in Toughened Epoxy Resins Aimed for Filament Winding of Type V Composite Pressure Vessels. *Polymer Testing*, v102, 2021.

[13] F. Hübner. Temperature-Dependent Fracture Behavior of Towpreg Epoxy Resins for Cryogenic Liquid Hydrogen Composite Vessels: The Influence of Polysiloxane Tougheners on the Resin Yield Behavior. *Polymer Testing,* v113, 2022.

[14] A. Bersani, et al. Long term elongation of Kevlar-49 single fiber at low temperature. *Cryogenics,* v3, 2013.

[15] G. Guillamet, et al. Damage occurrence at edges of non-crimp-fabric thin-ply laminates under off-axis uniaxial loading. *Composites Science and Technology*, v98, 2014.

MICRO–MESO SCALE NUMERICAL APPROACH FOR YARN CONSIDERING THE DAMAGE BEHAVIOR AND ITS FRICTION ANALYSIS

Yu WANG[1,2,*], Sascha KRUGL[2], Yanan JIAO[1], Peng WANG[2]

[1]School of Textile Science and Engineering, Tiangong University, Tianjin 300387, China
[2]Lpmt, Ensisa, Université de Haute-Alsace, Mulhouse F-68000, France

Keywords: Fiber/yarn, Micro–meso scale, Modeling, Stochastic damage, Friction simulation, Contact mechanism

Abstract
The production process of textile preforms involves a friction behavior that is exceedingly non-linear. This behavior is governed by several factors at the yarn level, which are in turn driven by interactions at the fiber level. The prediction approach for fiber and yarn level is an essential component in the process of enhancing the mechanical properties of the composites that have been produced. To optimize the production process, it is also a technique that is cost-effective. The friction that occurs between yarns has been shown to have a major impact on the velocity of friction, the amount of force that is applied, and the starting tension, according to study that was recently conducted on the subject of improving mechanical properties. It is possible to see these effects using either experimental or theoretical means. However, a single approach is not appropriate to investigate the causes of friction since there are several factors that are interrelated with one another. It should be considered to utilize a combination of modeling and experimental methodologies, based on the findings of past research, to accurately estimate the friction mechanism in complex situations.
The present research introduces an innovative multi-scale modeling approach that accurately predicts the friction and wear characteristics of fiber. The modeling approach encompasses the utilization of both geometric and mechanical components. A micro–meso scale yarn model is created by utilizing the Timoshenko beam element. The objective of the local geometry modification method is to enhance the robustness of contact behavior by utilizing yarn distance functions based on micro-CT reconstruction technology. Moreover, a stochastic damage mechanical model of the yarn was developed to replicate the friction and wear characteristics of the fiber, resulting in an improved depiction of actual situations. This modeling approach is used to determine the orthogonal friction behavior with various yarn constructions. Furthermore, the effectiveness of the simulation is validated by the experimental methodology. The model validation demonstrates that the suggested simulation technique properly predicts friction behavior. The friction and wear characteristics of yarn in various preform architectures are anticipated based on geometry and mechanics. This modeling method provides a helpful tool for understanding the mechanical response of yarns.

1. Introduction

Textile composites have gained a wide range of applications in the aerospace, automotive, energy and sports equipment industries, where their mechanical and lightweight properties are utilized to advantage. Textile composites consist of reinforcement and matrix components, where the reinforcement component plays a major role in load bearing and therefore the mechanical properties of the reinforcement are decisive for the mechanical properties of the final composite product. The textile reinforcement phase is made of several yarns interwoven according to a certain law, which inevitably undergo damage, stretching, bending, shearing and friction during the molding process. According to previous studies, yarn damage due to friction can be as high as 9-12% [1]. Furthermore, yarn consists of hundreds of fibers whose failure behavior is discontinuous due to inconsistencies in the mechanical

properties of the fibers. Thus, the research on the friction of fiber and yarn is quite meaningful to develop fiber-reinforced composites, especially for the prediction of friction and wear behavior of fibers and yarns [2,3].

In existing fiber/yarn friction testing methods, researchers usually carry friction and wear test instruments and build up experimental equipment close to the actual working conditions through customized fixture platforms. This kind of experimental method can effectively solve the problem of difficulty in testing accurately under complex mechanical conditions and can further explore the influence of multiple factors on friction and wear behavior [4,5]. However, due to the randomness of fiber properties, the experiments often show large inter-group differences and unstable results. Therefore, a numerical simulation model needs to be developed to efficiently predict the friction and wear behavior [6].

To accurately predict the frictional wear characteristics of fibers/yarns, an improved constitutive model based on damage-plasticity theory and a geometrical model similar to that of the actual yarns are developed. The model is demonstrated on HMWPE yarn using the explicit solver Abaqus/Explicit. Meanwhile, geometric and mechanical results were verified by micro-CT and experiments. Furthermore, the yarn wear behavior can be predicted for different force conditions, and the wear behavior will be predicted for different yarn geometrical parameters, including twist, twist direction, and Tex, and applied to the reinforced-phase molding process.

2. Simulation investigations

2.1 Constitutive law

According to the damage-plasticity theory, the strain tensor is split into an elastic part and a plastic part:

$$\varepsilon = \varepsilon^e + \varepsilon^p \tag{1}$$

where the superscripts “e” and “p” denote the elastic part and the plastic part. The parts should be analyzed, respectively [7].

For the elastic stage, the stress and strain can be expressed based on the generalized Hooke’s law as:

$$\sigma_{ij} = 2G\varepsilon_{ij}^e + \delta_{ij}\lambda\sum_k \varepsilon_{kk}^e, \quad i,j = 1,2,3 \tag{2}$$

$$\varepsilon_{ij} = \frac{1}{2G}\sigma_{ij}^e - \delta_{ij}\frac{\nu}{E}\sum_k \sigma_{kk}^e, \quad i,j = 1,2,3 \tag{3}$$

where the v is the Poisson ratio.

For the plastic stage, the introduction of a yield function Φ can be defined as:

$$\Phi(\sigma_{ij}, \sigma_y) = q - \sigma_y \tag{4}$$

where σ_y is yield stress and q is equivalent stress, which can be shown as:

$$q = \sqrt{\frac{3}{2}}\left\|S_{ij}\right\| \tag{5}$$

where S_{ij} is the deviatoric stress tensor, which can be expressed as:

$$S_{ij} = \sigma_{ij} - \frac{1}{3}\delta_{ij}\sigma_{kk} \tag{6}$$

It should be noted that, at any stage, no stress level is allowed above the current yield stress, Thus, any admissible stress must satisfy the restriction. Indeed, the yield criterion can be expressed by:

$$\Phi(\sigma_{ij}, \sigma_y) < 0 \Rightarrow \dot{\bar{\varepsilon}}^p = 0$$

$$\Phi(\sigma_{ij}, \sigma_y) = 0 \Rightarrow \begin{cases} \dot{\bar{\varepsilon}}^p = 0 & elastic \quad unloading \\ \dot{\bar{\varepsilon}}^p \neq 0 & plastic \quad loading \end{cases} \tag{7}$$

The plastic strain rate can be obtained, which is positive under tension and negative under compression.

$$\dot{\bar{\varepsilon}}^p = \dot{\gamma} sign(\sigma) \tag{8}$$

where γ is termed the plastic multiplier, which is non-negative. The sign is the signum function, which is distinguished +/-. Eventually, a phenomenon, the evolution of the yield stress accompanies the evolution of the plastic strain, is achieved. The yield stress is a given function.

$$\sigma_y = \sigma_y\left(\bar{\varepsilon}^p\right) = \sigma_y\left(\int_0^t \dot{\bar{\varepsilon}}^p dt\right) \tag{9}$$

Based on the plastic flow rule, the equivalent plastic strain rate is shown:

$$\dot{\bar{\varepsilon}}^{p} = \dot{\gamma} = \sqrt{\frac{2}{3}\dot{\varepsilon}_{ij}^{p} \cdot \dot{\varepsilon}_{ij}^{p}} \tag{10}$$

The ductile damage degradation model is adopted. The ductile criterion is a phenomenological model for predicting the onset of damage, which is used in current research. The model assumes that the equivalent plastic strain at the onset of damage, $\bar{\varepsilon}_{D}^{p}$, is a function of stress triaxiality and strain rate:

$$\bar{\varepsilon}_{D}^{p}(\eta, \dot{\bar{\varepsilon}}^{p}), \tag{11}$$

where η is the stress triaxiality, which is defined as:

$$\eta = \frac{\|S_{ij}\|}{q} \tag{12}$$

where q is the Mises equivalent stress. Furthermore, the displacement at failure can be shown as:

$$\bar{u}_{f}^{p} = \frac{2G_{f}}{\sigma_{y}} \tag{13}$$

where G_f is the fracture energy, which can be expressed as:

$$G_{f} = \int_{0}^{\bar{\varepsilon}_{f}^{p}} \sigma_{y} d\bar{u}^{p} \tag{14}$$

A damage variable d is introduced as:

$$d = \begin{cases} 0 & \sigma \le \sigma_{y} \\ \dfrac{2}{1+\exp\left(-d_{f}\left(\sigma-\sigma_{y}\right)^{2}\right)} - 1 & \sigma > \sigma_{y} \end{cases} \tag{15}$$

Where d_f is the damage factor, which can be explained as an input parameter according to the Weibull distribution law. The yarn stress after initial damage can be defined as:

$$\sigma = (1-d)\sigma_{y} \tag{16}$$

The detailed derivation process of the damage evolution equations can be referred to in the literature [8,9]. The above damage model is carried out by the user subroutine VUMAT of Abaqus.

2.2 Geometric description of virtual yarn

Fiber geometry plays a crucial role in determining the mechanical properties of yarns. Previous research has established that the arrangement of fibers at the quasi-fiber scale affects the geometry of the yarns [10]. However, to effectively model the mechanical behavior of yarns, it is important to simulate the virtual yarns with a high degree of accuracy. To achieve this, the authors of this study utilized a virtual yarn to model the mechanical behavior of a realistic yarn. The virtual fiber was modeled using chain-like beam elements in the Abaqus software, with each beam element representing a small segment of the fiber chain. By assembling a certain number of virtual fibers with twist angles, the authors were able to create a twisted yarn using a Python script. The assembly process was executed on Abaqus 2021 to ensure the accuracy of the simulation.

The central routine (f(u), g(u), h(u)) and cross-section (c(w,v)) of fibers are used to establish the geometric model:

$$\begin{cases} X = f(u) + c(\omega, v) \\ Y = g(u) + c(\omega, v) \\ Z = h(u) + c(\omega, v) \end{cases} \tag{17}$$

To maintain the proper alignment of the beam nodes, equations (19) and (21) were employed, which reflected the constraint relationship between them. The use of virtual yarns allowed the authors to model the mechanical behavior of yarns under different conditions and study the impact of fiber geometry on the properties of the yarn. The virtual yarns developed in this study provide a reliable means of simulating the behavior of real-world yarns, enabling researchers to study the impact of different parameters, such as fiber arrangement and twist angles, on yarn properties.

$$\theta_{0} = \pi - n \times \arcsin(z_{0} / r_{point}) \tag{18}$$

$$\begin{cases} x' = x_0 + \kappa \times Le \\ y' = r_{point} \times \cos\left(\theta_0 + \kappa\theta_t\right) \\ z' = r_{point} \times \sin\left(\theta_0 + \kappa\theta_t\right) \end{cases} \tag{19}$$

where, x', y' and z' are coordinates along x, y and z directions, separately. κ is the number of the element. $r_{point} = \sqrt{x_0^2 + y_0^2}$ is the distance between the node and the center of the circle on the section. θ_t and θ_0 are the twist of yarns and deflection angle of the element, which usually is normalized by n. Furthermore, the number of fibers can be obtained:

$$\pi \times \left(\frac{D_f}{2}\right)^2 \times n_f = \frac{\rho_f}{\phi_f} \tag{20}$$

where n_f and D_f are the amount and diameter of virtual fibers in the yarn, ϕ_f and ρ_f are the volume density and linear density of realistic yarn.
Particularly, the equations reflect the constraint relationship between beam nodes based on the rectangular coordinates:

$$\begin{bmatrix} y \\ z \end{bmatrix}^T \begin{bmatrix} \frac{1}{a^2} & 0 \\ 0 & \frac{1}{b^2} \end{bmatrix} \begin{bmatrix} y \\ z \end{bmatrix} = Q^T A Q = 1 \tag{21}$$

The Eigenvectors of $\boldsymbol{A}$ can be obtained as:

$$\mu_1 = \begin{bmatrix} 1 \\ 0 \end{bmatrix} \qquad \mu_2 = \begin{bmatrix} 0 \\ 1 \end{bmatrix} \tag{22}$$

3. Materials preparation and micro-CT

HMWPE (High Molecular Weight Polyethylene) of 135 Tex yarns composed of hundreds or thousands of fibers were selected as the experiment object, which is produced by Honeywell International, Inc., USA. All samples are both twisted yarns, according to the references showed that the strength of high-performance fiber yarns can be improved by a slight twist. The label “tpm” represents twist per meter of yarn. Each twist level of HMWPE yarns exhibits different tensile mechanical properties.
The Micro-CT technology was employed to observe the geometry of yarn. One 100tpm (twist per meter) yarn sample with a length of 50 mm was scanned by an X-ray CT machine (Xradia-510 versa, Zeiss). The X-ray source emitted a cone-beam which passed through the sample and was then absorbed by the receiver plate. The radiographs were acquired with a voxel size of 5 μm, a beam energy of 50 kV and a current of 80 μA. A total of 1160 projections were acquired and then stitched for the image reconstruction. Model reconstruction and image processing were carried out through Dragonfly software (version 2020.1, Object Research Systems (ORS) Inc.)

4. Consistency analysis

4.1 Geometric verification

To validate the precision of the model, a thorough analysis was conducted, comparing the simulation results with experimental data. This analysis encompassed several aspects, such as the geometric properties and mechanical response. The intersection area is determined as a distinctive indication of the geometric properties of the yarn. Figure 1 (a) and (b) display a Micro-CT picture and a simulation model of yarns. The statistical data for each cross-section is represented by the cross-section regions, such as in Figure 1 (c). This figure displays a scattering map that illustrates the link between the experimental value and the two averages: the average of simulation and the average of experimental data. Each point in the figure corresponds to a distinct intersection value. The blue dot represents the experimental value, the blue line represents the simulation's average, and the green line represents the experimental average. The data illustrates a discrepancy of 7.4% between the average obtained from the experiment and the average obtained from the simulation.

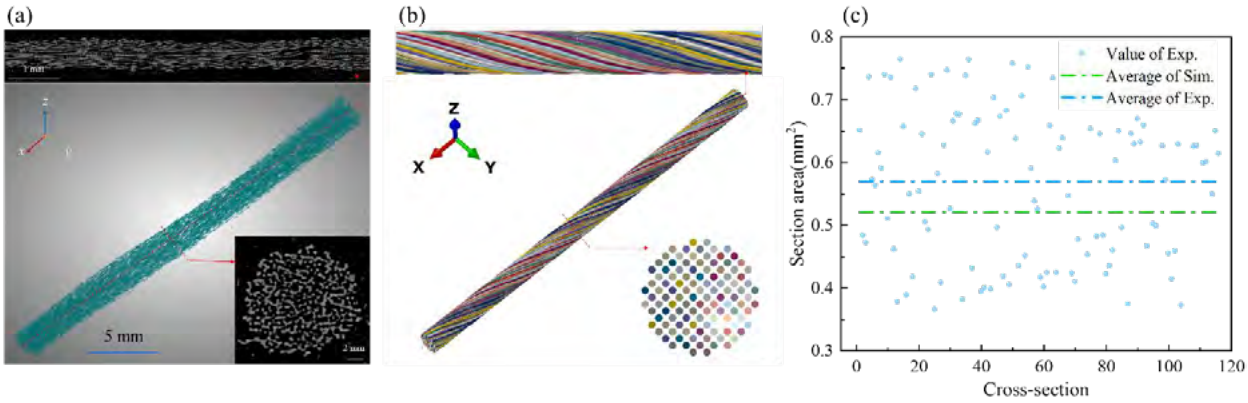


Figure 1. The geometric comparison results between simulation and experiment: (a) the experimental value, (b) the simulated value and (c) cross-sectional statistics.

4.2 Mechanical verification

Figure 2 illustrates the correlation between the friction force and the yarn's location. The green and blue core points represent experimental and simulated data points. They clearly illustrate the difference between static and active friction, as well as the turning point or mutation point on the curve. These points indicate the transition from static to motion friction, reflecting a change in the state of the friction force. Generally, the correlation between friction and shift is not always linear, as friction can vary with increasing shift, particularly in situations involving distinct friction stages, such as static and moving friction. To facilitate a comprehensive comparison between the experiment and simulation findings, an adjustment operation was conducted. The experimental and simulation corrections are depicted by the green and blue curves, respectively, in Figure 2. Additionally, the expected intervals of the results are also displayed. The simulation results may be derived from the diagram, which falls within the expected range of the experiment. This suggests that the simulations exhibit some resemblance to the experiment and provide a more accurate characterization of the yarn friction behavior. The overall friction strength steadily increases as the shift increases, reaching maximum static friction during the active friction phase, and then declines to attain stability. During the time of active friction, there is a 13% disparity in the friction of the yarn.

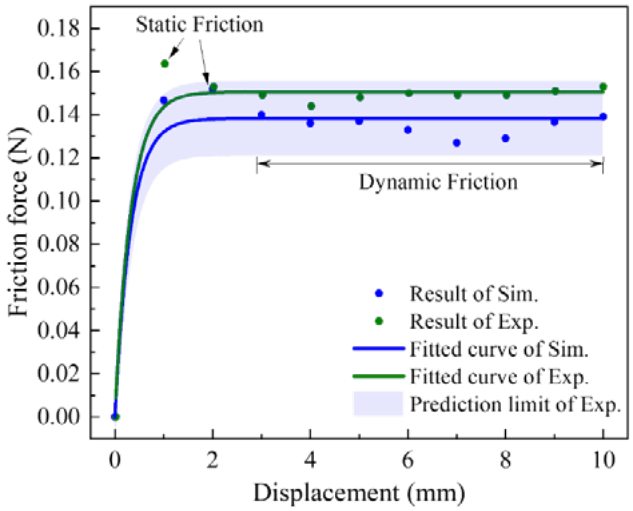


Figure 2. Experiment and simulation results of friction behavior.

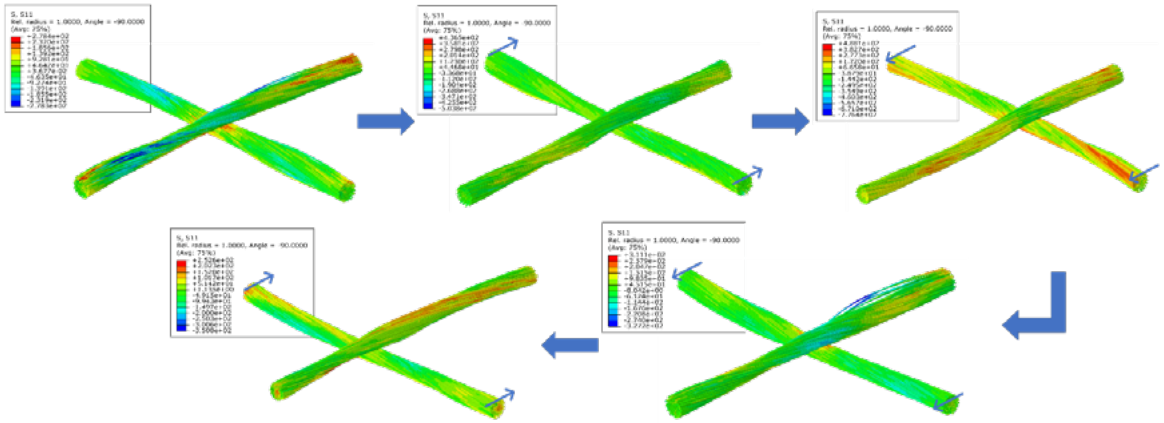


Figure 3. Morphology of different stages of friction simulation.

Figure 3 shows the evolution of stress along the longitude of yarn direction during the orthogonal friction. The upper yarn is applied to the normal load by displacement, and the lower yarn is applied to the cyclic displacement. The maximum longitudinal stress (S11) was close to the tensile strength of warp yarns before the breakage. As the friction force increased, the damage accumulation occurs for each fiber. Eventually, the fiber will completely fail.

5. Conclusions

This paper proposes a novel friction simulation model for twisted yarns, based on the Timoshenko beam principle and damage-plasticity theory. The proposed model is able to effectively predict the friction wear behavior considering the contact behavior. Further, the effect of yarn parameters on friction and wear behavior can be explored. There is excellent agreement in characterization parameters including the mechanical and geometrical behavior between the experimental measurement and the simulation. Furthermore, the model adds a damage factor to consider the damage behavior, furthermore, the yarn wear behavior can be predicted for different force conditions, and the wear behavior will be predicted for different yarn geometrical parameters, including twist, twist direction, and Tex, and applied to the reinforced-phase molding process.

Acknowledgments

The authors thank the joint support from the China Scholarship Council (Project No. 202108120054). Special thanks to Prof. Libo Yan and senior research group members from the department of Organic and Wood-Based Construction Materials, Technische Universität Braunschweig for their help in improving the research.

References

[1] Almeida JHS, Ribeiro ML, Tita V, Amico SC. Damage modeling for carbon fiber/epoxy filament wound composite tubes under radial compression. Composite Structures 2017;160:204–10. https://doi.org/10.1016/j.compstruct.2016.10.036.

[2] Vu AN, Grouve WJB, de Rooij MB, Akkerman R. A mesoscopic model for inter-yarn friction. Composites Part A: Applied Science and Manufacturing 2024;180:108070. https://doi.org/10.1016/j.compositesa.2024.108070.

[3] Vu AN, Grouve WJB, Akkerman R. Modeling of yarn interactions for non-axisymmetric biaxial overbraiding simulations. Composites Part A: Applied Science and Manufacturing 2023;167:107421. https://doi.org/10.1016/j.compositesa.2022.107421.

[4] Pascoe MW, Tabor D, Bowden FP. The friction and deformation of polymers. Proceedings of the Royal Society of London Series A Mathematical and Physical Sciences 1956;235:210–24. https://doi.org/10.1098/rspa.1956.0077.

[5] Das A, Choong GYH, Dillard DA, De Focatiis DSA, Bortner MJ. Characterizing friction for fiber reinforced composites manufacturing: Method development and effect of process parameters.

Composites Part B: Engineering 2022;236:109777. https://doi.org/10.1016/j.compositesb.2022.109777.
[6] Vanaerschot A, Cox BN, Lomov SV, Vandepitte D. Stochastic multi-scale modelling of textile composites based on internal geometry variability. Computers & Structures 2013;122:55–64. https://doi.org/10.1016/j.compstruc.2012.10.026.
[7] Feng D-C, Wu G, Sun Z-Y, Xu J-G. A flexure-shear Timoshenko fiber beam element based on softened damage-plasticity model. Engineering Structures 2017;140:483–97. https://doi.org/10.1016/j.engstruct.2017.02.066.
[8] Qian Y, Li Z, Zhou X, Xia T, Zhang Y, Yang Z, et al. The strength prediction model of unidirectional fiber reinforced composites based on the renormalization group method. Composites Science and Technology 2024;253:110639. https://doi.org/10.1016/j.compscitech.2024.110639.
[9] Wang Y, Li X, Xie J, Wu N, Jiao Y, Wang P. Numerical and Experimental Investigation on Bending Behavior for High-Performance Fiber Yarns Considering Probability Distribution of Fiber Strength. Textiles 2023;3:129–41. https://doi.org/10.3390/textiles3010010.
[10] Wang Y, Jiao Y, Wu N, Xie J, Chen L, Wang P. An efficient virtual modeling regard to the axial tensile and transverse compressive behaviors of the twisted yarns. Journal of Industrial Textiles 2022;52:15280837221137353. https://doi.org/10.1177/15280837221137353.

allows design engineers to immediately test a new workflow using different failure models and routines – allowing for faster dissemination and reach of the state-of-the-art models.

This framework was developed building on the existing experience of the team on building composite failure models for large structures and coarse finite element models. It aims at reducing the researcher development overhead while retaining all the performance benefits, and usability of user subroutines. We present the framework using well-known and well-tested failure models against a comprehensive set of suitable of finite element models across the scale and complexity spectra. We believe that this framework has the potential to promote composite failure model development, interoperability between composite researchers and composite engineers, and benchmark and testing of the state-of-art on composite failure analysis.

2. The framework

2.1. Architecture and concept

The concept makes use of the best hardware in the most efficient way possible. This means that all the computational grunt work needs to be off-loaded into distributed computing systems, alleviating the computational burden off the engineer/researcher (Figure 1).

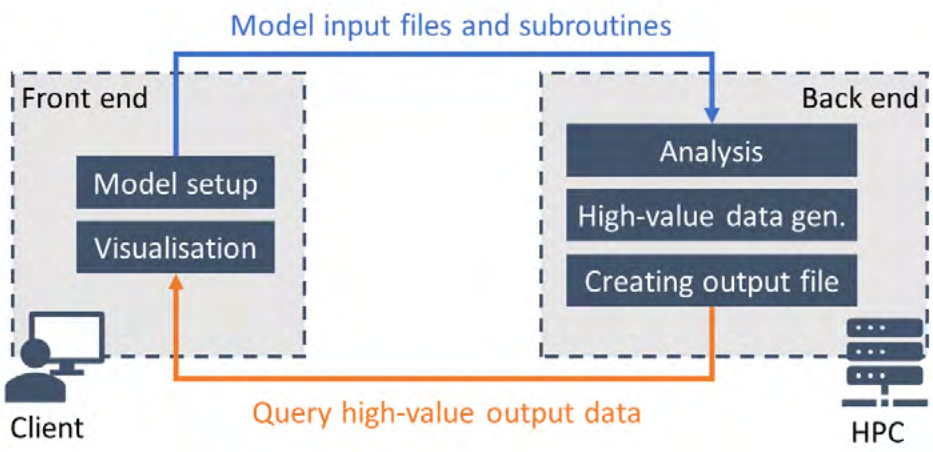


Figure 1. Separation of concerns: HPC platform handles the heavy computations; the user machine is tasked only with visualization.

We implemented the proposed framework within Abaqus but in a such way that is solver backend agnostic. This leaves the possibility of supporting multiple solver backends (both commercial and open-source).

2.2. Implementation

The framework builds up modularly from core abstractions (matrices and math algorithms) all the way to fracture plane rotations and stress transformations. These modules or components that make up the framework allow the developer to express the physical processes in a cleaner way. The framework currently defines two simulation modalities: (i) damage initiation – computes the failure indices for all damage modes and prints output; (ii) damage evolution – uses the failure indices to simulate the propagation of failure across the plies and the elements. What modules or components are used will depend on how the solver interface is implemented, and what simulation modality the user requires. The organization of the framework is depicted in Figure 2.

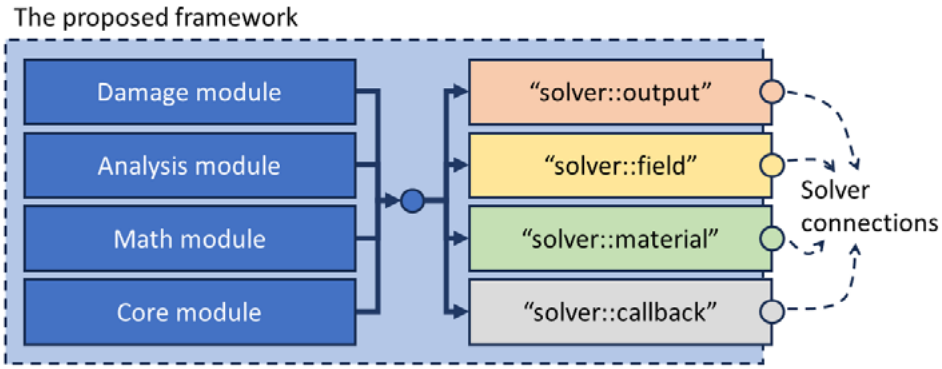


Figure 2. Modular architecture and solver agnostic connection points

The implementation of the Abaqus Standard interface to the proposed framework makes use of user subroutines and the new "uniquelibs" feature that allows libraries to be loaded at runtime (rather than copying source files, or compiled user subroutine binaries). In this way, the user subroutines can utilize all the tools and abstractions the framework provides.

Currently the Abaqus interface to the framework has the following entry points:

- For "solver::output" – UVARM (damage initiation);
- For "solver::field" – USDFLD (damage evolution – uses the previously converged strain and stress state);
- For "solver::material" – UMAT (damage evolution – uses the current strain state).
- For "solver::callback" – UEXTERNALDB (used for debug purposes only).

These Abaqus user subroutines act as interfaces that make use of the damage initiation and evolution algorithms within the framework as depicted in Figure 3.

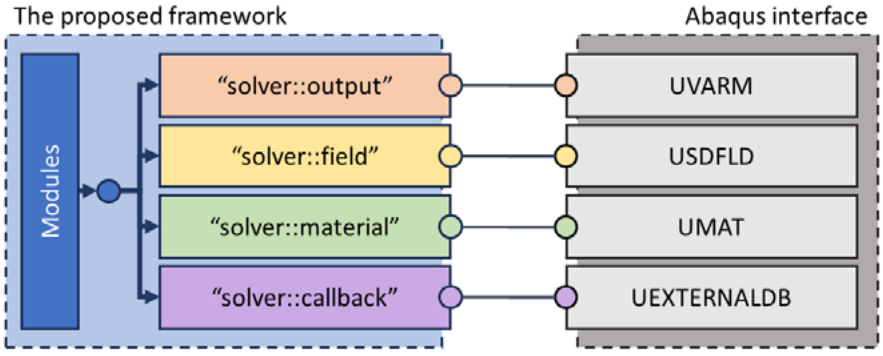


Figure 3. Abaqus interface and visual representation of the interaction with the framework

2.3. Use cases

The framework is built as an open-source project with the intention of promoting community interaction. This will ensure continuous evolution of the framework in a way that best serves the composite material community.

Therefore, we anticipate the following use cases:

- Basic user – only wants to use the framework for simulation and make use of all the failure models implemented;
- Researcher – someone who will use the framework but also develop their own models, extensions or algorithms;
- Developer – someone interested in the technology that wants to help maintain, improve the framework.

Additionally, the framework is designed to enable interaction in the form of feedback, models, code, or even with ideas and suggestions.

3. Examples

We have used the framework to run several models with both simulation modalities (damage initiation and evolution). The failure models used in the following examples are described in detail in [3].

This framework was built with the intention of running very large industrial-scale models (such as an entire wing-box). Figures 4 and 5 show that the framework can handle a full wing-box model with 15 million degrees of freedom (model from [1,2]).

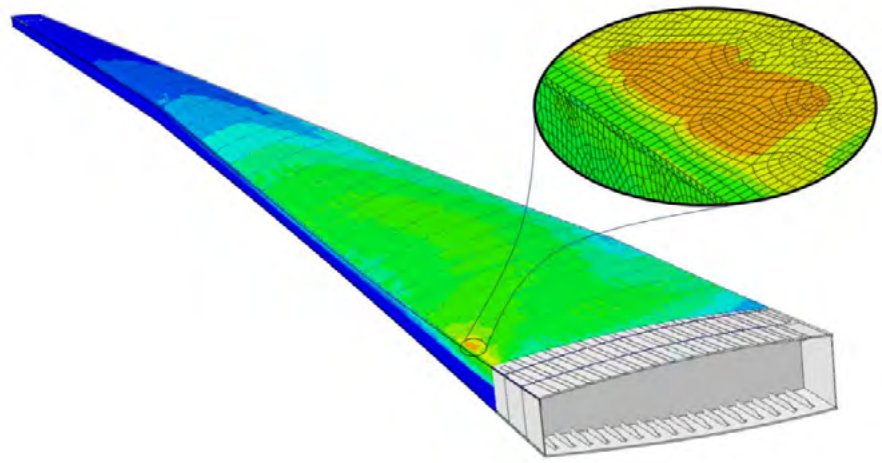


Figure 4. Compressive damage developing on upper cover of wing-box (with mesh detail)

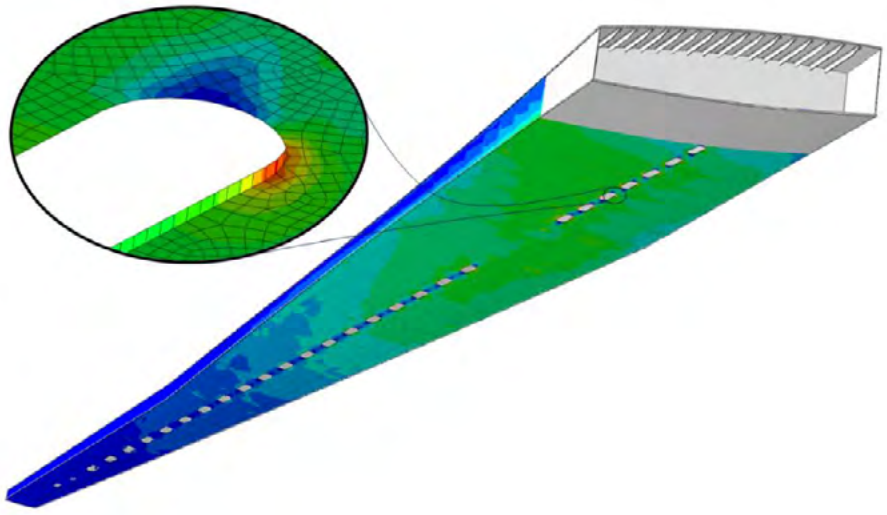
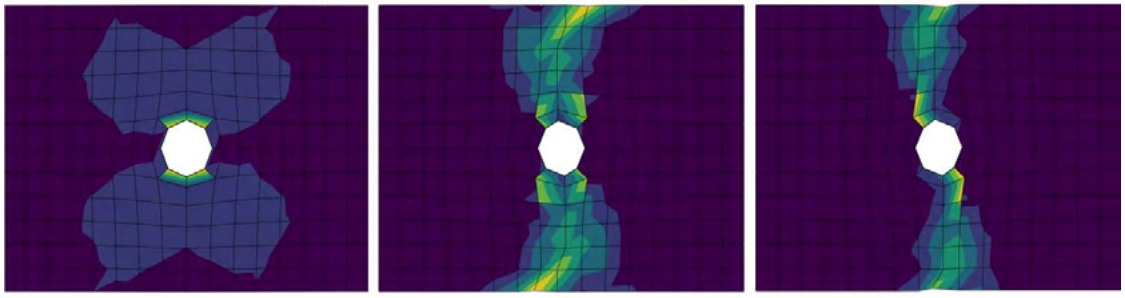


Figure 5. Tensile damage developing on manhole on lower cover of wing-box (with mesh detail)

In addition, the framework is also meant to work across scales. Therefore, we also studied what can be small structural details in the very large model of the wing-box, meshed with an equivalent level of detail. See Figure 6 for representative results. The model presented here is an open-hole compression (OHC) specimen based on [4] using the IM7-8552 material system.



a) UVARM b) USDFLD c) UMAT

Figure 6. Through-thickness maxima of fibre kinking damage index and variables of OHC models at the last increment (compression loading along horizontal direction). OHC models meshed in accordance with the level of detail of full-scale wing-box model.

3. Conclusions

This work introduces a new composite damage analysis framework targeting HPC platforms. The new framework creates a platform for researchers to implement their existing and new composite failure models such that:

- All failure models are tested under the same conditions and compared/benchmarked in a structured manner;
- The failure models – containing only the high-level physical model for different failure modes – makes direct use of the HPC capabilities of the architecture;
- Engineers can readily test various models and implementations; thus, bringing state-of-the-art research closer the real-world applications.

When compared to traditional Abaqus user subroutine workflows, this framework provides the following advantages:

- Modern C++ codebase following proven coding standards and practices and with easy interoperability with a huge ecosystem of external C/C++ libraries;
- Comprehensive test suite and visualisations;
- A set of useful abstractions to make writing failure models faster and safer.

We believe that this framework has the potential to become an important tool for the design of composite structures. Furthermore, with suitable community support and interaction, the proposed framework can bring together decades of knowledge into a user-friendly and robust library of failure models.

Acknowledgments

This work is made possible with the funding of the Engineering and Physical Sciences Research Council (EPSRC) United Kingdom, under the project “Vera: A new paradigm to enable efficient design of VERy large Aircraft structures - the key for innovative aircraft design concepts” (EP/W022508/1).

References

[1] S. T. Pinho, M. Matos, R.O.S.S. da Costa, A. Ibbotson, M. Ostergaard. Enabling multiscale analysis of very large composite structures. COMPOSITES 2021, 22-24 September 2021, Göteborg, Sweden

[2] S. T. Pinho, R.O.S.S. da Costa, M. Matos, A. Ibbotson, M. Ostergaard. Multiscale analysis of an aircraft wingbox. ECCM20. 26-30 June 2022, Lausanne, Switzerland

[3] R.O.S.S. da Costa, S. T. Pinho, M. Matos, A. Ibbotson, M. Ostergaard. A high-performance simulation framework for very large composite structures. Submitted to Composite Structures.

[4] Lee, J. and Soutis, C. (2008). Measuring the notched compressive strength of composite laminates: Specimen size effects. Composites Science and Technology, 68(12), pp.2359–2366.

THE INFLUENCE OF THE CRUSH PLUGS ON THE ENERGY ABSORPTION OF CARBON/EPOXY COMPOSITE CIRCULAR TUBES UNDER AXIAL CRUSHING

Serdar Demir[1] and Nuri Ersoy[1]

[1] Dept. of Mechanical Engineering, Bogazici University, Istanbul, Bebek, 34342, Turkey
Email: serdar.demir1@std.bogazici.edu.tr, nuri.ersoy@bogazici.edu.tr Web Page: http://www.kompozit.boun.edu.tr/

Keywords: CFRP composites, Woven prepregs, Crush plugs, Axial-crushing, Finite element analysis

Abstract
In this study, an investigation of the effects of innovative crush plugs on composite circular tubes subjected to axial quasi-static crushing is presented. The composite tube specimens in the study are manufactured from Carbon-Fibre Reinforced Plastic (CFRP) plain weave woven fabric prepregs. The crushing characteristics of composite tubes are investigated both experimentally and numerically using Finite Element Method (FEM) simulations for axial crushing tests. After FE model is validated with experimental results, the effect of the suggested novel plugs are investigated numerically using the FE models. Suggested novel plug geometries includes two crushing zone curves and channels that steers the crushed tube through during crushing and can lead to more fragmentation behavior and higher energy absorption characteristics along with progressive crushing. FEM simulations are carried out in Abaqus/Explicit software with stacked-shell approach, using cohesive zone method (CZM) to model delamination and using a built-in subroutine for continuum damage mechanics (CDM) of fabric composites to model intralaminar damage.

1. Introduction

CFRP composites are increasingly replacing traditional metallic materials in various industrial applications due to their promising attributes. Their outstanding mechanical properties and lightweight nature render them highly advantageous, particularly in crashworthy structures. In such applications, components must possess high specific energy absorption (SEA) capacity and stable progressive crushing behavior to effectively mitigate the impact of crash incidents. Well-designed CFRP composite crashworthy structures meet these criteria owing to their superior characteristics. However, estimating energy absorption values and predicting the crushing behavior of composite structures poses significant challenges due to the involvement of numerous complex damage modes, including in-plane and interlaminar damages, which encompass fiber and matrix damage, as well as delamination respectively [1-5].

A review of literature reveals studies investigating the progressive crushing behavior and morphology of CFRP structures, commonly categorizing the progressive crushing behavior into three modes: splaying, fragmentation, and local buckling [1, 2, 6]. These modes may occur simultaneously during a crushing incident. Various design parameters of CFRP structures significantly influence energy absorption characteristics and crushing behavior. These parameters include composite material in-ply properties, microstructure, geometry of the composite structure, crushing conditions, and trigger mechanisms [1, 2 ,5-10].

Trigger mechanisms play a pivotal role in composite crashworthy structures, influencing both the initial peak force in load displacement curves and crush reaction forces, thereby affecting the energy absorption rate of CFRP structures. They initiate the crushing of composite structures and facilitate stable, progressive crushing behavior by aiding in the initial crushing of tubes, thereby averting catastrophic failure. Trigger mechanisms are typically classified into two types: conventional trigger mechanisms and external trigger mechanisms. Conventional trigger mechanisms are commonly integrated into composite structures by shaping the structure's tip through machining, often forming steeple or chamfered shapes.

External trigger mechanisms involve an external structure that guides the composite component during crushing, facilitating progressive crushing behavior. Typically applied to tubular composite structures, their geometry affects the crushing behavior and can enhance energy absorption characteristics. Several studies in the literature examine the effects of external crush plugs. Siromani et al. [11] studied the axial crushing behavior of circular graphite/epoxy tubes with chamfered ends using basic outward and inward crush plugs with varying crushing zone radii. They found that inward crush plugs exhibited the best performance, and the energy absorption rate could be adjusted based on the crushing zone radius. Jiang et al. [12] explored the crushing of CFRP fabric square tubes with various plugs including circular convex, circular concave, square convex, square concave plugs, and ditch plugs with narrow and wide channels. They suggested that ditch plugs offer superior performance, although the load-displacement curves fluctuate more due to the observed progressive folding behavior of the tubes. Ren et al. [13] investigated the effects of different triggers applied to the tip of the tube, such as sawtooth, chamfer, square holes, and channel holes triggers, on square tube CFRP composites crushed with ditch-type plugs. They also observed folding behavior in the crushing morphology of the specimens. Tong and Xu [14] examined the crushing of CFRP braided circular tubes with innovative crush plugs, including conventional outward plugs and outward plugs with semi-circle cavities, which guide the tube downwards after the crash event.

This study examines the crushing behavior of Ø40 mm CFRP fabric composite tubes employing various innovative crush plugs. Recently, Demir et al. [15] investigated the axial quasi-static crushing of composite tubes and explored the effects of different modeling techniques, including mesh density and the virtual debris wedge approach in FEM simulations. In this current investigation, similar manufacturing and testing methods, as well as modeling techniques, are adopted to investigate the effect of crush plugs. Initially, Ø40 mm composite tubes are experimentally tested under quasi-static axial crushing conditions. The experimental setup includes crushing the tubes without using any crush plug and utilizing basic outward and inward crush plugs with a 2 mm radius on the crushing surfaces. In the numerical study, the model is validated by comparing with the experimental results. The crushing simulation of composite tubes is conducted using FEM with Abaqus/Explicit software. Following validation, the model is utilized to simulate and analyze the crushing behavior of tubes employing channel crush plugs.

2. Experimental Study

Ø40 mm CFRP composite tubes are fabricated using KORDSA OM10 carbon fiber prepregs, featuring a plain weave of 3K carbon fiber tows and an epoxy matrix. The prepregs have a nominal areal weight of 200 g/m² [15]. The manufacturing process involves roll-wrapping six layers of prepregs onto an aluminum mandrel, followed by the application of heat shrink tapes on the surface. The roll-wrapped tubes are then cured in a vacuum oven at 130°C, following the recommended curing cycle. Upon completion of the curing process, the products are released from the aluminum mandrels and cut into smaller specimens with a length of 40 mm using a water-cooled diamond disc. The dimensions of the circular tube specimens are depicted in Figure 1.a. These specimens undergo quasi-static compression tests at a constant crushing rate of 2 mm/min [15]. The tests include axial crushing using basic inward and outward crusher plugs with a 2 mm radius on the crushing zone, as well as crushing without plugs using only test rigs. The test setups are illustrated in Figure 1.b-d.

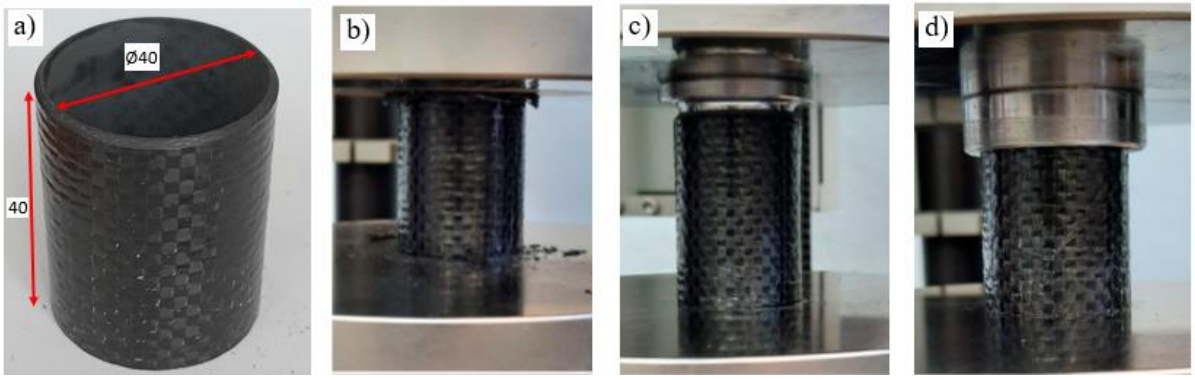


Figure 1. Manufactured crush tube specimen and test setups; a) Whole specimen b) Test setup without using crush plug, c) Outwards crushing test setup, d) Inwards crushing test setup.

Tip of the tube specimens are 45° chamfered using a lathe as illustrated in Figure 2.a, to prevent catastrophic failure during tests. During the crushing tests, the crush plugs are placed at the top of the tubes. Basic outwards and inwards crush plugs utilized in tests are illustrated in Figure 2.a and 2.b.



Figure 2. Trigger mechanisms on experimental tests; a) Chamfer trigger, b) Outwards crush plug, c) Inwards crush plug.

3. Finite Element Analysis

Following the same modelling method stated in Demir et al.'s study [15], the axial crushing of composite tubes are modelled in Abaqus/Explicit software adopting the stacked shell model approach. Interlaminar behavior of plies are modelled with Cohesive Zone Method (CZM) by generating cohesive interactions between the surfaces of the plies. In the CZM method used to model interlaminar delamination behavior, cohesive contacts based on traction-seperation law are generated between surfaces of the plies. To model mixed delamination, damage initiation behavior is modelled by quadratic stress damage initation criterion and damage evolution is modelled according to Benzeggagh-Kenane damage evolution law. Softening behavior is set as linear softening in the model and B-K coefficient is selected as 2.284 [15, 17]. Interlaminar behavior properties are listed in Table 1.

Table 1. Interlaminar material properties of composite tubes [15, 17]

Description	Mode I	Mode II	Mode III	Unit
Penalty Stiffness	2×10^6	1×10^6	1×10^6	[N/mm³]
Damage Initiation	54	70	70	[MPa]
Fracture Energy	0.504	1.566	1.566	[kJ/mm²]

Intralaminar damage behavior of the composite plies are modelled by using built-in ABQ_PLY_FABRIC subroutine [15-17]. ABQ_PLY_FABRIC built-in subroutine defines the material behaviour of composite plies adopting a continuum damage material model. Input values of the intralaminar properties of composite tubes are illustrated in Table 2.

Table 2. Intralaminar material properties of composite tubes [15, 17]

Description	Symbol	Value	Unit
Density	ρ	1.56	g/cm³
Young Modulus along fiber direction 1	E_1	65.1	GPa
Young Modulus along fiber direction 2	E_2	64.4	GPa
Shear Modulus	G_{12}	4.5	GPa
Principal Poisson Ratio	v_{12}	0.037	-
Tensile Strength along fiber direction 1	X_{1+}	776	MPa
Compressive Strength along fiber direction 1	X_{1-}	704	MPa
Tensile Strength along fiber direction 2	X_{2+}	760	MPa
Compressive Strength along fiber direction 2	X_{2-}	698	MPa
Shear Stress at the initiation of shear damage	S	95	MPa
Tensile fracture energy per unit area along fiber direction 1	G_f^{1+}	125	kJ/m²
Compressive fracture energy per unit area along fiber direction 1	G_f^{1-}	250	kJ/m²
Tensile fracture energy per unit area along fiber direction 2	G_f^{2+}	95	kJ/m²
Compressive fracture energy per unit area along fiber direction 2	G_f^{2-}	245	kJ/m²
Shear damage equation parameter	α_{12}	0.18	-
Max shear damage	d_{12}^{max}	0.99	-
Initial effective shear yield stress	$\tilde{\sigma}_{y0}$	185	MPa
Hardening equation coefficient	C	1053	-
Hardening equation power term	p	0.41	-
Element deletion flag	1DelFlag	1	-
Maximum value of damage variables	d_{max}	0.99	-

In constructing the FE models, each ply is first modeled individually as solid layers and then meshed with continuum shell elements (SC8R) using the stacked shell modeling approach, thereby representing the plies as homogeneous orthotropic layers. These continuum shell elements possess the geometric attributes of 3D elements while exhibiting constitutive behavior akin to conventional shell elements. To expedite FEM simulation results, composite tubes are modeled using a quarter-model approach. Material properties are defined by assigning homogeneous continuum shell sections to each ply, thereby specifying ply orientations.

Individual plies are modelled with a thickness of 0.2 mm and meshed with approximately 1.0×1.0 mm sized elements. A rigid plate is generated to model the test rig beneath the composite tube. Tie contacts are used between the bottom nodes of the tube and bottom rigid surface, which is meshed with R3D4 rigid elements and fixed boundary condition. Crushing rate is choosen to be 1 m/s as recommended in the literature [15]. In order to define the interaction between applied rigid crush plugs and tubes, “Tangential Behaviour” contact with penalty stiffness and “Normal Behavior” contact is defined between the tubes and rigid parts. The friction coefficient is selected as 0.2 for the interaction between parts. Also contacts with “Tangential Behaviour” and “Normal Behavior” are defined for the cohesive interactions between plies with friction coefficient of 0.3 [15]. Semi-autoamtic mass-scaling method is

used and applied to whole model with the target increment of 1e-7. To be able to model delamination, crushing behavior and initation of crushing, the surfaces of the upper elements of last 2 mm's are not included into cohesive interactions. CAE model of the quarter-model composite tubes and rigid bottom plate is illustrated in Figure 4.

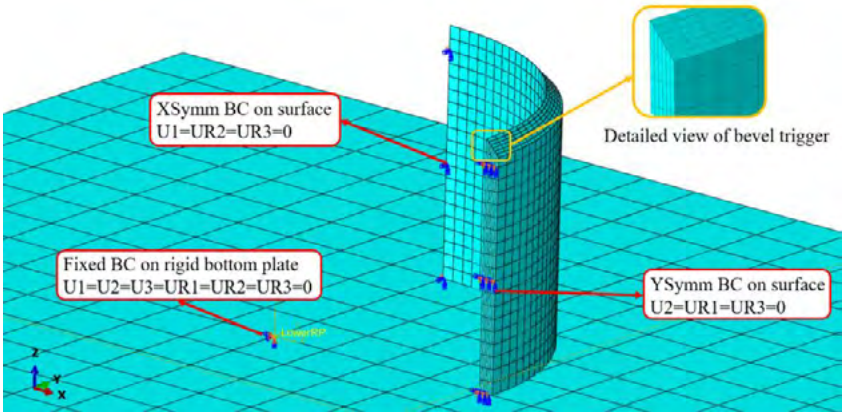


Figure 4. CAE model of the quarter-model of composite tubes and rigid bottom plate

To integrate crush plugs into the simulations, the inner surfaces of the plugs, which come into contact with the specimen during crushing are modeled using rigid surfaces that are meshed with R3D4 elements, with dimensions of 0.2×0.2 mm in critical radius zones and 0.5×0.5 mm in flat surfaces. The model for the axial crushing of Ø40 mm composite tubes is validated by comparing experimental tests with FE simulations. For modeling axial crushing using only test rigs, the virtual debris wedge method is applied, as recommended in the literature [15, 18, 19, 20]. Following validation, the performance of novel plugs is investigated through FEM simulations. These novel plugs include a channel that guides the composite tube wall through two curves with a 2 mm radius. Two novel channel plugs, crushing the tubes outward and inward, respectively, are examined. The rigid surfaces representing benchmark plugs and virtual debris wedge rigid surfaces are depicted in Figure 5, along with the rigid surfaces of the novel plugs.

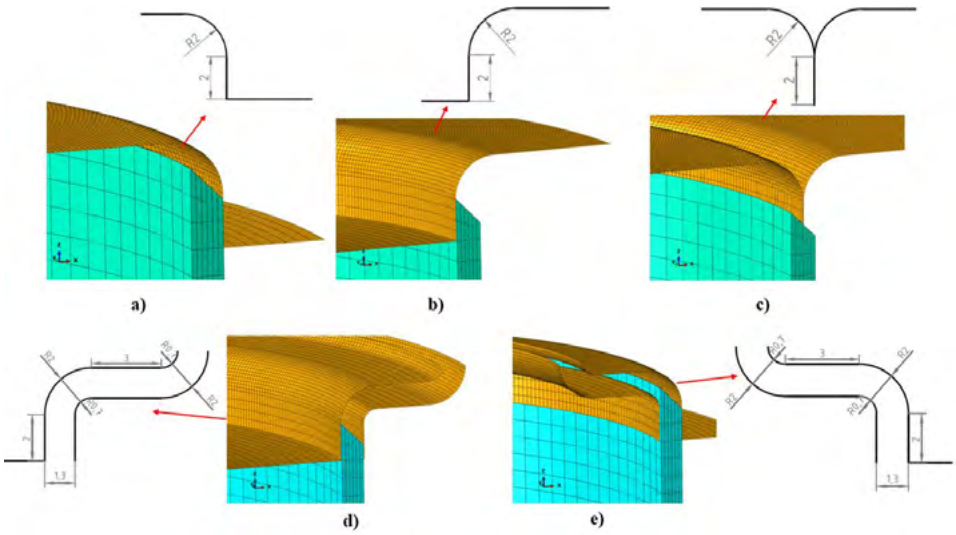


Figure 5. Rigid upper surfaces generated to model crush plugs and virtual debris wedge; a) Inwards crush plug (ICP), b) Outwards crush plug (OCP), c) Virtual debris wedge (VDW), d) Outwards channel crush plug (OCCP), e) inwards channel crush plug (ICCP)

4. Results and Discussion

In the first phase of the study, the experimental and simulation results of the benchmark specimens are compared. Load-displacement curves and SEA-displacement curves obtained from FEA simulations and experimental tests are illustrated together in Figure 6 for inwards crushing, outwards crushing and crushing without plugs respectively. The experimental tests without any plugs are compared with virtual debris wedge simulations.

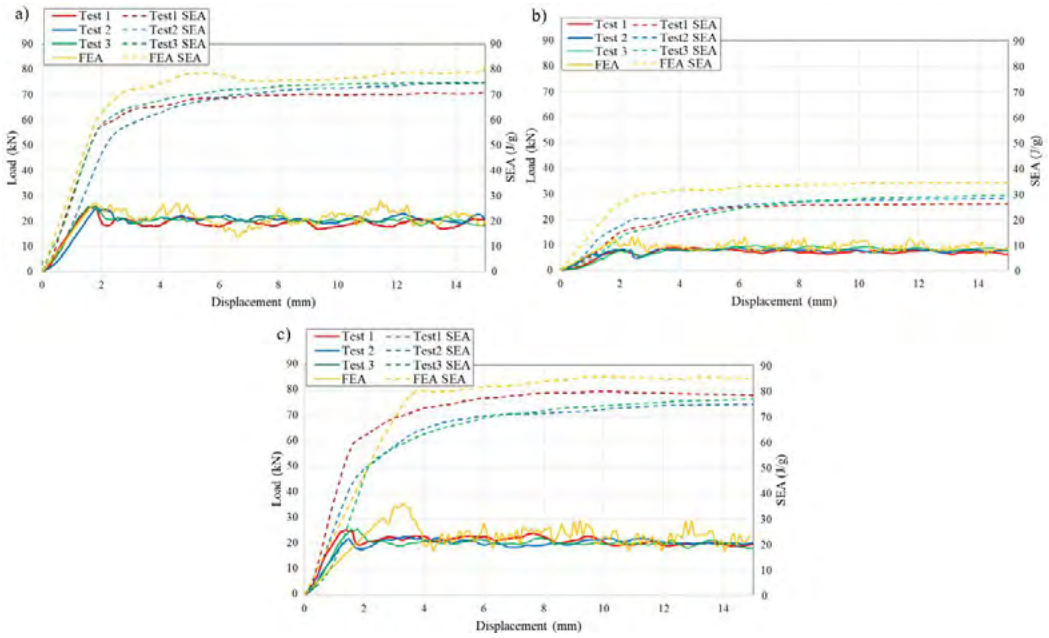


Figure 6. Load-displacement, SEA-displacement curves of benchmark models; a) crushing with no plugs (virtual debris wedge simulation (VDW)), b) Outwards crushing (OCP), c) Inwards crushing (ICP)

Evidently, the load-displacement curves derived from FEA simulations closely match those observed in the experimental tests, particularly during the progressive crushing phase. However, simulations incorporating outward and inward crushing plugs show slightly elevated peak forces compared to the experimental results. As a result, the SEA-displacement curves in these simulations also exhibit a minor deviation. Furthermore, the crushing morphologies obtained from FEA simulations accurately mirror the experimental morphologies, as depicted in Figure 7.

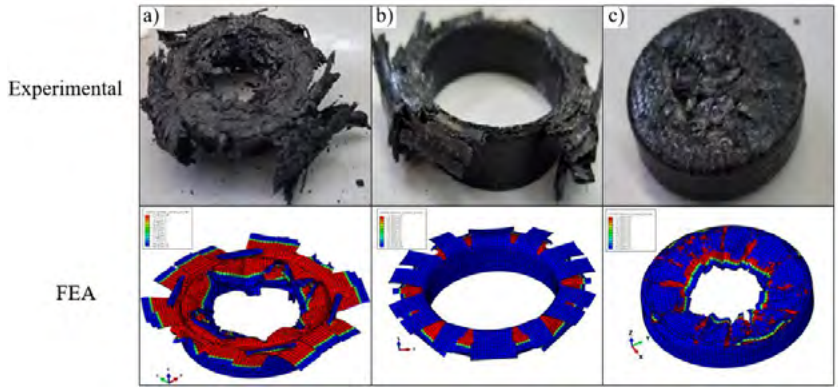


Figure 7. Experimental and FEA crush morphologies for benchmark specimens; a) crushing with no plug, b) outwards crushing, c) inwards crushing

After benchmarking study completed, the numerical simulations of the novel plugs are carried out. The load-displacement, SEA-displacement curves and crushing morphologies are illustrated in Figure 8. Novel outwards and inwards plug simulation results are also compared with basic outwards and inwards plug test results in Figure 8.

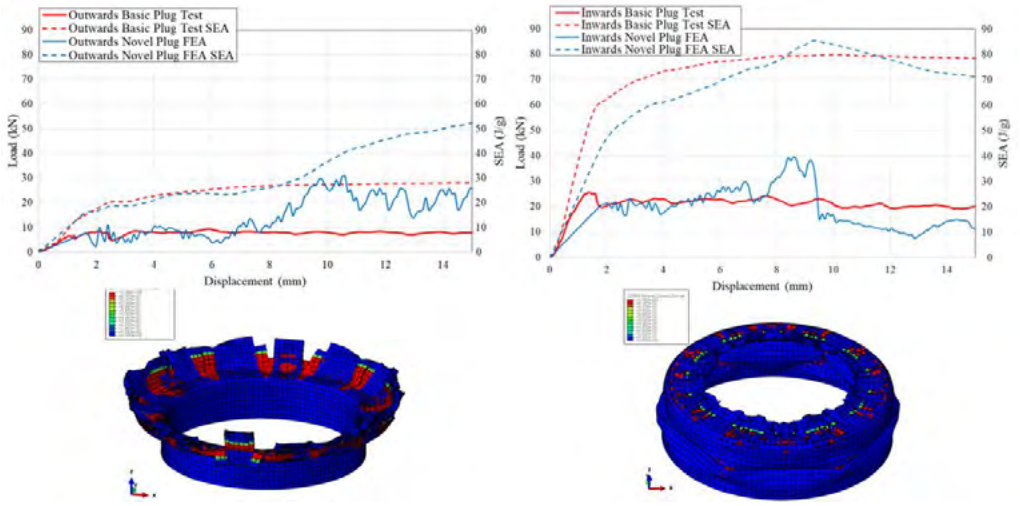


Figure 8. Load-Displacement, SEA-Displacement curves of novel plug simulations compared with basic plug test results and crush morphologies of the novel plug simulations; Outwards Channel Crush Plug (OCCP) (left), Inwards Channel Crush Plug (ICCP) (right)

Analyzing the load-displacement curves reveals that the simulations using the novel channel plugs exhibit similar behavior to those with the basic plugs within the first 8 mm. However, once the tube reaches the second turn in the channel section, the loads begin to increase. Upon examining the crushing morphologies, it is observed that the tube crushed with the outward channel plug takes on the shape of a crown, whereas the tube crushed with the inward channel plug shows signs of local buckling before the composite tube reaches the second radius. Following buckling, the loads tend to decrease, resulting in a reduction in SEA-displacement curves as well. The SEA values for all simulations and the mean values of experimental tests are evaluated in Table 3.

Table 3. SEA values of the experimental tests and simulations

	No Plug Test	OCP Test	ICP Test	VDW Sim.	OCP Sim.	ICP Sim.	OCCP Sim.	ICCP Sim.
SEA (J/g)	73.59	28.74	76.66	77.61	34.39	84.64	52.47	70.88

5. Conclusion

This study examines the impact of novel inward and outward crusher plugs on the axial crushing behavior of CFRP woven composite tubes using Abaqus/Explicit FEA software. Initially, the models are validated against experimental tests conducted with basic crush plugs and without any plugs. The simulation results obtained with the novel channel plugs demonstrate behavior consistent with the conventional plugs during the initial phase of crushing. However, once the tube reaches the second turn in the channel section, the loads, hence SEA values begin to increase. Evidently, crush plugs featuring channels significantly influence the crushing behavior and energy absorption values of composite tubes. As a future endeavor, optimizing crush plugs utilizing channel geometries could be explored to achieve more efficient crashworthy structure assemblies, suitable for use in transportation vehicles and various industries.

References

[1] D. Hull. A unified approach to progressive crushing of fibre-reinforced composite tubes. *Composites Science and Technology*, 40:377-421, 1991.
[2] G. L. Farley. *Energy-absorption capability of composite tubes and beams*. Ph.D. dissertation, VA: Virginia Tech, Blacksburg, 1989.
[3] J. Carruthers, A. Kettle, A. Robinson. Energy absorption capability and crashworthiness of composite material structures: a review. *Applied Mechanics Reviews*, 51:635-649, 1998.
[4] C. Bisagni. Experimental investigation of collapse modes and energy absorption characteristics of composite tubes. *International Journal of Crashworthiness*, 4(14):365-378, 2009.
[5] P. Thornton. Energy Absorption in Composite Structures. *Journal of Composite Materials*, 13(3):248-262, 1979.
[6] S. Ramakrishna. Microstructural design of composite materials for crashworthy structural applications. *Materials & Design*, 18(3):167-173, 1997.
[7] A. G. Mamalis, M. Robinson, D. E. Manolakos, G. A. Demosthenus, M. B. Ioannidis, J. Carruthers. Review, crashworthy capability of composite material structures. *Composite Structures*, 37(2):109-134, 1997.
[8] D. Schmuesser and L. Wickcliffe. Impact energy absorption of continuous fiber composite tubes. *Journal of Engineering Materials and Technology*, 109(1):72-77, 1987.
[9] H. Hamad, J. Coppola, D. Hull, Z. Maekawa and H. Sato. Comparison of energy absorption of carbon/epoxy and carbon/PEEK composite tubes. *Composites*, 23(4):245-252, 1992.
[10] P. H. Thornton and P. J. Edwards. Energy absorption in composite tubes. *Journal of Composite Materials*, 16(6):541-545, 1982.
[11] D. Siromani, G. Henderson, D. Mikita, K. Mirarchi, R. Park, J. Smolko, J. Awerburch and T. M. Tan. An experimental study on the effect of failure trigger mechanisms on the energy absorption capability of CFRP tubes under axial compression. *Composites Part A: Applied Science and Manufacturing*, 64:25-35, 2014.
[12] H. Jiang, Y. Ren, B. Gao, J. Xiang and F. G. Yuan. Design of novel plug-type triggers for composite square tubes: enhancement of energy-absorption capacity and inducing failure mechanisms. *International Journal of Mechanical Sciences*, 131-132:113-136, 2017.
[13] Y. Ren, H. Jiang and Z. Liu. Evaluation of double- and triple-coupled triggering mechanisms to improve crashworthiness of composite tubes. *International Journal of Mechanical Sciences,* 157-158:1-12, 2019.
[14] Y. Tong and Y. Xu. Improvement of crash energy absorption of 2D braided composite tubes through an innovative chamfer external triggers. *International Journal of Impact Engineering*, 111:11-20, 2017.
[15] S. Demir, N. Ersoy and M. C. Engül, Axial quasi-static crushing of composite tubes: An investigation on the influence of the modeling techniques. *Journal of Reinforced Plastics & Composites*, 0(0):1-19, 2023.
[16] V. Sokolinsky, K. Indermuehle and J. Hurtado, Numerical simulation of the crushing process of a corrugated composite plate. *Composites Part A: Applied Science and Manufacturing*, 42(9):1119-1126, 2011.
[17] G. Zhou, G. Sun, G. Li, A. Cheng and Q. Li, Modelling for CFRP structures subjected to quasi-static crushing. *Composite Structures*, 184:41-55, 2018.
[18] M. C. Engül, S. Demir, N. Ersoy. The Influence of Geometry on the Energy Absorption Capability of Composite Structures Made of Woven Fabric Prepregs. In *23th International Conference on Composite Materials (ICCM/23)*, Belfast, 2023.
[19] C. McGregor, R. Vaziri and X. Xiao. Finite element modelling of progressive crushing of braided composite tubes under axial impact. *International Journal of Impact Engineering*, 37(6):662-672, 2010.
[20] M. Engül and N. Ersoy. From flat plates to sinusoidal structures: Influence of geometry on energy absorption capability of carbon/epoxy composites. *Journal of Composite Science*, 7(56): 1-17, 2023.

MODELLING OF SHORT- AND LONG-TERM BOND BEHAVIOR IN CONCRETE STRUCTURES STRENGTHENED WITH EXTERNALLY BONDED CFRP COMPOSITES

Aloys Dushimimana[1]*, José Sena-Cruz[1], Anastasios P. Vassilopoulos[2],
Luís Correia[1], João Miguel Pereira[2]

[1]ISISE/IB-S/ARISE, Department of Civil Enginnering, University of Minho, Guimarães, Portugal
Email: aloysdushimimana@yahoo.fr, jose.sena-cruz@civil.uminho.pt, lcorreia@civil.uminho.pt, jpereira@civil.uminho.pt, Web Page: https://isise.net/
[2]Composite Construction Laboratory (CCLab), Department of Civil Engineering, Ecole Polytechnique Fédérale de Lausanne (EPFL), Station 16, Lausanne CH-1015, Switzerland
Email: anastasios.vassilopoulos@epfl, https://www.epfl.ch/en/

Keywords: Numerical modeling, Carbon fiber, Concrete, Epoxy adhesive, Water exposure

Abstract
In the context of structural rehabilitation of concrete structures, carbon fiber reinforced polymer (CFRP) composites are usually bonded to concrete substrates using the externally bonded reinforcement (EBR) technique. Although this is a commonly used method in various applications, only a few studies have investigated the long-term performance of such joints. In this study, numerical models to simulate the short- and long-term performance of the EBR CFRP-to-concrete bondline are developed. Using these models, the performance of the bonding before and after four years of water exposure is assessed. The numerical results from both models are compared with results from an experimental investigation previously performed by the authors' research group, which shows a good agreement.

1. Introduction

Concrete is used extensively in engineering structures that need to be in operation for several decades. Various strengthening techniques have been implemented in the past to extend the service life of reinforced concrete (RC) structures. One of the best candidate materials for strengthening RC structures is carbon fiber reinforced polymer (CFRP) composites. CFRP composites show excellent durability performance; furthermore, they possess very high stiffness and high strength-to-weight ratios [1]. There are two main strengthening techniques using CFRP composites for the strengthening of RC structures: (i) externally bonded reinforcement (EBR) and (ii) near-surface mounted (NSM) [1][2]. In both techniques, an epoxy adhesive is required to bond the CFRP to the concrete substrate. In the case of the EBR technique, the CFRP laminate is bonded to the concrete substrate, whereas in the case of NSM, the CFRP laminate is inserted in a groove pre-cut into concrete [3].

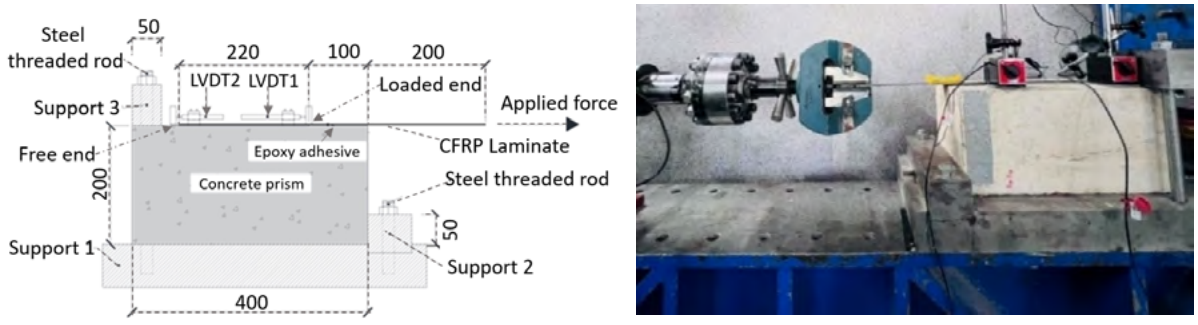
Despite the successful application of the above techniques, the existing literature still lacks sufficient data about the durability/long-term response of the applied strengthening techniques. In fact, the question of how long the epoxy adhesive can keep binding the concrete to the CFRP laminate, allowing the composite action between both parts, needs to be addressed to better understand the durability and long-term performance of EBR and NSM techniques. This work attempted to develop numerical models addressing the durability of the EBR CFRP-to-concrete bond for up to 4 years of water exposure. Experimental data on the durability of the EBR CFRP-to-concrete under accelerated aging test protocols already exist, e.g., [4], as well as under natural aging test protocols [5] [6] [7]. However, a very few numerical models addressing bond durability exist, e.g., in [8][9] and are unfortunately based on short-

term experimental data. Hence, the developed models in the present work contribute to increasing the availability of numerical data regarding the durability of the EBR CFRP-to-concrete bond by using data from long-term exposure. Constitutive models for each bond constituent material (concrete, epoxy adhesive, CFRP laminate) are first developed considering the yearly degraded properties of the materials. These constitutive models are developed referring to existing equations in the literature. Both concrete and epoxy adhesive are modeled using the well-known concrete damage plasticity (CDP) model [10], while the CFRP laminate is assumed to behave linearly up to failure. The added novelty lies in assessing the effects of the degradation of the material properties themselves on the bond performance by using the properties of the materials at the bondline rather than adopting the commonly known cohesive model. That is, the constitutive models are developed referring to the data from material property testing. This work comprises of the following sections: Section 1 introduces the existing work, highlights the gap, and the strategies used for addressing the gap; Section 2 describes the materials and methods adopted. Furthermore, results are presented and discussed in Section 3, followed by conclusions in Section 4.

2. Materials and methods

2.1. Experimental Program

An experimental campaign was previously conducted by the authors' group [6] where, in the first phase, 3 concrete cylinders, 5 epoxy adhesives, 6 CFRP laminates, and 2 concrete elements strengthened with CFRP laminates according to externally bonded reinforcement (EBR) technique (each element being strengthened by two CFRP laminates yielding to 2 tests per element), were tested to examine their responses before water exposure. In the second phase, the specimens were immersed in tap water controlled at 20 °C for up to four years. That is, 12 concrete cylinders, 20 epoxy adhesives, 24 CFRP laminates, and 8 concrete elements (strengthened with CFRP laminates) were immersed in water for later testing. Each year, these specimens were tested to assess the effect of water ingress on their long-term mechanical properties. The results from testing of concrete, epoxy adhesive, CFRP laminates, and bond in the strengthened elements are provided in the recently published work by the authors' research group [6] (i.e., see E2 data in Table 3, Table 4 and Table 5 of [6]). The bond test (single lap shear test) procedure for the elements with EBR is summarized in Fig. 1, and more details of this test can be found in [6].



(a) (b)

Figure 1. Single lap shear test: (a) specimen geometry and test setup (all units in [mm]), (b) photograph of the full test configuration [6].

2.2. Developed numerical models

A summary of the constitutive models used in this study is provided in Fig. 2. Concrete behavior under compression and tension was predicted using Saenz model [11] and the model by Horjidik [12] as shown in Fig. 2a,b respectively. The input parameters for both models were as follows: for concrete under compression and tension, the experimentally recorded maximum concrete compressive and tensile

strengths and elastic modulus before exposure (short-term value) and after each year of exposure (long-term values) for up to 4 years (see values for E2 in the previously published work [6]) were used in developing the relations shown in Fig. 2a,b.

Furthermore, epoxy adhesive behavior under compression and tension was modeled using the Saenz [11] and Belarbi and Hsu [13] models, as in Fig. 2c,d, respectively. The CFRP laminate was modeled as a linear elastic material up to failure. Similar to the case of concrete model, the input parameters for the adhesive from experimental results before and after water exposure (compressive strength, tensile strength, and elastic modulus) were used as inputs to produce the relations shown in Fig. 2c,d.

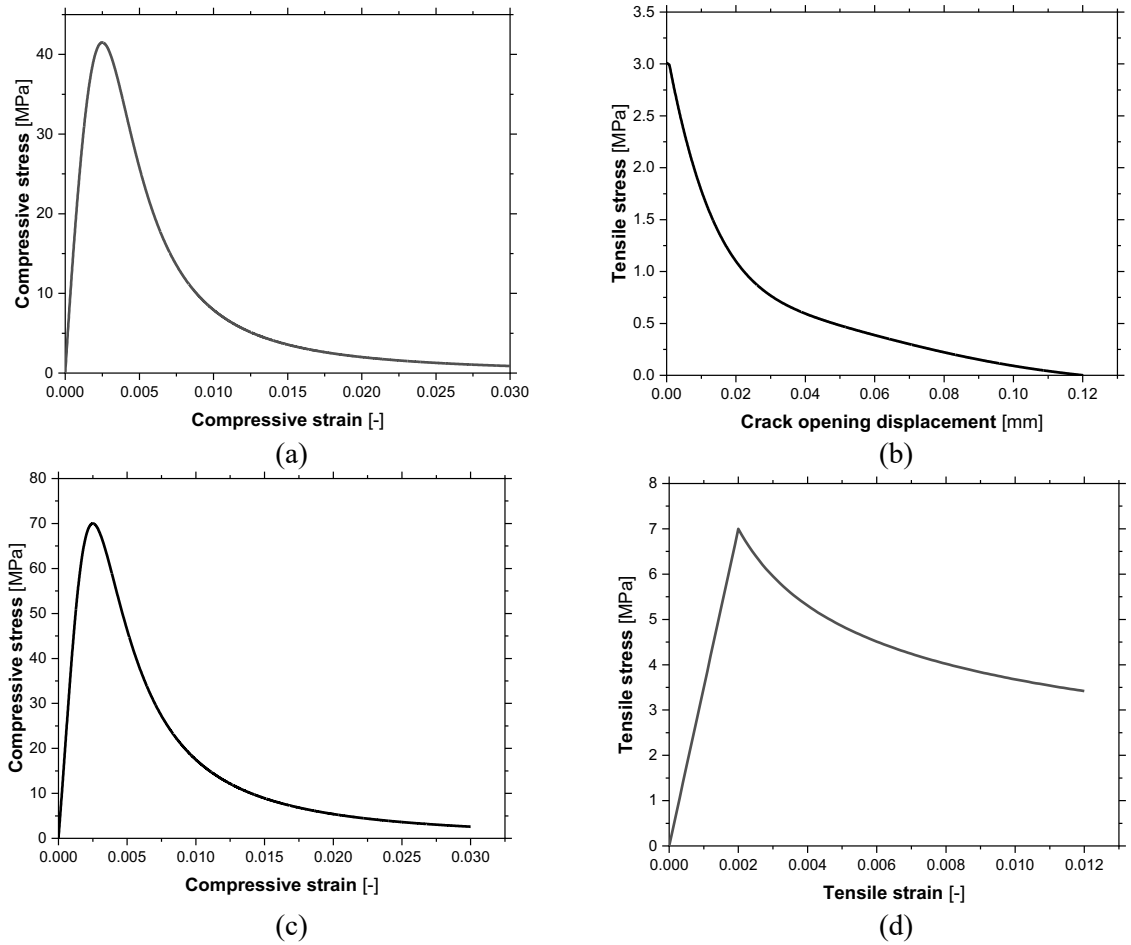


Figure 2. Developed material constitutive models: (a) concrete in compression, according to Saenz et al. [11], (b) concrete in tension, according to Horjidk [12], (c) epoxy adhesive in compression, according to Saenz et al. [11], (d) epoxy adhesive in tension, according to Belarbi and Hsu [13].

2.2.1. EBR CFRP-to-concrete model

The finite element method (FEM) using ABAQUS software was used to simulate the short and long-term performance of the bond between concrete and CFRP laminate. A perfect bond was assumed between the concrete-epoxy adhesive and the CFRP laminate-epoxy adhesive interfaces. Therefore, tie constraints were used to tie the materials at these defined interfaces. The material parameters used for defining the CDP model [10] and other input properties to the EBR CFRP-to-concrete bond model are summarized in Table 1.

Table 1. CDP model parameters used for concrete and epoxy adhesive

Material	Concrete damage plasticity (CDP) model parameters										
	Plasticity flow parameters					Compression			Tension		
	D_a	e	fb_0/fc_0	K	V_p	CC_C			CC_t		
						SS_C	ε_{in}	d_c	SS_t	ε_{Tcr} or w_t	d_t
Concrete	38	0.1	1.16	0.6667	0.0	Saenz et al. [11]			Horjidk [12]		
Adhesive	38	0.1	1.16	0.6667	0.0	Saenz et al. [11]			Belarbi and Hsu [13]		

D_a: Dilation angle, e: eccentricity, fb_0/fc_0: the ratio of initial equibiaxial yield stress to initial uniaxial yield stress in compression, K: ratio of the second stress invariant on the tensile meridian to the one on the compressive meridian, Vp: viscosity parameter, , CC_C: constitutive law in compression, CC_t: constitutive law in tension, ε_{in}: inelastic strain, d_c: compression damage, SS_C: stress-strain curve in compression, SS_t: stress-strain (or displacement) curve in tension, w_t: crack opening width, ε_{Tcr}:cracking strain, d_t: tension damage.

3. Results and Discussion

The results from the EBR CFRP-to-concrete bond are analyzed in this section. Comparative graphs between experimental and FE model curves are shown in Fig. 3 for the short-term behavior of the studied strengthening system. The maximum values are also compared in Table 2. It can be seen that experimental and FEM data are in very good agreement (with only a 5% difference). Particularly, the average curve in Fig. 3a corroborates well with the FEM model curve shown in Fig. 3b, which shows the model is very promising in predicting the behavior of non-exposed specimens.

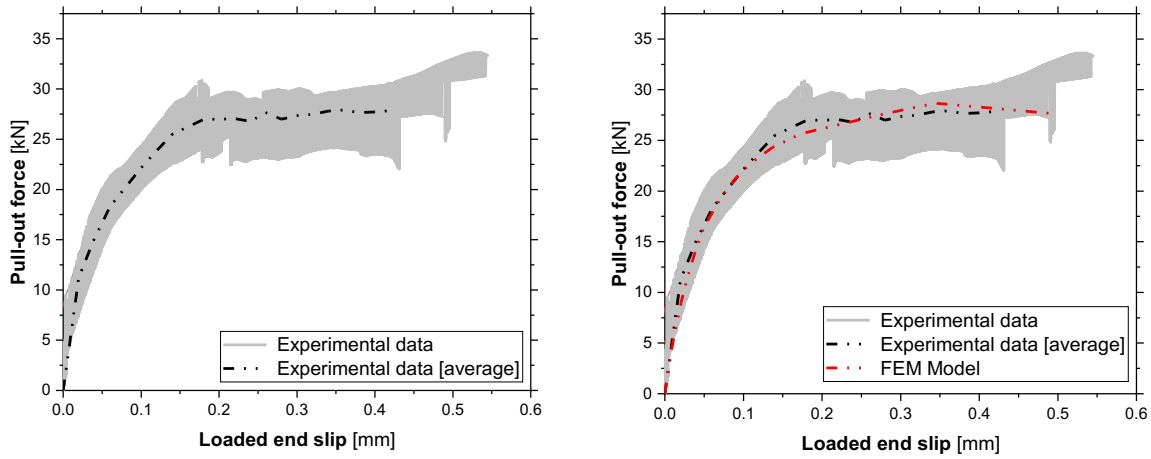


Figure 3. Short-term EBR CFRP-to-concrete bond responses: (a) experimental data (shaded area represents the four curves from four tests), (b) experimental *vs.* FEM model data before exposure

The pull-out force *vs.* loaded end slip relationships for the case of long-term exposure are presented in Fig. 4 (that is, experimental *vs.* FEM model results for the first (Fig. 4a), second (Fig. 4b), third (Fig. 4c), and fourth (Fig. 4d) years of exposure), and their average maximum pull-out values are compared with those from experimental tests in Table 2. Based on Fig. 4., the FEM predicted responses agree well with the experimental results as the FEM curve falls within the shaded area representing the four curves from the experimental tests, though there is a slight difference in terms of the average experimental data and the numerical FEM data curves. Despite this, it can be noted that the results from the FEM model are promising as the maximum values and those from experimental tests are close to each other. This is clearly shown in terms of percentage difference that varies between 1.68 and 11.96% (Table 2).

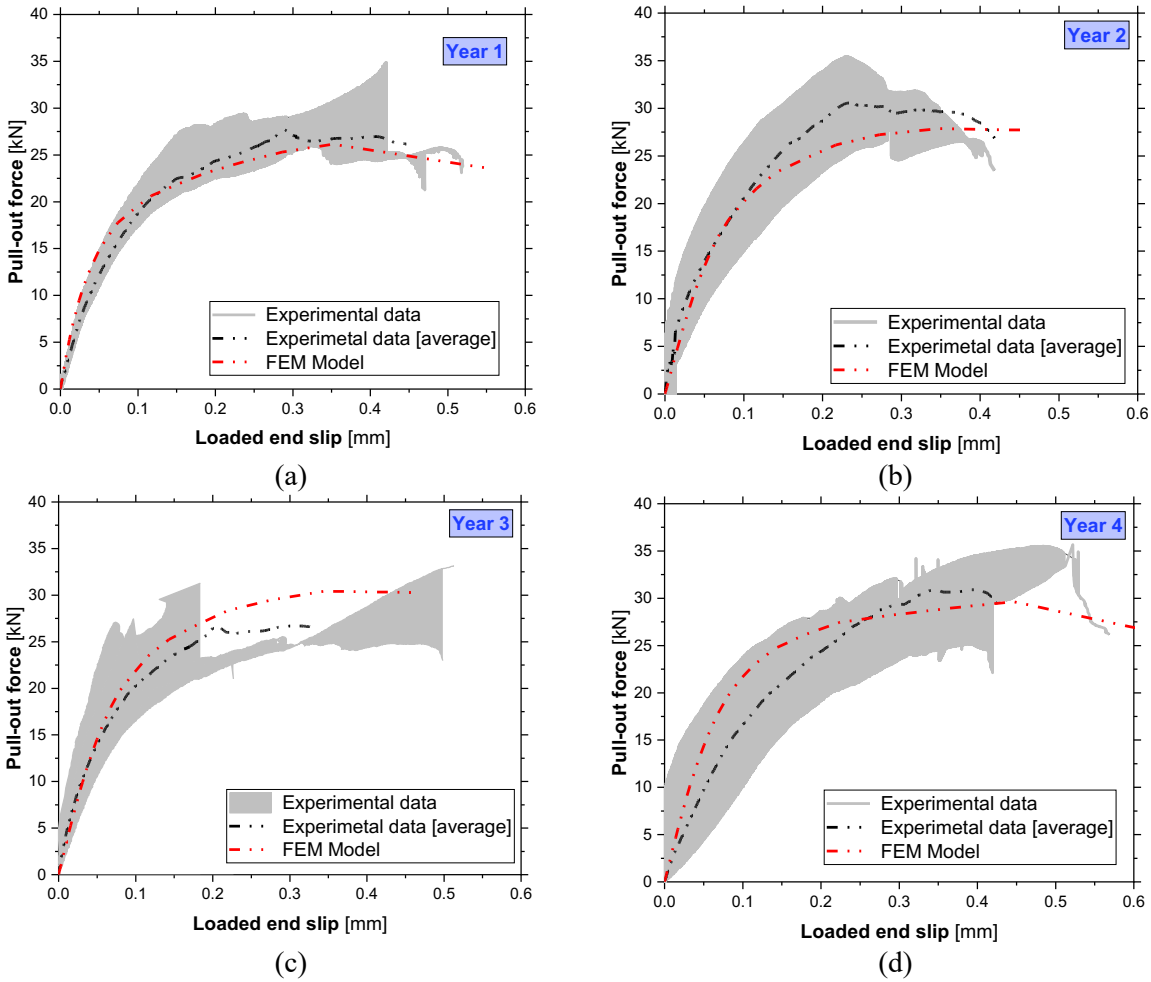


Figure 4. Long-term EBR CFRP-to-concrete bond responses: Experimental *vs.* FEM model data (a) after 1 year, (b) after 2 years, (c) after 3 years, and (d) after 4 years of exposure

Table 2. Comparison of pull-out forces (kN) from experimental tests with those from FEM modelling

Exposure time (in years)	Experimental result	FEM model result	Difference (%)
0	30.20	28.67	5.07
1	27.86	26.14	6.17
2	31.06	28.52	8.18
3	27.18	30.43	11.96
4	29.14	29.63	1.68

On the other hand, comparison of the concrete substrate's tension and compression damages, as well as the substrate displacement at the failure stage for the case of non-exposed specimens, are presented in Fig. 5a,b, and c, and for the case of water exposed specimens (at the fourth year of exposure) in Fig. 5d,e, and f. respectively. It is observed, for both non-exposed and exposed specimens, that concrete damages severely at the loaded end and this damage propagates toward the free end, thereafter, reaching a complete failure, which is the concrete cohesive failure. This type of failure was also observed during the experimental tests. Hence, it can be noted that the type of failure is well predicted by the developed model; also, the failure mode for the specimens immersed in water does not change with time.

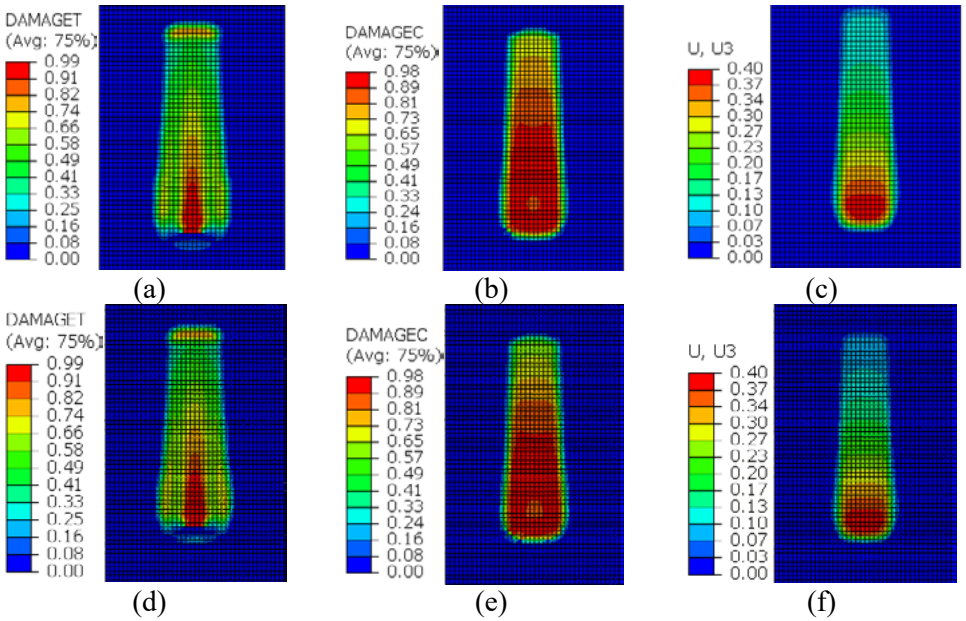


Figure 5. Failure modes from the FEM model: i) Before exposure: concrete (a) tension and (b) compression damages, and (c) concrete substrate displacement [mm]; ii) after 4 years of exposure: concrete (d) tension and (e) compression damages, and (f) concrete substrate displacement [mm].Note: The direction of the applied pull-out force is from the top to bottom of each image.

4. Conclusions

In this study, finite element modeling of the bond between concrete and carbon fiber reinforced polymer (CFRP) laminates applied using externally bonded reinforcement (EBR) technique was developed. The developed models addressed the bond performance under short-term (before water exposure) and long-term (after water exposure) cases. These models were validated using experimental data previously published by the authors' group. The key findings are as follows.

1. The numerical models of the CFRP-to-concrete bond in non-immersed and immersed (in tap water conditioned at 20 °C for different exposure durations) cases are developed. The yearly predicted pull-out force *vs.* slip curves corroborated well with those observed during the experimental program.

2. The developed models revealed that the damage of concrete started from the loaded end and propagated toward the free end. Concrete cohesive failure was predicted as the prevailing failure mode for all considered exposure durations and matched with that observed during experimental program.

3. The developed model that only considers the material properties (without using cohesive model) led to a very good agreement with the observed data from the experimental program. This shows that modeling the epoxy adhesive with its own properties rather than using the commonly known cohesive model is promising.

Acknowledgements
This work was carried out in the scope of the projects FRPLongDur POCI-01-0145-FEDER-016900 (FCT PTDC/ECM-EST/1282/2014) and DURABLE-FRP (PTDC/ECI-EGC/4609/2020 / DOI: 10.54499/PTDC/ECI-EGC/4609/2020) funded by national funds through the Foundation for Science and Technology (FCT) and co-financed by the European Fund of the Regional Development (FEDER) through the Operational Program for Competitiveness and Internationalization (POCI) and the Lisbon Regional Operational Program and partially financed by the project POCI-01-0145-FEDER-007633 and by FCT/MCTES through national funds (PIDDAC) under the R&D Unit Institute for Sustainability and Innovation in Structural Engineering (ISISE), under reference UIDB/04029/2020 (DOI: 10.54499/UIDB/04029/2020). This work was financed by national funds through FCT under a grant agreement [DFA/BD/08403/2021] attributed to the first author.

Part of this work was conducted at Ecole Polytechnique Fédérale de Lausanne (EPFL), Lausanne, Switzerland, in the scope of a short-term scientific mission sponsored by COST via CERTBOND action. The first author would like to acknowledge the support provided by CERTBOND action, also, the supports provided by the CCLab lab (at EPFL), and Prof. Anastasios Vassilopoulos (at EPFL) are highly acknowledged.

References

[1] CEB-FIP, fib90 Bulletin:Externally Applied FRP reinforcement for Concrete structures, 2019.
[2] J.S. Cruz, J. Barros, Bond Between Near-Surface Mounted Carbon-Fiber- Reinforced Polymer Laminate Strips and Concrete, J. Compos. Constr. 82 (2004) 1513–1521. https://doi.org/10.1016/j.compstruc.2004.03.047.
[3] A. Dushimimana, J. Sena-cruz, L. Correia, J.M. Pereira, Effects of long-term exposure of NSM CFRP-to-concrete bond to natural and accelerated aging environments, Compos. Struct. (2024) 118174. https://doi.org/10.1016/j.compstruct.2024.118174.
[4] M. Leone, S. Matthys, M.A. Aiello, Effect of elevated service temperature on bond between FRP EBR systems and concrete, Compos. Part B Eng. 40 (2009) 85–93. https://doi.org/10.1016/j.compositesb.2008.06.004.
[5] A. Dushimimana, L. Correia, R. Cruz, J.M. Pereira, J. Sena-Cruz, Durability of CFRP-Concrete Bond in EBR and NSM Sysytems under Natural Ageing for a Period of Three Years, in: Proc. 20th Eur. Conf. Compos. Mater., CC BY-NC 4.0, Lausanne, Switzerland, 2022: pp. 1–8. https://doi.org/https://doi.org/10.5075/epfl-298799_978-2-9701614-0-0.
[6] A. Dushimimana, J. Sena-Cruz, L. Correia, J.M. Pereira, S. Cabral-Fonseca, R. Cruz, Durability of bond between EBR-CFRP laminate and concrete after four years of natural outdoor and accelerated ageing exposures, Constr. Build. Mater. 427 (2024). https://doi.org/10.1016/j.conbuildmat.2024.136213.
[7] R. Cruz, L. Correia, S. Cabral-Fonseca, J. Sena-Cruz, Durability of bond of EBR CFRP laminates to concrete under real-time field exposure and laboratory accelerated ageing, Constr. Build. Mater. 377 (2023). https://doi.org/10.1016/j.conbuildmat.2023.131047.
[8] J.P. Firmo, M.G. Roquette, J.R. Correia, A.S. Azevedo, Influence of elevated temperatures on epoxy adhesive used in CFRP strengthening systems for civil engineering applications, Int. J. Adhes. Adhes. 93 (2019) 102333. https://doi.org/10.1016/j.ijadhadh.2019.01.027.
[9] M.R.T. Arruda, J.P. Firmo, J.R. Correia, C. Tiago, Numerical modelling of the bond between concrete and CFRP laminates at elevated temperatures, Eng. Struct. 110 (2016) 233–243. https://doi.org/10.1016/j.engstruct.2015.11.036.
[10] Y. Tao, J.F. Chen, Concrete Damage Plasticity Model for Modeling FRP-to-Concrete Bond Behavior, J. Compos. Constr. 19 (2015) 1–13. https://doi.org/10.1061/(asce)cc.1943-5614.0000482.
[11] L. Saenz, Discussion of Equation for the stress-strain curve of concrete by Desayi, P. and Krishnan, S., ACI J. 61 (1964) 1229–1235.

[12] D.A. Hordijk, Local approach to fatigue of concrete, Diss. Delft Univ. Technol. (1991) 41. http://resolver.tudelft.nl/uuid:fa87147b-8201-47ed-83d7-b812b09c5fbb.
[13] A. Belarbi, T.T.C. Hsu, Constitutive Laws of Concrete in Tension and Reinforcing Bars Stiffened By Concrete, Struct. J. 91 (1994) 465–474.

ANNEALING EFFECTS ON MECHANICAL PERFORMANCE AND FAILURE CHARACTERISTICS OF CF/PEKK AEROSPACE COMPOSITES: A THOROUGH EXPLORATION

Sinem Elmas [1,2], Buse Atac [1,2], C. Orhun Senol [1,2], Serra Topal [1,2], Mehmet Yildiz [1,2], Hatice S. Sas [1,2*]

[1]Faculty of Engineering and Natural Sciences, Sabanci University, Orhanli-Tuzla, 34956, Istanbul, Turkey
[2]Sabanci University Integrated Manufacturing Technologies Research and Application Center & Composite Technologies Center of Excellence, Teknopark Istanbul, Pendik, 34906, Istanbul, Turkey
*corresponding author: hatice.sas@sabanciuniv.edu

Keywords: CF/PEKK Composite; Annealing; Bending & Compression Properties; Acoustic Emission Inspection

Abstract
This study examines the effect of annealing on carbon fiber-reinforced polyether ketone ketone (CF/PEKK) composites under flexural and compressive loads using reference, pre-damaged, and annealed specimens. Annealing recovers pre-existing damages in the composite specimens in both loading scenarios. Additionally, annealing increases glass transition temperature (T_g) and degree of crystallization, as a result of dynamic scanning calorimetry (DSC) analysis. Furthermore, acoustic emission (AE) inspection reveals that CF/PEKK composite specimens are dominated by fiber-related failure under flexural loading and matrix-related failure under compressive loading. Pre-damages influence the failure cumulative counts and initiation times, but annealing restores cumulative count percentages to reference specimens' levels by relieving residual stresses and changing microstructure.

1. Introduction

Thermoplastic composites (TPCs) offer key benefits over thermoset composites, including mechanical properties meeting aeronautical standards, room temperature storage, weldability, recyclability, and efficient processing methods [1]–[3]. Within the thermoplastic polymer options for aircraft components, the Polyether-ketone-ketone (PEKK), a semicrystalline polymer becomes prominent due to its features with a glass transition temperature (T_g) of 160°C, a moderate processing range (330–380°C), and high strength and stiffness, and strong mechanical properties [4].

The Vacuum Bag Only (VBO) process is known as a rapid and cost-effective manufacturing method, generally used for thermoset composite manufacturing. However, there are few studies about TPCs manufacturing by the VBO process. Zhang et al. [5] studied void reduction during VBO processing of high-performance carbon fiber-reinforced thermoplastic composites of varying thicknesses, establishing a processing window for thick composites with low void content. Swamy et al. [3] described process design strategies to enhance air removal during VBO consolidation of CF/PEKK laminates.

It is important to understand failure behavior in thermoplastic composites (TPCs) to ensure safety and reliability, particularly since micro-cracks in the matrix can trigger catastrophic failure [6]. The AE method, a passive non-destructive evaluation (NDE) technique, is commonly used to identify and classify damage types, aiding in the monitoring of damage formation and evolution under diverse loading conditions by recording elastic waves generated by sudden energy release due to damage [7].

During both the manufacturing and service life of composite structures, various types of damage can occur under different loading conditions. Composite structures are engineered to endure different loading types, notably flexural and compression loads, each leading to distinct failure modes critical for structural performance during phases like takeoff, landing, turbulence, and maneuvers [8]. Repair methods are essential for the repair of damages, maintaining the structural integrity of composite materials, and minimizing. TPCs can be reshaped and repaired quickly due to their ability to melt and

reform with heat [9]. Annealing is a significant thermal treatment conducted above the glass transition temperature (T_g) of the semicrystalline thermoplastic matrix. Annealing reduces residual effects, and increases crystallinity, leading to enhanced structural performance [10]. While annealing typically served as a post-manufacturing process [11], [12], it holds potential as an effective repair method for addressing widespread matrix damages occurring during the operation or manufacturing of large-scale TPCs.

This study aims to explore how annealing affects pre-damages in TPCs and understand their mechanical behavior using AE inspection of CF/PEKK composites made through the VBO process. To achieve this, pre-damages are induced in composite specimens based on identified loads from AE inspection and subsequently, these specimens are subjected to annealing. Three-point bending, and compression tests are carried out to analyze how pre-damage and annealing affect the mechanical performance of CF/PEKK specimens. Mechanical tests are assisted with AE inspection to highlight the damage mechanism of reference, pre-damaged, and annealed CF/PEKK composite specimens. Moreover, dynamic scanning calorimetry (DSC) analyses are performed to assess the microstructural and thermal quality of the VBO-manufactured thermoplastic composite, including changes in glass transition temperature (T_g) and crystallization degree due to annealing.

2. Materials and Method

2.1. CF/PEKK Composite Manufacturing

CF/PEKK composites are produced using the vacuum-bag-only (VBO) process with Toray Cetex®TC1320 carbon fiber reinforced poly-ether-ketone-ketone unidirectional tape as shown in Figure 1. The layup configuration follows a quasi-isotropic and symmetric pattern with a stacking sequence of $[0/45/90/(-45)_2/90/45/(0)_2/45/90/-45]_s$. After the vacuum bag layup is completed, the vacuum is set at 1 atmosphere (atm) and maintained for 24 hours for debulking before being placed in the oven, and the vacuum level is maintained at this pressure during the oven cycle. The oven temperature is gradually increased to 250°C at a rate of 4°C/min, then further increased to 378°C at a rate of 3°C/min. The laminates are held at this temperature for 90 minutes before being cooled to room temperature at a constant rate of 3°C/min.

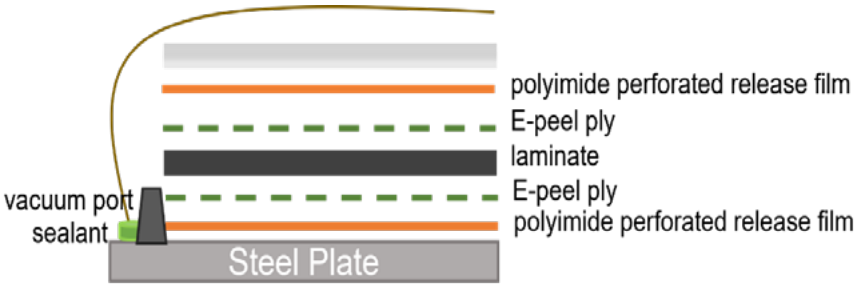


Figure 1. VBO process

2.2. Thermal and Mechanical Characterization of CF/PEKK Composites

DSC measurements are conducted using the Mettler Toledo DSC^{+3} instrument to assess thermal behavior and determine the degree of crystallization.
Three-point bending and compression tests are conducted on Instron 5982 Universal Testing Machine with a 100kN load cell, followed by ASTM D790 and ASTM 6641 standards, respectively.

2.3. Failure Monitoring by Acoustic Emission (AE) Inspection

Three-point bending and compression tests are assisted with AE inspection to detect detailed failure. During mechanical characterization experiments, AE data are continuously captured using a system equipped with two wideband piezoelectric sensors (PICO-200–750 kHz, Mistras) and AEwin PCI2 software. These sensors are positioned on the composite laminates during tests, and placed equidistant from the supporting spans for both three-point bending and compression tests Figure 2. Post-processing

involves using Noesis 7 software to extract waveforms and MATLAB for clustering acoustic events using the Calinski-Harabasz criterion to determine optimal clusters based on amplitude and peak frequency [13]. The k-means clustering algorithm categorizes acoustic events by assigning data points to the cluster with the nearest mean [14]

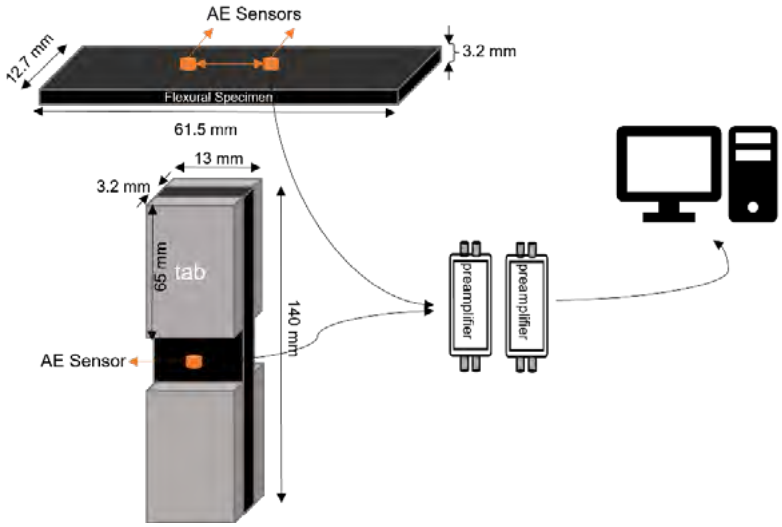


Figure 2. The mechanical test setups with acoustic emission sensor placements for a. three-point bending and b. compression tests

AE analysis is also used to determine optimal pre-load levels for generating pre-damage under bending and compressive loads. Three clusters are identified to address matrix, interface, and fiber-related failures under both loadings. The preloads are identified according to the corresponding load to strain level which failure initiates, therefore pre-loads of 1200 N and 19000 N are selected for flexural and compression specimens, respectively.

2.4. Annealing

Annealing is carried out to mitigate pre-existing damages and restore mechanical integrity, thermoplastic composite specimens undergo annealing in an oven for one hour at 180°C which is 20°C above the T_g of PEKK resin [11], with heating and cooling rates maintained at 8°C/min.

3. Results and Discussion

The compressive stress-strain and AE cumulative count curves of CF/PEKK specimens are presented in Figure 3. The reference CF/PEKK specimen is demonstrated a maximum compressive strength of 548 MPa, and the compressive strength of the CF/PEKK specimen is decreased by 7.66% to 506 MPa due to pre-damages, followed by a 2.00% improvement to 516 MPa after annealing. Additionally, pre-damages significantly affected the compressive strain properties of the specimens and decreased to 1.08% which indicates increased brittleness of the thermoplastic matrix. Cumulative count results are revealed that CF/PEKK specimens predominantly fail due to matrix cracking under compressive load. However, the response is slightly different in the pre-damaged specimen. Induced pre-damages are led to a reduction in the cumulative counts of matrix cracking, but an increase in the interface and fiber-related failures significantly. In contrast, the annealed sample maintains a high percentage of matrix-related failure, since annealing strengthens the matrix, enhancing composite resilience under compressive loading.

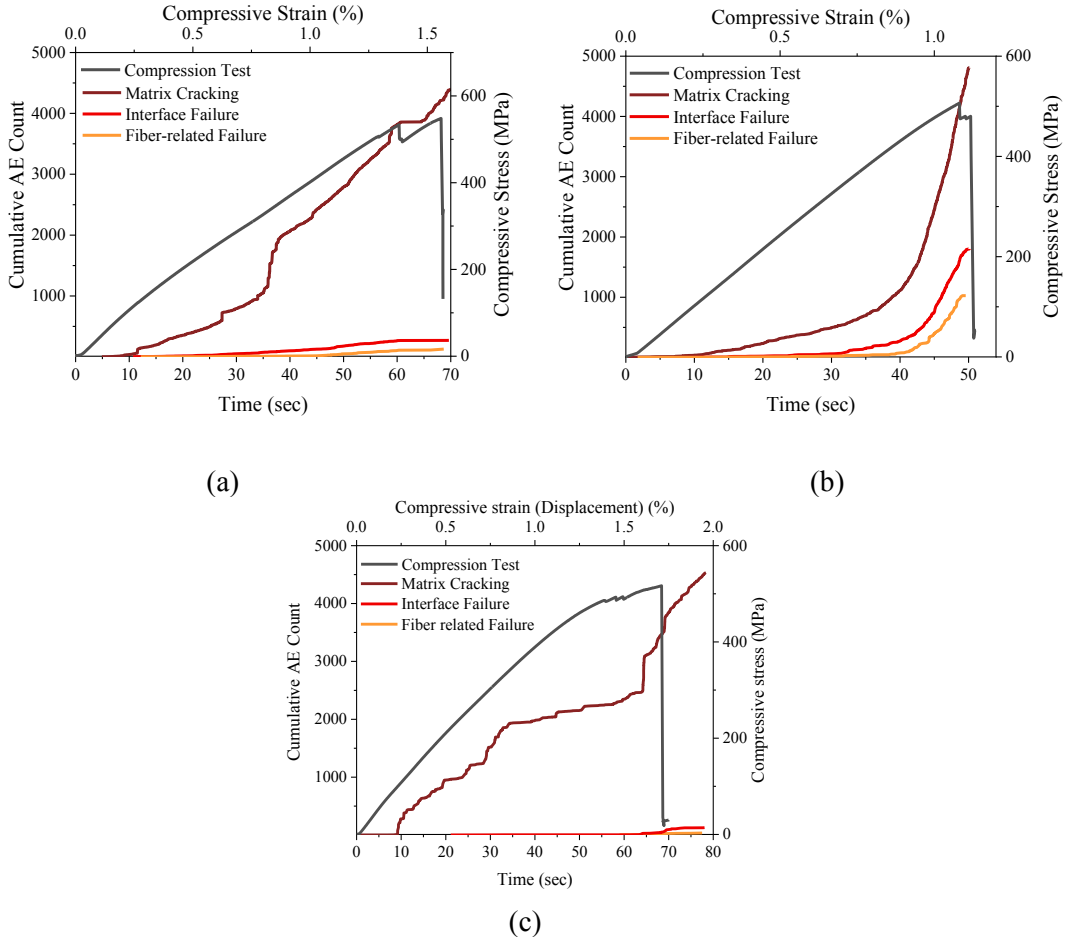


Figure 3. Cumulative AE counts and compression stress-strain curves for; (a) reference, (b) pre-damaged, (c) annealed CF/PEKK composite specimens

The bending stress-strain and AE cumulative count curves of CF/PEKK specimens are presented in Figure 4. Similar to compressive properties the reference specimen is exhibited the highest flexural strength with a strength value of 955 MPa and the flexural strength is decreased by 10% to 859 MPa in the pre-damaged specimen. After annealing the strength is recovered to 865 MPa. The cumulative acoustic counts are revealed that all samples predominantly fail due to fiber-related issues under bending load, highlighting the strong influence of fiber quality on composite performance. The cumulative counts of matrix and interface-related failures are increased significantly in the pre-damaged sample which indicates micro-crack formations in the matrix by preload. Annealing is reduced the cumulative counts of matrix cracking and interface-related failure, demonstrating improved bonding between fibers and matrix.

The mechanical analysis and AE inspection results are showed that the presence of damage, particularly in the PEKK matrix, acted as a stress concentrator, limiting the even distribution of applied load during analysis. The initiation of micro-cracks from the pre-damage led to failure at a lower strength under both loading conditions [15]. However, annealing redistributed internal stresses and induced stress relaxation, influencing the overall mechanical and failure behavior.

The mechanical results are also supported by DSC analysis, with a glass transition temperature (T_g) and degree of crystallinity (X_c) improvement. The annealed specimen is exhibited an X_c of 21.61% compared to the reference specimen's crystallinity degree, 19.70%. This increase is attributed to the annealing process which induces partial melting and recrystallization. As a result, the more ordered crystalline structure restricts the mobility of the amorphous chains, leading to an increase in T_g to 160.93 °C from 155.59 °C in the reference specimen.

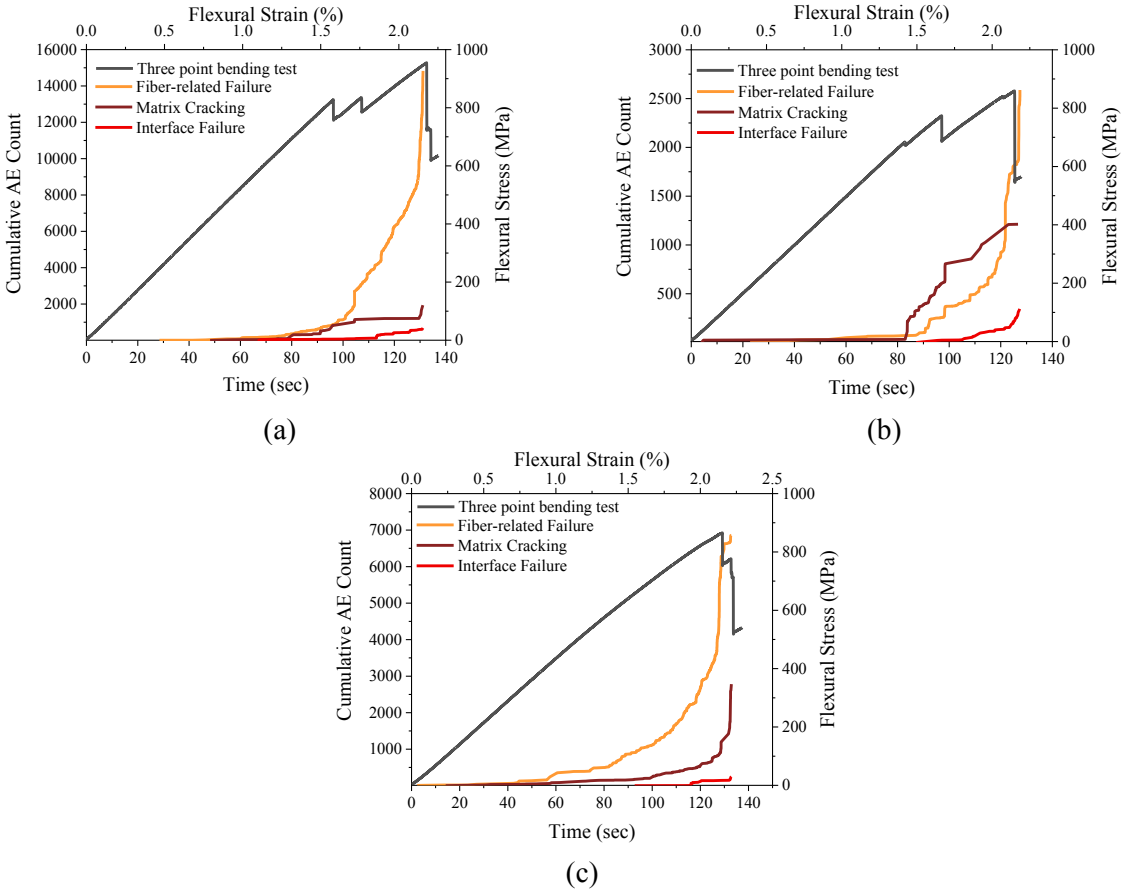


Figure 4. Cumulative AE counts and bending stress-strain curves for; (a) reference, (b) pre-damaged, (c) annealed CF/PEKK composite specimens

Conclusion

This study investigates how annealing affects pre-existing damages and the mechanical behavior of CF/PEKK composites. Three-point bending and compression tests assisted with acoustic emission (AE) inspection provide insights into pre-existing damages and annealing effects. Fiber-related failures dominate under bending load, while matrix-related failures prevail under compressive loading. However, cumulative count results demonstrate annealing improves structural integrity and mechanical behavior, valuable for repair methods in aerospace and other industries.

Acknowledgments

The authors thank to TUBITAK for their support. This study was supported by the Scientific and Technological Research Council of Turkey (TUBITAK) under Grant Numbers 221M565 and 218M709.

References

[1] L. Amedewovo, A. Levy, B. de Parscau du Plessix, L. Orgéas, and S. Le Corre, "Online characterization of moisture transport in a high-performance carbon fiber-reinforced thermoplastic composite at high temperatures: Identification of diffusion kinetics," *Compos. Part B Eng.*, vol. 256, no. December 2022, p. 110629, 2023, doi: 10.1016/j.compositesb.2023.110629.

[2] L. Amedewovo *et al.*, "A methodology for online characterization of the deconsolidation of fiber-reinforced thermoplastic composite laminates," *Compos. Part A Appl. Sci. Manuf.*, vol. 167, no. December 2022, p. 107412, 2023, doi: 10.1016/j.compositesa.2022.107412.

[3] J. N. Swamy, W. J. B. Grouve, S. Wijskamp, and R. Akkerman, "An experimental study on the role of different void removal mechanisms in VBO processing of advanced thermoplastic composites," *J. Reinf. Plast. Compos.*, 2023, doi: 10.1177/07316844231159134.

[4] R. L. Mazur, G. M. Cândido, M. C. Rezende, and E. C. Botelho, "Accelerated aging effects on carbon fiber PEKK composites manufactured by hot compression molding," *J. Thermoplast. Compos. Mater.*, vol. 29, no. 10, pp. 1429–1442, 2016, doi: 10.1177/0892705714564283.

[5] D. Zhang, D. Heider, and J. W. Gillespie, "Void reduction of high-performance thermoplastic composites via oven vacuum bag processing," *J. Compos. Mater.*, vol. 51, no. 30, pp. 4219–4230, 2017, doi: 10.1177/0021998317700700.

[6] E. F. Sukur, S. Elmas, M. Seyyednourani, V. Eskizeybek, M. Yildiz, and H. S. Sas, "Effects of meso- and micro-scale defects on hygrothermal aging behavior of glass fiber reinforced composites," *Polym. Compos.*, vol. 43, no. 11, pp. 8396–8408, Nov. 2022, doi: 10.1002/pc.27011.

[7] S. Akgun, C. O. Senol, G. Kilic, I. E. Tabrizi, and M. Yildiz, "A novel damage evaluation of CFRPs under mode-I loading by using multi-instrument structural health monitoring methods," *Eng. Fract. Mech.*, vol. 286, no. April, p. 109291, 2023, doi: 10.1016/j.engfracmech.2023.109291.

[8] E. F. Sukur, S. Elmas, M. Seyyednourani, V. Eskizeybek, M. Yildiz, and H. S. Sas, "A rational study on the hydrothermal aging of AFP manufactured CF/polyetherketoneketone composites with in situ consolidation supported by acoustic emission inspection," *J. Appl. Polym. Sci.*, vol. 139, no. 29, pp. 1–14, 2022, doi: 10.1002/app.52480.

[9] J. Barroeta Robles, M. Dubé, P. Hubert, and A. Yousefpour, "Repair of thermoplastic composites: an overview," *Adv. Manuf. Polym. Compos. Sci.*, vol. 8, no. 2, pp. 68–96, 2022, doi: 10.1080/20550340.2022.2057137.

[10] F. Ahmadi, "STUDY OF PROCESS-INDUCED STRESSES AND DEFORMATIONS IN THERMOPLASTIC MATRIX COMPOSITES," 2023.

[11] W. Yu, X. Wang, X. Yin, E. Ferraris, and J. Zhang, "The effects of thermal annealing on the performance of material extrusion 3D printed polymer parts," *Mater. Des.*, vol. 226, p. 111687, Feb. 2023, doi: 10.1016/J.MATDES.2023.111687.

[12] M. Regis, A. Bellare, T. Pascolini, and P. Bracco, "Characterization of thermally annealed PEEK and CFR-PEEK composites: Structure-properties relationships," *Polym. Degrad. Stab.*, vol. 136, pp. 121–130, Feb. 2017, doi: 10.1016/j.polymdegradstab.2016.12.005.

[13] T. Caliñski and J. Harabasz, "A Dendrite Method Foe Cluster Analysis," *Commun. Stat.*, vol. 3, no. 1, pp. 1–27, 1974, doi: 10.1080/03610927408827101.

[14] S. Gul, I. E. Tabrizi, B. S. Okan, A. Kefal, and M. Yildiz, "An experimental investigation on damage mechanisms of thick hybrid composite structures under flexural loading using multi-instrument measurements," *Aerosp. Sci. Technol.*, vol. 117, Oct. 2021, doi: 10.1016/j.ast.2021.106921.

[15] M. McElroy, W. Jackson, R. Olsson, P. Hellström, S. Tsampas, and M. Pankow, "Interaction of delaminations and matrix cracks in a CFRP plate, Part I: A test method for model validation," *Compos. Part A Appl. Sci. Manuf.*, vol. 103, pp. 314–326, 2017, doi: 10.1016/j.compositesa.2017.09.011.

EFFECTS OF TEMPERATURE, WATER ABSORPTION AND WEAK INTERPHASE STRENGTH ON THE DAMAGE TOLERANCE OF GFRP

Dennis Gibhardt[1*], Lennart Braun[1], Friedrich M. Kassing[1] and Bodo Fiedler[1]

[1] Hamburg University of Technology, Institute of Polymers and Composites, Denickestraße 15, 21073 Hamburg, Germany
Email: dennis.gibhardt@tuhh.de, Web Page: https://www.tuhh.de/kvweb/en/home

Keywords: Fracture Toughness; Sizing, Composite, Impact Damage, Environmental Aging

Abstract
Due to the success of glass fiber-reinforced polymers (GFRP) in many industries, their durability, reliability, and sustainability are increasingly important requirements. The polymer matrices and multi-scale composites undergo various fracture and aging processes during their service life. The already complex damage behavior is additionally influenced by harsh environmental conditions (humidity, water, temperature). However, there is little consensus in the literature on how environmental conditions affect the damage tolerance of different composite materials. Obviously, polymer type, fiber type, interphase, layer structure, etc. have an enormous influence and can sometimes even lead to opposite effects. Therefore, the present study specifically investigates the aging and temperature related changes in mode I and mode II fracture toughness and energy release rates (ERR) of epoxy infused GFRP laminates based on thick non-crimp fiber fabrics It is shown that mode I and II properties mostly follow opposite trends when exposed to high temperatures or water aging. Furthermore, the effects of temperature and wet-aging clearly affect the damage pattern and propagation in response to low-velocity impacts. However, residual compressive strength is shown to be little affected, as the main drivers strength and fracture toughness follow opposite trends.

1. Introduction

Because of their favorable specific mechanical properties and comparatively attractive price/performance ratio, glass fiber-reinforced polymers (GFRP) are the most widely used composites in energy, mobility, and civil applications. However, the composites are often exposed to harsh environmental conditions in most relevant applications [1]. Consequently, the structural design must take into account the potential degradation caused by aging processes under the given service conditions. In this context, damage- and fracture-related parameters such as fracture toughness and energy release rates (ERRs) are of particular importance as they are essential for structural integrity and durability during service life. However, comparably few studies have been published on the effects of temperature or water aging on these properties [2-4]. In addition, the studies that have been conducted show conflicting results. This may be due to the dependence on several potentially conflicting factors, such as matrix strength and ductility [5], the additional influence of composite layup, layer thickness, fiber volume fraction, fiber distribution or type, and specific interphase properties [6].
Therefore, the present study investigates the effects of various ambient temperatures between -30 °C and 70 °C, water absorption, and specific interphase aging [7] on the damage tolerance of GFRP laminates made from current E- and E-CR glass fibers. Experimentally, single-edge-notch bending (SENB), double cantilever beam (DCB), end-notch flexure (ENF), and low-velocity impact (LVI) tests are performed and analyzed. Based on the test campaign, matrix- and interphase-driven changes of the fracture behavior are identified and separated.

2. Materials and Methods

2.1 Materials and Manufacturing

Three different types of commercially available glass fibers with epoxy compatible sizings are used for the preparation of 4 mm thick GFRP laminates using a vacuum assisted resin transfer molding (VARTM) process. For DCB (ASTM D5528) and ENF (ASTM D7905) tests, SE 2020 E-CR glass (3B-Fibreglass, Belgium) and NEG 2002 E-glass (Nippon Electric Glass, Japan) based fiber fabrics (U-V-E, Saertex GmbH & Co. KG, Germany) with a nominal areal weight of 1166 g/m² are used as input for unidirectional laminates. To introduce an intrinsic pre-crack, polytetrafluoroethylene (PTFE) film stripes of 10 µm thickness (Goodfellow GmbH, Germany) are placed in the symmetry layer between the second and third plies. The laminates for the LVI tests are based on bi-axial fabrics (X-E, Saertex GmbH & Co. KG, Germany) with a nominal areal weight of 610 g/m² and E-CR glass fibers E6 396 (Jushi, China). All laminates, $[0]_4$ and $[\pm 45/90/0]_{2s}$, are infused with EPIKOTE™ Resin MGS™ RIMR 135 and the amine hardener EPIKURE™ Curing Agent MGS™ RIMH 137 (Westlake Epoxy., USA). Therefore, the mold filled with the dry fabrics is pre-heated to 50 °C and the resin is subsequently drawn through under full vacuum. The curing involves two steps: Curing at 50 °C for eight hours under overpressure of two bar followed by a post-curing at 80 °C for 15 hours. Both types of laminates have a fiber volume fraction of 46-47 % and a dry glass transition temperature (T_g) of about 89 °C.
Pure, 4 mm thick epoxy plates are manufactured using the same VARTM setup and curing cycle. The SENB specimens (ASTM D5045) are machined using an Euromod 35 mill (Isel Germany AG, Germany) with 1.8 mm diamond-coated bits. The sharp crack is introduced with a razor blade immediately prior to testing.

2.2 Aging and testing methods

In order to investigate different types of environmental aging effects on the fracture toughness and damage tolerance GFRP and its constituents, three different kinds of aging approaches are applied. In addition to the classical aging of the composites immersed in a distilled water bath at room temperature (RT) for almost half a year (165 days), a novel fiber pre-aging method is applied to the fiber fabrics [7] in the case of the DCB and ENF tests. Contrary to the classical method, this specific sizing and interphase aging method allows to obtain composites with aged interphase properties (aging of the fabrics in humid air at 50 °C and 80 % relative humidity (RH) for five weeks). The results of the pre-aged specimens are marked with PreHA. After fiber pre-aging, the fabrics are dried and then infused with resin using the same VARTM process as described above. As a result, these laminates have the same dry matrix properties, but only weakened interphases. Further details on the process, the fabrication and the effects on the static and fatigue properties (tensile, transverse tensile and tensile-tensile fatigue) of unidirectional (UD) GFRP composites can be found in Gibhardt et al. [7]. Here, it was also shown that the pre-aging process has no negative effects on the fiber strength. All DCB, ENF and SENB tests are performed on a Z10 universal testing machine (Zwick-Roell, Germany) equipped with a thermal chamber and the specific test setups.
The 150x100x4 mm³ laminates for the LVI tests were aged in distilled water at 40 °C for 69 days to accelerate the absorption process without affecting the aging behavior by too high temperatures. Dry and aged specimens are impacted with LVI according to ASTM 7136 using an Instron 9450 weight impact tower and an impact energy of 18 J. The impactor had a semi-spherical tip with a diameter of 16 mm. In addition, the specimen chamber is equipped with a thermal conditioning system to cool or heat the ambient air. Specimens are held at the specific impact test temperature for at least ten minutes prior to impact. Compression after impact (CAI) tests were then performed in accordance with ASTM 7137 using a Z400 universal testing machine (Zwick-Roell, Germany) equipped with a CAI fixture in accordance with the standard. Both the fracture mechanics-related parameters and the impact behavior are additionally analyzed under the influence of different ambient test temperatures (between -30 °C and 70 °C).

3. Results and Discussion

The critical ERR (G_{IC}) for the neat resin and the SE 2020 based UD composites are shown in Figure 1 for several different testing conditions. With about 800 J/m² the ERR of the RIMR135/H137 epoxy is within the range typically reported in the literature [2,8,9]. The results show a clear increase in fracture

toughness with increasing temperature and water aging. These results are consistent with those proposed by authors such as Pitaressi et al. [3] and Han et al. [2]. During wet aging, the epoxy absorbed approximately 3.1 m% water to saturation. This increases the G_{IC} value by about 30 % and corresponds to a temperature increase of about 20-30 °C in dry conditions. Considering also the results at higher temperatures (e.g., 145% increase at 70 °C), a clear nonlinear behavior is evident. The increased mobility of the polymer network at temperatures close to the T_g leads to more pronounced yielding and softening of the epoxy. At high temperatures and due to water absorption, the plasticizing effects reduce brittleness and also increase the damage tolerance of the epoxy. At low temperatures, however, the effects are less pronounced. This is because the mobility of the network is not significantly reduced beyond a certain distance from the T_g.

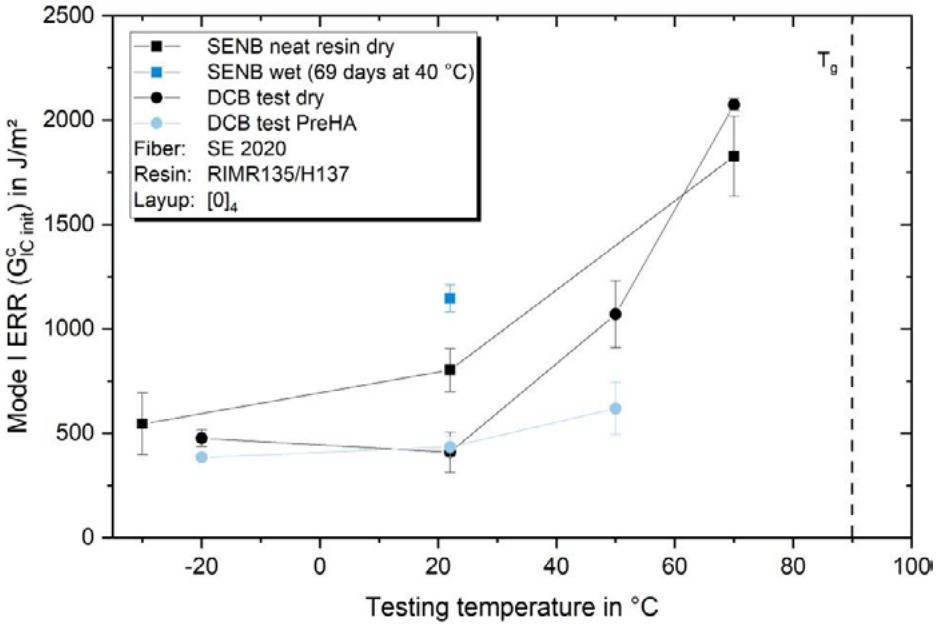


Figure 1: Mode I ERRs of the neat epoxy and the SE 2020 based composites in relation to the testing temperature and aging condition.

Comparison with the DCB tests indicates that the mode I composite fracture properties closely follow the matrix properties over the temperature range tested. The fracture analysis of the dry composites showed that the matrix failure was mainly in the resin-rich region between the middle layers. The use of the novel fiber pre-aging method additionally allows to analyze the effect of a weak interphase. Here, it can be highlighted that the toughness increase of the epoxy matrix is only decisive if the interphase is sufficiently robust. In the case of the SE 2020 composite, it can be seen that the RT and cold temperature behavior is not changed. However, as the test temperature increases, the weakened interphase is unable to transfer the increased resin ERR to the composite. Under these conditions, fracture occurs more frequently at the fiber/matrix (F/M) interphase.
The test results for the DCB mode I and ENF mode II tests of the composites are shown in more detail in Figures 2 and 3. First, it becomes clear that the effects of the individual conditions under mode II loading exhibit a uniform trend for both composites, while under mode I, there are more pronounced differences for the NEG system. The mode I initiation ERRs in dry conditions at RT are with about 400 to 550 J/m² well in line with typical values reported for GF/EP composites at crack initiation [4,10]. Wet aging of the composite at RT for almost half a year and wet pre-aging of the fibers reduce the mode I ERR of the NEG composite by about 16 % and 35 %, respectively. Consequently, the reduction by combining both pre-aging and additional wet-aging is even higher at about 42 %. This indicates that the mode I ERR depends on the matrix and the interphase properties. However, a weak interphase quality (strength) significantly reduces the mode I ERR of the NEG 2002 composite.

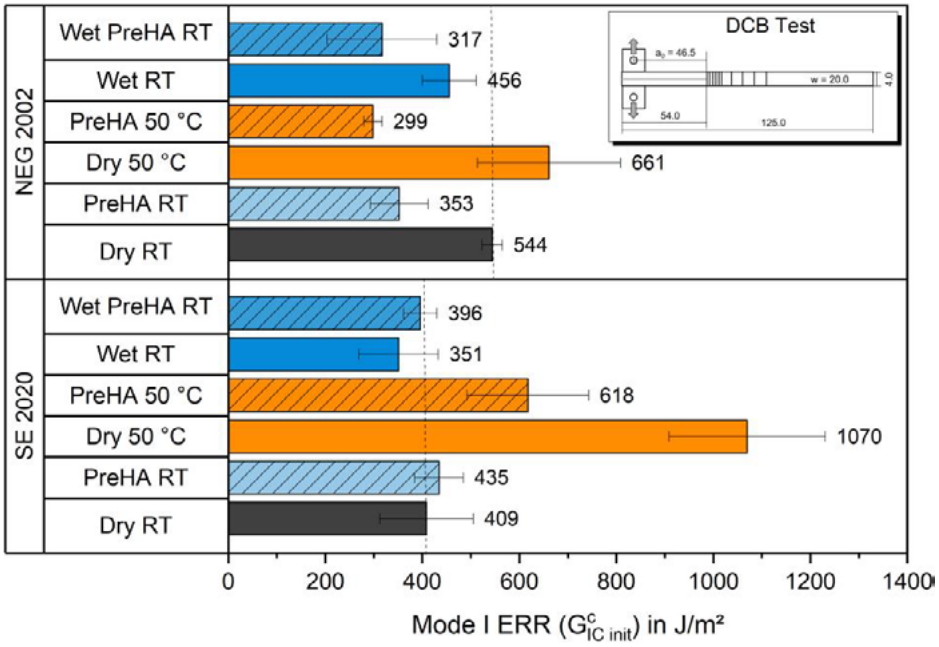


Figure 2: Mode I ERRs of the the SE 2020 and NEG 2002 based composites (aging 165 days at RT).

This observation can be confirmed for the SE 2020 composites only in the case of the tests at elevated temperatures (50 °C), where again, a reduction of about 42 % was found due to humid pre-aging. The RT tests showed only marginal differences in the mean values with overlapping standard deviations. Reasons for this could be both the significantly higher residual interphase strength (≥ 40 MPa after pre-aging and ≥ 50 MPa after wet aging at RT [7]) of the SE 2020 system, a potentially lower T_g of the pre-aged interphase, and the relatively small number of three samples per configuration. The fact that the SE 2020 reference and the pre-aged composites have the same initiation ERR is noteworthy because the crack surfaces after pre-ageing show mainly blank fibers after pre-aging. Consequently, it could be hypothesized that the majority of the energy consumed in the DCB test is associated with matrix fracture in the resin-rich regions and the geometry influence of, for example, the stitching. In this case, the difference between mode I crack growth in the brittle resin or in the interphase with still acceptable quality is small.

The results obtained by ENF tests demonstrate that the mode II ERR is more related to the F/M interphase properties than the mode I ERR. Humid pre-aging and the resulting lower interphase strength reduce the mode II ERR uniformly for both composites. The fracture toughness increase and yield strength decrease of the matrix due to water absorption and testing at elevated temperatures affect the mode II ERR in combination less within the tested range. These effects could partially neutralize each other. The reduction in mode II composite fracture toughness due to the decrease in interphase strength caused by wet pre-aging is between 12 % and 22 % for dry tests at RT. Increasing the test temperature alone reduces mode II fracture toughness by about 16 %, while the combination with weakened interphase results in reductions between 30 % and 40 %. Wet aging of the composite slightly increases the mode II ERR by about 5 %. Furthermore, the weakening effect of a weakened interphase predominates for the combination of both aging procedures (reduction between 22 % and 28 %). The pronounced differences between the wet-aged and pre-aged conditions and between the wet-aged standard and pre-aged composite also highlight the resilience of the F/M interphase to water aging at moderate temperatures ≤ 22 °C.

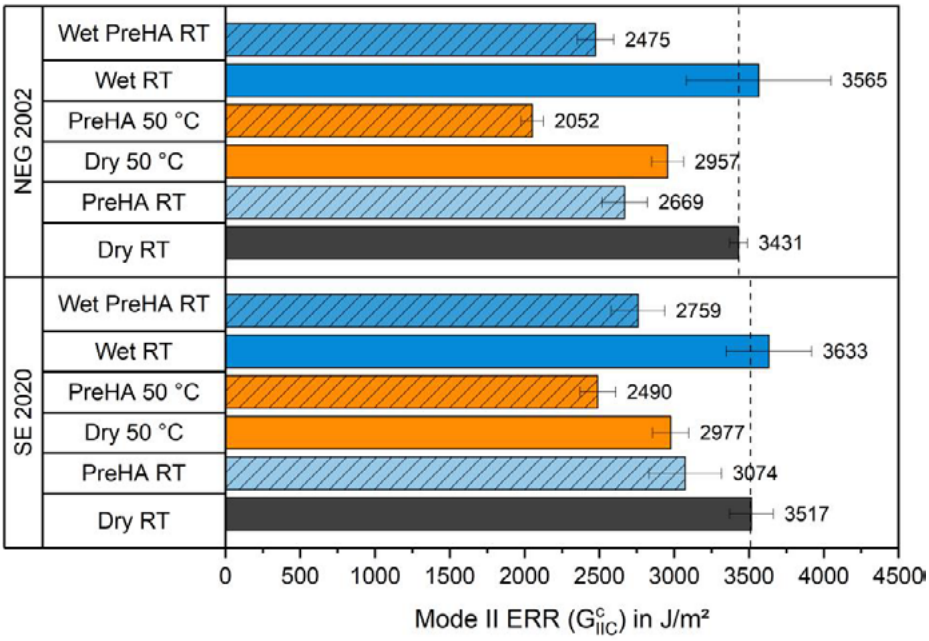


Figure 3: Mode II ERRs of the the SE 2020 and NEG 2002 based composites (aging 165 days at RT).

Looking at the fracture analysis of the mode II fracture paths, it is clear that the number of mode II matrix fractures increases with temperature and water absorption. Contrary to what is intuitively expected, the occurrence of this type of fracture reduces the mode II ERR. Thus, it consumes less energy than the pronounced interphase delaminations found for the reference. This behavior is associated with a significant decrease in the shear yield strength, which appears to dominate the global mode II ERR of the composite. Typically, for all failure paths, ply jumps and mode II cracks under 45° can be detected at the stitching yarns. Depending on the quality of their interfacial bond with the resin, these areas can either be the origin of damage or partially stop crack growth. Finally, it should be noted that crack growth in an ENF test is usually unstable after the maximum load is reached. The higher the nonlinearity of the stress-strain curves, the more likely stable crack growth is. For the GFRPs tested, a non-linear flattening or plateau followed by a drop is the norm for all conditions.

The results of an LVI test series are presented and discussed below to provide a first insight into the effects of the typical operating conditions of temperature and moisture absorption described above on damage resistance. Damage is evaluated in terms of the projected delamination area on the front surface and the projected crack propagation area on the back surface based on high resolution transmitted light scans. The results are shown in Figure 4. The effects of temperature and water absorption are clearly visible for both types of damage. Wet laminates always show slightly less delamination and crack propagation area than dry laminates at the same impact temperature. Temperature has the most significant effect on backside matrix crack propagation, as the affected area decreases by about 40 % from -30°C to 70°C. These results can be explained by a combination of increased resin mode I ERR and strain to failure in contrast to the simultaneous decrease in resin strength and stiffness with increasing temperature and water content. As a result, the deformation at high temperatures is much more localized, resulting in a greater indentation depth at the front and a greater dome height at the back. The interlaminar stresses are not high enough to cause large delaminations in the upper half of the composite, which is consistent with the findings of Körbelin [11] for high performance CFRP composites.
Pure resin fracture in the resin-rich regions between the fiber bundles is completely suppressed at elevated temperatures due to the high fracture toughness and correspondingly high allowable strain to failure. Intralaminar matrix fracture, if it occurs, is confined to the dense bundles. The small effect of temperature and water absorption on the delamination size in the lower half is due to the opposing effects of decreasing mode II ERR at the delamination surface and simultaneously decreasing global stiffness

of the laminate. The higher the temperature, the lower the resulting stresses between the plies. Therefore, delaminations at low temperatures, which imply higher mode II ERR and higher interlaminar stresses, grow to a similar extent as those at high temperatures, which imply lower mode II ERR and lower interlaminar stresses. Figure 5 gives a detailed view of the LVI damage by microscopic images of the cross section through the central impact region.

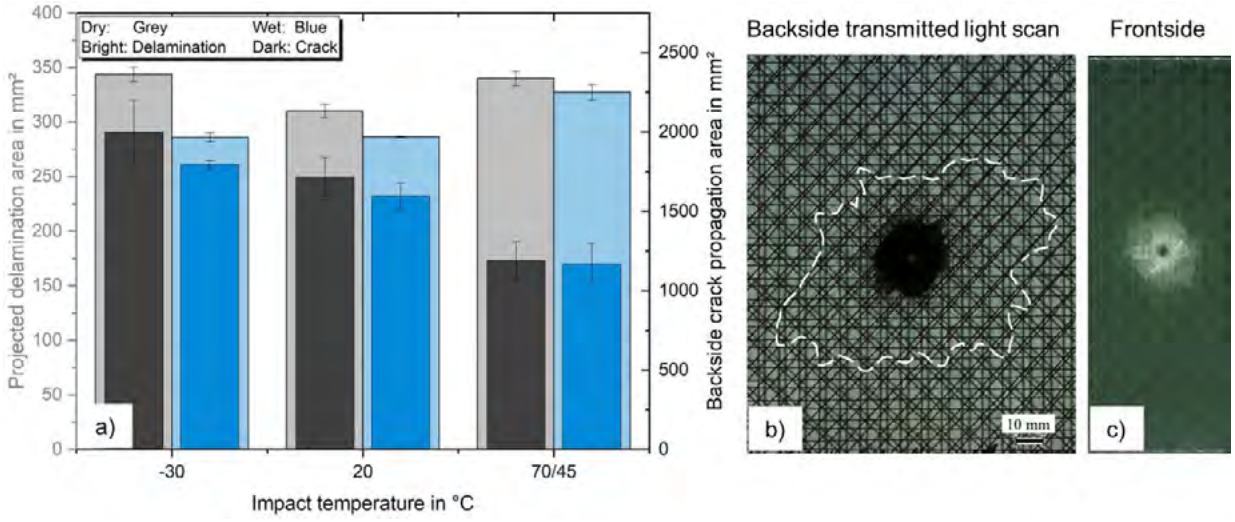


Figure 4: Projected delamination (bright) and backside crack propagation (dark) areas of dry (grey) and wet (blue) QI-composites after a low-velocity impact with 18 J a). Backside transmitted light scan b) and frontside reflected light scan c) after impact at 20 °C under dry reference conditions.

The effects of impact damage on residual compressive strength and typical failure by local buckling around the impact area are shown in Figure 6. Similar to the results of Körbelin [11] for CFRP, the residual compressive strength of dry GFRP at room temperature is not significantly affected by the impact temperature. The standard deviations of all dry tests overlap. Similarly, there is no difference between the wet laminates, but the residual strength is always slightly lower than for the dry laminates. These results can be explained by the relatively similar size of the delaminations near the neutral plane, which is related to the global buckling resistance [12]. In the wet case, the reduced flexural stiffness and the reduced fiber and interphase strengths affect the compressive strength of the composite. However, the global effect is relatively small after short-term aging at 40 °C for 69 days.

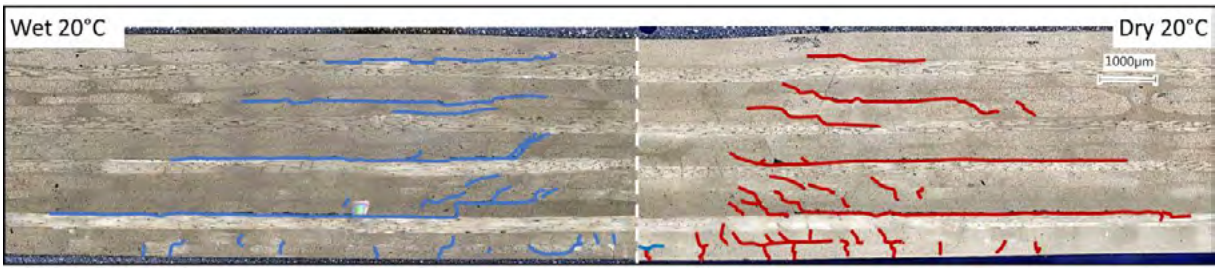


Figure 5: Comparison of representative microscopic cross sections of the impacted area (central cut) after impact at 20 °C for dry and wet conditions. Delaminations and cracks are highlighted.

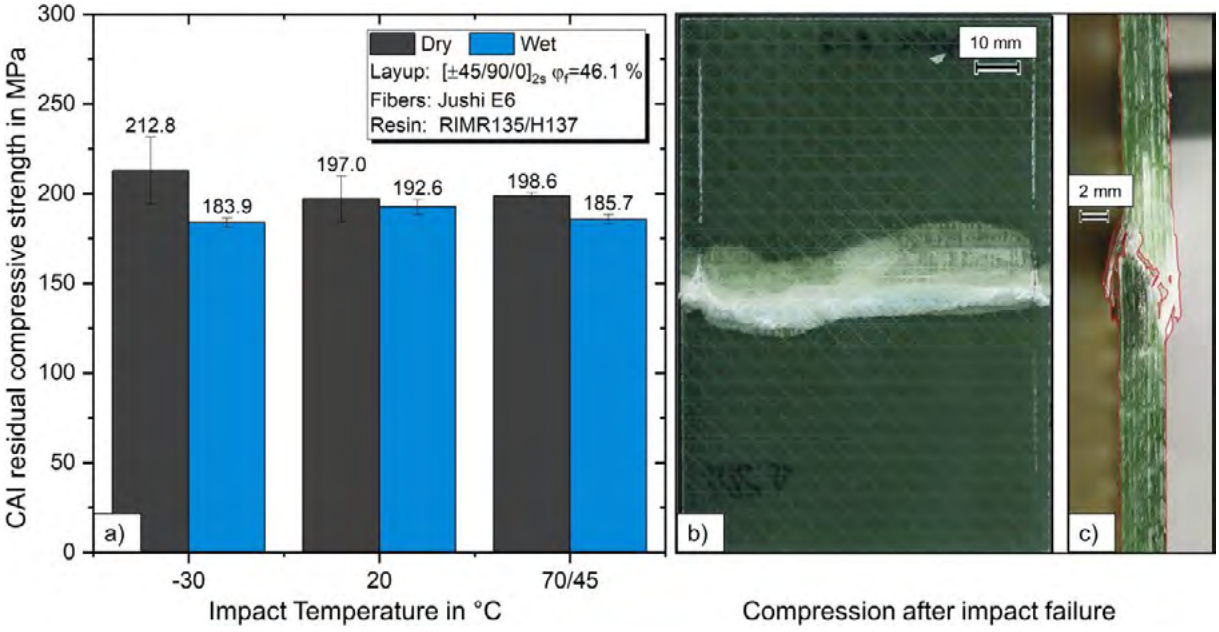


Figure 6: Residual compressive strength of the different GFRP/impact configurations after an 18 J low-velocity impact a) and representative pictures of the CAI test failure b, c).

4. Conclusions

Investigations of the interlaminar fracture properties highlighted the opposing effects of ambient temperature and water-induced aging on mode I and II ERR. Water absorption and increasing temperatures increase the fracture toughness of the resin and significantly delay damage initiation, which dominates the mode I ERR of the composite. Mode II ERR, on the other hand, is controlled by the shear yield strength and stiffness of the resin and especially of the interphase. Their decreasing tendency outweighs the increasing fracture toughness of the resin at the composite level. For fabric-based composites with highly inhomogeneous fiber (volume) distributions (dense bundles vs. interspace), the interphase effects are limited because a significant amount of matrix resin is always involved in the fracture process.

Furthermore, the damage and fracture-related effects of temperature and water-based aging could be successfully transferred to explain the change of LVI damage appearance in GFRP. It became clear that the impact damage depends on the structural response of the laminate, which in turn is also related to the environmental temperature and aging condition. As the main driving factors of fracture toughness and strength are subject to a contradictory dependence, the residual compressive strength determining largest delaminations grow to a similar extent. Consequently, no significant effect of the laminate condition during the impact event on the residual strength could be detected, even though the micro- and macroscopic damage differs significantly.

Acknowledgments

The authors would like to thank J. Körbelin for the in-depth discussions and valuable input about the fracture toughness and damage behavior of composites.

References

[1] A. E. Krauklis, O. Starkova, D. Gibhardt, G. Kalinka, H. A. Aouissi, J. Burlakovs, A. Sabalina, and B. Fiedler. Reversible and irreversible effects on the epoxy GFRP fiber–matrix interphase due to hydrothermal aging. *Composites Part C: Open Access* 12, 2023. doi: 10.1016/j.jcomc.2023.100395

[2] J. T. Han and K. Cho. Nanoparticle-induced enhancement in fracture toughness of highly loaded epoxy composites over a wide temperature range. *Journal of Materials Science* 41(13): 4239–4245, 2006. doi: 10.1007/s10853-006-6219-2

[3] S. Alessi, M. Di Filippo, G. Pitarresi, M. Scafidi, and A. Toscano. Fracture Toughness of Hydrothermally Aged Epoxy Systems with Different Crosslink Density. *Procedia Engineering* 109(8): 507–516, 2015. doi: 10.1016/j.proeng.2015.06.257

[4] R. Khan. Experimental investigation of mixed mode fracture toughness of glass fiber/epoxy laminates with sea water absorption. *Polymer Composites* 42(6): 2808–2816, 2021. doi: 10.1002/pc.26015

[5] S. M. Lee. Mode II Interlaminar Crack Growth Process in Polymer Matrix Composites, *Journal of Reinforced Plastics and Composites* 18(13): 1254–1266, 1999. doi:10.1177/073168449901801308

[6] R. F. Teixeira, S. T. Pinho, and P. Robinson. Thickness-dependence of the translaminar fracture toughness: Experimental study using thin-ply composites. *Composites Part A: Applied Science and Manufacturing* 90(4): 33–44, 2016. doi: 10.1016/j.compositesa.2016.05.031

[7] D. Gibhardt, C. Buggisch, L. Blume-Werry, and B. Fiedler. Influence of Sizing Aging on the Strength and Fatigue Life of Composites Using a New Test Method and Tailored Fiber Pre-Treatment: A Comprehensive Analysis. *Journal of Composites Science* 7(4), 2023. doi: 10.3390/jcs7040139

[8] W. Araki, T. Adachi, M. Gamou, and A. Yamaji. Time-temperature dependence of fracture toughness for bisphenol A epoxy resin. *Proceedings of the Institution of Mechanical Engineers, Part L: Journal of Materials: Design and Applications* 216(2): 79–84, 2002.

[9] S. Chandrasekaran, N. Sato, F. Tölle, R. Mülhaupt, B. Fiedler and K. Schulte. Fracture toughness and failure mechanism of graphene based epoxy composites. *Composites Science and Technology* 97(16): 90–99, 2014. doi: 10.1016/j.compscitech.2014.03.014

[10] S. Samborski, A. Gliszczynski, J. Rzeczkowski, and N. Wiacek. Mode I Interlaminar Fracture of Glass/Epoxy Unidirectional Laminates. Part I: Experimental Studies. *Materials* 12(10), 2019. doi: 10.3390/ma12101607

[11] J. Körbelin. Damage tolerance of high-performance composites. PhD thesis. *TUHH Universitätsbibliothek*, 2022. doi: 10.15480/882.4276

[12] J. Körbelin, C. Dreiner, and B. Fiedler. Impact of temperature on LVI-damage and tensile and compressive residual strength of CFRP. *Composites Part C: Open Access* 3(12), 2020. doi: 10.1016/j.jcomc.2020.100074.

ON THE TRANSVERSE SHEAR FAILURE IN UNIDIRECTIONAL FIBRE-HYBRID COMPOSITE LAMINAE WITH PERIODIC MICROSTRUCTURES

Giuseppe Romano[1*], Yang Yang[1], Zhenmin Zou[1,2], Prasad Potluri[2,3], Kali-Babu Katnam[1,2]

[1] Department of Solids and Structures, The University of Manchester, Manchester, M13 9PL, UK
[2] Northwest Composites Centre, The University of Manchester, Manchester, M13 9PL, UK
[3] Department of Materials, The University of Manchester, Manchester, M13 9PL, UK
[*]Corresponding authors: Email: giuseppe.romano@manchester.ac.uk, Web Page: https://www.linkedin.com/in/giusepperomano92/

Keywords: Fibre-hybrid polymer composites, RUC modelling, micromechanics, micro-stress fields, Transverse shear failure

Abstract
Traditional thermosetting composites have high specific strength and stiffness but exhibit poor damage tolerance. To address this, fibre hybridisation emerges as a cost-effective strategy. This study investigates the transverse shear failure of fibre-hybrid unidirectional composite laminae, specifically primary E-glass fibres with secondary fibres embedded in an epoxy matrix (*i.e.,* E-glass/secondary/epoxy). The study employs a 2D plane-strain hexagonal fibre-packing to estimate micro-stress fields, transverse shear modulus, and transverse shear strength of the fibre-hybrid unidirectional composite laminae. By predicting and comparing the properties and micro-stresses of fibre-hybrid unidirectional composite laminae to non-hybrid E-glass/epoxy unidirectional composite laminae, this research aims to understand the influence of matrix plasticity and secondary fibre properties on the transverse failure of fibre-hybrid unidirectional composite laminae. It also aims to enhance the understanding of the phenomena that contribute to the increased damage tolerance of fibre-hybrid composite laminae.

1. Introduction

Experimentally, fibre hybridisation has been successfully used to enhance thermosetting composite damage tolerance by introducing energy dissipation (*i.e.,* conducive failure modes) mechanisms to hinder crack grow from the micro (*i.e.,* fibre-matrix debonding and matrix cracking) to the meso-level (*i.e.,* delamination) [1–3]. Katnam, Dalfi and Selver used E-glass and S-glass fibres commingled with PP fibres in an epoxy matrix and tested the compression after impact behaviour of different UD and woven composites [1–3]. However, even if experimental work has been conducted certain aspect remain novel and computational models have not been fully explored to examine those aspects [4,5]. Therefore, this study aims to investigate the effect of matrix plasticity on the transverse shear behaviour of different fibre-hybrid composite laminae using 2D plane strain computational micromechanical models with periodic microstructure.

2. Methodology

2.1. Hexagonal RUC

Fibre-hybrid unidirectional laminae are investigated using two-dimensional repeating unit cell (2D RUC) models to predict the lamina's transverse shear elastic modulus, strength, and matrix micro-stress

fields. In this study, 2D RUCs with a periodic microstructure (*i.e.,* hexagonal fibre packing) are generated in *Abaqus/Standard*. These 2D RUCs accommodate fibre hybridisation by incorporating a secondary fibre in the middle of the RUC, surrounded by primary E-glass fibres at the corners. The stiffness ratio between the secondary and primary fibres is defined as β_E. Figure 1 illustrates a hybrid lamina with intra-laminar fibre hybridisation, featuring primary E-glass fibres and secondary fibres, Figure 1 (a), along with a 2D RUC with a periodic hexagonal packing microstructure used for micromechanical analysis Figure 1 (b). The coordinate system (x_i) in Figure 1 aligns with the principal material coordinate system of the unidirectional fibre-hybrid lamina.

Constituent material properties (*i.e.,* fibres and matrix) [6,7] are given in Table 1, where σ_{sut} and σ_{suc} are the tensile and compressive strength, respectively. Table 2 presents the stiffness of the secondary fibre, with the Poisson's ratio of the secondary fibre being the same as that of the primary fibre.

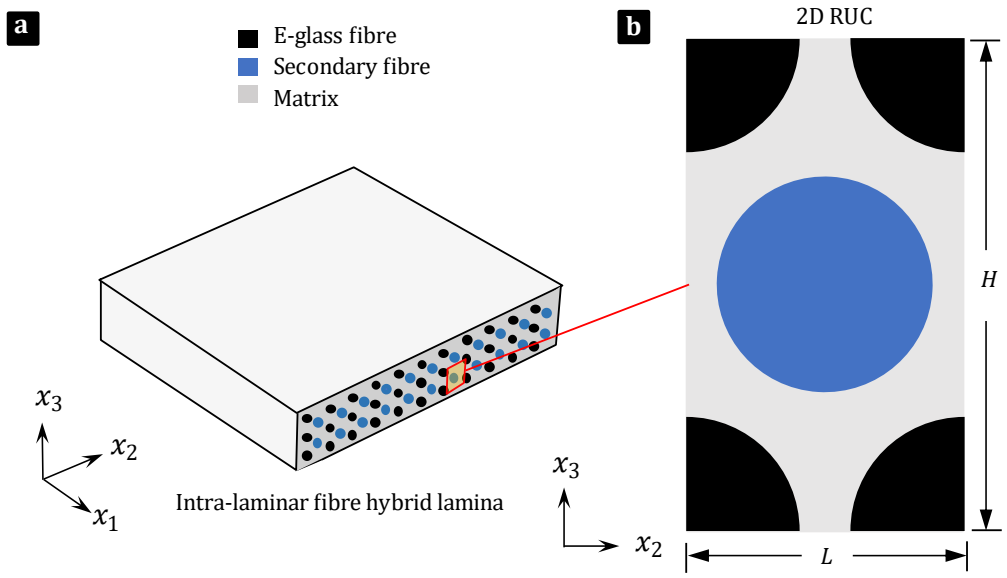


Figure 1. The fibre-hybrid modelling approach: (**a**) Lamina and (**b**) 2D fibre-hybrid hexagonal RUC with E-glass/secondary/epoxy.

Table 1. Material properties of the constituents [6,7]

	E (GPa)	ν	σ_{sut} (MPa)	σ_{suc} (MPa)
Epoxy	3.35	0.35		
E-glass	74	0.2	80	120

Table 2. The secondary fibre stiffness in comparison with that of the primary E-glass fibre.

$\beta_E = E_{fS}/E_{fG}$	5	1	0.1	0.03
E_{fS} (GPa)	370	74	7.4	2.22

Within the model, the fibres are assumed to be continuous, homogeneous, isotropic, and defect-free with circular cross-sections. The matrix is considered homogeneous, isotropic, elastic-plastic, and void-free. A perfect fibre-matrix interface is assumed. The variation in material properties and diameter of each fibre type is considered negligible. Both the fibres and the matrix are assumed to be linear elastic. The diameters of the primary (E-glass) and secondary fibres are assumed to be 10 µm. The total fibre volume

fraction (V_f), which is the sum of the E-glass fibre volume fraction (V_{fG}) and the secondary fibre volume fraction (V_{fP}), is assumed to be 0.6 in all the laminae analysed. Matrix plasticity has been implemented using the Drucker–Prager yield criterion [7,8], (Eq. 1):

$$t - p\tan\gamma - c = 0 \tag{1}$$

In Eq.1, p is the hydrostatic stress, t is the deviatoric stress, γ is the slope of the linear yield surface in the $p-t$ stress plane, c is the cohesion of the material. The matrix is assumed as linear elastic perfect plasticity, *i.e.,* no hardening is considered.

2.2. Periodic Boundary Conditions

The RUC model is implemented in *ABAQUS/Standard*. A *python* script is used, and the displacement-based periodic boundary conditions (PBCs) are imposed by generating matching nodes on the opposite edges. Considering plane strain conditions, the 2D RUC is analysed with a structured quad mesh with CPE4R (a 4-node bilinear plane strain element with reduced integration). Figure 2 (a) shows the partition strategy used to guarantee the generation of a periodic mesh, Figure 2 (b), and the simple shear loading boundary condition, Figure 2 (c). The domain is meshed such that all the nodes $n^-$and n^+ on the opposite edges are perfectly aligned, Figure 2 (b) [5].
The periodic displacement conditions are imposed by using Eq. 2 [9]. Periodic boundary conditions guarantee traction and displacement continuity conditions between opposite edges.

$$u_i(\boldsymbol{x} + \Delta\boldsymbol{x}) - u_i(\boldsymbol{x}) = \hat{\varepsilon}_{ij}\Delta x_j \qquad (i,j = 1,2,3) \tag{2}$$

In Eq. 2, u_i is the displacement in the x_i direction, $\boldsymbol{x} + \Delta\boldsymbol{x}$ and $\boldsymbol{x}$ are the position vectors of the points on the opposite faces of the RVE, and $\hat{\varepsilon}_{ij}$ is the macro-strain components. In the case of a 2D domain as in Fig. 2, the application of PBCs can be defined by Eq. 2 [7,10]:

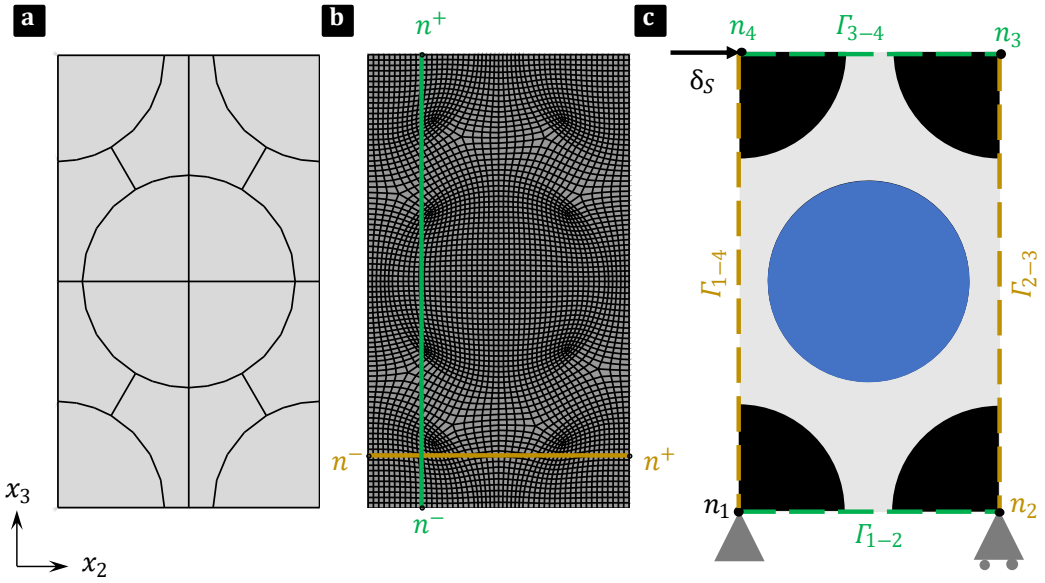


Figure 2. Modelling strategy used: (**a**) model partition (**b**) mesh generated and (**c**) shear loading boundary conditions.

2.3. Homogenization

With the periodic displacement conditions (Eq. 2), the homogenised lamina properties are obtained by applying a uniform macro-stress ($\hat{\sigma}_{ij}$) or macro strain ($\hat{\varepsilon}_{ij}$) state and then calculating the unweighted volume average of the micro-stresses (σ_{ij}) and micro-strains (ε_{ij}) within the RVE volume (Ω), using Eqs. 3 and 4 [5] .

$$\hat{\sigma}_{ij} = \frac{1}{\Omega}\int_{\Omega} \sigma_{ij} d\Omega \tag{3}$$

$$\hat{\varepsilon}_{ij} = \frac{1}{\Omega}\int_{\Omega} \varepsilon_{ij} d\Omega \tag{4}$$

In this study, the transverse shear elastic modulus ($\hat{G}_{23}$) and the transverse shear strength ($\hat{S}_{23}$) have been predicted. The transverse shear elastic modulus ($\hat{G}_{23}$) is defined as the ratio of the homogenised shear stress ($\hat{\sigma}_{23}$) to the homogenised shear strain ($\hat{\varepsilon}_{23}$) in the elastic region of the shear stress-strain plot. The transverse shear strength ($\hat{S}_{23}$) is measured as the maximum homogenised shear stress ($\hat{\sigma}_{23}$) that the RUC can support before failure.

2.4. Model validation

Model validation has been performed by comparing the transverse shear elastic modulus $\hat{G}_{23}$ and the transverse shear strength $\hat{S}_{23}$ predicted using the 2D RUC against data available in the literature [6,7]. The predicted values are in excellent agreement with the ones available in the literature, as shown in Table 3.

Table 3. Predicted transverse shear modulus and shear strength compared against Yang [6,7].

	RUC	Yang [6,7]	Relative variation (%)
$\hat{G}_{23}$ (GPa)	4.21	4.67 ± 0.07	-10
$\hat{S}_{23}$ (MPa)	60.77	62.19 ± 1.52	-2

3. Results and Discussion

In this section the lamina transverse shear stiffness, lamina transverse shear strength, and normalised von Mises matrix stresses (*i.e.,* per unit MPa of macro transverse shear, with and without matrix plasticity) for different secondary fibre stiffness to the primary fibre (E-glass) stiffness ratio (β_E) are investigated.

3.1. Lamina properties

Table 4 presents the predicted transverse shear modulus and transverse shear strength for various fibre-hybrid E-glass/secondary/epoxy unidirectional composite laminae using the developed 2D RUCs. The stiffness ratio β_E *i.e.*, E_{fS}/E_{fG} , the secondary fibre stiffness to the primary fibre (E-glass) are used: 5, 1, 0.1 and 0.02. The transverse shear stiffness is significantly affected by the stiffness of the secondary fibre volume fraction, especially when the secondary fibre stiffness is comparable or lower than the one of the matrix. The lamina transverse shear strength has been predicted by determining the maximum transverse shear stress that the lamina can bear before failure. The transverse shear strength has been shown to be highly dependent on the matrix properties and not affected by the fibre type used, while the stiffness highly depends on the material properties of the fibres.

Table 4. Predicted transverse shear modulus and transverse shear strength for different β_E (*i.e.*, E_{fS}/E_{fG}).

$\beta_E = E_{fS}/E_{fG}$	5	1	0.1	0.02
$\hat{G}_{23}$ (GPa)	4.45	4.21	2.73	1.26
$\hat{S}_{23}$ (MPa)	60.77	60.77	60.74	60.59

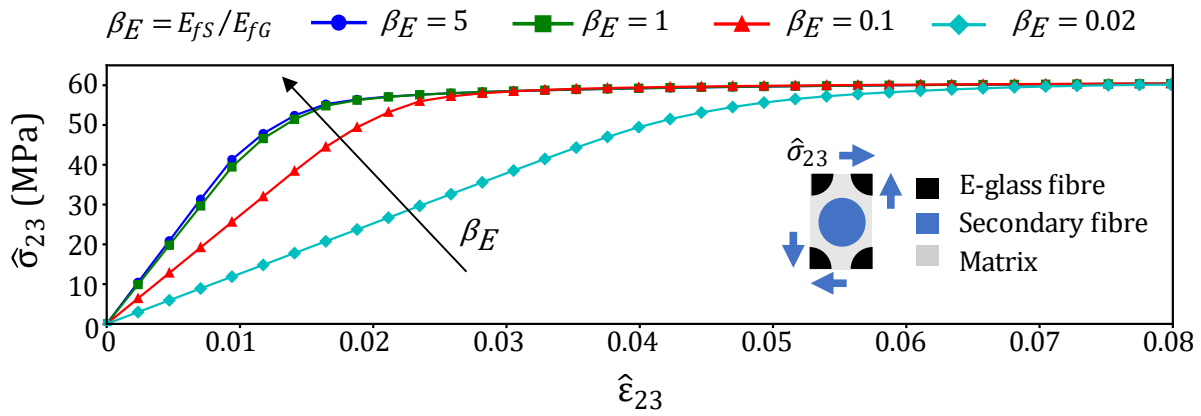


Figure 3. The transverse shear-strain curve for different β_E (*i.e.*, E_{fS}/E_{fG} , the secondary fibre stiffness to the primary fibre (E-glass) stiffness ratio: (**a**) β_E = 5, (**b**) β_E = 1, (**c**) β_E = 0.1, and (**d**) β_E = 0.02.

3.2. Matrix stress-fields

The von Mises matrix stress has been normalised first in the elastic regions using a unit MPa of macro-transverse shear (*i.e.*, $\hat{\sigma}_{23} = 1$ MPa), Figure 4 (a-d). This normalization has been used to understand where plasticity is most likely to initiate. To investigate the effect of matrix plasticity on the normalised von-Mises matrix micro stress distribution, a macro-transverse shear stress of 50 MPa (*i.e.*, $\hat{\sigma}_{23} = 50$ MPa) has been used, as shown in Figure 4 (e-h). This macro-stress state is enough high to introduce significant plastic deformation within the matrix. The maximum normalised von Mises matrix micro-stress occurs in the regions where the inter-fibre distance is minimal and the fibres are aligned with the loading direction [11]. The maximum stress is not significantly altered when the secondary fibre is 5 times stiffer and 10 times less stiff than the primary E-glass fibre, while when the secondary fibre is softer than the matrix, the normalised von Mises matrix micro-stress is significantly altered and a larger volume of the matrix is subjected to higher stress compared to the case when only E-glass fibres are used, as shown in Figure 4 (c).

The matrix plasticity is significantly affecting the matrix von Mises micro-stress fields and the position of the maximum normalised von Mises matrix micro-stress, as shown in Figure 4 (e-h). Moreover, the matrix plasticity is reducing the normalised stress within the matrix when β_E = 0.02. The asymmetrical stress distribution during matrix plastic deformation is due to the differing matrix strengths under compression and tension. Now, the maximum stress is located in the matrix region which goes under compression state. Moreover, matrix plastic deformation seems to be beneficial when the secondary fibre is soft (*i.e.*, β_E = 0.1 and 0.02), by reducing the matrix stress amplification significantly in proximity of the soft secondary fibre. Then having a secondary soft fibre opens the door for a solution to benign the matrix micro stress fields.

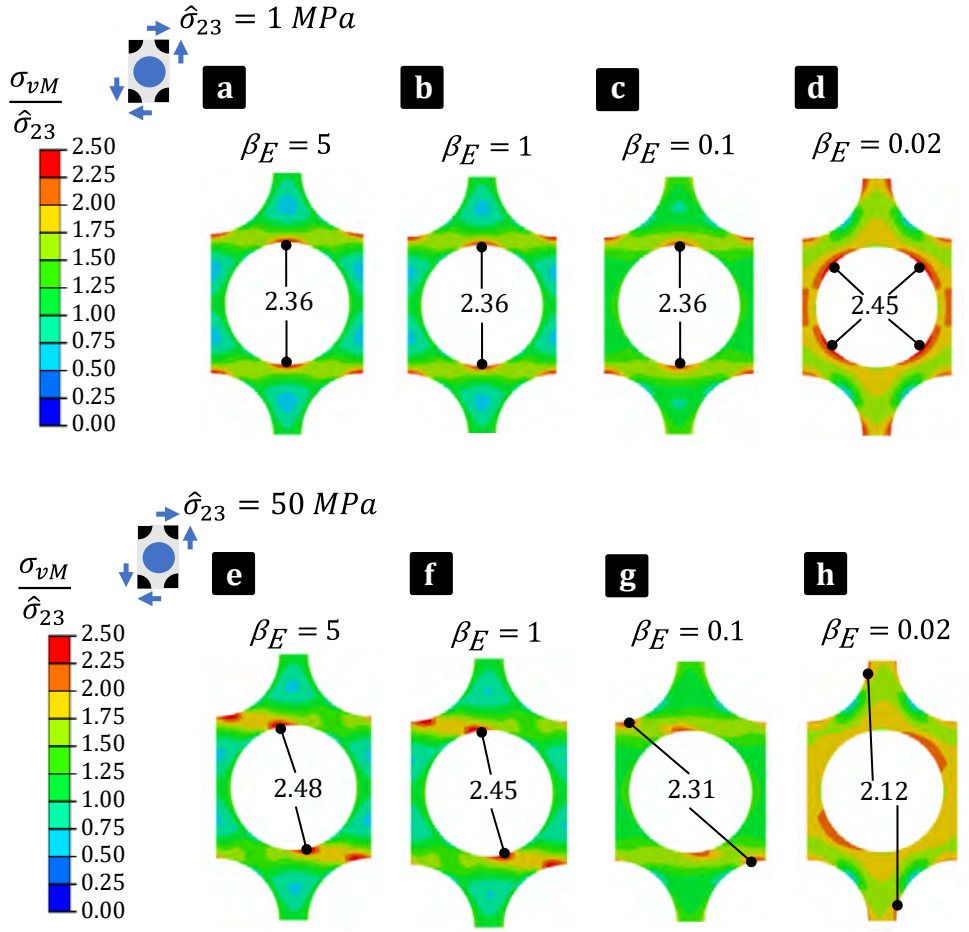


Figure 4. The normalised von Mises matrix micro-stress fields ($\sigma_{vm}/\hat{\sigma}_{23}$) per unit macro shear ($\hat{\sigma}_{23} = 1$ MPa) for different β_E (*i.e.*, E_{fS}/E_{fG} , the secondary fibre stiffness to the primary fibre (E-glass) stiffness ratio: (**a**) β_E = 5, (**b**) β_E = 1, (**c**) β_E = 0.1, and (**d**) β_E = 0.02; and for ($\hat{\sigma}_{23} = 50$ MPa), for (**e**) β_E = 5, (**f**) β_E = 1, (**g**) β_E = 0.1, and (**h**) β_E = 0.02

3.3. Fibre-matrix interfacial stresses

The normalised interfacial normal and shear stresses ($\sigma_n/\hat{\sigma}_{23}$, and $\tau_{nt}/\hat{\sigma}_{23}$) measured counterclockwise for the bottom left corner fibre and the middle fibre are given in Figure 5.Only a quarter of the fibres is studied because of symmetry in stress distribution. Figures 5 (a) and (b) reports the normalised Interfacial stresses for $\hat{\sigma}_{23} = 1$ MPa, while Figures 5 (c) and (d) report the normalised interfacial stresses for $\hat{\sigma}_{23} = 50$ MPa. The maximum normalized normal stress ($\sigma_n/\hat{\sigma}_{23}$) is at the minimum inter-fibre distance and aligned with the loading direction, *i.e.*, $\theta = 60°$, when the fibres are stiffer than the matrix [11]. On the other hand, when the secondary fibre is less stiff than the matrix, the peak $\sigma_n/\hat{\sigma}_{23}$ location changes, as illustrated in Figure 4 (a). Matrix plasticity is not affecting the normalised interfacial normal and normalised shear stresses for the E-glass corner fibres, Figures 4 (a) and (c), and the normalised shear stresses for the middle fibres (d). On the other hand, matrix plasticity is altering the $\sigma_n/\hat{\sigma}_{23}$ for the middle secondary fibre, when the secondary fibre stiffness is significantly lower than the E-glass fibre and even lower than the matrix stiffness (*i.e.*, $\beta_E = 0.02$), Figures 4 (b). The secondary fibres exhibit a compressive $\sigma_n/\hat{\sigma}_{23}$ at $\theta = 0°$, which could hinder and delay fibre-matrix interface debonding.

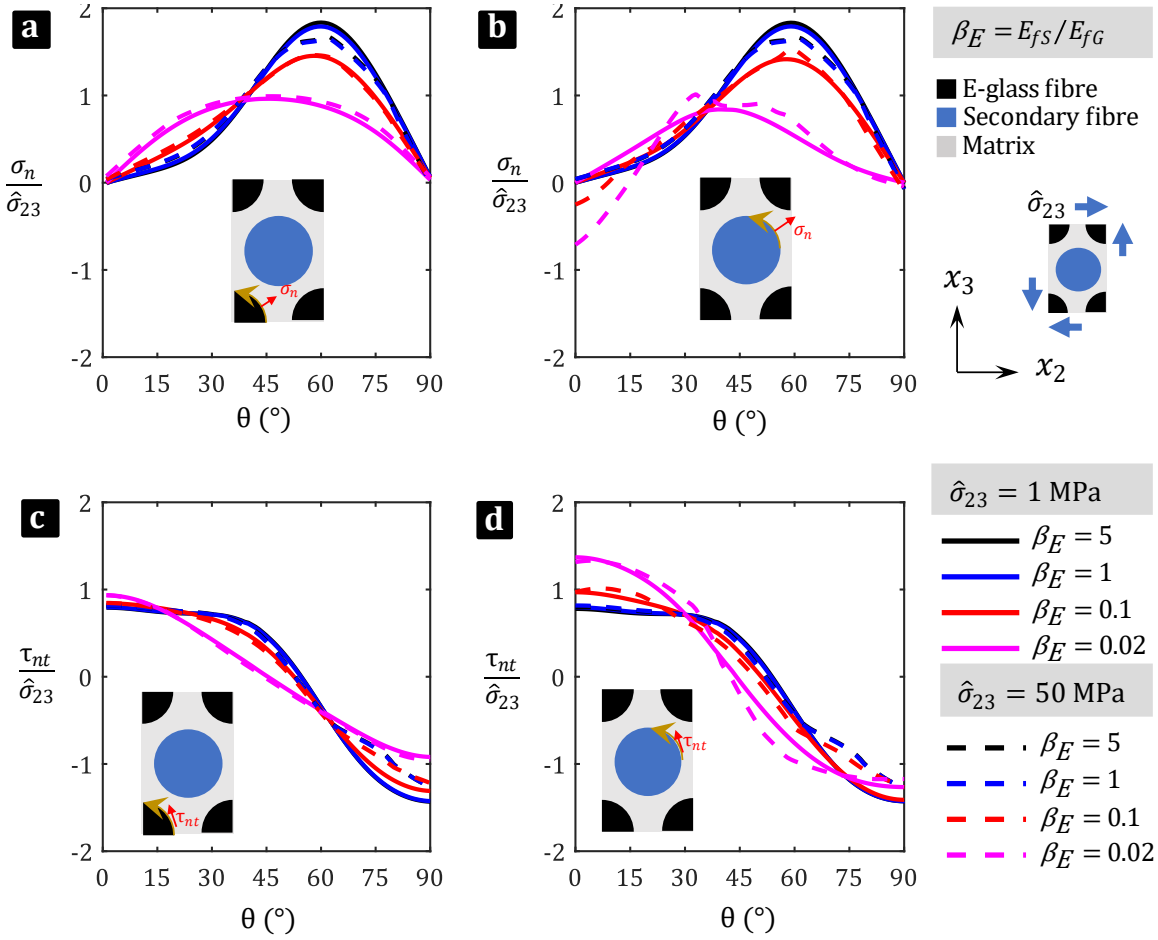


Figure 5. The normalised interfacial normal stresses ($\sigma_n/\hat{\sigma}_{23}$, and $\tau_{nt}/\hat{\sigma}_{23}$) for $\hat{\sigma}_{23} = 1$ MPa and $\hat{\sigma}_{23} = 50$ MPa for different β_E (*i.e.*, E_{fS}/E_{fG} , the secondary fibre stiffness to the primary fibre (E-glass) stiffness ratio: normalised interfacial normal stresses for **(a)** bottom left corner fibre and (**b**) middle fibre; normalised interfacial shear stresses for **(c)** bottom left corner fibre and **(d)** middle fibre

4. Conclusions

This study investigated the transverse shear behaviour of fibre-hybrid unidirectional thermosetting composite laminae with primary (E-glass) fibres combined with secondary fibres in an E-glass/secondary/epoxy fibre-hybrid system using 2D hexagonal fibre packing. The micromechanical analysis led to the following conclusions:

- The transverse shear stiffness $\hat{G}_{23}$ is highly depending on the stiffness on the secondary fibres, while the transverse shear lamina strength $\hat{S}_{23}$ is not affected and depends mainly on the matrix properties.
- Matrix plasticity significantly alters matrix micro-stress fields, especially when the secondary fibre stiffness is comparable to or lower than that of the matrix.
- The effect of matrix plasticity on interfacial stress is negligible, except for the normalised interfacial normal stress component for the secondary fibre when its stiffness is lower than that of the matrix.

Thus, matrix plasticity and fibre properties play a significant role on the transverse shear behaviour and failure of the fibre-hybrid unidirectional composite laminae. Future studies should investigate the effect of matrix plasticity on other independent and combined loading cases. Additionally, the effect of fibre-matrix interface debonding should be examined to predict the nine engineering constants and all strength components for different fibre-hybrid composite laminae.

Acknowledgments
We would like to acknowledge the Department of Mechanical, Aerospace, and Civil Engineering at The University of Manchester for granting a scholarship (MACE strategic support studentship) to support this research. Romano acknowledges Hexagon Manufacturing Intelligence, Inc., who granted him a software license of Digimat through the student ambassador program. All the authors acknowledge the assistance given by Research IT and the use of the Computational Shared Facility at The University of Manchester.

References

[1] Katnam KB, Dalfi H, Potluri P. Towards balancing in-plane mechanical properties and impact damage tolerance of composite laminates using quasi-UD woven fabrics with hybrid warp yarns. Composite Structures 2019;225:111083. https://doi.org/10.1016/j.compstruct.2019.111083.
[2] Selver E, Potluri P, Hogg P, Soutis C. Impact damage tolerance of thermoset composites reinforced with hybrid commingled yarns. Composites Part B: Engineering 2016;91:522–38. https://doi.org/10.1016/j.compositesb.2015.12.035.
[3] Dalfi H, Katnam KB, Potluri P. Intra-laminar toughening mechanisms to enhance impact damage tolerance of 2D woven composite laminates via yarn-level fiber hybridization and fiber architecture. Polymer Composites 2019;40:4573–87. https://doi.org/10.1002/pc.25325.
[4] Banerjee S, Sankar BV. Mechanical properties of hybrid composites using finite element method based micromechanics. Composites Part B: Engineering 2014;58:318–27. https://doi.org/10.1016/j.compositesb.2013.10.065.
[5] Romano G, Rao YN, Liu C, Katnam KB, Zou Z, Potluri P. On the Micro-Stress Fields in Fibre-Hybrid Polymer Composite Laminae with Periodic Microstructure Under Transverse Tension and Transverse Shear Loading. Appl Compos Mater 2024. https://doi.org/10.1007/s10443-024-10213-4.
[6] Yang L, Yan Y, Ran Z, Liu Y. A new method for generating random fibre distributions for fibre reinforced composites. Composites Science and Technology 2013;76:14–20. https://doi.org/10.1016/j.compscitech.2012.12.001.
[7] Yang L, Wu Z, Cao Y, Yan Y. Micromechanical modelling and simulation of unidirectional fibre-reinforced composite under shear loading. Journal of Reinforced Plastics and Composites 2015;34:72–83. https://doi.org/10.1177/0731684414562873.
[8] Alejano LR, Bobet A. Drucker–Prager Criterion. Rock Mechanics and Rock Engineering 2012;45:995–9. https://doi.org/10.1007/s00603-012-0278-2.
[9] Xia Z, Zhang Y, Ellyin F. A unified periodical boundary conditions for representative volume elements of composites and applications. International Journal of Solids and Structures 2003;40:1907–21. https://doi.org/10.1016/S0020-7683(03)00024-6.
[10] Xia Z, Zhang Y, Ellyin F. A unified periodical boundary conditions for representative volume elements of composites and applications. International Journal of Solids and Structures 2003;40:1907–21. https://doi.org/10.1016/S0020-7683(03)00024-6.
[11] Hojo M, Mizuno M, Hobbiebrunken T, Adachi T, Tanaka M, Ha SK. Effect of fiber array irregularities on microscopic interfacial normal stress states of transversely loaded UD-CFRP from viewpoint of failure initiation. Composites Science and Technology 2009;69:1726–34. https://doi.org/10.1016/j.compscitech.2008.08.032.

AN ENERGY-CONSERVING CYCLE JUMP AND LOAD APPLICATION TECHNIQUE FOR HIGH-CYCLE FATIGUE SIMULATIONS UNDER GENERAL LOADING CONDITIONS

G. Hacker[1], G. Just[2], S. Scheffler[1], I. Koch[2], M. Gude[2], R. Rolfes[1]

[1]Institute of Structural Analysis, Leibniz University Hannover, Appelstraße 9a, 30167 Hannover, Germany
Email: g.hacker@isd.uni-hannover.de, Web Page: https://www.isd.uni-hannover.de/
[2]Institute of Lightweight Engineering and Polymer Technology, Technical University Dresden, Holbeinstraße 3, 01307 Dresden. Germany
Email: gordon.just@tu-dresden.de, Web Page: https://tu-dresden.de/ing/maschinenwesen/ilk

Keywords: cycle jump technique, fatigue damage modelling, cohesive zone models

Abstract
For high cycle fatigue simulations, cyclic loads are often replaced by constant envelope loads using a cycle jump technique. However, this simplification cannot be used under general loading conditions where the local stress ratios can substantially deviate from global load ratios. The local stress ratios have to be determined for every material point individually by periodically performing a full loading-unloading cycle. Usually, commercial finite element (FE) solvers use time integration methods that are not energy-conserving, so that the simulation of such a loading-unloading cycle produces a numerical energy error. In this contribution, a new cycle jump and load application technique for high cycle fatigue simulations under general loading conditions is presented. It combines the simulation of full load cycles to determine local stress ratios with cycle jumps to save computational costs. The new technique is characterized by its energy-conserving behavior which is reached by a complete unloading of the FE model after each cycle jump and a modified formulation of the element residual vectors. By using user-defined elements, this modified formulation can also be used with commercial FE solvers.

1. Introduction

The importance of structural components made of fiber-reinforced composites is continuously increasing in several engineering disciplines like aircraft or automotive. Composite structures usually experience cyclic loadings with variable load characteristics during their service life causing various damage modes like matrix cracking or delamination [1]. In Addition to knowledge of possible damage mechanisms, the use of accurate and reliable fatigue damage models (FDM) must be ensured during the design process of safety-relevant composite structures [2].

A well-established method for the numerical simulation of cyclic delamination growth is the use of so-called cohesive zone models (CZM), where a damage growth rate $\partial D/\partial N$ is used to describe the cyclic degradation of the interface stiffness. This damage rate can be a function of several fatigue-relevant parameters like the mixed mode ratio and the stress ratio [3].

In a numerical high-cycle fatigue analysis, it is computationally inefficient to simulate each load cycle individually. Instead, cycle jump techniques are used. The most common technique is to replace cyclic loads with a constant envelope load, which is equal to the maximum load F_{max} of the represented cyclic load (Figure 1a). It has to be assumed that the local stress ratio at every material point is equal to the global load ratio given as an input to the model, which may not be true if a complex inhomogeneous stress field prevails in the structure [4]. A simple method to determine the local stress ratios is the “Min-

Max Load" approach by Raimondo and Bisagni [5], in which a finite element (FE) analysis is conducted with two models of the component in parallel. A constant maximum load F_{max} is applied to one model, while a constant minimum load F_{min} is applied to the other model (Figure 1b). By sharing information about the local stress states, the local stress ratios can be determined. However, the Min-Max Load approach is limited to components experiencing only cyclic loads that are in phase. Under general loading conditions, various dephased cyclic loads as well as static loads can act on a structural component. The "In-Situ" approach by Nojavan et al. [6] uses a global load profile with a full loading-unloading cycle, followed by a cycle jump ΔN, as plotted in Figure 1c. The stress states at every material point have to be saved during the simulation of a full loading cycle so that the local stress ratios can be subsequently determined. Joosten et al. [7] took up this approach and defined a stress ratio and an effective mixed mode ratio for a CZM under general loading conditions with a 3D stress state.

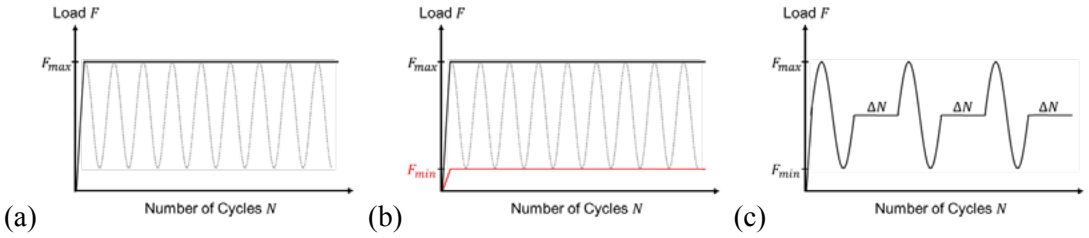


Figure 1. Three approaches to apply a cyclic load in a FE analysis: (a) Envelope Load, (b) Min-Max Load [5], (c) In-Situ Analysis [6]

A nonlinear FE solver is required for the numerical simulation of delamination using a CZM. Common commercial FE solvers use time integration schemes for nonlinear analyses that are not energy-conserving. Thus, the simulation of a full load cycle inevitably produces a numerical energy error, which is accumulated if a loading profile with several full load cycles as plotted in Figure 1c is simulated.

In this paper, a cycle jump technique with a new global load profile is presented allowing the simulation of any number of full load cycles without producing numerical energy errors. In Section 2, the global load profile and the implementation into commercial FE solver ABAQUS/Standard are explained. The energy-conserving property of the new technique is demonstrated by means of a simple one-element test in Section 3. In Section 4, concluding remarks and an outlook to future works are given.

2. Cycle Jump and Load Application Technique

2.1. Global Load Profile

The global load profile is plotted in Figure 2. The applied load F, which can be either a force or a displacement, represents a cyclic load with a maximum load of F_{max} and a minimum load of $F_{min} > 0$. One cycle consists of five steps illustrated by the circled numbers in Figure 2.

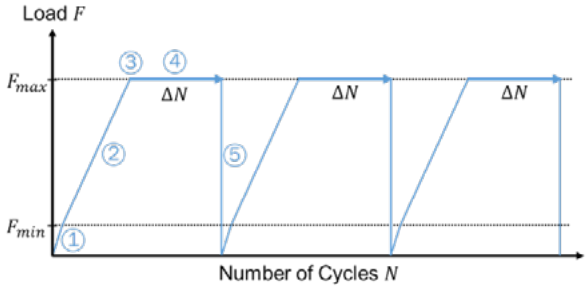


Figure 2. Illustration of global load profile

Starting from an unloaded state, the load is incrementally increased up to F_{min} in the first step. In the second step, the load is further increased up to F_{max} while the stress values are recorded. The local stress ratios R_s are determined from the recorded stress values in the third step. After that, the cycle jump ΔN can be performed. In the fifth step, the model is completely unloaded. It is worth mentioning that in the load profile shown in Figure 2, only the loading phase of the represented cyclic load is covered in the second step. It is assumed, that during the unloading phase, the same stress states occur. If multiple dephased loads or loads with various cycle lengths act on a component, step 2 has to cover a full loading-unloading cycle of that load with the longest cycle length in order to record all stress states occurring during the cycle.

2.2. Energy Conservation

In a nonlinear FE analysis, the displacement field is computed iteratively. The displacement field for the next iteration $\boldsymbol{u}^{(n+1)}$ is updated from the displacement field of the current iteration $\boldsymbol{u}^{(n)}$ by

$$\boldsymbol{u}^{(n+1)} = \boldsymbol{u}^{(n)} + \Delta\boldsymbol{u}. \tag{1}$$

The displacement increment $\Delta\boldsymbol{u}$ can be calculated by

$$\Delta\boldsymbol{u} = \boldsymbol{A}^{-1}\boldsymbol{r}, \tag{2}$$

where **A** is the tangential matrix and **r** is the residual vector. If a non-energy-conserving time integration scheme like the explicit or implicit Euler scheme is used, the simulation of a full loading-unloading cycle leads to a hysteresis curve, because the linearization of the loading and unloading path are not equal. If however, the residual vector $\boldsymbol{r}$ is set to

$$\boldsymbol{r} = -\boldsymbol{A}\boldsymbol{u}^{(n)}, \tag{3}$$

the new displacement field will be $\boldsymbol{u}^{(n+1)} = \boldsymbol{0}$ which is equal to the unloaded initial state. Equation (3) is thus used in step 5 of the previously described load profile to set the whole system back to its initial state without producing or dissipating energy.

2.3. Implementation into ABAQUS

The load profile described in section 2.1. is implemented in a Fortran module. The module is used by the ABAQUS subroutines UEL and UAMP (user-defined amplitude) for exchanging information, as illustrated in Figure 3. The UAMP is linked to the boundary condition where the load is applied to the FE models. It gets all relevant input properties like the maximum load F_{max}, the load ratio R_L or the total number of cycles N_{tot} via the input file and transfers it to the cycle jump module, from where it gets back the amplitude value.

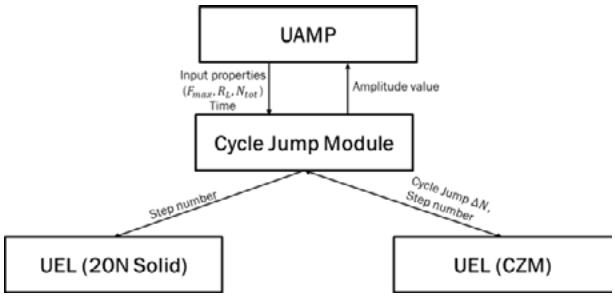


Figure 3: Exchange of information between different subroutines

In order to use equation (3), the whole FE model has to consist of user-defined elements (UEL). The solid user elements need information about the step number of the load profile, so that equation (3) can be used only in step 5. The CZM is also implemented in user elements exchanging information on the step number and the value of the cycle jump ΔN with the cycle jump module.

3. One-Element Test

The energy conservation of the new load application method is demonstrated in a simple one-element test in ABAQUS. The FE model consists of a single cubic 20-node solid (user) element with an edge length of 1mm, as illustrated in Figure 4. One side of the cube is clamped while the opposite side is loaded with a periodic cosine-shaped displacement with a load ratio $R_L = 0.1$ (
Figure *5*a). The presence of middle nodes in a 20-node element enables a constriction of the cube under tensional loading constituting a geometric nonlinearity. A transversally isotropic linear elastic material model is assigned to the cube. The "fiber direction" corresponds to the load direction. Deliberately, no kind of damage model was used here in order to not mix the energy dissipating effect of the damage model with possible numerical energy errors.

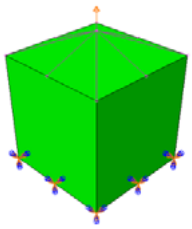


Figure 4: *One element test*

As plotted in Figure 5b, the reaction force caused by the periodic cosine-shaped displacement load is linearly increasing over the number of cycles, which means an unphysical production of energy. If however, the cosine-shaped displacement load is replaced by a periodic displacement load with the load profile presented in section 2.1, the maximum reaction force remains constant, as plotted in Figure 6. The deformation behavior is energy-conserving here.

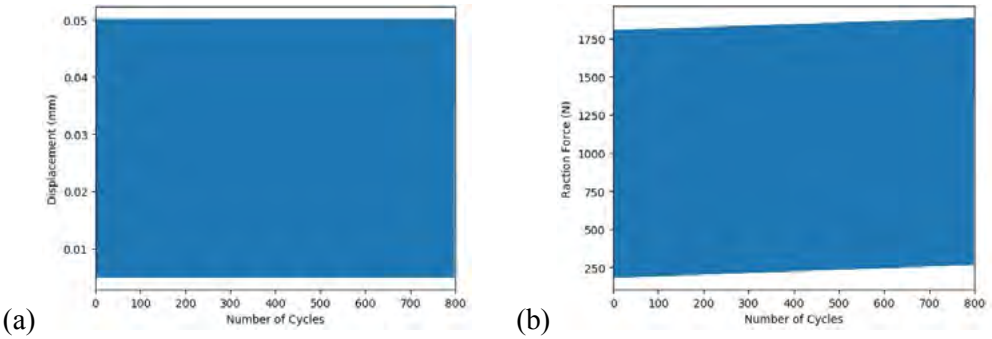


Figure 5: Non energy conserving behaviour of the cube loaded by a cosine shaped displacement (a) with an increasing reaction force (b)

4. Conclusion and Outlook

A new cycle jump and load application technique for high cycle fatigue simulations under general loading conditions based on the in-situ approach by Nojavan et al. [6] was presented. The in-situ" approach enables the determination of local stress ratios under general loading conditions, which have an important impact on the fatigue damage rate of a CZM. However, using this approach in a commercial FE solver causes a numerical energy error.

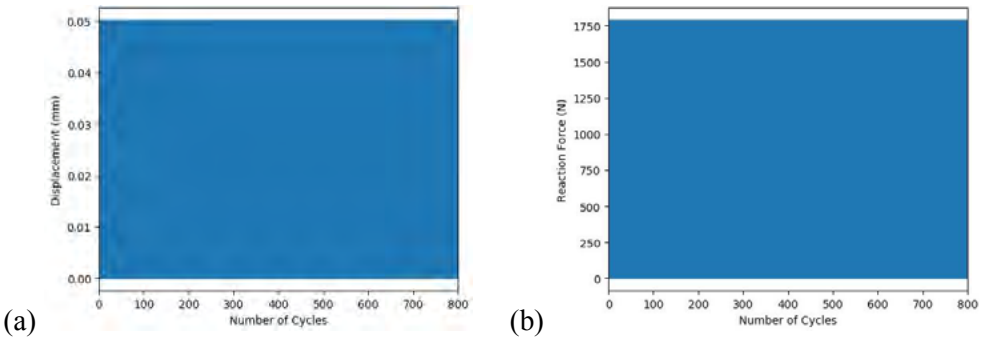


Figure 6: Energy conserving behaviour of the cube loaded by the newly developed load profile (a) with a constant reaction force

It was shown in a simple one-element test, that the energy produced by the simulation of a loading-unloading cycle accumulates with the number of simulated cycles and can no longer be neglected after comparatively few cycles. To overcome this, an additional step was added to the load profile, where the FE model is completely unloaded to its initial state. This is realized by modifying the formulation of the element residual vectors. This modified element formulation requires the exclusive use of user-defined elements and is limited to elastic material behavior.

For future works, the numerical simulation of microcracked-induced delamination (MCID) under cyclic loading can be a possible application example, where the use of the newly developed energy-conserving cycle jump and load application technique is required. Previous studies by the authors showed a variable mixed ratio during the process of delamination propagation under static loading [8]. It is assumed, that under cyclic loading, also the stress ratios will change and significantly deviate from the global load ratio, especially if the global load ratio is negative.

Acknowledgments
The authors gratefully acknowledge the financial support of the German Research Foundation (DFG) within the Research Grant 457043708.

References

[1] G. Just, I. Koch, M. Brod, E. Jansen, M. Gude and R. Rolfes. Influence of reversed fatigue loading on damage evolution of cross-ply carbon fibre composites. *Materials*, 12(7):1153-1174, 2019.
[2] M. Brod, G. Just, A. Dean, E. Jansen, I. Koch, R. Rolfes and M. Gude: Numerical modelling and simulation of fatigue damage in carbon fibre reinforced plastics at different stress ratios. *Thin-walled structures,* 139:219-231, 2019.
[3] C. G. Dávila, C. A. Rose, G. B. Murri, W. C. Jackson and W. M. Johnston. Evaluation of fatigue damage accumulation functions for delamination initiation and propagation. *NASA Technical Report*, NASA/TP–2020-220584, 2020.
[4] M. Brod, A. Dean, S. Scheffler, C. Gerendt and R.Rolfes. Numerical modeling and experimental validation of fatigue damage in Cross-Ply CFRP composites under inhomogeneous stress states. *Composites Part B,* 200:10850, 2020.
[5] A. Raimondo and C. Bisagni. Fatigue analysis of a post-buckled composite single-stringer specimen taking into account the local stress ratio. *Composites Part B*, 193:108000, 2020.
[6] S. Nojavan, D. Schesser, Q.D. Yang. An in situ fatigue-CZM for unified crack initiation and propagation in composites under cyclic loading. *Composite Structures*, 146:34-49, 2016.
[7] M. W. Joosten, C.G. Dávila, Q. Yang. Predicting fatigue damage in composites subjected to general loading conditions. *Composites Part A*, 156:106862, 2022.
[8] G. Hacker, M. Brod, G. Just, S. Scheffler, I. Koch, R. Rolfes, M. Gude. Numerical simulation of microcracked-induced delamination in cross-ply-laminates under static loading using cohesive zone models. In *Proceedings of the 20th European Conference on Composite Materials: Composites Meets Sustainability,* volume 4, pages 334-341, 2022

STRUCTURAL DAMAGE IDENTIFICATION OF COMPOSITE STIFFENED PANELS BASED ON MACHINE LEARNING

First Huaixiang. Sun[1], Second Xiaodong. Wang[1] , Third Zhidong. Guan[1]

[1]School of Aeronautic Science and Engineering, Beihang University, 100191, China
Email: sunhuaixiang@buaa.edu.cn

Keywords: Composite stiffened panels, Damage identification, Machine learning, Structural strain responses

Abstract
Damage identification in composite structures is both a focal point and a challenge in the field of structural health monitoring. This study presented a data-driven method for damage identification in composite stiffened panels based on structural strain responses under load. Damage-inclusive models with various types and locations of damage were established using finite element methods to generate the original damage-strain dataset. Five machine learning models with different strain input processing methods were developed and trained, including Graph Neural Network (GNN), Decision Tree (DT), Random Forest (RF), Artificial Neural Network (ANN), and K-Nearest Neighbors (KNN). Comparative analysis of their predicitons revealed that the GNN model, which incorporated the structure's geometric characteristics through graph-based strain input, performed best. The capability of GNN model to handle missing strain data was further analyzed, and the results validated the accuracy and robustness of the proposed data-driven method.

1. Introduction

Composite materials, with high specific properties and exceptional design flexibility, are ideally suited to lightweight applications such as aerospace. In particular, composite stiffened panels with superb load-bearing capacity and excellent post-buckling characteristics [1], are widely used in aircraft structures. However, during the entire lifecycle of production, processing, and cyclic loading in aircraft structures, composite materials often incur damages such as low-velocity impact-induced dents, delamination, and debonding [2]. These damages are not only difficult to detect visually but also significantly impair the structural strength and stiffness. Therefore, there is an urgent need to develop an efficient and reliable damage identification technology for composite stiffened panels to assess structural integrity and prevent catastrophic failures.

Non-destructive testing (NDT) techniques are currently the most widely used methods for assessing the safety and integrity of aircraft structures. Common techniques include visual inspection, acoustic emission, infrared thermography, optical interferometry, ultrasonic testing, radiography, and vibration/modal analysis [3]. However, these NDT techniques have limitations due to their inherent characteristics, and most require operators to possess considerable experience and expertise [4]. In this context, strain-based damage detection methods have garnered attention due to the ease of signal acquisition, high sensitivity to local damage, and low operational costs [5]. This approach involves deploying strain sensors on structures to collect raw strain data, which is then analyzed to extract features indicative of structural damage. To accurately identify structural damage from strain responses, it is crucial to select appropriate computational methods to extract damage features from the collected strain signals.

Recently, machine learning (ML) algorithms have demonstrated unique advantages in establishing mappings between structural responses and damage characteristics. These efficient and adaptable methods have been progressively applied in advanced research fields, including composites damage identification [6]. For example, Song et al. [7] developed an artificial neural network (ANN) to elucidate the relationship between the electrical resistance and strain in carbon fiber-reinforced composites, facilitating real-time monitoring of damage under simple loading conditions. Almeida et al. [8] employed a supervised learning model based on the K-Nearest Neighbors (KNN) algorithm to process acoustic emission signals collected during tests, investigating the correlation between these signals and composite material damage. Pham V T et al. [9] developed a highly robust damage identification model by establishing a nonlinear mapping between the vibration data features of composite cables and structural damage using a Multi-Layer Perceptron (MLP) and Graph Neural Networks (GNN). The integration and application of emerging ML technologies in the field of composite damage identification have received increasing attention. However, most prior studies have focused on specific structures or components, with insufficient research on damage identification in typical structures such as composite stiffened panels. Moreover, previous research often relied on specific ML algorithms, and the variations in training outcomes due to different algorithms and data processing techniques have not been sufficiently explored.

This study utilizes data-driven methods to analyze the strain response of composite stiffened panels for structural damage identification, aiming to explore the differences in training outcomes attributable to various ML algorithms and data processing approaches. Initially, the finite element method is employed to construct the stiffened panel models featuring skin-stiffener debonding and stiffener damage, from which strain response data at monitoring points under compressive load are extracted and processed to compile the damage-strain response dataset. Subsequently, GNN, Decision Tree (DT), Random Forest (RF), ANN, and KNN models are established and trained using strain responses processed in various ways as inputs to predict the type and location of structural damage, followed by the assessment and comparison of prediction accuracy of each model. Finally, the performance of GNN model is further evaluated, particularly its capability to handle missing strain data, thereby validating the model's robustness.

2. Model Establishment

2.1. Damage-inclusive finite element model

A finite element model of a stiffened panel with three stiffeners was constructed, featuring a panel size of 300mm*300mm and incorporating three T-shaped stiffeners. The adhesive layer between the panel and stiffeners has material properties of E = 250 GPa, $G_1 = G_2 = 100$ GPa, and the panel and stiffeners are made of X850, with its mechanical properties detailed in Table 1. Fixed boundary conditions were implemented via coupling constraint, while compressive loads were applied at the loading end in the direction of the stiffeners via the RP-1 reference point. Strain gauges were strategically placed at intervals of 50mm along one side of the T-shaped stiffeners and on the external side of the web, totaling 36 monitoring points as depicted in Figure 1 (a).

Two types of damage were preset in the stiffened panel: debonding of the panel and stiffeners, and impact damage to the web of the stiffeners, achieved by applying a stiffness reduction method [10]. Considering the randomness of damage locations in practical engineering applications, the stiffened panel structure was divided into zones. The specific location of identified damage is characterized by the corresponding area, with the damaged areas schematically shown in Figure 1 (b). Two sets of varying magnitudes of compressive loads were applied to models with different types of damage (including undamaged case), to expand the dataset.

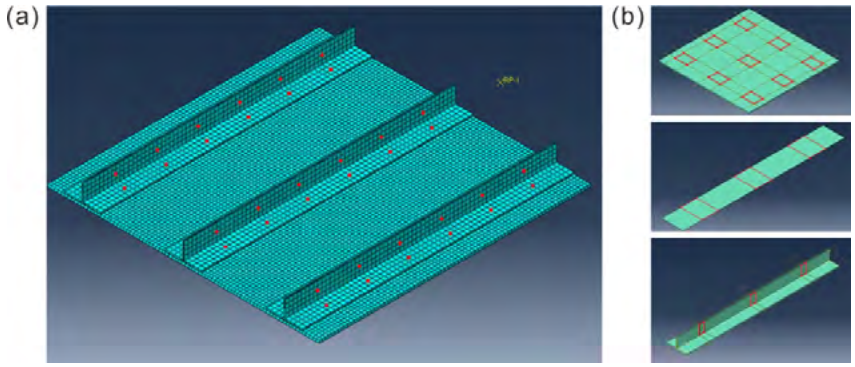


Figure 1. (a) Layout of strain-monitoring points. (b) Schematic diagram of the damaged area.

Table 1. Material properties of X850.

E_1 (GPa)	$E_2 = E_3$ (GPa)	$G_{12} = G_{13} = G_{23}$ (GPa)	$Nu_{12} = Nu_{13} = Nu_{23}$
135	8.8	4.5	0.33

2.2. Data processing

Data augmentation can rapidly generate sufficient and efficient datasets from a limited original dataset, which is critical for enhancing the performance of data-driven models. By adding noise to the strain data, this study simulates engineering strain gauge data errors and the variability in strain values due to differing damage locations within the same zone. The random method from the numpy library was employed to augment the data, ultimately generating 5700 training datasets. Cross-validation was utilized to divide the obtained dataset into three subsets: training, validation, and test, with a ratio of 7:2:1. The strain data were standardized using the min-max normalization method to analyze the relative magnitudes of structural responses, thereby reflecting information on the damage. The dimensions and magnitudes of the features were standardized to effectively enhance the convergence speed and learning stability of the ML models.

Labels for the dataset were encoded using one-hot encoding, mapping nine types of debonding damage models, nine types of rib damage models, and one undamaged model into discrete 19-bit binary-coded categories. This digital representation eliminates ordinal relationships among labels and converts categorical features into binary vector representations, thus enhancing the sparsity of the feature vector and enabling the models to process and interpret these features more effectively.

2.3. Machine learning model

This study examines the damage identification performance of five machine learning models. For the GNN, the input data are normalized strain measurements transformed into a graph structure, where relationships between nodes represent spatial information inherent in the structure itself. In contrast, the DT, RF, ANN, and KNN models use raw one-dimensional data with 36 components as input. All five models use structural strain responses as inputs to produce outputs of 19-component one-hot encoded damage labels.

A key feature of GNN is its ability to incorporate original topological information through graph-structured data inputs, thereby integrating the spatial relative positions of strain measurement points into the original graph features. Initially, the input graph features are passed through a 1*1 convolutional layer that transforms dimensions while preserving spatial information, converting the channel count of input features to the dimensions of hidden layer. Following a nonlinear transformation by the activation function, the conv2 layer converts the dimensions of the hidden layer to the number of output categories,

which is then passed to the next layer's activation function. Subsequently, information is transmitted from source nodes to target nodes and aggregated via maxpooling from adjacent nodes. Considering both training performance and computational cost, the selected model configuration was set with hidden_size=16, learning_rate=0.01, lr_decay=0.3, and num_epochs=50, using a combination of Leaky_ReLU and Linear activation functions, with learning rate decay applied every 10 epochs. The other four models were developed using the scikit-learn package, with the ANN model structured as 36-64 (ReLU)-32 (Tanh)-19 (Softmax); key parameters for each network are provided in Table 2.

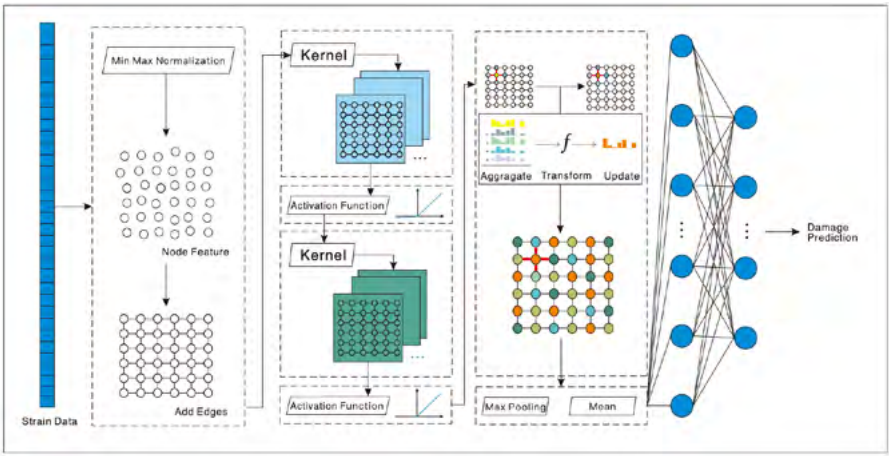


Figure 2. Framework of proposed GNN model.

Table 2. Critical parameters of ML models.

ML model	Critical parameters
Decision Tree	Max_depth=10
Random Forest	N_estimators=50, mini_samples_split=10, mini_samples_leaf=5
ANN	lr=0.1, optimizer=Adam, loss=categorical_crossentropy, epochs=50
K_Neighbors	N_neighbors=2, weights='uniform' , metric='manhatan' , p=2

3. Results and discussions

3.1. Comparison of predicted results across different models

This section explores the optimal method for processing structural strain response data in machine learning by comparing the predicted outcomes resulting from different data processing approaches. Specifically, the GNN processes graph-structured strain data considering inter-node relationships, DT and RF make decisions through feature splitting and selection, ANN establish nonlinear relationships by learning weights and biases from raw feature data, and KNN calculates feature similarity using appropriate distance metrics.

Accuracy is initially used to assess the proportion of correctly predicted samples by the classifiers, with the comparative predictive accuracies of the five models presented in Table 3 following cross-validation. The results indicate that the GNN model achieves optimal prediction on the training, validation and test sets. The DT model, constrained by the complexity of its network structure, showed the lowest predictive accuracy. The RF model, which adds complexity to the DT framework, achieved a training accuracy of 94.94% but performed poorly on the validation and test sets. The ANN model, after appropriate optimization of network structure and parameters, exceeded 90% accuracy across all datasets, with minimal variation among them. The KNN model, second only to the GNN in predictive precision, achieved an accuracy of 95.26% on the training set, likely due to the algorithm's consideration of sample

similarity. The core challenge in damage identification based on structural strain responses is how to process raw strain inputs to adequately extract damage information contained within the strain responses. Unlike the other four models, which use raw strain inputs, the GNN introduces physical information of original structure, establishing strain nodes graph which representing the geometric spatial relationships among the measurement points. This approach significantly enhances the predictive performance of the damage identification model.

Table 3. Comparison of prediction accuracy of five ML models.

	Training Accuracy	Validation Accuracy	Testing Accuracy
Decision Tree	86.17%	78.25%	77.37%
Random Forest	94.94%	86.67%	88.95%
ANN	92.03%	91.75%	92.81%
K_Neighbors	95.26%	92.19%	93.51%
GNN	97.59%	94.56%	95.61%

To further compare the predictive efficiency of five ML models for three types of damage: debonding, stringer damage, and undamaged. The prediction results for each model across varying types and locations of damage were aggregated and represented in grouped box plots as shown in Figure 3. The debonding and stringer damage consist of nine damage zones each, whereas the undamaged model shows no variation in damage location, hence is represented by a single horizontal form line in the box plots. Comparing the predictive performances of the five models, the DT model exhibits poor predictive performance in the undamaged cases and low accuracy rates for both debonding and stringer damage, with notable variability. The RF model shows some improvement overall, yet it still achieves less than 70% accuracy for the undamaged cases and displays considerable variability in the accuracy for debonding. Compared to these, the ANN model improves the dispersion of accuracy for debonding damage, but the average predictive accuracies, especially for the undamaged model, remain low. The KNN model achieves high accuracy for debonding and stringer damage but shows two outliers in its predictions for the nine stringer damage scenarios and achieves less than 90% accuracy for undamaged cases. The GNN model demonstrates the best overall predictive performance, with an impressive 94% accuracy for the undamaged model and the highest accuracy and lowest variability for both debonding and stringer damage. Accurately identifying whether a structure is damaged is crucial for structural health monitoring. The GNN model significantly enhances its predictive performance by analyzing the relative magnitude and spatial relationships between data, effectively accomplishing the task of binary classification.

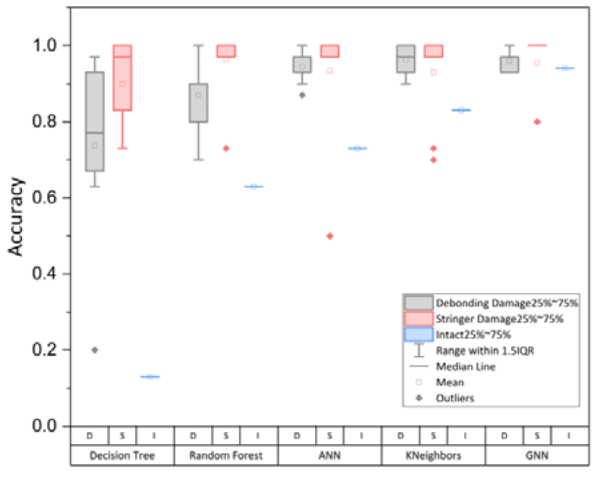


Figure 3. Grouped box plots of the results of the five model predictions.

3.2. Robustness analysis of GNN model

This section further evaluates the the proposed GNN model, which demonstrated the best predictive outcomes. The model's prediction accuracy and the learning curves of the loss function are shown in Figure 4. Both the training and validation loss curves exhibited a smooth decline until convergence, their similar trends indicating that there is no overfitting in the training process. Furthermore, in practical engineering applications of composite stiffened panels, strain data are often acquired from strain gauges mounted on the structure's surface. Due to various factors such as environmental conditions and human error, strain gauges may exhibit inaccurate readings or even become damaged, affecting structural health monitoring. Therefore, the model's ability to correctly predict damage when strain gauges are impaired is a critical metric for assessing its performance. This subsection considers two scenarios of strain gauge impairment: 1) random damage occurring in 0, 1, or 2 out of 36 strain gauges; 2) random damage occurring in 1 of 36 strain gauges. Datasets for both scenarios were generated by assigning zero values to the affected strain gauges in the test set using random numbers, and instances where more than one strain gauge is damaged are typically preventable with timely maintenance, thus these scenarios adequately represent realistic conditions. The model's prediction accuracy results, as shown in Table 4, indicate that under both scenarios of strain gauge damage, the model achieved approximately 80% accuracy in predicting various damages, demonstrating its stability in handling noisy inputs. Figure 5 further assesses the prediction results through a normalized confusion matrix. The confusion matrix, in table form, uses predicted and actual values as its axes, with each cell's normalized value representing the proportion of predictions corresponding to the true labels.

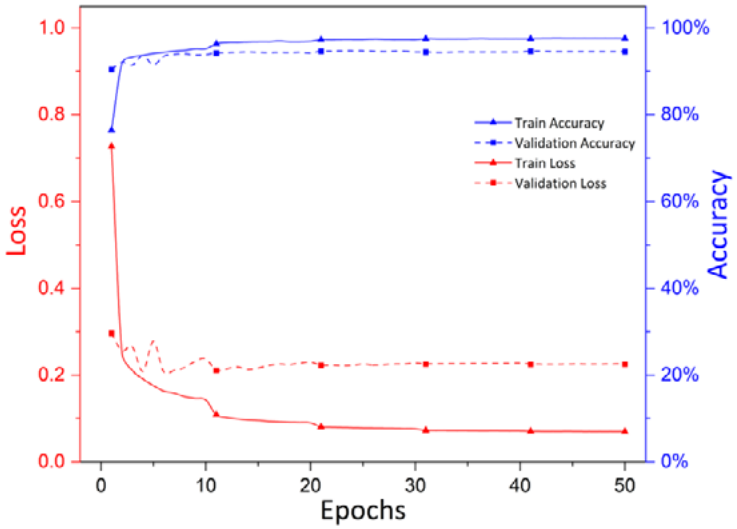


Figure 4. Learning curves of model accuracy and loss function.

Table 4. Model training effect considering strain gage damage scenario.

	Accuracy	Debonding Accuracy	Stringer Accuracy	Intact Accuracy
Case 1	84.74%	90.00%	80.00%	80.00%
Case 2	82.81%	85.93%	79.63%	83.33%

The confusion matrix clearly shows that, despite data loss, the model still maintains a high prediction accuracy for debonding damage, with 90% and 85.93% for the two cases. However, for stringer damage and undamaged scenarios, data loss significantly reduces prediction accuracy. This occurs because the GNN model distinctly extracts structural strain response features for these scenarios: undamaged cases show a uniform strain distribution, whereas regions near stringer damage exhibit significant differences compared to other areas. Consequently, missing data values set to zero result in strain inputs that do not

match the learned damage features, thus reducing prediction accuracy. Furthermore, it is notable that under conditions of data loss, the model's prediction accuracy significantly decreases for label 10 and 12, 16 and 18, which involve stringer damage. An analysis of the model's geometric structural features reveals that these groups correspond to four types of damage located near the vertices on both sides of the stiffened panel. The similarity in spatial structures among these damage scenarios results in similar strain response datasets, complicating the machine learning model's ability to accurately map strain responses to damage conditions, especially in cases of data loss. This underscores the importance of considering geometric spatial features in addressing related challenges. Overall, the model demonstrates strong robustness and maintains stability in the presence of data loss, noise, or other disturbances, exhibiting excellent generalizability.

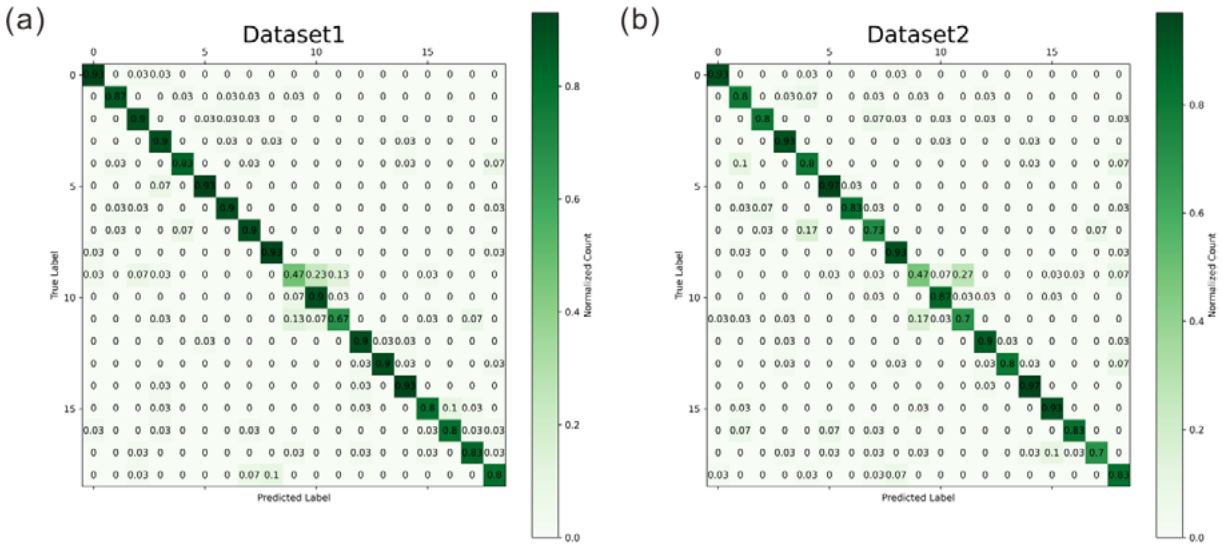


Figure 5. Confusion matrix of model predictions with impaired strain gages. (a) Case 1. (b) Case 2.

4. Conclusions

This study employs five machine learning models to identify damage in composite stiffened panels with debonding between the panel and stiffeners, and stiffener damage. A finite element model of the damaged composite stiffened panels was developed, incorporating different types of damage across nine zones. Thirty-six strain response monitoring points were placed on three ribs of the stiffened panel structure to capture and process the strain responses under compressive loads, thereby creating a damage-strain dataset. Five data-driven models were developed, including GNN, DT, RF, ANN, and KNN, using strain responses obtained via the finite element method as inputs to predict the types and locations of damages in the stiffened panels. The predictive results from the five models indicate that the GNN, utilizing graph-structured strain responses as inputs, achieves the highest accuracy and lowest variability in predicting debonding and stiffener damage. Notably, it exhibits a significant performance advantage, especially in predicting the presence of damage, over the other four models that input strain data as one-dimensional vectors. Furthermore, the GNN model's accurate predictions for datasets with missing strain data validate its high noise resistance and robustness.

Acknowledgments

This work was supported by Young Elite Scientists Sponsorship Program by CAST (2021QNRC001).

References

[1] Y. Feng, H. Zhang, X. Tan, T. An, Y. He and J. Zheng. Investigation on the buckling and postbuckling performance of aero stiffened composite panels under axial compression. *Polymer Composites*, 39(7):2547-2559, 2018.
[2] R. B. Heslehurst. *Defects and damage in composite materials and structures*. CRC press, Boca Raton, 2014.
[3] K. Diamanti and C. Soutis. Structural health monitoring techniques for aircraft composite structures. *Progress in aerospace sciences*, 46(8):342-352, 2010.
[4] J. Zhou, Z. Li and J. Chen. Damage identification method based on continuous wavelet transform and mode shapes for composite laminates with cutouts. *Composite Structures*, 191:12-23, 2018.
[5] L. Grassia, M. Iannone, A. Califano and A. D'Amore. Strain based method for monitoring the health state of composite structures. *Composites Part B: Engineering*, 176:107253, 2019.
[6] A. Malekloo, E. Ozer, M. AlHamaydeh and M. Girolami. Machine learning and structural health monitoring overview with emerging technology and high-dimensional data source highlights. *Structural Health Monitoring*, 21(4):1906-1955, 2022.
[7] D. Y. Song, N. Takeda and A. Kitano. Correlation between mechanical damage behavior and electrical resistance change in CFRP composites as a health monitoring sensor. *Materials Science and Engineering: A*, 456(1-2):286-291, 2007.
[8] R. S. Almeida, M. D. Magalhães, M. N. Karim, K. Tushtev and K. Rezwan. Identifying damage mechanisms of composites by acoustic emission and supervised machine learning. *Materials & Design*, 227:111745, 2023.
[9] V. T. Pham, Y. Jang, J. W. Park, D. J. Kim and S. E. Kim. Cable damage identification of cable-stayed bridge using multi-layer perceptron and graph neural network. *Steel and Composite Structures, An International Journal*, 44(2):227-240, 2022.
[10] P. Gaudenzi, P. Perugini and A. Riccio. Post-buckling behavior of composite panels in the presence of unstable delaminations. *Composite Structures*, 51(3):301-309, 2001.

CONTENTS

NOVEL JOINT INTERFACE DESIGN STRATEGIES FOR STRENGTH IMPROVEMENT IN FDM PRINTED SINGLE LAP ADHESIVE JOINTS

Ishan Manoj[1], Atul Jain[1]

[1]Department of Mechanical Engineering, Indian Institute of Technology Kharagpur, INDIA-721302

Email: manoj.ishan@iitkgp.ac.in

Keywords: Adhesive Joints, Dmage Modelling, 3D Printing, Joint design, Finite Element Analysis

Abstract

This paper introduces a geometrical grading technique aimed at enhancing joint performance through a novel joint interface design. The implementation and demonstration of this technique are discussed. The design aspects of various fused deposition modelling (FDM) printed single lap joints (SLJs) were analyzed to understand their strengths and failure mechanisms. The study focuses on evaluating the failure behavior dissimilar FDM printed SLJs, using two commonly used thermoplastics, polylactic acid (PLA) and polyamide (PA), through numerical and experimental methods. Computational damage modeling, incorporating cohesive zone modeling (CZM) and ductile damage, has been utilized to investigate the failure load and failure mechanisms of polymer joints. Experimental studies have been carried out to validate these computational models confirming very good match. The research delves into understanding failure initiation and damage progression, specifically evaluating how geometric grading parameters and bonding substrates influence the failure load. The optimized toothed-shaped interface in dissimilar PLA-PA single lap joints (SLJs) shows a substantial improvement, with enhancements in strength and failure strain of approximately 46% and 480%, respectively, compared to the baseline PLA-PA SLJs.

1. Introduction

The presence of joints in structures is common as it is challenging to construct any structure without joints. The size of print beds and budgetary constraints prevent contemporary manufacturing techniques, such as additive manufacturing, from producing entire structures [1]. Hence, design requirement of joint is imperative to ensure a structure's overall strength and durability.

Single-lap adhesive joint (SLJ) are easiest and dependable technique for joining similar and dissimilar adherends. However, sudden material mis-match and eccentricity of applied load in SLJs causes peak stress to originate at the bond-layer and decreases the load bearing capacity, causing premature failure of SLJs [2]. Hence, it is a common practice to geometrically grade adherend or adhesive based on stress transfer mechanism complexity. Fused deposition modelling (FDM) [3] allows to achieve intricate geometries at a lower fabrication cost. These meticulously designed optimized adherends, can then be joined together using adhesive joining processes.

A thorough examination of the strength and failure analysis of different SLJs that include adherends made by 3D printing is presented in this paper. The analysis involves evaluating the strength of joints and identifying the reasons for their failure. It also involves developing new joints using knowledge gained from traditional SLJs and confirming their effectiveness through computer simulations and experiments. In addition, a thorough study is performed to examine the failures of the innovative interface-tailored SLJs. This analysis specifically focuses on assessing how the geometrically graded

tooth characteristics affect the load at which failure occurs and the resulting strain. This study presents computational simulations that incorporate cohesive zone and ductile damage modeling to evaluate the initiation and spread of failure. The objective of the research is to improve the maximum load capacity and deformation properties, prolong the time it takes for damage to start and advance, and get a more profound comprehension of design factors in dissimilar 3D-printed SLJs.

A notable deficiency in the existing literature is the lack of comprehensive analysis of failure causes in dissimilar SLJs using 3D printed adherends. Current research predominantly emphasizes stress analysis rather than going into the complexities of failure analysis. Furthermore, the primary emphasis in this area of study has been on the connection of different materials, such as metal-to-metal or metal-to-composite surfaces. As a result, there is a lack of knowledge regarding the fundamental reasons for failure in 3D printed SLJs. The absence of understanding has impeded the enhancement of 3D printing skills to effectively tackle these modes of failure. In order to fully utilize the potential of 3D printing technology in improving joint strength, it is crucial to thoroughly comprehend the capabilities and failure analysis of FDM printed adherends. This is especially important for adherends that have geometrically graded interfaces combined with adhesive bonding.

The paper presents a detailed examination into the failure mechanisms and root causes of different SLJs made of FDM-printed Polylactic acid (PLA) and Polyamide (PA) that are bonded using adhesive bonding. The discrepancy in modulus between PA and PLA is substantial, validating the selection of these two materials to exemplify the difficulties associated with differing adherends. The decreased flexural rigidity of the PA adherend led to significant tensile stress, resulting in noticeable deformation in the bond-layer close to the left free edges [4,5]. The insufficient strength of the adhesive, along with significant peeling and shearing stress, resulted in a cohesive breakdown in the non-customized SLJ. An asymmetrical stress distribution was caused by the difference in stiffness between the adherends, resulting in increased stress concentration on the adherend with lower stiffness. These observations support the need to apply geometric grading to the different adherends in order to reduce the risk of premature SLJ failure and improve the strength of the joint [6,7]. The second and third structures of the SLJ unique showcase customized interfaces that incorporate an innovative toothed design. The second SLJ structure, known as "*P/PA-A-N/PLA*", incorporates positive interlocking teeth on the PA adherend and negative interlocking teeth on the PLA adherend (Figure 1). The third SLJs, also known as *"P/PLA-A-N/PA*," consist of interlocking teeth that are oriented in opposite directions. The PLA adherend has positive interlocking teeth, while the PA adherend has negative interlocking teeth.

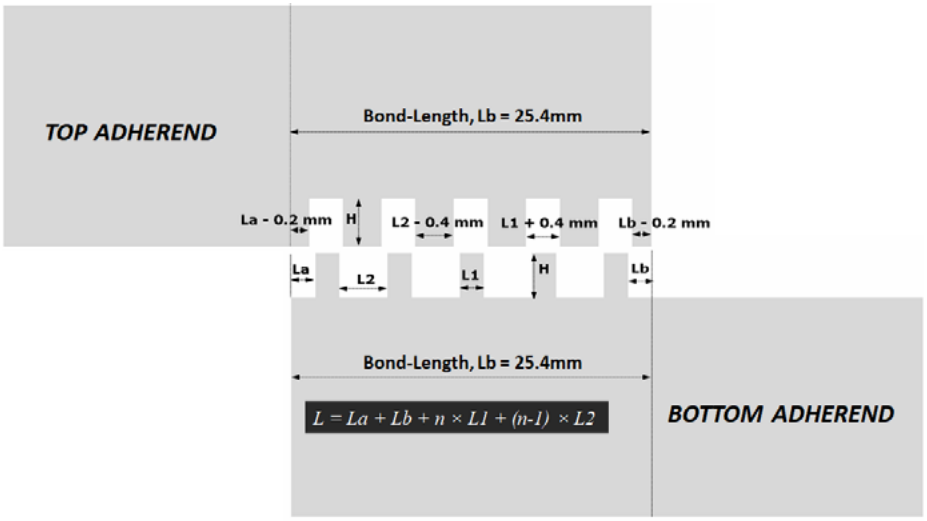


Figure 1: Represntative image of positive and negative interlocking teeth graded on bond-layer interface.

CONTENTS

2. Materials and Methods

Commonly used thermoplastic filaments; freshly extruded Polyamide (PA) and Polylactic acid (PLA) were used for this study.

Specimens were 3D printed using line infill, which had a density of 100%. The fused material lines were deposited primarily in a parallel manner in this configuration, resulting in the formation of successive stacked layers that ultimately constitute the final specimen. CURA software was utilized to process the 3D model of the adherend, ensuring the correct printing method. The 3D-printed adherends were given sufficient time to cool down after the printing process before being removed from the print bed. The introduction of an MK2a heat bed in the printer has significantly contributed to reducing the occurrence of warping in the specimens. A glass cage was used to prevent moisture absorption during the printing of specimens on the FDM printer. Open-source Creality CR-10 3D printer was used for the printing. The printing parameters used for the test samples are listed in table 1.

Table 1: FDM Printing Parameters.

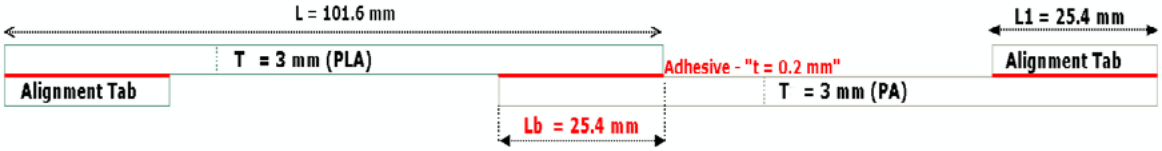
Printing Parameters	**Neat PLA**	**Neat PA**
Infill Density	100%	100%
Infill Pattern	Line	Line
Nozzle Diameter (mm)	0.4	0.4
Nozzle Extrusion Temperature (ºC)	210º	240º
Raster Orientation	0º	0º
Bed Temperature (ºC)	60º	80º
Deposition Layer Height (mm)	0.1	0.1
Printing Speed (mm/s)	20	20

Initially, the uniaxial tensile parameters, such as Young's modulus, elongation at break, and ultimate tensile strength, were determined by experimental means from the tensile test results. Tensile tests are repeated three times for each SLJ configuration using servo-hydraulic tensile testing equipment (Instron 3365) equipped with a 5 kN load cell. The obtained material properties for PLA and PA are listed in table 2.

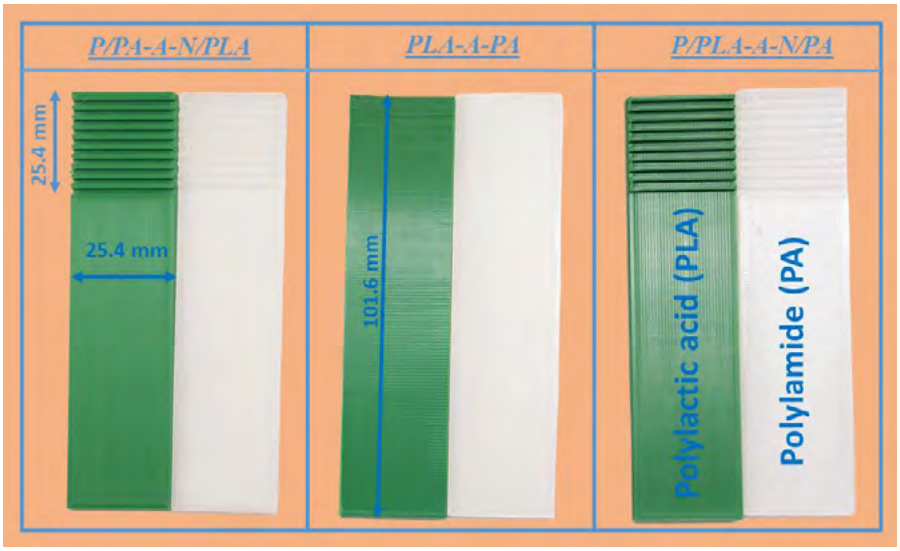
Table 2: Extracted material property of FDM printed PLA and PA from uniaxial tensile test.

Material Property	**FDM printed PLA**	**FDM printed PA**
Young’s Modulus (MPa)	1778.68 ± 63.21	293.27 ± 9.46
Ultimate Tensile Strength (MPa)	65.5 ± 9.84	42.76 ± 1.60
Fracture Strain (%)	7.54 ± 0.46	326.01 ± 47.51

Subsequently, adherends and SLJs were fabricated. The dimension of SLJs manufacture by FDM are depicted in Figure 2. The width of the SLJs is 25.4 mm. The ASTM D638-14 Type V, which is the established standard for assessing the tensile strength of polymers, was chosen because there are no special standards available for thermoplastics.



(a)



(b)

Figure 2: (a) Dimensions of SLJs (b) FDM printed SLJs for experimental validation.

The adhesive "*Momentive RTV 106*" is utilized to attach adherend due to its ductility and excellent temperature resistance [8]. This is a single-component, pre-mixed silicone rubber adhesive sealant that offers strong bonding to plastics, ceramics, and glass surfaces.

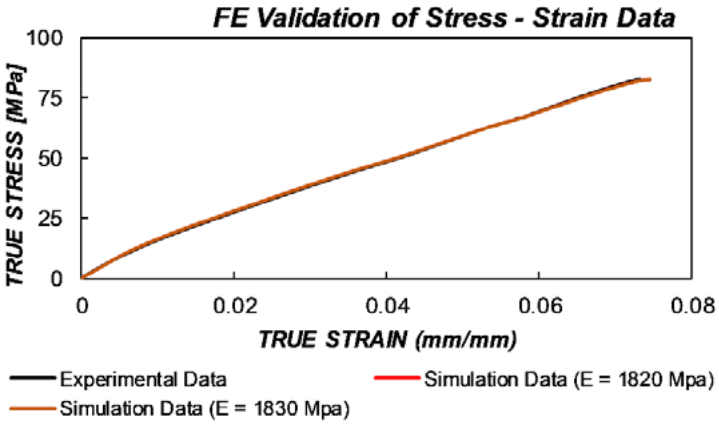
3. Numerical Approach

Abaqus CAE 6.21 [9] was used to create two-dimensional finite element (FE) models for all SLJ configurations. The purpose of these computer models is to forecast the point at which a system or structure will fail and determine the specific way in which it will fail. Finite Element Analysis (FEA) was used to analyze the impact of geometric parameters related to positive and negative interlocking teeth on enhancing the strength of *"P/PA-A-N/PLA*" and *"P/PLA-A-N/PA*" SLJs.

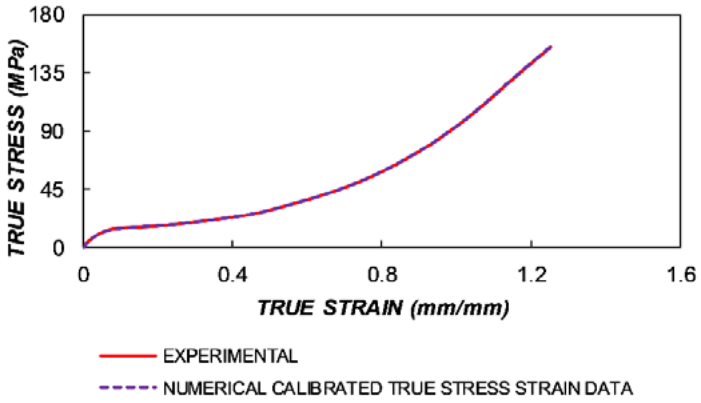
The failure of the adhesive material is simulated using cohesive zone modeling (CZM) with element-based criteria. The governing principle of CZM involves the application of cohesive elements or a surface approach, where cohesive forces exist between the failure surface to accurately model the start and propagation of damage [10]. CZM with a mixed-mode formulation was employed, which had a triangular shape.The adhesive was composed of a uniform layer of cohesive components that extended throughout its entire thickness. A four-node two-dimensional (COH2D4) element was employed to create a mesh for the adhesive layer. The cohesive properties for the finite element simulation of the "Momentive RTV 106" adhesive were obtained from the literature [11].

The behavior of 3D printed PLA and PA was simulated using multi-linear elasto-plastic data that included a ductile damage criterion. The ductile damage criterion is both computationally stable and very easy to implement. Thermoplastics, like PLA and PA, can display either brittle or ductile characteristics depending on how they are processed. FDM-printed thermoplastics such as PLA, PA, and others often exhibit elasto-plastic characteristics (Figure 3). The ductile damage criterion facilitates

a seamless shift from elastic to plastic behavior.The materials PLA and PA were simulated using four-node planar strain elements (CP4ER). The mesh was adequately adjusted with 16 elements over the thickness of the adherend in order to decrease the size of the elements in areas with significant stress gradients.



(a)



(b)

Figure 3: Computational vs experimental validation of obtained elasto-plastic dataset for (a) 3D printed polylactic acid (PLA) and (c) 3D printed polyamide (PA).

The lower adherend's right vertical end moved to the right, but the upper adherend's left vertical end did not move horizontally in the X-direction ($U_X = 0$). In order to preserve grip-related boundary conditions, the lateral displacement in the Y-direction ($U_Y = 0$) for the upper and lower adherends was restricted to 25.4 mm. The boundary conditions used in this study closely resemble those used in experimental tensile testing.

4. Results and Discussion

The primary investigation was on a specific type of SLJ that had an uncustomized interface, known as *PLA-A-PA* SLJ. The PA adherend had substantial longitudinal deformation in comparison to PLA. The decreased flexural rigidity of the PA adherend led to significant tensile stress, resulting in noticeable deformation in the bond-layer near the left free margins. The insufficient strength of the adhesive, along with significant peeling and shearing stress, resulted in a cohesive failure in the *PLA-A-PA SLJ* under normal conditions. The variation in stiffness between the adherends resulted in an uneven distribution of stress along the bond-layer, with the lower stiffness adherend experiencing higher levels of stress. These observations support the need to apply geometric grading to the different adherends in order to reduce the risk of premature SLJ failure and improve the strength of the joint.

The correlation between the strength of the "*P/PA-A-N/PLA*" joint and various geometric parameters is determined. The customized SLJs exhibited intricate failure modes, showcasing several interacting damage modes that varied based on the geometric parameters' values. The ideal joint configuration, determined by adjusting the tooth geometric parameter to achieve the highest load, includes the following coefficients: The values are as follows: *H = 1.4 mm, L1 = 1 mm, L2 = 1.4 mm, La = 0.6 mm, and n = 10.* (Figure 4)

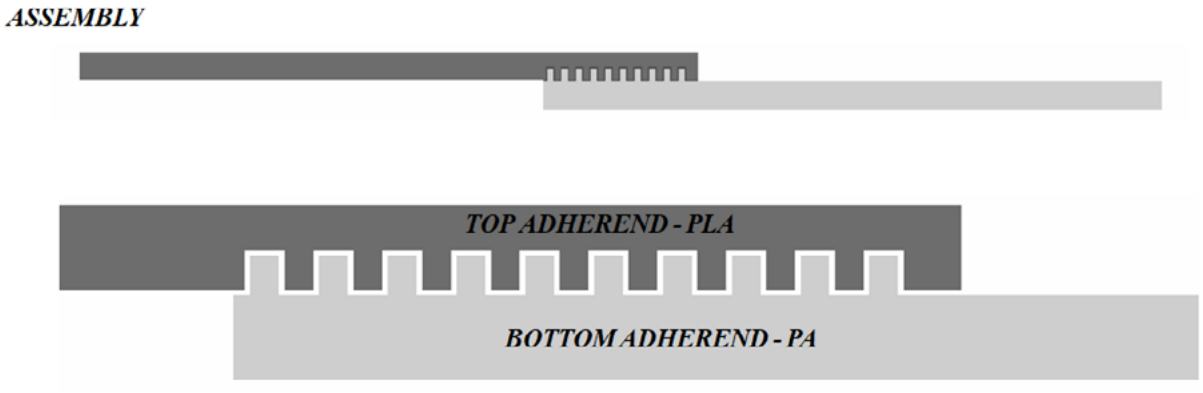


Figure 4: Optimal tooth coefficients obtained after calibrating tooth parameters for strength

The modification of tooth geometry parameters in the "*P/PLA-A-N/PA*" SLJ exhibits a more pronounced deviation in failure load in comparison to the "*P/PA-A-N/PLA*" SLJ. The incorporation of positive interlocking teeth on the PLA adherend enhances the failure load in comparison to the baseline "*PLA-A-PA*" SLJ (Figure 5). Nevertheless, the enhancement in the strength of the joint is greater when positive interlocking teeth are incorporated into the adherend made of PA. The differential in stiffness between PLA and PA is the main reason for this divergence. Introducing interlocking teeth to PLA, which is already a hard material, often enhances its stiffness. On the other hand, removing material from the PA adherend reduces its stiffness.

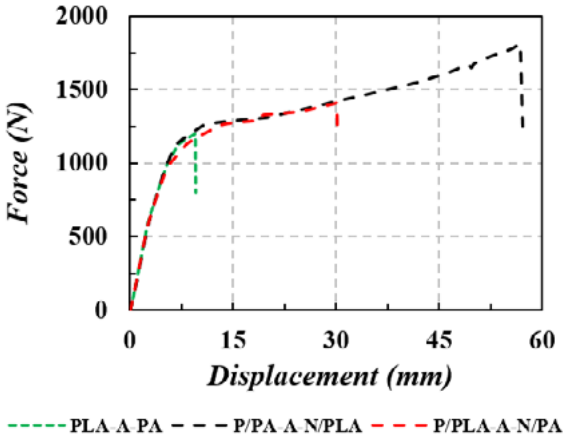


Figure 5: Computation load vs displacement curve for all the three realized SLJs configuration

The addition of interlocking teeth on the PA adherend is efficient in increasing the bending stiffness of the PA adherend, therefore improving the overall global rigidity. In contrast, the act of removing material from the adherend made of PA decreases the rigidity of the adherend, which is already less rigid. The observed augmentation in failure load and strain in the "*P/PLA-A-N/PA*" configuration is attributed to a synergistic effect of the geometrical interlocking mechanism and adhesive bonding. The importance of geometric tooth characteristics in enhancing interfacial stiffness is evident in both

customized setups. Moreover, it is important to mention that the most efficient arrangement, obtained by modifying tooth geometric characteristics, remained consistent for both customized setups.

The customized SLJs exhibit exceptional durability due to a gradual deterioration process, which is made possible by the inventive tooth-interface design utilized. This design approach enables the creation of localized tensile and compressive stresses along certain tooth edges, substantially reducing the concentration of maximum peel and shear stresses inside the adhesive layer. The failure originates in the bond layer located close to the unfixed border of the flexible PA adherend. The main reason for this phenomenon is the significant uniaxial straining that the PA adherend undergoes, which is in contrast to the stronger PLA adherend. Afterwards, the damage slowly advances towards the center of the bond layer, finally extending to the interlocking teeth, indicating a combined failure of the tooth-interface joint. The occurrence of many sequential failures significantly prolongs the time it takes for the joint to completely fail, leading to significant enhancements in total strength.

In all three situations, the finite element analysis overestimated the failure loads in comparison to the experimental data (Figure 6). For the numerical simulations, it is assumed that the adherend is isotropic. The parameters of the 0° raster orientation were used as input. FDM printed plastics exhibit anisotropy, which poses challenges in managing print orientations for intricate designs. In customized joints, teeth were printed at a right angle to the direction of applied force. In addition, the use of FDM printing for PA materials can result in various issues such as warping and delamination, which can have a detrimental impact on the overall strength of the printed object. In addition, Momentive RTV106 exhibited reduced adherence to PA. Furthermore, it is recognized that triangle cohesive laws tend to overestimate the failure load, especially for extremely flexible adhesives like Momentive RTV106 [12].

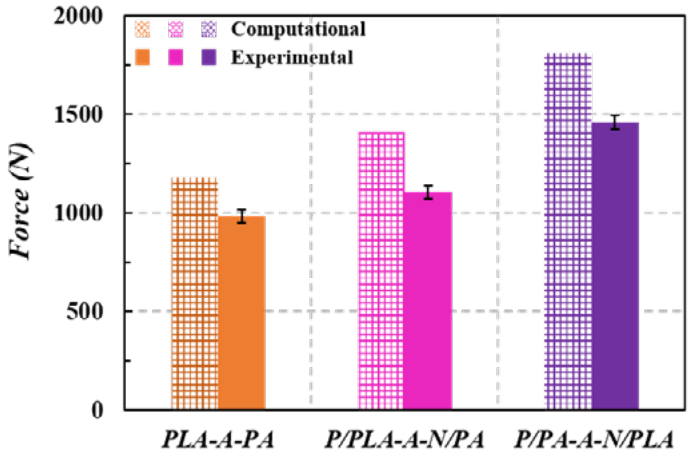


Figure 6: Experimental vs numerical comparison of failure load for all the three realized SLJs

The experimental findings and numerical modeling of the baseline *PLA-A-PA* SLJ demonstrate cohesive failure processes. Examination of the failure surface of *PLA-Adhesive-PA* SLJ reveals that certain adhesive material remains partially connected to the interface of the bond layer. The examination of the compromised surface of the "*P/PA-A-N/PLA* and *P/PLA-A-N/PA*" reveals a combined failure that impacts both the adhesive layer and the interfacial teeth. There are visible signs of the adhesive partially clinging to the interface between the bonded layers. These signs are accompanied by an uneven surface at the interface, which is generated by the breaking of interfacial teeth. This failure mode allows for the simultaneous utilization of adhesive bonding and geometrically interlocked joint technologies, resulting in the development of more reliable SLJs. Both numerical and experimental findings indicate that the failure of PA teeth in customized designs is attributed to the lower strength of PA compared to PLA.

5. Conclusions

This work presents a novel geometrically graded interface for connecting dissimilar parts that have been printed using FDM technology. The primary objective is to enhance the durability of SLJs by postponing

the onset and advancement of failure. This was accomplished by integrating adhesive bonding with mechanical interlocking teeth in a hybrid joint configuration. The study assesses the influence of positive and negative interlocking teeth on the adherends in relation to failure load and mechanism. The following conclusion can be drawn from the study:

- Untailored *PLA-A-PA* SLJs exhibit the lowest load capacity because the PA adherend experiences significant longitudinal deformation induced by its lower bending rigidity.
- The strength of tailored *P/PA-A-N/PLA* and *P/PLA-A-N/PA* SLJs was higher compared to non-tailored SLJs. Remarkably, the inclusion of favorable interlocking teeth on the PA adherend substantially enhanced the strength of the joint in comparison to their placement on the PLA adherend.
- The ideal combination of joint settings, achieved by adjusting the tooth's geometric parameters, consists of the following values: H = 1.4 mm, L1 = 1 mm, L2 = 1.4 mm, La = 0.6 mm, and n = 10.
- The improved "*P/PA-A-N/PLA*" SLJ exhibited a significant 58.5% enhancement in average strength when compared to the baseline.
- The failure modes in the three numerical SLJ setups correspond to those found numerically.

References

[1] A. Nazir, J.Y. Jeng, A high-speed additive manufacturing approach for achieving high printing speed and accuracy, Proc. Inst. Mech. Eng. Part C J. Mech. Eng. Sci. 234 (2020) 2741–2749. https://doi.org/10.1177/0954406219861664.

[2] I. Manoj, S. Kumar, A. Jain, A numerical study on stress mitigation in through- thickness tailored bi-adhesive single-lap joints, J. Adhes. Sci. Technol. 0 (2023) 1–35. https://doi.org/10.1080/01694243.2023.2217674.

[3] A.K. Shah, A. Jain, Microstructure and mechanical properties of filament and fused deposition modelling printed polylactic-acid and carbon-fiber reinforced polylactic-acid, J. Reinf. Plast. Compos. (2023). https://doi.org/10.1177/07316844231167551.

[4] T. Zou, J. Fu, J. Qin, L. Li, Z. Liu, Failure analysis of composite-to-titanium single lap adhesive joints subjected to tensile loading, Eng. Fail. Anal. 129 (2021). https://doi.org/10.1016/j.engfailanal.2021.105734.

[5] A.M.G. Pinto, A.G. Magalhães, R.D.S.G. Campilho, M.F.S.F. de Moura, A.P.M. Baptista, Single-lap joints of similar and dissimilar adherends bonded with an acrylic adhesive, J. Adhes. 85 (2009) 351–376. https://doi.org/10.1080/00218460902880313.

[6] A.Y. Kanani, X. Hou, J. Ye, A novel dissimilar single-lap joint with interfacial stiffness improvement, Compos. Struct. 252 (2020). https://doi.org/10.1016/j.compstruct.2020.112741.

[7] S.M.J. Razavi, E. Esmaeili, M. Samari, S.M.R. Razavi, Stress analysis on a non-flat zigzag interface bonded joint, J. Adhes. 94 (2018) 199–217. https://doi.org/10.1080/00218464.2016.1257942.

[8] F. Aerospace, Silicone RTVs Custom Solutions for Today ' s Manufacturing Challenges, (n.d.).

[9] A. 6.21, ABAQUS / CAE User ' s Manual, 2021. https://www.3ds.com/support/hardware-and-software/simulia-system-information/abaqus-2021/.

[10] I. Manoj, A.K. Shah, A. Jain, Strength and failure assessments of 3D printed PLA single lap joints : Experimental and numerical analysis, Eng. Fail. Anal. (2024) 108257. https://doi.org/10.1016/j.engfailanal.2024.108257.

[11] E.A.S. Marques, L.F.M. Da Silva, M. Flaviani, Testing and simulation of mixed adhesive joints for aerospace applications, Compos. Part B Eng. 74 (2015) 123–130. https://doi.org/10.1016/j.compositesb.2015.01.005.

[12] J.J.M. Machado, E.A.S. Marques, M.R.G. Silva, L.F.M. da Silva, Numerical study of impact behaviour of mixed adhesive single lap joints for the automotive industry, Int. J. Adhes. Adhes. 84 (2018) 92–100. https://doi.org/10.1016/j.ijadhadh.2018.02.036.

MULTI-SCALE LEVEL PREDICTION OF CRACK GROWTH IN WIND TURBINE BLADE SHEAR-WEB JOINTS APPLYING COHESIVE ZONE MODELLING

Arturo Gomez[1], Christian Berggreen[2]

[1, 2] Department of Civil and Mechanical Engineering, Technical University of Denmark, DK-2800 Kgs. Lyngby, Denmark,
[1] eagme@dtu.dk, [2] cber@dtu.dk

Keywords: Fracture, Sandwich, Cohesive law, Shear web, Building block approach

Abstract
This manuscript presents the overview of the multi-scale level approach applied to the evaluation of disbond damage observed in the transition region of a large wind turbine blade. In particular in the bonded joint between the 3rd shear-web and the trailing edge sandwich panel. This work applies the Building Block Approach, adopted from the aircraft industry in the wind energy industry. It consists of performing a set of physical tests and virtual FEA simulations of increasing complexity to properly understand the fracture mechanism and its implications for the joint's integrity. Results from the experimental test campaign suggest that quasi-static and fatigue crack propagation are dominated by large fibre bridging. As a result, non-linear numerical models based on Cohesive Zone Modelling are been proposed at three different scale levels to analyze quasi-static and fatigue crack propagation in the adhesive interface. Correlation between experimental and numerical results seems promising although further improvements in the formulation and calibration of the fatigue model are still a matter of development.

1. Introduction

In wind turbines, a blade is a major structural/aerodynamic component with the primary function of transforming part of the kinetic energy of the incoming wind into rotatory kinetic energy in the turbine shaft. This is done by transferring the aerodynamic shear, bending and torsional loads along the blade to the center hub. A wind turbine's blade comprises two outer aerodynamic shells (upwind and downwind shells), spar caps to increase the blade's flexural stiffness and shear webs (typically two) which are bonded to the shells at the leading and trailing edges. Shear webs usually run almost the entire length of the blade from the transition zone (denoted by the shear web fish mouth). The cross-section of a typical blade is depicted in Figure 2.

Due to the increasing global demand for clean and sustainable energy, wind turbines have become more prevalent over the past few decades. This surge in interest has driven manufacturers to develop larger wind turbines that are more efficient and cost-effective than their smaller counterparts. However, the continuous increase in size has resulted in higher loads, which require additional strengthening. This challenge is addressed by adding a third shear web to the blades. Unfortunately, this leads to a failure phenomenon known as shear web disbonding, where cracks in the adhesive interface between the shear web footing and spar cap propagate due to large deflections in the aerodynamic skins near the third shear web. If the crack grows too large this could compromise the integrity of the blade, eventually causing the wind turbine to collapse. A detailed discussion of the type of loads and structural response that trigger shear web disbond in wind turbine blades can be found in (Jensen et al., 2023)

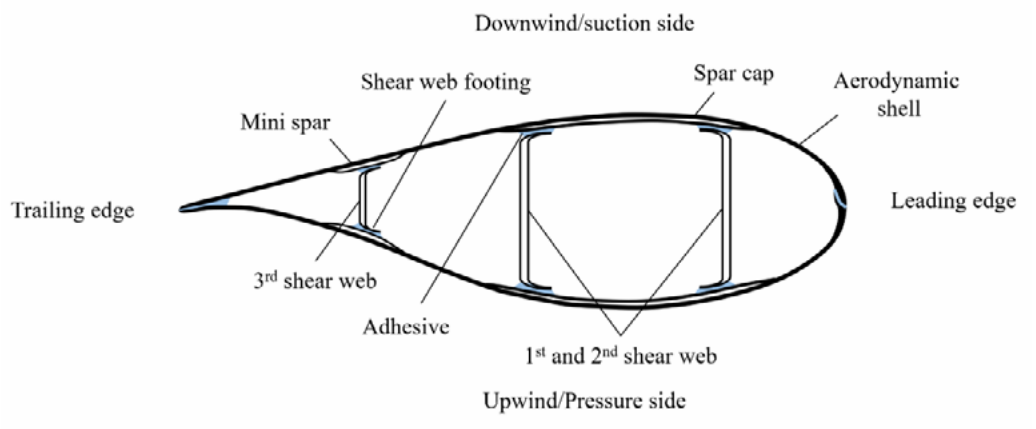


Figure 1. Example of a wind turbine blade section

To address this issue, Bladena has partnered with wind turbine owners and operators, The Technical University of Denmark (DTU) and Aalborg University, to initiate the CORTIR-II project, which aims to investigate shear web disbond in large wind turbine blades. The project is divided into four stages to investigate the issue in detail. It starts with characterisation and moves on to sub-component testing with more detail, before finally conducting large-scale testing. The current manuscript focused on the first three stages but further details and partial results about the large-scale testing can be found in (Waldbjørn et al., 2023).

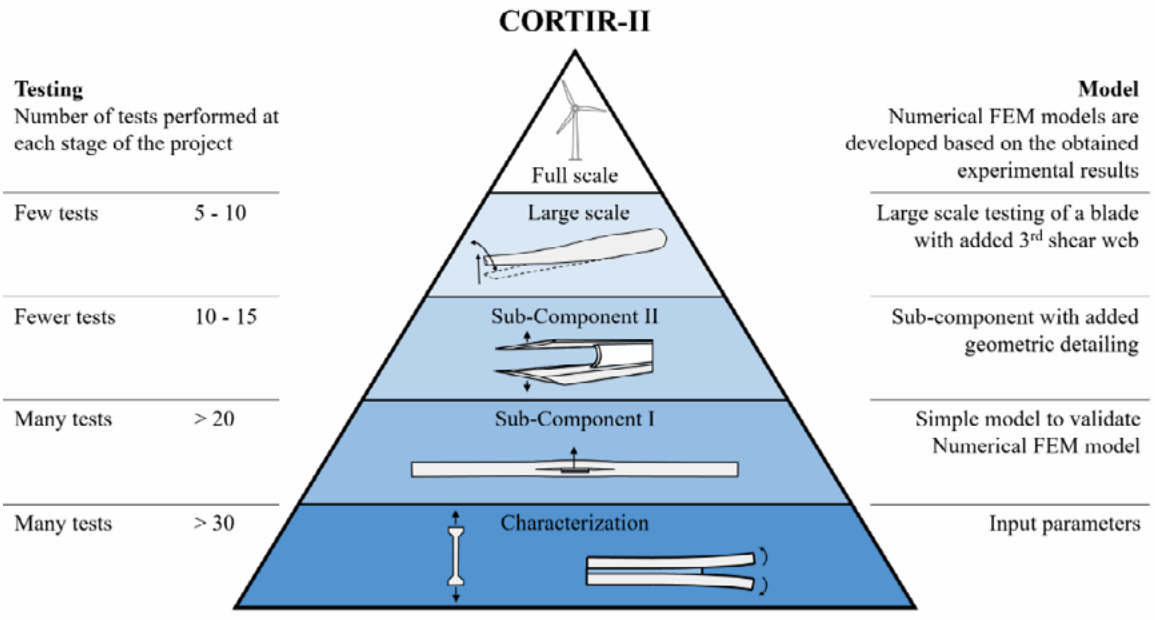


Figure 2. Building block approach applied to CORTIR-II project

2. Fiber bridging at different scale levels

The joint interface studied here is the same as in the real 3rd shear web for the 34 m balde (laminate materials and thickness and stacking sequence are the same). The top laminate is made from a triaxial/biaxial E-glass fabric with the following stacking sequence 8[45/0/-45/ ±45] and an average cured thickness of 10 mm. The bottom laminate is made from biaxial E-glass fabric with a stacking sequence of 10[±45] and an average cured thickness of 6.8 mm.

Quasi-static and fatigue fracture testing of the joint interface has been carried out at three different scale levels. At the most fundamental level, fracture characterization has been carried out using the

Double Cantilever Beam with Uneven Bending Moments (DCB-UBM) method, which is a novel test method for mixed-mode fracture. The DCB-UBM test, as introduced by (Sørensen, 2022), involves the application of uneven bending moments to the crack flanks' tips in the specimen (Figure 3.a.). By adjusting the ratio of these applied moments, crack propagation can occur under different fracture modes, ranging from pure mode I to pure mode II. Since the load applied to the specimen solely originates from bending moments, both the energy release rate and the mode-mixity angle remain unaffected by the crack length. Another advantage of employing pure bending moments for loading, particularly in cases involving large process zones, is that the applied load remains constant throughout the entire process zone.

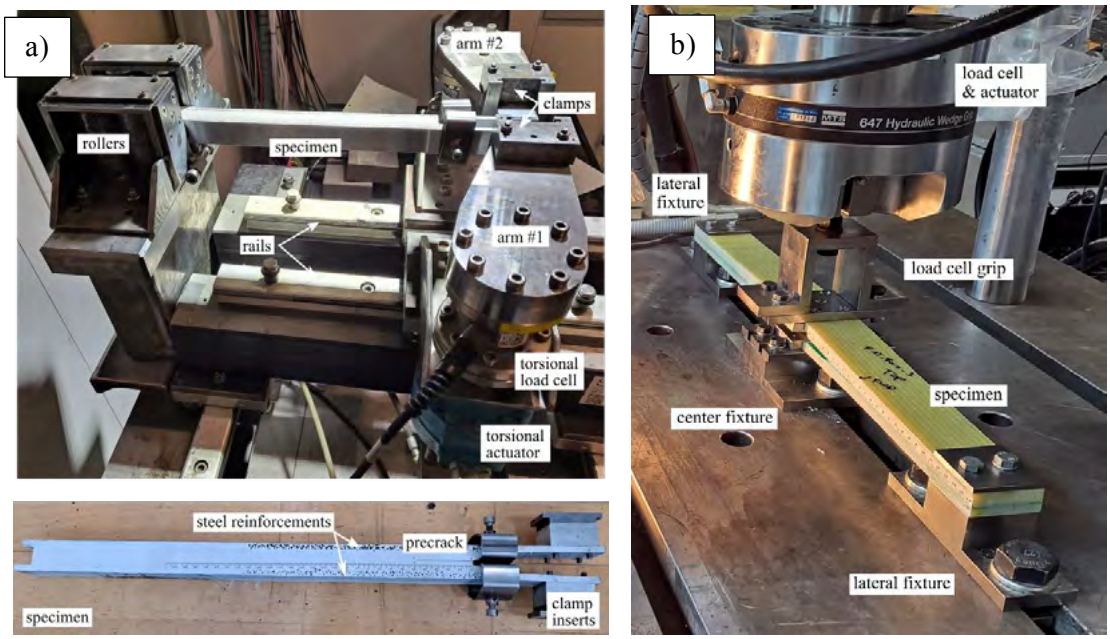


Figure 3. Test set-up. a) DCB-UBM, b) MTT

Subsequently, two subcomponent scale levels have been carried out to study. The first, using a Modified Tear Test (MTT) with simplified geometry and loading in which the variation of fracture mode mixites is accounted during the crack propagation process. The Modified Tear Test (MTT) is derived from the Sandwich Tear Test (STT) method in which the upper laminate is pulled upwards, so the in-plane membrane forces escalate significantly as the test proceeds (Figure 3.b). This escalation leads to an increase in the mode-mixity angle, transitioning from an initial pure mode I opening condition to mixed fracture modes (opening and shear). Finally, the second subcomponent test or Shear Web Disbond Test (SWDT) is based on a more complex geometry and loading conditions which replicates a simplified portion of a real 3rd shear web paying particular attention to the bonded interface between the shear web flange and the blade outer shell. The top laminate and shear web flange have the same composite layup as those used in level-I and level-II tests.

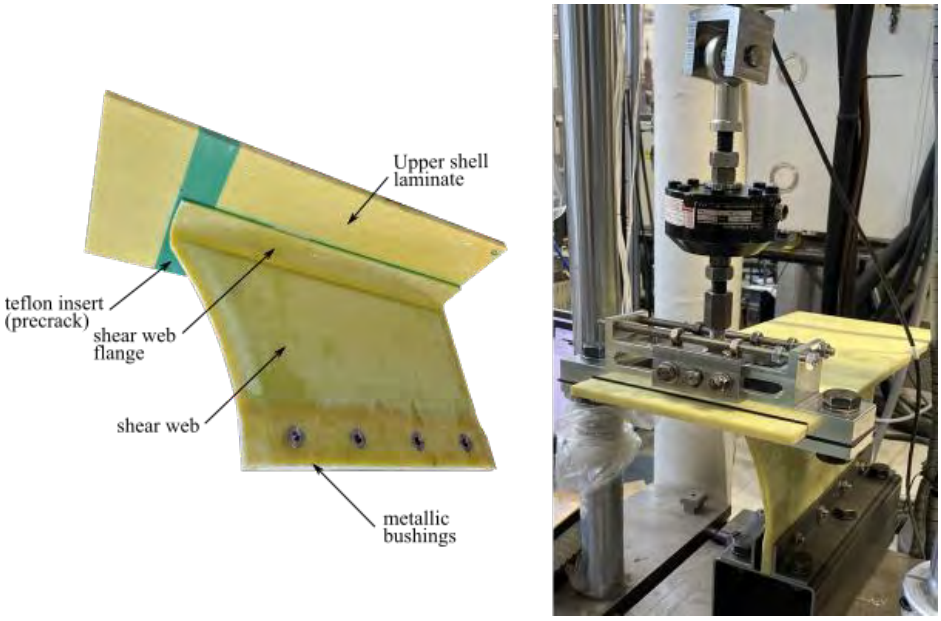
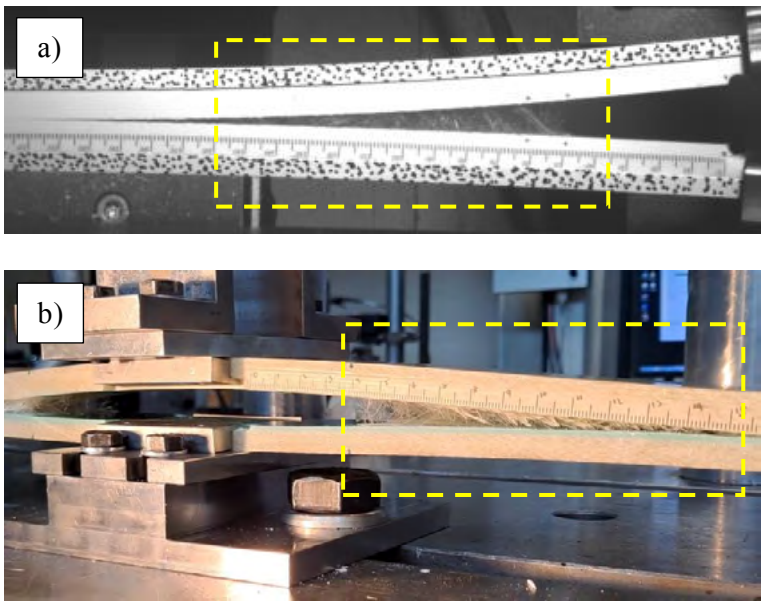


Figure 4. SWDT experimental set-up

Tests at all different scale levels for quasi-static and fatigue crack growth show the presence of large fibre bridging zones which dominate the fracture process. In short, the fibre bridging phenomenon occurs when the fibres in neighbouring laminate plies bridge the debonding plane, serving as crack arrestors. As a result of fibre bridging, the debonding resistance, inter-laminar fracture toughness and fatigue crack growth are enhanced.



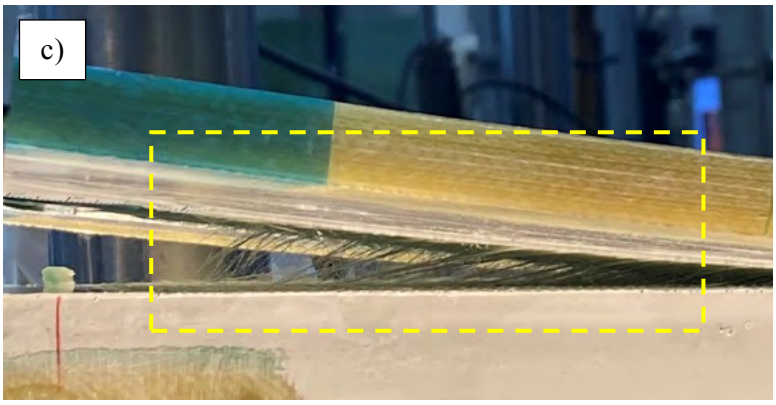


Figure 5. Fiber bridging at different scale level tests.
a) DCB-UBM, b) MTT, c) SWDT

3. Modelling fiber bridging with the cohesive zone approach

The non-linear nature of the fiber bridging phenomena can be addressed by Cohesive Zone Modeling (CZM). In this approach, the fracture process zone (FPZ) is substituted with a cohesive region, where the exchange of stress between the two artificial crack surfaces is defined using a relationship between the traction and separation of the FPZ. This relationship is then incorporated into the non-linear constitutive behaviour of the material. In practical FEA analysis, the cohesive zone model is commonly applied by a single layer of cohesive elements, which are placed along the expected path of crack propagation. It is generally agreed that the key parameters of traction-separation law can be obtained from direct experimental testing (Sørensen, 2022) although some other studies have used calibration methods based on trial-and-error search methods (Barbero et al., 2013) or a combination of both.

An extension of this quasi-static method is to consider the degradation of the traction-separation response due to fatigue cycles. This degradation as proposed by (Khoramishad et al., 2010) follows a predefined power law such that coefficients must be calibrated against experiments.

For the DCB-UBM and MTT cases, two-dimensional FEA models were generated in Abaqus 2021. The laminates and adhesive layer are modelled as separate geometric bodies joined at the interface using a tie constraint. The laminates are modelled as orthotropic materials while the adhesive material and the material for the doubler stiffeners an isotropic materials. Quasi-static tests are run using the standard/linear solver while the fatigue test uses an explicit solver. For the fatigue model, the damage criteria are described in section 2.2. was implemented in a VUSDFLD Fortran subroutine and computational time is accelerated by applying the cycle jump technique (Moslemian et al., 2011) within the subroutine. An example of the good correlation that can be achieved between experimental and FEA model results is presented in Figure 6.b. for a DCB-UBM test.

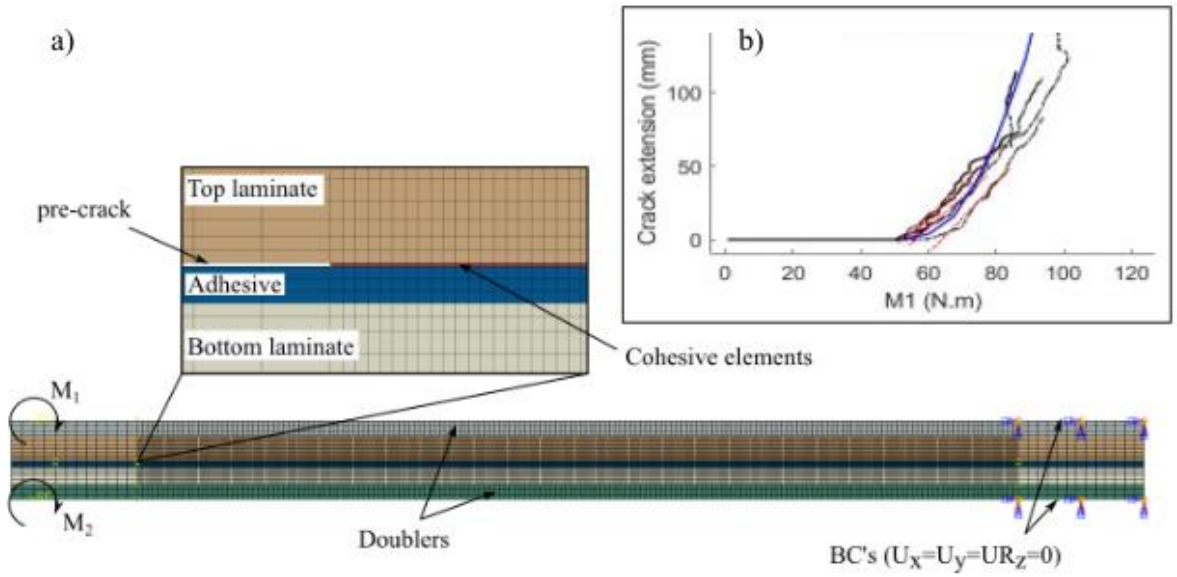


Figure 6. a) FEA model for DCB-UBM test using the CZM, b) Comparison between FEA model and test results for a quasi-static DCB-UBM test. Experimental (black), FEA (blue). a) MR = -1.2

In the case of the SWDT a fully detailed 3D FEA model was implemented in Abaqus to study the behaviour of the shear web specimen and the fracture behaviour at the bondline in both quasi-static and fatigue loading conditions. A detailed 3D CAD model was initially prepared in SolidWorks which includes the most important geometrical features of the specimens (e.g. shear web flange, local reinforcements, core-laminate transition, laminate drop-offs, insert holes). Each part was imported independently in Abaqus as a 3D solid and modelled with 8-node linear brick elements with reduced integration (C3D8R). Contact interactions and tie constraints were applied between interacting bodies as required. The bondline is modelled using cohesive elements using the same traction separation in the same way as in the previous scale levels a 3D FEA model is adopted due to the level of detail required to reproduce the geometry and load pattern. A more extensive description of the results and limitations of the current implementation can be found in (Gomez & Berggreen, 2023).

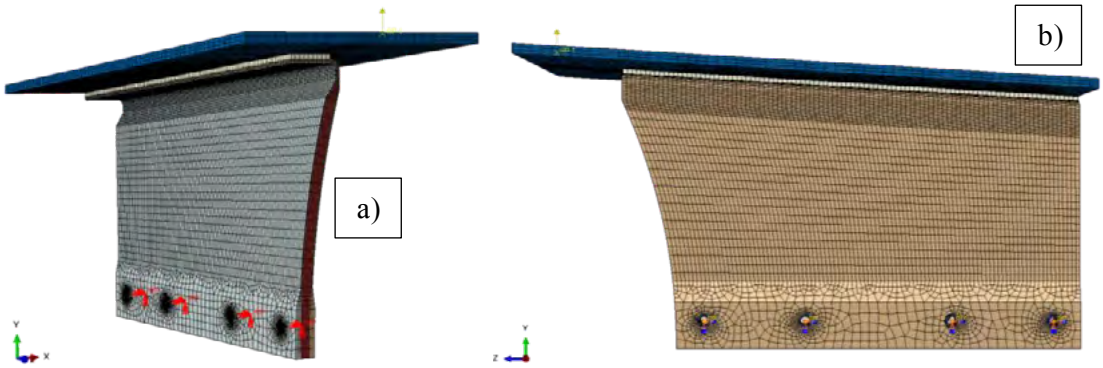


Figure 7. Detailed 3D FEA model of the SWD test. a) Isometric view, b) Left view

Conclusions

A building block methodology has been implemented to study crack initiation and propagation in bonded joints of glass fibre laminates and epoxy adhesives, typically encountered in shear webs in wind turbine blades. The phenomena have been studied from an experimental and numerical perspective at three different levels of complexity. Tests show that the crack propagation behaviour is dominated by a large fibre bridging zone in the bondline which acts as a toughening mechanism, particularly at small mode mixites phase angles (mode I opening-dominated fracture). It was also possible to obtain the traction-separation law directly from the experiments for a range of phase angles by measuring crack tip displacements and applying a data reduction method. The proposed 2D FEA models capture with accuracy the crack onset and crack propagation observed in experimental testing. A novel approach to model fatigue crack growth in the bondline was successfully implemented through a material user subroutine in which a fatigue damage law is coupled with the cycle jump technique. The same 2D FEA model was used to calibrate the fatigue damage law parameters using trial-and-error search methods. However, it was not possible to find a combination of material parameters that fully validate the experimental data. Implementation of the CZM into a full 3D method is still an active subject of research with promising applications for detailed component analysis.

References

Barbero, E. J., Cosso, F. A., Roman, R., & Weadon, T. L. (2013). Determination of material parameters for Abaqus progressive damage analysis of E-glass epoxy laminates. *Composites Part B: Engineering*, *46*, 211–220. https://doi.org/10.1016/j.compositesb.2012.09.069

Gomez, A., & Berggreen, C. (2023). Cohesive zone modelling to predict crack growth under fatigue loading. *IOP Conference Series: Materials Science and Engineering*, *1293*(1), 012012. https://doi.org/10.1088/1757-899x/1293/1/012012

Jensen, F. M., Arconada, J. O., Werk, M., Berggreen, C., Sørensen, J. D., Zhong, G., & Haans, W. (2023). Torsional Effects on Wind Turbine Blades and Impact on Field Damages. *IOP Conference Series: Materials Science and Engineering*, *1293*(1), 012005. https://doi.org/10.1088/1757-899x/1293/1/012005

Khoramishad, H., Crocombe, A. D., Katnam, K. B., & Ashcroft, I. A. (2010). Predicting fatigue damage in adhesively bonded joints using a cohesive zone model. *International Journal of Fatigue*, *32*(7), 1146–1158. https://doi.org/10.1016/J.IJFATIGUE.2009.12.013

Moslemian, R., Karlsson, A. M., & Berggreen, C. (2011). Accelerated fatigue crack growth simulation in a bimaterial interface. *International Journal of Fatigue*, *33*(12), 1526–1532. https://doi.org/10.1016/J.IJFATIGUE.2011.06.006

Sørensen. (2022). Cohesive laws for assessment of materials failure: Theory, experimental methods and application. *Downloaded from Orbit.Dtu.Dk On*. www.risoe.dtu.dk

Waldbjørn, J. P., Berggreen, C., Ahmed, S., & Nagy, T. (2023). Large-scale fatigue testing of a retrofitted 3 rd shear web in a 34m wind turbine blade section . *IOP Conference Series: Materials Science and Engineering*, *1293*(1), 012026. https://doi.org/10.1088/1757-899x/1293/1/012026

STUDY ON BUCKLING BEHAVIOR OF COMPOSITE SANDWICH STRUCTURE WITH CORRUGATED CORE UNDER HYDROSTATIC PRESSURE

Na-hyun Jeon[1], Hui-Jin Um[1], Shin-Ji Hwan[2] and Hak-Sung Kim[1,3]

[1]Department of Mechanical Convergence Engineering, Hanyang University, 222 Wangsimni-ro, Seongdong-gu, Seoul, Republic of Korea
Email: nahyun.j11@gmail.com, Web Page: http://mcdm.hanyang.ac.kr/
Email: gog9057@gmail.com, Web Page: http://mcdm.hanyang.ac.kr/
[2]Agency for Defense Development, 18 Changwon, Gyeongnam, Republic of Korea
Email: naraboja@add.re.kr, Web Page: http://www.add.re.kr
[3]Hanyang Research Center for Advanced Semiconductor Packaging, Hanyang University, 222 Wangsimni-ro, Seongdong-gu, Seoul, Republic of Korea
Email: kima@hanyang.ac.kr, Web Page: http://mcdm.hanyang.ac.kr/

Keywords: Hydrostatic buckling, Carbon fiber reinforced plastic (CFRP) composites, Sandwich structure, Corrugated core, Finite element analysis (FEA)

Abstract
In this study, buckling behaviors of composite cylinder and sandwich structure with corrugated core (SSCC) were investigated through finite element analysis (FEA). The composite cylinder and sandwich structure skins were composed of twill woven carbon fiber reinforced plastic (CFRP) composites and cores of sandwich structure were composed of 3D printed CFRP composites with continuous carbon fiber filament. In the case of SSCC, corrugated cores could be split according to their length, and split cores were rotated by 18 degrees. To derive critical buckling pressure, FEA simulation was conducted for composite cylinder and sandwich structures. As a result, the SSCC showed higher critical buckling pressure than that of the composite cylinder. Furthermore, different buckling behaviors were observed with number of cores. Critical pressure was improved with more split cores. Especially, sandwich structure with maximum multiple cores showed about 2 times higher critical buckling pressure compared to the sandwich structure with single core.

1. Introduction

Underwater vehicles are designed with cylindrical structures that have relatively small external diameters than length to operate smoothly in underwater environments. These cylindrical structures are vulnerable to external loads due to their geometry, and buckling can occur at lower strength than the material's strength [1,2,3]. Therefore, buckling analysis under hydrostatic pressure should be considered to design underwater vehicle.

Various studies have been conducted to apply carbon fiber reinforced plastic (CFRP) composites to hulls such as ships and underwater vehicles (UVW) in the marine field due to their advantages such as high mechanical properties with light weight and corrosion resistance etc. [4,5,6]. C. J. et al., investigated effect on winding angle of CFRP composites, so they anlayzed buckling characteristics and failure of thick-walled filament wound CF/epoxy cylinders under external hydrostatic [7]. Lee et al. studied optimization of composite sandwich cylinders to increase the design load considering buckling and material failure [8].

In our previous study, energy storage-corrugated lattice core sandwich structures were designed to not only protect battery but also achieve superior mechanical properties [9]. Moving forward, the buckling behaviors of composite cylinders and sandwich structures with corrugated cores were analyzed for application in underwater vehicles. To anlayze buckling behavior of composite cylinder, linear buckling analysis was referenced in our study under samd boundary and load conditions [5]. Additionally, buckling behaviors of sandwich structures with corrugated lattice core was analyzed according to core length under hydrostatic pressure through FEA.

2. Finite Element Analysis

2.1. Buckling simulation

To analyze buckling of structure, finite element analysis was performed using the commercial program ABAQUS for two structures: single composite cylinder (SCC) structure and sandwich structures with corrugated core (SSCC). The SCC structure was designed with thickness of 1.5 mm, external diameter of 210 mm and length of 450 mm. The SSCC are divided into two skins and core parts, which had thickness of 1.5 mm and 2 mm, repectively. It was modeled with the same external diameter of 210 mm and length of 450 mm. The core of sandwich structure was designed in our previous study [9] (shown in Fig 1.(a)) and it can be split along its length. In this study, while maintaing the same overall length, the core was divided into several segments of equal legnth. Each divided core segment was placed with rotation angle of 18 degrees in the sandwich structure. The core number by length is noted such as C1, C2. The geometry of single core was presented in Fig 1.(b) and separated cores rotated by 18 degrees also in Fig 1.(c).



Figure 1. Geometrical model of (a) corrugated core (cross section), (b) single core of C1, and (c) separated cores of C2.

The SCC and skins of SSCC were characterized by the properties of CF/epoxy twill prepreg (CPF-3327, 353 gsm; TB Carbon, Korea), and the corrugated cores by the properties of continuous carbon fiber (CCF) filament (Markforged, USA) provided by the manufactures (Table 1). To calculate eigenvalue in FEA, both structures were modeled using continuum shell elements (SC8R), and end cover was modeled using shell model (S4R). The boundary conditions were set such that one end was fixed while the other end allowed only axial displacement. The pressure applied to the external face contacted with water such as outer skin and end cover (Fig 2.).

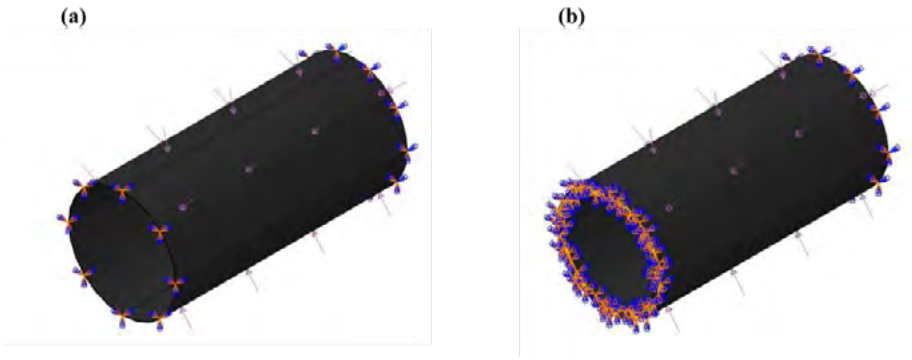


Figure 2. Simulation conditions of (a) composite cylinder structure and (b) sandwich structure with corrugated core.

Table 1. Material properties provided by manufacturer.

Properties	Symbol	CF/epoxy twill	CCF filament
Elastic modulus [GPa]	E_1	56.0	60.0
	E_2	56.0	22.4
Shear modulus [MPa]	G_{12}	4.6	5.0
	G_{13}	4.6	5.0
	G_{23}	2.3	2.5
Poisson's ratio	ν_{12}	0.3	0.33
Tensile strength [MPa]	X^T	430	726
	Y^T	430	115
Compressive strength [MPa]	X^C	340	320
	Y^C	340	131

3. Result and Discussion

3.1. Linear buckling of cylindrical composite

As a results of the linear buckling analysis for a SCC made with twill woven fabric, buckling deformation occured in the cylinder's overall shape. The Fig 3. shows displacement magnitude of the composite cylinder buckling with scale factor of 20. The red region showed significant deformation, while the blue region showed relatively less deformation, displaying a four-lobed shape in the first mode (Fig 3.). The critical buckling pressure derived from the linear analysis was 0.3 MPa. Furthermore, large mode shape has more

3.2. Buckling analysis of sandwich structure with corrugated core

The buckling analysis of the sandwich structure showed more complex buckling shapes compared to a composites cylinder due to the support by the core. Because the internal core supporting the skin enhanced buckling load, SSCC have critical load more than 10 times that of the composite cylinder. The Fig 4. presents the critical load of the first buckling mode of the sandwich structure according to core length, and it also shows first buckling mode shape. In Fig 4., a sandwich structure with a single core (C1) showed buckling across the entire skin similar to composite cylinder (SCC). However, as the number of separated and rotated cores increased, localized buckling behavior was observed. Furthermore, as the number of cores increased, there was a significant increase in the critical buckling load. The sandwich structure with the most separated cores at a core length of 50 mm (C9) showed more than 1.7 times increase in critical bucking strength compared to the structure with a single core (C1).

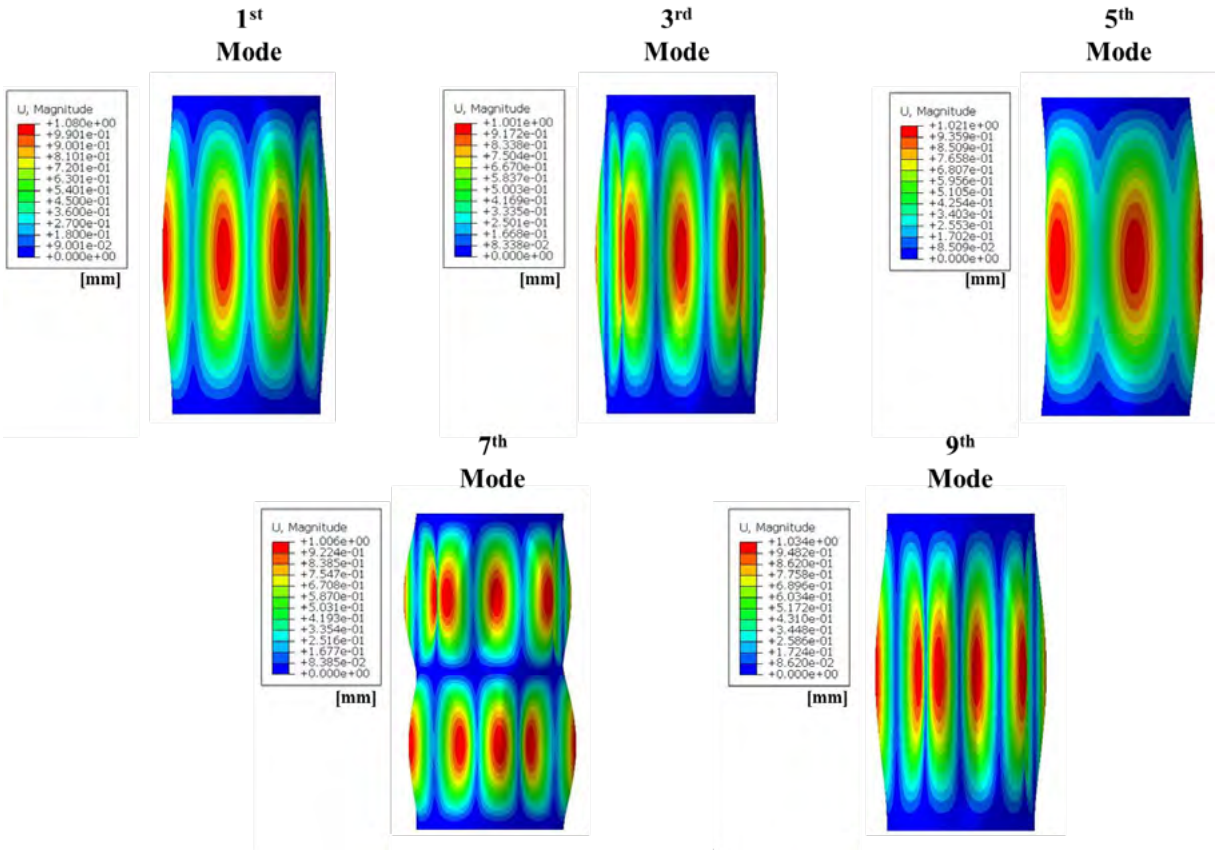


Figure 3. Linear buckling mode shape of cylindrical composite

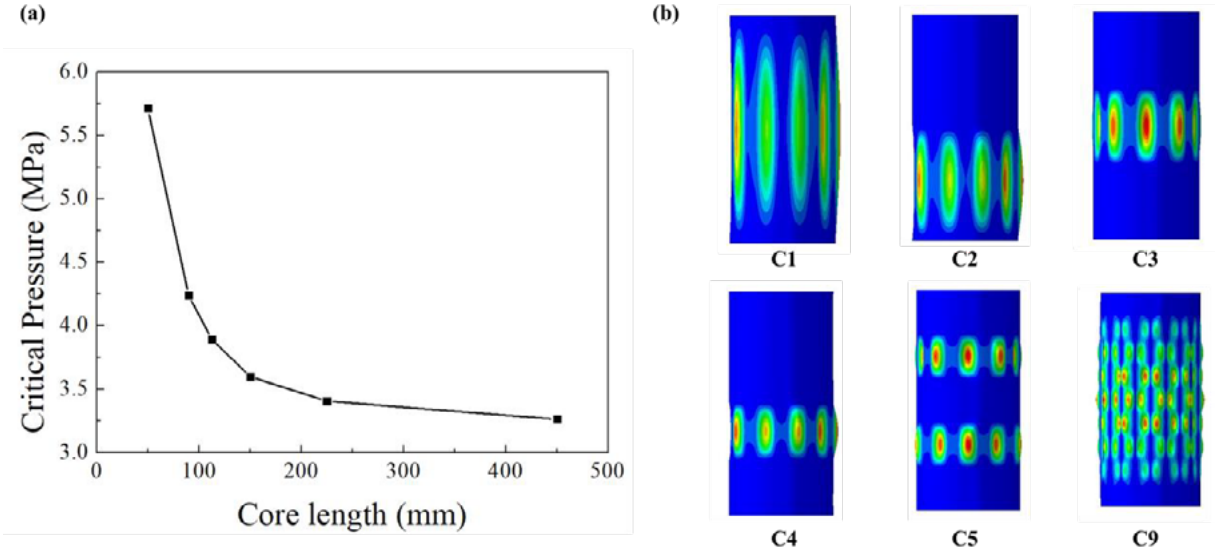


Figure 4. Linear buckling simulation results of sandwich structure according to core length: (a) critical pressure, and (b) first mode shape.

4. Conclusion

In this work, a sandwich structure which was designed with corrugated core was applied to underwater vehicle, and a buckling analysis under hydrostatic pressure was conducted using FEA. For cylinders composed with twill woven CFRP composites, the buckling load was around 0.3 MPa. On the other hand, buckling load of SSCC was enhanced more than 10 times that of the composite cylinder due to the internal core supporting the skin enhanced. Moreover, the critical buckling pressure increased as having more split cores. However, in the case of buckling failure, the actual buckling occurs at a lower pressure than the linear buckling pressure due to the nonlinearity in the manufacturing process such as imperfection. Additionally, to analyze failure of SSCCs under hydrostatic pressure, the relationship between buckling and material failure should be considered. Therefore, it will be anlyzed and verified in nonlinear analysis of composite cylinder and sandwich structures to predict the actual buckling pressure with experiment in next step.

Acknowledgments

This work was supported by the Agency For Defense Development by the Korean Government(UD230502DD) and it also supported by Korea Insititute of Energy Technology Evaluation and Planning (KETEP) grant funded by the Korea government(MOTIE)(2021202080090, Development and Demonstration of Energh-Efficiency Enhanced Technology for Temperature-Controlled Transportation and Logistics Center).

References

[1] X. Zuo, J. Zhang, W. Tang, Y. Li and H. Li. Buckling behavior of steel-composite cylinders under external pressure, *Thin-Walled Structures*, 181:110011, 2022.
[2] H. Y. Kim, Y. K. Shin, S. Y. Kim, B. Y. Chung, J. H. Jo and H. S. Kim. Structural Design of Small Submarine Pressure Hull, *Journal of the Society of Naval Architects of Korea,* 49(2):116-123, 2012.
[3] S. Xu, J. Lin, B. Liu, Y. Garbatov, Y. Wang and C. Guedes Soares, Experimental and numerical buckling analysis of cylindrical pressure hulls with multi-circular openings, *Ocean Engineering*, 214:107689, 2020
[4] X. Zhang, Z. Li, P. Wang, and G. Pan, Experimental and numerical analyses on buckling and strength failure of composite cylindrical shells under hydrostatic pressure, *Ocean Engineering*, 249:110871, 2022
[5] S. H. Hur, H. J. Son, J. H. Kweon, and J. H. Choi, Postbuckling of composite cylinders under external hydrostatic pressure, *Composite Structures*, 86:114-124, 2008
[6] X. Zhang, Y. Liu, Z. Chen, Z. Yang, R. Hu, and G. Pan, Buckling and material failure analyses for ring-stiffened composite shells subjected to hydrostatic pressure, *Applied Ocean Research*, 146:103944, 2024
[7] C. J. Moon, I. H. Kim, B. H. Choi, J. H. Kweon, and J. H. Choi, Buckling of filament-wound composite cylinders subjected to hydrostatic pressure for underwater vehicle applications, *Composite Structures*, 92:2241-2251, 2010
[8] G. C. Lee, J. H. Kweon, and J. H. Choi, Optimization of composite sandwich cylinders for underwater fehicle application, *Composite Structures*, 96:691-697, 2013
[9] H. J. Um, N. H. Jeon, J. H. Shin, and H. S. Kim, High-performance multifunctional energy storage-corrugated lattice core sandwich structure via continuous carbon fiber (CCF)/polyamide6 (PA6) 3D printing, *Advanced Composite and Hybrid Materials*, 6:182, 2023

TEMPERATURE DISTRIBUTION ESTIMATION USING NEURAL NETWORKS IN COMPOSITE MATERIALS MANUFACTURING: A SOFT COMPUTING APPROACH

Jhonny de Sá Rodrigues[1], Paulo Teixeira Gonçalves[2], and N. D. Gonçalves[3]

[1]LAETA - Associate Laboratory for Energy, Transports and Aerospace, Porto, Portugal, email: jsrodrigues@inegi.up.pt
[2]LAETA - Associate Laboratory for Energy, Transports and Aerospace, Porto, Portugal, email: prgoncalves@inegi.up.pt
[3]LAETA - Associate Laboratory for Energy, Transports and Aerospace, Porto, Portugal, email: ngoncalves@inegi.up.pt

Keywords: Automated Fibre Placement, Physics-Informed Neural Networks, State estimation, Model Predictive Control, Soft computing.

Abstract
As the demand for high-performance composite structures increases, the manufacturing of composite materials continues to be a very active research field, seeking to attend to such demand by improving the quality of manufactured components with reduced costs. One of the research topics involves manufacturing process control. Controlling such processes can be challenging due to the difficulty of placing sensors at the required locations, so a technique known as virtual sensing is preferred. This technique implyes having a detailed model of the process, and such model requires running in real time along the process itself. Depending on the process complexity, the model cannot run in real time, so alternative methods must be researched. In this work, a soft computing approach is presented based on artificial neural networks trained using physics equations. The goal is to determine the temperature distribution along a composite material inside a mould. This approach also includes a framework to define an adimentional set of geometry and the thermal properties of the materials involved.

1. Introduction

Before a composite process begins to produce structures, some studies are performed to determine the optimal manufacturing conditions. A recently developed strategy to address such topics is the Virtual Testing [1, 2, 3]. It has been developed as an approach that employs simulation tools for analyzing composite structures, beginning with conceptualization and, more recently, throughout the production process.

During the conceptualization part, researchers develop advanced numerical simulations [4], not only for design purposes but also to determine appropriate manufacturing process conditions to attend to the strict design requirements of high-performance structures.

Once those conditions are determined, the next step is to produce the structure. Typically, the manufacturing process conditions won't change once the process starts. This is due to the difficulty of placing sensors to monitor its progress, which allows a system to compute control actions by closing a control loop, which increases the probability of producing a structure that does not meet the required performance.

To close the control loop, a typical strategy consists of using a state estimator. The state estimator uses the gathered information about the process input variables and boundary variables to estimate its state. To achieve that goal, this strategy requires a model to simulate the process in real time, which can be challenging to implement.

This work explores a framework for a state estimation strategy using Physics-Informed Neural Networks (PINN). Recently, PINNs have been implemented to solve problems by fast computing system predictions [5, 6, 7]. It bases its predictions on the initial state of a process and its interactions with its bounds by proposing a Neural Network as the solution to the differential equation that describes the process. As a demonstration, it is used in the heating stage of a Resin Transfer Mould process.

2. Physics-Informed Neural Networks

To understand the working strategy of a PINN, it is recommended to first understand the formulation of an artificial neural network.

2.1. Artificial Neural Networks

Artificial Neural Networks have been developed since the 1950's inspired by rats cortex functioning [8, 9]. A Neural Network is a set of simple computational units, perceptrons, Fig. 1a, where a set of inputs is multiplied by weights and its sum with a bias is sent to an activation function.

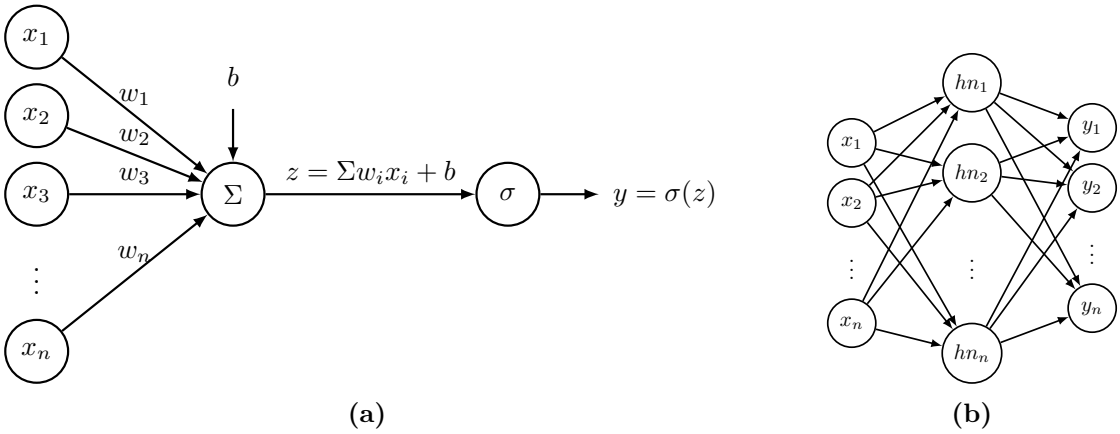


Figure 1: Graphical representation of a Perceptron (1a), and a Neural Network (1b)

In Neural Network a set of inputs can feed a set of perceptrons, forming a layer, and an entire neural network is composed of multiple of those layers, Fig 1b.

For the training process for the neural network, it is generally required to have a set of data with real inputs and real results from such input data over the real system. Then, weights w_n are initialized with a random number. The input data x_n is evaluated to obtain a result y_n. Such result is compared with the real result that such input is supposed to obtain. The difference between those values are used by an optimization algorithm to compute a net set of weights w_n

to reduce such gap. The process is repeated until that gap is zero or lower than a tolerance value.

2.2. Physics-Informed Neural Networks

The concept of a PINN is similar to that of a regular neural network. A PINN was first suggested in 1998 as an alternative to solving differential equations [10]. The training stage is the main difference between a regular neural network and a PINN. For a PINN, the training data does not have the output values; instead, the network has to solve a differential equation that is forced to be zero. For the PINN strategy, the neural network is suggested as a solution for the differential equation shown in Eq. 1; the solution is of the form of $f(x) = \mathcal{N}(X, w, b)$.

$$\frac{\partial f(x)}{\partial x} - g(x) = 0 \tag{1}$$

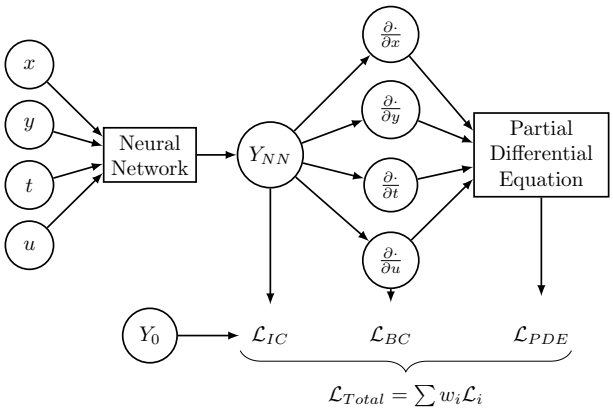


Figure 2: Physics-Informed Neural Network graphical representation

The differential equation is evaluated by deriving the found solution $f\mathcal{N}(X, w, b)$ with respect to the input variables, evaluating the input data values, and then checking the error generated by evaluating the differential equation. This derivative is possible by applying the chain rule or, more recently, by using an automatic differentiation algorithm [11].

3. Methods and materials

In this section, we present the details of the problem used to test the proposed methodology, which aims to utilise a dimensionless model compatible with neural networks.

3.1. Framework

Let's suppose a two-dimensional heat transfer problem, whose general equation is presented in Eq. 2.

$$\frac{\partial T}{\partial t} = \frac{k}{\rho\, c_p}\frac{\partial^2 T}{\partial x^2} + \frac{k}{\rho\, c_p}\frac{\partial^2 T}{\partial y^2}, \tag{2}$$

where T is the temperature of the material, t is the time, k is the thermal conductivity, ρ is the material density, and c_p stands for the specific heat capacity.

Let's suppose that the problem is a rectangle in which x direction has a length of L and the

y direction has a length of H, where $L > H$. The goal is to use the x direction length as a reference, so the following variables change are proposed: Eq. 3 and Eq. 4.

$$x = \chi\, L \tag{3}$$

$$y = \psi\, H \tag{4}$$

where $H = a \cdot L$, and a is a proportioonal constant, and χ and ψ are dimensionless variables in the following range $[0, 1]$. On the other hand, for the time variable change, as it has to maintain the dimensionless nature of the main equation, the proposed variable change is expressed in Eq. 5.

$$\frac{\rho \cdot c_p \cdot L^2}{k}\tau, \tag{5}$$

where τ is the temporal dimensioless variable in the range $[0, \infty)$. The last variable change is related to the temperature, where a dimensionless temperature variable in the range of $[0, 1]$ is proposed as shown in Eq. 6.

$$\theta = \frac{T - T_o}{T_m - T_o} \tag{6}$$

where θ is the dimensionless temperature, T is the temperature at a specific location, T_m is the maximum expected temperature, and T_o is the minimum temperature. Replacing Eq. 3, Eq. 4, Eq. 6 and Eq. 5 into Eq. 2 and making all the variable manipulation, we can obtain the dimensioless expression presented in Eq. 7.

$$\frac{\partial \theta}{\partial \tau} = \frac{\partial^2 \theta}{\partial \chi^2} + \frac{1}{a^2}\frac{\partial^2 \theta}{\partial \psi^2}, \tag{7}$$

where the coefficient a^2 stands to correct the geometrical difference between the x and y directions.

3.2. Case of study

Resin Transfer Moulding is a composite manufacturing process that consists of injecting resin into a mould filled with a type of reinforcement. In some cases, the mould needs to be at a certain temperature for the process to take place. Let's consider a section at the interface between the mould and the composite material as presented in Fig. 3. We would apply the framework presented in Section 3.1 for the material 1.

For material 2, as it is a composite, it is expected that the thermal properties, specifically the thermal conductivity, will be different for the x and y directions. The same framework is applied, according to the thermal and physical properties of material 2 presented in Table 1.

When working with a composite material, the framework has to be applied to both materials, always referencing material 1 for the properties and the length along the x direction. For this case, the differential equations to be solved by the PINN strategy for material 1 and material 2 are Eq.8 and Eq. 9 respectively.

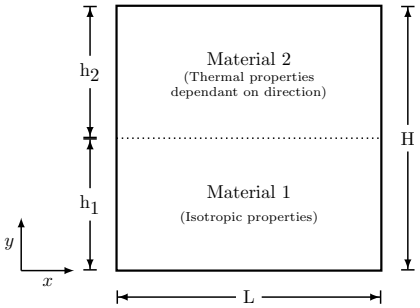


Figure 3: Schematic of the interface mould-composite

Table 1: Material's properties

Property	**Material 1**	**Material 2**
Thermal conductivity	1.0	10.0 (x direction)
		0.01 (y direction)
Specific heat	1.0	15.0
Density	1.0	5.0

$$\frac{\partial \theta}{\partial \tau} = \frac{\partial^2 \theta}{\partial \chi^2} + 400\,\frac{\partial^2 \theta}{\partial \psi^2} \tag{8}$$

$$\frac{\partial \theta}{\partial \tau} = 0.13\,\frac{\partial^2 \theta}{\partial \chi^2} + 0.053\,\frac{\partial^2 \theta}{\partial \psi^2}, \tag{9}$$

where the geometrical factor is reflected as the coefficient of the second term in Eq. 8, the coefficient of the first term of Eq. 9 stands for the property correction, and a combination of geometrical and property coefficients is present at the second term of the same equation.

For demonstration purposes, the boundary conditions in this case will be defined as follows:

- The initial condition will be set to a uniform temperature of 0.2
- The right-hand side of the domain will be adiabatic, as well as the left-hand side od the domain
- The bottom surface will be set at a constant temperature of 0.6
- The upper surface will be set at a constant temperature of 0.2

4. Results

The neural network architecture used consists of 4 inputs, 3 hidden layers of 15 neurons each, and one output. The inputs are: x coordinate, y coordinate, t time step, and the initial temperature T_0 for each pair of coordinates x, y. A set of 121 collocation points was selected, dividing the x direction into 11 parts as well as the y direction and 301 time steps. 50000 epochs were used to train the entire model. Fig. 4 shows the loss evolution along the training stage of the neural network.

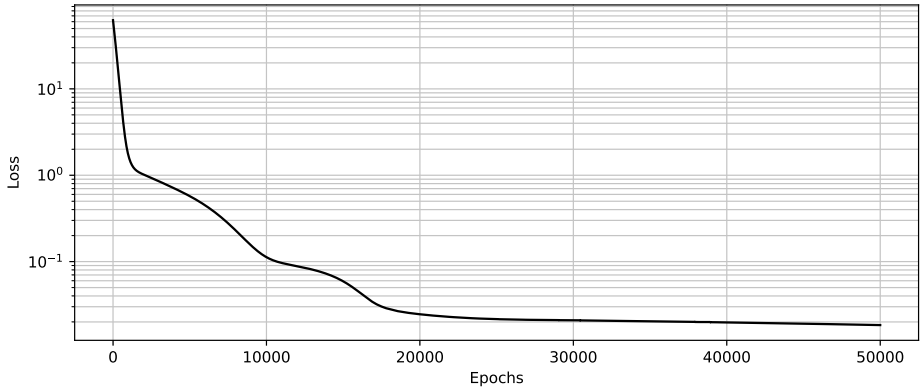
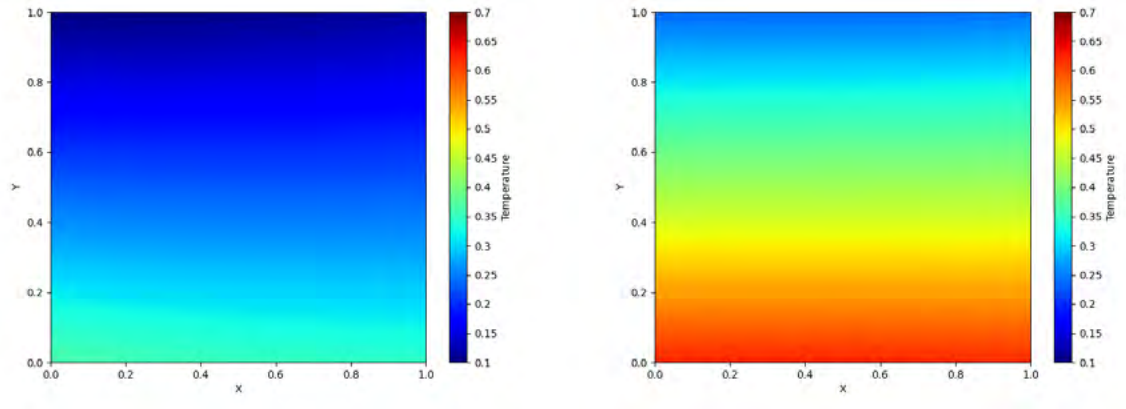


Figure 4: Train loss along the 50000 epochs



(a) **(b)**

Figure 5: Temperature distibution for the initial conditions (5a). Temperature distibution for the final conditions (5b)

The results presented in Fig. 5a show the temperature distribution at the initial conditions. The non-uniformization of data can be attributed to the randomness of the initialization of the neural network.

Fig. 5b shows the temperature distribution after a simulation of 1.5 τ. It is visible that the lower half of the domain has a higher and more consistent temperature compared to the upper half, due to the difference between the thermal conductivities of both materials.

5. Conclusions

In this work, a neural network was trained using the proposed framework. This framework allows us to address the orthotopic nature of composite materials, referring to their thermal properties, to handle the physics of the problem.

The framework allows the inputs of the resulting neural network to be on the same scale, guaranteeing the numerical stability of the method.

This framework can be scalable to any geometry in a two-dimensional plane, allowing its implementation to solve similar problems. On the other hand, as the framework does not depend on

units, it can be used to comprare two similar systems with different dimensions.

Acknowledgments
This work has been supported by the European Union under the Next Generation EU, through a grant of the Portuguese Republic's Recovery and Resilience Plan (PPR) Partnership Agreement, within the scope of the project PRODUTECH R3 - "Agenda Mobilizadora da Fileira das Tecnologias de Produção para a Reindustrialização", Total project investment: 166.988,71 Euros; Total Grant 97.111.730.27 Euros.

References

[1] R. J. D'Mello, M. Maiarù, and A. M. Waas. "Virtual manufacturing of composite aerostructures". en. In: *The Aeronautical Journal* 120.1223 (Jan. 2016), pp. 61–81. ISSN: 0001-9240, 2059-6464. DOI: 10.1017/aer.2015.19.

[2] Royan J. D'Mello and Anthony M. Waas. "Virtual curing of textile polymer matrix composites". en. In: *Composite Structures* 178 (Oct. 2017), pp. 455–466. ISSN: 02638223. DOI: 10.1016/j.compstruct.2017.05.045.

[3] Morten G. Ostergaard et al. "Virtual testing of aircraft structures". en. In: *CEAS Aeronautical Journal* 1.1-4 (Sept. 2011), pp. 83–103. ISSN: 1869-5582, 1869-5590. DOI: 10.1007/s13272-011-0004-x.

[4] Jhonny de Sá Rodrigues et al. "Modelling the Heating Process in the Transient and Steady State of an In Situ Tape-Laying Machine Head". In: *Journal of Manufacturing and Materials Processing* 6.1 (Jan. 2022), p. 8. ISSN: 2504-4494. DOI: 10.3390/jmmp6010008.

[5] Jochen Stiasny and Spyros Chatzivasileiadis. "Physics-informed neural networks for time-domain simulations: Accuracy, computational cost, and flexibility". In: *Electric Power Systems Research* 224 (Nov. 2023), p. 109748. ISSN: 0378-7796. DOI: 10.1016/j.epsr.2023.109748.

[6] Jonas Nicodemus et al. "Physics-informed Neural Networks-based Model Predictive Control for Multi-link Manipulators". In: *IFAC-PapersOnLine*. 10th Vienna International Conference on Mathematical Modelling MATHMOD 2022 55.20 (Jan. 2022), pp. 331–336. ISSN: 2405-8963. DOI: 10.1016/j.ifacol.2022.09.117.

[7] Florian Arnold and Rudibert King. "State–space modeling for control based on physics-informed neural networks". In: *Engineering Applications of Artificial Intelligence* 101 (May 2021), p. 104195. ISSN: 0952-1976. DOI: 10.1016/j.engappai.2021.104195.

[8] Frank Rosenblatt. *A perceiving and recognizing automation*. Tech. rep. Cornell Aeronautical Laboratory, Jan. 1957.

[9] Jean Rabault et al. "Deep reinforcement learning in fluid mechanics: A promising method for both active flow control and shape optimization". In: *Journal of Hydrodynamics* 32 (2020). Publisher: Springer, pp. 234–246.

[10] I.E. Lagaris, A. Likas, and D.I. Fotiadis. "Artificial neural networks for solving ordinary and partial differential equations". In: *IEEE Transactions on Neural Networks* 9.5 (Sept. 1998). Conference Name: IEEE Transactions on Neural Networks, pp. 987–1000. ISSN: 1941-0093. DOI: 10.1109/72.712178.

[11] Lawrence CW Dixon. "Use of automatic differentiation for calculating Hessians and Newton steps". In: *Automatic Differentiation of Algorithms: Theory, Implementation, and Application* (1991), pp. 114–125.

FATIGUE NOTCH SENSITIVITY OF WOVEN CFRP LAMINATE UNDER DIFFERENT *R*-RATIO LOADINGS - EXPERIMENT AND MODELING -

M. Kawai

Department of Engineering Mechanics and Energy, University of Tsukuba, Tsukuba 305-8573, Japan
Email: mkawai@kz.tsukuba.ac.jp

Keywords: fatigue, notch effect, fading notch sensitivity, stress ratio, analytical model

Abstract
Constant amplitude fatigue tests are performed on notched specimens of a woven fabric carbon/epoxy laminate for different notch sizes and stress ratios, respectively, and the effects of these factors on the notched fatigue behavior are examined. A new model applicable to the notched fatigue of compsoites is developed which can predict the notched S-N relationship for any notch size and stress ratio by means of the unnotched S-N relationship for the same value of stress ratio. The capability of the model to predict the notch sensitive and insensitive bounds of fatigue life for a given composite with help of the unnotched fatigue bahavior is highlighted. It is shown that the proposed method can successfully predict the notched fatigue life of the woven CFRP laminate for different notch sizes and stress ratios.

1. Introduction

Structural components in engineering applications often contain notches or holes. Because of stress concentration caused by those stress risers, the local failure in machines and structures during service is apt to initiate at the edges or in the vicinity of the notches or holes involved. The degree of reduction in strength of a carbon fiber-reinforced plastic (CFRP) laminate due to a notch is governed by the intensity of stress concentration in the vicinity of the notch that is affected not only by the inherent elastic anisotropy but also by the multiple non self-similar cracking in the composite laminate. This suggests that a CFRP laminate exhibits a notch sensitivity within the notch sensitive and insensitive bounds, depending on stacking configuration as well as on damage in the vicinity of notch tips. A more important suggestion in the present context is that the notch sensitivity of a CFRP laminate may not be constant but it may be changed during service depending on the accumulation of damage at notch tips as well as in the ligaments that controls the progressive dissipation of local strain energy.

The notch effect in fatigue of CFRP laminates is practically very important for accurate evaluation of their fatigue lives [1]. Notched fatigue of composites is considered to be affected by the stress ratio of fatigue loading, since the difference in load waveform has a significant influence on the fatigue strength in their unnotched configuration [2, 3]. The change in notch sensitivity during fatigue loading, however, has not quantitatively been examined for carbon fiber composites subjected to different *R*-ratio loadings. In order to fully understand and quantify the wear-in and wear-out behaviors of notched CFRP laminates [4], we need more systematic studies on their notched fatigue behaviors from both experimental and modeling points of view.

In the present study, fatigue tests are performed on unnotched and notched woven fabric carbon/epoxy laminate specimens for different notch sizes as well as for different stress ratios, respectively, including tension-tension (T-T), tension-compression (T-C) and compression-compression (C-C) waveforms, at room temperature. Experimental results show a gradual decrease in sensitivity to a notch during fatigue

loading, regardless of stress ratio. A measure of fatigue notch sensitivity is defined, and it is successfully used to quantify the transient notch effect on fatigue by contrasting the observed unnotched and notched S-N relationships for each of different R-ratios. A simple and effective model is developed to predict the notched fatigue life of a given composite for any notch size as well as for any stress ratio. A further development into a more general version is attempted that allows describing the gradual decrease in fatigue notch sensitivity with cyclic loading. It is also demonstrated that the general notched fatigue life prediction model can describe the wear-in behavior of residual notch strength of the woven composite taking into account the effect of R-ratio.

2. Specimen and experimental procedure

2.1. Material

Carbon fiber plain weave roving fabric laminates were used. The woven prepreg cloths were made of carbon fibers T300 (Toray) and thermosetting epoxy resin #2500 with the curing temperature of 130°C. A woven CFRP laminate consists of 12 sheets of prepregs aligned in the same orientation and molded using an autoclave.

Central circular-hole specimens were employed. The length and width of the circular hole specimens are identical to those of the unnotched specimens (L = 10 mm, W = 10 mm). The circular holes were machined using a drill with a special jig. The relative notch sizes D/W, which are the ratios of the diameter D of the circular hole to the specimen width W, were set to D/W = 0.1, 0.2, and 0.4 for static tests and to D/W = 0.1 and 0.4 for fatigue tests.

2.2. Testing

Constant amplitude fatigue tests were performed under load control at room temperature with a sinusoidal waveform at a constant frequency of f = 10 Hz. To examine the effect of stress ratio (fatigue waveform) on S-N behavior, constant-amplitude fatigue tests were performed for different constant values of stress ratio R, which is equal to the ratio of minimum stress to maximum stress $\sigma_{min}/\sigma_{max}$, respectively. Fatigue tests on unnotched specimens were performed at R = 0.5, 0.1, -0.5, -0.7, -1, -2, 10, 2, and $\chi_0 = \sigma_0^C/\sigma_0^T$, respectively, and on notched specimens at R = 0.1, -0.5, $\chi_N = \sigma_N^C/\sigma_N^T$, -2, and 10, respectively. The stress ratios indicated by χ represent the critical stress ratios [5] which is equal to the ratio of compressive strength to tensile strength of the unnotched and notched specimens, respectively.

3. Experimental results and discussions

The notched fatigue behavior of the woven CFRP is gentle. The notched S-N relationships are close to those obtained by the parallel shift of the unnotched S-N relationship to their lower stress sides by the difference between the unnotched and notched strengths, regardless of stress ratio and notch size.

To observe the effect of stress ratio on the notched fatigue behavior, the notched S-N data are normalized using the associated static notched strength (ψ_N), and the results for D/W = 0.1 are shown in Fig. 1. We can see that the slope of the notched S-N relationship is the largest for the fatigue loading at the notched critical stress ratio, irrespective of notch size. This observation reveals that the concept of critical stress ratio [5], which was confirmed for the unnotched fatigue of the woven CFRP laminate, also holds true for the notched fatigue of the composite tested.

The difference in the shape of the S-N relationship between the unnotched and notched specimens is examined. For this purpose, the S-N data are normalized using their associated static strength. For the unnotched specimens, the fatigue stress is normalized using the unnotched strength (ψ_0). For the notched specimens, the normalization with respect to the static notched strength (ψ_N) and the normalization with respect to the notch insensitive strength (ψ_{NI}) are considered. The comparisons of the normalized notched and unnotched S-N data for R = 0.1 and 10 are shown in Fig. 2 and Fig. 3, respectively.

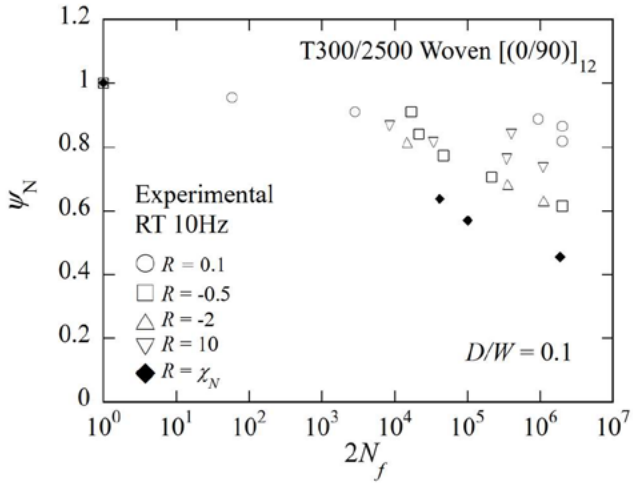


Figure 1. Comparison of notched S-N data for different stress ratios.

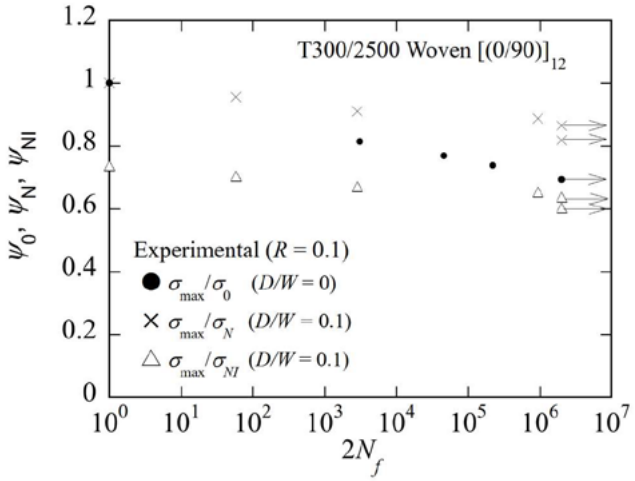


Figure 2. Notch effect on tensile fatigue for $R = 0.1$.

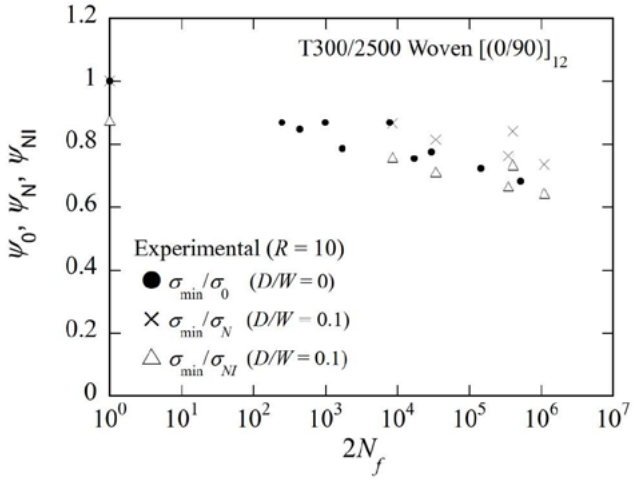


Figure 3. Notch effect on compressive fatigue for $R = 10$.

Compare the plots for the tensile fatigue at R = 0.1. The normalized S-N plots using ψ_{NI}, in which the fatigue stress is divided by the notch insensitive strength, start from the value of fatigue strength ratio smaller than 1 on the vertical axis since the notch insensitive strength is larger than the actual notched strength. In the range of low cycle fatigue, therefore, they are distributed away from the normalized S-N plots for unnotched specimens using ψ_0 to the lower side. As the number of cycles to fatigue failure increases, however, we can see that the normalized S-N plots using ψ_{NI} gradually approach the normalized S-N plots for the unnotched specimens. The latter observation suggests that the notched fatigue at R = 0.1 turns to be dominated by the unnotched fatigue of the ligaments in the high cycle range. In other words, the initial notch effect is fading and the notched fatigue behavior is changing to be notch insensitive.

Looking at the normalized S-N plots for the notched specimens using ψ_N for the tensile fatigue loading at R = 0.1, we can see that they start from the value of 1, since the fatigue stress is divided by the actual notched strength, along with the normalized S-N plots for the unnotched specimens using ψ_0. In contrast to the S-N plots using ψ_{NI} observed above, the normalized S-N plots using ψ_N gradually deviate from the normalized S-N plots for the unnotched specimens using ψ_0 to the upper side as the fatigue life increases. This observation means that the slope of the notched S-N relationship is smaller than that of the unnotched S-N relationship. Thus, the notched fatigue strength relative to the static strength at the onset of fatigue loading is larger than the unnotched fatigue strength. In other words, the fatigue notch sensitivity is lower than the static notch sensitivity for the tensile fatigue loading at R = 0.1.

The compressive notched fatigue behavior for R = 10 is complicated. In the case of the notch size D/W = 0.1, it is seen that the notched S-N data normalized using the notched strength and the notch insensitive strength (ψ_N and ψ_{NI}) are both distributed close to the normalized S-N data (ψ_0) for the unnotched specimens. A bit closer observation reveals that the normalized S-N data (ψ_N) with respect to the notched strength tend to be distributed slightly above the normalized S-N data (ψ_0) with respect to the unnotched strength in the range of high cycle fatigue. Conversely, the normalized S-N relationship with respect to the notch insensitive strength (ψ_{NI}) tends to be slightly below the normalized S-N relationship for the unnotched specimens in the high-cycle range. However, the difference in normalized stress in the high-cycle range is small in both cases using ψ_N and ψ_{NI}. This prompts us to consider that the notch effect may have substantially disappeared in the high cycle range.

Observing the results for D/W = 0.4, we can see the normalized S-N data using the notched strength are distributed slightly above the normalized S-N data for the unnotched specimens, similar to the case for D/W = 0.1. As for the normalized S-N plots with respect to the notch insensitive strength, we can see they are clearly away from the normalized S-N plots for the unnotched specimens to the lower side, and they seem to be almost parallel to each other up to the high cycle range. The latter observation suggests that the normalized S-N relationship using the notch insensitive strength does not fully approach the normalized S-N relationship of the unnotched specimens even in the high cycle range. This feature observed in the notched fatigue for D/W = 0.4 implies that the decrease in notch sensitivitywith fatigue is small and thus the notched fatigue behavior is moderately notch sensitive even in the high-cycle range. In another compression-dominated notched fatigue at the stress ratio R = -2, we observed similar effect of notch on fatigue behavior as well. The compressive notched fatigue behavior thus suggests an influence of notch size.

4. Modeling of notched fatigue behavior

4.1. Fatigue notch factor

In order to establish a quantitative relationship between the unnotched and notched S-N relationships for loading at the same stress ratio, the fatigue notch factor is defined as

$$K_{f(net)}(N_f) = \frac{\sigma^0_{\max}(N_f)}{\sigma^N_{\max(net)}(N_f)} \tag{1}$$

The fatigue notch factor expresses the extent to which the presence of a notch reduces the fatigue strength of a notched specimen from the fatigue strength of a unnotched specimen. It is an important quantitative measure of the effect of notch on fatigue. Note that the variables with the subscript of *net* are on the net-section basis.

4.2. Equivalent notched fatigue strength ratio

Normalizing the unnotched and notched fatigue stresses in Eq. 1 using the associated static strengths, we can obtain the relationship between the fatigue strength ratios for unnotched and notched specimens;

$$\psi_N(N_f) = \frac{1}{K_f^*(N_f)}\psi_0(N_f) \tag{2}$$

where

$$\psi_N = \frac{\sigma_{\max}^N}{\sigma_N} \tag{3}$$

$$\psi_0 = \frac{\sigma_{\max}^0}{\sigma_0} \tag{4}$$

$$K_f^*(N_f) = K_{f(net)}(N_f)\frac{\sigma_{N(net)}}{\sigma_0} \tag{5}$$

The modified fatigue notch factor defined by Eq. 5 has an important role to play, because it can be interpreted as a transformation that relates the normalized S-N relationship for notched fatigue to the normalized S-N relationship for unnotched fatigue;

$$K_f^*(N_f)\psi_N(N_f) = \psi_0(N_f) \tag{6}$$

Defining the left-hand side of Eq. 6 as

$$\psi_N^*(N_f) = K_f^*(N_f)\psi_N(N_f) \tag{7}$$

we can express Eq. 6 as

$$\psi_N^*(N_f) = \psi_0(N_f) \tag{8}$$

Eq. 8 explains that the modified notched fatigue strength ratio defined by Eq. 7 is equivalent to the unnotched fatigue strength ratio for loading at the same stress ratio. Therefore, the modified notched fatigue strength ratio defined by Eq. 7 may be called the equivalent notched fatigue strength ratio.

4.3. Notched S-N relationship

As observed above, the notched fatigue behavior can be identified with the equivalent unnotched fatigue behavior with the help of the equivalent notched fatigue strength ratio. For fatigue loading at a constant stress ratio R, the S-N relationship for unnotched specimens is expressed as

$$2N_f = f_R(\psi_0) \tag{9}$$

Making use of the concept of equivalent plain material given by Eq. 8, we can express the notched S-N relationship as

$$2N_f = f_R(\psi_N^*) \tag{10}$$

4.4. Specific forms

The S-N relationship of unnotched composites for fatigue loading at a constant stress ratio R can be well described by means of the following fatigue function [6]:

$$2N_f = f_R(\psi_0) = \frac{2}{(1+k)K}\frac{1}{\psi_0^{\,n}}\frac{\langle 1-\psi_0\rangle^a}{\langle \psi_0 - \psi_{0W}\rangle^b} \tag{11}$$

where the coefficients $(1+k)K$, a, b, n, and ψ_{0W} are determined by fitting to the unnotched S-N data for a stress ratio of interest. Using the equivalent notched fatigue strength ratio and the unnotched S-N function, we can express the notched S-N relationship as

$$2N_f = f_R(\psi_N^*) = \frac{2}{(1+k)K}\frac{1}{\psi_N^{*\,n}}\frac{\langle 1-\psi_N^*\rangle^a}{\langle \psi_N^* - \psi_{0W}\rangle^b} \tag{12}$$

for fatigue loading at R.

4.4.1. Notch sensitive S-N behavior

In the case of notch-sensitive fatigue, the equivalent notched fatigue strength ratio may be considered as the notch sensitive fatigue strength ratio; $\psi_N^*(N_f) = \psi_N(N_f)$. Accordingly, the notch-sensitive S-N relationship can be expressed as

$$2N_f = \frac{2}{(1+k)K}\frac{1}{\psi_N^{\,n}}\frac{\langle 1-\psi_N\rangle^a}{\langle \psi_N - \psi_{0W}\rangle^b} \tag{13}$$

4.4.2. Notch insensitive S-N behavior

For a notch insensitive fatigue behavior, the equivalent notched fatigue strength is given as $\psi_N^*(N_f) = \psi_{NI}(N_f)$. The baseline strength at the onset of fatigue of notched specimens is the static notched strength. Taking into account this initial condition, we can express the notch insensitive S-N relationship as

$$2N_f = \frac{2}{(1+k)K}\frac{1}{\psi_{NI}^{\,n}}\frac{\langle 1-\psi_N\rangle^a}{\langle \psi_{NI} - \psi_{0W}\rangle^b} \tag{14}$$

The notch insensitive S-N model may be identified with the vanishing notch sensitivity model [7].

4.5. Comparison with experimental results

The notch-sensitive and notch-insensitive S-N relationships provide the lower and upper bounds of notched fatigue life. The predicted notch-sensitive and notch-insensitive S-N relationships for the woven CFRP laminate are compared with the experimental results in Fig. 4 and Fig.5 for R = 0.1 and 10, respectively. We can see that the measured notched S-N data are distributed between the notch-sensitive and notch-insensitive S-N relationships, regardless of stress ratio.

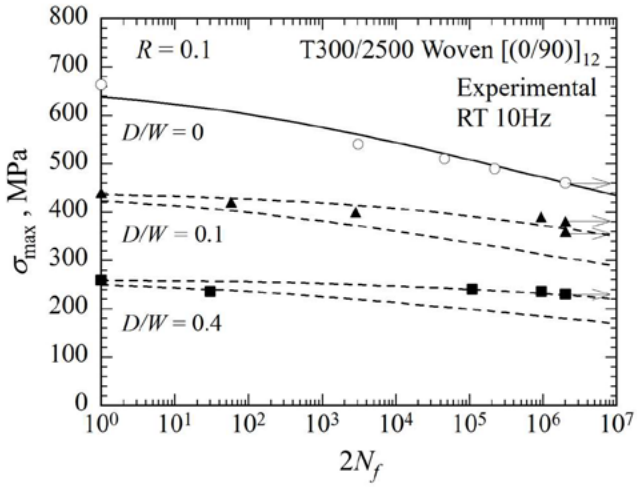


Figure 4. Notch sensitive and insensitive S-N relathionships for $R = 0.1$.

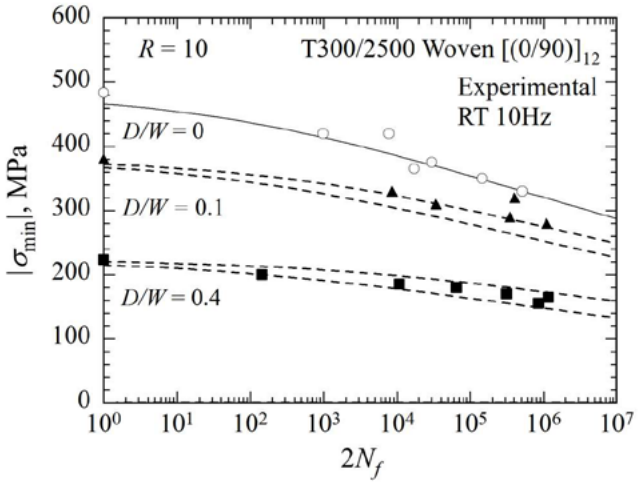


Figure 5. Notch sensitive and insensitive S-N relathionships for $R = 10$.

The notch-sensitive S-N relationship can be easily predicted utilizing the unnotched S-N relationship and the static notched strength. The notch sensitive S-N relationship represents the lower bound of notched fatigue life, and thus the use of it allows a conservative prediction of notched fatigue life, regardless of stress ratio. In case of no knowledge of the transition of fatigue notch sensitivity, therefore, the notch-sensitive S-N relationship is a safe choice. For compressive fatigue loading, as seen in Fig. 5, it is a good choice as well because the prediction is moderately conservative, not too much, and the degree of accuracy of prediction is acceptable. For tensile fatigue loading, however, the transition to notch insensitivity is rapid as seen in Fig. 4, so the use of the notch-sensitive S-N relationship for the actual notched fatigue behavior is too conservative while it is on the safe side. The latter observation suggests a need for developing a notched fatigue model that takes into account a stress-ratio dependent transition of fatigue notch sensitivity.

5. Conclusions

The effects of stress ratio and notch size on the fatigue behavior (S-N relationship) of plain weave roving fabric CFRP laminate were investigated in detail by experiments. Based on the comparison of the S-N relationships of unnotched and notched specimens for the same stress ratio, the fatigue notch factor was

defined, and the dependence on stress ratio and notch size was quantitatively elucidated. A method was developed to predict the S-N relationships of notched specimens for different constant values of stress ratio by means of the S-N relationships of unnotched specimens for the same stress ratios and the static notched strengths. It was shown that the notch insensitive and notch sensitive S-N relationships, which correspond to the upper and lower bounds of notched fatigue life, respectively, can be predicted easily using the unnotched S-N relationship and static notched strength and they actually bound the measured S-N data for notched specimens.

Further development into a more general methodology will be presented in which a gradually decreasing fatigue notch sensitivity is modelled taking into account the continuous reduction of notch sensitivity due to fatigue as well as its dependence on stress ratio. It allows to formulate a general notched fatigue life prediction method. The general notched fatigue life prediction method is applied to predict the S-N relationships corresponding to the experiments for different stress ratios, and they are evaluated by comparing with the experimental results. A capability of the gradually fading fatigue notch sensitivity model to predict the wear-in behavior of residual notch strength during fatigue loading is also demonstrated.

Acknowledgment
This study was supported by the Ministry of Education, Culture, Sports, Science and Technology of Japan under a Grant-in-Aid for Scientific Research.

References
[1] P.T. Curtis and B.B. Moore. A comparison of the fatigue performance of woven and non-woven CFRP laminates in reversed axial loading. *International Journal of Fatigue*, 9(2):67-78, 1987.
[2] M. Kawai. A phenomenological model for off-axis fatigue behavior of unidirectional polymer matrix composites under different stress ratios. *Composites Part A*, 35:955-963, 2004.
[3] M. Kawai. Fatigue of composites—life prediction methods—. In *Encyclopedia of Composites*, L. Nicolais and A. Borzacchiello Eds., John Wiley &Sons, Hoboken, New Jersey, 2012.
[4] K.L. Reifsnider, W.W. Stinchcomb and T.K. O'Brien. Frequency effects on a stiffness-based fatigue failure criterion in flawed composite specimens. In *Fatigue of Filamentary Composite Materials*, ASTM STP 636, K.L. Reifsnider and K.N. Lauraitis Eds. 171-184, 1977.
[5] M. Kawai and M. Koizumi. Nonlinear constant fatigue life diagrams for carbon/epoxy laminates at room temperature. *Composites Part A*, 38:2342-2353, 2007.
[6] M. Kawai and T. Taniguchi. Off-axis fatigue behavior of plain weave carbon/epoxy fabric laminates at room and high temperatures and its mechanical modeling. *Composites Part A*, 37(2):243-256, 2006.
[7] M. Kawai and T. Shiratsuchi. Vanishing notch sensitivity approach to fatigue life prediction of notched cross-ply CFRP laminates at room temperature. *Journal of Composite Materials*, 46(23):2935-2950, 2012.

MODELING MOISTURE-INDUCED DEFORMATION IN CFRP BASED ON TWO-PHASE DIFFUSION THEORY

Kazuya Kitamoto[1], Shu Minakuchi[2] and Tomohiro Yokozeki[2]

[1]Research and Development Directorate, Japan Aerospace Exploration Agency (JAXA),
2-1-1 Sengen, Tsukuba-shi, Ibaraki 305-8505, Japan
Email: kitamoto.kazuya@jaxa.jp
[2]Department of Aeronautics and Astronautics, The University of Tokyo,
7-3-1 Hongo, Bunkyo-ku, Tokyo 113-8656, Japan

Keywords: moisture absorption, swelling, CFRP, modeling

Abstract
Water or moisture absorption causes swelling and plasticization of polymers and polymer matrices. The swelling of composite structures is a dominant factor in deteriorating the observational accuracy of space telescopes. Prediction of long-term deformation behavior for stable composite structures is essential for feasibility studies of advanced space missions. This work developed a rational model of nonlinear and hysteretic deformation behavior during moisture absorption and desorption processes using a modified two-phase diffusion theory. The model was based on the findings of water-polymer interactions. The mechanism of water transport was identified by gravimetric analysis and molecular-scale analysis using NMR. Furthermore, macroscopic strain behavior measured by fiber optics sensing resulted from swelling responses induced by anti-plasticization and plasticization effects. The strain model was formulated using a piecewise linear function with respect to the moisture concentration of bound water, which responded to shrinkage due to anti-plasticization and swelling due to plasticization. Consequently, a model for nonlinear and hysteretic deformation behavior in CFRP was successfully developed.

1. Introduction

Carbon fiber reinforced polymer (CFRP) is used in precise structures for space optics due to its excellent material properties (e.g., high specific stiffness, high specific strength, and low thermal expansion). A stable composite structure is crucial for advanced observation missions that demand large optical systems for high pointing accuracy. The development of a model for the evaluation and prediction of the long-term deformation behavior of composite structures is essential for the feasibility studies of such missions. Polymers and polymer-based composites absorb water or moisture, causing physical swelling and plasticization, which can deteriorate the pointing accuracy of observation satellites [1–3]. The nonlinear, hysteretic, and irreversible deformation behaviors observed in polymers during moisture absorption and desorption cycles make predicting these behaviors challenging [1,4–6]. The mechanisms of water transport, swelling, and plasticization due to moisture absorption in the polymers have been experimentally studied [7,8]. Absorbed water in epoxy is categorized into bound water, which interacts with hydrophilic group sites through hydrogen bonding, and free water, which does not form such bonds and is stored in free volume. Advanced techniques such as Fourier transform infrared (FTIR) spectroscopy, nuclear magnetic resonance (NMR), and positron annihilation lifetime spectroscopy (PALS) have been used to investigate water-polymer interactions at the molecular scale [7,8]. Although such findings have partially advanced understanding of the mechanisms, there is no physics-based model that can explain the deformation behavior in connection with molecular-scale mechanisms during the entire process from moisture absorption to desorption.

This study focuses on the development of a rational model based on the physics for the nonlinear, hysteretic, and irreversible deformation behavior during moisture absorption and desorption in epoxy-based CFRP. The model employs a modified two-phase diffusion theory based on findings from analyses of water-polymer interactions at the molecular scale. Specifically, we identify the mechanisms of water transport and swelling through NMR and macroscopic strain measurements. The two-phase diffusion theory, which accounts for water-polymer interactions within a material, is modified based on NMR for water-transport modeling. The strain behavior, measured by optical fiber sensing, is modeled based on the modified two-phase diffusion theory. Lastly, the moisture-induced deformation behavior is evaluated to validate the model.

2. Material testing

The water-polymer interaction and macroscopic strain behavior are evaluated during moisture absorption and desorption in epoxy-based CFRP. Specifically, the state of absorbed water within the polymer is identified by NMR and the moisture-induced strain is measured using optical fiber sensing.

2.1. Sample preparation and moisture test conditions

CFRP samples for material testing were made using unidirectional carbon fiber/epoxy prepregs (T700S/2592, Toray) and were manufactured by a typical autoclave process. All samples were thoroughly dried in a vacuum oven at 100°C until their weight stabilized. For moisture absorption tests, the samples were placed in a constant temperature and humidity chamber at 40°C and 93%RH. For subsequent desorption tests, the samples were placed in a vacuum chamber set at 40°C. The sample's weights were measured using an electronic balance (BP211D, Sartorius). Moisture content $M(t)$ was determined from the gravimetric analysis according to Eq. (1).

$$M(t) = \frac{W(t) - W_{ini}}{W_{ini}} \times 100 \tag{1}$$

where $W(t)$ is the weight of the specimen at time t, and W_{ini} is the initial weight in the dry-out state.

2.2. Methods

Time-domain NMR (TD-NMR) was used to evaluate the mobility of water molecules in moisture-absorbed CFRP. The T_2 relaxation behavior of proton nuclei ^1H in CFRP samples was measured using the Bruker Minispec mq20 (Observation nuclei: ^1H, Resonance frequency: 20 MHz) by the solid echo method. The free induction decay (FID) was interpreted as a superposition of three components: the Hard component, which has extremely low mobility and derives from protons inherently present in the polymer matrix network; the Soft component, which has high mobility and derives from protons in free water; and the Middle component, which represents intermediate mobility and derives from protons in bound water. The moisture uptake of the sample was assumed to be the sum of that of the Middle and Soft components. The moisture content of each component is calculated as the product of its compositional proportion determined through NMR, and the moisture content of the sample is determined through gravimetric analysis. The moisture contents of bound water $M_{bound}(i)$ and free water $M_{free}(i)$ were estimated using Eq. (2), respectively.

$$\begin{aligned} &Bound\ (or\ free)\ water\ content\ M_{bound\ or\ free}(i) \\ &= \frac{Middle\ fraction\ (or\ soft\ fraction)(i)}{Middle\ fraction(i) + \ soft\ fraction(i)} \times Moisture\ content\ M(i) \end{aligned} \tag{2}$$

where i represents the sample number corresponding to different degrees of moisture absorption. Six levels of CFRP specimens (50 mm in length x 50 mm in width x 0.56 mm in thickness, 4 plies) were prepared. Strain measurements by optical fiber sensing were used to evaluate the swelling behavior of moisture-absorbed CFRP [1]. The moisture-induced strain in CFRP samples embedded with polyimide-coated fiber Bragg grating (FBG) sensors (coating diameter: 150 μm, grating length: 1 mm, Technica SA) was measured using an interrogator (sm125, Micron Optics). Two types of specimens (100 mm in length x 25 mm in width x 1 mm in thickness, 8 plies) were prepared for measuring the strain in the fiber and transverse directions.

2.3. Results and discussion

Figure 1 shows the moisture content as a function of the square root of time over the specimen's thickness. As shown in Figure 1(a), an initial increase in bound water is followed by a gradual rise in free water during moisture absorption. The bound water increased proportionately to the square root of time and reached saturation. The Fick-like behavior suggests that the diffusion in bound water is preferential in the water-transport kinetics during absorption. The desorption curve in Figure 1(b) indicates that the initial desorption rate is rapid, then gradually slows, and finally reaches an equilibrium moisture content of approximately 0.05 wt%. The TD-NMR results indicated that free water was rapidly desorbed and eventually completely removed, while bound water was gradually desorbed and remained even at desorption equilibrium. The observation suggests that the diffusion in free water is preferential in the water-transport kinetics during desorption.

Figure 2 shows the moisture-induced strain in the fiber and transverse directions as functions of moisture content. The strain varied nonlinearly with moisture content. During absorption, strain in the fiber direction increased slowly until moisture content exceeded 0.25 wt%, then rose significantly in proportion to moisture content up to 0.55 wt%, and the increase became more gradual above 0.55 wt%. Conversely, during desorption, the reduction in strain was small until 0.55 wt%, and thereafter, the strain decreased significantly in proportion to the moisture content. Similar to the TD-NMR results, desorption equilibrium was reached at a moisture content of approximately 0.05 wt%. The shrinkage strain was observed at the desorption equilibrium. Therefore, during absorption and desorption cycle, nonlinear, hysteretic, and irreversible strain behavior relative to moisture content were observed. The strain behavior in the transverse direction was similar to that in the fiber direction. Since swelling increases significantly at intermediate moisture content, where TD-NMR results show an increase in bound water, the swelling is attributed to this bound water. Conversely, since the change in swelling is small at high moisture content, where free water is dominant, free water does not induce swelling. In addition, since the residual water in desorption is identified as bound water (Figure 1(b)), the shrinkage can also be attributed to the bound water. It suggests that a low concentration of bound water, corresponding to residual water, can induce shrinkage. Other studies report that the shrinkage is an anti-plasticization effect, which enhances the mechanical properties by forming a secondary cross-linking network through interactions at multiple hydrophilic sites with a small amount of water [9,10].

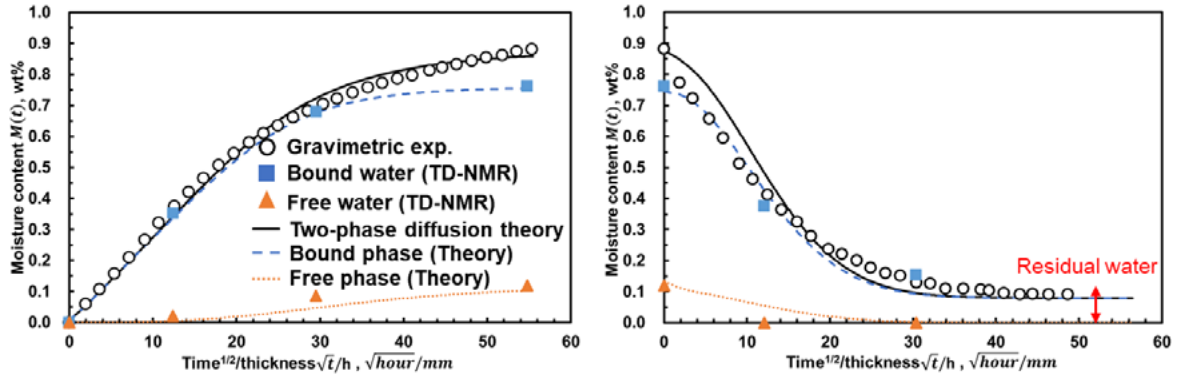


Figure 1. Bound and free water as a function of (a) moisture absorption and (b) desorption times. The white symbols indicate the moisture content determined by gravimetric analysis using Eq. (1), while the blue and orange symbols denote the moisture content of bound and free water, respectively, as determined by TD-NMR results using Eq. (2).

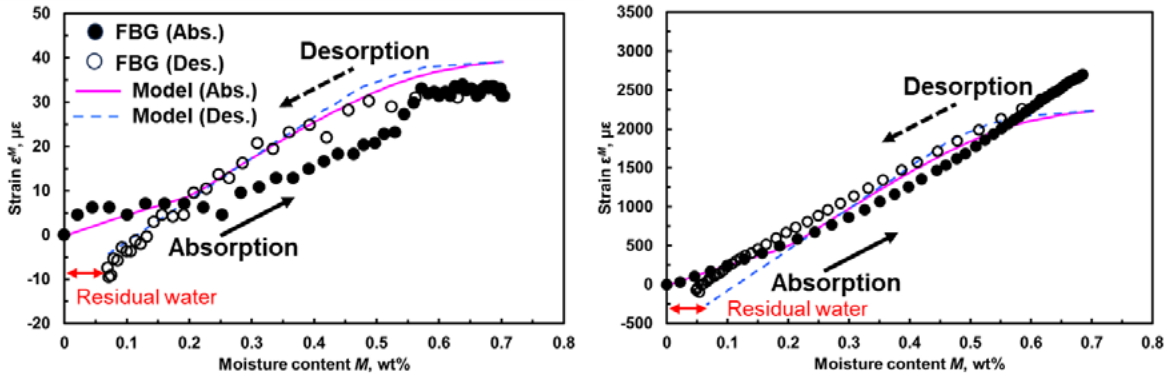


Figure 2 Moisture-induced strain as a function of moisture content in unidirectional composites. (a) Strain in the fiber direction and (b) in the transverse direction. Closed and open symbols correspond to the strain during moisture absorption and desorption, respectively.

3. Modelling

The mechanisms of water transport and swelling during moisture adsorption and desorption are strongly associated with the interactions between water molecules and polymers.

3.1. Water transport

The two-phase diffusion theory serves as a model for water transport that accounts for water-polymer interactions within a material during moisture absorption [11,12]. In this study, the water-transport model was conducted based on the two-phase diffusion theory (as interpreted by Popineau et al. [11]). The one-dimensional diffusion equation during absorption is described by Eq. (3).

$$D_{z,n}\frac{\partial^2 n}{\partial z^2} = \frac{\partial n}{\partial t} + \frac{\partial N}{\partial t}$$
$$\frac{\partial N}{\partial t} = bn - aN \tag{3}$$

where n and N represent the water concentration of bound and free water in the material, respectively. $D_{z,n}$ is the constant diffusion coefficient of bound water in the z (through-the-thickness) direction, b is a probability per unit time to become free water from bound water, a is a probability per unit time to become bound water from free water, t is time; z is the location in the through-the-thickness direction of the material. Next, the water-transport model during desorption must reflect that free water diffuses preferentially, while bound water reaches desorption equilibrium with a small amount of water remaining. Therefore, the two-phase diffusion model was modified during desorption as described in the following Eq. (4).

$$D_{z,N}\frac{\partial^2 N}{\partial z^2} = \frac{\partial N}{\partial t} + \frac{\partial (n - R_w)}{\partial t}$$
$$\frac{\partial (n - R_w)}{\partial t} = aN - b(n - R_w) \tag{4}$$

where $D_{z,N}$ is the constant diffusion coefficient of free water in the z direction, and R_w is residual water.

These differential equations were solved using the partial differential equations (PDE) function in a commercial finite element analysis software (COMSOL Multiphysics 6.2). The diffusion coefficients and the probability parameters (as described in Table 1) were determined using a nonlinear least squares method to fit the two-phase diffusion models (Eqs. (3), (4)) to the experimental data obtained from gravimetric analysis and TD-NMR. The theoretical curves are shown in Figure 1. Figure 1 shows that

the moisture contents in total, bound, and free water agree well with the results of gravimetric analysis and TD-NMR. during absorption and desorption.

Table 1. Parameters for two-phase diffusion model.

Process	Diffusion coefficient D_z, $\times 10^{-13}$ m^2/s	a, $\times 10^{-7}$ 1/s	b, $\times 10^{-7}$ 1/s	Equilibrium moisture content M_∞, wt%
Absorption	2.5	0.9	1.0	1.0
Desorption	30.6	2.6	6.7	0.05

3.2. Swelling

Modeling the swelling behavior during moisture absorption and desorption was conducted based on the two-phase diffusion models, which were applied to water transport in the previous section. It is assumed that only the epoxy matrix absorbs moisture, and that the moisture-induced strain solely responds to the bound water $n(z,t)$ of the two-phase diffusion models. Specifically, a piecewise linear function was used for a simplified modeling, in which the coefficient of moisture expansion (CME) $\beta_m(n)$ for the epoxy matrix varies at a specific threshold C_T of moisture concentration in the bound water as described in Eq. (5). Therefore, the moisture-induced strain response model was expressed as shrinkage due to anti-plasticization at moisture concentrations C_T or below and expansion due to plasticization at moisture concentrations above C_T.

$$\begin{gathered}\beta_m(n) = \beta_{m,ap} \quad if\ n \le C_T \\ \beta_m(n) = \beta_{m,p} \quad if\ n > C_T \\ \text{where,}\quad \beta_{m,ap} \le 0,\quad \beta_{m,p} \ge 0\end{gathered} \tag{5}$$

The CMEs ($\beta_{c,0}(n)$ and $\beta_{c,90}(n)$) of CFRP in the fiber and transverse directions when the moisture absorption of carbon fiber is negligible are expressed by the following Eq. (6) [13].

$$\begin{gathered}\beta_{c,0}(n) = \frac{V_m E_m \beta_m(n)}{\left(V_f E_f + V_m E_m\right) V_m s_m} s_c \\ \beta_{c,90}(n) = \frac{V_m \beta_m(n)(1+\nu_m)}{V_m s_m} s_c - \left(\nu_f V_f + \nu_m V_m\right)\beta_{c,0}(n) \\ s_c = s_f V_f + s_m V_m\end{gathered} \tag{6}$$

where, V is the volume fraction, E is the elastic modulus, ν is Poisson's ratio, and s is the specific gravity. Subscripts c, f, and m denote the CFRP, fiber, and matrix, respectively. The parameters (C_T, $\beta_{m,ap}$, and $\beta_{m,p}$) of the moisture-induced strain response model, as shown in Table 2, are determined using classical lamination theory so that the strains (ε_0^M and ε_{90}^M) in each direction of the laminated plates fit the material test results of unidirectional CFRP as described in Section 2. The curves in Figure 3 represent the moisture-induced strain response model. The developed model agrees well with the nonlinear, hysteretic, and irreversible strain behavior observed in experiments.

Table 2. Parameters for strain response model.

C_T, wt%	$\beta_{m,ap}$, $\times 10^{-6}$/wt%	$\beta_{m,p}$, $\times 10^{-6}$/wt%
0.05	-3800	3000

4. Conclusions

This study developed a rational model that can explain the nonlinear, hysteretic, and irreversible deformation behavior during moisture absorption and desorption in CFRP. The model modifies the two-phase diffusion theory based on findings from the analysis of water-polymer interactions at the molecular scale. The mechanisms of water transport and swelling were clarified through gravimetric and NMR analyses. The analysis shows bound water diffuses preferentially during absorption, whereas free water does during desorption, with some remaining strongly bound after long-term desorption. The strain model employed a piecewise linear function to respond to shrinkage due to anti-plasticization and

swelling due to plasticization, based on the water concentration of bound water. Consequently, we have successfully developed a model that reproduces nonlinear, hysteretic, and irreversible deformation behavior.

Acknowledgments
This work was supported by JSPS KAKENHI Grant Number JP22K04546.

References
[1] Kitamoto K, Minakuchi S and Yokozeki T. High-fidelity simulation model for moisture-induced deformation of CFRP structure considering anisotropic nonlinear moisture absorption-desorption characteristics. *Composites Part A: Applied Science and Manufacturing* 2023; 165:107324.
[2] Lallo MD. Experience with the Hubble Space Telescope: 20 years of an archetype. *Optical Engineering* 2012;51(1):011011.
[3] Anguita J, Smith C, Stute T, Funke M, Delkowski M and Silva S. Dimensionally and environmentally ultra-stable polymer composites reinforced with carbon fibres. *Nature Materials* 2020;19(3):317-322.
[4] Obeid H, Clément A, Fréour S, Jacquemin F and Casari P. On the identification of the coefficient of moisture expansion of polyamide-6: Accounting differential swelling strains and plasticization. *Mechanics of Materials* 2018;118:1-10.
[5] Adamson M, Thermal expansion and swelling of cured epoxy resin used in graphite/epoxy composite materials. *Journal of materials science* 1980;15:1736-1745.
[6] Lo S, Hahn H and Chiao T. Swelling of Kevlar 49/epoxy and S 2-glass/epoxy composites. *Progress in science and engineering of composites* 1982;987-1000.
[7] Ibrahim G, Casari P, Jacquemin F, Freour S, Clement A, Celino A and Khalil K. Moisture diffusion in composites tubes: Characterization and identification of microstructure-properties relationship. *Journal of Composite Materials* 2018;52(8):1073-1088.
[8] Bratasyuk N, Latyshev A and Zuev V. Water in Epoxy Coatings: Basic Principles of Interaction with Polymer Matrix and the Influence on Coating Life Cycle. *Coatings* 2023;14(1):54.
[9] Zhou J and Lucas J. Hygrothermal effects of epoxy resin. Part I: the nature of water in epoxy. *Polymer* 1999;40(20):5505-5512.
[10] Karuth A, Alesadi A, Vashisth, A, Xia W and Rasulev B. Reactive molecular dynamics study of hygrothermal degradation of crosslinke d epoxy polymers. *ACS Applied Polymer Materials* 2022;4(6):4411-4423.
[11] Popineau S, Rondeau-Mouro C, Sulpice-Gaillet C, Shanahan M. Free/bound water absorption in an epoxy adhesive. *Polymer* 2005;46(24):10733-10740.
[12] Carter H and Kibler K. Langmuir-Type Model for Anomalous Moisture Diffusion In Composite Resins. *J. Compos. Mater* 1978;12:118–131.
[13] Tsai SW and Hahn HT. Introduction to Composite Materials. Westport: Technomic, 1980.

A NEW SANDWICH SOLUTION COMBINING CMC AND CERAMICS FOR THE LINER OF RADIOACTIVE WASTE DISPOSAL CELLS

S.MIOT[1], E. PERRET[2], M. BOX[2], A. DEBELLE[3]

[1]IRT Saint Exupéry, Toulouse, FRANCE
stephanie.miot@irt-saintexupery.com, https://www.irt-saintexupery.com
[2]IRT Saint Exupéry, Talence, FRANCE
[3]Andra, Châtenay-Malabry, FRANCE

Keywords: Ceramic Matrix Composites, sandwich, instrumented test, parametric analysis, manufacturing defects

Abstract
A liner made of Ceramic Matrix Composites (CMC) and monolithic ceramic is currently being studied for a potential use in the micro-tunnels of a radioactive waste geological disposal facility. Proof of concept and representative specimens have been manufactured and mechanically tested. In parallel, a numerical model is being developed with the objective of designing an optimum liner in regards to the manufacturing constraints and the in-service load evolving over time.

1. Introduction

The French project called Cigéo [1], led by Andra (the French National Agency for Radioactive Waste Management), aims at creating and managing a deep geological disposal facility for intermediate-level long-lived (ILW-LL) and high-level (HLW) radioactive waste. The high-level waste (HLW) will be placed in horizontal micro-tunnels, known as cells, excavated deep (at ~ 500 m) in a clay layer. A liner will be inserted in the cells to facilitate the placing of the waste packages and allow their retrieval (if needed) during the Cigéo facility operation time (~100 years). To further increase the safety margins above the expected levels presented in the Cigéo licensing application file [2], the current carbon steel liners could be replaced by a ceramic liner. This substitution would limit the amount of $H_{2(g)}$ production that comes from steel corrosion under anoxic conditions. However, no monolithic ceramic can sustain the loading due to the rock convergence. Therefore, the use of Ceramic Matrix Composites (CMC) was proposed. Yet, to sustain the load, the required thickness of CMC makes the solution economically prohibitive.

An innovative solution, combining CMC and monolithic ceramic materials, has then been invented by the authors [3]. This sandwich solution consists of a thin outer skin made of CMC, a core made of several sections of a dense ceramic material, and a thicker inner skin in CMC. Two Proofs of Concept (PoC), shown in Figure 1, have been manufactured and mechanically tested. Different materials, manufacturing processes and dimensional tolerances were considered. Both PoC had a core made of alumina. The skins were either made of Carbon/Geopolymer (PyroKarb) or Oxide/Geopolymer (PyroXide), both materials being developed and commercialised by Pyromeral. Filament winding and hand lay-up fabrication methods have been investigated.

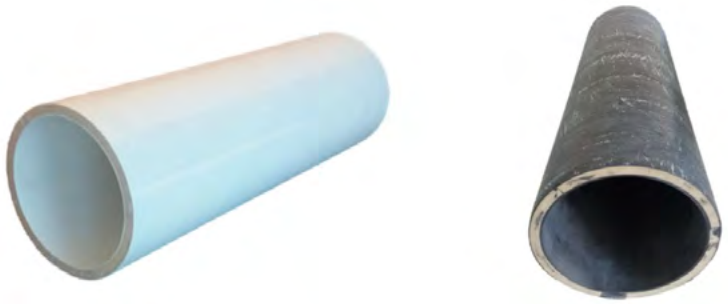


Figure 1. Proof of Concept made of PyroXide/alumina/PyroXide (left) and PyroKarb/alumina/PyroKarb (right)

The liner would be subjected to a non-uniformly distributed pressure applied to its external surface by the geological envrironment. The magnitude and the distribution of the pressure are governed by the motion of the rock around the liner that is strongly dependent on the mechanical response of the liner itself. Thus, two types of tests were considered to evaluate the response of the PoC in conditions aiming at approaching the in-service ones:

- a confinement test consisting in applying a uniformly distributed pressure on the external surface of the PoC,
- a compression test representing a severe anisotropic loading.

The in-service conditions would actually consist of the combination of both tests with a ratio between the two types of loading evolving with time.

Both tests were performed on the PoC, starting with the confinement test followed by the compression test. This latter enables a rich instrumentation set up, including Digital Image Correlation (DIC) as shown in Figure 2. DIC was used to identify the damage such as cracks in the ceramic core and debonding between the core and the skins. For instance, a discontinuity in the displacement field, due to a crack in the ceramic core, was observed in the superior part of the specimen (see Figure 2). Despite the damage, both PoC maintained their structural integrity after the two subsequent tests, which suggests a high technical potential of this sandwich architecture.



Figure 2. Compression test with digital image correlation (DIC) – test setting (left) and measured displacements (right).

Within the project, new PoC will be designed, manufactured then placed in Andra's Underground Research Laboratory (URL) for in-situ testing. The objective is to acquire data on the load generated by the rock convergence. The design of the POC must be optimised so that this latter sustains the load without any catastrophic failure occuring. The deformation of the PoC will provide essential information on the relationship between the rock convergence and the PoC stiffness that is needed for further design optimisation of the liner. Furthermore, designing composite structure must account for the manufacturing process, as technical constraints and fabrication defects will affect the mechanical performance. To tackle this issue, studies combining Finite Element Analysis (FEA) and experiments on representative samples are currently carried out and provide fundamental information on the influence of design parameters – such as dimensions or material orientation – and manufacturing tolerances and defects – such as skin/core bond quality.

2. Design and preliminary analysis of the representative annular technological specimen

Following the analysis of the PoC, a representative annular technological specimen (RATS) was considered to perform a deeper analysis of the mechanical behaviour of the sandwich structure. Design examples are presented in Figure 3. A numerical analysis was perfomed to evaluate the impact of the design parameters such as the skins thickness or the number of core sections. In addition, dimentionnal tolerances and manufacturing defects were considered.

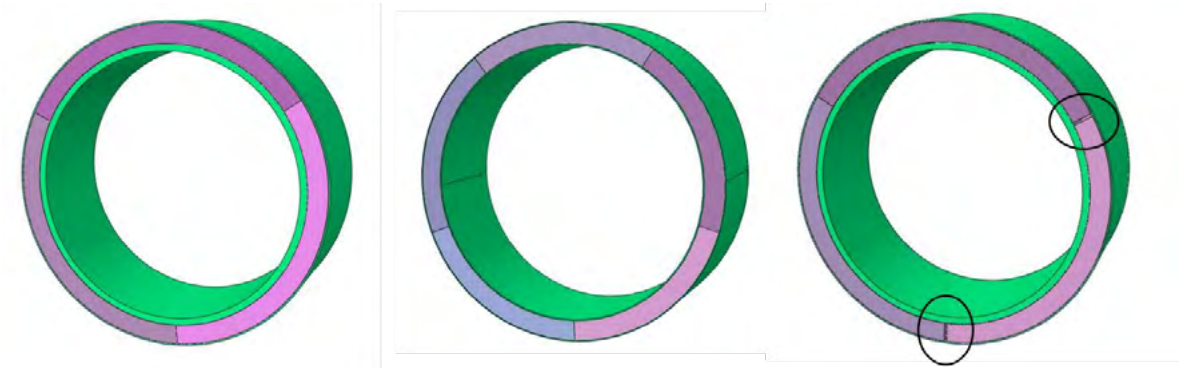


Figure 3. Example of 3 designs with a thick internal skin and 3 core sections (left), with a thin internal skin and 5 core sections (centre) and with 2 manufacturing defects (gaps between sections) (right)

The preliminary analyses highlight the influential parameters and phenomena that need to be investigated further. For instance, a combination of a thin internal skin and a ceramic core divided into 5 sections creates a compliant structure that tolerates a larger deflection; indeed, the core sections may slide along each other in this case. However, the stress in the skins may locally reach high levels, eventually leading to the failure of the composite. Figure 4 shows the displacement and stress fields in such a structure. The deformed shape is shown with a scale factor of 10 to underscore the critical areas. The highest levels of stress in the skins can be observed near the junctions between the ceramic sections. The tensile stress in the ceramic remains below the tensile strength estimated at 280 MPa by the ceramic manufacturer. On the other hand, a thick internal skin combined with a reduced number of core sections would be stiffer and the relative sliding of the core sections would be limited. Thus, the local stress in the skins would be reduced, but the bending load applied to the ceramic core would generate a higher risk of cracks occurring in the ceramic. Figure 5 shows a different deformed shape as the one seen in the previous example. The stresses, plotted with the same scale as in Figure 4, are lower in the internal skin but higher in the ceramic core compared to those obtained with the previous 5-section RATS. Although cracks in the ceramic core are not critical as the core is contained within the skins, these cracks lead to a reduction of the structure's stiffness and a change in the mechanical response of the 3-section structure that will ressemble the one of the 5-section RATS.

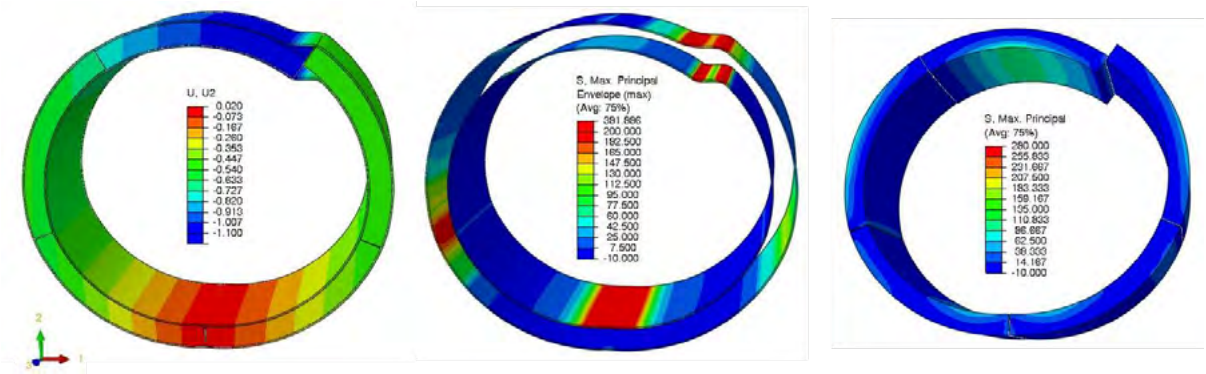


Figure 4. FEA of RATS with a thin internal skin and 5 core sections – predictions of displacement in mm (left), tensile stress in MPa in the skins (centre) and in the core (right) – scale factor = 10

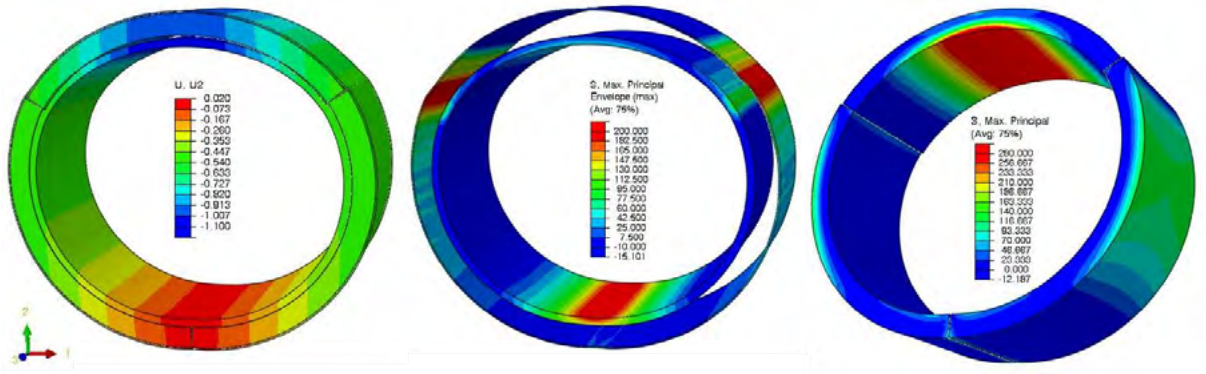


Figure 5. FEA of RATS with a thick internal skin and 3 core sections – predictions of displacement in mm (left), tensile stress in MPa in the skins (centre) and in the core (right) – scale factor = 10

The mechanical response of the structure would also be affected by the manufacturing defects. For instance, a weak bond – or an initial debonding – between the core and one of the skins would disrupt the load transfer. On the other hand, the debonding would provide more compliance to the system, as the displacement of its different parts would be facilitated in this case (see Figure 6).

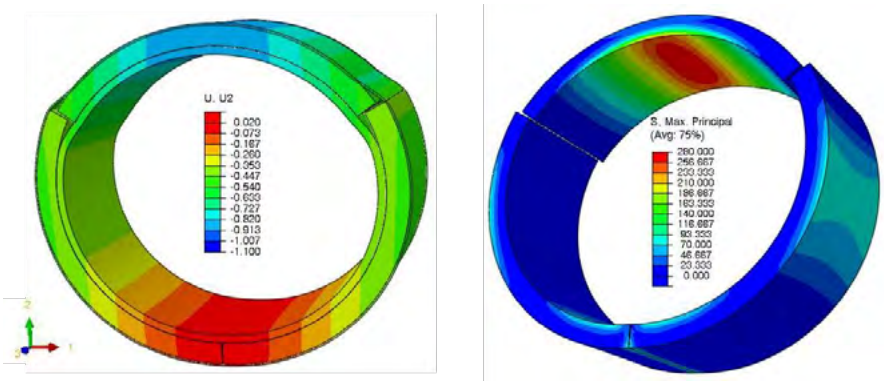


Figure 6. FEA of RATS with a thick internal skin, 3 core sections and an initial debonding between one of the sections and the internal skin – predictions of displacement in mm (left) and tensile stress in MPa in the core (right) – scale factor = 10

Table 1 summarises the design parameters and the potential manufacturing defects that were considered in the parametric study. The trends identified with the numerical model need to be confirmed by experiments.

Table 1. Design parameters and potential manufacturing defects that may influence the mechanical response of the RATS

	Design parameters	Manufacturing defects	Influence
Internal face	Internal diameter Internal skin thickness and lay-up		Global stiffness, stress in both skins and likelihood of damage in core or skin; thicker laminate can compensate for defects in core or in core/skin bond
		Initial debonding between core and internal skin	Disruption of load transfer between core and internal skin and higher levels of stress in the skins
	Number of core sections		Global stiffness and number of critical areas in the skins
		Junction with gaps between core sections	Disruption of load transfer between core and skin and higher levels of stress in the skins
	Core thickness		Global stiffness and load carrying capacity
		Bond between core and external skin	Disruption of load transfer between core and internal skin and higher levels of stress in both skins
External face	External skin thickness and lay-up		Thicker laminate can compensate for defects in core or in core/skin bond

3. Manufacturing process

The RATS were made of PyroKarb/Alumina/PyroKarb and manufactured in 4 steps as illustrated in Figure 7:

1. The elaboration of the internal skin by filament winding.
2. The positioning of the ceramic sections on the internal skin.
3. The elaboration of the external skin by filament winding.
4. The final processing stage (Pyromeral's Intellectual Property) including the separation of the RATS

Multiple RATS were manufactured with different skin thicknesses and lay-ups and variable dimensions of the core sections. As the skins were made by filament winding, the dimensions and material orientation were precisely controlled. On the contrary, the manufacturing process of the ceramic parts is not controlled as accurately. The geometrical tolerances then lead to variable adjustments of the core sections and a variable quality of bond between the core sections and the skins. These variabilities were observed on the final structure. Micro-computed tomography (μCT) was used to both identify and quantify the initial defects. An example is shown in Figure 8. The manufacturing process is under development and the quality of the RATS could be improved. However, the need for improvement will be determined by evaluating the required structural properties; the manufacturing tolerances will be then defined accordingly.

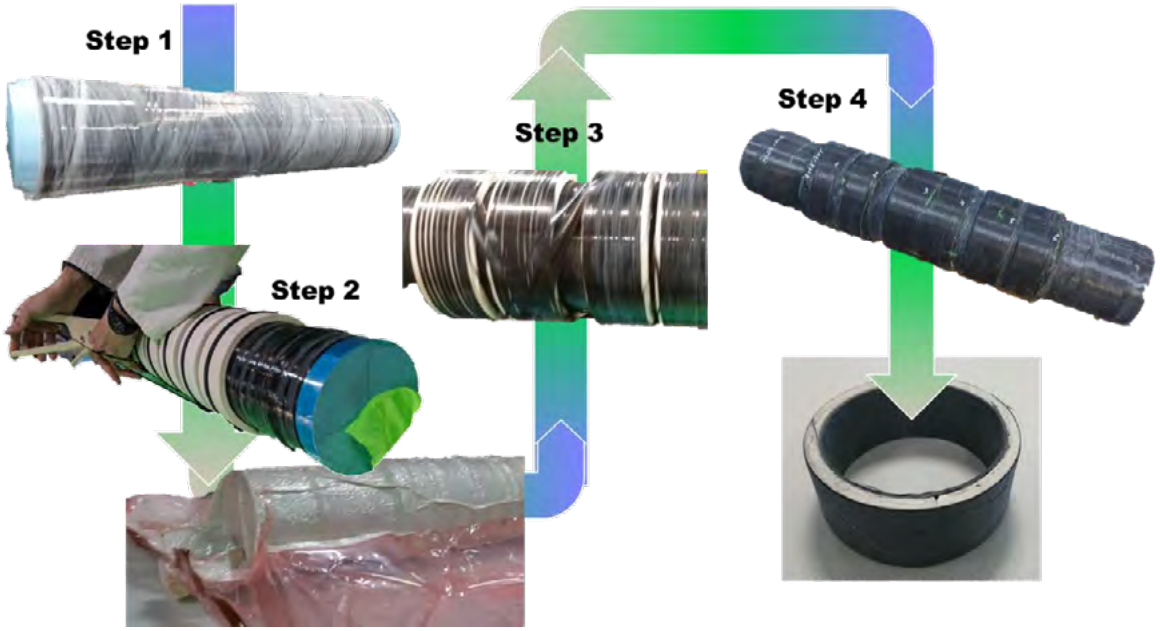


Figure 7. Manufacturing process of the RATS

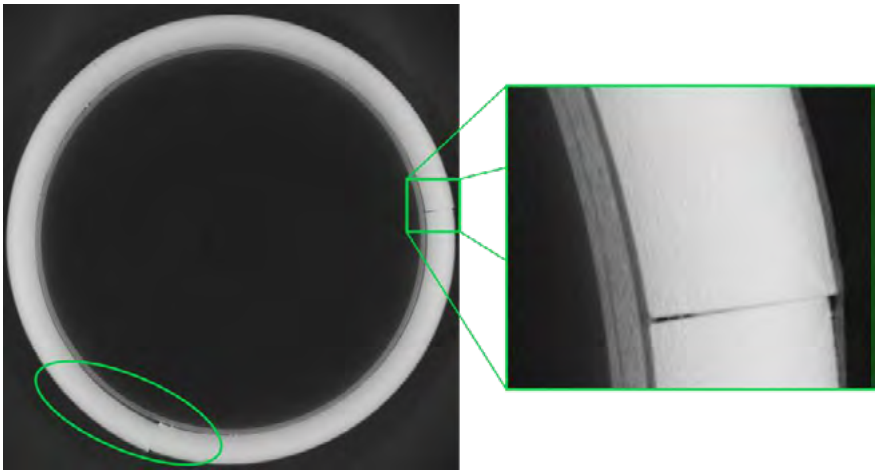


Figure 8. Observation by µCT of a RATS where defects including internal skin/core debonding and variable thickness of core section leading to gaps are readily visible

4. Experimental study

A compression test was specifically developed to characterise the mechanical response of the sandwich structure, analyse the influence of the design parameters and evaluate the impact of the manufacturing defects. Figure 9 shows the set-up with the relevant instrumentation including cameras to perform Digital Image Correlation (DIC) analysis, a microphone to capture Acoustic Emission (AE) and a Linear Variable Differential Transformer (LVDT) to measure the cylinder ovalisation.

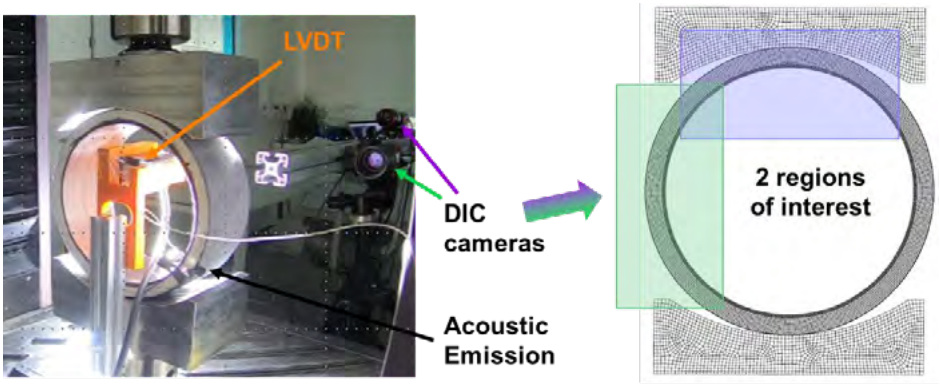


Figure 9. Compression test on RATS with dedicated instrumentation (LVDT, DIC, AE)

A cyclic compressive loading was applied to the RATS. The displacement was imposed at a rate of 0.2 mm/min until 2 mm, then at 0.5 mm/min until 4 mm. Unloadings were set at regular intervals of 0.2 mm until 2 mm, then at 0.5 mm between 2.5 mm and 4 mm. The force was measured by a 50 kN load cell. As shown in Figure 10, during this test, a sudden event was captured by the AE and corresponds to a drop in the Force/Displacement curve. The DIC analysis allowed the identification of this event: a crack occurred in the top section of the ceramic core that was loaded in bending. The crack triggered a debonding between the core section and the internal skin. The DIC residuals highlight the crack (see lower right-hand side image in Figure 10). The test continued and a new event occurred (after ~66 minutes), indicating additional damage that yet remains to be identified. A decrease in global stiffness is observed on the Force/Displacement curve. In particular, if we compare the initial slope at the beginning of the test (purple curve) with the slope at the beginning of the new cycles in black, the residual stiffness is about half of the initial one. However, the structure could still carry the load. The test was stopped to analyse the damage in the RATS. Further tests will be performed on the same specimen until complete failure.

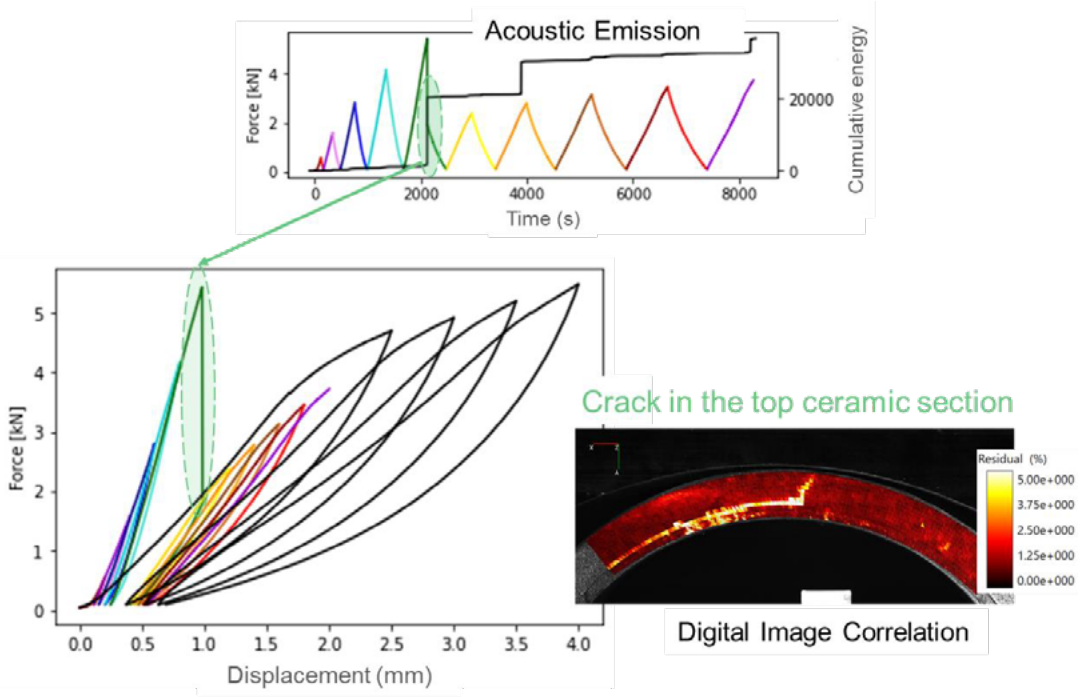


Figure 10. Compression test on RATS with instrumentation (LVDT, DIC, AE)

5. Conclusion

A sandwich tube was created to be evaluated as a potential liner for a micro-tunnel in a deep radioactive waste disposal facility. Two PoC were manufactured and mechanically tested under severe conditions: they exhibit a high technical potential, as both maintained their overall integrity. Subsequently, a smaller representative annular technological specimen was designed to perform further systematic and parametric studies and improve the understanding of the mechanical response of the sandwich structure. These RATS' skins were made of Carbon/Geopolymer and the core was made of alumina. Multiple RATS were manufactured. A comprehensive analysis based on µCT observations, FE simulations and experimental tests is in progress. The objective is to evaluate the influence of the various design parameters and the impact of the manufacturing tolerances and defects on the mechanical performance of the sandwich structure. A predictive model will then be proposed to help and design a liner that would be a compromise between the optimum design for a given load, the expected quality of the manufactured product and the evolving in-service load over time. New PoC will then be manufactured and placed in Andra's Underground Research Laboratory for in-situ testing to assess that this innovative component fulfil the safety requirements associated with the Cigéo project.

References

[1] ANDRA, The Cigéo project. https://international.andra.fr/solutions-long-lived-waste/cigeo.
[2] https://international.andra.fr/submission-application-authorization-create-cigeo
[3] Emilie Perret, Stéphanie Miot, Maxime Box, Raffaele D'Elia. Pièce cylindrique à structure sandwich, procédé de fabrication d'une telle pièce et son utilisation pour le stockage de déchets radioactifs. France, N° de brevet: FR3115533A1. 2023. ⟨hal-04329451⟩

Eshelby's inhomogeneity problem in complete Mindlin's first strain gradient elasticity theory

Koami P. DADABO, Napo BONFOH, Rodrigue MATADI-BOUMBIMBA, Hafid SABAR

Laboratoire d'Etudes des Microstructures et de la Mécanique des Matériaux (LEM3), CNRS, Arts et Métiers Paris Tech, Université de Lorraine, F-57000 Metz, France

pierre.dadabo@univ-lorraine.fr

napo.bonfoh@univ-lorraine.fr

rodrigue.matadi@univ-lorraine.fr

hafid.sabar@univ-lorraine.fr

Abstract

The solution of Eshelby's inhomogeneity problem in the second form of Mindlin's first strain gradient elasticity theory is developed to predict the effective elastic properties of micro or nanocomposites. Thanks to the Green's function technique, the local strain is expressed, in terms of an integral equation, for an ellipsoidal inhomogeneity embedded in an infinite homogeneous elastic medium subjected to non-homogeneous boundary conditions. The expression of the mean strain inside a spherical inhomogeneity with isotropic elastic behavior is acquired and depends on two characteristic length scale parameters and five elastic gradient constants introduced by the Mindlin's strain gradient elasticity theory. The effective bulk and shear moduli are predicted through Mori-Tanaka homogenization scheme for a two-phase composite, considering some simplified versions of the strain gradient elasticity theories: simplified strain gradient elasticity theory, reduced strain gradient elasticity theory and couple-stress theory. These predictions are then compared with those proposed by some investigations on the same topic.

Keywords

Heterogeneous materials, strain gradient elasticity theory, Eshelby's inhomogeneity problem, integral equation, Mori-Tanaka scheme.

1. Introduction

The prediction of the elastic behavior of heterogeneous materials based on the properties of their constituents and their microstructures is one of the interests of mechanics of materials. Eshelby's inclusion [1] and inhomogeneity models [2] provide a valuable tool for the development of micromechanical models for the prediction of the effective elastic properties through the chosen homogenization schemes. Classical models failed to account for the size effects of inhomogeneities on the effective elastic behavior of heterogeneous materials and high-order micromechanical theories such as strain gradient elasticity theories are investigated to this end. Recently, Bonfoh and Sabar [3] developed a new method based on the Eshelby's inhomogeneity issue, within the simplified strain gradient elasticity theory. This method is developed within a simplified version of Mindlin's first strain gradient elasticity theory with a unique material's characteristic length scale parameter. Sidhardh and Ray [4,5], solved the Eshelby's inclusion problem within Mindlin's first strain gradient elasticity theory with three characteristic's length scale parameters and suggested the necessity of multiple characteristics

length scale parameter for a relevant prediction of the size effects at different length scales for crystals, polymers and micro and nanocomposites. Mindlin's first strain gradient elasticity theory introduces five gradient constants and appears as the general and complete version to address these issues. In the present study, an Eshelby's inhomogeneity model is developed within a complete version of Mindlin's first strain gradient elasticity theory. Through Mori-Tanaka scheme, a relevant estimation of the size-dependent effective elastic moduli of micro or nanosized composites is provided for some simplified theories and compared with those issued from some investigations.

2. Eshelby's inhomogeneity problem within Mindlin's first strain gradient elasticity theory

2.1. Integral equation

Let us consider an elastic heterogeneous medium with a volume V and outer boundary ∂V. Its local linear elastic behavior is described by the elastic moduli tensors $\boldsymbol{C}(\boldsymbol{r})$ and $\boldsymbol{D}(\boldsymbol{r})$ at an arbitrary vector position $\boldsymbol{r}(x_1, x_2, x_3)$. The corresponding representative volume element (RVE) is subjected to non-homogeneous boundary conditions [6]: uniform strain $\boldsymbol{\varepsilon^0}$ and strain gradient $\boldsymbol{\kappa^0}$ prescribed at ∂V :

$$u_i(\boldsymbol{r}) = \varepsilon^0_{ij}\, x_j + \kappa^0_{ijq}\, x_j\, x_q \;\; ; \text{ for } \boldsymbol{r} \in \partial V \tag{1}$$

Considering the general Eshelby's equivalent inclusion method as suggested by [1], and based on the Green's function technique, an integral equation for an isotropic infinitely elastic RVE subjected to non-homogeneous conditions within the Mindlin's first strain gradient elasticity theory is obtained:

$$\begin{aligned} u_m(\boldsymbol{r}) &= u^0_i(\boldsymbol{r}) - \int_{V'} G^0_{km,l'}(\boldsymbol{r}-\boldsymbol{r}')\, \delta C_{klij}(\boldsymbol{r}')\, \varepsilon_{ij}(\boldsymbol{r}')\, dV' \\ &- \int_{V'} G^0_{km,l'n'}(\boldsymbol{r}-\boldsymbol{r}')\, \delta D_{klnijp}(\boldsymbol{r}')\, \kappa_{ijp}(\boldsymbol{r}')dV' \\ &+ \int_{\partial V'} \left\{ G^0_{km}(\boldsymbol{r}-\boldsymbol{r}')\, t^d_k(\boldsymbol{r}') + G^0_{km,q'}(\boldsymbol{r}-\boldsymbol{r}')\, q^d_k(\boldsymbol{r}')\, N_q \right\} dS' \\ &- \int_{\partial V'} \left\{ T^0_{im}(\boldsymbol{r}-\boldsymbol{r}')\, u^d_i(\boldsymbol{r}') + Q^0_{im}(\boldsymbol{r}-\boldsymbol{r}')\, u^d_{i,q'}(\boldsymbol{r}')\, N_q \right\} dS' \end{aligned} \tag{2}$$

where $\boldsymbol{N}$ stands for the outward unit normal vector to ∂V, $\boldsymbol{G^0_{km}}$ the Green's function tensor of the homogeneous reference medium (HRM) with elastic moduli tensors $\boldsymbol{C}^0$ and $\boldsymbol{D}^0$, $\delta\boldsymbol{C}(\boldsymbol{r}) = \boldsymbol{C}(\boldsymbol{r}) - \boldsymbol{C}^0$, $\delta\boldsymbol{D}(\boldsymbol{r}) = \boldsymbol{D}(\boldsymbol{r}) - \boldsymbol{D}^0$, the fluctuating moduli tensors.

The local displacements field is decomposed as:

$$u_i(\boldsymbol{r}) = u^0_i(\boldsymbol{r}) + u^d_i(\boldsymbol{r}) \tag{3}$$

and $\boldsymbol{u^d}$, $\boldsymbol{t^d}$ and $\boldsymbol{q^d}$, are respectively the fluctuating of displacements, Cauchy stress traction, double stress traction vectors, defined by:

$$t_i = \sigma_{ij}\, N_j - \left(\mu_{ijk}\, N_k\right)_{,j} + \left(\mu_{ijk}\, N_k\, N_l\right)_{,l} N_j \;\text{ and }\; q_i = \mu_{ijk}\, N_j\, N_k \tag{4}$$

with:

$$\tau_{ij} = C_{ijkl}\,\varepsilon_{ij} \;\;,\;\; \mu_{ijq} = D_{ijqklp}\kappa_{klp} \;\text{ and }\; \sigma_{ij} = \tau_{ij} - \mu_{ijq,q} \tag{5}$$

Moreover, the transformed traction tensors, $\boldsymbol{T^0}(\boldsymbol{r}-\boldsymbol{r'})$ and $\boldsymbol{Q^0}(\boldsymbol{r}-\boldsymbol{r'})$ are defined by:

$$\begin{aligned} T^0_{im}(\boldsymbol{r}-\boldsymbol{r'}) &= C^0_{klij}\,G^0_{km,l'}(\boldsymbol{r}-\boldsymbol{r'})\,N_j - D^0_{klnijp}\,G^0_{km,l'n'p'}(\boldsymbol{r}-\boldsymbol{r'})\,N_j \\ &- D^0_{klnijp}\,G^0_{km,l'n'j'}(\boldsymbol{r}-\boldsymbol{r'})\,N_p + D^0_{klnijp}\,G^0_{km,l'n'q'}(\boldsymbol{r}-\boldsymbol{r'})\,N_p\,N_q\,N_j \\ &+ D^0_{klnijp}\,G^0_{km,l'n'}(\boldsymbol{r}-\boldsymbol{r'})\left\{N_{p,q'}\,N_q\,N_j + N_p\,N_{q,q'}\,N_j - N_{p,j'}\right\} \end{aligned} \tag{6}$$

$$\text{and } Q^0_{im}(\boldsymbol{r}-\boldsymbol{r'}) = D^0_{klnijp}\,G_{km,l'n'}\,(\boldsymbol{r}-\boldsymbol{r'})\,N_p\,N_j$$

The topology of the considered Eshelby's inhomogeneity model consists of an ellipsoidal inhomogeneity (denoted by index I) with a volume V_I embedded in an infinitely homogeneous reference medium (denoted by index 0). The fluctuating tensors are defined as: $\delta\boldsymbol{C}(\boldsymbol{r}) = \Delta\boldsymbol{C^{I/0}}\,\theta^I(\boldsymbol{r})$ and $\delta\boldsymbol{D}(\boldsymbol{r}) = \Delta\boldsymbol{D^{I/0}}\theta^I(\boldsymbol{r})$ where $\theta^I(\boldsymbol{r}) = \begin{cases}1 & \text{if } \boldsymbol{r}\in V_I \\ 0 & \boldsymbol{r}\notin V_I\end{cases}$, is the Heaviside function of the inhomogeneity volume V_I.

In the absence of the double stress traction $\boldsymbol{q^d}$ at the boundary ∂V, the Green's tensor $\boldsymbol{G^0}$, the displacements field $\boldsymbol{u^d}$ and its gradients vanished at the infinite boundary ∂V. Eq.(2) therefore leads to:

$$\begin{aligned} \varepsilon_{mn}(\boldsymbol{r}) &= \varepsilon^0_{mn} + \left(\kappa^0_{mnl} + \kappa^0_{mln}\right)x_l - \int_{V_I'}\Gamma^0_{mnkl}(\boldsymbol{r}-\boldsymbol{r'})\,\Delta C^{I/0}_{klij}\,\varepsilon_{ij}(\boldsymbol{r'})\,dV' \\ &- \int_{V_I'}\Gamma^0_{mnkl,p'}(\boldsymbol{r}-\boldsymbol{r'})\,\Delta D^{I/0}_{klpijq}\,\kappa_{ijq}(\boldsymbol{r'})\,dV' \;\text{ and} \\ \kappa_{mnr}(\boldsymbol{r}) &= \kappa^0_{mnr} + \kappa^0_{mrn} - \int_{V_I'}\Gamma^0_{mnkl,r}(\boldsymbol{r}-\boldsymbol{r'})\,\Delta C^{I/0}_{klij}\,\varepsilon_{ij}(\boldsymbol{r'})\,dV' \\ &- \int_{V_I'}\Gamma^0_{mnkl,p'r}(\boldsymbol{r}-\boldsymbol{r'})\,\Delta\mathcal{D}^{I/0}_{klpijq}\,\kappa_{ijq}(\boldsymbol{r'})\,dV' \end{aligned} \tag{7}$$

where $\boldsymbol{\Gamma^0}$ is the modified Green's tensor, defined by:

$$\Gamma^0_{mnkl}(\boldsymbol{r}-\boldsymbol{r'}) = -\frac{1}{2}\left[G^0_{mk,nl}(\boldsymbol{r}-\boldsymbol{r'}) + G^0_{nk,ml}(\boldsymbol{r}-\boldsymbol{r'})\right] \tag{8}$$

In what follows, we are interested in the prediction of the first-order elastic properties of a heterogeneous material within Mindlin's first strain gradient elasticity theory. To this end, a remote uniform strain tensor $\boldsymbol{\varepsilon^0}$ $(\boldsymbol{\kappa}=0)$ is prescribed at the boundary of the RVE.

Within the present investigation, the Green's tensor $\boldsymbol{G^0}$ is decomposed as suggested by [7] :

$$G^0_{mk}(\boldsymbol{r}-\boldsymbol{r}') = G^c_{mk}(\boldsymbol{r}-\boldsymbol{r}') + G^G_{mk}(\boldsymbol{r}-\boldsymbol{r}') \tag{9}$$

Consequently, the uniform classical part $\boldsymbol{T^C}$ and the gradient part $\boldsymbol{T^G}$ of the Hill's polarization tensor $\boldsymbol{T}$ inside V_I read as:

$$\int_{V_I} \Gamma^C_{mnkl}(\boldsymbol{r}-\boldsymbol{r}')\, dV = T^C_{mnkl} \quad \text{and} \quad \int_{V_I} \Gamma^G_{mnkl}(\boldsymbol{r}-\boldsymbol{r}')\, dV = T^G_{mnkl}(\boldsymbol{r}') \quad \text{for} \quad \boldsymbol{r}' \in V_I \tag{10}$$

Assuming a constant elastic behavior per local phase and uniform characteristic length scale parameters (l_1 and l_2) inside the heterogeneous material, the volume average $\bar{\boldsymbol{\varepsilon}}^{\boldsymbol{I}}$ of the strain inside inhomogeneity volume V_I can be considered:

$$\begin{aligned}\bar{\varepsilon}^I_{mn} = \varepsilon^0_{mn} - T^C_{mnkl}\, \Delta C^{I/0}_{klij}\, \bar{\varepsilon}^I_{ij} - \frac{1}{V_I}\int_{S_I} T^G_{mnkl,p}(\boldsymbol{r})\, \Delta D^{I/0}_{klpijq}\, \varepsilon_{ij}(\boldsymbol{r})\, n_q\, dS \\ - \frac{1}{V_I}\int_{S_I}\left[T^G_{mnkl}(\boldsymbol{r})\, \Delta C^{I/0}_{klij} - T^G_{mnkl,pq}(\boldsymbol{r})\, \Delta D^{I/0}_{klpijq}\right] u_i(\boldsymbol{r})\, n_j\, dS\end{aligned} \tag{11}$$

The main difficulty of the complete expression of the volume average $\bar{\boldsymbol{\varepsilon}}^{\boldsymbol{I}}$ arises from the analytical evaluation of the surface integrals of Eq.(11), since the local fields $\boldsymbol{u}(\boldsymbol{r})$, $\boldsymbol{\varepsilon}(\boldsymbol{r})$ and $\boldsymbol{T^G}(\boldsymbol{r})$ are non-uniform inside the inhomogeneity.

2.2. Exact analytical solution for spherical Eshelby's inhomogeneity problem

We considered a spherical inhomogeneity with radius a. Thanks to Green's function [7], the components of Hill's polarization tensors for a HRM with an isotropic elastic behavior read as:

$$\begin{aligned}T^C_{mnkl} &= \frac{1}{30\mu_0(1-\nu_0)}\left[(8-10\nu_0)\, I_{mnkl} - \delta_{mn}\, \delta_{kl}\right] \quad \text{and} \\ T^G_{mnkl}(\boldsymbol{r}) &= -\alpha_0\, {l_1}^2[\varphi^I(r) - \Lambda^1(r)]_{,mnkl} + \frac{{l_2}^2}{\mu^0}[\varphi^I(r) - \Lambda^2(r)]_{,mnkl} \\ &+ \frac{1}{2\mu_0}\left[\Lambda^2_{nl}(r)\, \delta_{mk} + \Lambda^2_{ml}(r)\, \delta_{nk}\right]\end{aligned} \tag{12}$$

where $\alpha_0 = (1-2\nu_0)/2\mu_0(1-\nu_0)$; μ_0 and ν_0 are shear modulus and Poisson's ratio of the HRM, respectively. $I_{mnkl} = (\delta_{mk}\, \delta_{nl} + \delta_{nk}\, \delta_{ml})/2$ are the components of the four-order identity tensor, $\varphi^I(\boldsymbol{r})$ and $\Lambda^i(\boldsymbol{r})$ for $i = 1,2$, respectively Newtonian and Yukawa potential functions related to the characteristic length scale parameter l_i (l_1 and l_2) [3]:

$$\varphi^I(\boldsymbol{r}) = \frac{1}{4\pi}\int_{V_I'} \frac{1}{|\boldsymbol{r}-\boldsymbol{r}'|}\,dV' \quad \text{and} \quad \Lambda^i(\boldsymbol{r}) = \frac{1}{4\pi}\int_{V_I'} \frac{e^{-|\boldsymbol{r}-\boldsymbol{r}'|/l_i}}{|\boldsymbol{r}-\boldsymbol{r}'|}\,dV' \quad \text{for} \quad \boldsymbol{r} \in V_I \tag{13}$$

For a spherical inhomogeneity, these potential functions are expressed as [3]:

$$\varphi^I(\boldsymbol{r}) = -\frac{1}{6}(r^2 - 3a^2) \quad \text{and} \quad \Lambda^i(\boldsymbol{r}) = {l_i}^2 - {l_i}^2\,(l_i + a)e^{-\frac{a}{l_i}}\frac{\sinh(\boldsymbol{r}/l_i)}{\boldsymbol{r}} \quad \text{for} \quad \boldsymbol{r} \in V_I \tag{14}$$

Considering Eqs. (12)-(14), Eq. (11) becomes:

$$\begin{aligned}\bar{\varepsilon}^I_{mn} = {}& \varepsilon^0_{mn} - T^C_{mnkl}\,\Delta C^{I/0}_{klij}\,\bar{\varepsilon}^I_{ij} \\ & - \alpha_0\left[\left(\Delta a_1^{I/0} + 2\Delta a_2^{I/0}\right)R^1_{mn} + \left(\Delta a_1^{I/0} + 2\Delta a_3^{I/0}\right)R^2_{mn}\right. \\ & \left. + \left(2\Delta a_4^{I/0} + 2\Delta a_5^{I/0}\right)R^3_{mn} + \left(\Delta\lambda^{I/0} - \frac{\Delta a_1^{I/0} + 2\Delta a_2^{I/0}}{{l_1}^2}\right)(R^4_{mn} - R^5_{mn})\right] \\ & - \frac{1}{\mu_0}\left[\left(2\Delta a_4^{I/0} + 2\Delta a_5^{I/0}\right)(R^6_{mn} - R^7_{mn}) + \left(2\Delta\mu^{I/0} - \frac{2\Delta a_4^{I/0}}{{l_2}^2}\right)(R^8_{mn}\right. \\ & \left. - R^9_{mn})\right]\end{aligned} \tag{15}$$

where $\Delta a_i^{I/0} = a_i^I - a_i^0$, (for $i = 1,2,\dots,5$), $\Delta\mu^{I/0} = \mu_I - \mu_0$ and $\Delta\lambda^{I/0} = \lambda_I - \lambda_0$. The second-order tensors $\boldsymbol{R}^p$ (for $p = 1,2,\dots,9$) are introduced as:

$$\begin{aligned} R^1_{mn} &= \frac{1}{V_I}\int_{S_I} \Lambda^1_{mnp}(\boldsymbol{r})\,\varepsilon_{qq}(\boldsymbol{r})n_p\,dS \;;\; R^2_{mn} = \frac{1}{V_I}\int_{S_I} \Lambda^1_{mnl}(\boldsymbol{r})\,\varepsilon_{pl}(\boldsymbol{r})\,n_p\,dS\,; \\ R^3_{mn} &= \frac{{l_1}^2}{V_I}\int_{S_I} \Lambda^1_{mnklp}(\boldsymbol{r})\,\varepsilon_{kl}(\boldsymbol{r})\,n_p\,dS \;;\; R^5_{mn} = \frac{{l_1}^2}{V_I}\int_{S_I} \Lambda^1_{mnlp}(\boldsymbol{r})\,u_l(\boldsymbol{r})\,n_p\,dS\,; \\ R^6_{mn} &= \frac{1}{2V_I}\int_{S_I} \left[\Lambda^2_{mlp}(\boldsymbol{r})\,\varepsilon_{nl}(\boldsymbol{r}) + \Lambda^2_{nlp}(\boldsymbol{r})\,\varepsilon_{ml}(\boldsymbol{r})\right]n_p\,dS\,; \\ R^7_{mn} &= \frac{{l_2}^2}{V_I}\int_{S_I} \Lambda^2_{mnklp}(\boldsymbol{r})\,\varepsilon_{kl}(\boldsymbol{r})\,n_p\,dS\,; \\ R^8_{mn} &= \frac{1}{2V_I}\int_{S_I} \left[\Lambda^2_{ml}(\boldsymbol{r})\,u_l(\boldsymbol{r})\,n_n + \Lambda^2_{nl}(\boldsymbol{r})\,u_l(\boldsymbol{r})\,n_m\right]dS\,; R^9_{mn} = \frac{{l_2}^2}{V_I}\int_{S_I} \Lambda^2_{mnlp}(\boldsymbol{r})\,u_l(\boldsymbol{r})\,n_p\,dS \end{aligned} \tag{16}$$

2.3. Spherical and deviatoric parts of strain inside spherical inhomogeneity

Within an isotropic elastic behavior of spherical inhomogeneity, the mean strain tensor $\bar{\boldsymbol{\varepsilon}}^{\boldsymbol{I}}$ and the remote uniform strain tensor $\boldsymbol{\varepsilon}^0$ can be decomposed into spherical $\bar{\varepsilon}_s = \bar{\varepsilon}_{pp}/3$ and deviatoric $\bar{\boldsymbol{e}}$ parts as:

$$\bar{\varepsilon}_s = \frac{1+\alpha_0\,\eta_1\,\xi}{1+\alpha_0\,\eta_1\,\xi+\alpha_0\,\Delta\kappa^{I/0}\left(1+3\bar{D}_1+\alpha_0\,\xi\,(3{l_1}^2+\eta_1)\right)}\,\varepsilon_s^0 \quad \text{and}$$

$$\begin{aligned}\bar{e}^I_{mn} = e^0_{mn} &- \frac{(8-10\nu_0)\Delta\mu^{I/0}}{15\mu_0(1-\nu_0)}\,\bar{e}^I_{mn}\\ &- \alpha_0\left\{\left(\Delta a_1^{I/0}+2\Delta a_2^{I/0}\right)R^{1d}_{mn}+\left(\Delta a_1^{I/0}+2\Delta a_3^{I/0}\right)R^{2d}_{mn}\right.\\ &\left.+\left(2\Delta a_4^{I/0}+2\Delta a_5^{I/0}\right)R^{3d}_{mn}+\left(\Delta\lambda^{I/0}-\frac{\Delta a_1^{I/0}+2\Delta a_2^{I/0}}{{l_1}^2}\right)\left(R^{4d}_{mn}-R^{5d}_{mn}\right)\right\}\\ &-\frac{1}{\mu_0}\left\{\left(2\Delta a_4^{I/0}+2\Delta a_5^{I/0}\right)\left(R^{6d}_{mn}-R^{7d}_{mn}\right)\right.\\ &\left.+\left(2\Delta\mu^{I/0}-\frac{2\Delta a_4^{I/0}}{{l_2}^2}\right)\left(R^{8d}_{mn}-R^{9d}_{mn}\right)\right\}\end{aligned} \tag{17}$$

$\boldsymbol{R^{pd}}$ is the deviatoric part of the tensors $\boldsymbol{R^p}$, $\eta_1 = -\,l_1(a^2+3a\,l_1+3l_1^2)/(l_1+a)$, $\xi = a^2\,\bar{D}_3\left(\Delta\lambda^{I/0}+2\Delta\mu^{I/0}\right)+\left(5\Delta\lambda^{I/0}+10\Delta\mu^{I/0}-\frac{2(2\Delta a_4^{I/0}+2\Delta a_5^{I/0})}{{l_1}^2}\right)\bar{D}_2$ and

$$\begin{aligned}\bar{D}_1(r) &= \frac{1}{r}\frac{\partial\Lambda^1(r)}{\partial r}\bigg|_{r=a}\;;\quad \bar{D}_2(r)=\frac{1}{r^2}\left\{\frac{\partial^2\Lambda^1(r)}{\partial r^2}-\frac{1}{r}\frac{\partial\Lambda^1(r)}{\partial r}\right\}\bigg|_{r=a}\;;\quad \bar{D}_3(r)\\ &= \frac{1}{r^3}\left\{\frac{\partial^3\Lambda^1(r)}{\partial r^3}-\frac{3}{r}\frac{\partial^2\Lambda^1(r)}{\partial r^2}+\frac{3}{r^2}\frac{\partial\Lambda^1(r)}{\partial r}\right\}\bigg|_{r=a}\end{aligned} \tag{18}$$

3. Simplified theories

In the following, some simplified theories are investigated, to provide particular solution.

3.1. Simplified strain gradient elasticity theory (SSGET)

Initially promoted by Atlan and Aifantis [8], the SSGET is obtained by putting material's constants a_i of the gradient elastic moduli tensor $\boldsymbol{D}$ as: $a_1 = a_3 = a_5 = 0\;;\quad a_2 = \frac{\lambda}{2}\,l^2\;;\; a_4 = \mu\,l^2\;;\; l_1 = l_2 = l.$

3.2. Reduced strain gradient elasticity theory (RSGET)

Suggested by Lazar [9] to investigate straight dislocations problems, the RSGET is a generalization of the SSGET by putting: $a_1 = a_3 = a_5 = 0\;;\; a_2 = \frac{\lambda+2\mu}{2}\,{l_1}^2 - \mu\,{l_2}^2\;;\; a_4 = \mu\,{l_2}^2.$

3.3. Couple stress theory (CST)

Following Yury Solyaev et *al*. [10], the couple-stress theory can be deduced by putting: $a_1 = 4\mu\,\gamma\,l^2$; $a_2 = a_3 = -2\mu\,\gamma\,l^2$; $a_4 = -a_5 = 2\mu\,l^2\,(\gamma+1)$; $l_1 = 0$; $l_2 = l$ with $-1 < \gamma < 1$ for the positive definiteness of the strain density energy.

4. Comparisons with other models

Through Mori-Tanaka homogenization scheme, the solution of Eshelby's inhomogeneity problem is implemented to predict the effective properties of a heterogeneous materials. These predictions are then compared with those issued from uniform eigenstrain-based models suggested by Ma and Gao [11], SSGET and the recent model within SSGET developed by [3]. As depicted by Figures 1 and 2, the predicted elastic bulk and shear moduli are strongly depended on the inhomogeneity size a/l_i for $i = 1; 2$. Some significant deviations are noticed between results predicted by considered simplified models.

The predicted normalized effectives properties κ_{eff}/κ_M and μ_{eff}/μ_M tends asymptotically to the classical elasticity theory predictions when the ratio a/l_i tends to the infinity. As shown by Figures 1 and 2, for a Young's modulus ratio $E_I/E_M = 20$, Poisson's ratio $\nu_I = \nu_M = 0.3$ and $a/l_1 = 2$; $a/l_2 = 2$, these properties are enhanced by the volume fraction f of inhomogeneities, whatever the simplified theory.

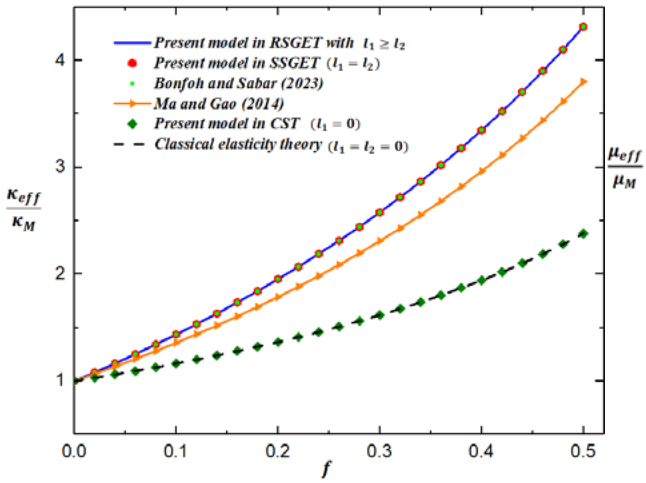


Figure 2: Normalized effective bulk modulus as a function of inhomogeneity volume fraction f $a/l_1(a/l_2 \text{ for } CST) = 2$.

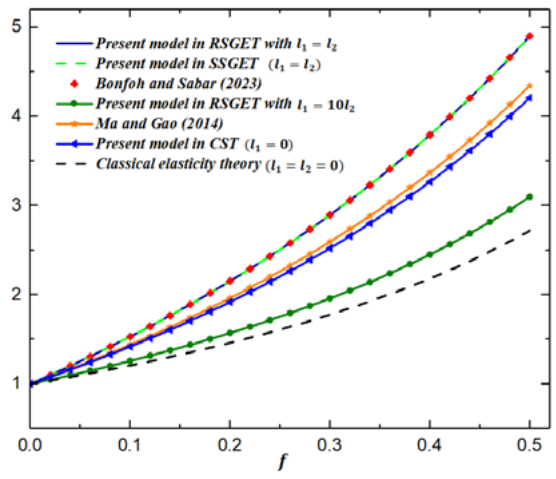


Figure 2: Normalized effective shear modulus as function of inhomogeneity volume fraction f $a/l_1(a/l_2 \text{ for } CST) = 2$.

5. Conclusion

The present micromechanics model provides an exact solution of Eshelby's inhomogeneity problem for a spherical inhomogeneity with an isotropic elastic behavior within the second form of Mindlin's first strain gradient elasticity theory. Some predictions of the present model within simplified versions of the theory, through Mori-Tanaka homogenization scheme, revealed the gradient effects on the effective bulk and shear moduli of two-phase composite. Within the simplified strain gradient elasticity theory, the predictions of Bonfoh and Sabar [3] are retrieved and significant deviations are noticed with other theories. The present micromechanical model can be extended to cylindrical or the ellipsoidal

inhomogeneities and also to an anisotropic elastic behavior per phase. Moreover, elastic mechanical problems such as: chiral materials, quantum dots or void materials can also be investigated.

References

[1] J. D. Eshelby. The determination of the elastic field of an ellipsoidal inclusion, and related problems. *Proc. R. Soc. London. Ser. A. Math. Phys. Sci.*, volume (241): 376–396, 1957.

[2] J. D. Eshelby. Elastic inclusions and inhomogeneities. *Sneddon R. Hill (Eds.), Prog. Solid Mech.*, North Holl. volume (2): 89–140, 1961.

[3] N. Bonfoh and H. Sabar. Exact solution of Eshelby's inhomogeneity problem in strain gradient theory of elasticity and its applications in composite materials. *Appl. Math. Model.*, volume (117): 1–26, 2023.

[4] S. Sidhardh and M. C. Ray. Inclusion problem for a generalized strain gradient elastic continuum. *Acta Mech.*, volume (229): 3813–3831, 2018.

[5] S. Sidhardh and M. C. Ray. Size-dependent Eshelby's ellipsoidal inclusion problem based on generalized first strain gradient elasticity theory. *Math. Mech. Solids*, volume (24): 2251–2273, 2019.

[6] X. L. Gao and S. K. Park. Variational formulation of a simplified strain gradient elasticity theory and its application to a pressurized thick-walled cylinder problem. *Int. J. Solids Struct.*, volume (44): 7486–7499, 2007.

[7] H. Ma, G. Hu, Y. Wei, and L. Liang. Inclusion problem in second gradient elasticity. *Int. J. Eng. Sci.*, volume (132): 60–78, 2018.

[8] S. B. Altan and E. C. Aifantis. On the structure of the mode III crack-tip in gradient elasticity. *Scr. Metall. Mater.*, volume (26): 319–324, 1992.

[9] M. Lazar. Reduced strain gradient elasticity model with two characteristic lengths: fundamentals and application to straight dislocations. *Contin. Mech. Thermodyn.*, volume (34): 1433–1454, 2022.

[10] Y. Solyaev. Self-consistent assessments for the effective properties of two-phase composites within strain gradient elasticity. *Mech. Mater.* 169, 104321, 2022.

[11] H. M. Ma and X.-L. Gao. A new homogenization method based on a simplified strain gradient elasticity theory. *Acta Mech.*, volume (225): 1075–1091, 2014.

CORK-BASED COMPOSITE MATERIALS SUITABLE TO PROTECT TYPE I HYDROGEN TANKS

G.J. de Antunes e Sousa[1,2,*], A.J.C. Silva[1,2] , G.F. Serra[1,2], F.A.O. Fernandes[1,2,3], and R.J. Alves de Sousa[1,2,3]

[1]Department of Mechanical Engineering (DEM), University of Aveiro (UA), Campus de Santiago, Aveiro, 3810-193, Portugal
[2]Centre for Mechanical Technology and Automation (TEMA), University of Aveiro (UA), Campus de Santiago, Aveiro, 3810-193, Portugal
[3]Intelligent Systems Associate Laboratory (LASI). University of Minho (UMinho), Campus Azurém, Guimarães, 4800-058, Portugal
* Email: gui.sousa@ua.pt

Keywords: Hydrogen storage, Cork agglomerates, Energy absorption, Thermal insulation, Mechanical characterization, Finite element analysis (FEA), Numerical modelling

Abstract
Since hydrogen presents more supply chain challenges than conventional fossil fuels, the project aims to investigate the safety of type I pressurized hydrogen storage tanks using composite materials based on cork agglomerates, particularly in accidents, fires, or explosions, as well as the relationship between their mechanical and thermal properties and their density. The samples underwent dynamic impact compression and thermal tests to assess thermal conductivity, diffusivity, volumetric specific heat, and fire behaviour. A numerical model was created using Finite Element Analysis (FEA) to confirm the mechanical results, indicating that agglomerated cork composite materials are suitable for coating type I hydrogen storage tanks. The numerical model validates that lower densities increase the energy absorption capacity during dynamic events because of the shear rate. Thermal diffusivity and volumetric-specific heat significantly impact fire behaviour more than thermal conductivity. To illustrate how agglomerated cork composite materials can be applied to hydrogen storage tanks and support a secure energy transition without jeopardizing the Sustainable Development Goals (SDGs) or the European Green Deal, a demonstrative prototype was developed. The coatings are practical and safe for the environment.

1. Introduction

The global population's rapid growth is exacerbating the scarcity of natural resources, and the high levels of greenhouse gas (GHG) and CO_2 emissions necessitate funding sustainable development and renewable energy sources. Hydrogen, the energy of the future, is highly regarded due to its energy efficiency and zero emissions. However, production, storage, transport, and usage safety conditions are less established than in conventional fuels. This study aims to develop materials and methods to make hydrogen storage reservoirs safer without compromising Sustainable Development Goals or the European Green Deal.

Hydrogen, the most abundant element in the universe, is the first and simplest atom, with only one proton and one electron. It is highly reactive and can be found in various inorganic and organic chemical substances, with water being the most common [8]. Hydrogen can be produced and stored in large quantities for long periods, making it a viable alternative to fossil fuels [2]. Its high specific energies make it an energy-efficient and relatively harmless element. However, its low density (0.089 kg/m^3) makes it challenging to develop mobile hydrogen tanks. Despite its low density, handling hydrogen

requires extreme caution due to its properties [12]. Hydrogen gas storage under pressure is the most established method due to its low density and high-pressure requirements [6]. Type I tanks, made of carbon or low-alloy steel, are used in industrial and commercial operations and operate between 200 and 300 bar. However, lighter composite materials have been developed due to weight requirements [1]. Hydrogen can cause explosions when it reacts with oxidizing substances like oxygen or chlorine, especially in enclosed spaces. Air-powered low-energy ignition sources initiate the burning of hydrogen, which diffuses four times faster than natural gas. This means that if a leak occurs, hydrogen will evaporate into thin air in seconds. The hydrogen flame is almost invisible during the day, increasing the fire risk. Safety mechanisms in hydrogen storage tanks mainly consist of pressure relief valves and temperature sensors to gradually release hydrogen into the atmosphere. However, these mechanisms have limitations in efficiency and size [9]. It is crucial to consider alternatives that can enhance the safety of hydrogen tanks and prolong their exposure to fire without causing damage. In a fire, it is difficult for operators of type I tanks to open the valve without jeopardizing their physical safety.

Cork is a natural substance that has been suggested for its potential to improve safety regulations for hydrogen storage tanks. Its mechanical and thermal properties make it an ideal material for insulating tanks, reducing the risk of explosions and slowing flame spread during fires. Cork's unique chemical composition, derived from its low polysaccharide content, provides exceptional thermal stability and is impermeable to gases and liquids [5]. Its moisture resistance and low solid fraction make it a suitable material for sealing. Additionaly, cork has inferior heat transfer properties due to its low solid fraction, low conductivity of gas, tiny cells that prevent gas convection, and radiation reduction from repeated absorption and reflection at the multiple cell walls [7]. Therefore, cork agglomerates, created by triturating leftover cork planks and combining them with a polymer binder, offer excellent options for coating type I hydrogen storage tanks due to their remarkable mechanical properties under compression and energy absorption [3,4,10]. This makes cork a promising material for improving safety regulations in type I hydrogen storage tanks.

In the academic sense, there has yet to be prior use of composites made of agglomerated cork to protect hydrogen storage tanks. The main goal of this project is to research and evaluate a composite material composed of cork agglomerates that may be applied to hydrogen storage type I tanks to increase their safety. Specifically, it is anticipated that the suggested composite will offer enhanced thermal insulation, function as a flame retardant, and possess a substantial energy absorption capability in case of an explosion.

2. Materials and Methods

2.1. Type I Tank

In order to characterize the tank that will be used in the project in terms of its physical, thermal, and chemical properties, two type I tanks were purchased from Luxfer Gas Cylinders (Luxfer, Nottingham). Technical characteristics for the two P3338N tanks are as follows: type 25E connection, 200 bar operating pressure, 660 mm height, 176 mm outer diameter, 12.91 kg net weight, 10 l water volume, and compliance with Directive 2010/35/EU. Luxfer claims that the building material is a unique 6061 aluminium alloy they created independently.

2.2. Design of Experimens (DOE)

Amorim Cork Composites (ACC, Mozelos) supplied materials for this research. The three types of materials that ACC made available will hereafter be referred to as kinds A, B, and C since they are products that ACC offers for sale and makes available on the market and for reasons of confidentiality. The most essential details and attributes of each material group are shown in **Table 1**.

Table 1. Design of experiments of the samples.

Material	**Density** [kg/m^3]	**Grain size** [mm]	**Binder**	**Binder** wt.%
A	210	2-4		15
B	300	2-5	PU Rigid	13
C	400	2-4		10

2.3. Dynamic Impact Compression Tests

The state-of-the-art drop tower Instron 9440 was used for impact testing. The impactor was raised to a height of roughly 750 mm and had an overall mass of 8.15 kg for experiments employing 60 J of impact energy. The cork samples were squares of 50 mm with a thickness of 25 mm. A 45 kN load cell and a position encoder incorporated into the machine were used to collect the load, position, and time data to create the time acceleration history, forced displacement, and stress-strain curves for each sample. A second impact of the same magnitude was made 30 to 40 seconds following the first impact. The objective of this effort is to ascertain how the density of the composites affects the mechanical response of cork agglomerates under dynamic loading. Since the absorbed energy is equal to the area under the stress-strain curve, the energy density (E_v), or the amount of energy absorbed per unit volume, may be calculated by integrating the following equation (Eq. 1):

$$E_v = \int_{\varepsilon_1}^{\varepsilon_2} \sigma(\varepsilon) d\varepsilon \tag{1}$$

where ε_1 and ε_2 are the lower and higher limits of integration and $\sigma(\varepsilon)$ is the equation for the stress-strain curve.

2.4. Thermal Tests

The method used to determine the samples' thermal conductivity and diffusivity was the transient plane heat source (hot disc) method. Materials with uniaxial structures that are homogenous, isotropic, or anisotropic can all be tested using this method. A sample with a tiny hot-disc probe placed in it can reach equilibrium at a specific temperature. The probe produces a dynamic temperature field inside the object. The temperature rise of the probe is measured as a function of time. The probe doubles as a self-heating heat source and temperature sensor. Next, the response is analysed using the model developed for that specific probe and the assumed boundary conditions. The Hot Disk software provides some suggested settings for each material class's heating power and heating duration, but it is up to the user to calibrate those values.

2.5. Fire Behaviour and Retardancy Tests

It is significant for one to understand that there are two different kinds of fire tests: fire behaviour tests and fire heat conduction tests. The fire behaviour testing aimed to evaluate the burned area and mass loss. The fire-related heat conduction tests aimed to evaluate the samples' thermal behaviour. The cork samples were 200 mm square, 15 mm thick for experiments on fire behaviour, and 10 mm thick for tests on heat conduction. No instrumentation was used in the first kind of test. The blowtorch was the only tool used and operated at maximum power. The distance between the samples and the flame was adjusted. It took two minutes for each test. At maximum power, tests were conducted at three distinct torch-to-sample distances: 200 mm (450 °C), 175 mm (580 °C), and 150 mm (700 °C). Due to a lack of infrastructure and technical conditions and the high cost required by companies specializing in this kind of testing, it was decided to conduct fire heat conduction tests following GTR-13 and NHTSA standards using a simple and basic setup. A surface temperature cycle was carried out after the distance between the material and the flame apparatus where adjusted: 0 to 1 minute: 200 mm and 415 °C; 1 to 3 minutes: 175 mm and 535 °C; 3 to 10 minutes: 150 mm and 650 °C; Over 10 minutes: cool down at

room temperature. **Figure 1** (a) shows a schematic illustration of the experimental setup, whereas **Figure 1** (b) shows the actual experimental setup.

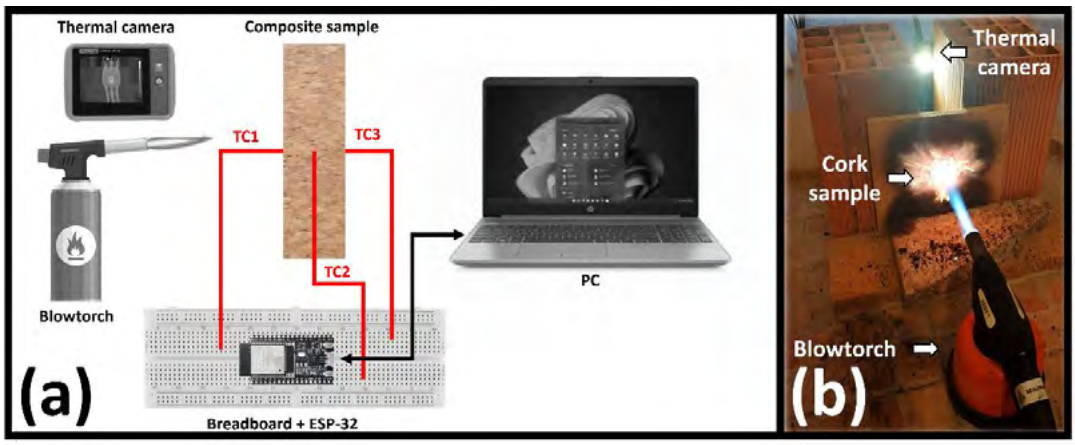


Figure 1. (a) Fire test schematic setup (TC stands for thermocouple) **(b)** Fire test experimental setup.

2.6. Numerical Model

This study uses the Hyperfoam model from the ABAQUS material library to study agglomerated cork as a hyperelastic material. This established nonlinear isotropic model explains the hyperelastic behaviour of elastomeric foams. The Mullins effect model is used with the Hyperfoam material model to expand the isotropic elastomeric foam model and accurately reflect the long-term energy dissipation and stress-softening effects in agglomerated cork. The stress softening phenomenon is replicated in the ABAQUS Mullins effect material model. The experimental testing allowed the conclusion that there is virtually minimal lateral deformation; hence, a negligible Poisson coefficient was considered [11]. Simulations of impacts were performed using the ABAQUS FE program's Explicit solver and large deformation option. To navigate the hourglass phenomenon, the sample was represented as an eight-node linear brick element with reduced integration (ABAQUS' C3D8R element).

3. Results and Discussion

3.1. Dynamic Impact Compression Tests and Numerical Comparision

Figure 2 suggests that the stress-strain curve becomes more “open” as sample density increases, resulting in more considerable stresses for more minor strains. **Table 2** shows impact testing mean parameters and associated standard deviations (SD), supporting the previous finding (Acc. stands for acceleration). Four isocurves have been constructed for dynamic impact testing at 200, 400, 600, and 800 kJ/m^3 energy densities. Given the nature of isocurves, it is reasonable to assume that they are roughly equivalent to straight lines. All four isocurves have a negative slope. As absorbed energy increases, the slope decreases. The energy densities of the samples decrease as their densities increase.

The outcomes of the simulation and the experiments were compared. The entire stress-strain curve (loading and unloading) is shown in **Figure 3** for both experimental and numerical methods. Overall, the FEA results are equivalent to those obtained experimentally despite the numerical results indicating slightly higher stresses and strains.

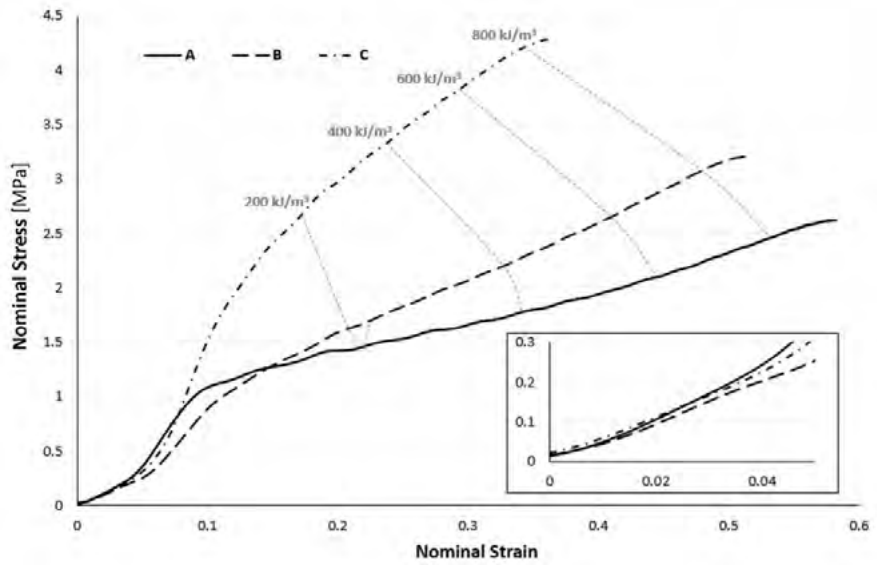


Figure 2. Nominal impact stress-strain curve for the three samples and four different energy levels.

Table 2. Data on the samples impact test that were performed.

Material	Density [kg/m³]	Peak Force [N]	SD Force	Peak Acc. [g]	SD Acc.	Peak Strain	SD Strain
Type A	210	6549.0	9.3	81.9	0.1	0.58	0.0034
Type B	300	8022.2	101.1	100.4	1.3	0.52	0.0053
Type C	400	10717.2	386.8	134.1	4.8	0.37	0.0058

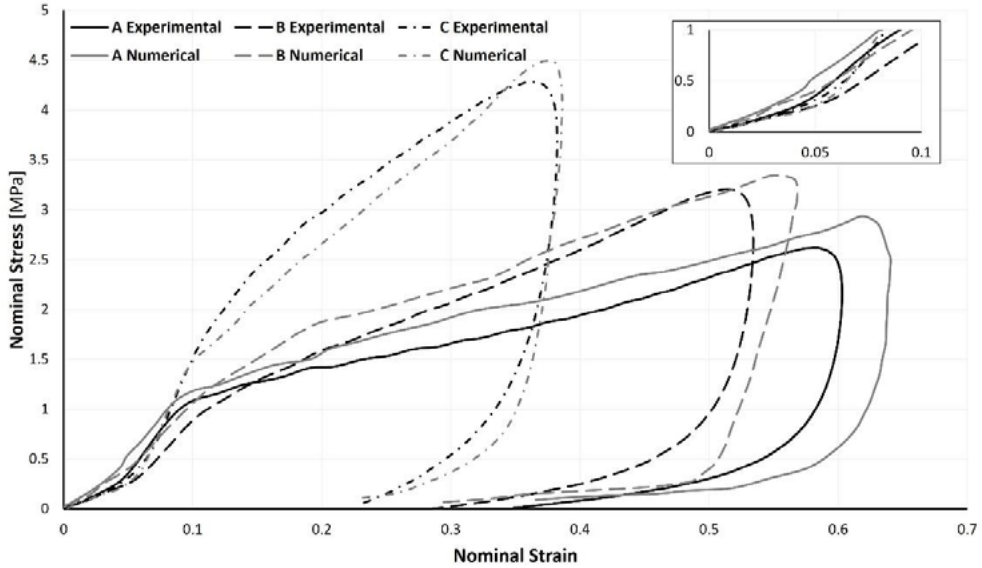


Figure 3. Comparison between experimental and numerical stress-strain curves (full impact test).

3.2. Thermal Tests

As predicted, it can be inferred from **Table 3** that thermal conductivity rises as density does. Although thermal conductivity rises with density, thermal diffusivity falls because the difference in densities in the samples is more significant than in thermal conductivity. Thermal diffusivity is reliant on both thermal conductivity and density. The sample with a density of 400 kg/m³ has a lower thermal diffusivity. Finally, it is found that an increase in density causes an increase in specific heat, or more precisely, volumetric heat capacity. This is particularly relevant since more heat will be required to raise the substance's temperature.

Table 3. Thermal properties of the samples.

Material	Thermal Conductivity [MW/m³·K]	Thermal Diffusivity [mm²/s]	Specific Heat [MJ/m³·K]
Type A	0.060	0.43	0.1393
Type B	0.066	0.23	0.2879
Type C	0.077	0.14	0.5668

3.3. Fire Retardancy Tests

3.3.1. Fire Behaviour Tests

Figure 4 shows that, as expected, bringing the torch closer to the sample results in a larger burned area. More importantly, it has been shown that improved fire behaviour, or a reduced burned area, is correlated with larger sample densities. A higher density leads to a lesser burned area. For example, a 400 kg/m^3 sample has a burned area equivalent to 39.8% and 53.3% of samples A and B's burned areas, respectively. However, as the distance from the blowtorch decreases, the relationship between the burned areas of samples C, A, and B increases. This leads us to the conclusion that the greater the distance from the torch, the more significant the difference between the burned areas of samples with different densities.

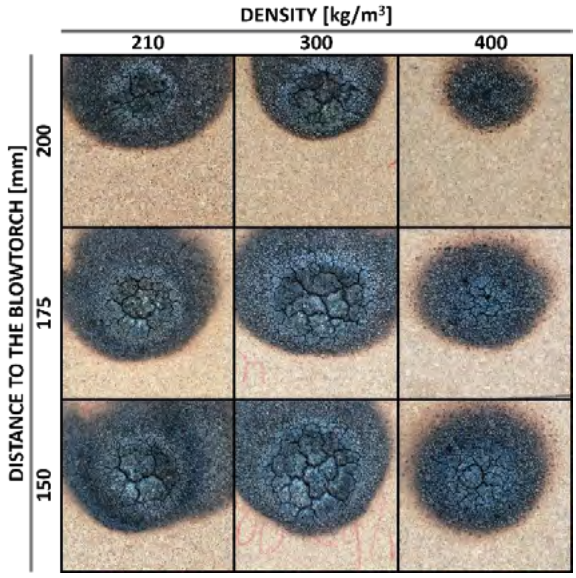


Figure 4. Samples' burnt area as a function of density and blowtorch distance.

A higher density also leads to less mass loss or more structural stability when a structure is exposed to fire. It is interesting to note that mass loss is decreased when the flame is positioned closer to the sample for the same density. There is less mass loss because the burned area grows as the flame gets closer to the sample. This indicates that the heat is dispersed more evenly throughout the sample rather than focused in one spot. It should be mentioned that a polyurethane-based binder, which makes up most of the mass burned by fire, has a melting point far lower than the temperature at which cork grains burn—roughly 100 °C.

3.3.2. Fire Heat Conduction Tests

Since the flame broke through the plate in Type A and Type B samples, the test had to be terminated after 355 and 310 seconds, respectively, and they could not withstand the entire fire test. It is still possible to get some intriguing findings. The examination of **Figure 5** and **Figure 6** indicates that a higher density results in better thermal insulation or lower temperatures on the interior surface. After 310 seconds of testing, samples A, B, and C each displayed an inner surface temperature of 271.8, 230.1, and 124.1 °C. This observation is exciting because sample C should have a greater inner surface temperature than the other samples. After all, it is supposed to have superior thermal conductivity and

is denser than the other samples. This discovery leads one to the intriguing conclusion that thermal conductivity has minimal bearing on the thermal behaviour of the burning samples. Consequently, this behaviour can be explained by thermal diffusivity and volumetric specific heat rather than thermal conductivity.

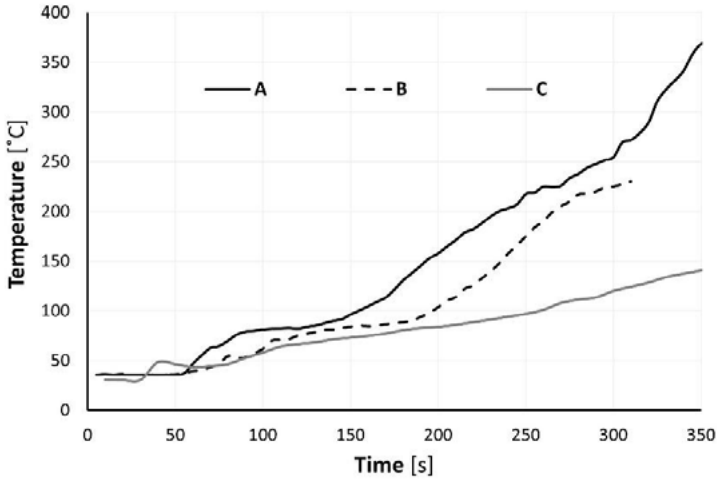


Figure 5. Density influence on the back surface temperature evolution.

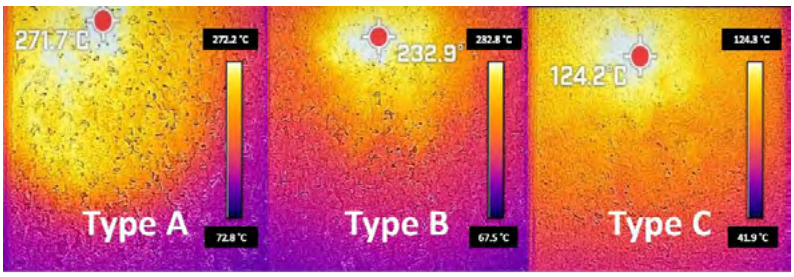


Figure 6. Back surface temperature after 310 seconds for all samples (recorded with Flir One).

Fire experiments were conducted for type C samples with thicknesses of 10, 15, 20, and 25 mm under the previously described conditions since sample C, with a density of 400 kg/m^3, shows the best thermal behaviour in a fire. **Figure 7** shows that a thinner thickness leads to higher interior surface temperatures. It is also evident that the temperature takes longer to reach its maximum as thickness increases. Samples with 10, 15, 20, and 25 mm thicknesses have maximum temperatures of 183.4, 123.5, 100.6, and 66.5 ºC, respectively. This graph only serves as a recommendation for temperature values on an experimental basis. A red line has also been added to show the maximum temperature the hydrogen storage tank can reach without jeopardizing its safety. This suggests that a covering thicker than 15 mm is required.

4. Conclusions and Prototype

The research was successful, in a very clear-cut and objective sense, because it validated using composite materials based on cork agglomerates for hydrogen tank linings to boost their safety. This investigation revealed that type C samples, which have a density of 400 kg/m3, are the best for composite materials because they simultaneously provide strong mechanical and thermal properties. Samples with this density exhibit significantly more intriguing thermal features, especially concerning thermal behaviour and fire resistance, even though they have a slightly lower energy absorption capacity and worse mechanical performance than other samples with lower densities.

More density has been shown to enhance heat conductivity, which has implications for thermal behaviour and fire resistance. Higher density, on the other hand, results in a lower thermal diffusivity. More density enhances fire resistance since it reduces mass loss and the burned area in terms of fire behaviour.

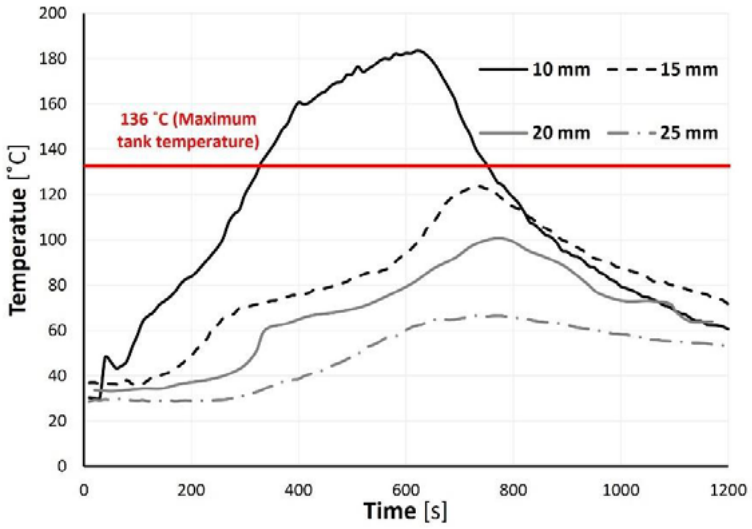


Figure 7. Thickness influence on the back surface temperature evolution of type C samples.

Further evidence that thermal conductivity has minimal bearing on the sample's response to fire comes from the finding that larger densities lead to lower inner surface temperatures. More important impacts are caused by specific heat and thermal diffusivity. The requirement for a coating thicker than 15 mm was also established. From a mechanical perspective, peak forces and acceleration increase with density. Lower density favours a better energy absorption capacity. It was found that a higher density causes a shorter dimensional recovery period during the rebound phase. Conversely, the almost immediate recovery from deformation is decreased with increasing density. The research was successful numerically because it was possible to improve and optimize an already-existing model for impact simulations. The current model can simulate the hit, recovery period, and second impact with remarkable accuracy. On the other hand, the numerical results indicate values that are marginally greater than those from the experimental campaign. Still, other numerical models encounter the same problem.

Coatings and their adhesion can be produced by various processes and technologies. The prototype type I hydrogen storage tank was covered using the most practical and affordable approach: folding and adhering plates. The SOUDAL 22A adhesive, specifically formulated for bonding composites comprised of cork agglomerates, was used in this instance. Notably, the coating was applied in sections to facilitate the appropriate curing of the coating. **Figure 8** shows the final prototype's 3D CAD model as well as the actual prototype, which is presently undergoing development and optimisation.



Figure 8. Real prototype currently in development and CAD 3D model of the prototype.

Acknowledgments
This Project had the support of the Agenda Illiance Project [C644919832-00000035 — Project nº46], financed by the PRR - Programa Recuperaçãoao e Resilência under the Next Generation EU Program financed by the European Union, and had logistical and laboratory at the Center for Mechanical Technology and Automation (TEMA).

References
[1] A. M. Abdalla, S. Hossain, O. B. Nisfindy, A. T. Azad, M. Dawod and A. K. Azad. Hydrogen production, storage, transportation and key challenges with applications: A review. *Energy Conversion and Management,* 165:602-627, 2018. https://doi.org/10.1016/j.enconman.2018.03.088.
[2] A. Léon. *Hydrogen Technology: Mobile and Portable Applications* (1st ed.). Springer, Berlin, 2008. https://doi.org/10.1007/978-3-540-69925-5.
[3] F. Fernandes, R. Pascoal and R. Alves de Sousa. Modelling impact response of agglomerated cork. *Materials & Design,* 58:499-507, 2014. https://doi.org/10.1016/j.matdes.2014.02.011.
[4] G. J. Antunes e Sousa, A. R. S. Rocha, G. F. Serra, F. A. O. Fernandes and R. J. Alves de Sousa. Shear Thickening Fluids in Cork Agglomerates: An exploration of Advantages and Drawback. *Sustainability,* 15:6764, 2023. https://doi.org/10.3390/su15086764.
[5] H. Pereira. *Cork: Biology, Production and Uses* (1st ed.). Elsevier, Amsterdam, 2007. https://doi.org/10.1016/B978-0-444-52967-1.X5000-6.
[6] J. Abe, A. Popoola, E. Ajenifuja and O. Popoola. Hydrogen energhy, economy and storage: Review and Recommendation. *International Journal of Hydrogen Energy,* 44(29):15072-15086, 2019. https://doi.org/10.1016/j.ijhydene.2019.04.068.
[7] L. J. Gibson and M. F. Ashby. *Cellular Solids: Structure and Properties* (2nd ed.). Cambridge University Press, Cambridge, 2014. https://doi.org/10.1017/CBO9781139878326.
[8] M. Hirscher and K. Hirose. *Handbook of Hydrogen Storage: New Materials for Future Energy Storage* (1st ed.). Willey-VCH, 2010. https://doi.org/10.1002/9783527629800.
[9] M. Zhang, H. Lv, H. Kang, W. Zhou and C. Zhang. A literature review of failure prediction and analysis methods for composite high-pressure hydrogen storage tanks. *International Journal of Hydrogen Energy,* 44(47):25777-25799, 2019. https://doi.org/10.1016/j.ijhydene.2019.08.001.
[10] P. Santos, S. Pinto, P. Marques, A. Pereira and R. Alves de Sousa. Agglomerated cork: A way to tailor its mechanical properties. *Composites Structures,* 178:277-287, 2017. https://doi.org/10.1016/j.compstruct.2017.07.035.
[11] R. Jardin, F. Fernandes, A. Pereira and R. Alves de Sousa. Static and dynamic mechanical response of differente cork agglomerates. *Materials & Design,* 68:121-126, 2015. https://doi.org/10.1016/j.matdes.2014.12.016.
[12] T. Santos. *Estudo de um sistema de armazenamento de hidrogénio para veículos* (Master's Thesis, ISEP). Repositório Científico do Instituo Politécnico do Porto, Porto, 2018. http://hdl.handle.net/10400.22/14233.

Tomography-based numerical reconstruction of fiber bundle and response of microstructural characteristics to mechanical behavior

Xinling song [1*], Audrey Hivet [1], Anwar Shanwan [1], Gilles Hivet [1]

1: LaMé, University of Orléans, Orléans, France
E-mail: xinling.song@univ-orleans.fr*, audrey.hivet@univ-orleans.fr, anwar.shanwan@univ-orleans.fr, gilles.hivet@univ-orlean.fr

Key words: Fibers, Composites, Mechanical behavior, Microscale, Modeling

Abstract
To understand the overall behaviour of fabrics in depth, it is necessary to study the behaviour of the fiber yarn (the basic unit) under different mechanical paths. Due to the limitations of experimentation, simulation becomes an effective tool to study the behaviour of fiber bundles under different stress conditions. The goal of this study is to create simulation tools to understand and model the behaviour of a fiber yarn in microstructure to build a constitutive law of the yarn. This work creates numerical fiber bundle based on tomography and combines micro-compaction experiments with 40 polyester fibers (15mm length, 0.5mm diameter). The initial numerical fiber bundle geometry is extracted with MATLAB and input into ABAQUS® to simulate the mechanical load as the experiments. The compaction behaviour curve and the microstructure of fiber bundle of simulation and experiment are compared after last compaction step. (i) From the compaction curves, the experimental and simulation results are approximate. (ii) In addition, in the final compaction step, the error of three fiber bundle samples between simulation and experiment is optimistic, with mean values of 27.95%, 14.07% and 19.6%, and standard deviations of 10.56 %, 7.89% and 11.6% with respect to the fiber diameter, respectively.

1. introduction

Composite materials are used for different industrial applications like transports. Among the most widespread, one can find composite materials based on fibrous reinforcements. But, the proper functioning of processes now results from know-how and experience resulting from an empirical approach, much more than from a complete mastery of the physical phenomena involved. The RTM (Resin Transfer Molding) manufacturing of composite parts starts usually by the preforming of dry or pre-impregnated fabrics according to a defined mold, sometimes complex, before the resin is injected. The mechanical behavior of the fabric is therefore crucial during the preforming process because it influences the next steps of the manufacturing process. However, a fibrous reinforcement is a complex structure since it results from the weaving of thousands of yarns, themselves made up of the assembly of tens of thousands of fibers of few microns diameter. Thus, the mechanical behavior of the reinforcements is obtained by a sum of responses obtained experimentally to specific loading path (compression, tension, bending, shear, etc.) [1]. These mechanical responses are subsequently modeled

by equations whose form is obtained by hypotheses on the most influent parameters [2, 3, 4], without a truly rigorous approach of the complex physics involved (large number of fibers, variability, undulation of fibers, sizing, etc.). This is particularly the case for compression behavior in which a direct relationship is assumed between the compression stiffness and the fibers volume fraction according to an empirical law. If this law works correctly, it requires an identification for each new type of yarn and does not allow to highlight the structural parameters, which can improve the structure performances and to anticipate the mechanical behavior of fabrics without having to create and test it.

The goal of this paper is therefore to be able to tackle this lack by studying the mechanical behavior of an assembly of quasi-parallel fibers which represent the fibrous structures most used for technical applications. In order to achieve this goal, several solutions exist; an experimental approach couldn't be sufficient as it requires a very important number of experiences, because there are many loading paths and an important number of undulations exist. It is therefore necessary to be able to use effective numerical approaches allowing a parametric study, i.e. carrying out many tests in a short time. The chosen strategy is therefore to be able to create a virtual estimator of the behavior of a fibrous assembly and to validate it by experiments. One of the most important difficulties to study the behavior of fiber assembly is undoubtedly the size of the fibers (a few micrometers) which make them very difficult to handle and observe individually. As the goal of this study is to understand the strain phenomenology of fibrous assemblies, a model of fibers is done at larger scale (500 microns) as a first approach; in a second time, simulations with fibers at a "real" scale are performed. To achieve this goal, many steps should by carried-out successfully. The first is to develop a numerical strategy to efficiently simulate, at the fiber scale, the strain of the architecture under various solicitation. The second step is to define experimental validations to ensure the reliability of this virtual estimator by comparing its results with experimental results. The third step aims to define indicators of the microstructure that allow to analyze the results. Finally, it is necessary to use this strategy to create any type of architecture with a defined parameters and apply different paths of loadings to analyze the mechanical response of the structure. A first numerical approach was established by the thesis of Oussama HAJI [5]. This approach allowed to highlight the feasibility of the first and the second step of the strategy, but it is now necessary to be able to improve them and especially to carry out the last two steps as well as to operate the entire strategy to carry out parametric studies and conclude on their influence on the mechanical behavior. The aim of this paper is to improve the accuracy of existing virtual numerical estimators from experimentation to post-processing, as well as numerical strategies. The developed accurate model approach allows understanding and modeling the mechanical behavior, to build a constitutive law of the yarn.

2.Experiment and simulation strategy

2.1. Tomography combines micro-compaction experiment

Two fiber bundle samples consisting of 40 dry polyester fibers, without matrix or sizing, were manually prepared, where a single fiber length is approximately 14-14.5 mm, with diameter of 0.5mm, density of 1.38e-09 T/mm^3, Young's modulus of 6 GPa and Poisson's ratio of 0.25 as shown in Fig.1(a). The sample contained only 40 fibers since considering that (i) the numerical virtual estimator is still in the validated stage, a large number of numerical simulations are required, with a reasonable number of fibers to control the simulation time; (ii) the fiber samples are prepared manually, so it is difficult to prepare a large number of fiber samples. The sample is placed in a transparent support of PMMA (Poly methyl methacrylate) as shown in Fig.1(a).

This study used an X-ray tomography system (model EasyTom Nano 160, Fig.1(b)) to scan the samples. The micro-compaction machine (Deben, Fig.1(c)) is equipped with two compaction plates, upper and lower. The upper compaction plate is always fixed, while the lower one is movable and connected to a piezoelectric linear motor installed at the bottom of the compaction machine. The sample is compressed vertically in the "scan channel". The sensor is located in the upper part of the machine Deben, and the sensor of 500N was used. To avoid the influence of inertial effects on the fiber rearrangement, it was crucial to maintain quasi-static compression. The speed of compaction was fixed to $V_{compaction}$=1 mm/min. The tomography scan sample at each compaction step (Fig.1 (d, e)), with the spatial resolution of 9 μm, tube tension of 60 KV and tube intensity of 100 μA. The slices (cross-sections) of the fiber bundle were obtained by three-dimensional reconstruction of the tomography data processing by using the software “Xact”.

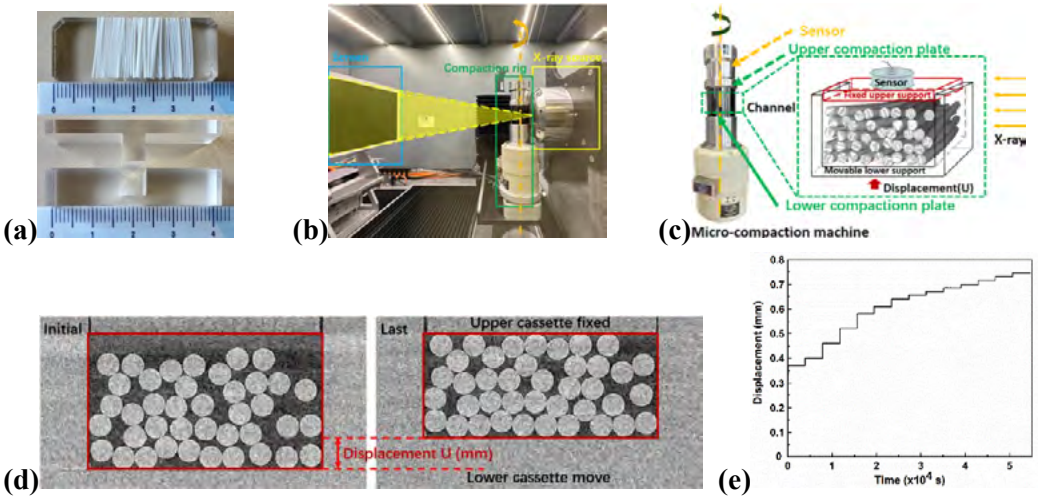


Figure 1. Tomography combines micro-compaction experiment. (a) The fiber bundle sample with cassette/compaction channel/ transparent support of compaction. (b)X-ray tomography system, (c) micro-compaction machine (Deben). (d, e) Compact path imposed by displacement.

2.2 Reconstruction fiber bundle with virtual numerical estimator

As mentioned above, the fiber bundle virtual numerical estimator was developed by O. Haji [5, 6], and includes two parts: reconstruction of numerical fiber bundle geometry and simulation compaction test with ABAQUS®.

The reconstruction step of numerical fiber bundle geometry consists of two steps: (i) tomography slices post-treatment and (ii) create fiber bundle centerline with MATLAB.

(i) Tomography slices post-treatment:

Firstly, the flow chart for post-treatment tomography slices of fiber bundle shown in Fig.2(a). According to the tomography slices of fiber section (horizontal, vertical), the shape of fiber vertical section could be considered ideal regular circle, then extract the fiber centerline to reconstruct the numerical fiber geometry. In order to improve the accurate of reconstruction step, it’s important to remove another part except fiber section, the 3 steps were performed for fiber bundle: (a) separation, the X-ray CT scan image manifest as an aggregation of pixel points. It can be seen that fibers and pores are composed of these distinct pixel points, and each one is characterized by varying the grayscale values. Therefore, by setting a grayscale threshold to make the separation between voids and fibers (only black and white exists). (b) elimination of compaction channel, here, the cassette and fibers both are white, this step

cloud avoid the influence of compaction channel during extract fiber centerline. (c) remove noise, this step plays the same role of avoiding the effects of noise in slices on the extracted fibers. Secondly, the fiber bundle centerline is extracted by detecting the center of the fiber cross-section based on the FIJI preprocessed image, and then connecting the center points of the same fiber.

(ii) Create fiber bundle centerline with MATLAB:

The fiber cross-section in each X-ray tomography slice can be approximated as a circle, and the center of this circle can be a pixel point coordinate. Therefore, the radius and the center of each circle can be defined by the "Imfindcircles" function in MATLAB. The principle used in this function for definition of the circle is the “Circle Hoff Transform (CHT)”, as shown in Fig.2 (b1). The detected section (circle) projected on the initial slice shown in Fig.2 (b2). The coordinates of the center point and the radius of each fiber cross-section are obtained by the CHT algorithm, but MATLAB cannot automatically determine which circles of different slices belong to the same fiber. Therefore, the determination method is shown in Fig.2 (b3, b4), for center point $\boldsymbol{C_{ij}}$ in slice $\boldsymbol{j}$ and the center point $\boldsymbol{C_{ij+1}}$ in slice $\boldsymbol{j+1}$ belonging to the same fiber **i**, the distance between the projection of $\boldsymbol{C_{ij}}$ and $\boldsymbol{C_{ij+1}}$ should be less than the diameter of fiber:$\left|\boldsymbol{C_{ij+1}} - \boldsymbol{C_{ij}}\right| < \emptyset$. In this study, the distance between the two slices was $d = 9$ µm, which is enough small compared to the fiber’s diameter $\emptyset = 500$ µm.

As mentioned earlier, the tomography images are composed of thousands of pixel points. As shown in Fig.2 (b5), when defining a circle, the position of the center coordinates in the slice calculated using the CHT algorithm can be divided into two cases: Case 1, the center of the circle is not on the pixel point and the actual center point is offset to the nearest pixel point when defining the center of the circle; Case 2, the center of the circle is on the pixel point and no offset occurs.

Therefore, when the center coordinates of fibers are connected, the form of the “folded” line (extracted line) in Fig.2 ((b5)-right) and Fig.2 (b6)) (before smooth centerline) is obtained, which does not correspond to the actual fiber morphology due to the uncertainty of 1 pixel on the center position. The oscillations amplitude depicted Fig.2 (b6)) are, indeed verified to be lower than 1 pixel. A smoothing step has then to be performed on them to obtain the consistent trajectory Fig.2 (b6)).

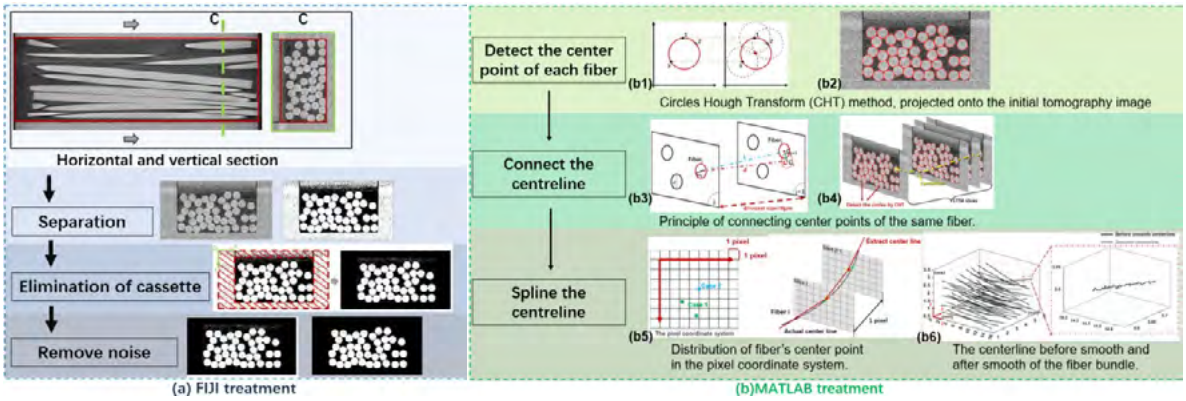


Figure 2. Flow chart for reconstruct numerical fiber bundle geometry (a) post-treatment tomography slices with FIJI, (b) create numerical fiber bundle centerline with MATLAB.

2.2.2 Numerical strategy

This study develops and enhances an existing simulation strategy [5, 6]. The simulation strategy, which is executed in ABAQUS®/EXPLICIT, shows that Explicit method can be used for quasi-static dynamics simulations under many contact conditions and that selection of appropriate simulation parameters can

optimize the computational time. The beam element used in the present strategy are B31 as they are more stable than B32, and the material damping coefficient $\alpha = 10^5$ and a compaction loading speed of $v = 10^3$ mm/min, can optimize the calculation time and avoid the inertia effect of the fibers [5,6] . In addition, for this simulation, other parameters were chosen: (i) the tangential contact was modeled by the Coulomb's friction law, where the friction coefficient was used with an average value of $\mu = 0.2$ according to Gassara [7]; (ii) the adhesion coefficient was assumed to be equal to the coefficient of friction; and (iii) the diameter of the beam elements of the single fibers was the same (0.5mm) and constant [5,6].

In order to improve even more the numerical simulation estimator, the selection of the size of the mesh elements of the fibers and the compaction channels (sample cassettes), the correction of initial penetration between the fiber bundles was set in next part.

When the mesh size is small enough, the accuracy of the calculation does not change significantly as the mesh continues to decrease, after the calculation of 3 beams compaction test, the sensitivity analysis the good range the for the mesh sizes is defined and will then be used for the compaction calculations. When the element size of the fibers is L_b=0.3 (a single beam contains 50 elements), the reaction force of compaction planes stabilizes and reaches a critical value for the mesh sensitivity. Since, the discrete rigid solid will have to be considered for the real compaction case, the mesh sensitivity of the discrete rigid is tested with a beam with a mesh size of 0.3mm and the same case. The reaction force results are basically the same as the reference with analytical rigid part when the mesh size of the discrete rigid part is 0.2mm. The considered Polyester fibers (Poisson's ratio = 0.25 [5]) for the validation experiments have a diameter of 500 µm and a density of 1.38×10^{-09} T/mm^3. In order to optimize the mechanical properties of the fibers as accurately as possible, mechanical tests were carried out. The tensile experiment was performed for single fiber, the resulted average Young's modulus is 6 ± 0.2 Gpa, and the average value of this parameter will be used in the simulation. In addition, the initial penetration (Fig.3) and contact control are manually proposed in the "*.inp*" file for the contact pairs between fibers [8].

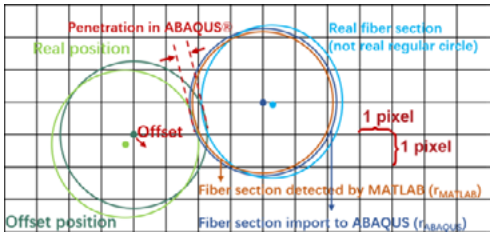


Figure 3. Penetration principle between fibers in ABAQUS®.

3.Indiacotor tools

Fiber Position Deviation Diameter Ratio (FPDDR) and Fiber Position Deviation Displacement Ratio (FPDUR) are the ratio of the average of the fiber position distance relative to the fiber diameter and displacement of compaction step in the experiments and simulations, respectively. Fig.4 shows FPDDR and FPDUR error proposed indicators to quantify the fiber position between simulation and experiment:

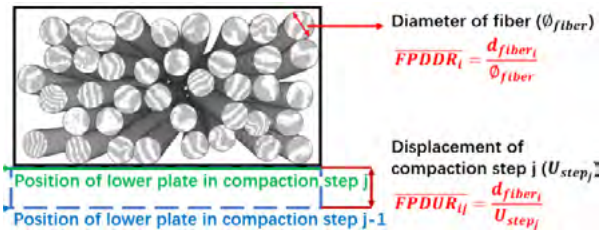


Figure 4. Indicators used to represent fiber position errors in experimental and simulation results.

4.Discussion

4.1 Imposing gravity simulation to the initial geometry

As mentioned before, the fiber's section is composed with thousands of pixel points, when reconstruct the fibers with MATLB, the fiber's centerline is not exactly coinciding with real one (Fig.2 (b5, b6)), where the deviation less than 1 pixel. Indeed, the initial fiber's section penetrated a little before calculation or miss the point of contact that exists in the real bundle geometry. After the introducing of the gravity force, the fibers move towards each other until their contact are each an equilibrium, the centerline before and after imposing gravity shown in the Fig.5, and the fiber position errors shown in the Tab.1 ($\boldsymbol{d_{fiber_i}}$: the distance between simulation and experiment for fiber $\boldsymbol{i}$). This clearly shows the influence of the voxel size but also that the initial modeling obtained for sample 1 and 2 is accurate since very small changes and the indicators are observed.

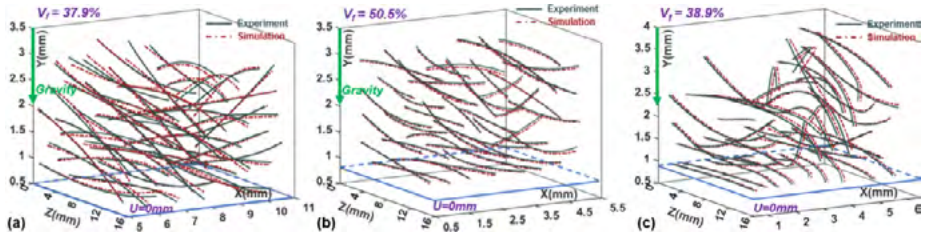


Figure 5. The centerline of fiber bundle after imposing the gravity field. (a) Sample 0 (Dr. Haji's sample), (b) Sample 1, (c) Sample 2.

Table 1. The position errors of fibers between experiment and simulation after imposing gravity.

	Sample 0		Sample 1		Sample 2	
Spatial resolution (μm)	15		9		9	
FPDDR (%)	μ =15.83	σ =5.50	μ =5.20	σ =1.20	μ =8.30	σ =2.45

4.2 Compaction simulation

The compaction simulation of sample 0, 1 and 2 were performed here, volume fraction in the function of compaction pressure the shown in Fig.6 (a1-c1), form the compaction curve, the consistency between the simulated and experimental values is interesting and acceptable. In addition, the 3D rendering fiber bundle of simulation and 3D reconstrued geometry of experiment of last compaction step were performed. The morphology of fibers in simulation and experiment are closely related.

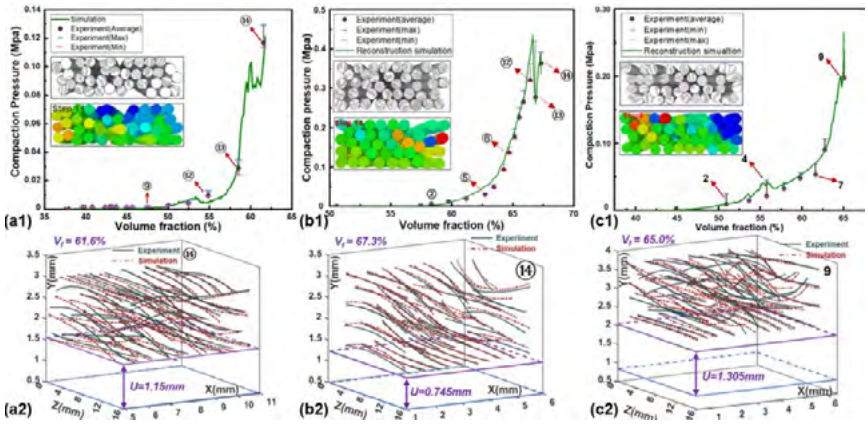


Figure 6. Compaction simulation for the 3 samples.

Furthermore, the centerline position for the last step shown in the Fig.6 (a2-c2). Even if the sample 2 results are not as accurate as for the sample 1, experimental and simulated results is good remains in good agreement which enables to confirm the potential of the strategy to model consistently the deformation of a fiber bundle during compaction. By introducing a gravity field into the three fiber samples, the contact between the fibers of Sample 1 is more stable. The more stable contact state results in the less error accumulation between the simulated and experimental fiber positions in the last compaction simulation. It is important to notice and confirm here that the initial errors of the reconstructed microstructure from the experimental one is of a main importance for the general consistency which is definitely a very good thing for the use of the strategy as a virtual estimator because this step does not exist for such simulations.

Table 2. The position errors of fibers between experiment and simulation of 3 samples for last compaction step.

Indicators (%)	Sample 0		Sample 1		Sample 2	
	μ	σ	μ	σ	μ	σ
FPDDR	27.95	10.56	14.07	7.89	19.60	11.60
FPDUR	12.15	2.59	9.44	5.40	7.51	4.45

5. Conclusion

Compaction experiments and simulations were carried out on three samples using the simulation strategy described above, with an initial volume fraction of 37.9%, 50.5%, 38.9%. The accuracy of the initial model was verified by imposing a gravity simulation. The contact position detected by post-treatment strategy could be verified by imposing the gravity filed to the fiber bundle geometry: the fibers move until the static equilibrium and the differences consequently point out the uncertainties of the reconstruction process. The average error (FPDDR: the error according to the fiber diameter) of the fiber position under imposing gravity simulation and the one extracted by tomography experiment for the three samples was 16%, 5%, and 8% of the fiber diameter, respectively. As expected the increase in the XCT resolution enables obtain a more accurate initial consistency which is very promising for the proposed strategy. This means that the initial contact introduced by the post-treatment strategy achieve the goal, with a very satisfying accuracy even if the errors couldn't be completely eliminated due to the necessary simplification of the modeling.

Even though, there is potential for improvement, the comparison between the simulated and experimental, in terms of macroscopic compaction behavior, and the position of the fibers after compaction is interesting and promising and enables to validate that the virtual numerical estimator, as well as the developed microstructural analysis tools are effective for the current work.

Acknowledgments

This work of the project supported by the China Scholarship Council (CSC), the project of "National constructed high-level university-sponsored graduate programs" (Funding number: 202008120116).

References

[1] Long A C, & Clifford M J. *Composites forming technologies*. 2007.

[2] Toll, S. Packing mechanics of fiber reinforcements. *Polymer Engineering and Science*, *38*(8), 1337–1350. 1998.

[3] Van Wyk, C. M. 20—NOTE ON THE COMPRESSIBILITY OF WOOL. *Journal of the Textile Institute Transactions*, *37*(12), T285–T292. 1946.

[4] Beil, N. B., & Roberts, W. W. Modeling and Computer Simulation of the Compressional Behavior of Fiber Assemblies. *Textile Research Journal*, *72*(4), 341–351. 2002.

[5] Haji Oussama. *A behaviour model of textile structures : Development, identification and implementation*. (thesis). 2018.

[6] Haji, O., Song, X., Hivet, A., Rolland du Roscoat, S., Orgéas, L., Sinoimeri, A., Hivet, G., & Blond, E. Modeling of Quasi-Parallel Fiber Networks at the Microscopic Scale. *Applied Composite Materials*, *30*(2), 653–675. 2023.

[7] Gassara, H. E. *Development of new measurement methods of transversal friction between fibers*. (thesis).2016.

[8] ABAQUS Documentation (6.5-1). (n.d.). In *ABAQUS documention (v6.5-1)*.

DESIGN APPROACH USING DAMAGE TOLERANT COMPOSITES MATERIALS WITH RISING FRACTURE RESISTANCE (R-CURVE BEHAVIOUR)

Bent F. Sørensen[1], Frode Grytten[2], Reidar K. Joki[3], Jens K. Jørgensen[4], Philippe Noury[5], Daan J. H. Cederløf[6]

[1]Technical University of Denmark, Wind and Energy Systems, Risø Campus, Roskilde, Denmark
Email: bsqr@dtu.dk, Web Page: http://www.wind.dtu.dk/
[2]SINTEF Industry, Department of Materials and Nanotechnology, PB 124 Blindern, Oslo, Norway
Email: frodegry@gmail.com, Web Page: https://www.sintef.no/en/
[3]JOKI Engineering, Storgata 26, 1607 Fredrikstad, Norway
Email: rkj@joki-engineering.no, Web Page: https://www.joki-engineering.no/
[4]SINTEF Industry, Department of Materials and Nanotechnology, PB 124 Blindern, Oslo, Norway
Email: Jens.Jorgensen@nammo.com, Web Page: https://www.sintef.no/en/
[5]DNV, Technology Centre, Oslo, Norway
Email: Philippe.Noury@dnv.com, Web Page: https://www.dnv.com
[6]DNV, Technology Centre, Oslo, Norway
Email: Daan.Jonas.Hottentot.Cederlof@dnv.com, Web Page: https://www.dnv.com

Keywords: delamination, fibre bridging, design, damage tolerance

Abstract
Composite structures can fail by delamination. For some composite materials, denoted damage tolerant materials, the fracture resistance increases with crack length (R-curve behavior). We consider three design approaches: Level 1 is a traditional linear elastic fracture mechanics design approach where the applied J integral value, J, should be kept below J_0, so that no crack growth occurs, and cyclic crack growth is assessed by the Paris-Erdogan relation of an unbridged crack. Level 2 is restricted to steady-state problems for which the J integral is independent of crack length, so that under monotonic loading unstable cracking will not occur unless J reaches J_{ss}. The design can be made using analytical models. Level 3 is design using cohesive laws. Level 3 is more general, but also more demanding; the cohesive laws must be known, and a numerical model must be used. We illustrate the Level 1 and Level 2 approaches by analyzing delamination crack growth from a ply-drop under static and cyclic loading. The Level 2 design stresses for both static and cyclic crack growth were significantly higher than that for Level 1. Finally, we discuss the implications regarding safety factors and the limitations of the proposed approaches.

1. Introduction

Failure of composite structures often involves delamination, which is crack growth between layers. Some composites have a relative brittle interface between layers, while others, denoted damage tolerant materials, demonstrate an increasing fracture resistance with crack extension (R-curve behaviour). A physical mechanism that can generate rising fracture resistance is large-scale bridging by fibres that cross over the crack and create tractions along the crack faces opposing the crack opening. The fracture resistance, characterized in terms of the J integral [1], rises from an initial value, J_0, (a sharp, unbridged crack) to a significantly higher steady-state value, J_{ss} (fully developed bridging zone) under monotonic loading [2]. Under cyclic loading, the crack growth rate is fastest in the beginning (sharp, unbridged crack) and decreases as the bridging zone becomes larger and reaches a

significantly slower growth rate as the bridging zone is fully evolved [3]. From an engineering standpoint, such material behaviours are highly desirable, since the increasing fracture resistance provides an additional intrinsic safety margin. However, current design approaches based on linear elastic fracture mechanics do not utilize these behaviours. This paper proposes a design approach to utilize the advantageous properties of damage tolerant composites, shifting from a "no crack growth" to a "controlled crack growth" philosophy, allowing for stable, but not unstable crack growth.

The paper is organised as follows. First, in Section 2, we describe in more details the fracture mechanics properties of damage tolerant materials that exhibit large-scale bridging. Next, in Section 3, we discuss how these properties can be utilized in engineering design and presents two novel design approaches. Section 4 includes a case study, delamination from a ply drop. Section 5 includes some considerations and suggestions for future work and Section 6 presents the main conclusions.

2. Design with damage tolerant materials

2.1. Utilization of R-curve

In this paper, we will make a sharp distinction between brittle materials and damage tolerant materials. By "brittle materials" we refer to those that follow linear elastic fracture mechanics (LEFM). Conversely, "damage tolerant materials" are characterized by R-curve behavior, i.e., the fracture resistance expressed in terms of the J integral, rises as the crack tip advances. Fig. 1 shows a schematic of R-curve behavior. In Fig. 1, the fracture resistance, J_R, is shown as a function of the end-opening, δ_n^* , the opening of the original crack tip. Crack growth starts when the value of the applied J integral reaches the value, J_0. With increasing loading, J_R rises, eventually reaching a steady-state value, J_{ss}, denoted the steady-state fracture resistance. Fig. 2 provides a visual representation of the mechanism of crack bridging that underpins the rising fracture resistance. The bridging zone spans the distance from the initial crack tip to the current crack tip. The fracture resistance J_R increases as the end-opening increases. Eventually, the bridging starts failing at the original crack tip, and now the bridging zone extends along with the crack tip at a constant, steady-state fracture resistance, J_{ss}.

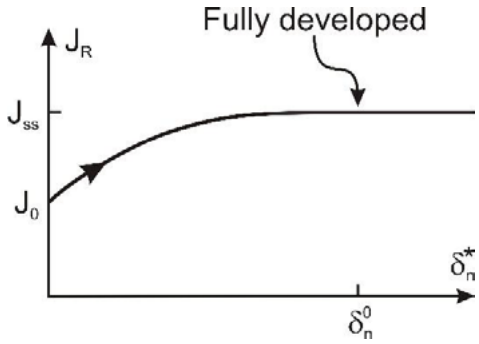


Figure 1. Schematic of R-curve behavior: The fracture resistance, J_R, starts from an initiation value, J_0, rises with crack opening, eventually reaching a constant, steady-state fracture resistance, J_{ss} as the bridging zone is full developed.

Fig. 3 shows the crack growth behavior for a crack in a damage tolerant material subjected to cyclic loading between fixed maximum and minimum J integral values, J_{max} and J_{min}, respectively. Initially, the crack starts growing as a sharp, non-bridged crack. As the crack tip advances and the bridging zone developed between the original crack tip and the current crack tip, the crack growth rate da/dN decreases (here, a is the crack length and N is the number of load cycles). In steady-state specimens (see Section 2.3 below) the crack growth rate attains a constant crack growth rate once the bridging zone is fully-evolved and the crack tip and bridging zone translate along the specimen in a self-similar manner. The crack growth rate at the onset of cyclic crack growth is denoted as da/dN_{nb} (subscript nb indicates "non-bridged") and crack growth rate of the fully-developed bridging zone is denoted as

da/dN_{fd} (subscript fd indicates "fully developed"). The crack extension corresponding to the onset of the fully-developed crack growth is denoted by Δa_{fd} and the associated number of cycles to reach the fully-developed bridging zone under cyclic loading is denoted N_{fd}. In general we expect theses parameters to be material constants but for mixed mode cracking they will depend on the mode mix.

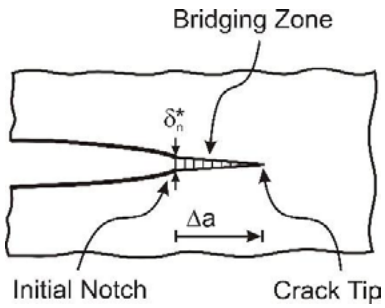


Figure 2. Schematics of a crack tip with a bridging zone. The bridging zone spans the distance from the original to the current crack tip position.

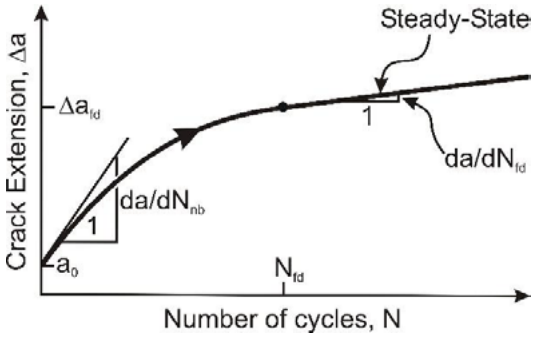


Figure 3. Schematic of cyclic crack growth with large-scale bridging in a steady-state specimen. The crack growth rate starts from an initial value, da/dN_{nb} (corresponding to an un-bridged crack), decreasing to a lower, constant growth rate, da/dN_{fd}, as the bridging zone becomes full developed.

It is clear that the presence of fibre bridging is beneficial from the perspective of engineering design: The rising fracture resistance can lead to crack arrest, or in the case of cyclic loading, substantially reduce the crack growth rate. The goal of this paper is to develop robust design guidelines that fully exploit the fracture mechanics of damage-tolerant materials, ensuring safety and reliability.

In the following, we will formulate design criteria for static loading corresponding to the maximum allowed applied load (avoiding unstable crack growth) and design criteria for the number of cycles between inspection intervals to ensure that unstable crack growth does not happen under cyclic loading. Our approach is categorized into three distinct levels of design methodology: Level 1, Level 2, and Level 3. These design approaches are described in the following sub-sections.

2.2. Level 1 design approach: Traditional LEFM

Level 1 is a traditional design where under static loading, the applied J integral value, J should be kept below J_0, so that no crack growth occurs. Crack growth under cyclic loading is assessed by the Paris-Erdogan relation [4] for unbridged crack, i.e., using Paris-Erdogan parameters fitted to da/dN_{nb}-data.

While the Level 1 design approach is universally applicable and inherently safe, it is also notably conservative for damage-tolerant materials. This conservatism stems from its failure to utilize the

potential benefits of increased fracture resistance and the deceleration of crack growth observed in cyclic loading of such materials.

2.3. Level 2 design approach: Steady-state specimens

The Level 2 design approach is restricted to a class of problems we call steady-state problems for which the J integral remains constant regardless of crack length. The concept of steady-state specimens was introduced by Suo *et al*. [2, 5]. For a steady-state specimen subjected to a monotonic increasing loading, the crack front will advance stably when J exceeds J_0 until the load is so high that the value of the applied J reaches J_{ss}. When J exceeds J_{ss}, the crack grows unstably. Consequently, for steady-state specimens, J_{ss} can be used as the critical value for the applied load in the prediction of the load-carrying capacity. Under cyclic loading, the crack growth in steady-state specimens will include both the initial region where the crack growth rate slows down and the fully-developed (steady-state) cyclic crack growth rate, da/dN_{fd}. Assuming the maximum permissible crack length is a_{max} (an example will be given in Section 3), and the initial unbridged crack length is a_0. Then, the total number of cycles required for the crack to extend from a_0 to a_{max} can be estimated by taking into account the effects of crack bridging:

$$N_i = N_{fd} + \frac{a_{max} - a_0 - \Delta a_{fd}}{da/dN_{fd}} \tag{1}$$

2.4. Level 3 design approach: Design using cohesive zone modelling

The Level 3 design approach involves numerical modelling with cohesive laws for the prediction of the load-carrying capacity of composite structures. The design approach is general, it is not restricted to steady-state specimens. Thus, it can provide precise predictions for structures that may fail under loads where the bridging zone has not yet fully developed. However, the development of cohesive laws based on experimental data - especially those pertaining to mixed-mode loading conditions - is still an emerging discipline. Similarly, modelling cyclic crack growth with cyclic cohesive laws has yet to reach a level of maturity suitable for standard engineering practice. Thus, although Level 3 design is expected to be more accurate and general than the Level 1 and Level 2 design approaches, it is not yet sufficiently mature to be used in engineering analysis of large-scale crack bridging problems. Consequently, we will not employ the Level 3 design approach in the analyses presented within this paper.

3. Case story: Delamination from a ply-drop

To demonstrate the practical application of the Level 2 design approach, we present a case study focusing on delamination crack growth originating from a ply-drop. A ply-drop is a common feature in composite structures designed to achieve targeted variations in thickness; this is typically accomplished by terminating a layer of the composite, known as "dropping" a ply. The geometry at the site of the ply-drop can lead to stress concentrations or even stress singularities upon loading, which in turn may initiate a delamination crack. This crack can then propagate along the interface between the terminated ply and the main laminate. We wish to analyse the delamination crack growth under both static and cyclic loading.

3.1. Problem description

An idealized situation of a delamination from a ply-drop is depicted in Fig. 4. The applied stress in the main laminate is $\bar{\sigma}$, the initial crack length is a_0, the thickness of the delaminated layer is h_1, the thickness of the main laminate is $h_2/2$, the width of the laminate is B and the Young's modulus of the laminate in the longitudinal direction (the x_1-direction in Fig. 4) is denoted E_{11}. Furthermore, the spacing to the next ply-drop is L. This implies that before the crack tip reaches the next ply drop, the

thickness of the delaminated part equals one ply thickness, $h_1 = t$, where t is the thickness of a single ply. Once the crack tip has advanced by the next ply-drop, the delaminated layer will include two plies, i.e., $h_1 = 2t$.

The problem (Fig. 4) has been analysed by fracture mechanics [6]. The model is actually a symmetric model with two delamination cracks propagating simultaneously, so that the specimen does not undergo bending. Still, the analytical model has been shown to give results that deviate only about 4 % from a J integral calculation obtained using an accurate finite element model of the ply-drop problem with one delamination crack (i.e., not assuming symmetry) [7]. The J integral evaluated along a path along the external boundaries gives:

$$J_{ext} = \frac{\bar{\sigma}^2 h_1}{2E_{11}} \frac{h_2}{(2h_1 + h_2)} \tag{2}$$

Note that the J integral result is independent of crack length and that the J integral value scales with the layer thickness h_1. For thick laminates ($h_2 \gg h_1$), J_{ext} scales linearly with h_1.

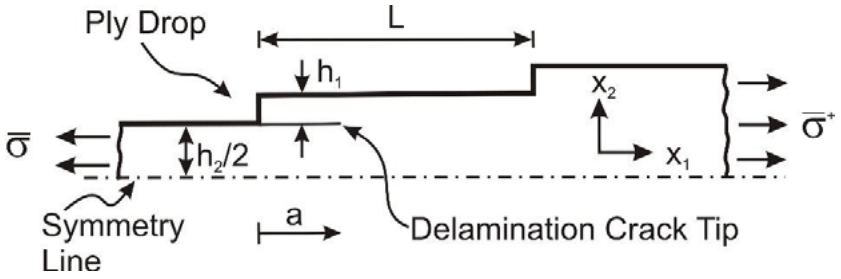


Figure 4. The idealized ply-drop problem with a delamination crack extending between along the interface between a surface layer and a main laminate. The thicknesses of the surface layer and the main laminate are h_1 and $h_2/2$ respectively, and the spacing to the next ply-drop is L.

For the present case, we will assume the following parameters: $h_1 = 1.5$ mm, $h_2 = 6.0$ mm, $B = 12.5$ mm, $L = 850$ mm and $E_{11} = 45$ GPa, corresponding to a unidirectional glass fibre/polyester polymer matrix composite. Additional fracture mechanics parameters will be taken from the literature. The static properties will be taken from Sørensen and Jacobsen [8] and the cyclic properties will be obtained from Holmes *et al*. [3].

The task is, for each design approach, to predict a maximum allowable stress for static loading and the number of cycles between inspection intervals assuming that the non-destructive inspection method can detect delamination cracks larger than the size, a_0. Thus, for the cyclic loading, we will calculate the number of cycles it takes for a crack to propagate from crack length a_0 to $a_{max} = L$. The logics is, that when the crack tip advances past the ply drop, $h_1 = 2t$, so that J_{ext} will increase significantly (nearly doubled, see eq. (2)), resulting in a much faster crack growth under cyclic loading.

3.2. Design using Level 1 design approach

For the prediction of the static strength, we rewrite (2) as follows:

$$\bar{\sigma}_i = \sqrt{\frac{2(2h_1 + h_2)}{h_2} \frac{J_0 E_{11}}{h_1}}, \tag{3}$$

where subscript *i* has been added to indicate the stress value that corresponds to the initiation of crack growth and we have set the J integral value equal to J_0. Moreover, we take the LEFM mode mixity, ψ,

for the delamination crack to be 50°. We obtain the value of J_0 for $\psi = 50°$ from Fig. 10 in Sørensen and Jacobsen [8] to be 250 J/m^2. Inserting values into (3) gives $\bar{\sigma}_i = 150$ MPa.

For cyclic loading, we use the experimental data of Holmes *et al*. [3] for J_{max} = 402 J/m^2 and a moment ratio $M_1/M_2 = 0.1$. Then from Fig. 11 in Holmes *et al*. [3] we find $da/dN_{nb} = 67$ x 10^{-4} mm/cycle. The number of cycles to grow the delamination crack from an initial length a_0 to the critical length, a_{max}, is

$$N_i = \frac{a_{max} - a_0}{da/dN_{nb}}. \tag{4}$$

Setting $a_{max} = L$ and (for simplicity) $a_0 = 0$, gives

$$N_i = \frac{L}{da/dN_{nb}}. \tag{5}$$

Inserting values gives $N_i = 127$ x 10^3 cycles = 0.123 x 10^6 cycles.

3.3. Design using Level 2 design approach

The J integral result (2) is valid also for the large-scale bridging situation. For the static analysis, we now set $J_{ext} = J_{ss}$. Then (2) can be rewritten as:

$$\bar{\sigma}_{fd} = \sqrt{\frac{2(2h_1 + h_2)}{h_2}\frac{J_{ss}E_{11}}{h_1}}, \tag{6}$$

where we have used the subscript fd to indicate that the bridging zone is assumed to be full developed. From Fig. 12 in Sørensen and Jacobsen [8] we find $J_{ss} = 2400$ J/m^2 for a tangential separation, δ_t, of 2 mm. Inserting values into (6) gives $\bar{\sigma}_{fd} = 460$ MPa.

For the cyclic loading, we find from Fig. 11 in Holmes *et al*. [3] that $da/dN_{fd} = 3.4$ x 10^{-4} mm/ cycle (i.e., only about 5 % of da/dN_{nb}), $N_{fd} = 100.000$ cycles, and $\Delta a_{fd} = 100$ mm. Furthermore, setting $a_{max} = L$ and (for simplicity) $a_0 = 0$, eq. (1) becomes

$$N_i = N_{fd} + \frac{L - \Delta a_{fd}}{da/dN_{fd}}. \tag{7}$$

Inserting values gives $N_i = 2.21$ x 10^6 cycles.

3.4. Safety factors and allowable design value

The DNV standard for composite components [9] can be used to determine allowable design values for both static and cyclic loading. This standard allows for designing structures or components with different safety requirements based on their assigned safety class, which is determined by the consequences of failures at the ultimate limit state (ULS). Structural reliability is maintained through the use of partial safety factors specified in the standard, which are adjusted to achieve specific reliability levels. Table 1 summarizes the assumptions from [9] and the main results for static loading. The maximum allowable design stress of the Level 2 design approach (fully utilizing the fracture resistance due to fibre bridging) for static loading is more than 2.5 times the design stress for the Level 1 design approach.

Table 1 Allowable design stresses for static loading obtained using partial safety factors from [9]

	Level 1	**Level 2**
Safety class	Normal	Normal
Failure type	Ductile	Brittle
Number of test repetitions	10	10
COV	15%	15%
k-factor for characteristic value	2.5	2.8
Partial resistance factor, γ_m	1.49	1.83
$J_{0\ mean}$ for Level 1 or $J_{ss\ mean}$ for Level 2	250 J/m^2	2400 J/m^2
$J_{0\ char}$ for Level 1 or $J_{ss\ mean}$ for Level 2	156 J/m^2	1392 J/m^2
$J_{0\ allowable}$ for Level 1 or $J_{ss\ allowable}$ for Level 2	105 J/m^2	761 J/m^2
Maximum allowable design stress	97 MPa	262 MPa

Table 2 presents the assumptions from [9] and the main results for cycling loading. Safety class, failure type and number of test repetitions are assumed identical to those of Level 1. The inspection interval of the Level 2 design approach is more than 20 times that associated with the Level 1 design approach.

Table 2 Inspection intervals for cyclic loading obtained using partial safety factors from [9]

	Level 1	**Level 2**
COV	5%	5%
k-factor for characteristic S-N curve	3.9	3.9
Partial fatigue safety factor, γ_{fat}	30	30
da/dN_{mean}	$67 \cdot 10^{-4}$ mm/cycle	$3.4 \cdot 10^{-4}$ mm/cycle
da/dN_{char}	$80.1 \cdot 10^{-4}$ mm/cycle	$4.06 \cdot 10^{-4}$ mm/cycle
Calculated number of cycles	$106 \cdot 10^3$	$2.09 \cdot 10^6$
Allowed number of cycles between inspections	$3.53 \cdot 10^3$	$69.7 \cdot 10^3$

4. Discussion

For the Level 1 design approach, the maximum allowable stress under static monotonic loading is determined based on the condition that there is no crack growth in a non-bridged crack, following traditional LEFM principles. The number of cycles until the crack reaches the next ply drop is calculated using the growth rate characteristic of a non-bridged crack. While these estimates are precise for brittle interface fractures, they tend to be overly conservative for damage-tolerant materials that display significant R-curve behavior.

Conversely, the Level 2 design approach sets the maximum stress under monotonic loading at the point where the bridging zone in damage-tolerant materials is fully developed. This approach is expected to yield a more accurate estimate of the structure's load-carrying capacity. Similarly, the prediction of the number of cycles between inspection intervals under cyclic loading is anticipated to be more precise. It is important to note that the Level 2 design stress and the number of cycles between inspection intervals are substantially higher than those suggested by the Level 1 approach, highlighting the conservative nature of the latter. However, the Level 2 results are finely balanced; a slight excess in the maximum allowable stress can lead to unstable crack growth, and if the actual number of load cycles surpasses the estimated threshold, the crack may extend beyond the next ply drop and propagate more rapidly. Therefore, the safety factors for design stress and number of cycles between inspections in the Level 2 approach should be selected with greater caution than those for Level 1.

An additional perspective to consider is the advancement of more damage-tolerant materials, such as composites that exhibit enhanced fibre bridging during delamination. The development of such

materials is particularly advantageous for large-scale composite structures like wind turbine rotor blades, which are manufactured in large sections and cannot be entirely free from manufacturing defects. The importance of creating composite materials with improved damage tolerance cannot be overstated. In parallel, design methodologies like the one outlined here must evolve to ensure that the benefits of increased fracture resistance can be fully utilized.

Future research should explore incorporating cohesive laws into a probabilistic load-resistance design format (LRDF) similar to DNV-ST-C501, and the facilitating the application of a Level 3 design approach.

5. Conclusions

The study has demonstrated that fibre bridging in damage-tolerant composite materials can markedly enhance fracture resistance during static loading, as evidenced by R-curve behavior, and can significantly decrease the crack growth rate under cyclic loading. The traditional design approach, referred to as Level 1 in this paper, does not incorporate these advantageous material properties during the design phase. However, an alternative design methodology, named Level 2, has been shown to fully exploit the characteristics of damage-tolerant materials.

Our case study, which examined delamination crack growth originating from a ply drop, revealed that the maximum allowable design stress for static loading in the Level 2 design approach is more than double that of the Level 1 approach. Similarly, the inspection interval for cyclic loading under the Level 2 approach can be extended to over ten times that of the Level 1 approach. The substantial benefits observed with the Level 2 approach suggest that it offers a compelling advantage and warrants further development and maturation for practical engineering applications.

Acknowledgements

This research was supported by the project DACOMAT (Damage Controlled Composite Materials), funded by the European Union's Horizon 2020 research and innovation programme under GA No. 761072.

References

[1] J. R. Rice, A path independent integral and the approximate analysis of strain concentrations by notches and cracks, *J. Appl. Mech*., Vol. 35, pp. 379-86, 1968.
[2] Z. Suo, G. Bao and B. Fan, Delamination R-curve phenomena due to damage, *J. Mech. Phys. Solids*, Vol. 40, pp. 1-16, 1992.
[3] J. W. Holmes, L. Liu, B. F. Sørensen and S. Wahlgren, Experimental approach for mixed-mode fatigue delamination crack growth with large-scale bridging in polymer composites, *Journal of Composite Materials*, Vol. 48, pp. 3111–28, 2014.
[4] P. Paris and F. Erdogan, A critical analysis of crack propagation laws, *Journal of Basic Engineering,* Series D, Vol. 85, pp. 528-34, 1963.
[5] G. Bao, S. Ho, Z. Suo and B. Fan, The role of material orthotropy in fracture specimens for composites", *Int. J. Solids Structures*, Vol. 29, pp. 1105-16, 1992.
[6] B. F. Sørensen, Microscale testing and modelling for damage tolerant composite materials and structures, IOP Conference Series: Materials Science and Engineering, Vol. 942, 012004, 2020.
[7] S. Goutianos, B. F. Sørensen, Fatigue crack growth rate at material and geometry transitions in glass-epoxy composites, *Composites Structures*, Vol. 275, 114445, 2021.
[8] B. F. Sørensen and T. K. Jacobsen, Delamination of fibre composites: determination of mixed mode cohesive laws, *Composite Science and Technology*, Vol. 69, pp. 445-56, 2009.
[9] DNV-ST-C501, Composite Components, 2022.

A NOVEL TEST LOAD FRAME FOR CHARACTERIZING THE BUCKLING RESISTANCE OF THICK SANDWICH PANELS

Antoniou A.[1], English N. [2], Ghiasvand S.[2] and Rosemeier M.[2]

[1]School of Mathematics and Physical Science, Department of Mechanics, National Technical University of Athens, Zografou 15780, Greece
Email: alexandros_antoniou@mail.ntua.gr, Web Page: http://mechan.ntua.gr
[2]Department of Rotor Blades, Fraunhofer Institute for Wind Energy Systems IWES, Am Seedeich 45, 27572 Bremerhaven, Germany
Email: malo.rosemeier@iwes.fraunhofer.de, Web Page: https://www.iwes.fraunhofer.de

Keywords: buckling resistance, wind turbine blades, stability analysis

Abstract
The latest design standards and guidelines for wind turbine rotor blades encourage model validation through sub-component testing, offering the incentive of lower material reduction factors. Structural stability, i.e., the buckling resistance, stands out among the critical design parameters. This aspect is crucial for the large, aerodynamic shell-like areas constructed from lightweight sandwich materials. In support of this model validation, our research introduces a novel test load frame designed to assess the stability of composite sandwich plates under quasi-static compressive loads. The load frame accommodates relatively thick plates with adjustable aspect ratios and aims to: (i) provide simply supported boundaries on all four edges, (ii) enable rapid installation of the specimen while accurately aligning the plate to the load axis, and (iii) allow for easy mounting in a standard universal testing machine. We successfully conducted a proof-of-concept test. For this purpose, a sandwich configuration consisting of glass, epoxy, and balsa wood was manufactured. It was tested quasi-statically to failure, while strains and out-of-plane deflections were monitored using a digital image correlation system. The critical buckling load was predicted using both an analytical orthotropic plate model and a finite element model, with the theoretical results overestimating the experimental values by 1.3% to 5.7%.

1. Introduction

Wind turbine blades are typically constructed from thin-walled cylindrical and airfoil-shaped shells, primarily composed of fiber-reinforced polymers (FRPs). These shells, susceptible to buckling [[1]-[2]], are designed with sandwich panels for enhanced stability, incorporating thin FRP skins and core materials like balsa wood, polyvinyl chloride (PVC), or polyurethane (PU) foam for lightweight purposes. Resin-filled grooves and holes in the core material aid resin infusion during manufacturing and accommodate the curvature of the shells. In [3], the importance of realistically representing core materials, considering resin uptake in sandwich constructions for wind turbine blades, was emphasized. Reducing resin uptake offers notable benefits to the specific flexural strength of the core [4]. However, the challenge lies in the complex experimental validation required to assess the impact of resin uptake on buckling resistance, particularly in adherence to the new design standard for blade structures [5][6]. This advocates for experimental validation to minimize partial material safety factors during the design process.

In response to this need, our research introduces a novel load frame designed for characterizing the buckling resistance of thick sandwich constructions [7]. This unique test frame accommodates simply supported flat plates with variable aspect ratios. The load frame can be mounted in standard universal testing machines. Moreover, we describe the proof of concept test and validate numerical and analytical predictions of the critical buckling resistance with the experimental results.

2. Methods

2.1 Experiment

2.1.1 Load frame design

The sandwich plate width and thickness can be adjusted at the lateral, as well as at the upper and lower boundaries, to accommodate variable plate dimensions. The frame can host spanning dimensions of 1.2m in height, 0.3m to 1.2m in width, and up to 0.05m in thickness. Its segmented, articulated roller bearing supports allow the plate edges to twist non-uniformly out of the plane at the load application and load reception positions. The tested plate is simply supported, with modular roller bearings for the horizontal edges and 'knife edges' for the vertical boundaries. The frame is optimized for compatibility with standard universal uniaxial testing machines, having clamping heads with flat bearing surfaces.

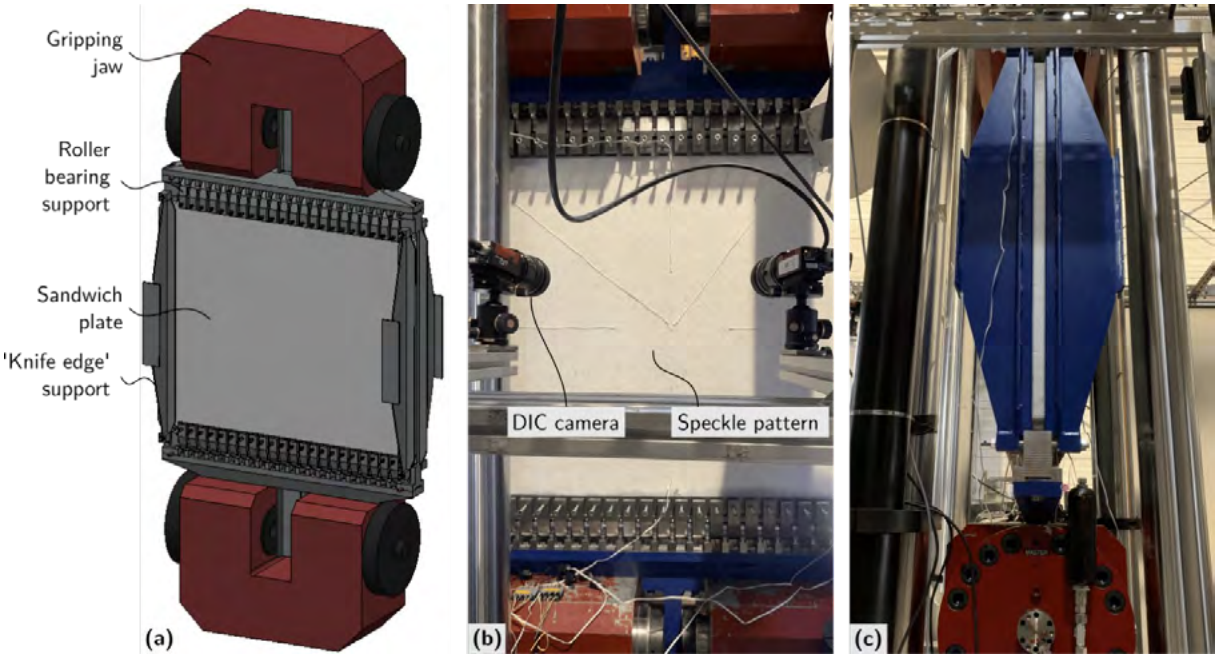


Figure 1. Load frame design: a. overview, b. front view (side B), and c. side view.

2.1.2 Manufacture of specimen

A sandwich panel of 1.2 m in width and 1.2 m in height was manufactured with Vacuum Assisted Resin Infusion Molding (VARIM) using E-glass fabrics of type SAERTEX X-E-778g/m^2 infused with epoxy resin of type Westlake EPIKOTE™ Resin MGS® RIMR035c with EPIKURE™ Agent MGS® RIMH037 for the skins and a balsa wood core of type BALTEK SB.100 with a nominal density of 148kg/m^3. The total thickness of the sandwich was measured to be 27.82 ± 0.42 mm around the plate edges (**Figure 2a)**. Additionally, the average thickness of the balsa wood, measured along the plate edges, was 24.86 mm, resulting in an average thickness of 0.74 mm per [±45$_2$] ply.

The layup was built symmetrically, i.e., [±45$_2$/Balsa/±45$_2$], with the last two biaxial plies rotated by 90° in the roll direction. During the infusion, a table was heated to 40°C. After the infusion, the sandwich was cured for 12 hours at 40°C.

About 25 mm balsa wood was removed from the load-introducing plate edges (**Figure 2b**) and replaced with short-glass-fiber-filled epoxy adhesive to enhance a smoother load transition in the sandwich structure, reducing the risk of local core crushing due to the low strength of the balsa wood. Afterwards, the panel was post-cured at 80°C for 7 hours.

2.1.3 Measurement instrumentation

A Digital Image Correlation (DIC) system was used to monitor the global displacement field from side B of the panel, where a fine black speckle pattern was applied over white ground paint (**Figure 1b**). Moreover, five pairs of axial Strain Gauges (SG) were mounted back-to-back on both sides of the plate (**Figure 2c**). SG1, SG2, and SG5 were aligned with the load axis (x-direction) while SG3, SG4, and

SG6 were applied at 90° to it. SG5 and SG6 were installed at the center of the plate, while all others were symmetrically placed around it, on a virtual circle with a radius of 150 mm.

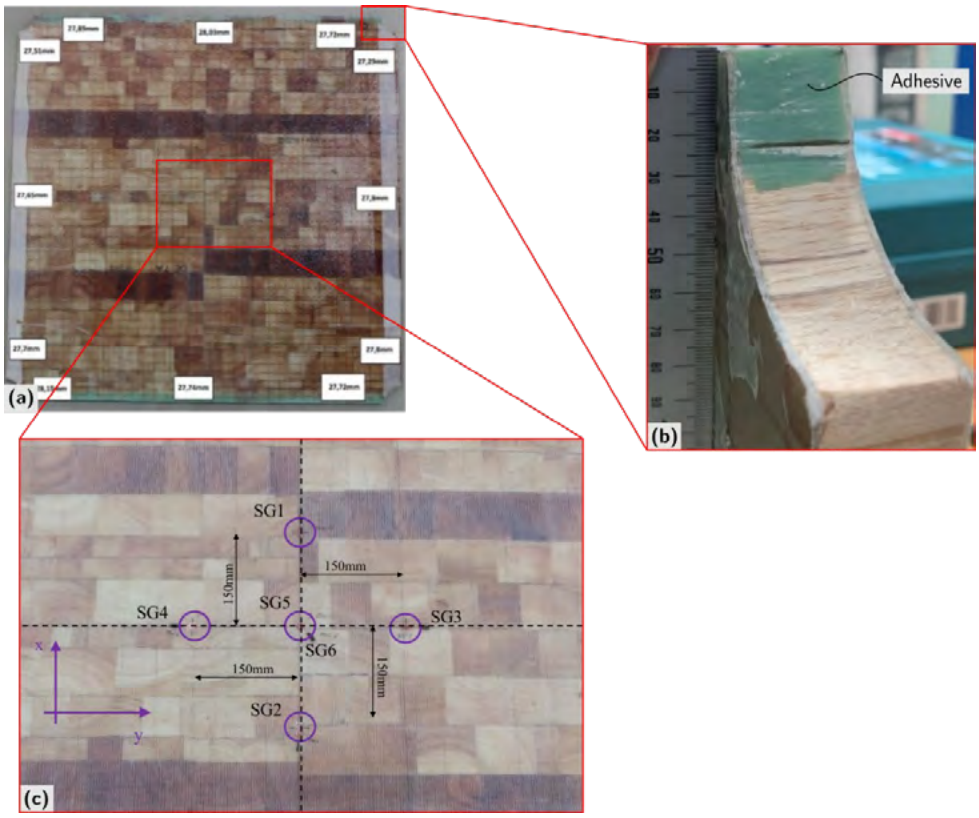


Figure 2. a. Sandwich plate thickness measurements at the edges, b. adhesive at edge, and c. strain gauge positions measured from the center of the sandwich plate.

2.1.4 Experimental determination of buckling resistance

The critical buckling load F_{cr}, i.e., the buckling resistance, was determined using two methods. The first method involves analyzing the experimentally recorded load versus in-plane displacement diagram of the plate. Although there is no drop in load, just a reduction in the stiffness of the plate as suggested by Zaal [12], the buckling load is identified at the ordinate of the intersection point between the tangents of the pre- and post-buckling gradients (**Figure 3a**). In the second method, as described by Schuette [13], the buckling load is defined as the level at which the compressive strain on the convex side of the buckle crest stops increasing and begins to decrease, a method known as strain reversal (**Figure 3b**).

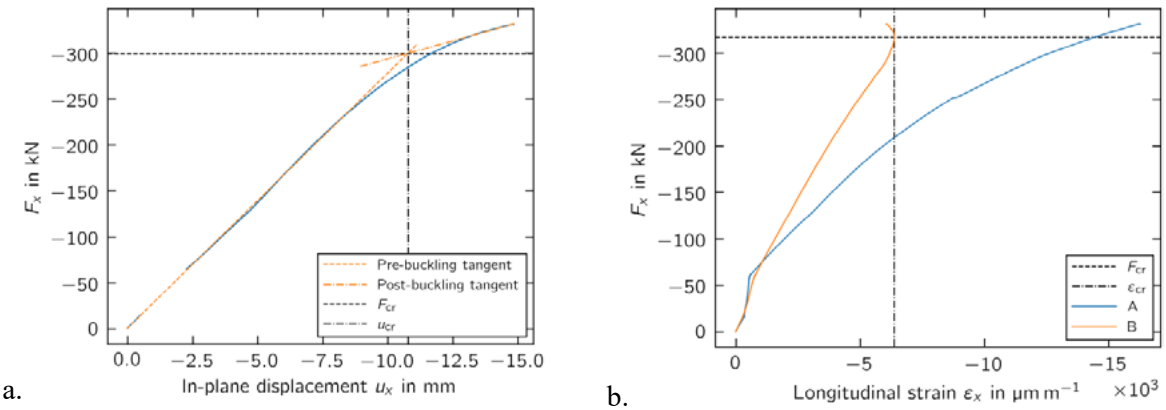


Figure 3. Experimental buckling loads: a. tangent method, b. strain reversal method.

2.2 Theoretical analyses

2.2.1 Material properties

The raw material properties listed in **Table 1** were used to calculate the lamina properties of the sandwich skin using a micro-mechanical approach, as introduced in [8]. Based on the thickness measurements, the skins were estimated to have a fiber volume fraction of 40%. The laminate properties (**Table 2**) were then calculated using Classical Laminated Plate Theory (CLPT). The raw material properties of the infusion resin and the adhesive were mechanically tested at Fraunhofer IWES according to international test standards. The glass fiber properties were sourced from the literature [8]. The balsa wood properties were derived from an experimental database using a curve-fitting approach that linearly correlates the material properties with the corresponding wood density [9].

Table 1. Raw material properties.

Material	E_{11} (MPa)	E_{22} (MPa)	E_{33} (MPa)	ν_{12} (-)	ν_{13} (-)	ν_{23} (-)	G_{12} (MPa)	G_{13} (MPa)	G_{23} (MPa)
Inf. Resin	3150	3150	3150	0.35	0.35	0.35	1167	1167	1167
Adhesive	4772	4772	4772	0.30	0.30	0.30	1835	1835	1835
Balsa	223	199	3784	0.43	0.06	0.06	22	203	197
Glass fib.	81000	81000	81000	0.22	0.22	0.22	33197	33197	33197

Table 2. Laminate properties.

Material	E_{xx} (MPa)	E_{yy} (MPa)	E_{zz} (MPa)	ν_{xy} (-)	ν_{xz} (-)	ν_{yz} (-)	G_{xy} (MPa)	G_{xz} (MPa)	G_{yz} (MPa)
Glass-FRP $[\pm 45_2]$	8807	8850	8830	0.62	0.18	0.18	9518	2523	2523

2.2.2 Analytical sandwich plate model

The critical buckling resistance was estimated for a simply supported plate considering an orthotropic model according to Wiedemann [10], as described in [3]. The materials used and the coordinate system are illustrated in **Figure 4**.

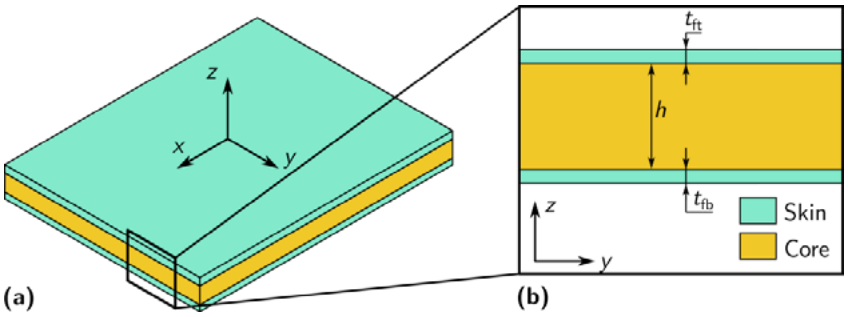


Figure 4. Sandwich plate model parameters; based on [3].

The critical buckling value k is defined as

$$k = \frac{p_{xcr} b^2}{\sqrt{B_x B_y}\pi^2} = \frac{1}{\Phi_x} + a_{wm}^2 \left(\frac{1}{\Phi_y} - \frac{H_1 + H_2 - 2(v + \hat{v})}{(H_1 H_2 - (v + \hat{v})^2)\Phi_x \Phi_y} \right) \quad (1)$$

where p_{xcr} is the critical buckling resistance and b the width of the sandwich plate. The help functions H_1 and H_2 are defined as

$$H_1 = \frac{\Phi_y\left(1+\frac{\hat{v}}{a_{wm}^2}\right)+1}{\Phi_x} \tag{2}$$

and

$$H_2 = \frac{\Phi_x(1+\hat{v}a_{wm}^2)+a_{wm}^2}{\Phi_y} \tag{3}$$

The buckling ratio a_{wm} is given by

$$a_{wm} = \frac{a}{mb}\sqrt[4]{\frac{B_y}{B_x}} \tag{4}$$

where a is the length of the sandwich plate and m the number of buckling half waves. Poisson's ratio is determined as

$$v = \frac{D_{12}}{\sqrt{B_y B_x}} \tag{5}$$

and the drill stiffness number as

$$\hat{v} = \frac{D_{66}}{\sqrt{B_y B_x}} \tag{6}$$

where D_{ij} represents the terms of the bending stiffness matrix of the sandwich as described in [11], which can be determined using Classical Laminated Plate Theory (CLPT). B_x and B_y denote the matrix elements D_{11} and D_{22}, respectively. The core number in each plane direction is defined as

$$\Phi_y = \frac{\pi^2 B_y}{K_y b^2} \tag{7}$$

and

$$\Phi_x = \frac{\pi^2\sqrt{B_y B_x}}{K_x b^2} \tag{8}$$

where the shear stiffness is defined as

$$K = \frac{G_c d^2}{h} \tag{9}$$

where G_c is the through-the-thickness core shear stiffness (G_{13} and G_{23} in **Table 1**) and d is defined as

$$d = h + \bar{t_f} \tag{10}$$

with $\bar{t_f}$ as the arithmetic mean thickness of the two skins t_{ft} and t_{fb}. h denotes the thickness of the core.

2.2.3 Finite element model

A three-dimensional finite element model was developed in ANSYS to predict the bifurcation load, i.e., the buckling resistance, of the sandwich plate. The material properties used are detailed in **Table 1** and **Table 2**. Each skin layer of the model was represented by a single element in the thickness direction. The adhesive at the top and bottom of the test plate at the load introduction points was also modeled. In

total, 68,375 eight-node brick elements of type SOLID185 were utilized. At the virtual panel edges, the rotational degrees of freedom were left free, simulating the degrees of freedom provided by the test load frame. A compressive force was applied vertically at the top of the plate (**Figure 5**).

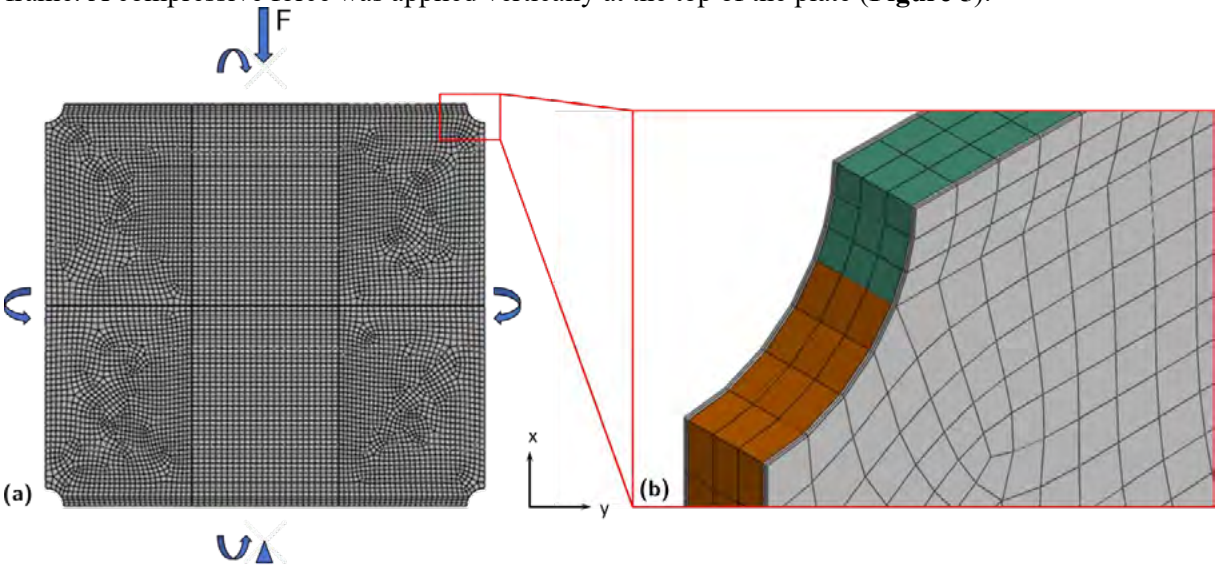
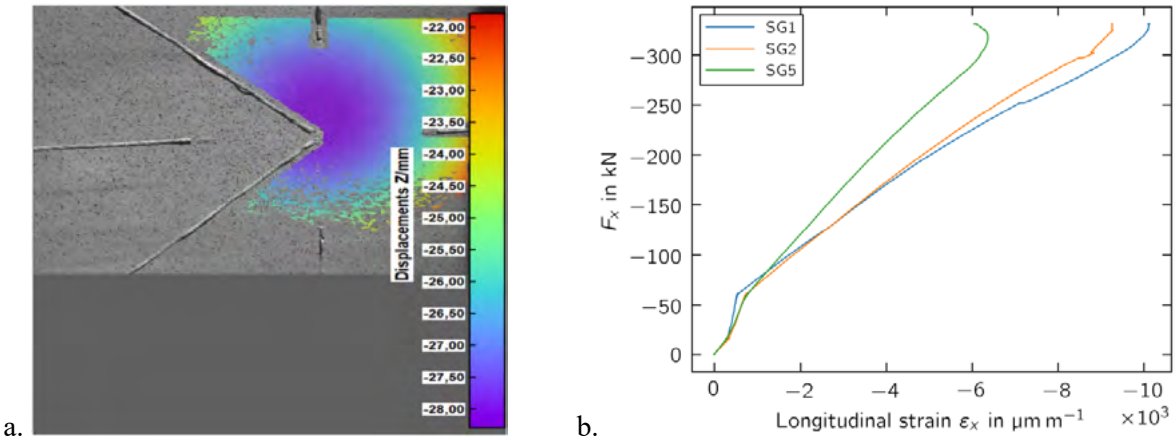


Figure 5. Finite element model of the plate: a. boundaries and mesh, b. zoom-in of corner.

3. Results and discussion

From the DIC displacement recordings, it is clear that the plate was deforming according to the first buckling eigenmode (**Figure 6a**). The negative displacement indicates that the monitored surface (side B) was deflecting out-of-plane towards the viewer. This observation is corroborated by the strain gauge measurements along the load axis. The diminishing recordings suggest that, although the plate was under compression, the developed dimple caused side B to bend out-of-plane, adding positive deformation to the overall negative displacement. This phenomenon explains the strain reversal that occured at the buckling load, as defined in Chapter 2.1.4., before the final collapse (**Figure 6b**).

Based on the force-displacement diagram shown in **Figure 3a**, it is evident that the panel exhibits limited post-buckling performance in terms of displacement. After a slight drop in stiffness, the plate failed, as illustrated in **Figure 7**. Delaminations were observed at the lower right edge of the plate at side A, and cracks along the lower edge of side B, which ultimately led to the final failure.



a. b.

Figure 6. Side B: a. out-of-plane displ., b. strain-gauges along load axis

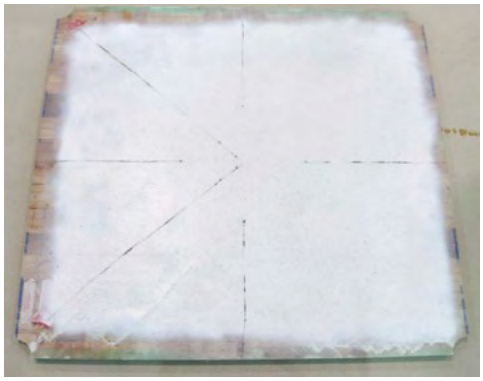
a.  b. 

Figure 7. Post-mortem specimen: a. Side A, b. Side B

The theoretical buckling load predictions are presented in Table 3, alongside the experimentally determined buckling loads.

Table 3. Summary of theoretical and experimental buckling loads

	Tangent of pre- & post buckling (Exp.)	Strain reversal (Exp.)	Analytical model	Linear bifurcation analysis (FE)
F_{cr} in kN	299	310	314	316

The theoretically determined buckling loads overestimate the experimentally determined buckling loads by 1.3% to 5.7%. The tangent method yields a more conservative buckling load than the strain reversal method. Both the analytical and numerical predictions are in good agreement with each other, differing by only 0.6%.
The lower experimental values could be a result of imperfections in the plate geometry, structure, and load introduction. The analytical and numerical models do not account for these imperfections, hence they predict higher buckling loads. However, it is noteworthy that in this proof-of-concept case, the discrepancy was relatively small.

4. Conclusions

A novel test load frame was introduced to enhance the experimental design validation of the critical buckling load of thick composite sandwich plates, as found in wind turbine blades. A proof-of-concept test was successfully conducted, confirming the expected performance and validating both analytical and numerical predictions. The compressed sandwich panel deformed in the anticipated first buckling eigenmode, as recorded by a DIC (Digital Image Correlation) system. Moreover, the theoretically determined buckling loads overestimated the experimentally determined buckling loads by 1.3% to 5.7%, while the analytical and numerical predictions were in good agreement with each other.
Future finite element analyses should consider geometric imperfections to further reduce the remaining discrepancy between the model and experiment.

Acknowledgments

Fraunhofer IWES acknowledges the financial support provided by the German Federal Ministry for Economic Affairs and Energy (BMWi) for the ReliaBlade project (grant number 0324335A).

References

[1] M. Rosemeier, M. Bätge. A concept study of a carbon spar cap design for a 80m wind turbine blade. *The Science of Making Torque*, In J. Phys.: Conf. Ser. 524 012039, 2014.
[2] M. Rosemeier, P. Berring and K. Branner. Non-linear ultimate strength and stability limit state analysis of a wind turbine blade. *Wind Energ.*, volume (19): 825–846, 2016.
[3] M. Rosemeier, P. Buriticá, A. Antoniou. Impact of resin uptake of core materials on buckling of wind turbine blades. *J Phys Conf Ser*. 2018; 1037(4): 1-13.

[4] Cao, D., Malakooti, S., Kulkarni, V.N., Ren, Y., Liu, Y., Nie, X., Qian, D., Griffith, D.T. and Lu, H., 2022. The effect of resin uptake on the flexural properties of compression molded sandwich composites. *Wind energy*, *25*(1), pp.71-93.
[5] IEC, IEC 61400-5 - Wind energy generation systems - Part 5: Wind turbine blades, 1st ed. Geneva, Switzerland: International Electrotechnical Commission, 2020.
[6] DNV-ST-0376, *Rotor blades for wind turbines*, DNV, 2024
[7] Rosemeier M, Antoniou A, Gebauer T, 2022, DE102020127065B4 Vorrichtung und Verfahren zum Einspannen eines Prüfkörpers
[8] A. Krimmer. *Mikromechanische Modellierung von Fasergelege-Kunststoff-Verbunden auf Basis von Normprüfungen unter Berücksichtigung der in-situ-Eigenschaften der Matrix* Doctoral thesis (TU Berlin), Berlin, 2014.
[9] D. G. Merida, *Theoretical and experimental determination of balsa wood elastic properties to supplement the stiffness prediction of a physically based FRP sandwich model*, Bachelor Thesis, Hamburg University of Applied Sciences, 2021.
[10] J. Wiedemann, *Leichtbau: Elemente und Konstruktion*, Springer-Verlag, Heidelberg, 2007
[11] R. M. Jones, *Mechanics of composite materials - Second Edition*, Taylor & Francis, NY, 1999
[12] K. Zaal, Buckling and postbuckling of a square plate subjected to uniform edge loads – an experimental investigation. ASL-138 Technion Israel Inst. of Technology, Dept. of Aeronautical Engineering, 1988.
[13] E. H. Schuette, Charts for the Minimum-Weight Design of 24S-T Aluminum-Alloy Flat Compression Panels with Longitudinal Z-Section Stiffeners, NACA ARR L5F15, 1945 (Wartime Report).

VIRTUAL TESTING OF THE TRANSVERSE CRACKING MECHANISMS OF THIN PLY THERMOPLASTIC AND THERMOSET MATRIX LAMINATED COMPOSITES UNDER CRYOGENIC THERMOMECHANICAL LOADING

Timothée Klein[1,2,3], Christophe Bois[1,2], Jean-Christophe Wahl[1,2] and Caroline Petiot[3]

[1]Univ. Bordeaux, CNRS, Bordeaux INP, I2M, UMR 5295, F-33400, Talence, France
Email: timothee.klein@u-bordeaux.fr
[2] Arts et Metiers Institute of Technology, CNRS, Bordeaux INP, Hesam Universite, I2M, UMR 5295, F-33400 Talence, France
[3] Airbus Central Research and Technology, Toulouse, France

Keywords: Thin Ply, Transverse cracking, Thermoplastics, Thermosets, Micromechanical modeling, FEA, Cryogenic

Abstract
The development of linerless liquid hydrogen composite tanks is a major challenge for improving the performance, lightweight and cost of Hydrogen-powered commercial aircraft. Since the tightness must be provided by the composite itself, an in-depth understanding of the damage mechanisms of laminated composites at cryogenic temperatures is desired. The aim of the present study is to propose a micromechanical numerical approach in order to analyze the effect of matrix type on the development of transverse cracks in various ply thicknesses under cryogenic thermomechanical loading. Experimental results have shown that the decrease in ply thickness leads not only to the delay of the transverse crack initiation thresholds, but also to a transition to a more diffuse and progressive cracking, particularly in the case of the thermoplastic matrix. Numerical results indicate that even at cryogenic temperature, the elasto-plastic behavior of the matrix plays a significant role on both the magnitude of thermal residual stresses and the resulting transverse crack initiation thresholds and propagation.

1. Introduction

Airbus aims to lead the decarbonization of the aviation sector by building the world's first Hydrogen-powered commercial aircraft. The use of liquid hydrogen as a fuel is very promising thanks to its high energy density and renewable production potential. The development of linerless liquid hydrogen composite tanks is a major challenge for improving the performance of low-carbon commercial aircraft. Since the tightness must be provided by the composite itself, an in-depth understanding of the damage mechanisms and resulting permeability of laminated composites at cryogenic temperatures is desired. Indeed, it has been shown that under thermomechanical loading, the main types of damage are transverse cracking and micro-delamination [1]. This leads to the creation of crack networks which, if they coalesce in the thickness, constitute leak paths [2]. Experimental results have shown so far that at ambient temperature, the decrease in ply thickness leads not only to the delay of the transverse crack initiation thresholds, but also to a transition from an almost instantaneous crack propagation though the thickness of the ply to a more diffuse and progressive cracking initiated by fibre/matrix decohesions [3], [4]. The reduction in ply thickness implies a greater importance of microstructure morphology on the laminate's mechanical behaviour and damage. Scale separation is thus harder, and it becomes necessary to explicitly represent the microstructure across the various constituents in the modelling [5], [6]. However, these experimental and numerical studies were carried out at room temperature, and mostly on epoxy-type thermosetting resin composite systems [5], [6], [7]. The present study therefore proposes an evaluation of this type of behavior and modeling in the context of two laminated composites, composed either of a thermoset or a thermoplastic resin. In both materials, ply thicknesses of 70µm, 140µm and

280µm will be considered, and measurements will be performed at cold and cryogenic temperatures (-130°C, -196°C). First, the studied materials, experimental protocols and main results will be presented. Then, a micromechanical finite element model developed will be introduced to help understand the effect of ply thickness but especially the micro-constituent properties on transverse cracking mechanisms.

2. Materials and experimental observations

Two carbon fibre (CF) composites with thermoset (CF/TS) and thermoplastic (CF/TP) matrices are considered in this study. For the CF/TS material, tensile test specimens were extracted from plates obtained from unidirectional prepreg material followed by autoclave curing. Plates of CF/TP material were manufactured using an Automated Fibre Placement (AFP) process, followed by heated press consolidation. Materials were chosen so as to have a thin unit ply thickness similar between the two of them: approximately 70µm. The samples manufactured were all checked by C-Scan and microscopic observations to guarantee the quality of their initial state and cutting directions. All specimens to be tested were dried in a silica gel desiccator prior to testing.

2.1 Transverse cracking tests

Tensile tests with microscopic monitoring of the cracking process under thermomechanical loading were set up to study the evolution of transverse cracks at cryogenic temperatures (-196°C and -130°C). They consist of successive incremental loading steps in tension, all at cryogenic temperature. After each thermomechanical loading step, damage within the sample is monitored by observing the sample's polished edge with an optical microscope (see Figure 1) [8], [9]. The stacking sequence $[0/90/0/90_2/0/90_2]_s$ enables three different ply thicknesses to be studied: thin (90 alone), intermediate (90_2) and thick (90_4) (see Figure 1). Each test is stopped before reaching failure of the sample. The polished edge monitored during the test is then subjected to an abrasion and polishing cycle to remove a surface layer containing damages that initiated due to edge effects and did not propagate through the material. This is particularly relevant for thin plies, which have shown to exhibit a higher tendency of developing this type of damage [3], [7], [10], [11]. Accounting for those edge effects would lead to a significant overestimation of the damage effectively developing in the thinner plies, as well as an underestimation of the transverse crack initiation threshold. Damage in each ply and material at a given longitudinal strain ε_x is quantified through the use of the reduced crack density $\bar{\rho}$ $[-]$:

$$\bar{\rho} = \sum_n \frac{L_c^n}{h_{ply}^n} \cdot \frac{h_{ply}}{L_{obs}} \tag{1}$$

Where L_c^n is the crack n's length, normalized by the local ply thickness h_{ply}^n. This allows to account for partial cracks that do not fully propagate across the ply thickness (see Figure 3). The sum of all partial crack's relative lengths is then divided by the total observed length L_{obs} multiplied by the average ply thickness h_{ply} to obtain a non-dimensional number. Only the cracks that are present within the bulk of the material, after final polishing are counted.

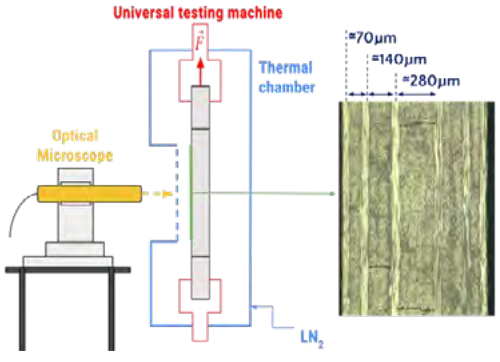
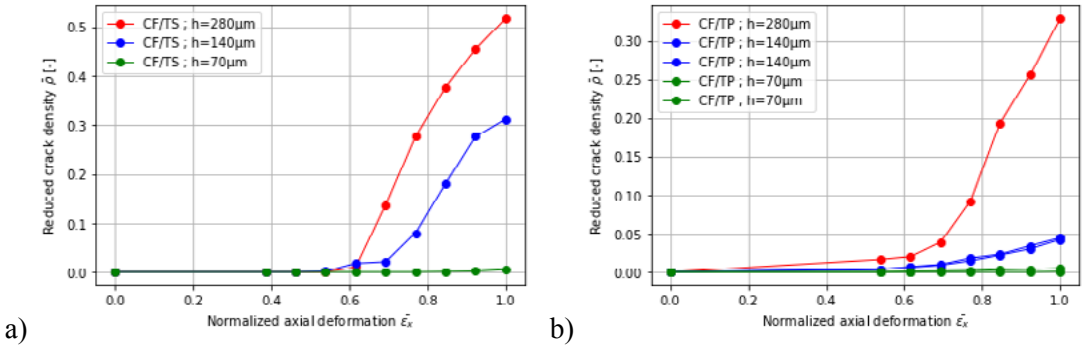


Figure 1. Diagram of the experimental setup used for transverse cracking tests at -130°C and -196°C

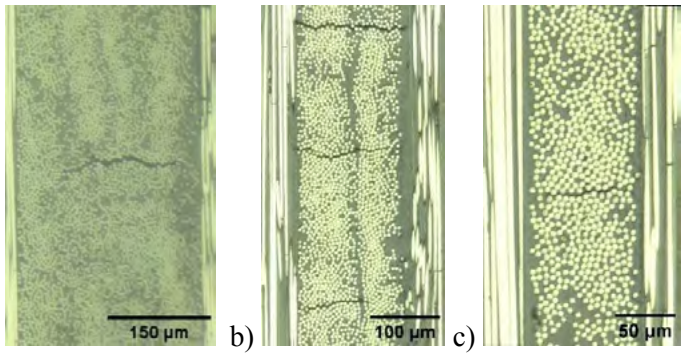
Results show that temperature, ply thickness and matrix type play a significant role in the initiation and propagation of transverse cracks. Indeed, little to no transverse cracks were observed at -130°C up to deformations close to the sample failure, while numerous of them develop in both materials in both thick (280µm) and intermediate (140µm) plies at -196°C. Very few cracks were observed in the thin (70µm) plies (see Figure 2). Transverse cracking does not initiate with the thermal loading alone. Figure 2 shows that the reduction in ply thickness shifts crack density curves towards higher loading levels, delaying transverse cracking thresholds and reducing cracking rates for both materials.



a) b)

Figure 2. Reduced crack density as a function of normalized axial strains applied to the laminate for the three ply thicknesses considered, at -196°C for the CF/TS (a) and CF/TP (b) materials. The normalization is identical for each figure.

An interesting observation is that the CF/TP material not only presents a smaller crack density than the CF/TS material (Figure 2), but also a transition from a majority of fully developed cracks in the thick ply, to partial ones that do not propagate through the entirety of the intermediate and thin plies' thickness, as shown in Figure 3. Damages initiated by fibre/matrix decohesions no-longer propagate quasi-instantaneously, but progressively extend during loading. Such partial cracks were indeed observed in other studies, yet for thin plies (<100µm) and only at ambient temperatures [3], [4], unlike in the present study under cryogenic conditions.



a) b) c)

Figure 3. Microscopic observations of partial cracks observed in the bulk of CF/TP samples after transverse cracking tests: thick 280µm ply at -130°C (a); intermediate 140µm ply (b) and thin 70µm ply (c) at -196°C.

2.2 Elastic and elasto-plastic mechanical testing properties

To feed numerical models, tension tests up to failure were performed on composite samples (250x25mm² equipped with tabs) of both materials to determine the mechanical properties at three temperatures (20°C, -130°C and -196°C) on lamination specimens $[0]_{16}$, $[90]_{16}$ and $[\pm45]_{4s}$ enabling longitudinal, transverse and shear moduli to be determined.

Tension tests were also performed on neat TP resin samples according to ISO 527-2, at four different temperatures (T_{hot}, 20°C, -130°C and -196°C). T_{hot} being a temperature comprised between the TP material's T_g and consolidation temperature.
All tests were carried out at a constant crosshead speed of 0.5 mm/min. Two samples were tested for each configuration. Strain and temperature were measured using strain gauges and thermocouples respectively. At 20°C and T_{hot}, strains were also measured using an extensometer, allowing to reach deformations up to 25%, after which the test was stopped if failure was not reached.
Some of the experimental results for both neat TP resin samples and CF/TP $[90]_{16}$ tensile tests are presented in Figure 5.

3. Computational micromechanics strategy

In this study, a 2D micro-mechanical finite element (FE) model was developed, consisting in a representative volume element (RVE) of a thin 90° ply surrounded by two homogenized 0° plies (Figure 4a). Each of the three ply thicknesses tested experimentally can be represented numerically, namely $h_{ply} \in \{70; 140; 280\}\mu m$. The RVE is rectangular with length $L_{RVE} = 2 \cdot h_{ply}$, and the adjacent ply thickness is kept at $h_{ply} = 70\mu m$ similarly as in experiments.

The adjacent plies are assumed to be homogenous with transversally isotropic thermo-elastic properties. The temperature-dependent elastic properties of adjacent plies were measured experimentally as described in the previous section. The thermal expansion coefficients (CTEs) are determined either from documentation available from the manufacturer or experimental measurements that were performed. The interface with the 90° ply is assumed perfect, as no micro-delaminations were observed experimentally.
Fibres are distributed randomly within the RVE, while respecting a prescribed fibre volume fraction V_f and constraints on the minimum distance between two fibres' external surface and with the matrix's edges ($> 0.05R$). The fibre radius R is constant. The transversally isotropic thermo-elastic properties of the carbon fibres were taken from the literature, and are considered independent from temperature.
The matrix behavior was modelled using a pressure-dependent hyperbolic Drucker-Prager model with regularized damage [7], [12] and associated flow. Properties in function of temperature are considered rate independent and are either based on tensile tests performed on neat TP specimens or from literature, as well from UD composite tensile tests. Numerous studies propose to extend the stress/strain curves measured experimentally until a perfectly plastic behavior is reached (horizontal tangent) [5], [7], [13]. This is motivated by notable size-effects observed in neat resin mechanical tests [14], [15], [16], and by the fact that at micrometric scales, much higher strains are encountered than those conventionally observed in thick specimen testing. Whether this is still the case at cryogenic temperatures is yet to be verified, and will be discussed in the next sections.
Nevertheless, the way in which the tests are extended has a strong influence on the levels of plastic stress and strain achieved. Kohler [7] suggests using a second-order polynomial fit. A more conventional approach is Voce's law [13], [17], where true stresses σ_t asymptotically tend towards a plastic plateau as true strains ε_t increase, following an exponential law:

$$\sigma_t = A(T) \cdot \left(1 - e^{-B(T) \cdot \varepsilon_t}\right) \tag{2}$$

Where $A(T)$ and $B(T)$ are temperature-dependent parameters to be determined experimentally. They govern the initial linear elastic $E \approx A(T) \cdot B(T)$ and final plastic plateau $A(T)$ of the curve. This empirical law has proved to be the most consistent with the tension tests performed on our TP neat resin samples, and will be kept in the present study.
Once the ultimate strain ε_u^m and stress σ_u^m are reached, an exponential softening, energy based regularized damage model reduces the stiffness of the matrix elements.

The brittle behavior of the fibre–matrix interface [6], [18] was modelled using the linear softening, energy based, cohesive model. The interface is first linear elastic with a stiffness of $K = 10^8$ [MPa/mm]

that ensures displacement continuity between the fibre and the matrix. The onset of damage is dictated by a quadratic stress criterion. The shear strength τ_s was assumed to be equal to 3/2 of the normal strength τ_n, based on the experimental results obtained by Ogihara and Koyanagi at ambient temperatures [19]. Once the damage begins, the interface stiffness is progressively degraded following a damage variable d whose rate is controlled by the mixed-mode critical energy release rate of the cohesive element according to the Benzeggagh-Kenan (BK) law [20]. Mode I and Mode II fracture energies are complex to measure experimentally and are generally set using an inverse identification between experimental measurements and numerical models [18]. Regarding mode II, as contact is present, the friction dissipates some energy and can generate plastic deformations within the matrix due to contact stresses. These additional dissipation mechanisms corroborate the assumption of a larger mode II fracture energy. Various ratios can be found across literature [5], [7], [18], yet for simplicity a ratio of 1.5 will be kept in the present study.

Abaqus Finite Element code is used. Adjacent plies are meshed using linear quadrilateral generalized plane strain elements CPEG4R. For higher mesh quality, triangular linear elements CPEG3 are used to discretize the matrix. Finally, fibres are meshed using quadratic quadrilateral elements CPE8R allowing for a better approximation of their curved geometry (Figure 4a). Typical element size of 1µm are used in the fibres, 0.5µm in the matrix. Element size gradually increases from the interface to the free edges in the adjacent plies.

In order to represent the behavior in the bulk of the material, while maintaining reasonable calculation times, a 2D Generalized Plane Strain modeling strategy was chosen. Periodic boundary conditions are applied on the RVE's lateral edges (Figure 4a) and the top and bottom surfaces are kept free, similarly as in experiments. The model was implemented using Abaqus/Standard with an implicit dynamic resolution scheme. Geometric non-linearities (i.e. large deformation assumptions) are considered due to large strains encountered. Each simulation consists in a first thermal step between the stress-free temperature T_0 down to the considered temperature. During that first step, the RVE remains unconstrained to allow for thermal contraction. This is followed by a mechanical displacement-controlled loading step along the $\vec{x}$ direction (Figure 4a), until the desired macroscopic strains ε_{max} are reached.

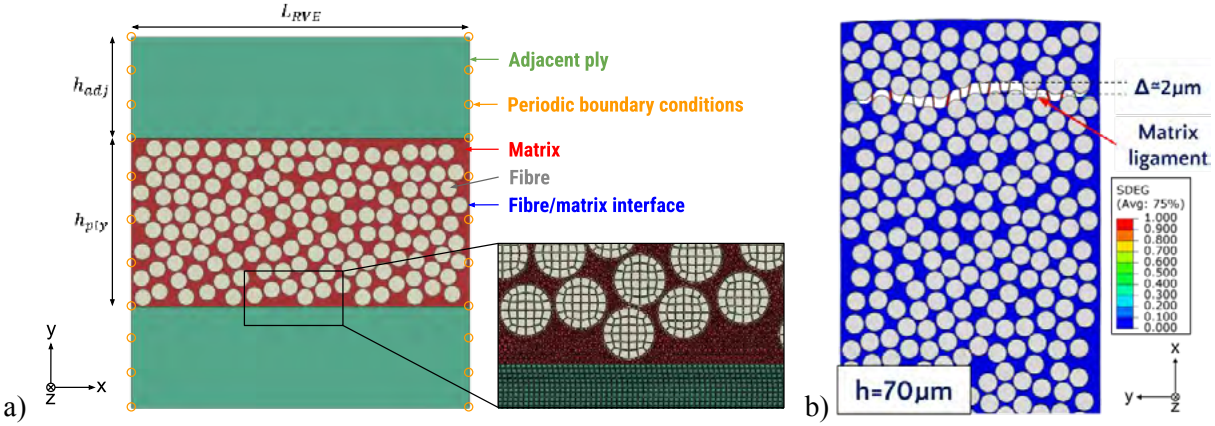


Figure 4. (a) RVE of the composite laminate with stacking sequence $[0/90_n]_s$ and associated length and boundary conditions. Detail of the finite element discretization.
(b) Numerical result at -196°C close the sample failure of a thin ply (70µm) subject to axial loading along the $\vec{x}$ direction (vertical). Matrix ligaments subject to large deformations are visible, along with their corresponding damage variable (SDEG). Adjacent plies are not represented.

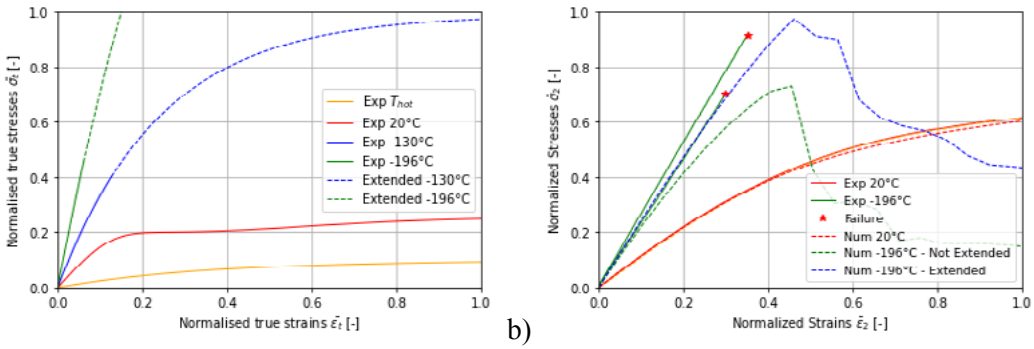
4. Numerical results and discussion

The consideration of a thermoplastic matrix at cryogenic temperatures underlines and amplifies certain difficulties and limitations associated with this type of numerical approach. First, the vast majority of micromechanical models presented in literature consider epoxy-type resins, whose properties are very often set to those obtained by Fiedler et al. [14]. Thermo-elastic properties are considered as independent

of temperature (moduli and CTE) and the stress-free temperature T_0 is set to that of the glass-transition temperature T_g [5], [6], [7]. This approximation is acceptable as long as properties do not vary significantly across the studied temperature range. On the contrary, thermoplastics can exhibit higher CTEs than those conventionally found in epoxy-type polymers and increased ductility at high temperatures. This is particularly the case for semi-crystalline thermoplastics where T_0 is no longer equal to the T_g but is often considered to be equal to the peak crystallization temperature $T_c > T_g$ [21], [22]. In order not to over-estimate thermal residual stresses, the present model needs thus to account for the variation of the thermo-elasto-plastic properties of the considered polymers from the rubbery state after manufacturing, down to the rigid glassy state at cryogenic temperature.
A second limitation is related to the matrix energy release rates G_m. For un-toughened epoxy resins, G_m is typically in the range of $10^0 - 10^2 [J/m^2]$ [7], [23], [24]. Authors generally study the effect of various energy release rates, yet never to magnitudes of $[kJ/m^2]$ that are typically encountered in thermoplastics [25], [26], [27]. Whether such high values are still encountered at cryogenic temperatures has yet to be evaluated.

4.1 Extension of the resin elasto-plastic curves

Whether the elasto-plastic curves of the resin should be extended or not as proposed by other studies, even at cryogenic temperatures, can be evaluated by modeling the tensile tests performed at various temperatures on unidirectional $[90]_{16}$ laminated composites. The model used here is the one described in the previous section yet without the presence of adjacent plies, and will be referred to as the UD90 model. It has been noted that, provided the RVE is sufficiently large, little effect of the RVE size was observed on the macroscopic behavior of the system before damage onset and localization. A model with dimensions of 100x50µm² was therefore used.
Figure 5a presents the normalized experimental tensile curves of the neat TP resin samples performed at T_{hot}, 20°C, -130°C and -196°C. The proposed extension of the experimental curves at cryogenic temperature based on Voce's law (eq.2) is presented alongside. As one can see at cryogenic temperatures, the plastic plateau is reached at very high stresses (not fully shown at -196°C) that seem unlikely to be encountered in a real microstructure. In addition, the extrapolation is performed on a very small part of the fully extended curve, making uncertainty about the latter all the more significant.
Figure 5b) presents experimental tensile curves at 20°C and -196°C of the CF/TP unidirectional $[90]_{16}$ laminated composite samples along with numerical results. In this configuration, the 90° ply is free to contract in all directions due to thermal expansion coefficients. From a macroscopic point of view, one could say that no stresses should build. Nevertheless, at microscopic scales, significant stresses are reached. So much that, at cryogenic temperatures and when the elasto-plastic curves of the neat TP resin are taken "as is" (i.e. not extended and damage initiates at the experimentally determined ultimate stresses) from experimental measurements, tensile tests of UD plies cannot be reproduced numerically with high fidelity. Indeed, the micro-stresses within the matrix rapidly reach the limit stresses observed on the macroscopic resin samples, and premature plasticity is obtained. This leads to an overly non-linear macroscopic behavior of the system at cryogenic temperature (see Figure 5b for the "non-extended" properties), even when parameters of the Drucker Prager model are adjusted. This behavior is observed regardless of the properties of the cohesive zones selected and independently of the stress-free temperature T_0. This excessive softening behavior can be suppressed when the elasto-plastic properties of the TP matrix are extended at cryogenic temperatures, as seen in Figure 5b. In this case, the initial thermal loading and parameters of the plasticity model affect only slightly the macroscopic behavior of the system at 77K. Indeed, stresses reached after thermal loading remain well below the matrix extended ultimate stresses, and the overall system behaves rather elastically with a brittle failure controlled by the cohesive zones, as observed experimentally.
This suggests that properties of the matrix should be extended as proposed by other authors [5], [7], [14], even at cryogenic temperatures. The way to extend these properties at cryogenic temperatures remains an open issue.



a) b)

Figure 5. Normalized stress-strain curves of neat TP resin samples (a) and CF/TP UD $[90]_{16}$ tensile tests (b) at different temperatures. T_{hot} is comprised between material's T_g and consolidation temperature. In (a), experimental results (full line) are extended (dashed lines) at cryogenic temperature using Voce's law (eq.2). In (b), numerical results are presented in dashed lines, with the extended matrix properties (green) or not (blue).

4.2 Polymer fracture toughness

Before diving into the modeling of transverse cracks within constrained 90° plies, it is important to study the capability of the present approach to solve the crack initiation and propagation, based on the input matrix fracture energy. As said before, the matrix's mode I fracture toughness G_m is provided as an input parameter. In order to decrease mesh dependencies in the damage localization, Bažant and Oh's crack band model [28] stipulate that under mode I loading, the area under the stress-strain curve once damage initiates should be equal to G_m/l_e^m where l_e^m is the characteristic element length in the direction along the crack path. In common FEM softwares, it is defined as a function of the element's volume V_e^m in 3D and cross-sectional area A_e^m in 2D: $l_e^m = \sqrt[3]{V_e^m}\big|_{3D} = \sqrt{A_e^m}\big|_{2D}$. Elements should thus have an aspect ratio as close to 1 as possible. Assuming a linear damage softening law, the strain at which an element is fully damaged (i.e. damage variable $d = 1$) when subject to a unidirectional tensile load is: $\varepsilon_f^m = \frac{2G_m}{l_e^m \sigma_u^m} + \varepsilon_u^m$, where ε_u^m is the strain at which damage onsets [29]. Using properties classically used in literature for thermosets at ambient temperatures ($G_m = 0.1\,N/mm$, $\sigma_u^m = 100\,MPa$ and $l_e^m = 1\mu m$), it is common to obtain failure strains up to $\varepsilon_f^m = 2$. The corresponding length of the ligament upon full damage depends whether geometrical non-linearities are accounted for or not, i.e. whether the small or finite deformations theory is used. When considering small deformations, the length becomes $\Delta L_f^{eng} = l_e^m \varepsilon_f^m \approx 2\mu m$, which is large yet reasonable when considering classical crack opening displacements that are in the same order of magnitude (see Figure 4b). It is no longer acceptable when true strains (i.e. finite deformations) are used: $\Delta L_f^{true} = l_e^m \cdot \left(e^{\varepsilon_f^m} - 1\right) \approx 6.4\mu m$.

This explains the presence of matrix ligaments (see Figure 4b) that require large crack openings in order to be fully damaged, and thus to dissipate the desired energy. This issue is further enhanced when mesh size (i.e. l_e^m) decreases and matrix fracture toughness increases to values expected for thermoplastics. Here, it is almost impossible to completely damage matrix ligaments, no matter whether geometrical non-linearities are accounted for or not. The model thus does not dissipate the desired damage energy, making comparisons of various matrix fracture toughness impractical.

The present approach thus appears incapable of describing the brittle fracture of highly energetic dissipative processes, as the characteristic length scales required for the damage process to occur are larger than the crack openings observed experimentally.

4.3 Thermal residual stresses and matrix plasticity model

In spite of the limitations presented above, a qualitative analysis of the transverse cracking mechanisms at various temperatures and ply thicknesses can be performed. Here, the properties of the resin are fully extended, and the matrix energy release rate G_m will be kept to a small value typically used in literature, namely 0.12N/mm in order for the matrix elements to reach full damage and dissipate the entire input

fracture energy. The model will be the one described in the section 3, consisting of a 90° ply surrounded by homogenized adjacent plies (Figure 4a).
As pointed out by Kohler et al. [30], the implementation of thermal residual stresses is not trivial and their magnitude can generate significant stresses leading to the formation of transverse cracks in the 90° ply during the thermal step. The magnitude of those stresses is directly driven by the stress-free temperature T_0, the CTEs of the micro-constituents, the elasto-plastic properties of the matrix (and thus the extension or not of the experimental curves) and the ultimate stress at which damage onsets in the CZMs (τ_{CZM}) and in the matrix (σ_u^m). The energy release rates of both the CZM (G_{CZM}) and the matrix (G_m) does not have a significant impact on the thermal residual stresses. The ply thickness has also little impact on them. Surprisingly, even at cryogenic temperatures, the plasticity model used significantly affects the average thermal residual stresses built during the thermal step, leading to an important effect on the transverse crack initiation threshold. More specifically, for the same model parameters, changing from a pressure-independent plastic model with isotropic hardening based on Von-Mises' yield criterion to a pressure-dependent hyperbolic Drucker-Prager plastic model can lead to a 15% decrease in average thermal residual stresses, and a transverse crack initiation threshold increased by a factor 3. This is observed even when the matrix properties have been extended, where the plasticity model showed no impact on the behavior of the UD90 model. This underlines the need for precise knowledge of the elasto-plastic and thermal behavior of components over the entire temperature range, from T_0 and even down to cryogenic temperatures. Complementary tests (DMA, CTE, compression) therefore seem necessary to restrict the range of uncertainties.
Whether non-linear geometry is accounted for or not does not influence the thermal residual stresses. It was nevertheless observed that considering small deformations leads to a decrease of the transverse crack initiation thresholds by approximately $\Delta\varepsilon = 0.05\%$. It also leads to the formation of non-physical deformation in certain highly deformed elements, supporting the idea that finite deformations theory should be used.

5. Conclusion and perspectives

The present study aims at improving the understanding of transverse cracking of thin plies in cryogenic environments, and to investigate the influence of the damageable elasto-plastic properties of the polymer resin. Experimental tests at -130°C and -196° on two carbon fiber composites with thermoset (CF/TS) and thermoplastic (CF/TP) matrices demonstrated the significant influence of temperature and ply thickness on transverse cracking mechanisms. In particular, the appearance of partial cracks was noted in the case of intermediate and thin (<140µm) plies of the CF/TP composite, whose initiation is driven by microstructural variability. A micromechanical finite element numerical model has been developed, allowing to model the initiation and propagation of transverse cracks without presupposing their path, and to study the influence of the matrix. It was noted that, even at cryogenic temperatures, experimentally measured resin properties need to be extended to higher strain levels, and that the plasticity model chosen has a significant influence on both the level of thermal residual stress reached at -196°C and the resulting transverse cracking threshold. However, further experimental measurements are required to narrow down the range of possible values defining the micro-constituents (matrix and interfaces).
This type of approach has nevertheless a number of limitations, which were highlighted by the study of a thermoplastic matrix composite at cryogenic temperature. First, this type of approach has a strong dependence on interfacial properties modeled by cohesive zones. It is very difficult to identify these numerically and experimentally, especially under cryogenic conditions. In addition, due to large element elongations required for the damage process to occur in the matrix, the small crack opening displacements ($\propto 1\mu m$) encountered in thin plies do not allow for the damage process to fully develop, and thus dissipate the entire input matrix fracture toughness. This modeling approach therefore appears incapable of describing the brittle fracture of highly energetic dissipative processes that are encountered in some thermoplastic resins.
It would thus be interesting to compare the present approach with other ones such as the Finite Fracture Mechanics (FFM), where a double criteria governs the initiation and propagation of damage, without the need to spread the damage over a certain characteristic length for it to be fully completed.

References

[1] J. A. Nairn, « Matrix microcracking in composites », in *Comprehensive composite materials. Vol.2, Polymer matrix composites*, vol. 2, Elsevier, 2000, p. 403-432.

[2] T. Yokozeki, T. Ogasawara, T. Aoki, et T. Ishikawa, « Experimental evaluation of gas permeability through damaged composite laminates for cryogenic tank », *Composites Science and Technology*, vol. 69, nº 9, p. 1334-1340, 2009.

[3] H. Saito, H. Takeuchi, et I. Kimpara, « Experimental Evaluation of the Damage Growth Restraining in 90° Layer of Thin-ply CFRP Cross-ply Laminates », *Advanced Composite Materials*, vol. 21, nº 1, p. 57-66, 2012.

[4] F. Laurin, A. Mavel, P. Paulmier, J.-M. Garcia, et M. Herman, « Experimental and numerical study on the transverse cracking in a composite material with a thermoplastic matrix. », *Proceedings of the 20th European Conference on Composite Materials - Composites Meet Sustainability*, vol. (Vol 1-6), juin 2022, doi: 10.5075/EPFL-298799_978-2-9701614-0-0.

[5] A. Arteiro, G. Catalanotti, A. R. Melro, P. Linde, et P. P. Camanho, « Micro-mechanical analysis of the in situ effect in polymer composite laminates », *Composite Structures*, vol. 116, p. 827-840, 2014.

[6] A. R. Melro, P. P. Camanho, F. M. Andrade Pires, et S. T. Pinho, « Micromechanical analysis of polymer composites reinforced by unidirectional fibres: Part II – Micromechanical analyses », *International Journal of Solids and Structures*, vol. 50, nº 11-12, p. 1906-1915, 2013.

[7] S. Kohler, J. Cugnoni, R. Amacher, et J. Botsis, « Transverse cracking in the bulk and at the free edge of thin-ply composites: Experiments and multiscale modelling », *Composites Part A: Applied Science and Manufacturing*, vol. 124, p. 105468, sept. 2019.

[8] T. Briand, « Effect of ply thickness and temperature on transverse cracking process in composite laminates », présenté à 22nd International Conference on Composite Materials (ICCM22), Melbourne, août 2019.

[9] Y. Accettura, J. Vereecke, T. Briand, C. Bois, et J.-C. Wahl, « Experimental methods dedicated to the study of cracking process in laminated composites subjected to thermomechanical loadings », in *The 16th CRYOGENICS*, Dresden, 2023.

[10] A. Parvizi, K. W. Garrett, et J. E. Bailey, « Constrained cracking in glass fibre-reinforced epoxy cross-ply laminates », *J Mater Sci*, vol. 13, nº 1, p. 195-201, janv. 1978, doi: 10.1007/BF00739291.

[11] T. Klein, C. Bois, J.-C. Wahl, et C. Petiot, « Comparaison de l'endommagement sous chargement thermomécanique cryogénique de composite stratifié à matrice thermoplastique ou thermodurcissable. », présenté à Comptes Rendus des JNC 23, Besançon, 2023.

[12] R. Higuchi, T. Yokozeki, K. Nishida, C. Kawamura, T. Sugiyama, et T. Miyanaga, « High-fidelity computational micromechanics of composite materials using image-based periodic representative volume element », *Composite Structures*, vol. 328, p. 117726, 2024.

[13] J. I. Múgica, C. S. Lopes, F. Naya, M. Herráez, V. Martínez, et C. González, « Multiscale modelling of thermoplastic woven fabric composites: From micromechanics to mesomechanics », *Composite Structures*, vol. 228, p. 111340, 2019, doi: 10.1016/j.compstruct.2019.111340.

[14] B. Fiedler, M. Hojo, S. Ochiai, K. Schulte, et M. Ando, « Failure behavior of an epoxy matrix under different kinds of static loading », *Composites Science and Technology*, vol. 61, nº 11, p. 1615-1624, 2001, doi: 10.1016/S0266-3538(01)00057-4.

[15] J. Misumi, R. Ganesh, S. Sockalingam, et J. W. Gillespie, « Experimental characterization of tensile properties of epoxy resin by using micro-fiber specimens », *Journal of Reinforced Plastics and Composites*, vol. 35, nº 24, p. 1792-1801, 2016, doi: 10.1177/0731684416669248.

[16] E. M. Odom et D. F. Adams, « Specimen size effect during tensile testing of an unreinforced polymer », *J Mater Sci*, vol. 27, nº 7, p. 1767-1771, 1992, doi: 10.1007/BF01107202.

[17] H. S. Da Costa Mattos, J. F. S. Brandão, F. C. Amorim, P. V. S. Araújo, et J. M. L. Reis, « A unified expression to estimate the stress-strain curve of polyamides at different temperatures », *Mater. Res. Express*, vol. 6, 2018, doi: 10.1088/2053-1591/aae564.

[18] M. Herráez, D. Mora, F. Naya, C. S. Lopes, C. González, et J. LLorca, « Transverse cracking of cross-ply laminates: A computational micromechanics perspective », *Composites Science and Technology*, vol. 110, p. 196-204, 2015, doi: 10.1016/j.compscitech.2015.02.008.

[19] S. Ogihara et J. Koyanagi, « Investigation of combined stress state failure criterion for glass fiber/epoxy interface by the cruciform specimen method », *Composites Science and Technology*, vol. 70, nº 1, p. 143-150, 2010, doi: 10.1016/j.compscitech.2009.10.002.
[20] Benzeggagh M.L. et Kenane M., « Measurement of mixed-mode delamination fracture toughness of unidirectional glass/epoxy composites with mixed-mode bending apparatus », *Compos Sci Technol*, vol. 56, nº 4, p. 439-449, 1996, doi: 10.1016/0266-3538(96)00005-X.
[21] P. P. Parlevliet, H. E. N. Bersee, et A. Beukers, « Residual stresses in thermoplastic composites-A study of the literature-Part I: Formation of residual stresses », *Compos Part A Appl Sci Manuf*, vol. 37, p. 1847-1857, 2006.
[22] M. Péron *et al.*, « Measurement and prediction of residual strains and stresses during the cooling of a glass fibre reinforced PA66 matrix composite », *Composites Part A: Applied Science and Manufacturing*, vol. 137, p. 106039, 2020, doi: 10.1016/j.compositesa.2020.106039.
[23] T. H. Hsieh, A. J. Kinloch, K. Masania, A. C. Taylor, et S. Sprenger, « The mechanisms and mechanics of the toughening of epoxy polymers modified with silica nanoparticles », *Polymer*, vol. 51, nº 26, p. 6284-6294, 2010.
[24] A. R. Melro, P. P. Camanho, F. M. Andrade Pires, et S. T. Pinho, « Micromechanical analysis of polymer composites reinforced by unidirectional fibres: Part I – Constitutive modelling », *International Journal of Solids and Structures*, vol. 50, nº 11-12, p. 1897-1905, 2013.
[25] G. Christoph et G. Hartwig, « Fracture Behavior of Polymers at Cryogenic Temperatures », in *Advances in Cryogenic Engineering Materials*, L. T. Summers, Éd., Boston, MA: Springer US, 1996, p. 7-12. doi: 10.1007/978-1-4757-9059-7_2.
[26] D. R. Moore, « The Time and Temperature Dependence of Fracture Toughness for Thermoplastics », *Polymer Testing*, vol. 5, nº 4, p. 255-268, 1985.
[27] L. Laiarinandrasana, G. Boisot, C. Fond, et G. Hochstetter, « Toughness improvement of polyamide 11 assessed via quasistatic tensile tests on notched round bars », présenté à Fracture of materials and structures from micro to macro scale - ECF 18, Dresden, Germany, 2010.
[28] Z. P. Bazant et B. Oh, « Crack band theory for fracture of concrete », *Matériaux et Constructions*, vol. 16, p. 155-177, 1983.
[29] M. Herráez, C. González, et C. S. Lopes, « A numerical framework to analyze fracture in composite materials: From R-curves to homogenized softening laws », *International Journal of Solids and Structures*, vol. 134, p. 216-228, mars 2018, doi: 10.1016/j.ijsolstr.2017.10.031.
[30] S. Kohler, « Multiscale experimental characterisation and modelling of transverse cracking in thin-ply composites », Ecole Polytechnique Fédérale de Lausanne, 2019.

ANALYTICAL AND NUMERICAL MODELING OF ARAMID HONEYCOMB CORES

Dr.-Ing. Jens Bold[1]

[1]Boeing Research & Technology Europe, Integrated Vehicle Systems – Structure Technologies, Boeing Deutschland GmbH, Brabanter Strasse 4, 80805 München, Germany
Email: jens.bold@boeing.com, Web Page: http://www.boeing.com

Keywords: Honeycomb core, Testing, Homogenization, Modeling, Cuntze-Bold

Abstract
Aramid honeycomb cores are widely used in combination with composite face sheets for various sandwich structure applications due to their exceptional stiffness-to-weight ratio. Although numerical simulation techniques for the material and failure behavior of composite skins are well-established, modeling the honeycomb core continues to present a challenge. The honeycomb core is often modelled at meso-scale using shell elements, with geometry and material properties evaluated through a combination of tests and assumptions. However, this approach becomes computationally expensive for simulating large structures. In this study, a new method is presented where the honeycomb core is homogenized using orthotropic solid elements, incorporating an advanced material and failure model. The effective core material properties used in the model were determined for an aramid honeycomb core by tension, compression, and shear testing on coupon level. Furthermore, effective material values obtained from analytical calculations were compared with the experimental results to assess the accuracy of the analytical methods. The new developed model was finally validated by four-point-bending testing. This method aims to replace current expensive simulation involving shell elements for the core with a more computationally efficient solution using orthotropic solid elements.

©2024 | 3_BOLD_Jens_DG2Q9.pdf

1. Introduction

In various load bearing applications across aerospace, automotive, marine, and civil engineering, the utilization of honeycomb sandwich structures is prevalent [1]. Main reasons for this are their exceptional stiffness-to-weight ratio and weight specific bending strength. When confronted with high requirements for lightweight design, impregnated aramid papers are commonly chosen for the honeycomb core material, owing to their outstanding stiffness-to-weight ratio. This was also the case in the Ba-varian-funded project BayLu25-BLANCA, which is a collaborative effort on opti-mizing load introductions in sandwich structures, involving the University of the Bun-deswehr Munich (UniBw M), the testing facility GMA, the small and medium-sized enterprise GERG, and the aircraft manufacturer Boeing This work presents the inves-tigations on sandwich structures within the projects scope.

Aramid honeycomb cores exhibit orthotropic structural behavior [2], which is caused by both the inherent nature of the aramid paper material [3] and the manu-facturing process of the honeycomb core. Manufacturing of aramid cores is com-monly done using the expansion process, illustrated in Fig. 1. In a first step, an adhe-sive is applied to the aramid paper sheets, which are subsequently laminated into a stack. After curing, the stack is expanded to achieve the specified cell configuration. Various cell shapes are available for honeycomb cores, with the most common ge-ometry being the hexagonal cell. Subsequent to shaping, the honeycomb structure is immersed multiple times in a resin bath until the desired density is reached, followed by curing in an oven. Notably, the walls where the aramid papers are bonded together have a higher thickness than the single paper cell walls. This causes a pronounced orthotropic structural behavior with higher mechanical properties in the L-direction.

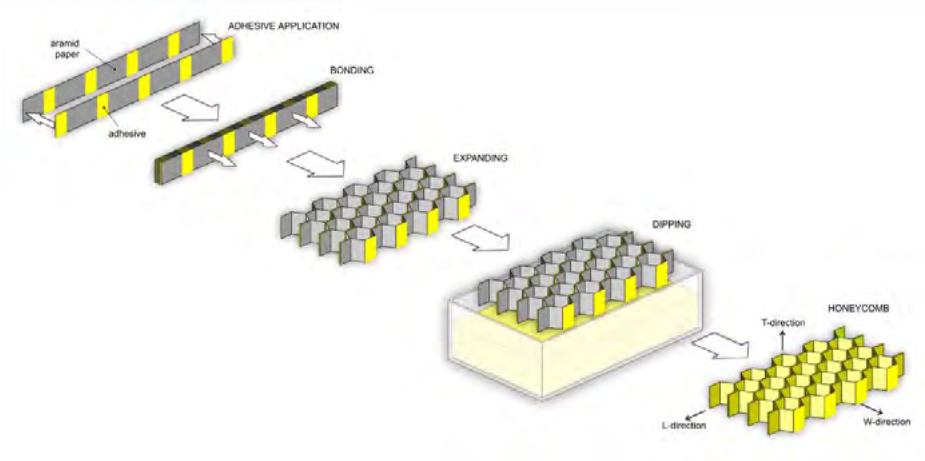


Figure 1. Manufacturing process of aramid honeycomb cores

For simulating a honeycomb core there are two main approaches. One method is to simulate the honeycomb core at meso-scale using shell elements [3,4]. This approach requires detailed modeling and fine discretization of the cell walls to accurately pre-dict the structural behavior. A high computational effort is therefore needed, which can become problematic, particularly for simulating large structures. This drawback can be mitigated by homogenizing the honeycomb structure to a 3D-continuum, integrating an appropriate material and failure model. This approach allows for a significantly coarser discretization, thereby reducing computational time. In addition, the homogenization approach requires fewer material data input as for detailed me-so-scale modeling. To describe the honeycomb structure behavior with 3D-solid ele-ments, the input depicted in Fig. 2 is needed.

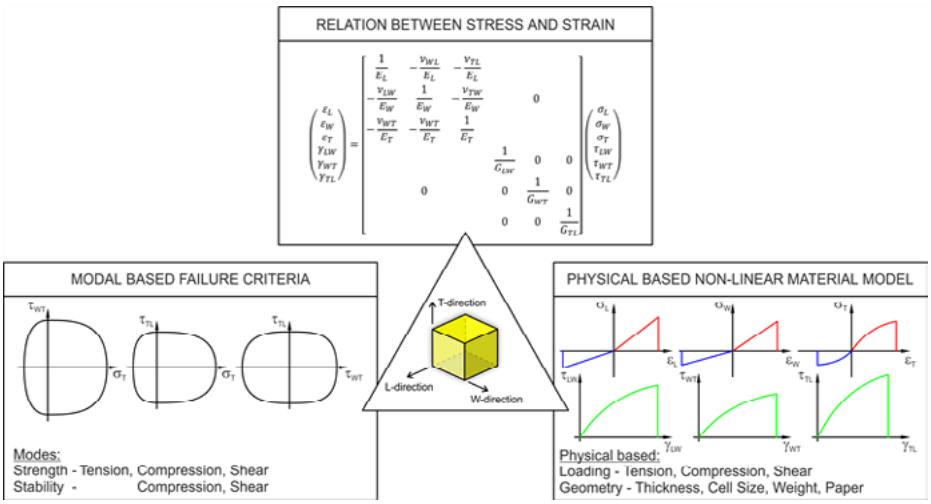


Figure 2. Input for homogenized honeycomb core model

The effective orthotropic properties of the honeycomb core must be determined to describe the stress-strain relation. This can be done by experiments [3,4], analytical models [5-7] or numerical homogenization [8,9]. Moreover, a failure criterion is need-ed to predict the honeycomb core failure modes as well as a non-linear material model to describe the elastoplastic behavior.
In this study, the homogenization approach was used for modeling the honey-comb structure since it allows highly efficient simulation. The effective orthotropic properties of a honeycomb core were determined by experimental testing and com-pared to analytical solutions. Furthermore, a material- and failure model was devel-oped for the homogenized honeycomb core. The models were then validated by four-point testing.

2. Honeycomb Core Testing

In honeycomb core datasheets, typically only the stiffness and strength values for out-of-plane compression and shear are provided [10,11]. These are the most im-portant properties for dimensioning honeycomb cores in sandwich structures [3]. However, there are also applications where the in-plane properties are relevant. An example is the core-forming process, in which the honeycomb core is largely de-formed to complex shapes, such as for airframe sandwich panels [12]. To compre-hensively describe the honeycomb behavior, both out-of-plane and in-plane proper-ties were considered in this work. Testing was conducted by the project partner GMA, utilizing universal testing machines (Zwick Z010, Z330) under nominal environmen-tal conditions. In addition, digital image correlation measurements were performed by the UniBw M for the non-standard tests. A hexagonal para-aramid (Twaron®) /phenolic honeycomb core was used in this work, with a cell size of 3.2 mm, density of 40 kg/m3 and a thickness of 10 mm. The experimental results are presented in the following sections.

2.1. Out-of-Plane Testing

For characterizing the out-of-plane behavior, tensile and compression tests were con-ducted in T-direction of the honeycomb core, while shear tests were performed for the LT- and WT-directions. The standard ASTM C297 [13] was used for the tensile tests in T-direction and ASTM C365 [14] was utilized for the compression tests. In both load cases, the honeycomb core was tested with face sheets (“stabilized”). Further-more, the machine displacement was used for calculating the strains. To ensure accu-racy, the measured displacements were corrected by the hinge tolerances in the test fixture. The resulting stress-strain curves are depicted in Fig. 3.

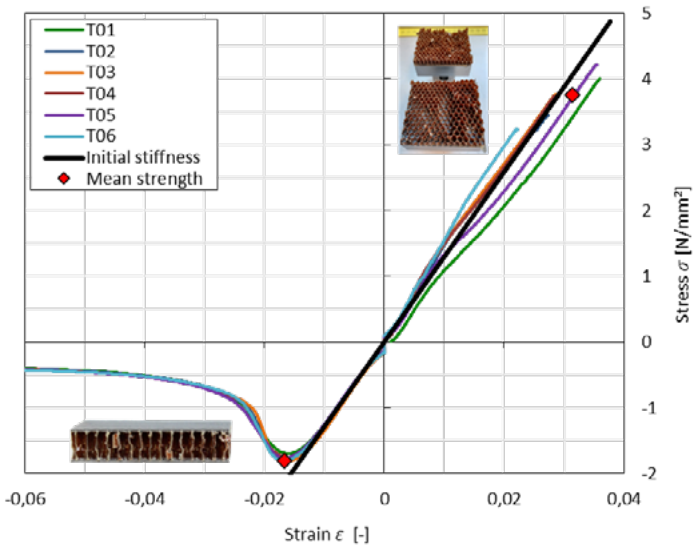


Figure 3. Stress-strain curves of the out-of-plane tensile and compression tests in T-direction

Under tensile loading, the honeycomb structure exhibits linear elastic behavior until reaching a brittle failure of the core cell walls. Core rupture failure also occurs in compression, but here subsequently leading to a nearly constant stress plateau due to the formation of plastic hinges [5]. Comparing both load cases showed that the initial stiffnesses are similar, whereas the tensile strength is approximately twice as high compared to compression.
The shear behavior in LT- and WT-directions was investigated following ASTM C273 [15]. In both directions, the stress-strain curves can be approximated by a bilinear curve, as depicted in Fig. 4. The initial linear part ends with a stability failure onset [16]. This was also observed by finite element analysis of the honeycomb cell walls. It is further evident that stability failure in LT-direction occurs at lower stress levels than in WT-direction. However, the shear strength and the initial stiffness are higher in LT-direction due to the increased cell wall thickness in L-direction. Notably, the evaluated out-of-plane core properties are within a similar range to the effective properties given in comparable core datasheets [10,11].

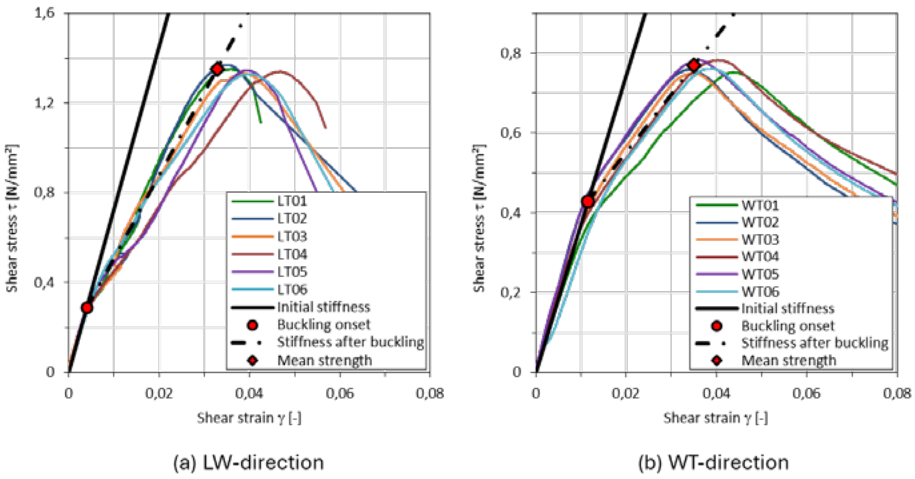


Figure 4. Stress-strain curves of the out-of-plane shear tests in LT- and WT-direction

2.2. In-Plane Testing

The in-plane behavior was investigated by tensile and compression loading in L- and W-direction, as well as by in-plane shear tests in LW-direction. The tests in L- and W-directions were conducted based on ASTM C363 [17]. According to this standard, pins are used for constraining the core specimens in the test fixture. In case of the tensile tests, it was necessary to adhesively bond the pins to the cell walls to prevent failure at the clamping area. The tensile and compression test setups and the resulting stress-strain curves are depicted in Fig. 5.

In tension, failure was caused in both L- and W-directions by bond rupture between the cell wall nodes. Contrary, for compression no rupture occurred in W-direction since the honeycomb core is compressed to the initial stacked aramid paper configuration. The initial stiffness and failure load in W-direction were found to be about three times lower than in L-direction. This was observed for both tensile and compression loading. Furthermore, comparing both load cases showed that the initial stiffnesses are nearly the same, while the compression strength is approximately half that of the tensile strength.

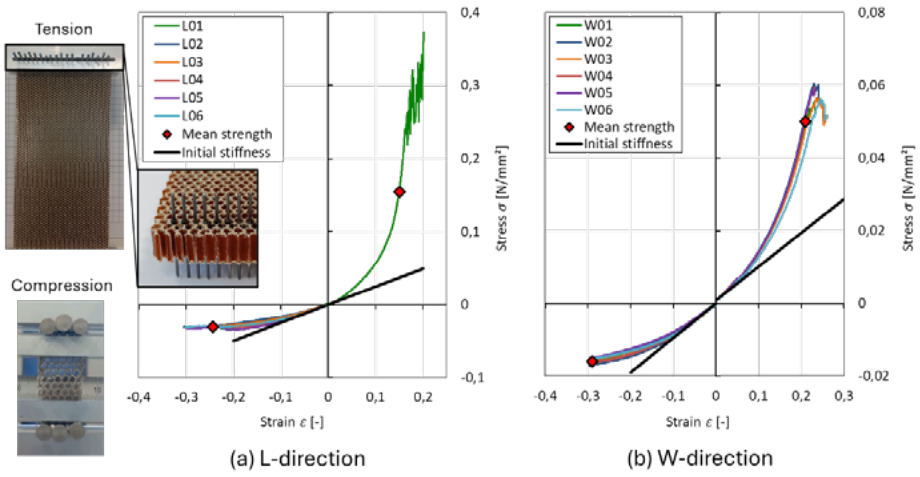


Figure 5. Stress-strain curves of the in-plane tests in L- and W-direction

For investigating the in-plane shear behavior no standard is currently available. Therefore, a new picture frame setup explicitly tailored for testing honeycomb cores was developed in this study. The specimen is mounted in the test fixture using pin rows positioned on all four sides (Fig. 6). In these areas a potting material (Neukasil SN 2907, Altropol Kunststoff GmbH) is used to clamp the specimen.

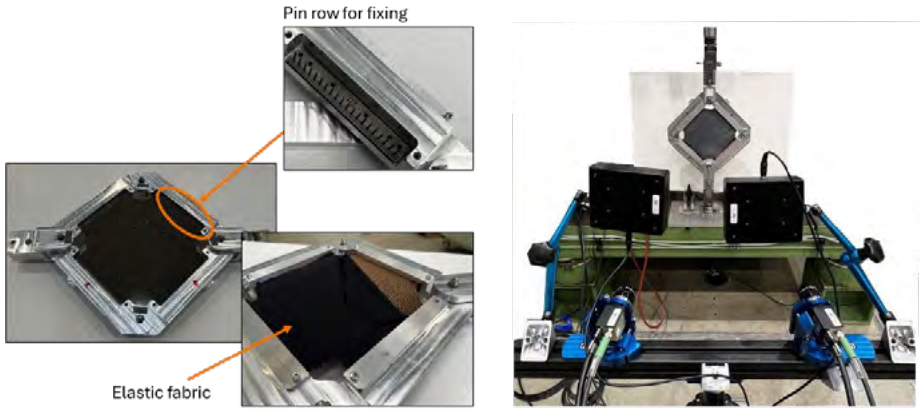


Figure 6. Picture frame test setup for in-plane shear testing

To assess the uniformity of the shear strain distribution, a digital image correlation (DIC) system (Q400D, Limess GmbH) was used. DIC requires a surface on which it can monitor deformations. Therefore, an elastic fabric, consisting of a cotton-elastane mix, was bonded on the honeycomb surface using a spray adhesive. Moreover, a white speckle pattern was sprayed on the fabrics surface for the DIC-measurement. Two 12-megapixel cameras equipped with standard lenses were utilized for this purpose. The resulting in-plane shear strain field is exemplary shown for the linear elastic region in Fig. 7.

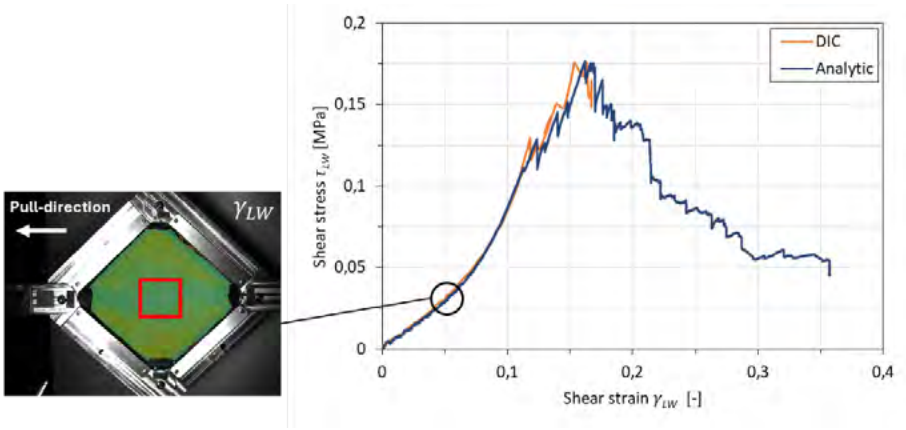


Figure 7. Stress-strain curves of the in-plane shear tests in LW-direction measured with DIC and compared to an analytical solution

At the border areas the shear strain is as expected higher, while the middle region shows a nearly homogeneous strain condition. This uniform region was selected for evaluating the shear strain. An alternative to obtain the shear strain is through analytical calculation. By using the machine displacement δ_f as an input and considering the kinematics of the picture frame, the shear strain and stress can be calculated with Eqs. (1) and (2) [18]. Comparing the analytic solution with the DIC results showed a very good agreement, thereby validating the accuracy of the conducted measurements.

$$\gamma_{LW} = \frac{\pi}{2} - 2cos^{-1}\left[\frac{1}{\sqrt{2}} + \frac{\delta_f}{2L_f}\right] \tag{1}$$

$$\tau_{LW} = \frac{F_f}{\left(\sqrt{2} + \frac{\delta_f}{L_f}\right) L_e t_h} \tag{2}$$

3. Analytical Models for Effective Core Properties

To reduce the number of tests, analytical models can be used to predict the effective orthotropic core properties. Numerous approaches have been developed for this in literature. In the present work, three widely used models are considered, namely Gibson and Ashby [5], Malek and Gibson [6] and Sorohan [7]. The models in [6,7] are based on the work by Gibson and Ashby [5] and consider further influences and corrections. As an input, the core cell geometry and the solid cell wall material data are used. For regular hexagonal honeycomb cores, the models assume that the cell walls containing two bonded papers (aligned in L-direction) have double thickness and that the cell angle Θ equals to 30° [5-7] (Fig. 8). Upon comparison, the analytical results derived from these assumptions did not align well with the observed test results. Therefore, the real thickness and the cell angle Θ of the investigated honeycomb core were measured.

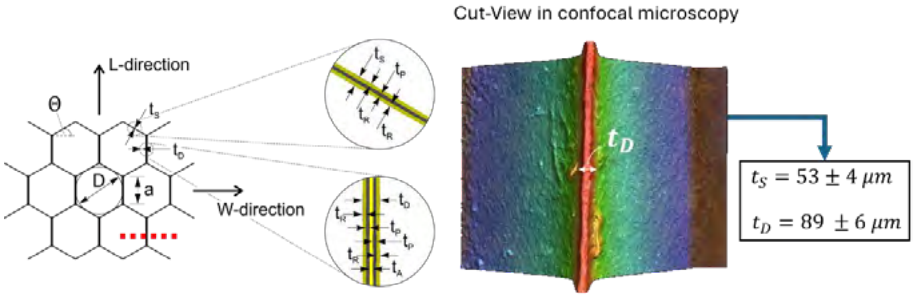


Figure 8. Thickness measurement of the single and double paper cell walls of the honeycomb core

For the thickness measurement, the core was cut along its height and analyzed by confocal laser scanning microscopy (CLSM), as depicted in Fig. 8. Evaluating the single and double wall areas revealed that the thickness of the cell walls aligned in L-direction is only around 70% higher than that of the single paper walls. Furthermore, measuring the cell angle Θ with a microscope indicated an angle of 37.5°. The real cell angle can also be determined by analytical calculation of stiffness ratios for different cell angles and subsequent comparison with the test results. This is exemplary shown in Fig. 9 for the stiffness ratios E_L/E_W and G_{LT}/G_{WT}, calculated with the model proposed by Gibson and Ashby [5].

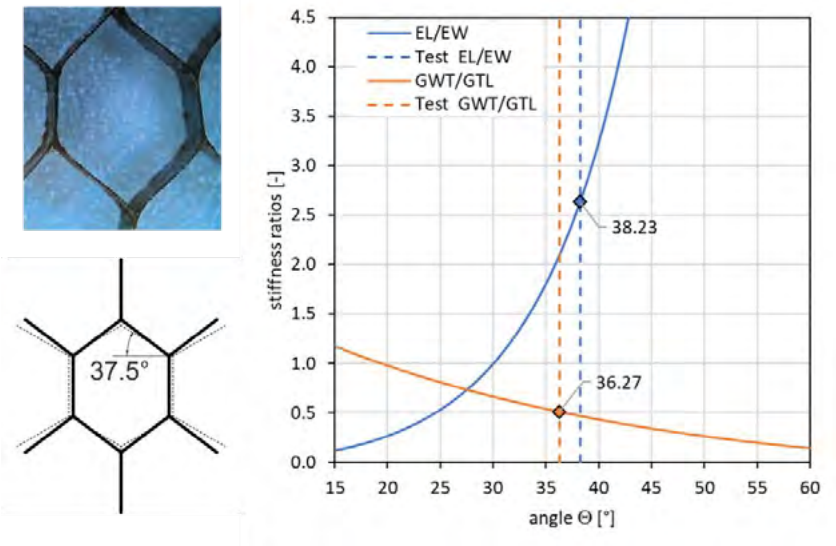


Figure 9. Determination of the cell angle Θ by optical measurement and analytical calculation

Considering the measured thicknesses and cell angle Θ, the effective Young's moduli were calculated with the analytical models for all directions and compared with the test results (Fig. 10). For directions where both tension and compression tests were conducted, the mean stiffness values are given in the following charts.

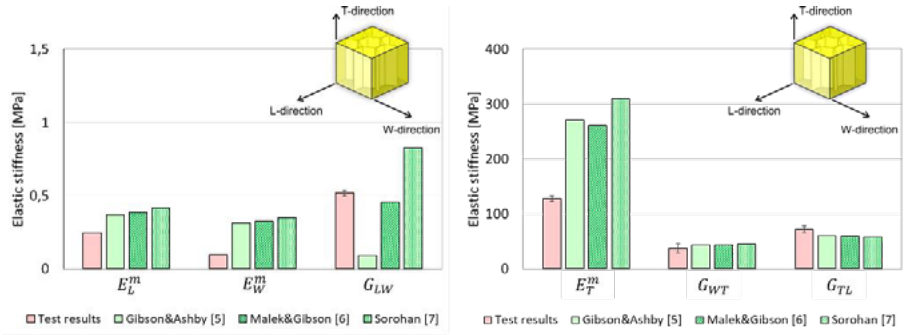


Figure 20. Comparison of effective Young's moduli between test results and analytical models

Using the models in [5-7] resulted in similar stiffness values in most cases. However, for the in-plane shear stiffness G_{LW} and the out-of-plane stiffness E_T, the analytical formulae suggested by Malek and Gibson [6] provides a better prediction. Furthermore, comparing the analytical solutions with the test results showed an overall good agreement. A larger deviation is present for E_T, which needs to be further investigated.

Based on the presented results, a method was developed for honeycomb core testing and analysis (Fig. 11). The approach suggests to only conduct the standard out-of-plane tests and additionally to measure the cell wall thicknesses. With this input, the real cell angle Θ can be determined by calculating the stiffness ratios and comparing it with corresponding analytical solutions, such as in [6]. The analytic model can then be used to calculate all remaining effective elastic properties of the honeycomb core. Afterwards, the effective properties can be utilized for numerical analysis of the honeycomb core. The developed material- and failure model for the numerical analysis is presented in the following chapter.

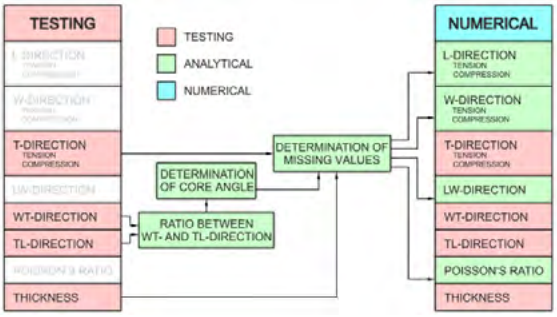


Figure 31. Method for honeycomb core testing and analysis

4. Non-Linear Material Model and Failure Criterion

4.1. Non-Linear Material Model

For modeling the elastoplastic behavior, the Bold non-linear material model for unidirectional and woven composite materials [19] was used. A significant advantage of this model is that it only requires measurable physical properties as input. These are initial stiffness E^{in}, failure stress R^{fr} and elongation at failure ε^{fr}. Unlike many other elastoplastic models, such as Ramberg and Osgood [20], no tuning parameter is needed here. The base form of the material model is shown in Eq. (3).

$$\sigma(\varepsilon) = E^{in}\varepsilon\left(\frac{R^{fr}}{E^{in}\varepsilon^{fr}}\right)^{\frac{\varepsilon}{\varepsilon^{fr}}} \tag{3}$$

This model was applied for all loading types and directions except for the out-of-plane shear loading cases. Regarding the shear behavior in LT- and WT-direction, the following bilinear model was used, here exemplary shown for LT.

$$\tau_{31} \leq R_{TL}: \qquad \tau_{31} = G_{TL}^{in}\gamma_{31} \tag{4}$$

$$R_{TL} < \tau_{31} \leq R_{TL}^{res}: \qquad \tau_{31} = R_{TL} + G_{TL}^{res}\left(\gamma_{31} - \gamma_{31}^{fr}\right) \tag{5}$$

Applying the material model for the investigated honeycomb core showed a good agreement with the experimental stress-strain-curves. This is illustrated in Fig. 12 for tensile and compression loading in L-, W-, T-direction, and in Fig. 13 for the shear behavior.

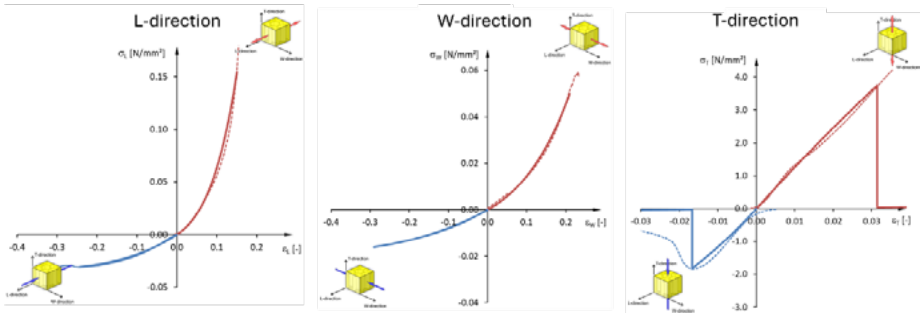


Figure 42. Bold non-linear material model applied to tensile and compression loading in L-, W-, T-direction

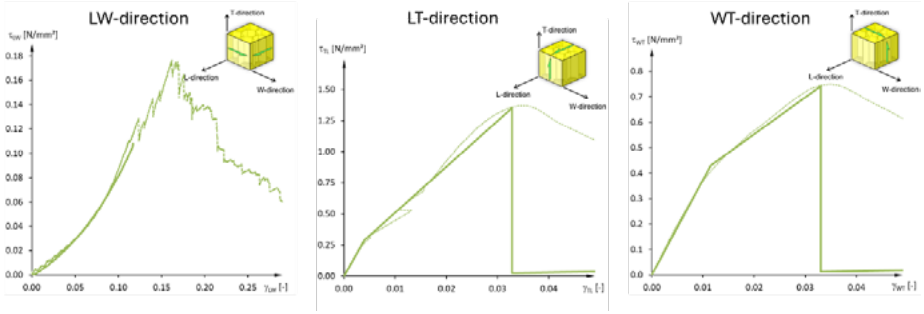


Figure 53. Bold non-linear material model applied to shear loading in LW-, LT-, WT-direction

4.2. Failure Criterion

To model the failure modes of an aramid honeycomb core, it's crucial to account for its orthotropic behavior. A new failure criterion was therefore developed, based on the Cuntze failure criterion for woven materials [21]. This modal-based failure criterion was adapted by considering the most relevant failure modes of honeycomb cores in a sandwich structure. These are failure due to out-of-plane tension (CTF1), compression (CTF2) and two for shear (CSF1 and CSF2). In-plane failure was neglected, given that the core's deformation within a sandwich structure is constrained by the stiff face sheets. Moreover, the friction parameters in the Cuntze-model were set to 0, considering the absence of a matrix in this application. With that, efforts were calculated for the out-of-plane failure modes using Eqs. (6-9).

CTF1: $\sigma_3 \geq 0$ $$Eff^{TF1} = \frac{\sigma_3}{R_T^t} \quad (6)$$

CTF2: $\sigma_3 < 0$ $$Eff^{TF2} = \frac{|\sigma_3|}{R_T^c} \quad (7)$$

CSF1: $$Eff^{SF1} = \frac{|\tau_{31}|}{R_{TL}} \quad (8)$$

CSF2: $$Eff^{SF2} = \frac{|\tau_{23}|}{R_{WT}} \quad (9)$$

The efforts are then combined in the failure criterion, by using the parameter m, which describes the interaction between the failure modes (Eq. (10)). Based on applications in [19, 21], the m value was set to 2 for this study.

$$Eff^m = (Eff^{TF1})^m + (Eff^{TF2})^m + (Eff^{SF1})^m + (Eff^{SF2})^m \leq 1 \quad (10)$$

It should be noted that for other applications the in-plane failure modes could also be considered in the same manner as it was done here for the out-of-plane failure modes.

4.3. Validation

The developed material- and failure model for hexagonal aramid honeycomb cores was validated by four-point-bending-testing (4PB) of sandwich plates. The woven CFRP system Teijin - Q110-2/2TW-285-38-10/HTS40-6k was utilized for the face sheets, with different layups for lamination. This resulted in a total face sheet thickness of 0.915 mm. Moreover, testing was conducted based on ASTM C393 [22].

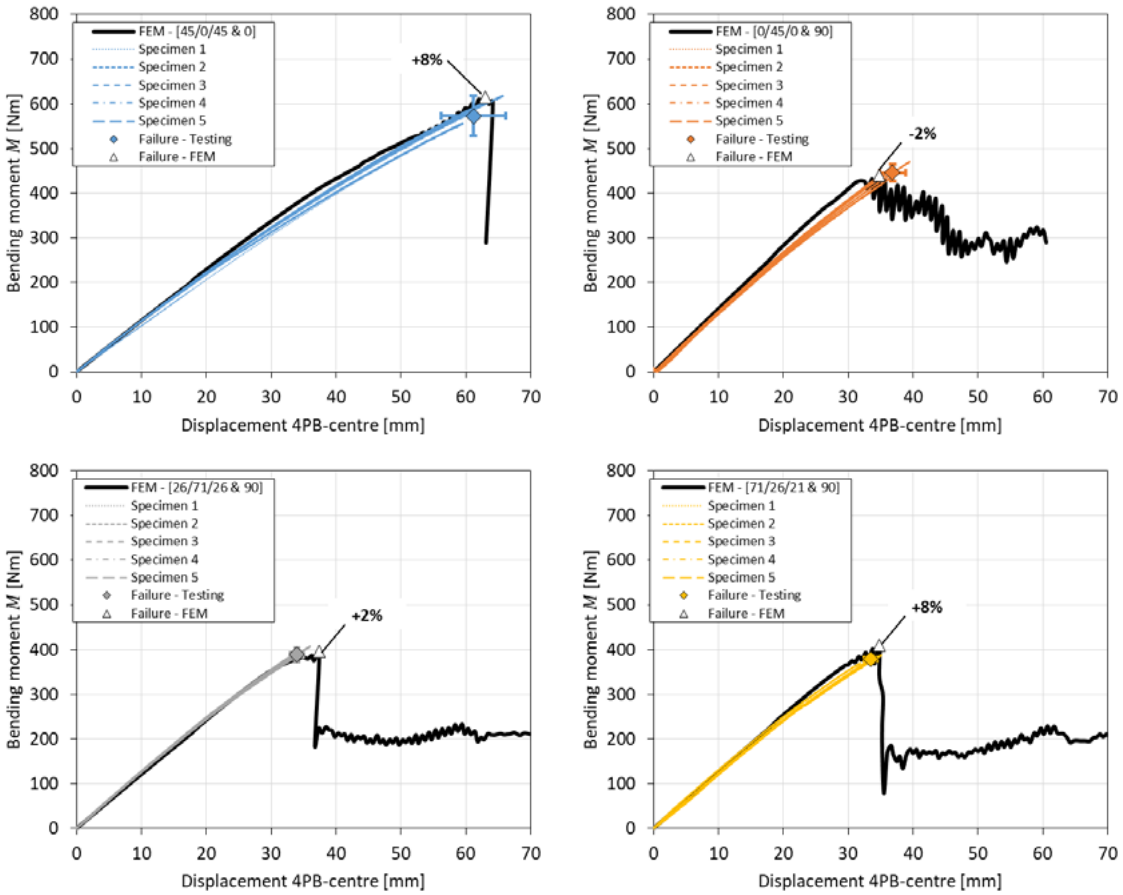


Figure 64. Bending moment-displacement test results of 4PB-experiments compared with FE-simulation

Comparing the bending moment-displacement curves between FE-simulation and 4PB-tests at the middle position demonstrated a good alignment (Fig. 14). Furthermore, the FE simulation accurately identified the failure mode at the expected location, which in this instance was core shear failure. This is illustrated in Fig. 15 by overlaying FE-simulation and experiment using the failure index.



Figure 75. Comparison between FE-simulation and experiment using numerical failure index plot

5. Conclusion and Outlook

The out-of-plane and in-plane behavior of a hexagonal aramid core was investigated by experimental testing. The obtained effective orthotropic core properties were sub-sequently used for modeling a homogenized core. Moreover, a comparison of the test results with existing analytical models was conducted to assess the model accuracy to predict the effective core properties. It was found that only after considering the real cell wall thicknesses and cell angles, the models allow a generally good prediction of the effective elastic properties. Based on these results, a method was developed for core testing and analysis. The proposed approach recommends to only conduct the standard out-of-plane tests alongside measurements of the cell wall thicknesses. With this input, the real cell angle can be calculated, enabling the use of analytical models to predict the unknown elastic in-plane properties. The core properties can then be used for an orthotropic material- and failure criterion. In this study, the Bold non-linear material [19] and the Cuntze modal based failure criterion for woven material [21] were adapted for honeycomb cores. The validity of the developed simulation approach was confirmed through four-point-bending-testing. In future investigations, the developed method will be validated for other honeycomb core configurations. In addition, the analytical models will be further improved to also predict stability and strength failure.

Acknowledgments

This study is part of the research project BLANCA, which is funded by the Bavarian Ministry of Economic affairs, Regional development and Energy (StMWi) within the program BayLu-25. The authors thank Teijin Aramid and Teijin Carbon Europe for providing honeycomb core and prepreg materials free of charge.



References

[1] Zenkert D.: The Handbook of Sandwich Construction (1997).

[2] Karakoç, A., Freund, J.: Experimental studies on mechanical properties of cellular structures using Nomex® honeycomb cores. Composite Structures 94(6), 2017–2024 (2012). https://doi.org/10.1016/j.compstruct.2012.01.024

[3] Seemann, R.: A Virtual Testing Approach for Honeycomb Sandwich Panel Joints in Air-craft Interior. Springer Vieweg, Heidelberg (2019). https://doi.org/10.1007/978-3-662-60276-8

[4] Heimbs, S.: Sandwichstrukturen mit Wabenkern: Experimentelle und numerische Analyse des Schädigungsverhaltens unter statischer und kurzzeitdynamischer Belastung. Dissertati-on, Technischen Universität Kaiserslautern (2008).

[5] Gibson, L.J., Ashby, M.F.: Cellular Solids, Structure and Properties. Cambridge University Press, New York (1997). https://doi.org/10.1017/CBO9781139878326

[6] Malek, S., Gibson, L.: Effective elastic properties of periodic hexagonal honeycombs. Mechanics of Materials 91, 226–240 (2015). https://doi.org/10.1016/j.mechmat.2015.07.008

[7] Sorohan, S., Constantinescu, D.M., Sandu, M., Sandu, A.G.: On the homogenization of hexagonal honeycombs under axial and shear loading. Part I: Analytical formulation for free skin effect. Mechanics of Materials 119, 74-91 (2018). https://doi.org/10.1016/j.mechmat.2017.09.003

[8] Kumar, A., Muthu, N., Narayanan, R.G.: Equivalent orthotropic properties of periodic honeycomb structure: strain-energy approach and homogenization. International Journal of Mechanics and Materials in Design 19, 137–163 (2022). https://doi.org/10.1007/s10999-022-09620-x

[9] Stocchi, A., Colabella, L., Cisilino, A., Álvarez, V.: Manufacturing and testing of a sand-wich panel honeycomb core reinforced with natural-fiber fabrics. Materials and Design 55, 394-403 (2014). https://doi.org/10.1016/j.matdes.2013.09.054

[10] Schütz Composites: Coremaster CN1 Technical data sheet. https://www.schuetz-composites.net/de/honeycombs/cormaster-cn1/. Accessed 15 Dec 2023

[11] Hexcel: HexWeb® HRH-36 Technical data sheet. https://www.hexcel.com/user_area/content_media/raw/HRH_36_eu.pdf. Accessed 15 Dec 2023

[12] Castanié, B., Bouvet, C., Ginot, M.: Review of composite sandwich structure in aeronautic applications. Composites Part C: Open Access 1, 100004 (2020). https://doi.org/10.1016/j.jcomc.2020.100004

[13] ASTM International: Standard Test Method for Flatwise Tensile Strength of Sandwich Constructions. ASTM C297/C297M-16, West Conshohocken, PA, United States (2016)

[14] ASTM International: Standard Test Method for Flatwise Compressive Properties of Sand-wich Cores. ASTM C365/C365M-22, West Conshohocken, PA, United States (2022)

[15] ASTM International: Standard Test Method for Shear Properties of Sandwich Core Materi-als. ASTM C273/C273M-20, West Conshohocken, PA, United States (2020)

[16] Bianchi, G., Aglietti, G.S., Richardson, G.: Static Performance of Hot Bonded and Cold Bonded Inserts in Honeycomb Panels. Journal of Sandwich Structures and Materials 13, 1 (2011).https://doi.org/10.1177/1099636209359840

[17] ASTM International: Standard Test Method for Delamination Strength of Honeycomb Core Materials. ASTM C363-00, West Conshohocken, PA, United States (2000)

[18] Jauffrès, D., Morris, C.D., Sherwood, J.A., Chen, J.: Simulation of the thermostamping of woven composites: Determination of the tensile and in-plane shearing behaviors. Internatio-nal Journal of Material Forming 2, 161 (2009). https://doi.org/10.1007/s12289-009-0590-x

[19] Bold, J.: Vergleich des Impaktverhaltens von monolithischer und hybrider CFK-Platte unter Verwendung eines neuen Werkstoffmodells. PhD Thesis, Deutsches Zentrum für Luft- und Raumfahrt e.V., Köln (2019).

[20] Ramberg, W., Osgood, W.R.: Description of stress-strain curves by three parameters. NACA, Washington, D.C. (1943).

[21] Cuntze, R.: Comparison between experimental and theoretical results using Cuntze's failure mode concept model for composites under triaxial loadings. Journal of Composite Materials, SAGE Publications (2012).

[22] ASTM International: Standard Test Method for Core Shear Properties of Sandwich Constructions by Beam Flexure. ASTM C393/C393M-20, West Conshohocken, PA, United States (2020)

Influence of water aging on mechanical behavior and damage mechanisms of windturbine blades in marine environment

El Hadji Amadou BA[1], Khalid AOUJDAD[2], Florian GEHRING[1], Alexandre VIVET[1], Mounsif Ech-Cherif EL-KETTANI[2], Damien LEDUC[2], Pierre MARECHAL[2]

1 : Normandie Univ, ENSICAEN, UNICAEN, CEA, CNRS, CIMAP, 14000 Caen, France
e-mail : elhadji-amadou.ba@etu.unicaen.fr
florian.gehring@unicaen.fr
alexandre.vivet@unicaen.fr

2 : LOMC : Normandie Univ, UNIHAVRE, CNRS, LOMC, 76600 Le Havre, France
e-mail : khalid.aoujdad@etu.univ-lehavre.fr

Abstract

The implementation of in-situ integrity monitoring of wind turbine blade structures used in the marine environment requires an understanding of the strucure damage kinetics. These structures mainly elaborated with sandwich composite materials.This study focuses on the influence of water aging of sandwich structures immersed in seawater heated to 40°C on their mechanical behavior and the evolution of various types of damage. The 4-point bending behavior of structures samples after aging was analyzed. Monotonic and repeated progressive loading tests were carried out. Damage initiation and propagation were monitored by acoustic wave recording. Water absorption monitoring on the test specimens showed that the water content equilibrium is reach after 15 weeks. After 15 weeks, begin the second phase of hydric aging. The two stages were identify in water aging influence on sandwich behaviour. The water content equilibrium time apprears to be the threshold. The K-means classification method was used to obtain the acoustic wave average parameters signatures of the 5 damage mechanisms : matrix cracking, fiber/matrix decohesion, skin/shell decohesion, delamination and fiber breakage. During the first phase, the structure absorbs water. This phase is characterized by an initial change in the structure behavior, with an increase in dissipated energy and in the average amplitudes of the damage classes. After water content has stabilized, the mechanical behavior of the structures is characterized by a decrease in energy and average amplitudes with aging. The study also shows that aging accelerates material failure under load.

Keywords : Sandwich structure, damage mechanisms, acoustic emission, bending tests, water aging

1. Introduction

The law on energy transition [1], passed on August 17, 2015 voted by the French National Assembly, aims to boost the share of green energy in France's energy mix [2]. With this in mind, the wind power sector (marine and terrestrial) is therefore aiming to produce 10 GigaWatts of electricity by 2050. As a result, innovative projects such as COSPHI are developped. The COPSHI project, supported by LABEX EMC3 (https ://www.labex-emc3-gsmes.fr/labex-emc3/), aims to work on a in-situ method to monitor offshore wind blade turbine integrity in service. When in service, these blades are subjected to coupled mechanical and environmental stresses, leading to damage and aging of the structures. Understanding sandwich structure behavior and damage are essential to optimize the service life of wind turbine structures.

Sandwich panels mechanical properties is characterized by bending tests. The stiffness values of the sandwich structure depend essentially on the stiffness of the skins and the mechanical properties of the core [3, 4, 5, 6]. Studies on the mechanical behavior under static and dynamic 4-point bending loading of sandwich structures with glass composite skins in a polyester matrix with a PVC core were carried out [7]. The main goal is to characterize the stiffness, energy dissipation and damping of this sandwich structure, and at the same time to monitor the evolution of damage by acoustic emission. Indeed, the use of acoustic emission enables a better understanding and monitoring of damage on composite sandwich structures [8]. A classification of the various damage classes is made using the K-means method [9, 10, 11, 12]. This method consists in segmenting the data (acoustic waves bursts) collected by the sensors into classes using "moving center" classification algorithms. These algorithms perform iterations of data partitioning, minimizing the distance variance intra non overlaping clusters. At the same time, post-mortem microscopic observation of the samples tested and advanced knowledge of damage patterns enabled to associate a damage mechanism with each class obtained [13, 14, 15]. In general, most of the damage observed and identified by acoustic emission on the composite samples tested was matrix cracking, decohesion between the fibers and the polymer resin matrix, delamination and fiber breakage. Fiber breakage is considered to be the most energetic form of damage, occurring mainly just before structural failure. This is in contrast to matrix cracks, which are diffuse in time and very low in energy [13, 14, 15]. In sandwich structures, the same types of damage can be found, plus decohesion between the skins and the core. These interfaces, which are sometimes glued together, represent an additional source of fragility for the structure.

The aim of this article is to understand to what extent the hydric ageing of sandwich structures with glass/polyester composite skins in seawater at 40°C affects the overall mechanical behaviour of these structures. and the evolution of damage mechanisms.

2. Structure and Methodology

2.1. Sandwich structure

Despite the wind turbine blade structural complexity, the work focus on a representative sandwich structure panel. The skins are unidirectional fiberglass laminates with an isophthalic unsaturated polyester resin suitable for marine environment. The reinforcement weight ratio was set at 35%. The density of the glass/polyester composite skins is 1550 kg/m^3. The core is a closed-cell rigid foam of SAN (styrene acrylonitrile) polymer, suitable for the marine environment, with a density of 85 kg/m^3. The sandwich plates were processed by under vaccum contact molding at a pressure of 1 bar at room temperature for 24 h. After demolding, the sheets were post-cured for 1 hour at 130°C to achieve complet cross-linking of the resin.

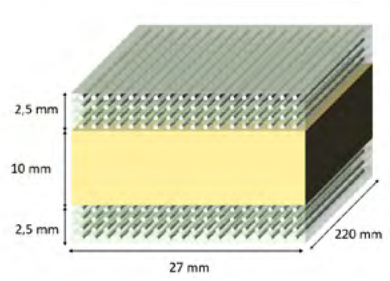


Fig. 1. – Sandwich structure used in this study

2.2. Mechanical testing

An experimental behavior characterization protocol has been set up to reproduce some of the stresses experienced by a wind turbine blade in service. The sandwich structures were subjected to 4-point bending tests in accordance with ISO standard NFT54-606 on a servo-hydraulic machine equiped with a 100kN force cell. The experimental data base is composed of monotonic loading controlled at 2 mm/min and repeated progressive loading (RPL). The dimensions used for the sandwich samples, in line with the standard, are : length 220 mm, width 27 mm, total thickness 15 mm, core thickness 10 mm. The span of the sandwich specimens tested was 190 mm, and the distance between the two upper supports was 100 mm.

2.3. Acoustic emission

Bending tests are coupled with acoustic emission recording to monitor damage mechanisms. Two piezoelectric transducers, 20 mm in diameter and with a bandwidth of 20 kHz to 1 MHz, are placed on the tension skins of the sandwich specimens. These sensors convert the mechanical waves generated by the damage into acoustic waves. The acoustic signals are pre-amplified with a gain of 40 dB before acquisition on a PC running Noesis software. Acoustic signals were classified using a K-means method, enabling the acquired data to be partitioned into K groups. A maximum number of iterations of 1000 was used as an additional stopping criterion. The 5 most commonly accepted descriptors in the literature are used, namely amplitude (dB), rise time (µs), duration (µs), number of strokes and energy of acoustic signals (aJ). This method was applied to classify the signals into 5 classes associated with 5 damage mechanisms in sandwich structures, in order of severity : matrix cracking, fiber/matrix decohesion, core/skin decohesion, delamination and fiber breakage.

2.4. Damage and energy dissipation parameters of the sandwich structure

Using normal stress curves in the skin under tension and deflection under support, we were able to determine the evolution of quantities associated with the mechanical behavior of structures as a function of water aging time. As the behavior is non-linear, the evolution of the variables is analyzed as a function of the residual deflection after unloading.

2.4.1. Damage rate "d"

Damage is classically defined by the decrease in stiffness obtained during the unloads of a RPL test (Eq. 1).

$$d(f) = 1 - \frac{Z(f)}{Z_0} \quad \text{(Eq. 1)}$$

With :

- d(f) : damage rate
- Z(f) : specific unloading stiffness module (MPa/mm)
- f : permanent displacement (mm)
- Z_0 : modulus of initial specific rigidity (MPa/mm)

The specific stiffness modulus Z(f) is determined by calculating the slope at unload of the RPL loops of the normal stress curve in the skin in tension as a function of permanent deflection. The start of unload is assumed to be a linear elastic zone. The damage rate d(f) varies between 0, representing the initial state, and 1, representing complete failure of the sandwich structure at the end of the test.

2.4.2. Cumulative surface energy dissipated

During a bending test on a sandwich specimen, the foam core of the structure contributes to energy dissipation [16]. The dissipated cumulative surface energy, E_{diss}, quantifies this energy dissipation. This energy quantifies all dissipative phenomena such as plastic phenomena, viscoelastic deformations and the progression of damage. This energy is determine by calculation of the cumulative difference between the area under the loads and unloads (Eq. 2). This calculation allow to measure the structure's capacity to dissipate energy following the evolution of mechanical damage. This dissipation may be linked to elasto-plastic or visco-elastic phenomena, or to damage to the sandwich structure.

$$E_{diss} = E_{def} - E_{res} \quad \text{(Eq. 2)}$$

With :

- E_{diss} : cumulative surface energy dissipated (mJ/m^2)
- E_{def} : surface energy of deformation (mJ/m^2)
- E_{res} : surface energy restored (mJ/m^2)

3. Results and discussion

3.1. Hydric aging

After immersion in distilled water maintained at 20°C, regular monitoring of the mass of sandwich specimens shows that the time required to reach water saturation is 2500 hours (15 weeks) (Fig.2). To sum up, the immersion of sandwich structures in water first causes an absorption phenomenon through the diffusion of water in the pores of the foam and in the pores of the skin. The equilibrium is reached after 15 weeks and the maximal water weight content is 9 %.

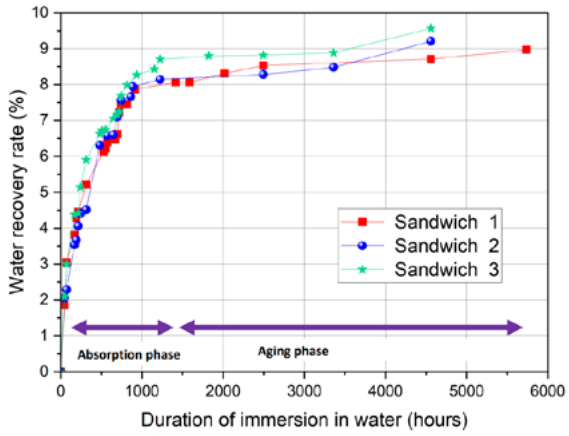


Fig. 2. – Water uptake curves for sandwich samples at 20°C

The sandwich specimens used to characterize flexural behaviour are immersed in seawater at 40°C to accelerate aging. According to the literature, the mineral salts present in seawater do not change the maximum water content, even if they modify absorption through accelerated diffusion by ions [17, 18]. Nevertheless, diffusion phenomena are accelerated by temperature [18, 19]. Consequently, the first sandwich structure characterization occurs after 16 weeks of immersion.

3.2. Study of dissipated energy and damage

The curves in Fig. 3 show the evolution of the cumulative dissipated surface energy of sandwich specimens under 4-point repeated progressive bending loading for aging periods ranging from 0 to 88 weeks. Firstly, the energy dissipation by the structure during the water absorption phase is studied, and secondly the study focuses on the aging phase from 16 to 88 weeks.
The study showed a 3-stage evolution. During the absorption phase (<16weeks), for all deflections, the aging causes a diminution of cumulative energy. In contrario, a aging time longer than 16 weeks tends to decrease the energy whatever the deflection. Between 60 and 88 weeks, a final major change is observed, with a significant increase in dissipated energy close to structural failure. Aging shows that under bending loads, dissipation close to sandwich failure accelerates.
The curves in Fig. 4 show the evolution of the damage rate of sandwich specimens under 4-point bending repeated progressive loading for aging periods ranging from 0 to 88 weeks. The study of the influence of water aging on the damage rate is divided into two parts. The first is carried out during the first 16 weeks, during which the immersed sandwich structure absorbs water, and the second is carried out between 16 and 88 weeks.
Over the first 16 weeks, the damage rate curves remained virtually unchanged. At the start of the test, damage to the sandwich structure increased significantly, with a permanent deflection, i.e. a rate of over 0.2. Damage continues to growth slower until the end of the test. Between 16 and 88 weeks of water aging, the damage rate curves also remain virtually unchanged. In short, water aging has few influence on the kinetics of damage evolution during the absorption phase and for longer aging periods.

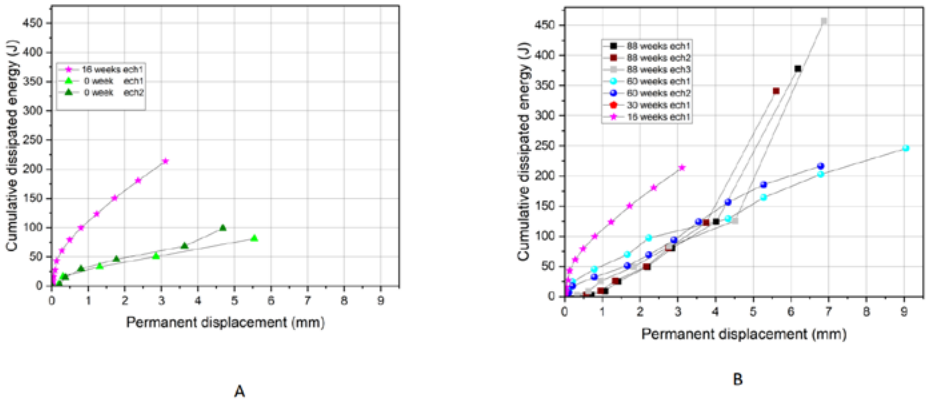


Fig. 3. – Evolution of cumulative dissipated energy during a RPL bending test of sandwich structures as a function of water aging. A : absorption phase, B : aging phase

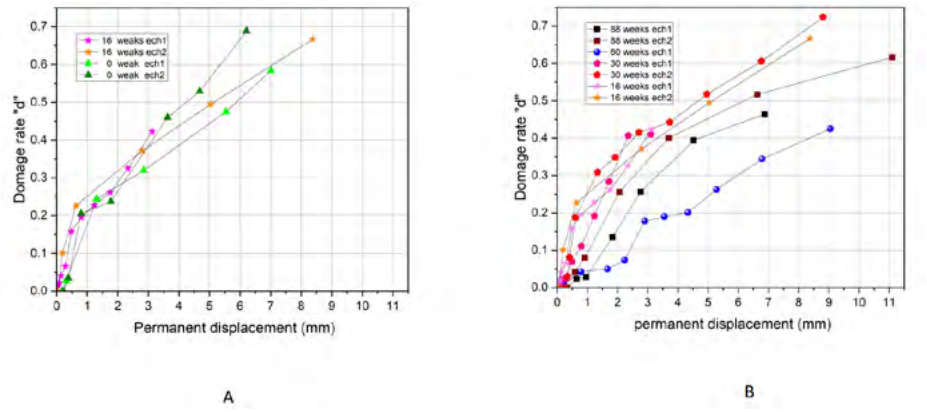


Fig. 4. – Evolution of the damage rate during a RPL bending test of sandwich structures as a function of water aging. A : absorption phase, B : aging phase

3.3. Damage monitoring by acoustic emission

The damage evolution is monitoring using acoustic wave emission during flexural tests. The 5 parameters previously mentioned, namely amplitude (dB), rise time (µs), duration (µs), number of hits and energy (aJ), were used by applying the unsupervised K-means classification method. Fig. 5 to Fig. 9 are average acoustic signatures of damage clusters associated with a type of damage. For each damage mechanism, the evolutions of the acoustic signatures are first observed during the water absorption phase (between 0 and 16 weeks) and during the aging phase from 16 to 88 weeks.

Polyester resin cracking and glass fiber breaks in composite skins are considered to be volume damage. Decohesion between glass fibers and polyester resin, decohesion between composite skins and foam core, and delamination are thus considered to be interfacial damage. The descriptor most affected is sound intensity. Observations are in line with those observed for dissipated energy.Two distinct phases are observed, with sound intensity increasing during the absorption phase (<16 weeks) then decreases until 88 weeks for all damage classes.



Fig. 5. – Evolution of acoustic signatures associated with polyester matrix cracking as a function of water ageing

Between 16 and 60 weeks, the intensity of the sound remains unchanged, but decreases sharply thereafter. Between 16 and 88 weeks of ageing, there is a small variation in wave energy, characterized by a slight increase with ageing (Fig. 5).

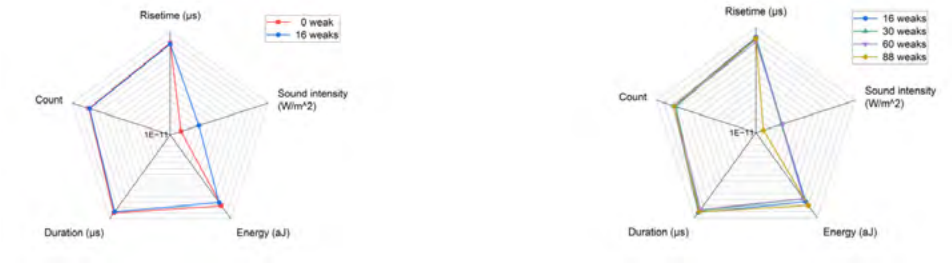


Fig. 6. – Evolution of acoustic signatures associated with decohesion between glass fibres and polyester matrix as a function of water ageing

During the aging phase up to 88 weeks, signal energy decreases slightly. Between 16 and 60 weeks, the intensity decreases slightly, and beyond that it decreases sharply. Between 16 and 88 weeks of aging, wave energy remains unchanged (Fig. 6).



Fig. 7. – Evolution of acoustic signatures associated with decohesion between glass/polyester UD skins and SAN foam core as a function of water ageing

During the aging phase up to 88 weeks, signal energy remains unchanged. Between 16 and 60 weeks, the intensity decreases progressively, and beyond that it decreases sharply. Between 16 and 88 weeks of aging, wave energy decreases slightly (Fig. 7).



Fig. 8. – Evolution of acoustic signatures associated with delamination in UD glass/polyester skins as a function of water ageing

During the aging phase up to 88 weeks, signal energy remains unchanged. Between 16 and 60 weeks, the intensity decreases progressively, and beyond that it decreases sharply. Between 16 and 88 weeks of aging, wave energy decreases slightly (Fig. 8).



Fig. 9. – Evolution of acoustic signatures associated with glass fiber breakage as a function of water aging

During the aging phase up to 88 weeks, signal energy remains unchanged. Between 16 and 60 weeks, the intensity of the sound remains unchanged, but decreases significantly thereafter. Between 16 and 88 weeks of aging, there is a small variation in burst energy, characterized by a slight increase with aging (Fig. 9).
During the absorption phase, continuous water absorption in the pores of the sandwich structure changes the acoustic impedance of structure, thereby modifying the propagation of acoustic waves resulting from mechanical damage. The sandwich structure itself

remains unaffected, which explains why, under 4-point bending loading, the damage propagation is low. This non-degradation of the sandwich structure at this stage of aging explains why the evolutions between surface and interface damages are the same. Between 16 and 88 weeks, the 9 % water weigth ratio content of the sandwich structure causes degradation at the interlaminar, intralaminar and skin-core interfaces. Water aging induces plasticization of the polyester matrix and hydrolysis of the polyester chains, leading to long-term depolymerization. Plasticization of the matrix is seen in the drop of its glass transition temperature T_G [17]. Experimental measurements of the evolution the value of T_G according aging time confirm this observation (not showing here).This embrittlement of the polyester resin accelerates the phenomena of decohesion between the glass fibers and the matrix, and interlaminar decohesion. Since glass fibers are inert, this explains why water aging has few influence on the development of glass fractures. Water absorption causes differential hygroscopic expansion between the glass/polyester composite skins and the foam core, which in turn causes differential swelling responsible for brittleness at these interfaces. As a result, water aging degrades the interfaces between skin and core. The embrittlement of all these interfaces is accompanied by a small increase in energy dissipation and a small increase in damage. The energy stored in the interfacial bonds once broken leads to an increase in the energy dissipated [20]. The hypothesis that the evolution of decohesions is guided by an energy criterion can be posed.

4. Summary

The aim was to study the influence of hydric aging on the behaviour and evolution of structural damage in sandwiches. The sandwich structure, which is representative of wind turbine blade structures on a laboratory scale, is made up of unidirectional laminated composite skins of glass fibers in an isophthalic polyester resin, and a rigid SAN (styrene acrylonitrile) polymer foam core. The sandwich structure was water-aged by immersion in seawater at 40°C. Through 4-point bending tests with monotonic loading and progressive repeated loading, damage parameters and dissipated energy were assessed. Acoustic emission is used to monitor the evolution of damage mechanisms. Water absoption test point out the water content equilibrium is reached after 15 weeks. Water aging increases energy dissipation during the absorption phase, with few change between 16 and 60 weeks, and a significant increase beyond 60 weeks. Experimental characterization shows a sudden increase of cumulative energy close to structure final failure. The kinetics of damage evolution remained unchanged throughout the hydric aging of the sandwich structure. Acoustic emission, using the non-overlapping K-means classification method, revealed the presence of 5 clusters of acoustic waves in the sandwich structure. These clusters are associated to the following damage mechanisms : matrix cracking, fiber/matrix decohesion, skin/shell decohesion, delamination and fiber breakage. No new damage mechanisms appear with water ageing, although variations in the waves parameters were observed. The descriptor most affected is sound intensity and, to a lesser extent, the energy of acoustic signals. During the absorption phase, there is a significant increase in sound intensity for all damage mechanisms. Between 16 and 60 weeks, for surface damage, i.e. polymer matrix cracking and glass fiber breakage, sound intensity remains unchanged. For interfacial damage, i.e. both types of decohesion and delamination, sound intensity decreases progressively. Acoustic signal energy either decreases slightly or remains unchanged for all damage mechanisms. Beyond 60 weeks, sound intensity decreases sharply for all types of damage, while waves energy either decreases slightly or remains unchanged.
The results show that the 88 weeks hydric aging of sandwich samples in 40°C seawater mainly degraded the interfaces of the structure. This degradation of the interfaces was accompanied by an increase in energy dissipation [20]. The causes of this interface degradation during water ageing can be multiple, such as plasticization and hydrolysis of the polyester matrix chains [17]. Differential swelling between the skins and the core due to differential expansion is at the root of decohesions between skins and core.

Acknowledgment

The authors acknowledge the financial of the French Agence Nationale de la Recherche LabEx EMC3 through the project COSPHI (Grant No. 10-LABX-0009), and the Normandy Region (Réseau d'Intérêt Normand - Label d'excellence).

©2024 | 3_BA_El Hadji Amadou_3UYWR.pdf:6

Références

[1] "Loi n°2015-992 titre v : Favoriser les énergies renouvelables pour diversifier nos énergies et valoriser les ressources de nos territoires," 2015.

[2] Agence De l'Environnement et de la Maîtrise de l'Energie, "L'énergie éolienne," 2016.

[3] K. Djama, *Comportement mécanique d'un panneau sandwich à peaux hybrides et à âme renforcée par des connecteurs en GFRP : étude expérimentale et numérique*. PhD thesis, Université de Lyon, Dec. 2019.

[4] A. Amrane, *Etude du comportement en flexion d'un panneau à fibres naturelles courtes*. PhD thesis, Normandie Université ; Université des Sciences et de la Technologie d'Oran Mohamed-Boudiaf (Algérie), June 2021.

[5] L. Mezeix, C. Bouvet, and D. Poquillon, "Matériaux élaborés à partir de fibres enchevêtrées pour une application coeur de structure sandwich = porous materials made with entangled fibers network for an application as core material for sandwich structures," in *JNC 16, Toulouse, France*, 2009.

[6] A. Mir, B. Bezzazi, R. Zitoune, and F. Collombet, "Caractérisation mécanique d'un panneau sandwich à âme en liège et peaux jute/époxy," in *JNC 17, Poitiers, France*, 2011.

[7] I. Ben Ammar, C. Karra, A. El Mahi, R. el Guerjouma, and M. Haddar, "Mechanical behavior and acoustic emission technique for detecting damage in sandwich structures," *Applied Acoustics*, vol. 86, p. 106–117, 12 2014.

[8] W. Harizi, J. Anjoul, V. Acosta Santamaría, Z. Aboura, and V. Briand, "Mechanical behavior of carbon-reinforced thermoplastic sandwich composites with several core types during three-point bending tests," *Composite Structures*, vol. 262, p. 113590, 01 2021.

[9] M. Ng, "A note on constrained k-means algorithms," *Pattern Recognition*, vol. 33, pp. 515–519, 03 2000.

[10] A. Likas, N. Vlassis, and J. Verbeek, "The global k-means clustering algorithm," *Pattern Recognition*, vol. 36, pp. 451–461, 08 2002.

[11] X. Tong, J. Zhang, L. Yao, B. Li, and S. Lv, "Cluster analysis of acoustic emission signals of 2d-c/sic under tensile loading," *Guti Lixue Xuebao/Acta Mechanica Solida Sinica*, vol. 35, pp. 109–114, 04 2014.

[12] O. Ismaili, V. Lemaire, and A. Cornuéjols, "Classification à base de clustering ou décrire et prédire simultanément," in *Treizièmes Rencontres des Jeunes Chercheurs en Intelligence Artificielle (RJCIA 2015), Rennes, France*, 2015.

[13] Huguet, "Use of acoustic emission to identify damage modes in glass fibre reinforced polyester," *Composites Science and Technology*, vol. 62, pp. 1433–1444, 08 2002.

[14] N. Godin, S. Huguet, R. Gaertner, and L. Salmon, "Clustering of acoustic emission signals collected during tensile tests on unidirectional glass/polyester composite using supervised and unsupervised classifiers," *NDT E International*, vol. 37, pp. 253–264, 06 2004.

[15] N. Osa-Uwagboe, A. Udu, V. Silberschmidt, K. Baxevanakis, and E. Demirci, "Damage assessment of glass-fibre-reinforced plastic structures under quasi-static indentation with acoustic emission," *Materials*, 07 2023.

[16] P. Lhuissier and L. Laszczyk, "Caractérisation des structures sandwich," *Techniques de l'ingénieur Étude et propriétés des métaux*, 2012.

[17] N. Tual, *Durability of carbon/epoxy composites for tidal turbine blade applications*. PhD thesis, Université de Bretagne occidentale - Brest, 2015.

[18] A. Le Guen-Geffroy, P. Davies, P. Y. Le Gac, and B. Habert, "Influence of seawater ageing on fracture of carbon fiber reinforced epoxy composites for ocean engineering," vol. 1, pp. 198–214, 09 2020.

[19] L. Le Gué, E. Savina, M. Arhant, P. Davies, N. Gayet, and B. Vincent, "Degradation mechanisms in pbsat nets immersed in seawater," *Polymer Degradation and Stability*, vol. 225, p. 110788, 04 2024.

[20] Y. Monerie, *Fissuration des matériaux composites : rôle de l'interface fibre/matrice*. PhD thesis, UNIVERSITE AIX-MARSEILLE II, 2000.

ON DESIGN AND OPTIMIZATION OF FLAX AND HYBRID COMPOSITE TUBULAR STRUCTURES SUBJECT TO AXIAL CRUSHING

M. Capretti[1], G. Del Bianco[1], V. Giammaria[1] , S. Boria[1] and V. Castorani[2]

[1]School of Science and Technology, Mathematics Division, University of Camerino
Via Madonna delle Carceri 9, Camerino, 62032, Italy
[2]HP Composites S.p.A., Department of Research & Development
Via del Lampo S.N., Z.Ind.le Campolungo, 63100 Ascoli Piceno, Italy

Email: monica.capretti@unicam.it, giulia.delbianco@unicam.it, valentina.giammaria@unicam.it, simonetta.boria@unicam.it, v.castorani@hpcomposites.it

Keywords: natural-fiber composites, hybrid composites, crashworthiness, energy absorption, tubular structures

Abstract
Natural fibers are pivotal in the development of green composites, offering lightweight and sustainable solutions. However, their mechanical performance often falls short of synthetic counterparts. The combination of natural and synthetic fibers in hybrids balances performance with environmental impact, resulting in improved sustainability and properties such as lightweight and crashworthiness. This study focuses on the crashworthiness of chamfer-triggered circular tubes made from flax/epoxy and hybrid carbon-flax/epoxy, highlighting the potential of natural fibers compared to carbon in energy-absorbing composite structures during axial crushing. The energy-absorbing capabilities of these composite tubes are investigated through both experimental and numerical methods. Performance results under quasi-static and dynamic loading conditions are compared. Starting from the mechanical characterization of composite materials, a finite element model of these structures is developed to simulate their crushing behavior using LS-DYNA. The numerical and experimental results are compared to validate the effectiveness of the designed models, showing a high consistency of results indicating good model predictability. Concurrently, an optimization procedure is conducted using LS-OPT to identify optimal material parameters to accurately predict experimental responses and damage mechanisms.

1. Introduction

The recent adoption of natural fiber composites (NFCs) as a sustainable alternative to synthetic ones has garnered significant attention from research and various industries, including the automotive sector [1]. This interest stems from their notable specific strength, energy absorption capability, and design flexibility, alongside their improved sustainability compared to conventional materials. The diminished environmental impact ensured by substituting synthetic fibers with natural ones yields benefits for pollution issues like waste reduction, landfill management, toxicity mitigation, and the reduction of greenhouse gas emissions. When evaluating their eco-friendliness it is crucial to consider the entire lifecycle from raw material extraction and fiber processing to textile and apparel manufacturing, distribution, consumer use, and end-of-life disposal. In this regard, the life cycle assessment (LCA) is essential to evaluate the products environmental impact across their entire life span, from raw materials extraction to end-of-life, providing insight into its environmental performance [2]. First, the extraction of raw materials for reinforcements of NFCs is simpler and more environmentally friendly than petroleum-based fibers. Moreover, natural fibers are biodegradable, being able to decompose naturally over time through biological processes. Despite the advantages of incorporating natural fibers, their exclusive application in high-performance composites is hindered by challenges, such as limited thermal stability, sensitivity to humidity, inferior durability compared to synthetic counterparts, along with

inadequate adhesion with different types of matrices due to their hydrophilic nature. All these aspects lead to a reduction in the final mechanical properties of the composite. To overcome these issues, researchers proposed several solutions like the hybridization of plant fibers with synthetics, the application of polymer coatings, and the use of advanced manufacturing techniques [3].
In the automotive industry, among natural reinforcements, bast fibers such as flax, hemp, jute, and kenaf are the most commonly used. Several prominent car manufacturers incorporate NFCs into body panels (door and window frames, columns, ceilings, seat backs, trunk liners, etc.) [4]. However, the use of purely reinforced natural fiber composites in structural applications, such as crash-boxes, side impact, and pillar structures, is still not entirely feasible and remains a future challenge due to poorer mechanical performance compared to synthetic. Therefore, the hybridization of natural and synthetic fibers is one of the most promising strategy to obtain improved mechanical properties, such as strength, stiffness, toughness, and impact resistance, while also offering other benefits such as reduced weight, cost-effectiveness, and environmental sustainability. Components designed to withstand axial or lateral crushing are commonly thin-walled structures, such as tubes, cones, truncated cones, square frusta, and grooved or un-grooved pyramids. Circular and square sections are the most common adopted for composites striking a balance between performance and ease of manufacturing [5]. The present study concentrates on investigating structures with circular cross-sections, considering both axial dynamic and quasi-static loading scenarios. Furthermore, a finite element (FE) modeling of these composites is designed to simulate the crushing behavior of tested samples through LS-DYNA [6]. Material properties are determined from experimental mechanical characterization. The aim is to establish a robust correlation between experimental and numerical results, validating the efficiency and predictability of models. In this regard, an optimization tool (LS-OPT) [7], is used to determine the best unknown parameters required by the material card, performing a surrogate-model (Kriging) based strategy, i.e., Efficient Global Optmization (EGO) [8].

2. Materials And Experimental Methods

The crashworthiness performance of circular tubes made from flax (F), carbon (C), and hybrid (H) reinforced toughened epoxy resin was evaluated under both quasi-static and dynamic conditions. The experiments aimed to investigate the behavior of tubular structures reinforced with flax fibers during axial crushing. The primary objective was to understand how composites containing flax fibers respond during crushing compared to tubes made exclusively with carbon reinforcements. This involved conducting quasi-static compression tests to assess the effectiveness of natural fibers in crashworthiness applications, studying their failure mechanisms and energy absorption capability, as well as comparing their performance under dynamic loading conditions.
Laminated tubes were produced by HP Composites SpA using a Prepreg composed of flax and carbon balanced woven fabric (weight distribution: 50% warp and 50% weft) with a toughened epoxy resin. They consist of five, six, and four layers for flax, carbon, and hybrid reinforcements (CF_2C and FC_2F), respectively. Different numbers of layers were used to achieve comparable wall thicknesses for flax and carbon fiber cases, as well as for the two hybrid configurations. Specifically, technical features of the used composites are detailed in Table 1.

Table 1. Features of material laminates for the used Prepregs.

Fiber	Grammage [g/m^2]	Resin Content	Average layer thickness [mm]
Flax	350	52 %	0.56
Carbon	384	38 %	0.45

The curing cycle was performed in autoclave at 135 °C for 90 min under 6 bar, with a vacuum bag on the components. A gradual thermal process was employed, characterized by low heating (3 °C/min) and cooling (4 °C/min) rates, ensuring a uniform temperature distribution aiming at preventing deformations of the specimens.
In particular, four material configurations of laminated circular tubes were investigated. Materials differ in reinforcement type, comprising flax, carbon, and hybrid fibers. In the hybrid case, the variation also encompasses different stacking sequences. For the dynamic experiments, each configuration included

two samples tested for each energy level, while three specimens were tested under quasi-static compression. The tubular specimens had a length (L) of 100 mm and an internal diameter (D) of 70 mm. Additionally, to initiate failure and thereby prevent catastrophic crushing, all tubular samples were triggered with a single 45° external chamfer (bevel) at the top, as outlined in Figure 1. Additional details on the geometry and stacking sequence of tubes are reported in Table 2.

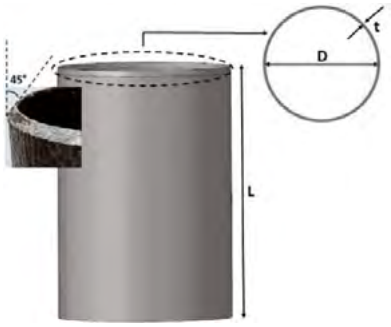


Figure 1. Geometry of tubes under axial crushing. L: length, D: internal diameter, t: thickness.

Table 2. Tested tubes under dynamic (D-) and static (S-) axial crushing. F: flax, C: carbon, H: hybrid. From H1 to H6, the reinforcement sequence is CF_2C, from H7 to H10 is FC_2F.

Specimens	Number of layers	Stacking sequence
D-F1, D-F2, D-F3, D-F4; S-F1, S-F2, S-F3	5	[0°/45°/0°/45°/0°]
D-C1, D-C2, D-C3, D-C4, D-C5, D-C6; S-C1, S-C2, S-C3	6	$[0°/45°/0°]_S$
D-H1, D-H2, D-H3, D-H4, D-H5, D-H6; S-H1, S-H2, S-H3	4	$[0°/45°]_S$
D-H7, D-H8, D-H9, D-H10; S-H7, S-H8, S-H9	4	$[0°/45°]_S$

2.1 Mechanical characterization

Firstly, PrePreg comprising flax and carbon woven fabric with a toughened epoxy resin were mechanically characterized through tensile and compression tests, using a Zwick Z100 electromechanical machine. The aim was to acquire input data for simulating composite structure behavior and validating the reliability of numerical material models. Tensile tests were conducted on 8-layers tabbed standard rectangular specimens following ASTM Standard D3039. These experiments, with the warp direction aligned either parallel (0°) or perpendicular (90°) to the test direction, provided data on modulus, ultimate strength, yield stress, and strain in both warp and weft directions. In contrast, in accordance with ASTM Standard D3518, samples with the fiber aligned at 45° to the test direction, determined shear properties of materials. Compression tests according to the ASTM Standard D6641 allowed to complete the mechanical characterization necessary to model the material card. The material properties of the carbon and flax composites, obtained from these tests, are reported in Table 3.

Table 3. Experimental tensile properties of carbon (C) and flax (F) laminates. E_T: tensile modulus; σ_T: tensile strength; ε_T: ultimate tensile strain; E_C: compression modulus; σ_T: compression strength; ε_C: ultimate compression strain; G: shear modulus; τ: shear strength; ε_T: ultimate shear strain.

	E_T [GPa]	σ_T [MPa]	ε_T	E_C [GPa]	σ_C [MPa]	ε_C	G [GPa]	τ [MPa]	ε_S
C	59.4±2.9	993±9	0.016	57.4±2.5	468 ±15	0.009	3.3±0.1	58	0.050
F	9.9±0.6	138±14	0.018	9.0 ±0.2	99±8	0.077	1.7± 0.1	40±1	0.085

2.2 Quasi-static axial crushing

The quasi-static axial crushing tests were conducted using a 200 kN dynamometer GALDABINI machine. The average test speed was 15 mm/min for a set maximum displacement of 80 mm. The load applied and the displacement over time of the cross-head were monitored and recorded using an automated data acquisition system. To prevent the sliding of samples, each one was constrained on the bottom end (10 mm length) during the test using a support fixture.

2.3 Dynamic axial crushing

The dynamic experimental tests were performed using a Drop Tower Machine (Instron 9450), equipped with a total mass of 59.128 kg. The recorded initial velocities were 5.82 m/s, 6.88 m/s, and 7.80 m/s, for impact energies of 1000 J, 1400 J, and 1800 J respectively. The maximum energy level is applied exclusively to carbon and hybrid tubes externally reinforced with carbon, as they are capable of withstanding higher loads compared to the others. The remaining tubes had already reached a displacement of half the tube length with the previous impact energy. Each sample was supported at the bottom end, as in the quasi-static scenario.

3.Crashworthiness

Crashworthiness of a component is defined as the ability of absorbing energy, typically converting kinetic energy mainly into internal one, during an impact event. The standard load-displacement response of a composite under axial crushing can be divided into: (1) the pre-crushing zone, extending from the origin to the peak load, (2) the crushing zone, defined by the average crush load, and (3) the post- crushing zone, representing compaction or failure. The crashworthiness performance of the tested tubes is evaluated here through parameters, that can be defined from the load-displacement curve.

- The peak load (P_{max}) is the maximum load, at least excluding a possible compaction zone.
- The total absorbed crush energy (AE) is the amount of energy absorbed during the impact event: $AE = \int_0^{\Delta x_{max}} P\, d\Delta x$, where Δx_{max} is the maximum displacement, and P represents the load.
- The specific absorbed energy (SEA) is the ratio of AE and the mass of crushed specimen (m), measured as $m=\rho\, A\, \Delta x_{max}$, where ρ is the material density, and A is the cross-sectional area: $SEA = \frac{AE}{m}$.
- The average crush load (P_{avg}) is the ratio of the absorbed energy (AE_{post}) in the crushing zone and the related displacement (Δx_{post}): $P_{avg} = \frac{AE_{post}}{\Delta x_{post}}$.
- The crush force efficiency (CFE) is the measure of variation of P_{avg} from P_{max}, $CFE = \frac{P_{avg}}{P_{max}}$.

The higher the SEA, the better the energy absorption capability. Conversely, it is important to limit the magnitude of P_{max} to minimize the deceleration experienced by the crushed structure. Specifically, a CFE value close to unity indicates a reduction in deceleration changes. This aspect is crucial in automotive applications for protecting vehicle passengers.

4. Numerical modeling

The Finite Element (FE) models (see Figure 2) created in Altair HyperMesh were simulated using the commercial solver LS-DYNA. The tube was modeled using two (for flax and hybrid) and three (for carbon) cylindrical shell layers. To define composite numerical model, the PART COMPOSITE card was used, so that the laminate thickness was defined by the sum of each individual layer. Two rigid walls were designed to model the plate load test and ground floor, respectively - one planar and the other rigid. To the moving rigid wall the same constant velocity was assigned as in the experimental test, as well as the mass in case of dynamic loading conditions. The specified boundary conditions required constraining nodes in the lower part of the tube, as in the physical test. This involved constraining translational degrees of freedom. The design of the single 45° external chamfer followed the scheme proposed in [9], as shown in Figure 2. Moreover, a wavy mesh was employed for the entire length of the tube (except for the short trigger zone), extending to the lower band constrained by the fixture, where a flat mesh is used. This mesh design characterized as a tailored approach to capture the experimental

trend aiming at reaching a greater load-displacement response stability. All elements were defined as fully integrated quadrilater shell elements (ELFORM=16).
The LS-DYNA material card MAT54/55 (MAT ENHANCED COMPOSITE DAMAGE) was used for modeling all composite materials. MAT54/55 is the most commonly used material model in crash simulations among those directly avaliable in LS-DYNA for describing composites.This model is specifically designed for orthotropic unidirectional fiber composite material, exhibiting linear behavior until fracture. On the other hand, due to the fewer parameters to be set compared to other more complex models, it is successfully used here to model flax/epoxy composites as well. This adopted simplified method should provide a reasonable compromise between accuracy and computational cost, especially when an optimization strategy must be performed. The CRIT material card parameter was set equal to 54, referring to in the failure criterion of the Chang-Chang model [10].
The CONTACT_AUTOMATIC SURFACE_TO_SURFACE TIE-BREAK (OPTION=8) was used to replicate the bonding between each pair of adjacent plies, considering both normal and shear forces on the interface surfaceAdditionally, to avoid the interpenetration of the inner and outer layers during the splaying, the CONTACT_SINGLE_SURFACE (OPTION=8) was implemented.

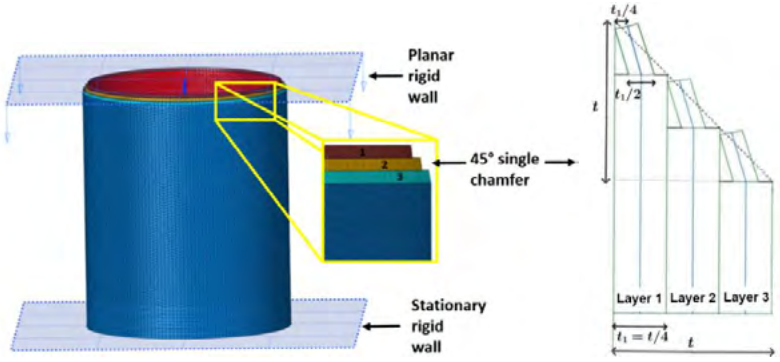


Figure 2. Shell finite element model for axial crushing of a 45° chamfered-tube (carbon fiber case).

5. Material card optimization

Most of the parameters of the material cards were experimentally determined (see Table 3). However, some of them require an optimization strategy for tuning to achieve an accurate reproduction of crushing behavior. A manual calibration process through a trial-and-error approach would be inefficient and finding a global optimum challenging. Hence, an EGO approach was pursued to precisely identify optimal material parameters for the considered composite materials. The parameters DFAILT and DFAILC, i.e., the maximum strain for fiber tension and compression respectively, and DFAILS, i.e., the maximum shear strain, were selected to be optimized, resulting as the most influential from a preliminary sensitivity analysis. The EGO algorithm based on Kriging model, as surrogate model, and expectation improvement (EI) criteria, as acquisition function. The LS-OPT software is used to perform the optimization procedure. It was performed in two steps, as shown in Figure 3.

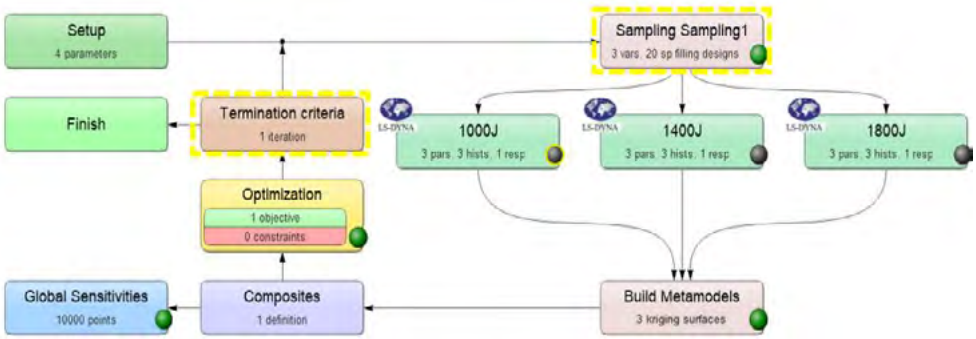


Figure 3. LS-OPT flowchart for the EGO strategy (1st step). The 2st step differs for yellow blocks.

The initial step consisted of a single iteration, which entailed sampling the design space to generate a set of training points for assessing the objective function. A space-filling design approach was used to locate 20 sample points within a four-dimensional search space, adhering to the following variables bounds: $0.01 \leq DFAILT \leq 0.15$, $-0.8 \leq DFAILC \leq 0$, $0.01 \leq DFAILS \leq 0.15$. The training data with the observed responses were then used by a Kriging model to predict the value of the objective function at each point of the search domain. Hence, the EI function was built over the same domain and its optimization provided the infill point to be evaluated through FEM simulation. Step 2 consists of 100 iterations, with one function evaluation per iteration. An infill point was added at each iteration and the best design is updated only if the simulated infill point had a better objective function value than the previous best design. In either case, the new data was used to update the Kriging approximation model. The infill procedure was repeated until it met the termination criterion [11].

6. Results and discussion

The stress-displacement curves from experimental tests are illustrated in Figure 4. Across all materials, a consistent trend emerged between quasi-static and dynamic responses, except for carbon fiber. Notably, carbon fiber exhibited strain-rate sensitivity [12], resulting in a higher loading capacity in the quasi-static scenario. Consequently, there was a 15% decrease in SEA compared to the quasi-static value, attributed to larger delaminations leading to folding observed in the dynamic tests. All tubular samples crushed in a progressive manner. In particular, they presented similar crushing modes, with the main energy absorption mechanisms given by splaying.

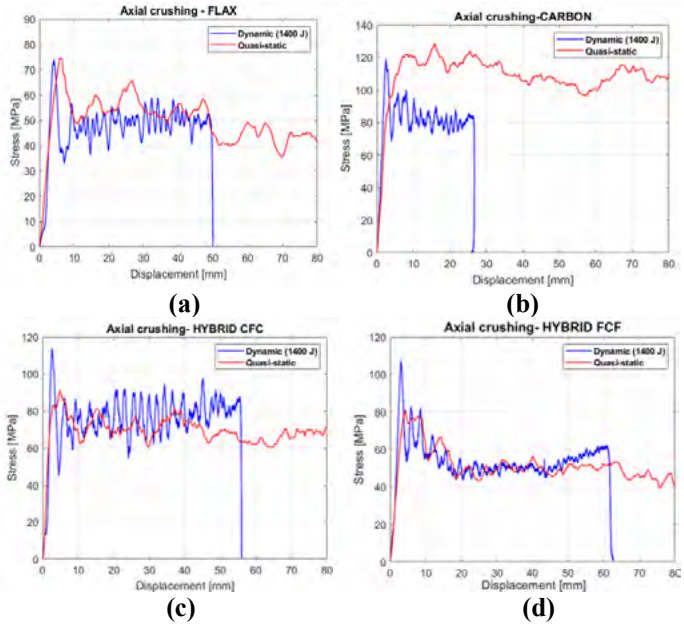
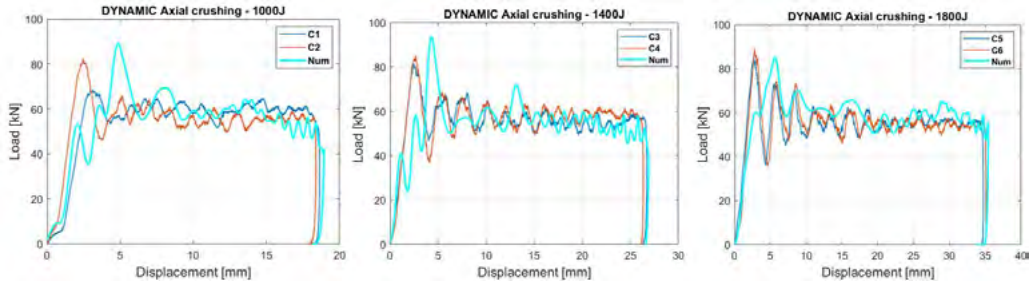


Figure 4. Comparison of stress-displacement curves of quasi-static (red) and dynamic (blue), at 1400 J, axial crushing tests: (a) flax, (b) carbon, hybrid (c) CFC, (d) FCF.

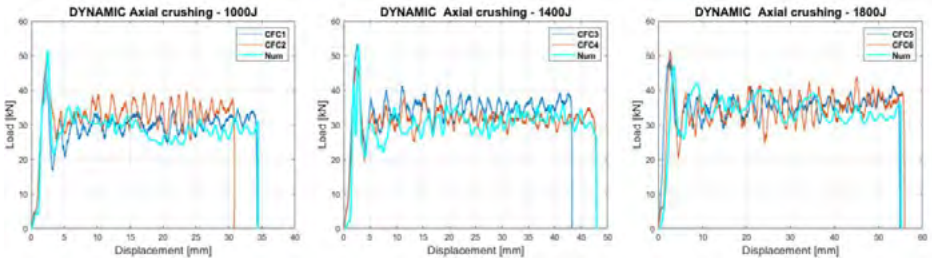
For the sake of brevity, numerical results only for dynamic tests are presented here and compared with the experimental outcomes to evaluate the accuracy of the designed models coupled with the optimization strategy. Load-displacement reponses from experiments and numerical outcomes are depicted in Figures 5-7.

From a quantitative point of view, SEA and CFE values were evaluated to analyze the energy absorption performance of structures and efficiency during crushing. Notably, numerical simulations exhibited SEA and CFE values that closely matched the experimental ones, as shown in Table 5. The designed FE models effectively captured the experimental trends and can thus be considered effective tools for predicting the behavior of composite materials under axial crushing.



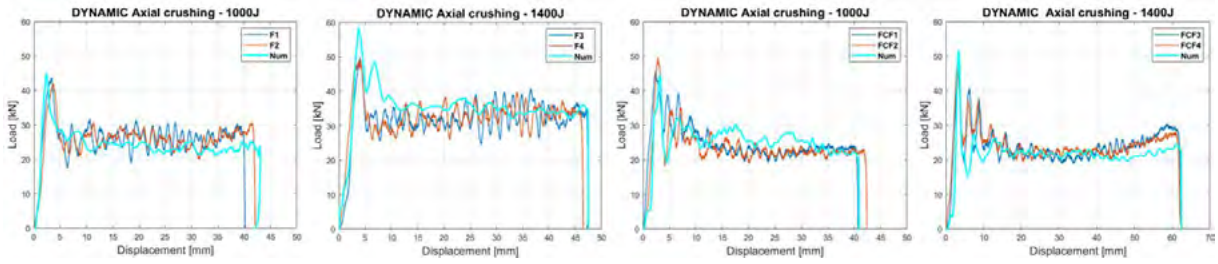
(a) **(b)** **(c)**

Figure 5. Experimental and numerical load-displacement curves of dynamic axial crushing: carbon samples impacted at (a) 1000 J, (b) 1400 J, and (c) 1800 J.



(a) **(b)** **(c)**

Figure 6. Experimental and numerical load-displacement curves of dynamic axial crushing: hybrid CFC samples impacted at (a) 1000 J, (b) 1400 J, and (c) 1800 J.



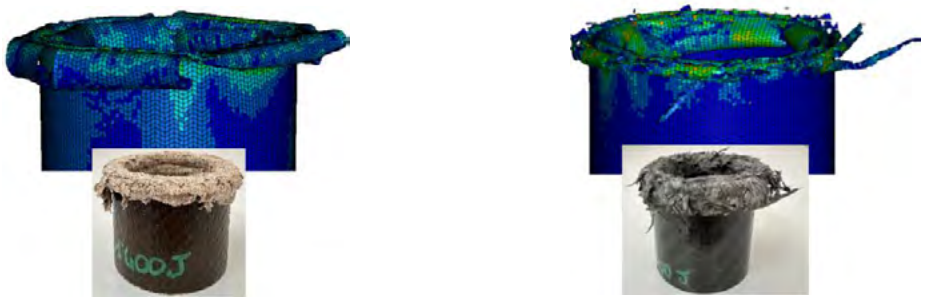
(a) **(b)** **(c)** **(d)**

Figure 7. Experimental and numerical load-displacement curves of dynamic axial crushing: flax samples impacted at (a) 1000 J, (b) 1400 J, and hybrid FCF at (c) 1000 J, (d) 1400 J.

Table 5. Comparison of numerical and experimental dynamic results.

	1000 J		1400 J		1800 J		
Fiber	**SEA [J/g]**	**CFE**	**SEA [J/g]**	**CFE**	**SEA [J/g]**	**CFE**	
Carbon	63.2	0.8	64.0	0.7	62.1	0.7	*Experimental*
	64.3	0.7	67.5	0.7	65.7	0.7	*Numerical*
Flax	32.7	0.6	38.0	0.7			*Experimental*
	30.8	0.6	36.5	0.6			*Numerical*
CFC	53.1	0.7	55.8	0.7	55.4	0.7	*Experimental*
	54.3	0.6	53.6	0.6	53.3	0.7	*Numerical*
FCF	40.1	0.5	39.7	0.5			*Experimental*
	40.9	0.5	35.7	0.4			*Numerical*

Moreover, numerical results demonstrated the ability of the designed models to replicate tube crushing behavior and associated damage mechanisms for both flax and carbon fiber, as illustrated in Figure 8. Specifically, the simulations successfully captured the splaying mode, reproducing the outward and inward splaying of composite fronds.



(a) (b)

Figure 8. Experimental and numerical damage progression of (a) flax and (b) carbon tubes impacted at 1400 J.

3. Conclusions

A comparative analysis of carbon, flax, FCF, and CFC tubes regarding their load-displacement responses and crashworthiness performance, evaluated in terms of SEA and CFE values, has been conducted from both experimental and numerical perspectives. It emerged that the two hybrid solutions perform better compared to the pure flax case, with CFC emerging as the superior configuration, exhibiting results closely aligned with carbon. Finally, the integration of numerical simulations with the EGO strategy enabled an accurate reproduction of the crushing behavior of tested samples, ensuring both qualitative and quantitative accuracy.

References

[1] M. Shuda, L. Drzal, R. Dipa, A. Mohanty, and M. Manjusri. Natural-fiber composites in the automotive sector. In *Properties and Performance of Natural-Fiber Composites.* Woodhead Publishing, Oxford UK, 2008.

[2] A.S. Ead, R. Appel, N. Alex, C. Ayranci, J.P. Carey. Life cycle analysis for green composites: A review of literature including considerations for local and global agricultural use. *Journal of Engineered Fibers and Fabrics.* 16, 2021.

[3] S. Owonubi, S. Agwuncha, C. Anusionwu, N. Revaprasadu, R. Sadiku. Improving the Mechanical Properties of Natural Fiber Composites for Structural and Biomedical Applications. In *Renewable and Sustainable Composites*. 2019.

[4] V. Naik, K.K Mohan and V. Kaup. A Review on Natural Fiber Composite Material in Automotive Applications. *Engineered Science*. 18: 1-10, 2021.

[5] M. Capretti, G. Del Bianco, V. Giammaria, S. Boria. Natural Fiber and Hybrid Composite Thin-Walled Structures for Automotive Crashworthiness: A Review. *Materials*, 17(10): 2246, 2024.

[6] LS-DYNA keyword user's manual. Material Models, r12 ed. *Livermore Software Technology*. 2020

[7] LS-Opt user manual. A design optimization and probabilistic analysis tool for the engineering analyst, Version 6.0. *Livermore Software Technology Corporation*. 2019.

[8] D.R. Jones, M. Schonlau, W.J. Welch. Efficient global optimization of expensive black-box funtions. *J Global Optim*. 13(4):455–92. 1998.

[9] J. Huang and X. Wang. Numerical and experimental investigations on the axial crushing response of composite tubes. *Composite Structures*, 91(2): 222-228, 2009.

[10] F.K. Chang and K.Y. Chang. A progressive damage model for laminated composites containing stress concentrations. *Journal of Composite Materials*, 21(9): 834-855, 1987.

[11] E. Raponi, M. Bujny, M. Olhofer, N. Aulig, S. Boria, and F. Duddeck. Kriging-assisted topology optimization of crash structures. *Comput Methods Appl Mech Engrg,* 348:730–52, 2019.

[12] S. Boria, G. Belingardi, and A. Scattina. Thermosetting and thermoplastic impact attenuator under axial loading. *Multiscale and Multidiscip. Model. Exp. and Des*. 2:129-139, 2019.

Mechanochromic hybrid composites for structural health monitoring

Mohammad Fotouhi[1], Ali Tabatabaeian[2], Philip Harrison[2] and Erik Schlangen[1]
[1]*Faculty of Civil Engineering and Geosciences, Delft University of Technology, Delft, The Netherlands*
[2] *School of Engineering, University of Glasgow, Glasgow, UK*

Corresponding author:
m.fotouhi-1@tudelft.nl Web Page: https://www.tudelft.nl/en/chairs0/material-health-monitoring

Keywords: Structural health monitoring, Mechanochromic, Hybrid Composites

Abstract
The present paper reports an overview of mechanochromic self-reporting thin-ply hybrid composite sensors, which are designed to visually indicate overload in structures. These sensors, made from combinations of high-strain and low-strain materials, change appearance earlier than the final fracture, providing a clear visual cue of damage like delamination or strain overload. They can be used for various applications, for example, overload monitoring, and to detect barely visible impact damage in composites.

1. Introduction

The development of mechanochromic composites for structural health monitoring (SHM) presents a novel and efficient approach to improving the safety and performance of various structures in industries like aerospace, civil, and automotive. These are based on self-reporting polymer composites which provide a light-weight sensor with an easy-to-read visual cue. These composites can sense their state of health, such as damage or deformation, through changes in colour or appearance, and do not require external data acquisition systems. They offer a user-friendly, cost-effective, and environmentally sustainable solution for SHM, with the potential for significant technological and economic benefits [1].
As summarised in figure 1, the mechanochromic composites are categorized into two primary groups: chemical-based and physical-based colors. Chemical-based colors involve the use of pigments or dyes that change color upon mechanical excitation, often through the rupture of micro-capsules or fibers containing dyes. These can be used in various composites and coatings for metals and concrete, providing a visible response to mechanical stimuli [2]. Physical-based colors, on the other hand, arise from the interaction of light with the material's structure, as seen in phenomena like the iridescent colors of butterfly wings or peacock feathers. These structural color materials can change color under different stimuli like electricity, heat, light, and strain, offering an eco-friendly alternative to traditional pigments and dyes [3].

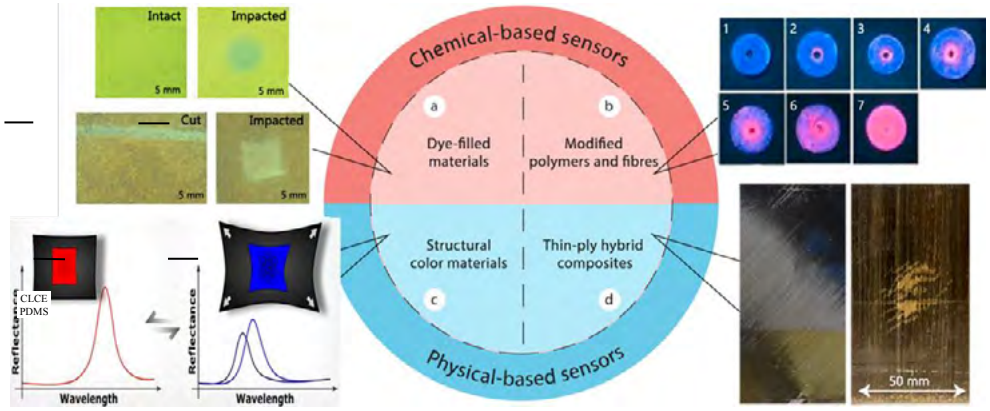


Figure 1. Examples of different mechanochromic approaches for SHM applications: a) characterisation of impact damage and cuts in polymer composites prepared with microcapsules [4], b) color changing process in composites under compression, increasing from left to right, indicating the fluorescent activation [5], c) a structural color patterns that are either always visible or reversibly revealed or concealed upon

mechanical deformation [6], d) comparison of the visual damage detection in a structure with (right) and without (left) hybrid composite sensors under the same impact loading condition [7].
The present paper reports a critical overview of mechanochromic self-reporting thin-ply hybrid composite sensors, which are designed to communicate visual information for SHM purposes. These sensors, made from combinations of high-strain and low-strain materials, change appearance earlier than the final fracture, providing a clear visual cue of damage like delamination or strain overload. They can be used for various applications, for example, overload monitoring [3], and to detect barely visible impact damage in composites [8].

2. Mechanochromism based on Glass/Carbon Hybridisation

Thin-ply hybrid composite sensors have been developed as an easly-implementable approach for visual indication of overload. These sensors are made using commercial prepregs and the sensing mechanism is activated via fracture. Different types of failure in a three-layer uni-directional hybrid laminate made from high-strain-material and low-strain-material are shown in figure 2. Damage and failure mechanisms lead to a visual indication of strain overload, where delamination is suppressed and several low strain fractures occur, followed by stable localised pull-out. This is achieved by choosing appropriate material properties, relative low-strain-material to high-strain-material thicknesses and absolute thickness of the low-strain-material [9].

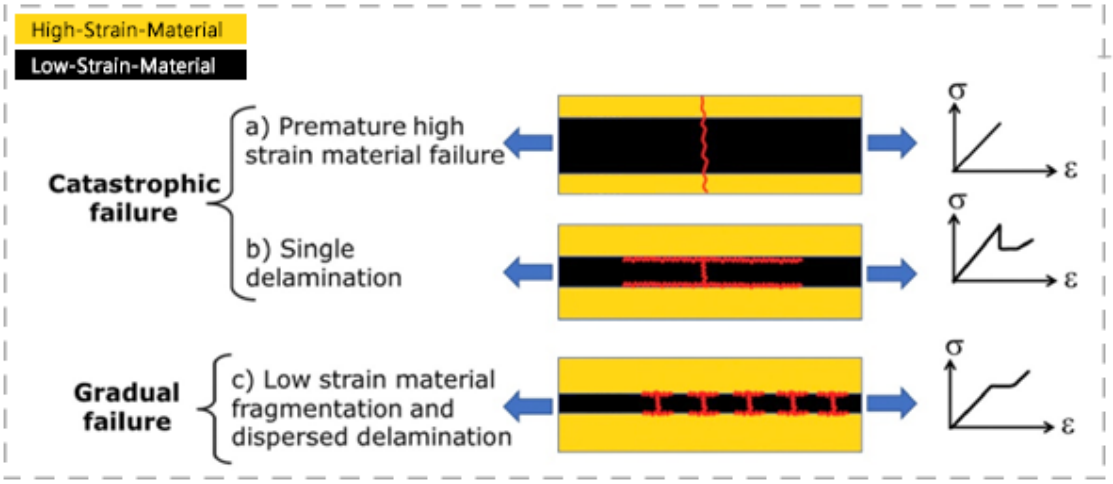


Figure 2. Different failure mechanisms in a three layer uni-directional hybrid composed of high-strain-material and low-strain-material (red lines indicate fracture) (a) single crack through the whole specimen, (b) single crack in the low-strain-material followed by instantaneous delamination, and (c) multiple fracture and localised stable pull-out of the low-strain-material [10]

Figure 3 shows two different designs of the uni-directional hybrid composite sensors, where the visual change is achieved by a purpose-designed, thin interlayer of glass/carbon-epoxy hybrid composite loaded by a predefined strain value. Light passes through the translucent glass layer and is absorbed by the intact carbon layer, creating a dark appearance. Figure 3(a) shows fragmentation of the low strain material followed by gradual, dispersed delamination [11]. The incident light is reflected from the locally damaged glass/carbon interface around the carbon layer fractures, creating light stripes. Figure 3(b) shows another type of failure in thicker carbon layers: a single fracture of the low-strain-material is followed by sudden delamination [12]. Both can act as good overload indicators since it is easy to visually monitor the delamination through the translucent glass layer.
Hybrid sensors can also be used for fatigue life monitoring, where an increase in the delamination area can be correlated to the number of cycles, as shown in Figure 4 [13].

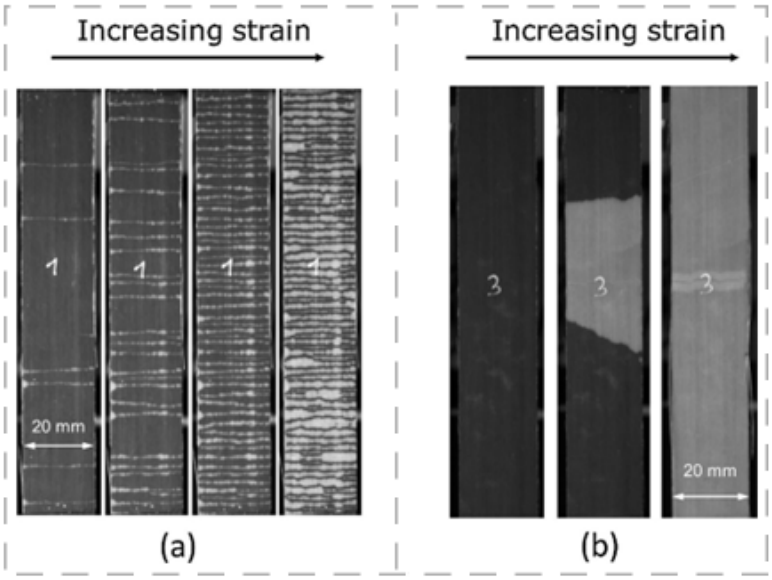


Figure 3. Visual indication of damage in thin-ply glass/carbon hybrids: (a) carbon layer fragmentation followed by stable, dispersed delamination [11], (b) carbon layer fracture followed by sudden delamination [12].

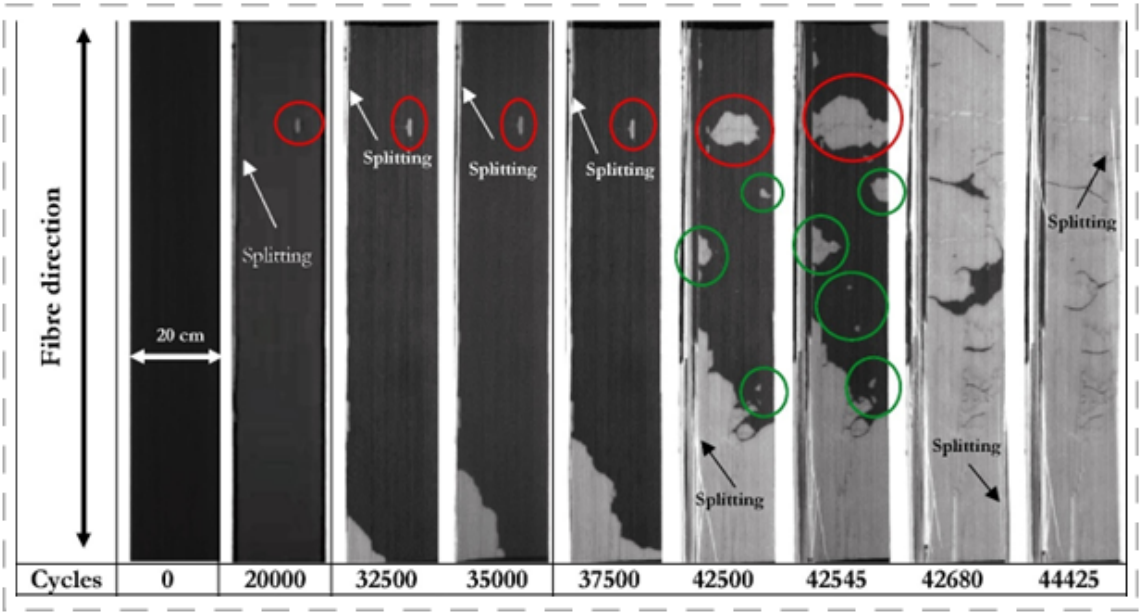


Figure 4. Fatigue life monitoring in a uni-directional thin-ply glass/carbon hybrid composite at 90% stress level of the carbon fragmentation initiation [13].

Multidirectional pseudo-ductile thin-ply hybrid laminates with improved ductility and notch insensitivity have also been developed [10,14]. These multidirectional laminates showed similar damage mechanisms to the uni-directional laminates but have the advantage of being able to monitor damage evolution, as the damage can be observed around the notches before any catastrophic failure occurs, as shown in Figure 5. Typically, hybrid composite sensors are either bonded directly onto the structures' surface or they are incorporated into the structure as a sensing layer (see Figure 6). By combining different sensing materials activated by different strains, they can provide a more detailed picture of the overload. Also, by designing an array of sensors orientated in different directions, the overload direction can be monitored. A sensor mounted on a component is subjected to the same strains as the material below. Carbon and glass layers serve as the 'sensing' and 'outermost' layers in this case.

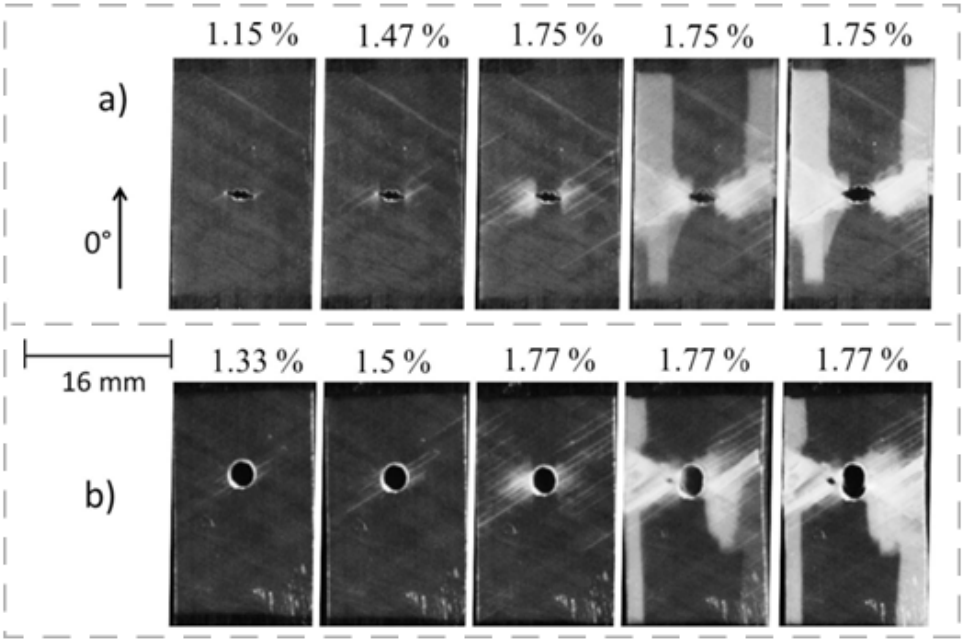


Figure 5. Visual indication of damage in (a) sharp notched and (b) open-hole ±60QI/Hexcel laminates, at different strains in tensile test [14].

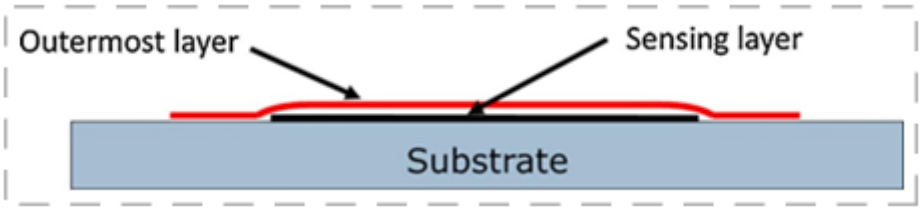


Figure 6. Schematic of a hybrid composite strain overload sensor attached to a substrate material [3].

Unlike other mechanochromic systems reviewed in previous sections the simplicity and practicality of glass/carbon hybrid sensors has led to their relatively rapid use in SHM. For example, a set of short and long sensors made of single ply XN80/EPOXY were applied on some commercially available CFRP bike handlebars, and both handlebar structures with and without sensors were tested under a three-point bending load. Figure 7 shows the force-displacement response of the tested structures, here the activation point for long sensors is between 1500 N and 2000 N. The graph also shows the load (1000 N) prescribed for testing Racing Bicycle handlebars according to the European Standard (EN14781) [15]. Results of this test suggested that sensors did not induce any noticeable increase in stiffness.

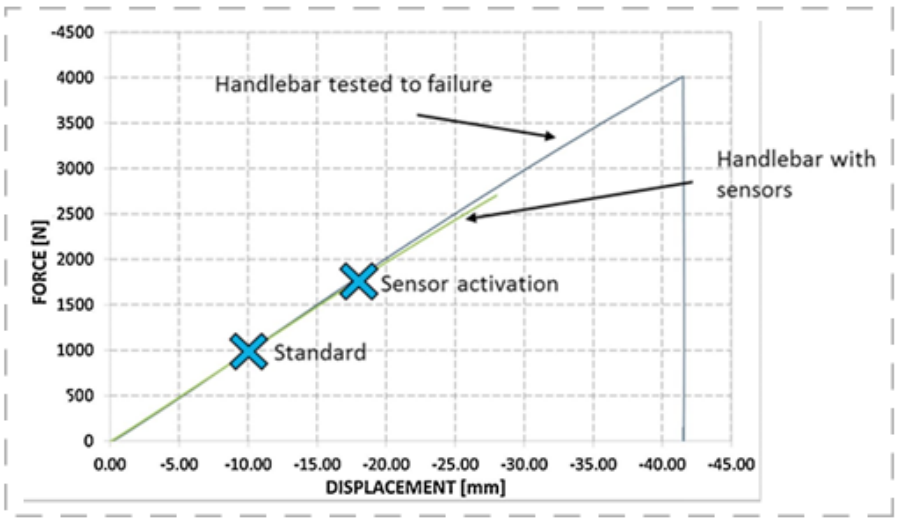


Figure 7. Force-displacement response of the tested CFRP bike handlebars [3].

Figure 8 illustrates a handlebar equipped with both short and long sensors. Here the first fracture of the long sensor was observed at 1750 N. The self-reporting concept could be successfully achieved by using long sensors, providing a warning to the user that a critical loading condition had occurred.

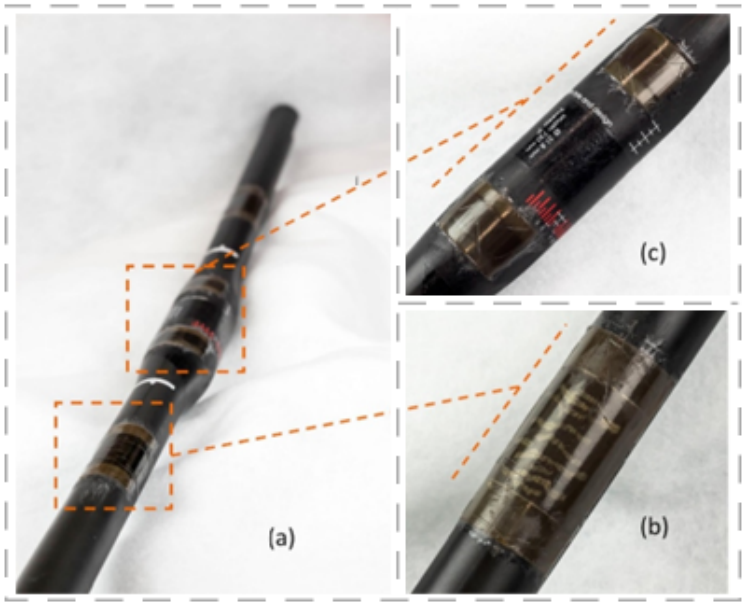


Figure 8. Bike handlebar eqipped with hybrid composite sensors: (a) MTB Racing flat handlebar, fitted with (b) long (c) short sensors [3].

A bonded composite patch is one method used to repair cracks in aluminium panels used in aerospace structures. However, in the case of standard repair techniques, damage beneath the repair patch cannot be detected by simple visual inspection alone. Therefore, hybrid composite sensors can be used as a composite repair patch which can self-report critical situations, e.g. an overload or crack extension in the substrate. As discussed earlier, these sensors are designed such that they do not change the local strain distribution. Nevertheless, in case of a repair patch, it is necessary to have enough stiffness so that the load in the substrate damaged area is reduced and carried instead by the patch. The practicality of the concept was investigated by applying a hybrid composite sensor on an aluminium panel with a 20mm initial crack length (see Figure 9).

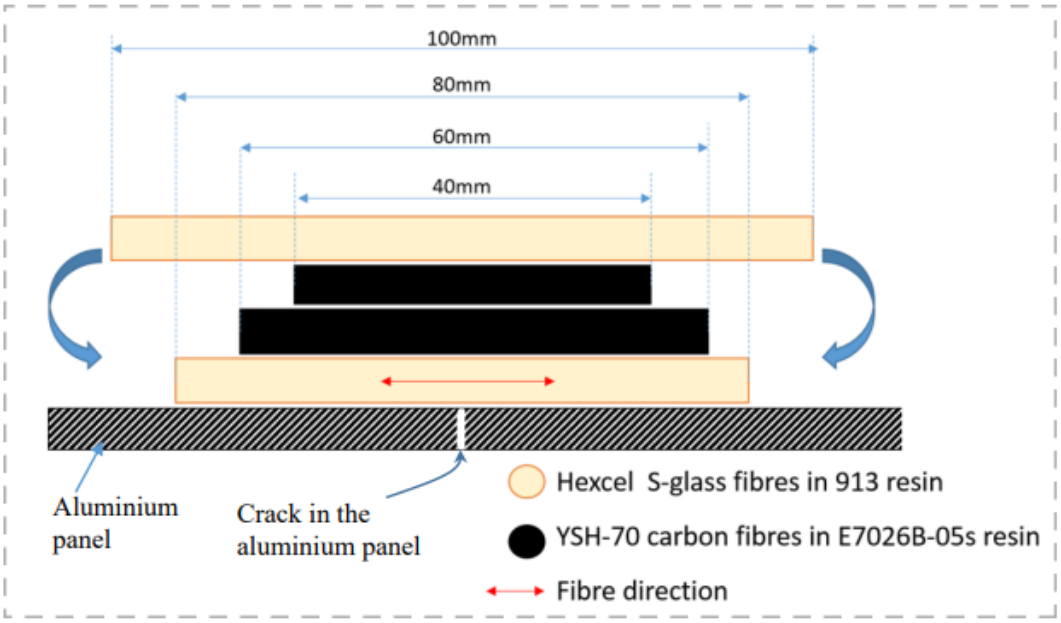


Figure 9. Schematic of hybrid composite repair patch [16].

During the quasi-static tensile test, changes in appearance were evident above the threshold load in the repaired specimen (see Figure 10). By overloading the specimen, crack propagation began beneath the repair patch. Figure 10 shows a change of appearance due to delamination, induced by fractured carbon at the centre of the specimen (above the crack), demonstrating the self-warning ability of the repair patch.

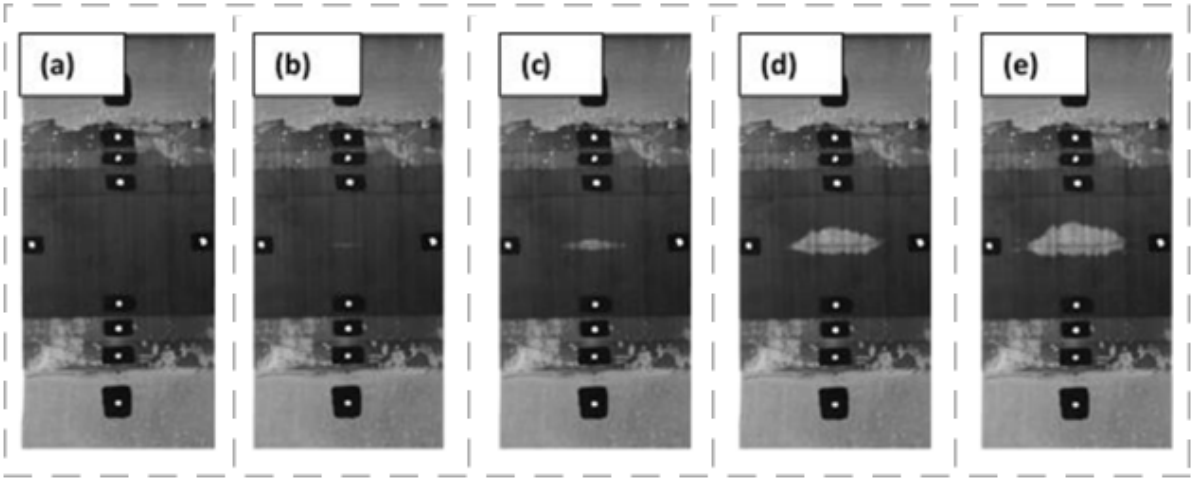


Figure 10. Self-reporting hybrid composite sensors subjected to increasing loads: (a) 195 MPa; (b) 197 MPa; (c) 304 MPa; (d) 336 MPa; (e) 340 MPa (99% failure load) [16].

A hybrid sensor was also used to detect BVID, which can have a noticeable influence on the mechanical performance of laminates, especially the compressive strength which may decrease by up to 60% compared with an undamaged laminate [17]. A hybrid composite layer composed of a unidirectional ultra-high modulus carbon (YS-90)/epoxy and a S-glass/epoxy material was used. It was applied to detect BVID in a quasi-isotropic $[45/0/90/-45]_{4S}$ laminate fabricated from unidirectional T800 carbon/MTM49-3 epoxy prepreg. Figure 11 shows an example of the impacted-face-, back-face and c-scans for samples subjected to a 12-Joule drop tower test. The c-scan reveals significant delamination damage for all samples, and the delamination size is slightly higher in the original sample compared to the sensor integrated sample. However, there is no change in the appearance of the original sample on either the front or back faces. In contrast, for the sample with the sensor, a visible colour change is observable on both faces. As discussed, these colour changes are due to damage induced in the hybrid sensors. The size of the visible damage area on the front face corresponds to the level of the impact energy.

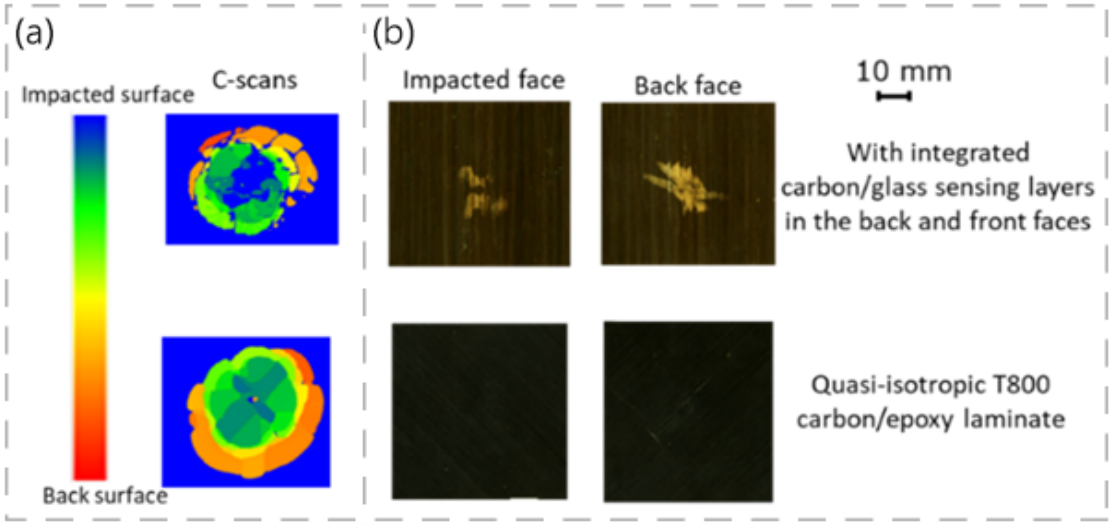


Figure 11. A carbon/epoxy composite (substrate) with integrated impact detector hybrid composite. a) Schematic 3D view, and b) impacted and back faces of specimens with (up) and without (bottom) sensors [18].

A hybrid composite composed of a layer of unidirectional S-glass/epoxy and another layer of unidirectional ultra-high modulus (UHM) carbon/epoxy was used for improving the performance of damaged concrete beams post-retrofitting, to showcase the practical use of mechanochromic composite for both strengthening and structural health monitoring purposes. As depicted in figure 12, when subjected to a strain beyond the strain to failure of the UHM carbon layer, the mechanochromic composite changes its appearance, indicating an overload of the structure.



Figure 12. Colour change in the composite of the retrofitted sample, showing the location and size of the developed underneath cracks [19].

3. Conclusions

The results demonstrated that mechanochromic composites serve as both reinforcement and passively activated, visually readable sensors. The dynamic color change phenomenon provides valuable insights into structural performance, acting as a passive indicator of stress accumulation and potential failure. These glass/carbon hybrid sensors are simple and easy to implement, making them attractive for use in SHM. Practical applications were discussed, including damage monitoring of a bike handlebar and repair of a damaged aluminum panel and a concrete beam. Currently, hybrid composite sensors are developed only for static overload sensing, are not reversible, and are limited to specific strain ranges due to the low strain of carbon fiber. They cannot be fabricated using conventional hand layup or liquid infusion methods because of the thin ply requirement of the sensing layer. Future studies should investigate the performance of purposely pre-damaged sensors in BVID detection to determine precise thresholds for different damage modes, such as delamination and fiber breakage. Additionally, hybrid composite sensors should be tested under various environmental conditions to develop high-performance, function-oriented sensors.

Acknowledgments

The authors acknowledge the funding provided by the UK Engineering and Physical Sciences Research Council (EPSRC) programme Grant EP/V009451/1 on Next generation of high-performance impact resistant composites with visibility of damage.

References

[1] Tabatabaeian, A., Liu, S., Harrison, P., Schlangen, E. and Fotouhi, M., 2022. A review on self-reporting mechanochromic composites: An emerging technology for structural health monitoring. Composites Part A: Applied Science and Manufacturing, 163, p.107236.

[2] Calvino, C., Neumann, L., Weder, C. and Schrettl, S., 2017. Approaches to polymeric mechanochromic materials. Journal of Polymer Science Part A: Polymer Chemistry, 55(4), pp.640-652.

[3] Rev, T., Jalalvand, M., Fuller, J., Wisnom, M.R. and Czél, G., 2019. A simple and robust approach for visual overload indication-UD thin-ply hybrid composite sensors. Composites Part A: Applied Science and Manufacturing, 121, pp.376-385.

[4] Calvino C, Henriet E, Muff LF, Schrettl S, Weder C, Calvino C, et al. Mechanochromic Polymers Based on Microencapsulated Solvatochromic Dyes. Macromol Rapid Commun 2020;41:1900654.

[5] Toivola R, Lai PN, Yang J, Jang SH, Jen AKY, Flinn BD. Mechanochromic fluorescence in epoxy as a detection method for barely visible impact damage in CFRP composites. Compos Sci Technol 2017;139:74–82. https://doi.org/10.1016/j.compscitech.2016.11.026.

[6] de Castro, L.D., Engels, T.A., Oliveira Jr, O.N. and Schenning, A.P., 2024. Sticky Multicolor Mechanochromic Labels. ACS Applied Materials & Interfaces, 16(11), pp.14144-14151.

[7] Tabatabaeian A, Fotouhi S, Harrison P, Fotouhi M. On the Optimal Design of Smart Composite Sensors for Impact Damage Detection. 20th Eur. Conf. Compos. Mater. (ECCM20), Lausanne, Switz., 2022.

[8] Fotouhi, S., Jalalvand, M., Wisnom, M.R. and Fotouhi, M., 2023. Smart hybrid composite sensor technology to enhance the detection of low energy impact damage in composite structures.

Composites Part A: Applied Science and Manufacturing, 172, p.107595.
[9] Jalalvand M, Czél G, Wisnom MR. Damage analysis of pseudo-ductile thin-ply UD hybrid composites - A new analytical method. Compos Part A Appl Sci Manuf 2015;69:83–93. https://doi.org/10.1016/j.compositesa.2014.11.006.
[10] Fotouhi M, Jalalvand M, Wisnom MR. High performance quasi-isotropic thin-ply carbon/glass hybrid composites with pseudo-ductile behaviour in all fibre orientations. Compos Sci Technol 2017;152:101–10.
[11] Czél G, Jalalvand M, Wisnom MR. Design and characterisation of advanced pseudo-ductile unidirectional thin-ply carbon/epoxy–glass/epoxy hybrid composites. Compos Struct 2016;143:362–70. https://doi.org/10.1016/J.COMPSTRUCT.2016.02.010.
[12] Czél G, Wisnom MR. Demonstration of pseudo-ductility in high performance glass/epoxy composites by hybridisation with thin-ply carbon prepreg. Compos Part A Appl Sci Manuf 2013;52:23–30.
[13] Suwarta P, Fotouhi M, Czél G, Longana M, Wisnom MR. Fatigue behaviour of pseudo-ductile unidirectional thin-ply carbon/epoxy-glass/epoxy hybrid composites. Compos Struct 2019;224:110996. https://doi.org/10.1016/j.compstruct.2019.110996.
[14] Fotouhi M, Jalalvand M, Wisnom MR. Notch insensitive orientation-dispersed pseudo-ductile thin-ply carbon/glass hybrid laminates. Compos Part A Appl Sci Manuf 2018;110:29–44. https://doi.org/10.1016/j.compositesa.2018.04.012.
[15] Wilson D. Bicycling science, 3rd edn, 2004.
[16] Jalalvand M, Wu HWML, Sheibanian F, Fotouhi M, Wisnom MR. Self-warning hybrid composite patches for repairing cracked aluminium panels. ECCM 2018 - 18th Eur. Conf. Compos. Mater., 2020, p. 24–8.
[17] Cantwell WJ, Morton J. The impact resistance of composite materials — a review. Composites 1991;22:347–62. https://doi.org/10.1016/0010-4361(91)90549-V.
[18] Fotouhi M, Pui W, Fotouhi S, Jalalvand M, Wisnom MR. Detection of Barely Visible Impact Damage Using a Smart Hybrid Composite Surface Layer. Twenty-Third Int. Conf. Compos. Mater., Belfast: 2021.
[19] Fathi A, Mohammadi R, Schlangen E, Fotouhi M, Flexural Performance of Damaged Concrete Prisms Retrofitted Using Mechanochromic Glass/Carbon Hybrid Composites, Concreep12 conference, June 5 –7, 20244.

THE EFFECTS OF AGEING TESTS ON THE FLEXURAL PERFORMANCE OF FLAX FIBRE COMPOSITES

Maria Morissa Lu[1,2] and Aart Willem van Vuure[1]

[1]Department of Materials Engineering (MTM), KU Leuven, Leuven, Belgium
Email: mdlu1@up.edu.ph, Web Page: https://des.uplb.edu.ph
[2]Department of Engineering Science (DES), University of the Philippines Los Baños (UPLB), Laguna, Philippines
Email: aartwillem.vanvuure@kuleuven.be, Web Page: https://www.mtm.kuleuven.be

Keywords: Flax fibre, Polymer-matrix composites, Moisture sorption, Durability

Abstract
This study investigates the changes in the transverse flexural properties of flax fibre composites induced by accelerated and natural ageing methods. The reductions in flexural strength and modulus of composites, ranging from 14% – 48% and 6% – 57%, respectively or even an increase in flexural properties after the cyclic ageing test, show the diverse effects of the tests on flax composites. Moreover, the water immersion test seems to be predictive of the long-term durability of flax composites in natural conditions. The simplicity of water immersion makes it a suitable method for evaluating the baseline durability of these materials in outdoor environments. Overall, the results suggest that uncoated flax composites can withstand extreme humidity changes, but perhaps not in applications wherein composites come in contact with liquid water for long periods.

1. Introduction

In natural fibre composites (NFCs), moisture exposure enables water sorption by the hydrophilic fibres, potentially disrupting fibre/matrix interfacial adhesion [1]. Moisture sorption of NFCs affects them by swelling of the reinforcing fibres, leading to a microcrack formation at the interface and thus compromising the mechanical properties of the composites [1–2]. The degradation of the fibre/matrix interface is a primary failure mode in NFCs following water ageing tests [3–4].

Several researchers have studied NFCs moisture durability through water immersion, cyclic exposure to high and low humidity environments and natural ageing tests. Despite extensive research on NFCs durability, there is still a lack of understanding on how these different test results relate to each other. There is a lack of comprehensive data concerning the ageing damage and degradation mechanisms suffered by NFCs subjected to the different ageing tests. Therefore, this study aims to compare the changes in flexural properties of flax fibre composites caused by accelerated and natural ageing methods and to determine each method's similarity with the other ageing protocols. It would help choose the best durability study to be used for NFCs.

2. Experimental procedure

Untreated unidirectional (UD) flax fibre (Flax Tape 200, Lineo) was used in this study. Before composite manufacturing, the fibres underwent conditioning at 80% relative humidity (RH), resulting in 10% moisture content, to assess the impacts of utilising non-dry fibres on the ageing behaviour of the composites. The matrices used were unsaturated polyester resin ((Synolite 1967-N-1, DSM), peroxide curing agent (Butanox M-50, Nouryon), inhibitor (NLC-10, Nouryon) and cobalt-free accelerator (Nouryact CF-32, Nouryon)) and epoxy resin ((Epikote 828 LV), hardener (Vestamin® IPD, Evonik)). The polyester matrix was prepared using 1 wt% curing agent, 1 wt% accelerator, and 0.6 wt% inhibitor. The epoxy matrix was formulated with a resin-to-hardener weight ratio of 100:23, according to the

manufacturer's specifications. The UD flax fibre-reinforced polyester and epoxy composite laminates with dimensions of 300 mm x 300 mm and a thickness of 2 mm were fabricated using a vacuum-assisted resin infusion technique. During the infusion process, a vacuum pressure of 0.6 bar was applied for both composites. The flax/polyester composites were cured at room temperature for 24 hours, followed by post-curing at 70°C for 12 hours in an oven. The flax/epoxy composites were cured at 70°C for 4 hours on a hot plate and post-cured at 150°C for 1 hour in a hot press under a pressure of 15 bar to prevent the evaporation of sorbed moisture from the non-dry fibres.

The moisture durability tests used in the study were long-term moisture cycling (CYC), water immersion (IMM), natural ageing under the shade (SHA) and natural ageing exposed to sunlight (NAT) tests (Figure 1). The long-term moisture cycling was performed over 40 weeks using 20 cycles of "wet-dry" conditions in an oven with potassium nitrate and potassium fluoride salt solutions. The wet/humid condition held the temperature at 40°C and used 89% RH. The dry condition maintained 40°C and 23% RH. The IMM test was conducted by immersing samples in distilled water at 20 ± 1°C for 30 days.

An outdoor ageing test was conducted in Leuven, Belgium, from September 2019 to June 2020. The test included a shaded ageing (SHA) component, where samples were kept shaded, and a natural ageing test (NAT) component, where samples were unshaded. The SHA and NAT used similar experimental setups, with the SHA test eliminating direct solar radiation effects for comparison to the NAT test and accelerated tests, which only examine temperature and moisture influences. This way, it was possible to evaluate the influences of solar radiation, temperature, and moisture, including water immersion, on the aged samples.

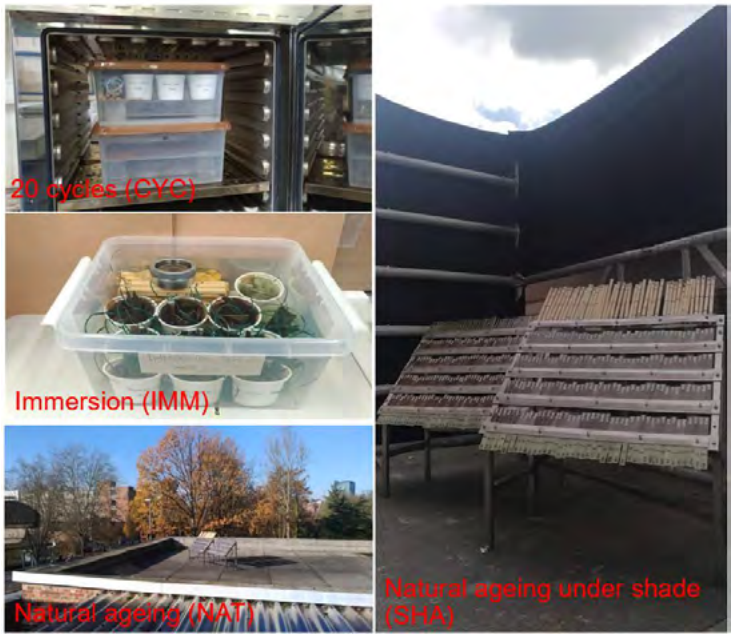


Figure 1. Ageing test setups: long-term moisture cycling (CYC), water immersion (IMM), natural ageing under the shade (SHA) and natural ageing exposed to sunlight (NAT), of uncoated samples.

3. Results

The transverse flexural properties of the composites after ageing tests are presented in Figure 2. Similar results were obtained for samples which were prepared with fibres that were dried before composite manufacture, albeit with lower mechanical properties, due to the initial damage resulting from fibre swelling [5]. Composites manufactured using non-dry fibres exhibited superior flexural performance compared to those made with dried fibres, a trend observed consistently across both flax/polyester and flax/epoxy composite systems. This enhancement in flexural properties can be attributed to the reduced swelling and shrinkage of composites reinforced with non-dry fibres during the different ageing tests.

©2024 | 3_LU_Maria Morissa_9XW3W.pdf:2

It is apparent that there are differences among the ageing tests for both the flexural strength and modulus of the composites. The IMM samples exhibited flexural properties similar to those of NAT-exposed samples. This suggests that the water immersion protocol, although accelerated, induced a degree of degradation representative of natural ageing exposure.

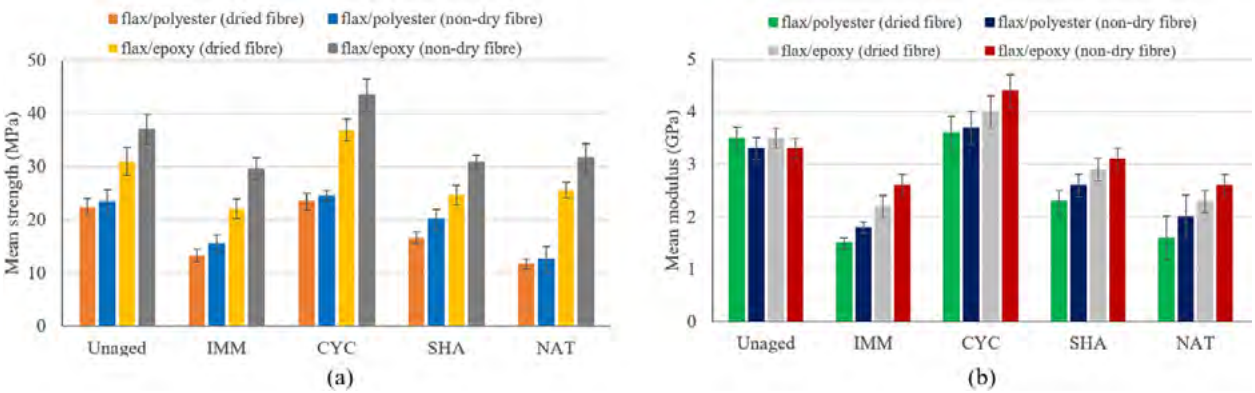


Figure 2. Transverse flexural properties of composites made of dried and non-dry fibres after the ageing tests: (a) mean flexural strength and (b) mean flexural modulus of composites.

Unexpectedly, as discussed in the literature [5], the CYC test did not reduce the transverse flexural properties of the composites after 20 cycles. Instead, the test increased both the mean strength and modulus, especially for flax/epoxy composites compared to unaged samples, likely due to some hornification mechanism in the fibres and/or post-curing of the resin. Because similar results were obtained for pre-cycled fibres, which were then converted into composite and tested for ageing, the main strengthening/stiffening effect seems to be within the fibres [5].

The transverse strength and modulus of SHA samples were similar to those of NAT samples, especially for flax/epoxy composites. Despite a 47% decrease in the strength of aged epoxy resin after NAT testing (Figure 3), exposure to solar radiation did not significantly reduce the transverse flexural properties of the composites.

The flax/epoxy composite exhibited higher transverse flexural strength across all ageing conditions compared to the flax/polyester composite. This can be attributed to the inherently higher strength of the neat epoxy resin versus the polyester resin, as shown in Figure 3. The epoxy matrix also likely formed a stronger interfacial bond with the flax fibres than for polyester. An increase in resin modulus was observed during the CYC, SHA, and NAT tests (see Figure 3), which could be explained by post-curing effects [6–7].

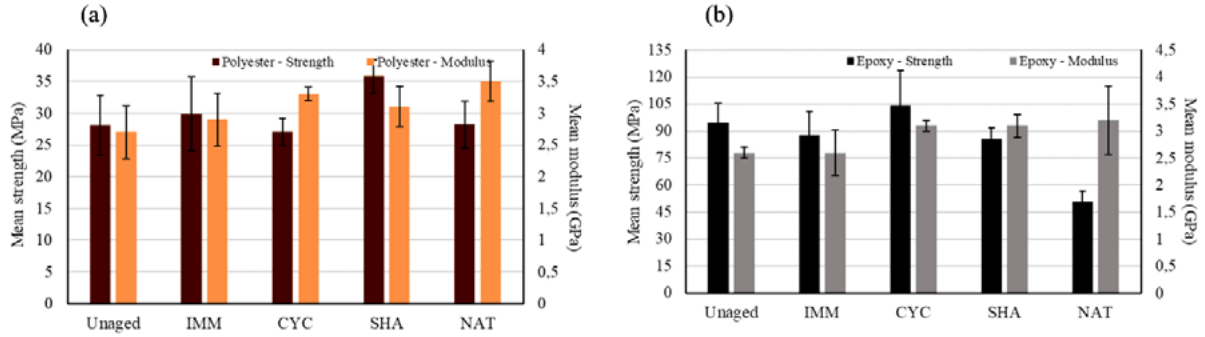


Figure 3. Flexural behaviour of reference materials after the different ageing tests: (a) neat polyester resin and (b) neat epoxy resin.

Visual observation revealed colour fading in aged composites (Figure 4). After 20 cycles, the CYC test produced only slight colour changes in all composites compared to SHA and NAT samples. After ten months of NAT testing, the flax/epoxy composites appeared darker yellow than the flax/polyester composites. This suggests that direct sunlight radiation during the NAT test caused colour changes to a dark yellow in the epoxy composites. In contrast, the ageing under the SHA test induces a light yellow colour for flax/epoxy composites. The yellowing of the composites during NAT testing correlates directly with the severe yellowing of the resins, especially the epoxy resin, as shown in Figure 4.

The significant colour change of the epoxy resin after the NAT test supports the decreased flexural strength observed for NAT-tested epoxy samples compared to those without direct sun exposure (SHA test). These results clearly demonstrate that solar radiation exposure causes reduced strength in the used epoxy resin.

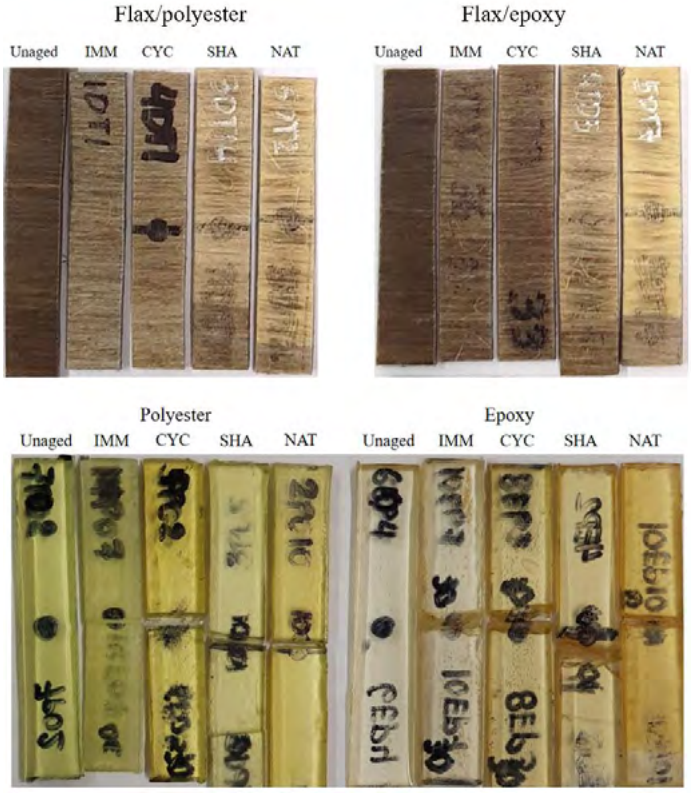


Figure 4. Comparison of the change in appearance of the composites and resins after the different ageing tests.

Figure 5 presents the SEM images showing the microstructure of unaged and aged composite samples. The images include aged flax/polyester and flax/epoxy samples from the IMM and NAT tests. SEM images of composites aged under the SHA test are not shown, as the surface microstructures were comparable to those resulting from the IMM and NAT tests. This similarity in the surface microstructure following IMM, SHA, and NAT testing aligns with the declining flexural properties exhibited across all three ageing methods, as presented in Figure 2.

The ageing tests revealed notable differences in the microstructure properties of the composites. As seen in Figure 5, the unaged samples of both composites displayed generally good fibre/matrix bonding. However, the two ageing methods, IMM and NAT, substantially increased the damage in the composites. The flax/polyester samples showed more extensive cracking and degradation than the flax/epoxy samples after both ageing tests. These microstructural defects accounted for the reductions

in flexural properties, with the flax/polyester composite exhibiting a sharper decline in flexural properties relative to the flax/epoxy composite. The greater susceptibility of the flax/polyester composite to ageing damage indicates inferior durability compared to the flax/epoxy composite under these testing conditions.

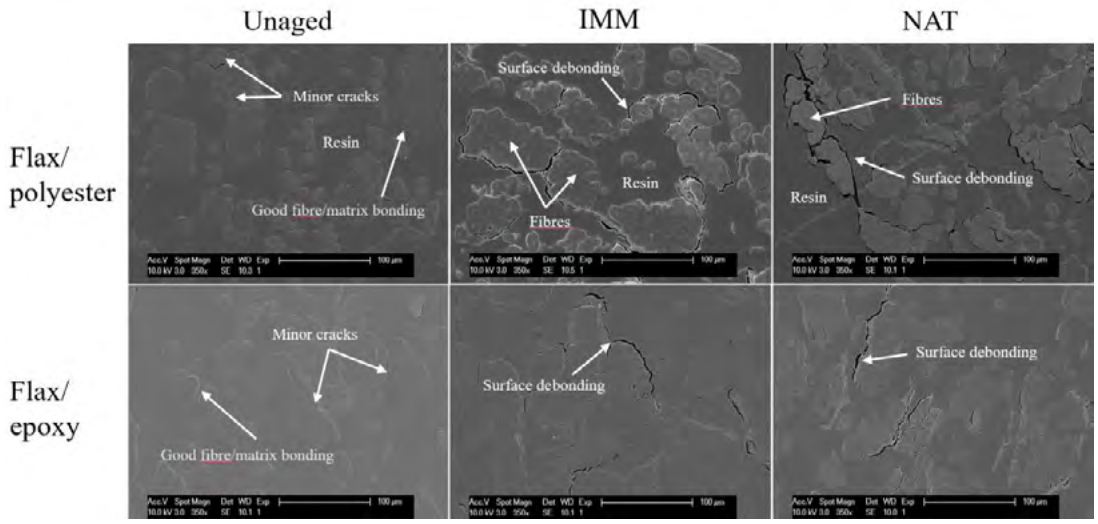


Figure 5. SEM images of flax/polyester and flax/epoxy composites' cross-sections before and after the immersion (IMM) and natural ageing (NAT) tests.

3. Conclusions

Across ageing methods, flax/epoxy composites outperformed flax/polyester, aligning with their superior starting mechanical properties. Microstructure analysis confirmed interfacial debonding as the key failure mode, arising from moisture-driven swelling differences between fibre and matrix. Overall, uncoated flax fibre composites demonstrate the potential to be used in environmental conditions even with extremely varying humidity values but are less suitable in applications wherein composites come in contact with liquid water for long periods. In the latter case, the use of water barrier coatings should certainly be considered.

The composite durability tests performed in this study offer insights toward optimising flax fibre composites for enhanced durability under long-term, real-world service conditions. The diverse effects of various ageing tests on the flax fibre composites highlight the importance of selecting appropriate testing protocols that suitably replicate application-specific exposure scenarios of composites.

The immersion test as accelerated test method, appeared to give the best prediction of real outdoor testing conditions for the uncoated samples. Cyclic moisture loading surprisingly lead to improved composite properties after 20 cycles of loading. This effect may be related to a "hornification" of the fibres and is currently topic of further research.

Acknowledgments

The authors would like to acknowledge the financial support of the EU-H2020 BBI project "SSUCHY" [grant number 744349]; and The University of the Philippines.

References

[1] Azwa ZN, Yousif BF, Manalo AC, Karunasena W. A review on the degradability of polymeric composites based on natural fibres. Mater Des 2013;47:424–442.

[2] Yan L, Chouw N, Jayaraman K. Flax fibre and its composites – A review. Compos Part B Eng 2014;56:296–317.

[3] Dhakal HN, Zhang ZY, Richardson MOW. Effect of water absorption on the mechanical properties of hemp fibre reinforced unsaturated polyester composites. Compos Sci Technol 2007;67: 1674–1683.

[4] Lu MM, Van Vuure AW. Effects of water immersion ageing on composites made of non-dry flax fibres. Mater Today: Proc 2020;31:S206–08.

[5] Lu MM, Van Vuure AW. Long-term moisture cycling performance and unexpected strengthening of non-dry flax fibre composites. Ind Crops Prod 2023;195:116486.

[6] Hunter-Alarcón RA, Vizán A, Peréz J, Leyrer J, Hidalgo P, Pavez B, da Silva LFM. Effect of the natural aging process on the shear strength of FRP composite single lap joints. Int J Adhes Adhes 2018;86:4–12.

[7] Marouani S, Curtil L, Hamelin P. Ageing of carbon/epoxy and carbon/vinylester composites used in the reinforcement and/or the repair of civil engineering structures. Compos Part B Eng 2012;43:2020–30.

MECHANICAL PROPERTIES OF CIPP: A COMPARATIVE ANALYSIS OF TEST METHODS, SPECIMEN GEOMETRY AND LINER MATERIALS

Ana Skender[1], Marina Frančić Smrkić[2] and Viktorija Ukalović[3]

[1]Faculty of Civil Engineering, Department of Engineering Mechanics, University of Zagreb, Fra Andrije Kačića Miošića 26, Zagreb, Croatia
Email: ana.skender@grad.unizg.hr, Web Page: https://www.grad.unizg.hr/en/ana.skender
[2]Faculty of Civil Engineering, Department of Engineering Mechanics, University of Zagreb, Fra Andrije Kačića Miošića 26, Zagreb, Croatia
Email: marina.francic.smrkic@grad.unizg.hr,
Web Page: https://www.grad.unizg.hr/en/marina.francic_smrkic
[3]Faculty of Civil Engineering, Department of Engineering Mechanics, University of Zagreb, Fra Andrije Kačića Miošića 26, Zagreb, Croatia
Email: vukalovic@student.grad.hr, Web Page: https://www.linkedin.com/in/viktorija-ukalović-ab28b62a6/

Keywords: Cured-In-Place Pipe (CIPP), tensile test, three-point bending test, ring stiffness test, modulus of elasticity

Abstract

This study focuses on the mechanical properties of installed cured-in-place pipe (CIPP) liners as determined by various tests. The experimental methods used include tensile tests on longitudinal specimens, three-point bending tests on hoop curved specimens and ring stiffness tests on whole pipe segments. The variability of the mechanical properties can be caused by defects, different strain rates during tests, anisotropic properties and specimen geometry. Finite element (FE) simulations of the three-point bending test on curved specimens and the ring stiffness test were performed in Abaqus to evaluate the influence of specimen geometry. The longitudinal, flexural and ring moduli of synthetic felt and GRP CIPP specimens cut from pipes with different nominal diameters and wall thicknesses were determined experimentally. There is good agreement between the experimental results and the theoretical relationships. Since the ring stiffness method is a simple method and the cut pipe segment is approximately the same as for curved specimens, the ring modulus can be considered a reliable parameter for hoop performance.

1. Introduction

The cured-in-place pipes (CIPP) have been used as a trenchless (“no dig”) rehabilitation method for water and sewer pipelines since the 1970’s. This technology is often used to address issues such as leaks, corrosion, and structural damage to concrete pipelines. A thermoset resin-saturated liner (flexible tube) is inserted into the damaged pipe by mechanical pulling or inversion. The liner is inflated to the inner surface of the pipe by air or water pressure and then cured by heat or ultraviolet (UV) light to obtain a hardened liner inside. The heat curing method is a traditional, low-cost curing method with a significant carbon footprint and energy consumption. The UV curing method, on the other hand, is characterized by fast curing, a lower carbon footprint and higher costs. The liner serves as a resin carrier and can be a synthetic fiber needle felt liner or GRP (glass reinforced polymer) liner. The fiber reinforcement reduces the thickness of the inner pipe and at the same time increases its mechanical properties. Resin systems mostly used are styrene-free Vinylester or styrenated Polyester. Laboratory tests are performed on specimens taken from full-length liners to verify that the installed liner fulfils the performance

requirements. The modulus of elasticity serves as an indicator of the load-bearing capability. To accurately characterize the mechanical performance of CIPP, various test methods are used, including tensile, three-point bending and ring stiffness tests [1] [2]. The expressions used to calculate the longitudinal, flexural and ring moduli are valid if linear elastic behavior and small deflections are assumed. Each test method includes a specific specimen geometry and test conditions such as strain rate. For example, the three-point bending tests can be performed on curved specimens cut in the circumferential (hoop) direction or on flat longitudinal specimens. Current quality control methods are predominantly based on hoop performance [3]. The apparent values of the flexural modulus determined on curved specimens are converted to the flexural modulus that would be obtained on an equivalent flat specimen using a theoretical correction factor. In practice, the modulus values obtained from different tests differ, although ideally they should be the same for a homogeneous, isotropic material. The variability of mechanical properties can be caused by common installation defects such as cracks and impregnation imperfections [4], different strain rates, anisotropic properties and specimen geometry [5]. In this study, the longitudinal, flexural and ring moduli of synthetic felt CIPP specimens cut from pipes with different nominal diameters and wall thicknesses were experimentally determined. The three-point bending tests were also carried out on GRP CIPP specimens. The specimens were not produced in the laboratory but were taken on site and represent realistic mechanical properties of installed CIPP. The resin system used was polyester and the reinforcement consisted of E-glass fibers. Finite element (FE) simulations of the three-point bending test on curved specimens and the ring stiffness test were performed in Abaqus to evaluate the influence of the specimen geometry. The aim of this study is to provide an understanding of the mechanical properties of CIPP as determined by various tests related to the effects of specimen geometry, test conditions and liner material.

2. Experimental setup, procedure and data

2.1. Tensile test

The tensile tests were performed on parallel-sided specimens cut in the longitudinal direction of the pipe in accordance with EN 1393 [6]. The tests were carried out in the tensile zone of the Zwick/Roell universal static machine using an extensometer (Figure 1, left). The speed of the tests was 5 mm/min. Eight series of synthetic felt CIPP specimens were prepared from pipes with different nominal diameters (d_n) and wall thicknesses (h). The composite thickness is then determined by subtracting the known thickness of the membrane layer ($e_1 = 0.5$ mm). The length and width of the specimens were $l = 300$ mm and $b = 25$ mm respectively. The gauge length was set at $l_G = 100$ mm. The number of specimens in each series was five. The average values of the measured dimensions of the width b and the composite thickness $e_{c,m}$ were used to determine the tensile stresses and strains. The modulus of elasticity was determined as the slope of the stress/strain curve (Figure 1, right) in the strain interval between $\varepsilon_1 = 0.05\%$ and $\varepsilon_2 = 0.25\%$.

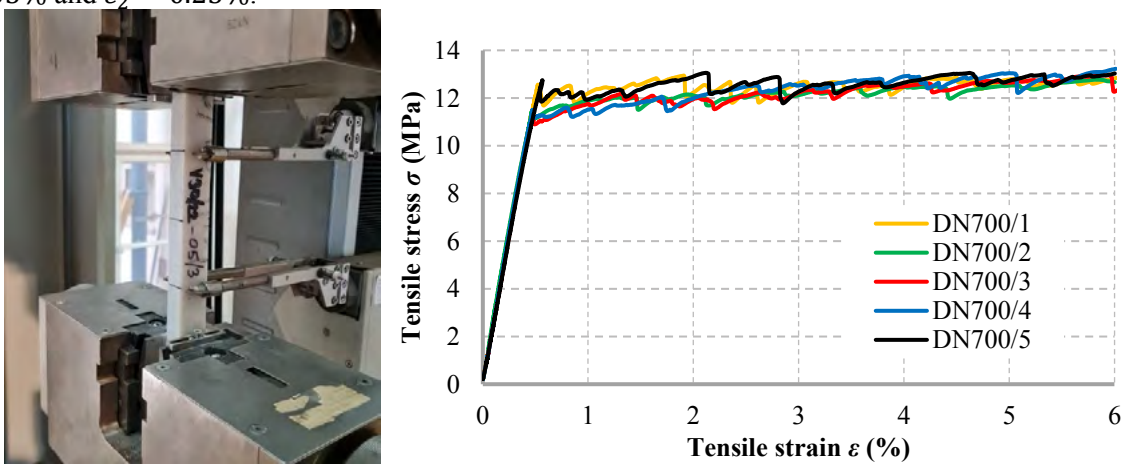


Figure 1. Tensile test on CIPP specimen (DN700/15): test setup (left) and stress/strain curves (right)

2.2. Three-point bending test

The three-point bending tests were performed on curved specimens (Figure 2, left) in accordance with EN ISO 178 [7] and EN ISO 11296–4 [8]. The tests were carried out in the compression zone of the Zwick/Roell universal static machine. An HBM LVDT WA 50 mm was used to measure the displacement in the middle of the span. The speed of the tests was 10 mm/min. Eight series of CIPP specimens made of synthetic felt were cut from the circumferential direction of pipes with the same nominal diameters and wall thicknesses as in the tensile tests. The specimens were taken from the same locations as the specimens for the tensile tests. The same synthetic felt liner material was used for the bending and tensile specimens. The number of specimens in each series was five.

The nominal distance L between supports was set at 16 times the composite thickness $e_{c,m}$ to minimize the influence of shear strain on deflection (less than 1.2 %). L_2 is the true span of the curved specimen and R_2 is the radius of curvature of the specimen calculated at the mid-thickness of the composite. The width b of the curved specimens is generally set at 50 mm. The total chord length of the specimen L_3 is equal to 20 times the total thickness. Both supports and the loading edge have a cylindrical shape with a radius of 5 mm.

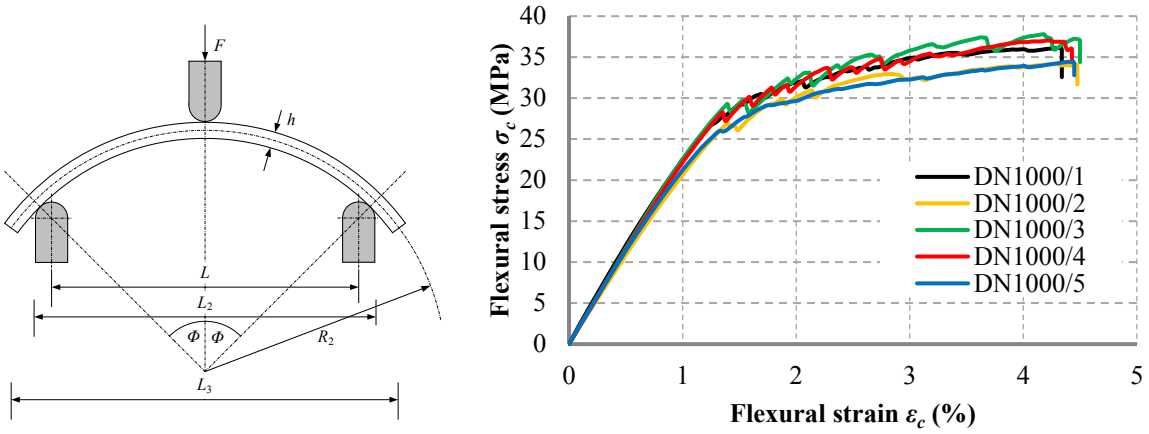


Figure 2. Three-point bending test setup for curved specimens (left) and stress/strain curve for DN1000/21 (right).

For the range of typical values of the diameter to thickness ratio for CIPP from 40 to 80 [5], the apparent flexural stress σ_c and strain ε_c are calculated as for flat specimens as follows

$$\sigma_c = \frac{3FL_2}{2be_{c,m}^2} \tag{1}$$

$$\varepsilon_c = \frac{6se_{c,m}}{L_2^2}. \tag{2}$$

F is the applied force and s is the deflection in the middle of the span. The apparent flexural modulus E_c is determined as the slope of the flexural stress/strain curve (Figure 2, right) in the strain interval between $\varepsilon_1 = 0.05\%$ and $\varepsilon_2 = 0.25\%$.

In 1998, a correction factor C_E was introduced by Niemann that corrects the apparent modulus obtained from a curved specimen E_c and gives the apparent modulus obtained from an equivalent flat specimen E_f. This factor can be found in the standard in the following form [8]

$$C_E = \frac{E_c}{E_f} = \frac{(L_2/d_m)^3 \cos^2 \phi}{1{,}5[\phi - (L_2/d_m)\cos \phi]}. \quad (3)$$

The mean pipe diameter is equal to $d_m = 2R_2$. The half angle ϕ, as defined in Figure 2 (left) and calculated from the formula $\sin \phi = L_2/d_m$, should not exceed 45° according to the standard. This corresponds to an upper limit for the true span to mean diameter ratio L_2/d_m of 0.71 and an underestimated value of the modulus before correction for curvature $E_c = 0.41E_f$.
A correction factor C_σ that corrects the apparent stress obtained from a curved specimen σ_c to the equivalent for a flat specimen, σ_f is given in the following form

$$C_\sigma = \frac{\sigma_c}{\sigma_f} = \left[1 + \frac{e_{c,m}}{3d_m}\right] / \cos \phi. \quad (4)$$

A further five series of curved GRP CIPP specimens were also tested in a three-point bending test. As the liner material is reinforced with glass fibers, the wall thicknesses are reduced compared to synthetic felt CIPP. The influence of curvature is less pronounced, as the values of the mean diameter to composite thickness ratio $d_m/e_{c,m}$ are closer to and above 100 and the values of the half angle ϕ are up to 10°.

2.3. Ring stiffness test

The initial specific ring stiffness of CIPP was determined in accordance with EN 1228 [9] using the same Zwick/Roell machine. A pipe segment of 300 mm length (L) is compressed over its entire length to achieve a change in mean diameter of 3% (Figure 3, left). The load was applied under displacement control so that a change in the mean diameter of 3% is reached in 60 seconds. The test is carried out two more times on the same specimen, which is rotated by 60° (a, b and c). The specimen must be allowed to recover between the individual tests. The ring stiffness is calculated using the following expression

$$S = \left(0.0186 + 0.025\frac{y}{d_m}\right) \cdot \frac{F}{L \cdot y}. \quad (5)$$

F is the applied force and y is the deflection of the pipe. The average of the three values represents the initial specific ring stiffness of the specimen. The force/deflection curve for a synthetic felt CIPP specimen DN300-1/6 is shown in Figure 3 (right). Two pipe segments with the same diameter and thickness were taken from the same location and tested for ring stiffness. A pipe segment with the same nominal diameter and thickness was taken from the same location, cut into five curved specimens and tested in a three-point bending test.

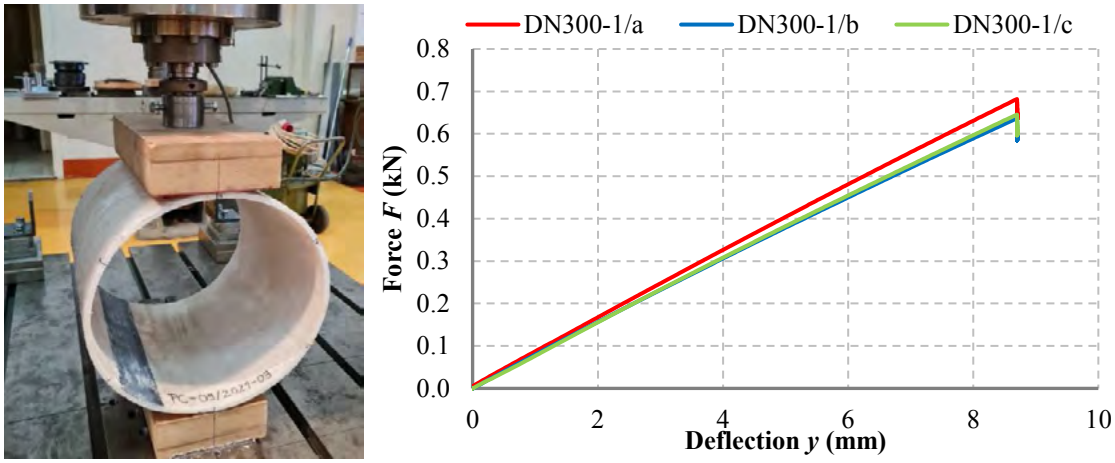


Figure 3. Test setup (left) and force/deflection curve (right) in the ring stiffness test.

The apparent modulus of elasticity can also be calculated based on the initial ring stiffness as follows

$$E_r = \frac{S \cdot d_m^3}{I} = \frac{12 \cdot S \cdot d_m^3}{e^3}. \quad (6)$$

3. Finite element analysis

Finite element (FE) simulations of the three-point bending test on curved specimens and the ring stiffness test were performed to compare different test methods for determining the modulus of elasticity of CIPP specimens. The analytical expressions (Eqs. 1, 2 and 6) used in both methods to calculate the modulus of elasticity are valid if an isotropic linear elastic material is assumed. Therefore, the synthetic felt CIPP material was modelled in FE models as an isotropic, linear elastic material with $E = 2500$ MPa and $\nu = 0.25$. The aim was to evaluate the influence of the specimen geometry.
Two different pipe segments (DN200 and DN1000) were modeled considering a typical span-to-diameter ratio of synthetic felt CIPP specimens in practice. The dimensions of the curved segments and the distances between the supports are given in Table 1. The FE simulations of the ring stiffness test were carried out for pipes with the same diameters and wall thicknesses from Table 1 and a length of 300 mm.

Table 1. Geometry of the curved segments in a three-point bending simulation.

Pipe segment	b (mm)	h (mm)	R_2 (mm)	L (mm)	L_2 (mm)	L_2/d_m	$C_E = \frac{E_c}{E_f}$
DN200	15	5.9	97.0	90.3	98.4	0.51	0.68
DN1000	50	21	490	329.2	340	0.35	0.84

Numerical models were created using Abaqus/Standard. The CIPP segments were meshed with 8-node linear bricks labeled C3D8R. All other instances apart from CIPP were modelled as analytical rigid surfaces in all simulations. The contact between the supports and the curved instance was modelled as frictionless. Due to the symmetry, the ring stiffness simulations were performed using one eighth of the pipe. In the simulations of the three-point bending test, the supports were fixed and a displacement was defined at the loading nose. In the simulations of the ring stiffness test, a displacement was defined on the upper plate. The numerical models of the three-point bending test and the ring stiffness test are shown in Figures 4 and 5.

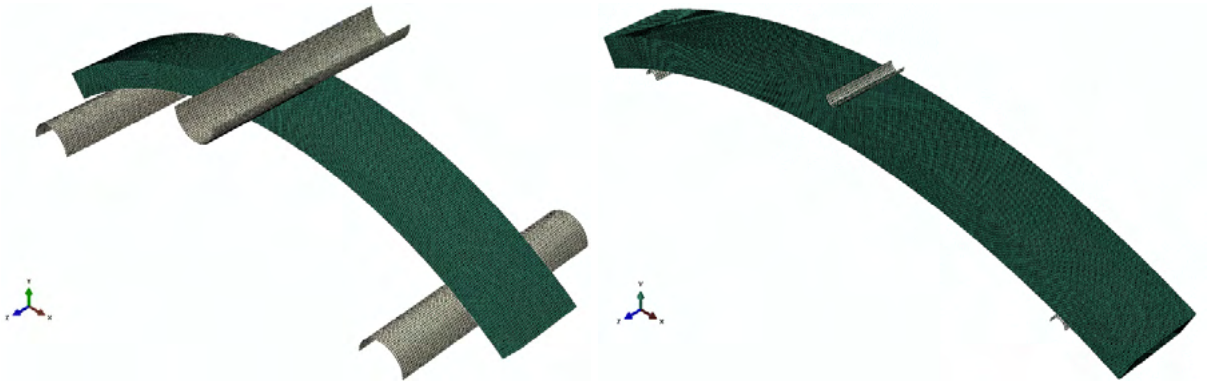


Figure 4. Numerical models of the three-point bending test for DN200 (left) and DN1000 (right).

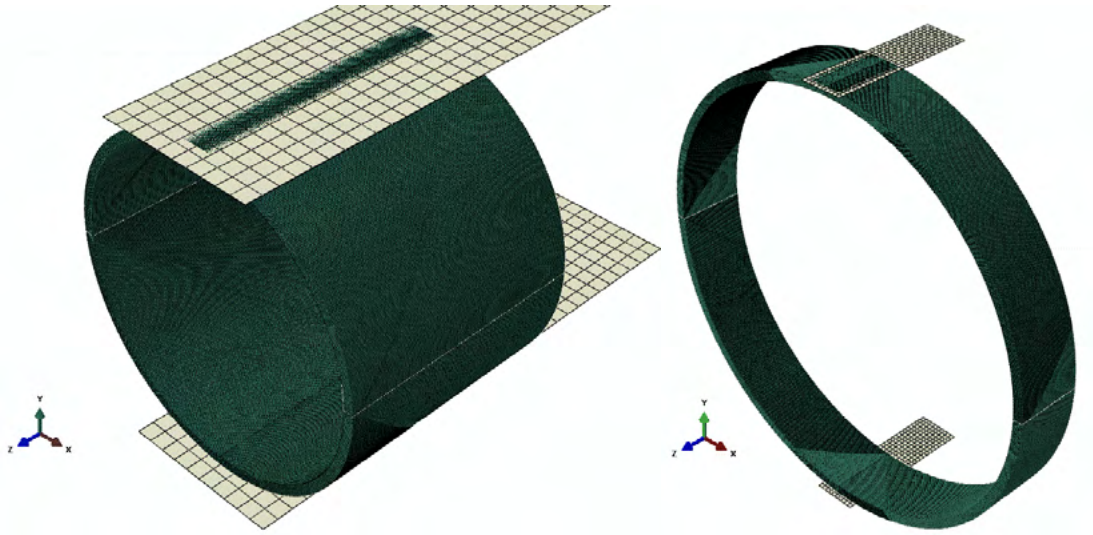


Figure 5. Numerical models of the ring stiffness test for DN200 (left) and DN1000 (right).

The theoretical relationship between the flexural moduli obtained from curved and flat specimens with regard to the ratio L_2/d_m is shown graphically in Figure 6. The correction factors for DN200 and DN1000 calculated according to Eq. 3 are given in Table 1. The results of the finite element analysis (FEA), i.e. the values of the displacement and the reaction force of the moving analytical rigid surface in the three-point bending test simulations, were used to calculate the flexural stress and strain according to Eqs. 1 and 2. The numerical flexural modulus was determined as the slope of the flexural stress/strain curve. For both values of the true span-to-mean diameter ratio L_2/d_m, the underestimation of the value $E = 2500$ MPa corresponds to the values in Table 1. The theoretical correction factor accurately takes into account the geometry of the curved specimen (Figure 6).

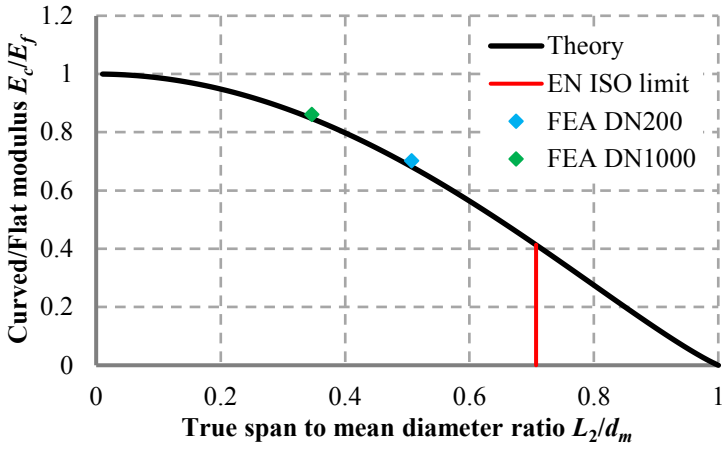


Figure 6. Comparison of apparent flexural moduli obtained from three-point bending tests on curved and flat specimens.

The values of displacement and reaction force from the moving analytical rigid surface in the ring stiffness test simulations were used to calculate the ring stiffness according to Eq. 5. The values of the modulus of elasticity calculated on the basis of the ring stiffness according to Eq. 6 deviate from the value $E = 2500$ MPa by approx. 2%. The correction factor E_c/E_f can also serve as a theoretical relationship between the flexural modulus obtained from a curved specimen and the modulus obtained from the ring stiffness test.

4. Experimental results and discussion

The apparent values of the flexural modulus determined from the three-point bending test on curved specimens are listed in Table 2. These values were corrected for curvature using a correction factor from Eq. 3. The corrected values of the flexural modulus E_f, obtained from an equivalent flat specimen are compared with the apparent longitudinal modulus E_L, obtained by tensile tests. Ideally, they should be the same for a homogeneous, isotropic material. Considering the variability of the CIPP material due to defects and anisotropic properties as well as different strain rates during the tests, there is a good agreement between the flexural and longitudinal modulus. The curved and longitudinal specimens taken from the DN500 pipe segment obviously do not represent the same material, even though they were taken from the same location.

Table 2. Results of the three-point bending and tensile tests (synthetic felt CIPP).

Pipe segment	h_n (mm)	L_2/d_m	$C_E = \frac{E_c}{E_f}$	E_c (MPa)	E_f (MPa)	E_L (MPa)	$\frac{E_f}{E_L} - 1$
DN500	10.5	0.34	0.853	3560	4180	2450	71%
DN1000	21	0.35	0.844	2320	2730	3130	-13%
DN600	12	0.37	0.826	3590	4360	3530	24%
DN800	18	0.38	0.817	2290	2810	2670	5%
DN400	9	0.39	0.808	3300	4100	4120	0%
DN700	15	0.43	0.768	2530	3280	2600	26%
DN300	6	0.46	0.736	2350	3200	3330	-4%
DN200	4.5	0.51	0.678	1680	2460	2650	-7%

The apparent values of the flexural modulus obtained from the three-point bending tests on curved and equivalent flat GRP CIPP specimens are given in Table 3. The influence of curvature is practically eliminated as the values of the correction factor are very close to 1.

Table 3. Results of the three-point bending tests (GRP CIPP).

Pipe segment	h_n (mm)	$d_m/e_{c,m}$	L_2/d_m	$C_E = \frac{E_c}{E_f}$	E_c (MPa)	E_f (MPa)
DN400	3.0	94	0.18	0.96	9600	10100
DN500-1	4.2	95	0.17	0.96	12300	12800
DN500-2	4.2	99	0.17	0.96	12900	13300
DN1000	6.3	140	0.11	0.98	15200	15500
DN1200	7.0	151	0.11	0.98	15100	15300

The apparent value of the flexural modulus E_f, obtained from an equivalent flat specimen is in good agreement with the apparent ring modulus E_r, obtained by ring stiffness tests (Table 4).

Table 4. Results of the three-point bending and ring stiffness tests (synthetic felt CIPP).

Pipe segment	h_{nom} (mm)	L_2/d_m	$C_E = \frac{E_c}{E_f}$	E_c (MPa)	E_f (MPa)	E_r (MPa)	$\frac{E_r}{E_f} - 1$
DN300-1	6	0.38	0.817	2920	3580	3640	+2%
DN300-2						3450	-4%

5. Conclusions

In this study, the mechanical properties of installed cured-in-place pipe (CIPP) liners are evaluated as determined by various tests. The experimental methods used include tensile tests on longitudinal specimens, three-point bending tests on hoop curved specimens and ring stiffness tests on whole pipe segments. The specimens tested in this study were taken on site and represent realistic mechanical properties of installed CIPP. The experimental results are in good agreement with the theoretical relationships. The question arises as to whether the flexural modulus of GRP CIPP should be corrected for curvature in the test reports. Which method provides the most reliable value of the modulus of elasticity in the context of quality control varies from country to country. The current quality control methods in Croatia are based on three-point bending tests on curved specimens. The ring stiffness test is performed on whole pipe segments and is a mandatory quality control test for thermoplastic pipes in Croatia. Since it is a simple test method and the cut pipe segment is approximately the same as for curved specimens, the ring modulus can be considered a reliable parameter for hoop performance.

Acknowledgments
The authors gratefully acknowledge the support from Aktiv Global d.o.o. and Solmex d.o.o.

References

[1] T. Abel. Laboratory tests and analysis of CIPP epoxy-resin internal liners used in pipelines – part I: comparison of tests and engineering calculations. *Studia Geotechnica et Mechanica*, 43(2): 169-180, 2021.
[2] F. Gras-Travesset, A. Andreu-Torras and M. A. Perez. A novel test procedure for evaluating the performance of composite cured-in-place-pipe liners in water pressure pipe rehabilitation. *Case Studies in Construction Materials*, 19, 2023.
[3] D.P. Kozman. Bonded or Unbonded Liners? How Longitudinal Bending Impacts Pipe Lining Design and Performance. In *Pipelines 2020*, 263-270, 2020.
[4] S. Das, A. Bayat, L. Gay, M. Salimi and J. Matthews. A comprehensive review on the challenges of cured-in-place pipe (CIPP) installations. *Journal of Water Supply: Research and Technology—AQUA*, 65(8): 583-596, 2016.
[5] J. Gumbel and D. Chrystie-Lowe. Determination of hoop strength and stiffness in short and long term testing of pipes and liners. In *NO DIG BERLIN 2015*, 2015.
[6] EN 1393:2003, Plastics piping systems – Glass-reinforced thermosetting plastics (GRP) pipes – Determination of initial longitudinal tensile properties, CEN.
[7] EN ISO 178:2019, Plastics – Determination of flexural properties, CEN.
[8] EN ISO 11296-4:2018, Plastics piping systems for renovation of underground non-pressure drainage and sewerage networks – Part 4: Lining with cured-in-place pipes, CEN.
[9] EN 1228. Plastics piping systems – Glass-reinforced thermosetting plastics (GRP) pipes – Determination of initial specific ring stiffness, CEN.

IMPACT OF PRE-EXISTING DELAMINATION DEFECTS ON THE EVOLUTION OF BUCKLING IN COMPOSITES

Swami S. Venkat[1], Sven Scheffler[1], P. M. Anilkumar[1], Emmanuel Baranger[2] and Raimund Rolfes[1]

[1]Leibniz Universität Hannover, Institute of Structural Analysis, Appelstraße 9A, 30167 Hannover, Germany, Web Page: https://www.isd.uni-hannover.de/en/
[2]Université Paris-Saclay, CentraleSupélec, ENS Paris-Saclay, CNRS, LMPS - Laboratoire de Mécanique Paris-Saclay, 91190, Gif-sur-Yvette, France, Web Page: https://lmps.ens-paris-saclay.fr/en

Keywords: Delamination, Buckling, Cohesive Zone Model, Finite Element Method

Abstract
The integrity of wind and aerospace structures encounter significant challenges due to various damage mechanisms, including delaminations. Delaminations pose critical threat to safety and reliability of the structure due to challenges in detecting them and the severe detriment they cause to mechanical performance, especially under compressive loads. As delamination advances under service loads like impact or fatigue, the vulnerability of the structure to buckling failure increases, due to possibility of its critical buckling load falling below the encountered service load. This work elucidates the phenomenon on a classic case of column buckling with the aid of a quasi-static 'Effect of Defect' study. A serie of finite element analyses have been carried out which involved maintaining a constant applied load while progressively increasing the delamination sizes in the models. The investigation systematically evaluates the influence of through thickness position of the delamination on the laminate behaviour. It was observed that near surface delamination induces local buckling initially, followed by mixed local/global buckling failure. On the other hand midplane delamination tends to global buckling. Also owing to initial thin sublaminate buckling, the near surface configurations exhibit axial stiffness reductions and are prone to unstable growth, even for smaller delamination sizes. The study also outlines how the observed results provide a foundation for future investigations into analyzing delaminated laminates under fatigue loading conditions.

1. Introduction

Fiber reinforced composites, owing to their exceptional specific stiffness and strength, have found a wide range of applications, particularly in aerospace and wind energy sectors. Their excellent in-plane properties are however not matched by their through-thickness properties, making them prone to delaminations, which continues to be a major concern for designers [1]. Delaminations may occur due to impact loads or develop under static/fatigue loads, due to factors such as matrix cracks, free edge effects or the propagation of interfacial defects introduced during manufacturing [2, 3]. These delaminations can significantly decrease the stiffness and load-carrying capacity of composite structures, especially under compression loads, by potentially instigating sublaminate buckling and subsequent delamination propagation [2, 4]. A number of numerical works have investigated the influence of through-width delaminations on buckling and post-buckling behavior of composite laminates and they are well documented in literature [2, 4, 5, 6, 7]. Apart from nonlinear finite element (FE) analysis [2, 4, 6, 7], other approach like layerwise B-spline finite strip method (FSM) [5] has also gained attention over the years. For the simulation of delamination propagation techniques such as virtual crack closure technique (VCCT) [5, 6] and cohesive zone model (CZM) [2, 4, 7] have been utilized.

Wang et al. [5] employed B-spline FSM for deformation analysis and VCCT to compute the energy release rate along the delamination front. By comparing local laminate surface strains with experiments

conducted by Kutlu et al. [8], they demonstrated that their method yields a good prediction of buckling loads corresponding to thin and thick sublaminate. Similarly Liu et al. [6] used VCCT approach to compute energy relase rate for crack propagation in a geometric nonlinear FE analysis and made a comparison of their prediction with the results in [5]. Although VCCT has shown good agreements for these simple 3D cases and 2D plane strain (geometry and loading invariant along the width) problems, they still have difficult propagating cracks when the crack front is not aligned with the mesh and require additional techniques such automated and robust remeshing procedures [9] or gradual release of forces [10]. Finally, such linear elastic fracture mechanics (LEFM) techniques cannot predict crack nucleation and needs an initial crack in the model.

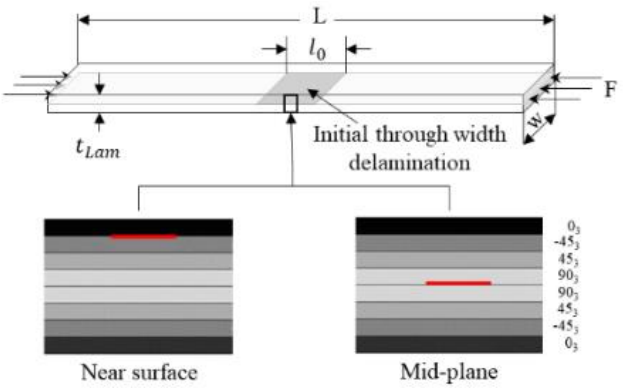
Alternatively, in few studies [2, 4, 7], researchers have used CZM within a geometrically nonlinear FE framework to simulate delamination propagation, employing a fracture mode-dependent traction-separation law for CZM. In one such studies, Mekonnen et al. [2] demonstrated that the through-thickness location of delamination can influence the buckling mode. It was also reported that the sequence of events involving thick sublaminate buckling and delamination propagation can vary based on delamination length and through-thickness location (for upto intermediate locations). In another study Nikrad et al. [7] has shown that off-centre delamination can produce asymmetric instability configuration and may also trigger asymmetric delamination growth. Though accurate energy dissipation in CZM requires multiple elements in fracture process zone [11], CZM does not require adaptive remeshing procedures for capturing different fracture modes and can predict crack initiation as well as propagation [4].

Although previous studies provide a thorough understanding of numerical modeling for the discussed problem, their focus has primarily been on determining the critical buckling load associated with the given delamination configurations. However, during the operational lifespan of a composite structure it is generally the known design limit load (DLL) that sets the requirement for critical buckling load [12]. Under the action of service loads which usually do not exceed the DLL the delaminations can grow in length and reach a critical length when their buckling load falls below the DLL. In this context an Effect of Defect study has been carried out, involving a series of analyses with a constant applied load and increasing delamination lengths in the models. The significance of this study lies in its departure from the conventional way in which the critical buckling load is predicted for a given delamination length. Instead, the focus is on predicting the critical delamination length for a given load, thereby paving the way towards the concept of slow-growth damage tolerance, which has been largely unexplored until now [12]. A nonlinear FE framwork, coupled with CZM has been employed in this work to analyse the buckling evolution and delamination propagation. In Section 2 the methodology has been discussed which comprises the general aspects of the study and the modelling framework. The subsequent section (section 3) presents and discusses the results. The paper ends with a section on conclusions along with the outlook in section 4.

2. Methodology

2.1. General Aspects of Parameteric Study

This study examined the evolution of buckling in composite laminates as the length of delamination was increased in the models under a constant applied load. The Figure 1 depicts the details such as layup, geometry, applied load and locations of delaminations examined in this study. The selection of delamination locations represents two extreme cases: the near-surface delamination results in two sublaminates with most asymmetric bending stiffness, while the midplane delamination results in sublaminates with symmetric bending stiffness.



Layup	$[0_3/-45_3/45_3/90_3]_s$
L	100 mm
l_0	Starting with 10 mm
w	20 mm
t_{Lam}	3.144 mm
t_{Ply}	0.131 mm
F	8 KN

Figure 1. Details of the parametric study

2.2. Modelling Framework

The FE modelling was conducted employing a commercially available software package, ABAQUS 2023. Figure 2 illustrates the schematic representation of the steps followed in the analysis. The first step involved setting up of the FE model. The deformed configuration of a FE model with an initial delamination has been depicted in Figure 3.

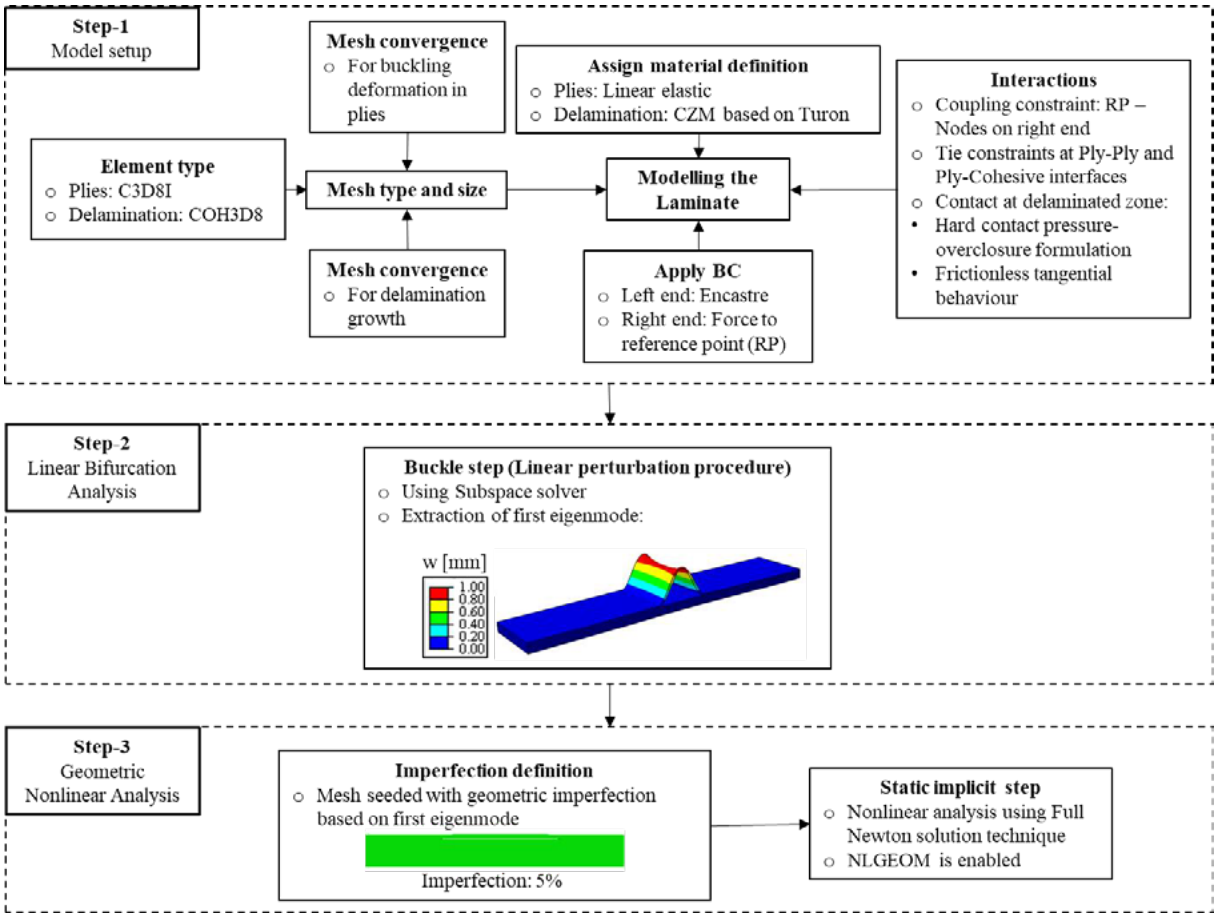


Figure 2. Flowchart of the FE framework

The laminate was modeled using the eight-noded incompatible mode solid element (C3D8I), chosen for its capacity to alleviate shear locking during bending [13]. To simulate delamination growth, zero-thickness eight-noded cohesive elements (COH3D8) were placed in the plane along the initial

delamination. The plies were modeled as linearly elastic and transversely isotropic. To accurately model the fracture mode dependent delamination growth, a static CZM based on Turon et al. [14] was used. This damage model was chosen for its accuracy in predicting the mixed mode delamination growth in composite laminates [14]. The computational algorithm of the damage model was implemented as a user-defined material subroutine (UMAT) in Abaqus/Implicit, tailored for the COH3D8 elements. The mesh sizes for solid and cohesive elements were selected based on mesh convergence studies focusing on buckling deformation and delamination growth, respectively. The first convergence study showed that modelling each three ply sublaminate (e.g. 0_3) using a single element through the thickness and in-plane mesh size of 0.5 mm was sufficient to produce converged buckling results. To conduct accurate delamination analysis the mesh size must be sufficiently fine to ensure that enough interface elements exist within the fully developed prozess zone length near the crack tip [15]. The mesh size was determined through a convergence study conducted on the mode I double cantilever beam (DCB) test, as this mode typically governs the minimum mesh density requirement [11]. Finally the converged mesh size of 0.1 mm along the propagation direction and 0.5 mm along the width direction was utilized in the fine mesh region in the model. The model's interactions and boundary conditions (BC) have also been detailed in Figure 2 and depicted in Figure 3.

In the nonlinear analysis, laminate buckling is only initiated through geometric or loading imperfections [2]. A geometric imperfection was defined based on the linear bifurcation analysis as illustrated in the second step of Figure 2. Due to its plausible shape and lowest eigenvalue, only the first mode was selected for defining the geometric imperfection. In line with the study by Mohammadi et al. [4], 5% of the calculated deformation of the first eigenmode was applied to the mesh for nonlinear analysis. The final third step involved performing the geometric nonlinear analysis as detailed in Figure 2.

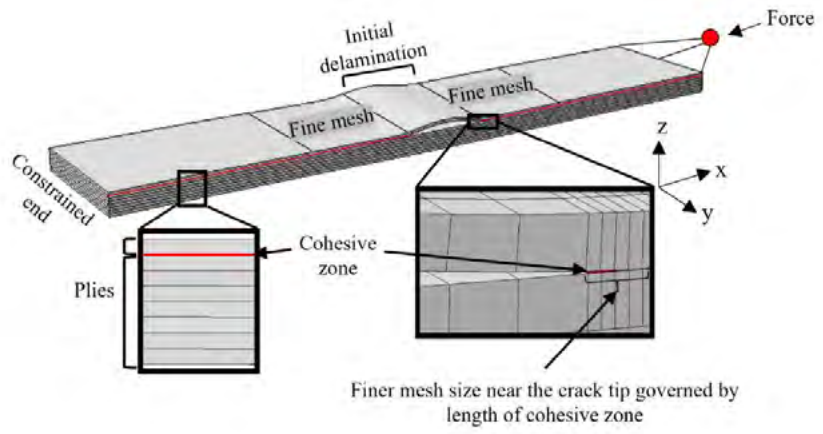


Figure 3. FE model depicting the mesh and the boundary conditions

3. Results and Discussion

Following the methodology outlined in the previous section, the FE analyses were carried out, and a comprehensive discussion of the obtained results is presented in this section.

3.1. Near Surface Delamination

For near surface delamination, in Figure 4 a) the evolution of out-of-plane displacement, *w* is depicted in relation to delamination lengths, while Figure 4 b) displays delamination growth using the damage variable, *d* across various delamination lengths. Figure 5 illustrates axial stiffness change with the normalized delamination length. In these figures, the delamination length has been normalized with respect to the laminate length.

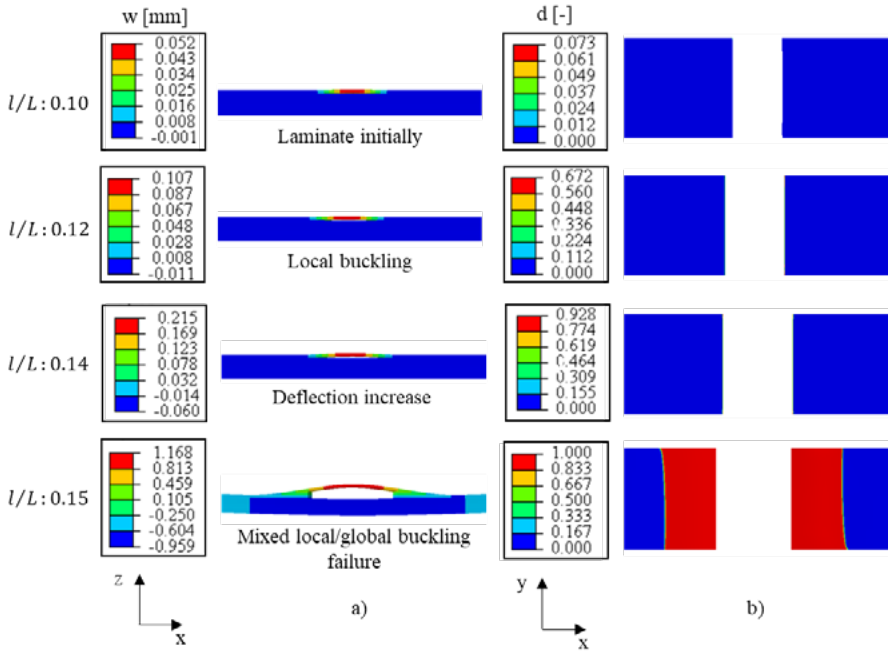


Figure 4 a) Evolution of out-of-plane displacement, *w* with the delamination length and b) Damage variable, *d* showing delamination growth for different delamination length. The delamination length is normalized with respect to length of the laminate

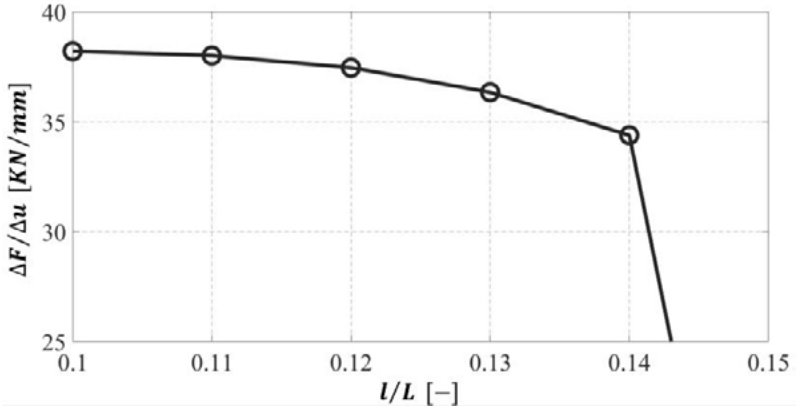


Figure 5 Axial stiffness drop with the normalized delamination length

Near-surface delamination results in two sublaminates: an upper thin sublaminate with lower bending stiffness and a lower thick sublaminate with higher bending stiffness. Due to its lower bending stiffness and presence of geometric imperfection (as illustrated in Figure 2), bending is induced in the upper sublaminate, even at the lowest normalized delamination length of 0.10. This is confirmed by out-of-plane displacement value of the upper sublaminate of 0.052 mm (Figure 4 a). Subsequently as the delamination length is increased, the upper sublaminate undergoes local buckling. Figure 4 a) illustrates that local buckling occurs at a normalized delamination length of 0.12, with the upper sublaminate displaying an out-of-plane displacement of 0.107 mm, exceeding 25% of its thickness (that is 0.393 mm). However, it should be noted that determining the precise point of local buckling is challenging due to the presence of geometric imperfection. Future research will explore this further, aiming to determine whether a discrete bifurcation point corresponding to local buckling can be identified for lower magnitudes of imperfection.

With the further increase in delamination length it is noticed that out-of-plane displacement of upper sublaminate continues to increase beyond the point of local buckling. At a normalized length of 0.14, out-of-plane displacement of upper sublaminate increases to a value of 0.215 mm and that of lower sublaminate also increases marginally to 0.056 mm. The impact of the increased out-of-plane displacement is clearly evident in the reduction of axial stiffness by around 10.5% as the normalized length increases from 0.10 to 0.14 (Figure 5). At a normalized length of 0.15, the delamination extends on both ends by 11 mm (Figure 4 b)) , causing the out-of-plane displacement in lower sublaminate also to increase significantly. At this point, the laminate is considered to have undergone mixed local/global buckling failure. In the Figure 5 this is indicated by the sudden drop in the value of axial stiffness. It should be noted that for normalized delamination lengths below 0.15, damage is only seen at the corners of the delamination tip (not clearly visible), as indicated by the values in the legend (Figure 4 b)).

From the results, it can be concluded that in this scenario of near-surface delamination, the laminate experiences local buckling initially as the delamination length increases. Following local buckling the out-of-plane displacement continues to increase with the delamination length. This trend persists until a critical length is reached and beyond this length, the laminate experiences significant delamination growth, leading to what is termed as mixed local/global buckling failure of the laminate.

3.1. Midplane Delamination

For midplane delamination, in Figure 6, evolution of out-of-plane displacement, *w* has been shown in relation to normalized delamination length. Figure 7 illustrates axial stiffness change with the normalized delamination length. The midplane delamination divides the laminate into two sublaminates with identical bending stiffnesses. Consequently, the laminate does not demonstrate local buckling, as seen in the previous configuration. Instead, both sublaminates deform in the same direction, as illustrated in Figure 6. This suggests that for this configuration the laminate is prone to undergo what is known as the global buckling failure. The Figure 6 also shows that the mode shape changes as the normalized delamination length increases from 0.10 to 0.20. At a normalized length of 0.20, the laminate shows an S-shaped deflection, and beyond that the magnitude of out-of-plane displacment continues to increase following the same deformation pattern as the delamination length increases.

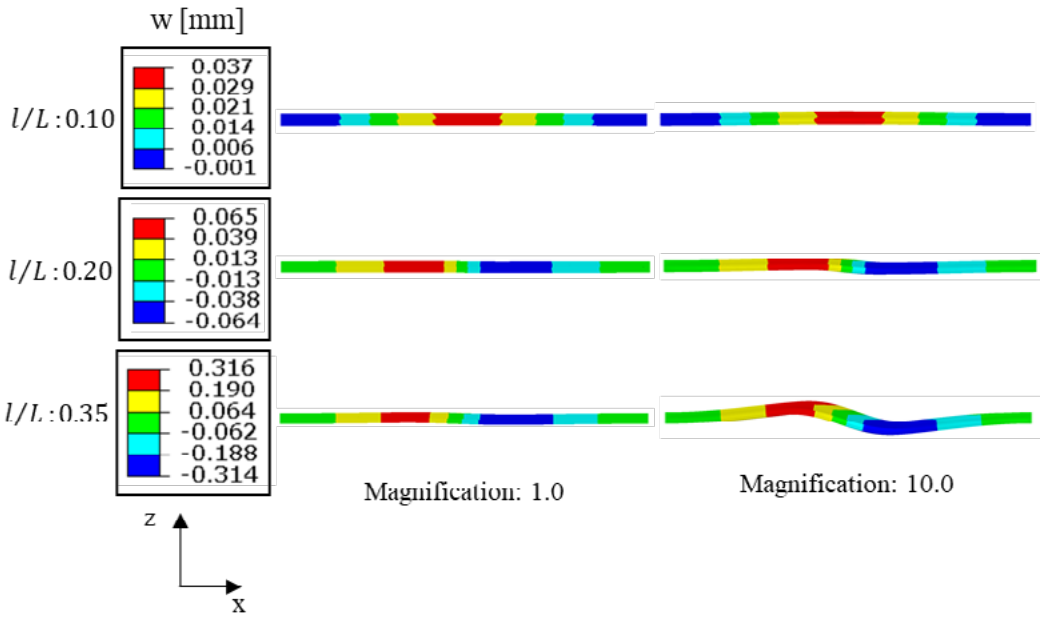


Figure 6. Evolution of out-of-plane displacement (w) with the normalized delamination length. The plots compare two levels of magnification for improved visualization.

The Figure 7 indicates that increasing the normalized delamination length from 0.10 to 0.15 does not show any visible change in its axial stiffness, unlike the near surface case where the laminate failed when the delamination was increased to same length. This shows that the mode of buckling has a significant influence on the behaviour of the laminate. Even beyond the normalized delamination length of 0.15, the drop in axial stiffness occurs gradually with the delamination length and at a normalized length of 0.35, only the delamination tip displays some damage, without significant extension of the delamination to cause a sudden drop in axial stiffness.

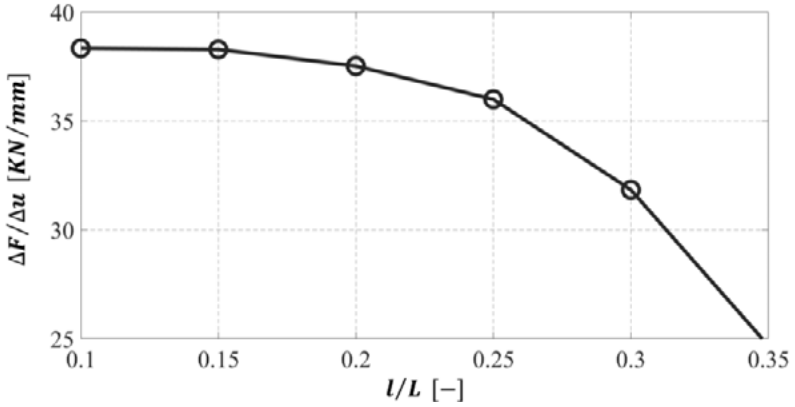


Figure 7. Axial stiffness drop with the normalized delamination length

4. Conclusions

The conclusions from the current study are summarized below:

- For the near-surface delamination, the laminate initially experiences local buckling as the delamination length increases. The out-of-plane displacement continues to grow with the delamination length until reaching a critical size. Subsequently, significant delamination growth occurs, leading to a mixed local/global buckling failure of the laminate.Due to local buckling the delamination growth and, consequently, laminate failure occurs at shorter delamination lengths compared to midplane delamination configuration.
- In the case of midplane delamination, where the two sublaminates have identical bending stiffnesses, the laminate does not demonstrate local buckling but rather tends toward global buckling. The global mode was found to be less critical, as unlike near-surface delamination, there's no substantial reduction in laminate axial stiffness for shorter delamination lengths. With further increases in length, there's a gradual decline in laminate stiffness, yet for the considered load no significant delamination growth was observed even at larger delamination lengths.

These findings are useful for the subsequent investigation on the impact of delamination defects under fatigue loading. In this future study, the near surface delamination scenario is considered relevant due to its tendency for local buckling, which acts as the main mechanism for driving delamination growth. Other areas of investigation include examining the impact of intermediate delamination, conducting a study on imperfection sensitivity and studying the influence of a stiffer lower sublaminate in the context of near-surface delamination.

Acknowledgments

The authors are grateful to the the International Research Training Group 2657 (IRTG 2657) funded by the German Research Foundation (DFG) (Grant reference number 433082294).

The authors also acknowledge the compute cluster of the Leibniz University Hannover, which was mainly used to perform the presented simulations. The compute cluster is partly funded by DFG – Project-IDs INST 187/742-1 FUGG and INST 187/592-1 FUGG.

References

[1] B. L. Bak, C. Sarrado, A. Turon und J. Costa, Delamination Under Fatigue Loads in Composite Laminates: A Review on the Observed Phenomenology and Computational Methods, *In Applied Mechanics Reviews,* volume(66), 20 june 2014.

[2] A. A. Mekonnen, K. Woo, M. Kang und I.-G. Kim, Effects of Size and Location of Initial Delamination on Post-buckling and Delamination Propagation Behavior of Laminated Composites, *International Journal of Aeronautical and Space Sciences,* volume(21), pp. 80-94, 13 July 2019.

[3] A. Brunner, *Experimental study of delamination in cross-ply laminates. In Delamination Behaviour of Composites (pp. 281–309)*, Elsevier, 2008.

[4] B. Mohammadi und F. Shahabi, „On computational modeling of postbuckling behavior of composite laminates containing single and multiple through-the-width delaminations using interface elements with cohesive law," *Engineering Fracture Mechanics,* volume(152), pp. 88-104, 2016.

[5] S. Wang und Y. Zhang, „Buckling, post-buckling and delamination propagation in debonded composite laminates Part 2: Numerical applications," *Composite Structures,* volume (88), pp. 131-146, March 2009.

[6] P. Liu, S. Hou, J. Chu, X. Hu, C. Zhou, Y. Liu, J. Zheng, A. Zhao und L. Yan, „Finite element analysis of postbuckling and delamination of composite laminates using virtual crack closure technique," *Composite Structures,* volume (93), pp. 1549-1560, May 2011.

[7] S. Nikrad, S. Keypoursangsari, H. Asadi, A. Akbarzadeh und Z. Chen, „Computational study on compressive instability of composite plates with off-center delaminations," *Computer Methods in Applied Mechanics and Engineering,* pp. 429-459, October 2016.

[8] Z. Kutlu und C. Fu-Kuo, „Composite panels containing multiple through-the-width delaminations and subjected to compression. Part II: Experiments & verification," *Composite Structures,* volume(31), pp. 297-314, 1995.

[9] N. Viera De Carvalho, R. Krueger und G. D. L. Mabson, „Combining Progressive Nodal Release with the Virtual Crack Closure Technique to Model Fatigue Delamination Growth Without Re-meshing," in *AIAA/ASCE/AHS/ASC Structures, Structural Dynamics, and Materials Conference*, American Institute of Aeronautics and Astronautics, 2018.

[10] C. Dávila, „From S-N to the Paris law with a new mixed-mode cohesive fatigue model for delamination in composites," *Theoretical and Applied Fracture Mechanics,* volume(106), April 2020.

[11] P. W. Harper und S. R. Hallett, „Cohesive zone length in numerical simulations of composite delamination," *Engineering Fracture Mechanics,* volume(75), pp. 4774-4792, November 2008.

[12] J.-A. Pascoe, „Slow-growth damage tolerance for fatigue after impact in FRP composites: Why current research won't get us there," *Procedia Structural Integrity,* volume(28), pp. 726-733, 2020.

[13] SIMULIA User Assistance 2023, *ABAQUS/Standard User's Manual, Version 2023*, Dassault Systèmes Simulia Corp, United States, 2023.

[14] A. Turon, E. V. González, C. Sarrado, G. Guillamet und P. Maimí, „Accurate simulation of delamination under mixed-mode loading using a cohesive model with a mode-dependent penalty stiffness," *Composite Structures,* volume(184), pp. 506-511, 15 January 2018.

[15] A. Turon, C. Dávila, P. Camanho und J. Costa, „An engineering solution for mesh size effects in the simulation of delamination using cohesive zone models," *Engineering Fracture Mechanics,* volume(74), pp. 1665-1682, July 2007.

Material Characterization on Temperature Dependency of Fatigue Stiffness Degradation of CFRP Laminate Manufactured by Filament Winding Using Three-point Bending Test

Takeshi Watanabe[1], Ryoma Aoki[2], Tomohiro Yokozeki[2], and Yuta Urushiyama[1]

[1]Honda R&D Co., Ltd., 4630 Shimotakanezawa, Haga-machi, Haga-gun, 321-3393 Tochigi, Japan
Email: takeshi_watanabe@jp.honda, Web Page: https://global.honda/en/RandD/
[2]Department of Aeronautics and Astronautics, The University of Tokyo, 7-3-1 Hongo, Bunkyo-ku, Tokyo 113-8656, Japan

Keywords: Residual strength, Fatigue, Temperature dependency, Composite vessel, Filament winding

Abstract
A temperature dependency of a stiffness degradation during fatigue of a carbon fiber reinforced plastics manufactured by filament winding and the residual mechanical property after fatigue was experimentally studied. A coupon specimen was made with a towprepreg and prepared using a plate-type mandrel for filament winding. The stacking sequence of the laminate was $[45/-45]_{2s}$ in order to focus on the matrix resin cracks and interface fracture between fiber and matrix resin as major dominants of intralaminar fracture. Fatigue test was performed under the temperature of -40 ℃, +85 ℃ and room temperature (RT) using a three-point bending test. The residual property was evaluated by a tensile test at RT. The stiffness degradation during fatigue at -40℃ was more likely to occur than at RT and showed more brittle characteristics. On the other hand, the fatigue stiffness degradation at +85 ℃ was less likely to decrease than at RT and showed more toughness. The residual strength at the same residual stiffness after fatigue at -40 ℃ and +85 ℃ decreased in comparison with that at RT. This suggested that the temperature dependency of the mechanical properties of the matrix resin influenced the damage propagation during fatigue of the composite laminate.

1. Introduction

A type-IV high-pressure vessel is becoming a mainstream for a hydrogen storage system of automotive application in order to achieve both of a pressure resistance and weight reduction. The reinforcement shell of the vessel is made of carbon fiber reinforced plastics (CFRP) manufactured by filament winding. The performance requirement of the composite high-pressure vessel is characterized by low-cycled fatigue due to high ratio of residual burst strength after durability to initial one. In order to achieve further weight reduction of CFRP, it is required that building an analytical method that can predict precisely not only initial burst strength but also residual one after durability. In addition, in order to verify a certification test and to ensure an end-of-life performance of high-pressure vessel by numerical analysis, it will become necessary to take into account for the effect of environment temperature and loading sequence on fatigue damage inside CFRP.

We have studied a residual strength after fatigue for CFRP in in-plane share direction, which is strongly related with matrix resin cracks and interface fracture between fiber and matrix resin as major dominants of intralaminar fracture shown in the reference [1] and [2]. Characterization of stiffness degradation of filament-wounded CFRP during fatigue using three-point bending test and residual strength after fatigue damage were investigated experimentally. And we have also reported a possibility of numerical prediction of residual mechanical property after fatigue using the finite element analysis with material damage models, which were based on Ladevèze model for static analysis and dd/dN model for fatigue analysis.

In this study, fundamental efforts to realize the extension of the numerical analysis method of fatigue stiffness reduction and residual strength to temperature dependency was described. A coupon specimen with layup of $[45/-45]_{2s}$ were made with a towprepreg and filament winding using a flat

plate mandrel. Fatigue stiffness degradation under the temperature condition of -45 ℃ and +85 ℃ using a three-point bending test was understood experimentally and compared with that at room temperature. In addition, the residual strength in the case of the same stiffness degradation rate after fatigue at each temperature was evaluated using a tensile test at room temperature, and the effect of the environment temperature during fatigue on the residual strength was investigated.

2. Materials and experimental method

2.1. Materials and specimen preparation by filament winding

Figure 1 shows the method for producing a laminated flat plate of CFRP by filament winding to obtain a coupon specimen. The towprepreg, which was carbon fiber (T720SC-36000-50C, Toray Co., Ltd.) pre-impregnated with uncured epoxy resin, was used. The glass transition temperature of the cured epoxy resin was about 120 ℃. The towprepreg was supplied to a filament winding machine and wound onto a steel flat mandrel (380 mm in length and width, 10 mm thickness) alternately in the 0 degree and 90-degree direction to obtain the layup of $[0/90]_{2s}$. The filament-wounded mandrel was lapped in a bagging film and cured at 110 ℃ for 8 hours. Then, the laminated flat plate was removed from the mandrel and the coupon specimen with the layup of $[45/-45]_{2s}$ was cut out from the laminated plate by adjusting the cutting angle. The dimensions of specimen were 250 mm in length and 25 mm in width, The thickness was approximately 2.4 mm after molded.

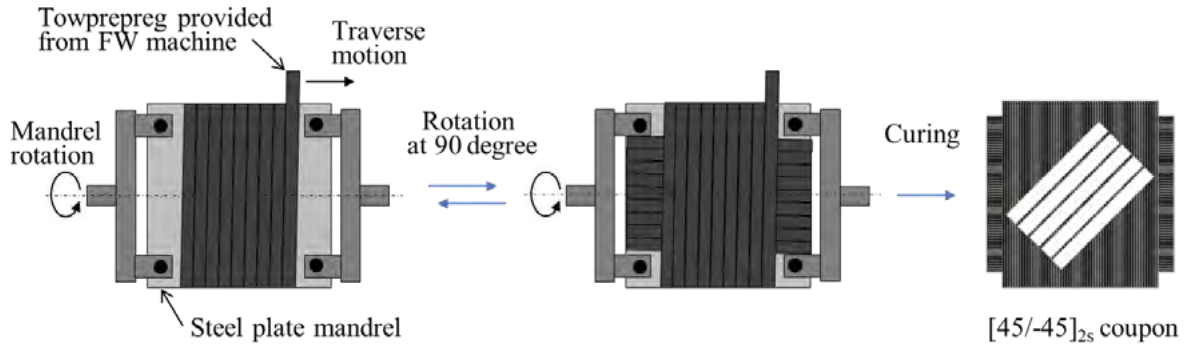


Figure 1. Preparation of coupon specimens manufactured by filament winding.

2.2. Characterization of stiffness degradation due to fatigue damage

Fatigue test was performed at room temperature, -40 ℃ and +85 ℃ using a three-point bending method. The stress conditions for fatigue test were set based on the strength of static three-point bending test shown in Table 1. Cyclic loading was applied using a sine wave with a stress ratio of 0.1 and a frequency of 2 Hz until failure occurred. The radius of the indenter and support point for the three-point bending test was 5 mm, and the indenter position was at the longitudinal center of the coupon specimen. The distance between the supports was 96 mm, and the distance between the indenter and the support was 48 mm. The maximum and minimum values of the applied load and the indenter stroke were measured for each cycle of the fatigue test, and the slope of the load amount with respect to the stroke amount of each cycle was defined as the bending stiffness of that cycle. The residual stiffness obtained by normalizing the bending stiffness of each cycle by the initial bending stiffness was plotted against the number of cycles and this was taken as the stiffness reduction characteristic.

2.3. Evaluation of residual strength after fatigue damage

The residual strength after fatigue was evaluated by a tensile test after adjusting the ratio of the residual stiffness to 0.8 by a pre-fatigue bending test under the conditions shown in Table 2. The strain in the tensile direction at the center of the specimen during the tensile test was measured using an extensometer with the gauge length of 25 mm, and the test speed was 1.5 mm/min.

Table 1. Static bending strength of filament wound CFRP coupon with $[45/-45]_{2s}$ layup.

	Temperature		
	-40 ℃	RT	+85 ℃
Bending strength (MPa)	232.5	193.7	126.5

Table 2. The conditions of pre-fatigue bending test.

	Temperature		
	-40 ℃	RT	+85 ℃
Fatigue stress (MPa)	116.3	116.2	75.9
Stress ratio for static strength	0.50	0.60	0.60
Target ratio of residual stiffness after fatigue	0.80	0.80	0.80

3. Results and discussion

3.1. Effect of temperature on stiffness degradation of CFRP due to fatigue damage

Figure 2 shows a stress-failure number diagram of filament wound CFRP when performing the three-point bending fatigue test at RT, -40℃ and +85℃. The vertical axis is the fatigue stress ratio relative to the static strength, and the horizontal axis is the number of the cycle which the fracture occurred. There is a large variation in the fracture cycle at each temperature, but this is thought to be caused by fiber gaps, voids and interlaminar defects that generated in the specimens due to filament winding process. At a low temperature of -40 ℃, fatigue failure tended to occur at a lower fatigue stress level than at RT. On the other hand, the number of the failure cycle at of 85℃ tended to be longer that at RT. Figure 3 shows the stiffness degradation characteristics due to fatigue damage at (a) RT, (b) -40 ℃ and (c) +85 ℃. The vertical axis means the ratio of the residual stiffness G/G_0 obtained by normalizing the bending stiffness of each cycle by the initial stiffness, and the horizontal axis means the number of fatigue cycles normalized by the fracture cycle N/N_f. At RT, there was a rapid decrease in stiffness of about 5 to 10 % at the beginning of the fatigue cycle up to N/N_f of 0.1. During N/N_f was from 0.2 to 0.9, the stiffness showed a constant and gradual decrease. After N/N_f was 0.9, at which the residual stiffness reached to 0.65, the stiffness decreased sharply again, leading to failure. Then, the behavior of the stiffness degradation characteristics until fracture was consistent regardless of the ratio of fatigue stress. At a low temperature of -40 ℃, a greater decrease in stiffness than at RT was observed at the beginning of the cycle until N/N_f reached 0.1. Although the subsequent stiffness reduction behavior matched the trend at RT, there was a large variation in stiffness reduction. On the other hand, at a high temperature of +85 ℃, the rapid stiffness degradation at the beginning of the cycle was alleviated, and the subsequent stiffness reduction until N/N_f reached to 0.9 also showed a gradual tendency compared to RT. In-plane share damage progression involves matrix resin cracking and fiber-resin interface failure, both of which are influenced by the mechanical properties of the matrix resin. The glass transition temperature of the matrix resin used in this study was about 120 ℃, and at -40 ℃ it has a higher elastic modulus and strength but more brittle behavior, whereas at +85 ℃, it has a lower elastic modulus and strength but more ductile behavior. It is thought that this temperature effect on the mechanical properties of the matrix resin contributes to the stiffness degradation characteristics due to fatigue damage observed in this experiment.

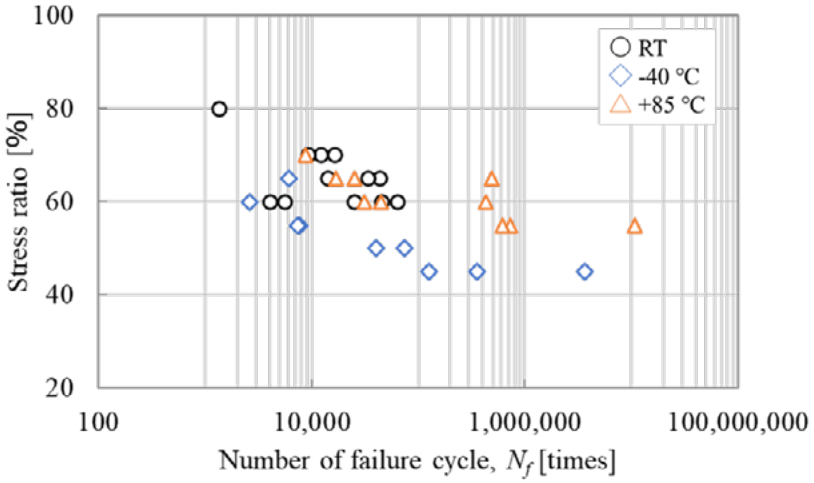
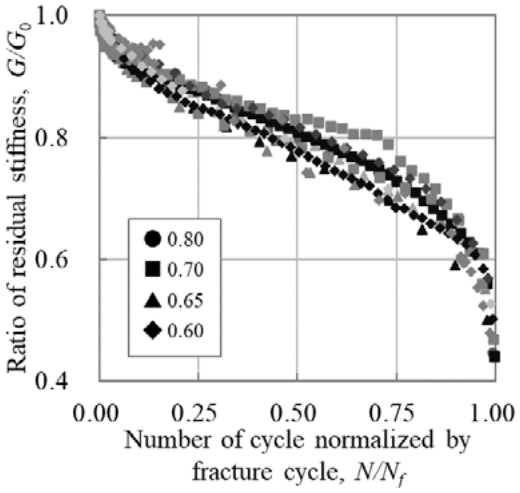
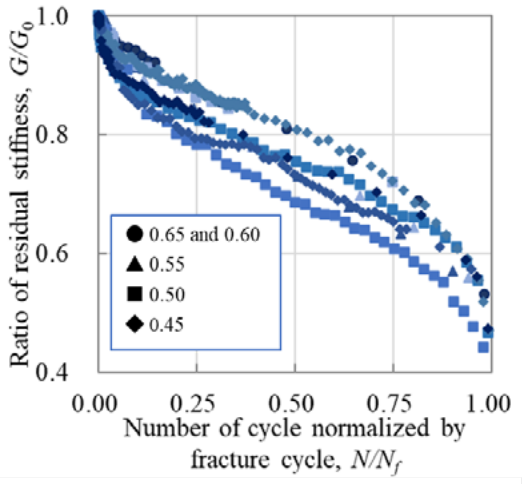


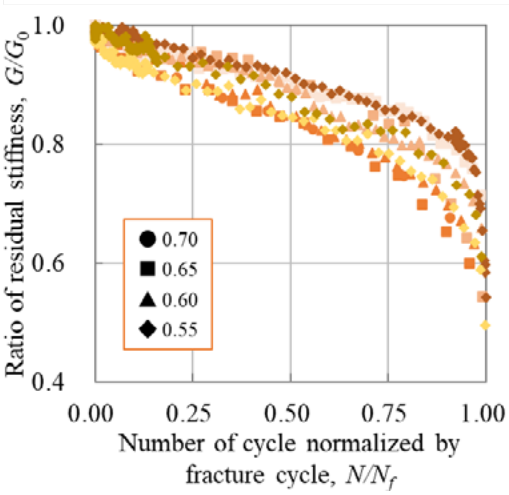
Figure 2. Fatigue life diagram of filament wound CFRP coupon with $[45/-45]_{2s}$ layup.



(a) RT



(b) -40 °C



(c) +85 °C

Figure 3. Stiffness degradation curves of filament wound CFRP coupon with $[45/-45]_{2s}$ layup.

3.2. Comparison of residual strength after fatigue damage at each temperature

Table 3 shows the residual tensile strength of CFRP coupon with $[45/-45]_{2s}$ layup after the bending fatigue test under the conditions shown in Table 2.

In all three temperature conditions, the residual strength after fatigue damage decreased compared to the initial strength. However, the ratio of the residual strength showed different values depending on each fatigue temperature, which was 87 % at RT, 73 % at -40 ℃ and 70 % at +85 ℃ respectively. Observation of the cross-section of the coupon near the indenter after fatigue damage revealed that the amount of resin cracking on the tension side directly below the indenter was small at -40 ℃ and the amount of the plastic deformation was extremely small. In contrast, at 85 ℃, the number of resin cracking near the indenter was greater than at -40 ℃, and the amount of plastic deformation after fatigue was also very large. From the above, it was confirmed that even if the residual stiffness after fatigue is the same, the state of fatigue damage and plastic deformation differs depending on the temperature of the fatigue test environment, and this affects the residual strength.

Table 3. Residual tensile strength of CFRP with $[45/-45]_{2s}$ layup after bending fatigue test.

	Initial	Temperature during fatigue		
		-40 ℃	RT	+85 ℃
Residual strength (MPa)	79.8	69.6	58.2	55.5
Remaining ratio with respect to initial strength (%)	-	87	73	70

4. Conclusions

The effect of environmental temperature on the stiffness degradation due to fatigue damage was experimentally investigated using CFRP coupon with $[45/-45]_{2s}$ layup manufactured by filament winding and three-point bending test. At a low temperature of -40 ℃, the stiffness degradation at the initial stage of fatigue was greater than that at room temperature, but the behavior of stiffness reduction during steady stage was the same as room temperature. On the other hand, at a high temperature of +85 ℃, the stiffness degradation at the initial stage and subsequent steady stage tended to be more alleviated and gradual than at room temperature.

After conducting preliminary fatigue test at each temperature until the residual stiffness reached 0.8, the residual strength was evaluated. As a result, the residual strength decreased from the initial strength at all temperatures, and the ratio of residual strength differ depending on the environmental temperature. From the cross-sectional observation of the post-fatigue coupons, it was confirmed that the state of fatigue damage and plastic deformation differs depending on the temperature of the fatigue test environment, and that this affects the residual strength.

References

[1] T. Watanabe, R. Aoki, T. Yokozeki and Y. Urushiyama. Evaluation of Residual Tensile Property after Three-point Bending Fatigue Test Using CFRP Laminates Manufactured by Filament Winding Process. The 14th Japanese Conference of Composite Materials, 2023.

[2] T. Watanabe, R. Aoki, T. Yokozeki and Y. Urushiyama. Simulation of residual property after fatigue in CFRP laminates manufactured by filament winding process using intra-laminar damage models. The 9th International Conference on Fatigue Composites, p12-13, 2023.

Fatigue Failure Mechanisms and Lifing Method of 2.5D CMCs under Combined Loading

Chao You[1,2*], Zikai Zhou[1,2], Xiguang Gao[1,2], Yingdong Song[1,2,3]

[1] Jiangsu Province Key Laboratory of Aerospace Power System, College of Energy and Power Engineering, Nanjing University of Aeronautics and Astronautics, Nanjing 210016, P.R. China
Email: chaoyou@nuaa.edu.cn
[2] Key Laboratory of Aero-engine Thermal Environment and Structure, Ministry of Industry and Information Technology, Nanjing 210016, P.R. China
Email:1741454573@qq.com
[3] State Key Laboratory of Mechanics and Control Mechanical Structures, Nanjing University of Aeronautics and Astronautics, Nanjing 210016, P.R. China
Email: gaoxiguang@nuaa.edu.cn
Email:ydsong@nuaa.edu.cn

Keywords: Ceramic matrix composites, Fatigure-creep coupling, Trapezoidal-wave fatigue

Abstract

In this study, the fatigue-creep interaction behavior of 2.5D ceramic matrix composites (CMCs) under anaerobic environment at 1100℃ was carried out. The influence of creep loading on fatigue properties of CMCs was studied by comparing fatigue life, hysteresis loop shape, hysteresis dissipation energy accumulation rate and fracture micromorphology of fatigue specimens under sine-wave and trapezoidal-wave fatigue loading. The results show that the fatigue-creep coupling damage has a great influence on the fatigue life of 2.5D CMCs. In addition to the hysteretic dissipation energy caused by friction during sine-wave fatigue loading, the damage accumulated during load holding is the main factor affecting the fatigue life of CMCs.

1. Introduction

Ceramic matrix composite (CMCs) has the characteristics of low density (approximately 1/3 of traditional superalloy), high temperature resistance and oxidation resistance. The application of CMCs is expected to bring a higher turbine inlet temperature. Therefore, CMCs is regarded as the ideal high temperature material for hot sections of aeroengines[1-3]. In the mid-1990s, GE, Safran, Rolls-Royce[4-9] and other companies have invested a lot in the development of CMCs components. GE applied CMC chambers, high-pressure turbine guide blades and high-pressure turbine outer rings to the GE9X engine,which saves $1 million in fuel costs per aircraft every 10 years and the rotor blades, mixer and center cone components prepared by Safran were tested on the CFM56 engine on the ground, and the nozzle were also tested on the A320, A380 and other aircraft.

As one of the most important hot-end components, turbine rotor blades are mainly subjected to centrifugal load and high service temperature during operation, which may result in complex failure modes of the blade due to fatigue or creep damage [10,11]. Under such complex working conditions, the failure mechanism of CMCs is significantly different from that of metals, and there is a lack of effective fatigue life prediction methods, which impedes the application of CMCs on rotor blades. Therefore, it is important to study the fatigue-creep failure mechanism of CMCs and establish the corresponding fatigue life prediction methods.

By far, scholars have conducted a lot of studies on the fatigue behavior and failure mechanism of CMCs[12-16], the results show that CMCs mainly includes several basic damage forms, such as matrix cracking, interface debonding, interface wear and fiber fracture. In addition, some scholars further studied the effects of loading frequency and load holding time on the fatigue life of CMCs[17-20]. The above studies usually focus on single factors such as fatigue or creep, and the studies on the fatigue-creep coupling failure of CMCs under complex working conditions are extremely lacking. Based on the above research background, the failure mechanism of 2.5D CMCs under fatigue-creep coupling load at high temperature and anaerobic environment is studied in this paper.

2. Material and experimental procedures

2.1. Test material and technology

The 2.5D CMCs used in this paper is composed of silicon carbide fiber, silicon carbide matrix and boron nitride interface. The general preparation steps are as follows: Firstly, the plate preform was processed by 2.5D twill weaving process. The boron nitride interface was then deposited on the fiber surface of the preform by Chemical Vapor Infiltration (CVI), and the silicon carbide substrate was deposited on the boron nitride interface. Finally, a plate-like specimen with the thickness of 3 mm was prepared by surface machining.

The size of the specimen used in this paper was based on the existing design standards, considering the internal size of the high temperature furnace and the vacuum environment chamber. The total length of the specimen is 200mm, the length of the test section is 80mm, the width of the clamping end is 12mm, and the width of the test section is 6mm. The 2.5D CMCs plate specimen was shown in Figure 2.1.

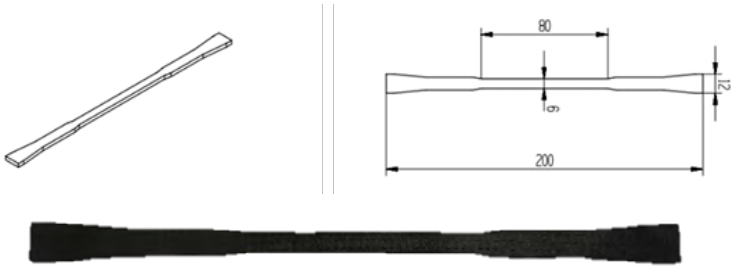


Figure 2.1 2.5D CMCs fatigue specimen

2.2. High temperature anaerobic fatigue test platform

In order to carry out high temperature anaerobic fatigue test of 2.5D CMCs, a set of high temperature anaerobic environment test system was built as shown in Figure 2.2. This test system mainly includes high temperature furnace, empty chamber, vacuum pump, temperature control chamber, water cooling, high purity argon filling device and fatigue loading system.



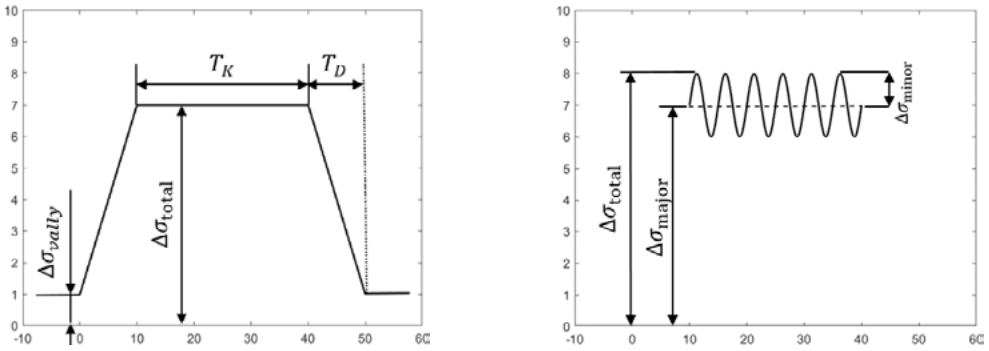
Figure 2.2 High temperature anaerobic fatigue test system

2.3. Load conditions

In order to investigate the effects of fatigue-creep interaction of CMCs, the fatigue tests carried out in this paper were divided into sine-wave and trapezoidal-wave fatigue tests. The fatigue life and failure modes resulting from the two loading waves were compared in this study to clarify the effects of load holding on fatigue life of CMCs at high temperature.

Figure 2.3(a) shows the diagram of the sine-wave fatigue load.It is mainly defined by five characteristic parameters, namely the median value of fatigue load $\Delta\sigma_{major}$, the amplitude of fatigue load $\Delta\sigma_{minor}$,the loading frequency f (cyclic load period T=1/f),the peak value of fatigue load is defined as $\Delta\sigma_{total}$=$\Delta\sigma_{major}$+$\Delta\sigma_{minor}$ and the stress ratio is defined as $R = (\Delta\sigma_{major}\text{-}\Delta\sigma_{minor})/(\Delta\sigma_{major}+\Delta\sigma_{minor})$.

Figure 2.3 (b) is a schematic diagram of the trapezoidal-wave fatigue load, which is mainly defined by four characteristic parameters, including the peak fatigue load $\Delta\sigma_{total}$, the valley fatigue load $\Delta\sigma_{vally}$, the load holding time T_K, the load loading (unloading) time T_D and the stress ratio defined as $R_T = \Delta\sigma_{vally}/\Delta\sigma_{total}$.



（a）Trapezoidal wave　　（b）Sinusoidal wave

Figure 2.3 Fatigue load spectra with different waveforms

Based on the above definition, the sine-wave and trapezoidal-wave fatigue tests under anaerobic environment at 1100℃ was carried out in, in which the $\Delta\sigma_{total}$ of sine-wave fatigue load was 60%-92% of the tensile strength of CMCs, with the f and R being set as 10Hz and 0.1 respectively. Based on the results of sine-wave fatigue test, the $\Delta\sigma_{total}$ of trapezoidal wave was set as 75% of the tensile strength of CMCs,in which the effect of fatigue-creep coupling on the material can be clearly shown .The T_K was set as 30s or 60s. The T_D was set as 0.1s and the R_T was set as 0.1. The complete load parameters of the two waveform fatigue tests are shown in Table 2.1.

Table 2. 1 Loading parameters of fatigue test with different waveforms

Test waveform	sine wave	trapezoidal wave
Hold time (loading frequency)	10Hz	30s/60s
Fatigue peak load	60%-92% tensile strength	75% tensile strength
Stress ratio	0.1	0.1
Number of specimens	14	2/2

3. Results

The S-N curve of anaerobic sine-wave fatigue of 2.5D CMCs at 1100℃ was shown in Figure 3.1. It can be seen from the figure that the fatigue limit (corresponding to 10^6 cycles) of the material under anaerobic conditions at 1100℃ is between 60% and 70% of the tensile strength. It can also be seen that the fatigue life of CMCs is less affected by the change of load, as the fatigue peak load decreases from 75% to 60% of the tensile strength, the fatigue life of the specimen is only increased by one order of magnitude. The fatigue life of most specimens is in the order of 10^4 to 10^5.

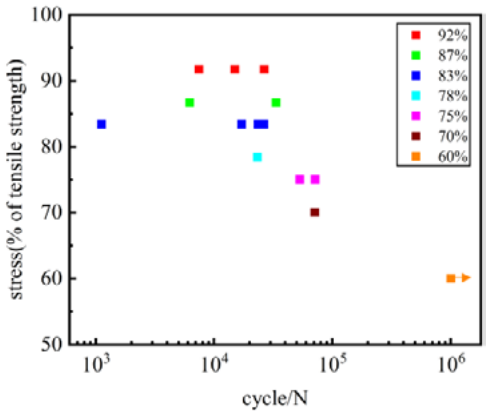
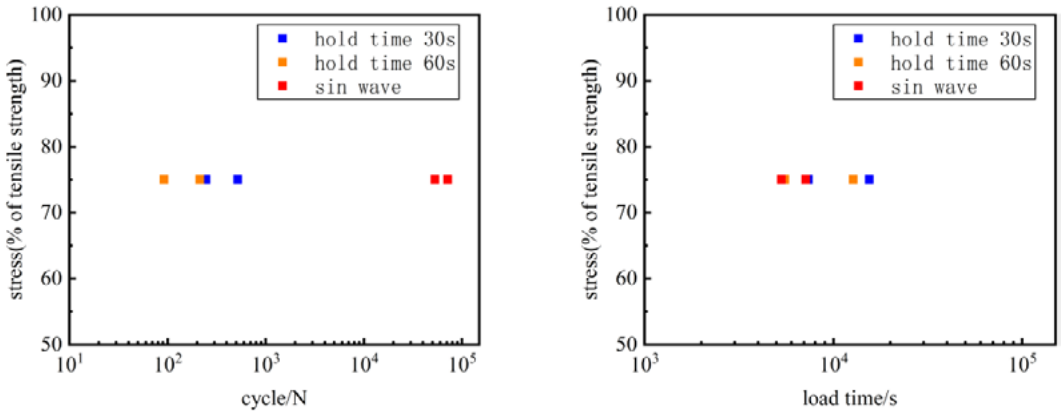


Figure 3.1 S-N curve under sine wave at 1100℃

Figure 3.2(a) summarizes the fatigue life test data of CMCs under trapezoidal-wave loading and 10Hz sine-wave loading (same peak load) under anaerobic environment at 1100℃. As can be seen from the figure, the dispersion of fatigue life cycles of CMCs under trapezoidal-wave loading is less than 4 times (same load holding time). In addition, it can be seen that the fatigue life cycles resulting from 30s holding time is about twice that with 60s. Compared with the fatigue life of sine-wave loading under the same peak load, the sine-wave fatigue life cycles is about 100~1000 times that of the trapezoid-wave loading condition. However, if the number of fatigue cycles is converted into loading time (unit:s), the trapezoidal-wave loading (including 60s and 30s load retention) shows a good consistency with the 10Hz sine-wave loading condition, as shown in Figure 3.2 (b).

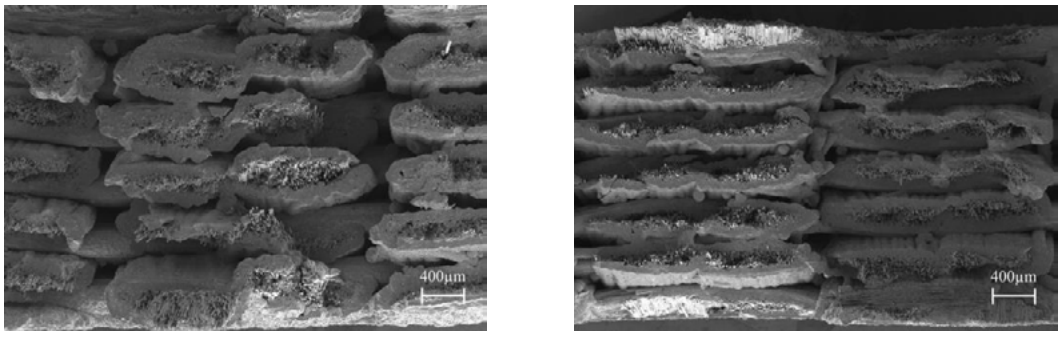


（a）S-N curve　　（b）S-T curve

Figure 3.2 2.5D CMCs trapezoidal wave and sine wave fatigue life curve

In order to study the difference of fatigue failure mechanism between trapezoidal wave loading and sine wave loading, the fracture characteristics of the two fatigue loading specimens were compared and analyzed in this paper, as shown in Figure 3.3. As can be seen from the figure, no clear difference in the overall morphology of fatigue failure fractures under the two waveforms can be found, with no obvious

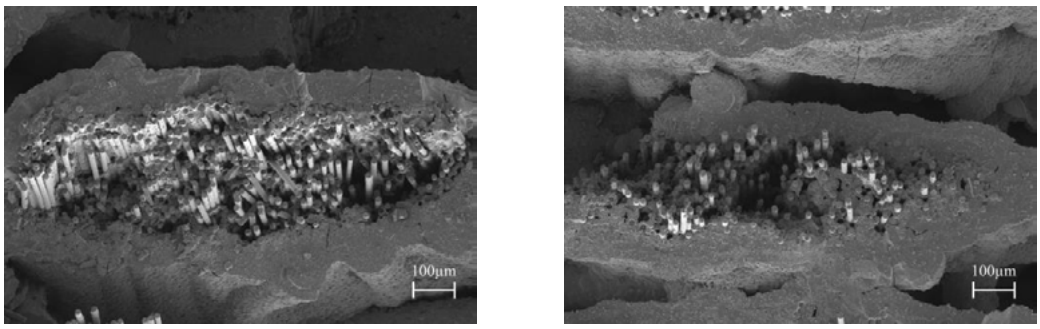
transverse tearing of weft yarns. The main fracture locations are between two adjacent weft yarns, and the fracture of warp yarns is the main failure mode.



（a）Sine wave （b）Trapezoidal wave

Figure 3.3 Overall appearance of fatigue failure fracture with different waveforms

Figure 3.4 compares the fracture surface morphology of warp yarns between the sine-wave and trapezoidal-wave fatigue loading specimens.It can be seen that the trapezoidal-wave loading and unloading with fewer times produces the fiber pulling out with the same length as the sine-wave loading. It can also be seen that under the condition of the same temperature and load amplitude, trapezoidal-wave load retention can also promote the damage of CMCs.

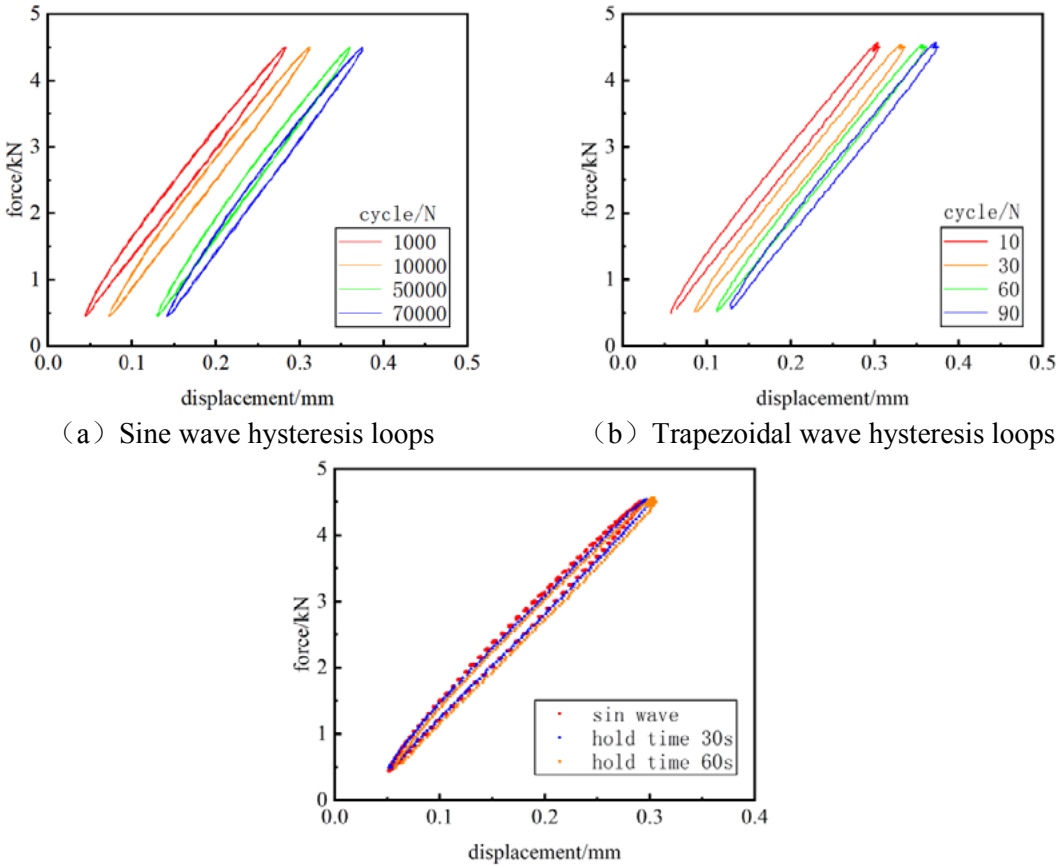


（a）Sine wave （b）Trapezoidal wave

Figure 3.4 Local appearance of fatigue failure fracture with different waveforms

Figure 3.5 further compares the force-displacement hysteresis curves of 2.5D CMCs under sine-wave and trapezoidal-wave fatigue loading. As can be seen from the figure, 2.5D CMCs exhibit similar fatigue hysteresis laws under different fatigue load waveforms. Further analysis shows that under the same loading time, although the number of cycles of trapezoidal-wave loading is less than that of sine-wave loading, the accumulated residual deformations of specimens under these two loading conditions remain consistent, about 0.1mm. For instance, Figure 3.5 (c) compares the hysteresis shapes of different loading waveforms at the same loading time (300s). It can be seen that the hysteresis loops of different waveforms coincide well, and that the trapezoidal-wave load retention does not significantly affect the shape of the hysteresis loop, with a limited deformation (about 0.001mm) resulting from load retention occurring at the maximum load.

In summary, trapezoidal-wave load retention has no effect on the hysteresis loop of CMCs. Therefore, the difference in cycle number of fatigue test between the two waveforms may be caused by creep damage，and the influence of this factor should be considered for more accurate fatigue life prediction.



（a）Sine wave hysteresis loops （b）Trapezoidal wave hysteresis loops

（c）Hysteresis loops with different waveforms at the same loading time

Figure 3. 5 Hysteresis loops of different waveforms

4. Conclusion

In conclusion, the number of fatigue life cycles of CMCs under trapezoidal-wave loading decreases by 10^2-10^3 orders of magnitude compared with that under sine-wave loading. Although the characteristics reflected on the fracture surface of CMCs under different loading waveforms are similar, it can be inferred that the load-holding process in trapezoid-wave loading tends to significantly promote the damage accumulation in CMCs, showing a non-negligible fatigue-creep interaction effects. However, the traditional law of hysteretic dissipation energy accumulation based on the number of loading cycles can only reflect the energy dissipation caused by friction during fatigue loading, and cannot consider the damage of CMCs caused by load retention. It is found that if the number of fatigue life cycles is equivalently converted to the loading time, the hysterical dissipation energy accumulation law and stiffness attenuation law of CMCs during fatigue loading have good consistency under different load conditions, which is promising in providing a method of quantifying equivalent damage of different fatigue loading waveforms.

References

[1] Nakamura, T., et al., Development of CMC turbine parts for aero engines. 2014. 47(1): p. 29-32.
[2] DiCarlo, J.A. and M. Van Roode. Ceramic composite development for gas turbine engine hot section components. in Turbo Expo: Power for Land, Sea, and Air. 2006.
[3] Grady, J.E. CMC technology advancements for gas turbine engine applications. in Pacific Rim Conference on Ceramic and Glass. 2013.
[4] Ohnabe, H., et al., Potential application of ceramic matrix composites to aero-engine components. 1999. 30(4): p. 489-496.
[5] Lamouroux, F., et al., An improved long life duration CMC for jet aircraft engine applications. 2001: p. 783-788.
[6] Cormen, S. and K.J.C.C.M.I. Lutra, Development history of GE's prepreg melt infiltrated ceramic composite material and application. 2018. 5: p. 325-328.
[7] Watanabe, F., T. Nakamura, and Y. Mizokami. Design and testing for ceramic matrix composite turbine vane. in Turbo Expo: Power for Land, Sea, and Air. 2017. American Society of Mechanical Engineers.
[8] Watanabe, F., T. Nakamura, and K.-i. Shinohara. The application of ceramic matrix composite to low pressure turbine blade. in Turbo Expo: Power for Land, Sea, and Air. 2016. American Society of Mechanical Engineers.
[9] Lacombe, A., et al. Ceramic matrix composites to make breakthroughs in aircraft engine performance. in 50th AIAA/ASME/ASCE/AHS/ASC Structures, Structural Dynamics, and Materials Conference 17th AIAA/ASME/AHS Adaptive Structures Conference 11th AIAA No. 2009.
[10] Naeem, M., R. Singh, and D.J.I.j.o.F. Probert, Implications of engine deterioration for a high-pressure turbine-blade's low-cycle fatigue (LCF) life-consumption. 1999. 21(8): p. 831-847.
[11] Salam, I., A. Tauqir, and A.J.E.f.a. Khan, Creep-fatigue failure of an aero engine turbine blades. 2002. 9(3): p. 335-347.
[12] Marshall, D.B. and A.G.J.J.o.t.A.C.S. Evans, Failure mechanisms in ceramic-fiber/ceramic-matrix composites. 1985. 68(5): p. 225-231.
[13] Marshall, D.B. and W.J.J.o.t.A.C.S. Oliver, Measurement of interfacial mechanical properties in fiber-reinforced ceramic composites. 1987. 70(8): p. 542-548.
[14] Evans, A., F. Zok, and R.J.A.M.e.M. McMeeking, Fatigue of ceramic matrix composites. 1995. 43(3): p. 859-875.
[15] Paar, R., et al., Influence of fibre properties on the mechanical behaviour of unidirectionally-reinforced ceramic matrix composites. 1998. 250(2): p. 209-216.
[16] Sørensen, B.F., J.W. Holmes, and E.L.J.J.o.t.A.C.S. Vanswijgenhoven, Rate of strength decrease of fiber-reinforced ceramic-matrix composites during fatigue. 2000. 83(6): p. 1469-1475.
[17] Mall, S., J.M.J.C.s. Engesser, and technology, Effects of frequency on fatigue behavior of CVI C/SiC at elevated temperature. 2006. 66(7-8): p. 863-874.
[18] Mehrman, J., et al., Influence of hold times on the elevated-temperature fatigue behavior of an oxide–oxide ceramic composite in air and in steam environment. 2007. 67(7-8): p. 1425-1438.
[19] Ruggles-Wrenn, M., et al., Effect of frequency and environment on fatigue behavior of a CVI SiC/SiC ceramic matrix composite at 1200 C. 2011. 71(2): p. 190-196.
[20] Ikarashi, Y., T. Ogasawara, and T.J.J.o.t.E.C.S. Aoki, Effects of cyclic tensile loading on the rupture behavior of orthogonal 3-D woven SiC fiber/SiC matrix composites at elevated temperatures in air. 2019. 39(4): p. 806-812.

NUMERICAL MODELING OF AGING EFFECTS BASED ON THE MECHANICAL BEHAVIOR OF FUNCTIONALLY GRADED MATERIALS

Julia Petro*[,1,2], Eric Helfer[1], Petra Christöfl[1], Gernot Oreski[1,3] , Margit Lang[1] and Thomas Antretter[2]

[1]Polymer Competence Center Leoben GmbH, Sauraugasse 1, A-8700 Leoben, Austria
*Email: julia.petro@pccl.at, Web Page: http://www.pccl.at
Email: eric.helfer@pccl.at, Web Page: http://www.pccl.at
Email: petra.christoefl@pccl.at, Web Page: http://www.pccl.at
Email: gernot.oreski@pccl.at, Web Page: http://www.pccl.at
Email: margit.lang@pccl.at, Web Page: http://www.pccl.at
[2]Chair of Mechanics, Montanuniversität Leoben, Franz Josef Strasse 18, 8700 Leoben, Austria
Email: thomas.antretter@unileoben.ac.at, Web Page: http://www.unileoben.ac.at
[3]Institute of Materials Science and Testing of Polymers, Montanuniversität Leoben, Otto-Glöckel-Straße 2, 8700 Leoben, Austria
Email: gernot.oreski@unileoben.ac.at, Web Page: http://www.unileoben.ac.at

Keywords: Functionally graded materials, Nano-indentation, material degradation, Xenon arc test.

Abstract
Consideration of material degradation is important when designing structural polymeric components exposed to outdoor environmental conditions. This is necessary to be able to guarantee safe and reliable performance of these components over their intended lifespan. Thus, a systematic approach is required to generate relevant mechanical property degradation data and model it in a way that can be implemented in design analysis simulations. In this study, aging effects have been assessed using nanoindentation measurements throughout the cross-section of a PC/PBT (polycarbonate-polybutylene terephthalate) material plate. Accelerated artificial weathering with State-of-the-Art Xenon arc lamps has been used to age the material according to ISO 4892-2 standard. The variation of the elastic modulus through-the-thickness of the plate has been evaluated showing a significant increase at the exposed side of the plate compared to the unexposed one. A modeling framework is presented to capture the degradation of mechanical properties through-the-thickness of the plate. A gradient is defined to represent the degradation of the modulus through the material thickness using a user subroutine (USDFLD) in Abaqus, where the definition of the material properties is dependent on a field variable via a predefined function. The results show that the model prediction is dependent on element size and therefore, a sensitivity analysis was carried out. A defined load case, i.e. cooling from room temperature (RT) to -40°C is analyzed using a virgin homogenized material definition for the plate versus a functionally graded material model.

1. Introduction

Functionally graded materials (FGM) are composite materials that exhibit innovative characteristics, featuring a gradual variation in material properties along specified dimensions [1]. In general, these materials are designed to combine strengths of multiple materials to statisfy a functional requirement [1–3]. The main advantage of FGM is the seamless transition of properties from one material to another, resulting in the elimination of stress singularities at the interfaces between different materials which are commonly found in composites, especially in ultra-high temperature environments [1, 4, 5]. Bhavar et

al. [2] described the different types of FGM and their manufacturing methods. On the other hand, several studies have focused on the characterization, modeling and analysis of parts with respect to various aspects, including testing, manufacturing, homogenization of particulate FGM, issues with heat transfer, residual stresses and fracture [3, 4, 6]. Exponential and power-law functions are commonly used to describe the varying material properties of FGMs [7–12]. Similarly, surface aging causes variation of material properties throughout the depth of designed polymeric parts [13, 14]. Polymers exhibit sensitivity to various types of radiation, including ultraviolet and gamma rays [13, 14]. Typically, these external stimuli have a greater impact on the surface of the polymer than on its bulk; however, this can have a significant impact on the overall performance of these materials depending on the application and its use-environment. A comprehensive evaluation of these aging consequences necessitates the assessment of the variation in chemical and morphological modifications in conjunction with the corresponding physical properties, enabling the determination of a characterization profile from surface to bulk [13].

In contrast to metals and ceramics, nanoindentation (NI) has not been widely used to measure the mechanical properties of polymeric materials because the viscoelastic behavior of these materials during deformation causes difficulties [13]. Nevertheless, NI is a powerful and versatile technique for polymer surface characterization [15, 16]. NI has been adapted to detect and analyze early changes in mechanical properties induced by aging mechanisms for polymers [17], as long as macrostructural factors such as cracks are not present [16, 18]. Christöfl et al. [19, 20] have shown that NI can be a reliable method to reproduce the viscoelatic properties of semi-crystalline thermoplastics, such as polyoxymethylene (POM), as well as amorphous thermoplastics, such as poly(methyl metacrylate) (PMMA).

In this paper, NI measurements are used to determine the Young's modulus profile through the thickness of an artificially weathered polycarbonate-polybutylene terephthalate (PC/PBT) material plate. A simulation approach, inspired by FGM modeling techniques, is implemented in a commercial finite element (FE) simulation software to describe the varying modulus through the thickness of the material plate.

2. Materials and Methods

2.1. Material Preparation

The virgin material used in this study is an unreinforced, UV stabilized resin. It is an impact modified PC/PBT flame retardant injection moldable grade blend. Common applications for this material include switches, housings, and coils in the electrical industry.

Tensile test specimens were injection molded standard dogbone type (1A) specimens in accordance with ISO 527-2. Tests were performed under standard laboratory conditions of 23 °C and 50 % relative humidity at a loading rate of 1 mm/min for Young's modulus evaluation, followed by a test rate of 50 mm/min. Strain measurements were acquired and analyzed using the Digital Image Correlation (DIC) technique with an ARAMIS 4M system developed by GOM.

Thermal expansion measurements were performed using a Dantec Q400 TCT (Dantec Dynamics, Ulm, Germany) DIC system. For these measurements, 30 × 30 × 3 mm^3 specimens were cut from injection molded plates. The test program had a defined temperature range of -40 °C to 140 °C at a heating rate of 1 °K/min.

For the nanoindentation (NI) tests, samples were prepared from a 3 mm thick injection molded plates. These plates were aged using an ATLAS Xenontester 440 according to the ISO 4892-2 standard settings summarized in (Table 1) for a total of 3000 hours. After cutting the samples from the aged plates as shown in (Figure 1a), they were embedded in Technovit epoxy resin. The prepared embedded sample was then ground with silicon carbide up to a grain size of 4000 and polished with 1 µm diamond polishing paste. NI measurements were performed on the polished surface using an Anton Paar UNHT^3 nanoindenter according to the measurement scheme presented in (Figure 1b). The measurements were performed under standard laboratory conditions of 23 °C and 50 % relative humidity at a loading rate of 20 mN/min and 30 s holding phase using a sphero-conical diamond indenter tip with a diameter of 10 µm.

Table 1. Accelerated aging conditions as per ISO 4892-2 standard.

Exposure period	Relative humidity (%)	Black-standard temperature (°C)	Chamber temperature (°C)	Irradiance	
				Broadband (W/m^2)	Narrowband (W/(m^2 nm))
102 min dry	50 ± 10	65 ± 3	38 ± 3	60 ± 2	0.51 ± 0.02
18 min water spray	-	-	-	60 ± 2	0.51 ± 0.02

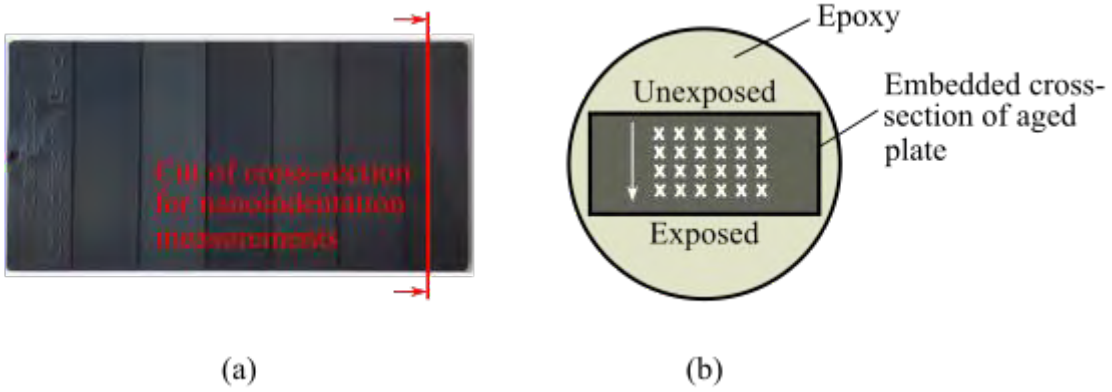


Figure 1. a) Top view of PC/PBT material plate. b) Schematic diagram for the embedded cross-section of PC/PBT sample with exemplary indents marked as "x".

2.2. Tensile test results

The virgin material properties obtained from these tests are presented in (Table 2).

Table 2. PC/PBT blend virgin material properties.

Elastic modulus (MPa)	Poisson's Ratio (-)
2102	0.3911

2.3. Coefficient of thermal expansion (CTE) results

The results of the CTE measurements on the virgin material are presented in (Figure 2).

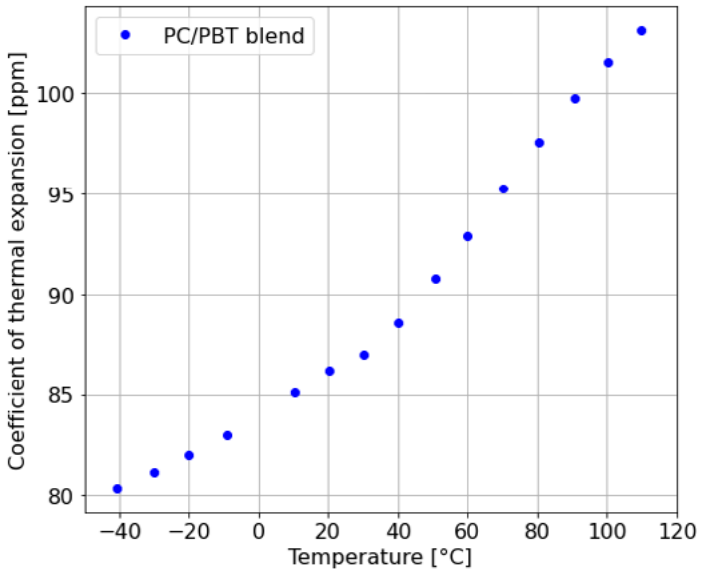


Figure 2. Coefficient of thermal expansion (CTE) measurements for PC/PBT material.

2.4. Nanoindentation results

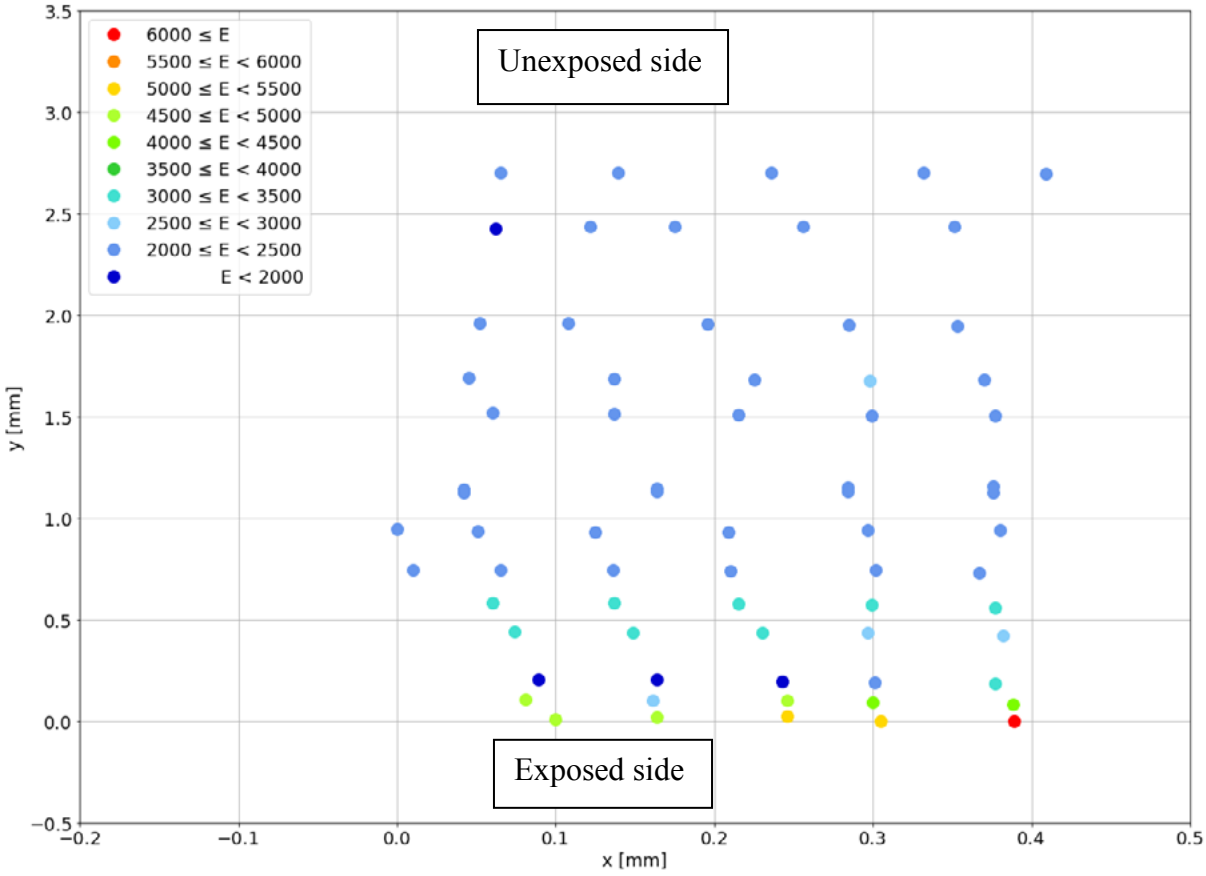


Figure 3. Nanoindentation results of the aged sample: Young's modulus variation through-the-thickness in MPa.

NI curves were evaluated using the method of Oliver and Pharr [21], where the reduced elastic modulus E_r in N/mm^2 is calculated using the following equation (Eq. 1),

$$E_r = \frac{\sqrt{\pi}}{2\beta}\frac{S}{\sqrt{A_p(h_{max})}} \quad (1)$$

where, S is the contact stiffness of the upper portion of the unloading curve at the maximum indentation depth in N/mm, A_p (h_{max}) is the contact area of the indenter tip in mm^2 as a function of h_{max} , which is the contact depth of the indenter at the maximum force in mm, and β is a dimensionless geometry factor equal to 1 for a sphero-conical tip. The method used assumes that unloading is purely elastic, which is not the case for viscoelastic polymers. As clarified in our previous work [20], the Oliver and Pharr approach with a longer hold phase is good enough for a quatitative analysis as in this work. For more sophisticated modulus evaluation, other methods such as the creep method or dynamic methods would be appropriate. This was not possible in this work due to time and equipment limitations.
The evaluated measurements for the elastic modulus are shown in (Figure 3). A gradient throughout the thickness of the plate can be observed, indicating material surface embrittlement at the UV exposed side of the plate compared to the unexposed side.

3. Simulations

In this section, a modeling framework is presented to capture the degradation of mechanical properties through-the-thickness of a PC/PBT plate.

3.1. Model setup

The setup for the finite element model (FEM) is presented as a global model in (Figure 4). In order to reduce computational effort, symmetric boundary conditions are assumed and therefore, only a quarter of the model is analyzed. The dimensions of the quartered plate are 30 × 30 × 3 mm^3. The mounting of the global model is represented by a fixed boundary condition at the edges of the plate, as illustrated in (Figure 4). 8-node linear brick elements, with reduced integration, and hourglass control are used in this model.

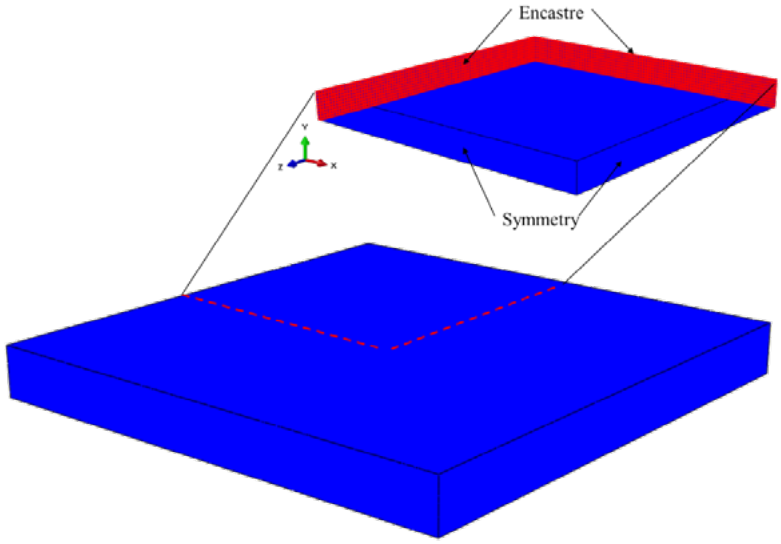


Figure 4. FE model setup and definition of boundary conditions.

3.2. Material modeling

The evaluated nanoindentation measurements at each depth are used to calculate a representative, averaged value for the Young's modulus, as depicted in (Figure 5). An optimization scheme using Genetic Algorithm (GA) is implemented to find a least squares fitting function to represent the material

degradation profile of the elastic modulus evaluated through the thickness of the plate. The function takes an exponential form, see (Eq.2). The fitted coefficients are given in (Table 3).

$$E(y) = ae^{by} + ce^{dy} + k \tag{2}$$

where, y is the position of the material point within the plate thickness, a, b, c, d and k are fitting parameters.

Table 3. Fitting parameters for the functionally graded material: PC/PBT blend

a	b	c	d	k
2435.42	-2.71	783.98	-3834.19	2241.92

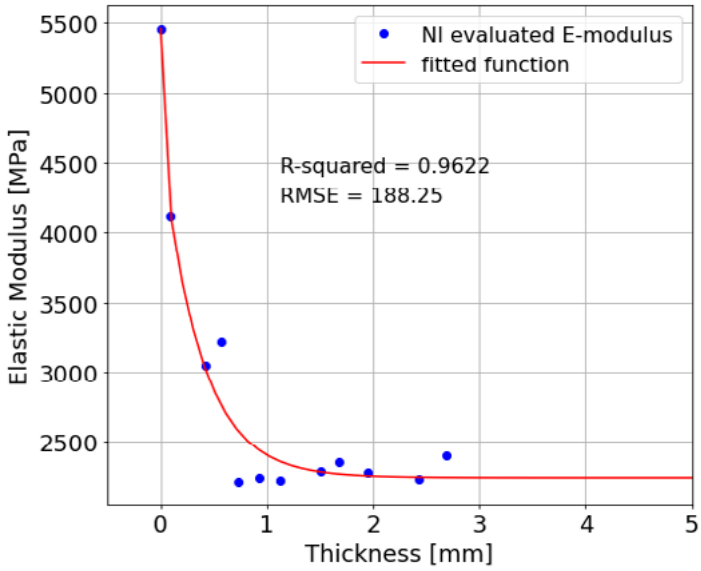


Figure 5. Fitting function for the Young's modulus variation through the thickness of the plate.

A gradient is defined to represent the degradation of the modulus through the material thickness using a user subroutine (USDFLD) in Abaqus 2019. Here, the definition of the Young's modulus in the through thickness dimension is dependent on a field variable, which is calculated using the fitted function presented in (Eq.2) and (Figure 5).

3.3. Loading conditions

The load case is defined by applying a thermal profile to cool the plate from room temperature (RT) to -40 °C. The load case is analyzed using a virgin homogenized material definition for the plate as described in (Table 2) versus a functionally graded material model.

3.4. Numerical results

The numerical results of five models with refined meshes are compared below, see (Figure 6). The element sizes and corresponding number of elements are listed in (Table 4). The model prediction shows element size dependency and therefore, a mesh sensitivity analysis is carried out. The results are found to be accurate enough at an element size of h = 0.125 mm.

Table 4. Mesh information summary for the analyzed models.

Model	Element size, h (mm)	Number of elements, N
1	0.5	21600
2	0.35	66564
3	0.25	172800
4	0.125	1382400
5	0.1	2700000

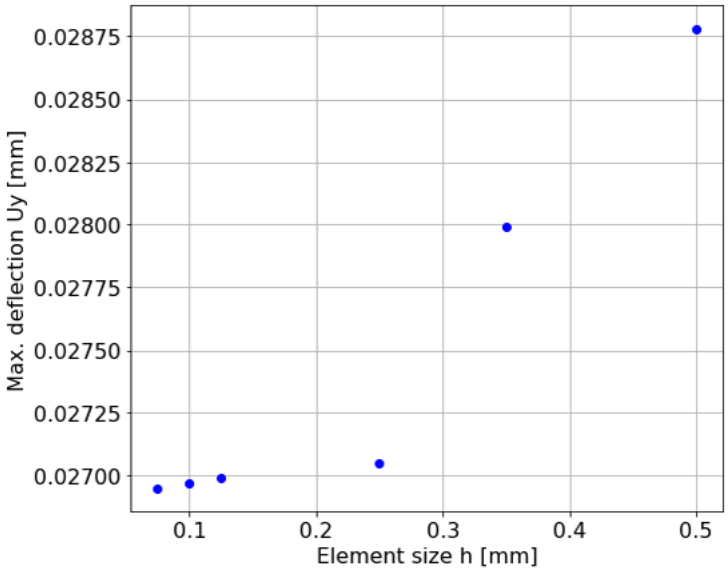


Figure 6. Max. deflection obtained from different mesh sizes.

(Figure 7) shows a contour plot of the deformation results for a homogeneous plate with virgin, non-degraded material properties (see, Table 2) and a functionally graded material plate (material model see Section 3.2). In the case of the homogeneous plate, the deformations are symmetrical, as expected. However, in the case of the functionally graded material plate, non-symmetrical deformations are observed due to the increase in Young's modulus closer to the UV-exposed surface. To further illustrate this deflection asymmetry in the case of the FGM plate vs. the homogeneous virgin material, the deflection through the thickness of the plate in both cases is plotted against the nodal coordinate in the thickness direction, as shown in (Figure 8). In the case of the homogeneous virgin material, zero deflection is observed at the line of symmetry, which is exactly the mid-plane of the plate (at y =1.5 mm), while in the case of the FGM plate, the plane of zero deflection is shifted toward the exposed side of the plate by 0.2163 mm.

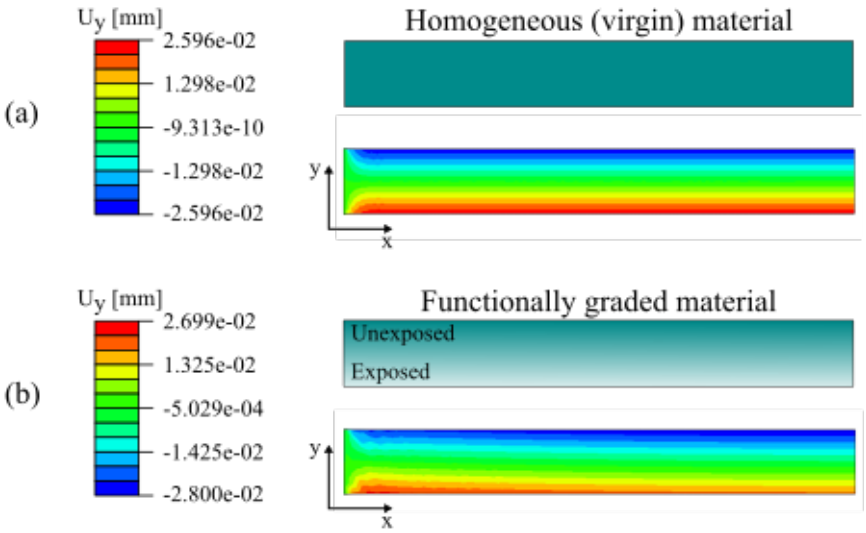


Figure 7. Deformation results when cooling from room temperature to -40 °C: (a) Homogeneous (virgin) material properties, (b) Aged material, modelled as functionally graded material.

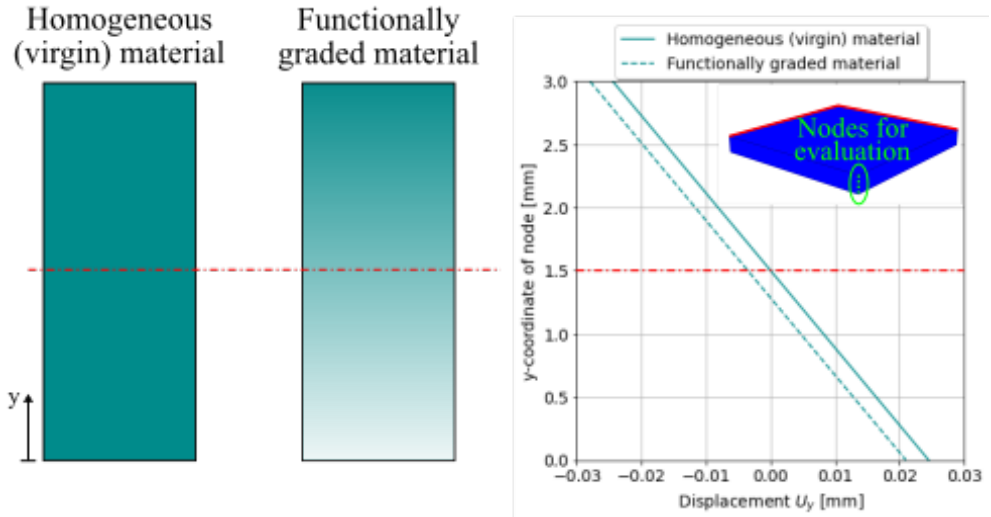


Figure 8. Deflection through the thickness of the plate: Homogeneous (virgin) material vs. Functionally graded material (FGM).

4. Conclusions and Outlook

Surface aging effects are determined using through-thickness nanoindentation measurements of a polymer plate. These effects are captured in numerical simulations using the FGM modeling approach in a thermo-mechanical simulation, where, non-symmetric deformations are observed in the case of the FGM plate compared to the results for the virgin material. This indicates that it is necessary to consider material degradation in order to assess the lifetime of the designed part. However, the methodology used has been shown to be highly dependent on the element size and therefore the computational effort for complex geometries is expected to be significant. The effect of the element type and formulation used on the simulation results obtained would be further investigated in the future, as well as the effect of aging on the thermal properties of the material, i.e., CTE measurements and its inclusion in the material model.

Acknowledgments
The research work of this paper was performed at the Polymer Competence Center Leoben GmbH (PCCL, Austria) within the framework of the COMET-program of the Federal Ministry for Transport, Innovation and Technology and the Federal Ministry of Digital and Economic Affairs with contributions by Fronius International GmbH. The PCCL is funded by the Austrian Government and the State Governments of Styria, Lower Austria and Upper Austria.

References

[1] J. Kim, W. I. Lee, and S. W. Tsai, "Modeling of mechanical property degradation by short-term aging at high temperatures," *Composites Part B: Engineering*, vol. 33, no. 7, pp. 531–543, 2002, doi: 10.1016/S1359-8368(02)00036-7.
[2] V. Bhavar, P. Kattire, S. Thakare, S. patil, and R. K. Singh, "A Review on Functionally Gradient Materials (FGMs) and Their Applications," *IOP Conf. Ser.: Mater. Sci. Eng.*, vol. 229, p. 12021, 2017, doi: 10.1088/1757-899X/229/1/012021.
[3] V. Birman and L. W. Byrd, "Modeling and Analysis of Functionally Graded Materials and Structures," *Applied Mechanics Reviews*, vol. 60, no. 5, pp. 195–216, 2007, doi: 10.1115/1.2777164.
[4] S.-H. Chi and Y.-L. Chung, "Mechanical behavior of functionally graded material plates under transverse load—Part I: Analysis," *International Journal of Solids and Structures*, vol. 43, no. 13, pp. 3657–3674, 2006, doi: 10.1016/j.ijsolstr.2005.04.011.
[5] M. Niino and S. Maeda, "Recent development status of functionally gradient materials," *ISIJ International*, vol. 30, no. 9, pp. 699–703, 1990, doi: 10.2355/isijinternational.30.699.
[6] S.-H. Chi and Y.-L. Chung, "Mechanical behavior of functionally graded material plates under transverse load—Part II: Numerical results," *International Journal of Solids and Structures*, vol. 43, no. 13, pp. 3675–3691, 2006, doi: 10.1016/j.ijsolstr.2005.04.010.
[7] Z.-H. Jin and G. H. Paulino, "Transient thermal stress analysis of an edge crack in a functionally graded material," *International Journal of Fracture*, vol. 107, no. 1, pp. 73–98, 2001, doi: 10.1023/A:1026583903046.
[8] Z.-H. Jin and R. C. Batra, "STRESS INTENSITY RELAXATION AT THE TIP OF AN EDGE CRACK IN A FUNCTIONALLY GRADED MATERIAL SUBJECTED TO A THERMAL SHOCK," *Journal of Thermal Stresses*, vol. 19, no. 4, pp. 317–339, 1996, doi: 10.1080/01495739608946178.
[9] F. Delale and F. Erdogan, *The Crack Problem for a Nonhomogeneous Plane*. London: Routledge, 1983. [Online]. Available: https://search.ebscohost.com/login.aspx?direct=true&scope=site&db=nlebk&db=nlabk&AN=365065
[10] P. Gu and R. J. Asaro, "Crack deflection in functionally graded materials," *International Journal of Solids and Structures*, vol. 34, no. 24, pp. 3085–3098, 1997, doi: 10.1016/S0020-7683(96)00175-8.
[11] F. Erdogan and B. H. Wu, "CRACK PROBLEMS IN FGM LAYERS UNDER THERMAL STRESSES," *Journal of Thermal Stresses*, vol. 19, no. 3, pp. 237–265, 1996, doi: 10.1080/01495739608946172.
[12] Z.-H. Jin and N. Noda, "Crack-Tip Singular Fields in Nonhomogeneous Materials," *Journal of Applied Mechanics*, vol. 61, no. 3, pp. 738–740, 1994, doi: 10.1115/1.2901529.
[13] A. C. Tavares, J. V. Gulmine, C. M. Lepienski, and L. Akcelrud, "The effect of accelerated aging on the surface mechanical properties of polyethylene," *Polymer*

Degradation and Stability, vol. 81, no. 2, pp. 367–373, 2003, doi: 10.1016/S0141-3910(03)00108-3.

[14] G. M. Odegard and A. Bandyopadhyay, "Physical aging of epoxy polymers and their composites," *J Polym Sci B Polym Phys*, vol. 49, no. 24, pp. 1695–1716, 2011, doi: 10.1002/polb.22384.

[15] B. D. Beake and G. J. Leggett, "Nanoindentation and nanoscratch testing of uniaxially and biaxially drawn poly(ethylene terephthalate) film," *Polymer*, vol. 43, no. 2, pp. 319–327, 2002, doi: 10.1016/S0032-3861(01)00600-0.

[16] P. Christöfl *et al.,* "Nanoindentation for Fast Investigation of PET Film Degradation," *JOM*, vol. 74, no. 6, pp. 2287–2294, 2022, doi: 10.1007/s11837-022-05278-0.

[17] D. C. Miller, M. Owen-Bellini, and P. L. Hacke, "Use of indentation to study the degradation of photovoltaic backsheets," *Solar Energy Materials and Solar Cells*, vol. 201, p. 110082, 2019, doi: 10.1016/j.solmat.2019.110082.

[18] T. Pertin, G. Minatchy, M. Adoue, A. Flory, and L. Romana, "Investigation of nanoindentation as a fast characterization tool for polymer degradation study," *Polymer Testing*, vol. 81, p. 106194, 2020, doi: 10.1016/j.polymertesting.2019.106194.

[19] P. Christöfl *et al.,* "Morphological characterization of semi-crystalline POM using nanoindentation," *International Journal of Polymer Analysis and Characterization*, vol. 26, no. 8, pp. 692–706, 2021, doi: 10.1080/1023666X.2021.1968122.

[20] P. Christöfl, C. Czibula, M. Berer, G. Oreski, C. Teichert, and G. Pinter, "Comprehensive investigation of the viscoelastic properties of PMMA by nanoindentation," *Polymer Testing*, vol. 93, p. 106978, 2021, doi: 10.1016/j.polymertesting.2020.106978.

[21] W. C. Oliver and G. M. Pharr, "Measurement of hardness and elastic modulus by instrumented indentation: Advances in understanding and refinements to methodology," *J. Mater. Res.*, vol. 19, no. 1, pp. 3–20, 2004, doi: 10.1557/jmr.2004.19.1.3.

EXPERIMENTAL AND NUMERICAL PROBABILISTIC MULTISCALE INVESTIGATION OF SHORT-FIBER REINFORCED POLYMERS

B. Rohrmüller[1], J. Hohe[1], L. Kärger[2] and C. Beckmann[1]

[1]Fraunhofer Institute for Mechanics of Materials IWM, Freiburg, Germany
Email: benedikt.rohrmueller@iwm.fraunhofer.de, Web Page: www.iwm.fraunhofer.de
[2]Karlsruhe Institute of Technology (KIT), Institute of Vehicle System Technology (FAST), Karlsruhe, Germany

Keywords: Uncertainties, Multiscale simulation, Probabilistic assessment, Short fiber-reinforced polymers, Composites

Abstract
Short-fiber reinforced composites are used in lightweight construction due to their numerous advantages: they have a high strength-to-weight ratio together with a low specific density and can be manufactured cost efficiently in complex geometries. Standard manufacturing technologies like injection-molding can be used. In this contribution, the material uncertainty of a short fiber reinforced composite material is investigated by mechanical characterization and multiscale simulations based thereon. The objective is to assess the propagation of uncertainties across the scales. Uncertainties in short-fiber reinforced composites can be caused by a scatter in the material properties but especially by a local variation in the fiber orientation and fiber density.
Experimental results of mechanical testing showed a scatter of the mechanical properties inside a plate and between different plates. This scattering is mainly caused by the scattering of the fiber orientation. Microstructure generation and simulation enable the investigation of the local microstructure influence.

1. Introduction

The material investigated has a heterogeneous microstructure consisting of a phenolic-resin polymer matrix reinforced with short glass fibers. The material compounding and manufacturing was done in a thermoset injection-molding process at Fraunhofer ICT, Pfinztal, Germany [1]. Due to the material flow in the manufacturing process, this composite has an uncertainty in the fiber orientation distribution. This leads to an uncertainty in the mechanical properties. The material is characterized experimentally on plates manufactured under constant conditions to investigate the scatter of the material behavior. Additionally plates with different fiber volume contents are manufactured. The characterization of the uncertainty of the mechanical properties is done by experiments on different levels of structural hierarchy. Large scale tensile, compression and shear tests are performed on different plates to investigate the scatter between different plates. Small scale tensile tests are performed to investigate the scatter of the mechanical properties inside a plate [2]. Additionally microscale tensile tests are performed to investigate the debonding between fiber and matrix at the fiber-matrix interface.
The experimental microstructure is rebuilt for numerical simulations. Finite element simulations of the microstructure are performed to investigate the influence of the scattering of the fiber orientation distribution and the fiber volume content. The microstructure simulations require different material models for fibers, matrix and the intermediate fiber-matrix interface. The fiber-matrix interface is modeled by a cohesive zone model. The microstructure simulations form the basis for multiscale simulations with a consideration of the uncertainty of the fiber orientation and fiber volume content.
Microstructure motivated representative volume element (RVE) simulations can be utilized to study the effect of the fiber orientation on the macroscale (see e.g. [4],[5]). The term statistical volume element

(SVE) is often used for microstructures that are not individually representative of a material because they are too small. Only the sum of all SVEs is in turn representative of a material. [6] However, the scattering of the material behavior can be investigated with SVE simulations.
In this work, experimental tensile test results on a short fiber reinforced polymer on two different scales are shown. In a second step, microstructure simulations using the finite element method (FEM) are performed to further investigate the material scattering. They form the basis for a microstructurally motivated investigation of the scattering of material properties.

2. Experimental investigation

2.1. Material

The material under investigation is a short fiber reinforced polymer consisting of glass fibers and a phenolic resin matrix. The manufacturing was done by a thermoset injection molding process [1]. The material was characterized on rectangular plates of size 480 x 190 mm² and thicknesses of 2 and 3 mm. The plates possess a fiber mass content of 37.5 wt%.

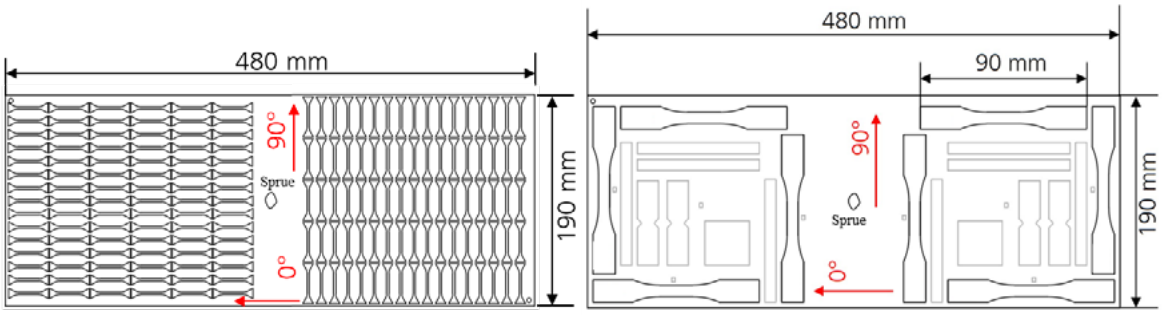


Figure 1. Sample plan with sprue in the middle of the plates.

2.2. Experiments and evaluation

Two sizes of tensile test specimens were taken from the plates. Miniature samples of a cross-section of 2 x 2 mm² and a length of 36 mm and shortened ISO size samples (3 x 10 mm² and 90 mm length). The sample plan is shown in Figure 1. The miniature samples were taken from two half plates of 2 mm thickness to investigate the material scatter inside a plate. 90 miniature samples were taken in 0° and 85 in 90°. The shortened ISO size samples were taken from seven different plates to investigate the scatter between different plates. From every plate were taken four 0° samples and four 90° samples. A total of 28 0° ISO samples and 28 90° ISO samples were tested. The samples were cut out by water jet cutting.

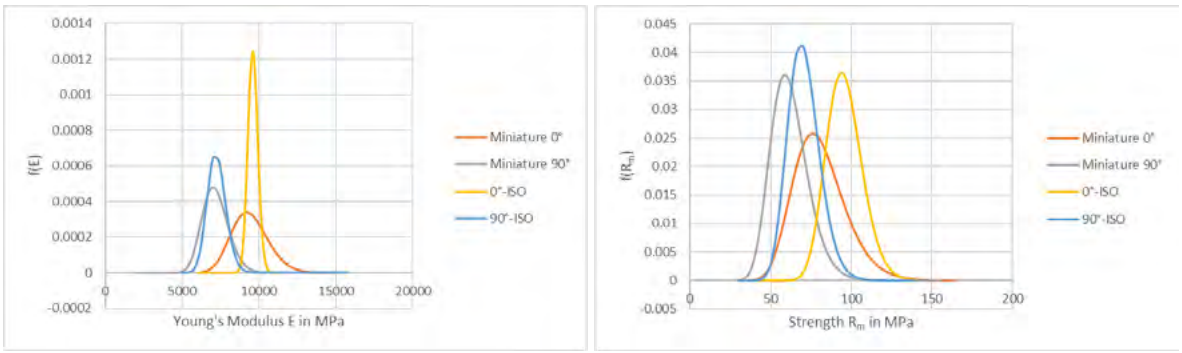


Figure 2. Experimental data.

A statistic evaluation of the experimental tensile test results is given in Figure 2. The distribution functions of the Young's modulus and strength are shown. A Log-normal distribution is used for every distribution. More details of the experimental results are given in [2]. Both sizes of tested samples show higher Young's modulus and strength values in 0° direction which coincides with the flow direction of the material. The tests on the miniature samples show a larger scatter than the tests of the ISO size samples. Compared to the ISO specimen tests, the 0° tests on the miniature specimens show a slightly lower stiffness. This could be due to the fact that the 0° ISO specimens were only taken at the edges of the plate and not in the middle. In addition, the tests of the miniature samples showed a lower strength. As the material is brittle, edge effects from the sampling could play a greater role.

3. Simulation investigation

3.1. Microstructure simulation

Microstructures with fibers and matrix are used as the basis for FEM-simulations. Short fiber microstructures with given fiber volume content and fiber orientation distribution are generated using the sequential addition and migration method of Schneider [3]. The generated microstructures are used as geometry for FEM simulations in Abaqus. Material models for fibers (linear elastic), matrix (elastic-plastic with damage) and interface (cohesive zone contacts) are used in the simulation.
Microstructures are generated on a representative volume element (RVE) scale. To include a scatter of the mechanical properties, the evaluation of the RVEs is done on a statistical volume element (SVE) subscale. An example microstructure of the size 0.6 x 0.6 x 0.1 mm³ is shown in Figure 3 with the separation in SVEs for the evaluation. The SVEs are only representatives of the material as a whole.

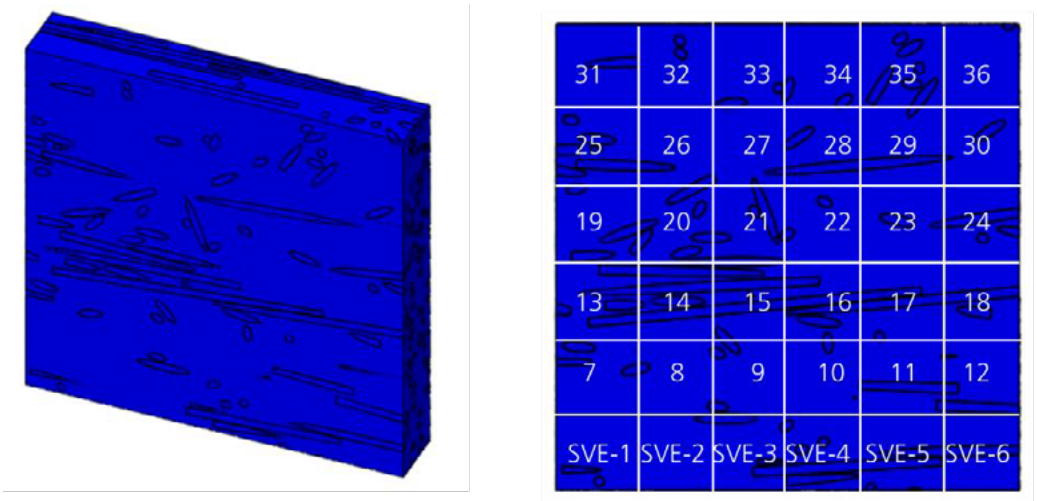


Figure 3. Microstructural RVE, separated in SVEs for evaluation.

The RVE is loaded in tension and shear directions as shown in Figure 4. Most fibers are arranged in xx-direction, which is the flow direction in the manufacturing process. Additionally, the stress-strain curves for all SVEs are given. Stresses and strains of every SVE are determined by averaging over the individual elements. The ij-th component of the stress tensor is determined by

$$\bar{\sigma}_{ij} = \frac{1}{V_{\mathrm{SVE}}} \int_{V_{\mathrm{SVE}}} \sigma_{ij} \, \mathrm{d}V \cong \frac{1}{V_{\mathrm{SVE}}} \sum_{k=1}^{n_{\mathrm{SVE}}} \sigma_{ij}^{(k)} V^{(k)} \tag{3}$$

with n_{SVE} as the number of elements in the SVE and V_{SVE} as the volume of the SVE. The strain is determined in the same way.

$$\bar{\varepsilon}_{ij} = \frac{1}{V_{\mathrm{SVE}}} \int_{V_{\mathrm{SVE}}} \varepsilon_{ij} \, \mathrm{d}V \cong \frac{1}{V_{\mathrm{SVE}}} \sum_{k=1}^{n_{\mathrm{SVE}}} \varepsilon_{ij}^{(k)} V^{(k)}. \tag{3}$$

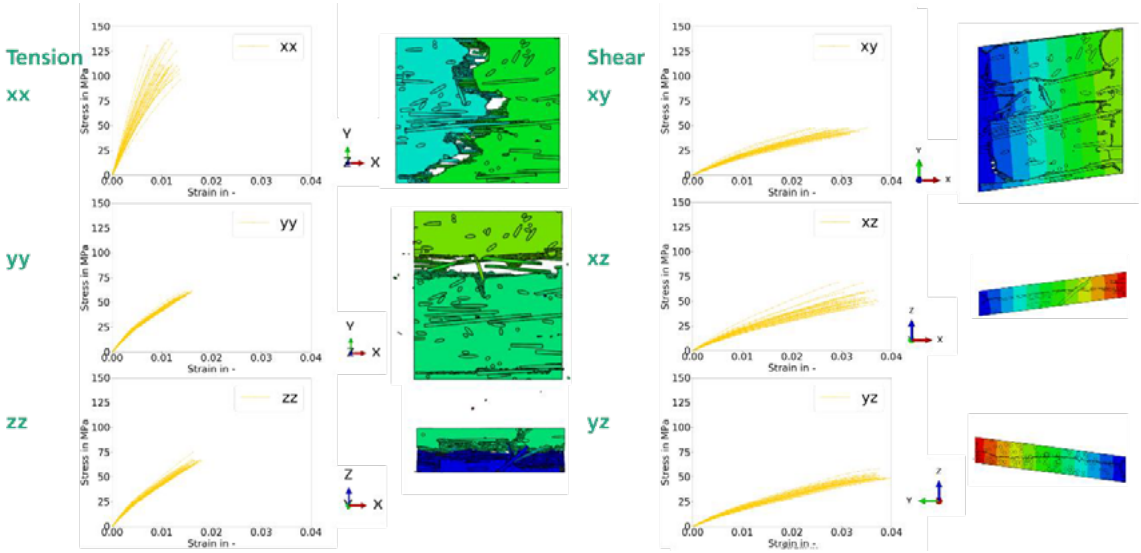


Figure 4. Tension and shear loading evaluations of SVEs with RVE from Figure 3.

4. Discussion

The experimental results show a higher scatter for the mechanical properties of the miniature samples than for the ISO size samples. This means the flow-induced variation of the fiber orientation inside a plate is larger than the variation between the same positions of different plates.

The evaluation of the microstructure simulation on the SVE scale enables the consideration of the scattering of the mechanical properties. The SVE evaluation shows a high scattering of the stress-strain curves in the xx-direction (flow direction) of the material. This can be explained by the fact that the fibers in the flow direction have the largest reinforcing effect and deviations therefore also have a greater influence. The scatter of the shear loading is relatively similar. Slightly higher scatter in the shear load in the xz- and yz-directions can be caused by the stronger influence of the boundary conditions, because the geometry is thinner in the z-direction. Also the correlation between fiber orientation and mechanical properties can be investigated in detail.

5. Conclusions

For short fiber reinforced composites, microstructure simulations provide a way of predicting the production-related scattering of material properties. They thus form a basis for probabilistic multiscale simulations in virtual process chains.

Acknowledgments
The present work has been funded by the Deutsche Forschungsgemeinschaft (DFG, German Research Foundation) under Grant no. 464119659. The financial support is gratefully acknowledged.

References

[1] R. Maertens, W.V. Liebig, P. Elsner and K.A. Weidenmann. Compounding of short fiber reinforced phenolic resin by using specific mechanical energy input as a process control parameter. J. Compos. Sci., 5, 127, 2021.
[2] B. Rohrmüller, F. Kneisel, J. Hohe and C. Beckmann. Experimental investigation of the uncertainty of disordered fiber-reinforced injection-molded components. UNCECOMP Proceedings, 2023.
[3] M. Schneider. The sequential addition and migration method to generate representative volume elements for the homogenization of short fiber reinforced plastics. Comput. Mech. 59(2):247–263, 2017.
[4] J. Köbler, M. Schneider, F. Ospald and H. Andrä. Fiber orientation interpolation for the multiscale analysis of short fiber reinforced composite parts. *Comput Mech*, 61:729-750, 2018.
[5] K. Breuer, A. Spickenheuer and M. Stommel. Statistical analysis of mechanical stressing in short fiber reinforced composites by means of statistical and representative volume elements. *Fibers*, 9(32): 1-17. 2021.
[6] A. Couture, V. François, J.-C. Cuillière and P. Pilvin. Automatic statistical volume element modeling based on the unified topology model. *International Journal of Solids and Structures*, 191-192:26-41, 2020.

EFFICIENT APPROACH TO THE DIMENSIONING OF HYBRID METAL-FRP INTERFERENCE-FITTED CONNECTIONS WITH HIGH CIRCUMFERENTIAL SPEED

Leon Schröder[1], Sebastian Spitzer[2], Michael Schiffner[1] and Maik Gude[1]

[1]Institute of Lightweight Engineering and Polymer Technology, TU Dresden, Holbeinstr. 3, 01307 Dresden, Germany, Email: leon_heinrich.schroeder@tu-dresden.de, Web Page: https://tu-dresden.de/ing/maschinenwesen/ilk
[2]Chair of Lightweight Design, Universität Rostock, Albert-Einstein-Str. 2, 18059 Rostock, Germany
Email: sebastian.spitzer@uni-rostock.de, Web Page: https://www.cld.uni-rostock.de

Keywords: press fit, fibre reinforced polymer, centrifugal force

Abstract *(max 200 words)*
This paper proposes an analytical method for the efficient prediction of the effective joint pressure in interference fits of metal/fibre reinforced polymer (FRP) joints. The approach can be used by engineers to efficiently estimate key design parameters such as laminate structure or wall thickness. A simplified model for describing joints with anisotropic material behavior is developed using analytical models of press-fitted isotropic cylinders known from DIN 7190 for interference fits, among others. The model is based on various assumptions about the structural behavior of the FRP component. The presented calculation method enables the calculation of joint pressure curves that are dependent on circumferential speed with minimal computational effort. These curves can be used to draw conclusions about functionality and load transferability within a defined speed range by comparing them with the loads that need to be transferred. To ensure accuracy, the analytical calculation approach is checked against the results of a corresponding numerical simulation. This paper presents practical design recommendations for metal/FRP interference fits with high circumferential speeds. The recommendations are derived based on a parameter variation analysis. The aim is to facilitate the time and computationally efficient design of hybrid press-fitted shaft-hub connections in metal-FRP designs considering the deformation induced by centrifugal force during operation.

1. Introduction

Fibre reinforced polymer (FRP) structural components have the potential to achieve high circumferential speeds due to their high density-related mechanical properties, such as strength and stiffness, which reduce centrifugal forces and induced stresses. These materials are particularly suitable for use in rotating components, as future demands will require higher circumferential speeds and reduced rotating mass or moment of inertia to meet technical and economic criteria.

Interference fits, also known as press-fits, represent an attractive solution for lightweight design, as they connect without the need for additional fasteners or connection elements that would otherwise require significant design space. Furthermore, the load can be applied to a defined area of the FRP, which is advantageous as stress peaks are avoided. This reduces system mass and centrifugal forces, leading to reduced energy consumption and stresses during operation.

However, the use of hybrid interference fit connections in metal/FRP designs presents challenges due to the anisotropic behaviour of FRP materials. Existing analytical approaches do not consider this issue [1-3] or have other disadvantages, such as high computational effort or the inability to consider

the influence of rotation [4-8]. Moreover, at high circumferential speeds, the outer part experiences radial deformation, resulting in a decrease in the effective joint pressure. This can cause the outer part to slip or even lift off [3]. The subsequent discussion explores a simplified analytical approach that considers these effects for anisotropic hybrid metal/FRP interference-fitted connections.

2. Hybrid Interference fits with high circumferential speed.

2.1 Hybrid interference fits

The force transmission in a press-fit connection is achieved through surface friction between the connection partners. The transmittable force F_T is determined by Coulomb's law for static friction $F_T = \mu_{sf} \cdot F_N$ with the static friction coefficient μ_{sf}. The contact pressure F_N is a result of the interference between the inner and outer parts, which is specifically set during the joint process [3].

This paper investigates Type A connections (cf. Figure 1) since it is assumed that they reach the highest circumferential speeds. The induced stresses in the tangential direction are limiting, especially for the metal part. Therefore, Type A is chosen because the induced stresses in solid shafts are much lower than in hollow shafts according to Type B and Type C. This is justified by simple calculations of rotating circular disks [9].

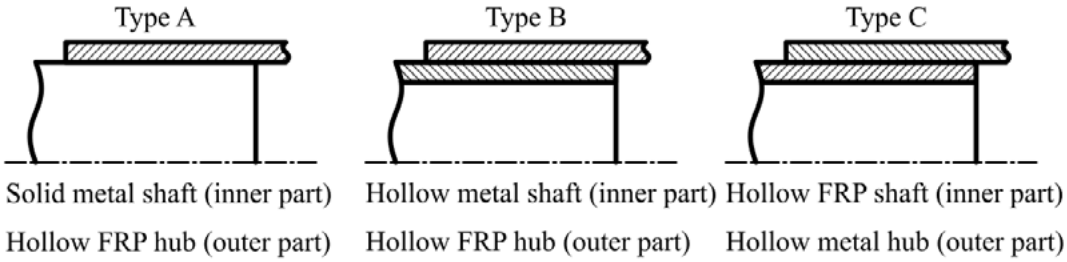


Figure 1. Different designs for hybrid metal-FRP-interference fits

2.2. Interference fits with isotropic components

The analytical calculation of interference fits for isotropic connection parts of the same material, whether solid or hollow, is a well-established practice described in DIN 7190. However, the calculation under the influence of centrifugal forces is limited to designs where the inner part I and the outer part A have the same modulus of elasticity, Poisson ratio, and density, i.e $E_I = E_A$, $\nu_I = \nu_A$ and $\rho_I = \rho_A$ [1]. Additional literature sources [2,3] offer an analytical approach to the isotropic properties of both the inner and outer parts.

Consideration based on the joint pressure, as described in [2]:
The minimum joint pressure $p_{\min}$ required to transmit the axial force F_{ax} and the torsional moment M_t can be calculated from equation

$$p_{\min} = \frac{1}{\mu_{sf} \cdot \pi \cdot D_F \cdot L_F} \sqrt{F_{ax}^2 + \frac{4 \cdot M_t^2}{D_F^2}} \tag{1}$$

where D_F is the diameter and L_F is the length of the interference fit. The calculation of the angular velocity for lift-off ω_{ab} with the outer diameter of the outer part D_{aA} is given by:

$$\omega_{ab} = \frac{4}{D_{aA}} \sqrt{\frac{E_A \cdot \xi}{K \cdot \rho_A}}. \tag{2}$$

That requires the determination of the relative stiffness factor ξ and the support factor K:

$$\xi = \frac{1}{E_A}\left[\left[\frac{E_A}{E_I}\left(\frac{1+Q_I^2}{1-Q_I^2} - \nu_I\right) + \frac{1+Q_A^2}{1-Q_A^2} + \nu_A\right] p_{min} + \frac{K \cdot D_F^2 \cdot \omega^2 \cdot \rho_A}{16 \cdot Q_A^2}\right], \tag{3}$$

$$K = 3 + \nu_A + (1-\nu_A)\cdot Q_A^2 - \frac{E_A \cdot \rho_I}{E_I \cdot \rho_A} \cdot Q_A^2 \cdot [1 - \nu_I + (3+\nu_I)\cdot Q_I^2], \tag{4}$$

$$Q_A = \frac{D_F}{D_{aA}} \text{ with } Q_I = 0\,. \tag{5}$$

The following equation enables the calculation of the joint pressure at standstill p_{still} using $p_\omega = p_{min}$:

$$p_\omega = p \cdot \left[1 - \left(\frac{\omega}{\omega_{ab}}\right)^2\right]. \tag{6}$$

Additionally, it facilitates the determination of the joint pressure at any arbitrary angular velocities ω.

Consideration based on the interference, as described in [3]:
The effective interference is calculated based on the expansions and constrictions of the inner and outer parts, separately, according to the influencing factors: joint pressure ($\Delta D_{aI,p}$ and $\Delta D_{iA,p}$), centrifugal force ($\Delta D_{aI,rot}$ and $\Delta D_{iA,rot}$) and temperature ($\Delta D_{aI,T}$ and $\Delta D_{iA,T}$). The equations used are as follows:

$$\Delta D_{aI,p} = -\frac{p}{E_I} \cdot D_F \cdot \left(\frac{1+Q_I^2}{1-Q_I^2} - \nu_I\right), \tag{7}$$

$$\Delta D_{iA,p} = \frac{p}{E_A} \cdot D_F \cdot \left(\frac{1+Q_A^2}{1-Q_A^2} + \nu_A\right), \tag{8}$$

$$\Delta D_{aI,rot} = \frac{\rho_I \cdot \omega^2}{2 \cdot E_I} \cdot \left(\frac{D_F}{2}\right)^3 \cdot (1-\nu_I), \tag{9}$$

$$\Delta D_{iA,rot} = \frac{\rho_A \cdot \omega^2 \cdot D_F}{E_A} \cdot \left[2 \cdot c_1 \cdot \left(\frac{D_{aA}}{2}\right)^2 + (c_1 - c_2) \cdot \left(\frac{D_F}{2}\right)^2\right], \tag{10}$$

$$\Delta D_{aI,T} = D_F \cdot \alpha_A \cdot \Delta\theta_A\,, \tag{11}$$

$$\Delta D_{iA,T} = D_F \cdot \alpha_I \cdot \Delta\theta_I \text{ with} \tag{12}$$

$$c_1 = \frac{3+\nu_A}{8} \text{ and } c_2 = \frac{1+3\cdot\nu_A}{8}. \tag{13}$$

When considering influencing factors, it is important to note that joint pressure can be reduced by the centrifugal force of the outer part, but can also be increased by the thermal expansion of the inner part. The effective interference during operation is determined by the superposition of these effects. The following equation allows the recalculation from the effective interference $P(n,T)$ at a specific rotational speed n and temperature T back to the joint pressure $p(n,T)$:

$$p(n,T) = \frac{P(n,T)}{D_F \cdot \left[\frac{1}{E_A} \cdot \left(\frac{1+Q_A^2}{1-Q_A^2} + \nu_A\right) + \frac{1}{E_I} \cdot \left(\frac{1+Q_I^2}{1-Q_I^2} - \nu_I\right)\right]}. \quad (14)$$

The temperature difference required to join the interference fit $\Delta\theta_F$ (cooling of the inner part) can be calculated from the required interference at standstill with the isotropic temperature expansion coefficient of the inner part α_I as follows [5]:

$$\Delta\theta_F = -\frac{\Delta D_{aI,p} + \Delta D_{iA,p}}{D_F \cdot \alpha_I}. \quad (15)$$

2.3. Interference fits with orthotropic components

The literature provides calculation methods and design recommendations, although their practical applicability is often limited due to underlying assumptions and simplifications. For instance, [4] presents an analytical method for calculating torsionally loaded interference fits, which enables the determination of stresses in finitely extended, orthotropic connection partners. Various assumptions are necessary due to the complexity of the differential equation systems involved. These assumptions limit the use of the calculation method to preliminary design applications. Further details on this calculation approach can be found in [5], which does not provide consideration of rotational stresses.

Other calculation approaches pose similar challenges for engineers, as they are often only applicable to specific use cases or involve significant simplifications. For instance, the calculation of radial and tangential stresses in cylinders under internal pressure can be performed assuming a unidirectional laminate, as described in [7]. Another method for calculating pressed anisotropic laminates is presented in [8], wich requires a significantly higher calculation effort. These models describe cylinders with infinite expansion, making it impossible to consider the axial stress distribution curves.

In order to take into account the influence of temperature, [6] proposes a method for the calculation of stresses in thick-walled, anisotropic cylinders. The calculation includes the effects of axial force, torsional moment, internal and external pressure, and centrifugal force. However, solving the differential equations results in systems of equations that are difficult to solve analytically [4].

This paper focuses solely on the force transmission of the interference fit and not on the strength analysis of the part. Therefore, the stress distribution in the laminate and resulting failure indices are not considered. Simply the elastic properties of the connecting parts are used to determine the force transmission. The presented analytical calculation approach requires the determination of the laminate engineering constants of the FRP part. The ABD-matrix describes the stiffness of a multiaxial laminate made up of several unidirectional layers. It allows the calculation of the averaged engineering constants for the laminate [10].

3. Results

3.1 Analytical calculation of the joint pressure considering the centrifugal force

The presented analytical model combines the advantages of low computational effort and ease of design studies in the early stages of the development process, based on state-of-the-art methods for calculating interference fits.

The following assumptions have been made:

I. Both connection partners are considered to be infinitely extended, isotropic cylinders.
II. The FRP connection partner is described by the engineering constants of the multilayer composite in the circumferential direction.

III. Both connection partners are subjected to purely elastic deformation.
IV. The reduction in joint pressure due to relaxation of the matrix is neglected.
V. In the case of longitudinal compression joints, the influence of the compression process is neglected.
VI. The leveling of roughness (smoothing) is neglected.

The calculation procedure is based on the calculation of isotropic interference fits. An estimation of the properties through the engineering constants of the laminate in the tangential direction t with $E_A = E_t$ and $\nu_A = \nu_t$ is used to consider the anisotropic behavior. This is based on the assumption that the properties in the tangential direction determine the behavior of the interference fit and its load transferability. The calculation procedure can be summarized as follows:

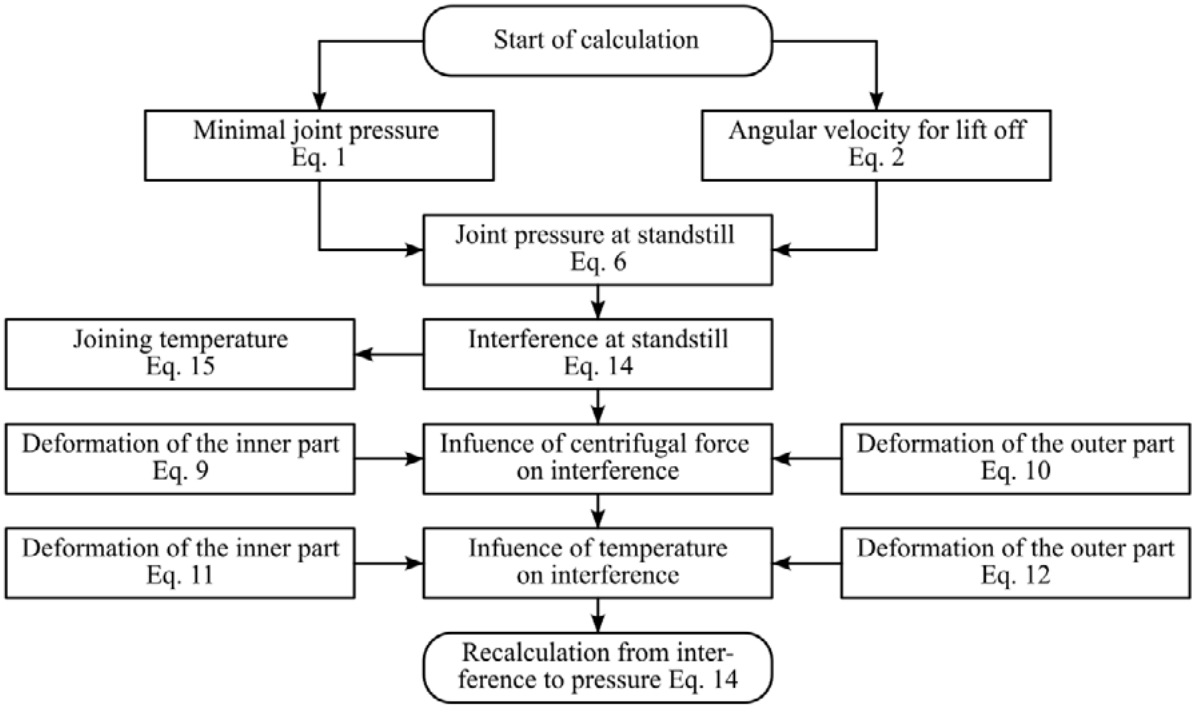


Figure 2. Calculation procedure for hybrid metal-FRP interference-fitted connections with high circumferential speed

3.2 Numerical Model

To verify the analytical approach, an FE model of interference-fitted cylinders was created (cf. Figure 3). Simplifications III to VI also apply, while simplifications I and II are no longer valid due to the modeled joint length and direction-dependent properties of the FRP.

In the first load step, the joint interference is eliminated by the contact definition, and the circumferential speed is increased to the analytically calculated lift-off speed in five subsequent load steps. An outer shaft edge is subject to a boundary condition that restricts the axial and tangential degrees of freedom in a cylindrical coordinate system. The shaft is modelled with a length of $3 \cdot L_F$ to minimize the impact of the boundary condition on the compressed area.

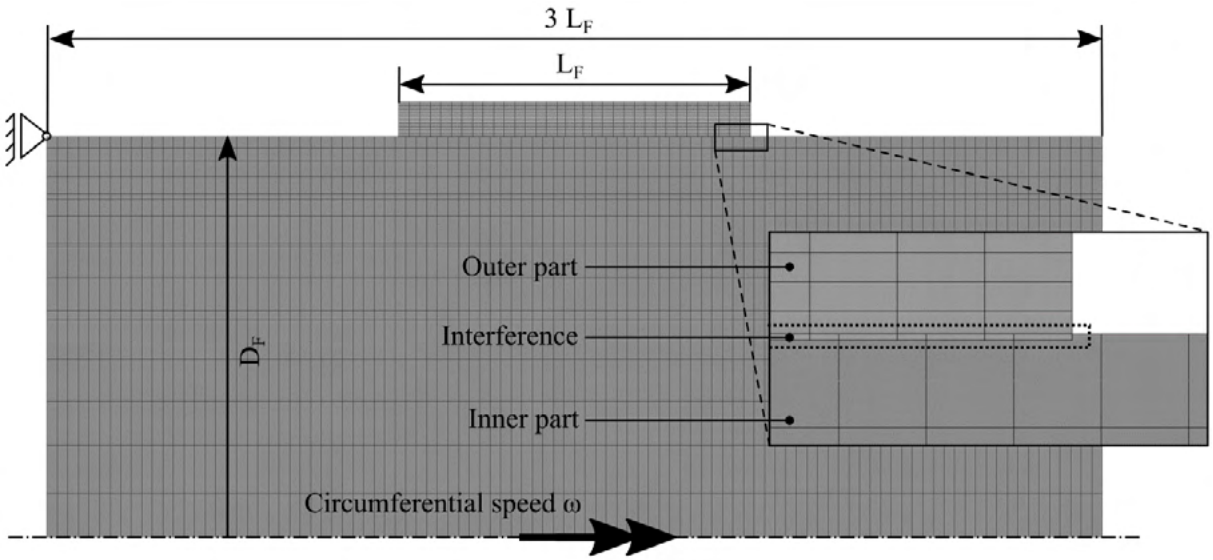


Figure 3. Section cut of the numerical model

3.3 Comparison of analytical and numerical results and investigation of different designs

To evaluate whether the assumption II can be used as an approximation, several compression joints are simulated by varying stiffness-relevant parameters. Starting from a reference Design 1, the fibre type (Design 2), laminate structure with 90° for the tangential orientiation and 0° for the axial direction (Design 3) and wall thickness of the laminate (Design 4) are varied according to Table 1.

Table 1. Parameter study for different designs.

	Stiffness relevant parameters			E_t [GPa]	P [mm]
	Fibre	Laminate	Thickness [mm]		
Design 1	UMS45	$[90_4/0]_S$	10	197,9	0,241
Design 2	IMS65	$[90_4/0]_S$	10	136,0	0,431
Design 3	UMS45	$[90_5/0_3/\pm45]_S$	10	137,5	0,411
Design 4	UMS45	$[90_4/0]_S$	10	198,9	0,168

Figure 4 illustrates the comparison between the analytical and numerical results of the circumferential speed-joint pressure curves. The dimensioning speed describes the highest angular velocity that provides enough pressure to transfer the loads according to equation (1).

Designs 1, 2 and 3 exhibit good correlation. However, Design 3 shows discrepancies of 3% up to 11% between the analytical and numerical calculations at low speeds and standstill. A similar observation was made in [5] regarding the analytical model for determining the joint pressure from [4] (without considering centrifugal forces). The cause of this discrepancy lies in the neglect of the radial strain of the laminate. The calculation approach used in this paper also does not provide a physically correct description of the radial strain. This is because the modulus of elasticity in the laminate thickness direction is overestimated with the assumption II $E_A = E_t$, which leads to an overestimation of the joint pressure.

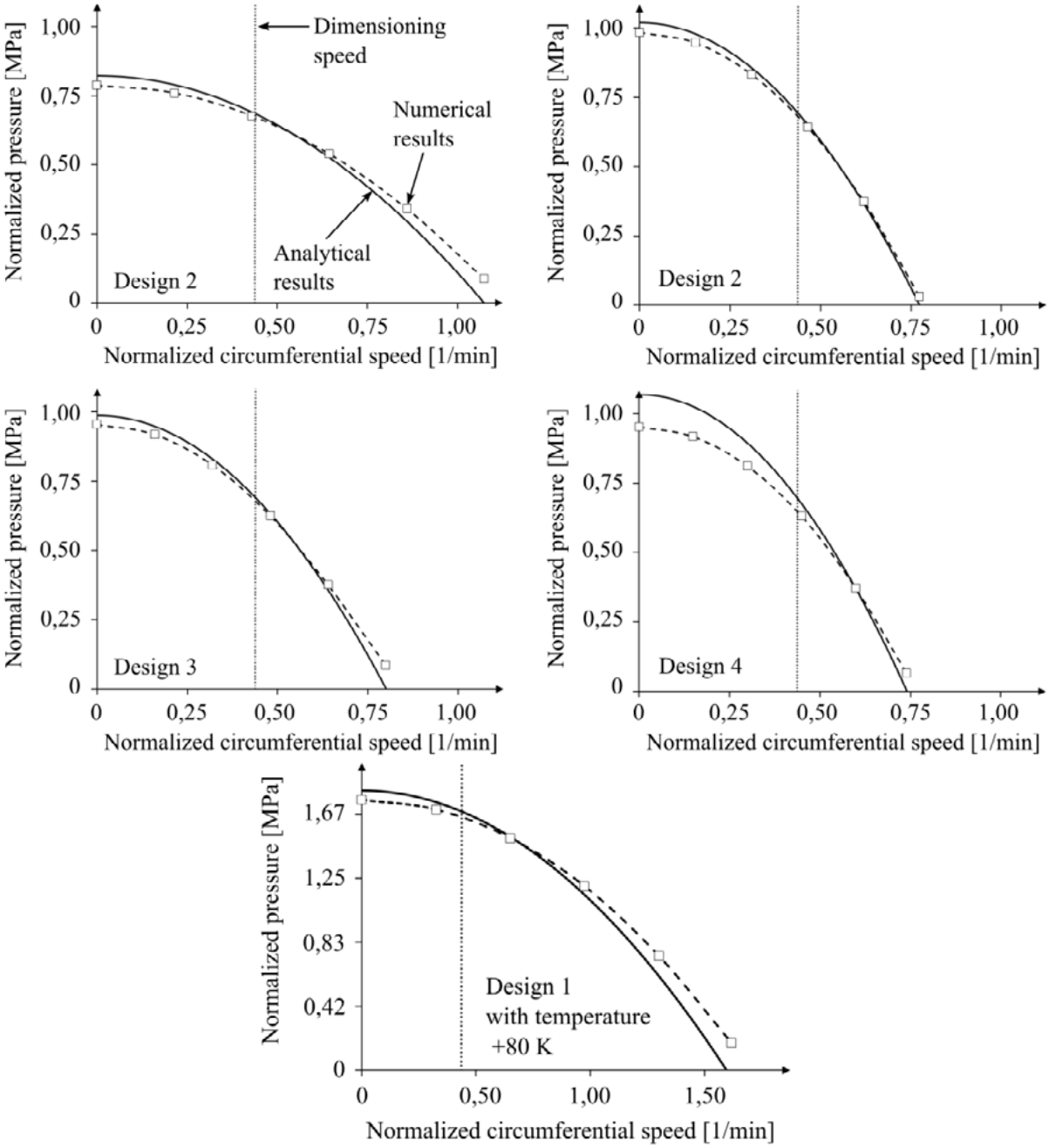


Figure 4. Analytically and numerically determined joint pressure curves of steel-CFRP press fits over the speed with variation of stiffness-relevant parameters.

4. Design recommendations for high circumferential speeds

Based on the presented results, the following observations can be made (comparisons with Design 1):

- When joining fibre types of lower stiffness, a higher joint pressure is required due to the steeper drop in joint pressure that occurs when the speed is increased (cf. Figure 3, Design 2). As a result, the interference to be set also increases (cf. Table 1).
- Laminate structures with a lower proportion of 90° layers require a higher joint pressure at standstill. This is because there is a steeper drop in joint pressure when the speed is increased, (cf. Figure 3, Design 3). The interference to be set also increases (cf. Table 1).

- Increasing the wall thickness results in a higher required joint pressure during joining. This is due to the steeper drop in joint pressure when the speed is increased (cf. Figure 3, Design 4). The interference to be set is reduced accordingly (cf. Table 1).
- The rise in operating temperature causes an increase in joint pressure across all speeds, resulting in a higher lift-off speed (cf. Figure 4, Design 1) with temperature +80 K.

Design recommendations for metal/FRP interference fitted connections with high circumferential speed under the influence of temperature are as follows:

- The use of high-stiffness fibre types is recommended for FRP joint partners as it leads to a smaller reduction of joint pressure at high circumferential speeds. However, the decreasing strength of high-stiffness fibre types should be considered.
- The use of laminates with a high proportion of 90° layers results in less reduction of joint pressure at high circumferential speeds. When developing a laminate structure, it is important to consider additional loads such as axial forces and torsional moments.
- Increasing the wall thickness of the hub laminate is a suitable measure for reducing the necessary interference during manufacturing. It is important to note that an increase in speed results in a steeper decrease in joint pressure.
- The properties of the interference fit are influenced by the operating temperature due to the different thermal expansions of the connection partners. This can be used to adjust the properties of the joint without design adaptation. For example, high speed ranges may only be approached at defined operating temperatures.

5. Conclusion

This paper addresses the challenge of designing efficient connections for rotating components using fibre-reinforced polymer materials, which offer high strength and stiffness. Interference fits, which connect parts without additional fasteners, are explored for their potential to reduce mass and energy consumption. However, designing hybrid metal/FRP interference fits is complex due to the anisotropic nature of FRP and the influence of high circumferential speeds on joint pressure.

The study focuses on hybrid connections with solid metal shafts and hollow FRP-hubs, assuming they reach the high circumferential speeds according to the stress distribution. Analytical approaches for isotropic and orthotropic components are discussed, highlighting existing limitations in practical applicability. The paper proposes a simplified analytical model considering centrifugal forces and anisotropic behavior to calculate joint pressure.

Numerical models validate the analytical approach, revealing discrepancies primarily due to neglected radial strain in the laminate. Design recommendations emphasize factors influencing joint pressure, such as fibre type, laminate structure, and wall thickness. For high-speed applications, using high-stiffness fibre types, incorporating more tangential layers in laminates, and decreasing wall thickness of the FRP-hub are suggested. Additionally, considering operating temperature effects on joint properties offers optimization opportunities.

In conclusion, the paper provides insights into efficiently dimensioning hybrid metal-FRP interference-fitted connections for high circumferential speeds, offering practical design recommendations to meet technical and economic criteria.

Acknowledgments

Supported by:

Federal Ministry for Economic Affairs and Climate Action

on the basis of a decision by the German Bundestag

The work took place as part of the project "Laufräder und Rotoren für Wasserstoffverdichtung & Probabilistische Auslegung von Turbinen" (TurboHyTec). The project is funded by the Bundesministerium für Wirtschaft und Klimaschutz (BMWK).

References

[1] Norm DIN 7190-1: Pressverbände - Teil 1: Berechnungsgrundlagen und Gestaltungsregeln für zylindrische Pressverbände. Ausg. 02.2017. Berlin: Beuth Verlag.
[2] Leidich, E.: Welle-Nabe-Verbindungen. In: Konstruktionselemente des Maschinenbaus 1. Berlin Heidelberg: Springer-Verlag, 2016, S. 493-570.
[3] Niemann, G.; Winter, H.; Höhn, B. und Stahl, K.: Maschinenelemente 1 Konstruktion und Berechnung von Verbindungen, Lagern, Wellen. 5. Aufl. Berlin: Springer Vieweg, 2019.
[4] Fischer, T.: Der Pressverband als torsionsbelastete Krafteinleitung in Faser-Kunststoff-Verbund-Wellen. Dissertation, Technische Universität Darmstadt, 2004.
[5] Fahr, P.: Beitrag zur Gestaltung und Auslegung rotationssymmetrischer dickwandiger Pressverbindungen mit orthotropen Fügepartnern. Dissertaion, Technische Universität München, 2018.
[6] Jakobi, R.: Zur Spannungs-, Verformungs- und Bruchanalyse an dickwandigen, rohrförmigen Bauteilen aus Faser-Kunststoff-Verbunden. Düsseldorf: VDIForschungsberichte, Reihe 5, Nr. 126, 1987.
[7] Forbig, F.: Einsatz von faserverstärkten Kunststoffen bei modernen Welle-Nabe-Verbindungen. Konferenz: 5. VDI-Tagung Welle-Nabe-Verbindungen, Nürtingen, Deutschland, 2012.
[8] Lee, S. und Lee. D.: Torque transmission capability of composite–metal interference fit joints: Composite Structures. 2007, Nr. 78, S. 584–595.
[9] Balke, H.: Einführung in die Technische Mechanik Festigkeitslehre. 3. Aufl. Berlin Heidelberg: Springer-Verlag, 2014.
[10] Schürmann, H.: Konstruieren mit Faser-Kunststoff-Verbunden. 2. Aufl. Berlin: Springer-Verlag, 2007.

Mechanical Performance and Damage Analysis of Multi- Jointed Carbon Fiber-Reinforced Thermoset Composites under Transverse Impact and Low-Temperature Conditions Assisted with Acoustic Emission Analysis

Mahsa Seyednourani [1]*, Sercan Akgun [2], Hasan Ulus [3], Mehmet Yildiz [4], Hatice S. Sas[5]

[1] Faculty of Engineering and Natural Sciences, Sabanci University, Tuzla, Istanbul 34956, Turkey, Mahsa@sabanciuniv.edu
[2] Faculty of Engineering and Natural Sciences, Sabanci University, Tuzla, Istanbul 34956, Turkey, sercan.akgun@sabanciuniv.edu
[3]Selcuk University, Huglu Vocational School, Konya 42700, Turkey, hasanulus@selcuk.edu.tr
[4]Faculty of Engineering and Natural Sciences, Sabanci University, Tuzla, Istanbul 34956, Turkey, meyildiz@sabanciuniv.edu
[5]Faculty of Engineering and Natural Sciences, Sabanci University, Tuzla, Istanbul 34956, Turkey, haticesas@sabanciuniv.edu

Keywords: Bolted joints, Low-velocity impact, Tensile test, Low-temperature, Damage mechanism

Abstract

Jointed structures become inevitable due to high-strength requirements and the need for assembly, especially in large parts. Industrial applications often highlight the significance of multi-bonded joints, leading to the development of stronger and more durable structures. The exploration of jointed structures becomes even more critical in understanding their behavior under various conditions. In this study, carbon fiber-reinforced thermoset composites manufactured via the automated fiber placement process with a cross-ply ($[0/90°]_{4s}$) lay-up are employed. The study focuses on a multi-bolted joint, employing two bolts symmetrically positioned. Specifically, a 10J impact energy and a temperature of -55°C are chosen to simulate transverse impact and low-temperature conditions, respectively. The mechanical performance of the jointed composite laminates is investigated through a tensile test. The results are then compared with reference jointed composite laminates to assess the effect of impact and operating temperature on the structural integrity and performance of the composites. To gain insights into the damage mechanisms and propagation during the tensile test, in-situ acoustic emission analysis is performed at both room and low temperatures. It is shown that the joint strength is significantly influenced by the operating temperature and the joint's load-bearing capacity is less enhanced when impacted transversely at low temperature, compared to the enhancement observed solely due to low temperature condition. The mentioned effects are further explained and verified by damage mechanism evaluation using acoustic emission.

1. Introduction

Joints have found wide-ranging application in the assembly of substantial components in aerospace applications, primarily as a consequence of the constraints due to design, cost and maintenance associated with the manufacturing of oversized parts [1]. On the other hand, the use of jointed materials become more preferrable to achieve the high strength. The composite material with the advantage of high strength and lightweight become the main source to apply the joints . However, the joining process leads to discontinuity and reduced mechanical performance compared to a single-piece component. The discontinuity offered by joints makes them vulnerable points in terms of damage initiation and failure

of the structure [2]. Each joining methodology offer advantages and drawback, for the case of bolted joints, the drilled holes perform as stress concentration points and weaken the structure due to damages induced by the opening a hole [3]. Moreover, enhanced load-bearing capacity is attainable through multi joints commonly employed in practical applications. Multi joints distribute loads across multiple paths, leading to altered load distribution and diverse failure modes. Typical failure modes in multi-bolt joints encompass net-section failure, shear-out, and bearing failure. While net-section failure and shear-out can result in abrupt and catastrophic failures, bearing failure is preferred in structural applications, underscoring the critical need for accurate prediction of failure modes [4]. On the other hand, composite structures exhibit susceptibility to impact events and are often subjected to fluctuating temperatures during their operational lifespan. The impact-induced damage can be further compounded by exposure to varying operating temperatures, leading to altered damage mechanism and failure modes [5]. This phenomenon becomes particularly significant in cases involving structures with potential stress concentration areas, such as multi-jointed structures. Several studies investigate the effect of temperature on joints strength [6,7]. Ulus studied the temperature dependent behavior of hybrid, bolted and bonded BFRP composites from room temperature to 150°C, comparing tensile strength with DMA results for SLJ composites. Adhesive bonded joints had higher strength below Tg, while bolted joints performed better above Tg up to 50°C; hybrid joints prevented sudden failure by transferring load from adhesive to bolt [8]. The effect of impact and the combined effect with temperature are investigated in studies mostly focused on adhesively bonded joints [9–18]. Sayman et al. studied single lap joints bonded with adhesive using glass fiber-epoxy composites under varied conditions (surface type, temperatures, impact energies). They found that load-carrying capacities decrease at low and high temperatures and with lower impact energies (5 J, 10 J, 15 J), but increase at 20 J due to adhesive perforation, with rough surfaces showing higher capacities than smooth surfaces [11]. In another study done by Sayman et al. investigated adhesively bonded joints post-axial impacts at -20°C to 80°C and impact levels ranging 10J to 25 J, finding high-energy impacts beyond specific temperature limits cause immediate failure. Deviations from room temperature negatively affect tensile strength, particularly at lower temperatures, reducing load carrying capacities [12]. Akderya et al. investigated thermal aging effects on adhesively bonded glass fiber/epoxy composite joints at -18°C, 25°C, and 70°C, observing increased load capacity at -18°C but decreased capacity with impact application (5-30 J). Tensile tests at different temperatures revealed reduced load capacity with higher impact energies, particularly at 18°C and 70°C, compared to room temperature [13]. Considering all the studies available in literature, the combined effect of impact, temperature of laminates on mechanical performance of composites with multi bolted joints remain still unclear. This study investigates the impact of transverse impacts and low-temperature conditions (-50°C) on the residual tensile strength of multi-bolted CFRP composite laminates. Specifically, cross-ply laminates arranged in jointed configurations undergo impact testing at room temperature (RT), followed by subsequent tensile strength assessment at both RT and low temperature (LT). The study employs acoustic emission analysis to explore damage mechanisms and conduct failure analysis comprehensively.

2. Experimental Methodology

2.1. Manufacturing of Laminates and Joint preparation

HexPly 8552 carbon/epoxy unidirectional prepreg spool fiber tapes were employed to fabricate composite laminates. The lay-up process was conducted utilizing an advanced Coriolis automated fiber placement (AFP) robot. Each laminate layer comprised 8 tows per course, with a tow preg width of 6.35 mm and a feeding rate set at 0.1 m/s. The resulting 16-layer laminates were arranged in a cross-ply (CP) configuration with a lay-up sequence of $[0/90°]_{4s}$, ensuring varied fiber orientations, and subjected to 1 atm pressure using vacuum bagging for 24 hours at room temperature, followed by autoclave curing according to the prepreg manufacturer's instructions. The cured thermoset composite laminates attained final dimensions of 900 mm × 600 mm, with an average thickness measured at 3 mm at three different points on the laminate. Subsequently, the laminated composites were cut into 100 mm x 150 mm sizes using a Kuka KR16 robot equipped with a high-performance water jet for precise composite specimen

cutting, intended for impact testing, and further trimmed to dimensions of 36 mm × 150 mm to serve as the adherends of single lap joints (SLJs). The geometric characteristics of multi-bolted joints are depicted in Figure 1. The holes are drilled utilizing a DMG Mori Seiki Lasertec 65 3D Hybrid Process Machine, operating at a cutting speed of 90 m/min and a feed rate of 0.005 mm/rev. Assembly of the adherends, sized at 150 mm × 36 mm × 3 mm, involved the utilization of an M6 stainless steel bolt, nut, and two washers with a 6 mm internal diameter and 18 mm external diameter. The bolted joints were torque tightened to a level of 15 N × m using a torque control wrench.

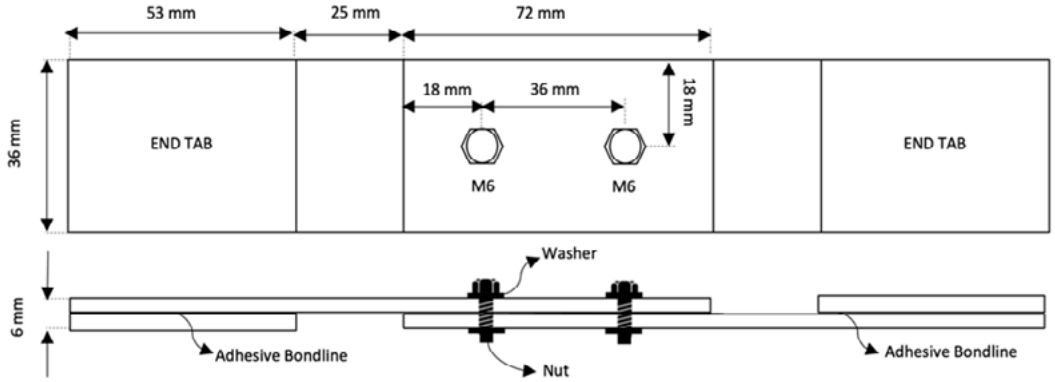


Figure 1. Schematics of front and top view of SLJ specimen

2.2. Impact Testing and Tensile-after-Impact Testing

Barely visible low-velocity impact tests at 10 J are conducted using a hemispherical steel impactor (16 mm diameter and 2.5 kg mass) with 2.83 m/s velocity and 40.7 mm height, tests followed ASTM D7136 with 3 repetitions for OB joint types. Following impact testing, tensile tests were conducted to evaluate residual mechanical properties. Specimens were tested using an Instron universal testing machine at a constant crosshead speed of 1 mm/min, following ASTM D3039 standards. Load-displacement curves were recorded to analyze the residual strength and stiffness of the laminates after impact. Three specimens were tested for each joint type.

2.3. Acoustic Emission Monitoring

Damage mechanisms in tensile after impact tests, for both impacted and non-impacted specimens, relied on AE. Mistras PCI-2 AE system with PICO-200–750 kHz sensors captured AE data continuously. The Physical Acoustics 0/2/4 voltage preamplifier enhanced signal detection by 20 dB. AE sensors' sensitivity was evaluated per ASTM E976-10. Digital conversion used an 18-bit A/D converter. System parameters included a 45 dB threshold, 50 µs PDT, 150 µs HDT, and 200 µs HLT, with a 2 MHz data collection rate per sensor. Post-experiment analysis involved noise elimination, Bessel bandpass filtering (from 20 kHz to 800 kHz), and MATLAB for pattern recognition based on features like weighted peak frequency and amplitude. Clustering, using the unsupervised k-means algorithm and Calinski-Harabasz criteria, performed as three clusters for OB joints.

3. Results and Discussion

The maximum load carried by multi bolted SLJ with cross-ply laminates is represented in Figure 2(a). For intact joints the maximum load at RT is 23940 which increases up to 26875 as it is exposed to LT. this can be explained by the effect of LT on matrix shrinkage, the shrinkage tightens the bond between matrix and fiber and strengthen the interface region. Thus, the maximum load capacity increases by 12%. The same scenario is valid for impacted laminates as exposed to LT the load carrying capacity of the joint increases by 9%. It can be understood that, although the 10J impact considered as low velocity impact with barely visible damage, the damage induced by 10J to interface region reduce the load

bearing capacity by 3% when exposed to LT. This happens when the 10J impact at RT reduces the maximum load by only 0.4%. Figure 2(b) depicts the maximum displacement or the displacement at failure. The maximum displacement decreases by 13.9% and 12.5% for impacted joints at RT and LT respectively. However, the effect of impact and operating temperature reduce the displacement decrease rate to 10.5%. In other words, the LT increases the stiffness and load bearing capacity for both intact and impacted joints while the displacement decreases due to brittle behavior at LT.

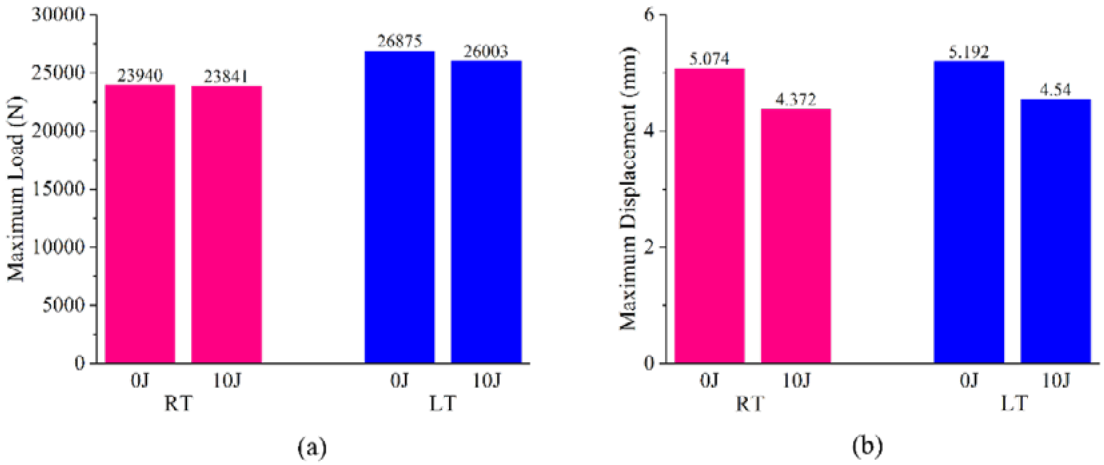


Figure 2. The maximum load bearing capacity (a) and maximum displacement (b) of multi-bolted SLJ for intact and 10J impacted joints at RT and LT.

Figure 3 presents the damage classification of SLJs based on peak frequency and amplitude under different conditions: RT with 0J impact (a), RT with 10J impact (b), LT with 0J impact (c), LT with 10J impact (d). In RT conditions, non-impacted joints exhibit higher amplitudes (reaching a maximum of 120 dB) compared to the 10J impacted joints (maximum amplitude around 90). This difference is due to pre-existing damage between the bolts in impacted joints, allowing for lower amplitude hits before failure point during AE monitoring. Under LT conditions, the maximum amplitudes for non-impacted and 10J impacted joints are almost the same, both around 120. This indicates that the rigidity of the material in cold conditions leads to consistent amplitude levels for AE signals, regardless of low velocity impact energy. The observed behavior suggests that even when impacted in cold conditions, the multi-jointed laminate remains relatively rigid, resulting in consistent AE signal amplitudes reflecting the internal damage mechanisms. Figure 4 illustrates the distribution hit fractions of each cluster for RT-0J (a), RT-10J (b), LT-0J (c), LT-10J (d). The graph indicates that fiber failure is the predominant type of failure observed in both non-impacted and 10J impacted joints under RT and LT conditions, owing to the alignment of fibers with the applied load. Since the load is mainly bearing with reinforcing fibers, the total AE hits related to matrix and interfacial failure are lower compared to fiber failure. In non-impacted joints (Figure 4(a) and (b)), there is a transition to matrix-related failure events under LT conditions due to the increased sensitivity of the matrix to crack initiation, stemming from its molecular composition. Moreover, differences in the coefficients of thermal expansion between the matrix and fibers result in thermally induced residual stresses, facilitating damage initiation and progression [8]. Conversely, there is no significant change observed between RT-10J and LT-10J joints, attributed to pre-existing damage in the matrix and interface influenced by the applied impact energy.

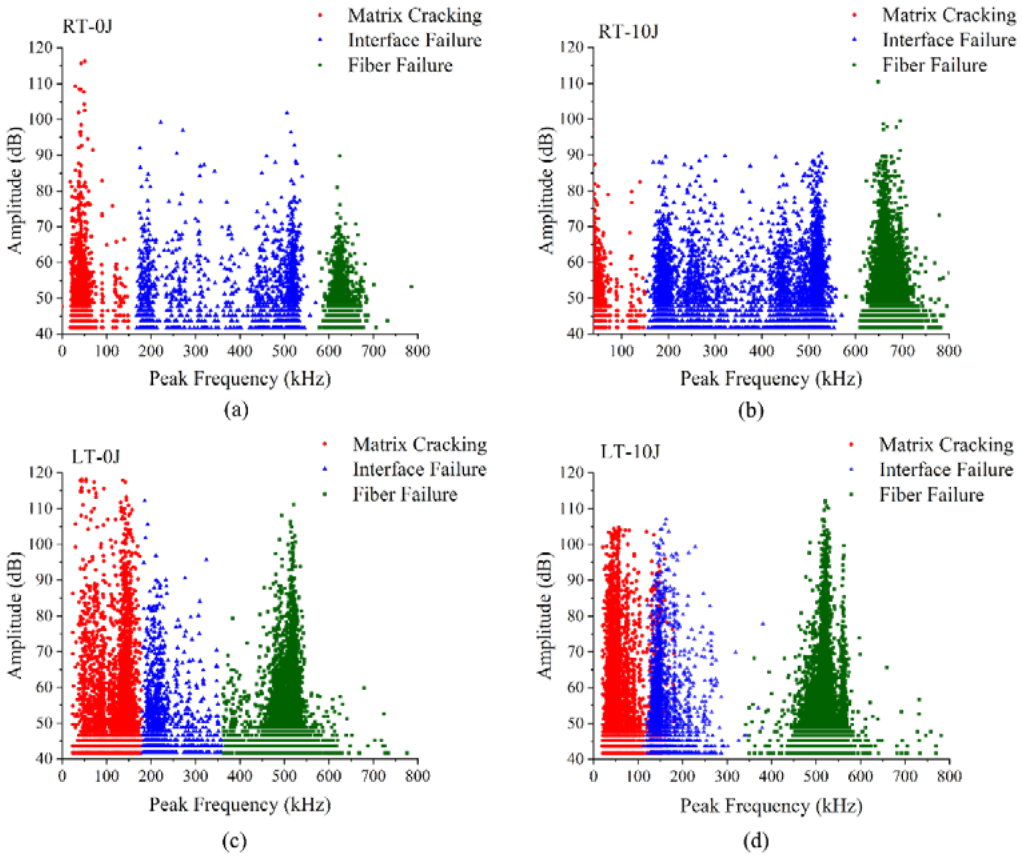


Figure 3. Peak Frequency vs Amplitude based failure classification of SLJ specimens.

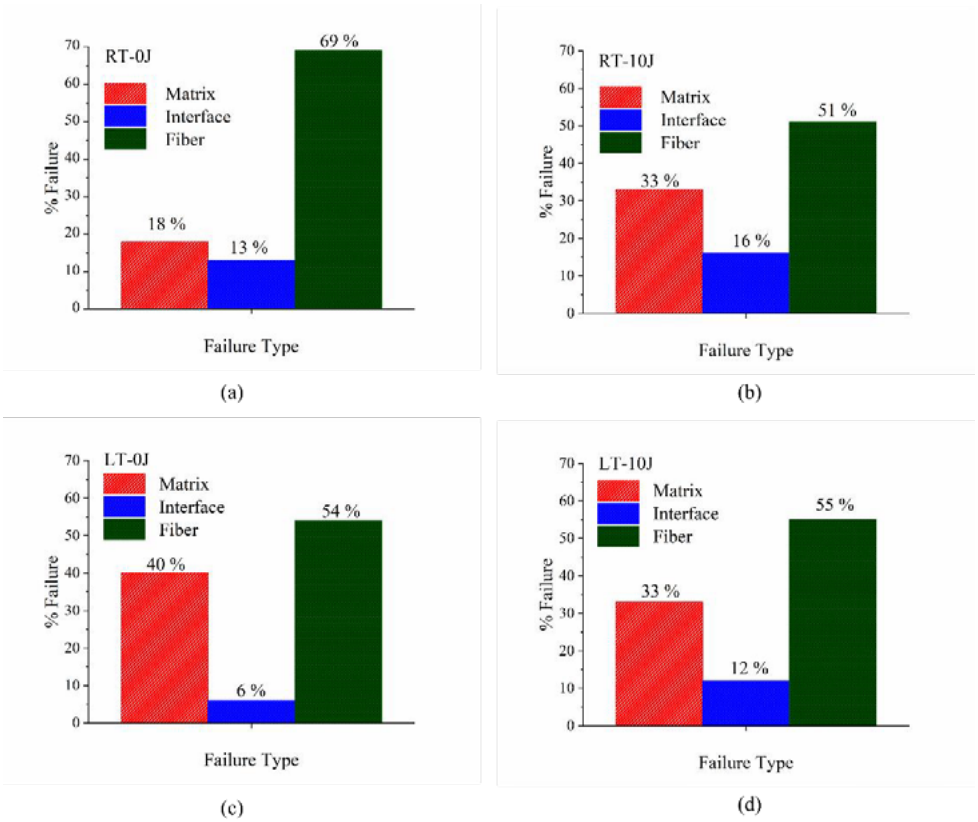


Figure 4. Average hit fractions of all three classified failure types of SLJ specimens.

4. Conclusions

In conclusion, this study focuses on the effect of impact loading and operating temperature on multi bolted joints. The residual strength of intact and 10J impacted joints are evaluated at both RT and LT. Furthermore, the failure analysis is conducted by using acoustic emission evaluation. The conclusion is as following:

- In multi-bolted joints, the influence of impact loading on the joint's maximum load-bearing capability is negligible at room temperature (RT) but becomes significant at low temperature (LT). This implies the importance of barely visible damage induced to the jointed structures at low operating temperatures. This assertion is confirmed through a separate comparison between intact and impacted joints exposed to LT. Moreover, the combined effect of impact load and temperature results in a reduced enhancement of load-bearing capacity compared to the effect of temperature alone.
- The assessment of damage mechanisms involved comparing the acoustic emission hits collected from three distinct clusters representing matrix cracking, interface failure, and fiber-related failure. The combined effect of impact and temperature results in the increase for matrix cracking and reduction in interface and fiber related failure.
- It is noteworthy that the effect of impact in LT is more pronounced with higher interface related failure, and leads to less enhancement in load bearing capacity compared to intact joints at LT.
- The introduction of impact loading decreases the displacement at failure in both Rt and LT. However, the combined effect of impact and low temperature weakens the effect of impact loading by less reduction in failure displacement, a phenomenon explained by evaluating damage mechanism. The impacted joints at LT experience less interface related failure compared to the same impacted joints at RT.

Acknowledgments

This research is partially supported by the Scientific and Techno-logical Research Council of Turkey (TUBITAK) under TUBITAK 1001 program (Grant no: 221 M565) and TUBITAK 2244 - Industrial Ph.D. Fellowship Program Roketsan Missiles Inc. and Sabanci University (Grant no: 118C049).

References

[1] Groche P, Wohletz S, Brenneis M, Pabst C, Resch F. Joining by forming—A review on joint mechanisms, applications and future trends. J Mater Process Technol 2014;214:1972–94. https://doi.org/10.1016/J.JMATPROTEC.2013.12.022.

[2] Cao Z, Cardew-Hall M. Interference-fit riveting technique in fiber composite laminates. Aerosp Sci Technol 2006;10:327–30. https://doi.org/10.1016/J.AST.2005.11.003.

[3] Kim JH, Lopez-Cruz P, Heidari-Rarani M, Lessard L, Laliberté J. An experimental study on the mechanical behaviour of bonded and hybrid bonded-bolted composite joints using digital image correlation (DIC) technique. Compos Struct 2021;276:114544. https://doi.org/10.1016/J.COMPSTRUCT.2021.114544.

[4] Liu F, Shan M, Zhao L, Zhang J. Probabilistic bolt load distribution analysis of composite single-lap multi-bolt joints considering random bolt-hole clearances and tightening torques. Compos Struct 2018;194:12–20. https://doi.org/10.1016/J.COMPSTRUCT.2018.03.100.

[5] Seyyednourani M, Akgun S, Ulus H, Yildiz M, Sas HS. Experimental investigation on Compression-After-Impact (CAI) response of aerospace grade thermoset composites under low-temperature conditions assisted with acoustic emission monitoring. Compos Struct 2023;321:117260. https://doi.org/10.1016/J.COMPSTRUCT.2023.117260.

[6] Soykok IF, Sayman O, Ozen M. Low temperature and tightening torque effects on the failure response of bolted glass fiber / epoxy composite joints 2012. https://doi.org/10.1177/0021998312463828.

[7] Grant LDR, Adams RD, da Silva LFM. Effect of the temperature on the strength of adhesively

bonded single lap and T joints for the automotive industry. Int J Adhes Adhes 2009;29:535–42. https://doi.org/10.1016/J.IJADHADH.2009.01.002.

[8] Ulus H. An experimental assessment of hybrid bolted/bonded basalt fiber reinforced polymer composite joints' temperature-dependent mechanical performances by static and dynamic mechanical analyses. Int J Adhes Adhes 2022;114. https://doi.org/10.1016/j.ijadhadh.2022.103120.

[9] Kaybal HB, Ulus H, Eskizeybek V, Avcı A. An experimental study on low velocity impact performance of bolted composite joints part 1: Influence of halloysite nanotubes on dynamic loading response. Compos Struct 2021;258:113415. https://doi.org/10.1016/J.COMPSTRUCT.2020.113415.

[10] Kaybal HB, Ulus H, Eskizeybek V, Avcı A. An experimental study on low velocity impact performance of bolted composite joints-part 2: Influence of long-term seawater aging. Compos Struct 2021;272:113571. https://doi.org/10.1016/J.COMPSTRUCT.2021.113571.

[11] Sayman O, Arikan V, Dogan A, Soykok IF, Dogan T. Failure analysis of adhesively bonded composite joints under transverse impact and different temperatures. Compos Part B Eng 2013;54:409–14. https://doi.org/10.1016/J.COMPOSITESB.2013.06.017.

[12] Sayman O, Soykok IF, Dogan T, Dogan A, Arikan V. Effects of axial impacts at different temperatures on failure response of adhesively bonded woven fabric glass fiber/epoxy composite joints. J Compos Mater 2015;49:1331–44. https://doi.org/10.1177/0021998314533598.

[13] Akderya T, Kemiklioğlu U, Sayman O. Effects of thermal ageing and impact loading on tensile properties of adhesively bonded fibre/epoxy composite joints. Compos Part B Eng 2016;95:117–22. https://doi.org/10.1016/J.COMPOSITESB.2016.03.073.

[14] Huang W, Sun L, Li L, Shen L, Huang B, Zhang Y. Investigations on low-energy impact and post-impact fatigue of adhesively bonded single-lap joints using composites substrates. J Adhes 2020;96:1326–54. https://doi.org/10.1080/00218464.2019.1602767.

[15] Huang W, Sun L, Liu Y, Chu Y, Wang J. Effects of low-energy impact at different temperatures on residual properties of adhesively bonded single-lap joints with composites substrates. Compos Struct 2021;267:113860. https://doi.org/10.1016/J.COMPSTRUCT.2021.113860.

[16] Borba NZ, Körbelin J, Fiedler B, dos Santos JF, Amancio-Filho ST. Low-velocity impact response of friction riveted joints for aircraft application. Mater Des 2020;186. https://doi.org/10.1016/j.matdes.2019.108369.

[17] Vaidya UK, Gautam ARS, Hosur M, Dutta P. Experimental–numerical studies of transverse impact response of adhesively bonded lap joints in composite structures. Int J Adhes Adhes 2006;26:184–98. https://doi.org/10.1016/J.IJADHADH.2005.03.013.

[18] Kemiklioğlu U, Baba BO. Mechanical response of adhesively bonded composite joints subjected to vibration load and axial impact. Compos Part B Eng 2019;176:107317. https://doi.org/10.1016/J.COMPOSITESB.2019.107317.

INVESTIGATING THE MODE-I FAILURE BEHAVIOUR OF THICK ADHESIVE JOINTS USING A COUPLED COMPUTATIONAL/EXPERIMENTAL APPROACH

Akash Sharma[1], Ali Shivaie Kojouri[2], Jialiang Fan[3], Anastasios P. Vassilopoulos[4], Veronique Michaud[3], Kalliopi-Artemi Kalteremidou[2], Danny Van Hemelrijck[2], Wim Van Paepegem[1],
[1]Department of Materials, Textiles and Chemical Engineering, Ghent University, Technologiepark–Zwijnaarde 46, B-9052 Zwijnaarde, Belgium
[2]Department of Mechanics of Materials and Constructions (MeMC), Vrije Universiteit Brussel, Brussels, Belgium
[3]Laboratory for Processing of Advanced Composites (LPAC), Institute of Materials (IMX), Ecole Polytechnique Fédérale de Lausanne (EPFL), Lausanne, Switzerland
[4]Composite Construction Laboratory (CCLab), Ecole Polytechnique Fédérale de Lausanne (EPFL), Lausanne, Switzerland

Keywords: Mode I loading, Thick adhesive joints, Drucker-Prager plasticity, Thermal residual stresses, Pre-cracking

Abstract

Wind turbine blades are manufactured by molding them in two halves and joining them using thick adhesive joints. The failure of these adhesive joints, particularly in the trailing edge of the blades, compromises the structural integrity of the wind turbine. Therefore, comprehending the mechanisms of failure in adhesive joints is critical to designing wind turbine blades efficiently. For this purpose, the present study proposes a novel approach that integrates computational and experimental methods to enhance the overall understanding of the factors that influence the failure of thick adhesive joints. The experimental specimens consist of two cross-ply glass fibre composite laminates bonded with a ~10 mm thick layer of an epoxy-based adhesive. The specimens are cured at 70°C. After curing, a pre-crack is generated within the adhesive layers of each specimen. The specimen is subjected to Double Cantilever Beam (DCB) tests at room temperature to induce mode I failure. The load-displacement curves of the DCB specimens are obtained. The strain in the adhesive layer is determined using the Digital Image Correlation (DIC). Finite Element (FE) models of the DCB specimens having virtually generated pre-cracks are created to predict the experimental load-displacement curves. So far, most researchers have employed the cohesive zone model for the adhesive in such numerical studies. However, epoxy-based adhesives typically exhibit plastic deformation. Hence, the Drucker-Prager plasticity criteria are utilised to model the mechanical response of the adhesive. Also, it is crucial to assess the influence of thermal residual stresses that arise from the thermal mismatch between composites and adhesives, an aspect that has not been adequately addressed in the literature. Thus, appropriate thermal expansion coefficients are assigned to both composites and adhesives. Furthermore, a cool-down is simulated before mechanical loads to mimic the temperature transition from curing to room temperature. A very good agreement is observed between the experimental and numerical results. A satisfying correlation is also observed between the FE analysis and the DIC, further verifying the effectiveness of the proposed modelling strategy.

1. Introduction

Thick adhesive joints are used to create bonds between the two halves of the wind turbine blades [1]. Adhesive bonding offers remarkable durability, resilience to fatigue, and the ability to distribute stress evenly in the joined area, but it also meets the requirement for lightweight blades. [2]. Despite these advantages, the failure of the thick adhesive joints in the trailing edge of the wind turbine blade compromises the structural integrity of wind turbines [3–6]. Understanding the mechanisms of mode I failure in adhesive joints is crucial for efficiently designing wind turbine blades [7,8]. Therefore, the current research uses a combined computational and experimental approach to investigate the mode I failure behaviour of the thick adhesive joints.

In this context, the elastoplastic mechanical properties of the adhesives, T-stresses and the existence of residual stresses influence the failure behaviour of adhesive joints [9,10]. The non-linear mechanical behaviour of commercial-grade adhesives can be ascribed to their epoxy content, which is well-known for its elastoplastic characteristics [11]. The residual stresses are primarily caused by the thermal expansion/contraction caused by the prevalent mismatch in the thermal expansion coefficients of the adherends and the adhesive during the post-curing cool-down [12–17]. The T-stress, which refers to the stress acting parallel to the crack plane in an adhesive layer that connects two adherends, significantly affects the directional stability of the crack path. Therefore, it is essential to evaluate the T-stress accurately to comprehend the crack propagation in thick adhesive joints. [18–20].

Finally, researchers usually create pre-crack in the thick adhesive joint specimens for the DCB tests [10,19,21]. To the best of the authors' knowledge, the current literature has not addressed the potential influence of pre-crack generation on the mode I behaviour of the thick adhesive joints. Therefore, the influence of the aforementioned factor was incorporated by creating virtual pre-cracks through Finite Element (FE) modelling. Subsequently, virtual DCB tests were performed on the aforesaid FE models. The FE results were thoroughly compared with experimental results to evaluate the accuracy of the modelling approach. The experimental campaign involved the Double Cantilever Beam (DCB) tests on Glass Fibre Reinforced Polymer (GFRP) composites bonded using an epoxy-based adhesive layer, which was pre-cracked in the middle. The computational results were extensively verified against the experimental results. The results obtained, as well as the insights from the findings, are presented below.

2. Experiments

2.1. Characterisation of materials

2.1.1 Adhesive

Tensile and compressive tests were performed on the bulk adhesive specimen to determine the material properties of the Sika power®-830 adhesive. The adhesive is categorised as epoxy-based. The compressive tests were conducted following the ASTM D695 standard. The tensile tests adhered to the ASTM D638-22 standard [10].

a) b)

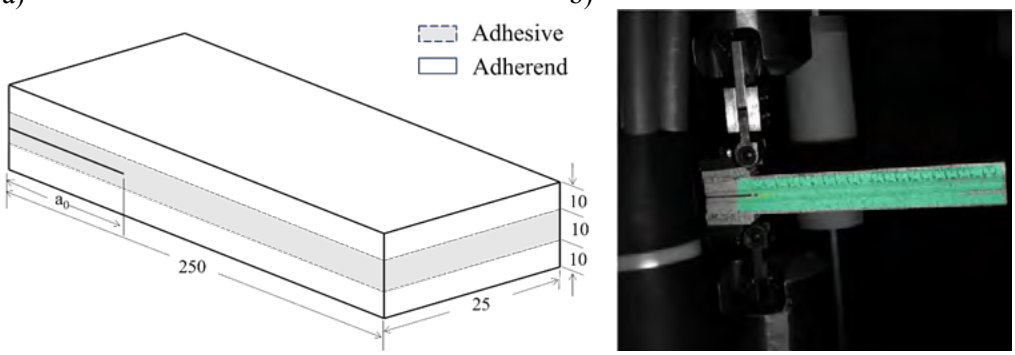


Figure 1. Double Cantilever Beam specimen: a) Schematic description (all dimensions are in mm); b) Experimental set-up

2.1.2 Composite

The adherends used in the current research were cross-ply ($[90/0]_{7s}$) GFRP Composite laminates. The UD glass fabric with an aerial weight of 425 g/m^2 was used as reinforcement. The infusion process utilised EPIKOTE Resin MGS RIMR 135 epoxy resin in conjunction with EPIKURE MGS RIMH 137 as the curing agent. The manufactured composite laminates had a fibre volume fraction of 50.8%. Experiments, as well as FE-based homogenisation, were carried out to obtain the elastic properties of the cross-ply GFRP composite laminate. In addition, Table 1 and Table 2 display the properties of the adhesive and composite.

Table 1. Properties of the Sika power®-830 adhesive

Properties	Sika power®-830 epoxy adhesive
E,GPa	2.6*
ν	0.4*
G, N.mm^{-1}	0.001§
α, 10^{-6}/°C	78.2*
σ_t, σ_c, MPa	[40/60]*
β/K	23.2°/0.89
Plastic strain at failure, -	0.0118*

*Experimental value; # These values were estimated based on analytical expressions; § Assumed value

Table 2. Properties and thermal expansion coefficients of cross-ply $[0/90]_{7s}$ GFRP laminate

Properties	cross-ply $[0/90]_{7s}$ GFRP laminate
E_{XX}*, GPa	24.7
E_{YY}†, E_{ZZ}†, GPa	24.3, 12.7
ν_{XY}†, ν_{XZ}†, -	0.13
G_{XY}*, G_{XZ}†, GPa	3.2
G_{YZ}*, GPa	3.5
α_{XX}, (10^{-6}/°C) †	14.9
α_{YY}, (10^{-6}/°C) †	15.3
α_{ZZ}, (10^{-6}/°C) †	38.1

† Homogenised values, *Experimental values

2.2. Double Cantilever Beam tests

The samples consisted of two composite adherends joined together by the adhesive layer (Figure 1a). The specimen was heated to 70 °C and maintained at that temperature for four hours for curing. More details regarding the manufacturing method can be found in the study by Fan et al. [10]. Figure 1b shows the experimental setup. The adhesive layers in each specimen had a pre-crack. The pre-crack length a_0 varied from 24 mm to 52 mm. Also, all the pre-cracks had a thickness of ~1 mm. The crack length (a_0) for each specimen were: 24 mm for specimen-1, 29 mm for specimen-2, 34 mm for specimen-3, 39 mm for specimen-4, 48.5 mm for specimen-5, and 52 mm for specimen-6. The rest of the dimensions remained the same.

3. Computational simulations approach

The Finite Element (FE) models of the DCB specimens were meshed with 8-noded hexahedral elements with reduced integration (C3D8R). The dimensions of the FE models were the same as the experimental specimens. As shown in Figure 2, the X-direction is the direction parallel to the crack plane. The Z-direction is along the thickness of the DCB FE models. Finally, the Y-direction is along the width. Note that six FE models were created from the aforesaid model through the virtual pre-crack generation, each corresponding to specimens 1 to 6.

The adhesive and composite sections of the model were assigned appropriate material models. The adhesive was assigned with the built-in Abaqus Drucker-Prager plasticity model and the ductile damage criterion in combination. The details of the above models are given in [22]The built-in isotropic thermal expansion model was used to compute the thermal stresses in the adhesive. The composite was assigned a linear elastic and orthotropic material model. In addition, the orthotropic thermal expansion model was used to compute the thermal stresses in the composite. In the devised simulations approach, the model was first exposed to a thermal load representing the specimen's cooling down process.

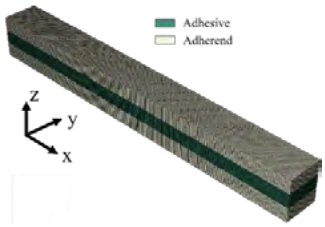


Figure 2. Finite element model for the DCB specimen.

Then, a pre-crack was created by eliminating the relevant elements from the adhesive layer. Finally, mechanical forces were applied to trigger mode I failure. Thus, the simulations were performed in three stages: i) application of thermal load, ii) creation of a virtual pre-crack, and iii) mechanical load application. The first two stages of the simulations were carried out in Abaqus/standard module. Subsequently, the results from the end of the pre-crack generation stage were imported into Abaqus/explicit. The mechanical loads were applied using the Multiple Point Constraint available in Abaqus. The mass scaling factor 0f 1000 was utilised in this step. The ratio between kinetic and internal energy in the third step needed to be low to maintain the quasi-static nature of the FE simulations. The aforementioned ratio was significantly below the recommended allowable limit of 10% [23], ranging from 1-4% for all the numerical results presented in this paper. The boundary conditions of each step are highlighted in Figure 3. The following sections describe the results relevant to each step.

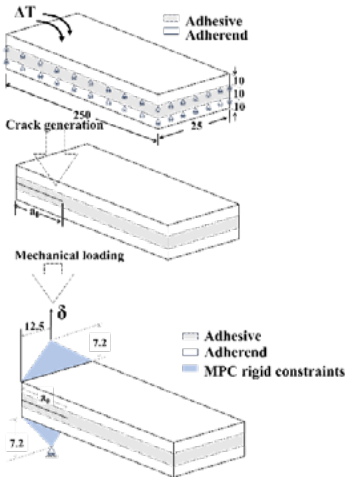


Figure 3. Description of the applied boundary conditions on the DCB FE model

4. Results and discussion

4.1 Effect of thermal loading

The FE model was subjected to a temperature difference of -50 °C. Due to thermal loading, the composite experienced a thermal strain of -747 με (THE_{XX}), while that in the adhesive layer was -391 με. Also, the thermal strain observed in the through-thickness direction (THE_{ZZ}) was -1900 με. The aforesaid thermal strain contours are highlighted in Figure 4.

a) b)

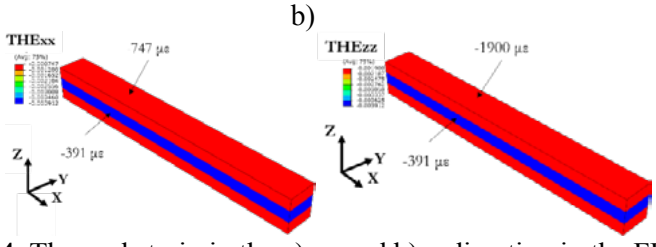


Figure 4. Thermal strain in the a) x- and b) z-direction in the FE model

4.2 Effect of pre-cracking

The thickness of the pre-crack was set at 1 mm, which corresponded to the thickness of the saw employed to produce the pre-crack in the experimental samples. Furthermore, the element size in the adhesive layer of the FE models was set at 1 mm. Therefore, after removing the elements at the location of the pre-crack, the resulting virtual pre-crack had a thickness of 1 mm. Figure 5 highlights the subsequent stages of the virtual pre-crack generation. The stress contours shown belong to the surface Y=0. The through-thickness stresses in the middle of the adhesive layer were approximately 7-12 MPa when the virtual pre-crack was first formed. The virtual pre-crack generation led to unbalanced forces. As a result, the adhesive surfaces on either side of the crack tried to move closer together. The stress values mentioned earlier became negative, approximately -2.5 MPa, due to stress redistribution. The crack closure continued until the mechanical equilibrium was reinstated. At the end of the virtual pre-crack generation, the compressive through-thickness stresses reached -17 MPa (Figure 5).

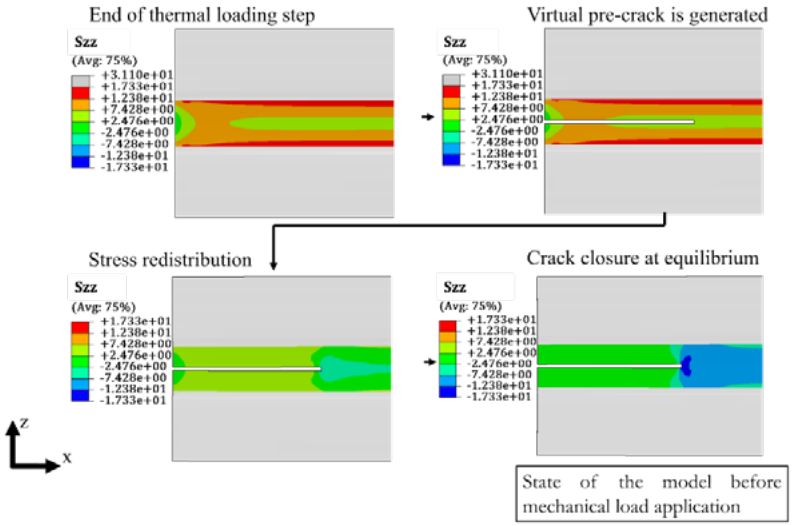


Figure 5. Effect of the virtual pre-crack generation on stresses at the crack tip

4.3 Load-displacement curves

The load-displacement curves for the FE simulations were created by plotting the vertical reaction force of the loading point against the relative displacement between the loading point and the bottom fixed point (refer to Figure 3) for each crack length.

To emphasise the influence of the adhesive's plasticity on the overall mode I behaviour, Figure 6a displays the plastic strains at different increments of the FE simulation of specimen-1. According to the figure, the plastic strain reached its highest value at the crack tip. Once the plastic strain near the crack tip reached a value of 0.0118, the same as the adhesive's plastic strain at failure, the damage to the elements near the crack tip began. Due to a very low fracture energy of 0.001 N/mm, the damage at the crack-tip element quickly evolved, resulting in the continuous removal of the adjacent elements at the crack-tip. During the loading process, the plastic strain of the adjacent elements along the line parallel to the crack tip consistently reached the point of failure strain. As a result, these elements were continuously removed, resembling the propagation of a crack. Figure 6a clearly shows that the crack extended through the centre of the adhesive layer (refer to 'crack propagation' in Figure 6a).

Figure 6b compares experimental and numerical load versus displacement curves. The FE simulations predicted load-displacement curves that matched the experimental results, and the crack length influenced the slope of the numerical load-displacement response. Thus, Figure 6b shows that the FE results correlate well with the experimental specimen behaviour.

a) b)

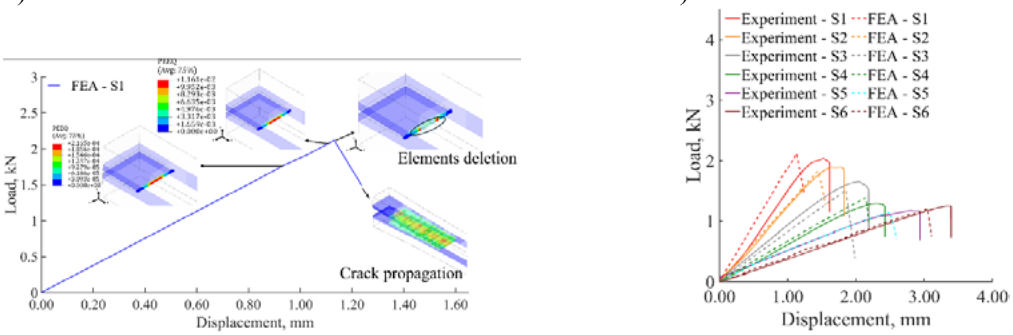


Figure 6. Finite Element Analysis (FEA) and experimental results: a) Evolution of the plastic strain around the crack tip; b) FEA versus Experimental load-displacement curves

4.4 Comparison with DIC

The displacement contours were extracted for specimen-3 for the load step at which the maximum load occurs during the experiment (i.e., peak-load step). Three linear trajectories were established in the experimental sample and FE model of specimen-3 [Figure 7 (a, b)]. Subsequently, the vertical displacements along the top trajectory (V^{top}) and the bottom trajectory (V^{bottom}) were extracted using DIC. The relative displacement (V^{top} - V^{bottom}) was calculated and plotted against the horizontal distance (in the X-direction) from the crack tip in the specimen. Relative displacement was favoured over absolute displacement to avoid the influence of rigid body movements during the experiments. Later, the abovementioned process was repeated for the FE model.

a) b)

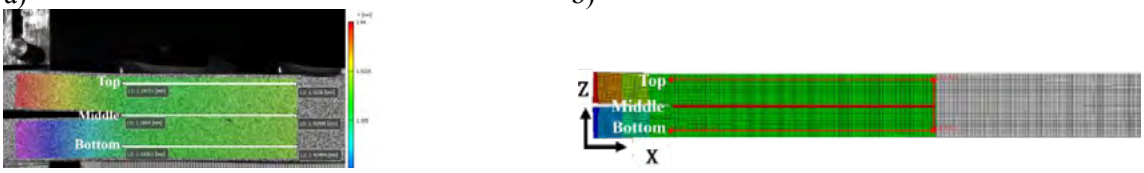


Figure 7. Description of trajectories for a) an experimental specimen and b) an FE model

The comparison between Finite Element Analysis (FEA) and DIC highlighted a significant discrepancy (Figure 8a). In the abovementioned scenario, the FE simulations were once again carried out, and the deformations resulting from thermal loads and the subsequent stress redistribution were neglected, similar to the DIC analysis. This was accomplished by deactivating the result update while importing the FE results into the Abaqus/explicit [24]. Figure 8b shows that upon removing the influence of the factors above, the relative displacements obtained from the FE model were consistent with those obtained from DIC.

a) b)



Figure 8. Relative displacement versus distance from crack tip plot a) FEA with the influence of thermal load and pre-cracking b) FEA without the influence of thermal load and pre-cracking around the crack tip

5. Conclusion

The present computational approach is unique for its capability to simulate thermal loading and generate virtual pre-cracks. The generation of virtual pre-cracks caused the adhesive surfaces to close, resulting in stress redistribution. Due to the virtual pre-cracking, the tensile opening stresses at the crack tip were transformed into compressive stresses. A notable difference between the FEA- and DIC-based results was observed. However, ignoring the influence of thermal loads and virtual pre-crack generation in an FE simulation yielded numerical results that matched the results provided by the DIC. Additionally, the FE models accurately predicted experimental load-displacement curves. The crack length significantly influenced the slope of both experimental and numerical curves, with longer cracks resulting in decreased slopes. Moreover, crack propagation was governed by the adhesive's plastic deformation. The strong correlation between the experimental and computational results confirms the effectiveness of the proposed modelling strategy.

Acknowledgments

The authors acknowledge funding under the Lead Agency scheme from the Research Foundation - Flanders (FWO Vlaanderen) through the project grant G031020N and the Swiss National Science Foundation (SNF) through the project grant 200021E_18944/1 with the title "Combined numerical and experimental approach for the development, testing and analysis of thick adhesive joints in large wind turbine blades".

References

[1] P. Zuo and A.P. Vassilopoulos. Review of fatigue of bulk structural adhesives and thick adhesive joints. *International Materials Reviews*, 66(5):313–338, 2021.

[2] R. Larson, A. Bergan, F. Leone and O.G. Kravchenko. Influence of stochastic adhesive porosity and material variability on failure behavior of adhesively bonded composite sandwich joints. *Composite Structures*, 306:, 2023.

[3] M.A. Eder, R.D. Bitsche and F. Belloni. Effects of geometric non-linearity on energy release rates in a realistic wind turbine blade cross section. *Composite Structures*, 132:1075–1084, 2015.

[4] P.U. Haselbach and K. Branner. Initiation of trailing edge failure in full-scale wind turbine blade test. *Engineering Fracture Mechanics*, 162:136–154, 2016.

[5] F. Lahuerta, N. Koorn and D. Smissaert. Wind turbine blade trailing edge failure assessment with sub-component test on static and fatigue load conditions. *Composite Structures*, 204:755–766, 2018.

[6] P.U. Haselbach, M.A. Eder and F. Belloni. A comprehensive investigation of trailing edge damage in a wind turbine rotor blade. *Wind Energy*, 19(10):1871–1888, 2016.

[7] M.A. Eder and R.D. Bitsche. A qualitative analytical investigation of geometrically nonlinear effects in wind turbine blade cross sections. *Thin-Walled Structures*, 93:1–9, 2015.

[8] J. Shmueli, M.A. Eder and A. Tesauro. A versatile stereo photogrammetry based technique for measuring fracture mode displacements in structures. *Precision Engineering*, 39:38–46, 2015.

[9] F.M. Jensen, B.G. Falzon, J. Ankersen and H. Stang. Structural testing and numerical simulation of a 34 m composite wind turbine blade. *Composite Structures*, 76(1–2):52–61, 2006.

[10] J. Fan, A.P. Vassilopoulos and V. Michaud. Mode I fracture of thick adhesively bonded GFRP composite joints for wind turbine rotor blades. *Composite Structures*, 327:117705, 2024.

[11] D.V. Srinivasan and A.P. Vassilopoulos. Manufacturing and toughening effects on the material properties of wind turbine blade adhesives. *Polymer Testing*, 116:, 2022.

[12] F.S. Jumbo, I.A. Ashcroft, A.D. Crocombe and M.M. Abdel Wahab. Thermal residual stress analysis of epoxy bi-material laminates and bonded joints. *International Journal of Adhesion and Adhesives*, 30(7):523–538, 2010.
[13] T. Holst, F. Sayer and A. Antoniou. Modelling of chemical shrinkage evolution with curing degree of a filled epoxy adhesive. In: *IOP Conference Series: Materials Science and Engineering*, IOP Publishing Ltd, 2020.
[14] C. Ma, Y. Tian, Y. Gong, J. Zhang, H. Qi and C. Wang. Study of the effect of curing residual stress on the bonding strength of the single lap joint using a high-temperature phosphate adhesive. *Materials*, 11(7):, 2018.
[15] A. Agha and F. Abu-Farha. Experimental methods to capture curing induced effects in adhesive bonded joints. *International Journal of Adhesion and Adhesives*, 104:, 2021.
[16] L.F.M. da Silva and R.D. Adams. Joint strength predictions for adhesive joints to be used over a wide temperature range. *International Journal of Adhesion and Adhesives*, 27(5):362–379, 2007.
[17] K.B. Sim, T.H. Lee, G.Y. Han and H.J. Kim. Thermal expansion and mechanical properties of urethane-modified epoxy bonded CFRP/steel joints at low and high temperatures for automotive. *Composite Structures*, 322:, 2023.
[18] N.A. Fleck, J.W. Hutchinson and Z. Suo. Crack path selection in a brittle adhesive layer. *Int. J. Solids Structures*, 27(13):1683–1703, 1991.
[19] R. Lopes Fernandes, M.K. Budzik, R. Benedictus and S. Teixeira de Freitas. Multi-material adhesive joints with thick bond-lines: Crack onset and crack deflection. *Composite Structures*, 266:, 2021.
[20] B. Chen and D.A. Dillard. The effect of the T-stress on crack path selection in adhesively bonded joints. *International Journal of Adhesion & Adhesives*, 21(5):357–368, 2001.
[21] A. Shivaie Kojouri, H. Khosravi Rikaee, K.A. Kalteremidou and D. Van Hemelrijck. Experimental evaluation of J-integral in elastic and elastic–plastic polymers by means of digital image correlation and higher-order eigenfields under mode-I. *Engineering Fracture Mechanics*, 291:, 2023.
[22] A. Sharma and S. Daggumati. Computational micromechanical modeling of transverse tensile damage behavior in unidirectional glass fiber-reinforced plastic composite plies : Ductile versus brittle fracture mechanics approach. *International Journal of Damage Mechanics*, 29(6):943–964, 2020.
[23] A. Sharma, S. Daggumati, A. Gupta and W. Van Paepegem. On the prediction of the bi-axial failure envelope of a UD CFRP composite lamina using computational micromechanics: Effect of microscale parameters on macroscale stress–strain behavior. *Composite Structures*, 251(October 2019):112605, 2020.
[24] Abaqus, 6.23 documentation, Dassault Systemes Simulia Corporation (2023). 2023.

EFFECTS OF BRAIDING ARCHITECTURES IN THE MECHANICAL PROPERTIES AND DAMAGE MECHANISMS OF 3D BRAIDED COMPOSITES

Shenghao Zhang[1], Xinyi Song[1], Jin Zhou[1],*, Di Zhang[1], Xiaohui Yang[2], Longteng Bai[2], Jun Wang[2], Zhongwei Guan[3]

[1]School of Mechanical Engineering, Xi'an Jiaotong University, Xi'an 710049, China.
[2]Key Laboratory of liquid rocket Engine Technology, Xi'an Aerospace Propulsion Institute, Xi'an, China
[3] Advanced Materials Research Centre, Technology Innovation Institute, Abu Dhabi, UAE.

[*] *Corresponding E-mail: jin.zhou@xjtu.edu.cn*

Keywords: 3D braided composites; Finite element; Mechanical properties; Progressive damage.

Abstract

The tensile properties and resulting damage mechanisms observed in three-dimensional four-directional (3D4d), three-dimensional five-directional (3D5d) and three-dimensional six-directional (3D6d) braided composites have been studied experimentally and numerically. Finite element (FE) models have also been established using a continuous damage mechanics methodology, with user-defined subroutines being developed to define the damage criteria and the associated stiffness degradation in the yarns and matrix. The bridging and Chamis models are used to define the mechanical properties of yarns. The proposed method is then used to predict the tensile properties and damage development in these novel 3D braided composites. The FE models are subsequently validated by comparing the results of the simulations with experimental data. It has been shown that the maximum longitudinal tensile strength is associated with the 3D4d braided composites, whereas the maximum longitudinal tensile modulus is exhibited by the 3D5d braided composites. In contrast, the 3D6d braided composites exhibit the lowest values for each of these test parameters. It has been shown that the 3D4d braided composites tend to fracture along the braiding angle, whereas axial splitting occurs in the 3D5d braided composites and transverse failure predominates in the 3D6d braided composites.

1. Introduction

Three-dimensional (3D) braided composites are currently attracting significant attention in both the academic and industrial sectors due to their high specific strength and modulus, exceptional impact resistance, and design versatility [1-4]. However, their complex meso-structure frequently results in a mechanical behavior that is challenging to predict [5]. Therefore, it is necessary to study the mechanical properties and damage mechanisms of such composites in order to guide their design and use in load-bearing applications.

Recently, a number of studies have been undertaken to experimentally investigate the mechanical properties of 3D braided composites [6-8]. In addition to investigating the quasi-static mechanical properties of three-dimensionally braided composites [9-11], their response to complex loading and environmental conditions has also been studied in the past [12-14]. In addition, the damage mechanisms occurring in 3D braided composites has been analyzed using acoustic emission (AE), computed tomography (CT), scanning electron microscope (SEM) and other advanced tools [15-17]. Measuring the mechanical properties and subsequent internal failure processes in braided composites is both expensive and challenging. Additionally, these properties are known to vary with changes in the braiding

angle and fiber volume fraction [18, 19]. As a result of their high accuracy and cost-efficient nature, finite element (FE) models are regularly used to study the mechanical behavior of 3D braided composites [20-23]. For example, Du et al. [24] developed a parametric FE model for a 3D6d braided composite. Their investigations highlighted a reduction in the longitudinal mechanical properties of such composites with increasing braiding angle. In contrast, increasing the fiber volume fraction resulted in an increase in these properties. Li et al. [25] found that decreasing the braiding angle and increasing the fiber volume fractions lead to notable enhancements in the strength and modulus of the 3DR5d braided composites. In summary, the previously-mentioned studies mainly focus on the variation of mechanical properties with void content, fiber volume fraction and braiding angle. However, the effect of modifying the braiding architecture on the mechanical properties of 3D braided composites is also likely to be significant and should be studied.

This paper describes the development of FE models for 3D4d, 3D5d, and 3D6d braided composites, with the aim to investigate the effect of varying braiding architecture on mechanical response. The FE models are used to predict the mechanical properties and damage behavior of these three braided composites under longitudinal tensile loading, and the models are then validated against experimental data. Differences in the tensile properties and resulting damage mechanisms observed in the different braiding architectures are investigated in detail.

2. Materials and geometric structure

2.1. Materials

In the present study, 3D braided composites, with a theoretical internal braiding angle of 20° are investigated. These braided composites are designated as 3D4d-20°, 3D5d-20° and 3D6d-20°. The 3D braided fabrics were prepared using T700-3K carbon fiber yarns (Toray®, Tokyo, Japan) through the 4-step 1×1 procedure [26]. The preforms were then impregnated using with a TDE86 resin matrix (Jingdong®, Tianjin, China) [27] the resin transfer molding (RTM) technique.

These 3D braided composites comprise of fiber bundles and a matrix, which can be considered to be transversely-isotropic and isotropic, respectively. Tables 1 and 2 present the mechanical properties of the carbon fibers and epoxy resin investigated here. The impregnated fiber bundle is composed of fibers and matrix and its mechanical properties can be calculated using the bridging model [28] and Chamis model [29].

Table 1. Mechanical parameters and fracture energy densities of the fiber

Components	E_{f1} (GPa)	E_{f2} (GPa)	ν_{12}	ν_{23}	G_{f12} (GPa)	G_{f23} (GPa)	X_{ft} (GPa)	X_{fc} (GPa)	G_{Lt} (N/mm)	G_{Lc} (N/mm)	G_{Tt} (N/mm)	G_{Tc} (N/mm)
T700	230.0	18.2	0.27	0.30	36.6	7.0	4.9	1.4	12.78	6.26	0.13	1.15

Table 2. Mechanical parameters and fracture energy density of the matrix

Components	E_m(GPa)	ν_m	T_m(GPa)	C_m(GPa)	S(MPa)	G_{mt}(N/mm)	G_{mc}(N/mm)
TDE-86	3.45	0.35	0.08	0.18	0.2	1.0	1.0

2.2. Geometric structure

As a result of the periodic nature of 3D braided composites, it is possible to predict their mechanical properties by selecting a representative volume element (RVE), and in doing so, greatly improve the calculation efficiency. The geometric relationships between the yarns in the RVE are shown in Fig. 1.

It is evident that differences in three braiding architectures are associated with the presence of axial yarns or warp yarns. The braiding yarns 1, 2 ,3 ,4 signify that the braiding yarns have four different distribution patterns in a 3D space. Considering the extrusion deformation of the yarns, several assumptions are applied to model the geometrical configurations in this study, as proposed by Li [25]. The braiding yarns are assumed to have hexagonal cross-sectional shapes, the axial yarns are presumed to be square and the warp yarns are assumed to have a quadrilateral configuration.

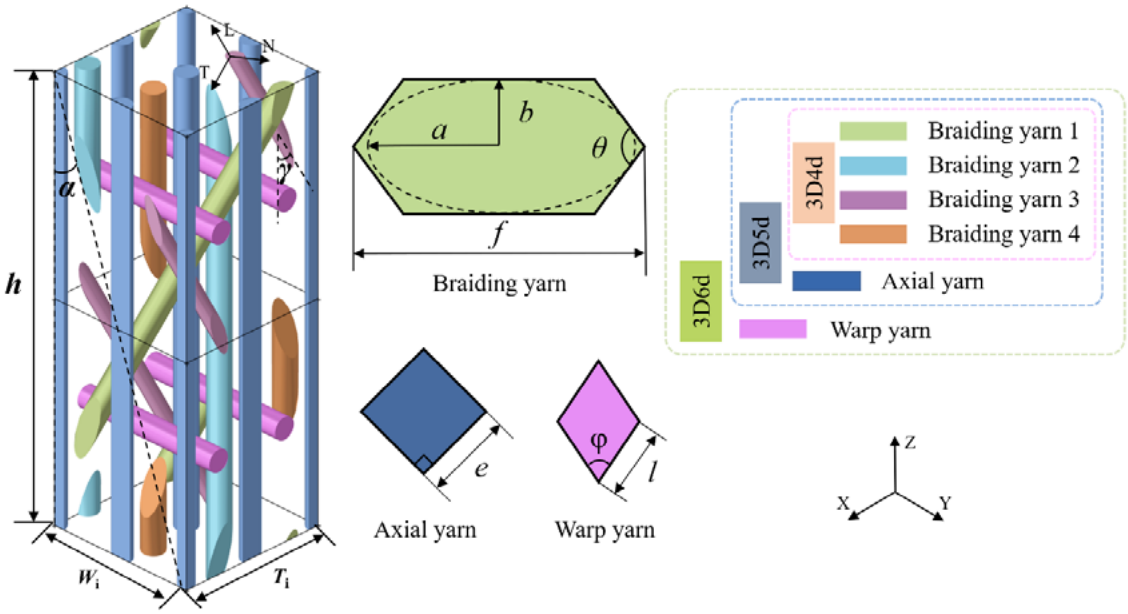


Fig. 1. RVE structure of the braided composites

Parameters, such as the width (W_i), thickness (T_i), height (h) and internal braiding angle (γ), are used to define the size of the RVE. The relationships between these parameters are given in Eqs. (1) - (3).

$$W_i = T_i = 2\sqrt{2}(2+r)b \tag{1}$$

$$\tan\gamma = \frac{\sqrt{2}W_i}{h} \tag{2}$$

$$\tan\alpha = \frac{\sqrt{2}}{2}\tan\gamma \tag{3}$$

where r represents the section factor of the axial yarn, which should be zero in the 3D4d composite model; b is the short half-axis of the cut ellipse in the braided yarn section. The geometrical relationships of the yarns can be inferred as follows.

$$a = b\sqrt{r^2+4r+3}\cos\gamma \tag{4}$$

$$\theta = 2\arcsin\left(\frac{1}{\sqrt{1+\cos^2\gamma}}\right) \tag{5}$$

$$f = 2b\cos\gamma \tag{6}$$

$$e = rb \tag{7}$$

$$l = \frac{1}{2\sin\alpha}\left(\frac{W_i}{2} - \frac{a\sin\theta}{\cos\alpha}\right) \tag{8}$$

$$\varphi = 2\alpha \tag{9}$$

where a is long half-axis of the cut ellipse in the braided yarn section; θ and f are the incline angle and side length of the hexagon; e and l are the side length of the axial and warp yarns.

Based on the equations outlined above, the parameterized RVE of each of the 3D braided composites can be created using SolidWorks software. Periodic meshing is required, as periodic boundary conditions need to be imposed on the established RVE models. The 3D four-node tetrahedral (C3D4) element is chosen to mesh the RVE models using the Hypermesh software to generate the periodic meshes.

3. Numerical Model Implementation

3.1. Failure criteria

The stress states in the fiber bundles and the matrix in different regions are unequal since the meso-structure of a 3D braided composite is complex, but they are closely related to each other, which determines the complexity of the damage process in the 3D braided composites. Therefore, a suitable damage criterion is required to accurately predict damage initiation based on the mechanical properties of the composites. In the current study, the Hashin criterion [30, 31] was used to predict tensile damage in the fiber bundles in the L-direction. This approach has been used with great success in previous studies. For the T and N-directions, the Hou failure criteria [32] are adopted. The matrix was modelled using Christensen's criterion [33], which can be used to predict damage and yielding in isotropic materials subjected to various stress states. And a bilinear constitutive relation was determined to describe the constitutive responses before and after failure in the composites. Then, the progressive damage model was implemented through a user-defined subroutine (UMAT) coded in Fortran within the commercial software ABAQUS 2021 [34].

3.2. Boundary conditions

In order to accurately analyze the mechanical properties of three-dimensional braided composites, it is necessary to establish the exact boundary conditions of the RVE. Based on the symmetry of the material microstructure, Li et al. [35, 36] proposed periodic boundary conditions, which ensure that the unit cell satisfies stress continuity and deformation coordination at the same time. In this paper, the nodal displacement constraint relationships for symmetric nodes on parallel faces were imposed using a Python script within ABAQUS 2021 [34]. Finally, the average stress and strain were determined through the following equations.

$$\begin{aligned} \bar{\sigma}_{ij} &= \frac{1}{V}\int_V \sigma_{ij}\mathrm{d}V \\ \bar{\varepsilon}_{ij} &= \frac{1}{V}\int_V \varepsilon_{ij}\mathrm{d}V \end{aligned} \tag{10}$$

where V is the volume of RVE.

3. Results and Discussion

3.1. Mechanical properties

The predicted longitudinal tensile responses of the three different braiding architectures were compared with the experimental data to validate the proposed FE models, in Table 3 and Fig 2. It is evident that the predicted stress-strain curves initially exhibit linear growth with increasing strain, followed by a

rapid drop at the peak stress. The model clearly predicts that the three composites fail in a brittle fracture manner, which is consistent with the experimental observations. It is worth pointing out that the greatest error between the FE simulation and the experimental results remains less than 5 %.

Table 3. Comparison of the predicted results with the experimental data

Test	Strength (MPa)			Modulus (GPa)		
	FE	Exp	Relative error	FE	Exp	Relative error
3D4d-20°	1123.95	1079.35	4.13 %	112.17	117.42	-4.47 %
3D5d-20°	951.65	960.66	-0.94 %	114.41	120.13	-4.76 %
3D6d-20°	787.76	754.34	4.43 %	94.78	98.44	-3.72 %

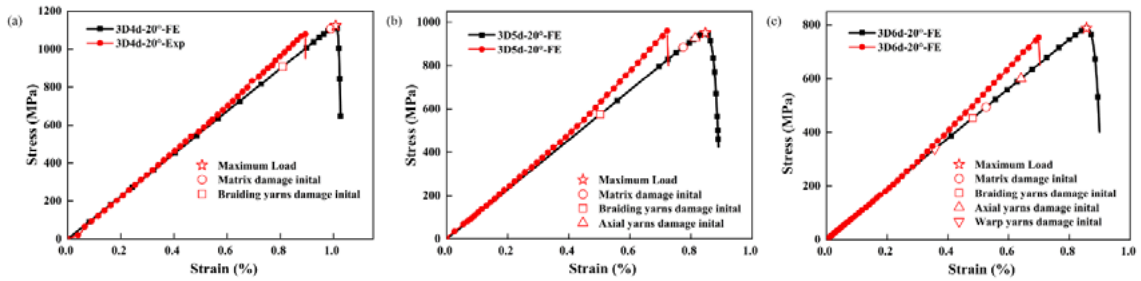


Fig. 2. Comparison of the predicted results with the experimental data (a) 3D4d-20°, (b) 3D5d-20° and (c) 3D6d-20°

The mean and variance of longitudinal tensile properties of the three types of 3D braided composite are compared in Fig. 3. An examination of the figure shows that the highest tensile strength is associated with the 3D4d-20° composite, whilst the 3D5d-20° exhibits the highest tensile modulus. The tensile strength of the 3D5d-20° composite is only 3%lower than the 3D4d-20° composite, whereas its tensile modulus is almost 14% greater. This evidence suggests that the axial yarns exert only a minimal influence on the longitudinal tensile strength, but have a much greater effect on the longitudinal tensile stiffness of these 3D braided composites. The tensile strength and modulus values of the 3D6d-20° composite are the lowest of those measured here, being approximately 21 %, 12 % lower than its 3D5d-20° counterpart, respectively. This suggests that the warp yarns reduce the tensile properties of these 3D braided composites.

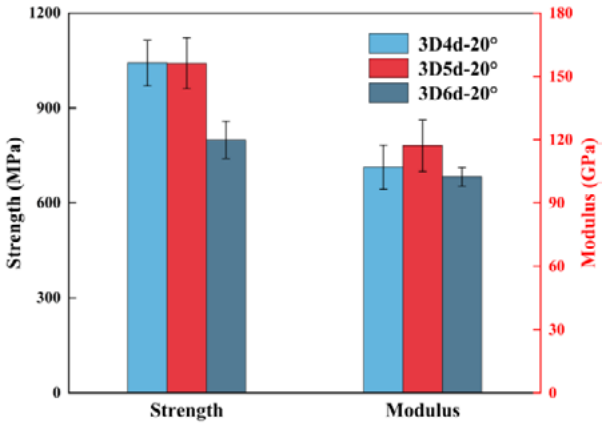


Fig. 3. The longitudinal tensile strength and modulus of the 3D braided composites

3.2. Damage mechanisms

Figs. 4 (a)-(c) present the external damage morphologies in the three braided composites under tensile loading. Here, the predominant tensile failure modes in the 3D4d-20° braided composite are fiber fracture perpendicular to the loading direction and tension-shear failure roughly parallel to the internal braiding angle. The effect of the braiding yarn on the failure mode is readily apparent. For the 3D5d-20° braided composite, the damage mode is mainly fiber fracture perpendicular to the loading direction and splitting along the longitudinal direction, suggesting that the axial yarns play a major role. For the 3D6d-20° braided composite, the warp yarns prevent crack propagation in the longitudinal direction, so that transverse fiber fracture occurs. Figs. 4(d)-(e) show the predicted damage patterns, which agree well with the experimental results. These findings suggest that the proposed FE models are capable of accurately predicting the mechanical behavior of these 3D braided composites under longitudinal tensile loading.

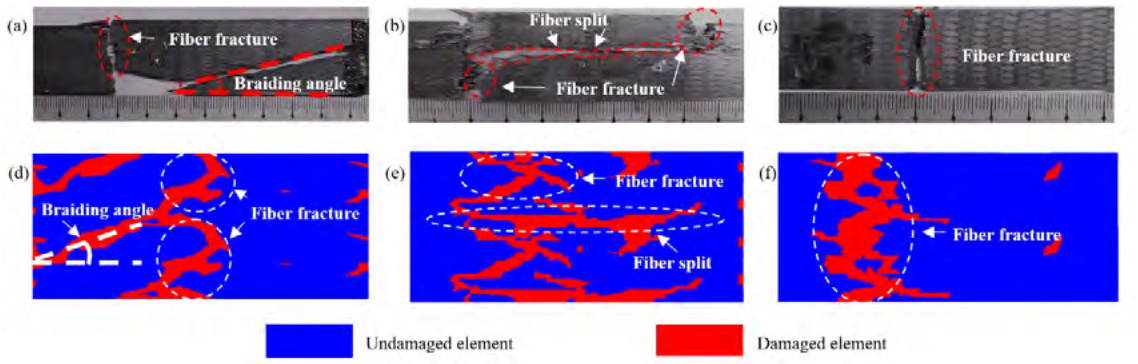


Fig. 4. Longitudinal tensile fracture morphology (a) 3D4d-20° (Exp), (b) 3D5d-20° (Exp), (c) 3D6d-20° (Exp), (d) 3D4d-20° (FE), (e) 3D5d-20° (FE), (f) 3D6d-20° (FE)

4. Conclusions

The longitudinal tensile responses of three types of braided composite have been studied both experimentally and numerically. Finite element models have been developed and validated against the corresponding experimental results and the damage mechanisms occurring in the composites have been highlighted. It has been shown that the tensile strength of the 3D4d-20° braided composite and the tensile modulus of 3D5d-20° braided composites are the highest among the three composites, whereas the 3D6d-20° braided composite exhibits the lowest strength and modulus. The difference between the tensile strength of the 3D5d-20° and 3D4d-20° composites is less than 3%. This suggests that the axial yarns enhance the longitudinal tensile stiffness of 3D braided composites, but the warp yarns weaken the longitudinal tensile mechanical properties.

The tensile damage mechanisms differ between the three braided composites, due to the presence of the axial and warp yarns. In the 3D4d composites, the braiding yarns play a major role in determining the tensile response. The observed damage modes are therefore fiber fracture perpendicular to the loading direction and tension-shear failure along the braiding angle. The failure patterns observed in the 3D5d composites are dominated by fiber fracture perpendicular to the loading direction and longitudinal cracking. This is attributed to the influence of the axial yarns, which direct the evolution of damage along them. In contrast, the failure modes observed in the 3D6d composite are characterized by fiber fracture along the transverse direction, primarily due to the abrupt failure of the warp yarns during initial loading.

Acknowledgments

This work was supported by the Natural Science Basic Research Program of Shaanxi [Program No. 2023-JC-QN-0042].

References

[1] Shi DQ, Zhang B, Liu CQ, Wang LY, Yang XG, Luo RY. In-situ study on compressive behaviors of different types of 3D SiC/SiC composites using X-ray computed tomography and digital image correlation. *Journal of Materials Research and Technology*, 22:3475-88, 2023.
[2] Song XY, Zhang D, Zhou J, Chen XF, Zhang SH, Bai LT, et al. Hierarchical multi-scale analysis of the effect of varying fiber bundle geometric properties on the mechanical properties of 3D braided composites. *Composite Structures*, 322:117375, 2023.
[3] Long J, Xu F, Wu YY, Sun BZ, Gu BH. Thermal oxygen coupling effects on multiple-layer degradation behaviors and full-field crack evolutions of 3D5d braided composites. *Composites Science and Technology*, 233:109922, 2023.
[4] Long J, Xu F, Huang SW, Wu TW, Sun BZ, Gu BH. Compressive anisotropy effects and crack evolution mechanisms of 3D5d braided composites induced by thermo-oxidative ageing. *Composites Science and Technology*, 240:110102, 2023.
[5] Bilisik K, Sahbaz N. Structure-unit cell-based approach on three-dimensional representative braided preforms from four-step braiding: Experimental determination of effects of structure-process parameters on predetermined yarn path. *Textile Research Journal*, 82:220-41, 2011.
[6] Kalidindi SR, Abusafieh A. Longitudinal and Transverse Moduli and Strengths of Low Angle 3-D Braided Composites. *Journal of Composite Materials*, 30:885-905, 1996.
[7] Zuo HM, Li DS, Jiang L. Experimental study on compressive fatigue behavior and failure mechanism of 3D five-directional braided composites. *Composites Part A: Applied Science and Manufacturing*, 139:106097, 2020.
[8] Wu YY, Guo JH, Xun LM, Sun BZ, Gu BH. Anisotropic degradation mechanism on low-velocity impact of 3D braided composites after thermo-oxidative ageing. *Thin-Walled Structures*, 182:110204, 2023.
[9] Zheng YY, Sun Y, Li JL, Liu LM, Li C, Liu JL, et al. Tensile response of carbon-aramid hybrid 3D braided composites. *Materials & Design*, 116:246-52, 2017.
[10] Zhang D, Zheng XT, Zhou J, Song XY, Jia P, Liu HB, et al. Effect of Braiding Architectures on the Mechanical and Failure Behavior of 3D Braided Composites: Experimental Investigation. *Polymers*, 14:1916, 2022.
[11] Huang H, Shan ZD, Liu JH, Sun Z, Guo ZT, Gong H, et al. A unified trans-scale mechanical properties prediction method of 3D composites with void defects. *Composite Structures*, 306:116574, 2023.
[12] Karnik IT, Tallman TN. An experimental study on the effect of fatigue loading on electrical impedance in open-hole carbon nanofiber-modified glass fiber/epoxy composites. *Composite Structures*, 276:114463, 2021.
[13] Singh A, Reynolds N, Keating EM, Barnett AE, Barbour SK, Hughes DJ. The effect of braid angle on the flexural performance of structural braided thermoplastic composite beams. *Composite Structures*, 261:113314, 2021.
[14] Zhang XH, Gao HS, Wen ZX, Li MY, Zhou XG, Yue ZF. Effect of film cooling holes on the mechanical properties of 3D braided SiCf/SiC composites at 1350 °C in air. *Ceramic International*, 46:7982-90, 2020.
[15] Zhang PF, Zhou W, Yin HF, Shang YJ. Progressive damage analysis of three-dimensional braided composites under flexural load by micro-CT and acoustic emission. *Composite Structures*, 226:111196, 2019.
[16] Xun LM, Huang SW, Sun BZ, Gu BH. Torsional cracks development in carbon-fiber 3-D braided composite tubes. *Thin-Walled Structures*,184:110477, 2023.
[17] Zuo HM, Zhu H, Li DS, Jiang L. Study on in-plane compression properties and numerical modeling of three dimensional five-directional braided composites. *Thin-Walled Structures*, 168:108232, 2021.

[18] Du XB, Zhu H, Ai J, Li DS, Jiang L. Parameterized meso-scale modeling and experimental study on the tensile damage evolution and strength of 3D five-directional braided composites. *Materials & Design*, 205:109702, 2021.
[19] Li ZJ, Liu ZG, Wang Y, Yi YP, Wang YB. Process-structure-performance modelling and progressive damage analysis of 3D rotary-four-directional rectangular braided composites under tensile load. *Materials & Design*, 225:111523, 2023.
[20] Ghaedsharaf M, Brunel JE, Lebel LL. Fiber-level numerical simulation of biaxial braids for mesoscopic morphology prediction validated by X-ray computed tomography scan. *Composites Part B: Engineering*, 218:108938, 2021.
[21] Zhang YY, Li HM, Liu X, Gao YH, Guan CY. Trans-scale elastic-plastic damage analysis of 3D tubular braided composites with void defects. *International Journal of Mechanical Sciences*, 274:112288, 2023.
[22] Yang ZQ, Sun Y, Huang SQ, Yang ZH. A higher-order three-scale reduced homogenization approach for nonlinear mechanical properties of 3D braided composites. *International Journal of Mechanical Sciences*, 208:106684, 2021.
[23] Ai J, Du XB, Li DS, Jiang L. Parametric study on longitudinal and out-of-plane compressive properties, progressive damage and failure of 3D five-directional braided composites. *Composites Part A: Applied Science and Manufacturing*, 156:106840, 2022.
[24] Du XB, Li DS, Jiang L, Fang DN. Numerical investigation on tensile behavior of three-dimensional six-directional braided composites. *International Journal of Mechanical Sciences*, 237:107815, 2023.
[25] Li ZJ, Dai HL, Liu ZG, Wang Y. Micro-CT based parametric modeling and damage analysis of three-dimensional rotary-five-directional braided composites under tensile load. *Composite Structures*, 309:116734, 2023.
[26] Pandey R, Hahn HT. Designing with 4-step braided fabric composites. *Composites Science and Technology*, 56:623-34, 1996.
[27] Liu BC, Bickerton S, Advani SG. Modelling and simulation of resin transfer moulding (RTM)—gate control, venting and dry spot prediction. *Composites Part A: Applied Science and Manufacturing*, 27:135-41, 1996.
[28] Huang ZM. A bridging model prediction of the ultimate strength of composite laminates subjected to biaxial loads. *Composites Science and Technology*, 64:395-448, 2004.
[29] Chamis CC. Mechanics of Composite Materials: Past, Present and Future. *Journal of Composites Technology & Research*, 11:3-14, 1989.
[30] Kaddour AS, Hinton MJ. Maturity of 3D failure criteria for fibre-reinforced composites: Comparison between theories and experiments: Part B of WWFE-II. *Journal of Composite Materials*,47:925-66, 2013.
[31] Kaddour AS, Hinton MJ, Smith PA, Li S. A comparison between the predictive capability of matrix cracking, damage and failure criteria for fibre reinforced composite laminates: Part A of the third world-wide failure exercise. *Journal of Composite Materials*, 47:2749-79, 2013.
[32] Hou JP, Petrinic N, Ruiz C, Hallett SR. Prediction of impact damage in composite plates. *Composites Science and Technology*,60:273-81, 2000.
[33] Christensen RM. 2013 Timoshenko Medal Award Paper—Completion and Closure on Failure Criteria for Unidirectional Fiber Composite Materials. *Journal of Applied Mechanics*, 81, 2013.
[34] ABAQUS/CAE 2021, Simulia. https://www3dscom/products-services/simulia/products/abaqus/. Accessed date: 17/10/2023.
[35] Li SG, Wongsto A. Unit cells for micromechanical analyses of particle-reinforced composites. *Mechanics of Materials*, 36:543-72, 2004.
[36] Li SG. Boundary conditions for unit cells from periodic microstructures and their implications. *Composites Science and Technology*, 68:1962-74, 2008.

NUMERICAL INVESTIGATION OF THE FLEXURAL BEHAVIOR OF STEEL PLATES REINFORCED WITH HYBRID FLAX/CARBON COMPOSITE PATCHES

M.A. Tazi[1], M. Jebli[1], S. Teixeira de Freitas[2,3], P. Casari[4], S. de Barros[1]

[1]Cesi Lineact, France.
Email: matazi@cesi.fr
Email: mjebli@cesi.fr
Email: sdebarros@cesi.fr
[2]IDMEC, Instituto Superior Técnico, Lisbon, Portugal.
Email: sofia.teixeira.freitas@tecnico.ulisboa.pt
[3] Delft University of Technology, Delft, The Netherlands
[4]GeM, Nantes University, France
Email: Pascal.Casari@univ-nantes.fr

Keywords: Steel reinforcement, Hybrid carbon/flax composite, Patch, FEA, Flexural test.

Abstract
For strengthening or rehabilitation of existing structures, patches of fiber-reinforced polymers (FRP) materials are being adhesively bonded to the existing metallic structures. So far, Carbon FRP (CFRP) are the main composite materials industrially implemented for metal structural reinforcement, due to their reliability and high mechanical performances. However, multiple researchers have highlighted the negative environmental impact of synthetic composite materials, and interest is shifting towards the use and development of bio-based composite materials. This paper presents an FE numerical investigation of the use of Hybrid Carbon/Flax FRP as an alternative solution for structural reinforcement of steel plates under flexural loading. Four different configurations of patches are studied to be bonded to steel rectangular plates, and three point bending tests are numerically modelled to simulate the flexural behaviour of the assemblies. Compared to the unreinforced steel plate baseline, reinforcements C5, F5, CFFFC, and FFFCC exhibited improvements of 149%, 120%, 137%, and 145% in bending stiffness, respectively.

1. Introduction

Advanced composite materials have been employed in the civil engineering industry for many years [1]. One of the most popular use of composites in the civil engineering field is the repair and upgrading of beams in bridges and buildings. Although not as widespread as the upgrading of reinforced concrete structures, carbon fiber reinforced polymer (CFRP) is becoming a very attractive solution for the retrofitting of metallic beams, especially for cases where there are severe access constraints, or associated high costs with installation time [2]. Various research findings have established the effectiveness of strengthening metallic structures by bonding CFRP strips and proved that the load-carrying capacity and post-yielding flexural stiffness of steel beams can be significantly improved [2,3,4]. Design guidance documents have been published regarding the use of CFRP for the rehabilitation and upgrading of metallic civil engineering structures by CIRIA [5] and ICE [6].

©2024 | 3_TAZI_Mohamed Amine_2MIF4.pdf

Nevertheless, researchers have lately highlighted the important negative environmental impact of synthetic composite materials, and interest is shifting towards the use and development of natural-based composites [7]. Flax fiber has attracted increasing attention as a reinforcement material because of its low environmental impact, weight and cost compared to traditional carbon or glass fiber. The main drawbacks of flax fibers, like many other natural fibers, are their lower mechanical properties (elastic module, strength, etc.), and poor hygrothermal behavior. Natural fiber reinforced polymers (NFRP) are therefore limited to sub-structural applications such as interior automotive or aircraft parts, sports, music instruments, among others [8].

Hybridizing flax and carbon fibers is considered an interesting and effective method to overcome the mechanical shortcomings of flax fibers. By investigating the right hybrid modes and stacking sequences, hybridization technique may combine the advantages of both flax fibers (environmental friendliness, low cost) and carbon fibers (higher mechanical properties and hygrothermal resistance).

In this paper, a 3D solid FE model was built, to investigate the flexural behavior of a steel rectangular plate, reinforced by bonding a composite patch on its tension flange. Four different patch configuration consisting of CFRP, FFRP and hybrid Carbon/Flax composites are studied. Three point bending tests are numerically simulated to assess and compare the flexural stiffness values of the modelled specimens.

2. FE Modelling

2.1. Model description

A 3D solid model is designed to investigate the flexural behaviour of a steel rectangular plate, reinforced by bonding a smaller rectangular composite patch to its tension flange. Three point bending tests are modelled to assess the flexural gain of the assemblies and compare them to those of a non-reinforced reference steel plate. Figure.1 presents the geometries of the designed specimens and their dimensions. Four different composite configurations are studied, and consist of either carbon fiber reinforced epoxy (CFRP), flax fiber reinforced epoxy (FFRP), or hybrid carbon-flax reinforced epoxy. All modelled composite patches contain five plies. According to a previous work from the authors [9], and a study by Wang et al. [10], CFRP and FFRP plies are chosen to be 0.3mm and 0.5mm thick, respectively. Table.1 presents relevant details of the used configurations.

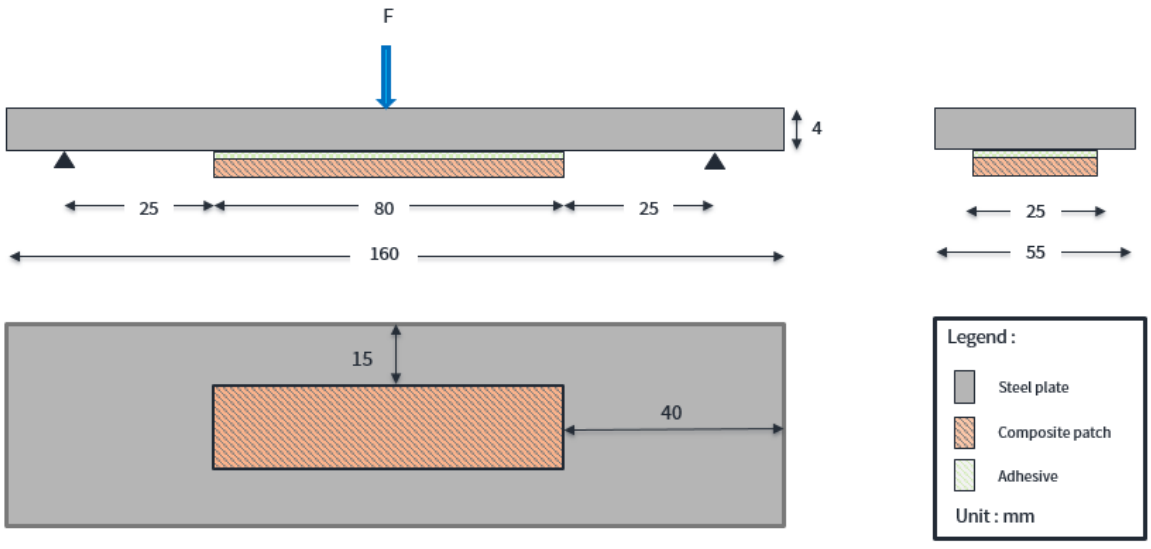
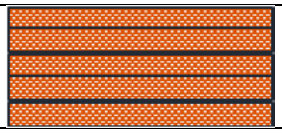
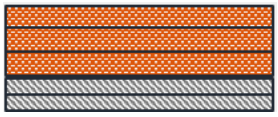


Figure 1. Schematic of a composite-strengthened steel plate.

Table 1. Composite patch configurations.

Configuration name	Representation	Nominal thickness [mm]	CFRP relative thickness	Number of CFRP plies	Number of FFRP plies
C5		1.5	1.5	5	0
F5		2.5	0	0	5
CFFFC		2.1	0.6	2	3
FFFCC		2.1	0.6	2	3

2.2. Material properties

2.2.1. Steel

A36 steel is a very commonly used material in bridge construction, and is chosen as the metallic substrate to be reinforced. Since the purpose of the study is to assess flexural gain, its behaviour is approximated with a simple bilinear elastic-plastic law, in accordance with material properties provided by the American Society of Testing and Materials (ASTM A36 Steel) [11]. Figure.2 displays the stress-strain behaviour and table.2 summarizes the used steel mechanical properties for FE modelling.



Figure 2. Stress-Strain bilinear law for A36 Steel.

Table 2. Mechanical properties of A36 Steel and adekit a-140 adhesive.

Mechanical properties	Value	
	A36 Steel	Adekit a-140
Young's Modulus [GPa]	200	2.5
Poisson Ratio	0.26	-
Yield Tensile Strength [MPa]	250	-
Ultimate Tensile Strength [MPa]	450	30

2.2.2. Composite patch

Unidirectional carbon fibers and bidirectional flax fibers with an epoxy matrix are used as reinforcement materials for the steel substrate. Table.3 summarizes their mechanical elastic properties, which were experimentally characterized in previous studies [12], [13]. We note that all laminates have 0° ply orientation relative to the longitudinal axis of the steel plate.

Table 3. Mechanical properties of composite materials.

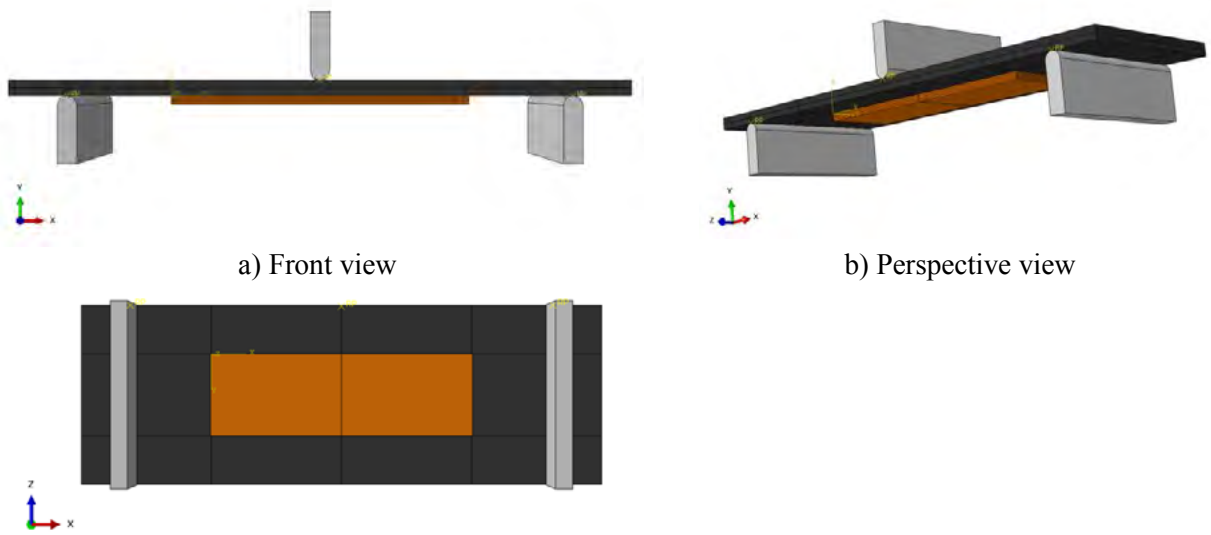
Mechanical properties	Symbol	Values	
		CFRP	FFRP
Elastic tensile Modules [GPa]	E_1	105.5	13.81
	E_2	7.2	13.81
	E_3	7.2	5.32
Shear Modules [GPa]	G_{12}	3.4	1.58
	G_{13}	3.4	1.64
	G_{23}	2.52	1.64
Poisson ratios	ν_{12}	0.34	0.144
	ν_{13}	0.34	0.51
	ν_{23}	0.378	0.51

2.2.3. Adhesive (cohesive contact)

A cohesive contact interaction has been created between the top surface of the composite patch and the bottom surface of the steel substrate, to simulate the bond behaviour which would result from using the epoxy adhesive adekit a-140. Table.2 gives relevant mechanical properties of the adhesive. The cohesive zone was modelled as an elastic non-damageable interaction, because we are exclusively interested in assessing the flexural gain prior to debonding in this study. Traction-separation stiffness coefficients were all taken equal to the young's modulus of the adhesive, in accordance with the values provided by the supplier data sheet [14], $K_{nn} = K_{ss} = k_{tt} = 2500$ MPa.

2.3. Three point bending test

Three point bending test set up is designed to assess the flexural behavior of the reinforced steel plates. Figure.3 gives a visual representation of the CAE model. Fixtures were designed as rigid body parts. Contact interactions were created between the fixtures and the steel plate, and consist of a normal "hard" contact behavior and tangential friction behavior, with a friction coefficient equal to 0.15, as advised from literature for steel-steel contact [15]. 6mm displacement loads are imposed for all studied configurations.



a) Front view

b) Perspective view

c) Bottom view

Figure 3. Visual representation of the CAE model.

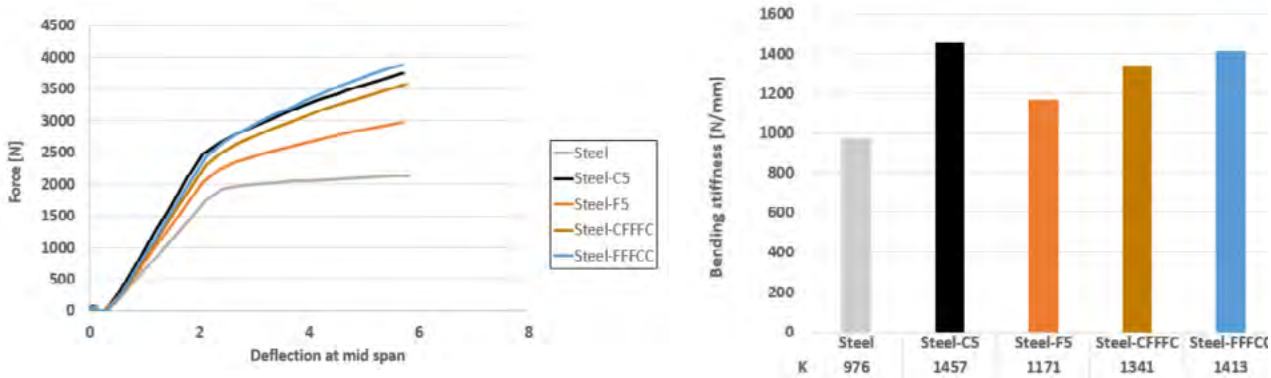
3. Numerical results and discussion

3.1. Force-deflection results

Figure.4.a) represents the force-deflection curves numerically obtained. In order to compare the flexural gain due to the bonding of the composite patches, we calculate the bending stiffness K within the elastic domain (between 0.5 – 2mm of deflection) with the following equation:

$$K = \frac{p}{w} \tag{1}$$

Where p is the applied load measured at the reference point of the moving fixture, and w is the deflection at mid span of the composite plate.
The bending stiffness values, depicted in Figure 4.b), highlight significant enhancements for steel plates reinforced with used configurations. Specifically, compared to the unreinforced steel plate baseline, reinforcements C5, F5, CFFFC, and FFFCC exhibit improvements of 149%, 120%, 137%, and 145% in bending stiffness, respectively. We note that the higher flax fiber ply thickness, acts like a geometrical compensation for their lower mechanical properties compared to carbon fiber plies.



a) Force-deflection curves

b) Bending stiffness for each configuration

Figure 4. Force-deflection simulation results.

3.2. Evaluation of zone of maximal stress

Figure.5 shows the longitudinal stresses S_{11}, along the thickness of the composite patches, at the end of the load history, for the four tested configurations. We notice that the patches are exclusively loaded in tension, which is due to the higher traction forces of the steel bottom flange compared to the compression of the composite patch top surface because of the curvature. From figure.5, we can also perceive that the highest stresses in the patches are contained in their bottom surfaces. This explains the high values of bending stiffness increase obtained with the CFFFC and FFFCC configurations.

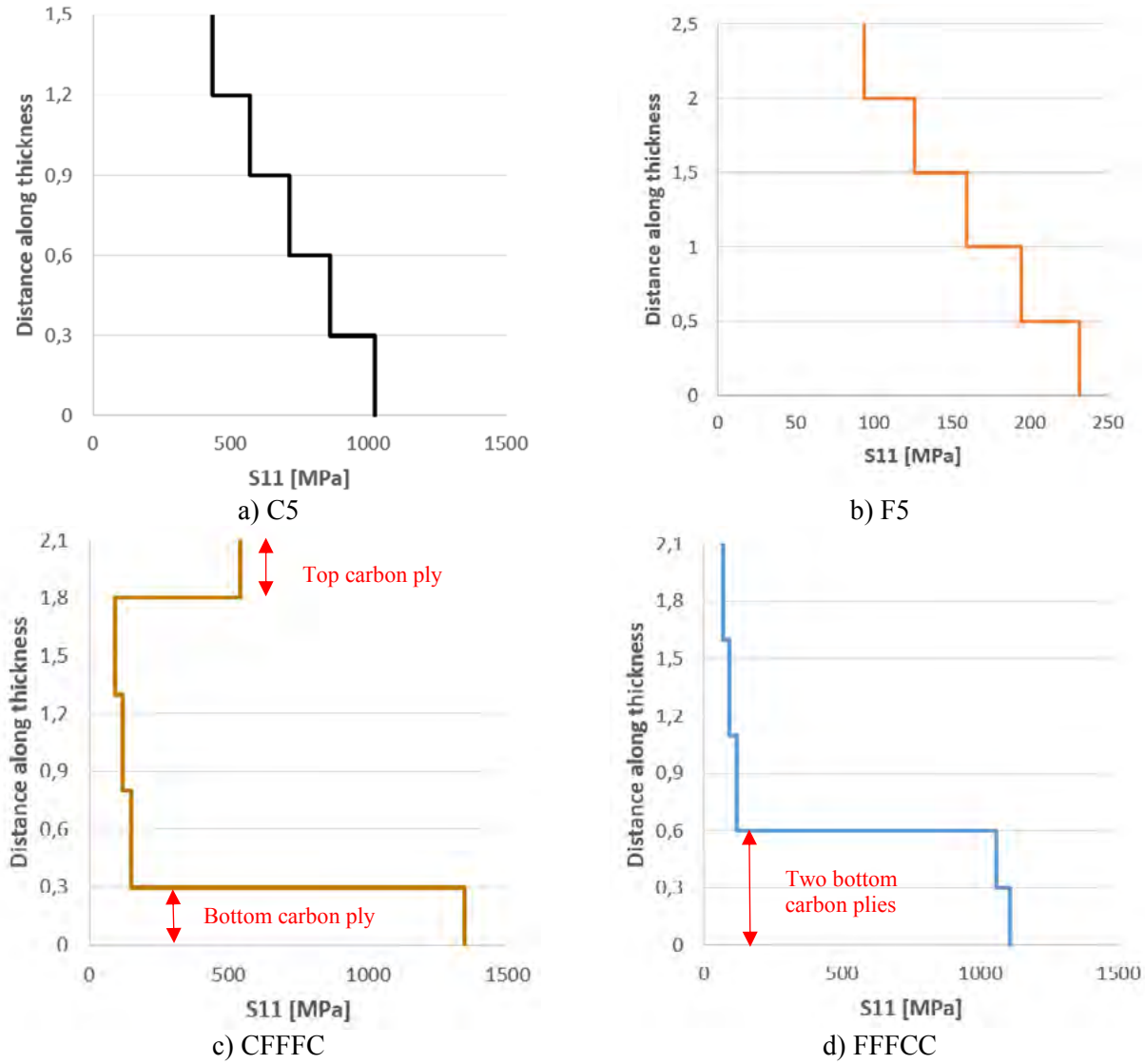


Figure 5. Distance along the thickness of the composite patches vs longitudinal stresses at mid-span

4. Conclusion

The aim of this work is to establish a finite element model to investigate the flexural stiffness gain of a steel plate reinforced by bonding a composite patch to its tension flange. Four different patch configurations consisting of CFRP and FFRP have been used, namely C5, F5, CFFFC and FFFCC. From the analysis of the obtained results, the following conclusions are drawn:

- Compared to the unreinforced steel plate baseline, reinforcements C5, F5, CFFFC, and FFFCC exhibit improvements of 149%, 120%, 137%, and 145% in bending stiffness, respectively. It is of interest to note that we achieve relatively close flexural stiffness gain with hybrid carbon/flax configuration compared to C5, while substituting 60% of carbon fibers with flax fibers.
- For various composite manufacturing processes, the choice of number of used fiber plies is the main design parameter. This study highlights the fact that natural fibers usually achieve a higher thickness per ply compared to synthetic composites, which is an interesting way of geometrically compensate their lower mechanical properties in flexural loading.
- FFFCC configuration showed the best mechanical performances after C5. Indeed, since both carbon plies are place at the bottom surface where maximal stresses evolve. Moreover, Flax fibers are the ones in contact with the steel interface, which limits risks of galvanic corrosion caused by carbon-steel contact.

Acknowledgements
The authors acknowledge Fundação para a Ciência e a Tecnologia (FCT) for its financial support via the project LAETA Base Funding (DOI: 10.54499/UIDB/50022/2020).

References

[1] L. Hollaway, *Polymer Composites for Civil and Structural Engineering*. Dordrecht: Springer Netherlands, 1993. doi: 10.1007/978-94-011-2136-1.
[2] J. Deng and M. M. K. Lee, "Behaviour under static loading of metallic beams reinforced with a bonded CFRP plate," *Composite Structures*, vol. 78, no. 2, pp. 232–242, Apr. 2007, doi: 10.1016/j.compstruct.2005.09.004.
[3] D. Guo, H.-P. Wang, Y.-L. Liu, W.-Y. Gao, and J.-G. Dai, "Structural behavior of CFRP-strengthened steel beams at different service temperatures: Experimental study and FE modeling," *Engineering Structures*, vol. 293, p. 116646, Oct. 2023, doi: 10.1016/j.engstruct.2023.116646.
[4] P. Colombi and C. Poggi, "An experimental, analytical and numerical study of the static behavior of steel beams reinforced by pultruded CFRP strips," *Composites Part B: Engineering*, vol. 37, no. 1, pp. 64–73, Jan. 2006, doi: 10.1016/j.compositesb.2005.03.002.
[5] T. Stratford, J. Cadei, and L. Hollaway, "CIRIA C595 – STRENGTHENING METALLIC STRUCTURES USING EXTERNALLY-BONDED FRP," in *Advanced Polymer Composites for Structural Applications in Construction*, Elsevier, 2004, pp. 693–700. doi: 10.1533/9781845690649.7.693.
[6] S. S. J. Moy, *FRP composites, life extension and strengthening of metallic structures: ICE design and practice guides*. London: Thomas Telford, 2001.
[7] S. Vigneshwaran *et al.*, "Recent advancement in the natural fiber polymer composites: A comprehensive review," *Journal of Cleaner Production*, vol. 277, p. 124109, Dec. 2020, doi: 10.1016/j.jclepro.2020.124109.
[8] M. D. Banea, "Natural Fibre Composites and Their Mechanical Behaviour," *Polymers*, vol. 15, no. 5, Art. no. 5, Jan. 2023, doi: 10.3390/polym15051185.
[9] M. A. Tazi *et al.*, "Experimental evaluation of interface adhesion of a flax fiber composite patch with epoxy and polyurethane adhesives for the reinforcement of steel structures," *International Journal of Adhesion and Adhesives*, vol. 129, p. 103559, Feb. 2024, doi: 10.1016/j.ijadhadh.2023.103559.
[10] A. Wang, X. Liu, Q. Yue, and G. Xian, "Tensile properties hybrid effect of unidirectional flax/carbon fiber hybrid reinforced polymer composites," *Journal of Materials Research and Technology*, vol. 24, pp. 1373–1389, May 2023, doi: 10.1016/j.jmrt.2023.03.078.
[11] A01 Committee, "Specification for Carbon Structural Steel." ASTM International. doi: 10.1520/A0036_A0036M-19.

[12] D. Scida, A. Bourmaud, and C. Baley, “Influence of the scattering of flax fibres properties on flax/epoxy woven ply stiffness,” *Materials & Design*, vol. 122, pp. 136–145, May 2017, doi: 10.1016/j.matdes.2017.02.094.
[13] S. Rahimian Koloor, A. Karimzadeh, N. Yidris, M. Petrů, M. Ayatollahi, and M. Tamin, “An Energy-Based Concept for Yielding of Multidirectional FRP Composite Structures Using a Mesoscale Lamina Damage Model,” *Polymers*, vol. 12, no. 1, p. 157, Jan. 2020, doi: 10.3390/polym12010157.
[14] “fr-np-ind-adekit-a140-1-h9940-1.pdf.” Accessed: May 12, 2024. [Online]. Available: https://fra.sika.com/dam/dms/fr01/v/fr-np-ind-adekit-a140-1-h9940-1.pdf
[15] J. J. Arnoux, G. Sutter, G. List, and A. Molinari, “Friction Experiments for Dynamical Coefficient Measurement,” *Advances in Tribology*, vol. 2011, pp. 1–6, 2011, doi: 10.1155/2011/613581.

Proceedings of the 21st European Conference on Composite Materials
Volume 3 - Material and Structural Behavior – Simulation & Testing

THERMOSET AND GLASS FIBER COMPOSITE FLEXIBILIZATION USING PARTIALLY REACTED SUBSTRUCTURES (PRS)

Hans Wittich, Louisa Christensen, Julian Karsten and Bodo Fiedler

Institute of Polymers and Composites, Hamburg University of Technology, Denickestrasse 15
21073 Hamburg, Germany
Email: wittich@tuhh.de, Web Page: https://www.tuhh.de/kvweb/en/home

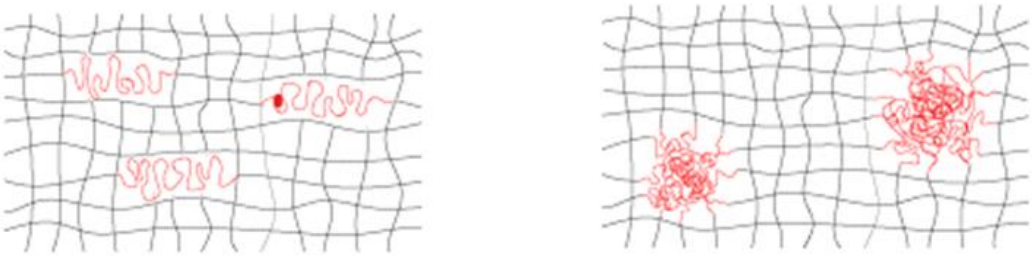
Keywords: composite, fber reinforced, epoxy, flexibilizer, fracture toughness

Abstract
The goal of this work is to modify glassfiber-reinforced plastics (GFRP) with a procedure which has already increased the fracture toughness in tests with pure resin, while the glass transition temperature Tg was not decreased. To increase the fracture toughness, a flexibilizer is used. But instead of simply adding it to the resin and hardener, a procedure with a two-step synthesis is used. A prereaction of resin and flexibilizer leads to the formation of partially reacted substructures (PRS), which are fully crosslinked in the next step by adding resin and hardener, so that the PRS form as domains in the composite. By vary curing temperature, curing degree and weight portions of the PRS the best possible combination can be chosen. Dynamic mechanical thermal analysis (DMTA), SEM, and Double Cantilever Beam (DCB) analyses provide information on T_g, PRS size and interlaminar toughness G_{Ic}. The interlaminar toughness reaches a value of 490,05 ± 40,91 J/m^2, which is an increase of 38% compared to the reference of homogeniously distributed flexibilizer and 118% compared to specimens without any flexibilizer. T_g can be increased by 7% compared to the reference of homogeniously distributed flexibilizer.

1. Introduction

The fracture toughness as a characteristic value depends on the molecular structure. In contrast to elastomers and thermoplastics, thermosets have a dense polymer network. The dense cross-linking prevents plastic deformation during crack propagation, which is why thermosets are brittle and have a lower fracture toughness. One advantage, however, is their high adaptability to specific load cases. The fracture toughness can be increased through the use of flexibilizers. These react chemically in a similar way to normal hardeners, but are characterized by longer-chain molecules that expand the polymer network and lead to greater mobility. However, the increase in fracture toughness is accompanied by a reduction in thermal resistance and thus the glass transition temperature. As a reduction in important mechanical properties such as strength or stiffness occurs in this area, a high value for the glass transition temperature is important for the safe use of the component.

Sharifi et al [1] have developed a two-stage synthesis that eliminates this contradictory dependency and prevents a reduction in the glass transition temperature. Instead of mixing all components - resin, hardener and flexibilizer - directly with each other and allowing them to crosslink, pre-crosslinking of resin and flexibilizer takes place. Partially reacted substructures (PRS) are formed during pre-crosslinking. An intermediate step in the production process causes the resin and flexibilizer to pre-crosslink and form partially reacted substructures (PRS). In the composite, the PRS are then locally concentrated in spherical form, as can be seen in Figure 1.



(a) Statistically distributed flexibilizer units. **(b)** Locally concentrated flexibilizer units in domains.

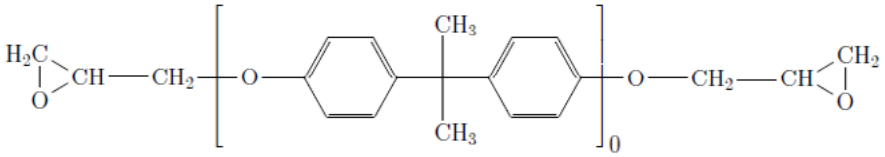
Fig. 1: Comparison of the schematic polymer networks of a (a) reference sample to the (b) Sample with formation of PRS domains based on [1].

These are mixed with resin and hardener and fully cross-linked. This intermediate step in the production process causes domains of locally concentrated flexibilizer units to form in the composite. The aim of this work is to transfer and test this principle of two-stage synthesis to a composite with glass fibers. For this purpose, the formation of the PRS in the pure resin is first examined in two preliminary test series as a function of the previously selected influencing factors - crosslinking temperature, crosslinking time or degree of crosslinking, weight proportion of the PRS in the composite -. The most suitable combination of these parameters is produced as a glass fiber composite in the main series of tests and examined with regard to domain formation and the resulting characteristic values for fracture toughness and glass transition temperature.

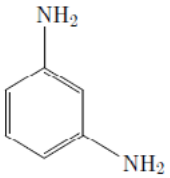
2. Experimental approach

2.1. Materials

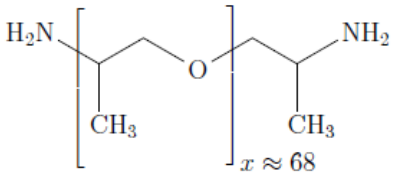
The resin used in this study is EPON 162 from HEXION, which belongs to the group of bisphenol A diglycidyl ethers (DGEBA).



The hardener used, DETDA 80 from Lonzacure, belongs to the group of diamine hardeners, which differ in the position of the amino groups. The mixture consists of approx. 80 % 3,5-diethyltoluene-2,4-diamine and approx. 20 % 3,5-diethyltoluene-2,6-diamine. In DETDA 80, the two amino groups are meta-positioned.



In addition, the flexibilizer JD-4000 from Huntsman is used. The repeating segments, which form no cross-links, create a flexibilizing effect.



For the main tests, glass filament fabrics from Interglas Porcher Industries are used for the reinforcement. The unidirectional fabric (Interglas 92145, Aero, FK 144, LW, UD) has a area weight of 220 g/m^2 and a warp thread in the 90° direction.

2.2. Processing

In the first series of preliminary tests, samples are prepared for combinations of crosslinking temperature, degree of crosslinking and a fixed weight proportion of the PRS.
First, the degree of crosslinking of the resin and flexibilizer is determined over time using the Netzsch Kinetics Neo software [2] in order to remove the pre-crosslinked PRS from the oven accordingly.

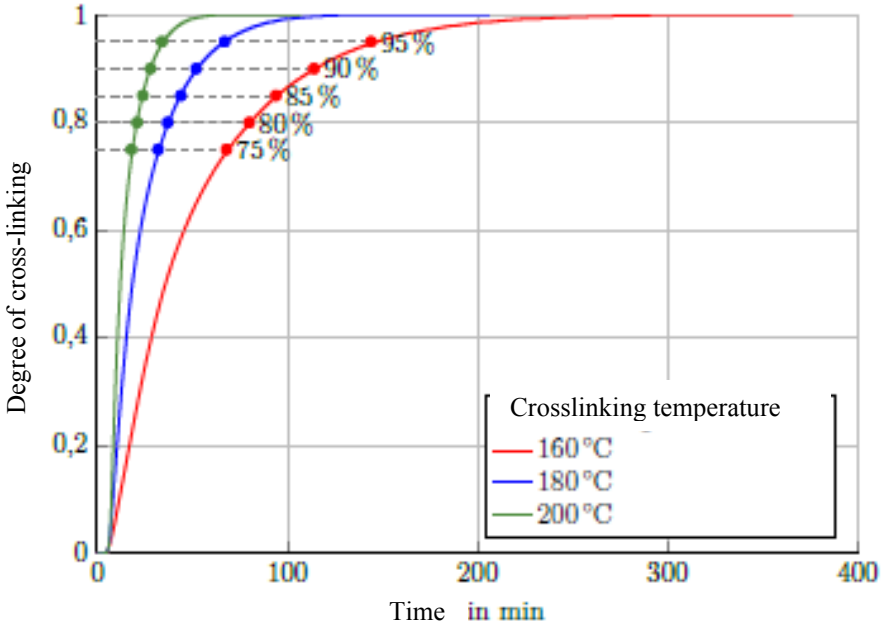


Fig. 2: Degree of crosslinking of the PRS of EPON 162 and JD-4000 simulated in Kinetics Neo at different crosslinking temperatures as a function of time.

The two components are mixed together superstoichiometrically (0.344 : 1) and mixed in a speed mixer at 3500 rpm for 2 min. For pre-crosslinking, the PRS are placed in an aluminum crucible in the oven, whereby three different crosslinking temperatures of 160 °C, 180 °C and 200 °C must be observed. The aluminum crucibles are removed from the oven at the predetermined times at the corresponding crosslinking levels of 75 %, 80 %, 85 %, 90 % and 95 % and cooled at room temperature. The PRS are then mixed with appropriate quantities of resin and hardener. Care must be taken to compensate for the over-stoichiometric proportion of the resin in order to achieve a stoichiometric mixture.
For the main series of tests, sheets of glass fiber reinforced plastic (GRP) with a unidirectional layer structure of $[0_{16}]$ are manufactured. The individual steps are illustrated in Figure 3. The individual matrix components are initially mixed as in the preliminary test series. However, the finished uncrosslinked mixtures are applied to the rollers of an impregnating roller mill in order to wet the individual glass fiber fabrics. The impregnating roller mill is made by EXAKT and is operated at room temperature with a gap width of 240 µm. The continuous rolling process removes air inclusions from the mixture. After

complete wetting, the fabrics are placed by hand on a Teflon foil covered metal plate and applied in the direction of the fibers using a roller. The metal plate ensures an even distribution of pressure and vacuum in the autoclave. After every four layers, an intermediate vacuum is applied for 7 minutes in order to achieve uniform consolidation and a reduction in air inclusions (debulking). In addition, after the eighth layer, two cut Teflon foils are inserted into the laminate, which later serve as artificial cracks in the tests. After the plates have been fully cross-linked in the autoclave and demolded, they are machined to the samples sizes needed.



Fig. 3: Sequence for manual lamination with (a) impregnation using a rolling process, (b) manual unrolling, (c) pulling intermediate vacuum, (d) vacuum bag for autoclave, (e) autoclave.

The samples are named according to the selected parameters. They are named in the following order: crosslinking temperature - degree of precrosslinking - weight percentage of PRS. Examples of sample naming are shown in Table 1.

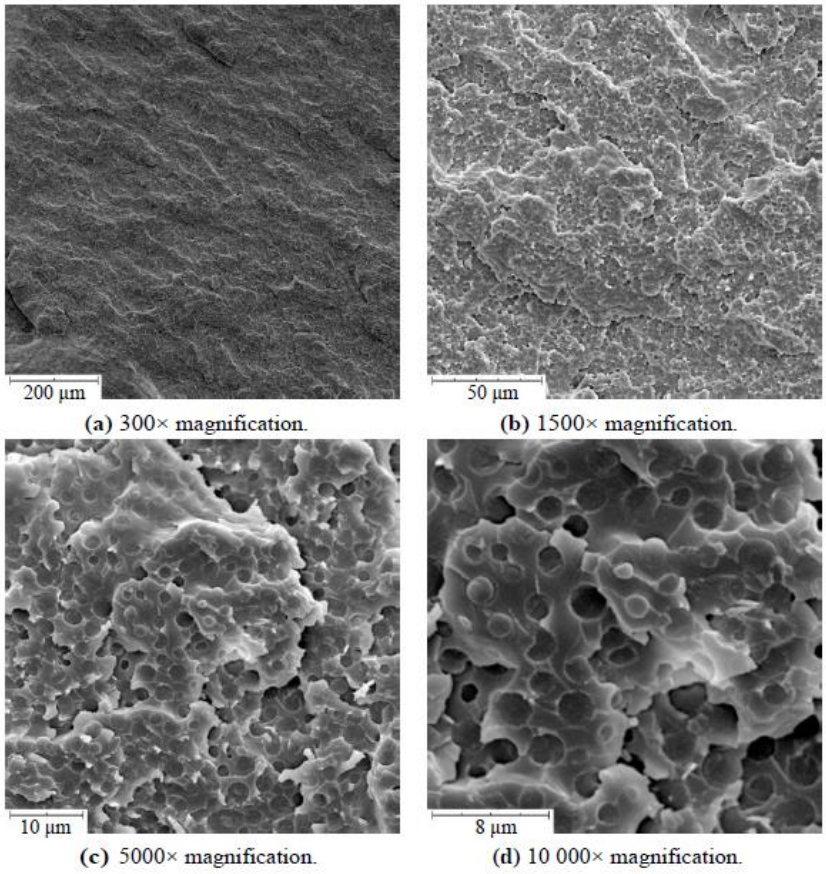
Table 1: Nomenclature of the samples used.

Sample name	Cross-linking temperature in °C	Degree of cross-linking in %	Weight percentage of PRS in wt%
160-75-20	160	75	20
180-80-10	180	80	10
200-95-20	200	95	20

In addition to the samples with PRS, references are also produced. The proportion of flexibilizer in these is the same as that contained in the samples with PRS. With a weight proportion of 30 wt%, the designations are accordingly Ref 30 or Ref 00 for samples without any flexibilizer.

3. Results and discussion

In this preliminary test series, not including the reference samples, 15 samples with combinations of crosslinking temperatures of 160 °C, 180 °C and 200 °C, crosslinking degrees of 75 %, 80 %, 85 %, 90 % and 95 % and a fixed weight fraction of PRS of 20 wt% were tested for the size of the PRS and the glass transition temperature. The PRS were evaluated with regard to their size using SEM analysis. On average, these were 1.57 ± 0.23 µm in size. As no trends were discernible and the size values were very close to each other, it can be assumed that different crosslinking temperatures and degrees of crosslinking did not have a significant effect on the PRS size. The DSC results also showed no significant differences in relation to the glass transition temperatures of the PRS samples. Here too, the crosslinking temperature and degree of crosslinking do not appear to have affected the measurement. As the 180-80-20 sample reached a maximum value of 214.7 °C, this parameter combination should be decisive for the next series of tests. With this combination, PRS with an average diameter of 1.66 ± 0.49 µm were determined. All samples produced from then on should therefore have a crosslinking temperature of 180 °C and a degree of crosslinking of 80 %.



(a) 300× magnification. (b) 1500× magnification.
(c) 5000× magnification. (d) 10 000× magnification.

Fig. 4: SEM images of sample 200-80-20 at different magnifications.

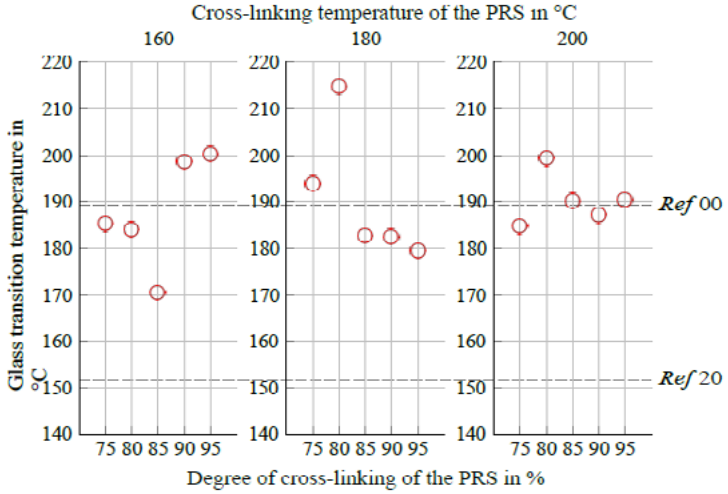


Fig. 5: Glass transition temperatures of the individual parameter combinations with a PRS weight fraction of 20 wt%.

In the second series of preliminary tests, the PRS sizes were influenced by the different weight proportions. Up to a weight fraction of 30 wt%, the size of the PRS increases from 0.91 ± 0.17 µm at 180-80-10 to a maximum value of 2.55 ± 0.72 µm. At 40 wt% the size decreases again, while in the 180-80-50 samples no more PRS can be determined. A significant trend can therefore be recognized, which leads to the largest PRS at 30 wt%. By forming the PRS, the glass transition temperature can be increased by around 20 °C to 30 °C compared to the corresponding reference. The flexibilizer units only

weaken the network locally and mean that the remaining polymer network can still exhibit high thermal resistance.

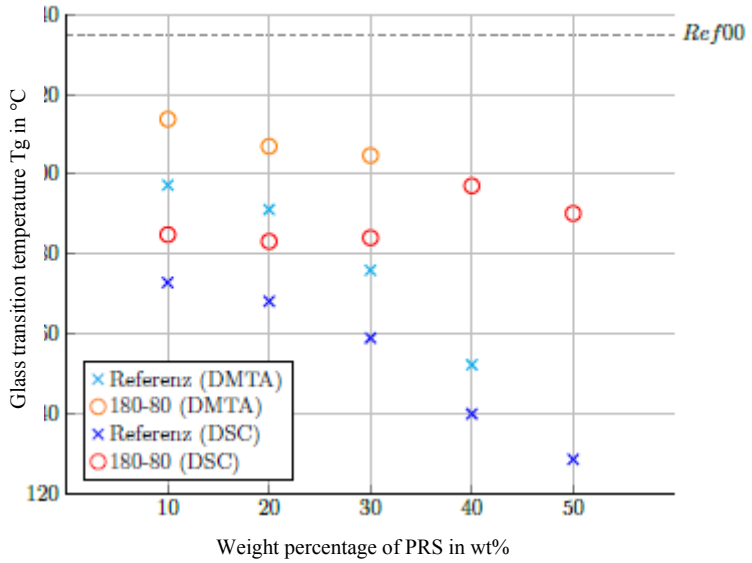


Fig. 6: Glass transition temperatures of DSC and DMTA in comparison.

In notched three-point bending test (SENB) light microscopic images of the fracture surfaces also confirm that the samples behave increasingly ductile with increasing flexibilizer content. While the K_{Ic} values show no significant change, G_{Ic} exhibit a clear increase with the amount of PRS. This is due to more energy absorbed during crack propagation and a more ductile behaviour.

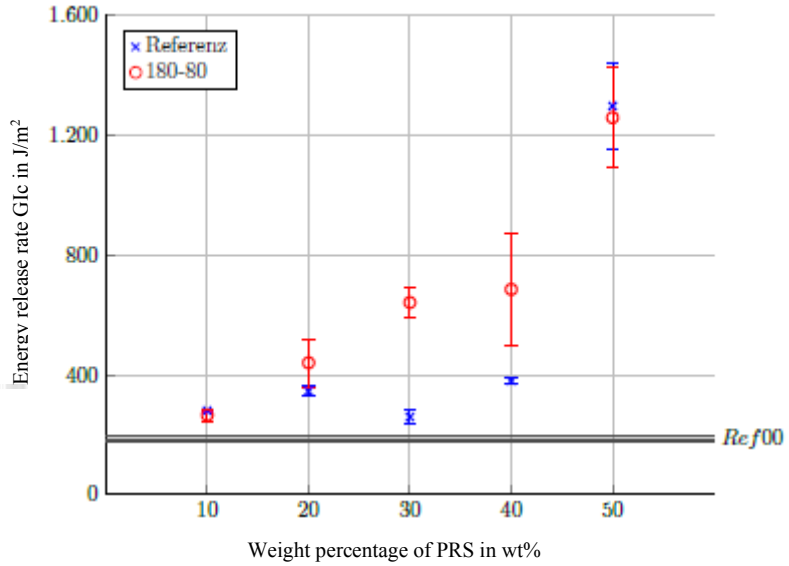


Fig. 7: Energy release rates of the samples from the second series of preliminary Tests measured by SENB.

In the main test series with the glass-fiber composite laminate, PRS were also detected in the samples of 180-80-10 and 180-80-30. No PRS could be detected in 180-80-50. Due to the dominance of the fibers in the SEM images, no meaningful size determination could be carried out, but their formation is nevertheless reflected in the results of the DCB and DMTA tests.

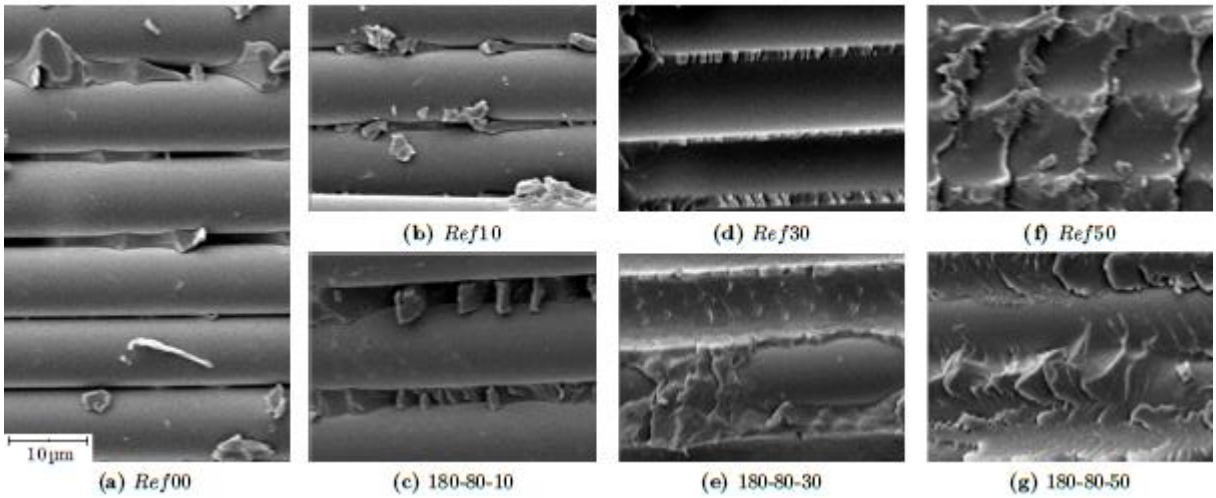


Fig. 8: SEM images of the delamination fracture surfaces of glass fiber composite samples.

180-80-30 also achieved the highest increases in the DCB results. While the samples with 10 wt%, both Ref 10 and 180-80-10, showed no significant increases compared to Ref 00, the samples with 50 wt% were able to achieve a significant increase compared to Ref 00, but not with each other. The 180-80-50 samples could not achieve an increase in interlaminar toughness compared to Ref 50, as no PRS could be detected in either the pure resin or the laminate.

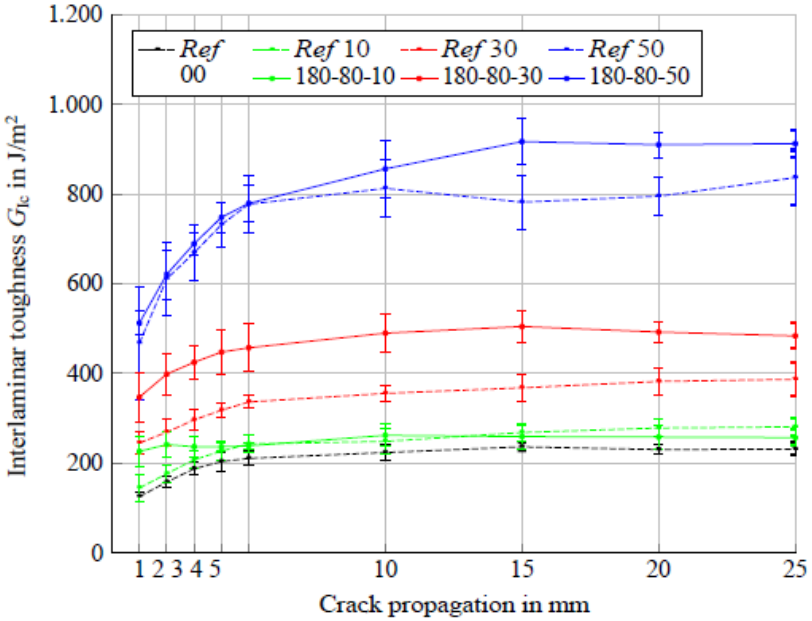


Fig. 9: Representation of G_{Ic} as a function of the crack propagation.

By introducing the unidirectionally oriented fibers, the stiffness at room temperature is increased compared to the pure resin samples. The glass transition temperatures are therefore also slightly higher. Figure 10 shows the glass transition temperatures of the samples measured with the DMTA. Due to the formation of PRS, an increased glass transition temperature can be measured in all three cases. An increase of 4 % is achieved with a weight proportion of 10 wt% and 7 % with 30 wt%. At 50 wt%, however, PRS does not form, so the increase of 5 % is not as high. The principle therefore only works up to a certain weight proportion.

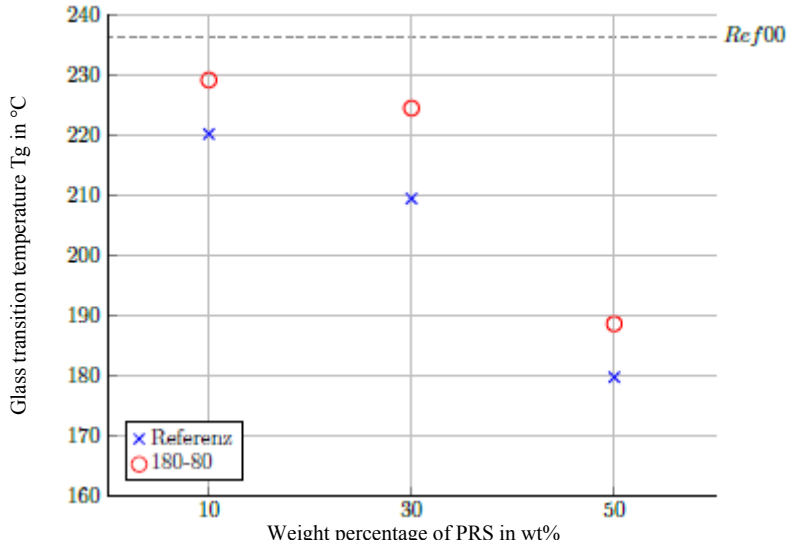


Fig. 10: Glass transition temperatures of the samples in the main test series determined with the DMTA.

4. Conclusions

The aim of this work was to transfer the principle of two-stage synthesis from the pure resin to the fiber composite in order to prevent a simultaneous reduction in the glass transition temperature while increasing the fracture toughness. The influencing factors for the formation of PRS were selected as 160 °C, 180 °C and 200 °C for the crosslinking temperature, 75 % to 95 % in 5 % steps for the degree of crosslinking and 10 wt% to 50 wt% in 10 wt% steps for the weight proportion of PRS in the composite. In two preliminary test series, these parameters were varied in pure resin tests in order to make the best possible selection for the main test series in the composite with glass fibers. The first series of preliminary tests resulted in PRS with an average size of 1.57 ± 0.23 µm at a fixed weight fraction of 20 wt%. No significant differences were found for the variation of crosslinking temperature and degree. The analysis using DSC also revealed no trends. Since sample 180 °C-80 %-20 wt% showed a maximum value, 180 °C and 80 % were used for further tests to vary the weight fraction. In the second series of preliminary tests, the PRS sizes were influenced by the different weight proportions. At 30 wt%, a maximum value of 2.55 ± 0.72 µm was achieved. No PRS could be detected for a weight proportion of 50 wt%. By forming the PRS, an increase in the glass transition temperature could be achieved for all parameter combinations compared to the respective reference. In the main test series, PRS were also detected in the fiber composite. Using DMTA, , the reference values decreased, while the values of the PRS samples were higher with increasing flexibilizer content. By forming PRS, 180 °C-80 %-30 wt% achieved the highest increase of 7 °C to 224.6 °C. Sample 180 °C-80 %-30 wt% also achieved the best results in the DCB test with regard to the percentage increase due to PRS formation. While at a weight fraction of 10 wt% the content was not high enough to achieve significant increases, 180 °C-80 %-30 wt% with a value of 490.05 ± 40.91 kJ/m^2, achieved an increase of 38% compared to the sample with 30 wt% uniformly distributed fexibilizer and 118% compared to the sample without any fexibilizer, confirming that the principle of two-step synthesis is applicable to the fiber composite.

References

[1] Sharifi, Majid ; Jang, Changwoon ; Abrams, Cameron F. ; Palmese, Giuseppe R.: Epoxy Polymer Networks with Improved Thermal and Mechanical Properties via Controlled Dispersion of Reactive Toughening Agents. In: Macromolecules 48 (2015), Nr. 20, S. 7495–7502. http://dx.doi.org/10.1021/acs.macromol.5b00677. – DOI 10.1021/acs.macromol.5b00677. – ISSN 0024–9297

[2] Moukhina, Elena ; Rampke, Thomas ; NETZSCH-Gerätebau GmbH (Hrsg.): Netzsch Kinetics Neo Software Demonstration: Kinetics Neo: Demo & Ringversuche. 2019

SIMULATION OF SELF-HEATING IN UNIDIRECTIONAL COMPOSITE MATERIAL UNDER FATIGUE LOADING OBSERVED BY INFRARED THERMOGRAPHY

Y. Yan[1], ML. Pastor[2], E. Abisset-Chavanne[3], XJ. Gong[4]

[1]Institut Clément Ader (ICA), Université de Toulouse, CNRS UMR 5312, IMT Mines Albi, INSA, ISAE-SUPAERO, UPS, Université de Technologie Tarbes Occitanie Pyrénées, 1 rue Lautréamont, 65016 Tarbes Cedex, France
Email: yan.yan@iut-tarbes.fr
[2]Institut Clément Ader (ICA), Université de Toulouse, CNRS UMR 5312, IMT Mines Albi, INSA, ISAE-SUPAERO, UPS, Université de Technologie Tarbes Occitanie Pyrénées, 1 rue Lautréamont, 65016 Tarbes Cedex, France
Email: marie-laetitia.pastor@iut-tarbes.fr
[3]Arts et Metiers Institute of Technology, CNRS UMR 5295, Bordeaux INP, HesamUniversite, I2M, F-33400 Talence, France
Email: emmanuelle.abisset-chavanne@ensam.eu
[4]Institut Clément Ader (ICA), Université de Toulouse, CNRS UMR 5312, IMT Mines Albi, INSA, ISAE-SUPAERO, UPS, Université de Technologie Tarbes Occitanie Pyrénées, 1 rue Lautréamont, 65016 Tarbes Cedex, France
Email: xiaojing.gong@iut-tarbes.fr

Keywords: self-heating; IR thermography; composite material; thermodynamic model; fatigue degradation

Abstract
The infrared radiation (IR) thermography method has been applied to study the fatigue behavior of composite laminates by observing the temperature variation on the specimen surface during fatigue process, which is called self-heating phenomenon. Theories and models were proposed based on self-heating to evaluate the fatigue progress and predict the fatigue limit. In this work, a thermodynamic model was proposed to simulate the fatigue behavior and the self-heating temperature of composites, considering the effect of viscoelasticity. Two stiffness degradation laws determined by traditional fatigue tests and rapid fatigue tests based on thermography were implemented in the model, and the simulation results were compared with the experimental data. Results show that with the help of a rapid fatigue test based on thermography, a stiffness degradation law can be determined, and the process of building a thermodynamic fatigue model is greatly shortened.

1. Introduction

Carbon fiber reinforced polymer matrix composites (CFRPs) have been widely used in aerospace, automotive engineering and advanced sports equipment due to their high specific mechanical properties and their good corrosion resistance. Under complex serving conditions, composite structures can be subject to cyclic stresses, which can cause important and serious damages. Therefore, a comprehensive study of composite materials' fatigue behavior is necessary. However, the classic fatigue test to obtain fatigue limit and S-N curve is long and expensive, especially it takes months under low-stress levels.

During the last years, contributions have been made to find a rapid way to shorten the fatigue test process. The fatigue limit of material can be determined using advanced characterization technologies rather than practicing a traditional fatigue test. Among them, infrared radiation (IR) thermography is promising.

Indeed, during mechanical tests, a phenomenon called self-heating has been observed in homogenous metallic at first, then polymeric material and heterogeneous polymer CFRPs. So, the surface temperature rise of a sample can be recorded by an IR camera. Some research shows a connection between the self-heating temperature and fatigue limit [1]. Several thermography methods based on the self-heating principles have been developed to predict fatigue life such as Luong's method [2], Risitano's method [3] and Krapez's method [4]. Based on these works, recently, Huang [5] proposed a methodology based on IR thermography to determine the fatigue limit of CFRPs within a fairly short period. By applying a series of stair-like fatigue stress to a single specimen, a relationship between the stabilized self-heating temperature and the fatigue stress level can be found. Then the fatigue limit and the fatigue life in term of S-N curve [6] can be determined by a thermographic data treatment method. These methods provide a rapid and accurate prediction of the fatigue life.

Self-heating, a process characterized by energy dissipation, is influenced by many factors, such as the intrinsic properties of the material, the loading conditions, and the surrounding environment. Considering the nature of the material, for CFRPs, the viscoelastic and plastic behavior of polymer matrix can generate significant heat under cyclic loading. The damages such as the fiber breakage, delamination, matrix and matrix/fiber cracking can also produce heat with the fatigue process continuing. To describe this complex behavior, a fatigue model combined with a thermodynamic model has to be proposed. Shojaei et al. [7] considered fatigue, creep, and plasticity in a continuum damage mechanics model for polymers, and used thermodynamics principles to derive a constitutive relation between self-heating and dissipative energy, which predicts the temperature rise in polymers. Mirzaei et al. [8] investigated the self-heating phenomenon in laminated composites under fatigue loading and developed a generated-dissipated energy (GDE) model considering the viscoelastic behavior of polymer matrix to calculate the generated and dissipated energy.

These studies can help to build a model to describe the self-heating phenomenon in the fatigue process. However, still large amount of experimental works needs to be conducted to obtain the necessary parameters in the model, such as the material degradation laws during fatigue, the fatigue limits, etc. In this work, the rapid fatigue test based on thermography is applied to shorten this period of experiment. The purpose of this work is to explain this thermodynamic behavior in the first place, then develop a model to predict the fatigue process of CFRPs and the self-heating temperature, with the constrain of the need of as few experiments as possible for model parameters identification. By applying the rapid fatigue test based on thermography, the experimental time can be shortened to several hours and the fatigue model can be built and put to use within a short time. The comparison between the experimental data and simulation results of the self-heating temperature variation has been done to validate the methodology of modeling.

2. Thermography framework

To build the self-heating model, two aspects were considered: (i) the simulation of the fatigue process of CFRPs, including the material degradation and damage evolution, and (ii) the thermal behavior during the fatigue process. Considering the principle of the self-heating phenomenon in a material under cyclic loading, from the thermodynamic laws, the basic rules of self-heating modeling include heat generation and dissipation. To simplify the heat generation, the viscoelastic behavior of the polymer matrix is first considered for a unidirectional CFRP. For the heat dissipation, the conduction and convection were considered. The first law of thermodynamics defines an energy balance in a given system. Eq. 1 describes the energy balance in an arbitrary control volume:

$$\frac{dE}{dt} = \frac{dW}{dt} - \frac{dQ}{dt} \tag{1}$$

where E is the total internal energy, W represents the mechanical work due to the cyclic loadings, and Q is the thermal energy.

In recent studies [9,10], mechanical work W is considered as the energy generated by the viscoelastic behavior of polymer matrix, which is caused by the hysteresis between the cyclic load and the resulting displacement. To calculate the mechanical work, the hysteresis between the stress and resulting strain should be determined, as it is shown in Eq. 2.

$$\sigma = \sigma_0 \sin(\omega t) \rightarrow \varepsilon = \varepsilon_0 \sin(\omega t + \delta) \begin{cases} \delta = 0 & \text{for perfect elastic materials} \\ 0 < \delta < \dfrac{\pi}{2} & \text{for viscoelastic materials} \\ \delta = \dfrac{\pi}{2} & \text{for perfect viscous materials} \end{cases} \tag{2}$$

where σ is a fatigue stress in a sinus form, σ_0 is the amplitude of stress, while ε is a resulting strain with a lag phase δ, ε_0 is the amplitude of the strain.

For each loading cycle, the energy can be calculated and divided into two parts: elastic energy and generated energy (Eq.3). The elastic energy is stored inside the material and then totally released at the end of each cycle, while the generated energy due to viscoelastic behavior is transformed into heat. The heat generated by viscoelasticity behavior is not the only heat source during the fatigue test but the primary heat source throughout the whole fatigue cycle [11].

$$\begin{aligned} &\int_0^{\varepsilon_0} \sigma d\varepsilon = \int_0^{\pi/2\omega} \sigma \frac{d\varepsilon}{dt} = \omega \varepsilon_0 \sigma_0 \int_0^{\pi/2\omega} \left(\cos \omega t \sin \omega t \cos \delta + \sin^2 \omega t \sin \delta \right) dt \\ &= \underbrace{\varepsilon_0 \sigma_0 \frac{\cos \delta}{2}}_{\text{elastic energy}} + \underbrace{\varepsilon_0 \sigma_0 \frac{\pi \sin \delta}{4}}_{\text{generated energy}}. \end{aligned} \tag{3}$$

Generally, three heat dissipation behaviors are considered for the thermal energy Q: convection, conduction, and radiation [12]. Since the self-heating temperature of composite material under low frequency fatigue is relatively low, the heat dissipation through radiation can be ignored. To calculate the heat dissipation through convection for an elementary volume on the surface of the specimen, considering the shape of specimen used in the following experimental and simulation work, the heat transfer equation for a vertical plate is used, as shown in Eq. 4.

$$E_{\text{convection}} = ha\left(T_s - T_\infty\right) = \frac{Nu \cdot k_{\text{air}}}{l} a\left(T_s - T_\infty\right) \tag{4}$$

where the heat convection coefficient (h) between the composite laminate and air can be calculated by Nusselt number (Nu) and the heat conduction coefficient of the air (k_{air}), l is the length of elementary volume, a is the area of the elementary volume surface, T_s and T_∞ represent the surface temperature and environment temperature, respectively.

The Fourier law stated in Eq. 5 is employed to calculate the dissipated energy through heat conduction for an elementary volume:

$$E_{\text{conduction}} = 2k_{\text{ply}} a \left(\frac{\partial T}{\partial x} + \frac{\partial T}{\partial y} \right) \tag{5}$$

where k_{ply} represents the heat conduction coefficients of the composites, which differ according to the direction of the fiber. It can be calculated by Eq. 6:

$$k_{ply} = k_l \cos^2\theta + k_t \sin^2\theta \tag{6}$$

where θ represents the angle of the orientation of the fibers, k_l and k_t are the heat conduction coefficients in the longitudinal and transversal direction of the fibers, respectively, calculated by the following equation (7):

$$\begin{aligned} k_l &= k_m\left(1-V_f\right)+k_f V_f \\ k_t &= \frac{k_m + k_f - V_f\left(k_m - k_f\right)}{k_m + k_f + V_f\left(k_m - k_f\right)} \end{aligned} \tag{7}$$

where k_m and k_f are the heat conduction coefficients of matrix and fiber, V_f and V_m are the volume ratio of fiber and matrix, respectively [12].

3.Self-heating model

Based on the thermodynamic rules, the whole self-heating model can be considered as a combined model that can calculate step by step the fatigue process and the heat generation and dissipation condition, and finally the temperature variation, as shown in Figure 1. It consists two main parts: the first is for the fatigue damage process, within which the stress calculation, material degradation and failure criterion were considered; and the second is to calculate heat variation, then the self-heating temperature can be determined. This framework has been widely used in the internal energy variation of a structure under statical or dynamic mechanical tests [8]. It is a modular and flexible framework since the researchers can modify any of the thermodynamic principles according to their real conditions.

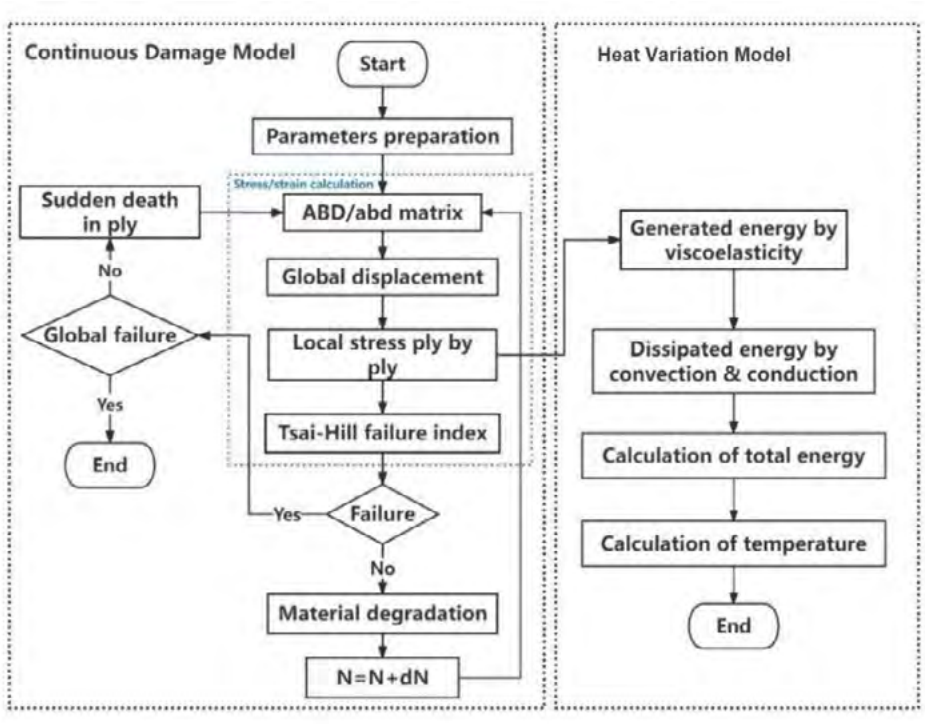


Figure 1. The calculation process of continuous fatigue damage and thermodynamic behavior.

In this model, the stress and strain calculation for each step during the fatigue process can be done by using the commercial software ABAQUS. In the first step, build an analysis model in ABAQUS based on the material properties, ply sequences and loading conditions in Huang's experimental work [13],

with specimen's dimension of 150 mm*25 mm*1.04 mm. A stair-like fatigue stress was applied to the model and during each iteration, the associated strain in each ply can be calculated using the ABD/abd matrix. Afterwards, with the information of stress and strain in each ply, the failure condition in each ply was checked. Then the material properties were upgraded based on the failure condition. If no failure happened, the material degradation rules were employed to do a deduction on the material properties due to the fatigue process, then the fatigue process continued in the next loop. Otherwise, the failure in the whole system should be checked to determine whether the fatigue process is stopped. To reduce the computational cost of the proposed coupled modeling approach, a cyclic jump approach is also incorporated and dN is set to 100. Then the whole process was repeated until the final failure of the entire composite structure. At the same time, in each step, the results of stresses and the strain calculation are transferred to the heat variation model to calculate the energy generated by viscoelasticity. Then considering the energy loss due to conduction and convection, the total energy variation was able to be calculated. Finally, the self-heating temperature can be determined.

The C3D8T element type was selected, which is an 8-node trilinear element coupled with temperature and displacement. A convergency test was done to well choose the element size to keep a balance between the simulation precision and computation time. A UMAT subroutine was designed to model the thermodynamic fatigue behavior of the composite samples for a 3D thermal-stress coupled analysis in ABAQUS software. Fatigue-induced stresses were replicated by applying the peak load onto the specimen. Benefiting from the inherent symmetry of the samples, only a quarter-section was used for computational modeling, ensuring efficiency.

During the fatigue modeling of CFRPs, it is crucial to understand how the material's properties evolve with the fatigue process. In this work, a continuous damage law based on traditional fatigue experiments has been applied firstly to describe the degradation in modulus of the material as a function of the number of fatigue cycles n, fatigue load σ and stress ratio κ, as it shown in Eq. 8.

$$E(n,\sigma,\kappa)=\left[1-\left(\frac{\log(n)-\log(0.25)}{\log\left(N_f\right)-\log(0.25)}\right)^{\lambda}\right]^{1/\gamma}\left(E_s-\frac{\sigma}{\varepsilon_f}\right)+\frac{\sigma}{\varepsilon_f} \tag{8}$$

where E_s represents the statical modulus and ε_f is the final displacement under the statical tensile test. λ and γ are parameters to be determined by experimental data fitting. The fitting method can be found in Shokrieh's work [14,15]. A normalized form of Eq. 8 which depends on the values of γ and λ is shown in Eq. 9. All different curves of degradation under different stress states collapse to a single curve.

$$k(n)=\frac{E(n)-\frac{\sigma}{\varepsilon_f}}{E_0-\frac{\sigma}{\varepsilon_f}}=\left[1-\left(\frac{\log(n)-\log(.25)}{\log\left(N_f\right)-\log(.25)}\right)^{\lambda}\right]^{\frac{1}{\gamma}} \tag{9}$$

Since the previous method to determine the degradation law demands the experimental data of classic fatigue tests, it still costs of large time. As mentioned before, Huang [13] roposed another law of modulus degradation which indicates the relationship between stiffness degradation and stable self-heating temperature, as shown in equation (10). Different levels of fatigue stress were applied to a single specimen and each stress level lasted for 10000 cycles to attend the stabilization of self-heating temperature, so the whole process took only hours, which greatly shortened the experimental process.

$$\frac{E(n)}{E_s}=k'(n)=1-p\Delta T_{stab}n^{1/q}\quad(q\geq 1) \tag{10}$$

where $k'(n)$ is the normalized stiffness at the n^{th} cycle, ΔT_{stab} is the stable temperature variation during the rapid fatigue test, p and q are material parameters to be determined by the fitting process.

4.Results and discussion

In the experimental works of Huang [13], classic fatigue tests were practiced. The necessary parameters are determined by applying a fitting method to the results of classic fatigue tests. The fatigue test data under the stress levels of 70% of the ultimate tensile strength (UTS) and 85%UTS were chosen to fit the law, as it shown in Figure 2, with λ=0.2006, γ=4.424 and the R-square of the fitting results is 0.947, which means a good fitting degree.

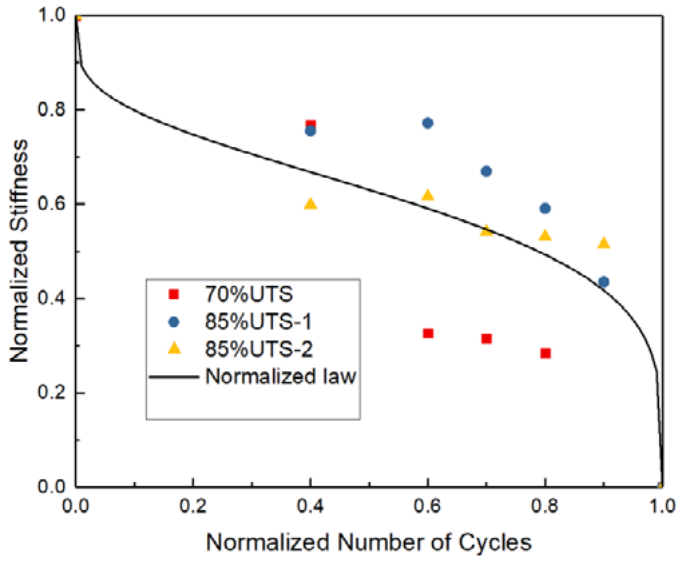


Figure 2. Fitting result with the normalized degradation law.

Applying the rapid fatigue test data in [5], as shown in Fig. 3 (a), a surface fitting process can be performed to obtain the model parameters, as shown in Fig. 3 (b), with p=1.87*10^{-2}(°C ×Cycle$^{1/q}$)$^{-1}$, and q=4.75.

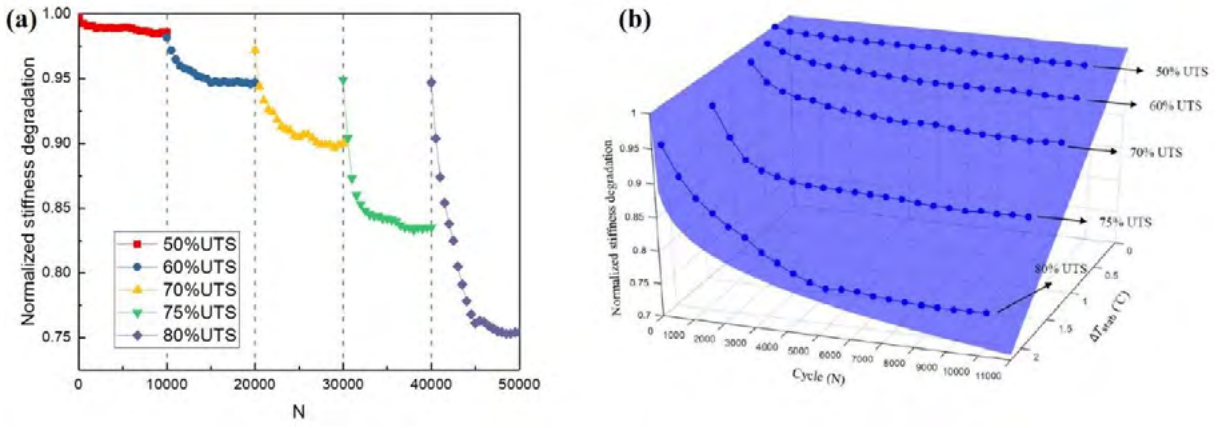


Figure 3. (a) Stiffness degradation determined by rapid fatigue test; (b) Fitting results of rapid fatigue tests.

The two stiffness degradation laws were then integrated into the self-heating model to simulate the temperature variation during the rapid fatigue test. The results are shown in Fig. 4, in which the dots represent the temperature variation captured by the IR camera, while the line and dotted line represent

the simulation results by using Shokrieh's model and Huang's model, respectively. The results show that the two simulation results have a good correlation at different stress levels, which means the model obtained by the rapid thermography method can well describe the stiffness degradation as the classic degradation model does. With the application of the stiffness degradation model based on the thermography method, only one group of fatigue experiment is needed and the experimental time can be reduced to hours to build a fatigue model. Meanwhile, by comparing the experimental data and simulation results, at a relatively low stress level, the results fit well, but with the stress level increased, the difference between them grew. This indicates that at low stress levels, viscoelasticity is the main reason for the self-heating phenomenon. But when the stress level increases, or the damage accumulates to a certain level, some other heat is generated due to the plasticity of matrix, fiber breakage, friction of the cracks and delamination, etc. These heat sources will be taken into consideration and added to the model in the following works.

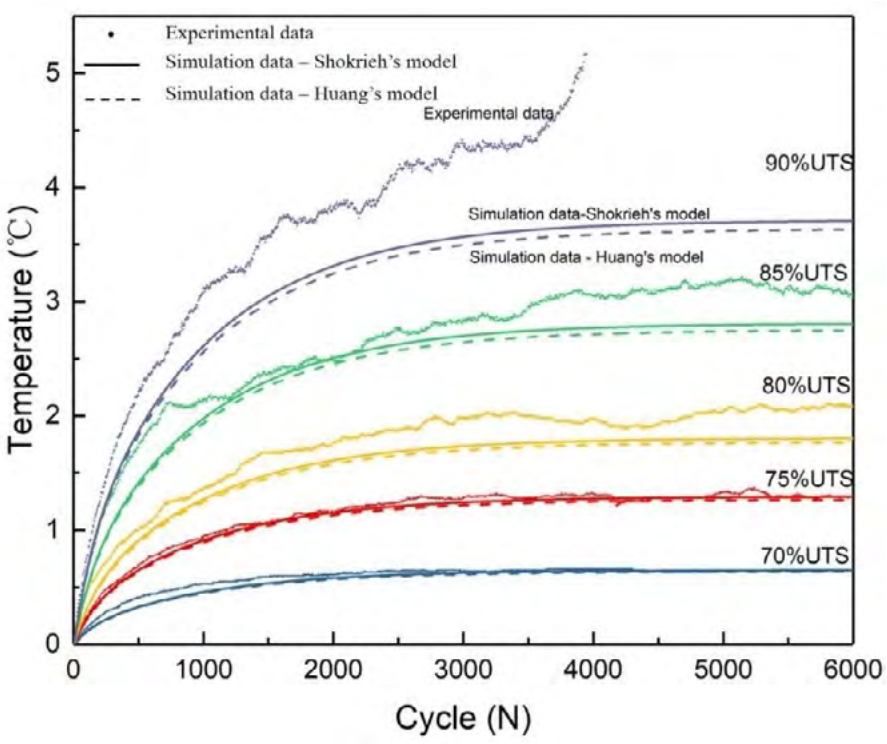


Figure 4. Comparison between the experimental and simulation data.

5. Conclusions

In this work, a self-heating model was built to simulate the fatigue behavior and the heat generation and dissipation during the fatigue process, as well as the self-heating temperature variation on the surface of the specimen. To simulate the fatigue process, two stiffness degradation laws based on the traditional fatigue test data and the rapid fatigue test data, respectively, were applied to the model. The viscoelasticity of the polymer matrix was considered as the main heat generation during the fatigue process, and there was also heat dissipation by conduction and convection. The comparison between the simulation results showed that the two degradation laws were equivalent for describing the evolution of material properties during the fatigue process. With the help of the thermography method in a rapid fatigue test, the determination of material degradation can be greatly shortened compared to the traditional fatigue test, only one group of rapid fatigue test based on thermography and the experimental time is greatly shortened to several hours, which will help build the fatigue model more efficient. Compared to the experimental data, the simulation results showed good fitness at the beginning while at high stress levels, the viscoelasticity was not the only heat generation source. Some other heat sources exist and have to be determined in the future work.

Acknowledgments
The author Yan Yan is supported by the China Scholarship Council for 3 years study at the University of Toulouse.

References

[1] S. Mortazavian, A. Fatemi, S. R. Mellott, A. Khosrovaneh. Effect of cycling frequency and self-heating on fatigue behavior of reinforced and unreinforced thermoplastic polymers. *Polymer Engineering & Science*, volume(55):2355-2367, 2015.
[2] M. P. Luong. Fatigue limit evaluation of metals using an infrared thermographic technique. *Mechanics of Materials*, volume(28):155-163, 1998.
[3] G. Fargione, A. Geraci, G. La Rosa, A. Risitano. Rapid determination of the fatigue curve by the thermographic method. *International Journal of Fatigue*, volume(24):11-19, 2002.
[4] J. Krapez, D. Pacou, G. Gardette. Lock in thermography and fatigue limit of metals. In *Office National D'etudes et de Recherches Aerospatiales onera publications*, voulme 187, 2000.
[5] J. Huang, M. L. Pastor, C. Garnier, X. Gong. Rapid evaluation of fatigue limit on thermographic data analysis. *International Journal of Fatigue*, volume(104):293-301, 2017.
[6] Z. J. Jia. Determination of fatigue properties of Multidirectional composite laminates (MD) based on thermography measurements, Doctoral thesis, Toulouse University 3, 2022.
[7] A. K. Shojaei, P. Volgers. Fatigue damage assessment of unfilled polymers including self-heating effects. *International Journal of Fatigue*, volume(100):367-376,2017.
[8] A. Mirzaei, M. Shokrieh. Simulation and measurement of the self-heating phenomenon of carbon/epoxy laminated composites under fatigue loading. *Composite Part B: Engineering*, volume(223):109097, 2021.
[9] T. L. Bergman, F. P. Incropera, D. P. DeWitt, A. S. Lavine. *Fundamentals of heat and mass transfer*. John Wiley & Sons, USA, 2011.
[10] J. P. Holman. *Heat transfer*. McGraw-Hill Press, New York, 2015.
[11] A. Katunin, A. Wronkowicz. Characterization of failure mechanisms of composite structures subjected to fatigue dominated by the self-heating effect. *Composite Structures*, volume(180):1-8, 2017.
[12] A. Mahmoudi, B. Mohammadi. Theoretical-experimental investigation of temperature evolution in laminated composites due to fatigue loading. *Composite Structures*, volume(225):110972, 2019.
[13] J. Huang. Rapid determination of fatigue behaviour for carbon fiber reinforced polymer laminates based on thermodynamic phenomena observed by IR thermography. Doctoral thesis, Toulouse University 3, 2019.
[14] B. Mohammadi, B. Fazlali, D. Salimi-Majd. Development of a continuum damage model for fatigue life prediction of laminated composites. *Composites Part A: Applied Science and Manufacturing*, volume(93):163-176, 2017.
[15] M. M. Shokrieh, L. B. Lessard. Progressive fatigue damage modeling of composite materials, Part I: Modeling. *Journal of Composite Materials*, volume(34):1056–80, 2000.

DEVELOPMENT OF A MODULAR AND FLEXIBLE CONSTRUCTION SYSTEM FOR A SELF-SUPPORTING AND MODULAR BRIDGE FORMWORK MADE OF GLASS FIBRE-REINFORCED PLASTICS

Zhikun Yang[1], Oliver Kruse[1] and Christian Lauter[1]

[1]PHWT Institute, Department Design, Lightweight and Fibre-reinforced plastics, PHWT, Am Campus 2, 49356 Diepholz, Germany
Email: yang@phwt.de, o.kruse@phwt.de, lauter@phwt.de, Web Page: http://www.phwt.de/

Keywords: Lightweight design, Bridge, Formwork, Composites, Glass fibre-reinforced plastic, GFRP, concrete, hybrid structure

Abstract
This research examines the potential of glass fibre-reinforced polymers (GFRP) as bridge formwork in concrete bridge construction, with a particular focus on load-bearing capacity and modular design. It concludes with a preliminary exploration of GFRP-concrete hybrid structures. Previous work identified the potential of glass fibre-reinforced polymer as a formwork material for bridges through market research and technical exchange. The mechanical properties of standard GFRP profiles were determined in the interim through laboratory experiments, with the flexural modulus of GFRP ranging from 20 GPa to 45 GPa, depending on the fibre arrangement and reinforcement used. The experimental data was then combined with the boundary conditions of the bridge structure to create computational and finite element analysis models. Subsequently, a self-supporting, modular formwork system, comprising approximately 4-5 basic elements, was developed. The system is constructed from GFRP material and its feasibility was verified by constructing a bridge model.

1. Introduction

The repair and replacement of bridges is a crucial task in Germany's highly dense transport network. Extensive renovation work is necessary due to unforeseeable loads when the infrastructure was planned and built decades ago, such as increased traffic and the intensive use of road de-icing salt. For example, statistics indicate that there are approximately 120,000 bridges in Germany. Of these, 86% are concrete bridges. On a scale of 1.0 (Excellent condition) to 4.0 (Insufficient condition), more than 10% of the bridges on federal trunk roads and motorways no longer have a sufficiently safe load-carrying capacity and are in urgent need of repair and maintenance [1]. One potential solution is to use innovative materials and construction methods to build longer-life bridges more efficiently.

2. Current technology

The potential of fiber reinforced polymer (FRP) in construction has been extensively researched and developed in recent decades [2]. The high strength-to-weight ratio, high environmental stability and other properties of this material make it the most advantageous alternative to steel reinforcement in concrete structures [3] [4].The Acciona company manufactures beams, cables, bars or forged structures made of carbon fibre, glass fibre and polymers materials as a replacement for traditional steel and concrete materials in construction projects. In the 21st century, the potential of FRP materials in the field of traditional concrete construction, represented by bridges, has been further investigated [5] [6] [7]. In 2017, a road bridge with GFRP as the superstructure support was constructed in Poland. The bridge, with a load capacity of 40 t, is a 22.0 m long, 10.5 m wide, single-span, simply supported girder bridge. The bridge superstructure is composed of four GFRP composite beams and a 0.18-metre-thick concrete slab [8]. In 2020, construction company Kaj Bech built a pedestrian bridge made entirely of

GFRP in Sønder Felding, Denmark. The bridge is 5.5 m long and 2.5 m wide and has a total weight of just 625 kg, but it can carry up to 8 t [9]. This research presents the development of a self-supporting GFRP bridge formwork. The basic bridge formwork elements are standard profiles available on the market, and the modular design is the basic principle. The formwork will serve as the outer surface of the future concrete structure and will not be removed after the concrete has been poured and hardened. In addition to its protective function, the formwork will be equipped with sensors that will provide information about the condition of the bridge at any time.

3. Materials and methods

This research used standard GFRP profiles, comprising glass fibre and polyester resin, to investigate the mechanical properties of the materials and the standard profiles. Additionally, a preliminary research was conducted on the GFRP-concrete hybrid structure formed by fresh concrete poured onto the GFRP material.

3.1. GFRP and concrete

Compared to other fibre-reinforced plastics (FRP), GFRP can be used to produce large continuous profiles through automated pultrusion moulding processes. Their cross sections have relatively high design flexibility. This process enables continuous longitudinal arrangement of glass fibres along the profile, resulting in high strength and stiffness with a flexural elastic modulus ranging from 20 GPa to 45 GPa. This makes it an ideal choice for applications re-quiring high structural performance. Additionally, GFRP is highly resistant to corrosion and its polyester matrix provides exceptional UV resistance, making it an excellent option for protecting the exterior surfaces of bridges. Therefore, fiberglass plastic was chosen as the material for the bridge formwork. In this research were standard pultruded GFRP profile from Fiberline Building Profiles A/S, Denmark selected for the material tests.

The concrete of grade C35/45 produced by Dammer Betonwerk GmbH & Co. KG, Germany has been selected for use in conjunction with GFRP material and subjected to static loading experiments. The cement utilised in the concrete is of the CEM III/A 42.5 N variety. This cement is a blast furnace cement with an initial strength that is typical of the category and a high final strength. It is frequently used in the construction of buildings and civil engineering projects, as well as in road construction and the creation of carriageway surfaces. It demonstrates good resistance to frost and de-icing salts [10]. The concrete has a maximum particle diameter of 8 mm and a flow class of F3 for fresh concrete, as well as an exposure class of XC4, XD3, XF3 for the final hardened concrete. These exposure classes are suitable for resisting corrosion of the reinforcement due to carbonation, chloride corrosion of the reinforcement and frost attack in a humid and saline environment. [11] [12]

3.2. Methods

The cross-section of a GFRP double T profile with thicknesses of 6 mm is divided into five distinct areas, as shown in Figure 1.

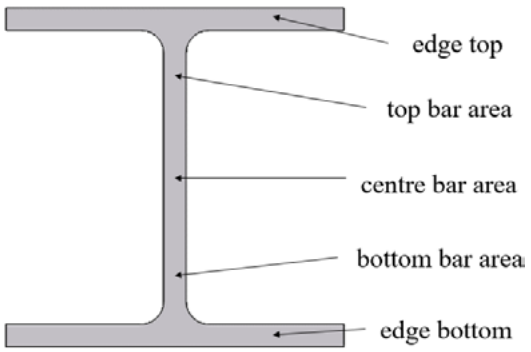


Figure 1. Five distinct areas in the cross-section of a GFRP double T profile: edge top, top bar area, centre bar area, bottom bar area, edge bottom

In order to analyse the reinforcement of the profiles, samples were selected from different areas and subjected to X-ray tests in the direction of the sample thickness. A four-point bending test was conducted on GFRP samples using a ZwickRoell LTM10 machine in order to determine their mechanical properties edge fibre elongation ε (1), bending stress σ_f (2) and flexural tensile modulus E_f (3) [13]. The experimentally determined material parameters are imported into the finite element method (FEM) simulation analysis model for the purpose of analysing and optimising the load capacity of individual formwork elements, the modularity of formwork and complete formwork systems.

$$\varepsilon = \frac{4.7sh}{L^2} \tag{1}$$

$$\sigma_f = \frac{FL}{bh^2} \tag{2}$$

$$E_f = \frac{0.21L^3}{bh^3}\left(\frac{\Delta F}{\Delta s}\right) \tag{3}$$

A preliminary investigation was conducted on the bond between concrete and GFRP using 3-point flexure tests [14] [15]. The formation of a GFRP-concrete hybrid structure begins with the combination of GFRP material and fresh concrete. This is followed by the hardening of the concrete on the GFRP material, which ultimately results in the formation of the hybrid structure. Two research directions have been identified with regard to the process of combining GFRP and fresh concrete. These are unbonded and bonded. In the unbonded method, the surface of the GFRP material is processed to form specific projections (T-slots). Fresh concrete is then poured directly onto the surface of the GFRP material, creating a mechanical interlock between the two components when the concrete hardens. Bonding is the process of applying an epoxy resin adhesive to the surface of the GFRP material, followed by the pouring of fresh concrete directly onto the wet epoxy resin adhesive [16]. In this research, an unbonded solution was selected. However, the GFRP material is a sheet with no T-slots, necessitating modifications to this solution, showed in Figure 2. Four distinct surface treatments were applied to the GFRP sheets. The first surface treatment is devoid of any alteration to the initial surface condition of the profile, which was manufactured by pultrusion. The second, third, and fourth methods used 2K epoxy resin adhesive to bond and cure alkali-resistant glass fibre wool, alkali-resistant short glass fibre bundles (13 mm long), and basalt grit (5–8 mm in diameter), respectively, to the surface of the GFRP sheets.



Figure 2. Four surface treatments (a), in the mould, fresh concrete is poured onto the surface treated GFRP sheet (b), GFRP-concrete hybrid structure formed after the concrete hardened in 28 days (c)

A GOM ARAMIS measuring system is used to determine the deformation of the entire surface of the concrete-GFRP composite struc-ture, the formation and development of cracks, and the relative displacement of the concrete and GFRP parts.

4. Experiments and results

The results section of the research primarily concerns X-ray inspection, the testing of the mechanical properties of the material, and the static load analysis of GFRP-concrete.

4.1. Reinforcement of the profiles

Four distinct types of fibre reinforcement for the GFRP-profiles in question have been identified through X-ray inspection, and are listed in Figure 3 using the symbols A, B, C and D, respectively.

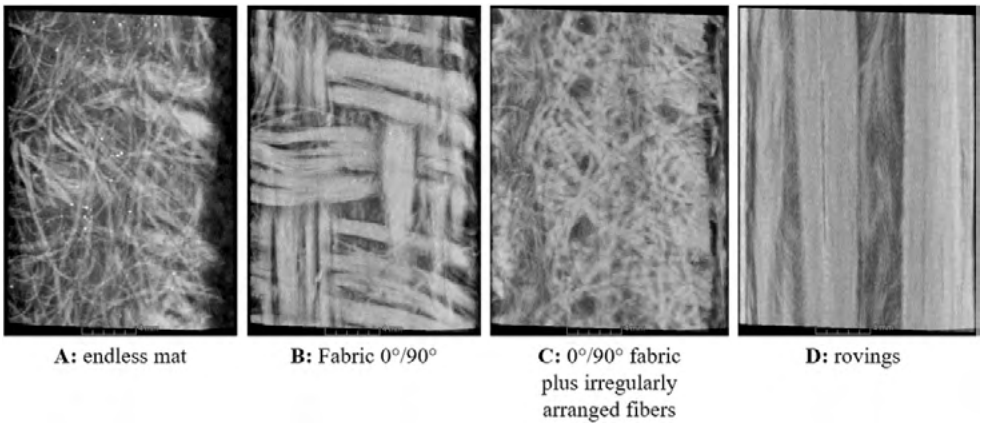


Figure 3. Four types of fibre reinforcement, endless mat (A), fabric 0°/90° (B), 0°/90° fabric plus irregularly arranged fibers (C), rovings (D)

Samples with a thickness of 6 mm were selected at the edge of the double-T profile and in the ribbed plate area. The arrangement and thickness of the different fibre reinforcements were recorded and measured.

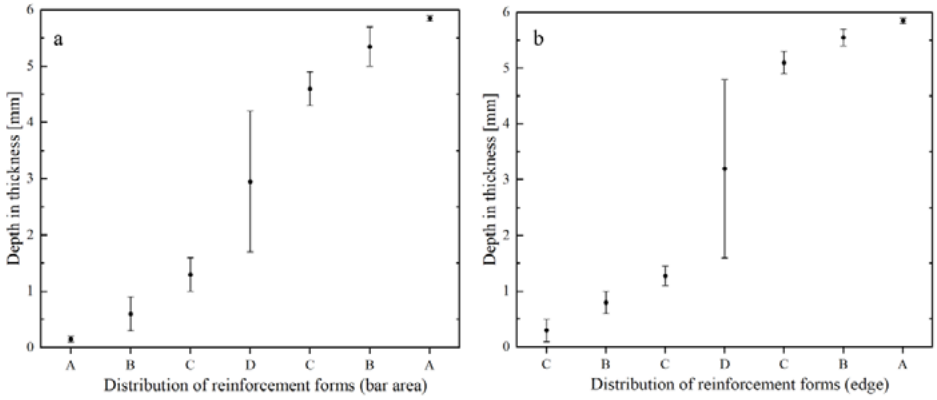


Figure 4. Method of reinforcement and thickness of fibres used in the bar area (a) and edge (b)

Figure 4 showed that the double-T profile exhibits a different fibre reinforcement distribution in the bar area and edge. The fibre reinforcement in the bar area is distributed in a symmetrical manner, with the central ply serving as the boundary. The predominant type of fibre reinforcement is rovings, accounting for approximately 43% of the total fibre reinforcement. At the edge, the fibre reinforcement exhibits a symmetrical distribution bounded by the central ply, although it differs slightly from the bar area. Firstly, the one side does not utilise endless mat. Secondly, the proportion of each fibre reinforcement is different, as the main fibre reinforcement is also rovings but accounts for 55% of the total fibre reinforcement. This is evidenced by the proportion of rovings being increased while the proportion of other fibre reinforcements is reduced.

4.2. Mechanical properties of GFRP

The material's flexural tensile modulus is determined through four-point bending experiments.

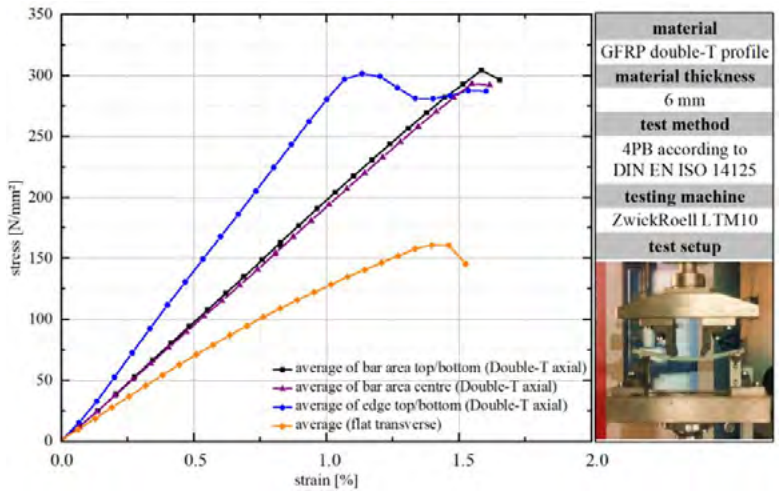


Figure 5. The axial stress and strain diagrams for the material in the bar and edge of the Double-T profile and transverse stress and strain diagram for the material of flat profile

The axial bending tensile modulus of the profile bar is experimentally measured to be around 19,000 MPa and the top and bottom edge positions can reach 28,000 MPa. In the transverse direction is lower and around 14,000 MPa. The axial direction represents the principal direction of fibre reinforcement of the profile, with the primary reinforcement material being rovings. Concurrently, the B, C and D fibre reinforcement methods are used for supplementary transverse reinforcement. Figure 6a presents the digital model of the modular formwork system established. A single module, as illustrated in Figure 6b, was selected for real load simulation in accordance with the dimensions of the laboratory prototype, combined with material experimental data. The results demonstrate that the GFRP formwork has an excellent load-carrying capacity, with a deflection of approximately 1 mm, which is less than the industry requirement of L / 300 (L: span). The results were validated by subjecting the prototype to load testing following the placement of concrete.

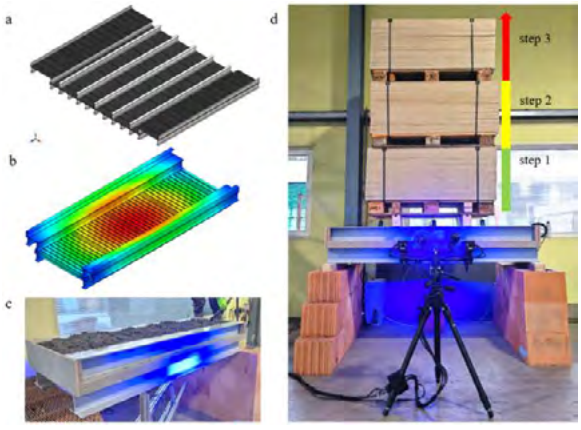


Figure 6. Digital model of the modular formwork system (a), realistic load simulation of a single module of the formwork with laboratory prototype dimensions (b), the assembly and concreting of prototypes of single modules (c), Prototype real load test (d)

4.3. GFRP-Concrete hybrid structure

The connection behaviour of GFRP-concrete hybrid structures was observed through the implementation of static loading experiments. The flexural tensile strength of concrete is approximately

6 N/mm², which is considerably less than the flexural tensile strength of GFRP material, which is 240 N/mm². The experiments were conducted using a load control mechanism, whereby the load was incrementally increased from zero at a rate of 1100 N per second until the experimental samples failed, i.e., the concrete fractured partially.

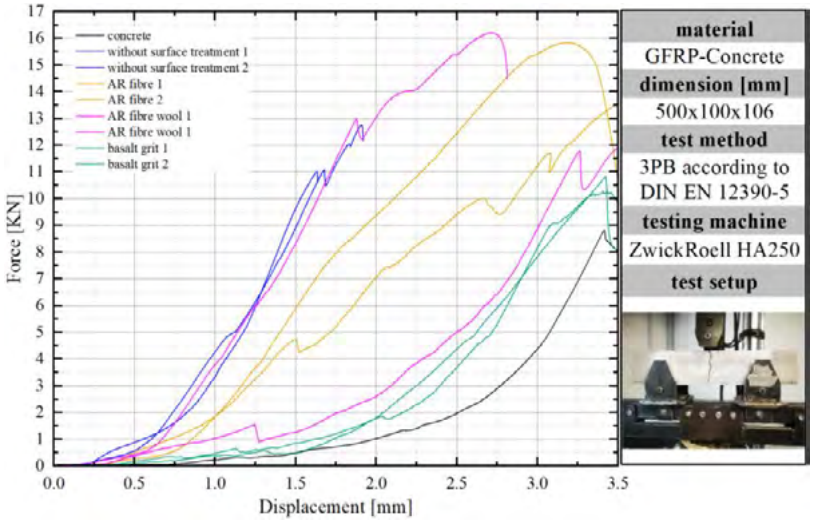


Figure 7. Force and displacement diagrams for GFRP and concrete hybrid structures

The force and displacement diagrams in Figure 7 demonstrate that the damage loads for the pure concrete specimens were below 9 kN, while the failure loads for the GFRP-concrete hybrids of the same dimensions were above 10 kN. GFRP-concrete hybrid mechanisms with alkali-resistant glass fibre wool and alkali-resistant short glass fibre bundles surface treatments can reach a failure load of 15 kN. The GFRP-concrete hybrids exhibited multiple load fluctuations before failure, but no cracks were observed. Photographs captured by the GOM ARAMIS measuring system illustrate the appearance and evolution of cracks in the GFRP-concrete hybrid structure subjected to static loading. The relative displacements of the GFRP and concrete areas were quantified at points L/4, L/2, and 3L/4 of the supported section of the GFRP-concrete hybrid structure, showed in Figure 8. A single crack was observed in all GFRP-concrete hybrid structures throughout the course of the experiment, with the initial appearance occurring at the contact surface of the hybrid structure in the middle of the structural support. This crack then progressed rapidly towards the point of application of the concrete side load within a short period of time. The GFRP material remained unscathed until the point of failure.

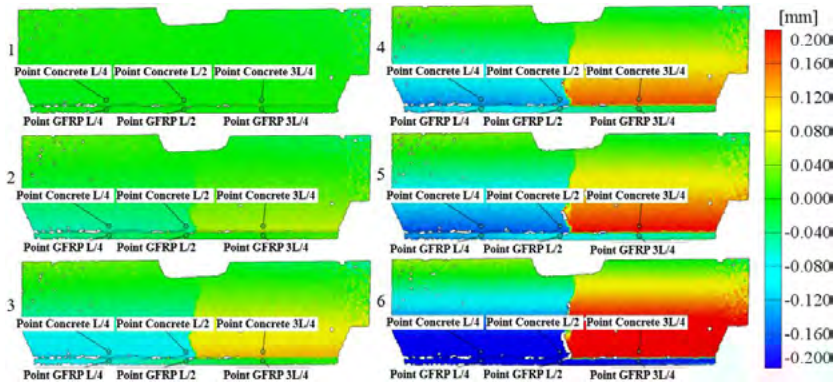


Figure 8. The surface displacement of a GFRP-concrete hybrid structure under static loading is analysed in stages, demonstrating the formation and development of cracks and the relative displacement between the two materials

The relative displacement between GFRP and concrete throughout the static loading experiment was quantified by recording the relative displacement between points, showed in Figure 9.

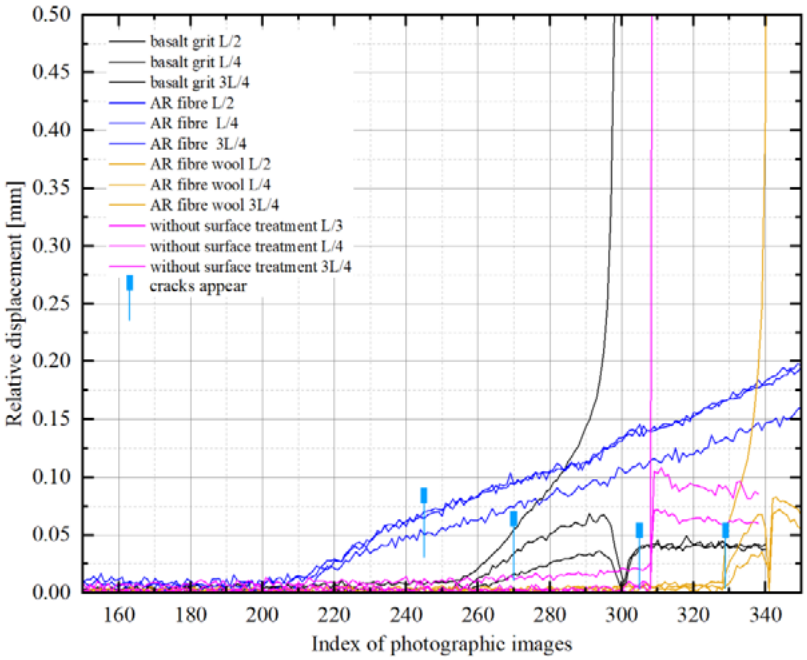


Figure 9. The relative displacements of the GFRP-concrete hybrid structure at L/4, L/2 and 3L/4 of its support section during the static loading experiments and the points of occurrence of cracks

The experimental results demonstrate that the GFRP-concrete hybrid structures exhibit relative displacements at the interface between the GFRP and concrete elements prior to the formation of cracks. The relative displacements at different measurement points of the same sample exhibit variability, yet the underlying trend remains consistent. Relative displacements and their trends are not uniform across samples that have undergone different surface treatments. The maximum relative displacements before the appearance of cracks were 0.069 mm for samples treated with AR fibre and 0.058 mm for samples treated with basalt grit, while the maximum relative displacements for the other two treatments were less than 0.050 mm. The state of a GFRP-concrete hybrid structure prior to the emergence of cracks under static loading can be described as an elastic composite exhibiting relative displacement. In this state, the two components are rigidly coupled in the vertical direction, while there are constrained relative displacements in the horizontal direction. [17]

5. Conclusions

This research demonstrates the feasibility of large continuous profiles produced by an automated pultrusion process as a bridge formwork. In addition to sufficient load-bearing capacity compared to traditional formwork, GFRP formwork can be used as permanent formwork to protect the concrete from environmental damage. A novel approach to the repair and reinforcement of concrete structures has emerged in recent years. This involves bonding GFRP or CFRP materials to the areas of the concrete elements that are subject to tensile stresses. The direct pouring of fresh concrete into the GFRP formwork in this research allows for intervention in the concrete building from the beginning of construction, thereby maximising the protection of the concrete and reducing the stress of subsequent repairs. Furthermore, the use of this material can result in a reduction in construction costs during the construction phase, due to its light weight and simple modular installation.

Subsequent research will investigate methods for establishing permanent and stable connections between concrete and GFRP profile surfaces. Ultimately, in future construction, the formwork system and cured concrete will share the load-bearing function of the bridge. This combination allows for

achieving the load-bearing capacity of conventional bridges, reducing the investment for concrete and reinforcement, and possibly dispensing with the use of reinforcement altogether.

Acknowledgments
This Project is supported by the Federal Ministry for Economic Affairs and Climate Action (BMWK) on the basis of a decision by the German Bundestag. The authors would like to acknowledge Central Innovation Programme for SMEs (ZIM), LohrElement GmbH, Autmaring Engineering GmbH and Dammer Betonwerk GmbH & Co.KG for their support of this research.

References

[1] Bundesanstalt für Straßenwesen (BASt), Accessed: May 01, 2024. [Online]: https://www.bast.de/DE/Statistik/Bruecken/Brueckenstatistik.pdf?__blob=publicationFile&v=21
[2] F. Yan, Z. Lin, and M. Yang, Bond mechanism and bond strength of GFRP bars to concrete: A review, *Composites Part B: Engineering*, vol. 98, pp. 56–69, Aug. 2016.
[3] E. Cosenza, G. Manfredi, and A. Nanni, *Composites in construction, a reality : proceedings of the international workshop, July 20-21, 2001, Capri, Italy*. Reston, Va.: American Society of Civil Engineers, 2002.
[4] J. Figueiras, 2001 International Conference Composites in Construction (2001.10.10-12, and (2001.10.10-12 CCC 2001, *Composites in construction : proceedings of the International Conference Composites in Construction - CCC2001, Porto, Portugal, 10-12 October 2001*. Lisse: Balkema, 2001.
[5] D. Bačinskas *et al.*, Structural Analysis of GFRP Truss Bridge Model, *Procedia Engineering*, vol. 172, pp. 68–74, 2017.
[6] T. Siwowski, M. Rajchel, and L. Wlasak, Experimental research on static and dynamic performance of a novel GFRP bridge girder, *Composite Structures*, vol. 259, p. 113464, Mar. 2021.
[7] B. Stankiewicz, Composite GFRP Deck for Bridge Structures, *Procedia Engineering*, vol. 40, pp. 423–427, 2012.
[8] T. Siwowski and M. Rajchel, A Polish approach to FRP bridges, *Selected Scientific Papers - Journal of Civil Engineering*, vol. 12, Dec. 2017.
[9] Fiberline Building Profiles A/S, Accessed: May 01, 2024. [Online]: https://fiberline.com/de/projekte/bruecken/gfk-profile-sind-die-zukunft-des-brueckenbaus
[10] DIN EN 197-1:2011-11, Cement - Part 1: Composition, specifications and conformity criteria for common cement; German version.
[11] DIN EN 206:2021-06, Concrete - Specification, performance, production und conformity; German version.
[12] DIN 1045-2:2023-08, Concrete, reinforced and prestressed concrete structures - Part_2: Concrete; German version.
[13] DIN EN ISO 14125:2011-05, Fibre-reinforced plastic Composites - Determination of flexural properties (ISO 14125:1998 + Cor.1:2001 + Amd.1:2011); German version.
[14] DIN EN 12390-1:2021-09, Testing hardened concrete - Part 1: Shape, dimensions and other requirements for specimens and moulds; German version.
[15] DIN EN 12390-5:2019-10, Testing hardened concrete Part 5: Flexural strength of test specimens; German version.
[16] E. Schaumann, Hybrid FRP-lightweight concrete sandwich system for engineering structures, Jan. 2008.
[17] D. Zhou, M. Pahn, and W. Kurz, Beitrag zur Berechnung von Verbundträgern mit elastischem Verbund: Genaue Methode und ein Näherungsverfahren, *Stahlbau*, vol. 83, no. 4, pp. 278–288, Apr. 2014.

EXPERIMENTAL AND NUMERICAL ANALYSES ON THE THERMAL DISTRIBUTION WITHIN HYBRID FRP SANDWICH PANELS UNDER DIFFERENT CLIMATIC CONDITIONS

Marco Abreu Filho[1*], João M. Pereira[1], Miguel Azenha[1], José Sena-Cruz[1]

[1]ISISE/IB-S/ARISE, University of Minho, Azurém, 4800-058 Guimarães, Portugal
[*]Email: marcoabreufilho@civil.uminho.pt

Keywords: Fibre-reinforced polymer (FRP), Hybrid FRP Sandwich Panels; Thermal Distribution Analysis; Environmental Thermal Loads; Numerical Modelling

Abstract
Fibre-reinforced polymers (FRP) show valuable features for civil engineering applications. However, the response of these structures to temperature fluctuations is often oversimplified. Structures experience daily, seasonal, and yearly variations in environmental temperature that can significantly impact their behaviour. This study investigates the thermal distribution across a hybrid FRP sandwich panel, comprising glass-FRP face sheets/webs and a polyurethane foam core, complemented by a top layer of steel fibre-reinforced self-compacting concrete, under controlled climatic conditions (constant and variable thermal loads). Through a combination of experimental analyses and numerical simulations, the research provides insights on the thermal distribution within this type of sandwich panel. Moreover, the investigation highlights the lack of established guidelines to predict temperatures in FRP composite materials, underscoring the importance of calibrated numerical models to accurately predict thermal distributions. This research contributes with valuable insights to enhance the understanding and prediction of thermal distributions in FRP composite structures, crucial for ensuring their structural integrity and performance under service environmental conditions.

1. Introduction

Fibre-reinforced polymer (FRP) composites, composed of fibres (providing strength and stiffness) and resin (ensuring fibre protection and binding) [1], have garnered growing attention in the construction sector, e.g. [2, 3]. This advanced material shows valuable features for structural applications, such as: (i) high overall durability [4], (ii) easy in-situ installation [4], (iii) high strength-to-weight ratio [1], (iv) corrosion resistance [5], and (v) excellent fatigue resistance [6]. Considering the numerous advantages offered by FRP materials, significant research efforts have been directed towards improving the understanding of their mechanical properties and structural behaviour [7, 8]. However, the response of these structures to environmental effects and temperature fluctuations is often oversimplified [8]. In fact, the behaviour and response of FRP structures under environmental thermal loads are still not fully investigated and understood [9].

Structures are subject to daily, seasonal, and annual environmental thermal conditions that influence their behaviour [10, 11]. The non-uniform temperature distribution resulting from temperature variations cause the structure to undergo thermal stresses [11]. In addition, in some cases temperature fluctuations can exert a more significant influence on the structural response than operational loads, becoming one of the main factors leading to deformations [10, 11]. This is particularly relevant considering how the mechanical properties of polymer composites are known to be strongly temperature-dependent; thus, minor temperature variations can lead to changes in their mechanical properties [12]. The significance of this issue has been identified by the CEN WG4.T2 project team, responsible for developing the CEN/TS 19101:2022 - Design of fibre-polymer composite structures [13], published in November 2022, as an urgent problem to be addressed.

The main objective of this work is to develop and refine numerical models of a specific FRP sandwich structure under controlled climatic conditions, allowing accurate prediction of thermal distribution in response to environmental thermal loads considering the effects of radiation, convection, and

conduction. The validation of these models involved a meticulous analyses of experimental results, focusing on the thermal analysis of a hybrid FRP sandwich panel, composed of a glass-FRP (GFRP) face sheets/webs and a polyurethane (PUR) foam core, complemented by a top layer of steel fibre reinforced self-compacting concrete (SFRSCC).

2. Experimental campaign

Two hybrid web-core FRP sandwich panels, with a cross section of 0.5 m width and 0.3 m height and a length of 1.5 m, were used. The panels were originally developed as part of the research project "Easyfloor-Development of Composite Sandwich Panels for Building Floor Rehabilitation" and consisted of a 6 mm thick GFRP face sheets/webs fabricated via the pultrusion method, a PUR closed-cell foam core and a 20 mm SFRSCC top layer (Figure 1). Further details about the sandwich panels, namely design, manufacturing, material characterization and structural and fire performance can be found in [14, 15]. Six Platinum 385 PT100 Resistance Temperature Detector (RTD) sensors, model NB-PTCO-002, were strategically installed inside the samples for monitoring the temperature evolution. These sensors were positioned along the vertical central axis of the cross section, as shown in Figure 1.

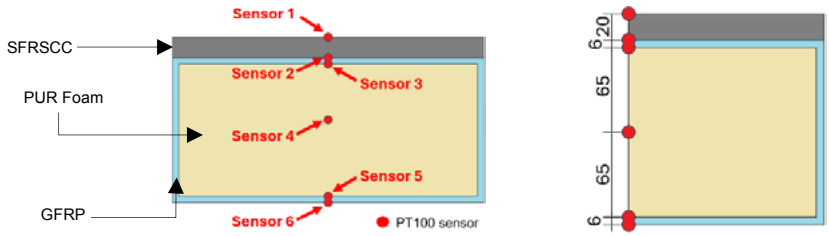


Figure 1. Experimental specimens: a) sensors numbering; b) sensors position (dimensions in mm).

The experimental campaign was developed using a FITOCLIMA 6400EC25 climatic chamber, with dimensions of 2400 mm (length) × 1800 mm (width) × 2000 mm (height), range of temperature between -25±1 ºC and +80±1 º C and range of relative humidity between 30±2 % and 98±2 %. The temperature distribution within the specimens was monitored, under various conditions, which were carried out across a four-stage experimental campaign, as described in the following:

- **Stage I** consisted of reaching the equilibrium 20 °C and maintain it for 24 hours. Subsequently, the temperature was gradually increased at a rate of 0.33 °C per minute until it reached 40 °C. Likewise, the temperature of 40 °C was maintained for 24 hours. Afterwards, a controlled reduction in temperature began, at a rate of 0.33 °C per minute, returning to the initial temperature of 20 °C. The temperature was maintained again for a further 24 hours.
- **Stage II** included reestablishing equilibrium at 20 °C. Subsequently, the temperature was gradually reduced at a rate of 0.076 °C per minute until it reached -15 °C. Following this, the temperature underwent a controlled rise at a rate of 0.076 °C per minute, until it reached 40 °C. The heating process spanned over 12 hours, followed by a 12-hour cooling period. This 24-hour cycle was repeated 10 times. (For stages I and II, both specimens were placed inside the climatic chamber in a way to maximize the open space around the specimen's sides, as shown in Figure 2a).
- **Stage III** initiated from equilibrium at 20 °C, maintaining this temperature throughout the whole stage. The process involved subjecting the specimens to a 1000 W high-pressure sodium lamp (HPS) with a spectrum from UV to IR for 12 hours, followed by a 12-hour period without lamp exposure, completing a full 24-hour cycle. This pattern was repeated for 5 cycles. To optimize lamp exposure, only one specimen was kept inside the climatic chamber, centrally positioned, as shown in Figure 2b, with the lamp positioned 50 cm above the specimen.
- **Stage IV** is similar to Stage II. Additionally, the process included subjecting the specimen to the HPS lamp for 12 hours, followed by a further period of 12 hours without the lamp. This sequence completed a full 24-hour cycle. This cyclical exposure pattern was repeated for a total of 10 cycles. In particular, the activation of the lamp was synchronized with the increase in temperature, while the deactivation coincided with the decrease in temperature. The experimental setup was the same as in Stage III (Figure 2b).



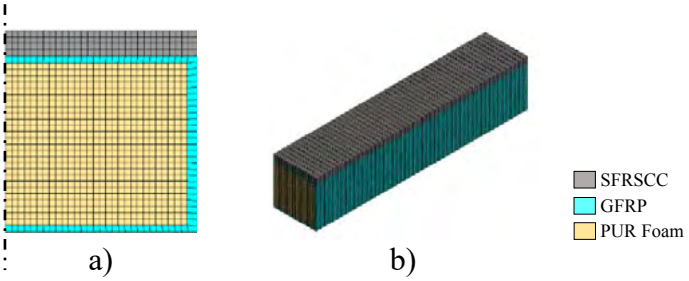
a) b)

Figure 2. Setups for the experimental campaign: a) Stages I and II; b) Stages III and IV.

The data acquisition for this experimental campaign was conducted using a DataTaker DT85M device, recording data at a rate of 2 readings per minute. Additionally, two PT100 RTD Platinum 385 sensors were strategically positioned within the climatic chamber to improve temperature monitoring.

3. Numerical models

The DIANA finite element software [16] was used to develop numerical models to investigate the non-linear transient heat transfer phenomena for the specimens studied. The main objective of these models was to reproduce the observed experimental behaviours and subsequently validate their accuracy.
Given the non-uniform incidence of the lamp on the specimens, a 3D model was employed and meshed using twenty-node isoparametric hexahedron elements (CHX20H). Utilizing the central axis of symmetry, half of the cross-section and longitudinal length were modelled (Figure 3), employing element dimensions of 5 × 5 × 10 mm³ (width × height × length). The elements were optionally elongated to reduce the computational processing time.



a) b)

Figure 3. Developed numerical models – mesh adopted: a) front view; b) isometric view.

The properties of the materials used in these models are presented in Table 1. The GFRP properties were collected from the characterization made in [14, 15], while the properties for the other materials were estimated based on literature [9, 17, 18, 19]. The temperature data acquired within the climatic chamber was incorporated into the model as a convective boundary condition, applied uniformly throughout the model, excluding the axis of symmetry. The heat transfer coefficients for SFRSCC and GFRP were 30 W/m²°C and 40 W/m²°C, respectively, for simulations within the climate chamber as forced convection is involved. The lamp's irradiation pattern was simulated using a Gaussian curve and was introduced into the model as a heat flow boundary condition, exclusively affecting the top surface of the model. The lamp produced a heat flux of 595 W/m² at its central point, with this intensity dissipating in a range of 40 cm from the centre. Thus, the models comprehensively considered the interaction of thermal conduction, convection, and radiation phenomena.

Table 1. Thermal properties of the materials that constitute the panels.

Material	Density [kg/m³]	Specific Heat [J/kg°C]	Thermal Conductivity [W/m°C]
SFRSCC	2420	900	1.55
GFRP	1890	1053	0.2495
PUR Foam	60	1450	0.03

4. Results and discussion

Within this section, an in-depth analysis of the main findings derived from the results of the four phases of the experimental campaign, along with the numerical results, will be carried out. It will culminate in an evaluation of the thermal distribution within the specimens, with considerations made in light of current standards. Starting with the results obtained from the Stage I of the experimental campaign, Figure 4 highlights the results obtained for sensor 1 and sensor 6 (as indicated in Figure 1a) of both specimens (P1 and P2) for Stage I.

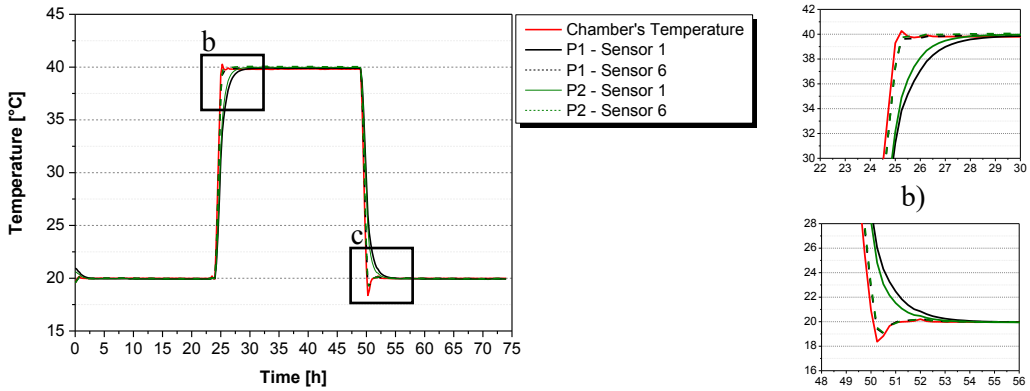


Figure 4. Stage I - Sensors 1 and 6: a) overview; b) detail b; c) detail c.

As evidenced by the Figure 4, the sensors positioned within the outermost layers indicate that the SFRSCC layer displayed a slower rate of heat exchange with its surroundings compared to the GFRP bottom face sheet. Specifically, sensor 1, located at the highest point of the SFRSCC layer, at the top of the specimen, took approximately 6 hours to achieve thermal equilibrium during heating, transitioning from 20 °C to 40 °C. Similarly, it required about 5 hours to reach equilibrium during cooling, from 40 °C to 20 °C. In contrast, sensor 6 at the outermost GFRP laminate (GFRP bottom face sheet) at the specimen base reached thermal equilibrium almost simultaneously with the climatic chamber in both heating and cooling phases, suggesting a higher convective heat transfer coefficient for GFRP compared to SFRSCC. Additionally, the entire specimen reached thermal equilibrium in approximately 7 hours during heating and 8 hours during cooling. Moreover, experimental data from panels P1 and P2 exhibited consistent results.

Furthermore, noteworthy is the observation that the highest and lowest temperature peaks depicted by the red line (representing internal temperature sensors) during heating and cooling processes, respectively, signify the climatic chamber's efforts to balance temperatures between those recorded by the sensors and the adjustments made to increase or decrease the temperature to the targeted one.

Advancing to Stage II, Figure 5 shows the data collected from sensors 1, 4, and 6, representing the outermost points at the top of the specimen in the SFRSCC layer, the innermost within the PUR foam, and the GFRP bottom face sheet at the panel, respectively.

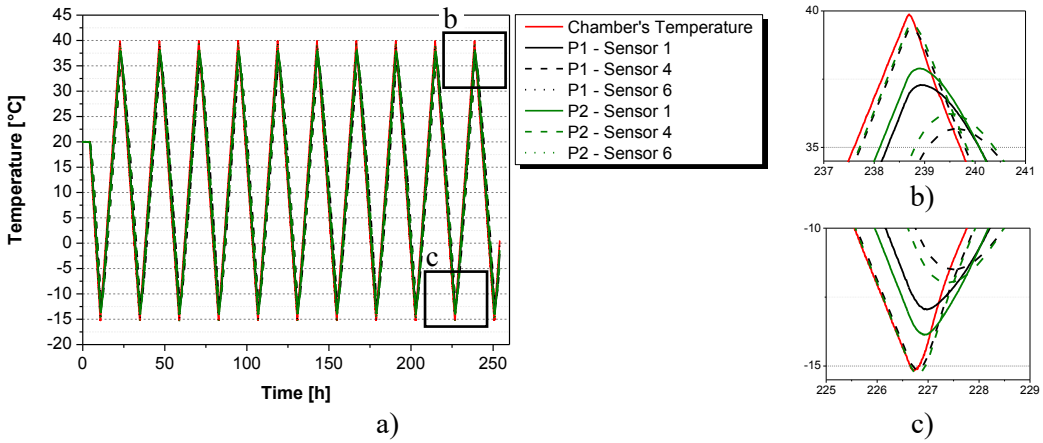
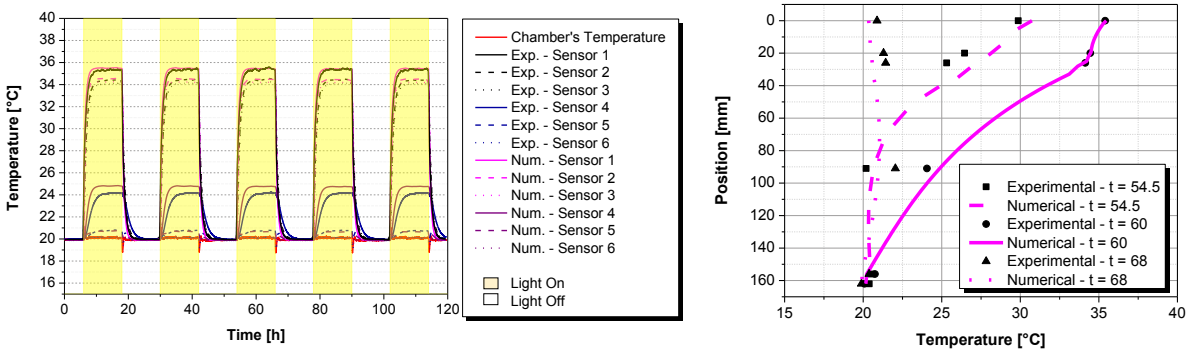


Figure 5. Stage II - Sensors 1,4 and 6: a) overview; b) detail b; c) detail c.

Stage II confirmed the findings from Stage I. The sensors positioned in the outermost layers clearly indicated that the SFRSCC layer exhibited a lower heat transfer rate with the surrounding environment compared to the GFRP. In contrast with the previous stage, constant temperature plateaus were not maintained during Stage II. Consequently, the maximum and minimum temperatures recorded by the various sensors differed.

Specifically, sensor 1 registered a maximum temperature of around 37.3 °C and a minimum temperature of approximately -12.5 °C throughout the process. Sensor 6 recorded a maximum temperature of approximately 39.4 °C and a minimum temperature of roughly -15 °C during the process. Sensor 4, located at the innermost part of the specimen, recorded a maximum temperature of about 35.6 °C and a minimum temperature of approximately -11.5 °C throughout this stage. This analysis provided valuable insights into the heat exchange occurring between the test specimens and their surroundings, as well as within the specimens themselves. Furthermore, it is noteworthy that the experimental data collected from test panels P1 and P2 exhibited consistent results, like the previous stage.

In the sequence of the experimental campaign, Figure 6a presents Stage III results for the 6 sensors, both experimental and numerical. In addition, Figure 6b presents the thermal profiles obtained for three specific points of interest: t = 54.5 hours, t = 60 hours, and t = 68 hours. These time instances correspond, respectively, to half an hour after the initiation of exposure to the lamp during the third cycle, six hours after the start of lamp exposure in the third cycle, and the midpoint between the interruption of lamp exposure in the third cycle and the moment when the specimen returns to thermal equilibrium at 20 °C.



a) b)

Figure 6. Stage III - Sensors 1 to 6: a) overview; b) thermal profiles.

As depicted in the figure above, the proximity of the upper sensors to the lamp resulted in a more pronounced influence, as expected. This influence progressively diminished with the depth of the sensors within the specimen. Notably, sensor 6, situated farthest from the lamp, showed no noticeable impact, maintaining a temperature nearly identical to that of the climatic chamber. Sensor 1, for instance, required approximately 4 hours of lamp exposure to reach its maximum recorded temperature, reaching around 35.5 °C. In contrast, sensor 4, positioned more centrally within the specimen, needed roughly 6 hours of lamp exposure to reach its maximum recorded temperature, approximately 24.2 °C. Throughout the experiment, the specimen exhibited a temperature gradient of 15.5 °C across its cross-section.

Furthermore, upon deactivating the lamp, sensor 1 needed about 4.5 hours to return to thermal equilibrium with the climatic chamber. On a broader scale, the entire test specimen required approximately 7.5 hours to achieve a steady state after the lamp exposure ended.

Moreover, the numerical simulation demonstrated a considerable level of accuracy compared to the experimental results for most sensors. During this phase, sensor 4 emerged as the most critical point for the analysed time instants. However, the observed disparity did not exceed 4.9%, corresponding to an approximate temperature variation of 1.08 °C between the numerical and experimental data.

Concluding the experimental campaign, Figure 7 presents the experimental and numerical results acquired for sensors 1, 2, and 6, for Stage IV. These correspond to the outermost sensor located at the top of the specimen in the SFRSCC layer, the sensor positioned between the top layer and the laminate at the top face sheet of the GFRP component's panel, and the outermost sensor at the bottom face sheet of the specimen, respectively. Additionally, Figure 7d depicts the thermal profiles for four specific points of interest: t = 218 hours, t = 224 hours, t = 230 hours, and t = 236 hours. These time instants

correspond, respectively, to the midpoint between the 10th negative peak and the preceding positive peak, the 10th negative peak, the midpoint between the 10th negative peak and the 10th positive peak, and the 10th positive peak.

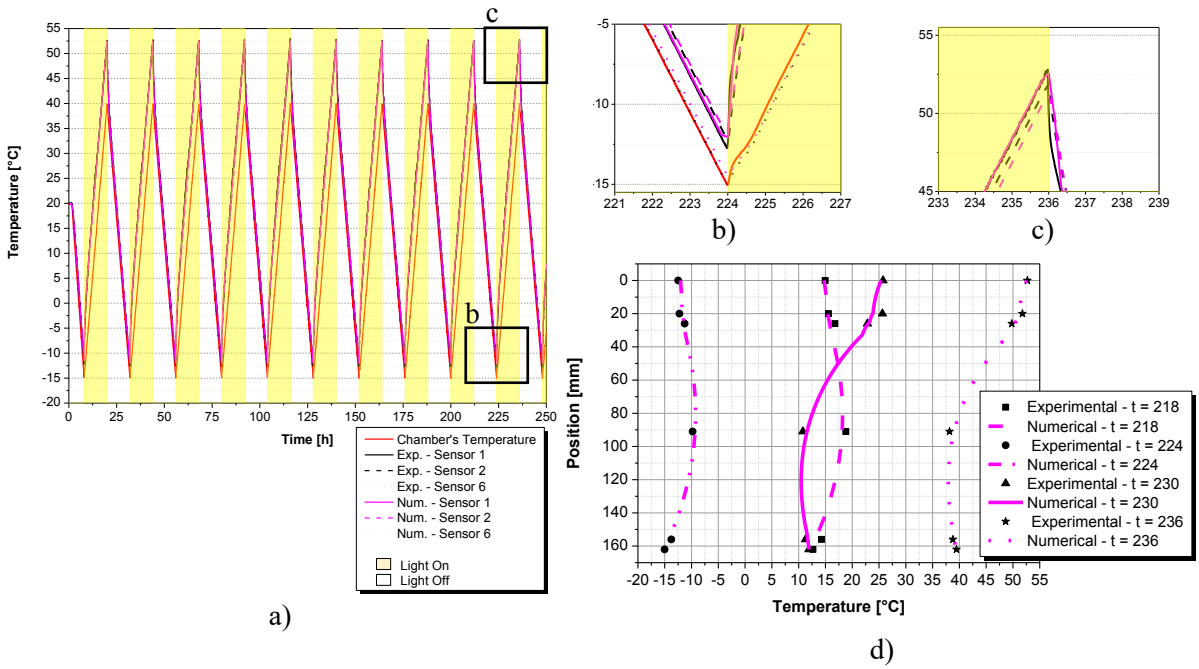
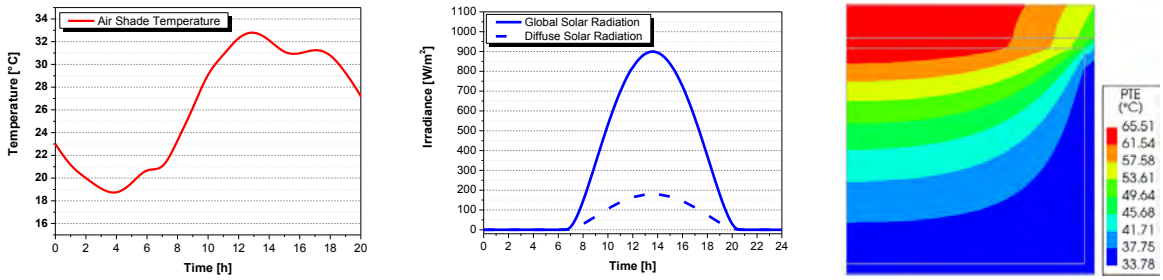


Figure 7. Stage IV - Sensors 1, 2 and 6: a) overview; b) detail b; c) detail c d) thermal profiles (all sensors).

The figures above depict temperature fluctuations within the specimen, influenced by cyclical thermal loads and exposure to the HPS lamp. At this Stage, sensor 1 reached a peak temperature of around 52.7 °C, surpassing the climate chamber's set temperature by 12.7 °C, with a minimum of approximately -12.6 °C. Sensor 6, however, recorded a maximum of about 39.5 °C and a minimum of -14.9 °C, closely mirroring the climate chamber's conditions. Positioned between the SFRSCC layer and the top GFRP face sheet, sensor 2 registered a maximum of approximately 52.2 °C and a minimum of about -12.2 °C. The maximum temperature gradient across the specimen's cross-section during this phase was approximately 14.5 °C. The numerical simulation closely matched experimental results; particularly highlighting sensor 2 as critical at t = 230 h (Figure 7d). The observed discrepancy did not exceed 6.8%, equivalent to a temperature variance of approximately 1.74 °C between numerical and experimental data. However, it's worth highlighting that during Stage IV, the applied temperature peaked at 40 °C, while the HPS lamp managed to emit a heat flow of 595 W/m² at its focal point, gradually dissipating over a 40 cm radius from the centre.

Finally, it is important to acknowledge the potential of the discussed numerical models, which have shown a high level of compatibility with the experimental data. They provide a promising way to explore the complexities of temperature distribution within the specimens. Once calibrated and validated, these models can be applied to practical scenarios, providing insights into how temperature gradients manifest in the specimens under real-world climatic conditions. Transitioning from the controlled environment of the climate chamber to simulations in the external environment, where the forced convection rate is expected to be lower, the following heat transfer coefficient values were used: 15 W/m²°C for SFRSCC and 25 W/m²°C for GFRP. All other parameters of the numerical model remain unchanged.

In Guimarães, Portugal, where the research centre (ISISE) conducting the test is situated, summer months witness solar radiation reaching up to 900 W/m² (which would have a near uniform incidence on the specimen, in contrast with the lamp). Furthermore, in 2023, the city experienced a maximum temperature of 33 °C. Figure 8c illustrates the thermal distribution of the test specimen under the most extreme conditions recorded in Guimarães in 2023, considering air temperature data from [20] (Figure 8a) and estimated solar radiation for a clear day in August/2023 at latitude 41.442, corresponding to Guimarães (Figure 8b).



a) b) c)

Figure 8. Guimarães worst-case scenario in 2023: a) solar radiation; b) air shade temperature; c) thermal distribution within the specimen.

Figure 8c indicates that under these extreme conditions, the specimen in Guimarães would reach a maximum temperature of 65.5 °C, while the GFRP structure would peak at 65.2 °C. Additionally, a thermal gradient exceeding 30 °C would be observed.

In Europe, the EN 1991-1-5 standard provides principles and guidelines for calculating thermal actions on buildings, bridges, and other structures, including their components. Although this standard does not address FRP composites, for comparative purposes, the most extreme scenario in terms of maximum temperature for a structure in Portugal would involve bridge decks, with the deck *type 1* (steel decks) being the most critical. The maximum temperature for such decks is calculated using the equation:

$$T_{e,max} = T_{max} + 16 \quad (1)$$

In this equation, $T_{e,max}$ represents the maximum temperature of an exposed surface, and T_{max} represents the maximum air shade temperature, determined by the Portuguese national annex for the specific zone. For Guimarães, this value is set at 40 °C.

According to EN 1991-1-5, the worst-case scenario would predict a maximum temperature of 56 °C for a structure in Guimarães, Portugal. However, the numerical analysis indicated that the specimen under study would reach 65.5 °C, surpassing the predicted worst case by 9.5 °C. It's crucial to emphasize that EN 1991-1-5 does not include provisions for FRP materials, thus its applicability to our case study is not fully covered. The *type 1* deck, exemplified in this context, regards to steel decks (steel box girder, steel truss or plate girder). As expected, the unique thermal properties of the hybrid panel's diverse components will yield a distinct thermal response.

5. Conclusions

This work provides insights into the thermal distribution over hybrid FRP sandwich structures subjected to different thermal loads. The experimental data obtained from both panels were consistent between themselves. Particularly noteworthy was the observation that the SFRSCC layer displayed a lower rate of heat transfer to the surrounding environment compared to the GFRP. Furthermore, the conducted numerical simulations demonstrated a very good agreement with experimental results, validating the developed models.

Numerical simulations demonstrated that under the most extreme conditions for Guimarães in 2023 (with an air shade temperature of 33 °C and maximum solar irradiation of 900 W/m²), a peak temperature of 65.5 °C would be reached at the upper surface of the specimen's cross-section. In contrast, with even higher air shade temperatures (40 °C), in accordance with the EN 1991–1–5, a bridge deck *type 1* (which regards to steel decks and represents the worst-case scenario for maximum temperature of a structure in Portugal) would reach a maximum temperature of 56 °C, indicating a shortfall of 9.5 °C.

It is essential to emphasise the lack of established guidelines for predicting temperatures in FRP composite materials. Moreover, this research demonstrates that even the most extreme scenarios in current standards for other materials may underestimate maximum temperatures if applied to FRP materials. Therefore, calibrated finite element-based numerical models serve as crucial tools for analysing thermal distribution in FRP composite structures. This significance is underscored considering that CEN/TS 19101:2022 provides a temperature conversion factor accounting for material property changes by temperatures diverging from 20 °C under service conditions. A discrepancy of more than 9 °C would be substantial in this context.

Acknowledgments
This work was partly financed by FCT / MCTES through national funds (PIDDAC) under the R&D Unit Institute for Sustainability and Innovation in Structural Engineering (ISISE), under reference UIDB/04029/2020 (doi.org/10.54499/UIDB/04029/2020), and under the Associate Laboratory Advanced Production and Intelligent Systems ARISE under reference LA/P/0112/2020. The 1st author wish also to acknowledge the grant 2022.13310.BD, provided by Fundação para a Ciência e a Tecnologia, IP (FCT), financed by European Social Fund and national funds through the FCT/MCTES. Acknowledgments are extended to LEST – Laboratório de Estruturas, for their technical and material support.

References

[1] S. Moy, "Advanced fiber-reinforced polymer (FRP) composites for civil engineering applications," in *Developments in Fiber-Reinforced Polymer (FRP) Composites for Civil Engineering*, pp. 177–204, 2013.
[2] C. E. Bakis *et al.*, "Fiber-Reinforced Polymer Composites for Construction-State-of-the-Art Review," *Journal of Composites for Construction*, vol. 6, no. 2, pp. 73–87, 2001
[3] B. Jurkiewiez *et al.*, "Static behaviour up to failure of a full-scale GFRP-concrete hybrid footbridge," *Eng Struct*, vol. 199, 2019.
[4] G. Carra and V. Carvelli, "Ageing of pultruded glass fibre reinforced polymer composites exposed to combined environmental agents," *Compos Struct*, vol. 108, pp. 1019–1026, 2014.
[5] H. Xin *et al.*, "Moisture diffusion and hygrothermal aging of pultruded glass fiber reinforced polymer laminates in bridge application," *Compos B Eng*, vol. 100, pp. 197–207, 2016.
[6] P. Kumar, K. Chandrashekhara, and A. Nanni, "Structural performance of a FRP bridge deck," *Constr Build Mater*, vol. 18, no. 1, pp. 35–47, 2004.
[7] G. Vizentin and G. Vukelic, "Failure analysis of FRP composites exposed to real marine environment," in *Procedia Structural Integrity*, pp. 233–240, 2021.
[8] B. M. Shahrooz *et al.*, "Durability of FRP composite bridge decks-construction and temperature effects," *Int. J. Materials and Product Technology*, vol. 28, no. 1, pp. 66–88, 2007.
[9] E. Lepretre *et al.*, "Design Approach for FRP Structures: A Focus on Thermal Design," in *10th International Conference on FRP Composites in Civil Engineering. CICE 2021*. Springer Science and Business Media Deutschland GmbH, pp. 2446–2457, 2022.
[10] Q. Xia *et al.*, "Experimental Study of Thermal Effects on a Long-Span Suspension Bridge," *Journal of Bridge Engineering*, vol. 22, no. 7, 2017.
[11] Y. Xia *et al.*, "Field monitoring and numerical analysis of Tsing Ma suspension bridge temperature behavior," *Struct Control Health Monit*, vol. 20, no. 4, pp. 560–575, 2013.
[12] B. Stankiewicz, "Durability of glass fiber-reinforced polymer bridge panel based on differential thermal analysis, dynamic mechanical analysis, and differential scanning calorimetry analysis," *J Compos Mater*, vol. 51, no. 16, pp. 2301–2313, 2017.
[13] CEN - European Commitee for Standardization, "TS 19901: Design of fibre-polymer composite structures," 2022.
[14] T. Silva *et al.*, "Flexural Creep Response of Hybrid GFRP–FRC Sandwich Panels," *Materials*, vol. 15, no. 7, 2022.
[15] M. Proença *et al.*, "Experimental study on the fire resistance of all-composite and hybrid web-core sandwich panels for building floors," *Compos Struct*, vol. 337, Jun. 2024.
[16] DIANA, *DIANA User's Manual - Release 10.8*. 2023.
[17] H. Zhang *et al.*, "Experimental study of the thermal conductivity of polyurethane foams," *Appl Therm Eng*, vol. 115, pp. 528–538, 2017.
[18] B. Nagy *et al.*, "Thermal properties and modeling of fiber reinforced concretes," in *Energy Procedia*, pp. 2742–2747, Nov. 2015.
[19] I. Asadi *et al.*, "Thermal conductivity of concrete – A review," *Journal of Building Engineering*, vol. 20. Elsevier Ltd, pp. 81–93, 2018.
[20] "Historical weather data for guimarães | Visual Crossing." Accessed: Apr. 16, 2024. [Online]. Available: https://www.visualcrossing.com/weather-history/guimar%C3%A3es/metric/2023-08-01/2023-08-31

©2024 | 3_ABREU FILHO_Marco_3Q7AU.pdf:8

DESIGN ASSESSMENT OF COMPOSITE PATCH REPAIR ON STEEL STRUCTURES BASED ON TOUGHNESS TESTS USING A NEWLY DESIGNED NON-STANDARD "EQUIVALENT INTERFACE" SPECIMEN

M. Deydier[1], S. Paboeuf[1], Q. Sourisseau[2], E. Leprêtre[2] and T. Balutch[3]

[1]Bureau Veritas, Research Department, 4 Rue Duguay Trouin 44800 Saint Herblain, France
Email: maxime.deydier@bureauveritas.com, stephane.paboeuf@bureauveritas.com
[2]MAST/SMC, Université Gustave Eiffel, 44344 Bouguenais, France
Email: quentin.sourisseau@univ-eiffel.fr, emilie.lepretre@univ-eiffel.fr
[3]CESMAN, Naval Group, Rue de l'Halbrane, 44340 Bouguenais, France
Email: thomas.balutch@naval-group.com

Keywords: composite patch, repair, cohesive model, toughness tests

Abstract
Classic repairs of corroded steel plates consist in cropping and renewing steel plates. Such repairs involve hot work which may not be compatible with Floating, Production, Storage and Offloading (FPSO) capacities content. It is necessary to carry out long operations of emptying, cleaning, and inerting in capacities surrounding the repair, implying long durations for which the production must be stopped. By using adhesively bonded repairs, described as cold work, tanks do not have to be emptied, and production can continue during repair.
In the Joint Industry Project (JIP) StrengthBond Offshore (SBO), a robust methodology for the design assessment of composite patch repairs on steel structure was developed. Typical stress approaches and energy approaches have first been tested using standard specimens for model calibration but the correlation with large scale samples (2 m) was not accurate enough. Thus, a new specimen called "equivalent interface", which includes several interfaces, was designed to be representative of the type of failure for this application, and used in toughness tests. Finally, a cohesive zone model was identified based on these toughness tests, in order to define a reliable failure criterion that can be used to design large composite repairs on steel structures with more confidence.

1. Introduction

Initiated in 2019, the JIP StrengthBond Offshore (SBO) developed a robust methodology for the strength assessment of composite patch repair bonded on corroded steel plates [1]. Several designs, with different geometries and manufacturing processes, were investigated with a large experimental and numerical campaign. Determination of failure of such composite/steel assembly is complex as it involves mixed material interfaces.

When designing bonded assemblies, simple approach involves stress analysis with analytical [2] or numerical models. Nonetheless, these approaches are limited when studying complex geometries and loadings, as is the case with large composite patch repairs. In our study, fracture mechanics approach in Finite Element (FE) and cohesive zone model were chosen to characterise the interfaces' behaviour involved in the patch repair resistance. Cohesive elements can predict both the delamination onset and crack propagation [3]. When modelling such elements, several methods exist to calibrate the parameters from behaviour laws, referred as cohesive laws. The inverse method, used in [4], where a high number of simulations is performed until fitting of both numerical and experimental results coincide, is the

method commonly used. Other calibration methods, as well complete methodology from characterisation to application on large scale steel-steel specimens are described in [5]. Experiments used to calibrate cohesive laws are typically toughness tests from standards ([6], [7], [8]). However, these tests require similar upper and lower adherents made of a single material and are thus non-suitable to model mixed material interface. A new specimen, named Equivalent Interface (EI), was designed during the JIP SBO to be used in toughness tests in order to characterise mixed-material interfaces as encountered in the composite patch repair. The objective of this specimen was also to limit the number of specimens needed for the characterisation campaign, by obtaining the critical energy release rate (ERR) of the weakest interface with a single specimen, rather than testing each interface. Cohesive laws calibrated with this new specimen are finally implemented in numerical models of large scale composite patch repair and compared to experimental results.

2. Method

2.1. Materials

The application described in this paper is on a composite patch repair on a steel substrate. Substrates were made of Strenx 1100 steel, with a minimum yield strength of 1100 MPa. The composite patch is composed of Carbon Fibre Reinforced Polymer (CFRP) with Unidirectional (UD) plies mainly, to restore the steel stiffness and some Glass Fibre Reinforced Polymer (GFRP) plies at the steel interface to prevent galvanic corrosion and to soften the interfacial stresses. UD carbon were oriented in the direction of the tensile loading. The composite patch was manufactured with infusion process using bi-component epoxy resin.

2.2. Equivalent Interface specimen

The objective of this specimen named equivalent interface (EI) specimens was to obtain the toughness of the weakest interface of the composite patch repair on steel plates. Thus, it had to be representative of where the failure would occur. The EI specimen included the several interfaces of the patch: steel/GFRP, GFRP/GFRP, GFRP/CFRP, CFRP/CFRP. Teflon inserts were placed at each interface. A large plate was manufactured by vacuum hand lay-up and cut into multiple EI specimens illustrated in Figure 1. The materials (resin, fibres) and the surface preparation, described in [5] were identical between EI and large composite patch specimens.

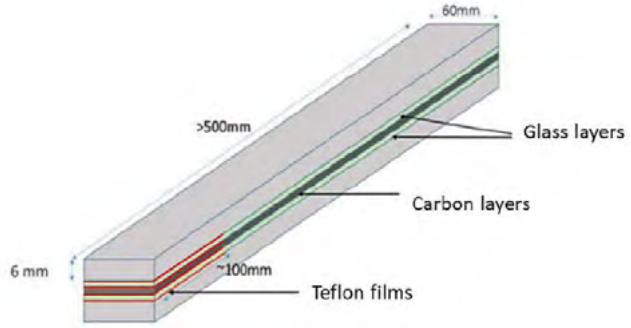


Figure 1. Equivalent interface specimen

2.3. Toughness tests

The EI specimens described earlier were used in toughness tests, namely Double Cantilever Beam (DCB) for mode I crack propagation, End Notch Flexure (ENF) for mode II and Mixed Mode Bending (MMB) for mixed mode I+II. From these tests, force-displacement curves, in pure mode I, pure mode II and mixed mode at ratio 50% and 75% mode II (ratio G_{II}/G_{tot}, ERR of mode II over total ERR) were obtained. Compliance Calibration Method was used to determine toughness values in pure mode I G_{Ic} and mode II G_{IIc} as described in [5]. Experimental set-ups of both DCB and ENF tests are shown in Figure 2.

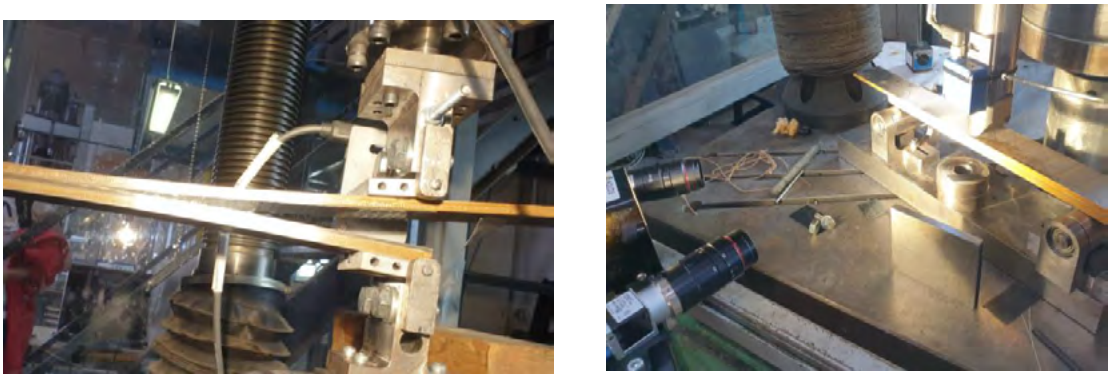


Figure 2. Experimental set-ups of DCB test (left) and ENF test (right) using EI specimens

2.4. Finite element models of EI specimens with cohesive elements

Finite models were performed in Siemens Simcenter Nastran with the SOL402 solver. Formulation of the cohesive elements is based on the continuum damage mechanics initially developed by the Ladevèze's team in Cachan [9]. Implementation in Nastran is further detailed in [3] with behaviour laws description.

The elements used in the model were solid volume elements. Isotropic properties were used for the steel substrates and 3D orthotropic properties used for the carbon and glass plies. In-plane properties were based on experimental tests while out-of-plane properties were calculated from BV rules NR546 [10]. Geometry and boundary conditions are shown in Figure 3. As Teflon was inserted at every interface except the CFRP/CFRP middle interface, contact was applied at each interface except this middle interface where nodes were merged. Contact surfaces were applied with default parameters from SOL402 solver and no friction was used. In the case of MMB setting, the beams of the test bench were modelled using rigid elements. A cohesive element layer was introduced at the interface between steel and the first ply of GFRP.

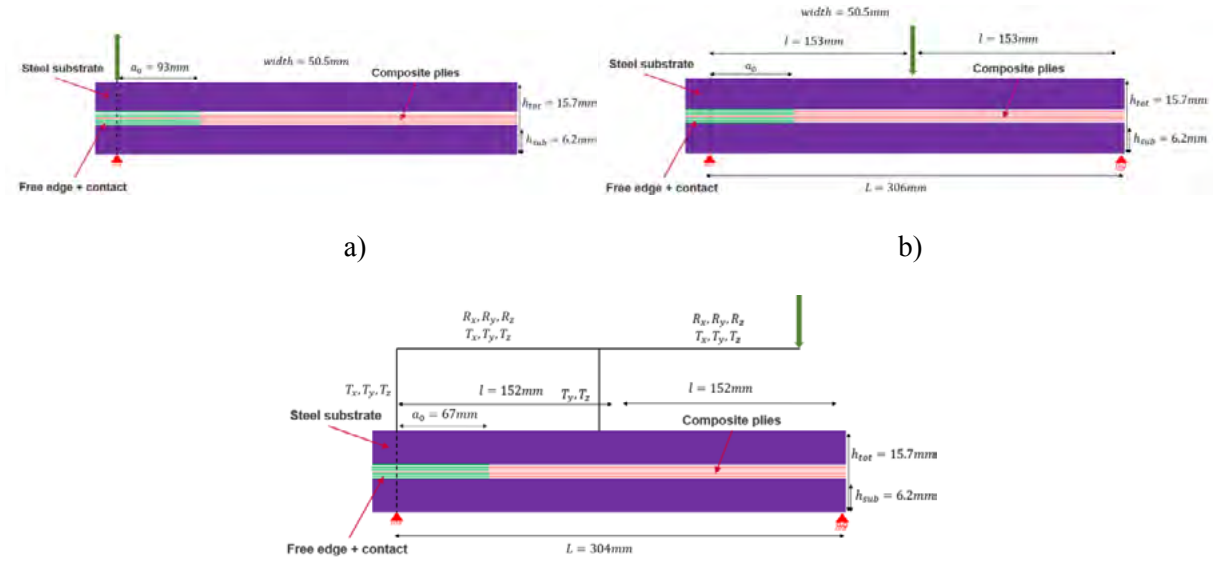


Figure 3. Geometry and boundary conditions of the used finite element model for: a) the DCB model, b) ENF model, c) MMB model

Figure 4 shows the mesh used for the ENF model (a similar mesh was used for the DCB and MMB models). Only one element in the thickness of each composite ply is considered. A mesh sensitivity study was carried out in the direction of crack propagation, resulting in a mesh size of 1 mm in this direction for each toughness test.

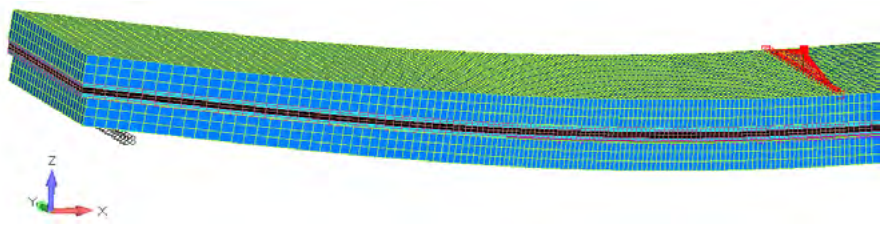


Figure 4. Illustration of ENF model mesh

2.5. Methodology for cohesive parameters calibration

A bilinear cohesive law shape was used for modelling the crack propagation for all modes. Thus, 3 different parameters had to be calibrated in pure mode I and II: the critical ERR G_c, the initial stiffness K and the critical stress before damaging σ_c. An example of mode I cohesive law is shown in Figure 5. Damage is referred as d.

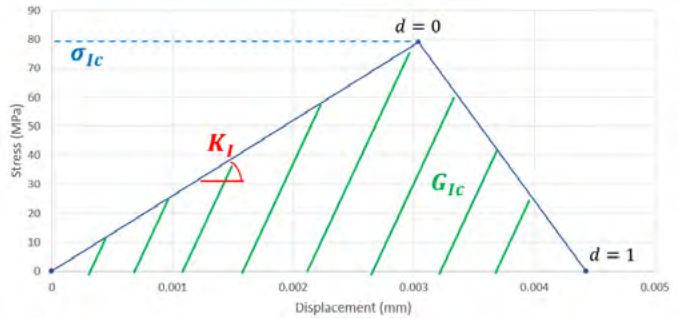


Figure 5: Example of bilinear cohesive law in mode I

The inverse method was used for the calibration of the cohesive law parameters. The toughness in pure mode I and II was determined thanks to the fracture mechanics tests, and the two other parameters from each mode were determined by fitting the numerical and experimental force-displacement curves. For MMB tests, the coupling between the modes is calibrated through a single parameter α determined by inverse method. The complete methodology is described below:

1. Measure the toughness experimentally from DCB, ENF, MMB using the EI specimen,
2. Assess the mesh sensitivity for all models,
3. Determine the cohesive law in mode II, with the only given value being G_{IIc},
   a. Evaluate the stiffness K_{II} sensitivity in ENF models,
   b. Evaluate the critical shear stress τ_c sensitivity in ENF models,
   c. Determine the cohesive law in mode II with optimal stiffness and critical shear stress,
4. Determine the cohesive law in mode I, with the only given value being G_{Ic},
   a. Evaluate the stiffness K_I sensitivity in DCB models,
   b. Evaluate the critical peel stress σ_c sensitivity in DCB models,
   c. Determine the cohesive law in mode I with optimal stiffness and critical peel stress,
5. Implement the resulting cohesive laws in mode I and II in MMB models and evaluate the sensibility of the coupling parameter,
6. Determine the optimal coupling parameter in MMB models for mixed mode.

2.6. Validation with large scale specimens

2.6.1. Specimen presentation

Large specimens were manufactured by infusion to validate the approach. Two different geometries were tested during the experimental campaign, corresponding to two different scarf angles (to minimise stress concentration at the edges), as illustrated in Figure 6, with the same thickness in the middle section of the composite patch. The length of the composite patch was 1.4 m, with a width of 50 mm for both geometries.

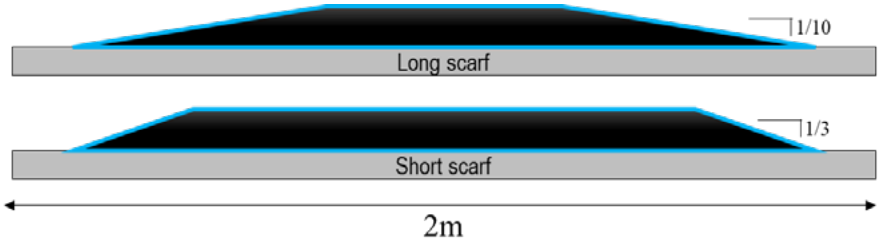


Figure 6. Illustration of long scarf and short scarf geometries

These specimens were tested both in tensile loading and bending loading, which provided four different configurations to compare numerical and experimental results.

2.6.2. Modelling of large scale specimens

The entire model was done with solid volume elements. The composite part of the specimen was modelled with 1 element per layer in the thickness and 3D orthotropic properties, similarly to the EI models. Two plies of GFRP were placed at the interface, as in EI specimens, and two other plies covering everything at the top for protection purposes. Two different positions were tested in two separate models for the cohesive element layer: at the steel/GFRP interface and the first two GFRP/GFRP plies, in separate models. A mesh sensitivity analysis was also performed. An illustration of the mesh is given in Figure 7, along with the 2 different cohesive element layer configurations. Boundary conditions and loadings are illustrated in Figure 8. The loading was applied as follows:

- Tensile: Clamp modelled by rigid element, with loading applied on it. All rotations and all displacements blocked on rigid element, except x-translation.
- Bending: Loading applied on rigid element at the mid-length. All rotations and all displacements blocked on rigid element, except z-translation.

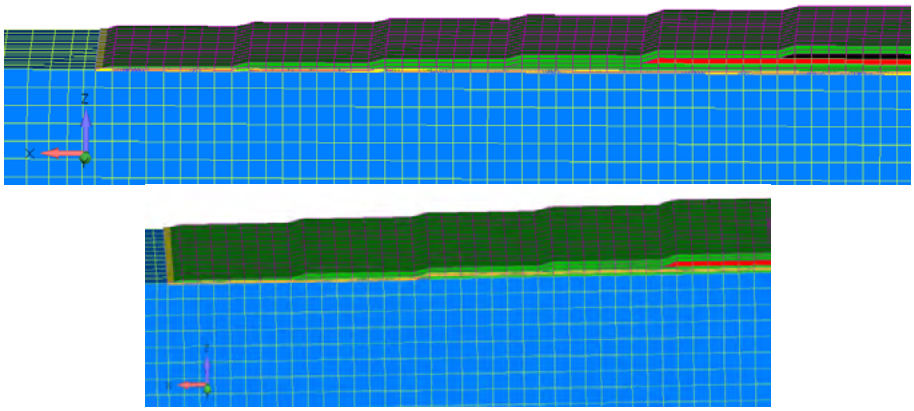


Figure 7. Illustration of mesh of the composite patch on steel substrate model with cohesive element layer in yellow at the steel/GFRP interface (top) and GFRP/GFRP interface (bottom)

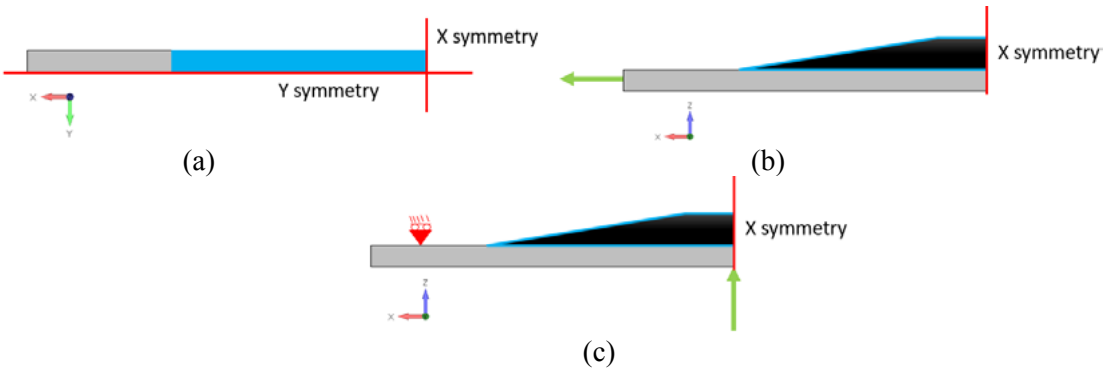


Figure 8: (a) symmetries used on both models; (b) loadings, boundary conditions on tensile model and (c) loadings, boundary conditions on bending model

3. Results

3.1. EI Model results and cohesive parameters

For DCB and ENF models where a stiffness sensitivity analysis was performed, it was found that the stiffness (values from 10^2 to 10^6 MPa/mm) had almost no influence on numerical force-displacement curves. The critical ERR has a lot of influence on the results but it was fixed from the experimental tests. Thus, the calibration of the cohesive parameters to fit to experimental results was done mostly by varying the critical stress before damaging, σ_c for DCB and τ_c for ENF.

Results for the DCB peel critical stress sensitivity is shown in Figure 9 where experimental and numerical force-displacements curves are plotted. All DCB specimens had the same initial crack size. For DCB models, it is clear that a small critical stress of 2 MPa represents well the experimental behaviour, with a progressive damaging that starts early in the tests. For ENF models, four configurations were used based on the standard, with four different initial crack sizes. Numerical results, with dots, represent well the behaviour of the tests. In the tests, there was a smaller slope at the starts from the testing set-up that induced some lateral offset but passed 0.5 mm displacement, the global stiffnesses of both numerical and experimental curves coincide. The calibration of the critical shear stress was done based on the failure load at one configuration and tested on the other three ones. It showed failure load difference between numerical and experimental below 5% for all configurations.

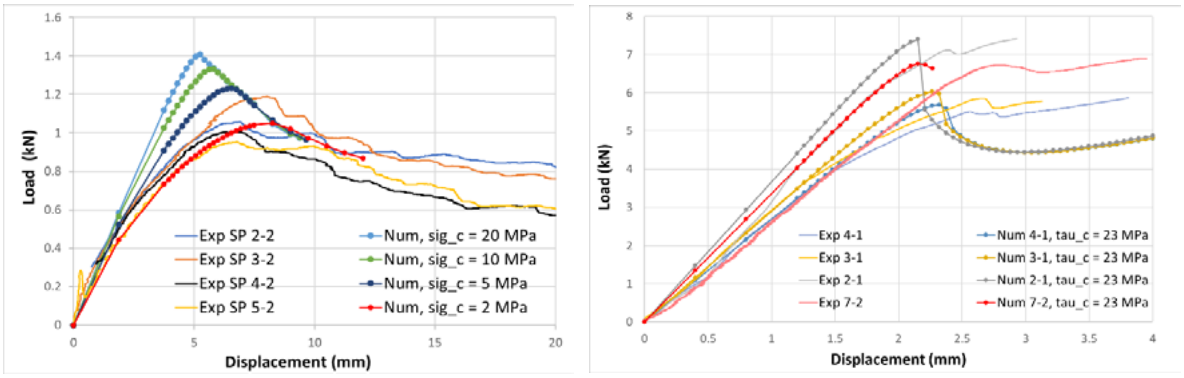


Figure 9. Comparison of numerical and experimental force-displacement curves for DCB (left) and ENF (right) at $\tau_c = 23$ MPa

The coupling parameter was also calibrated from MMB tests using inverse method and the final cohesive parameters are reported in Table 1.

Table 1. Resulting cohesive parameters from EI specimens

	Critical ERR (kJ/m^2)	*Critical stress* (MPa)	*Stiffness* (MPa/mm)	*Coupling parameter*
Mode I	1.74	2	1 000	0.6
Mode II	1.46	23	158 000	

3.2. Results on large scale specimens

For tensile and bending models, there was a competition between the two cohesive layer positions, as was observed during experiments where the failure occurred between the steel and first GFRP ply but also between the first two GFRP plies. The first cohesive elements to be damaged and reaching failure were those below the introduction of 0° UD CFRP plies in the patch.

Detailed results concerning the failure loads of the long scarf specimen in tensile loading are presented in Table 2. It can be seen that the failure loads for both cohesive layer position is quite close but failure would first occur at the interface between the first two GFRP plies for this configuration.

Table 2: Failure loads of tensile tests on long scarf specimens at both cohesive interfaces for different mesh sizes

Interface 1st GFRP ply/2nd GFRP ply			
Mesh size (mm)	*Failure load* (kN)	*Difference compared to finest mesh*	*Difference compared to experiments*
1	821	+0.3%	+4.2%
0.5	**818**		**+3.8%**

Interface steel/1st GFRP ply			
Mesh size (mm)	*Failure load* (kN)	*Difference compared to finest mesh*	*Difference compared to experiments*
2	857	+2.9%	+8.6%
1	828	+0.5%	+5.1%
0.5	832		+5.6%

Results of all configurations are summed up in the Table 3. They correspond to the lowest failure load of the 2 different cohesive element layer position. It can be seen that the difference with experimental results is below 25% in all cases. The behaviour in tensile loading, which is the main global loading on FPSO main deck, is also better represented in the models compared to bending loading.

Table 3. Comparison of numerical and experimental failure loads for all 4 configurations

Numerical and experimental failure loads comparison				
	Tensile loading		*Bending load*	
	Long scarf	*Short scarf*	*Long scarf*	*Short scarf*
Experimental (kN)	787	489	30	34
Numerical (kN)	818	406	37	27
Difference	+4%	-17%	+24%	-21%

4. Conclusions

The methodology presented in the paper with the newly designed equivalent interface specimens allowed to predict the failure loads of composite patch repair of corroded steel plates. The approach is based on fracture mechanics and the use of cohesive elements. The equivalent interface specimen is a non-standard symmetric specimen made of steel substrate and several composite plies, representative of the composite patch where failure occurred. This specimen was used in toughness tests to determine cohesive laws in mode I, mode II and in coupled mode I+II with an inverse method to fit numerical and experimental force-displacement curves. These laws were then input in the large specimens' model with composite patch on steel substrate. While methods using stress criteria or cohesive laws from standard specimens (steel/steel or GFRP/GFRP substrates) gave failure loads 50% above the experimental values, cohesive elements with equivalent interface laws resulted in smaller differences with experiments. For the tensile loading, the loading type most encountered for FPSO repair, the difference between numerical and experimental failure loads was below 20% for two different composite patch geometries.

The methodology to assess the strength of composite repair on steel structures was successfully applied for this design. To complete the design assessment methodology, durability of such repairs should be the subject of future work.

Acknowledgments

This work was carried out in the project JIP Strength Bond Offshore initiated by Bureau Veritas in 2019 and completed in 2023. The authors wish to acknowledge the partners of this project for their support: Bureau Veritas, TotalEnergies, Petrobras, Naval Group, Siemens, InfraCore Company and ColdPad.

References

[1] Q. Sourisseau, E. Lepretre, S. Chataigner, X. Chapeleau, M. Deydier and S. Paboeuf. A new adhesively bonded composite repair for offshore steel structures: strength assessment and fatigue. In *11th International conference on FRP composites in civil engineering, CICE,* 2023

[2] L.F.M Da Silva, P.J.C Das Neves, R.D. Adams and J.K. Spelt. Analytical models of adhesively bonded joints-Part I: Literature survey. *International Journal of Adhesion and adhesives*, Volume 29, Issue 3, pages 319-330, 2009.

[3] M. Bruyneel, J.P. Delsemme, A.C. Goupil, P. Jetteur, C. Lequesne, T. Naito and Y. Urushiyama. Damage modeling of laminated composites: Validation of the inter-laminar damage model of Samcef at the coupon level for UD plies. In *16th European conference on composite materials, ECCM16,* 2014.

[4] M. Deydier, S. Paboeuf and Q. Sourisseau. Application of cohesive elements on large bonded steel patch specimens, based on cohesive law calibrated with standard tests. In *International conference on Durability, Maintenance and Repair of Structures, DRMS,* 2023.

[5] Q. Sourisseau. Development of a robust methodology for the design assessment of bonded reinforcements on steel structures: Use of cohesive zone model and distributed optical fiber for characterization. *Engineering Sciences, PhD Thesis*, 2022.

[6] ASTM. *D5528 Standard Test Method for Mode I Interlaminar Fracture Toughness of Unidirectional Fiber-Reinforced Polymer Matrix Composites*, November 2013.

[7] ASTM. *D7905 Standard Test Method for Determination of the Mode II Interlaminar Fracture Toughness of Unidirectional Fiber-Reinforced Polymer Matrix Composites*, October 2014.

[8] ASTM. *D6671 Standard Test Method for Mixed Mode I-Mode II Interlaminar Fracture Toughness of Unidirectional Fiber Reinforced Polymer Matrix Composites*, April 2019.

[9] O. Allix and P. Ladevèze. Interlaminar interface modelling for the prediction of delamination. *Composite Structures*, 22:235-242, 1992.

[10] Bureau Veritas. *NR546 Hull in composite, plywood and high-density polyethylene materials*, November 2022.

THERMO-OXIDATION AGING OF EPOXY POLYMER UNDER HIGH-SPEED AIR FLOW

Aurélien Doriat[1], Marco Gigliotti[1], Marianne Beringhier[1], Gildas Lalizel[1], Eva Dorignac[1], Patrick Berterretche[1], Matteo Minvervino[2].

[1]Institut Pprime, CNRS, ISAE-ENSMA, Université de Poitiers, 1, Avenue Clément Ader, BP40109, 86961, Chasseneuil Futuroscope, France
Email: aurelien.doriat @ensma.fr
[2]Safran Aircraft Engine – Safran Group, Rond point Rene Ravaud-Reau, 77550, Moissy Cramayel Cedex, France

Keywords: Thermo-oxidation, Epoxy, Experimental work, Environmental aging

Abstract
Carbon fiber-reinforced epoxy composites are used in warm aero-engine parts to reduce weight and allow for more complex and efficient shapes. In these parts, the surrounding aero-thermal environment may promote high temperatures (over 100°C in an aircraft engine) leading to thermo-oxidation phrenomena. Thermo-oxidation may promote material properties change and embrittlement, leading to material degradation. Nevertheless, the laboratory aging studies have been carried out in oven only (in atmospheric condition or under oxygen pressure), but the parts in real conditions are exposed to temperature but also to air flow. The aim of this article is to understand the effect of the airflow and the influence of the aero-thermal boundary conditions on thermo-oxidative aging of the materials. As a first step, the polymer matrix was studied by comparing oven and wind tunnel aged samples. The wind tunnel aged sample showed faster degradation when aged in the wind tunnel which is mainly due to the temperature and pressure field in the flow.

1. Introduction

Composites, including carbon fiber-reinforced epoxy composites, have a multitude of applications in fields such as sports (sailing, automotive sports, and cycling) and transportation (cars, helicopters, and aircraft). These applications are often subjected to harsh conditions, necessitating the control of polymer aging. Humidity, ultraviolet radiation, and high temperatures can lead to thermo-oxidation, which can result in polymer matrix degradation. This study will investigate thermo-oxidation of epoxy polymer materials at high temperature.

Depending on the environment, samples can be exposed to different range of temperature. The degradation rate is proportional to the chemical kinetics which basicly follow an Arrhenius law with the temperature until the appartition of the first craks. The thermo-oxidation is faster close to the glassy transition temperature [1] [2] [3]. Temperature is also used as an acceleration factor to reduce the duration of test, nevertheless, at low or high temperature other phenomenom can occur such as physical aging, humidity aging (low temperature) or reticulation [4]. An other important parameter is the oxygen pressure. This parameter is widely used to accelerate the test as the oxidation rate is linked to the oxygen quantity available at the interface [3] [5] [6]. The chemical reactions are faster as more oxygen can react inside the polymer.

Thermo-oxidation results in a change in the chemical bonds (and thus chemical functional groups), which ultimately leads to yellowing in all polymers [7] [8]. The chemical changes also resulted in mechanical changes. The competition between chain scission and crosslinking outcomes in a modification of the glass transition temperature (and other phase transitions) [9] [10] [11]. Consequently, the polymer becomes harder and the modulus of elasticity increases [10] [2] [11]. The

polymer embrittlement alters the failure properties [12]. Furthermore, some decohesion between fibers and the polymer matrix can affect the failure properties even more.
Temperature and pressure are the most important factors to control the oxidation rate. In real conditions, specially in an aircraft, the composite parts are exposed to high temperature, variable pressure but also to an airflow. The effect of the airflow is still unknown whereas the boundary layer can increase the friction coefficient and mass transfer du to the velocity gradient near the wall. In order to understand the effect of airflow, this study will focus on the aging of the polymer matrix. The application to composites will be considered in a subsequent study. This work aims to give first answer on the effect of airflow on the thermo-oxidation of polymer.
Two set of samples will be examined. The first one will be aged in an oven under atmospheric condition and used as our reference. The second set will be aged inside a wind tunnel to reproduce the airflow aging condition.
To characterize the thermo-oxidation, mechanical property measurement will be done. The indentation technique has been demonstrated to be an effective method for characterizing thermo-oxidation processes, and linked to chemical modifications [13] [14] [15] [16].
The first part of the article will present the experiment and focus on the wind tunnel used to age the sample. Then, the indentation measurements on both samples aged in an oven and a wind tunnel will be shown. Finally, the effect of the temperature and the airflow on the aging will be discussed.

2. Experimental set-up and method

2.1. Materials and aging

In this study, an aromatic diamine epoxy resin was employed, exhibiting chemical similarities to both the DGEBF-CAF resin and the PR520 resin manufactured by Syensqo, which are commonly utilized in the aerospace industry [17] [18]. Samples, provided by SAFRAN Aircraft Engine company, were received in the form of 5mm thick rectangular blocks, with the exposed surface area measuring 8*8mm in a square configuration.
Reference samples were exposed to atmospheric air conditions at 150°C in an oven for durations ranging from 20h to 80h. The ventilation oven is set at a level where the oxygen is renewed and no flow is created around the sample.

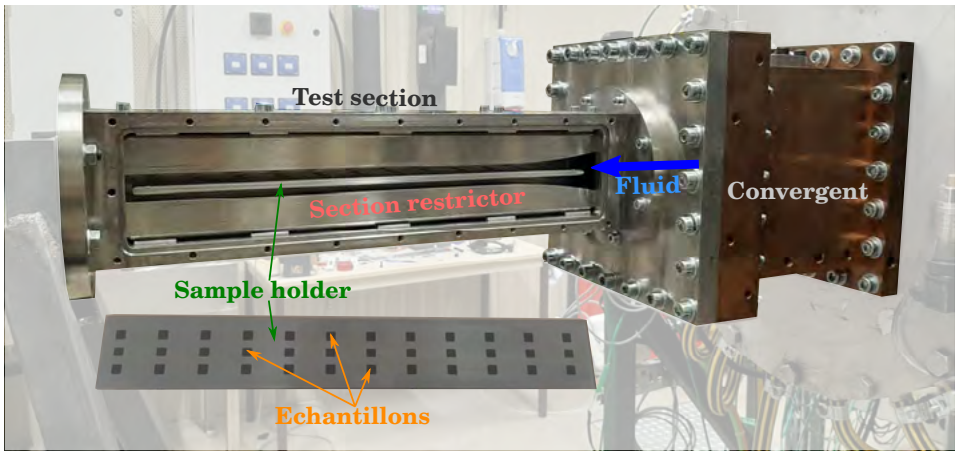


Figure 1. BATH wind tunnel geometry and samples positions.

The other set of samples have been aged in the BATH (Banc AéroTHermique) wind tunnel (for the detail of the bench, see [19]). A test section has been designed to put the sample inside the airflow (same aerothermal condition on each side) and avoid temperature gradient inside a sample. Fig.1 shows the geometry of the wind tunnel with the convergent shape until a constant reduced section to accelerate the flow until Mach 1. The samples are positioned inside the flow in a mount. This set-up avoid temperature gradient inside the sample. Both face of the samples are aged with the same airflow conditions.
Nevertheless, the samples undergoes different aerothermal conditions. The flow rate and the total temperature (flow temperature at static conditions) are the two regulated parameters inside the wind

tunnel: the pressure and temperature field is then a function of the flow and the geometry. It is not possible to adjust the temperature and pressure for each sample.
Fig.2(a) shows the temperature and Fig.2(b) the pressure and mach number for each samples estimated by numerical simulation (RANS simulation, StarCCM+). The increase of the Mach number in the constant test section is due to the thickening of the boundary layer conjugated with the decrease of the static pressure. The constant total pressure shows the lack of shock inside the canal where as the slighty decrease at the end is due to viscious friction.

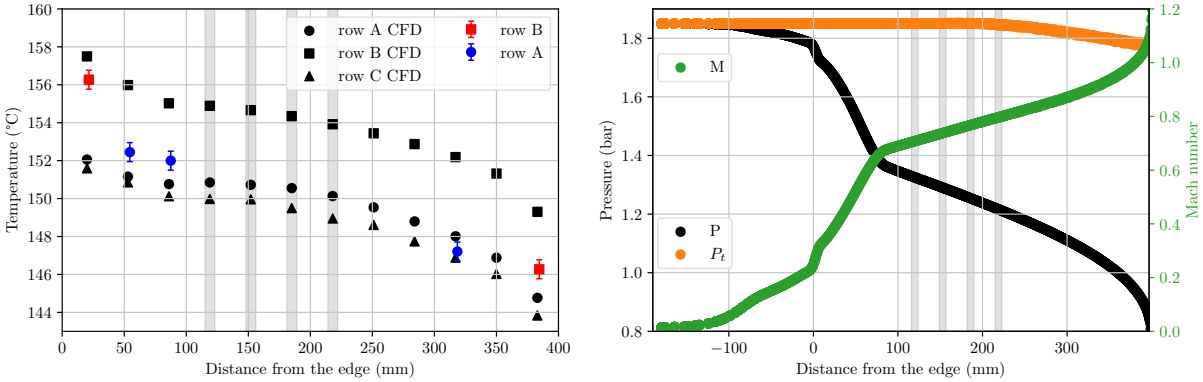


Figure 2. (a) Temperature insidethe samples in the wind tunnel. The black dots are from numerical simulation and colored dot from measurement which validate the simulation. (b) Mach number M, static pressure P and total pressure P_t profiles inside the wind tunnel. In both figures, the gray vertical lines shows the position of the samples.

The temperature inside the sample is not constant because the wind tunnel is inside a room at ambient temperature. The test section wall promotes thermal losses by convection with the environment and therefore conductive heat transfer inside the sample. The decrease of temperature between samples are due to the thickening of the boundary layer and therefore the reduction of the heat transfer coefficient coupled to the conductive losses. Nevertheless, only 2°C gap is noticed between studied samples. The simulation tends to overestimate the measurement between 1°C to 2°C. Small temperature (2°C to 5°C) deviation is noticed between oven and wind tunnel aging.

2.2. Indentation test

Nanoindentation analyses were conducted using the NanoTest Vantage instrument by MicroMaterials. Sample preparation involved halving the samples, put side by side them with an elastic band, and applying a coating (image of the sample Fig.3). This preparation strategy was employed to mitigate edge effects during indentation close to the interface, achieved by applying resin coating on the opposing side of the interface. The measurement surface underwent polishing to minimize roughness to levels below 10nm, thereby mitigating the influence of surface irregularities on nanoindentation measurements (refer to [20] [17]) for comprehensive details on sample preparation).

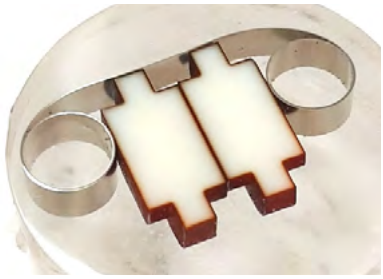


Figure 3 : Aged sample cut and coated.

Nanoindentation experiments utilized a spherical indenter with a radius of 5µm. The tests were conducted with force control, reaching a maximum force of 5mN over a 20s duration due to the

viscoelastic properties of the polymer. The velocity during both the loading and unloading phases was set at 0.5µm/s. Data collected during the unloading phase were employed to calculate the reduced elastic indentation modulus (E_{red}) using the method outlined by Oliver and Phar [21]:

$$E_{red} = \frac{\sqrt{\pi}\frac{dF}{dh}}{2\,\beta\sqrt{A_p}} \quad (1)$$

with $\frac{dF}{dh}$ the slope at the beginning of unload, A_p surface contact between the indenter and the sample and β, the indenter geometrical parameter ($\beta = 1$ for revolution indenter). Based on the properties of the indenter, the elastic indentation modulus *EIT* is estimated (Eq.2) :

$$\frac{1}{E_{red}} = \frac{1-\nu_{ind}^2}{E_{ind}} + \frac{1-\nu_{poly}^2}{EIT} \quad (2)$$

with $E_{ind} = 1141GPa$ and $\nu_{ind} = 0.07$ the elastic modulus and Poisson coefficient of the diamond indenter and $\nu_{poly} = 0.4$ the Poisson coefficient of the polymer (value from technical data).
The elastic indentation modulus profile of the oxidized layer was characterized at intervals of 5µm from the sample edge, with measurements taken every 15µm. This experimental profiling was repeated 10 times at intervals of 50µm. Each profile presented in this study represents the average of 10 profiles. Vertical error bars denote one standard deviation, with measurement uncertainty being at least 10 times lower than the variation observed between measurements.

3. Results

Samples aged 20h, 40h, 60h and 80h in oven and in BATH wind tunnel are compared to understand the effect of the airflow on thermo-oxidation aging. During the aging of thick samples, an oxidized layer appears because the chemical reaction are faster then oxygen diffusion, therefore, the oxygen affects the bulk more lately. Inside the oxidized layer, a mechanical property gradient can be measured. The indentation shows an increase in the elastic modulus due to the stiffening of the sample.

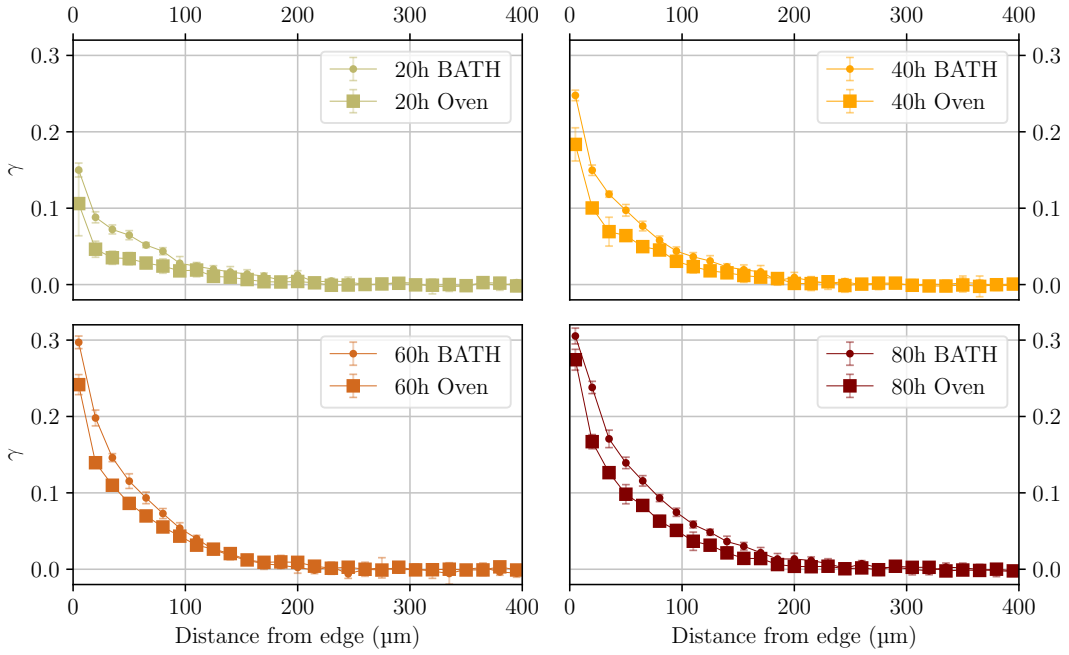


Figure 4. Adimensional indentation modulus profiles (γ, Eq.3) for samples aged during four times (20h, 40h, 60h, 80h) in the oven and in the wind tunnel (BATH).

Fig.4 shows the indentation modulus for samples aged the same duration in oven or in the wind tunnel. The parameter γ is plotted to avoid the dependency of the materials :

$$\gamma = \frac{EIT}{EIT_0} - 1 \quad (3)$$

with EIT_0 the indentation modulus of the virgin sample (it is estimated by averaging the 5 last measurements of the profiles).

For all exposure duration, the sample aged in the wind tunnel shows a higher value of indentation modulus which means a higher degradation and so a more oxidized layer. It can be interesting to extract a modulus increase factor Γ from each profile since each sample has been aged in a different position due to the experimental set-up. The modulus increase factor Γ is the ratio of the indentation modulus for the sample aged in the BATH wind tunel γ_{BATH} over the sample aged in the oven γ_{oven} : $\Gamma = \frac{\gamma_{BATH}}{\gamma_{oven}}$.

The modulus increase factor Γ is the average of each values computed from the experimental data shown in Fig.4 until a depth of 100µm.

Tab.1 summarises the modulus increase factor Γ and the aerothermal conditions enconters by the sample for four different aging times.

Exposure time (h)	Γ	T (°C)	P (bar)
20	1.78 ± 0.20	155,0	1,29
40	1.47 ± 0.13	154,3	1,25
60	1.32 ± 0.06	155,3	1,32
80	1.38 ± 0.11	154,7	1,21

Table 1. Experimental estimation of the modulus increase factor Γ from the samples aged in the wind tunnel and aerothermal aging conditions (temperature and pressure).

The effect of temperature, pressure and airflow will be discussed in the next section to explain this fater aging.

4. Discussion

The accelerated aging observed in this study may be attributed to the temperature, pressure, or airflow. Previous results (Fig.2(a)) have demonstrated slight differences in temperature-induced aging between oven and wind tunnel conditions. A time-temperature equivalence law will be employed to eliminate the influence of temperature on the results [22] [4]. For two aging temperatures T_A and T_B and aging durations t_{T_A} and t_{T_B}, the equivalence is given by Eq.4 :

$$\alpha_{\boldsymbol{T}}(T_A)t_{T_A} = \alpha_{\boldsymbol{T}}(T_B)t_{T_B} \quad (4)$$

with $\alpha_{\boldsymbol{T}}(T)$ the accelerating factor due to the temperature (Eq.5) :

$$\alpha_{\boldsymbol{T}}(T) = \exp\left(-\frac{E_a}{R}\left(\frac{1}{T} - \frac{1}{T_{ref}}\right)\right) \quad (5)$$

$E_a = 1.63\ 10^4 J\ mol^{-1}$ the activation energy, $R = 8.31 J\ mol^{-1}K^{-1}$ the universal gas constant, T and $T_{ref} = 126°C$ two temperatures.

It is then possible to calculate the time that should be considered to compensate the temperature difference between a sample aged in oven at 150°C and a sample in BATH wind tunnel. The temperature is not precisely known as explain with Fig.2(a). We considered the sample exposed at the higher at 155°C and at the lower at 152°C to take into count the uncertainy between reality and fluid simulation. By using Eq.4, it is possible to calculate the time that the sample should be exposed to compensate the temperature difference. Eq.5 is used to calculate the accelerating factor α_T value at the different temperatures. For example, the 40h aged sample at BATH should be compared to the sample aged between $\frac{\alpha_{\boldsymbol{T}}(152)}{\alpha_{\boldsymbol{T}}(150)} t_{152} = \mathrm{t}_{150} = 1.2 \times 40h = 48\mathrm{h}$ and $\frac{\alpha_{\boldsymbol{T}}(155)}{\alpha_{\boldsymbol{T}}(150)} t_{155} = \mathrm{t}_{150} = 1.5 \times 40h = 60\mathrm{h}$ in the oven at 150°C. In other words, the sample aged 48h at 150°C is equivalent to the sample aged 40h at 152°C.

The corresponding indentation modulus can be estimated by interpolating normalized indentation modulus γ over the time for each distance from the edge. Then, the equivalent indentation modulus is between $\gamma(t = 48h, x = 5\mu m) = 0.22$ and $\gamma(t = 60h, x = 5\mu m) = 0.26$ for the measurement at a

distance of 5 µm from the edge. For this example, the resulting modulus increase factor Γ_T, which traduce the variation of the indentation modulus whithout the temperature influence is between 0.96 and 1.13. This factor traduces if in addition of the temperature, there is still a faster oxidation. If the factor Γ_T is lower or equal to 1, the temperature is the only accelerating factor. If the factor is greater than 1, there is another cause of the acceleration.
This approach is employed for all the samples presented in Fig.4 to eliminate the influence of temperature. The calculated value of the modulus increase factor Γ_T (without temperature effect) is then used to assess whether there is a discernible difference in the rate of aging between the samples aged in the wind tunnel and those aged in the oven, once the temperature offset has been accounted for.
As illustrated in Tab.2, the modulus increase factor exceeds 1 in most of the case. It is also important to note that the temperature difference is not the only factor responsible for this acceleration.

Exposure time (h)	$\Gamma_{T=155°C}$	$\Gamma_{T=152°C}$	P (bar)
20	0.76	0.95	1,29
40	0.96	1.12	1,25
60	0.99	1.13	1,32
80	0.96	1.13	1,21

Table 2. Experimental estimation of the modulus increase factor Γ_T from the samples aged in the wind tunnel with corrected temperature offset and aerothermal aging conditions (pressure).

The pressure at the interface may also be a contributing factor in this aging acceleration. The more oxygen at the interface, the more oxygen is thus available for the chemical reaction and the easier it is for oxygen to go inside the sample by diffusion. The oxidized layer of the sample aged in the wind tunnel exhibits a greater modulus increase with more oxygen at the interface than the oxidized layer from sample aged in the oven.

The last parameter to be considered is the mass transfer due to the airflow. Due to the viscosity of the fluid, boundary layers are created close to the wall, exhibiting velocity, temperature, and mass gradients. The mass gradient induces a higher mass transfer exchange within the sample, analogous to heat transfer with the temperature gradient. The current study is unable to distinguish the effect of pressure from the boundary layer effect. However, further investigations are ongoing to identify the oxygen boundary condition and distinguish these two parameters.
Ultimately, the aging temperature difference between the oven and the wind tunnel represents a significant contributing factor to the acceleration of the aging process but it is not the only one. Additionally, the static pressure in BATH is higher than in the oven due to the link between airflow speed and static pressure, as well as the influence of convective mass transfer on accelerated aging. Further investigations are underway to ascertain the role of pressure and mass transfer at the interface. In real operating environments, such as turbine fan blades, local pressure and temperature may vary due to the slowing down of the flow and its subsequent understanding. This could explain the faster aging observed in laboratory tests than in real operating environments.

5. Conclusions

This article reports on a study of thermal oxidation aging in a realistic environment for an aircraft engine application. Both oven and wind tunnel aging tests were conducted. A test section was designed for wind tunnel aging with the objective of achieving the most controlled aerothermal conditions possible. These conditions were characterized in terms of temperature and pressure, as these two parameters exert the most influence on thermo-oxidative aging. The results demonstrated a faster rate of aging compared to the results obtained from oven tests.
To compare samples exposed in the oven and in the wind tunnel, indentation modulus measurements were made in the oxidized layer. The gradient of mechanical properties in the sample provides an indication of the degree of aging. The results demonstrated that the samples subjected to wind tunnel aging exhibited accelerated aging. This is primarily attributable to the slightly elevated temperature in

the wind tunnel relative to that in the oven. Furthermore, in the context of fluid flow, pressure and convective mass transfer have been identified as factors that accelerate the aging process.
Given the current understanding of the aging behavior of the polymer, it is crucial to ascertain whether the composite exhibits similar characteristics and to determine whether the carbon fibers influence oxidation. At present, tests on composite samples are being conducted.

Acknowledgments
This work was supported by the French government program "Investissements d'Avenir" (EUR INTREE, reference ANR-18-EURE-0010). This work was supported by Safran Aircraft Engine. This work pertains to the French government program "Investissements d'Avenir" (LABEX INTERACTIFS, reference ANR-11-LABX-0017-01). The authors thank SAFRAN Aircraft Engines for providing the polymer material.

References

[1] B. Dao, J. Hodgkin, J. Krstina, J. Mardel and W. Tian, "Accelerated aging versus realistic aging in aerospace composite materials. II. Chemistry of thermal aging in a structural composite," *Journal of applied polymer science,* vol. 102, p. 3221–3232, 2006.

[2] G. A. Schoeppner, G. P. Tandon and K. V. Pochiraju, "Predicting thermooxidative degradation and performance of high-temperature polymer matrix composites," in *Multiscale modeling and simulation of composite materials and structures*, Springer, 2008, p. 359–462.

[3] T. K. Tsotsis, S. Keller, K. Lee, J. Bardis and J. Bish, "Aging of polymeric composite specimens for 5000 hours at elevated pressure and temperature," *Composites Science and Technology,* vol. 61, p. 75–86, 2001.

[4] M. C. Celina, "Review of polymer oxidation and its relationship with materials performance and lifetime prediction," *Polymer Degradation and Stability,* vol. 98, p. 2419–2429, 2013.

[5] Y. Kobayashi and S. Kobayashi, "Accelerated thermo-oxidative aging for carbon fiber reinforced polycyanate under high pressure atmosphere," *Advanced Composite Materials,* vol. 26, p. 451–464, 2017.

[6] G. P. Tandon, K. Pochiraju, P. W. R. Beaumont and C. H. Zweben, "7.8 Environmental Durability of Polymer Matrix Composites," in *Comprehensive Composite Materials II*, Elsevier, 2018, p. 131–158.

[7] J. L. Down, "The Yellowing of Epoxy Resin Adhesives: Report on High-Intensity Light Aging," *Studies in Conservation,* vol. 31, p. 159–170, 1986.

[8] C. Wu, B. C. Meng, L.-h. Tam and L. He, "Yellowing mechanisms of epoxy and vinyl ester resins under thermal, UV and natural aging conditions and protection methods," *Polymer Testing,* vol. 114, p. 107708, 2022.

[9] M. Celina, J. Wise, D. K. Ottesen, K. T. Gillen and R. L. Clough, "Correlation of chemical and mechanical property changes during oxidative degradation of neoprene," *Polymer Degradation and Stability,* vol. 68, p. 171–184, 2000.

[10] N. Rasoldier, X. Colin, J. Verdu, M. Bocquet, L. Olivier, L. Chocinski-Arnault and M. C. Lafarie-Frenot, "Model systems for thermo-oxidised epoxy composite matrices," *Composites Part A: Applied Science and Manufacturing,* vol. 39, p. 1522–1529, 2008.

[11] S. Terekhina, M. Mille, B. Fayolle and X. Colin, "Oxidation induced changes in viscoelastic properties of a thermostable epoxy matrix," *Polymer Science Series A,* vol. 55, p. 614–624, 2013.

[12] B. Fayolle, X. Colin, L. Audouin and J. Verdu, "Mechanism of degradation induced embrittlement in polyethylene," *Polymer Degradation and Stability,* vol. 92, p. 231–238, 2007.

[13] G. Mertz, F. Hassouna, P. Leclère, A. Dahoun, V. Toniazzo and D. Ruch, "Correlation between (nano)-mechanical and chemical changes occurring during photo-oxidation of filled vulcanised

styrene butadiene rubber (SBR)," *Polymer Degradation and Stability,* vol. 97, p. 2195–2201, 2012.

[14] L. Olivier, N. Q. Ho, J. C. Grandidier and M. C. Lafarie-Frenot, "Characterization by ultra-micro indentation of an oxidized epoxy polymer: Correlation with the predictions of a kinetic model of oxidation," *Polymer Degradation and Stability,* vol. 93, p. 489–497, 2008.

[15] J.-F. Larché, P.-O. Bussière, S. Thérias and J.-L. Gardette, "Photooxidation of polymers: Relating material properties to chemical changes," *Polymer Degradation and Stability,* vol. 97, p. 25–34, 2012.

[16] M. Gigliotti, M. Minervino, M. C. Lafarie-Frenot and J. C. Grandidier, "Effect of Thermo-oxidation on the local mechanical behaviour of epoxy polymer materials for high temperature applications," *Mechanics of Materials,* vol. 101, p. 118–135, 2016.

[17] M. Pecora, O. Smerdova and M. Gigliotti, "In-situ characterization of the local mechanical behaviour of polymer matrix in 3D carbon fiber composites by cyclic indentation test," *Composite Structures,* vol. 244, p. 112268, 2020.

[18] P. B. Stickler and M. Ramulu, "Investigation of mechanical behavior of transverse stitched T-joints with PR520 resin in flexure and tension," *Composite Structures,* vol. 52, p. 307–314, 2001.

[19] A. Subramanian, E. Dorignac and G. Lalizel, "Contribution to Aerothermal Study of a Film Cooling Geometric Design using ZnO Phosphorescence Thermography and Numerical Simulations," 2022.

[20] M. Minervino, "Effets de la thermo-oxydation sur le comportement mécanique de matériaux composites pour applications aéronautiques," 2013.

[21] W. C. Oliver and G. M. Pharr, *Improved technique for determining hardness and elastic modulus using load and displacement sensing indentation experiments,* vol. 7, 1992, p. 1564–1580.

NUMERICAL MODELING OF THE IN-PLANE SHEAR BEHAVIOR OF WOVEN THERMOPLASTIC COMPOSITES AT HIGH TEMPERATURE

Ramak Hossein Abadi[1*], Kalliopi-Artemi Kalteremidou[1] and Danny Van Hemelrijck[1]

[1] Department of Mechanics of Materials and Constructions (MeMC), Vrije Universiteit Brussel, Brussels, Belgium
[*]Email: ramak.hossein.abadi@vub.be

Keywords: Thermoplastic composite, High temperature, Finite element model, Bias extension test

Abstract
This paper investigates the in-plane shear behavior of flax fiber-reinforced polypropylene composites at a high temperature by linking numerical modeling tools with experimental results. For this purpose, the bias-extension experiment is performed on composite specimens at 160 °C. The study employs the Digital Image Correlation (DIC) technique to measure local deformations and strains on the specimen's surface during the test. Additionally, the Finite Element (FE) method is used to simulate the experiment. A hypo-elastic material model is implemented into the Finite Element model through a VUMAT subroutine to represent the material's in-plane shear behavior. The study compares the force-shear angle variations derived from the test and the numerical model.

1. Introduction

The mechanical behavior of fiber rainforced thermoplastic composites, particularly their response to in-plane shear deformation, is an important area of investigation for optimizing manufacturing processes like thermoforming. In-plane shear, characterized by the rotation of fibers within the composite structure, influences the material's overall performance [1]. One commonly employed method to study the in-plane shear behavior of composites is the bias-extension experiment [2]. This experiment involves subjecting composite samples to tensile loading, with the fibers being initially oriented at ±45 degrees with respect to the loading direction. Based on the Pin-Jointed Net (PJN) theory, a key requirement of this test is using an initial gauge length H that is at least two times larger than the specimen width W [2]. In addition, the PJN model assumes that fibers are inextensible and that there is no slip between them. These criteria ensure creating a pure shear region C (Figure 1) during the loading of the specimen. In such a condition, the existing four triangular regions B have half the shear value of region C. Lastly, two undeformed triangular regions A with zero shear values also exist, as shown in Figure 1.

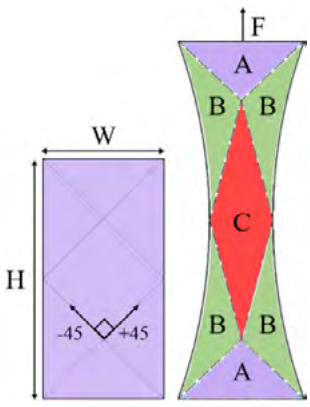


Figure 1. Pin-jointed net theory.

Thermoforming involves heating a thermoplastic composite sheet and shaping it into a mold to produce complex geometries. The material experiences various deformation modes during this process, with in-plane shear being the dominant one. Numerical simulations can be used to simulate and optimize the process parameters [3, 4]. Capturing the complex behavior of the composites during the thermoforming process is an essential step in simulating the process, which can be done by developing a constitutive model. By accurately characterizing the forming behavior of composite materials, manufacturers can tailor the thermoforming processes to optimize part quality, minimize defects, and enhance mechanical properties [5].

This paper investigates the in-plane shear behavior of flax fiber-reinforced polypropylene composites. For this purpose, first the bias-extension experiment was performed at 160 °C. The Digital Image Correlation (DIC) technique was continuously measuring the local deformations on the specimen's surface. This method provides full-field displacement and strain distributions on the specimen's surface as it deforms [6]. The Finite Element (FE) method was used in the next step to develop a numerical model of the bias extension experiment. This study examines the capability of a hypo-elastic shear model to represent the material behavior by developing a VUMAT subroutine. Based on the results, the suggested material model can be employed to simulate the samples' in-plane shear behavior during thermoforming.

2. Material and Methods

The tested samples were cut from a 4-ply spread tow woven composite laminate, made from polypropylene matrix and reinforced with flax fibers (40% fiber volume fraction), with an average thickness of 2.4 millimeters. The gauge section of the specimens was coated with two thin layers of white paint, followed by spraying a single layer of black paint to generate a speckle pattern for the DIC measurements. Additionally, four white points were marked on the specimen's surface (Figure 2 (left)) to measure the shear angle in zone C using the marker tracking method. An Instron universal testing machine with a TA Instruments climate chamber and a 10-kN load cell were used for the thermo-mechanical tests (Figure 2 (right)). During the experiments, the fibers were oriented at ±45 degrees with respect to the applied load, the climate chamber was set at 160 °C, and the displacement rate was 10 mm/min. The image acquisition frequency of the DIC measurements was 1 Hz. The experiment was repeated two times. In each test, a type-K thermocouple was connected to the sample to measure the temperature history. The measurements were logged using the 8000 Micro-Measurements data logger with a data sampling frequency of 1 Hz.

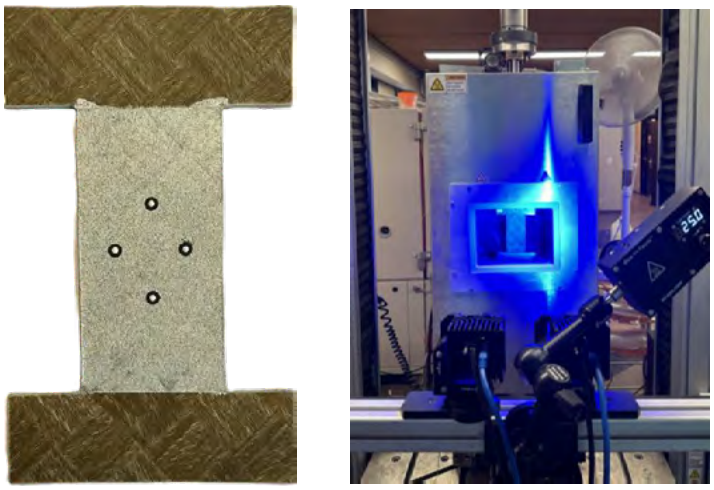


Figure 2. (left) Bias extension specimen, (right) clamped specimen inside the oven and DIC cameras.

3. Finite Element Model

A finite element model of the sample was developed in ABAQUS to investigate the in-plane shear behavior. A mesh sensitivity analysis was performed to ensure the solution is independent of the mesh size. Boundary conditions were defined so as to simulate the loading conditions at the top and the constraints at the bottom of the sample. A VUMAT subroutine has been introduced to the FE analysis to include a hypo-elastic material model into the composite's response [7]. The in-plane shear modulus constants, obtained from the force versus shear angle results, are incorporated in the VUMAT subroutine. The in-plane shear modulus in this simulation is given by (MPa):

$$G_{12}(\gamma) = 374.90\,\gamma^4 - 633.56\,\gamma^3 + 396.29\,\gamma^2 - 99.07\,\gamma + 9.96 \quad (1)$$

where γ represents the shear angle and defined as the angle between the two fiber directions during deformation. The model is compared with the experimental results by evaluating the obtained force-shear angle curves.

4. Results

An overview of the results obtained from both the experimental investigations and the finite element simulations is provided in this section. Figure 3 presents the average load-shear angle curve of the two specimens tested at 160 °C and at a 10 mm/min displacement rate. The results include the variation in the repeated tests using error bars. The initial load increase is due to the static friction between yarns and plies [8]. After that, the yarns are relatively free to rotate around their crossover points. Towards the end of the curve, at an approximate shear angle of 40° (identified as the locking angle), where the fibers come into contact and resist further deformation, a significant increase in the measured load is observed.

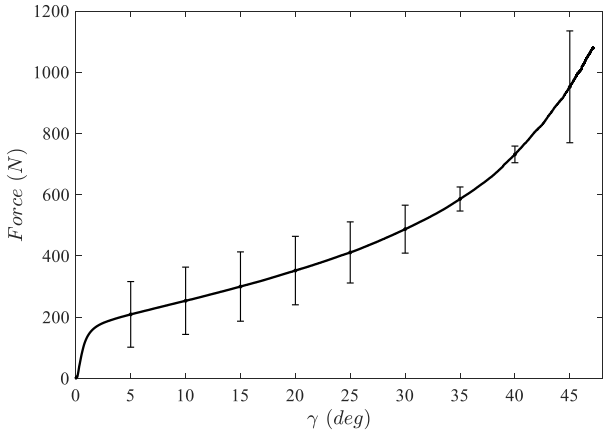


Figure 3. Average experimental force-shear angle curve with the corresponding variations.

Figure 4 shows the shear angle distribution obtained at 30 mm of displacement using the DIC method. As seen in this figure, the deformed shape matches well the predictions of the PJN theory. A pure shear zone is present at the center of the specimen. A gradient of deformation decreasing towards the four semi-shear triangular regions and two triangular regions that exhibit almost no shear are also evident.

Figure 5 illustrates a comparison between the load versus shear angle curves derived from the experimental data and the finite element simulation. The results indicate that the simulation underestimates the stiffness of the specimen, with the difference becoming more pronounced at higher shear angles. This difference reveals the need for further refinement of the finite element model to more accurately represent the in-plane shear mechanical behavior of the material at high temperatures.

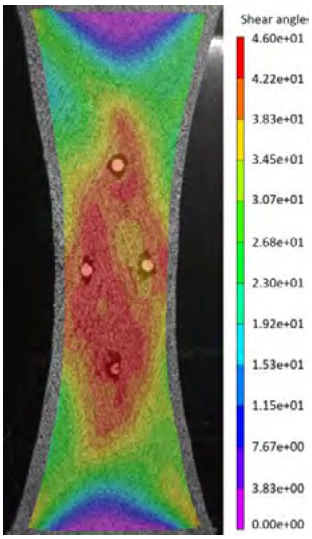


Figure 4. Shear angle distribution obtained by DIC at a displacement of 30 mm.

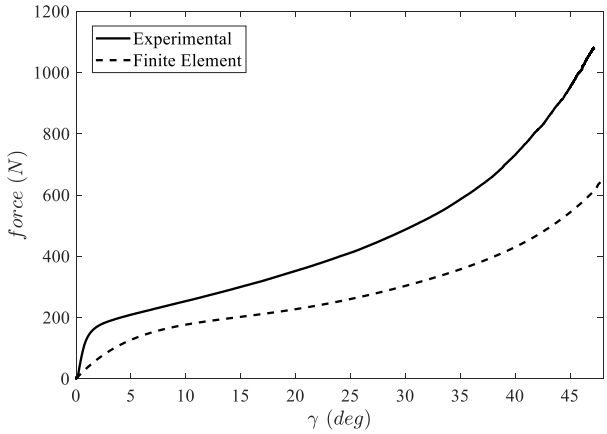


Figure 5. A comparison between the force-shear angle curves derived from the FE analysis and the experiments.

5. Conclusions

This paper investigates the in-plane shear behavior of flax fiber-reinforced polypropylene composites at high temperatures by linking numerical modeling tools with experimental results. The bias-extension experiment is used to investigate the behavior of a specimen at 160 °C and 10 mm/min displacement rate. The study applies the Digital Image Correlation (DIC) technique to observe local deformations and strains on the surface of the specimens. The FE method is used to simulate the tests, incorporating a hypo-elastic material model through a VUMAT user material subroutine. Based on the results, the comparison between the experimental and FE force-shear angle predictions shows that the finite element model underestimates the shear stress and predicts, hence, a lower shear stiffness. A possible reason for this miscalculation of the numerical model is that the reorientation of the fibers during the test is not taken into account [9]. Accordingly, the effect of the fiber reorientation will be examined in follow-up studies.

Acknowledgments

This publication was supported by the STOEMP project "Stamping of thermoplastic composite materials" and STOEMP 2 project "Stamping-overmoulding of thermoplastic composites" coordinated by Solvay and funded by Innoviris. The authors gratefully acknowledge W8SVR GmbH for providing the materials.

References

[1] M. Machado, M. Fischlschweiger and Z. Major. A rate-dependent non-orthogonal constitutive model for describing shear behaviour of woven reinforced thermoplastic composites. *Composites Part A: Applied Science and Manufacturing*, 80, 194-203, 2016.

[2] P. Boisse, N. Hamila, E. Guzman-Maldonado, A. Madeo, G. Hivet and F. Dell'Isola. The bias-extension test for the analysis of in-plane shear properties of textile composite reinforcements and prepregs: a review. *International Journal of Material Forming*, 10, 473-492, 2017.

[3] M. Limaye, SA. Pradeep, A. Kothari, S. Savla, A. Agha, S. Pilla, G. Li. Thermoforming process effects on structural performance of carbon fiber reinforced thermoplastic composite parts through a manufacturing to response pathway. *Composites Part B: Engineering*. 235, 109728, 2022.

[4] AJ. Thompson, JP. Belnoue, SR. Hallett. Modelling defect formation in textiles during the double diaphragm forming process. *Composites Part B: Engineering*. 202, 108357, 2020.

[5] M. Machado, L. Murenu, M. Fischlschweiger, Z. Major. Analysis of the thermomechanical shear behaviour of woven-reinforced thermoplastic-matrix composites during forming. *Composites Part A: Applied Science and Manufacturing*, 86, 39-48, 2016.

[6] MA. Sutton, JJ. Orteu, H. Schreier. Image correlation for shape, motion and deformation measurements: basic concepts, theory and applications. *Springer Science & Business Media*, 2009.

[7] M. Nasri, C. Garnier, F. Abbassi, AR. Labanieh, O. Dalverny and A. Zghal. Hybrid approach for woven fabric modelling based on discrete hypoelastic behaviour and experimental validation. *Composite Structures*. 209, 992-1004, 2019.

[8] T. Baumard, G. Menary, O. De Almeida, P. Martin, F. Schmidt, J. Bikard. Experimental characterization and modeling of the temperature and rate-dependent shear behaviour of powder-impregnated glass fiber/PA66 woven semipregs. *Composites Science and Technology*, 180, 23-32, 2019.

[9] A. Aridhi, M. Arfaoui, T. Mabrouki, N. Naouar, Y. Denis, M. Zarroug and P. Boisse. Textile composite structural analysis taking into account the forming process. *Composites Part B: Engineering*. 166, 773-84, 2019.

STATIC AND FATIGUE MULTI-AXIAL TRACTION/TORSION LOADING OF 3D REINFORCED COMPOSITE MATERIALS

A. Kobeissi[1], Z. Aboura[1], F. Rasselet[2], W. Harizi[1], and K. Khelil[1]

[1]Université de Technologie de Compiègne, Roberval (Mechanics, Energy and Electricity), Centre de Recherche Royallieu CS 60319, 60203 Compiègne Cedex, France
Email: alaa.kobeissi@utc.fr
[2]Département Mécanique des Matériaux et Composites, Safran Aircraft Engines, Site de Villaroche Rond-Point René Ravaud,Moissy Caramayel, France
Email: francois.rasselet@safrangroup.com

Keywords: 3D woven, Fatigue, Multi-axial, Traction/Torsion, Failure Envelop

Abstract

In this study, the failure analysis of 3D carbon fibre composite subjected to multiaxial traction/torsion (σ11/τ13) loadings is investigated. A rectangular specimen undergoes fatigue cyclic loading to understand how the material responds to such complex stress conditions. Various measurement techniques like stereo Digital Image Correlation (stereo-DIC), Acoustic Emission (AE), and in-situ microscopic observation track the material properties evolution after each cycle (N). Tests are conducted for different ratios of σ11/τ13. Furthermore, the damage mechanism, including its type and localization, is identified based on the material's meso-structure. The localization of damage in such specific areas of the specimen was attributed to both normal and shear stress distributions according to the numerical finite element model, rendering this observation more comprehensible.

1. Introduction

Over the past decade, three-dimensional (3D) composites have been gradually introduced into numerous applications, particularly in aeronautics. The incorporation of 3D weaving architectures into composite materials induces mechanical behavior and damage mechanisms that are entirely different from those of conventional unidirectional and bidirectional composites [1]. Thus, characterization methods, mechanical behavior, and damage mechanisms of two-dimensional composites cannot be directly extrapolated to 3D woven composites due to significant differences in their structure and behavior. Therefore, an effort is currently underway to understand the mechanical behavior of these materials. Most of these studies focus on quasi-static uniaxial loads, fatigue, and impacts, but very few have been conducted on multiaxial loading applied to 3D woven composites. Traditionally, material properties are determined using conventional uniaxial tests. However, these tests often inadequately represent the true material behavior, which is significantly influenced by the loading conditions experienced in real-world engineering applications. A more effective strategy for accurately characterizing mechanical behavior involves employing biaxial tests, which closely mimic the actual loading states encountered by composite structures. Among various biaxial testing methods, prominent ones include (i) proportional axial tensile and torsion tests conducted on tubular specimens [2], (ii) biaxial tensile tests utilizing cruciform specimens [3]. Despite the inherent complexities associated with specimen preparation and test setup, the application of these methods to composite materials has facilitated the determination of multi-axial combined in-plane tensile and in-plane shear stress failure envelopes.

In this study, the mechanical behavior of 3D woven composites subjected to tensile/torsional loading conditions is investigated. Initially, a description of the materials and equipment used is presented. Preliminary static tests are then discussed, establishing a damage threshold envelope. Based on this, fatigue tests are addressed, detailing the loading conditions and results obtained accompanied by analysis.

2. Material and equipment

The material under investigation consists of 3D woven intermediate modulus (IM) carbon fibers combined with epoxy resin. Rectangular specimens are cut from the thickness (plane 1,3) and equipped with aluminum grips (gage length of 220 mm, width of 38 mm, and thickness of 9 mm). Multi-axial tests, including monotonic and fatigue tests, are conducted using a hydraulic tension/torsion machine with a capacity of 100 kN in tension and 1000 Nm in torsion. The tests are followed by observations conducted using in-situ video microscopy, digital image correlation (DIC), and acoustic emission (AE). Figure 1 illustrates the material meso-structure and the equipment used for conducting the tests, providing a visual representation of the experimental setup employed in the study.

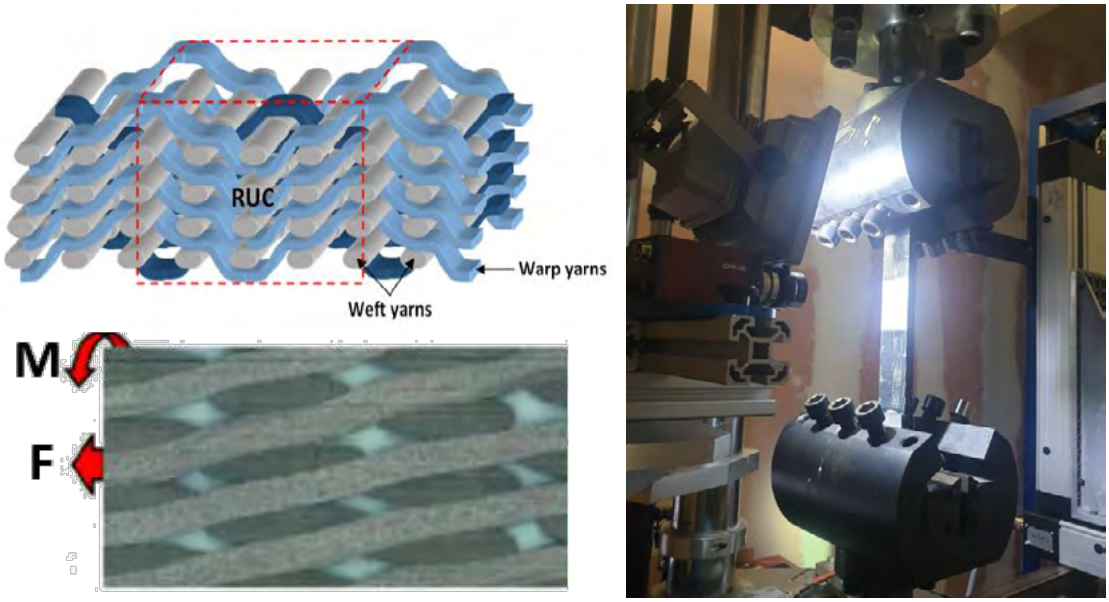


Figure 1. Material structure and used equipment

3. Experimental procedure and stress calculation

The first part of the study focused on determining the σ11-τ13 damage threshold envelope of the material. Static tension/torsion tests were conducted for various stress ratios σ11/τ13. A criterion based on the cumulative energy of the AE signals was utilized to determine this threshold, supplemented by microscopic observations to confirm damage initiation. This phase aimed to select stress levels to be applied during fatigue testing. The protocol followed during fatigue tests is illustrated in Figure 2 and consists of three parts: (i) scanning the specimen in its initial state using a video microscope, (ii) performing two static tests (pure tension and torsion) at stress levels below the damage threshold to measure the material's elastic moduli, deformations, and torsion angle in the usable region of the specimen, (iii) conducting a number N of sinusoidal fatigue cycles at a frequency of 2Hz and a load ratio R=0.05. Acoustic signals are recorded during the tests, along with the tensile and torsional stiffness derived from the angle measurement and displacement of the actuator. These three steps are repeated

until a significant decrease is observed in either of the two moduli E1 or G13 (approximately 20% of the initial value).

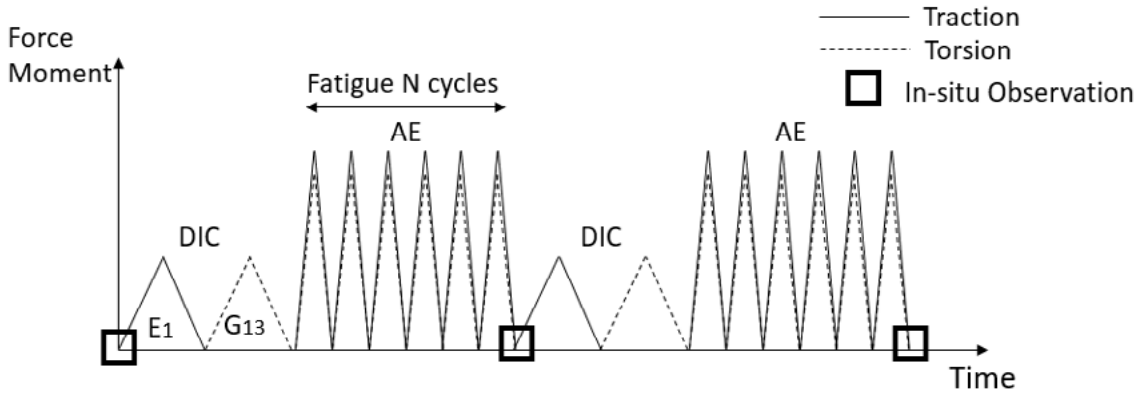


Figure 2. Fatigue test protocole

The load and moment to be applied to the specimen are determined based on Lekhnitskii's theory [4] and the works of Gong et al. [5]. A relationship between the maximum shear stress in the central zone of the specimen and the applied torque is established according to the following equations:

$$\tau_{13} = \frac{M_{eff}}{b\,h^2} k1 \tag{1}$$

$$M_a = M_{eff} + \frac{\frac{b\theta}{3L}\sqrt{1+\frac{1}{\varphi^2}}+\frac{1}{\varphi^2} ln\left(\varphi+\sqrt{1+\varphi^2}\right)}{\left(\frac{4}{E_{xx}hb^2}\right)} \tag{2}$$

Where Ma represents the applied moment, Meff is the effective moment inducing shear stresses, ϕ depends on the torsion angle of the bar (θ) and the length of the specimen (L) that has undergone twisting during torsion, b is the width of the sample, and Exx is the Young's modulus in the direction of the torsion axis. Considering the normal stresses, the relationship between the force to be applied and the average stress at the center of the specimen is given by the classical relation in equation 3. The results obtained from these analytical relationships linking torque and stress have been verified through finite element elastic calculations. A more detailed explanation of the calculation is presented in previous works [6].

$$\sigma = \frac{F}{S}\ ,\ S = bh \tag{3}$$

4. Results and discussion

4.1. Static tests

A previous study by the authors [6] identified four points on the material damage threshold envelope. Nine additional points were added in this study, including repeatability tests. Based on the obtained envelope, three distinct zones were defined for fatigue testing: (i) Zone A, which considers the variation of τ13 for pure torsion tests, (ii) Zone B, which refers to the effect of σ11 for high shear stresses, and (iii) Zone C, which refers to the effect of σ11 for mid-range shear stresses, as illustrated in Figure 3. The fatigue stress levels are chosen according to the stress levels at the damage initiation threshold.The choice of those 3 Zones allows for the study of the effect of shear stress τ13 during multiaxial testing. The elliptical shape of the failure envelope illustrates how the σ11/τ13 ratio would affect the material response.

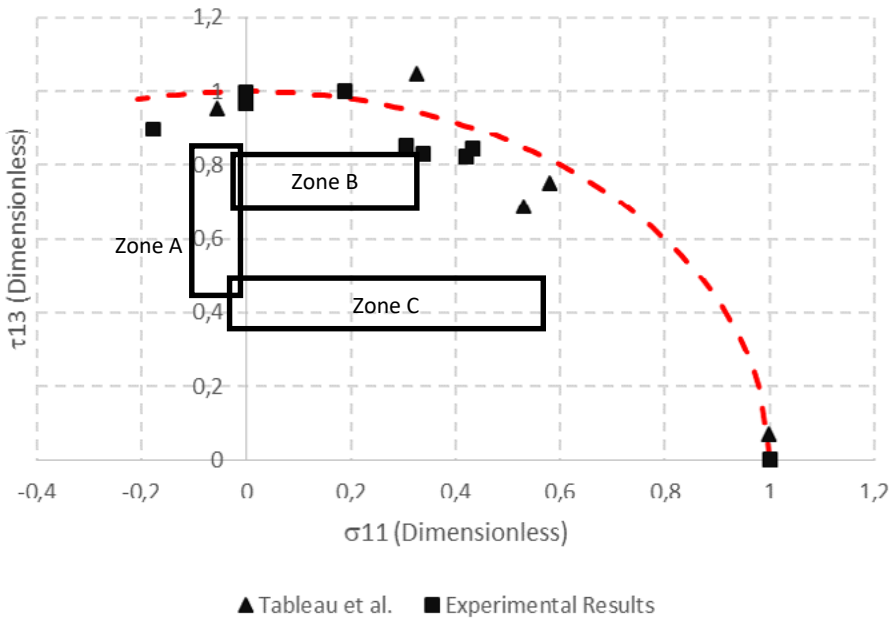


Figure 3. Damage threshold envelope of the 3D composite

4.2. Fatigue tests

The results obtained for the different zones indicate that the material damage is primarily influenced by the torsion of the specimen. Figure 4 illustrates the evolution of material stiffness (normalized) after each N fatigue cycle for the three different zones (two tests are considered per zone).

The trend curves reveal that in zone B (variation of σ11 for high τ13), the stiffness G13 decreases similarly, regardless of the σ11 value, suggesting that the test is primarily influenced by shear stress. In Zone C, where σ11 is varied and τ13 is fixed at a mid-range level, the effect of σ11 is noticeable at the beginning of the fatigue cycles, where a high applied normal stress leads to a lower shear modulus (as shown at 200,000 cycles). However, after a high number of fatigue cycles, the results show a similar shear modulus for both normal stress levels (700,000 cycles). In Zone A (pure torsion), the stiffness evolution depends on the level of applied τ13: a rapid loss is observed for high τ13, while the opposite is observed for low τ13. An example of the shear strain distribution for the specimen subjected to high τ13 shear stresses is illustrated in Figure 5. The figure depicts the localized concentration of shear strain along the warp direction resulting from the evolution of damage in the material after 190,000 cycles. This distribution is compared to the shear stresses at the beginning of the test for the same loading level. Considering the tensile behavior of the material, the evolution of Young's Modulus shows that the material retains its properties throughout the tests. A slight decrease is observed for specimens heavily damaged in shear.

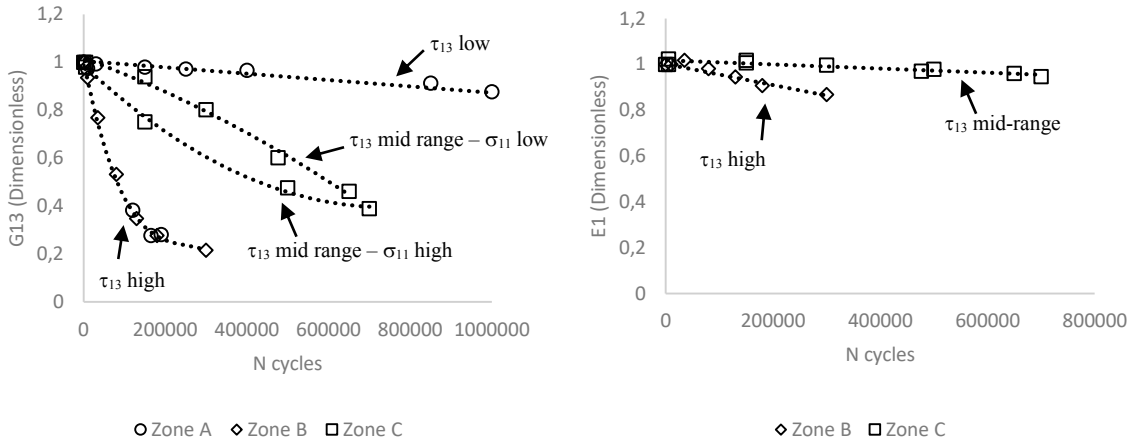


Figure 4. Damage threshold envelope of the 3D composite

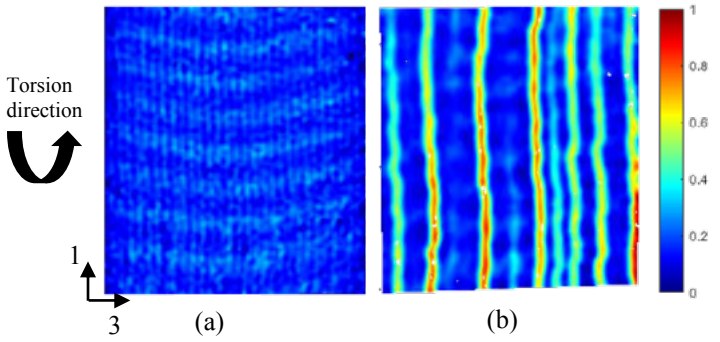


Figure 5. Shear strain distribution under torsion loading : (a) initial, (b) after fatigue

For the failure analysis, in-situ microscopic observations reveal that the cracks tends to initiate on the edge of the the weft fibers and propagates through the matrice to rejoin another crack. Macroscopically, the inspection shows a localized damage in the central zone and at two opposite diagonal sides of the specimen, while the rest show minimal damage. To better understand this localization, a numerical Finite Element model was developed using ABAQUS. The rectangular-shaped specimen is subjected to simultaneous traction/torsion loading applied on the aluminum tabs, with the composite modeled as a 3D orthotropic material.

The numerical results show a maximum homogeneous shear stress in the central zone, which explains the damage observed in that area. Additionally, the normal stress σ11 exhibits maximum values on both corners of the specimen. This localization of stress is attributed to the torsion effect of the bar. The normal stresses generated from the torsion of the bar combine with the stresses from traction to induce damage on two sides of the specimen, while others remain undamaged. A representation of both experimental damage and numerical stress distributions is illustrated in Figure 6.

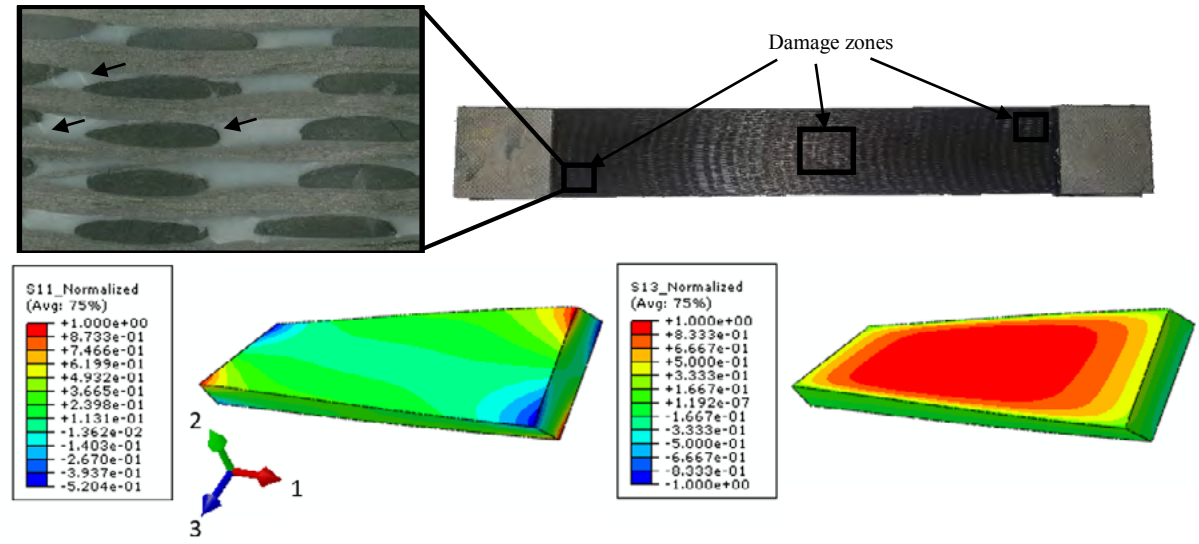


Figure 6. Damage localization and numerical stress distribution

3. Conclusions

The study focuses on investigating the damage of 3D woven composite materials. Static tension/torsion tests were conducted to determine the damage threshold envelope of the material. Based on this envelope, the effect of out-of-plane shear stress τ13 is analyzed in fatigue through different σ11/τ13 ratios. The evolution of the material's tensile and shear stiffness during fatigue testing highlights that the degradation of mechanical properties is primarily due to the effect of torsion. The in-situ investigation revealed the damage mechanism and localization, which aligns well with the stress distribution obtained in the numerical model.This study will contribute as a database for validation of phenomenological fatigue damage models.

Acknowledgments
Authors extend their sincere appreciation to Safran Aircraft Engines (Safran Group) for their funding and provision of materials, which were instrumental to this research.

References

[1] Mouritz, AP., Bannister, MK., Falzon, PJ, Leong, KH. Review of applications for advanced three-dimensional fibre textile composites, *Composites Part A: Applied Science and Manufacturing*, 30, 1999, p. 1445-1461.
[2] W. Hufenbach, W. Błażejewski, L. Kroll, R. Böhm, M. Gude, and A. Czulak, Manufacture and multiaxial test of composite tube specimens with braided glass fiber reinforcement, *Journal of Material Processing Technology*, vol. 162–163, pp. 65–70, May 2005, doi: 10.1016/j.jmatprotec.2005.02.212
[3] A. Kobeissi, P. Rahme, L. Leotoing, and D. Guines, Strength characterization of glass/epoxy plain weave composite under different biaxial loading ratios, *Journal of Composite Materials*, vol. 54, no. 19, pp. 2549–2563, Aug. 2020, doi: 10.1177/0021998319899135.
[4] S. Lekhnitskii, Theory of elasticity of an anisotropic elastic body. San Francisco: Holden-Day Inc., 1963.
[5] Gong XL, Laksimi A, Laï DW, Benzeggagh ML. Stress analysis in unidirectional composite plates under torque loadings: experimental observation. *Journal of Reinforced Plastic and Composites*, 1995.

[6] N. Tableau, Z. Aboura, K. Khellil, F. Laurin, and J. Schneider, "Multiaxial loading on a 3D woven carbon fiber reinforced plastic composite using tensile-torsion tests : Identification of the first damage envelope and associated damage mechanisms," *Composite Structures*, vol. 227, p. 111305, Nov. 2019, doi: 10.1016/j.compstruct.2019.111305.

NUMERICAL SIMULATION OF FATIGUE DAMAGE ACCUMULATION OF ORTHOTOPICALLY VISCOELASTIC CFRP LAMINATES CONSIDERING TEMPERATURE ELEVATION CAUSED BY ENERGY DISSIPATION

KUDO Natsuko[1], HUACHAO Deng[2] and KOYANAGI Jun[3]

[1]Department of Materials Science and Technology, Graduate School of Tokyo University of Science, 6-3-1 Niijuku, Katsushika-ku, Tokyo 125-8585, Japan
Email: 8219b01@alumni.tus.ac.jp, Web Page: https://www.rs.tus.ac.jp/koyanagi/home.html
2Department of Materials Science and Technology, Tokyo University of Science, 6-3-1 Niijuku, Katsushika-ku, Tokyo 125-8585, Japan
Email: dhc19911202@rs.tus.ac.jp, Web Page: https://www.rs.tus.ac.jp/koyanagi/home.html
3Department of Materials Science and Technology, Tokyo University of Science, 6-3-1 Niijuku, Katsushika-ku, Tokyo 125-8585, Japan
Email: koyanagi@rs.tus.ac.jp, Web Page: https://www.rs.tus.ac.jp/koyanagi/home.html

Keywords: Temperature elevation, Dissipated energy, Strength degradation

Abstract

The observed temperature elevation during CFRP fatigue testing poses a significant challenge in accurately predicting fatigue. The temperature increase in laminates is attributed to the inelastic deformation of the resin. This inelastic deformation increases dissipated energy and subsequently leads to a rise in temperature. At lower frequencies of fatigue testing, a balance is achieved between heat release and dissipated energy generation, minimizing the temperature rise. However, at higher frequencies, the temperature of the laminate increases due to the heightened generation of dissipated energy. Therefore, it is crucial to consider this temperature rise when discussing CFRP fatigue. In this study, plastic deformation was introduced as a notable addition. Additionally, the code was modified to relate dissipated energy to temperature rise. In this modified code, as dissipated energy increases, the temperature also increases. In this study, we simulate cyclic loadings of epoxy resin at frequencies of 1 Hz, and 20 Hz. Since heat dissipation is considered, temperature elevation was different for each frequency.

1. Introduction

The number of cracks in fatigue tests of CFRP depends on its frequency[1, 2]. This is due to two reasons. The first is the inelastic deformation of the resin. When the frequency is low, the inelastic deformation of the resin increases. Since more inelastic deformation leads to more damage, the number of cracks is increased at lower frequencies. The second is temperature elevation. As the frequency increases, the temperature increases. As the temperature increases, the damage increases faster. At low frequency loads, the temperature does not rise due to high heat release. Therefore, the number of cracks increases due to inelastic deformation of the resin. At high frequency loads, the temperature elevation of the CFRP occurs because the heat generation is greater than the heat release. Therefore, cracks increase due to temperature elevation.

In the author's previous work[1, 2], a code was developed to predict the degradation of CFRP using Hashin's law. In this code, entropy based on dissipated energy causes strength degradation. In some

studies, entropy generation can be used as a failure criterion[3, 4, 5, 6, 7]. The code incorporated five Maxwell element models. However, in this paper, damage is only related to dissipated energy and omits consideration of temperature changes and permanent plastic deformation. In this study, plastic deformation was introduced as a notable addition. Additionally, the code was modified to relate dissipated energy to temperature rise. In this modified code, as dissipated energy increases, the temperature also increases. The temperature rise, according to the temperature-time conversion law, accelerates the movement of the dashpot, thereby amplifying dissipated energy. This implies that dissipated energy increases exponentially with rising temperature. This increase in entropy generation further accelerates the decrease in intensity. Furthermore, since heat dissipation is considered, frequency influences the number of fatigue failures. This study is unique in allowing for a comprehensive fatigue failure simulation that considers both temperature and frequency.

This study simulates the behavior of epoxy resin, commonly used in CFRP laminates. Dissipated energy is calculated by inelastic strain and stress, and it is used in calculating the heat generation. Surface heat transfer is considered on the model's surface. Using the model which considers heat release and heat generation, we simulate cyclic loadings at 1Hz and 20Hz. As a result, the loading at 20Hz has higher temperature than 1Hz. This suggests that fatigue failure with temperature elevation can be reproduced.

2. Numerical Method

2.1. Plastic deformation

Resin deformation can be divided into two types: elastic deformation and inelastic deformation. In previous study[8, 9], Maxwell elements are used for simulating the behavior of resin. However, in the previous study, the dissipated energy in the simulation depended solely on the stress level, thus it could not account for the influence of frequency. In this study, we use both maxwell elements and following plastic deformation equation.

$$\Delta\varepsilon_{\mathrm{p}} = \left(\alpha \times \varepsilon^{n} \exp\left(-\left(\frac{\varepsilon}{\varepsilon_0}\right)^{m}\right) + \beta\left(1 - \exp\left(-\left(\frac{\varepsilon}{\varepsilon_0}\right)^{m}\right)\right)\right) \times |\Delta\varepsilon|. \tag{1}$$

where $\Delta\varepsilon_{\mathrm{p}}$, ε and $\Delta\varepsilon$ represent the plastic strain increment, strain, strain increment and α, β, m, n, and ε_0 are fitting parameters. Positive and negative of the plastic strain increment are determined by stress. The validity of this equation will be discussed in a subsequent study, but for now, we will adopt it.

2.2. Time–temperature superposition principle

A polymeric material commonly follows the time–temperature superposition principle (TTSP)[10, 11]. Based on Arrhenius' equation, the following equation is used to simulate the resin behavior.

$$\log \alpha^{TR}(T) = \frac{\Delta H}{2.303R}\left(\frac{1}{T} - \frac{1}{T^{R}}\right). \tag{2}$$

where α^{TR}, ΔH, R, T and $T^{R}$are time factor, the activation energy, he gas constant 8.314 $\times 10^{-3}$ [kJ/(K mol)], test temperature, and reference temperature. In this study, the activation energy is 150kJ/mol, and the reference temperature is 333K.

2.3. The calculation flow of UMAT

Figure 1 shows the Viscoelastic/plastic model consisting of 15 Maxwell elements and a plastic element. Figure 2 shows the calculation flow of updating stress which is based on the model (Figure 1). In terms of the viscoelastic model part, the flow closely resembles that of the previous study[8, 9]. However, the

novel point of this flow is the calculation of plastic strain by using Eq. 1 which is independent for time increment.

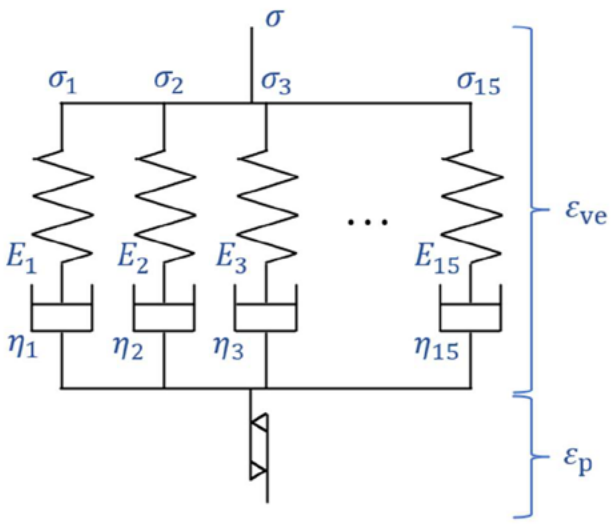


Figure 1. The Viscoelastic/plastic model.

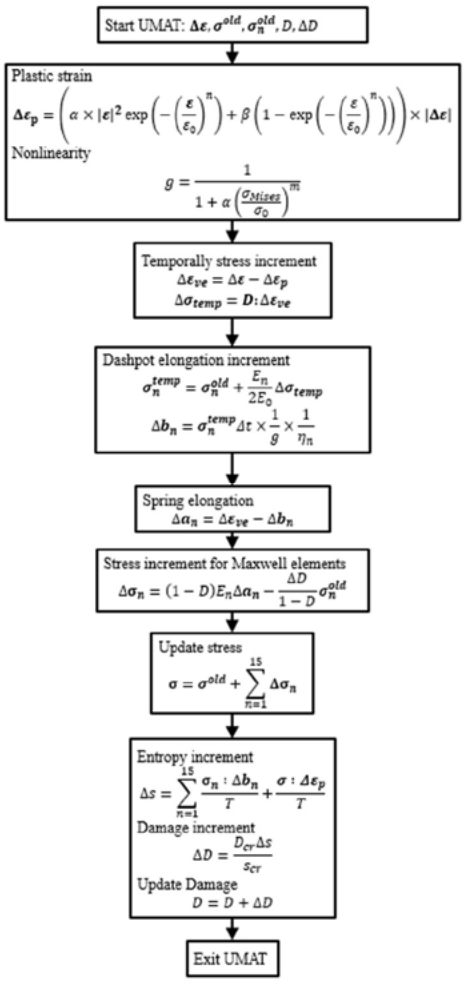


Figure 2. Calculation flow of updating stress.

3. Numerical Results and Discussions

As shown in Figure 3, dimensions of the resin in the simulation are 1 mm × 1 mm × 1 mm and boundary conditions are applied on surfaces ADHE, ABCD and DCGH. Heat transfer is given in the surfaces ABFE, BCGF, EFGH. The displacement boundary conditions is employed on surface EFGH at frequencies of 1 Hz and 20 Hz. The cyclic displacement is 0.01 mm for 30s. The cyclic loading behavior is simulated using Abaqus (2020, Dassault Système). The stress is calculated using a user-subroutine UMAT of Abaqus. UMAT is based on the calculation flow (shown in Figure 2.) and the material properties used in the calculation is shown in Table 1.

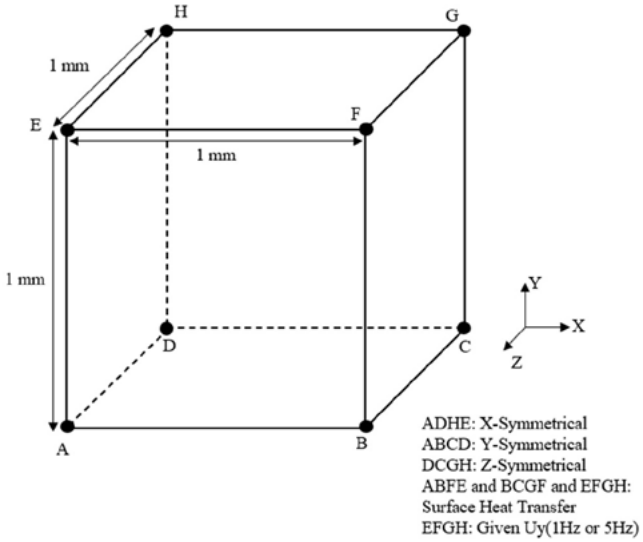


Figure 3. Boundary condition.

Table 1. Material properties of matrix resin.

n	E_n(MPa)	η_n(MPa·s)	Elasticity	
1	220	3.16E+01	E_n(MPa)	3300
2	220	1.26E+03	ν	0.3
3	220	3.16E+04	Nonlinearity	
4	220	2.51E+05	σ_0(MPa)	70
5	220	1.26E+06	α	2
6	220	6.31E+06	m	7
7	220	2.51E+07	Plastic strain	
8	220	1.00E+08	α	0.04
9	220	2.00E+08	β	0.0002
10	220	2.00E+09	ε_0	0.035
11	220	6.31E+09	m	6
12	220	2.00E+10	Damage variables	
13	220	2.51E+11	α_d	1000
14	220	3.16E+12		
15	220	7.94E+13		

Figure 4 shows the result of temperature elevations in cyclic loadings. The heat release and the heat generation are balanced at both 1 Hz and 20 Hz, but the temperature elevation at 20 Hz is higher than that of 1 Hz. Because the resin follows TTSP, the higher temperature, the movement of dashpot of the model (shown in Figure 1) is accelerated. Consequently, this leads to a higher dissipation of energy, resulting in a larger damage variable. The result suggests that the transverse cracking behavior of CFRP laminates under cyclic loading at different frequencies can be simulated by considering heat release and plastic deformation which are related to temperature elevation.

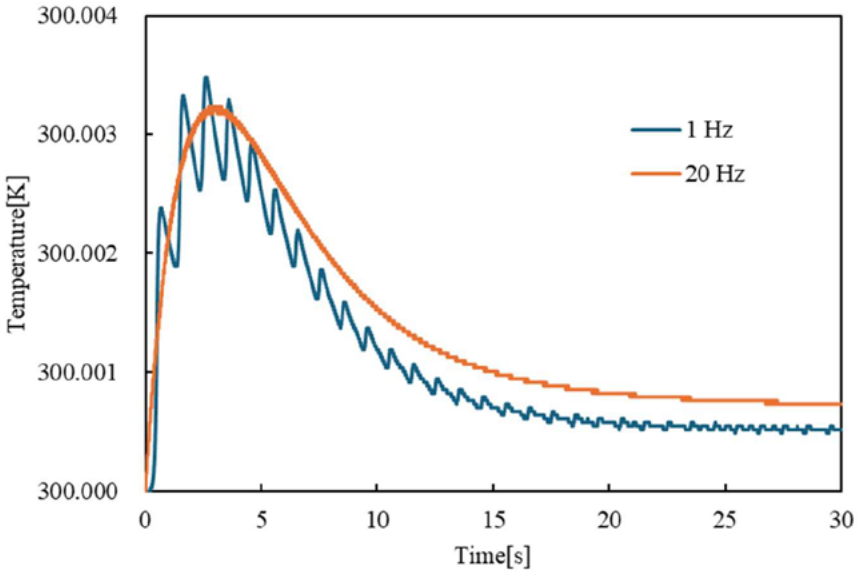


Figure 4. Result of cyclic loading simulation considering temperature elevation.

4. Conclusions

The plastic deformation is added to the previous study in order to consider the temperature elevation of epoxy resin under cyclic loading. It's because plastic deformation is independent of time increment, different temperature elevations occur depending on the frequencies of the cyclic loadings. Dissipated energy calculated in the suggested model increases exponentially with higher temperatures. the results suggest that this model can simulate the transverse cracking behaviors of CFRP laminates.

References

[1] J. Koyanagi, A. Mochizuki, R. Higuchi, V.B.C. Tan, and T.E. Tay. Finite element model for simulating entropy-based strength-degradation of carbon-fiber-reinforced plastics subjected to cyclic loadings. *International Journal of Fatigue,* volume:107204,2022.

[2] H. Deng, A. Mochizuki, M. Fikry, S. Abe, S. Ogihara, and J. Koyanagi. Numerical and Experimental Studies for Fatigue Damage Accumulation of CFRP Cross-Ply Laminates Based on Entropy Failure Criterion. *Materials,* volume (1)2023.

[3] S. Iwamoto, Y. Oya, and J. Koyanagi. Evaluation of Microscopic Damage of PEEK Polymers under Cyclic Loadings Using Molecular Dynamics Simulations. *Polymers,* volume (22)2022.

[4] A. Mahmoudi, and B. Mohammadi. On the evaluation of damage-entropy model in cross-ply laminated composites. *Engineering Fracture Mechanics,* volume:106626,2019.

[5] N. Takase, J. Koyanagi, K. Mori, and T. Sakai. Molecular Dynamics Simulation for Evaluating Fracture Entropy of a Polymer Material under Various Combined Stress States. *Materials,* volume (8)2021.

[6] M. Naderi, M. Amiri, and M.M. Khonsari. On the thermodynamic entropy of fatigue fracture. *Proceedings of the Royal Society A: Mathematical, Physical and Engineering Sciences,* volume (2114):423-438,2009.
[7] N. Kudo, R. Fujita, Y. Oya, T. Sakai, H. Nagano, and J. Koyanagi. Identification of invisible fatigue damage of thermosetting epoxy resin by non-destructive thermal measurement using entropy generation. *Advanced Composite Materials,* volume (2):233-249,2024.
[8] H. Deng, K. Toda, M. Sato, and J. Koyanagi. Micro-Scale Numerical Simulation of Fatigue Failure for CFRP Subjected to Multiple-Amplitude Cyclic Loadings Based on Entropy Damage Criterion. *Materials,* volume (18)2023.
[9] M. Sato, K. Hasegawa, J. Koyanagi, R. Higuchi, and Y. Ishida. Residual strength prediction for unidirectional CFRP using a nonlinear viscoelastic constitutive equation considering entropy damage. *Composites Part A: Applied Science and Manufacturing,* volume:106178,2021.
[10] Y. Miyano, M. Nakada, and R. Muki. Applicability of Fatigue Life Prediction Method to Polymer Composites. *Mechanics of Time-Dependent Materials,* volume (2):141-157,1999.
[11] J. Koyanagi, S. Yoneyama, A. Nemoto, and J.D.D. Melo. Time and temperature dependence of carbon/epoxy interface strength. *Composites Science and Technology,* volume (9):1395-1400,2010.

A STUDY ON FATIGUE RESISTANCE AND STRUCTURAL INTEGRITY IN WEB-CORE COMPOSITE BRIDGE DECK PANELS

O. Karpenko[1], T.Peeters[2], E. Gommers[3], T. White[4], L. Tromp[5], M. Pavlović[6]

[1]Delft University of Technology, Stevinweg 1, 2628CN Delft, The Netherlands,
Email: o.karpenko@tudelft.nl, Web Page: https://www.tudelft.nl/staff/o.karpenko/
[2]Delft University of Technology, Stevinweg 1, 2628CN Delft, The Netherlands,
Email: t.peeters-1@tudelft.nl
[3]Delft University of Technology, Stevinweg 1, 2628CN Delft, The Netherlands,
Email: e.s.gommers@student.tudelft.nl
[4]Delft University of Technology, Stevinweg 1, 2628CN Delft, The Netherlands,
Email: t.j.white@student.tudelft.nl
[5]Royal HaskoningDHV, Rotterdam, The Netherlands.
Email: liesbeth.tromp@rhdhv.com
[6]Delft University of Technology, Stevinweg 1, 2628CN Delft, The Netherlands,
Email: m.pavlovic@tudelft.nl, Web Page: https://www.tudelft.nl/staff/m.pavlovic/

Keywords: GFRP, Web-to-Flange Junctions, fatigue, experiments

Abstract
The presented research aims to examine local fatigue failure modes of Glass Fiber-polymer Composite (a.k.a. GFRP), particularly how the bending of the Web-to-Flange Junctions (WFJ) and tensile loading of the material affects the composite's fatigue resistance. By conducting experimental analyses, the study investigates GFRP's efficacy both as a material and as a component element, drawing parallels with Eurocode standards for steel and concrete.
The coupon tests under static and fatigue loading conditions provided an empirical data on the Ultimate Limit State (ULS) and fatigue resistance of the GFRP composites, including a better understanding of the effects of variation in the facing's thicknesses in the web-core composite on the fatigue response. Subsequent three-point bending tests on the WFJ provided the insights into the strength of WFJ with the first indications on the governing failure mechanisms in the WFJ.

1. Introduction

For civil engineering applications, the renovation of existing bridges and the design of new structures demand innovative and sustainable materials. Glass Fiber-reinforced Polymer (GFRP) composites have emerged as a leading material in this transformation due to their durability, corrosion resistance, and lightweight properties, which are particularly advantageous for bridge construction [1]. GFRP composites represent a promising alternative to traditional materials like timber, steel, and concrete, which are susceptible to deterioration and corrosion over time [2]. The lighter weight of GFRP not only reduces installation costs but also minimizes the load on foundation structures. By replacing old bridges with GFRP structures, municipalities can achieve substantial improvements in durability and a reduction in maintenance costs [3].
Despite these benefits, the integration of GFRP into existing design frameworks like the Eurocode [4]for composite structures introduces complexities. The specificity required in the design guidelines can lead to increased construction costs and project delays. As noted by authors in [5], current design recommendations do not fully accommodate the unique properties of GFRP, necessitating additional research and modification of design codes to enhance their applicability to GFRP-based structures.
Focusing on the structural design innovations, this study examines the material and component properties of web-core panels in GFRP bridge decks. These panels employ unidirectional (UD) fabrics

on the facings to address bending and mitigate local buckling, while incorporating multidirectional laminates in the webs for effective shear transfer. For the continuous connections between the flanges and webs, components known as Web-to-Flange Junctions (WFJs) are constructed using 'wrap-layers', GFRP fabrics wrapped around foam blocks during production to form the outer layers of the webs and inner layers of the facings. To facilitate the design verification of WFJ components, more comprehensive information is required regarding their fatigue behavior. Currently, the existing design codes lack Stress-life (S-N) curves specifically tailored for WFJ components. Conducting fatigue tests on these components can provide the necessary data to establish an S-N curve, thereby aiding in the design process.

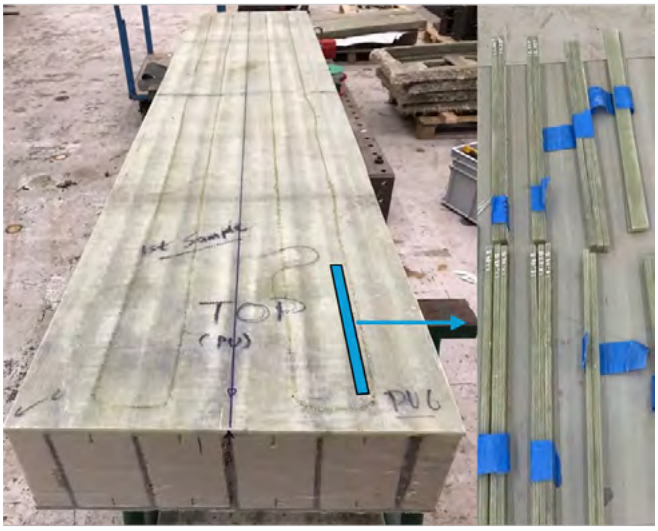


Figure 1. Coupons cut out from the sandwich panel.

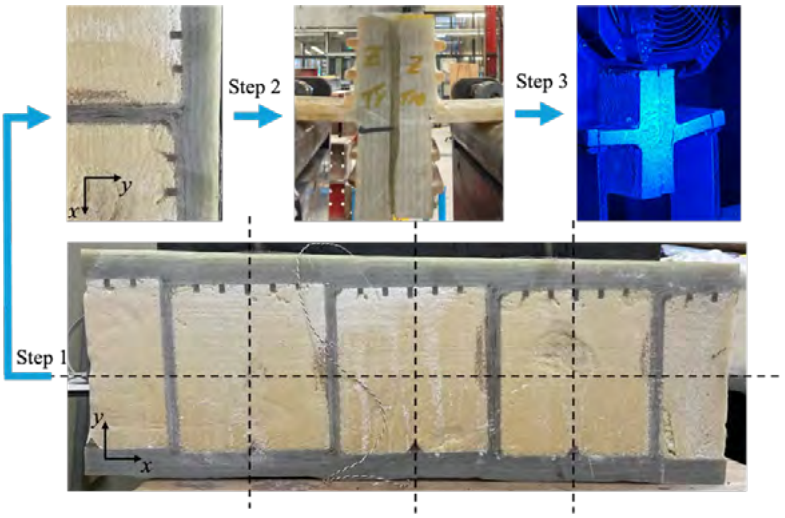


Figure 2. Extraction of web-facing junctions from the sandwich panel.

2. Materials and experimental methods

The coupons and the components (WFJs) are cut out of the GFRP bridge decks, as shown in Figure 1 and Figure 2. The bridge deck is manufactured with vacuum-infused GFRP panels and polyurethane resin that has a core of polyurethane (PU) foam. The deck laminate consists of a Z-shaped layering approach and integrates three types of fibre fabrics. Surrounding the foam blocks are layers of E-glass fabric angled at [+/-45 degrees]. Along the length, three layers of UD E-glass fabrics are laid, with overlaps of two blocks at the top and bottom. The Z-shaped configuration also includes two additional

layers of E-glass fabric oriented at [0/90 degrees] that overlap by 2.5 blocks. Facings have a higher volume fraction of the fibres compared to the webs, due to the production process. The top and the bottom facing of the deck have the lay-up of $[((0/90)_2/0_3)_4/0/90/\pm 45]$ and the web - $[\pm 45_2/(0/90)_2/\pm 45_2]$. The material properties of the composite plies can be found in [6].

2.1. Material tests on coupons

The coupons are cut out from the top and bottom facings of the sandwich panels of the deck as shown in Figure 1. The coupons are extracted from a scaled deck by a factor of 0.5 and the thickness of the coupon specimens is twice as low compared to the thickness of the tests on the WFJs.

The samples are precisely cut using a water jet technique with the dimensions of the coupon specimens to comply with ISO 527 – 4 standard [7] as shown in Figure 3. Owing to the Z-shape layup method used in the decks' production, specimen thicknesses ranged between 9 and 12 mm. The variance in coupon thickness introduces complications in the testing process, requiring the adjustments of modified testing techniques. These complications primarily occur in the gripping area of the testing apparatus, where the specimen's variable thickness causes uneven stress distribution due to a non-uniform clamping surface. Such stress concentrations can induce premature failure of the specimens at the clamping points, thereby complicating the assessment of material properties. Figure 4a highlights the thickness differences in the specimen cross-section A-A. To overcome the thickness transition issues, a mould is designed from timber, shown in Figure 4b. The specific purpose of this mould is to apply a two-component epoxy system [8] at the clamping points to have a flat surface to clamp the specimen in. This resin is fast curing and reaches its full strength in 3 days, after which it is strong enough to resist the high clamping force of the hydraulic wedge grips. Before the specimens are placed in the mould, surface preparation is performed on the regions near the clamps to prevent slipping between the resin and the specimens during testing.

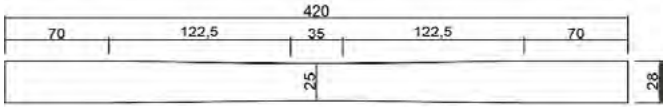
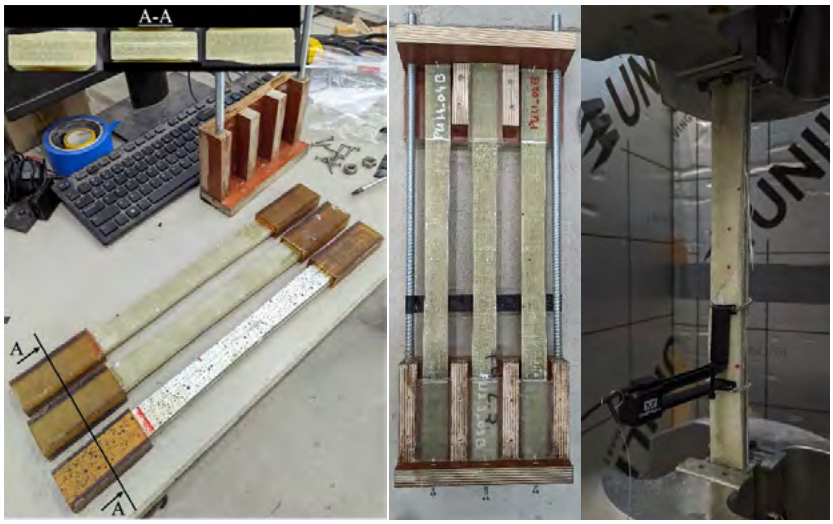


Figure 3. Coupon specimen dimensions.



a) Specimen preparation b) Mould design c) Test set-up

Figure 4. Material coupon tests.

Static and fatigue tests are performed on a universal testing machine with a 100kN load cell. The test set-up is shown in Figure 4c. Each static test is subjected to a uniform loading rate of 1 mm/min until the point of failure. The tensile-tensile fatigue tests are performed under the loading ratio of 0.1

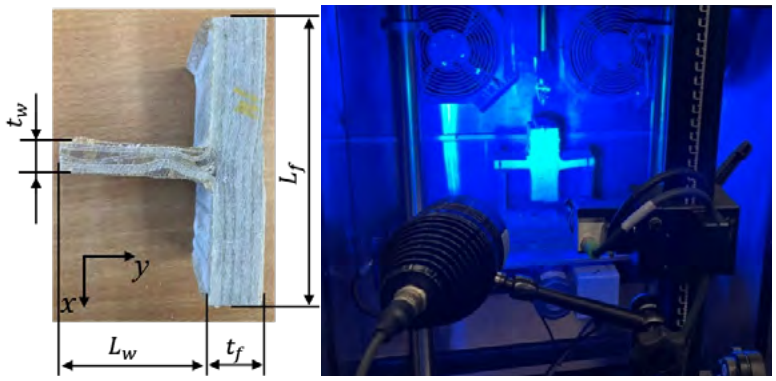
considering the three loads of 52%, 37% and 22% of the ultimate load capacity. For every load level a total of 3 successful tests are required, slipped specimens or specimens failing in the clamps are disregarded. The sinusoidal constant amplitude is utilized with frequencies of 2 to 6 Hz, depending on the load levels. During the fatigue tests, an extensometer is used with a gauge length of 50 mm, as shown in Figure 4c.

2.2. Component tests

The bridge deck's web-core sandwich panel contains WFJs, referred to as components, which are shown in Figure 2. The preparation process for these components involves several key steps: 1) Cutting the GFRP panels both in the XZ plane and through the thickness in the YZ plane, specifically between the web sections; 2) Removing the PU foam and using a structural adhesive quick set epoxy to bond the web-facing components together. Steel tabs 25x6x80 mm^3 are also glued in areas designated for load and supports; 3) Applying a thin layer of white, non-reflective paint on one side of the specimens, followed by a random black pattern using a spray gun. This is crucial for detecting crack initiation with the Digital Image Correlation (DIC) system.

Figure 5a shows the specimens' average dimensions, including a width of 50.02±0.53 mm, flange length and thickness ($L_f = 140 \pm 9.16$mm, $t_f = 26.22 \pm 2.25$mm), and web length and thickness ($L_w = 72.45 \pm 3.65$mm, $t_w = 12.86 \pm 2.16$mm).

For testing, a universal testing machine equipped with a 15kN load cell and a total span of 175 mm is used (see Figure 5b). A DIC system featuring a 50.6 MPa camera and polarized blue LED lights captures full-field displacements on the specimens' side surfaces during tests, synchronizing photos with load and displacement data.



a) Specimen dimensions b) Test set up.

Figure 5. Component tests.

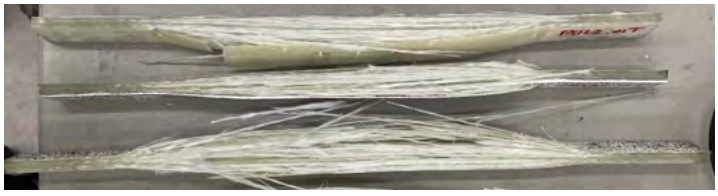


Figure 6. Delamination and fibre failure. Static material tests.

3. Results and discussion

3.1. Material coupon tests

Prior to fatigue tests, static tests are conducted on a set of three specimens to determine the failure loads and stresses. The failure modes are visually inspected, which included delamination and fibre breakage, and consistent across all tests and are shown in Figure 6. The analysis of the specimens is detailed in Figure 7, where the average failure load, displacement and stress are F_{max}=137.68kN, $w_{max} = 11.89$mm and $\sigma_{max} = 577.75$MPa, respectively. The tensile stress is calculated by dividing the applied

load by the initial cross-sectional area at the failure region of the specimen. All three tests show a linear relationship between the applied load and displacement.
Figure 8 illustrates the fatigue response of the tested coupons. Each load level is evaluated with three specimens, resulting in a total of nine tests. The analysis of the material's fatigue performance is carried out in accordance with ASTM E739-10 [9] standards, which involves establishing the S-N relationship through linear regression. The S-N relationship is presented in the following format:

$$\log N = A + B(\log \sigma) \quad (1)$$

where σ is the maximum cyclic stress; N is the number of cycles to failure; A and B are the fitting parameters.
The plot in Figure 8 includes data points, a solid black line representing the logarithmic fit to the data, and dashed black lines are representing the 95% confidence bands for the fit. The fit equation is indicated in Figure 8.

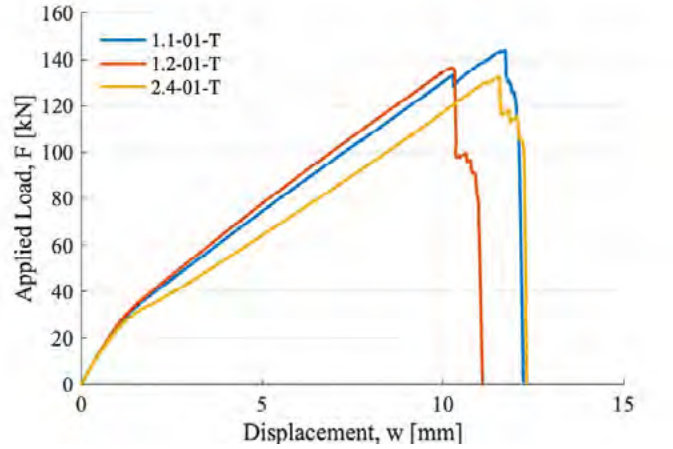


Figure 7. Load-Displacement curves. Static material tests.

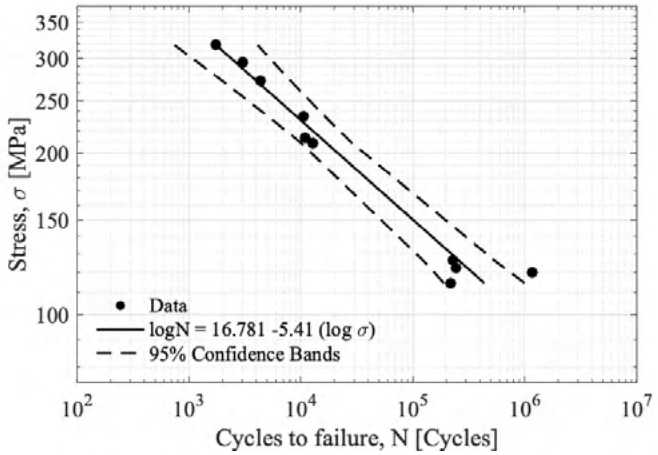


Figure 8. S-N curves of the material tests.

The fatigue tests are force controlled and are set to 30 kN, 50 kN and 70 kN. A higher force resulted in immediate failure of the ±45° plies at the outer surface. Due to large thickness differences in the specimens the forces are converted to stresses where the areas are evaluated at the location of failure, shown in Figure 9. Almost all locations of failure are concentrated in the middle region of the coupon with the narrowed cross-section according to ISO 527 – 4 to trigger the failure in this region. Due to some margins in the cutting process not all specimens had the smallest cross-section precisely in the middle, this explains why the failures don't occur precisely in the middle.

The governing failure modes occurring during the fatigue tests are delamination and/or fibre breakage respectively. This can also be seen in Figure 9. In some cases the fibre breakage progressed through the specimen in longitudinal direction towards the clamped region, while in most cases the specimen broke in the middle straight away. This progress of fibre breakage and delamination towards the clamps is better visible on the side view which is shown in Figure 9d.



Figure 9. Damage of the coupons subjected to fatigue loading of a)30kN b) 50kN c) 70kN d) Side view
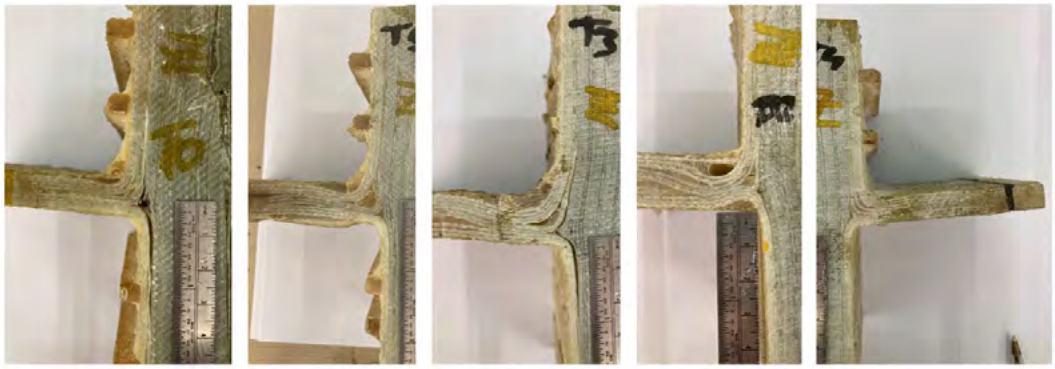


Figure 10. Failure initiation and delamination. Static component tests.

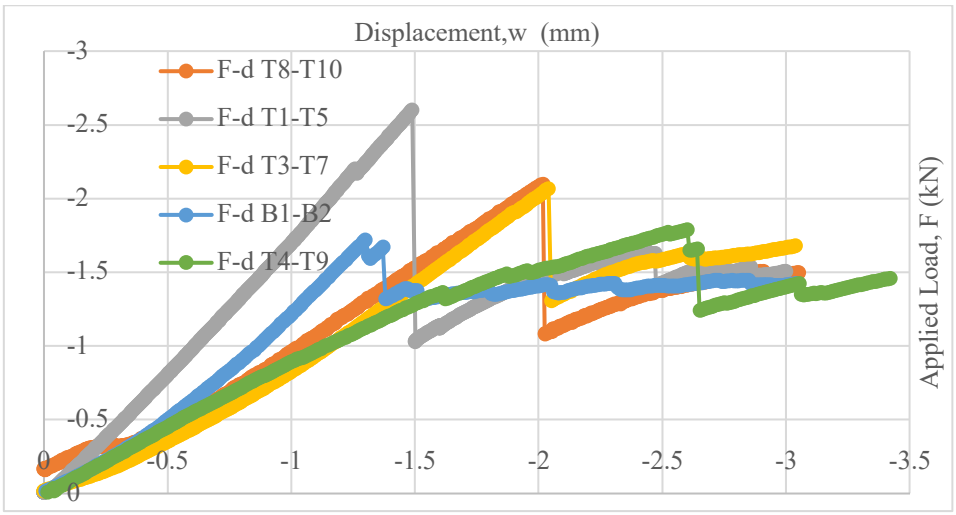


Figure 11. Load-Displacement curves. Static component tests.

3.2. Component tests

Static tests are conducted on 5 pairs of WFJ, in which one out of two connected together WFJ failed during each test. The failure modes are visually inspected, shown in Figure 10, which are similar across all the tests with the delamination between the 'Wrap' and 'UD'-layer of the WFJ. The Force-Displacement plots of the specimens are shown in Figure 11 indicating an average failure load, displacement and nominal bending stress are F_{max}=2.04kN, w_{max} = 1.90mm and σ_{max} = 50.90MPa, respectively. The nominal bending stress is determined by multiplying the reaction force from the support by the distance from the support to the beginning of the radius to obtain the bending moment. This is then divided by the elastic section modulus of the web just before the junction. All five tests show a linear relationship between the applied load and displacement.

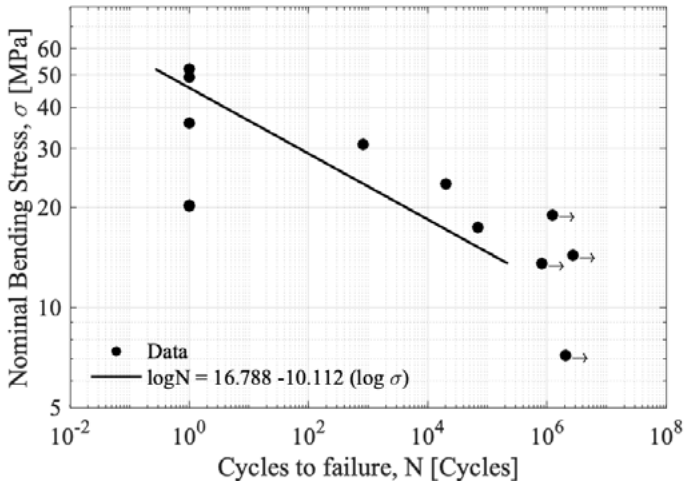


Figure 12. S-N curves of the component tests.

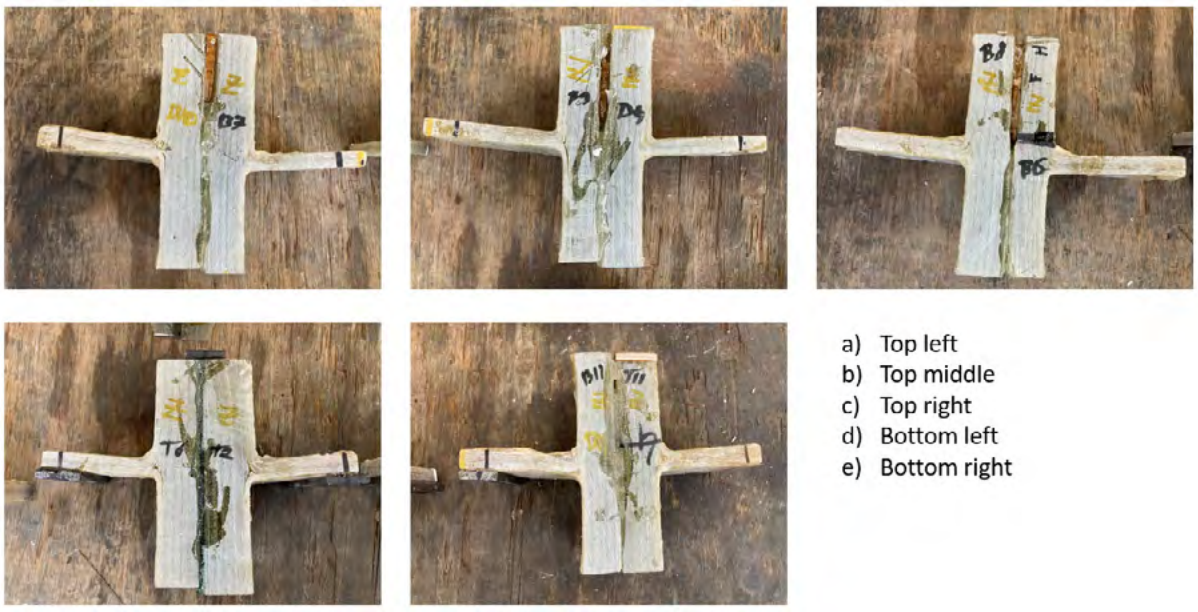


Figure 13. WFJ Component damage, fatigue tests.

The analysis of the WFJ component fatigue tests is presented in Figure 12. The tests are force-controlled with an R = 0.1. The plot includes data points along with a solid black line that represents the logarithmic

fit to the data. All the data points, except for one ($\sigma_{nom} = 7.16$MPa) are included in the fit. The equation for the fit is also shown in Figure 12.
Multiple WJF have failed at the first cycle with the applied load of 50% to 70% of ULS. Those specimens had a resin reach region in the corners of WJF, as shown in Figure 12a) and b). The specimens indicated with the arrow are stopped at around 10^6 cycles and are indicated as outruns. Similar to the static tests, the fatigue tests revealed the same failure mode: delamination between the 'wrap' and 'UD' layers, see Figure 13. The criteria for failure in the fatigue tests is determined to be crack initiation between these layers, specifically when the tangential strain in the crack direction (measured using a virtual extensometer with a 10 mm gauge length on DIC data via GOM correlate software) exceeded 0.1215% strain from the static tests. The stress correlated with the number of cycles until failure represents the nominal bending stress at the initial load cycle. Compared to the static tests, crack initiation often occurred in both junctions during the fatigue tests. This is likely due to the lower occurring stresses and longer testing times, allowing for stress redistribution and crack initiation in both junctions. However, despite quick crack initiation at low stress levels, crack growth was retarded, and no complete failure of the junction occurred in any fatigue tests.

4. Conclusions

The experimental analysis of GFRP material and WFJ components in web-core composite bridge deck panels reveals consistent failure modes across all specimens, characterized by delamination and fiber breakage during material fatigue tests, and delamination between the 'wrap' and 'UD' layers in component fatigue tests. WFJ components typically initiated fatigue under low bending stresses yet did not experience the abrupt failures with the retardation of crack propagation in between the UD layers. Although the coupon fatigue tests indicated a steep fatigue slope of 5.41, it's important to note that the material coupons tested were half the thickness of the actual deck laminate, which may influence the results' applicability to real-world scenarios.

Acknowledgments

The authors would like to express their gratitude to Rijkswaterstaat, the Directorate-General of the Ministry of Infrastructure and Water Management of the Netherlands for the financial support, and FibreCore Europe for the production of the panels.

References

[1] D. K. Rajak, D. D. Pagar, P. L. Menezes, and E. Linul, "Fiber-reinforced polymer composites: Manufacturing, properties, and applications," *Polymers*, vol. 11, no. 10. MDPI AG, Oct. 01, 2019. doi: 10.3390/polym11101667.
[2] L. C. Bank, *Composites for Construction: Structural Design with FRP Materials*. John Wiley & Sons, 2006.
[3] J. Qureshi, "Fibre-Reinforced Polymer (FRP) in Civil Engineering," in *Next Generation Fiber-Reinforced Composites - New Insights*, IntechOpen, 2023. doi: 10.5772/intechopen.107926.
[4] Technical Specification CEN/TS 19101, "Design of fibre-polymer composite structures".
[5] A. V. Movahedi-Rad, T. Keller, and A. P. Vassilopoulos, "Fatigue damage in angle-ply GFRP laminates under tension-tension fatigue," *Int J Fatigue*, vol. 109, pp. 60–69, Apr. 2018, doi: 10.1016/j.ijfatigue.2017.12.015.
[6] O. Karpenko, T. Peeters, A. Christoforidou, and M. Pavlović, "Fatigue of web-core composite bridge decks: an experimental and numerical study," Rio de Janeiro, brazil: International Conference on Fiber-Reinforced Polymer (FRP) Composites in Civil Engineering (CICE 2023), 2023. [Online]. Available: https://doi.org/10.5281/zenodo.8066285
[7] ISO 527-4: 2023, "Part 4: Test conditions for isotropic and orthotropic fibre-reinforced plastic composites."
[8] Poly Service, "POLY-POX THV 500 - HARDER 455."
[9] ASTM E739-10, "Standard Practice for Statistical Analysis of Linear or Linearized Stress-Life (S-N) and Strain-Life (ε-N) Fatigue Data."

NONLINEAR DYNAMIC RESPONSE OF 2.5D WOVEN SIC/SIC CERAMIC MATRIX COMPOSITES: EXPERIMENTAL AND NUMERICAL INVESTIGATION

Maojing.RAN[1,2], Lu.ZHANG [1,2], Xiguang.GAO [1,2], Yingdong.SONG [1,2,3]

[1] Key Laboratory of Aero-engine Thermal Environment and Structure, Ministry of Industry and Information Technology, College of Energy and Power Engineering, Nanjing University of Aeronautics and Astronautics, Nanjing, China
Email: maojingran@nuaa.edu.cn
[2] Jiangsu Province Key Laboratory of Aerospace Power System, College of Energy and Power Engineering, Nanjing University of Aeronautics and Astronautics, Nanjing, China
Email: Luzhang@nuaa.edu.cn
[3] State Key Laboratory of Mechanics and Control Mechanical Structures, Nanjing University of Aeronautics and Astronautics, Nanjing, China
Email: gaoxiguang@nuaa.edu.cn
Email:ydsong@nuaa.edu.cn

Keywords: Nonlinear dynamic, ceramic matrix composite, constitutive mode

Abstract

During the service life of high-performance engines, essential components in the high-temperature parts undergo simultaneous exposure to high temperatures and aerodynamic vibrations. Elevated vibrations in high-temperature conditions not only influence engine performance, but also expedite structural fatigue, resulting in premature failure. Selected SiC/SiC composite materials, renowned for their superior high-temperature performance, present considerable advantages and application potential. However, under such multi-field coupling hush service conditions, ceramic matrix composites (CMCs) demonstrate complex dynamic nonlinear and hysteresis behavior, which limits the ability to predict material failure. Thus, establishing a dynamic failure model and efficient computational methods for high-temperature CMCs are crucial. These advancements will accelerate structural material design and validation, enabling real-time monitoring and prediction of failure behavior in high-temperature composites, with significant engineering application potential.

To address the aforementioned challenges, this study developed mechanical loading and vibration experiment systems to obtain constitutive and dynamic data, respectively, at 1100℃. Tension and loading-unloading mechanical tests were conducted to obtain the tensile curves and skeleton curves for 2.5D CMCs at 1100℃. These data were used to establish arbitrary cyclic tensile and compressive constitutive model. A numerical model was stablished to simulate the stress-strain curves. This model integrated matrix cracking, interface friction and fiber fracture, and is applicable to 3D stress states. The calibrated parameter values in the constitutive model were applied to calculate the response of CMCs to dynamic loading at 1100℃. Combining the constitutive model and an explicit dynamic numerical method, a nonlinear dynamic simulation model was established for CMCs structures, to predict the first-order natural frequency and amplitude of 2.5D CMCs at 1100℃. This work contributes a better understanding of the CMCs' behavior under high-temperature dynamic loads.

1. Introduction

Ceramic-matrix composites (CMCs) have become indispensable in replacing high-temperature alloys in aero-engines due to their high strength, temperature resistance, excellent toughness, crack resistance,

and low density. Exposed to prolonged high temperatures and vibrations, aero-engines exhibit significant behavioral changes, necessitating a nonlinear dynamic calculation methodology to accurately assess CMCs' responses in such environments.

The theoretical framework for analyzing composite materials has evolved considerably. Love [1] introduced the classical laminate-plate theory, simplifying calculations significantly. This theory was further developed by Mindlin [2] and Naghdi [3], who included considerations for transverse shear and extrusion, thus enhancing dynamic response accuracy. Advances by Nagesh and Hanagud [4] using finite element methods revealed natural frequency reductions due to delamination. Librescu and Nosier [5] further refined dynamic equations with transverse shear deformation and higher-order effects, surpassing classical theory accuracy.

Recent studies have further examined the vibrational behaviors of composites under varied conditions. Lee et al. [6] analyzed carbon-fiber epoxy composite plates in supersonic airflow at different temperatures, while Xia et al. [7] developed models for wall plate vibrations under constant temperatures, linking decreased vibration frequency to thermal stresses. Fu et al. [8] created a dynamic model for composite beams across different temperatures.

Experimental validations by Spivey et al. [9] on aircraft structures under thermal loads confirmed the effectiveness of finite element methods, clarifying modal characteristics in high-temperature environments. Jeyaraj et al. [10] observed natural frequency variations in composite plates across temperatures. Birman et al. [11] studied the impact of matrix cracking on woven CMCs, finding minimal effects on stiffness and natural frequency. Gao et al. [12] introduced a three-dimensional shear lag model to analyze the vibration response of unidirectional CMCs, integrating multiscale simulation with finite-element methods.

While much research has focused on laminate-plate composites, the dynamic responses of CMCs with complex woven structures in high-temperature environments have received less attention.

This study conducts tensile, loading and unloading, and vibration tests on 2.5D woven SiC/SiC composites under high-temperature conditions to establish a macroscopic intrinsic model, assess high temperature's impact on natural frequency, and predict the first-order natural frequency and amplitude.

2. Methods Experiment

2.1. Specimen and Material

The material investigated in this study comprised a 2.5D woven shallow-bend SiC/SiC ceramic matrix composite (CMCs). In order to enhance the material's mass density, we utilized Chemical Vapor Infiltration (CVI). Through multiple cycles of vapor deposition applied to the preform surface using CVI, the preform was filled with SiC matrix, effectively compacting the CMCs. Consequently, CMCs composite plates were produced, boasting a density of approximately 1.8 g/cm³ as determined by displacement method.

The 2.5D woven SiC/SiC composites were prepared with a thickness of 3 mm, and for processing the CMCs test pieces, waterjet cutting [13], selected for its superior processing efficiency and cutting precision, was employed.

The specimens obtained through water cutting were utilized for mechanical property tests, and their dimensions and physical conFigureurations are depicted in Figure 1. The overall length of the specimen measured 200 mm, with a clamping end length of 25 mm, width of 12 mm, test section length of 100 mm, and width of 6 mm.

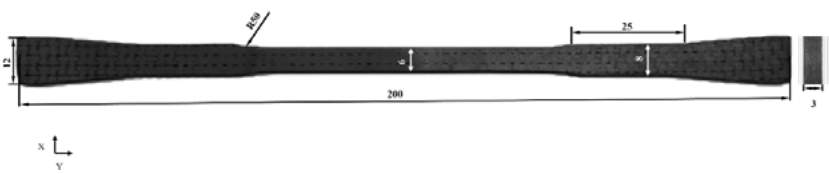


Figure 1. Dimensional drawing and picture of the dog bone specimen of 2.5D woven CMCs(mm)

Additionally, water jet cutting was utilized to procure rectangular specimens for dynamic response testing. These specimens measured 143 mm in length, 10 mm in width, and 3 mm in thickness. The clamping end was positioned on one side of the rectangle, featuring a clamping length of 20 mm, as depicted in Figure 2.



Figure 2. Dimensional drawing and picture of the rectangular specimen of 2.5D woven CMCs (mm)

2.2. Experimental Method

2.2.1. Intrinsic structure response test

Tension and loading-unloading mechanical tests were performed to obtain the tensile curves and skeleton curves for 2.5D CMCs at 1100℃. These data were utilized to establish an arbitrary cyclic tensile and compressive constitutive model.

To conduct static tensile, loading, and unloading tests on 2.5D woven SiC/SiC composites at 1100℃, a test system illustrated in Figure 3 was devised in this study. The test system primarily comprised a fatigue testing machine, high-temperature furnace and temperature control device, vacuum apparatus, water circulation cooling system, and strain measurement device.

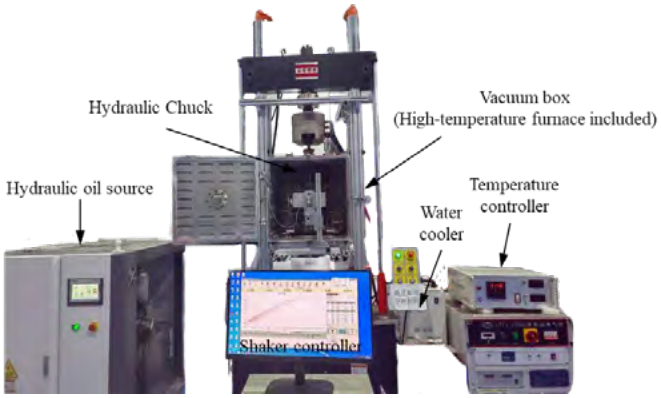
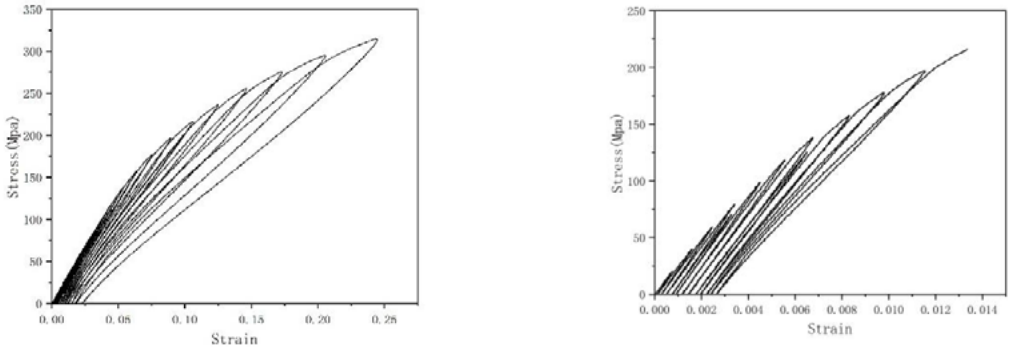


Figure 3. High temperature tensile, loading and unloading test system

The tensile test was executed under force loading at a loading rate of 0.05 kN/s until fracture occurred in the test specimen. For loading-unloading tests, force-controlled loading was employed at a loading rate of 0.05 kN/s, and loading paths were governed by a programmed sequence. Initially, tensile loads were applied until reaching the specified load, followed by unloading and reloading according to the program's parameters. Multiple loading-unloading cycles with decreasing maximum loads were included to validate the arbitrary nature of loading-unloading and the randomness of vibrational loads, thereby mitigating potential anomalies, as depicted in Figure 4.



(a) 25℃ (b) 1100℃

Figure. 4 Loading and unloading curves and skeleton curves of SiC/SiC composite.

The skeleton curves depicting cyclic loading and unloading stress–strain behaviors of the 2.5D woven CMCs at various temperatures closely mirrored the overall shape and trend observed in the monotonic tensile curve. These curves exhibited three distinct segments: initial linear, nonlinear, and secondary linear sections. The specimens' strength under cyclic loading and unloading conditions notably lagged behind that of monotonic tensile test specimens. This disparity stemmed from frictional forces between internal fibers, the matrix, and the interfacial layer, encompassing warp and weft yarns along with different transverse and longitudinal layers. Such frictional forces dissipated energy, consequently diminishing material strength [14-16].

At room temperature, the stress–strain curves of the 2.5D woven CMCs in the low-load range of the skeleton curves displayed almost linear profiles with minimal hysteresis, suggesting negligible frictional damage and energy dissipation. Conversely, in the high-load range, hysteresis loops formed in the cyclic loading and unloading stress–strain curves, with the loop area expanding alongside increasing loads. This occurrence arose from heightened interfacial frictional damage as load intensified, leading to gradual reduction in interfacial shear stress and increased interfacial debonding length. Consequently, residual strain and energy dissipation during loading and unloading augmented, contributing to a decline in material elastic modulus. Notably, the history of maximum load influenced the hysteresis loop's configuration [17].

In scenarios where tensile stress persisted at the maximum load point of the hysteresis loop, the stress–strain curve followed a monotonic tensile trajectory. This was attributed to the Ceramic-matrix's low fracture toughness, rendering it resistant to damage under cyclic loading, thereby exhibiting a "memory effect" within the hysteresis loop [18].

Comparatively, the high-temperature cyclic loading and unloading stress–strain curve largely retained its characteristics observed at room temperature. However, it no longer precisely mirrored the hysteresis loop of room-temperature loading and unloading, particularly in traversing through the historical maximum load point. This deviation became more pronounced with escalating temperatures. The weakening of initial interfacial bonding, expansion of interfacial slip zones, and exacerbation of interfacial wear at higher temperatures led to additional material damage during unloading and reloading processes. This observation underscores that elevated temperatures exacerbate material degradation [19].

2.2.2. Dynamic tests

Experimental setups suitable for high-temperature vibration tests were developed for 2.5D woven SiC/SiC composite flat-plate structures at 1100℃, as shown in Figure 5. This apparatus, designed to facilitate vibration performance testing, incorporated a vibrator, a high-temperature furnace, and precision measurement equipment, among other components. The system enabled vibration tests and dynamic response analyses under elevated temperatures.

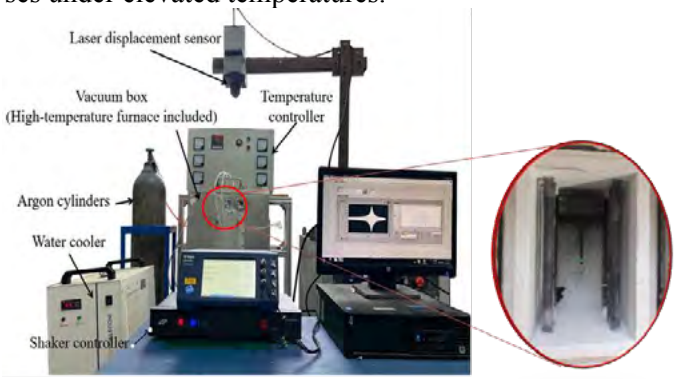


Figure. 5. High-temperature vibration experiment system

The high-temperature furnace, equipped with water cooling and gas filling functionalities, maintained a controlled environment. It featured quartz glass windows and a high-temperature resistant glass cover plate to minimize heat loss while ensuring a sealed environment. The vibration table, connected to the furnace through a vacuum-sealed interface, supported fixtures made of 310S stainless steel.

During the experiments, the vibrator's sampling frequency was set to 8192 Hz with an accuracy of 0.1μm. Initial tests involved a rapid sinusoidal sweep across a broad frequency range to estimate the first-order resonance frequencies of the undamaged CMCs. Subsequent tests increased the vibration load to

examine the material's nonlinear stress-strain characteristics. The acceleration excitation of the vibration table was set to 5 m/s², scanning frequencies near the first-order resonance frequency at a rate of 0.5 Hz/s. This method successfully captured the first-order natural frequency of the material at 1100℃. Fourier transform analysis converted time-domain data to frequency-domain signals for precise vibration analysis.

Figure 6 illustrates the vibration sweep tests on the 2.5D woven CMCs plates, demonstrating how frequency sweeping through the first natural frequency induced resonance and a significant displacement increase at 25 ℃ and 1100 ℃. This result confirmed the test data's integrity and showed a gradual increase in the first-order natural frequency with rising temperature, which, however, decreased at 1100 ℃. This behavior reflects changes in material stiffness due to temperature variations, influencing the natural frequency. Below 1100 ℃, as temperature increases, the difference in thermal expansion coefficients between the fibers and matrix decreases, enhancing material stiffness and increasing natural frequency. Above 1100 ℃, however, high temperatures cause SiC matrix degradation, fiber damage, and matrix cracks, reducing the composite's structural stiffness and lowering its natural frequency.

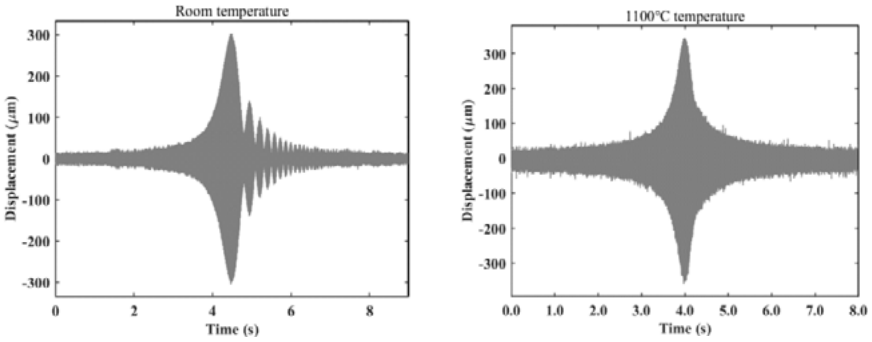


Figure. 6 Vibration time domain plot

2.3. Numerical modeling

The vibrations of CMCs beams involve individual units undergoing arbitrary cyclic tensile and compressive loads. Accurate simulation of these vibrations necessitates an intrinsic model that captures the repetitive stress behaviors under vibrational conditions. Establishing this model requires high-temperature tensile tests on 2.5D woven CMCs.

We utilized the cyclic loading and unloading stress-strain curves from these tests to model the behavior of 2.5D woven CMCs at high temperatures. This model, derived from the skeleton curves' trends, establishes a relationship between the historical maximum strain and the stress-strain response during each cycle.In the low-load range, linear fitting addressed the loading and unloading behaviors, where the modulus decreased in line with the skeleton curve. At high loads, direct fitting of the hysteresis loop was impractical due to the lack of a memory effect and material damage from high temperatures. However, the sub-loop displayed nearly linear behavior with minimal hysteresis, suggesting that friction damage had largely stabilized after the initial cycle. This finding highlighted the role of historical maximum stress in assessing material damage.

In conclusion, the completion of fitting arbitrary cyclic tensile and compressive stress–strain curves for 2.5D woven CMCs in 1100℃ environments provides a comprehensive understanding. Based on this macroscopic intrinsic model, stress at a given time can be calculated when the stress and strain at that time, the strain at a previous time, and the historical maximum stress and its corresponding strain are known., as shown in Eqs. 1:

$$^{t+\Delta t}\sigma = f(^{t}\sigma, ^{t}\varepsilon, ^{t+\Delta t}\varepsilon, \varepsilon_{\max}, \sigma_{\max}) \tag{1}$$

A finite-element model of the CMCs beam, matching the dimensions of the test specimens, was developed to simulate the effects of sinusoidal gravity fields at varying frequencies. This model helps to mimic the conditions of vibration tests effectively.

The structure of the cantilever beam is simple, and during its bending vibration, normal stress acts along the axial direction. Thus, each small element on the beam can be considered to undergo arbitrary tensile

and compressive behavior. Therefore, it is reasonable to use a CMCs arbitrary loading and unloading constitutive model considering temperature effects for dynamic response calculations, which can reduce computational complexity.
The vibration of the fixture base has been reflected in the equation through the global inertial load , and the displacement of the vibrator is very small and can be ignored in the simulation. Hence, this boundary condition is set:

$$u(x = 0) = v(x = 0) = w(x = 0) = 0 \tag{2}$$

$$\boldsymbol{f} = (0, 0, f)^T = (0, 0, \bar{f} \sin \omega t)^T \tag{3}$$

Based on the principle of virtual displacement, the dynamic control equation for CMCs is established as follows:

$$\int_\Omega \sigma_{ij} \delta \varepsilon_{ij} dV - \int_\Omega \rho \ddot{u}_i \delta u_i dV - \int_\Omega c \dot{u}_i \delta u_i dV - \int_{\Gamma 2} q_i \delta u_i ds - \int_\Omega \rho \bar{f} \sin(\omega t) \delta u_i dV = 0 (i, j = 1, 2, 3) \tag{4}$$

Where u, v, and w represent displacements in the x, y, and z directions, respectively.

By balancing (stress) differential equations and geometric differential equations, the control equation is simplified to:

$$\boldsymbol{K}^T \delta \boldsymbol{a} - \ddot{a}^T \boldsymbol{M}^T \boldsymbol{a} - \dot{\boldsymbol{a}}^T \boldsymbol{C}^T \delta \boldsymbol{a} = \boldsymbol{Q}^T \delta \boldsymbol{a} \tag{5}$$

Where:

$$\begin{cases} \boldsymbol{M} = \sum_e \int_{\Omega^e} \rho \boldsymbol{G}^{eT} \boldsymbol{N}^{eT} \boldsymbol{N}^e \boldsymbol{G}^e \mathrm{d}V \\ \boldsymbol{C} = \sum_e \int_{\Omega^e} c \boldsymbol{G}^{eT} \boldsymbol{N}^{eT} \boldsymbol{N}^e \boldsymbol{G}^e \mathrm{d}V \\ \boldsymbol{K} = \sum_e \int_{\Omega^e} \boldsymbol{G}^{eT} \boldsymbol{B}^{eT} \boldsymbol{\sigma}^e \mathrm{d}V \\ \boldsymbol{Q} = \sum_e \int_{\Gamma^e} \boldsymbol{G}^{eT} \boldsymbol{N}^{eT} \boldsymbol{q} \mathrm{d}S \end{cases} \tag{6}$$

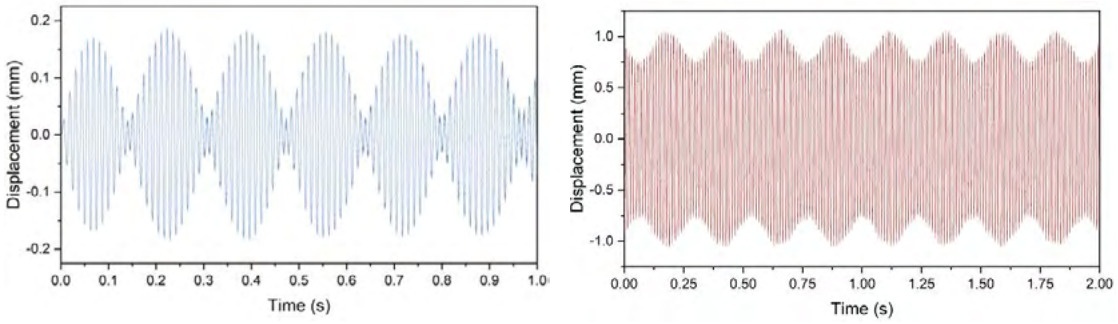
It should be noted that K here is not the stiffness matrix, but a vector with the same dimensions as the degrees of freedom of the structure. Writing the dynamic equation in this form facilitates the subsequent solution of the dynamic equation. Although not a stiffness matrix, it effectively reflects the stiffness of CMCs, and material nonlinearity is manifested in K.
This study employs the center difference method to solve the dynamic equations. This method is based on the finite difference method rather than the derivative of displacement with respect to time. The velocity and acceleration are obtained using the first-order and second-order derivatives of displacement, respectively. Utilizing the center difference method not only avoids matrix inversion but also accelerates the calculation speed and does not produce mathematical discontinuity points in the calculation process of the intrinsic model, effectively avoiding iterative operations and saving space in the calculation. This method is very suitable for calculating the nonlinear vibration response of CMCs.
Based on the established macroscopic arbitrary tensile and compressive intrinsic model of 2.5D woven CMCs in different temperature environments, a self-developed solver was programmed to import the material properties. Subsequently, leveraging the theory of the central difference method, self-developed solver was developed to calculate the vibration response.

3. Conclusions

The nonlinear constitutive behavior of CMCs is calculated using the shear-lag model, and the parameters involved in the calculation are shown in Table 1.

Table 1. Parameters of constitutive model.

Item	Value	Item	Value
E_m / GPa	369.75	τ_i /MPa	50
E_f / GPa	223.80	r_f / μm	6
α_m /$\times 10^{-6}$ / ℃	4.53	L_{sat} / mm	0.54
$\alpha_f \times 10^{-6}$ / ℃	0.1252	ΔT / ℃	-1000
ν_f	0.2	σ_{mR} /MPa	140
ν_m	0.8	m	2



(a) dynamic response with small damage (b) dynamic response with large damage

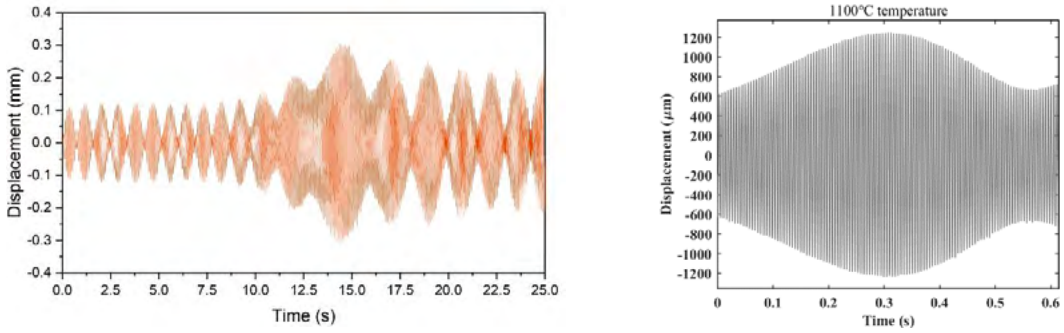


Figure.7.. Simulation dynamic responses of the CMCs

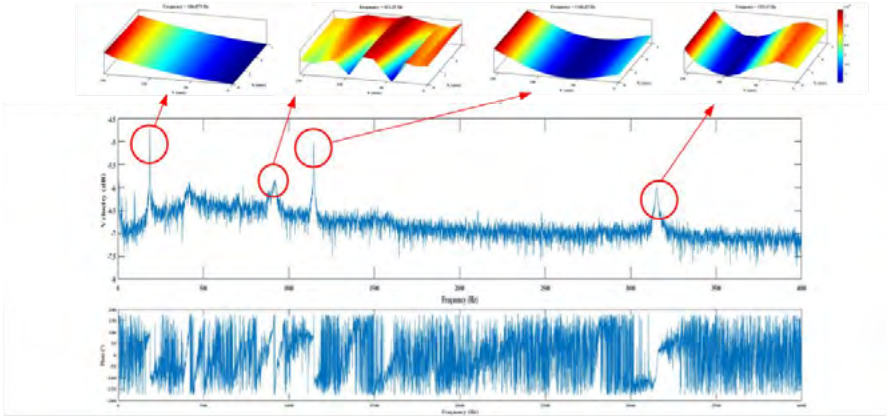


Figure. 8.. Simulation of nonlinear dynamic response

Table 2. First-order natural frequency test and simulation comparison and deviation.

Tmperature (℃)	25	1100
Experiment (Hz)	212	198
Simulation (Hz)	211.9	199

Acknowledgments
The authors are grateful for the financial supports provided from the National Science and Technology Major Project (Grant No. Y2019-I-0018-0017).

References
[1] A.E.H. Love, On the Small Free Vibrations and Deformations of the Elastic Shells, 1988.
[2] R.D. Mindlin, Influence of Rotatory Inertia and Shear on Flexural Motions of Isotropic, Elastic Plates, Journal of Applied Mechanics, vol. 18, 1951.
[3] P.M. Naghdi, ON THE THEORY OF THIN ELASTIC SHELLS, Quarterly of Applied Mathematics, vol. 14, 1955.
[4] S. Hanagud, Delaminations in smart composite structures - A parametric study on vibrations, 1990.
[5] L. Librescu, A. Nosier, Response of laminated composite flat panels to sonic boom and explosive blast loadings, AIAA Journal, vol. 28, 1990, pp. 345-352.
[6] W. Xia, Z. Yang, Vibration Analysis to Composite Panels in Thermal Environment, Chinese Journal of Applied Mechanics, 2005.
[7] Y. Fu, Y. Chen, J. Zhong, Analysis of nonlinear dynamic response for delaminated fiber–metal laminated beam under unsteady temperature field, Journal of Sound & Vibration, vol. 333, 2014, pp. 5803-5816.
[8] N.D. Spivey, HIGH-TEMPERATURE MODAL SURVEY OF A HOT-STRUCTURE CONTROL SURFACE, 2010.
[9] I. Lee, D.M. Lee, I.K. Oh, Supersonic Flutter Analysis of Stiffened Laminated Plates Subject to Thermal Load, Journal of Sound & Vibration, vol. 224, 1999, pp. 49-67.
[10] P. Jeyaraj, N. Ganesan, C. Padmanabhan, Vibration and acoustic response of a composite plate with inherent material damping in a thermal environment, Journal of Sound & Vibration, vol. 320, 2009, pp. 322-338.
[11] V. Birman, L.W. Byrd, Effect of Matrix Cracks on Damping in Unidirectional and Cross-Ply Ceramic-matrix Composites, Journal of Composites Materials, vol. 36, 2002, pp. 1859-1877.
[12] X. Gao, D. Han, J. Chen, H. Dong, Y. Song, Numerical and experimental study on the nonlinear dynamic response of a Ceramic-matrix composites beam, Ceramics International, vol. 44, 2018.
[13] J. Jiao, H.P. Qiu, X.Q. Li, J.H. Luo, Y. Wang, The pyrolysis processing of polycarbosilane studied by TG, XRF, IR, XRD, and XPS, Key Engineering Materials, vols. 512-515, 2012, pp. 965-970.
[14] J.W. Lee, I.M. Daniel, Progressive transverse cracking of crossply composite laminates, Composites Part B Engineering, vol. 34, 2003, pp. 473-480.
[15] S.S. Lee, W.W. Stinchcomb, Damage Mechanisms and Fracture Modes in Nicalon / CAS-II Laminates, Key Engineering Materials, vols. 120/121, 1996, pp. 227-256.
[16] S. Zhu, M. Mizuno, Y. Kagawa, Y. Mutoh, Monotonic tension, fatigue and creep behavior of SiC-fiber-reinforced SiC-matrix composites: a review, Composites Science & Technology, vol. 59, 1999, pp. 833-851.
[17] J. Wang, Y. Xiao, K. Inoue, M. Kawai, Y. Xue, Modeling of nonlinear response in loading-unloading tests for fibrous composites under tension and compression, Composites Structures, vol. 207, 2018, pp. 894-908.
[18] H. Mei, L. Cheng, Comparison of the mechanical hysteresis of carbon/ceramic-matrix composites with different fiber preforms, Carbon, vol. 47, 2009, pp. 1034-1042.
[19] S. Zhang, X. Gao, H. Dong, Y. Song, S. Pang, Effects of gradual matrix crack closure on the constitutive behavior of SiC/SiC composites upon unloading, Ceramics International, vol. 43, 2016, pp. 1839-1842.

NUMERICAL INVESTIGATION OF CAVITY GROWTH SUBSEQUENT TO RAPID GAS DECOMPRESSION OF CO2 IN HIGH-DENSITY POLYETHYLENE

Houssem Eddine Rekik[1], Ali M. Alghamdi[1], Xiaole Li[1], Gilles Lubineau[1]

[1]Mechanics of Composites for Energy and Mobility Lab, King Abdullah University of Science and Technology (KAUST), Thuwal, 23955-6900, Kingdom of Saudi Arabia
Email: houssem.rekik@kaust.edu.sa
Email: ali.alghamdi.2@kaust.edu.sa
Email: xiaole.li@kaust.edu.sa
Email: gilles.lubineau@kaust.edu.sa

Keywords: CO_2, HDPE, RGD, Multiphysics, Diffusion

Abstract

Rapid Gas Decompression (RGD) is a concern when using polymeric material in gas transport pipelines. To better understand the mechanism of RGD, this study investigates high-density polyethylene (HDPE) liners used in pressurized CO_2 pipelines for carbon capture and sequestration (CCS). We propose a coupled deformation-diffusion model tailored for polymeric materials under pressurized gas conditions. An extensive parametric study was performed using the model to assess cavity growth in relation to variations in maximum pressures and depressurization rates. The results were consistent with the experimental observations, emphasizing the potential of such numerical model in estimating RGD damage and maintaining the integrity of polymeric materials in gaseous environments.

1. Introduction

The energy industry is particularly interested in pressurized CO_2 pipelines for carbon capture and sequestration (CCS). These pipelines play a pivotal role in various CCS applications, with two prominent ones being sustainable hydrogen production (SHP) and enhanced oil recovery (EOR)[1]. Carbon steel is widely used in many oil and gas operations due to its low cost and strong performance, which is complemented by extensive familiarity with its operational and maintenance procedures. However, the presence of water and impurities in captured CO_2 can drastically increase the corrosion rate of steel pipelines. This corrosion not only compromises the integrity of the pipelines but also poses environmental and safety risks[2]. Composite pipelines, on the other hand, exhibit superior performance compared to steel in numerous aspects, including weight, spoolability, ease of installation, reduced greenhouse gas emissions during production, longevity, and maintenance expenses. High-Density Polyethylene (HDPE) is the main liner material used in these pipes. HDPE is widely used in industrial pipelines due to its mechanical properties, barrier properties, chemical resistance, and low cost [3], [4].

Nonetheless, challenges arise in terms of chemical compatibility, permeability, low-temperature performance, and resistance to rapid gas decompression (RGD) when using polymeric materials in gas transportation [5], [6]. The permeation of gases through polymer materials, particularly under high temperatures and pressures, is an important consideration for system integrity [7]. HDPE is utilized in environments where it is exposed to corrosive fluids at high pressures and temperatures up to 300 bar and 85°C and. Rapid Gas Decompression (RGD) refers to the phenomenon in which pressurized gases absorbed into a polymer material are suddenly released due to a rapid decrease in external pressure. This phenomenon can result in structural damage or failure [8], [9].

The goal of this study is to investigate the viability of HDPE liners for CO_2 composite pipelines, driven by the pressing need to address critical challenges in carbon capture and sequestration (CCS) during the ongoing energy transition. In this work, we propose a coupled deformation-diffusion model tailored for polymeric materials under pressurized gas conditions. Our proposed model offers insights into the effects of rapid gas decompression (RGD) on HDPE liner materials. Through a comprehensive parametric study, we investigate how environmental factors such as maximum pressure and depressurization rate affect the integrity of HDPE liners in a harsh CO_2 environment.

2. Methodology

In this section, we present the different components of the coupled model and its numerical implementation.

2.1. Problem description

Here, we propose a coupled diffusion-deformation model to assess the growth of a pre-existing cavity within the polymer. This cavity may arise from manufacturing defects or nucleate due to prior rapid gas decompression (RGD) events. We proceed with the assumption of a perfectly spherical cavity, and that the surrounding area of the cavity is initially free of residual stresses. To mimic a pipe liner (Figure 1), we adopt a rectangular HDPE coupon, with one dimension smaller than the other two representing the thickness.

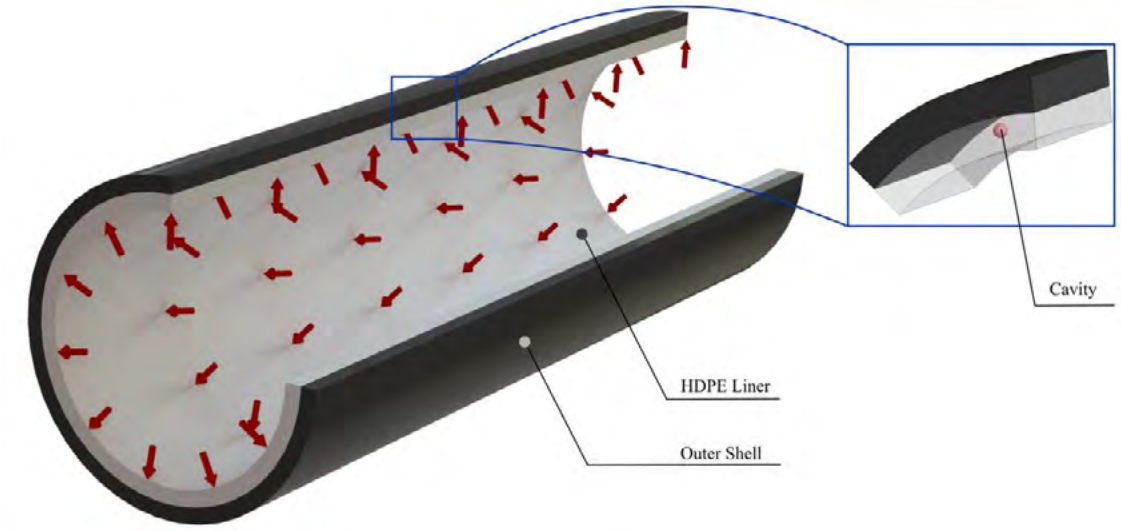


Figure 1. Schematic of a Pipe with HDPE liner under CO_2 pressure. The detail shows a coupon with a spherical cavity

For numerical simulations, we consider a 2D square Representative Volume Element (RVE) containing a single cavity. The RVE is subjected to CO_2 pressure from both faces along the thickness while being periodic along the other faces. (See Figure 2).

The substantial difference in scale between liner thickness (on the order of millimeters) and cavity size (on the order of micrometers) complicates the implementation of the entire structure, resulting in numerical problems. Consequently, we adopted a global-local approach (see Figure 3), where we first obtain the solution for the larger scale without the cavity, and then use it to solve for the smaller scale problem. The global solution is transfered to the local problem as boundary conditions. This method not only overcomes numerical challenges but also significantly reduces computation time, as we can derive an analytical solution for the large scale problem.

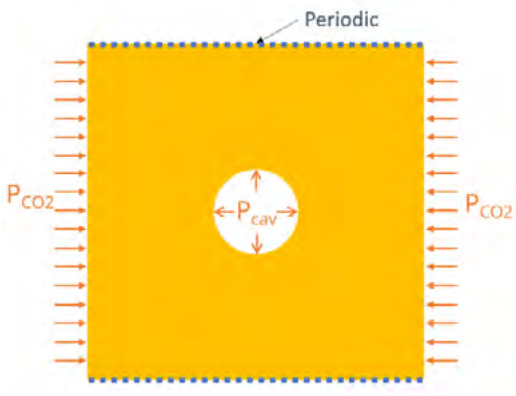


Figure 2. Boundary conditions of the RVE

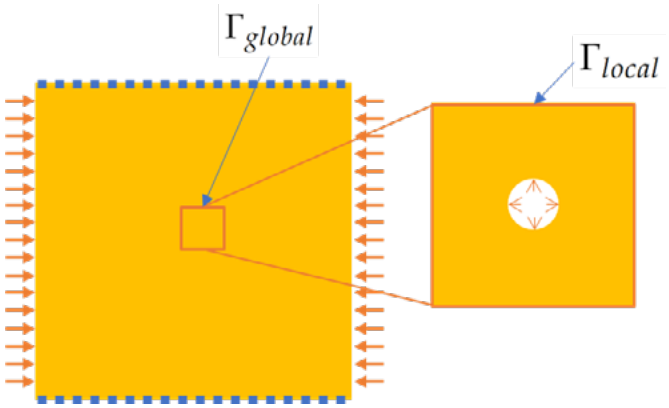


Figure 3. Schematic representation of the Global-Local modeling approach

2.2. Governing equations

In this section, we describe the governing equation for the coupled multiphysics model, which incorporates deformations and CO_2 gas transport in the HDPE. From a mechanical standpoint, the RVE is subjected to pressure boundary conditions on the inner and outer surfaces, and on the cavity boundary, where the gas accumulates. Further, periodicity is imposed on the other surfaces. The boundary value problem for deformation is governed by the following equations.

$$\begin{aligned} &\underline{div}\,\underline{\underline{\sigma}} = \underline{0} && \forall \underline{x} \in \Omega \\ &\underline{\underline{\sigma}}.\underline{n} = -p\underline{n} && \forall \underline{x} \in \partial\Omega_T \end{aligned} \tag{1}$$

Where $\underline{\underline{\sigma}}$ is the stress tensor, $\underline{n}$ is the outward normal at point of the boundary, and p is the prescribed pressure at the pressurized boundaries $\partial\Omega_T$.

For the constitutive law, we assume an elastoplastic material with nearly perfect plasticity. The yield stress σ^y of HDPE at a temperature T was obtained using the law given by [10] expressed as

$$\sigma^y(T) = 112.85 - 0.305T \tag{2}$$

In terms of gas transport, we assume that CO_2 transport in HDPE under the given conditions is governed by Fickian diffusion. We prescribe the Dirichlet BC on the pressurized surfaces, including the cavity boundary. For periodicity, we assume continuity of concentration and a zero gap for normal flux. The following equations give the boundary value problem for diffusion.

$$\begin{aligned} &\frac{\partial c}{\partial t} + div\underline{J} = 0 && \forall (\underline{x},t) \in \Omega \times [0,T] \\ &\underline{J} = -D\underline{\nabla c} && \forall (\underline{x},t) \in \Omega \times [0,T] \\ &c(\underline{x},0) = 0 && \forall \underline{x} \in \Omega \\ &c(\underline{x},t) = c_d && \forall (\underline{x},t) \in \partial\Omega \times [0,T] \end{aligned} \tag{3}$$

Where c is the gas concentration, $\underline{J}$ is the diffusive flux, D is the diffusion coefficient, and c_d is the prescribed concentration at the boundary.

The cavity is modeled as a closed sink where gas accumulates, resulting in pressure buildup. Assuming the gas behaves ideally, the ideal gas law, $PV = nRT$, can be used to calculate the pressure at the cavity's surface. The total number of moles inside the cavity is obtained by mas conservation law which states that: the evolution of the mass inside the cavity is equal to the total flux crossing the boundary. Thus, the number of of moles is obtained by solving

$$\frac{d\,n_{cav}}{dt} = \int_{\partial\Omega_{cav}} \underline{J}.\underline{\nu}\, dS \tag{4}$$

Where $\underline{\nu}$ is the outward normal at the cavity boundary.

The gas pressure and the gas concentration at the pressurized boundaries are coupled via Henry's law

$$\begin{aligned} c_g &= P_g\ S \\ c_{cav} &= P_{cav} S \end{aligned} \tag{5}$$

Where S is Henry's Solubility.

2.3. Numerical Implementation

The model was implemented in COMSOL Multiphysics software due to its simplicity in solving coupled physics. For the cavity growth assessment, we focus only on the depressurization period where the cavity will be expanding due to the difference between the loading pressure and cavity pressure. Furthermore, due to the simplicity of the global problem we get an analytical solution for the stress and for the concentration. Thus, we only have to simulate the local part. For the deformation part, the stress is uniform and it's given as

$$\underline{\underline{\sigma}} = -p\,\underline{e_x} \otimes \underline{e_x} \tag{6}$$

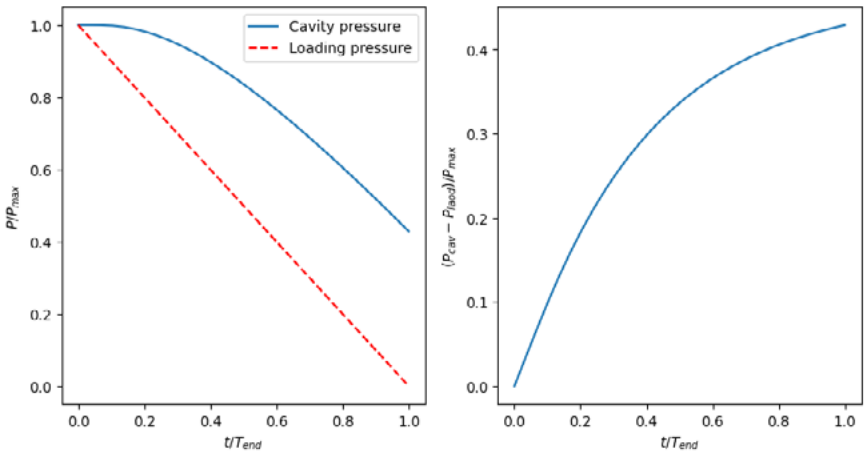
And for diffusion, the concentration of CO_2 is given at any time during the depressurization $0 \le t \le T_{dp}$ and at any position x along the thickness by the following expression

$$\frac{c(x,t)}{c_{\max}} = 1 - r\,t + \sum_{k=1}^{\infty} \frac{4r}{(2k+1)^3 \pi^3} \mathrm{Sin}\left((2k+1)\pi x\right)\left(1 - e^{-(2k+1)^2 \pi^2 t}\right) \tag{7}$$

The depressurization was assumed to be of the form $P_g = P_{\max}(1 - r\,t)$, where $P_{\max}$ is the saturation pressure and r is the depressurization rate.

3. Results

In this section, we present the results obtained from various parametric studies conducted using the model described earlier to evaluate cavity growth in HDPE liners. For each simulation, we calculate the final cavity volume after complete depressurization. Additionally, we focus our study on a single point that is located at the mid-thickness, as it represents the position experiencing the most severe pressure accumulation. For all the reported results, the temperature was kept constatnt at $T = 85°C$ and the coupon thickness was set to 1 mm.



(a) (b)

Figure 4. (a) Normalized Cavity pressure and loading pressure versus normalized time. (b) difference between cavity and load normalized pressures versus time

3.1. Maximum Pressure difference

The analytical solution for diffusion provided in the previous section provides quick insight into the pressure profile at the cavity during depressurization. Figure 4 exhibits the cavity and load pressure profiles (4a), as well as their differences across the depressurization time (4b). We see that difference is maximum at the end of depressurization (Figure 4b). As a result, we anticipate that the cavity will expand the most when the loading pressure hits zero. Afterwards, the gas will continue to evacuate slowly and the cavity will relax.

3.2. Results objectivity

To ensure the objectivity of our results, we must verify that the local RVE size (referred to as the scale size) does not impact the results. Therefore, we perform a sensitivity analysis to assess the effect of the scale size. We conduct simulations with various initial cavity sizes and scale sizes. Employing an almost instantaneous depressurization rate, which is anticipated to induce the most significant change in cavity volume. Figure 5 illustrates the relative change in volume as a function of the scale size for different levels of initial cavity sizes. We observe that the results saturates for higher scale size. For the following simulations, we fix the scale size to 100um.

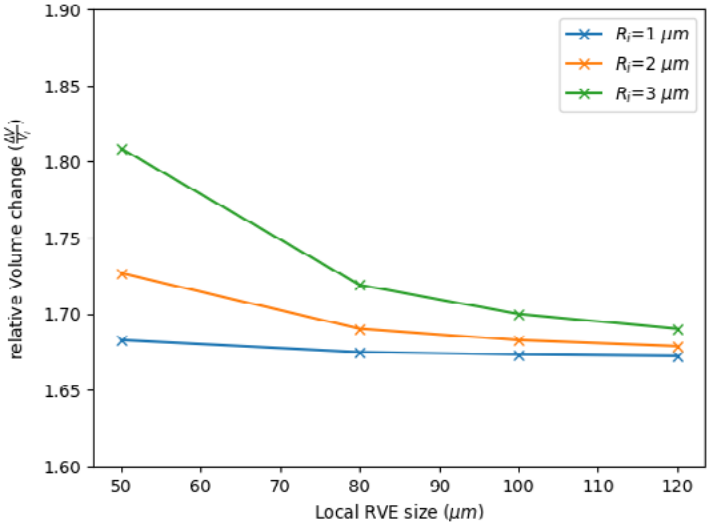
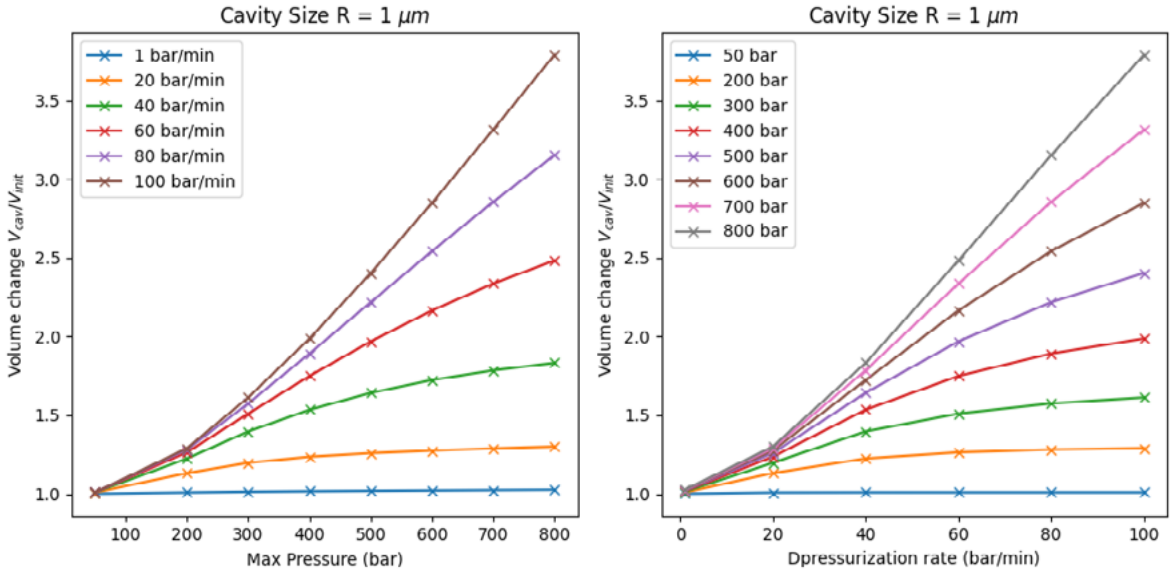


Figure 5. The relative change in the cavity volume for various local RVE size.

3.3. Parametric study

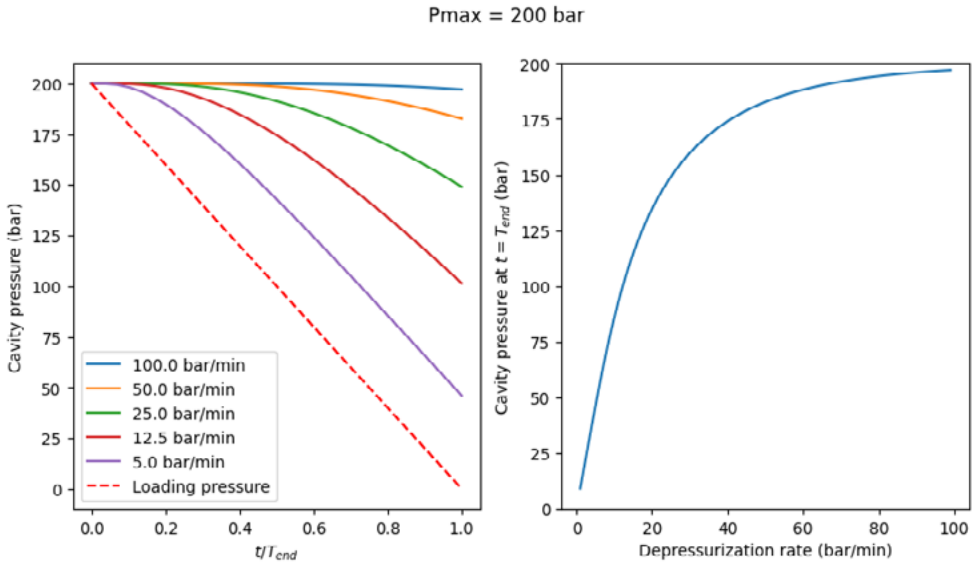
In this section, we conduct multiple simulations with varying depressurization rates and maximum pressures, while keeping the initial cavity size fixed at 1 µm. The results are presented in Figure 6. Our findings indicate the absence of cavity growth for low maximum pressures (<100 bar) and slower depressurization rates (<1 bar/min). Above these thresholds, the model starts to predict volume change in the cavity. The damage becomes more severe when going to high pressures and high rates. Additionally, the figure reveals a saturation feature, particularly evident for medium pressures and rates. This suggests that damage is limited for a fixed parameter (maximum pressure or depressurization rate). In other words, for a set rate (resp. maximum pressure), the cavity growth is limited to a certain value, even for higher pressures (resp depressurization rates).



(a) (b)

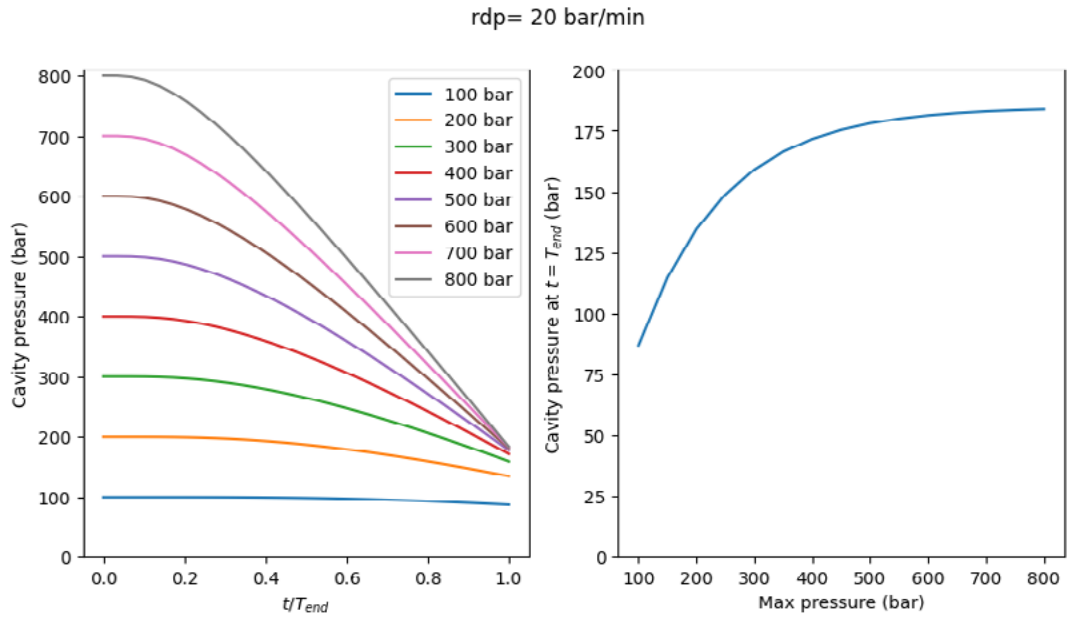
Figure 6. Parametric study results for Maximum pressure and the depressurization rate. (a) we plot the cavity growth vs the maximum pressure for different levels of depressurization rate. (b) we plot the cavity growth vs the depressurization rate for different levels of maximum pressure.

To explain the saturation features, we plot the cavity pressure at the end of depressurization against various depressurization rates (Figure 7) and maximum pressures (Figure 8). Figure 7 shows that the change in final cavity pressure is significant at low rates before saturating to the maximum loading pressure. This revealed that before reaching a critical depressurization rate (depending on the maximum pressure), we detect a change in cavity expansion as the rate increases. Following that, the cavity growth becomes less sensitive to the depressurization rate. A similar observation is made with the variation of the maximum pressure (Figure 8), where we can plainly see that the final cavity pressures concentrate to a particular level when the rate is fixed and the maximum pressure is varied.



(a) (b)

Figure 7. (a) Plot of the cavity pressure evolution with different depressurization rates. (b) Plot of the cavity pressure at the end of depressurization versus the depressurization rates



(a) (b)

Figure 8. (a) Plot of the cavity pressure evolution with different maximum pressures. (b) Plot of the cavity pressure at the end of depressurization versus the maximum pressure

Conclusions

In this study, we present a coupled multiphysical model that assesses the growth of a pre-existing defect in polymeric materials under rapid gas decompression. Our model effectively illustrates the impact of both the depressurization rate and the maximum pressure on cavity growth. Notably, it accurately captures the phenomenon where slow decompression limits the defect growth. Similar behavior is observed concerning the loading pressures. Furthermore, our model predicts saturation behavior for medium depressurization rate and load pressure. These parametric study results are in accordance with the phenomena observations. Therefore, it demonstrates the model's utility in predicting rapid gas decompression damage, and offering quantification of the cavity growth. Notably, our model's applicability extends to various polymeric materials in gas environments, provided no chemical reactions occur. Overall, our findings suggest promising potential for using this model to anticipate and manage rapid gas decompression-induced damage in practical applications.

Acknowledgement

The research reported herein was supported by King Abdullah University of Science and Technology (KAUST), under award number BAS/1/1315-01-01.

References

[1] H. C. Lau, S. Ramakrishna, K. Zhang, and A. V. Radhamani, "The role of carbon capture and storage in the energy transition," *Energy and Fuels*, vol. 35, no. 9, pp. 7364–7386, May 2021, doi: 10.1021/acs.energyfuels.1c00032.

[2] I. Energy Agency, "Technology Perspectives Energy Special Report on Carbon Capture Utilisation and Storage CCUS in clean energy transitions." [Online]. Available: www.iea.org/t&c/

[3] J. Mason, "Thermoplastic Liners For Oilfield Pipelines," in *Oil and Gas Pipelines: Integrity and Safety Handbook*, wiley, 2015, pp. 447–456. doi: 10.1002/9781119019213.ch31.

[4] J. Conley, B. Weller, and A. Sakr, "RECENT INNOVATIONS IN REINFORCED THERMOPLASTIC PIPE."

[5] E. Schlangen, M. Lukovic, B. Šavija, and O. Copuroglu, "Nano-Indentation Testing and Modelling of Cement Paste," in *CONCREEP 10*, Reston, VA: American Society of Civil Engineers, Sep. 2015, pp. 1028–1031. doi: 10.1061/9780784479346.122.

[6] L. B. Hill, X. C. Li, and N. Wei, "CO2-EOR in China: A comparative review," *International Journal of Greenhouse Gas Control*, vol. 103. Elsevier Ltd, Dec. 01, 2020. doi: 10.1016/j.ijggc.2020.103173.

[7] A. Dargahi, M. Duncan, J. Runka, A. Hammami, and H. E. Naguib, "Supercritical CO2 permeation in polymeric films: Design, characterization, and modeling," *Mater Des*, vol. 227, Mar. 2023, doi: 10.1016/j.matdes.2023.111715.

[8] M. Gerland, S. A. E. Boyer, and S. Castagnet, "Early stages of cavitation in a stretched and decompressed poly(vinylidene fluoride) exposed to diffusive hydrogen, observed by Transmission Electronic Microscopy at the nanoscale," *Int J Hydrogen Energy*, vol. 41, no. 3, pp. 1766–1774, Jan. 2016, doi: 10.1016/j.ijhydene.2015.11.015.

[9] B. Dewimille, J. Martin, and J. Jarrin, "Behaviour of thermoplastic polymers during explosive decompressions in a petroleum environment," *Journal de Physique IV Proceedings*, vol. 111, no. C7, p. 3, 1993, doi: 10.1051/jp4:19937243ï.

[10] N. Merah, F. Saghir, Z. Khan, and A. Bazoune, "Effect of temperature on tensile properties of HDPE pipe material," *Plastics, Rubber and Composites*, vol. 35, no. 5, pp. 226–230, 2006, doi: 10.1179/174328906X103178.

MECHANICAL CHARACTERIZATION AND MODELING OF FIBER REINFORCED POLYAMIDES IN CONTACT WITH COOLANT

Gilles ROBERT[1], Florent ALEXIS[1]

[1]Application Center, DOMO Chemicals, avenue Ramboz, Saint Fons, France
Email: gilles.robert@domo.org, Web Page: https://www.domochemicals.com/en

Keywords: Polyamide 6.6, coolant, ethylene glycol, short fibers, meta-models

Abstract
Mechanical and viscoelastic behavior of fiber reinforced polyamide 6.6 has been characterized before and after hydrolytic ageing. The level of properties achieved has been shown to depend only on the average molecular weight, and not the couple time/temperature used for ageing. Results have then been inserted into a meta modeling approach based on a generalized time temperature superposition method that was proven effective for several water, ethylene glycol and coolant concentrations, and easily adaptable to aged materials.

1. Introduction

Many short fibers reinforced polyamide 6.6 parts under the hood are in contact with coolant. It is true for internal combustion engines, or batteries electric and hybrid vehicles, not to mention fuel cells. The interactions between polyamide and coolant main components, water and ethylene glycol include plasticization, which decreases strongly the compound's glass transition temperature and hence mechanical properties in standard operating conditions. They also include chemical degradation, through hydrolysis of the polyamide chains[1]. Simulation of parts in contact with coolant is key to optimize their design. To perform it accurately, all the relevant parameters must be taken into account, and a specific simulation chain must be developed.

To face this challenge, a collaborative project has been built. Project team includes OEMs, Renault and TOYOTA, the tier one supplier SOGEFI Filtration, two French academic labs, CEMEF and LEM3, ADI a toolmaker, NOVITOM, specialized in analytical techniques involving synchrotron X-rays beams, AROBAS technologies, Hexagon Manufacturing Intelligence, editor of the Software Digimat™ and DOMO chemicals as material supplier and project coordinator. Project was funded by Banque Publique d'Investissement, and local communities Grand Lyon and Auvergne Rhône Alpes.

One of the main challenges before these new simulations become a reality is the reinforced materials characterization and modeling. In parts, local water or ethylene concentrations, temperatures and average molecular weight are highly variable. The influence of all these parameters must be characterized, and a way to manage them in simulations must be found. This is the target of this study.

2. Materials and methods

The materials under investigation are commercial compounds of polyamide 6.6 reinforced with glass fibers, TECHNYL A218 V30 34NG. They are used to mold plaques with the following geometry: length 360mm, width 100mm, thickness 3mm. The gating system ensures that fiber orientation is homogenous over the volume. The fiber orientation is measured using high resolution CT-scans performed in ESRF and post processed to extract fiber orientation tensors in the thickness of the plaques. Figure 1 illustrates the orientation across the specimens for two different specimens locations and demonstrates orientation homogeneity across the plaque. All the specimens machined have been cut along the symmetry axis of the plaque, between the two points where fiber orientation have been characterized. Three different orientations have been machined: 0°, 45° and 90°. Unfilled specimens made with the same formulation as the reinforced compounds, without glass fibers, have also been molded.

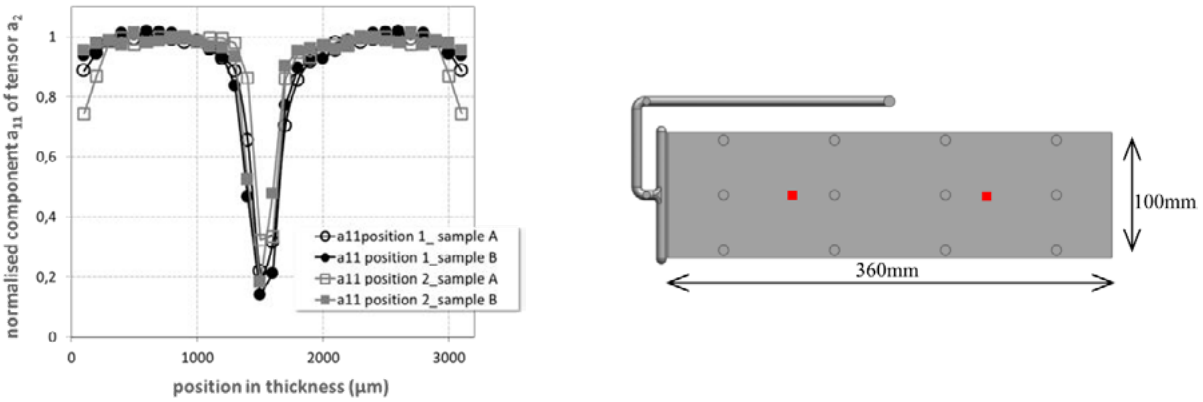


Figure 1. orientation tensors in two different locations of a plate illustrated above for a short fiber reinforced polyamide 6.6 reinforced with 30% of glass fibers

Aging of materials have been performed in autoclaves, at temperatures ranging from 110°C to 125°C, in contact with a mixture of ethylene glycol and water. Volume ratio used is 50% of each liquid. The ethylene glycol used is a commercial product, CCI L255N. Times used at each temperature have been adjusted to reach after treatment 68%, 56%, 44% and 32% of the initial average molecular weight in number. At a temperature of 120°C, the different times used are 408h, 624h, 948h and 1800h. For three of the molecular weight targeted, several couples time-temperature have been obtained.
Specimens molded and machined have been characterized using tensile tests for reinforced compounds and DMTA for unfilled specimens. Tensile tests have been realized using a specific experimental setup. Longitudinal and transverse strain have been measured using a first camera. A second camera is used to measure the strain in the thickness thanks to a PROVISYS video extensometer. This leads to true strain – true stress tensile curves. The longitudinal strain rate is also kept constant during the whole tensile test. DMTA tests are frequency scans between 0,01Hz and 20Hz, led at several constant temperatures between -100°C and 210°C. After tests, a time-temperature superposition procedure is applied in order to create a mastercurve, following a method classical in polymer science [2].

3. Consequences of hydrolysis on viscoelastic properties

Viscoelastic properties have been characterized at different levels of hydrolysis and compared with the properties of a material saturated with coolant, but without any significant loss of its average molecular weight M_n.

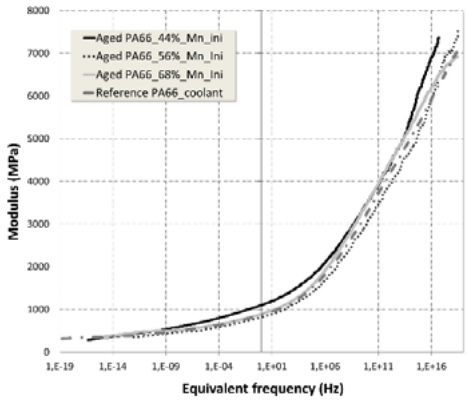


Fig. 2a: mastercurves obtained on PA66 saturated with coolant at different levels of average molecular weights after ageing

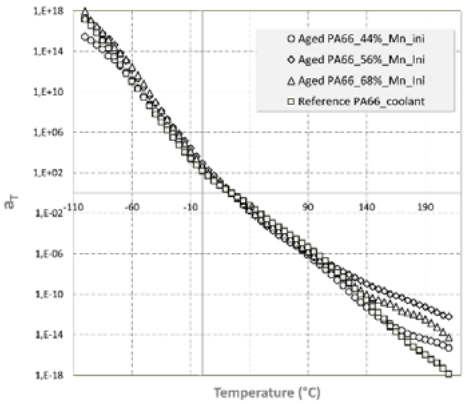


Fig. 2b: shift factors computed during the building of mastercurves on PA66 saturated with coolant after ageing

Results are illustrated on figure 2 for both the mastercurve and the shift factors associated. The mastercurves and shift factors are extremely similar to each other. Hydrolysis effects on viscoelastic properties are weak or even negligible. The only temperature range where curves can be differentiated is above 140°C, which is (a) the maximum usage temperature of reinforced PA6.6 in contact with coolant ; (b) a temperature where coolant desorption in the material is fast and makes the DMTA results questionable anyway. In conclusion, it is safe to say that viscoelastic processes are not strongly affected by hydrolysis in the average molecular weight domain explored and useful temperature range.

4. Consequences of hydrolysis on tensile properties

The first key result obtained comes from the comparison of materials aged in different conditions: 110°C/1392h, 115°C/936h, 120°C/624h, 125°C/432h. The final average molecular weight in number M_n of all these materials is 56%±1% of their initial average molecular weight. Results are pictured below on figure 3a and 3b. The main conclusion is that the mechanical behavior depends only on the average molecular weight, and not on the aging temperature or aging time. On figure 3a, the tensile curves obtained with the different aging conditions can't be differentiated. On figure 3b, failure strains for a 45° orientation are given for various temperatures and compared with the reference without hydrolysis. It can be checked on the figure that there is no noteworthy influence of aging conditions on failure strain, as long as the same average molecular weight is achieved.

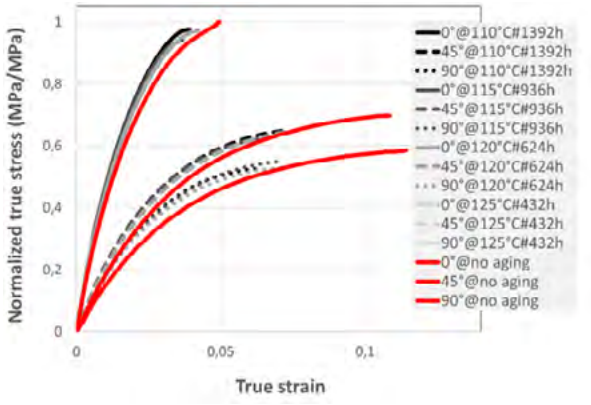


Fig. 3a: Tensile curves measured at 23°C and $10^{-3}s^{-1}$ for three different orientations on a 30% fibers reinforced PA6.6. Red curves: material saturated with coolant without hydrolysis. Grey curves: hydrolysed materials saturated with coolant

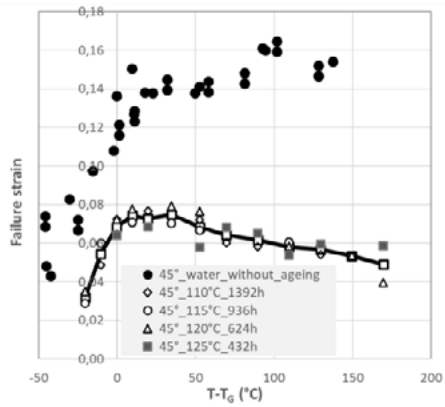


Fig. 3b: failure strain after aging in coolant for 30% glass fibres reinforced PA6.6. Comparison of several couples temperature/time leading to the same average molecular weight. Results are given for a fibre orientation of 45°.

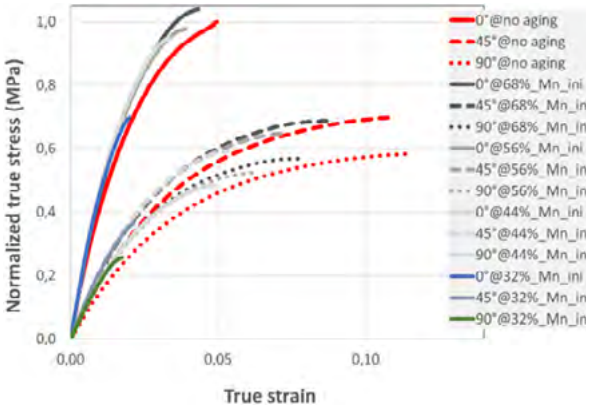


Fig. 4a: Tensile curves measured at 23°C and 10-3s-1 for three different orientations on a 30% fibers reinforced PA6.6 at different levels of hydrolytic ageing

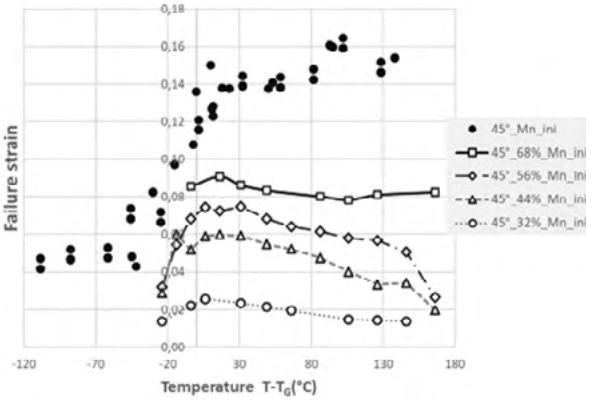


Fig. 4b: progressive embrittlement after aging in coolant for 30% glass fibers reinforced PA6.6 with a fiber orientation of . 45°

The main consequence of hydrolytic aging is a progressive embrittlement of the material. The tensile curves shape is not modified significantly by aging. Oppositely, failure strain decreases strongly. It becomes very low for the minimum value of average molecular weight studied, as shown by figure 4.
An interesting effect is the difference of performance evolution after ageing for different fibers orientations. This effect is stronger at high temperature and is illustrated on figure 5 for a tensile test temperature of 120°C. In initial conditions failure strain at 45° and 90° are bigger than for longitudinal orientation. Aging leads to a decrease in failure strain that reaches 80% of the initial value for longitudinal orientations, and 96% for transverse orientations. It leads to lower failure strain at high temperature for orientations of 45° or 90° compared to longitudinal orientations. This means that in these conditions the loss of matrix ductility is partially compensated by fibers, that hinder crack propagation[3].

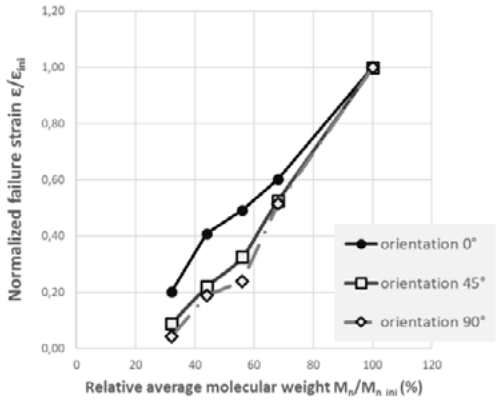


Fig. 5: relative loss of failure strain for different glass fibers orientations after hydrolytic ageing

5. Framework for material modeling and meta-modeling

Materials of this study have been characterized in order to obtain data for integrative finite elements simulation, using Digimat™ Software. Integrative simulation takes into account the forming process to predict the final mechanical performance of a part. To do so, Digimat uses the information generated during process simulation about fiber orientation to compute on every integration point of the finite elements mesh the behavior of the anisotropic composite material[4]. It uses Mori-Tanaka model to compute composite properties from fibers orientation, aspect ratio and mechanical properties on one hand, and matrix constitutive model on the other hand. Information about fiber properties are extracted from CT-scans and fiber length measurements. Tensile data on reinforced materials are used to reverse engineer matrix constitutive model. Digimat allows to use the model defined in equations (1) and (2) where E is matrix modulus in given conditions of temperature and strain rate, R_E is the elastic limit, R_∞ is the hardening modulus, m the hardening exponent, and p the plastic strain.

$$\sigma = E.\varepsilon \text{ if } \sigma \leq R_E \tag{1}$$

$$\sigma = R_E + R_\infty[1 - e^{-m.p}] \text{ if } \sigma \geq R_E \tag{2}$$

Having the possibility to express all these parameters as a function of temperature, strain rate and plasticization is important for industrial applications, especially in the context of parts in contact with coolant, where temperature, water and ethylene glycol concentrations are highly variable. A meta-modeling approach has been developed using a generalized time-temperature superposition method initially proposed by Billon and coworkers[5,6] and adapted to the present case. The different parameters can be plotted as a function of $\dot{\varepsilon}.a_T/a_{T_G}$ a generalized strain rate, where $\dot{\varepsilon}$ is the strain rate, a_T and a_{T_G} are the shift factors corresponding to the horizontal frequency shift applied between the temperature T or glass transition temperature T_G and the reference temperature used to build the storage modulus

mastercurve. The glass transition temperature definition used here is the temperature where the tan δ peak reaches a maximum for a frequency of 1Hz.

It appears that all the parameters of the elastoplastic models can be adjusted accurately when a generalized time-temperature superposition method is used. In this paper, a focus will be done on the yield R_E, but all the other parameters follow the same trends. A first key result is that in the case of water, materials containing various levels of water concentration follow the same mastercurve as illustrated by figure 6a. This result is valid for a wide range of aliphatic and semi-aromatic polyamides, and for mixtures such as PA6/PA6.6 or PA6.10/PA6.6. Figure 6.b shows another key result: the meta-modeling approach can be considered as valid even when applied to ethylene glycol or a mixture of water and ethylene glycol.

Data coming from reverse engineering can be adjusted using a purely phenomenological equation given in (3), with five adjustable parameters R_{E_0}, ΔR_E, β, λ and μ.

All the different parameters evolution with the generalized strain rate $\dot{\varepsilon}.a_T/a_{T_G}$ are available on both virgin materials and aged materials after hydrolysis. An interesting point is that the different parameters stabilize very quickly for limited agings, while failure behavior goes on evolving.

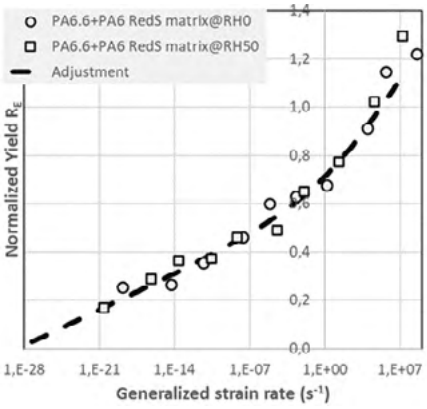


Fig. 6a: evolution of the yield R_E as a function of generalized strain rate for a blend of PA6 and PA66 and two different water concentrations (0,3% and 3% in the polymer)

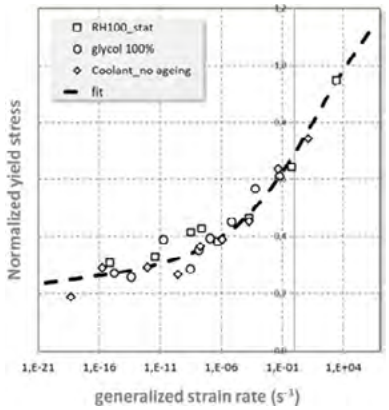


Fig. 6b: evolution of the yield R_E as a function of generalized strain rate for PA66 plasticized with different substances

$$R_E = R_{E_0}.\left(1+\beta.\ln\left(\frac{\dot{\varepsilon}.a_T}{a_{T_G}}\right)\right) + 0{,}5.\Delta R_E.\left(1+\tanh\left(\lambda/2.\left(\ln\left(\frac{\dot{\varepsilon}.a_T}{a_{T_G}}\right)-\mu\right)\right)\right) \quad (3)$$

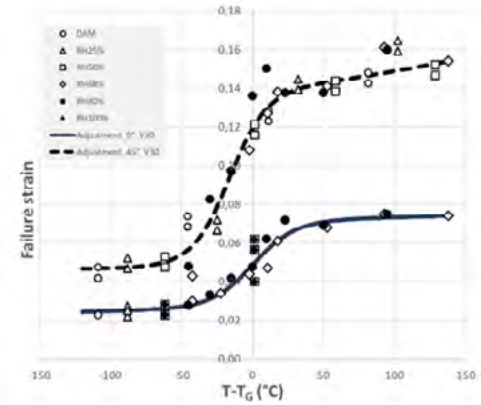


Figure 7: evolution of failure strain as a function of T-T_G for two different glass fibers orientations

Failure behavior can also be modeled in a simple way, at least if only moderate strain rates, lower than $10^{-2}s^{-1}$, are considered. Several levels of water concentration in the matrix have been tested on PA6.6 reinforced with various fibers concentrations and orientations. The figure 7 illustrates the results obtained for a 30% GF material with fibers oriented at 0° or 45°, for water concentrations in the matrix ranging from 0,3% to 8,4% and strain rates ranging from $10^{-4}s^{-1}$ to $10^{-2}s^{-1}$. As can be observed, failure behavior of all specimens follow the same global mastercurve, and failure depends on T-T_G.

6. Extension to general mixtures of polyamide 6.6/water/ethylene glycol and related assumptions

In an industrial part, local concentrations of water or ethylene glycol are far from constant. Solutions have to be found to parameterize matrix local constitutive models. Some assumptions have been made from the available results to generalize them.

(a) the results obtained for variable water concentrations, polyamide 6.6 saturated with ethylene glycol and coolant can be extrapolated to any water or ethylene concentration. If $a_T(T)$ and a_{T_G} are known, determining the parameters of an elastoplastic model is possible.
(b) The shift factors $a_T(T)$ do not depend on aging. Those determined without significant hydrolysis can be used for any average molecular weight.
(c) Failure behavior depends on T-T_G for any molecular weight and can be predicted if T_G is known.

From these assumptions, all that is needed to complete the available results is a mapping of viscoelastic properties at various water and ethylene glycol concentrations, and for any average molecular weight. This mapping is now available, and the material models are ready to be tested in full scale finite elements simulations.

7. Conclusion

A meta-modeling strategy has been developed in order to model the behavior of generic mixtures of polyamide 6.6, water and ethylene glycol with or without hydrolysis. It is based on a generalized time temperature superposition method which has been proven effective for several polyamide matrixes and several water concentrations already. The effect of hydrolysis on the properties is now also taken into account. It is too soon to know which level of accuracy these material models will allow on finite elements simulations, but the first case studies are running, and a final evaluation of the full simulation workflow is under way.

Acknowledgments

The authors wish to thank the Banque Publique d'Investissement, region Auvergne Rhône Alpes and Grand Lyon which funded our research.

References

[1] Ledieu B., PhD dissertation, Ecole Nationale Supérieure d'Arts et Métiers (2010).
[2] Ferry J.D., Viscoelastic Properties Of Polymers, John Wiley & sons, New York (1980).
[3] Rolland H. Saintier N., Raphaël I., Lenoir N., King A., Robert G., Composites Part B Engineering, **143**, 217 (2018).
[4] https://nexus.hexagon.com/documentationcenter/bundle/Digimat_2024.1_MF_User_Guide/resour--ce/Digimat_2024.1_MF_User_Guide.pdf.
[5] Baquet E., PhD dissertation, Ecole des Mines de Paris (2011).
[6] Maurel-Pantel A., Baquet, E., Bikard J., Billon N., Applied Mechanics and Materials, **70**, 393 (2011).

MULTISCALE MODELING AND EXPERIMENTAL ASSESSMENT OF DAMPING IN UNIDIRECTIONAL FIBER REINFORCED COMPOSITES

Tsilat Shiferaw[1], Pauline Butaud[1], Morvan Ouisse[1], Vincent Placet[2]

[1]Supmicrotech, Université de Franche-Comté, CNRS, Institut Femto-st, F-25000 Besançon, France
Email: tsilat.shiferaw@femto-st.fr
Email: pauline.butaud@femto-st.fr
Email: morvan.ouisse@femto-st.fr
[2] Université de Franche-Comté, CNRS, Institut Femto-st, F-25000 Besançon, France
Email: vincent.placet@femto-st.fr

Keywords: Multiscale modeling, Homogenization, Damping

Abstract

The dynamic mechanical properties of fiber reinforced composites could depend on several factors including geometrical parameters, fiber volume fraction, orientation and other aspects. This paper focuses on determining the impact of volumetric fraction of fibers on the dynamic mechanical properties of composites. The study involves analyzing the dynamic properties of composites reinforced with unidirectional fibers using a multiscale numerical model. Additionally, the results are compared with experimental approaches to assess and validate the accuracy of the model.

1. Introduction

Composite materials are increasingly crucial in various sectors as the demand for materials with enhanced properties growths. Recent improvements have focused on enhancing properties such as high damping capacity, flexural modulus, specific strength, and corrosion resistance to compete with some conventional materials [1]. These enhancements are influenced by several factors, including the fabrication method, fiber length, fiber weight ratio, fiber orientation, fiber and matrix nature, and the interfacial interaction between the fiber and matrix [2].

With a growing need for materials sourced from renewable origins, bio-based composites are becoming increasingly popular. Plant fibers, serving as an alternative to widely used glass fibers and even in certain conditions carbon fibers, are gaining attention due to their sustainability, renewability, environmental friendliness, lightweight nature, and cost-effectiveness [3]. The distinctive focus lies on the unique properties of these plant fibers, highlighting their contribution to the overall composite's profile. Additionally, bio-based composites exhibit superior damping properties compared to conventional alternatives [4]. Despite these promising advantages, there remains a gap in our comprehensive understanding about the origin of the damping in plant fiber composites.

In addressing this gap, a multi-scale finite element method is proposed in this study to assess the damping behavior of composite materials. This approach operates on two distinct scales: micro-level and macro-level. The micromechanical approach examines the overall composite behavior by analyzing the properties of its constituents (fiber and matrix) within a representative volume element (RVE). Conversely, the macromechanical approach simplifies the composite's heterogeneous structure by substituting it with a homogeneous medium possessing anisotropic properties [5]. Homogenization plays

a pivotal role in multiscale modeling, enabling the derivation of properties for a homogeneous model at a specific scale from a heterogeneous model constructed at a lower scale [6].

This proposed modeling methodology serves as a complementary approach to experimental techniques for assessing composite damping behavior. Commonly used techniques in the experimental approach include dynamic mechanical analysis (DMA) and modal analysis [7]. DMA, conducted within a lower frequency range, focuses on controlled volume fractions of fibers in both synthetic and bio-based composites, aiming to measure their viscoelastic properties. Meanwhile, modal analysis, performed under free-free boundary conditions and covering a broad frequency spectrum, is employed to identify the dynamic properties of the composites at the macroscale.

2. Finite element model

Understanding and modeling natural fiber reinforced composites has become a significant challenge in bio-based materials research. Both bio-based and synthetic composites possess complex properties, making it difficult to accurately evaluate their overall characteristics using traditional methods designed for metals [8]. Consequently, more efficient techniques are needed to characterize composite materials due to their intricate microstructure. Among the methods proposed multi-scale modeling is employed to analyze the constituent materials (fibers and matrices) and predict their characteristic behavior.

2.1. Multi-scale modeling

Analyzing the dynamic behavior of a complex structure can pose challenges, especially when dealing with numerous small components or when assembly properties are unknown. In such cases, the concept of homogenization becomes crucial [9]. Homogenization techniques offer a solution by simplifying the complex structure into a single material with macroscopic properties that reflect its overall behavior. This simplification proves especially useful within composite laminas, where the distribution of fibers across the cross-section tends to be random. To simplify analysis, many micromechanical models presume a periodic layout of fibers, enabling isolation of a RVE or unit cell. This RVE shares identical elastic constants and fiber volume fraction with the composite.

In order to analyze an RVE, careful consideration of the applied boundary conditions is essential. Additionally, selecting the appropriate RVE that matches the assumed fiber distribution is critical for obtaining reliable results [10]. Commonly employed periodic fiber arrangements include the square array and the hexagonal array. As shown in Figure 1, we have chosen to investigate a unidirectional fiber inside a square array of quadrilateral elements, which correspond to the fiber volume fraction of interest.

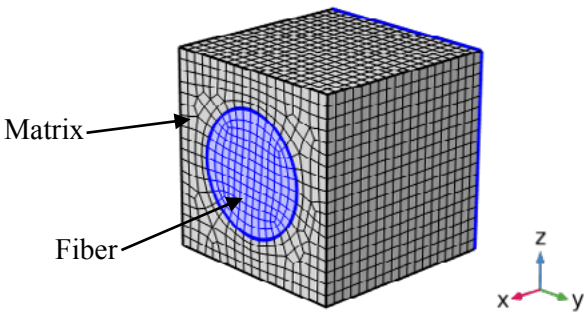


Figure 1. RVE meshed with COMSOL

One way to think of composite materials is as a periodic array of RVEs. Therefore, applying periodic boundary conditions (PBC) to the RVE models becomes imperative. These boundary conditions require the imposition of continuity criteria at the RVE boundaries connected to neighboring RVEs, ensuring

the integration of all individual RVEs into a structural continuum body [11]. The periodic boundary conditions are expressed as:

$$u_{dst} - u_{src} = \bar{\varepsilon}\,(X_{dst} - X_{src}). \quad (1)$$

where $\bar{\varepsilon}$ is the average strain, u_{dst} and u_{src} are the displacement components at the destination and source faces of the RVE respectively, and X is the postion. To fulfill this requirement, we utilized the cell periodicity feature in COMSOL®, with steps provided in Figure 2. At the microscale, homogenized properties are computed through a complex stationary analysis, neglecting the dynamics effects occuring at the scale of the cell.

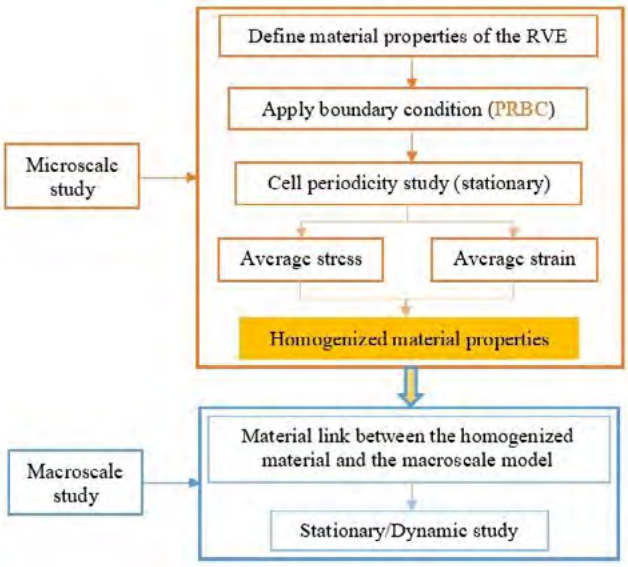


Figure 2. Steps performed on COMSOL

In the study of the micromechanics of fiber-reinforced materials, it is convenient to use an orthogonal coordinate system that has one axis aligned with the fiber direction. In this setup, the x-axis coincides with the fiber direction, while the y and z axes lie within the plane of the RVE and are perpendicular to the fibers, as illustrated in Figure 1. For our analysis, we consider dimensions of l = 10 µm for a square RVE, with fiber radii corresponding to volume fractions ranging from 30 to 70%. The simulations have been performed on a glass fiber reinforced epoxy with the elastic stiffness and damping properties represented in table 1 [12].

Table 1. Basic properties of glass fibre-reinforced epoxy

Properties	Glass fiber	Epoxy
$\boldsymbol{E}$ $\boldsymbol{(GPa)}$	72.4	2.76
$\boldsymbol{G}$ $\boldsymbol{(GPa)}$	30.2	1.02
$\boldsymbol{\nu}$	0.2	0.35
$\boldsymbol{\eta}$	0.0018	0.015

3. Results

In Figure 3, as expected, we observe that as the volume fraction of fiber varies between 30% to 70%, the stiffness of the composite increases by 58% in the longitudinal direction and by 70% in the transverse direction. In terms of shear modulus, there is a 68% increase in the fiber direction and a 62% increase in the transverse direction. To confirm our findings, we compare them with those from Devireddy, S. B. R., & Biswas, S. [13], showing a strong agreement between the two sets of results.

Once we obtain the complex modulus from the elasticity matrix, we proceed to calculate the loss factor by taking the ratio between the imaginary and real parts of the modulus. As shown in figure 4, it is

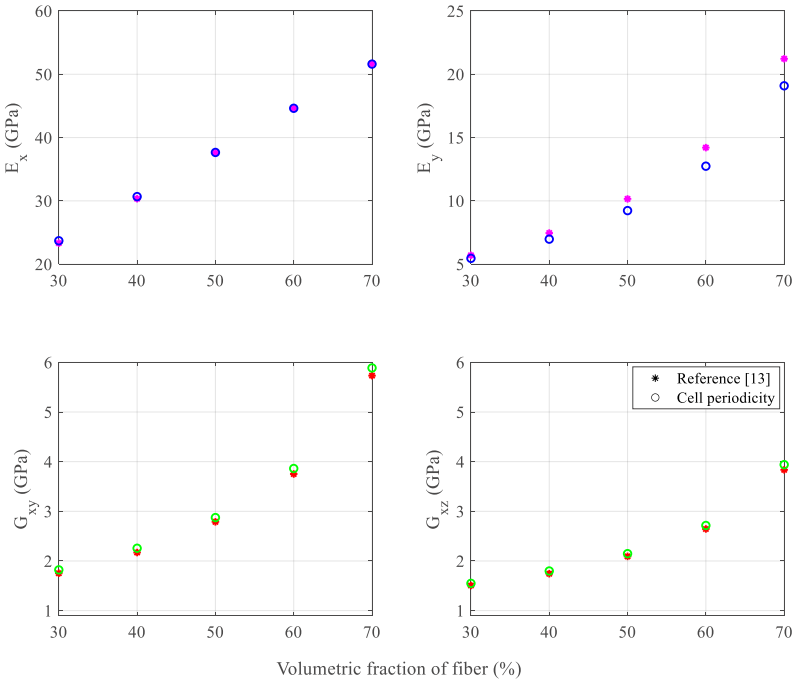


Figure 3. Evolution of Young's modulus and shear modulus with increasing volume fraction

evident that the damping of the composite decreases by 39% for 0° orientation of the fiber as the volume fraction of the fiber increases from 30% to 70%, with a similar decrease of 24% observed in the transverse direction of the fiber. Similarly, examining the shear modulus reveals a decrease of 17% in the longitudinal direction and 6.9% in the transverse direction of the fiber. These results are then compared with the findings presented by Rezaei A. et al. [14].

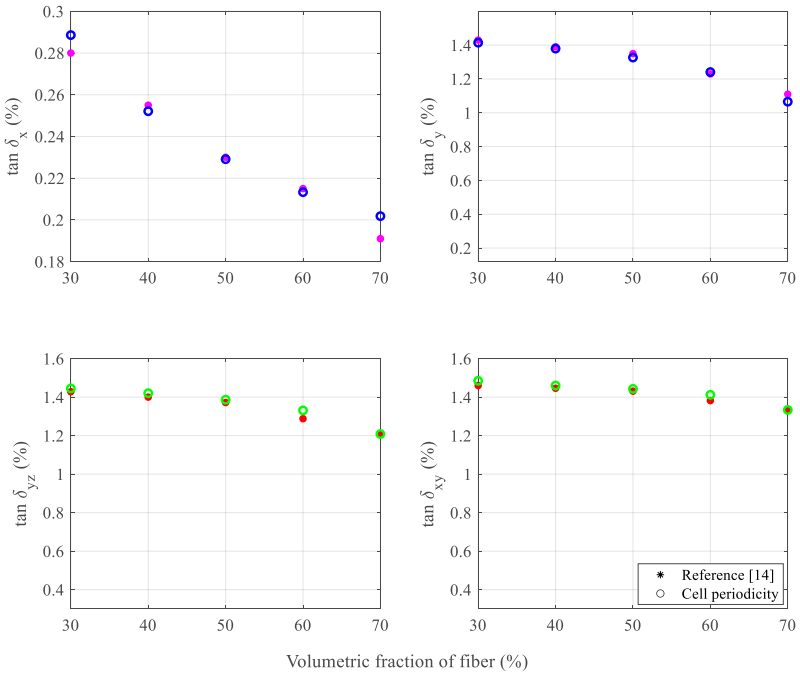


Figure 4. Evolution of damping with increasing volume fraction

Now that we have obtained the effective properties of the composite material from our micro-scale study, we can construct a macro-scale model where the composite consists of homogeneous effective properties determined from the homogenization study. We considered the same glass-epoxy composite, modeled as a solid plate measuring 300 mm * 200 mm * 1.5 mm, and subjected to fixed-free boundary conditions. Here, we conducted a complex eigenfrequency analysis to determine the composite's overall damping property.

We conduct a similar study for the flax fiber reinforced epoxy composite. Although information on the damping properties of flax fibers is limited, some literatures suggest that the damping value ranges from 0.9% to 11% [15,16]. For our simulations, we selected a value of 0.9%. Figure 5 illustrates a comparison between the damping values of glass fiber reinforced epoxy composites and those of flax fiber reinforced epoxy composites. Eigenfrequency study indicates that at each frequency, the loss factor for the flax-epoxy composite exceeds that of the glass-epoxy composite.

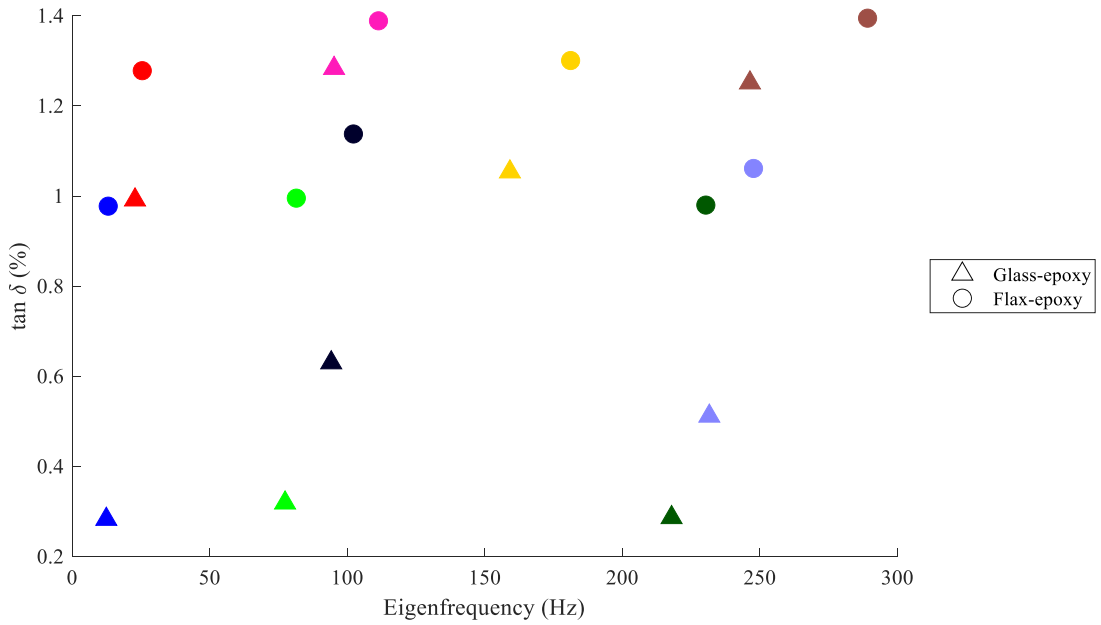


Figure 5. Damping properties of unidirectional fiber reinforced epoxy composites

These findings are consistent with the experimental research conducted by Duc F. et al [4], where they perfomed DMA tests at 1 Hz and ambient temperature. The incorporation of flax fibers into epoxy leads to a notable increase of 52% in the composite's damping values compared to those achieved with glass fibers. This highlights the enhanced damping characteristics offered by flax fiber reinforcement, affirming its potential for improving composite materials' performance in various applications.

4. Conclusions

In this paper, we propose a multi-scale model to simulate the damping behavior of fiber reinforced composite materials. At the micro-scale, the constituents of a composite are simulated as isotropic materials to obtain homogenized elastic properties. These properties are then utilized in a macro-scale study to determine the overall damping of the composites.

Using the proposed method, we investigated the impact of fiber volume fraction on the behavior of a unidirectional fiber reinforced composite. Our findings highlight the significant role of fiber volume

fraction, showing that higher fiber fractions result in increased stiffness and decreased damping, considering that the damping values of the matrix is dominant over the damping of the fiber.

Our analysis suggests that with accurate information, the multi-scale approach can serve as an effective tool for predicting the dynamic mechanical properties of composites. This numerical method can also incorporate an interface between the fiber and the matrix, aiming for an optimal balance between rigidity and damping in the composite.

Acknowledgments

This project has received funding from ANR JCJC MIDIFIC.

References

[1] Mulenga, T. K., Ude, A. U., & Vivekanandhan, C. (2021). Techniques for modelling and optimizing the mechanical properties of natural fiber composites: A review. *Fibers*, *9*(1), 6.

[2] Jeyapragash, R., Srinivasan, V., & Sathiyamurthy, S. J. M. T. P. (2020). Mechanical properties of natural fiber/particulate reinforced epoxy composites–A review of the literature. *Materials Today: Proceedings*, *22*, 1223-1227.

[3] Deeraj, B. D. S., Joseph, K., Jayan, J. S., & Saritha, A. (2021). Dynamic mechanical performance of natural fiber reinforced composites: A brief review. Applied Science and Engineering Progress, 14(4), 614-623.

[4] Duc, F., Bourban, P. E., Plummer, C. J. G., & Månson, J. A. (2014). Damping of thermoset and thermoplastic flax fibre composites. *Composites Part A: Applied Science and Manufacturing*, *64*, 115-123.

[5] Xia, Z., Zhang, Y., & Ellyin, F. (2003). A unified periodical boundary conditions for representative volume elements of composites and applications. International journal of solids and structures, 40(8), 1907-1921.

[6] Conejos, F., Balmes, E., Tranquart, B., Monteiro, E., & Martin, G. (2021). Viscoelastic homogenization of 3D woven composites with damping validation in temperature and verification of scale separation. Composite Structures, 275, 114375.

[7] Liu, T., Butaud, P., Placet, V., & Ouisse, M. (2021). Damping behavior of plant fiber composites: A review. Composite Structures, 275, 114392.

[8] K Jagath Narayana and Ramesh Gupta Burela. Multi-scale modeling and simulation of natural fiber reinforced composites (bio-composites). In Journal of Physics: Conference Series, volume 1240, page 012103. IOP Publishing, 2019.

[9] Pierre Millithaler. Dynamic behaviour of electric machine stators: modelling guidelines for efficient finite-element simulations and design specifications for noise reduction. PhD thesis, Besançon, 2015.

[10] Chin-Teh Sun and Rajesh S Vaidya. Prediction of composite properties from a representative volume element. Composites science and Technology, 56(2):171– 179, 1996.

[11] Narayana, K. J., & Burela, R. G. (2019, July). Multi-scale modeling and simulation of natural fiber reinforced composites (Bio-composites). In *Journal of Physics: Conference Series* (Vol. 1240, No. 1, p. 012103). IOP Publishing.

[12] Chandra, R., Singh, S. P., & Gupta, K. (2003). Prediction of damping in three-phase fibre-reinforced composites. *Defence Science Journal*, *53*(3), 325.

[13] Devireddy, S. B. R., & Biswas, S. (2014). Effect of fiber geometry and representative volume element on elastic and thermal properties of unidirectional fiber-reinforced composites. *Journal of Composites*, *2014*.

[14] Rezaei, A., Goroz Gómez, D., Gilabert, F., Desmet, W., & Van Paepegem, W. (2016). Micro-scale finite element simulation of the viscoelastic damping in unidirectional fiber reinforced composites. *Leuven, Belgium: Katholieke Univ Leuven, Dept Werktuigkunde*, 1757-66.

[15] Reda, A., Dargent, T., & Arscott, S. (2023). Dynamic micromechanical measurement of the flexural modulus of micrometre-sized diameter single natural fibres using a vibrating microcantilever technique. *Journal of Micromechanics and Microengineering*, *34*(1), 015009.

[16] Davies, G. C., & Bruce, D. M. (1998). Effect of environmental relative humidity and damage on the tensile properties of flax and nettle fibers. *Textile Research Journal*, *68*(9), 623-629.

DESIGN AND TEST OF A WITNESSING COUPON FOR FILAMENT-WOUND TOW PREG CFRP PARTS

Georg Söllinger[1], Matthias Redl[2] and Matthias Lechner[3]

[1] Materials and Processes, Peak Technology, Technologiepark Straße 6, Holzhausen, Austria
Email: georg.soellinger@peaktechnology.at, Web Page: http://www.peaktechnology.at
[2] Development Engineering, Peak Technology, Technologiepark Straße 6, Holzhausen, Austria
Email: matthias.redl@peaktechnology.at, Web Page: http://www.peaktechnology.at
[3] CTO, Peak Technology, Technologiepark Straße 6, Holzhausen, Austria
Email: matthias.lechner@peaktechnology.at, Web Page: http://www.peaktechnology.at

Keywords: Filament Winding, Witnessing Coupon, Material Testing, Tow Preg, In-Plane Shear Test

Abstract

Due to high complexity, expensive filament-wound CFRP products such as Composite-Overwrapped Pressure Vessels (COPVs) Spacecraft Structures require appropriate witnessing coupons, such that in case of deviating manufacturing processes the part can be released for use by verifying the structural behaviour of the witnessing coupon via destructive testing.

A tubular coupon with a ±45 degree cross-ply layup with an inner diameter of 50 mm was designed based on the standardized coupon for in-plane shear testing as per ASTM D3518 [1]. To avoid stress concentrations and guarantee homogeneous shear loading in the gage section, the layup of the clamping section was reinforced with staggered hoop layers.

In a preliminary test campaign several coupons were manufactured and submitted to tests. This campaign confirmed the coupon design not only to be suitable for witnessing and controlling serial production but also to result in similar structural properties as evaluated on comparable flat coupons.

1 Introduction

Since components such as Composite-Overwrapped Pressure Vessels (COPVs) or large tubular composite structures used for aerospace applications, as shown in Figure 1, have either undergone costly preceding processes or are simply expensive due to their size and the associated material costs, appropriate process control is essential.

To avoid scrapping such high-priced components, e.g., most commonly due to deviations of the autoclave cure cycle, a witnessing coupon was developed. Its aim is to verify both the quality of the filament winding- and the subsequent autoclave curing process.

The component, for which the witnessing coupon was designed, is filament-wound with a Toray T800SC-Epoxy tow preg. However, the test method presented in this article can also be applied to other materials.



a: Composite-Overwrapped Pressure Vessel

b: Space Structure

Figure 1. High-Priced Filament-Wound Space Components

2 Methodology

2.1 Prerequisites

The requirements considered in the design of the witnessing coupon are:

- to allow a similar manufacturing process by filament winding and autoclave curing,
- to allow simple structural testing of both fiber- and resin-dominated properties, and
- to allow simple and quick processing with low material consumption, resulting in low cost.

These are answered by a coupon combining the testing of both fiber- and resin-dominated properties: The fiber-dominated properties are required to verify the use of an acceptable raw material- and filament winding quality, while the resin-dominated properties verify the acceptance of the curing process. These material properties are inherited by the in-plane shear behaviour of the composite, as standardized, e.g., according to ASTM D3518 [1] by tensile testing of flat plates with a layup of ± 45 degree. The principle of this test method is the baseline for the design of the witnessing coupon.

2.2 Coupon Design

Based on experience, the manufacture of flat coupons by filament winding using tow preg is leading to several unwanted effects, which are not present in rotationally symmetric parts:

- The tow preg tends to be necking when wound over a flat mandrel. This is leading to gaps of adjacent tows, see Figure 2.

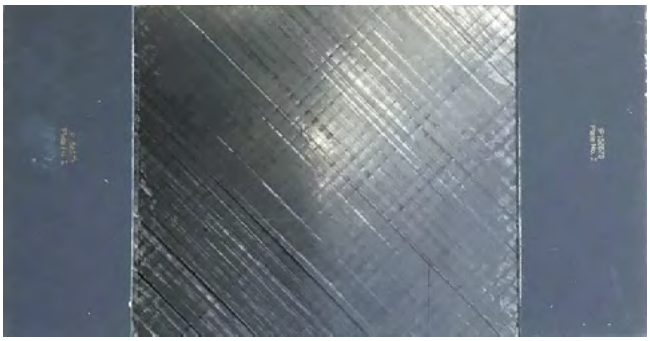


Figure 2. Gaps between adjacent Tows on Flat ASTM D3518 In-Plane Shear Coupon Plate

- Due to setting effects the remaining pretension applied to the tows at the winding process is dissimilar for subsequent layers, potentially leading to process-induced deformations of the manufactured coupon plates.

- Even though considered as negligible for this test method [1], edge effects are present on flat coupons, including the necessity to cut the fibers to get individual coupons out of the test plate such as shown in Figure 2.
- In addition to these effects, flat coupons require additional process steps such as tab-bonding, including surface preparation, and cutting of individual coupons is needed prior to testing of the coupons, increasing manufacturing complexity and cost.

To overcome all these issues a tubular coupon geometry as shown in Figure 3 was established.

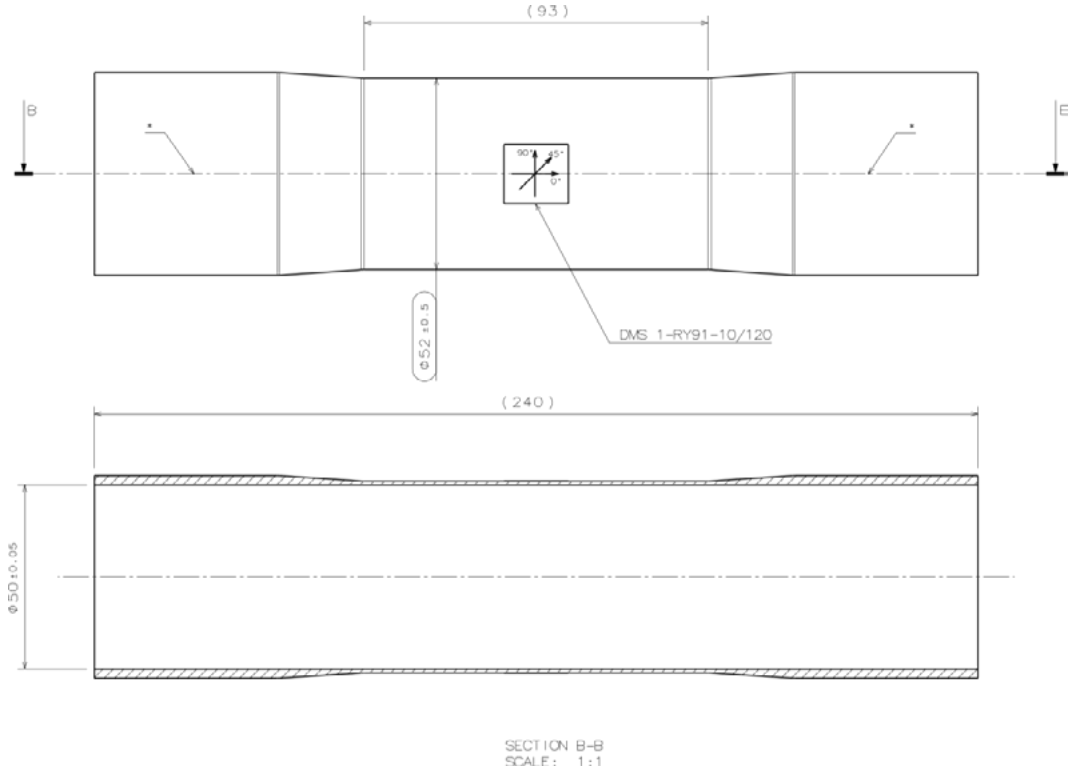


Figure 3. In-Plane Shear Witnessing Coupon

The coupon is entirely rotationally symmetric with an inner diameter of 50 mm and a layup of $(\pm 45 \text{ degree})_2$ in the gage section. The ends of the tube are reinforced locally with staggered hoop layers, which are evenly distributed in the ±45 degree layers outside of the gage section, allowing homogeneous load introduction to the gage section similar as tabs for flat coupons. If wound on a sufficiently long mandrel, several coupons could be manufactured at a time in near-net shape, including the local reinforcements with the above-mentioned hoop layers. After curing, only a cutting operation is required to trim the coupons to final length.

Two mechanical locking assemblies clamp the tube from the inside during tensile testing and allow load transmission through friction. Therefore, the coupons do not require any machining operation prior to test.

2.3 Test Method

The test method for determination of in-plane shear properties by tensile testing of ±45 degree laminates as defined in ASTM D3518 [1] is considered as baseline for test execution and evaluation.

For strain measurement, each tube is instrumented with a 3-grid strain gauge rosette *HBK 1-RY91-10/120* with a gauge length of 10 mm and a resistance of 120 Ω, applied in axial direction in the middle of the gage section, see Figure 3. The displacement rate during tensile testing is defined as

2 mm/min. Since it is assumed that a fiber scissoring effect occurs on the ±45 degree layup, no ultimate failure of the coupon is expected. Therefore, the test is aborted at 5 mm crosshead displacement of the universal testing machine, ending up in an Engineering Shear Strain of approximately 1 % and 2 %.

The following parameters are evaluated, see Figure 4:

- Principal Strains and Maximum Shear Strain
  Based on the strain signals of the strain gauge rosette, the Principal Strains ϵ_1 and ϵ_2 are derived as defined in [2]. The Engineering Shear Strain γ_{12} is calculated as defined in [1].
- Shear Modulus G_{12}^{s}
  The Shear Modulus is evaluated in an Engineering Shear Strain range between $0.002 < \gamma_{12} < 0.006$.
- Offset Shear Strength $F_{12}^{s,0.2\%}$
  The Offset Shear Strength is evaluated at 0.2 % plastic shear deformation as defined in [1].

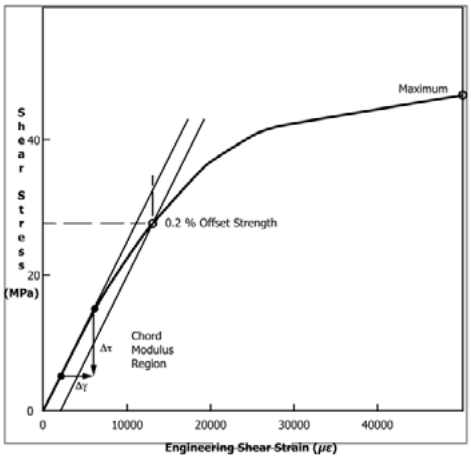


Figure 4. Illustration of Shear Modulus- and Offset Shear Strength Evaluation [1]

The following effects expectedly could be identified with the presented witnessing coupon test, when compared to the structural response of a set of reference coupons:

- Winding angle (fiber-dominated)
  If process- or winding machine errors lead to a change in the planned ±45 degree layup angle on the witnessing coupon, the evaluated Shear Stiffness of the coupon would change.
- Temperature and consolidation during cure cycle (resin-dominated)
  An improper cure, e.g., due to loss of vacuum or insufficient cure time, is expectedly resulting in a softening of the coupon. This would be manifested in both a reduced Offset Shear Strength and Shear Stiffness.
- Resin batch quality (resin-dominated)
  Significant changes of the resin quality would expectedly end up in both a reduced Offset Shear Strength and Shear Stiffness.

The fiber batch quality itself cannot be tested with the presented method. However, this is not required, as a Certificate of Conformity (including material test reports for the neat fiber) is required for every batch of raw material supplied for aerospace applications.

2.4 Implementation into Manufacturing Process

Two witnessing coupons are manufactured before and/or after the space component. The filament winding of both the space component and its witnessing coupons is conducted on a numerically controlled winding robot with a customized filament winding head, that lays four tows at a time. Curing is conducted in an autoclave oven for 135°C / 3 h, with a preliminary dwell at 90°C, where the witnessing coupons and the component get cured in the same vacuum bag. After application of strain

gauges one coupon is submitted to a destructive test to verify the in-family behaviour against already tested coupons, whereas the second coupon is delivered together with the component to the customer. It could be tested upon request, e.g., in case of deviating transportation- or storage conditions of the space component.

2.5 Verification Tests

Prior to initiating the manufacture of the space components, a test campaign was carried out. Aim of this verification tests were:

- in addition to the virtual testing to validate the function of the coupon geometry in practice,
- to capture the structural response (Shear Stress vs. Shear Strain curves) of at least ten (10) coupons, being the baseline for comparison of the witnessing coupons in terms of in-family behaviour, and
- to derive robust acceptance limits with statistical validity.

Therefore, 15 coupons were manufactured and submitted to tests. 3x2 coupons of which were manufactured together with prototype space components, the remaining coupons were manufactured in individual manufacturing batches.

The tests were conducted with a universal testing machine *Hegewald & Peschke Inspekt 200*, being equipped with a 100 kN load cell, see Figure 5. Data acquisition of the strain gauge rosette was performed with a *HBK Quantum X MX1615B* amplifier. Strain control via the strain gauges was not feasible in the test configuration. Hence, the test was conducted up to a pre-defined crosshead displacement. To avoid parasitic bending moments the locking assemblies were fixed to the universal testing machine with each one uniball clevis.



a: Coupon

b: Tensile Testing in Universal Testing Machine

Figure 5. Tubular In-Plane Shear Witnessing Coupon

3 Results

3.1 Test Results and Discussion

The Shear Stress vs. Principal- and Engineering Shear Strain curves of the tested coupons are displayed in Figure 6, while the test results are summarized in Table 1. Coupon 10 could not be evaluated due to a strain gauge failure and is therefore not considered.

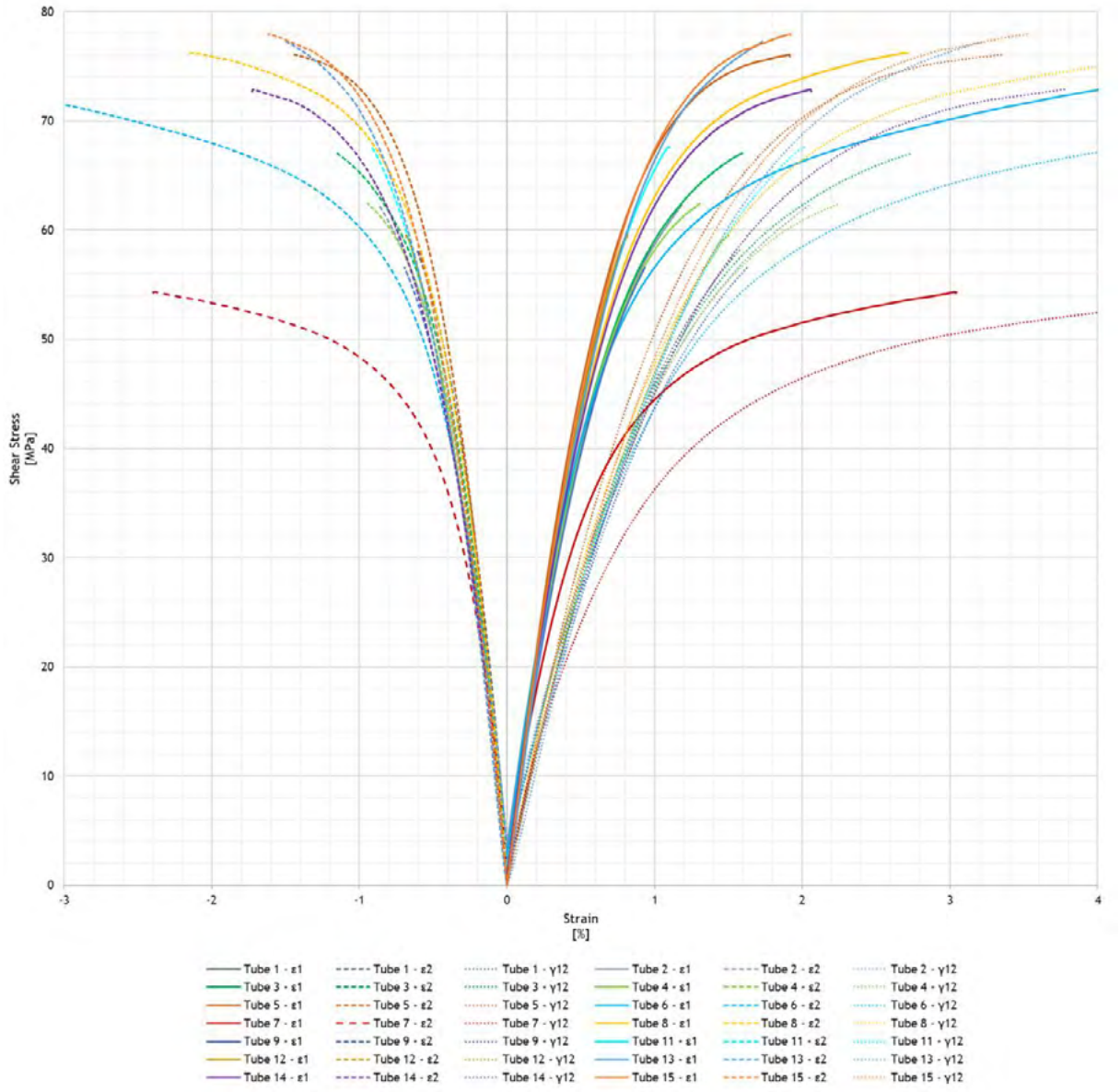


Figure 6. Shear Stress vs. Principal- ($\boldsymbol{\epsilon_1}$, $\boldsymbol{\epsilon_2}$) and Engineering Shear Strain ($\boldsymbol{\gamma_{12}}$) of Witnessing Coupon in Universal Testing Machine

The following observations are derived:

- Except of Coupon 7 the structural response of all coupons is similar.
- As mentioned in Section 2.3 the tests are terminated at a crosshead displacement of 5 mm. However, e.g., Coupon 6 and Coupon 8 are straining significantly more than others. On Coupon 6 the issue is originating from the strain gauge. The scatter on the other coupons is expected to originate in slipping and / or setting effects of the clamping.

- Coupon 7 shows an out-of-family behaviour of the Shear Stress vs. Principal Strain response. Also, the Offset Shear Strength and the Shear Modulus are significantly lower than for all other coupons. The root-cause was found in the autoclave cure being terminated four (4) consecutive times, always caused by a loss of vacuum.
  Coupon 9 was cured together with Coupon 7. In the first curing attempt the vacuum bags of both coupons were experiencing a leak right after the end of the 90°C dwell. On all further attempts Coupon 7's leaking vacuum bag was causing the termination of the cure cycle.
  The out-of-family behaviour of Coupon 7 is concluded to originate from the four consecutive cure cycles with improper consolidation due to loss of vacuum. Since the vacuum pressure on Coupon 9 remained OK and the termination of the first cure cycle happened at an early stage of the cure before passing the resin's gel point, it behaved in-family.
  This observation confirms that the in-plane shear witnessing coupon is capable to reveal improper curing of the composite, in this case an improper consolidation due to a loss of vacuum.
- The 13 valid test results were used to define acceptance criteria for the witnessing test, which are based on the average Shear Modulus and the A-Basis of the Offset Shear Strength of the verification test campaign.

Table 1. Results of In-Plane Shear Witnessing Coupon Verification Test
Note: the color distribution helps to visualize the distribution between minimum and maximum.
Note 1: A-Basis evaluated based on [3], Chapter 8, considering a Gaussian Distribution

Test Coupon [-]	Shear Strength $F_{12}^{s,0.2\%}$ [MPa]	Shear Modulus G_{12}^{s} [GPa]	Comment [-]
1	55.2	4.61	Valid
2	54.8	4.37	
3	52.5	4.83	
4	52.3	4.69	
5	58.4	5.45	
6	51.5	4.34	
~~7~~	~~40.9~~	~~3.65~~	Invalid, Vacuum Loss at Cure
8	56.5	4.97	Valid
9	51.1	4.63	
~~10~~	~~N/A~~	~~N/A~~	Invalid, Strain Gauge Failure
11	56.6	4.91	Valid
12	57.0	5.14	
13	55.3	5.05	
14	54.5	4.68	
15	58.1	5.14	
Average	54.9	4.83	
Std Deviation	2.45	0.32	
A-Basis (1)	46.0	3.66	

3.2 Potential for Material Characterization

To assess the potential of the presented test method for material characterization, the discussed results were compared against the flat-plate results tested according to ASTM D3518 and used for sizing of the space components, see Table 2. The comparison shows that the flat coupons as shown in Figure 2 result in a lower standard deviation but also in a reduced performance in their structural response. Both tendencies were expected, since the tubular coupons were manufactured with a different raw material batch and in different filament winding/curing lots. This explains an increased standard deviation compared to the flat coupons, which are manufactured from one flat plate made of the same material

and as part of the same process. Parasitic side effects, as present in the flat plate testing and described in Section 2.2, are non-existent in the tubular coupons, which explains the better average structural properties.

Table 2. Comparison of In-Plane Shear Test on Flat vs. Tubular Coupon
Note 1: A-Basis evaluated based on [3], Chapter 8, considering a Gaussian Distribution

Shape	Flat Coupon	Tubular Coupon	Flat Coupon	Tubular Coupon
Structural Property	Offset Shear Strength $F_{12}^{s,0.2\%}$ [MPa]		Shear Modulus G_{12}^{s} [GPa]	
Average	49.9	54.9	4.41	4.83
Std Deviation	0.81	2.45	0.09	0.32
No Coupons	10	13	10	13
A-Basis (1)	46.7	46.0	3.97	3.66

Based on these observations, the coupon design was already applied successfully to derive the in-plane shear characteristics of a novel raw material, comprising of an Ultra-High Modulus (UHM) Carbon Fiber, which was used for the manufacture of the space structure shown in Figure 1.a.

4 Conclusions

A witnessing coupon in tubular shape was designed based on the standardized coupon for in-plane shear testing as per ASTM D3518. The tube design is of low complexity, allows near-net shape manufacture and low additional manufacturing efforts prior to testing. The interface towards the universal testing machine functions based on locking assemblies, which allow load introduction to the coupon by friction.

Since in-plane shear properties are both dependent on fiber- and resin quality, the presented coupon allows the verification of:

- Winding angle (fiber-dominated)
- Temperature and consolidation during cure cycle (resin-dominated)
- Resin batch quality (resin-dominated)

An incident during the cure of one test coupon confirms the ability of the presented test method to detect faulty consolidation quality.

The tubular design is not subjected to unwanted side effects such as tow gapping and edge effects as present on comparable flat coupons. This was confirmed by comparing the test results of the tubular coupons against those of flat coupons manufactured from the same tow preg. Expectedly, the strength and stiffness of the tubular coupons show a higher standard deviation, since they are manufactured individually and of different raw material batches. As the tubular coupon better reflects the production of filament-wound components, the test method could be used not only for process control but also for characterizing new types of materials.

References

[1] ASTM D3518/3518M-13: Standard Test Method for In-Plane Shear Response of Polymer Matrix Composite Materials by Tensile Test of a ±45° Laminate. ASTM International, 2013
[2] Methods of Obtaining Magnitude and Direction of Principal Stress (Rosette Analysis). https://product.kyowa-ei.com/en/learn/strain-gages/kfgs_rosetteanalysis, Kyowa Electronic Instruments Co., Ltd., 2024
[3] MIL-HDBK-17-1F: Composite Materials Handbook Volume 1: Polymer Matrix Composites: Guidelines for Characterization of Structural Materials. Department of Defense, 2002

FINITE FRACTURE MECHANICS FRACTURE CRITERION FOR FREE EDGE DELAMINATION

Mohammad Burhan[1], Tommaso Scalici[2], Zahur Ullah[1], Zafer Kazancı[1], and Giuseppe Catalanotti[2]

[1]Advanced Composites Research Group, School of Mechanical and Aerospace Engineering, Queen's University Belfast, Belfast, BT9 5AH, UK
mburhan01@qub.ac.uk, z.ullah@qub.ac.uk, z.kazanci@qub.ac.uk
[2] Facoltà di Ingegneria e Architettura, Università degli Studi di Enna Kore, Cittadella Universitaria, Enna, 94100, Italy
tommaso.scalici@unikore.it, giuseppe.catalanotti@unikore.it

Keywords: Interlaminar stresses, Energy release rate, Semi-elliptical crack, Free edge effect, Finite Fracture Mechanics

Abstract
The interlaminar stresses at the dissimilar interface near the free edges of the composite laminates are weakly singular due to the material mismatch. These stresses can induce delamination between the dissimilar plies. The free edge delamination is investigated in the present study in the framework of Finite Fracture Mechanics. Dimensional analysis is performed to evaluate the two quantities (interlaminar stresses and incremental energy release rate) required for the FFM criterion for any arbitrary load and ply thickness. The non-dimensional functions of these quantities are determined semi-analytically by utilising the expressions derived from dimensional analysis and Finite Element models. The energy release rate is calculated by considering a semi-elliptically shaped crack emanating from the dissimilar interface at the free edge. Since the crack has two dimensions the FFM system of equations leads to infinitely many solutions. Therefore, a hypothesis is made to introduce an additional inequality that the crack extension occurs homothetically, i.e., the crack retains its aspect ratio while extension. The unknown variables (failure load and crack nucleated dimensions) are determined by solving an optimisation problem to find the minimum load corresponding to a specific crack and satisfying both the stress and energy criterion. The prediction of a failure of laminate exhibiting free edge effects using introduced 3D FFM criterion is compared against experimental results from literature and good agreement is attained.

1. Introduction

The traditional Composite Plate Laminate Theory (CPLT) is not suitable for the evaluation of the free edge stresses due to its two-dimensional nature. Also, the exact solution of these stresses does not exist. Therefore, different closed-form analysis [1] and numerical approaches [2] have been developed to compute interlaminar stresses. The prediction of delamination due to singular nature of interlaminar stresses is not feasible using either traditional strength-of-materials or fracture mechanics-based criterion. Therefore, there exist non-local strength-of-materials [3,4] and fracture mechanics-based [5,6] criterion to predict the free edge delamination induced by free edge stresses. However, all of them depend on having the pre-requisite information about the characteristic length to function. To avoid this issue, Leguillon [7] proposed a new coupled criterion within the framework of Finite Fracture Mechanics (FFM), which supports the idea that both stress and energy criteria are necessary and together they form a sufficient one. FFM yields both failure load and its corresponding unknown finite crack size. Therefore, avoiding the prior requirement of an unknown length parameter.
The present paper introduces a 3D FFM criterion for the free edge delamination for symmetric angle-ply laminates. A semi-elliptically shaped crack is assumed to emanate from the free edge and the energy release rate (ERR) is calculated using Virtual Crack Closure Technique (VCCT) through a three-dimensional numerical model built in Abaqus. This type of crack provides flexibility to calculate mixed-mode energy release rates. The interlaminar stresses are computed, from the integration points within a

thin resin-rich layer introduced at the interface, using a second finite element model. Using the equations from dimensional analysis, an average quadratic stress and mixed-mode energy criteria are established. The non-dimensionalised functions from the dimensional analysis let's to work and solve the system of equations semi-analytically. Finally, the results obtained by FFM are compared to experimental results found in literature to validate the criterion using different laminate configurations. This approach can accurately predict free edge delamination onset provided the interlaminar strengths and the interfacial fracture toughness are available

2. Theory

2.1. Semi-analytical framework

Consider a symmetric angle-ply laminate with length L, width $2W$, and h as ply thickness. The symmetry only holds through the thickness. This reduces the required FEM modelling to half ($0 < z < 2h$) and the resulting two-layer laminate with appropriate boundary conditions is illustrated in Fig. 1 for interlaminar stress calculations and in Fig. 2 for ERR calculations. A thin resin-rich layer is introduced at the $(+\theta/-\theta)$ interface for computation of interlaminar stresses. A parametric study of the thickness of the resin-rich layer revealed that the thickness of resin-rich layer of 2% of parent ply thickness is enough to calculate interlaminar stresses precisely. The interlaminar stresses are calculated within this layer at the integration points by using commercial Finite Element Analysis (FEA) software Abaqus. The 3D model in Abaqus uses 8-node linear brick, reduced integration, C3DR8 element.

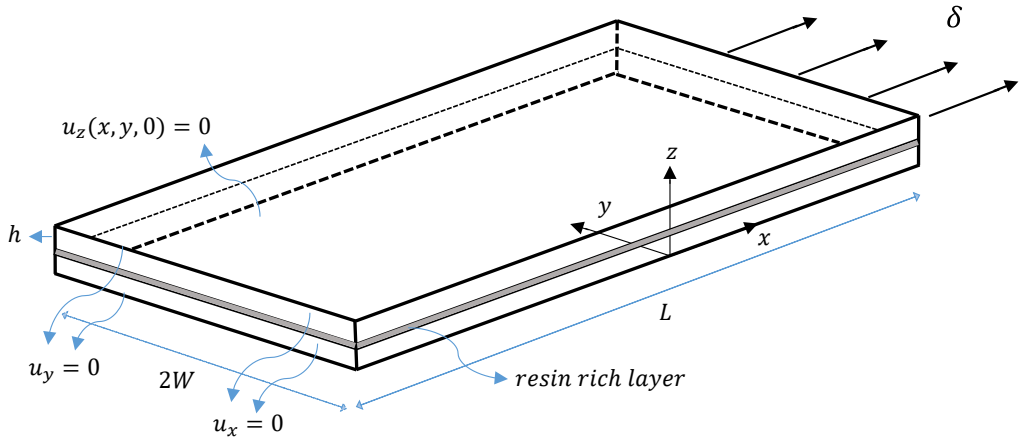


Fig. 1: The boundary conditions used for the half-uncracked model with a transitioned resin rich layer at the $(+\theta/-\theta)$ interface.

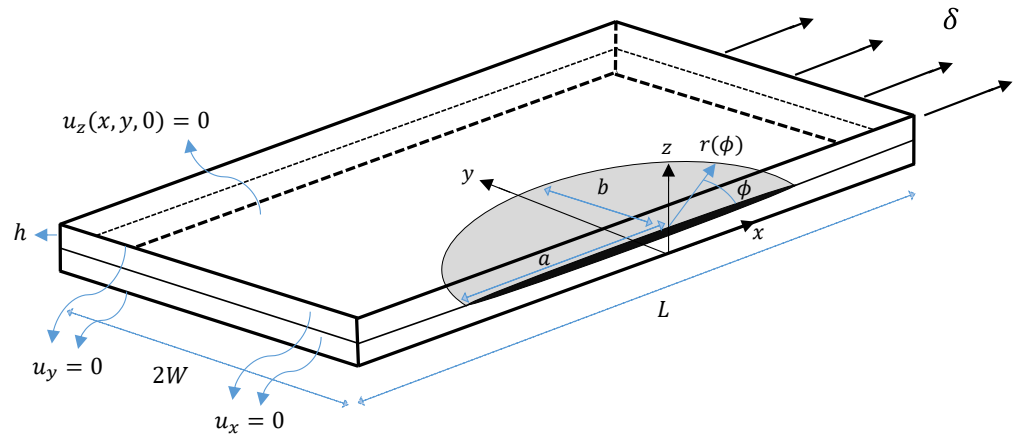


Fig. 2: The boundary conditions for a half-cracked model considering only one semi-elliptical crack at the $(+\theta/-\theta)$ interface.

The ERR for mode I, II and III along the semi-elliptical crack front are calculated using Abaqus in-built Virtual Crack Closure Technique (VCCT) for a given remote load. Due to symmetry only through the

thickness, the top half of the laminate ($0 < z < 2h$) is modelled. The adjacent cracks in the top half of the laminate are assumed to be far from each other without influencing the stress distributions of each other. Therefore, only one crack is considered for the fracture mechanics analysis. This is illustrated in the Fig. 2 along with the appropriate boundary conditions used. The 3D model for the ERR computation incorporates 8-node linear brick, reduced integration, C3DR8 elements.
For the general representation of unknown interlaminar stresses, dimensional analysis is performed. For a material $(E_1, E_2, G_{12}, \upsilon_{12}, \upsilon_{23})$, ply thickness h, ply orientation θ, and remote load σ_∞, interlaminar stress component is written as:

$$\sigma_{ij} = \sigma_{ij}\begin{pmatrix}\sigma_\infty, y, h, \theta, \\ E_1, E_2, G_{12}, \upsilon_{12}, \upsilon_{23}\end{pmatrix}, \tag{1}$$

where y is a distance from the free edge. The material invariant 3D trace $\Im$ [8] is used instead of elastic properties for carbon fibre reinforced polymer (CFRP) composites. The CLPT is employed to generate the trace-normalized 3D stiffness components for various CFRP composite materials, and the **Master ply** is defined based on the average values of these components. The incorporation of the trace enables the calculation of individual elastic constants for any CFRP using their individual traces and the **Master ply**. Following the sequential elimination, Eq.(1) in terms of non-dimensionalised groups for a given material and ply orientation can be written as:

$$\pi_\sigma = \pi_\sigma\left(\frac{\sigma_{iz}}{\sigma_\infty}, \frac{y}{h}\right) \quad i \in \{x, y, z\}, \tag{2}$$

The interlaminar stress components for a symmetric laminate at $(+\theta/-\theta)$ interface is written as:

$$\sigma_{iz} = \sigma_\infty\, \chi_{iz}\left(\frac{y}{h}\right), \tag{3}$$

where χ_{iz} is a non-dimensional stress function component.
To derive a general expression for ERR for a symmetric angle-ply laminate at $(+\theta/-\theta)$ interface, the procedure is analogous to interlaminar stresses. The ERR (G) is a function of the following input parameters:

$$G = G\begin{pmatrix}\sigma_\infty, a, b, \phi, \theta, h, W, L, \\ E_1, E_2, G_{12}, \upsilon_{12}, \upsilon_{23}\end{pmatrix}, \tag{4}$$

where ϕ is a polar angle along crack front (see Fig. 2) and a, b are the semi-axes of a semi-elliptical crack. For a long laminate $(L \gg a, h)$, $(W \geq 3b)$ with given material and ply orientation, Eq.(4) is expressed in the following dimensionless form:

$$\pi_G = \pi_G\left(\frac{G\Im}{{\sigma_\infty}^2 h}, \alpha, \beta, \phi\right). \tag{5}$$

Finally, the ERR of a semi-elliptical crack front at the $(+\theta/-\theta)$ interface of a symmetrical angle-ply laminate is written as:

$$G_i = \frac{{\sigma_\infty}^2 h}{\Im}\psi_i^2(\alpha, \beta, \phi), \qquad i \in \{I, II, III\}, \tag{6}$$

where ψ_i is a non-dimensional correction factor and subscripts (I, II, III) refer to different modes of fracture.
The stress functions χ_{iz} and correction factors ψ_i need to be calculated only once using Eq.(3) and (6), respectively, after the interlaminar stresses and ERR are computed numerically (using Abaqus) for a given material system and ply orientation. These non-dimensional functions can then be used to compute the interlaminar stresses and ERR for any arbitrary load and ply thickness without re-solving the underlying boundary value problem. Therefore, the current framework reduces the numerical effort significantly.

2.2. Finite Fracture Mechanics

Finite Fracture Mechanics (FFM) is a coupled stress and energy criterion proposed by Legullion [7], that predicts the spontaneous nucleation of a finite crack at initiation. FFM yields both, the prediction of the unknown finite crack size and corresponding failure load if two necessary stress and energy

conditions are fulfilled simultaneously. As a result, it only requires intrinsic material properties such as fracture toughness and strength.

The average stress criterion based on single interlaminar stress component for the free edge delamination is written as [3]:

$$\frac{1}{y_0}\int_0^{y_0} \sigma_{iz}\, dy = \overline{\sigma}_{iz} \geq S_i, \tag{7}$$

where y_0 is a critical distance and S_i the corresponding strength. Based on Eq.(7), the average stress criterion for the nucleation of a finite semi-elliptically shaped crack is written as:

$$\frac{1}{A}\int_{-a}^{a}\int_0^{b/a\sqrt{a^2-x^2}} \sigma_{iz}\, dy\, dx \geq S_i, \tag{8}$$

where $A = \pi ab/2$ is the finite area of a semi-elliptical crack. Eq.(8) can be written explicitly for remote stress σ_∞ using Eq.(3) and the stress criterion is written as:

$$\sigma_\infty \geq \frac{A\, S_i}{\int_{-a}^{a}\int_0^{b/a\sqrt{a^2-x^2}} \chi_{iz}\, dy\, dx}. \tag{9}$$

The energy condition for a structure with no inherent flaw such as laminate exhibiting free edge effects is written as:

$$\overline{G} = \overline{G}_I + \overline{G}_{II} + \overline{G}_{III} \geq G_c, \tag{10}$$

where G_c is mixed-mode interface fracture toughness and $\overline{G}$ is the total incremental ERR (IERR) relating the total change in energy $\Delta\Pi$ to the finite size ΔA of an emerging crack and is written as:

$$\overline{G}_i = -\frac{\Delta\Pi_i}{\Delta A}, \quad i \in \{I, II, III\}. \tag{11}$$

For the limiting value $\Delta A \to 0$, IERR $\overline{G}$ becomes Griffith's ERR G and vice-versa. Therefore, IERR can be interpreted as the integral average of G:

$$\overline{G}_i = \frac{1}{\Delta A}\int_0^{\Delta A} G_i\, dA. \tag{12}$$

Combining equations (6), (10), and (12):

$$\overline{G} = \frac{2{\sigma_\infty}^2 h}{\pi ab\Im}\int_{-a}^{a}\int_0^{b/a\sqrt{a^2-x^2}} \left({\psi_I}^2 + {\psi_{II}}^2 + {\psi_{III}}^2\right) dy\, dx \geq G_c. \tag{13}$$

Also, the normalised IERR, denoted by Λ, from Equation (13) can be written as:

$$\Lambda = \frac{\overline{G}\Im}{{\sigma_\infty}^2 h} = \frac{1}{A}\int_{-a}^{a}\int_0^{b/a\sqrt{a^2-x^2}} \left({\psi_I}^2 + {\psi_{II}}^2 + {\psi_{III}}^2\right) dy\, dx. \tag{14}$$

Equation (13) is the mixed-mode energy condition for nucleation of semi-elliptically shaped crack at a given interface in laminates exhibiting free edge effects. For angle-ply laminates only interlaminar shear stress σ_{xz} is predominant and stress condition (9) should be written for the corresponding interlaminar shear strength S_x. Consequently, these laminates have insignificant contribution to ERR in mode I along semi-elliptical crack front. Therefore, by means of both stress and energy subcriteria, the FFM criterion for angle-ply laminate reduces to:

$$\begin{cases} \dfrac{2\sigma_\infty}{\pi ab}\displaystyle\int_{-a}^{a}\int_0^{b/a\sqrt{a^2-x^2}} \chi_{xz}\, dy\, dx \geq S_x \\ \dfrac{2{\sigma_\infty}^2 h}{\pi ab\Im}\displaystyle\int_{-a}^{a}\int_0^{b/a\sqrt{a^2-x^2}} \left({\psi_{II}}^2 + {\psi_{III}}^2\right) dy\, dx \geq G_c \end{cases}. \tag{15}$$

By assuming linear behaviour between individual modes of fracture toughness, the interfacial fracture toughness G_c, considering negligible mode I contribution in angle-ply laminates, is written as [9]:

$$G_c = \left(G_{IIc} + (G_{IIIc} - G_{Ic}) \frac{\overline{G}_{III}}{\overline{G}} \right), \tag{16}$$

For the AS1/3501-6 laminate, according to [9], the mode III fracture toughness is approximately equal to 1.5 times mode II fracture toughness ($G_{IIIc} \sim 1.5 G_{IIc}$), and thus Eq.(16) can be written in terms of G_{IIIc}.

The system of equations (15) represents the 3D FFM criterion that can be used to predict the critical remote stress load σ_∞^c and its corresponding area of finite crack A^c (expressed in the form of a^c and b^c). For a given interface properties (S_x, G_{IIIc}), two equations in (15) has three unknown variables (σ_∞^c, a^c, b^c), that corresponds to the critical state and hence infinite many solutions exist. Furthermore, as semi-elliptical crack is assumed to nucleate, Eq.(15) poses a challenge in determining the dimensions and shape of the crack during extension. Therefore, the unique solution of (15) is determined by solving a standard non-linear optimisation problem that satisfies both stress and energy conditions for a minimum remote stress. Also, the issue with crack front shape is resolved by assuming the homothetic crack extension, i.e., semi-elliptical crack extends in a self-similar manner by keeping the aspect ratio constant.

3. Results

The interlaminar stresses and ERR are determined using semi-analytical framework, as discussed in Section 2.1. The material system considered is AS1/3501-6 with $[\pm \mathbf{15_n}]_\mathbf{s}$ layup. The elastic constants for AS1/3501-6, listed in Table 1, are adopted from a closely related material system (AS4/3501-6), that exhibit similar properties [10] and are taken from [11].

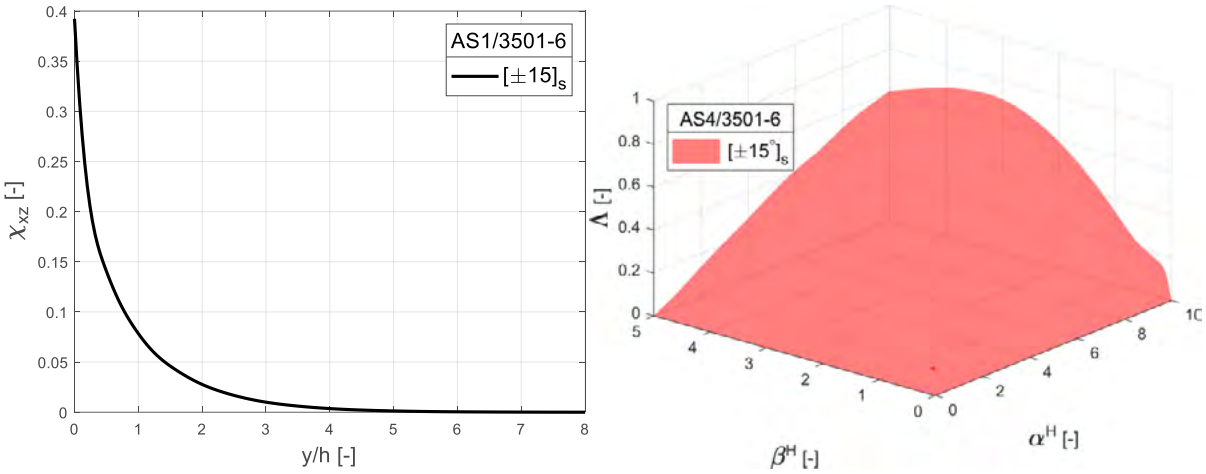
Table 1: Elastic properties of AS4/3501-6 graphite/epoxy composite system.

Laminate	E_1 (GPa)	E_2=E_3 (GPa)	υ_{12}=υ_{23}	G_{12}=G_{23} (GPa)	υ_{23}	S_x (GPa)	G_{IIIc} (N/mm)
AS4/3501-6	144	9.65	0.31	5.24	0.52	110	0.37

The normalised interlaminar shear stress distribution as a function of normalised distance from free edge for the selected laminate configuration is illustrated in Fig. 3 (a). The interlaminar shear stress is only concerned due to its prominent significance in angle-ply laminates. It is evident that there exists a stress singularity at the free edge that decreases rapidly as towards inside of the laminate. The normalised IERR corresponding to total mode (I, II, III) is presented in Fig. 3 (b) as a function of homothetic crack parameters, denoted by α^H and β^H. The homothetic coordinate system represents here that each point within the domain is a potential crack initiation configuration which must have extended through propagation of semi-similar semi-elliptical cracks, i.e., aspect ratio remained constant. The normalised IERR increases with α^{H} and decreases slightly at higher values of β^{H}.

Following the implementation of standard non-linear optimisation to 3D FFM equations (15), the system yields the failure stresses along with finite crack size. The intrinsic properties (S_x, G_{IIIc}) are generally unknown and therefore are evaluated by a reverse fit for a given different ply thicknesses considered. A unique couple (S_x, G_{IIIc}) can be found by minimising the deviation between experimental results and predictions for both failure stresses and crack initiation length. The identified couple are listed in Table 1.

For the selected laminate, the failure stress prediction as a function of normalised ply thickness n is shown in Fig. *4* and is compared against the experimental results taken from literature [12]. The current prediction of 3D FFM is also compared with the predictions of quadratic stress criterion from [12]. The current fracture predictions are in good agreement with the experiments in the sense that size effects are well reproduced. The corresponding finite delamination size is plotted also in the same figure. The absolute values of which increase with increasing normalised ply thickness n, while normalised values decrease.



(a) (b)

Fig. 3: Normalised (a) interlaminar shear stress distribution as a function of normalised distance from free edge and (b) IERR as a function of normalised homothetic crack parameters α^H and β^H, for the selected laminate.

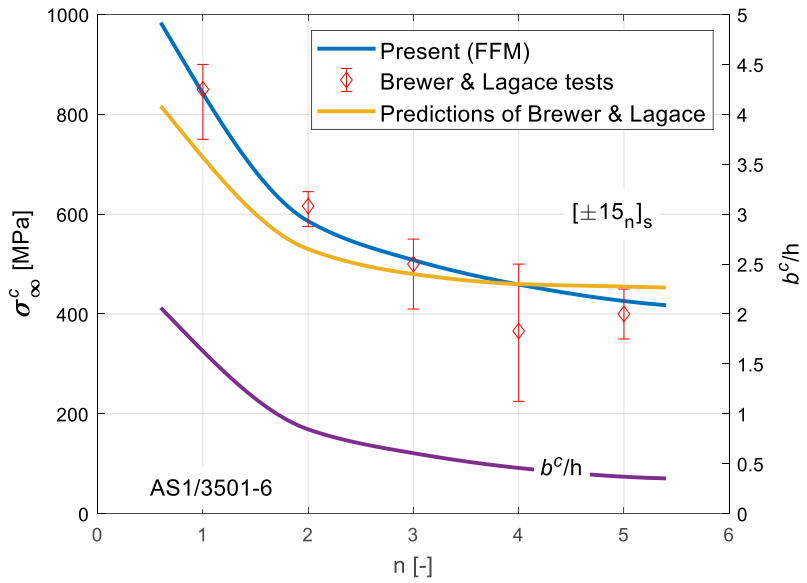


Fig. 4: Predicted failure stresses (blue line) in comparison to experimental tests (error bars) and corresponding normalised crack width onset (right y-axis) with respect to normalized ply thickness n for as1/3501-6 laminate with $[\pm 15_n]_s$ layup.

4. Conclusions

The present paper predicts the free edge delamination of symmetric angle-ply laminates by introducing a 3D FFM fracture criterion. Semi-elliptical crack is considered to emanate from free edge and the issue of crack front extension is solved by hypothesising homothetic crack extension, i.e., aspect ratio remains constant while propagation. Since the crack has two lengths that leads FFM to have an infinite many solutions, the system of equations of the criterion is solved using a standard optimisation technique. The intrinsic interfacial material properties (interlaminar strength and toughness) are identified by minimising the deviation between the proposed FFM criterion and experimental test results. The predicted results are compared against experiments available in literature and good agreement is obtained.

Acknowledgments
This study was conducted as part of the Belfast Maritime Consortium UKRI Strength in Places project, 'Decarbonisation of Maritime Transportation: A return to Commercial Sailing' led by Artemis Technologies, Project no. 107138.

References

[1] Kassapoglou C, Lagace PA. Closed Form Solutions for the Interlaminar Stress Field in Angle-Ply and Cross-Ply Laminates. J Compos Mater 1987;21:292–308. https://doi.org/10.1177/002199838702100401.

[2] Pipes RB, Pagano NJ. Interlaminar Stresses in Composite Laminates Under Uniform Axial Extension. J Compos Mater 1970;4:538–48. https://doi.org/10.1177/002199837000400409.

[3] Kim RY, Soni SR. Experimental and Analytical Studies On the Onset of Delamination in Laminated Composites. J Compos Mater 1984;18:70–80. https://doi.org/10.1177/002199838401800106.

[4] Lagunegrand L, Lorriot T, Harry R, Wargnier H, Quenisset JM. Initiation of free-edge delamination in composite laminates. Compos Sci Technol 2006;66:1315–27. https://doi.org/10.1016/j.compscitech.2005.10.010.

[5] Rybicki EF, Schmueser DW, Fox J. An Energy Release Rate Approach For Stable Crack Growth in the Free-Edge Delamination Problem. J Compos Mater 1977;11:470–87.

[6] Wang A, Crossman FW. Initiation and Growth of Transverse Cracks and Edge Delamination in Composite Laminates Part 1. An Energy Method. J Compos Mater 1980;14:71–87.

[7] Leguillon D. Strength or toughness? A criterion for crack onset at a notch. Eur J Mech A/Solids 2002;21:61–72. https://doi.org/10.1016/S0997-7538(01)01184-6.

[8] Tsai SW, Melo JDD. An invariant-based theory of composites. Compos Sci Technol 2014;100:237–43. https://doi.org/10.1016/j.compscitech.2014.06.017.

[9] Reeder JR. 3D mixed-mode delamination fracture criteria - An experimentalist's perspective. Am Soc Compos - 21st Tech Conf Am Soc Compos 2006 2006;1:129–45.

[10] Kuo YM, Lin HJ, Wang CN, Liao CI. Estimating the elastic modulus through the thickness direction of a uni-direction lamina which possesses transverse isotropic property. J Reinf Plast Compos 2007;26:1671–9. https://doi.org/10.1177/0731684407081450.

[11] Zywicz E. On the equivalence of stress- and strain-based failure criteria in elastic media. Eur J Mech A/Solids 1999;18:391–8. https://doi.org/10.1016/S0997-7538(99)00129-1.

[12] Brewer JC, Lagace PA. Quadratic Stress Criterion for Initiation of Delamination. J Compos Mater 1988;22:1141–55. https://doi.org/10.1177/002199838802201205.

ANALYSIS OF LAMINATES WITH TRANSVERSE CRACKS AND INDUCED DELAMINATIONS: STRESS DISTRIBUTION, EFFECTIVE PROPERTIES AND ENERGY RELEASE RATE

Vladimir Vinogradov

School of Engineering, Newcastle University, Newcastle upon Tyne, NE1 7RU, U.K.
Email: vladimir.vinogradov@newcastle.ac.uk

Keywords: generic laminates, transverse cracks, delaminations, variational analysis, effective properties.

Abstract
An approximate stress field in laminates with parallel intralaminar cracks and local delamination is derived using the principle of minimum complementary energy. Simple matrix expressions are obtained that define the effective compliance matrix, thermal expansions and curvatures, and specific heat of a cracked laminate. The method allows to analyze laminates with various stacking sequences and cracking patterns at negligible computational costs. Results for the stress distribution are presented for symmetric and non-symmetric crack, as well as the corresponding energy release rate associated with interlaminar crack propagation.

1. Introduction

Delamination cracks in fiber reinforced composite laminates can form at various stages of the laminate service and often present the main reason for final failure. Whether the delamination cracks are formed due to monotonous, cyclic or thermal loadings, it is desirable to know their effect on the mechanical properties of the cracked laminate and the stress distribution perturbation due to the cracks.

The variational approach adopted in this paper was originated by Hashin [1] for a symmetric cross-ply $[0_n/90_m]_S$ is one of the most accurate methods to analyze the stress fields in a cracked laminate. The main idea of the approach consists of developing a stress state that satisfies all equilibrium, boundary and traction continuity conditions, and minimizes the complimentary energy of the laminate in attempt to have the best approximation for the stresses. It has been widely used and extended to different cases. One can refer to work by Nairn, who has extensively used the variational analysis, extended it to thermal loading, and used it with an energy based fracture criterion to describe crack accumulation in cross-ply laminates (see, e.g. [2] and references therein). Li and Hafeez [3] looked at a general symmetric cross-ply with symmetric periodic arrangement of transverse cracks. Vinogradov and Hashin [4] looked at an angle-ply laminate with cracks in the middle ply. Recently, the method has gained more attention, e.g. [5,6]. Vinogradov [7] expanded the approach to estimate the effective thermoelastic properties of generic laminates with parallel but not necessarily coplanar matrix cracks. Fikry et. al. [8] developed a variational analysis to explain an experimentally observed crack pattern in unidirectional laminate with a resin pocket.

The variational analysis has also been applied to study effects of delamination cracks [9,10] on the effective properties of cross-ply laminates and associated energy release rate. The present work extends the approach to generic laminates and arbitrary transverse and delamination crack pattern and in-plane loadings.

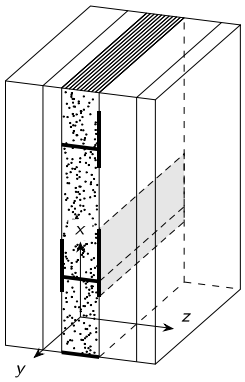


Figure 1. Schematic presentation of a cracked laminate with transverse and delamination cracks.

2. Problem formulation

2.1. Admissible stress field and energy functional

Consider an n-ply laminate sample in the xy plane under a uniform in-plane membrane forces N_{xx}, N_{yy}, N_{xy} and moments M_{xx}, M_{yy}, M_{xy}. We next impose an arbitrary state of damage in a family of plies defined by a certain fiber orientation θ, when the intralaminar cracks are parallel to the fiber direction, but not necessarily coplanar. One can then rotate the coordinate system such that the crack surfaces are normal to the x-axis and the cracked plies become 90° plies (see Figure 1). The front of interlaminar cracks is assumed to be parallel to axis y.

For an arbitrary orientation of plies in the laminate, when there are no cracks, the in-plane stresses $\sigma_{xx}^{0(m)}$, $\sigma_{yy}^{0(m)}$ and $\sigma_{xy}^{0(m)}$ in any ply (m) are linear function of the transverse coordinate z, which can be obtained from a simple analysis using the classical laminate theory, and the rest of the stress tensor components σ_{yz}^{0}, σ_{xz}^{0} and σ_{zz}^{0} are equal to zero. The cracks introduce stress perturbations, which are denoted $\sigma_{ij}^{(m)}$, and the total in-plane stresses in the cracked material become

$$\sigma_{ij}^{C(m)}(x,z) = \sigma_{ij}^{0(m)}(z) + \sigma_{ij}^{(m)}(x,z), \quad \text{for} \quad i,j = x,y \tag{1}$$

It is assumed that the in-plane perturbation stresses $\sigma_{xx}^{(m)}$, $\sigma_{yy}^{(m)}$ and $\sigma_{xy}^{(m)}$ in ply m are linear functions of z everywhere in the cracked laminate, i.e. for any x. According to this assumption the in-plane perturbation stresses can be expressed in terms of yet unknown functions $\phi_i^{(m)}(x)$ and $\psi_i^{(m)}(x)$:

$$\sigma_{ij}^{(m)}(x,z) = \phi_{ij}^{(m)}(x) + \psi_{ij}^{(m)}(x)z, \quad \text{for} \quad i,j = x,y \tag{2}$$

The out-of-plane stresses σ_{xz}, σ_{yz} and σ_{zz} are derived from (2) using differential equilibrium equations

$$\sigma_{ij,j}^{(m)} = 0, \quad \text{for} \quad i,j = x,y,z \tag{3}$$

which are integrated considering traction continuity at the ply interfaces. The result is expressed in a matrix form:

$$\sigma^{(m)} = A_0^{(m)}(z)\phi(x) + A_1^{(m)}(z)\phi'(x) + A_2^{(m)}(z)\phi''(x), \tag{4}$$

where $\sigma^{(m)}(x,z) = \left[\sigma_{xx}, \sigma_{yy}, \sigma_{zz}, \sigma_{yz}, \sigma_{xz}, \sigma_{zz}\right]^T$ is a (6×1) vector of the stress components in ply m, $\phi(x)$ is a $(6N \times 1)$ vector of all the unknown functions:

$$\phi^T(x) = \left[\phi_1^{(1)}, \psi_1^{(1)}, \phi_2^{(1)}, \psi_2^{(1)}, \phi_6^{(1)}, \psi_6^{(1)}, \ldots\right]^T, \tag{5}$$

and A_0, A_1 and A_2 are $(6 \times 6n)$ z-dependant matrices, whose elements are explicitly given in [7].

The complementary energy of a cracked laminate is now expressed in terms of the perturbation stresses:

$$\boldsymbol{U_C = U_C^0 + \frac{1}{2}\int_V \sigma^T S \sigma dV = U_C^0 + \frac{1}{2}\int_L \sum_{p,q=0,1,2} \phi^{pT} M_{pq} \phi^q dx}, \tag{6}$$

where U_C^0 is the complementary energy of the uncracked laminate, $S(x,z)$ is the local compliance matrix, ϕ^p denotes the p-th derivative of $\boldsymbol{\phi(x)}$, and

$$\boldsymbol{M_{pq} = \sum_{m=1}^{n} \int_{z_m}^{z_{m+1}} A_p^{(m)^T}(z)\, S^{(m)}\, A_q^{(m)}(z) dz}. \tag{7}$$

Here $\boldsymbol{z_m}$ and $\boldsymbol{z_{m+1}}$ are $\boldsymbol{z}$-coordinates of the top and bottom interfaces of ply $\boldsymbol{m}$. The elements of matrices $\boldsymbol{A}$ and $\boldsymbol{M}$ have simple analytical expressions and can be found in [7]. For monoclinic and higher ply material symmetries the matrices $\boldsymbol{M_{01}}$, $\boldsymbol{M_{10}}$, $\boldsymbol{M_{21}}$ and $\boldsymbol{M_{12}}$ vanish, leading to the following expression for the complementary energy:

$$\boldsymbol{U_C = U_C^0 + \frac{1}{2}\int_L F(x) dx}, \tag{8}$$

where

$$\boldsymbol{F(x) = \phi^T M_{00} \phi + \phi^T M_{02} \phi'' + \phi''^T M_{20} \phi + \phi'^T M_{11} \phi' + \phi''^T M_{22} \phi''}. \tag{9}$$

The problem is to determine unknown functions $\boldsymbol{\phi(x)}$ that minimize the energy functional (8).

2.2. Constraints

The perturbation stresses must satisfy global equilibrium constraints as well as zero traction on the delamination surfaces. The overall membrane perturbation forces N_{xx} and N_{xy} and moments M_{xx} and M_{xy} must vanish independently of crack geometry and must remain zero for any x due to the plate equilibrium constraints:

$$\frac{\partial N_{xx}}{\partial x} = \frac{\partial N_{xy}}{\partial x} = \frac{\partial M_{xx}}{\partial x} = \frac{\partial M_{xy}}{\partial x} = 0,$$

that hold due to independence of the stress field of y. Therefore, taking the corresponding rows of (2) and integrating them over the laminate thickness, we obtain

$$\begin{bmatrix} N_i \\ M_i \end{bmatrix} = \sum_{m=1}^{n} \int_{z_m}^{z_{m+1}} \sigma_i^{(m)} \begin{bmatrix} 1 \\ z \end{bmatrix} dz = B_0^T\, \phi(x) = 0\,, \quad \text{for } i = xx, xy \tag{10}$$

forming four linear constraints for the unknown functions $\phi(x)$.

Force N_{yy} and moment M_{yy} are treated differently, since they are not subjected to any differential constraints. According to Saint-Venant's principle, away from the y-edge of the laminate plate, where the forces are applied, a different but statically equivalent distribution is formed. If the edge effects and y-dependence of the stress field close to the force application are ignored, only the total force and moment should vanish:

$$\int_L N_{yy} dx = \int_L \int_{-\frac{h}{2}}^{\frac{h}{2}} \sigma_{yy}\, dz\, dx = 0, \quad \text{and} \quad \int_L M_{yy} dx = \int_L \int_{-\frac{h}{2}}^{\frac{h}{2}} \sigma_{yy}\, z\, dz\, dx = 0, \tag{11}$$

which after substitution of the corresponding stress in (2) and explicit integration over the laminate thickness can be written in the matrix form:

$$B_y^T \int_L \phi(x) dx = 0, \tag{12}$$

where B_y is a constant matrix. In case of a periodic crack geometry, the above integral should be evaluated over the length of the periodic cell.

In the regions with delamination cracks, zero traction conditions are also required. For each delamination crack at interface z_d with the normal in the z-direction, one has:

$$\sigma_{xz}(x, z_d) = \sigma_{yz}(x, z_d) = 0, \tag{13}$$

which, given the shear stresses are proportional to the first derivative of $\phi(x)$, is written in the matrix form as

$$B_1^T \phi'(x) = 0. \tag{14}$$

Additionally, we require

$$\sigma_{zz}(x, z_d) = 0, \tag{15}$$

which also should hold for each delamination crack and is combined to a system of second order differential constraints

$$B_2^T \phi''(x) = 0. \tag{16}$$

Linear equations (10), differential equations (14) and (16) and integral relations (12) form a set of constraints that the admissible stress field must satisfy.

3. Energy minimization

Consider now a fragment of a laminate between two (adjacent) transverse cracks that can serve as a periodic cell or representative volume element, such that the cracked laminate can be reconstructed by either translation of the fragment or reflection about its end planes. The fragment is then divided into several intervals having different delamination geometries; the interval boundaries can be defined by the tips of the delamination cracks. In each interval different delamination arrays impose different constraints on the stress field, hence different solutions for $\phi(x)$.

Let us write the energy functional as a sum of energies of the intervals

$$U_C = U_C^0 + \sum_{k=1}^{n_{int}} \int_{L_k} \frac{1}{2} F^{(k)}(x) dx, \tag{17}$$

where the Lagrangian $F^{(k)}(x)$ for interval k is defined by (9) expressed in terms of functions $\phi^{(k)}(x)$, n_{int} is the number of intervals with different delaminated interfaces in the periodic cell. The constraints are also written for different intervals:

$$\begin{aligned} B_0^T \phi^{(k)}(x) &= 0, \\ {B_1^{(k)}}^T \phi'^{(k)}(x) &= 0, \\ {B_2^{(k)}}^T \phi''^{(k)}(x) &= 0. \end{aligned} \tag{18}$$

Matrix B_0 is the same for all intervals, however matrices $B_1^{(k)}$ and $B_2^{(k)}$ are written with superscript (k) to emphasize that they depend on the locations of the delamination cracks. The integral constraints defined in (12) obtain the form

$$B_y^T \sum_{k}^{n_{int}} \int_{L_k} \phi^k(x) dx = 0. \tag{19}$$

Finally, the problem is formulated as following: determine vector functions $\phi^{(k)}$ that minimize the perturbation part in (17) subject to constraints (18) and (19):

$$\min_{\phi^{(k)}} \sum_{k=1}^{n_{int}} \int_{L_k} \frac{1}{2} F^{(k)}(x) dx, \quad \text{s.t.} \quad (18) \text{ and } (19). \tag{20}$$

The constrains are now added to the perturbation energy with Lagrange multipliers to form the extended Lagrangian:

$$U_C' = \sum_{k=1}^{n_{int}} \int_{L_k} \left[\frac{1}{2} F^{(k)}(x) + \omega_0^{(k)^T} B_0^T \phi^{(k)} + \omega_1^{(k)^T} B_1^{(k)^T} \phi'^{(k)} + \omega_2^{(k)^T} B_2^{(k)^T} \phi''^{(k)} \right]$$
$$+ \omega_y^T B_y^T \sum_{k}^{n_{int}} \int_{L_k} \phi^{(k)}(x) dx \,. \tag{21}$$

Here ω_0, ω_1 and ω_2 are Lagrange multipliers for constraints (18) that must hold at every point x along the fragment, hence they are functions of x. Constraints (19), however, are integral constraints and the corresponding Lagrange multipliers ω_y are constant.

Perturbing the unknown functions and requiring that the corresponding perturbation of the Lagrangian in (21) vanishes when the unknown functions are the minimizers, we arrive at the following Euler-Lagrange equations

$$M_{00}\phi + (M_{02} + M_{20} - M_{11})\phi'' + M_{22}\phi'''' + B_0\omega_0 - B_1\omega_1' + B_2\omega_2'' + B_y\omega_y = 0 \tag{22}$$

where the superscript (k) is omitted for simplicity. Together with constraints (18) they form a system of ordinary differential equations with constant coefficients for $\phi(x)$, $\omega_0(x)$, $\omega_1(x)$ and $\omega_2(x)$. The constant Lagrange multipliers ω_y will be treated as known and determined later using (19).

The differential constraints in (18) can be integrated:

$$\begin{bmatrix} B_0^T \\ B_1^T \\ B_2^T \end{bmatrix} \phi = \begin{bmatrix} 0 \\ c_1 \\ c_{20} + c_{21}x \end{bmatrix} = \begin{bmatrix} 0 \\ c_1 \\ c_{20} \end{bmatrix} + \begin{bmatrix} 0 \\ 0 \\ c_{21} \end{bmatrix} x \tag{23}$$

where c_1, c_{20} and c_{21} are some constants. The above can be written as

$$B^T\phi = p(x) \tag{24}$$

which defines matrix B and vector $p(x)$. One can also introduce vector

$$\omega = \begin{bmatrix} \omega_2 \\ -\omega_2 \\ \omega_2 \end{bmatrix} \tag{25}$$

With help of those definitions the system of equations can be written in the following convenient form:

$$\begin{aligned} M_{00}\phi + B\omega &= -(M_{02} + M_{20} - M_{11})\phi'' - M_{22}\phi'''' - B_y\omega_y \\ B^T\phi &= p \end{aligned} \tag{26}$$

The vector multipliers $\omega(x)$ can be excluded from the first system of equations yielding the resultant equations

$$M_{00}\phi + P(M_{02} + M_{20} - M_{11})\phi'' + PM_{22}\phi'''' = B(B^T M_{00}^{-1} B)^{-1} p - PB_y\omega_y \tag{27}$$

where $P = I - B(B^T M_{00}^{-1} B)^{-1} B^T M_{00}^{-1}$ is the orthogonal projection matrix. The solution of the above system of differential equations is a combination of a homogeneous and particular solutions

$$\phi = \phi_h + \phi_p \tag{28}$$

Here ϕ_h is the solution of the homogeneous equation obtained by setting the right-hand-side of (27) to zero

$$\phi_h = \sum_i c_{h,i}\, v_i \exp(r_i\, x) \tag{29}$$

with v_i being the i-th eigenvector, r_i – corresponding eigenvalue, $c_{h,i}$ – an arbitrary scalar constant. The particular solution for the current ODE and linear in x right-hand-side of (27) has the form

$$\phi_p = M_{00}^{-1}\left[B(B^T M_{00}^{-1} B)^{-1} p(x) - PB_y\omega_y\right] \tag{30}$$

Finally, the yet unknown constants c_h, c_1, c_{20}, c_{21} and ω_y are determined from boundary conditions at the end planes of the fragment, comprising zero (total) traction conditions on transverse crack surfaces and periodic or symtery boundary conditions, continuity of traction at the interfaces between intervals of different delamination geometries and the integral constraint (19). Typically, these physical boundary conditions do not suffice to determine the constants and should be supplemented by natural boundary conditions, obtained as part of perturbed functional (21). Alternatively, the complementary energy can be expressed as a quadratic form in the vector of all the unknown constants c, and minimized over c, while subject to the above set of physical boundary conditions which are linear in c, using again the method of Lagrange multipliers. Details of the procedure can be found in [7].

Once the unknown constants are obtained, functions $\phi(x)$ and the stress tensor components can be calculated, as well as the minimum value of the energy functional. The minimum value of the complementary energy defines the lower bound for the effective ABD* compliance matrix and elastic properties of the cracked laminate.

4. Numerical examples

The derived solution for the stress distribution and effective properties of a laminate is concise and requires negligible computational efforts. At the same time, the method is very robust and applicable to a variety of crack geometries and laminate systems. It has also been shown [7] that the results for effective thermomechanical properties of laminates with transverse cracks (no delamination cracks) agree very well with experimental data.

Figures 2-4 show the results of axial stress σ_{xx} in $[\pm 45/90_2]_S$ GFRP laminate due to axial tensile loading in three different developed delamination crack geometries: symmetric, antisymmetric (T-type) and periodic Z-type delamination. The thick black solid line indicates the locations of cracks. In these examples, the plies are subdivided, and more nonlinear stress distribution in the thickness direction is revealed, with clear stress concentrations (singularities) at the tips of the delamination cracks and significantly higher stress concentrations at the tips of transverse cracks arrested at ply interfaces without initiating delaminations (Figure 3).

The energy release rate associated with interlaminar crack propagation is obtained by differentiating the complementary energy respect to the crack length. The results for the three cracking patterns are shown in Figure 5. While the energy release rate at delamination initiation is approximately the same for the three cases, they demonstrate quite different behavior at the advanced stages of crack propagation.

5. Conclusion

An analytical solution based on the principle of minimum complementary energy is proposed for an approximate stress field, effective elastic properties and energy release rate of an arbitrary laminate with transverse cracks and delaminations. Using Lagrange multipliers, linear, first and second order differential and integral techniques are imposed on the admissible stress field to satisfy equilibrium and conditions and traction free crack surface conditions. The computational costs required to solve the problem are negligible in comparison to the Finite Element method due to the fact that the solution is analytical in each ply. At the same time the method allows application of so called “ply refinement technique” for more accurate stress distributions, which reveal different stress intensities around the transverse and delamination crack tips, and different crack patterns in general, as well as a strong dependence of the associated energy release rate on the formed crack geometry.

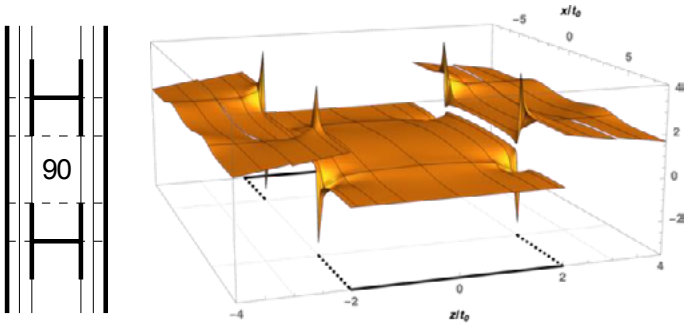


Figure 2. Distribution of σ_{xx} in cracked $[\pm 45/90_2]_S$ due to N_{xx}: symmetric delamination.

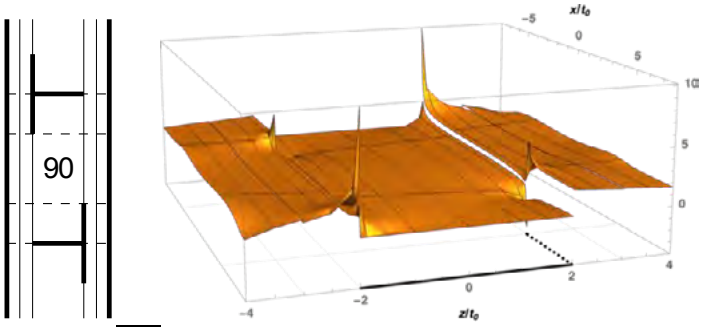


Figure 3. Distribution of σ_{xx} in cracked $[\pm 45/90_2]_S$ due to N_{xx}: antisymmetric delamination.

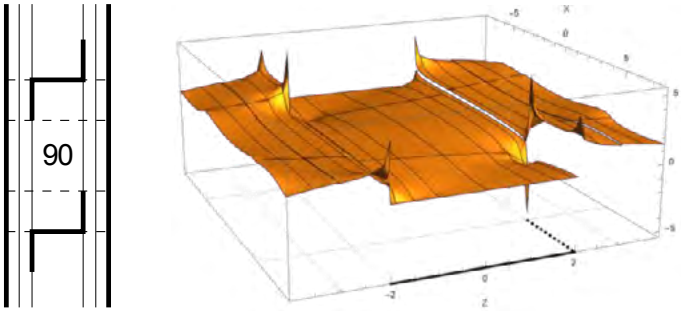


Figure 4. Distribution of σ_{xx} in cracked $[\pm 45/90_2]_S$ due to N_{xx}: Z-type delamination.

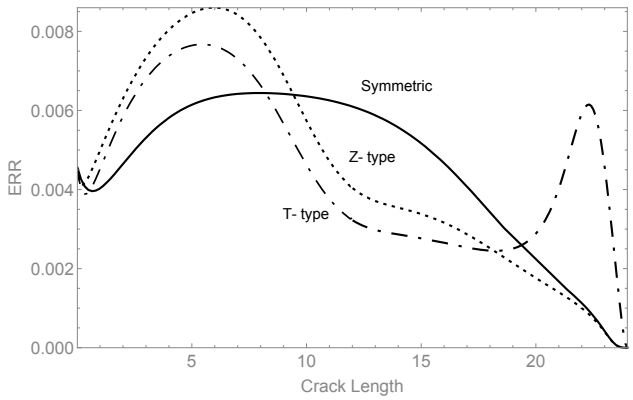


Figure 5. Energy release rate at constant axial load for the three cracking patterns.

References

[1] Z. Hashin, Analysis of cracked laminates: a variational approach. *Mechanics of Materials*, 4(2):121–136, 1985. https://doi.org/10.1016/0167-6636(85)90011-0.
[2] J.A. Nairn and S. Hu,Matrix microcracking, in: R. Talreja (Ed.), Elsevier Science, 1994: pp. 187–243.
[3] S. Li and F. Hafeez, Variation-based cracked laminate analysis revisited and fundamentally extended. *International Journal of Solids and Structures*, 46(20):3505–3515, 2009. https://doi.org/10.1016/j.ijsolstr.2009.03.031.
[4] V. Vinogradov and Z. Hashin, Variational analysis of cracked angle-ply laminates. *Composites Science and Technology*, 70(4):638–646, 2010. https://doi.org/10.1016/j.compscitech.2009.12.018.
[5] M. Hajikazemi and M.H. Sadr, A variational model for stress analysis in cracked laminates with arbitrary symmetric lay-up under general in-plane loading. *International Journal of Solids and Structures*, 51(2):516–529, 2014. https://doi.org/10.1016/j.ijsolstr.2013.10.024.
[6] Z.Q. Huang, J.C. Zhou, X.Q. He and K.M. Liew, Variational analysis for angle-ply laminates with matrix cracks. *International Journal of Solids and Structures*, 51(21):3669–3678, 2014. https://doi.org/10.1016/j.ijsolstr.2014.06.028.
[7] V. Vinogradov, A variational method for analysis of laminates with parallel arrays of intralaminar cracks. *International Journal for Numerical Methods in Engineering*, 120(5):666–705, 2019. https://doi.org/10.1002/nme.6152.
[8] M.J.M. Fikry, V. Vinogradov and S. Ogihara, Experimental observation and modeling of resin pocket cracking in unidirectional laminates with ply discontinuity. *Composites Science and Technology*, 218:109175, 2022. https://doi.org/10.1016/j.compscitech.2021.109175.
[9] J.A. Nairn and S. Hu, The initiation and growth of delaminations induced by matrix microcracks in laminated composites. *International Journal of Fracture*, 57(1):1–24, 1992. https://doi.org/10.1007/BF00013005.
[10] S.-H. Lim and S. Li, Energy release rates for transverse cracking and delaminations induced by transverse cracks in laminated composites. *Composites Part A: Applied Science and Manufacturing*, 36(11):1467–1476, 2005. https://doi.org/10.1016/j.compositesa.2005.03.015.

Mechanical performance analysis of 3D printing PLA/flax composite sandwich with different core geometries

Zhenyi Wang[1], Daniel Scida[2], Mustapha Assarar[2], Pierre-Antoine Adragna[1], and Xiao-lu Gong[1,*]

[1]University of Technology of Troyes, LASMIS, 12 Rue Marie Curie, 10000, Troyes, France
[2]University of Reims Champagne-Ardenne, ITheMM EA 7548, 51097, Reims, France
[*]Corresponding author: gong@utt.fr

Abstract

Natural fiber-reinforced composite materials present several advantages, such as low density and environmental friendliness. In particular, sandwich composite materials based natural fibers have gained significant traction in various industries due to their good characteristics, offering an exceptionally high stiffness-to-weight ratio and energy absorption capabilities. Their lightweight nature and high strength-to-weight ratios make them ideal candidates for various applications, including aerospace, automotive, and medical industries. For this purpose, four core geometries of sandwich composites composed with flax fiber reinforced PLA were considered: sinusoidal (SN), triangular (TR), double triangular (DT), and trapezoidal (TP). This study used the FDM technique to manufacture the sandwich structures and to assess and compare their properties with mechanical testing. The experimental results show that the trapezoid structure exhibited the best maximum load and load-displacement fitted stiffness among all the structures considered.

Keywords: 3D Printing, Sandwich structures, Flax fiber

1. Introduction

Synthetic fibers reinforced petrochemical polymer matrices pose a threat to the environment when they reach the end of their useful life. Environmental concerns and the issues of pollution are driving the development of sustainable materials suitable for emerging applications. There is a growing emphasis each year on the adoption of biodegradable or eco-friendly products sourced from renewable materials. Recent years have

witnessed a surge in the utilization of environmentally responsible polymers and composites within industrial sectors. This shift is not only motivated by the ecological harm caused by plastics but also by the risk of depleting oil reserves and the unchecked proliferation of landfills. With the increasing frequency of environmental disasters and the looming specter of global warming, governments are increasingly compelled to champion the use of biodegradable and eco-friendly materials in industrial contexts[1][2].

Natural fiber-reinforced polymer composites are considered promising alternatives to petroleum-based synthetic fiber-reinforced composite materials. The former exhibits satisfactory mechanical, thermal, and acoustic properties, and thus, they have been used as structural materials in constructions, furniture, automobiles and aircraft, etc[3][4]. Commonly used natural fibers are sourced from materials such as wood, flax, jute, sisal, abaca, and cotton. These natural fibers are characterized by their environmental friendliness, widespread availability, renewability, cost-effectiveness, and lightweight properties[5] [6] [7] .

PLA (Polylactic acid) is a biodegradable, thermoplastic polymer that is commonly used in Fused Deposition Modeling (FDM) 3D printing method[8].The origins of PLA lie in replenishable sources such as tapioca roots, corn starch, or sugarcane, facilitating production in diverse hues and qualities. In contrast to alternative 3D printing substances, PLA boasts several merits, including its minimal toxicity, commendable mechanical attributes, and facile processing[9]. Exhibiting a remarkable strength-to-weight ratio, PLA combines strength and rigidity with lightweight properties. Moreover, it demonstrates impressive resistance to impacts and fatigue, rendering it capable of enduring repeated stress without succumbing to breakage. These characteristics render PLA highly suitable for applications where robustness and rigidity hold significance, such as in structural components or operational prototypes.

Nowadays, polymer materials like PLA find increasing utility, particularly in crafting minor structural elements susceptible to modest loads. In this study, the cores and panels of sandwich structures were concurrently fabricated using a 3D printer employing FDM, utilizing flax-reinforced PLA material. Based on four different core models, sandwich structure samples[10] were manufactured from iso-mass configurations and then compressive tests were carried out. The aim was to compare the performance and characteristics of these different natural-fiber-reinforced composite sandwich structures.

2. Sample preparation and testing method

2.1 Material properties

The tested materials are flax fiber reinforced polymer composites based on short fibers of flax and polylactic acid (PLA)

The PLA/flax fiber filament was purchased from the Nanovia company in France. Each roll weighs approximately 500g, with a filament diameter of 1.75mm ± 0.05mm.

According to the technical specifications, tensile coupons were tested for flax fiber reinforced materials, and the mean value of the results is depicted in Table 1, where fy, y, fu, u, and E refer to the yield strength, yield strain, tensile strength, ultimate strain, and elastic modulus, respectively.

Table 1: Tensile properties of PLA flax reinforced composite

Material	Thickness(mm)	Width(mm)	f_y(MPa)	ϵ_y(%)	f_u(MPa)	ϵ_u(%)	E(GPa)
PLA/flax	4.00	10.00	13.76	0.46	41.31	2.46	3.11

2.2 Design and optimization of sandwich structure geometries

Four different core patterns of sandwich composites composed with flax fiber reinforced PLA were considered: sinusoidal (SN), triangular (TR), double triangular (DT), and trapezoidal (TP), as shown in Figure.1. The masses of these geometries were controlled to be consistent to better compare the effects of different patterns on the mechanical properties of the samples. So a python model has been developed to define samples with different sandwich core geometries of the same length, width and height with the same guaranteed mass. In order to reach iso-mass configurations (with a tolerance below 3%), it was necessary to define the following parameters to describe each structure: the length L, the width b, the thickness of core structure e_c, and the thickness of skin structure e_s.

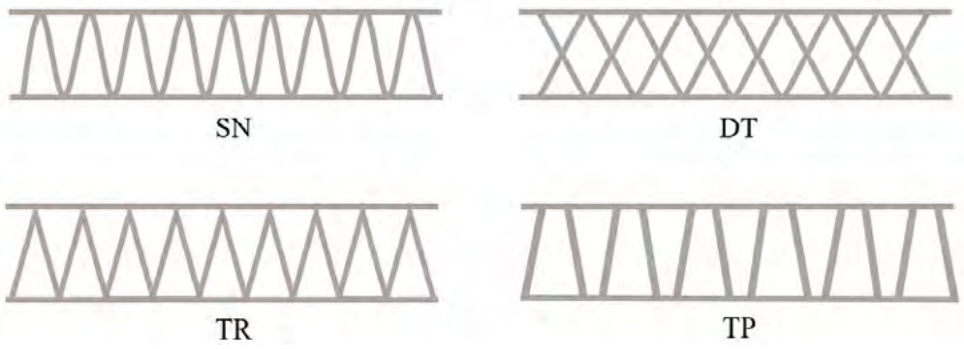


Fig. 1. 4 different core geometries of sandwich structures

2.3 Manufacturing process

The experimental study is made on FDM printed part. 3D printing is mostly used by importing CAD files into slice software such as ideamaker or curamaker, slice and use the resulting gcode file for printing. In this paper, MATLAB programming is used to draw the print path to generate the gcode file instructions directly. This way of printing can avoid line crossing during the printing process. The printing material is a 1.75 mm ABS filament from 3D Printing machine. The printer is a semi-professional RAISE2 from RAISE3D. Printing parameters are as follows, nozzle diameter is 0.8 mm, printing head

temperature is 215°C, bed temperature is 65°C, printing speed is 40 mm/s except for the first layer that is printed at 15 mm/s. For each geometry, 5 separate samples have been printed for conducting the experiments in the later section. Table 2 shows the real parameters measured for these samples fabricated.

Table 2: Parameters of different geometries

	L(mm)	b(mm)	h(mm)	e_c(mm)	e_s(mm)	m(g)
SN	139.27±0.05	29.89±0.01	31.00±0.04	1.66±0.01	1.66±0.01	45.97±0.14
TR	139.28±0.03	29.91±0.03	31.06±0.04	1.69±0.02	1.64±0.02	46.38±0.21
DT	139.29±0.06	29.90±0.02	31.13±0.02	1.75±0.02	1.63±0.01	46.33±0.27
TP	139.21±0.07	29.92±0.03	31.03±0.01	2.51±0.02	1.70±0.02	45.74±0.25

2.4 Compressive tests

A universal mechanical testing machine Instron 3300 has been used to realized the compressive tests. The compressive load is applied gradually and uniformly to the specimen at a constant rate, with a cross-head speed of 2mm/min. For each core geometries path, five specimens were tested for each set of samples according to ASTM D695 standard. Load application continues until the specimen undergoes significant deformation or failure. Figure shows the experimental machine assembly used, and the DT sandwich structure undergoing compressive tests.

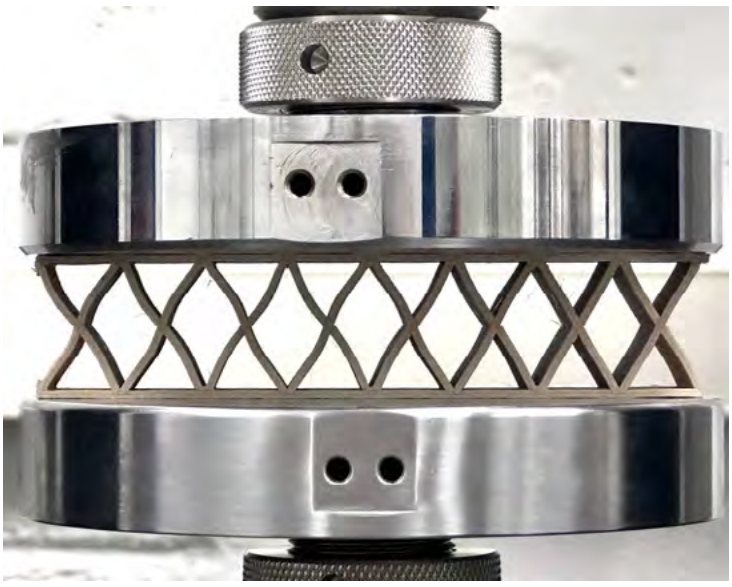
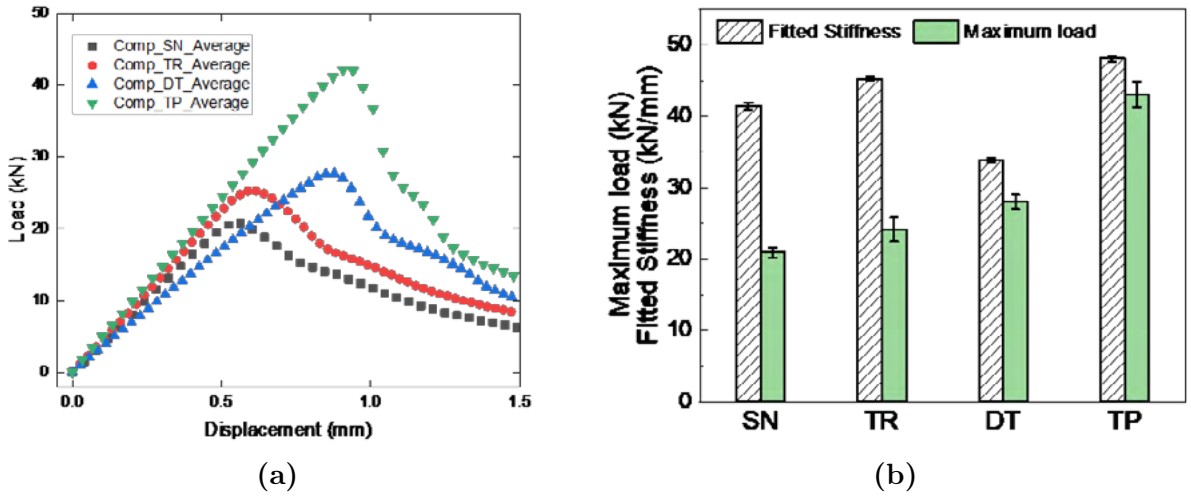


Fig. 2. DT sandwich structure undergoing compressive tests

3. Results and discussions

The Figure 3 illustrates the load-displacement curves obtained from compressive tests conducted on the four investigated core patterns. As depicted in Figure 3a, the axial

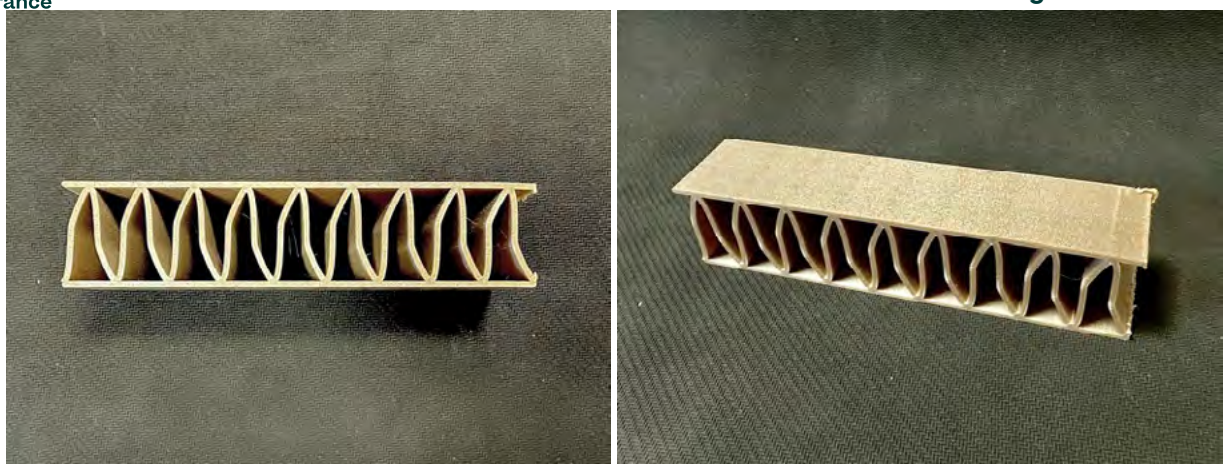
load-displacement curves of the sandwich structures exhibit a linear segment during the initial loading phase. Subsequently, as the load increases, localized buckling occurs in both the skin and core, resulting in a reduction in the slope of the curves. With further continued loading, the local buckling of the specimen became more serious, and the load-displacement curves decreased slowly. The experimental findings indicate that among all the structures examined, the trapezoid structure demonstrated the highest maximum load and stiffness that best fit the load-displacement relationship, with the best compressive mechanical performance. One possible explanation for this observation could be attributed to the greater number of contacts between the skin and core of the compressive side of the trapezoid pattern, totaling 12, as opposed to the remaining three patterns which each have 9 contacts. Furthermore, it's worth mentioning that certain structures seem to have minimal influence on the fitted stiffness, similar to the apparent akin Young's modulus. The load-displacement curves of SN and TR geometries are close to each other, probably because their geometries are also very similar. The core thickness of TP is 1/3 higher than the other three, but the fit stiffness does not increase significantly, so the relevance of the core thickness parameter needs to be further investigated and discussed.



(a) (b)

Fig. 3. (a) Averaged load(kN)-displacement (mm) curves with four different patterns (b) Fitted stiffness (kN/mm) and maximum load (kN) of four different patterns with error bar

At the beginning of the experiment, the sample is uniformly pressurized from above, and as the force increases, the displacement of the sample in the y-axis direction correspondingly increases. After that, the sandwich structure starts to bend internally, and eventually the force reaches its highest point and starts to drop slowly. The color change of the bent part of the sandwich structure can be clearly observed according to the Figure 4, which describe the damage of this part. To delve deeper into the microscopic alterations occurring during this process, future investigations can employ a broader array of analytical techniques. This may encompass leveraging advanced microscopy methodologies to meticulously scrutinize distinct stages of damage progression.



(a) (b)

Fig. 4. A sample of PLA/Flax with sinus structure after compressive tests

4. Conclusion

In summary, we explored various core geometries of biobased sandwich structures using PLA/Flax fiber. We designed and optimized samples of the same length, width and height with different sandwich core geometries: sinus, triangular, double triangular, trapezoid, for the same total mass. Utilizing continuous extrusion printing optimized by MATLAB, the gcode has been regenerated automatically and these samples have been manufactured sequentially. Through experimentation, we investigated the compressive mechanical properties of samples with different core patterns, aiming to compare the performance and characteristics of natural fiber-reinforced composite sandwich structures under different core patterns. Among these patterns, the trapezoid pattern exhibited superior performance relatively, this may be related to the number of contact points between sandwich core and skin. Based on experimental observations, this study provides insights for further analysis and research into the failure mechanisms of such materials in the future.

References

[1] M. Huda, L. Drzal, D. Ray, A. Mohanty & M. Mishra, 'Natural-fiber composites in the automotive sector,' in *Properties and performance of natural-fibre composites*, Elsevier, 2008, pp. 221–268.

[2] G. S. Mann, L. P. Singh, P. Kumar & S. Singh, 'Green composites: A review of processing technologies and recent applications,' *Journal of thermoplastic composite materials*, 33, no. 8, pp. 1145–1171, 2020.

[3] P. R. Oliveira, M. May, T. H. Panzera & S. Hiermaier, 'Bio-based/green sandwich structures: A review,' *Thin-Walled Structures*, 177, p. 109 426, 2022.

[4] M. Staiger & N. Tucker, 'Natural-fibre composites in structural applications,' in *Properties and performance of natural-fibre composites*, Elsevier, 2008, pp. 269–300.

[5] G. Chen, A. Gupta & T. H. Mekonnen, 'Silane-modified wood fiber filled epdm bio-composites with improved thermomechanical properties,' *Composites Part A: Applied Science and Manufacturing*, 159, p. 107 029, 2022.

[6] A. K. Mohanty, F. Wu, R. Mincheva *et al.*, 'Sustainable polymers,' *Nature Reviews Methods Primers*, 2, no. 1, p. 46, 2022.

[7] C. Baley, 'Analysis of the flax fibres tensile behaviour and analysis of the tensile stiffness increase,' *Composites Part A: Applied Science and Manufacturing*, 33, no. 7, pp. 939–948, 2002.

[8] L. Azzouz, Y. Chen, M. Zarrelli *et al.*, 'Mechanical properties of 3-d printed truss-like lattice biopolymer non-stochastic structures for sandwich panels with natural fibre composite skins,' *Composite Structures*, 213, pp. 220–230, 2019.

[9] B. Tymrak, M. Kreiger & J. M. Pearce, 'Mechanical properties of components fabricated with open-source 3-d printers under realistic environmental conditions,' *Materials & Design*, 58, pp. 242–246, 2014.

[10] Z. Yan, C. Shen, H. Fang, L. Xie, X. Bao & H. Wang, 'Compressive performance of full-scale gfrp composite sandwich wall panels with wood core,' *Journal of Building Engineering*, p. 108 979, 2024.

OPTIMISING INTERMITTENT INTERFACES IN FIBRE-REINFORCED COMPOSITES: STRIKING THE BALANCE BETWEEN STRONG AND WEAK FIBRE-MATRIX INTERFACES

S. AhmadvashAghbash[1], M. Mehdikhani[1] and Y. Swolfs[1]

[1]Department of Materials Engineering, KU Leuven, Kasteelpark Arenberg 44, 3001 Leuven, Belgium
Email: sina.ahmadvashaghbash@kuleuven.be, Web Page: https://www.mtm.kuleuven.be

Keywords: Interface, Microscale modelling, Carbon fibre, Epoxy, Cohesive zone modelling

Abstract
While a strong fibre-matrix interface yields a composite with high strength and stiffness, it often leads to brittle failure and limited energy absorption. By deliberately weakening the interface, one can enhance toughness by creating longer debond lengths and subsequent pull-out mechanisms. However, this strategy comes with the drawback of reducing both strength and stiffness, necessitating a careful balance between these competing factors in composite design. Drawing inspiration from nature's mechanisms to enhance toughness, the overarching objective of this study is to thoroughly comprehend and leverage the potential of intermittent interfaces to engineer fibre-reinforced composites with an outstanding combination of mechanical properties. The proposed microscale numerical model proves invaluable in enhancing the efficacy of subsequent experimental pursuits in manufacturing intermittently-treated fibre-reinforced composites. This finite element model addresses the research question of identifying the mechanisms behind intermittent interfaces with a synergistic blend of high strength, stiffness, and toughness. It also investigates how design parameters, such as the length and interval length of intermittent areas and their locations relative to the fibre break plane, influence the mechanical behaviour of these composites. The model predictions reveal that the proposed intermittent approach results in larger debond lengths and, consequently, higher energy dissipation values.

1. Introduction

One of the most ambitious goals in structural materials is to achieve exceptional mechanical properties with an ideal combination of low density, high strength, and high toughness. The strength and toughness of different materials, including fibre-reinforced composites, are usually intertwined. The amount of stress that a material can support without cracking and then fracturing increases when the strength of the material is high; however, toughness increases only when the energy required to cause a crack to grow to fracture also increases and is coupled to more deformation of the material. This intricate relationship implies that enhancing one attribute inevitably comes at the expense of the other. However, natural materials, such as bone, have exceptional properties that can combine both high strength and high toughness by an ingenious structural design [1]. For biomaterials, strategies to achieve unification between structure and mechanical properties have been through millions of years of evolution. Nacre is a good example of a material that combines strength, stiffness, and toughness. When this material is subjected to stress and a crack is produced, it follows a complex path to grow in a very complex pattern [2]. The tortuous crack paths and pull-out of the mineral platelets provide a major contribution to toughening. The result is a material with a toughness of at least an order of magnitude higher than either of its constituents [3].

High toughness holds particular significance in applications which suffer impact or for components where fracture could have catastrophic consequences. Composite materials emerge as a compelling

alternative to traditional counterparts, offering superior strength-to-density ratios that translate to reduced fuel consumption, especially in the aviation and automotive sectors. Carbon and glass fibre-reinforced composites, in particular, are light, stiff and strong. However, their brittleness remains a limitation.

The pioneering work of Atkins (1975) [1] described theoretically the failure mechanism of composites reinforced with long fibres with alternate sections of high and low adhesion, showing its capability for improving composite toughness without a reduction of stiffness and strength. Although he was only able to produce irregular intermittent areas of lengths around 19 to 51 mm on thick boron fibres (diameter 140 µm) and on monofilament tapes (not individual fibres), the translaminar fracture toughness of boron/epoxy unidirectional composites increased from 50 kJ/m² to 150 kJ/m² while retaining rule-of-mixtures tensile strength, demonstrating the validity of the approach.

The intricate nature of crafting alternative sections brought this field to a standstill for years. Only in 2017 did Grappe et al. [2] propose a new attempt to obtain intermittent sizing on CF yarns for composite applications. The approach consisted of an intermittent spray sizing of CF bundles (80k individual filaments) and was developed specifically for sheet moulding with the aim of improving diffusion of resins on the alternate sections without sizing. Although the aim of this research was to improve composite processability only, an increment of 100% and 60% for the tensile strength and tensile modulus, respectively, was reported when compared with untreated samples. No description of the mechanisms that allowed the significant improvement in the mechanical performance was given. More recently, in 2018, Greenfeld et al. [2] proposed an intermittent approach on single fibres for the first time, by creating beads of cured epoxy evenly distributed on a single glass fibre [26]. Pull-out and fragmentation tests showed an improvement in toughness while keeping tensile strength. However, this approach is based on mechanical interlocking created by the beads during failure, producing energy dissipation due to the deformation of the matrix during pull-out of the fibres and not to the development of a tortuous crack path for energy dissipation (“brick and mortar” concept).

Inspired by nature’s strategies to increase toughness, this study proposes a novel numerical approach for the development of tough CF composites, creating micro mechanisms for energy dissipation at the interface of individual fibres while maintaining good load transfer. This can be achieved by creating areas of high and low shear strength in an orderly position on brittle fibres, controlling the local damage process to promote crack propagation (low shear stress areas), as well as inhibiting crack propagation and sustaining the filament strength (high shear stress areas). Our approach consists of defining the best compromise between strong and weak fibre/matrix interfaces distributed alternatingly along single fibres to improve the toughness of composites. While an interface with high shear strength produces composites with high strength and stiffness, brittle failure and low energy absorption, an interface with low shear strength produces large delamination and high energy absorption (given an optimum length) but reduces the strength of the composite. If we are keen to tailor the interface and balance these two areas of high and low shear strength, then an advancing crack tip will be blunted by fibre debonding in the weak interface regions, whereas the strong part of the interface can prevent the debond length from becoming too large.

An intermittent interface influences the longitudinal crack growth (mode II) produced by shear debonding, generating a tortuous path which increases the surface area that must be created during fracture until the crack reaches the strong areas. In this way, the strong regions ensure that the filament strength is taken, while the weak areas weaken the running crack, creating a complex pattern for crack evolution. Then, strong interfacial areas can maximise the use of fibre strength, while the weak interface can increase energy absorption.

2. Numerical model

A modelling approach (as exemplified in [3,4] for a continuous interface) is imperative to comprehensively understand how intermittent surfaces impact the adhesion between carbon fibres and

polymer matrices so that the experimental methods, such as plasma activation and deposition processes, are guided and optimised.

A single-fibre model is generated to establish and validate the methodology. Considering a cylindrical coordinate system, r and θ are the radial and angular coordinates, respectively, and z-axis is the axial (fibre) direction of the composite (see Fig. 1a). The length and the radius of the model were set to 6 *mm* and 0.5 *mm*, respectively. These large dimensions help to diminish the apparent stiffness loss of the simulated specimen due to a fibre break and debonding. The nodes on the $\theta = 0°$ and 30° planes are constrained in the direction. At the plane, a z-symmetry boundary condition is applied, excluding the broken fibre surface (traction-free). The outer cylindrical surface ($r = 0.5$ *mm*) is traction-free, enabling Poisson contraction. The plastic response of the epoxy matrix is modelled using the Abaqus plasticity model. The engineering constants for the transversely isotropic CF, macroscale epoxy properties and their thermal expansion coefficients are given in [4].

The fibre-matrix interface of the broken fibre is modelled by adopting a surface-based cohesive contact with a bilinear traction-separation law. The mixed-mode debond initiation is based on the quadratic traction criterion. An energy-based damage evolution with a linear softening law is considered for debond propagation. The contact definition in our proposed model couples the cohesive zone model with the Coulomb friction model as of the initial step (thermal cooldown of −100 °C), leading to a continuous transition from debond initiation to its completion and then frictional sliding. Fig. 1a-b illustrates the conceptual foundation of this numerical investigation, depicting the assigned interfacial properties for both weak and strong interfaces using cohesive surface pairs. A high initial penalty stiffness is assigned to eliminate interpenetration of the crack faces. The simulations are performed in Abaqus/Standard 2023, using quadratic, reduced integration hexahedral elements (C3D20R). Fig. 2 shows the mesh quality with a highly dense mesh assigned to the broken fibre and the matrix in the vicinity of the interface, which is gradually coarsened out radially away from the interface using a logarithmic bias.

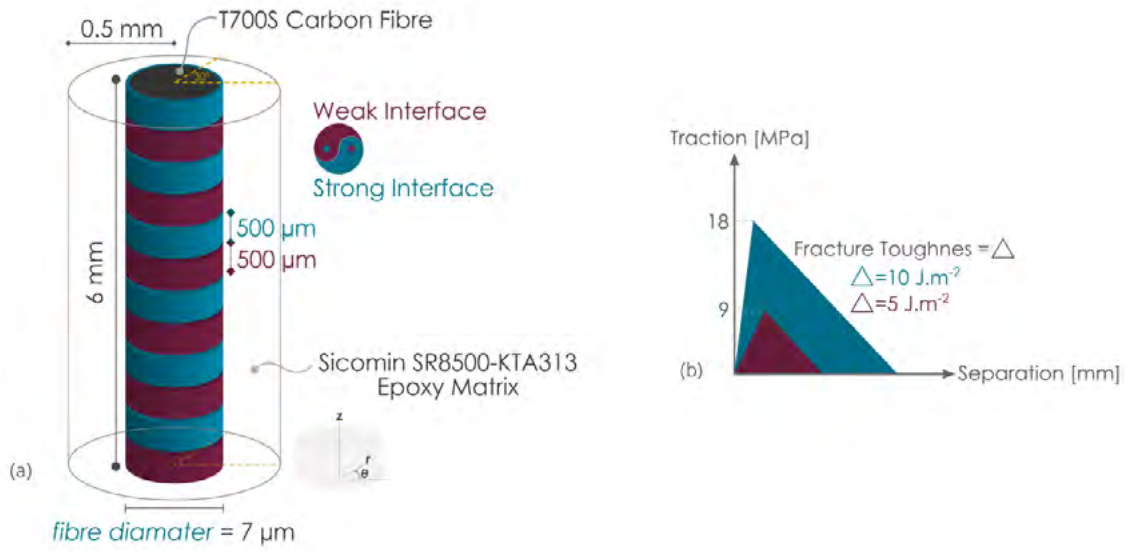


Figure 1. (a) Schematics (at adjusted scale for enhanced clarity) of the microscale model for intermittent fibre-matrix interfaces, and (b) assigned bilinear cohesive zone models for the weak and strong interfaces.

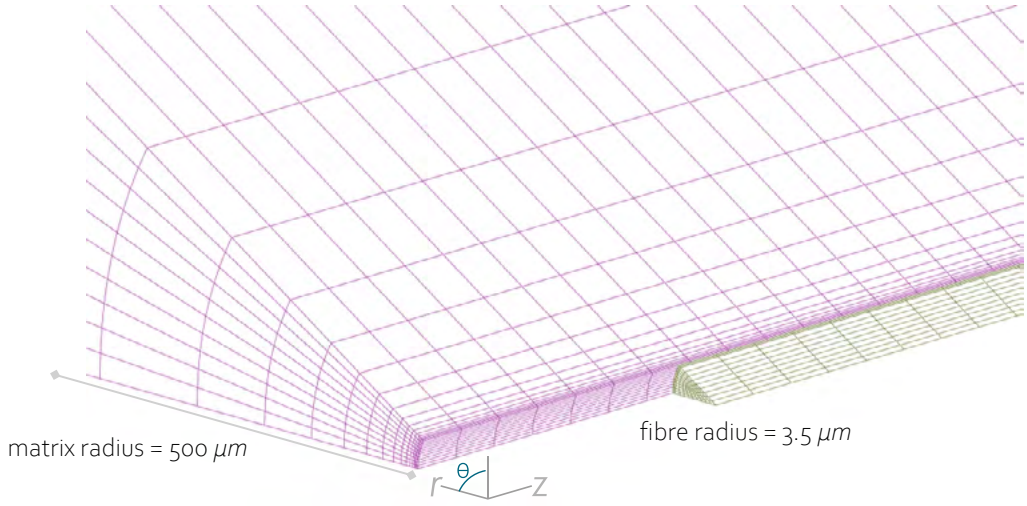


Figure 2. The FE model and mesh quality visualisation of a 30°-wedge single fibre-epoxy model for intermittent interfaces with the frictionally-slided debonded broken fibre at the end of a simulation ($\varepsilon = 2\%$).

Six models have been developed for the initial analysis. Among these, two focus on *continuous* (or *uniform*) interfaces, distinguished by their interfacial properties—one characterised by high interfacial properties (*strong*) and the other by low interfacial properties (*weak*) as shown in Fig. 1b. The remaining four models adopt an intermittent approach, featuring intermittent lengths of either 100 or 1000 μm. These intermittent models are further differentiated based on whether the weak or strong interface is adjacent to the fibre break plane.

Fig. 3 illustrates the interface status of the "100-μm intermittent model" as strain levels increase, notably featuring a weak interface positioned adjacent to the fibre break plane. In this depiction, an interface damage parameter of 1 signifies complete debonding of the interface. Observably, interfacial debonding initiates from the side adjacent to the fibre break plane, particularly from a weak interface. Subsequently, the adjacent weak interface, separated by a strong interface, undergoes debonding as strain increases, albeit without achieving full debonding initially. At higher strain levels, the central strong interface initiates debonding, merging with the debonding of the first weak interface, ultimately connecting these two weak interfaces and resulting in fully debonded regions. For fibre axial stress, all Gaussian points' stress is averaged within each layer of the cross-section. As seen from the longitudinal stress recovery profile of the broken fibre (Fig. 4), the proposed intermittent approach will result in a larger debond length (~4-4.7 *mm* compared to 1.1 *mm*) and, consequently, higher energy dissipation values.

Moreover, it is imperative to investigate the significance of the quality of the first neighbouring interface adjacent to the fibre break plane and its correlation with the interfacial debond length. As seen in Fig. 4, when the initial interface is weak, the increase in debonding length is only marginally larger compared to a strong initial interface, particularly with a small intermittent size (e.g., in 100-μm model). However, this discrepancy amplifies notably with larger intermittent sizes, such as in 1000-μm model.

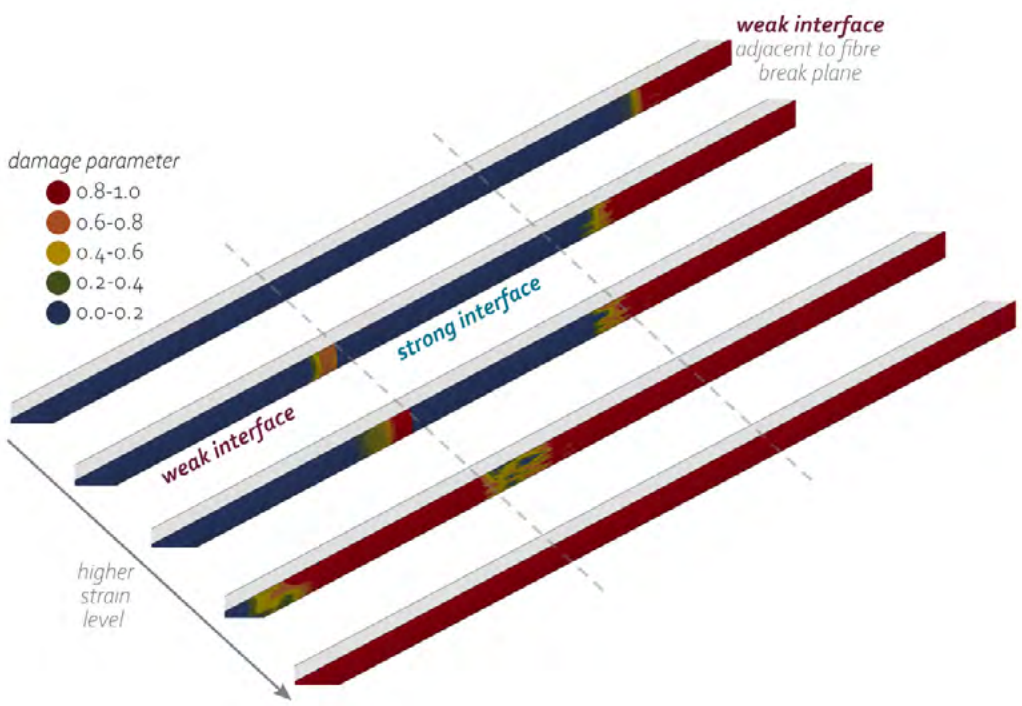


Figure 3. The progressive debonding of weak interfaces, subsequent to the debonding of the intermediate strong interface, leading to their eventual merging within the "100-μm intermittent" model, delineated against strain progression.

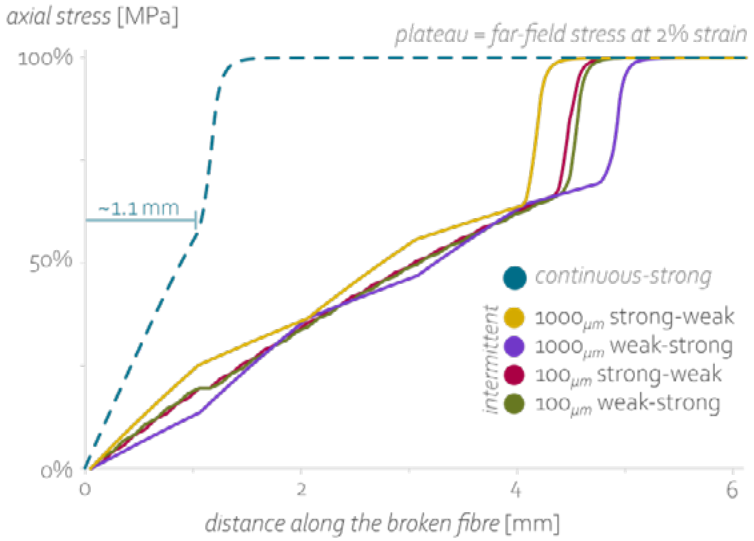


Figure 4. The load-displacement response across varying lengths (100 μm and 1 mm) of intermittent interfaces and the interface quality adjacent to the fibre break plane. Note that the debond length corresponds to the slipping extent of the *contact status output*, aligning with the linear segment of the stress recovery profiles.

3. Conclusions

As a general approach, it is possible to weaken the interface, but this is accompanied by a significant reduction in strength and stiffness; therefore, intermittent modulation of fibre-matrix interfaces provides an interesting compromise, as a propagating crack tip can be blunted by fibre debonding in the weak

interface regions, while the strong area of the interface can limit the extent of the debond length and preserve the overall strength and stiffness. In a nutshell, the strong interface can maximise the use of the fibres, while the weak interface can improve energy absorption. This study underscores the potential of intermittent interfaces in advancing the performance of composites, offering a pathway towards achieving a harmonious blend of stiffness, strength, and toughness.

Through stress recovery profiles, it became evident that the proposed intermittent approach facilitates larger debond lengths and, subsequently, higher energy dissipation values, offering potential enhancements in composite performance. Additionally, the investigation emphasised the critical role of the quality of the initial neighbouring interface adjacent to the fibre break plane, showcasing its correlation with debond length. These findings underscore the significance of tailored interface design strategies in optimising composite properties and advancing materials engineering. Moreover, this numerical model plays an essential role as the guideline for experimental methods in creating regular and precise intermittent areas (with controlled height at the nano/micro scale) on an individual fibre using a combination of techniques such as micro-plasma and the formation of a precursor micro/nano layer during the spreading of a molten thermoplastic. Moreover, the stress recovery library, within the feasible range of interfacial properties, as reported in [5], can be utilised in the KU Leuven strength model to predict the optimal longitudinal tensile strength.

Acknowledgements
The work leading to this publication was performed within the framework of the BioInter project and has received funding from the Luxembourg National Research Fund (Fonds National de la Recherche - FNR) under the CORE 2021 scheme, as well as from FWO (Fonds Wetenschappelijk Onderzoek) in Belgium, under approval number G005323N. MM gratefully acknowledges his FWO postdoctoral fellowship ToughImage (1263421N).

References
[1] A. G. Atkins. Intermittent bonding for high toughness/ high strength composites. *Journal of Materials Science*, 10:819–832, 1975.
[2] I. Greenfeld, W. Zhang, X. M. Sui and H. D. Wagner. Intermittent beading in fiber composites. *Composites Science and Technology*, 160:21–31, 2018.
[3] S. AhmadvashAghbash, B. Fazlali, M. Mehdikhani and Y. Swolfs. Finite element analysis of the effect of longitudinal debonding on stress redistributions around fibre breaks in randomly packed fibres. *Composites Science and Technology* 227:109586, 2022.
[4] S. AhmadvashAghbash, C. Breite, M. Mehdikhani and Y. Swolfs. Longitudinal debonding in unidirectional fibre-reinforced composites: Numerical analysis of the effect of interfacial properties. *Composites Science and Technology* 218:109117, 2022.
[5] S. AhmadvashAghbash, I. Verpoest, Y. Swolfs and M. Mehdikhani. Methods and models for fibre-matrix interface characterisation in fibre-reinforced polymers: a review. *International Materials Reviews*, 68(8):1245–1319, 2023.

Analysis of electrical performance of carbon fiber composites for heat generation in de-icing applications

Nawres J. Al-Ramahi[1,2], Patrik Fernberg[1], Roberts Joffe[1]
[1]Division of Materials Science, Luleå University of Technology, SE-971 87 Luleå, Sweden
[2]Institute of Technology / Baghdad, Middle Technical University, Baghdad, Iraq
Email: nawres.al-ramahi@ltu.se
Email: patrik.fernberg@ltu.se, Web Page: https://www.ltu.se/en/staff/p/patrik-fernberg
Email: roberts.joffe@ltu.se, Web Page: https://www.ltu.se/en/staff/j/roberts-joffe

Keywords: Electrical resistance, Temperature distribution, Electrical resistivity, Carbon fiber, Finite element method.

Abstract
A study was conducted on the electrical behavior of carbon fiber composite for anti-icing applications in structures like wind turbine blades and aircraft wings. Both experimental and numerical methods were used to analyze how different layer orientations ($[0_2]_T$, $[90_2]_T$, $[0/90]_T$, $[\pm45]_T$, $[0/45/-45/90]_T$) and plate dimensions affect the electrical resistance and heat generation of the carbon fiber composite. To simulate this behavior a numerical model using the finite element method (FEM) with Thermal-Electric element (Coupled-Field Solid) was used. The capacity of the carbon fiber composite laminate to generate heat under electrical load was predicted. A good agreement between experimental results and numerical simulations was obtained. This study found that the 0° layer had the lowest electrical resistance and highest heat generation capacity compared to other layups with the circuit configuration studied. The 90° layer demonstrated very high electrical resistance due to inter-fiber dominated behavior. The conclusion based only on the performance to generate heat under electrical load is that unidirectional lamina with 0° fiber orientation is best suited for this task. However, complete design should consider various mechanical and thermal loads. The results provide valuable insights into the performance of carbon fiber composite for de-icing applications in various structures.

1. Introduction

The remarkable mechanical and electrical properties of carbon fibers promote use of carbon fiber-reinforced plastics (CFRPs) in various applications where multi-functionality is required. These materials are utilized in various ways, such as de-icing aircraft components, preventing icing on wind turbine blades, design of heated CFRP molds. Additionally, the advancement of specialized non-destructive testing techniques, like electrical measurements, has allowed for the detection and assessment of damages in CFRPs [1]. The heating systems play a crucial role in maintaining the operational efficiency and safety of both wind turbines and aircraft, especially in cold climates. In these applications, the growth of ice on critical surfaces can compromise performance, increase energy consumption, and pose significant safety risks. In wind turbine applications, icing on the blades can disrupt airflow, decrease aerodynamic efficiency, and lead to structural concerns. Similarly, for aircraft, ice formation on wings, engines, and other surfaces can decline lift, increase drag, and impact control, posing serious risks during flight. Consequently, it is very important to focus on how to improve the performance of these heating systems. More specifically, for CFRP based on continuous fibers discrete conductive pathways (fibers) are distributed within an insulating matrix, providing the entire CFRP with local conductive or insulating properties [2,3]. Moreover, it has been observed that CFRP has a much higher electrical conductivity along the direction of the fibers, while the conductivity is significantly lower perpendicular to the fiber orientation [4]. It is commonly assumed in the field of CFRP that, in ideal conditions and without considering capacitive or inductive couplings between fibers, electrical current flows primarily through individual carbon fibers due to the insulating properties of the surrounding polymer material. Theoretically, in a scenario where carbon fibers were perfectly straight

and did not come into contact with adjacent fibers, CFRP would exhibit extremely high insulating characteristics in a direction perpendicular to the fibers. Nevertheless, it is important to note that the assumption of perfectly unidirectionally aligned fibers in an CFRPs is in practice never completely fulfilled. In reality, individual carbon fibers do not completely follow the same alignment and they can also have a tendency to exhibit waviness along fiber direction. As a result of this characteristic, there are occasions where adjacent fibers come into contact with each other, allowing for the flow of electric current between them [5].

Unidirectional carbon fiber-reinforced plies are expected to conduct electricity similarly in transverse and out-of-plane directions (as both are perpendicular to the fiber orientation). However, the potential presence of resin in between layers, e.g. in multi-directional composites or in textile based composites, acts as an insulator and hinders flow of current in an out-of-plane direction, resulting in even lower conductance than in the transverse direction [6]. Since the conductance in both directions is affected by the contact between fibers, the overall electrical impedance of a CFRP sample depends on the electric resistance of all fibers present [7].

There are a number of studies [8–11] that are dealing with the prediction of heat generation by CFRP subjected to the electrical load. A numerical model is presented in [8] to calculate temperature distribution during induction heating with a circular coil. The study shows the significance of including temperature-dependent thermal properties in the numerical model, while the addition of temperature-dependent electrical conductivity may not be important given its negligible influence on the calculated heat generation and temperature. The feasibility of simulating temperature distribution in the induction heating of carbon fiber-reinforced polymer woven fabric using a finite element model with a simplified unidirectional layer representation is demonstrated in [9]. The simulation shows good agreement in predicting peak temperature, with around a 10% difference in comparison with the experimental results. Another numerical model is presented in [10] to calculate temperature and heating power distribution in cross-ply CFRP plates during induction heating. Different fibre volume fractions and layer thicknesses were used in experiments which were validated by the numerical model. The model in [11] represents CFRP as a network of discrete resistors, with local currents determined by Kirchhoff's circuit laws and temperature distribution calculated using the finite difference method. The current and temperature distribution in CFRP during induction heating were simulated. This model complements traditional finite element simulations, providing an understanding of current paths and heating patterns on a tow size level. Experimental thermographic recordings during induction heating experiments support the validity of the model.

The above studies render a lot of useful results for particular cases, however, the influence of fiber orientations on the electrical conductivity of CFRP composites, especially in scenarios where fibers are not perfectly aligned, has not been carried out. The coupling capacitance between fibers in CFRP composites and its effect on electrical current flow has not been properly studied either. The current work tries to address some of these issues to generate more knowledge for future studies related to the conductivity of composite laminates with defects as well as recommendations for efficient repairs of composites to maintain the same performance.

2. Experimental work

The fast-curing carbon fiber prepreg (T700S/ #2300) was used to manufacture composite laminates. The sandwich panels made of glass fiber composites and foam core (supplied by PODCOMP, in Piteå) were used as a support material for the carbon fiber layers (to simulate the structure of the turbine blade). To ensure good connection between the carbon fibers and the stainless-steel electrodes, the metal stripes were embedded between the carbon layers. The distance between the metal stripes defines the effective width of the plate. The whole assembly (carbon fiber layer, glass fiber panel, and stainless-steel electrodes) were placed in a hot press (Phi Pasadena Hydraulics, inc) at 130°C, 3 bar for 30 minutes.

Two different distances between the metal stripes (16 cm and 28 cm) were employed to see if it has any effect on heat generation. Five different fiber lay-ups ($[0_2]_T$, $[90_2]_T$, $[0/90]_T$, $[\pm45]_T$, $[0/45/-45/90]_T$) were

used to study how fiber orientation and lay-up affects electrical performance and consequently temperature generation.

To initiate the experiment to measure electrical conductivity and temperature generation, the electrodes (stainless-steel stripes) are connected to a power supply (metal bolts were used to ensure a stable connection between the wires and the electrodes). To prevent the heat reflection into the thermal camera from the surfaces around the sample, a protective shield was used (box made out of glass fiber sandwich panels), as shown in Fig.1. 2 voltage was applied on all the plates in order to accurately comparison for the results. A thermal camera (FLIR series-A6000) and ResearchIR software were used to monitor the temperature generation and distribution within the plate.

To determine the resistance of the plate, various voltage values were systematically applied to the plate while measuring the corresponding currents. By plotting the relationship between electrical voltage and current, it is possible to determine the slope of the curve which represents the resistance. The resistance value for each tested plate is adjusted to exclude additional wire resistance from measurements (by subtracting the wire resistance from measured values).

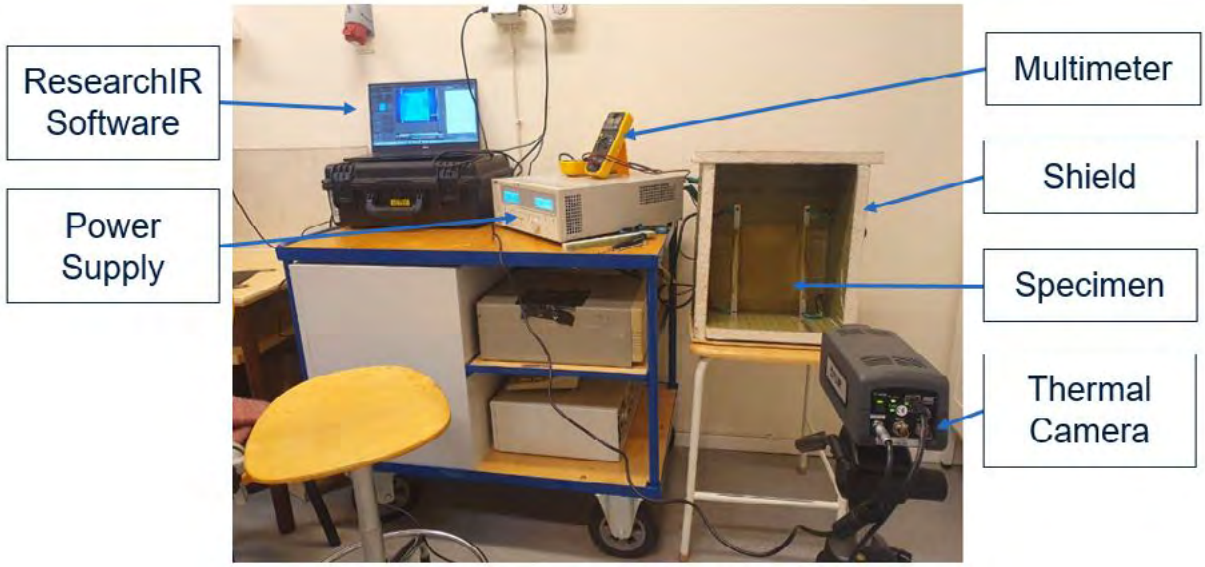


Figure 1. Experimental set-up for the test.

3. Finite element model

In this study, the numerical analysis of thermal and electrical performance for a rectangular carbon fiber composite plate with different fiber orientations in layers and various plate dimensions subjected to an electrical field (by applying voltage) was carried out. The simulations were done by using a commercial FEM package ANSYS 2023 R1 (utilizing APDL codes). A 3D coupled-field solid element (SOLID226) [12] with twenty nodes were used to create the uniform mesh for the whole plate with the same element size. The convergence of the results was obtained by monitoring the influence of the mesh size on the thermal value. In this simulation, two different materials are used through the thickness of the plate in order to simulate the real scenario of the turbine blades which consists of glass and carbon fiber layers. The same geometry and dimensions of the experimental specimens are used with the following boundary conditions applied: the electrical load is applied on both ends of the plate (at the same location as the electrode in the experimental setup in the locations X=-L/2 and X=L/2). The surface loads are applied on the outer areas of the plate which has convection with the surrounding air. The mechanical, thermal, and electrical properties are supplied to the program for the standard linear orthotropic material model implemented in ANSYS in order to be used for simulations.

4. Results and discussion

As was mentioned earlier the aim of the study is to gain a better understanding of how different layer orientations and sample dimensions (plate sizes) affect the electrical resistance of the composite and the amount of heat it produces. Thus, the analysis is focused on the comparison of the experimental results of the electrical resistance, temperature generation and distributed within the carbon layer of the flat plate. The comparison between experimental and numerical results is presented for these parameters.

4.1 The effect of fiber orientation

The comparison between different carbon layer orientations is discussed in this section. The results of the experiment are presented in Table 1. It was found that the plate with a $[0_2]_T$ layup exhibited the lowest electrical resistance compared to other configurations. Accordingly, the $[0_2]_T$ plate showed the highest heat generation capacity compared to other layups with the circuit configuration studied as shown in Fig. 2. The electrical resistance of the cross-ply laminates, $[\pm45]_T$ and $[0/90]_T$, were higher than the resistance of unidirectional $[0_2]_T$ lamina by 80% and 97% respectively. While, the quasi-isotropic laminate $[0/45/-45/90]_T$ showed only a 2% difference in resistance when measured in absolute values, but it is important to consider the effect of any changes in the cross-sectional area of the plate. Thus to exclude the effect of change in the cross-section area of the plate the value should be normalized with respect to thickness. Once this normalization is applied, the difference in resistance is actually increased to 102%. Notably, the $[90_2]_T$ layer alone demonstrated a very high electrical resistance, approximately 2000 times higher than that of the $[0_2]_T$ laminate. This is expected, since ideally, no electrical current should pass through the $[90_2]_T$ layer (fibers are insulated by matrix). However, due to inevitable small misalignments, waviness of carbon fibers resulting in inter-fiber contact points along the length of continuous fibers, current may flow from one fiber to another even in 90° layer. This inter-fiber behavior also results in the electric conductance of the out-of-plane direction being very similar to that of the transverse direction.

Table 1. Electrical resistance for different laminates

Stacking sequence	Thickness (mm)	Width (mm)	Distance between the electrodes (mm)	Resistance (ohm)
$[0_2]_T$	0.5	200	160	0.0647
$[0/90]_T$	0.5	200	160	0.1275
$[45/-45]_T$	0.5	200	160	0.1185
$[90_2]_T$	0.5	200	160	134.37
$[0/45/-45/90]_T$	1	200	160	0.0653

Furthermore, it was observed from Fig. 2 that the temperature increase for the $[0_2]_T$ plate was approximately twice as high as that for the $[0/90]_T$ plate under the same applied electrical voltage. While it is approximately 40% and 4.5 times higher than the $[45/-45]_T$ and $[90_2]_T$ plates respectively. However, the $[0_2]_T$ showed only a 25% higher than for the quasi-isotropic laminate $[0/45/-45/90]_T$ which is related to an increase in the contact points between the fibers, but at the same time, more layers are needed to reach the same temperature as for $[0_2]_T$. Consequently, in general, a lower electrical current (approximately around 25% of the value compared to laminates with different layups) needed to be applied to the $[0_2]_T$ plate to achieve the same temperature increment as for the other laminates.

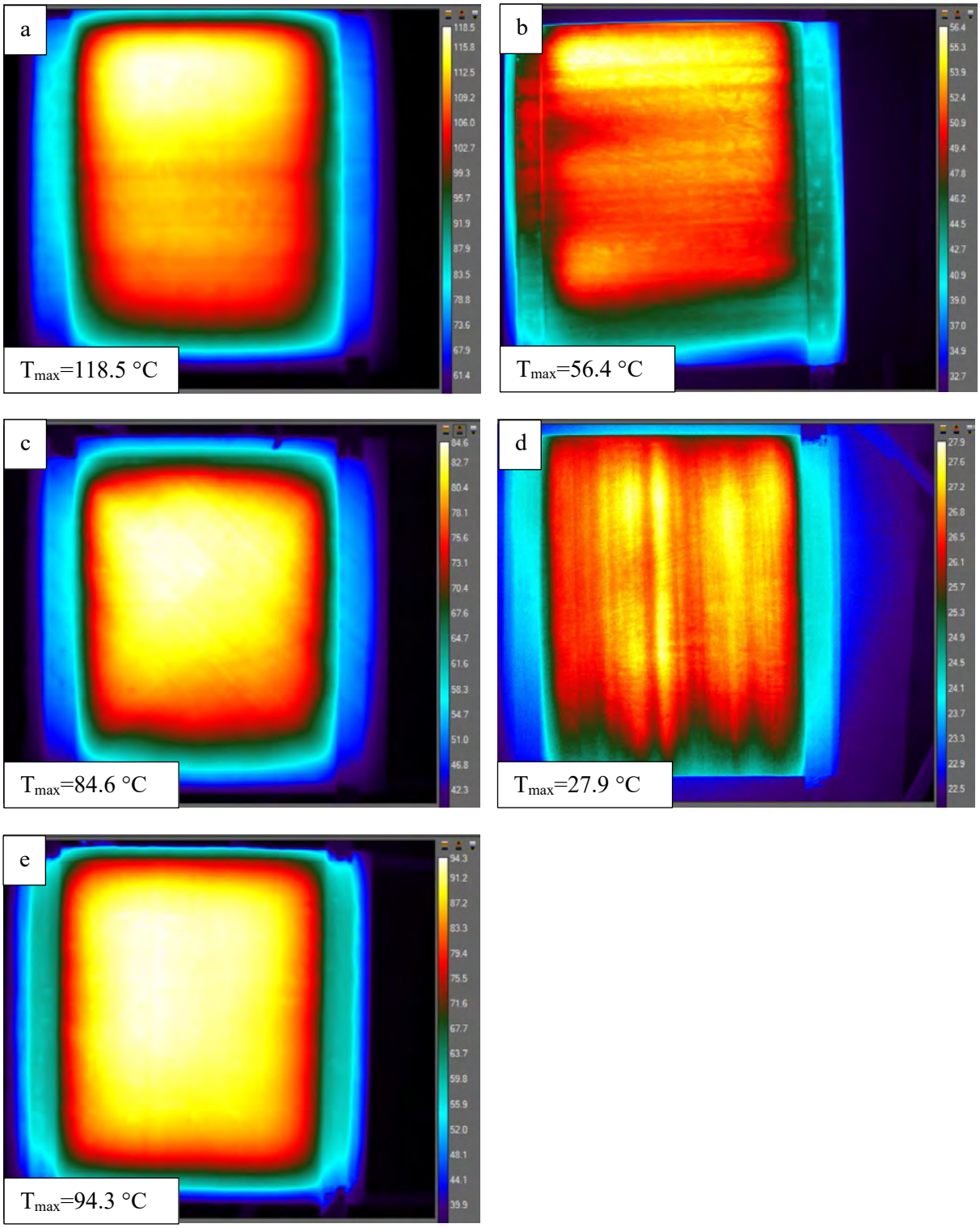


Figure 2. The experimental results of thermal distribution and the maximum temperature under the same applied electrical voltage (2 V) for different carbon layer orientations: a) $[0_2]_T$, b) $[0/90]_T$, c) $[\pm45]_T$, d) $[90_2]_T$, e) $[0/45/-45/90]_T$.

4.2 The effect of plate size

In this section, the comparison between two carbon fiber composite plates with different widths is discussed. The results of the experiment are presented in Fig. 3. The results show that increasing the length of the plate by 80% leads to an increase of the plate resistance by 65%. It results in a reduction in temperature by 53% compared with the original size of the plate (160mm). This is somewhat expected since the cross-section area for the current flow is unchanged and the resistance is increasing due to the longer fiber.

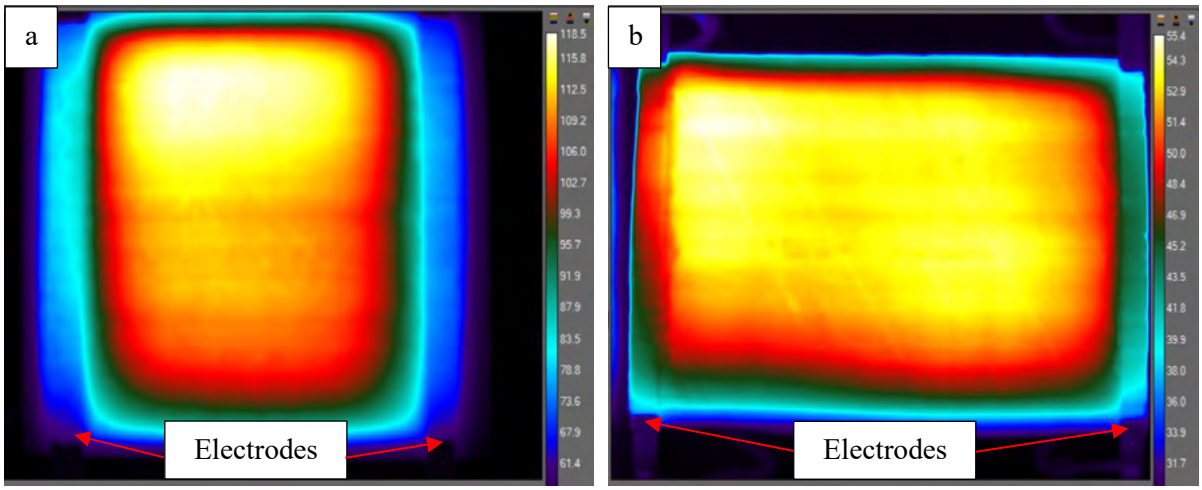
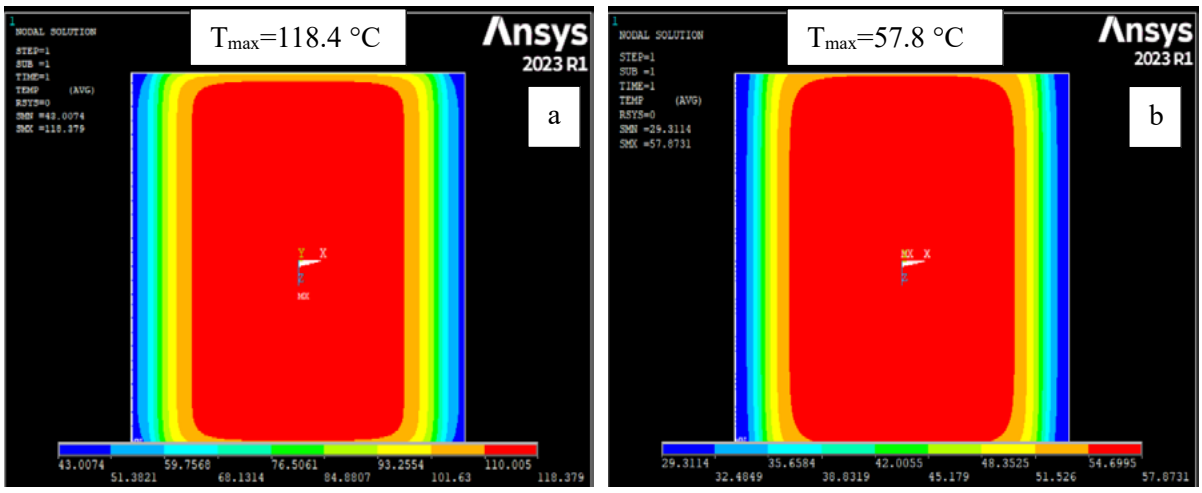


Figure 3. The experimental results of thermal distribution and the maximum temperature under the same applied electrical voltage (2 V) for different distances between the electrodes: a) 160 mm, b) 285 mm.

4.3 Comparison between the experiment and numerical simulations

The numerical simulation results for the laminates with the same stacking sequence as used in experiments are presented in this section, see Fig. 4. The results showed a very good agreement with the experimental results (Fig. 2). The maximum difference between experiment and simulation is around 3.5% which is acceptable accuracy. Thus, the developed model can be considered as validated and it can be used for further calculation for laminates with defects as well as repaired plates (this work is planned as a future study).



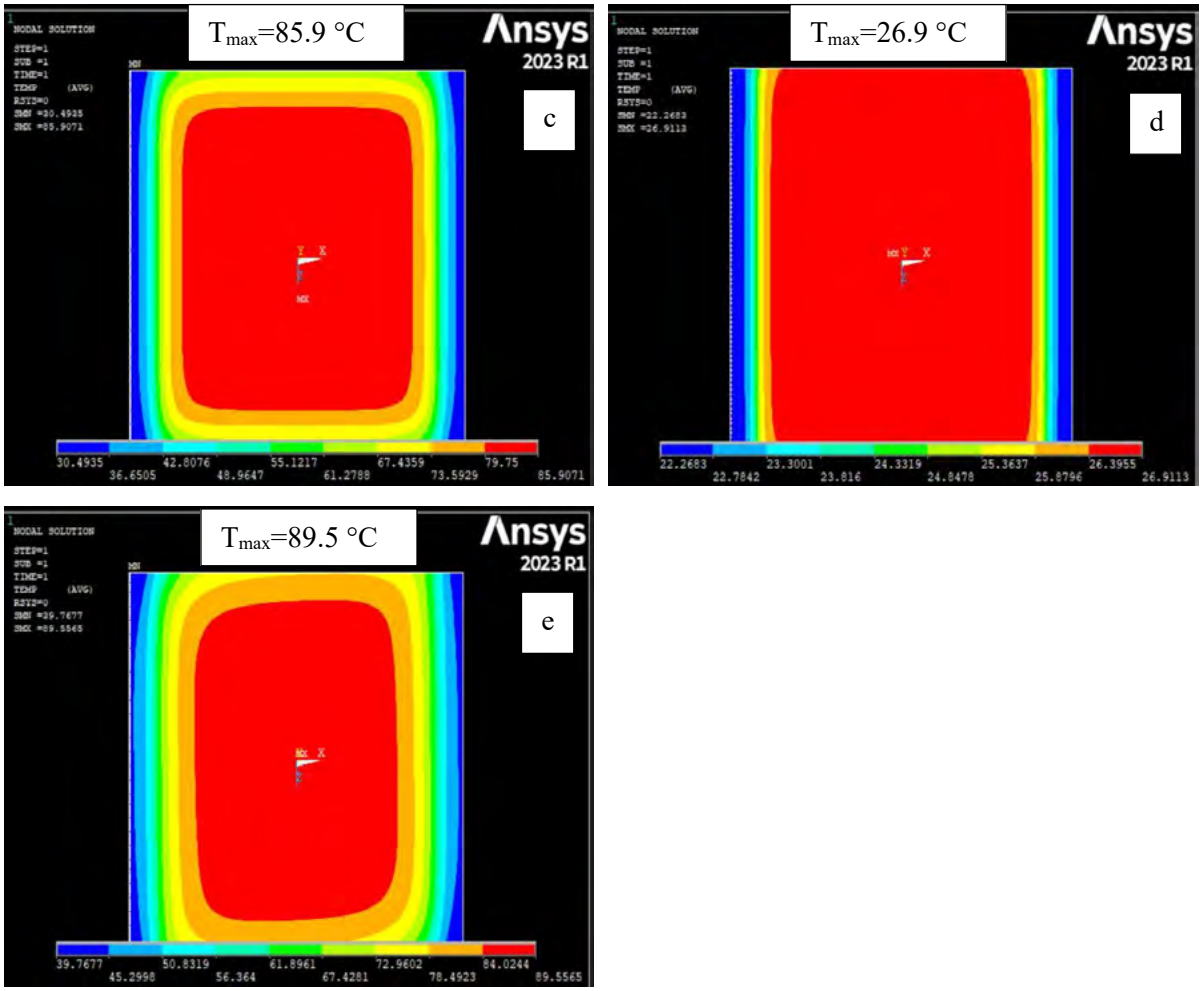


Figure 4. The numerical results of thermal distribution and the maximum temperature under the same applied electrical voltage (2 V) for different carbon layer orientations: a) $[0_2]_T$, b) $[0/90]_T$, c) $[\pm45]_T$, d) $[90_2]_T$, e) $[0/45/-45/90]_T$.

5. Conclusions

This study has shown that the highest surface temperatures, yielding in suitable composites for electrical and thermal applications, is the prepreg-based unidirectional lamina with fiber aligned at 0°. However, when designing laminates for particular application (e.g. multi-axial mechanical loads) it is crucial to take into account various factors such as mechanical and thermal loads, expected location, direction, and the potential risk of damage. Additionally, the design of the plate should aim to cover the necessary area using the shortest possible fiber length to improve heat generation. This investigation offers useful observations regarding the electrical performance of carbon fiber composites which can be used to define recommendations for design of composites with multi-functional properties for application in different structures.

Acknowledgement

The authors would like to acknowledge Nour Labidi, a Master's student for help with experiments. The authors also express gratitude to Birgitha Nyström from PODCOMP for providing the glass fiber sandwich panels. Additionally, thanks are due to Greger Nilsson from Blade Solutions company for his valuable guidance as an advisor and insightful discussions on the results.

References

[1] Kupke M, Schulte K, Schüler R. Non-destructive testing of FRP by d.c. and a.c. electrical methods. Compos Sci Technol,61:837–47, 2001.
[2] Athanasopoulos N, Kostopoulos V. Damage detection via Joule effect for multidirectional carbon fiber reinforced composites. Appl Phys Lett,101, 2012.
[3] Galehdar A, Rowe WST, Ghorbani K, Callus PJ, John S, Wang CH. The effect of ply orientation on the performance of antennas in or on carbon fiber composites. Progress in Electromagnetics Research,116:123–36, 2011.
[4] Li X. Eddy Current Techniques for Non-destructive Testing of Carbon Fibre Reinforced Plastic (CFRP). University of Manchester:1–185, 2012.
[5] Schueler R, Joshi SP, Schulte K. Damage detection in CFRP by electrical conductivity mapping. Compos Sci Technol,61:921–30, 2001.
[6] Shin YC, Novin E, Kim H. Electrical and thermal conductivities of carbon fiber composites with high concentrations of carbon nanotubes. International Journal of Precision Engineering and Manufacturing,16:465–70, 2015.
[7] Zappalorto M, Panozzo F, Carraro PA, Quaresimin M. Electrical response of a laminate with a delamination: modelling and experiments. Compos Sci Technol,143:31–45, 2017.
[8] Lundström F, Frogner K, Andersson M. Numerical modelling of CFRP induction heating using temperature-dependent material properties. Compos B Eng,220, 2021.
[9] Lundström F, Frogner K, Andersson M. Analysis of the temperature distribution in weave-based CFRP during induction heating using a simplified numerical model with a cross-ply representation. Compos B Eng,223, 2021.
[10] Lundström F, Frogner K, Andersson M. A numerical model to analyse the temperature distribution in cross-ply CFRP during induction heating. Compos B Eng.202, 2020.
[11] Lundström F, Frogner K, Andersson M. A resistor network model for analysis of current and temperature distribution in carbon fibre reinforced polymers during induction heating. J Compos Mater,56:3159–83, 2022.
[12] ANSYS 16–Structural Analysis Guide, (2014-2015). n.d.

NUMERICAL PREDICTION OF FATIGUE DAMAGE PGOGRESS AND RESIDUAL STRENGTH AFTER FATIGUE IN COMPOSITE PRESSURE VESSEL

Ryoma Aoki[1], Tomohiro Yokozeki[2], Tetsuya Matsuda[3], Masahito Ueda[4], and Wataru Iwase[5]

[1]The University of Tokyo, 7-3-1 Hongo, Bunkyo, Tokyo Japan
Email: r.aoki@aastr.t.u-tokyo.ac.jp
[2]The University of Tokyo, 7-3-1 Hongo, Bunkyo, Tokyo Japan
Email: yokozeki@aastr.t.u-tokyo.ac.jp
[3]University of Tsukuba, Tennodai 1-1-1, Tsukuba, Ibaraki, Japan
Email: matsuda@kz.tsukuba.ac.jp
[4]Nihon University, 1-8-14 Kanda-surugadai, Chiyoda, Tokyo, Japan
Email: ueda.masahito@nihon-u.ac.jp
[5]Yachiyo Industry Co., Ltd., 2-2-11 Hirosedai, Sayama, Saitama, Japan
Email: wataru_iwase@yachiyo-ind.co.jp

Keywords: High-pressure hydrogen tank, Fatigue damage, Stiffness degradation, Residual strength after fatigue

Abstract

Type IV tanks, composed of a plastic liner and CFRP, are expected to greatly enhance hydrogen storage capacity. However, CFRP high-pressure tanks have shown damage like matrix cracking and delamination under typical operating pressures, escalating with repeated loading. Cracks and delamination within the tank can diminish structural rigidity, potentially reducing strength compared to the original state, even if total tank failure is prevented. To tackle this, the development of numerical analysis techniques considering fatigue-induced residual strength is vital, not only to adjust the design safety factor for failure strength but also to meet the growing demand for further lightweight solutions. This study endeavored to forecast the internal damage progression due to internal pressure fatigue and the residual burst pressure following fatigue in composite tanks. By employing static damage analysis using the fatigue damage distribution derived from fatigue analysis as initial values, residual strength predictions were conducted. Consequently, it was demonstrated that the residual burst pressure post-fatigue decreased due to heightened tank susceptibility to deformation from fatigue damage.

1. Introduction

CFRP (Carbon Fiber Reinforced Plastic) is expected to be used in the structural components of high-pressure hydrogen tanks due to its high specific strength and specific stiffness. Type IV tanks, consisting of a plastic liner and CFRP, are anticipated to significantly improve hydrogen storage capacity. However, in the CFRP high-pressure tanks, damage such as matrix cracking and delamination has been observed under normal operating pressures, with further progression under repeated loading. Cracks and delamination occurring within the tank can reduce structural stiffness, leading to a potential decrease in strength compared to the initial state, even if complete tank failure is averted. To address this, the development of numerical analysis techniques considering fatigue-induced residual strength is crucial,

not only to accommodate potential relaxation in the design safety factor for failure strength but also to meet the growing demand for further lightweight.

In this study, we defined an intralaminar damage model based on continuum damage mechanics to analyze the damage evolution in composite laminates under fatigue loading. We employed a methodology that combines these damage models with finite element analysis [1]. Additionally, we created a finite element analysis model simulating a tank structure manufactured through filament winding. Applying fatigue analysis to the 2D tank model, we evaluated the stiffness values for each fatigue cycle and attempted to predict the residual strength after fatigue. For residual strength prediction, we performed fatigue analysis up to a predetermined target fatigue cycle, used the evaluated damage variables as initial values for strength prediction, and assessed the internal pressure until the tank burst.

2. Numerical simulation method

2.1. Continuum damge mechanics and static damage model

In continuum damage mechanics, the deterioration behavior of materials due to damage occurring within the material is described by a parameter called the damage variable, which is used to formulate the residual stiffness. The damage variable represents the extent of damage, with 0 indicating an undamaged state and 1 indicating a state where the load transfer capability is completely lost due to full damage. In this study, to describe the intralaminar damage occurring within composite materials, three components of in-plane damage variables, d_{ij} (ij = 11: fiber direction, ij = 22: transverse direction, ij = 12: shear direction) are utilized.

The model for damage progression under static loading is presented in Eqs. (1) to (3) [1,2]. Taking into account the brittle fracture in the fiber direction, the damage variable $d11$ abruptly increases from 0 to 1 when fiber failure occurs. The thermodynamic force at d_{11}=1 is determined from the fiber direction strength obtained from tensile testing of 0° unidirectional specimens (see Table I). Damage evolution laws for the transverse and shear directions are formulated as second-order functions of the square root of the equivalent thermodynamic force Y_{12}+b_2Y_{22}. The parameters of the model are determined through best fitting to experimental results. The experimental data used consisted of stress-strain curves obtained from tensile loading-unloading tests conducted on various types of laminates.

$$d_{11} = \begin{cases} 0 & \text{if } Y_{11} < Y_{11}^{s} \\ 1 & \text{if } Y_{11} \geq Y_{11}^{s} \end{cases} \tag{1}$$

$$d_{12} = f_1\left(\sqrt{Y_{12} + b_2 Y_{22}}\right)^2 + f_2\sqrt{Y_{12} + b_2 Y_{22}} + f_3 \tag{2}$$

$$d_{22} = b_3 d_{12} \tag{3}$$

2.2. Fatigue dmage model and simulation method for prediction of residual strength

In this study, a fatigue simulation based on continuum damage mechanics was applied [3]. Intralaminar damage, predominantly characterized by resin cracking, was considered dominant, with the influence of fiber direction properties deemed insignificant. Thus, fatigue damage calculations were conducted for in-plane shear d_{12}, and transverse direction d_{22}. Fatigue simulation was performed using the fatigue damage models proposed by Ref. [3]:

$$\frac{d(d_{12})}{dN} = c_{1,12}\tilde{Y}\exp\left(-c_{2,12}\frac{d_{12}}{\sqrt{\tilde{Y}}}\right) + c_{3,12}d_{12}\tilde{Y}^2 \tag{4}$$

$$\frac{d(d_{22})}{dN} = b_3 \frac{d(d_{12})}{dN} \tag{5}$$

For the determination of parameters ($c_{1,12}$, $c_{2,12}$, $c_{3,12}$) of the fatigue model, data of normalized stiffness from three-point bending fatigue tests conducted on laminates with two different curvatures were utilized.

In this fatigue analysis, it was assumed that fatigue damage progresses at the point where maximum load is applied during fatigue loading, and a method of repeating the analysis at the maximum load was adopted. The flow of this analysis begins with performing finite element analysis with the maximum load starting from cycle number $N = 1$. Subsequently, the damage variables d_{ij} are computed for every ΔN cycles. At cycle number N^k where the analysis is conducted, a stiffness matrix utilizing the damage variables d_{ij} is created, finite element analysis is performed, and the displacement field is converged. Upon convergence, the damage after ΔN^k cycles is updated using the following equation.

$$d_{ij}^{k+1} = d_{ij}^{k} + \left.\frac{d(d_{ij}^{k})}{dN}\right|_{N^k} \times \Delta N^k \tag{6}$$

The updated damage variables d^{k+1} are used as inputs to proceed with the calculation steps for the next N^{k+1} cycles. This procedure is repeated until the desired number of cycles is reached.

This study presents an overview of the proposed residual strength calculation method. To predict the residual strength, damage occurring in CFRP is represented using damage variables d_{ij} based on continuum damage mechanics. In the proposed residual strength calculation, fatigue analysis based on continuum damage mechanics is applied as a method to predict fatigue damage. Initially, fatigue damage analysis is conducted up to a specific number of cycles, and the post-fatigue damage variables for each element of the FEM model are outputted. Subsequently, this data is provided as the initial damage state for each element of the FEM model, and residual strength is predicted by conducting static damage analysis using the static model.

3. Static burst simulation

3.1. FEM model and simulation condition

Figure 1 illustrates the FEM model of the composite tank utilized in this study. The laminate configuration of the tank model is summarized in Table 1. A 2D mesh is converted into a 3D model with thickness in the θ direction in cylindrical coordinates, with each layer having a thickness of 1°. Analysis was conducted with boundary conditions to achieve axisymmetric analysis for this FEM model. Additional boundary conditions include imposing symmetry conditions assuming symmetry along the longitudinal direction and restraining the radial displacement to 0 at the tip of the dome section. In the static analysis, the internal pressure was gradually increased from 0 MPa across the entire inner surface to simulate a burst test. The analysis was continued until the tank deformed significantly or the calculation no longer converged.

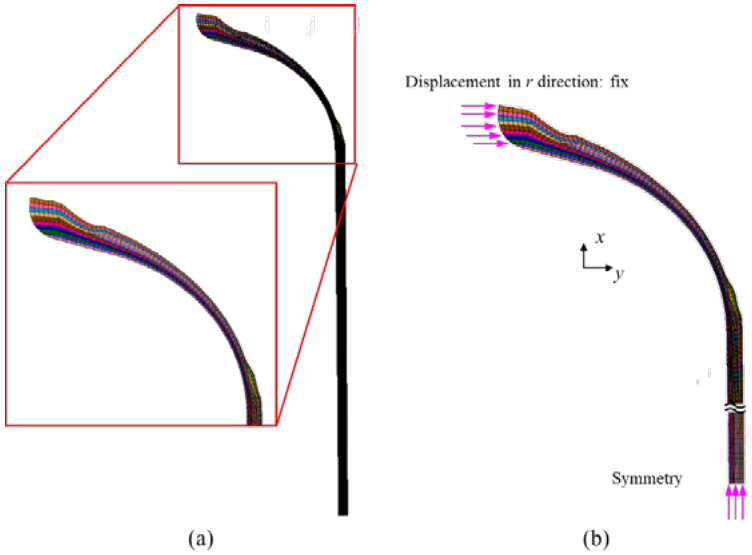


Figure 1. (a) FEM model of composite tank and (b) boundary conditions.

Table 1. Stacking sequence of composite tank.

	Numberof ply	Angle [deg.]
Helical	2	21.0
Hoop	3	88.9
Helical	4	17.0
Hoop	2	88.9
Helical	2	30.0
Helical	2	15.1
Hoop	2	89.0
Helical	2	73.0
Helical	2	15.1
Hoop	2	89.0

3.2. Results

Figure 2 and Figure 3 depict the damage distributions at failure obtained from the static damage analysis. When the internal pressure was increased from 0 MPa to 70.2 MPa, Figures 2 and 3 represent contour plots of the damage variables d_{11} (fiber direction damage) and d_{22} (transverse direction damage), respectively. Regarding the fiber direction damage, it can be observed that as the internal pressure is increased to a certain extent, fiber rupture occurs in the hoop layer at the center of the cylinder section, leading to significant deformation of the cylinder section and subsequent propagation of fiber rupture throughout the cylinder section. On the other hand, for the transverse direction damage d_{22}, although there are localized areas of failure at some parts of the tip, damage and failure predominantly occur in the helical layer of the cylinder section prior to fiber rupture. Eventually, it was confirmed that failure occurred throughout the entire cylinder section up to 70.2 MPa. In this analysis, the pressure of 70.2 MPa, at which significant deformation occurred, was predicted as the burst pressure of the tank in numerical analysis.

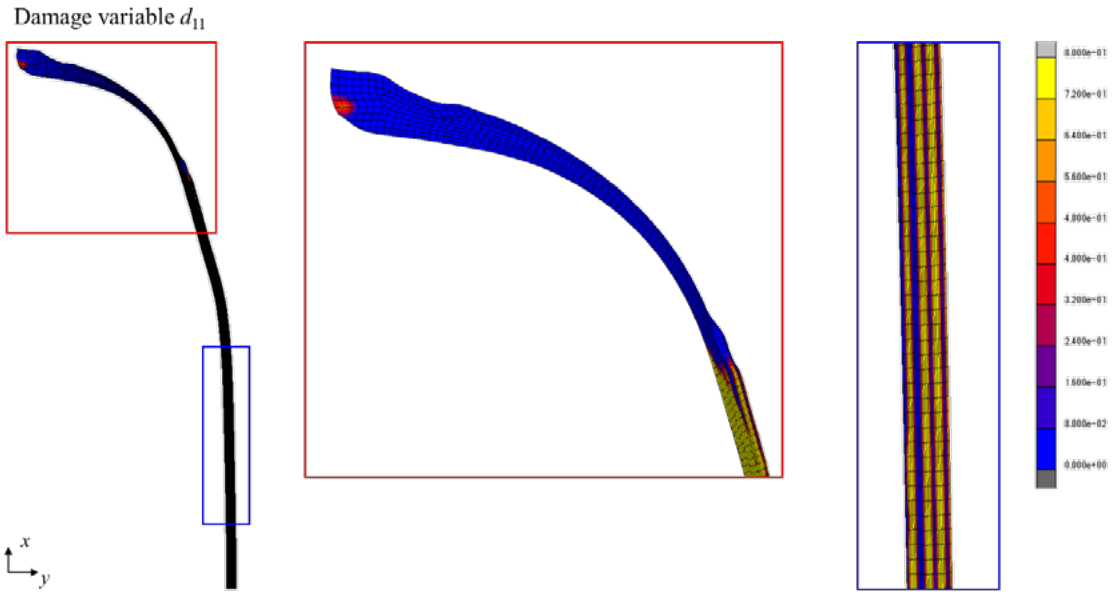


Figure 2. Damage distribution d_{11} at tank burst.

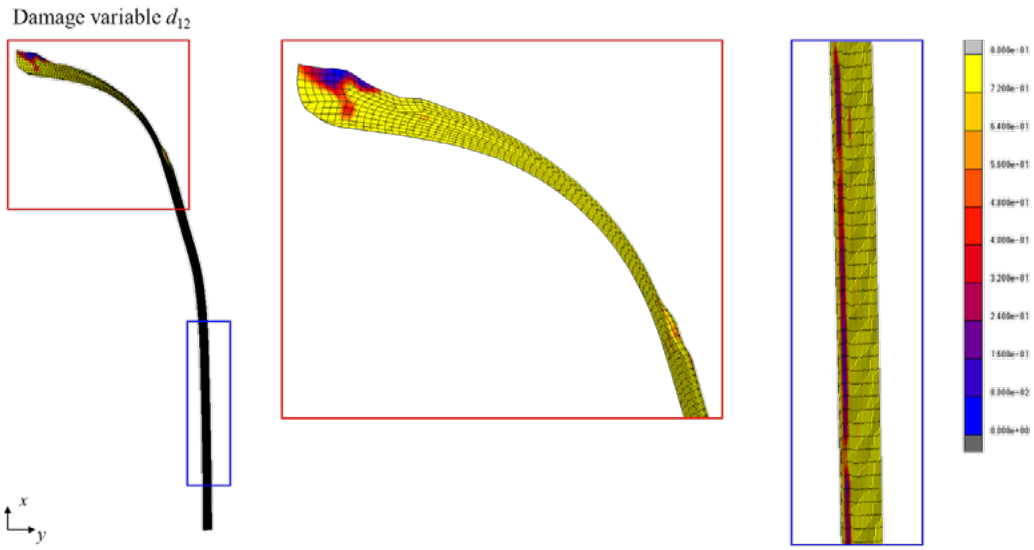


Figure 3. Damage distribution d22 at tank burst

4. Fatigue simulation

4.1. Simulation condition

Regarding the conditions for fatigue analysis, the same boundary conditions as those for static damage analysis were applied. Symmetry conditions were imposed assuming symmetry along the longitudinal direction, and constraints were applied to fix the radial displacement to 0 at the tip of the dome section. For the internal pressure, it was gradually increased from 0 MPa across the entire inner surface until reaching the target pressure. In fatigue analysis, the analysis was continued until the tank deformed significantly and the calculation no longer converged or until the target number of cycles was reached. For the fatigue conditions, internal pressure levels of 30%, 50%, and 70% were considered, with corresponding maximum internal pressures of 21, 35, and 49 MPa, respectively, for each fatigue cycle. The target number of cycles was set to 10,000 cycles for all internal pressure levels, and fatigue analysis was conducted accordingly.

4.2. Results

Figure 4 and Figure 5 show damage distributions of resin in the dome and cylinder parts, respectively, obtained from fatigue analysis. They present contour plots of the damage variable d_{22} at cycle numbers of 1 cycle and 10,000 cycles. When considering the 50% internal pressure level, at 1 cycle, except for the region where the dome tip is fixed, damage occurs predominantly in the outermost layer of the bent portion, resulting in resin cracking. As the fatigue cycles increase, it can be observed that the region of failure in the bending portion of the dome expands longitudinally. At the 30% internal pressure level, almost no resin damage occurs even at 10,000 cycles, whereas at the 70% level, matrix failure is widespread.

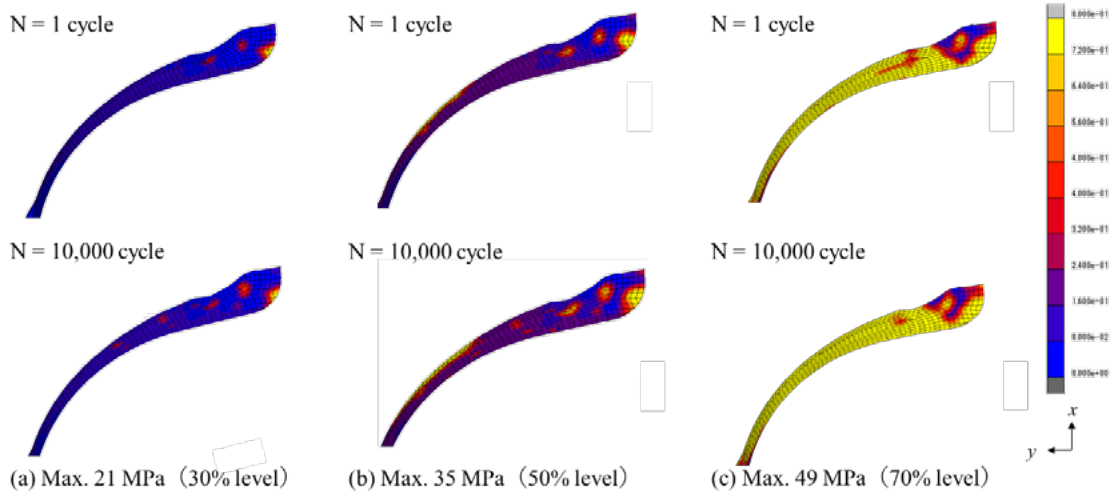


Figure 4. Fatigue damage distribution d_{22} in dome section of composite tanks.

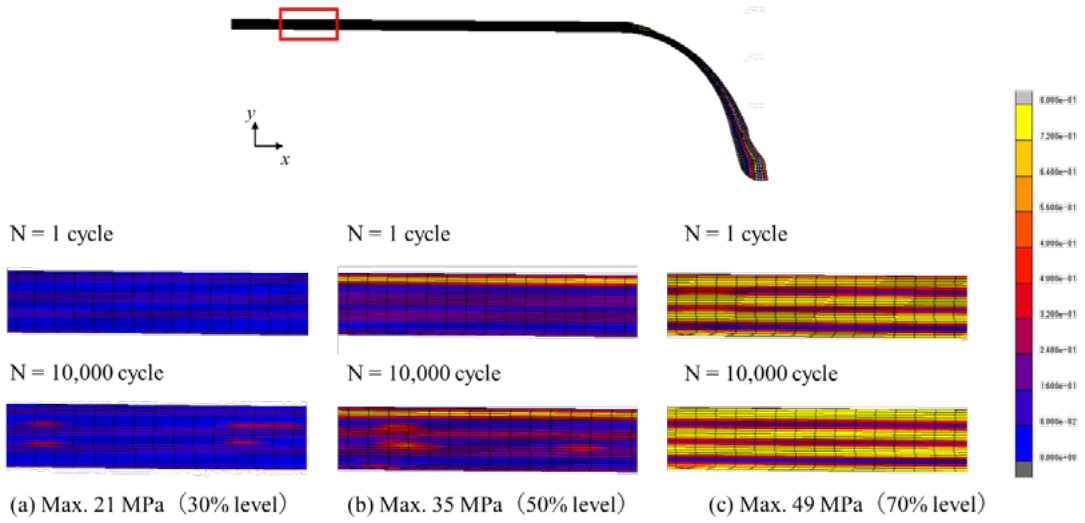


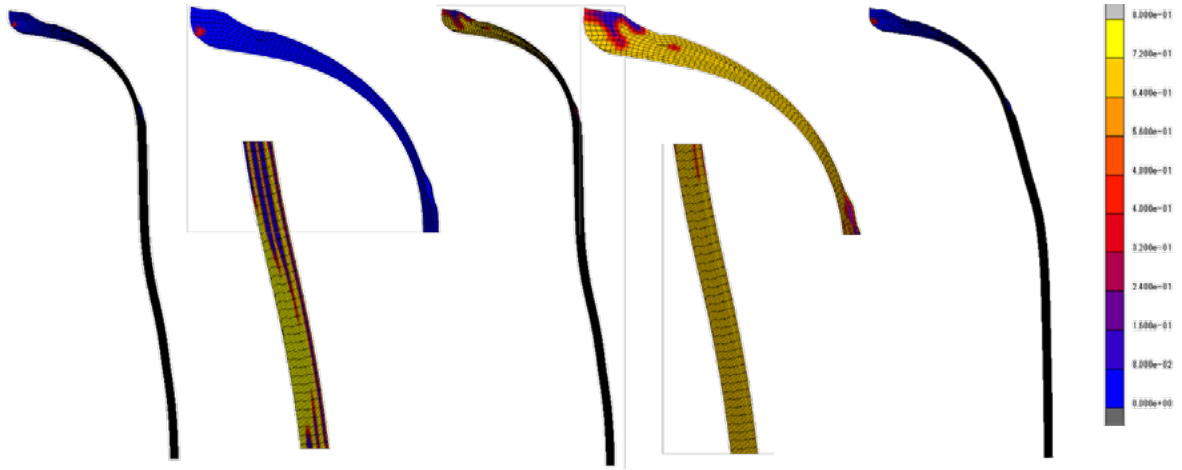
Figure 5. Fatigue damage distribution d_{22} in cylinder section of composite tank.

5. Prediction residual burst pressure after fatigue

We conducted a prediction of residual strength under the fatigue analysis conditions presented in the previous section, specifically focusing on the 50% internal pressure level condition. Following fatigue analysis of 10,000 cycles at the 50% internal pressure level, we performed static damage analysis using

the resulting damage distribution as the initial state.

The results of residual strength prediction at the 50% internal pressure level are shown in Figure 6. In burst failure after fatigue at the 50% internal pressure level, similar to the case without fatigue, fiber failure occurred in the hoop layer at the center of the cylinder, leading to final rupture. After fiber fracture in the cylinder section, significant deformation of the cylinder section occurred, and the propagation of fiber fracture within the cylinder section was observed. The burst pressure after fatigue at the 50% internal pressure level was 61.2 MPa, approximately 13% lower compared to the case without fatigue. Deformation is prone to occur due to resin damage caused by fatigue, resulting in an increase in stress along the fiber direction, which likely led to earlier rupture compared to the fatigue-free case.



(a) Case: 50% level
Damage variable d_{11}

(b) Case: 50% level
Damage variable d_{22}

(c) Case: No fatigue

Figure 6. Damage distribution at tank burst in residual strength prediction.

6. Conclusions

This study attempted to predict the internal damage progression due to internal pressure fatigue and the residual burst pressure after fatigue in composite material tanks. The internal damage of composite material tanks was represented using damage variables based on continuum damage mechanics. We applied damage progression models under static loading and fatigue loading based on continuum damage mechanics. A two-dimensional finite element model of the composite material tank was created, and static damage analysis was first conducted to predict the burst pressure. Subsequently, fatigue analysis under three internal pressure conditions was performed to predict the fatigue damage progression inside the tank. Finally, an attempt was made to predict the residual burst pressure after fatigue. By conducting static damage analysis using the fatigue damage distribution obtained from fatigue analysis as initial values, predictions of residual strength were made. As a result, it was demonstrated that the residual burst pressure after fatigue decreased due to the increased susceptibility of the tank to deformation caused by fatigue damage.

Acknowledgments

This study was supported by a project (JPNP20003) commissioned by the New Energy and Industrial Technology Development Organization (NEDO).

References

[1] Ladeveze, P., Le Dantec, E.: Damage modeling of the elementary ply for laminated composites, Composites Science and Technology 43:257-267 (1992).

[2] Aoki, R., Higuchi, R., Yokozeki, T., Aoki, K., Uchiyama, S., & Ogasawara, T.: Damage-mechanics mesoscale modeling of composite laminates considering diffuse and discrete ply damages: Effects of ply thickness. Composite Structures, 277, 114609 (2021).

[3] Aoki R., Higuchi R., Yokozeki T.: Fatigue Simulation for progressive damage in CFRP Laminates using intra-laminar and inter-laminar fatigue damage models, Internal Journal of Fatigue 143: 106015 (2021).

DESIGN, MANUFACTURING AND TESTING OF 3D PRINTED VARIABLE-STIFFNESS LAMINATES FOR OPTIMUM DYNAMIC RESPONSE

M. Iragi[1], A. McCloskey[1], J. Rodríguez[1], M. Mateos[1] and L. Aretxabaleta[1]

[1]Mondragon Unibertsitatea, Loramendi kalea 4, 20500, Arrasate-Mondragón, Spain
Email: miragi@mondragon.edu, Web Page: http://www.mondragon.edu

Keywords: 3D printing, continuous fibre-reinforced polymers, variable-stiffness, vibration, natural frequency

Abstract
In the present study, variable-stiffness 3D printed continuous carbon fibre-reinforced thermoplastic laminates were designed, manufactured, and tested, to improve the dynamic behaviour of plates. The fibre trajectory of the variable-stiffness laminates was described by a curvilinear function; this way, the design-oriented model could be parametrized based on the finite element method. Fibre orientation angles were considered as design variables. A genetic optimisation algorithm was used to obtain the laminate configuration for different optimisation cases over the first two natural frequencies for a plate with one embedded edge and three free edges. Finally, the most promising laminates were printed and tested. The non-conventional 3D printed laminates showed an improvement of the individual natural frequencies of more than 25%, a combined increase of the first two natural frequencies of more than 10%, and a spacing of the first two natural frequencies of up to 45% compared to the quasi-isotropic reference laminate. This study is a contribution to the design and manufacture of 3D printed continuous fibre composites, and an additional step towards producing high-performance functional components for actual applications using 3D printing.

1. Introduction

The 3D printing technology of fused filament fabrication of continuous fibre-reinforced thermoplastics shows great potential for the production of the next generation of lightweight structural parts [1]. One of the most promising possibilities offered by this technology is its ability to steer fibres through curved tracks making it suitable for manufacturing variable-stiffness (VS) laminates [2]. These laminates can be used to customise the behaviour of panels, such as the vibration behaviour [3]. The effectiveness of these laminates in improving vibration performance has already been studied in recent years for traditional composites [4,5]. However, the applicability of 3D printing technology to manufacture non-conventional laminates for vibration attenuation has not been explored to date.

The aim of the present study, therefore, is to evaluate the capacity of continuous fibre 3D printing to manufacture variable-stiffness laminates that enhance the dynamic response of structural components. To this end, we designed, manufactured, and tested variable-stiffness plates with optimised vibration behaviour (natural frequencies). The performance of these non-conventional laminates was compared to that of a reference constant-stiffness quasi-isotropic laminate.

2. Problem statement and methodology

In this study, rectangular plates with a length L of 180 mm and a width W of 90 mm were analysed, resulting in a L/W ratio of 2. The boundary conditions were one embedded edge and three free edges, as shown in Figure 1.

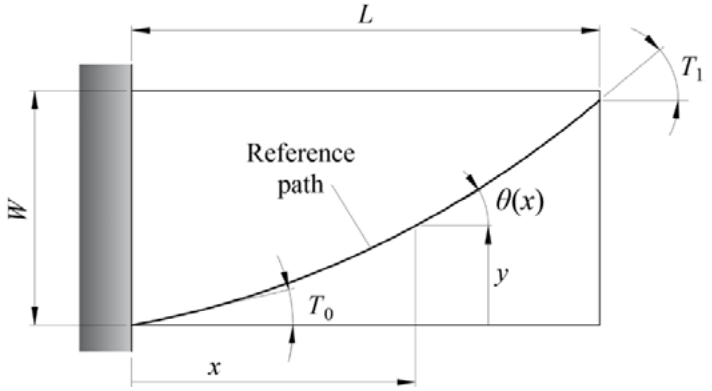


Figure 1. Embedded plate configuration and $\langle T_0|T_1\rangle$ reference fibre path.

To manufacture the laminates, we used the fused filament fabrication (FFF) 3D printing technology of preimpregnated filament from Markforged®. Among the materials available for this technology, continuous carbon fibre reinforced polyamide (cCF/PA) was chosen because of its higher stiffness. Previous studies [1,6] analysed and reported on the microstructure, content, and mechanical behaviour of cCF/PA. This technology includes bottom and top layers of Onyx™, a polyamide 6 reinforced with carbon micro-fibres. In this study, only a top and bottom layer of Onyx were included. Curvature radii of up to 1 mm can be created with this technology; however, radii smaller than 15 mm should not be used to avoid twisting and fibre breakage [7]. The 380 µm diameter filament is flattened during the process to a thickness of 125 µm (the printed layer's thickness) and a bead width of about 0.9 mm.

The widely used definition of fibre orientation proposed by Gürdal and Olmedo [8] was applied in the steered-fibre layers. The orientation angle $\theta(x)$ of the reference fibre path varies linearly with respect to the x-position, from T_0 at the embedded edge to T_1 at the opposite free edge (Figure 1 and Eq. 1). By shifting the reference path in the direction of the y-axis, the entire steered-fibre layer is produced. As a result, each layer's orientation is specified by just two parameters (T_0 and T_1), which are referred to as $\langle T_0|T_1\rangle$. Layers having equal but opposing orientations, $\pm\langle T_0|T_1\rangle$, are typically combined by employing this solution.

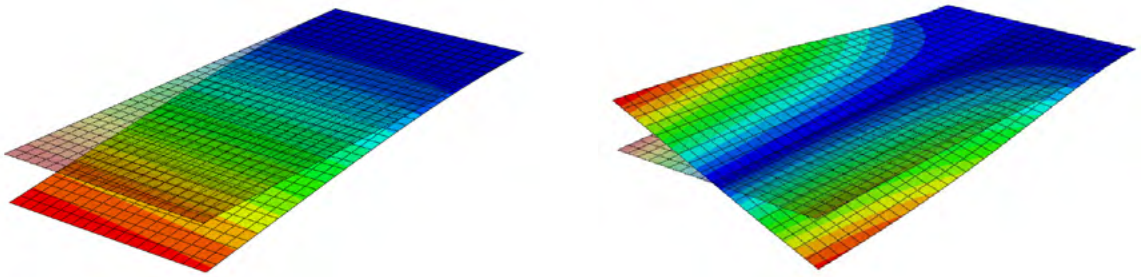
$$\theta(x) = \frac{(T_1 - T_0)}{L}x + T_0 \tag{1}$$

The designed laminates are symmetrical and balanced with 18-ply (16 cCF/PA and two outer Onyx), resulting in a nominal sample thickness of 2.25 mm. A quasi-isotropic (QI) laminate of $[0/45/90/\text{-}45]_{2s}$ stacking sequence was assumed as the reference laminate. The designed VS laminate consists of 2 pairs of steered-fibre layers on each face and eight inner layers of straight-fibres, in a $[\pm\langle T_{10}|T_{11}\rangle/\pm\langle T_{20}|T_{21}\rangle/0/45/90/\text{-}45]_s$ stacking sequence. Straight-fibre layers were included to minimise the effect of manufacturing constraints in the steered-fibre layers and to stiffen the weaker directions.

With this approach, the design variables of the VS laminate were reduced to four, the orientation of the outer steered-fibre layers: $\pm\langle T_{10}|T_{11}\rangle/\pm\langle T_{20}|T_{21}\rangle$. These orientations were determined by optimisation studies in the 0°–90° range of $\langle T_0|T_1\rangle$ potential angles using the commercial finite element method (FEM) package Abaqus and the genetic algorithm (GA) optimization method implemented in Matlab programming platform. The parametric FEM model configuration was implemented in a user-developed

Python script for Abaqus. Reduced integration quadrilateral shell elements (S4R) were used in the model, with a general edge length of 5 mm. Each element of the FEM model was associated with a specific lay-up based on the centroid position of each element. Optimisation of the fibre orientation was carried out using the GA method implemented in Matlab. For each individual of a generation, the Python script was adapted and its behaviour (natural frequencies) was determined. The GA Matlab code was configured with a number of generations of 20 and a population size of 100.

Figure 2 shows the first two vibration modes of the QI laminate determined by FEM. The first is the fundamental bending mode with a natural frequency f_1 of 50.7 Hz. The second is the fundamental torsional mode, with a natura frequency f_2 of 175.4 Hz. Four cases were studied for the design of the laminate using the FEM-GA optimisation method, depending on the objective: (1) f_1 maximisation, (2) f_2 maximisation, (3) $f_2 - f_1$ maximisation (i.e. maximise the separation between the two natural frequencies), and (4) equally weighted maximisation of f_1 and f_2.



(a) (b)

Figure 2. First two modes of the QI laminate determined by FEM: (a) first fundamental bending mode at 50.7 Hz, and (b) second mode, torsional, at 175.4 Hz.

Finally, the most promising laminates were manufactured and tested. The plates were made 30 mm longer so that they could be clamped between two steel profiles bolted to a test platform (Figure 3). The natural frequencies were obtained from the characteristic frequency response functions (FRF). A medium-sized impact hammer (B&K 8206-003 REF) was used to excite the plate and the response was measured with a light triaxial accelerometer (B&K 4525 B REF). To minimise the influence of the accelerometer mass, it was placed close to the mounting, at 30 mm from the embedment in the x-axis and 20 mm from the free side in the y-axis (Figure 3). Excitation was performed with an impact hammer at a point symmetrical to the accelerometer position. The signals were recorded and processed in the PULSE Labshop spectrum analyser. A time period of 4 s was measured for a frequency resolution of 0.25 Hz and a frequency range of 1600 Hz was obtained with a sampling frequency of 4096 Hz.

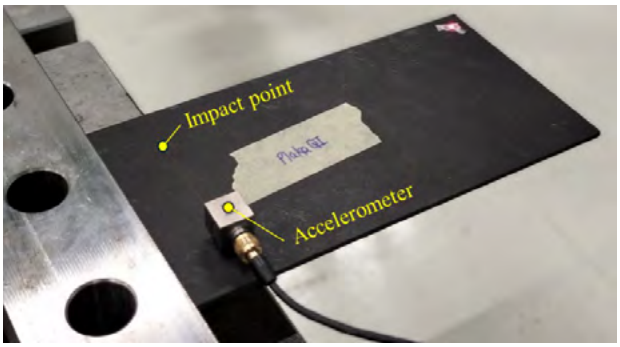


Figure 3. Experimental set-up of the measurements of the dynamic behaviour of the plates.

3. Results and discussion

The optimal fibre orientations and natural frequencies obtained with the FEM-GA method are shown in Table 1 for the four cases considered, as well as the results for the reference QI laminate.

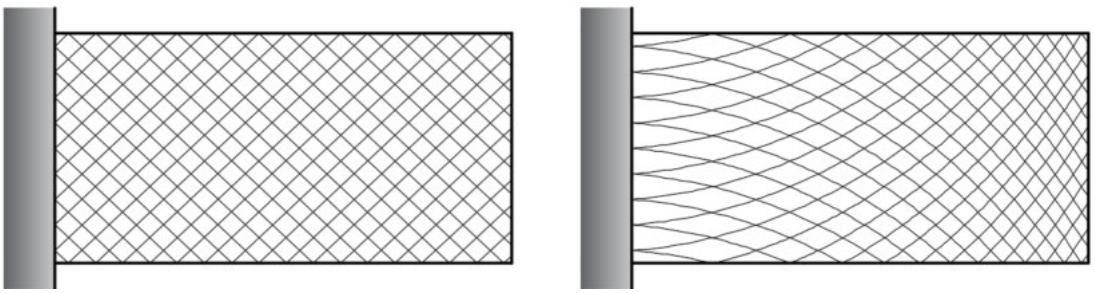
Table 1. Results obtained with the FEM-GA method: optimal fibre orientations and the corresponding first two natural frequencies.

Case	Objective	$\pm\langle T_{10}\|T_{11}\rangle$ / $\pm\langle T_{20}\|T_{21}\rangle$ (º)	f_1 (Hz)	f_2 (Hz)
Ref.	QI reference	-	50.7	175.4
1	f_1 maximisation	$\pm\langle 0.3\|0.3\rangle$ / $\pm\langle 0.1\|0.4\rangle$	69.0	126.5
2	f_2 maximisation	$\pm\langle 32.8\|54.8\rangle$ / $\pm\langle 32.6\|56.6\rangle$	42.7	226.3
3	Δf maximisation	$\pm\langle 45.6\|39.1\rangle$ / $\pm\langle 42.9\|46.8\rangle$	37.3	223.6
4	f_1 & f_2 maximisation	$\pm\langle 4.8\|50.5\rangle$ / $\pm\langle 2.7\|73.0\rangle$	60.9	201.1

The first case, which seeks to maximise the first natural frequency f_1, gives a result that tends towards a constant-stiffness (CS) laminate with fibres oriented in the longitudinal direction (0°). This is consistent because it is a bending mode. With this configuration, the first natural frequency increases by 36%, while the second natural frequency decreases by 28% compared to the QI laminate. For the maximisation of the second natural frequency f_2 of the torsional mode (Case 2), the optimal result is a VS laminate with fibres oriented from approximately 33° at the embedded edge to 55° at the outer free edge (Table 1). In this case, the second natural frequency increases by 29% versus QI, while f_1 decreases by 16%.

To maximise the separation between the first two natural frequencies (Case 3), the model proposes a solution that tends towards a CS laminate with straight-fibres with an orientation close to 45° (Table 1). With this configuration, the natural frequencies separation is increased by 49% compared to the QI laminate. Finally, in Case 4, where weighted maximisation of the first two natural frequencies is sought, the FEM-GA method results in a VS laminate with steered-fibre having a longitudinal orientation at the embedded edge and an oblique orientation at the free edge. With this configuration, the natural frequencies are increased by up to 20% compared to the QI laminate.

The two most interesting configurations (Cases 3 and 4) and the QI reference laminate were manufactured and tested. The configuration of these laminates is shown in Table 2 and Figure 4. For Case 3, which seeks to maximise the separation between natural frequencies, a CS laminate was manufactured with the outer layers at ±43 (Figure 4a), the optimal orientation determined with the FEM-GA method. For Case 4, where weighted maximisation of the first two natural frequencies is sought, a VS laminate with steered-fibre outer layers was manufactured at $\pm\langle 4.2|57.2\rangle$ (Figure 4b). Unlike the initial optimisation where the laminate contained two pairs of different steered-fibre layers, in this case we opted for two pairs of the same type of steered-fibre layer, as the results are similar but the fabrication is simpler. The manufacturing by 3D printing of the steered-fibre layer is shown in Figure 5.



(a) (b)

Figure 4. Configuration of the manufactured laminates: (a) ±43 fibre orientation for the CS laminate, (b) $\pm\langle 4.2|57.2\rangle$ steered-fibre layers configuration for the VS laminate.

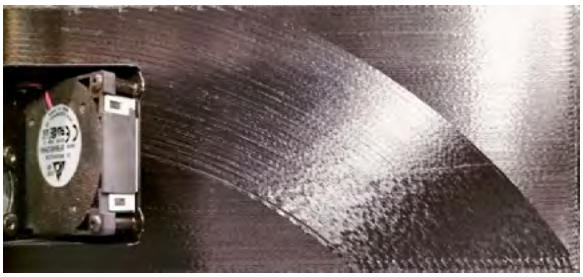


Figure 5. Manufacturing by 3D printing of the steered-fibre -⟨4.2|57.2⟩ layer.

The results of both the FEM model and the tests for the three laminates are given in Table 2, and the measured experimental FRFs are shown in Figure 6. The natural frequencies determined with the model are slightly higher than those measured in the test (below 10%). This may be due to factors such as the difficulty of reproducing an ideal embedding in tests, the low interlaminar properties of the printed material or the influence of defects produced in 3D printing. The difference is smaller for the torsional mode (mode 2), less than 4%. This may be because this mode is less sensitive to the way the plate is embedded.

Table 2. Characteristics and results of the three laminates manufactured and tested.

Laminate type	Objective	Stacking sequence	f_1 (Hz)		f_2 (Hz)	
			Test	Model	Test	Model
QI	Reference	$[0/45/90/-45]_{2s}$	47.5	50.7	172.5	175.4
CS	Δf max.	$[\pm 43_2/0/45/90/-45]_s$	35.0	38.2	216.0	224.3
VS	f_1 & f_2 max.	$[\pm\langle 4.2\|57.2\rangle_2/0/45/90/-45]_s$	54.5	59.7	192.0	198.6

Experimental results confirm the behaviour predicted by the FEM model (Table 2 and Figure 6). The CS laminate extends the frequency range between the first two modes by 45% compared to the QI laminate. It is also observed in the FRF of the CS laminate that the third mode is close to the second mode (Figure 6). This is because this laminate configuration causes the third mode, corresponding to a bending mode, to experience a decrease in its natural frequency, approaching the torsional mode.

In the VS laminate, the experimental results also evidence an increase in the natural frequencies of the first two modes, as shown in Table 2 and Figure 6. The first natural frequency increases by 15% and the second by 11%. The reason for this improvement is a favourable stiffness distribution that favours both bending and torsional modes. This requires an orientation of the fibres from an oblique orientation at the free edge to a longitudinal orientation at the embedded edge.

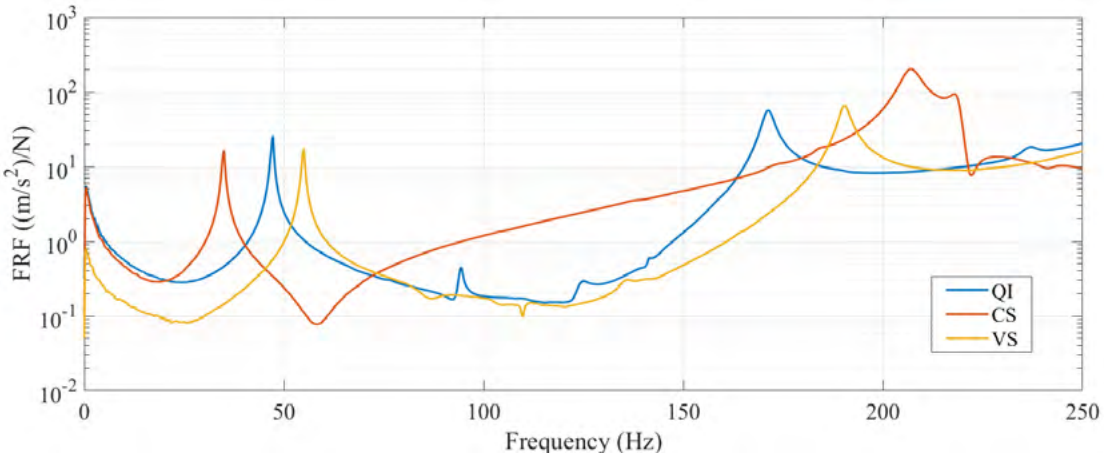


Figure 6. Experimental FRFs of the three types of laminates for a range between 0 and 250 Hz. The displacement of the modes can be observed relative to the QI laminate.

4. Concluding remarks

This study has demonstrated that continuous fibre 3D printing technology is valid to manufacture non-conventional laminates that improve the dynamic response of structural components. Compared to a constant stiffness QI laminate, the first two natural frequencies can be increased by more than 10% or spaced by up to 45%.

These results encourage further progress in the use of 3D printing to manufacture high-performance functional components in real applications, with emphasis on capabilities of this technology such as: high steering capacity of the fibre path, higher damping properties of thermoplastic matrices compared to thermosets, and the potential to print multi-material and functionally graded structures.

Acknowledgments
This work was finantially supported by the Basque government under MATFUN KK-2021/00066, and by the Provincial Council of Gipuzkoa under NUCAVA.

References

[1] M. Iragi, C. Pascual-González, A. Esnaola, C.S. Lopes and L. Aretxabaleta. Ply and interlaminar behaviours of 3D printed continuous carbon fibre-reinforced thermoplastic laminates; Effects of processing conditions and microstructure. *Additive Manufacturing*, 30, 100884, 2019.
[2] M. Iragi, C. Pascual-González, A. Esnaola, U. Morales, J. Aurrekoetxea, C.S. Lopes and L. Aretxabaleta. Design, manufacturing and testing of 3D printed variable-stiffness laminates for improved open-hole tensile behaviour. *Additive Manufacturing*, 63, 103418, 2023.
[3] M.M. Abdalla, S. Setoodeh and Z. Gürdal. Design of variable stiffness composite panels for maximum fundamental frequency using lamination parameters. *Composite structures*, 81(2):283-291, 2007.
[4] M.A. Antunes, P. Ribeiro, J.D. Rodrigues and H. Akhavan. Modal analysis of a variable stiffness composite laminated plate with diverse boundary conditions: experiments and modelling. *Composite Structures*, 239, 111974, 2020.
[5] A. Sabido, L. Bahamonde, R. Harik and M.J. van Tooren. Maturity assessment of the laminate variable stiffness design process. *Composite Structures*, 160, 804-812, 2017.
[6] C. Pascual-González, M. Iragi, A. Fernández, J.P. Fernández-Blázquez, L. Aretxabaleta and C.S. Lopes. An approach to analyse the factors behind the micromechanical response of 3D-printed composites. *Composites part B*, 186, 107820, 2020.
[7] H. Zhang, J. Chen and D. Yang. Fibre misalignment and breakage in 3D printing of continuous carbon fibre reinforced thermoplastic composites. *Additive Manufacturing*, 38, 101775, 2021.
[8] Z. Gürdal, R. Olmedo, In-plane response of laminates with spatially varying fiber orientations - variable stiffness concept. *AIAA Journal*, 31 (4), 751–758, 1993.

CHARACTERIZATION OF FATIGUE-DRIVEN DELAMINATION IN MODE II

A.Arrese*1, F. Mujika1, L. Carreras2 and J. Renart 2

[1]Materials Mechanics Group
University of the Basque Country (UPV/EHU)
Plaza Europa 1, 20018 Donostia-San Sebastián, San Sebastián, Spain
[2]AMADE, Polytechnic School (II), University of Girona,
Carrer Universitat de Girona, 4,
E-17003 Girona
*ainhoa.arrese@ehu.es

Keywords: Mode II, Fatigue, Composite Material

Abstract
Understanding the behavior of composite laminates against fatigue crack initiation and growth is essential to accurately predict component life and establish safe maintenance periods.

In this paper we present and validate an extrapolation procedure to characterize the mode II fatigue behavior based on the $\boldsymbol{J}_{0i}$ **-**$\boldsymbol{C}_{0i}$ and $\boldsymbol{\Delta}_{0i}$ **-**$\boldsymbol{C}_{0i}$ master curves.

The extrapolation procedure, based on compliance variation, assumes that all effects associated with damage are included in the equivalent crack length. In this method, new factored expressions of compliance ($\boldsymbol{C}_{0i}$), *J*-Integral ($\boldsymbol{J}_{0i}$) and crack tip displacement ($\boldsymbol{\Delta}_{0i}$) are defined. According to their polynomial expressions with respect to the equivalent crack length, invariant relationships between $\boldsymbol{J}_{0i}$ **-**$\boldsymbol{C}_{0i}$ and $\boldsymbol{\Delta}_{0i}$ **-**$\boldsymbol{C}_{0i}$ are obtained for a given material system and test configuration.

Once the master curves have been calibrated, the extrapolation procedure enables the characterization of a material system's fatigue behavior by determining the Paris law during the fatigue test. This is done by monitoring only the test compliance and the maximum load concerning the number of cycles.

1. Introduction

The use of composite materials in structural components within the automotive and aeronautical industries has been increasing due to their numerous advantages, such as high stiffness, superior fatigue resistance, and significant potential for weight reduction. However, composite materials are prone to delamination damage because of their low interlaminar strength in the thickness direction, which can occur during both manufacturing and service. Additionally, delamination damage can propagate during use due to fatigue loading, which can impact the service life of the component. Therefore, it is

crucial to understand the initiation and growth behavior of delamination damage to accurately predict component life and establish safe maintenance intervals. [1].

In composite laminates, crack growth is assessed through fatigue tests using the energy release rate G as the loading parameter to obtain the experimental fatigue crack propagation curve da/dN versus G. While there is no standardized method to characterize the fatigue behavior of composite laminates under Mode II loading, the End-Notched Flexure (ENF) test setup is the most widely used for Mode II fatigue-induced delamination studies. [2,3].

Measuring crack growth under cyclic loading in Mode II is challenging because the crack propagates without a clear opening, making visual inspection difficult. To address this, numerous researchers have proposed various compliance-based strategies to monitor crack length during fatigue testing. [4,5]. These methodologies eliminate the need for visual inspection, enabling uninterrupted testing and providing real-time experimental data..

Renart et al. [4] proposed a procedure to determine the crack length of a specimen by continuously monitoring its compliance. They defined a dynamic compliance to avoid the effects of initial nonlinearities that can occur during experimental tests, as the ratio between displacement and load amplitudes.

On the other hand, de Moura et al [5] proposed and validated a data reduction procedure based on the equivalent crack concept, taking into account the effect of the fracture process zone (FPZ).

The aim of this work is to validate the extrapolation procedure based on the master curves recently presented [6], to characterize the fatigue behavior in mode II.

2. Metodology

Recently, a compliance-based data reduction method has been proposed to determine the energy release rate J and the relative crack tip displacement Δ in both Mode I and Mode II as a function of the equivalent crack advance[7,8]. This method, based on beam theory, assumes that all effects associated with damage development are included in the equivalent crack length obtained from the compliance variation. Analytical expressions have been derived for the compliance C, the relative displacement at the crack tip Δ, and the J-Integral, all as functions of the elastic properties of the adherends, the test configuration, the cross-sectional dimensions of the specimens, the applied load, and the equivalent crack length (a_e).

By rewriting the expressions of C, the Δ and the J-Integral in the form of a multiplication of separate functions, new factored expressions are defined with respect to the applied load and the adhesive and adherend thicknesses, of the compliance ($\boldsymbol{C}_{0i}$), the J-Integral ($\boldsymbol{J}_{0i}$) and the crack tip displacement $\boldsymbol{\Delta}_{0i}$.

Assuming that all effects associated with damage are included in the equivalent crack length, and according to the polynomial expressions of $\boldsymbol{J}_{0i}$, $\boldsymbol{C}_{0i}$ and $\boldsymbol{\Delta}_{0i}$ with respect to it, invariant relationships between $\boldsymbol{J}_{0i}$ -$\boldsymbol{C}_{0i}$ and $\boldsymbol{\Delta}_{0i}$ -$\boldsymbol{C}_{0i}$ are obtained for a given material system and test configuration.

Assuming the invariant character of the curves $\boldsymbol{J_{0i}}$ **-**$\boldsymbol{C_{0i}}$ and $\boldsymbol{\Delta_{0i}}$ **-**$\boldsymbol{C_{0i}}$, the *Master Curves* for mode II are extracted from the data of a single specimen following the flow chart shown in Fig. 1.

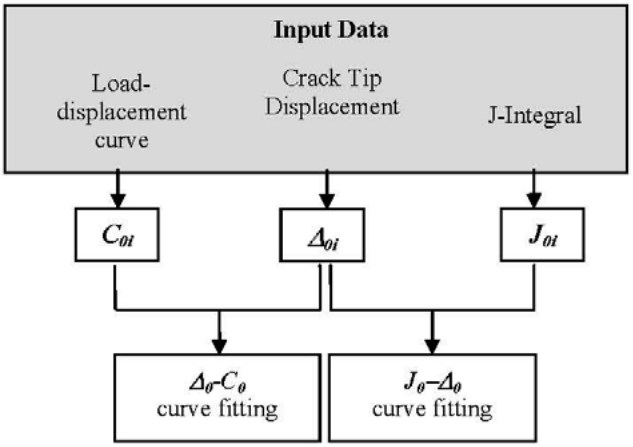


Figure 1. Flowchart to obtain the Master Curves

Once the *Master Curves* have been obtained, following the extrapolation procedure shown in Fig. 2, the results can be extrapolated to different specimen configurations by processing only the test compliance and the maximum load with respect to the number of cycles.

In this case, by applying the extrapolation procedure, both the *J*-integral as a function of the number of cycles and the crack growth rate are obtained.

$$J = \frac{3{P_{max}}^2}{w^2(2h)^3}\ \boldsymbol{J}_0(a_e) \tag{1}$$

$$\frac{da}{dN} = \frac{1}{2J_0}\frac{dC_0}{dN} \tag{1}$$

It is also feasible to experimentally analyze the fatigue-induced degradation of the Cohesive Zone, assessing the impact of severity on the variation of cohesive laws and the evolution of cohesive stress over the number of cycles.

$$\tau_{max} = \frac{6P_{max}}{w(2h)}\ \frac{\boldsymbol{J}_0(a_e)}{\Delta_0(a_e)} \tag{2}$$

$$\Delta_{t\,max} = \frac{P_{max}}{w(2h)^2}\ \Delta_0(a_e) \tag{2}$$

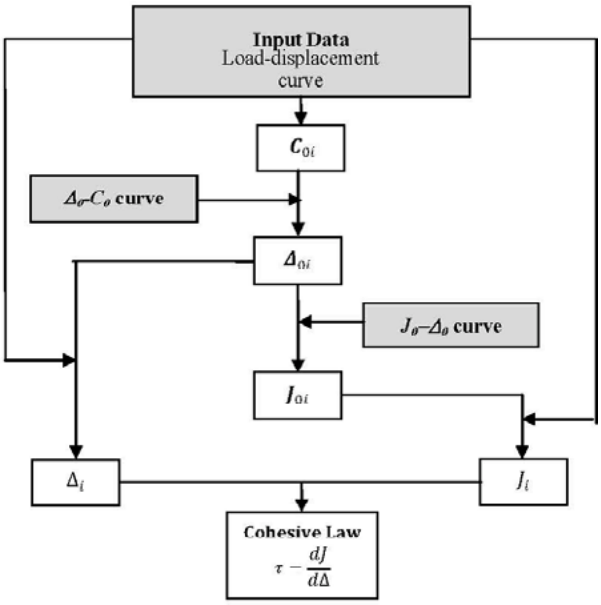


Figure 2. Flowchart for extrapolating the cohesive law

3. Verification of the proposed method and results

In the ENF mode II fracture test, the range of the crack growth rate curve obtained in a single test under constant cyclic displacement is very narrow; therefore, Carreras et al [1] proposed a methodology to measure, in a single test, a region of the crack growth rate curve more extensive than that achieved in a constant cyclic displacement test. The procedure consists of varying the applied displacement, δ_{min} and δ_{max}, keeping constant the displacement ratio, $R= \delta_{min}/\delta_{max}$.

The validity of the extrapolation method for characterizing mode II delamination growth is evaluated by comparing the crack growth rate curves obtained by the extrapolation procedure with those obtained by [1] for variable cyclic displacement tests.

The unidirectional carbon fiber/epoxy specimens tested were 25 mm wide, 3 mm thick and 200 mm long, with an initial crack of 35 mm.

In the ENF test, **Fig.** 3, the support span was 2L = 120 mm and the support rollers had a radius of 5 mm.

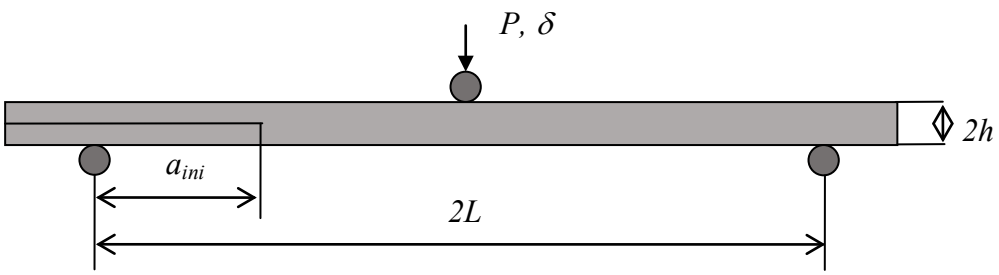


Figure 3. ENF test configuration.

Fig.4 shows the J_{0i} -C_{0i} and Δ_{0i}-C_{0i} curves for different mode II fatigue tests with variable cycling displacement, where the properties of the adherend and the initial crack are maintained.

According to **Fig. 4**, it is found that the curves J_{0I}-C_{0I} and Δ_{0I}-C_{0I} are invariant for a given material system and test configuration also in fatigue.

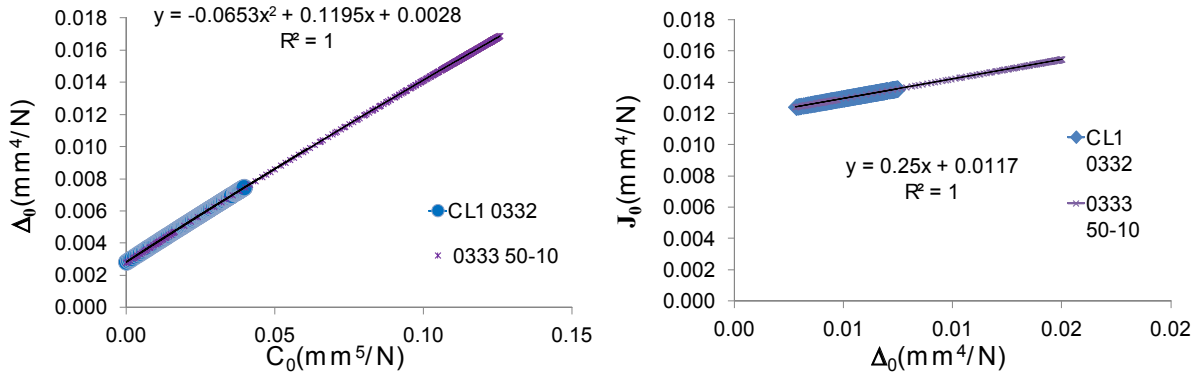


Figure 4. Master Curves J_{0I} -C_{0I} and Δ_{0I} -C_{0I} in mode II.

Applying the extrapolation procedure described above, **Fig. 5** shows the results obtained for the test where the severity varies from %50 to %10.
As observed, the results align with those obtained in [1], indicating that the extrapolation method yields suitable results in fatigue as well.

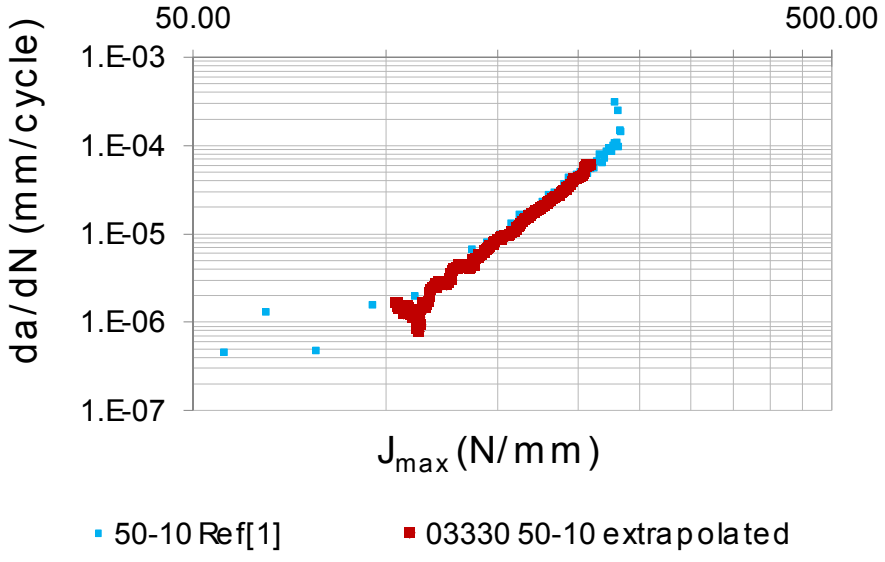


Figure 5. Experimental fatigue crack propagation curve.

Finally, in **Fig. 6a**, the Fatigue-Induced Degradation of the Cohesive Zone is depicted for tests conducted under constant cyclic displacement for varying severities. In **Fig. 6b** the variation of cohesive stress as a function of the number of cycles and severity is illustrated.

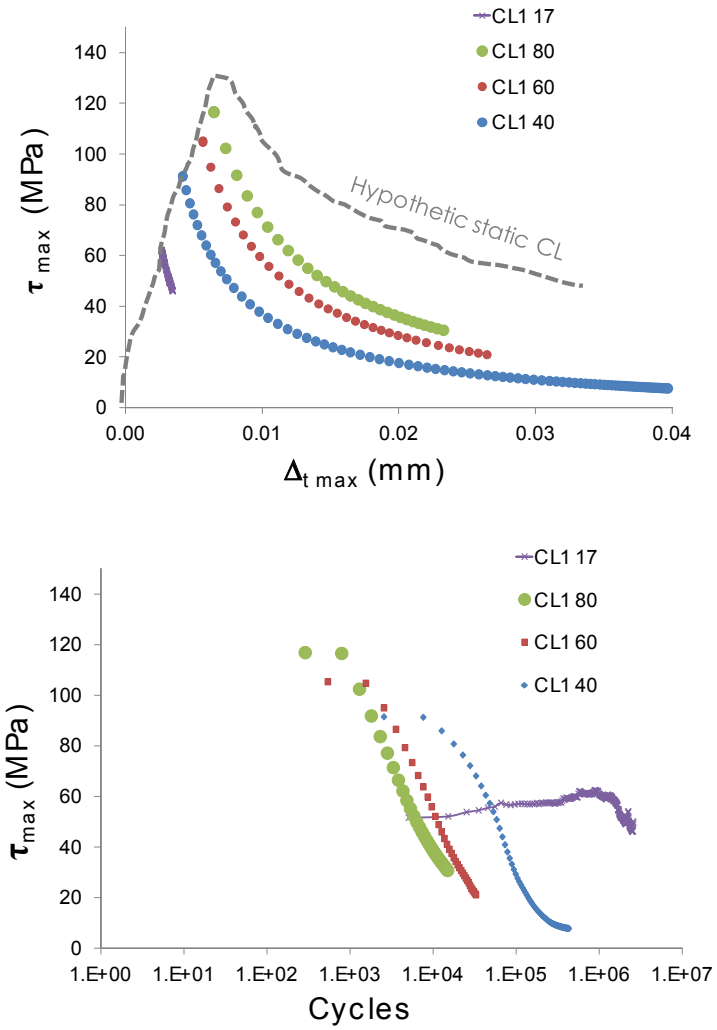


Figure 6. Experimental Fatigue-Induced Degradation of the Cohesive Zone

3. Conclusions

The extrapolation method has been validated to predict the fatigue behavior of composite laminates by determining the experimental fatigue crack propagation curve da/dN versus J, monitoring only the compliance and the maximum load per cycle. The degradation of the Cohesive Zone by Fatigue has also been experimentally determined, analyzing the effect of severity both on the variation of the cohesive laws and on the evolution of the cohesive stress as a function of the number of cycles.

References

[1] L. Carreras, J. Renart, A. Turon, J. Costa, Y. Essa, F. Martin de la Escalera, *Int. J. Fatig.* 95 (2017) 185-193, https://doi.org/10.1016/j.ijfatigue.2016.10.017

[2] A. Argüelles, J. Viña, A. Fernandez-Canteli, I. Vi˜na, J. Bonhomme, *Mech. Mater*. 43 (2011) 62- 67, https://doi.org/10.1016/j.mechmat.2010.10.001
[3] A. Argüelles, P. Coronado, A.F. Canteli, J. Viña, J. Bonhomme, *Int. J. Fatig*. 56 (2013) 54-59, https://doi.org/10.1016/j.ijfatigue.2013.08.001.
[4] J. Renart, J. Vicens, S. Budhe, A. Rodriguez-bellido, J. Comas, J.A. Mayugo, J. Costa, *Int. J. Fatig*. 82 (2016) 634-642, https://doi.org/10.1016/j.ijfatigue.2015.09.021
[5] M.F.S.F. de Moura, M.A.L. Silva, A.B. de Morais, J.J.L. Morais, *Eng. Fract. Mech*. 73 (2006) 978-993, https://doi.org/10.1016/j.engfracmech.2006.01.004
[6] A. Arrese, U. Garitaonaindia, I. Adarraga and F. Mujika, *Materiales Compuestos* (Online first). URL https://www.scipedia.com/public/Arrese_et_al_2022a
[7] A. Arrese, A. Boyano, J. de Gracia, F. Mujika, *Composites Science and Technology*, 152, pp. 76- 84, (2017) https://doi.org/10.1016/j.compscitech.2017.09.012
[8] A. Arrese, N. Insausti, F. Mujika, M. Perez-Galmés, J. Renart, *Composites Science and Technology*, 170, pp. 42-50, (2019) https://doi.org/10.1016/j.compscitech.2018.11.031

Implementation of Second-Order Homogenisation using Shell Elements for Woven Composites

Athira Anil Kumar[1], Aewis K.W. Hii[1], Stephen R. Hallett[1] and Bassam El Said[1]

[1] Bristol Composites Institute, University of Bristol, BS8 1TR, United Kingdom
Email: athiraanil.kumar@bristol.ac.uk, aewis.hii@bristol.ac.uk,
Stephen.Hallett@bristol.ac.uk, Bassam.ElSaid@bristol.ac.uk
Website: https://www.bristol.ac.uk/composites/

Keywords: Multiscale modelling, Second-order homogenisation, Woven composites, Shell elements

Abstract
Composite materials are extensively used in aerospace, automotive, and construction for their higher strength-to-weight ratio, corrosion resistance, and good fatigue properties. However, their limitations in load-bearing applications, such as poor impact performance and delamination resistance is due to a lack of through-thickness reinforcement in the laminated pre-preg material format. 3D woven composites by contrast, offering through-thickness reinforcement via binder yarns, enhance inter-laminar toughness, impact, and energy absorption, making them ideal for impact-critical structures. Despite these advantages, accurately modelling these composites is challenging due to their complex internal structure and multi-scale nature. Traditional first-order homogenisation is limited by its assumptions on scale separation and representative volume element size, particularly when structural scales are similar to substructural scales. To overcome these issues, advanced second-order homogenisation techniques have been developed, integrating strain gradients and higher-order deformation modes to improve accuracy in bending-dominated scenarios. The current study implements a thick-shell based second-order framework for modeling 2D and 3D woven composites, evaluating their mechanical performance through ASTM standardized tests and comparative studies. It highlights the limitations of conventional shell elements in capturing through-thickness stress variations, suggesting the need for a solid-element based, second-order homogenisation framework for thick structures, indicating future research directions.

1. Introduction

3D-woven composites are becoming prominent in multiple industrial applications, including aerospace, due to their enhanced mechanical properties. As summarised by Tong et al. [1], this includes higher delamination toughness, and better impact damage resistance and post-impact mechanical properties due to the presence of through-thickness reinforcements. As a result, these materials have been used in high loading and impact-prone aerospace structures, such as wing panel joints, landing gear braces, and turbofan engine blades. Manufacturing of woven composites is also cost efficient, since components with complex geometries can be woven to near-net shape, thus providing design flexibility. These advantages also come with challenges, especially when it comes to mathematical modelling, due to their complex internal architecture, and multi-scale behaviour.

Meso-scale deformations have significant effect on global performance, and therefore these deformations need to be modelled accurately in a multi-scale manner. Even though the complex internal architecture can be accurately predicted through experiments and simulation, this information is not enough to predict the final structural behaviour. In conventional solid mechanics problems, scale separation between material properties and global structure is possible using an equivalent constitutive model. This kind of separation is not possible in 3D woven composites since the material behaviour is dependent of manufacturing process and final structural geometry, and therefore the properties can not be calculated at a scale larger than that of the constituents. On the other hand, building detailed models for the full scale structure including all the complex internal architecture is not computationally feasible.

Hence, there is a need for multiscale modelling methods which can link the constituents across the multiple length scales [2].

2. Computational Homogenisation

Homogenisation based approaches are a good choice for problems where scale separation hypothesis is valid. Among the different homogenisation methods presented in literature, computational homogenisation is one of the most accurate schemes to upscale the non-linear behaviour of a well-defined microstructure. It involves solving a set of nested boundary value problems, where both the fine and coarse scale models are solved concurrently. This allows for the evaluation of effective properties from a digital definition of microstructure, without explicit description of all heterogeneities at structural level. This approach is also known as the FE^2 method, as proposed by Smit et al. [3] and Feyel et al. [4].

The first-order (1OH) framework is well-established and has been developed over time for large deformations and with nonlinear behaviour at the fine scale (Fig. 1). However, the assumptions on which the framework is built upon presents certain limitations [5]:

- Separation of scales principle assumption remains valid only in cases where macro-gradients are small and material failure does not occur. So, even if there are higher-order deformation modes like bending at the macroscale, the assumption leads to constant macroscopic deformation gradients (tension, compression and shear) over the RVE length scale.
- Dimensions of the RVE have no effect on the averaging procedure, i.e. if we increase the scale of the microstructure, it will give us the same results. For example, even though 1OH can distinguish between an RVE with a large void and a small void, it can't predict the effects of position of the void. Hence, microstructural and geometrical size effects cannot be accounted for.
- 1OH is not applicable in cases where the substructural length scale becomes comparable with length scale associated with macroscopic spatial variability in the loading, due to the highly localized deformation.

2.1. Second-Order Homogenisation

The second-order homogenisation (2OH) framework was developed to address the limitations mentioned in the previous section. The 2OH framework takes into account the strain gradient, which is the gradient of the macroscopic deformation gradient tensor, thus partly alleviating the assumption of separation of scales (Fig. 1) [6].

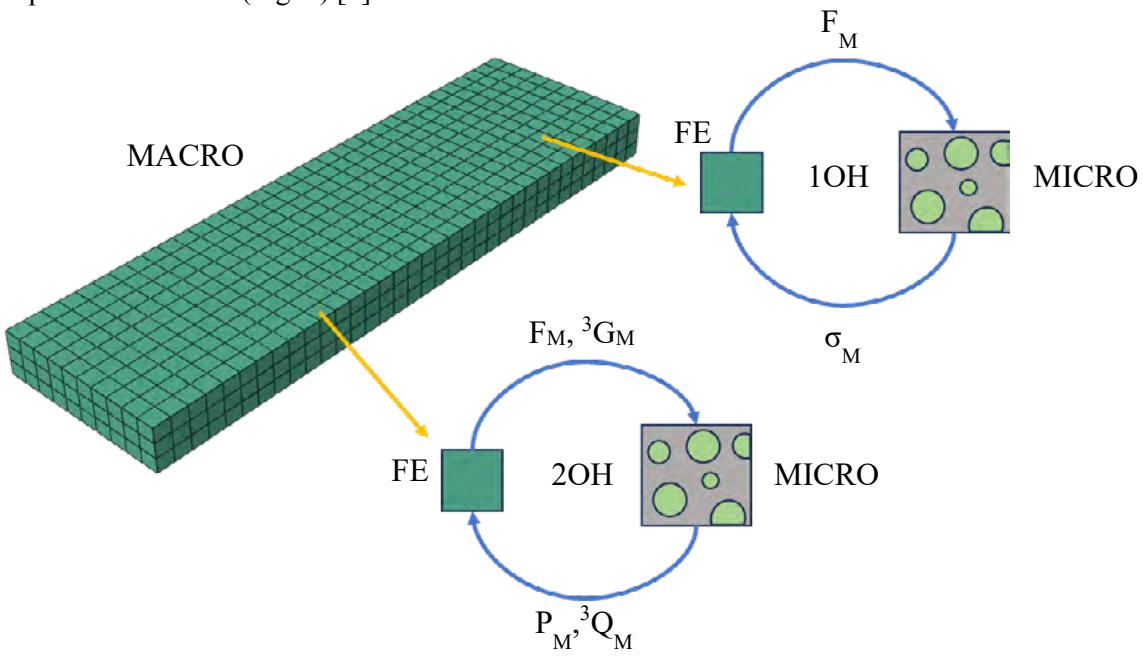


Figure 1. First (1OH) and second (2OH)-order computation homogenisation of continua

Here, the deformation at the mesoscale can be written as:

$$\Delta\vec{x} = F_M \cdot \Delta\vec{X} + {}^1/_2\,\Delta\vec{X} \cdot {}^3G_M \cdot \Delta\vec{X} + \vec{w} \tag{1}$$

Using this Taylor series expansion, the macro-scale kinematics are determined through the deformation gradient tensor F_M and its Lagrangian gradient ${}^3G_M = \vec{\nabla}_{0M}F_M$. (3) is applied to a representative part of the microstructure, such that a classical boundary value problem is obtained at the micro-scale. The macroscopic kinematics are transferred to the RVE through a set of boundary conditions, i.e

$$\vec{u}^* = \vec{f}(\vec{X}, F_M, {}^3G_M) \tag{2}$$

The second-order framework employs higher-order continuum models like strain gradient continuums or shell models at the macroscale, while maintaining first-order for the small-scale boundary value problem. This framework uses an averaging of the Representative Volume Element (RVE) stress field to generate macroscopic and higher-order stress tensors. Unlike the first-order approach, 2OH incorporates a specific length scale defined by the RVE size, which is bounded by macroscopic strain variations and statistical representativeness. This method enhances the assessment of second-order constitutive relations, accommodates micro-length scales, and addresses issues like material gradient sensitivity and macroscopic problem ill-posedness due to localisation and mesh dependency.

2.1. Second-Order Homogenisation using Shell Elements

Shell models, a subset of strain gradient continuum models, are particularly effective in macroscale applications in industry due to their ability to incorporate bending deformations and non-zero strain gradients in a computationally efficient manner. These models are utilised in second-order homogenisation to capture non-linear fine-scale behaviors through numerical averaging, which is crucial for addressing heterogeneities in the through-thickness direction [7] . The homogenisation process within shell models involves discretising the global structure using shell elements, each linked to an underlying solid RVE that resolves full shell thickness. This integration process includes projecting shell basis modes onto the RVE using specific boundary conditions that align with macroscopic gradient averages. Upscaling then involves deriving equivalent shell stresses and constitutive properties from the fine-scale model, which is based on the modified Hill-Mandel condition that ensures consistent strain energy variation across scales [8].

The nonlinear shell homogenisation method developed by Hii and El Said [7] integrates accurate constitutive relations for transverse shear, membrane, and bending components using orthogonality conditions by Luscher et al. [9] This method introduces a novel volumetric constraint that enhances the projection of transverse shear strains to the fine scale, ensuring traction-free conditions on shell surfaces and eliminating spurious modes in RVE transverse shear responses, regardless of its size. Additionally, the framework is adaptable to include material and geometric nonlinearities across various scales, making it suitable for both thick and thin shells. The present study implements this framework to woven composites and the observations are explained in the next section.

3. Observations and Results

Weave models used in the study are built in SimTex (Simulation of Textile Composites), a software suite developed within Bristol Composites Institute. SimTex uses the multi-filament (MF) method to model the inter- and intra- yarn interactions occurring in textile composite fabrics and preforms during the weaving process, to obtain a realistic description of the fabric's internal architecture. SimTex can be used to model the internal architecture of 2D and 3D fabrics. The final simulated fabric geometry is extracted from MF model and is meshed using voxels, where the voxels are assigned yarn or matrix properties depending on the location of its centroid. The voxels must be small enough to represent the yarn cross-sectional geometries and prevent overlapping of element surfaces and stress discontinuities at the yarn-matrix boundaries.

©2024 | 3_ATHIRA ANIL KUMAR_Athira Anil_XUGSA .pdf:3

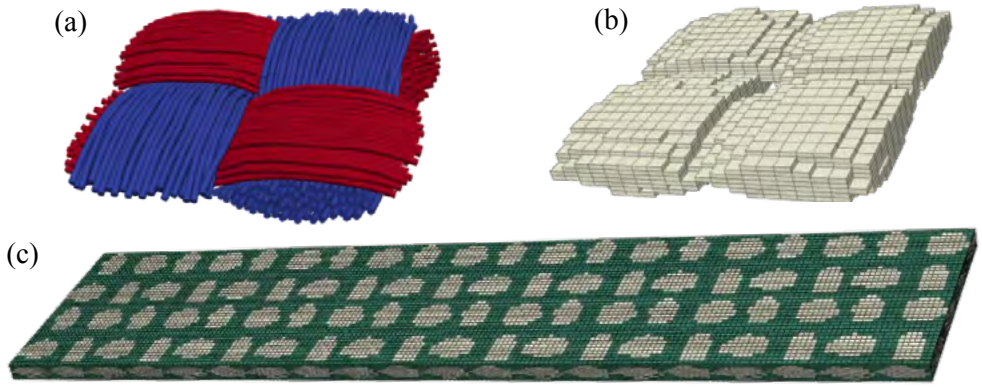


Figure 2. (a) Plain weave simulation and compaction, (b) Voxelised yarn elements, (c) Tessellated high-fidelity macroscale model

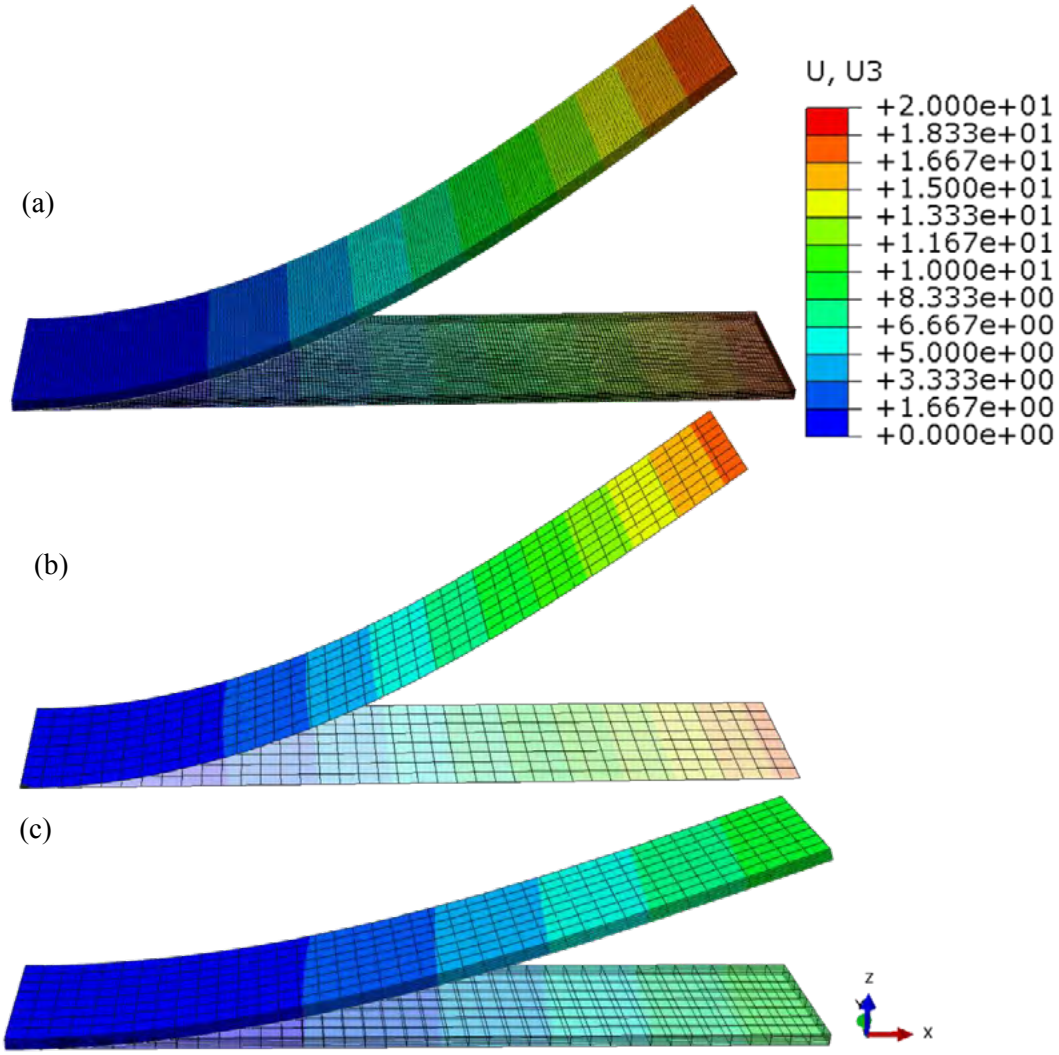


Figure 3. Macroscale models undergoing bending (a) high-fidelity plain weave model, (b) shell model based on 2OH of mesoscale plain weave RVE, (c) solid model based on 1OH of mesoscale plain weave RVE.

Prior to conducting the ASTM standard tests, a preliminary cantilever test was executed for a single-layer plain weave model. The comparative analysis revealed a strong correlation between the second-order response and the high-fidelity model, where the latter was constructed by tessellating the RVE in the in-plane direction. This test primarily aimed to assess the compatibility of the 2OH framework with woven composites, as evidenced by the U_3 responses depicted in Fig.3.

Four-point bending test of a single layer plain weave model showed promising results, where the 2OH response has a good agreement with the high-fidelity response, while the first-order response deviates significantly (Fig.4 (a)). This validates the proficiency of the 2OH framework in precisely replicating bending responses. On the other hand, a short beam shear test, which induces significant shear stress between the loading rollers, showed deviated responses for both 1OH and 2OH framework with respect to high-fidelity response (Fig. 4(b)). This test highlights the material's shear response due to its distinct through- thickness stress distribution, and shows the limitation of 2OH shell framework, since it can not capture this variability of stress. Similar responses were observed for multi-layer 2D and 3D woven cases.

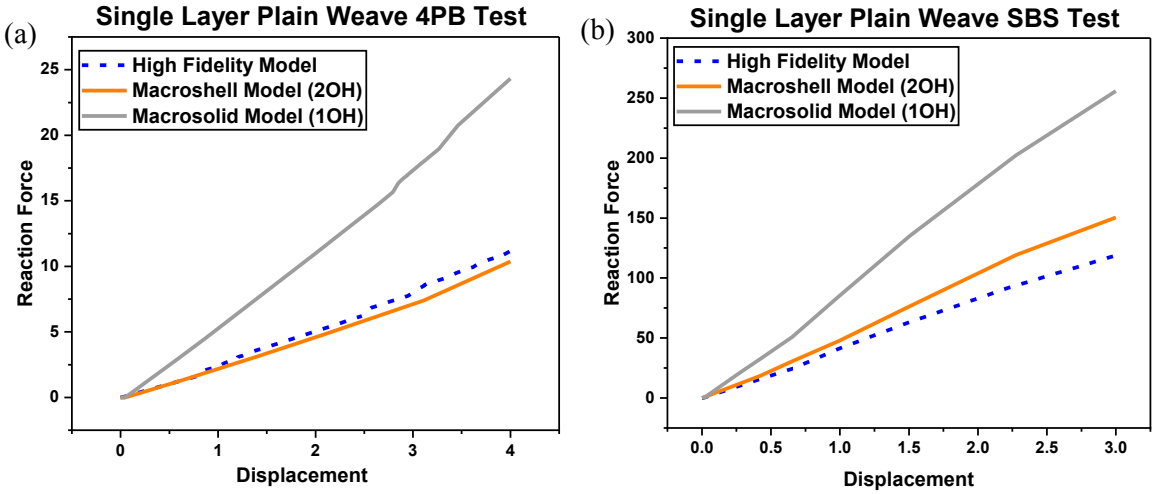


Figure 4. (a) 4 Point Bending and (b) Short Beam Shear responses of high fidelity, 2OH-based macroshell and 1OH-based macrosolid, single layer plain weave models

3. Conclusions

The present study implements a shell element-based second-order homogenisation framework to woven composites, and showcases its ability to capture complex responses like bending, which is not possible with the classical first-order framework. However, the use of shell elements at the macroscale makes it difficult to capture through-thickness variability of stresses, which is highlighted through the simulation of a short beam shear test, thus laying the groundwork for a multi-scale homogenisation framework using solid elements at the macroscale.

Acknowledgments

This work was supported by the UK Engineering and Physical Sciences Research Council (EPSRC) through the Programme Grant: 'Certification of Design: Reshaping the Testing Pyramid (CerTest – www.composites-certest.com), EP/S017038/1. The funding received is gratefully acknowledged.

References

[1] L. Tong, A. P. Mouritz, and M. K. Bannister, 'Chapter 5 - 3D Woven Composites', in *3D Fibre Reinforced Polymer Composites*, L. Tong, A. P. Mouritz, and M. K. Bannister, Eds., Oxford: Elsevier Science, 2002, pp. 107–136. doi: 10.1016/B978-008043938-9/50017-X.

[2] N. Isart, B. El Said, D. S. Ivanov, S. R. Hallett, J. A. Mayugo, and N. Blanco, 'Internal geometric modelling of 3D woven composites: A comparison between different approaches', *Composite Structures*, vol. 132, pp. 1219–1230, Nov. 2015, doi: 10.1016/j.compstruct.2015.07.007.

[3] R. J. M. Smit, W. A. M. Brekelmans, and H. E. H. Meijer, 'Prediction of the mechanical behavior of nonlinear heterogeneous systems by multi-level finite element modeling', *Computer Methods in Applied Mechanics and Engineering*, vol. 155, no. 1, pp. 181–192, Mar. 1998, doi: 10.1016/S0045-7825(97)00139-4.

[4] F. Feyel and J. L. Chaboche, 'FE2 multiscale approach for modelling the elastoviscoplastic behaviour of long fibre SiC/Ti composite materials', *Computer Methods in Applied Mechanics and Engineering*, vol. 183, no. 3–4, pp. 309–330, Mar. 2000, doi: 10.1016/S0045-7825(99)00224-8.

[5] M. Geers *et al.*, 'Computational homogenization of structures and materials', in *9e colloque national en calcul des structures*, Giens, France: CSMA, May 2009. Accessed: Jan. 01, 2023. [Online]. Available: https://hal.archives-ouvertes.fr/hal-01419916

[6] V. G. Kouznetsova, M. G. D. Geers, and W. A. M. Brekelmans, 'Multi-scale second-order computational homogenization of multi-phase materials: a nested finite element solution strategy', *Computer Methods in Applied Mechanics and Engineering*, vol. 193, no. 48–51, pp. 5525–5550, Dec. 2004, doi: 10.1016/j.cma.2003.12.073.

[7] A. K. W. Hii and B. El Said, 'A kinematically consistent second-order computational homogenisation framework for thick shell models', *Computer Methods in Applied Mechanics and Engineering*, vol. 398, p. 115136, 2022, doi: https://doi.org/10.1016/j.cma.2022.115136.

[8] E. W. C. Coenen, V. G. Kouznetsova, and M. G. D. Geers, 'Computational homogenization for heterogeneous thin sheets', *International Journal for Numerical Methods in Engineering*, vol. 83, no. 8–9, pp. 1180–1205, 2010, doi: 10.1002/nme.2833.

[9] D. Luscher, D. McDowell, and C. Bronkhorst, 'Essential features of fine scale boundary conditions for second gradient multiscale homogenization of statistical volume elements', *International Journal for Multiscale Computational Engineering*, vol. 10, pp. 461–486, Jan. 2012, doi: 10.1615/IntJMultCompEng.2012002929.

©2024 | 3_ATHIRA ANIL KUMAR_Athira Anil_XUGSA .pdf:6

ADVANCING THE UNDERSTANDING OF EDDY CURRENTS IN CFRPs USING THROUGH TRANSMISSION EDDY CURRENT TECHNIQUE

Atul Sharma[1], Robert Hughes[1] and Anthony Peyton[2]

[1]Ultrasonics and Non-destructive Testing (UNDT) Group, University of Bristol, UK, BS8 1TR
Email: atul.sharma@bristol.ac.uk, robert.hughes@bristol.ac.uk
[2]Electromagnetic Sensing Group, University of Manchester, UK, M139PL
Email: a.peyton@manchester.ac.uk

Keywords: Non-destructive Testing (NDT), Carbon fibre reinforced polymers (CFRPs), eddy currents, penetration depth, stacking sequence, ply orientation, structural performance.

Abstract

Performing non-destructive testing (NDT) on carbon fibre reinforced polymers (CFRPs) is challenging. Eddy current testing (ECT) offers a promising approach for inspecting CFRPs. However, due to their low and anisotropic conductivity, a complete understanding of how eddy currents flow in these materials is missing, preventing accurate inversion and characterization of parts. This study explores, how the magnetic field is attenuated through CFRPs as a function of stacking sequence. A through transmission ECT measurement was employed involving different orientations of ply layers. Starting with two uni-directional plies, we progressively altered the layers arrangement, studying the impact of relative orientation of plies on eddy current behaviour. The experimental results reveal that CFRP samples with (0/90) ply orientation exhibits a higher degree of magnetic field shielding compared to those with (0/0) ply orientation, indicating that stacking sequence and symmetry between the layers significantly influence the penetration depth of magnetic fields. This knowledge is crucial for improving ECT simulation models, sensor designs and improving quality control of CFRP composites, enhancing their structural performance in diverse engineering applications.

1. Introduction

A major concern for composite manufacturers is how to enhance the structural performance of CFRP composites, which are now widely used in the aerospace and automotive industries [1]. NDT of the CFRP components is required to ensure that those manufactured of CFRP material are fit for purpose. However, the lack of NDT techniques for the characterization of CFRP composites is a significant challenge for many real-world uses of the material, particularly in the aerospace sector.

Numerous NDT techniques have been developed to non-destructively characterise CFRP structures, including ultrasonics, scanning acoustic microscopy, embedded optical fibre, microwave technology scanning to optimise CFRP manufacturing [2]. Because eddy current testing (ECT) is quick, easy, portable, and non-contacting, it has become popular for in-service inspection and quick quality control in the manufacturing of CFRPs [2,3]. ECT offers advantages in cost, development time, and efficiency compared to other more developed and extensively used non-destructive testing methods.

ECT relies on electromagnetic principles and can only be used with electrically conductive materials. CFRPs present a challenge for ECT because their low electrical conductivity. Although carbon fibres themselves are electrically conductive, the resin matrix in these composites is electrically insulating, resulting in a low overall electrical conductivity [4]. This disparity in electrical conductivity is also

influenced by the orientation of the fibres; typically, the electrical conductivity of CFRPs is several orders of magnitude higher along the fibre direction compared to perpendicular to it [4]. This makes it difficult to interpret the results from ECT. Furthermore, the physical structure and inherent anisotropy of CFRPs raise questions about how eddy currents actually flow within these materials, leaving the precise mechanism of eddy currents in CFRPs somewhat unclear. Some researchers have reported in finite element modelling (FEM), that orthogonal unidirectional ply layers exhibit stronger eddy current responses compared to other stacking sequences [5]. To evaluate whether this simulated effect is true and to better understand how eddy currents interact within CFRP, a through transmission ECT measurement is used to measure magnetic flux that passes through 2-ply structures. This knowledge is important for developing faster simulation models and optimizing sensor designs. This development can then be used to inspect CFRPs in a much more systematic way which can ultimately enhance the structural performance of CFRPs in a wide range of engineering applications.

This paper is organised as follows: Section 2 describes the theory behind this experimental study. Section 3 provides details of the through transmission ECT experimental system and the specifications of the CFRP samples. Section 4 shows the results of the experimental study. The conclusions are drawn in Section 5.

2. Theory

2.1 Eddy current testing (ECT)

In ECT, an alternating current is passed through the probe (transmitter coil). Due to faradays law of electromagnetic induction an alternating magnetic field is produced around the transmitter coil. When the coil is moved close to another electrical conductor, the alternating magnetic field around it permeates the material and, according to Lenz's Law, causes an eddy current to flow in the conductor. This eddy current, in turn, generates its own magnetic field. This ‘secondary' magnetic field opposes the 'primary' magnetic field, influencing the current and voltage flowing through the coils. Finally, electromagnetic induction in a receiver coil, or a set of coils, detects both the primary and secondary magnetic fields. Eddy currents exhibit a skin effect. That is, current density is maximum at the material surface and decreases exponentially with depth and it depends on frequency, conductivity, and permeability of the material [6]. In our work we used two sperate coils, the transmitter coil (T_x) for generating eddy currents in the material and the receiver coil (R_x) for detecting magnetic field leaking through the other side of the material. This type of system is commonly known as through-transmission system where one coil is used to excite the eddy currents and the other is used to sense changes in the test material. Figure 1 shows an eddy current system with transmitter and receiver coil in proximity to an electrically conductive sample.

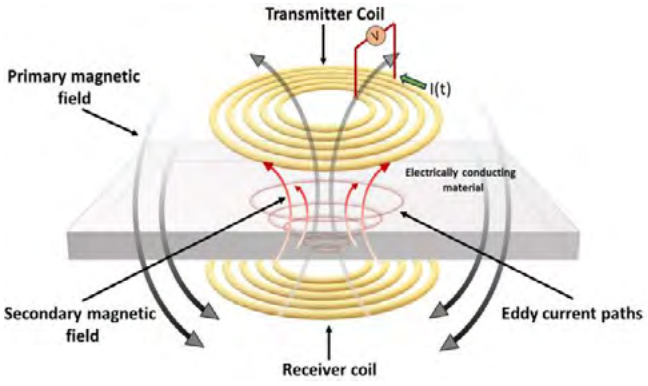


Figure 1 : Schematic of through transmission ECT

2.2 Transformer Model

When an inductor is brought into the proximity of another inductor, they both will electromagnetically couple with each other and there will be a certain amount of mutual inductance (M) between them. When an electrically conducting sample is bought between the two inductors it changes the coupling coefficient (k) between the two inductors which is an important parameter for our experimental study. The coupling interaction can be modelled as a transformer circuit shown in figure 2. The mutual inductance, M, between the circuits is defined as

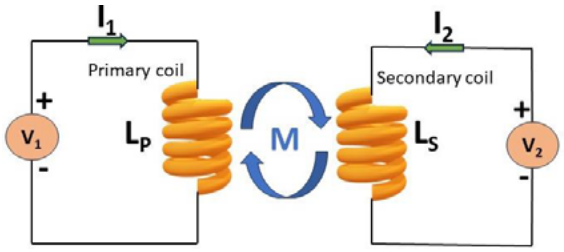


Figure 2: Simple transformer circuit model

$$M = k\sqrt{L_p L_s} \tag{1}$$

where k is the coefficient of coupling between the two inductors.

Kirchhoff's laws are used to find out the relationship between k and other parameters.

$$V_1 = i\omega L_p I_1 + i\omega M I_2 \tag{2}$$

$$V_2 = i\omega M I_1 + i\omega L_s I_2 \tag{3}$$

Using (1) (2) and (3) and $I_2 = 0$ as there is no current in the secondary coil, we get,

$$k = \frac{V_2}{V_1}\sqrt{\frac{L_p}{L_s}} \tag{4}$$

The values of V_1 and V_2 are voltages in the primary and secondary coil.

3. Experimental method and Sample preparation

3.1 Through-transmission measurement

A through transmission ECT measurement was developed consisting of two PCB coil (T_x and R_x) and a 3D printed rig which holds the two coils. PCB coils are used due to their efficient manufacturability and precise alignment capabilities. It also consists of a Zurich Instruments HFLI2 lock-in Amplifier which houses an integrated excitation function generator and measurement scope, which monitors the complex voltage across both Tx and Rx coils via the Howland current source (SonEMAT Ltd, Coventry, UK), which, for a constant output excitation waveform, is proportional to the electrical impedance of the coils testing CFRP sample at different frequencies.

The input voltage (1V) excited by the amplifier is converted to the sensor coil's equivalent frequency current excitation (30 mA). The current source is mounted directly above the Tx coil to eliminate the detrimental high-frequency shunt effects generated by the connecting cables. A frequency sweep was performed using LABONE software of the lock-in amplifier and the voltages on the T_x and R_x coil were measured. The collected data is saved in MATLAB for post-processing.

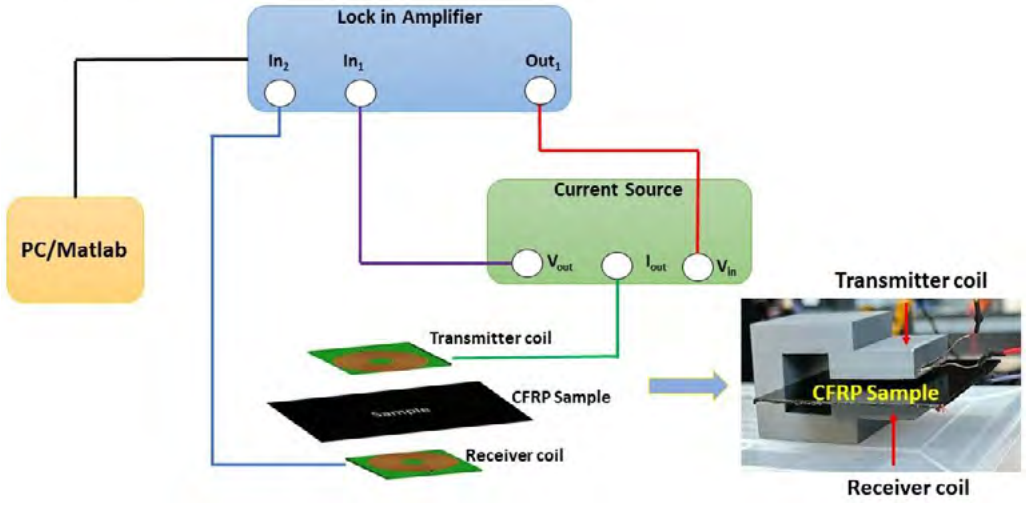


Figure 3 : Schematic diagram of the experimental setup showing through transmission ECT measurement with 3D printed rig

3.2 CFRP Samples

Seven CFRP samples are used in this study. These samples are all defect-free, 2-layered with the first layer being 0 degree and second layer changing from 0 to 90 with an increment of 15 degrees. This will give 7, 2-layerd samples with different orientation. The samples are IM7/8552 prepreg manufactured in-house with specific ply structures (0/0, 0/15, 0/30, 0/45, 0/60, 0/75, 0/90) as shown in table 1.

Table 1: Specification of two-layer, defect-free samples

Sample	No. of Layers	First Layer (degrees)	Second Layer (degrees)	Material
0/0	2	0	0	IM7 8552 Prepreg
0/15	2	0	15	IM7 8552 Prepreg
0/30	2	0	30	IM7 8552 Prepreg
0/45	2	0	45	IM7 8552 Prepreg
0/60	2	0	60	IM7 8552 Prepreg
0/75	2	0	75	IM7 8552 Prepreg
0/90	2	0	90	IM7 8552 Prepreg

4. Results and Analysis

One of the critical properties for this experimental study is the coupling coefficient (k) between the 2 coils (Tx and Rx) as described in section 2.2.

Figure 4 shows the coupling coefficient (k) against the relative angle of the samples at three randomly selected frequencies (0.9 MHz, 1 MHz, 1.8 MHz), with both coils having N=30 turns and resonance frequency of 12.4 MHz. The data reveals that, at each frequency, the 0/90 sample has the lowest coupling coefficient. Since the coupling coefficient is related to magnetic flux through Faraday's Law of Electromagnetic Induction which states that voltage induced in the coil is proportional to the rate of

change of magnetic flux through the coil [6]. This suggests that inserting a 0/90 sample between the coils disrupts the coupling more than a 0/0 sample, which has a higher coupling coefficient at these frequencies. The most likely reason for this is that in a 0/90 orientation, there are more contact points among the fibres as shown in Figure 5. This led to stronger eddy currents circulating in closed loops as shown in figure 5, thereby creating stronger opposing magnetic field, reducing the primary magnetic field from the transmitter coils, thereby diminishing the magnetic flux that penetrates to the other side of the sample. In contrast, the (0/0) ply orientation samples screen the magnetic flux to a lesser extent because their orientation allows for fewer circular eddy currents. This observation suggests that the (0/90) ply orientation yields higher current densities, a finding consistent with the finite element method (FEM) study conducted by Qiuji et al. [4].

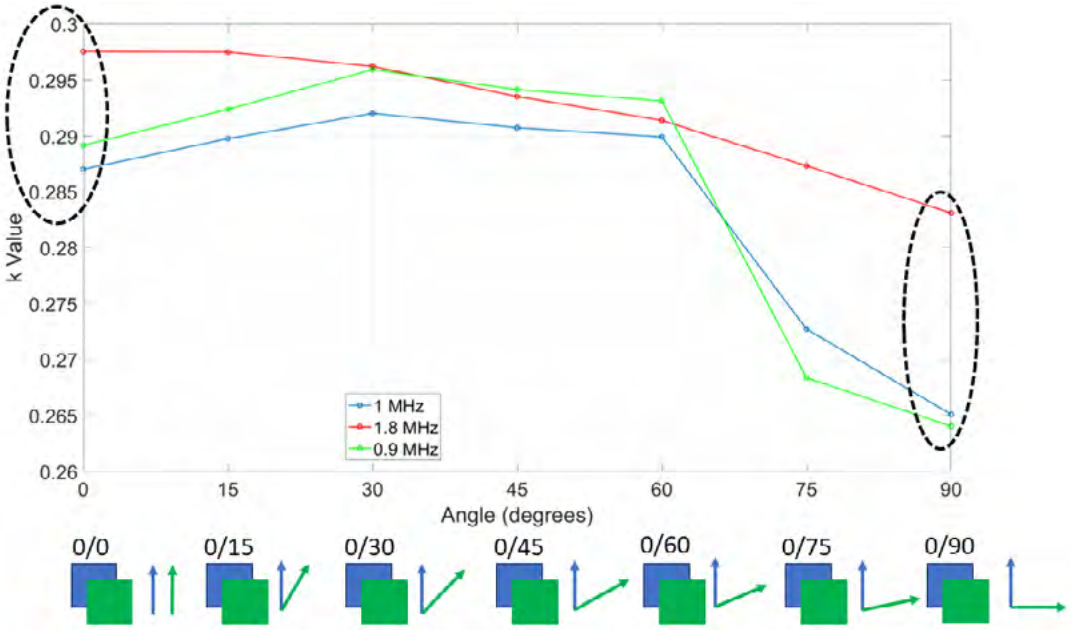


Figure 4 : Coupling coff (K). vs Ply orientation for N=30

It is also observed that there are different values of coupling coefficient (k) for different orientations of samples which signifies that stacking sequence plays an important role in shielding the magnetic field reaching the other side which ultimately affects the depth of penetration in CFRPs.

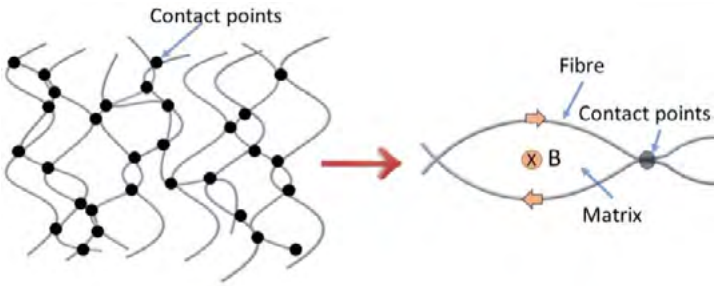


Figure 5 : Contact points and possible eddy current paths in CFRP layers

5. Conclusion and Future works

This work has developed a through-transmission ECT methodology to evaluate the electromagnetic interactions within CFRPs and how the stacking sequence in CFRPs affect the ECT response.

The proposed methodology shows that (0/90) ply orientation shields more magnetic field as compared to their (0/0) ply orientation. This also suggests that in (0/90) ply orientation there are higher current densities between the interfaces. It means that stacking sequence/symmetry plays a significant role in shielding the magnetic field reaching the other side which ultimately affects the depth of penetration in CFRPs. It is clear that frequency also plays a significant role in the penetration depth in these materials in a way that is not yet fully understood.

Future works will include finite element method FEM models to validate the experimental findings and a systematic study will be conducted to enhance existing FEM models, optimize sensor configurations, and eventually improving the structural performance of CFRP composites in diverse engineering applications.

References

[1] X. E. Gros, K. Ogi, and K. Takahashi, “Eddy current, ultrasonic c-scan and scanning acoustic microscopy testing of delaminated quasi-isotropic cfrp materials: A case study,” *Journal of Reinforced Plastics and Composites*, vol. 17, no. 5, pp. 389–405, 1998.

[2] E. P. Papadakis, “quality degradation due to shipment of nonconforming product under statistical process control in the absence of quarantining,” *Materials Evaluation*, Vol. 51(11), pp. 1274–1278, 1994.

[3] F. Burdekin, “Ndt in perspective,” *British Journal of NDT*, Vol. 32(11), pp. 563-567, 1990.

[4] J. Cheng, X. Xu, H. Ji, T. Takagi, and T. Uchimoto, “Research advances in eddy current testing for maintenance of carbon fiber reinforced plastic composites,” *International Journal of Applied Electromagnetics and Mechanics*, vol. 51, pp. 261–284, 07 2016.

[5] Q. Yi, P. Wilcox, and R. Hughes, “Modelling and evaluation of carbon fibre composite structures using high-frequency eddy current imaging,” *Composites Part B: Engineering*, vol. 248, p. 110343, 2023.

[6] P. J. Shull, *Non Destructive Evaluation, Theory, Techniques and Applications*, publisher = CRC Press, year = 2002.

UNDERSTANDING FATIGUE DELAMINATION CRACK GROWTH IN A WIND TURBINE ROTOR BLADE THROUGH AN ELEMENT TESTING

Ashish K. Bangaru, Seyed Sina Samareh-Mousavi, Xing-Yuan Miao, Bent F. Sørensen and Malcolm McGugan

Department of Wind and Energy Systems, Technical University of Denmark, Risø Campus, Frederiksborgvej 399, 4000 Roskilde, Denmark
Email: akba@dtu.dk, seysa@dtu.dk, ximi@dtu.dk, bsqr@dtu.dk and mamc@dtu.dk

Keywords: Delamination, Element test specimen, Cyclic loading, Fatigue crack growth, Wind turbine rotor blade

Abstract
A novel element test specimen, considered to be representative of a thick composite laminate in a wind turbine rotor blade, is investigated in cyclic loading for fatigue delaminations. The element test specimen has an embedded artificial defect to mimic the delaminations in the spar cap of a 31 m wind turbine rotor blade. The aim was to measure the growth rate of delamination cracks and the temperature rise during the cracks propagation. It was noticed that four delamination cracks initiated and propagated, out of which two cracks were along the embedded defect interface planes and the other two originated from the crack-tips of a transvers tunneling crack in the resin pocket. The initial difference in the crack lengths of the four cracks translated throughout the cyclic loading. Initiation and propagation of multiple delamination cracks documented by the optical images were well correlated by the temperature distribution recorded from the thermal images.

1. Introduction

Fatigue failure in large composite structures like wind turbine rotor blades, typically made from fibre reinforced polymers, is one of the major design concerns. With the current trend in increasing sizes of the rotor blades, a full-scale blade test becomes quite challenging as it demands many resources, high costs, and a great deal of time. The conventional method for designing against fatigue failure involves several tests performed at various length scales and is referred to as the building block approach [1] or the testing pyramid approach [2]. At the pinnacle of the testing pyramid, very few full-scale blade tests are performed as in comparison with the base of the pyramid where numerous coupon tests are performed. The intermediate level involves testing of smaller blade sections like critical substructures, subcomponents that are connected by adhesive bondlines to evaluate their structural integrity [3].

On the similar lines of substructure tests, element tests aim to understand the evolution of multiple damage mechanisms and their interaction. An element test specimen can be designed for specific damage types to understand and document the details of the interaction between the damages. It is worth mentioning that the damage evolution in these element tests should be predicted using material laws such as cohesive laws, crack growth laws etc. measured from the material characterization tests at the bottom of the test pyramid.

Delamination is one of the common damage types seen in composite structures [4]. The damage is progressive in nature and leads to unfavorable conditions such as loss of stiffness, cause vibrations, can even promote buckling and may eventually lead to final collapse of the rotor blade [5, 6, 7]. Jensen et

al. [8] investigated a 34 m full-scale blade under flap-wise loading and observed that post outer skin debonding delamination buckling led to the final failure of the blade. Haselbach et al. [9] uncovered that near surface delamination of about 30% of spar cap width led to crack growth at normal operating conditions. Lee and Park [10] tested a 48.3 m blade in static loading after cyclic testing and attributed delamination as the root cause for the blade collapse.

Samareh-Mousavi et al. [11] tested a 31 m wind turbine rotor blade with an artificial defect embedded in the spar cap under cyclic flap-wise bending. Noticing multiple delaminations that grew from the artificial defect, an element test specimen was manufactured based on the design analysis by Erives et al. [12]. This study is an experimental investigation to understand the evolution of multiple delaminations and their interaction by isolating the complexities like curvatures, ply drops etc. those are pertinent to a full structure.

The current paper is organized as follows; an introduction along with a brief motivation behind the study is presented in section 1 followed by the material system and experimental setup in section 2. Results of delaminations crack growth and thermography are discussed in section 3. Lastly, conclusions are summarized in section 4.

2. Materials and testing

2.1. Material system

The material investigated was a glass fibre/epoxy composite made up of E-glass fabric, E-1182 Saertex, and Hexion RIMR 035c epoxy. For the layup, a total of 16 UD layers were used. The central 8 UD layers were cut at half-length and then wrapped by a 35±15 µm thin Teflon slip foil (which acts as a defect) on one side of the cut fabrics as shown in Figure 1. A plate with dimensions of approximately 600 mm x 600 mm was manufactured by vacuum assisted resin transfer molding process. The plate was cured for 19 hrs. at 40°C followed by a post-cure for 10 hrs. at 80°C. Tabs covering a length of 70 mm each on both sides of the plate were glued onto the plate and thereafter, test specimens of dimensions 500 mm × 50 mm were cut from the plate. Figure 1 shows the geometry of the element specimen.

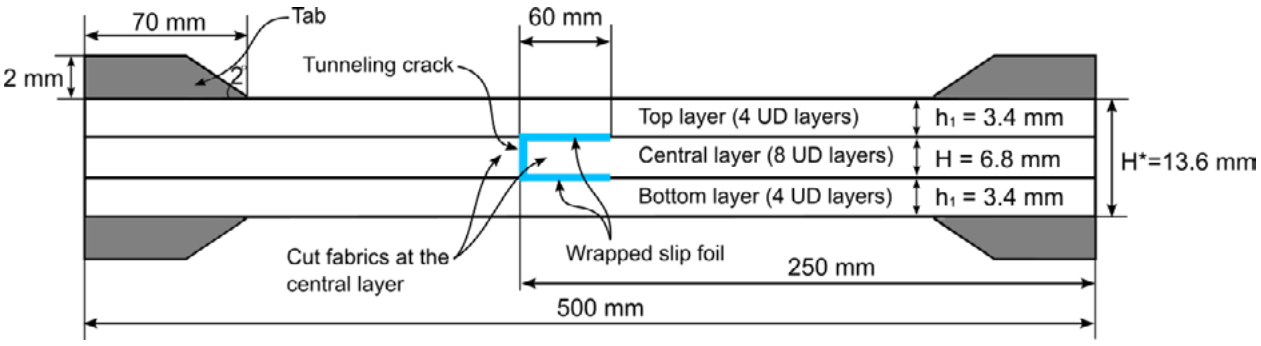


Figure 1. A schematic illustration of the geometry of the element test specimen. The artificial defect is a tunneling crack and two delaminations made by a slip foil, shown in thick light blue colored lines.

2.2. Test setup

An experimental campaign was carried out on a universal servo-hydraulic Instron 250 kN test machine equipped with a 100 kN load cell. Cyclic tension-tension loading test was performed on the element test specimen with a load ratio, $R = F_{max}/F_{min} = 0.1$ (F being the applied force), and at a frequency of 2 Hz. A strain level of 0.3% was applied for the first load cycle and the test ran up to 10,000 cycles. Digital image correlation, white light and infrared imaging were used as instrumentation. As shown in Figure 2, one optical camera (Nikon D7200 with 4000×6000-pixel resolution) and one thermal camera (Optris PI 640i equipped with a 640×480-pixel resolution and 40mK thermal sensitivity uncooled detector) were

placed in a way to observe cracks propagation from the sideways i.e., thickness view of the specimen, while the second optical and thermal cameras look at the front and back surfaces of the test specimen.

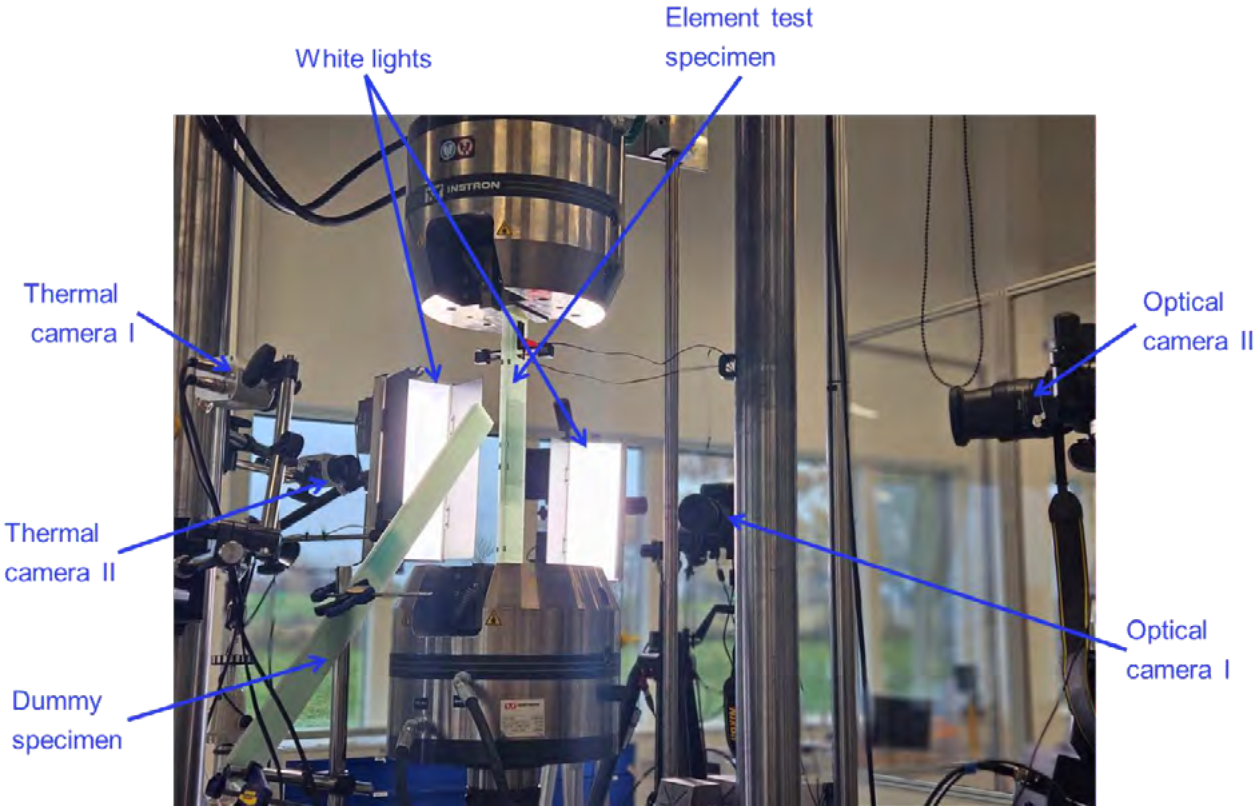
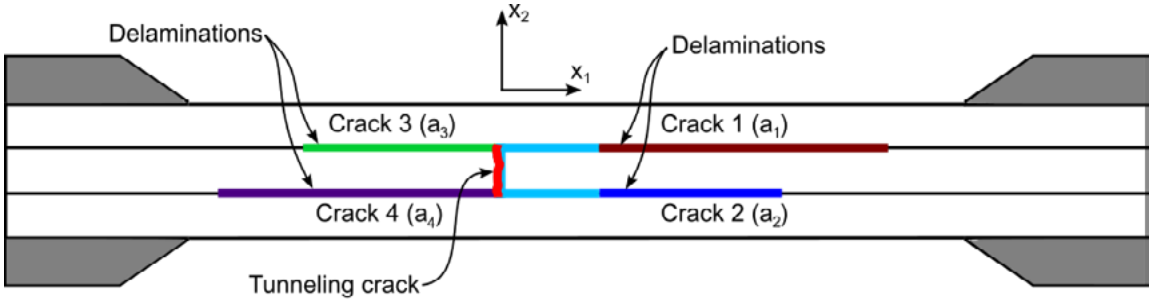


Figure 2. Test setup used for monitoring fatigue delaminations in the element test specimen.

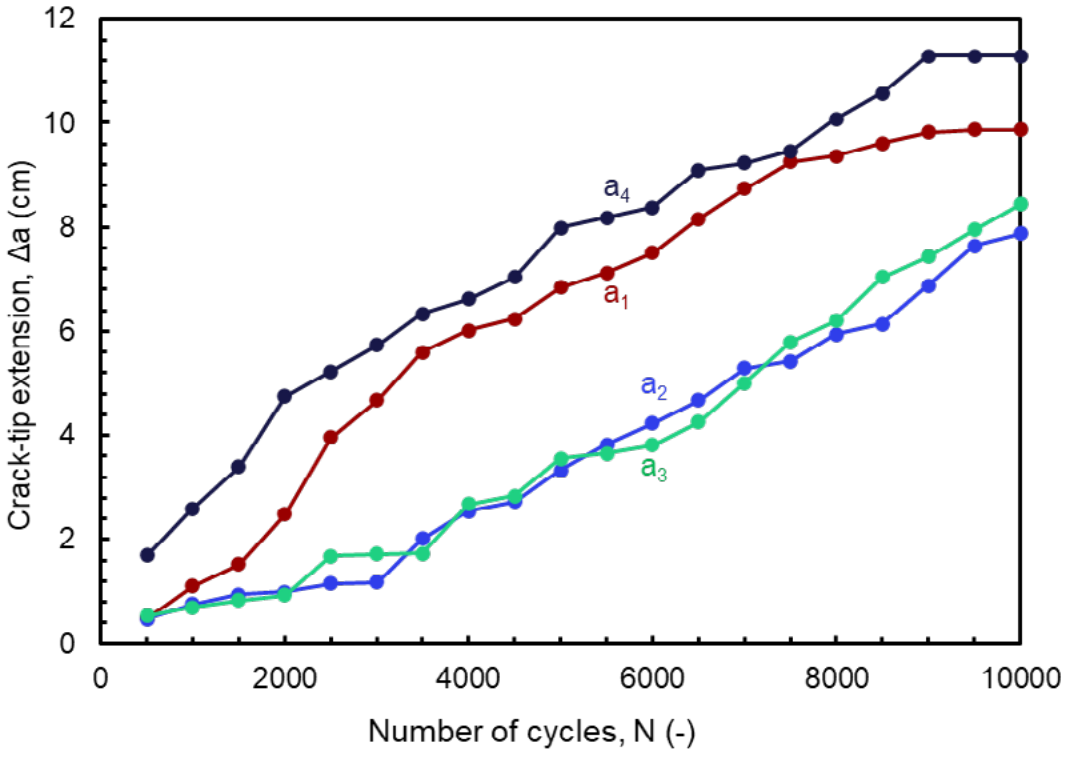
3. Results and discussion

3.1. Crack growth

A total of four delamination cracks initiated and propagated in the element test specimen as shown in Figure 3(a). Two cracks (a_1 and a_2) along the slip foil planes and the other two (a_3 and a_4) originating from the crack-tips of a tunneling crack in the resin pocket that is located in between the cut central layers. The crack-tip extension recorded for each delamination crack against the number of load cycles, viewed from the thickness side is plotted in Figure 3(b). The cracks a_1 and a_4, propagated approximately at the same rate and were longer than, a_2 and a_3, which were also found to grow in tandem. The difference between the crack growth rates of a_1, a_4 and a_2, a_3 is attributed to the initial cracking length differences observed during the early load cycles.



(a)



(b)

Figure 3. a) Schematics of the multiple delamination cracks observed in the element test specimen and b) measured crack-tip extension of each delamination plotted as a function of number of load cycles.

3.2. Infrared thermography

Figures 4 and 5 show the fatigue crack propagation from the initial pre-cracks in comparison with the corresponding thermal images at the same cycles from the front and side faces, respectively. Since the thermal and optical cameras were pointed to the opposite faces, the thermal images were mirrored vertically to facilitate comparison. The temperature range of the color bar is considered constant to have consistent and comparable thermal images over time, that covers temperature variation from the beginning to the end of the test. In Figure 4, the temperature contours on the front face show highest temperatures around the initial pre-crack fronts and tunneling crack at the early cycles. As cracks propagate, the distances between four crack fronts increases and as a result, large area of the specimen warms up. In addition, several hot spots evolve which distance from each other by cycles and their positions correlate with the crack fronts during the test. Several mechanisms could be involved in heat generation and temperature evolution such as viscoelastic hysteresis dissipation, friction between the crack faces and crack growth energy release. With increasing crack lengths, stress free region in the middle layer enlarges in the x_2-direction (Poisson's effect) and its load is transferred to the upper and lower layers which means higher cyclic stress range and more hysteresis dissipation. The higher hysteresis dissipation and larger rubbing faces can explain an overall warmer region in the middle of the specimen. At the very tip of the crack fronts, stress is singular which dissipates high amount of hysteresis energy and crack growth related energy release in a small volume. The trace of higher heat dissipation near crack fronts was observed with a delay in the thermal images due to low thermal conductivity of the glass fiber composites.

The surface temperature field is influenced by material thermal conductivity, depth of crack from surface and the rate of heat dissipation. Moreover, the area near to tunneling crack is consistently hot from the

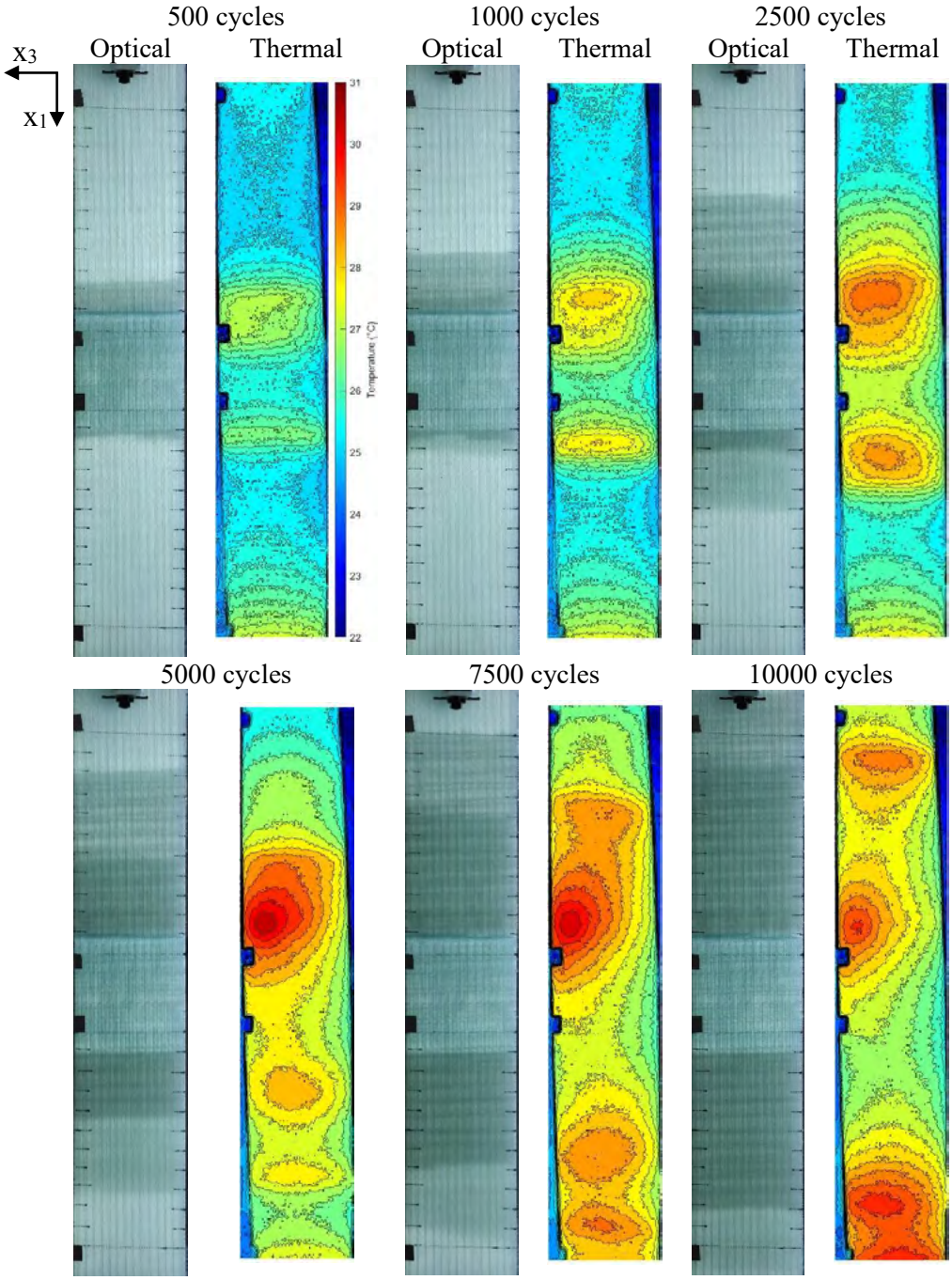


Figure 4. Comparison of multiple delamination cracks from the optical images (taken from front face) with their corresponding thermal images (taken from back face) at different load cycles.

beginning to the end that significantly affects temperature field. More investigation and post-mortem analysis is essential to uncover the dominant heat source near to the tunneling crack.

Figure 5 shows the optical photos taken from the right side and thermal images from the opposite side. The positions of four crack fronts are shown with arrows in the optical photos. The crack growth can be tracked from thermal images, however hot spots do not precisely follow the crack fronts' positions, due to variation of the crack front position along the specimen's width (in x_3-direction). Like the front face, the tunneling crack is observed as the hottest point on side face thermal images and its reason is unclear

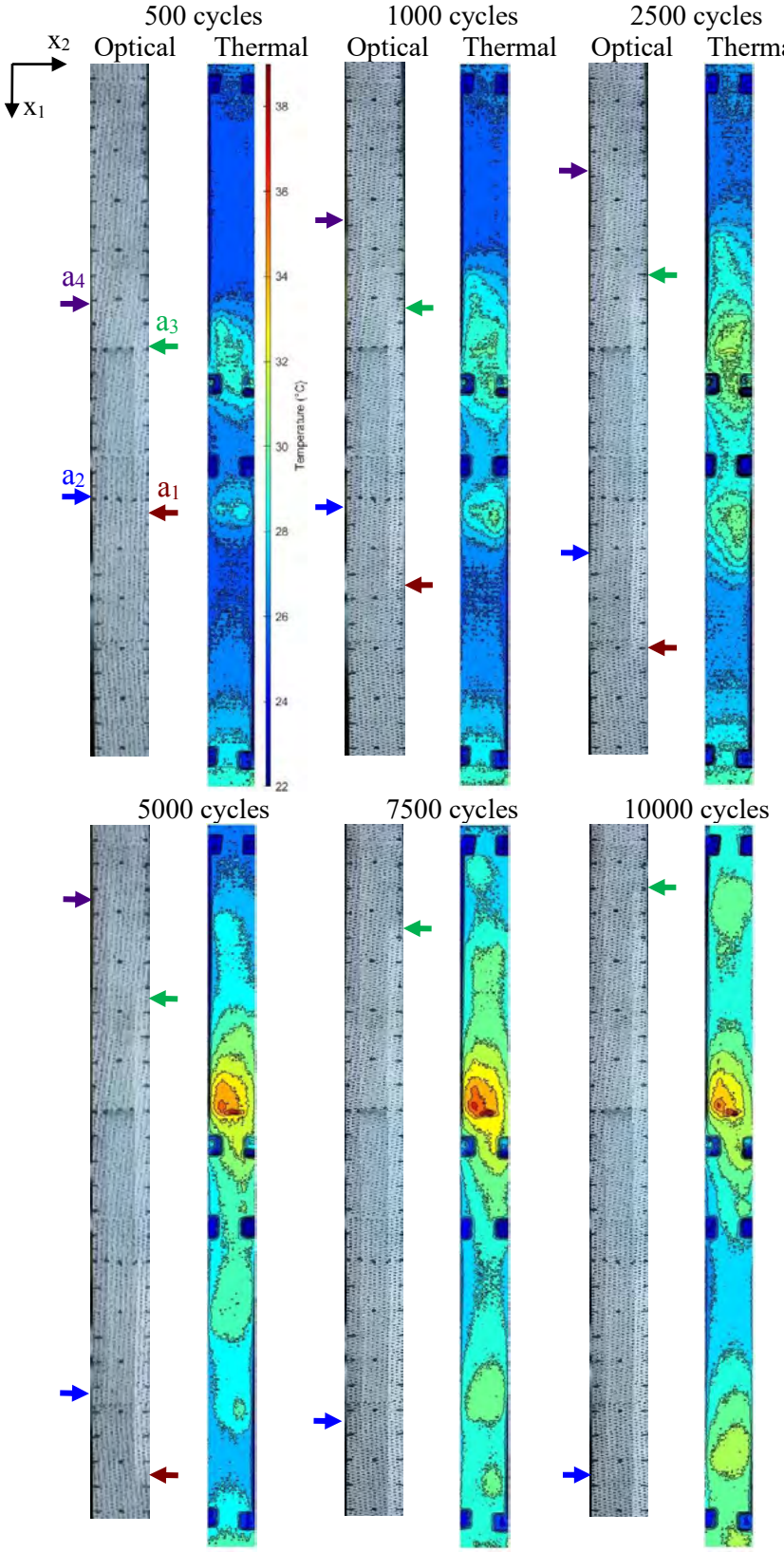


Figure 5. Comparison of multiple delamination cracks from the optical images with their corresponding thermal images viewed from the sideways. The arrows indicate each delamination crack-tip position.

for the authors. Due to significantly higher temperature near to the tunneling crack, it is difficult to distinguish temperature contours around the crack fronts at the early cycles. However, hot spots related

to crack fronts are observed by increasing the distance of crack fronts from the initial pre-cracks and the tunneling crack positions. Moreover, it is observed in the side face thermal images that the temperature is higher very close to the crack tips and decreases towards specimen's front and back faces that explain the difference of maximum temperature in the front and side faces.

4. Concluding remarks

Fatigue delaminations were investigated under cyclic loading on an element test specimen with an intentionally embedded defect (in the form of a slip foil) that is intended to imitate a thick laminate in main spar of the wind turbine rotor blade.Two cracks were found to initiate and propagate from the tips of the slip foil, and further, two more cracks initiated and propagated from the tips of the tunneling crack in the resin pocket. Out of the four cracks, set of two cracks each recorded approximately same crack-tip growth when plotted as a function of number of load cycles. The difference between the crack lengths observed is attributed to the initial cracking difference occurred from the early load cycles. The hot regions detected on the thermal images were well correlated by the position of crack-tips seen in the optical images, however, further investigation is needed to know the source of increasing heat dissipation near the tunneling crack.

Acknowledgments

This work is carried as a part of the research supported by the AINDT project (Artificial Intelligence-based Non-Destructive Techniques for reduced service costs for wind turbine blades) through the Innovation Fund Denmark (0224-0011A). The author would like to acknowledge the assistance provided by Christian H. Madsen, for manufacturing of the element test specimens, and Steffen Rasmussen, and Nicolai Frost-Jensen Johansen for the experimental test setup. Further, the author would also like to thank the associate professor Xiao Chen for the scientific discussions throughout the work.

References

[1] J. R. Soderquist, "Design/certification considerations in civil composite aircraft structure," SAE Trans., vol. 96, pp. 1248–1254, 1987, Accessed: Feb. 16, 2021. https://www.jstor.org/stable/44473034.
[2] J. Rouchon, "Certification of large aircraft composite structures, recent progress and new trends in compliance philosophy," in 17th ICAS Congress, 1990, vol. 1, pp. 1439–1447.
[3] S. Laustsen, E. Lund, L. Kühlmeier, and O. T. Thomsen. "Development of a High-fidelity Experimental Substructure Test Rig for Grid-scored Sandwich Panels in Wind Turbine Blades," Strain, 50(2) (2014), 111-131.
[4] N. J. Pagano and G.A. Schoeppner. "Delamination of Polymer Matrix Composites: Problems and Assessment". In: Comprehensive Composite Materials (2000), pages 433–528.
[5] L. C. T. Overgaard and E. Lund. "Structural collapse of a wind turbine blade. Part B: Progressive interlaminar failure models". In: Composites Part A: Applied Science and Manufacturing 41.2 (2010), pages 271–283.
[6] Xiao Chen. "Experimental investigation on structural collapse of a large composite wind turbine blade under combined bending and torsion". In: Composite Structures 160 (2017), pages 435–445.
[7] J. Yang et al. "Structural investigation of composite wind turbine blade considering structural collapse in full-scale static tests". In: Composite Structures 97 (2013), pages 15–29.
[8] F. M. Jensen et al. "Structural testing and numerical simulation of a 34 m composite wind turbine blade". In: Composite Structures 76.1-2 (2006), pages 52–61.
[9] P. U. Haselbach, R. D. Bitsche, and K. Branner. "The effect of delaminations on local buckling in wind turbine blades". In: Renewable Energy 85 (2016), pages 295– 305.
[10] H. G. Lee and J. Park. "Static test until structural collapse after fatigue testing of a full-scale wind turbine blade". In: Composite Structures 136 (2016), pages 251–257.

[11] S. S. Samareh-Mousavi et al. "Monitoring fatigue delamination growth in a wind turbine blade using passive thermography and acoustic emission." Structural Health Monitoring (2024): 14759217231217179.
[12] R. Erives et al. "Design of an element test specimen for fatigue delamination growth of a thick laminate." IOP Conference Series: Materials Science and Engineering. Vol. 1293. No. 1. IOP Publishing, 2023.

INFLUENCE OF FLUID PROPERTIES ON TRANSVERSE FABRIC COMPRESSIBILITY DURING IN-SITU IMPREGNATION

M. Bender[1], E. Fauster[2]

[1] Processing of Composites Group, Department of Polymer Engineering and Science, Montanuniversität Leoben, 8700 Leoben, Austria
marcel.bender@unileoben.ac.at, https://www.kunststofftechnik.at/en/verbundwerkstoffe
[2] Processing of Composites Group, Department of Polymer Engineering and Science, Montanuniversität Leoben, 8700 Leoben, Austria
ewald.fauster@unileoben.ac.at, https://www.kunststofftechnik.at/en/verbundwerkstoffe

Keywords: In-situ impregnation, Transverse fabric compressibility, Test fluid influence

Abstract
In this study, the influence of different fluids on the transverse compressibility behaviour of technical reinforcing fabrics was investigated. Specifically, a glass fibre woven and a non-crimp fabric with comparable fibre areal weight, were studied in a novel test-rig with in-situ impregnation of the samples under transverse load. Four test fluids with varying viscosity and polarity, respectively, were chosen to analyse the influence of fluid viscosity and polarity on the relaxation behaviour. In addition, silicone oil with four different levels of viscosity across three orders of magnitude was used to isolate the influence of fluid viscosity, as no significant difference in polarity was observed.
A qualitative analysis showed that the fabrics reacted significantly different to the impregnation, as with lower flexibility and increasing viscosity, hydrostatic effects in the compressed area counteracted a lubricating effect. However, only in the fabric with lower fibre bundle flexibility a slight to significant relative pressure relaxation was measured only as a result of fluid polarity.
In addition, the viscosity of the fluid had no significant effect on the relative relaxation at the same polarity, but with increasing viscosity the time to reach pressure equilibrium increased significantly.

1. Introduction

Process optimization of composites manufacturing requires fundamental understanding of the most relevant phenomenological mechanisms. This involves reliable data on material behaviour and a good understanding of the process. To determine this data under process-like conditions, a novel in-situ test method was proposed [1]. The present work uses this test method and a broad selection of fluids to analyse the influence of fluid viscosity and polarity on transverse fabric compressibility.

2. Materials and methods

Two glass fibre textiles were selected in order to simplify the transfer of this research into industrial applications and to take account of the more than 90% mass share of glass fibres in the global composites market [2]. The materials are characterised by a comparable fibre areal weight (FAW) of around 300 g/m² and at the same time represent the most frequently used textile reinforcement structures, i.e. woven (WF) and non-crimp fabrics (NCF), for structural and mechanically stressed components. In addition, the selected WF corresponds to the textile used in the latest international benchmark exercise (IBE) [3] and therefore allows for comparability of the results. The following table provides an overview of important textile parameters of the two materials.

Table 1. Overview of the analysed textile reinforcements with their respective FAW according to the technical data sheet labelled (*), as well as their measured average FAW and coefficient of variation (CV) labelled (**).

Manufacturer	Textile name	Fibre material	Textile structure	FAW (*) [g/m²]	FAW (**) [g/m²]	CV (**) [%]	Data sheet
Hexcel Corporation	01202	GF	Twill 2/2 (WF)	290	291.36	0.56	[4]
Saertex GmbH	X-E-302	GF	Bi-axial (NCF)	302	305.14	0.23	[5]

Both materials are slightly heavier than the specification, but the deviation is very small at approximately 0.5% (Hexcel) and 1.0% (Saertex) and the variability is very low for both materials. This aspect is very important for the significance of the measurements, as the expected influence of fluid polarity on the compaction behaviour is likely to be very small.
Table 2 lists the fluids used for the in-situ impregnation tests, their average dynamic viscosity and the CV from 10 consecutive measurements. The viscosity measurements were carried out at 20 °C in a shear rate range of 1-500 1/s in 15 logarithmically distributed steps.

Table 2. Overview of test fluids with their average dynamic viscosity.

Manufacturer	Fluid name	Material	Dynamic viscosity [mPa·s]	CV [%]	Data sheets
Carl Roth GmbH + Co. KG	n-Decane	n-Decane	0.94	1.34	[6]
-	Tap water	H_20	1.03	0.97	-
DOW Europe GmbH	Si-oil 10	Silicone oil 10 m·Pas	10.29	0.36	[7]
DOW Europe GmbH (mixture)	Si-oil 71	Silicone oil 71 m·Pas	69.06	0.19	-
DOW Europe GmbH	Si-oil 100	Silicone oil 100 m·Pas	105.88	0.04	[8]
Sigma-Aldrich	PEG 400	Polyethylene glycol	117.87	0.02	[9]
DOW Europe GmbH	Si-oil 1000	Silicone oil 1000 m·Pas	1071.60	0.27	[10]

In order to achieve a better understanding of the comparisons made in the following, the viscosity curves of the test fluids are illustrated in Figure 1. Particular attention is drawn to the fluid groupings i) tap water & n-Decane at 1 mPa·s, as well as ii) PEG 400 & Si-oil 100 at around 100 mPa·s. Due to the almost identical to closely related viscosity within their respective grouping, differences in the compaction behaviour cannot be attributed to this parameter and could therefore indicate another influencing factor, such as polarity.

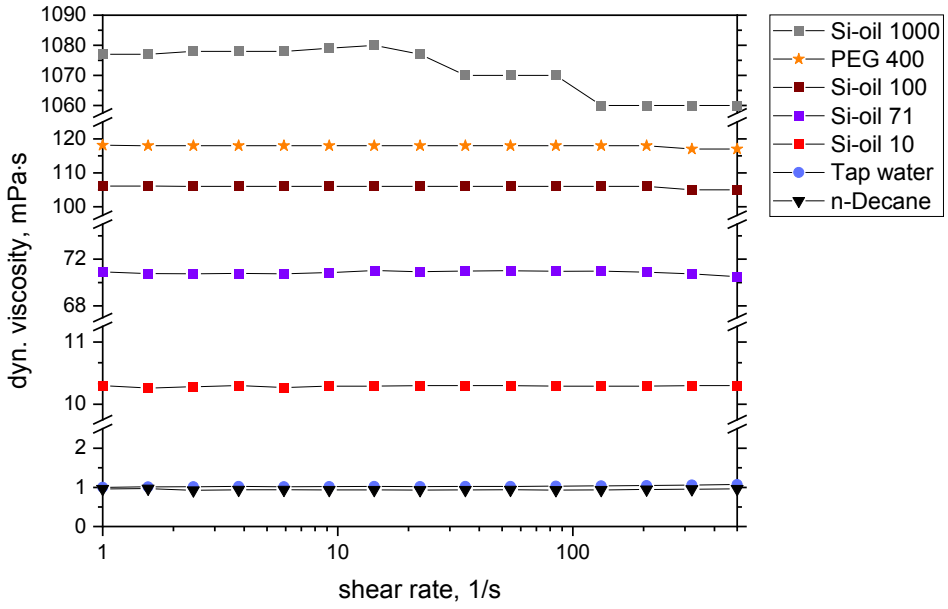


Figure 1. Dynamic viscosity of the test fluids in a shear rate range relevant for the applied in-situ impregnation method.

Figure 1 also shows that all fluids exhibit an almost constant dynamic viscosity within the measuring range, with the sole exception of Si-oil 1000, which shows a small drop at higher shear rates. This however can be attributed to the test method, in which a modular compact rheometer from Anton Paar, type MCR 501, was used in combination with a double-slit measuring system, specifically DG26.7/T200/AL, in accordance with DIN 54453 [11] and ISO/WD 3219-2 [12]. The use of this double-slit measuring system enables the measurement of dynamic shear viscosity in a wide range, especially for fluids with very low viscosity values, e.g. water and n-Decane. However, the measurement data sheet for DG26.7/T200/AL [13] states, that this method is only applicable for fluids with a viscosity of less than 200 mPa·s, which may explain a change in the result for increasing shear rates.

Both textiles were tested with all liquids using the in-situ impregnation method [1], as detailed in Figure 2. This method allows to test the effects of fluids of different viscosity and polarity on textile structures with different fibre bundle fixation to gain a deeper understanding of the underlying mechanisms.

In order to ensure comparability with each other and with the results of the IBE, the dry and the wet stress relaxation phase were set at 1800 s [3]. Furthermore, the impregnation phase was selected so that complete impregnation at 2 bar injection pressure was achieved under the plunger, which was indicated for all fluids after 900 s at the latest by a fluid outflow over the entire circumference of the plunger. For the Si-oil 1000 the impregnation phase had to be extended to 1800 s due to the high viscosity and thus slow impregnation of the test specimen. Due to limited fluid quantities, especially of n-Decane and Si-oil 10, it was not possible to use the longer impregnation phase for all fluids.

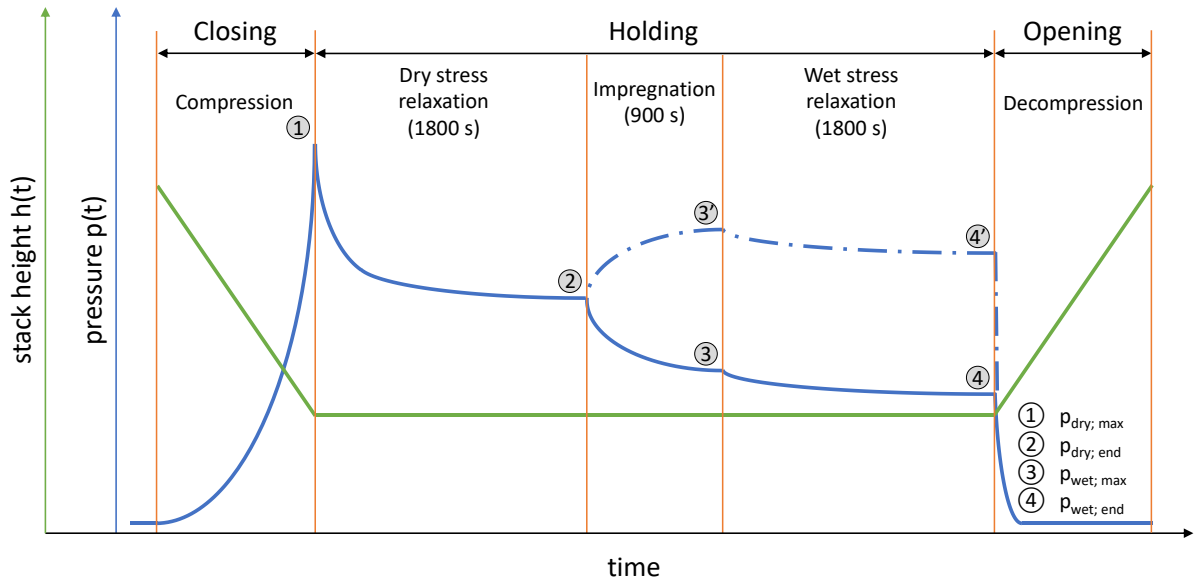


Figure 2. Schematic in-situ impregnation method and characteristic points during the test as detailed in [1]. Paths 3 and 3' show two possible pressure responses to the impregnation of a specimen with a test fluid. The exact characteristic of the measured behaviour depends on the respective fixation of the fibre bundles (textile structure) as well as the viscosity and polarity of the test fluid.

The test specification regarding the specimen were adopted from the IBE for both fabrics, test specimen of 14 layers each with 120 mm x 120 mm were prepared, which enables direct comparability within the measurement series and with the IBE [3].
In order to reduce the negative influence of manual movement during the stacking process and thus reduce the scattering of the tests, 7 layers of textiles were simultaneously cat by a CNC-based cutting system (Zünd Systemtechnik AG, type G3) and stacked uniformly in a 7+7 configuration.
All test fluids were degassed at 0.05 bar pressure for one hour, to avoid any effect of air bubbles during the impregnation stage. Furthermore, the injection set-up was completely disassembled and thoroughly cleaned, and all fluid lines were replaced while changing test fluids, to avoid any cross-contamination.
Before each test every specimen was weighed and its FAW was calculated. The average results are listed in Table 1. The specimen was then transferred to the thoroughly cleaned test area and the testing procedure was started. After each test the saturated weight of every specimen was also noted, as any significant change would indicate a measurement error such as dry spots or fibre wash-out.
For each fluid and textile combination, a set of ten successful in-situ impregnation tests were conducted. Obvious measurement errors such as a premature start of impregnation due to a leaking magnetic valve or insufficient fluid quantity in the pressure pot were declared as incorrect and not evaluated.

3. Results

It is known that the relationship between the fibre volume fraction (FVF) and the compression pressure follows a power law equation [14]. For this reason, even small fluctuations in the dry weight and thus the FVF at a certain gap height, especially at high FVF, lead to large variations in the compaction pressure. As an example,
Figure 3 displays all individual test data of the relaxation behaviour of both textiles with tap water and n-Decane as test fluids. One way to reduce the effects of these fluctuations and improve the conclusion drawn is to normalize the pressure data by the maximum compacting pressure $p_{dry;\,max}$, or point ① as shown in Figure 2. This does not change the qualitative character of the statement, but increases the distinctness of small effects by suppressing a significantly larger basic variation.

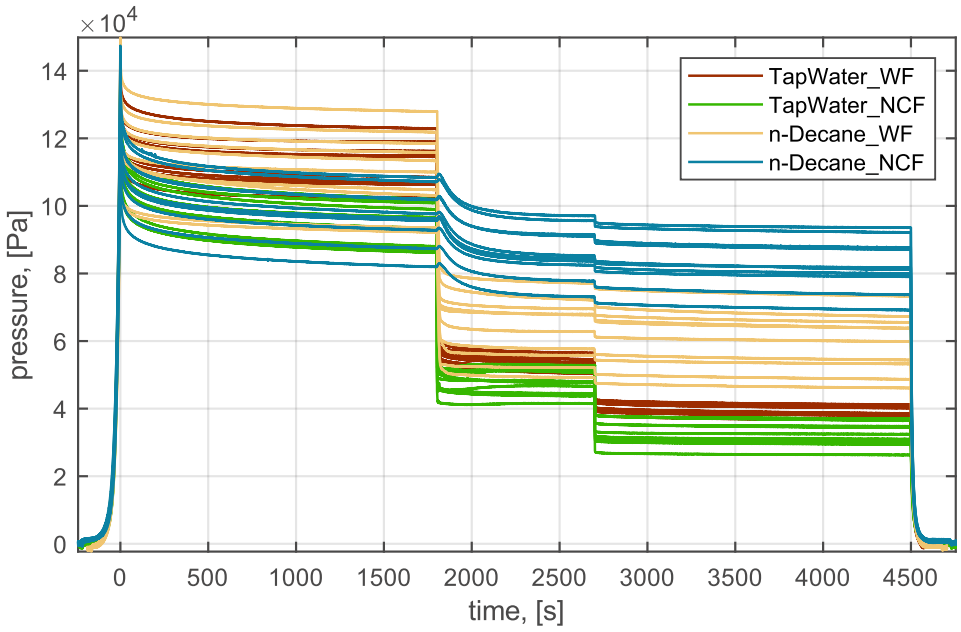


Figure 3. Individual relaxation characteristics of both textiles with tap water and n-Decane as test fluids.

It becomes clear, that due to the considerable scatter of $p_{dry;\,max}$ not all four characteristics can be distinguished. However, if all relaxation measurements are normalised to their respective $p_{dry;\,max}$, as shown in Figure 4, subtle details can be recognized. For this reason, only the normalised pressure characteristics are shown in the following.

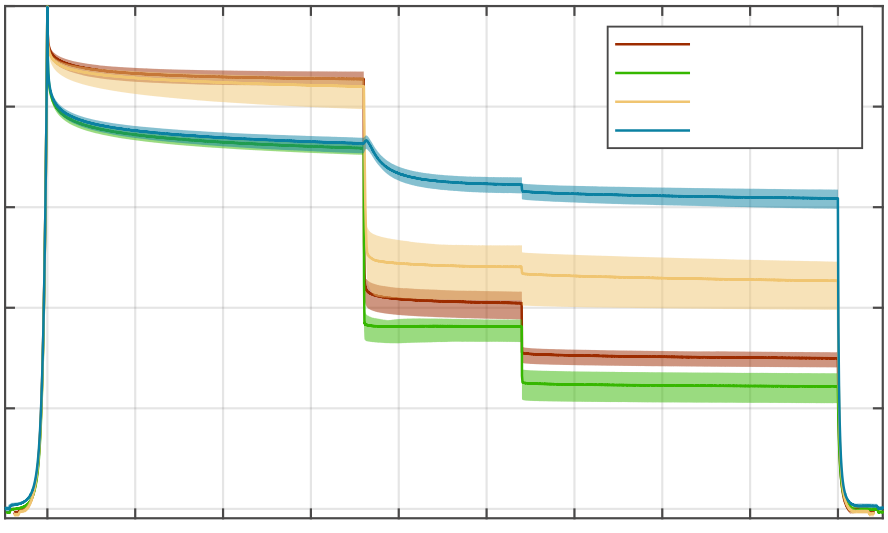


Figure 4. Min-max-envelopes of the relaxation characteristics of both textiles with tap water and n-Decane.

©2024 | <Sans lien d'intersection>

As expected, the dry compressibility behaviour is identical for both textiles, with only very small min-max deviations from the arithmetic mean, which are characterised by the coating and the relative dry relaxation, which is about twice as high for the NCF. This changes drastically with the start of impregnation. For the WF, there is an immediate drop in pressure for both fluids with a fluid viscosity at around 1 mPa·s, with tap water showing a slightly higher relaxation. However, this does not apply to the NCF. The combination NCF and tap water shows a relative relaxation comparable to that of the WF with tap water. Opposite to this the combination NCF and n-Decane shows a relative relaxation which is significantly lower, compared to the combination WF and n-Decane, and even shows a slight pressure increase at the start of impregnation phase. It also takes considerably longer to reach pressure equilibrium during the impregnation phase. In addition, the pressure drop at the end of the impregnation phase is significantly lower with n-Decane than with tap water. Overall, tap water leads to lower $p_{wet;\,end}$ values than n-Decane with approximately the same remaining pressure level of around 25-30% for both textile structures. In comparison, impregnation with n-Decane leads to drastically different results for different textile structures, not only in the relaxation behaviour during impregnation, but also in the remaining pressure level of about 45% for NCF and 60% for the WF.

Increasing the fluid viscosity from 10 mPa·s to approximately 100 mPa·s changes the results significantly, as can be seen in Figure 5.

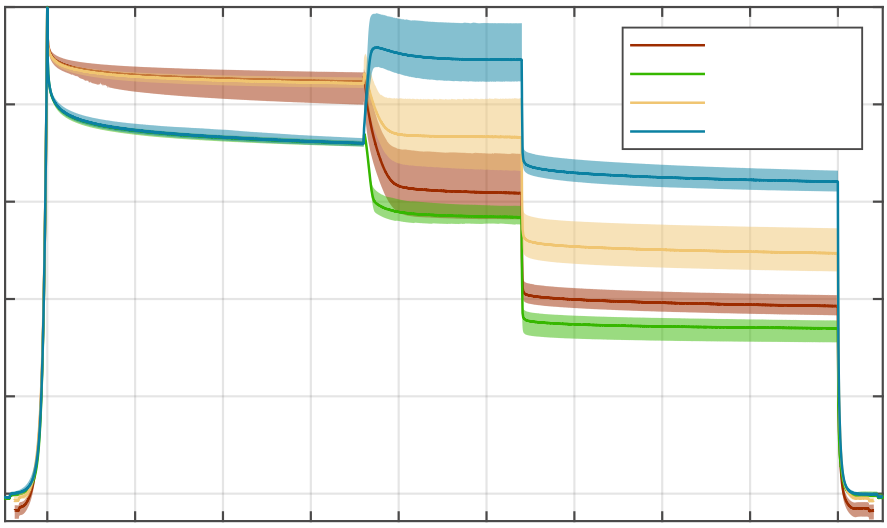


Figure 5. Min-max-envelopes of the relaxation characteristics of both textiles with PEG 400 and Si-oil 100.

It becomes clear, that only the combination of the non-polar silicone oil with NCF leads to an increase in relative pressure during the impregnation phase. This increase for NCF and Si-oil 100 is most likely due to opposing effects of textile relaxation due to nesting and fibre reorientation and the build-up of a pressure field in the impregnated areas. The other three combinations again show a drop in relative pressure after the start of impregnation, as the pressure release due to a lubrication effect is significantly greater than a pressure increase due to the build-up of a pressure field in the compressed area. The total pressure release of the combination of Si-oil 100 and NCF could most likely also be achieved dry relaxation over the whole test time, while a significant lubrication effect can be recognised in all other combinations.

This leads to an interesting result, because although NCF showed the highest relative relaxation during the initial dry relaxation phase, the significantly different behaviour during the impregnation phase leads to NCF showing the highest and also the lowest relaxation characteristics of the four combinations, only depending on the test fluid.
In addition, a further effect can be observed due to the increased fluid viscosity, as this is equivalent to a slower flow front propagation. Due to the generally lower permeability of the WF compared to the NCF, it takes longer to reach pressure equilibrium, which was less pronounced at lower viscosity, but is now clearly visible.

In addition to comparative measurements of two fabrics in combination with four fluids, the relaxation characteristics of the WF with four silicone oils with viscosity of 10 .. 1000 mPa·s were compared. As the high viscosity of Si-oil 1000 meant that complete impregnation was not fully achieved during the impregnation phase under the stamp, it was extended to 1800 s. Figure 6 shows the results of these tests.

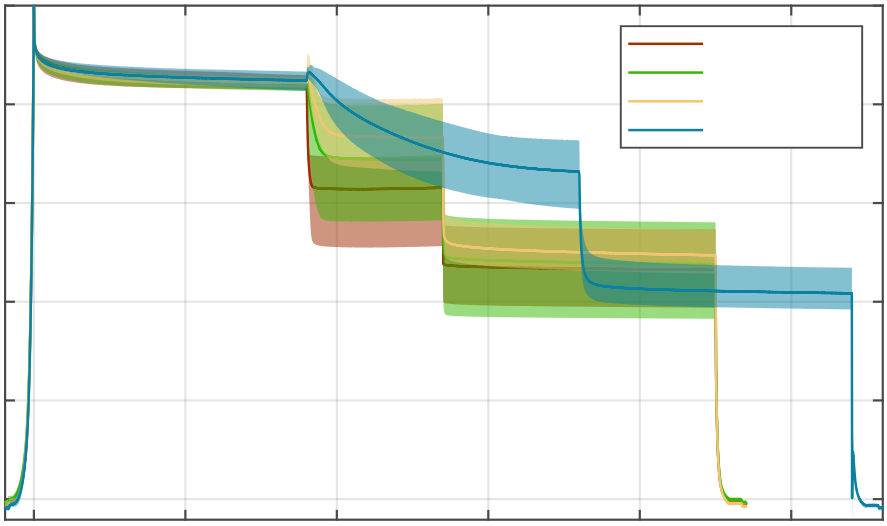


Figure 6. Min-max-envelopes of the relaxation characteristics of the WF with all four silicone oils, Si-oil 10, Si-oil 71, Si-oil 100, Si-oil 1000, spanning two decades of fluid viscosity, without significant differences is fluid polarity.

There is no significant difference in $p_{wet;\,end}$ for all four fluids, although their respective viscosity differs significantly. However, as the viscosity of the fluid increases, the time until pressure equilibrium is reached increases. Furthermore, it can be seen that there is no significant difference in the remaining pressure level at the end of the test, even though the test time for one fluid was increased by 20%. It can be deduced that there is no residual nesting potential after the introduction of the silicone oil, which acts as a lubricant, as soon as pressure equilibrium is reached in the impregnation phase.

4. Conclusion

A qualitative analysis of the in-situ relaxation characteristics of two textile structures with eight different test fluids was conducted. The relaxation characteristics during the different stages of the in-situ impregnation method were compared in each case of two fluids with comparable viscosity, but significantly different polarity. It became clear that even though the fluid viscosity within the

groupings were very close, significantly different relaxation behaviours could be observed, which must be caused by another fluid property, most likely polarity. This is especially pronounced for NCF, as very little up to a high relative pressure relaxation can be observed, which is not the case for the WF, as differences in fluid polarity result in only minor relaxation differences.
Also, the impregnation characteristics of four silicone oils with comparable polarity, but viscosity spanning two decades were analysed. In this case three aspects became obvious. First of all, the relative relaxation during the impregnation phase decreased with increasing fluid viscosity, while overall relative relaxation at the end of the wet holding phase was almost identical. Second, the time necessary to reach a pressure equilibrium during the impregnation stage increases with higher viscosity. Third, the remaining relative pressure level seems to be independent on the fluid viscosity and previous relaxation characteristics.
As the qualitative analysis has shown interesting, novel aspects of the influence of fluid properties on transverse fabric compressibility during in-situ impregnation, a quantitative study with the aim to develop a theoretical model to predict textile behaviour should be conducted.

References

[1] Bender M, Fauster E (2023) Novel test-rig for compaction behaviour analysis of textile reinforcements for improved RTM-process replication. Advanced Manufacturing: Polymer & Composites Science 9(1). doi:10.1080/20550340.2023.2263828
[2] JEC Observer: Overview of the global composites market 2023-2028 (2024). JEC Composites Magazine. JEC, 251 Boulevard Pereire, 75017 Paris
[3] Yong A, Aktas A, May D, Endruweit A, Lomov SV, Advani S, Hubert P, Abaimov SG, Abliz D, Akhatov I, Ali MA, Allaoui S, Allen T, Berg DC, Bickerton S, Caglar B, Causse P, Chiminelli A, Comas-Cardona S, Danzi M, Dittmann J, Dransfeld C, Ermanni P, Fauster E, George A, Gillibert J, Govignon Q, Graupner R, Grishaev V, Guilloux A, Kabachi MA, Keller A, Kind K, Large D, Laspalas M, Lebedev OV, Lizaranzu M, Long AC, López C, Masania K, v. Michaud, Middendorf P, Mitschang P, van Oosterom S, Schubnel R, Sharp N, Sousa P, Trochu F, Umer R, Valette J, Wang JH (2021) Experimental characterisation of textile compaction response: A benchmark exercise. Composites Part A: Applied Science and Manufacturing 142:106243. doi:10.1016/j.compositesa.2020.106243
[4] Hexcel Corporation (2020) HexForce 01202 TF970; Technical Data Sheet
[5] SAERTEX GmbH & Co. KG (2023) X-E-302g/m²-1270mm; Technical Data Sheet
[6] ROTH (2015) n-Decane ROTICHROME(r) GC
[7] DOW (2017) XIAMETER™ PMX-200 Silicone Fluid, 10 cSt
[8] DOW (2017) XIAMETER™ PMX-200 Silicone Fluid, 100 cSt
[9] Sigma-Aldrich (2021) Polyethylene glycol 400 for synthesis
[10] DOW (2017) XIAMETER™ PMX-200 Silicone Fluid, 1000 cSt
[11] DIN Deutsches Institut für Normung e. V. (1982) Prüfung von Metallklebstoffen und Metallklebungen: Bestimmung der dynamischen Viskosität von anaeroben Klebstoffen mittels Rotationsviskosimetern [zurückgezogen], Berlin. Beuth Verlag GmbH (DIN 54453:1982-01). Accessed 12 December 2023
[12] DIN Deutsches Institut für Normung e. V. (1994) Polymere/Harze in flüssigem, emulgiertem oder dispergiertem Zustand: Bestimmung der Viskosität mit einem Rotationsviskosimeter bei definiertem Geschwindigkeitsgefälle, Berlin. Beuth Verlag GmbH 83.080.10(EN_ISO_3219:1994). Accessed 12 December 2023
[13] Anton Paar GmbH Measuring System Data Sheet: DG26.7/Q1 - SN36535. 3338, Ostfildern
[14] Pearce N, Summerscales J (1995) The compressibility of a reinforcement fabric. Composites Manufacturing 6(1):15–21. doi:10.1016/0956-7143(95)93709-S

MICROMECHANICAL PROPERTY CHARACTERISATION OF WATER ABSORPTION IN CARBON FIBRE EPOXY COMPOSITES USING NANOINDENTATION

Jasmine Bone[1], Hannah Zhang[2] and Stefanos Giannis[2]

[1]School of Mechanical Engineering Sciences, Faculty of Engineering and Physical Science, University of Surrey, Stag Hill, Guildford, Surrey, UK
Email: jasmine.bone@surrey.ac.uk, Web Page: https://www.surrey.ac.uk/people/jasmine-bone
[2]National Physical Laboratory, Hampton Road, Teddington, Middlesex, UK

Keywords: polymer composite, durability, diffusion, nanoindentation, interphase

Abstract

Polymer composite material properties such as strength and stiffness can be degraded over time due to moisture absorption. While macroscale mechanical tests exist to measure the change in bulk properties due to moisture, the microscale effects of moisture diffusion have not been well characterised. This insight would allow better modelling of degradation. To characterise this on a micromechanical level, unidirectional carbon fibre epoxy composites were immersed in water at elevated temperatures to simulate accelerated ageing, and a method has been developed using nanoindentation to measure changes in hardness, modulus, and viscoelastic behaviour at various depths through the material's thickness. These micromechanical results were correlated with macroscale mechanical tests (four-point bend flexure) and optical microscopy to assess microstructural changes over time. The findings highlight the micromechanical response of carbon fibre epoxy composites to water uptake, providing deeper insights into degradation mechanisms. This knowledge is essential for developing predictive models and optimising the design of composite structures for improved durability in various environments.

1. Introduction

Carbon and glass fibre epoxy composites are commonly used in structures that require a resistance to environmental degradation, such as in marine, offshore, construction or aerospace applications, where their performance can degrade due to moisture absorption [1], [2], [3]. Understanding these degradation mechanisms in different environments is crucial for durability assessment and good predictive modelling of lifetime. Traditional accelerated ageing tests for polymers evaluate the rate of diffusion through the material [1], [4], [5], [6], [7], but do not fully explain how moisture uptake degrades these materials.

The absorption of water in polymer and polymer composite materials has been found to reduce the strength and the glass transition temperature (T_g) [8], [9], [10], due to a decrease in molecular friction, increased mobility of the polymer chains, and therefore plasticisation of the polymer matrix. This plasticisation is often reversible, and the properties are recovered once moisture is removed. Epoxy polymers are hydrophilic due to the presence of polar groups on the polymer chain available for hydrogen bonding [11], but more permanent chemical degradation is possible due to hydrolysis. In polymer composite materials, carbon fibres are typically considered to be inert to chemical degradation, whereas E - glass fibres have been shown to be susceptible to degradation due to moisture exposure where there is leaching of alkali oxides from the fibre surface [8].

Previous research on a carbon fibre epoxy composite material suggests moisture absorption causes significant degradation at the fibre-matrix interface, reducing the bulk flexural strength and modulus [12]. This has been evidenced by scanning electron microscopy analysis of the fracture surfaces after failure in mechanical testing, where fibre – matrix adhesion is disrupted after prolonged exposure. However, this is only a qualitative measure, therefore micromechanical testing is required to determine a more quantitative measure of degradation around the interface, and through the thickness of a material.

Nanoindentation has been shown to be an effective tool for assessing the viscoelastic and mechanical properties of materials and has shown use for assessing the composite interface and interphase regions [13]. One recent study uses this technique to investigate the through thickness micromechanical property characterisation to assess the manufacture of CF/PEKK composites under either automated tape placement or compression moulding [14]. The method enables indents in an array at various locations through a composite cross section to evaluate the differences in hardness and elastic modulus in the bulk resin and close to the fibre surfaces, in this interphase region.

In this research, specimens of a unidirectional carbon fibre epoxy composite pultrusion were subjected to an accelerated ageing regime, using immersion in water at elevated temperature. Testing through the thickness was then conducted using nanoindentation on different locations through the cross section of the composite material. The nanoindentation results are complemented by macroscale mechanical testing (four-point bend flexure) and optical microscopy to correlate changes in mechanical properties with variations at the microstructural level, through the thickness of the material, as well as compared between materials exposed for increased exposure times. Measurement of the micromechanical response of carbon fibre epoxy composites to water uptake offers a more nuanced understanding of the underlying degradation mechanisms. This improved understanding is required for the development of predictive models for the mechanical performance of these materials due to exposure to moisture, aiding in the design and optimisation of composite structures for enhanced durability.

2. Materials and Methods

2.1. Materials

For this work, an Easycomposites unidirectional (UD) pultruded carbon fibre epoxy resin strip with dimensions 2 mm thickness, 12 mm width and 2 m long has been used. This material was purchased from the manufacturer's agent.

All test specimens were cut to size from these strips prior to exposure using a CompCut diamond saw. The material was tested as received as well as the conditioned state following accelerated ageing procedures. For the Easycomposites material the specimens only had two cut surfaces at the end of the strips, transverse to the length, due to the pultrusion width being suitable for testing.

2.2 Accelerated ageing

Composite specimens were immersed in a water bath in distilled water at 60°C in a Grant GD120 bath. Specimens were immersed for pre-determined time intervals of 28 and 84 days, with the moisture content determined by gravimetric measurements. This procedure was based on guidance for water absorption in plastics from ISO 62 [15]. Specimens were removed from the water bath, surface water dried off, and each weighed prior to either returning to the water bath immediately or storing in deionised water at room temperature prior to testing within 72 hours. The moisture content of the specimens was calculated as a weight percentage of the material (Equation 1):

$$Moisture\ content(\%) = \frac{m_w - m_d}{m_d} \times 100\% \quad (1)$$

Where m_w is the mass of the aged specimens, and m_d is the mass of the unaged specimens prior to any testing. It has been assumed that there is no mass change due to leaching from the specimens.

2.3 Macroscale mechanical testing

Four-point bend flexure tests were conducted following BS EN ISO 14125 [16]. Tests were carried out on an Instron 4507/5570R machine with a 20kN load cell. The test speed was at 2 mm/min, and the test spans were 81 mm and 27 mm. The specimens were placed on the four-point bend fixture with a linear variable displacement transducer (LVDT) mounted underneath the central span to measure the deflection due to flexure in the centre of the bending beam. This enabled determination of both the flexural strength and flexural modulus of the unaged and aged composite specimens. Specimens for this test were cut to dimensions 2mm × 12 mm × 100 mm as per the standard recommendations using a CompCut diamond saw.

2.4 Micromechanical testing: Nanoindentation

Samples measuring approximately 10 mm in length (12 mm width and 2 mm thick) were cut from the pre-immersed CF epoxy strips with a hand saw and were mounted in epoxy resin, exposing the cross-section of the laminate. These were polished with silicon carbide discs, followed by diamond suspension polishing down to 1 µm particle size. The nanoindentation tests were performed using a UNHT CSM Nanoindenter, with a diamond Berkovich-type indenter tip.

Load – unload indentation cycles were performed at a frequency of 10 Hz, load rate of 4 mN/min, to 400 nm depth, and a dwell period of 30 s, in order to produce indents of a 2 – 3 µm diameter size; this was to ensure indents smaller than the comparable 10 µm fibre diameter. This was influenced by the nanoindentation method used by Perez et al. [14]. The elastic modulus and hardness values were then determined using the load – displacement curves, from the method defined by Oliver and Pharr [17].

All samples were indented as marked in Figure 1. Each sample was indented at four locations, from the top edge of the cross section, approximately 50 µm from the edge, through to approximately 350 µm, 650 µm, and finally to the centre at 950 µm into the cross section. At each location, a series of indentations were performed: two individual indents on resin rich areas to measure the bulk matrix hardness and elastic modulus, two individual indents on the fibres to measure the same for the fibres, and finally a 5 x 5 array of indentations to obtain hardness and elastic modulus values of the composite material. A micrograph using an optical microscope was taken of each location.

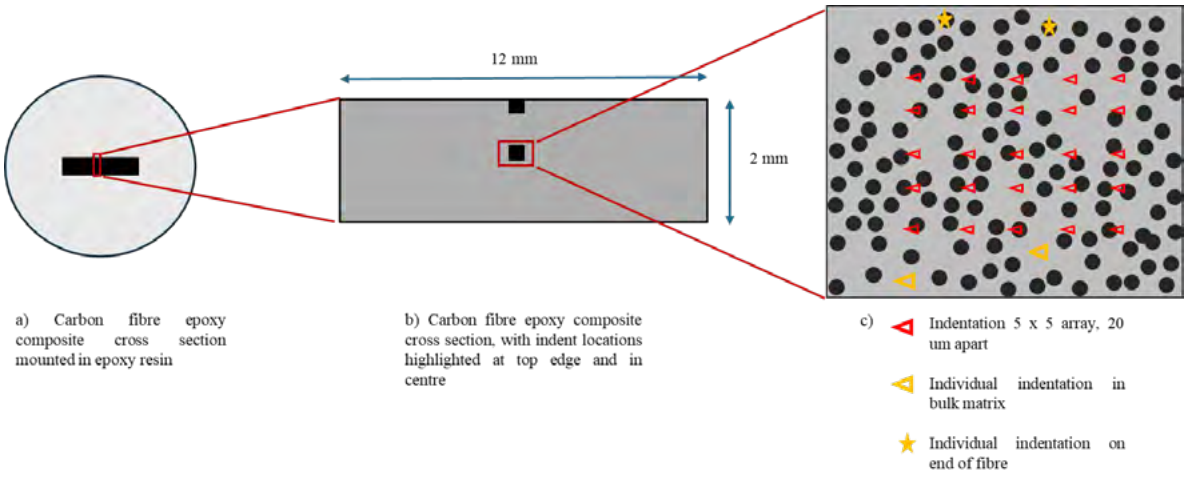


Figure 1 *Schematic example of the indentations performed on the carbon fibre epoxy composite cross section, showing the individual bulk matrix and fibre indents, the 25 indents in an array, and the location of these indents at both the top edge and the centre of the cross section*

3. Results and discussion

3.1 Accelerated ageing

The results of the accelerated ageing tests, as further discussed by this author in a previous paper [12] and reproduced in Figure 2, show how as moisture content increases, the flexural strength and flexural modulus of the carbon fibre epoxy composite material were reduced, as was the glass transition temperature (T_g). Microscopy suggested that interfacial degradation due to moisture absorption was the likely cause of this, therefore nanoindentation could provide further insight into this degradation.

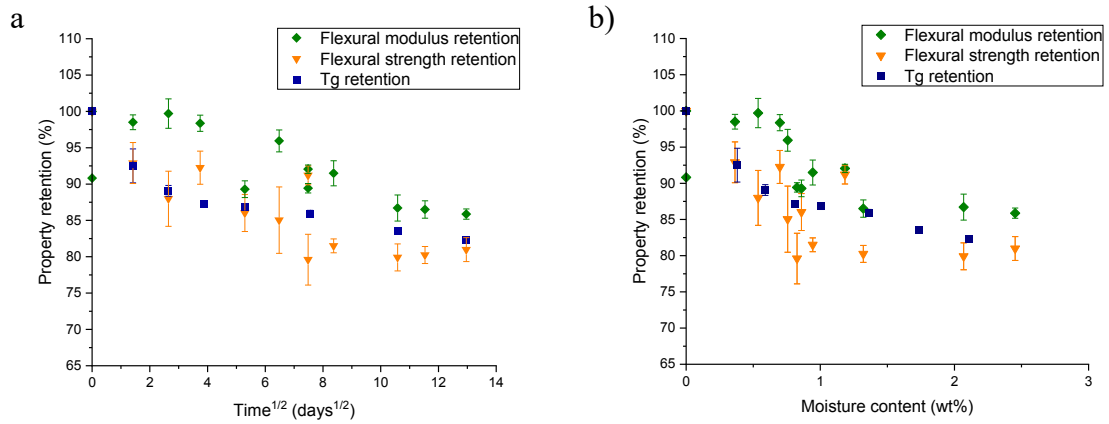


Figure 2 *Changes in material properties of the carbon fibre epoxy composite with increase exposure time, and increase in moisture content* [12]

3.2 Nanoindentation: load – displacement curves

The load – displacement curves from the nanoindentation tests are shown in Figure 3. These show three distinct regions for the responses of either “matrix”, “interphase”, or “fibre”, as measured by the initial individual indentations at specific matrix and fibre locations to establish these bounds of the measurements. Indentations from the 5 × 5 array may be assigned any of the three measurement responses, depending on if the indentation is made in a bulk matrix area, on a fibre, or in a matrix region but close in proximity to a fibre surface.

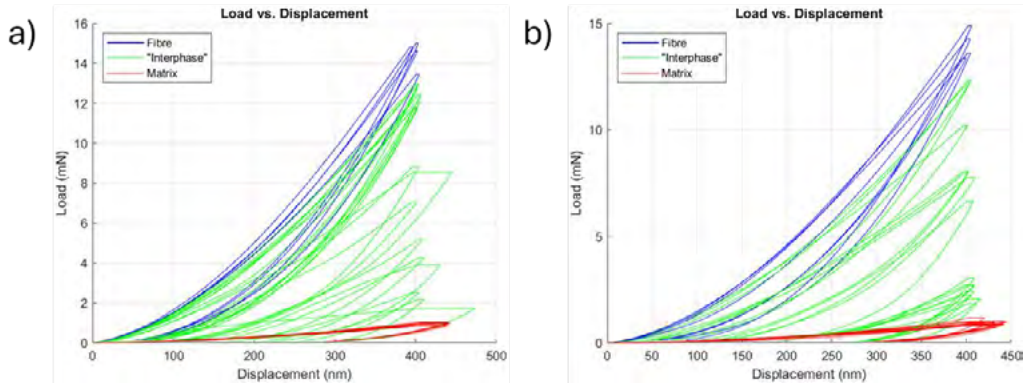


Figure 3 *Load – displacement from indents in the unaged carbon fibre epoxy composite, a) at the top edge and b) in the centre of the cross section.*

The fibres show a stiffer response and have the largest elastic recovery, as was found by Perez et al [14]. Additionally, the fibres showed a higher load response of 13 – 15 mN. Due to this elastic response, no indentations were left permanently in the fibres, which is why no indents are visible in the fibres on the micrographs of the indentation arrays. In contrast, the indents in the matrix regions are clearly observed in the images in Figure 4.

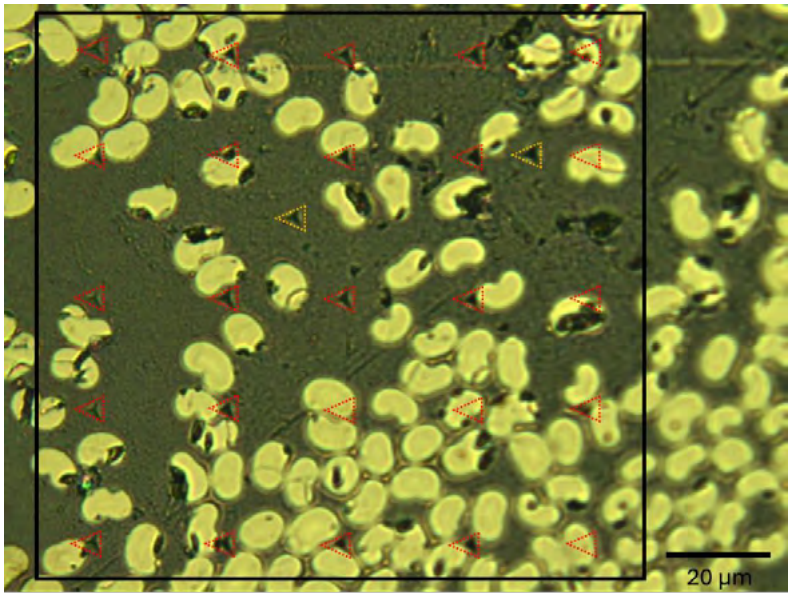


Figure 4 Micrograph of unaged carbon fibre epoxy composite cross section, with the 5 x 5 indentation array highlighted in red, and the matrix indents highlighted in orange.

Unlike the fibres, for the matrix behaviour, which is the bulk matrix response where indents resulted in similar load – displacement curves, there is a clear hysteresis loop which is due to the viscoelasticity in the polymer. This can be seen in Figure 3, where the load – displacement plot shows that the indent depth is retained at 280 - 320 nm, after the indenter tip has been withdrawn. In contrast to the fibres, the load response for the bulk matrix was much lower, at 0.8 – 1.2 mN.

The regions labelled as “interphase”, are those where the response is clearly neither bulk matrix or fibre but within a range of mechanical results, with hardness values between 0.3 and 5.5 GPa, and a load response over a range over 1.2 mN and less than 13 mN, due to close proximity to a fibre surface. While still indenting into a resin matrix area, these indents show a stiffer response than the bulk matrix due to this fibre proximity. Comparable results have been found for polymer composite materials in the

literature, where the distinction between matrix, interphase and fibre responses is clear [14], [18]. In this work, for all indentation locations in the sample, and across the variously aged samples, this response of fibre, bulk matrix, and interphase was observed in the load - displacement curves.

3.3 Nanoindentation: mechanical property results

When comparing the measured hardness and modulus values for indents on each sample at different locations, the results are mixed. The average hardness and modulus values for the bulk matrix are shown in Table 1. Firstly, for the unaged specimen, the values measured at the top edge were 0.24 GPa hardness and 4.50 GPa elastic modulus. At the centre of the specimen, the values were 0.22 GPa hardness and 5.44 GPa modulus. It may have been expected that the properties through the specimen would be of equal value, however the measured discrepancy shows the microscale differences in material properties, which could be attributed to variations in polymer crystallinity due to the manufacture process. However, the measurements of bulk matrix hardness and modulus were averaged only over a small number of indentations, and the modulus values show a larger error.

Table 1. Hardness and elastic modulus results from nanoindentation tests on CFRP samples

Specimen	Hardness (GPa)	Modulus (GPa)
Unaged top	0.24 (± 0.013)	4.50 (± 0.22)
Unaged middle	0.22 (± 0.017)	5.44 (± 1.46)
28-day aged top	0.22 (± 0.011)	4.83 (± 0.72)
28-day aged middle	0.23 (± 0.010)	4.90 (± 0.75)
84-day aged top	0.21 (± 0.006)	4.85 (± 0.81)
84-day aged middle	0.20 (± 0.042)	4.47 (± 0.83)

For specimens that had been immersed in water for 28 days, the bulk matrix hardness at the top edge of the specimen was 0.22 GPa, and modulus 4.83 GPa, whereas in the centre of the specimen was 0.23 GPa and 4.90 GPa for the hardness and modulus respectively. After a total of 84 days of exposure in water, the indentation results were 0.22 GPa hardness and 4.85 GPa elastic modulus at the top edge of the specimen, and 0.20 GPa hardness and 4.47 GPa modulus. The slight changes in values of the specimens exposed for 28 days show lower hardness and modulus at the tope edge compared to the middle, suggesting the water diffusion front was at a higher concentration at the surface and so reduced the mechanical properties compared to the centre. After 84 days immersion, the mechanical properties were reduced compared to 28 days, suggesting greater degradation due to moisture ingress, however it cannot be concluded that the indents show the reduction in mechanical properties through the thickness from the edge to the centre of the specimen.

The bulk mechanical properties after immersion in water for 28 days, when tested in flexure showed a reduction of 12% in strength, and 9% modulus with a 1wt% increase in moisture content [12]. After 84 days immersion, and a 1.5wt% increase in moisture, the properties reduced by 20% strength and 12% modulus. In previous work, when dried out to remove the water, flexural tests were repeated to ascertain the recoverability of these mechanical properties, or if moisture diffusion had caused a permanent degradation and therefore reduction in properties [19]. The results showed a permanent degradation in strength and modulus of 5% after 28 days immersion in water, and microscopy of the fracture surfaces indicated some interfacial degradation even after 7 days immersion in water. This supports the hypothesis from the nanoindentation results – where specimens are dry – that there is not only a permanent reduction in mechanical properties compared to unaged specimens but suggests a more nuanced understanding through the thickness of the material. However, due to small number of indents this is not particularly a statistically significant comparison, therefore further testing is planned for a larger array on indents, in addition to further analysis of the “interphase” indents in relation to their distance from the fibres and resulting hardness and modulus.

4. Conclusions

Nanoindentation is a useful tool for the micromechanical characterisation of through thickness properties in a polymer composite material. In this work, the nanoindentation tests supported bulk scale flexural tests results from previous work [12], where the moisture diffusion in a carbon fibre epoxy UD material caused a permanent reduction in strength and modulus. The nanoindentation tests indicated a reduction in bulk matrix properties from the top edge of the specimen cross sections to the centre due to moisture absorption, but it is not yet clear if this is indeed an effect of water uptake and the diffusion front, or if it is merely variations in the material crystallinity.

Therefore, further work is planned to relate the measured hardness and stiffness data to the distance of the indents from the fibre surface. This will better assess the "interphase" region and highlight the degradation in this region, as suggested by bulk testing and microscopy of fracture surfaces. This also requires improved image analysis. Additionally, further work has begun to increase the statistical relevance of the measured through thickness changes in hardness and modulus by using a NanoTest to conduct 20 x 20 indent arrays through the samples.

References

[1] P. Davies and Y. Rajapakse, *Durability of composites in a marine environment*, Springer International Publishing, 2014

[2] P. Davies and Y. Rajapakse, *Durability of composites in a marine environment 2*, Springer International Publishing, 2018

[3] L. C. Hollaway and J. Cadei, 'Progress in the technique of upgrading metallic structures with advanced polymer composites', *Progress in Structural Engineering and Materials*, vol. 4, no. 2, pp. 131–148, 2002

[4] J. M. Zhou and J. P. Lucas, 'Hygrothermal effects of epoxy resin. Part I: the nature of water in epoxy', *Polymer (Guildf)*, vol. 40, no. 20, pp. 5505–5512, 1999.

[5] M. Cavasin, M. Sangermano, B. Thomson, and S. Giannis, 'Exposure of glass fiber reinforced polymer composites in seawater and the effect on their physical performance', *Materials*, vol. 12, no. 5, 2019

[6] C. Humeau, P. Davies, and F. Jacquemin, 'Moisture diffusion under hydrostatic pressure in composites', *Mater Des*, vol. 96, pp. 90–98, 2016

[7] W. R. Broughton, B. C. Duncan, *Absorption and In Polymeric Materials,* NPL Measurement Good Practice Guide No . 102, 2007

[8] W. R. Broughton, A. S. Maxwell, *Accelerated Environmental Ageing of Polymeric Materials*, NPL Measurement Good Practice Guide No . 103, 2007

[9] A. Zafar, F. Bertocco, J. Schjødt-Thomsen, and J. C. Rauhe, 'Investigation of the long term effects of moisture on carbon fibre and epoxy matrix composites', *Compos Sci Technol*, vol. 72, no. 6, pp. 656–666, 2012

[10] N. Tual, N. Carrere, P. Davies, T. Bonnemains, and E. Lolive, 'Characterization of sea water ageing effects on mechanical properties of carbon/epoxy composites for tidal turbine blades', *Compos Part A Appl Sci Manuf*, vol. 78, pp. 380–389, 2015

[11] P. Alam, C. Robert, and C. M. Ó Brádaigh, 'Tidal turbine blade composites - A review on the effects of hygrothermal aging on the properties of CFRP', *Compos B Eng*, vol. 149, no. April, pp. 248–259, 2018

[12] J. E. Bone *et al.*, 'On the relationship between moisture uptake and mechanical property changes in a carbon fibre/epoxy composite', *J Compos Mater*, vol. 56, no. 14, pp. 2189–2199, Jun. 2022

[13] R. F. Gibson, 'A review of recent research on nanoindentation of polymer composites and their constituents', *Compos Sci Technol*, vol. 105, pp. 51–65, Dec. 2014

[14] H. Pérez-Martín, P. Mackenzie, A. Baidak, C. M. Ó Brádaigh, and D. Ray, 'Microstructural and micromechanical property characterisation of CF/PEKK composites using nanoindentation', *Mater Des*, vol. 234, Oct. 2023

[15] ISO 62: 1999, Plastics - Determination of water absorption

[16] ISO 14125. Fibre-reinforced plastic composites — Determination of flexural properties. 1998

[17] G.M. Pharr, W.C. Oliver, F.R. Brotzen, On the generality of the relationship among contact stiffness, contact area, and elastic modulus during indentation, *J. Mater. Res*. 7 (1992) 613–617

[18] A. Molazemhosseini, H. Tourani, M. R. Naimi-Jamal, and A. Khavandi, 'Nanoindentation and nanoscratching responses of PEEK based hybrid composites reinforced with short carbon fibers and nano-silica', *Polym Test*, vol. 32, no. 3, pp. 525–534, 2013

[19] J. Bone, *On the Effect of Accelerated Ageing and Moisture Absorption in Polymer Composites,* Doctoral Thesis, 2021

MECHANICAL BEHAVIOUR OF BAMBOO FIBRES AT THE MICRO SCALE BY APPLYING A DIGITAL IMAGE PROCESSING ANALYSIS

Carlos I. Cardona[1], Carlos A. Ibarra[2], David Ruch[3] and C.A. Fuentes[4]

[1] Luxembourg Institute of Science and Technology (LIST), Department of Materials Research and Technology, 5, rue Bommel L-4940 Hautcharage, Luxembourg
University of Luxembourg, Department of Physics and Materials Science, 2, place de l'Université L-4365 Esch-sur-Alzette, Luxembourg
Email: carlos.cardona@list.lu, Web Page: https://orcid.org/0000-0002-0825-4254
[2] Luxembourg Institute of Science and Technology (LIST), Department of Materials Research and Technology, 5, rue Bommel L-4940 Hautcharage, Luxembourg
Universidad Autónoma de Manizales, Experimental and Computational Mechanics Laboratory, Edificio Fundadores 17001, Colombia
Email: carlos.ibarram@autonoma.edu.co
[3] Luxembourg Institute of Science and Technology (LIST), Department of Materials Research and Technology, 5, rue Bommel L-4940 Hautcharage, Luxembourg
Email: david.ruch@list.lu, Web Page: https://orcid.org/0000-0001-8797-6820
[4]Luxembourg Institute of Science and Technology (LIST), Department of Materials Research and Technology, 5, rue Bommel, L-4940 Hautcharage, Luxembourg
KU Leuven, Department of Materials Engineering, Kasteelpark Arenberg 44/bus 2450, 3001 Leuven, Belgium
Email: carlos.fuentes@list.lu, Web Page: https://orcid.org/0000-0002-0766-9079

Keywords: Digital Image Analysis, Reverse Engineering, Natural Fibres, Failure Modes.

Abstract: The characterization of natural fibers, particularly in understanding their morphological features, and their influence in their mechanical behavior, faces several challenges. On the morphology perspective factors as aspect ratio, geometrical transitions of the organic geometry, presence of defects play a role in the material response. Moreover, the degree of crystallinity, molecular alignment, presence of amorphous regions and elementary fiber arrangement, too. Conventional methods for measuring natural fiber geometry, e.g. micro tomography, can be time-consuming, labor-intensive, and costly, involving complex sample preparation and data analysis procedures. These limitations become more pronounced when physics-informed models require extensive sources of smoothed geometrical data to accurately predict the behavior of natural fibers. An exploratory study was conducted in this work to study samples of bamboo fibers *Guadua Angustifolia* via fracture patterns 3D reconstruction, to provide insights into stress occurrence, fracture mode, crack propagation. This study employs a reverse engineering method, incorporating digital image analysis for measuring the fibers 3D geometry. A monitoring system was developed to reconstruct the fiber's fracture areas which were contrasted with the stress-strain functions and resilience. These findings indicate that the proposed approach can identify failure modes, opening avenues for advanced studies in fracture mechanics of natural fibers.

1. Introduction

The precise understanding of natural fiber's mechanical behavior is challenging given the intricate connection between the mechanical properties and geometry. Firstly, factors such as the variability in the cross section, defects induced from the fiber's extraction process may act as a source uncertainty in the mechanical characterization. Secondly, testing conditions such as gauge and span length can influence the probability that the fiber fracture at different points resulting in a challenge for studying mechanical stress evolution and fracture. Therefore, it is crucial to address with precision the nature of the variability in mechanical properties, whereas notably existing literature emphasizes significant

differences in the tensile strength of natural fibers of the same species and bunch, such as bamboo ranging from 391 to 700 MPa [1, 2]. This fact highlights the necessity of accurately creating 3D reconstructions of the fiber, particularly in the regions where fractures occur. These detailed analyses are made possible by the micro-scale robotized monitoring equipment developed for this research. Gaining a precise understanding of the variability in the mechanical properties of natural fibers is essential for identifying the true origins of failure. This knowledge is crucial for developing composite materials that incorporate natural fibers.

In estimating the mechanical properties of complex natural fibers, digital image correlation (DIC) analysis demonstrates potential for analyzing intricate behavior at the microscale, specifically in the context of elastic local behavior. However, DIC encounters challenges when estimating fracture metrics, as the misalignment that occurs during sample damage in tensile testing complicates the identification of patterns in the final failure mode [3, 4, 5]. These issues underscore the necessity of proposing methods that further complement the DIC technique in studying the fracture geometry of tested fibers. For instance, in the case of hemp fibers, strain maps obtained through the DIC technique indicate that fractures can occur at the interface, but the specific fracture areas could not be evaluated. Therefore, alternative approaches are needed to conduct tests that effectively monitor the damage shape, as fractures can occur at various points and no clear strategy currently exists for identifying damage patterns [5]. The Digital Image Correlation (DIC) technique, while widely used for strain measurement, faces certain limitations when it comes to analyzing fracture events. At the point of fracture, the rapid release of energy can pose challenges for the DIC system. To accurately capture the dynamics of fracture, the recording system requires a higher sampling rate, which can be achieved by using high-speed cameras. However, the use of high-speed cameras often necessitates additional hardware for data acquisition, increasing the complexity and cost of the setup.

While DIC has limitations in capturing the rapid dynamics of fracture, analyzing the fracture surfaces offers an alternative approach to understanding fracture modes without requiring high-speed cameras. Complementary to the DIC technique, the proposed methodology presents an opportunity to develop reverse engineering protocols assisted by image processing techniques. This study aims to correlate the fracture geometry with the fiber toughness.

2. Materials and Methods

2.1. Geometrical characterization of the samples

Bamboo technical fibers *Guadua Angustifolia* were selected bamboo for being studied by a robotized micro-scale geometrical characterization device was developed for the mechanical analysis of natural fibers in the frame of this project. Using this technology, a 3D reconstruction protocol was implemented for estimating volume shape applying a reverse engineering approach to generate a digital mesh of the fibre subsequently converted into a CAD model. The protocol was calibrated contrasting the measurements of one technical fibre of 580 μm average major diameter with a high-resolution tomography (voxel size:700 nm) equipment with 3% of relative error. For the calculation the cross section was measured and compared at 8 points of the length of the sample (See **Figure 1**).

The implemented 3D reconstruction method was applied to calculate an easier to handle geometry compared to micro-cT in terms of computational cost. A typical scan plus reconstruction of a 3D fibre using tomography specialized equipment should take 1.5 hours. Our scanning process using the developed technology reduces this time to (10-15 minutes). For the case of tomography, the resulting DICOM files conversion for obtaining a STL file geometry, mesh errors, overhangs and thin walls can put challenges in the verification and repair for getting the geometry. We point out that our purpose we are oriented to study the external volume and surface of the fibre. In that sense a protocol was implemented to defeature unnecessary details in the studied samples to increase the computational efficiency in the study of the geometry. Due to confidential reasons the process to obtain the mesh is not disclosed in the present manuscript. We point out that for this study the geometry of interest is the shape

external surface of the technical fibers without taking into consideration the middle lamella, elementary fibers, and lumens.

Once the fibre is scanned with our device scanning with triangle geometrical elements, a mesh regularization process is applied to smooth the geometrical transitions of the geometry. The generated mesh was assessed and regularized using Meshmixer software and repaired using Spaceclaim from Ansys 2024 r1 to provide a more homogeneous size of elements. This process was done fixing remaining crossed facets of the mesh and then applying automated skin surface generation. Then, the geometry is converted into a CAD model covered in the surface by the generated skin patches. The reduce the computational cost of the fibre model.

From the tensile tests that will be exposed in the section 2.2, samples of bamboo fibers 5, 9 and 15 were selected for stress-elongation analysis after exploratory experiment. A 2.0 mm extra length from each of the fibers was separated and 3D scanned for having the reference pristine cross-section measurement for each fiber. From the scanned length three cross sectional areas are measured at three different measuring planes over the skinned surfaces, with average diameters ($d1$=226 μm, $d2$= 119.45 μm) micrometers (See scanned samples and shapes in **Figure 2**). Considering the typical irregular cross-sectional shape of the fibers we point out the importance of properly recognize two diameters.

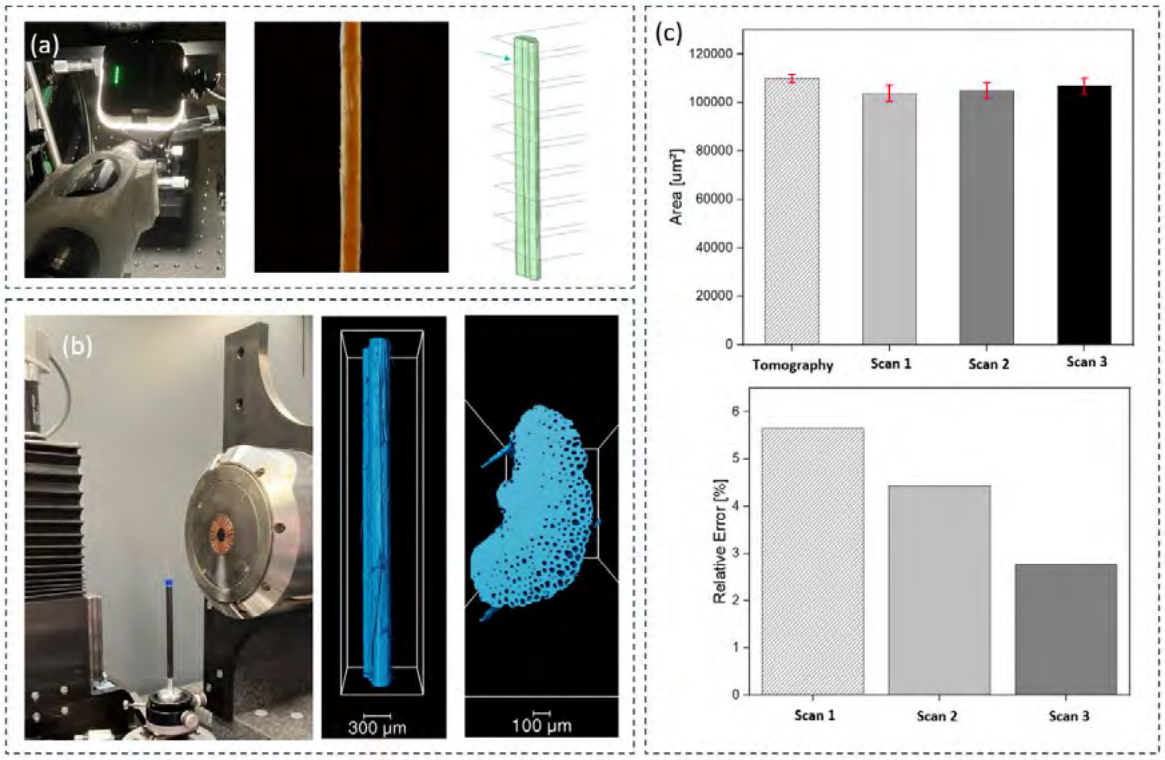


Figure 1. Calculation of the cross-sectional area of bamboo fibers. a) Geometrical measurements of the samples with the developed device. b) Comparison with micro-tomography. c) Comparison of cross-sectional area measurements between CT and the developed protocol.

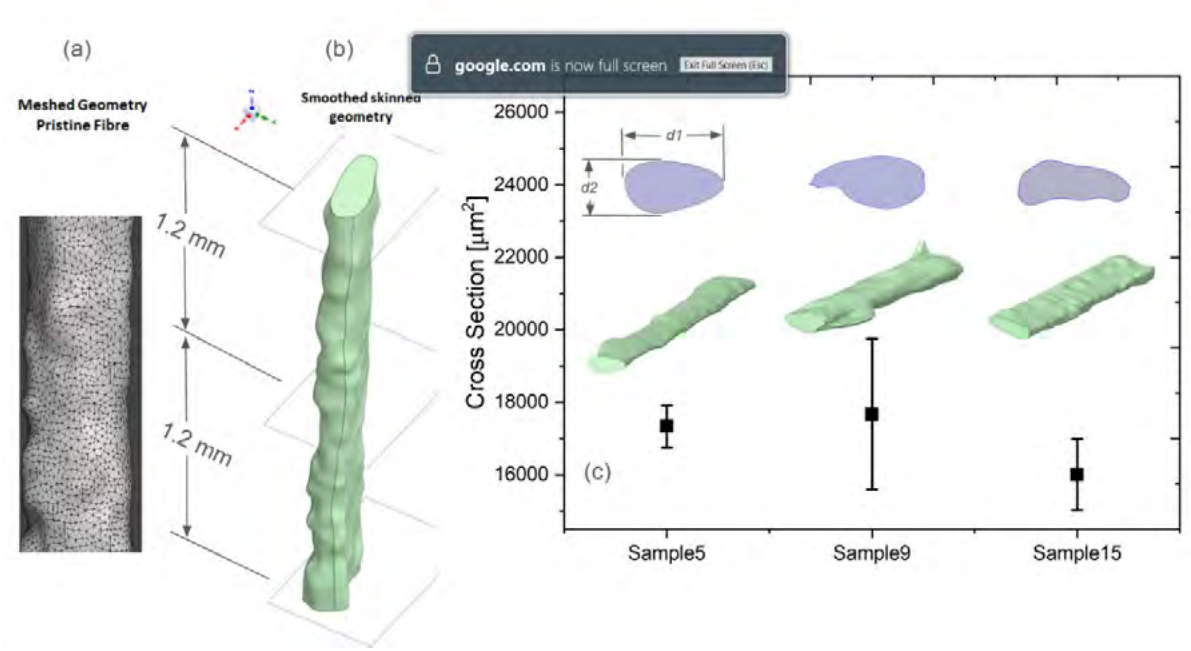


Figure 2. Cross sectional measurements applied in samples for stress-elongation analysis of section 2.2. a) Mesh obtained after measuring with the device). b) Reconstructed fiber skinned geometry c) Cross sectional area and cross sectional shapes for samples 5, 9 and 15.

2.2. Tensile tests and fracture digital reconstruction

A population of 20 bamboo technical fibers randomly selected were experimented in single fibres tensile testing ($d1$=226 μm, $d2$= 119.45 μm). From this population ten fibers were tested with a gauge length of 15 mm and other ten fibers with 20 mm. Following the initial analysis, nine technical bamboo fibers that presented similar trends in their force-displacement behavior were chosen among these for the calculations. We highlight that these samples did not present damage in the gripping zones and not slippage was evidenced in the tests.

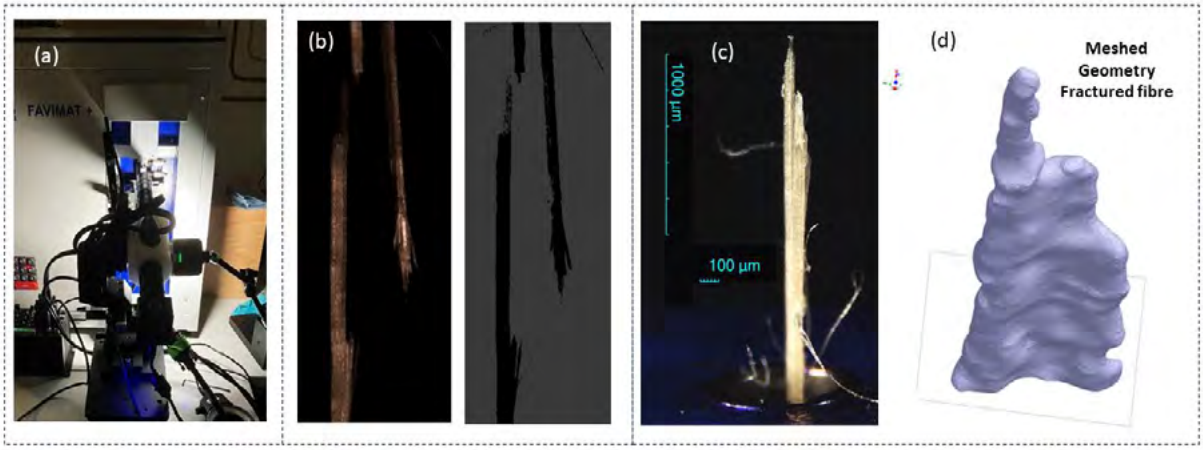


Figure 3. a) Tensile test and recording of the sample failure with the device. b) Image segmentation of the damage mode. c) Image of the fracture 2.4 um/ pixel d) Meshed geometry calculated with the implemented reverse engineering protocol.

The nine selected samples were categorized in tree groups as follows; Group 1 fibers were tested with a 15 mm gauge length and 23 mm span length, while Groups 2 and 3 fibers were tested with a 20 mm gauge length and 28 mm span length. All single-fiber tests were conducted using a TEXTECHNO FAVIMAT tensile testing machine equipped with a 3200 cN capacity load cell, a 0.2 mm/min load rate,

and Plexi polymer 4 mm gripping clamps. From each defined group one representative sample was selected for scanning the damage shape of the resulting damage mode for the 3D reconstruction of the damaged region were the fracture propagated. This selection enabled the categorization of fibers into three groups for 3D reconstruction of the damaged regions. Video recordings of the tests were taken to capture the resulting fractures, with the goal of determining the 3D reconstruction of the fiber at the tip after testing. An explanation of the process is depicted in **Figure 3**.

According to the sample shape, the fracture paths are determined in the CAD model obtained from the mesh. The generated skin divided into surfaces are used to cover the model. To represent the fracture paths and evaluate the area of influence.

3. Results and discussion

After executing the single fiber tests, the force-displacement functions up to the fracture force were obtained and gathered in three groups, as depicted in **Figure 4a**, **b** and **c**. The working hypothesis for the proposed methodology is that samples with similar cross sections and same testing conditions should exhibit a similar characteristic fracture pattern. The resulting testing conditions were established after testing 20 bamboo fibers chosen. The fibers passed the loop test applied to verify that each one did not have preexistent breaks as applied in the methodology for quality assessment of bamboo technical fibers used in epoxy composites samples for flexural characterization [3]. As can be seen in **Figures 4a group 1**, **4b** group 2 and **4c** group3 samples that presented similar force-displacement measurement concerning slopes were conveniently grouped. The sample that exhibited a clear fracture was chosen to be measured and as a representative sample from each group. For the case of the group 1 sample 5, in the group 2 sample 9 and from the group 3 sample 15, as shown in **Figure 4a**, **b** and **c**, respectively. One part of the divided fiber after the damage was chosen for the observation to see in detail the shape in microscope and having initial insights concerning the path in which the crack passes. In the case of samples 5 and 9 the ends these fibers seem to become more sharp suggesting that these shapes have defibrillation appearance with pulled out elementary fibers (see ref [3] description of elementary fibers). Distinctly, Sample 15 is showed to have asymmetric dome appearance at the tip suggesting that probably this fiber of damage was partially presenting defibrillation for the lateral right side see **Figure 4c**.

For each group, one sample was chosen in the group for a microscopic image-measurement with a resolution of 3.45 μm/pixel, to visualize the fracture shape. The morphology of bamboo fractures has been evidenced by SEM measurements as investigated by [3]**.** However, for the reverse engineering of the fracture and modeling purposes it is required to develop cost and time-effective geometry informed models to construct enough databases with smoother and easier to manage geometrical approximations.

Stress-strain function up to the failure was calculated for the selected fibers (samples 5, 9 and 15) and are represented in **Figure 5a** and using calculated cross section in the section in **Figure 2b**. for each sample. The tensile strength of these fibers resulted in mean value of 585.08 ± 50.69 MPa with elongations to failure 1.67 ± 0.17 % elongation. Likewise, the mean of the young modulus among these was obtained to be 35.15 ± 3.83 GPa.

For the scanned fractured fibers and damages, the peak force is represented with respect to the strain value for samples 5, 9 and 15. Sample 15 exhibited the lowest peaks of force, followed by sample 9 and sample 15 (see **Figure 5b**). Fracture of sample 5 seems to be a semi clean shape with almost symmetric appearance, sample 9 appears to be with some symmetric trend with Y shape and sample 5 seems to be asymmetric. In this case it can be inferred that sample 15 can be more influenced by normal stress and more stress transfer capacity in longitudinal direction. Meanwhile samples 9 and 5 seem to be influenced by a combination of shear and normal stress.

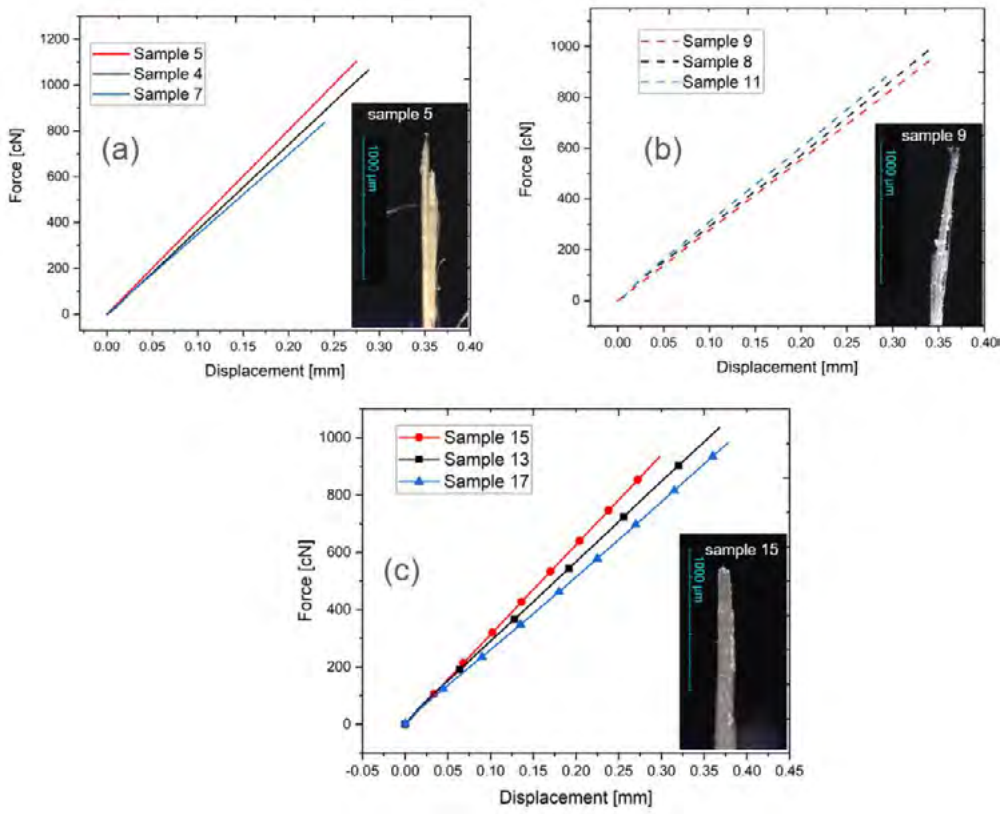


Figure 4. Force displacement functions for the single fiber tensile testing experiments a) Samples of the group 1. b) Samples of the group 2. c) Samples of the group 3

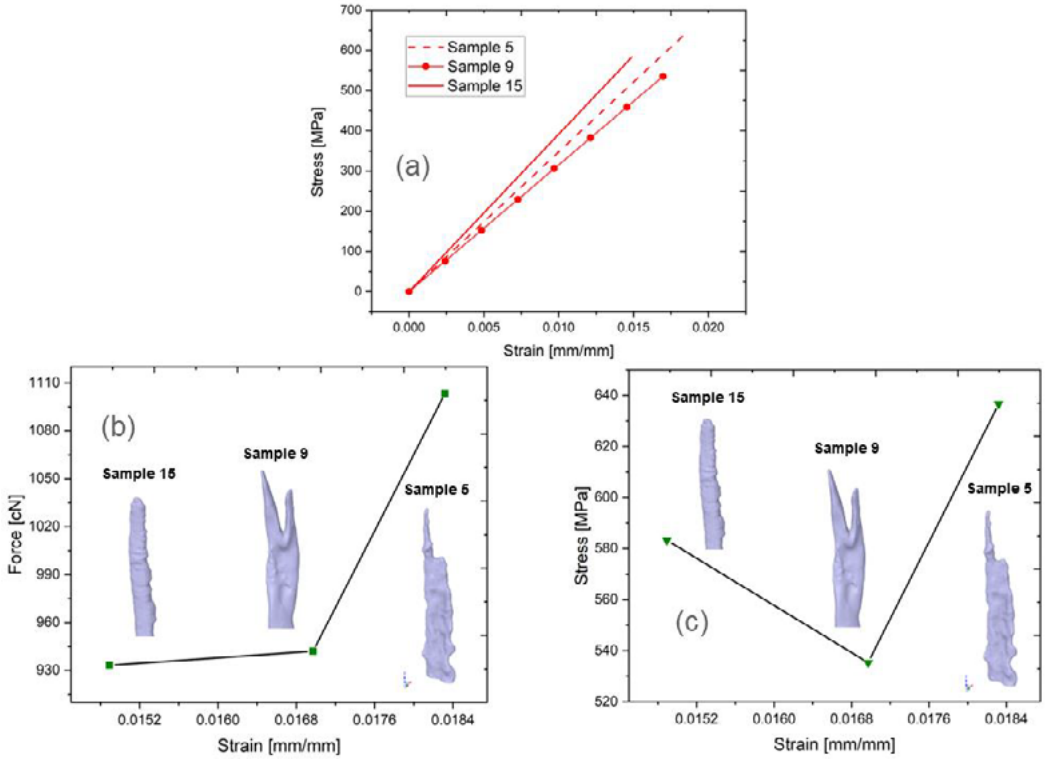


Figure 5. Samples 5, 9 and 15 a) Stress-strain function. b) Force vs strain to failure. c) Stress vs strain to failure

A defibrillation failure results in a larger elongation which is logical since the shear articulate bigger displacements and more force is required to conduct the failure. Moreover, the force-elongation ratio was calculated in the group of samples to monitor the damage. According to the findings, fibers that fail via defibrillation have bigger ratio which can be an indicator of stiffness. Considering the analysis the area in the zone of damage can be linked to the force to determine an approximation of the stress in the surface area.

In what concerns to toughness the area under the curve of the stress-strain was used to determine the Toughness of each sample which from bigger to smaller resulted to be 5.83 J/m^3 (**Sample 5**), 4.54 J/m^3 (**Sample 9**) and 4.34 J/m^3 (**Sample 15**), as depicted in **Figure 6a, b** and **c**.

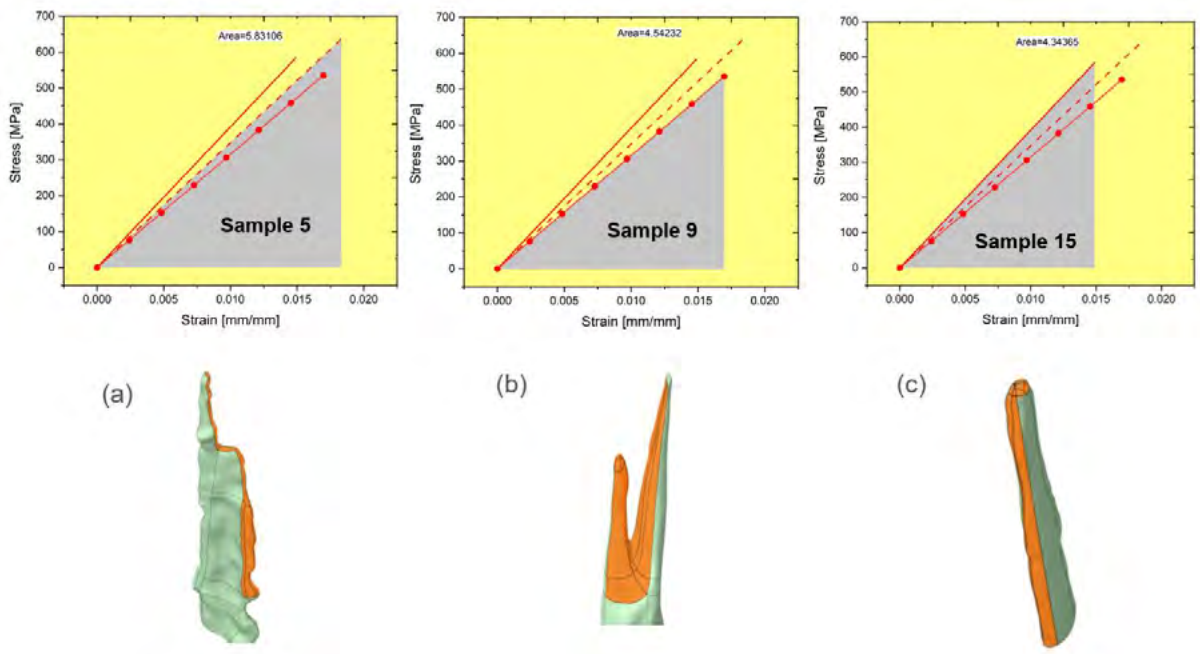


Figure 6. Toughness of selected samples and their damage shapes and fracture paths represented in orange color, calculated with the protocol. a) Sample 5. b) Samples 9. c) Sample 15

4. Conclusions

This investigation presents a novel methodology for the geometrical and micromechanical characterization of bamboo fibers (*Guadua angustifolia*) using fracture geometrical measurements. The primary aim of this methodology is to expedite material studies and gain deeper insights into failure mechanics. The geometry of bamboo fibers was determined using a calculated mesh generated from advanced digital image processing techniques. During single fiber tensile testing, samples exhibited failures that directly correlated with the resilience of the material and the specific fracture areas. Notably, sample 9 and sample 15 showed 22.11% and 25.51% less toughness, respectively, compared to sample 5.

Damage modes such as defibrillation and semi-clean failure were categorized and quantified in the geometrical representation at the tip of the fracture damage. These damage morphologies align with the failure modes reported in the literature, where semi-clean failure and defibrillation have been studied using SEM microscopy. The expertise gained from this investigation suggests the establishment of new standards for experimenting with bamboo natural fibres and analysing data sets of geometries to create predictive models. Moreover, topological information patterns are being measured with the device for the implementation of machine learning models for composite modelling applications. Also, future works will be undertaken to complement the methodology with Digital Image Correlation technique. The contribution of this work is oriented to the development physics-informed models.

Acknowledgments

The authors extend a gratitude message to the Luxembourg National Research Fund (FNR) for the funding of project SusPoCo (Sustainable Polymer Composites) under the agreement (PRIDE21/167482260).

References

[1] L. Osorio, E. Trujillo, F. Lens, J. Ivens, I. Verpoest, and A. W. Van Vuure, "In-depth study of the microstructure of bamboo fibres and their relation to the mechanical properties," Journal of Reinforced Plastics and Composites, vol. 37, no. 17, pp. 1099–1113, Sep. 2018, doi: 10.1177/0731684418783055..

[2] K. Haag and J. Müssig, "Scatter in tensile properties of flax fibre bundles: influence of determination and calculation of the cross-sectional area," J Mater Sci, vol. 51, no. 17, pp. 7907–7917, Sep. 2016, doi: 10.1007/s10853-016-0052-z.

[3] L. Osorio, E. Trujillo, A. W. Van Vuure, and I. Verpoest, "Morphological aspects and mechanical properties of single bamboo fibers and flexural characterization of bamboo/ epoxy composites," Journal of Reinforced Plastics and Composites, vol. 30, no. 5, pp. 396–408, Mar. 2011, doi: 10.1177/0731684410397683.

[4] D. Ren, Z. Yu, W. Li, H. Wang, and Y. Yu, "The effect of ages on the tensile mechanical properties of elementary fibers extracted from two sympodial bamboo species," Ind Crops Prod, vol. 62, pp. 94–99, 2014, doi: 10.1016/j.indcrop.2014.08.014.

[5] C. A. Fuentes et al., "Effect of the middle lamella biochemical composition on the non-linear behaviour of technical fibres of hemp under tensile loading using strain mapping," Compos Part A Appl Sci Manuf, vol. 101, pp. 529–542, Oct. 2017.

ACCELERATED AGEING OF A PULTRUDED FRP COMPOSITES PA6/GF

Hussein Chebbo[1,2]*, Romain Léger[1], Arnaud Regazzi[1], Stéphane Corn[1] ,Didier Perrin[2], Patrick Ienny[1]

[1] LMGC, IMT Mines Ales, Univ Montpellier, CNRS, Ales, France
[2] Polymers Composites and Hybrids (PCH), IMT Mines Ales, Ales, France
* hussein.chebbo@mines-ales.fr

Keywords: Pultruded composite, Hygrothermal effect, Mechanical testing

Abstract: Nowadays, mobility is experiencing numerous transformations driven by the need to reduce carbon footprint. The INFRAlight project aims to develop an environmentally friendly composite railway infrastructure to reduce the carbon footprint in economic development. Rails are subjected to severe natural and mechanical weather conditions such as temperature variations, relative humidity, UV radiation. Therefore, the study of durability under severe service conditions is essential to the industrial exploitation of these materials. One of the materials considered for this application is a pultruded fibre-reinforced plastic (FRP) made of polyamide 6 (PA6) and glass fibres (GF). Literature shows that the durability of pultruded composite materials is still an understudied topic. However, several studies have shown that PA6 polymers are sensitive to moisture, leading to changes in their physicochemical properties and a decrease in their mechanical properties. In this study, accelerated hygrothermal ageing at 70 °C and 80 %RH was applied to the PA6/GF pultruded composites. The results show a decrease in mechanical properties during water absorption, followed by a recovery upon drying, highlighting the reversibility of the ageing process.Viscoelastic characterisation from vibration analysis complement these results to understand the effect of moisture on the material.

1 Introduction

Polyamide 6 (PA6) reinforced with glass fibres (GF) is widely used in many industrial sectors due to its mechanical performance and chemical properties. Pultrusion is a continuous process for producing composite profiles with uniform cross-sectional areas.. However, several studies have shown that PA6 intensively absorbs water due to the presence of amide groups (-HN) in the amorphous part of the polymer. Initially,water occupy the available space (free volume) and then form hydrogen bonds.As more molecules accumulate,the polymer's chain mobility is activated, reducing the attraction between molecules and increasing flexibility.This phenomenon explains the plasticization of PA6 after the absorption of water.This sensitivity to hygrothermal conditions has a significant impact on its mechanical and physicochemical properties. This effect has been extensively studied in the literature [1,2]. For example Taktak et al. [4] observed a loss of approximately 60% in tensile strength and 74% in Young's modulus for PA6 specimens subjected to hydrothermal ageing at temperatures between 70°C and 90°C, while Pivdiablyk et al. [3] showed a decrease of the shear modulus, shear stress at yield and shield stress at rupture for woven PA6/GF composites after hygrothermal ageing (-40°C<T<80°C)and (0<RH<85%).

This paper aims to study the effect of water absorption at 70°C and 80% RH on the mechanical and physicochemical properties of a PA6/GF pultruded composites to assess the suitability of such materials for outdoor use on rails. To evaluate this effect, mechanical tests, vibration analysis and dynamic mechanical analysis were performed before, during and after ageing.

2 Materials and methods

The material used in this study is a pultruded PA6/GF composite 100% UD. This pultruded material is made up of two types of rovings the first is a 2400 tex roving with 17 µm filaments and the second is a 4800 tex roving with 24 µm filaments.On the outer layers are found the 2400 roving and in the core the 4800 roving.This led to a fibre volume fraction of 68 %. The pultruded profiles were cut, using water jet cutting, into specimens of different sizes in three orientations 0°, 45° and 90° relative to the fibre orientation. All cut specimens were then conditioned in a regulated room at 22 °C and 50 %RH to ensure that the specimens were in the same initial state. Table 1 shows the dimensions of the different samples.

Samples	Length (mm)/length between stubs (mm)	Width(mm)	Thickness(mm)
Fibre orientation 0°	250/150	25	2
Fibre orientation 45°	100/50	20	2
Fibre orientation 90°	90/50	20	2

Table 1: Dimensions of samples in the different orientations

2.1 Sorption

Moisture absorption tests were conducted by placing the specimens in climatic chambers at 70 °C and 80 %RH. The percentage of water absorbed was periodically measured by weighting the specimen with a scale of 0.1 mg accuracy (Sartorius Secura225D-1S) according to ASTM D5229/D 5229M-92 standard specifications [5]. The absorption curves were then obtained by the gravimetric method by averaging the percentage of water absorbed on five samples. The moisture content of a sample at a given duration, M_t was determined as follows:

$$M_t(\%) = \left(\frac{W_t - W_0}{W_0}\right) \times 100 \quad (1)$$

Where W_t and W_o are the weights of the sample at a given time and before ageing, respectively.

After reaching the saturation point, quasi-static mechanical tests were conducted on half of the specimens and the rest were placed for 50 days in a desiccator which in turn was placed in an oven for drying at 70 °C and 0 %RH. Desorption was monitored through gravimetric analysis until an equilibrium state was reached. The mechanical properties were also examined to evaluate the reversibility of the ageing process.

2.2 Quasi-static mechanical analysis

All tensile tests were conducted according to ISO 527-4 on an MTS Criterion C45.105 tensile machine equipped with a 100 kN load cell at a speed of 3 mm/min for specimens with a 0° fibre orientation, and 1 mm/min for specimens with a 45° or 90° fibre orientation. This difference in the loading speed aims to match the same strain rate for all the tested samples (0.0003 s^{-1}). These different tests were instrumented by a digital image correlation (DIC) technique to evaluate the in-plane strain tensor. Young's modulus was calculated using linear regression between 0.05 % and 0.25 % strain on five samples in each case and the shear modulus G_{LT} was calculated from tensile test results for each sample as follows:

$$\frac{1}{G_{LT}} = \frac{4}{E_{45}} - \frac{1}{E_L} - \frac{1}{E_T} + 2\frac{\nu_{LT}}{E_L} \quad (2)$$

Where E_L, and E_T are Young's moduli measured from tensile tests in the longitudinal and transverse directions, E_{45} is the apparent modulus measured from the off-axis test, and ν_{LT} is the Poisson's ratio measured from tensile tests in the transverse direction.

2.3 Vibration analysis

The viscoelastic parameters (elastic modulus and damping factor) of the composite specimens were determined using impulse modal analysis. The principle of this non-destructive method is to study the dynamic behaviour of a coupon through its natural vibration modes. In practice, the samples were suspended with elastic bands to simulate free-free boundary conditions. The samples were subjected to

a longitudinal or transverse mechanical impulse using an impact hammer. An accelerometer positioned on the sample captured its transient vibratory response(in traction/compression and flexion). Through signal acquisition and Fast Fourier Transform (FFT) analysis, the frequency response function can be determined. Considering sample dimensions, the dynamic elastic modulus is calculated from beam theory as follows:

$$E_t = 4 \times \rho \times L^2 \times f_t^2 \quad (3)$$

$$E_f = 0.946 \times \rho \times \frac{L^4}{e^2} \times f_f^2 \quad (4)$$

Where E_t and E_f are the dynamic elastic modulus in traction/compression and flexion, respectively, ρ is the material density, L the sample length, e the sample thickness and f_t, f_f the resonance frequencies of the first tensile and first flexural vibration modes, respectively.

2.4 Dynamic mechanical analysis

This technique allows for the characterisation of the viscoelastic parameters of the material. The viscoelastic behaviour is evaluated through forced dynamic tension-compression testing as a function of temperature. After verifying the linear domain range, a displacement amplitude of 1 µm was imposed at a frequency of 10 Hz to the PA6/GF composites with fibre orientations of 90°. A heating rate of 2 °C/min was applied to identify the evolution of the glass transition temperature T_g. The dimensions of the specimens used for this test were 60 × 10 × 2 mm. The complex dynamic elastic modulus E^* and loss factor $\tan(\delta)$ can be written as:

$$E^* = E' + iE'' \quad (5)$$

$$\tan(\delta) = \frac{E''}{E'} \quad (6)$$

Where E' is the storage modulus (real part) related to the material elastic behaviour, and E'' is the loss modulus (imaginary part) related to the material viscous behaviour. The loss factor $\tan(\delta)$ represents the ratio of the viscous to elastic effects.

3 Results and discussion

3.1 Water sorption

Around 30 specimens were aged in a climate chamber at 70 °C and 80 %RH. The absorption curves of PA6/GF in different orientations are shown in Figure 1. It's apparent that the water uptake of PA6/GF follows a two-stage process: an initial stage leading to maximum moisture absorption where the absorption phase appears to be linear with the square root of time. However, in the second stage, the diffusion behaviour shows a decreasing trend after reaching maximum moisture absorption. A similar behaviour was already observed by Lin Sang [6] where the moisture diffusion was investigated for woven carbon fabric reinforced PA6 after hydrothermal ageing. This loss was attributed by the authors to the cleavage reactions of macromolecular chains during ageing, known as leaching. Both phenomena start at the same time when the composite to hygrothermal ageing. The phenomenon of sorption is predominant at short times and becomes less and less important (Fickian behaviour),while leaching is initially very slight and then becomes more pronounced and predominant.

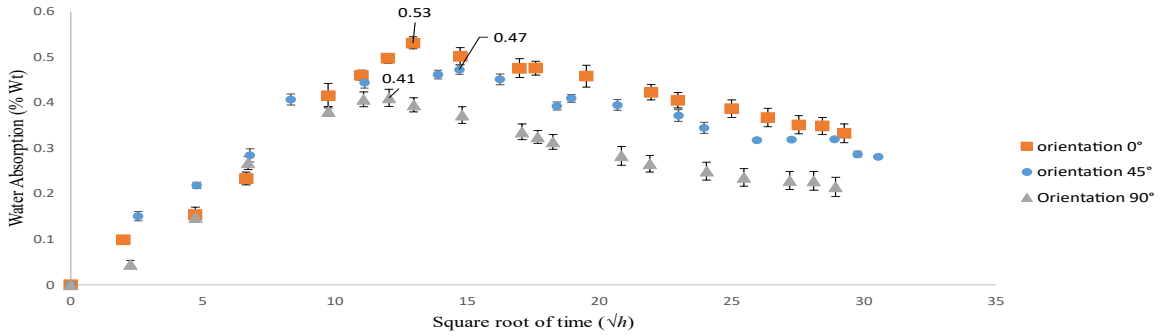


Figure 1 : Moisture uptake curves of PA6/GF specimens in three orientations 0°, 45°, 90°.

3.2 Water desorption

To examine the reversibility of ageing mechanisms, the PA6/GF specimens were dried at 70 °C and 0 % RH. The desorption curves show that the amount desorbed at equilibrium is 0.81 % for the specimens with a 0° fibre orientation, 0.92 % with a 45° fibre orientation, and 0.86 % with a 90° fibre orientation, different from the saturation values reached during the absorption phase. This saturation is confirmed by the vibrational analysis data that shows that dynamic moduli in bending and tension reach constant values at these points.

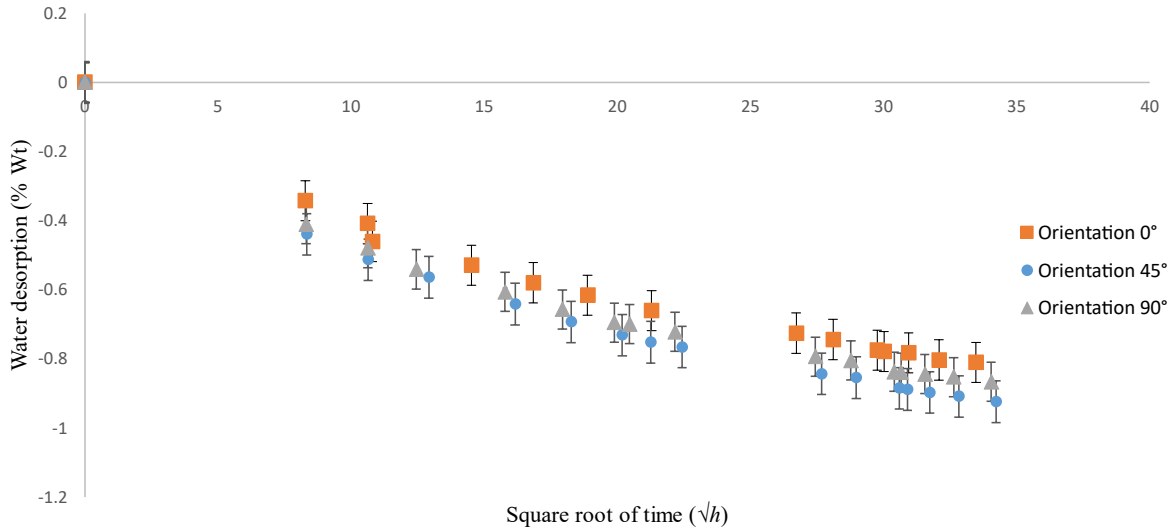


Figure 2. Desorption curves of PA6/GF after drying.

3.3 Quasi-static mechanical properties

Uniaxial tensile tests were conducted on unaged (reference condition), aged and dried states. Figures 3 and 4 summarise the mean values and standard deviation of the quasi-static mechanical properties.

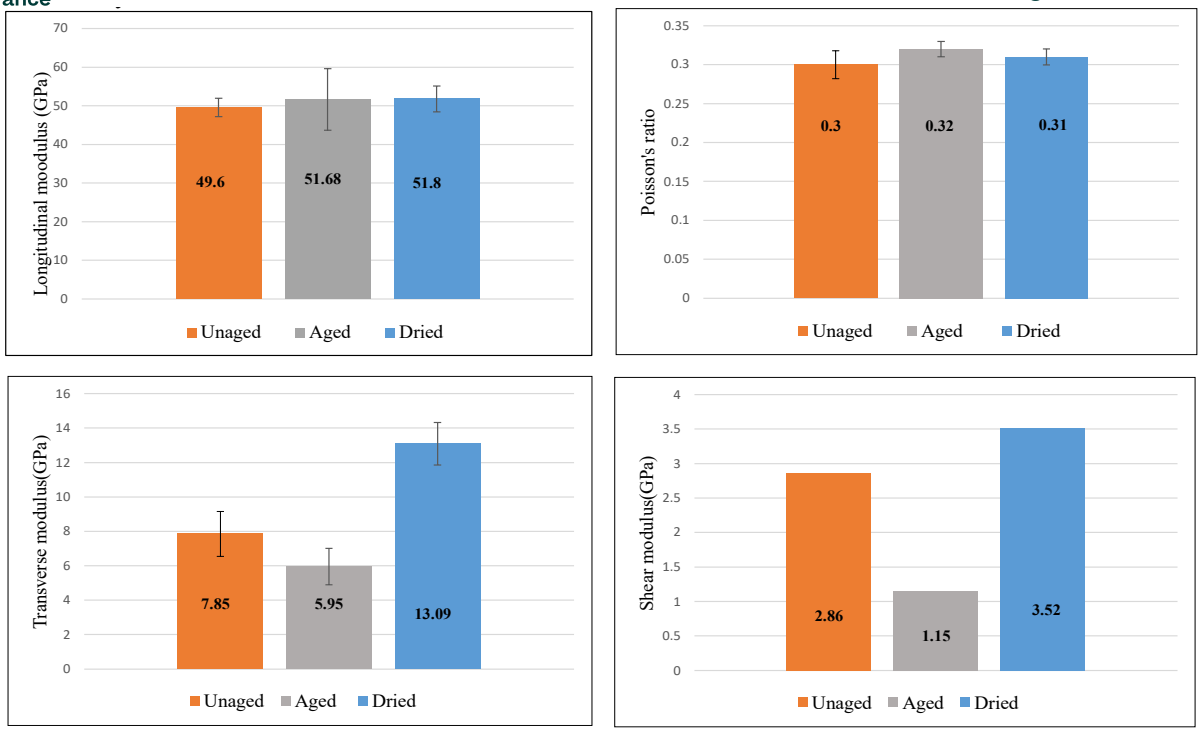


Figure 3: Comparison of elastic properties between unaged, aged, and dried samples.

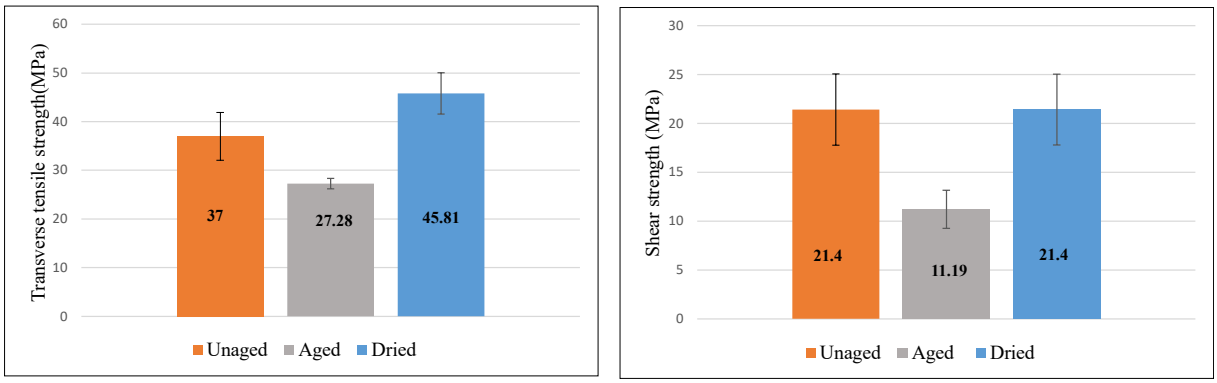


Figure 4: Comparison of ultimate properties between unaged, aged, and dried samples.

First, tests carried out on the materials along fibre directions allow to obtain the longitudinal modulus and the Poisson's ratio. No difference is observed for these parameters between the unaged, aged, and dried state. This result confirms that the mechanical performance PA6/GF along the fibre direction is dominated by the glass fibre which is unaffected by the absorption of water.
The second test is the transverse tensile test. A decrease in transverse modulus from 7.85 GPa to 5.95 GPa (24.2% loss) is observed as well as a decrease of transverse tensile strength from 37 MPa to 27.28 MPa (27% loss). Then this value increases respectively to 13.09 GPa and 45.81 MPa after drying.
The third test shows the same trend where the shear modulus decreased from 2.86 GPa to 1.15 GPa (60% loss) and the shear strength from 21.4 MPa to 11.19 MPa (48% loss). After drying, these values increase respectively to 3.52 GPa and 21.4 MPa.
During ageing, water diffuses into the composite mainly through the resin, even though diffusion may also occur at the resin/fibre interfaces. Water absorption in the resin leads to a decrease in its inherent rigidity due to plasticization (increased mobility of macromolecular chains). After drying PA6 polymer gains a certain rigidity leading to an increase in the mechanical properties of the PA6/glass fibre in the directions 90° dominated by the matrix behaviour. This gain of properties after drying is due to an additional water loss related to the difference between storage conditions (22°C,50% RH) and drying conditions.

3.4 Vibration analysis

To gain a deeper understanding of how hygrothermal ageing impacts the mechanical properties of PA6/GF, non-destructive testing by impulse modal analysis was conducted. Figures 4 and 5 display the evolution of the dynamic elastic modulus during ageing and drying, respectively in tensile and flexural mode. Each point reflects the average of five measurements. For specimens with fibre orientations at 0°, it can be observed that the longitudinal modulus did not vary during ageing and drying, confirming that glass fibres, which are not affected by water absorption dominate the mechanical properties in this orientation. But for the other orientations, Young's modulus decreases with ageing, due to a plasticisation of the matrix. Once saturation is reached and samples dried, an increase in this modulus is observed, confirming the gain of rigidity of the material as observed with the quasi-static tests.

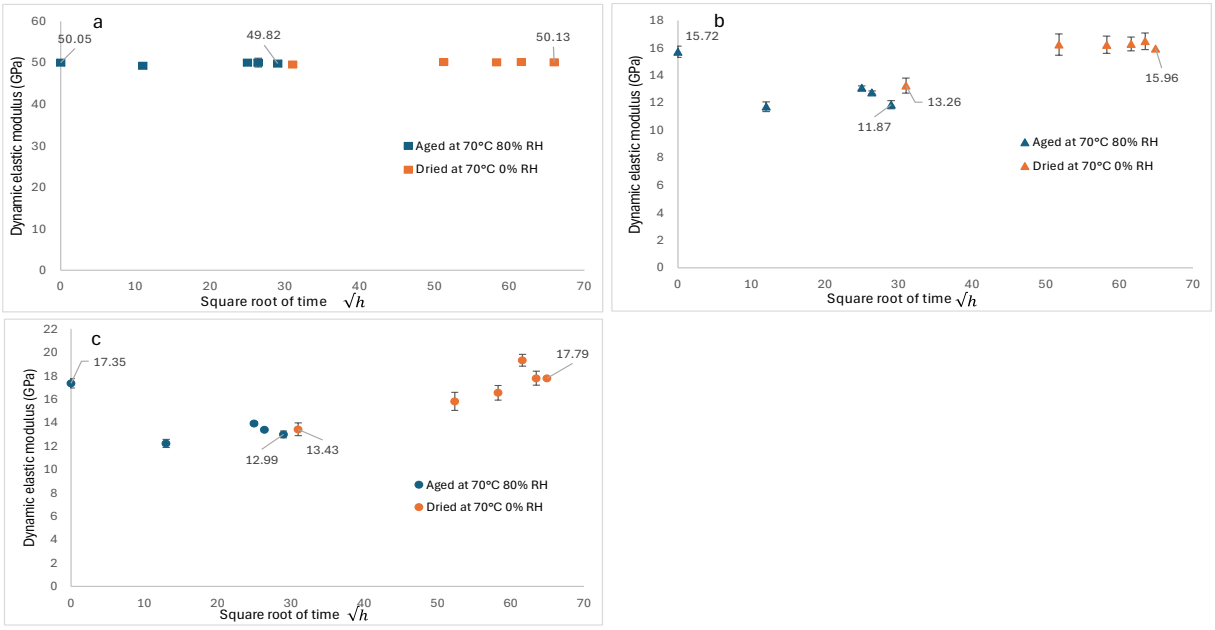


Figure 5:Evolution of dynamic elastic modulus in traction mode during ageing and drying for samples with a) 0° fibre orientations b) 90° fibre orientations c) 45° fibre orientations.

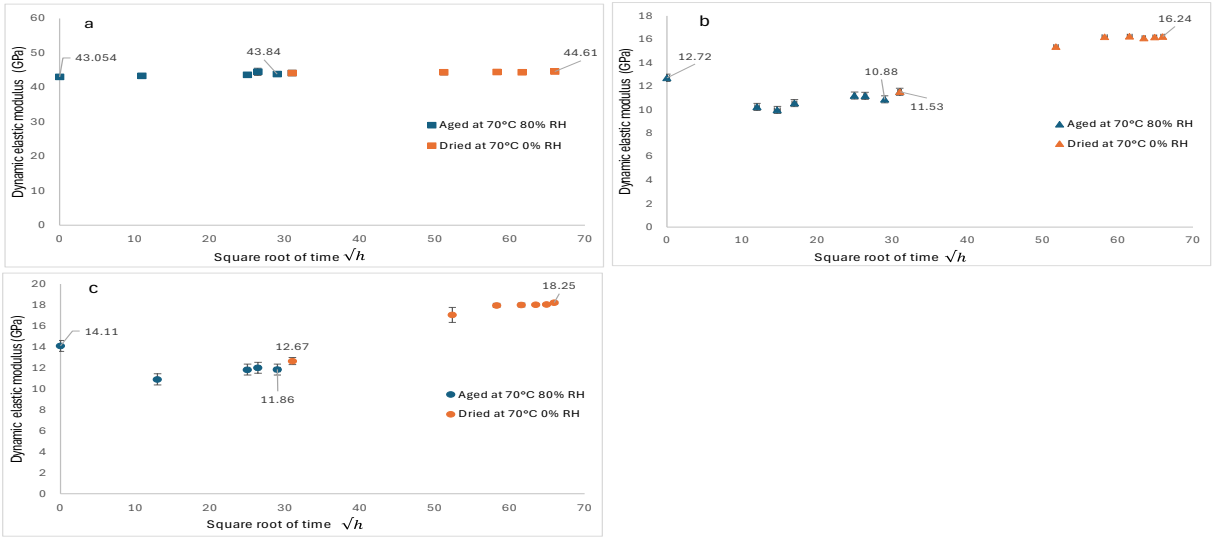


Figure 6: Evolution of dynamic elastic modulus in flexion mode during ageing and drying for samples with a) 0° fibre orientations b) 90° fibre orientations c) 45° fibre orientations.

3.5 Dynamic mechanical properties

Many studies confirm that hygrothermal ageing induces physical and chemical degradation which can affect the mechanical response of the composite material. A DMA test was conducted to identify changes of storage modulus (E') and loss factor tan(δ) between the unaged and the aged states.

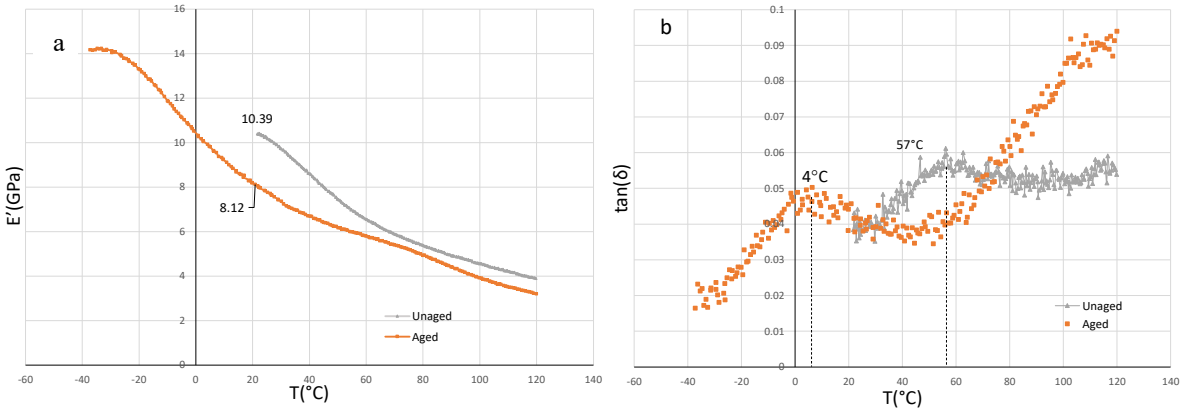


Figure 7:DMA (a) storage modulus and (b) loss factor results of unaged and aged PA6/GF fibres.

Figure 7 shows a 22 % decrease in the storage modulus at 20 °C from 10.4 GPa to 8.1 GPa due to ageing. The results indicate a pattern like that observed in quasi-static experiments and vibrational analysis, with a 24.2% (Figure 3) and a 25.5% (Figure 5) decrease respectively in the quasi-static and dynamic transverse modulus. This decline is attributed to the influence of water, caused by the plasticizing impact of molecules within the polyamide [7]. Besides, there is a significant decrease in T_g (i.e. the temperature corresponding to the peak of the loss factor) from 57°C to 4°C after ageing. The decrease of T_g can be related to the increase in the mobility of the PA6 polymer chains due to the formation of hydrogen bonds between the amide groups and water [8][9].

The results obtained from this article show that the absorption curve of PA6/GF at 70°C and RH=80% shows two stages: the first is a rapid water uptake and the second is a mass loss due to polymer degradation. This water uptake leads to a decrease in mechanical properties especially for samples with fibre orientations of 90° and 45°due to a plasticization effect. Then DMA test shows a decrease in the Tg,this effect is widely shown in the literature where the water absorbed breaks the secondary bond between the polar groups leading to a decrease in the Tg.

4 Conclusion

In this study, hygrothermal ageing of pultruded PA6/GF in the different orientations at 70°C and 80% RH were investigated. The absorption curves exhibit two distinct phases: an initial stage in which water absorption rises until it reaches a peak, followed by a subsequent phase characterized by a steady decline in mass relative to the square root of time.

To study the effect of water molecules on the mechanical properties of pultruded PA6/GF, tensile tests, and vibrational analysis were evaluated. A decrease in the mechanical properties for the specimens with 90° and 45° of fibre orientations is observed, while these properties are not affected for the specimens with 0° of fibre orientations. DMA analysis shows a significant decrease in the T_g due to an increase in the mobility of PA6 chains. This study will be complemented by a numerical model to predict the response of the material after other hygrothermal conditions.

5 References

[1] Le Gac, P. Y., Arhant, M., Le Gall, M., & Davies, P. (2017). Yield stress changes induced by water in polyamide 6: Characterization and modeling. *Polymer Degradation and Stability*, *137*, 272–280. https://doi.org/10.1016/j.polymdegradstab.2017.02.003

[2] Mortazavian, S., Fatemi, A., & Khosrovaneh, A. (2015). Effect of Water Absorption on Tensile and Fatigue Behaviors of Two Short Glass Fiber Reinforced Thermoplastics. *SAE International Journal of Materials and Manufacturing*, *8*(2), 435–443. https://doi.org/10.4271/2015-01-0546

[3] Pivdiablyk, I., Rozycki, P., Jacquemin, F., Gornet, L., & Auger, S. (2020). Experimental analysis of mechanical performance of glass fibre reinforced polyamide 6 under varying environmental conditions. *Composite Structures*, *245*. https://doi.org/10.1016/J.COMPSTRUCT.2020.112338

[4] Taktak, R., Guermazi, N., Derbeli, J., & Haddar, N. (2015). Effect of hygrothermal aging on the mechanical properties and ductile fracture of polyamide 6: Experimental and numerical approaches. *Engineering Fracture Mechanics*, *148*, 122–133. https://doi.org/10.1016/j.engfracmech.2015.09.001

[5] Standard Test Method for Moisture Absorption Properties and Equilibrium Conditioning of Polymer Matrix Composite Materials 1, n.d.)

[6] Sang, L., Wang, Y., Wang, C., Peng, X., Hou, W., & Tong, L. (2019). Moisture diffusion and damage characteristics of carbon fabric reinforced polyamide 6 laminates under hydrothermal aging. Composites Part A: Applied Science and Manufacturing, 123, 242–252. https://doi.org/10.1016/j.compositesa.2019.05.023

[7] Vlasveld, D. P. N., Groenewold, J., Bersee, H. E. N., & Picken, S. J. (2005). Moisture absorption in polyamide-6 silicate nanocomposites and its influence on the mechanical properties. *Polymer*, *46*(26), 12567–12576. https://doi.org/10.1016/j.polymer.2005.10.096

[8] Arhant, M., Le Gac, P. Y., Le Gall, M., Burtin, C., Briançon, C., & Davies, P. (2016). Effect of sea water and humidity on the tensile and compressive properties of carbon-polyamide 6 laminates. *Composites Part A: Applied Science and Manufacturing*, *91*, 250–261. https://doi.org/10.1016/j.compositesa.2016.10.012

[9] Lei, Y., Zhang, T., Zhang, J., & Zhang, B. (2021). Dimensional stability and mechanical performance evolution of continuous carbon fiber reinforced polyamide 6 composites under hygrothermal environment. *Journal of Materials Research and Technology*, *13*, 2126–2137. https://doi.org/10.1016/j.jmrt.2021.06.012

A SEMI-ANALYTICAL MODEL FOR CRACK KINKING OUT OF THE INTERFACE OF BIMATERIAL ANISOTROPIC LAYERS

Carmine Contaldi[1], C. Berggreen[2], B.N. Legarth[3], R. Massabó[4]

[1]Department of Civil and Mechanical
Engineering, Technical University of Denmark, Kgs. Lyngby, Denmark
Email: carco@dtu.dk, Web Page: https://orbit.dtu.dk/en/persons/carmine-contaldi
[2]Department of Civil and Mechanical
Engineering, Technical University of Denmark, Kgs. Lyngby, Denmark
Email: cber@dtu.dk, Web Page: https://orbit.dtu.dk/en/persons/christian-berggreen
[3]Department of Civil and Mechanical
Engineering, Technical University of Denmark, Kgs. Lyngby, Denmark
Email: bnle@dtu.dk, Web Page: https://orbit.dtu.dk/en/persons/brian-nyvang-legarth
[4]Department of Civil, Chemical and
Environmental Engineering, University of Genova, Genova, Italy
Email: roberta.massabo@unige.it, Web Page: https://dicca.unige.it/roberta.massabo@unige.it

Keywords: Anisotropy, Crack kinking, CSDE, Debond, Interface fracture mechanics

Abstract
Bimaterial interface cracks in composite materials can either continue propagating along the interface or deviate their path, an event known as crack kinking, which can heavily impact structural integrity. To understand the crack kinking phenomenon, in literature is proposed a linear mathematical model based on six coefficients, which depend only on the kink angle and material properties. While earlier studies offer limited data on these coefficients for specific bimaterials, our work presents a verified semi-analytical approach that served as the foundation for the newly developed Matlab app introduced to compute coefficients for a wider range of bimaterial combinations.

1. Introduction

Composite materials have a big importance in various industries due to their exceptional combination of high stiffness and low weight. However, their widespread application is often hindered by susceptibility to damage, including debonding and cracking. These issues are critical and challenging to detect, potentially compromising structural integrity significantly. This vulnerability to damage, which arises from factors such as manufacturing processes, fatigue cycles, and impacts, highlights the importance of understanding and mitigating these risks. An intriguing phenomenon in this regard is crack kinking, where cracks deviate into adjacent layers at specific angles. Therefore, the understanding of the behavior and propagation path of the kink crack can be helpful to mitigate the damage in bimaterial layers.

The mathematical model for addressing kinking in isotropic bimaterial solids was formulated by Hutchinson and He [1] and extended further by He et al. [2], who, under linear elastic fracture mechanics (LEFM) assumptions, connected linearly the complex stress intensity factor (SIF) of the interface, the complex SIF of the kink crack and in-plane stress at the crack. The relationship is based on three complex coefficients which depend on the kink angle Ω and the Dundurs' parameters α and β. The values of several coefficients were tabulated for limited combinations of α and β by Hutchinson and He in [3], while other values were provided in a plot by He et al. [2] for many values of α and $\beta = 0$.

Subsequently, Wang [4] and Wang et al. [5] further expanded the kinking model to include interface cracks occurring between two dissimilar anisotropic elastic solids. In addition to the Dundurs'

parameters and kink angle, the coefficients now also rely on dimensionless parameters λ and ρ defined in [6], which give information on the anisotropy level.
However, despite these advancements, a straightforward method for determining coefficients for the kinking model for generic bimaterial layers remained non-existent. Yet, more recently Jakobsen et al. [7] proposed and verified a semi-analytical alternative strategy based on finite element (FE) analyses and algebraic manipulation to find the coefficients in isotropic elastic bimaterials. The approach was adopted also by Noijen et al. [8] who built a Response Surface Model (RSM) [9], thanks to which it is possible to obtain immediately the solution of the coefficients for any isotropic bimaterials as a function of α, β and Ω.
In this work, the same semi-analytical approach is adopted, and its functionality is verified for anisotropic materials. Based on the obtained results, a newly developed Matlab app is introduced to compute the coefficients of the kinking model straightforwardly for various bimaterial combinations.

2. Mathematical model of a crack kinking out of an interface

The Dundurs' parameter α and β, the oscillatory index ϵ, the dimensionless anisotropic parameters λ and ρ for anisotropic bimaterial solids are defined in [6].

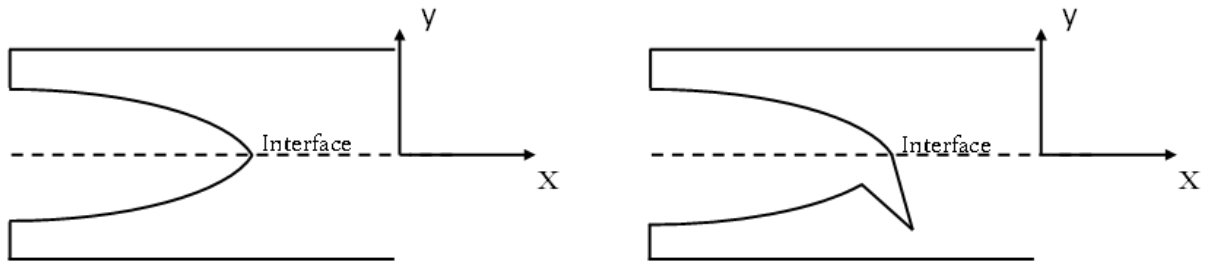
The mixed-mode angle ψ measures the type of loading acting at the crack tip. For the interface crack in a bimaterial it is defined as follows:

$$\tan(\psi) = \frac{\mathrm{Im}\left(Kl^{i\epsilon}\right)}{\mathrm{Re}\left(Kl^{i\epsilon}\right)} \tag{1}$$

where K is the complex SIF of the interface crack, with $K = K_1 + iK_2$; l is a characteristic length for the problem of the interface crack. If $\psi = 90°$, the loading condition is a pure mode-II, while if $\psi = 0°$ it is pure mode-I. The characteristic length must be chosen accurately because it can shift the value of ψ.
The event of a crack kinking out from an interface is illustrated in Figure 1. Phenomenon of a crack kinking out from an interface.The complete 2D model formulated by Hutchinson and He [1], and extended further by He et al. [2], describes the phenomenon and defines the kink crack complex SIF as a linear combination of the interface complex SIF and the crack tip in-plane stress through the complex coefficients c , d and b. It is the following:

$$K^{kink} = cKa^{i\epsilon} + \overline{dK}a^{i\epsilon} + b\sigma_0\sqrt{a} \tag{2}$$

where a represents the length of the kink crack; σ_0 is the in-plane stress generated by either residual stresses or external loads; the overline represents the complex conjugate; K^{kink} is the complex SIF at the kink crack, with $K^{kink} = K_I + iK_{II}$.



a) Interface crack b) Crack kinking from an interface

Figure 1. Phenomenon of a crack kinking out from an interface.

The coefficients c, d and b used in Eq. (2) are complex and defined as follows:

$$\begin{aligned} b &= b_1(\alpha,\beta,\lambda_j,\rho_j,\Omega) + ib_2(\alpha,\beta,\lambda_j,\rho_j,\Omega) \\ c &= c_1(\alpha,\beta,\lambda_j,\rho_j,\Omega) + ic_2(\alpha,\beta,\lambda_j,\rho_j,\Omega) \\ d &= d_1(\alpha,\beta,\lambda_j,\rho_j,\Omega) + id_2(\alpha,\beta,\lambda_j,\rho_j,\Omega) \end{aligned} \tag{3}$$

where the subscript j = 1, 2 refers to material above and below the interface, and Ω is the kink angle.

If Eq. (2) is expanded, it becomes:

$$\begin{aligned} K_I^{kink} &= c_{11}\mathrm{Re}\left(Ka^{i\epsilon}\right) + c_{12}\mathrm{Im}\left(Ka^{i\epsilon}\right) + b_1\sigma_0\sqrt{a} \\ K_{II}^{kink} &= c_{21}\mathrm{Re}\left(Ka^{i\epsilon}\right) + c_{22}\mathrm{Im}\left(Ka^{i\epsilon}\right) + b_2\sigma_0\sqrt{a} \end{aligned} \tag{4}$$

where Re and Im denote, respectively, the real and imaginary parts of the complex terms. The new coefficients correspond to:

$$\begin{aligned} c_{11} &= \mathrm{Re}(c+d) = c_1 + d_1 \\ c_{12} &= -\mathrm{Im}(c+d) = -c_2 - d_2 \\ c_{21} &= \mathrm{Im}(c-d) = c_2 - d_2 \\ c_{22} &= \mathrm{Re}(c-d) = c_1 - d_1. \end{aligned} \tag{5}$$

3. Methodology

3.1. Analytical approach

The method proposed by Jakobsen et al. [7] and adopted also by Noijen et al. [8] consists in solving a 6x6 linear system to find the coefficients $b_1, b_2, c_{11}, c_{12}, c_{21}, c_{22}$. These coefficients are determined by constructing six equations based on Eq. (2) or Eq. (4), each corresponding to three loading conditions with different ψ values, ensuring that the determinant of the system matrix is non-zero.

Jakobsen et al. [7] solved the system in two steps by decoupling the problem. The first step consisted in deriving the coefficients c_1, c_2, d_1 and d_2 by solving a 4x4 linear system obtained setting the value of $\sigma_0 = 0$. The second step is built upon the solutions of the first one and is a 2x2 linear system to find coefficients b_1 and b_2.

However, Noijen et al. [8] directly solved the 6x6 system in one step, employing a strategy that eliminates the need to search for loading conditions with a null in-plane stress σ_0.

The 6x6 linear system is the following:

$$\underbrace{\begin{bmatrix} c_{11} \\ c_{12} \\ c_{21} \\ c_{22} \\ b_1 \\ b_2 \end{bmatrix}}_{\boldsymbol{c}} = \underbrace{\begin{bmatrix} f_1^{\psi_1} & f_2^{\psi_1} & 0 & 0 & f_3^{\psi_1} & 0 \\ 0 & 0 & f_1^{\psi_1} & f_2^{\psi_1} & 0 & f_3^{\psi_1} \\ f_1^{\psi_2} & f_2^{\psi_2} & 0 & 0 & f_3^{\psi_2} & 0 \\ 0 & 0 & f_1^{\psi_2} & f_2^{\psi_2} & 0 & f_3^{\psi_2} \\ f_1^{\psi_3} & f_2^{\psi_3} & 0 & 0 & f_3^{\psi_3} & 0 \\ 0 & 0 & f_1^{\psi_3} & f_2^{\psi_3} & 0 & f_3^{\psi_3} \end{bmatrix}^{-1}}_{\boldsymbol{F}} \underbrace{\begin{bmatrix} K_I^{kink,\psi_1} \\ K_{II}^{kink,\psi_1} \\ K_I^{kink,\psi_2} \\ K_{II}^{kink,\psi_2} \\ K_I^{kink,\psi_3} \\ K_{II}^{kink,\psi_3} \end{bmatrix}}_{\boldsymbol{K^{kink}}} \tag{6}$$

with the components of the matrix $\boldsymbol{F}$ to be:

$$\begin{aligned} f_1 &= [K_1\cos(\epsilon\log(a)) - K_2\sin(\epsilon\log(a))] \\ f_2 &= [K_2\cos(\epsilon\log(a)) + K_1\sin(\epsilon\log(a))] \\ f_3 &= \sigma_0\sqrt{a}\,. \end{aligned} \tag{7}$$

The superscript ψ_j with $j = 1,2,3$, refers to the three needed loading conditions.

3.2. Numerical procedure

The components of matrix $\boldsymbol{F}$ and vector $\boldsymbol{K^{kink}}$ are found by solving three different FE models: the *interface crack* model, *interface stress* model and the *kink crack* model.
The *interface crack* model represents the crack at the interface of a bimaterial structure. It is used to obtain the relative displacement δ_x and δ_y of the crack flanks. These values are post-processed with the crack surface displacement extrapolation (CSDE) method [10] to calculate the energy release rate (G_{i_j}) and the phase angle (ψ_j) of the interface crack for the given loading condition. These values are needed to compute the SIFs of the interface crack.
The *kink crack* model represents the crack kinking from the interface into one of the layers. It is used to compute the SIFs at the tip of the kink crack at various kink angles.
The *interface stress* model is similar to the interface crack model but without a crack. It is used to obtain σ_0, which represents the stress in the direction of the interface (σ_{xx}). This value is obtained at the node of the material where the crack is assumed to kink and at the same location as the interface crack tip.

3.3. Iterative process and curve fitting

The analytical and the numerical procedures were performed in an iterative loop for many bimaterial combinations, and the coefficients obtained were stored in a large set of data. Then, these values were used to create 8D fitting polynomials able to find straightforwardly the value of the six coefficients without going through the classic procedure. During the iterative process, while α and β were left varying through their entire range, to limit the computational time, it was only possible to cover a limited domain for λ_j and ρ_j of the materials of the two layers. The domains are described below:

$$\begin{gathered}\lambda_1 \in [0.05, 1] \\ \lambda_2 \in [0.05, 1.5] \\ \rho_1 \in [1, 2.75] \\ \rho_2 \in [0.25, 3]\,.\end{gathered} \tag{8}$$

4. Developed tool

The developed tool is a simple Matlab app which contains a tabbed panel where the plot of the desired coefficients is shown. The required inputs include α, β, $\lambda_1, \lambda_2, \rho_1, \rho_2$ and the desired kink angles Ω, which can be specified with maximum and minimum values and a step size for the range between them. Additionally, the outputs include the values of the coefficients at the specified parameters and the coefficient of determination (R^2), which measures the accuracy of the regression model.
The app performs polynomial curve fitting on sub-domains created from values in Eq. (8) to enhance the accuracy. Subsequently, the input values are substituted into the polynomial equation to determine the coefficients.
In Figure 2 a screenshot of the Graphic User Interface (GUI) of the Matlab app is presented.

5. Conclusions

The reliability of the semi-analytical method proposed in [7] to determine the coefficients of the kinking model was verified for anisotropic bimaterial layers. A Matlab app was developed to find the coefficients for a much wider range of anisotropic and Dundurs' parameters, respectively λ_j, ρ_j and α, β, in order to make the model applicable for broader and realistic material configurations.

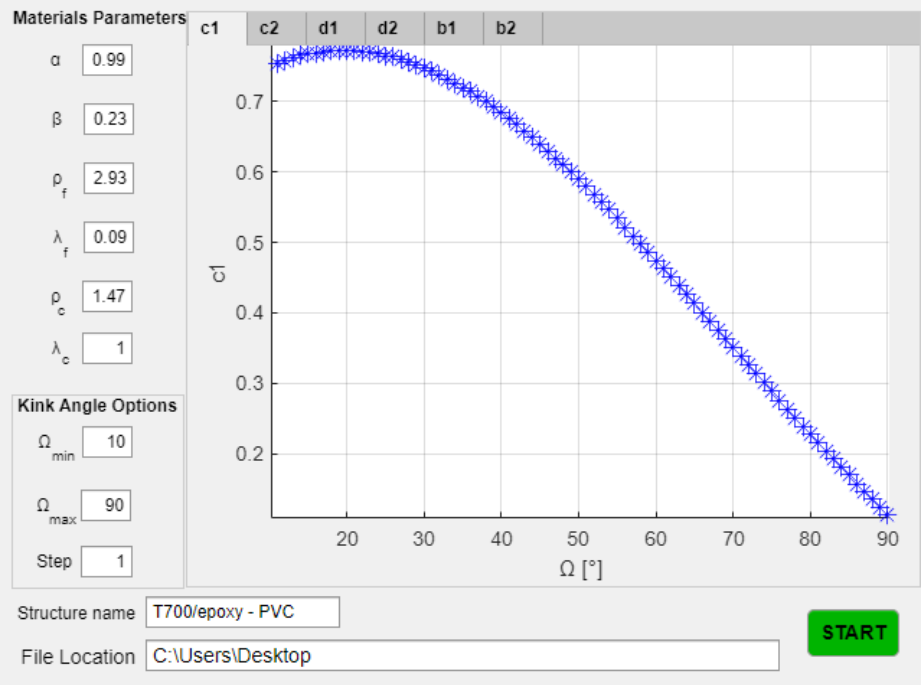


Figure 2. Screenshot of the GUI of the developed Matlab app to compute the coefficients.

References

[1] M.-Y. He and J. W. Hutchinson, "Kinking of a Crack Out of an Interface," *Journal of Applied Mechanics,* vol. 56, no. 2, pp. 270-278, 1989.

[2] M.-Y. He, A. Bartlett, A. Evans and J. W. Hutchinson, "Kinking of a Crack Out of an Interface: Role of In-Plane Stress," *Journal of the American Ceramic Society,* vol. 74, pp. 767 - 771, 1991.

[3] M.-Y. He and J. W. Hutchinson, "Kinking of a Crack out of an Interface: Tabulated Solution Coefficients," Harvard University, 1988.

[4] T. Wang, "Kinking of an interface crack between two dissimilar anisotropic elastic solids," *International Journal of Solids and Structures,* vol. 31, no. 5, pp. 629-641, 1994.

[5] T. C. Wang , C. F. Shih and Z. Suo, "Crack extension and kinking in laminates and bicrystals," *International Journal of Solids and Structures,* vol. 29, no. 3, pp. 327-344, 1992.

[6] Z. Suo, "Singularities, Interfaces and Cracks in Dissimilar Anisotropic Media," *Proceedings of the Royal Society of London. Series A, Mathematical and Physical Sciences,* vol. 427, no. 1873, pp. 331-358, 1990.

[7] J. Jakobsen, J. Andreasen and E. Bozhevolnaya, "Crack kinking of a delamination at an inclined core junction interface in a sandwich beam," *Engineering Fracture Mechanics,* vol. 75, no. 16, pp. 4759-4773, 2008.

[8] S. Noijen, O. van der Sluis, P. Timmermans and G. Zhang, "A semi-analytic method for crack kinking analysis at isotropic bi-material interfaces," *Engineering Fracture Mechanics,* vol. 83, pp. 8-25, 2012.

[9] R. L. Mason, R. F. Gunst and J. L. Hess, Statistical Design and Analysis of Experiments: With Applications to Engineering and Science, John Wiley and Sons, 2003.

[10] C. Berggreen, "Damage Tolerance of Debonded Sandwich Structures," Technical University of Denmark, Copenhagen, DK, 2004.

EXPERIMENTAL AND NUMERICAL COMPARISON OF FIBRE/MATRIX DEBOND EXTENSION IN ULTRA-THIN PLIES AFTER TENSION-TENSION CYCLIC TESTING

S. Sánchez-Carmona[1], C. Sandino[2], E. Correa[3], M.L. Velasco[4], A. Barroso[5]

[1,2,3,4] Grupo de Elasticidad y Resistencia de Materiales, Departamento de Mecánica de Medios Continuos y Teoría de Estructuras, Escuela Técnica Superior de Ingeniería, Universidad de Sevilla, Camino de los Descubrimientos, 41092, Sevilla, España
[1] Email: sscarmona@us.es, Web Page: https://prisma.us.es/investigador/7003
[2] Email: csandino@us.es, Web Page: https://prisma.us.es/investigador/5831
[3] Email: ecorrea@us.es, Web Page: https://prisma.us.es/investigador/931
[4] Email: mvelasco7@us.es, Web Page: https://prisma.us.es/investigador/4308
[5] Email: abc@us.es, Web Page: https://prisma.us.es/investigador/350

Keywords: ultra-thin plies, cross-ply laminates, microscopical inspection, longitudinal debonds

Abstract
Ultrathin layers (UTP) are present in a relevant number of studies, from quasi-static to cyclic loading. Important through-the-thickness stresses may especially appear in the 90º ply block of a cross-ply laminate when there is a relevant restraint between the 0º and 90º ply block thicknesses. This leads to a biaxial stress state even only due to the residual thermal stresses due to the curing process.
In this study, the biaxial stress state that occurs in an ultra-thin 90º ply block of a cross-ply laminate was completely defined after its thermal and mechanical edge-effect analysis. Once the laminates were cured, the samples were carefully inspected by optical microscopy, showing longitudinal fibre/matrix debonds in the ultra-thin 90º ply block (parallel and aligned to the fibre direction of the 0º ply block). These non-conventional damages that appeared were registered, and the specimens were also mechanically loaded. In a second stage T-T cyclic testing was performed and the total extension of the debonds was monitored up to a permanent growth stage. These experimental results were compared with numerical analyses of the Energy Release Rate (G) using a BEM model to predict the fibre/matrix interface crack growth under the biaxial stress state. The results showed that there is an excellent agreement when the biaxial stress state (caused by the edge effect phenomenon) is considered in the numerical model.

1. Introduction

During the performance of micromechanical studies on the appearance of fatigue damage in cross-ply laminates containing ultra-thin plies (Sánchez-Carmona et al. [1]), 'non-conventional damages' were detected in the 90° ply-block of the tested laminates. These damages were longitudinal fibre-matrix interface debonds, i.e. debonds parallel to the 0° layers of the laminate.

In Sánchez-Carmona et al. [2] an explanation was given for the appearance of these debonds based on the stress state caused in the 90º ply-block by the so-called edge effect, Mittelstedt et al. [3]. Specifically, the presence of this effect produces, among others, the appearance of an out-of-plane transverse tension component in the 90º layer, which is found to be greater as the thickness of the 90º layer increases. These stresses derived from the edge effect are generated both by residual thermal curing stresses and by mechanical loads. As a consequence, the 90º ply block is subjected to a state of transverse biaxial stresses capable of causing longitudinal debonds.

This fact was the starting point for the present work. A detailed microscopic observation of the 90º ply block of cross-ply laminate specimens was carried out in order to find fibre-matrix debonds in quasi-isolated fibres in the post-curing situation. Later, these specimens were subjected to T-T cyclic loads and the growth of the previously detected debonds was monitored, Section 2. In addition, a BEM model was developed, based on previous works by the authors, see for instance Sandino et a [4], in order to find an explanation for their extension, Section 3.

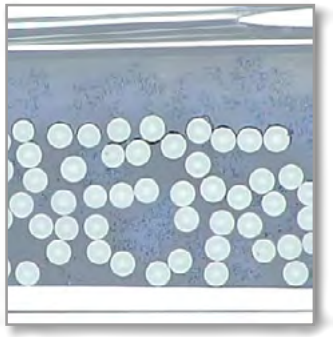


Figure 1. Longitudinal debonds observed in a UTP 90º ply block of a cross-ply laminate.

2. Experimental study

The study carried out focuses, in a first stage, on the observation of longitudinal debonds in cross-ply laminate specimens, just after the material has been cured. The cross-ply laminate selected was $[0_4/90/0_4]$, manufactured with T700S/TP402 carbon/epoxy prepreg unidirectional tape supplied by North Thin Ply Technology. 150 g/m^2 pre-preg was used for the 0° layers and 30 g/m^2 for the 90° layers, Figure 2. The manufacturing was carried out by manual stacking and the laminate was cured in an autoclave following the recommendations provided by the supplier.

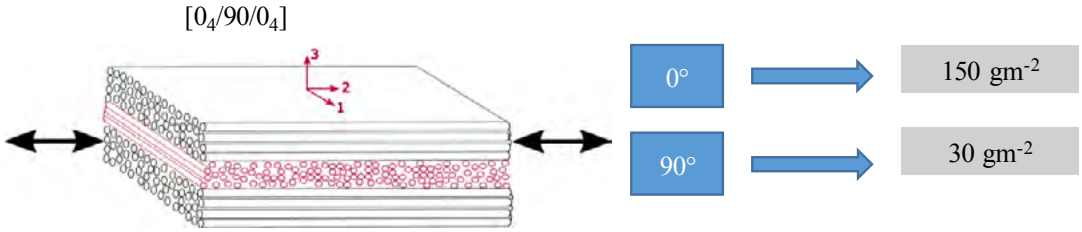


Figure 2. Scheme of the cross-ply laminate stacking sequence used for the experimental study.

After manufacturing, the specimens were sanded, polished and microscopically inspected. Longitudinal debonds were observed, as expected given the configuration of the laminate and the ultra-thin 90º ply used. The proximity of neighbouring fibres to those housing longitudinal debonds was analyzed and a selection was made of the debonds that may be considered as quasi-isolated. Specifically, 22 debonds were chosen. The extension of these debonds was measured. An example of a debond detected during this stage is presented in Figure 3. The results of the experimental measurements carried out show an average debond extension θ_t=189.1º (CV=11.9%).



Figure 3. Experimental measurement of a quasi-isolated debond detected after curing.

In a second stage, the specimens were subjected to 100 T-T loading cycles (σ_m=36.9 MPa, R=0.1). The tests were carried out with intermediate stops at N=5, 10 and 50, measuring the growth of the selected debonds after each step and of course at the end of the test. As remarkable results, it should be mentioned that the debonds grew only during the first cycles. Specifically, an important part of the debonds just grew during the first 5 loading cycles and the rest reached their final length in the second step, not growing after 10 cycles. Secondly, it was found that the average extension of the set of debonds in this cyclic loading stage was θ_t=239.5º (CV=6.2%).

From the comparison of the average values between the post-curing stage and the cyclic loading stage it is immediately evident that the scatter is considerably reduced from the first stage to the second. There are a few connected elements that explain this fact. First of all, it must be taken into account that the debonds found in the post-curing stage were not perfectly symmetrical; this lack of symmetry depends on the local configuration and distance of the neighboring fibres since the debonds are not completely isolated. Secondly, it is very interesting to observe that as the number of cycles increases, the debonds become more symmetrical, therefore reaching a more homogeneous group of debonds, which explains the reduction in the scatter of the results.

3. Numerical study

The objective of the numerical study was to be able to create a model that could reproduce the growth and extension of the longitudinal debonds. To this end, a single fibre BEM model was chosen. This model considers the presence of a fibre-matrix interface crack that grows under a biaxial stress state both in Modes I and II, Sandino el al [4].

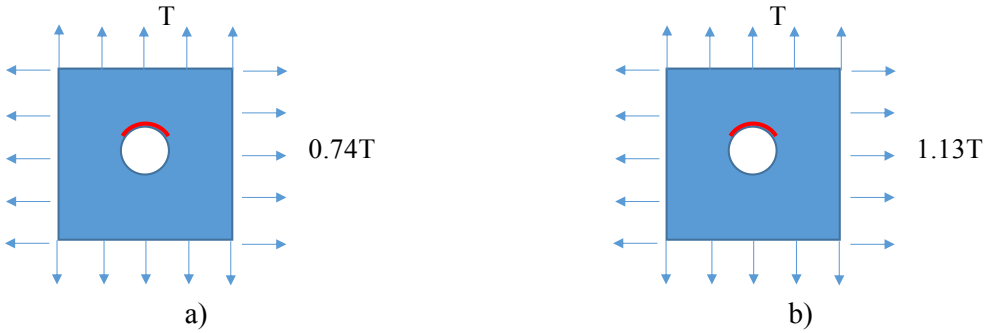


Figure 4. Biaxial stress states: a) Case 1, b) Case 2.

The key point in the model definition was the estimation of the external loads to which it should be subjected. The stress situation of the post-curing case (case 1) and the stress situation during the loading cycles (case 2) were analyzed. Specifically:
Case 1: Residual thermal stresses provoked by the cooling thermal decrement (both at mesomechanical and micromechanical level) and thermal edge effect stresses. The resulting biaxial stress state is a T-nT type, Figure 4a, with a biaxiality ratio n=0.74. This stress state justifies the preferential appearance of a longitudinal debond once the corresponding critical values at the interface are overcome.
Case 2: Partially relaxed residual thermal stresses provoked by the cooling thermal decrement (both mesomechanical and micromechanical), the mechanical load and the edge effect stresses (both thermal and mechanical). The resulting biaxial stress state is a T-1.13T type, Figure 4b.

Using Irwin's approach [5] for calculating the Energy Release Rate, G, of the fibre-matrix interface crack, and the proposal of Hutchinson and Suo [6] for estimating its critical value, G_c, it was possible to make a prediction of the debonds growth. Specifically, Figure 5 presents the results (G versus $\theta_d = \theta_t/2$), of the model associated with Case 1 verifying that, for values of the parameter λ in the expected range for the expected bi-material system [4], it is expected that the final extension of the debonds after curing should be within $195° \leq \theta t \leq 215º$, showing an excellent fit with the experimental observations under the hypotheses assumed.

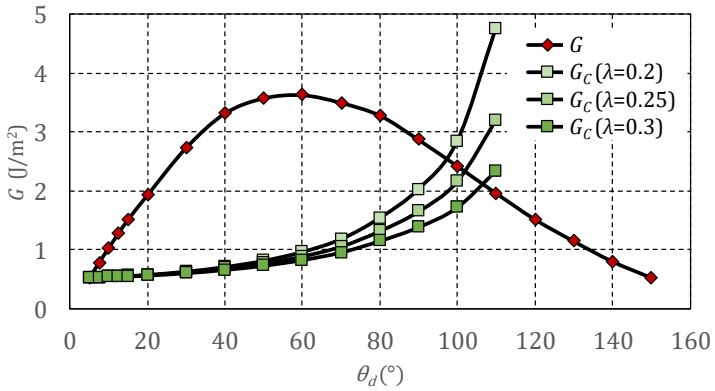


Figure 5. Energy Release Rate distribution versus semi-debond extension in the post-curing situation.

4. Conclusions

The appearance and growth of non-conventional (longitudinal) debonds in a cross-ply laminate with an UTP 90º layer was studied. An experimental campaign, microscopically detecting the longitudinal debonds nucleated during the cooling down stage after the curing process, and monitoring their growth under T-T cyclic loads, was performed. A numerical BEM model was carried out predicting the extension of the observed debonds. The key point for the agreement between the experimental and the numerical results was the consideration of the complex biaxial stress state locally acting in the surroundings of the 90º ply block fibres highly conditioned by the edge effect phenomenon.

Acknowledgments

This work was supported by the Consejería de Economía y Conocimiento Junta de Andalucía [P18-FR-3360] corresponding to the I+D+I Programa Operativo FEDER 2014-2020; Spanish Ministry of Universities ['Margarita Salas' grants for the training of young doctors] funded by the Spanish Recovery, Transformation and Resilience Plan and Next Generation EU; and Spanish Ministry of Science, Innovation and Universities [PID2021-126279OB-I00] corresponding to the State Plan 2021-2023: Knowledge Generation Projects.

References

[1] S. Sánchez-Carmona, E. Correa, A. Barroso, and F. París, "Experimental observations of fatigue damage in cross-ply laminates using carbon/epoxy ultra-thin plies," *Compos Struct*, vol. 306, no. 116564, 2023, doi: 10.1016/j.compstruct.2022.116564.

[2] S. Sánchez-Carmona, A. Barroso, V. Mantic, E. Correa, and F. París, "Non-conventional failures caused by the edge effect in cross-ply laminates made of ultra-thin plies," *Composites Part B*, vol. 254, no. 110576, pp. 1–10, 2023, doi: 10.1016/j.compositesb.2023.110576.

[3] C. Mittelstedt and W. Becker, "Free-edge effects in composite laminates," *Appl Mech Rev*, vol. 60, no. 1–6, pp. 217–245, 2007, doi: 10.1115/1.2777169.

[4] C. Sandino, E. Correa, and F. París, "Inter-fibre failure under biaxial loads in glass–epoxy composite materials: Effect of the presence of a nearby fibre," *Theoretical and Applied Fracture Mechanics*, vol. 127, Oct. 2023, doi: 10.1016/j.tafmec.2023.103956.

[5] G. Irwin, "Analysis of Stresses and Strains Near the End of a Crack Traversing a Plate," *J Appl Mech*, 1957, [Online]. Available: http://asmedigitalcollection.asme.org/appliedmechanics/article-pdf/24/3/361/6750462/361_1.pdf.

[6] J. W. Hutchinson and Z. Suo, "Mixed Mode Cracking in Layered Materials," *Advances in Applied Mechanics*, vol. 29, no. C, pp. 63–191, Jan. 1991, doi: 10.1016/S0065-2156(08)70164-9.

THERMO-MECHANICAL STUDY OF OXIDE/OXIDE CMCs USING IN-SITU MICRO-CT TESTS AND DIGITAL VOLUME CORRELATION

T. Drouin[1], F. Laurin[2] , F. Guillet[1] and G. Couégnat[3]

[1]Commisariat à l'Énergie Atomique et aux énergies alternatives
Centre d'études du Ripault, Place Raoul Dautry, 37250 Monts, France
Email: thomas.drouin@cea.fr , françois.guillet@cea.fr
[2] ONERA - University of Paris-Saclay
29 Avenue de la Division Leclerc, 92320 Châtillon, France
Email: frederic.laurin@onera.fr
[3] Laboratoire des Composites Thermostructuraux (LCTS)
Université de Bordeaux, 3 Allée de La Boétie, 33600 Pessac, France
Email: couegnat@lcts.u-bordeaux.fr

Keywords: Oxide/Oxide Ceramic Matrix Composites (CMC), Digital Volume Correlation (DVC) CT-Scan in-situ tests, Finite Elements (FE), Constitutive law, Thermo-mechanical properties.

Abstract *: Mechanical testing of materials implies the measurement of the displacement field resulting from the application of a force or a displacement at sample boundaries. Different techniques can be used to access the displacement field, but all rely on hypotheses on the field for lack of a complete full field measurement. This study considers the usage of computed tomography (CT) to access macroscopic displacement field through the Digital Volume Correlation (DVC) method. The material considered is a laminate oxide/oxide ceramic matrix composite for which accessing the 3D displacement field during a mechanical test as well as damage (cracks) which are known to develop to accompodate the strain is particularly relevant. The in-situ testing equipment and the CT sequipment used are described, as well as the method used to measure the displacement fields. Although measurements parameters and analysis protocol are still under optimization, a first result of the displacement field is presented.Although this result is in line with expectations, further progress is expected. Influence of the 3D image constrast and noise on the displacement field precision is discussed.*

1. Introduction

Ceramic Matrix Composites (CMCs) are lightweight materials with excellent mechanical properties at elevated temperature, making them promising candidates for various advanced applications. Oxyde/Oxyde (Ox/Ox) laminates are particularly relevant for moderate thermo-mechanical loadings due to their favourable balance of mechanical properties and cost. However, these materials experience damage even at low load levels, resulting in an highly non-linear behaviour. The determination of a constitutive law requires a precise understanding of their mechanical behaviour, including at the ply level, as well as rigorous observation and measurement of their damage mechanisms.

X-Ray Computed Tomography (CT) is a widely recognized imaging method allowing access to a material structure in 3D provided local absorption coefficients provide enough contrast in the resulting 3D image. In the same way that the observation of a surface speckle pattern can be used to compute a displacement field during a mechanical test [1], the material structure may provide a natural pattern that can be used to compute a 3D displacement field through Digital Volume Correlation (DVC), [2]. In addition to the 3D determination of the displacement field, the advantage of CT is that temperature has no effect whatsoever on X-Ray absorption and material contrast. Thus temperature measurements are no different than room temperature measurements if the X-Ray absorption of the furnace windows is put aside. This allows to overcome experimental issues related to measuring strain fields at elevated temperatures (strain gauges, high-temperature speckles for 2D Digital Image Correaltion (DIC)...) and

it is one of his most important adavantage oindustrial this application. However, in situ mechanical testing requires a specific device which will be discussed further on.

The material considered is this study is a quasi-isotropic 2D woven Ox/Ox laminate. Our primary objective is to identify a constitutive law (eg ONERA Damage Model (ODM) [3]) through mechanical tests and measurements carried using CT in situ testing to access 3D displacement fields.. The goal of this study is first and foremost to optimize CT parameters and DVC analysis and then conduct a series of various tests such as tension, flexion, torsion, etc.

First, the computed tomography setup (*section 2.1*) is presented. This specific device can reach a resolution of 15-30 µm on macroscopic samples (dimension 50 mm). The CMC ox/ox material and the sample geometry considered for the tensile tests are then presented (*section 2.2*) to conducted tensil test. The DVC method is briefly discussed, key aspects like regularisation being of primary importance (*section 2.3*). As the mechanical test has to be paused during CT scans, a protocol had to be defined in order to limit the influence that the CT scans may have on the stress/strain behaviour characterisation (*section 3.1*). Finally, a DVC analysis of a tensile test on [-45°,45°] layup CMC ox/ox sample is then shown and discussed (*section 3.2 and 3.3*).

2. Experiemental setup and methodology

2.1 Experimental Setup

The tomography device considered in this study is a Nikon C3 equipped with two X-Ray tubes : a 450 kV microfocus (max resolution 60 µm) with rotating anode and a 225 kV microfocus (max resolution 5 µm). This device is much larger in dimensions compared to standard laboratory µCT scanners (Figure 1). Featuring a cone-beam geometry, it is equipped with a Varex 1611 detector (4k pixels, 41cm x 41cm) placed on a 4 positions translation which allows to image a width of 1600 cm. In this study, only single detector position scans are considered in order to minimize scan durations and complexity. This equipment is primarily designed to study the interior of industrial parts and assemblies such as hydrogen tanks. With the addition of a Deben 25 kN open frame rig, it can perform standard as well as complex in-situ mechanical tests (tension, torsion, tension/torsion, pure bending) on samples similar if not identical to those tested in stand alone mechanical testing machines.. Top and bottom jaws are mounted on rotation stages which allow a full 360° rotation to perform the CT scan as well as apply torsion up to 100 N.m. It is also equipped with an air-cooled furnace allowing in-situ tests up to 1200°C. Two windows limit the amount of matter that the X-Rays have to go through and thus the additional absorption brought by the furnace.

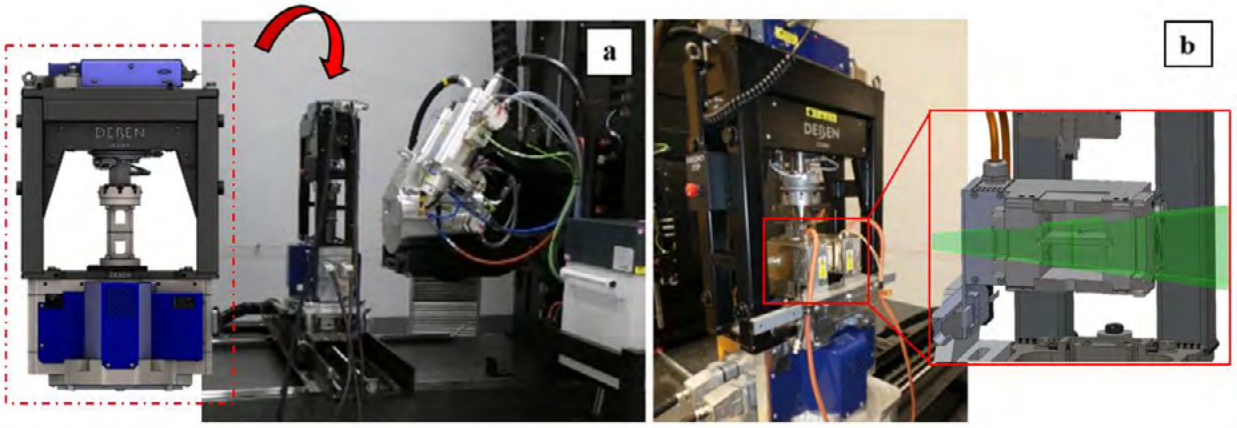


Figure 1. CT-Scan with in-situ mechanical testing machine inside (a) and his air cooled furnance (b)

Several parameters have to be taken into account when considering CT scans. The first one is the total amount of time it takes it perform the whole test. Each point on the force/displacement curve is measurement from a single scan. Considering that the whole curve should be sampled by about ten

points and that an experiment should not exceed one day, this leads to a typical CT scan duration of about 1/2 hr. A small voxel size (high resolution) ensures a better constrast in between pores and material and also discontinuities in fiber density in the threads. However, high resolution and high contrast is maximum at low energy and power which, when considering a fixed scan time, lead to more noise when compared to higher energies (X-Ray yield increase with energy) and power. Moreover, a low X-Ray intensity leads to an increase in the detector gain in order to be able to measure a projection and thus increase the detector reading noise. Scan parameters considered in this paper are not yet fully optimized and we expect to obtain better results in the future. Nevertheless, these results illustrate very well the analysis conducted. The overall scan time was 35 minutes, tube voltage was set to 210 kV, power was set to 30 W and geometric resolution to 12.7 µm. At this power, the focus size is expected to be wider than the geometric resolution, but as the resolution loss is not straightforward to estimate it was decided to use a small geometric resolution even if the real resolution is greater. The number of projections used to reconstruct the 3D volume by backprojection is 2,100.

2.2 Sample

Rectangular shape specimens without fillets are used in this study and present the following dimensions: l x w x h with l = 160 mm length, w = 20 mm width, and h = 3.30 mm thickness. This thickness corresponds to a 2D woven laminate made of 16 plies oriented at $[(+45°/-45°)_4]_s$. These specimens have the advantage of failing in the Region Of Interest (ROI) (110 mm of total length) without the need for fillet machining, unlike their counterparts at $[0/90]_s$, and they present a slightly higher theorical strain at faillure in tension ($5.0x10^{-3}$ compared to $3.5x10^{-3}$ for $[0/90]_s$). This is an interesting testing case (but more complex to conduct than a classical cross-ply tensile test with a simili quasi linear behaviour) because it allows for a larger deformation range and a high non linear part before failure [4], allowing to study the different damage occurring in the material.

To avoid some sliding during the tensile test, copper interleafs of 0.1 mm thickness have been glued between grips and sample. To address issues arising from too small sample sizes, as highlighted by [5], the samples used in this study will present a minimum size larger than 1.5 times the Representative Elementary Volume of the ply (REV) (Figure 2). Considering a $[\pm 45°]_s$ laminate, this imposes to consider a larger specimen because the REV expressed in the specimen axis is larger (7.5 mm x $\sqrt{2}$) than that associated to a cross-ply laminate.

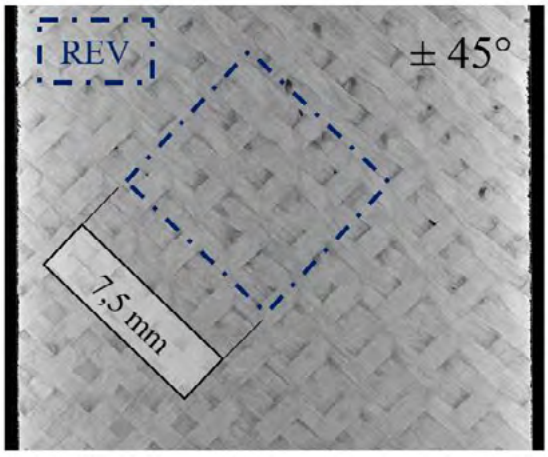


Figure 2. REV of 2D Ox/Ox CMC on ± 45° oriented ply draw to illustrated sample type use in this study, (8 hrs scan)

The maximum volume obtained by backprojection of is 4000x4000x4000 pixels, which, at a resolution of 12.7µm/voxel, allows us to study approximately a 50x50x50 mm area at the center of the sample (Figure 3).The edges of the observed zone at the top and bottom (rotated here by 90° in the illustration)

exhibit artifacts due to the conical shape of the X-ray beam. The anlysed ROI is thus reduced to 200x1500x3500 pixels to avoid these artifacts, as well as the periphery of the sample which is affected by beam hardening. The volume obtained after crop is still large (2Go for each volume, 16 bytes integer format).

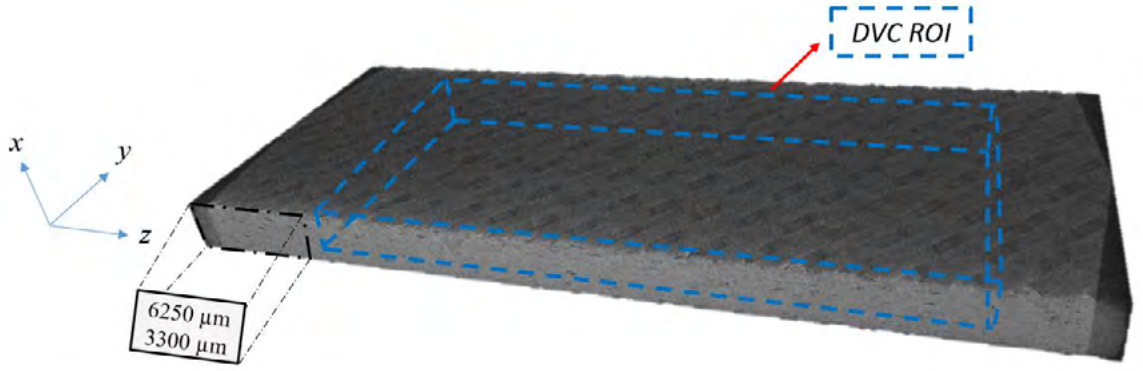


Figure 3. 3D volume of the total ROI. A 3D Gaussian convolution of isotropic width of 2 voxels has been applied so as to improve the 3D visual of the scan.

2.3 Global DVC principle

There are two possible approaches: global or local, which mainly differ in how the displacement field is computed. In the local approach, the studied zone **Ω** is subdivided into small zones of interest Ω_i. For each of these small zones, the average mechanical transformation is estimated between the reference state and the deformed state. This approach has the advantage of being easier to implement and can be easily parallelized, and this is the reason why it is currently the most used correlation method, particularly in commercial software. However, although the results can be interpolated over the entire reference zone **Ω**, the continuity of the displacement field between sub-volumes is not. In contrast to local methods, global methods rely on defining a continuous kinematic field *u(x)* over the entire region of interest examined.The formalism of this method is thoroughly described in [6]. The main advantage of this approach lies in ensuring the continuity and regularity of *u(x)* on **Ω**, thanks to local support from finite elements. This aspect is moreover interesting in the determination of constitutive equations, because the same finite elements framework can be used for DVC and numerical computations. In this study, we will consider a global DVC method using and a tetrahedral mesh created with the software “GMSH”, which will serve as local support for finite elements. The global DVC software used is "Kintsugi" [7], which is mechanically regularized [8]. In u nutshell, a rigid registration of rigid body movements is performed beforehand to estimate rigid translations and compute an initial solution for the DVC algorithm. The DVC is then conducted in a pyramidal manner to help the system to gradually converge from the largest to the smallest regularization length, starting from binned volumes to full volume.

3. Results and discuss

3.1 Tensile test

In this paper, results obtained on an in-situ tensile test are presented. The aim of this test, as explained in the introduction, is to validate the DVC displacement field analysis before conducting extensive campaigns on more complex tests (torsion, pure bending, etc.) and at higher temperatures (until 1000°C). The test curve for the ±45° specimen is reported in Figure 4, plotting the tensile force as a function of the applied displacement of the test machine crosshead. It should be noted that two discharges were made during the two nights that interrupted this three-day test, which enabled 22 scans of 35 minutes each to be performed (originally planned for 10 scans and 1 day). These scans are numbered S01, S02.... and are represented by dotted lines. In order to summarise the information presented, only the DVC

displacement fields of the scan indictaed with a black dotted line are discussed in the rest of this study. Scan denoted "S22" represents the post-mortem scan.

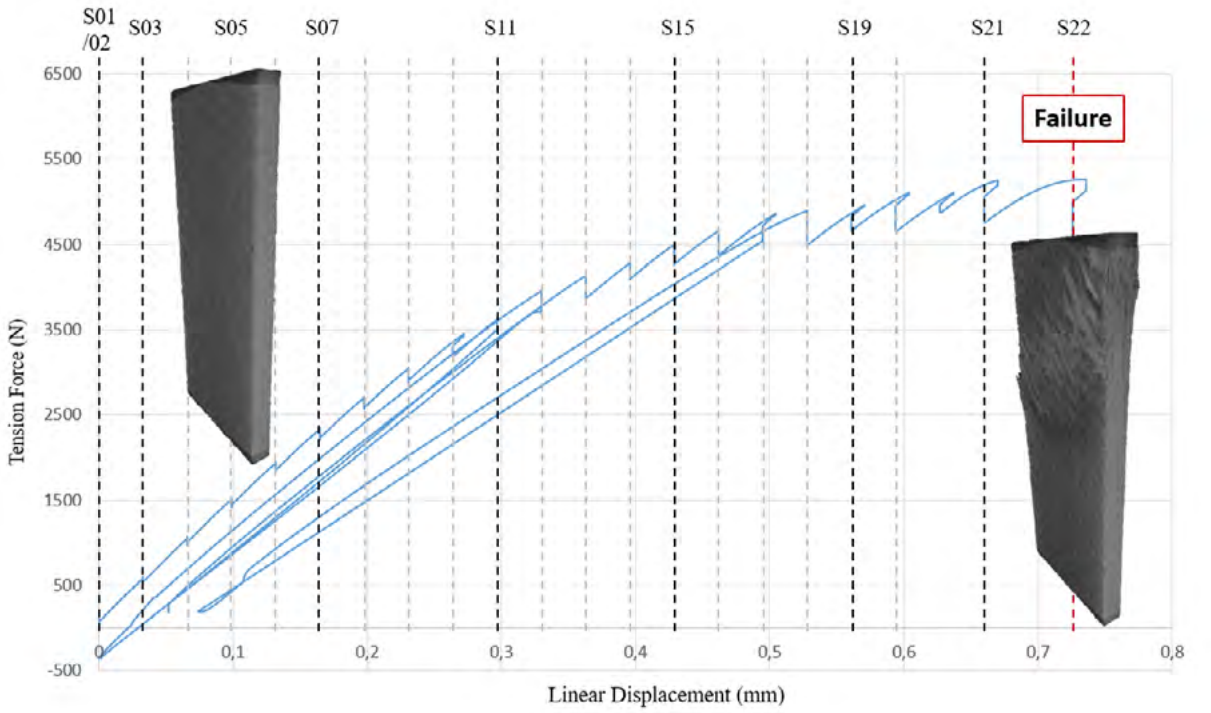


Figure 4. Experimental curve with each scan conduct during the tensile test (scans S01 to S22)

This test have been conducted at 0.1 mm/min linear tension rate and with a 33µm step between each scan. Only scans S21 and S22 were carried out with a step of 66µm so as to achieve failure faster. It is important to point out, at this stage, that force variations of the order of $\Delta F = 150$ N (*i.e.* ± 75 N) are observed during each scan when the sample is rotated 360° and the CT scan is performed. As lateral misalignment of top and bottom would only mainly result in lateral force, this variation is attributed to an overall distance variation between top and bottom during the full turn. It is however estimated from the stiffness of the material at less than 5 µm and is acceptable. An increasing relaxation during the test is also noticeable during the pauses before the scans and adds to the phenomenon of force variation observed. This could be due to over-critical cracking of the material during these tension maintenance phases. As for the discharges carried out during the night breaks, they make it possible to appreciate the loss of linearity of the behaviour, which is due to the decrease of the apparent modulus by the damage that has occurred within the material. They also highlight a fairly significant residual displacement.

3.2 Uncertainties on measurements and noise

Two scans S01 and S02 have been conducted at the initial state (0mm of linear displacement) to estimate the displacement uncertainty. This study is performed on a small crop in center of the ROI (200x400x400 voxels) and it is shown on Figure 5. DVC have been carried out with a mesh size of 16 pixels and 128 pixels of regularisation length. The DVC displays high extremum values at the edges and on the surface of the crop, as well as a spread which originates from the noise which is quite noticeable on the tomograms. The standard deviation of the displacement along the tension direction Z is -0.15 voxels, the mean displacement value being -0.55 voxels. These values are calculated with an offset of 10 pixels towards the inside of the ROI so as to avoid the artifacts observed at the free edges/surfaces. The standard deviation measured is consistent with what is expected and is a satisfactory value, even if the regularization length has to be kept quite large due to the noise on the 3D images.

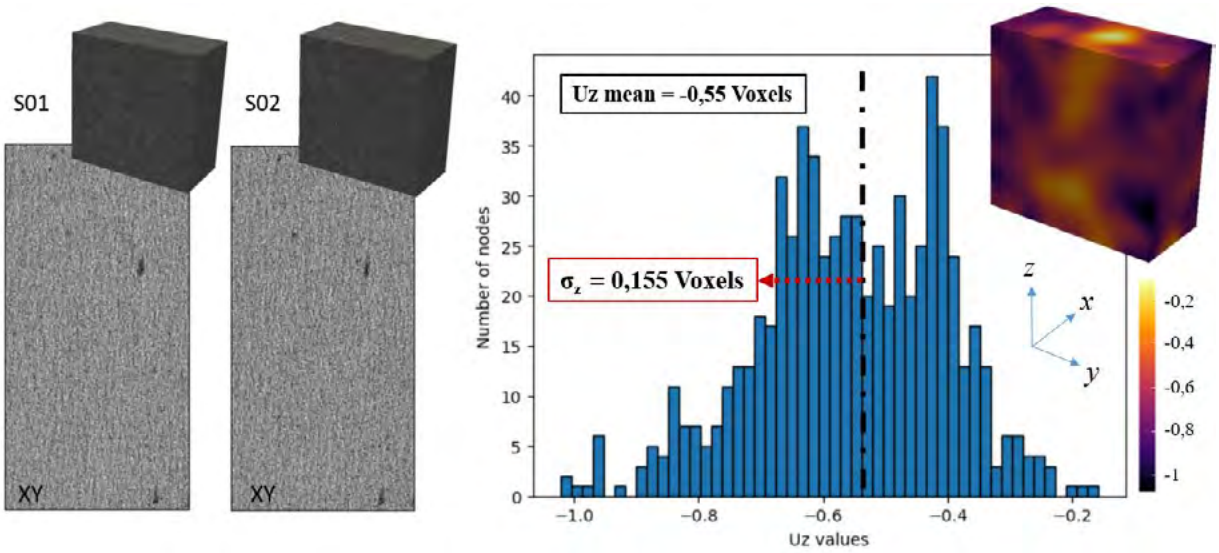


Figure 5. Small crop taken in the middle of the ROI (left) and histogram of Uz values with his mean and his standard deviation (right).

The theoretically zero deviation from the average can be explained by a dilatation of the X-ray tube target, which may result in a shift of focus of a few µm. This can happen during the first few hours of emission (in our case, 1 hour of conditioning was carried out before the S01 scan, which precedes the S02 scan).

3.3 DVC Results on displacement field and strain measurement

The displacement fields in the tensile test direction (noted U_z and expressed in voxels), determined with DVC comparing each scan with the reference scan, are presented on Figure 6. Theses displacement fields have been determined considering a mesh size of 16 pixels and 128 pixels of regularisation length (which corresponds nearly to the width of one fiber bundle of the laminate fabric). The poor quality of image contrast inside a fiber bundle and the noise impede to conduct DVC on smaller regularisation length. This is not an issue for this first test, because a tensile test just requires to evaluate the relevance of the global, smooth, displacement field measured by DVC. In order to optimise computation time, 3D volumes have been binned, which is equivalent to conduct DVC on 8 pixels mesh size and 64 pixels of regularisation length.

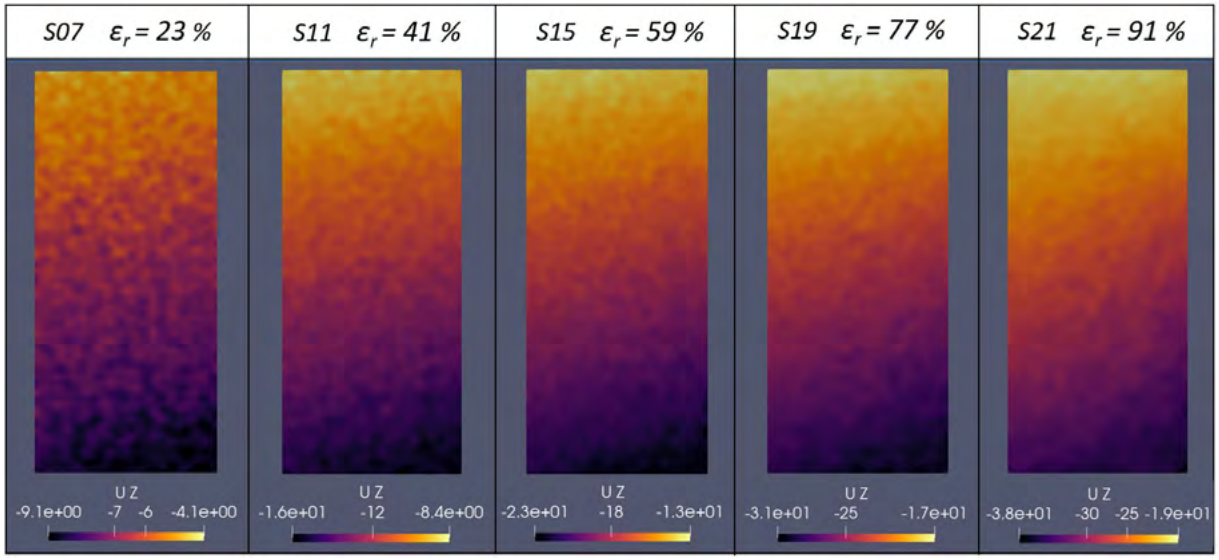


Figure 6. U_z displacement field in DVC ROI at different percents of strain at failure ε_r

In order to assess the relevance of the displacement field measurements, a 200x400x400 voxels ROI is considered to compute an averaged displacement value at the centre of the specimen. Assuming that the CT-Scan is halfway up the specimen and that there is no rigid body movement (*e.g.* slippage), this should be equal to half the machine top jaw displacement value. The tensile force curve is then plotted against the linear machine displacement value and that obtained with the DVC, as reported in Figure 7.

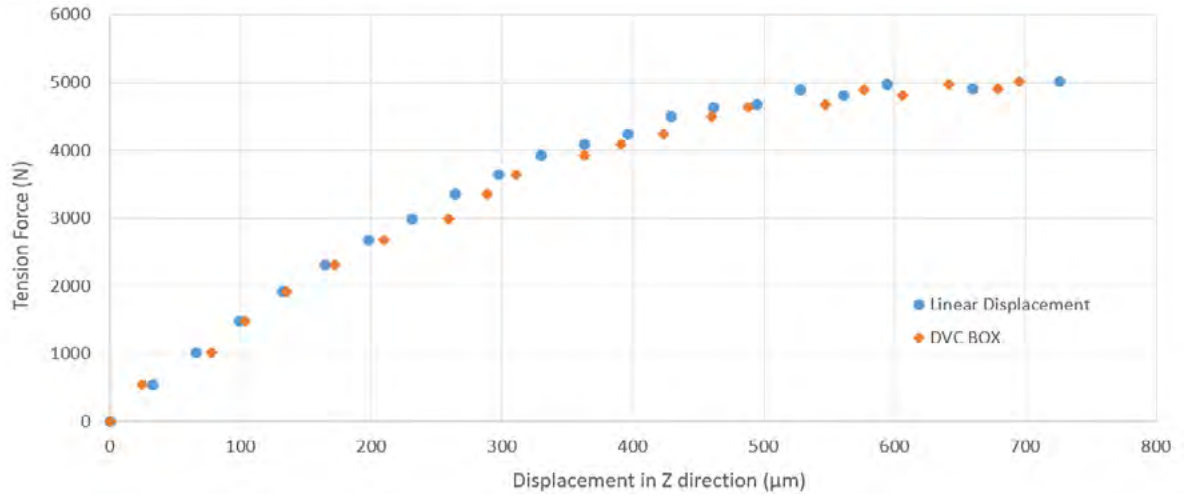


Figure 7. Tension force ploted against linear (U_z) displacement measured by testing machine curse (linear displacement) and DVC (DVC BOX)

The displacement curve measured with the DVC is in very good agreement with the linear displacement imposed by the testing machine. The small discrepancies observed can be explained by the force variations occurring during CT scans. If slippage had occurred, there would have been a clear offset between these two curves. In our case, therefore, it can be concluded that slippage is either almost non-existent or perfectly symmetrical between the two jaws during loading (which is very unlikely).

In order to minimize the effect of the spread of the displacement values on strain, the mean tensile strain value ε_{zz} is estimated from the displacement field *Uz* over the height of the scanned ROI. This value is computed considering the difference between the top and the bottom mean *Uz* values of the DVC ROI (i.e. 3500 voxels in Z direction). The different values obtained are plotted for each scan from S01 to S21 on Figure 8.

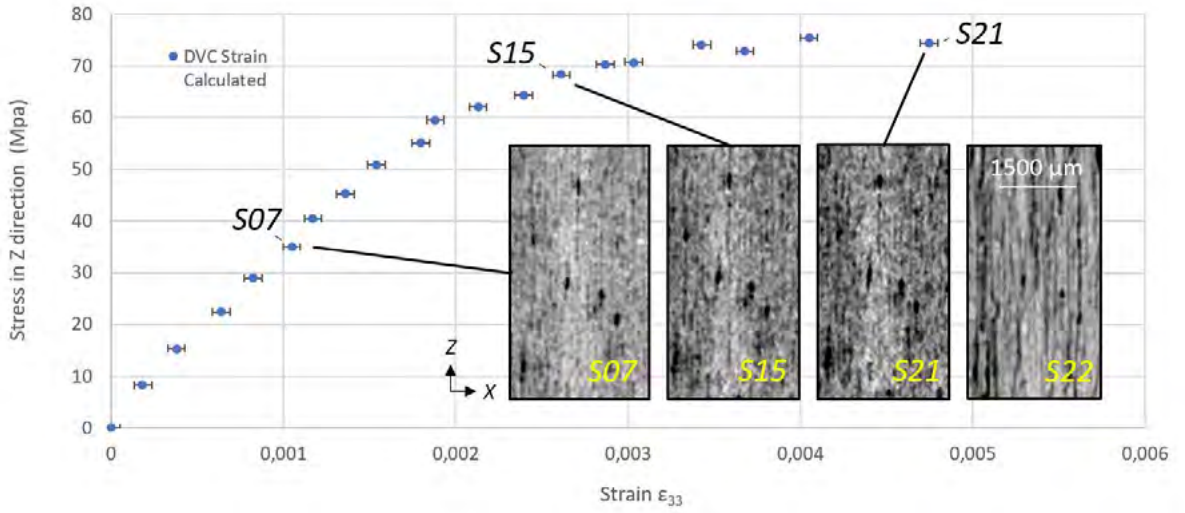


Figure 8. Stress/Strain curve in tensile direction (Z) with strain calculated by DVC in the total length of the "DVC ROI"(3500 voxels) and local damage evolution along the tensile test (viewed with 3D gaussian convolution of 2 pixels to reduce noise).

The non-linear behaviour in tension after the damage threshold (≈ $1.5x10^{-3}$) is in good agreement with classical mechanical tests performed previously in the laboratory. The damage seems to correspond to the global (45° oriented) and local fracture facies, with the development of increasing delamination cracks from the initial voids as described by [2]. Delamination seem to originate from, or at least is predominant, pores in between plies as can seen on Figure 8, although this phenomenon does not seem to be systematic.

4. Conclusion and perspective

This first result show that a full DVC analysis carried out on CT scans on a sample undergoing a mechanical test make it possible to obtain a full 3D displacement field on a macroscopic region while retaining an alsmost microscopic resolution. While the result presented here show a noise level that prevents from allowing the displacement field to vary locally, parameters have since been optimized and we expect that the final regularization length to consider (128 pixels reported here) can be decreased. A full signal/noise ratio analysis is being performed with formulae suggest by [9]. When the optimal parameters are determined, it will be also possible to analyse local damage more accurately (measurement of delamination, crack orientation and growth, etc…). Whereas a time/signal quality compromise will probably still limit the analysis, measurements of 3D displacement fields using in situ CT scans will give valuable insights on more complex tests like tension-traction combined tests, pure beding, etc. It is even more true when considering temperature experiments up to 1000°C.

References

[1] F. Hild : S. Roux. Digital Image Correlation: from Displacement Measurement to Identification of Elastic Properties – a Review. *Strain : an internal journal for experimental mechanics* , Volume 42, issue 2, pages 69-80, 2006

[2] Ante Buljac, Clément Jailin, Arturo Mendoza, J Neggers, T. Taillandier-Thomas, et al.. Digital Volume Correlation: Review of Progress and Challenges. *Experimental Mechanics*, 58 (5), pages 661-708, 2018

[3] C. Ben Ramdane : Etude et modélisation du comportement mécanique de CMC oxyde/oxyde, Doctorate thesis, Université de Bordeaux, 2014.

[4] F. Laurin ; N. Tableau ; M Kaminski ; Z Aboura ; F Bouillon : Validation of the onera damage model through comparisons with multi-instrumented structural tests on interlock woven ceramic matrix composites, *16th European Conference on Composite Materials*, June 2014, SEVILLE, Spain.

[5] N. Guel : Comportement mécanique de composites oxydes : relations procédé microstructure-propriétés, Doctorate thesis, Institut National des Sciences Appliquées de Lyon, 2018.

[6] D. Claire, F. Hild, and S. Roux. A finite element formulation to identify damage fields : the equilibrium gap method. *International journal for numerical methods in engineering*, 61 (2), pages 189–208, 2004.

[7] C. Billard : Analyse du comportement thermomécanique d'un composite C/C de l'ambiante jusqu'à 1000 ◦ C par suivi in-situ et modélisation, Doctorate thesis, Université de Bordeaux, 2021

[8] A. Mendoza, J. Neggers, F. Hild, and S. Roux. Complete mechanical regularization applied to digital image and volume correlation. *Computer Methods in Applied Mechanics and Engineering*, 355 : 27-43, 2019

[9] H.Leclerc, J-N.Périé, F.Hild, S.Roux : Digital volume correlation: what are the limits to the spatial resolution ?. *Mechanics & Industry,* 13, pages 361–371, 2012

CONTENTS

Hierarchical natural fibre composites based on cellulose nanocrystals modified luffa structures for acoustic panels

S. Ekbatani[1], D. Papageorgiou[1], H. Zhang[1*]

[1] School of Engineering and Materials Science, Queen Mary University of London, London, United Kingdom
* Corresponding author (han.zhang@qmul.ac.uk)

Keywords: Luffa fibres, porous structure, sound absorption, surface roughness

Abstract
This study investigates the effect of integrating cellulose nanocrystals on the sound absorption properties of luffa, a natural porous material. Employing locally deposited cellulose nanocrystals (CNCs), we developed a hierarchical natural fibre composite and evaluated the effects of CNC loadings (1 and 3 wt.%) on acoustic performance using the impedance tube method. The impact of panel density and thickness on sound absorption has also been evaluated. Modification of luffa with 3 wt.% CNC led to a 13% increase in the average sound absorption coefficient compared to the unmodified luffa, across the frequency range of 300 Hz to 2000 Hz. In particular, the addition of 1 wt.% CNC has significantly enhanced the sound absorption coefficient, reaching 0.8 at 1550 Hz. The study demonstrates the capabilities of integrating bio-based nano-reinforcements such as CNC in natural materials for tailored acoustic properties, offering a promising approach to developing eco-friendly acoustic materials with enhanced performance.

1. Introduction

The use of modern materials that provide improved sound absorption has become necessary due to the significant health risks associated with noise pollution [1]. One typical method of noise reduction is the use of porous materials, such as polyurethane foams , which have the unique property of converting sound waves into heat [2, 3].

More recently, the selection of acoustic materials is undergoing a significant change towards bio-based alternatives, mostly due to the negative environmental and health effects linked to synthetic options like polyurethane (PU) foam. The porous and hierarchical structures of many natural materials made them an interesting option for sound absorption, while the sound absorption coefficient of panels produced from natural fibre such as coir and tea leaf has been examined [4, 5].

However, limited research can be found on the acoustic properties of luffa fibre and composite materials [5, 6], although their highly porous structures could be highly efficient in such applications. In addition, to the best of our knowledge, no research has been conducted on the use of nanofillers to tailor the interface and tune the sound absorption properties of luffa panels, nor has the significance of employing green nanofillers such as cellulose nanocrystals (CNCs) been emphasised.

Due to their large surface area [7, 8], CNCs are also expected to adhere to the cellular walls of the luffa structure. This adherence can potentially increase the density and hierarchy of the luffa's internal network. The nanomodifications to the micro-architecture are expected to affect the sound wave interference and absorption in the material, thus leading to a change in the total sound absorption coefficient.

In this work, hierarchical natural fibre composites based on luffa and CNCs were fabricated and characterised. Different CNC loadings (1 and 3 wt.%) have been deposited onto the luffa structure, with

various panel thicknesses ranging from 6 to 12 mm manufactured. The acoustic properties have been characterised using an impedance tube method, with an systematic analysis conducted to evaluate the impact of various CNC loadings on the acoustic efficiency.

2. Materials and methods

2.1. Unmodified Luffa and CNCs Modified Luffa

The luffa sponge, derived from the matured fruit of the luffa plant, was used as the primary material. Commercially sourced dry luffa sponges used in this work have an average length of 10 cm and a diameter of 6 cm. For CNCs modification, 1 wt.% and 3 wt.% cellulose nano crystals (CNCs) solutions in water were prepared. Luffa sponges were soaked in the solutions for one hour, then left at room temperature for one day, followed by drying in an oven at 80°C for 24 hours to ensure complete drying.

2.2. Preparation of samples for sound absorption test

Cylindrical luffa sponges were halved longitudinally, and the residual seeds were extracted. The desirable thickness was achieved by layering different amounts of sponges in compression moulding, with spacers to achieve final sample thicknesses ranging from 6 mm to 12 mm. The luffa layers were compression moulded into flat sheets using a Dr. Collin P300E press (Germany) at 120°C and 30 bar pressure for a duration of 20 minutes. For testing purposes, the sheets were subsequently prepared into 100 mm-diameter discs.

3. Characterization

3.1. Bulk density

The density of various thickness samples was calculated by dividing the mass of the disc (g) by its volume (cm^3). The average density values were taken from three samples.

3.2. Scanning Electron Microscopy

The morphology of the unmodified and CNC-luffa surfaces was examined using a Scanning Electron Microscope (SEM) (FEI Inspect-F, Netherlands) to examine the impact of CNCs coating on the surface and the structure of luffa samples.

3.3. Sound absorption measurements

Sound absorption tests were conducted using the one-microphone impedance tube method, in accordance with ASTM C384 [9] (Figure 1). The standing wave apparatus was made of polycarbonate tube (wall thickness of 3 mm) with an inner diameter of 9.4 cm and length of 100 cm. A circular 10 cm diameter luffa sample was inserted inside the tube and sealed with an 8mm thick polycarbonate backing plate from the outside. A loudspeaker on the other side of the tube to produce the sinus sound using a function generator (RS PRO GFG-8216A). The oscilloscope (RS PRO RSDS 1052 DL + 50MHz) was used to measure and record the maximum (V_{max}) and minimum (V_{min}) amplitudes in volts as the microphone moved along the tube. The sound absorption coefficient (SAC) was calculated using SWR(x) as the standing wave ratio at position x and α_n as the SAC (equation 1 and 2).

$$SWR(x) = V_{max}(x)/V_{min}(x) \quad (1)$$

$$\alpha_n = 1 - ((SWR - 1)/(SWR + 1))^2 \quad (2)$$

The SAC (α_n) was measured at frequencies between 300 and 2000 Hz, while the noise reduction coefficient (NRC) was calculated for the complete range.

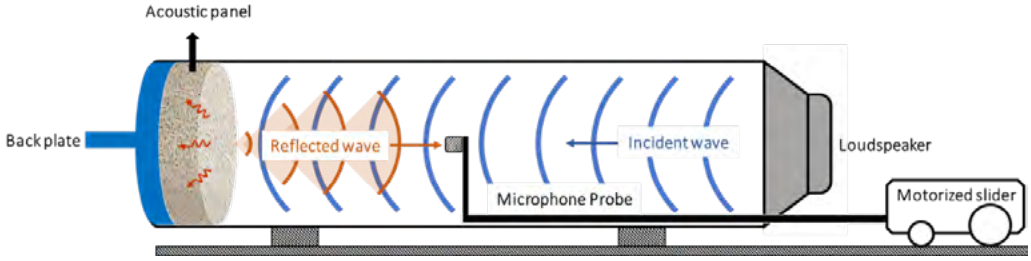


Figure 1. Schematic diagram of the instrumentation for the impedance tube method used in measuring sound absorption coefficients.

4. Results and Discussion

4.1. Morphologies and structures of neat and modified luffa

Figure 2 shows the surface of the luffa fibre, with an uneven and a porous structure observed. With the CNC deposited onto the luffa surface, a fine and relatively uniform coating can be found from the SEM images, with an increased surface roughness. The dimensions of certain cavities in luffa structures have been reduced slightly, while evidence of CNC exposed at cavities was also noticed.

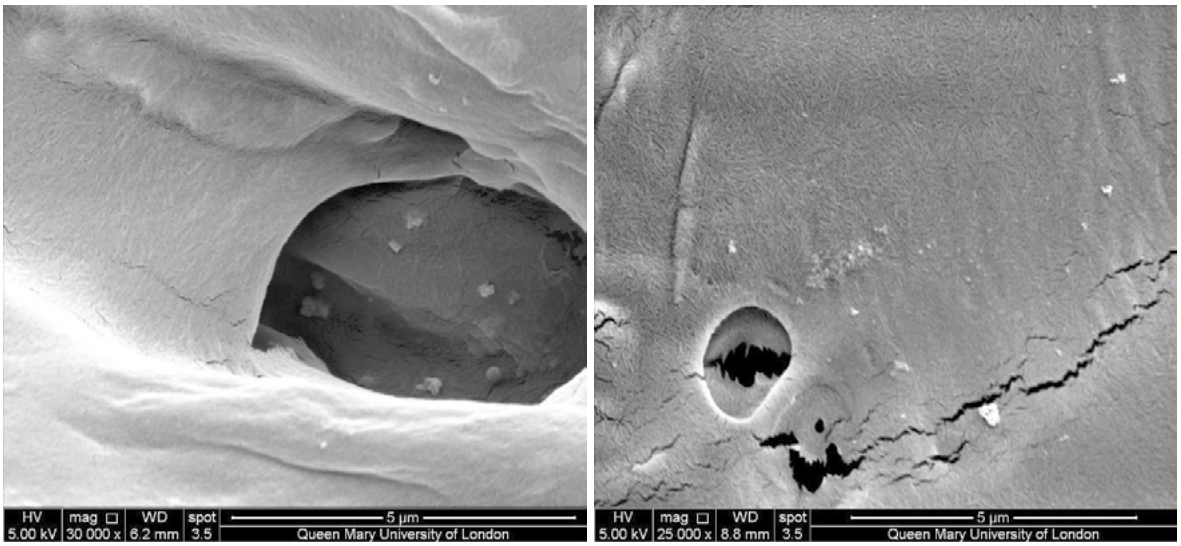


Figure 2. SEM images of neat luffa (left) and 1 wt.% CNC coated luffa (right).

4.2. Sound absorption properties

The neat luffa samples without any modifications, exhibited a noise reduction coefficient (NRC) of 0.46 in Figure 3, although a relatively large variation can be found due to the porous and varied structures between samples. When introducing CNC at concentrations of 1 and 3 wt.% to the luffa samples, a slightly improved NRC was obtained, with values slightly above 0.5 for both cases, in the frequency range of 300 to 2000 Hz.

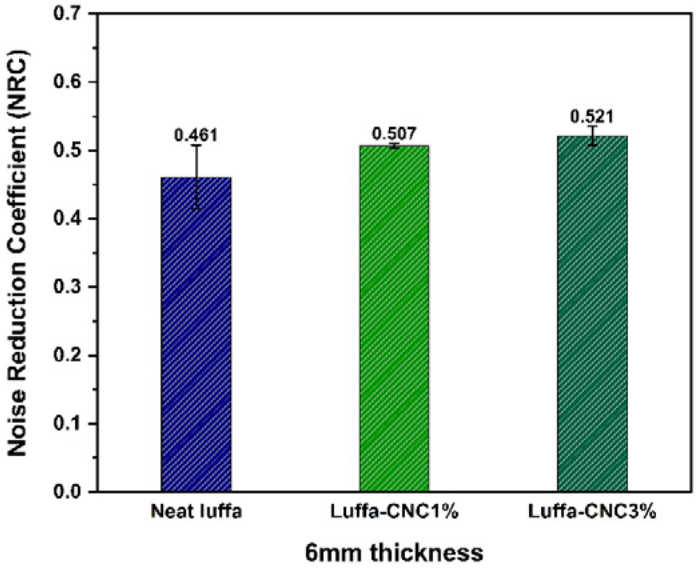


Figure 3. Noise Reduction Coefficient (NRC) comparison among unmodified luffa and CNC-enhanced luffa composites.

The effect of CNC on luffa structures has been examined with a series of panel thicknesses. In Figure 4, it can be seen that the addition of 1 wt.% CNC clearly enhanced the sound absorption values across all thicknesses. As acoustic waves enter these fibrous materials, the airflow inside the pores causes the cellular walls to vibrate and experience friction. This interaction results in the generation of a high resistance, converting sound energy into heat energy, thus increasing the reduction of sound vibrations [10]. The introduction of CNC is expected to enhance the sound energy dissipating process, hence increase the sound absorption properties. In addition, the modified surface feature of CNC is also expected to affect the reflection patterns of sound waves hence the dampening of the structure. It is worth noting that the SAC value was approaching to 0.8 at the frequency 1550 Hz, highlighting the potential of developed hierarchical natural fibre composites in acoustic applications.

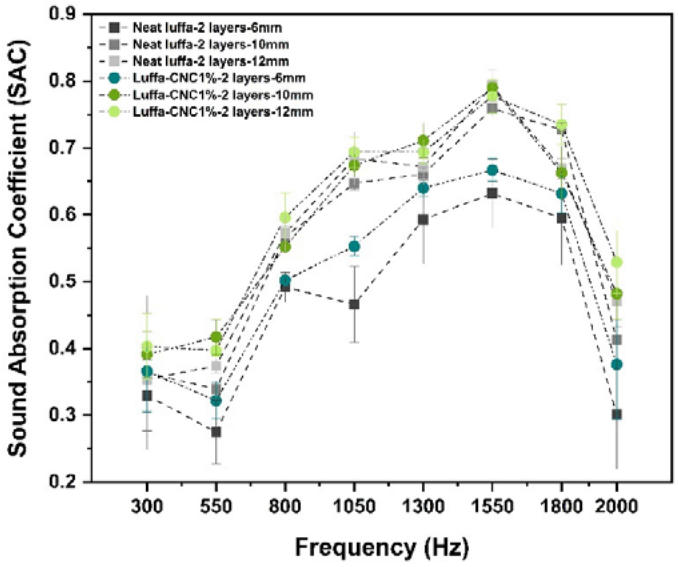


Figure 4. Effect of CNCs modification on the sound absorption coefficient of the luffa panels over various panel thicknesses.

Table 1 summarises the calculated density, porosity, and NRC of the fabricated panel. It is commonly observed that a greater sample thickness is often associated with a higher sound absorption coefficient. The improvement with increased thickness is believed due to the increased porosity in luffa's structure, as seen by the porosity values. However, with the introduction of 1 wt.% CNC, an increased NRC can be found for the panels with same thickness due to enhanced sound energy dissipation, despite the slightly reduced porosity.

Table 1. Panels characteristics and NRC values of neat and CNCs-modified luffa panels.

Sample Name	Thickness (mm)	Calculated density (g/cm³)	Porosity (ε)	NRC (300 Hz - 2000 Hz)
Neat luffa	6	0.239 (±0.0193)	0.730	0.46 (±0.047)
	8	0.218 (±0.0527)	0.753	0.55 (±0.009)
	10	0.150 (±0.0151)	0.830	0.56 (±0.017)
	12	0.165 (±0.0053)	0.813	0.57 (±0.023)
Luffa-CNC1%	6	0.279 (±0.0219)	0.686	0.51 (±0.003)
	8	0.251 (±0.0074)	0.718	0.58 (±0.011)
	10	0.201 (±0.0135)	0.774	0.59 (±0.012)
	12	0.193 (±0.0114)	0.784	0.60 (±0.012)

5. Conclusions

This study demonstrated the capability of luffa sponge as a highly efficient porous material for sound absorption applications, especially when modified with cellulose nanocrystals (CNC). The addition of 1 and 3 wt.% CNC resulted in enhancements in sound absorption coefficients, particularly in the frequency range of 1050-1550 Hz, with the NRC value of 0.52 achieved.

References

[1] T. Zhu, S. Chen, W. Zhu, Y. Wang, and Y. Jiang, "Sound Absorption Property of Polyurethane Foam with Polyethylene Fiber," *Materials Science,* vol. 25, no. 1, 2019, doi: 10.5755/j01.ms.25.1.19720.

[2] M. J. Cops, J. G. McDaniel, E. A. Magliula, D. J. Bamford, and J. Bliefnick, "Measurement and analysis of sound absorption by a composite foam," *Applied Acoustics,* vol. 160, 2020, doi: 10.1016/j.apacoust.2019.107138.

[3] J. Lee and I. Jung, "Tuning sound absorbing properties of open cell polyurethane foam by impregnating graphene oxide," *Applied Acoustics,* vol. 151, pp. 10-21, 2019, doi: 10.1016/j.apacoust.2019.02.029.

[4] M. Hosseini Fouladi, M. Ayub, and M. Jailani Mohd Nor, "Analysis of coir fiber acoustical characteristics," *Applied Acoustics,* vol. 72, no. 1, pp. 35-42, 2011, doi: 10.1016/j.apacoust.2010.09.007.

[5] H. Koruk and G. Genc, "Investigation of the acoustic properties of bio luffa fiber and composite materials," *Materials Letters,* vol. 157, pp. 166-168, 2015, doi: 10.1016/j.matlet.2015.05.071.

[6] Y. Chen *et al.*, "A novel sound absorbing material comprising discarded luffa scraps and polyester fibers," *Journal of Cleaner Production,* vol. 245, 2020, doi: 10.1016/j.jclepro.2019.118917.

[7] X. Xu, F. Liu, L. Jiang, J. Y. Zhu, D. Haagenson, and D. P. Wiesenborn, "Cellulose nanocrystals vs. cellulose nanofibrils: a comparative study on their microstructures and effects as polymer reinforcing agents," *ACS Appl Mater Interfaces,* vol. 5, no. 8, pp. 2999-3009, Apr 24 2013, doi: 10.1021/am302624t.

[8] D. Bondeson, A. Mathew, and K. Oksman, "Optimization of the isolation of nanocrystals from microcrystalline cellulose by acid hydrolysis," *Cellulose,* vol. 13, no. 2, pp. 171-180, 2006, doi: 10.1007/s10570-006-9061-4.

[9] Standard Test Method for Impedance and Absorption of Acoustical Materials by Impedance Tube Method, doi: 10.1520/c0384-04r16.

[10] A. Suthatho, P. Rattanawongkun, N. Tawichai, S. Tanpichai, A. Boonmahitthisud, and N. Soykeabkaew, "Low-Density All-Cellulose Composites Made from Cotton Textile Waste with Promising Thermal Insulation and Acoustic Absorption Properties," *ACS Applied Polymer Materials,* vol. 6, no. 1, pp. 390-397, 2023, doi: 10.1021/acsapm.3c02076.

INFLUENCE OF LARGE-SCALE FIBRE BRIDGING IN THE CRACK GROWTH RATE OF MIXED-MODE DELAMINATION OF A UNIDIRECTIONAL GLASS-EPOXY COMPOSITE

Ruben I. Erives, Bent F. Sørensen

Department of Wind and Energy Systems, Technical University of Denmark,
Frederiksborgvej 399, 4000 Roskilde, Denmark
Email: riea@dtu.dk, Web Page: https://wind.dtu.dk/

Keywords: Composite fatigue, Crack Growth Rate, Fibre bridging

Abstract
In the present research the influence of large-scale fibre bridging on the crack growth rate in mixed-mode delamination of unidirectional glass-epoxy composites was investigated. The study employed double cantilever beam specimens subjected to cyclic even and un-even bending moments, i.e., steady-state specimens. In the study, the bridging ligaments at fracture process zone (developed after several cycles) were cutoff and the tests are then subject to the same previous load. This led to an accelerated crack growth rate. Varying the length of the bridging zone (while keeping everything else, e.g., load, the same) has a strong effect on the crack growth rate.

1. Introduction

There is a large interest in understanding the propagation of delamination in composite materials under cyclic loading. For instance, in wind turbine rotor blades, delamination of the main spar-cap is of great concern, especially considering the continuous trend of upscaling to very large blades, exceeding 100m in length.

Predicting the crack growth rate (CGR) of a delamination crack is a difficult task given the large uncertainty of the external loading, e.g., variable amplitude loading history, as well as the uncertainty on the material response to loading, i.e. the CGR. Currently, most predictive models of composite delamination are based on the Paris-Erdogan relationship [1] [2] [3] [4] [5]. However, implicit in this relationship is the assumption of small-scale fracture (i.e., the assumption that the size of the fracture process zone (FPZ) is negligible in comparison with all other geometric dimensions). This is, however, not valid for delamination cracks with a large-scale fracture process zone, which is observed in most fibre reinforced polymer (FRP) composites due to fibre bridging.

Although fibre bridging is a toughening mechanism with positive effects on the material's resistance to fracture, the effect of fibre bridging on cyclic crack growth is not sufficiently well understood, and there are no design criteria that accounts for large scale fibre bridging. This means that fibre bridging as a toughening mechanism is largely, if not completely, under-exploited. Promising ideas for developing materials with passive crack arrest and crack stability [1] [6] among other can be derived from an understanding of fibre bridging.

Fibre bridging can affect the crack propagation in two stages, during the formation of a large-scale fracture process zone and during propagation of the fully developed FPZ, where the CGR is near-constant. In the later, fibre bridging enhances crack resistance by shielding the crack-tip from the remote load [7]. In the former, the formation of a large-scale fracture process zone dissipates energy due to the presence of different damage mechanisms, e.g., fibre full out. When a delamination crack is initiated, a crack front is formed. Then, the FPZ is only composed by the crack front and is thus negligible in size. However, with increasing number of load cycles the crack-tip advances leaving bridging ligaments in its wake. The zone from the microscopic crack-tip (in the fracture plane) until the last active (loaded)

bridging ligament becomes the new large-scale FPZ. Ligaments are created until a certain crack separation is reached and the ligaments are overloaded and break. At this stage, the FPZ is fully developed, and the small-scale fracture assumption is no longer valid, so the entire fracture process zone needs to be modelled. From this point, the FPZ will translate in a self-similar fashion in steady-state specimens, at the same, near-constant CGR as the crack-tip. Note that for non-steady-state specimens, the bridging length will not be constant [8]. In a crack propagation curve, the previously described process would resemble that of the schematic shown in Figure 1.

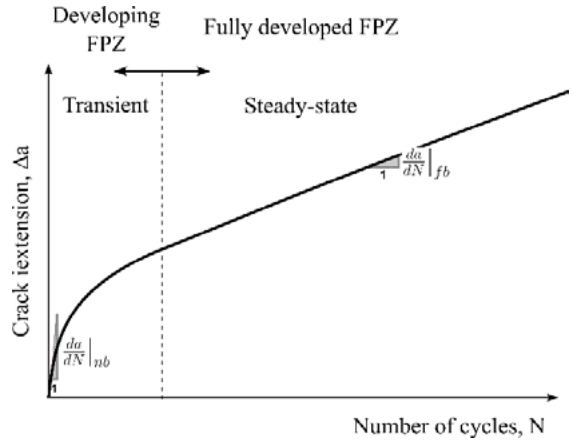


Figure 1. Schematic of the crack length of FRP composites undergoing delamination with fibre bridging

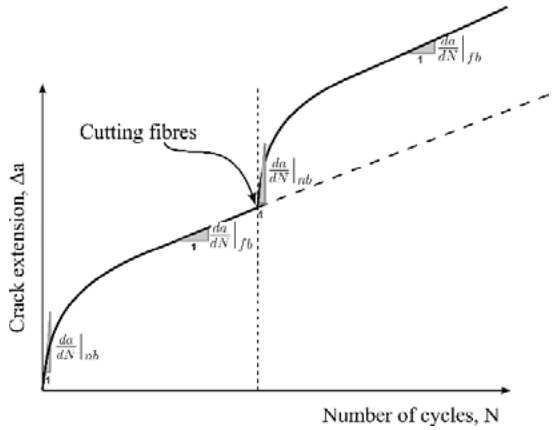


Figure 2. Visual illustration of proposed hypothesis

The scenario described above has been documented for glass-fibre composites where testing was conducted on double cantilever beams (DCB) specimen loaded by un-even bending moments (DCB-UBM), which is a steady-state specimen [9]. There are however, only few experimental studies on cyclic crack growth in composites under large-scale bridging [10] [11].

In the present work, we have conducted series of cyclic DCB experiments with un-even bending moments (DCB-UBM) to investigate the effect of fibre bridging on the crack growth rate of a delamination crack at different mixed-mode values. In particular, we have modified the length of the bridging zone by cutting off fibre ligaments, and studied how this affected the crack growth rate.

2. Problem statement

The hypothesis to be tested can be summarised as follows:

The development of the fracture process zone (from a “sharp” crack tip to large-scale fracture process zone) under cyclic loading leads to the shielding of the crack-tip, and thus slows the initial crack growth rate $da/dN|_{nb}$(where the subscript nb stands for “no-bridging”) until the fracture process zone (FPZ) is fully developed. Once the FPZ is fully developed it retains its characteristic length (length of the fully developed fracture process zone) and starts translating. The crack-growth rate takes a constant value $da/dN|_{fd}$ (where fd stands for “fully developed”) provided the cyclic loading remains constant. This is schematically illustrated in Figure 2.

In the present work we have tested the hypothesis using the following procedure; First, a DCB is subject to a cyclic loading with a fixed ratio of maximum and minimum values of the applied load (in the form of bending moments) until it develops its FPZ. Second, the test is stopped, and the length of the bridging zone is reduced by cutting the bridged ligaments (details of this procedure are given in the methods section). Third, the specimen is loaded again under the same applied cyclic loading as previously until its FPZ is fully developed, which is when da/dN becomes constant again. This sequence is conducted once for the nominal mode I, and twice for the mixed-mode.

3. Methods

3.1. Materials

DCB specimens were manufactured using a unidirectional (UD) glass fabric (E-1182 Saertex) embedded in Epoxy Hexion. The curing process involved 12 hours at 40°C followed by 10 hours at 80°C. The laminate was constructed with 20 layers, incorporating a 20 mm long Teflon insert of 15µm thickness in the middle plane to serve as the crack initiator. All laminates utilized strands of glass fibres, oriented perpendicular to the UD direction, as backing, all of which were positioned facing downwards at every laminae. The nominal dimensions of the specimens were a length (L) of 500 mm, a width (W) of 30 mm, and a thickness corresponding to 20 layers (~17 mm) [12].

3.2. Experimental setup and instrumentation

The DCB specimens were fixed at the uncracked end and subjected to uneven bending moments at the cracked end to induce mixed-mode conditions, in accordance to the test configuration described in [9]. A schematic of the test configuration is shown in Figure 2. The cyclic loading is imposed using a hydraulic cylinder which pulls on a wire that is attached to the lever arms (fixed in length). The loading ratio was set at R=0.1, a commonly used value in the literature for comparative analysis, with a cyclic loading frequency of 2 Hz to minimize frequency effects. A lower frequency also helped to minimize dynamic conditions arising from the inertia of the lever arms.

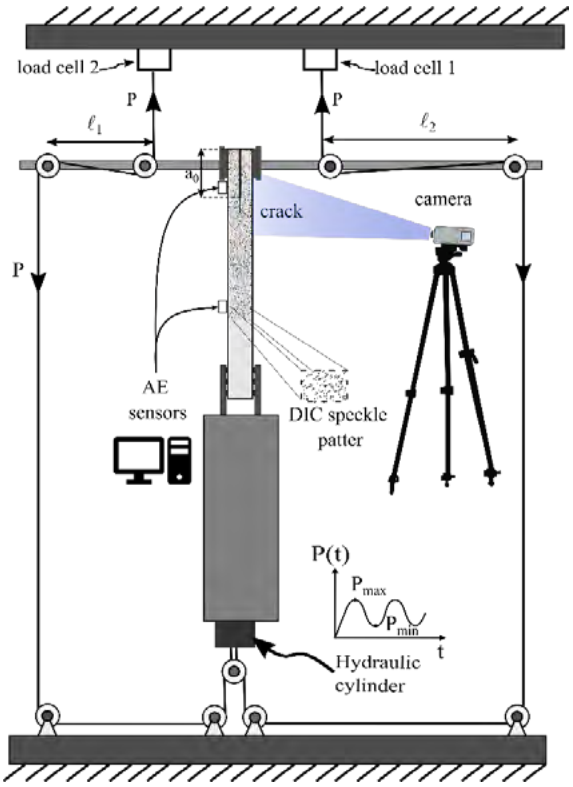


Figure 3. Schematic of cyclic tests configuration using a DCB with un-even bending moments

Table 1. DIC experimental set-up

Image resolution	3296 x 2472 pixels
Field-of-view	~90-120 mm
Image scale	~750 Pixel/mm
Image acquisition	Logarithmic*
Stand-off distance	≈ 200 mm
Patterning technique	Ink-pad speckle

Table 2: List of DIC-parameters

DIC software	GOM Correlate 2019 [13]
Subset size	~50 pixels
Subset interpolation	Bicubic
Extensometer size	10x100 mm
Displacement noise floor	~1-6 µm

*Pictures were taken at the maximum and minimum amplitude every cycle for cycles 1-100, then every 10 cycles for cycles 100-1000, then every 100 cycles for cycles 1000-10,000, then every 1000 for cycles 10000-100000, and every 10,000 afterwards.

The test setup was instrumented with a machine vision camera (EVO8050) aimed at the crack. All specimens were marked with an ink speckle pattern pad from iMetrum [14] on the visible side of the DCB where images were captured at maximum and minimum amplitude following a logarithmic cycle increment*. The images were analysed using GOM Correlate Pro 2019 [13] software for a 2D digital

image correlation (DIC) analysis to obtain displacement fields of the visible surface of the DCB. The optical experimental setup and the parameters used for the DIC measurement of the opening displacement are detailed in Table 1 and Table 2.

Some of the specimens where also instrumented with acoustic emission (AE) sensors (two daisy-chained 1283 USB AE nodes from MISTRAS group physical acoustics each with R15-alpha sensors). The sensors were located 10 mm, and 110 mm ahead of the crack initiator. The AE win set-up file for the tests specified a detection threshold of 45 dB and a hit data set including rise time, counts, MARSE energy, duration, amplitude, and average carrier frequency.

3.3. Automatic crack tip location measurements based on DIC

With a full-field displacement measurement of a the measured DCB surface, a "continuous virtual extensometer" can be used to post process the opening displacements. The virtual extensometer was created using two parallel curves aligned with the crack plane. In an unloaded state the initial distance between the parallel lines is Δ_0. As soon as the DCB is loaded, the separation between the parallel lines i.e., $\Delta u_i = u_i^+(x_1) - u_i^-(x_1)$ will take on values larger than zero in the locations where a crack has formed. The largest positive location in the x_1 direction along the crack plane where $\Delta u_i > 0$ can thus be considered as the current position of the crack-tip. In practice, a small threshold value (as small as possible, but larger than the measurement noise floor) must be used to identify such a transition given the displacement noise from DIC measurements. We used a value of ~2 times the displacement noise floor, which is between 1-6 μm depending on the image quality of at a given test set-up and current cycle. Effects such as light variation, and machine vibration can lead to lower image quality, and therefore higher displacement noise floor. A schematic of the procedure is shown in Figure 3.

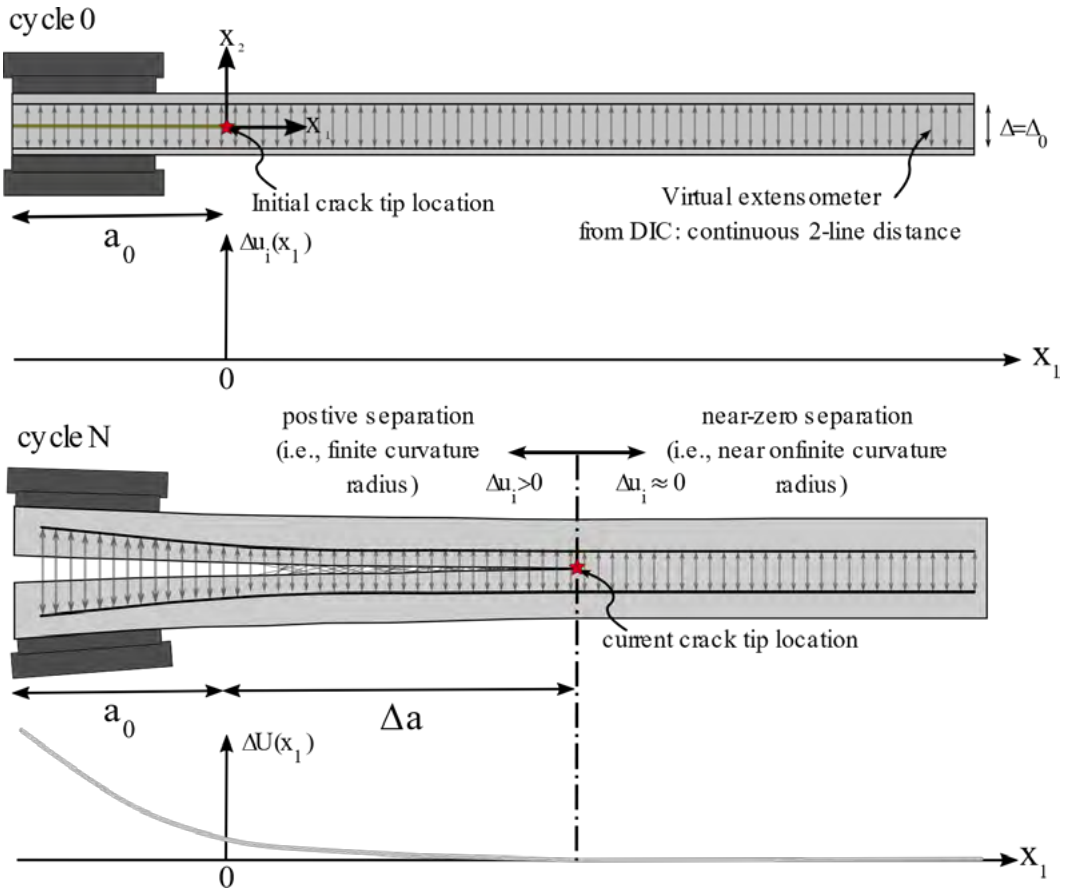


Figure 4. Schematic of the determination of the crack-tip location as a function of the cycle count

3.4. Cutting fibre bridging to restore FPZ

To cut the bridged ligaments of the test specimens after their initial block of cyclic loading the following procedure was implemented. After stopping and unloading the specimen, the test setup is change towards nominal mode I. Prior to loading the specimen (in nominal mode I) a clamp was placed at the current crack-tip ($x_1 = \Delta a$) location so that the crack tip is prevented from experience any opening. The specimen is then loaded so that the ligaments are visible, which are then cut-off using a thin razor blade (blade thickness of 10 μm, which is thinner than the original slip foil acting as the crack starter).

3.5. Data analysis

The nominal mode mixity of the specimens was calculated using an analytical solution for orthotropic DCB-UBM specimen [15] as:

$$\psi(\lambda, M_1/M_2) = tan^{-1}\left\{\lambda^{-1/4}\frac{\sqrt{3}}{2}\frac{1+M_1/M_2}{1-M_1/M_2}\right\}, \quad \text{for } |M_1| < M_2, \tag{1}$$

where M_1 and M_2 are the applied moments, and λ is an elastic non-dimensional parameter $\lambda = E_{11}/E_{22}$.

The maximum and minimum values of the fracture resistance (J_{max}, and J_{min} respectively) were calculated from an analytic solution of the J-integral for a DCB-UBM specimen [16].

$$J = \frac{21(M_1^2 + M_2^2) - 6M_1M_2}{4B^2H^3E_1'}, \quad \text{for } |M_1| < M_2, \tag{2}$$

where B is the width of the specimen, $2H$ is the height of the specimen, and E_1' is the young's modulus under plain strain.

4. Results and discussion

The crack growth as a function of the number of cycles is shown in Figure 3 for the specimen loaded under nominal mode I, and in Figure 4 for the one loaded with a mixed mode. The data corresponding to the crack growth is shown in blue curves. The different shades of blue indicate different blocks, where the dark blue corresponding to the first cyclic block, and the lighter curves correspond to sub-sequent blocks. The end of each block, which is when the ligaments are cut-off, is marked with a vertical dashed line. Note that the process of stopping and cutting off the developed fibre ligaments is carried once for the specimen under nominal mode I, and twice for the specimen under mixed mode. In Figure 3 the cumulative energy obtained from the AE sensors is superpose to the crack growth rate and shown with red curves. The same convention of colour shades is followed.

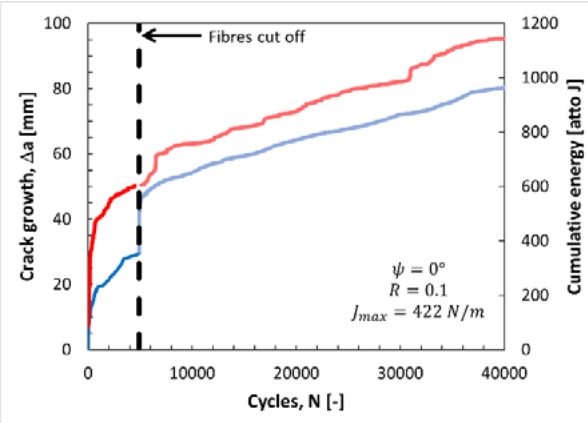


Figure 5. The crack growth as a function of the number of cycles of the nominal mode I ($\psi = 0°$) test specimen shown in shades of blue, where the darker blue represents the first block, and the light blue the subsequent block. The red curve represents the cumulative energy from the AE sensors.

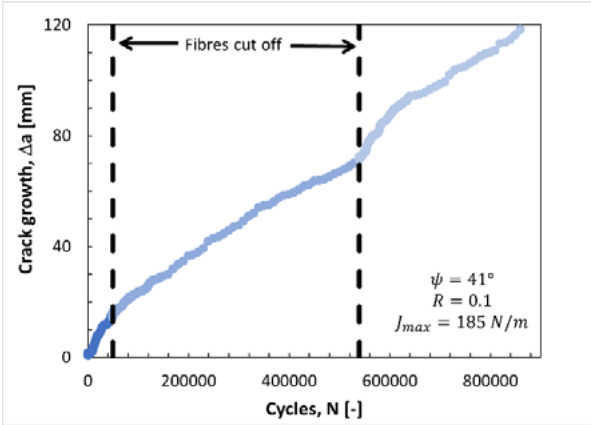


Figure 6. The crack growth as a function of the number of cycles of the mixed mode ($\psi = 41°$) test specimen shown in shades of blue, where the darker blue represents the first block, and the lighter blue the subsequent blocks.

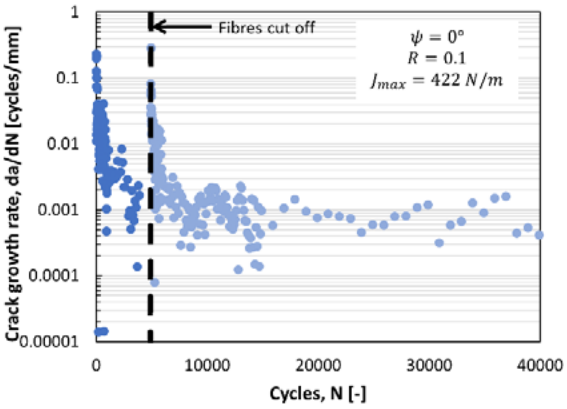


Figure 7. Crack growth rate as a function of the number of cycles of the nominal mode I ($\psi = 0°$) test specimen shown in dark blue markers for the first block and light blue for the subsequent block.

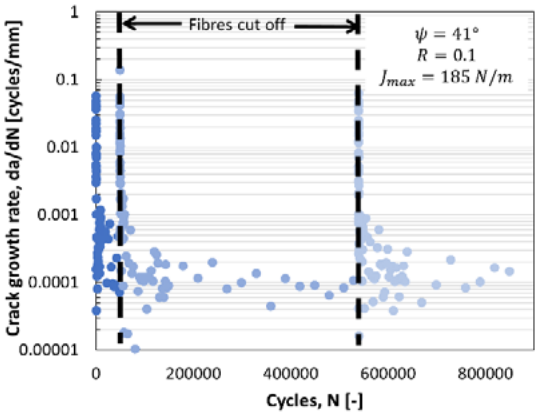


Figure 8. Crack growth rate as a function of the number of cycles of the mixed mode ($\psi = 41°$) test specimen shown in dark blue markers for the first block and lighter blue markers for the subsequent blocks.

In Figure 5 and Figure 6 the crack growth rate as a function of the number of cycles is shown for the specimen under nominal mode I, and mixed mode respectively. The same plotting convention as in the previously shown figures is used.

The CGR of the initially unbridged crack is in the order of 0.1 mm/cycle (or higher), while the CGR of the fully developed bridged crack is 0.0001-0.001 mm/cycle, i.e., a growth rate of ~100 times that of the unbridged crack.

The effect of cutting off the fibres is very clear, specially from the crack growth rate data. It is worth noting that such the effect of cutting off the fibres is not always easy to identify directly from the crack growth data. Take the first time the fibres were cut off in the mixed-mode specimen, with the current x and y scales in the figure its effect on Δa are not easy to appreciate (Figure 5). However, the higher CGR after cutting off fibres is evident, see Figure 8. It is worth noting that, a similar behaviour i.e., rapid increase after fibres are cut-off, can be seen in the cumulative energy obtained from the acoustic

emission signals. Although we have chosen to present the cumulative energy only (Figure 4), the same pattern was found in all the recorded AE signals i.e., duration, amplitude, amplitude frequency, hit count, and rise.

5. Conclusions

Experimental evidence of the effect of large-scale fibre bridging in the crack growth rate of a delamination crack in a UD composite has been presented. It can be concluded that the crack growth rate of a delamination crack with large-scale fibre bridging depends strongly on the size of the FPZ.

Acknowledgments

We would like to acknowledge the AINDT project (number 0224-00110A), which is funded by the Innovation Fund Denmark for providing resources for the current article.

References

[1] B. Cox and D. Marshall, Concepts for bridged crackc in fracture and fatigue, *Acta metall. mater.,* vol. 42, no. 2, pp. 341-363, 1994.

[2] A. Turon, J. Costa, P. P. Camanho and C. G. and Davila, Simulation of Delamination in Composites Under High-Cycle Fatigue, *Composites Part A,* vol. 38, no. 11, pp. 2270-2282, 2007.

[3] H. P. and S. Hallett, A fatigue degradation law for cohesive interface elements - Development and application to composite materials, *Int. J. Fatigue,* vol. 32, no. 11, pp. 1774-1787, 2010.

[4] A. Pirondi and F. and Moroni, A Progressive Damage Model for the Prediction of Fatigue Crack Growth in Bonded Joints, *The Journal of Adhesion,* vol. 86, no. 5-6, pp. 501-521, 2010.

[5] A. Turon, P. Camanho, J. Costa and D. C.G., A damage model for the simulation of delamination in advanced composites under variable-mode loading, *Mechanics of Materials,* vol. 38, no. 11, pp. 1072-1089, 2006.

[6] B. Cox and D. Marshall, Stable and unstable solution for bridged cracks in various specimens, *Acta metall mater,* vol. 39, no. 4, pp. 579-589, 1991.

[7] B. N. Cox, Extrinsic factors in the mechanics of bridged cracks, *Acta metall. mater.,* vol. 39, no. 6, pp. 1189-1201, 1991.

[8] Z. Suo, G. Bao and B. Fan, Delamination R-curve phenomena due to damage, *J. Mech. Phys. Solids,* vol. 40, pp. 1-16, 1992.

[9] J. W. Holmes, L. L., B. F. Sørensen and S. Wahlgren, Experimental approach for mixed-mode fatigue delamination crack growth with large-scale bridging in polymer composites, *Journal of Composite Materials,* vol. 48, no. 25, pp. 3111-3128, 2014.

[10] S. M. Jensen, L. Carreras, B. Bak, C. Lequesne and E. Lindgaard, A crack growth rate model with load history effects for mode I fatigue-driven, *International Journal of Fatigue,* 2023.

[11] S. Jensen, B. Bak, J. Bender and E. L. L. Carreras, Transient delamination growth in GFRP laminates with fibre bridging under variable amplitude loading in G-control, *Composites Part B,* vol. 225, 2021.

[12] R. Erives, B. F. Sørensen and S. Goutianos, Extraction of mix-mode cohesive laws of composites undergoing delamination with large scale bridging, *Composites Part A: Applied Science and Manufacturing,* vol. 165, 2023.

[13] GOM Correlate Pro, GOM Metrology ZEISS, 2023. [Online]. Available: https://www.gom.com/en/products/zeiss-quality-suite/gom-correlate-pro.

[14] imetrum, [Online]. Available: https://www.imetrum.com/.

[15] B. F. Sørensen, K. Jørgensen, K. Jacobsen T. and C. Østergaard, DCB-specimen loaded with uneven bending moments, *International Journal of Fracture,* vol. 141, no. 1-2, pp. 163-176, 2006.

[16] S. B. F. and J. T. K., Characterizing delamination of fibre composites by mixed mode cohesive laws, *Composites science and technology,* vol. 69, no. 3-4, pp. 445-456, 2009.

CONTENTS

©2024 | 3_ERIVES ANCHONDO_Ruben_N48TU.pdf:8

INVESTIGATION ON GNP LAYER AS PROTECTION AGAINST HIGH THERMAL FLUXES IN CFRP COMPOSITES

Fabrizia Cilento [1], Barbara Palmieri[1], Claudio Leone[2], Silvio Genna[3], Michele Giordano[1], Alfonso Martone[1]
[1]Institute of Polymers, Composite and Biomaterials (IPCB), National Research Council of Italy, 80055 Portici, Italy
fabrizia.cilento@ipcb.cnr.it; barbara.palmieri@ipcb.cnr.it; michele.giordano@cnr.it; alfonso.martone@cnr.it
[2]University of Campania Luigi Vanvitelli, Department of Engineering, via Roma 29, 81031 Aversa (CE), Italy
claudio.leone@unicampania.it
[3]University of Rome Tor Vergata, Department of Enterprise Engineering, via del Politecnico 1, 00133 Rome, Italy
silvio.genna@uniroma2.it

Keywords: Graphene protective coating, radiative flux, CFRP

Abstract
The demand for lightweight multifunctional materials is increasing in the automotive and aerospace industries. Protective coatings are required for polymer-based composite materials, especially in the case of high-temperature applications. Carbon fibre reinforced Plastic (CFRP) exhibits poor performance when exposed to high temperatures, mainly due to the decomposition of the organic matrix, resulting in a deterioration of the material's mechanical performance. In this work, graphene nanoplatelet (GNP)/Epoxy nanolayered films are employed as barrier coatings from radiative thermal fluxes (TBCs) to mitigate the thermal degradation in CFRP. The performance of the composite to high-power radiative heat flux has been investigated by laser spot heating tests and the post-heat mechanical response has been assessed through flexural elastic modulus and post-heat interlaminar shear strength (ILSS). The performance has been assessed for two levels of protection, considering #1 to #2 GNP layers. When exposed to heat fluxes, a significant reduction of the maximum temperatures on the heated surface and the damaged area is observed in the protected samples compared to the unprotected CFRP. This effect improves with the increasing level of protection. Mechanical tests on burned samples at 100 kW/m^2 showed a significant increase of the post-heat flexural elastic modulus and post-heat ILSS in the case of #1 GNP-layer protection of +260% and +90% respectively compared to the unprotected sample, which further improves with increasing thickness of the protective layer.

1. Introduction

Carbon fibre-reinforced plastic (CFRP) finds applications in various sectors thanks to its high specific strength and stiffness, good fatigue, and chemical resistance. However, their applications are still limited by the poor thermomechanical behaviour of the polymer matrix, characterised by very low thermal conductivity and low thermal stability. Composite components placed in proximity to a heat radiative flux can deteriorate and experience failure [1], [2]. To preserve the mechanical performance of CFRP composites from exposure to high temperatures thermal barrier coatings (TBCs) may be applied on the surface of the laminates. This system provides additional thermal conductivity and gas/liquid barrier, without impacting the structural properties of the material. TBCs mitigate the thermal degradation in composites protected, showing a steep thermal gradient through their thickness [3]. Anisotropic thermal conductivity and barrier to vapour and gases are required for managing the conductive heat exchange, blocking the oxygen and pyrolysis products' and reflecting the incoming radiative heat flux. Coatings with brick-and-mortar architecture are suitable for this application thanks to intrinsic properties that such

kind of architecture may exhibit [4], [5]. But even if the thermal barrier properties of such thin films have been published [6], [7], no works have been devoted to evaluating the effect of the application of such coating as protective layers of CFRP composites. To guarantee a safe application of CFRP in different sectors, it is necessary to investigate the mechanical and thermal properties as well as the degradation mechanism of the material in case of heat-induced damage. One-sided thermal loads, such as hot engine gases and electronic components overheating, cause a temperature gradient through the material. When striking the material on the front side, the absorbed thermal radiation is conducted to the back side. Consequently, thermal, chemical, and physical decomposition processes occur and the damaged material loses its mechanical performance [8]. Up to now, investigations on the thermal degradation of CFRP with and without coating are mostly conducted in the context of fire scenarios. However, other heat sources responsible for thermal degradation can affect the service life of a composite. Indeed, the thermal degradation processes and damage progress depend on the heat flux and can affect the mechanical properties differently. A laser heating test is a reasonable-cost method to investigate the thermal degradation of CFRP with and without protection and allows for modulating the desired heat flux.
In this work, graphene nanoplatelet (GNP)/epoxy nanolayered films are evaluated as barrier coatings to radiative thermal fluxes (TBCs) to mitigate the thermal degradation of Carbon fibre reinforced Plastic (CFRP). The GNP protective film was bonded on the surface of the CFRP laminate with a compression moulding process using a platen press and cured for 1 hour at 120°C with a pressure of 3 bar. Samples protected with #1 GNP layer (60 μm thickness) and #2 GNP layers (120 μm thickness) have been fabricated and tested. The performance of CFRP composite to high-power radiative heat flux has been investigated by laser spot heating tests of a duration of 15 min and magnitudes ranging from 25 to 150 kW/m^2 and the post-heat mechanical response has been assessed through flexural elastic modulus and post-heat interlaminar shear strength (ILSS).

2. Materials and methods

Carbon fibre pre-pregs are supplied by Technologycom S.r.l. They consist of high-strength carbon fabrics twill 2/2 of 600 g/m^2, impregnated with a standard epoxy resin.
GNP/Epoxy films consist of flexible and conductive free-standing sheets with an average thickness of 62 ± 7 μm and a nominal nanoplatelet/epoxy resin content ratio of 70/30 wt/wt. The films are produced by a top-down fabrication process based on a spray deposition process of a dilute solution of GNP/Epoxy/Acetone followed by a calendering process. The complete procedure is illustrated in [9].
Composite laminate panels with different levels of protection (#0,#1 and #2 GNP/Epoxy layers) are fabricated by a compression moulding process using a platen press and cured for 1 hour at 120°C with a pressure of 3 bar. In the case of coated samples, the films are easily integrated into the panel, by overlaying them on the pre-preg surface. The adhesion is guaranteed without the addition of any binder. According to the test, 8 plies (C8) and 24 plies (C24) are used to fabricate balanced laminates, obtaining samples with different thicknesses as reported in Table 1.
Specimens of dimensions 50 x 50 mm^2 were tested for 15 minutes changing the heat flux in the range of 25-150 kW/m^2 (i.e. by changing the laser power percentage). The irradiated area was set at 28% of the total area, by considering the laser spot of 30 mm diameter. In Table 1 the test conditions are summarised. During the heating tests, an IR camera (FLIR A655SC), was adopted to monitor the temperature on the specimen surface exposed to the laser radiation. On the surface opposite to the irradiated one, two K-type thermocouples (TESTO, 0602 064, -50 to +400 °C, accuracy class 2) were adopted to monitor the temperatures in real-time. They were placed at the centre of the irradiated area (10 mm from the centre) and bonded with epoxy adhesive.
Residual mechanical properties were performed on C8 samples tested at 100 kW/m^2 and were evaluated with dynamic mechanical analysis using TA Instrument DMA-Q800 equipped with a dual cantilever clamp. Rectangular specimens of 35 x 15 mm^2 were cut from the central area of the burned coupons. Tests were conducted with an initial amplitude of 20 μm, at room temperature. Data were elaborated according to the ASTM D790 standard for the flexural behaviour of composites [10].
The ILSS of C24 composites tested at 100 kW/m^2 was determined using the short-beam shear (SBS) test method following the ASTM D2344 standard. The interlaminar shear is generated indirectly through

the three-point bending of specimens in the SBS method. The tested specimens were compliant with the dimensions of 36 × 12 × h mm^3 where h was the actual thickness of the specimens.
The ILSS (MPa) values were calculated by Equation (1):

$$\mathrm{ILSS} = \frac{3P_{max}}{4bh} \tag{1}$$

where P_{max} (N) is the maximum load, b (mm) is the sample width, and h (mm) is the actual thickness of specimens.

Table 1. List of tested samples and performed test (*T*=Laser heating test, *ILSS*=Interlaminar shear test, *E'*=Elastic behaviour from DMA test)

Sample code	N° layers	N° plies	Thickness [mm]	Power density [kW/m^2]				
				25	50	75	100	150
G0-C8	#0	8	1.70±0.22	*T*	*T*	*T*	*T, ILSS, E'*	*T*
G1-C8	#1	8	1.75±0.13	*T*	*T*	*T*	*T, ILSS, E'*	*T*
G2-C8	#2	8	1.82±0.18	*T*	*T*	*T*	*T, ILSS, E'*	*T*
G0-C24	#0	24	6.31±0.35	*T*	*T*	*T*	*T, ILSS, E'*	*T*
G1-C24	#1	24	7.13±0.51	*T*	*T*	*T*	*T, ILSS, E'*	*T*
G2-C24	#2	24	4.39±0.12	*T*	*T*	*T*	*T, ILSS, E'*	*T*

3. Results

Samples with #0, and #1 GNP/Epoxy layers were tested at different laser power densities, while sample #2 GNP/Epoxy was only at 100 kW/m^2. The maximum temperatures recorded on the face exposed to the radiative source have been acquired and reported in Table 2.
Protection with the #1 GNP layer guarantees a significant reduction in the maximum temperature with respect to the value reached by the unprotected sample for all power densities. In the case of an incident power of 150 kW/m^2, a high temperature was measured due to the occurrence of swelling of the protection with a sudden release of pyrolysis products that produced an immediate flame on the surface of the sample.

Table 2. Maximum temperatures recorded on the face exposed to the heat flux for samples C8

	#0	#1		#2	
Laser power [kW/m^2]	$T_{max,\#0}$ [°C]	$T_{max,\#1}$ [°C]	$\Delta T/T_{\#0}$ [-]	$T_{max,\#2}$ [°C]	$\Delta T/T_{\#0}$ [-]
25	360.6	255.1	-29%	-	-
50	501.8	410.5	-18%	-	-
75	571.2	493.0	-14%	-	-
100	659.5	593.9	-10%	526.1	-20%
150	897.8	1366.0	52%	-	-

By increasing the thickness of the protection (#2 layers), a further reduction (-20%) of the maximum temperature was found at 100 kW/m^2. The highest the thickness of the protection, the lowest the maximum temperature reached on both sides of the samples. The time-temperature history during the test performed at 100 kW/m^2 on both the uncoated CFRP (#1-C8) and 2-layer coated CFRP (#2-C8) samples is reported in Figure 1a-b. Temperatures are acquired by an IR camera within the circle of radius 20 mm centred in the laser beam spot. In both cases and for all the distances, *R*, from the centre of the laser beam, the temperatures rapidly increase up to a plateau, indicating that the thermal equilibrium is achieved and remains almost constant up to laser irradiation off. After the heating phase, the temperature rapidly drops to the ambient one. The maximum temperatures, measured at the laser beam centre, are considerably different, reaching the value of 675°C for the unprotected specimen and ≃500°C for the specimen protected with #2 graphene layers. In addition, the initial heating rate reduces by 60% from 10°C/s to 25°C/s, when the coating is applied, indicating that the graphene layer significantly delays the heating time. On the surface opposite to the heating source, recorded temperatures follow the same dynamic maintaining a noticeable difference in the maximum temperatures reached during the test of about 120°C. Also, a significant reduction in the heating rate (40%) is observed in the case of the coated sample.

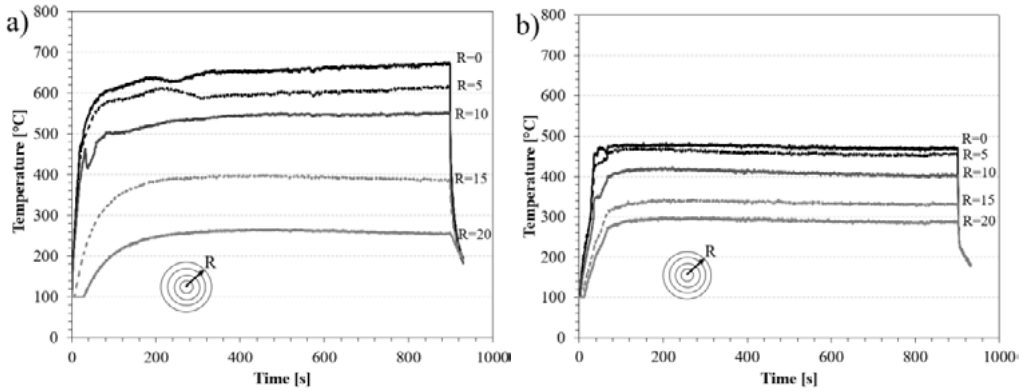


Figure 1. Evolution of temperature with time of the upper face at different distances R from the centre of the laser beam for (a) #0-C8 and (b) #2-C8

The spatial distribution of temperatures after 13 minutes of both uncoated and coated samples is reported in Figure 2. The shape of the curve significantly modifies from the uncoated to the coated sample. As stated before, the peak temperature is achieved for all cases under the laser beam and reduces at an increasing distance from the centre. By increasing the coating thickness, the curve flattens, and the maximum temperature approaches the average value. The ratio between the average and maximum temperatures are 0.65, 0.70, and 0.75 for #0-C8, #1-C8 and #2-C8 respectively.

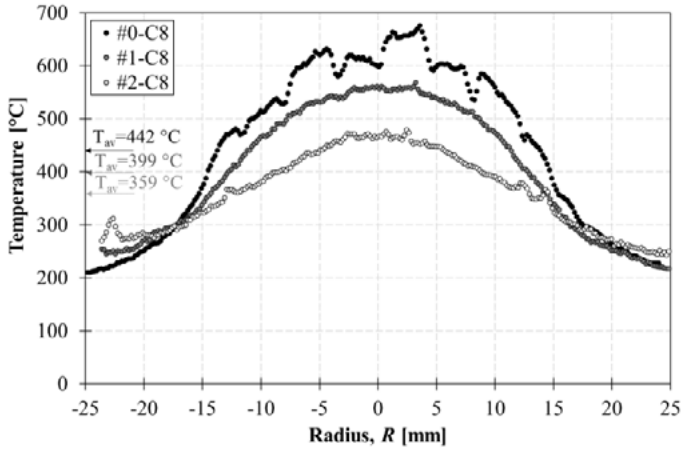


Figure 2. Spatial temperature distribution after 13 min of #0-C8, #1-C8 and #2-C8 samples.

The typical damage progression visually detected on both sides of the specimen as a function of the protection level is shown in Figure 3. Due to the different optical properties of the resin and burned carbon textile, it is possible to evaluate and compare the level of damage of the tested samples. The damaged area is clearly visible and identifiable from an optical analysis of the sample on both the upper and lower surfaces of the uncoated sample. In the case of coated samples, the presence of the GNPs-rich layer makes the evaluation of upper surface damage status not straightforward. However, they do not experience severe damage on the lower surface. In the case of #1-C8, the lower face only turns brown (Figure 3b), while in the case of #2-C8, no visible damages are observed (Figure 3c).

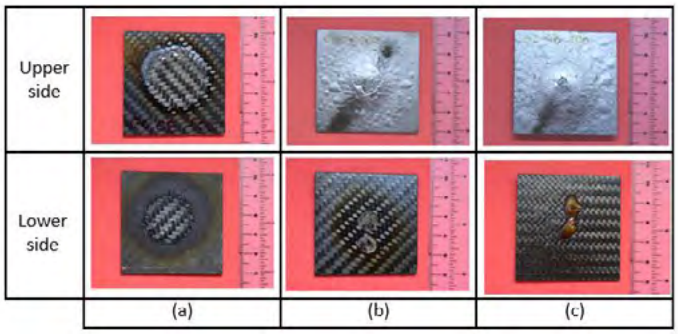


Figure 3. Optical damage of tested samples (a) #0-C8; (b) #1-C8; (c) #2-C8

Figure 4a shows the ILSS values for C24 samples tested at 100 kW/m^2. Samples coated with GNP layers showed higher values of ILSS compared to the unprotected CFRP. In the case of the #2-C24 sample, the ILSS increases by 71% compared to the unprotected CFRP, while in the case of the#1-C24 by 48%. In addition, it is found that the ILSS is 43% and 50% of the pristine value (53 MPa) for #1-C24 and #2-C24 respectively.

An inspection of the cross-section of C24 samples tested at 100 kW/m^2, further highlighted the effect of protection of the GNP layers. A sensible reduction of the damaged area can be detected with increasing thickness of the coating: the laser imprint is visible in the unprotected sample and tends to vanish for #1-C24 and #2-C24 samples.

Similarly, the beneficial effect of GNP layer protection on the elastic properties was found and reported in Figure 4b. Indeed, the residual elastic modulus of samples tested at 100 kW/m^2 is reduced by 88% compared to the reference unexposed CFRP (20 GPa), as shown in Figure 4. The effect of protection is clear in the case of #1-C8 and #2-C8, where the residual elastic modulus is 45% and 50% of the pristine value respectively. In the latter case, the elastic modulus is 4 times higher than the unprotected sample [11].

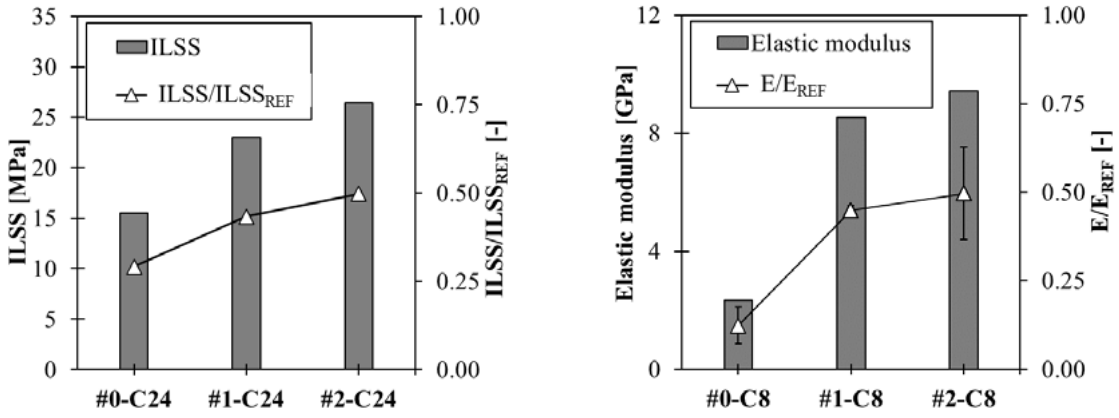


Figure 4. ILSS of C24 samples (a) and residual elastic modulus of C8 samples (b)

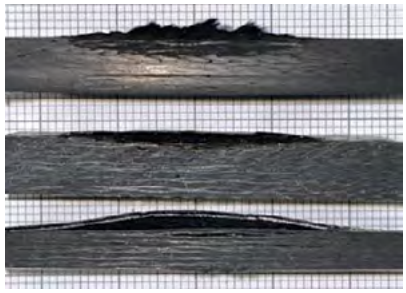


Figure 5. Cross section of #0-C24 (a) #1-C24 (b), #2-C24 (c) samples

4. Discussion

Experimental results show a sensible reduction of the maximum temperatures on both the upper and lower surfaces and an improvement of the mechanical properties of the protected samples, compared to the unprotected laminate.

The heat dissipation mechanism in the graphene-coated sample is based on different mechanisms.

(i). Unlike uncoated CFRP, in graphene-coated samples, the temperature field is uniform since the thermal energy spreads on the entire surface of the specimen thanks to the anisotropic thermal conductivity of graphene coating [12]. The effect of heat spreading increases with the increasing thickness of the coating and efficiently contributes to preventing major damage to the composite by removing the temperature peaks.

(ii). In addition, radiative heat transfer mechanisms should be considered. When panels are thermally loaded from one side, the incident radiation is reflected, emitted, or absorbed by the surface. Given the lower emissivity coefficient of graphene coating compared to the CFRP, the energy absorbed by the coated sample is much lower. Graphene layers efficiently reflect electromagnetic waves thanks to the laminated nanostructure made of GNPs well-aligned in the planar direction [13]. Consequently, they act as shielding against thermal radiation not only reducing the absorbed energy but also reducing the peak temperatures, preventing severe damage and preserving the structural properties.

5. Conclusions

In the present work, the ability of GNP coating to protect CFRP panels from high-power radiative fluxes was investigated. A testing procedure based on laser irradiation has been adopted for the verification of the performances of uncoated and coated CFRPs.

The experimental analysis showed that thanks to the high degree of orientation of highly conductive GNPs within the coating, the maximum temperature, and the temperature gradient onto the exposed heat flux surface are mitigated by spreading the thermal energy over the sample volume. The high anisotropy between the in-plane and cross-plane thermal conductivity of the graphene layer makes the heat diffusion capacity the main protection mechanism significantly reducing the thermal degradation of the material. Non-destructive analysis revealed that the presence of the coating on the surface subjected to laser irradiations preserves the sample from through-thickness damages at an energy level of 100 kW/m^2.

Finally, the graphene-based coating preserves the mechanical performance of CFRP when it is exposed to high heat fluxes. Specimens extracted from the damaged samples showed a residual mechanical performance four times higher than the CFRP without protection, with a residual mechanical performance of up to 50% of the pristine value.

Graphene coatings act as TBCs slowing down the degradation rate of components caused by heat flux and decreasing the surface temperature of the protected material. The coatings improve the operating temperature range, performance, and efficiency of CFRP laminates.

Acknowledgements

The authors are particularly grateful to the CIRTIBS Research Centre, University of Campania Luigi Vanvitelli, for providing part of the equipment to develop this research work.

References

[1] Z. Zhang, C. Wang, G. Huang, H. Liu, S. Yang, and A. Zhang, "Thermal degradation behaviors and reaction mechanism of carbon fibre-epoxy composite from hydrogen tank by TG-FTIR," *J. Hazard. Mater.*, vol. 357, pp. 73–80, 2018, doi: https://doi.org/10.1016/j.jhazmat.2018.05.057.

[2] C. A. Griffis, J. A. Nemes, F. R. Stonesifer, and C. I. Chang, "Degradation in Strength of Laminated Composites Subjected to Intense Heating and Mechanical Loading," *J. Compos. Mater.*, vol. 20, no. 3, pp. 216–235, May 1986, doi: 10.1177/002199838602000301.

[3] H. Kim, J. Kim, J. Lee, and M. W. Lee, "Thermal barrier coating for carbon fiber-reinforced composite materials," *Compos. Part B Eng.*, vol. 225, p. 109308, 2021, doi: 10.1016/j.compositesb.2021.109308.

[4] Y.-C. Wang, T.-K. Huang, S.-H. Tung, T.-M. Wu, and J.-J. Lin, "Self-assembled clay films with a platelet–void multilayered nanostructure and flame-blocking properties," *Sci. Rep.*, vol. 3, no. 1, p. 2621, 2013, doi: 10.1038/srep02621.

[5] F. Cilento, A. Martone, and M. Giordano, "Insights on Shear Transfer Efficiency in ' Brick-and-Mortar ' Composites Made of 2D Carbon Nanoparticles," *Nanomaterials*, vol. 12, no. 8. 2022. doi: 10.3390/nano12081359.

[6] J. Han, G. Du, W. Gao, and H. Bai, "An Anisotropically High Thermal Conductive Boron Nitride/Epoxy Composite Based on Nacre-Mimetic 3D Network," *Adv. Funct. Mater.*, vol. 29, no. 13, p. 1900412, Mar. 2019, doi: https://doi.org/10.1002/adfm.201900412.

[7] J. Li *et al.*, "Synergistic enhancement of gas barrier and aging resistance for biodegradable films with aligned graphene nanosheets," *Carbon N. Y.*, vol. 172, pp. 31–40, 2021, doi: https://doi.org/10.1016/j.carbon.2020.09.071.

[8] T. M. Vetter, J. Bibinger, F. Zimmer, S. Eibl, and H. J. Gudladt, "Characterization of one-sided thermal damage of carbon fiber reinforced polymers by means of depth profiles," *J. Compos. Mater.*, vol. 54, no. 24, pp. 3699–3713, 2020, doi: 10.1177/0021998320917190.

[9] F. Cilento, A. Martone, M. G. Pastore Carbone, C. Galiotis, and M. Giordano, "Nacre-like GNP/Epoxy composites: Reinforcement efficiency vis-à-vis graphene content," *Compos. Sci. Technol.*, vol. 211, p. 108873, Jul. 2021, doi: 10.1016/j.compscitech.2021.108873.

[10] ASTM INTERNATIONAL, "Standard Test Methods for Flexural Properties of Unreinforced and Reinforced Plastics and Electrical Insulating Materials. D790," *Annu. B. ASTM Stand.*, pp. 1–12, 2002, doi: 10.1520/D0790-17.

[11] F. Cilento, C. Leone, S. Genna, M. Giordano, and A. Martone, "Graphene NanoPlatelet-based coating as thermal protection from high-power radiative fluxes," *Compos. Struct.*, vol. 319, no. May, p. 117157, 2023, doi: 10.1016/j.compstruct.2023.117157.

[12] F. Cilento, A. Martone, F. Cristiano, A. Fina, and M. Giordano, "Effect of Matrix Content on Mechanical and Thermal Properties of High Graphene Content Composites," *MATEC Web Conf.*, vol. 303, no. 201 9, p. 01002, 2019, doi: 10.1051/matecconf/201930301002.

[13] F. Cilento, C. Curcio, A. Martone, A. Liseno, A. Capozzoli, and M. Giordano, "Effect of Graphite Nanoplatelets Content and Distribution on the Electromagnetic Shielding Attenuation Mechanisms in 2D Nanocomposites," *J. Compos. Sci.*, vol. 6, no. 9, p. 257, 2022.

ROBUST SKIN: A MULTIDISCIPLINARY APPROACH TO ROBUST MEMBRANE WING DESIGN FOR SUSTAINABLE URBAN MOBILITY

R. Fachtan[1*], M. Failner[1], and H. Ruckdäschel[1]
M. Toenjes[2], W. Machunze[3], U. Beier[3]
[1]Neue Materialien Bayreuth GmbH, Bayreuth, Germany
[2]Technical University of Munich, Germany; [3]Airbus Defence and Space GmbH, Munich, Germany
* Corresponding author (robin.fachtan@nmbgmbh.de)

Keywords: ultra-lightweight skins, robust skin, membranes, bionic, aerospace

Abstract
Eco-efficient electrical low speed flight concepts like City-Airbus NextGen need ultra lightweight load adapted designs combined with a high robustness. SoA monolithic fiber reinforced or sandwich design do not provide sufficient robustness. This research focus on the investigation of a disruptive skin architecture combining robust membrane materials with a hierarchical reinforcement. 5 different membrane material classes covering a wide range of relevant properties (stiffness, elongation at break, energy absorption, area weight) were processed and tested. Numerical simulation based design investigations show that the hierarchical reinforced membrane materials concept provide a much higher robustness (e.g. for an Endumax membrane concept up to 3*) with equal weight compared to SoA building methods. In conclusion, the study presents a promising approach to the synergy of material design, processing, and simulation for an eco-efficient flight concept. The detailed exploration of material properties and their integration into innovative wing structures positions this research as a significant contribution to the field of composite materials and aeronautical engineering.

1. Introduction

With the trend to eco-efficient travel and also new technologies available the idea of urban air mobility is becoming more tangible than ever. Nevertheless those low-velocity public aircrafts require different construction concepts than those used in commercial aviation to date. As often in research there is the idea to borrow from nature and e.g. employ bionic wings similar to the wings of a dragonfly (see Figure 1, left). The idea hereby would be to transfer the composition of a hierarchic gride-like reinforcement structure combined with a flexible but also tough membrane to wings for the new aircraft type. Though similar approaches have been used for e.g. sails with reinforcement of carbon fibre rods or fibres and a flexible membrane, a bionic approach has never been used in commercial aviation.

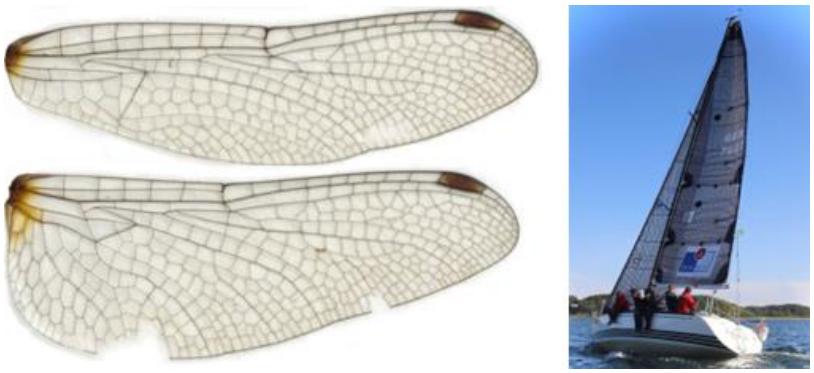


Figure 1. Dragonfly wings (left) [1], carbon fibre reinforced sails (right) [2]

The resulting findings serve as an initial assessment of such a covering material with the aim of achieving a technology readiness level of TRL 2-3 and address the technological trend of "unmanned flight" as well as the trend towards increasing the eco-efficiency of flight.

2. State of the art

State of the art lightweight building concepts consist either of monolithic fiber reinforced skin materials with stringer reinforcement or of sandwich structures. These minimize skin ripple under the acting flight and air loads and therefore keep drag as low as possible during cruise flight. Furthermore, this design takes into account the robustness requirements with regard to impact events in the context of high speeds. If you adopt the designs according to the lower acting loads to save weight, this leads to thinner skins and hence to lower robustness. Thus slow-flying sports aircraft in ultralight construction with significantly lower air loads and also wing span already take already different approach and use membranes to cover a supporting structure. For the urban aircrafts addressed in the publicly funded project *Robust Skin*, an unreinforced covering solution was yet not an option. Instead the goal was a simulation-supported development of material and process solution for damage-tolerant hybrid materials consisting of a highly flexible fibre-reinforced soft component (e.g. fibre reinforced elastomeric materials - FRE) and a load-bearing rod structure (e.g. C-fibres with duromeric matrix). Though some approaches of combining robustness with flexibility (e.g. carbon fibres in flexible epoxy matrices) have already been made in literature [3-5] non of them yet targeted a hierarchical bionic approach for an aircraft wing.

3. Materials, processing and investigation methodologies

3.1 Materials

To determine suitable ultra-light yet robust membrane materials also considering ecological aspects, multiple material classes were investigated of which 4 shall be further described. An overview to the examined material compositions is given in the following:

A. Carbon reinforced EPDM: *Rubber with unidirectional carbon fiber reinforcement, resulting in a combination of robustness and stiffness.*

For the EPDM trial series a EPDM film AA9KFZ from KRAIBURG Holding SE & Co. KG with a thickness of 0.35 mm, a density of 1 g/cm³ and a modulus of (30 – 40 MPa) has been used. Amongst others three different reinforcing fibre materials have been combined with the EPDM:

- Hexcel coorporation CFRP prepreg (HexPly® M21)
- A non impregnated spread tow from ZOLTEK Corp. (Zoltek PX35) with a width of 40 mm
- 3K-Rovings from Teijin Limited (Tenax HTA 40 / 3k / 200 tex)

B. Endumax: *A fabric composed of stretched ultra-high-molecular-weight polyethylene (UHMW-PE) fibers, which has a very high weight-specific tensile strength and robustness.*

The second approach was done with a UHMW-PE fabric from Teijin Limited with a width of 133 mm and a thickness of 100 µm which were consolidated together with LDPE-foils provided by Teijin with a thickness of 8 µm. The LDPE-foils act as a binder during the consolidation process to reach the desired final thicknesses. Additionally Flexon as an UHMW-PE fabric with additional erosion and UV-protection already in use in sails industry was investigated.

C. Twaron: *An elastomer-embedded aramid fabric with high intrinsic robustness*

As the third approach an aramid fabric was considered, since these have very good impact properties (e.g. use in ballistic applications). The used fabric from Teijin Limited (Twaron T750, 3360 dtex - Type 1000) has a areal wight of 460 gsm and a thickness of 0.65 mm. The aramid fibres in this fabric have a rubber coating.

D. NorthThinPly (NTPT): *An ultra-thin ply epoxy CFRP enabling ultra-lightweight membranes*
NTPT offers high-performance composite materials for sailing and other applications. The in delivery state uncured prepregs comprise of UD-carbon fibres and an epoxy-based matrix system

E. Reference-Sandwich:
In order to be able to compare the membrane materials with regards to an extremely light (755 gsm) fibre composite sandwich, a reference sandwich was manufactured using thin-layer CFRP (45 gsm) with a tough cryomatrix and a light Nomex honeycomb. The target design of membrane plus stiffeners in the background should achieve this weight as a reference value, but exhibit improved damage tolerance under impact.

3.2 Processing

A. EPDM
The elastic EPDM needed to be reinforced with fibres to improve its mechanical properties. Consolidation was done by a static press process. The process parameters that have been found to lead to the best results are given in **Table 1**.

Table 1. Process parameter used in the static press process

Specimen Type	*Temperature* (°C)	*Pressure* (bar)	*Time* (min)	Use of additional vacuum
EPDM + HexPly®	180	7	120	No additional vacuum
EPDM + Zoltek PX35	140	15	30	Additional vacuum
EPDM + Tenax 3K	140	15	30	Additional vacuum

The schematic structure of the EPDM reinforced with HexPly® is shown in Figure 2. The prepregs are placed on both the top and bottom side to avoid warping of the samples.



Figure 2. Structure of EPDM + HexPly®

B. Endumax
The UHMW-PE was consolidated in a static press process using the parameters specified by the vendor (T = 130 °C, p = 10 bar and t = 120 min). Due to the resistance to bird strike in the subsequent application, two LDPE-foils were placed over each of the individual fabric layers. The centre layer again consists of two films (see also Figure 3).

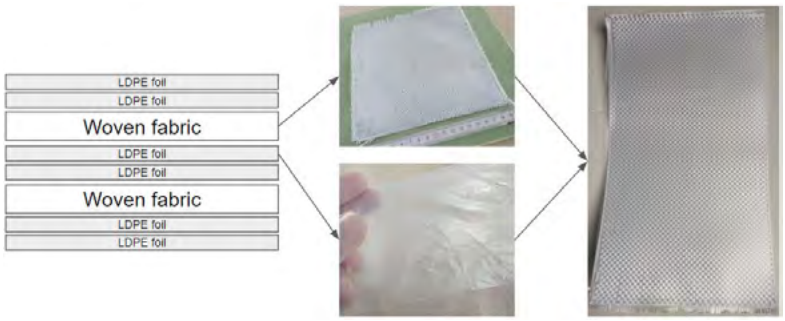


Figure 3. Schematic illustration of the composition of the samples made of Endumax UHMW-PE

C. Twaron

Due to the already high areal weight a single layer was used and the material was tested as delivered without any processing needs.

D. NorthThinPly

The prepregs have been processes in a static press process with parameters provided by NTPT. Two different layer compositions have been produced:

- NTP1: QI-layup with 8-layers (each 40 gsm) resulting in a total areal weight of 320 gsm
- NTP2: 0°/90° layup with 4-layers (each 20 gsm) resulting in a total areal weight of 80 gsm

3.3 Microscopic examinations

Digital microscopy images of the fibre-reinforced EPDM from Kraiburg were taken. The analyses were carried out on a Keyence 3 digital microscope VHX-7000. The advantage over optical microscopy is the sample preparation, as no embedding resin is required. The samples were cut to size using special fibre scissors and then fixed to the sample plate. In addition to being analysed using a digital microscope, selected samples were examined using a Zeiss EVO MA15 scanning electron microscope (SEM).

3.4 Set-up for static tensile tests and impact testing under pre-loading conditions

For a first material screening tensile tests according to ASTM D3039 are done. Therefore the specimens are tensioned until failure at constant displacement of 2 mm/min. According to the general design concept, first a pretension of 100 N is applied on the test coupon after which a physical extensometer is attached to the test coupon for an exact strain measurement.
The concept to consider the pretension load of the investigated membrane materials is also considered for the impact testing. Therefore an impact device was designed enabling impact testing on thin membranes that are bi-axially stressed before and during impact. The achieved continous impact area is 100 * 100 mm. Four load cells are installed on the clamping interfaces to measure the preload of the membrane. Here 2 manual applied pre-load settings are tested: 1 kN/1 kN and 1 kN/2 kN. Furthermore the load cells measure the force time signal during the impact with 4.8 kHz. In order to limit the strain/stress concentrations near the clamping area's due to bi-axial loading, a cruciform coupon shape is required as shown in **Figure 4** (right). The impactor radius is 15.75 mm having a weight of 1.917 kg. The lowest possible impact energy is 2 J.

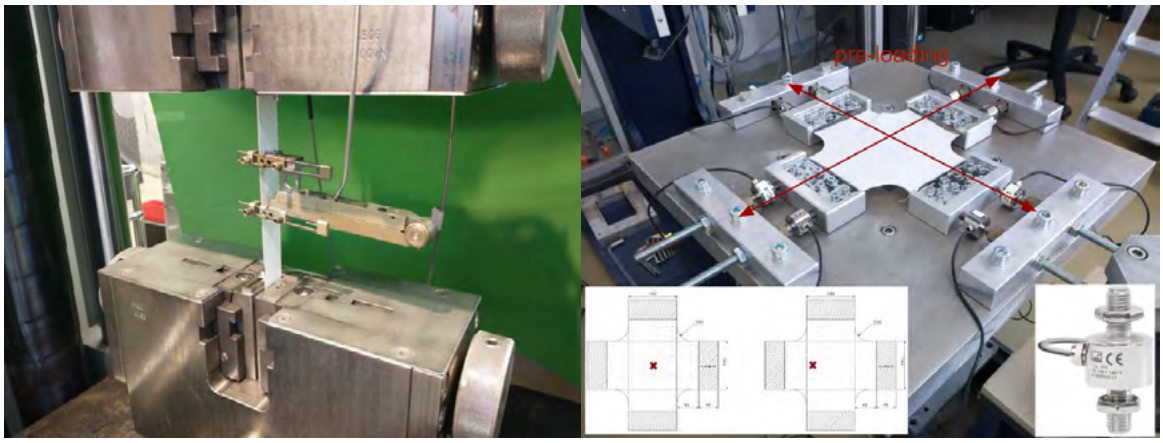


Figure 4. Static (left picture) and non-standard dynamic impact test device (right picture)

4. Results and discussion

4.1 Analytical investigations of processed materials

Digital microscope images of EPDM with the both non pre-impregnated 3K rovings and Zoltek PX35 were done in order to investigate the fibre-matrix adhesion. Unfortunately a bad adhesion (black cavities) between the Zoltek spread tow and the EPDM was detected in Figure 5 (right). For the 3K rovings especially at 140 °C and additional vacuum a good wetting of the outer fibres of the roving could be detected (left), though black areas are also detectable within the roving. Yet further SEM investigations show for the 3K rovings a poor wetting of the fibres within the rovings, resulting in unsufficient load transfer. Although progress had already been made in the impregnation process during the project, it was not possible to produce sufficiently good samples. Therefore, these were not subjected to mechanical testing. However, further optimisation could still lead to progress here.

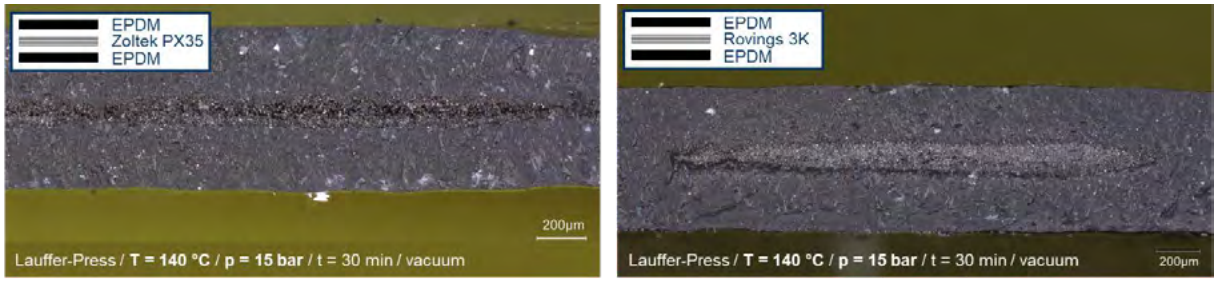


Figure 5. Digital microscopy images of the EPDM reinforced with the both non-pre-impregnated Zoltek PX35 spread tow (left) and 3K rovings (right)

4.2 Static tensile tests

Figure 6 shows the result summary for static tensile tests for the selected membrane materials. The materials Endumax and Twaron offer a very good compromise between strength, rigidity and elongation at break. EPDM/HexPly® material configurations show during the tests (in fiber direction and transversal) a high scattering and by far not the expected high elongation in transverse tension. In conjunction with the in Figure 5 shown process results and the low elongation at break this material class was not pursued further for the subsequent robustness and aging tests.

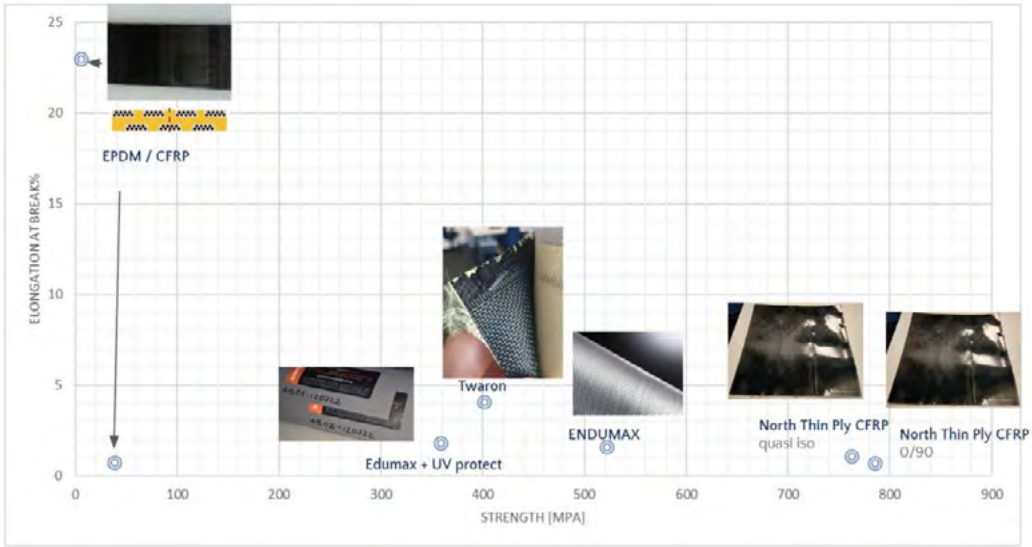


Figure 6. Results of static tensile testing

4.3 Validation of low velocity impact without and with grid reinforcement

Figure 7 shows for the example of ENDUMAX on the left hand side the force time signal of one load cell for different impact energies. The impact load is increased on the coupon in 1 J steps until the coupon is penetrated as shown on the right side. The very local penetration leads to a sudden drop of the force signal down to 0 N as no interaction between impactor and coupon exists anymore.

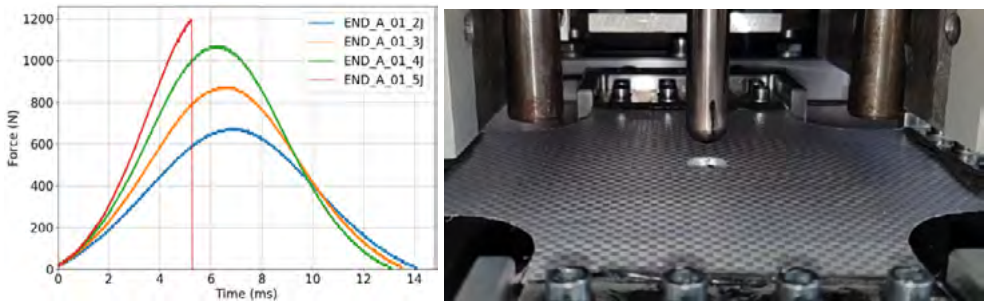
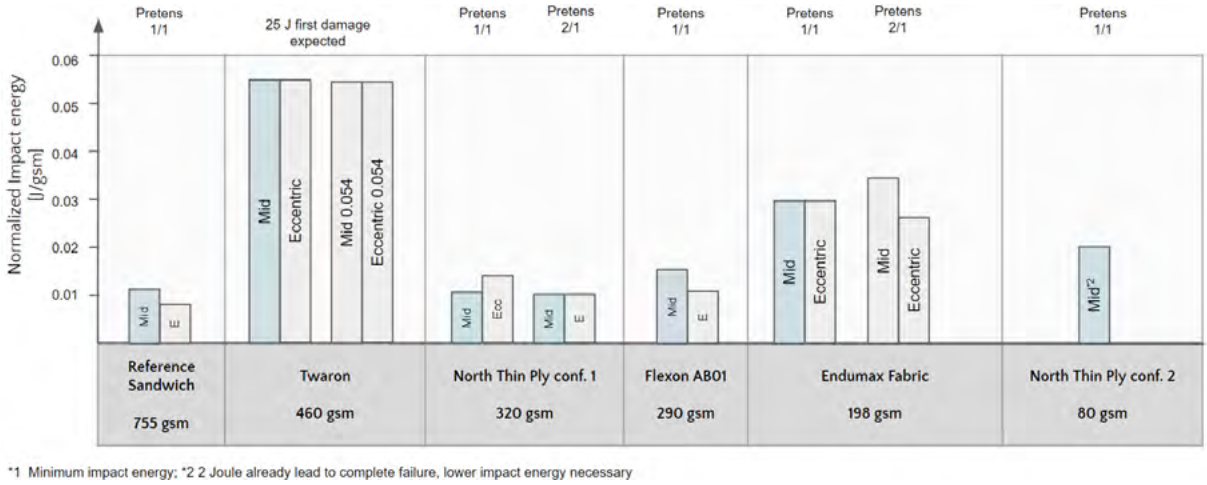


Figure 7. Force signal of load cells (left), penetrated ENDUMAX fabric [5 J impact] (right)

For a better robustness comparability of the tested membrane materials the respective energies leading to penetration are summarized in Figure 8 in a normalized way considering their areal weight. An ultra lightweight sandwich reference architecture (see also 3.1 Materials) was also tested in this campaign showing a very low impact resistance. Twaron, which could not even be penetrated in the test device up to 20 J impact energy, has the best normalized impact behavior of all materials. The Endumax material also performs very well. For both the choosen pre-tension (1 kN / 1 kN & 2 kN / 1 kN) as well the position (mid & 30 mm eccentric) of the impact have only a marginal influence on the overall results.



*1 Minimum impact energy; *2 2 Joule already lead to complete failure, lower impact energy necessary

Figure 8. Summary of impact tests on membrane materials – normalized impact energy [J/gsm]

To prove the influence of reinforcements on the impact performance, Endumax and NTPT1 coupons were equipped with rectangular struts (4 & 10 mm edge length, 3 different positions) which are bonded on the backside of the membrane. As expected the direct impact on the grid structure increases the impact energy leading to penetration for both materials. Tests with distance (15 mm & 50 mm) of the impact position to the grid element showed very similar penetration energies.

4.4 Numerical simulation

Various numerical simulations on different levels supported the experimental investigations to cover the mechanical requirements regarding stiffness and damage tolerance. The design approach of a thin membrane covering a reinforcing grid structure required the consideration of both a global stiffness requirement and a local stiffness requirement to ensure a low skin waviness for the aerodynamic surface.

Therefore, complete homogenization ("smeared modelling") of all components of the “Robust Skin” was not a sufficient solution, as this would not be usable for the optimization or local adaptation of the reinforcement structure, taking into account the aerodynamic requirements. The discrete reinforcements (grid structures) were modelled as computationally efficient beam elements for the stiffness investigations. Shell elements were used to model the thin membranes. The two components were perfectly connected using tie interactions. This approach ensured low computational costs for studying many parameters and later transferring the approach to larger models. Using the described approach, different regular grid patterns were evaluated for their stiffness in a periodic unit cell model. An uniform pressure distribution was chosen to represent flight loads to evaluate skin waviness and global stiffness. Parallel to that, the impact tests and further coupon tests were simulated to calibrate energy-based continuum damage models for the membrane materials. Finally, the modelling approaches were transferred to a larger scale represented by a wing box section. This was simplified as a connection of two panels in the form of the “Robust Skin” material solution with I-beams as spars. The unit cell simulations showed that a multi-hierarchical reinforcement grid is the preferred solution for a weight-efficient fulfillment of the waviness requirement as the allowable maximum size of a non-reinforced skin field is comparably small to the overall dimensions. Despite a non-regular, fully load path-optimized structure with a large number of hierarchies would be able to reach higher lightweight design potential, the solution was restricted for the demonstrator to a regular iso-grid with two hierarchies due to manufacturing reasons. The resulting unit cell of the demonstrator grid consists of an Endumax membrane and CFRP hollow profiles with quadratic cross-sections shown in the Figure 9 (left).
A full panel of multiple cells was modelled on the wing box level to predict the impact behavior for boundary conditions that are closer to the real application than the impact investigations on coupon level. The wing box was loaded by uniform pressure at the top and bottom to introduce pre-tension similar to flight conditions. After application of the surface pressure, the structure was impacted with the same geometry and kinetic energy as in the coupon tests.

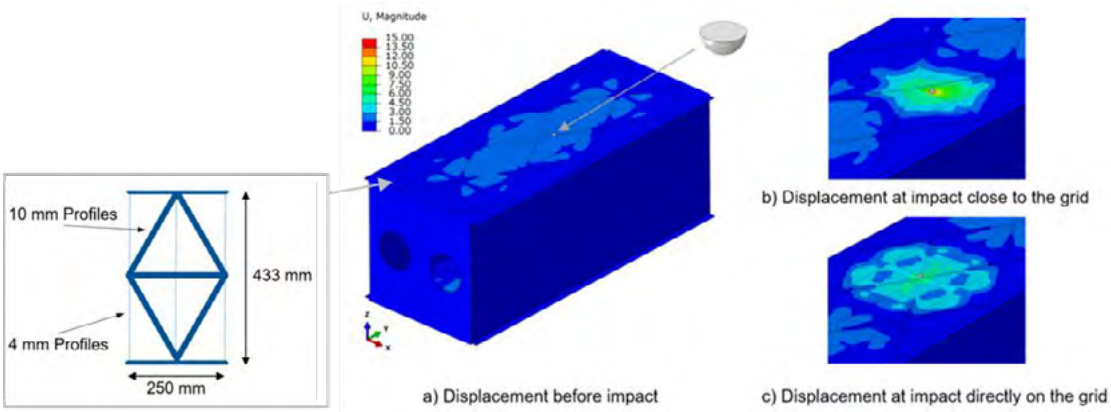


Figure 9. Resulting unit cell of the grid (left); displacement in mm before and after impact (right)

Figure 9 (right) shows the displacement due to the surface pressure before impact and the resulting impact for a kinetic energy of 8 J at two different impact locations. In both cases, there was no element that was fully damaged. While one element of the membrane reached 30% of the allowable damage for the impact close to the grid, the damage initiation criterion (maximum stress) was not even reached for the impact directly on the grid. These findings show that the results from the coupon impact tests should be transferable to the actual application of the “Robust Skin” while being more conservative.

5. Summary and outlook

Based on a numerical design, an demonstrator was built showing a possible architecture for ultra lightweight Robust Skins. In detail an Endumax membrane was hierarchically reinforced with 4 mm and 10 mm quadratic CFRP rods which are connected with 3D printed PA11 node-elements and bonded using a paste adhesive (**Figure 10**).

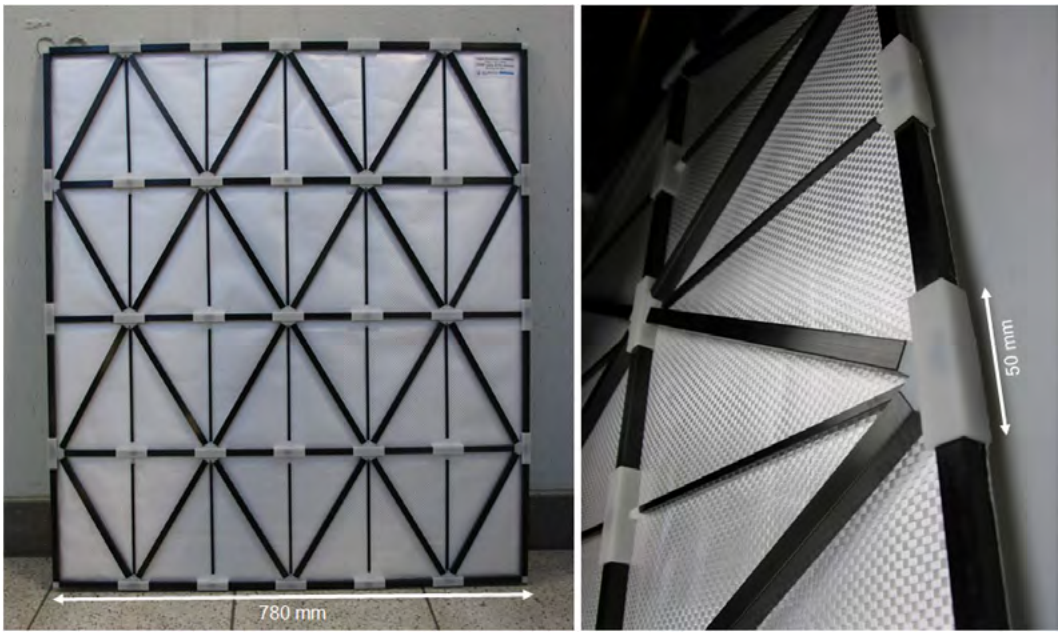


Figure 10. Demonstrator showing the global architectural concepts (left) und detail thereof (right)

A numerical sized reference use case of a wing box cover comparing SoA materials & architectures with Robust Skin concepts, show that the Robust Skin architecture can be realized weight neutral combined with a much higher robustness. To validate the approach, a detailed sizing and design loop within a program developing low speed vehicles need to be done considering all relevant aspects like e.g. load introductions. Furthermore aspects with regards to aging, lightning strike protection as well as paint application need to be investigated. In conclusion, the study presents a promising approach to the synergy of material design, processing, and simulation for an eco-efficient flight concept. The detailed exploration of material properties and their integration into innovative wing structures positions this research as a significant contribution to the field of composite materials and aeronautical engineering.

Acknowledgments
We would like to extend our sincere gratitude to BFS – Bayerische Forschungsstiftung for their support and funding of the project Robust Skin. Their commitment in advancing ultra lightweight and robust skin materials for low speed air vehicles has been instrumental in bringing this initiative into fruition. We also express our appreciation to all stakeholders and participants who contributed their time, expertise and resource to the success of this project. Together we made significant strides showing the potential of disruptive lightweight and robust skin architectures.

References

[1] R. A. Nonenmacher, CC BY-SA 3.0 <http://creativecommons.org/licenses/by-sa/3.0/>, via Wikimedia Commons, https://upload.wikimedia.org/wikipedia/commons/c/cf/Dragonfly_ran-004.jpg
[2] UK Sailmakers International, X332 SOPHIE , https://www.uksailmakers.com/wp-content/uploads/2022/10/X332-Sophie-682x1024.jpg
[3] S. Callens, O. K. Bergsma. Two-matrix Composites: Carbon Fiber Micropultrusions Embedded in Flexible Epoxy Matrices. In *Composites Part A Applied Science and Manufacturing*, 114, 2018.
[4] V. V. Vasil'ev, V. A. Salov. Development and examination of a two-matrix glassfiber composite with high transverse strain. In *Mech Compos Mater,* 20, 463–467,1985.
[5] I. J. Maqueda. High Strain Composites and Dual-Matrix Composite Structures. Dissertation (Ph.D.), California Institute of Technology. 2014

FATIGUE INVESTIGATION OF SELF-HEALING ADHESIVES FOR WIND TURBINE APPLICATIONS

Jialiang Fan[1], Anastasios P. Vassilopoulos[2], Veronique Michaud[1]

[1]Laboratory for Processing of Advanced Composites (LPAC), Ecole Polytechnique Fédérale de Lausanne (EPFL), Lausanne, Switzerland – jialiang.fan@epfl.ch.
[2]Composite Construction Laboratory (CCLab), Ecole Polytechnique Fédérale de Lausanne (EPFL), Lausanne, Switzerland.

Keywords: Fatigue, Composites, TDCB, Self-healing, Adhesive

Abstract
The failure of thick adhesive joints within wind turbine rotor blades (WTRBs) is often observed, and their performance could be improved by developing self-healing adhesives that heal small cracks before failure. Self-healing epoxy adhesives that were developed from earlier experiments, containing poly(ε-caprolactone) (PCL) microparticles and fumed silica are used here to fabricate Tapered Double Cantilever Beam (TDCB) specimens to investigate their fracture and fatigue performance. The fracture toughness showed ca. 60 % recovery with good healing repeatability through three healing phases. The fatigue crack growth (FCG) curves of virgin and healing phases exhibited similar slopes and the healing efficiency is thus the comparison of the stress intensity factor difference (ΔK) at the same crack growth rate, hence 58 %.

1. INTRODUCTION

The rated power of a wind turbine is determined by the length of wind turbine rotor blades (WTRBs). The urge for energy production led to a continuous increase of the blades' length over the last few decades with contemporary WTRBs reaching or exceeding 100 m [1]. WTRBs consist of composite shells and webs and large quantities of structural adhesives (hundreds of kg) are required to fabricate adhesive joints connecting them together [2]. The adhesive layer thickness can be up to 30 mm depending on the size and the position within the WTRBs [3].

Epoxy structural adhesives with low shrinkage rates are widely used for WTRB manufacturing. Although commercial state-of-the-art adhesives with high fracture toughness have been developed [4], failure of thick adhesive joints was still observed from post-mortem examinations and full-blade experiments [5], [6], mainly induced by voids and the complex stress state within the adhesive layers. Depending on the size and shape of voids, they may form crack initiation sites and influence the crack propagation path [7]. Developing new formulation adhesives with self-healing capabilities in addition to the usual processing and service requirements, as well as moderate cost, is one possible strategy to delay fracture by healing the crack and therefore improve the thick adhesive joint performance.

The new formulation adhesives should meet the requirements throughout the manufacturing process and the use phase, including low curing temperature, sufficient rheological yield stress, good adhesion, adequate tensile properties, good fracture and fatigue resistance. The adequate rheological properties are essential for the manufacturing process. One critical fabrication step is the mix of structural adhesives with an adhesive batch blender and dispensing adhesives through tubes on the composite shell and web surfaces, which have variable shapes. Therefore, the flow of adhesives on the vertical surface has to be prevented until the next step, during which the separated parts are assembled together. This is achieved by adding fillers into the adhesives to form a 3D filler network. Nanofillers with high surface-to-volume

ratios are optimal as only a small amount of nanofiller is sufficient to achieve the desired properties. Fumed silica with a relatively low cost is one promising candidate for the development of a new adhesive formulation [8].

Self-healing epoxies have been intensively studied, and one method is to add thermoplastic into epoxy blends, where the thermoplastic serves as the healing agent, flowing upon moderate heating to fill cracks. Cohades et al. [9] investigated epoxy/thermoplastic blends with low-melting temperature thermoplastic, PCL, which was introduced into epoxy through melting at a high temperature (120 °C). The morphology of the blend was determined by the PCL concentration. Good mechanical properties and high healing efficiency were achieved with a complex morphology, i.e. bi-continuous phases composed of PCL-rich matrix and cross-linked epoxy-rich spheres. This method is suitable for structures with long design lifetime, since it can heal cracks several times. However, due to the size of WTRBs, the curing temperatures of the adhesives need to be low to minimize energy demand. As a result, the phase separation approach is not applicable in this case, and a filler replacement method is proposed. Cryo-milled PCL microparticles are added into the adhesive to replace some of the fumed silica with dual purposes: acting as fillers to achieve sufficient yield stress by synergizing with fumed silica, and acting as the healing agents. The healing principle is the differential expansive bleeding phenomenon [10]. The expansion of the PCL liquid phase at high temperatures is greater than the epoxy phase due to the liquid transition and the higher expansivity. Therefore, the PCL phase could flow into the crack region and heal the crack after cooling. A formulation was developed that fulfills the requirements for application, mechanical and adhesive properties, as compared to a benchmark commercial epoxy.

The fracture and fatigue behavior of thick adhesive joints is critical for WTRBs, since their design lifetime is 20-30 years. Therefore, the fracture and fatigue behavior of self-healing adhesives needs to be investigated before their application to joints. TDCB is a commonly used configuration for self-healing investigations under both quasi-static and fatigue loadings. However, the TDCB fatigue investigations are mainly focused on the epoxy system with external healing agents contained in microcapsules, hollow fibers, and networks [11]–[13]. The fatigue investigations on repeatable epoxy/thermoplastic blends using TDCB specimens are rare.

This research thus investigates the fracture and fatigue behavior of self-healing adhesives developed for WTRBs with TDCB specimens to study their healing efficiency under quasi-static and displacement control fatigue loading.

2. MATERIALS AND METHODS

The baseline epoxy (BL) was provided by Sika Technology AG (mixing ratio 100:36.7 by weight). CAB-O-SIL® M-5 fumed Silica was purchased from Thermo Scientific. CAPA® 6500 PCL pellets were provided by Nordmann Switzerland AG, which were cryo-milled by Axalta Polymer Powders Switzerland Sàrl. The microparticles smaller than 150 μm were collected and used as the fillers.

The optimized adhesive determined by earlier investigations contains 20 wt% PCL microparticles, 4 wt% fumed silica, 55.6 wt% BL resin, and 20.4 wt% BL hardener. High temperature benefits the dispersion of fumed silica, while the PCL microparticles need to be processed at low temperatures (room temperature, RT). Consequently, the adhesive was processed in 4 steps: First, the BL resin and half amount of the fumed silica were mixed together with a mechanical stirrer at an elevated temperature (60 °C). An IKA T-25 Ultra-Turrax® disperser (at 24000 rpm, 20 mins) and Branson Digital Sonifier® SFX 550 (ultrasonic homogenizer) were used in sequence to disperse the fumed silica and break the agglomerate of fumed silica. The ultrasonic homogenizer was operated at 30% power and the pulsed mode with 15 s on and 60 s off. The total accumulated pulsed time was 10 mins. Second, the PCL microparticles were added to the fumed silica and BL resin mixture at RT. Only a mechanical stirrer with a cooling water bath was used and the speed was controlled (< 600 rpm) with several pauses to avoid heat accumulation. The total mixing time was 15 mins. Third, the other half amount the fumed silica was mixed with the BL hardener, using a mechanical stirrer and the same ultrasonic homogenizer in the first step with the same operation parameters. The last step is to mix the two components with a

vacuum mixer. The container was also surrounded with a cooling water bath and the new adhesives were mixed at 150 rpm for 10 mins. The mixture was then transferred to a silicon mold. TDCB specimen was cured at RT for 48 h and post-cured at 70 °C for 4 h. After demolding, the pre-crack (5 mm) was cut with a 0.16 mm thick jewelry saw. The detailed TDCB dimensions are shown in Figure 1 [14].

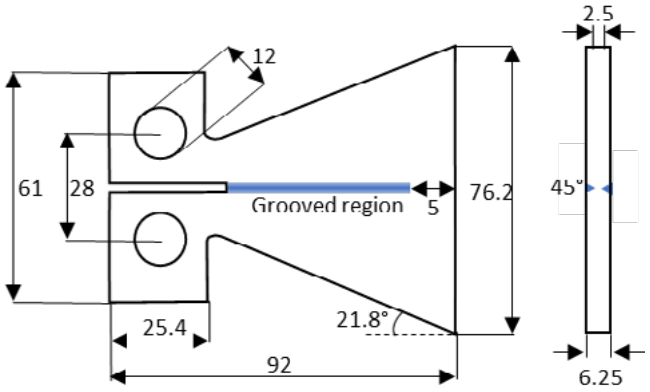


Figure 1: TDCB specimen sketch with dimensions (unit:mm) [14].

The fracture toughness recovery was first investigated through TDCB tests under quasi-static loading. The experiments were conducted with a universal testing machine (Walter + Bai AG, Switzerland, 125 kN capacity) and a 1 kN load cell (± 1 % accuracy). The load cell speed is 0.24 mm/min. After this, the specimen was dismounted and then it was clamped and put into an oven to heal at elevated temperature (120 °C for 1 hour), finally the specimen was cooled down to room temperature inside the oven. The specimens were fractured under the same conditions as the virgin specimens. Three specimens were studied and for each specimen, the healing process was repeated three times.

Table 1. Summary of TDCB fatigue test methodology and outcomes.

Specimen	Virgin	Healing phase 1	Healing phase 2	Healing phase 3
Static loading Speed	0.24 mm/min	0.24 mm/min	0.24 mm/min	0.24 mm/min
Max static loading force	120 N	80 N	80 N	80 N
R_d	0.5	0.5	0.5	0.5
Frequency	5 Hz	5 Hz	5 Hz	5 Hz
Total number of cycles	$3.62*10^5$	$3.80*10^5$	$8.30*10^4$	$5.80*10^4$
Max displacement	1.060 mm	0.714 mm	0.948 mm	0.780 mm
Final crack length	44 mm	42 mm	44 mm	42 mm
ΔK at the final cycle	0.43 MPa√m	0.27 MPa√m	0.33 MPa√m	0.28 MPa√m
Pairs' law equation with fitting parameters	$\frac{da}{dN} = 10^{-2.41}\Delta K^{6.77}$	Including 3 phase data: $\frac{da}{dN} = 10^{-0.84}\Delta K^{6.55}$		

The fatigue experiments were conducted with an MTS Landmark servo-hydraulic testing machine. The load cell was calibrated to 5 kN load capacity. The frequency was 5 Hz and the sample was loaded under displacement control at a constant amplitude with $R_d = \frac{D_{max}}{D_{min}} = 0.5$, where D_{max} and D_{min} are the max and min displacement. The virgin specimen was loaded to 120 N at 0.24 mm/min and the displacement between 20 and 120 N was considered as the $D_{max,virgin}$. When the crack length is larger than 50% of the total length, there is an increasing deviation of the stress intensity factor values compared with the calculated values [14]. Therefore, the fatigue experiment of the virgin specimen was stopped when the crack propagated approximately 15 mm (near the middle of the specimen). The healing process was the same with the quasi-static tests. To achieve a similar crack growth rate for the healed specimen compared to the virgin specimen, the healed specimen was loaded to 80 N and the displacement between 20 and 80 N was set as the $D_{max,healed}$. The crack length was measured with Image J with the help of a stamped ruler on the specimen surface. The healing specimen fatigue experiments were stopped when the crack

was approaching the final crack front of the one in the virgin specimen fatigue experiment. The healing process was also repeated three times, and the experiments conducted after each healing process are named as healing phase 1, 2 and 3 respectively. The summary of the test methodology is presented in Table 1.

The crack growth rates were calculated based on ASTM E647-23a [15]. The initial and final points of crack growth rate were calculated by the secant method, while the remaining points were calculated by the incremental polynomial method with 3, 5, and 7 consecutive crack length data points depending on the data availability. For example, the second point is calculated with 3 successive points. Due to the shape of the TDCB specimens, the stress intensity factor (K) is only related to the load (P) (equation 1). Here, $\alpha = 11.2 \cdot 10^{-3}\ \mathrm{m}^{-3/2}$. ΔK is then calculated based on the max and min load in one cycle (equation 2) and equation 3 shows the Paris' law, which presents the relation between crack growth rate ($\frac{da}{dN}$) and ΔK. C and m are Paris' law parameters.

$$K = \alpha \cdot P \tag{1}$$

$$\Delta K = \alpha \cdot (P_{MAX} - P_{MIN}) \tag{2}$$

$$\frac{da}{dN} = C\Delta K^m \tag{3}$$

3. RESULTS AND DISCUSSION

The virgin and three healing phase loading curves of one sample under quasi-static loading are plotted in Figure 2. The virgin fracture toughness was calculated using equation 1 with the virgin peak load. The average fracture toughness is 1.96 ± 0.13 MPa√m, which is adequate for real applications. The three healing phase curves shown in Figure 2 are consistent with each other, representing no degradation and good healing repeatability. The healing efficiency is calculated based on the fracture toughness (K_{Ic}) recovery as outlined in equation 4. The average healing efficiencies of the three phases are 62 ± 5 %, 61 ± 8 %, 61 ± 6 % separately. The high healing efficiency demonstrates the potential of prolonging the service life of thick adhesive joints. Therefore, the fatigue behavior was investigated to evaluate the recovery of fatigue properties.

$$\eta_{static} = \frac{K_{Ic,healed}}{K_{Ic,virgin}} = \frac{P_{c,healed}}{P_{c,virgin}} \tag{4}$$

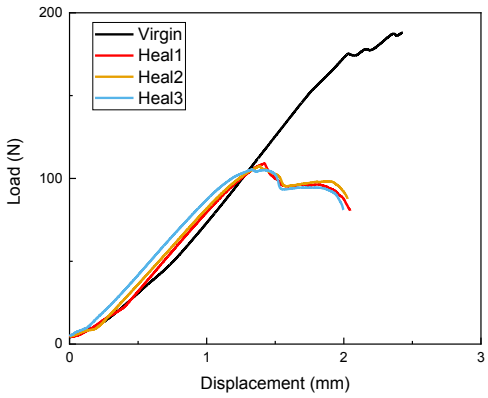


Figure 2: The virgin and three healing phase loading curves of one self-healing TDCB specimen.

A picture captured at the last cycle of the virgin phase is shown in Figure 3. The upper fixture remains stationary, while the lower fixture undergoes the predefined sinusoidal cyclic displacement with constant amplitude. The force is transferred with the load pins. The crack propagates within the grooved plane. The determination of the crack front relies on the contrast in color, i.e. the white and gray regions, as observed in the red rectangle. The crack length is the distance between the loading axis and the crack front, and the final crack front is near the middle of the specimens.

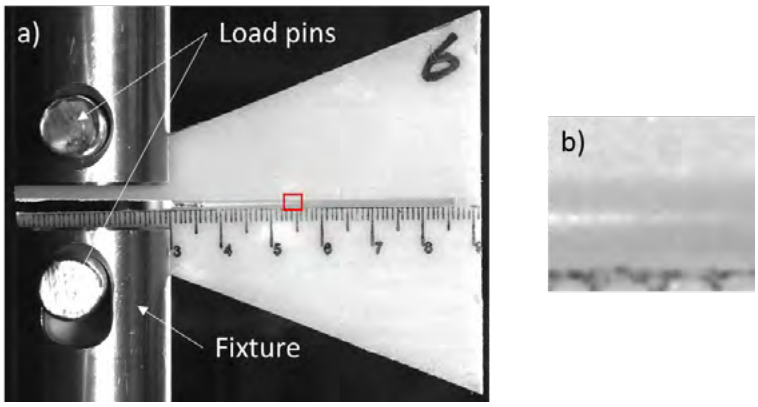


Figure 3: a) A typical picture captured at the last cycle during the virgin specimen fatigue experiments, and b) the picture enlargement within the red rectangle.

The evolution of the crack length of the virgin and three healing phases is thus presented in Figure 4. The corresponding maximum load values are also depicted in Figure 4. The crack length (closed symbols) steadily increases with a progressively decreasing crack propagation rate for both virgin and healed specimen results. The corresponding maximum cyclic force (open symbols) decreases with a progressively decreasing rate. After each healing process, the crack is healed and the crack propagation restarts from the pre-crack, as observed in Figure 4. The healing phase 1 shows lower crack propagation rates compared with phase 2 and 3. This may be attributed to the undesired specimen bending during the second healing process.

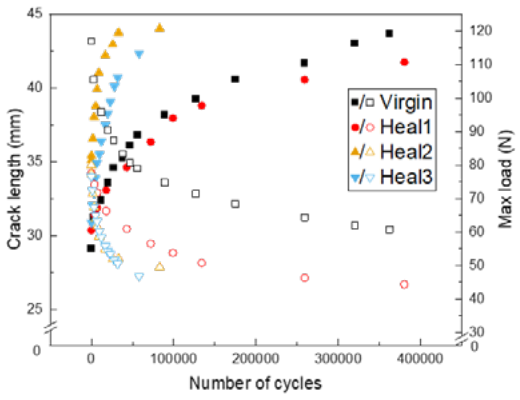


Figure 4: Crack length and the max load evolution with number of cycles for virgin and three healing phases. Solid points are the crack length and the hollow points are the corresponding max load in the corresponding cycle.

Figure 5 presents the FCG curves of the virgin and three healing phases. The typical FCG curves can be separated into three regions, i.e. subcritical, linear, and unstable phases. The data shown here mainly falls into the linear region. All the FCG curves exhibit comparable ranges of crack propagation rates, but all three healing phase curves are positioned to the left of the virgin curve. The healed FCG curves

are plotted using data acquired by restarting the crack propagation from the pre-crack and allowing the crack to propagate within the previously healed region. The healed FCG curves exhibit higher crack growth rates than the virgin curve at the same ΔK, indicating partial recovery of the fatigue properties after healing. The specimen would eventually break after a certain number of cycle loading at a specific ΔK, without the healing intervention. However, by applying the aforementioned healing process, the crack could be healed and restart from the initial point. Although the healed crack would propagate faster within the healed region, the overall fatigue lifetime could be extended with multiple healing processes.

Since the fatigue experiment of the virgin specimen was terminated when the FCG only reached the intermediate crack propagation rate (> 10^{-5} mm/cycle), the FCG curve at lower ΔK cannot be plotted. Therefore, the overlap of virgin and healing FCG curves only occurs within the range of 0.4 MPa√m < ΔK < 0.6 MPa√m. More investigations are necessary to start the virgin fatigue experiments at lower ΔK to complete the full curves.

The first healing phase FCG curve shows similar trends with the virgin one, The bending of the specimen during the second healing process only results in a shift of the second and third FCG curves to a higher ΔK range with higher crack growth rates. The slope of the curves and the healing efficiency (the relative position compared to the virgin curve) are similar for all three phases. Consequently, all the data were considered when calculating the Paris' law parameters.

The data points that may represent the transition between the three regions are not included for the Paris' law fitting, as they exhibit very high or low crack growth rates. The fitting equations are presented in Table 1. The slopes (m value) of the two fitting curves are similar to each other. Therefore, the healing efficiency can be calculated by comparing the ΔK at the same crack growth rate using equation 5. The fatigue healing efficiency (η) is thus 58 %, which is consistent with the healing efficiency obtained from quasi-static experiments.

$$\eta_{fatigue} = \frac{\Delta K_{healed}}{\Delta K_{virgin}} = \frac{\sqrt[m]{\frac{da}{dN} \cdot \frac{1}{C_{healed}}}}{\sqrt[m]{\frac{da}{dN} \cdot \frac{1}{C_{virgin}}}} = \sqrt[m]{\frac{C_{virgin}}{C_{healed}}} \tag{5}$$

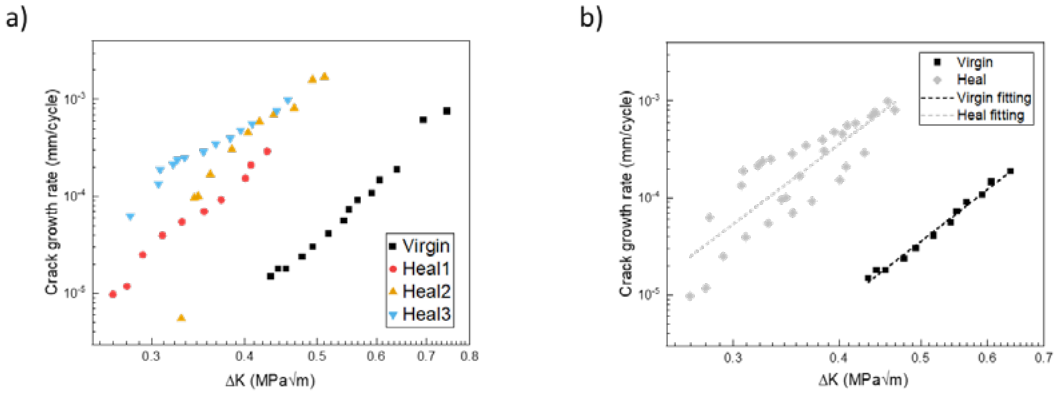


Figure 5: a) Crack growth rate vs. ΔK of virgin and three healing phases b) the comparison of the Paris' law fitting curves and experimental data points.

4. CONCLUSIONS

The self-healing adhesive TDCB experiments were conducted under quasi-static and constant amplitude loading conditions. High fracture toughness recovery (ca. 60%) with good healing repeatability was obtained from quasi-static experiments. Consequently, the fatigue property recovery was further investigated by comparing the relative position of FCG curves. The specimen bending problem that occurred in the second healing process may be the reason for the higher propagation rates in the second and third healing phase fatigue experiments. However, the bending had limited influence on the FCG curves. All the FCG curves of the three healing phases exhibit similar slopes, as reflected in the similar slope values (parameter m) of the Paris' law fitting equations. Therefore, the fatigue healing efficiency was calculated by comparing the ΔK values at the same crack growth rate, resulting in a value of 58 %, which is consistent with the quasi-static investigations. Further experiments with double cantilever beam specimens are required to understand the fatigue behavior of thick adhesive joints fabricated with self-healing adhesives. The healing repeatability and bending influence will also be studied with several TDCB specimens through multiple healing processes under fatigue loading.

Acknowledgments

The authors would like to acknowledge funding under the Lead Agency scheme from the Research Foundation - Flanders (FWO Vlaanderen) through the project grant G031020N and the Swiss National Science Foundation (SNF) through the project grant 200021E_189444 with the title "Combined numerical and experimental approach for the development, testing and analysis of thick adhesive joints in large wind turbine blades". The authors also acknowledge the experimental assistance provided by the technical team of the structural engineering experimental platform (GIS-ENAC at the Ecole Polytechnique Fédérale de Lausanne (EPFL), Switzerland). The authors would like to acknowledge Sika Technology AG and Nordmann Switzerland AG for providing materials and support. The authors acknowledge Axalta Polymer Powders Switzerland Sàrl for the particle cryo-milling process.

References

[1] S. Yao *et al.*, Aero-structural design and optimization of 50 MW wind turbine with over 250-m blades, *Wind Engineering*, **46**, no. 1, Feb. 2022, pp. 273–295, (doi: 10.1177/0309524X211027355.)

[2] K. P. Subrahmanian and F. Dubouloz, Adhesives for bonding wind turbine blades, *Reinforced Plastics*, **53**, no. 1, Jan. 2009, pp. 26–29, (doi: 10.1016/S0034-3617(09)70044-X.)

[3] International Electrotechnical Commission, IEC 61400-5:2020 Wind energy generation systems - Part 5: Wind turbine blades. Geneva, 2020. Accessed: Jun. 01, 2021. [Online]. Available: https://webstore.iec.ch/publication/33236

[4] HIGH PERFORMANCE TOUGHENING AGENT FOR SikaPower® EPOXY ADHESIVES. [Online]. Available: https://gbr.sika.com/dam/dms/gb01/p/SmartCore%20Tech%20-%20SikaPower%20Epoxy%20Adhesives.pdf

[5] D. A. Griffin, The challenges of wind turbine blade durability, *DNV*, May 15, 2023. Accessed: Sep. 14, 2023. [Online]. Available: https://www.dnv.com/Publications/the-challenges-of-wind-turbine-blade-durability-243601

[6] A.-H. I. Mourad, A. Almomani, I. Ahmad Sheikh, and A. H. Elsheikh, Failure analysis of gas and wind turbine blades: A review, *Engineering Failure Analysis*, **146**, Apr. 2023, p. 107107, (doi: 10.1016/j.engfailanal.2023.107107.)

[7] J. Fan, A. P. Vassilopoulos, and V. Michaud, Mode I fracture of thick adhesively bonded GFRP composite joints for wind turbine rotor blades, *Composite Structures*, **327**, Jan. 2024, p. 117705, (doi: 10.1016/j.compstruct.2023.117705.)

[8] H. Barthel, M. Dreyer, T. Gottschalk-Gaudig, V. Litvinov, and E. Nikitina, Fumed silica – rheological additive for adhesives, resins, and paints, *Macromol. Symp.*, **187**, no. 1, Sep. 2002, pp. 573–584, (doi: 10.1002/1521-3900(200209)187:1<573::AID-MASY573>3.0.CO;2-1.)

[9] A. Cohades, E. Manfredi, C. J. G. Plummer, and V. Michaud, Thermal mending in immiscible poly(ε-caprolactone)/epoxy blends, *European Polymer Journal*, **81**, Aug. 2016, pp. 114–128, (doi: 10.1016/j.eurpolymj.2016.05.026.)

[10] X. Luo, R. Ou, D. E. Eberly, A. Singhal, W. Viratyaporn, and P. T. Mather, A Thermoplastic/Thermoset Blend Exhibiting Thermal Mending and Reversible Adhesion, *ACS Appl. Mater. Interfaces*, **1**, no. 3, Mar. 2009, pp. 612–620, (doi: 10.1021/am8001605.)
[11] E. N. Brown, S. R. White, and N. R. Sottos, Retardation and repair of fatigue cracks in a microcapsule toughened epoxy composite—Part II: In situ self-healing, *Composites Science and Technology*, **65**, no. 15, Dec. 2005, pp. 2474–2480, (doi: 10.1016/j.compscitech.2005.04.053.)
[12] S. Neuser and V. Michaud, Fatigue Response of Solvent-Based Self-Healing Smart Materials, *Exp Mech*, **54**, no. 2, Feb. 2014, pp. 293–304, (doi: 10.1007/s11340-013-9787-5.)
[13] E. N. Brown, S. R. White, and N. R. Sottos, Fatigue crack propagation in microcapsule-toughened epoxy, *J Mater Sci*, **41**, no. 19, Oct. 2006, pp. 6266–6273, (doi: 10.1007/s10853-006-0512-y.)
[14] E. N. Brown, Use of the tapered double-cantilever beam geometry for fracture toughness measurements and its application to the quantification of self-healing, *The Journal of Strain Analysis for Engineering Design*, **46**, no. 3, Apr. 2011, pp. 167–186, (doi: 10.1177/0309324710396018.)
[15] ASTM, Standard Test Method for Measurement of Fatigue Crack Growth Rates. ASTM International, West Conshohocken (PA), Jun. 2023. (doi: 10.1520/E0647-23A.)

MOISTURE ABSORPTION COMPARISON BETWEEN BULK ADHESIVES AND ADHESIVELY BONDED JOINTS IN DIFFERENT ENVIRONMENTS

Arij FAWAZ[1] , Emilie LEPRETRE[2] , Xavier CHAPELEAU[3] and Sylvain CHATAIGNER[4]

[1]MAST/SMC, COSYS/SII-I4S, Université Gustave Eiffel, Bouguenais 44344, France
Email: arij.fawaz@univ-eiffel.fr
[2]MAST/SMC, Université Gustave Eiffel, Bouguenais 44344, France
Email: emilie.lepretre@univ-eiffel.fr
[3]COSYS/SII-I4S, Université Gustave Eiffel, Inria, Bouguenais 44344, France
Email: xavier.chapeleau@univ-eiffel.fr
[4]MAST/SMC, Université Gustave Eiffel, Bouguenais 44344, France
Email: sylvain.chataigner@univ-eiffel.fr

Keywords: Adhesively bonded joints, Epoxy adhesive, Durability, Moisture diffusion, Interphase.

Abstract
The use of adhesively bonded composite reinforcements is increasing in various industries for which they encounter diverse environmental conditions throughout their operational lifespan. Moisture absorption stands as a common aging factor leading to the deterioration and weakening of mechanical properties in these materials. Moreover, there is limited knowledge regarding the durability of bonded joints in wet environments. Consequently, moisture diffusion continues to hinder their widespread application across multiple fields. This study will focus on studying the durability of bulk adhesives and adhesively bonded joints under various wet conditions: exposure to 98% relative humidity, immersion in artificial sea water as well as in demineralized water.

In this study, water diffusion was first examined in bulk adhesives, and subsequently in two bonded assemblies having different adhesive thicknesses. Gravimetric measurements were carried out to obtain the corresponding diffusion coefficients. The experimental results revealed Fickian behavior for the studied epoxy bulk adhesives, while a non-Fickian diffusion was obtained for the studied methacrylate adhesive. Regarding the bonded assemblies, those with a 1 mm adhesive thickness exhibit faster diffusion compared to those with a 3 mm adhesive thickness.

1. Introduction

Adhesively bonded joints are increasingly being used in several fields such as aerospace, transport and marine sectors. Their widespread use in many civil engineering applications is due to several advantages. Indeed, compared to the traditional joining techniques (like fastening and riveting) they provide lightweight structural assemblies and allow dissimilar materials joining with no damage during manufacturing process. Moreover, they also permit to obtain more uniform stress distributions along the bonded zone.

Bonded assemblies are exposed to several environmental conditions such as high humidity levels specially in marine environment. Thereby, they should be designed to withstand such environmental conditions. Hence, predicting the long-term behavior of adhesively bonded joints in different environmental conditions is of crucial interest.
Water sorption by polymers is considered as one of the major setbacks in adhesive's application under humid conditions. Water and humid air are known to cause a reduction in strength, durability and service

life of adhesives joints [1]. Moisture degradation of adhesives can result in a decrease in their mechanical properties and can cause both reversible effects, such as plasticization and swelling, as well as irreversible ones, like hydrolysis and oxidation. The detrimental effects are more significant in adhesive joints since degradation of the interface between adhesive and adherend could initiate an interfacial failure. Some authors in the literature found that water penetration is faster in bonded joints than in bulk adhesives [2,3]. This phenomenon was attributed to the presence of interphase and/or interface between adherends and adhesive within the bonded assembly. Furthermore, it was found that in thinner joints, where the ratio of the interphase's thickness to adhesive's thickness is larger than that for thicker joints, there is a greater uptake of water.

Although it has been reported in the literature that water diffusion is often governed by Fick's laws, several authors have demonstrated deviations from Fickian diffusion. Other models have been developed for these cases, such as the Langmuir model [4], the dual Fickian diffusion [5] and the delayed dual Fickian [6].

This paper initially outlines the experimental investigation of water sorption behavior for three structural bulk adhesives using a high-precision balance. Then, the same procedure is also carried out for bonded assemblies with steel substrates and epoxy adhesive, where a comparison of the water sorption profiles for different bonded joint thicknesses is conducted. Additionally, another comparison is made between different humid environments.

2. Experimental methods

2.1. Materials and sample preparation

In this study, three commercial adhesives were used: two epoxy-based adhesives labeled as E1 and E2, and a methacrylate adhesive marked as M. The selection of these materials was driven by their industrial interest and also by their frequent applications in marine environment, which represents the case and condition of this research.

Bulk adhesive discs have been manufactured by pouring the adhesives into circular molds. To facilitate the demolding process, the used molds were made from non-adherent materials: Teflon molds for the M and E1 adhesives and modified polyethylene molds for the E2 adhesive. The discs made for both adhesives E2 and M have the same diameter d of 80 mm and the same thickness e of 1 mm ($\pm$ 0.05 mm). For the adhesive E1, the discs have a diameter of 70 mm and a thickness of 2 mm ($\pm$ 0.09 mm). The dimensions were selected with an aim to consider a 1D surface diffusion i.e., along the thickness direction ($d>>>e$), this allows to simplify the studied diffusion phenomena (figure 1).

The E2 discs were cured at 80°C for 3 hours, the E1 discs were cured at 80°C for 16 hours and the methacrylate adhesive was cured at 25°C for 24 hours according to their technical data sheets. According to [7], taking a slightly higher curing time than that suggested in technical data sheet is much more preferable.



Figure 1. 1D water diffusion through the thickness e of bulk adhesive discs .

Regarding the bonded assemblies, E1 was used as an adhesive, with stainless steel plates serving as adherends. Stainless steel was specifically chosen to prevent corrosion, which could complicate the studied mechanisms of water diffusion. Before bonding, the metallic substrates were sanded using a sandblasting machine, achieving an average roughness of 3.5 µm (± 0.5 µm). Then, they were cleaned with acetone. The bonded joints were manufactured in two different thicknesses of 1 mm (± 0.1 mm) and 3 mm (± 0.5 mm) as shown in figure 2-B. Two temporary steel wedges with these thicknesses were used to ensure a consistent adhesive thickness throughout the bonded assembly. All the bonded joints have the same length of 80 mm (± 7 mm) and the same width of 5 mm (± 0.5 mm), as shown in figure 2-A. These dimensions allow for the adoption of the assumption of 1D surface diffusion, i.e., along the width (where width <<< length).

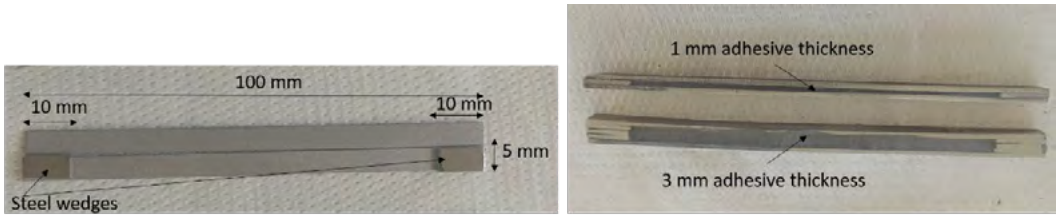


Figure 2. Dimensions of bonded assemblies: (A) 5 mm width and 80 mm length, and (B) two different thicknesses of 1 mm and 3 mm.

2.2. Aging conditions and gravimetric measurements

Before aging, methacrylate samples were dried in an oven at 50 °C until a constant mass was obtained, while the epoxy adhesives discs were placed in a desiccation chamber for 4 weeks (figure 3). No drying process was conducted for the bonded assemblies since the mass loss of E1 bulk specimens during drying was found to be minimal. Thus, the bonded joints were immediately submerged in water after curing to prevent any humidity absorption.

During drying, specimens were periodically weighed on a 10^{-3} g resolution balance (Kern PLJ 2000-3A having a maximum weighing range of 2.1 kg) for the E2 and M discs, and a 10^{-4} g resolution balance (with 610 g of maximum weighing range) was used for the bonded joints and E1 discs. The water content M_t (%) is determined using equation (1) where $m(t)$ is the mass of the sample at a time t while m_0 corresponds to the weight of totally dried specimen (i.e., for $M_t = 0$).

$$M_t\ (\%) = \frac{m(t)-m_0}{m_0} \times 100 \qquad (1)$$

Following drying, the E1 disc specimens were investigated under three different aging environments, which include immersion in demineralized water (DW), immersion in seawater (SW), and exposure to 98% relative humidity (RH) (figure 4). The bonded assemblies, E2 and M discs were placed only in DW and SW. The artificial seawater was prepared by dissolving sodium chloride (NaCl) into pure water following the reference salinity value of 3.5% provided by the ASTM D 1141 standards [8].



Figure 3. Drying process of (A) Epoxy adhesives in dessication chamber, and (B) Methacrylate adhesive in an oven at 50°C.

In each environment, a repeatability study was generated using five disc samples and five bonded assemblies (table 1). This was done to enhance confidence in the results. The total number of produced bulk adhesive discs was 45 (three adhesives, three wet environments and five specimens), while the number of bonded assemblies was 20 (two thicknesses of bonded joints, two wet environments and five specimens).

Table 1. Summary of the number of samples used for each sample type and for various aging environments

	Bulk adhesives			Bonded joints with E1 adhesive	
	E1 adhesive	E2 adhesive	M adhesive	1 mm adhesive thickness	3 mm adhesive thickness
SW	5 samples	5 samples	5 samples	5 samples	5 samples
DW	5 samples	5 samples	5 samples	5 samples	5 samples
98% RH	5 samples	5 samples	5 samples	-	-

To ensure the contact of all discs specimens' faces with water and achieve uniform diffusion, a small support (blue element in figure 3-B) was used to maintain the specimens vertically. During this wet aging process, the temperature was maintained at 50°C by placing all the specimens in a hygrothermal chamber (figure 4). This temperature is at least 20°C below the glass transition temperature Tg of all the adhesives used. The primary purpose of increasing the temperature is to accelerate diffusion, as highlighted in the study of [9].

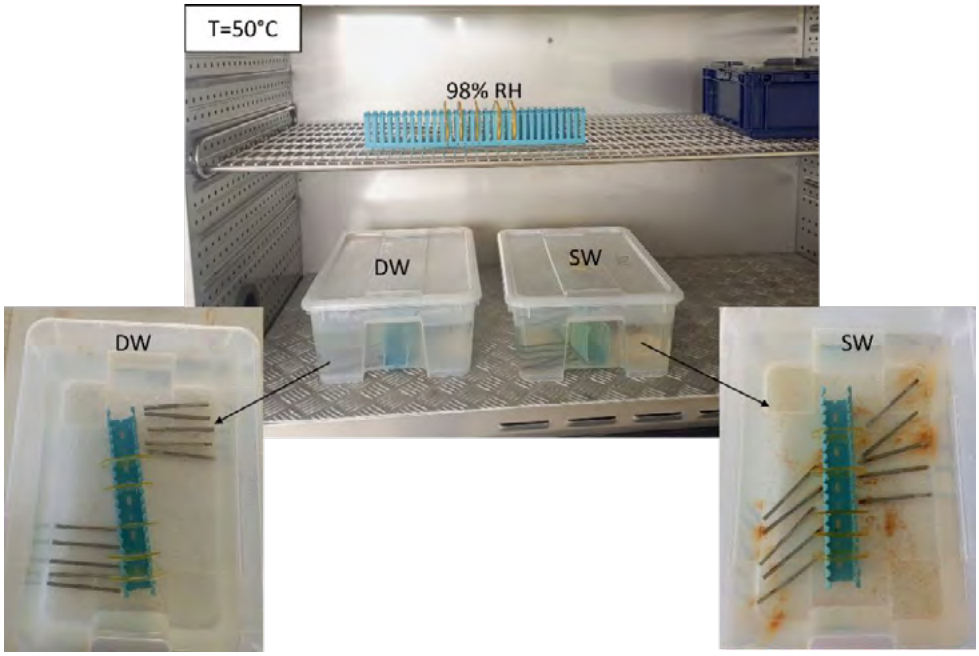


Figure 4. E1 discs and bonded assemblies placed in DW and SW, with E1 discs alone subjected to 98% RH. All the samples were in a hygrothermal chamber at 50°C.

After placing all the specimens (bulk adhesives and bonded joints) in the previously mentioned humid environments, they were taken off at different times, wiped off with tissues to dry their surfaces and weighed using the aforementioned balances. Thereby, the water gain can be calculated using equation (1) where m_0 is defined as the initial dry mass before aging. Once the saturation is reached, M_t will be equal to the saturation moisture content M_s.

Regarding the calculation of diffusion coefficient, the formula proposed by Crank [10], who defines a solution for the Fick model, is used. This formula corresponds to a 1D diffusion that takes place along the sample thickness *e* for the discs and along the sample's width for bonded assemblies.

3. Results and discussion

3.1. Gravimetric measurements for bulk adhesives

Using equation (1), the variation of the macroscopic water content *M(t)* can be graphically represented for M, E2, and E1 discs. These are respectively depicted in figures 5-A, 5-B and 6 that illustrate the evolution of weight gain with the square root of time over the adhesive thickness. Note, measurements for the E1 discs are still under progress as saturation was not obtained for the moment.

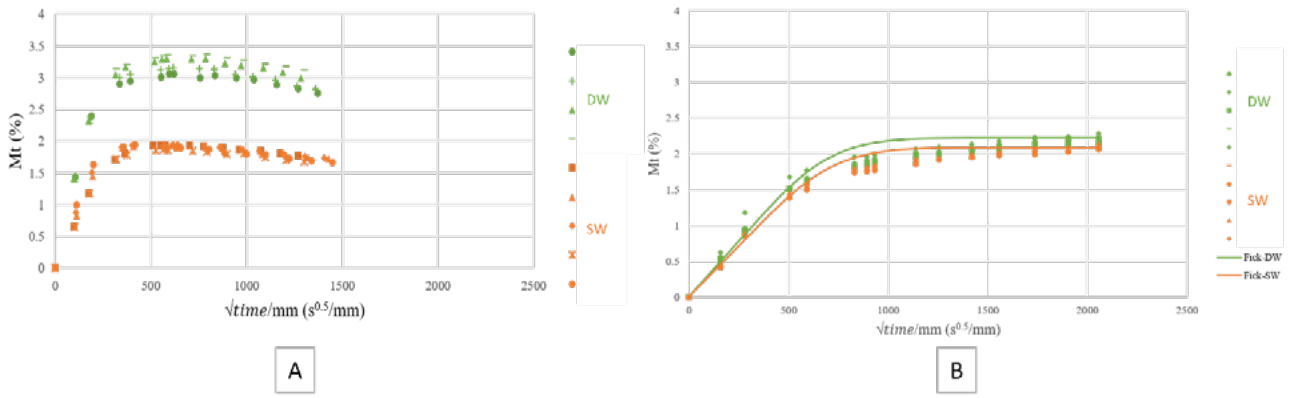


Figure 5. Sorption curves in SW and DW for the (A) M and (B) E2 discs.

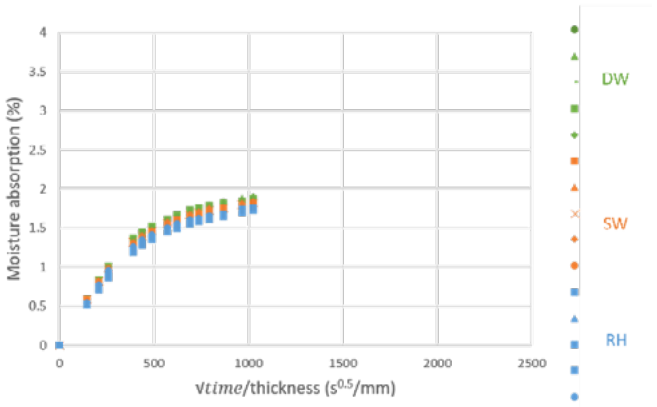


Figure 6. Sorption curves for the E1 discs under three wet conditions: immersion in SW, immersion in DW, and exposure to 98% RH.

These curves depict the absorption process for the epoxy adhesives E1 and E2, revealing two distinct stages. Initially, water uptake results in a linear increase in weight gain relative to the square root of time across the adhesive thickness. Subsequently, a plateau emerges, indicating saturation (figures 5-B and 6). For the methacrylate adhesive, the water absorption curve denotes that after immersion in water, the samples' mass increases linearly with the square root of time in the initial stage. Then, the water uptake begins to decrease after 10 days of wet aging in both SW and DW environments (figure 5-A). A small dispersion in results was obtained for all the disc adhesives.

Results of the gravimetric measurements reveal that the water uptake curves of the adhesives E1 and E2 follow Fickian diffusion, indicating non-anomalous water diffusion behavior. Indeed, the theoretical Fickian curve is distinguished by two phases: initially, a linear increase in water uptake over the square root of time is observed, succeeded by a slower absorption rate leading to a plateau, indicating saturation.

However, the water absorption profile displays a non-Fickian behavior for the M adhesive, as evidenced by a loss of mass observed after 10 days of wet aging. According to [11], this can be attributed to an initiation of material dissolution within the samples, altering the obtained weight change profile to be lower than the theoretical Fick curve. Indeed, a hydrolysis reaction occurred, causing a break in the macromolecular chain and resulting in a reduction in the rate of cross-linking. This reaction also led to the release of molecules into the water, leading to a loss of mass. This is considered as an irreversible consequence of the water diffusion within adhesives.

From the diffusion curves below, the diffusion coefficients can be calculated for the E2 and M adhesives in SW and DW. Table 2 presents the mean values of the obtained diffusion coefficients D and the mean water content at saturation M_s.

Table 2. Diffusion parameters for the M and E2 adhesives in two wet conditions (DW and SW).

	M adhesive		E2 adhesive	
Aging environment	DW	SW	DW	SW
D (mm^2/s) 10^{-7}	92.0 ± 6.20	78.1 ± 5.20	3.82 ± 0.23	3.62 ± 0.12
M_S (%)	2.92 ± 0.16	1.73 ± 0.03	2.22 ± 0.05	2.09 ± 0.03

In both SW and DW environments, the mean diffusion coefficient D of the methacrylate adhesive exceeds that of the epoxy adhesive E2. Additionally, as indicated in table 2, the diffusion coefficient is slightly larger in DW than in SW for the E2 adhesive (5.5% difference). However, a more significant contrast in diffusion coefficients between SW and DW is observed for the M adhesive, where D is 17.8% larger in DW compared to SW. For the E1, the samples are not saturated yet, but based on figure 6, it can be noticed, from a first inspection, that diffusion exhibits a slightly faster rate in DW compared to SW, with SW showing faster diffusion than in the 98% RH environment.

To summarize, the diffusion coefficient for epoxy adhesive E2 is slightly greater in DW compared to SW. A more pronounced contrast emerges with the methacrylate adhesive, consistently showing a higher diffusion coefficient in DW than in SW. It is important to note that the diffusion coefficient of these adhesives is primarily influenced by the chemical nature of these polymers. For the E1 adhesive, diffusion is ongoing, but initial findings suggest that the diffusion coefficient is higher in DW than in SW. Moreover, it appears to be greater in SW than in a 98% RH environment. These results deals with some authors in the literature who found that moisture ingress is more important in deionized water than in seawater [12].

3.2. Gravimetric measurements for bonded assemblies

The water absorption profiles for bonded assemblies, placed in SW and DW, with 1 mm and 3 mm thicknesses of adhesive, are illustrated in figures 7 and 8, respectively.

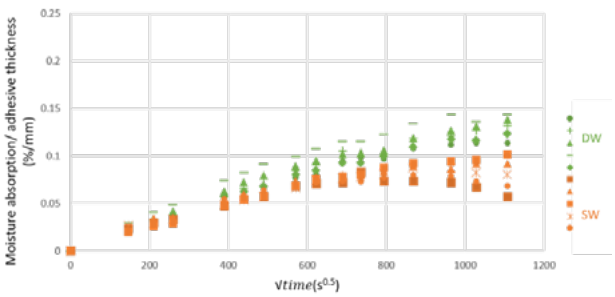


Figure 7. Water sorption curves of bonded assemblies with 1 mm adhesive thickness in SW and DW.

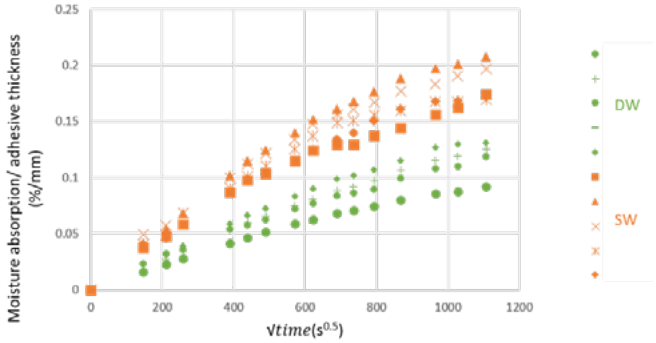


Figure 8. Water sorption curves of bonded assemblies with 3 mm adhesive thickness in SW and DW.

The stainless steel adherends of the bonded assemblies placed in SW began to corrode after 10 days of immersion (figures 7 and 8). After 25 days, corrosion became more significant, leading to a noticeable loss of mass in the water absorption profile. This loss of material due to corrosion exceeded the mass of water absorbed by the bonded joint. Consequently, it is not possible to determine a conclusive value of the diffusion coefficient for these bonded assemblies immersed in SW. However, normalization with respect to the volume of adhesive in each bonded assembly (considering the exposure surface and the primary diffusion-driving distance, which is the width for bonded joints) should be performed to be able to compare the diffusion rate between DW and SW for the 3 mm joints as well as the diffusion rate between bulk adhesives and bonded assemblies. This normalization is intended to account for uncertainties in the dimensions of the bonded assemblies.

In contrast, no corrosion was observed in the bonded joints placed in DW. Hence, only results for bonded assemblies in DW can be adopted and analyzed further. However, since diffusion is still active, the value of the diffusion coefficient for these bonded assemblies cannot be determined at this stage. The corresponding macrospcopic absorption curves are depicetd in figure 9. Nonetheless, it is evident that diffusion occurs slightly faster in the thinner adhesive joint (figure 9), despite the observed dispersion. This dispersion can primarily be attributed to uncertainties in the dimensions of the bonded joints. Further data is required for a more accurate comparison where the exact value of diffusion coefficient can be calculated.

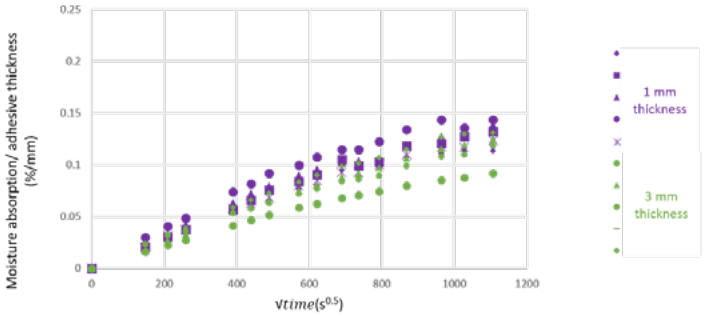


Figure 9. Water sorption curves of bonded assemblies in DW with 1 mm and 3 mm adhesive thicknesses.

4. Conclusion

In this study, the diffusion kinetics were compared at the same temperature of 50°C for three distinct adhesives: two epoxy resins, labeled as E1 and E2, and a methacrylate adhesive, labeled M. Bulk adhesives and bonded assemblies were investigated. Gravimetric measurements demonstrate that the water absorption within bulk epoxy adhesives obeyed the Fickian diffusion. This means that water sorption occurs in the polymer matrix without considering specific interactions between water and polymer chain. However, a degradation happened to the bulk methacrylate adhesive due to the water

penetration and a loss of mass initiates after 10 days of immersion. A faster diffusion is observed in the E2 bulk adhesive with respect to that of the methacrylate adhesive. Moreover, diffusion occurs more rapidly in DW than in SW for all the adhesives, consistently with existing literature.

Since adhesives are rarely used alone in real-life applications, ungoing investigations are carried out to study the diffusion process in bonded assemblies, where the interfaces (the weak points of bonded joints affecting their durability) become relevant. At this stage, slightly faster diffusion was observed in thinner joints. However, the diffusion process is still active, so further data is needed to calculate and compare diffusion rates more accurately.

The achievements of this study could be extended to predict the water uptake in bonded joints and the remaining mechanical strength in long-term aged adhesively bonded joints. For this, mechanical investigations are under investigations to correlate diffusion kinetics to mechanical degradation.

Acknowledgments
The authors would like to acknowledge the technical teams of the MAST/SMC laboratory and COSYS/SII laboratory at Université Gustave Eiffel, as well as the 'Région Pays de La Loire' for co-funding this study.

References
[1] D. R. Lefebvre, K. M. Takahashi, A. J. Muller, and V. R. Raju, “Degradation of epoxy coatings in humid environments: the critical relative humidity for adhesion loss,” *Journal of Adhesion Science and Technology*, vol. 5, no. 3, pp. 201–227, Jan. 1991, doi: 10.1163/156856191X00152.
[2] M. P. Zanni-Deffarges and M. E. R. Shanahan, “Diffusion of water into an epoxy adhesive: comparison between bulk behaviour and adhesive joints,” *International Journal of Adhesion and Adhesives*, Centre National de la Recherche Scientifique, Ecole Nationale Superieure des Mines de Paris, Centre des Matériaux P.M. Fourt, B.P. 87, 91003 Evry Cedex, France, pp. 137–142, 1995.
[3] R. Grangeat, M. Girard, F. Jacquemin, and C. Lupi, “Method of characterizing the interphase’s mean water diffusion properties of a bonded assembly in immersion,” *The Journal of Adhesion*, vol. 98, no. 3, pp. 207–226, Feb. 2022, doi: 10.1080/00218464.2020.1828080.
[4] S. Popineau, C. Rondeau-Mouro, C. Sulpice-Gaillet, and M. E. R. Shanahan, “Free/bound water absorption in an epoxy adhesive,” *Polymer*, vol. 46, no. 24, pp. 10733–10740, Nov. 2005, doi: 10.1016/j.polymer.2005.09.008.
[5] W. K. Loh, A. D. Crocombe, M. M. Abdel Wahab, and I. A. Ashcroft, “Modelling anomalous moisture uptake, swelling and thermal characteristics of a rubber toughened epoxy adhesive,” *International Journal of Adhesion and Adhesives*, vol. 25, no. 1, pp. 1–12, Feb. 2005, doi: 10.1016/j.ijadhadh.2004.02.002.
[6] A. Mubashar, I. A. Ashcroft, G. W. Critchlow, and A. D. Crocombe, “Moisture absorption–desorption effects in adhesive joints,” *International Journal of Adhesion and Adhesives*, vol. 29, no. 8, pp. 751–760, Dec. 2009, doi: 10.1016/j.ijadhadh.2009.05.001.
[7] M. Lettieri and M. Frigione, “Effects of humid environment on thermal and mechanical properties of a cold-curing structural epoxy adhesive,” *Construction and Building Materials*, vol. 30, pp. 753–760, May 2012, doi: 10.1016/j.conbuildmat.2011.12.077.
[8] D19 Committee, “Practice for the Preparation of Substitute Ocean Water.” ASTM International. doi: 10.1520/D1141-98R21.
[9] A. Q. Barbosa, L. F. M. Da Silva, and A. Öchsner, “Hygrothermal aging of an adhesive reinforced with microparticles of cork,” *Journal of Adhesion Science and Technology*, vol. 29, no. 16, pp. 1714–1732, Aug. 2015, doi: 10.1080/01694243.2015.1041358.
[10] J. Crank, *The mathematics of diffusion*. Oxford university press, 1979.
[11] J. Zhou and J. P. Lucas, “The effects of a water environment on anomalous absorption behavior in graphite/epoxy composites,” *Composites Science and Technology*, pp. 57–64, 1995.
[12] R. S. Ashofteh and H. Khoramishad, “Creep behavior of polymeric adhesive joints exposed to different environmental conditions,” *Polymer Composites*, vol. 41, no. 8, pp. 3218–3226, Aug. 2020, doi: 10.1002/pc.25613.

TOPOLOGY OPTIMIZATION AND NUMERICAL MODELLING OF STRUCTURAL BATTERIES

P. Fernandes[1,2], B. Maia[1,2], J. Pedro[1], R. Santos[1,2] and N. Correia[1,2]

[1] INEGI - Institute for Science and Innovation in Mechanical and Industrial Engineering, Porto, 4200-465, Portugal
[2] LAETA – Associated Laboratory for Energy, Transports and Aerospace
Email: pnfernandes@inegi.up.pt, Web Page: https://www.inegi.pt/en/

Keywords: Structural batteries, Topology optimization, Numerical modelling.

Abstract
Composite materials have drawn significant attention due to their versatility and tailored properties, offering an avenue for optimized performance in various applications. In this field, topology optimization has evidenced its capacity to provide new optimal designs, even considering the intricate interplay between material constituents, microstructure, and orientation that profoundly impact composite structures' overall behaviour and performance.
Focused on sustainability goals, structural batteries emerged as a potential solution for achieving efficient energy storage systems and increasing demand for mass electrification. Despite the novelty, interest and relevance of both these fields of research, the application of topology optimization methods to the design and development of structural batteries is still a largely unexplored field.
Therefore, this research demonstrates the possibility of applying topology optimization and novel numerical modelling approaches to the design and development of structural batteries, aiming to bridge the gap between two relevant fields of research. By delving into the methodologies of topology optimization for composite structures and fundamentals of numerical modelling in structural battery development, this study seeks to uncover unexplored synergies, identify new challenges, and pave the way for innovative opportunities in the pursuit of efficient structural battery designs aligned with sustainability goals.

1. Introduction

The successful harness and usage of renewable energy sources hold a pivotal role and contribution on the battle against climate change. Nonetheless, their effectiveness is highly dependent on the development of efficient energy storage systems, a crucial component of the future power grid that facilitates the storage of energy during off-peak periods and its release when high demand arises [1], [2]. This would enable a seamless integration of intermittent renewable sources, such as solar and wind power, enhancing energy independence and resilience.

Among the traditional electrical energy storage systems, lithium and sodium-based batteries emerged as the most used options owing to their superior energy and power densities, as well as longer life cycle [3]. However, the occurance of dendtritic growth, thermal runaway, overcharging, and the failure of individual components is a brief list of the physical phenomena that may occur during the operation of these batteries, affecting both their performance and safety [4]. These drawbacks are aggravated by the environmental impact of the extraction of essential raw-materials, such as cobalt and lithium, required for the lithium-ion batteries (LIBs) industry.
An overview of the state-of-the-art identifies the combination of the electrochemical performance of LIBs with lightweight composite engineering materials as one of the possible approaches to overcome these issues [5], [6], leading to the concept of structural batteries. The multi-functionality of having a

single component capable of simultaneously supporting mechanical loads while storing electrical energy leads to an improved efficiency, reducing raw-material consumption, carbon footprint, and fuel consumption, when applied to transportation industries, mitigates most of the drawbacks that characterize conventional batteries [7], [8].

Therefore, structural batteries are a recent development with the potential to revolutionize the design and implementation of energy storage systems, particularly in the mobility sector with focus on electric vehicles, hinging on the associated weight reduction. Fulfilling both structural and energy requirements represents a significant challenge, evidencing the need for a comprehensive understanding of the multi-physical phenomena that characterize their functioning, and that may be used to support their design and development [9].

Within the scope of this work, research on the numerical modelling techniques capable of representing the distinct physical phenomena that occur during the operation of structural batteries will be reviewed. Furthermore, their interaction with topology optimization techniques will also be explored. This possible link is justified by the similarity of objectives that usually motivate the use of topology optimization during structural design, such as the minimization of mass, and by the potential application of this method to multiple fields of research. Therefore, the following sections will provide a summarized overview of the research focused on the development of structural batteries, their associated numerical modelling techniques, and on topology optimization. Finally, a discussion on the possible interaction of these three fields will be presented and discussed, followed by the key conclusions.

2. Structural batteries

Conventional and all-solid-state batteries share a common composition: the cathode, the electrolyte, and the anode. The primary distinction relies on the type of electrolyte used. Conventional batteries use liquid electrolytes for lithium transport, requiring the inclusion of a separator to prevent short-circuiting [10], which can raise safety concerns due to inadequate thermal stability, parasitic reactions, and the flammability of organic solvents [3], [11]. As a suitable alternative, the concept of all-solid-state batteries emerged, utilizing non-flammable solid-state electrolytes to promote the movement of cations while improving the stability against dendrite formation, enhancing compatibility with high-potential electrodes, and enabling the development of higher energy-density batteries [12]. Their functioning are strongly dependent on well-designed cell configurations and comprehensive electrochemical reactions or physic interactions at the electrode/electrolyte interfaces, including physical contact and chemical and electrochemical stability [13].

One of the most promising designs, under the scope of a multi-functional composite structure, explores the potential of reinforcements, such as carbon fibres, to serve as electrodes while the matrix functions as the electrolyte [5], [14]. This dual strategy integrates both structural and energy storage capabilities, showcasing their combined potential. A key aspect of this strategy involves careful consideration of interface design to ensure that it does not compromise electrochemical performance.

In the subsequent sub-sections, a concise overview of recent research on the numerical modelling of structural batteries will be provided, with the purpose of highlighting the different physical phenomena that must be considered for their correct representation.

3. Numerical modelling of structural batteries

The state-of-the-art numerical modelling techniques used to represent structural batteries build upon the methods developed for their predecessors. Within the scope of this research, LIBs will be focused, which consist of two porous electrodes, each comprising various interpenetrating phases, such as active particles, a conductive binder matrix, and a liquid electrolyte. Their functioning relies on interplays of electrochemical reactions, ion transport, and heat generation. Therefore, to accurately capture these behaviors and battery performance, numerical modelling techniques usually address the isolated or coupled representation of chemical, electrical, and thermal physical phenomena. In research addressing the chemical behaviour of conventional batteries, it is common to focus on the representation of the

reactions occurring at the electrode/electrolyte interfaces, usually based on the Butler-Volmer equation [REF], with the purpose of determining the electrode kinetics and the movement of ions within the electrolyte, including the rate of electrochemical reactions and the distribution of ions. On the electrical behaviour, the challenge is mainly based on the accurate representation of mass transport, charge transfer, and electrical conductivity within the battery system, as the cyclic charging and discharging induces mechanical degradation, constraining the lifespan of LIBs. Finally, research on the numerical modelling of thermal phenomena with emphasis on accurately estimating the heat generation and transfer that occurs during the operation of the battery, usually oriented towards the design and development of efficient thermal management systems.

The three phenomenological fields mentioned are the common building blocks for the numerical modelling of the multi-physical nature of conventional batteries, with research commonly addressing their combination and interaction. Initial research on the numerical representation of the electrochemistry of conventional batteries dates back to the work of Newman et *al.* [15], further developed in [16], [17], with the deployment of a framework approach suitable for individual LIB cells. In this research, the authors proposed a one-dimensional (1-D) macroscopic model, where concentrated solution theory is used to describe the transport in the solution phase, while porous electrode theory is used to describe the composite positive electrode, which may consist of a solution phase, solid active-material phase, and any conductive filler or binding additives.
In addition, Golmon et *al.* [18] utilized a multi-scale approach to represent the influence of electrochemical processes on the mechanical behaviour of the battery, such as the resulting deformation, and *vice-versa*, studying also the influence of external mechanical loads on the electrical performance of the battery. A similar approach was proposed by Bower et *al.* [19] in later research, addressing the resulting stresses that may be installed during charge and discharge cycles, estimating the influence of lithiation phenomena in the electrode materials. This interaction between electrochemical and mechanical behaviour has been one of the major concerns of the research developed since then, addressing possible enhancements through the extension of the multi-scale approaches implemented [20]–[22], accounting for the material degradation during operation [23] and non-linear behaviour [24], as well as the influence of lithiation on mechanical stresses, elastic or plastic deformation, and the resulting crack initiation and propagation [25]–[33]. A similar trend is observed in the research related to the thermochemical behaviour of conventional batteries, accounting for the heat generation and resulting temperature gradients on the material thermal expansion and, consequent, mechanical stresses [34], [35].

The numerical modelling of structural batteries adds an additional dimension to the representation of these components, introducing their mechanical behaviour. Additionally, the use of materials with structural functionalities leads to slight changes in the phenomena represented. For instance, electrochemical or diffusion models add the complexity of Li (de-)intercalation with fibre reinforcements [36], the initiation and propagation of cracks due to the material dissimilarities [37]–[39], including the different thermal expansion coefficients [40]–[42], and respective extension of these phenomena into multiple scales [43], [44].

A different modelling approach that deserves to be mentioned within the scope of structural battery development is the use of Density Functional Theory (DFT). DFT explores the quantum mechanical modelling of the electronic structure and properties of materials at the atomic level. Within the scope of structural battery development, this method allows the tailoring of properties suitable for improved energy storage, which include the prediction of electronic conductivity, ion mobility, and stability. In [45], simulations were performed to predict the behavior of the employed materials for a lithium iron phosphate ($LiFePO_4$) cathode, considering the relationship between the chemical potentials, carriers density, and electronic density of states.
Falta concluir. O que este estudo demonstrou.

4. Topology optimization

Topology optimization is one of the three sub-fields of structural optimization, amongst size and shape optimization, and it is applied in the early stage of structural design, aiming to find an optimal distribution of material [46], [47]. According to an objective function and considering the division of the design domain into multiple regions, this optimization method adjusts the material density at each location, defining which regions should have material and which should not [48]. Resources efficiency and minimization of mass are objectives shared by multiple applications, motivating vast research on the use of topology optimization across diverse fields of research, which are summarily reviewed in this section.

Novel research on the field of topology optimization has focused on its synergy with additive manufacturing, specifically through the introduction of process manufacturing constraints and requirements into the formulation of the problem statement. The challenges involved in this development have been reviewed by Zhu et *al.* [49], Prathyusha and Babu [50], and Liu et al. [51] with a particular focus on either the usage of multi-scale or hierarchical structural optimization design approaches, allowing the integration of material and process limitations during the design of lightweight structures. With a similar objective, although not narrowed to additive manufacturing, Wu et *al.* [52] and Esfarjani et *al.* [53] reviewed the use of topology optimization in the design of multi-scale and metamaterial structures. In addition to classifying the optimization methods based on the use of homogenization-based, density-based, and inverse homogenization methods, these reviews highlight the diverse application of multi-scale approaches not only in structural design but also on the improvement of the thermal and electrical conductivities, thermal expansion, fluid permeability, and phononic and photonic material behaviours. The inclusion of complex material behaviour, such as buckling, geometric and non-linearities, and plasticity, is also identified as a natural development to be pursued in the field, including the introduction and refinement of the constraints associated to these physical phenomena, namely stress constraints, and adequate and failure criteria [54], [55].

Moreover, Fawaz et *al.* [56] reviewed the intrinsic limitations associated to the conventional use of topology optimization for structural design based on Finit Element Method (FEM), which may not be suitable to represent both the multi-disciplinary and -physical nature governing the functioning of a structural battery. For instance, the FEM does not consider the conservation law at each finite element [57], which may lead to numerical instabilities of the conjugate heat transfer problems [58]. The possible use of an extended FEM method (XFEM) has also been explored in combination with the level-set method for the optimization of steady-state and transient single-flow heat transfer problems [57], [59], [60], accounting for phase changes [61]. Finally, the integration of the Lattice Boltzmann method into topology optimization of flow channels in two-dimensional thermo-fluid problems has been explored in [62]–[64], allowing the use of a mesoscale method intended to solve the governing equations of transport problems at the macroscale [65], [66].

With particular concern on composite structures and their anisotropic behaviour, Gandhi and Minak [67] reviewed the use of topology optimization considering continuous fibre-reinforced polymers, adopting a simultaneous or sequential definition of both material distribution and orientation. The approach highlighted to address this issue is the use of continuous parametrization to define the fibre orientation as an angle [68], [69]. However, it faces challenges due to non-convex optimization and sensitivity to initial configurations [70], leading to suboptimal solutions [71]. In this case, further relaxing the design space, as proposed by the free material optimization process [72], [73], is suggested as a possible solution to be explored.

5. Discussion: on the topology optimization of structural batteries

The diverse range of applications studied in the literature, in conjunction with their respective multiphysical nature, demonstrates the versatility of topology optimization. Furthermore, the case studies mentioned in this article overlap with the physical nature of the phenomena used to model the behaviour of both conventional and structural batteries, suggesting the potential use of this method to support their design and development.

In recent research, topology optimization has been applied to the design of auxiliary systems, usually related to thermal management of the battery, such as cooling plates and circuits [74]–[77], to the structural design and protection of the battery against external loads, such as carrying packs and external casings [78], [79], or a combination of both structural and thermal functions combined [80]–[82].

However, scarce research can be found on the direct application of this method to design structural batteries. Mitchel and Ortiz [83] proposed the topology optimization of a silicon anode for LIBs, adopting a combined influence of electrical and structural properties in the objective function. The solution obtained allowed a material distribution capable of providing a compromise between structural performance, in terms of rigidity, and direct conduction pathways. Roy et *al.* [84] proposed the use of topology optimization framework to design porous electrodes. On one hand, the porosity of the electrode improves the electrochemical transport, while its surface area increases the electrochemical activity. This framework has been demonstrated on two applications: a porous electrode driving a steady Faradaic reaction, and a transiently operated electrode in a supercapacitor. In low-conductivity materials, the electrode designs obtained are characterized by a hierarchy of length scales and present reduced energy losses in half-cells. Pejman and Najafi [85] proposed a multi-objective multiphysics density-based topology optimization framework to design the structural battery electrolyte, considering electrochemical, thermal, and structural interactions. The objective function utilized aimed at maximizing the ionic conductivity while minimizing its compliance, imposing constraints on the volume fraction and maximum allowable temperature. In this research, Pejman and Najafi proposed as future work the inclusion of two-way coupling between the physical modules. Therefore, it would allow the damage initiated in the microstructure to have a quantified influence on the ionic conductivity and stiffness, as well as the temperature increase to influence the generated strain state due to thermal expansion.

Despite the limited research available on the junction of both fields of research, topology optimization suggests having the required versatility to cover the multiphysical domains that characterize the functioning of structural batteries.

6. Conclusions

The present article provides a summarized overview of the state-of-the-art on the numerical modelling of structural batteries, highlighting the multiphysical domains that describe their functioning, and on the field of topology optimization, showcasing its versatility and potential application in multiple fields, to draw the reader's attention to the largely unexplored potential synergies between this method and application.

Acknowledgements

B. Maia gratefully acknowledges the financial support from FCT - Fundação para a Ciência e a Tecnologia, I.P., under the scope of the Ph.D. Grant 2023.01813.BD, co-financed by the European Social Fund through NORTE 2020.
The remaining authors gratefully acknowledge the financial support provided by the project NGS – New Generation Storage project, within the scope of the Resilience and Recovery Program, identified through the code of operation 02/C05-i01.01/2022.PC644936001-00000045.

References

[1] X. Luo, J. Wang, M. Dooner, and J. Clarke, “Overview of current development in electrical energy storage technologies and the application potential in power system operation,” *Appl. Energy*, vol. 137, pp. 511–536, 2015, doi: https://doi.org/10.1016/j.apenergy.2014.09.081.
[2] X. Hu, L. Xu, X. Lin, and M. Pecht, “Battery Lifetime Prognostics,” *Joule*, vol. 4, no. 2, pp. 310–346, 2020, doi: https://doi.org/10.1016/j.joule.2019.11.018.

[3] B. A. Maia, N. Magalhães, E. Cunha, M. H. Braga, R. M. Santos, and N. Correia, "Designing Versatile Polymers for Lithium-Ion Battery Applications: A Review," *Polymers (Basel).*, vol. 14, no. 3, 2022, [Online]. Available: https://www.mdpi.com/2073-4360/14/3/403

[4] Y. Chen *et al.*, "A review of lithium-ion battery safety concerns: The issues, strategies, and testing standards," *J. Energy Chem.*, vol. 59, pp. 83–99, 2021, doi: https://doi.org/10.1016/j.jechem.2020.10.017.

[5] F. Danzi, R. M. Salgado, J. E. Oliveira, A. Arteiro, P. P. Camanho, and M. H. Braga, "Structural Batteries: A Review," *Molecules*, vol. 26, no. 8, 2021, [Online]. Available: https://doi.org/10.3390/molecules26082203

[6] S. Ansari, A. Ayob, M. S. Hossain Lipu, A. Hussain, and M. H. M. Saad, "Remaining useful life prediction for lithium-ion battery storage system: A comprehensive review of methods, key factors, issues and future outlook," *Energy Reports*, vol. 8, pp. 12153–12185, 2022, doi: https://doi.org/10.1016/j.egyr.2022.09.043.

[7] H. Yang, "A Review of Structural Batteries Implementations and Applications," in *2020 IEEE Transportation Electrification Conference & Expo (ITEC)*, 2020, pp. 223–228. doi: 10.1109/ITEC48692.2020.9161663.

[8] Y. D. Yücel, D. Zenkert, R. W. Lindström, and G. Lindbergh, "LiFePO4-coated carbon fibers as positive electrodes in structural batteries: Insights from spray coating technique," *Electrochem. commun.*, vol. 160, p. 107670, 2024, doi: https://doi.org/10.1016/j.elecom.2024.107670.

[9] L. Su *et al.*, "Tailoring Electrode–Electrolyte Interfaces in Lithium-Ion Batteries Using Molecularly Engineered Functional Polymers," *ACS Appl. Mater. \& Interfaces*, vol. 13, no. 8, pp. 9919–9931, 2021, doi: 10.1021/acsami.0c20978.

[10] Y.-K. Liu, C.-Z. Zhao, J. Du, X.-Q. Zhang, A.-B. Chen, and Q. Zhang, "Research Progresses of Liquid Electrolytes in Lithium-Ion Batteries," *Small*, vol. 19, no. 8, p. 2205315, 2023, doi: https://doi.org/10.1002/smll.202205315.

[11] Y. Jia, B. Liu, Z. Hong, S. Yin, D. P. Finegan, and J. Xu, "Safety issues of defective lithium-ion batteries: identification and risk evaluation," *J. Mater. Chem. A*, vol. 8, no. 25, pp. 12472–12484, 2020, doi: 10.1039/D0TA04171H.

[12] B. M. Gomes, J. F. Ribeiro Moutinho, and M. H. Braga, "A perspective on the building blocks of a solid-state battery: from solid electrolytes to quantum power harvesting and storage," *J. Mater. Chem. A*, vol. 12, no. 2, pp. 690–722, 2024, doi: 10.1039/D3TA04228F.

[13] S. Lou *et al.*, "Interface Issues and Challenges in All-Solid-State Batteries: Lithium, Sodium, and Beyond," *Adv. Mater.*, vol. 33, no. 6, p. 2000721, 2021, doi: https://doi.org/10.1002/adma.202000721.

[14] L. E. Asp and E. S. Greenhalgh, "Structural power composites," *Compos. Sci. Technol.*, vol. 101, pp. 41–61, 2014, [Online]. Available: https://doi.org/10.1016/j.compscitech.2014.06.020

[15] J. Newman and W. Tiedemann, "Porous-electrode theory with battery applications," *Am. Inst. Chem. Eng. J.*, vol. 21, no. 1, pp. 25–41, 1975, [Online]. Available: https://doi.org/10.1002/aic.690210103

[16] M. Doyle, T. Fuller, and J. Newman, "Modeling of Galvanostatic Charge and Discharge of the Lithium/Polymer/Insertion Cell," *J. Electrochem. Soc.*, vol. 140, no. 6, 1993, [Online]. Available: https://dx.doi.org/10.1149/1.2221597

[17] M. Doyle and J. Newman, "The use of mathematical modeling in the design of lithium/polymer battery systems," *Electrochim. Acta*, vol. 40, no. 13, pp. 2191–2196, 1995, [Online]. Available: https://doi.org/10.1016/0013-4686(95)00162-8

[18] S. Golmon, K. Maute, and M. L. Dunn, "Numerical modeling of electrochemical–mechanical interactions in lithium polymer batteries," *Comput. Struct.*, vol. 87, no. 23, pp. 1567–1579, 2009, [Online]. Available: https://doi.org/10.1016/j.compstruc.2009.08.005

[19] A. F. Bower, P. R. Guduru, and V. A. Sethuraman, "A finite strain model of stress, diffusion, plastic flow, and electrochemical reactions in a lithium-ion half-cell," *J. Mech. Phys. Solids*, vol. 59, no. 4, pp. 804–828, 2011, [Online]. Available: https://doi.org/10.1016/j.jmps.2011.01.003

[20] B. Wu and W. Lu, "A battery model that fully couples mechanics and electrochemistry at both

particle and electrode levels by incorporation of particle interaction," *J. Power Sources*, vol. 360, pp. 360–372, 2017, [Online]. Available: https://doi.org/10.1016/j.jpowsour.2017.05.115

[21] B. Wu and W. Lu, "A consistently coupled multiscale mechanical–electrochemical battery model with particle interaction and its validation," *J. Mech. Phys. Solids*, vol. 125, pp. 89–111, 2019, [Online]. Available: https://doi.org/10.1016/j.jmps.2018.12.005

[22] P. Gupta and P. Gudmundson, "A multi-scale model for simulation of electrochemically induced stresses on scales of active particles, electrode layers, and battery level in lithium-ion batteries," *J. Power Sources*, vol. 511, 2021, [Online]. Available: https://doi.org/10.1016/j.jpowsour.2021.230465

[23] G. Bucci, S. P. V Nadimpalli, V. A. Sethuraman, A. F. Bower, and P. R. Guduru, "Measurement and modeling of the mechanical and electrochemical response of amorphous Si thin film electrodes during cyclic lithiation," *J. Mech. Phys. Solids*, vol. 62, pp. 276–294, 2014, [Online]. Available: https://doi.org/10.1016/j.jmps.2013.10.005

[24] G. Bucci, Y.-M. Chiang, and W. C. Carter, "Formulation of the coupled electrochemical–mechanical boundary-value problem, with applications to transport of multiple charged species," *Acta Mater.*, vol. 104, pp. 33–51, 2016, [Online]. Available: https://doi.org/10.1016/j.actamat.2015.11.030

[25] D. Grazioli, O. Verners, V. Zadin, D. Brandell, and A. Simone, "Electrochemical-mechanical modeling of solid polymer electrolytes: Impact of mechanical stresses on Li-ion battery performance," *Electrochim. Acta*, vol. 296, pp. 1122–1141, 2019, [Online]. Available: https://doi.org/10.1016/j.electacta.2018.07.234

[26] D. Grazioli, V. Zadin, D. Brandell, and A. Simone, "Electrochemical-mechanical modeling of solid polymer electrolytes: Stress development and non-uniform electric current density in trench geometry microbatteries," *Electrochim. Acta*, vol. 296, pp. 1142–1162, 2019, [Online]. Available: https://doi.org/10.1016/j.electacta.2018.07.146

[27] X. Zhang, W. Shyy, and A. M. Sastry, "Numerical Simulation of Intercalation-Induced Stress in Li-Ion Battery Electrode Particles," *J. Electrochem. Soc.*, vol. 154, no. 10, 2007, [Online]. Available: https://dx.doi.org/10.1149/1.2759840

[28] K. Zhao, M. Pharr, S. Cai, J. J. Vlassak, and Z. Suo, "Large Plastic Deformation in High-Capacity Lithium-Ion Batteries Caused by Charge and Discharge," *J. Am. Ceram. Soc.*, vol. 94, no. 1, pp. 226–235, 2011, [Online]. Available: https://doi.org/10.1111/j.1551-2916.2011.04432.x

[29] D. R. Baker, M. W. Verbrugge, and A. F. Bower, "Thermodynamics, stress, and Stefan-Maxwell diffusion in solids: application to small-strain materials used in commercial lithium-ion batteries," *J. Solid State Electrochem.*, vol. 20, pp. 163–181, 2015, [Online]. Available: https://doi.org/10.1007/s10008-015-3012-7

[30] A. F. Bower, P. R. Guduru, and E. Chason, "Analytical solutions for composition and stress in spherical elastic–plastic lithium-ion electrode particles containing a propagating phase boundary," *Int. J. Solids Struct.*, vol. 69–70, pp. 328–342, 2015, [Online]. Available: https://doi.org/10.1016/j.ijsolstr.2015.05.018

[31] L. Anand, "A Cahn–Hilliard-type theory for species diffusion coupled with large elastic–plastic deformations," *J. Mech. Phys. Solids*, vol. 60, no. 12, pp. 1983–2002, 2012, [Online]. Available: https://doi.org/10.1016/j.jmps.2012.08.001

[32] R. Xu and K. Zhao, "Corrosive fracture of electrodes in Li-ion batteries," *J. Mech. Phys. Solids*, vol. 121, pp. 258–280, 2018, doi: https://doi.org/10.1016/j.jmps.2018.07.021.

[33] Y. Zhang, C. Zhao, and Z. Guo, "Simulation of crack behavior of secondary particles in Li-ion battery electrodes during lithiation/de-lithiation cycles," *Int. J. Mech. Sci.*, vol. 155, pp. 178–186, 2019, [Online]. Available: https://doi.org/10.1016/j.ijmecsci.2019.02.042

[34] F. Larché and J. W. Cahn, "A linear theory of thermochemical equilibrium of solids under stress," *Acta Metall.*, vol. 21, no. 8, pp. 1051–1063, 1973, [Online]. Available: https://doi.org/10.1016/0001-6160(73)90021-7

[35] Y. Jia, X. Gao, J.-B. Mouillet, J.-M. Terrier, P. Lombard, and J. Xu, "Effective thermo-electro-mechanical modeling framework of lithium-ion batteries based on a representative volume element approach," *J. Energy Storage*, vol. 33, 2021, [Online]. Available:

https://doi.org/10.1016/j.est.2020.102090
[36] G. G. Botte, "Modeling volume changes due to lithium intercalation in a carbon fiber," *Electrochim. Acta*, vol. 50, no. 28, pp. 5647–5658, 2005, [Online]. Available: https://doi.org/10.1016/j.electacta.2005.03.058
[37] A. Pupurs and J. Varna, "Modeling mechanical stress and exfoliation damage in carbon fiber electrodes subjected to cyclic intercalation/deintercalation of lithium ions," *Compos. Part B Eng.*, vol. 65, pp. 69–79, 2014, [Online]. Available: https://doi.org/10.1016/j.compositesb.2013.11.007
[38] J. Xu and J. Varna, "Matrix and interface microcracking in carbon fiber/polymer structural micro-battery," *J. Compos. Mater.*, vol. 53, no. 25, pp. 3615–3628, 2019, [Online]. Available: https://doi.org/10.1177/0021998319843616
[39] D. Carlstedt and L. E. Asp, "Thermal and diffusion induced stresses in a structural battery under galvanostatic cycling," *Compos. Sci. Technol.*, vol. 179, pp. 69–78, 2019, [Online]. Available: https://doi.org/10.1016/j.compscitech.2019.04.024
[40] F. Dionisi, R. Harnden, and D. Zenkert, "A model to analyse deformations and stresses in structural batteries due to electrode expansions," *Compos. Struct.*, vol. 179, pp. 580–589, 2017, [Online]. Available: https://doi.org/10.1016/j.compstruct.2017.07.029
[41] M. Zhuo, D. Grazioli, and A. Simone, "Active material utilization and capacity of fiber-based battery electrodes," *Electrochim. Acta*, vol. 333, p. 134929, 2020, [Online]. Available: https://doi.org/10.1016/j.electacta.2019.134929
[42] D. Carlstedt, J. Xu, K. Runesson, F. Larsson, and L. E. Asp, "Unit cells for multiphysics modelling of structural battery composites," 2019.
[43] S. Duan *et al.*, "Three-dimensional reconstruction and computational analysis of a structural battery composite electrolyte," *Commun. Mater.*, vol. 4, 2023, [Online]. Available: https://doi.org/10.1038/s43246-023-00377-0
[44] S. Yin *et al.*, "Fabrication and multiphysics modeling of modified carbon fiber as structural anodes for lithium-ion batteries," *J. Power Sources*, vol. 476, p. 228532, 2020, [Online]. Available: https://doi.org/10.1016/j.jpowsour.2020.228532
[45] B. A. Maia, B. M. Gomes, A. N. Guerreiro, R. M. Santos, and M. H. Braga, "Cathodes pinpoints for the next generation of energy storage devices: the LiFePO4 case study," *J. Phys. Mater.*, vol. 7, no. 2, p. 25001, 2024.
[46] R. C. Alderliesten, "Designing for damage tolerance in aerospace: A hybrid material technology," *Mater. Des.*, vol. 66, no. PB, pp. 421–428, 2015, doi: 10.1016/j.matdes.2014.06.068.
[47] Z. Meng and B. Keshtegar, "Adaptive conjugate single-loop method for efficient reliability-based design and topology optimization," *Comput. Methods Appl. Mech. Eng.*, vol. 344, pp. 95–119, 2019.
[48] W. Zhang, J. Yang, Y. Xu, and T. Gao, "Topology optimization of thermoelastic structures: Mean compliance minimization or elastic strain energy minimization," *Struct. Multidiscip. Optim.*, vol. 49, no. 3, pp. 417–429, 2014, doi: 10.1007/s00158-013-0991-9.
[49] J. ZHU, H. ZHOU, C. WANG, L. ZHOU, S. YUAN, and W. ZHANG, "A review of topology optimization for additive manufacturing: Status and challenges," *Chinese J. Aeronaut.*, vol. 34, no. 1, pp. 91–110, 2021, doi: 10.1016/j.cja.2020.09.020.
[50] A. L. R. Prathyusha and G. R. Babu, "A review on additive manufacturing and topology optimization process for weight reduction studies in various industrial applications," *Mater. Today Proc.*, vol. 62, pp. 109–117, 2022.
[51] J. Liu *et al.*, "Challenges in topology optimization for hybrid additive-subtractive manufacturing: A review," *Comput. Des.*, p. 103531, 2023.
[52] J. Wu, O. Sigmund, and J. P. Groen, "Topology optimization of multi-scale structures: a review," *Struct. Multidiscip. Optim.*, vol. 63, pp. 1455–1480, 2021.
[53] S. M. Esfarjani, A. Dadashi, and M. Azadi, "Topology optimization of additive-manufactured metamaterial structures: A review focused on multi-material types," *Forces Mech.*, vol. 7, p. 100100, 2022.
[54] A. Ferrer, P. Geoffroy-Donders, and G. Allaire, "Stress minimization for lattice structures. Part

I: Micro-structure design," *Philos. Trans. R. Soc. A*, vol. 379, no. 2201, p. 20200109, 2021.
[55] H. Yu, J. Huang, B. Zou, W. Shao, and J. Liu, "Stress-constrained shell-lattice infill structural optimisation for additive manufacturing," *Virtual Phys. Prototyp.*, vol. 15, no. 1, pp. 35–48, 2020.
[56] A. Fawaz, Y. Hua, S. Le Corre, Y. Fan, and L. Luo, "Topology optimization of heat exchangers: A review," *Energy*, vol. 252, p. 124053, 2022.
[57] L. Bush and V. Ginting, "On the application of the continuous Galerkin finite element method for conservation problems," *SIAM J. Sci. Comput.*, vol. 35, no. 6, pp. A2953–A2975, 2013.
[58] T. E. Bruns, "Topology optimization of convection-dominated, steady-state heat transfer problems," *Int. J. Heat Mass Transf.*, vol. 50, no. 15–16, pp. 2859–2873, 2007.
[59] Y. Lin, W. Zhu, J. Li, and Y. Ke, "A stabilized parametric level-set XFEM topology optimization method for thermal-fluid problem," *Int. J. Numer. Methods Eng.*, vol. 123, no. 4, pp. 924–952, 2022.
[60] P. Coffin and K. Maute, "A level-set method for steady-state and transient natural convection problems," *Struct. Multidiscip. Optim.*, vol. 53, pp. 1047–1067, 2016.
[61] R. Merle and J. Dolbow, "Solving thermal and phase change problems with the extended finite element method," *Comput. Mech.*, vol. 28, pp. 339–350, 2002.
[62] F. Dugast, Y. Favennec, C. Josset, Y. Fan, and L. Luo, "Topology optimization of thermal fluid flows with an adjoint Lattice Boltzmann Method," *J. Comput. Phys.*, vol. 365, pp. 376–404, 2018.
[63] K. Yaji, T. Yamada, M. Yoshino, T. Matsumoto, K. Izui, and S. Nishiwaki, "Topology optimization in thermal-fluid flow using the lattice Boltzmann method," *J. Comput. Phys.*, vol. 307, pp. 355–377, 2016.
[64] J. Rokicki, "Adjoint lattice Boltzmann for topology optimization on multi-GPU architecture," *Comput. Math. with Appl.*, vol. 71, no. 3, pp. 833–848, 2016.
[65] G. G. McNamara and G. Zanetti, "Use of the Boltzmann equation to simulate lattice-gas automata," in *Lattice Gas Methods For Partial Differential Equations*, CRC Press, 2019, pp. 289–296.
[66] S. Girimaji, "Lattice Boltzmann method: Fundamentals and engineering applications with computer codes." American Institute of Aeronautics and Astronautics, 2013.
[67] Y. Gandhi and G. Minak, "A review on topology optimization strategies for additively manufactured continuous fiber-reinforced composite structures," *Appl. Sci.*, vol. 12, no. 21, p. 11211, 2022.
[68] E. Lindgaard and E. Lund, "Optimization formulations for the maximum nonlinear buckling load of composite structures," *Struct. Multidiscip. Optim.*, vol. 43, pp. 631–646, 2011.
[69] M. Bruyneel and C. Fleury, "Composite structures optimization using sequential convex programming," *Adv. Eng. Softw.*, vol. 33, no. 7–10, pp. 697–711, 2002.
[70] Z. Qiu, Q. Li, Y. Luo, and S. Liu, "Concurrent topology and fiber orientation optimization method for fiber-reinforced composites based on composite additive manufacturing," *Comput. Methods Appl. Mech. Eng.*, vol. 395, p. 114962, 2022.
[71] J. Stegmann and E. Lund, "Discrete material optimization of general composite shell structures," *Int. J. Numer. Methods Eng.*, vol. 62, no. 14, pp. 2009–2027, 2005, doi: 10.1002/nme.1259.
[72] W. Alt, A. Ben-Tal, M. Kočvara, A. Nemirovski, and J. Zowe, *Free material design via semidefinite programming: the multiload case withcontact conditions*. Universität Erlangen-Nürnberg. Institut für Angewandte Mathematik, 1997.
[73] J. Zowe, M. Kočvara, and M. P. Bendsøe, "Free material optimization via mathematical programming," *Math. Program.*, vol. 79, no. 1, pp. 445–466, 1997.
[74] A. Frank, J. Sturm, M. Steinhardt, A. Rheinfeld, and A. Jossen, "Impact of current collector design and cooling topology on fast charging of cylindrical lithium-ion batteries," *ECS Adv.*, vol. 1, no. 4, p. 40502, 2022.
[75] C.-M. Lai and J. Teh, "Network topology optimisation based on dynamic thermal rating and battery storage systems for improved wind penetration and reliability," *Appl. Energy*, vol. 305, p. 117837, 2022.

[76] R. Guo and L. Li, "Heat dissipation analysis and optimization of lithium-ion batteries with a novel parallel-spiral serpentine channel liquid cooling plate," *Int. J. Heat Mass Transf.*, vol. 189, p. 122706, 2022.
[77] X. Mo, H. Zhi, Y. Xiao, H. Hua, and L. He, "Topology optimization of cooling plates for battery thermal management," *Int. J. Heat Mass Transf.*, vol. 178, p. 121612, 2021.
[78] S. Kambampati, J. S. Gray, and H. A. Kim, "Level set topology optimization of load carrying battery packs," *Int. J. Heat Mass Transf.*, vol. 177, p. 121570, 2021.
[79] W. Mingkai, S. Zhang, J. Diepolder, and F. Holzapfel, "Battery package design optimization for small electric aircraft," *Chinese J. Aeronaut.*, vol. 33, no. 11, pp. 2864–2876, 2020.
[80] S. Kambampati, J. S. Gray, and H. A. Kim, "Level set topology optimization of structures under stress and temperature constraints," *Comput. Struct.*, vol. 235, p. 106265, 2020.
[81] M. Astaneh, J. Andric, L. Löfdahl, and P. Stopp, "Multiphysics simulation optimization framework for lithium-ion battery pack design for electric vehicle applications," *Energy*, vol. 239, p. 122092, 2022.
[82] R. Pejman, J. Gorman, and A. R. Najafi, "Multi-physics design of a new battery packaging for electric vehicles utilizing multifunctional composites," *Compos. Part B Eng.*, vol. 237, p. 109810, 2022.
[83] S. L. Mitchell and M. Ortiz, "Computational multiobjective topology optimization of silicon anode structures for lithium-ion batteries," *J. Power Sources*, vol. 326, pp. 242–251, 2016.
[84] T. Roy, M. A. Salazar de Troya, M. A. Worsley, and V. A. Beck, "Topology optimization for the design of porous electrodes," *Struct. Multidiscip. Optim.*, vol. 65, no. 6, p. 171, 2022.
[85] R. Pejman and A. R. Najafi, "Multiphysics topology optimization of a multifunctional structural battery composite," *Struct. Multidiscip. Optim.*, vol. 66, no. 3, p. 46, 2023.

MODELLING OF TRANSVERSE CRACKING RESISTANCE REDUCTION AT ELEVATED TEMPERATURES AND AFTER ISOTHERMAL HEAT TREATMENTS

Vivek Richards Pakkam Gabriel[1], Patrik Fernberg[1] and Janis Varna[1,2]

[1] Department of Engineering Sciences and Mathematics, Luleå University of Technology, SE-97187 Luleå, Sweden.
Email: vivek.pakkam@ltu.se, patrik.fernberg@ltu.se, janis.varna@ltu.se
[2]Laboratory of Experimental Mechanics of Materials, Riga Technical University, LV-1048 Riga, Latvia.

Keywords: Polymer-matrix composite, Transverse cracking, Statistical methods, CT analysis.

Abstract
Under harsh service conditions, polymer composites can suffer damage that results in stiffness reduction. Hence it is critical to predict the damage development in composites exposed to thermal and mechanical loads. In response to this, the current paper focus on investigation and modelling of accumulation of transverse cracks in heat resistant carbon fiber cross-ply laminates subjected to mechanical loading at different elevated temperatures before and after a heat treatment. Weibull theory based modelling was applied to model transverse crack density growth in cross-ply composites subjected to static tensile loads. In the proposed two-parameter Weibull failure initiation stress approach, the shape parameter m is assumed to remain constant, but the effect of heat treatment and test temperature on local crack initiation is modelled as a scale parameter σ_0 dependency, generally described by polynomial expansion.

1. Introduction

Due to excellent mechanical and chemical properties and low density, polymer composites are favoured materials in many high-performance structural application areas e.g. aeronautics, space, sports equipment and automotive. Besides relatively high cost for materials and manufacturing, the maximum use temperature of polymer composites is often the limiting factor when determining what material to use. A possibility to extend the upper limit of the temperature use range of composites is by using temperature resistant polymers like cyanate ester, bismaleimide and polyimides, with high glass transition temperatures as matrix in the composites. A carbon fiber reinforced heat resistant polymer is employed in the presented work. The presented work, originally published and more extensively covered in recent publications [1,2], is on two temperature related phenomena that empirically was found to influence transverse crack density (= *number of cracks / unit length*) growth during thermo-mechanical tensile loading; the test temperature, and a long-term so-called Heat Treatment (HT) of the composite. Heat Treatment in this context refers to an extended exposure (500 h or more) of the test specimen to a temperature of 150°C in air without any external loading applied.

With the ambition to move from zero damage concept towards controlled progressive damage concept also at elevated temperatures, it is essential to characterise and predict the damage development. The first mode of damage during tensile loading are transverse/intralaminar cracks developed in off-axis layers with respect to the main loading direction. Typically, such transverse crack development is preceded by micro-scale debonds that coalesce to produce through-the-thickness cracks with potential to grow along fibers in the layer. With continuous loading the number of transverse cracks increases, each with further potential of initiating local delaminations growing at the interface between two layers. All the mentioned damage modes lead to degradation of thermo-elastic constants of the laminates [3,4].

Two important stages in transverse crack formation must be considered when analysing data and establishing models: a) initiation and b) propagation. Transverse crack initiation is the micro-scaled process involving coalescence of pre-existing defects, flaws or fiber/matrix debonds [5] created by in-plane stresses leading to a damage entity on a homogenized ply scale. The process of creating flaws of

sufficient size to propagate along fibers is not studied in detail in the current paper but is instead described using a failure stress distribution approach [6]. The nominal ply stress required for transverse crack initiation in the abovementioned sense only weakly depends on ply thickness and properties of adjacent plies [7,8]. Propagation of the developed mesoscale damage entity along the fiber direction is usually analysed using energy release rate (ERR) based criteria, leading to the well established $1/\sqrt{t}$ dependence of the required propagation stress on the ply thickness, t. So-called "thin" plies are defined as plies where the initiation stress is lower than the propagation stress. Conversely, for "thick" 90-layers (as considered in the current work), the nominal ply stress required for crack initiation is larger than the stress required for propagation. In "thick" plies, the initiated crack reaches a critical size in ply thickness direction and instantly grows in both ply thickness and fiber direction [9]. The transverse stress required to initiate a crack in a given position in the homogenized layer of a composite with "thick" plies consequently also will be the transverse failure stress in this position. Therefore, the failure initiation transverse stress is called in following "failure stress".

The available literature studying the influence of test temperature on damage development rates during quasi-static tensile loading are non-conclusive in the sense that some reports [10,11] showed that the elevated test temperatures reduced transverse cracking whereas few others [12] showed increase in transverse cracking tendency. This suggests that the transverse cracking characteristic depends on the used material system and the test temperature. In [13,14], the heat treatment of composites at elevated temperatures for several hours, increased the transverse cracking tendency in subsequent quasi-static tensile loading at Room Temperature (RT). To the authors knowledge, only a few studies have been performed to study and predict the crack density growth during quasi-static loading at different temperatures of heat treated composite laminates. The current work presents the systematic investigation on the effects of 1) test temperature T_{test}; 2) long term heat treatment before tensile testing, on transverse cracking in quasi-static tensile loading in heat resistant polymer cross-ply laminates. A two-parameter Weibull failure stress distribution model has been proposed to account for the temperature effects. For that, the Weibull scale parameter was assumed to be temperature dependent and defined using polynomial expression.

2. Methodology to predict crack initiation

To model crack initiation one can start by stating that fiber clusters and defects/voids are statistically distributed in the 90-layer implying that different locations within the layer has different failure stress. Such layer may be viewed as a connected chain of elements, each with certain length but with a statistically distributed failure stress. To ensure that each element will not have more than one crack, the element length can be selected based on experience as being equal to the layer thickness, t_{90}. By doing so the cumulative probability of failure P_f at transverse stress σ_T can be defined as the fraction of elements failed at that stress level or in terms of crack density,

$$P_f = \frac{\rho}{\rho_{max}}, \tag{1}$$

where ρ is the crack density at σ_T and the maximum possible crack density, $\rho_{max} = 1/t_{90}$ [15].
The distribution of failure stress in each element can also be defined using a Weibull failure stress distribution model [16,17]. Applying this methodology, consequently denoted "P_f approach" in the current paper, gives that the P_f of an element also may be expressed as

$$P_f = 1 - \exp\left(-\left(\frac{\sigma_T}{\sigma_0}\right)^m\right) \tag{2}$$

where σ_T denotes the thermo-mechanical transverse stress in 90-layer, and m and σ_0 denotes the Weibull shape and scale parameter respectively. The approach taken hereafter, also supported by findings of Sun et al [11], is to assume that the shape parameter, m, describing the variability of the failure stress in elements remains constant and is not affected by temperature effects such as test temperature or heat treatment.

The reference Weibull parameters, m and σ_0 are determined at reference conditions (as-manufactured specimens tested at RT) using data points from the low crack density region where the thermo-mechanical transverse stress is close to the stress in undamaged laminate σ_{T0}. In ln-ln axes, Eq. 2 becomes,

$$\ln\left(-\ln\left(1-P_f\right)\right) = m\, ln\sigma_{T0} + m\, ln\sigma_0 \tag{3}$$

allowing parameters m and σ_0 to be determined from a linear fit of experimental results. To address the empirically observed differences in cracking tendency at different temperatures and HT, the scale parameter is assumed to be dependent on T_{test} and HT and was defined using a polynomial expression,

$$\sigma_0^* = \sigma_0\left[1 - c\Delta T - df(T_{tr}, t_{tr}) + c_1\Delta T^2 + d_1 f^2(T_{tr}, t_{tr}) + \phi\left(\Delta T, f(T_{tr}, t_{tr})\right) + ..\right], \tag{4}$$

where ΔT is the difference between the T_{test} and a reference temperature T_R (RT in this case), T_{tr} and t_{tr} is the temperature and time of the HT and the functional dependence $f(T_{tr}, t_{tr})$ must be found experimentally. By incorporating the modified scale parameter from Eq. 4 in Eq. 2, one obtains,

$$P_f = 1 - \exp\left(-\left(\frac{\sigma_T}{\sigma_0^*}\right)^m\right). \tag{5}$$

In Eq. 4, the effects of ΔT and HT were defined separately due to the experimental time scale of those effects and also interaction between those effects were defined using the term $\phi\left(\Delta T, f(T_{tr}, t_{tr})\right)$. Definition of ϕ is suggested as, $\phi = e\Delta T\, f(T_{tr}, t_{tr})$. Parameters c, c_1, d, d_1 and e can be determined from empirical fitting.

3. Materials and conditioning

Cross-ply laminates with layups $[0/90_2]$s and $[0/90/0/90_{0.5}]$s and UD $[0_6]$, were manufactured by RTM using UD carbon fiber fabric as reinforcement to a polymer with bismaleimide formulation. Laminate properties, t_{90} and V_f, alongside with elastic constants and CTE used in the analysis are presented in Table 1 [1].

Table 1. Laminates and thermo-elastic ply constants used in stress calculations [1].

Plate	Layup	t_{90} (mm)	V_f (%)	E_1 (GPa)	E_2 (GPa)	ν_{12}	G_{12} (GPa)	α_1 (10^{-6} 1/°C)	α_2 (10^{-6} 1/°C)
Plate 1	$[0/90_2]$s	0.80	46	106.94	9.41	0.33	4.42	0.90	38.73
Plate 2	$[0/90_2]$s	0.73	52	120.08	9.92	0.32	4.96	0.60	35.88
Plate 3	$[0/90_2]$s	0.64	58	133.22	10.45	0.31	5.58	0.37	33.00
Plate 4	$[0/90/0/90_{0.5}]$s	0.16	57	131.03	10.36	0.32	5.47	0.40	33.48
Plate 5	$[0_6]$	1.00	60	137.60	10.08	0.30	5.81	0.30	30.20

The edges of samples (dimensions 180 mm and width 10-15 mm) were grinded and polished to minimize edge effects and to facilitate optical observation of edge damage development. Transverse cracks were manually counted using optical microscope (Zeiss Axioskop) either removing the specimen from the testing machine or inspecting edge replicas (Struers Repliset-T3) at RT. The crack density was calculated from the average of number of cracks over 50 mm gauge length on both specimen edges. Two specimen conditioning treatments were considered: As-Manufactured (AM) specimens with no

treatment and specimens after an extended HT. During HT, specimens taken from Plate 2, 3 and 4 were subjected to 150℃ at ambient air conditions for up to 1000 hours.

4. Quasi-static tensile test methodology

Quasi-static tensile tests were conducted on specimens where distance between grips was 100 mm at a constant cross-head displacement rate of 2 mm/min. The strain was measured using an extensometer, with gauge length of 50 mm. Tests were performed at RT, 90℃ and 150℃ using a stepwise loading procedure. Each step involves a tensile loading and unloading sequence, gradually increasing the strain level to introduce damage in 90-layer [5]. After each sequence, the edges of the tested specimen were observed for damage. Sequences were repeated until failure in or along 0-layer bundles occurred. During ET tests, the specimen was mounted in the test machine at RT. The environmental chamber, along with the specimen, was heated to desired temperature while keeping a constant, very small load (2N). Once thermal equilibrium was achieved, the specimen was loaded to the damage inducing strain level and subsequently unloaded. The specimen was thereafter allowed to slowly cool down inside the chamber to RT and observed for damage state at RT. The procedure was repeated for all incremental strain levels.

5. Results and discussion

5.1. Transverse cracking in quasi-static tensile tests

Crack density growth as a function of the calculated thermo-mechanical transverse stress in the 90-layer is shown in Figure 1. The crack density growth rate is rather similar at RT and ET, the main difference is that the stress required to reach certain crack density is lower at ET. This implies that transverse cracking initiation resistance is lower at ET. Similar observations were made for heat treated specimens. Though the crack density growth rate in heat treated specimens was similar as for AM specimens, the value of crack density at any stress level was higher for heat treated compared to AM specimens tested under same conditions. Possible reasons could be continued post curing, causing resin embrittlement [18], and/or certain extent of oxidation on specimen edges and surfaces during HT.

6. Identification of model parameters

Following sections presents a) determination of Weibull parameters at reference state, b) determination of temperature dependent model and c) applicability of the developed model, demonstrated by using independently determined parameters to predict cracking development in a laminate with same constituents but different layup and fiber content.

The reference Weibull parameters at RT of all AM (reference condition) plates are given in Table 2. They are determined using experimental data corresponding to $0.20 < P_f < 0.50$. The reason for the selected regions was a compromise between the requirement for remaining within the low crack density region ($0.05 < P_f < 0.3$) and having a statistically representative number of data points.

Table 2. Reference Weibull parameters of AM composites at RT from [1].

Plate	Shape parameter m	Scale parameter σ_0 (MPa)
Plate 1	6.18	124.01
Plate 2	3.27	141.91
Plate 3	4.71	126.99
Plate 4	4.91	191.27

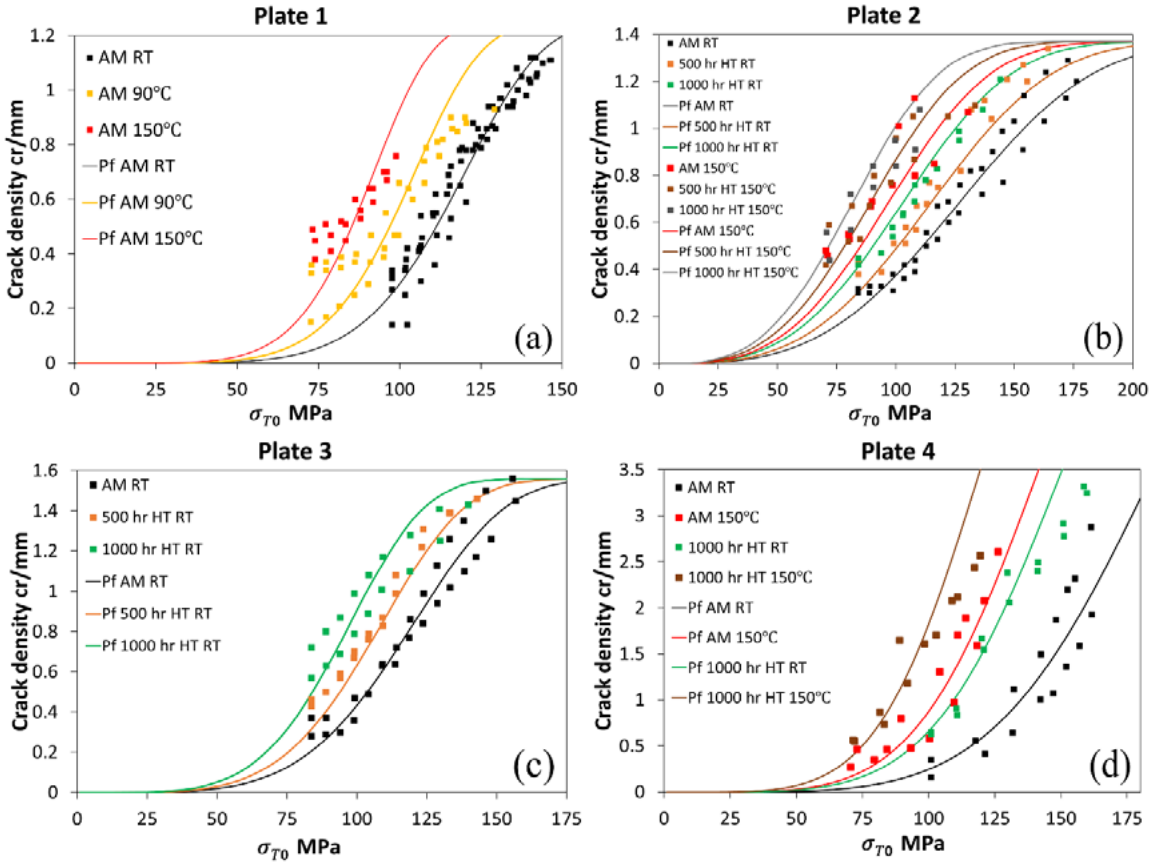


Figure 1. Crack density versus thermo-mechanical transverse stress in 90-layer. Coloured symbols are data points, solid lines are predictions. In legend, AM and HT refer to as-manufactured and heat treated specimens respectively, tested at different temperatures mentioned as RT, 90°C and 150°C. [1]

To determine model parameters only related to T_{test} effect, Eq. 4 may be written as,

$$\sigma_0^* = \sigma_0[1 - c\Delta T + c_1\Delta T^2]. \tag{6}$$

Scale parameter σ_0^* value was determined by finding a good fit for crack density growth versus σ_{T0} data of Plate 1 at elevated temperatures using Eq. 5. Determined σ_0^* showed clear reduction with increasing T_{test}. Graphical representation of the ΔT and $c\Delta T - c_1\Delta T^2$ (obtained from $1 - \sigma_0^*/\sigma_0$) relationship displays a highly linear relationship, see Figure 2a, hence $\boldsymbol{c_1 = 0}$. This suggests that including the quadratic term is not necessary for the given material. Linear fit of data gives value of $\boldsymbol{c = 0.00183}$.

In case of heat treated specimens tested at reference (RT) test conditions, Eq. 4 simplifies to,

$$\sigma_0^* = \sigma_0[1 - df(T_{tr}, t_{tr}) + d_1 f^2(T_{tr}, t_{tr})]. \tag{7}$$

The scale parameter σ_0^* dependence on HT was found by fitting crack density versus σ_{T0} at RT for Plate 2 specimens. In the current work, the only varying parameter in HT is treatment time, the temperature is constant at 150 ℃. The dependence on treatment temperature is consequently not known. Therefore, $df(T_{tr}, t_{tr})$ & $d_1 f^2(T_{tr}, t_{tr})$ in Eq. 7 becomes $d(T_{tr})t_{tr}$ & $d_1(T_{tr}){t_{tr}}^2$. Thereafter, by plotting $d(T_{tr})t_{tr} - d_1(T_{tr}){t_{tr}}^2$ (obtained from $1 - \sigma_0^*/\sigma_0$) against the t_{tr} in hours, see Figure 2b, the relationship is found to be rather linear and the quadratic term in expansion is again not required. A linear fit gives the value $\boldsymbol{d(T_{tr} = 150\,℃) = 0.000188}$.

Then the σ_0^* for heat treated specimens static tested at 150 ℃ for Plate 2 was obtained from fitting the experimental data. The interaction term between test temperature and heat treatment, $e\Delta Tf(T_{tr}, t_{tr})$ in Eq. 4 can be written as $e(T_{tr})\Delta T t_{tr}$ for cases where a single heat treatment temperature is considered. By using the σ_0, σ_0^*, c, c_1, d and d_1 values obtained, $e(T_{tr})\Delta T t_{tr}$ can be determined using Eq. 4. The obtained $e(T_{tr})\Delta T t_{tr}$ values are plotted against t_{tr} in Figure 2c. A rather linear behaviour with respect to t_{tr} is observed and linear fit gives, $\boldsymbol{e = 0.000069}$. The nonzero value of e indicates that the scale parameter reduction for heat treated specimens at elevated temperatures is more than just a sum of the HT and T_{test} caused reduction.

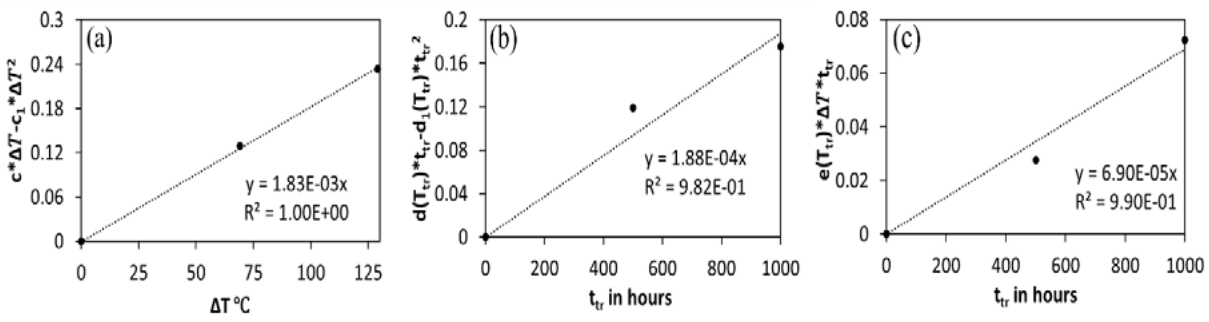


Figure 2. Graphical representation for determination of a) c b) $d(T_{tr})$ c) $e(T_{tr})$ parameters.

6.5. Verification of the HT and T_{test} dependent damage model

Simulations based on probability of failure P_f (Eq. 5) were used to produce predictions presented in Figure 1a-d. The predicted crack density using the scale parameter modified by Eq. 4 is consistent with test results. Interestingly, one can see that by using $c,\ d(T_{tr}),\ e(T_{tr})$ parameters obtained from tests on Plate 1 and 2 to predict the cracking developments of Plates 3 and 4 specimens, the crack density predictions are in good agreement, see Figure 1c and 1d. This is not surprising: all plates have the same reinforcement, interface and matrix.

7. Conclusion

Effect of test temperature and iso-thermal heat treatment on transverse cracking in 90-layer of carbon fiber reinforced polymer cross-ply laminate subjected to quasi-static tensile loading was studied. The transverse crack density growth in as-manufactured and heat treated specimens tested at different temperatures was analysed against the thermo-mechanical transverse stress in 90-layer. It was found that both elevated test temperature and heat treatment reduced the transverse cracking resistance. Methodology to predict transverse cracking was developed using a two-parameter Weibull model. In the model the Weibull scale parameter was assumed to be temperature dependent and defined using polynomial expansion. Model parameters in polynomial expansion were determined from experimental test results of Plates 1 and 2. The scale parameter was found to be linearly decreasing with the increase in tested test temperature range and heat treatment hours. The developed model to predict transverse cracking considering the temperature effects was validated against Plates 3 and 4 with same materials constituents but with different layup and fiber content.

Acknowledgement

The presented work was funded by Swedish Aeronautical Research Program NFFP 7&8 and GKN Aerospace, Sweden. The authors would like to acknowledge, Amirabbas Razkordanisharahi and Alessia Cardin for their contribution in experiments.

References

[1] V. R. Pakkam Gabriel, V. I. Petkov, P. Fernberg and J. Varna. Effect of heat treatment and test temperature on transverse cracking tensile loading. Composites Part A, 181: 108149, 2024.
[2] V.I Petkov, V. R. Pakkam Gabriel and P. Fernberg. Semantic segmentation of progressive micro-cracking in polymer composites using Attention U-Net architecture. Tomography of Materials and Structures, 5:100028, 2024.
[3] J. Varna. Crack separation based models for microcracking. Comprehensive Composite Materials II, 2:192-220, 2018.
[4] A. Parvizi and J. E. Bailey. On multiple transverse cracking in glass fiber epoxy cross-ply laminates. Journal of Material Science, 13:2131-2136, 1978.
[5] F. París, J. Cano and J. Varna. The fiber-matrix interface crack – a numerical analysis using boundary elements. International Journal of Fracture, 82(1):11-29, 1996.
[6] V. R. Pakkam Gabriel, M. S. Loukil and J. Varna. Analysis of intralaminar cracking in 90-plies of GF/EP laminates with distributed ply strength. Journal of Composite Materials, 55(26):3925-3942, 2021.
[7] M. Herráez et. al. Transverse cracking of cross-ply laminates: A computational micromechanics perspective. Composite Science and Technology, 110:196-204,2015.
[8] L. D. Stasio, J. Varna and Z. Ayadi. Effect of the proximity to the 0°/90° interface on Energy Release Rate of fiber/matrix interface crack growth in the 90°-ply of a cross-ply laminate under tensile loading. Journal of Composite Materials, 54(21):3021-3034, 2020.
[9] A. Parvizi, K. W. Garrett and J. E. Bailey. Constrained cracking glass fiber-reinforced epoxy cross-ply laminates. Journal of Material Science, 12:195-201, 1978.
[10] S. Kobayashi and N. Takeda. Experimental characterization of microscopic damage behavior in carbon/bismaleimide composite – effects of temperature and laminate configuration. Composites: Part A Applied Science and Manufacturing, 33(11):1529-1538, 2002.
[11] Z. Sun, I. M. Daniel and J. J. Luo. Statistical damage analysis of transverse cracking in high temperature polymer composite laminates. Mater Science and Engineering, 341:49-56, 2003.
[12] Y. Matsuhisa and J. King. Effects of temperature on monotonic and fatigue properties of carbon fiber epoxy cross ply laminates. Journal of Physics IV France, 3(C7):1657-1660, 1993.
[13] H. Z. Ammar. Composites with bundle mesostructured: Elastic properties and damage. PhD Dissertation, Luleå University of Technology, Sweden, 2016.
[14] D. Q. Vu, M. Gigliotti and M. C. Lafarie-Frenot. The effect of thermo-oxidation on matrix cracking of cross-ply [0/90]s composite laminates. Composites: Part A, 44:114-121, 2013.
[15] K. L. Reifsnider and R. Jamison. Fracture of fatigue-loaded composite laminates. International Journal of Fatigue, 4(4):187-197, 1982.
[16] P. W. M. Peters. The strength distribution of 90° plies in 0/90/0 Graphite-Epoxy laminates. Journal of Composite Materials, 18(6):545-556, 1984.
[17] P. W. Manders, T. W. Chou, F. R. Jones and J. W. Rock. Statistical analysis of multiple fracture in 0°/90°/0° glass fiber/epoxy resin laminates. Journal of Material Science, 18:2876-2889, 1983.
[18] R. J. Morgan, E. E. Shin, B. Rosenberg and A. Jurek. Characterization of the cure reactions of bismaleimide composite matrices. Polymer, 38(3):639-646, 1997.

DIRECT PARAMETER IDENTIFICATION FOR HIGHLY NON-LINEAR STRAIN RATE DEPENDENT CONSTITUTIVE MODELS USING MACHINE LEARNING

J. Gerritzen[1], A. Hornig[1,2,3], P. Winkler[2] and M. Gude[1]

[1]Technische Universität Dresden, Institute of Lightweight Engineering and Polymer Technology (ILK), Holbeinstr. 3, 01307 Dresden, Germany
Email: johannes.gerritzen@tu-dresden.de, Web Page: https://tu-dresden.de/ing/maschinenwesen/ilk
[2]Center for Scalable Data Analytics and Artificial Intelligence (ScaDS.AI) Dresden/Leipzig, Germany
[3]University of Oxford, Department of Engineering Science, Parks Road, Oxford OX1 3PJ, United Kingdom

Keywords: Direct parameter identification, Machine learning, Convolutional neural networks, Strain rate dependency, Fiber reinforced plastics

Abstract
Fiber reinforced plastics (FRP) exhibit strongly non-linear deformation behavior. To capture this in simulations, intricate models with a variety of parameters are typically used. The identification of values for such parameters is highly challenging and requires in depth understanding of the model itself. Machine learning (ML) is a promising approach for alleviating this challenge by directly predicting parameters based on experimental results. So far, this works mostly for purely artificial data. In this work, two approaches to generalize to experimental data are investigated: a sequential approach, leveraging understanding of the constitutive model and a direct, purely data driven approach. This is exemplary carried out for a highly non-linear strain rate dependent constitutive model for the shear behavior of FRP.
The sequential model is found to work better on both artificial and experimental data. It is capable of extracting well suited parameters from the artificial data under realistic conditions. For the experimental data, the model performance depends on the composition of the experimental curves, varying between excellently suiting and reasonable predictions. Taking the expert knowledge into account for ML-model training led to far better results than the purely data driven approach. Robustifying the model predictions on experimental data promises further improvement.

1. Introduction

The stress response of FRP to shear deformation is highly dependent on both deformation state and velocity. In order to model the behavior of FRP structures and thus allow for predictive analyses, a variety of models have been published, accurately capturing this non-linear and strain rate dependent stress-strain-behavior [1, 2]. Due to the inherent complexity of these models, they, however, pose a high initial hurdle when it comes to their application to new materials. One significant aspect in that matter is the determination of governing parameters from experimental results. This typically requires in depth knowledge of the intended constitutive model and thus significantly impedes the application of novel, potentially better suited models.
A promising approach of democratizing this expert knowledge lies in the application of ML. Its application to parameter identification (PI) has recently received an increasing amount of research interest [3, 4]. Especially the field of so called direct inverse PI, in which governing parameters are directly predicted from the material behavior, i.e. stress-strain-curve, promises to facilitate the application of novel models. It has been successfully used by several authors for PI on artificial data [5, 6]. However, the application of models for direct inverse PI to experimental data remains highly challenging.

In this work two ML-based approaches to realize this goal are investigated on the example of a recently proposed highly non-linear constitutive model for the strain rate dependent shear behavior of FRP [7]: 1. A convolutional neural network (CNN) taking several stress-strain-curves as input, directly mapping them to the corresponding parameter set. 2. A sequential approach in which a rate independent parameter set is predicted for each curve and the results are passed on to a second stage of the network, extracting rate dependency parameters. Both approaches are trained on purely artificial data and the better suited one is subsequently tested on real-world experimental data. The methods are compared in terms of prediction accuracy and interpretability.

2. Methodology

2.1. Constitutive model from [7]

The material model for which parameters shall be extracted contains a direct dependency of shear stress response τ to shear strain input γ given by

$$\tau(\gamma) = G/a\ (1 - \exp(-a \cdot \gamma)) \tag{1}$$

with the initial slope G, representing the shear modulus, and the decay parameter a. Dependency of these parameters on the strain rate $\dot{\gamma}$ is modeled by a Johnson-Cook approach using the respective scaling parameters A_G and A_a:

$$G(\dot{\gamma}) = G_0(1 + A_G \ln \dot{\gamma}/\dot{\gamma}_0) \tag{2}$$

$$a(\dot{\gamma}) = a_0(1 + A_a \ln \dot{\gamma}/\dot{\gamma}_0)\,. \tag{3}$$

Using the four parameters G_0, a_0, A_G and A_a alongside the strain rate of the reference and current experiment, the stress response under out of plane shear can be accurately calculated [7].

2.1. Model setup

For the identification of the strain rate dependency of material parameters, two approaches are investigated. Firstly, a sequential one subsidizing the steps from the classical approach by models that are individually trained and ensembled afterwards. This allows for a better insight into the workings of the final model. Secondly a direct training of the ensembled model. This is done to prevent error accumulation throughout the different sub-models. The fundamental model layout and subdivisions are shown in Figure 1.

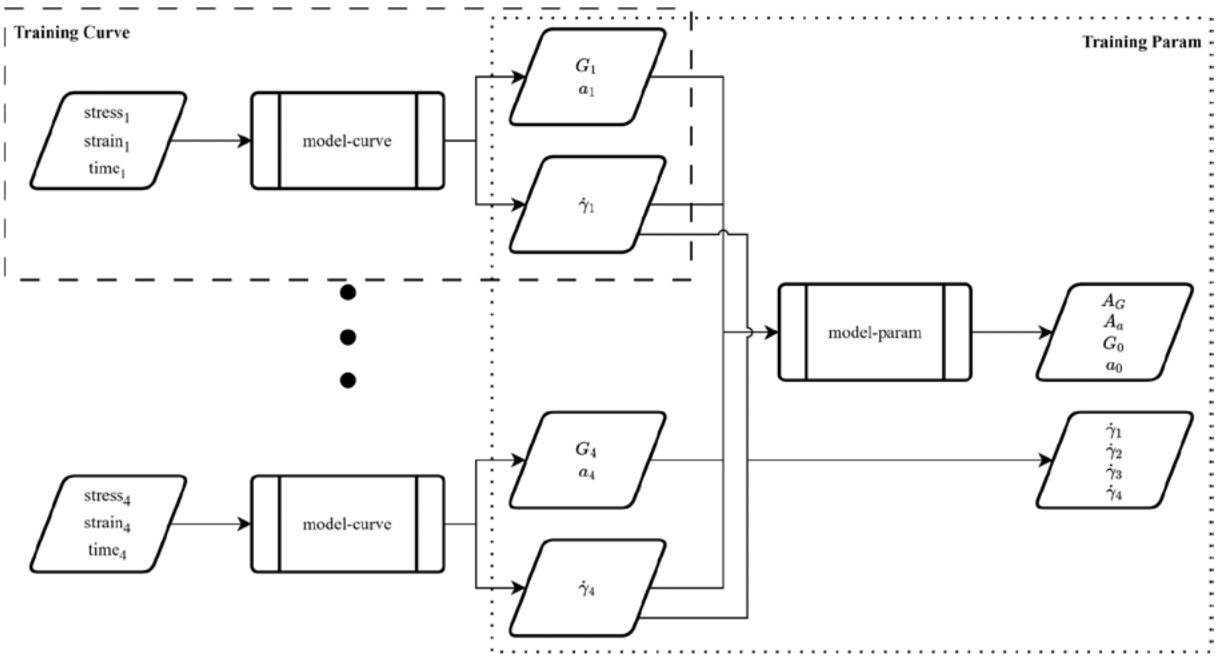


Figure 1. Fundamental layout of ensemble model

For both approaches the ensemble model takes four arrays containing time, strain and stress information as input. These are separated and each individual array is passed to `model-curve`. This maps the arrays to three scalar variables. For the first approach, this sub-step is trained a priori on a specific dataset, allowing for the interpretation of the output from `model-curve` as the governing parameters G, a and the strain rate $\dot{\gamma}$. In the second approach, this is just one of many hidden layers. The outputs of the four `model-curves` are concatenated and passed to `model-param` to extract the desired rate dependency parameters.
The fundamental architecture of `model-curve` is based on a proposition from [8], which was found in [6] to perform well for parameter identification on purely virtual data. The initial curve is first processed by two convolutional layers, each followed by max pooling. The output of this is piped through two dense layers before it is passed to the output layer. The addition of a second dense layer in comparison to [8] was found to significantly increase performance in preliminary studies. For `model-param`, a fully connected network with two hidden layers was chosen.

2.2. Creation of artificial training data

A total of three artificial datasets is required to train the full model according to the two defined approaches. All datasets are generated using the open-source Python library numpy [9]. After their creation, each dataset was split in training and test set with a ratio of 80:20.
For the sequential approach, a set of 100,000 individual time-strain-stress curves is generated, using the constitutive model from Eq. 1. Parameters G and a were drawn from a uniform distribution in the ranges 1000 to 4000 MPa and 25 to 115 respectively. For the strain rate a log-uniform distribution was used with a range 1e-4 to 5 1/s. To make the virtual data similar to the experimental ones, firstly a uniformly distributed time array was created, with the maximum time corresponding to the maximum strain of 20% at a given strain rate. From time and strain rate, strain values were calculated. These in turn were used to calculate corresponding stress using Eq. 1. To both strain and stress Gaussian noise was added. Finally, random data points from the aligned arrays were dropped until the desired input length of 201 was reached. The arrays of shape (201, 3) were used as input to predict corresponding parameters and strain rate with shape (3,).
Using Eqn. 2-3, 25,000 data points were created for training of `model-param`. The four parameters A_G, A_a, G_0 and a_0 were drawn from uniform distributions with the respective ranges 0.05 to 0.1, 0.025 to 0.05, 1000 to 2000 MPa and 25 to 75. The four strain rates were chosen from four increasing log-uniform intervals. Using Eqn. 2-3, four values for G and a were determined. Gaussian noise was added to these values. Since the number of strain rates is not suitably large to assume a zero mean of the noise values, a post hoc least-square fit is performed to determine the final set of parameters A_G, A_a, G_0 and a_0.
For the direct training, a similar approach can be taken. Notably, the individual parameters G and a used for creation of stress in step 1 of the sequential approach were not chosen randomly but taken as the values determined in step 2. However, these intermediate values were not added to the training data. To ensure comparability, a total of 25,000 series of four time-strain-stress curves were created.

3. Results

3.1. Model instantiation and training

The individual models are implemented using the open-source Python library tensorflow [10]. Well suited hyperparameters were determined on a subset of the training data using the hyperparameter optimization tool OmniOpt [11] and kept constant across both approaches. The used parameters are given in Table 1.

Table 1. Hyperparameters for models

`model-curve`				`model-param`	
filters_1	filters_2	neurons_1	neurons_2	neurons_1	neurons_2
49	24	187	172	20	20

All models were trained with an initial learning rate of 2.54e-4 using `adam` optimizer [12] and the respective dataset. The training was continued until no improvement of the mean squared error of the respective parameter predictions on the test set occurred for 50 consecutive epochs. Afterwards the best state, regarding the test set, achieved during training was restored.

3.2. Performance on virtual data

3.2.1. Sequentially trained model

To assess the final performance of the fully trained model it is evaluated on both train and test set. The parameters are used alongside the strain data from the input to obtain modeled stress responses. From this, the root mean squared error (RMSE) between input stress curve and modeled stress, hereafter referred to as "curve RMSE", is averaged across the entire data points in the dataset. The averaged curve RMSE on training and test set is 0.933 and 0.928 MPa respectively, with mean stress values of 33.2 and 32.9 MPa in the datasets.

In Figure 2 the virtual test series with overall best, median and worst curve RMSE from the test set are shown. In the best case results, the model works perfectly, despite the extremely similar stress-strain-curves at rates 1 and 2. For the median result, excellent agreement is achieved for all but the highest strain rate, at which the stress response is underestimated by 2.5 MPa. In the worst case, the model is not able to pick up on the curves' intricacies. However, the artificial input curves exhibit behavior that is not observed in the experiments described in [7]: individual curves from different strain rates intersect one another, leading to a dependency of the maximum stress with strain rate, which first increases, then plateaus and decreases and then begins to increase again. Such behavior cannot be captured by the constitutive model used here and is thus attributed to the significant noise in creating the training data.

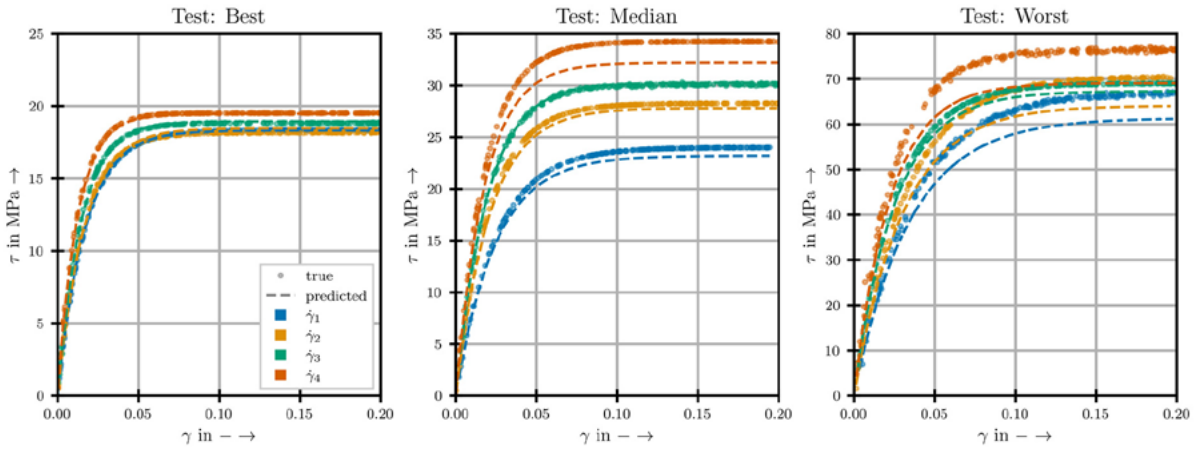


Figure 2. Resulting stress-strain-curves from predictions of the sequential model for artificial data

Given the sequential setup of the model, further insight into the models' individual performance is possible. In Figure 3 the distribution of the curve RMSEs with respect to the true parameter values is shown. From this it becomes clear that the combination of very high G values and low a values pose the highest challenge for the `model-curve`. For `model-param` no clear tendencies of the error to correlate with the input parameters was observed.

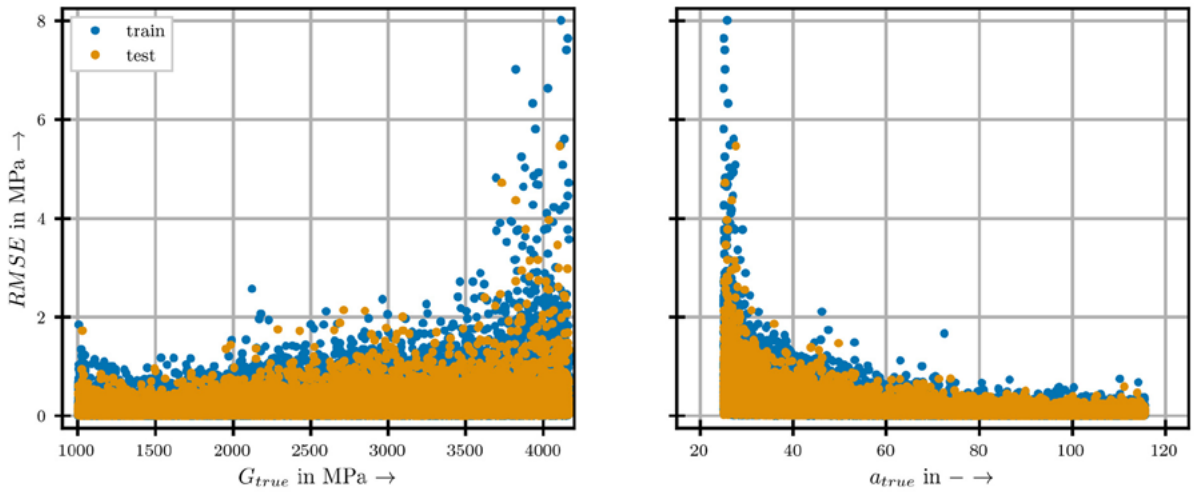


Figure 3. Distribution of error on resulting curves with respective input parameters

However, the specific input and output data of `model-param` for the three shown curves in Figure 4 show that while `model-curve` accurately extracts parameters and rate, represented by the agreement between true and intermediary values, `model-param` introduces a considerable error, leading to a significant deviation between predicted curve and input values. This is most notable at the model predictions for the G parameter of the worst example.

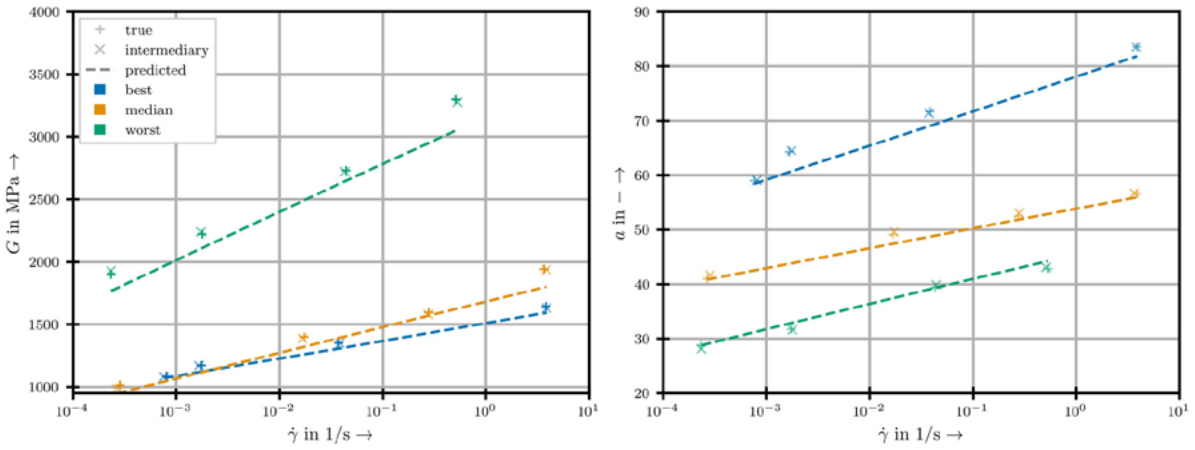


Figure 4. Predictions of sequential model corresponding to results shown in Figure 2.

3.2.2. Directly trained model

The directly trained model reaches a curve RMSE of 3.44 MPa on the training data and of 3.40 MPa on the test data. The results for best, median and worst data series are shown in Figure 5. In the best case, all four input curves lie very close together. Still, the model is not able to extract a set of parameters, leading to the excellent agreement observable with the sequential model. Already in the median case, modeling results and input stress deviate significantly. Additionally, the model does not capture the tendency of stress rising with strain rate, leading to a mismatch between input and output regarding ordering of highest stress response. This observation is strongly intensified by the worst case, where the predictions for lowest rate 1 lead to almost the maximum stress response.

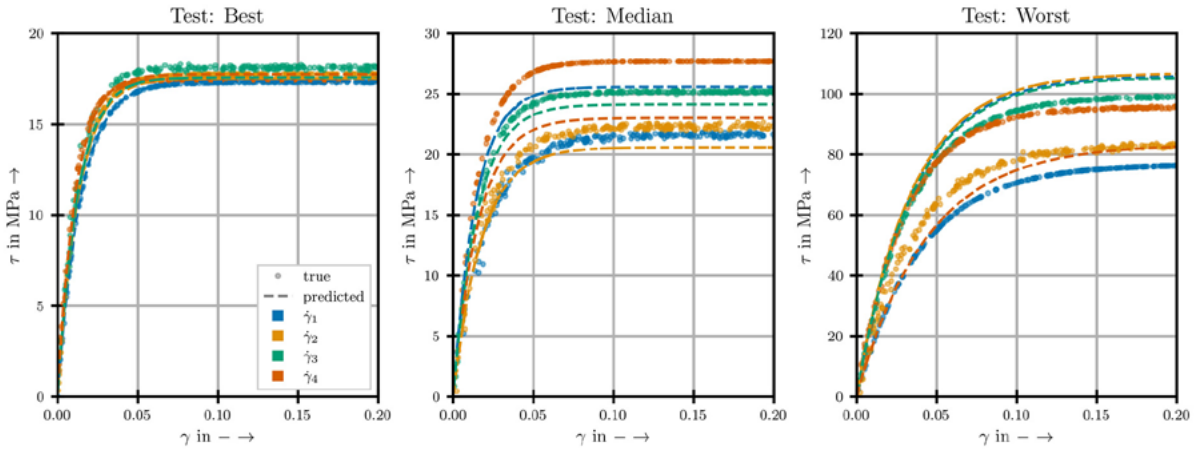


Figure 5. Resulting stress-strain-curves from predictions of the direct model for artificial data

3.2. Performance of the sequential model on experimental data

For the analysis of experimental data, existing results from [7] were used. Several individual tests across four strain rates were conducted. To evaluate them using the full model, the experiments were grouped by strain rate and then composed so that each data point contained one sample of each strain rate. Possible effects from sampling were considered by evaluating the full model on all possible combinations of experimental curves.

Similar to the behavior on artificial data, the direct model could not extract meaningful parameters from the experimental data; the tendency to mismatch rate and stress maxima persisted. Therefore, this approach is not further investigated here.

The sequential model is significantly better, achieving an average curve RMSE of 3.29 MPa at an average stress of 22.1 MPa. In these data, all test series containing one specific curve have a higher error than all others. This indicates some fundamental deficiency here. After removing this individual curve from the dataset, the average curve RMSE drops to 2.17 MPa. From the comparison of the experimental series on which the sequential model achieved the best, median and the worst performance it becomes clear that the composition of experimental curves plays a significant role in the model's predictive capabilities. On the best combination excellent agreement is achieved. On the median and worst combination, stress response is underestimated at the lowest and overestimated at the highest strain rate. For the two intermediate strain rates, good agreement can be observed.

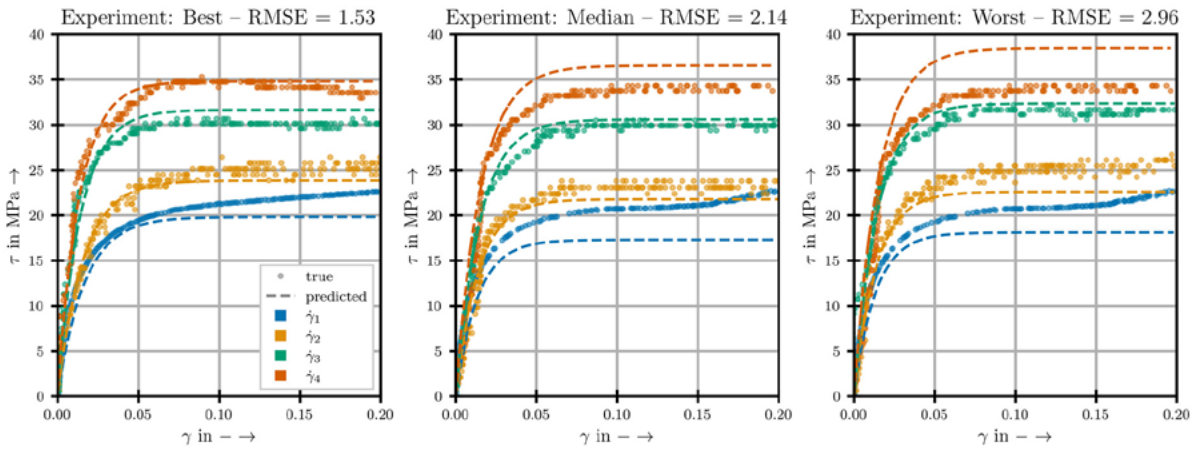


Figure 6. Resulting stress-strain-curves from predictions of the sequential model for experimental data

4. Conclusions

To alleviate the current hurdle in the form of PI for applying novel material models, the potential of two ML approaches has been investigated. Using the example of a highly non-linear, strain rate dependent constitutive model, artificial training data have been generated and used for training the ML models. In doing so, it was highly important to consider intricacies from the experimental data. Especially the inconsistent number of individual datapoints per experiment had to be considered in order to align artificial and experimental data. Additionally, several sources of noise had to be incorporated throughout the generation process to ensure applicability of the final ML model to experimental data.

By following two approaches for the model training, the importance of incorporating existing expert knowledge into the training procedure could be elucidated for the field of direct inverse PI. When pursuing the purely data driven approach, the amount of training data available did not lead to a model capable of extracting the key features from the provided data. This led to unphysical model predictions. Given the setup of the model, further insight into the cause of this problem and potential mitigations could not be obtained.

By including domain knowledge, such as the internal workings of the constitutive model, into ML-model setup and training significantly better results were achieved. The sequential training of task specific sub-models proved to be far more data efficient. Based on the same amount of data as the purely data driven training, meaningful material parameters could be extracted from the data and unphysical predictions were avoided. Furthermore, the composition of smaller expert models enabled insights into the full model's behavior. Regions in the training domain that were especially challenging for sub-models could be identified and can potentially be used to further refine training data and procedure.

Using the model sequentially trained on purely artificial data, it was possible to extract material parameters from experimental data that lead to a well fitting prediction of the stress response to a given strain load. Here, it was found that the composition of experimental data across four strain rates played a significant role in the ML model's performance. Still, the model gave reasonable predictions across all experimental data except for one individual test, that had to be removed.

Based on the presented findings, including domain knowledge into the ML model setup and training is highly recommended. Great potential for future work is expected to arise from extended ML approaches that allow for an arbitrary number of experimental curves per strain rate and should thus reduce the current dependency of prediction quality on the combination of individual curves.

Funding

This research was funded by the Deutsche Forschungsgemeinschaft (DFG, German Research Foundation) – Project-ID 418701707—TRR 285/2—sub-project A03.

Acknowledgments

The authors gratefully acknowledge the computing time made available to them on the high-performance computer at the NHR Center of TU Dresden. This center is jointly supported by the Federal Ministry of Education and Research and the state governments participating in the NHR (www.nhr-verein.de/unsere-partner).

References

[1] Z. Zhai, B. Jiang and D. Drummer. Nonlinear Material Model for Quasi-Unidirectional Woven Composite Accounting for Viscoelastic, Viscous Deformation, and Stiffness Reduction. *Polymers,* volume 10(8):903, 2018. DOI: https://doi.org/10.3390/polym10080903.

[2] M. Zscheyge, R. Böhm, A. Hornig et al. Rate dependent non-linear mechanical behaviour of continuous fibre-reinforced thermoplastic composites – Experimental characterisation and viscoelastic-plastic damage modelling. *Materials & Design,* volume 193:108827, 2020. https://doi.org/10.1016/j.matdes.2020.108827.

[3] S. Sessa, N. Vaiana, M. Paradiso and L. Rosati. An inverse identification strategy for the mechanical parameters of a phenomenological hysteretic constitutive model. *Mechanical Systems and Signal Processing,* volume 139:106622, 2020. DOI: 10.1016/j.ymssp.2020.106622.

[4] R. Schulte, C. Karca, R. Ostwald, and A. Menzel. Machine learning-assisted parameter identification for constitutive models based on concatenated loading path sequences. *European Journal of Mechanics - A/Solids*, volume 98:104854, 2023. DOI: 10.1016/j.euromechsol.2022.104854.

[5] E. Asaadi, D. N. Wilke, P. S. Heyns and S. Kok, The use of direct inverse maps to solve material identification problems: pitfalls and solutions. *Structural and Multidisciplinary Optimization*, volume 55(2):613–632, 2017. DOI: 10.1007/s00158-016-1515-1.

[6] P. Meißner, T. Hoppe, T. Vietor. Comparative Study of Various Neural Network Types for Direct Inverse Material Parameter Identification in Numerical Simulations. *Applied Sciences*, volume 12(24):12793, 2022. DOI: 10.3390/app122412793.

[7] J. Gerritzen, A. Hornig, B. Gröger and M. Gude, A data driven modelling approach for the strain rate dependent 3D shear deformation and failure of thermoplastic fibre reinforced composites: Experimental characterisation and deriving modelling parameters, *Journal of Composites Science* volume 6(10):318, 2022. DOI: 10.3390/jcs6100318.

[8] B. Zhao, H. Lu, S. Chen, J. Liu and D. Wu, Convolutional neural networks for time series classification. *Journal of Systems Engineering and Electronics*, volume 28(1):162-169, 2017. DOI: 10.21629/JSEE.2017.01.18.

[9] C.R. Harris, K.J. Millman, S.J. van der Walt et al. Array programming with NumPy. *Nature*, volume 585:357–362, 2020. DOI: 10.1038/s41586-020-2649-2

[10] M. Abadi, A. Agarwal, P. Barham et al. TensorFlow: Large-scale machine learning on heterogeneous systems. In 12th Symposium on Operating Systems Design and Implementation, pages 265-283, 2016. DOI: 10.5281/zenodo.4724125

[11] P. Winkler, N. Koch, A. Hornig, J. Gerritzen. OmniOpt – A Tool for Hyperparameter Optimization on HPC. In *H. Jagode, H. Anzt, H. Ltaief, P. Luszczek (eds) High Performance Computing. ISC High Performance 2021. Lecture Notes in Computer Science*, volume 12761, pages 285-296, 2021. DOI: 10.1007/978-3-030-90539-2_19

[12] D.P. Kingma and J. Ba. Adam: A Method for Stochastic Optimization (Version 9). *arXiv*, 2014. DOI: https://doi.org/10.48550/ARXIV.1412.6980

Warpage modelling of carbon fibre-reinforced SMC components in automotive applications

Shubham Gorde[1,*], Constantin Krauß [1], Alexander Bernath[2] , Marcel Olma[1], Korbinian Suckfüll[3], Sebastian Schmitz[3] and Luise Kärger[1]

[1]Institute of Vehicle Systems Engineering and Lightweight Engineering, Karlsruhe Institute of Technology, Karlsruhe, Germany
[2]Simutence GmbH, Karlsruhe, Germany
[3]Toray Industries Europe GmbH, Germany
*Corresponding author Email: shubham.gorde@kit.edu, Web Page: https://www.fast.kit.edu

Keywords: Finite element method, compression molding, carbon fibre-reinforced SMC (C-SMC), residual stresses, warpage modelling, mapping & homogenization

Abstract
This paper presents a finite element-based warpage simulation method for carbon fibre-reinforced SMC (C-SMC) components for automotive application. In the SMC process, one of the main problems is dimensional distortion of the composite component which is an inherent response of the residual stresses that occur due to chemical and thermal shrinkage of the thermoset resin. To tackle this problem, the curing and cooling behaviour of the composite needs to be predicted in a warpage analysis. For this purpose, material characterization is performed to obtain the thermal and chemical properties, and to parametrize the material models for cure kinetics and time- and temperature-dependent resin modulus. Additionally, material properties of the resin in the glassy and rubbery state, the mechanical properties of the fibres and the fibre volume content are required as input in the thermo-mechanical simulation of warpage in Abaqus. In conjunction with the mapped fibre orientation distributions from the SMC process simulation, local homogenization of the aforementioned properties is performed to correctly define the material behaviour during warpage. The warpage of complex automotive composite structure is analysed and a comparison between the experimentally measured and the numerically predicted displacement field is provided.

1. Introduction

Sheet Molding Compound (SMC) is a ready-to-mold, discontinuous fibre reinforced polymer made from thermoset sheets under pressure and temperature by compression molding. These SMC parts offer superior weight-specific properties at relatively low cost and the ability to form complex geometries during compression molding, which is not possible with continuous reinforcement. These properties make them attractive for applications in the aerospace and automotive industries. After manufacturing, process-induced deformations such as shrinkage or warpage can occur and lead to the loss of the component's dimensional stability. Therefore, it is important to perform numerical simulations of the different process steps, including SMC process simulation, mapping & homogenization, and warpage simulation, and to combine these steps to avoid loss of information. In this way, the process-induced deformations together with the accumulated residual stresses can be predicted in advance.

Due to the reorientation of the fibres as consequence of the compression molding process, it is necessary to take the fibre orientations into account in the warpage simulation. The simulation steps of process simulation, mapping and warpage simulation must therefore be linked together. This results in a consistent CAE chain which makes it possible to transfer the information between the simulation steps [1 - 4], as shown in Figure 1. Görthofer et al. [1] and Meyer et al. [2] already present CAE chains for SMC, but warpage of SMC was not yet included. As warpage simulation generally uses a different mesh than the process simulation, the use of an intermediate mapping step is required. The fibre orientation tensor field is imported from the process simulation [5, 6] and mapped onto the warpage mesh using the

Mapping library MpCCI MabLib [7]. All necessary interface operations, such as mapping, clustering of orientation states and homogenization, are bundled in a self-developed plugin for the commercial FE tool ABAQUS. The purpose of this manuscript is to present the FEM-based warpage methodology, including flow-induced process effects, and to demonstrate its application to a complex automotive component. The methodology is explained in Section 2, followed by numerical simulation and experimental validation in Section 3. For accurately predicting the warpage behaviour of C-SMC components, an anisotropic material model which is explained in Subsection 2.2 is implemented in Abaqus using UMAT subroutine.



Figure 1. Virtual CAE chain using the example of an automotive control arm.

2. Methodology

2.1. Workflow

Warpage modelling for C-SMC requires the fibre orientation tensor distribution from moulding simulation which are mapped onto the warpage mesh [1, 4], cf. Fig. 2. The effective material properties of the composite are determined by homogenization of the mechanical, thermal and chemical properties in addition to the fibre orientation distributions from the process simulation [1, 2, 4], in order to correctly define the material behaviour during warpage. The material models and experimental characterization for cure kinetics, cure shrinkage, and cure- and temperature-dependent modulus are explained in Subsection 2.2.

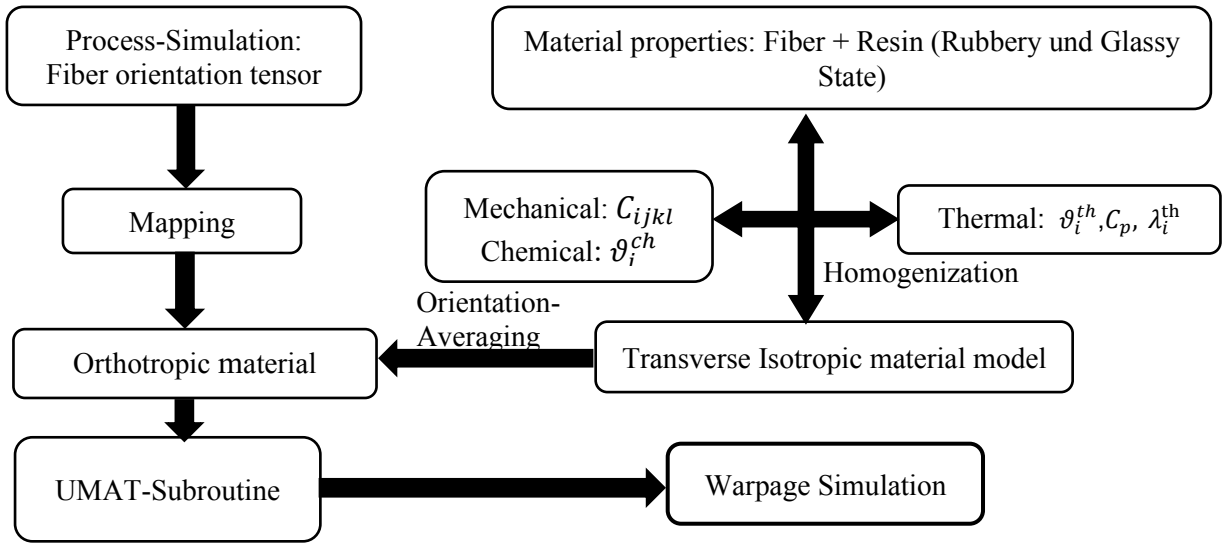


Figure 2. Workflow for the warpage modelling

In this work, the Tandon-Weng approach [8] is used for stiffness homogenization. It is based on the Eshelby tensor for unidirectional inclusions and considers the volume content of the fibres and the aspect ratio, as well as the stiffness of fibres and resin. This homogenization leads to the effective mechanical

property of the stiffness tensor C_{ijkl}. For the thermal properties, the specific heat is averaged over the volume, as it is a scalar and isotropic property. The thermal conductivity is calculated using the Clayton approach [9]. For the coefficient of thermal expansion, Schapery's energy-based approach is used [10]. Chemical shrinkage is averaged over the volume. This homogenization leads to the effective thermal properties such as the thermal conductivity ϑ_i^{th} and the specific heat C_p, as well as the coefficient vector of the thermal expansion $\lambda_i^{\text{th}}$and the chemical shrinkage ϑ_i^{ch}. The homogenized material properties are further averaged based on the fibre orientation tensor to describe the orthotropic behaviour required for SMC molded parts.

2.2. Material behaviour

The material system used for this analysis is a carbon fibre reinforced vinyl ester SMC stack with a weight percentage of 57% carbon fibres. This resin system was analysed with Toray using a differential scanning calorimeter for the cure kinetics and glass transition. A thermomechanical analysis was used for the coefficient of thermal expansion. A rheometer was used for the shrinkage measurement. Finally, a dynamic mechanical analysis was used for the elastic modulus characterization. The properties are summarized in the Table 1.

Table 1. Material Properties

	Fibre	Resin
Modulus (GPa)	250	Unrelaxed: 3.982 Relaxed: 1.125
Poisson's Ratio	0.3	0.3
Density (kg/m^3)	1800	1162

2.2.1. Cure Kinetics

The curing kinetics are calculated using the Kamal-Malkin kinetics model [11], which calculates the rate of change by

$$\frac{d\alpha}{dt} = (K_1 + K_2 \cdot \alpha^m) \cdot (1-\alpha)^n \tag{1}$$

with the empirical parameters m and n [10]. The parameters K_1 and K_2 are often specified by an Arrhenius approximation in the form.

$$K_i = A_i \cdot \exp\left(-\frac{E_i}{R \cdot T}\right) \tag{2}$$

where α is the degree of cure, $\frac{d\alpha}{dt}$ is the cure rate, E_i is the activation energy, and A_i are fitting constants. The mechanical properties of the thermoset matrix material depend on the degree of cure, due to the crosslinking in the reaction kinetics of the matrix. The cure-dependence of the glass transition temperature T_g is modelled using the DiBenedetto approach [12,13],

$$\frac{T_g - T_{g,0}}{T_{g,\infty} - T_{g,0}} = \frac{\lambda \cdot \alpha}{1-(1-\lambda)\cdot\alpha} \tag{3}$$

Here, λ is a model parameter which is 0.3. $T_{g,0}$= -44.04 °C and $T_{g,\infty}$=148.42 °C are the initial and final glass transition temperatures, respectively. $T_{g,0}$ is determined from cyclic DSC measurement, as shown in Figure 3. $T_{g,\infty}$ is the temperature at the maximum loss factor in the DMA measurement of temperature sweeps when the sample is fully cured, as shown in the Figure 4.

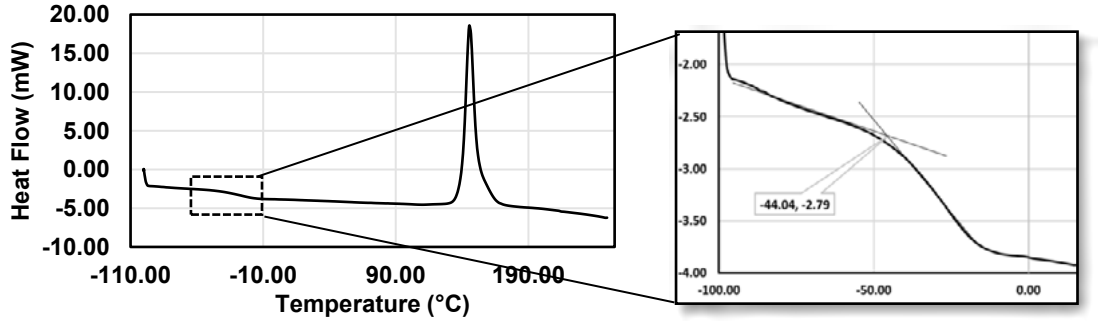


Figure 3. Cyclic DSC measurement

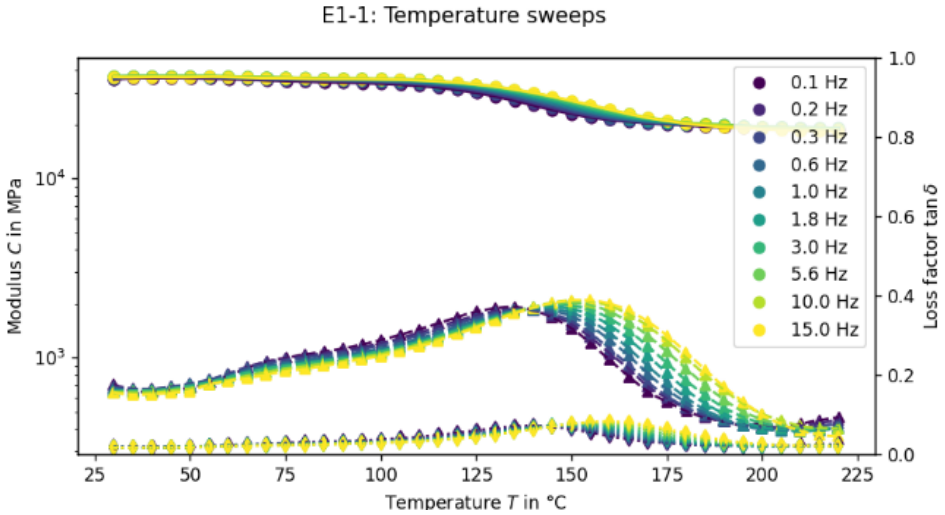


Figure 4. DMA Temperature Sweep

2.2.2. Thermal model

For the numerical simulation of the warpage of thermoset SMC components, thermal properties such as specific heat capacity, thermal conductivity, and coefficient of thermal expansion are required. These thermal properties are determined from material characterization in cooperation with Toray. The properties are given in Table 2.

Table 2. Thermal Properties

	Fibre	Resin
Coefficient of thermal expansion (1/K)	3.8×10^{-7}	3.908×10^{-5}
Specific Heat (J/Kg/K)	760	1310
Thermal Conductivity (m/W/K)	1.3	0.15

As discussed in subsection 2.2, the effective thermal conductivity is calculated with reference to Clayton [9]. For the coefficient of thermal expansion, the energy-based approach of Schapery [10] is used.

2.2.3. Chemical Shrinkage model

From PVT measurements, shrinkage is calculated to a value of -1.106% for the full cure cycle. The homogenization of chemical shrinkage is carried out using the volume averaging method, which is given by,

$$\vartheta_i^{\mathrm{ch}} = \varphi_{\mathrm{f}}\vartheta_{\mathrm{f},i}^{\mathrm{ch}} + \varphi_{\mathrm{m}}\vartheta_{\mathrm{m},i}^{\mathrm{ch}}\,. \tag{4}$$

Here $\vartheta_{\mathrm{f},i}^{\mathrm{ch}}$ and $\vartheta_{\mathrm{m},i}^{\mathrm{ch}}$ are the coefficients of chemical shrinkage for fibre and matrix, respectively. Since there is no shrinkage of the fibres, the effective shrinkage coefficient can be modified to

$$\vartheta_i^{\mathrm{ch}} = \varphi_{\mathrm{m}}\vartheta_{\mathrm{m},i}^{\mathrm{ch}} \tag{5}$$

with φ_{m}=1- φ_{f}. This is a simplified approach because the chemical shrinkage actually depends also on the fibre orientation.

2.2.4. Orthotropic CHILE Model

The Cure Hardening Instantaneously Linear Elastic (CHILE) model developed by Johnston is used to capture the stress evolution of the resin [14]. In case of C-SMC composite material, DMA experiments have shown a temperature dependency of the modulus. Therefore, the CHILE model is modified to fit a linear temperature dependency before the glass transition and used to model the cure-dependent mechanical behaviour of the composite material [14, 15, 16]. The models by Johnston [14] are extended and implemented to represent the orthotropic material behaviour for discontinuous carbon fibre reinforced vinyl ester resin SMC components. The stress evolution of the modified CHILE model is given by,

$$\sigma(t) = \int_0^t E(T,\alpha)\,\frac{\partial\varepsilon(\xi)}{\partial\xi}\mathrm{d}\xi, \tag{6}$$

where ξ is the time, $E(T,\alpha)$ is the instantaneous modulus of elasticity, which depends on the temperature T and the degree of cure $\alpha \in [0;1]$. The modified CHILE model assumes a monotonic increase in the resin modulus during curing according to

$$E(T,\alpha) = \begin{cases} E_1, & T^* < \Delta T_{\mathrm{c}_1} \\ E_2 + \dfrac{T^* - \Delta T_{\mathrm{c}_2}}{\Delta T_{\mathrm{c}_1} - \Delta T_{\mathrm{c}_2}}\,(E_1 - E_2), & \Delta T_{c_1} \le T^* < \Delta T_{\mathrm{c}_2} \\ E_3 + \dfrac{T^* - \Delta T_{\mathrm{c}_3}}{\Delta T_{\mathrm{c}_2} - \Delta T_{\mathrm{c}_3}}\,(E_2 - E_3), & \Delta T_{c_2} \le T^* < \Delta T_{\mathrm{c}_3} \\ E_3, & T^* \ge \Delta T_{\mathrm{c}_3} \end{cases}, \tag{7}$$

with $T^* = T - T_g$. The glass transition temperature T_g is calculated according to Equation (3). In DMA measurements, temperature sweep is carried out on carbon fibre reinforced SMC composite sample from 20 °C to 220 °C at frequency 1 Hz. Figure 5 reveals a tri-linear temperature dependency of the modulus of fibre reinforced vinyl ester resin. The modified CHILE model is fitted to the DMA experiments yielding the parameters: $\Delta T_{c_1} = -116.82$ °C, $\Delta T_{c_2} = -18.37$ °C, $\Delta T_{c_3} = 22.75$ °C, $E_1 = 34189.2$ MPa, $E_2 = 30906.99$ MPa, $E_3 = 16637.2$ MPa. In this model, the rubbery modulus E_3 is active as long as T_{g} has not exceeded the current temperature by a certain value ΔT_{c_3}. The stiffness is equal to the glassy modulus E_1 if the temperature T reaches a value below T_{g} - ΔT_{c_1} during cooling.

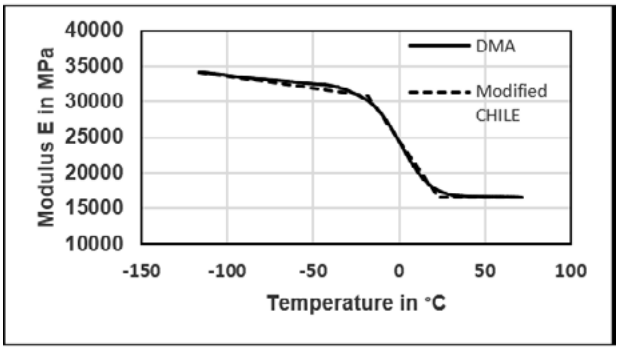


Figure 5. Temperature dependence of Modulus fitted to DMA.

2.2.5. Total strain

In the SMC process, the component undergoes chemical and thermal shrinkage in addition to the mechanical deformations, e.g. caused by the holding pressure. Thus, the complete change in elongation is given by,

$$\Delta\varepsilon_{ij} = \Delta\varepsilon_{ij}{}^{\mathrm{mech}} + \Delta\varepsilon_{ij}{}^{\mathrm{th}} + \Delta\varepsilon_{ij}{}^{\mathrm{ch}} . \tag{8}$$

The change in thermal expansion is given by,

$$\Delta\varepsilon_{ij}{}^{\mathrm{th}} = \vartheta_i^{\mathrm{th}}\Delta T . \tag{9}$$

The change in chemical elongation is given by,

$$\Delta\varepsilon_{ij}{}^{\mathrm{ch}} = \vartheta_i^{\mathrm{ch}}\Delta\alpha . \tag{10}$$

A subroutine was created for the modified CHILE model and implemented in ABAQUS. The homogenization is performed according to the method presented by Görthofer et al [1, 2] as explained in the Subsection 2.1.

2.2.6. Reverse Homogenization

The characterization is done on the C-SMC composite material. Therefore, a reverse homogenization is carried out to get the neat resin properties [18]. This is an iterative process in which the properties of the carbon fibre and the C-SMC composite material are known, and the resin properties are calculated. The workflow for the reverse homogenization is shown in Figure 6.

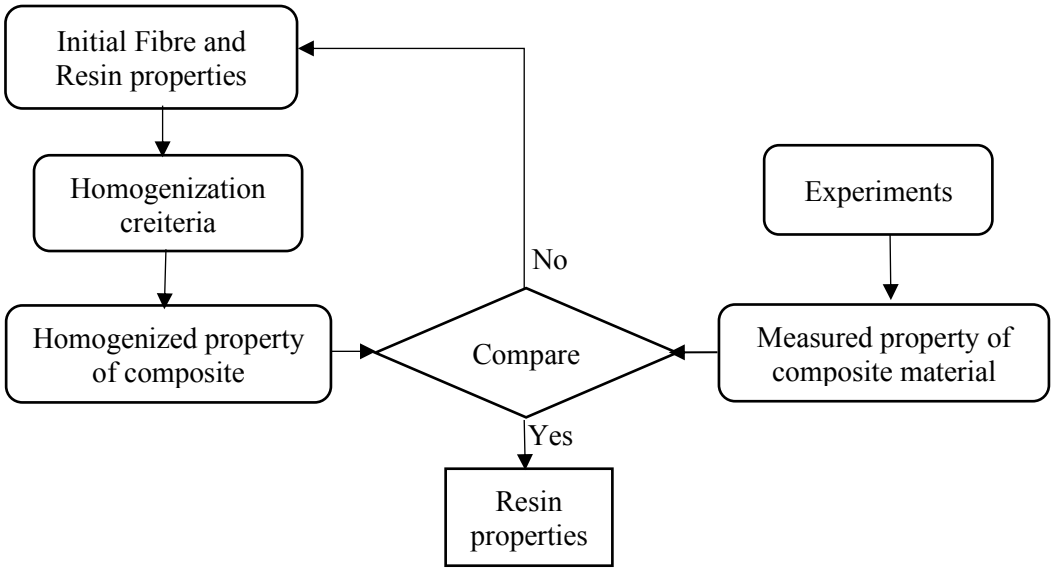


Figure 6. Reverse homogenization method

3. Numerical Simulation and Experimental Validation

The warpage analysis begins immediately after mold filling and includes the process steps of mold holding, curing, transfer and cooling outside the mold. The warpage analysis is carried out with the FE software ABAQUS 2021 (Dassault Systémes, USA). The simulation model is a section of a control arm of an automotive component, as shown in Figure 7. There are four steps in the simulations, namely mold holding, curing, transfer and cooling. During the mold holding and curing step, the displacements are blocked on the entire surface of the component, as it is still in the closed mold during the actual process. The surface temperature is set at a constant 140 °C. The curing step lasts 360 seconds, followed by a transfer step for 5 seconds and then a cooling step outside the mold. During cooling, a convection boundary condition is specified for the temperature field. The effective material properties are determined using the described schemes. For the mechanical model, the modified CHILE model is used in an orthotropic formulation. The orientation distribution is clustered into 100 sub-regions based on the fibre orientation tensors from mould filling simulation. According to the 100 material sections, 100 orthotropic materials are created that describe the thermomechanical material behaviour for the corresponding fibre orientation state.

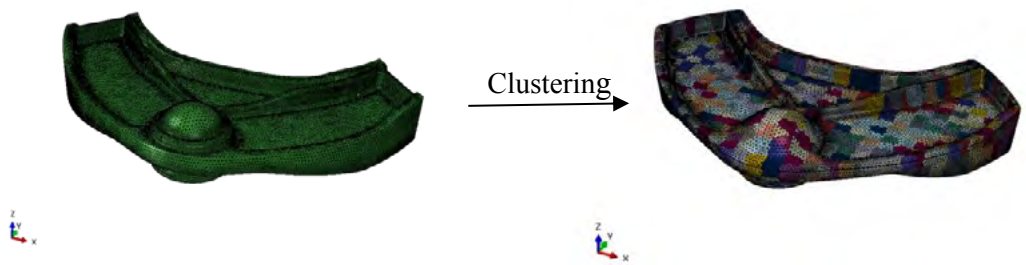


Figure 7. FE model of SMC Automotive suspension control arm showing orthotropic material clustering

An SMC suspension control arm was manufactured at Fraunhofer ICT, and measurements are conducted using GOM 3D ATOS scanner. Figure 8 shows a comparison between experimentally measured and numerically predicted displacements of the suspension control arm. The left-side figure shows the deviation of the manufactured part over the nominal geometry, and the right-side figure shows the deviation of the predicted shape of the component over the nominal geometry. The different deviation points in the figure indicate displacement values at specific locations. By comparison, it can be seen that the displacement values are qualitatively in reasonable agreement with the experimental results, but simulation underpredicts the deformation. In future work, the packing step after complete mold filling will be considered, which takes into account the additional holding pressure and may thus reduce the difference between simulation and experiment.

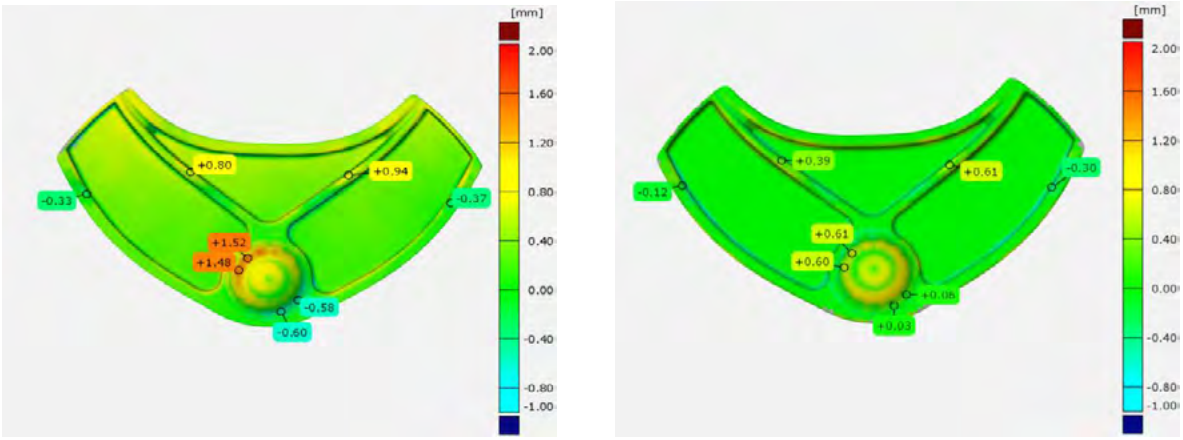


Figure 8. Comparison of experimentally measured (left) and numerically predicted (right) process-induced displacements of the SMC suspension control arm.

4. Conclusion

An orthotropic modified CHILE model has been implemented for process-induced warpage simulation of SMC components. The model is able to capture the distortion of fibre-reinforced SMC component as a function of process parameters, process-induced fibre orientation distributions and curing reaction. A consistent CAE chain approach is used to transfer the moulding simulation results onto the warpage mesh via mapping. The simulation methodology is applied for stress-deformation analysis of an automotive component suspension control arm, produced by compression molding of discontinuous carbon fibre-reinforced vinyl ester thermoset. The resulting fibre orientation distribution affects the warpage simulation results such as residual stresses and final shape of the part. The experimental results are qualitatively in good agreement with the deformations predicted by the simulations. However, the simulation underpredicts the deviation. In the future, a further developed viscoelastic material model for the matrix can also be used to capture the time-dependent behaviour of the matrix more accurately.

Acknowledgments

The authors gratefully acknowledge the financial support provided by the German Federal Ministry for Economic Affairs and Climate Protection (BMWK) for the research project EcoDynamicSMC (Project No. 03LB3023H). Acknowledgments to the Fraunhofer ICT faculty, specially to Mr. Uwe Podwojewski for helping with the warpage experiments.

References

[1] Görthofer, J., Meyer, N., Pallicity, T.D., Schöttl, L., Trauth, A., Schemmann, M., Hohberg, M., Pinter, P., Elsner, P., Henning, F. and Hrymak, A., 2019. Virtual process chain of sheet molding compound: Development, validation and perspectives. *Composites Part B: Engineering*, *169*, pp.133-147.

[2] Meyer N, Gajek S, Görthofer J, Hrymak A, Kärger L, Henning F, Schneider M, Böhlke T, 2023: A probabilistic virtual process chain to quantify process-induced uncertainties in Sheet Molding Compounds. *Composites Part B: Engineering, 249*, p. 110380.
[3] Kärger, L., Bernath, A., Fritz, F., Galkin, S., Magagnato, D., Oeckerath, A., Schön, A. and Henning, F., 2015. Development and validation of a CAE chain for unidirectional fibre reinforced composite components. *Composite Structures*, *132*, pp.350-358.
[4] Gorde, S.S., Krauß, C., Bartkowiak, M. and Kärger, L., 2022. CAE-Simulationskette zur Werkzeug- und Prozessauslegung von Carbonfaser-SMC-Bauteilen. In *NAFEMS DACH Regionalkonferenz 2022: Konferenz für Berechnung & Simulation im Engineering, 4.-6. Oktober 2022, Bamberg, D* (p. 142).
[5] Meyer N, Ilinzeer S, Hrymak AN, Henning F, Kärger L: Non-isothermal direct bundle simulation of SMC compression molding with a non-Newtonian compressible matrix. Journal of Non-Newtonian Fluid Mechanics 310: 104940, 2022.
[6] Meyer, N., Schöttl, L., Bretz, L., Hrymak, A.N. and Kärger, L., 2020. Direct Bundle Simulation approach for the compression molding process of Sheet Molding Compound. *Composites Part A: Applied Science and Manufacturing*, *132*, p.105809.
[7] Wolf, K., Bayrasy, P., Brodbeck, C., Kalmykov, I., Oeckerath, A. and Wirth, N., 2017. MpCCI: Neutral interfaces for multiphysics simulations. In *Scientific Computing and Algorithms in Industrial Simulations* (pp. 135-151). Springer, Cham.
[8] Tandon, G.P. and Weng, G.J., 1984. The effect of aspect ratio of inclusions on the elastic properties of unidirectionally aligned composites. *Polymer composites*, *5*(4), pp.327-333.
[9] Clayton, W., 1971. Constituent and composite thermal conductivities of phenolic-carbon and phenolic-graphite ablators. In *12th Structures, Structural Dynamics and Materials Conference* (p. 380).
[10] Schapery, R.A., 1968. Thermal expansion coefficients of composite materials based on energy principles. *Journal of Composite materials*, *2*(3), pp.380-404.
[11] Kamal, M.R. and Sourour, S., 1973. Kinetics and thermal characterization of thermoset cure. *Polymer Engineering & Science*, *13*(1), pp.59-64.
[12] DiBenedetto, A.T., 1987. Prediction of the glass transition temperature of polymers: a model based on the principle of corresponding states. *Journal of Polymer Science Part B: Polymer Physics*, *25*(9), pp.1949-1969.
[13] Pascault, J.P. and Williams, R.J.J., 1990. Glass transition temperature versus conversion relationships for thermosetting polymers. *Journal of Polymer Science Part B: Polymer Physics*, *28*(1), pp.85-95.
[14] Johnston, A.A., 1997. *An integrated model of the development of process-induced deformation in autoclave processing of composite structures* (Doctoral dissertation, University of British Columbia).
[15] Johnston, A., Vaziri, R., & Poursartip, A. (2001). A plane strain model for process-induced deformation of laminated composite structures. *Journal of composite materials*, *35*(16), 1435-1469
[16] Khoun, K., 2009. Process-induced stresses and deformations in woven composites manufactured by resin transfer moulding.
[17] Advani, S.G. and Tucker III, C.L., 1987. The use of tensors to describe and predict fiber orientation in short fiber composites. *Journal of rheology*, *31*(8), pp.751-784.
[18] Gandhi, U., Song, Y.Y. and Mandapati, R., 2017. Semiempirical approach to predict shrinkage and warpage of fiber-reinforced polymers using measured material properties in finite element model. *Journal of Thermoplastic Composite Materials*, *30*(9), pp.1303-1319.

REMAINING USEFUL LIFE PREDICTION OF FLAX FIBRE BIOCOMPOSITES UNDER CREEP LOAD BY ACOUSTIC EMISSION AND DEEP LEARNING

J. Hao[1], M. Rupp[2], S. Lomov[3], C.A. Fuentes[4], and A.W. Van Vuure[5]

[1] Department of Materials Engineering, KU Leuven, Leuven, Belgium
Email: jianqun.hao@kuleuven.be, Web Page:
https://www.mtm.kuleuven.be/english/research/scalint/cmg/team-composite-materials/00145170
[2] Department of Materials Research and Technology, Luxembourg Institute of Science and Technology, Luxembourg
Email: matthias.rupp@list.lu, Web Page: https://www.mrupp.info/index.html
[3] Department of Materials Engineering, KU Leuven, Leuven, Belgium
Email: stepan.lomov@kuleuven.be, Web Page:
https://www.mtm.kuleuven.be/english/research/scalint/cmg/team-composite-materials/00005593
[4] Department of Materials Research and Technology, Luxembourg Institute of Science and Technology, Luxembourg
Email: carlos.fuentes@list.lu, Web Page: http://orcid.org/0000-0002-0766-9079
[5] Department of Materials Engineering, KU Leuven, Leuven, Belgium
Email: aartwillem.vanvuure@kuleuven.be, Web Page:
https://www.mtm.kuleuven.be/english/research/scalint/cmg/team-composite-materials/00017432

Keywords: Remaining useful life, flax fibre composite, creep, acoustic emission, deep learning

Abstract
This paper explores a strategy that integrates acoustic emission (AE) and deep learning techniques for the remaining useful life (RUL) prediction of flax fibre composite subjected to long-term flexural creep load. The AE and creep deformation data were acquired by monitoring the creep rupture (run to failure) tests under four different stress levels. Derivatives of cumulative AE features with respect to time, such as cumulative hit and count rates, are introduced to reflect the performance degradation rate of the materials. These proposed features appear to be more relevant for creep lifespan than traditional AE features. Long short-term memory networks and temporal convolutional networks are adopted to estimate the composite's remaining useful life. The two model's normalized root mean square errors are below 0.11, which demonstrates a satisfactory prediction accuracy in RUL of the samples subjected to different loading levels.

1. Introduction

Damage prognostics are crucial to ensure the structural integrity and reliability of natural fibre composites (NFC) during their in-service life. When subjected to long-term cyclic (fatigue) and/or constant (creep) loadings, NFC often experience a considerably dispersive lifespan due to the complex deterioration process, which is mainly caused by their non-homogenous characteristics at the composite level, coupled with the non-uniform nature of natural fibres in their micro-structure, component content, as well as the randomly distributed defects like kink bands. In this scenario, the traditional physical or empirical models can only provide a rough lifespan estimation for NFC, because most of the models are formulated in terms of the premeasured ultimate strength and predefined loading patterns [1]–[6], and overlook the impact of the uncertainty in the damage evolution and accumulation in NFC during their in-service life. Hence, it is necessary to explore a more versatile approach for damage prognostics of NFC under long-term load.

Acoustic emission (AE), a prominent technique in the domain of structural health monitoring, has been widely used in damage detection and identification of composite materials [7]–[13]. Due to increased requirements in the health management and maintenance of composite structures, efforts have also been

made in AE-based damage prognostics to predict the remaining useful life (RUL) and strength (RUS). Compared to simple empirical models considering only a single AE parameter such as energy [14], [15] or counts [16] for RUL prediction, AE-based data-driven models have been gaining increased interest due to their excellent capability of processing abundant data and mapping complex non-linear relationships. Long Short-Term Memory (LSTM) networks are a variety of recurrent neural networks (RNNs) that are capable of learning long-term dependency. They specialize in discovering the underlying patterns embedded in time series, which makes them suitable to track the degradation process and thus to predict the RUL [17]. Another popular type of neural network is the Convolutional Neural Network (CNN) which has been commonly used in Computer Vision. Motivated by its feature extraction ability and computational efficiency, 1D CNN has been introduced to signal processing in the context of structural health monitoring [18], [19]. To deal with the problem of temporal dependency existing in RUL prediction, the AE sequential data are often segmented by a time window with fixed or variable length and then fed as an input into the CNN models [20], [21]. More recently, a Temporal Convolutional Network (TCN) architecture integrated with dilated causal convolutions and residual blocks, was introduced for sequence learning tasks [22], [23] and so far has attracted considerable attention [24]–[27].

Despite the tremendous potential of data-driven models such as LSTM and TCN in damage prognostics, very few attempts have been made for RUL prediction in the field of composite materials, especially for natural fibre composites subjected to long-term creep load. In this study, AE sensors and Linear Variable Differential Transformer sensors were employed to detect damage activities and acquire creep deformation information in flax fibre composites during creep rupture tests, respectively. LSTM and TCN models were employed for RUL prediction, and the model performances were compared.

2. Materials and tests

2.1. Material system

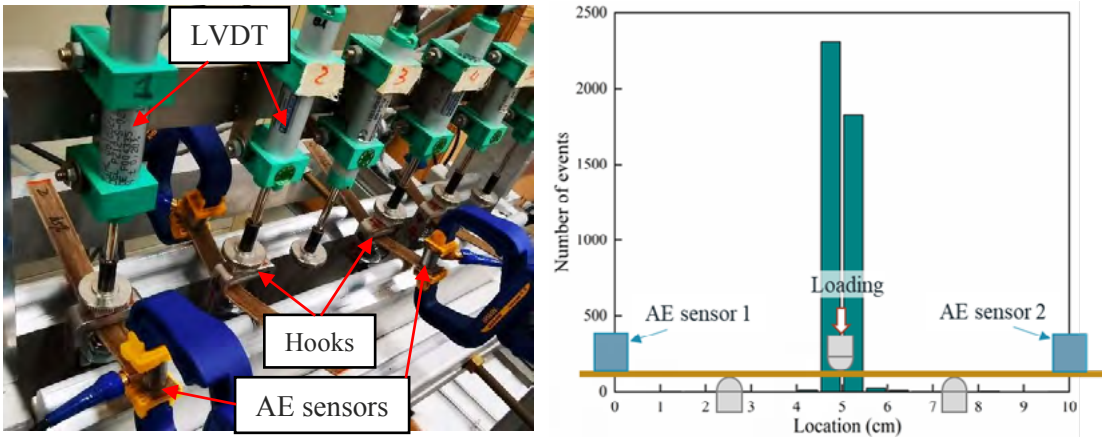
The composites were prepared with unidirectional flax fibre (Lineo Flaxtape 110), bound by polyoxymethylene (POM) (Hostaform C2521) through a film stacking method. The composite samples have a fibre volume fraction of ~40% and dimensions of 1.5 mm thickness, 10 mm width, and 120 mm length. The properties of the fibre and matrix as well as their composite are listed in Table 1 (the longitudinal strength and modulus of the fibre and matrix were measured by tensile tests, whereas the composites were characterized through flexural tests).

Table 1 Properties of flax fibre and POM as well as their composite

Materials	Longitudinal modulus (GPa)	Longitudinal strength (MPa)
Flax fibre	68 ± 3.4	533 ± 37
POM	~2.6	~62
Flax/POM composite	19.3 ± 1.7	201± 6.5

2.2. Creep rupture tests monitored by AE

The creep rupture tests were performed using a custom-designed flexural creep set-up placed in an environmentally conditioned room (23 ºC & 50% RH) as shown in Fig. 1 (a). Six Linear Variable Differential Transformer sensors (LVDT) with a resolution of 1 μm were attached on the set-up for measuring the sample deflection during creep loading. Several stainless-steel blocks with varying dimensions were fabricated to apply the constant creep load by connecting hooks positioned in the middle of the specimens. By adjusting the number of blocks, a weight resolution of 1N could be achieved for the sustained load. Four different stress ratios (the ratio of applied stress to the ultimate strength measured by quasi-static flexural tests), namely 90 %, 85%, 80% and 75%, were used to examine the applicability of the proposed strategy to the different samples with various damage accumulation pattern. Six specimens were tested for each loading condition.



(a) (b)

Fig. 1 (a) Creep tests monitored by AE and LVDT. (b) Distribution of AE sensors along sample lengthwise direction.

An AE device (Vallen AMSY-6 system) was used to monitor the creep rupture tests. The acoustic signal was captured by two AE-sensors Digital wave B-1025 with a broadband response from 50 - 2000 kHz, and subsequently amplified by preamplifier Vallen AEP4 with a 34 dB gain before being processed by AE-signal processor ASIP-2A. When the samples were loaded in 3-point bending mode during creep tests, the AE activities were concentrated in the middle of the sample where the damage generated, as shown in Fig. 1 (b) where two AE sensors were used for the damage localization. Only one sensor was used for each sample afterwards as the issue of disparity in detected signal energy due to varied source-detector distance (energy attenuation) caused by scattered damage locations barely existed. With four data acquisition channels configured in this Vallen system, four creep measurements could be performed synchronously, which significantly reduced the total experimental time.

3. Results and discussions

3.1. Data preparation

Unlike AE-based damage diagnostics for composite materials, where the damage modes are primarily identified by non-cumulative AE features (e.g., amplitude, rise time, counts, energy, frequency), damage prognostics rely more on cumulative features such as cumulative hits, cumulative counts and cumulative energy, which are sensitive to the damage evolution [28], [29]. Therefore, twenty-five AE features comprising thirteen non-cumulative features, six cumulative features and six cumulative features rates, were extracted based on the AE data, as presented in Table 2.

Table 2 Twenty-five extracted AE features

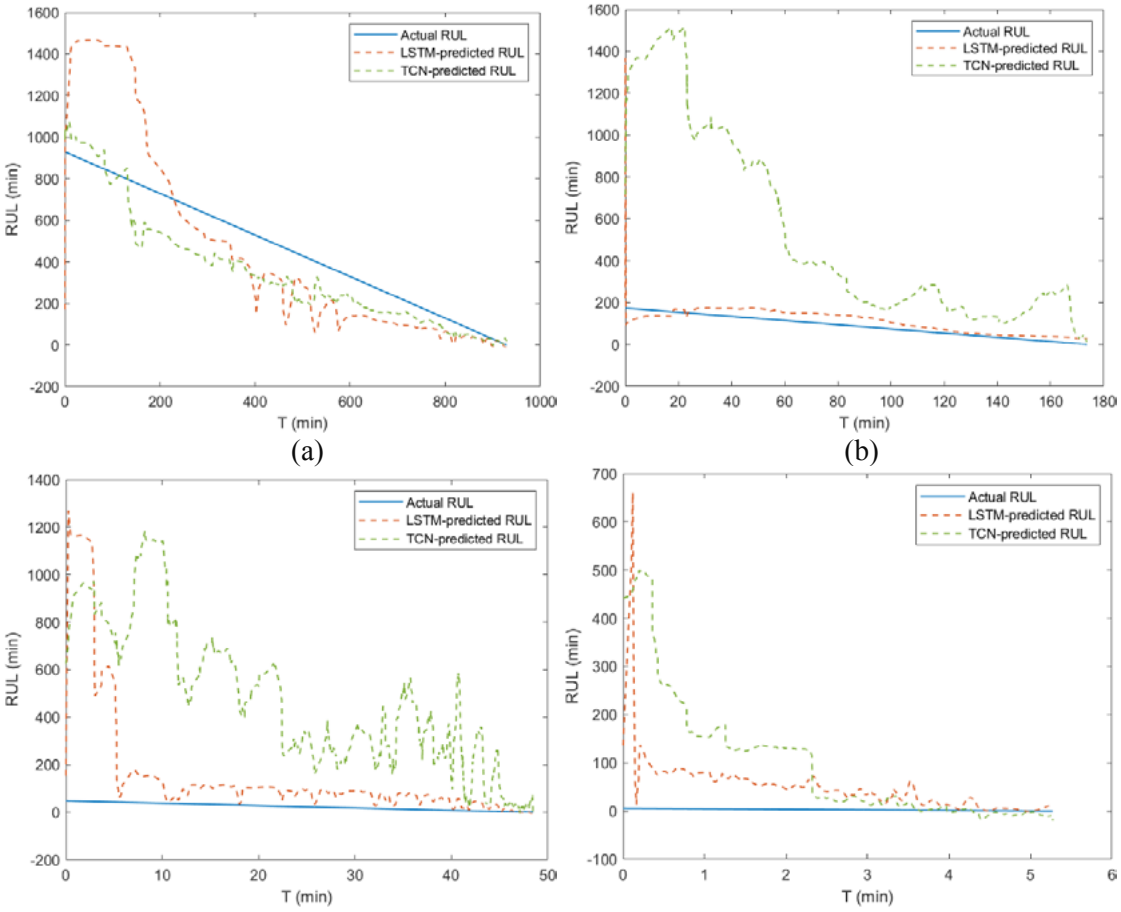
No.	Feature provided by Vallen system	No.	Extracted feature
1	Amplitude – A (dB)	14	Cumulative hits – Cum_Hits
2	Rise time – RT (μs)	15	Cumulative rise time – Cum_RT (μs)
3	Duration time – DT (μs)	16	Cumulative duration time - Cum_DT (μs)
4	Counts – C	17	Cumulative counts – Cum_C
5	Energy – E (eu)	18	Cumulative energy – Cum_E (eu)
6	Signal strength - SS(nVs)	19	Cumulative signal strength - Cum_SS (nVs)
7	Root mean square - RMS (μV)	20	Cumulative hits rate - Cum_Hits_rate (μs^{-1})

8	Peak frequency– FMAX (kHz)	21	Cumulative rise time rate – Cum_RT_rate
9	Frequency centroid of Gravity– FCOG (kHz)	22	Cumulative duration time rate- Cum_DT_rate
10	Cascade hits – CHIT	23	Cumulative counts rate – Cum_C_rate (μs^{-1})
11	Cascade counts - CC	24	Cumulative energy rate– Cum_E_rate (eu^{-1})
12	Cascade energy – CE (eu)	25	Cumulative signal strength rate - Cum_SS_rate (nV)
13	Cascade signal strength – CSS (nVs)		

Additionally, three creep deformation descriptors, namely creep strain, creep rate and creep ratio (the ratio of secondary creep strain to the instantaneous strain), were selected as the predictors.

3.2. RUL prediction based on LSTM and TCN

The Adaptive moment estimation (Adam) optimizer was used for training via gradient descent. All the hyperparameters of the two models were determined through a rough grid search on the data obtained from preliminary tests. In the LSTM model, 300 hidden units were set in a LSTM layer, followed by a FC layer with 50 neurons. The length of the AE sequential data is ~3500 in each measurement. To cover the complete historical data for the predictions at all timestamps, the filter size f of the TCN model was set as 5 and the number of convolutional layers (residual blocks) $K = 10$ was selected to achieve a receptive field $R = 1 + (f - 1)(2^K - 1) = 4093 > 3500$. The number of filters for each convolutional layer was set as 50. The initial learning rate was 0.01 for both LSTM and TCN models and reduced by a factor of 0.2 every 50 epochs. The maximum training epoch was set as 200 for LSTM and 100 for TCN as TCN converges more quickly. A dropout rate of 0.5 was used in both models to avoid overfitting.



(c) (d)

Fig. 2 RUL predictions of samples under four different stress levels by LSTM and TCN models based on fused data (a) Stress ratio of 75%. (b) Stress ratio of 80%. (c) Stress ratio of 85%. (d) Stress ratio of 90%.

Given the potentially consistent damage mechanisms and evolution pattern existing in the samples when subjected to different stress levels, an attempt was made to train the models using the data from twenty measurements (five out of six measurements at each stress level), whereas the remaining four measurements were held back for testing. However, poor predictions were obtained when the data from different stress levels were fused, see Fig. 2. The reason could be that the features from different stress levels vary widely with respect to time scales, from minutes (under a stress ratio of 90%) to days (under a stress ratio of 75%). The diversity of the features at different stress levels might exert a significantly greater influence on the models in training compared to the presumed consistent patterns.

Therefore, the models were trained using data from only the same stress level. A leave-one-out cross-validation method was adopted to estimate the generalization performance of the two models given the relatively small dataset (six measurements for each sample). That is, the data from five measurements of each stress level were used to train the models, and the remaining one measurement was used for testing. Each stress level sample comprises six predictions generated through the leave-one-out cross validation method.

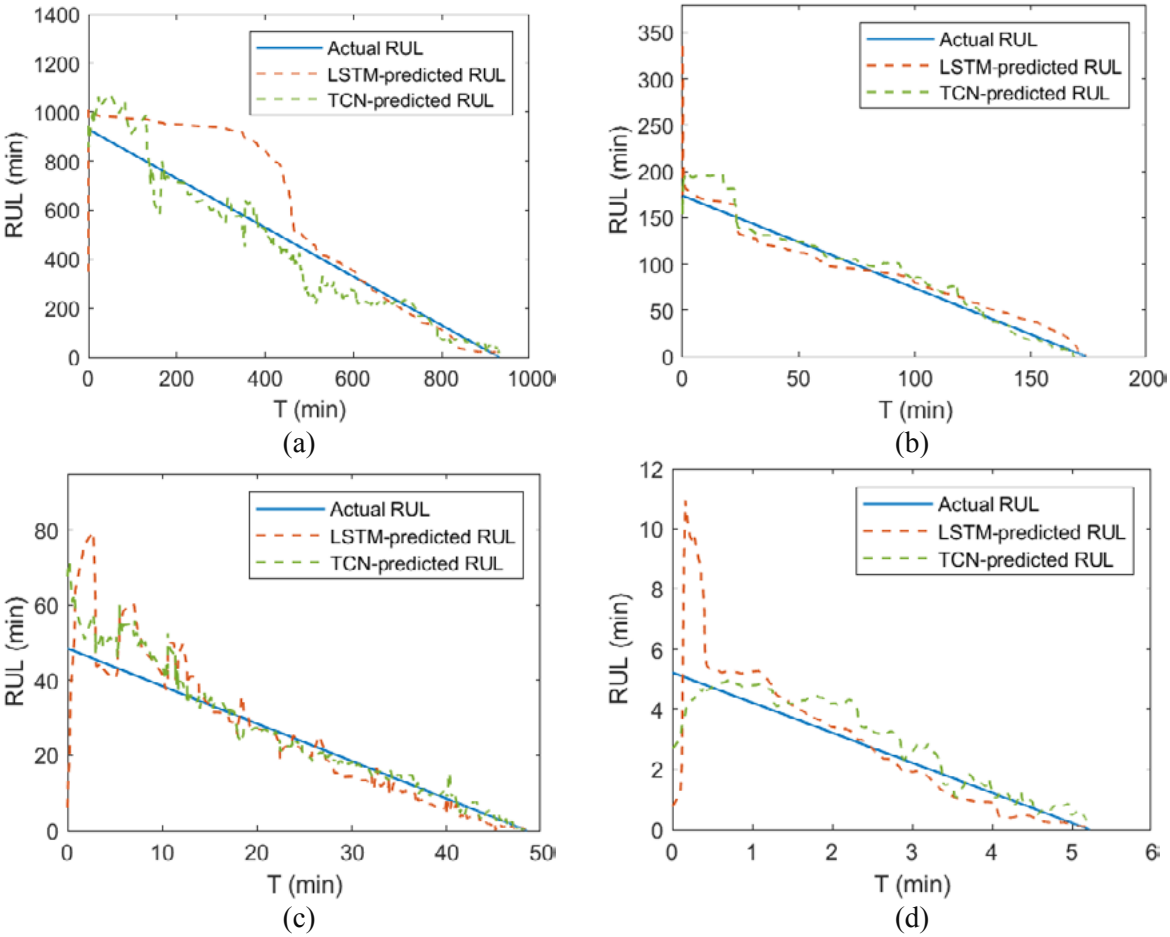


Fig. 3 Representative RUL predictions of samples under four different stress levels by LSTM and TCN. The RUL values at any moment t, were estimated based on the historical data up to t. (a) Stress ratio of 75%. (b) Stress ratio of 80%. (c) Stress ratio of 85%. (d) Stress ratio of 90%.

Fig. 3 presents the representative RUL estimations of the four samples by using LSTM and TCN (the models were trained using the data from the same stress ratio sample, respectively). In this case, the

predictions are much better than those shown in Fig. 2. It is found that the predicted values deviate noticeably from the actual RUL line in the early stage (most likely the primary creep stage) but converge to the actual RUL line when approaching the end of the creep life. The moderate performance in the early stage could be due to two reasons. Firstly, AE events generated sporadically in the early stage, leading to a relatively small number of AE events and thus limited information can be fed into the model for prediction. Secondly, the damage that occurred in the early stage when subjected to long-term creep load is mainly associated with matrix cracking based on our previous study [30]. For fibre reinforced composites, the performance degradation is less sensitive to the number of matrix failures, rather more dependent on the fibre-matrix interface and fibre failures as the load of composite materials is mainly borne by the fibres with the interface dominating the stress transfer. As the end-of-life approaches, increasing interface failures (interface debonding and fibre pull-out) as well as fibre fracture occur [30]. Consequently, better prediction results could be obtained with these more informative damage modes.

The normalized root mean squared error (NRMSE) is adopted to assess the model performance across the four samples under different stress ratios, formulated as follows:

$$NRMSE = \frac{RMSE}{T_L} = \frac{\sqrt{\frac{1}{N}\sum_{t=1}^{N}\left(\widehat{RUL_{(t)}} - RUL_{actual\,(t)}\right)^2}}{T_L} \quad (1)$$

Where $\widehat{RUL_{(t)}}$ is the estimated RUL and T_L the corresponding creep lifespan.

Each stress level sample comprises six predictions generated through the leave-one-out cross validation method. The corresponding NRMSE values are visually represented using a boxplot, as depicted in Figure 4 . It is clearly seen that the NRMSE values of the two models across all samples fall primarily within the range of 0.05 to 0.15. A minority of predictions exhibit errors exceeding 0.2. The mean NRMSE illustrated by a black dash line is used to represent the generalization performance of the two models for each sample. Notably, the mean errors of the both models for the four samples are less than 0.1. Among the four samples, the sample with a stress ratio of 80% exhibits the most favorable performance for both models, while higher mean NRMSE values are observed in samples with stress ratios of 75% and 85%, perhaps due to less patten diversity in the data of sample with stress ratio of 80%.

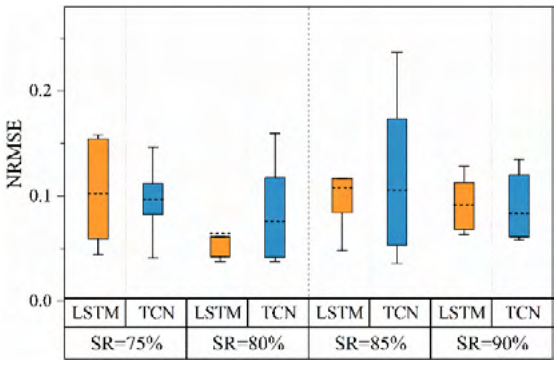


Fig. 4 The normalized RMSE of the two models for the samples under four different stress ratios.

4. Conclusions

In this study, the RUL of flax fibre composite subjected to creep load was predicted using LSTM and TCN deep learning models based on AE data and creep deformation. Cumulative feature rates, deemed crucial for RUL estimation, were proposed to reflect the performance degradation rate of the composites under creep load and were included as part of the input variables of the models. A specific evaluation metric, NRMSE, was adopted to assess and compare the model performance across four distinct samples with significantly different lifespans. Both models provided satisfactory accuracy in estimating RUL overall, with improved precision observed when more informative historical data was incorporated into the models

References

[1] J. A. Epaarachchi and P. D. Clausen, "An empirical model for fatigue behavior prediction of glass fibre-reinforced plastic composites for various stress ratios and test frequencies," *Compos. Part A Appl. Sci. Manuf.*, vol. 34, no. 4, pp. 313–326, 2003, doi: 10.1016/S1359-835X(03)00052-6.

[2] A. D'Amore and L. Grassia, "Comparative study of phenomenological residual strength models for composite materials subjected to fatigue: Predictions at Constant Amplitude (CA) loading," *Materials (Basel).*, vol. 12, no. 20, 2019, doi: 10.3390/ma12203398.

[3] A. D'Amore and L. Grassia, "A method to predict the fatigue life and the residual strength of composite materials subjected to variable amplitude (VA) loadings," *Compos. Struct.*, vol. 228, no. March, p. 111338, 2019, doi: 10.1016/j.compstruct.2019.111338.

[4] R. M. Guedes, "Lifetime predictions of polymer matrix composites under constant or monotonic load," *Compos. Part A Appl. Sci. Manuf.*, vol. 37, no. 5, pp. 703–715, 2006, doi: 10.1016/j.compositesa.2005.07.007.

[5] R. M. Guedes, "Creep and fatigue lifetime prediction of polymer matrix composites based on simple cumulative damage laws," *Compos. Part A Appl. Sci. Manuf.*, vol. 39, no. 11, pp. 1716–1725, 2008, doi: 10.1016/j.compositesa.2008.07.014.

[6] S. S. Samareh-Mousavi and F. Taheri-Behrooz, "A new phenomenological creep residual strength model for the life prediction of the laminated composites," *Fatigue Fract. Eng. Mater. Struct.*, vol. 44, no. 11, pp. 3152–3168, 2021, doi: 10.1111/ffe.13574.

[7] M. Kersani, S. V. Lomov, A. W. Van Vuure, A. Bouabdallah, and I. Verpoest, "Damage in flax/epoxy quasi-unidirectional woven laminates under quasi-static tension," *J. Compos. Mater.*, vol. 49, no. 4, pp. 403–413, 2015, doi: 10.1177/0021998313519282.

[8] C. Barile, C. Casavola, G. Pappalettera, and P. K. Vimalathithan, "Damage characterization in composite materials using acoustic emission signal-based and parameter-based data," *Compos. Part B Eng.*, vol. 178, no. September, p. 107469, 2019, doi: 10.1016/j.compositesb.2019.107469.

[9] S. Sikdar, D. Liu, and A. Kundu, "Acoustic emission data based deep learning approach for classification and detection of damage-sources in a composite panel," *Compos. Part B Eng.*, vol. 228, no. August 2021, p. 109450, 2022, doi: 10.1016/j.compositesb.2021.109450.

[10] M. Aslan, "Investigation of damage mechanism of flax fibre LPET commingled composites by acoustic emission," *Compos. Part B Eng.*, vol. 54, no. 1, pp. 289–297, 2013, doi: 10.1016/j.compositesb.2013.05.042.

[11] V. Carvelli, A. D'Ettorre, and S. V. Lomov, "Acoustic emission and damage mode correlation in textile reinforced PPS composites," *Compos. Struct.*, vol. 163, pp. 399–409, 2017, doi: 10.1016/j.compstruct.2016.12.012.

[12] N. Pei, S. Zhou, C. Xu, J. Shang, and Q. Wu, "Cluster analysis of acoustic emission signals for tensile damage characterization of quasi-static indented carbon/glass fiber-reinforced hybrid laminate composites," *Compos. Part A Appl. Sci. Manuf.*, vol. 150, no. June, 2021, doi: 10.1016/j.compositesa.2021.106597.

[13] F. E. Oz, N. Ersoy, M. Mehdikhani, and S. V. Lomov, "Multi-instrument in-situ damage monitoring in quasi-isotropic CFRP laminates under tension," *Compos. Struct.*, vol. 196, no. March, pp. 163–180, 2018, doi: 10.1016/j.compstruct.2018.05.006.

[14] S. Momon *et al.*, "Acoustic emission and lifetime prediction during static fatigue tests on ceramic-matrix-composite at high temperature under air," *Compos. Part A Appl. Sci. Manuf.*, vol. 41, no. 7, pp. 913–918, 2010, doi: 10.1016/j.compositesa.2010.03.008.

[15] E. Racle, N. Godin, P. Reynaud, and G. Fantozzi, "Fatigue lifetime of ceramic matrix composites at intermediate temperature by acoustic emission," *Materials (Basel).*, vol. 10, no. 6, 2017, doi: 10.3390/ma10060658.

[16] T. P. Philippidis and T. T. Assimakopoulou, "Using acoustic emission to assess shear strength degradation in FRP composites due to constant and variable amplitude fatigue loading," *Compos. Sci. Technol.*, vol. 68, no. 3–4, pp. 840–847, 2008, doi: 10.1016/j.compscitech.2007.08.012.

[17] J. Zhang, P. Wang, R. Yan, and R. X. Gao, "Long short-term memory for machine remaining life prediction," *J. Manuf. Syst.*, vol. 48, no. May, pp. 78–86, 2018, doi:

10.1016/j.jmsy.2018.05.011.
[18] S. Kiranyaz, T. Ince, O. Abdeljaber, O. Avci, and M. Gabbouj, "1-D Convolutional Neural Networks for Signal Processing Applications," *ICASSP, IEEE Int. Conf. Acoust. Speech Signal Process. - Proc.*, vol. 2019-May, pp. 8360–8364, 2019, doi: 10.1109/ICASSP.2019.8682194.
[19] S. Kiranyaz, O. Avci, O. Abdeljaber, T. Ince, M. Gabbouj, and D. J. Inman, "1D convolutional neural networks and applications: A survey," *Mech. Syst. Signal Process.*, vol. 151, p. 107398, 2021, doi: 10.1016/j.ymssp.2020.107398.
[20] H. Yang, F. Zhao, G. Jiang, Z. Sun, and X. Mei, "A novel deep learning approach for machinery prognostics based on time windows," *Appl. Sci.*, vol. 9, no. 22, 2019, doi: 10.3390/app9224813.
[21] D. Xu, P. F. Liu, and Z. P. Chen, "A deep learning method for damage prognostics of fiber-reinforced composite laminates using acoustic emission," *Eng. Fract. Mech.*, vol. 259, no. October 2021, 2022, doi: 10.1016/j.engfracmech.2021.108139.
[22] A. van den Oord *et al.*, "WaveNet: A Generative Model for Raw Audio," pp. 1–15, 2016, [Online]. Available: http://arxiv.org/abs/1609.03499.
[23] S. Bai, J. Z. Kolter, and V. Koltun, "An Empirical Evaluation of Generic Convolutional and Recurrent Networks for Sequence Modeling," 2018, [Online]. Available: http://arxiv.org/abs/1803.01271.
[24] R. Wan, S. Mei, J. Wang, M. Liu, and F. Yang, "Multivariate temporal convolutional network: A deep neural networks approach for multivariate time series forecasting," *Electron.*, vol. 8, no. 8, 2019, doi: 10.3390/electronics8080876.
[25] X. Lu, Y. Ling, and S. Liu, "Temporal Convolutional Network with Wavelet Transform for Fall Detection," *J. Sensors*, vol. 2022, 2022, doi: 10.1155/2022/7267099.
[26] Z. Gan, C. Li, J. Zhou, and G. Tang, "Temporal convolutional networks interval prediction model for wind speed forecasting," *Electr. Power Syst. Res.*, vol. 191, no. October 2020, p. 106865, 2021, doi: 10.1016/j.epsr.2020.106865.
[27] A. Pandey and D. Wang, "TCNN : TEMPORAL CONVOLUTIONAL NEURAL NETWORK FOR REAL-TIME SPEECH ENHANCEMENT IN THE TIME DOMAIN Department of Computer Science and Engineering , The Ohio State University , USA Center for Cognitive and Brain Sciences , The Ohio State University , USA," pp. 6875–6879, 2019.
[28] F. Lissek, A. Haeger, V. Knoblauch, S. Hloch, F. Pude, and M. Kaufeld, "Acoustic emission for interlaminar toughness testing of CFRP: Evaluation of the crack growth due to burst analysis," *Compos. Part B Eng.*, vol. 136, no. September 2017, pp. 55–62, 2018, doi: 10.1016/j.compositesb.2017.10.012.
[29] B. Xu, R. Blok, and P. Teuffel, "An investigation of the effect of relative humidity on viscoelastic properties of flax fiber reinforced polymer by fractional-order viscoelastic model," *Compos. Commun.*, vol. 37, no. October 2022, p. 101406, 2023, doi: 10.1016/j.coco.2022.101406.
[30] J. Hao, A. Prapavesis, S. V Lomov, C. A. Fuentes, A. W. Van Vuure, "Damage evolution in flax fibre composite under creep load," *Compos. Struct.*, vol. 329, no. August 2023, p. 117786, 2024, doi: 10.1016/j.compstruct.2023.117786.

DURABILITY UNDER HYGROTHERMAL EXPOSURE OF VACUUM INFUSED GFRP COMPOSITES PRODUCED WITH POLYESTER AND VINYL ESTER RESINS

Tarikul Hasan[1a], João R. Correia[1b], Mario Garrido[1c],
Susana Cabral-Fonseca[2d], José Sena-Cruz[3e], Marco Jorge[3f]
[1] CERIS, Instituto Superior Técnico, Universidade de Lisboa,
Av. Rovisco Pais 1, 1049-001, Lisbon, Portugal
Email: [a]tarikul.hasan@tecnico.ulisboa.pt, [b]joao.ramoa.correia@tecnico.ulisboa.pt,
[c]mario.garrido@tecnico.ulisboa.pt
[2]Departamento de Materiais, Unidade de Materiais Orgânicos,
Laboratório Nacional de Engenharia Civil, Av. do Brasil 101, 1700-066, Lisbon, Portugal.
Email: [d]sbravo@lnec.pt
[3] ISISE/ARISE, University of Minho, Azurém, 4800-058 Guimarães, Portugal
Email: [e]jose.sena-cruz@civil.uminho.pt, [f]marco@civil.uminho.pt

Keywords: glass fibre reinforced polymer, vacuum infusion, durability, thermomechanical properties, mechanical properties, hygrothermal ageing.

Abstract
The recent Technical Specification CEN/TS 19101:2022, "Design of fibre-polymer composite structures", provides moisture conversion factors for fibre-reinforced polymer (FRP) composites that were defined from data available in the literature. However, such data was found to present several limitations, namely (i) high scatter, (ii) few results for long-term exposure, and (iii) gaps for several combinations of constituent materials and manufacturing methods. In particular, very few data is available for relatively thick vacuum infused composites. This paper presents an ongoing study of the effects of hygrothermal exposure on the behaviour of glass-FRP (GFRP) composites. Relatively thick (6.5 mm) laminates were produced by vacuum infusion using (i) isophthalic polyester and (ii) vinyl ester. The laminates were immersed in water at different temperatures (20 °C, 40 °C and 60 °C) for 3, 6 and 12 months (data will be obtained for longer periods), during which water uptake measurements were conducted at regular intervals. For each period, the performance of the laminates was assessed through dynamic mechanical analysis (DMA), and tensile, compressive, and in-plane shear tests. Based on the mechanical test results, Arrhenius-type degradation models were developed and 50-year predictions were derived, later compared with the design provisions set out in CEN/TS 19101:2022.

1. Introduction

Fibre-reinforced polymer (FRP) composites offer several advantages for civil engineering applications, including lightness, high specific strength and stiffness, high resistance to corrosion and good performance under harsh environments [1,2]. Consequently, their application in the construction industry has increased in recent decades [3]. Despite their enhanced durability in service conditions, FRP composites may be susceptible to deterioration when exposed to different environmental agents, which can result in a reduction in thermomechanical and mechanical properties. These agents, acting individually or combined, include moisture [4,5], chemicals [6], ultraviolet radiation [7], thermal effects [8], thermal cycles [9], and freeze-thaw cycles [10].

Among the aformentioned environmental agents, moisture may be particularly harmful, as it can cause significant physical and chemical degradation, especially at elevated temperatures [4,5]. The physical degradation due to moisture involves phenomena such as plasticization, swelling and relaxation, and is

generally reversible upon drying. Irreversible chemical degradation mainly involves hydrolysis of the polymer matrix[11,12]. Moisture can also cause damage to the fibres and to the fibre-matrix interphace [13,14].

Several previous studies have investigated the effects of moisture exposure on the mechanical and thermomechanical properties of FRP composites [4,5]. However, several gaps exist in the literature, as noted in the test data survey that was carried out to derive a moisture conversion factor for the European Technical Specification CEN/TS 19101:2022 [5]. The following limitations in available data were then identified: (i) the FRP laminates used in previous studies are usually thinner (<4 mm) than those required for civil structural applications; (ii) few data is available for vacuum infused composites, dispite their relevance for construction; (iii) literature also lacks comprehensive comparative studies between different resin systems; (iv) the available data is often scattered and inconsistent; (v) most studies only address limited properties and short-term exposure. As a consequence, robust and validated degradation models and comprehensive design guidelines are not yet available. Addressing these literature gaps is very important to provide a solid ground for end users and engineers to make informed decisions regarding the use of FRP composites in construction and, thus, to promote the full utilization of their potential. The first step in that path is to properly and systematically measure the degradation of FRP composites exposed to different ageing conditions, including moisture.

In this context, this paper presents the results of an ongoing study about the hygrothermal durability of relatively thick glass-FRP (GFRP) composites produced by vacuum infusion using vinyl ester (VE) and unsaturated polyester (UP) resins. Both composite laminates were immersed in water at three temperatures for up to 12 months. After predetermined ageing periods, the degradation of their thermomechanical and mechanical properties was evaluated through DMA and tensile, compressive and in-plane shear tests. Additionally, the test results were used to develop Arrhenius-based models to predict the retention of selected mechanical properties after 50 years.

2. Experimental program

2.1. Materials

GFRP laminates were produced by vacuum infusion as large plates (5000 mm × 1250 mm) with a nominal thickness of 6.5 mm and subsequently cut into smaller plates with dimensions of 700 mm × 250 mm. The GFRP laminates comprise 14 layers of glass fibres (volume fraction of ~57%) and two different resin systems: unsaturated polyester (GFRP-UP) and vinyl ester (GFRP-VE). Both types of composite laminates have the same fibre architecture, thus enabling the direct comparison between them: eight layers of unidirectional fabrics (0°, 625 g/m^2), four quadriaxial fabrics (0°/+45°/90°/-45°, 835 g/m^2), and two outer layers of chopped strand mat (CSM, 300 g/m^2). Following production, both types of composite laminates were post-cured at 80 °C for a period of 12 hours. Polylite 720-691 resin (50-54% isophthalic polyester and 46-50% styrene) was used to produce the GFRP laminate with unsaturated polyester (GFRP-UP); this resin mixture included 1.5% (wt.%) of methyl ethyl ketone peroxide (MEKP, Ketanox B180). The resin used for producing the vinyl ester-based composites (GFRP-VE) was Derakane 411-200 (52% epoxy vinyl ester resin and 48% styrene), and this resin mixture included 1.5% (wt.%) of MEKP (Ketanox B180), 0.025% (wt.%) of dimethylaniline, 0.3% (wt.%) of cobalt octoate (with 1% cobalt), and 0.025% (wt.%) of 2,4-pentanodione.

2.2. Ageing procedure

The GFRP plates were immersed in demineralized water at three different temperatures of 20 °C, 40 °C and 60 °C. Water tanks with dimensions of 1000 mm × 600 mm × 500 mm were used, equipped with an electrical heater and controller to maintain the temperature at the desired level. To avoid the ingress of water along the lateral edges of the GFRP plates, they were coated with an epoxy resin (Icosit K-101 N), which promoted one-dimensional water diffusion through the composite laminates.

2.3. Test program

The initial characterization involved a series of thermomechanical (DMA) and mechanical tests, including tensile, compressive, and in-plane shear. Following a period of 3, 6 and 12 months (additional tests are

planned up to 240 months), two plates of each type of composite (GFRP-UP and GFRP-VE) were removed from the water tanks and subjected to similar tests in both wet and dry conditions. For the wet condition, specimens were tested within a short period after removal from the tanks and cutting to the appropriate size. For the dry condition, tests were carried out after 1.5 to 2 months of conditioning at room temperature, when constant mass was reached (mass change lower than 0.1% in 24 hours).

2.3.1. Thermomechanical tests

The DMA was conducted using a TA Instrument Q800 Dynamic Mechanical Analyser, in accordance with the recommendations of ISO 6721-1,5:2019. Specimens with dimensions of 60 mm × 10 mm × 4 mm (reduced thickness) were heated from 25 °C to 200 °C at a rate of 2 °C/min. During the tests, specimens were subjected to sinusoidal loading in a dual cantilever system, at a frequency of 1 Hz, with a strain amplitude of 15 μm. The glass transition temperature (T_g) was determined from the onset of the decay of the storage modulus (E') curve.

2.3.2. Mechanical tests

The tensile and compressive tests were performed according to ISO 527-4:2021 and ISO 14126:1999, respectively. Test specimens had rectangular shape, with dimensions of 300 mm × 25 mm × 6.5 mm (tensile tests) and 153 mm × 25 mm × 6.5 mm (compressive tests). Tests were performed in a universal testing machine (UTM) Instron 5989 (capacity of 600 kN), under displacement control. A video extensometer (VE, camera FLIR BFS-U3-51S5M-C; lens Fujinon HF25SA-1; software from MatchID—v2022.2) was used to measure axial strains.

The in-plane (IP) shear tests were carried out according to ASTM D5379/D5379M-19. Test specimens had rectangular shape, with dimensions of 76 mm × 19 mm, and comprised V-shaped notches at the mid-section (on both sides). Tests were performed in a UTM Instron 5982 (capacity of 100 kN), under displacement control. Strains in the notch region were also measured with the same video extensometer.

2.3.3. Mass uptake measurements

Mass uptake measurements were done in specimens immersed in demineralized water at the three different test temperatures (20 °C, 40 °C and 60 °C), following recommendations set in ASTM D5229/D5229-20 and ISO 62:1999. Squared shaped specimens of 60 mm × 60 mm were used and their lateral edges were coated with the above-mentioned epoxy resin. Prior to immersion, the specimens were dried at 40 °C until they reached constant mass (mass change lower than ± 1 mg in 24 hours).

3. Results and discussion

3.1. Initial characterization

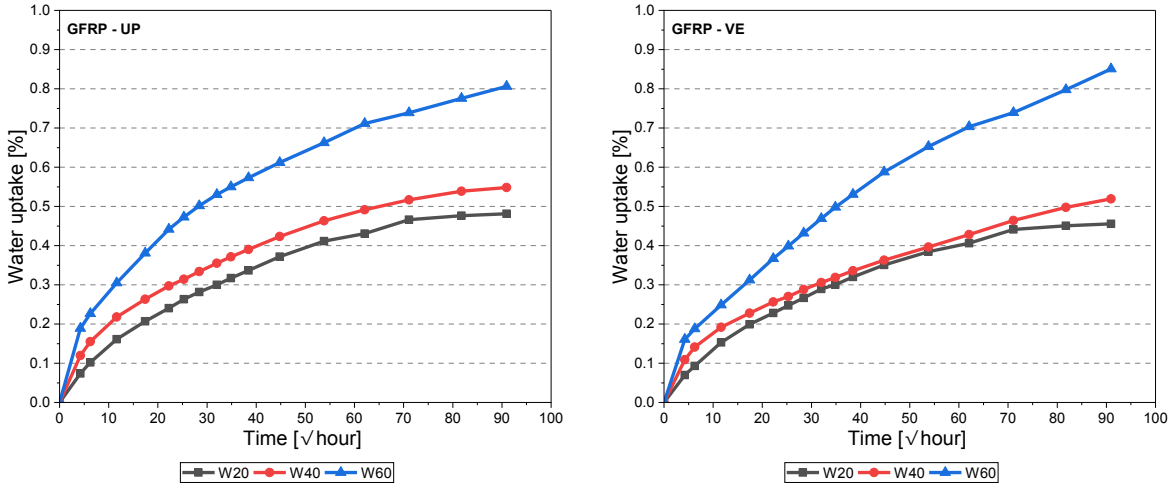
Table 1 presents the initial mechanical and thermomechanical properties of both composites, which were obtained along the main fibre reinforcement direction. For most mechanical properties, there are no significant differences between the two composites, produced with the alternative resin systems. However, with the exception of tensile strength, the mechanical properties of GFRP-VE are slightly higher, particularly in terms of compressive strength. This can be attributed to the superior performance of the VE resin in comparison to the UP resin. Also the T_g of GFRP-VE is significantly higher than that of GFRP-UP.

Table 1. Initial properties of GFRP composites with UP and VE resins (average ± standard deviation)

Properties	GFRP-UP	GFRP-VE
Tensile strength, σ_t [MPa]	844 ± 30	811 ± 22
Tensile modulus, E_t [GPa]	33.1 ± 0.5	35.1 ± 1.5
Compressive strength, σ_c [MPa]	470 ± 33	556 ± 45
Compressive modulus, E_c [GPa]	35.8 ± 1.9	39.2 ± 2.0
In-plane shear strength, τ [MPa]	148 ± 4	158 ± 3
In-plane shear modulus, G [GPa]	5.0 ± 0.4	5.4 ± 0.6
Glass transition temperature, T_g [°C]	86.0 ± 0.8	95.0 ± 0.2

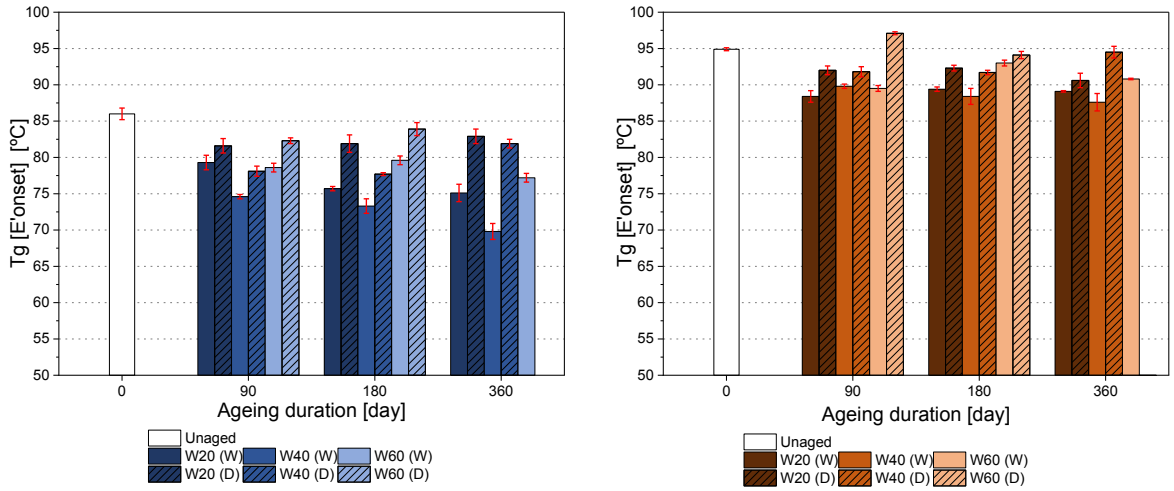
3.2. Water uptake

Figures 1a) and 1b) present the water uptake of GFRP-UP and GFRP-VE composites over the square root of time, respectively, which prompt the following comments: (i) for both composites, as expected, mass increased with increasing immersion temperature, especially from 40 °C to 60 °C; (ii) at 20 °C and 40 °C, GFRP-VE absorbed slightly less water than GFRP-UP, while at 60 °C the opposite trend was observed; (iii) after 345 days of ageing, the water uptake curves of GFRP-UP and GFRP-VE for 20 °C are approaching a plateau (0.48% and 0.46%, respectively), while for 40 °C and 60 °C they are still increasing. Overall, the performance of both composites in terms of water uptake is fairly similar.



a) b)

Figure 1. Water uptake: a) GFRP-UP, and b) GFRP-VE



a) b)

Figure 2. Changes in T_g: a) GFRP-UP, and b) GFRP-VE (tests for W60(D) not yet completed) (error bars correspond to one standard deviation).

3.3. Glass transition temperature

Figures 2a) and 2b) ilustrate the impact of hygrothermal ageing on the T_g of GFRP-UP and GFRP-VE. In the aforementioned figure, as well as in subsequent ones, the nomenclature W20 (W) and W20 (D) represents the results of tests conducted in water at 20 °C (W20) in either wet (W) and dry (D) conditions. Other codes have similar meanings for the corresponding temperatures. Figure 5 shows that: (i) for both composites, there was an overall reduction of T_g; (ii) the reduction in T_g was generally more pronounced for GFRP-UP than for GFRP-VE, reflecting the higher hygrothermal stability of the vinyl ester resin compared to its polyester counterpart; (iii) upon drying, a moderate to significant recovery in T_g occurred in both composites (more pronounced in

GFRP-UP), which can be attributed to the reversibility of physical degradation due to plasticization; (iv) increasing immersion temperature and duration did not necessarily result in an increasing reduction of T_g, which may be partly due to competing post-curing of the resins. In fact, the maximum reduction in T_g (16.2 °C) was observed for GFRP-UP after 12 months of immersion at 40 °C (in wet condition), while the lowest reduction (2.1 °C) was observed after 6 months of immersion at 60 °C (in dry condition); the largest reduction in T_g occurred during the first 3 months of immersion, after which only a slight variation was observed. For GFRP-VE, the highest reduction in T_g (7.3 °C) occurred after 12 months of immersion at 40 °C (also in wet condition), while an increase in T_g (2.2 °C) was observed after 3 monhts of immersion at 60 °C (in dry condition). For most immersion temperatures and conditions, the T_g exhibited a tendency to stabilize after 3 months of ageing.

3.4. Mechanical behaviour

3.4.1. Tensile strength

Figures 3a) and 3b) depict the impact of hygrothermal ageing on the tensile strength of GFRP-UP and GFRP-VE composites, respectively. Figure 3 shows that, for both composites: (i) the tensile strength exhibited a general decrease due to water immersion, (ii) the magnitude of such decrease was amplified by immersion temperatures, and (iii) the highest reductions occurred in wet condition, indicateting that some degradation was reversed when tested in a dry condition. This phenomenon aligns with the observations made regarding the T_g results. For immersion at 20 °C, the reduction in tensile strength was low and after 12 months it had not yet stabilized. At higher immersion temperatures, the reduction in tensile strength was significantly higher, most of it occurring during the first 6 months, after which it appears to be stabilizing (especially for 60 °C). For immersion temperatures of 20 °C and 40 °C, the GFRP-UP exhibited inferior performance relative to its GFRP-VE counterpart, while for 60 °C the trend was opposite (in the water uptake tests, the relative performance of both composites was similar). The lowest tensile strength retentions for the GFRP-UP and GFRP-VE composites were observed after 6 and 12 months of immersion at 60 °C (wet condition), with values of 62% and 54%, respectively; after 12 months of immersion at 20 °C, those figures were 93% and 98%.

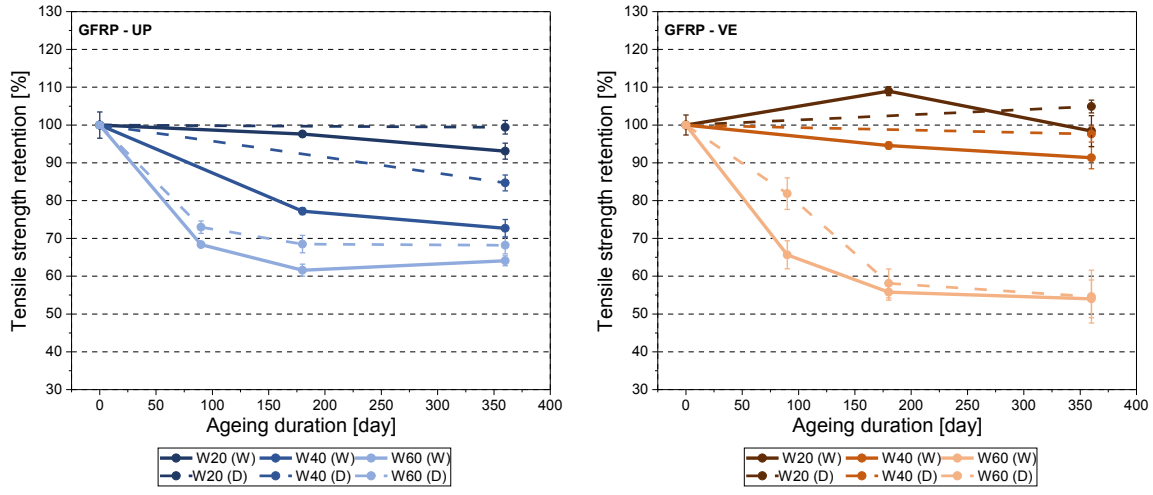


Figure 3. Tensile strength retention: a) GFRP-UP, and b) GFRP-VE (error bars correspond to one coefficient of variation (COV); some results for 3 months and 6 months of ageing are not yet available).

3.4.2. Compressive strength

Figures 4a) and 4b) illustrate the compressive strength retention of GFRP-UP and GFRP-VE composites, respectively, due to hygrothermal ageing. The impact of water immersion on compressive strength was found to be higher than that on tensile strength. This is attributed to the fact that the former property is more matrix-dominated, while the latter is more fibre-dominated. Although the scatter in compressive strength results was relatively high (due to the inherent variability of this property), similar variation trends to those reported above for tensile strength could be observed: (i) higher reductions for

higher water immersion temperature and for wet condition; (ii) partial reversibility of the degradation upon drying; (iii) larger reductions during the initial periods of ageing, especially at 60 °C; (iv) better performance of GFRP-VE for immersion at 20 °C and 40 °C and worse performance at 60 °C. The lowest compressive strength retention in the GFRP-UP and GFRP-VE composites occurred after 12 months of immersion at 60 °C (wet condition), with value of 45% and 39%, respectively; at 20 °C, those figures were 80% and 87%.

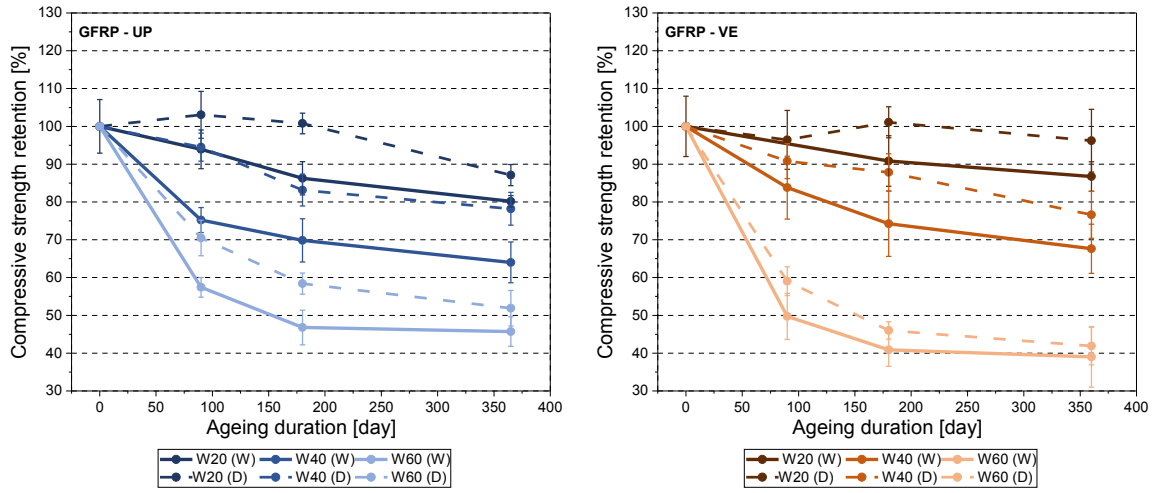


Figure 4. Compressive strength retention: a) GFRP-UP, and b) GFRP-VE (error bars correspond to one COV).

3.4.3. In-plane shear strength

Figures 5a) and 5b) present the changes in IP shear strength due to hygrothermal ageing. The overall variation trends are similar to those reported above for tensile and compressive strengths, with the IP shear strength presenting an intermediate reduction magnitude compared to those properties. As mentioned, the fibre architecture of the tested composites included quadriaxial fabrics, with significant fibre reinforcement at ±45º orientations, which resulted in a major influence of the fibre reinforcement in IP shear strength. This explains why this property was less affected by hygrothermal ageing than compressive strength. The lowest IP shear strength retention in the GFRP-UP and GFRP-VE composites occurred after 12 months of immersion at 60 °C (wet condition), with values of 61% and 58%, respectively; at 20 °C, those figures were much higher, respectively 94% and 97%.

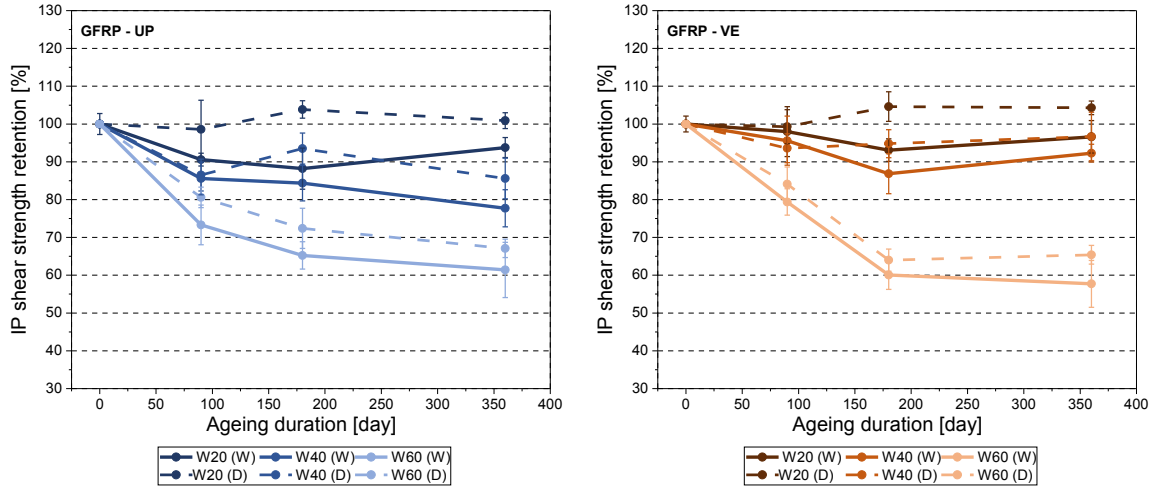
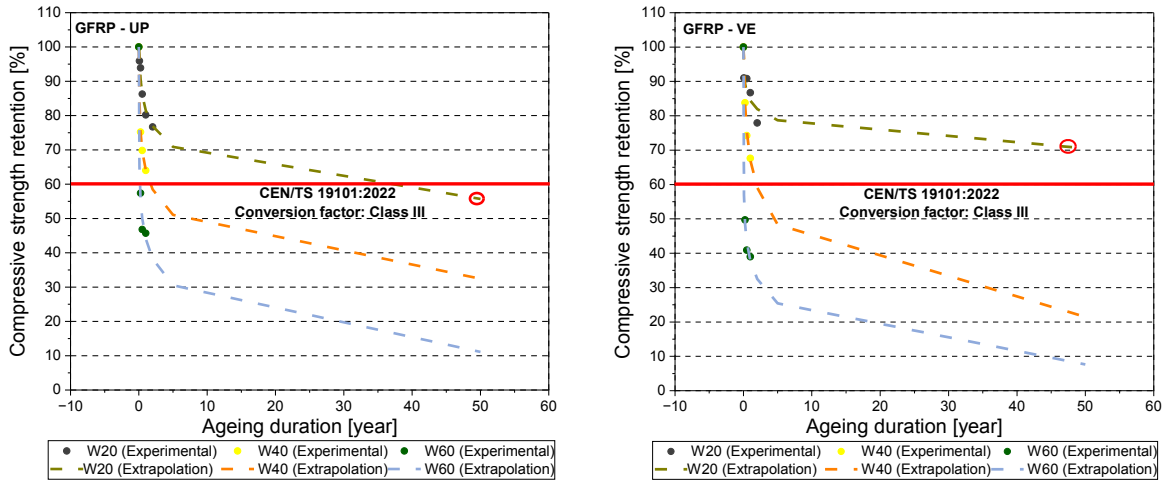


Figure 5. IP strength retention: a) GFRP-UP, and b) GFRP-VE (error bars correspond to one COV).

4. Arrhenius type degradation models

Figure 6 presents the Arrhenius-type degradation models developed for compressive strength (since this property presented the greatest depression in retention). The models were obtained by plotting property retention *versus* ageing duration (log scale) and applying curve fitting to the test data, i.e., the procedure detailed in Bank *et. al.* [15]. Using these models, 50-year predictions (extrapolations) were obtained and, for immersion at 20 °C, they (marked in red cicrcle) were compared with the conversion factor provided in CEN/TS 19101:2022. The compressive strength retention of GFRP-UP and GFRP-VE composites after 50 years was found to be 56% and 71%, respectively. These values are only slightly lower and moderately higher than the 60% retention set in CEN/TS 19101:2022 for the corresponding exposure class III (marked by a red line in Figure 6), which thus seems to cover the vacuum infused laminates used in this study.



a) b)

Figure 6. Compressive strength retention prediction: a) GFRP-UP, and b) GFRP-VE.

5. Concluding remarks

This paper presents the results of an ongoing study on the hygrothermal durability of GFRP composites produced by vacuum infusion using isophthalic polyester (GFRP-UP) and vinylester (GFRP-VE).

The results obtained so far indicate that both GFRP composites exhibited comparable performance in terms of water uptake, with slightly higher water uptake observed in GFRP-UP at 20 °C and 40 °C, and in GFRP-VE at 60 °C. A slight to moderate reduction in the glass transition temperature (T_g) was observed, with a more pronounced effect in GFRP-UP. However, upon drying, this reduction was partly recovered. For longer ageing periods and higher immersion temperatures, recovery of T_g was also observed, which may be attributed to post-curing phenomena.

The mechanical properties exhibited moderate to significant reductions, which varied according to the immersion temperature and duration, the test condition (wet or dry), and the type of resin system. Most of the degradation occurred during the initial stages of ageing, especially for higher immersion temperatures. As expected, the extent of the degradation consistently increased with the immersion temperature, e.g. the maximum reduction of compressive strength of GFRP-UP and GFRP-VE was by 55% and 61%, respectively, after 12 months of ageing at 60 °C and, upon drying, there was also significant property recovery, indicating that a part of the degradation was physical. The magnitude of the reduction in mechanical properties was found to be strongly influenced by the corresponding contribution of the fibres and polymer matrix, e.g. maximum observed reduction in tensile and compressive strengths of GFRP-VE were 46% and 61%, respectively, while the in-plane shear strength (in this case, with a relevant contribution of off-axis fibres) presented an intermediate level of degradation for most cases. In general, the GFRP-VE composite exhibited superior performance relative to GFRP-UP counterpart, namely at 20 °C and 40 °C.

Arrenhius-type models were developed based on the experimental results. These models provided 50-year compressive strength retention following water immersion at 20 °C of 56% and 71% respectively for GFRP-UP and GFRP-VE. These predicted (extrapolated) strength retentions are respectively slightly lower and moderately higher than the 60% retention set in CEN/TS 19101:2022 for exposure class III, which thus seems to cover the vacuum infused laminates used in this study.

Acknowledgements
The authors acknowledge the funding provided by Fundação para a Ciência e a Tecnologia (FCT) through project Durable-FRP (doi.org/10.54499/PTDC/ECI-EGC/4609/2020). The first author acknowledges the financial support provided by FCT through the PhD scholarship 2022.14644.BD. The first three authors acknowledge the funding provided by FCT to the CERIS research unit, through project UIDB/04625/2020 (doi.org/10.54499/UIDB/04625/2020). The last two authors acknowledge the funding provided by FCT to the ISISE research unit, through project UIDB/04029/2020 (doi.org/10.54499/UIDB/04029/2020) and the Associate Laboratory ARISE, under reference LA/P/0112/2020.

References

1. Bai, J. (Ed.). (2013). Advanced Fibre-Reinforced Polymer (FRP) Composites for Structural Applications. Woodhead Publishing, New Delhi.
2. Correia, J. R. (2015). In: Materials for Construction and Civil Engineering: Science, Processing and Design (Eds. F. Margarido & M. C. Gonçalves). Springer.
3. EMR Inc. (2022). Europe Composites Market Report and Forecast 2022-2027.
4. Sousa, J.M., Garrido, M., Correia, J.R. and Cabral-Fonseca, S. (2021). "Hygrothermal ageing of pultruded GFRP profiles: Comparative study of unsaturated polyester and vinyl ester resin matrices". Composites Part A: Applied Science and Manufacturing, 140, 106193.
5. Garrido, M., Sousa, J. M., Correia, J.R. and Cabral-Fonseca, S. (2022). "Prediction of long-term performance and definition of a moisture conversion factor for the durability design of pultruded GFRP profiles under hygrothermal exposure". Construction and Building Materials, 326, 126856.
6. Bazli, M., Ashrafi, H., and Oskouei, A.V. (2016). "Effect of harsh environments on mechanical properties of GFRP pultruded profiles". Composites Part B: Engineering, 99, 203-215.
7. Bazli, M., Ashrafi, H., Jafari, A., Zhao, X-L., Raman, R.K.S., and Bai, Y. (2019). "Effect of fibers configuration and thickness on tensile behavior of GFRP laminates exposed to harsh environment". Polymers, 11(9), 1401.
8. Correia, J.R., Gomes, M.M., Pires, J.M., and Branco, F.A. (2013). "Mechanical behaviour of pultruded glass fibre reinforced polymer composites at elevated temperature: Experiments and model assessment". Composite Structures, 98, 303-313.
9. Sousa, J.M., Correia, J.R., Cabral-Fonseca, S., and Diogo, A.C. (2014). "Effects of thermal cycles on the mechanical response of pultruded GFRP profiles used in civil engineering applications". Composite Structures, 116, 720-731.
10. Shahid, A.T., Hofmann, M., Garrido, M., Correia, J.R. and Rosa, I.C. (2023). "Freeze–thaw durability of basalt fibre reinforced bio-based unsaturated polyester composite". Materials, 16(15), 5411.
11. Antoon, M.K., Koenig, J.L. (1980). "The structure and moisture stability of the matrix phase in glass-reinforced epoxy composites". Journal of Macromolecular Science: Part C, 19(1), 135-173.
12. Mijović, K., Lin, K.F. (1985). "The effect of hygrothermal fatigue on physical/mechanical properties and morphology of neat epoxy resin and graphite/epoxy composite". Journal of Applied Polymer Science, 30, 2527-2549.
13. Karbhari, V.M. (Editor) (2007). Durability of Composites for Civil Structural Applications, Woodhead Publishing, Florida.
14. Pritchard, G. (Ed.) (1998). Reinforced plastics durability. Woodhead Publishing Limited, UK.
15. Bank, L. C., Gentry, T. R., Thompson, B. P., & Russell, J. S. (2003). "A model specification for FRP composites for civil engineering structures". Construction and Building Materials, 17(6–7), 405-437.

EFFECTS OF THERMAL CYCLES ON THE MECHANICAL AND THERMOMECHANICAL BEHAVIOUR OF VACUUM INFUSED GFRP COMPOSITES

Tarikul Hasan[1a], João R. Correia[1b], Mário Garrido[1c], Susana Cabral-Fonseca[2d], José Sena-Cruz[3e], Marco Jorge[3f]
[1] CERIS, Instituto Superior Técnico, Universidade de Lisboa,
Av. Rovisco Pais 1, 1049-001, Lisbon, Portugal
Email: [a]tarikul.hasan@tecnico.ulisboa.pt, [b]joao.ramoa.correia@tecnico.ulisboa.pt,
[c]mario.garrido@tecnico.ulisboa.pt
[2]Departamento de Materiais, Unidade de Materiais Orgânicos,
Laboratório Nacional de Engenharia Civil, Av. do Brasil 101, 1700-066, Lisbon, Portugal
Email: [d]sbravo@lnec.pt
[3] ISISE/ARISE, University of Minho, Azurém, 4800-058 Guimarães, Portugal
Email: [e]jose.sena-cruz@civil.uminho.pt, [f]marco@civil.uminho.pt

Keywords: glass fibre reinforced polymer, vacuum infusion, durability, mechanical properties, thermomechanical properties, thermal cycles.

Abstract
Fibre-reinforced polymer (FRP) composites exhibit high specific strength, lightness, high corrosion resistance, and have relatively low maintenance needs during service life, which has promoted their use in civil engineering structures. However, in the existing literature, there is limited data about the effects of dry thermal cycles (i.e., without moisture) on the degradation of FRP composites, namely those produced by vacuum infusion. To address this issue, this paper presents the findings of a study on the impact of thermal cycles on the mechanical (tensile, compression, flexure, in-plane shear and interlaminar shear) and thermomechanical (glass transition temperature) behavior of relatively thick (6.5 mm) glass-FRP (GFRP) laminates, produced by vacuum infusion, with unsaturated polyester and vinyl ester resins. The laminates were subjected to 100, 200 and 300 thermal cycles at temperatures ranging from -15 °C to 60 °C, each cycle lasting 12 hours. After each period, different tests were conducted to assess the changes in the above-mentioned mechanical and thermomechanical properties of the GFRP laminates caused by the exposure to thermal cycles. The results obtained show that the thermal cycles applied in this study caused only slight to moderate degradation of the properties of the vacuum infused GFRP laminates.

1. Introduction

The use of fibre reinforced polymer (FRP) composites in construction industry has increased over the last three decades [1], due to the advantages they provide over traditional materials, such as lightness, high specific strength and stiffness, and resistance to corrosion [2,3]. However, during their service life, FRP structures are exposed to different environmental agents that can be detrimental to them, namely moisture [4] and chemicals [5], ultraviolet radiation [6] and thermal effects [7], the latter encompassing thermal cycles [8] and, when combined with moisture, freeze-thaw cycles [9]. A thermal cycle refers to the (cyclic) change in temperature, with a given minimum and maximum temperature whose the magnitude depends on the climatic zone in which the FRP structure is located and on the specific exposure conditions for each structural component. As summarized below, thermal cycles can have different effects on FRP composites, both positive and negative.

In what concerns the exposure to the extreme temperatures of a given thermal cycle, at higher temperatures, as the glass transition temperature (T_g) of FRP composites is approached and eventually exceeded, they soften, and their mechanical properties are significantly reduced [12]. However, exposure to elevated temperatures and subsequent cooling can also promote post-cure phenomena, improving the mechanical properties and

increasing the T_g [13]. At subzero temperatures (below 0 °C), the polymer matrix hardens, causing microcracking [10]. Glass fibres and polymer matrices have different thermal expansion coefficients (e.g., 5×10^{-6} K^{-1} for E-glass and 30-200$\times10^{-6}$ K^{-1} and 30-50$\times10^{-6}$ K^{-1} for unsaturated polyester and vinyl ester resins, respectively [10,11]). Therefore, thermal cycles can cause fibre-matrix debonding due to the mismatch in expansion and contraction between the fibre reinforcement and the polymeric matrix. When the material repeatedly expands and contracts with varying temperature, cumulative damage can occur.

Several researchers have studied the effect of thermal cycles on FRP composites, namely Sousa *et al.* (2014), Grammatikos *et al*. (2016), etc. However, the available information on the effect of thermal cycles on FRP composites has several gaps: (i) the number of studies reported in the literature is still quite limited; (ii) most studies refer to FRP composites produced by pultrusion or hand layup, with very scarce data available for vacuum infusion, in spite of its relevance for civil engineering applications; (iii) comparative studies between different resin systems are also very rare, and (iv) most studies only address a limited number of properties. Therefore, an in-depth understanding of the effects of thermal cycles on FRP composites is necessary to promote their safe use in civil engineering structures, which are generally designed for 50 or 100 years.

To address the above-mentioned gaps, this paper presents a study about the effects of thermal cycles on relatively thick glass-FRP (GFPR) composites produced by vacuum infusion using two alternative resin systems, unsaturated polyester (UP) and vinyl ester (VE). Both composite materials were exposed to 300 thermal cycles and, periodically, subjected to various mechanical (tensile, compression, flexure, in-plane shear and interlaminar shear) and thermomechanical (dynamic mechanical analysis, DMA) tests to determine the impact of such exposure on their performance.

2. Experimental program

2.1. Materials

Composite laminates with 6.5 mm of nominal thickness were produced by vacuum infusion as large plates (5000 mm × 1250 mm) and later cut into smaller dimensions (700 mm × 250 mm). The composite laminates were produced using two alternative resin systems: unsaturated polyester (UP) and vinyl ester (VE). To enable a direct comparison of the two resin systems, both composites had similar fibre architecture, which included the following 14 layers of glass fibres: 8 layers of unidirectional fabrics (0°, 625 g/m^2), 4 quadriaxial fabrics (0°/+45°/90°/-45°, 835 g/m^2), and 2 outer layers of chopped strand mat (CSM, 300 g/m^2). This resulted in a fibre volume fraction of ~57%. After production, the composites were post-cured at 80 °C for a period of 12 hours. In the production of unsaturated polyester-based GFRP composites (GFRP-UP), Polylite 720-691 resin (50-54% isophthalic polyester and 46-50% styrene) was used, and this resin mixture included 1.5% (wt.%) of methyl ethyl ketone peroxide (MEKP, Ketanox B180). For vinyl ester-based GFRP composites (GFRP-VE), Derakane 411-200 (52% epoxy vinyl ester resin and 48% styrene) was used, and this resin mixture included 1.5% (wt.%) of MEKP (Ketanox B180), 0.025% (wt.%) of dimethylaniline, 0.3% (wt.%) of cobalt octoate (with 1% cobalt), and 0.025% (wt.%) of 2,4-pentanodione.

2.2. Ageing procedure

The ageing protocol used in this study was developed based on EN 13687-4:2002 and it considered the thermal variation applicable to various outdoor environments, i.e., covering a wide range of climates, for instance, in Lisbon (Portugal), Oslo (Norway) and Kuwait City (Kuwait), extreme negative air temperatures were recorded as -0.9 °C, -26.0 °C and -4.0 °C, respectively and extreme positive air temperatures were recorded as 44.0 °C, 34.6 °C and 52.1 °C, respectively. The temperature range of 75 °C (-15 °C to 60 °C) considered in this study is considerably higher, covering also the effects of temperature increase due to direct exposure to solar radiation. The thermal cycles, which were applied in a controlled environmental chamber (Aralab Testa CT 1000 EP20) are defined in Figure 1. Each cycle had a total duration of 12 hours, including (i) 1 hour of cooling from room temperature to -15 °C, (ii) 5 hours at -15 °C, (iii) 1 hour of heating from -15 °C to 60 °C (average rate of 1.25 °C/min), and (iv) 5 hours at 60 °C, with relative humidity of 50%. The composite laminates were subjected to a total of 300 thermal cycles. After each 100 cycles, batches of composite laminates were removed from the chamber and changes in their properties were assessed.

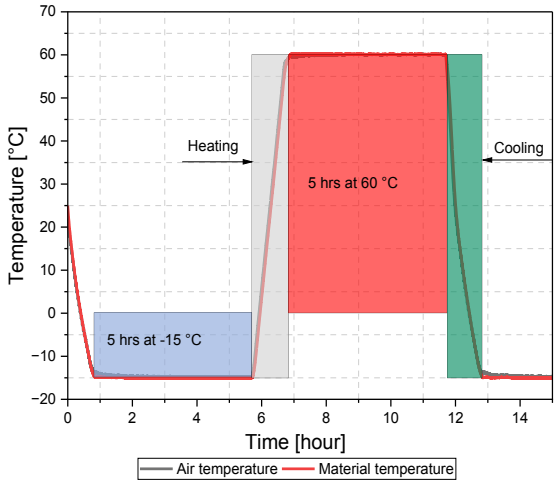


Figure 1. Phases of each thermal cycle

2.3. Test program

The test program first included tests on the unaged GFRP composites to evaluate different mechanical (tensile, compressive, flexural, in-plane shear and interlaminar shear) and thermomechanical (glass transition temperature, T_g) properties. After each 100 cycles, similar tests were repeated to assess the effects of thermal cycles in terms of retention of those properties (percentage of the initial values). For both composites, the mechanical and thermomechanical properties were determined along the longitudinal direction.

2.3.1. Thermomechanical tests

A dynamic mechanical analyser, model Q800 DMA (TA Instruments), was used to perform DMA tests, following the recommendations of the ISO 6721-1,5:2019. Each specimen had dimensions of 60 mm × 10 mm × 4 mm (thickness). During the tests, temperature ranged from 25 °C to 200 °C at a rate of 2 °C/min. Load was applied sinusoidally in a dual cantilever configuration, at a frequency of 1 Hz, with a strain amplitude of 15 µm. T_g was determined from the onset of the decay of the storage modulus (E') curve.

2.3.2. Mechanical tests

Tensile and compressive tests were performed in a universal testing machine (UTM) Instron 5989 (capacity of 600 kN), under displacement control, according to ISO 527-4:2021 and ISO 14126:1999, respectively. For both types of tests, specimens had rectangular shape, with dimensions of 300 mm × 25 mm × 6.5 mm (tension) and 153 mm × 25 mm × 6.5 mm (compression). A video extensometer (camera FLIR BFS-U3-51S5M-C; lens Fujinon HF25SA-1; software from MatchID—v2022.2) was used to measure axial strains.

Flexural, in-plane (IP) shear and interlaminar shear tests were carried out according to ISO 14125:1998, ASTM D5379/D5379M-19 and ISO 14130:1997, respectively. Rectangular shaped flexural and interlaminar shear test specimens had dimensions of 195 mm × 15 mm × 6.5 mm and 65 mm × 32.5 mm × 6.5 mm, respectively. Test specimens for in-plane shear tests also had rectangular shape, with dimensions of 76 mm × 19 mm, and comprised V-shaped notches at the mid-section section (on both sides); the main fibre direction was oriented parallel to the notch (i.e. the specimen height). Tests were performed in a UTM Instron 5982 (capacity of 100 kN), under displacement control. In IP shear tests, strains in the notch region were measured with the above-mentioned video extensometer.

3. Results and discussion

3.1. Initial characterization

Table 1 presents the initial properties of both types of composites. For most mechanical properties, differences between the two composites are relatively small. However, in general (except for tensile strength), GFRP-VE showed better performance than GFRP-UP. The most significant differences

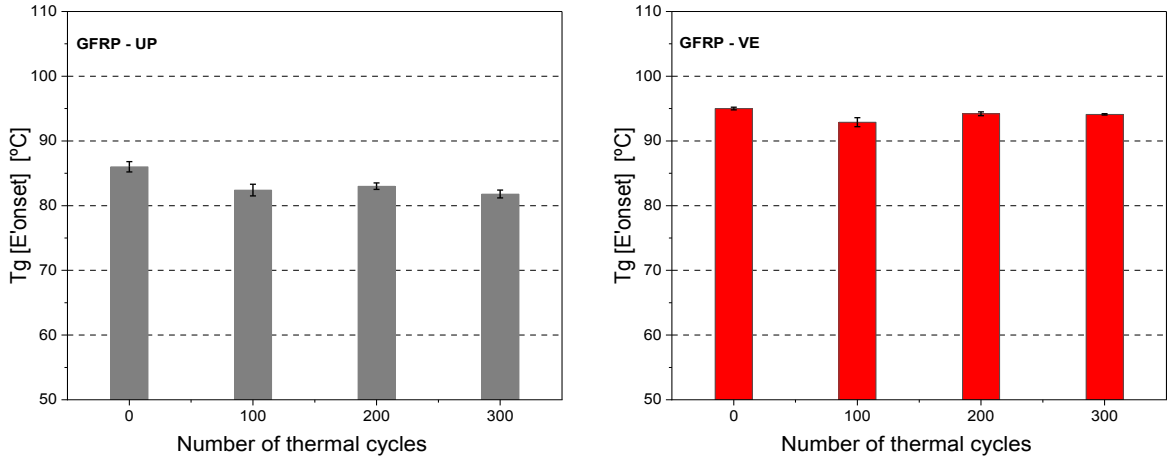
between the two composites refer to the compressive strength, which may result from a better performance of the VE resin system compared to its UP counterpart. Also, the glass transition temperature (T_g) of GFRP-VE is significantly higher than that of GFRP-UP.

Table 1. Initial mechanical properties and T_g of GFRP composites with UP and VE resins (average ± standard deviation)

Properties	GFRP-UP	GFRP-VE
Tensile strength, σ_t [MPa]	844 ± 30	811 ± 22
Tensile modulus, E_t [GPa]	33.1 ± 0.5	35.1 ± 1.5
Compressive strength, σ_c [MPa]	470 ± 33	556 ± 45
Compressive modulus, E_c [GPa]	35.8 ± 1.9	39.2 ± 2.0
In-plane shear strength, τ [MPa]	148 ± 4	158 ± 3
In-plane shear modulus, G [GPa]	5.0 ± 0.4	5.4 ± 0.6
Glass transition temperature, T_g [°C]	86.0 ± 0.8	95.0 ± 0.2

3.2. Glass transition temperature

Figures 2a) and 2b) illustrate the changes in T_g for GFRP-UP and GFRP-VE composites, respectively, due to the exposure to thermal cycles (TC). For both composites, TC caused slight reductions in their T_g, with the effect being more pronounced in GFRP-UP than in GFRP-VE. The maximum reductions in T_g were 4.2 °C (after 300 TC) and 2.1 °C (after 100 TC), respectively. In both composites, the highest reduction in T_g occurred during the first 100 TC, followed by a slight further reduction (in the case of GFRP-UP) or recovery (in the case of GFRP-VE). TC were reported to cause similar impact on the T_g of pultruded materials, with reductions of up to 7% for GFRP-UP and 3% for GFRP-VE [8,9].



a) b)

Figure 2. Changes in T_g: a) GFRP-UP, and b) GFRP-VE (error bars correspond to one standard deviation).

3.3. Mechanical behaviour

3.3.1. Tensile strength

Figures 3a) and 3b) present the variation of tensile strength for GFRP-UP and GFRP-VE composites, respectively, as a function of the number of thermal cycles (TC). Looking at these figures, it can be concluded that: (i) TC had no significant detrimental effect on the tensile strength of both composites; (ii) increasing number of TC did not cause a higher reduction in tensile strength; (iii) for GFRP-UP, the lowest retention (96.1%) was observed after 100 TC, which corresponded to a slight decrease in tensile strength (of a similar magnitude to the experimental scatter); in contrast, the tensile strength retention for GFRP-VE did not suffer any reduction; (iv) after 300 TC, the retention of tensile strength for GFRP-UP and GFRP-VE was 97.3% and 103.6%, respectively. These results indicate that both composites exhibited

excellent tensile strength retention, suggesting that TC did not affect the fibre-matrix bonding. Previous studies on the effects of TC on the tensile strength of pultruded GFRP-UP reported varying responses, including significant increase (by 11%) [8] and decrease (by 13%) [9], while results reported for pultruded GFRP-VE [8] were like those obtained here for vacuum infused materials.

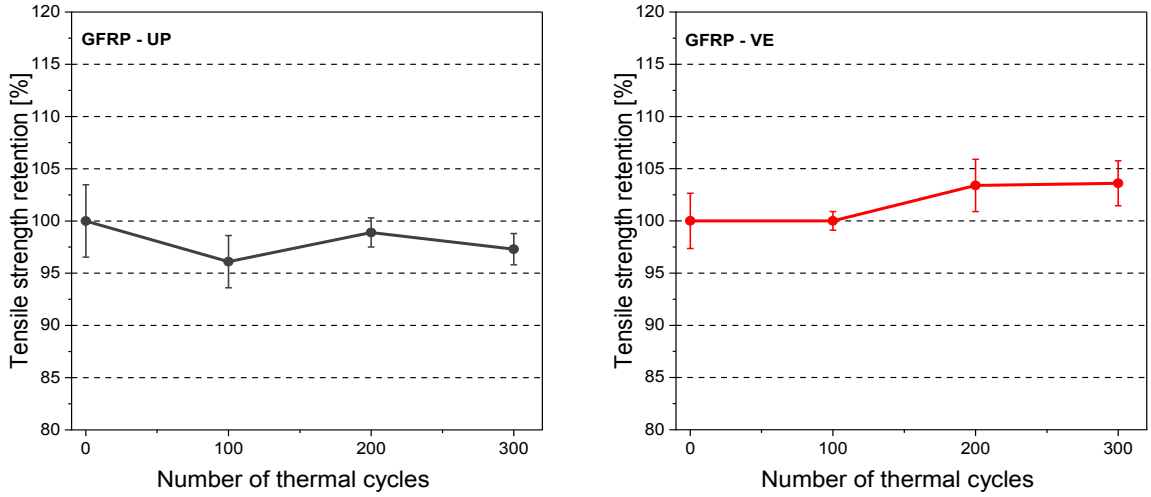


Figure 3. Tensile strength retention: a) GFRP-UP, and b) GFRP-VE (error bars correspond to one coefficient of variation, COV).

3.4.2. Compressive strength

The impact of TC on the compressive strength of GFRP-UP and GFRP-VE composites is depicted in Figure 4. The following trends were identified: (i) similar to tensile strength, the compressive strength was not significantly affected by TC; (ii) in fact, for most series, the composites showed negligible (GFRP-VE) to moderate (GFRP-UP) increase in compressive strength, which could indicate the occurrence of post-curing (although variations were of a similar order of magnitude to the experimental scatter); (iii) the maximum retention for GFRP-UP and GFRP-VE composites was 112.5% (after 300 TC) and 101.5% (after 200 TC); (iv) the lowest retention was 93.9% (after 300 TC) in GFRP-VE – again, this variation is of a similar magnitude to the experimental scatter, therefore it does not necessarily indicate the occurrence of damage such as fibre-matrix debonding or matrix micro cracking. It is worth mentioning that the compressive strength results presented relatively high scatter, due to the (well-known) inherent variability of this property.

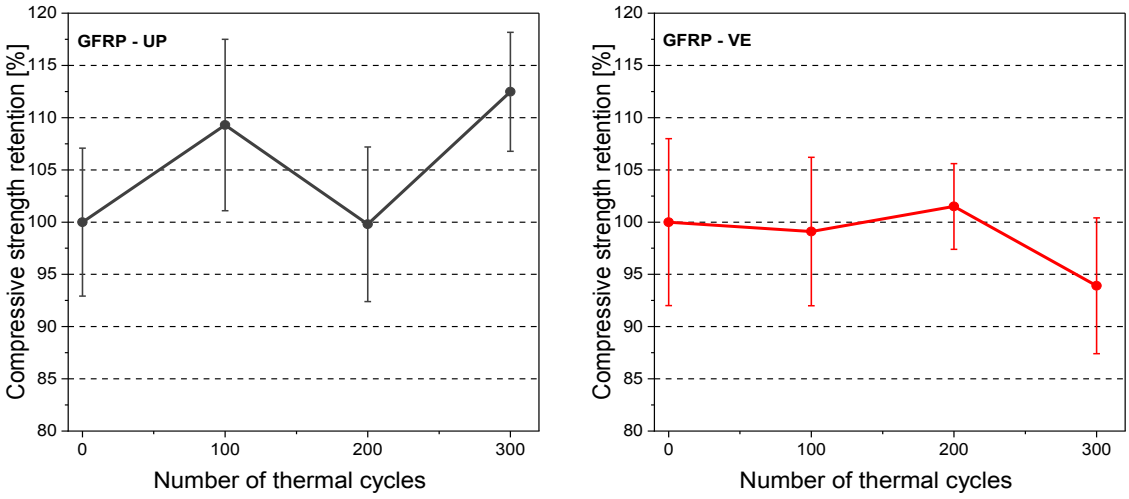


Figure 4. Compressive strength retention: a) GFRP-UP, and b) GFRP-VE (error bars correspond to one COV).

3.4.3. Flexural strength

For all number of cycles, flexural failure started at the upper laminae (in compression). Figures 5a) and 5b) show how the flexural strength varied throughout the ageing protocol, prompting the following remarks: (i) in comparison to tensile and compressive strengths, the flexural strength of GFRP-UP exhibited a more pronounced reduction, while GFRP-VE showed a similar level of retention, with only slight variations; (ii) the lowest retention values for GFRP-UP and GFRP-VE were 91% and 98%, respectively (after 200 TC), indicating that in the former composite some damage may have occurred (fibre-matrix debonding and micro cracking) – scanning electron microscopy (SEM) will be conducted to shade further light on this; (iii) the flexural strength of the composites presented moderate (GFRP-VE) to high (GFRP-UP) scatter; (iv) for both composites, the highest degradation in flexural strength was followed by an increase after 300 TC, with final retentions for GFRP-UP and GFRP-VE of 96% and 102%, respectively. Overall, these figures highlight, once again, a very good performance of both composites when subjected to TC, now in terms of flexural strength retention. Previous studies have reported much higher degradation (up to 16%) in the flexural strength of pultruded materials [8].

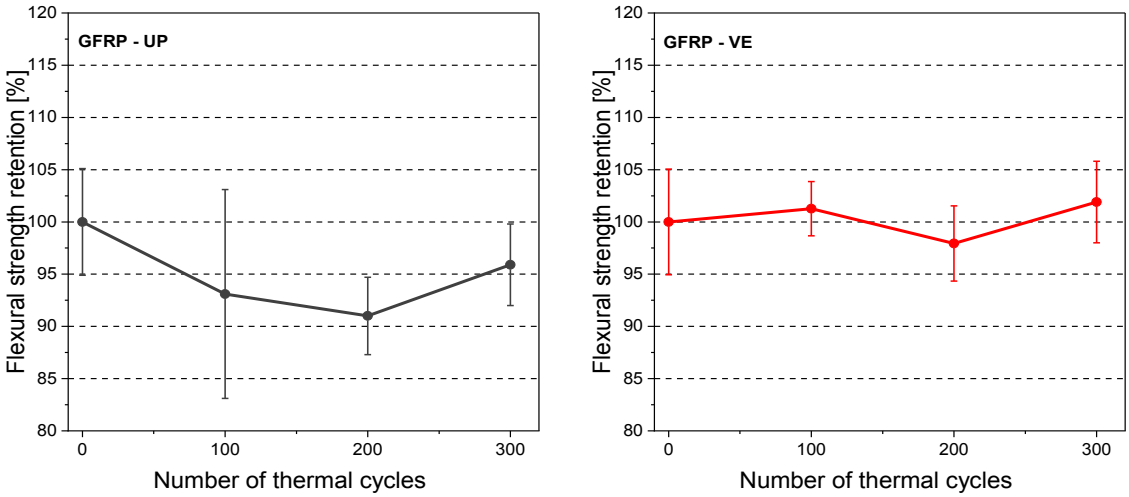


Figure 5. Flexural strength retention: a) GFRP-UP, and b) GFRP-VE (error bars correspond to one COV).

3.4.3. In-plane shear strength

The impact of TC on the in-plane (IP) shear strength is shown in Figures 6a) and 6b) for GFRP-UP and GFRP-VE composites, respectively. Here, the following trends are highlighted, largely similar to those previously mentioned for other properties: (i) both composites exhibited excellent resistance under TC, without relevant degradation of IP shear strength; (ii) retentions above 100% for various series (e.g., 104% after 200 TC for GFRP-UP and 107% after 100 TC for GFRP-VE) may indicate post-curing effects, although variations are often within the same order of magnitude as the experimental scatter. For these tests, it is worth noting the fibre architecture of the composite laminates, which included quadriaxial reinforcing mats, with fibres oriented at ±45°, thus resulting in a more fibre-dominated in-plane shear response. The excellent durability performance in terms of IP shear strength retention indicates that no relevant damage occurred in terms of fibre-matrix adhesion, even after 300 TC, in a manner similar to what was observed for tensile strength retention. Pultruded materials that were previously tested demonstrated excellent performance under exposure to TC, presenting similar retention of IP shear strength to the vacuum infused materials used in the current study [9].

3.4.3. Interlaminar shear strength

The interlaminar shear strength (ILSS) retention of GFRP-UP and GFRP-VE is presented in Figures 7. The ILSS of FRP composites depends on the adhesion at the interfaces between laminae, being also influenced by fibre bridging mechanisms. Figure 7 shows that the ageing protocol had no significant

adverse impact on the ILSS of the two composites. These results, together with the initial values of ILSS, are indicative of good fibre-matrix bonding, not significantly affected by exposure to TC, in agreement with previous observations in terms of tensile and IP shear strength retention. The changes in ILSS of GFRP-UP and GFRP-VE composites throughout the ageing protocol followed the same trend. The maximum retention was observed after 100 TC, with values of 111% and 112% for GFRP-UP and GFRP-VE, respectively. This may indicate the occurrence of post-curing. For both composites, the retention was followed by a continuous reduction until 300 FTC, for which retentions of 100% and 104% were obtained for GFRP-UP and GFRP-VE, respectively.

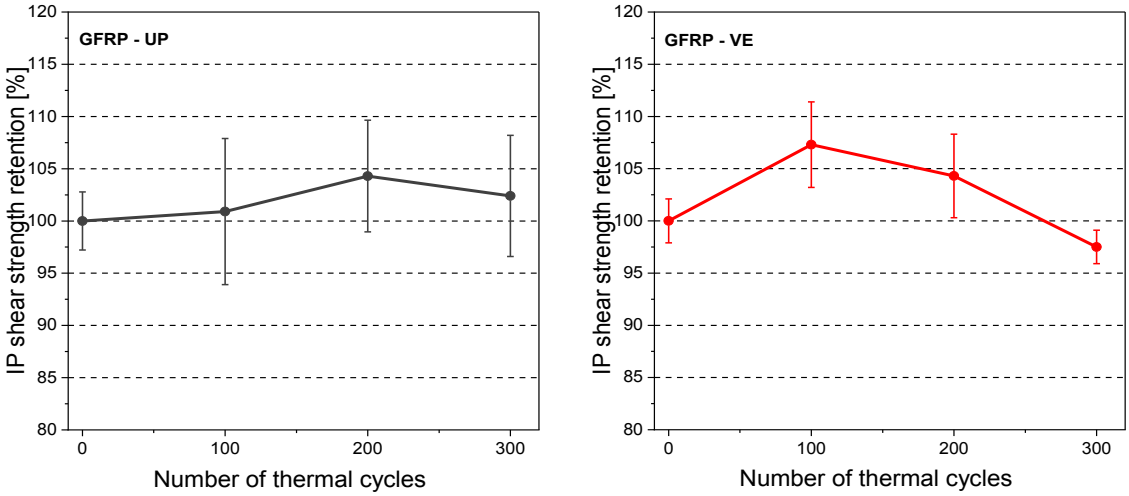


Figure 6. IP shear strength retention: a) GFRP-UP, and b) GFRP-VE (error bars correspond to one COV).

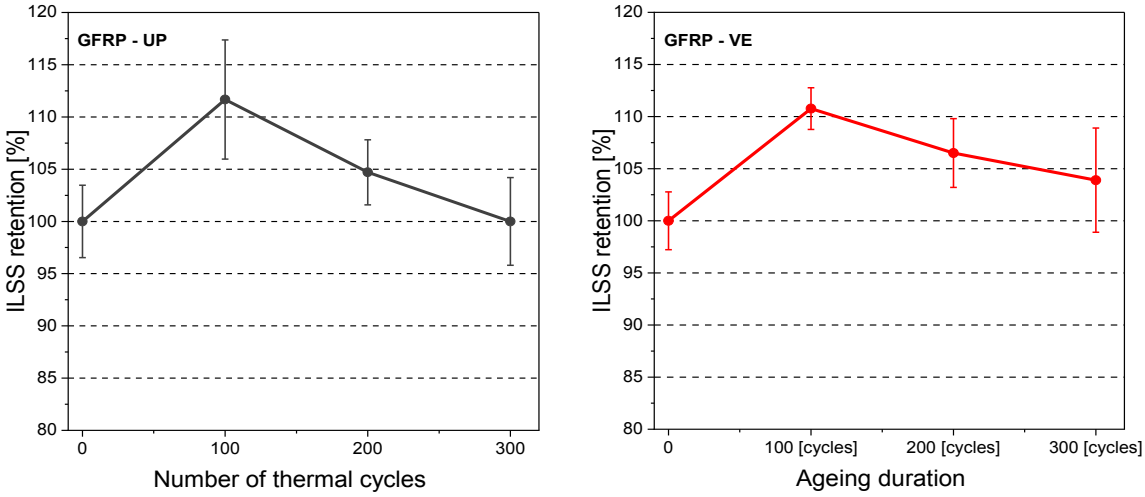


Figure 7. ILSS retention: a) GFRP-UP, and b) GFRP-VE (error bars correspond to one COV).

4. Concluding remarks

This paper presented a study about the effects of thermal cycles on the mechanical (tensile, compressive, flexural, in-plane shear and interlaminar shear strength) and thermomechanical (glass transition temperature, T_g) properties of relatively thick GFRP composites, produced by vacuum infusion, using two alternative resin systems, unsaturated polyester (GFRP-UP) and vinyl ester (GFRP-VE).

The T_g of both composites showed very slight changes due to exposure to thermal cycles, more pronounced in GFRP-UP, which exhibited a reduction from 86.0 °C to 81.8 °C. Most degradation occurred during the first 100 TC, which was followed by slight degradation (in the GFRP-UP) or recovery (in the GFRP-VE).

The mechanical characterization tests showed that exposure to the thermal cycles used in this study did not result in any significant negative impact on the mechanical properties of the composites, apart from flexural strength, for which the lowest retention for GFRP-UP was 91%. For all the other properties, the retentions were close to 100% and, some properties even increased (e.g., maximum ILSS retentions values of 112% and 111% for GFRP-UP and GFRP-VE, respectively), which may indicate the occurrence of post-curing. Overall, both composites presented excellent durability performance in response to thermal cycling, with no evidence of damage at the fibre-matrix interface or matrix micro-cracking. The variations in mechanical properties were not influenced by their inherent nature, which is to say that the properties were not influenced by whether the composite was matrix or fibre-dominated. Also, the two alternative resin systems demonstrated comparable retention of mechanical properties following thermal cycling.

Acknowledgements
The authors acknowledge the funding provided by Fundação para a Ciência e a Tecnologia (FCT) through project Durable-FRP (doi.org/10.54499/PTDC/ECI-EGC/4609/2020). The first author acknowledges the financial support provided by FCT through the PhD scholarship 2022.14644.BD. The first three authors acknowledge the funding provided by FCT to the CERIS research unit, through project UIDB/04625/2020 (doi.org/10.54499/UIDB/04625/2020). The last two authors acknowledge the funding provided by FCT to the ISISE research unit, through project UIDB/04029/2020 (doi.org/10.54499/UIDB/04029/2020) and the Associate Laboratory ARISE, under reference LA/P/0112/2020.

References

1. EMR Inc. (2022). Europe Composites Market Report and Forecast 2022-2027.
2. Bai, J. (Ed.): Advanced Fibre-Reinforced Polymer (FRP) Composites for Structural Applications, Woodhead Publishing, New Delhi, 2013.
3. Correia, J.R. (2015). “Fibre-Reinforced Polymer (FRP) Composites”. In: Materials for Construction and Civil Engineering: Science, Processing and Design (edited by F. Margarido, M.C. Gonçalves), Springer, 2015.
4. Sousa, J.M., Garrido, M., Correia, J.R. and Cabral-Fonseca, S. (2021). “Hygrothermal ageing of pultruded GFRP profiles: Comparative study of unsaturated polyester and vinyl ester resin matrices”. Composites Part A: Applied Science and Manufacturing, 140, 106193.
5. Bazli, M., Ashrafi, H., and Oskouei, A.V. (2016). “Effect of harsh environments on mechanical properties of GFRP pultruded profiles”. Composites Part B: Engineering, 99, 203-215.
6. Bazli, M., Ashrafi, H., Jafari, A., Zhao, X-L., Raman, R.K.S., and Bai, Y. (2019). “Effect of fibers configuration and thickness on tensile behavior of GFRP laminates exposed to harsh environment”. Polymers, 11(9), 1401.
7. Correia, J.R., Gomes, M.M., Pires, J.M., and Branco, F.A. (2013). “Mechanical behaviour of pultruded glass fibre reinforced polymer composites at elevated temperature: Experiments and model assessment”. Composite Structures, 98, 303-313.
8. Sousa, J.M., Correia, J.R., Cabral-Fonseca, S., and Diogo, A.C. (2014). “Effects of thermal cycles on the mechanical response of pultruded GFRP profiles used in civil engineering applications”. Composite Structures, 116, 720-731.
9. Grammatikos, S.A., Jones, R.G., Evernden, M., Correia, J.R. (2016). Thermal cycling effects on the durability of a pultruded GFRP material for off-shore civil engineering structures. Composite Structures. 153, 297-310.
10. Pritchard, G. (Ed.) (1998). Reinforced Plastics Durability. Woodhead Publishing Limited.
11. Karbhari, V.M. (Ed.). (2007). Durability of Composites for Civil Structural Applications. Woodhead Publishing.
12. Kodur, V.K., Bisby, L.A., and Foo, S.H. (2005). “Thermal behavior of fire-exposed concrete slabs reinforced with fiber-reinforced polymer bars”. ACI Structural Journal, 102 (6),799-807.
13. Jahani, Y., Baena, M., Barris, C., Perera, R., and Torres, L. (2022). “Influence of curing, post-curing, and testing temperatures on mechanical properties of a structural adhesive”. Construction and Building Materials, 324, 126698.

Quantifying the accuracy of different modelling techniques and element types to predict the structural performance of the DTU 12.6m wind turbine blade

Philipp U. Haselbach, Peter Berring, Anastasiia Larionova, Sergei Semenov,
Ana Margarida Antunes, Mohammad Hedayatzadeh and Kim Branner
Technical University of Denmark, Department of Wind Energy
Frederiksborgvej 399, 4000 Roskilde, Denmark
Email: phih@dtu.dk, Web Page: https://wind.dtu.dk/

Keywords: Wind turbine rotor blade, FEM, FEA, numerical modelling, conventional shell elements, continuum shell elements, layered solid elements, fibre composite structures, structural design, torsion

Abstract
Composite materials have gained widespread use in various engineering applications due to their unique combination of high strength, good fatigue resistance, lightweight and tailored properties. The accurate prediction of the mechanical behaviour of composite structures is essential for ensuring their structural integrity and optimal performance. Finite Element Analysis (FEA) is a widely employed numerical method for simulating the mechanical response of these structures. However, the choice of finite element type significantly influences the accuracy and reliability of the predictions.

This research employs a comprehensive validation approach, including experimental testing and benchmarking against numerical solutions, to assess the accuracy of predictions obtained from different finite element types. For this purpose, a wind turbine blade has been numerically and experimentally tested, subjected to flapwise, edgewise, torsional, and a combined flapwise-torsional load case.

The comparison reveals limitations in capturing the torsional behaviour of the wind turbine blade using shell elements, while solid elements perform well. This research provides valuable insights into selecting appropriate finite element types and modelling approaches for accurate and reliable predictions of the behaviour of composite structures commonly used in aerospace, automotive, and civil engineering applications.

1. Introduction

Over the last decades, wind turbines have significantly increased in size and capacity. With the increased capacity, the wind turbine rotor dimensions have also led to greater structural flexibility with its longer and slender wind turbine blades. Consequently, larger deflections and rotations occur, which presents a challenge for the accurate aeroelastic modelling of rotor blade structures. Nevertheless, the accurate and reliable prediction of the structural response of rotor blades is crucial for predicting the power output, stability, load conditions and structural integrity of wind turbines to ensure efficient and safe operation [1].

While current aeroelastic simulation tools for wind turbine applications typically rely on beam element models, higher fidelity models, such as conventional shell elements, continuum shell elements or layered solid elements, are used to discretise these complex curved, twisted and tapered structures made of fibre composite materials during the final structural design process.

2. Methodologies

This study investigates the reliability of different finite element types for predicting the mechanical behaviour of composite structures. The analysis encompasses various modelling techniques and investigates different element types to determine the accuracy of predicting the structural performance of the DTU 12.6m wind turbine blade [2].

Four distinct finite element formulations, namely beam elements, shell elements, continuum shell elements, and layered solid elements, are compared regarding their ability to capture the intricate behaviour of the DTU 12.6m wind turbine blade at full scale and predict its structural response under various loading conditions. The study focuses on quantifying the accuracy of different modelling techniques and element types to predict the blade's displacement and the ability to calculate its torsional performance numerically.

2.1 Numerical models

The numerical discretisation of the geometry of the DTU 12.6m wind turbine blade for all numerical models is derived from a basic structural blade model defined in DTU's in-house software; Blade Modelling Tool (BMT). The BMT allows the generation of different models originating from the same source, where the geometry, material properties and layup information are stored. Thus, a high level of conformity of the different models is ensured.

The commercial finite element package Abaqus/CAE is used as a pre/post-processing software with Abaqus/Standard as a solver [3] for this study. The entire blade geometry was modelled based on input data of 99 blade cross-sections generated by DTU's Wind HawtOpt2 [4] optimisation toolchain defining the aerofoil. These cross-sections describe the outer geometry (aerofoil) of the blade. For the discretisation with conventional shell elements, the aerodynamic blade profile is used as the reference surface, with the shell normal pointing from the reference surface towards the inner part of the blade. Simultaneously, an offset of half of the shell thickness from the shell's mid-surface is applied to ensure that the aerodynamic surface is the reference surface [5]. No offset is chosen for the shear webs, meaning that the geometrical middle of the shear webs is used as the reference surface. For the modelling approaches based on a volumetric geometry representation, cross-section curves are offset from the aerofoil according to the layup definition representing the laminates' thickness [6].

Each cross-section consists of 60 regions/sections to discretise the different cross-sectional properties and possible changes in the layup of the composite structure. The composite layup consists of 6 to 54 plies through the thickness, in which the material properties, layup and ply orientations are assigned automatically by the BMT. Subsequently, the 2D cross sections, defined by their aerofoil and the shear web shape at specific positions along the wind turbine blade span, are connected via a 3D lofting feature, creating a three-dimensional blade structure.

Figure 1 shows an overlay plot of a cross-section of the DTU 12.6m wind turbine blade, where both discretisation methods, volumetric (solid) and conventional shell elements with rendered shell element thickness, are compared. The plot clearly shows that the geometric discretisation only varies in areas where the layup thickness changes due to the different approaches of both methods to discretise the transition between individual sections.

The two beam models considered in the analysis, labelled "Abaqus beam" and "HAWC2", are also generated from the previously described cross-section geometries, from which mass and stiffness properties are calculated using the cross-sectional analysis tool BECAS [7]. Both beam models are based on Timoshenko beam elements – the "Abaqus beam" model uses B31 elements, and the "HAWC2" model uses the structural formulation from DTU Wind's aeroelastic code HAWC2, consisting of linear beam elements in a multibody floating frame of reference formulation [8].

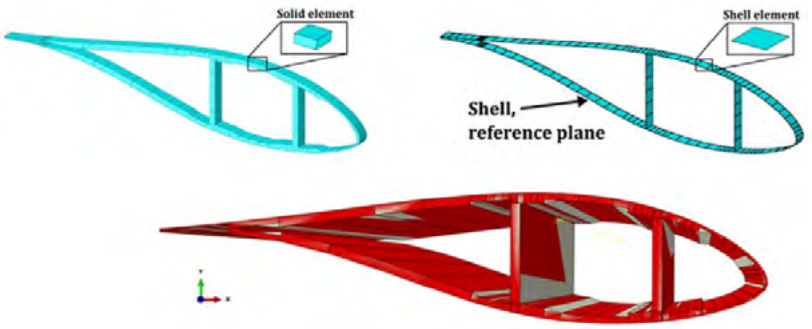


Figure 1. Cross-section of the DTU 12.6m wind turbine blade modelled with volumetric (solid) and conventional shell elements are compared by making an overlay plot of both discretisations (solid elements are grey and red, showing conventional shell elements with rendered thickness).

Figure 2 illustrates how the loads are applied to the volumetric and shell element models using coupling constraints. Here, the loads are applied to a central node (superior node) in the elastic centre calculated according to the computed elastic centre based on the strain gauge data from the Blade Property Extraction (BPE) test referring to SG (strain gauges) – explained in section 2.3 – or based on calculations according to the BECAS model (labelled BECAS) and distributed to coupled inferior nodes discretising the aerofoil geometry as shown in Figure 2. The coupled nodes' width reflects the wooden clamps used in the experimental setup to transmit the loads. The method aligns with previously conducted studies, as mentioned in [9].

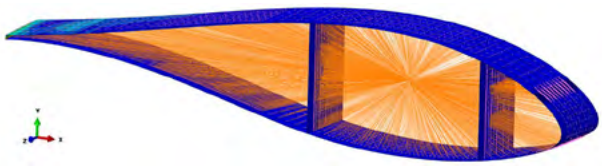


Figure 2. Blade model cross-section slice showing the coupling constraints connected to the shell nodes of the aerofoil with a central superior node in the elastic centre.

2.2 Experimental setup

The full-scale DTU 12.6m wind turbine blade experiments were conducted at the DTU Wind and Energy Systems' Large-Scale Facility at DTU Risø Campus. Here, the wind turbine blade was mounted on the test rig, as illustrated in Figure 3. Free-hanging weights were used to load the turbine blade at different locations depending on which load cases were tested. The weights were applied to metal load saddles with wooden clamps fitting the aerofoil geometry of the individual cross-sections attached to the blade, distributing the load over a cross-section. Load cells, installed between the load saddles and the weights, measured the loads applied to the blade. A digital image correlation (DIC) system based on an ARAMIS stereo camera system [10] was used to detect the translational and rotational displacement field at specific cross-sections along the blade. Moreover, strain gauges were installed to measure strains at specific locations.

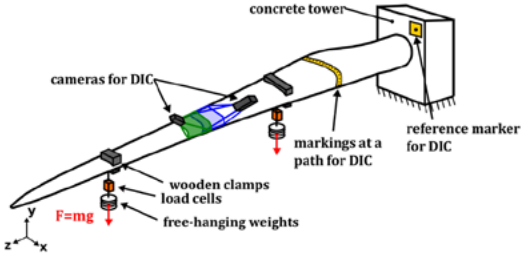


Figure 3. Illustration of the experimental setup for static test of the DTU's 12.6m wind turbine blade in suction-towards-pressure side (STP) loading (taken from [11]).

2.3 Blade property extraction method

At DTU Wind and Energy Systems, a method to determine the blade properties based on photogrammetry and/or strain measurement data has been developed. The blade property extractions (BPE) method allows for calculating the bending stiffness, the orientation of the principal axes, and the elastic centre of the wind turbine blade using standalone and combinations of different load scenarios as shown in Figure 4.

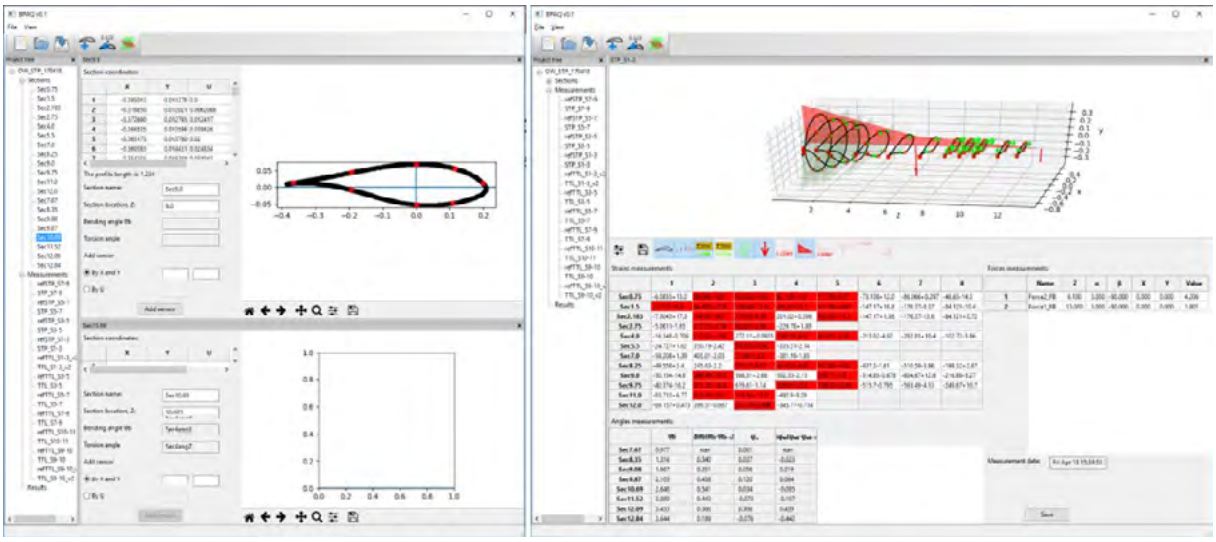


Figure 4. A Python-based code utilises cross-sectional strain measurements/displacement measurements to compute EI_x, EI_y, the principle bending axis's orientation and the elastic centre's location via the least squares method.

2.4 Test cases

A comprehensive validation approach is employed in this research, in which experimental tests are used to assess the accuracy of different finite element types to predict the response of the DTU 12.6m wind turbine blade. Various loading scenarios are considered, including flapwise, edgewise, torsional, and flapwise/torsional and combined flapwise/edgewise load cases. Some of these load cases are illustrated in Figure 5. Moreover, the eigenfrequencies/natural frequencies up to the first 10 natural modes of vibration obtained from an experimental test campaign are compared with numerical simulations of the different fidelity models, to benchmark the level of modelling/discretisation.

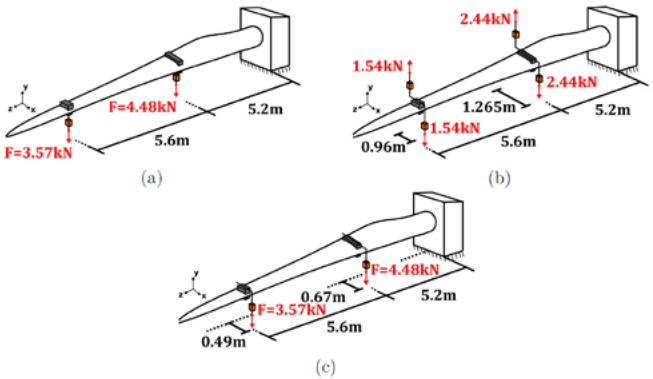


Figure 5. Illustrations of three load cases performed on the 12.6m turbine blade. (a) Suction-towards pressure side (STP) loading. (b) pure torsional (PT) loading. (c) Suction-towards pressure side with additional induced torsional (STP-tor) loading (taken from [11]).

3. Results and discussion

3.1 Blade properties:

Table 1 contains the centre of gravity and total mass of the blade calculated from the different finite element models and obtained experimentally. Here, it is evident that all numerical models deviate from the physical blade. The volumetric models underestimate the mass, whereas the conventional shell models (element type S4 & S8R) overpredict the mass. The reason for the higher mass of the shell model is inherent to the modelling approach, in which the aerodynamic blade profile is used as the top reference surface. Thus, a material overlap exists at the shear web and cap intersections, as well as in the leading and trailing edge regions, which can be visualised when rendering the shell element thickness. The beam elements underestimate the blade mass, partly because these models do not account for adhesive in the bondline of the trailing edge region (Figure 6). Due to the mass distribution difference, the centre of gravity along the blade span deviates. Consequently, the difference in centre of gravity and mass leads to differences in the eigenfrequencies, as shown in Figure 7.

Table 1: Blade properties

Element Type/Model	SC8R	C3D8R	C3D8I	S4	S8R	HAWC2/ BECAS	Abaqus beam	Test
Centre of gravity in m	3.48	3.48	3.48	3.23	3.23	3.379	3.379	3.59
Mass in kg	392.29	392.29	392.29	403.69	403.69	373.05	373.05	397.6

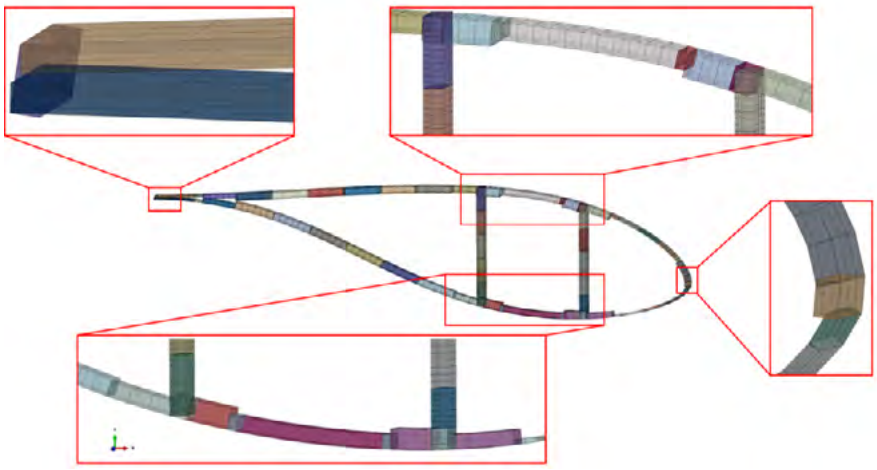


Figure 6. Blade cross-section rending of the shell element thickness visualises the material overlap at the shear web and cap intersections and in the leading and trailing edge regions.

3.2 Eigenfrequencies/natural frequencies

Figure 7 shows the eigenfrequencies of the DTU 12.6m blade based on experimental test data and numerical simulations using different element types for discretisation.

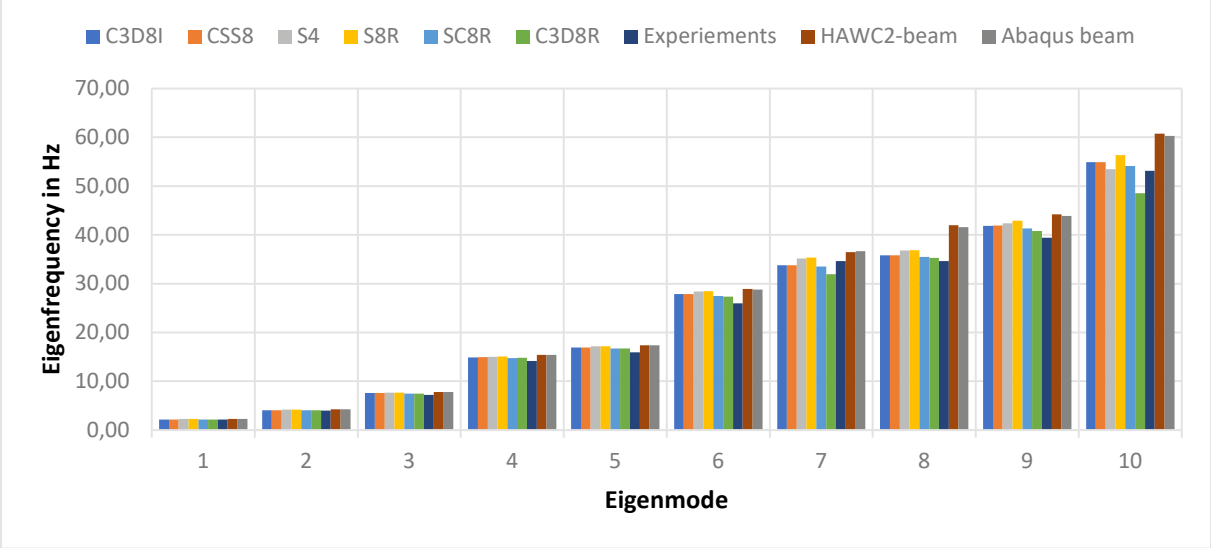


Figure 7. Eigenfrequencies of the DTU 12.6m blade based on experimental test data and numerical simulations using different element types for discretisation. Eigenmodes 1, 3, 5,6,8 and 9 have primarily a flapwise component, whereas mode 2 and partly mode 3 are edgewise mode shapes. Eigenmodes 7 and 10 are torsional modes.

3.3 Test cases

Flapwise, edgewise, torsional, and combined flapwise-torsional and flapwise/edgewise load cases have been considered numerically and experimentally. Strain gauge data and DIC measurements for the different load cases were utilised for computing the experimental cross-sectional displacements and rotations, as shown in Figure 8.

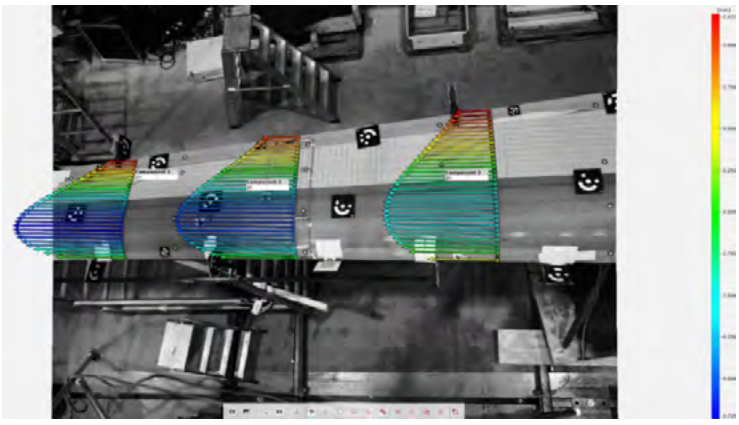


Figure 8. DIC Measurements from the STP load case utilised for computing cross sectional displacements and rotations.

The comparison study has concluded that, for predicting displacements, all numerical models show similar accuracy (see Figure 9), whereas the shell elements struggle to predict torsional response with the same accuracy as the volumetric elements do (see Figure 10). The beam elements are also less accurate than the volumetric discretisation via layered-solid or continuum shell elements.

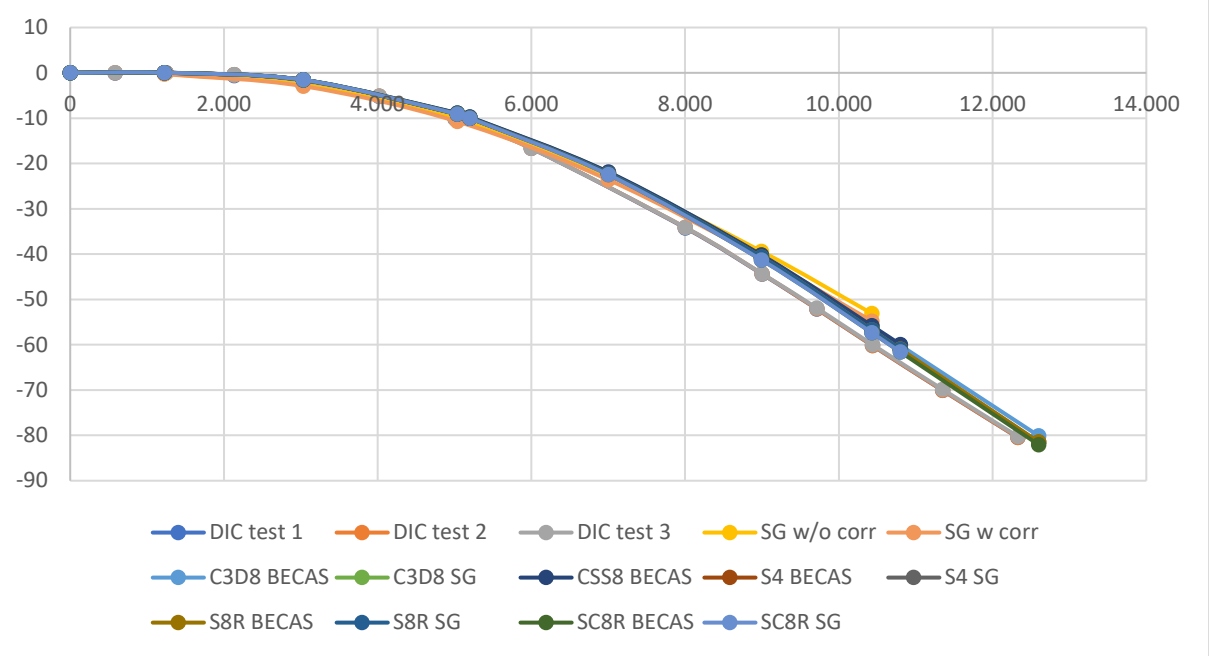


Figure 9. The depicted graphs show the displacement in y-direction in mm for the numerical predictions for different element types compared with the experimental test results for pure flapwise loading (STP load case).

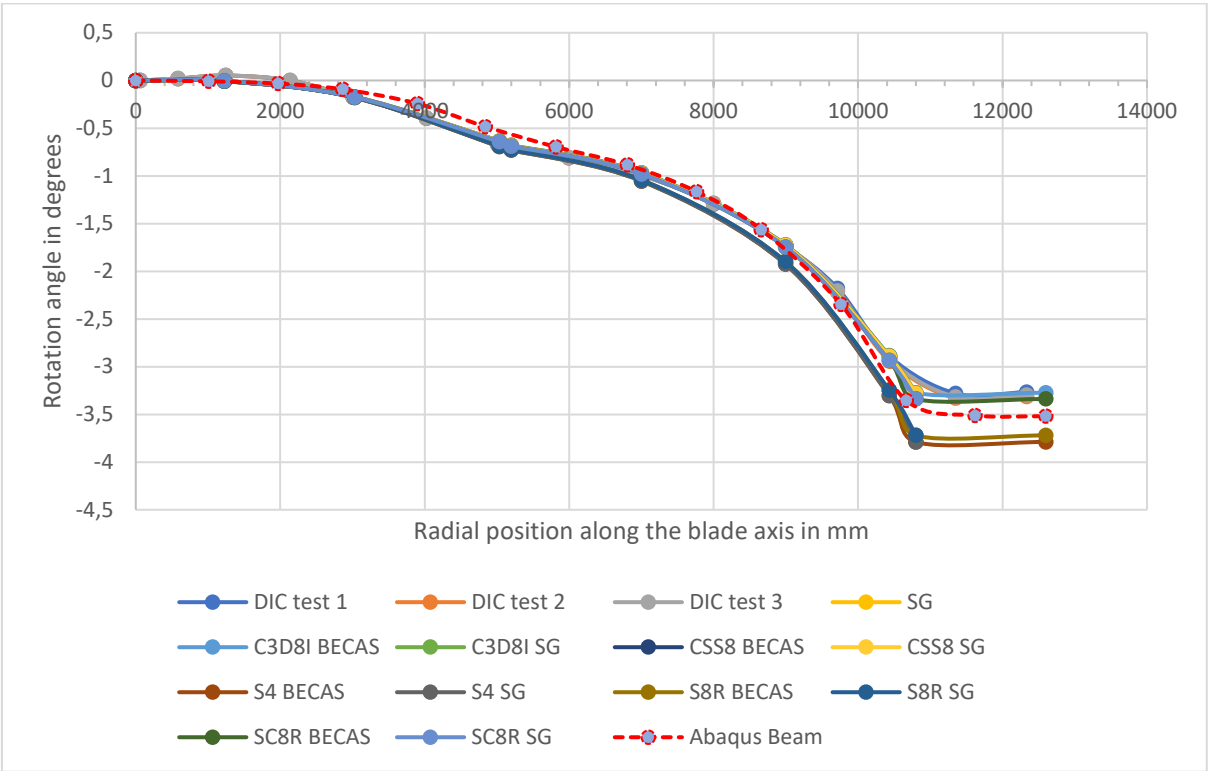


Figure 10. Rotation angle in degrees in spanwise direction (around the blade z-axis) showing numerical predictions for different element types compared with experimental for pure torsional loading (PT load case).

3. Conclusions

The comparison reveals limitations in capturing the torsional behaviour of the wind turbine blade using shell and beam elements, while solid elements perform well. These findings give valuable insights into selecting appropriate finite element types for accurate and reliable predictions of composite structures. While preliminary results have shown significant differences in computational time, more detailed and systematic investigations of factors such as mesh density and element size are needed to identify the sensitivity of each finite element type to these modelling parameters and evaluate the computational efficiency and accuracy of each finite element formulation, to provide a holistic understanding of their practical applicability.

Acknowledgements

We gratefully acknowledge the contributions of Christoffer Olesen Mæng and Simon Laulund Hummelgaard [8], who served as Master students assisting in post-processing data for this research. Their dedication and diligence contributed to the completion of this work. We also thank Energy Technology Development and Demonstration Programme (EUDP) for their support through the ReliaBlade - Improving Blade Reliability through Application of Digital Twins over Entire Life Cycle project with the grant-no. 64018-0068. EUDP is part of the Danish Energy Agency and funds work by enterprises and universities on demonstration of new green energy technologies. The support is gratefully acknowledged.

References

[1] Wang L, Liu X and Kolios A 2016 Renewable and Sustainable Energy Reviews 64 195–210
[2] Haselbach, P. U., Semenov, S., & Berring, P. (2020). DTU's blade research and demonstration platform. *IOP Conference Series: Materials Science and Engineering*, *942*(1), Article 012043. https://doi.org/10.1088/1757-899X/942/1/012043
[3] Abaqus Analysis User's Manual, SIMULIA User Assistance 2024, Dassault Systèmes (2024)
[4] Zahle, F. and Tibaldi, C. and Verelst, D.R. and Bak, C. and Bitsche, R.D. and Blasques, J.P.A.A., Aero-Elastic Optimization of a 10 MW Wind Turbine, 2015, Proceedings - 33rd Wind Energy Symposium, 201-223, American Institute of Aeronautics and Astronautics.
[5] Bitsche R.D. Modelling of Wind Turbine Blades with Abaqus, Composites Seminar, DTU Risø Campus Roskilde, Denmark, DTU Wind Energy - Technical University of Denmark (2015), pp. 1-14,
URL http://orbit.dtu.dk/files/106681216/Modelling_WTB_ABAQUS_Bitsche.pdf
[6] Blasques, J. P. (2012). User's Manual for BECAS: A cross section analysis tool for anisotropic and inhomogeneous beam sections of arbitrary geometry. Risø DTU – National Laboratory for Sustainable Energy. Risoe-R No. 1785(EN) ed.
[7] Kim, T., Hansen, A. M. and Branner, K. (2013). Development of an anisotropic beam finite element for composite wind turbine blades in multibody system. *Renewable Energy,* Volume 59: 172-183. doi: 10.1016/j.renene.2013.03.033.
[8] Philipp Ulrich Haselbach, An advanced structural trailing edge modelling method for wind turbine blades, Composite Structures, Volume 180, 2017, Pages 521-530, ISSN 0263-8223, https://doi.org/10.1016/j.compstruct.2017.08.029,
[9] Haselbach, P. U., Eder, M. A., and Belloni, F. (2016) A comprehensive investigation of trailing edge damage in a wind turbine rotor blade. *Wind Energy*, 19: 1871–1888. doi: 10.1002/we.1956.
[10] GOM Metrology, "ARAMIS Adjustable: The modular measuring system for 2D and 3D analyses," 1 2023.
[11] Christoffer Olesen Mæng, Simon Laulund Hummelgaard, Philipp Ulrich Haselbach, Peter Berring, Predicting torsional performance of wind turbine blades utilizing Finite Element analyses, February 2023, DTU Wind and Energy Systems.

Effects of continuous glass fiber incorporation to recycled PA6 polymer

Nahed HERMASSI[1], Yves GROHENS[2] , Noamen GUERMAZI[3] and Yves-Marie CORRE[4]

[1]Dupuy de Lôme Research Institute (IRDL),UBS Lorient, France
[1]Plateau technique Compositic (IRDL),UBS Lorient, France
Email: nahed.hermassi@univ-ubs.fr
[2]Dupuy de Lôme Research Institute (IRDL),UBS Lorient, France
[2]Plateau technique Compositic (IRDL),UBS Lorient, France
Email: yves.grohens@univ-ubs.fr
[3]LGME lab, National Engineering School of Sfax, University of Sfax, Sfax, Tunisia
Email: noamen.guermazi@enis.tn
[4]Dupuy de Lôme Research Institute (IRDL),UBS Lorient, France
[2]Plateau technique Compositic (IRDL),UBS Lorient, France
Email: yves-marie.corre@univ-ubs.fr

Keywords: Recycled PA6 matrix, Continuous Glass fiber , Fiber-matrix adhesion, Tensile fracture, Scanning electron microscopy (SEM).

Abstract
This study investigates the feasibility of producing composite materials by utilizing recycled plastic sourced from discarded fishing nets through a compression molding process. These composites would be further reinforced with unidirectional (UD) tape. The effects of processing parameters on mechanical properties were evaluated through tensile testing and SEM analysis. Three-layered tape composites exhibited noteworthy improvements over traditional semi-finished thermoplastics, particularly in tensile modulus and tensile strength except the elongation at break. Notable adhesion between fibers and matrix was seen even with minimal reinforcement. This finding underscores the potential for industrial application as locally reinforced plates, meeting standards in automotive or other industries. These results suggest a promising avenue for incorporating recycled plastic into composite manufacturing, offering both environmental advantages and superior mechanical properties.

1. Introduction

Environmental protection is currently a pressing concern across various industries, with a focus on curtailing carbon dioxide (CO2) emissions in order to combat climate change [1]. This is especially critical for the transportation sector, which ranks as the second largest contributor of anthropogenic greenhouse gas emissions in the European Union (EU). Road transportation alone accounts for approximately 93% of these emissions [2]. Due to recent regulations regarding CO2 emissions, the automotive sector is placing a significant focus on composite materials to further decrease the weight of the vehicle in the upcoming decade. Achieving lower vehicle mass primarily involves two key approaches: innovative design to optimize component performance and materials substitution, wherein traditional automotive materials like steel are replaced with lighter alternatives. Lighter metals such as aluminum and magnesium are increasingly utilized, along with high-strength steels in select applications. Polymer composite materials also hold promise for weight reduction in the automotive sector. Previous estimates indicate that extensive use of glass-reinforced polymers could lead to a 20–35% reduction in vehicle weight. The automotive industry has already gleaned benefits from composite materials in lower-performance applications over several decades.
Nowadays, thermoplastic matrices for semi-structural and structural applications are more and more gaining interest and material suppliers offer now a broad portfolio of semi-finished continuous fiber

thermoplastic products (organosheets, non-woven fiber consolidated sheets, unidirectional (UD) tapes...). Thermoplastic composites obviously show many advantages in several key manufacturing stages, especially a shorter processing time, easier assembly methods and good recyclability potential compared to thermoset composites. Notably, Wegmann in his study reveals that fully recycling aluminum, under ideal circumstances, yields substantial improvements in energy and CO2 balances, yielding optimal overall performance. Given the considerable energy and CO2 intensity associated with composite raw materials, integrating recycled materials into composite production is poised to reduce environmental impacts [3]. For example, repurposing old fishing nets into recycled PA6 and utilizing knitted glass fibers as fabric represent viable options [4]. So,This is our study as part of research work on composite materials.
Additionally, ongoing investigations into novel bio-based precursors for carbon fiber production and renewable resource utilization are underway within the automotive sector. Looking forward, leveraging cradle-to-cradle materials for sustainable products holds immense potential, contingent upon further advancements in recycling technologies to maximize efficacy.

2. Experimental

2.1. Materials

The tape utilized in this study consists of PA6/GF (6.35*35*0.2 mm), containing 60% weight of fibers. Table 1 presents the properties of the individual tape layer. Additionally, for purposes, a recycled PA6 derived from discarded fishing nets Fil & Fab FRANCE industry was selected to undergo processing and testing under the same conditions.

Table 1. Materials properties in this study.

Specimen Type	*E* (GPa)	*Rm* (MPa)	*A*(%)
UD Tape PA6/GF	74	2500	3.38
RECYCLED PA6	2.6	45	1.73

2.2. Compression molding

Parts were processed in an industrial way and with a large mold press with dimensions of 300x300 square meters, hrough four distinct stages:

1. Cutting the tape 35 mm.
2. Stacking and fixing the tape into the plate at 0°.
3. Transferring to press .
4. Thermoforming and part removal.

Industrial 50MT press can be observed on Figure 1 (a) and the resulting part is presented on Figure 1 (b). For each part, specimens were cut in the vertical area and prepared in the same conditions.



Figure 1. (a) Press Machine, (b) Part Molding .

13 layers of GF were 0° stacked and thermoformed (see Figure 1(b). These structures close to sandwich composite are investigated in this study. The 0° axis is defined as the main reinforced fiber axis for all composites. Then the stacked tape layers were dried by the oven for 24 h in 80°C.
The impact of molding temperature was examined while keeping process parameters and mold pressure constant (25 bars) across three distinct values: 230°C, 240°C, and 250°C. Besides, the effect of molding pressure was studied at constant process parametre and mold temperature (230°C) for 3 different values: 15, 20 and 25 bars [5]. Processing parameters of the press : heating, pressuring and thermoforming steps are summarized in Table 2.

Table 2. Processing parameters in this study

Processing Parameter	*Set-up condition*
Pre-Heat	3
Pressing Time	1
Full Pressing	2
Direct Cooling	10

2.3. Characterization

Tensile Test using MTS machine with a load cell of 5 kN. Those tests were conducted at a cross-head speed of 1 mm/min at room temperature by following the EN ISO 527 standard.
This morphological investigation is specifically centered on the SEM (Scanning Electron Microscope; Jeol JSM 6460LV) analysis applied to recycled PA6 materials reinforced with different percentages of tape. Employing SEM facilitates detailed imaging, enabling researchers to explore the subtle effects of reinforcement on the material's morphology. The specimens underwent coating with micrometer-thick layers of metallization, such as gold coating.

3. Results and discussion

3.1.Mechanical characterization

3.1.1.Effect of the process parameter on the mechanical behavior of recycled PA6

Figure 2 shows a conventional curve of recycled PA6 based on fishing nets after tensile testing [6], [7]. The x axis of this line chart represents the strain in percentage while the stress in MPa appears on the y axis. As you can see the green color indicated 230°C, the red color represented 240°C and 250°C represented by the black color. It may be clearly seen that T1 and T2 are the most successful temperatures for processing the recycled PA6 in compression molding. However T3 went up considerably then it dropped off in a weak value of stress-strain. T1 reached a peak before falling dramatically in contrast T2 continued to rising then it fell slightly.

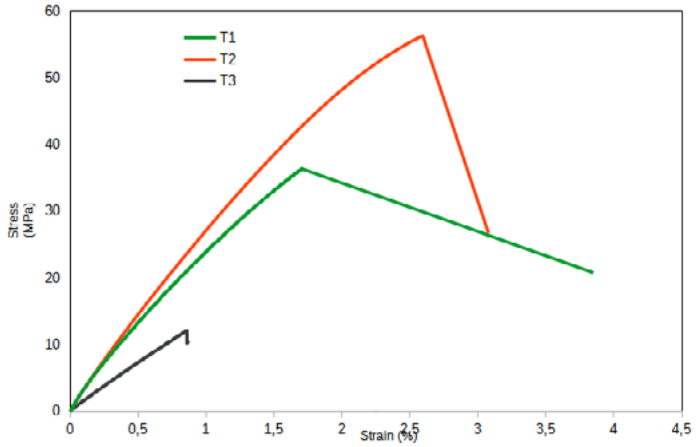


Figure 2. Effects of the temperature on the mechanical properties of the Recycled PA6 FN

Figure 3 represents the bar chart of the mechanical properties of the Recycled PA6 FN fig (a) indicating the tensile modulus, fig (b) represents the tensile strength and fig (c) shows the elongation at Break. The graph compared the different movements of the different mechanical properties. Fig 3 outlines that the best temperature for processing was the 240°C for both tensile strength and elongation at break However there's no significant difference in the modulus. Moreover, it appears that the recycled polymer is significantly affected at the temperature of T3,250°C.

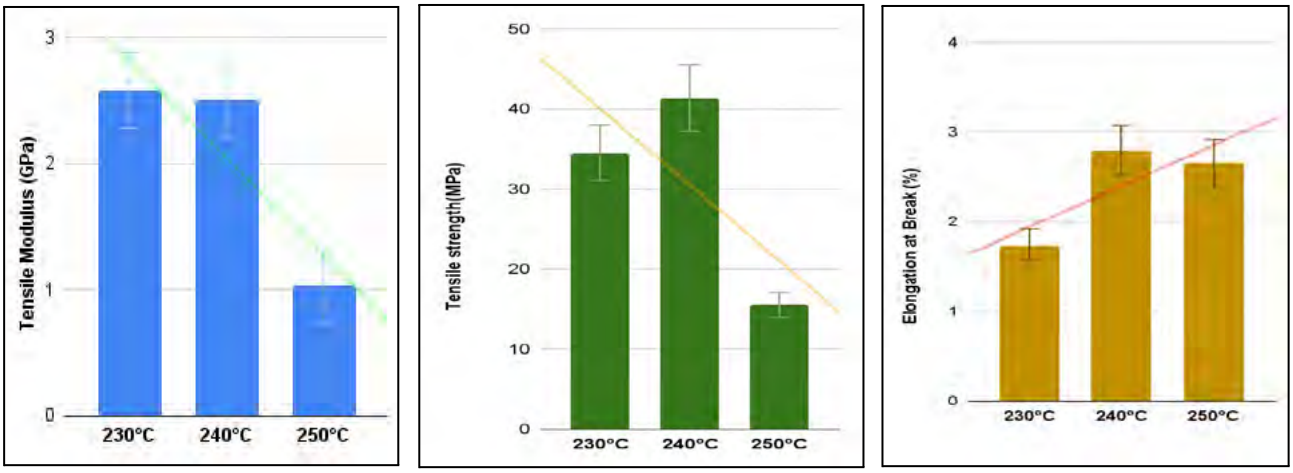


Figure 3. Effects of the temperature on the mechanical properties of the Recycled PA6 FN (a) Tensile modulus (b) Tensile strength(c) Elongation at Break

Table 2 includes the different values of modulus strength and elongation at break of the three process temperatures. As we can say 240°C is the best temperature to choose for processing a recycled PA6 with 2.51 GPa modulus, 41.38 MPa strength and 2.80 % of elongation at break. However T1 also has good properties with a slightly higher modulus (2.58 GPa) against T2.

Table 3. Effects of the temperature on the mechanical properties of he Recycled PA6 FN

Plastics	*E* (GPa)	*Rm* (MPa)	*A*(%)
Recycled PA6 FN T1	2.58 (±0.281)	34.52 (±5.65)	1.74 (±0.34)
Recycled PA6 FN T2	2.51 (±0.35)	41.38 (±11.85)	2.80 (±1.55)
Recycled PA6 FN T3	1.04 (±0.77)	15.53 (±2.,86)	2.65 (±0.392)

Figure 4 depicts a conventional curve of tensile test for a recycled PA6. It was clear to see a different behavior between the three pressure uses. At steady temperature (230°C), P2 under 20 bars of pressure increased vastly then it leveled out at a high value of stress of superior 40 MPa. However, both P1 at 15 bars and P3 at 25 bars exhibit similar behavior, they reached a peak P1 leveled out and P3 dropped off considerably Despite this, P1 is identified as the pressure level associated with a more stable behavior of recycled PA6 against P3.

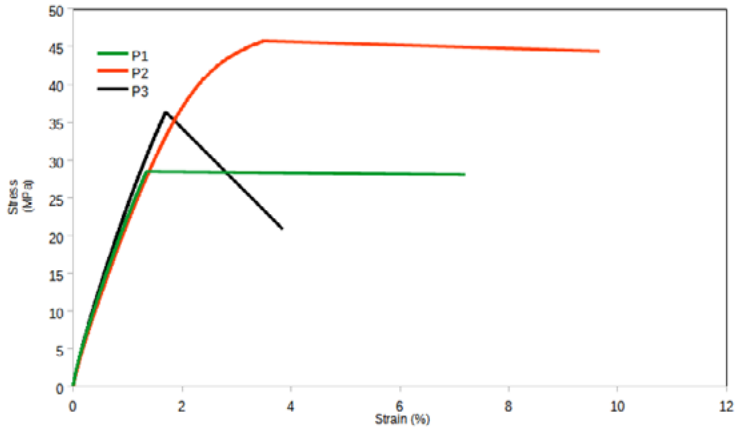


Figure 4. Effects of the Pressure on the mechanical properties of he Recycled PA6 FN

It was clearly observed (Fig 5) that 20 bars was the best pressure used in this study with a high level of strength and elongation at break against a moderate difference between the three pressure levels in modulus (see figure 5). P1 and P3 have a slight difference in modulus and strength and a considerable variation in elongation.

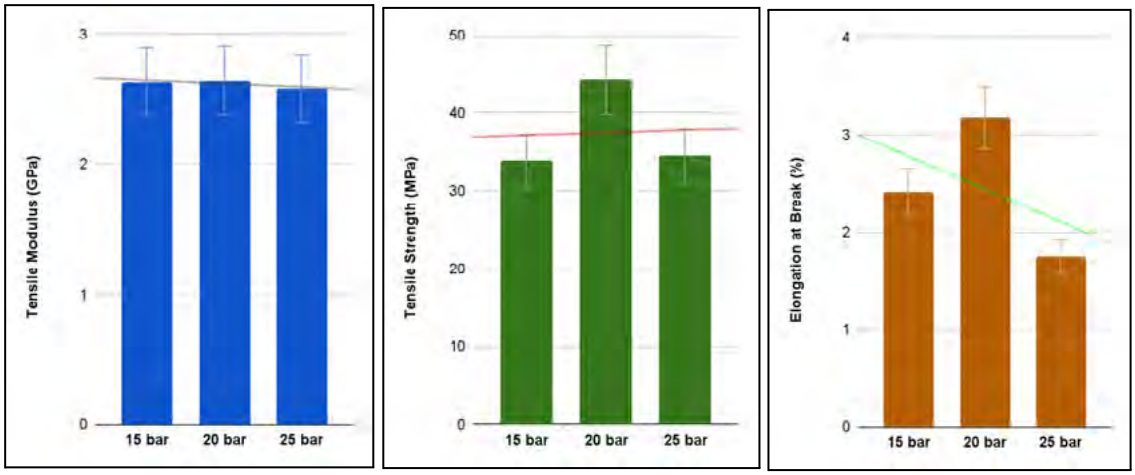


Figure 5. Effects of the pressure on the mechanical properties of the Recycled PA6 FN (a) Tensile modulus (b) Tensile strength (c) Elongation at Break.

Table 3 lists the different values of modulus strength and elongation at break of the three process pressures. It was evident that 20 bars is the best pressure for processing a recycled PA6 with 2.64 GPa modulus, 44.24 MPa strength and 3.17 % of elongation at break. However P1 has a slightly lower modulus with 2.63 GPa, strength and elongation at 33,86 MPa , 2.41 respectively. In his turn P3 has not a big difference in his mechanical properties in comparison to P1 or even P2. We can conclude that unlike temperature variation, pressure changes from 15 bars to 20 to 25 bars do not significantly affect mechanical properties. Additionally, the interval to explore lies between 20 and 25 bars.

Table 4. Effects of the pressure on the mechanical properties of he Recycled PA6 FN

Plastics	*E* (GPa)	*Rm* (MPa)	*A*(%)
Recycled PA6 FN P1	2.63 (±0.11)	33.86 (±6.13)	2.41 (±1.44)
Recycled PA6 FN P2	2.64 (±0.073)	44.24 (±4.99)	3.17 (±0.58)
Recycled PA6 FN P3	2.58 (±0.281)	34.52 (±5.65)	1.74 (±0.34)

3.1.1.Effects of continuous glass fiber incorporation to recycled PA6 polymer

Figure 6 shows a stress-strain curve of four specimens (red: tape rate 4 wt % , yellow : tape rate 8 wt %, green : tape rate 12 wt %, blue : reference with 0 wt% tape rate). the reinforced materials has increased considerably however the unreinforced material rose moderately.

It was evident that there was minimal effect, in variation of the percentage of tape, on the materials, except for a notable impact on resistance at the 12% tape level.

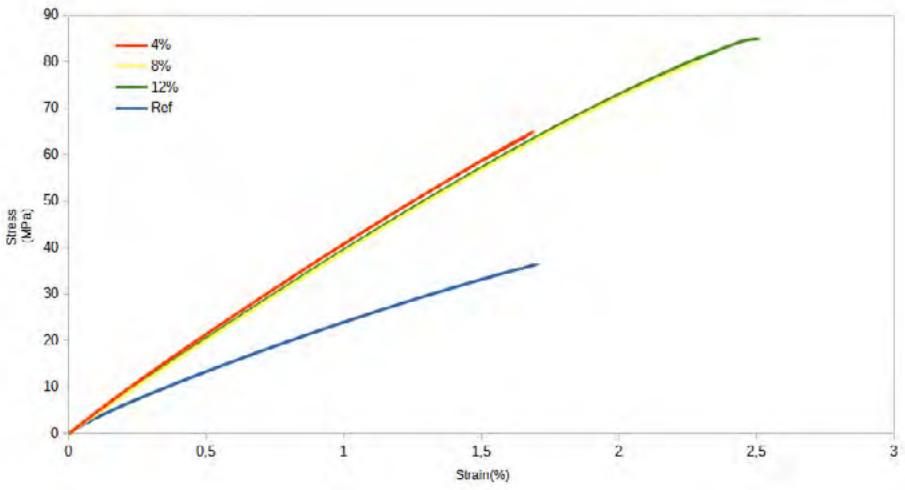


Figure 6. Effects of the tape rate on the mechanical properties of he Recycled PA6 FN

It was clear when we raised the percentage of tape there's increase in modulus and strength. However the elongation at break has different behavior. The augmentation of tape rate from 0% to 4% the elongation rose moderately. From 4% to 12% the properties have decreased significantly (see fig 7)

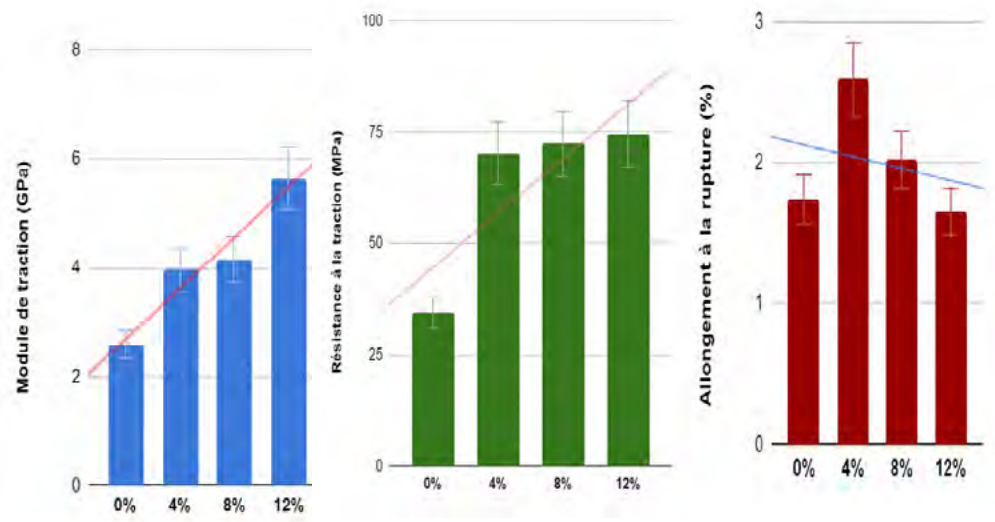


Figure 7. Effects of tape ratio on the mechanical properties of the Recycled PA6 FN

Table 4 lists the different values of the mechanical properties (E(GPa),Rm(MPa) and A(%)). The modulus and strength have increased depending on the percentage of reinforcement from 2.58 GPa to 5.64 GPa , from 34.52 MPa to 74.65 MPa respectively . However the elongation at break reached his maximum at 4 wt% by 2.59 % After that (for 8wt% and 12wt%) it declined to 1.65%. The two levels of tape reinforcement (8wt% , 12 wt%) significantly affect the modulus which increased by 118.6% , and the elongation which decreased by 5.17% respectively. However the tensile strength increased vastly for the first tape layer of 4 wt% by 103.5% and then increased a little between 4 wt % and 12 wt % with 5.7%. This may be due to the porosity and imperfection in the materials after reprocessing and manipulating the tape into plates.

Table 5. Effects of tape percentage on the mechanical properties of he Recycled PA6 FN

Plastics	*E* (GPa)	*Rm* (MPa)	*A*(%)
RECYCLED PA6	2.58 (±0.281)	34.52 (±5.65)	1.74 (±0,34)
PA6GF, 4wt%	3.96 (±0.84)	70.25 (±7,25)	2.59 (±0.3)
PA6GF, 8wt%	4.15 (±0.38)	72.26 (±6.34)	2.02 (±0.86
PA6GF, 12wt%	5.64 (±0,63)	74.65 (±7.33)	1.65 (±0.54)

3.2.SEM analysis

Fig 8 shows the SEM images of the fractured surface of the molded PA6 in different temperatures (230°C, 240°C and 250°C and different pressures (15 bars, 20 bars and 25 bars). The fractured surface of PA6 seems to be smooth and shows no apparent sign of plastics flowing, indicative to brittle failure of homogenous materials.

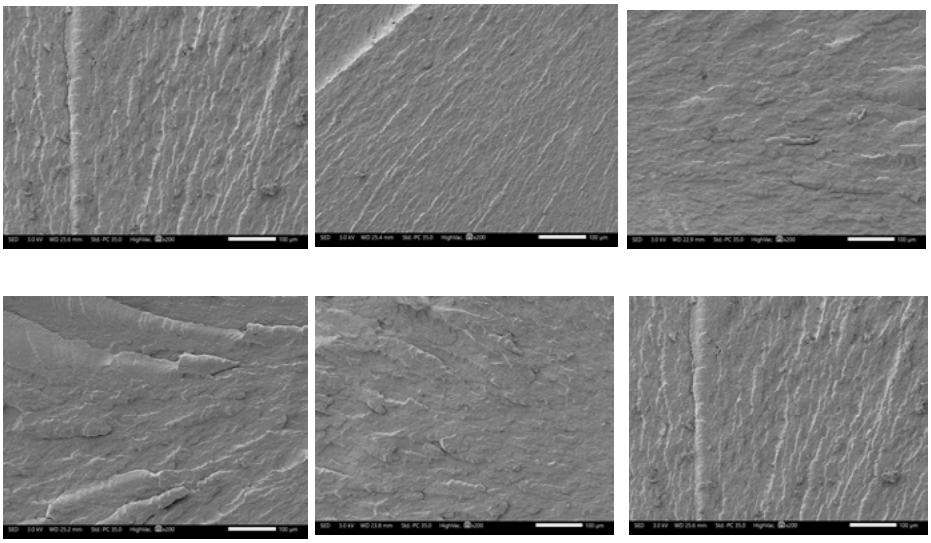


Figure 8. SEM images on Fracture surface of PA6 FN of different temperature (a) 230°C, (b) 240°C and (c) 250°C and different pressures (d)15 bars, (e) 20 bars and (f) 25 bars

To examine the microstructure and evaluate fiber-matrix adhesion, SEM examinations were conducted on tensile fracture surfaces of PA6/GF-containing specimens with varying weight percentages (4% 8% 12%) (refer to Fig.9.).
In instances of wt% PA6 reinforced with glass fiber, the matrix experienced restricted deformation, resulting in a brittle fracture.
Fiber debonding was observable (see Fig 9(a)), leaving a dark ring at the interface, consistent with findings in the study by many authors [8]. They attributed the presence of dark rings to the localized matrix deformation around fibers post-debonding. However, with most fibers being pulled out during deformation, the matrix stayed connected to the fibers, resulting in failure at the fiber-matrix interface. The surface of the fiber appeared clean and smooth , consistent with adhesion results indicating a lack of interaction between PA6-treated glass fibers. The figure 9 (b) shows the absence of the pulled-out fibers except for a few fibers. Moreover it revealed that failure predominantly took place within the matrix. Fig 9 (c) details the presence of a polymer sheath on fiber surfaces suggesting strong interactions , substantiated by differences in physical properties, notably density, in the proximity of the fiber surface compared to the bulk polymer.
The clear failure at the matrix emphasizes the importance of the interphase, highlighting a robust interfacial bond between the PA6 matrix and glass fibers in the composite material.

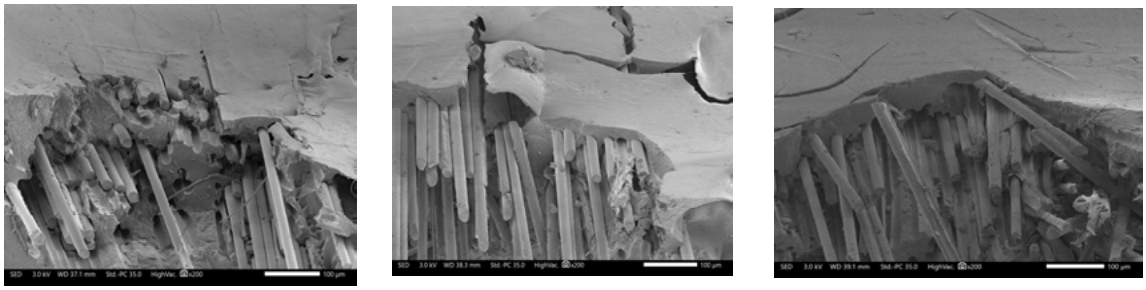


Figure 9. SEM images on Fracture surface of PA6/GF (a)at 4% , (b) 8% and (c) 12% weight ratio of reinforcement

4. Conclusions

This paper describe the main important advancement released still now for developing and characterizing a continuous glass fiber recycled thermoplastics polymers The main conclusion can be :

- There's always a big effect of the variation of temperature on the tensile properties of the recycled polymer PA6 FN
- In contrast there's no evident effect of the pressure on the recycled materials PA6 FN
- By addition of the different percentage of tape : the modulus rose slightly from 2.58 to 5.64 GPa , the strength increased significantly from 34.52 to 74.65 MPa and finally the elongation at break decreased slightly from 1.74 to 1.65%.

Acknowledgments
A paragraph (optional) at the end of the paper, before the references, can be used for acknowledgements.

References

[1] A. J. McMichael, R. E. Woodruff, et S. Hales, « Climate change and human health: present and future risks », *The Lancet*, vol. 367, nº 9513, p. 859-869, mars 2006, doi: 10.1016/S0140-6736(06)68079-3.
[2] G. Fontaras, N.-G. Zacharof, et B. Ciuffo, « Fuel consumption and CO 2 emissions from passenger cars in Europe – Laboratory versus real-world emissions », *Prog. Energy*

Combust. Sci., vol. 60, p. 97‑131, mai 2017, doi: 10.1016/j.pecs.2016.12.004.
[3] K. Kawajiri, M. Kobayashi, et K. Sakamoto, « Lightweight materials equal lightweight greenhouse gas emissions?: A historical analysis of greenhouse gases of vehicle material substitution », *J. Clean. Prod.*, vol. 253, p. 119805, avr. 2020, doi: 10.1016/j.jclepro.2019.119805.
[4] S. Wegmann *et al.*, « A life cycle analysis of novel lightweight composite processes: Reducing the environmental footprint of automotive structures », *J. Clean. Prod.*, vol. 330, p. 129808, janv. 2022, doi: 10.1016/j.jclepro.2021.129808.
[5] S. Liang, H. Nouri, et E. Lafranche, « Thermo-compression forming of flax fibre-reinforced polyamide 6 composites: influence of the fibre thermal degradation on mechanical properties », *J. Mater. Sci.*, vol. 50, nº 23, p. 7660‑7672, déc. 2015, doi: 10.1007/s10853-015-9330-4.
[6] F. Lv, D. Yao, Y. Wang, C. Wang, P. Zhu, et Y. Hong, « Recycling of waste nylon 6/spandex blended fabrics by melt processing », *Compos. Part B Eng.*, vol. 77, p. 232‑237, août 2015, doi: 10.1016/j.compositesb.2015.03.038.
[7] M. A. Abdelwahab, B. P. Chang, A. K. Mohanty, et M. Misra, « Waste valorization in sustainable engineering materials: Reactive processing of recycled carpets waste with polyamide 6 », *Polym. Test.*, vol. 114, p. 107681, oct. 2022, doi: 10.1016/j.polymertesting.2022.107681.
[8] G. Ozkoc, G. Bayram, et E. Bayramli, « Effects of polyamide 6 incorporation to the short glass fiber reinforced ABS composites: an interfacial approach », *Polymer*, vol. 45, nº 26, p. 8957‑8966, déc. 2004, doi: 10.1016/j.polymer.2004.10.026.

EFFECTS OF PLY THICKNESS AND 0-DEGREE LAYER RATIO ON FAILURE MODE AND STRENGTH OF NOTCHED COMPOSITE LAMINATES: EXPERIMENT AND HIGH-FIDELITY SIMULATION

Ryo Higuchi[1], Xin Lu[2], Ryoma Aoki[3], Tomohiro Yokozeki[4] and Tomonaga Okabe[5]

[1] Department of Aeronautics and Astronautics, The University of Tokyo, 7-3-1 Hongo, Bunkyo-ku, Tokyo, 113-8656, Japan
Email: higuchi@aastr.t.u-tokyo.ac.jp
[2] Department of Aeronautics and Astronautics, The University of Tokyo, 7-3-1 Hongo, Bunkyo-ku, Tokyo, 113-8656, Japan
Email: xinlu@g.ecc.u-tokyo.ac.jp
[3] Department of Aeronautics and Astronautics, The University of Tokyo, 7-3-1 Hongo, Bunkyo-ku, Tokyo, 113-8656, Japan
Email: r.aoki@aastr.t.u-tokyo.ac.jp
[4] Department of Aeronautics and Astronautics, The University of Tokyo, 7-3-1 Hongo, Bunkyo-ku, Tokyo, 113-8656, Japan
Email: yokozeki@aastr.t.u-tokyo.ac.jp
[5] Department of Aerospace Engineering, Tohoku University, 6-6-01, Aza-Aoba, Aramaki, Aoba-ku, Sendai, Miyagi, 980-8579, Japan
Email: tomonaga.okabe.a8@tohoku.ac.jp

Keywords: Thin-ply composites; Open-hole tension; Virtual testing, Nonlinear finite element method

Abstract
The aim of this study is to examine the effect of ply thickness and 0-degree ply ratio on the strength of the thin-ply composites in the open-hole tension (OHT) tests. To this end, we carried out OHT tests of a variety of layups having different ply thicknesses and 0-degree ply ratios. Based on the experimental results, we developed two types of high-fidelity simulation tools for the virtual testing of composite laminates; an in-house extended finite element method tool and a generic failure model implemented in the commercial software Abaqus. Two tools consider both geometric and material nonlinearities such as plasticity, non-Hookean behavior, intra/interlaminar cracking, and fiber tensile/compressive failures. Their prediction capabilities are verified against the open-hole tension experiments of several layups with a variety of 0-degree layer ratios in terms of stress-strain nonlinearity, damage propagation behavior, and ultimate strength.

1. Introduction

Due to the recent development of the spread-tow thin-ply technology [1,2], the design freedoms of ply thickness and stacking pattern per unit thickness in the composite laminated structure have been improved. Owing to this improvement, the nonconventional stacking sequence, which has never been applied to the aircraft structure so far, will be applicable. For instance, the extremely hard laminate with a high ratio of 0-degree ply can be used in the components where the loading direction is limited in a certain direction. This means that the excellent performance (specific stiffness and strength) in the fiber direction of unidirectional CFRP is able to be used more actively.

It is well known that the “in-situ” strength, which is defined as the stress and strain at ply failure within the laminates, depends on the ply thickness. Due to the high constraint from neighboring ply, the thin

ply laminates have high in-situ transverse and shear strengths [3-6]. The superior in-situ strength results in the superior laminated strength in most test cases such as non-hole tension/compression tests, open/filled-hole compression tests [7-10], and tapered laminates [11], however, it can negatively affect laminated strength in open/filled hole tention tests [7,12]. Another disadvantage to thin-ply technology is that numerous candidate stacking patterns must be reviewed in the design process. Therefore, for the optimization of the future design of CFRP laminated structures by tailoring the ply thickness and orientation, the development of a high-fidelity simulation method, which was thoroughly verified by experiments in various ply thicknesses and stacking sequences, is necessary.

This study aims to experimentally and numerically investigate the influence of ply thickness and 0-degree ply ratio on the failure mode and strength of open-hole tensile tests. Two types of high-fidelity virtual testing tools, an in-house tool and an Abaqus-implemented tool, were developed based on the experiments. In the experiment, we prepare the 6 types of CFRP laminates by changing the ply thickness from 0.05mm to 0.2mm and the 0-degree ply ratio from 10% to 67%. For all the layups, both the fracture tests and the interrupted tests are carried out to observe the progressive internal damage using X-ray radiography. These results are used to verify the prediction accuracy of the simulation tools. Based on the experimental results, we developed numerical tools considering both geometric and material nonlinearity, including plasticity, damage, and non-Hookean (NH) behavior. Using the developed scheme, the open-hole tensile strengths of the CFRP laminates are evaluated in the cases of various ply thicknesses and layups. From the sensitivity study on each model, the effects of each nonlinearity on the OHT strength are discussed.

2. Experiments

To examine the effects of ply thickness and 0°-layer ratio, five types of laminates are prepared: conventional QI laminates with three different ply thicknesses (QI50, QI100, QI200) and laminate with high and low 0°-layer ratios (H400, S400). The stacking sequences, the ratio of ply angle (0°: ±45°: 90°), and the maximum 0°-layer thicknesses of these laminates are summarized in Table 1. The material used for these laminates is thin-ply T800/epoxy unidirectional prepregs of 0.05 mm thickness (Industrial Technology Center in Fukui Prefecture). The OHT tests were carried out following JIS K7094 [32] using Instron 8802 and AG-250-X-plus (Shimadzu Corp.) under displacement control with a constant rate of 1.0 mm/min. The specimen geometry is illustrated in Fig. 1.

In order to capture damage propagation behaviors within the specimens in detail, the load was interrupted in some specimens, and X-ray inspection was conducted on them using a soft X-ray radiography system (M-100, SOFTEX, Inc.). For clear observation, the zinc iodide penetrant was immersed into the free edges including the hole edge of the specimens after unloading. The specimens were exposed to X-rays at 30kV, 1mA for 30sec.

Table 1. List of stacking sequences for OHT simulations.

Specimen ID	Layup	0°: ±45°: 90°	Max. 0° thickness
QI50	$[45/\mathbf{0}/-45/90]_{8S}$	25: 50: 25	50 μm
QI100	$[45_2/\mathbf{0_2}/-45_2/90_2]_{4S}$	25: 50: 25	100 μm
QI200	$[45_4/\mathbf{0_4}/-45_4/90_4]_{2S}$	25: 50: 25	200 μm
S400	$[(45_4/90_4/-45_4/45_4/-45_4)_2/45_4/0_4/-45_4/(45_4/-45_4)_3/\mathbf{0_4}]_S$	10: 80: 10	400 μm
H400	$[(45_2/90/-45_2/0_4)_2/(45/90/-45/\mathbf{0_4})_2]_S$	50: 37.5: 12.5	400 μm
XF600	$[45/90_2/-45/0_8/45/90/-45/0_8/45/90/-45/\mathbf{0_6}]_S$	68.75: 18.75: 12.5	600 μm

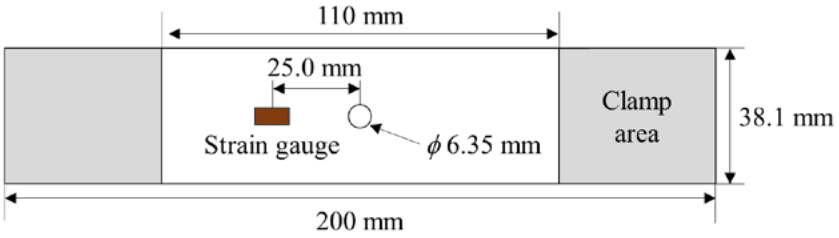


Figure 1. Geometry of OHT specimen.

3. Numerical methods

This study developed two types of virtual testing tools; an in-house extended finite element method (XFEM) tool and a generic failure model implemented in the commercial software Abaqus. The authors have developed the former tool so far [13,14] and newly developed the latter one by implementing the models in the former to the Abaqus.

3.1. In-house virtual test tool

The in-house virtual testing tool [13,14] is based on XFEM and introduces five models for material nonlinearities; plasticity, non-hookean effect, multiple intra-laminar cracks, delamination, and fiber tensile and compressive failure. The geometrical nonlinearity is also included. Table 2 summarizes the numerical models implemented in the developed in-house tool.

Table 2. Models implemented in in-house virtual testing tool.

Phenomena	Models
Plasticity	Pressure-dependent Sun-Chen model [15,16]
Non-hookean effect	Nondlinear elastic hardening model [17,18]
Intra-laminar cracking	XFEM with enhanced cohesive zone model [13,14]
Delamination	Interface element with enhanced cohesive zone model [19,20]
Fiber tensile failure	Weibull Criteria [21]
Fiber compressive failure	LaRC03 criteria with smeared crack model [22,23]

The XFEM can handle the intralaminar cracks and resultant displacement discontinuity independent from the mesh by introducing additional degrees of freedom and enriching the interpolation function in the solid elements. Furthermore, the interface elements for delamination are also enriched to deal with interaction between intra- and inter-laminar cracks. The detailed formulations can be referred to Refs. [13, 14]. In the proposed tool, the arbitrary crack shape is defined using multiple line segments on the base surface by the two level-set functions. All the elements are classified into normal, cut, and tip elements on the base surface. Three-dimensional elements are then created by extruding the two-dimensional elements. The schematic of the crack modeling strategy in the in-house XFEM tool is illustrated in Fig. 2.

3.2. Abaqus-implemented virtual test tool

This study develops a generic failure model (GFM) by implementing material models in in-house tool listed in Table 2. This study developed a generic failure model (GFM) by implementing material models in an in-house tool into Abaqus listed in Table 2. As shown in Table 2, most material models were implemented via the user-written FORTRAN subroutine VUMAT. One exception is the Weibull criterion for fiber tensile failure. Since it is a global criterion judging the probability of survival of the entire specimen by volume integration of the stress field, it was implemented by Python script as a post-process.

Particular attention was paid to the modeling of interaction between intra- and inter-laminar cracks. To this end, the partitioned interface element strategy is developed. The details are illustrated in Fig. 3.

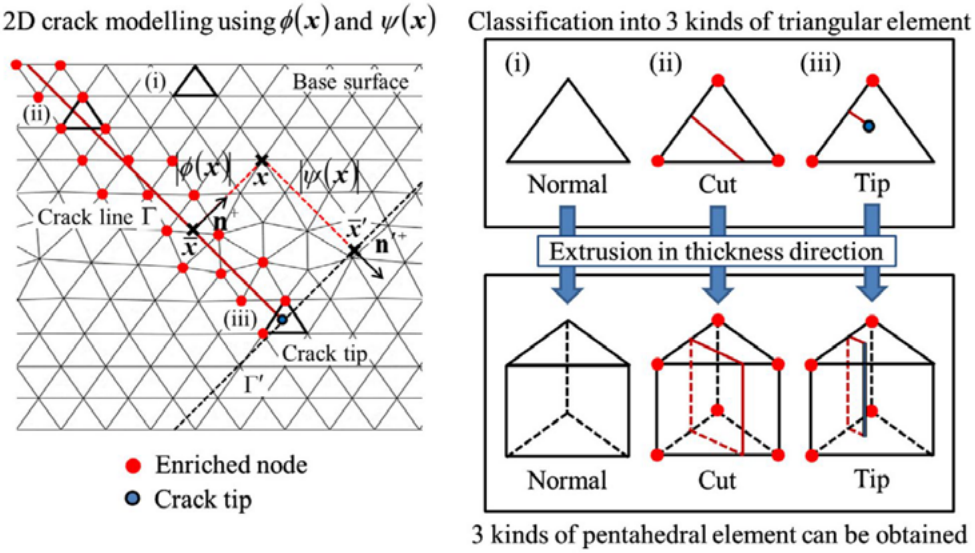


Figure 2. Schematics of intra- and inter laminar crack modeling in in-house virtual test tool [13].

Table 3. Models implemented in Abaqus virtual testing tool.

Phenomena	Models	Implementation
Plasticity	Pressure-dependent Sun-Chen model [15,16]	UMAT
Non-hookean effect	Nondlinear elastic hardening model [17,18]	UMAT
Intra-laminar cracking	Interface element with enhanced cohesive zone model [19,20]	UMAT
Delamination	Partitioned interface element with enhanced cohesive zone model	UMAT
Fiber tensile failure	Weibull Criteria [21]	Python script (Post process)
Fiber compressive failure	LaRC03 criteria with smeared crack model [22,23]	UMAT

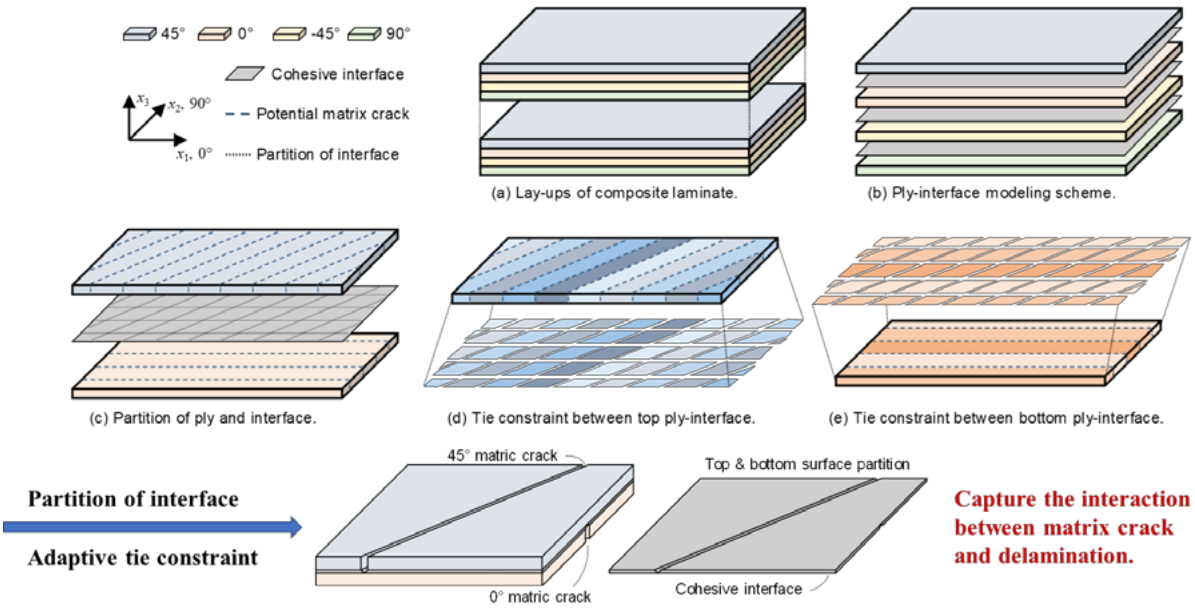


Figure 3. Schematics of intra- and inter laminar crack modeling in Abaqus virtual test tool.

Since mesh-independent crack modeling approaches such as XFFEM are hard to implement in commercial software, the developed tool employs the interface elements for intra-laminar cracks. It should be noted that such a modeling approach generally causes mesh inconsistency between the interface and neighboring plies with different fiber angles and makes it impossible to share the nodes between them. Generally, there are two ways to tackle this problem; (I) tying the ply and interface via the multi-point constraints, and (II) utilizing the surface-based interface (cohesive zone) modeling. However, they do not always provide accurate solutions for interactive propagation of intra- and inter-laminar cracks because results are dependent on the positional relationship between intralaminar crack and integration points on the interface. To tackle this problem, we proposed the partitioning of interface elements and setting tie constraints between each partitioned block of interface elements and corresponding neighboring ply elements. These procedures are automatically done by Python script as a pre-process.

4. Results and discussion

4.1. Effect of ply thickness (QI50, QI100, and QI200)

This section performs the OHT simulations in QI50, QI100, and QI200 cases using both proposed tools as the verifications of their prediction capabilities. The influence of ply thickness on the OHT strength and damage propagation behavior is also discussed via comparisons between the experimental and numerical results.

Experimental and predicted strengths and damage behaviors are compared in Table 4 and Fig. 4, respectively. It can be seen from Table 4 that the thinner ply-thickness results in lower OHT strength both in the experiment and simulation. This is because of the difference in internal damage. As shown in Fig. 4, even at 95% strength, only a few cracks happened in thin-ply laminates. In contrast, numerous cracks and delamination occurred in thick-ply even at 80% load level. In particular, these splittings in 0-degree plies can relieve the stress concentration around the hole and delay the fiber failure. By modeling these internal damages, both tools were able to capture the trend of damage behavior depending on the ply thickness (i.e., less damage in thinner ply) observed in the experiment and achieved high prediction accuracy within 15% for strength in all the cases. It should be noted that the Abaqus tool overestimated damage propagations in all the cases. This larger damage propagation caused a relaxation of stress concentration around the hole in the larger region, delayed fiber failure, and resulted in the overestimation of ultimate strength. One possible cause of the difference in prediction between in-house and Abaqus-implemented tools is the different spacing and positions of introduced cracks. Although a larger crack spacing is utilized in the Abaqus tool due to the lack of RAM, this undesirable problem will be relieved in the near future.

Table 4. Comparison of predicted and experimental OHT strength.

Specimen ID	OHT strength MPa (Error %)		
	Experiment	Sim. (in-house tool)	Sim. (Abaqus tool)
QI50	489.5	453.2 (-7.42)	554.7 (13.3)
QI100	508.4	459.2 (-9.68)	560.3 (10.2)
QI200	532.5	497.3 (-6.67)	571.2 (7.26)

4.2. Effect of 0-degree layer ratio (S400, H400, and XH600)

This section compares the experimental and numerical results of OHT tests in S400, H400, and XH600 cases. Here, sensitivity simulations were carried out using the in-house tool by omitting some material models to examine their effect on the damage and strength predictions. Comparisons of strength and stress-strain curves are provided in Table 5 and Fig. 5.

In the S400 case, significant softening happens in the stress-strain response due to the plastic behavior in the 45 plies. Therefore, both the stress-strain response and OHT strength were overestimated if the plasticity model was omitted.

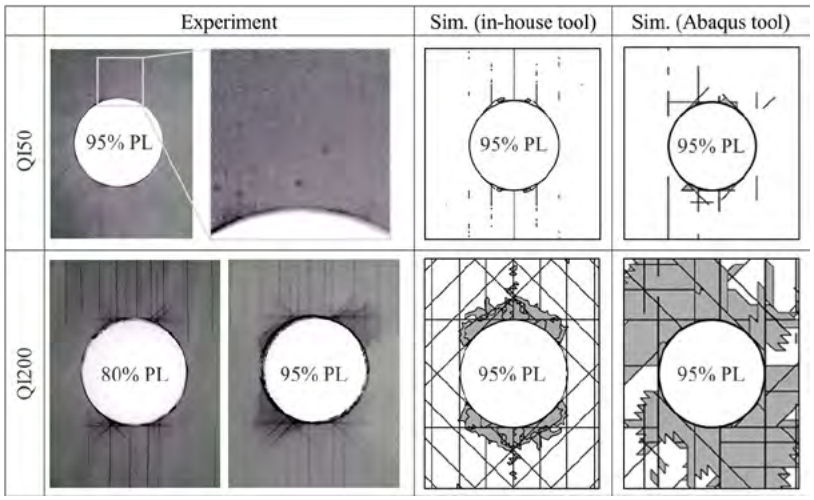


Figure 4. Comparisons of damage behaviors in QI50 and QI200 between experiment, simulation using in-house tool, and simulation using Abaqus-implemented tool.

Table 5. Comparison of predicted and experimental OHT strength.

Specimen ID	OHT strength MPa (Error %)				
	Experiment	Sim. (In-house tool)			
		w all models	w/o PLA	w/o NH	w/o GNL
S400	*313.6*	*287.0* (-8.54)	*305.0* (-1.81)	---	---
H400	673.6	695.2 (+3.20)	---	762.7 (+13.2)	---
XF600	**1363.6**	**1395.6** (+2.35)	**---**	**---**	**807.9** (-40.8)

Roman : Fiber failure mode, **Bold** : Splitting failure mode, *Italic* : Off-axis crack failure mode

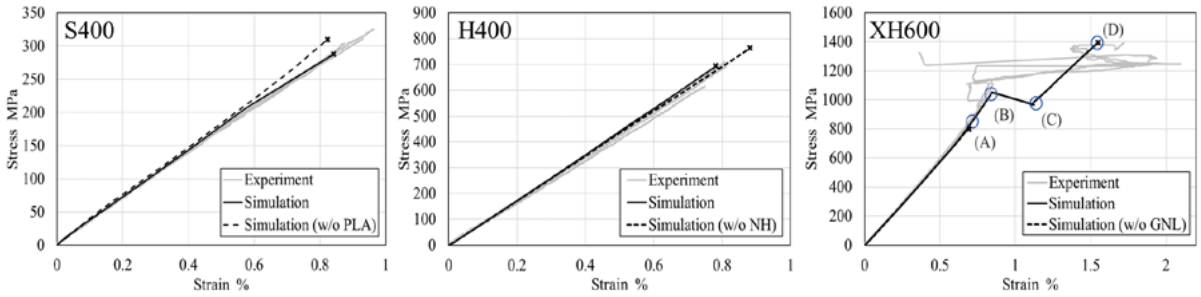


Figure 5. Comparisons of stress-strain curves in S400, H400, and XH600 cases.

In the H400 case, we compared the experiments and simulations with and without NH effect. If we neglect the NH effect (i.e., nonlinear elastic hardening in fiber direction), the stress-strain-response is underestimated, but the OHT strength is overestimated. This is because the local stress around the hole is underestimated without the NH effect. With the model for the NH effect, both the stress-strain response and OHT strength were well reproduced.

Finally, in the XH600 case, we compared the experiments and simulations with and without geometrical nonlinearity (GNL). As shown in Table 5, the strength is significantly underestimated if we neglect the GNL. In this laminate, the splittings in 0-degree layer were significantly extended with the accompanied delamination and fiber kinking (see Fig. 6). These accompanied delamination and fiber kinking highly depend on the out-of-plane deformation of the delaminated region. Therefore, without GNL, the out-of-plane deformation, delamination, fiber kinking, and the resultant ultimate failure are significantly underestimated.

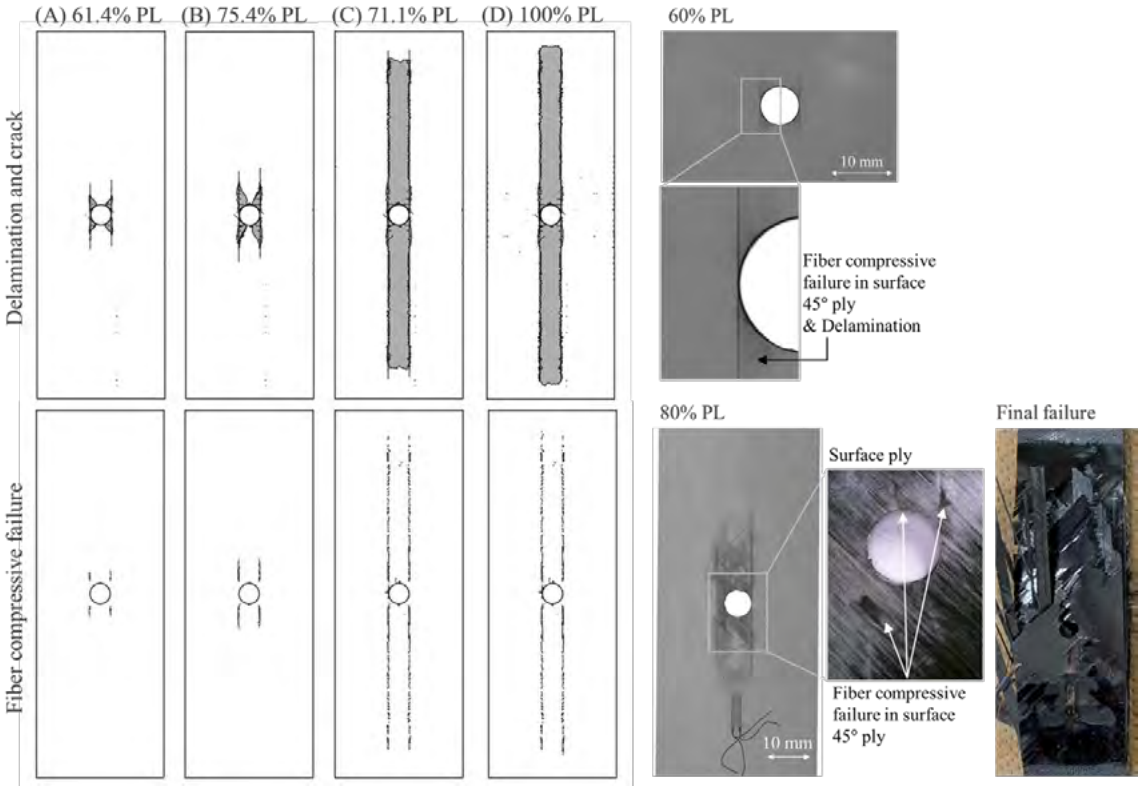


Figure 6. Comparisons of damage behaviors in XH600 case between experiment and simulation.

In summary, it was concluded that the OHT strengths of thin-ply laminate highly depend on the ply-thickness and layup, and, the proposed scheme can predict all OHT strengths very precisely by considering various material nonlinearity and GNL.

5. Conclusion

This study developed the virtual test tools for high-fidelity mesoscale simulation of composite laminates and examined the influences of ply thickness and 0-degree layer ratio on the damage behavior and the OHT strength. Two types of virtual test tools (the in-house XFEM tool and the Abaqus-implemented tool) were developed and verified in the OHT simulations of five types of layups. Based on the experimental and numerical results, we concluded that the OHT strengths highly depend on the ply-thickness and layup, and the proposed scheme can predict all OHT strengths very precisely by considering various material nonlinearity and GNL.

Acknowledgments

This study is based on the results obtained from a project, JPNP21014, subsidized by the New Energy and Industrial Technology Development Organization (NEDO).

References

[1] K. Kawabe, S. Tomoda, T. Matsuo. A pneumatic process for spreading reinforcing fiber tow. In *Proceedings of the 42nd international SAMPE symposium & exhibition*, pages 65-76, 1997.
[2] H. Sasayama, K. Kawabe, S. Tomoda, I. Ohsawa, K. Kageyama, N. Ogata. Effect of lamina thickness on first ply failure in multidirectionally laminated composites. In *Proceedings of the 8th Japan international SAMPE symposium & exhibition*, pages 18-21, 2003.

[3] G.J. Dvorak, N. Laws. Analysis of progressive matrix cracking in composite laminates II. First ply failure. *Journal of Composite Materials*, 21(4): 309-329. 1987
[4] P.P. Camanho, C.G. Dávila, S.T. Pinho, L. Iannucci, P. Robinson. Prediction of in situ strengths and matrix cracking in composites under transverse tension and in-plane shear. *Composites Part A: Applied Science and Manufacturing*, 37(2): 165-176, 2006.
[5] H. Saito, H. Takeuchi, I. Kimpara. Experimental evaluation of the damage growth restraining in 90 layer of thin-ply CFRP cross-ply laminates. *Advanced Composite Materials*, 21(1): 57-66, 2012.
[6] R. Higuchi, R. Aoki, T. Yokozeki, T Okabe. Evaluation of the in-situ damage and strength properties of thin-ply CFRP laminates by micro-scale finite element analysis. *Advanced Composite Materials*, 29(5): 475-493, 2020.
[7] S. Sihn, R.Y. Kim, K. Kawabe, S.W. Tsai. Experimental studies of thin-ply laminated composites. *Composites Science and Technology*, 67(6): 996-1008, 2007.
[8] T. Yokozeki, Y. Aoki, T. Ogasawara. Experimental characterization of strength and damage resistance properties of thin-ply carbon fiber/toughened epoxy laminates. *Composite Structures*, 82(3): 382-389, 2008.
[9] T. Yokozeki, A. Kuroda, A. Yoshimura, T. Ogasawara, T. Aoki. Damage characterization in thin-ply composite laminates under out-of-plane transverse loadings. *Composite Structures*, 93(1): 49-57, 2010.
[10] K. Takamoto, T. Ogasawara, H. Kodama, T. Mikami, S. Oshima, K. Aoki, R. Higuchi, T. Yokozeki. Experimental and numerical studies of the open-hole compressive strength of thin-ply CFRP laminates. *Composites Part A: Applied Science and Manufacturing*, 145: 106365, 2021.
[11] X. Hua, R. Higuchi, T. Yokozeki. Enhancement of tensile strength of tapered laminates by utilizing thin-ply composites. *Composites Part B: Engineering*, 248: 110372, 2023.
[12] R. Aoki, R. Higuchi, T. Yokozeki, K. Aoki, S. Uchiyama, T. Ogasawara. Effects of ply thickness and 0°-layer ratio on failure mechanism of open-hole and filled-hole tensile tests of thin-ply composite laminates. *Composite Structures*, 280: 114926, 2022.
[13] R. Higuchi, T. Okabe, T. Nagashima. Numerical simulation of progressive damage and failure in composite laminates using XFEM/CZM coupled approach. *Composites Part A: Applied Science and Manufacturing*, 95: 197-207, 2017.
[14] R. Higuchi, S. Warabi, A. Yoshimura, T. Nagashima, T. Yokozeki, T. Okabe. Experimental and numerical study on progressive damage and failure in composite laminates during open-hole compression tests. *Composites Part A: Applied Science and Manufacturing*, 145: 106300, 2021.
[15] C.T. Sun, J.L. Chen. A simple ow rule for characterizing nonlinear behavior of fiber composites. *Journal of Composite materials*, 23(10):1009-1020, 1989.
[16] T. Yokozeki, S. Ogihara, S. Yoshida, T. Ogasawara. Simple constitutive model for nonlinear response of fiber-reinforced composites with loading-directional dependence. *Composites science and technology*, 67(1): 111-118, 2007.
[17] T. Ishikawa, M. Matsushima, Y. Hayashi. Hardening non-linear fibe haviour in longitudinal tension of unidirectional carbon composites. Journal of materials science, 20(11): 4075-4083, 1985.
[18] T. Yokozeki, T. Ogasawara, T. Ishikawa. Effects of fiber nonlinear properties on the compressive strength prediction of unidirectional carbon fiber composites. *Composites science and technology*, 65(14): 2140-2147, 2005.
[19] X. Li, S.R. Hallett, M.R. Wisnom. Predicting the effect of through thickness compressive stress on delamination using interface elements. *Composites Part A: Applied Science and Manufacturing*, 39(2): 218-230, 2008.
[20] K.W. Gan, S.R. Hallett, M.R. Wisnom. Measurement and modelling of in terlaminar shear strength enhancement under moderate through-thickness compression. *Composites Part A: Applied Science and Manufacturing*, 49: 18-25, 2013.
[21] S.R. Hallett, B.G. Green, W.G. Jiang, M.R. Wisnom. An experimental and numerical investigation into the damage mechanisms in notched composites. *Composites Part A: Applied Science and Manufacturing*,40(5): 613-624, 2009.
[22] S.T. Pinho, L. Iannucci, P. Robinson. Physically based failure models and criteria for laminated fibre-reinforced composites with emphasis on fibre kinking. Part II: FE implementation. *Composites Part A: Applied Science and Manufacturing*, 37(5): 766-777, 2006.
[23] P. Maimi, P.P. Camanho, J.A. Mayugo, C.G. Davila. A continuum damage model for composite laminates: Part I - Constitutive model. *Mechanics of materials*, 39(10): 897-908, 2007.

Temperature-dependent changes in thermoplastic sandwich core properties and failure mechanisms using four-point tests with short specimens

A. Horn[1], C. Berggreen[1], E. A. Gomez Meisel[1] and B. N. Legarth[1]

Department of Civil and Mechanical Engineering, Technical University of Denmark, DK-2800 Kgs. Lyngby, Denmark
Email: alhor@dtu.dk, Web Page: https://construct.dtu.dk/
Department of Civil and Mechanical Engineering, Technical University of Denmark, DK-2800 Kgs. Lyngby, Denmark
Email: cber@dtu.dk, Web Page: https://construct.dtu.dk/
Department of Civil and Mechanical Engineering, Technical University of Denmark, DK-2800 Kgs. Lyngby, Denmark
Email: eagme@dtu.dk, Web Page: https://construct.dtu.dk/
Department of Civil and Mechanical Engineering, Technical University of Denmark, DK-2800 Kgs. Lyngby, Denmark
Email: bnle@dtu.dk, Web Page: https://construct.dtu.dk/

Keywords: thermoplastic, sandwich, honeycomb, four-point bending, core shear failure, low temperature, aircraft application

Abstract
Because of the emerging need for sustainable materials in the aircraft industry a promising composite material group is remeltable thermoplastic sandwich composites. To secure the useability of these sustainable thermoplastic composite materials, it is irrevocable to gain sufficient insight into the performance of these materials under versatile environmental conditions. In this investigation, the core properties, such as the ultimate core shear strength, the shear stiffness, and the associated failure mechanisms, at different temperatures are investigated by a four-point bending test series.
This series of tests can be seen as a step towards precise material characterization to ensure the development of a sustainable material alternative for structural aircraft parts, without compromising safety and reliability. Furthermore, critical aspects could be identified for prospective investigations.

1. Introduction

In order to the challenge of improving sustainability of structural airplane parts thermoplastic composite materials are a promising material alternative. In opposite to conventionally used thermoset based materials, such as epoxy or phenolic resin, thermoplastic materials will not receive irreversible chemical reactions. Due to that, thermoplastics can be remelted or restored to the flowable state. This ability offers new methodologies regarding recycling processes as well as other process options and new maintenance possibilities.
Sandwich materials have become standard material configurations, for designing parts with excellent strength-to-weight ratios. Their low mass compared to homogenous or stiffened structures as well as their high durability and reliability keeps them attractive for different industrial applications even beside the aerospace industry.

The aerospace industry is obliged to adhere to strict safety regulations. Sandwich materials in structural airplane parts, such as the shells of the vertical rudder, are continuously researched and improved to handle all the different conditions, which can appear during operation. One of the most critical aspects is the low temperature prevailing at flight altitude. Even at temperatures down to -55°C the sandwich material needs a good mechanical performance to ensure safety and reliability. To investigate the feasibilty of replacing conventional sandwich materials with more sustainable thermoplastic-based solutions it is important to investigate differences and similarities respectively of this promising material type compared with the conventionally used.

2. State of the Art

The two shells of a conventional rudder are both sandwich panels with two corresponding skin sheets on the outer surface. These sheets, also known as face sheets, are usually made of high-performance fiber-reinforced laminate. The high performance is reached by a fabric of carbon fibers embedded in an epoxy matrix. The face sheets are supported by a low-density core material. This low density is realized by using an aramid fiber paper material (known under the trade name Nomex®) coated with phenolic resin and arranged in a characteristic honeycomb geometry. To gain the so called sandwich effect, all corresponding layers has to be connected with each other, usually by an adhesive film. A general structure of sandwich materials is shown in figure 1. The major load case a sandwich material is supposed to, is bending. The bending deflection can be separated in a pure bending-related part and shear-related part. The amount of shear related effects for homogenous materials is very small and can be neglected. By using a low-weight core material the sandwich deformation gains an increasing amount of shear-related phenomena, which have to be considered.

The simplified first order shear deformation theory is highly coupled with two assumptions. The first is that the elastic modulus of the face sheets E_f should be much higher than the one of the core material E_c.

$$E_c << E_f \tag{1}$$

The second assumption is that the height of the core material t_c should be higher compared to the thickness of the face sheets t_f.

$$t_f << t_c \tag{2}$$

If both assumptions are fulfilled the stress contribution inside the material can be approximated like it is shown in figure 2. The bending stresses are just carried by both face sheets. The bending stresses inside the core material can be neglected. The shear load is completely carried by the core material because the face sheets are thin enough to not build up notable shear forces [1].

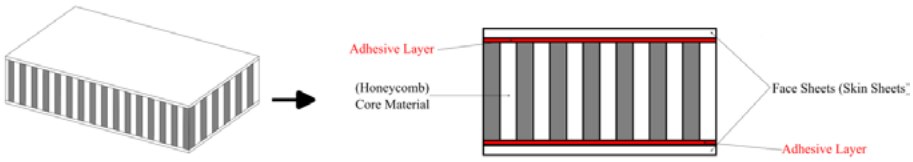


Figure 1. Sketch of general (honeycomb) sandwich structure

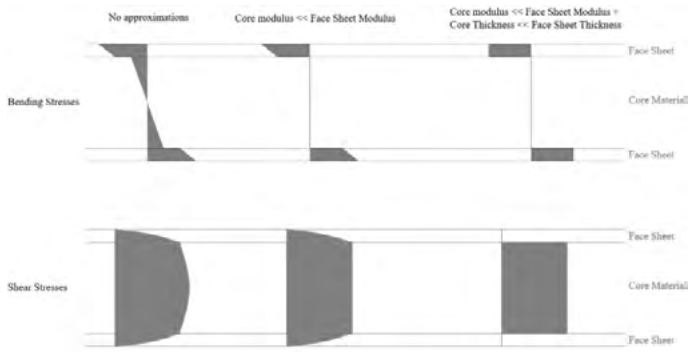


Figure 2. Approximated stress contributions

The mechanical properties of the face sheet laminate can be calculated well by using classical lamination theory (CLT). Also fiber reinforced composites consisting of thermoplastic matrix materials are already existing and are offered by the industry (e.g. by Toray Industries, Inc. or the Danish company Comfil ApS).
The honeycomb core material investigated in this approach is different from the conventional ones even beyond the material type. A specific production process also known as ThermHex process [2] realizes a semi-open folded honeycomb structure, characterized by two main differences [3]. Figure 3 shows schematically the folding process. Every row of cells obtain due to the continuous process covers, which are alternately pronounced on the upper and lower sides. This covers acting as additionally connection zones, therefore they increase the area of the core-face interface. Due to that characteristic, some known analytical calculation methods e.g. according GIBSON and ASHBY are not applicable for this core type [4]. The second difference related to conventional honeycomb cores is that the double cell walls are not connected over the complete surface. While conventionally produced cores are corrugated, stacked and connected over the full surface of double cell walls by an additional adhesive film, the folded structure just have connected zones at the upper and the lower area of the cells.
Another notable advantage of a sandwich material, which is completely thermoplastic-based, is the possibility to renounce the adhesive film for the core-face interface and realize the connection by a welding process instead.

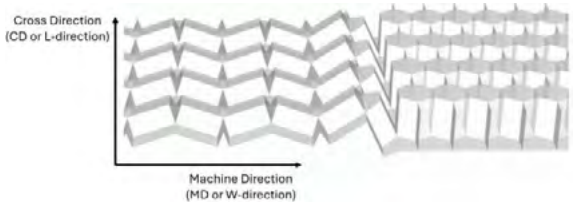


Figure 3. Process of semi-open folded honeycomb core (extracted and customized from [2])

3. Methodology

The focus for a promising material choice with respect to the use as aircraft structural part felt on two thermoplastic polymers as base material. Samples made of Polyetherimide (PEI) and Polphenylene Sulfide (PPS) were produced and provided by the company Econcore. Both polymers, regardable as high-performance thermoplastics, are characterized by a glass transition temperature, which is higher than the required operation temperature for structural airplane parts [5]. Furthermore they are less complicate to process caused by a lower melting point than other comparable high-performance thermoplastics. The core-face interface was realized in case of PPS with a welded connection. On the opposite, the PEI material is bonded together by using a thermoplastic adhesive layer.
As a first investigation to gain information about critical mechanism related to this type of sandwich materials a conventional four-point bending was chosen. In order to minimize the face sheet related proportion of the flexural rigidity and to provoce a core shear failure the decision of short sample design with a span length of 270mm was taken. The load introduction distance was 100mm. The bending test setup is located in a climatic chamber able to realize a temperature of -55°C. Tests were performed at low temperature as well as room temperature.
Three different basics are focused to compare. The first is a investigation of the failure mode, namely if the expected failure mode of core shear failure appears and if it is typically characterized. Second basic is the calculation of the ultimate core shear strength according ASTM C393 [6]. The standard prescribes a core shear failure for a properly determination. Another comparable core related property is the core shear stiffness. In order to determine it, the curvature in the area supposed to pure bending between the load introduction points was monitored by a digital image correlation system (DIC). To realize this, tracking dots are applied at the outer edges of the face sheets. With help of the curvature, the flexural rigidity can be calculated. With respect to the displacement the samples obtaining during the experiment as well as the known flexural rigidity, the shear stiffness can be calculated. Figure 4 shows the test setup inside the climatic chamber. Support point as well as load introduction points are supported by rotational bearings. To increase the load introduction surface additional load pads are applied. This helps to prevent local indentation phenomena. Figure 5 shows exemplarily a loaded test sample, where the for the DIC required tracking points as well as reference index respectively is shown.

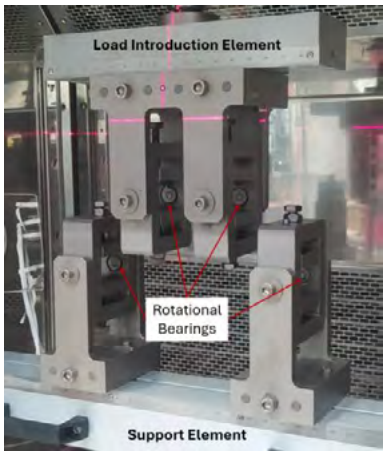


Figure 4. Four-point bending test setup



Figure 5. Loaded four-point bending test setup with PEI sample

4. Results

Figure 5 as well as figure 6 showing exemplarily the load-displacement behavior of PPS sandwichs and PEI sandwichs respectively. Due to the highly orthotropic character of honeycomb material a separation of properties with respect to the production direction and the transversal direction must be performed. The solid lines showing the low temperature tests, which can be directly compared with experimental results at room temperature visualized by dashed lines. Regarding the slopes, the curves are comparable with each other. An influence of low temperature effects the absolute force which is reached during the tests. However, all samples are subjected to a certain amount of variation, which causes that also these values are quite comparable.

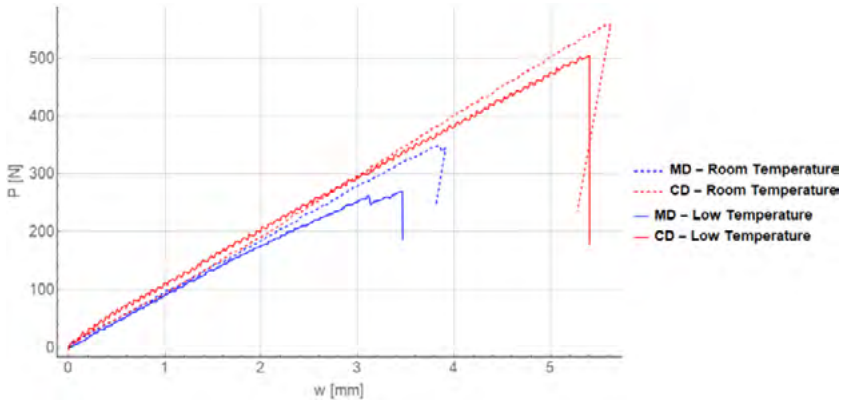


Figure 5. Exemplarily load-displacement curves of PPS

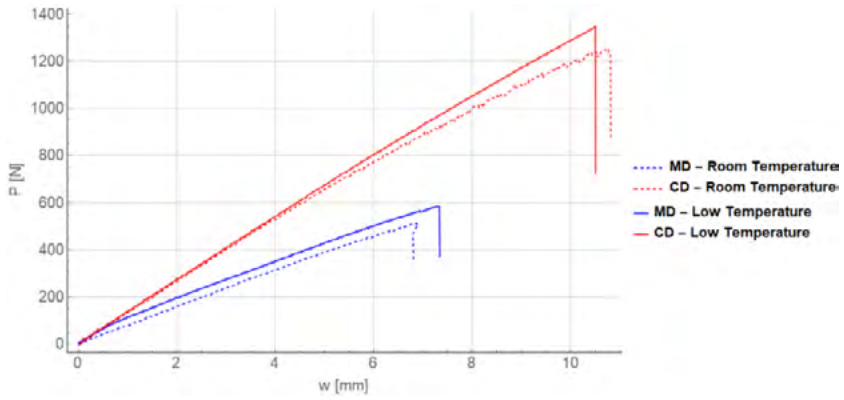


Figure 6. Exemplarily load-displacement curves of PEI

It is to note that the numerous values between both material types should not be compared directly because of differences in the geometry as well as the core density. A meaningful comparison is just possible within one material configuration between room temperature and low temperature.
In opposite to the numerous values, the failure mechanisms are representative for both material configurations and can be compared qualitatively. A buckling of the cell walls, initiating a critical failure of the core material is observable at all tested samples. The figures 7 and 8 are showing characteristic core shear failures of both material types. The shear crack is as expected in an approximate 45° angle. It is conspicuous that a development of the shear crack underneath the face sheets is observable. This phenomenon is more pronounced at low temperatures and independent of the type of core-face interface.



Figure 7. Core Shear Failure of PPS Sandwich



Figure 8. Core Shear Failure of PEI Sandwich

5. Discussion and Conclusion

The expectation of a more brittle behavior at low temperatures of -55°C was confirmed during the experiments. However, for a first investigation are these effects acceptable. All samples are supposed to a certain amount of variation, so that the results remain comparable independently of the test temperature. This also confirmes the promising character of PPS and PEI.
All in all, PPS shows a more brittle failure at lower loads than PEI, which is confirmed by lower values of the ultimate core shear strength in production direction at low temperatures. Due to increased brittleness at low temperatures, the relatively small connection zones between the double cell walls are supposed to fail earlier. A decreased shear stiffness can also be associated with this phenomena. It is planned that the PPS will additionally be modified and optimized regarding this brittle behaviour by a choice of certain additives.
The cell wall buckling as main driver of a critical core shear failure could be observed for both material types. It was observed that the failure starts in the immediate vicinity of the face sheets. The secondary source of a critical failure is the collapse of the core-face interface. Especially this phenomena will be investigated further to gain a more detailed knowledge about the failure mechanism and the associated useability of thermoplastic sandwich solutions for structural airplane parts.

Acknowledgments

Special thanks to all project partners of the work package EcoRudder of the Horizon Europe - Clean Aviation project FASTER H2 for a lot of knowledge exchange. Especially, the provision of test samples by Econcore was highly appreciated.

References

[1] D. Zenkert. *The Handbook of Sandwich Construction.* 1997
[2] Honeycomb cores for lightweight sandwich panels (Online), https://thermhex.com/ (Available at 07/05/2024)
[3] J. Pflug. *Continuously Produced Honeycomb Core Materials.* Leuven: Arenberg Doctoral School Dissertation. 2018
[4] L. Gibson and M. Ashby. *Cellular Solids - Structure and Properties.* Cambridge University Press 1997
[5] G. Wypych. *Handbook of Polymers*. Elsevier, 2016
[6] ASTM C393/C393M – 20, *Standard Test Method for Core Shear Properties of Sandwich Constructions by Beam Flexure* 2020

REVISITING CONSTRAINED-LAYER DAMPING IN HYBRID LIGHTWEIGHT LAMINATES: CHARACTERISATION, MODELLING AND DESIGN GUIDELINES

Alexander Jackstadt[1], Luise Kärger[1]

[1]Karlsruhe Institute of Technology (KIT), Institute of Vehicle System Technology - Lightweight Engineering, Rintheimer Querallee 2, 76131 Karlsruhe, Germany.
Email: alexander.jackstadt@kit.edu, Web Page: https://www.fast.kit.edu/english/lbt/

Keywords: Vibration, Damping, Plates

Abstract
Following the principle of constrained-layer damping (CLD), fibre metal elastomer laminates (FMELs) offer a high potential for damped lightweight structures, overcoming the undesirable vibration characteristics of conventional lightweight materials. This study investigates multiple hybrid CFRP elastomer metal laminates (HyCEMLs) regarding their damping behaviour. Following the viscoelastic material characterization of three different elastomer damping materials, different laminate lay-ups are investigated by employing a previously published analytical model based on a unified plate formulation. In particular, the free and forced vibration of simply-supported plates is investigated under consideration of the frequency-dependent material properties. The results include optimal laminate lay-ups for a maximized modal damping behaviour while maintaining a high static bending stiffness.

1. Introduction

The mechanical behaviour of fibre metal laminates (FMLs), such as glass fibre reinforced aluminium, has garnered significant attention from both academia and industry over the past decades. Their exceptional fatigue and impact resistance [1, 2] have enabled a wide range of structural applications, particularly in the aerospace sector [3]. Replacing the glass fibre-reinforced polymer (GFRP) plies with carbon fibre-reinforced polymer (CFRP) can greatly enhance mechanical properties like stiffness and strength, but it introduces corrosion issues at the aluminium interface and residual stresses due to differing thermal expansion coefficients. Incorporating elastomeric plies in these interfaces not only mitigates these issues [4] but also offers flexible options for enhancing and optimizing the vibration damping capabilities of FMLs through CLD [5]. Under bending loads, the highly compliant viscoelastic elastomer plies experience significant transverse shear deformations, allowing for substantial dissipation of vibration energy [6]. The damping behaviour of these HyCEMLs has been extensively studied in experimental studies such as [7–9], demonstrating the versatility and adaptability of the CLD mechanism in hybrid laminates. These studies also highlight the strong influence of material and laminate parameters on the achievable amount of damping in addition to cumbersome experimental characterisation procedures and thus motivate the use of computationally efficient analytical predictive models. This work employs an analytical model based on a unified plate formulation [10–12] to predict the vibration characteristics of different HyCEMLs including variations of the elastomeric damping material and overall laminate layup.

2. Materials

The HyCEMLs investigated in this contribution feature three individual constituents: CFRP, aluminum and an elastomeric damping material. The CFRP plies consist of cured unidirectionally reinforced

epoxy-based prepreg sheets HexPly M77/38/UD150/CHS-12K-70 by Hexcel with a nominal thickness of 0.15 mm. The aluminum plies are EN AW-2024 T3 ALCLAD AMS-QQA-250/5 alloy sheets with a thickness of 0.3 mm. Three different elastomeric damping materials are investigated within this study, all belonging to the KRAIBON® range of products by Gummiwerk KRAIBURG GmbH & Co. KG. An overview of the three compounds is given in Table 1.

Table 1: Properties of the three KRAIBON® compounds SAA9579/52, HAA9275/45 and HVV9632/59 studied in this work according to data sheets supplied by the manufacturer [13–15].

	SAA9579/52 (E1)	HAA9275/45 (E2)	HVV9632/59 (E3)
Base polymer	EPDM	EPDM	AEM
Mass density	$1180\,\mathrm{kg\,m^{-3}}$	$1250\,\mathrm{kg\,m^{-3}}$	$1350\,\mathrm{kg\,m^{-3}}$
Hardness	88 Shore A	98 Shore A	95 Shore A

Six different HyCEMLs, namely those listed in Table 2, are considered in this study. The laminates are manufactured as plates of dimensions 400 mm × 400 mm in a hot-mould process. The constituents are manually cut to dimensions and stacked in a heated plate tool, which has prior been treated with a release agent. The mould is heated to 150 °C and a pressure of 40 bar is applied upon closing, which is then retained for 300 s allowing for consolidation of all constituents.

Table 2: FMEL configurations and naming convention. The notation is adopted from Sessner [16]. Lower indices state the layer's thickness in mm and upper indices, if applicable, state the material orientation with respect to the x-direction. The index $(\,)_\mathrm{s}$ indicates symmetric stacks of CFRP plies.

Laminate	Abbreviation	Nominal thickness
$\left[\mathrm{A}_{0.3}/\mathrm{E1}_{0.5}/\left(\mathrm{C}^{0°}_{0.15}/\mathrm{C}^{90°}_{0.15}\right)_3/\mathrm{E1}_{0.5}/\mathrm{A}_{0.3}\right]$	A-E1-C-E1-A	2.5 mm
$\left[\mathrm{A}_{0.3}/\mathrm{E2}_{0.5}/\left(\mathrm{C}^{0°}_{0.15}/\mathrm{C}^{90°}_{0.15}\right)_3/\mathrm{E2}_{0.5}/\mathrm{A}_{0.3}\right]$	A-E2-C-E2-A	2.5 mm
$\left[\mathrm{A}_{0.3}/\mathrm{E3}_{0.5}/\left(\mathrm{C}^{0°}_{0.15}/\mathrm{C}^{90°}_{0.15}\right)_3/\mathrm{E3}_{0.5}/\mathrm{A}_{0.3}\right]$	A-E3-C-E3-A	2.5 mm
$\left[\left(\mathrm{C}^{0°}_{0.15}/\mathrm{C}^{90°}_{0.15}\right)_\mathrm{s}/\mathrm{E1}_{0.5}/\mathrm{A}_{0.3}/\mathrm{E1}_{0.5}/\left(\mathrm{C}^{0°}_{0.15}/\mathrm{C}^{90°}_{0.15}\right)_\mathrm{s}\right]$	C-E1-A-E1-C	2.5 mm
$\left[\left(\mathrm{C}^{0°}_{0.15}/\mathrm{C}^{90°}_{0.15}\right)_\mathrm{s}/\mathrm{E2}_{0.5}/\mathrm{A}_{0.3}/\mathrm{E2}_{0.5}/\left(\mathrm{C}^{0°}_{0.15}/\mathrm{C}^{90°}_{0.15}\right)_\mathrm{s}\right]$	C-E2-A-E2-C	2.5 mm
$\left[\left(\mathrm{C}^{0°}_{0.15}/\mathrm{C}^{90°}_{0.15}\right)_\mathrm{s}/\mathrm{E3}_{0.5}/\mathrm{A}_{0.3}/\mathrm{E3}_{0.5}/\left(\mathrm{C}^{0°}_{0.15}/\mathrm{C}^{90°}_{0.15}\right)_\mathrm{s}\right]$	C-E3-A-E3-C	2.5 mm

3. Methods

Experimental In order to determine, and later model, the damping behaviour of the elastomeric damping materials, dynamic mechanical analysis (DMA) is conducted for an experimental characterisation of the frequency-dependent viscoelastic materials. The DMA is conducted in tension mode with frequency sweeps ranging from 0.1 Hz to 10 Hz at discrete temperatures ranging from −80 °C to 80 °C in increments of 5 °C. Following the actual DMA experiments, time-temperature superposition (TTS) is applied, including horizontal and vertical shifts for the creation of mastercurves yielding the isothermal viscoelastic behaviour over a wide frequency range. More details on this procedure are given in Jackstadt [17].

Analytical In this study, the analytical model previously published by the authors in [10–12] is applied. Based on the Generalized Unified Formulation (GUF) by Demasi [18, 19], the Reissner's Mixed Variational Theorem (RMVT)

$$\int_\Omega \left(\delta\varepsilon_{\mathrm{pG}}^\top \sigma_{\mathrm{pH}} + \delta\varepsilon_{\mathrm{nG}}^\top \sigma_{\mathrm{nM}} + \delta\sigma_{\mathrm{nM}}^\top (\varepsilon_{\mathrm{nG}} - \varepsilon_{\mathrm{nH}})\right) \mathrm{d}V = \delta L_{\mathrm{ext}} - \int_\Omega \rho\, \delta u^\top \ddot{u} \mathrm{d}V \tag{1}$$

is considered in order to model the three displacement and three out-of-plane stress components based on the axiomatic approach

$$\begin{aligned} u_x^k(x,y,z) &= U_{x,\alpha_{u_x}}^k F_{\alpha_{u_x}}(z)\Phi_{u_x}(x,y) & \sigma_{xz}^k(x,y,z) &= S_{xz,\alpha_{\sigma_{xz}}}^k F_{\alpha_{\sigma_{xz}}}(z)\Phi_{\sigma_{xz}}(x,y) \\ u_y^k(x,y,z) &= U_{y,\alpha_{u_y}}^k F_{\alpha_{u_y}}(z)\Phi_{u_y}(x,y) & \sigma_{yz}^k(x,y,z) &= S_{yz,\alpha_{\sigma_{yz}}}^k F_{\alpha_{\sigma_{yz}}}(z)\Phi_{\sigma_{yz}}(x,y) \\ u_z^k(x,y,z) &= U_{z,\alpha_{u_z}}^k F_{\alpha_{u_z}}(z)\Phi_{u_z}(x,y) & \sigma_{zz}^k(x,y,z) &= S_{zz,\alpha_{\sigma_{zz}}}^k F_{\alpha_{\sigma_{zz}}}(z)\Phi_{\sigma_{zz}}(x,y) \end{aligned} \tag{2}$$

within each material layer k of the laminates. The simply-supported plate problem is solved using the Navier solution, yielding the in-plane dependencies Φ_i in Equation (2) as

$$\begin{aligned} \Phi_x &:= \Phi_{u_x}(x,y) = \Phi_{\sigma_{xz}}(x,y) = \cos\left(\frac{m\pi x}{a}\right)\sin\left(\frac{n\pi y}{b}\right) \\ \Phi_y &:= \Phi_{u_y}(x,y) = \Phi_{\sigma_{yz}}(x,y) = \sin\left(\frac{m\pi x}{a}\right)\cos\left(\frac{n\pi y}{b}\right) \\ \Phi_z &:= \Phi_{u_z}(x,y) = \Phi_{\sigma_{zz}}(x,y) = \sin\left(\frac{m\pi x}{a}\right)\sin\left(\frac{n\pi y}{b}\right) \end{aligned} \tag{3}$$

with a and b being the plate's in-plane dimensions. Following the layerwise assembly of the global stiffness and mass matrices as outlined in Jackstadt et al. [12], the eigenvalue problem

$$\left(\mathbf{K}_{mn}^*(\omega) - \lambda_{mn}^* \mathbf{M}_{mn}\right)\hat{\mathbf{U}}_{mn}^* = \mathbf{0} \tag{4}$$

taking into account the complex-valued stiffness matrix $\mathbf{K}_{mn}^*(\omega)$ due to the elastomer materials' viscoelasticity is solved, yielding natural frequencies

$$\omega_{mn} = \sqrt{\Re(\lambda_{mn}^*)} \tag{5}$$

and corresponding modal damping ratios

$$\xi_{mn} = \frac{\Im(\lambda_{mn}^*)}{\Re(\lambda_{mn}^*)}. \tag{6}$$

In the presence of harmonic loads, the system of equation reads

$$\left(\mathbf{K}_{mn}^* - \omega^2 \mathbf{M}_{mn}\right)\hat{\mathbf{U}}_{mn}^* = \hat{\mathbf{R}}_{mn}, \tag{7}$$

where the loads are summarized in the right-hand-side term $\hat{\mathbf{R}}_{mn}$.

4. Results

Experimental Figure 1 shows the mastercurves at room temperature of the three elastomer materials considered in this study, which have been determined from experimental DMA experiments. The three elastomers differ significantly in their stiffness as can be seen from the course of the storage modulus E'. This is particularly pronounced at lower frequency before the materials enter their glassy state. Furthermore, the materials exhibit different levels of material damping, expressed by their loss factor $\tan(\delta)$.

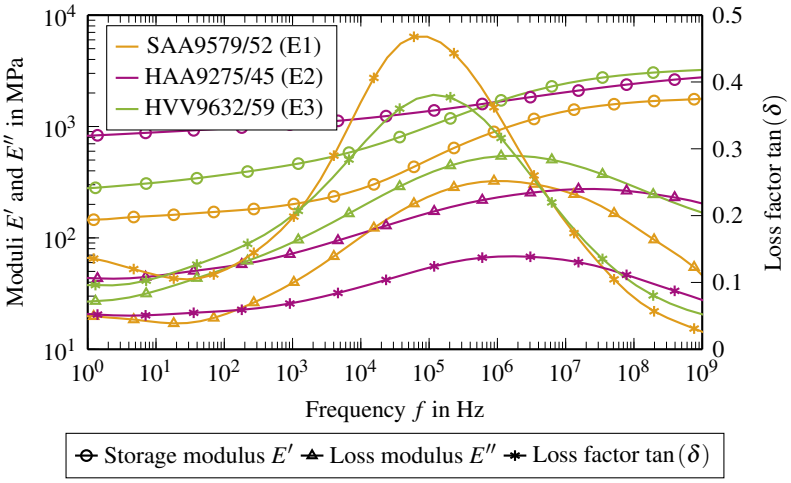


Figure 1: Master curves of the three elastomer materials at room temperature $T_R = 20\,°C$ generated from temperature and frequency sweeps in tension mode using TTS. [17]

Analytical For each of the six laminates under consideration, Figure 2 displays the natural frequencies and modal damping ratios corresponding to the first nine vibration modes of the simply-supported plates. It should be noted, that the order in which the modes occur is identical for all laminates.

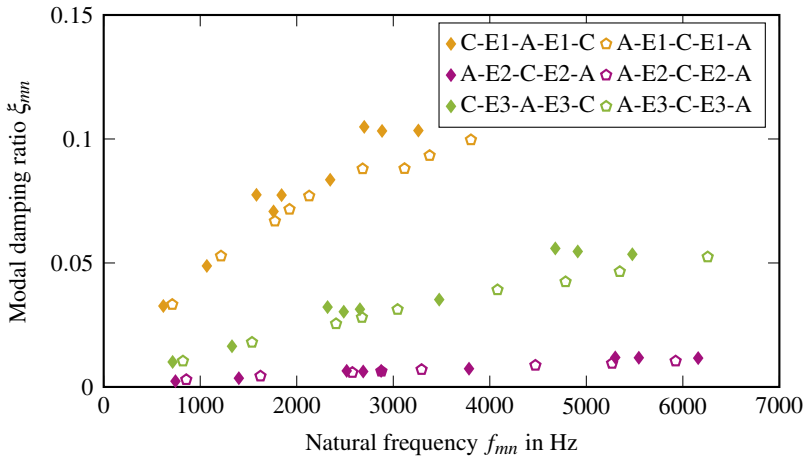


Figure 2: Modal damping ratios over corresponding natural frequencies of six different types of HyCEMLs. [17]

A clear differentiation between laminates incorporating distinct elastomer materials is evident. Specifically, laminates utilizing the same elastomer material display a consistent increase in modal damping ratios with increasing natural frequencies. Among these, the laminates incorporating the more compliant elastomer E1 demonstrate the highest modal damping ratios and relatively low natural frequencies. In contrast, the stiffer elastomer E2 results in the lowest modal damping ratios. Notably, the natural frequencies of laminates with elastomers E2 and E3 are comparable, yet the inclusion of elastomer E3 results in significantly higher modal damping ratios. These observations are consistent with the loss factors tan(δ) of the elastomer materials, as determined by DMA and depicted in Figure 1. Elastomer E1 exhibits the highest loss factor within the investigated frequency range, followed by elastomers E3 and E2. Irrespective of the specific elastomer used in the given HyCEMLs, laminates of type C-E-A-E-C show slightly higher modal damping compared to their A-E-C-E-A counterparts, albeit with a slight reduction in natural frequencies.

In order to investigate the response to forced vibration, the different HyCEMLs are excited by an harmonic force with amplitude $\hat{F}_0 = 10\,\mathrm{N}$ acting on the simply-supported plates. The structures' response is calculated as displacement amplitudes $|\hat{u}_z^*|$ and phase angles δ and shown in Figure 3 for a frequency-range of 1 Hz to 2000 Hz.

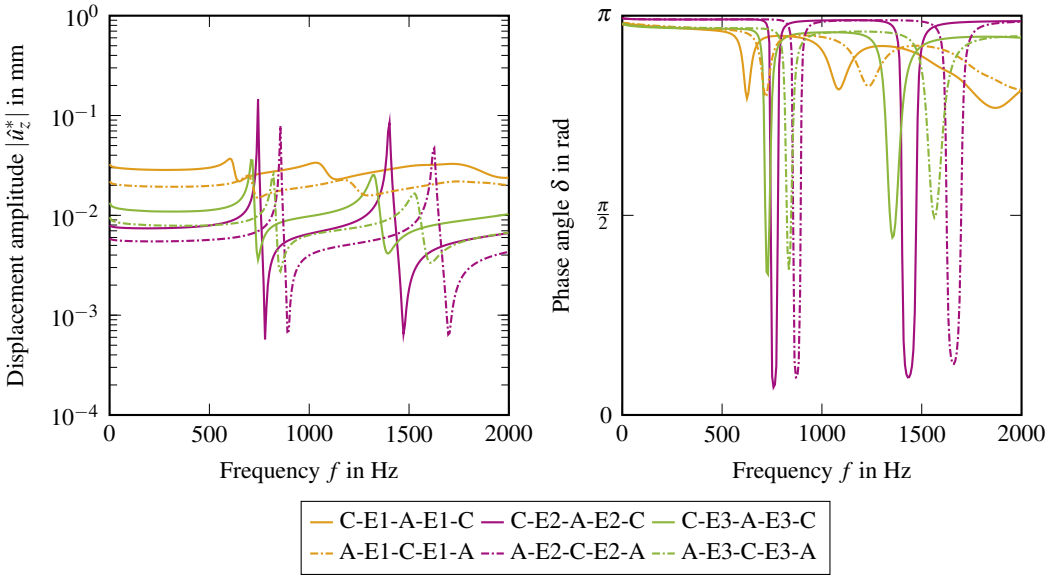


Figure 3: Frequency response to forced vibration of six different types of HyCEMLs in terms of transverse displacement amplitude and phase angle. [17]

In the left graph of Figure 3, the overall displacement amplitudes of the HyCEMLs are depicted. These amplitudes are influenced by the choice of elastomer material, with the most compliant elastomer, E1, producing the highest amplitudes. Near the natural frequency peaks on the response curve, however, laminates with stiffer elastomers, such as E2, exhibit the highest amplitudes. Additionally, these peaks are narrower compared to those of laminates with more compliant damping layers, indicating lower modal damping values. The right graph displays the phase angle between the applied oscillating force and the recorded displacement. Vibration modes can be identified by a phase angle shift δ of up to π, depending on the amount of damping featured by the mode at hand. Consequently, higher modal damping factors result in smaller phase angle shifts. At higher excitation frequencies, distinct modes become more difficult to identify, particularly for laminates with the highly compliant elastomer E1.
The results presented for the forced vibration of the six HyCEMLs are consistent with the findings from the preceding modal analyses. They confirm that the choice of elastomer material not only governs the overall level of vibration damping but also influences the structures' dynamic stiffness, as evidenced by the resulting displacement amplitudes. As elastomer materials can vary even more drastically in their stiffness, a parametric study is conducted, investigating how different laminate layups are influenced by a variation in elastomer stiffness. As an example, Figure 4 shows the influence of a variation in elastomer E1's stiffness in terms of a stiffness scaling factor κ_{E^*}, which is applied to the complex modulus

$$\tilde{E}^*(\omega) = \kappa_{E^*} E^*(\omega) = \kappa_{E^*}\left(E'(\omega) + \mathrm{i}E''(\omega)\right). \tag{8}$$

In general, the vibration characteristics of both types of laminates are influenced similarly by the stiffness variation of elastomer E1. Stiffening the damping plies in both cases leads to higher natural frequencies, with the higher modes experiencing more significant shifts. Conversely, reducing the stiffness decreases this mode dependency. Both increasing and decreasing the stiffness of the damping layers affect the

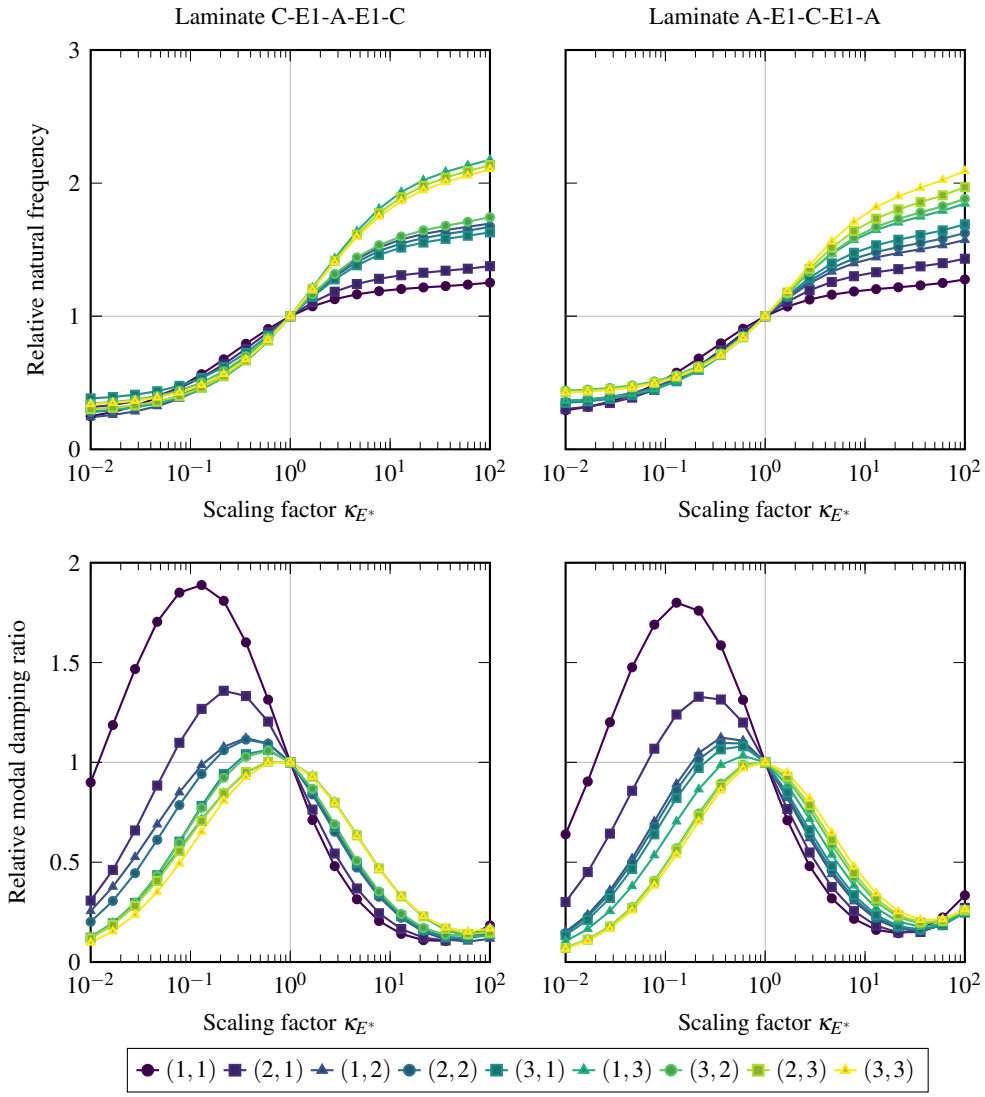


Figure 4: Relative natural frequencies and modal damping ratios for laminates C-E1-A-E1-C and A-E1-C-E1-A with varied complex stiffness in terms of κ_{E^*}. [17]

system within a specific range, showing convergence towards a plateau in both directions.
A different pattern emerges when considering the modal damping ratios in the graphs on the bottom of Figure 4, which also behave similarly for both types of laminates. Each of the nine modes examined exhibits a distinct maximum in their modal damping ratio within the range of the scaling factor κ_{E^*}. The peak modal damping for each mode occurs at different values of κ_{E^*}. While the higher modes do not surpass the damping achieved in the reference configuration ($\kappa_{E^*} = 1$), a significant increase in modal damping can be obtained for the first two vibration modes by using a more compliant elastomer. For the given plate dimensions and elastomer E1, an optimal modal damping appears to be achieved for the higher vibration modes, largely independent of the specific laminate layup.

5. Conclusion

In this study, an analytical model is employed to determine the vibration characteristics of different types of HyCEMLs. The findings indicate that the choice of elastomer material used largely dictates the resulting dynamic behaviour, whereas the overall laminate layup has a smaller influence. This correlation is confirmed under forced vibration and offers the possibility of designing CLD laminates, which offer high

bending stiffness under static loading while also being highly damped under vibration. A variation of the elastomers' complex stiffness whilst maintaining a constant loss factor shows the occurrence of a mode-dependent optimal elastomer stiffness for maximum damping, which is consistent with other reports in literature. Finally, the strong laminate and material dependencies illustrated in this study underline the necessity of efficient predictive models complementing experimental characterisation methods in the design phase of damped lightweight materials.

Acknowledgments

This work has been funded by the Deutsche Forschungsgemeinschaft (DFG, German Research Foundation) within the SPP1897 "Calm, Smooth, Smart – Novel approaches for influencing vibrations by means of deliberately introduced dissipation", project KA 4224/3-2 "HyCEML – Hybrid CFRP/elastomer/metal laminates containing elastomeric interfaces for deliberate dissipation" (Karlsruhe Institute of Technology). The work is also part of the Heisenberg project "Digitalization of fiber-reinforced polymer processes for resource-efficient manufacturing of lightweight components", funded by the DFG (project no. 798455807141). Furthermore, the authors would like to acknowledge Gummiwerk KRAIBURG GmbH & Co. KG for providing the elastomer material.

References

[1] T. Sinmazçelik, E. Avcu, M. Ö. Bora, and O. Çoban. A review: Fibre metal laminates, background, bonding types and applied test methods. *Materials & Design*, 32(7):3671–3685, 2011. ISSN 02613069. doi: 10.1016/j.matdes.2011.03.011.

[2] M. Sadighi, R. C. Alderliesten, and R. Benedictus. Impact resistance of fiber-metal laminates: A review. *International Journal of Impact Engineering*, 49:77–90, 2012. ISSN 0734743X. doi: 10.1016/j.ijimpeng.2012.05.006.

[3] J. Bienias, P. Jakubczak, and K. Dadej. Low-velocity impact resistance of aluminium glass laminates – Experimental and numerical investigation. *Composite Structures*, 152(15):339–348, 2016. ISSN 02638223. doi: 10.1016/j.compstruct.2016.05.056.

[4] M. Stoll, F. Stemmer, S. Ilinzeer, and K. A. Weidenmann. Optimization of Corrosive Properties of Carbon Fiber Reinforced Aluminum Laminates due to Integration of an Elastomer Interlayer. *Key Engineering Materials*, 742:287–293, 2017. doi: 10.4028/www.scientific.net/KEM.742.287.

[5] V. Sessner, M. Stoll, A. Feuvrier, and K. A. Weidenmann. Determination of the Damping Characteristics of Fiber-Metal-Elastomer Laminates Using Piezo-Indicated-Loss-Factor Experiments. *Key Engineering Materials*, 742:325–332, 2017. doi: 10.4028/www.scientific.net/KEM.742.325.

[6] H. Oberst. Über die Dämpfung der Biegeschwingungen dünner Bleche durch fest haftende Beläge. *Acta Acustica united with Acustica*, 2(4):181–194, 1952.

[7] V. Sessner, A. Jackstadt, W. V. Liebig, L. Kärger, and K. A. Weidenmann. Damping Characterization of Hybrid Carbon Fiber Elastomer Metal Laminates using Experimental and Numerical Dynamic Mechanical Analysis. *Journal of Composites Science*, 3(1):3, 2019. doi: 10.3390/jcs3010003.

[8] V. Sessner, W. V. Liebig, and K. A. Weidenmann. Modal damping behavior of plane and 3D curved constrained layer damping CFRP-elastomer-metal laminates. *Composites Part C: Open Access*, 2: 100037, 2020. ISSN 26666820. doi: 10.1016/j.jcomc.2020.100037.

[9] V. Sessner, W. V. Liebig, A. Jackstadt, D. Schmid, T. Ehrig, K. Holeczek, N. Gräbner, P. Kostka, U. von Wagner, K. A. Weidenmann, and L. Kärger. Wide Scale Characterization and Modeling

of the Vibration and Damping Behavior of CFRP-Elastomer-Metal Laminates—Comparison and Discussion of Different Test Setups. *Applied Composite Materials*, 28(5):1715–1746, 2021. ISSN 0929-189X. doi: 10.1007/s10443-021-09934-7.

[10] A. Jackstadt, W. V. Liebig, V. Sessner, K. A. Weidenmann, and L. Kärger. Application of a mixed variational higher order plate theory towards understanding the deformation behavior of hybrid laminates. *PAMM*, 19(1), 2019. ISSN 1617-7061. doi: 10.1002/pamm.201900048.

[11] A. Jackstadt and L. Kärger. Extension of an analytical solution of a unified formulation to the frequency response of composite plates with viscoelastic layers. *PAMM*, 20(1), 2021. ISSN 1617-7061. doi: 10.1002/pamm.202000234.

[12] A. Jackstadt, W. V. Liebig, and L. Kärger. Analytical modeling and investigation of constrained layer damping in hybrid laminates based on a unified plate formulation. *International Journal of Mechanical Sciences*, 216:106964, 2022. ISSN 00207403. doi: 10.1016/j.ijmecsci.2021.106964.

[13] Gummiwerk KRAIBURG GmbH & Co. KG. Technical Data Sheet KRAIBON® SAA9579/52, 2014.

[14] Gummiwerk KRAIBURG GmbH & Co. KG. Technical data sheet KRAIBON® HVV9632/59, 2017.

[15] Gummiwerk KRAIBURG GmbH & Co. KG. Technical data sheet KRAIBON® HAA9275/45, 2022.

[16] V. Sessner. *Charakterisierung und Modellierung des Dämpfungsverhaltens von hybriden Faser-Metall-Elastomer-Laminaten*. Dissertation, Karlsruhe Institute of Technology, Karlsruhe, Germany, 2021.

[17] A. Jackstadt. *Constrained-layer damping in hybrid fibre metal elastomer laminates and its tolerance to damage*. Dissertation, Karlsruhe Institute of Technology, Karlsruhe, Germany, 2024.

[18] L. Demasi. ∞^6 Mixed plate theories based on the Generalized Unified Formulation. Part I: Governing equations. *Composite Structures*, 87(1):1–11, 2009. ISSN 02638223. doi: 10.1016/j.compstruct.2008.07.013.

[19] L. Demasi. ∞^6 Mixed plate theories based on the Generalized Unified Formulation.: Part II: Layerwise theories. *Composite Structures*, 87(1):12–22, 2009. ISSN 02638223. doi: 10.1016/j.compstruct.2008.07.012.

ENGINEERED MYCELIUM FOR FIREPROOFING FLAMMABLE COMPOSITE MATERIALS AND STRUCTURES.

Everson Kandare[1], Nattanan Chulikavit[1], Cheng Wang[2], Tien Huynh[3], Anthony Chun Yin Yuen [4], Akbar Khatibi[1], Raj Das[1]

[1]School of Engineering, RMIT University, Bundoora, VIC 3083, Australia
Email: Everson.Kandare@rmit.edu.au, Web Page: https://www.rmit.edu.au/contact/staff-contacts/academic-staff/k/kandare-associate-professor-everson
[2]School of Mechanical and Manufacturing Engineering, University of New South Wales (Sydney), NSW 2052, Australia
Email: c.wang@unsw.edu.au, Web Page: https://research.unsw.edu.au/people/dr-cheng-wang
[3]School of Science, RMIT University, Bundoora, VIC 3083, Australia
Email: Tien.Huynh@rmit.edu.au, Web Page: https://www.rmit.edu.au/contact/staff-contacts/academic-staff/h/huynh-dr-tien
[4]Department of Building Environment and Energy Engineering, The Hong Kong Polytechnic University, Hung Hom, Kowloon, Hong Kong SAR, China
Email: anthony-cy.yuen@polyu.edu.hk, Web Page: https://www.polyu.edu.hk/en/beee/people/academic-staff/dr-yuen-chun-yin-anthony/

Keywords: Polymer composites, Flammability, Combustion, Fireproofing, Mycelium

Abstract
This study investigates the influence of deacetylation and hollow glass microsphere incorporation on the thermal stability and fire reaction properties of mycelium. Deacetylation, achieved through alkaline treatment of mycelium, enhances thermal stability and char formation by increasing chitosan content. Thermogravimetric analysis revealed improved char yields with increased deacetylation, correlating with enhanced fire reaction properties of mycelium. Microscale combustion tests using pyrolysis-combustion flow calorimetry revealed decreased heat release rates in deacetylated mycelium. Cone calorimeter tests simulating real-world fire scenarios, demonstrated superior fire performance in deacetylated mycelium, with delayed ignition and reduced flaming intensity. Incorporating deacetylated mycelium as fireproofing mats in glass fiber-reinforced polymer laminates improved fire safety by forming carbonaceous char at the heat-exposed surface. This research highlighted the potential of deacetylated mycelium as a sustainable fireproofing material for lightweight polymer composites in fire-prone environments, paving the way for effective bio-derived fireproofing solutions.

1. Introduction

Fibre-reinforced polymer (FRP) composites are increasingly used in engineering design, including civil infrastructure, where weight minimisation is a critical objective [1]. FRP composites have excellent structural efficiency making them desirable for applications requiring lightweight materials. Despite their adoption in various engineering fields, the use of FRP composites in fire-prone applications remains a significant challenge. In the event of exposure to high heat flux or radiant heat from a fire, the polymer matrix within the composites volatilizes into combustible gases, leading to ignition and flaming combustion [2]. A major issue during the flaming combustion of FRP composites is the emission of highly toxic gases, fumes, and sometimes heavy smoke due to incomplete combustion [2]. This issue is particularly critical in civil infrastructure, where fatalities and serious injuries in building fires are often caused by entrapment due to smoke-induced vision impairment or inhalation of toxic gases. Recent tragic examples, including the 2017 Grenfell Tower fire [3], where 72 people lost their lives, and 2010 Shanghai, China, apartment fire that killed at least 58 people and injured more than 70 others [4], highlight the risks posed by the use of flammable materials in civil structures.

The flaming combustion intensity for FRP composites, along with the amount of toxic volatiles or smoke produced, can be controlled by modifying the flammable polymer matrix using fire retardant additives [5]. These additives can be applied in the form of fire retardant nano- or microparticles incorporated into the polymer matrix, used for fibre treatment, or as fireproofing materials on the heat-exposed surface of the composite [6]. Generally, fire retardant additives for FRP composites involve materials that promote surface char formation reduce free radicals and fuel load thereby precluding fire propagation.

Currently, state-of-the-art fire retardant technology involves the use of phosphorous and nitrogen-based fire retardants, which, unfortunately, have been linked to reproductive and developmental issues, environmental persistence, and harm to aquatic organisms [7]. Therefore, it is imperative to develop new, biodegradable and environmentally sustainable fire retardants and fire proofing systems that are just as effective as their synthetic counterparts. Several bio-derived materials have potential for use as fire retardant additives or fireproofing systems for FRP composites. Some of these biodegradable fire retardants include dopamine, tannin, phytic acid, casein and mycelium [8]. Mycelium is particularly promising due to its high chitin content, which has been demonstrated to promote surface char formation, thereby insulating the underlying flammable composite. Additionally, mycelium can be grown from recovered organic waste, diverting waste from landfills. It also grows in the dark, without need for energy to support growth, further enhancing its sustainability and eco-friendliness.

Mycelium, the thread-like hyphae filaments of fungi, has chitin-constituted cell walls that exhibit promising fire-retardant properties. When exposed to heat, mycelium decomposes into a consolidated char. This surface char can slow down heat transfer to the flammable substrate and prevent the release of combustible volatiles into the combustion zone. When mycelium is treated with an alkaline medium such as sodium hydroxide (NaOH), deacetylation occurs, converting chitin into chitosan. Additionally, the alkaline-induced degradation of β-1,4-glycosidic chemical bonds produces low molecular weight hydroxyl-terminated polymer segments, which promote char formation [9]. The elevated char production underscores the potential of mycelium as an effective fireproofing material.

Limited research has focused on assessing the flammability characteristics of mycelium and its derivatives. This study investigated the correlation between thermogravimetric analysis (TGA) char yields and the flammability properties of mycelium. Micro-scale combustion properties of unmodified and deacetylated mycelium were evaluated using pyrolysis-combustion flow calorimetry (PCFC), while the flammability characteristics of mycelium were analyzed using a cone calorimeter. Additionally, the study explored the influence of hollow glass microspheres (HGM) on the thermal stability and flammability characteristics of mycelium. At high temperatures, HGM particles melt, forming viscous and potentially thermal insulative SiO_2 micro-architectures on the heat-exposed surface.

UL-94 flammability tests evaluated the flame spread characteristics of mycelium. Various parameters, including the duration of flame persistence, dripping behavior, and burning rate, were measured. The effectiveness of unmodified and deacetylated mycelium in fireproofing glass fibre-reinforced epoxy polymer (GFRP) composites was assessed using a cone calorimeter. Microstructural characterization of the char was conducted using scanning electron microscopy (SEM) to elucidate the mechanisms responsible for variations in char yields and the fire response of mycelium and its derivatives.

2. Methodology

A brief description of the materials and methodology followed in preparing the materials for experimental analysis is provided in this paper. For a detailed overview of the methodology, the reader is referred to a previous publication [10]. An isolated culture of mycelium fungi, *Ganoderma australe*, growing on malt extract agar was sourced from RMIT University's Fungal Culture Collection (Australia) and used as an inoculum. All materials used for cultivating mycelium were sterilised at 121°C for 30 min to prevent pathogenic or bacterial contamination. Blackstrap molasses (E&A Salce, Australia) was diluted to a 10 wt.% molasses/water solution using ionised water. A 3 cm-diameter circular disc of the fungal culture cut from the agar plate using the tip of a sterilised 50 mL centrifuge

tube was transferred to the centre of the PP container containing 350 mL diluted molasses. In the case of HGM-containing mycelium, 10 mL of HGM particles were sifted over molasses using a sieve. The PP container was sealed and incubated (temperature 25°C; white light) for 60 days. In the case of HGM-reinforced mycelium, 10 mL of the West System 411 HGM particles (ATL Composites, Australia) were sifted over molasses using a sieve. The residual molasses on mycelium biomass was rinsed with deionised water. Deacetylation was conducted at 40°C to preserve the microstural integrity of mycelium.

Some mycelium sheets were deacetylated using 2M reagent-grade sodium hydroxide, NaOH (Sigma Aldrich, Australia) at 40°C for 2 or 8 hr. Another batch of mycelium was deacetylated using 4M NaOH at 40°C over 2 hr. A standard nomenclature, concentration/temperature/time, was used to identify deacetylated mycelium. For example, mycelium deacetylated using 2M NaOH at 40°C for 2 hr was identified as 2M/40°C/2h. The unmodified (as-grown) and deacetylated mycelium sheets incorporating HGM particles were identified as Control-HGM and 2M/40°C/8h-HGM, respectively. Table 1 shows the deacetylation conditions, along with the identities of the mycelium samples. The calculation of the degree of deacetylation, DD, is explained in our previous publication [10].

Table 1. Deacetylation conditions (NaOH concentration and incubation time), biomass yields and the degree of deacetylation for mycelium sheets treated at 40°C.

Sample	[NaOH] (M)	Time (hr)	HGMs	[a]Biomass (%)	[b]DD (%)	[c]DD* (%)
Control	-	-	-	-	45 ± 3	48 ± 2
2M/40°C/2h	2	2	-	74 ± 4	56 ± 4	54 ± 4
2M/40°C/8h	2	8	-	62 ± 3	84 ± 2	83 ± 3
4M/40°C/2h	4	2	-	66 ± 1	75 ± 3	77 ± 2
Control-HGM	-	-	Yes	-	49 ± 1	46 ± 4
2M/40°C/8h-HGM	2	8	Yes	65 ± 3	86 ± 3	81 ± 2

[a]Biomass (%) is percent ratio of dry mass yield of a deacetylated to the unmodified mycelium.
[b]DD: degree of deacetylation (absorption peak intensity ratio of the C=O to OH bands).
[c]DD*: degree of deacetylation (integrated area ratio of the C=O and OH absorption bands).

Mycelium sheets were dried at 60°C over 3 hr and stored in hermetic plastic bags to prevent moisture absorption. Dry mycelium was used for microstructural characterization, thermal stability evaluation and microscale combustion calorimetry. For cone calorimetry tests, mycelium sheets were stacked and hot-pressed to form multi-layer laminates as described later.

The microstructure and morphology of both pristine mycelium sheets and residual char collected during TGA experiments at 600 or 850°C were characterised using the SEM (FEI Qanta 200) equipped with an Energy Dispersive X-Ray Spectrometer (SEM-EDS) and operated by the Aztec software. Mycelium sheets or residual char powder were bonded to an electrically conductive carbon tape which was then affixed to a sample holder. The sample was coated with iridium in a Leica ACE600 sputter coater operated at 8×10^{-3} mbar to achieve a coating thickness of ~5 nm.

The thermal stability of mycelium derivatives was evaluated using the Perkin Elmer STA 6000. Mycelium flakes (~12 mg) were placed into an alumina crucible which was then inserted into the TGA furnace. The furnace temperature was increased from 35 to 850°C at a rate of 30°C/min (flowing N_2 gas; 20 mL/min). A minimum of three repeat experiments were conducted for each mycelium sample. Microscale combustion properties of mycelium were evaluated using the Fire Testing Technology (Gosport, UK) supplied PCFC in accordance with the ASTM D7309-21 standard [11]. Mycelium flakes ~5 mg) were placed into the sample holder which was then inserted into the PCFC chamber. The chamber temperature was increased from 75 to 850°C at a rate of 1K/s under an N_2 (80 cm^3/min) and O_2 (20 cm^3/min) atmosphere. The combustion chamber temperature was maintained at 900°C.

Wet unmodified or alkaline-treated mycelium sheets were stacked to create multilayer mycelium only laminates. Mycelium laminate layups were hot-pressed at 60°C under 0.25 MPa compressive pressure for at least 3 hr, resulting in denatured and consolidated laminates of ~4.5 mm thickness. Mycelium laminates were transferred to a compression-loaded jig and further dried at 60°C in a conventional oven. Two mycelia only laminates were manufactured: unmodified (Control-Lam) and deacetylated (2M/40°C/8h-Lam). Fire reaction properties of the Control-Lam and 2M/40°C/8h-Lam mycelium only laminates were evaluated using the cone calorimeter operated at an incident heat flux of 35 kW/m^2. Consolidated mycelium-only laminates (unmodified and deacetylated) measuring 125 × 13 × 2 mm were evaluated under the UL-94 vertical flame test according to ASTM D3801-20 guidelines [12].

To assess their fireproofing efficacy, mycelium derivates were bonded onto the heat-exposed surface of the GFRP laminate. Due to their fragility, mycelium sheets required reinforcement prior to integration onto GFRP laminates. Two hot-pressed mycelium sheets (Control or 2M/40°C/8h) were bonded between 35 gsm chopped strand glass fibre veils (Glass Fibre Tissue & Veil, Australia) using epoxy. The glass fibre veil/mycelium/epoxy fireproofing mat was cured at ~23°C for 24 hr and post-curing at 60°C for 8 hr. The respective weight fractions of the glass fibre veil, mycelium, and epoxy matrix were 5, 31, and 64%. A baseline glass fibre veil/epoxy mat without mycelium was manufactured in the same way.

Eight-ply GFRP composites were manufactured via vacuum-assisted resin infusion using plain woven glass fabric (570 gsm) (Colan, Australia) and epoxy resin/amine hardener (West System 105/206) (ATL Composites, Australia). The glass fibre to epoxy weight ratio in the GFRP-Laminate, was 40:60. Fireproofing glass veil/epoxy mats with or without mycelium were then bonded onto the heat-exposed surface of the GFRP laminate. Fireproofed GFRP laminates were vacuum-bagged, cured at ~23°C for 24 hr and post-cured at 60°C for 8 hr. GFRP-Glass veil, GFRP-Control, and GFRP-2M/40°C/8h respectively refer to a GFRP laminate incorporating: a two-layer glass veil without mycelium; unmodified mycelium (Control); and deacetylated (2M/40°C/8h) fireproofing mats..

Fire properties of mycelium only laminates and the GFRP-Laminate were evaluated using square (85 × 85 mm) specimens in accordance with ISO 5660 [13]. Cone calorimeter specimens were wrapped in thin aluminium foil and horizontally mounted ~25 mm below the radiant cone heater, which was operated at 35 kW/m^2. Fire reaction properties of fireproofed GFRP laminates (100 × 100 mm) were evaluated under cone calorimeter conditions in accordance with ISO 5660 [13]. At least three experiments were conducted for each configuration.

3. Results and discussion

Mycelium-only laminates and mycelium fireproofed GFRP laminates are shown in Figure 1. A sideview image of the mycelium-only laminate revealed a consolidated structure layup suggesting strong bonding between mycelium in the absence of a binder. The two-layer mycelium/veil system bonded well to the GFRP laminate as shown in Figure 1(B).

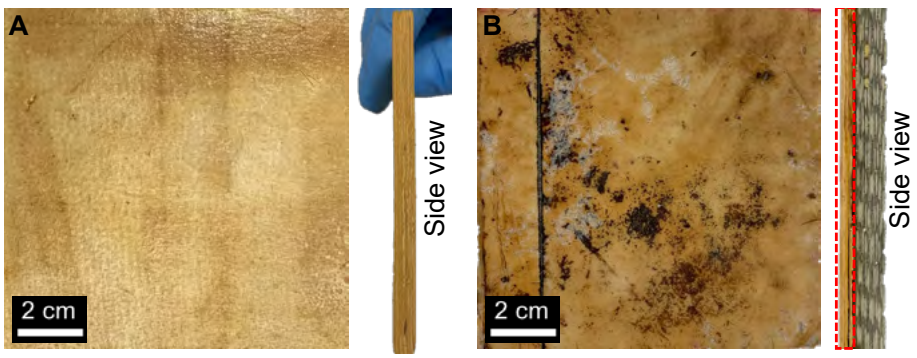


Figure 1. Top and side-view of (A) mycelium-only laminate and (B) mycelium fireproofed GFRP laminate. Dashed red lines in (B) indicate the fireproofing mycelium bonded to the GFRP laminate [10].

Figure 2(A) shows that under the mildest deacetylation conditions of 2M NaOH at 40°C for 2 hr, the filamentous hyphae network was preserved. Sample 2M/40°C/2h, had the highest biomass retention of 74% among all deacetylated mycelium samples. Increasing the deacetylation time from 2 to 8 hr or elevating the NaOH concentration from 2 to 4M caused the hyphae strands to fuse into micro-globular features, as revealed in Figures 2(B, C). Degree of deacetylation increased with time or NaOH concentration. However, harsher deacetylation conditions further reduced biomass yields. The reduction in biomass yields upon deacetylation was attributed to deproteinization caused by the cleavage of chemical bonds between chitin and proteins [14].

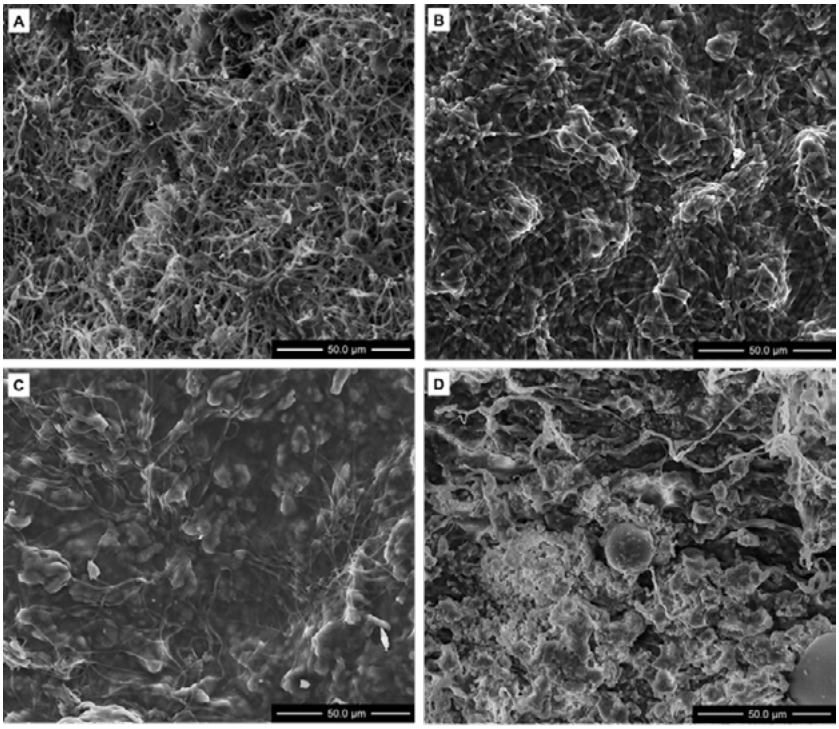


Figure 2. SEM images of deacetylated mycelium (A) 2M/40ºC/2h, (B) 2M/40ºC/8h, (C) 4M/40ºC/2h and (D) 2M/40ºC/8h-HGM. Spherical particles in (D) indicate HGM particles [10].

Deacetylation converted chitin components into chitosan, which has unique thermal degradation properties including the ability to form large quantities of surface char. TGA experiments revealed how different alkaline treatment conditions affected the thermal stability of mycelium. The TGA mass-temperature and derivative thermogravimetry profiles, Figure 3, showed five distinct mass loss events for unmodified mycelium, attributed to the decomposition of hydrophobins, dehydration, and the breakdown of fungal cell wall components [15]. The primary thermal degradation stage resulted in significant mass loss due to the decomposition of chitin, amino acids, and polysaccharides, followed by the formation of primary and secondary char.

Deacetylation had minimal impact on the thermal degradation temperatures and mass loss rates for the first two stages. However, the third mass loss event showed significant differences; for example, in the 2M/40°C/8h sample, the peak thermal degradation temperature occurred about 70°C earlier than in unmodified mycelium, indicating an earlier onset of primary thermal decomposition. Additionally, the mass loss during this stage was lower in deacetylated mycelia. The fourth and final mass loss events were largely similar across all samples, with the final event occurring between 600 and 835°C. These results suggest that while the overall thermal degradation mechanisms remain consistent, deacetylation particularly affects the primary thermal degradation stage and improves the primary char yield.

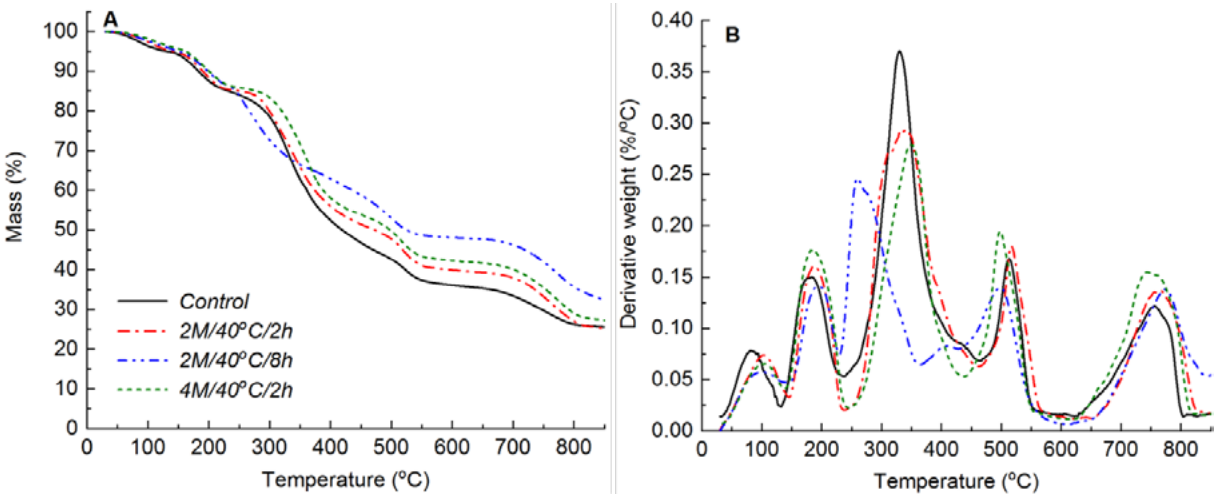


Figure 3. (A) Mass-temperature and (B) mass loss rate profiles for unmodified and deacetylated mycelium without HGM particles [10].

There were no significant differences in the TGA evaluated thermal stability of mycelium with and without HGM particles [10]. This was attributed to the relatively low content of HGM particles embedded in mycelium. However, microstructural analysis of residual char collected at 600°C revealed the presence of SiO_2 which later formed an integrated porous network at 850°C as shown in Figure 4.

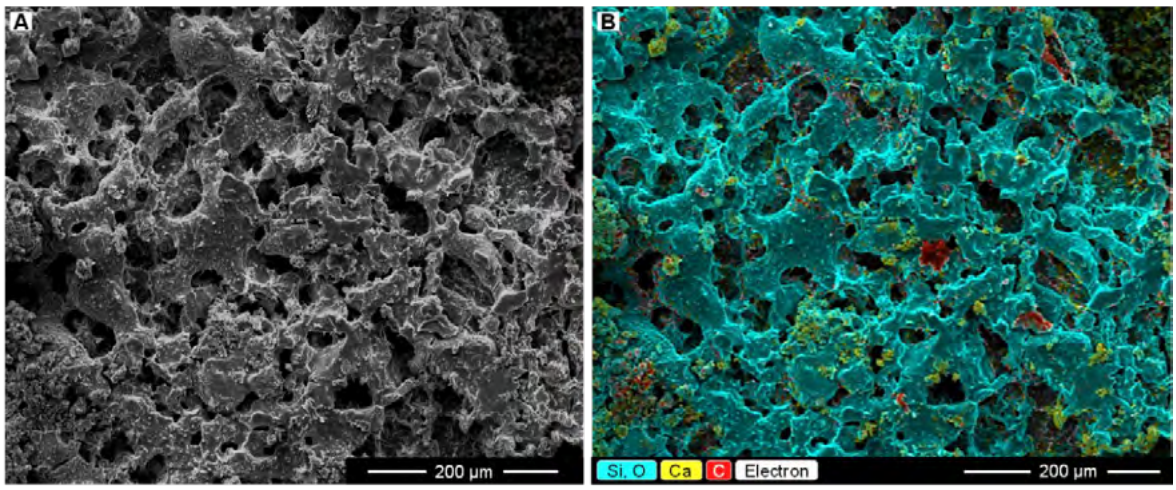


Figure 4. SEM (left) and EDS (right) image of the residual char for 2M/40°C/8h-HGM at 850°C [10].

The specific heat release rates (HRR) measured by PCFC for unmodified and deacetylated mycelium samples, shown in Figure 5(A), indicated lower HRRs for deacetylated samples. Five distinct combustion stages were identified, except for the 2M/40°C/8h sample, which exhibited unique thermal degradation pathways. The HRR-temperature profiles for samples under mild deacetylation conditions resembled that of unmodified mycelium, while harsher conditions significantly altered the profiles, particularly for 2M/40°C/8h, which had a notably lower peak HRR (pHRR). The TGA mass loss rate and PCFC HRR profiles for unmodified mycelium matched despite different heating conditions. While reductions in specific pHRR, shifts to higher peak HRR, and relatively lower heat release capacity indicate improved flammability for deacetylated mycelium, these metrics alone do not fully capture the material's combustion behavior. Consequently, cone calorimeter tests were necessary to evaluate the fire reaction properties of mycelium-only laminates and subsequently GFRP fireproofing efficacy of mycelium under conditions simulating a real fire.

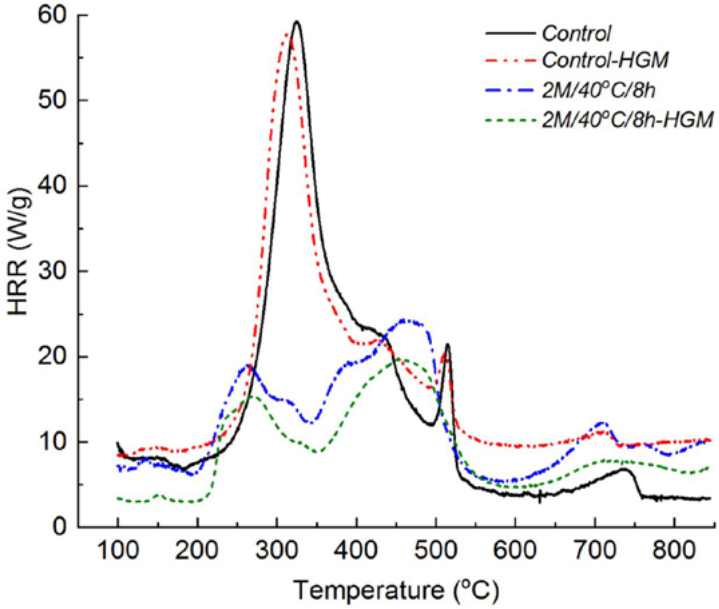


Figure 5. PCFC-measured specific HRR profiles of unmodified and deacetylated mycelium with (Control-HGM and 2M/40°C/8h-HGM) and without HGM particles (Control and 2M/40°C/8h) [10].

The cone calorimeter flammability characteristics of GFRP-Lam are compared to those of Control-Lam and 2M/40°C/8h-Lam in Figure 6. Sample 2M/40°C/8h-Lam was selected for fire reaction evaluation based on its high TGA char yield and lowest PCFC specific HRR. Control-Lam exhibited a sharp HRR spike shortly after ignition, reaching an average peak value of 149 kW/m^2 within 10 s, followed by a secondary peak event at around 50 s post-ignition. In contrast, 2M/40°C/8h-Lam showed no sharp HRR spike, maintaining HRR values below 50 kW/m^2 with broad peak events recorded at approximately 185 s and 398 s. Despite the greater total heat release from 2M/40°C/8h-Lam compared to Control-Lam, its flaming intensity was significantly lower due to enhanced char-forming characteristics. Further, both Control-Lam and 2M/40°C/8h-Lam exhibited substantially lower HRR profiles compared to GFRP-Lam, demonstrating mycelium as a potential fireproofing material for flammable composites. The deacetylated mycelium achieved UL94 V-0 rating suggesting superior resistance to flame spread [16].

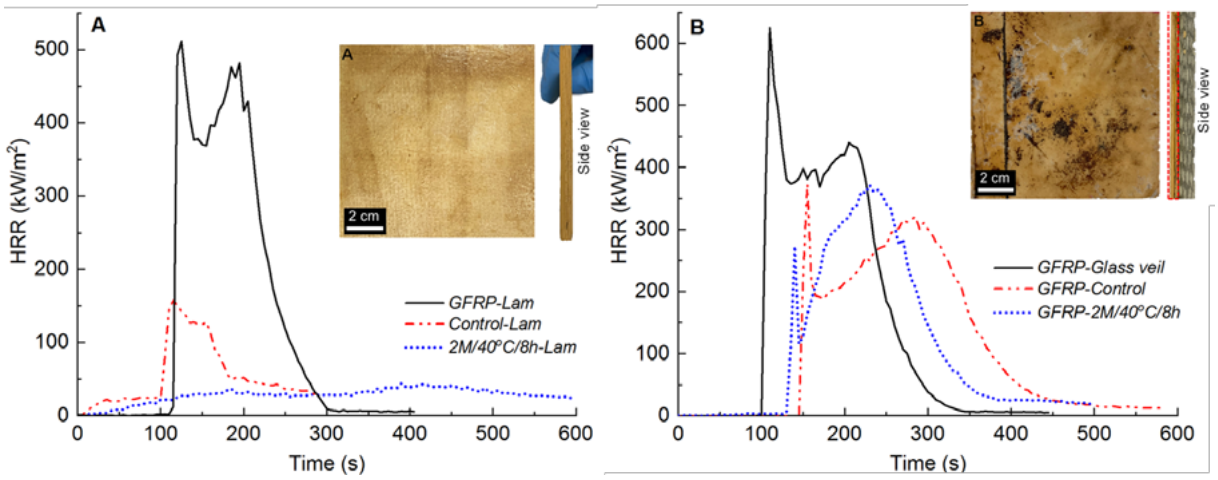


Figure 6. Cone calorimeter HRR profiles for (A) mycelium-only (Control-Lam and 2M/40°C/8h-Lam) and GFRP-Lam and (B) GFRP laminates fireproofed using the glass veil (GFRP-glass veil), unmodified (GFRP-Control) and deacetylated mycelium (GFRP-2M/40°C/8h) at 35 kW/m^2 [10].

4. Conclusions

This study investigated the impact of deacetylation on mycelium's fire reaction properties, correlating thermal degradation profiles with char yields. Increasing the degree of deacetylation through alkaline treatment enhanced thermal stability and char formation of mycelium. PCFC tests indicated improved combustion properties in deacetylated mycelium, with decreased heat release rates and combustion capacities. Cone calorimeter tests simulating real-world fire scenarios, revealed superior fire performance in deacetylated mycelium, particularly delaying ignition and reducing flaming intensity. Incorporating deacetylated mycelium as fireproofing mats in GFRP laminates improved fire safety by forming carbonaceous char at the laminate surface, suggesting its potential for protecting flammable polymer composites in fire-prone environments such as transport vehicles and buildings.

Acknowledgments

We acknowledge RMIT technical support in materials manufacturing, charactirisation and testing.

References

[1] H. Fang, Y. Bai, W. Liu, Y. Qi and J. Wang. Connections and structural applications of fibre reinforced polymer composites for civil infrastructure in aggressive environments. *Composites Part B: Engineering*. 164:129-143, 2019.
[2] J. Giebułtowicz, M. Rużycka, P. Wroczyński, DA. Purser and AA. Stec. Analysis of fire deaths in Poland and influence of smoke toxicity. *Forensic Science International*. 277:77-87, 2017.
[3] SM. Moore-Bick. Report of the Public Inquiry into the Fire at Grenfell Tower on 14 June 2017. Available: https://www.grenfelltowerinquiry.org.uk/phase-1-report. 2019.
[4] Farah M, Anita L. Eight detained after Shanghai apartment fire kills 53. *World News.* 2010; https://www.reuters.com/article/uk-china-fire-idUKTRE6AF1EJ20101116. Accessed 25/05/2024.
[5] SM. Seraji, P. Song, RJ. Varley, S. Bourbigot, D. Voice and H. Wang. Fire-retardant unsaturated polyester thermosets: The state-of-the-art, challenges and opportunities. *Chemical Engineering Journal.* 430:132785, 2022.
[6] S. Liang, NM. Neisius and S. Gaan. Recent developments in flame retardant polymeric coatings. *Progress in Organic Coatings*. 76(11):1642-1665, 2013.
[7] J. Andresen, A. Grundmann and K. Bester. Organophosphorus flame retardants and plasticisers in surface waters. *Science of The Total Environment*. 332(1-3):155-166, 2004.
[8] SH. Jeong, CH. Park, H. Song, JH. Heo, JH. Lee. Biomolecules as green flame retardants: Recent progress, challenges, and opportunities. *Journal of Cleaner Production*. 368:133241, 2022.
[9] S. Wang, L. Du, P. Zhu, Z. Jiang. Influence of hydroxyl-terminated phosphoramidates on the flame retardancy of microfiber synthetic leather. *Polymer Degradation and Stability*. 199:109897, 2022.
[10] N. Chulikavit, C. Wang, T. Huynh, ACY. Yuen, A. Khatibi, E. Kandare. Fireproofing flammable composites using mycelium: Investigating the effect of deacetylation on the thermal stability and fire reaction properties of mycelium. *Polymer Degradation and Stability*. 215:110419, 2023.
[11] ASTM D7309 - Standard Test Method for Determining Flammability Characteristics of Plastics and Other Solid Materials Using Microscale Combustion Calorimetry, 2013.
[12] ASTM D3801-20 Standard test method for measuring the comparative burning characteristics of solid plastics in a vertical position. American Society for Testing and Materials, 2020.
[13] ISO 5660-1 AMD:1 - Reaction-to-fire tests - Heat release, smoke production and mass loss rate — Part 1: Heat release rate (cone calorimeter method) and smoke production rate (dynamic measurement), 2019.
[14] M. Triunfo et al., Characterization of chitin and chitosan derived from Hermetia illucens, a further step in a circular economy process. *Scientific Reports*. 12(1):1-17, 2022.
[15] L. Winandy, F. Hilpert, O. Schlebusch, and R. Fischer. Comparative analysis of surface coating properties of five hydrophobins from Aspergillus nidulans and Trichoderma reseei. *Scientific Reports*. 8(1):12033, 2018.
[16] N. Chulikavit, T. Huynh, A. Khatibi, R. Das, and E. Kandare. Thermal degradation and flame spread characteristics of epoxy polymer composites incorporating mycelium. *Scientific Reports*. 13(1):17812, 2023.

INVESTIGATION OF ENERGY ABSORPTION AND ULTRASOUND-BASED DAMAGE RESPONSE OF 3D PRINTED COMPOSITE STAR HOURGLASS SHAPED LATTICE STRUCTURES

Amin Farrokhabadi[1], Houyu Lu[2], Dimitrios Chronopoulos[3]
[1] Mecha(tro)nic System Dynamics (LMSD), Ghent and Aalst Campuses, KU Leuven University, Belgium, Email: amin.farrokhabadi@kuleuven.be.
[2] Mecha(tro)nic System Dynamics (LMSD), Ghent and Aalst Campuses, KU Leuven University, Belgium, Email: houyu.lu@kuleuven.be.
[2] Mecha(tro)nic System Dynamics (LMSD), Ghent and Aalst Campuses, KU Leuven University, Belgium, Email: dimitrios.chronopoulos@kuleuven.be.

Keywords: Reinforced PLA, Additive manufacturing, Energy absorption, Star Hourglass Shaped Auxetic, Ultrasound.

Abstract
In this study, a novel combined auxetic honeycomb structure, featuring both star and hourglass shapes, is introduced. Experimental evaluations of quasi-static compressive loading applied to these structures in the vertical orientations are encompassed by the research. For specimen preparation, the manufacturing process involved fused filament fabrication, commonly known as 3D printing. During the test, the nonlinear response of the star-hourglass-shaped auxetic lattice subjected to compressive loading is analyzed at stepwise quasi-static tests. At each step, the send and receive signals are measured using the ultrasound sensor. The variation and reflection of the ultrasonic wave signals are used to evaluate the health status of the star-hourglass-shaped auxetic structure, as signal alterations are typically associated with damage. The performed experimental procedure is employed to assess the influence of damage and plasticity modes on wave response under compressive loading of the star-hourglass-shaped auxetic structures, which were fabricated with both pure and reinforced PLA materials. The findings indicate that in structures printed with pure PLA, plasticity dominates as the primary nonlinear phenomenon. Conversely, in lattice structures fabricated with reinforced PLA, damage events and fracture phenomena take precedence, outweighing the nonlinear response attributed to plasticity. Furthermore, it is demonstrated by obtained results that the energy absorption capabilities of composite structures surpass those of structures made exclusively with pure PLA.

1. Introduction

Cellular structures display several noteworthy characteristics, such as a robust strength-to-weight ratio, enhanced mechanical properties, effective energy absorption, sufficient fracture toughness, and heightened resistance to impacts [1]. Due to these benefits, cellular structures find widespread application across diverse industries including transportation, medical engineering, automotive production, and civil engineering [2]. An efficient strategy to alter the equivalent mechanical properties in different directions [3, 4] is to corrugate the cellular structures. The structures of this type are flexible along a corrugated wall (in the longitudinal direction) and provide the capability of adapting to deformations. Meanwhile, they exhibit stiff responses perpendicular to the corrugated wall (transverse directions) and provide a high load-bearing capacity [5]. Researchers have suggested several approaches to improve stiffness and boost energy absorption capacity within cellular structures [6]. Choudhry et al. [7] introduced innovative re-entrant auxetic honeycombs featuring vertical ribs and investigated their nonlinear responses under compression loads. Their findings revealed that these novel honeycombs exhibited superior energy absorption compared to traditional re-entrant honeycombs. Li et al. [8] conducted in-plane quasi-static compressive tests to explore the mechanical behavior and energy absorption capabilities of their honeycomb structures. They discovered that incorporating a variable cross-section design in the width direction boosted both compressive strength and energy absorption. Wang et al. [9] proposed a novel hierarchical lattice design by replacing the main straight beams of the face-centered cubic lattice with a string of higher-level circular beams to enhance energy absorption

capacity. Their results indicated that this hierarchical design, with an appropriate number of higher-level circular beams, could simultaneously improve specific energy absorption and crushing force efficiency. Reviewing the literature reveals that one of the critical issues about the behavior of cellular structures for real application is the scanning of the response of these structures for possible damage formations that are prone to them. Structural health monitoring (SHM) is a powerful approach to identifying structural damages and forecasting their remaining lifespan. By doing so, it ensures safety, reduces maintenance costs and downtime, evaluates the durability of structural components, and enhances the reliability and safety of structures [10]. The signals of guided wave propagation obtained by sensors include damage-sensitive information that can be exploited for damage detection [11]. Current methods for inspecting the structural health of lattice structures often rely on analyzing vibration signals [12]. Jose et al. [13] proposed using vibration parameters, such as natural frequency, damping ratio, and mode shapes, as inputs for a neural network model. The target output of this model was to predict the centroid coordinates of removed members in Cartesian space and to locate damage in lattice structures. Thankachan et al. [14] utilized vibrational modal frequencies or the first mode shape as inputs, and the Cartesian coordinates of the centroid of damaged members, along with the percentage reduction in cross-section, as outputs for a combination of an artificial neural network and a Cuckoo search algorithm. This was used to predict both the location and severity of damage in lattice structures. The review of existing literature reveals a gap in research concerning damage detection in lattice structures using ultrasound methods. Thus, this study introduces a novel combined auxetic honeycomb structure, incorporating both star and hourglass shapes. This innovative lattice design can be produced using 3D printing techniques, offering the flexibility to utilize either pure or reinforced filaments integrated with continuous fibers. The research encompasses experimental assessments of quasi-static compressive loading applied vertically to these structures. Specimen preparation involved fused filament fabrication, commonly referred to as 3D printing. During testing, the nonlinear response of the star-hourglass-shaped auxetic lattice under compressive loading is analyzed through stepwise quasi-static tests. At each step, ultrasound sensors measure both the transmission and reception of signals. Variations and reflections in these ultrasonic wave signals are utilized to assess the structural health of the star-hourglass-shaped auxetic lattice, as changes in signals typically indicate damage. The experimental procedure is employed to evaluate how damage and plasticity modes influence wave responses during compressive loading of the star-hourglass-shaped auxetic structures. These structures were fabricated using both pure and reinforced PLA materials.

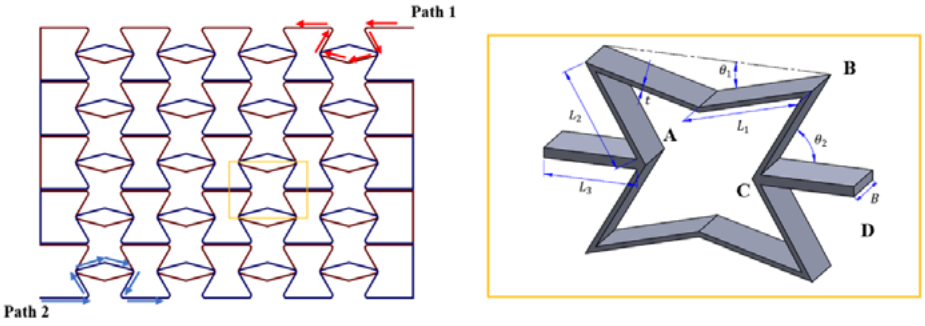
2. Star Hourglass Honeycomb structures

The star-hourglass honeycomb structure, illustrated in Figure 1, draws inspiration from a fusion of star-shaped and hourglass honeycomb configurations. Among the array of auxetic designs, star-shaped honeycombs stand out for their exceptional energy absorption capability, attributed to their remarkable flexibility and hinge movement during compression, resulting from plastic deformation angles. Similarly, hourglass honeycombs exhibit a notably high equivalent elastic modulus compared to other structures. This study introduces a pioneering combined star-hourglass honeycomb, which inherits the outstanding energy absorption and elastic modulus characteristics of both star-shaped and hourglass honeycombs simultaneously. The innovative structure aims to enhance equivalent material properties and plateau strength while maintaining a low weight compared to traditional materials like foam and honeycomb fillings. A crucial aspect of this proposed lattice structure is its compatibility with fabrication using 3D printing technology, utilizing either pure or reinforced filaments with continuous fibers, as depicted in Figure 1, enabling the creation of various automobile components. This structure holds potential for application in load-bearing engineering contexts, as well as in scenarios requiring energy absorption and crashworthiness, depending on the specific application requirements of this type of cellular structure.

3. Experimental methodology

3.1. Material properties of parent materials

To improve the energy absorption capacity of star-hourglass honeycomb structures composed of biodegradable thermoplastic PLA, polymers are reinforced with chopped carbon using the Fused Filament Fabrication (FFF) method. These fibers serve to enhance the mechanical properties of the 3D printed components. Tensile and compression test specimens are prepared according to ASTM D638 and ASTM D695 standards, respectively. These specimens undergo uniaxial tension and compression tests to characterize the properties of the materials utilized in this research.



(a) (b)

Figure 1. Configuration of star hourglass honeycomb structure (a) Printing paths, (b) Definition of geometrical parameter on an extracted unit cell.

3.2. 3D Printing of specimens

The specimens were manufactured using an FDM 3D printer, specifically the Quantum-2020 model, which utilizes standard 1.75 mm PLA filament as the substrate. The 3D printing G-Codes were generated using Simplify 3D software.

Table 1. General settings of the 3D printing process.

Parameter	Nozzle diameter	Air gap	Layer thickness	Bed temperature	Printing speed	Nozzle temperature
Value	1 mm	0.02mm	0.3 mm	65°C	10mm/s	210°C

Table. 1 summarizes the overall settings of 3D printing. Table. 2 also represents the geometrical parameters of the star hourglass honeycomb structure.

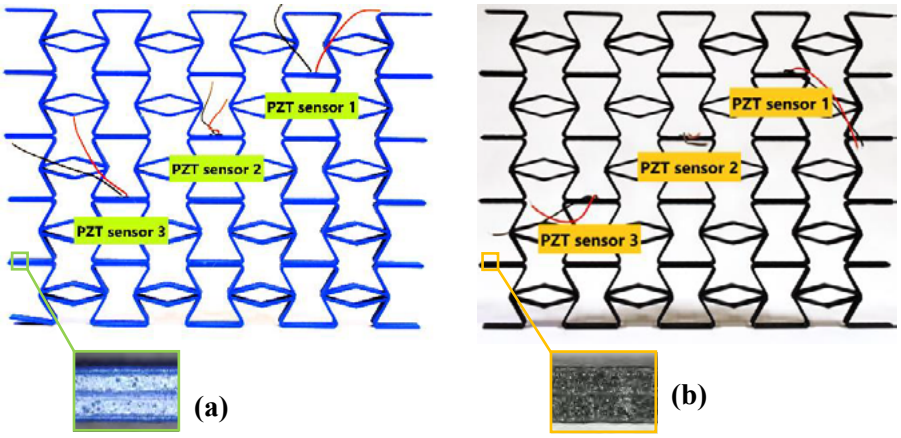


Figure 2. (a) star hourglass honeycomb structure fabricated by pure PLA, (b) star hourglass honeycomb structure fabricated by PLA reinforced by chopped carbon fibers.

Three specimens were prepared using the FDM process, which involves feeding filament through an extruder into a heated chamber. Within this chamber, pressure is applied to extrude the molten polymer through a nozzle. After each layer is deposited, the nozzle moves upward, allowing the adjacent layer to be placed atop the preceding one. The layer height for printing each specimen was set at 0.3 mm, and the thickness of the cellular wall remained consistent at 0.9 mm for all structures. Fig. 2 illustrates the 3D printer and the created cellular structures. Each structure is equipped with three PZT, arranged diagonally at equal distances, to coverage of the received ultrasonic waves throughout most structure areas, rather than just in a local area, enhancing the ability to monitor more structural paths. Furthermore, the use of multiple sensors enhances system redundancy, ensuring that even if one sensor fails or delivers poor-quality signals, other sensors can continue to provide critical monitoring data.

Table 2 Considered geometrical parameters for 3D printing structures.

L_1 (mm)	L_2 (mm)	L_3 (mm)	θ_1 (deg)	θ_2 (deg)	t (mm)	B (mm)	Total dimension (mm^3)
12.85	12.35	12	15	45	0.9	10	144×120×10

It should be noted that the measured mass of star hourglass honeycomb structures printed by pure PLA, and reinforced PLA by chopped carbon fibers are 32.66 gr, and 28.53 gr respectively.

4. Results and discussion

4.1. Characterization tests

To assess the material properties of the raw PLA material, specimens in both dog bone and cylindrical shapes are 3D printed using FDM technology. Tensile tests, following ASTM-D638 standards, and compression tests, following ASTM-D695 standards, are conducted on these specimens. A minimum of three samples are tested for each test category. The tests are performed using an Instron 5500R machine at a fixed crosshead speed of 5 mm/min. It is important to highlight that loading-unloading-reloading tests are conducted on both tensile and compression coupon tests to extract the necessary damage parameters and inelastic strains. The stress-strain responses of standard coupon tests for pure PLA and PLA reinforced with chopped carbon fibers are depicted in Figure 5. The material properties of PLA obtained from the conducted tensile tests are summarized in Table 3.

Table 3. Obtained material properties of Pure PLA and reinforced PLA by chopped carbon fibers using standard tensile and compression tests.

Material	***E*** **(GPa)**	***ν***	σ_{yt} **(MPa)**	ε_t **(%)**	σ_{ut} **(MPa)**	σ_{yc} **(MPa)**	ε_c **(%)**	σ_{ut} **(MPa)**
Pure PLA	$2.22^{\pm 0.1}$	0.3	$25.5^{\pm 1.2}$	$23.5^{\pm 0.01}$	$18.5^{\pm 0.5}$	$36.5^{\pm 1.1}$	$60\pm^{0.01}$	$60.42^{\pm 0.3}$
Chopped Carbon PLA	$3.1^{\pm 0.12}$	0.3	$62.8^{\pm 1.1}$	$10^{\pm 0.05}$	$58^{\pm 1.5}$	$79.1^{\pm 1.21}$	$55^{\pm 0.03}$	$86^{\pm 1.6}$

4.2. Compression tests

Typically, the energy absorption capacity of a specific structure is assessed through compression testing. This test generates a force-displacement curve, which serves as a representation of the structure's energy absorption characteristics. In this study, as depicted in Figure 3, the specimens underwent in-plane compression testing using the INSTRON-5500R compression test device. The velocity of the upper jaw displacement, applying quasi-static load, was set at 5 mm/min. Force-displacement curves were then obtained from the device, serving as the basis for further analysis and evaluation. For each material of the star-hourglass honeycomb structures, two specimens were tested. The specimens were compressed until they reached approximately 50% of their initial height. Figures 3 to 4 present the compression force-displacement curves obtained from both experimental and numerical testing of the star-hourglass honeycomb structures with various parent materials. In the results obtained, efforts were made to illustrate the different stages of structural deformation. Following compression loading in the y

direction, data from all three-star-hourglass honeycomb structures were recorded step by step to analyze the force behavior of the structures at different displacement rates.

4.2.1. Star hourglass honeycomb structure fabricated by pure PLA

According to the diagram depicted in Figure 3, for the star-hourglass honeycomb structure fabricated from pure PLA, the force initially increases from zero to 4 mm in the first elastic interval, indicating the structure's ability to withstand the applied load until signs of damage emerge at a displacement of 8 mm, leading to a notable reduction in force. The force remains relatively constant until reaching a displacement of 33 mm, where plasticity and damage become evident in the oblique struts. From the displacement range of 35 mm onwards, an upward trend in force is observed, continuing until all rows of the structure are compressed together.

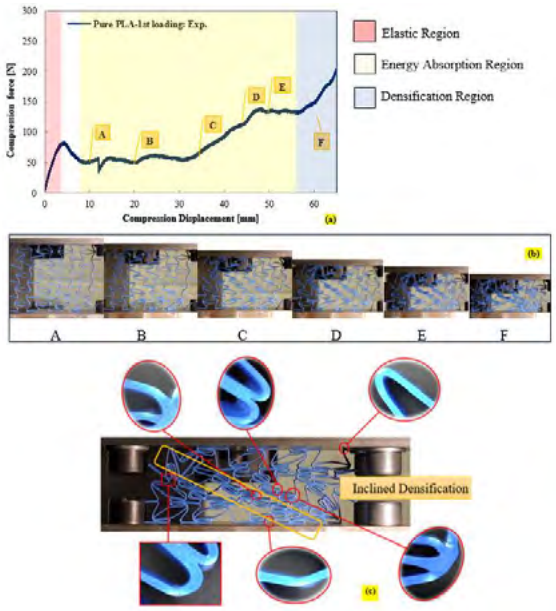


Figure 3. (a) Load- displacement and energy absorption diagram of compression test of star hourglass honeycomb structure sample fabricated by pure PLA in the y direction (b) deformation of star hourglass honeycomb structure at different displacement stage, (c) plasticity and damage phenomena (u_y=60 mm).

In the experimental test illustrated in Figures 3(a) and 3(b) A to F, the first zone represents the elastic response under the applied compressive load. As the oblique struts undergo compressive deformation, the star-shaped walls are compressed row by row, augmenting the load capacity of the structure. The second zone denotes the absorption zone, characterized by the appearance of inclined deformation zones. Plastic deformation and microcrack damage occur at the hinge connections of the inclined unit walls and horizontal struts. Deformation not only occurs within the deformation zone but also spreads obliquely to adjacent structural units as compression progresses, gradually widening the deformation zone. The layer-by-layer compression deformation characteristic of the inclined walls maintains stress at a constant level, resembling a shear zone until partial densification is reached within the inclined zone. Deformation outside the shear zone tends to be more homogeneous. Increasing compression distance leads to the piling up of unit walls, resulting in an expanding densification region until the entire structure is gradually compressed to a dense state at fixed ends. Force partially increases at locations where oblique struts are jointed, and the middle rows of the structure become densified. Once the middle rows of the structure are sufficiently densified, the structure's stiffness increases negligibly, while stress begins to rise continuously until the entire structure collapses, representing the third zone of the curve. Microcracks form in the tension side of the struts of the star-hourglass honeycomb structure at the last level of applied compression load for the first loading stage, as observed in Figure 3(c). While severe

failure at the hinges is not experienced, the formation of microcracks results in local stiffness reduction at the damaged location, which can affect the structure's response after recovery.

4.2.2. Star hourglass structure fabricated by reinforced PLA by chopped carbon fibers

According to the diagram depicted in Figure 4, during the first loading stage, the force initially rises from zero to 5 mm in the first elastic interval. The structure withstands the applied load until signs of damage emerge at a displacement of 9.5 mm, leading to a significant reduction in force. Subsequently, the force level remains relatively constant until reaching a displacement of 37 mm, where plasticity and damage occur in the oblique struts. Force begins to increase within the displacement range of 39 mm, and this upward trend continues until all rows of the structure are fully compressed together. In the experimental test response illustrated in Figure 4(a), the first zone highlighted in pink represents the elastic response under the applied compressive load. As shown in Figure 4(b), when the oblique struts undergo compressive deformation, the star-shaped walls are compressed row by row, resulting in an increase in the structure's load capacity. The second zone highlighted in white denotes the absorption zone, where the oblique struts are partially bending, but the horizontal struts of the cells are not yet deformed. Force increases partially at locations where oblique struts are jointed, and the middle rows of the structure become densified. Once the middle rows of the structure are sufficiently densified, the structure's stiffness increases negligibly, while stress begins to rise continuously until the entire structure collapses, representing the third zone of the curve.

4.3. Ultrasonic tests

Ultrasonic-guided waves are one of the most common inspection tools for collecting valuable data in engineering based on the SHM system. The damage will affect the material or structural properties, impacting wave propagation characteristics and showing a particular wave response [15]. In undamaged structures, ultrasonic waves propagate at a speed specific to their material characteristics. The waveform displays specific patterns influenced by the material's properties, such as density and elastic modulus. Damage such as cracks, voids, or corrosion alters these physical properties, thus impacting the speed and path of the sound wave propagation. During propagation, ultrasonic waves undergo absorption and scattering within the material, leading to attenuation of wave energy. When damage occurs within the structure, increased absorption and scattering in the affected area further intensify the attenuation of the waveform. Monitoring the extent of signal amplitude attenuation allows for an estimation of structural health. To evaluate the health of 3D printed auxetic structures under compression load, ultrasound signals of auxetic structures are obtained under different deformation levels. These signals are then analyzed, and the damage-sensitive features envelope and phase are extracted. The two auxetic structure samples connected to three PZT sensors are shown in Fig.2. The ultrasonic test is conducted as follows: a laptop is used to control the excitation signal. A Hanning windowed sinusoid with a frequency of 100 kHz and a duration of 6 cycles was applied as the excitation signal. The wave generator produces the excitation signal, which is displayed on the oscilloscope. The signal is then amplified by the signal amplifier and subsequently connected to the PLA auxetic structure through PZT sensor 1. Both PZT sensors 2 and 3 are utilized to capture the response signal. The ultrasonic signals at 100kHz response from PZT sensor. 3 (chopped carbon PLA) and sensor 2 (pure PLA), corresponding to the initial 35mm of deformation that includes key structural deformation stages and exhibits relatively better signal quality, were utilized as the raw wave signal. The two types of damage-sensitive features have been used to analyze the signal changes [15], which are the local envelope and phase, both are extracted from raw wave signal by using the Hilbert transform. Two sets of envelope and phase data vary with the deformation, with each deformation corresponding to a different distribution of the respective envelope and phase. The probability density function (PDF) distributions of envelope and phase with deformation ranging from 0 to 35 mm (chopped carbon PLA) and 0 to 34 mm (pure PLA) are shown in Fig. 5. It can be seen that the data distributions of the different envelopes (Fig. 5 (a) and (c)) and phases (Fig. 5 (b) and (d)) vary from each other, as they correspond to different levels of damage states. Theoretically, a greater disparity in the distribution shape indicates a larger deviation from the structure's initial health status. During the elastic phase, the PDFs of both the envelope and phase are similar, suggesting minimal

changes in the structure's properties. However, with increasing deformation, the PDFs of the envelope and phase for the two materials begin to exhibit significant fluctuations, particularly in the envelope. This often indicates that the structure is experiencing damage or the onset of plasticity. From compression tests, notable fluctuations in data distribution become apparent after the first peak on the force curve. Thus, we define the deformation at this first peak as the critical deformation.

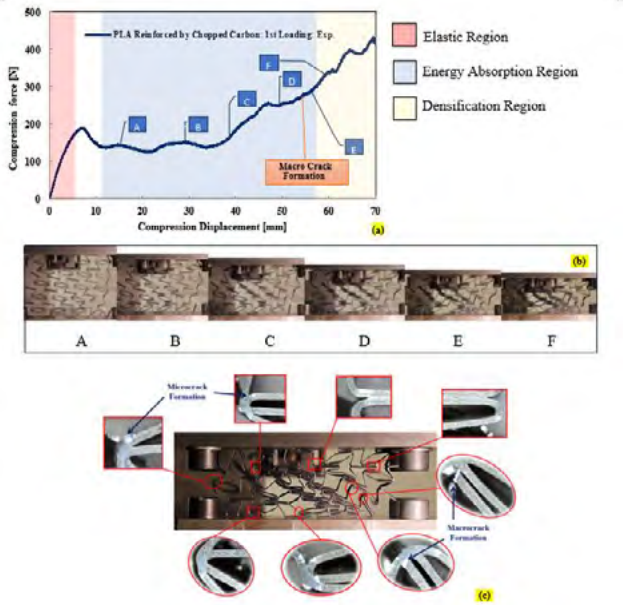


Figure 4. (a) Load- displacement and energy absorption diagram of compression test of star hourglass honeycomb structure sample fabricated by PLA reinforced by chopped carbon fibers (b) deformation of star hourglass honeycomb structure at different displacement stage, (c) plasticity and damage phenomena (u_y=62 mm).

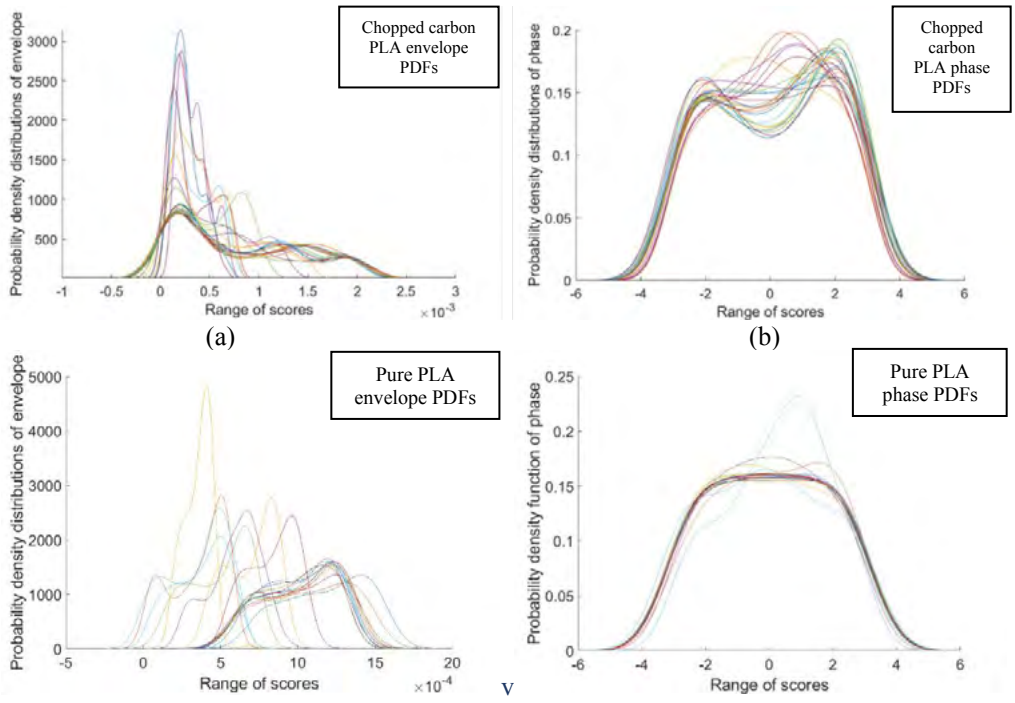


Figure 5. Two hourglass honeycomb structures' probability density distributions of the envelope (a) and (c), and phase (b) and (d).

Between reaching the critical deformation, the shape change of the distribution is minor, and after the critical deformation, significant changes in the PDFs' shape are observed. Specifically, the critical deformation for the hourglass honeycomb structure fabricated with pure PLA and chopped Carbon PLA

is 4.5 mm and 7.5 mm, respectively. Based on this way, a relatively conservative assessment of structural health status can be determined.

5. Conclusions

This paper represented the nonlinear response of an innovative lattice structure which was manufactured using 3D printing techniques. Experimental evaluations of quasi-static compressive loading applied to these structures in the vertical orientations are encompassed by the research. During the test, the nonlinear response of the star-hourglass-shaped auxetic lattice subjected to compressive loading is analyzed at stepwise quasi-static tests. Ultrasonic tests were conducted to obtain ultrasonic signals under various deformation states of two star hourglass shaped honeycomb structures. The Hilbert transform was employed to extract two damage-sensitive features: envelope and phase from ultrasonic signals. Based on the PDFs of the respective envelope and phase, along with the force curve, the critical damage or plasticity deformation was determined to assess the structural health status.

References

[1] A. Farrokhabadi, D. Chronopoulos, Composite curved hourglass cellular structures: Design optimization for stiffness response and crashworthiness performance, *Compos. Struct*., vol. 330, 117834, 2024.
[2] H. Gharehbaghi, and A. Farrokhabadi, Parametric study of the energy absorption capacity of 3D-printed continuous glass fiber reinforced polymer cruciform honeycomb structure, *Steel Compos. Struct*., vol. 49, no. 4, pp. 393-405, 2023.
[3] S. Mohammadi Ghalehney, M.H. Sadeghi, and H. Gharehbaghi, Mechanical Properties of 2D Re-Entrant Gradient Structures Produced by Additive Manufacturing, *Iran. J. Sci. Technol. Trans. Mech. Eng*., vol. 0 pp. 1–10, 2023.
[4] S. Rohani Nejad, M. Hosseinpour, and S.M.H. Mirbagheri, Experimental and Simulation Investigation on Energy Absorption of Cu Casting Lattice Structure during Compression, *Adv. Eng. Mater*., vol. 25, no. 16, 2300447, 2023.
[5] K. Lang and M. Su, Equivalent orthotropic model for corrugated plates based on simplified constitutive relation, *Heliyon*, vol. 8, no. 11, 11264, 2022.
[6] J. Shen, Q. Zeng, J. Wang, J. Ge, F. Gao, and J. Liang, Study of Mechanical Properties of a New 3D Re-Entrant Lattice Auxetic Structure Under Bending, *Adv. Eng. Mater*., vol. 25, no. 14, 2201509, 2023.
[7] N. K. Choudhry, B. Panda, and S. Kumar, In-plane energy absorption characteristics of a modified re-entrant auxetic structure fabricated via 3D printing, *Comp. Part B Eng*., vol. 228, 109437, 2022.
[8] A. Zara, I. Belaidi, S. Khatir, A. Oulad Brahim, D. Boutchicha, and M. Abdel Wahab, Damage detection in GFRP composite structures by improved artificial neural network using new optimization techniques, *Compos. Struct*., vol. 305, 116475, 2023.
[9] P. Wang, F. Yang, D. Ru, B. Zheng, and H. Fan, Additive-manufactured hierarchical multi-circular lattice structures for energy absorption application, *Mater. Des.,* vol. 210, 110116, 2021.
[10] S. Gopalakrishnan, M. Ruzzene, S. Hanagud, et al., Computational techniques for structural health monitoring, *Springer.*, 2011.
[11] I. Viktrov, Rayleigh and lamb waves: physical theory and applications, Chapter II, *Springer*., 1967.
[12] G. Wang, C. Xu, S. Zhang, Z. Zhou, L. Zhang, B. Qiu, J. Wan, H. Lei, Exploration of damage identification method for a large-span timber lattice shell structure in taiyuan botanical garden based on structural health monitoring, *Sensors*., vol. 23, 6710, 2023.
[13] C. Jose, P. Thankachan, T. M. Pillai, Structural health monitoring of lattice structure using artificial neural network, in: Proceedings of SECON'21: Structural Engineering and Construction Management, *Springer*., pp. 1081–1089, 2022.
[14] P. Thankachan, A. Fida, T. M. Pillai, Health monitoring of steel structures using cuckoo search algorithm-based ann, *Structures*., vol. 61, 105933, 2024.
[15] H. Lu, B. Chandran, W. Wu, J. Ninic, K. Gryllias, D. Chronopoulos, Damage features for structural health monitoring based on ultrasonic lamb waves: Evaluation criteria, survey of recent work and outlook, *Measurement*., vol. 114666, 2024.

EFFECT OF STIFFNESS VARIATION IN THE ADHESIVE ON PERFORMANCE OF COMPOSITE-METAL TUBULAR JOINTS

Olufemi Taylor[1], Maria Kashtalyan[2] and Mehmet Kartal[3]

[1]Centre for Micro- and Nanomechanics (CEMINACS), School of Engineering, University of Aberdeen, Aberdeen AB24 3UE, Scotland UK
Email: o.taylor.22@abdn.ac.uk, Web Page: https://www.abdn.ac.uk/people/olufemi.taylor
[2]Centre for Micro- and Nanomechanics (CEMINACS), School of Engineering, University of Aberdeen, Aberdeen AB24 3UE, Scotland UK
Email: m.kashtalyan@abdn.ac.uk, Web Page: https://www.abdn.ac.uk/people/m.kashtalyan
[3]Centre for Micro- and Nanomechanics (CEMINACS), School of Engineering, University of Aberdeen, Aberdeen AB24 3UE, Scotland UK
Email: mehmet.kartal@abdn.ac.uk, Web Page: https://www.abdn.ac.uk/people/mehmet.kartal

Keywords: fibre-reinforced composite, tubular joint, adhesive bonding, finite element modelling

Abstract
Reliable joining of fibre-reinforced polymer-matrix composites to metals remains one of the technological challenges to overcome when developing multi-material structures and components. In this paper, 2D (axisymmetric) finite element models of bio-inspired tubular metal-composite single lap adhesive joints are developed to study the effects of stiffness variation in the adhesive on joint performance. Axial tension, torsion and internal pressure are considered. Stiffness variation in the adhesive is implemented via the user defined field subroutine. Comprehensive parametric studies are facilitated via Python scripting. The developed models were extensively validated for different loading scenarios using results in the literature. Several profiles of stiffness variation in the adhesive have been examined and compared with a reference joint configuration without stiffness variation. Investigated stiffness variation profiles have been shown to reduce asymmetry of stress distributions in the adhesive and reduce maximum stresses in comparison with the reference joint configuration. The results demonstrate that a combination of overlap length and stiffness variation profile in the adhesive can reduce stresses and improve joint performance.

1. Introduction

Successful development of multi-material structures and components depends on reliable joining of fibre-reinforced polymer-matrix composites to metals, which remains one of the key technological challenges to overcome. Adhesive bonding has many advantages over other joining methods including lower fabrication costs, lower structural weight, better cost-effectiveness, unparalleled ability to join dissimilar materials such as metals and composites, and potential to disassemble them for recycling at the end of their service life [1, 2]. Stress distribution in adhesive joints, especially in lap joints, is non-uniform, with stress concentrations due to stiffness mismatch observed at the ends of the bonded area which often lead to premature failure of the joint. To eliminate these stress concentrations, several techniques have been proposed in the literature, either focusing on the adhesive, the adherend, or both. Several bio-inspired concepts such as functional grading [3], mechanical interlocking through surface patterning [4], adhesive patterning [5] and 3D metal pins [6, 7], to name but a few, are currently actively explored in metal-composite joint design with the view to achieve enhancements in joint performance and maximise recyclability.

Functional grading found in natural materials such as bones and teeth has evolved as a response to stress concentration at material interfaces and allows for a more balanced stress distribution across the joint. Inspired by nature, the concept of functional grading has been applied to the metal-composite adhesive joint design, pre-dominantly focusing on the adhesives [8]. Extensive analytical, numerical, and experimental studies of flat single lap joints with graded adhesives have been performed, demonstrating that varying stiffness properties of the adhesive with the overlap length along the bond line can reduce peak stresses at the overlap ends and improve performance of the joint. To achieve stiffness variation in the adhesive, several methods have been proposed, including adding microparticles such as glass beads or nanoparticles such as carbon black to the adhesive, using graded curing processes and/or adhesive mixes [8].

In this study, 2D (axisymmetric) models of bio-inspired tubular metal-composite single lap adhesive joints have been developed in Abaqus to study the effects of stiffness variation in the adhesive on the joint performance. Axial tension, torsion and internal pressure are considered. Stiffness variation in the adhesive is implemented via the user defined field subroutine. Python scripting is used to facilitate comprehensive parametric studies. The developed models have been extensively validated for different loading scenarios using results in the literature, including [9, 10]. Several profiles of stiffness variation in the adhesive have been examined and compared with a reference joint configuration without stiffness variation. Investigated joint configurations have been shown to reduce asymmetry of stress distributions in the adhesive and reduce maximum stresses in comparison with the reference joint configuration.

2. Methodology

Figure 1 shows a tubular single lap joint (TSLJ) comprising inner metal pipe of length L_t, radius R_i and thickness t_t, outer composite pipe of the same length and thickness, bonded together through a thin adhesive layer of thickness t_a and overlap length L_o. The joint is subjected to internal pressure P, axial load F and torsion T.

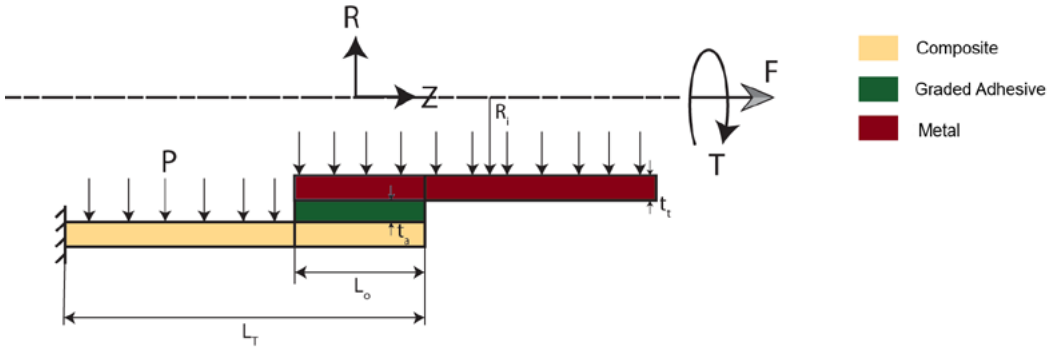


Figure 1. Tubular Single Lap Joint subjected to internal pressure axial loading and torsion

Young's modulus of the adhesive was assumed to vary with the axial coordinate z along the overlap length according to one of the five profile functions [11] given below by Eqs. (1)-(5), with Profile 5 taken as a reference configuration.

Profile 1 $$E_{f1} = E_{max} \exp\left[-4\ln\left(\frac{E_{max}}{E_{min}}\right)\left(\frac{z}{L_o} - \frac{1}{2}\right)^2\right] \quad (1)$$

Profile 2 $$E_{f2} = 4(E_{min} - E_{max})\left(\frac{z^2}{L_o^2} - \frac{z}{L_o}\right) + E_{min} \quad (2)$$

Profile 3 $$E_{f3} = 8(E_{max} - E_{min})\left(2\left(\frac{z}{L_o} - \frac{1}{2}\right)^4 - \left(\frac{z}{L_O} - \frac{1}{2}\right)^2\right) + E_{max} \quad (3)$$

Profile 4 $$E_{f4} = 12.8(E_{min} - E_{max})\left(\left(\frac{z}{L_o} - \frac{1}{2}\right)^6 + \left(\frac{z}{L_o} - \frac{1}{2}\right)^4\right) + E_{max} \quad (4)$$

Profile 5 $$E_{f5} = E_{max} \quad (5)$$

Figure 2 shows the above five stiffness variation profiles in the adhesive as a function of the normalized overlap length $\eta = z/L_o$. Out of the four grading profiles, profiles 1 and 3 are the least steep, profile 2 is moderately steep and profile 4 is the steepest.

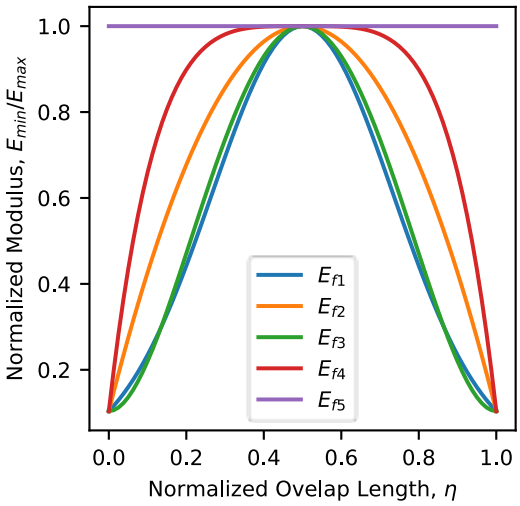


Figure 2. Normalized Young's modulus of the adhesive as a function of the normalized overlap length for five considered stiffness variation profiles.

Finite element (FE) modelling of the joint is performed in Abaqus [12] using four-node axisymmetric quadrilateral elements CAX4 for simulations involving axial tension and internal pressure and four-node generalized bilinear axisymmetric quadrilateral elements with twist CGAX4 for simulations involving torsion. Stiffness variation in the adhesive is implemented via the used defined field subroutine (USDFLD). Python scripting is used to facilitate comprehensive parametric studies. The developed FE model of TSLJ has been extensively validated for different loading scenarios using results in the literature, including [9, 10].

3. Results and discussion

Geometry of the joint is defined by the inner pipe radius $R_i = 8\,mm$, inner and outer pipes wall thickness $t_t = 2\,mm$, and adhesive layer thickness $t_a = 0.2\,mm$. A range of the overlap lengths was considered, taking values of $L_o = 10; 25; 50; 100; 200\,mm$, while the pipe lengths were taken as $L_t = L_o + 30\,mm$. Material properties of the metal pipe are taken as $E = 200\,GPa, \nu = 0.28$. The GFRP composite pipe was modelled as a unidirectional transversely isotropic GFRP material with the following material properties [13]: $E_1 = 20\,GPa$, $E_2 = E_3 = 5\,GPa$, $\nu_{12} = 0.3$, $\nu_{13} = \nu_{23} = 0.28$, $G_{12} = 2\,GPa$, $G_{13} = G_{23} = 1.5\,GPa$. Elastic properties of the adhesive are taken as [11]: $E_{min} = 0.280\,GPa$, $E_{max} = 2.7\,GPa$, $\nu = 0.35$. A displacement of 0.2 mm was applied to the metal end for tension cases, a rotation of 0.15 radians about the axis for torsion cases and a pressure of 10 MPa for internal pressure cases.

Figure 3 shows variation of shear stress τ_{rz} in the adhesive of a composite-metal tubular joint subjected to tensile loading as a function of the normalized overlap length. For all considered overlap lengths, the shear stress variation is strongly influenced by the stiffness variation in the adhesive, and the maximum stresses in the graded adhesives are reduced compared to the constant stiffness adhesive. Stiffness variation profiles 1 and 3, given by Eq. (1) and (3) respectively produce greater stress reduction compared to stiffness variation profiles 2 and 4, given by Eq. (2) and (4) respectively, but at the expense of slightly increasing stress values in the middle portion of the overlap length. For smaller overlap lengths of $L_o = 10\,mm$ and $L_o = 25\,mm$, the effect of stiffness grading in the adhesive on shear stress variation is felt throughout, however for longer overlap lengths of $L_o = 50;\ 100; 200\,mm$, stress variation away from the edges is largely unaffected by adhesive grading.

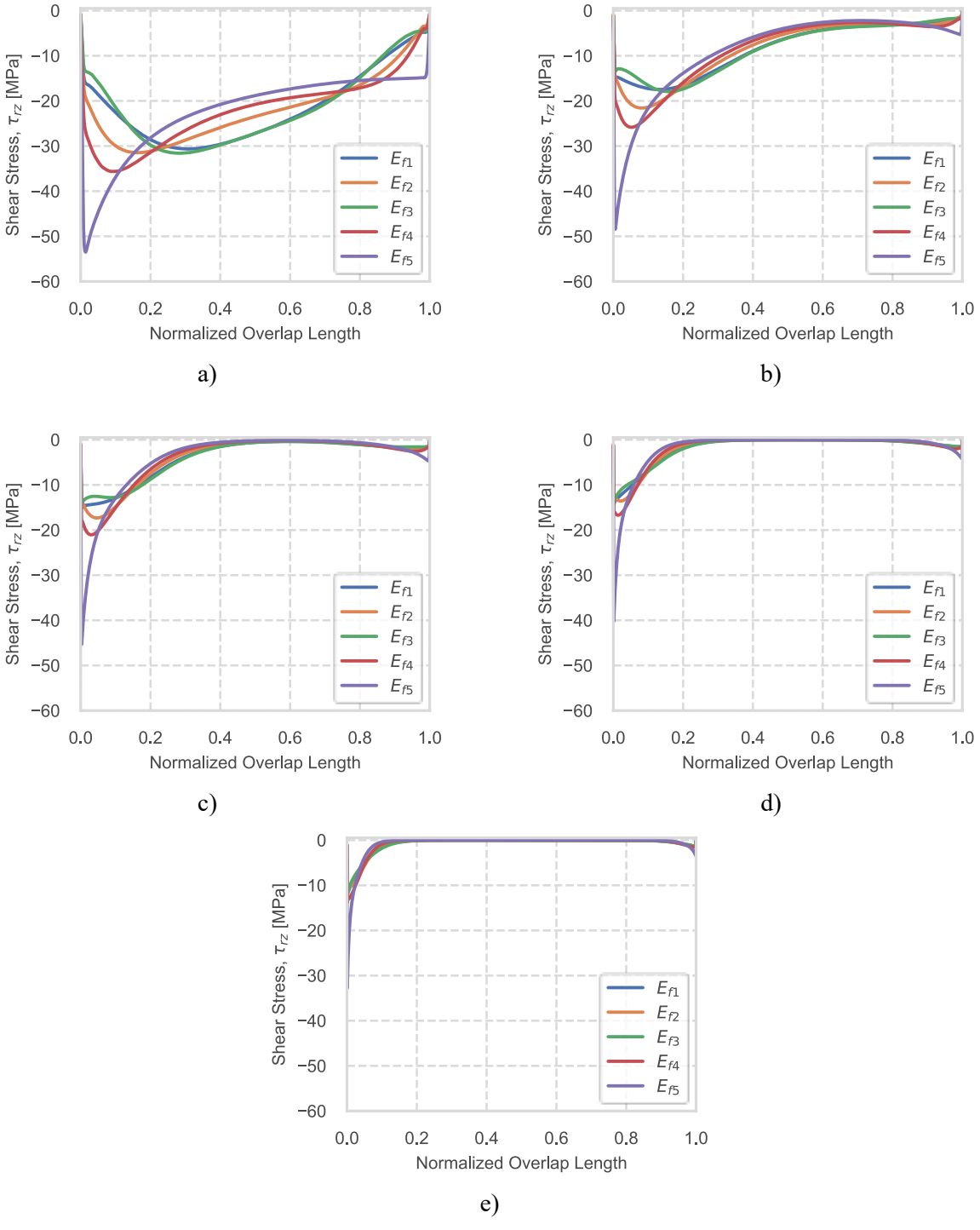


Figure 3. TSLJ under axial tension. Shear stress variation in the adhesive for five stiffness variation profiles and different overlap lengths: a) 10 mm; b) 25mm; c) 50 mm; d) 100 mm; e) 200 mm.

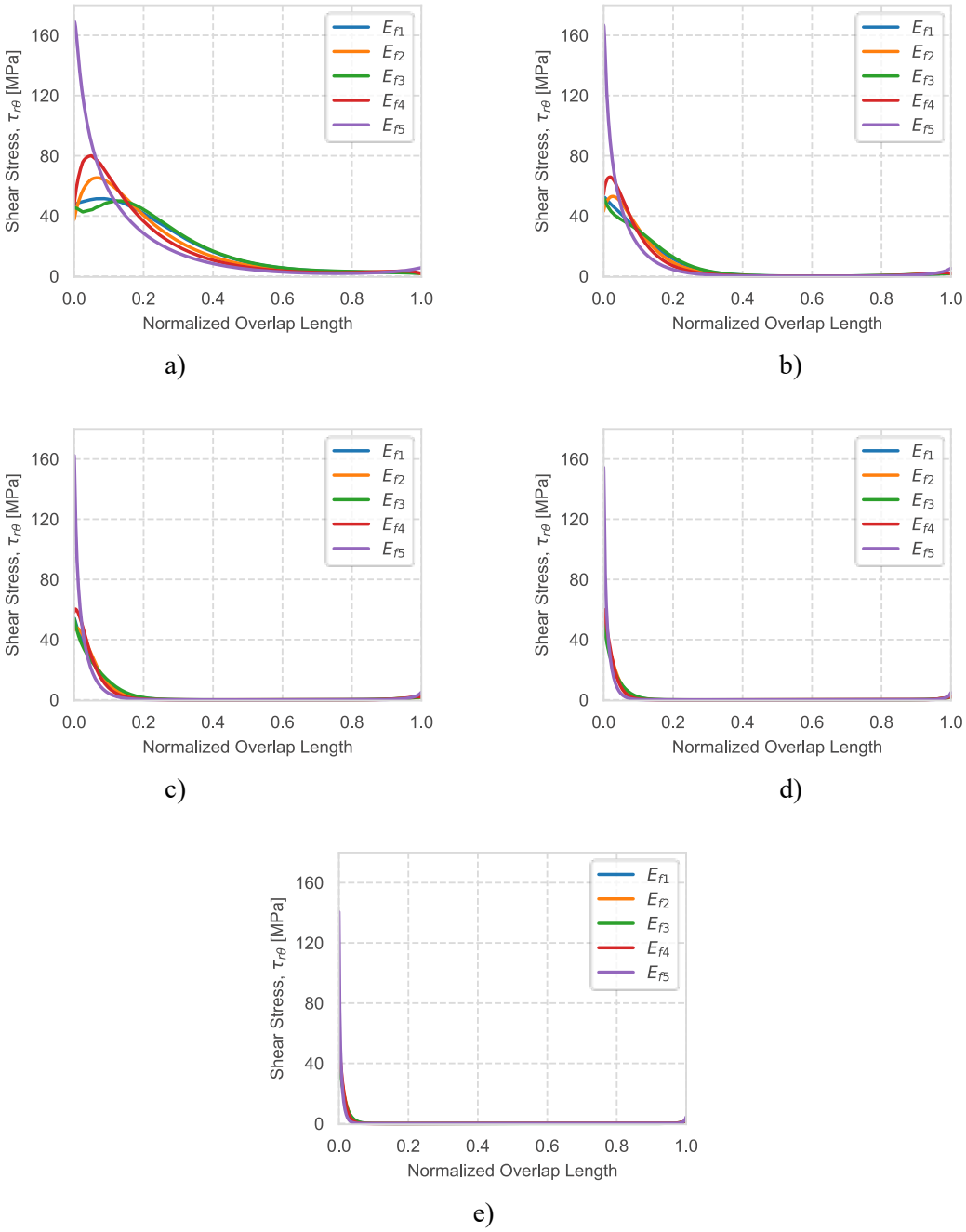


Figure 4. TSLJ under torsion. Shear stress variation in the adhesive for five stiffness variation profiles and different overlap lengths: a) 10 mm; b) 25mm; c) 50 mm; d) 100 mm; e) 200 mm.

Variation of shear stress τ_{rz} in the adhesive of a composite-metal tubular joint subjected to torsional loading is shown in Figure 4 as a function of the normalized overlap length. It is evident from Figure 4 that for all considered overlap lengths, stiffness grading in the adhesive significantly reduces the maximum shear stress compared to the reference configuration, and stiffness variation profiles 1 and 3 again perform better than stiffness variation profiles 2 and 4. For longer overlap lengths, shear stresses away from the internal edge $\eta = 0$ are largely unaffected by the grading profile and are similar to those in the reference case of the constant stiffness adhesive.

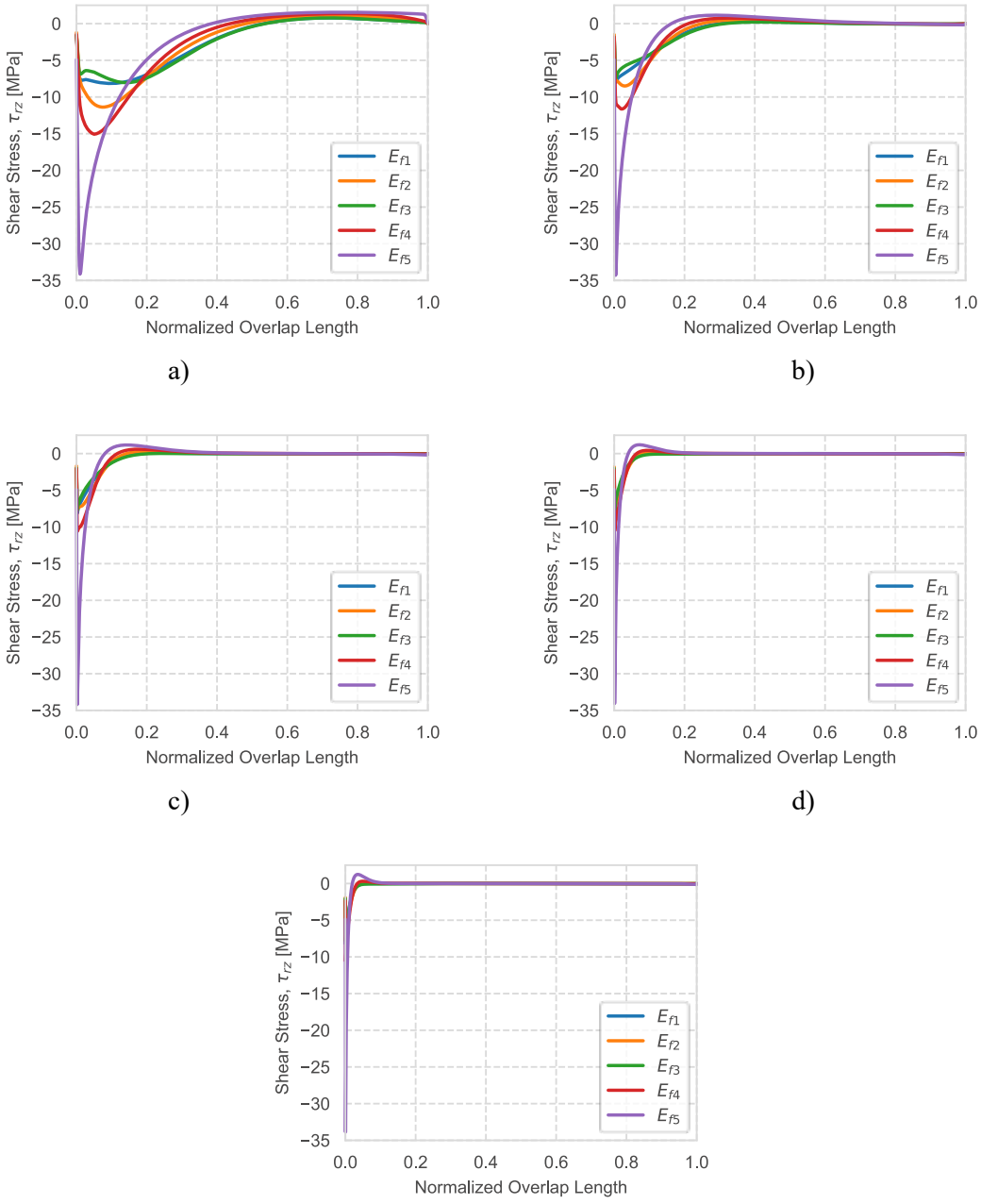


Figure 5. TSLJ under internal pressure. Shear stress variation in the adhesive for different stiffness variation profiles and different overlap lengths: a) 10 mm; b) 25mm; c) 50 mm; d) 100 mm; e) 200 mm.

Variation of shear stress τ_{rz} in the adhesive of a composite-metal tubular joint subjected to internal pressure is plotted in Figure 5 as a function of the normalized overlap length. Again, adhesive stiffness grading profiles 1 and 3 perform better at reducing the maximum shear stress in the adhesive than grading profiles 2 and 4. For longer overlap lengths, shear stresses away from the internal edge $\eta = 0$ are largely unaffected by the stiffness grading in the adhesive and are similar to those in the reference case of the constant stiffness adhesive.

4. Conclusions

In this study, finite element modelling of tubular single lap metal-composite adhesive joints has been performed with the view to study the influence of stiffness variation in the adhesive on joint performance. Several U-shaped profiles of stiffness variation in the adhesive have been examined and compared with a reference joint configuration without stiffness variation. All investigated stiffness profiles have been shown to reduce asymmetry of stress distributions and the maximum shear stress value in the adhesive layer under tensile loading, torsional loading and internal pressure. Stiffness variation profiles 1 and 3 were found to be more effective at reducing the maximum shear stress value in the adhesive than profiles 2 and 4. The results demonstrate that a combination of overlap length and stiffness variation profile in the adhesive can have beneficial effect on stresses in the adhesive and thus improve joint performance.

Acknowledgments

Financial support of this research by PTDF (Nigeria) is greatefully acknowledged.

References

[1] X. Shang, E.A.S. Marques, J.J.M. Machado, R.J.C. Carbas, D. Jiang, L.F.M. da Silva. Review on techniques to improve the strength of adhesive joints with compo-site adherends. *Composites Part B: Engineering*,117: 107363, 2019.

[2] Y. Wei, X. Jin, Q. Luo, Q. Li, G. Sun. Adhesively bonded joints – A review on design, manufacturing, experiments, modeling and challenges. *Composites Part B: Engineering* 111225, 2024.

[3] M.Q. dos Reis, E.A.S. Marques, R.J.C. Carbas, L.F.M da Silva. Functionally graded adherends in adhesive joints: An overview. *Journal of Advanced Joining Processes*, 2:100023, 2020.

[4] A. Hamilton, Y.Xu, M.E. Kartal, S. Kumar, N., Mulvihill. Optimisation of interlocking microstructured adhesive joints via finite element modelling, design of experiments and 3D printing. *International Journal of Adhesion and Adhesives*, 120:103292, 2023.

[5] I. Kaiser, C. Tan, K.T. Tan. Bio-inspired patterned adhesives single-lap joints for CFRP and titanium. *Composites Part B: Engineering*, 224: 109182, 2021.

[6] T. Bagnato, A.R. Ravindran, A. Mirabedini, R.B. Ladani, E. Kandare, A.C. Orifici, P.Chang, J. Wang, A. Mouritz. Superior interfacial toughening of hybrid metal-composite structural joints. *Composites Part A: Applied Science and Manufacturing*, 168:107479, 2023.

[7] J. Popp, D. Drummer. Influence of the textile reinforcement on the joint formation of pin-joined composite/metal parts. *Applied Composite Materials*, 2024.

[8] J.B. Marques, A.Q. Barbosa, C.I. da Silva, R.J.C. Carbas, L.F.M. da Silva. An overview of manufacturing functionally graded adhesives – Challenges and prospects. *The Journal of Adhesion* 97(2): 172-206, 2021.

[9] D.R. Barbosa, R.D.S.G. Campilho, R.J.B. Rocha, L.R.F. Ferreira. Experimental and numerical assessment of tensile loaded tubular adhesive joints. *Proceedings of the Institution of Mechanical Engineering, Part L: Journal of Materials: Design and Applications*, 233:452-464, 2019.

[10] A.M. Khan, S. Kumar. Mitigating edge effects in adhesively bonded composite tubular lap joints under axial, pressure and torsional loading via stiffness tailoring. In Proceedings of the 21st International Conference on Composite Materials (ICCM21), Xi'an, 20-25 August 2017.

[11] S. Kumar. Analysis of tubular adhesive joints with a functionally modulus graded bondline subjected to axial loads. *International Journal for Adhesion & Adhesives*, 29:785-795, 2009.

[12] Abaqus 6.14. Analysis User's Guide, Dassault Systèmes Simulia Corp., 2014.

[13] E.I. Avgoulas, M.P.F. Sutcliffe. A review of natural joint systems and numerical investigations of bio-inspired GFRP-to-Steel joints. *Materials*, 9: 566-588, 2016.

MODULAR FRAMEWORK FOR LIFETIME PREDICTION OF COMPOSITE MATERIALS AFFECTED BY THE ENVIRONMENT

Andrejs Krauklis* and Sotirios Grammatikos

ASEMlab – Laboratory of Advanced and Sustainable Engineering Materials, Department of Manufacturing and Civil Engineering, NTNU – Norwegian University of Science and Technology, 2815 Gjøvik, Norway
Email: andrejs.krauklis@ntnu.no, Email: grammatikos@outlook.com, Web Page: www.asemlab.no
*corresponding author, speaker

Keywords: lifetime prediction, polymer composite, environmental aging, accelerated testing methodology, multiscale modeling, durability

Abstract
Environmental aging significantly impacts composites, introducing uncertainty in material durability and compromising physico-mechanical properties, rending reliable prediction of a service life crucial. Experimental validation procedures for composites entail expensive and time-demanding testing programs bottleneck for innovation, thus turning modeling into an economically viable alternative capable of partially replacing extensive testing. A combination of accelerated testing methodologies alongside qualification by modeling, based in fundamental scientific principles, is seen as a viable long-term solution. Multiple approaches have been suggested to forecast long-term properties based on short-term measurements, aiming to streamline the assessment process by minimizing time and associated costs.

A modular lifetime prediction framework is presented herein, including insights into the environmental aging mechanisms of composite (micro-)constituents. Influence of factors on degradation rates, such as chemical composition, sizing quality, temperature, acidity, and mechanical stresses are considered. Lifetime is predicted by a diverse set of modeling tools, including degradation rate modelling, superposition principles, and parametrization techniques. The modular framework serves as a potentially valuable resource for both industry and academia, offering insights into predicting the lifetime of fiber-reinforced polymers. In addition, the duality of lifetime prediction is briefly discussed, presenting distinction in the definitions of integrity, failure criteria and end-of-life scenarios. Consequently, similar aging phenomena and modeling methodologies apply, whether prioritizing "safety" or "decomposition".

1. Introduction

Fiber-Reinforced Polymers (FPR) are used as structural materials due to their light weight and increased mechanical properties. During their service lifetime, exposure to environmental aging is common. Aqueous and humid environments, impacts of temperature, pH, and mechanical stresses result in the structural weakening of FRPs. The superior physico-mechanical properties of FRPs, such as strength and stiffness, are then compromised by the uncertainty of the material-environment interaction [1]. The presented modeling framework provides means of predicting the extent of such deterioration, and thus the expected lifetime.

Modeling emerges as an economically feasible alternative, complementing testing with simulation and accelerated testing methodologies, based on fundamental physico-chemical principles [2].

There are three microconstituents in an FRP, namely a polymer matrix, fiber reinforcement, and a multi-component sizing-rich interphase/interface. The interphase originates from the sizing (coating applied to the fiber surface), and is formed between the reinforcing fibers and the matrix polymer during the FRP manufacturing process. What complicates the prediction of composite aging is that each of the three microconstituents ages differently and may also affect the degradation rates of each other (coupling effects) [1]. Since the FRP composition is modular in its nature, a necessity for a modular modeling approach is called for, based on the understanding of the molecular mechanisms and kinetics of environmental aging of individual microconstituents [1]. The multiscale nature of lifetime prediction is shown in Figure 1.

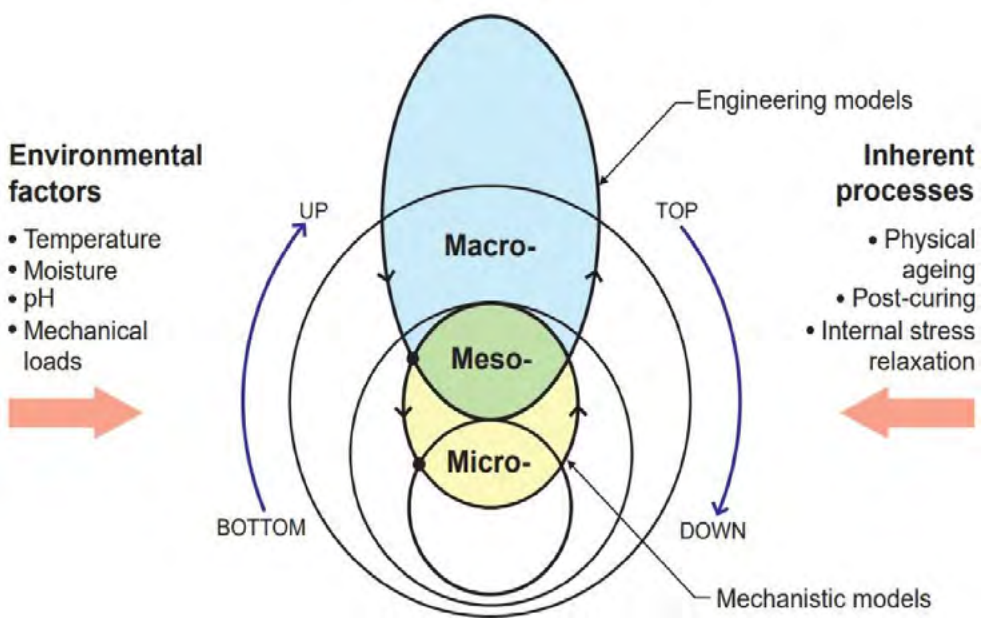


Figure 1. Multitude of scales involved in the Lifetime Prediction Modeling [3].

Many approaches have been proposed for predicting the long-term properties of polymers and FRPs based on short-term tests allowing for reduction of the time scales and costs required to obtain long-term data [4]. Accelerated testing methodologies enable the simulation of natural exposure effects within relatively short time frames [3]. The state-of-the-art modeling methodologies for predicting the lifetime of polymers and FRPs under environmental impact include the rate models (Arrhenius, Eyring, and Zhurkov); superposition principles (Time-Temperature, Time-Moisture, Time-Stress, and Time-Aging Time); Plasticity-controlled failure modeling methods and parametric methods (Larson–Miller, and Monkmann–Grant) [3]. The Modular framework presented herein is a multiscale modeling approach.

2. Methods

2.1. Modular Framework

The modular framework is a step towards the multiscale lifetime prediction and understanding of the composite aging phenomena [4]. The modular approach is schematically shown in Figure 2. Red colored modules are under development. QSPR stands for Quantitative Structure-Property Relationships.

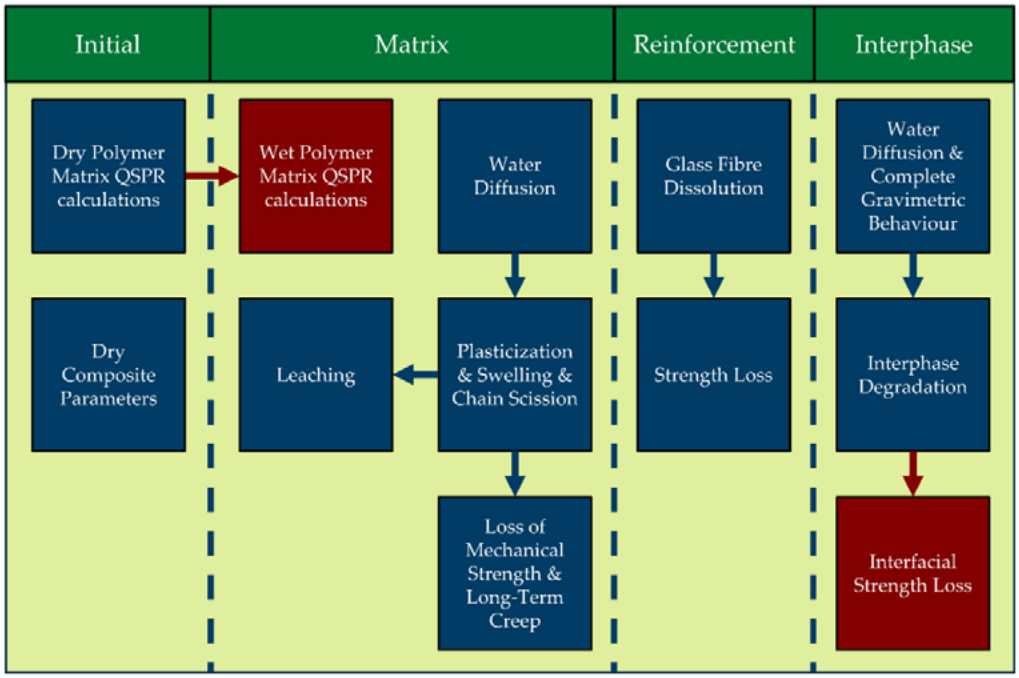


Figure 2. Modules of the framework for lifetime prediction of composite materials affected by humid/water environment [5].

As shown in Figure 2, modules are divided in four sections that relate to the overall composite configuration and modeling of environmental degradation of individual micro-constituents (polymer, fibers and interphase). Initial section covers such properties as volume and mass fiber fraction, the total number and surface area of fibers inside a composite, and the amount of sizing. Detailed instructions for determination of all these parameters can be found in [1]. More directions are provided in the following respective chapters.

2.2. Lifetime of Polymer Matrix

Service lifetime of polymers and polymer mixes are impacted by aging process. State-of-the-art multiscale and modular approaches of predicting environmental aging of polymeric and composite materials have been systematized and discussed, with this study providing a comprehensive overview of the broad possibilities and present limitations of the currently available models.

Polymer aging degradation rate is mainly influenced by factors like chemical formulation, environmental and material composition, acidity, mechanical stresses and temperature. Utilizing a spectrum of modeling tools, from simplified correlations to advanced simulations, enables lifetime prediction of polymer materials. Service life is forecasted using degradation rate models, superposition principles, and parametrization techniques, offering valuable insights for both the industry and academia [3].

The diffusion and leaching modules can employ both Fickian or non-Fickian diffusion [3]. As a result of diffusion and absorption of plasticizing molecules, e.g. water, plasticization and hygroscopic swelling may occur [2]. More detailed description can be found in [1].

Some polymers undergo irreversible degradation due to chain scission or hydrolysis, for example, polyamides. Such hydrolysis kinetics were described in detail in works by Mazan et. al. [6]. They developed a multiscale model for predicting the mechanical properties after hydrolytic degradation. The methodology described should apply to other thermoplastics that undergo hydrolysis. Mazan et al. have

reported that hydrolysis induced chain scission and chemicrystalization were the two main mechanisms of property change [7].

One of the promising methodologies to access the lifetime of polymers and the deterioration of properties, e.g. due to recycling and aging, has been identified to be the Quantitative Structure-Property Relationship (QSPR) approach for predicting properties of matrix polymers. Physical and chemical properties of the matrix polymer can be calculated as regression functions of the connectivity indices, based on the topological graph theory and Jozef Bicerano's QSPR approach [8]. Connectivity indices are derived from the chemical Lewis diagrams. Physical meaning of the connectivity indices is the description of electronic environment and the bonding configuration of atoms in the molecule, thus linking the microscale with the engineering properties on the macroscale, as shown in Figure 3.

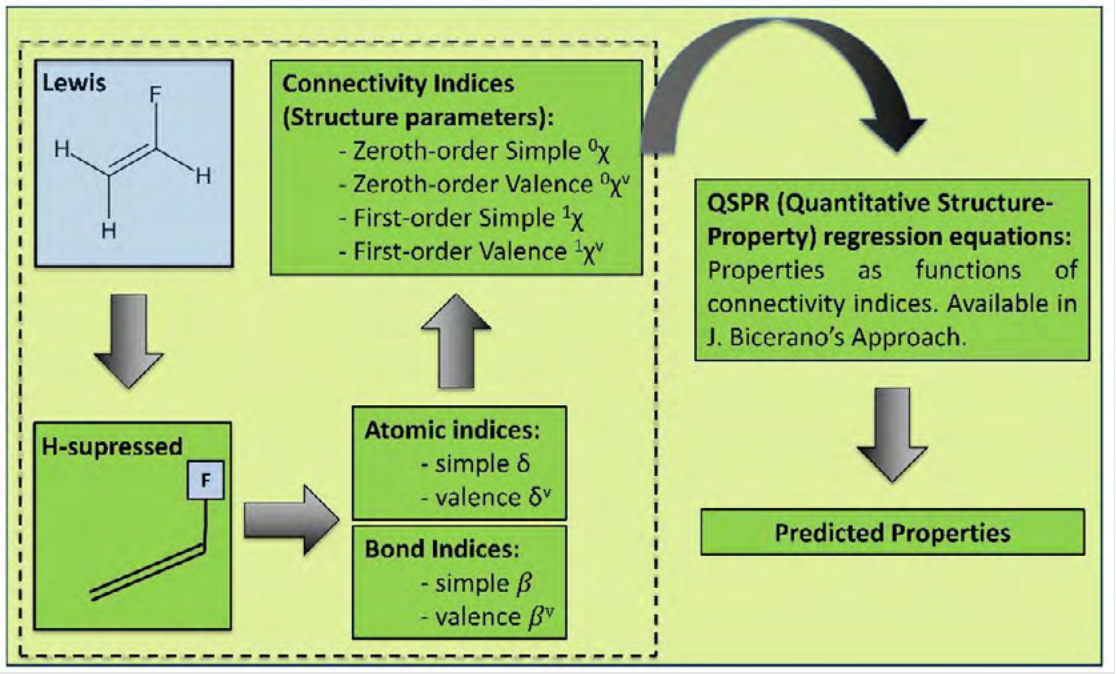


Figure 3. Quantitative Structure-Property Relationship (QSPR) approach; topological method and connectivity indices, reproduced from [5].

The method is based on the idea of a topological graph theory, allowing to describe a polymeric system as a number of parameters – connectivity indices, which are derived from the chemical Lewis diagrams. Physical meaning of the connectivity indices is the description of electronic environment and the bonding configuration of each non-hydrogen atom in the molecule. This approach should be considered as potentially useful for building the link from the microstructure up to the macro properties [2].

In addition, a variety of models can be employed in the above-mentioned modules. Rate Model such as Arrhenius is widely used when temperature is the dominant accelerating factor in aging. The Arrhenius relationship is widely used for lifetime predictions of polymers and composites through monitoring ultimate mechanical properties and their retention, e.g., tensile strength, interfacial shear strength, creep strength, and fatigue strength. However, the durability prediction methodology in most studies is based on the time shift concept [3]. For instance, for some polymers, time-temperature and time-temperature-plasticization superposition approaches might be considered and involved in evaluating the effect of physical effects on the polymers [9].

Finally, some multiscale approaches may be applied to study the complex nature of degradation of polymers, such as the Data-Driven Approach to Elucidate Degradation Trends described in [10]

2.3. Lifetime of Reinforcement

Carbon Fibers (CFs) are typically chemically inert in water, not showing any mechanical strength and stiffness changes. However, it was reported that some CF bundles had a water- and toluene-soluble binder [11]. Moreover, environmental degradation kinetic reaction models for aramid fibres have been presented by Horta et. al. in 2000 and 2003 [12,13]. Natural fibres on the other hand, are mainly affected by plasticization, hygroscopic swelling and biodegradation with microorganisms [14]. Lastly, Glass Fibers (GFs), the most common type of fiber reinforcement [15], are hydrophilic and hence susceptible to degradation when exposed to humid environments [16]. The fact that GFs degrade in aqueous environments has been known at the least since the 1970s [17,18]. However, the rates of hydrothermal degradation vary depending on the material grade and the sizing.

To predict lifetime of glass FRPs, an analytical toolbox consisting of seven modeling modules was presented in a recent work (2021) on the Modular Paradigm for GFRPs [19]. The seven developed modules of the Reinforcement Modular Group within the Modular Paradigm are shown in Figure 4.

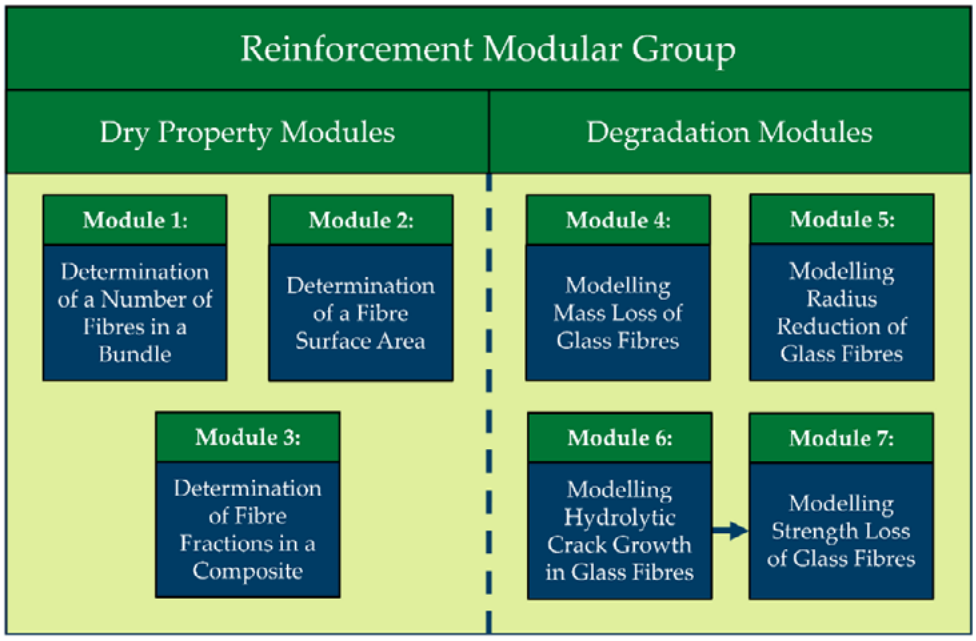


Figure 4. The seven developed modules for Reinforcement lifetime prediction within the Modular Toolbox [19].

Models that predict mass loss and radius reduction are the Contracting Cylinder model [20], the Shrinking Cylinder model [21] and the Dissolving Cylinder Zero-Order Kinetic (DCZOK) model [22].

The crack growth evolution can be modelled by micromechanical models that were proposed by Wierderhorn and Bolz in 1970 [18] and by Sekine and Beaumont in 1998 [23]. The modeling link between the dissolution chemistry-based kinetic models (DCZOK model) and the hydrolytic crack growth in GFs was only recently developed by Echtermeyer and Krauklis et al. in 2019 [11], even though it was initially proposed by Charles back in 1958 for bulk glass [24]. The established link enables prediction of the long-term deterioration of mechanical properties of the GFs due to hydrolytic crack growth by modeling the dissolution kinetics [11]. For FRPs, environmental parameters, such as pH, temperature, availability and composition of the environmental solution, and presence of mechanical stress, as well as fiber orientation play significant roles affecting the dissolution kinetics of GF in polymer composites [25].

2.4. Lifetime of the Interphase

The quality of the interfacial interaction is dependent on the adhesion and present flaws [26]. The FRP interphase may degrade due to hydrolysis, forming interphase flaws. These flaws may further develop into fiber-matrix debondings, matrix cracks and splittings along the fibers [27].

A mass balance approach has been proposed to deduce the hydrothermal aging of the interphase. Mass balance enabled deduction of the kinetics of the hydrolytic degradation of the sizing-rich composite interphase, the rate of dissolution being comparable to that of GFs hydrolytic dissolution [27].

There have been some attempts to quantitatively link the mass loss and the composite interfacial strength loss, but the proper model is yet to be established [28].

3. Discussion

Lifetime prediction modelling is complex due to the duality present in the definitions of failure criteria, integrity, and end-of-life, prioritizing either "safety" or "decomposition" scenarios, shown in Figure 5.

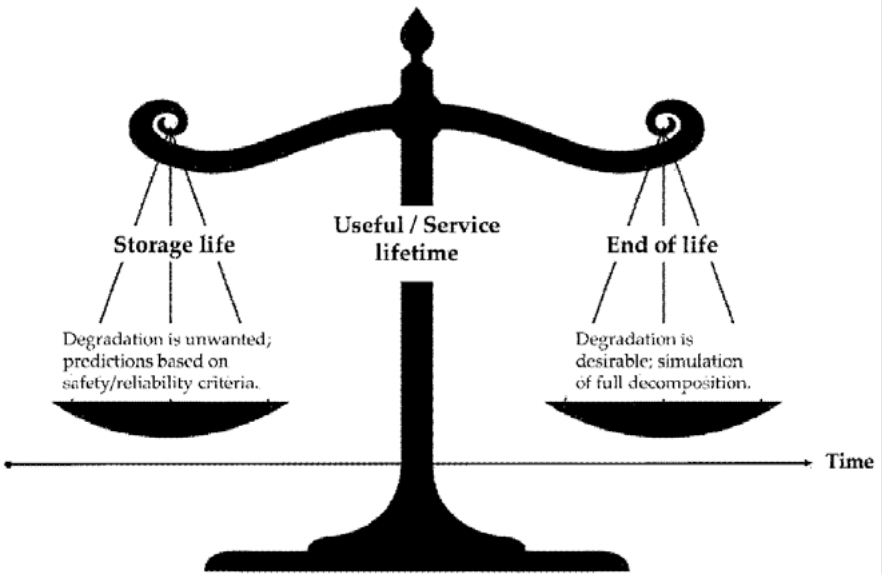


Figure 5. The complexity of Lifetime Prediction modelling is due to necessity to prioritize either “safety” or “decomposition” scenarios [2].

In other words, there are applications where degradation is unfavorable ("safety": structural polymers and FRPs) and is favorable ("decomposition": biodegradable plastics). In conventional structural applications, the aim is to ensure the integrity of the material within a valid lifetime safely, whereas in biodegradation tests (e.g., in compost or soil), the end of life (EoL) is defined by the "decomposition" criteria. While the criteria differ, the modelling approaches could be essentially the same in both scenarios. Future work should consider improvement of the individual modules [28], as well as their interconnectivity in the Lifetime Prediction Framework. For example, the missing link is the lack of understanding how the time-dependent aging of the interphase results in the deterioration of the FRP interfacial strength.

4. Conclusions

An overview of the state-of-the-art related to a modular framework for lifetime prediction of FRPs affected by the environment, has been presented. The underlying physical and chemical principles of the methodology were described. The modeling framework is able to account for the influence of various environmental factors such as pH, temperature, and mechanical stresses, as well as the effects of sizing protection and chemical composition.

Acknowledgments

This work has received funding from the European Union's Horizon Europe R&I program under grant agreement No 101058670 and the H2020 R&I program under the grant agreement No 101005435.

Andrey is grateful to Oksana for her support.

References

[1] A. E. Krauklis. *Environmental Aging of Constituent Materials in Fiber-Reinforced Polymer Composites*. Ph.D. Thesis, NTNU, Trondheim, 2019.
[2] A. E. Krauklis, C. W. Karl, I. B. C. M. Rocha, J. Burlakovs, R. Ozola-Davidane, A. I. Gagani, and O. Starkova. Modelling of Environmental Ageing of Polymers and Polymer Composites—Modular and Multiscale Methods. *Polymers*, 14:216-259, 2022.
[3] O. Starkova, A. I. Gagani, C. W. Karl, I. B. C. M. Rocha, J. Burlakovs, and A. E. Krauklis. Modelling of Environmental Ageing of Polymers and Polymer Composites—Durability Prediction Methods. *Polymers*, 14:907-942, 2022.
[4] A. T. Echtermeyer, A. I. Gagani, A. E. Krauklis and T. Mazan. Multiscale Modelling of Environmental Degradation—First Steps. In *Durability of Composites in a Marine Environment, vol 2*, pages 135-149, Springer, Berlin, 2018.
[5] A. E. Krauklis. Environmental Durability of Composite Materials: Analytical Modelling Toolbox. In *Proceedings of the Aachen Reinforced! Symposium*, Aachen, pages 62–70, 2021.
[6] T. Mazan, J. K. Jørgensen, and A. T. Echtermeyer. Aging of polyamide 11. Part 2: General multiscale model of the hydrolytic degradation applied to predict the morphology evolution. *J. Appl. Polym. Sci.* 132, 42630-42639, 2015.
[7] T. Mazan, J. K. Jørgensen, and A. T. Echtermeyer. Aging of polyamide 11. Part 3: Multiscale model predicting the mechanical properties after hydrolytic degradation. *J. Appl. Polym. Sci.* 132, 42792-42802, 2015.
[8] J. Bicerano. *Prediction of Polymer Properties, Ed. 3*. CRC Press, Boca Raton, 2002.
[9] D. Gibhardt, A. E. Krauklis, A. Doblies, A. Gagani, A. Sabalina, O. Starkova, and B. Fiedler. Time, temperature and water aging failure envelope of thermoset polymers. *Polymer Testing* 118, 107901, 2023
[10] E. Morel, V. Bellenger, and J. Verdu. Structure-water absorption relationships for amine-cured epoxy resins. *Polymer* 26, 1719–1724, 1985.
[11] A. T. Echtermeyer, A. E. Krauklis, A. I. Gagani, and E. Sæter. Zero Stress Aging of Glass and Carbon Fibers in Water and Oil—Strength Reduction Explained by Dissolution Kinetics. *Fibers* 7, 107-120, 2019.
[12] A. Horta, J. Coca, and F. Diez. Degradation mechanism and kinetics of a high thermally stable aromatic polyamide. *Adv. Polym. Technol.* 19, 120–131, 2000.
[13] A. Horta, J. Coca, and F. V. Diez. Degradation kinetics of meta- and para-aromatic polyamides. *Adv. Polym. Technol.* 22, 15–21, 2003.
[14] T. Fakhrul and M. Islam. Degradation Behavior of Natural Fiber Reinforced Polymer Matrix Composites. *Procedia Eng.* 56, 795–800, 2013.
[15] A. E. Krauklis, C. W. Karl, A. I. Gagani and J. K. Jørgensen. Composite Material Recycling Technology—State-of-the-Art and Sustainable Development for the 2020s. *J. Compos. Sci.* 5, 28-60, 2021.
[16] A. Tournie, P. Ricciardi and P. Colomban. Glass corrosion mechanisms: A multiscale analysis. *Solid State Ion.* 179, 2142–2154, 2008.
[17] A. Bledzki, R. Spaude and G. Ehrenstein. Corrosion phenomena in glass fibers and glass fibers reinforced thermosetting resins. *Compos. Sci. Technol.* 23, 263–285, 1985.
[18] S. M. Wiederhorn and L. H. Bolz. Stress Corrosion and Static Fatigue of Glass. *J. Am. Ceram. Soc.* 53, 543–548, 1970.

[19] A. E. Krauklis. Modular Paradigm for Composites: Modeling Hydrothermal Degradation of Glass Fibers. *Fibers* 9, 83-94, 2021.
[20] A. Khawam and D. R. Flanagan. Solid-State Kinetic Models: Basics and Mathematical Fundamentals. *J. Phys. Chem. B* 110, 17315–17328, 2006.
[21] S. T. Bashir, L. Yang, J. J. Liggat and J. L. Thomason. Kinetics of dissolution of glass fiber in hot alkaline solution. *J. Mater. Sci.* 53, 1710–1722, 2018.
[22] A. E. Krauklis and A. T. Echtermeyer. Long-Term Dissolution of Glass Fibers in Water Described by Dissolving Cylinder Zero-Order Kinetic Model: Mass Loss and Radius Reduction. *Open Chem.* 16, 1189–1199, 2018.
[23] H. Sekine and P. W. Beaumont. A physically based micromechanical theory of macroscopic stress-corrosion cracking in aligned continuous glass-fibre-reinforced polymer laminates. *Compos. Sci. Technol.* 58, 1659–1665, 1998.
[24] R. J. Charles. Static Fatigue of Glass. II. *J. Appl. Phys.* 29, 1554–1560, 1958.
[25] A. E. Krauklis, H. A. Aouissi, S. Bencedira, J. Burlakovs, I. Zekker, I. Bute, and M. Klavins. Influence of Environmental Parameters and Fiber Orientation on Dissolution Kinetics of Glass Fibers in Polymer Composites. *J. Compos. Sci.* 6, 210, 2022.
[26] R. Plonka, E. Mäder, S. Gao, C. Bellmann, V. Dutschk and S. Zhandarov. Adhesion of epoxy/glass fibre composites influenced by aging effects on sizings. *Compos. Part A Appl. Sci. Manuf.* 35, 1207–1216, 2004.
[27] A. E. Krauklis, A. I. Gagani and A. T. Echtermeyer. Long-Term Hydrolytic Degradation of the Sizing-Rich Composite Interphase. *Coatings* 9, 263-286, 2019.
[28] A. E. Krauklis, O. Starkova, D. Gibhardt, G. Kalinka, H. A. Aouissi, J. Burlakovs, A. Sabalina and B. Fiedler. Reversible and irreversible effects on the epoxy GFRP fiber-matrix interphase due to hydrothermal aging. *Composites Part C: Open Access* 12, 100395-100403, 2023.
[29] A. E. Krauklis. Predicting Environmental Ageing of Composites: Modular Approach and Multiscale Modelling. *Mater. Proc.* 6, 11, 2021.

FE MODELING OF DAMAGE DEVELOPMENT IN HYBRID CARBON/STEEL FIBER TEXTILE COMPOSITES USING FRACTURE MECHANICS AND COHESIVE ZONE APPROACH

Anish N. Kulkarni*, Olga Kononova, Vladislavs Jevstigņejevs and Andrejs Pupurs

Faculty of Civil and Mechanical Engineering, Riga Technical University, Kipsalas Street 6A, LV-1048, Riga, Latvia
*Email : anish-niranjan.kulkarni@rtu.lv, Web Page : https://ortus.rtu.lv/science/en/experts/38852

Keywords: Metal-composite joints, Textile composites, Mechanical testing, Finite element modeling, Damage development

Abstract
Joining of dissimilar materials such as metals and polymeric composites using bolting, riveting or adhesive joining results in abrupt change in mechanical properties at the joints causing stress concentration. Structural health of a hybrid metal-composite structure can be compromised by factors such as environmental degradation of adhesive or galvanic corrosion at the metal-composite joints. To solve these issues, metal-composite joints with textile mesostructure have been developed with hybrid carbon/steel fiber textile composites. The hybrid composites are tested under quasi-static tensile loading to study macro-mechanical properties and evolution of microdamage. Two configurations of woven hybrid composites are chosen for FE modeling of damage development. 3D representative volume elements are built such that resin-impregnated yarns are modelled as homogeneous orthotropic materials, and yarn/matrix-interface behavior is characterized by cohesive zone material modeling. During mechanical test simulation, stress-strain curves are plotted and damage schematics inside yarns and matrix are obtained. The FEM predictions match the experimental results of microdamage evolution, but they underestimate the experimental tensile strength values for hybrid composite configuration with stainless steel-fiber yarn in the warp-direction and carbon-fiber yarn in the weft-direction.

1. Introduction

Recent efforts to combine the use of metals and polymer-matrix composites in aerospace structures have led to the necessity of suitable metal-composite joining techniques. Jahn et al. [1] and Pramanik et al. [2] have reviewed the existing metal-composite joining techniques, among which the most common techniques are adhesive bonding and mechanical joining (bolting, riveting etc.). Although these techniques are effective in joining metal- and composite-parts, they have some serious drawbacks in terms of mechanical properties of joints. Adhesive metal-composite bonding results in an abrupt change of mechanical properties from the metal-side to the composite-side and the progressive environmental degradation of adhesive joints over time can be an issue [2]. In case of mechanical metal-composite joining using bolts or rivets, in addition to the abrupt change of mechanical properties and consequently high stress concentration at the joints, very poor notched strength of composite laminates as compared to their unnotched strength poses a serious threat to structural integrity of hybrid metal-composite structures [3].

While joining two dissimilar materials, their galvanic corrosion potential is an important factor which needs to be taken into consideration. This is critical while designing a metal-composite joint. In the case

of joining Al-alloys with carbon-fiber reinforced polymers (CFRP), Al-alloys must be coated at the joints, as the two materials have high galvanic corrosion potential [2,4,5]. On the contrary, alloys such as stainless steel are compatible with CFRP [5], and they can be joined together without any need of surface coating. In literature, there are multiple studies regarding CFRP-stainless steel hybrid stack-up or sandwich structures [6-8], where excellent joining is achieved using methods such as co-curing and weld-bonding.

In a similar study, Pupurs et al. [9] have recently developed CFRP-stainless steel hybrid joints with textile meso-structure. It is shown that epoxy-based hybrid composites with interwoven carbon-fiber yarns and stainless steel-fiber yarns possess mechanical properties intermediate to non-hybrid epoxy-based carbon-fiber and steel-fiber composites. The assembly of hybrid carbon/steel fiber textile composite with non-hybrid composites on either sides can act as a suitable metal-composite joint with gradual property change from the metal-side to the composite side.

In a follow-up study, Kulkarni et al. [10] have analyzed micro-damage evolution in hybrid carbon/steel fiber textile composites using experimental approach. A detailed description of possible damage modes in non-hybrid textile composites can be found in [11]. Similar damage modes have been reported in [10] for hybrid textile composites. Numerical study of mechanical behavior of hybrid carbon/steel fiber textile composites has been conducted in [12], where finite element models of the hybrid composites are developed, and their elastic properties are compared with the experimental values reported in [9].

The present work focuses on finite element modeling of microdamage in hybrid carbon/steel fiber textile composites. To evaluate damage inside fiber yarns and matrix, strength-based criteria are used. The yarn/matrix-interface is modelled with contact elements and yarn-matrix debonding is studied using cohesive zone material (CZM) modeling.

2. Materials and methods

Fabric reinforcements for the hybrid carbon/steel fiber textile composites were manufactured using T300 carbon-fiber yarns from Toray (Japan) and SY 11/1 stainless steel-yarns from Fujibo (Japan) and Bekaert (Belgium). The carbon-fiber yarns had a tow size of 1K with 7 μm individual filament diameter. The stainless steel-fiber yarns were 91 tex with 12 μm individual filament diameter. Two types of fabrics were manufactured - i) woven fabrics with plain weave pattern using manual weaving loom, and ii) knitted fabrics with plain weft knit pattern using manual knitting machine. Composite manufacturing was carried out using vacuum infusion of epoxy LY1564 resin (with XB 3404-1 hardener) into stacked dry fabric layers. The composite plates were oven-cured at 80 ^{o}C for 8 hours. Multiple configurations of knitted and woven composites with different meso-structures were manufactured. Composite specimens were tested under quasi-static tensile loading according to ASTM D3039 standard, and properties such as elastic modulus, tensile strength and strain-to-failure were obtained for each hybrid configuration. Additionally, micro-damage evolution with increasing level of applied strain was also studied. A detailed list of woven and knitted hybrid composite configurations, along with their mechanical properties obtained using experimental methods, can be found in [10].

For numerical analysis of mechanical properties and micro-damage evolution, two configurations among woven hybrid composites were chosen, namely, i) H5, with steel-fiber yarn in weft-direction and carbon-fiber yarn in warp-direction, and ii) H6, with carbon-fiber yarn in weft-direction and steel-fiber yarn in warp-direction. A schematic representation of the meso-structures of the two configurations is given in Fig. 1.

For FEM analysis, 3D representative volume elements (RVEs) for H5 and H6 were constructed in SolidWorks software and were imported in ANSYS Mechanical FEM software to generate element mesh and to apply boundary conditions. The curvature of warp yarns was modelled using a simple sine-wave function, whereas weft yarns were assumed to be straight. The yarns were embedded in a cuboidal matrix block, on which the relevant boundary conditions were applied. As shown Fig. 2, uniform displacement U_x along warp yarn-direction (X-axis) was applied on the right-face of the matrix block.

Symmetry boundary conditions were applied on the top-, bottom-, front- and left-faces, and U_z displacement coupling was applied at the back-face of the matrix block, allowing free contraction according to Poisson's effect along weft yarn-direction (Z-axis). Warp yarn-curvature and yarn cross-sections were calibrated according to optical microscopy images from the experimental results. Additional calibrations were performed by comparing elastic properties of the RVEs with the elastic properties obtained from the experimental results. The resin-impregnated carbon-fiber and stainless steel-fiber yarns were considered as homogeneous orthotropic materials with properties given in Table 1. Epoxy matrix was modelled as an isotropic material with Young's modulus $E = 3\ GPa$ and Poisson's ratio $\nu = 0.29$.



(a) (b)

Figure 1. Schematic representation of (a) H5 and (b) H6. Carbon-fiber yarns are shown in black, and steel-fiber yarns are shown in white. Yarns along X-axis are warp yarns and yarns perpendicular to X-axis (along Z-axis, not shown in the figure) are weft yarns.

Table 1. Material properties of resin-impregnated fiber yarns.

Material property	Notation	Unit	Carbon-fiber yarn	Stainless steel-fiber yarn
Longitudinal modulus	E_L	GPa	139.21	105.00
Transverse modulus	E_T	GPa	7.52	105.00
Longitudinal Poisson's ratio	ν_{LT}	-	0.22	0.30
Transverse Poisson's ratio	ν_{T3}	-	0.40	0.30
In-plane shear modulus	G_{LT}	GPa	3.43	40.38
Out-of-plane shear modulus	G_{T3}	GPa	2.69	40.38

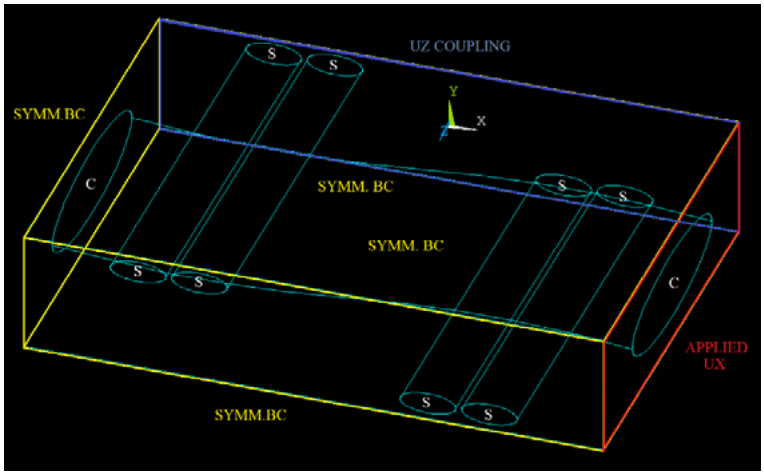


Figure 2. Representative Volume Element (RVE) of composite configuration H5. 'S' denotes steel-fiber yarn and 'C' denotes carbon-fiber yarn. Similar boundary conditions were applied for RVE of composite configuration H6.

During FE simulation, displacement U_x corresponding to 0.01% strain was applied at first time step. To study the quasi-static tensile test response of the FE model, value of applied strain was incremented by 0.01% at each subsequent time step until the model underwent final failure. To identify damage initiation sites inside fiber yarns and matrix, material strength limits were defined, and maximum stress criterion was used. To simulate progressive damage evolution, instant material stiffness reduction method was used such that material stiffness was reduced by 5% at every damage initiation instance. For analysis of yarn/matrix-interface debonding, contact elements were applied at the interface and CZM modeling was used. Bilinear material behavior with linear softening in the cohesive zone was defined by the values of maximum traction and critical energy release rates for normal separation and tangential slipping. Using the FEM solutions, stress-strain curves for H5 and H6 were plotted, and the schematics of i) damage status inside yarns and matrix and ii) contact status at yarn/matrix-interface were obtained.

3. Results and discussion

3.1. Stress-strain curves

To study mechanical behavior of FE models at the macro-scale, stress-strain curves were plotted for the two chosen composite configurations, and they were compared with the experimental results. Fig. 3 shows the comparison between experimental- and FEM stress-strain curves for H5 and H6.

In the case of composite configuration H5, FEM predictions for tensile strength and strain-to-failure in the warp direction are higher than the experimental values. The FEM model of H5 shows lower stiffness than experimental observation, but the difference in modulus values is small compared to the difference in FEM- and experimental modulus values for H6. For the FEM model of H6, the discrepancy in the use of input material properties for warp yarn (in this case, resin-impregnated stainless steel-fiber yarn) might have caused such a large difference in FEM- and experimental elastic modulus and tensile strength values along the warp-direction. Here, factors such as yarn twist, irregular fiber shapes and non-uniform fiber volume fraction should be considered, which cannot be replicated in the FEM analysis.

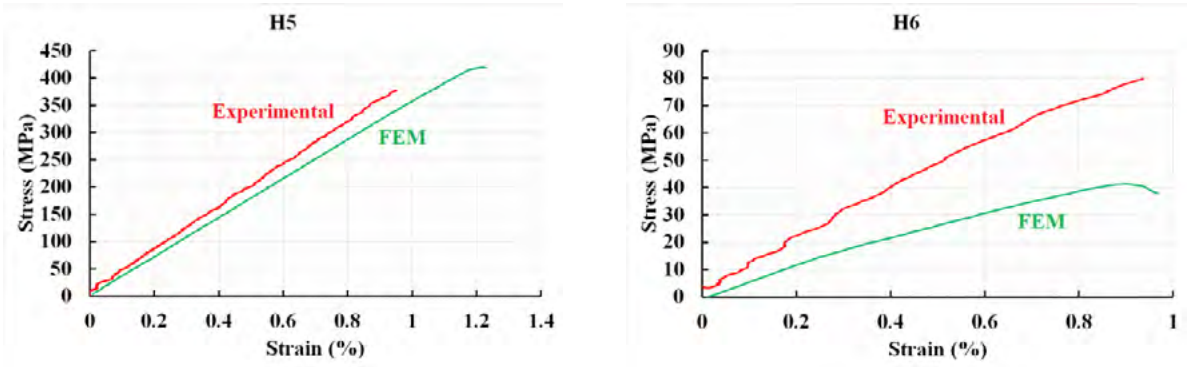
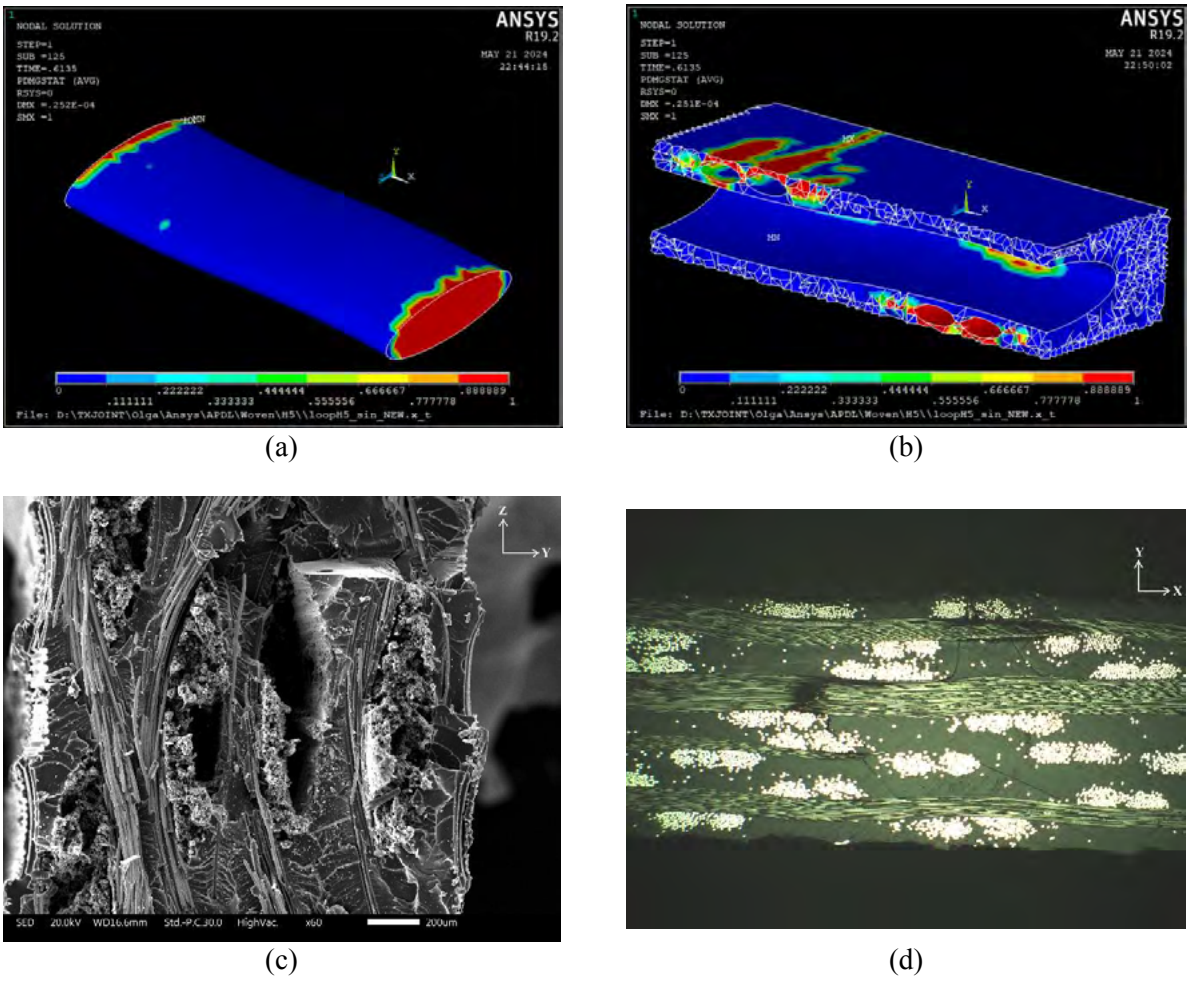


Figure 3. Stress-strain curves for composite configurations (a) H5 and (b) H6.

3.2. Microdamage studies

During quasi-static tensile loading simulation, microdamage inside yarns and matrix and debonding at the yarn/matrix-interface was monitored at each time step until final failure. Figs. 4 and 5 compare FEM damage status for yarn and matrix with experimental observations at the instance of final failure for H5 and H6. In composite configuration H5, the irregular damage of carbon-fiber warp yarns can be seen in Figs. 4(a) and 4(c). The matrix damage around weft yarns in FE model (refer Fig. 4(b)) is comparable with the matrix damage in optical microscopy image shown in Fig. 4(d). In composite configuration H6, partially damaged warp yarn/matrix-interface seen in Fig. 5(a) can be correlated with the yarn/matrix-interface in SEM fracture surface image in Fig. 5(c). The matrix damage surrounding warp yarns i.e.,

delaminations, can be seen in FE model (refer Fig. 5(b)) as well as in optical microscopy image (refer Fig. 5(d)). In terms of yarn/matrix-interface strengths, Figs. 4(c) and 5(c) depict that carbon-fiber yarn/epoxy-matrix interface is much weaker than the stainless-steel fiber yarn/epoxy-matrix interface.



(a) (b)

(c) (d)

Figure 4. Schematics of microdamage (at the instance of final failure) for composite configuration H5, (a) FEM warp-yarn damage, (b) FEM matrix damage, (c) SEM image of fracture surface, and (d) Optical microscope image of polished edge (For FEM damage schematics, 0 = No damage, 1 = Full damage).

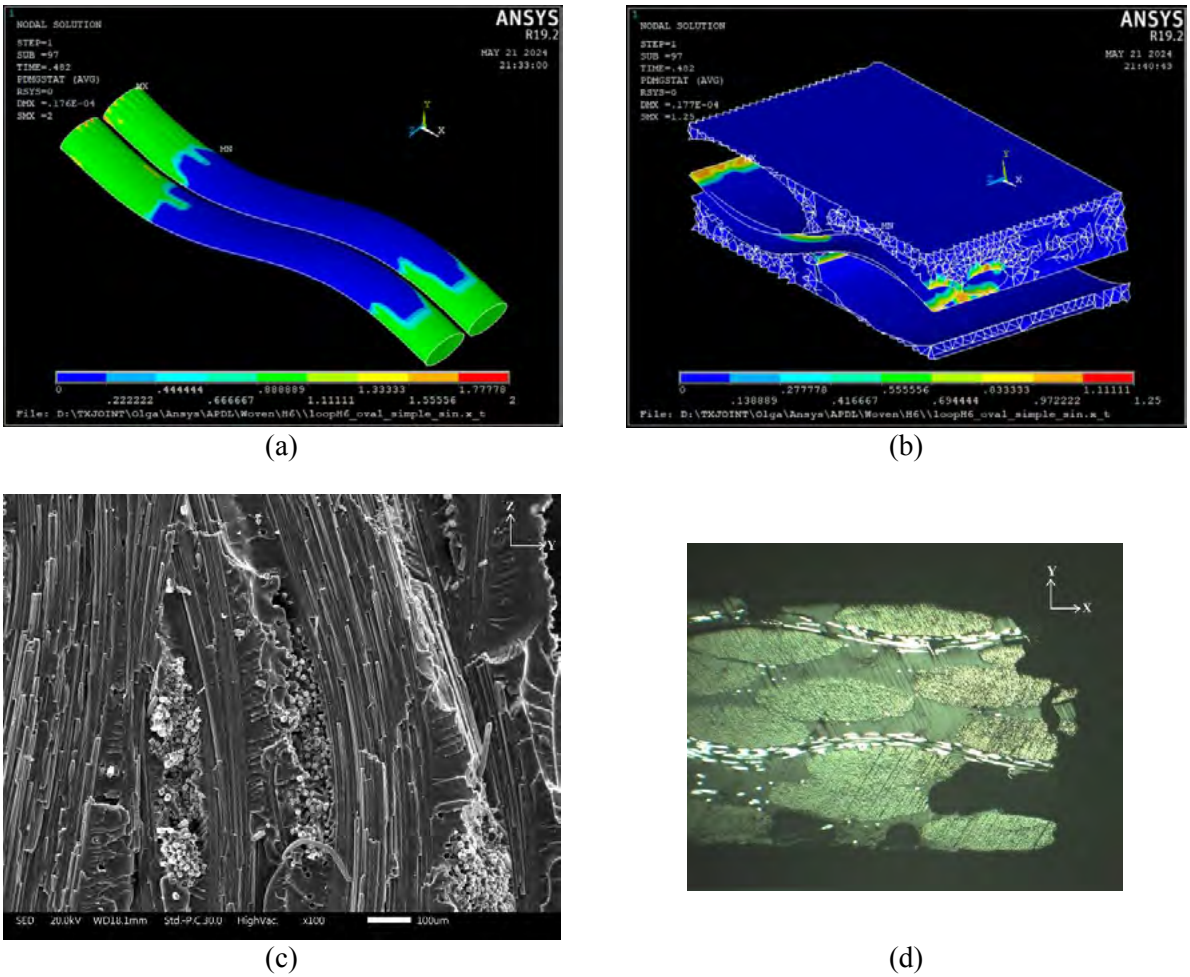


Figure 5. Schematics of microdamage (at the instance of final failure) for composite configuration H6, (a) FEM warp-yarn damage, (b) FEM matrix damage, (c) SEM image of fracture surface, and (d) Optical microscope image of polished edge (For FEM damage schematics, 0 = No damage, 1 = Partial damage, 2 = Full damage).

4. Conclusions

Damage development in hybrid carbon/steel fiber textile composites was studied using FE modeling. Representative volume elements were constructed for two configurations of hybrid woven composites and their mechanical response under quasi-static tensile loading was studied. To identify damage initiation sites inside fiber yarns and matrix, strength limits were defined, and maximum stress criterion was applied. Yarn/matrix-interface debonding was simulated by defining contact elements at the interface and by applying cohesive zone properties with bilinear material law. The macro-mechanical response of the hybrid composite FE models was captured by plotting stress-strain curves. For hybrid composite with stainless-steel fiber yarn in warp direction and carbon-fiber yarn in weft direction, FE model underestimates the experimental stiffness and strength values along warp direction by 50%. In terms of micro-damage evolution, FE models give accurate prediction of damage initiation sites and damage in fiber yarns and matrix at the instance of final failure.

Acknowledgments

This work has been supported by Latvian Council of Science, project LZP-2019/1-0357 “Development and behavior analysis of novel textile composite/metal joints with enhanced mechanical properties” and the European Social Fund within the Project No 8.2.2.0/20/I/008 “Strengthening of PhD students and academic personnel of Riga Technical University and BA School of Business and Finance in the

strategic fields of specialization" of the Specific Objective 8.2.2 "To Strengthen Academic Staff of Higher Education Institutions in Strategic Specialization Areas" of the Operational Programme "Growth and Employment".

References

[1] J. Jahn, M. Weber, J. Boehner and R. Steinhilper. Assessment Strategies for Composite-metal Joining Technologies - A Review. In *Procedia CIRP*, volume 50, pages 689-694, 2016.

[2] A. Pramanik, A. Basak, Y. Dong, P. Sarker, M. Uddin, G. Littlefair, A. Dixit and S. Chattopadhyaya. Joining of carbon fibre reinforced polymer (CFRP) composites and aluminium alloys – A review. *Composites Part A: Applied Science and Manufacturing*, 101:1-29, 2017.

[3] M. Saleh, Y. Wang, A. Yudhanto, A. Joesbury, P. Potluri, G. Lubineau and C. Soutis. Investigating the Potential of Using Off-Axis 3D Woven Composites in Composite Joints' Applications. *Applied Composite Materials*, 24:377–396, 2017.

[4] A.M. Joesbury. *New Approaches to Composite Metal Joining (Doctoral Thesis)*. Cranfield University, Cranfield, 2015.

[5] B. Hannemann, S. Backe, S. Schmeer, F. Balle and U.P. Breuer. New Multifunctional Hybrid Polymer Composites Reinforced by Carbon and Steel Fibers. In *Proceedings of the 20th International Conference on Composite Materials*, 2015.

[6] Q. Liu, J. Ma, L. Kang, G. Sun and Q. Li. An experimental study on fatigue characteristics of CFRP-steel hybrid laminates. *Materials and Design*, 88:643-650, 2015.

[7] A.M. Joesbury, P.A. Colegrove, P.V. Rymenant, D.S. Ayre, S. Ganguly and S. Williams. Weld-bonded stainless steel to carbon fibre-reinforced plastic joints. *Journal of Materials Processing Technology*, 251:241-250, 2018.

[8] Y. Shibuya, J. Zhang, Y. Sato and J. Yanagimoto. Evaluation of the mechanical properties and deformability of metal-based composite sheets made of thin stainless-steel sheets and carbon fiber reinforced plastics. *International Journal of Material Forming*, 15: 47, 2022.

[9] A. Pupurs, I. Bramane, I. Ļašenko, M. Maniņš, M. Irbe and A. Šņepts. Manufacturing and Experimental Testing of Composite/Metal Joints with Textile Mesostructure. In *ECCM 2022 - Proceedings of the 20th European Conference on Composite Materials: Composites Meet Sustainability*, volume 2, pages 540-546, 2022.

[10] A.N. Kulkarni, A. Pupurs, A. Šņepts and M. Irbe. Micro-damage Evolution in Hybrid Carbon/Steel Knitted and Woven Fabric Composites. In *Proceedings of the 23rd International Conference on Composite Materials*, 2023.

[11] L. Gorbatikh and S. Lomov. Damage accumulation in textile composites. In *Modeling Damage, Fatigue and Failure of Composite Materials*. Woodhead Publishing, pages 41-59, 2016.

[12] O. Kononova, V. Jevstigņejevs, A. Pupurs and A.N. Kulkarni. Modeling Micro-damage Development in Functionally Graded Knitted and Woven Carbon/Steel Fibre Composites. In *ECCM 2022 - Proceedings of the 20th European Conference on Composite Materials: Composites Meet Sustainability*, volume 4, pages 298-305, 2022.

COMPREHENSIVE ANALYSIS OF FATIGUE AND CREEP RELATIONSHIPS IN THERMOPLASTIC COMPOSITES: TOWARDS INNOVATIVE STRUCTURAL DESIGN APPROACHES.

F.Lamming[1,2], N.Bedrici[2], S. Gillet[2] and S.Joannès[1]

[1] ESTACA Campus Ouest - Parc Universitaire Laval-Changé - Rue Georges Charpak BP 76121 - 53061 Laval Cedex 9, France,francois.lamming@estaca.fr, https://www.estaca.fr/
[2] Mines Paris, Université PSL, Centre des Matériaux (MAT), UMR7633 CNRS, 91003 Evry, France, sebastien.joannes@minesparis.psl.eu, https://www.mat.minesparis.psl.eu/

Keywords: fatigue, creep, SFRT, microstructure, load ratio

Abstract
This work contributes to a more accurate prediction of the fatigue behaviour of structures, while reducing the number of characterisation tests on specimens for Short Fibre Reinforced Thermoplastic (SFRT) composites, based on nylon and short glass fibres. To achieve this, a more profound understanding of the oligocylic fatigue and creep damage mechanisms is required, both from a microstructural and a macroscopical perspective. Microscopically, no differences in fracture surfaces are observed. Macroscopically, a straightening of the S-t (Stress-time) curves is observed as the loading ratio increases. This relationship, highlighted by [5] through a strain-based criterion, paves the way for the development of a simplified fatigue model, suitable for use in the industrial world, based on creep calculation.

1. Introduction

1.1. Generalities

In order to address the challenges posed by global warming, there is a pressing need to enhance the energy efficiency of vehicles. This can be achieved by taking greater advantage of composite materials with an organic matrix, in particular a thermoplastic one. These materials are easily moldable and can significantly reduce structural weight, while offering good recyclability and high production rates. Initially intended for low-stressed components, thermoplastic composites, such as **PA66GF50**, are now well-suited to meet the requirements of parts subject to severe stresses and harsh environments. In order to guarantee user safety and to optimise maintenance, it is essential to effectively predict the service life of components under operating conditions.

Fatigue characterisation is a complex process: PA66GF50 is highly sensitive to external parameters such as **temperature**, **ambient humidity**, and **cyclic load ratio** [1], as well as intrinsic parameters such as **injection orientation** or **product thickness**. Numerous criteria have been proposed in the literature to predict component life [8]. These criteria establish a mathematical relationship between the **presumed life** (number of cycles or time to failure) and one or more observable or deducible quantities (strain, stress, energy, etc.) at the material's local scale. Prior to modelling and simulating the behaviour of a structure, it is essential to scale up to the representative specimen level. A robust criterion can predict and unify specimen life for a wide range of external and intrinsic parameters. Building upon this criterion, micromechanical models for life prediction have been developed [2,3]. These models enable the determination of the local life of a part without requiring the use of a complex and time-consuming damage model.

1.2. Criteria

In the work of [4], a criterion based on the mean strain rate (**2CMeanE**) was employed to estimate the life expectancy of representative specimens (**oligocyclic fatigue** and **creep)**. This criterion demonstrated satisfactory performance for cyclic load ratios between 0 and 1. Subsequently, a criterion based on the maximum strain rate (**2CMaxE**) was developed for load ratios between -1 and 1 [5]. This criterion is slightly more effective than energy-based criteria, such as **AED** [6], or **mixed criteria** (strain-energy) [7]. Indeed, it successfully grouped the results from 433 fatigue tests on representative specimens, with 86% of predicted life spans falling within a dispersion range of two. Furthermore, in comparison to more complex criteria [7,8], this criterion requires only two parameters and a single physical quantity for implementation, thus offering a simpler and more straightforward approach. Moreover, in contrast to the AED criterion [6], the 2CMaxE criterion is applicable to **creep** [5]. This requires the creep and fatigue deformation data to be expressed in the **time domain**. These results show the **link** between creep and fatigue.

To enhance the reliability of the 2CMaxE criterion [5], a range of load ratios and parameters related to environmental conditions are considered and incorporated into an experimental database.

1.3. S-t curves

From a macroscopic perspective, an upturn in the logarithmic **Wöhler curve** has been observed previously as the load ratio increases and approaches 1 (**pure creep**) [4]. It should be noted that the curves are time dependent, as the fatigue number of cycles is equal to the creep lifetime for our **1 Hz** frequency. An experimental campaign was conducted at room temperature for two conditions (**configuration 1**: 0% humidity and 0° orientation, **configuration 2**: 50% humidity and 90° orientation) to deepen the understanding of this phenomenon. Log-linear regressions for each curve are plotted according to the following law (Eq.1):

$$S_{max} = \sigma_{UTS} - b \log(t_f). \quad (1)$$

S_{max} represents the maximum applied stress, σ_{UTS} denotes the ultimate tensile stress (**NF EN 12003**), b is the slope of the curve et t_f fatigue life to failure. Given the significant uncertainties arising from the variability in fatigue life during tests, a correlation coefficient is provided for indicative purposes.

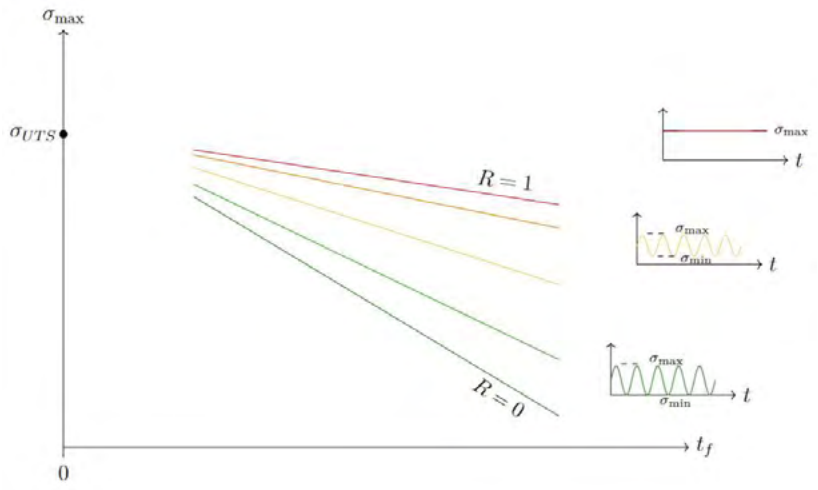


Figure 1. Illustration of the maximum stress - life curve for various load ratio values (R ranging from 0 to 1).

Under these conditions and for an identical lifespan, it is assumed that as one approaches a creep loading scenario, the maximum stress to be applied increases (Figure 1).

One author in the literature demonstrates a different behavioural pattern. Two distinct slopes are observed for fatigue loading, as evidenced by [9]. Other authors present an increase in fatigue strength with an increase in load ratio, although the softening of the slope is far less noticeable [7,10].

2. Methods

2.1. Material and conditioning

The material under study is a **polyamide 66** reinforced with **short glass fibres** with a fibre content of 50% by weight (**PA66GF50**), in the form of injection-molded plates with a thickness of 3 mm. The PA66 matrix is a semi-crystalline thermoplastic with visco-elasto-plastic mechanical properties. The material is conditioned at two **humidity levels**: **0%RH** and **50%RH**. The first conditioning involves heating the material to 80°C in an oven until mass stabilization is achieved. The second involves conditioning at 62%RH and 70°C until mass stabilization is achieved. **Dogbone-shaped** specimens used for fatigue tests were cut from the injection-molded plates with two different **angles** θ relative to the injection direction: 0° and 90°. Six specimens were cut from each plate.

2.2. Mechanical tests

Fatigue tests under load were conducted using an INSTRON 8801 hydraulic fatigue machine. All tests were performed at **room temperature** (T=23°C). Mass measurements indicated that the humidity variation during the test was negligible. The fatigue tests were conducted using a sinusoidal signal at a constant frequency of **1 Hz** to avoid **self-heating** and with a constant stress amplitude. Five load ratios were considered in this study, defined as the ratio between the maximum applied stress and the minimum stress: **R = 0** (R0), **R = 0.2** (R02), **R = 0.5** (R05), **R = 0.8** (R08), **and R = 1** (R1). For each load ratio and maximum applied stress level, a minimum of three tests were conducted. Furthermore, each curve includes a minimum of four levels of maximum applied stress.

3. Results

3.1. Microscopic observations

A microscopic investigation was conducted using a **Scanning Electron Microscope (SEM)** to analyse the fracture surfaces of various specimens. Thus, the objective was to gain insight into the observed decrease in fatigue life compared to creep loading (with identical maximum stress). A comparison of **fracture surfaces** obtained from fatigue (R0) and creep (R1) was performed, showing **no significant differences**, in accordance with the literature [2,11], whether under 0%RH and 0° conditions or at 80%RH (Figure 2a and b) and for orientations of 0° or 90°. At 0%RH, the surfaces only exhibit a **brittle looking zone** with numerous **pores** (micro and nanopores). At 80%RH, both ductile and brittle zones were observed in both cases, with no significant differences between fatigue and creep. **Extended plastic zones**, fibre-matrix interface debonding, and fractures were observed in both fatigue and creep conditions (Figure 2).

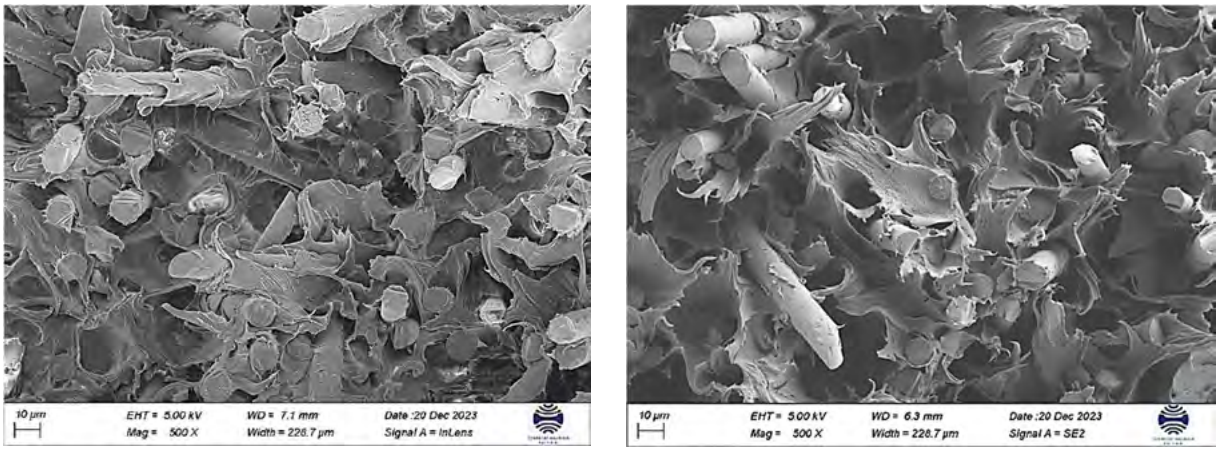


Figure 2. SEM images of ductile fracture surfaces. Fatigue (left), creep (right).

3.1. Macroscopic comparisons

The maximum stress, expressed as a percentage of the UTS stress, is plotted against time to failure. The parameters of the log-linear regressions are provided in Table 1. The **correlation coefficient** r^2 is also given, calculated using the formula (Eq.2):

$$r^2 = 1 - \frac{\sum_1^n \left(y_i - y_i^{pred}\right)^2)}{\sum_1^n (y_i - \bar{y_i})^2)} \quad (2)$$

The y_i values represent the values for point i, y_i^{pred} predicted value for point i calculated using a **log-linear regression** method. The $\bar{y_i}$ empirical mean is derived from the data. As expected, we observe an increase in the slope of the S-N curve as R increases from 0 to 0.2 and 0.5. However, as R approaches 1, a decrease in fatigue strength is observed, contrary to what was expected (Figure 1), for both conditioning levels. For the 0%RH conditioning, the upward trends cease beyond R05, with the R08 and R1 curves nearly overlapping.

With regard to the 50%RH conditioning (Figure 3), the curves from R0 to R08 exhibit a discernable **upward trend**. However, the creep curve shows a steeper slope and a considerably lower level than expected.

Table 1. Fatigue interpolation parameters, S-t curves, 50%RH, 90°

R	$\%\sigma_{UTS}$	b/σ_{UTS}	r^2
1	0.94	0.025	0.77
0.8	0.93	0.009	0.54
0.5	0.96	0.020	0.89
0.2	1.01	0.037	0.86
0	1.04	0.048	0,86

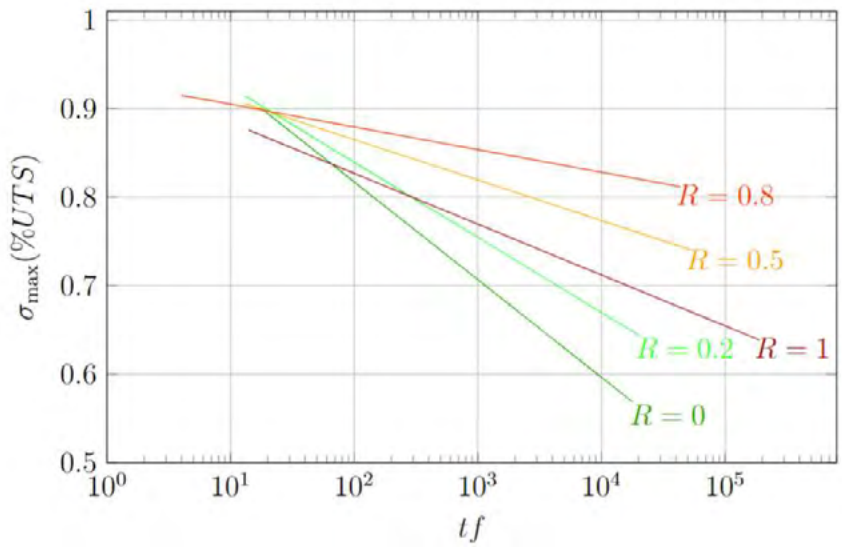


Figure 3.S-t curve (%UTS) – lifetime for several R values (R between 0(dark green) end 1 (dark red)), 50RH / 90°.

4. Discussions

A high degree of **dispersion** is observed, particularly evident in the creep curves, which introduces uncertainty into the analysis of the results, especially as R increases (highest for the creep curves) (Table 1).

While an upward trend in the slope can be confidently observed, it is more challenging to assert that the creep resistance level is below the other curves. To increase certainty regarding the slope and position of the curves, a new test campaign will be conducted.

5. Conclusion

The relationship between fatigue and creep is complex, both at the macroscopic and microscopic levels. From the microscopic perspective, **no significant differences** were observed in the fracture surface observations. Based on the similarity of the fracture surfaces between fatigue and creep, it can be inferred that similar damage mechanisms occurred. A **micro-tomography** observation campaign is planned to observe and quantify real-time differences in **damage mechanisms** between the two loading types (porosity rate, percentage of broken fibres, etc.), which may not be observable on fracture surfaces. From a macroscopic perspective, a **softening** of the S-t curves is observed for R ranging from 0 to 0.5 or 0.8 depending on the specimen type. However, the creep curve does not align with the expected level, which could indicate differences in damage mechanisms or simply the high measured dispersion. A similar test campaign at 80%RH is also planned to highlight the effect of ductile specimen behaviour on the curves' upward trend. Additionally, extra creep tests will be conducted to reduce **statistical uncertainty** regarding the obtained levels. A comparison of surface deformation fields between creep and fatigue will also be carried out using Digital Image Correlation (DIC).

The 2CMaxE criterion supports an **innovative numerical approach** to fatigue design (**oligocyclic**), leveraging insights gained from creep tests. These efforts contribute to better predicting the fatigue behaviour of structures while significantly reducing characterisation tests on specimens. Creep models capturing maximum average strain rate will be established. Post-processing using the experimentally determined criterion will predict the lifespan of complex components.

Acknowledgments

The authors would like to express their gratitude to the teams at the **ESTACA Laval laboratory** and the **Centre des Matériaux** of Mines Paris - PSL. In particular, they would like to acknowledge the invaluable assistance of **Raphaël DEFOSSEZ** during experiments.

References

[1] N. Jia et V. A. Kagan, « Mechanical Performance of Polyamides with Influence of Moisture and Temperature – Accurate Evaluation and Better Understanding », *in Plastics Failure Analysis and Prevention*, Elsevier, 2001, p. 95-104. doi: 10.1016/B978-188420792-1.50014-7.

[2] N. Fouchier, « Approche intégrée pour estimer la durée de vie en fatigue de pièces thermoplastiques renforcés fibres courtes dans un cadre viscoélastique haute température », 2019.

[3] A. Launay, M. H. Maitournam, Y. Marco, et I. Raoult, « Multiaxial fatigue models for short glass fibre reinforced polyamide. Part II: Fatigue life estimation », *Int. J. Fatigue*, vol. 47, p. 390-406, févr. 2013, doi: 10.1016/j.ijfatigue.2012.09.015.

[4] S. Gillet, T. Jacopin, S. Joannès, N. Bedrici, et L. Laiarinandrasana, « Short-term creep and low cycle fatigue unified criterion for a hybridised composite material », *Int. J. Fatigue*, vol. 155, p. 106571, févr. 2022, doi: 10.1016/j.ijfatigue.2021.106571.

[5] S. Gillet, F. L. Taussé Kamdoum, N. Bedrici, S. Joannès, et L. Laiarinandrasana, « Cyclic creep strain rate criterion for short-fibre reinforced thermoplastics: Validation of creep and fatigue performance across a wide range of load ratios », *Int. J. Fatigue*, vol. 183, p. 108257, 2024, doi: https://doi.org/10.1016/j.ijfatigue.2024.108257.

[6] F. E. Fiorini, L. M. Martulli, P. Steck, et A. Bernasconi, « A modified energy-based fatigue parameter for short fiber reinforced polymers: Performance analysis with varying thicknesses, load ratios, and fiber orientations », *Fatigue Fract. Eng. Mater. Struct.*, vol. 46, no 9, p. 3372-3386, 2023, doi: https://doi.org/10.1111/ffe.14072.

[7] I. Raphael, N. Saintier, H. Rolland, G. Robert, et L. Laiarinandrasana, « A mixed strain rate and energy-based fatigue criterion for short fiber reinforced thermoplastics », *Int. J. Fatigue*, vol. 127, p. 131-143, oct. 2019, doi: 10.1016/j.ijfatigue.2019.06.003.

[8] P. Santharam et al., « Fatigue criteria for short fiber-reinforced thermoplastic validated over various fiber orientations, load ratios and environmental conditions », *Int. J. Fatigue*, vol. 135, p. 105574, juin 2020, doi: 10.1016/j.ijfatigue.2020.105574.

[9] M. J. W. Kanters, T. Kurokawa, et L. E. Govaert, « Competition between plasticity-controlled and crack-growth controlled failure in static and cyclic fatigue of thermoplastic polymer systems », *Polym. Test.*, vol. 50, p. 101-110, avr. 2016, doi: 10.1016/j.polymertesting.2016.01.008.

[10] Mallick, P.K and Zhou, Yuanxin, « Effect of Mean Stress on the Stress-Controlled Fatigue of a Short {{E-glass}} Fiber Reinforced Polyamide-6,6 », *Int. J. Fatigue.*, vol. 26, p. 941-946, sep. 2004, doi: 10.1016/j.ijfatigue.2004.02.003.

[11] N. Selles, N. Saintier, et L. Laiarinandrasana, « Voiding mechanisms in semi-crystalline polyamide 6 during creep tests assessed by damage based constitutive relationships and finite elements calculations », *Int. J. Plast.*, vol. 86, p. 112-127, nov. 2016, doi: 10.1016/j.ijplas.2016.08.004.

NUMERICAL MODELLING AND EXPERIMENTAL COMPARISON OF A TENSILE TEST ON FLAX ROVING

T.Larquemin[1], A.Hivet[2] , G.Hivet[3] and D.Duriatti[4]

[1]LaMé, Université d'Orléans, 11 rue de Loigny-la-bataille, Chartres, France
Email: tiffany.larquemin@univ-orleans.fr,
[2]LaMé, Université d'Orléans, 11 rue de Loigny-la-bataille, Chartres, France
Email: audrey.hivet@univ-orleans.fr,
[3]LaMé, Université d'Orléans, 11 rue de Loigny-la-bataille, Chartres, France
Email: gilles.hivet@univ-orleans.fr,
[4]Teillage Vandecandelaere, 5 rue de l'Eglise, Bourguébus, France
Email: dduriatti@depestele.com, Web Page: http://groupe-depestele.com

Keywords: Numerical modeling, Behavior law, Flax roving

Abstract

Today, environmental considerations are leading manufacturers to integrate more and more composites based on plant fibre reinforcements, particularly from flax, into their production. However, predicting the behavior, mechanical characteristics and feasibility of parts remains complex. The step of shaping the dry reinforcement during the LCM (Liquid Composite Moulding) process is for example fundamental for the service life of the composite part. However, it is still difficult to accurately predict the final shape and integrity of the reinforcement. In order to study the behavior of a dry reinforcement under different stresses during shaping, this study proposes to carry out a numerical simulation on a mesoscopic scale of a 500tex flax roving supplied by the company Depestele in the context of tensile solicitation and to compare this simulation to the result of the associated experimental test. For this, a highly representative geometric model, taking into account the geometric variability of the roving and an adapted transverse isotropic hypoelastic behavior law are implemented. The comparison of the tensile curves shows a good correlation with the expected result.

1. Introduction

1.1. Context

The integration of composite parts based on fibrous reinforcement with natural fibers is increasingly popular with manufacturers, particularly for their damping properties. However, there is a major obstacle to the integration of this type of part, particularly in technical applications, which lies in the difficulty of having an efficient and controlled manufacturing process.

Indeed, the development of this type of part is carried out by LCM type processes which require imposing strong stresses on the dry reinforcement, particularly in tension, shear, and compression to keep it in the mold. However, to avoid damage to the reinforcement at this stage of the process, it is important to be able to characterize and predict the behavior of the dry reinforcement for this type of stress. The complexity of the implementation of reinforcement tests and the multiplicity of architectures lead to the desire to set up numerical simulations predictive of mechanical behavior. In order to accurately characterize the behavior of the reinforcement while guaranteeing reasonable calculation times, we place ourselves at the mesoscopic scale, i.e. the interlacing of the strands (here a linen roving)

modeled by an equivalent homogeneous material is considered. The implementation of the numerical simulation thus consists of determining and identifying the behavior of the equivalent homogeneous material of the strands and modeling the ERVs (Representative Elemental Volume) of the reinforcement from the strands. To do this, it is therefore necessary to have a geometry of the reinforcement, the strands, and an adapted law of behavior.

In this study, the strands are linen rovings. Rovings are assemblies of thousands of long staple fibers arranged in an almost parallel manner and held together in the transverse direction by a cohesive agent. The behavior law must therefore make it possible to model the behavior of the homogeneous material equivalent to a flax roving. An hypoelastic transverse isotropic law behavior already used by the team in the case of roving of synthetic fibers [1] will be adapted in this study to take into account the specificities related to flax.

Among these specificities is the high geometric variability of flax rovings (Figure 1) related to its structure and manufacturing process. Indeed, several categories of fibers can be identified within a flax stem. Inside the stems, bundles of fibres develop, which are aggregations of unitary fibres connected to each other by a membrane called the middle lamella [2]. Unit fibers are the shortest fibers that can be extracted from the stem and are the most studied because they have mechanical properties compared to their density comparable to glass fibers [3]. However, the difficulty of extraction without damage of this type of fiber and their short length (of the order of a few millimeters) do not make them good candidates for the manufacture of roving. However, the fibre bundles with the party lamella prevent good impregnation [4] for composite manufacturing. Thus, the fibers within the rovings are so-called technical fibers and are bundles that are not completely dissociated up to the unit fibers. However, for the manufacture of rovings, this incomplete dissociation, added to the initial variability of the cross-sections of the unit fibres, does not homogenize completely [5] and at the end of the chain creates the high cross-section variability of the flax rovings. However, the number of fibers in the transverse section varies little, since the linear mass is controlled and not very variable along the wire [5], so the variability of cross-section depends mainly on the internal arrangement. But in the case of a homogenization of a material by the apparent cross-section, this is not negligible.



Figure 1. Example of geometric variability observable on 20mm roving specimens

In addition to the geometric variability, we must add the variability of the mechanical properties of the natural fibers [6] and the various factors that can influence the results [7–10]. Although manufacturers homogenize the batches with fibres from different plots and years, which allows a certain reproducibility of the mechanical properties, there is still a certain variability in the mechanical properties that is difficult to link to the elements mentioned earlier. In addition, the particular structure of the rovings does not allow for extrapolation of the properties that will be obtained from the data on the unit fibres and the strength of the roving. These specificities make mechanical tests on the roving essential to obtain properties but also the exploitation of these tests difficult. The possibility of carrying out simulations considering these two types of specificities will make it possible to carry out more detailed inverse identifications to understand and interpret the behavior of this type of material. This is all the truer when certain quantities related to the properties of the materials will be strongly influenced by these variations in geometries during compression loading.

The aim of this study is to determine the tensile behavior of the equivalent homogeneous material to be implemented in the mesoscopic model. To do this, in order to overcome geometric effects and go back to the real behavior of the fibrous assembly, it is necessary to set up a numerical simulation taking into account the apparent geometric variability at the initial instant of the flax roving in the context of a uniaxial tensile test. A specimen is made from a roving and tested experimentally. A digital twin with the geometric variability of the specimen is recreated at the same time. The hypoelastic behavior law is modified to adapt to changes in geometries and the simulation results are compared to the experimental results.

1.2. Traction behaviour of flax roving

The study of the behavior of rovings is complex and this is why few studies are directly interested in the tensile behaviors of rovings, preferring to directly identify the behavior of reinforcements [11] or study the properties of unit fibers [3,12–14]. Nevertheless, it appears that the tensile loading curve of flax rovings has a typical shape (3 types appear in the literature [19] but type III is preponderant). Three phases during loading can be identified for type III, two non-linear phases which frame a linear phase from which the maximum stiffness K is extracted and for which an apparent modulus reported for the purpose of the roving can be identified. The initial non-linear phase is due to both the internal reorganization of the unit fibers and the structure within the roving (realignment in the direction of traction). The final nonlinear phase is due to fiber breaks and can be described by Weibull-type modeling [10].

It is found in the literature that the length of the gauge of the specimen influences both the breaking force and the stiffness. Concerning the breaking force, this result is classic and comes from the probability of the appearance of critical defects within a specimen which increases with the length of the gauge. In the case of stiffness, this result is less expected and comes from the internal organization of the roving and in particular from the role of the cohesive agent in the transmission of force between the technical fibers. For some rovings, it has been established that the shorter the gauge length, the closer the stiffness is to what is found for unit fibers. On the other hand, for longer gauge lengths, the stiffness decreases to a threshold value. As the influence of the gauge length is not implemented at this stage in the behavior law, the reconstruction length used here is the same as that used for the tests. Then there is the influence of various external factors such as the temperature and humidity of the test conditions, which are therefore controlled in our case.

1.3. Numerical modeling

The long-term objective of this mesoscopic modeling is to study the behavior of dry reinforcements. The variability in the cross-section of the rovings observed as soon as the coil comes out is also visible in the reinforcement and can be accentuated along the roving by the successive interlacing of the reinforcement patterns. However, in the case of rovings, tensile stiffness depends only on the number of technical fibers in tension in the roving. Thus, by the method of manufacture and the management of the titer in the rovings, it can be considered that each section of the roving is crossed by the same number of technical fibers. Therefore, if the shapes and sizes of the cross-sections change due to the different organization of the bundles, the tensile strength being carried by the number of technical fibers is not modified by these cross-section changes, which therefore requires an adaptation in the assignment of mechanical properties in the finite elements.

The behavior law used in this study is a transverse isotropic hypoelastic behavior law allowing to relate the stress increments to the increments of deformation in the base oriented by the fibers Here the base of the fibers is oriented in such a way that the longitudinal direction of the roving is in direction 1 and the transverse directions of the roving are in directions 2 and 3 (thickness and width of the roving respectively). This behavior law is implemented in a Vumat Abaqus.® for an explicit scheme and

elements of type C3D8R. The Vumat makes it possible to monitor the evolution of the material orientation of the fibers in the element being calculated [1]. Among the hypotheses for establishing this law, the absence of interaction between direction 1 and the transverse directions in the case of tensile stress implies the determination of a single coefficient (C1111). This coefficient is expressed by dividing the stiffness of the roving by the cross-section [1].

As explained above (I.1.1), the equivalent homogeneous material of a roving is modelled by the external roving shape (i.e. the apparent section of the roving) but as the variability of cross-sections is not due to a variation in the number of local technical fibres but to an internal arrangement linked to the architecture of the technical fibres (Figure 2), the difference in the size of the sections in the longitudinal direction should not lead to a variation in tensile stiffness at the level of the different sections. It will obviously be very different in compression.

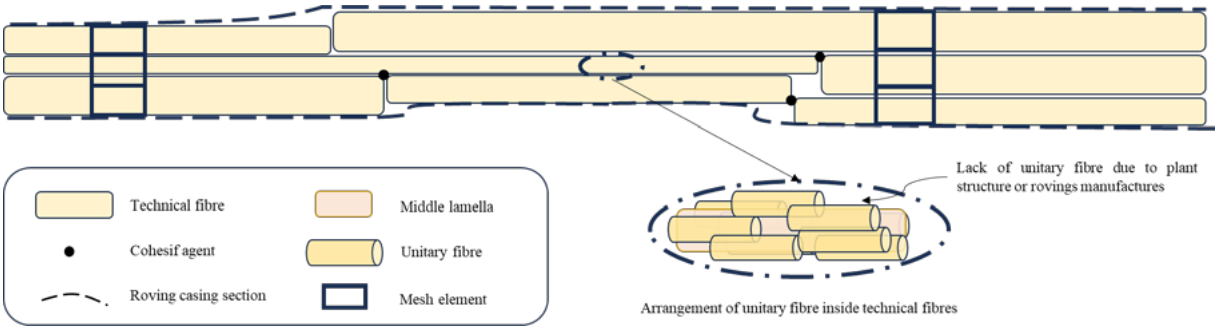


Figure 2. Schematic diagram for assigning element properties in the case of variable geometry section of the model.

The meshing made by the specific tool for fibrous reinforcement [15] requires that the model has the same number of elements in each section but with elements of different sizes between the sections. To obtain the same stiffness between sections of different sizes, the tensile modulus for each element must be related to the size of the section. This assignment of homogenized stiffness per section must be carried out both for the initial state and during the deformation of the sections. Thus, the allocation of the initial surface to which the elements belong at the beginning of the test is carried out and updated in the VUMAT and makes it possible to homogenize the resulting stress in each section. It should be noted that, while cross-section variations remain modest for tensile test, being able to manage the assignment of properties according to cross-section size will be all the more important for simulations of compression tests where the volume fractions of fibers and cross-section shapes vary greatly.

The adaptation of the hypoelastic behavior law to the geometric specificities of flax rovings is therefore possible by controlling the assignment of the properties of the elements according to the section to which they belong. Concerning the adaptation of this behavior law to the response of the tensile loading curve, this will be carried out in several steps. The first step, which is the one used for this study, consists in modeling the loading curve only by a linear approximation of stiffness K' without taking into account the nonlinear initiation of the breaking phase of the roving. The next steps will aim to integrate the two nonlinearities of the loading curve. To carry out this numerical simulation, it is therefore necessary to model a representative sample of the geometric variability of a flax roving and to carry out a uniaxial tensile test from which the stiffness on the loading curve will be recovered.

The numerical modeling of the tensile behavior of a flax roving requires both a precise geometry to reproduce the variability of the samples and a behavior law that allows to reproduce the behavior of the equivalent homogeneous material.

2. Material & Methods

2.1. Material of the study

A roving sample supplied by the company Depestele with a linear density of 500tex (kg/m) is prepared for tensile testing. The manufacturing protocol is similar to that used by Moothoo [16]. For the purpose of a 3D reconstruction using a digital microscope, the gauge length of the specimens is 20mm. The manufacturing protocol consists of gluing aluminum plate using Araldite to the sample. The length of the gauge is ensured by means of a template. A pre-tensioning force of 0.3 N is applied at the same time to each end of the specimen to ensure that the strand is straight and to ensure good repeatability of the initial state. After the manufacture of the specimen, a 24-hour drying period of the adhesive is necessary before the tensile test can be carried out. A 3D image of this specimen (Figure 3) is obtained using a Keyence digital microscope (VHX-5000) with a resolution of 2.21µm (XY plane) to obtain the geometric characteristics of our sample and allow the reconstruction of the model in numerical simulation.

2.2. Methods

2.2.1. Experimental tensile test

The test is carried out using a Zwick traction machine with a capacity of 5kN. The test is piloted in displacement with a crosshead travel speed of 6.66.10-5 $^{s-1}$. Before the test, a pre-tensioning of 2N is applied to the specimen. As the length of the gauge tested is small, a Sony α1 ILCE-1 camera with an RGB sensor, size 5760x5760 (pixels), is used to obtain the average deformation of the test specimen. The camera is placed in such a way that the resolution of the images is about 0.01mm/pixel. The synchronization between the camera and the traction machine is achieved with the timestamp of the images. The exploitation of the images by a Matlab code makes it possible to trace the loading curve of the test and to obtain the information necessary for the numerical simulation.

2.2.2. Numerical tensile test

The digital model of the specimen is obtained from a 3D image (Figure 3), reconstructed using Matlab. A preliminary study has determined that the roving sections shape are rectangular. The reconstruction therefore requires the ability to extract the thickness and width of sections from the specimen while maintaining geometric variability while smoothing the profile and eliminating artifacts from the image. For example, by eliminating groups of fibers that are not attached from one end of the specimen to the other and will therefore not participate in the tensile test. The selected cross-section profiles (1 per 0.8mm length) are then injected into CatiaV5 to reconstruct a volume model, which is itself reinjected into Abaqus®. Once the mesh has been obtained, the coordinates of the integration points (1 per C3D8R element) and the sections of the associated model are computed using a Matlab code and transcribed into a file allowing the reading by the Vumat during the calculation.

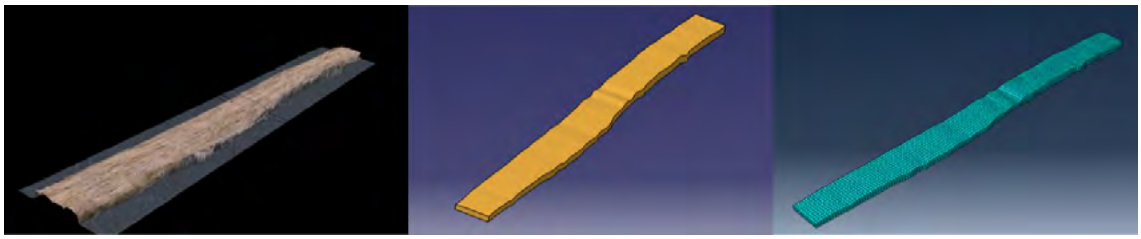


Figure 3. Reconstruction of the geometric model of the specimen from the 3D image of the digital microscope to the mesh model in Abaqus.

The material orientation of the elements is determined in the initial state using the GEOFAB software, which is a tool for modeling and meshing woven strands and reinforcements [1,15]. The material parameters used in the simulation are the flax density (1.4.10-9 t/mm2), the stiffness K' (in N) extracted from the tensile test and the value of the cross-sections (in mm2) calculated at the integration points. Displacement is applied to the nodes at the end of the model in the direction of pull. The total displacement is carried out in one step, from the preload to the length for which the non-linear failure of the roving is initiated. A damping of 10^4 as well as a shear modulus of 120MPa are applied for the stability of the calculation.

To illustrate the impact of taking into account the geometry of the roving, on the identification of the tensile property of the equivalent homogeneous material, two models are tested in simulation. A model with a behavior law (LDC1) that does not take into account the section variation, and which assigns to all the elements a stiffness dependent on the average cross-section of the specimen, and a modeling with a behavior law (LDC2) which allows to assign the initial stiffness of each element according to the size of the section to which it belongs.

3. Results & Discussions

The use of the camera images makes it possible to measure the length of the specimen after preload at 48.44mm. The exploitation of the 3D image under the microscope gives an average thickness of 0.59 ± 0.08 mm and an average width of 2.49 ± 0.2 mm. The test was conducted with an ambient temperature of 22°C and a humidity of 42.4%. The tensile curve obtained after the test has been used is given below (Figure 4).

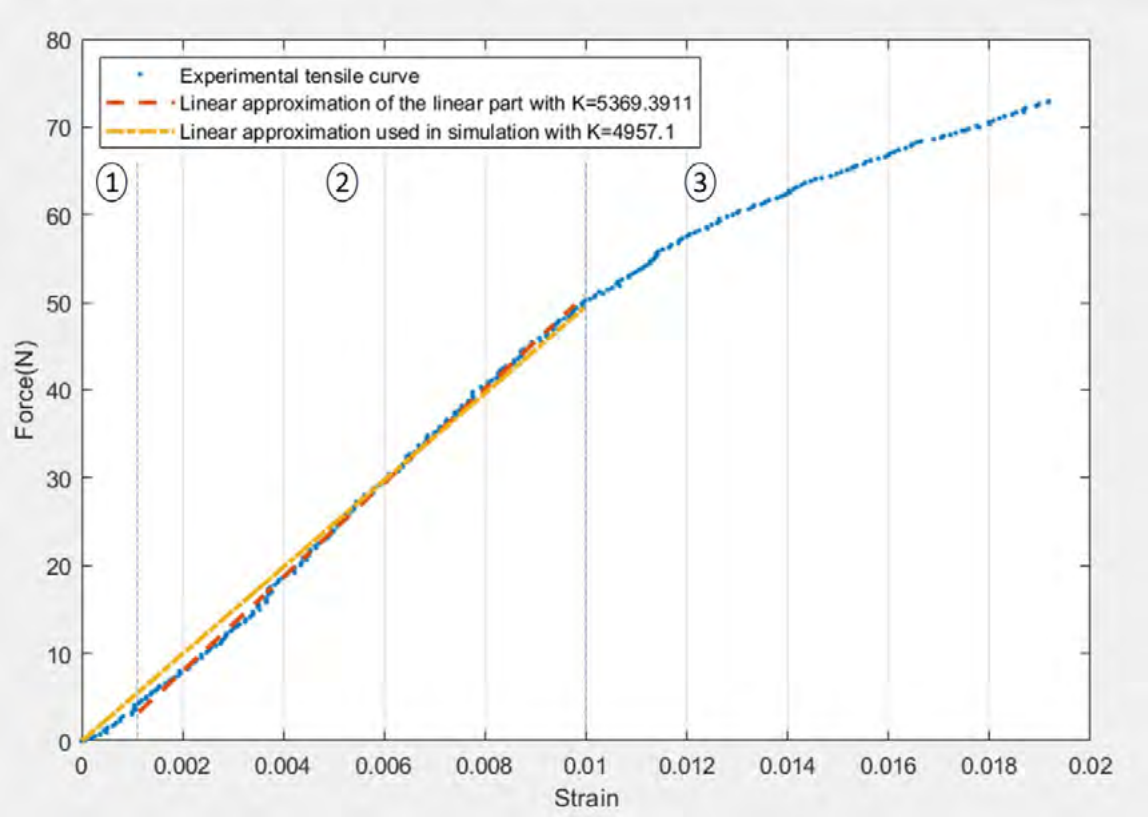


Figure 4. Experimental tensile curve obtained after exploitation of the test images.

The stiffness in the linear zone (2) is ... N and the linear approximation of the stiffness K' which was injected for the numerical test is 4957.1N. The simulation with a ... hours with LDC1 modeling and .. hours for modeling with LDC2. The tensile curves obtained are compared to those of the experimental test (Figure 5).

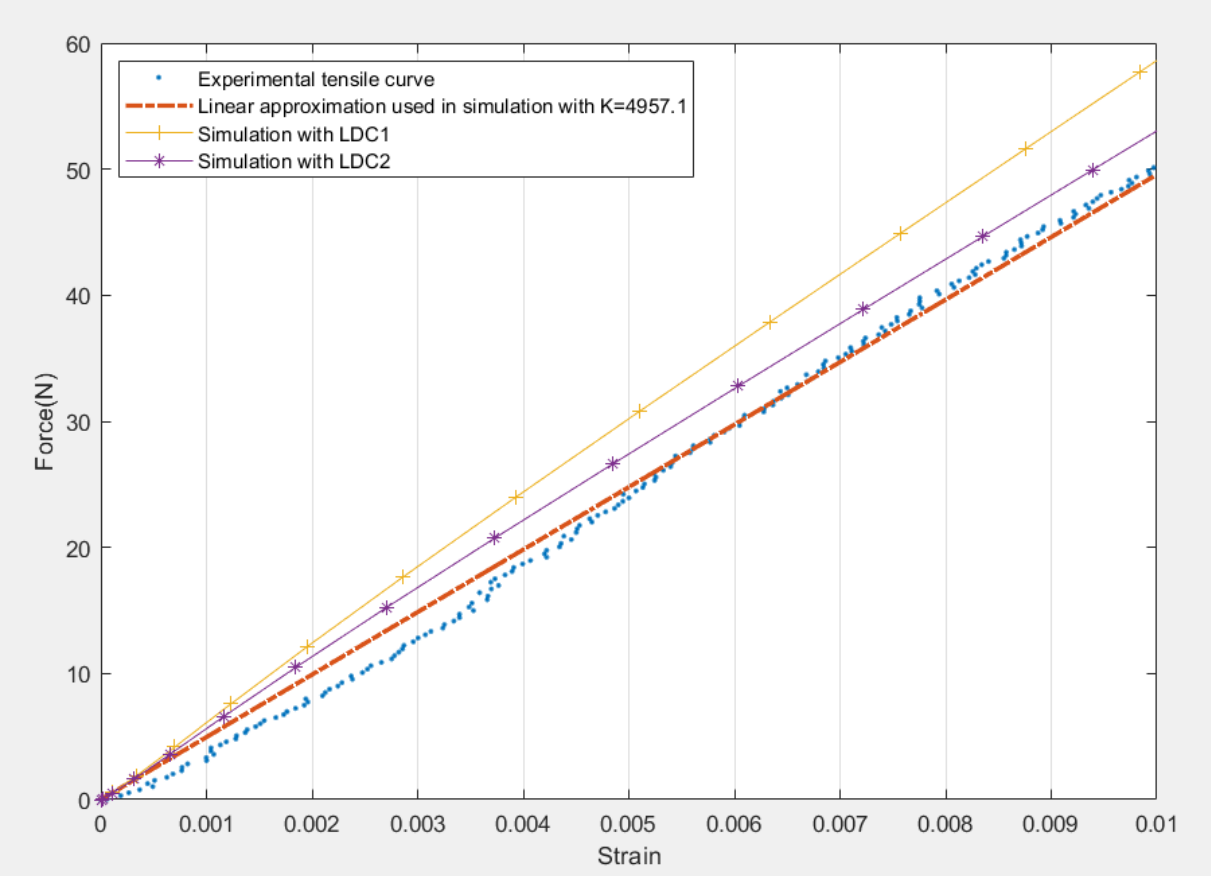


Figure 5. Comparison of experimental and numerical tensile curves

The figure shows a deviation in stiffness of 19.7% with the desired result for the modeling with LDC1 and a deviation of 8% with LDC2. The deviation obtained with the LDC2 modeling is due to the fact that the strand is slightly curved (Figure 3) and that the bending stiffness that comes into play is driven by the shear coefficient which has not been specifically identified for this material. This will therefore have to be taken into account in future modelling.

4. Conclusions and perspectives

The objective of this study was to have a numerical model of a flax roving to take into account the cross-sections variability, thus making it possible to identify more realistically the tensile behavior of the equivalent homogeneous material. A transverse isotropic hypoelastic behavior law that has already been used in the modeling of synthetic roving behavior has been used and adapted to the flax specificities. The tensile loading curve has been approximated linearly and the response of the numerical simulation is satisfactory from this point of view considering the future implementation of the realignment of the strand with the tension load. In the perspective of being able to achieve a fine inverse identification of the roving behavior, the realization of this step is encouraging. It is now necessary to tackle the modeling of the non-linear parts of the loading curve.

This first step paves the way for the modeling of a primary stress for LCM-type processes, compression loading.

References

[1] Wendling A, Daniel J L, Hivet G, Vidal-Sallé E and Boisse P 2015 Meshing Preprocessor for the Mesoscopic 3D Finite Element Simulation of 2D and Interlock Fabric Deformation *Appl Compos Mater* **22** 869–86
[2] Baley C, Morvan C and Grohens Y 2005 Influence of the Absorbed Water on the Tensile Strength of Flax Fibers *Macromolecular Symposia* **222** 195–202
[3] Martin N, Mouret N, Davies P and Baley C 2013 Influence of the degree of retting of flax fibers on the tensile properties of single fibers and short fiber/polypropylene composites *Industrial Crops and Products* **49** 755–67
[4] Coroller G, Lefeuvre A, Le Duigou A, Bourmaud A, Ausias G, Gaudry T and Baley C 2013 Effect of flax fibres individualisation on tensile failure of flax/epoxy unidirectional composite *Composites Part A: Applied Science and Manufacturing* **51** 62–70
[5] Blanchard J M F A, Sobey A J and Blake J I R 2016 Multi-scale investigation into the mechanical behaviour of flax in yarn, cloth and laminate form *Composites Part B: Engineering* **84** 228–35
[6] Omrani F, Peng W, Damien S, Ferreira M and Ouagne P 2017 Analysis of the deformability of flax-fibre nonwoven fabrics during manufacturing. *Composites Part B: Engineering* **116** 471–85
[7] Morgillo L, Brionne L, Melelli A, Ouagne P, Scheel M, Weitkamp T, Shah D U, Abida M, Beaugrand J and Bourmaud A 2023 Elucidating links between the mechanical performance of flax fibres and their structural defects *Industrial Crops and Products* **206** 117722
[8] Barbulée A, Jernot J-P, Bréard J and Gomina M 2014 Damage to flax fibre slivers under monotonic uniaxial tensile loading *Composites Part A: Applied Science and Manufacturing* **64** 107–14
[9] Nuez L, Richely E, Perez J, Guessasma S, Beaugrand J, D'Arras P, Bourmaud A and Baley C 2022 Exploring the effect of relative humidity on dynamic evolution of flax fibre's microfibril angle through in situ tensile tests under synchrotron X-ray diffraction *Industrial Crops and Products* **188** 115592
[10] Moothoo J, Allaoui S, Ouagne P and Soulat D 2014 A study of the tensile behaviour of flax tows and their potential for composite processing *Materials & Design* **55** 764–72
[11] Corbin A-C, Boussu F, Ferreira M and Soulat D 2020 Influence of 3D warp interlock fabrics parameters made with flax rovings on their final mechanical behaviour *Journal of Industrial Textiles* **49** 1123–44
[12] Baley C, Gomina M, Breard J, Bourmaud A and Davies P 2020 Variability of mechanical properties of flax fibres for composite reinforcement. A review *Industrial Crops and Products* **145** 111984
[13] Bourmaud A, Siniscalco D, Foucat L, Goudenhooft C, Falourd X, Pontoire B, Arnould O, Beaugrand J and Baley C 2019 Evolution of flax cell wall ultrastructure and mechanical properties during the retting step *Carbohydrate Polymers* **206** 48–56
[14] Charlet K 2008 *Contribution à l'étude de composites unidirectionnels renforcés par des fibres de lin : relation entre la microstructure de la fibre et ses propriétés mécaniques* phdthesis (Université de Caen / Basse-Normandie)
[15] Wendling A, Hivet G, Vidal-Sallé E and Boisse P 2014 Consistent geometrical modelling of interlock fabrics *Finite Elements in Analysis and Design* **90** 93–105
[16] Moothoo J 2013 *Analyse de la faisabilité d'éco-conception de pièces composites à base de ressources renouvelables pour applications médicales* These de doctorat (Orléans)

LIGHTNING STRIKE INDUCED AND IMPACT INDUCED DELAMINATION INVESTIGATION USING ADVANCED NON-DESTRUCTIVE TESTING METHODS

L.A.C. Lecointre[1], Y. Zhou[1], T. Yokozeki[1], S. Kamiyama[2], Shin-ichi Takeda[2], Mamoru Suyama[3], Naoki Hosoya[3]

[1]Department of Aeronautics and Astronautics, the University of Tokyo, Bunkyo-ku, Tokyo, Japan
Email: lea-lecointre@g.ecc.u-tokyo.ac.jp
[2]Aviation Technology Directorate, Japanese Aerospace Exploration Agency, Mitaka-shi, Tokyo, Japan
[3]Department of Engineering Science and Mechanics, Shibaura Institute of Technology, Koto-ku, Tokyo, Japan

Keywords: CFRP, delamination, Non-Destructive Testing, Lamb Waves, Thermography

Abstract
Despite having excellent mechanical performance and resistance to corrosion, Carbon Fibre Reinforced Composites are also particularly sensitive to delamination which may lead to their failure, and therefore represent a risk for their use. In order to prevent delamination, detecting and understanding them has been widely investigated by industrials and researchers. In this study, two types of delamination, one type induced by lightning strike test and one induced by impact test, are investigated by various classic and advanced NDT methods. Different features can therefore be extracted from healthy and delaminated zones, such as thermal propagation characteristics, ultrasonic wave attenuation or Lamb Wave propagation modes. The results allowed to emphasize the structural differences between lightning strike induced and impact induced delamination and to correlate various NDT techniques and their measured material features. This type of data fusion is partucilarly promising for improving the efficiency of defects detection by combining various methods, compensating for their respective weakness while emphasizing their strengths, and finally reduce the false positives and negatives.

1. Introduction

Carbon Fibres Reinforced Plastics (CFRP) have been increasingly attracting interest, particularly in the fields of aeronautics, aerospace and automobile, due to their outstanding mechanical performances combined with low weight. However, one of the main limitations to their use is their susceptibility to delamination, which present an important risk of structure failure. Delamination can be induced by various solicitations on the material, including mechanical solicitations (shock, fatigue, vibrations) but also thermal and even chemical solicitations [1–4].

The understanding of delamination generation, propagation or structure is an important area for research in order to prevent them. To detect delamination at any stage of the material fabrication and service, industrials and researchers developed Non-Destructive Testing (NDT) methods which have the ability to provide information on the inner structures while leaving them intact. Depending on their nature or the method involved, NDT techniques provide different aspects of the material characteristics. For example, Ultrasonic Testing (UT) provides information on the propagation of ultrasonic waves through the material, such as the waves dB attenuation or the presence of backwall echoes. InfraRed Thermography (IRT) provides information on the thermal propagation characteristics through the material. Radiographic Testing provides information on the material capacity to attenuate gamma rays, exactly in the way medical radiographies do with human body [2,5,6]. A very immediate but sometimes misconsiderated NDT method is visual inspection, which provides many information by just observing material surfaces state such as surface porosity, thickness variations, changes of colour, etc. Visual inspection can be assisted with more advanced methods such as 3D Optical Profilometers or Scanning Electron Microscopes (SEM), and many others [2,7].

In this research, CFRP samples which have been subjected to lightning strike in their centre are investigated using various NDT methods in order to collect a wide range of material characteristics in the healthy and defected zones. The comparison and correlation of these various material data, also called data fusion, allows to record particular features characterizing the lightning-strike induced delamination by selecting the best abilities of each NDT technique.
In the second part of this article, the experimental samples and the different NDT inspections are presented. The third part describes the analysis of the experimental data and the data fusion, with discussion points. The fourth and final part of this document gives a conclusion.

2. Experiment

2.1 Specimen preparation

In this experiment, two CFRP samples sized 150 per 150 mm have been used. The manufacturing was handmade in the Yokozeki laboratory at the University of Tokyo, Japan, by applying the resin on wowen carbon fibre fabric (TR3110M, TR30-3K, 200 GSM, Mitsubishi Rayon Co. Ltd.), stacking the prepregs in 0°/90° direction and then curing in hotpress. Instead of classic epoxy resin, the polyaniline-based resin PANI-DBSA/Phenol-DVB (PDPD) as described by Zhou and al. in [8] has been used in order to limit the damage from lightning strike test.
The two samples (respectively called LS-1 and LS-2) have been tested with a simulated Lightning Strike using the high impulse current generator (Otowa Electric Co.) at the National Composite Center at Nagoya University, Nagoya, Japan with a peak current at -40 kA [8]. The lightning strike induced a visible deformation of the samples surface, shown in figure 1.

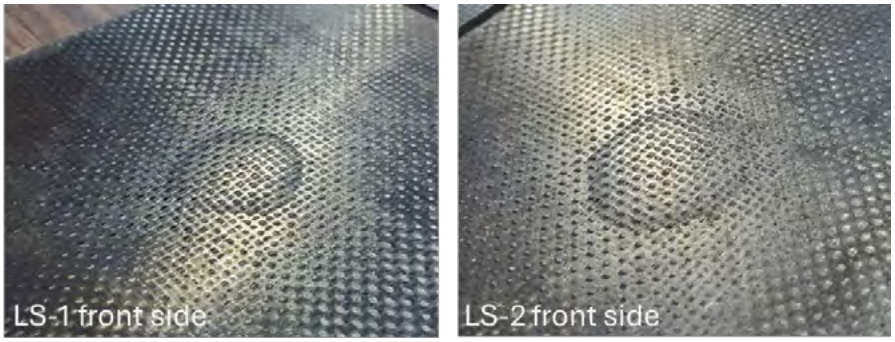


Figure 1: Visible deformation of the surface induced by the lightning strike

2.2 Visual Inspection

In addition to the eye inspection as shown in the figure, a 3D profilometry as also been performed on the 100 per 100 mm square at the centre of all samples using the Keyence VR-6000 profilometer located at the Chofu Aerospace Center Aerodrome Branch of the JAXA. The top and bottom surfaces thickness cartographies of all samples are shown in figure. It is to be noted that the back side results of LS-1 and LS-2 show a regular thickness difference, this is in fact due to the large surface deformation on the other side which unbalances the samples when set on this side. No deformation induced from the lightning strike is however detected. Some small small points are visible on all cartographies, they are surface irregularities also observable by eye and are attributed to the handmade resin application during the manufacturing. The Visual Inspection results are shown in the figures 2 and 3 where the color scale represents the thickness of every surface point. In the figure 3, the color scale has been replaced in order to allow a better visualization of the surface deformations induced by low velocity impact test.

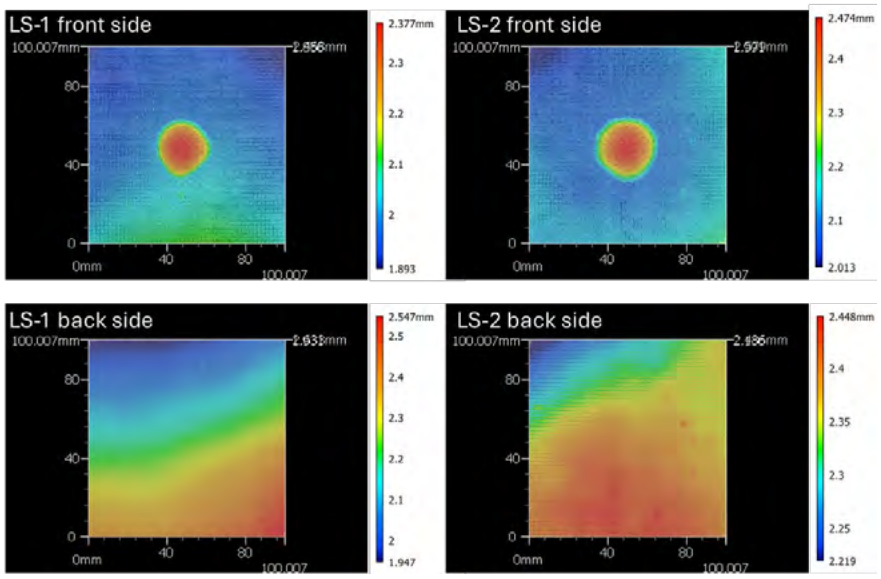


Figure 2: Profilometry measurement results in colour scale

2.3 Thermographic inspection

A thermographic inspection is performed on the four samples using the Thermal Wave Imaging system Echotherm coupled with MOSAIQ 4.0 analysis software located at the Chofu Aerospace Center Aerodrome Branch of the JAXA. The Echotherm system consists of a disposable hood containing an InfraRed camera and a flashlamp, connected to a display screen. The measurement is set to 10 to 18 seconds after flash. The video of thermal propagation recorded by the system shows a specific structure on the defected zone of LS-1 and LS-2 with three different zones: a dark ring on the periphery of the defect, a white ring inside the black ring, and a grey zone at the centre. These zones are shown in the parts a) of figures 3 and 4. The parts c) and b) of the figures 3 and 4 show respectively the log-log cooling plots at different points of the samples surface and the localization of these points.

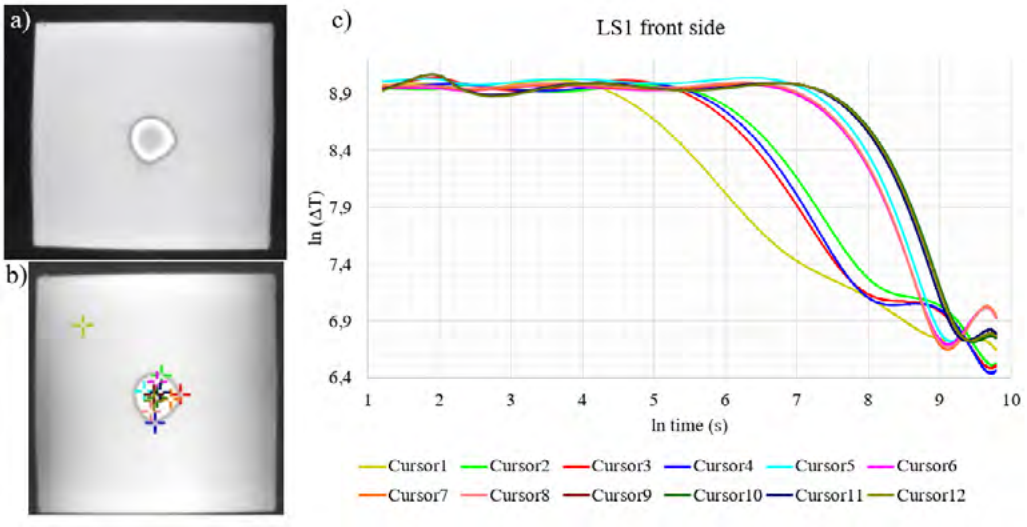


Figure 3: Thermographic Inspection results on LS-1 with a) the different aspects of cooling shown at the thermal video, b) localisation of the cooling curves cursos, c) cooling curves

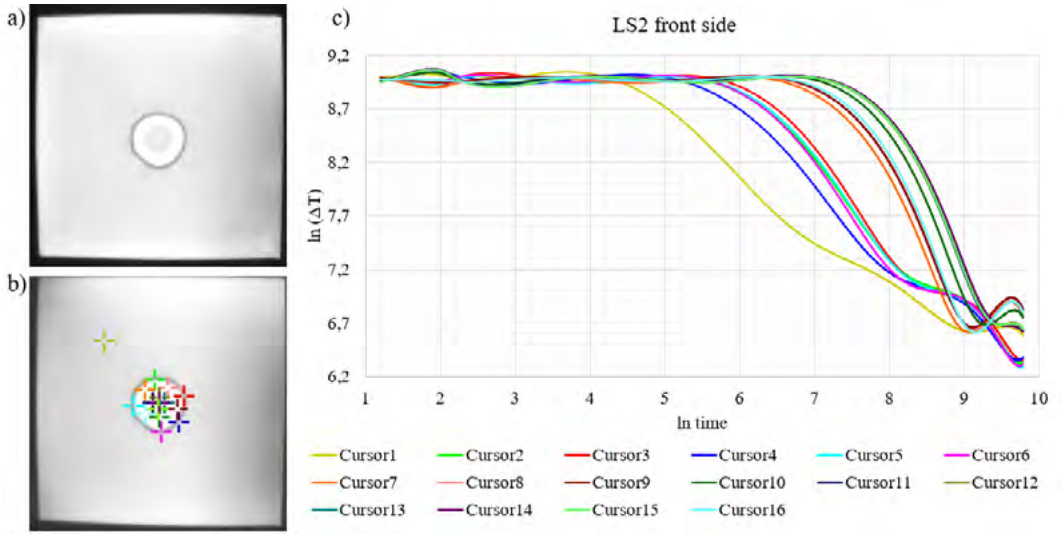


Figure 4: Thermographic Inspection results on LS-1 with a) the different aspects of cooling shown at the thermal video, b) localisation of the cooling curves cursos, c) cooling curves

2.4 Ultrasonic Testing inspections

Two methods have been used for Ultrasonic Inspection of the samples: a classic method consisting of a manual A-scan directly in contact with the samples using an Omniscan SX with an Olympus V201-RM 5 MHz delay line transducer located in Yokozeki Laboratory at the University of Tokyo, Tokyo, Japan. A-scan signals have been directly observed at different zones of the front and back sides of the samples. The second method, which is more innovative, uses Lamb Waves control with a fully non-contact system base on a Laser Induced Plasma Shock Wave (LIPSW) developed by Hosoya et al. [9,10]. Using sophisticated signal processing algorithm, this method is able to investigate various features of the Lamb Waves propagation through the specimen.

A-scan measurements shown that the backwall echo was detectable in all flat zones but not detectable in the thicker zone of the LS-1 and LS-2 samples. Therefore, measuring a thickness of delamination from this side was impossible. However, by measuring the signal on he back side, backwall echoes were found in the defected zone at respectively 1.79 mm and 2.02 mm for LS-1 and LS-2. Considering the thickness observed in the defected zone in figures , the defected zone is therefore estimated to be about 0.4 to 0.6 mm depth in both samples.

The LIPSW system method allows to record the Lamb Waves propagation field measured in the out-of-plane direction at the top surface. The Root Mean Square (RMS) of signals is shown in the left side of the figure 5 for LS-1 and LS-2. The cartography can be improved by measuring Damage Indexes from the algorithm. As an example, a Root Mean Squared Error (RMSE) cartography is shown in the right side of figure 5 for LS-1 and LS-2. The algorithm and the method for extracting RMSE cartography are described in [10].

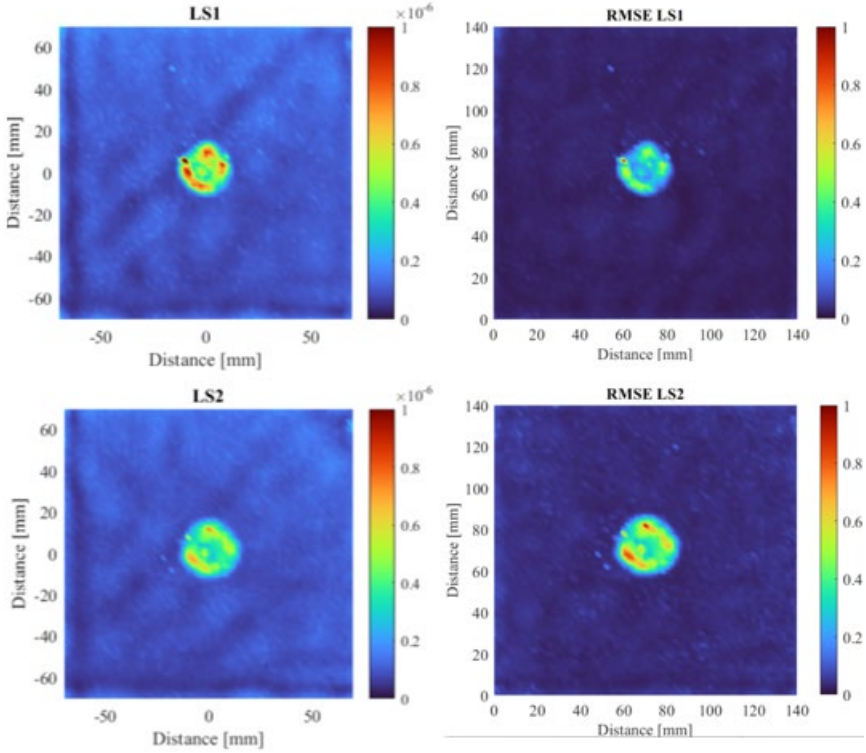


Figure 5: Lamb Waves measurement results shown as Damage Indexes cartographies with Root Mean Square on the left side and Root Mean Squared Error using a Wavelet Transform based algorithm on right side

3. Data fusion and discussion

The localization, size and shape of the defected zone are confirmed by Visual Inspection, Thermographic Inspection and LIPSW Inspection. For more quantitative study, quantitative data from Thermographic Inspection and LIPSW Inspection are calculated and compared.
Using the cooling curves, it is possible to measure the cooling slope and the breaking time which reflect the diffusivity of the heat through the sample. The thermal diffusivity α is calculated from the breaking time with the following equation:

$$\alpha = \frac{L^2}{\pi t^*} \quad (1)$$

Where α is the thermal diffusivity in mm²/s, L is the thickness in mm and t* the breaking time of the cooling curve.
The figure 6 shows the data fusion between the thermal diffusivity calculated in the four different zones: healthy, the black ring zone, the white ring zone and the grey centre (respectively represented in green, black, light blue and grey), and the RMSE value measured by LIPSW method for the same points. The LS-1 and LS-2 samples are fusionned for this figure as they are directly comparable and in order to increase the dataset. The four different zones are clearly visible on the graphe. It is to be noted that if considering only the thermal characteristics (looking at the x-axis), the healthy, grey and white zones may be difficult to distinguish. In a similar way, if considering only the LIPSW results (by looking at

the y-axis only), the white ring and the grey centre are difficult to distinguish, such as the healthy zone and the black ring.

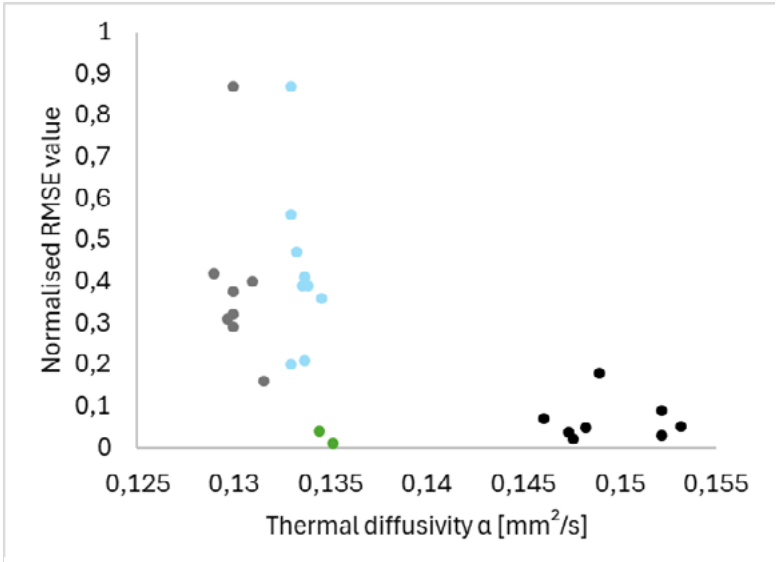


Figure 6: Classification of all LS-1 and LS-2 measurement points from LIPSW results (RMSE) and Thermographic results (thermal diffusivity)

4. Conclusions

In this study, several Non-Destructive Testing methods are used in order to investigate lightning strike induced delaminations in Carbon Fibre Reinforced flat samples. Visual Inspection using 3D optical profilometry, Ultrasonic Testing using manual A-scan and an innovate non-contact Lamb Waves method and Thermographic Inspection have been combined in order to characterize the delamination with various material features. The combination of Visual Inspection with manual Ultrasonic A-scan allowed to obtain good evaluation of the depth of the damage zones. Secondly, by combining quantitatively the Thermographic Inspection and the Lamb Waves Inspection results, interesting visualization of the different samples zones have been obtained. The thermal diffusivity calculated from Thermographic Inspection cooling curves and the Root Mean Squares Error of the Lamb Waves signals obtained from the Lamb Wavew Inspection, alone, do not give a clear representation of the different damaged zones. However, their combination allowed to obtain a better visualization of these zones. This shows the very promising outcomes that can be obtained by combining different characterization methods.

For further investigation, we are aiming to use similar methods using delaminations induced by impact. The data fusion of several Non-Destructive Testing characteristics may be able to give interesting information about the difference of delamination structure depending on their origin (thermal or mechanical), which is particularly useful for understanding the delaminations and therefore work for preventing them.

Acknowledgments

The current research project has been funded thanks to the Japan Society for the Promotion of Science under the Grant-in-Aid for Scientific Research programs (Grant No. JP22H01692).

References

1. Ufuk R, Bilge K, Kıral BE, Ereke M, Karabeyoğlu A. Fractographic Investigation of Cryogenic Temperature Mode-II Delamination Behavior of Filament Wound CFRP Laminates with Varied Resin Systems. J Compos Sci [Internet]. 2023;7(11). Available from: https://www.mdpi.com/2504-477X/7/11/450

2. Hellier CJ, editor. Handbook of Nondestructive Evaluation [Internet]. 3rd Edition. New York: McGraw-Hill Education; 2020. Available from: https://www.accessengineeringlibrary.com/content/book/9781260441437

3. Kamiyama S, Hirano Y, Ogasawara T. Delamination analysis of CFRP laminates exposed to lightning strike considering cooling process. Compos Struct. 2018 Jul;196:55–62.

4. Wang B, Zhu Y, Ming Y, Yao X, Tian X, Ziegmann G, Duan Y, Sun J. Understanding lightning strike induced damage mechanism of carbon fiber reinforced polymer composites: An experimental study. Mater Des. 2020 Jul;192:108724.

5. Beaumont P, Soutis C. The Structural Integrity of Carbon Fiber Composites, Fifty Years of Progress and Achievement of the Science, Development, and Applications. The Structural Integrity of Carbon Fiber Composites: Fifty Years of Progress and Achievement of the Science, Development, and Applications. 2016. 1 p.

6. Scott IG, Scala CM. A review of non-destructive testing of composite materials. NDT Int. 1982 Apr;15(2):75–86.

7. Duboust N, Ghadbeigi H, Pinna C, Ayvar-Soberanis S, Collis A, Scaife R, Kerrigan K. An optical method for measuring surface roughness of machined carbon fibre-reinforced plastic composites. J Compos Mater. 2017;51(3):289–302.

8. Zhou Y, Raghu SNV, Kumar V, Okada T, Yokozeki T. Simulated lightning strike investigation of CFRP comprising a novel polyaniline/phenol based electrically conductive resin matrix. Compos Sci Technol. 2021 Sep;214:108971.

9. Hosoya N, Mita M, Lecointre LAC, Tonegawa S, Higuchi R, Yokozeki T, Takeda S ichi. Lamb waves evaluation in CFRP plates with laser shock wave technique. Structures. 2023 Dec;58:105566.

10. Lecointre LAC, Higuchi R, Yokozeki T, Tonegawa S, Mita M, Hosoya N, Takeda S ichi. A NEW METHOD FOR DEFECTS DETECTION IN CFRP COMPOSITES USING WAVELET ANALYSIS AND NON-CONTACT LAMB WAVES PROPAGATION.

IMPACT BEHAVIOR OF HYBRID CFRP-ELASTOMER-METAL LAMINATES IN COMPARISON WITH CONVENTIONAL FIBER-METAL LAMINATES IMPACTED WITH DIFFERENT ENERGIES

Zhongyu Li[1]，Alexander Jackstadt[2]，Junyuan Zhang[3]，Jianfeng Wang[4,*], Bing Wang[5]，Luise Kärger[6]
[1]School of Automotive Engineering, Vehicle Engineering Department, Harbin Institute of Technology, West Wenhua Road 2, 264209, Weihai, China
Email: lizhongyu@hit.edu.cn, Web Page: https://homepage.hit.edu.cn/lizhongyu
[2]Institute of Vehicle System Technology, Lightweight Engineering, Rintheimer Querallee 2, D-76131 Karlsruhe, Germany
Email: alexander.jackstadt@kit.edu, Web Page: https://www.fast.kit.edu/english/lbt/5192_11940.php
[3]State Key Laboratory of Automobile Simulation and Control, Autobody Engineering Department, Jilin University, Renmin Street 5988, 130000, Changchun, China
Email: junyuan@jlu.edu.cn; Web Page: https://auto.jlu.edu.cn/info/1136/2325.htm
[4]School of Automotive Engineering, Vehicle Engineering Department, Harbin Institute of Technology, West Wenhua Road 2, 264209, Weihai, China
Email: wjfeee123@163.com, Web Page: https://homepage.hit.edu.cn/wangjianfeng?lang=zh
[5]National Key Laboratory of Science and Technology on Advanced Composites in Special Environments, Mechanics Department, Harbin Institute of Technology, Yikuang Street 2, 150001, Harbin, China
Email: wangbing86@hit.edu.cn, Web Page: https://homepage.hit.edu.cn/wangbing?lang=zh
[6]Institute of Vehicle System Technology, Lightweight Engineering, Rintheimer Querallee 2, D-76131 Karlsruhe, Germany
Email: luise.kaerger@kit.edu, Web Page: https://www.fast.kit.edu/english/lbt/5192_3870.php

Keywords: FML, Low-velocity impact, Elastomer, Energy dissipation, Impact energy

Abstract

This study investigates the low-velocity impact responses and damage mechanisms of HyCEMLs compared to conventional FMLs by considering variations in impact energy levels. Impact behavior with impact energies ranging from 3 J to 30 J is evaluated for FMLs and HyCEMLs by numerical and experimental methods. The force–time and energy-time histories are compared and discussed. Furthermore, damage mechanisms including metal plasticity, metal failure, delamination, and CFRP failure are revealed. The energy dissipation due to each mechanism is further quantified with regard to different impact energies. In addition, the energy release ratio of each component of the hybrid laminates after impact is evaluated in order to determine the recovery state of materials in potential applications. It is found that the initial damage force of HyCEML is increased, while the peak force and structural stiffness are reduced. The observed damage mechanism of FML and HyCEML are in competition during the impact and make different contributions to the total energy dissipation. The relation of those contributions varies with different impact energies. Additionally, the elastomer changes the damage mechanisms each component of the hybrid laminate which is useful to improve usage efficiency of hybrid materials. The findings of this work will assist in the assessment of impact damage resistance of hybrid laminates and provides added value for composite design engineers to design specific mechanisms for optimal energy dissipation based on given requirements.

1. Introduction

Fiber-metal laminates (FML) are a combination of sheets of fiber-reinforced polymer and metal, and can be found in various aerospace applications nowadays[1]. Carbon laminate aluminum reinforced epoxy (CLARE) is relatively new compared with glass laminate aluminum reinforced epoxy (GLARE), which is commonly used in the industry. CLARE shows even higher specific mechanical properties [2]. However, the combination of aluminum sheets with carbon fibers often leads to galvanic corrosion in the interface [3]. The big mismatch in thermal expansion coefficients between these materials leads to high residual stresses after curing in a hot mold [4]. One possible way to solve this problem is to introduce an elastomeric interlayer between the aluminum sheet and carbon fiber reinforced polymer (CFRP) ply. In addition, galvanic corrosion can be prevented [5], but also the damping behavior [6] and impact performance can be adjusted [7].

Impact response, damage mechanism and extent of damage change with the impact energy. Mohotti et al. [8] investigate the impact behavior of polyurea (rubber-like material) coated aluminum plates impacted at about 10 m/s. The introduction of polyurea is beneficial in reducing the permanent deformation of the aluminum. Sarlin et al. [9] conduct end notch flexure and single cantilever beam tests on three-layer steel-rubber-composite hybrid laminates and find that the interface strength between steel and rubber is higher than that of composite and rubber. Li et al. [10] investigated the impact behavior of hybrid CFRP-elastomer-metal laminates (HyCEML) and have reported how the elastomer influences the energy distribution and damage mechanisms under one specific impact energy.

There is insufficient literature on the impact behavior and particularly on the associated damage mechanisms of hybrid laminates with elastomer under LVI conditions to the authors' knowledge. The published literature shows that elastomers play an essential role in impact behavior, and the damage mechanisms of hybrid laminates are complex under dynamic loads. Impact energy has a strong influence on the response of the specimen. The damage mechanisms, including metal plasticity, CFRP failure, and delamination inside hybrid laminate, are competitive damage mechanisms that are changed by impact energies. It is also valuable to vary impact energy in the research for automotive applications, such as a stone impacting the battery container and pedestrian impacting the engine front hood.

This work investigates the low-velocity impact response of FML and HyCEML impacted with a wide range of energies. Impact responses, including force-time (*F-t*), energy-time (*E-t*), and critical characteristic parameters, are quantified and compared. The energy dissipated by aluminum plasticity, delamination, CFRP failure, aluminum failure, and viscosity is revealed. The contribution of each mechanism to the total energy dissipation of laminates impacted with different energies is quantified. It is found that each mechanism is a competitive failure mechanism. A comparative investigation of FML and HyCEML reveals the role of elastomer layers in changing the energy dissipation mechanism under different impact energies.

2. Materials and methods

A brief description of the materials and methods used in this work is presented here. Details can be found in the authors' previous work [10].

2.1. Materials

The configuration of the HyCEML plate investigated in this work is $\left[A_{0.3}/E_{0.5}/\left(C^{0°}_{0.15}/C^{90°}_{0.15}\right)_3/E_{0.5}/A_{0.3}\right]$ (A: aluminum; E: elastomer, C: CFRP) according to the nomenclature for hybrid laminates based on VDI 2014. Figure 1 illustrates the layup of HyCEML under investigation in this study. The metal layer used in this work is the aluminum alloy AL 2024-T3 with a thickness of 0.3 mm. The batch number of the elastomer is SAA9579-52 by KRAIBURG GmbH & Co. KG with a density of 1180 kg/m3, and the thickness of the elastomer layer is 0.5 mm. The CFRP prepreg named HexPlyM77/38/UD150/CHS-12K-70 by Hexcel is used and the nominal thickness of a single ply is 0.15 mm.

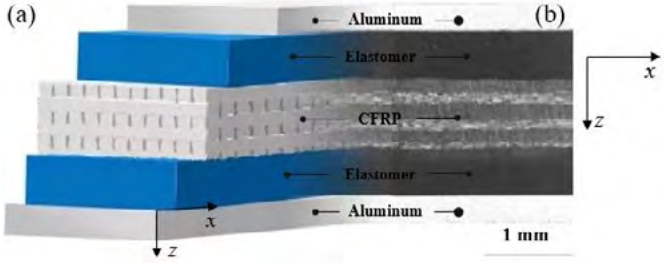


Figure 1. Hybrid CFRP-elastomer- metal laminates: (a) schematic cross-section of layup [10] (b) micrograph of cross section [11].

2.2. Methods

Drop weight impact tests are carried out referring to ASTM D7136 to investigate the dynamic response and damage mechanism of hybrid laminate subjected to out-of-plane LVI loading. A drop-tower machine Coesfeld Magnus 1300, Figure 2. (a), with the support fixture shown in Figure 2 (b) is employed. The specimen size is 150 mm × 100 mm, and the opening dimensions of the supporting window are 125 mm and 75 mm. The boundary conditions of the tests are shown in Table 1. The impactor's displacement over time and the contact force between the impactor and laminate are recorded during the impact. The absorbed energy during the impact is obtained by the continuous integration method on the force-displacement curve.

Table 1. Test parameters of HyCEML impact tests.

Impact energy (J)	Impactor mass (kg)	Impactor diameter (mm)	Impact velocity (m/s)
10	5.25	20	1.883
30	5.25	20	3.350

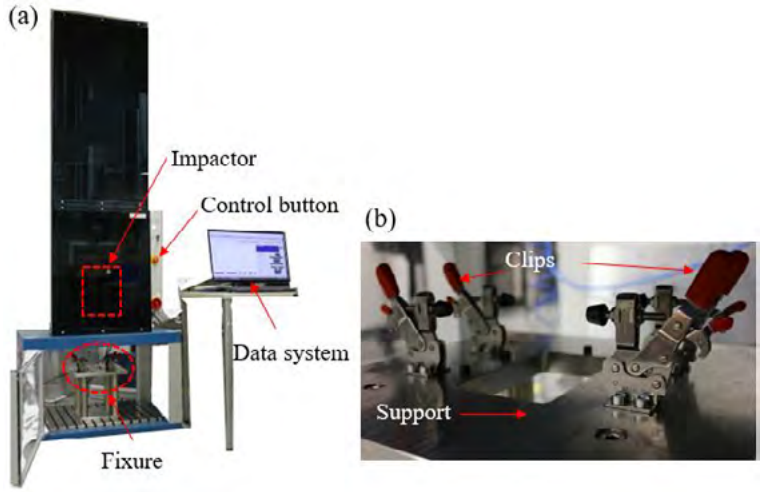


Figure 2. Drop weight testing equipment: (a) drop-weight tower (b) fixture for specimen.

The commercial finite element software Abaqus 2020, with explicit time integration, is adopted to investigate the impact behavior of HyCEML. The finite element (FE) model consists of an impactor with an initial velocity and a HyCEML plate with the dimensions 150 mm × 100 mm × 2.5 mm. The configuration of the plate is $\left[A_{0.3}/E_{0.5}/\left(C^{0°}_{0.15}/C^{90°}_{0.15}\right)_3/E_{0.5}/A_{0.3}\right]$. The details about the numetricla model are described in [10].

3. Results and discussion

In this section, the impact response for both, conventional FML and HyCEML, plates subjected to different impact energies is analyzed. The change of damage mechanisms and energy dissipation with the impact energy are investigated.

3.1. Impact history

The *F-t*, *F-u*, and *E-t* curves of hybrid laminates with elastomer and conventional FML subjected to different impact energy levels are analyzed. The impact behavior is compared for FML $\left[A_{0.3}/\left(C^{0^\circ}_{0.15}/C^{90^\circ}_{0.15}\right)_3/A_{0.3}\right]$ without elastomer and HyCEML $\left[A_{0.3}/E_{0.5}/\left(C^{0^\circ}_{0.15}/C^{90^\circ}_{0.15}\right)_3/E_{0.5}/A_{0.3}\right]$.

3.1.1. Force-time curves

The *F-t* curves of the HyCEML and FML plates subjected to impact energy levels ranging from 3 J to 30 J are shown in Figure 3. The *F-t* curves have a similar shape for the two laminates impacted with different energies. Up to 24 J, the *F-t* curves are almost symmetrical in ascending and descending parts. It is a typical curve under non-penetration condition [12]. The symmetry of the curve is not as pronounced as in the condition of 3 J, when the laminates are impacted with energies of more than 10 J and 15 J for FML and HyCEML, respectively. The oscillations represent progressive damage inside the laminates. Especially for the FML under impact energy of 30 J, the load drops dramatically. It is caused by partial penetration.

The value of F_{inc} (incipient damage force) is one important measure for the ability to impact resistance. The load drops at F_{inc}, cf. Figure 3, and the stiffness of the laminate decreases. This is caused by delamination inside the laminate. More damage modes will occur afterwards, such as the extension of delamination, matrix failure, fiber breakage and aluminum cracks. The curve fluctuates until it reaches the value of F_{max}.

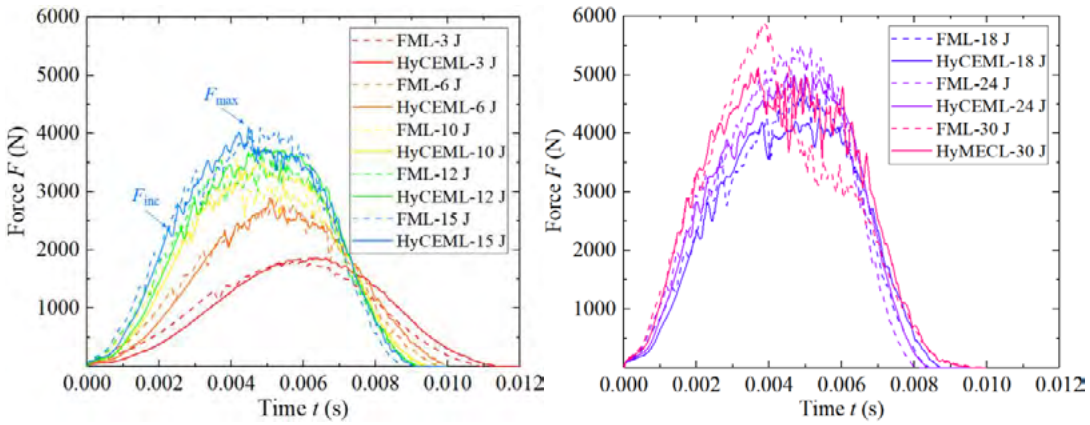


Figure 3. Force-time curves of FML and HyCEML impacted with energies ranging from 3 J to 30 J.

3.1.3. Energy-time curve

The *E-t* curves of FML and HyCEML impacted ranging from 3 J to 30 J are shown in Figure 4. The energy ascends to the maximum value E_{imp} (initial impact energy). Then it descends to the final value E_{abs}. The difference between the Eimp and Eabs is related to the elastic strain energy. It is found, that the dissipated energy of HyCEML is slightly lower than that of the FML. Especially at 12 J and 30 J levels, the final energy absorption is reduced by about 15% and 10%, respectively, compared with FML. This is mainly due to the stress and damage mechanism changes inside HyCEML.

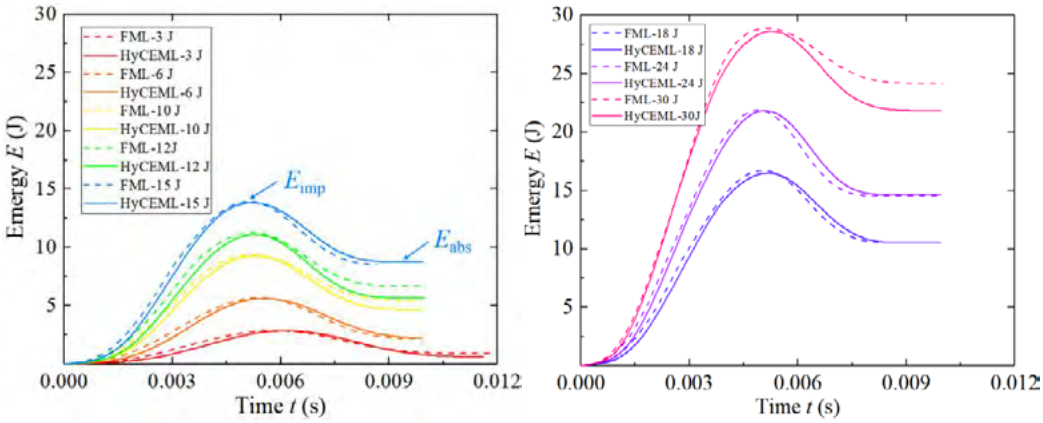


Figure 4. Energy-time curves of FML and HyCEML impacted with different energies.

3.2. Damage assessment

The main reason for the difference in impact behavior of FML and HyCEML is the changes in the internal damage mechanism after introducing the elastomer layer. This section will investigate the damage mechanism differences of these two laminates impacted with different energies. It should be noted that the interfaces between aluminum and elastomer and between CFRP and elastomer do not delaminate in this work. As seen in the *F-u* curves, the load oscillates significantly. This is mainly caused by four damage modes, namely aluminum yielding, aluminum crack, matrix failure, and delamination. Delamination includes interfaces between 0° and 90° CFRP and interfaces between CFRP and aluminum (only for FML).

3.2.1. Damage modes

This section investigates the differences in damage modes between FML and HyCEML impacted with energy from 3 J to 30 J. Plasticity and crack of the aluminum, delamination, and matrix failure are considered. Matrix failure is the primary intra-ply damage mechanism inside the CFRP under rebound conditions in this study.

Figure 5 shows the plastic strain (PEEQ) of the aluminum layers in hybrid laminates under different impact energies. It is found that the plastic strain of the aluminum layer increases with the impact energy. The difference in plastic strain between FML and HyCEML impacted with 3 J is small. However, there is a noticeable difference for 30 J conditions. Cracks occur in the bottom aluminum layer of FML due to the enormous plastic strain. There is no fracture in HyCEML, which shows that elastomer layers play an essential role in protecting the aluminum layers under high-energy impacts.

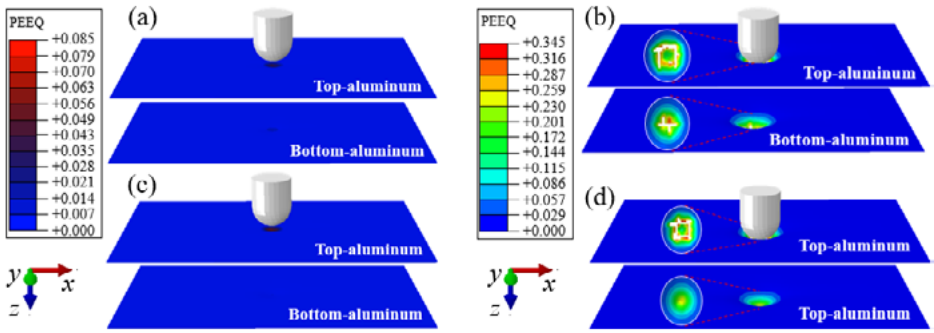


Figure 5. The plastic strain of aluminum layers in hybrid laminates subjected with different energies: (a) FML impacted with 3 J (b) FML impacted with 30 J (c) HyCEML impacted with 3 J (d) HyCEML impacted with 30 J.

Figure 6 shows the delamination between aluminum and CFRP and between 0° and 90° CFRP inside the laminates impacted with different energies. The degree of delamination damage (SDEG) varies from

0 to 1, with 0 representing no damage and 1 representing complete delamination. The delaminated area in FML and HyCEML increases with impact energy. The introduction of elastomer layers protects interfaces between aluminum and CFRP and interfaces between 0° and 90° CFRP. Tension failure is the primary damage mode for matrix failure. Figure 7 shows the matrix failure in the CFRP layers inside laminates impacted with different energies. The degree of tensile failure in the matrix (HSNMTCRT) varies from 0 to 1, with 0 representing no damage and 1 representing complete damage. The damaged area in HyCEML is larger than that in FML. This is caused by the elastomer layers, which increase the proportion of CFRP involved in the load-bearing, avoiding increased damage in the aluminum layers.

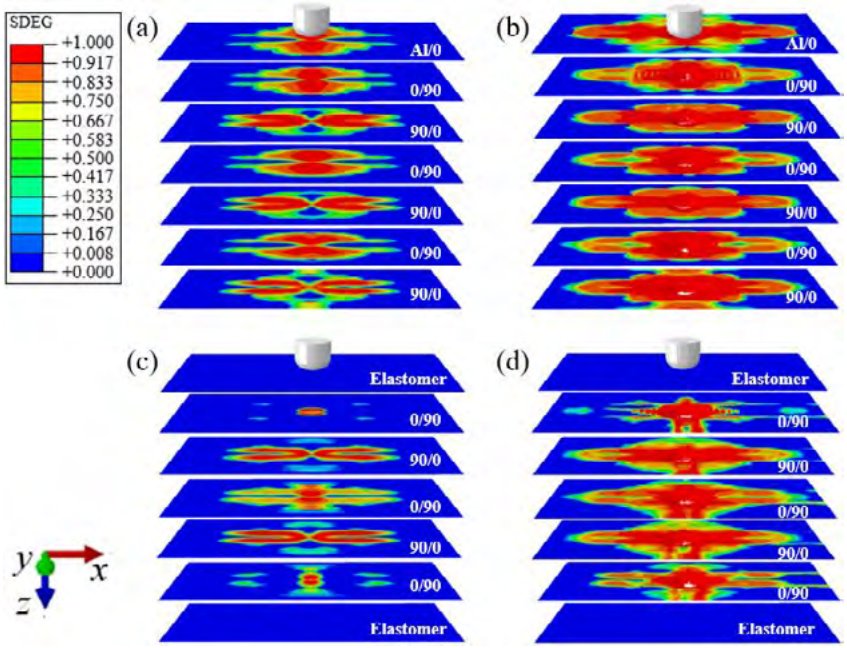


Figure 6. Delaminated area inside laminates impacted with different energies: (a) FML impacted with 3 J (b) FML impacted with 30 J (c) HyCEML impacted with 3 J (d) HyCEML impacted with 30 J.

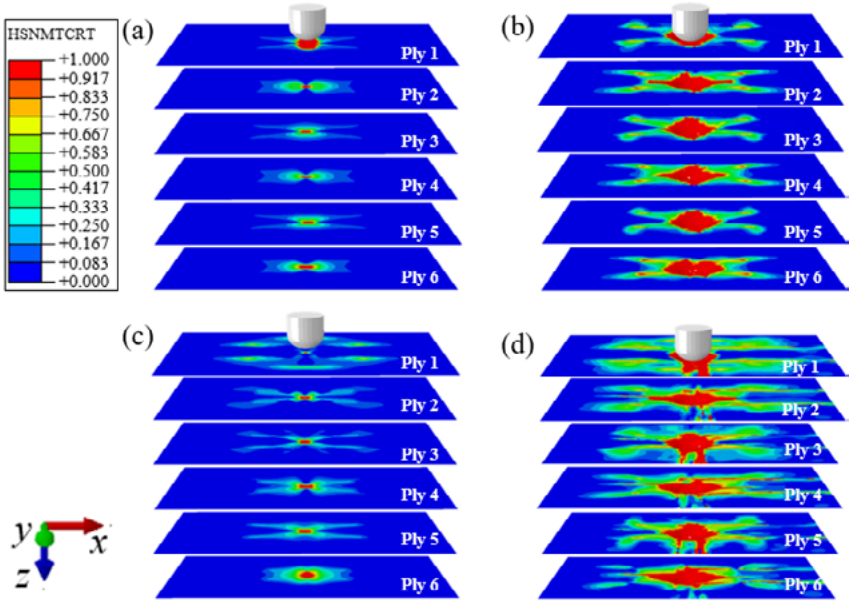


Figure 7. Matrix failure inside laminates impacted with different energies: (a) FML impacted with 3 J (b) FML impacted with 30 J (c) HyCEML impacted with 3 J (d) HyCEML impacted with 30 J.

3.2.2. Energy dissipation

In this section, five dissipative mechanisms and the total energy dissipation are quantified and compared for HyCEML and FML, impacted with different impact energies. The energy dissipated by the aluminum plasticity, delamination between 0° and 90° CFRP, and intra-ply failure of CFRP changes with the impact energy, cf. Figure 8. (a) - (c). The delamination between aluminum and CFRP (only in FML), and the viscosity of elastomer (only in HyCEML) is illustrated in Figure 8. (d). The energy dissipated by aluminum fracture is shown in in Figure 8. (e). Figure 8. (f) displays the total energy dissipation of FML and HyCEML under different impact energies. The proportion of each mechanism in the total energy dissipation in different impact conditions is quantitatively analyzed. The ratio of energy dissipated by each mechanism to the total energy dissipation is plotted in the form of a line chart, cf. Figure 8. (a) - (e).

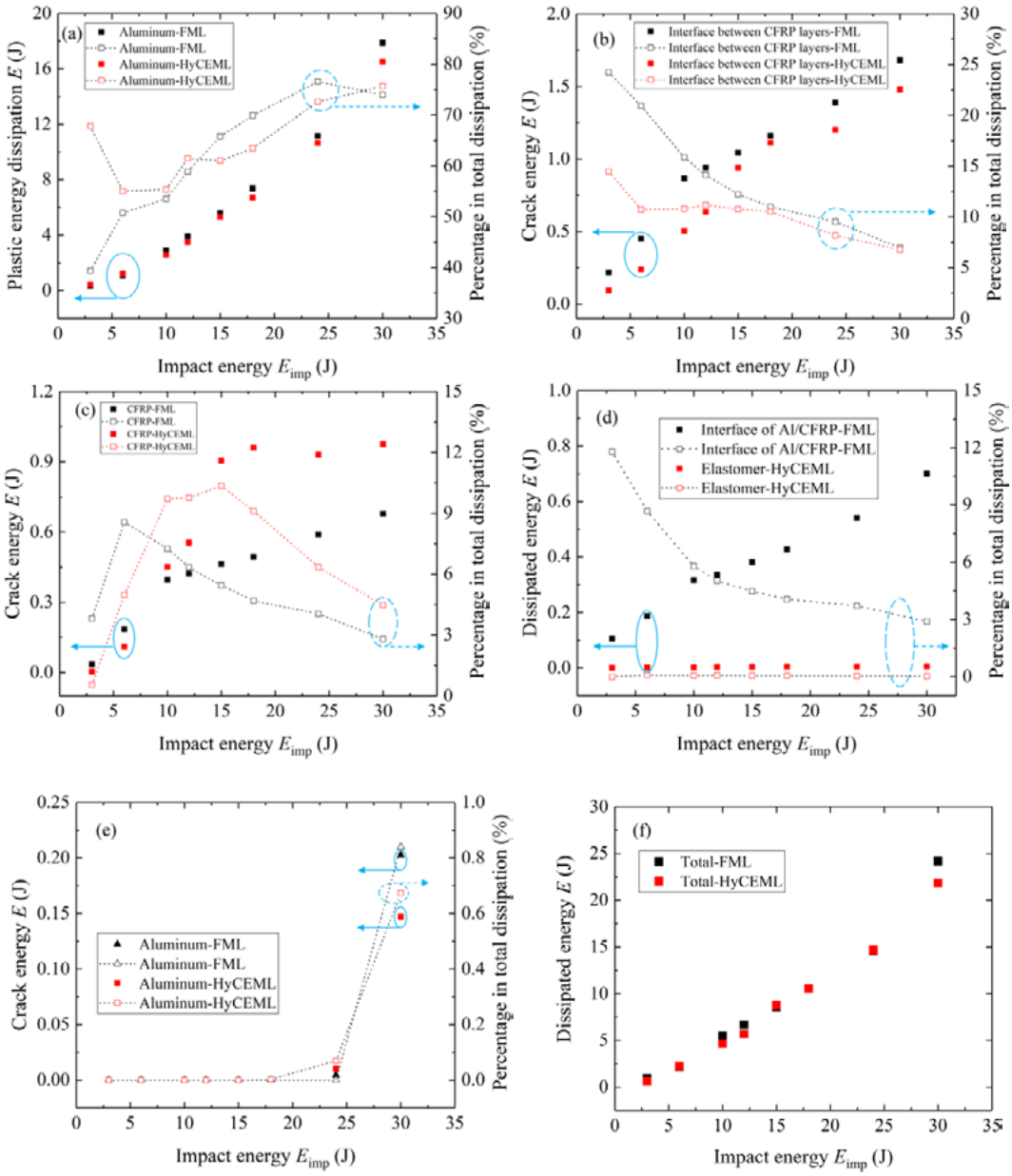


Figure 8. Energy dissipation comparison of FML and HyCEML under different impact energies.

Figure 8. (a) shows the relationship between the energy dissipated through plastic deformation of aluminum and the overall impact energy in FML and HyCEML. It is found that the energy dissipated

by aluminum plasticity in HyCEML is less than that in FML when the impact energy is greater than 10 J. Compared with Figure 8. (c), the energy dissipated by intra-ply failure of the CFRP, including matrix and fiber failure, in the HyCEML exceeds that in the FML. It shows that the elastomer layers make the impact energy more evenly distributed in the aluminum and in the CFRP. The energy dissipated by aluminum plasticity accounts for more than 50% of the total energy dissipation, even up to 77% at the impact energy level of 24 J. It is thus the most important energy dissipation mechanism. The energy dissipated by intra-ply failure of CFRP accounts for less than 12% of the total energy dissipation. The energy dissipation is more evenly distributed in these two primary mechanisms due to the introduction of the elastomer. The hybrid materials are efficiently taken advantage of. The overall load-bearing capacity of the hybrid laminate is improved.

The inter-ply damage of CFRP layers is the second most important energy dissipation mechanism in hybrid laminates. Figure 8. (b) shows the relationship between the energy dissipated by inter-ply damage of CFRP layers and impact energy in FML and HyCEML. Similarly, introducing elastomer layers also effectively reduces the delamination between 0° and 90° CFRP. It is due to the redistribution of impact energy among different dissipative mechanisms such as the aluminum plasticity, intra-ply damage of CFRP layers, and inter-ply damage of CFRP layers. In addition, the introduction of elastomers makes the in-plane dynamic load more uniform in every single ply, which is another crucial reason for the protection of the aluminum and the interfaces between CFRP layers.

The line charts in Figure 8. (a) - (e) describe the relationship of each dissipative mechanism and the impact energy. It is found that the proportion of energy dissipated by the aluminum increases with the impact energy. The proportions of delamination between 0° and 90° CFRP, between aluminum and CFRP gradually decreases with the impact energy. However, this does not occur monotonously. The energy dissipation due to the intra-ply damage of CFRP layers accounts for about 10% of the total dissipation of HyCEML at impact energy levels ranging from 10 J to 18 J, which is similar to the dissipated energy from inter-ply damage of CFRP layers. The introduction of elastomer layers changes the contribution of each damage mechanism to the total energy dissipation.

The energy dissipated by delamination between aluminum and CFRP is lower than that dissipated by delamination between 0° and 90° CFRP, cf. Figure 8. (d). However, considering that there are only two layers in FML, the damage degree of interfaces between aluminum and CFRP is also severe. The material corresponding to this interface is the elastomer in HyCEML. It can be found that the energy dissipated by viscosity is relatively small. The key role of the elastomer in HyCEML, thus, appears not to be dissipation by itself but rather as the distribution of load in order to enable other mechanisms to dissipate more energy.

Figure 8. (f) shows the total energy dissipation of FML and HyCEML impacted with different energies. It is found that the introduction of elastomer protects the hybrid laminate, especially at impact energies of 12 J, 10 J and 30 J. Under the other impact energy levels, even the total energy dissipation does not change much after the introduction of the elastomer, but the energy dissipated by each mechanism is changed concluded from Figure 8. (a) - (e). This is significant for the design of structures in which certain dissipative mechanisms are to be favored above others.

4. Conclusions

In this work, the impact behavior of hybrid CFRP-elastomer-metal laminates (HyCEML) and conventional fiber-metal laminates (FML) are compared in a wide range of impact energies by experimental and numerical methods. The damage modes of the hybrid laminate under low-velocity impact conditions are determined, and the energy dissipated by each mechanism under different impact energies is quantified.

The damage mechanisms of FML and HyCEML include metal plasticity, metal failure, delamination, CFRP failure. Each mechanism is a competitive failure mechanism and contributes a different proportion to the total energy dissipation under different impact energies. The elastomer layers change

the energy distribution in each component of hybrid laminates. The damage of the aluminum and delamination between 0° and 90° CFRP are reduced, and the usage efficiency of hybrid materials is improved due to the elastomer layer. The initial damage force of the laminate is increased, while the peak force and structural stiffness are reduced. The total energy dissipation decreases under large-energy impacts. Even if the total energy dissipation does not change under some impact energies, each mechanism's proportion of energy dissipated is changed.

Acknowledgments

The authors would like to acknowledge the funding of this work by the Natural Science Foundation Youth Project from Shandong Province (ZR2023QE336), the cooperative scientific research project of "Chunhui Program" of Ministry of Education (HZKY20220292), by the International Joint Laboratory on Digital laboratory of lightweight structure for green vehicle supported by Harbin Institute of Technology (ITCA10102001), by the Deutsche Forschungsgemeinschaft (DFG, German Research Foundation) in the SPP1897 "Calm, Smooth, Smart -- Novel approaches for influencing vibrations by means of deliberately introduced dissipation", project KA 4224/3-2 , grant no. 314969583, "HyCEML – Hybrid CFRP/elastomer/metal laminates containing elastomeric interfaces for deliberate dissipation" (Karlsruhe Institute of Technology). Furthermore, the authors would like to acknowledge Gummiwerk KRAIBURG GmbH & Co. KG for providing the elastomer material.

References

[1] T. Sinmazçelik, E. Avcu, M. Ö. Bora, et al. A review: Fiber metal laminates, background, bonding types and applied test methods. Materials & Design, 32(7): 3671-3685, 2011.
[2] K. Dadej, J. Bieniaś, B. Surowska. Residual fatigue life of carbon fibre aluminium laminates. International Journal of Fatigue, 100: 94-104, 2017.
[3] W. X. Wang, Y. Takao, T. Matsubara. Galvanic corrosion-resistant carbon fiber metal laminates. In Proceedings of The 16th International Conference on Composite Materials, 8-13,2007.
[4] C. T. Lin, P. W. Kao, M. H. R. Jen. Thermal residual strains in carbon fiber-reinforced aluminum laminates. Composites, 25(4): 303-307, 1994.
[5] M. Stoll, F. Stemmer, S. Ilinzeer, et al. Optimization of corrosive properties of carbon fiber reinforced aluminum laminates due to integration of an elastomer interlayer. Key Engineering Materials, 742: 287-293, 2017.
[6] W. V. Liebig, V. Sessner, K. A. Weidenmann, L. Kärger. Numerical and experimental investigations of the damping behaviour of hybrid CFRP-elastomer-metal laminates. Composite Structures, 202: 1109-1113, 2018.
[7] A. Khodadadi, G. Liaghat, A. Taherzadeh-Fard, et al. Impact characteristics of soft composites using shear thickening fluid and natural rubber-a review of current status. Composite Structures, 271: 114092, 2021.
[8] D. Mohotti, T. Ngo, S. N. Raman, et al. Plastic deformation of polyurea coated composite aluminum plates subjected to low velocity impact. Materials & Design, 56: 696-713, 2014.
[9] E. L. Sarlin, A. Luukkonen, M. S. Vippola, et al. Failure behavior of a three-layer steel/rubber/FRP hybrid structure. In Proceedings of the Seventh Asian-Australasian Conference of Composite Materials, 1-4, 2010.
[10] Z. Li, J. Zhang, A. Jackstadt, L. Kärger. Low-velocity impact performance of hybrid CFRP-elastomer-metal laminates in comparison with conventional fiber-metal laminates, Composite Structures, 287: 115340, 2022.
[11] V. Sessner, A. Jackstadt, W. V. Liebig, et al. Damping Characterization of hybrid carbon fiber elastomer metal laminates using experimental and numerical dynamic mechanical Analysis. Journal of Composites Science, 3(1): 3, 2019.
[12] G. C. Yu, L. Z. Wu, L. Ma, et al. Low velocity impact of carbon fiber aluminum laminates. Composite Structures, 119: 757-766, 2015.

BIAXIAL TESTING OF FRP LAMINATES OPTIMISED USING A RANGE OF FAILURE CRITERIA- DEVELOPMENT OF A BIAXIAL TESTING APPARATUS

T. Lorimer[1], T. Allen[1]

[1]Centre for Advanced Materials, Manufacturing and Design, University of Auckland, 314-390 Khyber Pass Road, Newmarket, Auckland 1023, New Zealand
Email: t.lorimer@auckland.ac.nz, Web Page: https://cacm.blogs.auckland.ac.nz

Keywords: Optimisation, Biaxial Loading, Failure Criteria

Abstract
Failure Criteria (FC) are commonly employed for the prediction of various forms of failure in Fibre Reinforced Polymers (FRP). However, they are usually extensions of criteria designed for isotropic materials and can struggle to accurately predict failure for FRP [1], [2]. Numerable factors, such as stacking sequence, loading direction, material characterization and the definition of failure significantly affect the accuracy and therefore the reliability of most common FC, particularly in complex load states [3], [4]
A testing apparatus and a cruciform specimen are developed for experimental in-plane biaxial testing at a lab-scale. The new biaxial testing apparatus is used to assess the accuracy of five common FC in terms of their predictions of failure load and their suitability within the objective function of a coupled FEA-GA optimisation approach.
Each FC is used to design an *optimal* cruciform specimen by specifying the stacking sequence of a laminate such that the highest load is carried by the specimen at failure.
Analysis of the results and comparison with earlier works suggest the Puck failure criteria is the most accurate and the most conservative, so, it is suggested as the most suitable.

1. Introduction

For a structural design object to efficiently perform its task, its allowable working loads must be based on some prediction of the limits of material strength [5]. This is true regardless of material or application. Well-established means of failure prediction for Fibre Reinforced Polymers (FRP) utilise Failure Criteria (FC), but previous works suggest they are not always reliable for multiaxial failure prediction [4], [6], [7], [8], [9], [10], [11]. Resultingly, in industry, FC are commonly only used as an initial sizing tool due to their inaccuracy, report Hinton et al. [12]. If the conditions under which a part might fail are not reliably identifiable, how can a designer hope to generate efficient responses to loading conditions? Structural Safety Factors (SFs) will need to include enlarged redundancy; thus, optimal structural efficiency cannot be achieved; Something which is crucial in high-performance applications, or more generally where structural mass affects energy efficiency.

Early work on biaxial testing by Hannon and Tiernan [13] investigated sheet metal specimens that exhibited anisotropy due to their manufacturing processes. Their review discussed developments in specimen and Biaxial Testing Apparatus (BTA) design and stressed the importance of testing materials in biaxial loading scenarios. Crucially, it was recognised that anisotropic materials would exhibit unique behaviour only captured by testing in multiaxial loading scenarios [13]. This behaviour is also observable in FRP laminates failure given the severely anisotropic nature of the uniaxial plies [14], [15]. Just as for metals, characterising FRPs using standard uniaxial tensile testing is insufficient to

reveal their true behaviour in biaxial and multiaxial loading [13], [16], [17]. However, FRP laminates strengths are often measured using individual coupon tests, the data from which is used to set global design allowables. This approach fails to characterise responses to biaxial loading or the effects of laminate configuration and can lead to failure in components expected to withstand loading according to their uniaxially loaded behaviour [13].

Despite the inaccuracy of FC, they still hold an important place in the design process for Large Composite Structures (LCSs), especially so in high-performnace applications. Testing full-scale LCSs is often too slow or expensive, so, considering and understanding the response of FRPs subject multiaxial loads is necessary [16], [18], [19]. Implementing FC into design and optimisation procedures is critical to estimating performance. Choosing the best FC for a high-performance structural optimisation case is essential as the better optimsed a structure can be, in terms of it strength to mass ratio, the better the structure can perform in a competitive setting.

This work investigates the effect of FC choice on optimised laminate specimens. Five FC; Puck (P) [20], Hashin (H) [21], Maximum Strain (MS) [22], Tsai-Hill (TH) [23], and Tsai-Wu (TW) [24] are substituted into the objective function of a Genetic Algorithm (GA) based optimisation approach for laminate stacking sequence and ply orientations. Each FC is used to optimise a newly developed biaixial cruciform specimen, tested to failure in a newly developed BTA. Test results are compared with simulated optimal laminate performance, and conclusions regarding the reliability of the investigated FC are drawn

2. Methodology

Following a review of literature looking at the application of multiple techniques for testing FRPs and other materials biaxially, a linkage-driven BTA has been chosen as the most suitable method for the testing in this work. This choice is made because of the relative inexpense of this type of apparatus compared to the independently actuated types and the ease of adaptation to the research centre's existing Instron 1185. Figure 1 shows the BTA built for this testing. It is a development of the linkage-driven design proposed by Ferron and Makinde [25].

The accompanying cruciform specimen (Figure 2) was developed concurrently with the BTA and was originally based on an optimised specimen designed by [26]. Specimen designs present in the literature usually target a gauge zone with as uniform a biaxial stress state as possible. However, the objectives of this work are to analyse the effects of FC choice in the context of LCS design where complex geometry and loading states are usually present, achieved by the addition of a central hole. Several design iterations were required, but the final specimen reliably fails in the gauge section and produces repeatable failure.

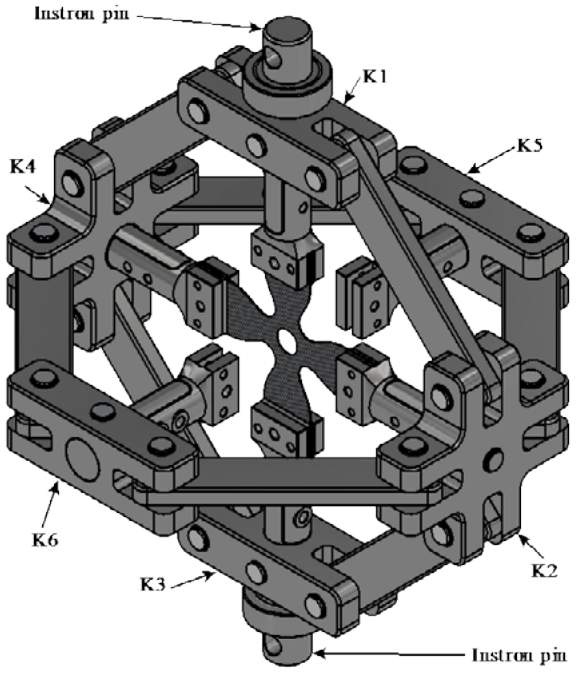


Figure 1: Illustration of the biaxial testing apparatus

For the specimen optimsation, a previously developed GA-based approach [27] has been coupled with an FEA solver (ABAQUS 2022). Five-layer laminates subjected to equal 1% tension-

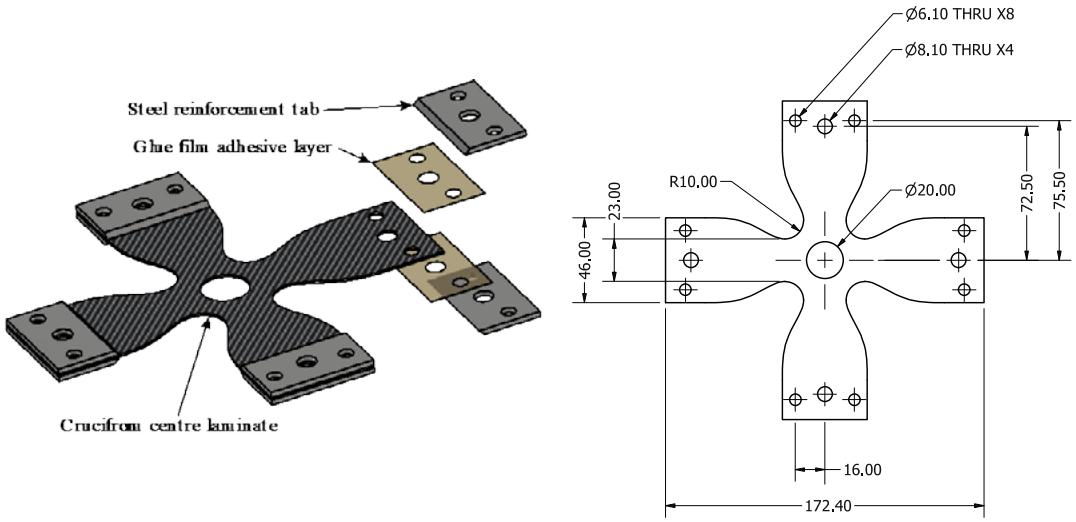


Figure 2: Novel cruciform specimen

tension displacement were optimised for maximum failure load. Five-layer laminates were chosen to exclude the possibility of trivial balanced laminates being returned by the optimisation while being within the ± 50 kN load range of the BTA. The material chosen was a unidirectional carbon-Epoxy 150 gsm pre-preg with properties shown in Table 1.

Table 1: CFRP material properties

E_{11}	E_{22}	G_{12}	ν_{12}	ρ
147 GPa	9 GPa	3.3 GPa	0.31	1500 kg m^{-3}
$\hat{\sigma}_{1T}$	$\hat{\sigma}_{1C}$	$\hat{\sigma}_{2T}$	$\hat{\sigma}_{2C}$	$\hat{\tau}_{12}$
2260 MPa	1200 MPa	50 MPa	190 MPa	100MPa
$\hat{\varepsilon}_{1T}$	$\hat{\varepsilon}_{1C}$	$\hat{\varepsilon}_{2T}$	$\hat{\varepsilon}_{2C}$	$\hat{\gamma}_{12}$
0.015	0.008	0.005	0.021	0.030

Each FC was substituted into the objective function (See Equation 1) of the GA-based optimisation approach to determine the failure load (F_F) at SF = 1.

$$F_F = \mathrm{SF} \times F_{1\%} \tag{1}$$

Where, SF is the safety factor determined by the FC and $F_{1\%}$ is the highest load experienced in either the *x*- or *y*-directions of the specimen at a 1% arm displacement. The FE model uses S4R shell elements with a 2D composite laminate applied. Displacements are applied to a point kinematically coupled to the edges of the arms at the extremities of the samples. The model used may be seen in Figure 3.

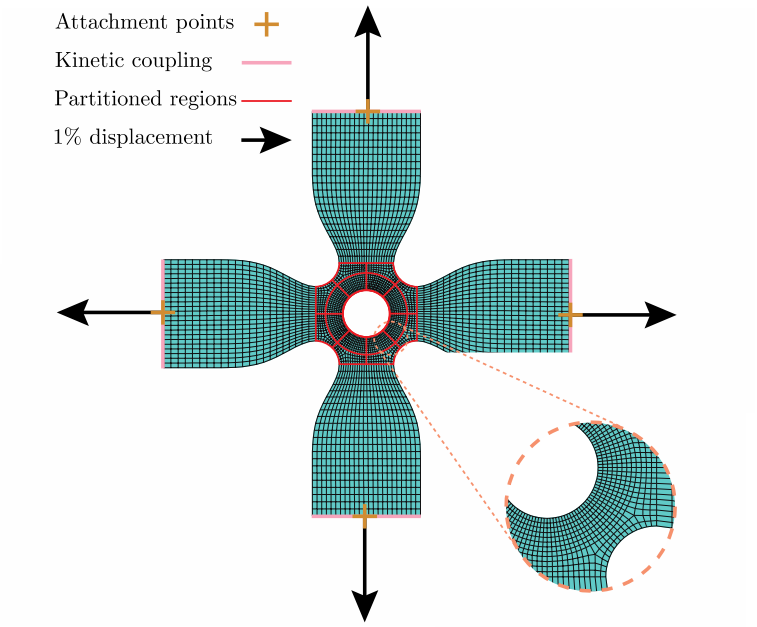


Figure 3: Modelling of the cruciform specimen in Abaqus 2022

3. Results & Discusssion

Seven distinct samples consisting of three specimens were tested to failure using the BTA. The first five samples each used one of the five FC being assessed. The last two sets were four-layer (not five as in the other samples) Cross-Ply (CP) and Dual-Bias (DB) laminates.

Table 2 shows the recorded and predicted failure loads for the CP and DB specimens. *NB:* These specimens are not optimised, but are included to assess the relative accuracy of the FC for standard *quasi-isotropic* laminate configurations.

Table 2: Comparison of recorded and predicted failure loads. CP and DB specimens

	Test mean	TW_P	TH_P	MS_P	P_P	H_P
CP F_F [N]	1849	4294	4532	19902	4142	4590
DB F_F [N]	4076	4344	4462	26258	3878	4462

Subscript P indicates a predicted load according to that FC

Mean error for the CP specimens sits at + 305 %. If MS is excluded as an obvious outlier, this drops to + 137 % error. In the DB case, mean error sits at + 113 % or + 5 % excluding MS. The strain paths generated in the cruciform specimens are aligned at 45° and so the much better accuracy in the DB case is thought to occur because the plies are subject to pure longitudinal (along the fibre) or transverse (across the fibre) stress. The plies would be expected to exhibit higher strength in this configuration and the FC are dealing with less complicated failure mechanisms. In these cases, Puck was found to be the most accurate FC at a still unreliable + 60 % strength prediction.

Figure 4 shows the mean recorded and predicted failure loads for all samples.

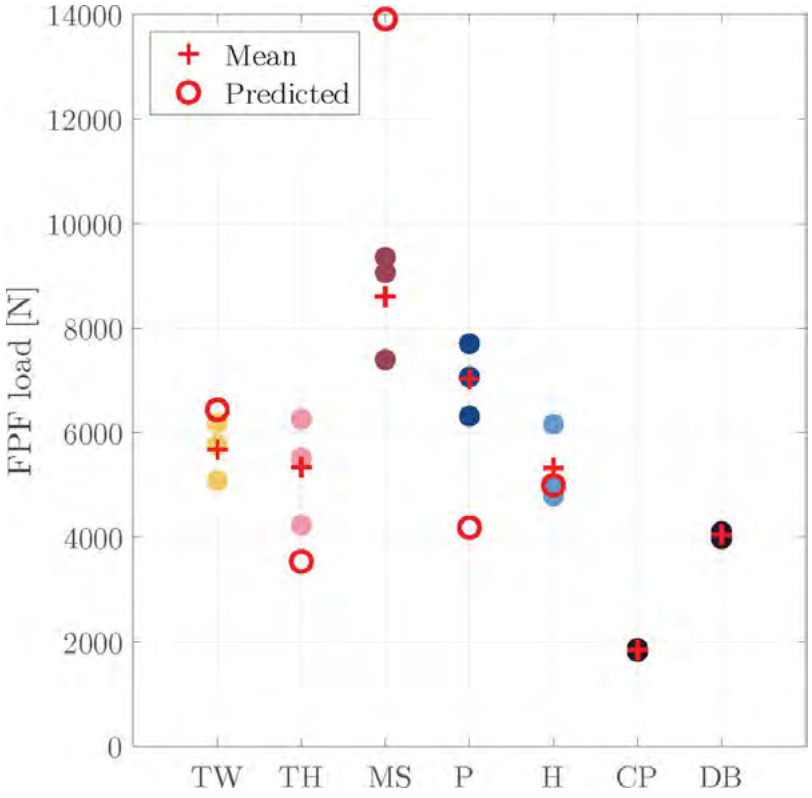


Figure 4: Crucifrom specimen test results

It can be seen that there a range of prediction accuracies associated with each FC. Also notable; the optimised specimens were much more spread out according to their actual failure loads, compared with the CP and DB specimens.

Table 3 shows the mean error of each FC.

Table 3: Mean prediction error by FC

	TW	TH	MS	P	H
Predicted Load [N]	6441	3538	13918	4189	4997
Recorded Load [N]	5681	5340	8607	7032	5326
Error	+ 13 %	- 34 %	+ 62 %	- 40 %	- 6 %

A Bayesian ANOVA was also conducted to assess the significance of choosing one FC relative to another for laminate design. Figure 5 shows how MS- and P-optimised specimens carried significantly higher load than the remaining three.

Here H is taken as the reference FC, It can be seen that MS and P were both significantly different but that using TW, TH, or H did not constitute a significant effect on part performance. This might suggest that MS was the most suitable FC as it produces the strongest laminates, but this is believed to be an isolated case and its poor accuracy means it could not be relied upon to determine structural performance with any confidence.

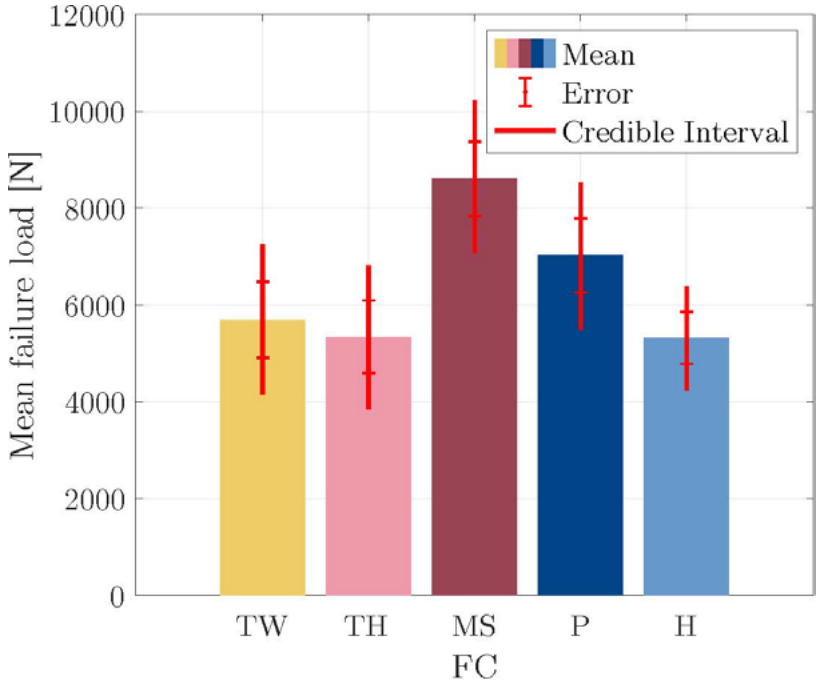


Figure 5: Bayesian ANOVA. FC effect relative to H

After analysing the results of this study and comparing to the results of the WWFE-I [28] and previous work by the author [27], P has been identified as the most favourable FC. It has proven to be the most conservative according to [27], the most accurate according to [28], and P-optimised specimens were the strongest while underpredicting failure load in this work.

4. Conclusions

In the realm of high-performance composite structural design, there must be reliable metrics for strength limit determination. While there are still underlying concerns as to the accuracy of even the most well-established failure criteria, as structures increase in size and complexity make-and-test design procedures become to costly or slow. This work investigated the impact of failure criteria choice within the objective function of an optimisation approach tasked with designing biaxial test specimens. Seven samples of cruciform speimens were tested using a newly implemented biaxial testing procedure and Puck's faiulure criteria was shown to be the most accurate and conservative, and is recommended for optimising the strength of complexly loaded complex geometry FRP laminates.

References

[1] G. C. Eckold, "Failure criteria for use in the design environment," *Failure Criteria in Fibre-Reinforced-Polymer Composites*, pp. 121–139, 2004, doi: 10.1016/B978-008044475-8/50006-8.

[2] W. E. Wolfe and T. S. Butalia, "A strain-energy based failure criterion for non-linear analysis of composite laminates subjected to biaxial loading," *Failure Criteria in Fibre-Reinforced-Polymer Composites*, pp. 353–378, 2004, doi: 10.1016/B978-008044475-8/50015-9.

[3] H. Dong, J. Wang, and B. L. Karihaloo, "An improved Puck's failure theory for fibre-reinforced composite laminates including the in situ strength effect," *Compos Sci Technol*, vol. 98, pp. 86–92, 2014, doi: 10.1016/j.compscitech.2014.04.009.

[4] A. S. Kaddour and M. J. Hinton, "Triaxial Failure Criteria for Polymer Composites : Part (a) of WWFE-II : Comparison Between Theories," in *18th International conference on composite materials*, 2011.

[5] M. J. Hinton and P. D. Soden, "Predicting failure in composite laminates: the background to the exercise," *Compos Sci Technol*, vol. 58, no. 7, pp. 1001–1010, 1998, doi: 10.1016/S0266-3538(98)00074-8.

[6] a S. Kaddour, "Multi-Axial Notched Strength Envelopes for Aerospace Composite Laminates," in *16th International Conference on Composite Materials*, 2007.

[7] A. S. Kaddour and M. J. Hinton, "Maturity of 3D failure criteria for fibre-reinforced composites: Comparison between theories and experiments: Part B of WWFE-II," *J Compos Mater*, vol. 47, no. 6–7, pp. 925–966, 2013, doi: 10.1177/0021998313478710.

[8] A. S. Kaddour and M. J. Hinton, "Failure criteria for composites," in *Comprehensive Composite Materials II*, Elsevier, 2017, pp. 573–600. doi: 10.1016/B978-0-12-803581-8.10354-6.

[9] A. S. Kaddour, M. J. Hinton, P. A. Smith, and S. Li, "A comparison between the predictive capability of matrix cracking, damage and failure criteria for fibre reinforced composite laminates: Part A of the third world-wide failure exercise," *J Compos Mater*, vol. 47, no. 20–21, pp. 2749–2779, Sep. 2013, doi: 10.1177/0021998313499476.

[10] A. S. Kaddour, M. J. Hinton, P. A. Smith, and S. Li, "The background to the third world-wide failure exercise," *J Compos Mater*, vol. 47, no. 20–21, pp. 2417–2426, Sep. 2013, doi: 10.1177/0021998313499475.

[11] M. J. Hinton and A. S. Kaddour, "Triaxial test results for fibre-reinforced composites: The Second World-Wide Failure Exercise benchmark data," *J Compos Mater*, vol. 47, no. 6–7, pp. 653–678, Mar. 2013, doi: 10.1177/0021998312459782.

[12] M. J. Hinton, A. S. Kaddour, and P. D. Soden, "The world-wide failure exercise. Its origin, concept and content," *Failure Criteria in Fibre-Reinforced-Polymer Composites*, pp. 2–28, 2004, doi: 10.1016/B978-008044475-8/50002-0.

[13] A. Hannon and P. Tiernan, "A review of planar biaxial tensile test systems for sheet metal," *J Mater Process Technol*, vol. 198, no. 1–3, pp. 1–13, 2008, doi: 10.1016/j.jmatprotec.2007.10.015.

[14] D. Zenkert and M. Battley, *Foundations of fibre composites: notes for the course: Composite lightweight structures*. DTU, 2006. [Online]. Available: https://books.google.co.nz/books?id=wGi8oAEACAAJ

[15] S. Grove, *Composite Materials and Structures for Engineering Students*. Kindle Direct Publishing, 2018.

[16] R. JONES Caroline; GREENE, "Pulled in different directions," *Materials world*, 2001.

[17] A. Pun, "Multiaxial fatigue models the real world," *Machine design.*, vol. 75, no. 9, pp. 26–28, 2003.

[18] W. M. Johnston, W. D. Pollock, D. S. Dawicke, and J. A. Wagner, "Biaxial Testing of 2195 Aluminum Alloy Using Cruciform Specimens," 2002. Accessed: Nov. 18, 2022. [Online]. Available: http://www.sti.nasa.gov

[19] Y. Ohtake, S. Rokugawa, and H. Masumoto, "Geometry Determination of Cruciform-Type Specimen and Biaxial Tensile Test of C/C Composites," *Key Eng Mater*, vol. 164–165, pp. 151–154, 1999, doi: 10.4028/www.scientific.net/kem.164-165.151.

[20] A. Puck and H. Schürmann, "Failure analysis of FRP laminates by means of physically based phenomenological models," *Failure Criteria in Fibre-Reinforced-Polymer Composites*, pp. 264–297, 2004, doi: 10.1016/B978-008044475-8/50011-1.

[21] Z. Hashin, "Failure criteria for unidirectional fiber composites," *Journal of Applied Mechanics, Transactions ASME*, vol. 47, no. 2, pp. 329–334, 1980, doi: 10.1115/1.3153664.

[22] H. Hahn, "Residual Stresses in Polymer Matrix Composite Laminates," *Journal of Composite Materials - J COMPOS MATER*, vol. 10, pp. 266–278, Mar. 1976, doi: 10.1177/002199837601000401.

[23] R. Hill, "A theory of the yielding and plastic flow of anisotropic metals," 1924. [Online]. Available: https://royalsocietypublishing.org/

[24] S. W. Tsai and E. M. wu, "A General Theory of Strength for Anisotropic Materials," *J Compos Mater*, vol. 5, no. 1, pp. 58–80, 1971, doi: 10.1177/002199837100500106.

[25] G. Ferron and A. Makinde, "Design and Development of a Biaxial Strength Testing Device," *J Test Eval*, vol. 16, no. 3, p. 253, 1988.

[26] D. A. A. Escarpita, "Experimental investigation of textile composites strength subject to biaxial tensile loads," Doctoral Thesis, Instituto tecnologico y de estudioa auperiore de monterrey, 2011.

[27] T. Lorimer and T. Allen, "The effect of failure criteria choice on optimised composite panels," in *Proceedings of the 20th European Conference on Composite Materials*, A. P. Vassilopoulos and V. Michaud, Eds., Lausanne: Composite Construction Laboratory, Jun. 2022, pp. 938–945.

[28] P. D. Soden, A. S. Kaddour, and M. J. Hinton, "Recommendations for designers and researchers resulting from the world-wide failure exercise," *Compos Sci Technol*, vol. 64, no. 3–4, pp. 589–604, 2004, doi: 10.1016/S0266-3538(03)00228-8.

METALLIZATION OF CARBON NANOTUBE FILMS AND THEIR APPLICATION IN THE LIGHTNING STRIKE PROTECTION OF CFRPS

Jiaqi XI[1], Wengang YANG[1] and Weibang LYU[1,2]

[1] Innovation Center for Advanced Nanocomposites, Suzhou Institute of Nano-Tech and Nano-Bionics, Chinese Academy of Sciences,Suzhou 215123, CHINA
[2]Division of Nanomaterials, Jiangxi Key Lab of Carbonene Materials, Jiangxi Institute of Nanotechnology, Nanchang 330200, CHINA
Email: wblv2013@sinano.ac.cn

Keywords: carbon nanotubes, composite materials, electrical properties, lightning strike protection, non-destructive examination

Abstract
Due to their poor conductivity, carbon fiber reinforced plastics (CFRPs) themselves cannot meet the lightning strike protection (LSP) requirement of modern aircrafts. Metal mesh is always introduced onto the surface of CFRPs for the LSP purpose. Carbon nanotube (CNT) films have been considered as the most promising alternatives for replacing the metal mesh considering that CNT films are lighter and more compatible with CFRPs. However, the conductivity of the CNT films is usually one or two orders of magnitude lower than that of metals like copper (Cu) and aluminum. In this study, CNT/Cu composite films were prepared by electrochemical deposition method, and their microstructure, electrical properties and current-carrying failure behavior were characterized. The results show that CNT/Cu composite films are flexible and have gradient microstructures, where the content of Cu gradually decreases from one side to another. The electrical conductivity of the composite films is 21.6 MS/m, their specific conductivity is 2 times of pure Cu, and the current carrying capacity and specific current carrying capacity are 1.4 times and 7 times of copper mesh, respectively. The simulated lightning tests show compared with copper mesh, CNT/Cu composite films are 61% lighter and possess better protection performance.

1. Introduction

Carbon Fiber Reinforced Plastics (CFRP) is known for its lightweight, high strength and stiffness, as well as strong corrosion resistance, and has long been one of the most important structural materials for aircrafts. For instance, on the Boeing 787, the use of CFRP has exceeded 50%, mainly in the fuselage and wings. Compared to traditional metal fuselages, CFRP has poorer electrical conductivity and cannot meet the lightning protection needs during flight. It is reported that commercial aircraft encounter lightning strikes on average every 3000 flight hours.[1] If the large current generated by a lightning strike is not dissipated in time, the complex electrical, magnetic, and thermal effects can cause the fibers in the composite material structure to break and the resin to decompose, leading to material failure and even serious flight safety accidents.[2] Currently, commercial aircraft primarily use a copper mesh lightning protection scheme,[3] which has disadvantages such as heavy weight and poor integration with CFRP, contradicting the design concept of lightweight aircraft.[4]

Carbon nanotubes (CNTs) have a unique one-dimensional nanostructure and have been proven to have superb mechanical and electrical properties.[5,6] In the last two decades, there has been numerous studies on using CNT films for the lightning protection of CFRP. For example, Dydek et al.[7] covered the CFRP

surface with CNT paper of varying SWCNT content, thickness, and areal density, showing that the electrical performance and lightning protection effect of the CFRP samples improved with the increase of SWCNT content, thickness, and areal density. Zhang et al. [8] interleaved CNT films between CFRP layers to improve their conductivity for lightning protection, obtaining composite materials with lightning protection performance, but the conductivity of the CNT films was lower than that of copper mesh, and their lightning protection was weaker than that of copper mesh. Theoretical studies have shown that the conduction mode of a single CNT exhibits quantum transport characteristics, with a conductivity that can reach 10^9 S/m, but when a large number of CNTs are made into a macroscopic film, the overall conductivity significantly decreases due to the presence of inter-tube contact resistance, with a conductivity of only 10^4 S/m, so the lightning protection effect of pure CNT film materials is still inferior to that of commercial copper mesh.[6] Additionally, based on the characteristics of the instantaneous current generated by lightning strikes, the lightning protection layer needs to quickly dissipate the large current on the surface of the aircraft structure.[4] To minimize damage to the fiber structure layer, the protective layer material needs to have both high conductivity and high current-carrying capacity.

This paper uses a single electrochemical deposition method to prepare CNT/Cu composite films. By optimizing the plating solution formula and electro-deposition process, the CNT/Cu composite structure is controlled, successfully preparing a composite structure with nano-sized Cu grains filled within the CNT network. The conductivity of this composite film is comparable to that of Cu, while its density is much lower than Cu. At the same time, the $CuSO_4$ aqueous plating solution used in the electro-deposition process contains no organic reagents, making the preparation process simple, and a capability for preparing meter-scale CNT/Cu composite films has been formed. Based on the electro-deposition method, CNT/Cu composite films were used to prepare CFRP lightning protection samples. In artificial lightning strike tests, the lightning protection performance of the CNT/Cu composite films was compared with that of commercial copper mesh and CNT/Cu composite films prepared by magnetron sputtering. The internal damage of the CFRP was characterized by CT scanning to evaluate its lightning protection effect, and the lightning protection mechanism of the CNT/Cu composite films was further explored by combining the results of the lightning protection tests and the structural characterization of the protective samples.

2. Materials and Methods

2.1. Preparation of CNT/Cu Composite Films

CNT films used for this study were made by using the Floating Catalyst Chemical Vapor Deposition (FCCVD) method and provided by Suzhou Jiedi Nanotechnology Co., Ltd., as shown in Figure 1(a). The thickness, areal density and electrical conductivity of this CNT film is 35 μm, 17.34 g/m^2 and 2.3 $\times 10^5$ S/m, respectively.

The CNT/Cu composite films were prepared by electrochemical deposition, as shown in Figure 1(b). A phosphor copper plate served as the anode, connected to the positive pole of the power source. CNT film was wetted with ethanol and tightly attached to the surface of a stainless steel plate, connected to the negative pole of the power source. Insulating tape was wrapped around the stainless steel surface surrounding the CNT film to ensure that Cu deposition only occurred on the designated area of the CNT film. An acidic $CuSO_4$ aqueous plating solution was used, with a deposition current density of 0.1 A/dm² and a deposition time of 6.5 hours. To minimize the impact of sample oxidation on electrical conductivity, the sample was quickly washed three times alternately in deionized water and ethanol after being removed from the plating solution, then immersed in a mixed solution of oleic acid and acetone for passivation (volume mixing ratio, oleic acid: acetone = 1:30), dried, and then reduced at 200°C in an H_2 atmosphere for 3 hours.

For comparison, magnetron sputtering was also adopted to metallized CNT films, as illustrated in Fig. 1c. In briefly, a CNT film with a thickness of 35 μm and a size of 350×350 mm was attached to the

roller of a roll-to-roll magnetron sputtering machine. The distance between the target material and the CNT film is adjusted, and the initial roller speed is set to 1 m/min to ensure that copper is uniformly sputtered onto the surface of the CNT film. After the vacuum level of the instrument body is reduced to 3.1×10^{-3} Pa, high-purity argon gas (Ar) with a flow rate of 160 sccm is introduced into the vacuum chamber. To effectively remove impurities from the surface of the copper target, a pre-sputtering of 10 minutes is required. Afterwards, the current is adjusted to 6 A, and the working vacuum level is set to 2.6×10^{-1} Pa.

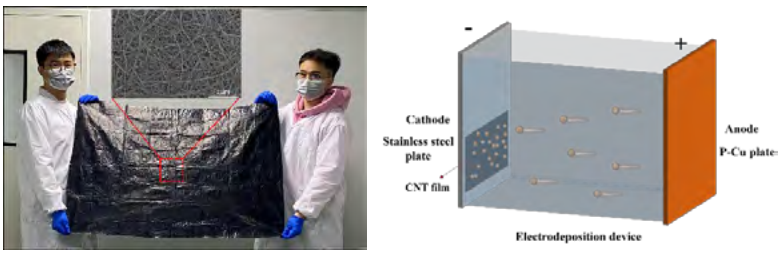


Figure 1. (a) Optical and SEM images of CNT film, and schematic diagrams of (b) electro-chemical deposition processing.

2.2. Preparation of Lightning Protection Layer Laminates

Unidirectional carbon fiber prepreg provided by Guangwei Composites, China was laid in the sequence of $[0,45,90,-45]_{3s}$. The conductive protection layer was directly covered on its surface and co-cured with the prepreg through vacuum bag hot pressing into laminates. The irregular edge areas were cut off, ultimately obtaining a test panel with dimensions of 300×300 mm^2 and a thickness of approximately 4mm. Four different sets of samples with various protection methods were set up: no protection (NP-CFRP), commercial copper mesh protection (Cu mesh-CFRP), CNT film protection (CNT-CFRP), and electro-deposited CNT/Cu composite film protection (CNT/Cu-CFRP). The commercial copper mesh was provided by Hefei Aerospace Electrophysics Technology Co., Ltd., with a specification of Cu-107 g/m², and the copper mesh composite adhesive film with epoxy resin had an areal density of 231 g/m². In addition, the resistance in the long intercept direction and short intercept direction was about 2.10 mΩ and 6.30 mΩ, respectively.

2.3. Characterizations and testing

The electrical conductivity (σ) of the CNT/Cu composite film and the current carrying capacity (J) was calculated by $\sigma=1/(R_{\square}\cdot t)$ and $J=I_{max}/(w\cdot t)$, where $R_{\square}$ is the sheet resistance of the composite film, measured by a multifunctional digital four-point probe, t and w are the thickness and width of the composite film, and I_{max} is the maximum current that can pass through the sample. When testing the current carrying capacity, the CNT/Cu composite film is cut into a size of 30×1 mm, and the two ends of the sample are attached to copper electrodes by using conductive silver paste. The current is increased at a rate of 0.01 A/s until the sample melts, where the current is recorded as I_{max}. Tests were performed within a homemade vacuum box.

Anisotropic electrical conductivity test of the laminated compostites. Laminates were cut into 10×10 mm^2 size using a water jet cutter. Remove the surface resin with 400-grit sandpaper. Based on the direction of the surface carbon fibers, divide into X and Y directions, with the thickness direction being Z. For each group of samples, apply conductive silver paste on both sides of the test surface and affix copper foil, dry it, and then test its resistance by the four-wire method. Calculate the electrical conductivity based on the shape parameters. To reduce errors caused by poor electrode contact, apply pressure to both ends of the sample during testing. After obtaining seven sets of data, remove the highest value and the lowest value, and the average of the remaining values is taken as the final test result.

The direct lightning effect test on CFRP samples refers to the standards SAE ARP 5416A-2013[24] and SAE ARP 5412-2013 [25], conducted by Hefei Aerospace Electrical Technology Co., Ltd. All test areas of the CFRP samples in this paper are chosen from the 2A zone of aircraft lightning effects. The test setup is shown in Figure 2(a), with an arc introduced in the middle of the sample and grounding around it. The current waveform combination is D+B+C*, and the component waveforms of the current are as shown in Figure 2 (b-d).

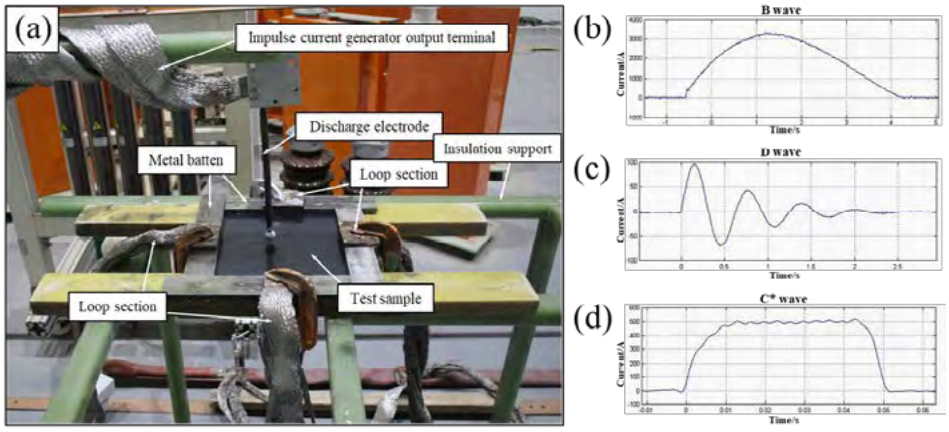


Figure 2. (a) Artificial simulation lightning strike test device, (b-d) Waveform of current components: (b) B wave, (c) D wave, (d) C* wave.

The microstructures and element distribution of the film and plates are analyzed by Scanning Electron Microscope (SEM, Hitachi S4800) and Energy Dispersive X-ray Spectrometer (EDS). The damage of the samples after the lightning strike tests were analized by using 3D confocal microscope (VX-250) and CT (FF35 CT Metrology).

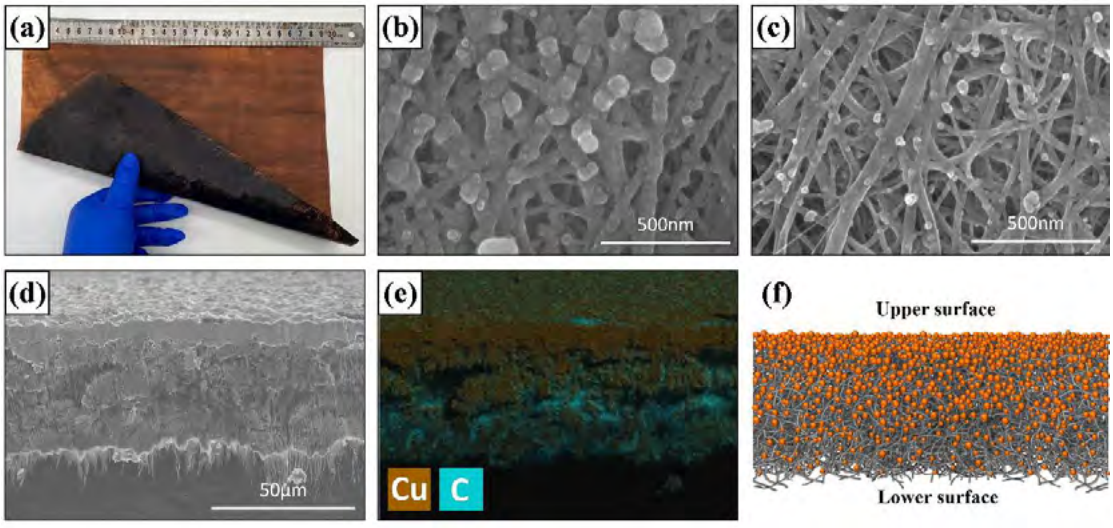


Figure 3. (a) CNT/Cu composite film sample prepared by electrochemical deposition, SEM images of (b) upper and (b) lower sur-faces of CNT/Cu composite film, (d) SEM images of the cross-section of CNT/Cu composite film and (e) elements distribution, (f) schematics of Cu distribution through the film thickness.

3. Results and discussions

3.1. Structural Characteristics of CNT/Cu Composite Films

During the electrochemical deposition processing, the nano-scale Cu grains reduced in the plating solution deposited onto the CNT film and entered into the internal network of the CNTs under the synergistic effect of a slow deposition rate provided by a small current density. As one side of the CNT film is tightly attached to the stainless steel plate, and the other side is in direct contact with the plating solution, the nano-scale Cu grains are enriched on the side of the film that contacts the plating solution, while the backside retains the porous network structure of the CNT. The prepared CNT/Cu composite film has good flexibility, as shown in Figure 3(a). The thickness of the film was increased from 35 μm to 50 μm. And the volume and areal density of the composite film is 1.8 g/cm^3 and 90 g/m^2, respectively.

Figures 3(b) and 3(c) show the SEM images of the upper and lower surfaces of the CNT/Cu composite film, respectively, where Cu grains with extremely small diameters can be seen attached to the CNT bundles. Figure 3(d) is an SEM image of the cross-section of the CNT/Cu composite film, showing the CNT network distributed throughout the entire thickness of the composite film, with nano-scale Cu grains filling the interior of the CNT network in the film. Figure 3(e) shows the distribution of Cu and C elements in the cross-section of the CNT/Cu composite film, where it can be seen that Cu relatively enriched on the upper side of the film. This indicates that the nano-scale Cu grains fill the network of the CNT film prepared by electrochemical deposition, forming a gradient structure with Cu enrichment on the upper surface and a porous CNT network retained on the lower surface, as shown in Figure 3(f).

3.2. Electrical Properties of CNT/Cu Composite Films

The electrical conductivity and specific electrical conductivity of for the CNT/Cu composite film compared to Cu is shown in Fig. 4(a). The electrical conductivity of the CNT/Cu composite film is 2.16 ×10^7 S/m, which is much higher than that of pure CNT films (2.3×10^5 S/m), while lower than that of pure Cu (5.7×10^7 S/m). However, as the CNT/Cu composite film has a much lower density (1.8 g/cm³) than metal conductors, at only the specific electrical conductivity is 12 S·m²/g, higher than that of pure Cu (6.36 S·m²/g). Fig. 4(b) compares the current carrying capacity and specific current carrying capacity for the CNT/Cu composite film and copper mesh. The current carrying capacity and specific current carrying capacity of the commercial copper mesh are 1.58×10^4 A/cm^2 and 1778 A·cm/g, respectively. The current carrying capacity of CNT/Cu composite film is 2.18×10^4 A/cm^2, and the specific current carrying capacity is 12132 A·cm/g, both higher than that of commercial copper mesh.

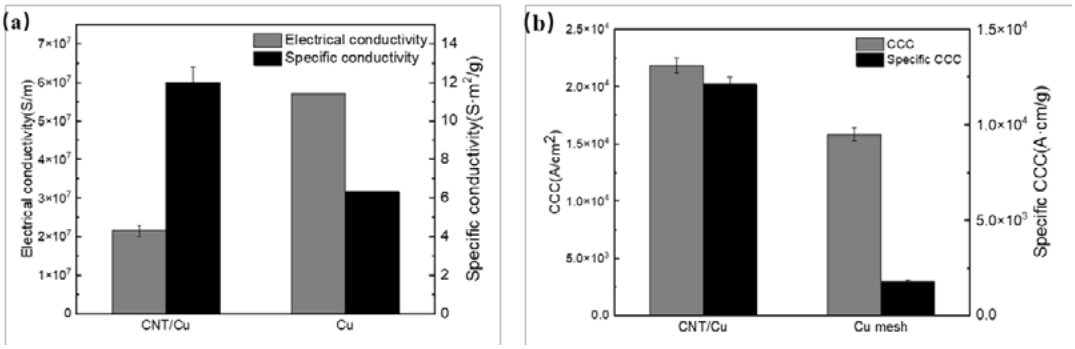


Figure 4. (a) Comparison of electrical conductivity between CNT/Cu composite film and Cu, and (b) comparison of current carrying capability between CNT/Cu composite film and Cu mesh.

To further investigate the failure behavior of CNT/Cu composite films and copper meshes under large current, a current density of 2.18×10^4 A/cm^2 was applied to two sets of samples. The commercial copper mesh failed and broke within 5 seconds, while the CNT/Cu composite film can sustain for much longer time. As shown in Fig. 5(a)-(d), the Cu in CNT/Cu composite film sample migrate from the middle to both ends of the test sample shortly after the large current passed through it. At around 30 seconds, the sample melted and broke at the initial migration location, and completely broke and failed at around 38

seconds. For the commercial copper mesh, the reason for the failure might be that the resistive heating greatly increase the atomic kinetic energy of Cu, promote Cu migration, and result in a local increase in resistance and a sharp rise in temperature, ultimately leading to failure. For the CNT/Cu composite film, Cu migrated first, while the CNT film maintained the conductive path, thereby prolonging the time until complete failure.

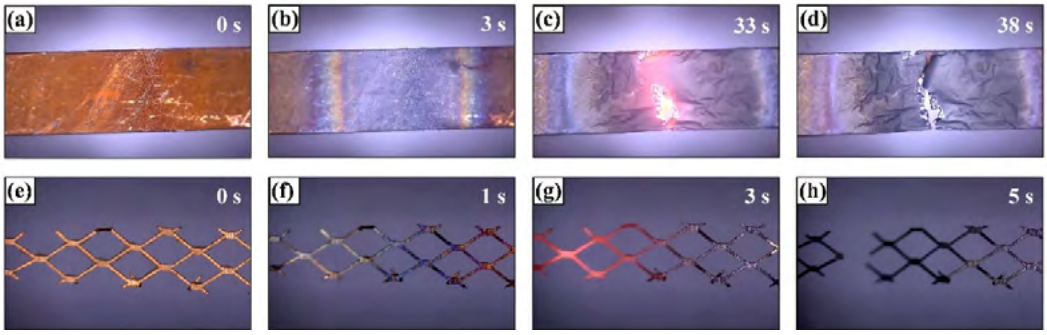


Figure 5. Failure of (a-d) CNT/Cu composite film and (e-h) Cu mesh under larger current.

3.3. LSP Performance of Laminated Composites

Fig. 6 shows the surfaces of different laminates after the lightning strike tests. The non-protected samples (NP-CFRP) had smaller damaged area, but much more carbon fibers were broken (Fig. 6a). The damage area of the CNT-CFRP (Fig. 6b) was slightly larger, and there still exist fiber breakage. The Cu mesh-CFRP (Fig. 6c) and CNT/Cu-CFRP (Fig. 6d) samples have larger damaged area while no obvious fiber breakage were observed, which meas that both the commercial copper mesh and the CNT/Cu composite films are effective in the lightning strike protection.

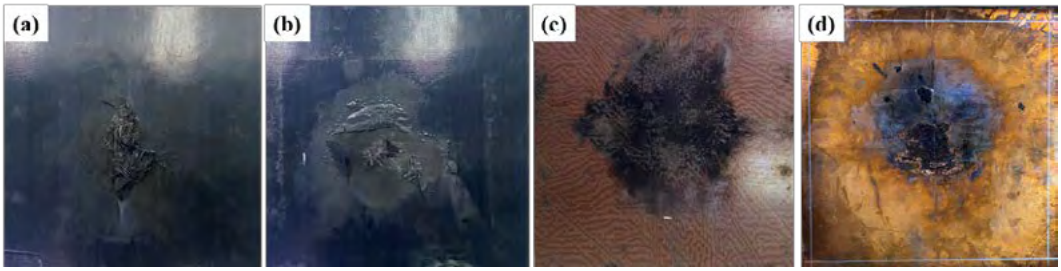


Figure 6. Surface morphology after lightning strike tests: (a) NP-CFRP, (b) CNT-CFRP; (c) Cu mesh-CFRP, (d) CNT/Cu-CFRP.

The damage pattern of CFRP due to lightning strikes is quite complex, including fiber sublimation fracture, resin matrix vaporization melting and carbonization, delamination, and so on. Surface damage analyses alone cannot adequately assess the protective effect. Therefore, CT scanning technology was utilized to characterize the internal damage of samples after the lightning strike test. Fig. 7 shows the CT scan cross-sectional images of four groups of CFRP samples with different protection methods as the depth changes. The damaged area of the four groups of samples decreases with increasing depth, among which the CNT/Cu-CFRP samples have a shallower damage depth and less internal delamination.

To further evaluate the effectiveness of lightning strike protection, cross-sectional CT scans were also performed to characterize the the depth of damage. From Figure 7 (the last column), it can be seen that there is a significant structural absence at the center of the lightning strike in NP-CFRP and CNT-CFRP, indicating a large amount of fiber fracture and resin sublimation. In contrast, Cu mesh-CFRP and CNT/Cu-CFRP samples show no significant damage in the thickness direction. Table 1 compares the damage rate of different laminates, which is defined as the (total damage thickness-protection layer

thickness)/(laminate thickness-protection layer thickness), where we can see that CNT/Cu composite layer has the best protection performance.

The EMI shielding performance of different protection films were also characterized and compared. As shown in Fig. 8, copper mesh film performs poorly due to the presence of macroscopic holes. CNT film shows better EMI shielding performance, and CNT/Cu composite film shows the best.

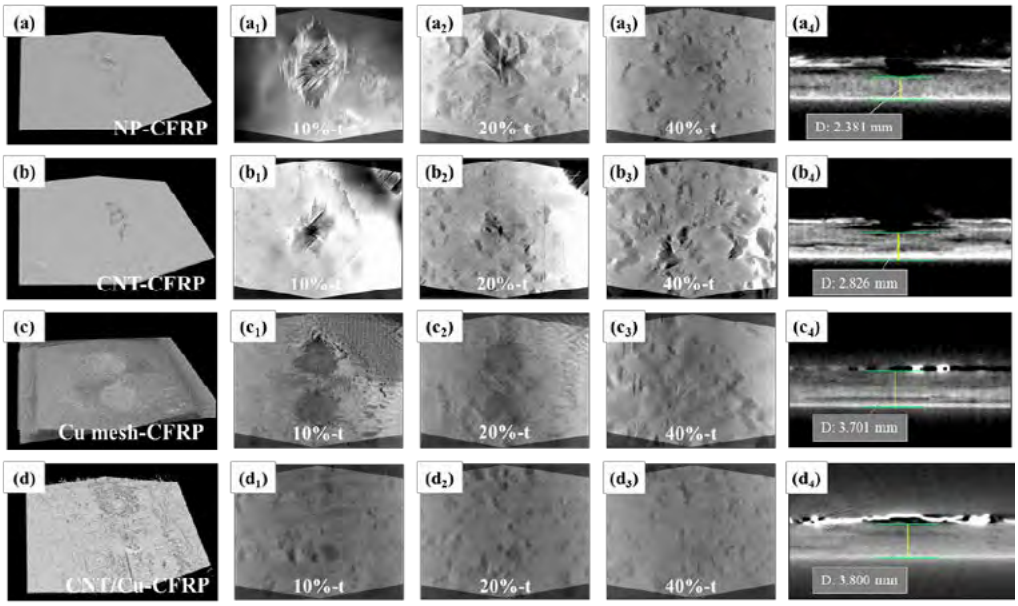


Figure 7. CT scanning of samples after lightning strike test: Overall damage morphology of (a) NP-CFRP ; (b) CNT-CFRP ; (c) Cu mesh -CFRP;(d) CNT/Cu-CFRP; and profile damage morphology varies by 10%, 20% and 40% with depth. (a4)-(d4) the cross-section of different samples.

Table 1. Analysis of damage depth of four groups of CFRP samples after lightning strike test

Samples	Total thickness/mm	Protective layer thickness/mm	Total damage thickness/mm	Damage rate/%
NP-CFRP	3.837	0	1.456	37.95
CNT-CFRP	3.915	0.035	1.089	27.16
Cu mesh-CFRP	4.372	0.218	0.671	10.91
CNT/Cu-CFRP	3.850	0.050	0.050	0

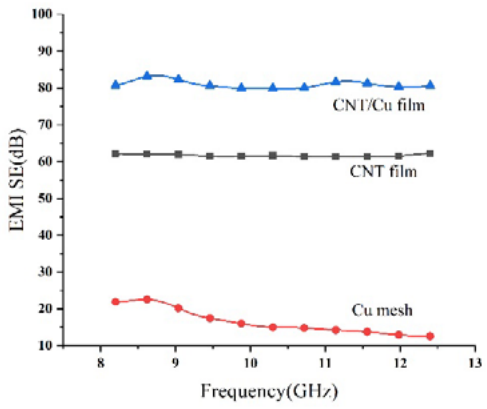


Figure 8. Electromagnetic shielding effect of different protective layers

3. Conclusions

In this study, a new method of protecting carbon fiber composite from lighting strike has been proposed. CNT/Cu composite films were prepared by using electrochemical deposition method, and their microstructure, electrical properties and current-carrying failure behavior were characterized. The results show that CNT/Cu composite films are flexible and have gradient microstructures, where the content of Cu gradually decreases from one side to another. The electrical conductivity of the composite films is 21.6 MS/m, their specific conductivity is 2 times of pure Cu, and the current carrying capacity and specific current carrying capacity are 1.4 times and 7 times of copper mesh, respectively. The lightning protection shielding profermance of CNT/Cu composite film were investigated and compared with that of CNT films and commercial copper mesh. It has been found that the CNT/Cu composite film (90 g/m^2) provides better lightning protection for carbon fiber laminates than commercial copper mesh (231 g/m^2). In addition, CNT/Cu film possesses much better EMI shielding performance than Cu-mesh. Although CNT/Cu composite film has demonstrated attractive performance, the underlying protection mechanism and the failure mechanism are still far to be understood. In addition, making continuous, uniform CNT films and CNT/Cu composite films are still challenging now. Further research efforts are needed to address these issues.

Acknowledgments
WB would like to acknowledge the support from the Jiangxi Double Thousand Talent Program.

References

[1] MA Uman, VA Rakov. The interaction of lightning with airborne vehicles. Progress in Aerospace Sciences, 2003. 39(1): 61-81.
[2] M Gagne, D Therriault. Lightning strike protection of composites. Progress in Aerospace Sciences, 2014. 64:1-16.
[3] ZJ Zhao, GJ Xian, JG Yu, et al. Development of electrically conductive structural BMI based CFRPs for lightning strike protection. Composites Science and Technology, 2018. 167: 555-562.
[4] V Kumar, T Yokozeki, C Karch, et al. Factors affecting direct lightning strike damage to fiber reinforced composites: A review. Composites Part B: Engineering, 2020. 183.
[5] S Iijima. Helical microtubules of graphitic carbon. Nature, 1991, 354(6348):56-58.
[6] S Zhang, N Nguyen, B Leonhardt, et al. Carbon-Nanotube-Based Electrical Conductors: Fabrication, Optimization, and Applications. Advanced Electronic Materials, 2019. 5(6).
[7] K Dydek, A Boczkowska, R Kozera, et al. Effect of SWCNT-tuball paper on the lightning strike protection of CFRPs and their selected mechanical properties. Materials, 2021. 14(11):3140.
[8] J Zhang, X Zhang, X Cheng, et al. Lightning strike damage on the composite laminates with carbon nanotube films: Protection effect and damage mechanism. Composites Part B: Engineering, 2019. 168: 342-352.

INVESTIGATING THE MECHANICAL PERFORMANCE OF BIO-COMPOSITES CONTAINING LONG NATURAL FIBERS: A STUDY ON ENVIRONMENTALLY FRIENDLY CHEMICAL AND PHYSICAL TREATMENTS FOR NATURAL FIBER REINFORCEMENT

A.R.Mahendran[1], G.Wuzella[1] , C. Beuc[1], S. Saravanamuthu[1], and H. Lammer[1]

[1]Wood K Plus, Competence Center for Wood Composites and Wood Chemistry, St. Veit an der Glan,Austria,Altenberger Strasse 69, Austria, Web Page: http://www.wood-kplus.at

Keywords: Long natural fiber, flax and hemp, fiber treatment, Bio-composites

Abstract

The growing usage of natural fiber-reinforced composites for structural purposes is being fueled by their impressive strength-toweight and stiffness-to-weight ratios, as well as their minimal environmental impact. Of all the bast fibers, flax and hemp stand out due to their remarkable tensile strength, making them ideal for situations where toughness and long-lastingness are crucial. Woven long continuous bast fibers are employed in situations demanding structural integrity and load-bearing capacity, facilitating improved load distribution within woven materials. These long continuous fibers also enhance resistance against creep, making them suitable for applications where dimensional stability is crucial. In the manufacturing of polymer matrix composites, the treatment of natural fibers with various chemicals is a pivotal step to enhance their properties. However, commonly used chemicals pose concerns related to health, environmental impact, and potential effects on fiber strength. In this study, we utilized eco-friendly chemicals such as oleic acid, coffee ground extract, citric acid, bee wax, and tartaric acid for flax fiber treatment. Characterization of the treated chemicals involved scanning electron microscopy (SEM) to observe morphological changes, x-ray diffraction (XRD) to assess crystallinity, and atomic force microscopy (AFM) to examine roughness. Composite manufacturing involved the use of a bio-based epoxy resin, "Greenpoxy," and mechanical property characterization. Flax fibers treated with oleic acid exhibited the highest flexural strength, with fiber volume fractions ranging between 35-37%, and calculated pore volume fractions between 5-7%. Additionally, we employed plasma vapor deposition as a physical treatment technique, offering advantages such as producing thin films with high purity, uniform thickness, and improved adhesion. The precursors were deposited onto the woven long fibers through plasma vaporization in a nanoscale, and subsequently, these treated fibers were integrated as reinforcement in the fabrication of bio-composites. Characterization of treated fibers involved SEM and XPS measurements to observe precursor deposition, revealing only marginal improvements in flexural strength within the composites. This investigation demonstrates the high potential of eco-friendly chemical treatments to enhance fiber properties without significantly affecting natural fiber characteristics. Moreover, these treatments contribute to improved mechanical strength and long term water resistance behavior.

1. Introduction

In the last six to seven decades, advancements in polymeric composite materials, predominantly utilizing synthetic fibers such as glass, carbon, and aramid, have enabled the substitution of numerous conventional metallic, polymeric, and ceramic materials. The adoption of advanced composites, particularly in transport sectors, as feasible substitutes for traditional materials primarily stems from

their remarkable mechanical properties and low density. This enables their application in structural roles where lightweight characteristics are essential to the ultimate design[1].

Owing to environmental concerns and the quest for alternatives to fossil-derived resources, a noticeable shift in materials science involves the growing fascination with and utilization of natural fibers sourced from wood or plants like hemp, flax, jute, kenaf, ramie, and sisal[2]. These natural fibers boast biodegradability[3] and suitable mechanical properties stemming from their abundant cellulose content, alongside sustainability[4], rendering them appealing substitutes for synthetic reinforcing fibers employed in polymer composites. Consequently, there has been a notable resurgence in the attention directed towards natural fibers over the last decade, especially for reinforcing polymeric materials. When paired with a degradable polymer matrix, natural fibers present themselves as a cost-effective, renewable, and less harmful option compared to synthetic fibers, all the while providing considerable specific strength and stiffness[5], [6].

The challenge with using natural fibers as reinforcement lies in their inherent hydrophilic nature, which can lead to weaker bonding interfaces within composites. However, various pretreatment methods are employed to address this issue by enhancing the adhesion between the fibers and the matrix. These pretreatments typically involve activating hydroxyl groups or introducing new functional groups that can effectively interlock with the matrix, thereby improving the overall performance of the composite material.

Chemical treatments aim to modify the chemical structure of the fibers, often by introducing functional groups that enhance compatibility with the matrix. This can involve processes such as grafting, acetylation, silane coupling, or alkali treatment[7]. The physical treatment using plasma, corona or chemical etching involves altering the surface characteristics of the fibers to improve adhesion with the matrix material. In our present study, we endeavor to modify the fibers using environmentally friendly chemicals. Additionally, we aim to perform surface modification on the natural fibers using plasma deposition techniques[8], utilizing renewable precursors in the process. The composites were fabricated utilizing a bio-based resin, and subsequently, the mechanical properties of these composites were examined and compared with those of the untreated natural fiber.

2. Experiment

2.1. Materials and Methods

The composites were manufactured using hemp textile fabric sourced from ecological textiles with a grammage of 600 GSM. Modification processes were conducted within a closed vacuum bag, with varying durations for each chemical treatment. The fibers underwent treatment with a range of chemicals including ethanol, citric acid, oleic acid, tartaric acid, bee wax, and coffee ground extract (Figure 1). For treatments involving oleic acid and bee wax, ethanol served as the medium. Treatment durations lasted 16 hours within the vacuum bag, followed by rinsing either with water or ethanol. Subsequently, the treated fibers were sealed in plastic bags for further analysis.

Surface properties of the treated fabrics were characterized using contact angle measurement, atomic force microscopy, scanning electron microscopy, x-ray diffraction studies, and thermogravimetric analysis. Microscopic studies provided insights into surface morphology, while thermal analyses offered insights into changes in thermal stability or fiber degradation post-chemical treatment. To conduct contact angle (CA) measurements, the fiber samples were compacted into uniform pellets, after which the CA was assessed for both untreated and treated fibers.

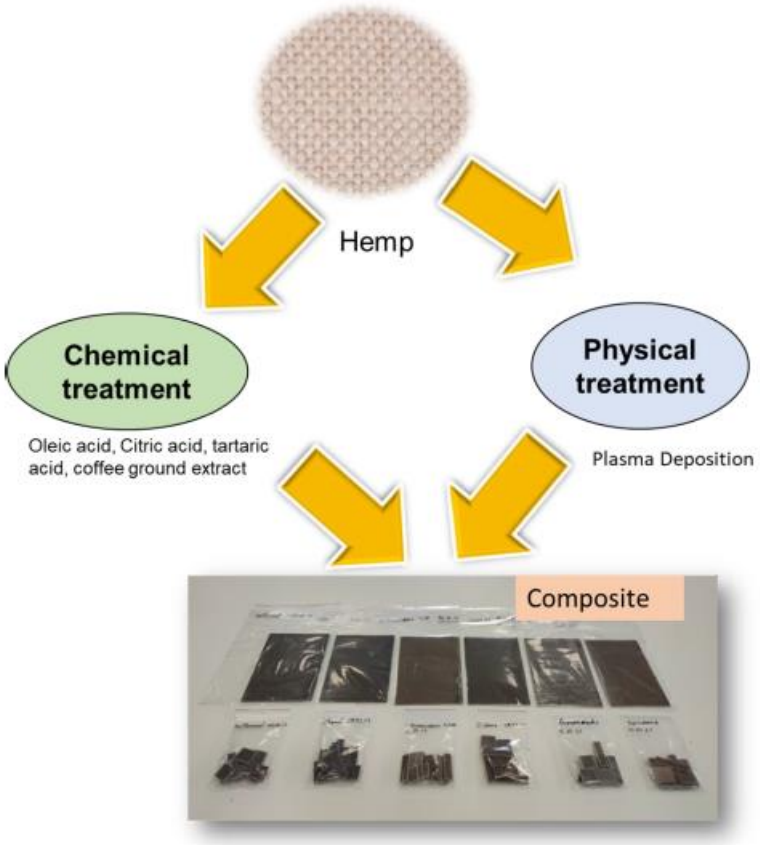


Figure 1: Functionalization of natural fibre and manfacturing composites using surface modified natural fibres

3. Results and Discussion

3.1 Fibre Characterization

Contact angle values for the treated fabrics were determined using various solvents, including water, ethylene glycol, and diiodomethane. The fiber samples were compressed into circular discs, and surface energy was calculated using the OWRK (Owens, Wendt, Rabel, and Kaelble) method based on the measured contact angles. The contact angle data is presented in Table 1.

The untreated fibers exhibited higher contact angles with water, primarily attributable to the water-repellent coating applied during the manufacturing process. Following surface treatment, a noticeable reduction in contact angle was observed, indicating significantly improved wettability. Notably, the fibers treated with oleic acid displayed surface energy values that met acceptable values, coupled with low contact angle values. Similarly, coffee ground extract treatment yielded promising surface energy values, signifying favorable interaction with the fiber matrix.

Table 1: Measured contact angle for the treated fibres and surface energy calculated using OWRK method

Sample	Water		Ethylene glycol		Diiodmethane		OWRK-Method			
	Contact angle [°]	Standard Deviation	Contact Angle[°]	Standard Deviation	Contact angle [°]	Standard Deviation	g_s [mN/m]	R^2	Disp. [mN/m]	Polar [mN/m]
Untreated fibre	121	9.0	68	4.3	63	1.6	32,93	0,45	32,06	0,86
Coffee Ground	111	4.9	74	5.1	57	2.0	30,76	0,82	30,69	0,08
Citric acid	99	12.4	69	5.5	72	5.0	24,26	0,98	22,84	1,43
Ethanol	110	12.5	75	3.2	61	4.0	28,68	0,42	28,66	0,02
Oleic acid	77	7.7	46	5.0	50	6.4	38,60	0,99	32,55	6,05
Tartaric acid	101	9.4	56	4.3	63	3.8	30,86	0,46	30,35	0,50

For Atomic Force Microscope (AFM) measurements, samples were analyzed using tapping mode, capturing both phase and amplitude images (See Figure 2 and 3). The amplitude image provided a visual representation of the contacted surface's shape, while the phase image offered insights into the sample's viscoelastic properties. In the phase image, darker areas indicated harder regions, while brighter areas corresponded to softer regions of the sample.

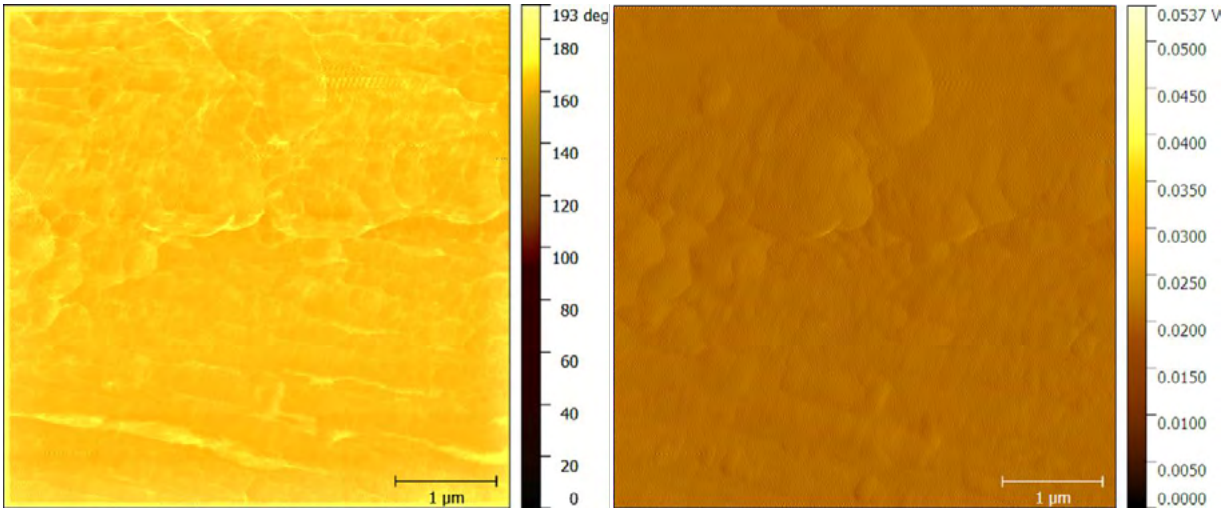


Figure 2. Phase and amplitude images of the untreated fibres in a tapping mode

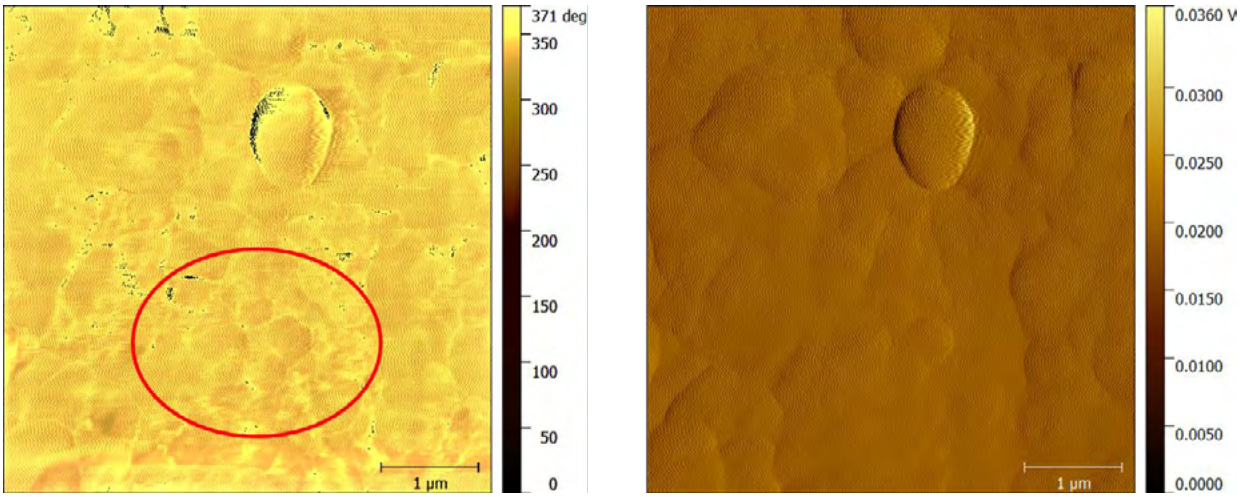


Figure 3. Phase and amplitude images of the oleic acid treated fibers in a tapping mode

The untreated fibers exhibited a finger-like pattern or morphology, which, notably, disappeared upon treatment with the specified techniques. In contrast, the fibers treated with oleic acid displayed a distinct domain-like structure on their surface.

The X-ray Diffraction (XRD) analysis indicates variations in crystallinity resulting from the different chemical treatment techniques (Figure 4). The calculated percentages of crystallinity for the samples are as follows: Untreated: 35.3% , Ethanol-treated: 27.1% , Coffee ground extract: 27.0% , Oleic acid: 32.4% , Tartaric acid: 36.5% , Citric acid: 33.0%. These results suggest that the chemical treatments induced changes in the cellulose structure within the natural fibers, particularly affecting the Cellulose II structure.

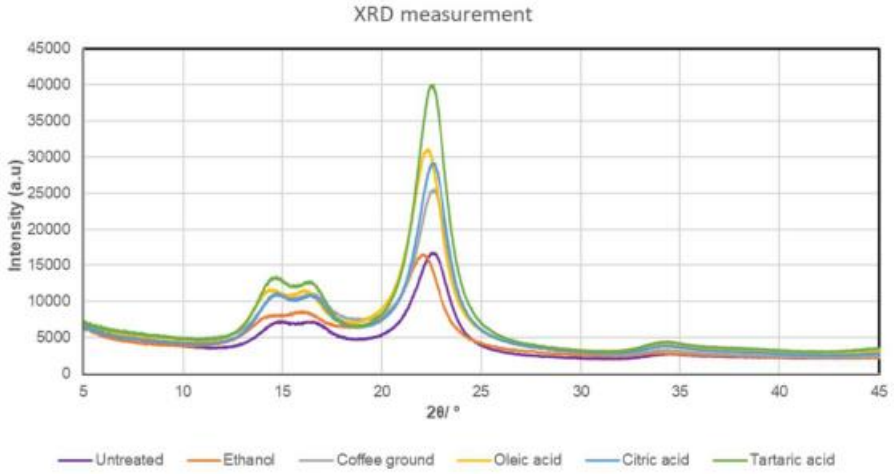


Figure 4. XRD measurement for the treated fabrics

3.2 Composite fabrication

Following the chemical modification, the fiber samples were used for manufacturing reinforced composites by impregnating them with a bio-based epoxy resin inside a vacuum bag. The bio-based resin is a two component resin and the curing agent is an amine derivative. Subsequently, the mechanical properties of the composite materials were evaluated. Additionally, long-term water absorption tests were conducted on the composite samples. This involved measuring changes in weight and thickness swelling of the composites after immersion in water.

Three-point bending tests were performed on the composites to assess how different chemical treatments impacted their mechanical properties. The results for flexural strength and modulus can be found in Figure 5 and Figure 6, respectively.

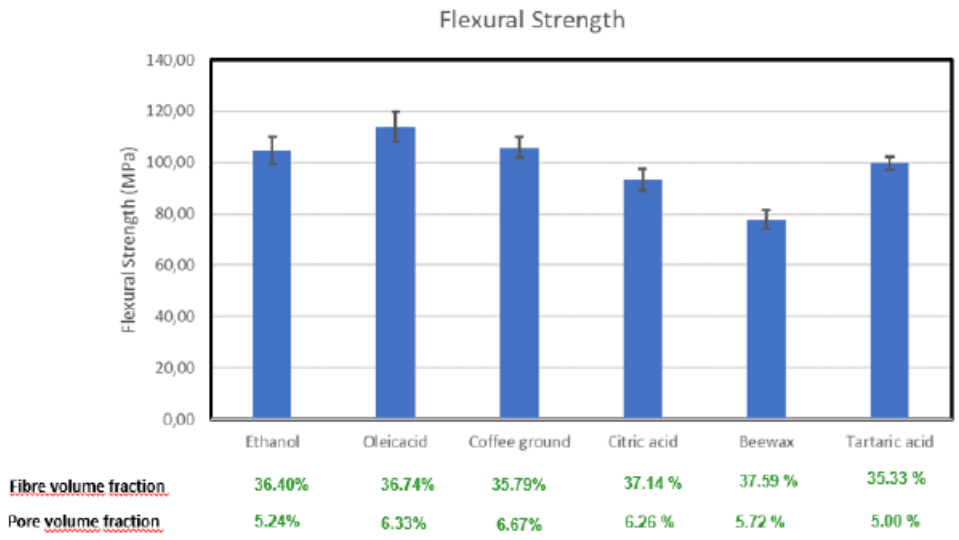


Figure 5: Flexural strengths of the composite made using treated fabrics with bio-based resins

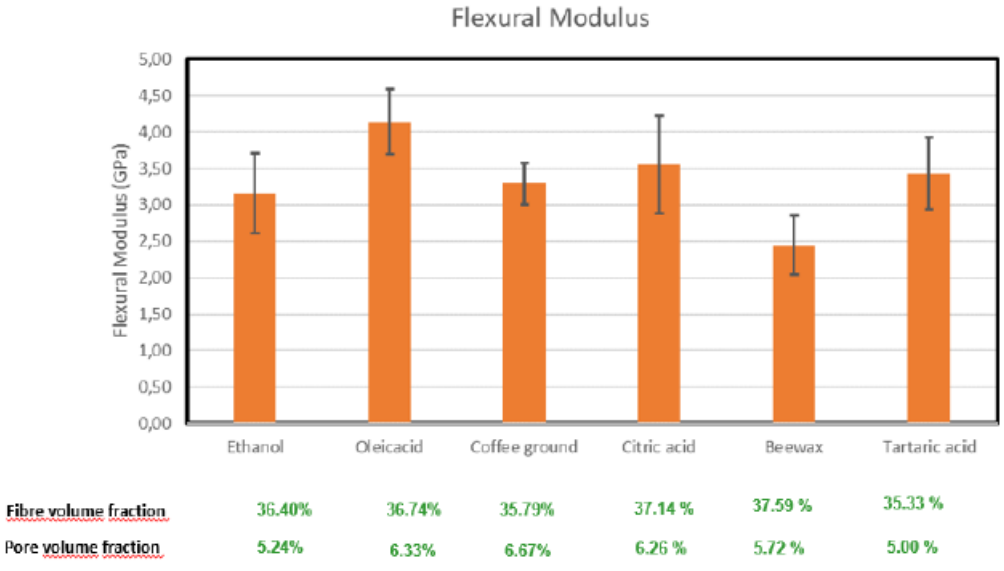


Figure 6: Flexural modulus of the composite made using treated fabrics with bio-based resins

The oleic acid treatment resulted in an increase in both flexural strength and modulus for the treated fabrics. Conversely, the bee wax treatment led to a decrease in flexural strength and modulus, likely due to uneven distribution of wax on the fiber surface. These findings suggest that oleic acid treatment is the optimal choice for treating hemp fibers, as it enhances their mechanical properties.

3. Conclusions

Positive improvements have been observed in the mechanical strength through the use of environmentally friendly chemical treatments.

- The utilization of the vacuum bagging technique demonstrated a viable approach to managing the chemicals.
- The chemical treatment resulted in alterations to the surface morphology of the fibers.
- Following the chemical treatment, there were slight changes observed in the thermal stabilities.
- The eco-friendly chemical treatment caused modifications in the crystallinity of the cellulose structures.
- Further optimization experiments are required for the chosen chemical treatment methods.

Acknowledgments

This work was by the Funded by the European Union Horizon Project ESTELLA.

References

[1] G. Cristaldi, G.; Latteri, A.; Recca, G.; Cicala, “Composites Based on Natural Fibre Fabrics,” *Woven Fabric Engineering*, pp. 317–342, 2010, doi: 10.5772/10465.

[2] C. W. Nguong, S. N. B. Lee, and D. Sujan, “A Review on Natural Fibre Reinforced Polymer Composites,” vol. 7, no. 1, pp. 52–59, 2013.

[3] J. Sahari and S. M. Sapuan, “Natural fibre reinforced biodegradable polymer composites,” *Rev. Adv. Mater. Sci*, vol. 30, pp. 166–174, 2011.

[4] R. Alex, R. Kessler, R. Kohler, G. Mayer, and M. Tubach, “Sustainability and profitability through intelligent value chain management in bast fibre processing,” *Journal of Natural Fibers*, vol. 1, no. 3, pp. 67–75, 2004, doi: 10.1300/J395v01n03_04.

[5] M. P. Staiger and N. Tucker, “Natural-fibre composites in structural applications,” in *Properties and Performance of Natural-Fibre Composites*, Elsevier Inc., 2008, pp. 269–300. doi: 10.1533/9781845694593.2.269.

[6] D. U. Shah, “Characterisation and optimisation of the mechanical performance of plant fibre composites for structural applications,” pp. 1–273, 2013.

[7] M. Rokbi, H. Osmani, A. Imad, and N. Benseddiq, “Effect of chemical treatment on flexure properties of natural fiber-reinforced polyester composite,” *Procedia Eng*, vol. 10, pp. 2092–2097, 2011, doi: 10.1016/j.proeng.2011.04.346.

[8] F. Palumbo, C. Lo Porto, F. Fracassi, and P. Favia, “Recent Advancements in the Use of Aerosol-Assisted Atmospheric Pressure Plasma Deposition,” *Coatings*, vol. 10, no. 5, p. 440, Apr. 2020, doi: 10.3390/coatings10050440.

ANALYSIS OF THE EFFECTS OF AUTOMATED FIBER PLACEMENT SINGULARITIES BY MULTI-INSTRUMENTATED TESTS ON PLANE AND OPEN-HOLE COUPONS UNDER COMPRESSION LOADING

L. Marquet[1], C. Fagiano[1], C. Huchette[1], J-M. García[1], A. Chiappini[2], A. Rassineux[3], S. Miot[2]

[1]DMAS, ONERA, Université Paris-Saclay, 29 avenue de la Divison Leclerc,
F- 92322 Châtillon, France
Email: **loic.marquet@onera.fr**, cedric.huchette@onera.fr, juan_manuel.garcia@onera.fr,
christian.fagiano@onera.fr
[2]IRT Saint Exupéry, 4 rue de Tarfaya, F-31405 Toulouse, France
Email: attilio.chiappini@airbus.com, stephanie.miot@irt-saintexupery.com
[3]Laboratoire ROBERVAL, UTC, Rue du docteur Schweitzer, CS 6039, 60203 Compiègne, France
Email: alain.rassineux@UTC.fr

Keywords: AFP, carbon fibre reinforced thermoset, gaps / overlaps, damage,

Abstract
This study analyses the impact of singularities caused by the automated fiber placement manufacturing process on the compression behavior of composite coupons. Compression tests are performed on plain and open-hole coupons with standard aeronautical stacking layups, featuring various configurations of gaps and overlaps. A rich multi-instrumentation is used for monitoring and better understanding the effects of singularities on the damage and failure scenario. Micro-computed X-ray tomography (CT-scan) observations performed at different loading steps allow the monitoring of damage within the core of the coupons. The failure scenario is characterized using acoustic emissions sensors and computed tomography observations. The instrumentation helps to understand the effective local loading state at the coupon-scale and highlights the necessity of numerical simulations for better understanding the effect of singularities.

1. Introduction

The aeronautic industry is continuously striving to produce the lightest products while ensuring their robustness. To do so, an increasing diversity of parts and structures are made out of carbon fibre reinforced plastics (CFRP) due to their high specific properties. However, CFRP can be difficult to shape. The complexity of the aforementioned parts and structures keeps increasing. Thus, new industrial processes are required to ensure the production reliability, quality and rate. One of the industrial process that fulfill these constraints is the automated fiber placement (AFP).

Developed from the 1980's, AFP process consists of the deposition of thin tows composed of continuous carbon fibre pre impregnated with matrix (prepreg). This automatic and robotic process allows the manufacturers new parts design opportunities thanks to specific features such as *(i)* the ability to individually stop and restart the deposition of each tow, *(ii)* the ability to control the deposition speed of each tow and *(iii)* the modularity of the process enabling to lay down from 1 up to 32 tows in parallel. (The tows width spans from some millimeters up to tenths of millimeters [1]). This robotized and automatized process ensure to the aerospace industrials a consistent and controlled quality of the produced parts, thus increasing the productivity by reducing the rework time caused by quality control and reducing the material waste. However, AFP induces unavoidable features such as gaps and overlaps. Gaps are created because of an intentional or unintended lack of material while laying down a ply to

build a laminate. Overlaps are created when two prepreg tows, belonging to the same ply, are superimposed. These singularities are induced because of the part design itself or because of non avoidable manufacturing errors. Some composite structures feature non developable surfaces. Therefore, the deposition trajectories that are designed to intersect each others induce gaps or ovelaps. Figure 1 presents two recovering strategies. On the left, the deposition of each tow is stoped as soon as it encounters another tow . That leads to a lack of material in a triangular region thus creates a gap. On the right, with a 100% recovering strategy, the tows are superimposed on each other in order to assure that no areas is let free of prepreg.

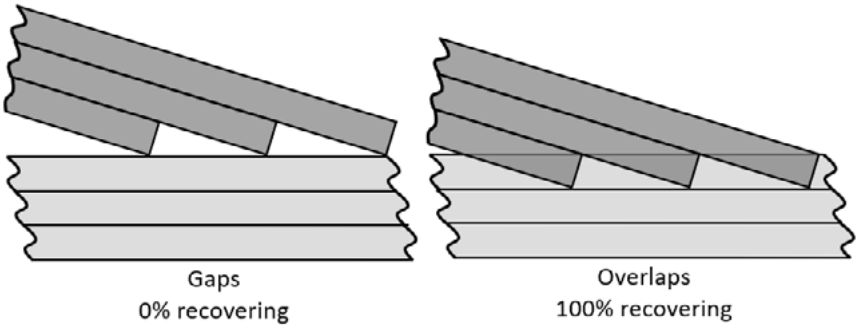


Figure 1. Scheme of the 0% recovering strategy (on the left) and scheme of the 100% recovering strategy (on the right)

Sawicki and Minguet [2] tested plain coupons embodying gaps and overlaps under compression. The presence of gaps or overlaps reduces the compression failure stress. In addition, with a wider singularity the failure stress reduction gets more important until a width limit of 2.54 mm. Turoski *et al*. [3] studied open-hole and plain coupons featuring differents gaps configurations under compression loading. The failure strength decreases for configurations with increasing number of gaps. Croft *et al.* [4] tested open-hole and plain coupons containing gaps and overlaps, as well as half gaps/ half overlaps placed in under compression loading. The effects of singularities is considered neglectable compared to the hole effects. In plain compression, the presence of gaps leads to the reduction of failure properties. The presence of overlaps leads to a slight increase of the failure properties which is in disagreement with the results of Sawicki and Minguet [2]. The authors concluded that the out-of-plane waviness induced by the presence of the singularities is one of the parameters that has the highest influence on the failure properties. Lan *et al*. [5], [6]studied the effect of out-of-plane waviness due to the presence of singularities through optical microscopy observation on the edge of specimens, which included various configurations of singularities in both number and type. Because of gaps, the thickness of the specimen is locally reduced and the empty area is filled by the adjacent plies leading to out-of-plane waviness. At the ply drop, the empty area left by the gap is filled with matrix creating matrix pockets. With the presence of overlaps, the thickness of the coupons is locally increased and the plies adjacent to the overlap are affected by out-of-plane waviness. Under loading, the thickness variation lead to stress concentration regions. The use of a caul plate during curing mitigates this effect. Due to the pressure applied by the caul plate, the matrix pockets are reduced. However, more severe out-of-plane waviness and ply thickness variation are observed within the specimen. In terms of mechanical properties, the caul plate mitigates the effects of singularities in coupons under tensile [5] and compression tests [6]. Del Rossi *et al.* tested configurations with multiple gaps and overlaps oriented along the length or the width of the specimens and located at different places along the length and the thickness of the laminate in [7]. Specimens are cured with a Caul plate and severe out-of-plane waviness is observed through optical microscopy.

It is clear that singularities affects the mechanical properties of AFP manufactured composites. However, it is not clear how the singularities affect the failure scenario. As the total failure of composite specimens under compressive load append abruptly, Woigk *et al.* [8] observed the edge of specimens under compression loading with high speed optical cameras and are able to characterize similarities and differences in the total failure evolution of specimens including gaps and overlaps under compression loading. However, these observation are influenced by the frame rate of the camera that limite the image

definition. This also limits the observable damage types to delamination and to the total failure of the specimen due to fiber breakage. There is a lack of work in the literature studying the damage and failure scenario of coupons under compression loading with gaps and overlaps.

However, in tensile test, many different experimental means were applied to monitor the damage and fialrue scenario of coupons including singularities : acoustic emission in the work of Anay *et al*. [9], DIC in the work of Falco *et al*. [10], optical microscopy in the work of Nguyen *et al.* [11] and CT-scan observation in the work of Falco *et al.* [12]. Overall, the exploration of different experimental means separately seems to be insufficient for properly assessing the effects of singularities on the failure scenario of AFP manufactured coupons.

The objective of the present study is to characterize experimentally the influence of the singularities on the mechanical properties and on the failure scenario of plain and open-hole coupons under compression loading by combining different experimental means. The second section describes the experimental campaign including the design of the coupons embodying singularities and the multi-instrumented set-up used to monitor the failure scenario of the specimens under compression. The third section presents the experimental results and the effects of the singularities.

2. Material and methods

2.1 Specimen design

To test various singulairities configurations, five different plates are manufactured using the AFP process. The plates are built with a 16 plies quasi-isotropic layup of prepreg. During curing, a caul plate is pressed to the plates to ensure a constant thickness of the laminate. 22 coupons are extracted from the plates. The specimens are 115 mm long and 25 mm wide with a nominal thickness of 2.944 mm. The open-holes specimens feature holes with a 4.8 mm in diameter.

Figure 2 presents the design of every specimen. Five designs for plain compression and six designs for open-hole compression. A scheme of singularities' positions within the coupons is indicated with a top view perspective and the layup of each configuration with the position of the singularities in the layup are presented. Plies with gaps are highlighted by stripped lines while overlaps are highlighted with a cross pattern. The rectangular gaps are made by the intentional omission of a tow during the AFP process while overlaps are fulfilled by the superposition of an extra two on top of the initial ply. The colors indicate the orientation of the plies that include singularities. To create design that are representative of industrial part designs, triangular gaps and overlaps are made by shifting tows during the deposition. These triangular gaps are placed at three different positions along the length of the specimens and are staggered along the thickness.

2.2 Test campaign

To achieve a better understanding of the effects of singularities on the failure scenario, observations at the inner core of the tested specimens are performed with a micro-computed X-ray tomograph (CT-scan). An initial CT-scan is performed before any loading to have an overview of the initial state of specimens. Then specimens are loaded until 90% of the failure load and scanned again. This load level is defined from a first batch of test until total failure of specimens and is the best compromise between a sufficient load level to able the observations of damage and a load level that does not lead to the total failure of specimen to ensure the ability to scan it again.

2.3 Experimental set-up

All the tests are carried out up to failure and are performed. The loading frame is a standard Zwick-Roell electromechanical testing machine with a capacitiy of 150 kN. Tests are equipped with a rich multi-instrumentation. The tests' set-up is presented in Figure 3. The multi-instrumentation consists of *(i)* two pairs of optical cameras used to establish two systems of stereo digital image correlation (SDIC) and *(ii)* two acoustic sensors mounted on the clamping jaws to record acoustic emissions. The optical cameras

are positioned following the scheme of Figure 4. The CT-scan were performed at Toulouse, France in IRT Saint-Exupéry facilities in an *EasyTom230* with a spatial resolution of 14 µm voxel.

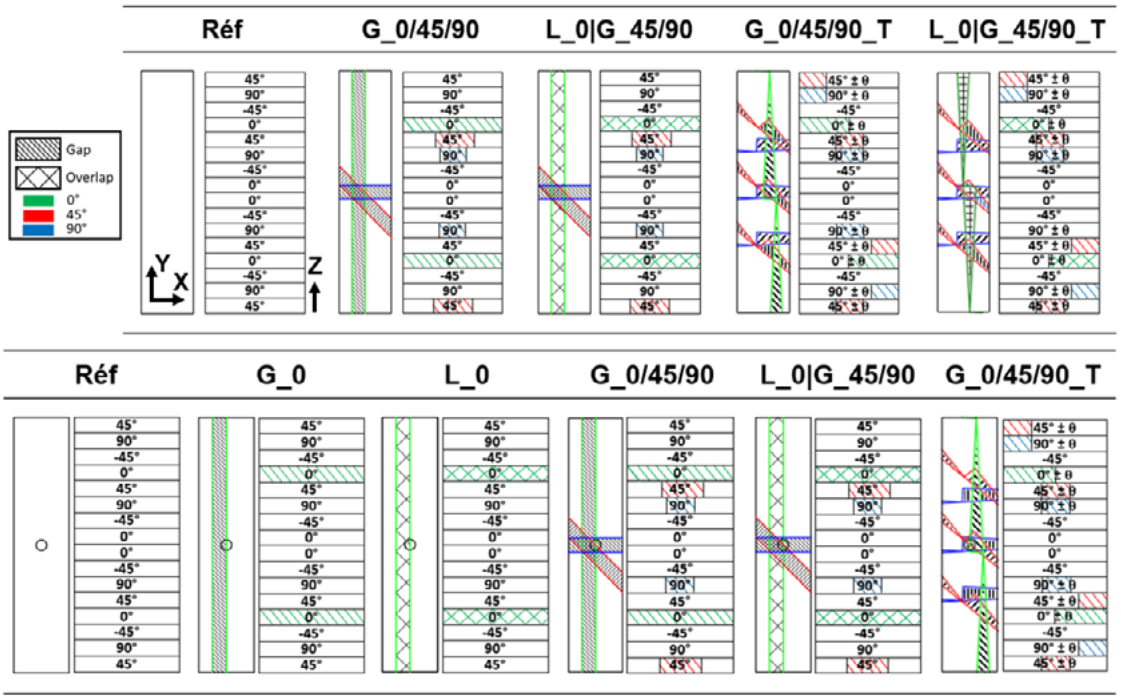


Figure 2. Design and layup of each type of specimen

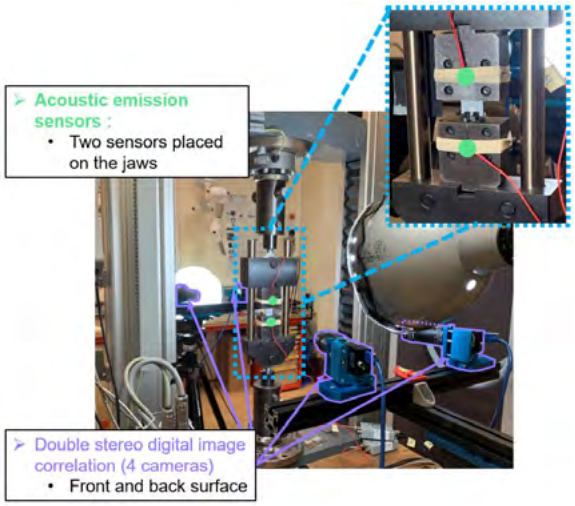


Figure 3. Experimental set-up

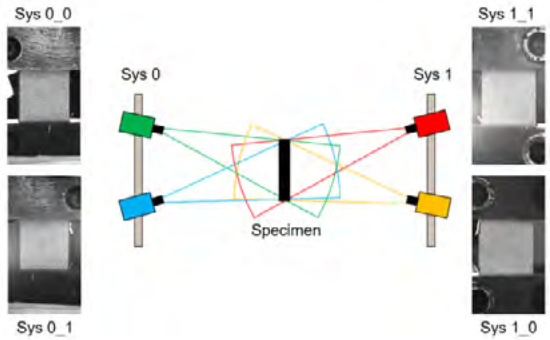


Figure 4. Scheme of the optical camera positions

3. Results

3.1. Mechanical properties under compression

For each configuration, one specimen is tested until failure and another one is tested until 90% of the failure load defined from the first test until failure. Table 1 presents the change in mechanical properties of each configuration and the change in the nominal volume of prepreg material for each configuration with respect to the reference configuration. The change in the volume of prepreg material is calculated from the theoretical layup. The nominal tow dimensions (6.35 mm in width, 0.184 mm in thickness) is considered. The prepreg volume is calculated only for the region of interest, which consists on the area between the jaws. This area is 25 mm wide (width of the specimens) and 27 mm long (distance between the jaws).

In term of compression modulus, the presence of gaps in 0°, 45° and 90° soften the coupons up to 9.4% reduction for G_0/45/90_T. The softening effect of gaps is more important for the configuration with triangular gaps than for the one with rectangular gaps. This might be explained by the misalignement of the fibre that is needed to creat such shape of singularity. The presence of overlaps in 0° (L_0|G_45/90 and L_0|G_45/90) counterbalances the softening effects of gaps. From the table, it is clear that neither the change in compression modulus, the failure strain or the failure stress is correlated with any change in prepreg volume. As an exemple, the OHC design G_0/45/90 present a reduction of 9.97% of the total material volume and a reduction of 12.36% of the material volume in the 0° plies while the reduction of compression modulus is of 3.9% and the reduction of failure strain and failure stress are of 15.1 and 14.6% respectively. In addition, an increase of the material volume in the 0° plies for L_0 does not induce an increase of the compression modulus or of the failure properties.

In open hole compression, the trends obtained in terms of failure properties change depending on the configuration follows those found in literature. The configuration with the greatest amount of gaps presents the lowest failure properites while the presence of overlaps reduces the gap effects. The effects of singularities is less important in plain compression than in open-hole compression. That may be explained by the hole effect that is more important than the effect of singularities. The presence of overlaps limits the softening effects of singulairites or increase the stiffness, as for the coupon L_0|G_45/90. The specimens with the most gaps present the lowest failure properties with a strain reduction of 15.1% and a failure stress reduction of 14.6% for the G_0/45/90 configuration. The reduction effect of triangular singularities on the failure properties is less severe than the rectangular singularities.

Table 1. Results of the compression test campaign and change in volume of material compared to reference coupons

Coupon type	Change in compression modulus [%]	Change in Ɛrupture [%]	Change in σmax [%]	Change in prepreg volume at 0° [%]	Change in prepreg volume at 45° [%]	Change in prepreg volume at 90° [%]	Change in total prepreg volume [%]
(PC) Ref	/	/	/	/	/	/	/
(PC) G_0/45/90	-8,3	29,3	18,5	-12,7	-16,47	-11,76	-10,90
(PC) L_0|G_45/90	-0,003	15,2	16,9	12,7	-16,47	-11,76	-4,55
(PC) G_0/45/90_T	-9,4	28,3	15,1	-7,22	-7,16	-6,52	-5,89
(PC) L_0|G_45/90_T	0,8	7,6	7,5	7,22	-7,16	-6,52	-2,28
(OHC) Ref	/	/	/	/	/	/	/
(OHC) G_0	-2,6	-3,5	-5,2	-12,36	/	/	-3,09
(OHC) L_0	-2	-2,3	-1,7	5,84	/	/	1,46
(OHC) G_0/45/90	-3,9	-15,1	-14,6	-12,36	-16,80	-10,71	-9,97
(OHC) L_0|G_45/90	4,2	-8,1	-3,1	12,36	-16,80	-10,71	-3,76
(OHC) G_0/45/90_T	-6,5	-6,9	-10,1	-6,73	-6,67	-5,32	-4,68

3.2. Failure scenario analysis

The experimental set-up for compression loading tests combines acoustic emission sensors and CT-scans to monitor the damage and failure scenario of specimens. Figure 5 presents two graphs with the curves of the normalized cumulative energy of acoustic emission (CEAE) function of the percentage of applied load normalized with respect of the failure load. The left graph presents the CEAE for all the PC specimens loaded until failure and the right graph present the CEAE for all the OHC specimens . It is worth noting that a steep increase of CEAE occurs after 90%/95% of the failure load. Indeed, these sudden increases are explained by high energy events. These high energy events might be related to damage mechanisms such as fibre breakage or delamination occurring before the total failure of the specimen.

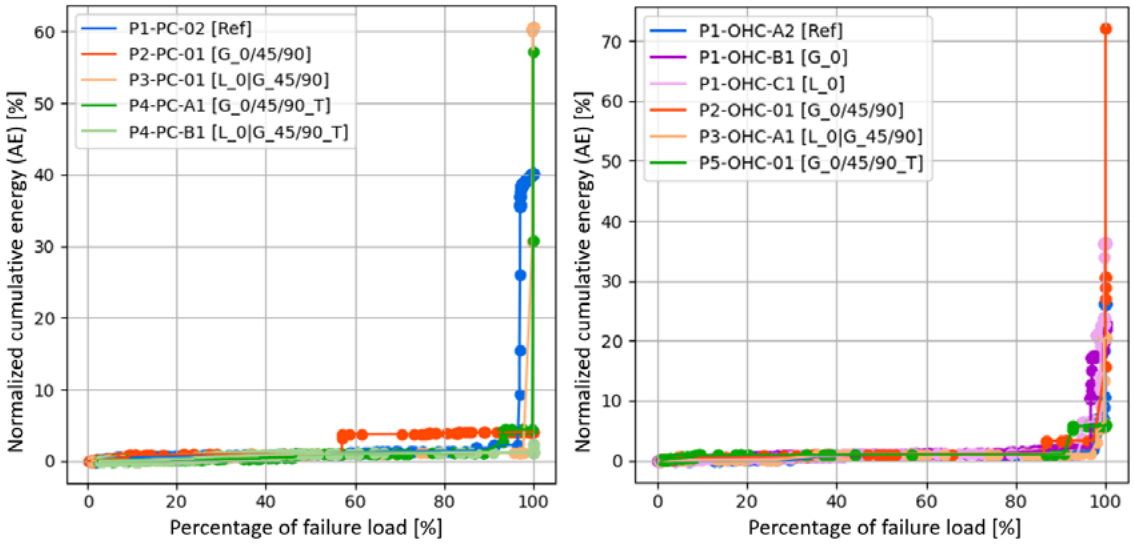


Figure 5. Normalized cumulative energy of acoustic emission function of the percentage of failure load for plain compression coupons (left) and open-hole compression coupons (right)

To confirm that no damage occurs before 90% of the failure load, the CT-scan results are *post* treated in order to obtain a projection along the whole thickness of the specimen of the inner core of the scanned specimen. Figure 6 presents the projection along the thickness of the specimen of P2-PC-03 at its initial state (Figure 6-A) and after a load step at 90% of the failure load (Figure 6-B). The position of the singularities (gaps at 0°, 90° and 45° in this configuration) are highlighted with dotted lines. Voids are clearly visible as black dots in the area where all the gaps intersect each others. Despite the use of a Caul plate during the curing, the matrix and the adjacent plies are not able to completely fill the gaps. No important cracks can be seen and no damage mechanism can be observed. The red arrows point to a tiny crack (0.1 mm) between tow voids that is present at the initial state but no clear extension of the crakc can be observed neither.

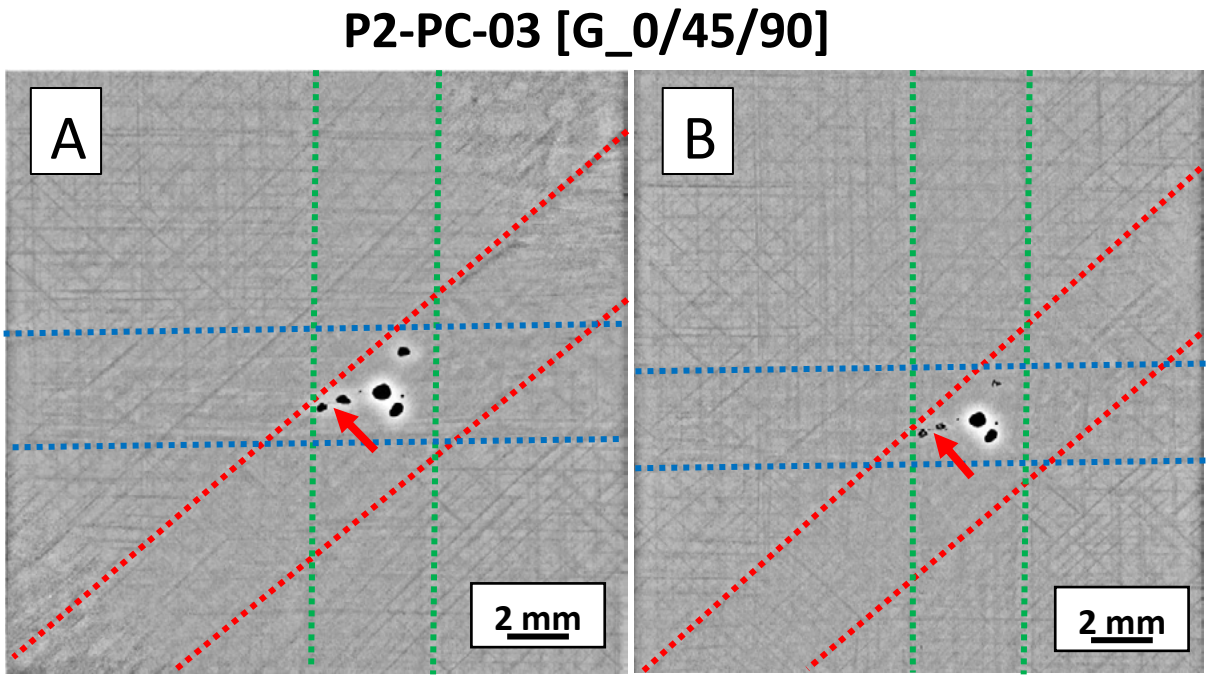


Figure 6. CT-scan image treatment result for a G_0/45/90 specimen at its initial state (A) and after a step loading to 90% of the failure load (B)

In plain compression, the results in failure stress and strain exhibit a certain disagreement with respect of those found in literature. The reference coupons present the lowest failure strain and failure stress while the configuration with the most gaps G_0/45/90 and G_0/45/90_T present the best failure properties with an increase of the failure strain up to 29.3% and 28.3% respectively. These results are not yet completely understood. To better understand the behavior of PC specimens, numerical simulation including boundary conditions measured from experiemental test will be performed. Preliminary analyses of the out-of-plane fields suggest that the loading seen by the speciments is not of pure compression.

5. Conclusions

A total of 5 configurations of plain coupons and 6 configurations of open-hole coupons including gaps and overlaps were tested experimentaly under compression loading up to failure and up to 90% of the failure load. The test were performed with a multi-instrumented set-up in order to monitor the failure scenario and characterize the effects of singularities on the mechanical properties and the failure scenario.

The effects of singularities are stronger on plain coupons than on the open-hole coupons due to the hole effect. However, the results from plain coupons test are unusual and requires deeper analysis. Numerical simulation including experimental boundary conditions computed with digital image correlation are considered in the future to better understand the test that were performed.

Despite the variation of the prepreg volume in the region of interest of the different specimens configurations, any correlation is found between variations in mechanical properties and variations in failure properties.

Regarding the effects of singularities on the mechanical and failure properties of open-hole specimens, the gaps reduce the stiffness and the failure properties of specimens under compression. The presence of overlaps along the loading direction limits the effects of gaps positioned along other directions. In addition, singularities positioned along the loading direction have the most important effect. The triangular singularities have a smaller effect than the rectangular singularities.

Coupling the analysis of acoustic emission data and the post treatment of CT-scan images able to state that no damage can be observed before 90% of the failure load. However, damage may appear after 90% of the failure laod as high energy acoustic events are recorded near 95% of the failure load for most of the specimens. A new CT-scan of the specimens after a new step load at 95% of the failure load could confirm these results and help to characterize the effects of singulairities on the failure scenario of coupons under compression loading.

References

[1] D. H.-J. A. Lukaszewicz, C. Ward, et K. D. Potter, « The engineering aspects of automated prepreg layup: History, present and future », *Compos. Part B Eng.*, vol. 43, nº 3, p. 997-1009, avr. 2012, doi: 10.1016/j.compositesb.2011.12.003.

[2] A. Sawicki et P. Minguett, « The effect of intraply overlaps and gaps upon the compression strength of composite laminates », in *39th AIAA/ASME/ASCE/AHS/ASC Structures, Structural Dynamics, and Materials Conference and Exhibit*, Long Beach,CA,U.S.A.: American Institute of Aeronautics and Astronautics, avr. 1998. doi: 10.2514/6.1998-1786.

[3] L. E. Turoski, « Effects of manufacturing defects on the strength of toughened carbon/expoxy prepreg composites », p. 137.

[4] K. Croft, L. Lessard, D. Pasini, M. Hojjati, J. Chen, et A. Yousefpour, « Experimental study of the effect of automated fiber placement induced defects on performance of composite laminates », *Compos. Part Appl. Sci. Manuf.*, vol. 42, nº 5, p. 484-491, mai 2011, doi: 10.1016/j.compositesa.2011.01.007.

[5] M. Lan, D. Cartié, P. Davies, et C. Baley, « Influence of embedded gap and overlap fiber placement defects on the microstructure and shear and compression properties of carbon–epoxy laminates », *Compos. Part Appl. Sci. Manuf.*, vol. 82, p. 198-207, mars 2016, doi: 10.1016/j.compositesa.2015.12.007.

[6] M. Lan, D. Cartié, P. Davies, et C. Baley, « Microstructure and tensile properties of carbon–epoxy laminates produced by automated fibre placement: Influence of a caul plate on the effects of gap and overlap embedded defects », *Compos. Part Appl. Sci. Manuf.*, vol. 78, p. 124-134, nov. 2015, doi: 10.1016/j.compositesa.2015.07.023.

[7] D. Del Rossi, V. Cadran, P. Thakur, M. Palardy-Sim, M. Lapalme, et L. Lessard, « Experimental investigation of the effect of half gap/half overlap defects on the strength of composite structures fabricated using automated fibre placement (AFP) », *Compos. Part Appl. Sci. Manuf.*, vol. 150, p. 106610, nov. 2021, doi: 10.1016/j.compositesa.2021.106610.

[8] W. Woigk, S. R. Hallett, M. I. Jones, M. Kuhtz, A. Hornig, et M. Gude, « Experimental investigation of the effect of defects in Automated Fibre Placement produced composite laminates », *Compos. Struct.*, vol. 201, p. 1004-1017, oct. 2018, doi: 10.1016/j.compstruct.2018.06.078.

[9] R. Anay *et al.*, « An experimental investigation concerning the effect of AFP defects on progressive damage in CFRP coupons », *Compos. Struct.*, vol. 279, p. 114725, janv. 2022, doi: 10.1016/j.compstruct.2021.114725.

[10] O. Falcó, J. A. Mayugo, C. S. Lopes, N. Gascons, et J. Costa, « Variable-stiffness composite panels: Defect tolerance under in-plane tensile loading », *Compos. Part Appl. Sci. Manuf.*, vol. 63, p. 21-31, août 2014, doi: 10.1016/j.compositesa.2014.03.022.

[11] M. H. Nguyen, P. Davidson, et A. M. Waas, « Experimental and numerical study on the tensile failure behavior of toughened-interlayer composite laminates with automated fiber placement (AFP) induced gap and overlap defects », *Int. J. Mater. Form.*, vol. 14, nº 1, p. 105-119, janv. 2021, doi: 10.1007/s12289-020-01581-w.

[12] O. Falcó, C. S. Lopes, F. Naya, F. Sket, P. Maimí, et J. A. Mayugo, « Modelling and simulation of tow-drop effects arising from the manufacturing of steered-fibre composites », *Compos. Part Appl. Sci. Manuf.*, vol. 93, p. 59-71, févr. 2017, doi: 10.1016/j.compositesa.2016.11.015.

MODELLING OF OXIDATION GRADIENTS OF EPOXY-DIAMINE NETWORKS ON BOTH SIDES OF THE GLASS TRANSITION TEMPERATURE: TOWARDS THE PREDICTION OF DEGRADATION OF THERMO-MECHANICAL PROPERTIES

J.P. Marquez Costa[1] and X. Colin[1]

[1]PIMM, Arts et Métiers Institute of Technology, CNRS, CNAM, HESAM, 151 Boulevard de l'Hôpital, 75013 Paris, France
Email: juan-pablo.marquez_costa@ensam.eu
xavier.colin@ensam.eu

Keywords: Epoxy-diamine networks, Thermal oxidation, Oxidation gradients, Kinetic modelling, Thermomechanical properties

Abstract
This article outlines a numerical calculation code developed within the framework of finite elements to simulate the thermal aging of epoxy-diamine networks on both sides of the glass transition temperature (T_g). This model couples, in an oxygen (O_2) balance equation, the diffusion of O_2 and its consumption by the chemical reaction with the epoxy matrix. The reliability of the oxidation rate expression has previously been checked for several epoxy-diamine networks. The code gives access to the oxidation gradients through the sample thickness, from which the gradients of properties of interest for the aeronautical field are deduced, *i.e.* T_g and elastic properties. The validity of the oxidation gradients is checked by calculating the corresponding values of the thickness of oxidized layer (TOL). The estimates of TOL are in good agreement with experimental measurements in the glassy state. In contrast, the calculations largely underestimate the experimental measurements in the rubbery state due to the sharp increase of the diffusion coefficient of O_2 above T_g.

1. Introduction

Carbon/epoxy composites are widely used for the design of structural parts in aeronautics because of their high specific properties. However, the long exposure to temperatures close to their glass transition temperature (T_g) can lead to potential risks. Among these risks, those related to the phenomenon of thermo-oxidative aging of the epoxy matrix are particularly critical [1]. Indeed, this aging causes a thin oxidized layer on the surface, leading to local weakening and stress gradients that could result in cracking. Over time, oxidation can reach the core of the parts following a progressive damage scenario and thus lead to their premature failure [2].
In this context, it is crucial to establish a link between the oxidation kinetics of epoxy matrices and the evolution of the thermomechanical properties of the composites. A compilation of thicknesses of oxidized layer (TOL) measured by optical microscopy, IR mapping or (nano or micro)-indentation on epoxy-diamine networks after thermal aging in air, clearly shows a break in the Arrhenius graph at neighbourhood of T_g, as shown in Figure 1. The jump in TOL is approximately of ~50 times when these materials reach their rubbery state.

©2024 | 3_Marquez-Costa_JuanPablo_YI97E.pdf

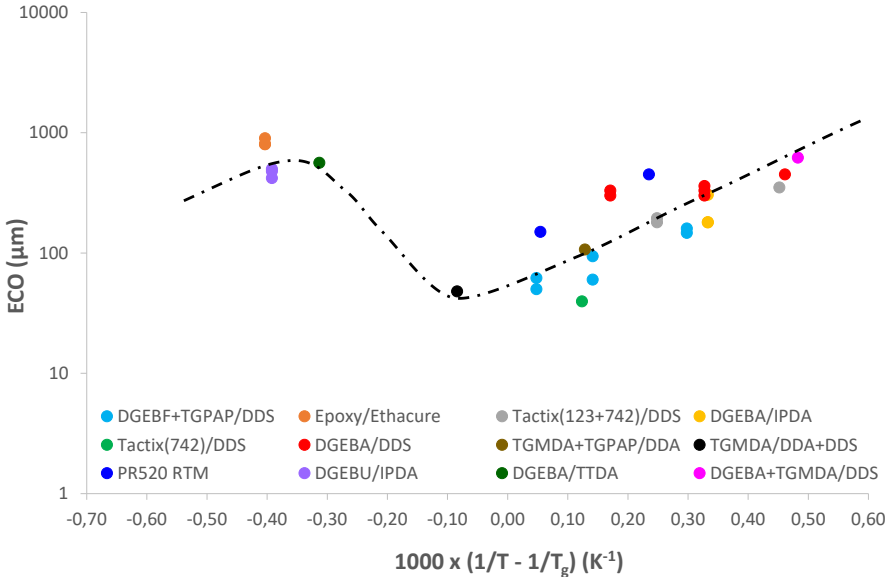


Figure 1. Variation of the thickness of the oxidized layer with the exposure temperature in air for epoxy-diamine networks. Data from 15 bibliographical references.

This jump in TOL above T_g is linked to higher molecular mobility and can have different origins. Any change in the oxidation mechanism with increasing temperature should be excluded because certain epoxy-diamine networks (cf. Figure 1) have very low T_g. Likewise, a slowdown in the rate of oxidation with increasing temperature is inconceivable from a kinetic point of view. Thus, the only realistic cause that could be envisaged would be a sudden acceleration of the diffusion of O_2 above T_g. In order to verify this hypothesis, numerical simulations are necessary. These simulations will not only allow us to better understand the kinetics of thermo-oxidation of the epoxy-diamine networks on either side of T_g, but also to predict the consequences of oxidation on the thermomechanical properties of the composites. Thus, the objective of this article is twofold : *(i)* the proposal of a kinetic model of thermo-oxidation of epoxy-diamine networks faithfully describing the oxidation gradients on either side of T_g, and *(ii)* the relationship between the evolutions of these gradients and the thermomechanical properties of interest for the aeronautical field, *i.e.* the T_g and the elastic properties. To achieve these two objectives, the article is divided into two main parts. First of all, Section 2 deals with the modelling of thermo-oxidation with a numerical calculation code developed by finite elements (FE). Section 3 aims to compare the predicted results using this code to experimental data. For this, TOL measurements will be used for checking the roboustness of the code. Then, the utility of the model for computing the evolutions of T_g and Young modulus (E) during aging will be discussed. Finally, conclusions and perspectives, aimed at predicting the lifetime of neat epoxy and/or epoxy/carbon composites, will be drawn up.

2. Modelling of the oxidation gradient

This section outlines a numerical computer code developed using EF to model the physico-chemical mechanisms involved in the thermo-oxidation of epoxy-diamine networks. It also presents a criterion for estimating the TOL, based on the code's results, to verify the predictive capacity of the kinetic model.

2.1. Description of the model

The propagation of the oxidation front is directly linked to the local concentration of O_2, which is governed by an O_2 balance equation coupling two main mechanisms: *(i)* the diffusion of O_2 and *(ii)* its consumption by the chemical reaction with the epoxy matrix. In the case of unidirectional diffusion (depending on the through-thickness coordinate), this balance equation is written such as:

$$\frac{\partial C(x,t)}{\partial t} = D\frac{\partial^2 C(x,t)}{\partial^2 x} - r(C(x,t)) \quad (1)$$

C(x,t) being the local O_2 concentration, r(C) the local oxidation rate, D the diffusion coefficient of O_2, x the though-thickness coordinate, and t the time.
A recent kinetic analysis of the so-called "*closed-loop*" oxidation reaction has resulted in a comprehensive analytical expression for r(C). Unlike previous versions of r(C), which were much simpler because they were based on simplifying assumptions, Eq. 2 makes it possible to describe all three stages of the oxidation kinetics, namely: the induction period, the sudden self-acceleration of oxidation at the end of this induction period, and the regime established (*i.e.* the steady state). This new equation has been verified for various epoxy-diamine networks on either sides of T_g [3,4].

$$r(C) = 2r_0 \frac{\beta C}{1+\beta C}\left(1 - \frac{\beta C}{2(1+\beta C)}\right)\left(\frac{1}{1+be^{-Kt}}\right)^2 \quad (2)$$

where K is an apparent first-order rate constant, β the inverse of the critical O_2 concentration delimiting the regimes in O_2 deficiency and excess, and r_0 the maximum rate of oxidation in O_2 excess.
To consider the strong coupling between the diffusion of O_2 and its chemical consumption through the thickness of the part and thus, to determine the gradients of C(x,t), we propose a 1D semi-numerical approach under FE to solve Eq. 1 [5]. Figure 2 shows the classical discretization scheme under FE applied to C(x,t). In the x direction, the part is discretized (*i.e.* splitted into thin elementary elements) for each node $x_i \subset [0, x_n = L]$ with $i \subset [0, n]$, L and n being respectively the thickness of the part and the number of elements. Analogically, a temporal discretization is also carried out for each time step $t_j \subset [0, t_m = t_f]$ with $j \subset [0, m]$, t_f and m being respectively the final time and the number of increments.

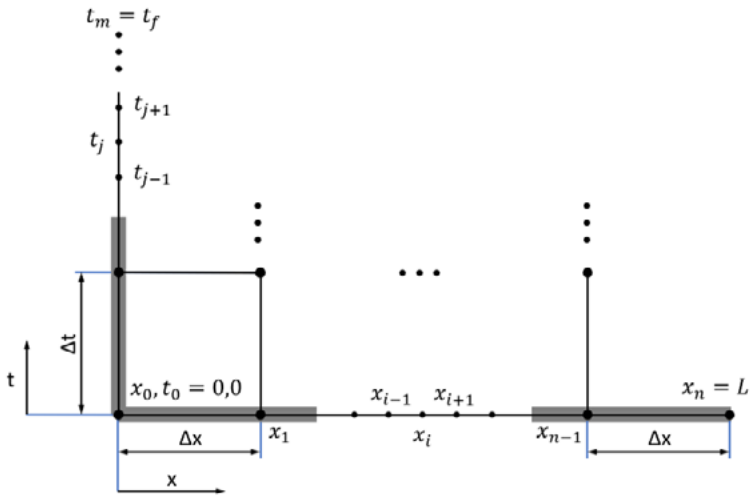


Figure 2. Scheme for discretizing the spatio-temporal problem [5].

Eq. 1 can be written as a variational problem with boundary conditions, whose approximate integral formulation is given by:

$$0 = \int_0^L \psi \left(\frac{\partial C(x,t)}{\partial t} - D\frac{\partial^2 C(x,t)}{\partial^2 x} - f(C(x,t))\right) dx \quad (3)$$

where ψ is a weighting function, and f(C(x,t)) represents the external forces of the problem to be solved. The problem is formulated as a minimization of the residual based on a Garlekin approach. Thus, the concentration $C(x_i,t) = C_i(t)$ in each node i is given by the shape function φ_i such as: $C(x,t) = \sum_i^n \varphi_i(x) C_i(t)$. Because of the EF framework, Eq. 3 can be rewritten in matrix form as follows:

$$M\dot{\boldsymbol{C}} + K\boldsymbol{C} = \boldsymbol{F} \tag{4}$$

with **C**=[C_0(t)…C_n(t)] the vector of O_2 concentrations and **F**=[f_0(t)…f_n(t)] the vector of external forces exerted at the nodes. M and K are the global mass and stiffness matrices of the problem to be computed by assembking the elementary matrices of all the elements of the domain [5]. Concerning the boundary conditions, Dirichlet initial conditions and Neumann spatial boundary conditions were used. Indeed, C(x,0) and f(x,0) are known at the initial time throughout the thickness of the sample, while C(0,t) and C(L,t) are also known at any time at the edges of the sample thanks to Eq. 5.

$$C(x,0) = S_0 p_0 \qquad C(0,t) = S_0 p_0 \qquad C(L,t) = S_0 p_0$$
$$f(x,0) = 2r_0 \frac{\beta C_0}{1+\beta C_0}\left(1 - \frac{\beta C_0}{2(1+\beta C_0)}\right)\left(\frac{1}{1+be^{-K_0 t_0}}\right)^2 \tag{5}$$

To solve the problem, firstly Eq. 4 can be directly solved at the initial time to get $\left.\frac{\partial C(x,t)}{\partial t}\right|_0$. Secondly, Eq. 4 can be iteratively solved by a Crack-Nicolson method to obtain C(x,t) for each time step.

2.2. TOL criterion from oxidation gradient

Solving the 1D problem presented in Paragraph 2.1 gives access to the evolution of the O_2 concentration gradient C(x,t) within the thickness of the sample. Numerical simulations have been carried out in air at 200°C for an epoxy-diamine network; the TACTIX(123+742)-DDS. Figure 3 shows the corresponding oxidation gradients. We see that C(x,t) is symmetrical in the thickness because of imposed boundary conditions. Over time, we clearly see that C(x,t) reaches a limit curve when the steady state is established. The shape of this gradient is strongly dependent on the values of the input parameters, in particular on β, r_0 and D.

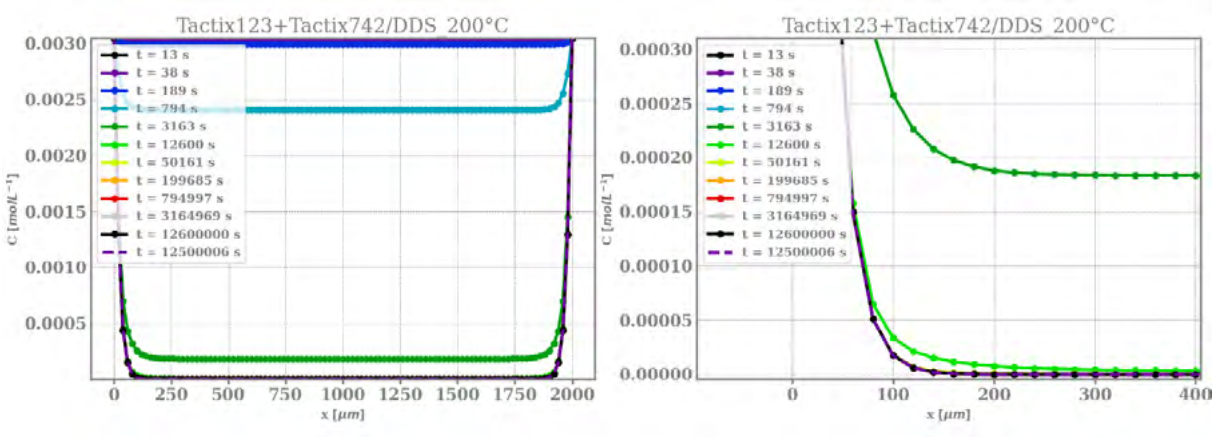


Figure 3. Calculation of the gradient C(x,t) for different exposure times in air at 200°C for the TACTIX(123+742)-DDS network.

Once r(C) calculated with Eq. 2, its temporal integration gives access to the total concentration of oxygen consumed by the chemical reaction, *i.e.* to the oxidation gradients Q(x,t):

$$Q(C) = \int_0^t r(C(x,t))dt = Q(x,t) \tag{6}$$

In order to propose a robust criterion valable to all epoxy-diamine systems for estimating the TOL and for validating the kinetic model, the Q(C) profiles are retained because this gradient can be accessible

experimentally with common laboratory physicochemical techniques, *e.g.* FTIR spectrometry. For it, the difference Q(x,t)-Q(L/2,t) was normalized between its maximum and minimum values in the steady state, as shown in Figure 4. This value has been estimated for each system as the difference between the concentration of oxidation sites PH on the surface when the oxidation reaction is complete and the initial O_2 concentration in the heart of the sample previous to oxidation. Then, an arbitraty criterion of around 0.05% has been considered, leading to the following expression for the estimate of the TOL evolution:

$$TOL(t) = Argmin([\,Q(x,t) - Q(L/2,t)]/[Q_{max} - Q_{min}] - 0.05\%)) \tag{7}$$

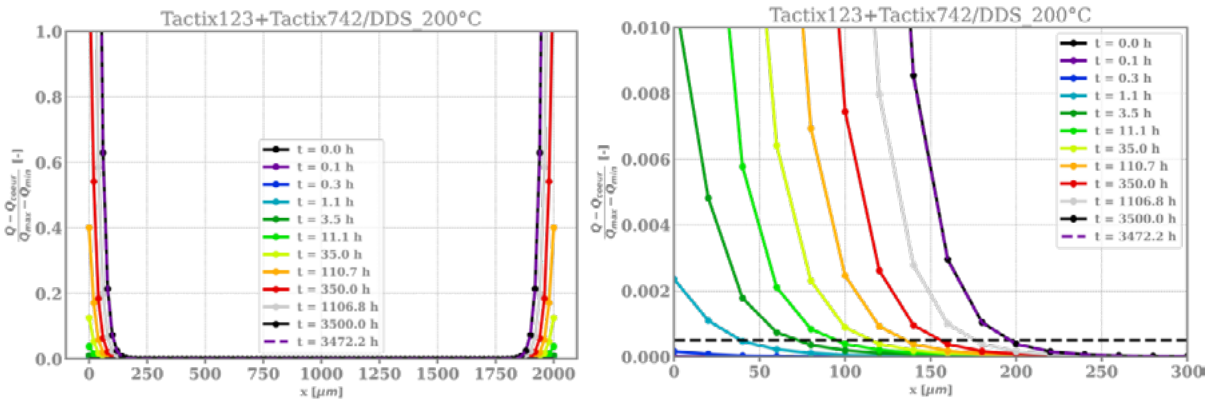


Figure 4. Calculation of the normalized oxidation gradient [Q(x,t)-Q(L/2,t)]/[Q_{max}-Q_{min}] and application of the criterion given in Eq. 7 for the estimate of TOL in air at 200°C for the TACTIX(123+742)-DDS network.

3. Comparison of simulations with experimental results

This section compares results from numerical simulations using the model described in Section 2 with experimental data, specifically TOL measurements. Additionally, the kinetic model is enhanced with structure/property relationships to predict the gradients of thermomechanical properties.

3.1. TOL confrontation

Figure 5 presents the confrontation of numerical simulations with experimental values of TOL (plotted using crosses). For numerical estimates, these TOL values were determined in the steady state using the criterion given in Eq. 7. The maximum TOL values calculated for epoxy-diamine networks with known parameters K, β, r_0, and D are plotted using filled dots. In this case, the diffusion coefficient D is assumed to be known and to follow a standard Arrhenius law in the glassy state, typically:

$$D(T) = 5.0\ 10^{-11} \times Exp\left[-\frac{41600}{R}\left(\frac{1}{T} - \frac{1}{T_g}\right)\right] \quad \text{for aliphatic diamines}$$
$$D(T) = 2.3\ 10^{-12} \times Exp\left[-\frac{9000}{R}\left(\frac{1}{T} - \frac{1}{T_g}\right)\right] \quad \text{for aromatic diamines} \tag{8}$$

In the glassy state (*i.e.* for $T<T_g$), numerical simulations give access to TOL values of the same order of magnitude as the experimental measurements. It can be shown that, as parameters β, r_0 et D follow an Arrhenius law, then the same is true for TOL [3]:

$$TOL = TOL_0\ Exp\left(\frac{E_{TOL}}{8.31 \times T}\right) \tag{9}$$

where TOL_0 et E_{TOL} are respectively the pre-exponential factor and the activation energy. Thus, TOL is a decreasing function of temperature. For epoxy-diamine networks exposed in air, we find that E_{TOL}≈40 kJ/mol. At this point, numerical simulations cannot account for the jump in TOL in the vicinity of T_g. As explained in the introduction, the main hypothesis to explain this jump is a sudden increase in D when the material goes from the glassy to rubbery state ($T>T_g$). To check this hypothesis, new simulations were redone in the rubbery state by increasing D from 10 to 100 times. The O_2 permeation measurements reported in the literature for all polymers confirm this hypothesis [6]. The new estimates of TOL are also plotted in Fig. 5 using filled squares. It is remarked a better agreement with the experimental results because the coupling between the chemical consumption and the diffusion of O_2 in the through-thickness direction of the sample is better respected.

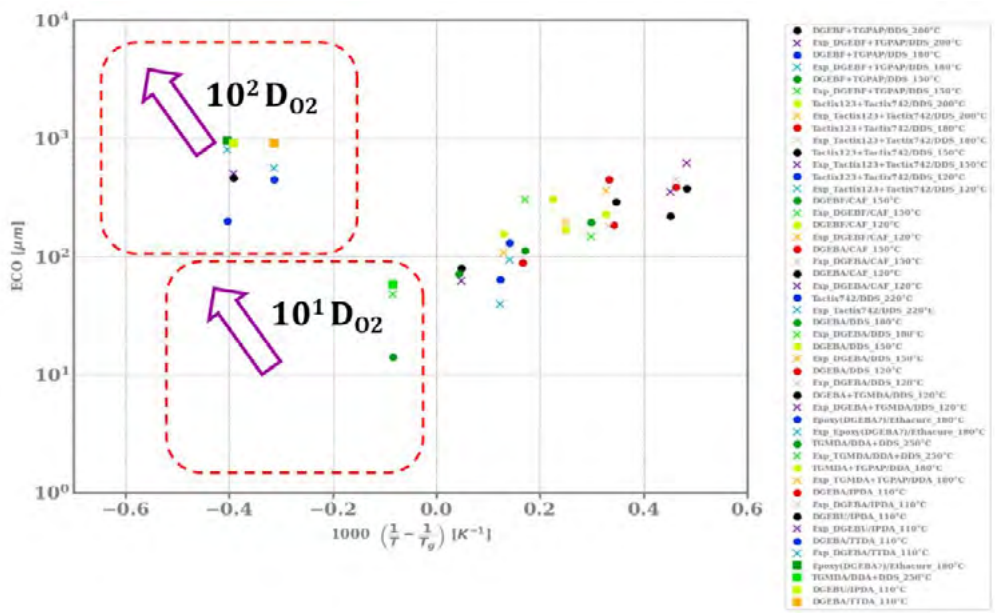


Figure 5. Variation of TOL with the reciprocal temperature for epoxy-diamine networks. Experimental values (crosses) compared to calculated values considering that D obeys an Arrhenius law below T_g (*i.e.* $1/T-1/T_g>0$) (filled circles) and increases suddenly by a factor of 10^1 to 10^2 above T_g (*i.e.* $1/T-1/T_g<0$) (filled squares). The arrows show the effect of the increase in D on the TOL estimates.

3.2. Prediction of degradation of thermomechanical properties

Some authors have shown that thermo-oxidation impacts the thermomechanical properties such as T_g and Young's modulus [7,8,9]. In fact, T_g decreases if chain scissions predominate over cross-linking [7]:

$$\frac{1}{T_g}=\frac{1}{T_{g0}}+\frac{2K_{DM}\,F}{3T_{gl}\,K}(3r_{S\infty}-2r_{X\infty})\left\{Kt+Ln\left[\frac{1+be^{-Kt}}{1+b}\right]-\frac{1}{1+be^{-Kt}}+\frac{1}{1+b}\right\} \quad (10)$$

where $r_{S\infty}$ and $r_{X\infty}$ are respectively the maximum ratess of chain scissions and crosslinking, K_{DM} a universal constant (K_{DM}≈3), F and T_{gl} two parameters linked to the rigidity of the chains of the macromolecular network. Figure 6 (left) shows the evolution of the gradient of T_g at 200°C in air for the TACTIX(123+742)-DDS network. The related thermo-oxidation kinetics were discussed in Paragraph 2.2 (Figures 3 and 4). A significant drop in T_g is observed at the sample edges, which lessens in deeper layers, leading to T_g values which remains almost unchanged in the sample core. Figure 6 (right) illustrates the decreasing evolution of the average value T_g in the whole sample, aligning well with experimental trends from literature.

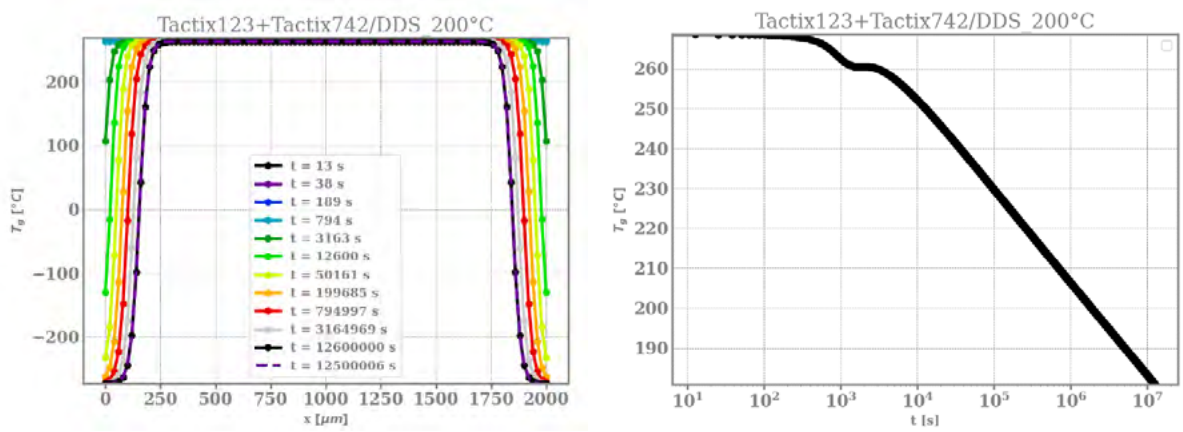


Figure 6. Left: Calculation of the gradient of $T_g(x,t)$ in air at 200°C for the TACTIX(123+742)-DDS network. Right: Evolution of the average value of T_g in the whole sample.

On the other hand, the Young's modulus increases due to an antiplasticization process. Indeed, although T_g decreases, the progressive disappearance of the sub-glass transition β (located around -70°C) ultimately leads to an increase in the Young's modulus between T_β and T_g. The Gilbert equation is generally used to account for this evolution [9]:

$$E(T) = E(0\ K)\left(1 - \alpha\frac{T}{T_g}\right) - \Delta E_\beta \tag{11}$$

where E(0 K) and E(T) are respectively the values of the Young's modulus at -273°C and at the study temperature, and ΔE_β is the drop in Young's modulus at the transition β. To our knowledge, there is still no kinetic law for describing the evolution over time of ΔE_β. However, it is possible to propose an arbitrary antiplastification law based on oxidation gradients. For this, the following relationship is used:

$$\Delta E_\beta = \Delta E_\beta^{max}\,(1 - \phi(x,t)) \tag{12}$$

where ΔE_β^{max} refers to the maximal modulus jump related to the transition β when the oxidation of the sample reaches the steady state. Φ represents the oxidation degree, whose value evolves between 0 and 1 according to normalized values of Q(x,t). Thus, when Q(x,t)-Q(L/2,t) reaches (Q_max-Q_min), it is assumed that Φ is equal to 1. According to Eq. 12, Figure 7 shows the gradienst of E (left) and the evolution of the average value of E in both the TOL and the whole sample, whose evolutions are in good agreement with experimental trends from literature [9].

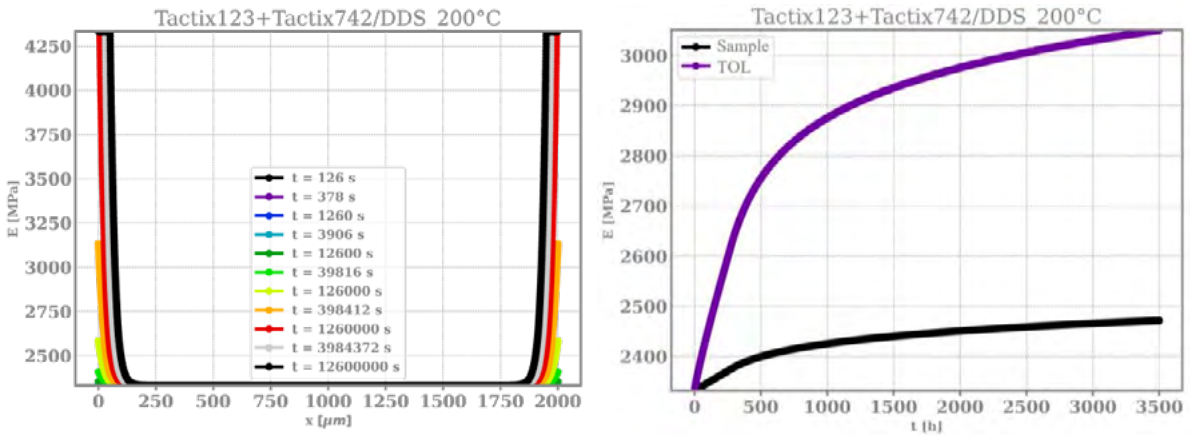


Figure 7. Left: Calculation of the gradient of E(x,t) in air at 200°C for the TACTIX(123+742)-DDS network. Right: Evolution of the average value of E in the TOL and the whole sample.

4. Conclusions and perspectives

A numerical calculation code based on finite elements was developed to solve a diffusion/reaction problem and simulate the oxidation gradients of the epoxy-diamine networks on either side of T_g. A physically-based criterion was chosen to calculate the thickness of oxidized layer (TOL) from the gradients of O_2 consummation. The robustness of this criterion was proven by comparing the estimates of the TOL with experimental measurements on many epoxy-diamine networks. The key role of O_2 diffusion has been highlighted, particularly in the rubbery state, for which the oxidation front evolves deeper in the sample compared to the glassy state. The consequences of oxidation on thermomechanical properties, in particular on T_g and E were then calculated. A significant reduction in T_g was thus shown at the edges, while in the heart of the sample, its value practically did not change. On the other hand, the consequences of oxidation on E has been computed assuming an arbitrary law to describe the effects of antiplasticization. The evolution of the average value E in the TOL and the whole sample have been obtained from the gradients of E, leading to an increase in E as consequence of local stiffness of oxidized layers. As perspectives, the computation of stress/strain states within the material is envisaged. This is, in fact, an important step in the lifetime prediction approach.

References

[1] T.K. Tsotsis and S.M. Lee. Long-term thermo-oxidative aging in composite materials: Experimental methods. *Compos. Sci. Technol.,* Vol. 32(11):1115–1135, 1998.
[2] X. Colin, A. Mavel, C. Marais and J. Verdu. Interaction between cracking and oxidation in organic matrix composites. *J. Compos. Mater*., Vol. 39(15):1371–1389, 2005.
[3] X. Colin, F. Essatbi, J. Delozanne and G. Moreau. A new analytical model for predicting the thermal oxidation kinetics of composite organic matrices. Application to diamine cross-linked epoxy. *Polym. Degrad. Stab*. Vol. 186:109513, 2021.
[4] X. Colin, F. Essatbi, J. Delozanne and G. Moreau. Towards a general kinetic model for the thermal oxidation of epoxy diamine networks. Effect of the molecular mobility around the glass transition temperature. *Polym. Degrad. Stab*. Vol. 181:109314, 2020.
[5] J.P. Marquez Costa and X. Colin. Modélisation des gradients d'oxydation des réseaux époxy-diamine de part et d'autre de la température de transition vitreuse. In 23èmes Journées Nationales sur les Composites, ENSMM, Besançon, France, 2023.
[6] D.W. Van Krevelen, K.Te Nijenhuis. *Properties of Polymers*. Elsevier, Amsterdam, 2009.
[7] X. Colin, J. Delozanne and G. Moreau. New advances in the kinetic modelling of thermal oxidation of epoxy-diamine networks. *Front. Mater*. Vol. 8:720455, 2021.
[8] M.C. Lafarie, J.-C. Grandidier, M. Gigliotti, L. Olivier, X. Colin, J. Verdu and J. Cinquin. Thermo-oxidation behaviour of composite materials at high temperatures: A review of research activities carried out within the COMEDI program. *Polym. Degrad. Stab.* Vol. 95(6):965–974, 2010.
[9] S. Terekhina, M. Mille, B. Fayolle and X. Colin. Oxidation induced changes in viscoelastic properties of a thermostable epoxy matrix. *Polym. Sci. Ser. A*. Vol. 55:614–624, 2013.

THE EFFECT OF PATTERN WIDTH ON THE PROPERTIES AND BEHAVIOR OF INTERFACIALLY ENGINEERED COMPOSITES WITH DESIGNED FAILURE

G. Zs. Marton[1,2], G. Szebényi[1,2,3]

[1]Department of Polymer Engineering, Budapest University of Technology and Economics, Műegyetem rkp. 3., H-1111 Budapest, Hungary
[2]MTA-BME Lendület Sustainable Polymers Research Group, Műegyetem rkp. 3., H-1111 Budapest, Hungary
[3]MTA-BME Lendület Lightweight Polymer Composites Research Group, Műegyetem rkp. 3., H-1111 Budapest, Hungary
Email: martong@pt.bme.hu
Email: szebenyi@pt.bme.hu

Keywords: interface engineering, designed failure, 3D printing, failure mode, interlayer material

Abstract
Without increasing the reliability of composites, their broader use in safety-critical components might be limited by their unfavorable failure process, which is mainly based on the interaction of different damage mechanisms from different sources and often occurs at random locations and without any particular sign. In our research, we developed and investigated a method that can be suitable for controlling and designing the failure process of composites in terms of pre-determined location and mode of failure. For this purpose, we manufactured UD carbon-fiber/epoxy composite plates, which contained a locally weakened adhesion zone formed by polycaprolactone (PCL) thermoplastic interlayer material. The failure mode and location of the composite specimens were evaluated under uniaxial tensile loading. The results show that the application of PCL interlayer material enables the design of the failure process of polymer composites, and it does not influence their mechanical properties significantly.

1. Introduction

Polymer composites, due to their complex microstructure and manufacturing technologies, are fundamentally affected by a wide variety of damage modes from different sources, such as defects in the raw material, manufacturing induced and in-service flaws, which differ significantly in their typical sizes, from nano to macro, and in their effect on the composite structure. The initiation and propagation of damage and the mode of failure that may occur, are essentially determined by the loading conditions and the structure of the composite [1, 2].

Damage in composites, especially delamination, is often difficult to detect and localize. However, its presence usually leads to a reduction in the effective strength and stiffness of the composite, and its propagation can lead to failure. Detecting these damages and investigating the residual mechanical properties of the composite are essential to ensure proper structural health monitoring, which is best achieved by using non-destructive testing methods [3].

Besides other NDT methods such as computed tomography, acoustic emission testing, and ultrasound testing, which are often used for the investigation of composite materials, the digital image correlation (DIC) technique is a cost-effective, relatively simple method - optical analysis of the mechanical

response to mechanical excitation - that can be used to detect damage at the meso- and macro-levels of a composite and to detect the propagation of damage. This information is provided by the high local strain values and the changes in the strain field observed during DIC-based full-field strain measurements [4, 5].

Another problem is that the failure of composites is challenging to predict and often occurs catastrophically. Therefore, to increase the reliability of composites, it is essential to influence their failure processes and make them more controllable. Failure can be partially localized by creating artificial damage, but this usually results in a significant loss of strength and cannot determine the mode of damage [6]. The failure process can be controlled by methods that aim to achieve pseudo-ductile behavior, where one possible method is the modification of interfacial adhesion, e.g., with nanofiber mats [7] or polymer films [8]. Applying polycaprolactone (PCL) thermoplastic interlayer material also seems successful in achieving pseudo-ductile behavior. PCL can be solved in the epoxy matrix. Thus, it does not create a new phase and applying it as interlayer material enables the influence of the failure process by the formation of locally weakened adhesion zones and the local modification of the matrix material [9, 10].

In the present research, we manufactured locally interfacially engineered composite plates containing PCL interlayer material. Our aim was to predefine the failure mode and location. The composite specimens were investigated under uniaxial tensile loading. Based on the measured data, the influence of the local modification of interfacial adhesion and the width of the weakened adhesion zone on the mechanical properties as well as the failure mode and position were evaluated.

2. Materials and methods

2.1. Materials

We applied IPOX MR 3010 (IPOX Chemicals Kft., Budapest, Hungary) DGEBA-based epoxy resin (EP) as matrix material of the composites, which was mixed with IPOX MH 3124 amine type curing agent in a weight ratio of 100:35. The reinforcement material was PX35FBUD0300 (Zoltek Zrt., Nyergesújfalu, Hungary) stitch-bonded unidirectional carbon fabric (309 g/m^2 surface weight), consisting of Panex35 50k rovings. As interlayer material, we used eMorph175N05 (Shenzhen Esun Industrial Co. Ltd., Shenzhen, China) poly (ϵ-caprolactone) (PCL) filament (1.75 mm diameter, 60°C melting temperature, 180°C printing temperature).

2.2. Sample production

Composite plates with [0°$_6$] layup sequence were manufactured by vacuum-assisted resin transfer molding (VARTM). For interfacially engineered composites, the PCL filament was printed directly on the surface of the carbon fabric by fused filament fabrication (FFF) method (Figure 1) using a CraftBot Plus 3D printer (CraftUnique Kft., Budapest, Hungary). Interlayer material was applied perpendicular to the fiber direction and placed only between the two middle plies.

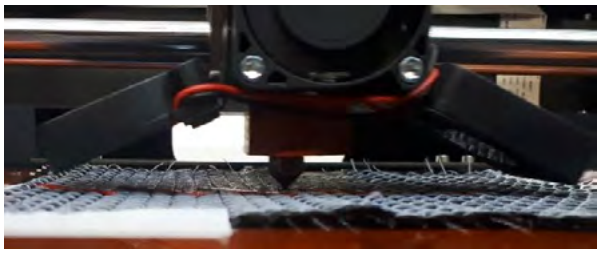


Figure 1. 3D printing of PCL interlayer material on the reinforcement fabric using FFF method

The thickness of the interlayer material, thus the weakened adhesion zone, was constantly 0.4 mm, only width differed in each plate. Plates containing 1, 2 and 3 mm wide interlayer material were produced.

Besides interfacially engineered composites, reference samples containing no interlayer material were also manufactured. Specimens prepared for the material testing were cut from the composite plates with a Mutronic Diadisc (Mutronic, Rieden am Forggensee, Germany) diamond disc cutter.

2.3. Methods

Initially, the fiber volume fractions of the composite plates were determined through density measurements conducted with a Sartorius Quintix 125D weighing scale (Sartorius Lab Instruments GmbH, Göttingen, Germany) following the rule of mixtures principle.

Tensile tests were performed according to ISO 527-4 standard using a Zwick Z250 (Zwick GmbH, Ulm, Germany) universal testing machine with a 250 kN load cell. During the tensile tests, 15 mm wide and 250 mm long specimens were investigated. The specimens were protected with bonded end-tabs, resulting in a free length of 150 mm. The test speed was set at 5 mm/min. Displacements were measured using a Mercury Monet (Sobriety, Kurim, Czech Republic) optical strain measuring system based on digital image correlation (DIC) featuring a 5 MPixel resolution IDS U3-3080CP-P-GL (Imaging Development Systems Inc., Obersulm, Germany) camera and two LED lights. Data acquisition was carried out with a frame rate of 10 Hz. The results were processed with Mercury RT-v2.9 software.

Before testing, the optical strain measurement system was calibrated in order to mitigate lens distortion and establish a correlation between the specimen's actual size and its representation in the recorded images. A gauge length of 75 mm was used for global strain measurement, applying a line probe within the software. Two additional line probes were used: one for further global strain measurement with a length of 50 mm, and another for local strain measurement in the region of the PCL interlayer material, covering 15 mm in length. DIC technique was used to generate a full-field strain map, where the calculated points were spaced at 20-pixel intervals, using a facet window size of 40 pixels × 40 pixels. For the DIC measurements, a high-contrast pattern was painted on the surface of the specimens.

3. Results and discussion

The results of the fiber volume fraction estimation based on density measurement showed that the average fiber volume fraction of the manufactured composite plates was 39.45±1.07 V/V%. The experienced differences do not affect the mechanical properties significantly, which enables the comparison of the different plates.

3.1. Tensile properties

Firstly, the tensile properties – tensile strength and modulus – of the different composite specimens were determined, and the effect of the PCL pattern width on them was evaluated (Figure 2).

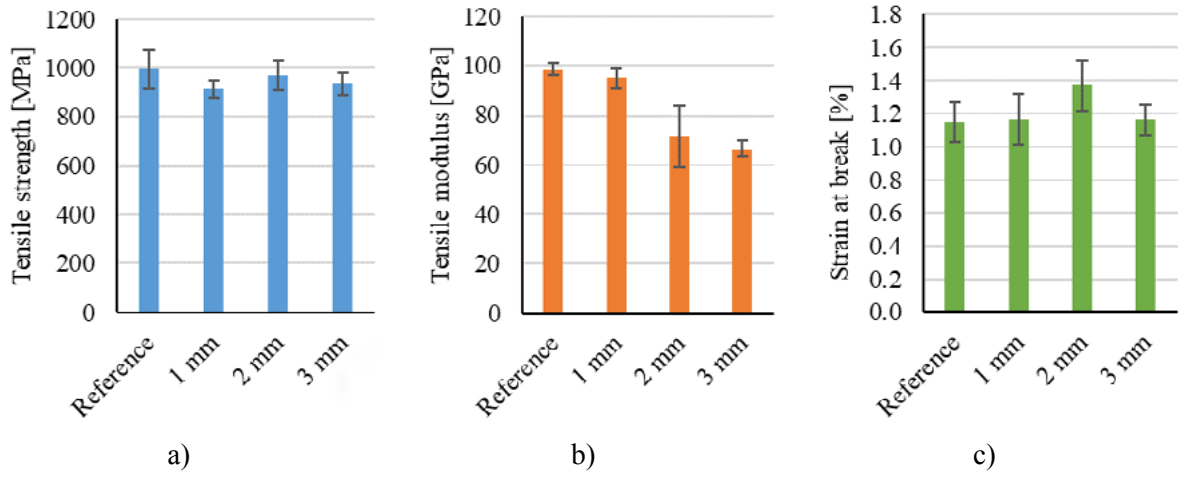


Figure 2. The effect of the width of PCL interlayer material on the tensile properties a) tensile strength, b) tensile modulus, c) strain at break

The results indicate that using PCL interlayer material does not significantly affect the tensile strength and the strain at break. On the other hand, using PCL causes a decrease in the tensile modulus, which is more significant with the increasing width of the interlayer material. This effect might be caused by the locally weakened adhesion, the fiber waviness and the resin-rich areas formed by the PCL interlayer material. During the tensile tests, we experienced that the interfacially engineered composites tend to fail in the region of the PCL interlayer material, and the frequency of the localized failure increases with the width of the PCL pattern.

3.2. Line probe tests

Following that, data obtained from Line Probe (LP) measurements, carried out by DIC during the tensile tests were analyzed to detect potential damage, particularly the formation of delamination. In the line probe test, elongation along three lines of varying lengths was measured. Line probes A2 and A3 provided insights into the global strain, while A1 specifically indicated local strain within the region of the interlayer material (Figure 3). The measured data was evaluated for the reference specimens as well.

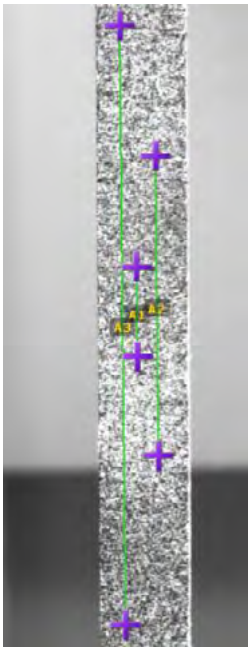


Figure 3. Arrangement of the line probes on the surface of the composite specimen: A1= 15 mm for local strain measurement, A2=50 mm and A3=75 mm for global strain measurement

The measured data indicate that the presence of the PCL interlayer material results in a deviation between the local and global strain values by locally increasing strain in the modified region. Higher strain values in the interfacially engineered region might lead to localized failure by reaching the failure strain earlier. In contrast, in the case of the reference sample, there is no significant difference in the elongations measured by the line probes. The only noticeable difference is that the line probe measuring local strain is affected by higher levels of noise (Figure 4).

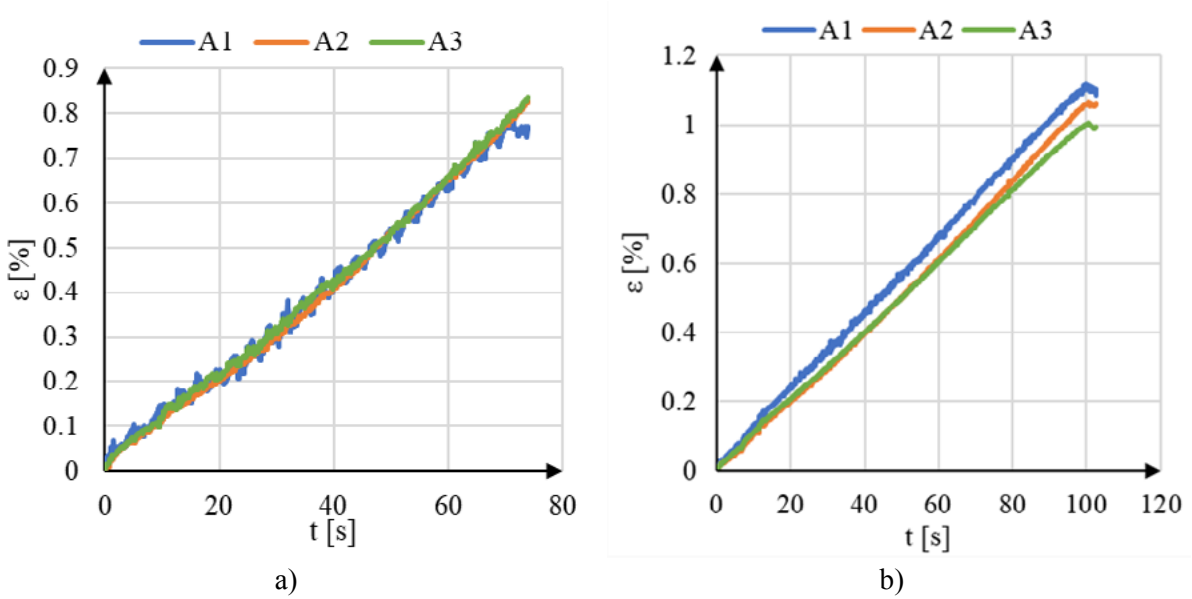


Figure 4. The results of the line probe test for a) a reference specimen, b) a specimen containing 3 mm wide, 0.4 mm thick PCL interlayer material

3.3. Full-field strain measurement

Then, strain fields were determined using the DIC technique, and the strain fields of the different composite specimens were compared at an identical global strain value of 0.7%. The results suggest that, while relatively homogenous strain fields belong to the reference composites, the presence of PCL interlayer material causes local high-strain values. These zones indicate the localization of damage and failure as well as the occurrence of local delamination. This effect was observed to become more significant with the increase in the PCL pattern's width. A characteristic strain field for a reference specimen and a specimen containing 3 mm wide and 0.4 mm thick PCL interlayer material can be seen in Figure 5.

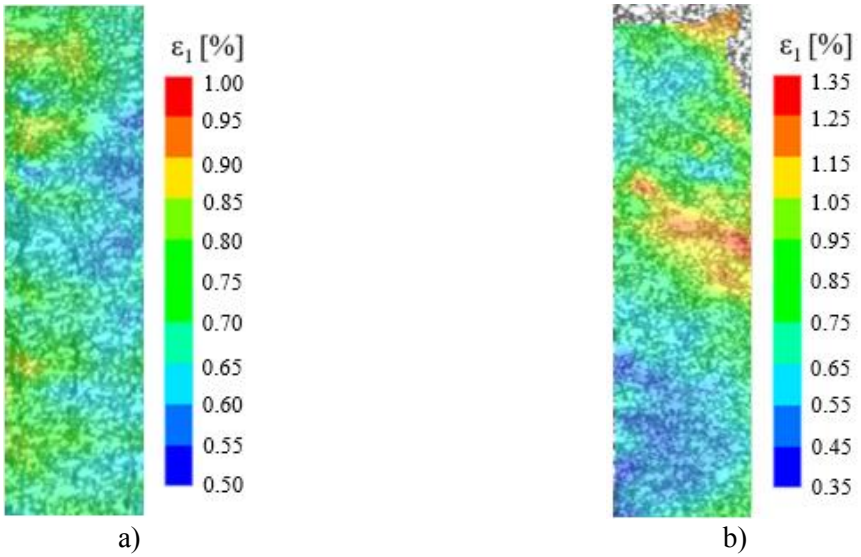


Figure 5. The results of the full-field strain measurement at 0.7% global strain for a) a reference specimen, b) a specimen with 3 mm wide and 0.4 mm thick PCL interlayer material

4. Conclusions

In our research, we manufactured locally interfacially engineered composites by applying 3D-printed PCL interlayer material in order to design their failure. We carried out tensile tests supported by DIC to investigate the effect of the pattern width of PCL on the mechanical properties and the failure process. The results show that the application of PCL interlayer material enables the design of the failure process of polymer composites, and it does not influence their mechanical properties significantly. The mechanism of the method can be explained with several effects of PCL: local modification of interfacial adhesion and the matrix material, as well as the formation of fiber waviness and resin-rich areas.

Acknowledgments

The research has been supported by the NRDI Office (OTKA FK 142540). Gábor Szebényi acknowledges the financial support received through the János Bolyai Scholarship of the Hungarian Academy of Sciences and ÚNKP-23-5-BME-415 New National Excellence Program. Project no. 2022-2.1.1-NL-2022-00012 „National Laboratory for Cooperative Technologies" has been implemented with the support provided by the Ministry of Culture and Innovation of Hungary from the National Research, Development and Innovation Fund, financed under the National Laboratories funding scheme. Project no. TKP-6-6/PALY-2021 has been implemented with the support provided by the Ministry of Culture and Innovation of Hungary from the National Research, Development and Innovation Fund, financed under the TKP2021-NVA funding scheme. Project no. KDP-IKT-2023-900-I1-00000957/0000003 has been implemented with the support provided by the Ministry of Culture and Innovation of Hungary from the National Research, Development and Innovation Fund, financed under the KDP-2023 funding scheme.

References

[1] R. Talreja and C. V. Singh. *Damage and Failure of Composite Materials*. Cambridge University Press, Cambridge, 2012.
[2] R. B. Heslehurst. *Defects and in Composite Materials and Structures.* CRC Press, Boca Raton, 2014.
[3] H. Towsyfyan, A. Biguri, R. Boardman and T. Blumensath. Successes and challenges in non-destructive testing of aircraft composite structures. *Chin. J. Aeronaut*, 33(3): 771–791, 2020.
[4] G. Szebényi and V. Hliva. Detection of Delamination in Polymer Composites by Digital Image Correlation—Experimental Test, *Polymers*, 11: 523/1-523/11, 2019.
[5] V. Hliva and G. Szebényi. Non-Destructive Evaluation and Damage Determination of Fiber-Reinforced Composites by Digital Image Correlation, *Journal of Nondestructive Evaluation*, 42: 43/1-43/15, 2023.
[6] J. Huang, Q. Wei, L. Zhuo, J. Zhu, C. Li and Z. Wang. Detection and quantification of artificial delaminations in CFRP composites using ultrasonic thermography, *Infrared Physics & Technology*, 130: 104579, 2023.
[7] K. Molnár, E. Kostakova and L. Mészaros. The effect of needleless electrospun nanofibrous interleaves on mechanical properties of carbon fabrics/epoxy laminates, *Express Polymer Letters*, 8(1): 62-72, 2014.
[8] S. G. Marino and G. Czél. Improving the performance of pseudo-ductile hybrid composites by film-interleaving, *Composites Part A.* 142: 106233/1-106233/16, 2021.
[9] B. Magyar, T. Czigány and G. Szebényi. Metal-alike polymer composites: The effect of interlayer content on the pseudo-ductile behaviour of carbon fibre/epoxy resin materials, *Composites Science and Technology*, 215: 109002/1-109002/8, 2021.
[10] G. Szebényi, B. Magyar and T. Czigány. Achieving Pseudo-Ductile Behavior of Carbon Fiber Reinforced Polymer Composites via Interfacial Engineering, *Advanced Engineering Materials*, 23: 2000822/1-2000822/7, 2020.

NEXTCOPV: Impact Behavior of Carbon Fiber/Epoxy Composite Overwrapped Tanks in Cryogenic Environments

A. Maziz[1], P. Gupta[1], TV. Birro [1], B.Derias[1], B Gely[1]

[1] Technology & Engineering Center, Capgemini Engineering,4 Av. Didier Daurat, Blagnac, France

Email: ammar.maziz@capgemini.com (https://orcid.org/0000-0001-6084-430X)
Email: prateek.g.gupta@capgemini.com (https://orcid.org/0000-0003-1118-9251)
Email :Thiago.vasconcellos-birro@capgemini.com (https://orcid.org/0000-0001-7872-9342)
Email: Bruno.derias@capgemini.com
Email : Benoit.gely@capgemini.com

Keywords: Carbon-reinforced plastic, composite tank, low-velocity impact, Cryogenic temperatures, Progressive damage

Abstract
This research investigates composite overwrapped tank structures produced through filament winding and exposed to cryogenic loads. A 3D-FE Model, including parameters of the mandrel trajectory for designing the dome, junction, and cylindrical shell, is coupled with thermal degradation to replicate physical variations. Intralaminar damages, such as matrix cracking and fiber failures, are predicted using 3D Hashin criteria. The numerical analysis employs a multi-step technique, using Abaqus/Standard for a general static step in thermal simulation and Abaqus/Explicit for impact events on the pre-stressed composite tank. The presented numerical results include contact force, displacement, energy dissipation, and predicted matrix damage in each layer of the tank. The impact of temperature changes on the tank's response to impacts is explored, and a detailed examination of damage zones on the structure reveals that damages increased as the temperature decreased for all test samples

1. Introduction

Hydrogen has gained significant attention in recent years as a promising energy vector, offering a sustainable and environmentally friendly alternative to conventional fossil fuels**[1]** Composite hydrogen tanks are crucial in developing and implementing hydrogen-based energy systems **[2]**. These tanks are designed to store hydrogen under high pressure, enabling its efficient use in various applications, such as transportation, stationary power generation, and portable devices. Composite materials, such as carbon fiber-reinforced polymers (CFRP), are utilized in the construction of hydrogen tanks due to their exceptional strength-to-weight ratio, corrosion resistance, and durability. These properties make composite tanks ideal for safely storing and transporting hydrogen while minimizing the overall system weight **[3,4]**. Hydrogen storage tanks play a crucial role in many applications, particularly in aerospace, where every gram counts. They are designed to safely and efficiently store hydrogen, enabling its use as fuel or as an energy source. Hydrogen can be stored in either gaseous or liquid form, each state having its own advantages and disadvantages. In aerospace, where lightweight design is essential to maximize aircraft range and energy efficiency, storing hydrogen in liquid form is of particular interest. For the certification of hydrogen storage tanks, it is essential that they comply with the relevant standards **[5]**. Therefore, it is crucial to develop a methodology for conducting impact studies before and after thermal degradation **[6]** following the injection and liquefaction of hydrogen in the tanks. This approach is indispensable to support the certification process and reduce the number of required testing campaigns.

2. Type of Hydrogen Tanks

All For hydrogen to serve as a fuel, it must be stored in tanks under considerable pressure. Currently, four main types of tank designs cater to this requirement: Type I, Type II, Type III, and Type IV, as shown in Figure 1. A Type III tank was developed, which is fully composite wrapped, including wrapping at the polar boss, but the liner is still a metallic one [7]. The liner acts as a barrier towards the hydrogen leak or permeation. As compared to Type I and Type II, it is much lighter and hence suitable for vehicle applications. The Type III tanks provide positive results up to a pressure of 450 bars only. Hence, a plastic liner with a complete composite wrap-based tank Type IV is developed [8]. Usually, the plastic liner is made of High high-density polyethylene (HDPE), and the composite used is generally.

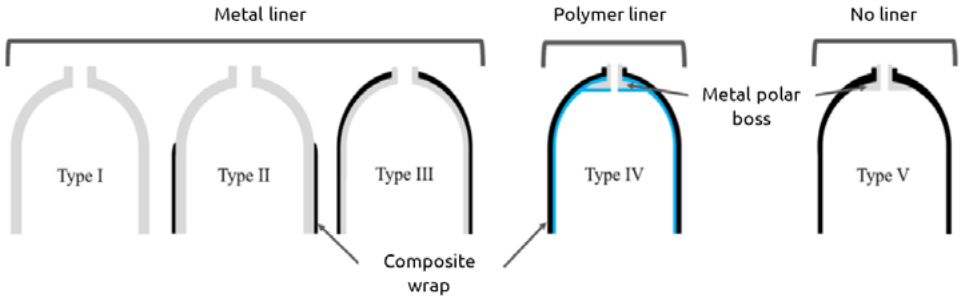


Figure 1. Types of pressure vessels

The transition of hydrogen from the gaseous state to the liquid state involves a significant reduction in volume, allowing for denser energy storage. Liquid hydrogen offers a higher energy density compared to gaseous hydrogen, meaning that a greater quantity of hydrogen can be stored in a smaller space. This is crucial for aerospace applications where weight and space are limiting factors. However, storing hydrogen in liquid form also presents technical challenges. Firstly, it requires extremely low temperatures to maintain hydrogen in a liquid state, typically around -253 degrees Celsius. This necessitates the use of sophisticated cooling systems, adding complexity and weight to the aircraft. Additionally, the process of liquefying hydrogen is energy-intensive, which can reduce the overall system efficiency.

Despite these challenges, liquid hydrogen remains a promising option for aerospace due to its high energy density. Advances in storage technologies and insulation materials could help overcome some of these obstacles in the future, paving the way for more widespread use of hydrogen as a clean and efficient fuel in aviation

3. Conditions for low velocity impact analysis

When dealing with hydrogen (especially for liquid) it is important to incorporate the cryogenic conditions into the simulation for the simple reason that the properties of the composite laminate have different properties at different temperature because of difference in the Glass Transition Temperature (Tg) of the epoxy. Li et al. [9] carried out experimental analysis on composite laminate at various temperatures ranging from 93k to 293k and compared with the RVE model which they developed. Authors presented temperature dependent constitutive damage laws. Since the properties of epoxy resin are dependent on temperature, a temperature dependent elastic-plastic model was developed to take into account this variation and the Young's Modulus is derived as follows:

$$E_m^T = E_m^0(a_{m_0} logT + b_{m_0})$$

where E_m^0 is the Young's modulus at the reference temperature and a_{m_0}, b_{m_0} are the curve fitting constants while T is the ambient temperature. Since the temperature dependence will change the hardening behaviour of the epoxy, the temperature dependent tensile and compressive strengths are provided by

$$\sigma_{m,t}^T = \left(\sigma_{m,t}^0 + H_t^0\left(1 - e^{-n^T \varepsilon^p}\right)\right)(a_{m_t} logT + b_{m_t})$$

$$\sigma_{m,c}^T = \left(\sigma_{m,c}^0 + H_c^0\left(1 - e^{-n^T \varepsilon^p}\right)\right)(a_{m_c} logT + b_{m_c})$$

Here $\sigma_{m,t}^T$ and $\sigma_{m,c}^T$ are the tensile and compressive yield stresses at the reference temperature T0, $H_t^0 and\ H_c^0$ are the hardening moduli in tension and compression at reference temperature.
However, the carbon fiber can be regarded as temperature-independent transversely isotropic material as its mechanical properties remain unchanged below 473K.
Using the RVE homogenization provided the effective properties of the composite laminate at 3 different temperatures , 293K, 193K and 93K have been adopted from the characterization experiments by Li et al [9], which are not shared in the article.

4. NEXTCOPV - Design of Tank

NEXTCOPV, the cutting-edge software for the design, simulation, and optimization of filament winding pressure vessels (COPVs), represents a significant leap forward in the field. Drawing on over a decade of experience in composite pressure vessels, the developers and mechanical engineers at Capgemini have successfully tackled the numerous challenges and complexities inherent in the design and simulation of COPVs. The outcome is a tool that revolutionizes the user experience, making the design process for COPVs simpler, faster, and more efficient. NEXTCOPV seamlessly integrates with Dassault Systems SIMULIA Abaqus Unified FEA, offering a robust and enduring solution. CAPGEMINI provide steadfast commitment for support, maintenance, and continuous development.

Several mathematical models have been implemented to achieve a realistic design, considering manufacturing parameters. The variation in thickness in the dome and the boss has been addressed, including a junction between the cylindrical part and the dome. To facilitate the ease of designing the COPVs with minimal knowledge in ABAQUS software, an user- interface (UI) is developed as an ABAQUS Plugin which directly takes input from the user. Due to this UI, it will help in fast optimization of the designs as presented in the process flow diagram below (Figure 2).

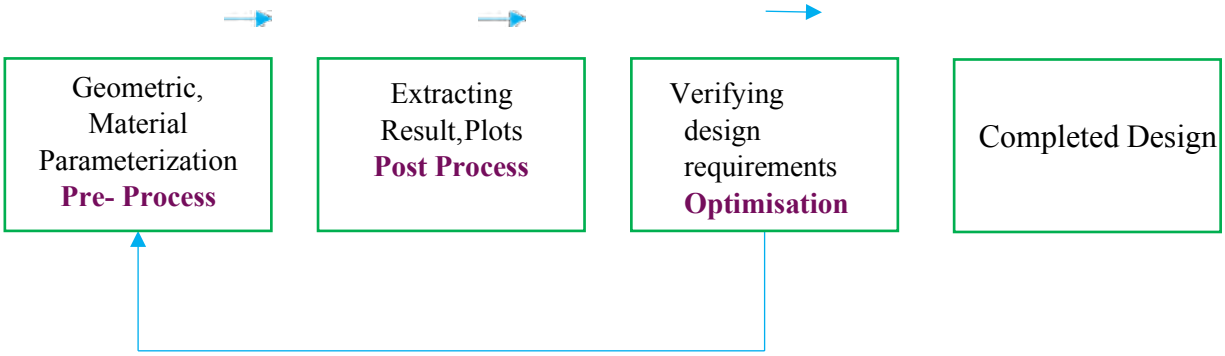


Figure 2. Process flow for the design using UI.

In the interface, there are 3 modules namely: Model setup, Geometry and Property. The 1st module is shown below (Figure 3). This allows user to select the type of theory amongst Constant Thickness and Variable Thickness. The user then can select the type of tank for the analysis. Type 3 is with a metal liner; Type 4 iswith a polymer liner while Type 5 has no liner. The user can also give the Part name and the internal pressure value which will be loaded as a ramp.

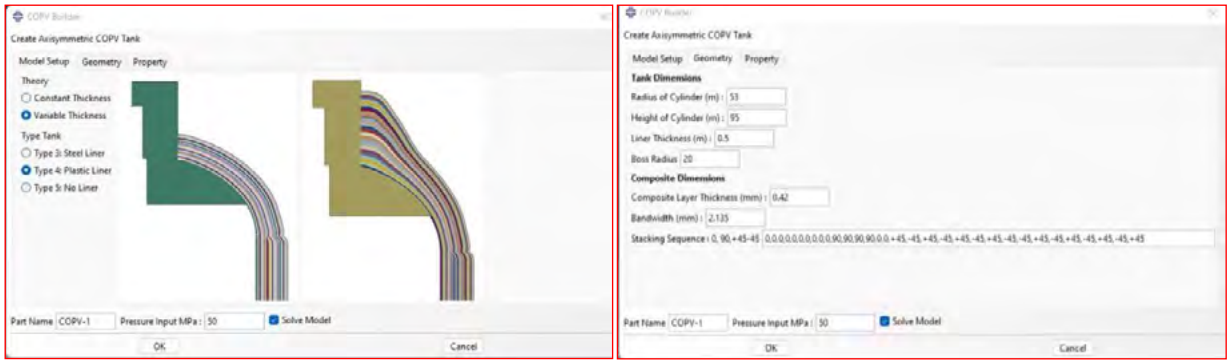


Figure 3. Model Setup and Geometry Modules.

Next, the geometry module allows the user to input all the geometrical parameters of the COPV (Figure 4). Lastly, the property module allows the user to input all the property parameters related to the composite/epoxy,liner and the plasticity related to the boss (see Figure 4). Once the user validates its options, the model is generatedalong with the mesh. An additional option is also given if the user wants to solve the model.



Figure 4. Property Module

5. FEM Modeling of Low Velocity Impact analysis

Curved composite laminates are brittle in nature and hence are prone to failure due to impact [10]. The impact caused on these structures can be due to low velocity Impact (LVI) or High Velocity Impact. The sensitivity towards the impact leads to over-dimensioning of the structure that further reduces the potential gain in ensure residual strength after the impact. In this study, LVI is of our interest. LVI occurs if the impact velocity is less than 10m/s and this can lead to Barely Visible Impact Damage (BVID) or directly failure of the structure. During the impact, the kinetic energy is converted into internal energy and an amount of this energy is stored as an elastic energy while the other part is dissipated by the damage. The damage in the structure can occur in terms of matrix crack, fiber fracture and delamination [11]. The first damage to appear is matrix cracking that occurs just below the impact zone. When these matrix crack grow during the fiber tension phase a disjointed strip between the plies is created that gives rise to interlaminar zone of tension stress between the two plies[11]. This further induces the phenomenon of delamination. In COPVs the resistance to LVI can depend on number of parameters like stacking sequence,thickness of each layer, properties of impactor, impact energy etc. For this analysis, progressive damage model is used to predict the damage onset and propagation of COPV before and after cryogenic load (see Figure 5).

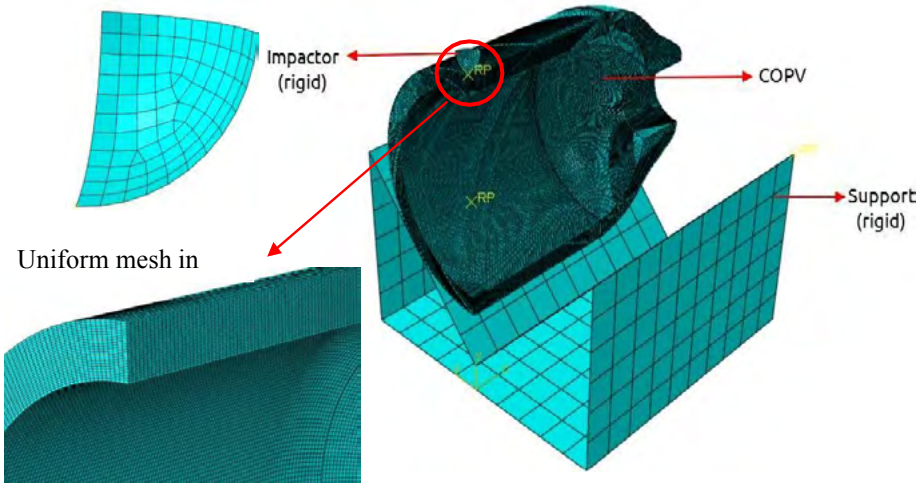


Figure 5. Low velocity impact model setup (1/4th model).

The impact is carried out at the middle of the cylindrical section and 1/4th model is used as shown in Fig.5 According to experimental setup [12] ASTM D7136/D7136M-05.

To save the computing time, a hemispherical impactor of diameter 16mm is selected which is impacted at various velocities (2m/s, 4m/s and 6m/s). These velocities account for the impact energies of 4J, 16J and 36 J respectively for the complete model.

Two models are developed with different stacking sequences. The 1st model has a stacking sequence of [0]10/ [+-45]2/ [0]2/ [+-45]3/ [45] while the 2nd model has a stacking sequence of [0]3/ [20]3/ [22]3/ [28]3/ 40/ [56]3/ [62]3/ [75]3/ [82] keeping all the remaining parameters same.

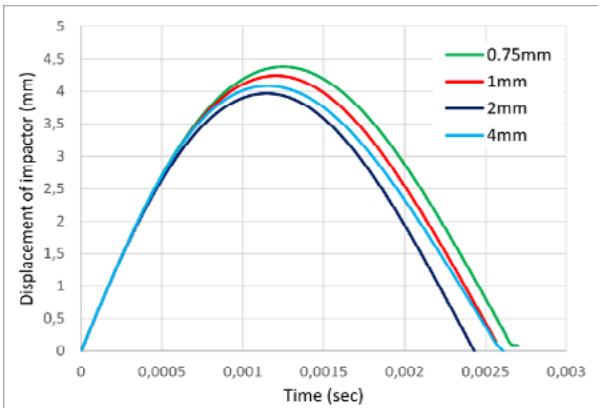
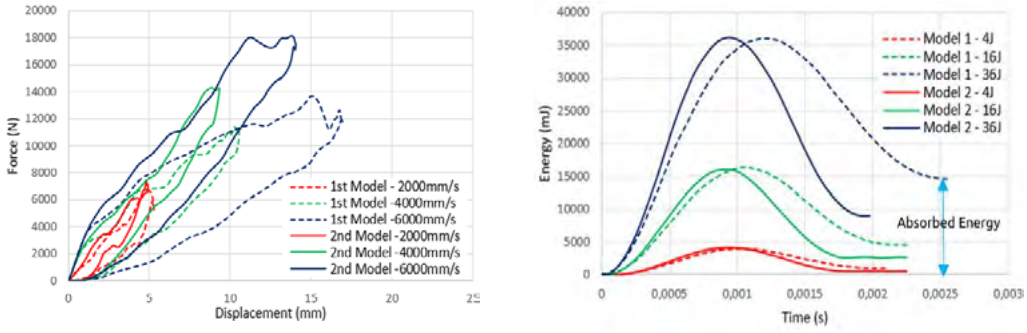


Figure 6. Mesh convergence

But before carrying out full analyses, mesh convergence studies are performed with element size 0.75mm, 1mm, 2mm and 4mm. The displacement of the impactor vs time is plotted in the Fig.6. Keeping in mind the complexity of the model and the computational time, mesh size of 1mm for the COPV is chosen for all the LVI analysis. but due to the complexity ofthe model, usage of continuum shells, and inability to reduce the mesh size less than 1mm, the percentage obtained is approximately 12%. Continuum shell elements SC8R are used in the tank accounting to a totalof 587,504 number of elements while rigid elements are used in the impactor and the support.



a) b)

Figure 7. Comparison of the results from two models: a) Force versus displacement b) Variations in energy.

As can be seen in Figure 7.a, the 2nd model resists more force due to the presence of the helical layers which also shows that instead of completely failing, the tank tries to resist the force over a period before rebound takes place. Figure 7.a provides the force vs displacement curves for both models at 3 different impact velocities. It can be observed that at low velocities or lower impact

energy there is no permanent displacement. But with increase in the energy a permanent displacement is observed. The ascending and descending part of the force displacement curve depict the loading and unloading. The ascending part relates to the stiffness and higher the peak force, stiffer the COPV is, and hence higher energy is needed to damage the COPV. Another information is about the energy absorbed which is area under the curve. Looking at the above figures it can be noticed that at lower energy of 4J, both models exhibit similar behaviour, but as the impact energy increases, the Model 2 shows a stiffer behaviour with higher peak force as compared to Model 1. However, the area of force-displacement for the 1st model at 36J is higher than that of 2nd model indicating that 1st model has absorbed higher energy which is validated by the energy-time graph. Clearly, Model 2 COPV which has helical layers is much stiffer than the model which has only 0° and 45° plies.

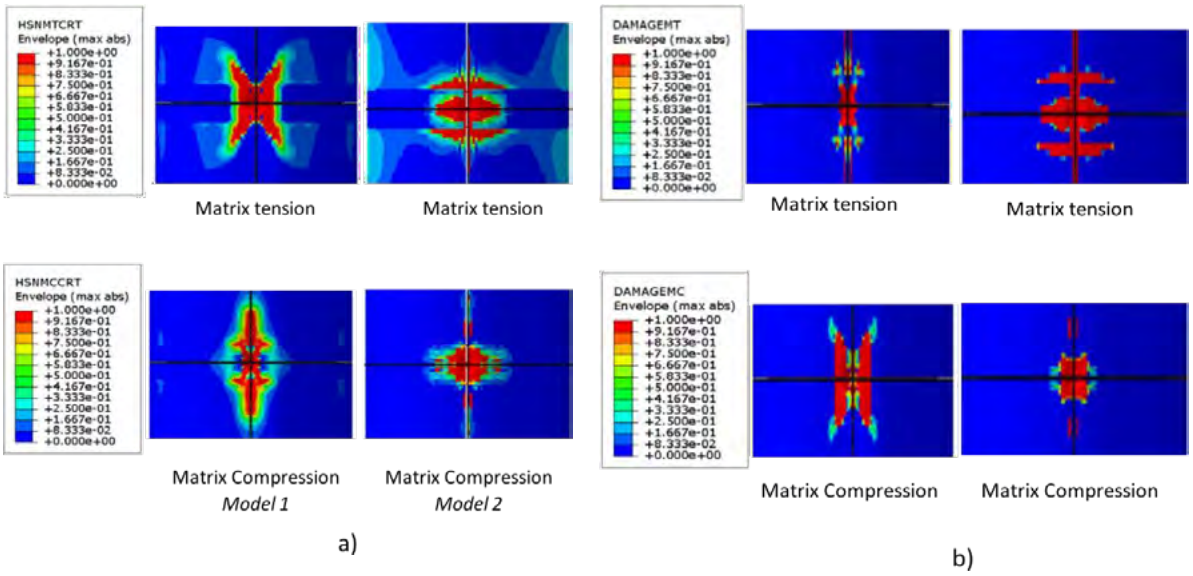


Figure 8. a) Hashin damage initiation; b) Damage evolution at 6m/s impact velocity at maximum displacement of the impactor

Fig.8(a) shows Hashin damage initiation for matrix under tension and compression and compares both the models subjected to impact velocity of 6m/s. This behaviour is captured as a complete model, and it is seen from the impacted side. As expected for the winding sequence that for the *Model 1*, damage initiates at 45° while for *2nd Model* it is more in the hoop direction. For the *2nd Model*, there is considerabledamage initiation on the non-impacted side under matrix tension when compared to the *1st Model*. This suggests that the 45° plies prevent the damage to initiate from the non-impacted side. The damage initiation due to matrix compression is small. Fig.8 (b) shows damage evolution of the matrix under tension and under compression for the *1st Model* at impact velocity of 6m/s. As the outer most layer in this model is at 45°, the damage of the matrix is along the direction of the fiber and hence the typical damage is observed under matrix compression [13]. In the stacking sequence of the *2nd Model*, since the outermost layer is oriented at 82°, we can observe the change in the damage for matrix under compression. It is, as expected, aligned more on the hoop or circumferential direction. Even thought the damage initiation under matrix compression is larger for both the models, the actual damage is relatively small. We also observe that there is damage in the axial direction as well in *Model 2*.

6. Cryo-impact analysis

After carrying out cryogenic and LVI studies, a multi-step analysis was carried out. From the Fig.9, it can be observed that after carrying out cryogenic analysis, the results from the last static step are

used as an input for the LVI. It can be observed that before the beginning of the LVI, at time step 0, there is already stress in the 1st stacking layer due to thermal loadings.

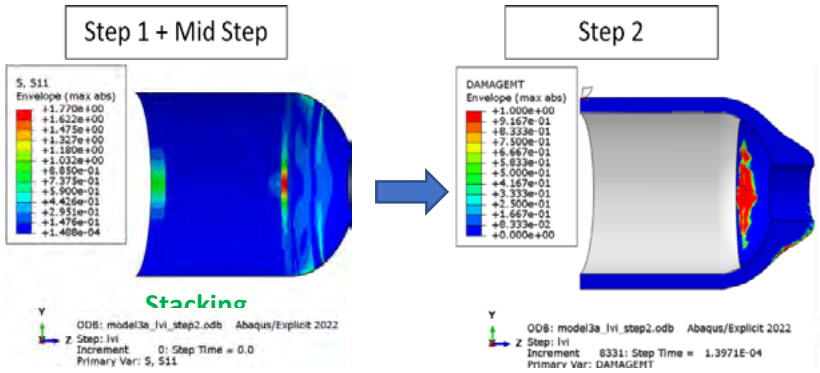


Figure 9. Behaviour under multi-step loading of cryo-impact damage.

After this, the LVI is performed which shows the damage in the impact region and as well as in the 1st layer of the dome. This is due to the lack of information on toughness and energy release rate of composite layers of the tank, which can affect the results. This is likely due to the stacking sequence, which can affect the composites under thermal conditions. The thermally induced effects are particularly severe on matrix damage, where the orientation of the carbon fibers varies in each layer. In these materials, low temperatures generate interlaminar residual thermal stresses that are significant enough to accelerate matrix cracking during LVI.

In future work, it is essential to thoroughly characterize the material to gain more detailed information on the behavior of carbon epoxy in a cryogenic environment. Additionally, several parameters related to fluid-structure interaction need to be implemented to predict the accuracy behaviour.

7. Conclusions

A study on the low-velocity impact of composite tanks, both with and without liquefied storage in a cryogenic environment, was conducted. It is well established that damage induced in COPV by low-velocity impact loads increases with impact energy. Results from this study showed that cooling the tank before impact has not similar effect on damage as increasing the impact energy, resulting in larger matrix cracking, while the energy absorbed by the composite is roughly proportional to the impact energy, the increased damage extent caused by low temperatures does not correspond to greater energy dissipation. This is due to the lower specific fracture energy of the epoxy matrix at cryogenic conditions. The embrittlement of the polymeric matrix, along with the interlaminar thermal stresses generated in the curved laminate at low temperatures, contributes to onset the damage.

8. Acknowledgments

The authors would like to express their sincere gratitude to the entire team of NEXTRUCTURES R&I Project for their valuable contributions and insightful discussions, the Research and Innovation department at the Technology Engineering Center (R&I TEC) and the Physical and Mechanical Engineering Unit for their sponsorship and support. The authors would also like to acknowledge Professor Frederic Lachaud from ISAE-SUPAERO, providing additional insights that enriched the discussion.

References :

[1] Cheng Q, Zhang R, Shi Z, Lin J. Review of common hydrogen storage tanks and current manufacturing methods for aluminium alloy tank liners. Int J Lightweight Mater Manuf 2024;7:269–84. https://doi.org/10.1016/j.ijlmm.2023.08.002.
[2] Hua TQ, Ahluwalia RK, Peng J-K, Kromer M, Lasher S, McKenney K, et al. Technical assessment of compressed hydrogen storage tank systems for automotive applications. Int J Hydrog Energy 2011;36:3037–49. https://doi.org/10.1016/j.ijhydene.2010.11.090.
[3] Knoell AC. Structural design and stress analysis program for advanced composite filament-wound axisymmetric pressure vessels (COMTANK). Comput-Aided Des 1973;5:267. https://doi.org/10.1016/0010-4485(73)90309-6.
[4] Boeing. Boeing breakthrough in all-composite cryogenic propellant tank advances technology readiness 2022.
[5] Perillo G, Grytten F, Sørbø S, Delhaye V. Numerical/experimental impact events on filament wound composite pressure vessel. Compos Part B Eng 2015;69:406–17. https://doi.org/10.1016/j.compositesb.2014.10.030.
[6] Voormeeren LO, Atli-Veltin B, Vredeveldt AW. Impact Resistance Cryogenic Bunker Fuel Tanks. Vol. 4B Struct. Saf. Reliab., San Francisco, California, USA: American Society of Mechanical Engineers; 2014, p. V04BT02A008. https://doi.org/10.1115/OMAE2014-23909.
[7] American Institute of Aeronautics and Astronautics, editor. Standard: Space Systems—Metallic Pressure Vessels, Pressurized Structures, and Pressure Components (ANSI/AIAA S-080A-2018). Stand. Space Syst. Press. Vessels Press. Struct. Press. Compon. ANSIAIAA -080A-2018, 12700 Sunrise Valley Drive, Suite 200, Reston, VA 20191: American Institute of Aeronautics and Astronautics, Inc.; 2018. https://doi.org/10.2514/4.105418.001.
[8] American Institute of Aeronautics and Astronautics, editor. Standard: Space Systems—Composite Overwrapped Pressure Vessels (ANSI/AIAA S-081B-2018). Stand. Space Syst. Overwrapped Press. Vessels ANSIAIAA -081B-2018, 12700 Sunrise Vally Drive, Reston, VA 20191: American Institute of Aeronautics and Astronautics, Inc.; 2018. https://doi.org/10.2514/4.105425.001.
[9] Li Y, Meng J, Luo J, Wang P, Ma J, Zhao Z, et al. Cryogenic mechanics and damage behaviors of carbon fiber reinforced polymer composites. Compos Part Appl Sci Manuf 2023;169:107484. https://doi.org/10.1016/j.compositesa.2023.107484.
[10] Bouvet C, Rivallant S, Barrau JJ. Low velocity impact modeling in composite laminates capturing permanent indentation. Compos Sci Technol 2012;72:1977–88. https://doi.org/10.1016/j.compscitech.2012.08.019.
[11] Maziz A, Tarfaoui M, Gemi L, Rechak S, Nachtane M. A progressive damage model for pressurized filament-wound hybrid composite pipe under low-velocity impact. Compos Struct 2021;276:114520. https://doi.org/10.1016/j.compstruct.2021.114520.
[12] Kara M, Kırıcı M, Tatar AC, Avcı A. Impact behavior of carbon fiber/epoxy composite tubes reinforced with multi-walled carbon nanotubes at cryogenic environment. Compos Part B Eng 2018;145:145–54. https://doi.org/10.1016/j.compositesb.2018.03.027.
[13] Maziz A, Tarfaoui M, Rechak S, Nachtane M, Gemi L. Finite Element Analysis of Impact-Induced Damage in Pressurized Hybrid Composites Pipes. Int J Appl Mech 2021;13:2150074. https://doi.org/10.1142/S1758825121500745.

MECHANICAL IMPACT OF EMBEDDED SENSORS IN FILAMENT WOUND THERMOPLASTIC COMPOSITE RINGS: NUMERICAL AND EXPERIMENTAL ANALYSES

B. MEEMARY[1], D. VASIUKOV[1], M. LAGARDERE[1], S. CHAKI[1]

[1] IMT Nord Europe, Institut Mines-Télécom, Univ. Lille, Centre for Materials and Processes, F-59000 Lille, France
Email: bilal.meemary@imt-nord-europe.fr, bilalmeemary97@gmail.com
Email: dmytro.vasiukov@imt-nord-europe.fr
Email: mylene.lagardere@imt-nord-europe.fr
Email: salim.chaki@imt-nord-europe.fr

Keywords: Thermoplastic filament winding, composite rings, embedded sensors, Structural Health Monitoring, finite element modeling, split-disk test

Abstract
Filament winding enables the integration of sensors within the core of composite structures during manufacturing for Structural Health Monitoring (SHM). This study proposes a split-disk test using fiber-reinforced polymer composite rings as an alternative to traditional filament wound pressure vessel testing methods. The research aims to evaluate the mechanical effects of embedding fiber optic sensors in various orientations within the rings through experimental analysis. Additionally, it seeks to predict the damage initiation and progression in composite rings using a finite element model of 3D Puck failure criteria and Element Weakening Method (EWM). Validation of this computational method was conducted via 3D Digital Image Correlation (3D DIC) and experimental tensile tests. Results reveal the numerical approach's capability to predict the low hoop strain field near the split area as indicated by the 3D DIC due to the local bending. The experimental data show that embedding fiber optic sensors has a minor influence on the apparent modulus and a negligible effect on the apparent strength of thermoplastic composite rings. However, parallel fiber optic installation aligned with the reinforced fibers is recommended over perpendicular orientations, given the former's less pronounced effects.

1. Introduction

Filament wound composite pressure products (such as vessels and pipes) are employed largely for high-pressure gaseous or liquid storage applications in aerospace, automotive and naval industries [1], [2], [3]. Given that composite tanks are subjected to harsh threats such as critical loadings, temperatures and bursting, a permanent in-situ and online monitoring approach of the structural integrity of storage tanks is of interest. This requires the development of a diagnostic and inspection technique for monitoring the state of health of the composite tank from the damage onset. SHM approach employed for filament wound products is established by the use of a complex strategy based on sensors. Before the employment of SHM technique, a fundamental step is required to understand the mechanical behavior of instrumented composite rings and study the potential influences of embedded sensors on the material degradation of fiber reinforced composite products.

For certification, filament wound pressure vessels must fulfill several mechanical tests, including the hydrostatic burst test for evaluating their circumferential tensile properties. However, the implementation of the burst test is very complicated due to several constraints such as the need for special facilities, trained personnel, and associated costs. To overcome these limitations, an alternative cost-effective testing method involving testing lab-scale specimens of filament wound composite rings cut from composite tubes, is proposed instead of testing the whole pressure vessel. This last test is known

as split-disk test. The split-disk test focuses on measuring the mechanical properties of a filament wound composite, mainly hoop tensile modulus, strength and strain [4], [5], [6].

The most common sensors used for the composite pressure tanks monitoring are fiber optic (FO) sensors [7], [8], [9], [10]. The fundamental reason to integrate a fiber optic sensor is that the sensor itself is a fiber which can easily fit with other fibers of the composite shell. Thanks to its small dimensions, it can be smoothly embedded into composite materials without causing any risk to the structure.

In recent studies, efforts are directed towards damage predictions of filament wound composites using classical failure criterias such as maximum stress, Tsai-Hill [11] and Tsai-Wu [12]. These criterias have the inconvenience of not taking into consideration the identification of failure mode such as matrix crack, fiber failure nor interlaminar failure. Therefore, a more advanced criteria based on the physical prediction mode of the damage onset is needed. The Puck failure criteria [13], based on Hashin criteria [14], is founded to overcome the aforementioned limitations.

In this paper, Puck criteria is coupled with EWM to predict damage initiation and growth in composite rings. Moreover, the mechanical impact of fiber optic sensors embedded in the core of thermoplastic composite rings is studied experimentally to assess their influence on the integrity of the structure.

2. Materials and methods

2.1. Materials and manufacturing of composite tubes

Composite tubes are manufactured using a filament winding technique with impregnated tape of glass fibers and polypropylene resin supplied by AVIENT (see Figure 1), ref Polystrand™ IE 7034B.

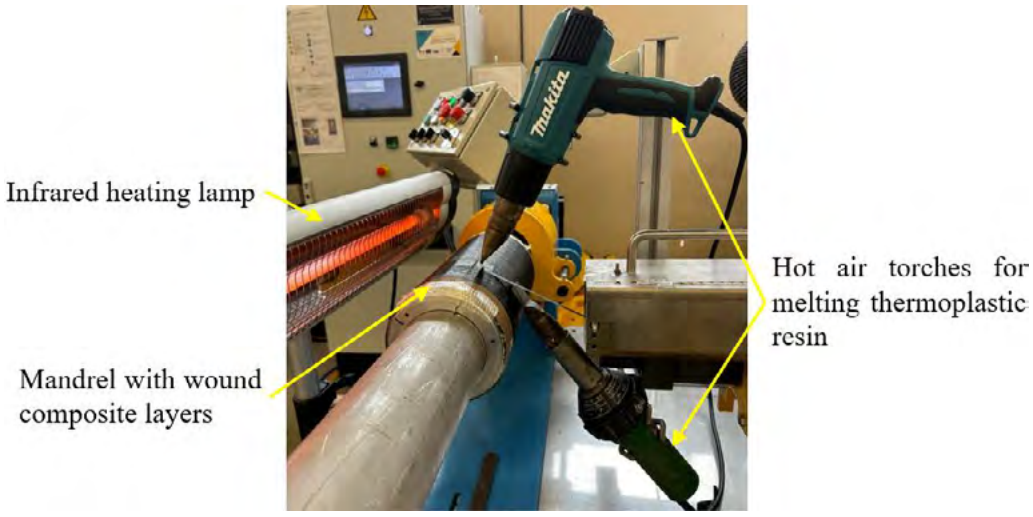


Figure 1. Filament winding process of thermoplastic composite tubes.

The main process-controlled parameters during the manufacturing are reported in Table 1 and include: filament winding angle, tape tension, number of layers, process temperature and the mandrel rotational speed. The tubes have a length of 275 mm and an internal diameter of 150 mm. Each layer has a theoretical thickness of 0.23 mm (initial tape thickness). For this study, only hoop winding is considered. The filament winding process requires to heat the incoming tape and the already deposited substrate up to the resin melting temperature. The tape is preheated to 100 °C, then hot air torches are used to heat locally the deposited tape on the mandrel until reaching the melting point at 200 °C. During winding, an infrared heating lamp is added behind the mandrel to maintain a high temperature of the composite layers, reduce the temperature difference and prepare the deposited layer to re-melt and to bond with the new layer. Once the tube is cooled down, it is put in the freezer for three hours to facilitate its unmolding. The process time for one tube manufacturing is in an average of 70 minutes.

Table 1. Manufacturing parameters of composite tubes.

Winding angle (°)	Winding tension (N)	Number of layers	Resin melting temperature (°C)	Rotation speed of mandrel (rpm)
88.8	40	6	200	5

2.2. Fiber optic sensors integration in composite tubes

Fiber optic cables are supplied by RS Components, France, with a core diameter of 125 μm. In total, seven fiber optic cables are embedded between the third and the fourth layer. Four tubes (T) are manufactured (see Figure 2 (a)). Two tubes (T1) and (T2) are instrumented with a total of six optical fiber sensors embedded circumferentially, thus in parallel to the reinforced glass fibers. Three rings from each tube are equipped with fiber optic sensors, while the remaining three rings within the same tube are sensor free. The goal of this division is to maintain the same manufacturing conditions with and without sensors. The third tube (T3) is instrumented with one fiber optic sensor embedded axially along the cylinder axis, thus perpendicular to the reinforced fibers. In tubes T1, T2 and T3, notches were introduced in ring specimens as recommended by the standards ISO 8521:2020 [15] to initiate damage in one localized zone that represents the Region of Interest (ROI) for the 3D DIC measurements. The tube (T4) is sensor free and three full ring specimens are extracted for testing and comparison with the numerical simulation. Four types of rings are tested: notched rings without sensors, notched rings with parallel FO sensors, notched rings with perpendicular FO sensors and full rings without sensors (see Figure 2 (b)). Three samples from each tube are used for fiber volume fraction (FVF) determination via burn-out tests. The location of FOs in the case of circumferential installation are positioned in the middle of the ring. In the case of axial installation, FOs are positioned in the middle of the notched area (in the most reduced section). The dimensions of notched rings are in accordance with the ISO 8521:2020 [15] standards, and are presented in Figure 2 (c) . Full rings are presented in Figure 2 (d). Tests are conducted on 15 or 35 mm wide cut-out rings from the manufactured cylinders.

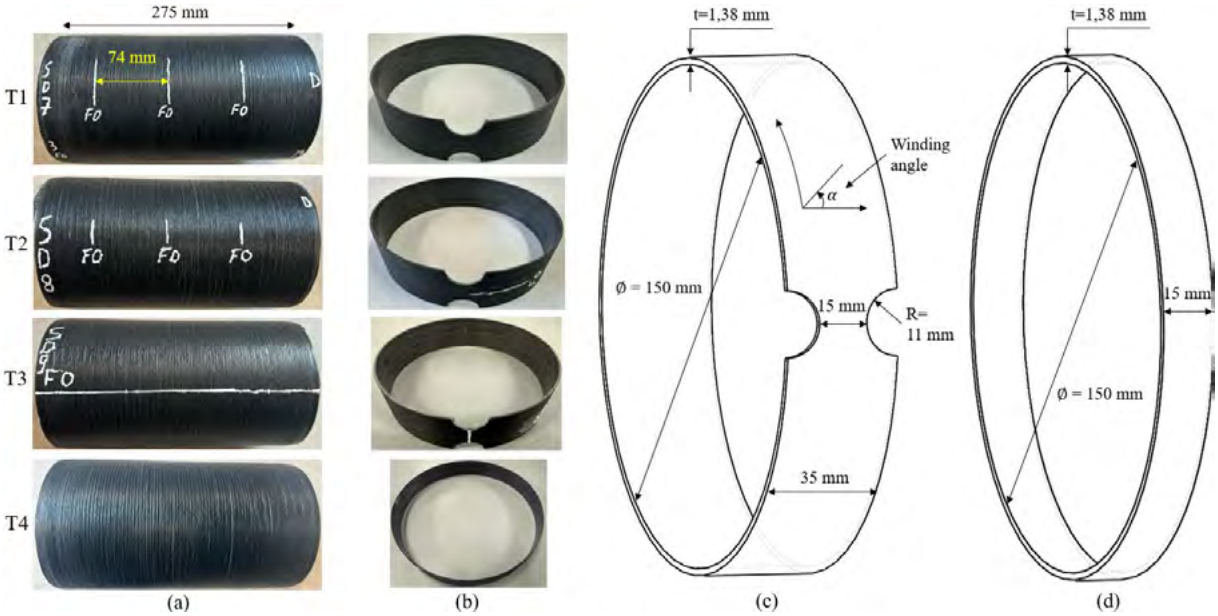


Figure 2. (a) Four manufactured thermoplastic composite tubes (white lines represent the location and direction of FO sensors); (b) four tested types of composite rings without and with FO sensors; (c) dimensions of notched composite rings; (d) dimensions of full composite rings.

2.3. Preparation of test composite rings

Rosette strain gauges are bonded using Loctite adhesive on the outer surface at an angular position of 10° with respect to the disks split line. The position of strain gauges for stiffness calculation is chosen as recommended by Zhao et al. [4] due to the absence of the influence of local bending. Apparent hoop modulus is measured by the real longitudinal strain gauges and virtual DIC longitudinal extensometer.

Three-dimensional DIC system equipped with two cameras is used to measure local hoop strain on the outer surface of the rings to accurately characterizing the complex three-dimensional deformations exhibited by non-planar structures. A black and white speckle pattern is applied to the tested ring specimens by covering only a 45° of the ring circumference around the notched zone for stereo images acquisitions. The covering area of speckles is defined as the ROI. A prepared notched and full ring specimens for testing are presented in Figure 3 (a) and (b), respectively, with added strain gauges and speckle pattern for DIC.

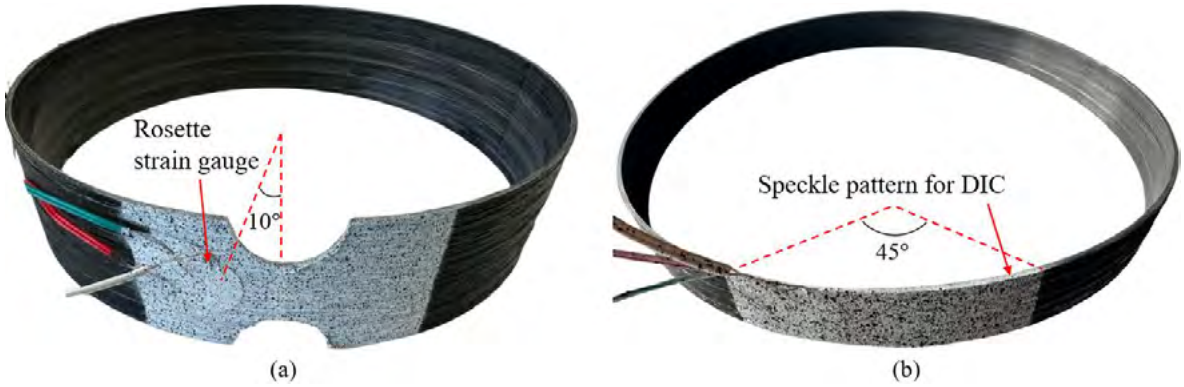


Figure 3. Ring specimens preparation before testing: (a) notched ring; (b) full ring.

2.4. Setup of split-disk test

The 3D DIC system with the split-disk setup mounted on the tensile test unit is presented on Figure 4 (a). The experiment is conducted on an Instron 1185 universal mechanical testing machine in accordance with ISO 8521:2020 standards [15]. The schematization of the 3D DIC system is shown in Figure 4 (b). Each specimen is loaded to the final failure by using a load cell of 100 kN. All tests are conducted under displacement control at a loading rate of 10 mm/min and at a room temperature of 23 °C. Due to the bending generated at the split line of separation of the two half-disks during testing, an apparent tensile strength and modulus are obtained.

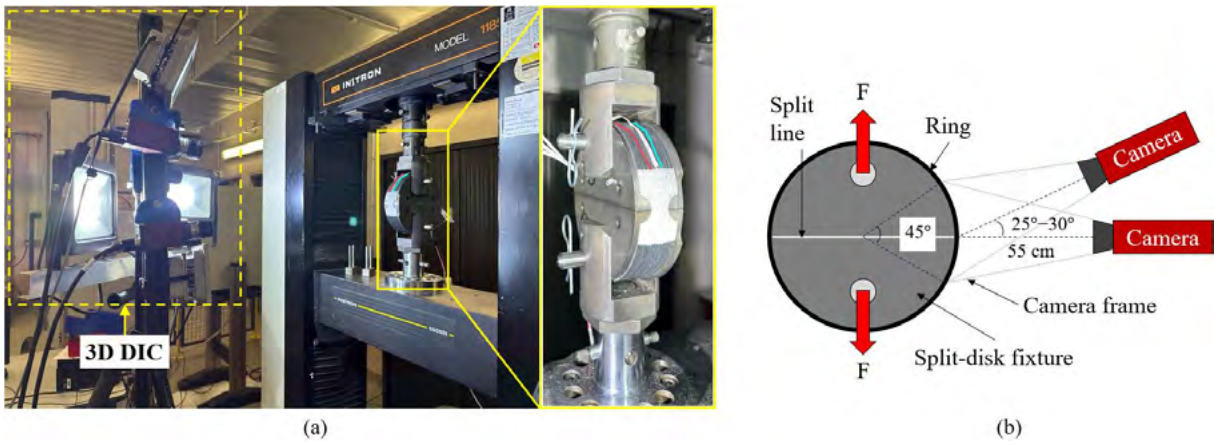


Figure 4. (a) Setup for split-disk testing in the tensile machine with 3D DIC system; (b) schematization of the 3D DIC system.

3. Results and discussion

3.1. Finite element analysis of full ring specimen

Finite element (FE) numerical simulation aims to: 1) analyze the hoop strain distribution along the circumference and compare it with full field strain obtained by 3D DIC, and investigate the bending effect; 2) evaluate the ultimate force predicted by the numerical model and compare it with the experimental results. Damage modeling is performed using a developed UMAT subroutine (User defined MATerial behavior) code on Fortran coupled with Abaqus FE commercial software. Damage modeling includes two parts: a damage initiation prediction using 3D Puck failure criteria and Progressive Failure Analysis (PFA) using Element Weakening Method (EWM).

3.1.1. Finite element model

A symmetrical FE model is developed to represent half of a ring, with a thickness of 1.38 mm, a width of 15 mm, and an internal diameter of 150 mm. The disk is treated as a discrete rigid part with a diameter of 150 mm. Contact properties are defined with tangential behavior and a low friction coefficient of 0.01, along with hard contact normal behavior between the disk and composite ring. Calibration of the assigned mechanical properties in the numerical model is achieved by comparing its force-displacement response with the experimental data from the tested full ring specimens. Considering the actual composition of the ring constituents, material heterogeneity through the thickness, and the presence of a resin layer on the outermost surface of rings as depicted by microscopic images due to manufacturing; the composite ring model is segmented into two equal parts through the thickness to take into account various areas dense in fibers and others in resin. The lower segment presents a FVF of 50 %, and the upper segment a FVF of 33 %, with material properties defined using the rule of mixture. The segments are composed of pure hoop layers with a 88.8° winding angle with respect to the ring main axis. The numerical model employs C3D8R elements for the composite ring, with a total of 56880 elements. The numerical model is able to render the complex mechanical behavior of the composite rings under an applied tension of an 8 mm displacement. The numerical predictions are compared to experimental results in terms of force-displacement response in Figure 5 (a). Tensile tests indicated an average failure load of 32096 N. In the numerical model, fiber failure, often considered the ultimate failure in fiber-reinforced polymers, is assumed to occur when fiber fracture extended across the specimen width in all plies, accompanied by a sudden drop of the displacement. Based on these assumptions, as shown in Table 2, the numerical model predicts failure at a maximum force of 30032.4 N, representing 6.4 % error compared to the average experimental results. Similarly, regarding displacement at failure, the simulations closely matched experimental values, with an average difference of less than 15 %. The numerical model predictions closely correspond to the observed mechanical response, providing validation of its accuracy and reliability in predicting the structural behavior of the composite rings.

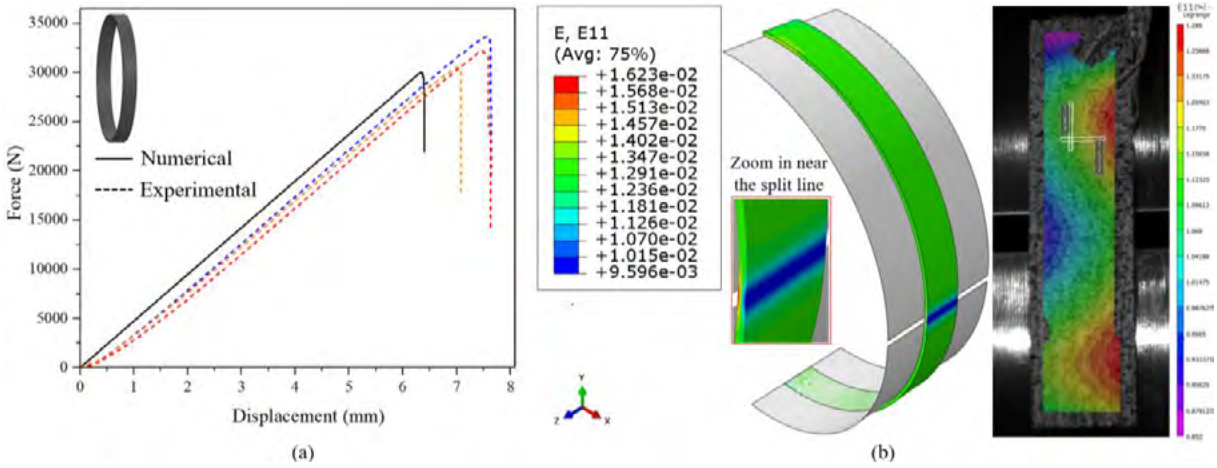


Figure 5. (a) Numerical and experimental force-displacement response of full ring specimen; (b) comparison between the first local strain E11 (in fiber direction) fields obtained numerically (left) and experimentally (right) for an applied load of 14.95 kN.

Table 2. Comparison between experimental and numerical simulation results.

Analysis method	Maximum load (N)	Maximum displacement (mm)
Experimental tests (mean values)	32096 ± 1563	7.44 ± 0.317
Finite element analysis	30032.4	6.403
Relative deviation (%)	6.4	13.9

Figure 5 (b) presents a comparison among the strain field predicted by the numerical simulation and 3D DIC measurements. This analysis involves evaluating the first local material coordinate strain E11 field at the outermost full ring specimen's surface. In general, there is a strong alignment between the predicted strain fields and the 3D DIC measurements. Particularly, at a load of 14.95 kN, the predicted and measured strain by 3D DIC at the location of strain gauge agree well with values of 1.32 % and 1.25 %, respectively. When focusing on the region surrounding the split line in the numerical simulation, the coupling of Puck criteria with the EWM demonstrates its ability to predict the high strain area at the inner surface and the low strain area at the outer surface, attributed to local bending. These findings are supported by the 3D DIC strain maps. Experimental results indicate localized bending near the split line, which can be characterized by the low strain area observed on the outermost surface at the same location.

Figure 6 illustrates a comparison between the typical failure observed numerically and experimentally. At maximum load, Figure 6 (a) depicts the final failure stage of the full ring close to the split line region, introduced by the fiber failure. During testing, the final failure occurs abruptly. Figure 6 (b) exhibits the final failure of the full ring, revealing a significant fiber breakage accompanied by delamination and matrix splitting. The predicted failure from FE simulation aligns well with experimental testing.

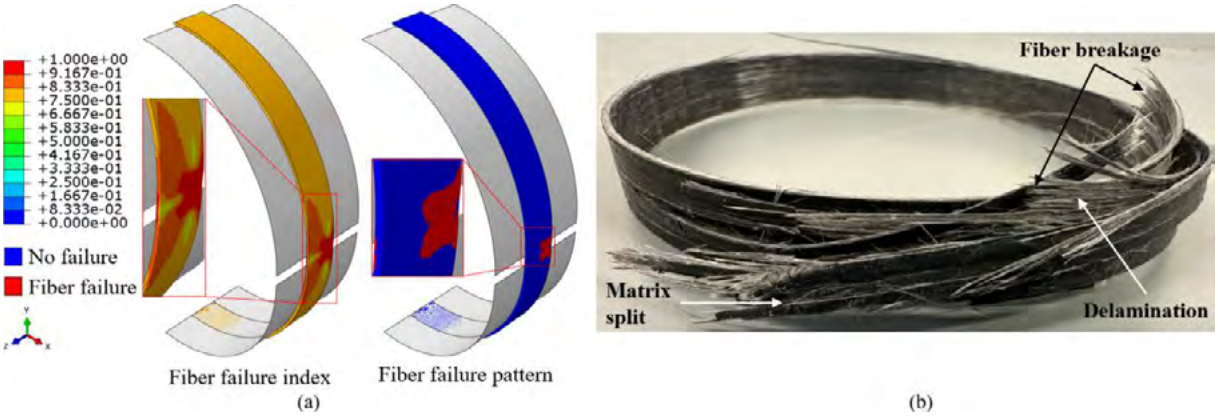


Figure 6. Comparison of damage: (a) fiber failure predicted by FE simulation; (b) failed ring.

3.2. Apparent hoop tensile properties for notched ring specimens

3.2.1. Apparent modulus

Longitudinal hoop strains measured by strain gauges and 3D DIC at an angular position of 10° serve for calculating the apparent hoop tensile modulus for the three different types of notched ring specimens. The theoretical modulus for each ring is determined using the rule of mixtures, considering the corresponding FVF for T1 (38.7 %), T2 (41.52 %), and T3 (42.61 %). The calculated apparent hoop modulus and theoretical modulus are shown in Figure 7 (a). Comparison of results shows that apparent hoop tensile modulus based on strain gauges and 3D DIC measurements are the highest for ring specimens without sensor. Apparent modulus decreases by 2.8% and 3% when a parallel FO is embedded among layers based on strain gauges and 3D DIC measurements, respectively. When FO sensor is embedded perpendicular to the orientation of reinforced fibers, the apparent hoop modulus is decreased by 7.52% and 7.67% based on strain gauges and 3D DIC, respectively. Based on these findings, 3D DIC exhibits strong agreement with strain gauges measurements, indicating its suitability for strain measurements in composite rings. Embedding FO sensors perpendicular to reinforced fibers degrades more the stiffness of the thermoplastic composite rings than the parallel FO embedment. In

other words, embedding FO sensors aligned with the reinforced fibers is the most effective way to minimize degradation of the composite's stiffness. Theoretical modulus cannot be compared since they are based only on the physical properties of the materials and do not depend on the existence of FO sensors within the composite rings.

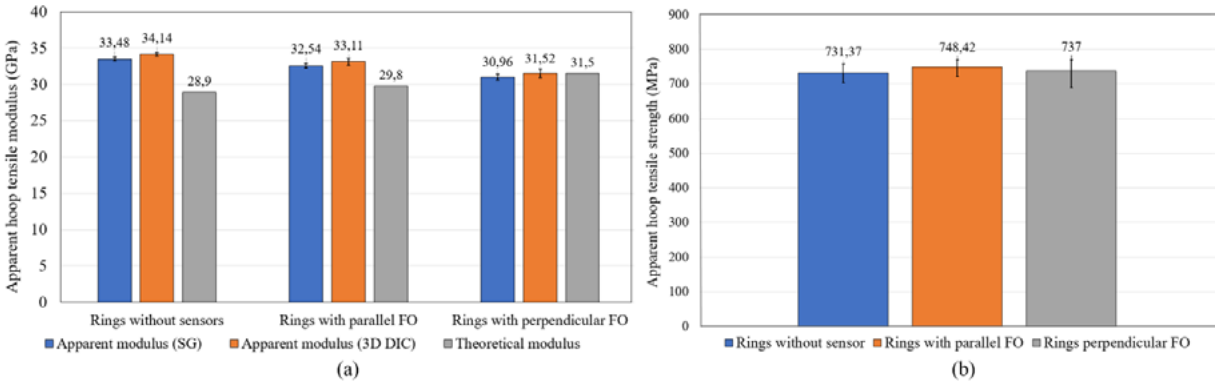


Figure 7. Comparison of the hoop tensile apparent properties for the three types of notched rings (a) calculated modulus based on hoop strains from strain gauges and 3D DIC, and the theoretical modulus; (b) calculated ultimate longitudinal strength.

3.2.2. Apparent strength

Apparent hoop tensile strength is calculated based on the average of the ratio between the half of the maximum load and the cross-sectional area of the notched zone at the split line. The theoretical tensile strength given by the material supplier is 765 MPa with a FVF of 45 %. Due to the existing bending moment in the notched zone during tension, the obtained apparent tensile strength is slightly underestimated for ring specimens without sensors with an average value of 731.37 MPa as can be seen in Figure 7 (b). The slight difference between the obtained tensile strength and that given by the supplier can also be influenced by other factors, including the discrepancy in FVF, as well as the presence of the notch, which initiate cracks earlier due to the emergence of matrix splitting in hoop direction near the notches at earlier load stages. The standard deviations of the three ring specimens types overlap with each other, indicating that the embedment of FO sensors does not influence the hoop tensile strength. Therefore, the embedment of FO sensors has no impact on the mechanical strength of the material.

4. Conclusions and perspectives

This paper presents a FE numerical simulation and an experimental analysis of filament wound thermoplastic composite rings. The numerical study investigates the implementation of 3D Puck failure criteria for damage initiation and EWM for damage progression prediction in full composite rings. The FE approach effectively predicts the low strain field at the outer surface near the split region when compared with 3D DIC, as well as the ultimate failure load with less than 7 % error with respect to tensile tests results. Experimental tests explore the mechanical impacts of embedding FO sensors within composite rings, examining two extreme cases: parallel and perpendicular orientations relative to the reinforced glass fibers. Results revealed that embedding FO sensor parallel to the reinforced fibers slightly reduces the apparent hoop tensile modulus by approximately 3 %, while the perpendicular orientation showed a reduction of about 7.5 %. However, the apparent hoop tensile strength remained unaffected by sensor embedding, as the standard deviation among each case overlapped. Overall, embedding FO sensors in the core of thermoplastic rings had a negligible impact on the filament wounded composite's mechanical performance, but parallel embedding is recommended for minimal disruption. The subsequent phase of this analysis involves conducting a finite element numerical study based on 3D Puck failure criteria and EWM to investigate the mechanical effects of FO sensors within composite rings using the embedded element method for modeling the presence of FO sensors.

Acknowledgments
Publication carried out as part of the CORENSTOCK Industrial Chair ANR-20-CHIN-0004-01, co-founded by the industrial company elm.leblanc "Group BOSCH", IMT (Institut Mines-Télécom), and its Schools IMT Nord Europe and École des Mines de Saint-Étienne, founded by the French National Research Agency, supported by the Carnot Institute Télécom & Digital Society, and endorsed by the EMC2 pole.

References

[1] P. Sharma *et al.*, « Effects of dome shape on burst and weight performance of a type-3 composite pressure vessel for storage of compressed hydrogen », *Compos. Struct.*, vol. 293, p. 115732, août 2022, doi: 10.1016/j.compstruct.2022.115732.
[2] S. Alam, G. R. Yandek, R. C. Lee, et J. M. Mabry, « Design and development of a filament wound composite overwrapped pressure vessel », *Compos. Part C Open Access*, vol. 2, p. 100045, oct. 2020, doi: 10.1016/j.jcomc.2020.100045.
[3] P. Sharma, P. Chugh, et S. Neogi, « Study to methodize the design of a safe Type-4 CNG storage vessel using finite element analysis with experimental validation », *Int. J. Press. Vessels Pip.*, vol. 192, p. 104425, août 2021, doi: 10.1016/j.ijpvp.2021.104425.
[4] Y. Zhao, P. Druzhinin, J. Ivens, D. Vandepitte, et S. V. Lomov, « Split-disk test with 3D Digital Image Correlation strain measurement for filament wound composites », *Compos. Struct.*, vol. 263, p. 113686, mai 2021, doi: 10.1016/j.compstruct.2021.113686.
[5] R. Rafiee, M. Maleki, et S. Rahnama, « Experimental study on the effect of hygrothermal environments combined with the sustained mechanical loads on the strength of composite rings », *Compos. Struct.*, vol. 258, p. 113397, févr. 2021, doi: 10.1016/j.compstruct.2020.113397.
[6] W. Gul, Y. E. Xia, P. Gérard, et S. K. Ha, « Characterization of Polymeric Composites for Hydrogen Tank », *Polymers*, vol. 15, nº 18, p. 3716, sept. 2023, doi: 10.3390/polym15183716.
[7] P. Gąsior *et al.*, « Validation of Selected Optical Methods for Assessing Polyethylene (PE) Liners Used in High Pressure Vessels for Hydrogen Storage », *Appl. Sci.*, vol. 11, nº 12, p. 5667, juin 2021, doi: 10.3390/app11125667.
[8] Z. Liang *et al.*, « FBG-based strain monitoring and temperature compensation for composite tank », *Aerosp. Sci. Technol.*, vol. 127, p. 107724, août 2022, doi: 10.1016/j.ast.2022.107724.
[9] X. Qu *et al.*, « Various static loading condition monitoring of carbon fiber composite cylinder with integrated optical fiber sensors », *Opt. Fiber Technol.*, vol. 83, p. 103685, mars 2024, doi: 10.1016/j.yofte.2024.103685.
[10] T. M. J. Gebhart, M. Seeberg, H. Çelik, R. Dahlmann, et C. Hopmann, « Advanced methods for the detection of measurement outliers in fibre optic strain measurements for non-destructive monitoring of the structural health of composite over-wrapped pressure vessels of type-IV », *Measurement*, vol. 226, p. 114133, févr. 2024, doi: 10.1016/j.measurement.2024.114133.
[11] V. D. Azzi et S. W. Tsai, « Anisotropic strength of composites: Investigation aimed at developing a theory applicable to laminated as well as unidirectional composites, employing simple material properties derived from unidirectional specimens alone », *Exp. Mech.*, vol. 5, nº 9, p. 283-288, sept. 1965, doi: 10.1007/BF02326292.
[12] S. W. Tsai et E. M. Wu, « A General Theory of Strength for Anisotropic Materials », *J. Compos. Mater.*, vol. 5, nº 1, p. 58-80, janv. 1971, doi: 10.1177/002199837100500106.
[13] A. Puck et H. Schürmann, « Failure analysis of FRP laminates by means of physically based phenomenological models », *Compos. Sci. Technol.*, vol. 62, nº 12-13, p. 1633-1662, sept. 2002, doi: 10.1016/S0266-3538(01)00208-1.
[14] Z. Hashin, « Failure Criteria for Unidirectional Fiber Composites », *J. Appl. Mech.*, vol. 47, nº 2, p. 329-334, juin 1980, doi: 10.1115/1.3153664.
[15] ISO 8521:2020, « Glass-reinforced thermosetting plastic (GRP) pipes — Test methods for the determination of the initial circumferential tensile wall strength ». Switzerland, juillet 2020. [En ligne]. Disponible sur: https://viewerbdc.afnor.org/pdf/viewer/C8ePvsO9H2w1?proxy=true

MICROMECHANICAL MODELING OF TRANSVERSE CRACKING WITH DIFFERENT METHODS FOR GENERATING RANDOM FIBER DISTRIBUTIONS

Mahoor Mehdikhani[1], Rui Guo[1], Christian Breite[1], Sina AhmadvashAghbash[1], Diego Celentano[2] and Yentl Swolfs[1]

[1]KU Leuven, Department of Materials Engineering, Kasteelpark Arenberg 44, 3001 Leuven, Belgium
Email: mahoor.mehdikhani@kuleuven.be, Web Page: https://www.mtm.kuleuven.be/english
[2]Pontificia Universidad Católica de Chile, Department of Mechanical and Metallurgical Engineering, Avenida Vicuña Mackenna 4860, Macul, Chile
Email: dcelentano@uc.cl, Web Page: https://www.ing.uc.cl/mecanica-y-metalurgica/

Keywords: Micromechanics, finite element modeling, transverse cracking, random fiber distribution, deep learning

Abstract
This study presents a modeling investigation into the initiation and propagation of transverse cracking in unidirectional fiber-reinforced composites, focusing on factors like fiber arrangement and matrix properties. Microscale computational models are created to address those challenges. Since existing fiber distribution generators are criticized for not representing features like resin-rich pockets, a deep learning approach is utilized to produce realistic microstructures for finite element modeling. A constitutive material model, incorporating epoxy plasticity and damage, successfully predicts the transverse crack formation and propagation under periodic boundary conditions. The study evaluates the impact of fiber arrangement on cracking behavior using microstructures generated by different methods, revealing similarities and differences in predicted outcomes. This research offers insights into enhancing the accuracy of computational models for simulating transverse cracking in composites.

1. Introduction

The initiation and propagation of transverse cracking in composites are governed by factors such as defects, arrangement of fibers, and properties of the matrix and fiber-matrix interface. Microscale computational models have been developed to simulate transverse cracking. The key challenges for such models lie in the 1) development of physics-based material models for the fiber, matrix, and interface and 2) generation of a representative volume element (RVE) that reflects the microstructure. In the existing models, fibers are often simplified to linear isotropic materials, while for the matrix, a few different plasticity and damage models have been proposed, such as those in [1, 2]. A vital challenge for these material models is the correct identification of the input parameters since those measured via macroscale testing do not always represent the behavior of the material at the microscale [3].

It is well established that the spacing between neighboring fibers determines the level of stress concentration between them. Therefore, predicting the transverse properties of composites depends heavily on the arrangement of fibers. Early models assumed regular distributions, i.e. square or hexagonal packings [7, 8], which led to poor estimation of transverse properties since in reality fibers are distributed in a random pattern [9, 10]. Usually, to achieve a random fiber distribution, a real microstructure is mimicked, like in [11], or random distribution generators are used. For the latter, a few methods have been proposed [12, 13], among which the one by Melro et al. [14] is commonly used.

Despite their high efficiency, these types of generators are criticized because they do not represent features like resin-rich pockets [15].

In the current study, micromechanical Finite Element (FE) models are developed to predict the transverse cracking and failure (transverse strength) of unidirectional fiber-reinforced composites, focusing on enhancing the two abovementioned issues. We have exploited deep learning to generate realistic images of transverse microstructures of unidirectional composites, yielding representative fiber distributions. Using these realistic GAN-generated microstructures, FE models for the simulation of transverse cracking are created. A constitutive material model, based on that developed by Morelle et al. [2], accounting for epoxy plasticity and damage, is implemented for the matrix. Applying periodic boundary conditions [6] to the RVEs, the implemented model can successfully predict the formation and propagation of transverse cracks. To evaluate the quality of our GAN-generated RVEs, experimental RVEs (from the real computed tomography images) as well as RMG-generated RVEs (based on the Melro's random generator [14]) are created for comparison. Analysis of different RVE generation methods demonstrates that the predicted transverse cracking behavior is similar in the deep-learning and real-image-based models, and slightly distinct from that in the random-generated one. A quantitative approach to compare the crack propagation path between these three microstructures is being developed.

2. Model development

2.1. RVE generation approaches

We employed three distinct methods to generate four periodic RVEs with a fiber volume fraction of approximately 51%: experimental, GAN-generated [16], and RMG-generated [15]. Each RVE measures 83.2 μm * 83.2 μm and contains over 100 fibers. As the validation outlined in [17-20], utilizing such large RVEs can effectively mitigate the influence of RVE size effects. The details of the generation algorithm are provided below.

- These microstructures are non-periodic for the experimental and GAN-generated microstructures; we use a Python script to convert them into periodic structures while preserving the original fiber distribution and minimizing variations in fiber volume fraction. According to our previous work [16], the calculated fiber diameter needs correction with an appropriate correction factor. However, this adjustment can lead to touching fibers, necessitating control measures to optimize finite element model generation. Moreover, in the process of creating periodic microstructures, it is necessary to iteratively adjust fiber positions to ensure the fibers on the model edges satisfy equation (1):

$$d_{i,j} \geq \left(1 + l_{ifd}\right) \cdot \left(r_i + r_j\right), \; for \; i \neq j \tag{1}$$

  where $d_{i,j}$ represent the distance between the i and j fibers, $r_{i,j}$ is their radius, and l_{ifd} corresponds to the ratio defining the minimal inter-fibre distance which is set to [0.05, 0.15] for the generation of high-quality elements. When we generate the periodic microstructures, the inter-fiber distance might not satisfy this requirement.

- For RMG-generated microstructures: these generated microstructures are periodic, but the fiber radius is constant. The inter-fiber distance is limited to the range of 0.1R and 0.3R, maintaining a constant fiber diameter (2R) of 6.5μm.

2.2. Constitutive material models

Fiber. Under the transverse tension, the fibers will not break and thus were considered linear elastic. Table 1 provides the properties of the fiber, matrix, and interface.

Table 1. The elastic material properties for carbon fiber, matrix, and interface.

Fiber properties [4]

Longitudinal Young's modulus (E_{11}^f)	238 GPa
Transverse Young's modulus ($E_{22}^f = E_{33}^f$)	28 GPa
Longitudinal Poisson's ratio (v_{12}^f/v_{31}^f)	0.28/0.02
Transverse Poisson's ratio (v_{23}^f)	0.33
Longitudinal shear modulus ($G_{12}^f = G_{31}^f$)	24 GPa
Transverse shear modulus (G_{23}^f)	7.2 GPa
Density (ρ^f)	1.8 g/cm^3
Matrix properties (RTM-6) [4, 21]	
Young's modulus (E^m)	3 GPa
Poisson's ratio (v^m)	0.34
Density (ρ^m)	1.14 g/cm^3
Drucker–Prager – Friction angle (β)	7.86 °
Drucker–Prager – Flow stress ratio (K)	1
Drucker–Prager – Dilatation angle (ψ)	0 °
Fiber-matrix interface properties [4]	
Elastic stiffness (K^i)	10^8 N/mm^3
Density (ρ^i)	1.14 g/cm^3
Mode I maximum traction [22]	50 MPa
Mode II & III maximum traction [22]	75 MPa

Matrix. A constitutive material model, based on that developed by Morelle et al. [2] and Chevalier et al. [4], accounting for epoxy's elasticity, plasticity and damage, is implemented for the RTM-6 matrix. This model accounts for yielding based on the linear Drucker-Prager criterion and isotropic strain hardening, which includes pre-peak hardening, softening, and rehardening. Moreover, failure is included based on critical equivalent plastic strain. Input parameters for the pre-failure phase are taken from compression tests, accounting for the compression-tension stress ratio. Macro-scale experimental results indicate that epoxy exhibits brittle fracture behavior at very low strains under uniaxial tension and can withstand larger strains in uniaxial compression and pure shear [4]. Consequently, a stress triaxiality-dependency is often assumed to predict its damage initiation. At the same time, epoxy demonstrates a strong size dependency [3, 5]. Sui et al. [5] showed that microscale epoxy fibers can reach 80% of strain before failure, suggesting that the stress triaxiality-dependency assumption may be invalid for microscale simulation. Therefore, in the definition of the epoxy material model, we assumed the same failure strain value for tension and compression. The elastic properties are given in Table 1. The governing equation for the linear Drucker-Prager model (available in Abaqus) is:

$$F = t + p\tan\beta - d = 0 \tag{1}$$

where t is the yield stress, p denotes the pressure, β corresponds to the friction angle, and d stands for the cohesion term. The friction angle β defines the slope of the yield surface in the t-p plane. The expression for t is:

$$t = \frac{\sigma_{eq}}{2}\left[1 + \frac{1}{K} - \left(1 - \frac{1}{K}\right)\left(\frac{I_3}{\sigma_{eq}}\right)^3\right] \tag{2}$$

where σ_{eq} is the von Mises equivalent stress, K is the stress ratio between yield stress under triaxial tension and triaxial compression, and I_3 is the third invariant of the deviatoric stress tensor. According to equation (2), with the fact $K = 1$ [4], we can obtain $t = \sigma_{eq}$.

The isotropic hardening law for the tension case is defined from the compression stress-strain curve. Consequently, the cohesion term d in equation (2) can be expressed as:

$$d = (1 - \frac{1}{3}tan\beta)\sigma_c \tag{43}$$

σ_c represents the compression yield stress and the data for σ_c is collected from the literature [4] at a strain rate of 10^{-4} s^{-1}. The associated flow rule is given by:

$$G = \sigma_{eq} + ptan\phi \tag{54}$$

Here, G represents the flow potential, and ϕ corresponds to the dilation angle. The value of ϕ is set as zero as plastic incompressibility was assumed. Along with the increase in plastic strain, it is essential to account for the damage initiation. To consider the matrix scale sensitivity, we assume that the failure strain for epoxy under tension is the same as in compression, specifically 0.572 [2, 4].

After failure initiation, the damage evolution follows a progressive procedure controlled by the damage variable (D). This variable increases as damage accumulates, according to the following expression:

$$\dot{D} = \frac{\dot{\bar{u}}^{pl}}{\bar{u}_f^{pl}} = \frac{L\dot{\bar{\varepsilon}}^{pl}}{\bar{u}_f^{pl}} \tag{6}$$

where L is the characteristic length, $\bar{\varepsilon}^{pl}$ and $\bar{u}^{pl}$, respectively, are the equivalent plastic strain and plastic displacement. Before the onset of the damage, $\dot{\bar{u}}^{pl}$=0, which means D is equal to 0. After the damage initiation, the damage variable $\dot{\bar{u}}^{pl}$ is equal to $L\dot{\bar{\varepsilon}}^{pl}$. When $\dot{\bar{u}}^{pl}$ reaches $\bar{u}_f^{pl}$, it indicates that the elements have reached the equivalent plastic displacement at failure and will be deleted. To determine the plastic displacement at failure, $\bar{u}_f^{pl}$, we can relate it to the yield stress and the fracture energy per unit area G_f:

$$G_f = \int_0^{\bar{u}_f^{pl}} \sigma_y \, d\bar{u}^{pl} \tag{75}$$

The value we set for G_f is 100 J/m^2.

Interface: To account for debonding at the interface between fibers and the matrix, zero-thickness cohesive elements (COH2D4) are inserted. These elements follow a bi-linear traction-separation law to describe their mechanical behavior. The initial response is linear, with a large stiffness value (K) equal to 10^8 MPa/mm. This choice ensures displacement continuity at the interface.
In our study, the quadratic nominal stress damage initiation criterion is used to determine the damage initiation as:

$$\left\{\frac{\langle t_n \rangle}{t_n^0}\right\}^2 + \left\{\frac{t_s}{t_s^0}\right\}^2 + \left\{\frac{t_t}{t_t^0}\right\}^2 = 1 \tag{86}$$

where $\langle t_n \rangle$ indicates the Macaulay brackets for the normal stress (they return zero if the term inside the brackets is negative). t_n^0, t_s^0, t_t^0 are the normal and shear strengths of the interface.
Once the damage initiation criteria are met, the cohesive element's elastic stiffness is degraded with a scalar damage variable D with the below equation [23].

$$D = \frac{\delta_m^f(\delta_m^{max} - \delta_m^0)}{\delta_m^{max}(\delta_m^f - \delta_m^0)} \tag{97}$$

δ_m represents the mixed mode effective separation: $\delta_m = \sqrt{(\delta_n)^2 + (\delta_s)^2 + (\delta_t)^2}$ and δ_m^{max} is the maximum effective displacement attained during the loading history. δ_m^0 and δ_m^f correspond to the effective displacement at the initiation of damage and complete failure, respectively.
δ_m^f can be defined by effective traction at the damage initiation T_{eff}^0 and critical energy G^c:

$$\delta_m^f = 2G^c/T_{eff}^0 \tag{108}$$

Here, the Benzeggagh-Kenane fracture criterion [24] is used, which assumes the critical fraction energies along the mode II (G_s^c) and mode III (G_t^c) are the same.

$$G^c = G_n^c + (G_s^c - G_n^c)(\frac{G_S}{G_T})^\eta \tag{11}$$

where G_S represents the sum of the two shear energies in two directions and G_T represents the sum of all fracture energies. For mode I fracture toughness (G_n^c), we set it as 10 J/m^2, while for Mode II & III fracture toughness (G_s^c), it is set as 50 J/m^2. η is a material parameter and is taken as 1.45 [24, 25].

2.3. Periodic boundary conditions

Periodic boundary conditions are employed with linear equations constrained in Abaqus. 4-node plane strain, reduced integration elements (CPE4R), and a few 3-node triangle elements (CPE3) are used to mesh the fiber and matrix. Using more than 2 elements in an area with possible stress concentration between the fibers is reasonable to capture the localized effects. The simulation was performed in Abaqus/Explicit to overcome the convergence issues as the damage considered in the matrix and interface.

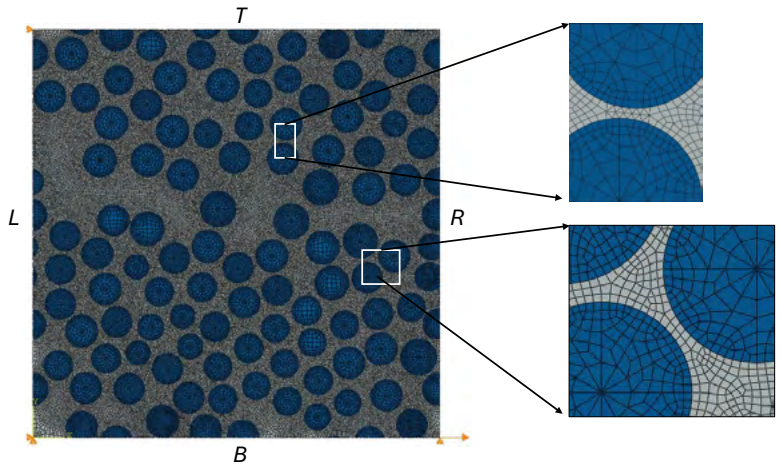


Figure 1. Periodic boundary condition for the RVE and their finite element discretization.

3. Results and discussions

Transverse tension loading simulations were conducted on three distinct types of microstructures: experimental, GAN-generated, and RMG-generated. Each type of microstructure was analyzed using four different RVEs. These RVEs demonstrated minor differences in their fiber volume fraction: 51.1%±1.0% for experimental, 50.5%±0.2% for GAN-generated, and 51.3%±0.3% for RMG-generated microstructures.

Figure. 2 illustrates the strain-stress curves for the different types of microstructures. We define failure of the RVEs as the point when the curve exhibits a notable drop, with the corresponding strain value referred to as the failure strain. From Figure 2a, it is evident that the strength and failure strain exhibit some variability across different RVEs. The mean strength is 60.2 MPa, with a standard deviation of 0.7

MPa. The mean failure strain is around 1.82%, with a standard deviation of 0.09%. For the GAN-generated RVEs (in Figure 2b), the mean strength and mean failure strain are 59.50 MPa and 1.73%, respectively. Their standard deviations are 0.13 MPa and 0.07%. For the RMG-generated RVEs, the mean strength is 59.5 MPa with a standard deviation of 0.4 MPa, and the mean failure strain is 1.75% with a standard deviation of 0.03%. We can observe that their mean strength values and failure strain are similar for all of these cases, as also concluded in [7]. However, their standard deviation values show differences, which can be attributed to the variation in their fiber volume fraction. Specifically, the trend of the standard deviation of strength follows the variation of fiber volume fraction. Interestingly, while the RMG-generated RVEs exhibit a relatively large variation in strength, their failure strain displays a relatively small variation and does not follow the fiber volume fraction variation trend. This suggests that the presence of resin-rich pockets might contribute to delaying failure, as similarly observed in [26].

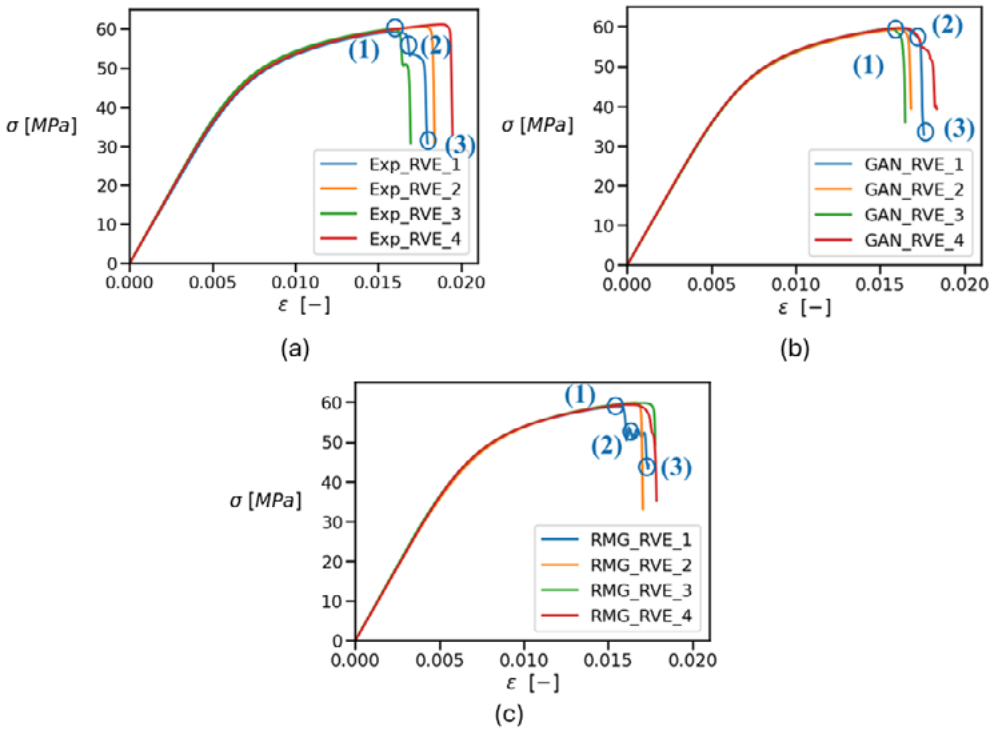


Figure 1. Comparison of stress-strain curves under transverse tension for (a) experimental microstructures, (b) GAN-generated microstructures, and (c) RMG-generated microstructures.

In Figure 3, we depict the damage evolution for the three different types of RVEs. Each case corresponds to the first RVE and is labeled Exp_RVE_1, GAN_RVE_1, and RMG_RVE_1. The results at points (1), (2), and (3) within each case correspond to the strength, matrix damage initiation, and RVE failure (), respectively (as highlighted in Figure 2). Across all three types of microstructures, stress values start to decrease during debonding initiation. These debonding areas primarily occur within the region of fiber clusters (as seen in the evolution process labeled (1) in Figure 3a-c). In the subsequent evolution process labeled (2) in Figure 3a-c, multiple debonding events occur near closely spaced fibers. During this phase, stress values rapidly decline, and the matrix undergoes deformation, reaching the matrix initial failure strain. As the loading continues, more matrix elements start to incur damage due to the accumulated effects of debonding and localized stress concentrations, eventually resulting in macroscopic transverse cracks.

Notably, the crack path does not traverse areas with large resin-rich pockets and initially occurs at the closely spaced fibers, consistent with observations in [27]. While some studies [28, 29] argue that resin-rich pockets significantly initiate damage evolution, an important consideration is that these pockets can exist only when the inter-fiber distance is decreased elsewhere, provided that the fiber volume fraction remains constant.

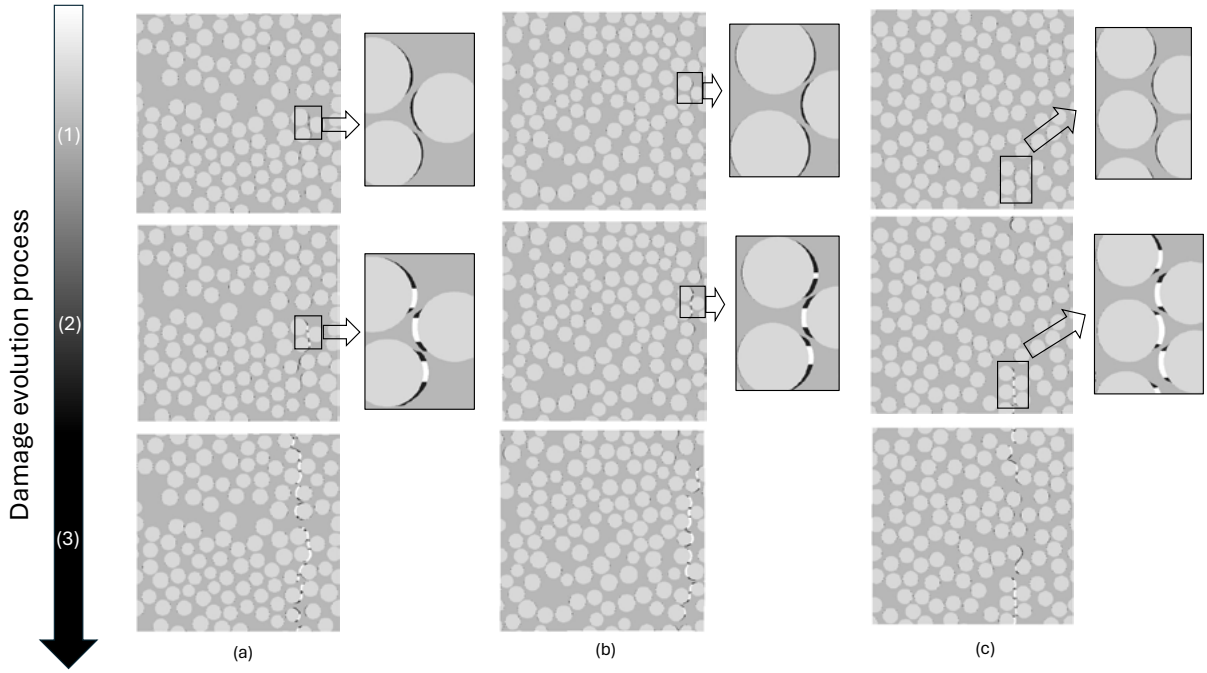


Figure 2. Comparison of damage evolution process under transverse tension for (a) experimental data, (b) GAN-generated microstructures, and (c) RMG-generated microstructures. (1), (2), and (3) correspond to the points indicated in the stress-strain curve in Figure 2.

4. Conclusions

The study compared the damage evolution process in three different unidirectional fiber-reinforced composite microstructures: realistic experimental data, deep learning-generated data, and RMG-generated microstructures. In our models, we first convert the non-periodic CT data into periodic data for real experimental and deep learning-generated cases. And then, for all three cases, four models are prepared, each containing more than 100 fibers to eliminate RVE size effects. Matrix scale effects are also considered, where the matrix exhibits strong nonlinear deformation at the micro-scale. We have found that the interface debonding predominantly occurs around the fiber cluster region. Stress values decrease when multiple debonding events happen at adjacent fibers. As loading continues, matrix damage initiates and more debonding happens, leading to the formation of unstable damage and eventual failure strain. Interestingly, debonding does not initially occur in the resin-rich pockets under transverse tension, so their existence might be able to inhibit damage propagation.

Acknowledgments

R. Guo would like to acknowledge his PhD scholarship from China Scholarship Council (202006430010). M. Mehdikhani and C. Breite acknowledge the Research Foundation Flanders for their FWO postdoc fellowships: ToughImage (1263421N), BIOPTOUGH (12B0624N), and COCOMI (1231322N) as well as the research stay grant (V435423N).

References

[1] A. R. Melro *et al.*, "Micromechanical analysis of polymer composites reinforced by unidirectional fibres: Part I - Constitutive modelling," *International Journal of Solids and Structures,* vol. 50, no. 11-12, pp. 1897-1905, Jun, 2013.

[2] X. P. Morelle *et al.*, "Mechanical characterization and modeling of the deformation and failure of the highly crosslinked RTM6 epoxy resin," *Mechanics of Time-Dependent Materials,* vol. 21, no. 3, pp. 419-454, Aug, 2017.

[3] T. Hobbiebrunken *et al.*, "Experimental determination of the true epoxy resin strength using micro-scaled specimens," *Composites Part a-Applied Science and Manufacturing,* vol. 38, no. 3, pp. 814-818, 2007.

[4] J. Chevalier *et al.*, "Multi-scale characterization and modelling of the transverse compression response of unidirectional carbon fiber reinforced epoxy," *Composite Structures,* vol. 209, pp. 160-176, Feb, 2019.

[5] X. M. Sui *et al.*, "Extreme scale-dependent tensile properties of epoxy fibers," *Express Polymer Letters,* vol. 13, no. 11, pp. 993-1003, Nov, 2019.
[6] Z. H. Xia, Y. F. Zhang, and F. Ellyin, "A unified periodical boundary conditions for representative volume elements of composites and applications," *International Journal of Solids and Structures,* vol. 40, no. 8, pp. 1907-1921, Apr, 2003.
[7] F. C. Huang *et al.*, "Transverse mechanical properties of unidirectional FRP including resin-rich areas," *Computational Materials Science,* vol. 198, Oct, 2021.
[8] D. F. Adams, and D. R. Doner, "Transverse normal loading of a unidirectional composite," *Journal of composite Materials,* vol. 1, no. 2, pp. 152-164, 1967.
[9] S. Li, "General unit cells for micromechanical analyses of unidirectional composites," *Composites Part a-Applied Science and Manufacturing,* vol. 32, no. 6, pp. 815-826, 2001.
[10] R. Cai, and T. Jin, "The effect of microstructure of unidirectional fibre-reinforced composites on mechanical properties under transverse loading: A review," *Journal of Reinforced Plastics and Composites,* vol. 37, no. 22, pp. 1360-1377, Nov, 2018.
[11] M. J. Pindera *et al.*, "Micromechanics of spatially uniform heterogeneous media: A critical review and emerging approaches," *Composites Part B-Engineering,* vol. 40, no. 5, pp. 349-378, Jul, 2009.
[12] M. Hojo *et al.*, "Effect of fiber array irregularities on microscopic interfacial normal stress states of transversely loaded UD-CFRP from viewpoint of failure initiation," *Composites Science and Technology,* vol. 69, no. 11-12, pp. 1726-1734, Sep, 2009.
[13] A. Wongsto, and S. Li, "Micromechanical FE analysis of UD fibre-reinforced composites with fibres distributed at random over the transverse cross-section," *Composites Part a-Applied Science and Manufacturing,* vol. 36, no. 9, pp. 1246-1266, 2005.
[14] L. Yang *et al.*, "A new method for generating random fibre distributions for fibre reinforced composites," *Composites Science and Technology,* vol. 76, pp. 14-20, Mar, 2013.
[15] A. R. Melro, P. P. Camanho, and S. T. Pinho, "Generation of random distribution of fibres in long-fibre reinforced composites," *Composites Science and Technology,* vol. 68, no. 9, pp. 2092-2102, Jul, 2008.
[16] R. Guo *et al.*, "Synthesising realistic 2D microstructures of unidirectional fibre-reinforced composites with a generative adversarial network," *Composites Science and Technology,* vol. 250, May, 2024.
[17] C. González, and J. Llorca, "Mechanical behavior of unidirectional fiber-reinforced polymers under transverse compression:: Microscopic mechanisms and modeling," *Composites Science and Technology,* vol. 67, no. 13, pp. 2795-2806, Oct, 2007.
[18] M. I. Okereke, and A. I. Akpoyomare, "A virtual framework for prediction of full-field elastic response of unidirectional composites," *Computational Materials Science,* vol. 70, pp. 82-99, Apr, 2013.
[19] L. Wu *et al.*, "From SEM images to elastic responses: A stochastic multiscale analysis of UD fiber reinforced composites," *Composite Structures,* vol. 189, pp. 206-227, Apr, 2018.
[20] N. K. Balasubramani *et al.*, "Micro-mechanical analysis on random RVE size and shape in multiscale finite element modelling of unidirectional FRP composites," *Composite Structures,* vol. 282, Feb, 2022.
[21] N. Klavzer *et al.*, "Nanoscale digital image correlation at elementary fibre/matrix level in polymer-based composites," *Composites Part a-Applied Science and Manufacturing,* vol. 168, May, 2023.
[22] A. Sharma, and S. Daggumati, "Micro-mechanical failure analysis of a uni-directional fiber reinforced composite ply-Cohesive elements & a ductile fracture mechanics approach," *Materials Today-Proceedings,* vol. 46, pp. 9927-9932, 2021.
[23] P. P. Camanho, and C. G. Dávila, *Mixed-mode decohesion finite elements for the simulation of delamination in composite materials*, 2002.
[24] M. L. Benzeggagh, and M. Kenane, "Measurement of mixed-mode delamination fracture toughness of unidirectional glass/epoxy composites with mixed-mode bending apparatus," *Composites Science and Technology,* vol. 56, no. 4, pp. 439-449, 1996.
[25] A. Arteiro *et al.*, "Micro-mechanical analysis of the in situ effect in polymer composite laminates," *Composite Structures,* vol. 116, pp. 827-840, Sep-Oct, 2014.
[26] R. Higuchi *et al.*, "High-fidelity computational micromechanics of composite materials using image-based periodic representative volume element," *Composite Structures,* vol. 328, Jan, 2024.
[27] H. Ahmadian, M. Yang, and S. Soghrati, "Effect of resin-rich zones on the failure response of carbon fiber reinforced polymers," *International Journal of Solids and Structures,* vol. 188, pp. 74-87, Apr, 2020.
[28] H. Ghayoor *et al.*, "Numerical analysis of resin-rich areas and their effects on failure initiation of composites," *Composites Part a-Applied Science and Manufacturing,* vol. 117, pp. 125-133, Feb, 2019.
[29] F. Sharifpour, J. Montesano, and R. Talreja, "Micromechanical assessment of local failure mechanisms and early-stage ply crack formation in cross-ply laminates," *Composites Science and Technology,* vol. 220, Mar, 2022.

On the Mode I Fracture Toughness of Metal-Composite Joints with untreated SLM 3D-Printed Ti6Al4V Substrates

Michele Gulino[1]*, Rosemere de Araujo Alves Lima[2], Fabrizio Moroni[1], Alessandro Pirondi[1] and Sofia Teixeira de Freitas[2,3]

[1]Department of Engineering for Industrial Systems and Technologies, University of Parma, Parma, Italy

Email: michele.gulino@unipr.it, fabrizio.moroni@unipr.it, alessandro.pirondi@unipr.it

[2]Faculty of Aerospace Engineering, Delft University of Technology, Delft, The Netherlands

Email: R.DeAraujoAlvesLima@tudelft.nl

[3]IDMEC, Instituto Superior Técnico, Universidade de Lisboa, Lisboa, Portugal

Email: sofia.teixeira.freitas@tecnico.ulisboa.pt

Abstract

Here we investigate the adhesive properties of Selective Laser Melted (SLM) titanium surfaces in metal-composite co-bonded joints without any prior surface treatment, to explore the inherent surface roughness of SLM parts to potentially create strong adhesive bonds.

Double Cantilever Beam (DCB) tests were carried out to assess the joints mode I fracture toughness involving untreated SLM titanium and woven Carbon Fibre Reinforced Polymer (CFRP) adherends, co-bonded with an epoxy film adhesive. The same type of DCB joints, but now with sandblasted SLM titanium adherends, were tested to compare the adhesion strength of the untreated SLM surface versus the sandblasted surface.

The findings reveal that joints with untreated SLM titanium adherends exhibit similar toughness to those with sandblasted SLM titanium adherends, indicating that the surface morphology of as-printed SLM titanium is suitable for manufacturing robust adhesive joints. The elimination of the surface treatment in the manufacturing of adhesive joints with SLM adherends could increase the interest of many industrial fields towards the use of adhesive bonding over other joining techniques.

Keywords

Fracture toughness, Ti6Al4V, Carbon Fibre Reinforced Polymer (CFRP), Selective Laser Melting (SLM), Co-bonding

1 Introduction

The rising adoption of Fibre Reinforced Polymers (FRPs) in manufacturing lightweight structures is evidence of their high strength and stiffness-to-weight ratios and consequent advantages over conventional materials. Indeed, FRP laminates are often joined with metals in large components to reduce costs and increase thermal resistance and crashworthiness [1], [2]. Adhesive bonding offers numerous advantages for joining FRPs, particularly in lightweight structures, by eliminating the need for drilling it minimizes the risk of introducing defects like delamination, which can compromise structural integrity, and becomes especially relevant for joining dissimilar materials. Additionally, it helps save weight, especially in scenarios where long bondlines would necessitate numerous rivets or bolts [3], [4].

One significant challenge of adhesive bonding compared to other joining methods is the necessity of surface treatments to ensure optimal adhesion, which are usually expensive, time-consuming and present difficult repeatability.

In this context, Selective Laser Melting (SLM) represents a strategic technology due to its inherently rough surface morphology [5], [6], [7], [8], which is often associated with good adhesion strength [3]. Nevertheless, the literature on adhesive bonding of as-printed SLM with FRP laminates is still quite limited and with a higher focus on metal-metal joints. Few works can be highlighted from literature:

- the work of Nguyen et al. [9], in which untreated SLM Ti6Al4V was either co-cured with CFRP or bonded using a film epoxy adhesive with another untreated SLM titanium adherend to form Double Cantilever Beam (DCB) joints. For the titanium-titanium joints, the fracture toughness was similar to the one indicated in the adhesive's datasheet. Also, they compared the results with the fracture toughness of grit-blasted titanium-titanium joints

©2024 | 3_MICHELE_Gulino_ABKO3.pdf

from the work of Brack and Rider [10], showing minor differences. For metal-composite joints, the innate surface morphology of the SLM process, together with sub-millimetric outward and inward features printed on the titanium adherend, promoted crack deflection in the composite adherend.

- another investigation on the topic was carried out by Fielden-Stewart [11], revealing that in SLM aluminum-CFRP secondary bonded joints printed with several build angles, the mixed-mode fracture toughness was higher for untreated joints compared to mechanically abraded joints, regardless of the build angle.

However, to the knowledge of the authors, a direct comparison of the mode I fracture toughness of co-bonded metal-composite joints with and without surface treatments has never been investigated.

Considering that the elimination of surface treatment in the manufacturing of adhesive joints could significantly increase the interest of many industrial fields in employing adhesive bonding over other techniques, such as mechanical fastening or welding, the use of as-printed SLM substrates can be a promising solution to promote their wider use.

Therefore, this research is part of a larger project aiming to 1) expand the literature in the field of SLM metal-composite joints and 2) develop a toughening technique for metal-composite joints, employing SLM to produce metal adherends with structured interfaces, enabling the composite to be co-bonded without the need for surface treatments.

For that, DCB joints with as-printed SLM Ti6Al4V adherends were compared to control joints where the titanium substrate is sandblasted after printing, given the fact that sandblasting is a well-known and often employed surface treatment for adhesive bonding [12].

2 Materials and method

The SLM Ti6Al4V substrates, measuring 130x25x6 mm³, were provided by 3T-Additive Manufacturing Ltd (Newbury, United Kingdom). They were manufactured using an M290 printer (EOS Gmbh, Krailling, Germany), with a 90° build angle and a layer thickness of 60 µm (**Figure 1**).

The CFRP adherend was made from woven GG630T (T700 carbon fibres) - DT120 prepregs supplied by Bercella Srl (Varano de' Melegari, Italy), with a stacking sequence of $[0\text{-}90]_{13}$. The number of plies (i.e., the thickness of the laminate) to obtain pure mode I, the bending and out-of-plane shear moduli of the composite, and Young's modulus of the Ti6Al4V adherends were determined with the same procedure used in the previous work by the authors [12], [13], [14].

To guarantee pure mode I on the crack tip of the dissimilar DCB joints, the resulting target thickness of the laminate is 8.23 mm, which rounds down to 8.11 mm with 13 plies, considering the estimated cured ply thickness of 0.624 mm MPa (**Table 1**).

Table 1 *- Mechanical properties of the CFRP: t_{ply} is the ply thickness expected after curing, E_{cfrp} and G_{cfrp} are the laminate's flexural and out of plane shear moduli considering a stacking sequence of $[0\text{-}90]_{13}$ and E_{ti} is the Young's modulus of the titanium.*

t_{ply} (1)	E_{ti} (2)	E_{cfrp} (2)	G_{cfrp} (2)
mm	MPa	MPa	MPa
0.624	118030	60079	2555

(1) CFRP datasheet values
(2) Experimental values [12]

Optical profilometries using Keyence VR-5000 wide-area 3D non-contact measurement system and contact angle measurements using KSV Instruments CAM 200 optical angle meter were performed on 2 spare titanium adherends, with 3 repetitions each.

2.1. Manufacturing of the DCB specimens

Half of the adherends were sandblasted with alumina particles at 0.5 MPa, with the nozzle at approximately 10 centimetres from the samples' surfaces. All the titanium adherends (sandblasted included) were cleaned with an ultrasonic acetone bath for 10 minutes before bonding to remove dirt and contaminants from the surface.

After that, a Teflon strip was inserted at the joints' tip, positioned 15 mm away from the load application point to simulate an artificial crack.

The joints were co-bonded using HexBond ST 1035 (Hexcel, Stamford, USA) epoxy adhesive film with a polyester carrier mat supplied by Bercella Srl. This bonding process occurred in an autoclave and vacuum bag setup, undergoing a curing cycle at 130°C for 2 hours under 6 bar of pressure.

©2024 | 3_MICHELE_Gulino_ABKO3.pdf:2

Following curing, the bonded joints were machined to the required dimensions, and a loading block was bonded to the CFRP adherend with EA Loctite 3425 (Henkel AG&CO. KGaA, Düsseldorf, Germany) bi-component paste epoxy (**Figure 1**). The thickness of the adhesive was not controlled with a spacer and it is assumed to be equal to the thickness of the adhesive carrier mat of 0.1 mm, measured with a micrometre after dissolving the epoxy matrix of the film adhesive in acetone.

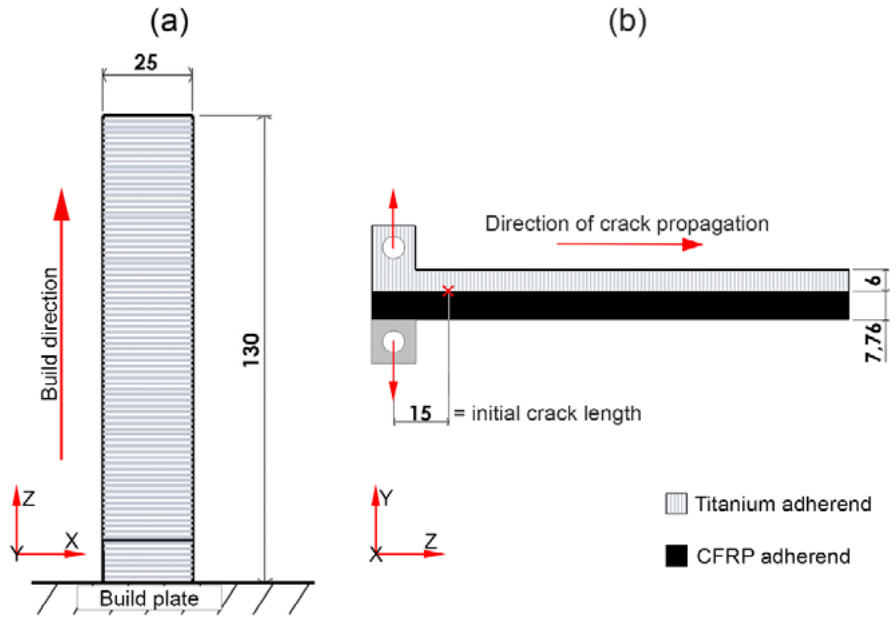


Figure 1 *– a) Titanium adherends, top view. b) Side view of the co-bonded joints. The titanium adherends were printed with an integrated loading block, which was then drilled to allow the positioning in the testing machine, whereas a separate loading block was glued onto the CFRP adherend. Grey lines representing the layers. Dimensions in millimetres.*

2.2 Testing setup

A speckle pattern was spray painted on one side of the DCB samples to evaluate the Crack Mouth Opening Displacement (CMOD), using a virtual extensometer via 3D Digital Image Correlation (3D DIC) with Vic3D software from Correlated Solutions Inc. The DIC cameras (5 megapixels sensor and lens with 23 mm of focal length) were positioned at 57.4 centimetres from the speckled surface and the pictures were taken with a 2 Hz frequency. The region of interest was defined around the load application line, and it was discretized using a 33 pixels subset size and 11 pixels step size.

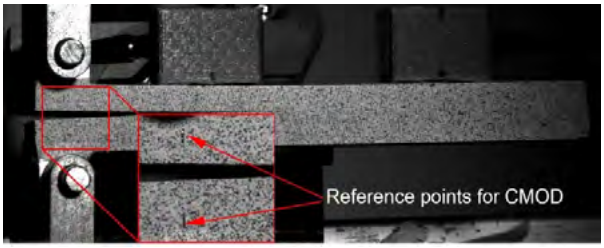


Figure 2 *– DIC evaluation of the CMOD, with region of interest highlighted in red. The relative displacement was evaluated in the 2 reference points aligned with the load line, as indicated in the figure.*

The joints underwent testing under displacement control at a rate of 2.5 mm/min using a Zwick-Roell electric testing machine, equipped with a 10kN load cell. The displacement rate was taken from the ASTM D3433 standard [15] for metal-DCB joints, since there is no standard available for metal-composite DCB testing. The DIC picture acquisition was

©2024 | 3_MICHELE_Gulino_ABKO3.pdf:3

synchronized with the load and displacement data from the testing machine. Testing concluded upon reaching a crosshead displacement of 6 mm.

2.3. Data reduction method

For the data reduction of the DCB tests, the Compliance Beam Based Method (CBBM) [16], [17] was employed, enabling the measurement of crack length a based on the DCB's compliance during testing.

In this study, the joint compliance was assessed through the linear regression analysis of the CMOD-load curve, evaluated during 14 unloading phases.

Knowing the crack length, the mode I fracture toughness G_{Ic} can be calculated as

$$G_{Ic} = \frac{F^2}{2B}\left[a^2\left(\frac{1}{E_{ti}I_{ti}} + \frac{1}{E_{cfrp}I_{cfrp}}\right) + \frac{6a}{5BG_{cfrp}}\left(\frac{1}{h_{ti}} + \frac{1}{h_{cfrp}}\right)\right] \qquad \text{Eq. (1)}$$

F is the test load, E are the elastic moduli of the adherends, I are the second moment of area of the cross-section of the adherends, and B is their width. The subscripts ti and $cfrp$ indicate the properties of the titanium and CFRP adherends, respectively.

3 Results and discussion

3.1 Titanium surface profilometries and water contact angle measurements

The surface profilometries of both as-printed and sandblasted samples are shown in **Figure 2**. The surface parameters and the contact angles of both types of samples are shown in **Table 2**.

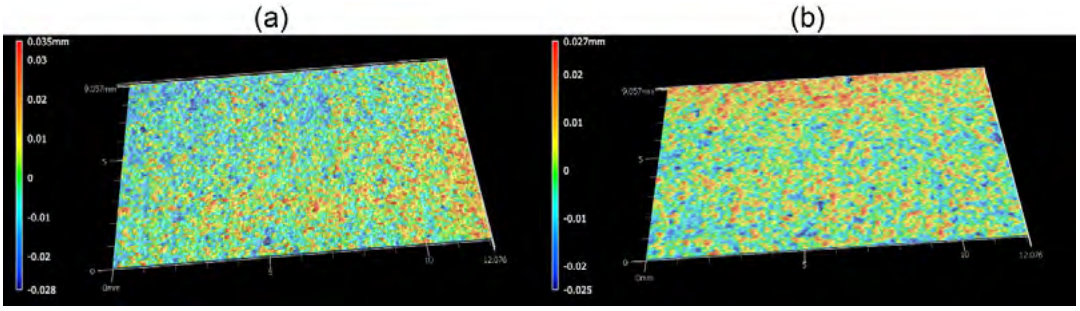


Figure 3 *– Surface profilometries of a) as-printed samples and b) sandblasted samples.*

Table 2 *– As-printed and sandblasted samples' surface parameters and distilled water contact angles.*

	Sa [µm]	Ssk [-]	Sku [-]	θ [°]
as-printed	9.26 ± 0.18	0.23 ± 0.08	3.63 ± 0.18	89.44 ± 3.86
sandblasted	7.13 ± 0.32	-0.1 ± 0.13	3.71 ± 0.43	77 ± 2.95

The optical profilometries shown in **Figure 2** reveal a noticeable contrast between the surfaces before and after sandblasting, with the latter exhibiting a smoother texture, indicated by the lower arithmetical mean height S_a. However, the sandblasting process does not alter the shape of the surface asperities significantly; these remain relatively sharp, as evidenced by S_{ku} values exceeding 3. The S_{sk} values, which indicate the skewness of the surface profile, generally hover around 0, meaning that the waviness is distributed symmetrically around the mid-plane for both surface types.

Regarding the water contact angle, **Table 2** shows a substantial improvement in surface wettability following sandblasting treatment. This enhancement could be attributed to the roughness of the SLM-printed substrates, where acetone cleaning alone may not effectively remove all contaminants from the deep valleys of the as-printed surface. Conversely, the lower contact angle observed on sandblasted surfaces suggests that an acetone bath adequately cleans this type of sample.

3.3 Fracture toughness of the titanium-CFRP joints

©2024 | 3_MICHELE_Gulino_ABKO3.pdf:4

The R-curves and the load-CMOD curves of the DCB samples are shown in **Figure 4**. When referring to the fracture toughness, the subscript T in place of I in G_{Tc} is used hereafter because a small percentage of mode II loading is expected since the actual thickness of the composite after curing was 7.76 mm (**Figure 1**) i.e., 5.7% lower than the target thickness of 8.23 mm.

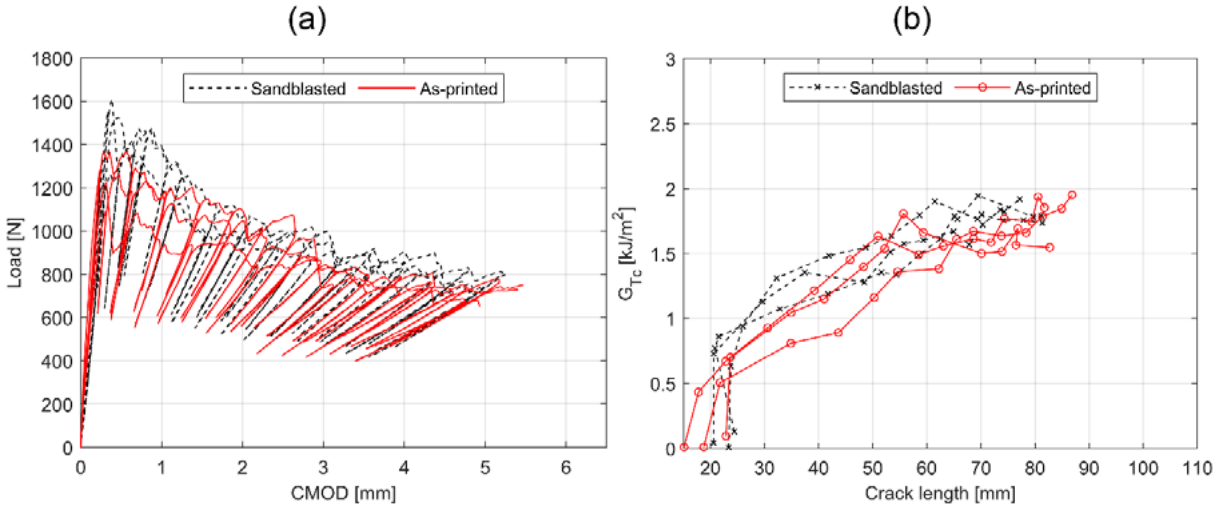


***Figure 4** – a) Load-CMOD curves with 14 unloading phases each. b) R-curves of the titanium-CFRP DCB samples, where the markers indicate the fracture toughness evaluated for a specific unloading. Three samples per batch were tested.*

A remarkable rising R-curve effect characterized the tests, which made the evaluation of a steady-state value of fracture toughness unfeasible. Hence, the values of initial and average fracture toughness (**Table 3**) are chosen to describe the behaviour of each batch of joints. The first unloading was not included in the calculation since it occurred in most of the samples' linear elastic phase of the test, with no visible crack propagation.

***Table 3** – Initial fracture toughness, average fracture toughness and maximum load of the titanium-CFRP DCB joints.*

	As-printed	**Sandblasted**
Initial G_{Tc} [kJ/m^2]	0.55 ± 0.14	0.71 ± 0.07
Average G_{Tc} [kJ/m^2]	1.42 ± 0.4	1.5 ± 0.36
Maximum load [N]	1317 ± 82	1536 ± 69

Figure 5 shows the fracture surfaces of the tested samples. The sandblasted samples consistently showed cohesive failure in the early stages of crack propagation, whereas in the as-printed samples the failure mode was mostly mixed cohesive-adhesive, probably due to less consistent adhesion. **Figure 6** makes a direct comparison of the R-curve of the sample AP2 with the correspondent fracture surfaces. AP2 was the one with the lowest values of fracture toughness (**Table 3**) associated with mostly adhesive failure in the first part of the test. Nevertheless, all 6 samples showed cohesive failure and small areas of CFRP first ply failure (region 2 in **Figure 6**) with an increase in fracture toughness. A final increase in the fracture toughness was observed when the crack deflection and further propagation within the composite layer occurred (region 3 in **Figure 6**). This failure mechanism is likely the reason behind the rising R-curve effect that characterized all the samples and led to comparable values of fracture toughness between the as-printed (1.42 kJ/m^2) and sandblasted (1.50 kJ/m^2) joints.

©2024 | 3_MICHELE_Gulino_ABKO3.pdf:5

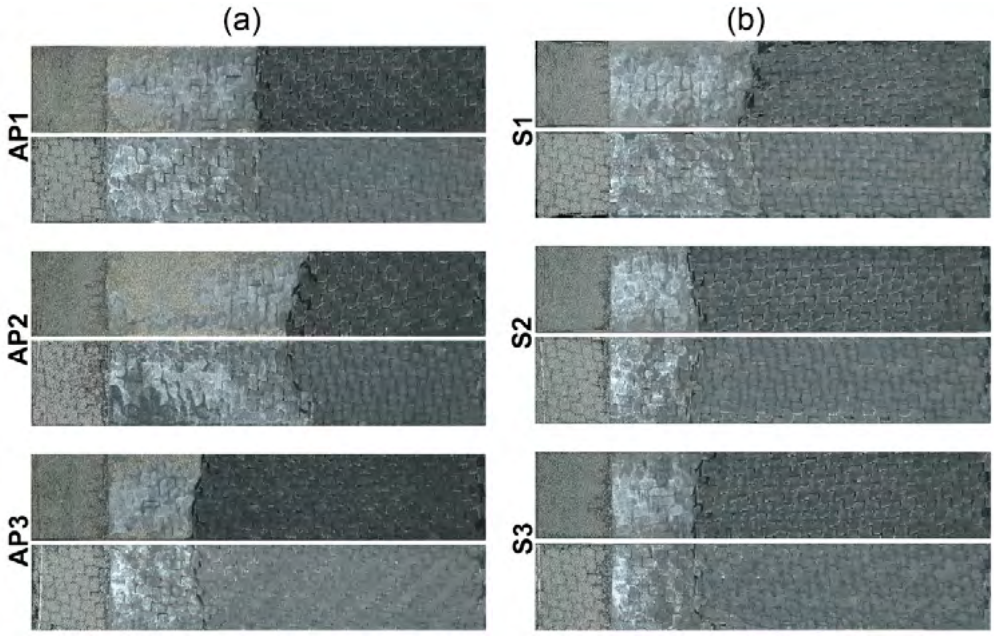


Figure 5 *– Fracture surfaces of the titanium-CFRP samples. "S" are the sandblasted joints and "AP" are the as-printed joints. For each joint, the titanium adherend is displayed above the CFRP adherend.*

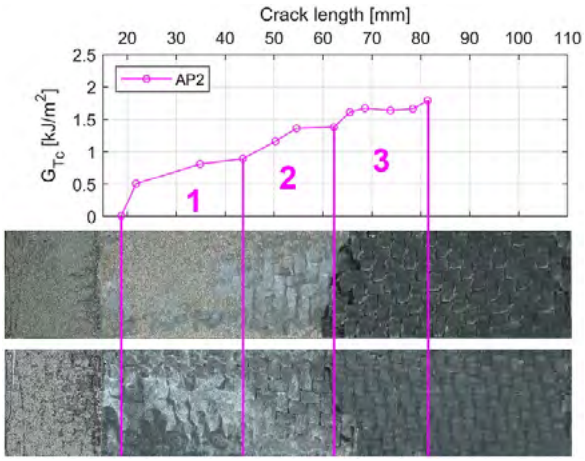


Figure 6 *- R-curve of sample AP2. The rising trend of the toughness is correlated to the transition from adhesive to cohesive failure (region "1"), then to cohesive and CFRP first ply failure (region "2"), eventually leading to crack deflection in the composite (region "3").*

4 Conclusions

The aim of this work was to evaluate the mode I fracture toughness of co-bonded joints involving untreated SLM Ti6Al4V and CFRP substrates using DCB tests. The untreated joints were compared with the same type co-bonded DCB specimens in which the SLM substrate was sandblasted. Both types of surfaces were characterized with optical profilometries and distilled water contact angle measurements. The following conclusions can be drawn:

- The as-printed surface has on average a 30 % higher roughness compared to the sandblasted surface, but the latter has a higher wettability (14% lower water contact angle), likely because the removal of contaminants on the titanium surface due to the mechanical treatment.
- In the first part of the crack propagation, the good wettability of the sandblasted surface is reflected in consistent cohesive failure, as opposed to mixed cohesive-adhesive failure of the as-printed samples. As the crack

©2024 | 3_MICHELE_Gulino_ABKO3.pdf:6

propagates, both sandblasted and as-printed joints show cohesive and CFRP first ply failure and eventually crack deflection in the composite adherend.

- Sandblasting leads to only a minor improvement of 6% in fracture toughness. It is believed by the author that the unstable crack propagation of the as-printed joints promoted dissipation phenomena, increasing the apparent fracture toughness of the as-printed joints. Nevertheless, the as-printed samples have worse wettability and higher percentage of adhesive failure compared to the sandblasted joints. This could be a concern for the long-term durability of the untreated samples since humidity can diffuse through the cracks at the adhesive-adherend interface, degrading the mechanical properties of the adhesive [18].

As a general conclusion, it was shown how the as-printed surface of SLM Ti6Al4V has great potential for the adhesive bonding of metal-composite joints, given its inherently rough surface morphology that can be exploited to avoid time-consuming treatments.

Acknowledgements

This research was carried as part of the project DOT13SJY60, Ministerial Decree No. 1061 of 10/08/2021 and funded under the "Programma Operativo Nazionale" (PON), Action IV.4 "PhD grant on Innovation Thematics". Support was provided by Bercella Srl and 3T-Additive manufacturing that kindly provided the materials for this research. The authors would like to thank Peter Jerrard, Matteo Menoni, and Ulderico Tarasconi for their invaluable help. This work was also supported by FCT, through IDMEC, under LAETA, project UIDB/50022/2020.

References

[1] Z. Wang, X. Jin, Q. Li, and G. Sun, "On crashworthiness design of hybrid metal-composite structures," *Int J Mech Sci*, vol. 171, Apr. 2020, doi: 10.1016/j.ijmecsci.2019.105380.

[2] R. Subbaramaiah, B. G. Prusty, G. M. K. Pearce, S. H. Lim, and R. S. Thomson, "Crashworthy response of fibre metal laminate top hat structures," *Compos Struct*, vol. 160, pp. 773–781, Jan. 2017, doi: 10.1016/j.compstruct.2016.10.112.

[3] da Silva L.F.M., Öchsner A., and Adams R.D., *Handbook of Adhesion Technology*. Springer Berlin Heidelberg, 2011. doi: 10.1007/978-3-642-01169-6.

[4] D. A. Dillard, *Advances in Structural Adhesive Bonding*, vol. 18, no. 1. Pergamon, 2011. doi: 10.1016/J.ENGFAILANAL.2010.09.010.

[5] A. M. Khorasani, I. Gibson, and A. R. Ghaderi, "Rheological characterization of process parameters influence on surface quality of Ti-6Al-4V parts manufactured by selective laser melting," *International Journal of Advanced Manufacturing Technology*, vol. 97, no. 9–12, pp. 3761–3775, Aug. 2018, doi: 10.1007/s00170-018-2168-6.

[6] G. Strano, L. Hao, R. M. Everson, and K. E. Evans, "Surface roughness analysis, modelling and prediction in selective laser melting," *J Mater Process Technol*, vol. 213, no. 4, pp. 589–597, 2013, doi: 10.1016/j.jmatprotec.2012.11.011.

[7] W. Cai, Q. Song, H. Ji, and M. K. Gupta, "Multi-perspective analysis of building orientation effects on microstructure, mechanical and surface properties of slm ti6al4v with specific geometry," *Materials*, vol. 14, no. 16, Aug. 2021, doi: 10.3390/ma14164392.

[8] M. Ahmed, M. A. Obeidi, S. Yin, and R. Lupoi, "Influence of processing parameters on density, surface morphologies and hardness of as-built Ti-5Al-5Mo-5V-3Cr alloy manufactured by selective laser melting," *J Alloys Compd*, vol. 910, Jul. 2022, doi: 10.1016/j.jallcom.2022.164760.

[9] A. T. T. Nguyen, M. Brandt, A. C. Orifici, and S. Feih, "Hierarchical surface features for improved bonding and fracture toughness of metal-metal and metal-composite bonded joints," *Int J Adhes Adhes*, vol. 66, pp. 81–92, Apr. 2016, doi: 10.1016/j.ijadhadh.2015.12.005.

[10] N. Brack and A. N. Rider, "The influence of mechanical and chemical treatments on the environmental resistance of epoxy adhesive bonds to titanium," *Int J Adhes Adhes*, vol. 48, pp. 20–27, 2014, doi: 10.1016/j.ijadhadh.2013.09.012.

[11] Z. Fielden-Stewart, T. Coope, D. Bacheva, and B. C. Kim, "Effect of the surface morphology of SLM printed aluminium on the interfacial fracture toughness of metal-composite hybrid joints," *Int J Adhes Adhes*, vol. 105, Mar. 2021, doi: 10.1016/j.ijadhadh.2020.102779.

©2024 | 3_MICHELE_Gulino_ABKO3.pdf:7

[12] M. Gulino, F. Moroni, and A. Pirondi, "Metal-metal and metal-composite joints with 3D printed aluminium substrates: effect of surface treatment on the mode I fracture toughness," *Journal of Adhesion*, 2023, doi: 10.1080/00218464.2023.2285074.

[13] W. Wang, R. Lopes Fernandes, S. Teixeira De Freitas, D. Zarouchas, and R. Benedictus, "How pure mode I can be obtained in bi-material bonded DCB joints: A longitudinal strain-based criterion," *Compos B Eng*, vol. 153, pp. 137–148, Nov. 2018, doi: 10.1016/j.compositesb.2018.07.033.

[14] ASTM E8/E8M-22, "Standard Test Methods for Tension Testing of Metallic Materials." doi: 10.1520/E0008_E0008M-13A.

[15] "ASTM D3433 - DCB Metal Joints".

[16] M. F. S. F. de Moura, R. D. S. G. Campilho, and J. P. M. Gonçalves, "Crack equivalent concept applied to the fracture characterization of bonded joints under pure mode I loading," *Compos Sci Technol*, vol. 68, no. 10–11, pp. 2224–2230, Aug. 2008, doi: 10.1016/j.compscitech.2008.04.003.

[17] R. D. F. Moreira, M. F. S. F. de Moura, and F. G. A. Silva, "A novel strategy to obtain the fracture envelope under mixed-mode I+II loading of composite bonded joints," *Eng Fract Mech*, vol. 232, Jun. 2020, doi: 10.1016/j.engfracmech.2020.107032.

[18] C. S. P. Borges, E. A. S. Marques, R. J. C. Carbas, C. Ueffing, P. Weißgraeber, and L. F. M. D. Silva, "Review on the effect of moisture and contamination on the interfacial properties of adhesive joints," *Proc Inst Mech Eng C J Mech Eng Sci*, vol. 235, no. 3, pp. 527–549, Feb. 2021, doi: 10.1177/0954406220944208.

©2024 | 3_MICHELE_Gulino_ABKO3.pdf:8

THE EFFECTS OF IN-SITU TEMPERATURE AND RELATIVE HUMIDITY ON THE TENSILE RESPONSE OF FLAX VS. GLASS FRP COMPOSITES

Valentin Perruchoud[1*], René Alderliesten[2] and Yasmine Mosleh[1]

[1] Biobased Structures and Materials, Faculty of Civil Engineering and Geosciences, Delft University of Technology, Stevinweg 1, 2628 CN Delft, the Netherlands
[2] Aerospace Structures and Materials, Faculty of Aerospace Engineering, Delft University of Technology, Kluyverweg 1, 2629HS Delft, the Netherlands

*Corresponding author E-mail: V.P.Perruchoud@tudelft.nl

Keywords: Structural biocomposite, Flax fibre reinforced epoxy, In-situ hygrothermal conditions, moisture durability

Abstract
The development of bio-based fibre-reinforced polymer composites (FPRs) has accelerated in recent years aiming at replacing synthetic FRPs in primary structures. Comparative case studies on biobased fibres (such as flax and hemp) indicate their potential to replace synthetic glass and carbon fibres in certain FRP structures as more sustainable and environmentally friendly alternatives. In those studies, the effects of in-situ hygrothermal conditions on the physical and mechanical performance of the natural fibre composites were generally overlooked, however, due to hygroscopicity of lignocellulosic natural fibres, flax fibre composites mechanical response is sensitive to its environmental temperature and relative humidity. To quantify and understand the effects of in-situ hygrothermal conditions on flax FRP composite, a quasi-static tensile testing campaign was conducted at various temperatures and relative humidities. Glass and flax FRP laminates were tested in cross-ply and angle-ply configurations. It was observed that the strength and stiffness of cross-ply and angle-ply FFRP laminates were significantly affected by relative humidity contrary to GFRP counterparts. All laminates exhibited strength and/or stiffness variation with temperature that can be attributed to the sensitivity of the common epoxy matrix. However, a distinct difference was observed between the flax and glass cross-ply laminates with the modulus of the flax FRP being highly affected by temperature and relative humidity while the glass FRP modulus was unaffected.

1. Introduction

In the quest for optimal performance in structural engineering, synthetic fibre-reinforced polymer composites (FRPs) have emerged as promising materials for light weight design of structures thanks to their high specific stiffness and strength. Regarding durability, synthetic FRPs do not rust or corrode or biologically decay unlike traditional materials such as steel or wood. Degradation in FRPs due to harsh environmental conditions can be mitigated by selecting a matrix system or coating designed to not degrade in the in-situ environmental conditions by preventing water diffusion through the matrix. Furthermore, the mechanical response of synthetic FRPs remains stable in most in-situ hygrothermal conditions because synthetic fibres such as glass are insensitive to moisture and have little stiffness variations with temperatures ranging from -20 to 50°C [1].

Due to recent sustainability and environmental concerns with synthetic FRPs, biobased FRPs have emerged as an alternative with the replacement of synthetic fibres such as glass by plant fibres such as flax. In addition to sustainability benefits, flax fibres have the structural advantages of being comparatively light [2] and effective at damping vibrations [3]. However in terms of durability, the cellulosic microstructure of flax fibres is hygroscopic resulting in a high moisture sorption in flax FRPs (FFRPs) [4] compared to the sorption in glass FRPs (GFRPs) [5]. This high moisture absorption and desorption induces swelling and shrinkage of the fibres, respectively, an order of magnitude larger than the swelling/shrinkage of the matrix [4]. Consequently, internal stresses are created, the fibre-matrix interface might get damaged, and the presence of water at the interface might reduce the fibre-matrix interface strength [6]. Furthermore, the stiffness and strength of single flax fibres are dependent on the moisture level in the fibres, with an increase in moisture reducing the modulus, and increasing the strength [7]. Regarding temperature (T), the mechanical properties of single flax fibres are affected with a significant reduction of modulus and strength between 20°C and 60°C [8].

Since the properties of flax fibres significantly vary at different in-situ temperatures and relative humidities due to their viscoelastic and hygroscopic nature it is pivotal to assess the mechanical response of biocomposites at different environmental conditions. As example, biobased FRP bridges and wind turbine are structural applications subjected to diurnal and seasonal variation of in-situ hygrothermal conditions.

In this study, we aim to evaluate how in-situ hygrothermal conditions impact the quasi-static tensile performance of composite laminates made from flax and glass fibres. Four FRP laminates were characterized at in-situ conditions ranging from -20 to 50C and 50% to 90% relative humidity. Cross-ply [0/90/0] and angle-ply $[+45/-45]_S$ laminates were manufactured and tested to highlight hygrothermal effects on fibres and the combination of matrix/interface, respectively. This experimental investigation helps to assess how the in-situ hygrothermal conditions affect the mechanical response of flax and glass FRP laminates.

2. MATERIALS AND METHODS

2.1 Composite laminates architecture/manufacturing

In this study, four types of composite laminates were manufactured by vacuum infusion. These include GFRP [0/90/0], GFRP $[(+45/-45)]_S$, FFRP $[0/90/0]_S$, FFRP $[(+45/-45)_2]_S$. The glass fibres employed are non-crimp high stiffness glass fabric with an aerial weight of 1260 g/m^2 manufactured by Kush Synthetics PVT.LTD. The flax fibres employed are quasi-unidirectional flax mat Amplitex, weighing 280 g/m^2 and manufactured by Bcomp (Switzerland). The epoxy resin system, SWANCOR 2511-1AL/BL, was used as matrix for manufacturing both GFRP and FFRP laminates. The method employed for manufacturing was vacuum assisted resin infusion (VARI) followed by autoclave post-cure at 70°C for 18 hours. The specimens were then cut into rectangular coupons of dimensions 250 × 15 mm using a waterjet cutter. Optical microscopy was utilized to qualitatively evaluate the consistency of the manufacturing quality. Differential scanning calorimetry (DSC) analysis was used to verify the completion of the epoxy curing. The fibre volume fraction was determined through density calculations at 42% and 53% for FFRP and GFRP laminates respectively.

2.2 Pre-conditioning protocol

Pre-conditioning was performed to ensure that the specimens are at equilibrium with the selected in-situ hygrothermal conditions during testing. To that end, the specimens were placed in a WK11-340/40 climate chamber at 50°C and at the desired relative humidity (RH) for at least two weeks to equilibrate the moisture content. To ensure that the specimens reach at least 90% of saturation, the moisture content was tracked by weight measurements initially at daily intervals and then 3 days intervals. Once the desired moisture content was reached the specimens were transferred to the climate chamber enclosing

the tensile testing setup set to the in-situ hygrothermal testing conditions. Specimens stayed at least 30 minutes in the climate chamber to equilibrate to the testing temperature.

2.3 Quasi-static tensile testing

Tensile testing was performed on an Instron 1251 with a 100 kN loadcell and equipped with hydraulic grips and a Klimaatkast Weisstechnik climate chamber enclosing the grip area. An extensometer is attached to the specimen with rubber bands to measure the strain. A thermocouple is attached with tape to the surface of the specimen to ensure the specimen is at the desired temperature during testing. Loading is performed at a rate of 2 mm/min up to failure. The in-situ hygrothermal conditions range from -20°C to +50°C and 50% to 90% RH to simulate common and extreme outdoor conditions.

3. Results

3.1. Effects of temperature and relative humidity on the tensile response of GFRP laminates

3.1.1. Cross-ply laminate

The stiffness of GFRP cross-ply laminate was observed to be negligibly affected by the temperature and the relative humidity with an overlap of all the stress-strain curves (figure 1). The highest ultimate tensile strength (UTS) was observed at -20°C and the lowest at 50°C showing an effect of temperature on UTS despite no remarkable effect on the modulus.

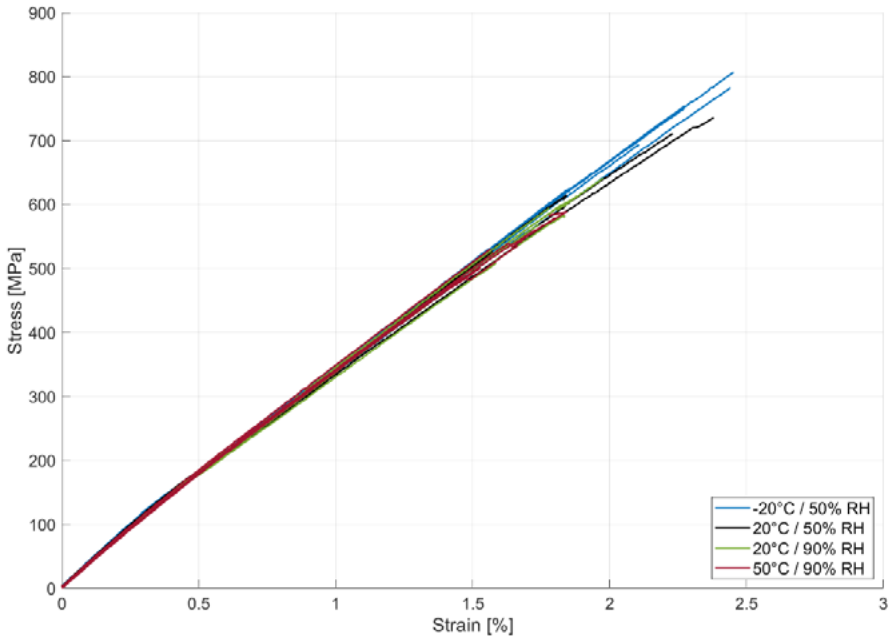


Figure 1. Stress-strain curves of the GFRP [0/90/0] laminate for 4 different in-situ hygrothermal conditions.

3.1.2. Angle-ply laminate

The stress-strain curves of the angle-ply GFRP laminate show three distinct responses governed by the in-situ temperature with a temperature increase resulting in lower modulus, lower UTS, and higher strain to failure (figure 2). The in-situ relative humidity had a negligible effect both at 20°C and 50°C.

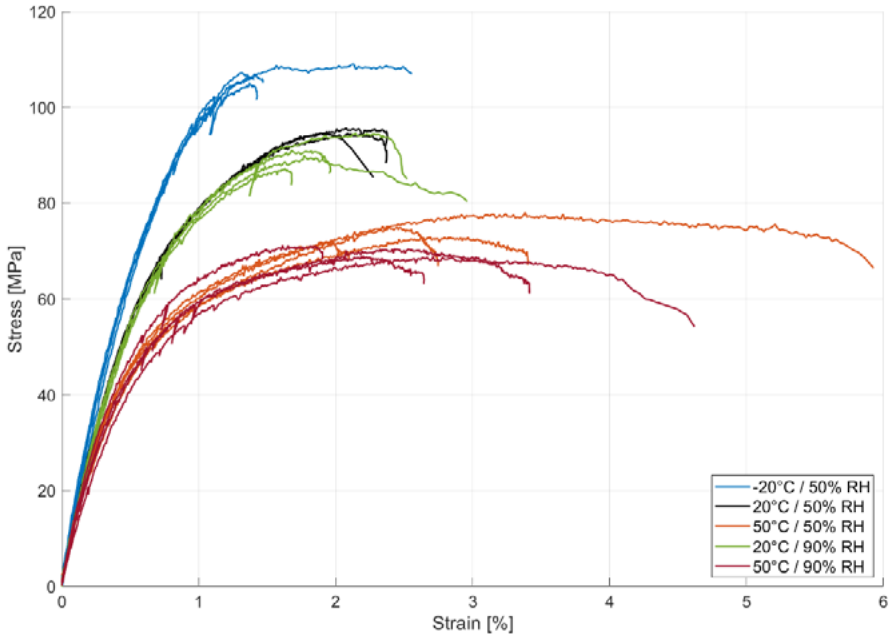


Figure 2. Stress-strain curves of the GFRP $[+45/-45]_S$ laminate for 5 different in-situ hygrothermal conditions.

3.2. Effects of temperature and relative humidity on the tensile response of FFRP laminates

3.2.1. Cross-ply laminate

The mechanical response of the cross-ply FFRP laminate was observed to be significantly dependant on the in-situ temperature and relative humidity (figure 3). The increase in temperature was observed to decrease the modulus and UTS of the laminate manifested by knock down effect on the entire stress-strain curve, observation valid at 50% and 90% RH. Interestingly, the high in-situ relative humidity of 90% caused the shape of the stress-strain curve to change compared to that at 50% relative humidity. The high relative humidity increased the UTS of the laminate.

3.2.2. Angle ply laminate

The angle-ply FFRP laminate exhibit three distinct yield plateau for the three in-situ temperatures (figure 4). The modulus was reduced by the increase in temperature and the increase in relative humidity. Remarkably high strains to failure were reached by the FFRP angle-ply laminate in particular at 50°C where the displacement limit of the tensile testing machine of 16% strain was reached by some specimens without failure. The flax fibre angle was measured on the post-mortem specimens of the angle-ply FFRP laminate (figure 5). At -20°C an angle of 45° was measured, corresponding to the flax fibre angle on the pristine specimens. At 20°C and 50°C the fibres show a permanent rotation of the fibres towards the loading direction.

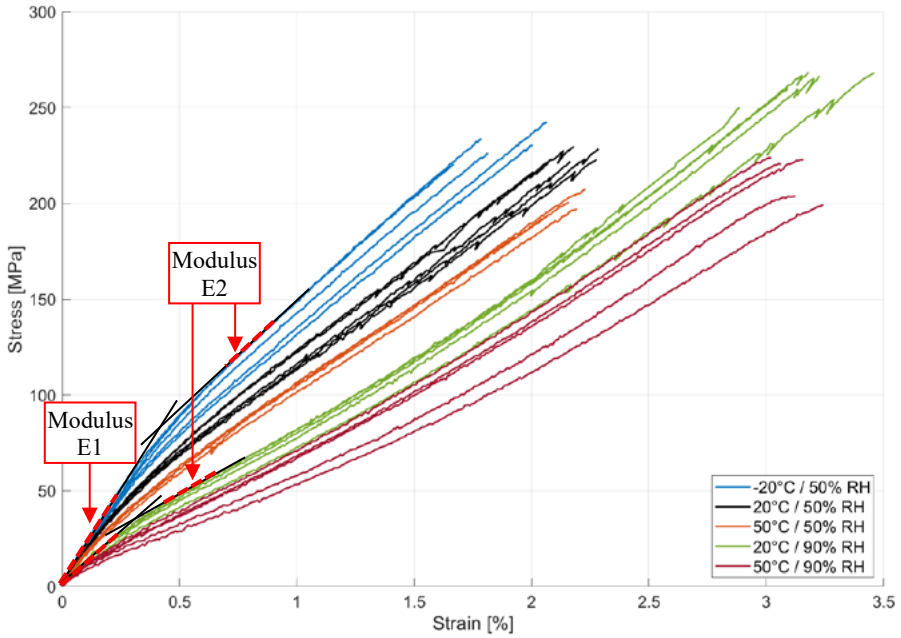


Figure 3. Stress-strain curves of the FFRP $[0/90/0]_S$ laminate for 5 different in-situ hygrothermal conditions.

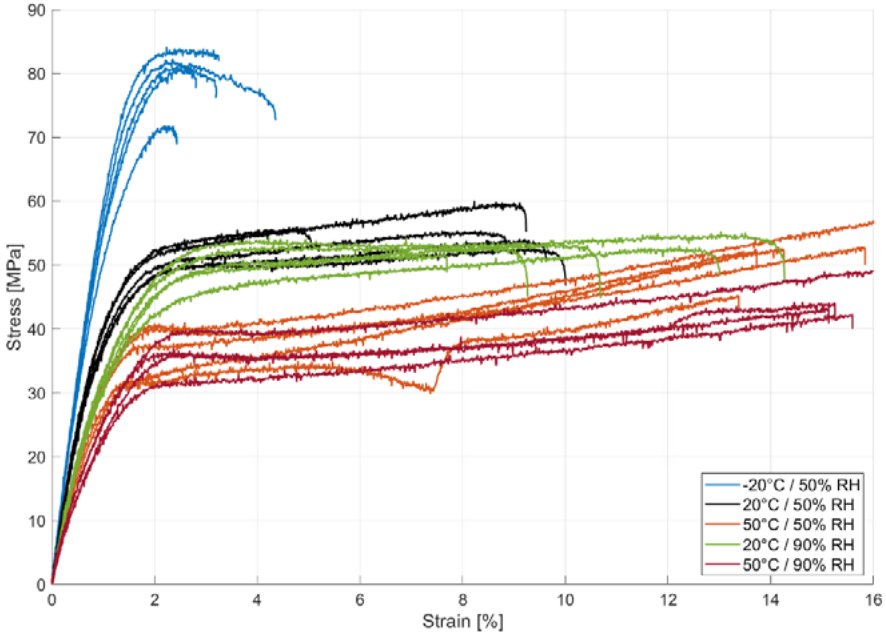


Figure 4. Stress-strain curves of the FFRP $[(+45/-45)_2]_S$ laminate for 5 different in-situ hygrothermal conditions. Beyond 6% strain the deformation was calculated based on the actuator displacement.

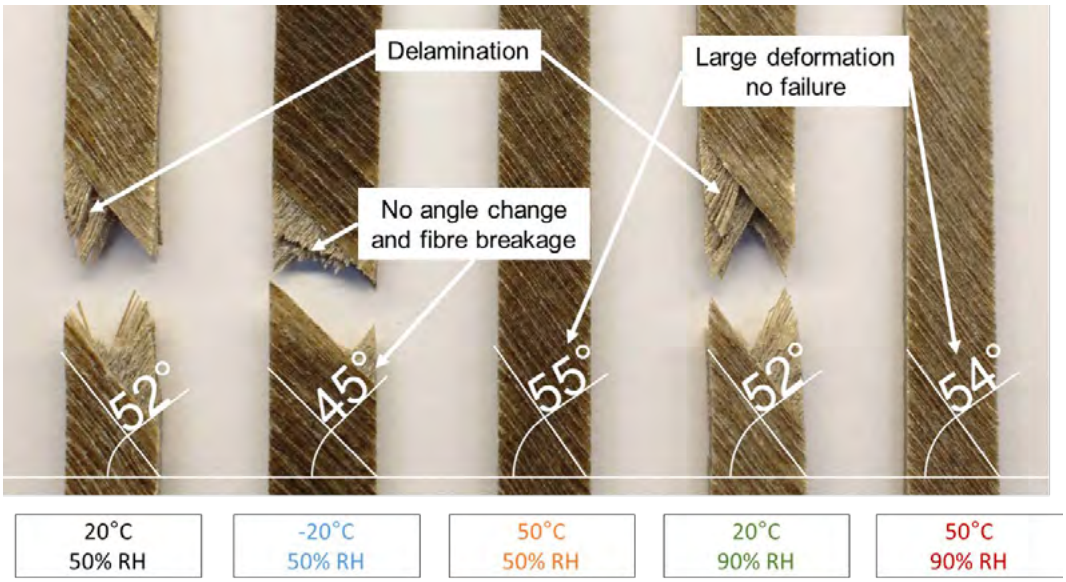


Figure 5. Pictures of post-mortem specimens and visual measure of fibre angle. Observation of different failure mechanisms (or no failure) for different in-situ temperatures.

4. Discussion

The characterisation of the four laminates at -20, 20, and 50°C showed a general trend of lower mechanical performance at higher temperatures (figure 6). While the GFRP and FFRP angle-ply laminates have a similar temperature effect on their modulus, likely due to the common temperature sensitive epoxy matrix system, the GFRP and FFRP cross-ply laminates have a distinct modulus sensitivity to temperature visible by comparing figure 2 with overlapping stress-strain curves and figure 4 with 3 distinct stress-strain curves. This observation suggests that the glass reinforcement is not sensitive to the in-situ temperature but the flax reinforcement is.

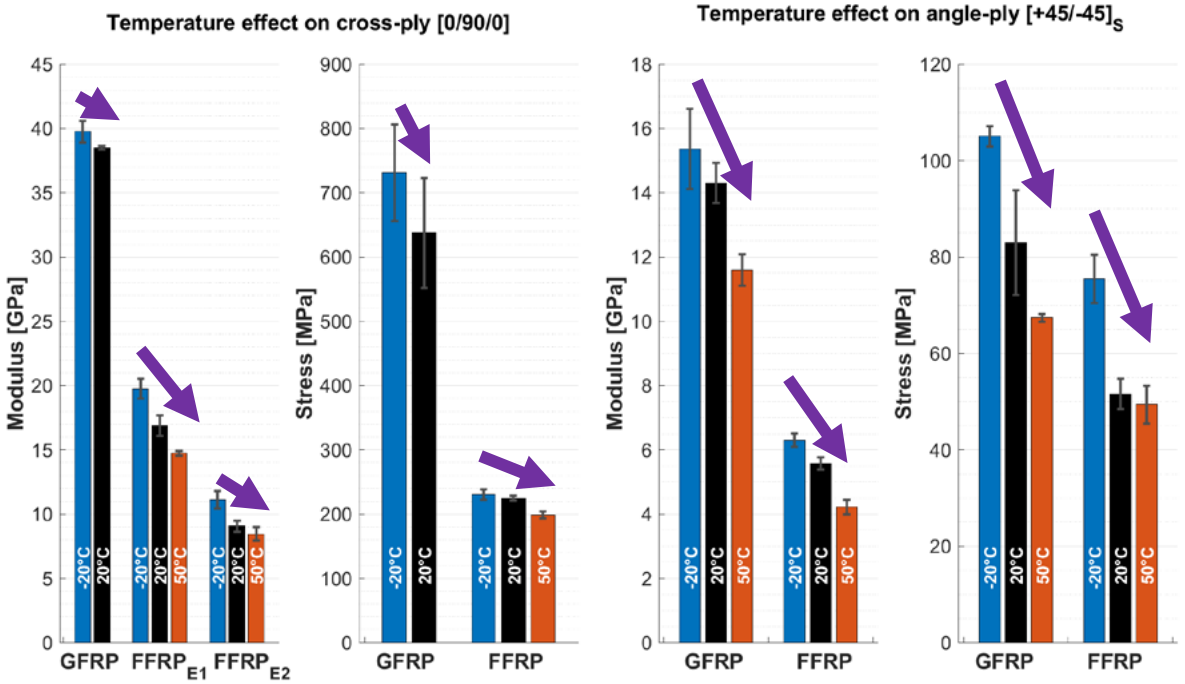


Figure 6. Tests at 50% RH. Decrease of stiffness and strength with increase of temperature. For cross-ply FFRP the E1 modulus is measured from 0 to 0.2% strain (before the knee) and the E2 modulus from 0.7 to 0.9% strain (after the knee) as indicated in figure 3. For the other laminates, the modulus is measured from 0 to 0.2% strain. The stress is measured at tensile failure.

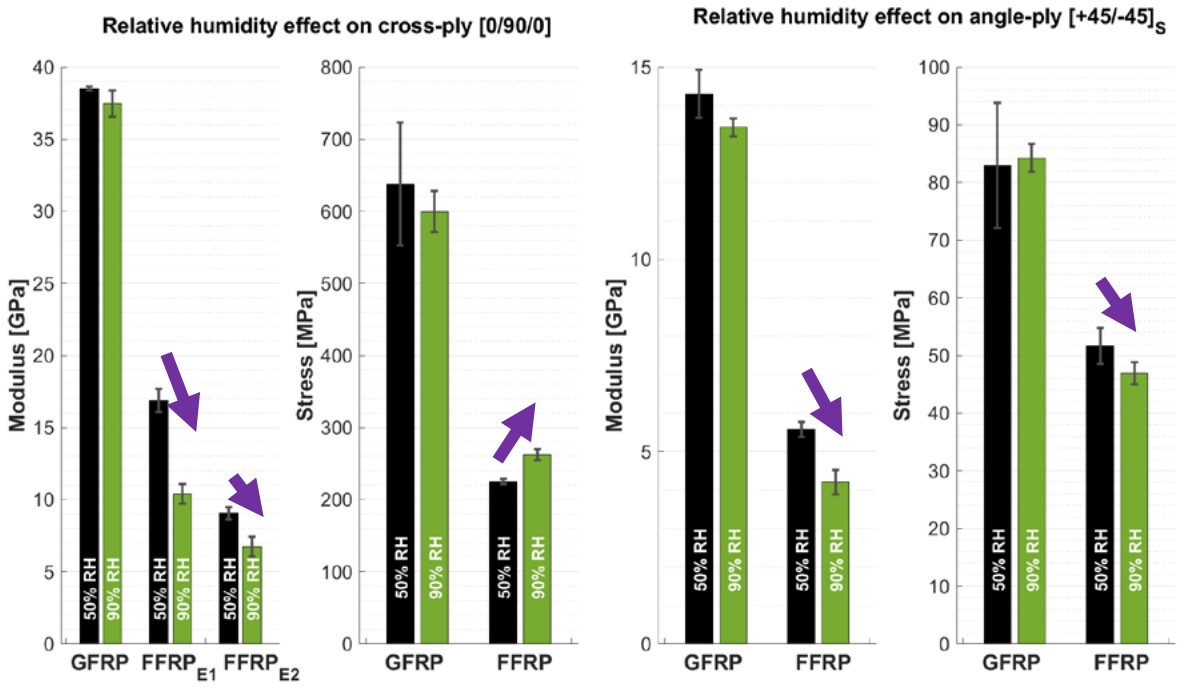


Figure 7. Tests at 20°C. Sensitivity of FFRPs stiffness and strength to relative humidity and insensitivity of GFRPs. For cross-ply FFRP the E1 modulus is measured from 0 to 0.2% strain (before the knee) and the E2 modulus from 0.45 to 0.65% strain (after the knee) as indicated in figure 3. For the other laminates, the modulus is measured from 0 to 0.2% strain. The stress is measured at tensile failure.

The characterisation of the four laminates at 50% and 90% RH showed that the effect of in-situ relative humidity is not significant on GFRP laminates (within standard deviation) but significant on FFRP laminates highlighting flax sensitivity to moisture and its consequences on the mechanical response of the composite (figure 7). Surprisingly, the shape of the cross-ply FFRP laminate stress-strain curve at 90% RH matches that of single flax fibres found in literature [9].

With the combination of in-situ temperature and relative humidity effects (50°C and 90% RH) the results of the FFRP laminates suggest a possible superposition of effects allowing modelling of hygrothermal effects by independent temperature and humidity knock-down factors. For example in figure 3, a factor could be applied on the 20°C/50% RH curve to obtain the same slope as the 50°C/50% RH curve. Then, the same factor could be applied on the 20°C/90% RH curve to obtain the slope of the 50°C/90% RH curve.

.

On the plastic region of the angle-ply FFRP laminate, a surprisingly high strain to failure was reached especially at 50°C with some specimens reaching more than 16% strain (figure 4). This large deformation cannot be solely explained by the fibre deformation as single flax fibre reach failure before 4% strain, even at 50°C [8]. However, a rotation of the flax fibres from the initial 45° to 55° (scissoring) was measured on the surface of the post-mortem specimens (figure 5). By trigonometry, this fibre rotation results in a longitudinal strain of 15.8% explaining the 16% strain reached. How such a large deformation can occur is not clear yet as the maximum strain reached by the equivalent GFRP angle-ply laminate is below 6%. The large rotation in the FFRP angle-ply laminate may be allowed by a weak flax fibre-matrix allowing for a relative displacement without failure which is exacerbated by elevated temperatures increasing matrix plasticity. The microstructure of the FFRP laminate may also contribute to allowing large fibre rotation because of larger spacing between fibres tows in FFRP than in GFRP, resulting in matrix rich areas susceptible to scissoring (figure 8). Also, low spacing between glass fibre tows in the fabric can also limit the scissoring effect.

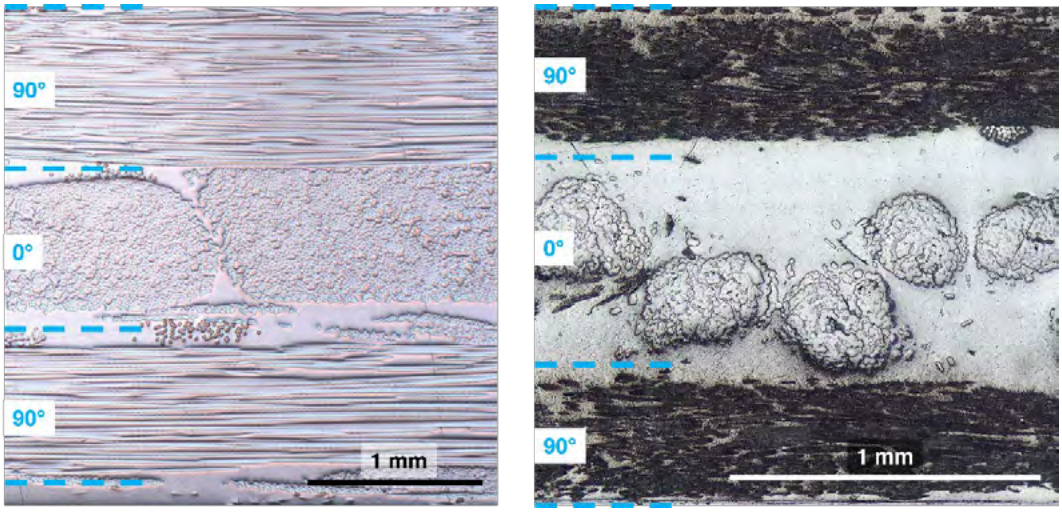


Figure 8. SEM images depicting microstructure of GFRP laminate (left) and FFRP laminate (right) demonstrating smaller spacing between glass tows compared to flax yarns. The delimitations of the plies and fibre angle relative to the observer are indicated.

4. Conclusions

In this study, we investigated the effects of in-situ temperature and relative humidity variations on the quasi-static tensile response of flax and glass FRP composites. Cross-ply and angle-ply laminates were manufactured, equilibrated to five different hygrothermal conditions with temperature and relative humidity ranging from -20 to 50°C and 50% to 90% RH, respectively and subsequently tested under controlled hygrothermal conditions. Below are the key findings:

- At higher in-situ temperatures, a general decrease in mechanical performance is noted across all laminates, with FFRP laminates displaying a more pronounced sensitivity, likely attributed to the cellulosic nature of the flax reinforcement.
- While the in-situ relative humidity had limited effects on the GFRP laminates, a significant effect of in-situ condition was observed on stiffness, strength, and strain to failure of FFRP laminates. Additionally, a change of the stress-strain curve shape was noted for the FFRP cross-ply laminate
- The in-situ temperature and relative humidity have distinct effects on the FFRP laminates. The results suggest that those effects can be modelled separately and superposed.
- For angle-ply laminates, the matrix sensitivity to in-situ environment has a large influence on the mechanical response of the composite while the hygrothermal sensitivity of the cross-ply laminates is predominantly dependant on fibre properties.
- Exceptionally large strains to failure, exacerbated at high temperatures, were measured with the FFRP angle-ply laminate and were accompanied by a fibre rotation. This large deformation is possibly attributed to scissoring in matrix rich region of the FFRP microstructure.

As a general conclusion, the results presented in this study show that the mechanical performance of FFRP laminates is sensitive to in-situ temperature and moisture conditions, and this to a significantly larger extent than in GFRP laminates. It is therefore pivotal for the safe and reliable use of biocomposites in structural applications to understand and account for in-situ hygrothermal effects.

Acknowledgments

The authors wish to thank the Suzlon company for the delivery of the epoxy resin used in the manufacturing of the specimens. Authors wish to sincerely thank the continuous support of all the technicians within the Macrolab/Stevinlaboratory of the faculty of Civil Engineering and Geosciences, and the ASM laboratory of the faculty of Aerospace Engineering at TU Delft.

References

[1] Y. Ou *et al.*, "Mechanical Characterization of the Tensile Properties of Glass Fiber and Its Reinforced Polymer (GFRP) Composite under Varying Strain Rates and Temperatures," *Polymers (Basel)*, vol. 8, no. 5, p. 196, May 2016, doi: 10.3390/polym8050196.

[2] W. Biswas and C. Dong, "Eco-Efficiency Performance for Multi-Objective Optimal Design of Carbon/Glass/Flax Fibre-Reinforced Hybrid Composites," *Sustainability*, vol. 16, no. 7, Art. no. 7, Jan. 2024, doi: 10.3390/su16072928.

[3] V. Krishnarajb, K. Kumar, and R. Zitoune, *Sound and Vibration Damping Properties of Flax Fiber Reinforced Composites*, vol. 97. 2014. doi: 10.1016/j.proeng.2014.12.285.

[4] M. Lu, C. Fuentes, and A. W. Vuure, "Moisture sorption and swelling of flax fibre and flax fibre composites," *Composites Part B: Engineering*, vol. 231, p. 109538, Nov. 2021, doi: 10.1016/j.compositesb.2021.109538.

[5] I. Rocha, S. Raijmaekers, R. Nijssen, F. Van der Meer, and L. J. Sluys, "Hygrothermal ageing behaviour of a glass/epoxy composite used in wind turbine blades," *Composite Structures*, vol. 174, Apr. 2017, doi: 10.1016/j.compstruct.2017.04.028.

[6] A. le Duigou, J. Merotte, A. Bourmaud, P. Davies, K. Belhouli, and C. Baley, "Hygroscopic expansion: A key point to describe natural fibre/polymer matrix interface bond strength," *Composites Science and Technology*, vol. 151, pp. 228–233, Oct. 2017, doi: 10.1016/j.compscitech.2017.08.028.

[7] G. C. Davies and D. M. Bruce, "Effect of Environmental Relative Humidity and Damage on the Tensile Properties of Flax and Nettle Fibers," *Textile Research Journal*, vol. 68, no. 9, pp. 623–629, Sep. 1998, doi: 10.1177/004051759806800901.

[8] A. Thuault, S. Eve, D. Blond, J. Bréard, and M. Gomina, "Effects of the hygrothermal environment on the mechanical properties of flax fibres," *Journal of Composite Materials*, vol. 48, no. 14, pp. 1699–1707, Jun. 2014, doi: 10.1177/0021998313490217.

[9] C. Baley, "Analysis of the flax fibres tensile behaviour and analysis of the tensile stiffness increase," *Composites Part A-applied Science and Manufacturing - COMPOS PART A-APPL SCI MANUF*, vol. 33, pp. 939–948, Jul. 2002, doi: 10.1016/S1359-835X(02)00040-4.

DECOMPOSITION OF FRACTURE MODES IN ASYMMETRIC DOUBLE CANTILEVER BEAM AND ASYMMETRIC END NOTCHED FLEXURE TESTS

F. Mujika[1] and A. Arrese[1]

[1]MECMAT group, Faculty of Engineering of Gipuzkoa, Department of Mechanical Engineering, University of the Basque Country (UPV/EHU), Plaza Europa 1, San Sebastián, Spain
Email: faustino.mujika@ehu.eus

Keywords: interlaminar fracture, mixed mode I/II, mode decomposition

Abstract
The double cantilever beam (DCB) test was designed to characterize interlaminar fracture in pure mode I and the end notched flexure test (ENF) was designed to analyse interlaminar fracture in pure mode II. Nevertheless, in the case of geometric, material or combined asymmetry of the cracked arms of the specimen, combination of modes appear in both test configurations. In the present study, some aspects of a new analytical model to decompose the energy release rate in mode I and mode II are presented. The model is based on the assumption of concentrated loads at the crack tip zone. The J integral is determined in the case of a small fracture process zone. Thus, J_I and J_{II} are obtained as a function of the loads and derivatives of the displacements at the crack tip. The calculation process is based on the derivatives of the complementary strain energy or coenergy in both, ADCB and AENF test configurations.

1. Introduction

Double Cantilever Beam and End Notched Flexure tests were designed for the determination of interlaminar fracture behavior in mode I and mode II of composite materials. The same configurations were used in the characterization of adhesive joints in modes I and II. When geometric or material symmetry does not exist, mixed mode fracture could appear. Recently, pure mode conditions have been related to the J-integral [1]. The same relation between thicknesses and flexural moduli was obtained for pure mode I and pure mode II of bimaterial specimen joints. The energy release rates (ERRs) that correspond to each specimen were obtained and the results were compared with numerical models, obtaining good agreement [2]. It is worth noting that numerical approaches were developed with cohesive elements. Thus, the results correspond to the J-integral determined by the cohesive law at the crack tip, while the results of the analytical approach correspond to the ERR (G) determined by the coenergy derivatives. The equivalence between J and G was established in cases of small and great fracture process zones (FPZs), provided that the global behaviour of the specimen was elastic. This equivalence is due to the equivalent crack length, which incorporates all sources of compliance changes in the specimen, was used for the determination of G.

The problem of the decomposition of fracture modes has been analyzed by several authors [3-7], following different approaches. In the present study, the decomposition in fracture modes I and II is analyzed in the case of the Asymmetric Double Cantilever Beam (ADCB) and the Asymmetric End Notched Flexure tests (AENF). The analytical model is based on the assumption that the crack tip effects are replaced by the resultant forces of stresses at that zone. The ERR that correspond to each mode, is determined analytically in a similar way as the virtual crack closure technique (VCCT) is applied in the

finite element method (FEM). Besides the forces at the crack tips, the displacement fields are also necessary for that calculation.

2. *J*-integral and VCCT

In the present section, it is shown that in the case of small fracture process zones (FPZ), the *J*-integral is equivalent to the virtual crack closure technique. Figure 1 shows the fracture process zone, the beginning of the FPZ, that is named *lagging crack tip*, and the end of the FPZ, that is named *leading crack tip*, according to the nomenclature used by Turón [8].

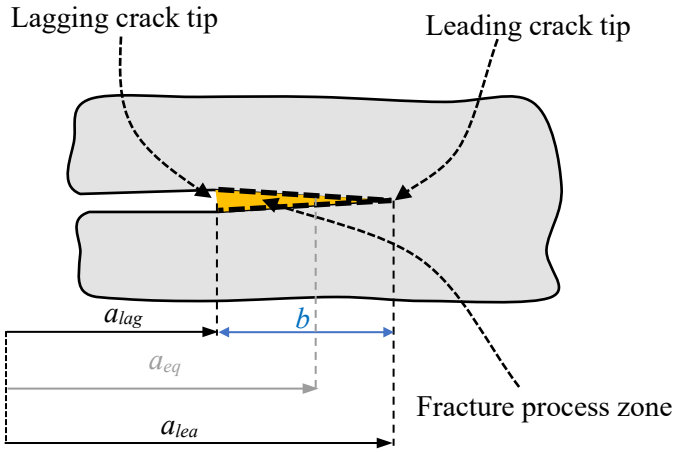


Figure 1. Fracture process zone and definition of crack lengths.

Being b the length of the fracture process zone, the *J*-integral can be expressed as [1]:

$$J = \int_0^{-b} \sigma \delta_{n,x} dx + \int_0^{-b} \tau \delta_{t,x} dx \tag{1}$$

where σ and τ are normal and shear stresses and δ_n and δ_t are the normal and tangential relative displacements of homologous points of the cohesive zone. Homologous points are defined as those that were the same point before fracture. In this way, the *J*-integral corresponds to the FPZ, and stresses and displacements refer to different points. As the relative displacements of the cohesive zone or FPZ are a function of the coordinate x:

$$d\delta_n(x) = \delta_{n,x} dx \text{ and } d\delta_t(x) = \delta_{t,x} dx \tag{2}$$

Furthermore, the integral limits in Eq. (1) change as follows:

$$\begin{cases} x = -b \Rightarrow \delta_n = \delta_n^*, \delta_t = \delta_t^* \\ x = 0 \Rightarrow \delta_n = 0, \ \delta_t = 0 \end{cases} \tag{3}$$

where δ_n^* and δ_t^* are the values at the lagging crack tip, i.e. at the beginning of the cohesive zone. Replacing Eqs . (2) and (3) in Eq. (1) the integral variables are the relative displacements:

$$J = \int_0^{\delta_n^*} \sigma d\delta_n + \int_0^{\delta_t^*} \tau d\delta_t \tag{4}$$

The derivation of Eq. (4) does not depend on the length of the cohesive zone. σ, τ, δ_n and δ_t correspond to the beginning of the FPZ. Therefore, Eq. (1) can be seen as a spatial interpretation of the *J*-integral,

evaluated in a given process configuration, taking into account all points of the FPZ. Alternatively, Eq. (4) can be seen as an evolutionary integral, taking into account the change of stresses and displacements at a fixed position as fracture process develops. This interpretation is applied to define the cohesive laws.

Figure 2 shows a fracture process zone of lengthe Δa, where stresses and relative displacements are linearly distributed, according to:

$$\sigma = \sigma_0\left(1+\frac{x}{\Delta a}\right) \quad \tau = \tau_0\left(1+\frac{x}{\Delta a}\right)$$
$$\delta_n = -\frac{\delta_n^*}{\Delta a}x \qquad \delta_n = -\frac{\delta_t^*}{\Delta a}x \tag{5}$$

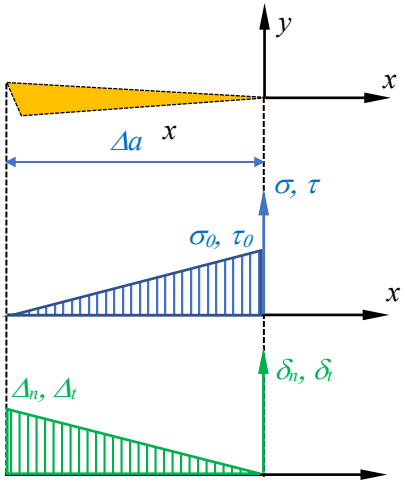


Figure 2. Linear stresses and displacements along the FPZ.

Replacing Eq. (5) in Eq.(1) and taking into account that $b = \Delta a$:

$$J = \tfrac{1}{2}\sigma_0\delta_n^* + \tfrac{1}{2}\tau_0\delta_t^*$$
$$\sigma_0 = \left[\frac{dF_n(x)}{wdx}\right]_{x=0} \qquad \tau_0 = \left[\frac{dF_t(x)}{wdx}\right]_{x=0} \tag{6}$$

where F_n and F_t are the normal and tangential forces, respectively. When $\Delta a \to 0$:

$$\left(dF_n\right)_{x=0} = F_n(0) - F_n(-\Delta a) = F_n(0) = F_n^*$$
$$\delta_n^* = \delta_n(-\Delta a) = \delta_n(-\Delta a) - \delta_n(0) = -\left(d\delta_n\right)_{x=0} \tag{7}$$

Eq. (7) can be extended to tangential components. Assuming crack closure, $dx = -da$. Replacing Eq. (7) in Eq. (6), the J-integral is:

$$J = \frac{1}{2w}F_n^*\left(\frac{d\delta_n}{da}\right)_{x=0} + \frac{1}{2w}F_t^*\left(\frac{d\delta_t}{da}\right)_{x=0} \tag{8}$$

Eq. (8) is the same as that of the virtual crack closure technique (VCCT). As the models of the present study are based on concentrated loads, Eq. (8) can be applied in the analytical approach. The relative normal displacement and its derivative are:

$$\begin{aligned}\delta_n &= v_1 - v_2 = (v_1 - v_2)_b + (v_1 - v_2)_s \\ \frac{d\delta_n}{da} &= (\theta_1 - \theta_2)_b + \left(\frac{dv_1}{da} - \frac{dv_2}{da}\right)_s\end{aligned} \tag{9}$$

where v_1 and v_2 are vertical displacements at the upper and lower sub-beams, respectively. The subscripts b and s refer to bending and shear, respectively. Grouping terms of each sub-beam, Eq. (9) can be expressed as:

$$\frac{d\delta_n}{da} = \left(\theta_{1b} + \frac{dv_{1s}}{da}\right) - \left(\theta_{2b} + \frac{dv_{2s}}{da}\right) = \phi_1 - \phi_2 \tag{10}$$

Moreover, the relative tangential displacement and its derivative are:

$$\begin{aligned}\delta_t &= u_1 - u_2 \\ \frac{d\delta_t}{da} &= \varepsilon_1 - \varepsilon_2\end{aligned} \tag{11}$$

In Eq. (11), ε_1 is the normal strain on the lower face of the upper arm and ε_2 is the normal strain at the upper face of the lower arm. Replacing Eqs. (9) and (11) in Eq. (8) it results:

$$J = \tfrac{1}{2} F_n^* (\phi_1 - \phi_2)_{x=0} + \tfrac{1}{2} F_t^* (\varepsilon_1 - \varepsilon_2)_{x=0} \tag{12}$$

According to Eq. (12) pure mode contributions are:

$$\begin{aligned}J_I &= \tfrac{1}{2} F_n^* (\phi_1 - \phi_2)_{x=0} \\ J_{II} &= \tfrac{1}{2} F_t^* (\varepsilon_1 - \varepsilon_2)_{x=0}\end{aligned} \tag{13}$$

Moreover, pure mode conditions can be formulated in the following manner:

1. Pure mode I occurs when $F_t^* = 0$ and $\varepsilon_1 = \varepsilon_2$ at the crack tip.
2. Pure mode II occurs when $F_n^* = 0$ and $\phi_1 = \phi_2$ at the crack tip.

It is worth noting that the force and deformation condition are both simultaneously satisfied in each case. The physical meaning is that if the force is zero, there is no cause to generate an associated deformation. Conversely, if the deformation is zero, there is no need of an associated force to prevent it.

3. Strain coenergy and partial derivatives

The complementary strain energy or coenergy of a laminated beam constituted by orthotropic layers, when normal forces are zero, axial-bending coupling and hygrothermal effects are zero, is given by [2]:

$$C = \tfrac{1}{2} d \int_{L_x} M^2 dx + \tfrac{1}{2} s \int_{L_x} V^2 dx \tag{14}$$

Where; M is bending moment; V is the shear force; d is the flexural flexibility, being: $d = (EI)^{-1}$; E is the bending modulus; I is the moment of inertia; s is the shear flexibility [2]; L_x is the length of the beam. We assume that the coenergy is a function of generalized applied forces F_j, the crack length a, and some unknown parameters λ_k, i.e. $C = C(F_j, a, \lambda_k)$. Then, a generalized displacement δ_j in the direction of the

generalized force F_j, the ERR G and the unknown parameters λ_k can be determined by the derivatives of the coenergy [2]:

$$\delta_j = \frac{\partial C}{\partial F_j} \qquad G = \frac{1}{w}\frac{\partial C}{\partial a} \qquad \frac{\partial C}{\partial \lambda_k} = 0 \tag{15}$$

4. Asymmetric Double Cantilever Beam Test: ADCB

Figure 2 shows the configuration of an Asymmetric Double Cantilever test. The asymmetry could be due to different thicknesses of the same material or due to the joint of two different materials. The rotation of the non-cracked part of the specimen indicates mode II.

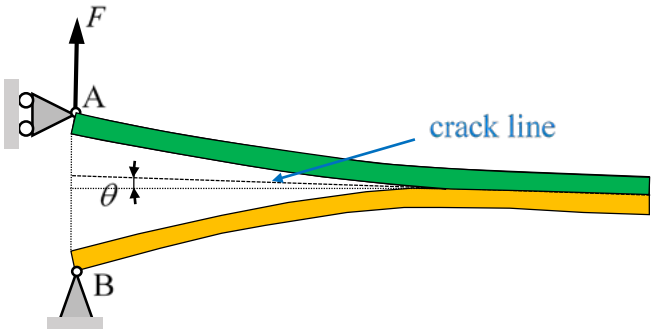


Figure 3. ADCB test configuration.

The rotation angle of the crack line can be determined by the Engesser-Castigliano's theorem given in Eq. $(15)_1$, being:

$$\theta = \frac{Fa^2}{4h}\left(h_1 d_1 - h_2 d_2\right) \tag{16}$$

Where h is the total thickness; h_i are the thicknesses of each arm, being i = 1, 2 the upper and lower cracked arms, respectively. In pure mode I, the cross section of the whole specimen at the crack tip is not plane due to crack tip effects. Then, the two sub-beams that constitute the specimen are assumed to be connected with normal concentrated forces [2] at a distance λ. In the case mode combination, horizontal forces are also added to the model, as shown in Figure 4.

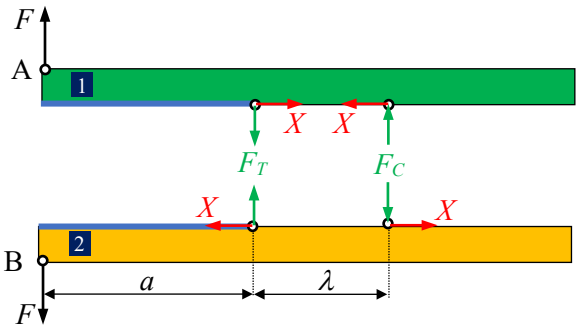


Figure 4. Forces in the ADCB configuration.

The distance λ and the force X are determined by stationary values of the coenergy C:

$$C_{,X} = 0 \rightarrow X$$
$$C_{,\lambda} = 0 \rightarrow \lambda \tag{17}$$

The relative angles and strains can be calculated by the Engesser-Castigliano's theorem, applying unit loads in the statically determined system to obtain the derivatives of the section forces and moments.

5. Asymmetric End Notched Flexure Test: AENF

Figure shows the AENF configuration. It is assumed that the contact in the cracked part exist only above the support A. In the case of pure mode, the hypothesis is correct. In the case of combined modes, it depend on the relative position of both sub-beams: when the most flexible sub-beam is in the lower part, the hypothesis is correct, as there is separation between both of them, as shown in Figure 5. In the opposite case, in a first approach, it can be assumed full contact between both sub-beams.

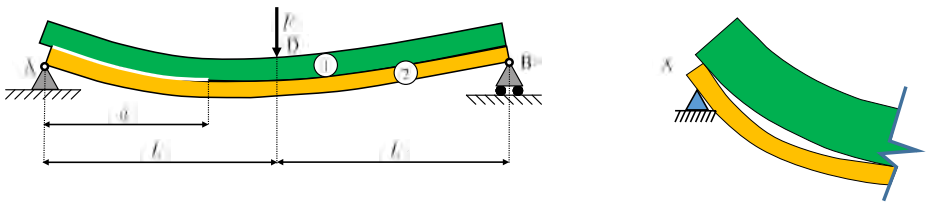


Figure 5. AENF configuration and separation between cracked arms.

In the case of pure mode II, we assume that the non-cracked part is a beam that satisfies the Euler-Bernoulli hypothesis, as the section at the crack tip remains plane. In the case of mode combination, it is assumed that mode II is related to the shear stress distribution that corresponds to the plane section hypothesis and mode I is related to normal vertical forces F_T and F_C that lead to the difference between bending angles at the crack end, as in the case of the ADCB test.

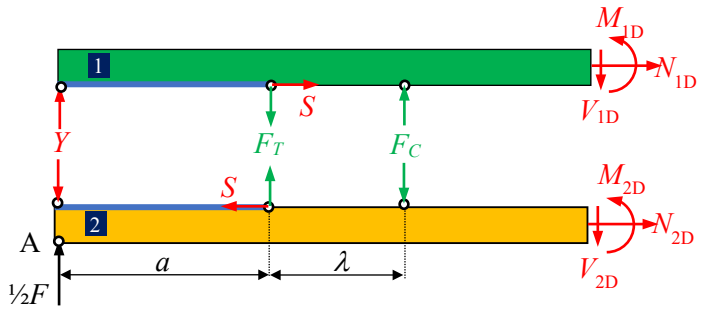


Figure 6. Forces and moments on the two sub-beams in the AENF configuration.

Figure 6 shows the force configuration assumed in the left half of the specimen, where N_{iD}, V_{iD} and M_{iD} correspond to the middle cross section D. Shear stresses that correspond to the complete beam are not included. These section forces and moments and shear stresses between both sub-beams, are determined by the classical beam theory [1,2]. The concentrated shear force S in this case is due to the equilibrium of the whole upper part: in the right half there is a uniform shear stress distribution over the length L, while in the left half, the shear stress distribution with the same value acts on the length (L-a). Then, S force equilibrates this difference, as occurs in an ENF test. The unknowns Y, F_T and F_C can be determined by the following equations:

$$\sum F_y = 0 \Rightarrow Y + F_C - F_T - V_{1D} = 0$$
$$\sum M_T = 0 \Rightarrow M_{1D} - V_{1D}(L-a) - \tfrac{1}{2}N_{1D}h_1 + F_C\lambda - Ya = 0 \tag{18}$$
$$C_{,Y} = 0$$

It is worth noting that N_{1D}, V_{1D} and M_{1D}, S and shear stresses do not depend on Y, as they are determined by equations that correspond to the whole specimen. Otherwise, bending moments and shear forces related to F_C and F_T, generate independent normal and shear stresses in each sub-beam.

6. Conclusions

Assuming a small fracture process zone, the J-integral can be used to determine the contribution of mode I or mode II as a function of concentrated forces and deformations at the crack tip. In mode I, the relative normal force and the relative angle between the elastic curves of each sub-beam at the crack tip are the main parameters. In mode II, J_{II} depend on the relative tangential force and the relative strains at the contact surfaces at the crack tip.

The models of ADCB and AENF where crack tip effects are incorporated as concentrated forces and the steps for their calculation have been described. When analytical approach is developed, the results can be compared with numerical results obtained applying the VCCT.

Acknowledgments

The authors gratefully acknowledge the financial support of the University of the Basque Country (UPV/EHU) in the Research Group GIU21/015 “Mechanics of Materials”.

References

[1] F. Mujika, P. Tsokanas, A. Arrese, P.S. Valvo and L.F.M. da Silva. Mode decoupling in interlaminar fracture toughness tests on bimaterial specimens. *Engineering Fracture Mechanics*, 290: 109454, 2023.
[2] F. Mujika, P. Tsokanas, A. Arrese and L.F.M. da Silva. Energy release rate in bimaterial specimens tested in pure modes I and II, Engineering Fracture Mechanics, 301: 110012, 2024.
[3] J.G. Williams. On the calculation of energy release rates for cracked laminates. *International Journal of Fracture*, 36: 101-119, 1988.
[4] M. Charalambides, A.J. Kinloch, Y. Wang and J.G. Williams. On the analysis of mixed-mode failure. *International Journal of Fracture*, 54: 269-291, 1992.
[5] V. Mollón, J. Bonhomme, A. Argüelles and J. Viña. Influence of the crack plane asymmetry over G_{II} results in carbon epoxy ENF specimens. *Composite Structures*, 94: 1187-1191, 2012.
[6] P.S. Valvo. On the calculation of energy release rate and mode mixity in delaminated laminated beams. *Engineering Fracture Mechanics*, 165: 114-139, 2016.
[7] P. Maimí, J. Renart, C. Sarrado, E.V. González. Characterization of debonding between two different materials with beam like geometries. *Engineering Fracture Mechanics*, 247: 107661, 2021.
[8] A. Turón. The role of the cohesive law shape and mixed-mode interpolation when modeling delamination failure involving large fracture process zones. *In Comptest 2023, Girona*, http://hdl.handle.net/10256/23154.

Stress Analysis of Thick Multilayered Laminated Composite and Sandwich Plates using Higher Order Zigzag Theory

Aamir Anwar Nezami[a], Shaikh Jahangir Hossain[b]

[a]*Department of Civil Engineering, Indian Institute of Technology Kharagpur, India*
Email: aamir.anwar47@gmail.com
[b]*Department of Civil Engineering, Indian Institute of Technology Kharagpur, India*
Email: sjh@civil.iitkgp.ac.in

Abstract

A higher-order zigzag theory is developed, which is independent of the number of laminae. This theory contains only five unknowns (three translations and two average cross-sections shearing strains). In various plate theories, the cross-sectional rotations are considered as the independent field, while in the present plate model, it is the average cross-section shearing strains. This higher-order zigzag theory formulation is motivated by elasticity solutions, revealing that the transverse shearing stresses are continuous at the interface of two different laminae. Therefore, the transverse shearing strain capture jumps at the interfaces and varies quadratically along the thickness of the plate. Numerical problems are solved analytically to assess the accuracy of the present theory, for thick laminated composites and sandwich plates of thickness ratio ($a/h = 4$). Results obtained for a cross-ply plate having all four sides simply supported and cylindrical bending case of angle-ply sandwich plates respectively, and are compared with exact three-dimensional elasticity (Exact-3D) solutions and various equivalent single-layer theories (ESL) such as First Order Shear Deformation Theory (FSDT), Murakami Zigzag Theory (MZT), and Sorrenti Enhanced-Refined Zigzag Theory (En-RZT). The numerical results show that the present theory captures very close to exact three-dimensional elasticity solutions for Laminated Composites and sandwich plates.

Keywords: Laminate, Sandwich, Zigzag, Enhanced-RZT

1. Introduction

Laminated composite plates are extensively used in engineering applications due to their high strength-to-weight ratio and customizable mechanical properties. These plates consist of layers of various materials, like fibers and resins, stacked together to achieve specific structural characteristics. Analyzing laminated composite plates involves examining their behavior under different loading conditions, including mechanical, thermal, and environmental factors. The main goals of this analysis are to understand the deformation patterns, stress distributions, failure modes, and overall performance of the plates. This is crucial for designing lightweight and efficient structures in industries such as aerospace, automotive, marine, and civil engineering. Laminated composite plates are manufactured using techniques that involve layering multiple plies of materials like glass, carbon, or aramid fibers, which are then bonded with polymer-based adhesives. These adhesives, typically low-strength polymers, contribute to the inherent weakness at the laminae interfaces, leading to reduced interlaminar strength and the occurrence of delamination and transverse cracking. Therefore, accurately predicting the interlaminar strains and stresses is essential for structural analysis and failure prediction in multi-layer thick composite and sandwich plates [15]. Significant shear deformation and discontinuities in material properties at inter-layer interfaces in multilayered laminated plates cause rapid changes in slope, a phenomenon known as the zigzag effect [1]. Various plate theories within ESL, such as CLPT, FSDT, and TSDT, have been developed, but none adequately capture the warping of in-plane displacements in thick laminated composites

and sandwich plates. The Zigzag theory represents a significant advancement in ESL theory by accurately capturing the warping of in-plane displacements in thick laminated plates. It also incorporates continuity functions to manage abrupt changes in transverse shear strains, ensuring the continuity of transverse shear stresses at the interfaces between layers [3]. The effectiveness of this model lies in its ability to provide accurate results while maintaining a fixed number of unknown variables, making it economical for analyzing general laminates with diverse material layers [6, 10, 2]. The Refined Zigzag Theory (RZT), developed by Tessler et al. [16] offers a crucial improvement by accurately simulating clamped boundary conditions. In RZT, in-plane strains exhibit a piecewise linear distribution across the laminate thickness, while transverse shear strains display discontinuities at layer interfaces but remain piecewise constant within each material layer. For thick plates, linear piecewise models are insufficient due to the nonlinear behavior observed in in-plane displacements. Di Sciuva [10] pioneered the development of a third-order zigzag plate model that captures nonlinear behavior in in-plane displacements throughout the thickness while satisfying stress continuity conditions at layer interfaces. Nemeth [7] further enhanced RZT by incorporating continuous piecewise-cubic zigzag functions, surpassing the limitations of piecewise-linear functions. Tessler et al. [14], and Iurlaro et al. [4] expanded the linear RZT model by including stretching effects, using cubic zigzag functions. Kreja [5] examined FSDT and zigzag theory. In his study of FSDT, he considered one classical and three different global shear coefficients, whereas, for Zigzag theory, he focused on MZT and RZT which share the same kinematics but different zigzag functions. Computational models for analyzing laminates with a larger number of layers, enhanced by the application of zigzag functions, tend to be very stiff while FSDT models with global shear correction coefficients performed better. Sorrenti et al. introduced Enhanced-RZT [12], which incorporates linear zigzag functions with improved coupling effects where RZT fails to provide the desired results for angle ply laminates. In recent developments, Sorrenti et al. introduced another version of Enhanced-RZT [13], featuring cubic zigzag functions. Additionally, Si et.al., [11] proposed a higher-order zigzag theory using $nine$ kinematic fields, although this approach comes with higher computational costs.

In this study, a higher-order zigzag theory that is independent of the number of laminae is developed, featuring just $five$ unknowns. This formulation is inspired by elasticity solutions, which reveal that transverse shearing stresses are continuous at the interfaces of dissimilar laminae. Consequently, the transverse shearing strain varies quadratically along the thickness of the plate, capturing jumps at the interfaces. The analytical solution of multilayered laminated composites and sandwich plate problems using this zigzag model is compared with various structural theories available in the literature, including FSDT, Murakami's Zigzag theory, the Enhanced-Refined Zigzag Theory by Sorrenti et al., and exact three-dimensional elasticity theory. These comparisons consider various stacking sequences, such as symmetric cross-ply and symmetric angle-ply.

2. Mathematical Formulation for Higher Order Zigzag Theory

Take into account that the laminated plate is made up of a finite number of linear-elastic anisotropic layers, each of which has distinct mechanical and physical characteristics. To prevent delamination or slide at any lamina interface, it is expected that the layers are perfectly bonded. The thickness of the k^{th} constituent layer and of the entire plate is denoted by $h_k (k = 1, 2, ..., N)$ and $h = \bigcup_{k=1}^{N} h_k$, respectively, where N denotes the total number of constituent layers

2.1. Kinematics

The elasticity solutions show that the transverse shearing stresses are continuous at the interface of two dissimilar laminae and assume zero values at the bounding surfaces of the plate in the absence of surface shear traction. Therefore, the transverse shearing strains encounter the jumps (i.e., discontinuity) at the interfaces. The simplest form of kinematics that accounts for these requirements can be achieved by superposing a piece-wise constant shearing strain field (i.e., different values in different laminae) on an overall quadratic varying field. We start with the following piece-wise quadratic distribution of the

transverse shearing strain fields in the thickness direction of the plate.

$$\begin{Bmatrix}\gamma_{xz}\\ \gamma_{yz}\end{Bmatrix} = \left(\begin{bmatrix}Q_{44}^{(m)} & Q_{45}^{(m)}\\ Q_{54}^{(m)} & Q_{55}^{(m)}\end{bmatrix}^{-1}\begin{bmatrix}(Q_s^{av})_{11} & (Q_s^{av})_{12}\\ (Q_s^{av})_{21} & (Q_s^{av})_{22}\end{bmatrix}\right)\begin{Bmatrix}\overset{0}{\gamma}_x\\ \overset{0}{\gamma}_y\end{Bmatrix} + 2z\begin{Bmatrix}\overset{1}{\gamma}_x\\ \overset{1}{\gamma}_y\end{Bmatrix} + 3z^2\begin{Bmatrix}\overset{2}{\gamma}_x\\ \overset{2}{\gamma}_y\end{Bmatrix} + \sum_{k=1}^{m-1}\begin{Bmatrix}\overset{0}{\gamma}_x^k\\ \overset{0}{\gamma}_y^k\end{Bmatrix}Y^-(z,k) + \sum_{k=m}^{N-1}\begin{Bmatrix}\overset{0}{\gamma}_x^k\\ \overset{0}{\gamma}_y^k\end{Bmatrix}Y^+(z,k) \tag{1a}$$

or in compact form written as :

$$\gamma(x,y,z) = \left(\mathbb{Q}_s^{(m)^{-1}}\mathbb{Q}_s^{av}\right)\overset{0}{\gamma}(x,y) + 2z\overset{1}{\gamma}(x,y) + 3z^2\overset{2}{\gamma}(x,y) + \sum_{k=1}^{m-1}\overset{0}{\gamma}^k(x,y)Y^-(z,k) + \sum_{k=m}^{N-1}\overset{0}{\gamma}^k(x,y)Y^+(z,k) \tag{1b}$$

with the various shear-constitutive coefficients defined as:

$$\mathbb{Q}_s^{av} := \begin{bmatrix}(Q_s^{av})_{11} & (Q_s^{av})_{12}\\ (Q_s^{av})_{21} & (Q_s^{av})_{22}\end{bmatrix} = \frac{1}{h}\sum_{k=1}^{N}\int_{z_k}^{z_{k+1}}\begin{bmatrix}Q_{44}^{(k)} & Q_{45}^{(k)}\\ Q_{54}^{(k)} & Q_{55}^{(k)}\end{bmatrix}dz;\ \ \mathbb{Q}_s^{m} := \begin{bmatrix}Q_{44}^{(m)} & Q_{45}^{(m)}\\ Q_{54}^{(m)} & Q_{55}^{(m)}\end{bmatrix} \tag{2}$$

In Eq. (1), m bears the affliation of the middle layer number. $\overset{1}{\gamma}_x(x,y)$, $\overset{1}{\gamma}_y(x,y)$, $\overset{2}{\gamma}_x(x,y)$, $\overset{2}{\gamma}_y(x,y)$ denote the independent shearing strain fields associated to the linear and quadratic through the thickness distribution, respectively. $\overset{0}{\gamma}_x^k$, $\overset{0}{\gamma}_y^k$ for $k = 1, N-1$ represent the independent interfacial shearing strain jump fields and $Y^+(z,k) = H(z - z_{k+1})$, $Y^-(z,k) = H(-z + z_{k+1})$ are the Heaviside-Unit-Step functions with $H(x) = 1$ for $x \geq 0$ and $H(x) = 0$ for $x < 0$.The independent averaged shearing-strain like variables $\overset{0}{\gamma}_x(x,y)$, $\overset{0}{\gamma}_y(x,y)$ are introduced in order to keep a balance between the piece-wise constant strain part in Eq. (1) for a general laminated situation. Using the static continuity conditions (i.e., $\tau_{xz}|_{z_{k+}} = \tau_{xz}|_{z_{k-}}$, $\tau_{yz}|_{z_{k+}} = \tau_{yz}|_{z_{k-}}$ for $k = 1, N-1$), one calculates the interfacial shearing strain jumps and then applying strain displacement relations we get the in-plane displacements and transverse displacements which involve only $nine$ fields (independent of a total number of layers). Now applying shear traction free conditions at the bounding surfaces(i.e.,$\tau_{xz}|_{z_1} = \tau_{xz}|_{z_{N+1}} = \tau_{yz}|_{z_1} = \tau_{yz}|_{z_{N+1}} = 0$) led the total number of independent fields (i.e., 9) may be reduced further to $five$. The geometric insight of different terms in Eq. (1) are illustrated in Fig. 1 for a five-layer symmetric angle-ply (30/-30/30/-30/30) laminate. Now, finally, we have the following five parametric displacement fields that are obtained:

$$\begin{aligned} U(x,y,z) &= u(x,y) - z\frac{\partial w}{\partial x} + g_{11}(z)\overset{0}{\gamma}_x + g_{12}(z)\overset{0}{\gamma}_y\\ V(x,y,z) &= v(x,y) - z\frac{\partial w}{\partial y} + g_{21}(z)\overset{0}{\gamma}_x + g_{22}(z)\overset{0}{\gamma}_y\\ W(x,y,z) &= w(x,y)\end{aligned} \tag{3a}$$

with $g_{11}(z)$, $g_{12}(z)$, $g_{21}(z)$, and $g_{22}(z)$ are the zigzag functions which depends upon the geometric properties (thickness of laminae) as well as material properties of each laminae and it yields continuous shear stresses at the interfaces of dissimilar lamiane when calculated using constitutive equations.

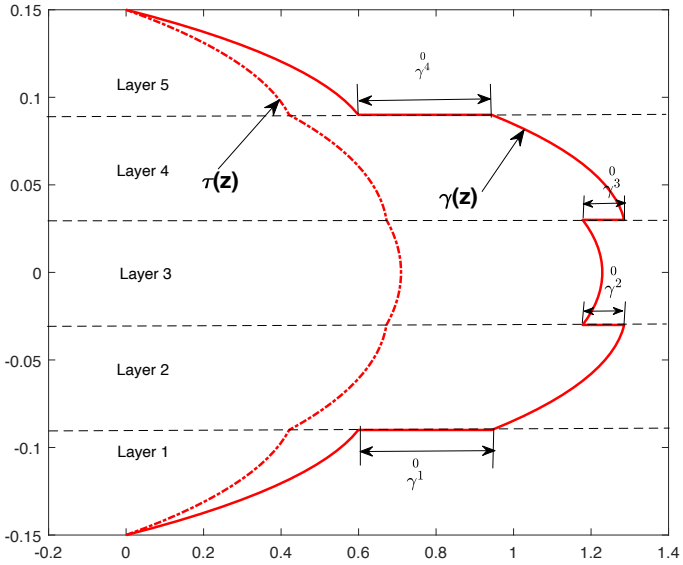


Figure 1: Geometric and kinematic Description of the plate

3. Numerical Results

Numerical studies have been carried out in order to assess the existing model's accuracy and reliability. The calculations were carried out in accordance with the methods Pagano [8],[9] devised for an exact three-dimensional elasticity solution. Pagano acquires the plot in the figure referred to as Exact-3D. Additionally, numerical outcomes from the En-RZT developed by Sorrenti et al. [12] and MZT developed by Murakami [6] are also shown. There are no in-plane prescribed tractions on the top and bottom surfaces, only sinusoidal distributed transverse load has been applied at the top and bottom surface of the plates. The total transverse load is equally divided into two parts. One half is applied on top and the other half on the bottom external surfaces in a three-dimensional solution.

Field Variables for Symmetric Cross-Ply Laminate having simply supported boundary conditions on all four sides. By using Navier's method to obtain the solutions for symmetric cross-ply orthotropic rectangular plates having simply supported boundary conditions (SS-1) under transverse bi-sinusoidal distributed load $q(x,y) = q_0 \sin\left(\frac{\pi x}{a}\right) \sin\left(\frac{\pi y}{b}\right)$, the equilibrium equations, and the boundary conditions can be satisfied by using the following sets of trigonometric functions:

$$\begin{aligned} u &= U_{mn} \cos\left(\frac{\pi x}{a}\right) \sin\left(\frac{\pi y}{b}\right), \quad v = V_{mn} \sin\left(\frac{\pi x}{a}\right) \cos\left(\frac{\pi y}{b}\right), \quad w = W_{mn} \sin\left(\frac{\pi x}{a}\right) \sin\left(\frac{\pi y}{b}\right), \\ \overset{0}{\gamma}_x &= \overset{x}{\gamma}_{mn} \cos\left(\frac{\pi x}{a}\right) \sin\left(\frac{\pi y}{b}\right), \quad \overset{0}{\gamma}_y = \overset{y}{\gamma}_{mn} \sin\left(\frac{\pi x}{a}\right) \cos\left(\frac{\pi y}{b}\right), \end{aligned} \tag{4}$$

Field Variables for Symmetric Angle-Ply Laminate having an infinite length in the y-directions and simply supported along the two opposite edges . Under transverse sinusoidal distributed load $q(x,y) = q_0 \sin\left(\frac{\pi x}{a}\right)$, the equilibrium equations and the boundary conditions can be satisfied by using the following sets of trigonometric functions.

$$[u, v, \overset{0}{\gamma}_x, \overset{0}{\gamma}_y] = [U_{mn}, V_{mn}, \overset{x}{\gamma}_{mn}, \overset{y}{\gamma}_{mn}] \cos\left(\frac{\pi x}{a}\right), \quad w = W_{mn} \sin\left(\frac{\pi x}{a}\right) \tag{5}$$

Normalized Values for Laminated Plates and Sandwich Plates. The displacements and stresses for Laminated Plates and Sandwich Plates are normalized throughout the problem unless stated otherwise, as given below:

Normalized Values for Laminated Plates

$$(u^N, v^N) = (100 \cdot E3)\frac{h^2}{q_0 a^3},\ w^N = (100 \cdot E3)\frac{h^3}{q_0 a^4},\ (\sigma^N_{xx}, \sigma^N_{yy}, \sigma^N_{xy}) = h^2\frac{q_0}{a^2},\ (\sigma^N_{xz}, \sigma^N_{yz}) = h\frac{q_0}{a} \quad (6)$$

Normalized Values for Sandwich Plates

$$(u^N, v^N) = E3\frac{h^2}{q_0 a^3},\quad w_N = E3\frac{h^3}{q_0 a^4},\quad (\sigma^N_{xx}, \sigma^N_{yy}, \sigma^N_{xy}) = h^2\frac{q_0}{a^2},\quad (\sigma^N_{xz}, \sigma^N_{yz}) = h\frac{q_0}{a} \quad (7)$$

3.1. Problem.1: Numerical examples on Cross-ply laminated plates

A simply supported laminated cross-ply rectangle plate (0°/90°/0°/90°/0°/90°/0°) are adopted. The thickness and the material properties of each layer are uniform. The size of the plate model: length along x-axes is $a = 1m$ while length along y-axes is $b = 3m$, thickness is $h = 0.25m$. The plate is subjected to bi-sinusoidal distributed load $q(x, y) = q_0 sin(\pi x/a) sin(\pi y/b)$. bending load is $q_0 = 1kN/m^2$. The material constants are, $E_1 = 172.4Gpa$; $E_2 = 6.89Gpa$; $E_3 = 6.89Gpa$; $G_{12} = 3.45Gpa$; $G_{13} = 3.45Gpa$; $G_{23} = 1.378Gpa$; $\nu_{12} = 0.25$; $\nu_{13} = 0.25$; $\nu_{23} = 0.25$;

3.1.1. Results for seven-layer laminated composite plate with the symmetric cross-ply stacking sequence having $a/h = 4$ and $b = 3a$

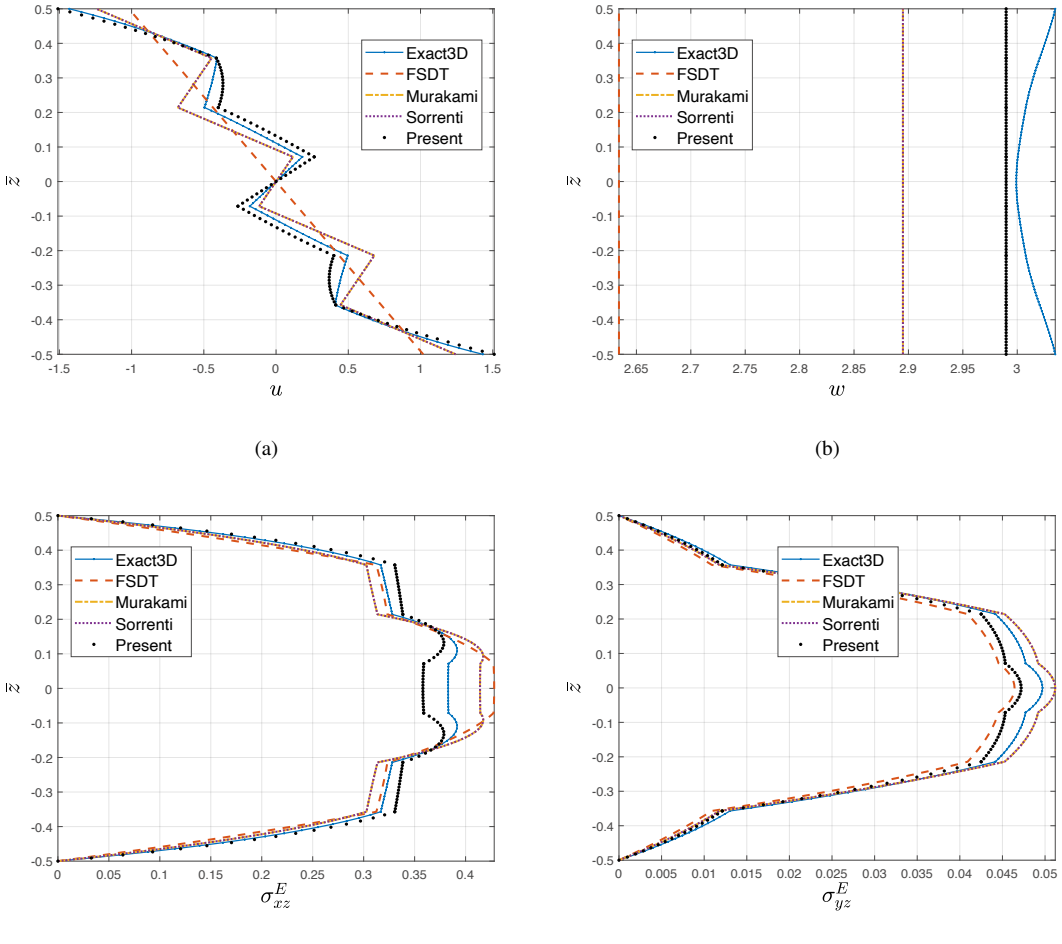
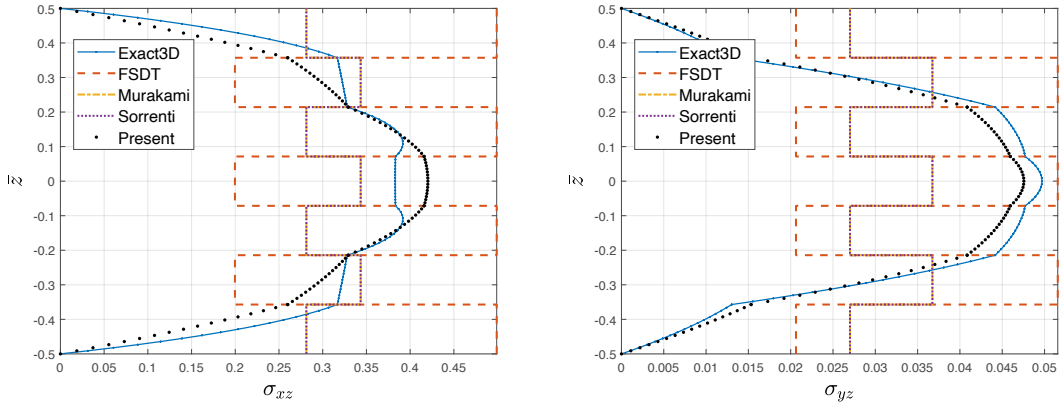


Figure 2: Dispacements $(2a, 2b)$, and transverse Shear stress as obtained from integration of equilibrium equations $(2c, 2d)$ for symmetric cross-ply seven-layer laminated plate for $a/h = 4$



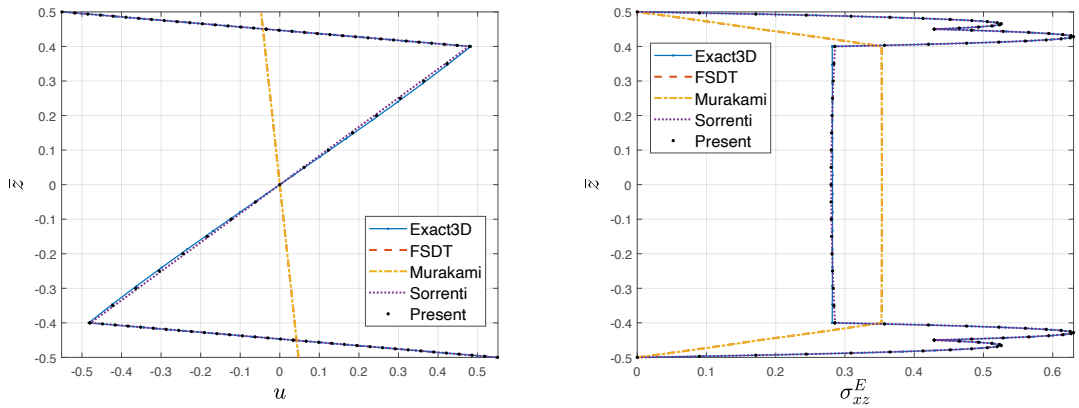
(e) (f)

Figure 2: Transverse Shear stress as obtained from Constitutive relations $(2e, 2f)$ for symmetric cross-ply seven-layer laminated plate for $a/h = 4$

3.2. *Problem. 2: Numerical examples on five-layer sandwich plates with the symmetric angle-ply configuration*

A five-layer sandwich plate with the symmetric angle-ply configuration (30°/-30°/$Core$/$-$30°/30°) simply supported on two opposite edges while infinitely long along y-directions are adopted. The thickness of skin is $h_{skin} = 0.05h$ and the thickness of core is $h_{core} = 0.8h$. The size of the plate model: length along x-axis is $a = 1m$, thickness is $h = 0.25m$. The plate is subjected to sinusoidal distributed load $q(x, y) = q_0 sin(\pi x/a)$, where $q_0 = 1kN/m^2$. The material constants for the face-sheets (transversely orthotropic) and core (isotropic) are given below. The superscript f and c are used for face-sheets and core respectively. $E_1^f = 110000Gpa$; $E_2^f = 7857Gpa$; $E_3^f = 7857Gpa$; $G_{12}^f = 3292Gpa$; $G_{13}^f = 3292Gpa$; $G_{23}^f = 1292Gpa$; $\nu_{12}^f = 0.33$; $\nu_{13}^f = 0.33$; $\nu_{23}^f = 0.49$; $E^c = 40.3Gpa$; $G^c = 12Gpa$; $\nu^c = 0.30$;

3.2.1. *Results for five-layer Sandwich plates with the symmetric angle-ply stacking sequence having* $a/h = 4$



(a) (b)

Figure 3: Displacement $(3a)$, and transverse Shear stress $(3b)$ as obtained from integration of equilibrium equations for the symmetric angle-ply five-layer sandwich plate for $a/h = 4$

Each of these numerical problems as shown above will provide valuable insights into the mechanical behavior and performance of the laminate under different layer-stacking configurations. σ_{xz}^{E}, and σ_{yz}^{E} represents the stresses obtained by integrating of equilibrium equations while σ_{xz}, and σ_{yz} are obtained from the constitutive equations.

4. Results and Discussions

For seven-layer symmetric cross-ply laminated composite plates, the results are shown in Fig. 2. The present model captures the in-plane displacements as shown in Fig. $2a$ very close to Exact-3D solutions. The FSDT fails to capture warping (zigzag effect). Murakami zigzag model and Sorrenti zigzag model get stiffened at the top and bottom of the laminate while the present model captures throughout the plate thickness. Fig. $2b$ shows the transverse displacements where the present model is very close to Exact-3D solutions. Fig. $2c$ and Fig. $2d$ results of transverse shear stresses obtained from the integration of equilibrium equations and the present model captures very close to Exact-3D solutions. Fig. $2e$ and Fig. $2f$ show the results of transverse shear stresses obtained from the constitutive equations and the present model captures very close to Exact-3D solutions and is continuous at the interfaces of the laminae and satisfies the shear stress-free conditions at the top and bottom surface, while other theories are piecewise constant in each lamina and fail to satisfy the continuity conditions at the interfaces and also fails to satisfy shear stress-free conditions at top and bottom surface of the laminate. For five-layer symmetric angle-ply sandwich plates, the results are shown in Fig. 3. The results in Fig. $3a$, and Fig. $3b$ show that the present model and Sorrenti model accurately captures the Exact-3D solutions while FSDT and Murakami Zigzag model fails to do so.

5. Conclusions

In this study, we propose a higher-order Zigzag Function-based formulation for thick and highly anisotropic multilayered laminated composite and sandwich plates. This advanced formulation effectively captures the warping of the plates, manifesting as zigzag effects in the in-plane displacements, and ensures continuity of transverse shear stresses at the interfaces of the laminated plates. Additionally, it satisfies the condition of zero shear stresses at the top and bottom surfaces of the plate. Unlike traditional linear zigzag theories, our approach is devoid of the stiffening effect that typically arises with an increased number of layers and does not require any shear correction factors. To validate the proposed formulation, we solved two problems with different stacking sequences: a symmetric cross-ply laminated composite plate and a symmetric angle-ply sandwich plate. The first case involves a seven-layer symmetric cross-ply laminated plate, which yields results closely matching the exact three-dimensional elasticity solutions. The second case analyzes a five-layer sandwich plate, with outcomes also aligning closely with exact three-dimensional elasticity solutions. These results underscore the robustness of the higher-order zigzag model, showcasing its exceptional performance even with highly anisotropic material properties and its immunity to the stiffening effect observed in other zigzag theories such as Sorrenti-En-RZT and Murakami Zigzag theory. This makes the proposed formulation a reliable and effective tool for analyzing complex laminated composite and sandwich plates.

References

[1] Erasmo Carrera. Historical review of Zig-Zag theories for multilayered plates and shells. *Applied Mechanics Reviews*, 56(3):287–308, 2003.

[2] Maenghyo Cho and R. Reid Parmerter. Efficient higher order composite plate theory for general lamination configurations. *AIAA Journal*, 31(7):1299–1306, 1993.

[3] U. Icardi and G. Zardo. C0 plate element for delamination damage analysis, based on a zig-zag model and strain energy updating. *International Journal of Impact Engineering*, 31(5):579–606, 2004.

[4] Luigi Iurlaro, Marco Gherlone, and Marco Di Sciuva. A mixed cubic zigzag model for multilayered composite and sandwich plates including transverse normal deformability. *11th World Congress on Computational Mechanics, WCCM 2014, 5th European Conference on Computational Mechanics, ECCM 2014 and 6th European Conference on Computational Fluid Dynamics, ECFD 2014*, (July):3614–3625, 2014.

[5] Ireneusz Kreja and Agnieszka Sabik. Equivalent single-layer models in deformation analysis of laminated multilayered plates. *Acta Mechanica*, 230(8):2827–2851, 2019.

[6] H. Murakami. Laminated composite plate theory with improved in-plane responses. *Journal of Applied Mechanics, Transactions ASME*, 53(3):661–666, 1986.

[7] Michael P Nemeth. Cubic Zig-Zag Enrichment of the Classical Kirchhoff Kinematics for Laminated and Sandwich Plates. *NASA Center for AeroSpace Information*, (May 2012), 2012.

[8] N. J. Pagano. Exact Solutions for Rectangular Bidirectional Composites and Sandwich Plates. *Journal of Composite Materials*, 4(1):20–34, 1970.

[9] N.J Pagano. Influence of Shear Coupling in Cylindrical. Bending of Anisotropic Laminates. 4(July):330–343, 1970.

[10] Marco Di Sciuva. Multilayered anisotropic plate models with continuous interlaminar stresses. *Composite Structures*, 22(3):149–167, 1992.

[11] Junling Si, Wanji Chen, Shujuan Yi, and Yong Yan. A new and efficient zigzag theory for laminated composite plates. *Composite Structures*, 322(March):117356, 2023.

[12] M. Sorrenti and M. Di Sciuva. An enhancement of the warping shear functions of refined zigzag theory. *Journal of Applied Mechanics, Transactions ASME*, 88(8):1–7, 2021.

[13] M. Sorrenti and M. Gherlone. A new mixed model based on the enhanced-Refined Zigzag Theory for the analysis of thick multilayered composite plates. *Composite Structures*, 311(August 2022), 2023.

[14] A. Tessler, M. Gherlone, D. Versino, and M. Di Sciuva. Analytical and computational perspectives of multi-scale theory for homogeneous, laminated composite, and sandwich beams and plates. *Civil-Comp Proceedings*, 99(January), 2012.

[15] Alexander Tessler. Refined zigzag theory for homogeneous, laminated composite, and sandwich beams derived from Reissner's mixed variational principle. *Meccanica*, 50(10):2621–2648, 2015.

[16] Alexander Tessler, Marco Di Sciuva, and Marco Gherlone. Refined Zigzag Theory for Laminated Composite and Sandwich Plates. *National Aeronautics and Space Administration*, 133(Technical Publication 215561):809–817, 2009.

ENVIRONMENTAL EFFECTS ON MECHANICAL PROPERTIES OF COMPOSITES MATERIALS – A NEW RECOMMENDED PRACTICE

Andreas T. Echtermeyer[1,2], Ramin Moslemian[3] and Philippe M. Noury[4]

[1]Structural Integrity Advisory, Energy Systems, Veritasveien 1, 1363 Høvik, Norway
Email: andreas.echtermeyer@dnv.com, Web Page: http://www.dnv.com
[2]Norwegian University of Science and Technology (NTNU), Trondheim, Norway
[3]Offshore and M/D Southern Europe, Energy Systems, DNV, 28-34 Rue du Château des Rentiers, 75013 Paris, France
Email: ramin.moslemian@dnv.com, Web Page: http://www.dnv.com
[4]Structural Integrity Advisory, Energy Systems, DNV, Veritasveien 1, 1363 Høvik, Norway
Email: philippe.noury@dnv.com, Web Page: http://www.dnv.com

Keywords: composite, polymer, environment, effect, recommended practice

Abstract
Composites provide an appealing substitute for metals, with excellent environmental resistance and stiffness-to-weight ratio. These distinctive qualities yield significant advantages in subsea structures, pipelines, and energy applications. However, resistance to challenging environments, high testing costs, and long-term efforts have hindered industry adoption. The DNV Recommended Practice (RP) addresses the critical challenge faced by several industries: The environmental exposure and degradation of composite materials. Models and assessment methodologies, supported by experiments, have been developed to enhance understanding and address the effects of fluid exposure and temperature in composites. Various methods have been developed to evaluate the chemical interactions with liquids and gas and to obtain Arrhenius-based Time-Temperature-Saturation-Superposition-dependent polymer and composite properties. The RP provides testing procedures for assessing the occurrence of chemical degradation. Other reversible interactions associated with swelling are addressed separately. Methods are given for polymers to obtain stiffness and strength over the design life. Cyclic fatigue and creep rupture are included, also covering applications both below and above the glass transition temperature. This RP establishes a reliable framework to quickly assess the mechanical properties of polymers and composites under various conditions, facilitating the qualification of new materials and technologies essential for high-risk transport, storage assets, and the energy transition.

1. Introduction

Reinforced and non-reinforced polymers have been offering an alternative to conventional material systems used by humankind from wood to stone and metals. It can be claimed that synthetic polymers made out of oil and gas since the early 20th century have been the foundation of our modern economy, enabling the emergence of consumerist societies. They have been used in consumer goods, electronics, construction, pharmaceuticals, pipelines, pressure equipment and many other applications.

One key feature of these materials compared to metals is their low reactivity to the environments they are exposed to. While corrosion has been a major challenge for metals, polymers and their products, such as composites, have been offering a way out of this challenge in industries such as water, oil and gas, and maritime.

With the age of fossil fuels approaching its end and with a dire need to decarbonize our economies, polymers and their products are key to the development of new green technologies, such as batteries, renewables, hydrogen, and carbon capture and storage.

Even though polymers do not corrode and have a low reactivity compared to metals, environmental exposures do impact them. Exposure to sunlight, water, oil and various chemicals can change their properties and their degradation. While we have extensive knowledge of the corrosion of metals, the environmental degradation of polymers and composites is still not very well understood and explored. Quantitative knowledge of the change in mechanical properties is essential for the acceptance of high-performance safety-critical applications.

Standards and recommended practices concerning the exposure and degradation of composite materials are essential for qualifying materials and determining design values in challenging environments. In addition, the industry's adoption of composites has been hindered by high testing costs, lengthy testing campaigns, and the inherent complexity of assessing composites' long-term durability under exposure. This challenge is particularly pronounced for high-risk assets such as deep-sea risers, subsea pressurized tanks, and large offshore floating fish-farming structures, where extensive test programs are necessary and where safety and reliability are paramount. There is today a pressing need for new standardized practices to ensure the efficient and reliable implementation of test programs tailored to any specific applications.

This conference paper gives a brief introduction to some of the main concepts used in the RP.

2. Core methodologies in the new RP

2.1. Organization of the RP

The RP is organized in eight main sections, as shown in Figure 1. Section 1 describes the objective and scope, as found in most standards and RPs. Section 2 describes methods to determine whether chemical interactions occur between polymers and fluid, as will be described further below. Section 3 addresses the changes of mechanical properties of polymers in the presence of temperature and a fluid. Sections 4 and 5 extend the content of Sections 2 and 3 for polymers to the case of more complicated composites.

Section 6 describes the procedure for confirmation testing, which is important from an RP point of view. Sections 2 to 4 describe theoretical procedures for predicting material performance under challenging environments. Some of the procedures are well-established, while others are relatively new. In addition, all procedures have some limits to their validity. The confirmation testing is used to show that the chosen approaches are valid for the particular polymer and fluid investigated.

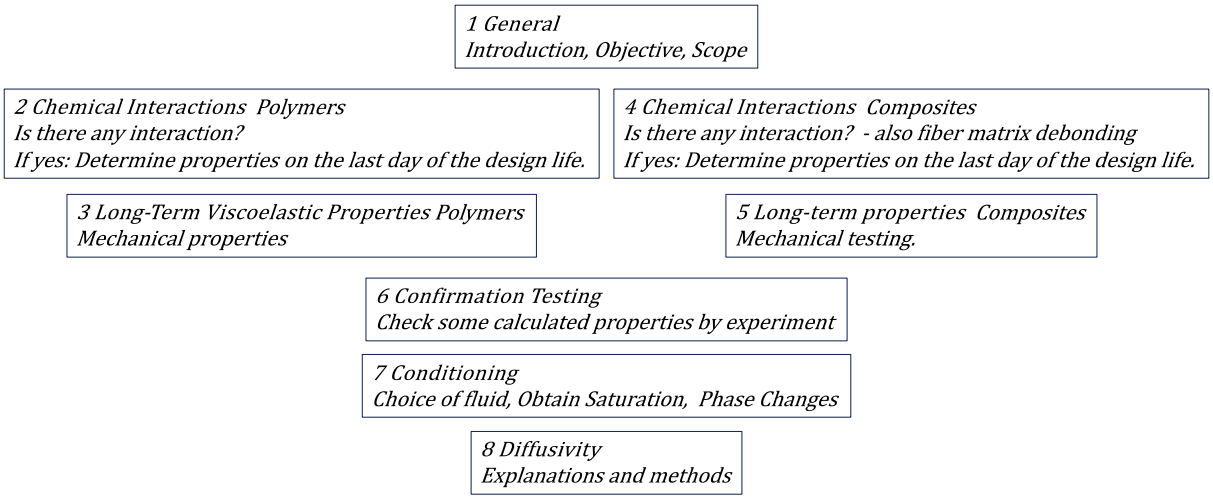


Figure 1. Organization of the recommended practice.

Section 7 describes how the test samples should be conditioned before mechanical testing is done. It describes mainly experimental details. One challenge with the conditioning is the time to reach saturation. It is important that the samples are fully saturated when being tested so that no concentration gradients of the fluid exist inside the sample. Section 8 gives some information on diffusivity, especially anisotropic diffusivity, and how saturation times can be calculated.

2.2. Chemical degradation

When a fluid diffuses into a polymer or composite, it causes swelling. The diffusion continues until the polymer is saturated, as shown in Figure 2 (blue line). This swelling changes the mechanical properties, as shown by the green line. Strength and modulus usually drop, while strain to failure would typically increase.

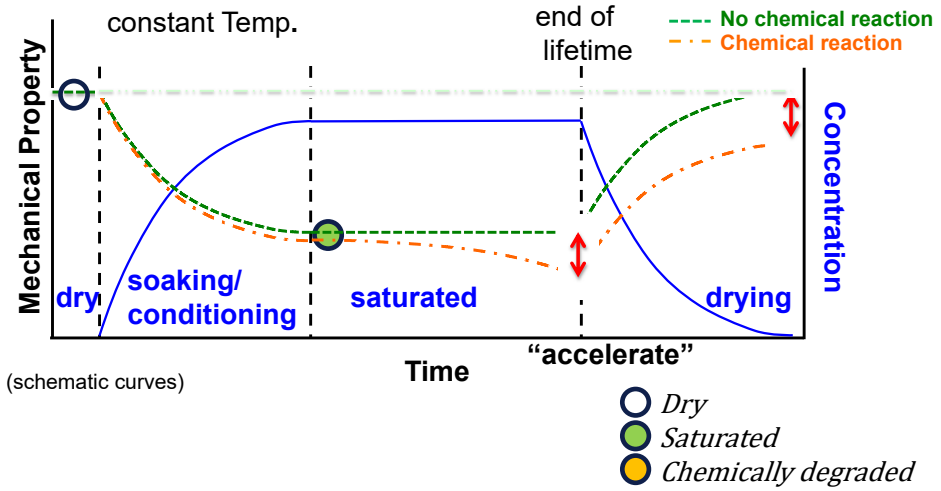


Figure 2. Schematic showing the change of a mechanical property with time due to saturating of the material with a fluid and chemical reaction with the material, from [1].

When saturation is reached, the properties no longer change if there is no chemical interaction between polymer and fluid. It is sufficient to test the material after saturation is reached, at the green point in Figure 2. Also note that if the fluid is removed, the mechanical properties change (almost) back to the original properties; the property changes are reversible.

A very different situation happens when chemical interaction happens between the polymer and the fluid. In that case, chemical bonds get broken or created. The change of properties is irreversible. The polymer continues to degrade after saturation is reached. If chemical degradation happens, the properties of the yellow dot at the end of the design lifetime need to be determined.

In most applications materials would be chosen that do not show chemical interactions with the polymer to avoid the extra degradation. It is, however, not trivial to proof that there is no chemical degradation. The RP provides procedures on how no chemical degradation can be demonstrated based on showing no change in fracture toughness characteristics within a test period of typically 1,000 to 10,000 hours, depending on the design lifetime and scatter of the test results.

If chemical degradation takes place the properties at the yellow point in Figure 2 have to be obtained in an accelerated way. The RP gives procedures on how this can be done by conditioning the sample in the fluid at higher temperatures using a modified Arrhenius approach. Mechanical properties can subsequently be measured on the conditioned/degraded samples.

The same approach described for polymers can also be used for composites. However, the RP also considers matrix fiber debonding as "chemical degradation", even though it may be caused by swelling stresses alone.

2.3. Master curves

Once the materials are conditioned for the case of chemical degradation or no degradation, the mechanical properties can be measured. The main approach in the RP is based on creating master curves according to the Arrhenius [2,3] or WLF method [4]. This method is well known. It was found that dry and saturated curves can also be superimposed on each other [5], as shown for compliance measurements in Figure 3.

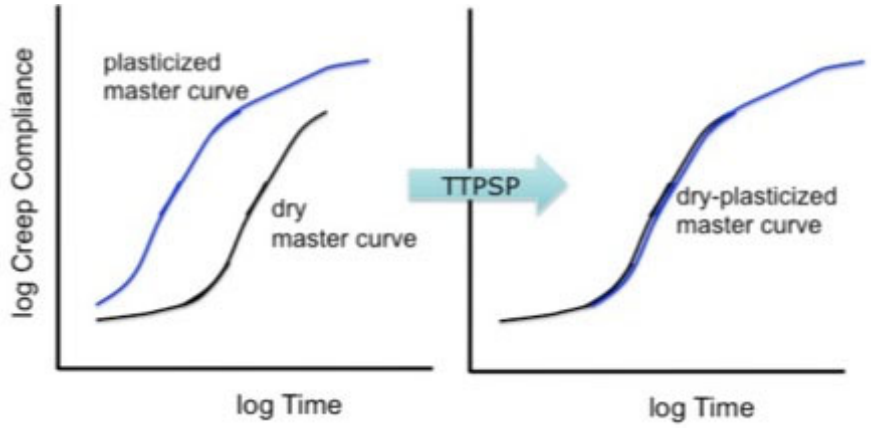


Figure 3. Schematic illustration of the Time – Temperature – Plasticization Superposition Principle (TTPSP) for the relaxation modulus from [1].

In most applications, obtaining strength over elastic properties is more important. This RP provides procedures for this, too, based on modified Arrhenius calculations or Prony series methods. Figure 4 shows cyclic fatigue SN curves of dry, wet, and re-dried epoxy. These data can easily be superimposed on a master curve [6]. Similar results were found for the interlaminar shear strength of glass fiber-reinforced epoxy [7].

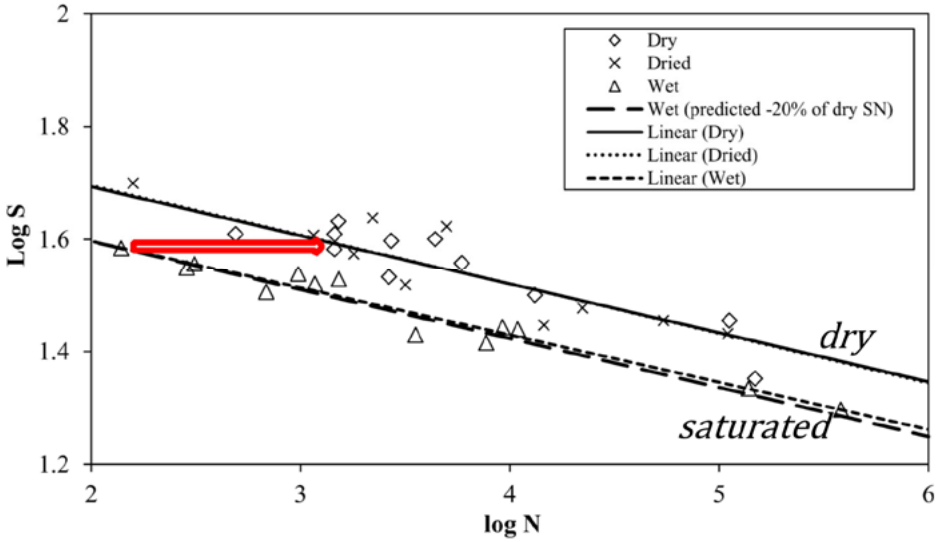


Figure 4. S-N curves of initial (dry), saturated and dried epoxy specimens. The curves can be superimposed to a master curve along the red arrow, modified from [5].

The approaches shown here are just a few examples. Other approaches could be added to the RP in the future and used for materials, provided the confirmation tests show that the approach is valid.

3. Industry examples

3.1 TCP

Thermoplastic composite pipes (TCPs) are increasingly used in subsea applications such as flowlines, jumpers, risers, and intervention lines due to their easy installation, resistance to corrosion, and versatility. However, their exposure to environmental factors presents significant challenges. The external cover of TCPs is predominantly subjected to seawater due to diffusion, while the internal laminates face various internal fluids, including both liquids and gases. These fluids can range from water and hydrocarbons to service fluids like methanol, as well as CO2 and H2, with temperatures fluctuating from a few degrees up to 120°C. The materials used in TCPs, such as HDPE, PA12, PEEK, and PVDF, along with reinforcing fibres like glass and carbon fibres, must withstand these harsh conditions. Understanding the environmental effects of seawater and internal fluids on these materials is crucial for ensuring the reliability and longevity of TCPs in demanding subsea environments.

3.2 Wind turbine roots

With the wind turbine blades increasing in size to improve efficiency and reduce the cost of wind energy, the root connections of the blades are increasingly exposed to large static and cyclic loads. These increasing loads, as well as the difficulty in sealing the root connections, leading to exposure to water and hydraulic oil, have led to a series of failures and design challenges. This has been especially the case for the leak of hydraulic oil to the root connections, leading to the softening of the thermoset resin used in the connections and a reduction in its load-carrying capacity.

3.3 Aquaculture

Aquaculture structures situated inshore or nearshore, with dimensions ranging from 40 to 60 meters, present significant economic and environmental risks due to their large sizes and high fish capacities. These structures are continuously exposed to seawater at temperatures between 0 and 30°C. They are typically constructed from conventional, low-cost thermoset composites, such as glass fibre combined with polyester or vinylester resins. While the evolution of properties of these materials is generally well understood in marine environments, and the reduction in fibre-dominated and resin-dominated properties is well documented, it is crucial to establish design allowable for these high-risk assets precisely. This involves accurate, reliable, time- and cost-efficient material properties determination, including those at the end-of-life, to be used in the design and for specific material systems to be used later in production. Moreover, the large structures are assembled using bonded or overlaminated joints, whose properties and capacities must be thoroughly evaluated to ensure reliability throughout their service life.

3.4 Deepwater H2 storage

With the emergence of green hydrogen and the need for storage of large amounts of it, concepts for storage of hydrogen offshore are gaining traction. Composite pressure vessels are popular for high-pressure hydrogen storage onshore for cars and refuelling stations and are naturally considered for offshore hydrogen storage underwater. However, the challenge of the impact of seawater on highly stressed composite materials remains to be solved. It is expected that over time, seawater will permeate through the material, impacting both the resin and fibres. However, there is limited knowledge of such interactions with the environment of subsea pressure vessels for hydrogen.

4. Conclusions

A Recommended Practice is about to be published that describes methods for analyzing polymers and composites to determine long-term properties in the presence of absorbed fluids in the material. A key issue is distinguishing reversible property changes due to fluid absorption when no chemical interaction is happening from irreversible changes when the fluid changes the chemical bonds of the polymer. Properties can be predicted based on Arrhenius and WLF methods, extended to account for fluid

interaction. The relevance and need for such an RP have been demonstrated by some industrial examples.

Acknowledgements
This work is part of the DNV-led Joint Industry Project "Affordable Composites" with nine industrial partners and the Norwegian University of Science and Technology (NTNU). The authors would like to express their gratitude for the financial support from the Research Council of Norway (Project No. 245606/E30 in the Petromaks 2 programme).

References

[1] DNV-RP-B302, Effects of the environment on mechanical properties of polymers and composite materials, DNV, 2024 (to be published)
[2] Emri, I. Rheology of Solid Polymers. Rheol. Rev. 2005, 2005, 49.
[3] Brinson, H.F.; Brinson, L.C. Polymer Engineering Science and Viscoelasticity; Springer US: Boston, MA, USA, 2015; ISBN 978-1-4899-7768-7.
[4] DNV-RP-B302, Williams, M.L.; Landel, R.F.; Ferry, J.D. The temperature dependence of relaxation mechanisms in amorphous polymers and other glass-forming liquids. J. Am. Chem. Soc. 1955, 77, 3701–3707
[5] Krauklis, A. E., Akulichev, A. G., Gagani, A. I., & Echtermeyer, A. T. (2019). Time–temperature–plasticization superposition principle: predicting creep of a plasticized epoxy. *Polymers*, *11*(11), 1848.
[6] Krauklis, A. E., Gagani, A. I., & Echtermeyer, A. T. (2018). Hygrothermal aging of amine epoxy: reversible static and fatigue properties. Open Engineering, 8(1), 447-454.
[7] Gagani, A. I., Mialon, E. P., & Echtermeyer, A. T. (2019). Immersed interlaminar fatigue of glass fiber epoxy composites using the I-beam method. International Journal of Fatigue, 119, 302-310.

EFFECTIVE PROPERTIES OF MAGNETOSTRICTIVE COMPOSITES THROUGH NUMERICAL HOMOGENISATION

Pantea Afshari[1], Iasonas Triantis[1], Asa Barber[1] and Hamed Yazdani Nezhad[4,*]

[1]Department of Engineering, School of Science and Technology, City, University of London, London, UK
[4]School of Mechanical Engineering, Faculty of Engineering and Physical Sciences, University of Leeds, Leeds, UK
*Corresponding author: h.yazdaninezhad@leeds.ac.uk

Keywords: magnetostrictive composite, finite element analysis, effective properties, RVE, periodic boundary condition (PBC)

Abstract
In the current research, the response of magnetostrictive composites to external magnetic fields has been investigated. The composite is comprised of magnetic particles embedded polymers, and is distinguished by their ability to undergo dimensional, elastic, and electromagnetic changes in the presence of a magnetic field. Contrasting with bulk magnetostrictive metals, such composites possess superior qualities, including high resistivity, lightweight composition, effective formability, and enhanced mechanical properties. The present study introduces a computational methodology aimed at extracting homogenised effective properties of the magnetostrictive composites, comprising of an elastic polymer reinforced by magnetostrictive particles. To achieve this, a representative volume element (RVE) is developed to model the random and repetitive heterogeneous magnetic microparticles within the polymer. Employing the finite element analysis in Abaqus, the RVE is analysed numerically, and its effective elastic and magnetic properties are extracted through the application of periodic boundary conditions (PBC). It is imperative to highlight the implementation of MATLAB and Python coding for generating randomly distributing particles within the RVE and for applying PBC. The emphasis is also made on the formulation of the PBC that allows the simulation of all modes pertaining to the spatial mechanical deformation arising from any arbitrary combination of mechanical and magnetic loading. Furthermore, investigations are carried out to study the influence of various parameters such as the volume fraction, morphology and distribution of the particles on the effective properties. To validate the numerical RVE model, its solution is compared with those derived from the analytical homogenisation method and the experimental data obtained from quasi-static uniaxial tensile testing of dogbone specimens (made of iron particles embedded polylactic acid polymers) subjected to magnetic fields. In conclusion, the comprehensive magneto-mechanical exploration offers a robust and nuanced understanding of the behaviour of magnetostrictive polymer composites for magnetic field assisted shaping (e.g. structural tailoring, novel morphing or draping during composite manufacturing) paving ways for innovative advancements, offering new avenues for exploration and technological breakthroughs in the realm of advanced magnetic composites.

1. Introduction

Magnetostrictive materials have gained significant attention due to their unique ability to alter dimensions, elasticity, and electromagnetic properties when exposed to magnetic fields. Traditionally, bulk magnetostrictive metals such as Terfenol-D have been widely studied and utilized in various applications, ranging from sensors to actuators. However, these materials often come with limitations related to flexibility and formability. To overcome these challenges, recent advancements have explored the development of magnetostrictive composites, which integrate magnetic particles within a polymer

©2024 | 3_PANTEA AFSHARI_Pantea_8WY9W .pdf

matrix. These composites present several advantages, including reduced weight, enhanced formability, and superior mechanical properties [1].
Understanding the equivalent properties of magnetostrictive composites is crucial for predicting their performance, optimizing design, and ensuring reliability in various applications. Magnetostrictive composites are heterogeneous materials composed of randomly distributed magnetic particles within a polymeric matrix. To predict the effective properties of these composites, numerical homogenization techniques based on finite element modeling (FEM) of a representative volume element (RVE) was utilized in the present work. The RVE represents the smallest region of the composite that can be considered homogeneous, effectively mirroring the overall properties of the original material. One of the major advantages of using numerical methods is the complete control they offer over the model. This allows for the application of various loads and boundary conditions, the use of different materials with different shape, size and distributions.

2. Finite element model of the magnetocomposite

In modeling the behavior of magnetostrictive composites, it is essential to understand the governing equations that describe the material's response to magnetic fields and mechanical stress. Magnetostrictive materials exhibit a nonlinear coupling between magnetic and elastic behavior. This nonlinear magnetostriction arises due to the dependence of the strain in the material on both the applied magnetic field and mechanical stress. However, under certain conditions, this complex nonlinear behavior can be approximated by linear relations.When the response of the magnetostrictive material involves only small deviations around an operating point, also known as a bias point, the nonlinear interactions can be effectively represented using linear coupled constitutive equations. This simplification is particularly useful for practical engineering applications, where it is often sufficient to consider the material's behavior near a specific working condition rather than over its entire operational range.
In this linear approximation, the magnetostrictive effect can be described by piezomagnetic relations. These relations are the linear counterparts to the nonlinear magnetostrictive effects and provide a manageable framework for finite element modeling. The piezomagnetic equations couple the mechanical and magnetic fields in a way that is analogous to the piezoelectric effect in electro-mechanical systems [2]. They can be expressed as:

$$\begin{aligned} \mathbf{S} &= c_{\mathrm{H}}\varepsilon - e_{\mathrm{HS}}^{T}\mathbf{H} \\ \mathbf{B} &= e_{\mathrm{HS}}\varepsilon_{\mathrm{el}} + \mu_0\mu_{\mathrm{rS}}\mathbf{H} \end{aligned} \tag{1}$$

where $\mu 0$ is the magnetic permeability of free space; c_H is the stiffness matrix; and μr_S is the relative magnetic permeability measured at constant strain and constant stress, respectively. The matrix e_{HS} is called piezomagnetic coupling matrix.

2.1. Distribution of Particles within an RVE

In the present study, a MATLAB code is employed to generate the Representative Volume Element (RVE). The random sequential adsorption (RSA) algorithm is utilized to position the inclusions within the RVE [3]. This algorithm introduces particles randomly into the RVE and adsorbs them into the system if they do not overlap with previously adsorbed particles.
The RSA algorithm operates iteratively, beginning with the creation of an inclusion particle within the unit cell. This process is repeated until the desired volume fraction is achieved. Each particle is randomly assigned a position within the unit cell. The algorithm then checks whether the new particle's location overlaps with any previously placed particles. If there is no overlap, the particle is accepted and incorporated into the RVE; if overlap occurs, the particle is discarded, and the search for a new particle position begins again.
Furthermore, to ensure that the RVE exhibits periodicity, the algorithm accounts for particles that may overlap with the boundaries of the unit cell. If a particle overlaps with one or more boundaries, it is replicated on the opposite faces of the unit cell to maintain periodicity. This approach ensures that the microstructure of the RVE accurately represents the infinite material and allows for the correct application of periodic boundary conditions during finite element analysis.

©2024 | 3_PANTEA AFSHARI_Pantea_8WY9W .pdf:2

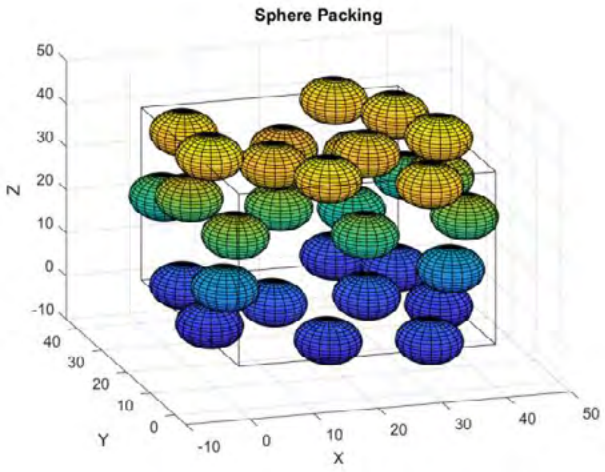


Figure 1. Representative Volume Element congaing randomly distributed spherical inclusions ($v_f = 0.25$)

2.2. Boundary Conditions

Composites can often be represented as a periodic array of RVEs or unit cells. To accurately simulate the responses of these composites, periodic boundary conditions (PBC) are applied [4]. The application of PBC ensures that the deformation mode remains consistent across the RVE and prevents interpenetration and separation between neighboring RVEs.

To implement periodic boundary conditions in ABAQUS, specific equations must be defined for each pair of nodes on opposite surfaces of the RVE. This process involves two key steps:

1. **Equal Meshing Pattern**: The meshing pattern on opposite surfaces of the RVE must be identical. This ensures that corresponding nodes on opposing faces can be correctly paired and constrained.
2. **Constrain Nodes by Periodicity Equations**: Once the meshing pattern is established, periodic boundary equations are applied to constrain all nodes on opposite surfaces. These equations ensure that the displacement and traction at each node on one surface are matched by the corresponding node on the opposite surface, maintaining periodicity.

The periodic boundary equation can be expressed as follows

$$u_i^{K^+} - u_i^{K^-} = \bar{S}_{ij}(x_j^{K^+} - x_j^{K^-}). \tag{2}$$

Where u is displacement and S is average strain tensor.

Since applying these constraints manually to each pair of nodes is impractical, they are implemented using Python scripting in ABAQUS. The next step is finding the averaged properties .

2.3. Calculation of Effective Properties

This section explains the calculation of the effective properties. We assume that the average mechanical and magnetic properties of our RVE are equivalent to those of a magnetic composite, as illustrated in Equation 3.

$$\langle T_{ij} \rangle = \overline{T_{ij}}, \quad \langle D_k \rangle = \overline{D_k}, \quad \langle \mathrm{H}_k \rangle = \overline{\mathrm{H}_k}, \quad \langle \mathrm{B}_k \rangle = \overline{\mathrm{B}_k}, \tag{3}$$

These average values can be defined as in Equation 4.

$$\overline{T_{ij}} = \frac{1}{|V|}\left(\int_V T_{ij}\, dV\right), \quad \overline{S_{ij}} = \frac{1}{|V|}\left(\int_V S_{ij}\, dV\right)$$
$$\overline{\mathrm{B}_i} = \frac{1}{|V|}\left(\int_V \mathrm{B}_i\, dV\right), \quad \overline{\mathrm{H}_i} = \frac{1}{|V|}\left(\int_V \mathrm{H}_i\, dV\right) \tag{4}$$

These calculations are repeated for every element or integration point in the FE model. In ABAQUS, the volume of the integration points can be requested. By multiplying the field values at each integration point by the corresponding integration point volume and summing these products, the total value is obtained. This total value is then divided by the total volume of the RVE, resulting in the average value of the property for the RVE.

3. Results and Discussion

In this research, Terfenol-D particles were chosen as inclusions within the polymer matrix to study the magnetostrictive behavior of the composite. Terfenol-D, known for its high magnetostrictive properties, was selected to enhance the composite's performance. The particles used in the study had a size of 10 micrometers.

The effective properties of the composite were determined for various volume fractions of Terfenol-D particles. To achieve this, different load cases were defined, and periodic boundary conditions were applied to the RVE in ABAQUS to simulate the material's response accurately. The periodic boundary conditions ensured that the deformation and stress distribution within the RVE correctly represented the behavior of an infinite composite material.

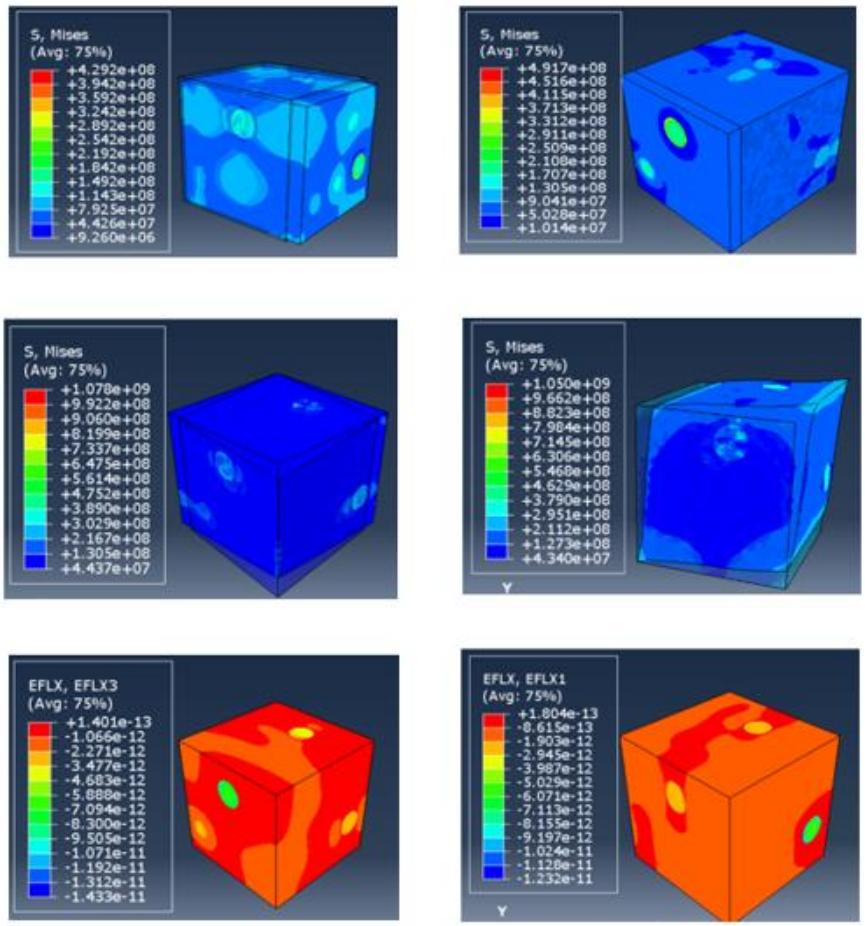


Figure 2. Different load cases defined for finding effective properties (v_f =0.1)

4. Conclusions

This research focused on determining the effective properties of magnetostrictive composites with Terfenol-D particles as inclusions. Through numerical homogenization techniques using finite element modeling, we analyzed the composite's behavior for different volume fractions of the particles. As expected, increasing the volume fraction of Terfenol-D significantly enhanced the magnetic properties of the composite. However, it was also observed that excessively high volume fractions led to increased stiffness, thereby reducing the composite's flexibility. These findings highlight the importance of

balancing magnetic performance with mechanical flexibility in the design of magnetostrictive composites. This research is currently undergoing further investigation to optimize the material properties for specific applications and to explore additional aspects of the composite's behavior under varied conditions.

Acknowledgments
The authors were grateful of the funding received by the UK Engineering and Physical Sciences Research Council for a Doctoral Training Programme (Grant Ref. EP/W524608/1)..

References

[1] Khayam, S.U.; Usman, M.; Umer, M.A.; Rafique, A. Development and characterization of a novel hybrid magnetorheological elastomer incorporating micro and nano size iron fillers. Mater. Des. 2020, 192.

[2] R. Pramanik and A. Arockiarajan, “Effective properties and nonlinearities in 1 3 piezocomposites, Smart Materials and Structures, vol. 28, no. 10, p. 103001, 2019.

[3] G. Catalanotti, On the generation of rve-based models of composites reinforced with long fibres or spherical particles, Compos. Struct. 138 (2016) 84–95. Mishra, R.K. et al. Functional Composite Materials, 2023. 4 (1), 6

[4] Bouaoune L, Brunet Y, Moumen AE, Kanit T, Mazouz H. Random versus periodic microstructures for elasticity of fibers reinforced composites. Compos B Eng 2016;103:68–73.

ENHANCING FATIGUE PERFORMANCE OF STRUCTURAL BIOCOMPOSITES BY PRE-STRAINING AND PRE-CREEPING METHODS

Valentin Perruchoud[1*], René Alderliesten[2] and Yasmine Mosleh[1]

[1] Biobased Structures and Materials, Faculty of Civil Engineering and Geosciences, Delft University of Technology, Stevinweg 1, 2628 CN Delft, the Netherlands
[2] Aerospace Structures and Materials, Faculty of Aerospace Engineering, Delft University of Technology, Kluyverweg 1, 2629HS Delft, the Netherlands

*Corresponding author Email: V.P.Perruchoud@tudelft.nl

Keywords: Structural biocomposite, Flax fibre reinforced polymer composite, Creep, Fatigue, pre-straining

Abstract
Synthetic fibre-reinforced polymer composites (FRPs) have long been favored in structural engineering for their exceptional mechanical properties. However, their environmental impact due to energy intensive manufacturing, and disposal has prompted exploration into sustainable biobased alternatives such as flax FRP composites (FFRPs). While using flax fibres as composite reinforcement has lightness and damping benefits from a structural point of view, it also introduces design challenges as the complex microstructure of flax fibres and flax FRPs induces a more viscoelastic fatigue response. Therefore, pre-straining and pre-creeping are proposed in this study as simple methods to improve fatigue performance by taking advantage of alignment mechanisms intrinsic to flax fibre and yarn microstructure. An experimental campaign was conducted on $[0/90/0]_S$ flax FRP laminates (hence, predominantly UD) to compare the tension-tension fatigue performance of reference specimens to pre-strained and pre-creeped specimens. It was observed that pre-straining and especially pre-creeping are effective at improving FFRPs fatigue performance with significant increase in fatigue life, increase in dynamic modulus, and decrease in accumulation of deformation (ratcheting).

1. Introduction

In the pursuit of peak performance in structural engineering, synthetic fibre-reinforced polymer composites (FRPs) have emerged as promising materials in multiple contexts, offering simultaneously high specific stiffness, and high specific strength along with design freedom. Currently, glass and carbon fibres dominate reinforcement of FRP composites for structural applications. While offering attractive mechanical properties, using synthetic fibres in large quantities is harmful to the environment as the production of those fibres consumes a large amount of energy and deplete non-renewable resources. Additionally, disposing of or incinerating synthetic FRP materials at the end of their lifespan causes environmental harm, and recycling them poses challenges. Consequently, numerous researchers and industries are exploring biobased FRPs as an alternative to synthetic FRPs where strong natural fibres such as flax are used as reinforcement instead of synthetic fibres, particularly glass fibres.

Elementary flax fibres have a complex microstructure mainly composed of cellulosic microfibrils [1] and those microfibrils are not naturally aligned with the axis of the flax fibres [2]. Coincidentally, cyclic

mechanical testing on single elementary fibres reveals a non-linear and viscoelastic behaviour with a peculiar increase of modulus [3], [4] suggesting that an alignment of the microfibrils occurs during loading. Direct observations of microfibrils angles during mechanical loading revealed that an alignment indeed occurs, however, the change of microfibrils angle is small and therefore unlikely to have a significant impact on the composite properties. Adding to the complexity of understanding the mechanics of flax FRP composites (FFRPs), flax fibres preforms utilized for manufacturing are often made of yarns in which a degree of twist is applied on the elementary flax fibres. This twist angle of the elementary fibre with respect to the yarn axis and the loading axis of the composite may again lead to alignment mechanisms upon loading but at a different scale due to unravelling of the twist [5].

Regardless of the exact mechanisms behind the viscoelasticity of flax fibres and its composites, this material must meet safety and serviceability requirements to be utilized in structural applications. In particular for fatigue applications, the fatigue life, stiffness (modulus) degradation, and accumulation of permanent deformation (ratcheting) must be within limits for structural design. Currently available results of FFRPs fatigue tests show that in predominantly UD laminates ratcheting is significantly larger than in glass FRP composites and that the modulus increases during fatigue while it decreases in glass FRPs [6].

In this paper we present two novel and yet simple methods aiming at improving the fatigue performance of FFRP composites by taking advantage of their intrinsic viscoelasticity and related alignment mechanisms within their intricate multi-scale microstructure. To demonstrate the effects of those two methods, namely pre-straining and pre-creeping, a fatigue experimental campaign was performed on $[0/90/0]_S$ FFRP laminates. Pre-strained and pre-creeped specimens were subjected to the same force-controlled tension-tension fatigue as reference specimens to measure the effects of the proposed methods. Results show that both methods are beneficial for fatigue performance, pre-creeping in particular.

2. MATERIALS AND METHODS

2.1 Composite laminates

In this study, the FFRP laminate employed is a 2.8 mm thick coupon with a narrow central cross-section and a wider cross-section towards the grips, as illustrated in figure 1, to prevent failure at the clamps' edges during fatigue testing which was observed in preliminary testing with rectangular coupons. Strain measurements are obtained using an extensometer in the narrow cross-section. The FFRP laminate comprises six layers of Bcomp quasi-unidirectional flax mat Amplitex, with an aerial weight of 280 g/m^2, stacked in a $[0/90/0]_S$ lay-up configuration. The choice of this lay-up configuration was driven by the aim to examine the mechanical behavior of flax fibers under loading along their primary axis, necessitating the inclusion of 0° layers. Although a strictly unidirectional lay-up was initially considered, preliminary testing showed susceptibility to fatigue-induced splitting in such specimens. Consequently, 90° layers were introduced to mitigate the occurrence of splitting phenomena.

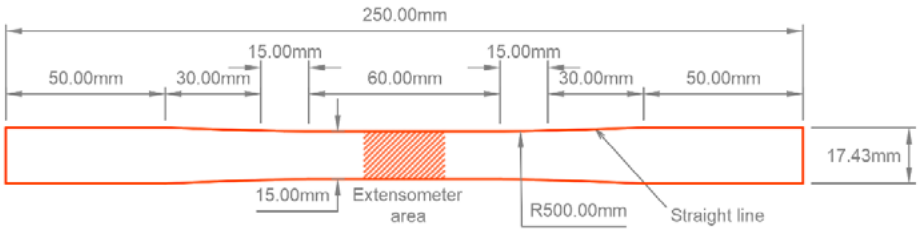


Figure 1. Specimen geometry.

FFRP plates were manufactured using a vacuum-assisted resin infusion process using the Swancor 2511-1 resin epoxy system. The infusion was followed by an 18-hour post-cure in an autoclave set at 70°C and 7 bars of pressure. Subsequently, the plates underwent cutting into test coupons utilizing a waterjet cutter. To ensure the completion of resin curing, a differential scanning calorimetry (DSC) analysis was conducted after the manufacturing process. This involved subjecting the specimens to three heating/cooling cycles between 0°C and 150°C, The midpoint of the stepwise change in the heat flow versus temperature curve in the first and third thermograms were measured to ascertain that the glass transition temperature (Tg) did not deviate by more than 3°C. Optical microscopy was employed to qualitatively assess the microstructure of pristine specimens, ensuring the absence of cracks or manufacturing defects/voids significant enough to impact fatigue damage. The fibre volume fraction was estimated at 42% based on calculations considering the density of the fiber mats, epoxy resin, and composites.

2.2 Pre-straining and pre-creeping protocols

For the experimental campaign, specimens were placed in an MTS 60 kN fatigue machine equipped with hydraulic grips (figure 2). An extensometer was attached to the specimens with rubber bands to measure the strain. As testing was not performed in an environmentally controlled environment, a thermocouple was installed to capture air temperature at proximity of the specimen and another thermocouple was installed on the specimen to measure its surface temperature.

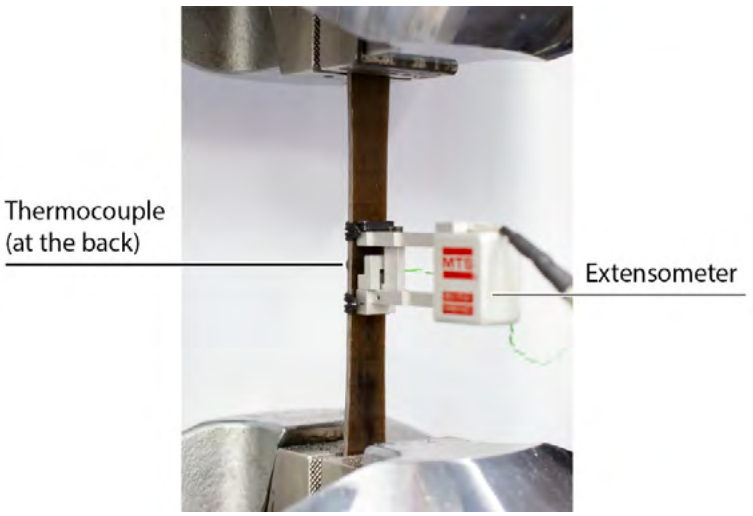


Figure 2. Tensile testing setup.

Loading prior to fatigue for the reference, pre-strained, and pre-creeped specimens are described in figure 3. All the loading and unloading were performed at a rate of 2 mm/min except for the pre-creeping plateau during which a constant force corresponding to the maximum fatigue load was maintained until a strain of 1.6% was reached.

The maximum stress reached during pre-straining corresponds to 80% of the material ultimate tensile strength (UTS). The start of fatigue testing, at the mean fatigue stress, is indicated by a star for each case in figure 3.

2.3 Fatigue testing protocol

Tension-tension fatigue tests were carried out under force control mode, employing a loading ratio (R) of 0.1 and a frequency of 5 Hz. The maximum fatigue load was set at 133 MPa corresponding to 60% of the UTS determined by quasi-static tensile testing at a loading rate of 2 mm/min. In the fatigue testing,

the data pulling was set such that 50 data points were recorded every cycle for the first 500 cycles and then 1 cycle was recorded every 1'000 cycles.

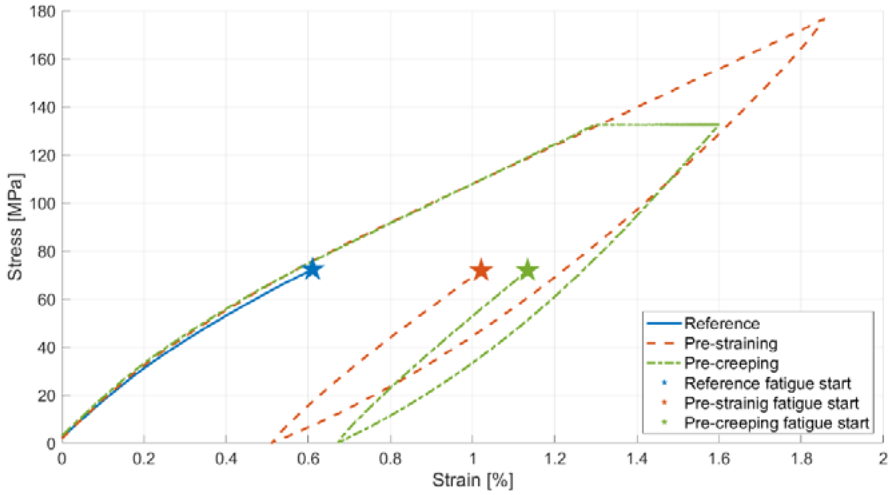


Figure 3. Depiction of pre-straining, pre-creeping and quasi-static ramp protocols before fatigue.

3. Results and discussion

Tests results were obtained with 3 repetitions for each fatigue case studied; reference, pre-straining, and pre-creeping symbolized by different colors. As the machine did not instantly reach the targeted fatigue force, all the analysis take the 10^{th} cycle as reference from which the minimum and maximum force remained constant.

3.1. Effect of pre-straining and pre-creep on the evolution of the dynamic modulus during fatigue

The dynamic modulus is defined here as the slope of the line connecting the top and bottom points of the hysteresis loop in a stress-strain graph. Figure 4 shows that the dynamic modulus as a general tendency to increase during fatigue but pre-straining and especially pre-creeping mitigate this increase in dynamic modulus. Furthermore, the dynamic modulus of pre-creeped specimens is significantly higher than the dynamic modulus of reference specimens and this throughout the entire fatigue life.

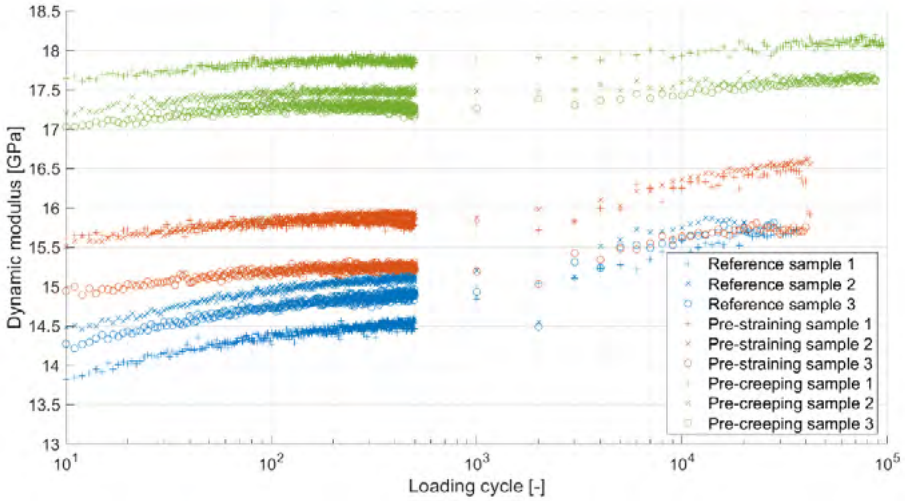


Figure 4. Effect of pre-straining and pre-creeping on dynamic modulus.

3.2. Effect of pre-straining and pre-creep on ratcheting

Ratcheting refers to an the incremental plastic strain accumulation during fatigue. Therefore, ratcheting is generally undesirable for structural applications as it creates significant deformation over the long-term. Here ratcheting is computed by measuring the shift in strain at the bottom of each hysteresis loop relative to the strain at loading cycle 10. Figure 5 shows that the ratcheting in the reference fatigue testing can be mitigated by the application of pre-straining. Furthermore, pre-creeping almost completely eliminates ratcheting and tends to a perfectly elastic behaviour with ratcheting values remaining below 0.05% strain for the entirety of the fatigue life.

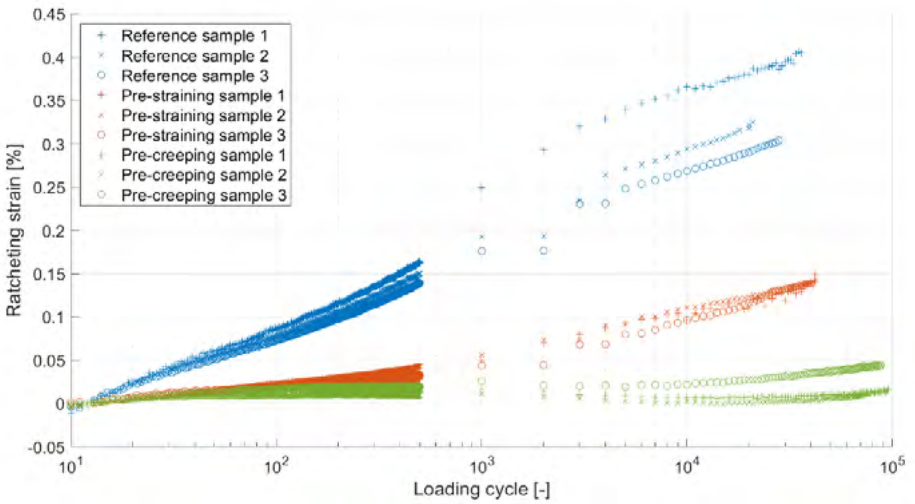


Figure 5. Mitigation of ratcheting with pre-straining and pre-creeping.

3.3. Ratio of inelastic work over total work

The ratio of inelastic work over total work is computed for individual loading cycles by dividing the area inside of the hysteresis loop by the area inside of the hysteresis loop plus the area below the hysteresis loop [7]. Figure 6 shows that this work ratio is decreasing during the entirety of the fatigue life indicating that most of the fatigue damage accumulation occurs towards the beginning of the fatigue life. The ratio is reduced by applying pre-straining or pre-creeping suggesting that less damage is accumulated at each loading cycle.

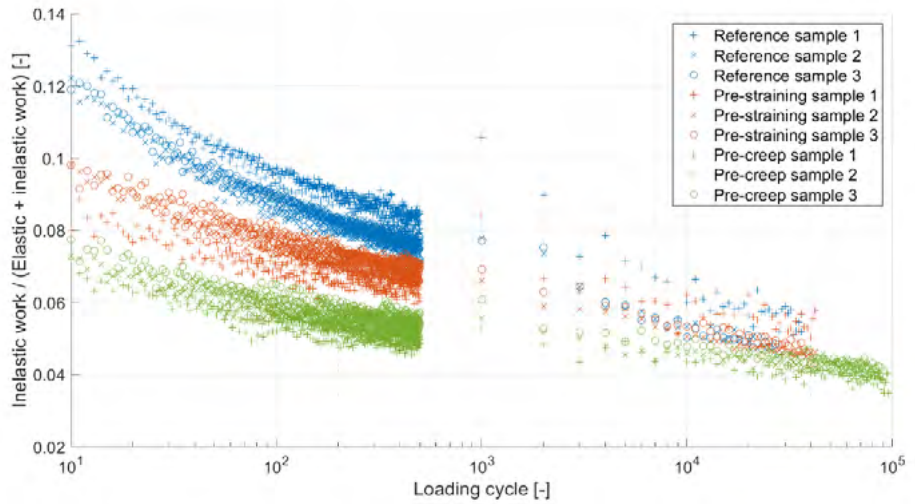


Figure 6. Effect of pre-straining and pre-creeping on the ratio of inelastic work over total work. The ratio is computed for individual loading cycles.

3.4 Effect of pre-straining and pre-creeping on fatigue life

Fatigue life results in figure 7 show that the pre-straining and pre-creeping methods have a significant impact on fatigue life. Pre-straining increases fatigue life by a factor of 1.3 compared to the reference specimens and remarkably pre-creeping increases the average fatigue life by a factor of 3. The comparatively large effect of pre-creeping compared to pre-straining highlights the importance of loading rate and viscous effects in FFRP composites. Given an alignment hypothesis, pre-creeping has a surprisingly significant impact, especially considering that the maximum strain achieved during pre-creeping is less than that reached during pre-straining.

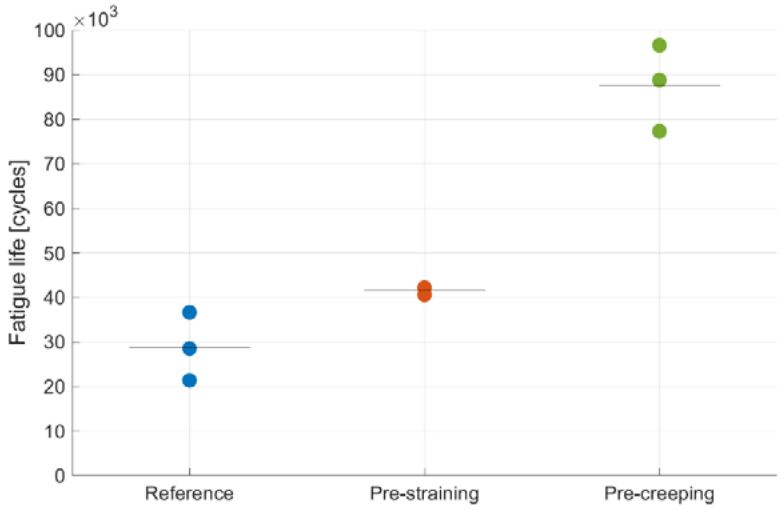


Figure 7. Effect of pre-straining and pre-creeping on the fatigue life .

3.5. Effects of temperature

Analysis of the recorded temperature during fatigue reveals that the air temperature in proximity to the specimen remained relatively constant at 22°C ± 2. However, the surface temperature of the specimen increased by up to 10°C between the first and the 2'000th loading cycle (figure 8) likely due to the 5 Hz testing frequency and associated dissipation of energy. Then, temperature slowly decreased during fatigue until final failure at which point the surface temperature was about 3°C lower than at cycle 2'000.

Assuming that the stiffness of FFRPs is sensitive to temperature [8], the temperature profile in figure 8 can be used to explain the different dynamic modulus trends at the beginning and end of life in figure 4. Furthermore, at cycle 2'000 the temperature peaks indicating the equilibrium between the heat generated by the specimen deformation and the heat of the specimen dissipated to its environment due to the temperature gradient. Since the temperature decreases after 2'000 cycles, it suggests that either less heat is generated by the specimen deformation or more heat is dissipated to the environment. The decrease of the inelastic work/total work ratio observed in figure 6 is in agreement with the hypothesis that less heat is generated by the specimen deformation of every next cycle.

Additionally, the uncontrolled air temperature affected the repeatability of pre-creeping even with a ±2°C variation. Since the end of pre-creeping was defined with a strain limit, the ambient temperature variation from run to run affected the repeatability of the pre-creeping duration by affecting the stiffness of the FFRP composite [8]. Combined with sample to sample variation it resulted in the shortest pre-creeping lasting 5 hours and the longest 15 hours.

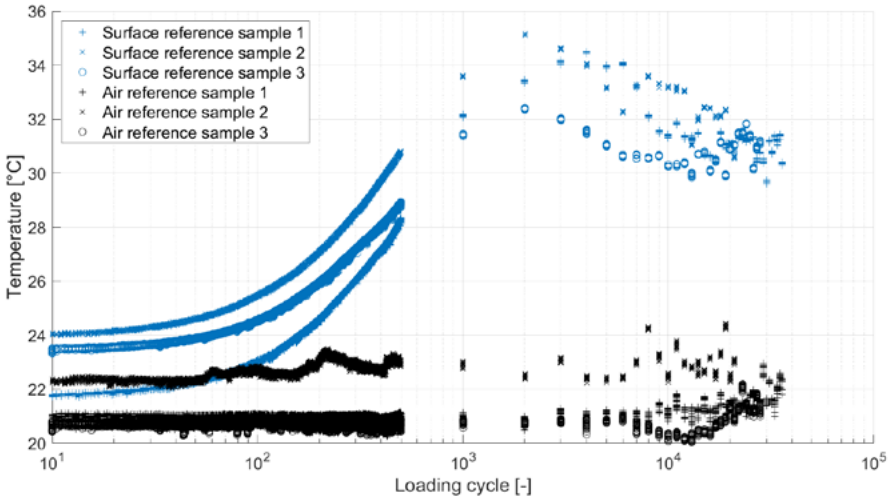


Figure 8. Comparison of the air temperature and the specimen surface temperature during fatigue

4. Conclusions

In this study, we presented a novel way of improving fatigue performance of structural flax fibre reinforced polymer composites. To this aim, we delved into the effectiveness of pre-straining and pre-creeping as methods for improving the fatigue performance of predominantly UD biobased FRP by taking advantage of the alignment mechanisms intrinsic to flax FRP composites. The main conclusion is that both methods, pre-straining and pre-creeping, have beneficial effects on the tension-tension fatigue performance of flax FRP composites with pre-creeping being the most effective.

The comparison of results of pre-strained and pre-creeped specimens highlighted the FFRPs mechanical response time dependency or viscoelasticity. Indeed, across all measured metrics - fatigue life, dynamic modulus, ratcheting - pre-creeping exerted a larger effect than pre-straining despite pre-straining inducing a higher maximum strain prior to fatigue. This implies that the loading rate plays a crucial role in any alignment mechanism occurring within flax FRP composites. By extension, the choice of the testing frequency is also susceptible to affects the fatigue response due to viscoelasticity. Additionally, flax FRPs were found to be sensitive to the temperature elevation generated by the 5 Hz testing frequency.

Acknowledgments

The authors wish to thank the Suzlon company for the delivery of the epoxy resin used in the manufacturing of the specimens. Authors wish to sincerely thank the continuous support of all the technicians within the Macrolab/Stevinlaboratory of the faculty of Civil Engineering and Geosciences, and the ASM laboratory of the faculty of Aerospace Engineering at TU Delft.

References

[1] Z. Zhang *et al.*, "High performances of plant fiber reinforced Composites—A new insight from hierarchical microstructures," *Composites Science and Technology*, vol. 194, p. 108151, Apr. 2020, doi: 10.1016/j.compscitech.2020.108151.

[2] E. Richely *et al.*, "Measurement of microfibril angle in plant fibres: Comparison between X-ray diffraction, second harmonic generation and transmission ellipsometry microscopies," *Composites Part C: Open Access*, vol. 11, p. 100355, Jul. 2023, doi: 10.1016/j.jcomc.2023.100355.

[3] C. Baley, "Analysis of the flax fibres tensile behaviour and analysis of the tensile stiffness increase," *Composites Part A-applied Science and Manufacturing - COMPOS PART A-APPL SCI MANUF*, vol. 33, pp. 939–948, Jul. 2002, doi: 10.1016/S1359-835X(02)00040-4.

[4] S. Ahmed and C. A. Ulven, "Dynamic In-Situ Observation on the Failure Mechanism of Flax Fiber through Scanning Electron Microscopy," *Fibers*, vol. 6, no. 1, Art. no. 1, Mar. 2018, doi: 10.3390/fib6010017.

[5] P. M. Giuliani, O. Giannini, and R. Panciroli, "Characterizing flax fiber reinforced bio-composites under monotonic and cyclic tensile loading," *Composite Structures*, vol. 280, p. 114803, Jan. 2022, doi: 10.1016/j.compstruct.2021.114803.

[6] Z. Mahboob and H. Bougherara, "Fatigue of flax-epoxy and other plant fibre composites: Critical review and analysis," *Composites Part A: Applied Science and Manufacturing*, vol. 109, pp. 440–462, Jun. 2018, doi: 10.1016/j.compositesa.2018.03.034.

[7] V. Perruchoud, R. Alderliesten, and Y. Mosleh, "Pre-straining as an effective strategy to mitigate ratcheting during fatigue in flax FRP composites for structural applications," *Heron*, vol. 68, Feb. 2024.

[8] V. Perruchoud, R. Alderliesten, and Y. Mosleh, "The Effects of In-Situ Temperature and Relative Humidity on Tensile Response of Flax vs. Glass FRP Composites," presented at the 21th European Conference on Composite Materials, ECCM 2024,

PROCESS SIMULATION CHAIN COMBINED WITH A STRUCTURAL SIMULATION TO CAPTURE THE ACTUAL PROCESS-INDUCED EFFECTS AND "AS-BUILD" CHARACTERISTICS

Maximilian Pollak[1], Franz Maier[1] and Roland M. Hinterhölzl[1]

[1] Research Group of Lightweight Design and Composite Materials, University of Applied Sciences Upper Austria, Stelzhamerstraße 23, 4600 Wels, Austria
Email: maximilian.pollak@fh-wels.at,
Web Page: https://fh-ooe.at/campus-wels/werkstofftechnik/werkstofftechnik/team

Keywords"As-built" Simulation, Process simulation, Mapping, FEA, Structural simulation, Diaphragm forming process

Abstract
This paper presents a structural "as-built" simulation of carbon fiber reinforced plastics (CFRP) manufactured in the diaphragm forming process, emphasizing the importance of accounting of process-induced effects for a more accurate prediction of the mechanical behavior. The study expands an existing draping simulation with a curing simulation and links it to an "as-built" structural analysis of a 3-point bending test. By transferring residual stresses, fiber orientations, and deformations from the process simulation to the structural simulation, a more precise depiction of manufacturing conditions were achieved. The results of the "as-built" simulation are validated against physical 3-point bending tests and compared to an "as-designed" simulation to highlight the impact of "as-built" characteristics. The methodology introduces an approach for transferring field quantities between simulation steps, utilizing a material point ID system and a mapping module developed in Python. The findings emphasize the need to consider process-induced effects such as folds and deviations, which influence damage initiation and progression in CFRP structures. The study concludes that "as-built" simulations align more closely with experimental observations compared to "as-designed" simulations, but further research is required to refine material parameters for damage behavior and improve simulation accuracy.

1. Introduction

To fully harness the potential of carbon fiber reinforced plastics (CFRP), it is crucial to find optimized, yet reliable designs. However, designing with CFRP poses challenges due to the inherent inhomogeneity, anisotropy, and process-induced effects and defects. Iterative product and process optimization, with loops of prototyping and testing, results in expensive and time-consuming part development [1]. Accounting for unknown inhomogeneities with generous safety factors further diminishes the lightweight potential. Process simulation is a common tool to overcome these challenges. By linking process simulations with structural simulations, an 'as-built'-simulation, accounting for process-induced effects, can be realized. Depending on the required level of detail, various process-induced effects can be used to model the 'as-built' characteristics. Residual stresses, local fiber orientations and macroscopic deformations are, among other effects, the most critical aspects for the structural performance of the part. By accurately modeling these effects, the presented approach aims to represent the manufacturing conditions. Furthermore, it can reduce development time and cost in processes, such as the depicted diaphragm forming process [2], [3], [4]

The diaphragm forming process is a cost-effective manufacturing process for CFRP that utilizes a single tool to create complex shapes. This makes it highly suitable for automated manufacturing, offering great potential for efficient and streamlined production processes[5], [6]. However, the complex interactions

between tools, materials, and process parameters can lead to significant deviations between the designed and the manufactured part [7].

In this study, an existing draping simulation of the diaphragm forming process, was extended with a curing simulation and further linked with a structural 'as-built' analysis of the 3-point bending test. This was done by transferring process-induced residual stresses, local fiber orientation and global deformations from the process simulation to the structural simulation. The results from this "as-built"-structural simulation were compared to the results of a 3-point-bending test of manufactured specimens and an "as-designed" simulation of the test. The simulation platform Abaqus 2019 with the Compro plug-in was used for the simulations.

2. Methods

2.1. Experimental Set-up

The "as-built "-simulation is a virtual model of the 3-point-bending test of a c-section part manufactured in the single diaphragm forming process. The part is stacked from three layers (90°, 0°, 90°) of unidirectional carbon fiber prepregs with a low temperature curing epoxy resin (*HexPly® M79/34%/UD300/CHS*). This stack is then positioned beneath the membrane of the diaphragm forming machine and draped over an aluminum tool geometry using vacuum pressure. After draping, the part is cured at 120°C for 19 minutes and cooled down for 25 minutes without vacuum pressure. The temperature and pressure curve during the process and the final part and tool geometry are shown in Figure 1.

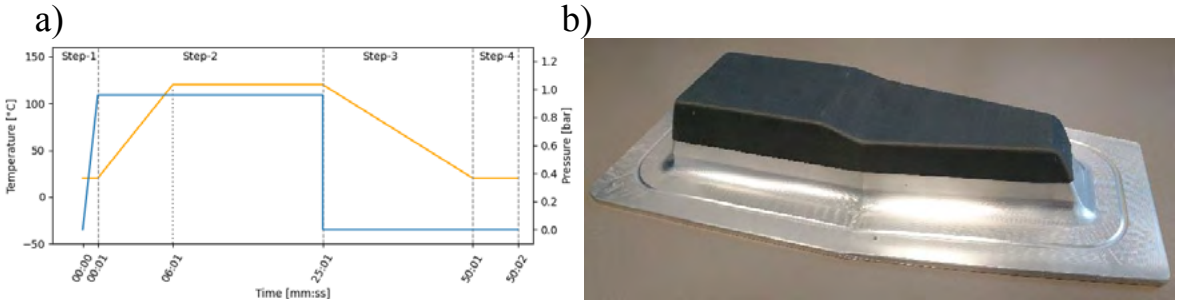


Figure 1: a) Temperature (orange) and vacuum pressure (blue) during process cycle where Step-1 represents draping process, Step-2 to Step3 curing and Step-4 demolding and b) final part and tool geometry

To validate the mechanical behavior and "as-built" (AB) characteristics the final part was tested in a 3-point bending test. Digital image correlation (DIC) was used to measure the strain distribution during the test. The setup of the 3-point-bending test and the corresponding dimensions are shown in Figure 2 a) and b) respectively.

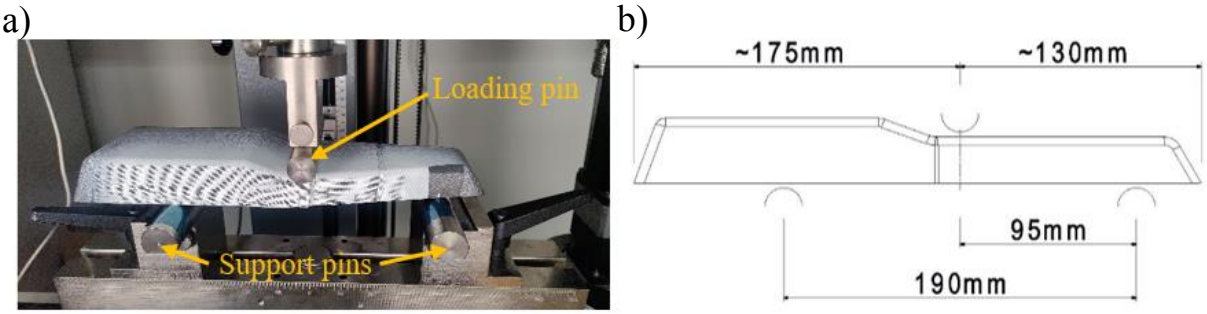


Figure 2: 3-point-bending test of a structural c-section part with DIC pattern and corresponding dimensions of the part, load and support pins.

2.2. Transfer of Field Quantities

In this work we transferred the deformed geometry, residual stresses, and local fiber orientations to link the simulation steps. Because continuum and shell elements were used in the simulation chain a method to transfer field quantities from conventional shell to continuum solid elements and vice versa was developed.

To account for process-induced deformations, the deformed mesh from the previous stage was used as a starting point for the next process stage. To change between element types the source mesh was thickened to generate solid elements or generating an off-set surface from solid elements to create a mesh with shell elements [8]. This operation can be done in *Abaqus CAE* and is shown in Figure 3.

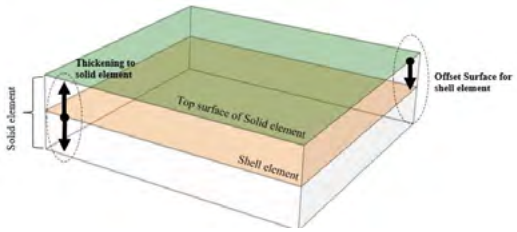


Figure 3: Visualization of thickening shell surface to solid element and offset surface from top surface of solid element to create shell element

Beside interpolation methods [9] we used a material point ID to transfer the field quantities. In Abaqus the material points of solid and shell elements with composite sections have identical coordinates (see Figure 4). Therefore, a material point identification numbering was introduced, which is composed of the element-, integration point-, layer- and section point-number. This is a fast and accurate method but can only be applied if the element basis does not change between simulation stages.

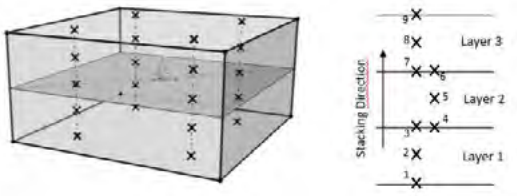


Figure 4: Material points of shell and solid elements with composite sections (left) and layer and material point numbering (right).

A 5-dimensional array is created to transfer stresses:

$$Array[E, IP, L, SP, 1{:}6] = [S_{11}, S_{22}, S_{33}, S_{12}, S_{13}, S_{23}]$$

and local fiber orientations:

$$Array[E, IP, L, SP, 7{:}12] = [e_{1x}, e_{1y}, e_{1z}, e_{2x}, e_{2y}, e_{2z}]$$

, where *E, IP, L, SP* refer to the element-, integration point-, layer- and section point-number, S_{xx} to the stress component in corresponding direction and *e1* and *e2* to the longitudinal and transversal fiber direction.

To automate the mapping process the mapping routine was implemented in a python module. By providing the file and instance name of the source data and the model and instance name of the target

model the routine automatically reads the data from the *Abaqus* output-file and writes them to a csv-file. The data can then be read from the user subroutine UEXTENALDB and will be provided for SIGINI and ORIENT user subroutine to transfer stresses and local fiber orientation, respectively.

2.3. "As-built" Simulation

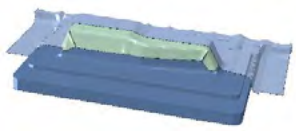
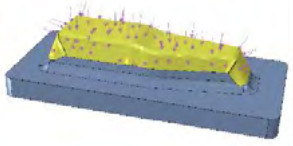
To capture the AB characteristics of the proposed c-section part (c.f. 2.1) and to provide practical computation time, the process simulation was divided into a macroscopic draping and curing simulation.

To model the uncured draping behavior of the prepregs the Abaqus FABRIC* material model can be used. This approach was proposed by [10], where they characterized the rate dependent in-plane tension, compression, bending and shear behavior of the M79 prepreg and demonstrated the applicability of this model.

The CHILE material model, implemented in the Compro Plug-In was used to model the curing behavior. This model requires solid elements to model the thermal and chemical shrinkage of the resin[11]. The cure kinetics and material parameters of the M79 prepreg were determined in a previous work [12] and were used for this model.

Finally, the results from the process simulation were used as a starting point for the structural simulation of the 3-point-bending test. A linear-elastic material model with the Hashin damage criteria and energy-based damage evolution law was used. The parameter for strength and fracture toughness were used from [13] where similar elastic properties to the M79 prepreg where used. In Table 1 the simulation stages of the process and AB simulation are summarized.

Table 1: Simulation stages of the process and "as-built" simulation

	Draping	Curing	3-point-bending
Material Model	*FABRIC	CHILE from Compro Plug-In	Linear-elastic, Hashin damage criteria, linear damage evolution
Element type	S4	C3D8	S4
Element size	3mm	3mm	3mm
Model	Dynamic, explicit	Standard & Explicit	Standard & Explicit
			

3. Results and Discussion

In Figure 5 left the reaction forces of the loading pin from the bending tests are shown. Almost linear-elastic behavior can be observed until 1.5-2mm displacement of the loading pin. After reaching 2mm displacement the slope begins to decrease indicating degradation. At 7mm displacement the maximum load capacity is reached, and the structure fails. At this point a crack at the bottom of the part underneath the loading pin appears, which can be seen in Figure 5 right from the DIC evaluation of the strain field.

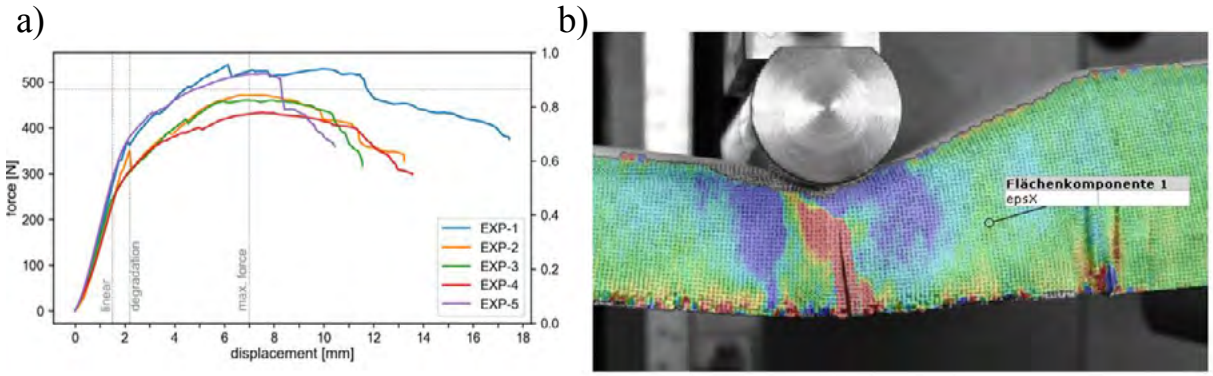


Figure 5: a) Force-displacement curves of bending test and b) DIC evaluation of strain distribution in transvers direction

By using the proposed method from section 2.2 for transferring field quantities, stresses and local fiber orientations can be transferred without errors. In ***Figure 6*** the results from a mapping procedure are visualized by a heat map of the part (left) and the stress distribution through thickness of an element at integration points from an source and target element (right). These results show that flawless transfer of the stresses from source to target has been achieved.

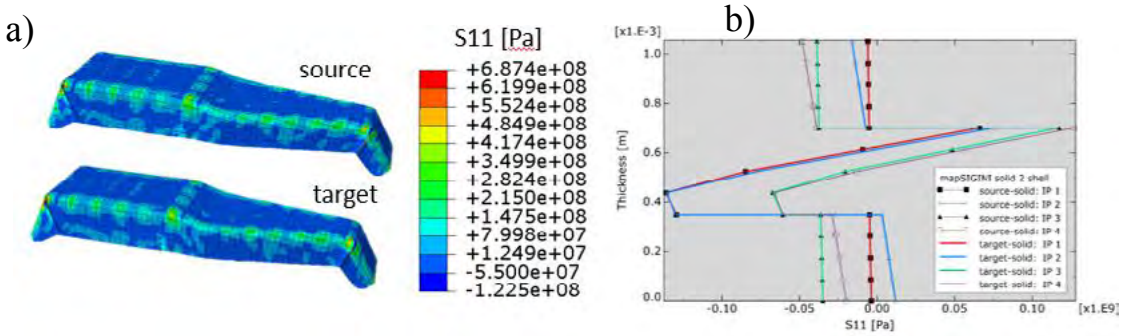


Figure 6: a) Heat map of S11 of source and target mesh from mapping procedure and b) stress distribution over thickness at integration points from source element (points) and target element (lines).

In Figure 7 the Hashin matrix tension criteria (MT) is plotted for an “as-designed” (AD)-simulation a), where no process-induced effects where included and three AB models b) - d). The “as-built”- models differ in mesh size and the presence of darts in the corners. By comparing the region where MT occurs in the models it can be observed that in the AD model the MT criteria initializes under the loading pin (Region 2 in Figure 7). Whereas in the “as-bulit” models the criteria initialize under the profile tapering of the c-section (Region 1 in Figure 7). This is because a fold developed during the process simulation and therefore shifts the area of damage. Furthermore, their is apparent that the fold is more pronounced with the 3mm mesh size, resulting in higher stress concentration.

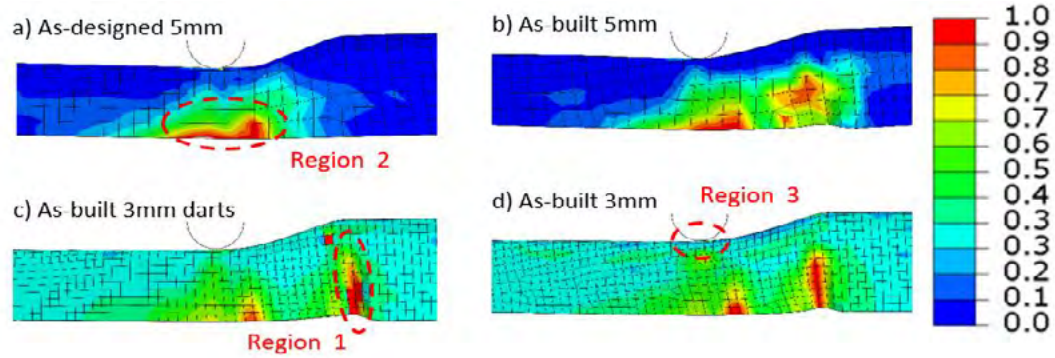


Figure 7: Initial Hashin criteria in fiber tension for "as-designed" and "as-built" simulations.

This fold could also be observed in the experiments but occurs as a smaller double waved fold (***Figure 8*** top). A much smaller mesh size would be required to reproduce this fold. However, comparing the areas of the strain distribution, good results can be observed.

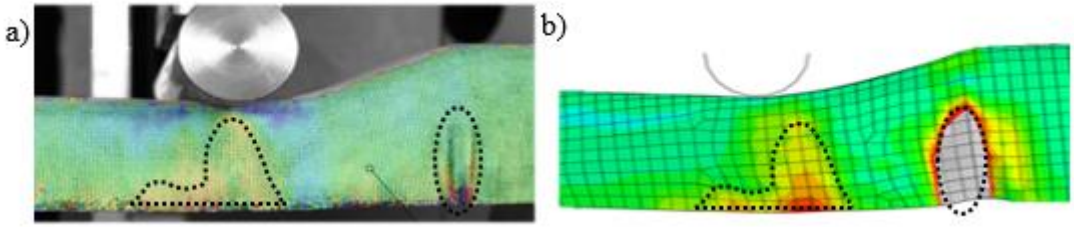


Figure 8: Transversal strain distribution of a) DIC evaluation and b) AB-simulation with identical marked areas (dotted lines)

Fehler! Verweisquelle konnte nicht gefunden werden. shows that in presence of AB characteristics, the maximum load is reduced significantly. Since crack propagation was neither modeled in the AB nor the AD simulation, the maximum load is compared before the crack initialization, observed in the experiment, at a displacement of 6.22 mm. At this position, the load capacity of the experiment is overestimated by 181% for the AD. The AB simulation provides more accurate results, overestimating the load capacity by 17%. This suggests that the material parameters do not fully represent the actual behavior of the structure. To further improve the results additional process-induced effects, like fiber waviness or voids, could be considered in the model.

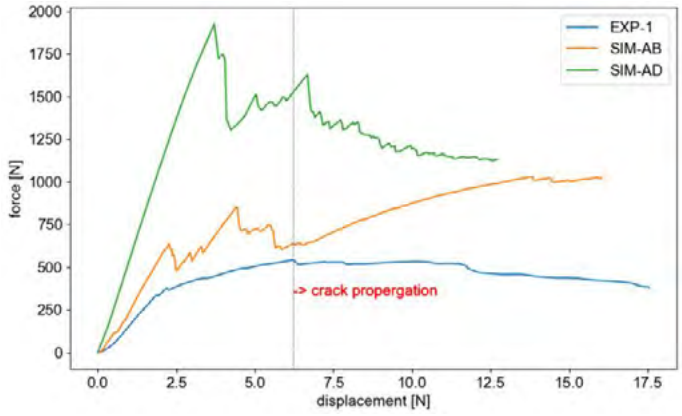


Figure 9: Load-displacement curves of experiment (EXP-1), "as-built"-simulation (SIM-AB) and "as-designed"-simulation

The initiation points of the Hashin criteria in region 1-3 (Figure 7) are are shown in Figure 10. If the damage characteristics, apparent as sudden drops in the force curve, are compared to the AB simulation, they appear at approximately the same displacement as in the experiment. However, the exsessive magnitude of the drops indicates improper material parameters.

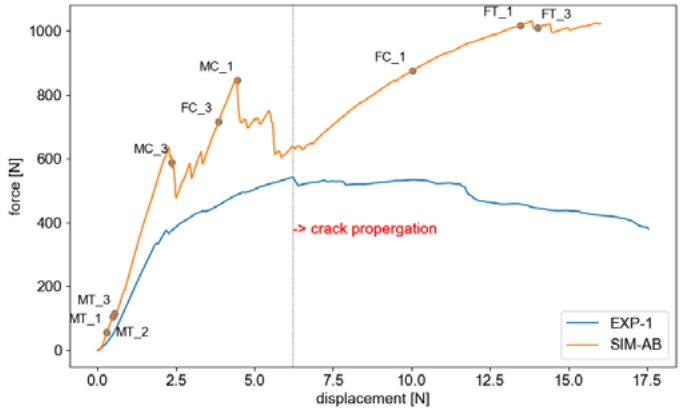


Figure 10: Load-displacement curves of experiment (EXP-1) and "as-built"-simulation (SIM-AB) with initiation points of Hashin criteria at region 1-3

4. Conclusion

In this study, a process simulation chain and "as-built" simulation for unidirectional epoxy prepregs manufactured with the diaphragm forming process were presented. The deformed shell mesh and local fiber orientations from the draping simulation were transferred to the curing simulation to model the thermal and chemical shrinkage. The results of the curing simulation were further used as initial conditions for a structural simulation of a 3-point-bending test to simulate the as-built characteristics of the part.

A material point ID of solid and shell elements was introduced to transfer field quantities with user subroutines in *Abaqus*.

We could show that a fold, which occurred during the process simulation, changed the location of damage initiation and progression of the structure. The as-built simulation was able to capture the damage events that could be observed in the experiments.

Compared to the as-designed simulation, the as-built simulations showed the correct damage initiation location and showed much more agreement in the force displacement curves of the loading pin.
Overall, the presented approach demonstrates the importance of including process-induced effects in the structural analysis for an accurate prediction of the part performance. But further research has to be made to determine material parameters for the damage behavior.

Acknowledgments
We thank our funding source, the Austrian Research Promotion Agency (FFG), for supporting us in the project ProSim (866878) and the Upper Austrian Government under the FTI-structural-funding program, for supporting us in the project IMP4Zero-E.

References

[1] I. Baran, K. Cinar, N. Ersoy, R. Akkerman, and J. H. Hattel, "A Review on the Mechanical Modeling of Composite Manufacturing Processes," *Archives of Computational Methods in Engineering*, vol. 24, no. 2, pp. 365–395, 2017, doi: 10.1007/s11831-016-9167-2.
[2] L. Kärger and A. Kling, "As-built FE simulation of advanced fibre placement structures based on manufacturing data," *Compos Struct*, vol. 100, pp. 104–112, Jun. 2013, doi: 10.1016/J.COMPSTRUCT.2012.11.024.
[3] N. Meyer *et al.*, "A probabilistic virtual process chain to quantify process-induced uncertainties in Sheet Molding Compounds," *Compos B Eng*, vol. 249, p. 110380, Jan. 2023, doi: 10.1016/J.COMPOSITESB.2022.110380.
[4] F. Henning, L. Kärger, D. Dörr, F. J. Schirmaier, J. Seuffert, and A. Bernath, "Fast processing and continuous simulation of automotive structural composite components," *Compos Sci Technol*, vol. 171, pp. 261–279, 2019, doi: 10.1016/j.compscitech.2018.12.007.
[5] J. Sun, Y. Gu, M. Li, X. Ma, and Z. Zhang, "Effect of forming temperature on the quality of hot diaphragm formed C-shaped thermosetting composite laminates," *Journal of Reinforced Plastics and Composites*, vol. 31, no. 16, pp. 1074–1087, 2012, doi: 10.1177/0731684412453778.
[6] H. E. N. Bersee, S. Lindstedt, G. Niño, and A. Beukers, "Diaphragm forming of thermoset composites," *ICCM International Conferences on Composite Materials*, pp. 1–11, 2007.
[7] F. Heinecke and T. Wille, "From As-Designed To As-Built Analysis Using an Multiscale Approach and Model Update," *EASN–5th Int. Workshop on Aerostructures*, pp. 1–10, 2015.
[8] Abaqus, "Abaqus Documentation Collection," Abaqus Documentation. [Online]. Available: https://help.3ds.com/2019/english/dssimulia_established/SIMULIA_Established_FrontmatterMap/sim-r-DSDocAbaqus.htm?contextscope=all&id=6e37335455a1420f9de68129400a122c
[9] S. M. Afazov, A. A. Becker, and T. H. Hyde, "Development of a Finite Element Data Exchange System for chain simulation of manufacturing processes," *Advances in Engineering Software*, vol. 47, no. 1, pp. 104–113, May 2012, doi: 10.1016/J.ADVENGSOFT.2011.12.011.
[10] J. Osterberger, F. Maier, and R. M. Hinterhölzl, "Application of the Abaqus *Fabric Model to Approximate the Draping Behavior of UD Prepregs Based on Suited Mechanical Characterization," *Front Mater*, vol. 9, no. May, pp. 1–13, 2022, doi: 10.3389/fmats.2022.865477.
[11] A. a Johnston, "An integrated model of the development of process-induced deformation in autoclave processing of composite structures," *University of British Columbia*, no. April, pp. 1–367, 1997.
[12] F. Silber, "Curing simulation and determination of process-induced deformations of a low-temperature curing prepreg," Fachhochschule Wels, 2021.

[13] H. Hu *et al.*, "Progressive Damage Behaviour Analysis and Comparison with 2D/3D Hashin Failure Models on Carbon Fibre–Reinforced Aluminium Laminates," *Polymers (Basel)*, vol. 14, no. 14, Jul. 2022, doi: 10.3390/polym14142946.

ANALYSIS OF MICRO-DAMAGE EVOLUTION IN INDUCTION-CURED THERMOSET COMPOSITES

Andrejs Pupurs, Viesturs Lācis, Alens Šņepsts, Anish N. Kulkarni and Mārtiņš Irbe

[1]Institute of High Performance Materials and Structures, Riga Technical University, Ķīpsalas 6A, Riga, Latvia
Email: andrejs.pupurs@rtu.lv, Web Page: http://www.rtu.lv

Keywords: induction heating, carbon fiber composites, epoxy, elastic properties, micro-damage

Abstract
In the present study a novel induction heating system for curing of carbon/epoxy composites has been developed and tested. Direct induction heating approach with carbon fibers acting as susceptors for heat generation was used. The novelty of the approach lies in the application of electromagnetic induction which is performed using a moving coil able to perform translation movement in x, y, z directions with respect to the plane of the manufactured plate. Intention of such design is to increase uniformity of induced temperature, which is known to be highly non-uniform as a result of material anisotropy which is in turn strongly related to laminate lay-up.
Carbon/epoxy cross-ply laminates made from unidirectional prepreg layers were manufactured using induction heating and with a pre-defined path of coil movement set up using Linux CNC software. Temperature distribution was monitored using a high resolution thermal imaging camera A6752sc from FLIR. Specimens from the induction cured laminates were cut and tested in uniaxial tensile loading to measure their elastic and micro-cracking properties. In addition DSC tests were performed to estimate the degree of cure of the specimens. The results were also compared with reference specimens, which were manufactured using conventional oven curing at a constant temperature.

1. Introduction

High performance lightweight composites, such as carbon fiber reinforced polymers are increasingly used in various engineering applications. Nevertheless, conventional manufacturing methods for production of lightweight composites are highly energy-consuming. For example, oven curing has been estimated to consume approximately 20 MJ/kg largely due to excess heating of chamber volumes and molds [1]. To reduce the high energy consumption in the composites manufacturing process alternative curing methods that can deliver heat directly to the composite part must be exploited. A highly promising direct curing method which stands out with low power consumption, ability to provide high heating rates, flexibility to deliver contactless energy to a targeted location in complex components and low health and safety requirements is electromagnetic induction heating [1-3].
Induction curing of thermoset composites holds a strong promise for fast, controlled and highly adjustable internal curing of high performance carbon fiber composite parts. Although carbon fibers have favourable electric conductivity and electromagnetic properties, the anisotropic nature of composite layer properties in fiber and transverse directions leads to significant difficulties to obtain uniform heating and a uniform degree of cure [4].
As part of a larger scale research project the non-uniformity of temperature distribution is solved by designing and applying in manufacturing a frame of a prototype with movable induction coil in 3 dimensions that uses feedback from thermal imaging camera to ensure even volumetric temperature distribution during the curing.

In the present study, the focus is on elastic and micro-cracking properties of carbon/epoxy UD, cross-ply composites manufactured with the above described induction heating rig with movable coil. Cross-ply composite plates of 300 x 300 mm were manufactured from UD carbon/epoxy prepregs. Tensile tests were performed on specimens from the manufactured plates to determine elastic properties. Loading-unloading tensile tests with increasing maximum strain levels were performed to study initiation and evolution of transverse matrix cracks. Additional characterization of the glass transition temperature and degree of cure were performed using DSC analysis.
Results were compared with corresponding reference materials manufactured from the same raw materials but instead using conventional oven curing.

2. Manufacturing

2.1. Material system

Composite laminates were made from UD carbon/epoxy prepregs XC130 from Xpreg. Carbon fibers were from Pyrofil high strength carbon fiber grade and the recommended pre-preg curing cycles range from minimum of 80°C to maximum of 120°C. The curing times accordingly correspond to a range between 1 to 16h depending on the temperature. In the present work, taking into consideration the capabilities and limitations of the manufacturing rig a curing cycle of 4 hours at 100°C temperature was selected and applied. A higher temperature would be preferable, however, it was not achievable with the present set-up consisting of a power supply, a coil and an electronic controler unit. One of the challenges was also the thickness of a non-inductive glass/epoxy base plate on which carbon pre-preg layers were placed and which acts as a spacer between the coil and carbon/epoxy laminate. It was found that 2 mm thickness suits well for effective application of heat to the carbon/epoxy laminate plate via induction.
Laminates with lay-up [0/90]s were manufactured. Each laminate consists of 4 UD layers each with approximate weight of 150 g/m^2. The plate size was 300 x 300 mm.

2.2. Induction heating system

In the present work, a custom made induction heating rig was built. The frame design is shown in Figure 1. The system consists of the main frame, thermal imaging camera and a control/inspection unit as shown in the figure. The frame was built in similarity to 3D printers and CNC machines capable of performing independent translation movements in x, y and z axis directions controled by Linux CNC software.

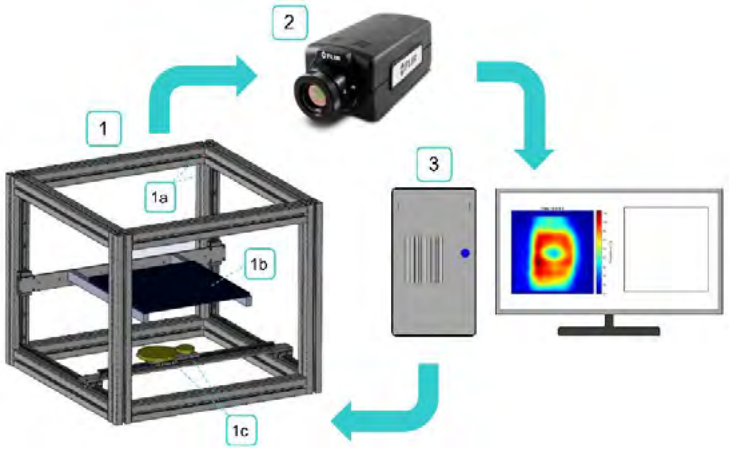


Figure 1. Drawing of an induction heating manufacturing rig: 1) main frame; 2) high resolution thermal imaging camera; 3) control and inspection unit

The size of the frame was 160 x 90 cm, and the height is approximately 60 cm. The diameter of induction coil was 150 mm. A control unit was built providing a constant frequency of electromagnetic field. The coil was connected to an adjustable power supply to control the output current of the induction coil.

2.3. Manufacturing process

As found in previous trials and in the literature [4,5], high non-uniformity of temperature is expected when the induction coil is static (no movement). The novelty of the present approach and test set-up is movable coil which can be pre-programmed to perform various heating paths in order to mitigate the non-uniformity. A trial circular heating path approximately following the inscribed circle inside the square plate of 300x300 mm was first applied leading to conclude that large cold spots near the plate corners are present irrespective of the coil output and speed of the movement. For better results of heating and curing uniformity, the heating path was applied in two consecutive rectangular paths each covering approximately one half of the composite plate, i.e., 150 x 300 mm. This approach according to observations on FLIR A6752sc thermal imaging camera during the induction heating led to the most uniform temperature distribution, however, with a drawback of increased time consumption to complete the curing of the whole 300 x 300 mm plate. The carbon/epoxy composite plate was placed on a non-conductive glass fiber base plate. Vacuum bag was applied for compacting the plate, however, only the vacuum film was put on top without any plate typically used to apply mechanical pressure as typically done in conventional hot-press manufacturing. This was done to enable a clear temperature distribution inspection with the FLIR A6752sc thermal imaging camera as shown in Figure 2.

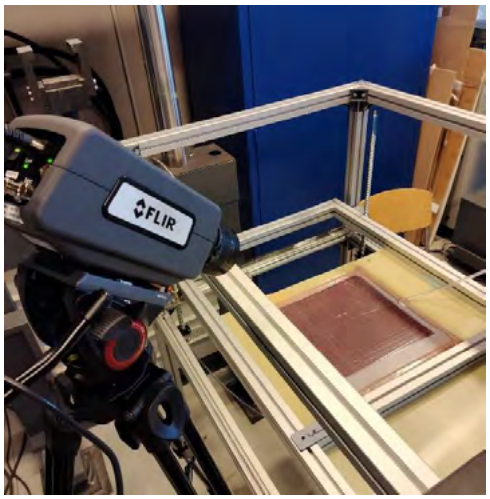


Figure 2. Overview of induction heating process: carbon/epoxy plate placed on a base plate and sealed in vacuum bag with thermal imaging camera placed to record temperature distribution from top view.

A constant output from the induction coil was applied to generate heat. Maximum temperature of 100°C was reached in a region approximately corresponding to the size of the coil. When the coil moved away from the heated part, a slight decrease of temperature was observed. An example temperature distribution is demonstrated in Figure 3.

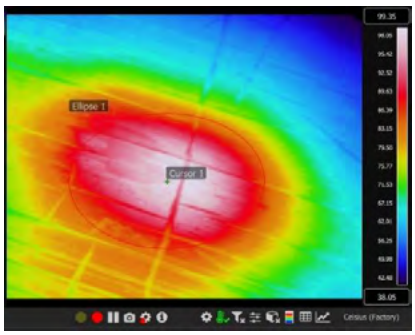


Figure 3. An instant temperature distribution during induction heating. Diameter of the highlighted region approximately corresponds to 150 mm.

As mentioned above, induction coil was following a programmed path of a rectangle corresponding to a half of the plate. In total, induction heating was applied for 4 hours on each half of the plate following the manufacturer's recommended curing cycle. It was clearly observed that the corners of the plate have significantly lower temperature, which was expected as it is typically difficult to induce the Eddy currents in the corners. For manufacturing of reference plates, a cross-ply plate with size of 150 x 300 mm was placed on a glass fiber/epoxy base plate and packed in a vacuum bag with no additional mechanical pressure applied to match conditions used in induction curing. Reference plates were cured in an oven at 100°C for 4 hours.

3. Experimental testing

3.1. Specimen preparation

After curing, plates were removed from the vacuum bag and specimens cut according to Figure 4. As shown in the figure, specimens were cut from regions which were in the central part of the plate where temperature distribution was the most uniform during the induction heating. In total 9 specimens from induction heated plate were obtained with size of 20 x 100 mm. Specimens were cut and their ends reinforced with tabs prior to testing. From the reference plate specimens with dimensions 20 x 150 mm were cut.

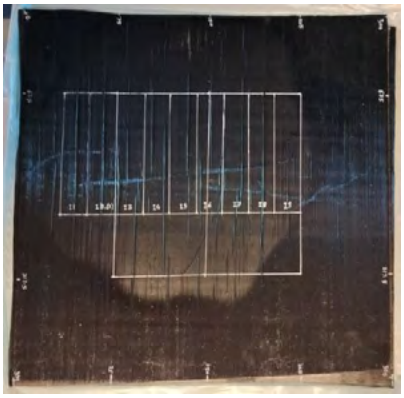


Figure 4. Specimens cut from the induction heated cross-ply laminate.

3.2. Testing procedure

Tensile tests were performed on tensile testing machine Zwick/Roell Z150 using 1% per minute tensile strain rate. At first, elastic modulus was measured, followed by cyclic loading/unloading cycles with increasing maximum strain level. Specimens were removed for optical microscopy inspection and reloaded in the testing machine to apply higher strain levels in the next step. The initiation of transverse cracking was monitored in optical microscopy by quantifying the amount of transverse (intralaminar) cracks in the 90° layers of the cross-ply laminate specimens. Additionaly DSC scans were performed on both induction heated and reference plate specimens to analyze the degree of cure in both composites. DSC tests were performed on specimens cut from area in vicinity to the ends of the tensile test specimens.

3.3. Results and discussion

The elastic modulus results are summarized in Figure 5. Specimen numbering corresponds to induction cured (I1 to I4) and oven cured (O1 to O4). In general, approximately 10% higher tensile elastic modulus was found for the oven cured (reference) materials as shown in Figure 5. These results also correlate well with the nominal glass transition temperature (Tg) obtained from DSC tests which are also plotted in the results summary in Figure 5. For the oven cured specimens, the nominal glass transition temperature Tg is slightly above 120°C while for the induction cured specimens the nominal Tg is approximately equal to 100°C.

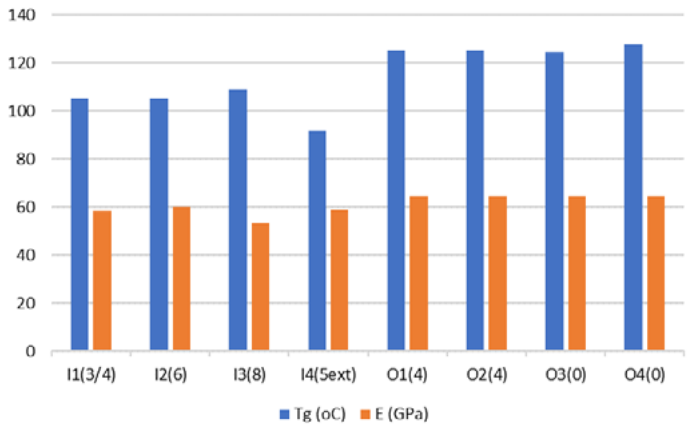


Figure 5. Summary of tensile elastic modulus and glass transition temperature from DSC tests.

Initiation and evolution of micro-damage was studied with optical microscopy and the results are summarized below in Table 1. Notation of specimens follows induction curing (I1, I2, I3, I4, I8) and oven curing (O1). According to the data summary in Table 1, micro-cracks (in form of transverse matrix cracks in the 90° layers) initiate at around 0.75% tensile strain for the oven cured (reference) specimens. For induction cured specimens, on the other hand, crack initiation takes place at significantly lower strain of 0.50% for several specimens. A significant increase of the amount of transverse cracks was observed for induction cured specimens at 0.8% strain. Such significant differences in micro-cracking were found to be related to significantly higher amount of voids in the induction cured specimens as shown in Figure 6, despite using the same vacuum pressure and curing temperature and time. Although at present only two plates have been tested, this observation deserves a more thorough study in the future work.

Table 1. Write your table caption here.

ε [%]	O1	I1	I2	I4	I3	I8
0.50	0	-	0	0	3	1
0.55	0	-	0	1	-	2
0.60	0	-	-	-	-	2
0.70	0	-	-	-	-	3
0.75	4	-	-	-	-	3
0.80	4	17	-	-	-	-

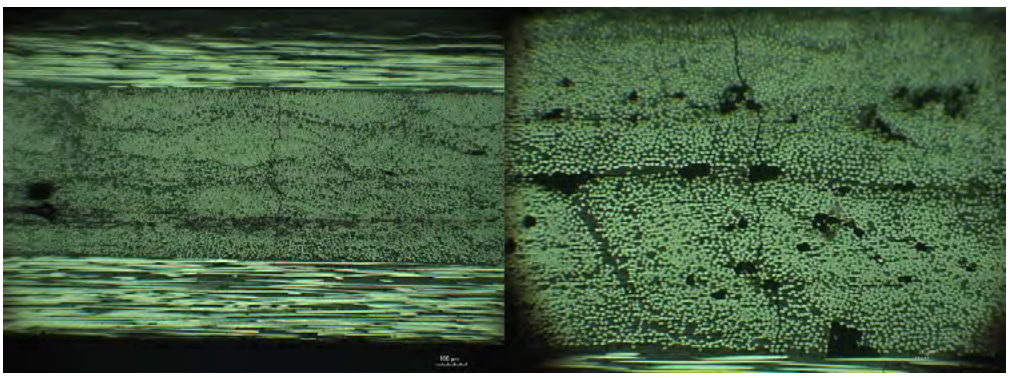


Figure 6. Comparison of micro-structure between oven cured (left) and induction cured (right) laminates showing significantly more voids in the latter.

4. Conclusions

The present study investigates elastic and micro-damage properties of induction heated cross-ply laminates and the results are compared with reference material manufactured using oven curing. In general, a higher elastic modulus was found for the oven cured material than for induction cured material. The found differences were also confirmed by DSC tests, which showed a higher nominal Tg, and thus presumably a higher degree of cure for the oven cured specimens than for induction cured specimens. Significant differences were also found in the microstructure in both materials. While oven cured specimens appeared to be in typical pre-pleg quality with a few voids, the induction cured specimens had a significant amount of voids which contribute to an earlier micro-crack formation. The future work will address improvement of the induction curing process to obtain a fully-cured condition and better uniformity of the temperature during induction heating. In addition, the observed high amount of voids in induction heated specimens needs a futher research.

Acknowledgments

This work was supported by Latvian Council of Science, project LZP-2022/1-0572 “Development of innovative induction-heating system for manufacturing of high-performance composites with improved mechanical properties”, project LZP-2022/1-0572.

References

[1] M.G. Collinson, M.P. Bower, T.J. Swait, C.P. Atkins, S.A. Hayes and B. Nuhiji. Novel composite curing methods for sustainable manufacture: A review. *Composites Part C: Open Access*, 9:art. no. 100293, 2022.

[2] T. Bayerl, M. Duhovic, P. Mitschang and D. Bhattacharyya. The heating of polymer composites by electromagnetic induction - A review. *Composites Part A: Applied Science and Manufacturing*, 57: 27-40, 2014.

[3] T.J. Ahmed, D. Stavrov, H.E.N. Bersee and A. Beukers. Induction welding of thermoplastic composites-an overview. *Composites Part A: Applied Science and Manufacturing*, 37(10):1638-1651, 2006.

[4] J.B. Khan, A.C. Smith, P.M. Tuohy, M. Gresil and C. Soutis. Three-dimensional finite-element analysis multiphysics modelling of electromagnetic Joule heating in carbon fibre composites. *IET Electric Power Applications*, 14 (10):1966-1973, 2020.

[5] F. Lundstrom, K.Frogner, M.Andersson. Analysis of the temperature distribution in weave-based CFRP during induction heating using a simplified numerical model with a cross-ply representation. *Composites Part B,* 223:art.no.109153, 2021.

ENHANCED ANALYTICAL MODELING OF CRACK PROPAGATION IN THROUGH-THICKNESS REINFORCED COMPOSITE LAMINATES

Albrecht Radtke, Philipp Weißgraeber

Chair of Lightweight Design, University of Rostock, Germany
Email : albrecht.radtke@uni-rostock.de, Web Page: https://www.cld.uni-rostock.de/

Keywords: Crack bridging, Delamination, Interlaminar fracture, DCB, Analytical modelling

Abstract
Fiber-reinforced composites are susceptible to failure by delamination. Hence, transverse reinforcements have been thoroughly researched, including the technology of z-pinning, with the insertion of pins in the thickness direction of laminate layups before curing. Such reinforcements act as strong crack bridging elements and enhance the interlaminar fracture behavior. To predict and design resulting delamination behavior, detailed models are needed. In this study a new enhanced model describing the delamination of pinned laminates for the example case of double cantilever beam tests is proposed. The new approach takes into account the cantilever beams' transverse compliance near the crack tip through an incorporation of a Winkler elastic foundation. Also first order shear deformation is introduced in the beam kinematic in order to also allow for accurate analyses for configurations with non-negligible shear compliance. To be able to investigate inter-laminar crack propagation in different composites featuring through-thickness reinforcements, an effective parametric iterative solving is implemented. The bridging zone is modeled by a linearly idealized bridging law. The models beam behavior at characteristic states of the crack propagation shows very good agreement with finite element reference simulations. The refined analytical model offers valuable insights for the design of composite laminates with enhanced resistance to delamination.

1. Introduction

Composite laminates are used in a wide range of applications, including aerospace, military, automotive and sports equipment due to their high ratio of mechanical performance to weight. With great in-plane properties they are however vulnerable to delamination damage, as they are usually not reinforced in through-thickness direction. There is a range of measures than can be utilized to add translaminar reinforcement to a composite laminate, including stitching, weaving and z-pinning. While the model proposed in this paper can be potentially applied to different kinds of translaminar reinforcement methods as well as crack bridging phenomenon in general, it's using the z-pin reinforcement as an example. This is a technique, in which pin shaped elements, made of either fiber-reinforced plastics or metal, are brought into usually uncured thermoset laminates in the through-thickness-direction (z) [1]. The pins are usually placed in the composite in a rectangular pattern, where the pins cross-sectional area per laminate area defines a z-pinning density. This measure has been shown to enhance the damage behavior through an increase in the apparent fracture toughness, while deteriorating the in-plane properties [2]. Song et al. [3] have proposed analytical model for the crack propagation in z-pinned double cantilever beams (DCB) under mode I loading and found good agreement with a finite element analysis and an experimental study. However, the model did not take into account shear deformations in the beams. Also the cantilevers are considered clamped at the crack tip, impeding rotation and elastic deformations at and in front of the crack tip due to the beams transversal compliance, as described by Kanninen et al. [4]. To account for these an enhanced model is proposed including first-order shear deformation theory (FSDT) [5] as well as adding a Winkler elastic foundation (WEF) to the uncracked zone of the cantilevers.

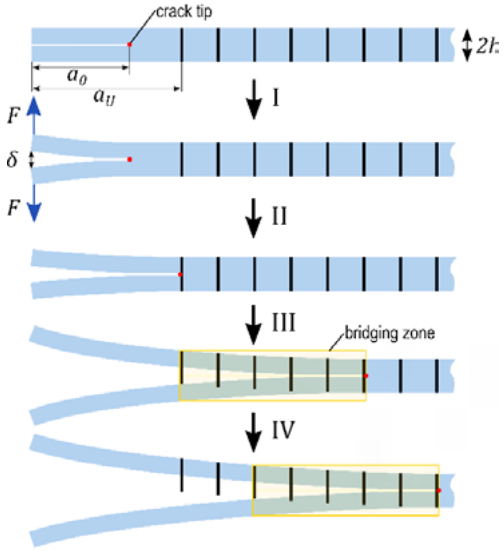


Figure 1. Characteristic phases testing a bridged DCB

2. Derivation of mechanical model for double cantilever beam

We study the case of a DCB that consists of two cantilever beams, each with a rectangular cross section described by height h and width b as depicted in Figure 1. In the initial (uncracked) state, the beams are connected along the interface, except for an initial crack with length a_0. The DCB features a transverse reinforcement starting from a_U on. During loading of the DCB crack opening deflection δ is applied at the cantilever ends, resulting in a transverse force F. The symmetry of the DCB is exploited.

2.1. Phases of bridged DCB testing

The bridged DCB test consists of different phases (see Figure 1.). Phase I starts in the unloaded state and is characterized by the linear-elastic deflection of the precracked end of the beam with the initial crack length a_0, when δ is increased. The DCB behavior in phase I is characterized by the beam compliance, given for Timoshenko beams on a Winkler elastic foundation by Kondo et al. [6]. Phase I ends when the fracture of the unbridged zone starts. There phase II concludes and the apparent crack length a_p increases with increasing δ. The critical force and corresponding deflection at the transition between phase I and II as well as all states in the unbridged crack propagation in phase II can be calculated from [6]

$$F_c = \sqrt{\frac{\mathcal{G}_{Ic} E_{fx} b^2 h}{12}} \left(\left(\frac{a}{h}\right) + \sqrt{\left(\frac{E_{fx}}{6E_z}\right)^{\frac{1}{2}} + \frac{1}{12}\frac{E_{fx}}{\kappa G_{xz}}} \right)^{-1} \tag{1}$$

At the end of phase II, the crack tip reaches the first row of the z-pin reinforcement at $a_p = a_U$. Then phase III starts, describing the crack propagation in the reinforced section of the DCB developing a bridging zone with a length of c_B. The total crack length then is $a = a_p + c_B$. Phase III proceeds up to the point when the first reinforcing elements are no longer exerting a bridging force, in this case, when the first row of pins is fully pulled out. Then phase IV, the migration of the bridging zone through the length of the DCB, succeeds, characterized by an increase in a_p.

2.2. Governing equations

To describe the behavior of crack propagation in the bridged zone, a model coupling the deflections of the three different zones, the unbridged (U), the bridged (B) and the foundation (F) is required (see Figure 2.). With constant material properties and beam cross section along the beam, the Timoshenko beam equations can be formulated as [7]:

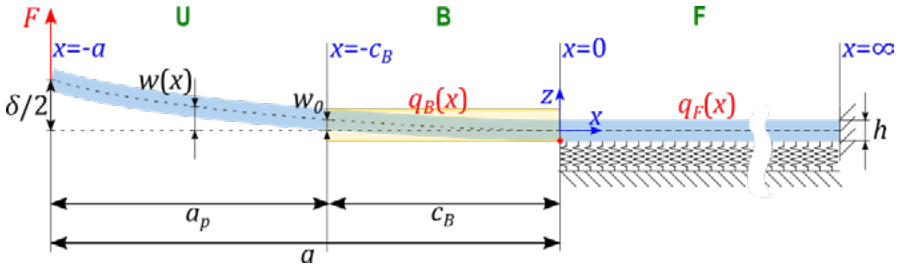


Figure 2. Schematic representation of a single bridged cantilever

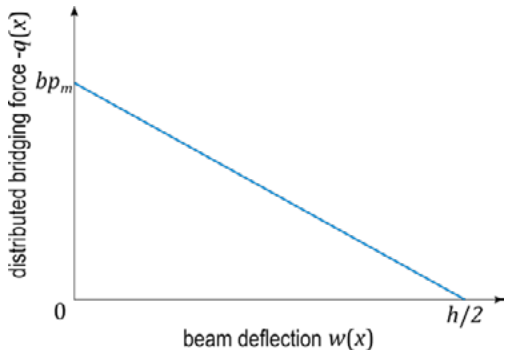


Figure 3. Linearly idealized pin-bridging law

$$E_{fx}\frac{\mathrm{d}^4 w}{\mathrm{d}x^4} = q(x) - \frac{E_{fx}}{\kappa A G_{xz}}\frac{\mathrm{d}^2 q}{\mathrm{d}x^2} \tag{2}$$

As in the unbridged zone (U) the cantilever doesn't feature a distributed load, the right hand side of this ODE vanishes. Taking into account the bending moment in the unbridged zone ($M_U(x) = F(x+a)$) the deflection is

$$w_U(x) = \frac{F}{E_{fx}I}\left(\frac{1}{6}x^3 + \frac{1}{2}ax^2\right) - \frac{Fx}{kAG_{xz}} + \frac{1}{E_{fx}I}C_1 x + C_2. \tag{3}$$

In the bridged zone (B) the bridging forces are characterized by the z-pins' pull-out behavior which can be idealized to a linear bridging law (see Figure 3.): [3]

$$q_B(x) = -bp_m\left(1 - \frac{2}{h}w_B(x)\right). \tag{4}$$

Here, $p_m = Nf_m$ is the maximum pin force per area, calculated from the number of pins per area N and the pin's maximum frictional pull-out-force f_m. In case not directly given, N can be calculated from the pin diameter d_{pin} (for circular pins) and the areal pinning density $\rho_{A,\mathrm{pin}}$ as $N = \frac{\pi d_{\mathrm{pin}}^2}{4\rho_{A,\mathrm{pin}}}$. Inserting this distributed bridging force into the governing ODE the bending deformation is obtained as

$$w_B(x) = C_3\cos(\gamma_1 x) + C_4\sin(\gamma_1 x) + C_5\cosh(\gamma_2 x) + C_6\sinh(\gamma_2 x) + h/2, \tag{5}$$

with

$$\gamma_1 = \sqrt{\frac{\alpha\beta_B}{2} + \sqrt{\left(\frac{\alpha\beta_B}{2}\right)^2 + \frac{\beta_B}{E_{fx}I}}}\,,\quad \gamma_2 = \sqrt{-\frac{\alpha\beta_B}{2} + \sqrt{\left(\frac{\alpha\beta_B}{2}\right)^2 + \frac{\beta_B}{E_{fx}I}}}$$
$$\alpha = \frac{1}{\kappa A G_{xz}},\quad \beta_B = \frac{2bp_m}{h}. \tag{6}$$

In the foundation zone (F) the transversal compliance of the beam can be accounted for by a distributed load

$$q_F(x) = -k_e w_F(x) \tag{7}$$

using a foundation stiffness obtained from the transversal stiffness of the beam and its thickness [4]

$$k_e = \frac{2E_z b}{h}\,. \tag{8}$$

The solution of the governing ODE requires to distinguish two cases in order to avoid complex solutions:

$$w_{F,A}(x) = \begin{cases} C_7 e^{-\psi_1 x} + C_8 e^{-\psi_2 x} + C_9 e^{\psi_1 x} + C_{10} e^{\psi_2 x} \\ \text{for } \dfrac{E_z E_{fx}}{24\kappa^2 G_{xz}^2} \geq 1\,, \\ C_7 e^{-\psi_3 x}\cos(\psi_4 x) + C_8 e^{-\psi_3 x}\sin(\psi_4 x) + C_9 e^{\psi_3 x}\cos(\psi_4 x) + C_{10} e^{\psi_3 x}\sin(\psi_4 x) \\ \text{for } \dfrac{E_z E_{fx}}{24\kappa^2 G_{xz}^2} < 1, \end{cases} \tag{9}$$

with

$$\psi_1 = \sqrt{\frac{\alpha\beta_F}{2} + \sqrt{\left(\frac{\alpha\beta_F}{2}\right)^2 + \frac{\beta_F}{E_{fx}I}}}\,,\quad \psi_2 = \sqrt{\frac{\alpha\beta_F}{2} - \sqrt{\left(\frac{\alpha\beta_F}{2}\right)^2 + \frac{\beta_F}{E_{fx}I}}}$$

$$\psi_3 = \frac{1}{\sqrt{2}}\sqrt{\sqrt{\frac{\beta_F}{E_{fx}I} + \frac{\alpha\beta_F}{2}}}\,,\psi_4 = \frac{1}{\sqrt{2}}\sqrt{\sqrt{\frac{\beta_F}{E_{fx}I} - \frac{\alpha\beta_F}{2}}}\,,$$

$$\beta_F = \frac{2E_z b}{h}. \tag{10}$$

2.3. Boundary conditions

To determine the deflections of the three beam zones, constants need to be calculated by boundary - , equilibrium - and continuity conditions. In both cases of the foundation zone solution for the far end boundary condition of

$$w_F(\infty) = 0\,,\quad \theta_F(\infty) = 0 \tag{11}$$

the ascending terms need to be eliminated leading to the simplification

$$C_9 = C_{10} = 0. \tag{12}$$

The eight remaining constants can then be determined through

$$\begin{gathered} w_U(-c_B) = w_B(-c_B), \\ \theta_U(-c_B) = \theta_B(-c_B), \\ M_B(-c_B) = a_p F(-c_B), \\ w_B(0) = w_F(0), \\ \theta_B(0) = \theta_F(0), \\ Q_B(0) = Q_F(0), \\ M_B(0) = M_F(0). \end{gathered} \tag{13}$$

One additional boundary condition is defined by the parameter controlling the DCB. Generally the test is controlled by the deflection at the loaded end

$$w_U(-a) = \delta/2. \tag{14}$$

2.4. Iteration solution of the crack propagation

The iterative solution of the crack propagation follows the phases described in 2.1. starting with the critical force and deflection for the end of phase I, the linear elastic deformation. Then for a range of

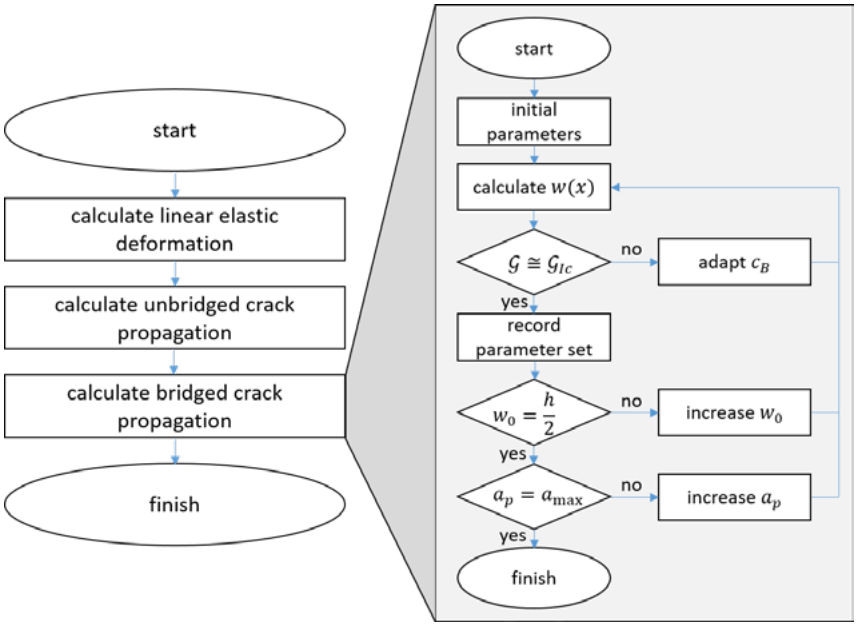


Figure 4. Flowchart of the schematic structure of the DCB crack propagation model

$a_0 < a_p < a_U$ forces and δ are calculated for phase II, the unbridged crack propagation. For phase III and IV, the crack propagation in the bridged zone, the steps shown in Figure 4. are performed. Starting from a w_0 slightly bigger than the $w(0)$ at state c) a corresponding c_B is determined, using a numerical root search method on the function

$$\frac{\mathcal{G}(c_B)}{\mathcal{G}_{Ic}} - 1 = 0. \tag{15}$$

This means, for that set of w_0 and c_B the Griffith criterion is fulfilled and the crack propagates. The energy release rate is calculated in displacement-controlled compliance approach [8]

$$\mathcal{G} = \frac{F^2}{2b}\frac{\mathrm{d}C}{\mathrm{d}a} = \frac{\delta}{2b}\frac{\mathrm{d}F}{\mathrm{d}a} \tag{16}$$

where the force is numerically differentiated with the symmetric difference quotient

$$\frac{\mathrm{d}F}{\mathrm{d}a} = \frac{F(c_B+\Delta) - F(c_B-\Delta)}{2\Delta}. \tag{17}$$

Subsequently w_0 is incrementally increased and the procedure repeated until $w_0 = h/2$, when the first pin row is fully pulled out and the bridging zone starts to migrate. There in phase IV a_p is incrementally increased and the calculation repeated until a defined $a_{\max}$ has been reached. It needs to be noted that in order to keep the assumptions for the far end (equation 11.) applicable, the crack is not allowed to run to the very end of the DCB. The solution is efficiently implemented in a Python routine.

3. Results and discussion

As a sample configuration the DCB definition used by Song et al. [3] based on experimental studies of Cartié [9] and a pin-bridging law by Dai et al. [10] was applied to the analytical model and investigated. The dimensions of the DCB and the material properties can be found in Table 1. The modelled DCB bridging behavior can be seen in Figure 5., where both the shear force and the zone lengths have been plotted over the increasing δ. The different phases described in section 2.1. can be observed. The linear increase of F over δ in phase I, the decline of the required force for crack growth with increasing a in phase II, followed by increase in force again as the bridging zone develops, exerting increasing bridging forces counteracting the crack propagation.

To validate the beam deflections determined by the solving of differential equations throughout the model run, an FE model was set up. It was built in Abaqus with a parametric Python script using beam

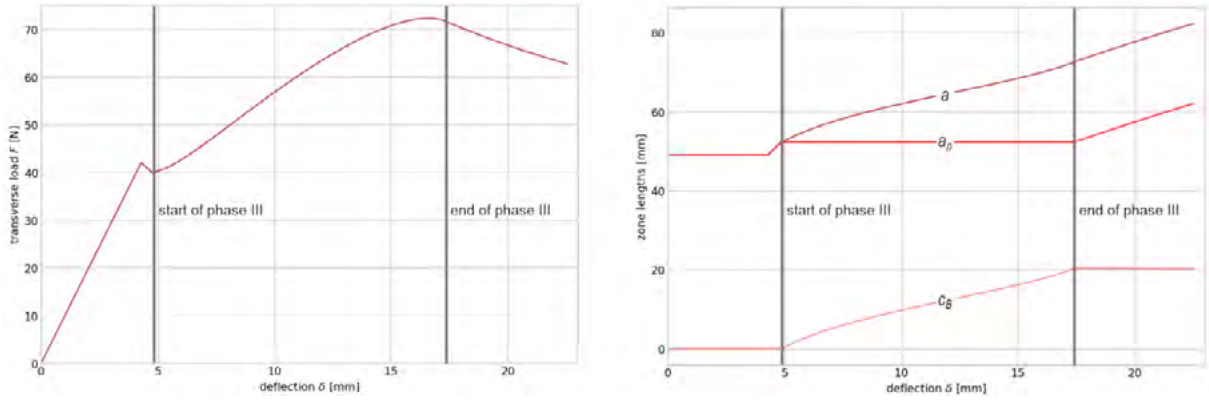


Figure 5. Force (left) and zone lengths (right) over deflection controlled crack propagation for sample configuration

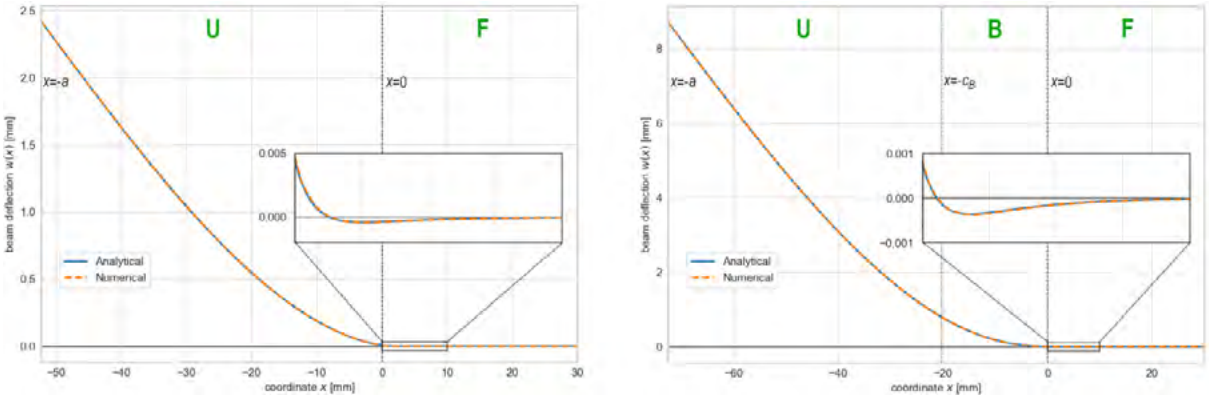


Figure 6. Comparison of deflection curves at start and end of phase III

Table 1. Dimensions and properties of sample configuration

b	20 mm
h	1.6 mm
a_0	49 mm
a_U	52.25 mm
$\rho_{A,\mathrm{pin}}$	0.5 %
d_{pin}	0.28 mm
f_m	19.27 N
E_{fx}	138 GPa
E_z	11 GPa
G_{xz}	4.4 GPa
ν_{xy}	0.34
$\mathcal{G}_{Ic}$	258 N/m

elements of the type B31, also featuring Timoshenko kinematics with shear deformation. The different zones were sectioned and both the pins as bridging elements and the foundation's springs were modelled as distinct axial connector elements, which were assigned the pin bridging law and the foundation spring stiffness, respectively. With the FE model characteristic states in the DCBs loading were statically simulated and compared to the results of the analytical model. The state directly before the crack starts to propagate into the bridged zone in the transition of phase II and III as well as the state, when the

bridging zone is fully built out and starts to migrate between phase III and IV where chosen. The first featuring only the unbridged and foundation zone, the later one utilizing all three zones defined. The resulting deflection curves can be observed in Figure 6. Both states show a very good agreement of the analytically and numerically determined deflections. The discretization of the elastic foundation in the FE model leads to minor offsets visible in the detail of the foundation zone. In the foundation a traction zone near the crack tip followed by a compression zone, characteristic for beams on WEFs, can be observed. The visible deflection of the beam's mid-plane at the crack tip $w(0) > 0$ as well as its slope result in an overall more compliant beam behavior compared to a model with a clamped boundary at the crack tip.

To investigate the importance of the implementation of the FSDT in the model, the configuration has also been processed in an ideally shear-stiff variant representing Euler-Bernoulli- instead of Timoshenko beam theory. In effect the DCB is stiffer, which was especially visible in phase I, where an increase in the critical force before unbridged crack growth could be observed. While $F_{c,\mathrm{TB}} = 42.06\,\mathrm{N}$ without FSDT it was $F_{c,\mathrm{EBB}} = 43.30\,\mathrm{N}$, an overestimation of about 2.95 %. A test with both shear deformation and elastic foundation taken out of consideration, so with a clamped crack tip, yielded a critical force of $F_{c,\mathrm{EBB,clamp}} = 44.99\,\mathrm{N}$, even 7 % higher than with the FSDT and WEF implementation.

4. Conclusions

An enhanced analytical model for the analysis of z-pin-bridged DCBs has been developed, taking into account shear deformations and compliance at and in front of the crack tip modelled with a WEF. The three-zone model has shown good agreement with reference FE simulations. Additionally the influence and importance of the model features are shown at hand of an exemplary case study. With this setup, the model can be applied to a wide range of DCB configurations, including non-isotropic and shear-compliant materials. Also the implemented z-pin bridging law can easily adapted to other transverse reinforcements or bridging phenomena's laws, opening a wide range of possibilities of application.

References

[1] A.P. Mouritz, Review of z-pinned composite laminates, *Composites Part A: Applied Science and Manufacturing*, Vol. 38: 2383-2397, 2007.
[2] L. Tong and A.P. Mouritz and M.K. Bannister, 3D fibre reinforced polymer composites, *Elsevier*, 2002.
[3] M. C. Song and B. V. Sankar and G. Subhash and C.F. Yen, Analysis of mode I delamination of z-pinned composites using a non-dimensional analytical model, *Composites Part B: Engineering*, Vol. 43: 1776-1784, 2012.
[4] M.F. Kanninen, An augmented double cantilever beam model for studying crack propagation and arrest, *International Journal of Fracture*, Vol. 9: 83-92, 1973.
[5] J.N. Reddy, Mechanics of laminated composite plates and shells: theory and analysis, *CRC Press*, 2003.
[6] K. Kondo, Analysis of double cantilever beam specimen, *Advanced Composite Materials*, Vol. 4: 355-366, 1995.
[7] A. Öchsner, Classical Beam Theories of Structural Mechanics, *Springer*, 2021
[8] T.L. Andersen, Fracture Mechanics: Fundamentals and Applications, *CRC Press*, 2005
[9] D.D.R. Cartié, Effect of z-fibres on the delamination behaviour of carbon-fibre/epoxy laminates, PhD thesis, Cranfield University, 2000.
[10] S.C. Dai, W.Yan, H.Y. Liu and Y.W. Mai, Experimental study on z-pin bridging law by pullout test, *Composites Science and Technology*, Vol. 64: 2451–2457, 2004.

MODELLING THE MECHANICAL BEHAVIOUR OF A CARBON/CARBON COMPOSITE MATERIAL FOR AERONAUTICAL STRUCTURES UNDER THE INFLUENCE OF ITS ENVIRONMENT

M. Rahard[1], M. Kaminski[1], J.-F. Maire[1], F. Laurin[1],
F. Bouillon[2], V.-I. Prisacari[3]

[1]DMAS, ONERA, Université Paris-Saclay, 92320, Châtillon, France
Email : mathis.rahard@onera.fr
[2]Safran Ceramics, a technology platform of Safran Tech,
105 avenue Marcel Dassault 33700 Mérignac , France
Email : florent.bouillon@safrangroup.com
[3]Safran Landing Systems, 7 rue Général Valérie André, 78140, Vélizy-Villacoublay, France
Email : vasile-ionut.prisacari@safrangroup.com

Keywords: Carbon/Carbon, Oxidation, Damage, Modeling

Abstract
The study focuses on developing a model for the specific lifetime of Carbon/Carbon (C/C) ceramic matrix composites in aeronautics braking systems, considering the effect of carbon oxidation on the thermo-mechanical properties. During the landing and taxi-out phases, brake temperatures range from 400°C to 800°C, leading to significant oxidation reactions with atmospheric oxygen. The literature review and the tests carried out in this study show that the duration but also the temperature of oxidation affect the mechanical properties. An in-depth understanding and advanced modeling approach are required to explain the results obtained. The modeling involves two main steps. First, the oxidation state of the material is estimated considering the environmental conditions. Then, the effects of oxidation on the mechanical properties are considered. A thermodynamically consistent behavior law based on the continuum damage framework has been developed, considering both the effects of mechanical loading and oxidation. The predictions of the model have been compared with the available test results and is able to reproduce the observed trends.

1. Introduction

Carbon-Carbon (C/C) composites are Ceramic Matrix Composites (CMCs), but with some specifities compared to classical C/SiC or SiC/SiC material [1]. C/C composites have found many applications in the aerospace industry. For instance, in nose cones for reentry vehicles and ballistic missiles, as well as in the leading edge of the Space Shuttle and in aircraft breaking systems which represent the largest consumption of this material. The latter is the practical application of the material in this study which constitutes the heat sink of the brake, as shown in Figure 1 [2], which captures the heat generated by braking, thus protecting other parts sensitive to high temperatures. However, C/C composite is susceptible to oxidation phenomena. Above 400°C, oxygen reacts strongly with carbon, which consumes the composite and degrades its mechanical properties. The C/C composite studied is a needle-punched 2.5D preform stacked in [0/±60] orientations, then densified by a CVI (Chemical Vapor Infiltration) process. The microstructure of the material under study is similar to that shown in Figure 2.

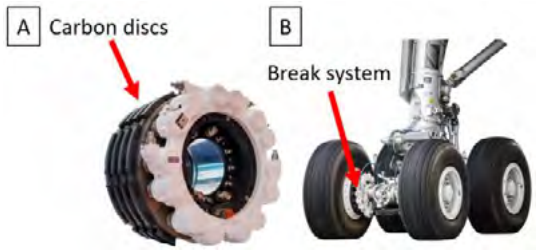


Figure 1. A- A330 break system. B- Wheel-integrated braking system [2].

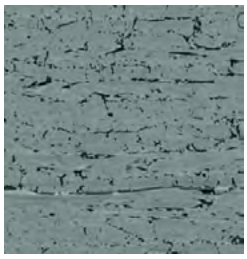


Figure 2. Material microstructure [3].



Figure 3. Pores due to CVI process [4].

The CVI densification process generates pores, as shown in Figure 3 [4], which facilitate oxidation ansd this promote the degradation of the mechanical properties. Therefore, the aim of this study is to propose a constitutive law able to describe the evolution of the mechanical properties (rigidity and damage) as a function of the oxidation. Firstly, the definition and the modelling of the oxidation state in /C composites is provided. Then, the influence of the oxidation on elastic properties and on the damage process are described. Finally, the model predictions are compared with experimental data.

2. Modeling the influence of oxidation on the mechanical behavior

2.1. Formalism for describing the oxidation state

The rate of oxidation is usually estimated by measuring the loss of mass, noted as Δm, compared to the mass of the material after manufacture. In standard application of brakes, the oxidation rate, also known as burn-off, does not normally exceed 5%. For C/C materials, three oxidation domains can be distinguished. Below 400°C, the oxidation reaction is not activated or takes a very long time. Between 400°C and 800°C, it can be reasonably assumed that oxidation is mainly uniform throughout the volume, due to the considerable pore rates. Above 800°C, surface oxidation phenomena predominate over volume mechanisms. In this study, the temperature range for describing oxidation corresponds to the second domain. The overall oxidation kinetics of C/C materials, denoted by the variable Δm, is assumed to follow an Arrhenius law [5], as reported in Eq 1., where E_a is the activation energy, the R perfect gaz constant, T the temperature, and A a material parameter to be defined :

$$\dot{\Delta m} = A \exp\left(-\frac{E_a}{RT(t)}\right) \tag{1}$$

Nevertheless, for the same mass loss obtained at different oxidation temperatures, the effect of oxidation on the mechanical properties are different, as shown in Figures 4 and 5. This means that the global variable Δm is not sufficient to describe the oxidation rate.

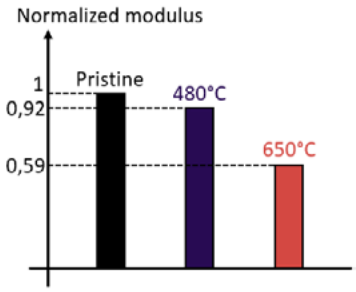


Figure 4. Effect of oxidation ($\Delta m = 5\%$) on the Young's modulus of the material under study.

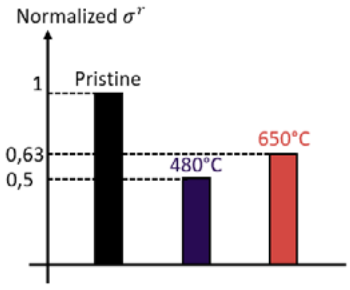


Figure 5. Effect of oxidation ($\Delta m = 5\%$) on the material's tensile strength σ^r.

To take account of this specifity, the idea is to create as many oxidation state variables as there are oxidation mechanisms to be described. In a first time, only two variables, homogeneous as mass loss, are considered : one to describe mechanisms occuring at low oxidation temperature (400°C), denoted Δm_1, and a second, Δm_2, for those occuring at higher temperature (800°C). Eq. 2 defines the evolution of these variables, and their relation to the measured global mass loss :

$$\Delta\dot{m} = \Delta\dot{m}_1 + \Delta\dot{m}_2 \quad \text{and} \quad \begin{cases} \Delta\dot{m}_1 = \zeta(T)\Delta\dot{m} \\ \Delta\dot{m}_2 = \big(1-\zeta(T)\big)\Delta\dot{m} \end{cases} \tag{2}$$

The term ζ corresponds to a logistic function, that allows the transition from one oxidation mechanism to another as a function of the oxidation temperature, as given in Eq. 3.

$$\zeta(T) = \frac{1}{2}\big(1-\tanh\big(\gamma(T-T_c)\big)\big) \tag{3}$$

Two coefficients control the transition between oxidation mechanisms: γ to calibrate the transition rate and T_c to define the transition temperature, as shown in Figure 6.

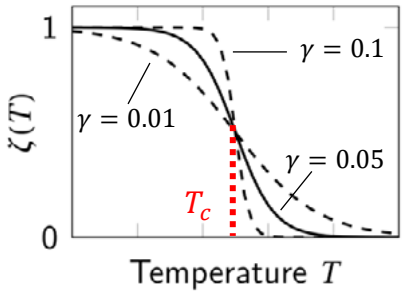


Figure 6. Representation of the logistic function ζ

Thanks to the introduction of the two variables Δm_1 and Δm_2, it is now possible to attribute different effects of oxidation on mechanical properties at low and high temperatures. Indeed, it is clear that the oxidation mechanisms associated with Δm_1 will predomine at temperatures lower than T_c, and vice versa the oxidation mechanisms associated with Δm_2 will predomine for temperatures higher than T_c.

2.2. Evolution law of the elastic compliance tensor due to oxidation without damage

In this part, we consider only the linear elastic part of the behavior (Eq. 4). The tensor $\mathbb{S}^0$ is the elastic compliance tensor at the initial state. The tensor $\mathbb{S}^{\mathrm{Ox}}$ corresponds to the one after oxydation. So, without oxydation $\Delta m = 0$, the two tensors are equal, meaning $\mathbb{S}^{\mathrm{Ox}} = \mathbb{S}^0$.

$$\boldsymbol{\varepsilon} = \mathbb{S}^{\mathrm{Ox}}(T, \Delta m_k) : \boldsymbol{\sigma} \tag{4}$$

The objective is to establish a law describing the evolution of the oxidized tensor $\mathbb{S}^{\mathrm{Ox}}$ as a function of temperature and the two mass losses associated to the different mechanisms. Considering the evolution of the compliance tensor as a function of time is a convient framework, as reported in Eq 5.

$$\frac{\mathrm{d}\mathbb{S}^{\mathrm{Ox}}(T, \Delta m_k)}{\mathrm{d}t} = \frac{\partial \mathbb{S}^{\mathrm{Ox}}}{\partial T}\dot{T} + \sum \frac{\partial \mathbb{S}^{\mathrm{Ox}}}{\partial \Delta m_k}\Delta\dot{m}_k \tag{5}$$

As described in Eq. 5, the evolution of the oxidized tensor due to the temperature is distinguished from the evolution due to the oxidation mechanisms. Firstly, the definition of the temperature-induced

variation of the compliance tensor is considered. Temperature has a particular effect on the C/C elastic stiffness. Research studies in the literature [4,6] indicate that the apparent stiffness increases with temperature up to about 1500°C, after which it decreases sharply, as shown in Figures 7 and 8.

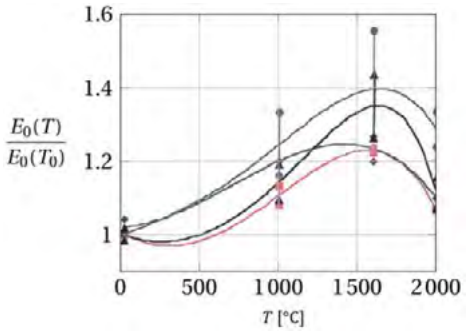


Figure 7. Effect of temperature on the stiffness of a C/C material [4]

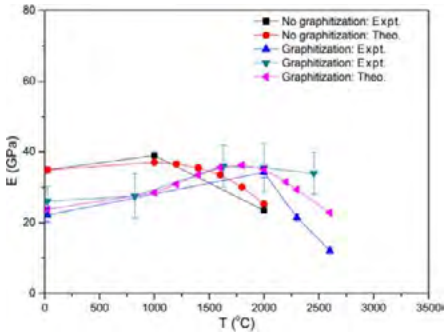


Figure 8. Effect of temperature and graphitization on the stiffness of a C/C material [6]

For now, the Young's modulus E_i and the shear modulus G_{ij} are assumed to be affected in the same way. The Poisson's ratios ν_{ij} are assumed to be constant due to measurement issues during experimental tests. Its means that all coefficients of $\mathbb{S}^{\mathrm{Ox}}$ are affected in the same manner. The chosen analytical expression for the Young's modulus is given by Eq. 6.

$$E^{\mathrm{Ox}}(T,\Delta m_k) = E^{\mathrm{Ox}}(T_0,\Delta m_k)\left(\frac{1}{1+\exp\left(\frac{T-T_s}{\alpha}\right)} + (T-T_0)\beta\right) \tag{6}$$

The coefficient T_s corresponds to the temperature at the maximum stiffness, α controls the shape of the peak, β controls the stiffness increase before the peak and T_0 is the ambient temperature.

Secondly, a definition of the oxidation-induced variation of the compliance tensor is considered. An expression for the evolution of the tensor $\mathbb{S}^{\mathrm{Ox}}$ due to oxidation is given by Eq. 7.

$$\sum \frac{\partial \mathbb{S}^{\mathrm{Ox}}}{\partial \Delta m_k}\Delta\dot{m}_k = \mathbb{S}^0(T)\,g\left(\Delta\dot{m}_k\right) \tag{7}$$

The effect of the oxidation on the evolution of the tensor $\mathbb{S}^{\mathrm{Ox}}$ is governed by the scalar function g expressed in Eq. 8. Two coefficients have been introduced : ξ_1 to calibrate the effect of the oxidation mechanism $\Delta\dot{m}_1$ on $\dot{\mathbb{S}}^{\mathrm{Ox}}$ and ξ_2 to calibrate the effect of $\Delta\dot{m}_2$.

$$g\left(\Delta\dot{m}_k\right) = \xi_1\,\Delta\dot{m}_1 + \xi_2\,\Delta\dot{m}_2 \tag{8}$$

To illustrate the oxidation process, let us consider an oxidation that takes place in an isothermal environment, *i.e.* $\dot{T} = 0$, and the temperature rise is instantaneous, as shown in Figure 9. The temperature T_{Ox} is the oxidation temperature. The time t_0 corresponds to the initial state and t_1 to the start of oxidation. The time $t_{\Delta m}$ corresponds to the time required to reach an oxidation rate of Δm and t is the current time after oxidation. Eq. 5 can be integrated with respect to the time through the oxidation path, between t_0 and $t > t_{\Delta m}$. At ambient temperature T_0, the material is not oxidized, or according to the Arrhenius law, over an extremely long time. So, the variation of $\mathbb{S}^{\mathrm{Ox}}$ between t_0 and t_1 as well as between $t_{\Delta m}$ and t can be neglected.

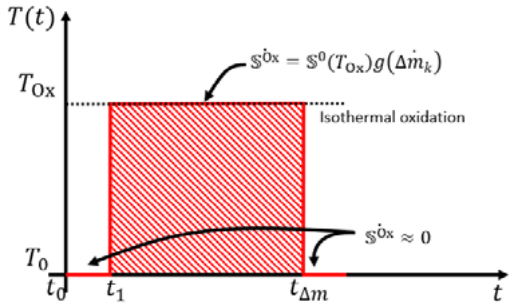


Figure 9. Thermal loading of the example

The calculations lead to Eq. 9, which describes the evolution of the normalized elastic modulus as a function of the oxidation rate, depending on the oxidation temperature T_{Ox}.

$$\begin{cases} \Delta m_1 = \zeta(T_{Ox})\Delta m \\ \Delta m_2 = \big(1 - \zeta(T_{Ox})\big)\Delta m \\ g(\Delta m_k) = \xi_1\,\Delta m_1 + \xi_2\,\Delta m_2 \\ \dfrac{E^{Ox}(T_{Ox}, \Delta m_k)}{E^0(T_{Ox})} = \dfrac{1}{1 + g(\Delta m_k)} \Leftrightarrow \dfrac{E^{Ox}(T_0, \Delta m_k)}{E^0(T_0)} = \dfrac{1}{1 + \dfrac{E^0(T_0)}{E^0(T_{Ox})} g(\Delta m_k)} \end{cases} \tag{9}$$

The expression for the shear modulus evolution is similarly assumed. Figure 10 shows the effect of the oxidation temperature T_{Ox} on the Young's modulus for several values of global mass loss. The purple crosses represent experimental measurements made at $\Delta m = 5\%$ for oxidation temperatures equal to 480°C and 650°C. The shape of the curves depends on the material coefficients γ, T_c, ξ_1 and ξ_2. For now, the lack of experimental data makes the identification of these coefficients difficult. Nevertheless, this model effectively describes the effects of oxidation on the elastic properties at low and high oxidation temperatures for a given mass loss. The decrease in the apparent modulus, shown in Figure 11, is similar to test results found in the literature for another C/C material [7].

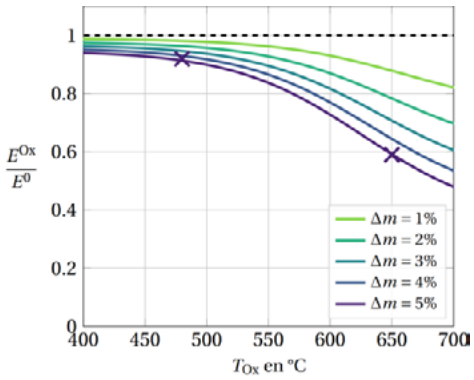


Figure 10. Evolution of the elastic modulus relative to the initial modulus as a function of T_{Ox} for several Δm.

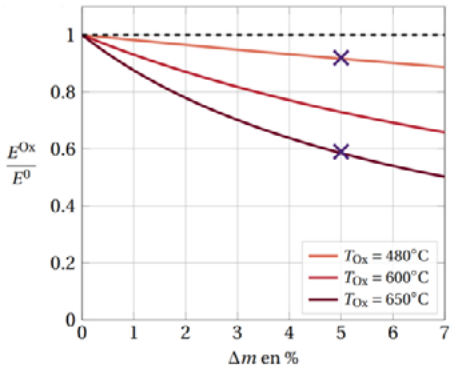


Figure 11. Evolution of the elastic modulus relative to the initial modulus as a function of Δm for several T_{Ox}.

2.3. Effect of oxidation on damage

The model considered to take into account the effect of damage on the material behaviour is OḊM for Onera Damage Model. This model was developed for static loading [9], and more recently for fatigue [10]. In this paper, only the static one part is considered for simulations. Some details about the

behaviour law, provided in Eq. 10, are given below. More details are provided in the literature [8,9,10].

$$\begin{gathered}\boldsymbol{\sigma} = \mathbb{C}^{\text{eff}} : (\boldsymbol{\varepsilon} - \boldsymbol{\varepsilon_0}) + \mathbb{C}^{\text{Ox}} : \boldsymbol{\varepsilon_0} \\ \mathbb{C}^{\text{eff}} = \left(\mathbb{S}^{\text{eff}}\right)^{-1} = \left(\mathbb{S}^{\text{Ox}} + \sum d_i \mathbb{H}_i\right)^{-1} \\ \dot{d}_i = (d_i^{\infty} - d_i) \left\langle \frac{\varepsilon_{\text{eq}_i}^{\max} - \varepsilon_{\text{eq}_i}^{0s}}{S_i^s} \right\rangle_+^{p_i^s} \left\langle \dot{\varepsilon}_{\text{eq}_i}^{\max} \right\rangle_+ \text{ and } \varepsilon_{\text{eq}_i} = \sqrt{y_i}\end{gathered} \tag{10}$$

Where $\boldsymbol{\sigma}$ is the stress, $\boldsymbol{\varepsilon}$ the total strain, $\boldsymbol{\varepsilon_0}$ the closure strain and $\mathbb{C}^{\text{Ox}}$ the non-oxidized elastic stiffness tensor. The effective tensor $\mathbb{C}^{\text{eff}}$ is degraded during the mechanical loading above a certain damage threshold. The scalar variables d_i are the damage variables representing the matrix meso-damages oriented at 0°, ±45° and 90° and an additional variable is considered through the out-of-plane direction of the material. The evolution of these variables is defined by non-linear differential equations, reported in Eq. 10. The different material parameters to be identified with the mechanical tests are: a threshold (occurence of the first crack) y_{0_i}, the kinetics of the damage evolution y_{c_i}, and the damage saturation d_i^{∞}. $\mathbb{H}_i$ are the effect tensors identified by homogenisation [8], using the elastic properties of the material. They are defined in such a way that the damage variables affect the elastic properties only when the cracks are opened, i.e. the unilateral aspect of the damage is guaranteed.

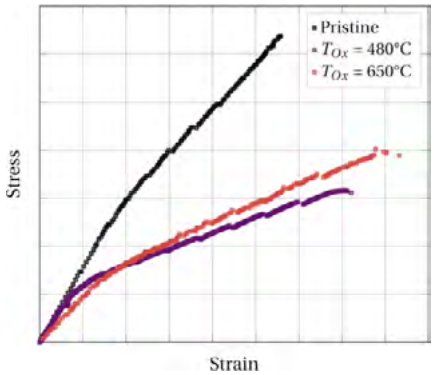


Figure 12. Envelope of the behaviour curves of the pristine and oxidized material ($\Delta m = 5\%$) for two different oxidation temperatures.

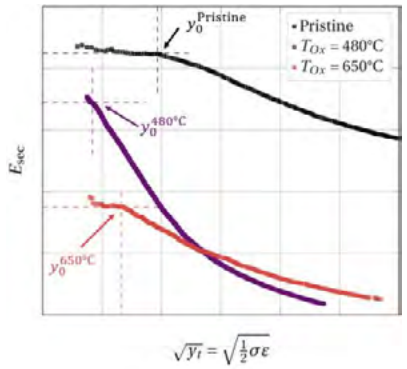


Figure 13. Evolution of the secant modulus during loading after oxidation as a function of the total energy.

Figure 12 shows the envelope of the behaviour curves. Linear elastic behaviour is at the beginning of the curves, followed by damaged behaviour. The damage threshold y_{0_i} can be measured graphically using Figure 13 from the point where the secant modulus drops.

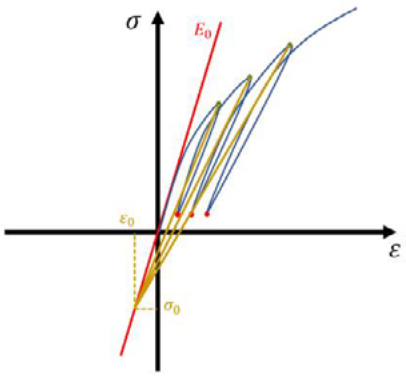


Figure 14. Definition of the closure strain.

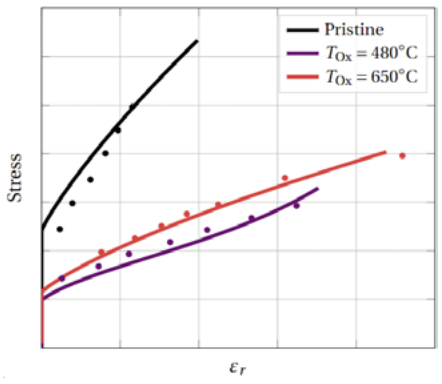


Figure 15. Identification of the closure strain using the measured permanent strains.

The damage threshold decreases as a function of oxidation, and appears to be lower at higher oxidation temperatures. This result needs to be confirmed by further measurements. An analysis of the effects of oxidation on the coefficients associated with the damage kinetics led to the conclusion that the damage saturation may not depend on the level of oxidation. The closure strain ε_0, defined in Figure 14, allows a precise description of the permanent strain after unloading. To identify the value of ε_0, the difference between the measured permanent strains, points reported in Figure 15, and those obtained numerically, lines in Figure 15, is minimized. Higher weights are affected to the measured large permanent strains in the minimization as their measurements are more reliable. Oxidation has therefore an important effect on the permanent strains. In addition, the closure strain allows residual strains to be accurately described in a simple manner.

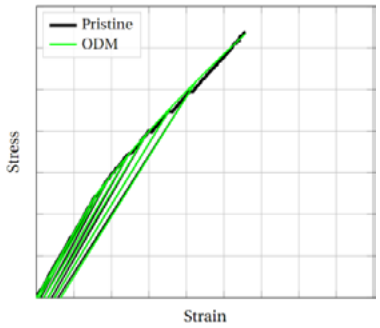


Figure 16. Stress-strain curve of the pristine material and the identified model.

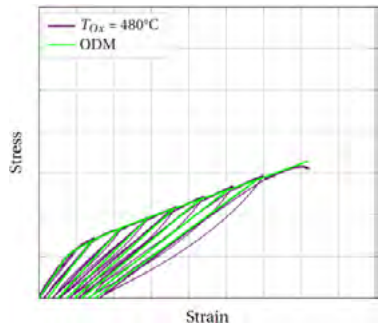


Figure 17. Stress-strain curve of the oxidized material ($T_{\mathrm{Ox}} = 480°C$, $\Delta m = 5\%$) and the identified model.

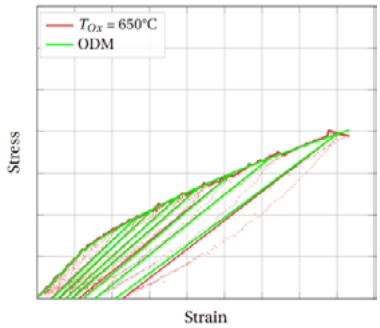


Figure 18. Stress-strain curve of the oxidized material ($T_{\mathrm{Ox}} = 650°C$, $\Delta m = 5\%$) and the identified model.

Once the damage threshold and closure strain have been identified graphically, the damage kinetics coefficient y_{c_i} can be determined. At this stage, all the coefficients are identified. The comparison between test and simulation for different oxidations can be seen in Figures 16 (pristine state with $\Delta m = 0\%$), 17 (oxidized at 480°C with $\Delta m = 5\%$), and 18 (oxidized at 650°C with $\Delta m = 5\%$) and the predictions are quite promising.

3. Conclusions

A formalism has been proposed to describe the oxidation state of C/C materials. For C/C materials, it has been established that for the same global mass loss, which is the commonly measured quantity to describe the oxidation state, is not fully relevant. Indeed, a high oxidation temperature degrades the elasticity tensor more than a low oxidation temperature for the same global mass loss. The main modeling idea is to assume that two oxidation mechanisms are in competition: at low temperatures, the mechanism noted $\Delta\dot{m}_1$ is larger than the mechanism $\Delta\dot{m}_2$, and vice versa at high temperatures. A Arrhenius-based model was proposed to predict the oxidation rate of each basic mechanism as a function of the oxidation time and the duration. Then, the effects of the oxidation states on the elastic properties but also on the damage indicators (onset of damage, permanent strain,) have been introduced in a continuum damage model. The predictions are in good agreement with the available experimental data, but additional tests are needed for validation.

In perspective, the effect of oxidation on the material parameters related to the damageable part of the model will be further investigated. This model is being implemented in a commercial finite element code. The effect of oxidation on fatigue behaviour will then be investigated.

References

[1] J.-C. Cavalier et F. Christin, *Matériaux composites thermostructuraux*, Plast. Compos., 1992, doi: 10.51257/a-v1-a7804
[2] Safran Landing Systems (safran-group.com)
[3] A. Raude, *Modélisation thermomécanique d'un composite carbone/carbone à texture complexe*, PhD thesis, Université de Bordeaux, 2018
[4] Mauchin, A. *Comportement mécanique à haute température de composites carbone/carbone*. PhD thesis, ENSIETA, 1997.
[5] M. Fradin, G. Couégnat, F. Rebillat, K. Haras, et G. L. Vignoles, *Designing porous C/C composites for oxidation resistance with an analytical model based on the kinetic and architectural features of fibers and matrix*, Compos. Part B Eng., vol. 263, p. 110825, 2023
[6] Cheng, T. *Understanding the ultra-high-temperature mechanical behaviors of advanced two-dimensional carbon-carbon composites*. Ceramics International, 46(13) :21395–21401., 2020
[7] X. Bertran, C. Labrugère, M. A. Dourges, et F. Rebillat, *Oxidation Behavior of PAN-based Carbon Fibers and the Effect on Mechanical Properties*, Oxid. Met., vol. 80, no 3-4, p. 299-309, 2013
[8] Maire, J. F. and Chaboche, J.-L. *A new formulation of Continuum Damage Mechanics (CDM) for composite materials*. Aerospace Science and Technology, (n°4) :247–257, 1997
[9] Marcin, L. *Modélisation du comportement, de l'endommagement et de la rupture de matériaux composites à renforts tissés pour le dimensionnement robuste de structures*, PhD thesis, Université Bordeaux 1, 2010.
[10] O. Sally, F. Laurin, C. Julien, R. Desmorat, et F. Bouillon, *Estimation de la rigidité résiduelle d'une structure composite oxyde/oxyde sollicitée en fatigue: comparaison essais/calculs*, 21ème Journées Nationales sur les Composites, École Nationale Supérieure d'Arts et Métiers (ENSAM) - Bordeaux, Jul 2019, Bordeaux, Talence, France. hal-02420768.

NONLINEAR DYNAMIC RESPONSE OF 2.5D WOVEN SIC/SIC CERAMIC MATRIX COMPOSITES: EXPERIMENTAL AND NUMERICAL INVESTIGATION

Maojing.RAN[1,2], Lu.ZHANG [1,2], Xiguang.GAO [1,2], Yingdong.SONG [1,2,3]

[1] Key Laboratory of Aero-engine Thermal Environment and Structure, Ministry of Industry and Information Technology, College of Energy and Power Engineering, Nanjing University of Aeronautics and Astronautics, Nanjing, China
Email: maojingran@nuaa.edu.cn
[2] Jiangsu Province Key Laboratory of Aerospace Power System, College of Energy and Power Engineering, Nanjing University of Aeronautics and Astronautics, Nanjing, China
Email: Luzhang@nuaa.edu.cn
[3] State Key Laboratory of Mechanics and Control Mechanical Structures, Nanjing University of Aeronautics and Astronautics, Nanjing, China
Email: gaoxiguang@nuaa.edu.cn
Email:ydsong@nuaa.edu.cn

Keywords: Nonlinear dynamic, ceramic matrix composite, constitutive mode

Abstract

During the service life of high-performance engines, essential components in the high-temperature parts undergo simultaneous exposure to high temperatures and aerodynamic vibrations. Elevated vibrations in high-temperature conditions not only influence engine performance, but also expedite structural fatigue, resulting in premature failure. Selected SiC/SiC composite materials, renowned for their superior high-temperature performance, present considerable advantages and application potential. However, under such multi-field coupling hush service conditions, ceramic matrix composites (CMCs) demonstrate complex dynamic nonlinear and hysteresis behavior, which limits the ability to predict material failure. Thus, establishing a dynamic failure model and efficient computational methods for high-temperature CMCs are crucial. These advancements will accelerate structural material design and validation, enabling real-time monitoring and prediction of failure behavior in high-temperature composites, with significant engineering application potential.

To address the aforementioned challenges, this study developed mechanical loading and vibration experiment systems to obtain constitutive and dynamic data, respectively, at 1100℃. Tension and loading-unloading mechanical tests were conducted to obtain the tensile curves and skeleton curves for 2.5D CMCs at 1100℃. These data were used to establish arbitrary cyclic tensile and compressive constitutive model. A numerical model was stablished to simulate the stress-strain curves. This model integrated matrix cracking, interface friction and fiber fracture, and is applicable to 3D stress states. The calibrated parameter values in the constitutive model were applied to calculate the response of CMCs to dynamic loading at 1100℃. Combining the constitutive model and an explicit dynamic numerical method, a nonlinear dynamic simulation model was established for CMCs structures, to predict the first-order natural frequency and amplitude of 2.5D CMCs at 1100℃. This work contributes a better understanding of the CMCs' behavior under high-temperature dynamic loads.

1. Introduction

Ceramic-matrix composites (CMCs) have become indispensable in replacing high-temperature alloys in aero-engines due to their high strength, temperature resistance, excellent toughness, crack resistance,

and low density. Exposed to prolonged high temperatures and vibrations, aero-engines exhibit significant behavioral changes, necessitating a nonlinear dynamic calculation methodology to accurately assess CMCs' responses in such environments.

The theoretical framework for analyzing composite materials has evolved considerably. Love [1] introduced the classical laminate-plate theory, simplifying calculations significantly. This theory was further developed by Mindlin [2] and Naghdi [3], who included considerations for transverse shear and extrusion, thus enhancing dynamic response accuracy. Advances by Nagesh and Hanagud [4] using finite element methods revealed natural frequency reductions due to delamination. Librescu and Nosier [5] further refined dynamic equations with transverse shear deformation and higher-order effects, surpassing classical theory accuracy.

Recent studies have further examined the vibrational behaviors of composites under varied conditions. Lee et al. [6] analyzed carbon-fiber epoxy composite plates in supersonic airflow at different temperatures, while Xia et al. [7] developed models for wall plate vibrations under constant temperatures, linking decreased vibration frequency to thermal stresses. Fu et al. [8] created a dynamic model for composite beams across different temperatures.

Experimental validations by Spivey et al. [9] on aircraft structures under thermal loads confirmed the effectiveness of finite element methods, clarifying modal characteristics in high-temperature environments. Jeyaraj et al. [10] observed natural frequency variations in composite plates across temperatures. Birman et al. [11] studied the impact of matrix cracking on woven CMCs, finding minimal effects on stiffness and natural frequency. Gao et al. [12] introduced a three-dimensional shear lag model to analyze the vibration response of unidirectional CMCs, integrating multiscale simulation with finite-element methods.

While much research has focused on laminate-plate composites, the dynamic responses of CMCs with complex woven structures in high-temperature environments have received less attention.

This study conducts tensile, loading and unloading, and vibration tests on 2.5D woven SiC/SiC composites under high-temperature conditions to establish a macroscopic intrinsic model, assess high temperature's impact on natural frequency, and predict the first-order natural frequency and amplitude.

2. Methods Experiment

2.1. Specimen and Material

The material investigated in this study comprised a 2.5D woven shallow-bend SiC/SiC ceramic matrix composite (CMCs). In order to enhance the material's mass density, we utilized Chemical Vapor Infiltration (CVI). Through multiple cycles of vapor deposition applied to the preform surface using CVI, the preform was filled with SiC matrix, effectively compacting the CMCs. Consequently, CMCs composite plates were produced, boasting a density of approximately 1.8 g/cm³ as determined by displacement method.

The 2.5D woven SiC/SiC composites were prepared with a thickness of 3 mm, and for processing the CMCs test pieces, waterjet cutting [13], selected for its superior processing efficiency and cutting precision, was employed.

The specimens obtained through water cutting were utilized for mechanical property tests, and their dimensions and physical conFigureurations are depicted in Figure 1. The overall length of the specimen measured 200 mm, with a clamping end length of 25 mm, width of 12 mm, test section length of 100 mm, and width of 6 mm.

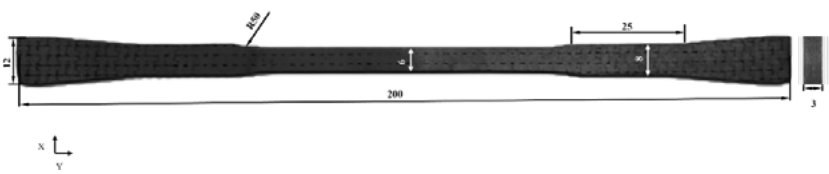


Figure 1. Dimensional drawing and picture of the dog bone specimen of 2.5D woven CMCs(mm)

Additionally, water jet cutting was utilized to procure rectangular specimens for dynamic response testing. These specimens measured 143 mm in length, 10 mm in width, and 3 mm in thickness. The clamping end was positioned on one side of the rectangle, featuring a clamping length of 20 mm, as depicted in Figure 2.



Figure 2. Dimensional drawing and picture of the rectangular specimen of 2.5D woven CMCs (mm)

2.2. Experimental Method

2.2.1. Intrinsic structure response test

Tension and loading-unloading mechanical tests were performed to obtain the tensile curves and skeleton curves for 2.5D CMCs at 1100℃. These data were utilized to establish an arbitrary cyclic tensile and compressive constitutive model.

To conduct static tensile, loading, and unloading tests on 2.5D woven SiC/SiC composites at 1100℃, a test system illustrated in Figure 3 was devised in this study. The test system primarily comprised a fatigue testing machine, high-temperature furnace and temperature control device, vacuum apparatus, water circulation cooling system, and strain measurement device.

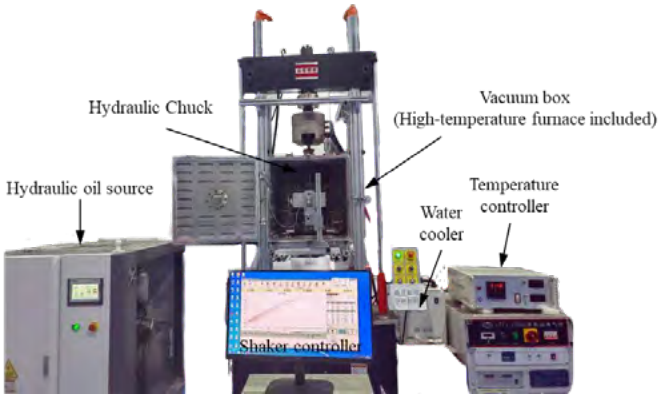
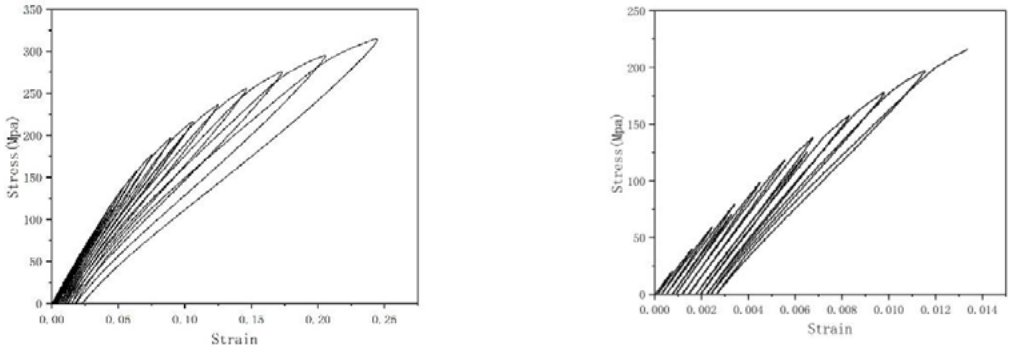


Figure 3. High temperature tensile, loading and unloading test system

The tensile test was executed under force loading at a loading rate of 0.05 kN/s until fracture occurred in the test specimen. For loading-unloading tests, force-controlled loading was employed at a loading rate of 0.05 kN/s, and loading paths were governed by a programmed sequence. Initially, tensile loads were applied until reaching the specified load, followed by unloading and reloading according to the program's parameters. Multiple loading-unloading cycles with decreasing maximum loads were included to validate the arbitrary nature of loading-unloading and the randomness of vibrational loads, thereby mitigating potential anomalies, as depicted in Figure 4.



(a) 25℃ (b) 1100℃

Figure. 4 Loading and unloading curves and skeleton curves of SiC/SiC composite.

The skeleton curves depicting cyclic loading and unloading stress–strain behaviors of the 2.5D woven CMCs at various temperatures closely mirrored the overall shape and trend observed in the monotonic tensile curve. These curves exhibited three distinct segments: initial linear, nonlinear, and secondary linear sections. The specimens' strength under cyclic loading and unloading conditions notably lagged behind that of monotonic tensile test specimens. This disparity stemmed from frictional forces between internal fibers, the matrix, and the interfacial layer, encompassing warp and weft yarns along with different transverse and longitudinal layers. Such frictional forces dissipated energy, consequently diminishing material strength [14-16].

At room temperature, the stress–strain curves of the 2.5D woven CMCs in the low-load range of the skeleton curves displayed almost linear profiles with minimal hysteresis, suggesting negligible frictional damage and energy dissipation. Conversely, in the high-load range, hysteresis loops formed in the cyclic loading and unloading stress–strain curves, with the loop area expanding alongside increasing loads. This occurrence arose from heightened interfacial frictional damage as load intensified, leading to gradual reduction in interfacial shear stress and increased interfacial debonding length. Consequently, residual strain and energy dissipation during loading and unloading augmented, contributing to a decline in material elastic modulus. Notably, the history of maximum load influenced the hysteresis loop's configuration [17].

In scenarios where tensile stress persisted at the maximum load point of the hysteresis loop, the stress–strain curve followed a monotonic tensile trajectory. This was attributed to the Ceramic-matrix's low fracture toughness, rendering it resistant to damage under cyclic loading, thereby exhibiting a "memory effect" within the hysteresis loop [18].

Comparatively, the high-temperature cyclic loading and unloading stress–strain curve largely retained its characteristics observed at room temperature. However, it no longer precisely mirrored the hysteresis loop of room-temperature loading and unloading, particularly in traversing through the historical maximum load point. This deviation became more pronounced with escalating temperatures. The weakening of initial interfacial bonding, expansion of interfacial slip zones, and exacerbation of interfacial wear at higher temperatures led to additional material damage during unloading and reloading processes. This observation underscores that elevated temperatures exacerbate material degradation [19].

2.2.2. Dynamic tests

Experimental setups suitable for high-temperature vibration tests were developed for 2.5D woven SiC/SiC composite flat-plate structures at 1100℃, as shown in Figure 5. This apparatus, designed to facilitate vibration performance testing, incorporated a vibrator, a high-temperature furnace, and precision measurement equipment, among other components. The system enabled vibration tests and dynamic response analyses under elevated temperatures.

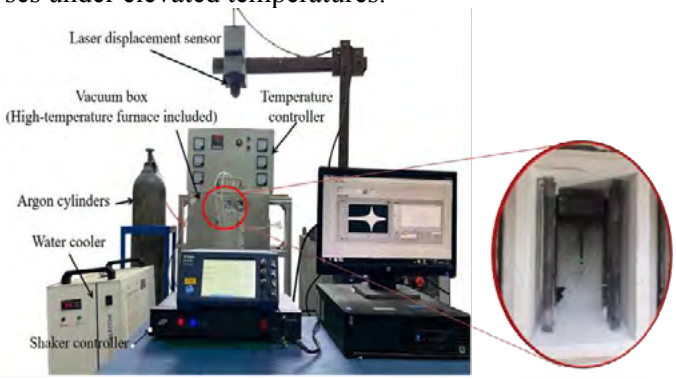


Figure. 5. High-temperature vibration experiment system

The high-temperature furnace, equipped with water cooling and gas filling functionalities, maintained a controlled environment. It featured quartz glass windows and a high-temperature resistant glass cover plate to minimize heat loss while ensuring a sealed environment. The vibration table, connected to the furnace through a vacuum-sealed interface, supported fixtures made of 310S stainless steel.

During the experiments, the vibrator's sampling frequency was set to 8192 Hz with an accuracy of 0.1μm. Initial tests involved a rapid sinusoidal sweep across a broad frequency range to estimate the first-order resonance frequencies of the undamaged CMCs. Subsequent tests increased the vibration load to

examine the material's nonlinear stress-strain characteristics. The acceleration excitation of the vibration table was set to 5 m/s², scanning frequencies near the first-order resonance frequency at a rate of 0.5 Hz/s. This method successfully captured the first-order natural frequency of the material at 1100℃. Fourier transform analysis converted time-domain data to frequency-domain signals for precise vibration analysis.

Figure 6 illustrates the vibration sweep tests on the 2.5D woven CMCs plates, demonstrating how frequency sweeping through the first natural frequency induced resonance and a significant displacement increase at 25 ℃ and 1100 ℃. This result confirmed the test data's integrity and showed a gradual increase in the first-order natural frequency with rising temperature, which, however, decreased at 1100 ℃. This behavior reflects changes in material stiffness due to temperature variations, influencing the natural frequency. Below 1100 ℃, as temperature increases, the difference in thermal expansion coefficients between the fibers and matrix decreases, enhancing material stiffness and increasing natural frequency. Above 1100 ℃, however, high temperatures cause SiC matrix degradation, fiber damage, and matrix cracks, reducing the composite's structural stiffness and lowering its natural frequency.

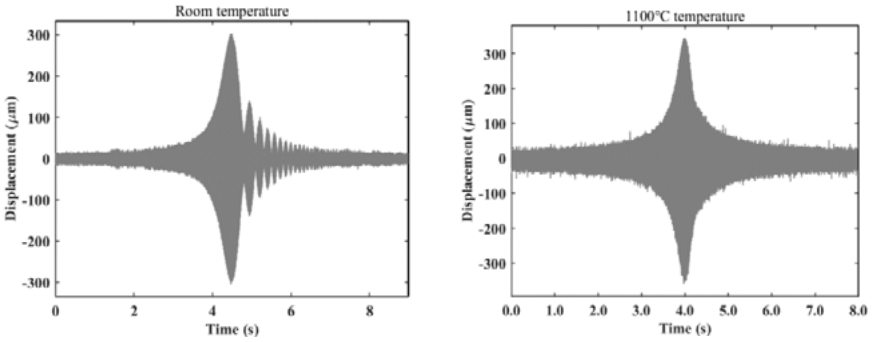


Figure. 6 Vibration time domain plot

2.3. Numerical modeling

The vibrations of CMCs beams involve individual units undergoing arbitrary cyclic tensile and compressive loads. Accurate simulation of these vibrations necessitates an intrinsic model that captures the repetitive stress behaviors under vibrational conditions. Establishing this model requires high-temperature tensile tests on 2.5D woven CMCs.

We utilized the cyclic loading and unloading stress-strain curves from these tests to model the behavior of 2.5D woven CMCs at high temperatures. This model, derived from the skeleton curves' trends, establishes a relationship between the historical maximum strain and the stress-strain response during each cycle.In the low-load range, linear fitting addressed the loading and unloading behaviors, where the modulus decreased in line with the skeleton curve. At high loads, direct fitting of the hysteresis loop was impractical due to the lack of a memory effect and material damage from high temperatures. However, the sub-loop displayed nearly linear behavior with minimal hysteresis, suggesting that friction damage had largely stabilized after the initial cycle. This finding highlighted the role of historical maximum stress in assessing material damage.

In conclusion, the completion of fitting arbitrary cyclic tensile and compressive stress–strain curves for 2.5D woven CMCs in 1100℃ environments provides a comprehensive understanding. Based on this macroscopic intrinsic model, stress at a given time can be calculated when the stress and strain at that time, the strain at a previous time, and the historical maximum stress and its corresponding strain are known., as shown in Eqs. 1:

$$^{t+\Delta t}\sigma = f(^{t}\sigma, ^{t}\varepsilon, ^{t+\Delta t}\varepsilon, \varepsilon_{\max}, \sigma_{\max}) \tag{1}$$

A finite-element model of the CMCs beam, matching the dimensions of the test specimens, was developed to simulate the effects of sinusoidal gravity fields at varying frequencies. This model helps to mimic the conditions of vibration tests effectively.

The structure of the cantilever beam is simple, and during its bending vibration, normal stress acts along the axial direction. Thus, each small element on the beam can be considered to undergo arbitrary tensile

and compressive behavior. Therefore, it is reasonable to use a CMCs arbitrary loading and unloading constitutive model considering temperature effects for dynamic response calculations, which can reduce computational complexity.
The vibration of the fixture base has been reflected in the equation through the global inertial load , and the displacement of the vibrator is very small and can be ignored in the simulation. Hence, this boundary condition is set:

$$u(x = 0) = v(x = 0) = w(x = 0) = 0 \tag{2}$$

$$\boldsymbol{f} = (0, 0, f)^T = (0, 0, \bar{f} \sin \omega t)^T \tag{3}$$

Based on the principle of virtual displacement, the dynamic control equation for CMCs is established as follows:

$$\int_\Omega \sigma_{ij} \delta \varepsilon_{ij} dV - \int_\Omega \rho \ddot{u}_i \delta u_i dV - \int_\Omega c \dot{u}_i \delta u_i dV - \int_{\Gamma 2} q_i \delta u_i ds - \int_\Omega \rho \bar{f} \sin(\omega t) \delta u_i dV = 0 (i, j = 1, 2, 3) \tag{4}$$

Where u, v, and w represent displacements in the x, y, and z directions, respectively.

By balancing (stress) differential equations and geometric differential equations, the control equation is simplified to:

$$\boldsymbol{K}^T \delta \boldsymbol{a} - \ddot{a}^T \boldsymbol{M}^T \boldsymbol{a} - \dot{\boldsymbol{a}}^T \boldsymbol{C}^T \delta \boldsymbol{a} = \boldsymbol{Q}^T \delta \boldsymbol{a} \tag{5}$$

Where:

$$\begin{cases} \boldsymbol{M} = \sum_e \int_{\Omega^e} \rho \boldsymbol{G}^{eT} \boldsymbol{N}^{eT} \boldsymbol{N}^e \boldsymbol{G}^e \mathrm{d}V \\ \boldsymbol{C} = \sum_e \int_{\Omega^e} c \boldsymbol{G}^{eT} \boldsymbol{N}^{eT} \boldsymbol{N}^e \boldsymbol{G}^e \mathrm{d}V \\ \boldsymbol{K} = \sum_e \int_{\Omega^e} \boldsymbol{G}^{eT} \boldsymbol{B}^{eT} \boldsymbol{\sigma}^e \mathrm{d}V \\ \boldsymbol{Q} = \sum_e \int_{\Gamma^e} \boldsymbol{G}^{eT} \boldsymbol{N}^{eT} \boldsymbol{q} \mathrm{d}S \end{cases} \tag{6}$$

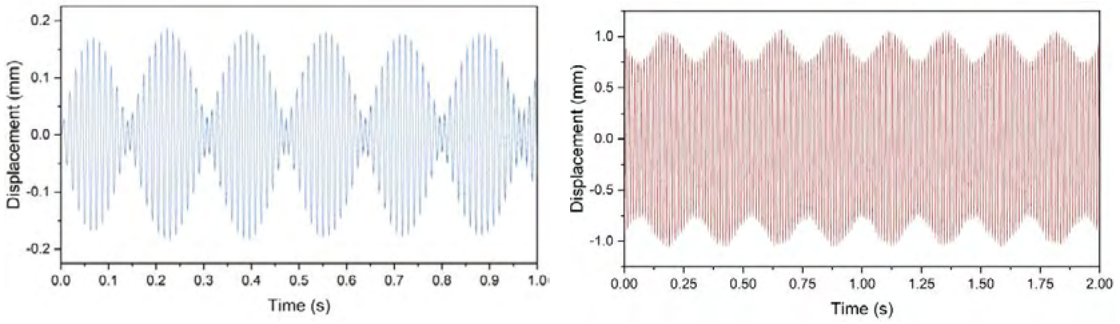
It should be noted that K here is not the stiffness matrix, but a vector with the same dimensions as the degrees of freedom of the structure. Writing the dynamic equation in this form facilitates the subsequent solution of the dynamic equation. Although not a stiffness matrix, it effectively reflects the stiffness of CMCs, and material nonlinearity is manifested in K.
This study employs the center difference method to solve the dynamic equations. This method is based on the finite difference method rather than the derivative of displacement with respect to time. The velocity and acceleration are obtained using the first-order and second-order derivatives of displacement, respectively. Utilizing the center difference method not only avoids matrix inversion but also accelerates the calculation speed and does not produce mathematical discontinuity points in the calculation process of the intrinsic model, effectively avoiding iterative operations and saving space in the calculation. This method is very suitable for calculating the nonlinear vibration response of CMCs.
Based on the established macroscopic arbitrary tensile and compressive intrinsic model of 2.5D woven CMCs in different temperature environments, a self-developed solver was programmed to import the material properties. Subsequently, leveraging the theory of the central difference method, self-developed solver was developed to calculate the vibration response.

3. Conclusions

The nonlinear constitutive behavior of CMCs is calculated using the shear-lag model, and the parameters involved in the calculation are shown in Table 1.

Table 1. Parameters of constitutive model.

Item	Value	Item	Value
E_m / GPa	369.75	τ_i /MPa	50
E_f / GPa	223.80	r_f / μm	6
α_m /$\times 10^{-6}$ / ℃	4.53	L_{sat} / mm	0.54
$\alpha_f \times 10^{-6}$ / ℃	0.1252	ΔT / ℃	-1000
ν_f	0.2	σ_{mR} /MPa	140
ν_m	0.8	m	2



(a) dynamic response with small damage (b) dynamic response with large damage

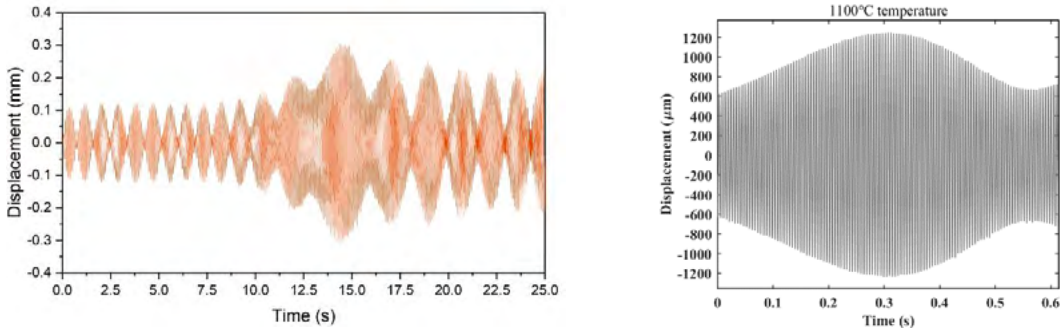


Figure.7.. Simulation dynamic responses of the CMCs

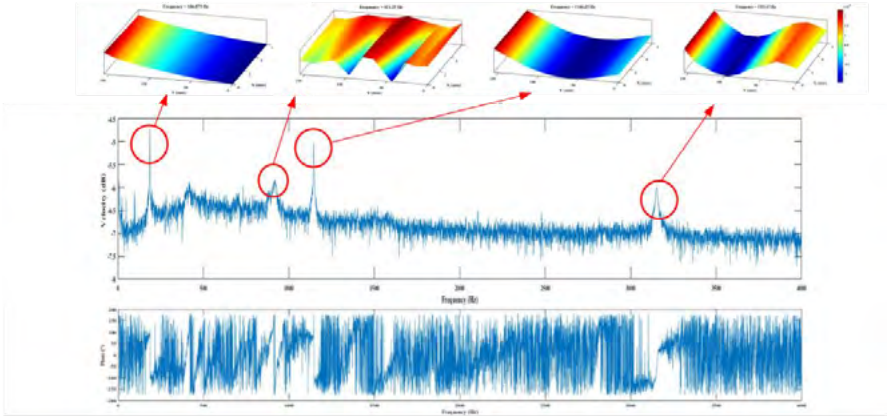


Figure. 8.. Simulation of nonlinear dynamic response

Table 2. First-order natural frequency test and simulation comparison and deviation.

Tmperature (°C)	25	1100
Experiment (Hz)	212	198
Simulation (Hz)	211.9	199

Acknowledgments
The authors are grateful for the financial supports provided from the National Science and Technology Major Project (Grant No. Y2019-I-0018-0017).

References
[1] A.E.H. Love, On the Small Free Vibrations and Deformations of the Elastic Shells, 1988.
[2] R.D. Mindlin, Influence of Rotatory Inertia and Shear on Flexural Motions of Isotropic, Elastic Plates, Journal of Applied Mechanics, vol. 18, 1951.
[3] P.M. Naghdi, ON THE THEORY OF THIN ELASTIC SHELLS, Quarterly of Applied Mathematics, vol. 14, 1955.
[4] S. Hanagud, Delaminations in smart composite structures - A parametric study on vibrations, 1990.
[5] L. Librescu, A. Nosier, Response of laminated composite flat panels to sonic boom and explosive blast loadings, AIAA Journal, vol. 28, 1990, pp. 345-352.
[6] W. Xia, Z. Yang, Vibration Analysis to Composite Panels in Thermal Environment, Chinese Journal of Applied Mechanics, 2005.
[7] Y. Fu, Y. Chen, J. Zhong, Analysis of nonlinear dynamic response for delaminated fiber–metal laminated beam under unsteady temperature field, Journal of Sound & Vibration, vol. 333, 2014, pp. 5803-5816.
[8] N.D. Spivey, HIGH-TEMPERATURE MODAL SURVEY OF A HOT-STRUCTURE CONTROL SURFACE, 2010.
[9] I. Lee, D.M. Lee, I.K. Oh, Supersonic Flutter Analysis of Stiffened Laminated Plates Subject to Thermal Load, Journal of Sound & Vibration, vol. 224, 1999, pp. 49-67.
[10] P. Jeyaraj, N. Ganesan, C. Padmanabhan, Vibration and acoustic response of a composite plate with inherent material damping in a thermal environment, Journal of Sound & Vibration, vol. 320, 2009, pp. 322-338.
[11] V. Birman, L.W. Byrd, Effect of Matrix Cracks on Damping in Unidirectional and Cross-Ply Ceramic-matrix Composites, Journal of Composites Materials, vol. 36, 2002, pp. 1859-1877.
[12] X. Gao, D. Han, J. Chen, H. Dong, Y. Song, Numerical and experimental study on the nonlinear dynamic response of a Ceramic-matrix composites beam, Ceramics International, vol. 44, 2018.
[13] J. Jiao, H.P. Qiu, X.Q. Li, J.H. Luo, Y. Wang, The pyrolysis processing of polycarbosilane studied by TG, XRF, IR, XRD, and XPS, Key Engineering Materials, vols. 512-515, 2012, pp. 965-970.
[14] J.W. Lee, I.M. Daniel, Progressive transverse cracking of crossply composite laminates, Composites Part B Engineering, vol. 34, 2003, pp. 473-480.
[15] S.S. Lee, W.W. Stinchcomb, Damage Mechanisms and Fracture Modes in Nicalon / CAS-II Laminates, Key Engineering Materials, vols. 120/121, 1996, pp. 227-256.
[16] S. Zhu, M. Mizuno, Y. Kagawa, Y. Mutoh, Monotonic tension, fatigue and creep behavior of SiC-fiber-reinforced SiC-matrix composites: a review, Composites Science & Technology, vol. 59, 1999, pp. 833-851.
[17] J. Wang, Y. Xiao, K. Inoue, M. Kawai, Y. Xue, Modeling of nonlinear response in loading-unloading tests for fibrous composites under tension and compression, Composites Structures, vol. 207, 2018, pp. 894-908.
[18] H. Mei, L. Cheng, Comparison of the mechanical hysteresis of carbon/ceramic-matrix composites with different fiber preforms, Carbon, vol. 47, 2009, pp. 1034-1042.
[19] S. Zhang, X. Gao, H. Dong, Y. Song, S. Pang, Effects of gradual matrix crack closure on the constitutive behavior of SiC/SiC composites upon unloading, Ceramics International, vol. 43, 2016, pp. 1839-1842.

IMPACT INDUCED PROGRESSIVE DAMAGE MODELLING IN WOVEN FIBRE REINFORCED COMPOSITES CONSIDERING STRAIN RATE SENSITIVITY

Theme : Material and Structural Behavior - Simulation & Testing

Sub theme : Fracture and damage

Keywords : woven FRP, strain rate dependent, impact damage, delamination, failure, damage

Type of submission : Oral communication

List of authors :
* Speaker
Jakov RATKOVIĆ[1]*, Darko IVANČEVIĆ[2]
[1] University of Zagreb Faculty of Mechanical Engineering and Naval Architecture, Department of Aeronautical Engineering, Ivana Lučića 5, Zagreb, CROATIA
[2] University of Zagreb Faculty of Mechanical Engineering and Naval Architecture, Department of Aeronautical Engineering, Ivana Lučića 5, Zagreb, CROATIA

In this study, progressive intralaminar and interlaminar damage models suitable for simulation of impact phenomena in woven fibre reinforced plastic (FRP) composites are introduced. In order to reduce costs of development and production of structural components in aeronautical, space, military and automotive industry, development of high-fidelity numerical models suitable for capturing the mechanical behaviour of FRP composites in all loading regimes is inevitable. Moreover, in order to accurately predict the load bearing capabilities and to be able to design the structural elements correctly, taking the strain rate effects in consideration is also imperative, as concluded in a large number of researches. Thus, by implementation of this comprehensive mesoscale numerical model in the commercial finite element method (FEM) software package Abaqus/Explicit as a VUMAT user-defined material model subroutine, an effort is made in advancing the current state of available woven FRP material models.
Intralaminar failure initiation and damage evolution is based on the Continuum Damage Mechanics (CDM) approach, whereas the interlaminar damage is modelled based on the Fracture Mechanics (FM), i.e., the Cohesive Zone Model (CZM) in the form of the decoupled bilinear traction-separation law. Both failure initiation and damage propagation are considered to be strain rate dependent. Hence, empirical logarithmic functions are utilized to scale both intralaminar material strengths and fracture toughness values based on the reference strain rate value and experimentally obtained data in quasi-static loading conditions. The fitting parameters of the empirical strain rate effect curves were then fitted according to dynamic experimental results. Material degradation is captured by a total of seven intralaminar damage variables, and a single interlaminar damage variable. Removal of both cohesive (representing interfaces) and solid (representing FRP plies) finite elements is utilized in order to simulate the complete failure of the material point. Characteristic finite element length is used in the CDM approach in order to overcome the mesh dependency of the solution. Inherent oscillations of numerically obtained values in explicit integration procedures are treated by a low-pass filter-like algorithm.
In order to verify and validate the developed model, impact simulations at various impact energies, i.e., initial velocities, were performed according to experimental and numerical investigations found in the available literature. The results obtained by utilization of developed material model demonstrate a good agreement with the referent ones.

Bibliographic reference

[1] L. A. Coles, A. Roy, and V. Silberschmidt, Ice Vs. Steel: Ballistic Impact of Woven Carbon/epoxy Composites. Part II – Numerical Modelling, *Engineering Fracture Mechanics*, 225; 106297, 2019.

[2] J. V. Calvo, N. Feito, M. Henar Miguélez and E. Giner. Modeling the delamination failure under compressive loads in CFRP laminates based on digital image correlation analysis. *Composite Structures*, 287; 115265, 2022.

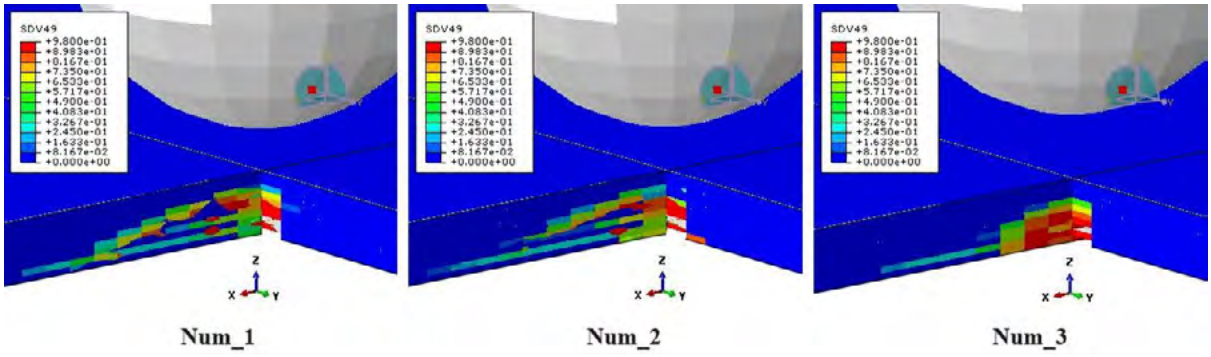
[3] X. Lu, M. Ridha, B.Y. Chen, V.B.C. Tan, T.E. Tay. On cohesive element parameters and delamination modelling. *Engineering Fracture Mechanics*, 206; 278–296, 2019.

[4] I. K. Giannopoulos, M. Yasaee, and N. Maropakis, Ballistic Impact and Virtual Testing of Woven FRP Laminates, *Journal of Composites Science*, 5(5); 115-129, 2021.

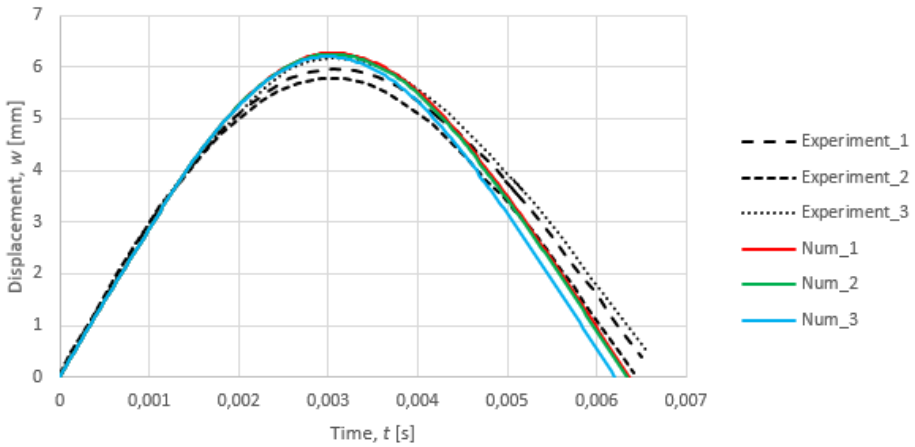
[5] M. Heidari-Rarani, M. Sayedian. Finite element modeling strategies for 2D and 3D delamination propagation in composite DCB specimens using VCCT, CZM and XFEM approaches. *Theoretical and Applied Fracture Mechanics*, 103(4); 102246, 2019.

Attached documents

Weft fibre tensile damage variable distributions for the three simulations



Displacement history - comparison of experimental and numerical results



ENHANCING THE REPAIR PERFORMANCES OF GLASS/EPOXY WIND-TURBINE BLADES USING A NOVEL RESISTANCE-WELDING APPROACH

Rishad Rayyaan[1], Yunhao Liang[2], Yu Shi[3]

[1]School of Design, University of Leeds, LS2 9JT, United Kingdom
Email: r.rayyaan@leeds.ac.uk, Web Page: https://ahc.leeds.ac.uk/design/staff/5835/dr-rishad-rayyaan

[2]Department of Physical, Mathematical and Engineering sciences, University of Chester, CH1 4BJ, United Kingdom
Email: y.liang@chester.ac.uk,

[3]Leeds Institute of Textiles and Colour, School of Design, University of Leeds, LS2 9JT, United Kingdom
Email: y.shi2@leeds.ac.uk, Web Page: https://ahc.leeds.ac.uk/design/staff/5709/professor-yu-shi-fimmm-ceng

Keywords: resistance welding, heating element, single lap shear, wind turbine blades, glass/epoxy composites

Abstract
Commercial wind turbine (WT) blades that are now being operational globally, are primarily made of glass-reinforced composites using epoxy or polyester matrix systems, mainly epoxy. The industry is rapidly growing (2100 TWh currently; 17% growth annually) with a forecast of 7400 TWh by 2030. The average lifespan of a WT is 20-25 years, which signifies the importance of repairing the damaged blades. Amongst the methods that have been exploited so far, resistance welding shows eminent potential, due to its ease of operation, promptness of the repair process, and cost effectiveness. Resistance welding was exploited previously for repairing thermoplastic composites. But in this project, repair of thermoset composites was evaluated using thermoplastic welding medium. The project focused on parametric optimisation of resistance welding, evaluation of welding via single lap shear strength, and COMSOL multiphysics modelling to examine the homogeneity of heat-distribution across the welding region. Stainless steel mesh and carbon nonwoven sheet were used as heating elements, while polymethyl methacrylate and thermoplastic polyurethane were used as welding medium. The highest single lap shear strength was shown as 6.4 MPa when nonwoven carbon sheet was used along with thermoplastic polyurethane. COMSOL modelling with a custom-designed heating element showed improvement in thermal homogeneity; however, further modifications will be required to better optimisation of welding.

1. Introduction

Wind turbines (WTs) are pioneering now globally in terms of renewable energy and this industry shares 7.33% of the global electricity generation, which is double of what was in 2015 before Paris Agreement [1]. For the EU including the UK, this figure is 17% [2]. Solar and wind energy are two of the major sources for renewable energy globally, which combinely share 23% of global energy market. The new target to meet by 2030 is to capture 42.5% of the energy market by renewable sources to meet the climate and energy goals [3]. While these stats implies a substantial growth of the WT industry, it can be envisaged that the necessity of operations, repair and maintenance of wind turbine blades (WTBs) will significantly rise [2]. Operations and maintenance may account for 25% to 40% of the levelised cost of energy [4].

As the necessity of the operations relating to repair and maintenance can be substantiated from the above discussion, it can also be noteworthy that the average lifespan of a wind-turbine blade is around 20 to 25 years [4]. In 2022, 19 gigawatt (GW) of WT plants were installed in the EU, and the figure will be 129 (GW) by the period of 2027 [2]. Understandably, the industry now heavily focuses on repair and maintenance of WT plants.

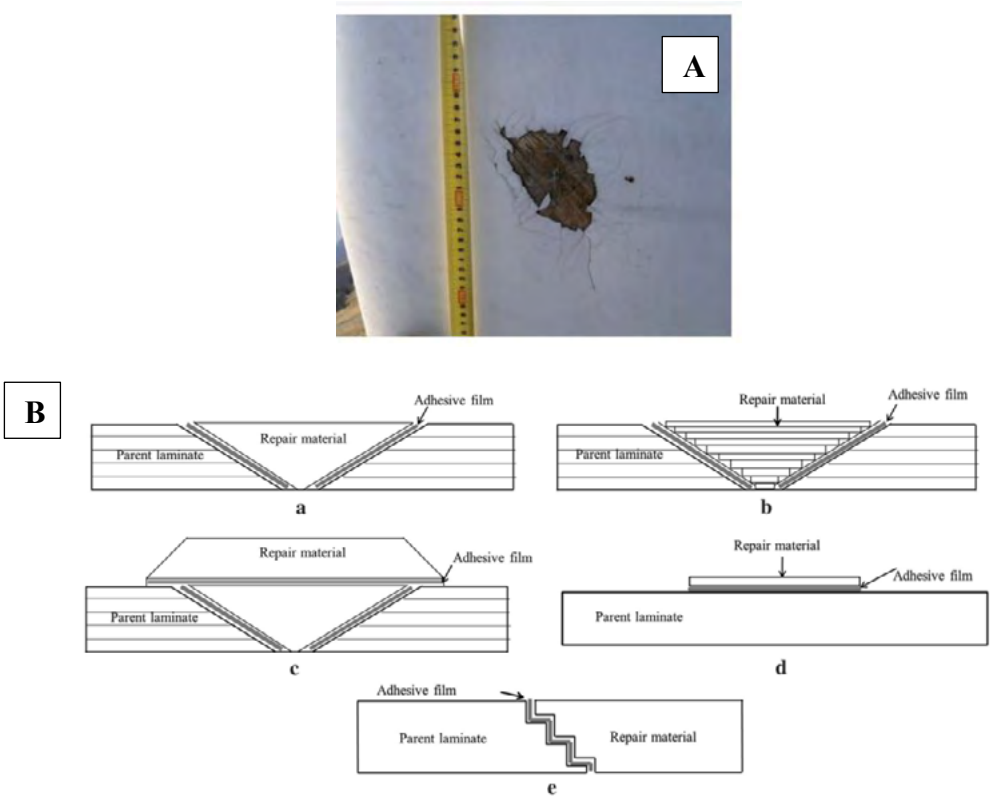


Figure 1 (A) A damaged WTB [15]; (B) Types of bonded joints [16]

This research work focuses on repairing wind turbine blades (WTBs) by bonded joints. As the blades are continuously operational and exposed to the environment, different types of damages including delamination, failure at joints, and leading-edge erosion occur frequently [5]. A typical example can be seen in **Figure 1**A. In terms of common damages and the corresponding repairs, Xiao et al. (2020) have conducted an intensive review, wherein, attaching repair patch to the damaged area has been shown as a frequently occurring repair method [6]. The most commonly used materials for WTBs are thermoset glass fibre/epoxy composites (GFC). Some of the common types of repair patches are shown in **Figure 1**B. RW is a technique, wherein, the damaged interface is subject to localised heating, with precision time, temperature, and an effective welding media, which joins the repair patch to the damaged surface. In this method, electrical energy is transmitted through an heating element (HE), which are commonly comprised of stainless-steel mesh (SSM), carbon nonwoven sheet (CNWS), or printed HE. The transmitted electrical current eventually generates heat energy within the HE, which is then dissipated to the welding medium, mainly polymeric materials, located on the top and/or at the bottom of the HE. A schematic diagram of a welding stack is shown in **Figure 2**. When the current passes through for a certain amount of time, the temperature rises up to the melting point of the polymers. When the molten polymers get cooled, it joins the repair patch to the damaged substrate. Normally, the heat generation and the melting of the polymers happen in less than 40 seconds of current flow, and the cooling down of the materials through convection (of heat to the surrounding air) also happens within a few minutes.

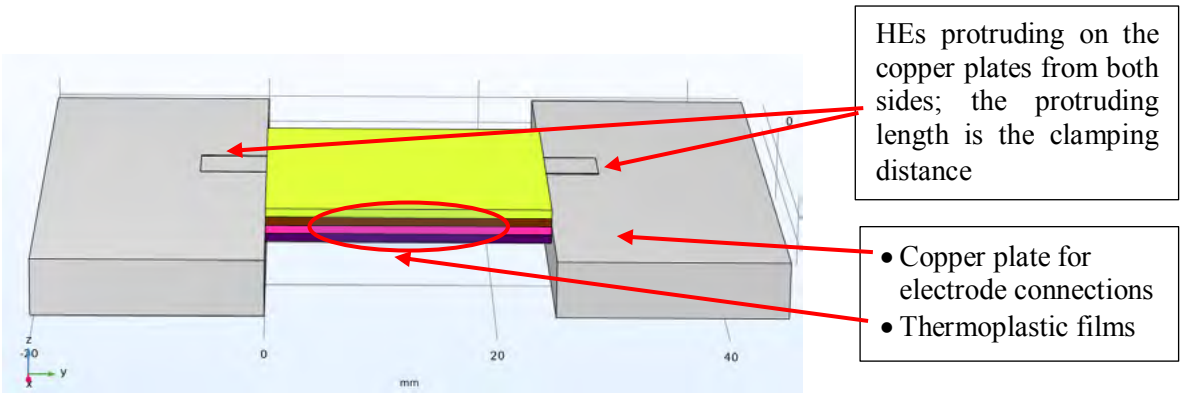


Figure 2 A schematic diagram of a single lap shear test coupon (Z-axis is magnified 5 times)

So far, a number of research works have been found to have critically evaluated resistance welding of thermoplastic composites with differet polymers as welding mediums and different HEs such as: CNWS, SSM and printed HE with conductive ink [7-13]. However, one research can be found from Yunhao and Shi (2023), wherein, two GFC composites were bonded via RW using SSM as a HE, and polymethyl methacrylate (PMMA) as a welding medium [14]. However, the homogeneity of heat distribution, evaluated via COMSOL multiphysics was found as an area of development. Due to the lack of homogeneity, the single lap shear strength was found as 3.6±0.3 MPa, which was less than the benchmark sample made by them: 5.1±0.4 MPa. The less strength was attributed to the 'edge-heating' phenomena as shown in **Figure 3**.

In this current study, resistance welding was evaluated via single lap shear strength, using SSM and CNWS as HEs. As welding medium, TPU film was used. Besides, a custom-designed HE was evaluated via COMSOL multiphysics modelling to improve the heat-distribution homogeneity.

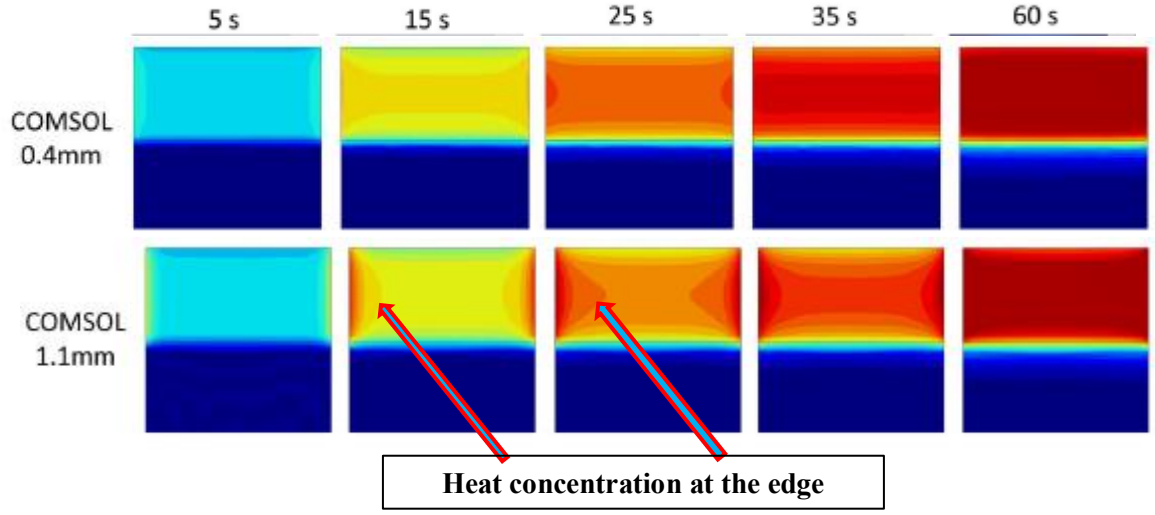


Figure 3 The surface between the upper PMAA film and the upper GFC panel; results from two clamping distances are shown [14]

2. Materials

2.1 Heating element

Plain woven SSM with 30 µm diameter and 110 µm opening width, 66 µm thickness with resistivity as shown in **Figure 4** A. Also, we have procured a range of nonwoven mesh with different areal densities (20 to 80 g/m2) and surface resistivity (27 to 0.4 ohm/square); an example is shown in **Figure 4**B. Secondly, carbon nonwoven sheet with 35 g/m2 areal density and 0.38 ohm/square and 0.48 ohm/square.

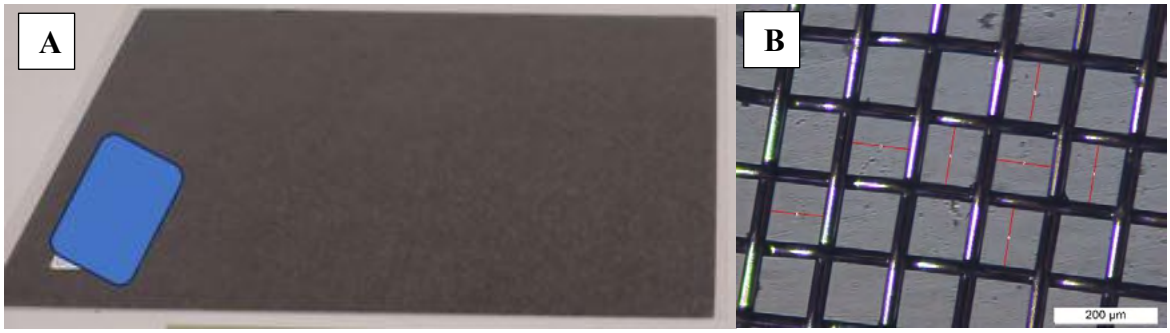


Figure 4 (A) SSM; and (B) Nonwoven Carbon mesh (A4 size)

2.2 Welding medium:

DUPONTTM TE-11C TPU films has been procured from DUPONT, as shown in **Figure 5**, with 133 g/m^2 areal density, 110 µm thickness, 160 ºC melting point, 270 ºC degradation temperature, and 1500 J/kg-K heat capacity.



Figure 5 TPU film

3. Experimentals

3.1 Composite panels:

Glass/epoxy preforms were purchased from SHD composites under the commercial brand name VTC 401, with 290 gsm (gram per square metre). The panels were made using vacuum bagging at the following curing cycle: 80 ºC for 4 hours and 120 ºC for 1 hour; the glass transition temperature, T_g, was 130 ºC. **Figure 6** shows the laminates. 8 layers of prepregs were used and the cured laminate thicknesses were measured as 1.77 ± 0.04 mm, with around 52% fibre volume fraction.

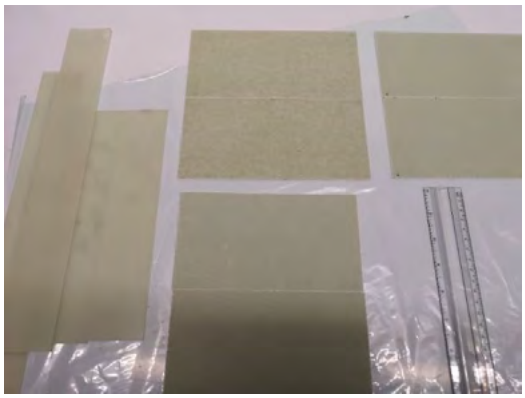


Figure 6 Glass/epoxy composite panels

3.2 Resistance welding

A welding rig has been constructed to produce test coupons for single lap shear (SLS) strength as shown in **Figure 7** A. The welding region of a test coupon was 25.4 mm^2. Firstly, the TPU films and the HEs were cut according to the appropriate sizes, as shown in **Figure 7** B to construct the welding stack. In this project, the typical welding stack was constructed with: 2 TPU films at the top, 2 SSMs or 1 CNWS in the middle, and 2 TPU films at the bottom. The stack was then placed between two laminates,

wherein, the HE protrudes at a certain length from the edges. Those two protruding HEs are then gets in contact with the copper plates from both sides by two side clamps, as shown in **Figure *8*** B. Finally, the copper plates were connected to the power supply unit (Elektro-Automatik 9080; 60A – 80V – 1500 W).



Figure 7 (A) RW setup, and (B) cut pieces of films and SSM

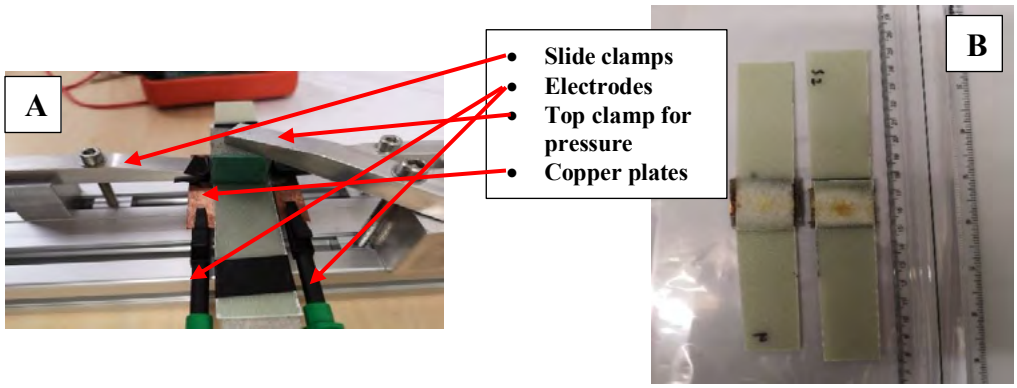


Figure 8 (A) The welding setup; and (B) Welded samples.

An important controlling point of this RW is to minimise heat dissipation via convection as much as possible. To do this, we have put a cement block on the top of the welding region, as shown in **Figure 9**.

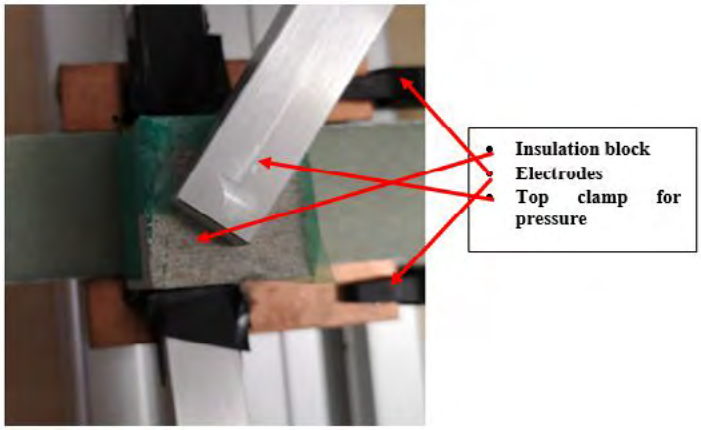


Figure 9 Top view of the RW rig

3.2 Single lap shear (SLS)

Single lap shear tests were carried out using an Instron 3369 machine, as shown in **Figure 10**.

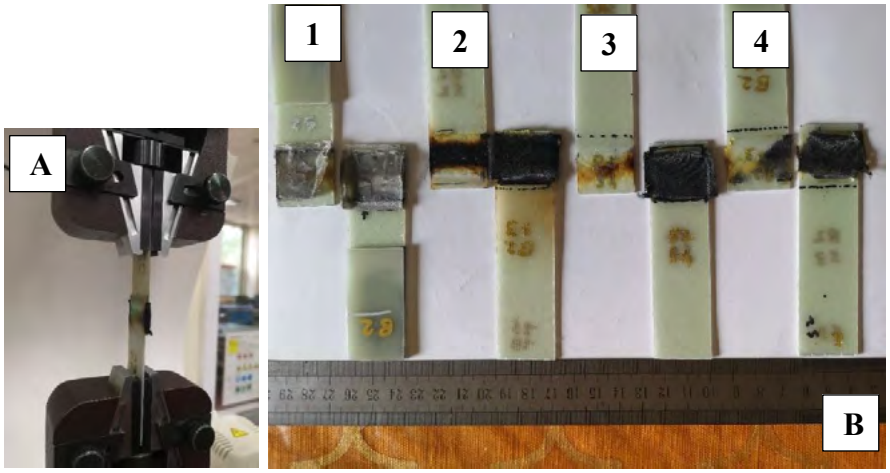


Figure 10 (A) Instron 3369 machine; and (B) SLS tested coupons



Figure 11 Damaged test coupons from SSM as HE; 50W, 1mm, 50s; 5.9 ± 0.3 MPa

4. Optimisation of welding parameters

$$Weight\ of\ the\ TPU\ films, m\ (in\ kg) = areal\ density\ \times area\ of\ film \times no.of\ layers$$

$$Heat\ required\ to\ melt\ the\ films, E = m \times c\ \times \Delta\theta \ldots\ldots\ldots\ldots \textbf{\textit{Equation 1}}$$

$$c = heat\ capacity\ in\ Jkg^{-1}K^{-1}$$

$$\Delta\theta = difference\ between\ room\ temp.\ and\ melting\ temp.$$

For each SLS test coupon, with a welding stack consists of 4 layers of TPU film, around 83 Joule heat will be required. To generate that heat, the following equation can exhibit the required power density:

$$E = P \times t \ldots\ldots\ldots\ldots\ldots\ldots\ldots\ldots\ldots\ldots \textbf{Equation 2}$$

$$or, R = \frac{V^2}{E}.t$$

$$Wherein, E = energy$$

$$P = power\ in\ watt, W$$

$$V = voltage\ in\ V$$

$$R = resistance\ in\ ohm, \Omega$$

$$t = time\ in\ seconds\ for\ the\ electricity\ to\ pass\ through$$

If electricity runs for 30 seconds and apply 5 volts, a resistance of 9Ω will generate the required amount of heat to melt the TPU films fully, for a typical SLS coupon made in this project. And with this setup, 2.8 Joule of heat will be produced in each second, and 1.9 Joule heat energy will be required to increase the overall temperature by each degree. Provided that some of the heat energy, for example, 15% will be dissipated via conduction and convection, the welding time can be increased by 5 sec to match that. Based on the above equations, two welded samples are shown in
Figure *8* B. The sample on the right has a brown patch visible in the mid region. This was due to running the current for a longer period (more than 50 seconds).

5. Discussion of single lap shear tests and COMSOL modelling

Table **1** summarises the results for SLS. It can be seen that the TPU and CNWS combination showed the best result among the lots. Compared to SSM and PMAA combination, TPU and CNWS showed better result due the presence of carbon fibres. The mechanical interlocking between carbon and thermoplastic polymers was better compared to that between SSM and polymers, due to lesser frictional coefficient of stainless-steel. Although, the tensile strength of PMAA is higher than that of TPU [17], PMAA was not used due to its unavailability for commercial grade films. **Figure 10B.1** shows a SLS

Table 1 Single lap shear strength results

Heating element	Welding medium	Single lap shear strength (MPa)	Welding thickness (mm)	Power density (watt)	Welding time (seconds)	Composite type	Fibre volume fraction
CNWS	TPU	6.4±0.8	1.2±0.15	50	50	GFC	53%
SSM	TPU	4.2±0.9	0.9±0.14	50	50	GFC	51%
SSM	PMAA	5.9±0.3	1.3±0.21	50	50	GFC	54%

coupon with SSM. The other three coupons (B.2, B.3, and B.4) are comprised of CNWS. It can be observed that the failure mode was cohesive. In terms of parametric optimisation, the calculations based on **Equation 1** and **Equation 2** did not take into account the heat dissipation from HE and welding regions to the air. Therefore, it was observed that when the welding time was 30s, the welding was not fully completed, but running for around 50 sec created some burning marks, as shown in **Figure 10B.2.** This probably had occurred from polymeric films being risen above their degradation temperature. **Figure 11** shows the damaged test coupons from SSM as HEs; the brown marks at the edges indicates heat-concentration during welding. Therefore, further optimisation will be required to obtain a better welded region, which may result in higher SLS strength. In order to further evaluate the welding parameters and to minimise 'edge-heating', a COMSOL multiphysics modelling is shown in **Figure 12**. The model still shows 'edge-heating' phenomena to some extent, but further modification of the custom-designed HE can potentially solve this problem.

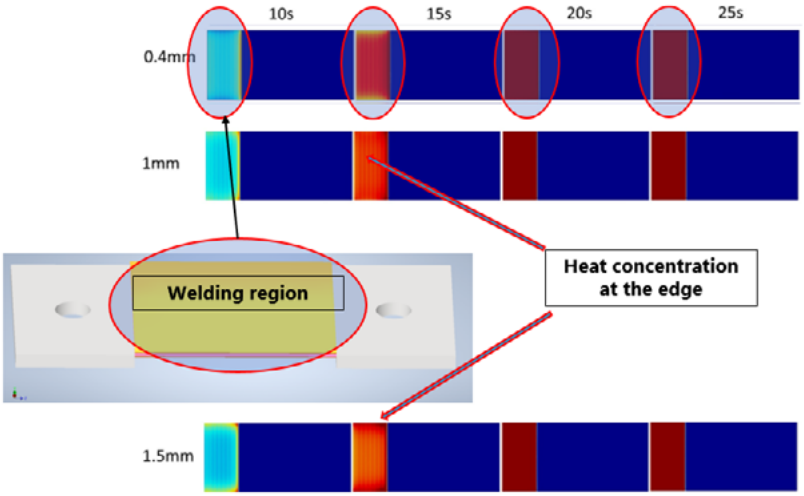


Figure 12 COMSOL modeling; custom-designed HE with PMAA film; the surface is in between the PMAA film and top GFC

6. Conclusion

A novel resistance welding solution has been investigated to provide repair services for thermoset glass/epoxy wind turbine blades, using thermoplastic welding medium. When stainless-steel mesh was used as a heating element along with polymethyl methacrylate (PMAA) film as a welding medium, the single lap shear strength was found to be 5.9 MPa. However, when carbon nonwoven sheet was used as a heating element with thermoplastic polyurethane (TPU) as a welding medium, the lap shear strength was found to be slightly higher, 6.4 MPa. Although the tensile strength of PMAA is higher than that of TPU, the higher lap shear strength from TPU and nonwoven sheet can be plausibly attributed to the better mechanical interlocking of the nonwoven carbon with the thermoplastic polymers. Fractography revealed some burning marks across the welded regions, which might be stemmed from lack of homogeneity towards heat-distribution. Hence, a custom-designed heating element was generated and

COMSOL multiphysics modelling was conducted, which still exhibited heat-concentration at the edges; however, in a lesser extent. Further modification of the heating element, thus, will be required to ensure a better homogeneity in heat distribution, which will eventually lead to obtaining an improved mechanical strength for the welded regions. Furthermore, thermoplastic films with higher load bearing properties, along with carbon nonwoven sheet as a heating element will potentially improve the welding strength. Further research of this project thus aims to produce a novel-designed heating element for resistance welding to repair offshore wind-turbine blades that will have superior bonding strength.

Acknowledgement
The research leading to this paper is part of the Romain project that has received funding from the European Union's Horizon Europe research and innovation programme. UK participants are supported by UKRI grant number: 10101311.

References

1. Fernandez, L., *Share of wind electricity generation worldwide 2010-2022*. 2023, Statista.
2. Costanzo, G., G. Brindley, and P. Cole, *Wind Energy in Europe*. 2023.
3. European_Environment_Agency. *Share of energy consumption from renewable sources in Europe*. 2024 [cited 2024 27/05/2024]; Available from: https://www.eea.europa.eu/en/analysis/indicators/share-of-energy-consumption-from?activeAccordion=ecdb3bcf-bbe9-4978-b5cf-0b136399d9f8.
4. Pfaffel, S., S. Faulstich, and K. Rohrig, *Performance and reliability of wind turbines: A review.* energies, 2017. **10**(11): p. 1904.
5. Wang, W., et al., *Review of the typical damage and damage-detection methods of large wind turbine blades.* Energies, 2022. **15**(15): p. 5672.
6. Xiong, X., et al., *Resistance welding technology of fiber reinforced polymer composites: a review.* Journal of adhesion science and technology, 2021. **35**(15): p. 1593-1619.
7. Totla, H.S., et al., *Resistance welding analysis of thermoplastic composite structures in aeronautical applications.* International Journal on Interactive Design and Manufacturing (IJIDeM), 2023: p. 1-13.
8. Wei, D., et al., *Influence of electrical heating metal mesh and power density on resistance welding of carbon fiber/PEEK composite.* Polymers, 2022. **14**(13): p. 2563.
9. Reis, J.P., M. de Moura, and S. Samborski, *Thermoplastic composites and their promising applications in joining and repair composites structures: A review.* Materials, 2020. **13**(24): p. 5832.
10. Brassard, D., M. Dubé, and J.R. Tavares, *Resistance welding of thermoplastic composites with a nanocomposite heating element.* Composites Part B: Engineering, 2019. **165**: p. 779-784.
11. Villegas, I.F. and H.E. Bersee, *Characterisation of a metal mesh heating element for closed-loop resistance welding of thermoplastic composites.* Journal of Thermoplastic Composite Materials, 2015. **28**(1): p. 46-65.
12. Deng, S., et al., *Thermoplastic–epoxy interactions and their potential applications in joining composite structures–A review.* Composites Part A: Applied Science and Manufacturing, 2015. **68**: p. 121-132.
13. Panneerselvam, K., S. Aravindan, and A.N. Haq, *Study on resistance welding of glass fiber reinforced thermoplastic composites.* Materials & Design, 2012. **41**: p. 453-459.
14. Liang, Y. and Y. Shi, *Computational and experimental study on the resistance welding process of a glass fiber-reinforced epoxy-based composite with thermoplastic interlayer adherent.* Polymer Composites, 2024.
15. Katsaprakakis, D.A., N. Papadakis, and I. Ntintakis, *A comprehensive analysis of wind turbine blade damage.* Energies, 2021. **14**(18): p. 5974.
16. Budhe, S., M. Banea, and S. de Barros, *Bonded repair of composite structures in aerospace application: a review on environmental issues.* Applied Adhesion Science, 2018. **6**: p. 1-27.
17. Olabisi, O. and K. Adewale, *Handbook of thermoplastics*. 2016: CRC press.

A NUMERICAL-EXPERIMENTAL METHODOLOGY TO DETERMINE THE TEMPERATURE-DEPENDENT THERMOPHYSICAL PROPERTIES OF CARBON FIBER REINFORCED COMPOSITE MATERIALS EXPOSED TO FIRE

Abderrahmane Rhardane[1], Benjamin Batiot[1], Thomas Rogaume[1], and Damien Halm[1]

[1]Institut PPrime / UPR3346 CNRS, Université de Poitiers, ISAE-ENSMA, 1 av. Clément Ader 86360 Chasseneuil-Futuroscope, France
Email: abderrahmane.rhardane@ensma.fr
Email: benjamin.batiot@univ-poitiers.fr
Email: thomas.rogaume@univ-poitiers.fr
Email: damien.halm@ensma.fr

Keywords: composites, fire, thermophysical properties, numerical-experimental, inverse analysis

Abstract
During a fire, the composite material is exposed to an external heat flux and a rising pressure, undergoing chemical and physical change that affects its thermal, mechanical and physical properties as temperature rises. To anticipate fire safety concerns, CFD simulations can be used at the structural scale in the design phase. The models developed for this goal require an identification of the thermophysical properties of the material, which can be obtained from experimental testing. This identification can be difficult, given their temperature-dependent change with the phases of thermal decomposition.

This paper proposes a simple methodology for this task. A thermophysical model combines mass-loss kinetics and heat transfer to simulate temperature change in the material. A modified cone calorimeter test provides the necessary experimental data for the calibration of the thermophysical properties using inverse analysis.

1. Introduction

High-pressure filament-wound composite cylinders have become the most common option for hydrogen fuel transport due to the lightweight nature and mechanical performance of the material. The alignment of carbon fiber-reinforced resin tapes in the direction of maximum stress provides a strong load-bearing element for the vessel. However, safety concerns dictate that the vessel should withstand its load-bearing capacity in the case of a fire. It is then of primordial importance that the material demonstrates high fire resistance, controlled by its thermophysical properties.
The identification of the thermophysical parameters can be difficult [1-3]. This is due to the fact that the properties of the material vary with the temperature as the mass undergoes thermochemical change under fire. Moreover, the coupling between the kinetics of decomposition that happen at the low scale and the global thermal behaviour at the larger scales must be taken into account. In the uncoupled analysis done by Hidalgo et al. [3], the heat equation is first solved with the assumption of an inert material and using effective thermophysical properties, then the remaining mass is estimated in the pyrolysis model. This of course assumes a decoupling between the two phenomena, which explains the further assumptions taken as the imposed heat flux changes. Tranchard et al. [2] used a two-step decomposition model as a basis for the thermal model, where temperature-dependent thermophysical properties of both virgin and fully degraded materials were measured. In this study, discrepancies between the experimental profiles

of temperature and those predicted by the model were found, highlighting the difficulty of accurately identifying the heat flux at the exposed surface.
In the proposed study, a multi-step kinetic model is also introduced and coupled with the thermal model where the thermophysical properties are expected to depend on the temperature and the mass loss kinetic aspect of decomposition. This comprehensive model is used to simulate a cone calorimeter test, where the temperature profiles are also experimentally measured at specific depths. This establishes a basis for the inverse analysis to identify the thermophysical properties at different steps of decomposition.

2. Model and boundary conditions

2.1. Thermal decomposition equations

In this model, the overall density of the material evolves as a function of the constituents of each reaction i, considering a unit volume, as shown in the following:

$$\frac{\partial \rho}{\partial t} = \rho_0 \sum_{i=1}^{N} \left(- \sum_{\gamma \in R_i} r_\gamma + \sum_{\delta \in P_i} \nu_\delta r_\delta \right) \tag{1}$$

where ρ_0 denotes the overall density of the virgin material, r_δ the production rate of products P_i and r_γ the consumption rate of the reactants R_i. ν_δ is a stoichiometric coefficient which takes into account the reduction of mass due to the decomposition and the evaporation of reaction gases. In a single-step kinetic model, it is assumed that a single reaction converts a homogeneous mass $\rho_{\gamma,0}$ into a product, with a remaining reactant mass $\rho_{\gamma,e}$. The mass loss rate follows an Arrhenius function [2]:

$$r_\gamma(t) = \frac{\partial \rho_\gamma}{\partial t} = -\rho_{\gamma,0} \left(\frac{\rho_{\gamma,0} - \rho_{\gamma,e}}{\rho_{\gamma,0}} \right)^{n_\gamma} A_\gamma \cdot e^{-\frac{E_{a,\gamma}}{RT}} \tag{2}$$

where R is the universal gas constant, A and E_a are the pre-exponential factor and the activation energy of the Arrhenius model, respectively. n is the reaction order. For a multi-step model, it is assumed that density ρ_0 undergoes consecutive steps of the same equation (Eq. 2), with the product of each step being the reactant of the next. It is therefore convenient to consider mass m as a vector for simple calculations. In the case where a reaction converts one reactant into a single product, the consumption and production rates are equal (with the stoichiometric coefficient dictating the conversion rate).

2.2. Heat transfer equations

From energy conservation principles, the heat equation governing temperature T evolution (including transient heat transfer) for a 1D system can be written as:

$$\rho_s C_{p,s} \frac{\partial T}{\partial t} = \frac{\partial}{\partial x} \left(\lambda_s \frac{\partial T}{\partial x} \right) + \dot{q} \tag{3}$$

The 3 thermal properties are the density ρ_s, heat capacity $C_{p,s}$ and conductivity λ_s. $\dot{q}$ is the heat source. To account for the enthalpy of reaction ΔH_r during pyrolysis, the heat source includes:

$$\dot{q}_{pyr} = \sum_{i=1}^{N} r_i \Delta H_{r,i} \tag{4}$$

Since the previous equation is applied to a homogenised material, the thermal properties are dependent on the evolution of the reaction steps as well as temperature. Due to the difficulty of measuring the said properties as the material undergoes decomposition, the mixture laws proposed by Tranchard et al. [2] are used, using only the apparent properties at the beginning and end of the reaction step. For instance, the heat capacity will be calculated using the following mixture law:

$$C_{p,s} = \frac{1}{\rho_s} \sum_{\delta=1}^{N} \rho_i C_{p,i} \tag{5}$$

where the densities are calculated from the reaction rates using Eq. (1).

2.3. Boundary conditions

The heat transfer thermal problem posed above is applied to a modified cone calorimeter test where the top surface of the sample is exposed to a uniform heat flux from the cone source, with conditions that allow for the exchange of heat through radiation and convection. The bottom surface, on the other hand, is isolated. In order to capture the evolution of temperature inside the material, a special mould was used whereby thermocouples can be inserted at specific distances inside the sample, as illustrated in Figure 1. The presence of the thermocouples is assumed not to disturb the heat transfer along the thickness.

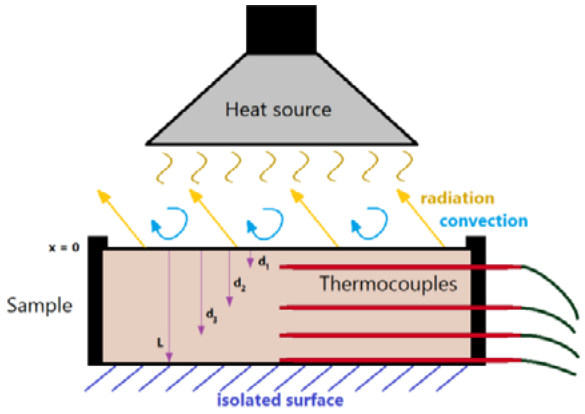


Figure 1. Modified cone calorimeter test with thermal boundary conditions shown.

The net heat flux on the surface exposed to the continuous heat source from the cone is the sum of both contributions from the convective and radiative heat transfer with the surrounding ambient air:

$$-\lambda_s \frac{\partial T}{\partial x}(x=0,t) = \dot{q}_{conv} + \dot{q}_{rad} \tag{6}$$

The convective part is expressed as a function of the temperature-dependent convective heat transfer coefficient $h(T)$:

$$\dot{q}_{conv} = h(T)(T - T_\infty) \tag{7}$$

while the radiative part includes both the flux from the energy source and the thermal radiation emitted by the surface following the Stefan-Boltzmann law:

$$\dot{q}_{rad} = \epsilon\sigma(T^4 - T_\infty^4) \tag{8}$$

where T_∞ is the ambient temperature of the gas flame, ϵ is the emissivity of the material, σ is the Stefan-Boltzmann constant. On the isolated back surface, the heat flux is null:

$$-\lambda_s \frac{\partial T}{\partial x}(x=L,t) = 0 \tag{9}$$

The kinetic parameters A_γ, $E_{a,\gamma}$, n_γ and ν_γ are first to be determined from a TGA decomposition curve, then the rest of the model's thermophysical properties must be identified by inverse analysis from the cone calorimeter test.

3. Materials and experimental data

The material used is a carbon fiber-reinforced thermoplastic resin (PA11) composite. Small scraps of the composite material were extracted for TGA under air atmosphere, with the temperature rising from 40°C to 900°C at a heating rate of 10°C/min. As shown in Figure 2, the decomposition shows 3 peaks. In the first step, oxidation of the resin in the range 300-380°C reduces the mass by about 3-4%. The higher peak in the second step represents the pyrolysis of the resin which accompanies a rapid decrease in mass, reaching a value of 0.08g.s^{-1} around 440°C. The third peak of resin decomposition is associated

with the oxidation of the residue between 480°C and 600°C. As the experimental curve from Figure 3 demonstrates, the final mass represents 69.37%, which is the mass of the non-decomposed carbon fibers. In the cone calorimeter test [5], samples of the same material of total surface 100mm² (with an exposed surface of 88.36mm², as required in ISO 5660 [6]) is used. Since the insertion of thermocouples leads to incorrect mass measurements, 2 sets of samples are used: the first is the standard test where the mass loss is measured accurately without interference from the thermocouples, and the second set where mass measurements are ignored, as thermocouples measure the evolution of temperature at 4 specific heights: 1mm, 3.3mm, 5.6mm and 6.6mm (using the middle of the top surface as a reference point). The cone calorimeter apparatus is conducted under air with a heat flux of 50kW.m^{-2}.
As shown in Figure 4 (below), a reduction in mass begins after about 30s, and the total mass gradually decreases until about 600s, reaching a value close to 68% of the initial mass. Figure 5 demonstrates that the mass loss kinetics in the cone calorimeter test undergoes 2 peaks, the first peak around 100s shows the decomposition of the top surface which then acts as an isolating barrier for the bottom surface, that is until enough heat is transferred to accelerate their decomposition as the peak is reached after 400s.

4. Simulation results: identification of the model parameters

4.1. Kinetic parameters

As shown in Figure 2, the TGA curve of the composite presents 3 different peaks. Therefore, the kinetic model includes 3 steps, each pertaining to a specific reaction that converts a part of a single reactant (the resin mass) into a single product with a stoichiometric coefficient to be identified.
Based on the work of Batiot et al. [9], the influence of each of the kinetic parameters can be analysed. Both A_γ and $E_{a,\gamma}$ have an impact on the peak temperature of the reaction step, while n_γ and ν_γ influence the shape and the height of the peak. Table 1 presents the parameters of the kinetic model found for the 3 steps through an inverse analysis using a Particle Swarm Optimization algorithm [10-11]. The reaction enthalpy for the pyrolysis step is taken from Dao et al. [12]. Figures 2 and 3 show a good agreement between the experimental and numerical curves of MLR and mass loss, respectively. Both peaks of the 1st and 3rd steps are accurately represented. The maximum mass loss rate of 0.08%/s in the 2nd peak was not reached. A decrease in ν_2 would lead to an increase in the peak value, but would reduce the amount of mass produced for the next step, thereby reducing the size of the last peak. Therefore, a compromise has been reached. Regardless, the mass loss is accurately represented in Figure 3, with a final mass of 68.6%, close to the experimental value of 68.2%.

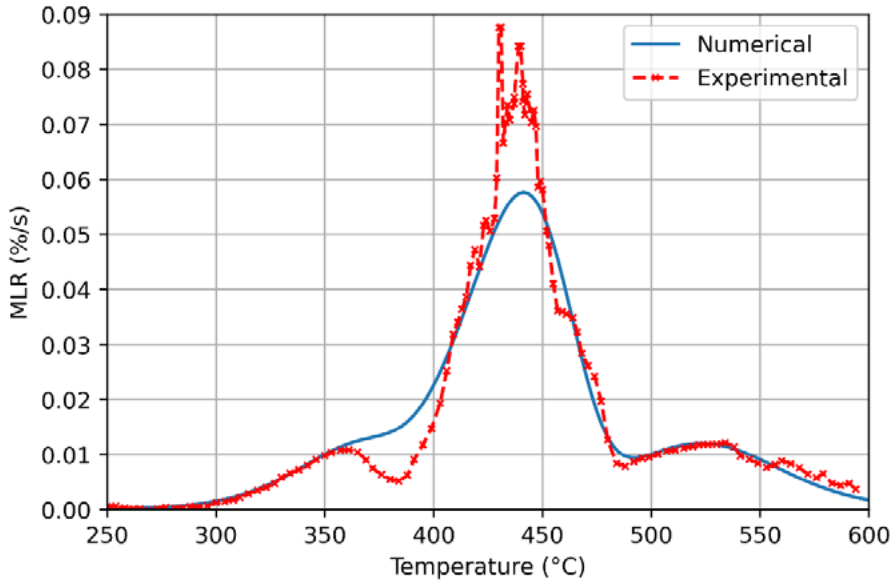


Figure 2. Thermal decomposition of the composite (TGA curve): normalized mass loss rate (MLR) as a function of temperature.

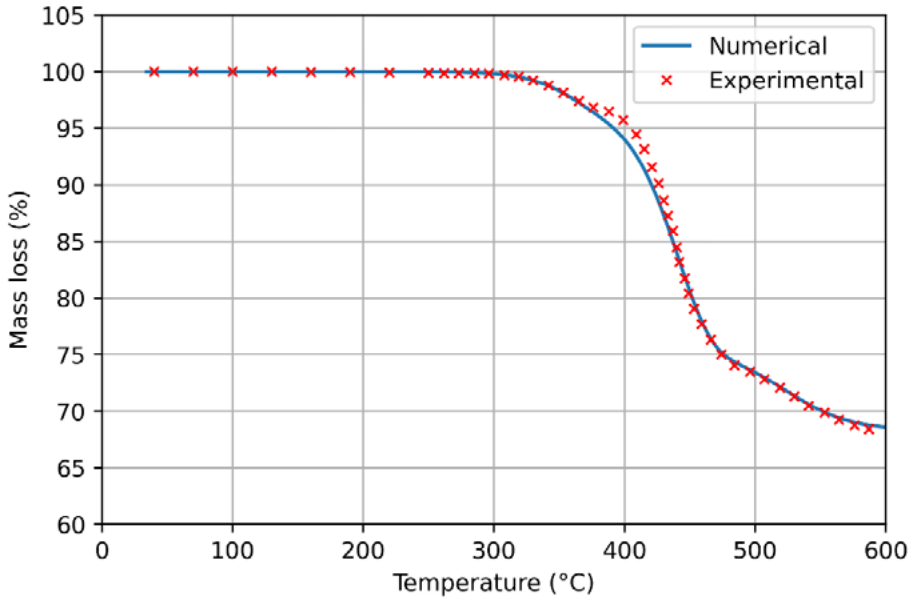


Figure 3. Thermal decomposition of the composite (TGA curve): normalized mass loss (ML) as a function of temperature.

Table 1. Kinetic parameters identified for the multi-step model.

Kinetic parameters	*Step 1*	*Step 2*	*Step 3*
A (s^{-1})	10^{10}	10^{11}	3.10^{10}
E_a ($kJ.mol^{-1}$)	139	171	174
n (-)	1	1	1.6
ν (-)	0.89	0.25	0.02

4.2. Thermophysical properties

The kinetic model is integrated in the thermal transfer equations of Section 2 where the decomposition reactions' rates help determine the evolution of the thermophysical properties. By using Eq. (5), these properties vary from the properties of an unaffected virgin material to those of a completely degraded material. Since decomposition is triggered at different times throughout the thickness of the sample, the same set of thermophysical properties will affect each of the temperature profile curves differently. Due to the coupling between the kinetic and thermal transfer models, thermophysical properties also have an effect on the mass loss measured by the cone calorimeter balance. For example, it is found that increasing λ_s or decreasing $C_{p,s}$ for the virgin material accelerate the mass loss rate without affecting the final value of the degraded material mass, and this has an incidence on the entire temperature profiles, particularly the lower temperatures. On the other hand, increasing λ_s or decreasing $C_{p,s}$ attributed to the degraded material has little incidence on the mass loss kinetics of the cone calorimeter, since by the time that these properties reach their degraded value, the mass at the end of the kinetic step had already been converted. The temperature curves are, however, greatly affected, particularly near thermal equilibrium. Evidently, the change in the material properties as previously stated leads to higher temperatures than necessarily found on the experimental curves. These facts help establish a strategy to identify appropriate intervals for the thermophysical properties in optimization by inverse analysis, first by determining the properties assigned to the virgin material leading to the correct mass loss kinetics, then identifying the properties of the degraded material that provide an accurate prediction of the temperature profiles. The optimized thermophysical properties found for the sample studied above are summed up in Table 2.

Table 2. Thermophysical properties identified through inverse analysis.

Thermal properties	*Virgin material*	*Degraded material*
ρ_s (kg.m^{-3})	1575	1100
$C_{p,s}$ (J.kg^{-1}.K^{-1})	2000	1350
λ_s (W.m^{-1}.K^{-1})	0.17	0.033
ϵ (-)	0.95	0.9

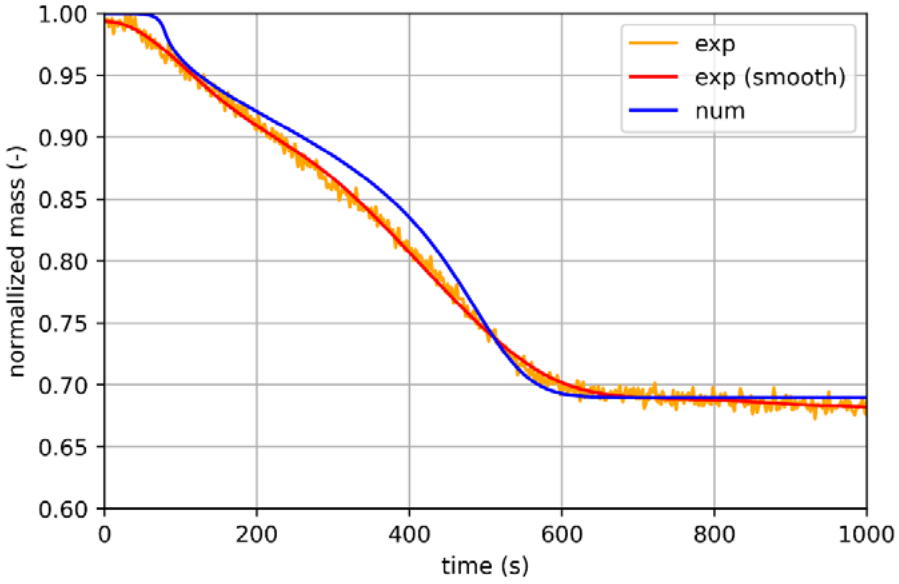


Figure 4. Normalized mass loss due to thermal degradation under the cone calorimeter test: comparison between experimental mass measurements and model simulation results.

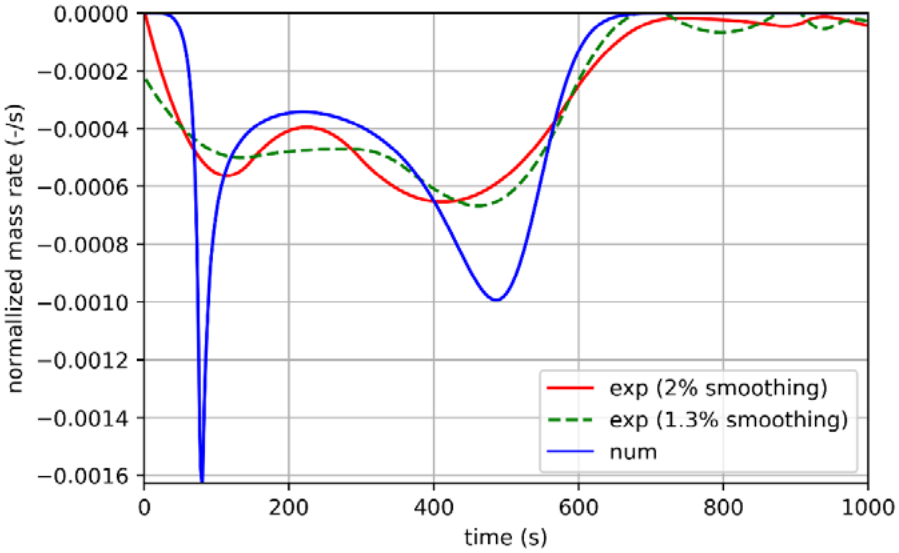


Figure 5. Normalized mass loss rate (MLR) due to thermal degradation under the cone calorimeter test: the experimental curve is derived using a de Boor-Cox algorithm with 2 smoothing ratios.

Figures 4 and 5 show respectively the mass loss and mass loss rate curves, measured experimentally by the cone calorimeter balance (the mass loss curve is first smoothed before derivation of MLR using a de Boor-Cox algorithm [7-8]).The comparison shows a fairly good reproduction of the curves by the model. The model also captures the two peaks shown in the MLR curve. The first peak is sharper in the model. As the first few layers degrade rapidly after ignition, their properties drop rapidly and isolate the rest of the material. This explains the delay in mass loss until after the first minute. The sharp peak leads to an intense increase in the temperature of the first layer, as shown in the temperature curve for a 1mm depth in Figure 6. While the model overestimate of the peak values in the MLR curve, the mass loss identified by the model neatly follows the experimental curve.
Figure 6 presents the temperature evolution curves within the 4 predefined depths of the material. For the lower depths (3.3, 5.6 and 6.6mm), the simulation curves are well-fitted to the experimental trends, demonstrating the ability of the algorithm to fairly represent the temperature profile within the material using a few parameters. Particularly notable are the temperatures reached near the end of the test, which match the temperatures measured within the material. At 1mm depth, the temperature is reached quicker than expected. This gap can be attributed to the sensitivity of measuring the temperature at a depth very close to the inflammable surface. If a heat barrier is formed, then the temperature would evolve slower than expected. Regardless, the simulation curve follows the trend of the experimental data after 600s.

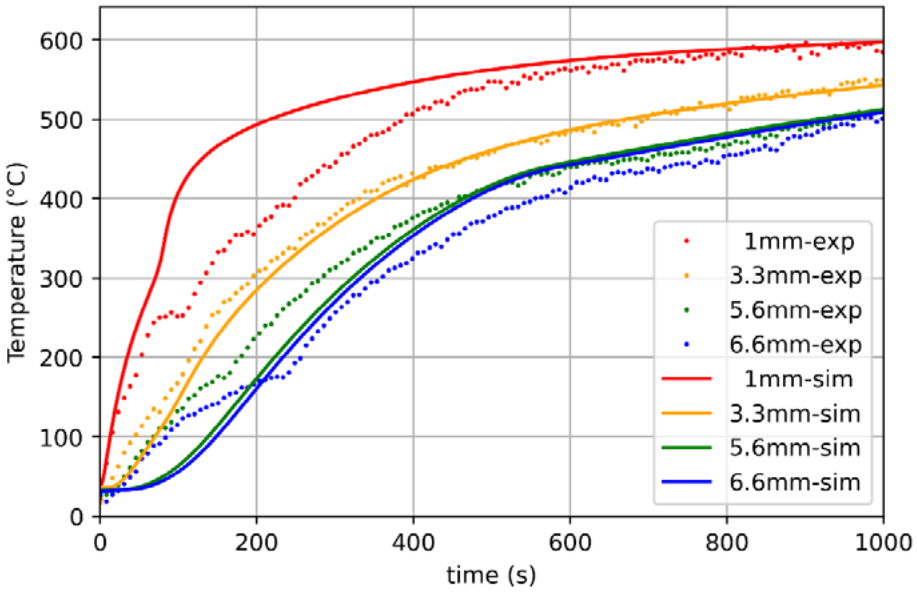


Figure 6. Evolution of temperature within the thickness of the material: comparison between measurements by thermocouples and model simulation results.

In the model presented above, a link is established between the thermal decomposition kinetics at the low scale and the thermal transfer phenomena at the upscale. For this reason, this homogenization nature provides a simple yet effective thermophysical model for predesign simulations at the structural scale.

5. Conclusions

A thermophysical model is described, combining multi-step kinetics that describe the decomposition of the material undergoing multiple chain reactions, coupled with thermal transfer modelling equations to determine the temperature mapping inside the bulk of the material. Simulations of the said model are run against experimental data obtained from TGA and a cone calorimeter test help identify the various parameters of the kinetic model, as well as the temperature-dependent thermophysical properties of the material. An example of an application on fiber-reinforced thermoplastic resin composite shows a good comparison between simulation results and experimental data.

Using the current model in an upscaling approach requires a reduction in the complexity of the model while keeping an accurate representation of small-scale phenomena as much as possible. In this regard, a sensitivity analysis can be applied to the model parameters to trace the most influential parameters to be kept in the simplified model.

Acknowledgment
The research leading to these results is supported by the Clean Hydrogen Partnership and its members in the framework of the project Road Trhyp. It has received funding from the European Union's Horizon Europe research and innovation programme under grant agreement N°10110142.

References
[1] H.B. Shim, M.K. Seo, S.J. Park, Thermal conductivity and mechanical properties of various cross-section types carbon fiber-reinforced composites. *Journal of materials science*. 37:1881-1885, 2002.
[2] P. Tranchard, F. Samyn, S. Duquesne, B. Estèbe and S. Bourbigot. Modelling Behaviour of a Carbon Epoxy Composite Exposed to Fire: Part I–Characterisation of Thermophysical Properties. *Materials*, 10(5):494, 2017.
[3] J.P. Hidalgo, P. Pironi, R.M. Hadden, S. Welch. A framework for evaluating the thermal behaviour of carbon fibre composite materials. In *Proceedings of the 2nd IAFSS European Symposium of Fire Safety Science.* Pages 195-200, 2015.
[4] B. Gentilleau, F. Touchard and J.C. Grandidier. Numerical study of influence of temperature and matrix cracking on type IV hydrogen high pressure storage vessel behavior. *Composite Structures*, 111:98-110, 2014.
[5] V. Babrauskas. Development of the cone calorimeter – a bench-scale heat release rate apparatus based on oxygen consumption. *Fire and Materials*. 8(2):81-95, 1984.
[6] ISO 5660-1:2015. Reaction-to-fire – Heat release, smoke production and mass loss rate. Part 1: Heat Release rate (cone calorimeter method) and smoke production rate (dynamic measurement). 3rd Edition, 2015.
[7] C. de Boor. On calculating with B-splines. *Journal of Approximation Theory*. 6(1):50-62, 1972.
[8] M.G. Cox. The numerical evaluation of B-splines. *MA Journal of Applied Mathematics*. 1:55-64, 1983.
[9] B. Batiot, T. Rogaume, A. Collin, F. Richard and J. Luche. Sensitivity and uncertainty analysis of Arrhenius parameters in order to describe the kinetic of solid thermal degradation during fire phenomena. *Fire Safety Journal*. 82:76-90, 2016.
[10] R.C. Eberhart and J. Kennedy. A new optimizer using particle swarm theory. In *Proceedings of the 6th international symposium on micro machine and human science*. Pages 39-43, 1995.
[11] D. Wang, D. Tan and L. Liu. Particle swarm optimization algorithm: an overview. *Soft Computing*, 22:387-408, 2018.
[12] D.Q. Dao, T. Rogaume, J. Luche, F. Richard, L. Bustamente Valencia and S. Ruban. Thermal decomposition of epoxy resin/carbon fiber composites: Influence of carbon fiber fraction on the fire reaction properties and on the gaseous species release. *Fire and Materials*. 40:27-47, 2016.

DIGITALIZED COMPOSITE MATERIAL AND PRODUCT DEVELOPMENT – STRATEGIES AND METHODS FOR MULTISCALE EXPERIMENTAL-NUMERICAL VALIDATION PROCESSES USING PLM AND MBSE APPROACHES

J. Richter[1], M. P. Dammann[2], M. Kluge[3], B. Saske[2], S. Arndt[3], A. Hornig[1,4], K. Paetzold-Byhain[2], N. Modler[1]

[1]Institute of Lightweight Engineering and Polymer Technology - ILK, TUD Dresden University of Technology, Holbeinstraße 3, 01307 Dresden, Germany
Email: jonas.richter@tu-dresden.de, Web: https://tu-dresden.de/ing/maschinenwesen/ilk
[2]Institute of Machine Elements and Machine Design, Chair of Virtual Product Development - VPE, TUD Dresden University of Technology, George-Bähr-Straße 3c, 01069 Dresden, Germany
Email: maximilian_peter.dammann@tu-dresden.de, Web: https://tu-dresden.de/ing/maschinenwesen/imm/vpe
[3]XPLM Solutions GmbH, Altmarkt 25, 01067 Dresden, Germany
Email: maximilian.kluge@xplm.com, Web: https://www.xplm.com/
[4]Center for Scalable Data Analytics and Artificial Intelligence Dresden/Leipzig - ScaDS.AI, TUD Dresden University of Technology, Strehlener Straße 12-14, 01069 Dresden, Germany
Email: andreas.hornig@ tu-dresden.de, Web: https:// www.scads.ai/

Keywords: experimental-numerical validation, event-driven process chains, model-based systems engineering, product lifecycle/data management, hybrid fiber-reinforced composite structures

Abstract
The management and digitalization of experimental-numerical validation and verification processes within product development (PD) for innovative, lightweight, high-performance composite materials is a major challenge due to increasing process chain complexity, highly heterogeneous data and the need to consider product-related data and processes over their entire life cycle. Methods for modeling the experimental and numerical validation process using Product Lifecycle Management (PLM) concepts to manage and integrate data and Model-Based Systems Engineering (MBSE) approaches to track data links and process steps are elaborated. A process roadmap is created including key processes, subprocesses and metadata for procedures in PD which are subsequently illustrated by an event-driven process chain showing linked processes, inputs/outputs, software needs and iteration points. This is used as a base to model key processes and their properties by creating customizable, connectable blocks in MBSE, where digital data is accessible through an interface linked by respective metadata in a PLM-tool. Excerpts of linked processes and respective metadata are exemplarily shown for a hybrid composite structure to illustrate the potential of the elaborated approaches for improved PD efficiency through data reuse, workflow execution, consistent data management and traceability.

1. Introduction

Within the product development processes for composite structures, the growing need for enhanced energy efficiency and reduced emissions increasingly gains attention. To achieve this, an optimized process chain, computer-aided methods, predictive modeling as well as sustainable digitalization and data management are considered vital, especially for the design phase with its multifaceted tasks: requirement analysis, product planning, specification and design on system level and subsequent, mechanical analysis, design, modeling and detailing of subsystems and components. Based on this, the process steps like manufacturing, experimental-numerical validation and verification are detailed. This information are being used back on system level, as described by the V-model approach [1]. Furthermore, processes and data related to the product lifetime and recycling also have to be managed. PLM offers new possibilities for such optimized PD processes but also affects the engineering workflows, regarding required skills, competencies, interdisciplinary, the design processes themselves and the tools for data analytics supporting data-driven processes [2]. To improve process efficiency, the data and metadata generated within a digitalized process chain have to be comprehensively structured by data and version management, following the FAIR principle [3].

1.1 Experimental and numerical validation in product development for composite materials

A key aspect within the product development process of composite materials is the experimental-numerical validation and verification, which is iteratively connected to the design of lightweight structures. The principle of this approach is based on the test/validation pyramid, which was introduced in [4] and is used to describe the building block approach [5]. On coupon level, the materials base properties are experimentally determined and transferred into the numerical processes to build up models and calibrate material cards. These processes continue on the structural element level where more application-oriented test setups and specimen geometries are used for advanced material and structure characterization [6]. Especially composite materials usually require considerable calibration and validation efforts for numerical models [7]. Furthermore statistical deviations in material properties and manufacturing influences often play a non-negligible role. On higher levels the focus shifts towards verification and certification using more complex components and tests [5].

The described experimental-numerical processes are very resource-intensive in terms of the physical testing requirements, costs and energy. To reduce these efforts, a shifting of the physical procedures towards a predictive virtual testing and certification is pursued [6, 8]. For this, a comprehensive data and revision or version management for highly heterogeneous linked data types like models, lists, tables, diagrams, images, scripts and other software specific data is required. The advantages of the processes according to the building block approach are their similarities and comparability, regarding testing type, specimen geometry, material model selection, modeling approach or numerical methods [6, 9, 10]. This emphasizes the potential for standardization with respect to process naming, categorization, definition of required input, output and metadata and structuring or management concepts within PLM and MBSE tools. Here, the metadata is assigned a special role: to create and save knowledge that is not directly included in the used data files and to ensure the FAIR principle.

1.2 Efficient product development with product lifecycle management and model-based systems engineering

The basis of efficient modern product development is PLM. PLM is understood as a strategic approach or a comprehensive management concept that relates specifically to technical products and the value-added processes associated with their manufacture and operation, as well as the information generated in the process [11]. The aim of PLM is to manage all information about a product and the associated production systems (and resources) consistently over the entire life cycle and to provide this information for all future tasks in the product development process [11]. This objective is realized by various IT systems that perform specific tasks and work together in a system landscape. Typical tasks are, for example, product data management (PDM), the management of customer relationships using customer relationship management (CRM) or systems that are used for the management of products in their utilization phase (maintenance, repair and overhaul (MRO)).

Within the PLM strategy, PDM is responsible for the consistent storage of the product model and the mapping of defined processes such as release and change management. Company-wide product information from all phases is processed in the value creation process [12]. This is the basis on which it is possible to keep product models consistent throughout their entire life cycle. The PDM forms the data backbone within the PLM strategy and enables the availability of information at the required time, in the required quality and in the right place. However, access to granularly related information across domain boundaries is difficult and not mapped in the data models of the PDM systems. The philosophy of systems engineering offers an approach to overcome this situation. In combination with the MBSE methodology, it is possible to model complex systems and map the relationship between properties at parameter level in the system model. The resulting system model can also be used to map the sources of the necessary information; while the documents continue to be stored in their domain-specific systems and are managed within the PLM strategy. If the resulting MBSE models are also integrated into the product data management, the system model can be understood as a special view of the product information that is implemented in a formalized manner (using SysML). The use of standardized, digitally linked models and workflows enables efficient and sustainable handling of process information and data.

2. Methods

2.1 Process roadmap and metadata categorization

The PD process consists of linked processes and subprocesses that either have to be run through linearly one after another, in parallel or iteratively through process loops and include a high amount of different input and output data. These among others include requirement analysis, decomposition of the overall system into substructures and individual components, loading and boundary definition, concept development and design, manufacturing, experimental characterization and all processes regarding modeling and simulation. A comprehensive process roadmap for the product development processes with focus on experimental-numerical validation processes has been elaborated. The main categories are defined based on the mid-level ontology Platform MaterialDigital Core Ontology (PMDco) [13] to standardize and link the semantic terminology. In order to subdivide the processes more specifically, the terminology has been extended. In the context of simulation, processes like simulation geometry modeling (meshing), sensitivity analysis, material card calibration, stability analysis, modal analysis, sub-modeling, virtual validation, mesh study, parameter optimization or stress prediction have been added. All of these processes contain descriptive property templates with features like characteristic name, process category, linked requirements, description (aims, methods, models), processing nodes (tools, equipment), revision/version, changes and other information like responsible person, confidentiality, organization, project assignment, priority, status, and remarks.
Additionally, the processes are connected with certain input and output objects regarding data such as requirement documents, literature, standards and legal documents, testing plans, CAD models, FE meshes, simulation files, evaluation data or other process related documents. A major focus for the description of this data lies on the definition of metadata. This gives information similarily to the process properties mentioned above in addition to the group classification and data type specification. The aim is to give the opportunity of including more specific information than usual, like material type, manufacturing parameters, types of element formulations, material models in FE simulation files, occurred errors or most important parameters from a data set, without the need to look into individual files or folders. The terminology of metadata descriptions is, like for the processes and their properties, again oriented and extended from the ontological classifications mentioned above [13] to structure and support digital system modeling and standardization.

2.2 Event-driven process chain

An event-driven process chain (EPC) is used as a method to capture and analyze existing processes. EPCs are a process modeling language that offer function elements (rounded box) which represent activities in the process and event elements (hexagonal box) which describe pre- or post-conditions of the function elements [14]. The elements are used alternately and are connected via control flow elements (arrow), which can be extended by connector elements (circle) that contain logical functions like AND, OR and XOR. The EPC is expanded to include swimlanes in which the data processing activities of various software tools that are involved in the process are compiled. The goal of this analysis is to capture the process and the included manual and automated data processing activities, as well as software tools and the produced documents and files that are inputs and outputs of the functions.
The analysis of the captured process leads to a complete overview of the involved stakeholders and domains, the system landscape, as well as generated data and information. The analysis of the EPC reveals a high degree of manual data processing activities together with unstructured and distributed data. In addition several process steps and data processing activities occur multiple times throughout the whole EPC, showing potential for a simplification of the representation of the process and the integration of the produced data in PLM/PDM systems. **Figure 1** shows a small excerpt of the EPC, namely the preparation of CAD-models and the following meshing for simulation on the left and the associated manual data processing activites for the model preparation in CAD-systems on the right.

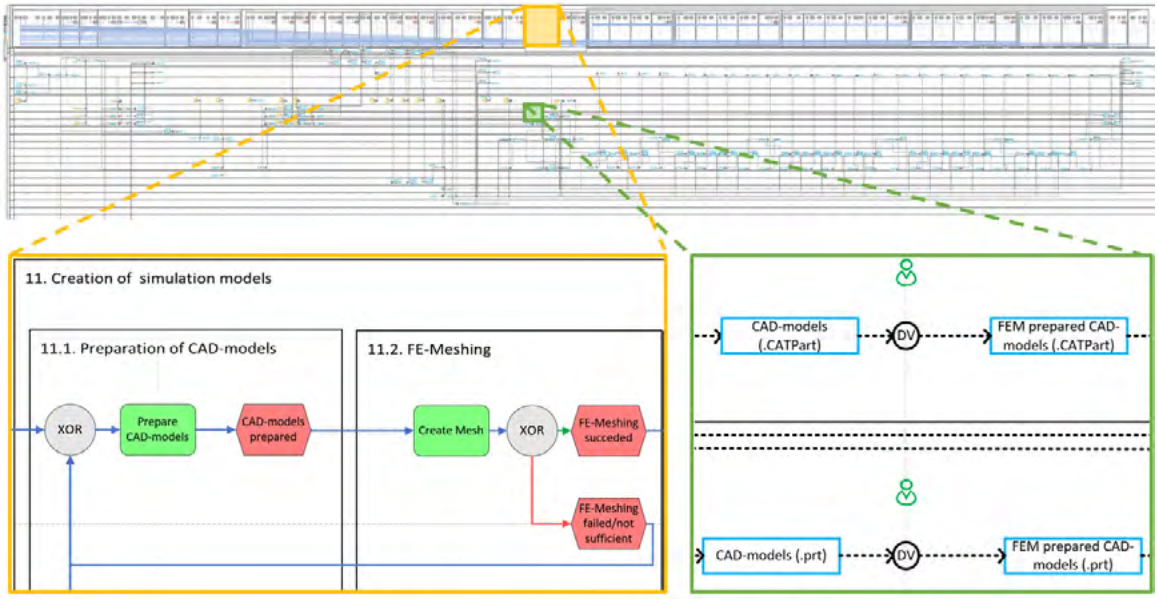


Figure 1. Exemplary EPC, left: excerpt of the EPC, right: excerpt of the data processing activites

2.3 Development of process chains with model-based systems engineering

New research focuses arise in the transfer of the MBSE methodology to the modeling of processes (not just product systems). Processes also access information from different sources, which are not always managed consistently and require network structures instead of hierarchichal structures as modeling basis. This is evident in the described EPC analysis. To reduce the complexity of the captured process, generalized process steps with a focus on the domain of experimental-numerical validation within the PD are defined and templates are developed (**Table 1**).

The process steps are modeled in the Software Enterprise Architect as SysML blocks and contain metadata as properties/values as well as proxy ports that can be utilized to model the information flow. In addition to the process steps, the input and output of the steps need to be captured for a consistent documentation of the development process – enabling future analysis and well-founded decision-making. These in-/outputs are categorized by the objects component and document (**Table 1**) which are modeled as blocks. A component describes a physical constituent of a product e.g. a part, assembly, system or material. Documents describe the data that is used and produced in the virtual product development (see chapter 2.1) and are further grouped into generalized categories, such as information documentation, scope statement, design geometry, testing plan, simulation model, simulation output data or process documentation. A document can contain a single file or also a group of files as data set. The documents can be linked to the components. Both component and document contain metadata (modeled as properties/values) and can be differentiated by definition of a group or type (before mentioned examples). It is important to note, that document blocks do not contain the actual documents, but only provide a link to e.g. PLM/PDM systems which handle the actual data, see chapter 2.4. Creation, manipluation and version control of data is still handled by the domain specific authoring systems.

Table 1. Overview of developed process steps and input/output objects

Process Steps	Input/Output Objects
Information research and analysis process Requirements management process Manufacturing process Mechanical testing process CAD modeling process Simulation geometry modeling process Simulation setup process Numerical simulation process Evaluating process	Component (part, assembly, system, material) Document (e. g. information documentation, scope statement, design geometry, testing plan, simulation model, simulation output, process documentation)

Through the application of the described approach it is possible to model the development process and the used input/output data for each process step including the defined properties/values (**Figure 2**). In addition the decisions and the development path can be captured and managed consistently. The MBSE model is completely machine-readable and provides a promising basis for assisted (e.g. through machine learning) analysis and process optimization or adaption to new challenges.

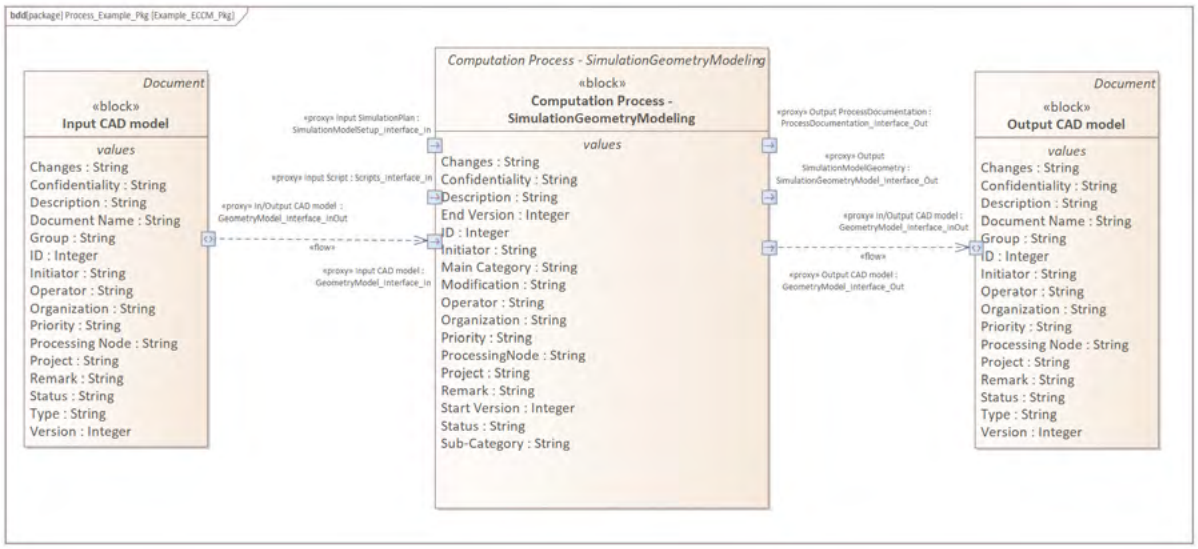


Figure 2. Exemplary blocks (document and process step) to model information flow in the process chain

2.4 Coupling of process information and digital data management

To enable access to the digital data used and generated as input or output documents respectively, a data model is used to implement a data management solution using Aras Innovator as a PLM/PDM system, which has been accordingly customized. With regard to relevant simulation data the model is structured by simulation studies and simulation tasks. Each task contains the document group classifications of design geometry (e. g. CAD model), simulation model geometry (e. g. FE-mesh), simulation model (e. g. an FE mesh with all defined loads, boundary condition and material cards), simulation output and task documents referencing other document types that are not models (**Figure 3**). These documents represent essential data necessary for the execution of typical simulation tasks. The coupling between the MBSE model in Enterprise Architect where only information about processes, documents and their links are modeled, and the PLM/PDM system with the actual data, is realized by a software interface provided by XPLM. The metadata for the documents between both is synchronized as the same entries to ensure consistency. Additionally, in each document block in the MBSE model a reference to the location of the stored related data is assigned which enables direct data access when modeling processes. The data can either be selected from files previously uploaded into Aras Innovator or uploaded directly when creating the document block in Enterprise Architect. A simulation task in context of the MBSE model is considered as a container consisting of the four process steps design, simulation geometry modeling, simulation model setup and numerical simulation. Whenever a new simulation task is defined in a typical workflow the respective template blocks are created as a base that can be individually extended, e. g. if further numerical processes are required to fulfil the task. The different simulation outputs can then be uploaded into the respective category within Aras Innovator. Additionally, the task has to be assigned to an existing or new simulation study. Documents that do not belong to a simulation process are structured in a general category that can be browsed according to the metadata information like group classification or data types.

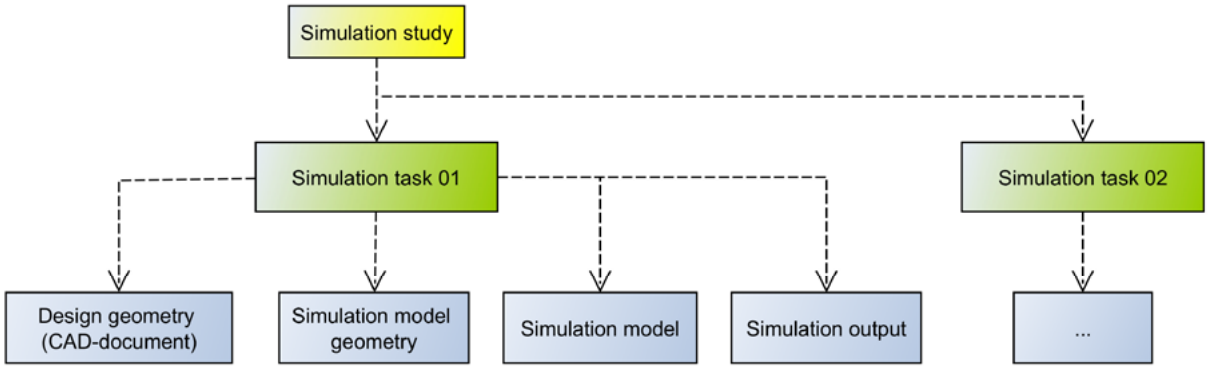


Figure 3. Customized structure for simulation data management in Aras Innovator

3. Results - Exemplary concept implementation and discussion

The elaborated concepts for process, object and metadata classifications, templates and links between MBSE and PLM/PDM tool have been investigated using the data from the design and experimental-numerical validation of an exemplary hybrid composite structure (**Figure 4**).

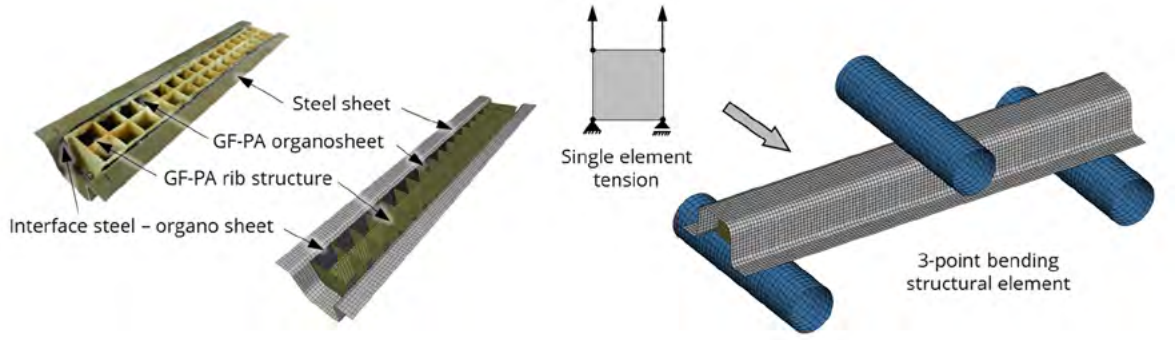


Figure 4. Exemplary simplified hybrid composite structure as an element of an A-pillar with data used for evaluation of the MBSE and PLM/PDM concepts

Starting with the requirements e. g. regarding maximum mass and energy absorption capability the component is designed and a comprehensive testing and simulation plan is derived to validate design variants. The processes conducted include e. g. specimen manufacturing and material characterization on coupon level with tensile, compression and shear tests to determine the required data for the components steel, organosheet, rib structure and interface. This data is used in the numerical material card calibrations where processes like single element tests for material model understanding, meshing, simulation model setup, parameter studies and optimizations take place. On structural element level the design is extended with more details and a prototype is manufactured and tested under low-velocity 3-point-bending conditions. On the numerical side the model setup process gets more complex and further processes like numerical contact investigation, error analysis in case of instability issues, model validation and stress prediction for other load cases are conducted. Here not only component- but also process-relevant requirements like demanded mesh size and percentage of allowed mass scaling effect can be necessary. Several iterations between design variants and numerical stress predictions take place and therefore a version management is crucial. In summary and based on the concepts described in chapter 2 the whole process chain for the development of the structure is captured and can be traced including all data used for a certain process step as well as information stored as metadata.

Figure 5 shows a simplified excerpt of the processes for the calibration of the material card regarding tensile properties on coupon level which are required to validate the product to be developed and functionalities on higher level within the building block approach. Additionally, exemplary documents that are used within the processes are connected as input and output. Both are modeled in MBSE as instances of the blocks defined in chapter 2.3. In this example, the documents “Coupon specimen CAD

model" or "Coupon specimen meshing script" are required for the simulation geometry modeling process "Coupon specimen mesh creation" for manual meshing or automated meshing using a parametric Python script. Here, an exemplary remark for the mesh size of 3 mm is added. In the simulation model setup process "Coupon specimen model setup" the boundary conditions are defined (e. g. load introduction and constraints) and a base material card is created by using the datasheet document "Organosheet properties" for the respective material (organosheet). In the subsequent numerical simulation process with the name "Parameter optimization", the software LS-OPT and LS-DYNA are used to calibrate the material card parameters by iteratively mathematically comparing the "Tensile test simulation optimization output" with the experimental "Tensile test results" (input document) which were generated in an earlier process. Another document "Optimization procedure documentation" is created as output that contains information about settings or changes that were made in the process step, e. g. as a tabular file. Finally the most relevant output is the "Calibrated organosheet material card", that can be either defined as new version of the document "Base organosheet material card" or as completely new object in case both have to be stored separately. The processes themselves can also have different versions, e. g. in a case where modeling issues are noticed within a numerical simulation process that have to be fixed within the simulation model setup process before the former process is repeated with the fixed model. This procedure is used to consider iterations and versioning in the MBSE model.

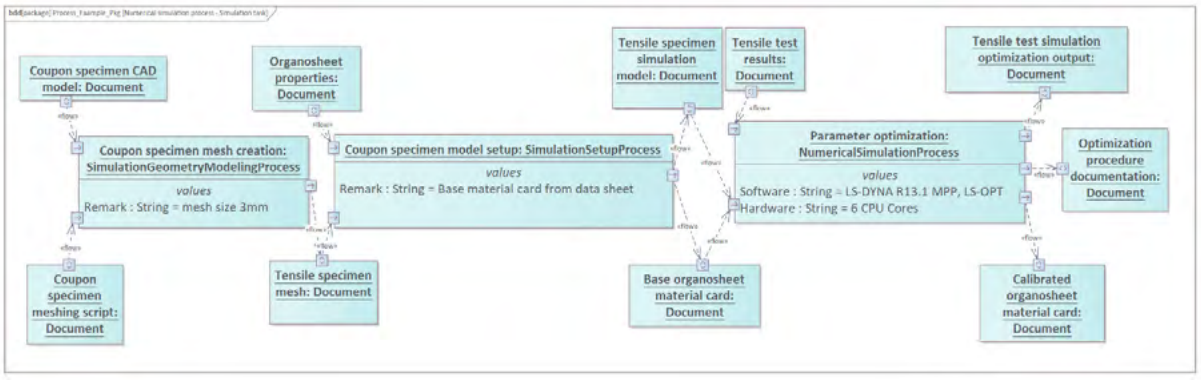


Figure 5. Simplified example of the process chain for a typical simulation task

4. Conclusion and outlook

A digital solution for modeling process steps and linked data generated within the PD with focus on experimental-numerical validation is proposed using MBSE and PLM/PDM approaches. The relevant processes, data and metadata are identified and classified to elaborate methods for improved data reuse according to the FAIR principle while using uniform vocabulary based on ontologies. The processes are visualized in an EPC together with the input/output and required software tools, giving an overview of involved stakeholders, domains, data and information in the system landscape and enable identification and analysis of dependencies and interactions of linked processes and data. The processes and their inputs/outputs, defined as objects, are further generalized and transferred into MBSE by modeling as SysML blocks with respective properties/metadata and proxy ports to model information flow. These customizable templates can be used for a consistent documentation of the development process to support consistent workflows, subsequent analysis, evaluation and decision-making improving data and information reusability when conducting similar processes. The MBSE model is flexible with regards to adaptation when executing and tracking process steps to suit individual needs. Since it is completely machine-readable, it is suitable for automated analysis (e. g. by machine learning) to optimize processes and derive or propose new process chains adapted to respective future use cases. The data used as input or output object for processes in MBSE can be manually linked and stored in a PLM/PDM tool which enables direct access during process modeling. Additionally, metadata is recorded containing important information about the object properties as well as links to connected processes or other objects, e. g. the links between a component and a CAE model or material model. This transforms data into information and subsequent knowledge improving its reusability.

An exemplary use case is introduced by means of the experimental and numerical processes required for the development of a hybrid composite structure and an excerpt of a process chain is shown. In this way, process steps are structured and executed in a consistent manner and the workflows including used data and information are managed, traceable and reusable to support future development processes. The open interfaces of the MBSE concept in combination with the linked data management allows to extent and specify the process modeling into further domains like manufacturing, design processes or other types of simulations (e. g. process simulation or computational fluid dynamics), taking into account the whole PD. Furthermore, the customizability of both used systems regarding user interface and script integrability enables the potential of creating automated workflows regarding simulations and data integration as well as coupling to other software tools.

Acknowledgements

The authors gratefully acknowledge the financial support for this research provided by the Federal Ministry of Economic Affairs and Climate Action under grant agreement no. 19S22006N ("Digitalization for Sustainability" – DigiTain) and would like to thank the "3D-Hybrid" project members of ILK for providing design, experimental and numerical data for the exemplary hybrid structure.



References

[1] Graessler, I. et al. (2018). V-Models for Interdisciplinary Systems Engineering. *International Design Conference – Design 2018*, 747-756.

[2] Cantamessa, M. et al. (2020). Data-driven design: the new challenges of digitalization on product design and development. *Design Science.*

[3] Wilkinson M. D. et al. (2016). Comment: The FAIR Guiding Principles for scientific data management and stewardship. *Scientific Data*.

[4] Rouchon, J. (1990). Certification of large airplane composite structures, recent progress and new trends in compliance philosophy. *Congress of the International Council of the Aeronautical Sciences (ICAS Proceedings), 17(2),* 1439-1447.

[5] US Dept of Defense (2002). Composite Materials Handbook-MIL 17, Volume II: Guidelines for characterization of structural materials. Routledge.

[6] Furtado, C. et al. (2019). Simulation of failure in laminated polymer composites: building-block validation. *Composite Structures, 226.*

[7] Zscheyge, M. et al. (2020). Rate dependent non-linear mechanical behaviour of continuous fibre-reinforced thermoplastic composites – Experimental characterisation and viscoelastic-plastic damage modelling. *Materials & Design*, *193.*

[8] Serra, J. et al. (2017). Validation and modeling of aeronautical composite structures subjected to combined loadings: The VERTEX project. Part 1: Experimental setup, FE-DIC instrumentation and procedures. *Composite Structures, 179*, 224-244.

[9] Amirth Jayasree, N. et al. (2017). Process analysis for structural optimisation of thermoplastic composite component using the building block approach. *Composites Part B, 126*, 119-132.

[10] Acosta, J.F. et al. (2017). Certification by Analysis—A Building Block Methodology for Composite and Metallic Aircraft Crashworthy Structures—Coupon Level. *Wichita State University, National Institute for Aviation Research.*.

[11] Gerhard, D. (2016). Daten und Informationsmanagement PDM/PLM. In: *Udo Lindemann (Hg.): Handbuch Produktentwicklung*, 215-246. München: Hanser.

[12] Eigner, M. (2009): Product Lifecycle Management. Ein Leitfaden für Product Development und Life Cycle Management. 2nd revised edition. Berlin, Heidelberg: Springer (VDI book).

[13] Bayerlein, B. et al. (2024). PMD Core Ontology: Achieving semantic interoperability in materials. *Materials & Design, 237.*

[14] Mendling, J. (2008). Event-Driven Process Chains (EPC). In: *Metrics for Process Models 6*, 17-57. Berlin, Heidelberg: Springer

3D PRINTING OF FOAMED PLA WITH VARIABLE MECHANICAL PROPERTIES FOR OPTIMISED LIGHTWEIGHT SANDWICH CORES

Jon Rodriguez[1], Mikel Iragi[1], Ondiz Zarraga[1], Jaione Iriondo[1], Aitziber Aizpuru[1] and Alex McCloskey[1]

[1]Mondragon Unibertsitatea, Mechanical and production engineering department, Loramendi kalea 4, Arrasate-Mondragon, Spain
Email: jrodriguezc@mondragon.edu, https://www.mondragon.edu

Keywords: 3D printing, PLA, foam, sandwich, tensile test, bending test, stiffness, Poisson, shear

Abstract
Recent advancements in additive manufacturing (AM) have facilitated the production of foamed biodegradable materials like Lightweight Polylactic Acid (LW-PLA). This study investigates the influence of density and infill angle on the elasticity modulus, shear modulus, and Poisson's ratio of foamed LW-PLA, aiming to establish the printing parameters to obtain the desired material properties. A screening of the manufacturing variables including flow rate, temperature, printing velocity, and raster width was conducted to obtain three part densities. Tensile tests, following ASTM D638-02a standards, were performed to determine elasticity modulus and Poisson's ratio, supplemented by Digital Image Correlation for Poisson's ratio assessment. Sandwich panels comprising aluminum skins and LW-PLA core were fabricated and subjected to bending tests, following ASTM D7250M-20 standards for three-point bending tests.

Results reveal significant variations in elasticity modulus and Poisson's ratio with respect to part density and infill angle, with higher density parts exhibiting elevated properties. Bending tests show the anisotropic nature of 3D printed LW-PLA.

1. Introduction

Fused deposition modelling (FDM) is a well-known additive manufacturing (AM) technology to print thermoplastic polymers. In this process, the material, typically in filament form, is fed through a heated nozzle, where it melts and is extruded onto a build platform. Once deposited, the material rapidly solidifies, gradually forming the desired object layer by layer [1].

Polylactic acid or Polylactide (PLA) is a biodegradable and bioactive thermoplastic derived from renewable resources, typically through the fermentation of corn starch or sugarcane into lactic acid. PLA is renowned for its eco-friendly characteristics, as it is compostable under industrial conditions, making it a sustainable alternative to traditional petroleum-based plastics. This versatile material is utilized in various applications, including packaging, food containers, disposable tableware, biomedical implants. The thermoplastic nature of PLA makes it suitable for AM, generating interest among researchers in a wide range of fields [2].

In an interesting review, Suteja and Soesanti [3] found 19 research works analyzing the influence of several printing parameters on the mechanical properties of PLA, and found that nozzle diameter, nozzle temperature, printing speed, filament feed rate, layer thickness and raster width are the most influential ones. Additionally, they observed that alternative printing strategies such as infill pattern, infill angle,

infill density, number of shells and build orientation also play a substantial role in influencing the mechanical properties.
In 2019 the company ColorFabb released the so-called lightweight PLA (LW-PLA) filament to manufacture foamed PLA by FDM [4]. The input filament material is saturated by a blowing agent which is activated when passed through the hot nozzle, obtaining a stochastic porosity distribution in the final part which is dependent on the printing conditions, mainly flow rate and temperature [5,6,7,8,9]. In all the referenced works, the printed maximum and minimum densities are around the one stated in the official technical datasheet of the material, which states that the maximum density achievable of the LW-PLA is 1240 kg/m^3 and the minimum 400 kg/m^3. However, there is a considerable difference between the measured densities by each author due to the difference in the printing strategy used by each researcher.

The special properties of having high stiffness-to-weight ratio and high bending strength-to-weight ratio make sandwich composite structures very suitable for many applications, reducing weight without compromising the mechanical performance. Therefore, they are widely used in all mechanical industrial sectors such as automotive, aerospace and construction [10]. The potential of LW-PLA material as a core of sandwich structures is considered in this study.

As mentioned above, the influence of the infill angle and part density on the mechanical properties was not studied in deep. In addition, due to the infill angle, the behaviour of the part might not be isotropic, and thus, the elasticity modulus, Poisson's ratio and the shear modulus will be independent. In order to analyze this behaviour, this study investigates the process-structure-property relationship of 3D Printed LW-PLA to manufacture desired material densities. Tensile and flexure samples were printed and tested to find static elastic modulus, shear modulus and Poisson's ratio.

2. Methodology

2.1. 3D Printing of Specimens

Printing parameters in FDM technology are abundant, so the first task was to define the variable parameters that allow to manufacture several densities using 3D printed LW-PLA and to establish the parameters that need to be kept constant, see Table 1. Printing temperature, flow rate, raster width and printing velocity were adjusted to manufacture three densities, see Table 2.

Literature states that the influence of the infill angle is significant in AM components [11], so it was taken as a variable to see the influence of it on the mechanical properties.

Determining the part density was straightforward, volume measurements were done with a digital caliper and weight measurements with a high precision scale. The achieved densities were: 450 kg/m^3, 610 kg/m^3 and 1115 kg/m^3. Three specimens for each configuration were manufactured to determine the mean density and the measured standard deviation was below 1%.

Table 1. Fixed parameters for 3D printing LW-PLA.

Parameters	Value
Fixed parameters	
Nozzle diameter	0.4 mm
Layer height	0.4 mm
Bed temperature	60°C
Overlap	30%
Build orientation	Flat
Number of shells	1
Infill density	100%
Infill pattern	Straight lines

Table 2. Variable parameters for 3D printing LW-PLA.

Parameters	Value
450 kg/m^3 part density	
Flow rate	50%
Printing temperature	230 °C
Raster width	1.15 mm
Printing speed	20 mm/s
610 kg/m^3 part density	
Flow rate	65%
Printing temperature	230 °C
Raster width	0.65 mm
Printing speed	60 mm/s
1115 kg/m^3 part density	
Flow rate	100%
Printing temperature	205 °C
Raster width	0.46 mm
Printing speed	20 mm/s

2.2. Tensile Test

The test methodology was established following the standard ASTM D638-02a [12] recommendations, type I specimen dimensions were used, with a nominal width and thickness of 19 mm and 3.2 mm, respectively. Three part densities and three infill angles were analyzed. Nine cases with three repetitions for each case, so 27 specimens were tested in total. The chosen infill angles are: ± 45º, 0º/90º and 0º. The three densities mentioned before were analyzed.

Tensile tests were performed on a Instron universal testing machine equipped with a 50 kN load cell and at a load-rate of 2 mm/min. Longitudinal and transverse strains were measured with a GOM-Aramis DIC system in order to obtain the Poisson's ratio. Only the linear elastic deformation region of the strain-stress curves was considered to obtain the elastic modulus and Poisson's ratio, disregarding the initial offsets or discontinuities.

2.3. Three Point Bending Test

The ASTM D7250M-20 [13] recommendations were followed to design the specimens. Sandwich beams were manufactured using aluminum face sheets and LW-PLA cores with variable density and infill angles, with thicknesses of 1 mm and 10 mm, respectively. All specimens have a width of 25 mm and length of 220 mm. The span length was defined at 75 mm. Only two densities were tested: 450 kg/m^3 and 1115 kg/m^3. The analyzed infill angles are the same as in the tensile tests, but they are only studied in cores with the highest density. Three specimens were used for each configuration, so a total of 12 specimens were tested. Figure 1 shows the experimental set-up.

The adhesion between the core and face sheet was done by applying Epoxy EA 9466 to the face sheet surfaces and after assembling the parts, pressure was applied during 24 hours using a glass with weight on top of it.

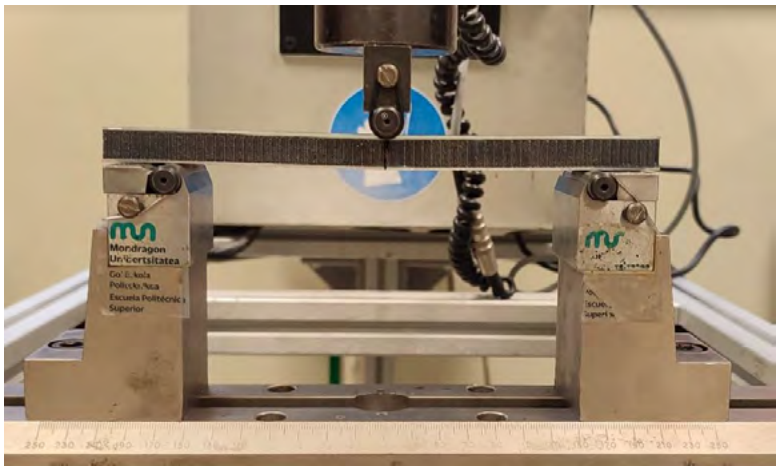


Figure 1: Three point bending test.

Bending tests were performed on a Instron universal testing machine at a load-rate of 0.5 mm/min. It is assumed that all the pure bending efforts are supported by the face sheets, so the bending stiffness is calculated by (Eq. 1),

$$D = \frac{E_{\text{face}}\,(h_{\text{tot}}^3 - h_{\text{core}}^3)\,b}{12} \tag{1}$$

where E_{face} is the elastic modulus of the aluminium, h_{tot} is the total thickness of the sandwich beam, h_{core} is the thickness of the core and b is the width of the beam. It is also assumed that all the shear efforts are assumed by the core, so the transverse shear stiffness is calculated by equation (Eq. 2),

$$U = \frac{S}{4\left(\frac{\Delta}{P} - \frac{2\,S^3}{96\,D}\right)} \tag{2}$$

where S is the span length, Δ is the measured displacement and P the applied load. Finally, the shear modulus of the core is calculated by equation (Eq. 3).

$$G = \frac{U\,(h_{\text{tot}} - 2\,h_{\text{face}})}{(h_{\text{tot}} - h_{\text{face}})^2\,b} \tag{3}$$

3. Results and Discussion

3.1. Tensile Test

The measured strain-stress curves for each configuration are illustrated in Figure 2.

It is observed that the highest yield strength is achieved in the highest density parts and infill angle of 0º, obtaining almost 10 times higher values than in the ±45º configuration. All the configurations showed a elongation strain of around 3% with a considerable plastified region before failure, and the lowest strains were measured in the infill angle of 0º. In Figure 3 the results for the elastic modulus and Poisson's ratio are displayed.

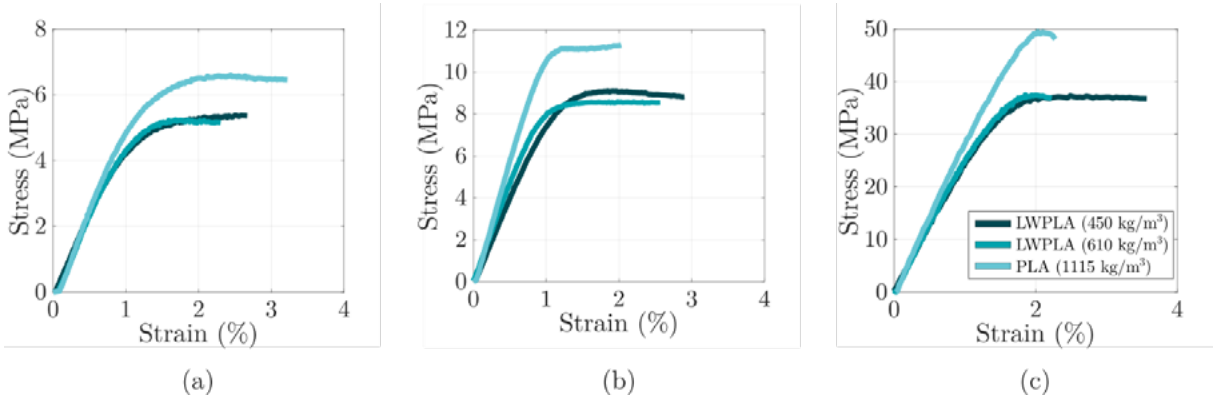


Figure 2. Strain-stress curves of tensile tests for several infill angles and part densities: (a) infill angle of ±45º, (b) infill angle of 0º/90º, and (c) infill angle of 0º.

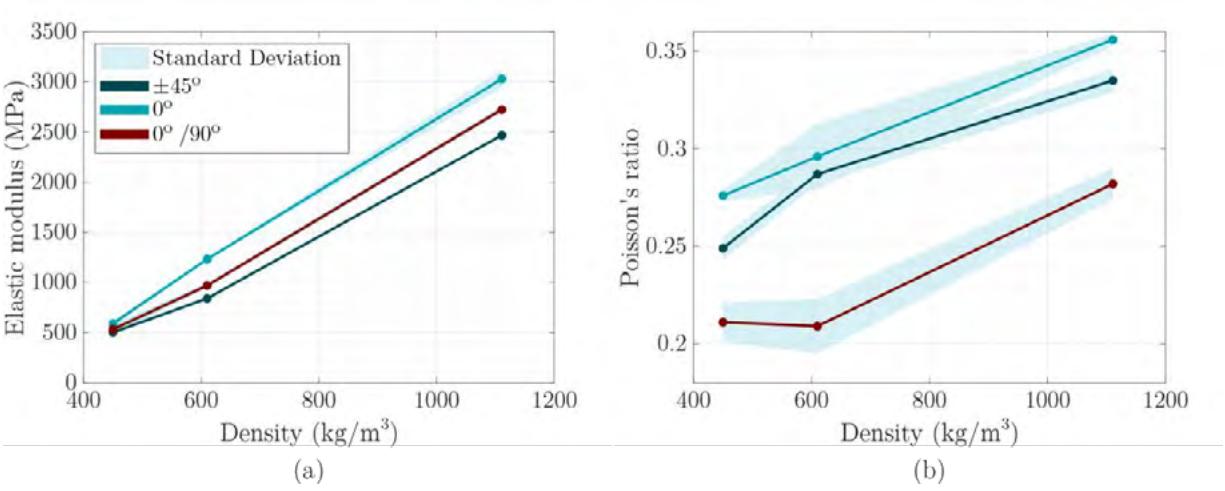


Figure 3. Tensile test results: (a) Elastic modulus and (b) Poisson's ratio.

The influence of the density is as expected, higher density parts are stiffer. However, the reason why the influence of the infill angle in low density parts is smaller is not straightforward. A hypothesis is that in fully foamed parts the infill cavities tend to homogenize. In foamed parts, the infill has numerous cavities minimizing the impact of the orientation of the interlayer gaps. In non-foamed parts interlayer gaps are the primary cavities and their orientation significantly affects the elasticity modulus of the part.

The Poisson's ratio results, ranging from 0.21 to 0.35, indicate the potential to attain a significantly broader range of values compared to those reported by Kanani and Kennedy [7], who measured values of 0.36 for foamed parts and 0.34 for non-foamed parts. Interestingly, in our tests, we observed an opposite trend, being the highest Poisson values obtained for the highest density parts.

3.2. Three Point Bending Test

In conventional foams, the isotropic relationship of equation (Eq. 4) is often considered to calculate the shear modulus [14],

$$G_{\text{iso}} = \frac{E}{2\,(1+\nu)} \tag{4}$$

where E is the elastic modulus and ν is the Poisson's ratio, both obtained in the tensile tests. In Figure 4 the measured shear moduli calculated using equation (Eq. 3) are compared with the shear modulus estimated using equation (Eq. 4).

The big differences between the measured shear moduli and isotropic values suggest that these parts posses anisotropic properties, but also that the assumption that all the bending stiffness is supported by the face sheets and that the core works in pure shear is incorrect. The bending stiffness of the face sheets is only 15 times bigger than the bending stiffness of the core. In the lowest density core case, the bending stiffness ratio goes up to 90, making the assumptions made by the standard more realistic, and thus, the differences in the measured and isotropic shear modulus are smaller.

It is also appreciated that the influence of the infill angle is small compared to tensile tests. When working on shear, the influence of the angle decreases.

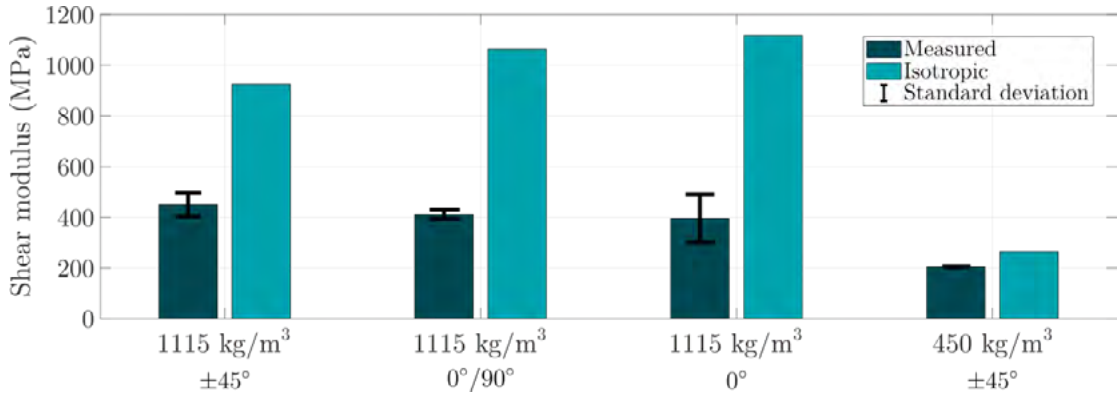


Figure 4. Three point bending results.

4. Conclusions

In this study, printing temperature, flow rate, raster width and printing velocity were adjusted to manufacture three densities and the influence of the infill angle and part density on the elastic modulus, Poisson's ratio and shear modulus of 3D printed LW-PLA was analysed. The tensile test and digital image correlation technique were employed to obtain the elastic modulus and Poisson's ratio and the three point bending test to get the shear modulus.

Non-isotropic properties were observed in the shear moduli of the high density parts in Figure 4, where almost two times bigger shear modulus was estimated in the isotropic material assumption respect to the one calculated using the equation (Eq. 3) of the standard ASTM D7250M-20. In low density parts, due to the bigger difference in the bending stiffness of the face sheets and the core, the shear modulus estimations using both assumptions are similar.

Moreover, the influence of the infill angle was only observed in the elasticity modulus of high density parts and in the Poisson's ratio of all density parts. However, the influence of the infill angle was minimum in the elastic modulus and in the shear modulus of fully foamed parts.

Aknowledgements
This work was financially supported by the Basque Government under MATFUN KK-2021/00066, and by the Provincial Council of Gipuzkoa under NUCAVA.

References

[1] B. N. Turner, R. Strong, and S. A. Gold. A review of melt extrusion additive manufacturing processes: I. Process design and modeling. *Rapid Prototyping Journal*, 20(3): 192–204, 2014.

[2] S. Divakara Shetty and N. Shetty. Investigation of mechanical properties and applications of polylactic acids - A review. *Materials Research Express*, 6(11), 2019.

[3] T. J. Suteja and A. Soesanti. Mechanical Properties of 3D Printed Polylactic Acid Product for Various Infill Design Parameters: A Review. In *Journal of Physics: Conference Series*, 1569(4) 2020.

[4] ColorFabb. *Technical datasheet LW-PLA*. Available: https://colorfabb.com/media/datasheets/tds/colorfabb/TDS_E_ColorFabb_LW-PLA.pdf

[5] I. Dinakaran, C. Sakib-Uz-Zaman, A. Rahman, and M. A. H. Khondoker. Controlling degree of foaming in extrusion 3D printing of porous polylactic acid. *Rapid Prototyp J*, 29(9): 1958–1968, 2023.

[6] A. Alduais and S. Özerinç. Tunable mechanical properties of thermoplastic foams produced by additive manufacturing. *Express Polym Lett*, 17(3): 317–333, 2023.

[7] A. Yousefi Kanani, A. E. W. Rennie, and S. Z. Bin Abd Rahim. Additively manufactured foamed polylactic acid for lightweight structures. *Rapid Prototyp J*, 29(1): 50–66, 2023.

[8] A. R. Damanpack, A. Sousa, and M. Bodaghi. Porous plas with controllable density by fdm 3d printing and chemical foaming agent. *Micromachines (Basel)*, 12(8), 2021.

[9] F. de Freitas and H. Pegado. Impact of nozzle temperature on dimensional and mechanical characteristics of low-density PLA. *International Journal of Advanced Manufacturing Technology*, 126(3–4): 1629–1638, 2023.

[10] D. Zenkert, *The Handbook Of Sandwich Construction*. Engineering Materials Advisory Services, 1995.

[11] F. He, H. Ning, and M. Khan. Effect of 3D Printing Process Parameters on Damping Characteristic of Cantilever Beams Fabricated Using Material Extrusion. *Polymers (Basel)*, 15(2), 2023.

[12] ASTM D638-02a. *Standard Test Method for Tensile Properties of Plastics*. ASTM International, 2002.

[13] ASTM D7250/D7250M – 20. Standard Practice for Determining Sandwich Beam Flexural and Shear Stiffnes. ASTM International, 2020.

[14] M. Assarar, A. El Mahi, and J. M. Berthelot. Evaluation of the dynamic properties of PVC foams under flexural vibration. *Composite Structures*, 94(6): 1919–1931, 2012.

ARREST OF UNSTABLE COMPRESSIVE CRACKS IN FIBRE REINFORCED POLYMERS USING PLY DISCONTINUITIES

B.P. Santos[1], E.S. Greenhalgh [2] and S.T. Pinho [3]

[1] Aeronautics Department, Imperial College London, South Kensington Campus, London, SW7 2AZ, UK
Email: b.santos22@imperial.ac.uk, Web Page: https://www.nextcomp.ac.uk
[2] Aeronautics Department, Imperial College London, South Kensington Campus, London, SW7 2AZ, UK
Email: e.greenhalgh@ imperial.ac.uk
[3] Aeronautics Department, Imperial College London, South Kensington Campus, London, SW7 2AZ, UK
Email: silvestre.pinho@ imperial.ac.uk

Keywords: Composite materials, Compression, Unstable failure, Crack arrest, Kink-band

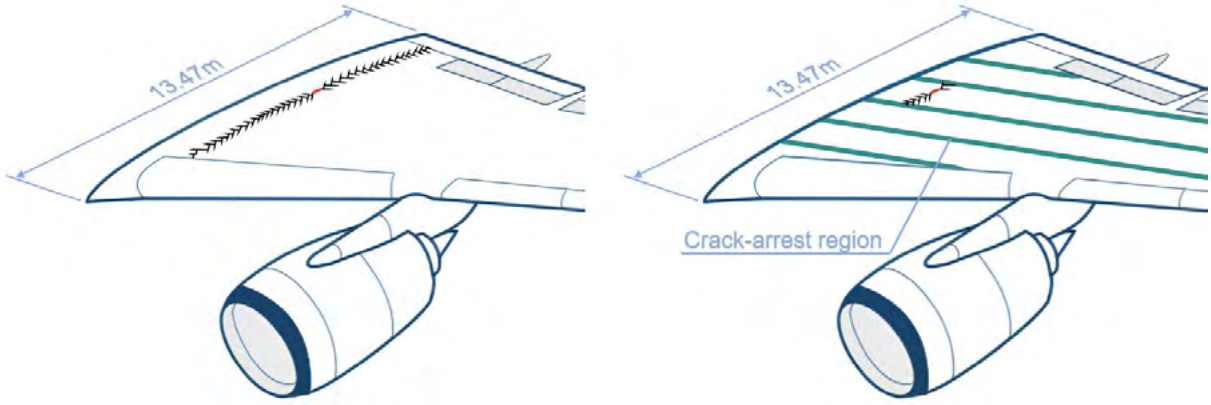
Abstract
The compressive properties of fibre-reinforced composites are significantly inferior to their tensile equivalent. This factor, allied to the 'no-damage growth' design philosophy currently used in aerospace, results in significantly oversized structures. The current work aims to improve the compressive response of composites by compartmentalizing unstable compressive failure in large fibre-reinforced structures. It proposes a ply-discontinuity feature capable of arresting unstable crack propagation in multidirectional Carbon Fibre-Reinforced Polymer (CFRP) laminates subjected to compressive loading. By replacing 0° oriented plies by carefully selected off-axis ones, the feature is capable of dispersing and dissipating compressive kink-band propagation energy as well as modifying the laminate's failure modes. Consequently, the laminate achieves arrest of rapidly growing unstable cracks (propagating at ~1 km/s) and the specimen's ultimate failure strain is increased. To validate the proposed concept, test specimens were designed and manufactured using IM7/8552 carbon-fibre reinforced epoxy. Through compressive tests, the feature's crack-arrest capability was shown, remarkably increasing by nearly a third the strain tolerance upon final failure, when compared to the respective baseline.

1. Introduction

Compressive performance, particularly in the presence of in-service damage, limits composite design. Factors such as a high sensitivity to manufacture defects and complexity in failure modes cause compressive strength of Fibre-Reinforced Polymers (FRPs) to be significantly inferior to their tensile performance [1-3]. Additionally, if compressive failure initiates in a component, there are no means to arrest such fracture. Thus, composites are currently constrained to a 'no-damage growth' design philosophy. Being able to tolerate and manage compression crack growth ('damage growth tolerance' philosophy) would enable the realisation of composites' full structural potential.

A key component of this design philosophy are crack-arrest methods, which seek to stop unstable failure growth, isolating damage and extending structural life after an initial failure event. Features with these capabilities have already been developed and are widely employed in other fields. In compressed-gas transmission pipelines, ribs are used to contain long tensile cracks in metallic pipes [4,5]. Similarly, in airplane fuselages tear straps are used to stop tear propagation in the composite skin [6]. Nevertheless, little to no study has been done on compression crack-arrest in fibrous composite laminates.

By developing a feature capable of arresting unstable compressive cracks in FRPs, this research aspires to pave the way to successful compartmentalisation of failure in large composite structures. Components designed through this method will remain fit for service after initial failure propagation, enabling safer designs while simultaneously reducing their weight. These developments shall be particularly advantageous in applications where catastrophic failure would lead to loss of lives, as is the case of airplane wings. Figure 1 exemplifies how such a feature would be able to avoid structural collapse in a damaged wing root.



(a) (b)

Figure 1. Visualisation of compressive-crack compartmentalisation on a damaged Airbus A350-1000 wing. (a) Crack propagation from the damaged region without crack arrest mechanisms, unrestrictedly expanding across the wing's chord and causing catastrophic failure. (b) Failure compartmentalisation by periodic crack-arrest bands, allowing the wing to remain in service.

2. Feature concept

Unstable compression crack propagation on CFRPs happens at a rate approaching 1 km/s [7]. Therefore, to stop this growth it is important to implement ways of dissipating or deflecting the energy associated to the propagation process. With that aim, a concept based on the idea of ply-discontinuity was developed. It is known that compressive kink-band failure is the main mechanism of crack growth in FRP compression [8]. This fracture mechanism tends to occur in 0° oriented plies, propagating perpendicular to the loading direction. Thus, by implementing regions where 0° plies are replaced by off-axis ones, the feature seeks to force the failure into following new paths, dispersing energy in the process. Moreover, lay-ups where 0° plies are the main loading component (hard lay-ups) have lower translaminar toughness than those where the load is supported only by off-axis plies (soft lay-ups). Therefore, by inserting discontinuities in the lay-up, the feature also implements regions of increased toughness that assist in fracture containment.

Notably, the feature does not introduce any new material types into the design. The sole presence of materials that have been previously certified and are already in use in the aerospace industry constitutes a remarkable advantage in the mechanism's incorporation into service. Furthermore, the usage of a single type of composite facilitates recycling and disposal processes.

3. Materials and methods

A compression specimen was designed to test the developed crack-arrest feature. The angle of the off-axis plies responsible for replacing 0° in the soft lay-up was defined as ±30°. A sandwich configuration with aluminium honeycomb core and IM7/8552 CFRP skins was chosen to prevent the composite laminate from global buckling during test. A notch was designed to induce initial failure in the gauge

region at an applied strain close to -3100με. This value was chosen for being slightly above the -2500με design limit load typically used in aerospace industry [9]. Figure 2 illustrates the specimen's geometry.

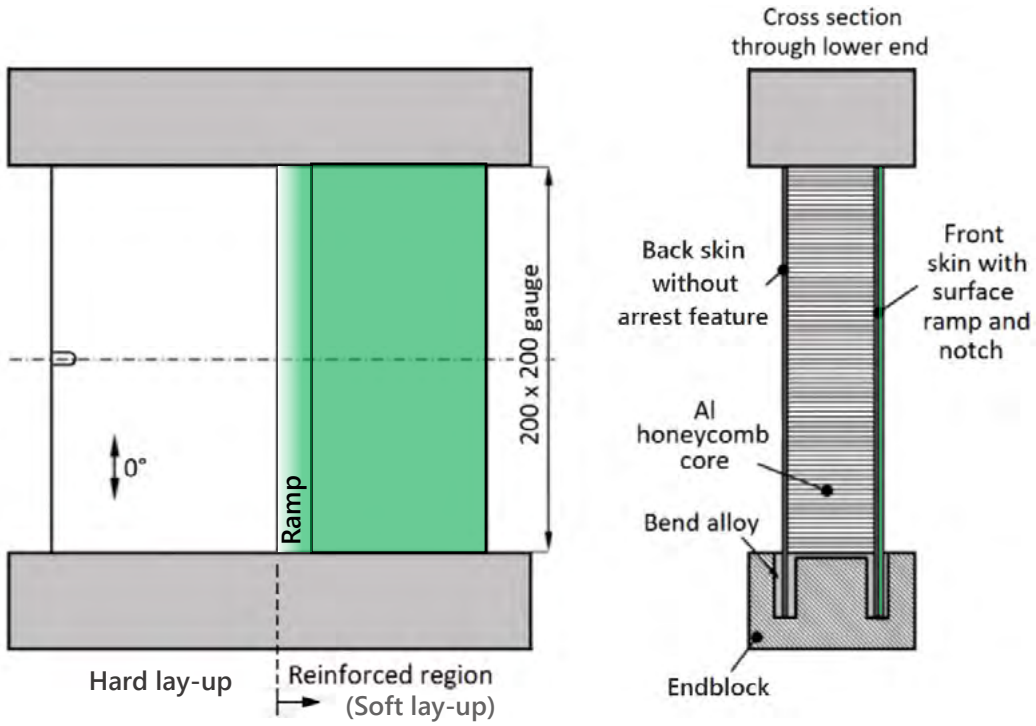


Figure 2. Compression test specimen geometry (crack-arrest region is presented in green).

While defining the skins' lay-up, a series of restrictions was defined to control test variables. Since the hard lay-up is multidirectional, while 0° layers were replaced by ±30°, the remaining plies were maintained continuous to conserve specimen integrity. Moreover, both hard and soft lay-ups were designed to be symmetrical to avoid compression-bending coupling effects. Finally, as a consistent stiffness was desirable throughout the specimen width, additional layers were added to the soft lay-up to compensate for the difference in stiffness induced by changing ply-orientation. To reduce stress concentration, the lay-up transition was designed to happen gradually, assuming the shape of a 'ramp'. Since the front skin of the of the crack-arrest specimen was defined as surface of interest, only this face possessed the arrest feature.

Two specimens were manufactured: a crack-arrest (CA) specimen, with the arrest feature lay-up presented, and a baseline (plain) specimen. The baseline consisted in a sandwich coupon with two hard lay-up skins and no ply-discontinuity, possessing an equivalent stifness to that of the CA specimen.

The specimens were tested in a 250 tonne screw-driven compression test machine under displacement control. Digital Image Correlation and strain gauges remote from the crack region were used to monitor mechanical behaviour and compute applied strain. C-scans and X-ray images of the fractured specimens were taken to achieve deeper understanding of the processes through which failure initiates and is subsequently arrested.

4. Results and discussion

As expected, the baseline specimen suffered an abrupt failure that propagated across the notched face's width, leading to almost complete loss of load-bearing capability. The failure of the CA specimen, however, was successfully stopped upon reaching the beginning of the arrest region. Following this

initial failure, additional strain was endured by the specimen, progressively causing smaller failure steps. Ultimate failure was achieved when the crack front reached the opposite end of the skin's width. Figure 3 represents both specimens after they had reached ultimate failure.

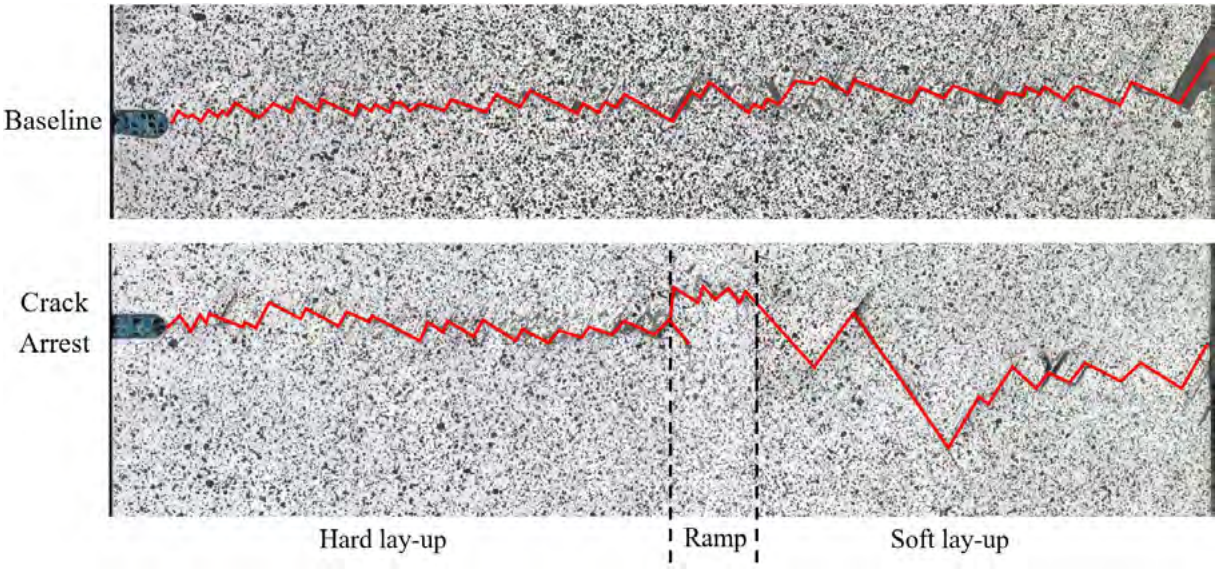


Figure 3. Fractured region of the test specimens, portraying the change in failure path caused by ply-discontinuity. Main visible failure paths are highlighted in red.

It was notable that, as seen in the baseline, initial fracture in the CA specimen grew perpendicular to load application direction. Similar fracture morphology was also observed between these failures, consistent with the baseline's suitability as comparison. Nevertheless, following the initial arrest, the subsequent failure in the CA specimen presented significant changes in both growth direction and fracture morphology. These behavioural changes hint as to the effects of the of ply replacement in obstructing the kink-band propagation.

Figure 4 presents the applied strain versus load of both specimens during test. It's important to note that the specimens' 200x200mm gauge area represents only a very small fraction of the dimensions of the structures they seek to represent. Therefore, even the loss of the entire 200mm section would not represent a significant reduction in the complete structure's load capacity. As of consequence, the most reliable way of analysing the specimens' performance is not through their load capacity but through their strain tolerance. This tolerance represents the structure's capability of being deformed before collapsing.

In Figure 4, it is possible to observe that both specimens showed similar elastic behaviour before initial failure. The baseline's failure happened at $\varepsilon_b^{ult} = -3070\mu\varepsilon$, while that of the CA specimen started at $\varepsilon^{ini} = -3600\mu\varepsilon$. The chart still portrays its subsequent growth steps, up to the ultimate failure at $\varepsilon^{ult} = -4065\mu\varepsilon$. It is notable that, although possessing the same stiffness as the baseline, the CA specimen presented an ultimate strain to failure nearly a third higher than it.

X-rays and C-scans were used to visualise subsurface damage in both specimens. The analyses showed that CA specimen's soft lay-up region presented considerably more extensive delamination than both the hard lay-up region and the baseline. Together with the more tortuous failure path caused by crack deflection, the increase in secondary damage surfaces contributed to energy dissipation, leading to the feature's success.

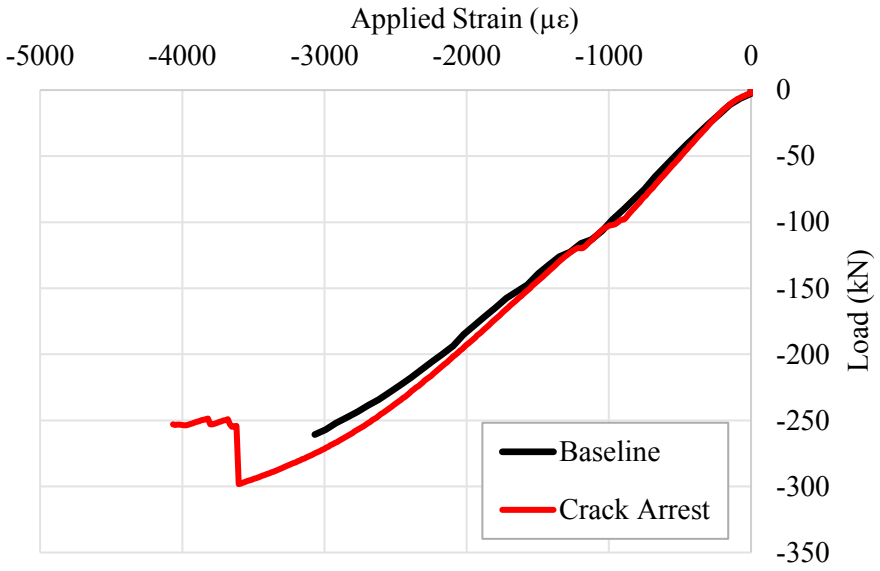


Figure 4. Evolution of applied strain in both specimen tests, evidencing feature-induced crack arrest and increase in strain tolerance.

5. Conclusions

A concept of crack-arresting feature for FRPs under compression was developed and tested. The concept was proven to successfully stop unstable compressive kink-band propagation, considerably delaying the specimen's ultimate failure and improving its strain tolerance. When compared to an equivalent baseline, the crack-arrest specimen showed a one third higher ultimate failure strain.

It was perceived that, by using discontinuity in fibre orientation, the feature can deflect the crack, forcing it to generate longer failure paths. Moreover, the soft lay-up suffered higher levels of secondary failure, contributing to energy dispersion. Therefore, by generating additional failure surfaces and imposing difficulties to crack propagation perpendicular to loading direction, the feature is able of dispersing enough energy to stop kink-band propagation.

Next research steps include fractographic analysis, to deduce the detailed failure mechanisms, followed by optimisation of the ply angles and stacking sequence. Through this process, crack-arrest effects will be maximised, whilst maintaining the same panel stiffness.

Acknowledgments

The authors kindly acknowledge the funding for this research provided by UK Engineering and Physical Sciences Research Council (EPSRC) programme Grant EP/T011653/1, Next Generation Fibre-Reinforced Composites: a Full Scale Redesign for Compression (NextCOMP), a collaboration between Imperial College London and University of Bristol. For the purpose of open access, the authors have applied a creative commons attribution (CC BY-NC 4.0) license to any author accepted manuscript version arising.

References

[1] S. Nunna, A.R. Ravindran, J. Mroszczok, C. Creighton and R.J. Varley. A review of the structural factors which control compression in carbon fibres and their composites, *Composite Structures*, 303, p.116293, 2023.

[2] C.V. Opelt, G.M. Cândido and M.C. Rezende. Compressive failure of fiber reinforced polymer composites – A fractographic study of the compression failure modes, *Materials Today Communications*, 15, pp.218-227, 2018.
[3] Q. Sun et al. Experimental and computational analysis of failure mechanisms in unidirectional carbon fiber reinforced polymer laminates under longitudinal compression loading, *Composite Structures*, 203, pp. 335–348, 2018.
[4] B.M. Albaghdadi and A.O. Cherniavsky. Possibility of using ribs to protect pipelines from the long crack propagation, *Bulletin of the South Ural State University. Ser. Mechanical Engineering Industry*, 16(3), pp.15-20, 2016.
[5] X.K. Zhu. State-of-the-art review of fracture control technology for modern and vintage gas transmission pipelines, *Engineering Fracture Mechanics*, 148, pp.260-280, 2015.
[6] A. Velicki and D.C. Jegley. PRSEUS structural concept development, *In 52nd Aerospace Sciences Meeting*, p. 0259, 2014.
[7] J. Ankersen et al. Dynamic fracture in CFRP panels under compressive loading. *Proceedings of the 15th European Conference on Composite Materials*. 2012.
[8] E.S. Greenhalgh. Failure analysis and fractography of polymer composites. *Elsevier*, pp.117-126, 2009.
[9] E.S. Greenhalgh. Technical Evaluation of DAMOCLES; Damage Management of Composite Structures for Cost-Effective Life-Extensive Service, Technical Report QinetiQ/FST/TR023421, 2002.

MICRO-SCALE FEA FOR CLARIFYING THE RELATIONSHIP BETWEEN ENTROPY GENERATION AND RESIDUAL STRENGTH OF POLYMER COMPOSITES

Mio SATO [1], Natsuko KUDO [2], Jun KOYANAGI [3]
[1]Japan Aerospace Exploration Agency, 6-13-1 Osawa, Mitaka-shi, Tokyo, Japan
Email: sato.mio@jaxa.jp
[2] Graduate school of Tokyo University of Science, 6-3-1 Niijuku, Katsushika-ku, Tokyo, Japan
Email: 8219B01@alumni.tus.ac.jp
[3] Tokyo University of Science, 6-3-1 Niijuku, Katsushika-ku, Tokyo, Japan
Email: koyanagi@rs.tus.ac.jp

Keywords: Polymer-matrix composites (PMCs), Damage mechanics, Finite element analysis (FEA), Viscoelasticity, Thermal entropy

Abstract
In this study, we estimate the residual strength of polymer composites after thermal shrinkage by correlating the amount of entropy generation during material deformation with material degradation. We propose a viscoelastic constitutive equation for viscoelastic media, grounded in the principles of irreversible thermodynamics and viscoelastic theory. Numerical simulations are conducted to investigate the residual strength after thermal shrinkage during molding. The results indicate that the residual strength decreases significantly with an increase in temperature difference during cooling due to increased entropy generation. This study highlights the importance of considering thermal shrinkage and its impact on material degradation for accurate residual strength prediction.

1. Introduction

In conventional studies concerning the durability of CFRP, particularly in terms of residual strength, the focus has typically been on assessing durability under specific loading conditions such as constant strain rate, cyclic loading, and creep, each considered independently [1]. To determine the essential durability, it is necessary to measure the residual strength after different load histories. For instance, if the material undergoes creep, followed by cyclic loading, then constant strain rate, and eventually fails, it stands to reason that the initial strength of the material would diminish due to the exposure to various loading conditions (Fig. 1). Utilizing traditional methods, the residual strength after such combined loading scenarios cannot be accurately determined. Therefore, even when the material is subjected to multiple and diverse loading conditions, there is a pressing need for a method capable of calculating the residual strength by establishing a universal failure criterion.

To discuss the lifetime (long-term durability) of composite materials, the viscoelastic properties must be considered because of the viscoelastic behavior of the polymer matrix. In discussing the lifetime of polymer composites, some studies have been conducted to describe their strength degradation by thermodynamic entropy, recently [2, 3]. Inelastic deformation of the material causes an irreversible structural change inside the material. Such an internal structural change is expressed by a thermodynamic internal variable based on Clausius-Duhem inequality (the second law of thermodynamics); i.e., deterioration of the material proceeds with the disorder of the system. The disorder in the system, which causes deterioration of the characteristics, is raised by the mechanical deformation and the entropy increases accordingly. The disorder in the degraded system continues to

increase to the critical state and causes the failure of the materials. Therefore, irreversible entropy in materials can be used as a criterion for evaluating lifetime of materials.

In order to effectively discuss and evaluate the residual strength of materials subjected to various loading conditions, it is imperative to develop a constitutive equation for the resin that comprehensively accounts for these diverse loads. To this end, we propose a viscoelastic constitutive equation for viscoelastic media, which is grounded in the principles of irreversible thermodynamics and viscoelastic theory. As an initial approach, we conduct numerical simulations to investigate the residual strength after thermal shrinkage during molding. It is anticipated that the residual strength after thermal shrinkage will be lower than the static tensile strength. Subsequently, we engage in a detailed discussion regarding the matrerial degradation due to the thermal shrinkage.

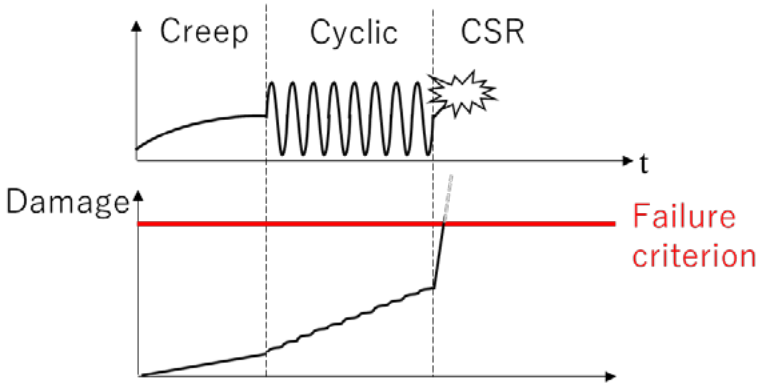


Figure 1. The concept of universal failure criterion.

2. Analysis

2.1 Constitutive equation

The generation of entropy up to the point of material failure (fracture entropy), denoted as s_{cr}, is described by Eq. (1), which is derived using the first and second laws of thermodynamics (Clausius-Duhem inequality) and Helmholtz free energy [4]. In this equation, t_f represents the time of material failure, W_d is the energy dissipated due to non-elastic deformation, T is the temperature, $\dot{\boldsymbol{V}}_k$ is the appropriate set of internal variables, $\boldsymbol{A}_k$ is the generalized thermodynamic force related to the internal variables, and $\boldsymbol{J}_q$ is the heat flux across the boundary. Eq. (1) encompasses mechanical dissipation from non-elastic deformation (the first term), non-recoverable energy such as damage stored within the material (the second term), and thermal dissipation due to heat conduction (the third term). In this study, we assume that the first and second terms are predominant during material deformation, thus defining the dissipated energy W until material failure as the sum of these two terms, as shown in Eq. (2). By using Eq. (2), the entropy generated up to material failure can be determined by measuring the dissipated energy and temperature during the material testing.

$$s_{cr} = \int_0^{t_f} \left(\frac{W_d}{T} - \frac{\boldsymbol{A_k}:\dot{\boldsymbol{V}}_{\boldsymbol{k}}}{T} - \frac{\boldsymbol{J_q} grad T}{T^2} \right) dt \tag{1}$$

$$s_{cr} = \int_0^{t_f} \left(\frac{W_d}{T} - \frac{\boldsymbol{A_k}:\dot{\boldsymbol{V}}_{\boldsymbol{k}}}{T} \right) dt$$

$$= \int_0^{t_f} \left(\frac{W}{T} \right) dt \tag{2}$$

We propose a viscoelastic model, described in Fig. 2, which is derived from Maxwell's model. This model incorporates 15 Maxwell elements. The overall strain, denoted as $\boldsymbol{\varepsilon}^{\mathrm{total}}$, is composed of both a viscoelastic strain, $\boldsymbol{\varepsilon}^{\mathrm{ve}}$, and a viscoplastic strain, $\boldsymbol{\varepsilon}^{\mathrm{vp}}$, as described in Eq. (3). Eq. (4) represents a

viscoelastic constitutive equation that takes into account the stress history, based on the formulation proposed by Schapery [5]. In this equation, D is a damage variable that incorporates the entropy-damage law, and E is the relaxation modulus, as outlined in Eq. (5). In Eq. (5) and Fig. 1, E^n represents the spring stiff ness of the n th Maxwell element, with each element having a stiffness value of 1/15 th of the initial stiffness of the entire Maxwell model. η^n denotes the viscosity coefficient of the nth Maxwell element, t is the time, t' is the time at which the strain is applied, and g is a nonlinear coefficient presented in Eq. (6). σ_{Mises} represents the von Mises stress, σ_0 is a specified stress value, and α_n is a nonlinear coefficient. The second term in Eq. (3) is defined by Eq. (7), where H^{irr} is the viscosity coefficient responsible for inducing irreversible strain. These material parameters are determined through experiments conducted on the matrix resin [3]. The damage variable D introduced by the fracture entropy is expressed by Eq. (8). There, D_{cr} is the critical damage, s is the current entropy and α_d is damage parameter. Matrix properties are shown in Tab. 1.

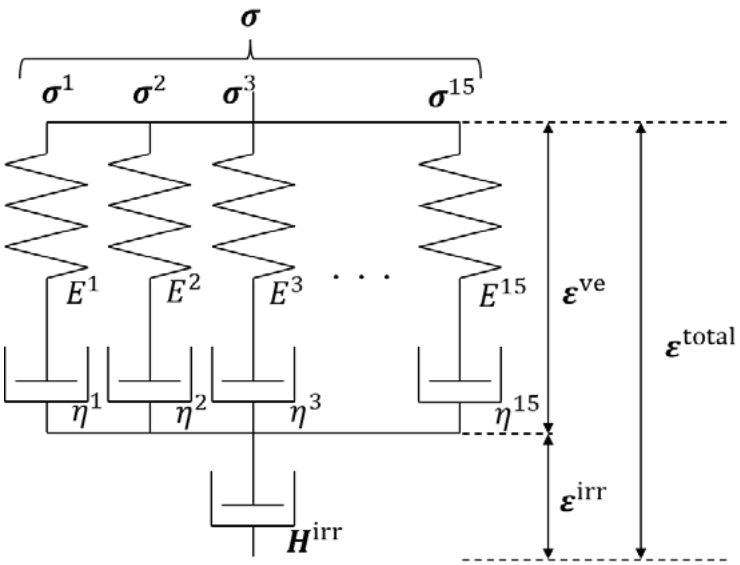


Figure 2. Viscoelastic model.

$$\boldsymbol{\varepsilon}^{\text{total}} = \boldsymbol{\varepsilon}^{\text{ve}} + \boldsymbol{\varepsilon}^{irr} \tag{3}$$

$$\sigma_{ij}(t) = (1 - D)\int_0^t E_{ijkl}(t - t')\frac{g d\varepsilon_{kl}^{ve}}{dt'}dt' \tag{4}$$

$$E_{ijkl}(t) = \sum_{n=1}^{15} E_{ijkl}^n e^{-tE^n/\eta^n} \tag{5}$$

$$g = \frac{1}{1 + \alpha_n\left(\frac{\sigma_{Mises}}{\sigma_0}\right)^m} \tag{6}$$

$$\varepsilon_{ij}^{irr} = \int_0^t \left(H_{ijkl}^{irr}\right)^{-1}\sigma_{kl}dt \tag{7}$$

$$D = D_{cr}\frac{s}{s_{cr}} = D_{cr}\frac{1}{s_{cr}}\frac{W}{T} \fallingdotseq W \times \alpha_d \tag{8}$$

Table 1. Matrix properties.

Maxwell element				
n	E^n [MPa]	η^n [MPa·s]	Elasticity	
1	284	4.5×10^2	E_0 [MPa]	4260
2	284	3.3×10^3		
3	284	1.2×10^5	Nonlinearity	
4	284	1.9×10^6	σ_0 [MPa]	70
5	284	1.8×10^7	α_n	2
6	284	1.4×10^8	m	7
7	284	8.5×10^8	Viscoplastic strain	
8	284	5.0×10^9	η^{irr} [MPa·s]	1.0×10^{23}
9	284	3.0×10^{10}		
10	284	1.9×10^{11}	Damage parameters	
11	284	1.4×10^{16}	α_d	1000
12	284	1.3×10^{19}		
13	284	2.1×10^{22}		
14	284	1.3×10^{26}		
15	284	2.5×10^{29}		

2.2 Micro-scale finite element model

A numerical analysis is performed using the ABAQUS 2020 software package. We create a three-dimensional (3D) unit cell model, as illustrated in Fig. 3, and applied periodic boundary conditions at all edges utilizing the key node method. The representative volume element (RVE) includes 34 carbon fibers with a diameter of 6 μm, embedded within a matrix resin. The dimensions of the 3D unit cell are 39 μm × 39 μm × 0.3 μm, resulting in a fiber volume fraction of 63%. The model consists of C3D15 elements, with a total of 38,322 elements and 173,760 nodes. The carbon fibers are modeled as anisotropic elastic materials (as detailed in Table 2), and the proposed constitutive equation is implemented in the matrix resin via the UMAT user subroutine.

In this study, three types of analysis conditions are performed. The first one involves a static tensile analysis conducted at room temperature (300K) to determine the static strength. The other two analyses consider the thermal shrinkage process during molding. For these analyses, the initial states are set at 400K and 350K, respectively, and the RVE model are cooled to 300K (ΔT are 100K and 50K, respectively). After cooling, the RVE model are left to rest for one hour before performing the static tensile analysis to evaluate the residual strength. The strain rate for the static tensile analysis is set at 0.001/sec. In the analysis of the thermal shrinkage process, the Arrhenius-type time-temperature superposition principle (TTSP) shown in Eq. (9) is adopted. There, α^{TR} is a time-accelerating factor, ΔH

is the activation energy, R is the gas constant, T^{R} is the reference temperature, and T is the current temperature. We assume that $\Delta H = 160$ kJ/mol from the result of dynamic mechanical analysis test, and $T^{\mathrm{R}} = 300$ K in this study.

$$\log\alpha^{\mathrm{TR}}(T) = \frac{\Delta H}{2.303R}\left(\frac{1}{T} - \frac{1}{T^{\mathrm{R}}}\right) \tag{9}$$

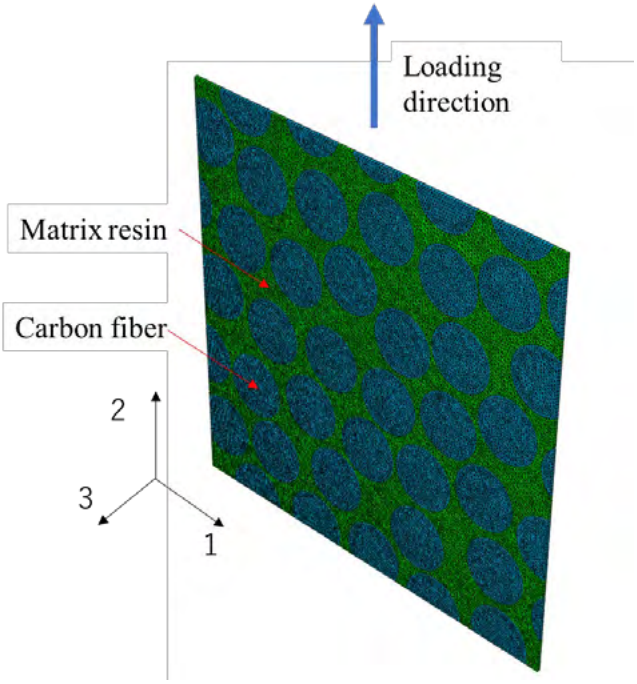


Figure 3. FEA model.

3. Result and Discussion

The results of the three analysis conditions are shown in Fig. 4. The static strength is found to be 68.6 MPa, while the residual strength after cooling with ΔT = 50K is 58.1 MPa, and with ΔT = 100K, it is 51.4 MPa. The greater the temperature difference during cooling, the more entropy (dissipated energy) is generated during thermal shrinkage, resulting in lower residual strength. In cases considering thermal shrinkage, the initial stiffness is reduced compared to the static analysis results due to viscoelastic behavior during cooling. The proposed model is capable of predicting the residual strength while accounting for the damage induced by thermal shrinkage.

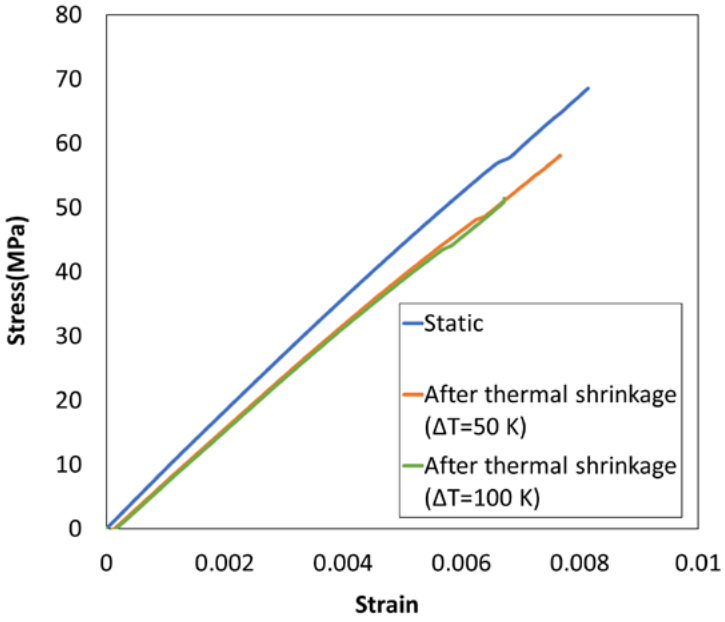


Figure 4. SS curve.

4. Conclusions

The study presented a comprehensive approach to evaluate the residual strength of polymer composites by incorporating a viscoelastic constitutive model based on irreversible thermodynamics and viscoelastic theory. The numerical analysis using ABAQUS revealed that the residual strength of polymer composites decreases as the temperature difference during cooling increases, due to higher entropy generation. The static strength is measured at 68.6 MPa, while the residual strengths after cooling with $\Delta T = 50K$ and $\Delta T = 100K$ are 58.1 MPa and 51.4 MPa, respectively. The proposed model effectively predicts the residual strength by accounting for the damage induced by thermal shrinkage, emphasizing the necessity to consider thermal effects in the design and analysis of polymer composites.

References

[1] R. Christensen et al., *International Journal of Fracture*, 143:35-39, 2007.
[2] EM Gune et al., Damage characterization in non-isothermal stretching of acrylics. Part I: Theory, *Mech Mater.* 43(12):979–91, 2011.
[3] M. Sato et al., Residual strength prediction for unidirectional CFRP using a nonlinear viscoelastic constitutive equation considering entropy damage. *Composites Part A*, 141:106178, 2021.
[4] M. Naderi et al. On the thermodynamic entropy of fatigue fracture. *Proc R Soc A Math Phys Eng Sci*, 466(2114):423–38, 2010.
[5] RA. Schapery, On the characterization of nonlinear viscoelastic materials. *Polym Eng Sci.* 9(4):295–310, 1969.

INTEGRATION OF CARBON FIBER AND FIBER OPTICAL SENSORS IN CONTINUOUS FIBER-REINFORCED ADDITIVELY MANUFACTURED PARTS

J. Seiffert[1], M. Bissinger[2] and Prof. K. Drechsler[3]

[1]Chair of Carbon Composites, School of Engineering and Design, Technical University of Munich, Boltzmannstr. 15, 85748 Garching, Germany
Email: jan.seiffert@tum.de, Web Page: https://www.asg.ed.tum.de/en/lcc/home/
[2]Chair of Carbon Composites, School of Engineering and Design, Technical University of Munich, Boltzmannstr. 15, 85748 Garching, Germany
Email: maximilian.bissinger@outlook.com, Web Page: https://www.asg.ed.tum.de/en/lcc/home/
[3]Chair of Carbon Composites, School of Engineering and Design, Technical University of Munich, Boltzmannstr. 15, 85748 Garching, Germany
Email: klaus.drechsler@tum.de, Web Page: https://www.asg.ed.tum.de/en/lcc/home/

Keywords: Continuous Fiber Additive Manufacturing, Structural Health Monitoring, Self-Sensing, Fiber Optical Sensors, 3D Printing, Carbon Fiber Sensors

Abstract
This study investigates the automated integration of fibrous sensors, including carbon fiber sensors (CFS) and fiber optical sensors (FOS), into continuous fiber-reinforced additively manufactured parts for enhanced structural health monitoring. Mechanical testing, in the form of tensile and 3-point bending tests, revealed that the presence of integrated CFS and FOS does not significantly impact mechanical properties, highlighting the potential for seamless integration without compromising structural integrity. FOS demonstrated high precision in strain measurements during tensile and bending tests, which strongly correlated with the reference measurement obtained through a video extensometer, even allowing for precise tensile and flexural modulus computation. Meanwhile, CFS exhibited linear piezoresistive behavior up to a particular strain limit, making them suitable for strain-sensing applications. Sensitivity coefficients of different CFS types were determined, which demonstrated the self-sensing capabilities of distinguishing between CFS integrated in different layers of 3-point bending specimens. These findings underscore the potential of additively manufactured sensor-integrated composites for structural health monitoring and multifunctionality across various engineering domains. Further advancements in sensor technology and additive manufacturing techniques hold promise for broader applications in aerospace, automotive, and civil infrastructure.

1. INTRODUCTION

Continuous fiber-reinforced polymer composites are increasingly utilized in various engineering applications due to their superior mechanical properties. To further enhance their functionality, integrating sensors directly into these composites is an area of growing interest. Hereby, fibrous sensors are of superior interest, as they can be integrated without compromising the structural integrity and the mechanical properties of the part. Carbon fibers are widely used as a reinforcement material, but due to their piezoresistive behavior, they can also be used as sensors (CFS), which is also referred to as self-sensing [1]. Some carbon fibers show linear piezoresistive behavior, which is a fundamental property for CFS and is influenced by the micro structure of the CFS as well as geometric effects, as was shown

by Horoschenkoff et al. [2]. CFS are sensitive to strain [3,4], temperature, and humidity [5]. Research on damage monitoring using CFS has also been conducted [6,7].
Likewise, FOS can be used to detect temperature and strain changes. More commonly, Fiber Bragg Grating sensors have been researched [8]. Still, the Rayleigh backscatter measurement technique has emerged in the last years [9,10], allowing the use of cost-effective, single-mode optical fibers as FOS.
In combination with additive manufacturing, FOS have been integrated into additively manufactured parts to measure strain and temperature [11]. With the development of continuous fiber additive manufacturing (CFAM) systems and commercially available systems, self-sensing of 3D printed structures with carbon fiber reinforcement has been in the spotlight of researchers recently [12–14].
In this study, a novel approach is presented for integrating CFS and FOS, using Rayleigh backscattering, into continuous fiber-reinforced parts additively fabricated via Fused Filament Fabrication (FFF). The aim is to evaluate the performance of CFS and FOS in measuring strain under tensile and bending loads.

2. MATERIALS AND METHODS

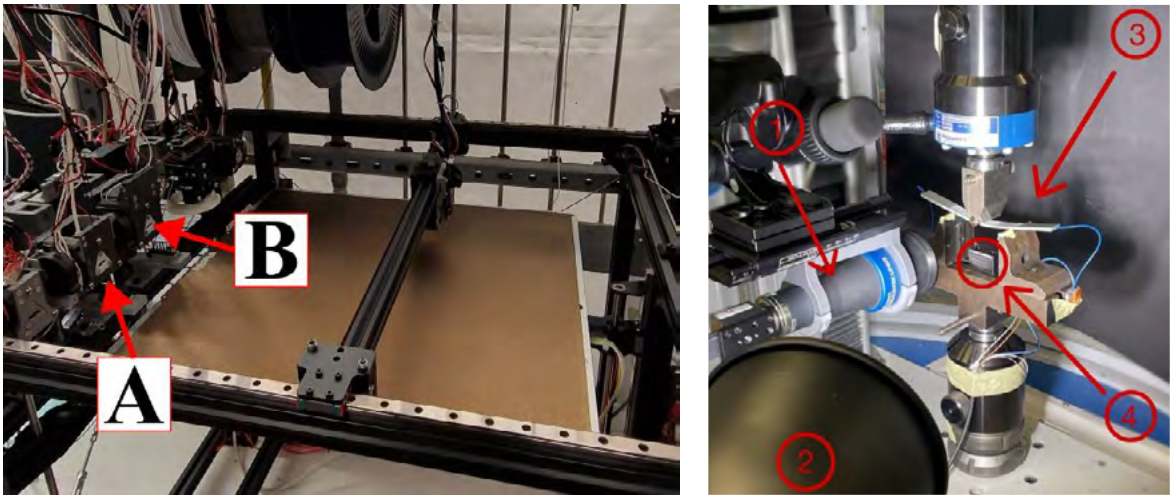
2.1 Specimen Fabrication

The specimens for the tensile and 3-point bending tests were designed in accordance with the standards DIN EN ISO 527-5 and DIN EN ISO 14125, respectively. A custom-built 3D printer, shown in **Figure 1**, was used to additively manufacture the specimens. The custom 3D printer is equipped with a tool-changer adapted from the concept and mechanisms of the jubilee tool-changer [15]. It can use up to five different tools and switch between them automatically during manufacturing. A continuous fiber printhead, provided by Anisoprint 3D Printing Technology Limited Company, and a direct-drive FFF printhead were used for the specimen fabrication. Anisoprint's Composite Carbon Fiber (CCF) was used as a CFS and as the reinforcement fiber. White PETG by Material4Print was used as a matrix material for the specimens. Thorlabs' SM1550P Polyimide-Coated Single Mode Fiber was used as a FOS.
For the tensile tests, the CFS and FOS were integrated in the mid-plane and centerline of the specimen. The FOS was integrated manually and overprinted by the direct-drive printhead. For the 3-point bending specimen, four different specimen types with sensors were manufactured. For types AN, AS and FO, the CFS and FOS were integrated in the first fiber layer on the tension side of the specimen during testing. For type A2S, the CFS was integrated in the second fiber layer on the tension side of the specimen, therefore being closer to the center of the specimen. The CFS in type AN was printed as one straight line in the centerline of the specimen. The CFS in types AS and A2S were printed as a grid with six gridlines centered around the centerline of the specimen. The CCF reinforcement fibers were printed in straight lines to reinforce the specimen unidirectionally in length direction only. The tensile specimen consisted of three thermoplastic layers on the bottom, mid-plane and top, and four reinforcement layers. The 3-point bending specimens were printed with two thermoplastic layers, bottom and top, and five reinforcement layers. The fiber volume content (FVC) was calculated and experimentally verified by burning the matrix and weighing the specimen using a high-accuracy scale. All specimen types and their respective specifications are shown in **Table 1**.
Each tip of a CFS was printed to extend approximately 20 mm outside the end of the specimen in order to electrically connect them. The matrix at the CFS' tips was removed by burning. The bare carbon fiber was then electrically connected and bonded to copper wires by means of DICO 200-05 highly conductive silver ink. A coreless termination fiber was spliced to one end of the FOS and a Logilink FPSLC01 G627.A2 fiber with an LC/APC connector to the other end.

Table 1: Specimen Specifications.

Specimen Type	Sensor type	Sensor location	Sensor length (mm)	FVC (%)	Test Standard	Specimen Dimension (L x W x T) (mm³)
AT	CFS (line)	Center plane, centerline	150	10.8	DIN 527-5	250 x 15 x 1.7

FOT	FOS (line)	Center plane, centerline	150	10.8	DIN 527-5	250 x 15 x 1.7
T	none	-	-	10.8	DIN 527-5	250 x 15 x 1.7
AL	CFS (line)	1st fiber layer, centerline	80	15.7	DIN 14125	120 x 15 x 2.0
AG	CFS (grid)	1st fiber layer, centered	420	15.7	DIN 14125	120 x 15 x 2.0
A2G	CFS (grid)	2nd fiber layer, centered	420	15.7	DIN 14125	120 x 15 x 2.0
FOB	FOS (line)	1st fiber layer, centerline	80	15.7	DIN 14125	120 x 15 x 2.0
B	none	-	-	15.7	DIN 14125	120 x 15 x 2.0



(a) **(b)**

Figure 1: (a) Custom 3D Printer. A: Direct-Drive FFF Printhead, B: Anisoprint's continuous fiber printhead. **(b)** Test Setup for AL type specimen. 1: video extensometer, 2: light source, 3: AL specimen under bending load, 4: reference block for video extensometer.

2.2 Experimental Setup and Analysis

A 100 kN universal test machine by Hegewald & Peschke was used for both tensile and 3-point bending tests. The test machine was equipped with a 10 kN or 2.5 kN load cell for tensile or 3-point bending tests, respectively. LabMaster control software was used to control the test machine and acquire data. A Real-Time Strain Sensor video extensometer (VE) by LIMESS GmbH was used for the reference displacement and strain measurement, as shown in **Figure 1**. The CFS' resistance measurement was conducted via a 4-wire setup by a QuantumX MX840B universal measuring amplifier. The FOS was connected to a LUNA ODiSI-A measurement system. LUNA ODisI-A Control Software v1.3.5 was used for the FOS setup, calibration, and data acquisition. Both tensile and 3-point bending tests were performed at room temperature and displacement-controlled at a speed of 2 mm/min.
The tensile stress and modulus were calculated according to eqs. (1) and (2), respectively.

$$\sigma = \frac{F}{wt} \tag{1}$$

$$E = \frac{\sigma'' - \sigma'}{\varepsilon'' - \varepsilon'} \tag{2}$$

F is the Force, σ is the tensile stress, w the width and t the thickness of the specimen. The Young's modulus or tensile modulus E is calculated between the strains $\varepsilon' = 0.0005$ and $\varepsilon'' = 0.0025$ and the respective tensile stresses σ' and σ'' at these strain values.
The flexural stress σ_f and strain ε_f in the outer surface of the specimen at mid-span, as well as the flexural modulus E_f were calculated according to eqs. (3),(4) and (5) respectively.

$$\sigma_f = \frac{3FL}{2wt^2} \tag{3}$$

$$\varepsilon_f = \frac{6st}{L^2} \tag{4}$$

$$E_f = \frac{L^3}{4wt^3}\left(\frac{\Delta F}{\Delta s}\right) \tag{5}$$

L denotes the span, s is the deflection of the centerline of the specimen at mid-span, Δs is the difference of deflections $s'' - s'$ at $\varepsilon'_f = 0.0005$ and $\varepsilon''_f = 0.0025$, which can be calculated using eq. (4). ΔF represents the difference in Force between s' and s''.
The LUNA ODiSI-A makes use of swept-wavelength interferometry to measure strain or temperature changes along a FOS. This is achieved by cross-correlating the current spectral response of the Rayleigh backscatter with a baseline measurement of FOS' Rayleigh scatter signature [16]. Changes in temperature or strain cause a spectral shift in the Rayleigh backscatter, which can be related to a temperature (ΔT) or strain using eq. (6). With the temperature kept constant at room temperature, the FOS' strain ε_{FOS} can be calculated using eq. (7):

$$\frac{\Delta\lambda}{\lambda} = -\frac{\Delta\nu}{\nu} = K_T\Delta T + K_\varepsilon\varepsilon_{FOS} \tag{6}$$

$$\varepsilon_{FOS} = -\frac{\bar{\lambda}}{cK_\varepsilon}\Delta\nu \tag{7}$$

where λ and ν are the mean optical wavelength and frequency, and K_T and K_ε are the temperature and strain calibration constants, respectively. The center wavelength of the scan is denoted as $\bar{\lambda}$, and c is the speed of light. The FOS strain was captured every 6 mm for the bending and every 10 mm for the tensile tests along the fiber length at approx. 1 Hz sampling rate.
The linear relation of carbon fibers' resistance to strain has already been shown in previous studies. This relation can be expressed as follows:

$$\frac{\Delta R}{R_0} = k\varepsilon \tag{8}$$

where k is the sensitivity coefficient, R_0 is the initial resistance at zero strain, and ΔR is the change in resistance.

3. RESULTS AND DISCUSSION

3.1 Mechanical Properties

Integrating sensors into structural parts may cause lower mechanical properties than non-sensor integrated parts. **Figure 2** denotes the tensile strength, tensile modulus, flexural strength, and flexural modulus of non-sensor integrated, FOS, CFS, and pure PETG specimens. The error bars show the standard deviation. It can be seen that there is no significant difference among the reinforced specimen types, which indicates that the integrated sensors do not significantly impact the mechanical properties. Values for pure PETG without fiber reinforcement were added for reference. The tensile properties were measured in tensile tests; the flexural properties were taken from the literature [17].

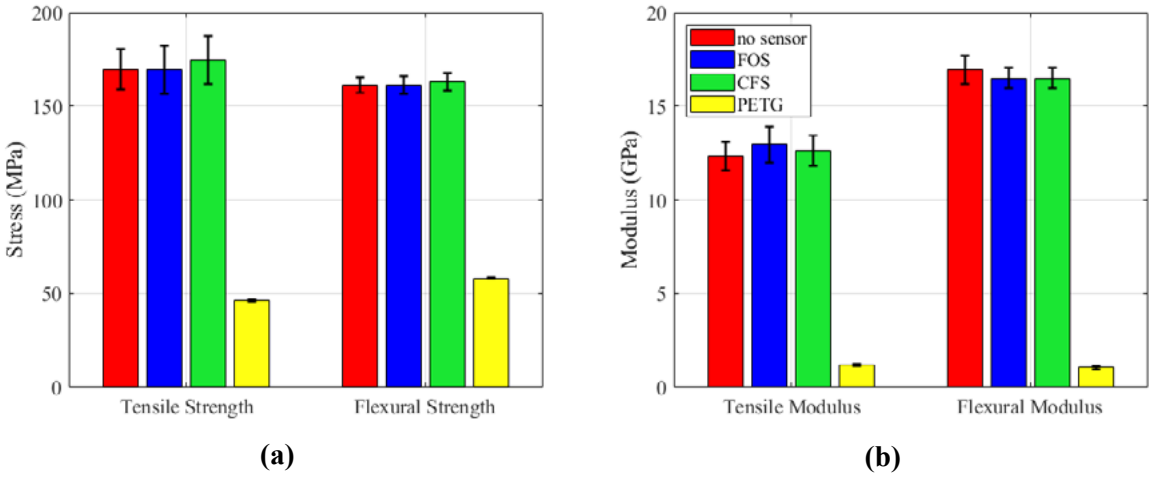


Figure 2: (a) Tensile and flexural strength of all specimen types. **(b)** Tensile and flexural modulus of all specimen types. PETG flexural values from [17].

3.2 FOS

Five specimens were tested in tensile tests. The LUNA ODiSI-A was set to measure the strain every 10 mm, resulting in about 25 measurement points inside the specimens. The strain along the FOS shows that measuring the strain inside the specimens is very precisely possible, as depicted in **Figure 3**. The strain increases over the glued-on tabs, which are used to clamp the specimen into the tensile test fixture of the test machine. The strain in the test region of the specimen has some minor deviations, but is primarily constant, as expected. The FOS strain was averaged to one value at each sampling point for each specimen. Plotting the force against the FOS strain measurement and the video extensometer (VE) strain measurement shows that the two strain measurements only differ slightly from each other when the force approaches the tensile strength of the specimen, as shown in **Figure 3**.

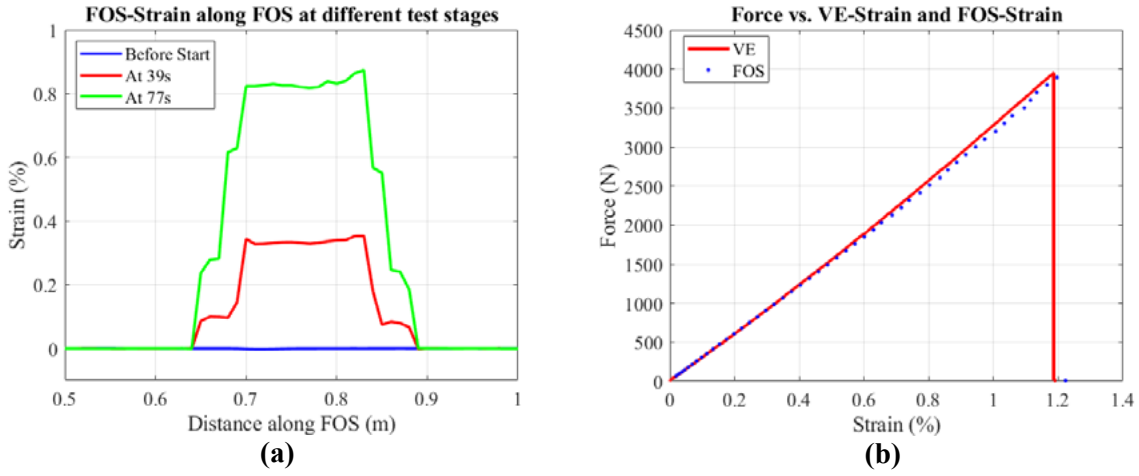


Figure 3: (a) FOS strain measurement at different times during the tensile test. **(b)** Force values plotted against the strain measured by the FOS and the VE.

Similarly to the tensile strain, the strain during the 3-point bending tests was captured, as shown in **Figure 4**. In order to compare the FOS strain measurement to the reference video extensometer strain measurement, the FOS strain was integrated and averaged over the test area. The averaged FOS strain and the reference VE strain were then plotted against time. It can be seen that the FOS is capable of

measuring the strain very well. Due to the LUNA ODiSI-A specifications, the FOS is limited to measuring up to a strain of 1%, which is clearly visible in the form of scatter in **Figure 4**.

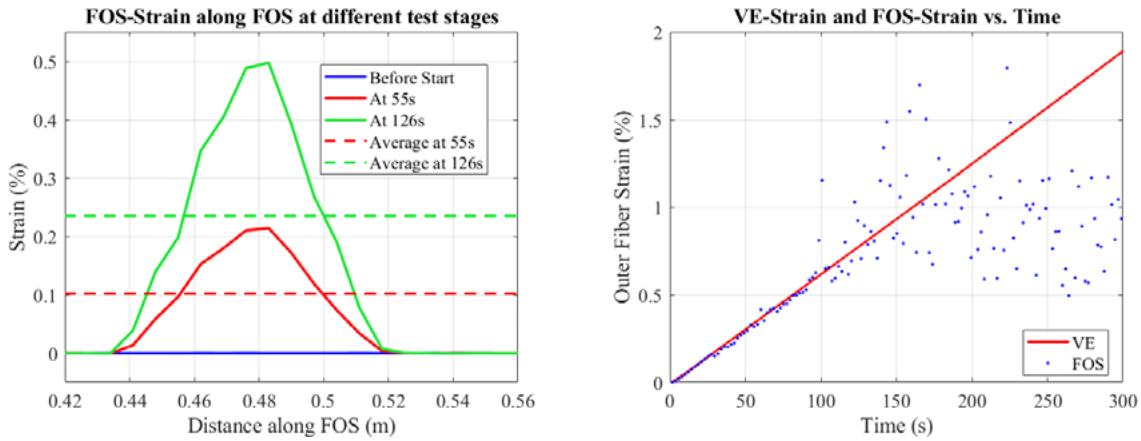


Figure 4: (a) FOS strain measurement at different times during the 3-point bending test. **(b)** Outer Fiber Strain computed by the FOS and the VE plotted against the time.

Considering the excellent correlation of the FOS and reference VE strain measurements, we calculated the average tensile and flexural modulus across all specimens using the VE and FOS strain measurements. The results are shown in **Table 2** and highlight the excellent capabilities of the FOS strain measurement. The modulus deviation is calculated as the difference between the two computed moduli divided by the VE modulus. The value represents the average across all specimens. The standard deviation refers to the modulus deviation across all specimens.

Table 2: Tensile and flexural modulus calculated by the VE and FOS. Modulus deviation and standard deviation refer to the FOS computation.

Specimen Type	VE Modulus (GPa)	FOS Modulus (GPa)	Modulus Deviation (%)	Standard Deviation (%)
FOT	12.402	12.404	-0.045	2.169
FOB	16.498	16.569	2.370	2.430

3.3 CFS

As expected, the resistance of the AT-type specimens increased linearly up to about 0.8% strain, as shown in **Figure 5**. The resistance thereafter started to grow exponentially, which was probably caused by fiber breakage in the CFS. The sensitivity coefficient for the AT-type specimens can be estimated as a linear regression and is denoted k_t along with its R²-value. Three different CFS-type specimens were tested in 3-point bending tests. The relative resistance change for one specimen of each type is plotted over the outer fiber strain (OFS) of the specimen, as shown in **Figure 5**. The corresponding force for each specimen is also shown in **Figure 5**. The sensitivity coefficient was approximated by linear regression and is denoted k_b. No significant difference can be seen between the AN- and AG-type specimens. The A2G-type is clearly distinctive, as it has a smaller sensitivity coefficient. This was expected because the sensor was integrated in the 2nd fiber layer, where the actual strain is less than the outer fiber strain, considering Hooke's law and linear stress distribution in the thickness direction of the specimen. The sensitivity coefficients for all CFS types are shown in **Table 3**.

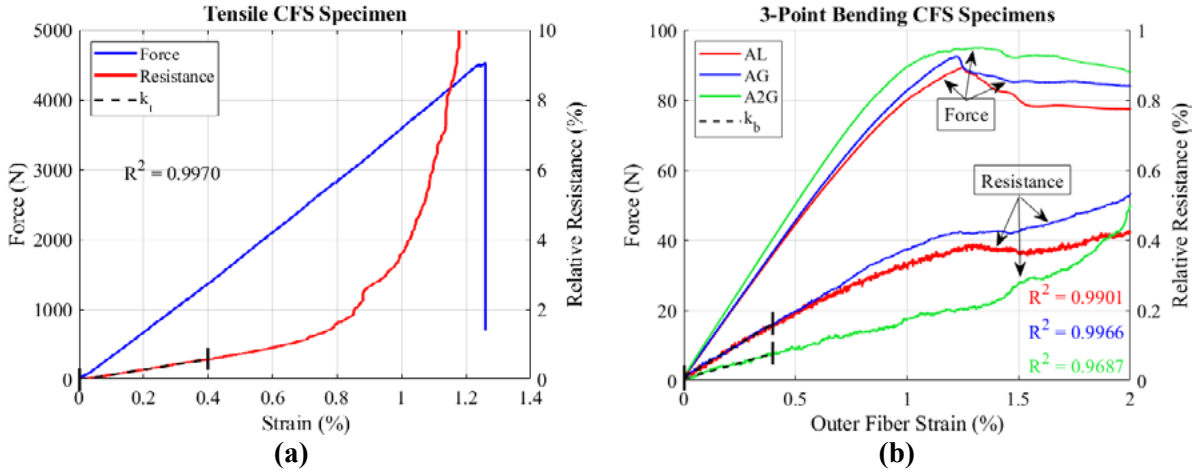


Figure 5: (a) Relative resistance and force plotted over OFS for an AT-type specimen. **(b)** Relative resistance and force plotted over OFS for each CFS-type during 3-point bending tests.

Table 3: Sensitivity coefficients for all CFS-type specimens.

Specimen Type	Sensor type	Sensor location	Sensitivity coefficient (-)	Standard Deviation (-)
AT	CFS (line)	Center plane, centerline	1.470	0.124
AL	CFS (line)	1st fiber layer, centerline	0.329	0.028
AG	CFS (grid)	1st fiber layer, centered	0.316	0.099
A2G	CFS (grid)	2nd fiber layer, centered	0.192	0.063

4. CONCLUSION

This study explored the integration of fibrous sensors, particularly carbon fiber sensors (CFS) and fiber optical sensors (FOS), into continuous fiber-reinforced additively manufactured (CFAM) parts. A custom-built 3D printer was used to fabricate the specimens, using the fully automated manufacturing process and showcasing the capabilities of CFAM. Three different specimen types for tensile and five different types for 3-point bending tests were manufactured to investigate the performance of the integrated sensors and the mechanical properties. The tensile and 3-point bending tests revealed that the presence of integrated sensors did not significantly affect the mechanical properties of the composite specimens. This indicates the potential for seamless integration of CFS and FOS without compromising the overall structural integrity of the composite material. The FOS demonstrated excellent performance in strain measurement during both tensile and bending tests, exhibiting high precision and correlation with the reference strain measurement obtained through a video extensometer. Furthermore, the FOS strain measurement was used to compute the tensile and flexural modulus, which resulted in a deviation of -0.045% and 2.370% compared to the reference tensile and flexural modulus, respectively. This highlights the reliability and accuracy of FOS in monitoring structural deformation and localized strain distribution within composite materials up to strains of 1%, using the LUNA ODiSI-A measurement system. Similarly, the CFS' resistance measurements exhibited linear behavior up to a specific strain limit. The sensitivity coefficients of four different CFS types were determined with high accuracy. The study also identified the influence of sensor location within the composite structure on the sensitivity coefficient values of CFS. It was shown that CFS integrated into different layers in a 3-point bending specimen can be clearly distinguished.

Overall, the findings of this research underscore the potential of integrating fibrous sensors into continuous fiber-reinforced additively manufactured parts. However, further research is necessary to investigate the capabilities of FOS and CFS in structural health monitoring applications, especially regarding fatigue loads and lifetime prediction.

Acknowledgments
This study was supported by the German Federal Ministry for Economic Affairs and Climate Action as part of the Central Innovation Programme for Small and Medium-sized Enterprises (ZIM). Special thanks to Fedor Antonov for the support and assistance with the Anisoprint CFAM system and printhead.

REFERENCES

[1] P. Scholle and M. Sinapius. A Review on the Usage of Continuous Carbon Fibers for Piezoresistive Self Strain Sensing Fiber Reinforced Plastics. *Journal of Composites Science*, vol. 5, no. 4, p. 96, 2021.
[2] A. Horoschenkoff and C. Christner. Carbon Fibre Sensor: Theory and Application, in *Composites and Their Applications,* N. Hu, Ed., InTech, 2012.
[3] Thomas Mäder, Daisy Nestler, and Bernhard Wielage. Strain Sensing using Single Carbon Fibres, In *Proceedings of the 18th International Conference on Composite Materials,* 2011.
[4] N. Angelidis, C. Y. Wei, and P. E. Irving. The electrical resistance response of continuous carbon fibre composite laminates to mechanical strain, *Composites Part A: Applied Science and Manufacturing*, vol. 35, no. 10, 1135–1147, 2004.
[5] N. Forintos and T. Czigany. Reinforcing carbon fibers as sensors: The effect of temperature and humidity, *Composites Part A: Applied Science and Manufacturing*, vol. 131, 2020.
[6] X. Wang and D. Chung. Self-monitoring of fatigue damage and dynamic strain in carbon fiber polymer-matrix composite, *Composites Part B: Engineering*, vol. 29, no. 1, pp. 63–73, 1998.
[7] A. Todoroki, M. Ueda et al.. Strain and Damage Monitoring of CFRP Laminates by Means of Electrical Resistance Measurement, *Journal of Solid Mechanics and Materials Engineering*, vol. 1, no. 8, pp. 947–974, 2007.
[8] D. Kinet, P. Mégret et al.. Fiber Bragg grating sensors toward structural health monitoring in composite materials: challenges and solutions, *Sensors (Basel, Switzerland)*, vol. 14, no. 4, pp. 7394–7419, 2014.
[9] M. Drissi-Habti and V. Raman. Fatigue Behavior of Smart Composites with Distributed Fiber Optic Sensors for Offshore Applications, *Journal of Composites Science*, vol. 6, no. 1, p. 2, 2022.
[10] X. Bao and Y. Wang. Recent Advancements in Rayleigh Scattering-Based Distributed Fiber Sensors, *Advanced Devices & Instrumentation*, vol. 2021, pp. 1–17, 2021.
[11] S. Mekid, A. M. Butt et al.. Integrity assessment under various conditions of embedded fiber optics based multi-sensing materials, *Optical Fiber Technology*, vol. 36, pp. 334–343, 2017.
[12] J. Akmal and M. Salmi. Additive manufacturing of self-sensing parts through material extrusion, *Virtual and Physical Prototyping*, vol. 19, no. 1, 2024.
[13] C. Luan, X. Yao et al.. Self-Sensing of Position-Related Loads in Continuous Carbon Fibers-Embedded 3D-Printed Polymer Structures Using Electrical Resistance Measurement, *Sensors (Basel, Switzerland)*, vol. 18, no. 4, p. 994, 2018.
[14] W. Ye, H. Dou et al.. Mechanical and self-sensing properties of 3D printed continuous carbon fiber reinforced composites, *Polymer Composites*, vol. 43, no. 10, pp. 7428–7437, 2022.
[15] J. Vasquez, H. Twigg-Smith et al.. Jubilee: An Extensible Machine for Multi-tool Fabrication. In *Proceedings of the 2020 CHI Conference on Human Factors in Computing Systems*, pages 1–13, 2020.
[16] LUNA Inc.. ODiSI-A Users Guide: User Guide ODiSI-A Software 1.3, Internet Source, 2013.
[17] Polymaker. PolyMax PETG Technical Data Sheet, Internet Source: https://us.polymaker.com/products/polymax-petg, 2024.

DURABILITY OF PULTRUDED GFRP LAMINATES UNDER ACCELERATED LABORATORY AND NATURAL ENVIRONMENTAL AGEING CONDITIONS

Omid Hassanshahi[1a], José Sena-Cruz[1b], Marco Jorge[1c], Luís Correia[1d], Cláudio Leite[1e]
Tarikul Hasan[2f], João Ramôa Correia[2g], Mário Garrido[2h], Susana Cabral-Fonseca[3i]

[1]ISISE/ARISE, University of Minho, 4800-058 Guimarães, Portugal
Email: [a]omid.hasanshahi@civil.uminho.pt, [b]jose.sena-cruz@civil.uminho.pt, [c]marco@civil.uminho.pt, [d]lcorreia@civil.uminho.pt, [e]pg47118@alunos.uminho.pt
[2] CERIS, Instituto Superior Técnico, Universidade de Lisboa,
Av. Rovisco Pais 1, 1049-001, Lisbon, Portugal
Email: [f]tarikul.hasan@tecnico.ulisboa.pt, [g]joao.ramoa.correia@tecnico.ulisboa.pt, [h]mario.garrido@tecnico.ulisboa.pt
[3] Laboratório Nacional de Engenharia Civil, Av. do Brasil 101, 1700-066, Lisbon, Portugal
Email: [i]sbravo@lnec.pt

Keywords: glass fibre reinforced polymer, pultrusion, durability, mechanical properties, hygrothermal ageing

Abstract
This paper investigates the durability of 8 mm thick pultruded glass fibre-reinforced polymer (GFRP) composite laminates manufactured with either unsaturated polyester or vinyl ester resins. Over a period of 12 months, a comprehensive set of experiments was carried out to assess the durability performance of these GFRP laminates under accelerated laboratory and natural environmental ageing conditions. The accelerated laboratory ageing included exposure to constant temperatures of -15 °C, 20 °C, 40 °C and 60 °C and water immersion at 20 °C. For natural ageing, four different locations in Portugal were selected to promote different levels of humidity, temperature fluctuations, freeze-thaw cycles, and UV radiation. Mechanical property retentions were evaluated, including tensile strength in the longitudinal pultrusion direction, compressive strength, flexural strength, in-plane shear strength and interlaminar shear strength. The highest reductions in mechanical properties occurred after immersion in water at 20 °C, when the specimens were tested under wet conditions, with the lowest property retentions being 63% for the interlaminar shear strength of the composite with vinyl ester matrix and 69% for the compressive strength of the composite with unsaturated polyester.

1. Introduction

The durability of fibre-reinforced polymer (FRP) composites is particularly critical in civil engineering applications, where the design service life is typically between 50 and 100 years. Furthermore, the assessment of the durability of composites is a complex study, as it depends on several aspects, e.g., polymer matrix, fibres, fibre-matrix interphase, processing method, quality control protocols, details, installation, maintenance and type of use [1, 2]. Among FRP composites, pultruded glass-FRP (GFRP) components are gaining popularity due to their desirable characteristics and relatively competitive cost compared to traditional materials like steel [3, 4].

Typically, composites are exposed to a variety of environmental conditions, frequently experiencing thermal effects (such as thermal cycles and freeze-thaw cycles), moisture, and UV radiation throughout their service life [5]. Thermal aging, involving prolonged exposure to elevated or sub-zero temperatures, and thermal cycling, characterized by temperature fluctuations, can significantly affect the mechanical properties of GFRP materials (CEN/TS 19101:2022). Particularly, elevated temperatures approaching or exceeding the glass transition temperature (T_g) lead to resin softening, contributing to material

degradation and reducing mechanical properties, e.g. [6-8]. Moisture diffusion is another primary cause of GFRP degradation, resulting in resin swelling, plasticization, cracking, hydrolysis, and/or fibre/matrix interface debonding, e.g. [9]. The combined effects of hot and humid climates exacerbate these challenges, while UV radiation accelerates polymer degradation, especially when combined with moisture and elevated temperatures, e.g. [10]. Given these complex interactions, assessing the durability of GFRP laminates requires comprehensive data and careful consideration.

Due to the lack of comprehensive and long-term durability results, targeted research is needed to gather durability data of GFRP composites tailored to civil engineering applications and to develop reliable degradation models for predicting long-term retention of mechanical properties. Furthermore, it is important to note that durability studies of pultruded GFRP laminates under various accelerated laboratory and natural aging conditions are rare, e.g. [11,12[].

To address the gaps identified in the literature, an extensive experimental campaign is being undertaken as part of the Durable-FRP research project. This test program aims to assess the durability of thick pultruded GFRP laminates composed of unsaturated polyester and vinyl ester matrices through laboratory (accelerated ageing) and in-situ field (natural ageing) tests, comprising both unloaded and loaded specimens during ageing. This paper presents selected preliminary results from this program, focusing on two types of pultruded GFRP laminates subjected to accelerated laboratory and natural ageing environments for over 12 months, without loading. The experimental program includes exposure to constant temperatures ranging from -15 °C to 60 °C, immersion in water at 20 °C (for which specimens were tested in “dry” and “wet” conditions), and natural ageing at four different locations in Portugal, characterized by different exposure to moisture, thermal fluctuations, freeze-thaw cycles, and UV radiation. Mechanical properties, including tensile (in the longitudinal direction), compression, flexural, in-plane shear, and interlaminar shear, were evaluated before and after exposure to these ageing environments.

2. Experimental Program

2.1. Materials

As mentioned, pultruded GFRP laminates manufactured with two distinct resin matrices were used: (i) unsaturated polyester (GFRP_UP) and (ii) vinyl ester (GFRP_VE). These laminates are composed of seven reinforcing layers, comprising four layers of chopped strand mat interspersed with layers of rovings in the pultrusion direction. The produced laminates have nominal dimensions of 250 mm of width and 8 mm of thickness.

Calcination tests carried out according to ISO 1172:2023 revealed fibre content (by mass) of 59% and 63% for GFRP_UP and GFRP_VE laminates, respectively. For the sake of simplicity in executing the experimental programs, 900 mm × 250 mm × 8 mm (length, width, thickness) plates were used.

2.2. Ageing Protocol

Firstly, all composites underwent a post-cure protocol after manufacturing and before any aging process. This involved exposing the laminates to 80 °C in a climatic chamber for 12 hours. Over 12 months, three types of ageing environments were simulated, both in laboratory and in-situ field conditions. The first group of specimens was subjected to constant temperatures of -15 °C (T-15), 20 °C (T20), 40 °C (T40), and 60 °C (T60) to assess the influence of exposure to those constant temperatures. The second group of specimens was completely immersed in demineralized water at 20 °C (hygrothermal ageing), and their mechanical properties were evaluated in the “dry” state (W20D), after reaching constant mass, and in the wet state (W20S), i.e., removed from water just before performing the mechanical tests. Finally, a third group of specimens underwent natural ageing in four different locations in Portugal, characterized by different exposure to moisture, thermal fluctuations, freeze-thaw cycles, and UV radiation. These locations included: (i) E2 - Elvas (warm and temperate climate; very high thermal amplitudes, the highest temperature in Portugal and UV radiation); (ii) E3 - Lisbon (mild Mediterranean climate in an urban area); (iii) E4 - Serra da Estrela (highest mountain in Portugal; high thermal amplitudes, lowest

temperatures in Portugal, UV radiation and freeze-thaw cycles); and (iv) E5 - Viana do Castelo (maritime moist environment – Atlantic Ocean). Note: E1 corresponds to T20.

2.3. Methods

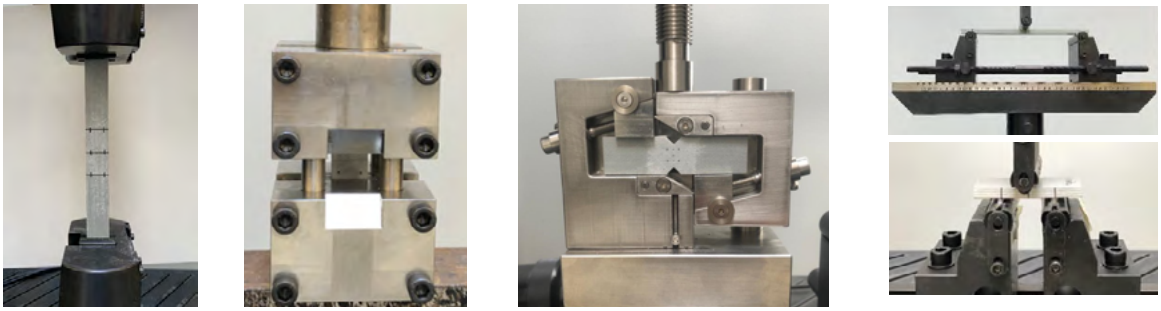
Several test methods were used to evaluate the durability of GFRP laminates in terms of their thermomechanical and mechanical properties.

The thermomechanical properties of unaged GFRP laminates were assessed using dynamic mechanical analysis (DMA). The DMA tests were conducted using a dynamic mechanical analyser, model Q800 DMA (TA Instruments), following the recommendations of ISO 6721:2019 (parts 1 and 5). Specimens measuring 60 mm × 10 mm × 4 mm were first prepared (in a CNC milling machine to reduce the laminate thickness from 8 mm to 4 mm on one surface) and then heated from 25 °C to 250 °C at a rate of 2 °C/min, while being subjected to a sinusoidal load in a dual cantilever-type clamp system, maintaining a constant frequency of 1 Hz and a strain amplitude of 15 µm. The glass transition temperature, T_g, was determined from the onset of the decay of the storage modulus (E') curve, considering the average from three replicates.

The mechanical properties of GFRP laminates before and after ageing were assessed using an MTS Exceed E45.105 universal testing machine with a load capacity of 100 kN (Figure 1), namely:

- Tensile tests in the 0° longitudinal direction (pultrusion direction), as per EN ISO 527-4:1997, with specimens of 300 mm × 25 mm × 8 mm, loaded at a rate of 2 mm/min.
- Compressive tests (in the 0° direction), as per ISO 14126:1999, with specimens of 153 mm × 25 mm × 8 mm, loaded at a rate of 1 mm/min.
- Flexural tests (in the 0° direction), as per EN ISO 14125:1998, with specimens of 240 mm × 15 mm × 8 mm, loaded at a rate of 5 mm/min.
- In-plane shear (IPS) tests, as per ASTM D5379/D5379M:2012, using specimens of 76 mm × 19 mm × 8 mm, which included a double V-notch at mid-span, loaded at a rate of 2 mm/min.
- Interlaminar shear tests (ILS) in the 0° longitudinal direction, as per ISO 14130:1997, with specimens of 80 mm × 40 mm × 8 mm, loaded at a rate of 1 mm/min.

Each test series comprised six specimens.



(a) (b) (c) (d), (e)

Figure 1. Mechanical tests: (a) tensile, (b) compressive, (c) IPS, (d) flexural, (e) ILS.

3. Results and Discussion

3.1. Initial Characterization

A glass transition temperature, T_g, of 80.6 °C (coefficient of variation, CoV=5.1%) was determined for the GFRP_UP composite, whereas for GFRP_VE a T_g of 101.0 °C (CoV=0.8%) was obtained. Table 1 presents the results of the mechanical properties in tension, compression, flexure, IPS, and ILS for unaged GFRP_UP and GFRP_VE. These results are based on the mean values obtained from six specimens, along with their corresponding CoV. In subsequent sections, these results are then compared with those obtained from the aged series exposed to various thermal conditions.

Table 1. Mechanical properties of references (unaged) series (REF) for both UP and VE matrices.

Test type	GFRP_UP		GFRP_VE	
	Mean value [MPa]	CoV [%]	Mean value [MPa]	CoV [%]
Tensile (0°) strength	426	1.7	456	1.7
Compressive strength	522	8.2	505	9.6
Flexural strength	519	6.1	539	3.4
In-plane shear strength	72.6	5.5	84.6	3.9
Interlaminar shear strength	21.9	3.3	42.1	3.2

3.2. Tensile strength

Figures 2a and 2b show the longitudinal tensile strength retention of GFRP_UP and GFRP_VE laminates, respectively. Overall, relatively low variations of the longitudinal tensile strength retention of the GFRP laminates for the two matrices and across the different laboratory ageing conditions was observed, with retention rates ranging from 86% to 100%. More relevant reductions were observed after exposure to the most extreme conditions, such as constant temperature at 60 °C (T60) and especially water immersion at 20 °C with wet conditions (W20S). Both GFRP_UP and GFRP_VE laminates exhibited relatively similar strength retention levels at different natural ageing environments, with low CoV values.

Under constant temperature exposure (T-15, T20, T40, and T60), the maximum reduction in longitudinal tensile strength was observed at 60 °C for both matrices, resulting in a retention rate of approximately 92%. This highlights the predominant influence of fibre characteristics over matrix properties on longitudinal tensile strength, given the architecture of the fibres used and the fact that literature reports lower degradation of glass fibres to these environments.

Under water immersion at 20 °C, both GFRP_UP and GFRP_VE laminates experienced a decrease in longitudinal tensile strength retention, particularly tested under wet (W20S) conditions, with retention rates of 86% and 89%, respectively. The difference in retention between dry (W20D) and wet (W20S) conditions was approximately 10% for GFRP_UP, while for GFRP_VE laminates, the difference between W20D and W20S was minimal. This may indicate that the degradation of UP composites was irreversible (hydrolysis), whereas in VE some was reversed on drying (plasticisation).

In the natural ageing environments (E2, E3, E4, and E5), both GFRP_UP and GFRP_VE laminates exhibited consistent longitudinal tensile strength retention levels, ranging from 92.9% (E4) to 95.7% (E5) for GFRP_UP and from 92.1% (E5) to 94.1% (E2 and E3) for GFRP_VE, with CoV values consistently below 4%. These results highlight the minor degradation of the pultruded GFRP laminates across diverse natural environmental conditions over a 12-month period.

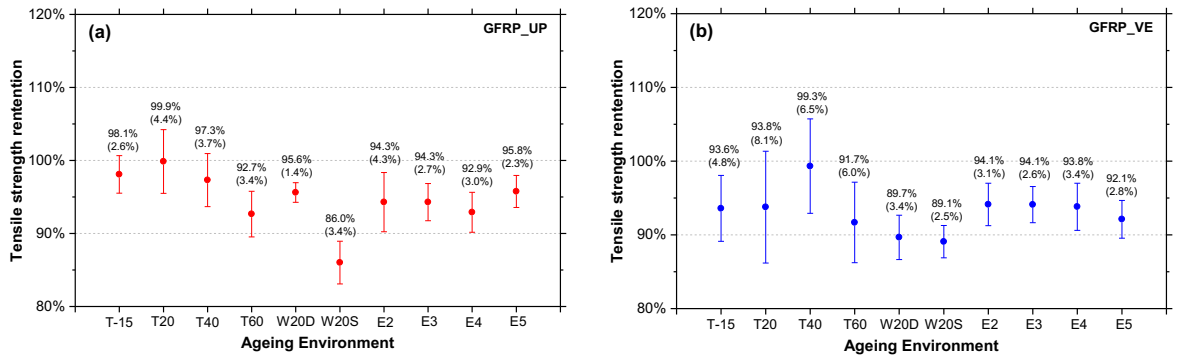


Figure 2. Tensile strength retention: (a) GFRP_UP; (b) GFRP_VE.

3.3. Compressive strength

As shown in Figure 3, both GFRP laminates exhibited an increase in longitudinal compressive strength retention across ageing environments, except for water immersion at 20 °C. GFRP_VE exhibited higher retention rates than GFRP_UP across all environments. Both materials demonstrated better performance at 40 °C, with a notable decline of ca. 15% drop at 60 °C, respect to 40 °C. The results show noteworthy dispersion, with a CoV that frequently exceeds 10%, reaching a maximum of 17.2%. This is consistent with previous studies [8,13]. Sun *et al*. [14] attributed this to local imperfections and material defects that affect compressive strength.

The water immersion at 20 °C resulted in a reduction in the compressive strength retention of both GFRP_UP and GFRP_VE of 31% and 19%, respectively. This reduction underscores the negative effect of moisture on the resin matrix of pultruded GFRP laminates over a period of 12 months. Furthermore, the drying process enabled an almost full recovery of initial compressive strength, for both cases (UP and VE), suggesting a strong impact of plasticization mechanisms on the "wet" condition results. This result is not fully consistent with the observations in section 3.2 (longitudinal tensile strength) and, thus, requires further investigation.

Both GFRP_UP and GFRP_VE laminates showed improved compressive strength retention in the four natural ageing environments, with values ranging from 102% to 118% for GFRP_UP and from 127% to 132% for GFRP_VE. Such increases, also observed in the thermal ageing environments, suggest that a relevant degree of resin post-curing occurred during environmental exposure.

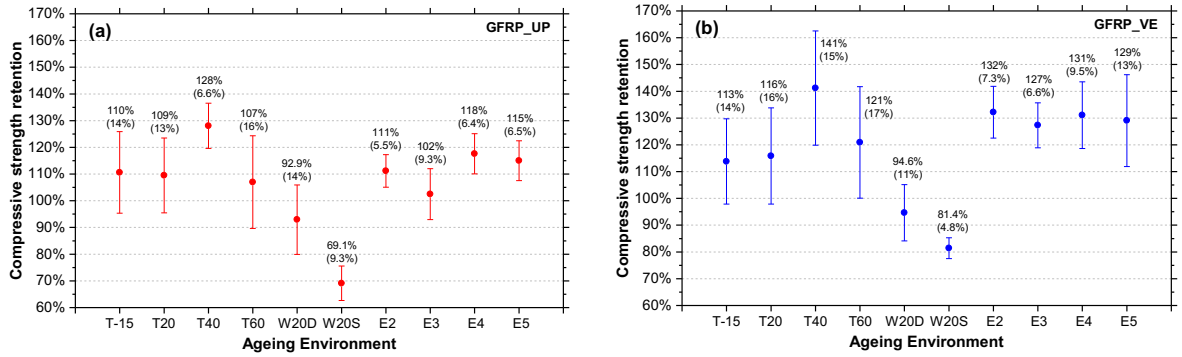


Figure 3. Compressive strength retention: (a) GFRP_UP; (b) GFRP_VE.

3.4. Flexural strength

Figure 4 presents the flexural strength retentions of both GFRP_UP and GFRP_VE composites. The flexural strength retention of a composite is influenced by various factors related to both the matrix and fibre components. In general terms, fibres contribute to tensile strength and stiffness in the tensioned zone (bellow the neutral axis), while the matrix provides support and stability to the reinforcing fibres in the compressed zone (above the neutral axis), with both materials and their interaction affecting the overall performance of the material under bending loads.

After exposure to constant temperatures, both composites (UP and VE) exhibited marginal variations in flexural strength retention, with generally consistent results, with CoV below 6%.

Upon immersion in water at 20 ºC, the GFRP_UP series showed slightly lower flexural strength retentions than GFRP_VE, with minimum retentions of 91% (GFRP_UP) and 93% (GFRP_VE) tested under wet conditions (W20S), with low CoV values.

In terms of natural ageing, the flexural strength retentions for both GFRP_UP and GFRP_VE laminates remained within similar envelopes, ranging from 94% (E2) to 103% (E4) for GFRP_UP and from 94% (E2) to 99% (E4) for GFRP_VE. The highest CoV observed was 7% for E2 in the GFRP_UP laminate.

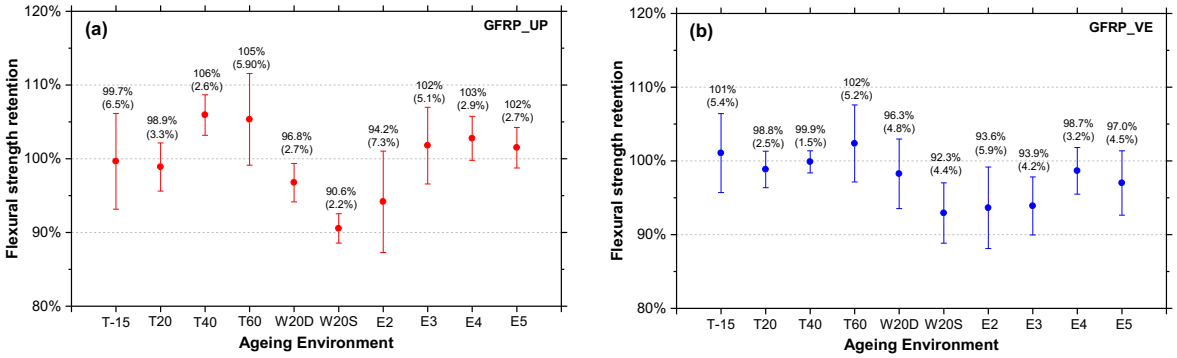


Figure 4. Flexural strength retention: (a) GFRP_UP; (b) GFRP_VE.

3.5. In-plane (IP) shear strength retention

The in-plane shear strength retention of GFRP_UP and GFRP_VE laminates is illustrated in Figure 5a and Figure 5b, respectively. Given the architecture of fibres adopted for the composite plates, this property is strong influenced by the matrix. Across the different environments, all series showed improved in-plane shear strength, except for the water immersion series (tested under wet conditions). Despite minor differences between the two materials, they exhibited similar responses to constant temperature exposure. The results for GFRP_UP showed the highest increase in this property (~17%) at a temperature of 40 °C, while GFRP_VE demonstrated similar increases for the T-15, T40, and T60 series. However, it should be emphasising the relatively high values of the standard deviations obtained.

Regarding water immersion, composites produced with both matrices experienced the highest reduction of IP shear strength tested under wet conditions, with a reduction in the two materials of approximately 8% and CoV values below 5%.

In terms of natural ageing, both GFRP_UP and GFRP_VE laminates displayed a consistent trend of improved IPS strength retention, akin to compressive strength, with values ranging from 106% (E3) to 117% (E4) for GFRP_UP, and from 100% (E5) to 108% (E4) for GFRP_VE.

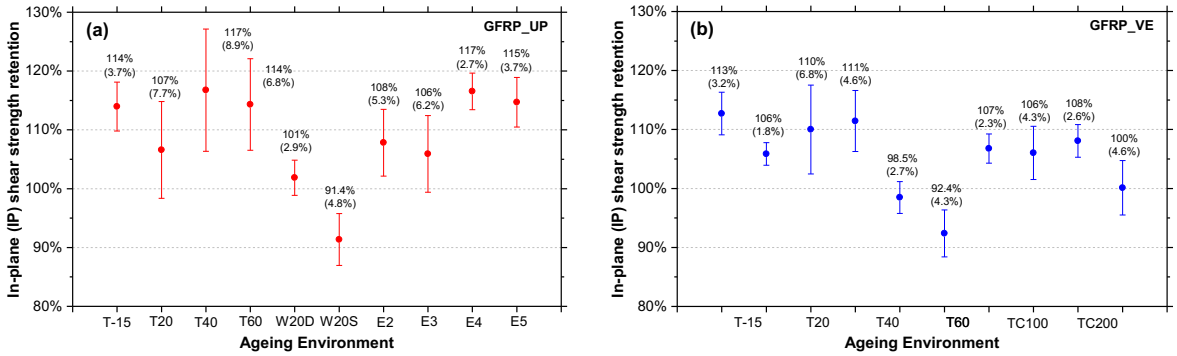


Figure 5. In-plane (IP) shear strength retention: (a) GFRP_UP; (b) GFRP_VE.

3.6. ILS strength response

The interlaminate shear (ILS) strength retention of GFRP_UP and GFRP_VE is depicted in Figure 6a and Figure 6b, respectively. Both laminate types show a trend in ILS strength that is comparable to that observed for compressive and flexural strengths, with minor variations. The ILS strength, reliant on laminae interface adhesion and influenced by fibre bridging mechanisms, is highly dependent on the matrix properties and the fibre-matrix interaction.

Under constant temperature, the ILS strength retention exhibited a nearly linear decrease with temperature rise from -15 °C to 40 °C, and an increase from 40 °C to 60 °C. The GFRP_UP series exhibited ILS strength retentions (slightly) above 100%, for both T-15 and T60 series. In contrast, for all other series, including all GFRP_VE series, strength retentions were below 100%, but above ~90%.

After exposure to water immersion for 12 months and for testing in wet conditions, GFRP_VE laminates experienced significant ILS strength reduction, with a minimum retention of 63%, compared to GFRP_UP laminates, which retained 84% of ILS strength. Notably, GFRP_UP laminates showed a maximum reduction of 69% in compressive strength retention, indicating vulnerability to high moisture content, which is partially reversed upon drying.

Following natural ageing, the ILS strength retention ranged from 90% (E2) to 103% (E4) for GFRP_UP, and from 87% (E3) to 97% (E4) for GFRP_VE.

Finally, the trend observed in ILS strength (higher retention in UP) is somehow opposite to that in compressive strength (higher retention in VE). Both properties are very much influenced by the matrix. Therefore, this requires further investigation.

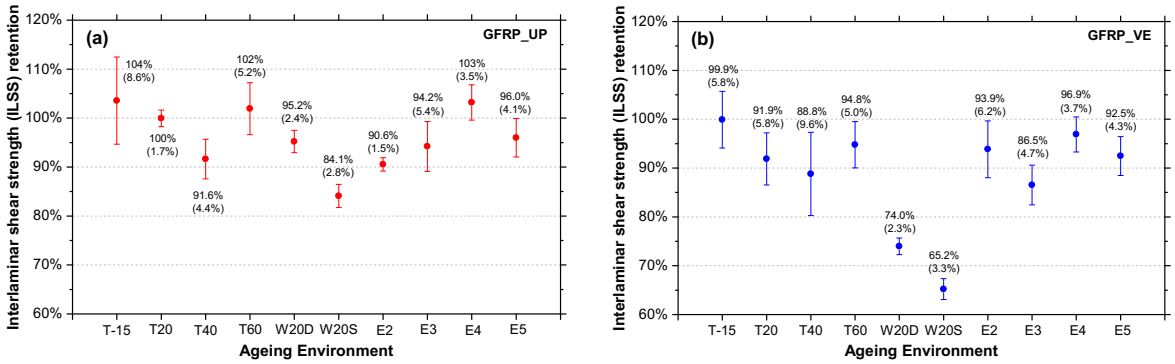


Figure 6. Interlaminar shear strength retention: (a) GFRP_UP; (b) GFRP_VE.

4. Conclusions

This study investigated the durability in terms of the changes in the mechanical properties of pultruded glass fibre-reinforced polymer (GFRP) laminates with unsaturated polyester (UP) and vinyl ester (VE) matrices, under accelerated and natural ageing conditions for 12 months.

Under constant temperature conditions very little reductions were observed for all the properties analysed.

The most significant reductions in mechanical properties were observed following immersion in water at 20 °C, under wet conditions. Notably, the lowest property retentions obtained in this study were found for the interlaminar shear strength of GFRP_VE laminates after water immersion in “wet” condition (63%), and for the compressive strength of GFRP_UP laminates under the same conditions (retention of 69%). However, the drying process allowed the almost full recovery of the initial properties, except in the case of ILS strength of GFRP_VE.

In terms of natural ageing, comprising different climates in Portugal (ranging from relative mild to extreme severe exposure) did not produce, so far, relevant mechanical degradation of both materials across all environments and properties compared to water immersion. The lowest retentions of 87% (GFRP_VE) and 91% (GFRP_UP) were observed in interlaminar shear strength in E3 and E2, respectively. In general, the natural weathering results were more comparable to those obtained in the constant temperature ageing environments, i.e., without water immersion. This highlights the potentially damaging effect of elevated moisture content in GFRP composites, while also suggesting that such high moisture levels may not be easily attained in some outdoor weathering scenarios.

Furthermore, these results highlight the complex interplay between environmental conditions, material characteristics, and mechanical performance of pultruded GFRP laminates. Further analysis and long-

term testing (ongoing) are necessary to deepen the understanding of such phenomena, but these initial findings provide valuable insights into their durability.

Acknowledgments
This work was carried out in the scope of the project DURABLE-FRP (PTDC/ECI-EGC/4609/2020, doi:10.54499/PTDC/ECI-EGC/4609/2020) funded by national funds financed by the European Fund of the Regional Development (FEDER) through the Operational Program for Competitiveness and Internationalization (POCI) and the Lisbon Regional Operational Program. It was also partly financed by FCT/MCTES through national funds (PIDDAC) under the R&D Unit Institute for Sustainability and Innovation in Structural Engineering (ISISE), under reference UIDB/04029/2020 (doi:10.54499/PTDC/ECI-EGC/4609/2020), under the Associate Laboratory Advanced Production and Intelligent Systems ARISE under reference LA/P/0112/2020, and under the R&D Unit Civil Engineering Research and Innovation for Sustainability (CERIS), under reference UIDB/04625/2020 (doi:10.54499/PTDC/ECI-EGC/4625/2020).

References

[1] Karbhari, V.M., Chin, J., Hunston, D., Benmokrane, B., Juska, T., Morgan, R., Lesko, J.J., Sorathia, U. and Reynaud, A.D., 2003. Durability gap analysis for fibre-reinforced polymer composites in civil infrastructure. *Journal of Composites for Construction*, *7*(3), 238-247.

[2] Sousa, J.M., Garrido, M., Correia, J.R. and Cabral-Fonseca, S., 2021. Hygrothermal ageing of pultruded GFRP profiles: Comparative study of unsaturated polyester and vinyl ester resin matrices. *Composites Part A: Applied Science and Manufacturing*, *140*, p.106193.

[3] Sousa, J.M., Correia, J.R., Cabral-Fonseca, S. and Diogo, A.C., 2014. Effects of thermal cycles on the mechanical response of pultruded GFRP profiles used in civil engineering applications. *Composite Structures*, *116*, 720-731.

[4] Jafari, A., Ashrafi, H., Bazli, M. and Ozbakkaloglu, T., 2019. Effect of thermal cycles on mechanical response of pultruded glass fibre reinforced polymer profiles of different geometries. *Composite Structures*, *223*, p.110959.

[5] Bazli, M., Jafari, A., Ashrafi, H., Zhao, X.L., Bai, Y. and Raman, R.S., 2020. Effects of UV radiation, moisture and elevated temperature on mechanical properties of GFRP pultruded profiles. *Construction and Building Materials*, *231*, p.117137.

[6] Bazli, M., Ashrafi, H., Jafari, A., Zhao, X.L., Gholipour, H. and Oskouei, A.V., 2019. Effect of thickness and reinforcement configuration on flexural and impact behaviour of GFRP laminates after exposure to elevated temperatures. *Composites Part B: Engineering*, *157*, 76-99.

[7] Bai, Y., Vallée, T. and Keller, T., 2008. Modelling of thermal responses for FRP composites under elevated and high temperatures. *Composites Science and Technology*, *68*(1), 47-56.

[8] Correia, J.R., Bai, Y. and Keller, T., 2015. A review of the fire behaviour of pultruded GFRP structural profiles for civil engineering applications. *Composite Structures*, *127*, 267-287.

[9] Böer, P., Holliday, L. and Kang, T.H.K., 2013. Independent environmental effects on durability of fibre-reinforced polymer wraps in civil applications: A review. *Construction and Building Materials*, *48*, 360-370.

[10] Carra, G. and Carvelli, V., 2014. Ageing of pultruded glass fibre reinforced polymer composites exposed to combined environmental agents. *Composite Structures*, *108*, 1019-1026.

[11] Cabral-Fonseca, S., Correia, J.R., Rodrigues, M.P. and Branco, F.A., 2012. Artificial accelerated ageing of GFRP pultruded profiles made of polyester and vinylester resins: characterisation of physical–chemical and mechanical damage. *Strain*, *48*(2), 162-173.

[12] Garrido, M., Sousa, J.M., Correia, J.R. and Cabral-Fonseca, S., 2022. Prediction of long-term performance and definition of a moisture conversion factor for the durability design of pultruded GFRP profiles under hygrothermal exposure. *Construction and Building Materials*, *326*, p.126856.

[13] Bai, Y. and Keller, T., 2011. Delamination and kink-band failure of pultruded GFRP laminates under elevated temperatures and compression. *Composite Structures*, *93*(2), 843-849.

[14] Sun, W., Vassilopoulos, A.P. and Keller, T., 2015. Effect of temperature on kinking failure mode of non-slender glass fibre-reinforced polymer specimens. *Composite Structures*, *133*, 178-190.

DESIGN AND DAMAGE ASSESSMENT IN EARTHQUAKE-RESISTANT COMPOSITE PIPE JOINTS

Kaveh Shahidi [1], Nuri Ersoy[2], Gulum Tanircan[3] and Hakan Mis [3]

[1]Department of Mechanical Engineering, Bogazici University, Istanbul, Turkey,
Email: Kaveh.shahidi1@std.bogazici.edu.tr
[2]Department of Mechanical Engineering, Bogazici University, Istanbul, Turkey,
Email: Nuri.ersoy@bogazici.edu.tr
[3]Department of Earthquake Engineering, Bogazici University, Istanbul, Turkey
Email: Gulum.tanircan@gmail.com
[4] Superlit Pipe Industry Inc., Duzce, Turkey
Email: Hmis@superlit.com

Keyword, GFRP, filament-wound pipe, FE modeling, earthquake-resistant composite pipes, angular deflection, seismic pipe joint, damage modeling

Abstract
This research tackles the gap in earthquake-resistant composite pipelines by developing a novel glass fiber-reinforced composite (GRP) pipe connection system. Aligned with seismic guidelines, it introduces an innovative linear and angular deflection solution for GRP pipe joints, ensuring flexibility to endure various deformations during earthquakes. It aims to design a pipe joint capable of withstanding seismic loads and ground deformations by simplifying assembly and disassembly through the omission of bolts in joints. The study involves the mechanical characterization of composite specimens and rings cut from filament-wound pipes to verify the mechanical performance of composite pipes and the structural optimization of earthquake-resistant composite pipes and joints. Notably, finite element models of ring compression tests on filament-wound pipe rings successfully predict stiffness and strength. The methodology integrates composite micromechanics theories and literature to establish initial reference values of material properties, employing an iterative process with the stress homogenization method, validated by comparing simulation results with experimental data. The optimization process includes stress analysis using the Finite Element Method to determine optimal wall thicknesses and improve the position and shape of sealing and lock rings. This proposed pipe joint model aims to advance the engineering design of earthquake-resistant composite pipes, offering valuable insights for assessing the risk of significant ground deformation in pipelines.

1. Introduction

Standardized composite tests offer a general understanding of the strength and stiffness of filament-wound fiber-reinforced pipes but do not account for the behavior of individual layers under load due to variations in fiber orientation and resin type. Specialized tests are necessary to measure individual layer properties for optimized pipe design. Unlike flat composites, acquiring layer characteristics in cylindrical filament-wound composite pipes is more complex. Ply properties are refined through iterative Finite Element simulations and experimental data using initial estimates from literature and micromechanics theories [1]. These refined properties validate material accuracy and predict pipe behavior in various designs.

Designing pipe joints for seismic events necessitates a multidisciplinary approach to address challenges like permanent ground deformation (PGD) caused by faulting, liquefaction, lateral spread, slope failure, or settlement. PGD is most severe at boundary conditions, requiring meticulous design considerations.

This study presents a unique push-on spigot and socket joint for segmented pipelines, designed using Finite Element Analysis. These socket joints allow for elongation, contraction, and rotation during ground deformation, while the boltless design ensures easy assembly.

2. Material and methods

2.1. Determining the in-plane ply properties for finite element modeling

A modeling method is outlined to determine material properties for finite element modeling of Fiber Reinforced Polymer (FRP) pipes. Initially, ply properties are estimated based on previously published studies and available literature on mechanical tests conducted on unidirectional (UD) and angle-ply composite laminates [2] due to the wide range of reported material properties for FRP pipes. Table 1 summarizes the ply properties of the GFRP composites used in piping systems.

Table 1. Material properties of E-glass/UPR epoxy laminate.

E_1 [Gpa]	45.6
E_2 [Gpa]	16.2
G_{12} [Gpa]	5.5
ν_{12}	0.278
ν_{23}	0.4
X_T [Mpa]	1280
X_C [Mpa]	825
Y_T [Mpa]	65.2
Y_C [Mpa]	194
S [Mpa]	51.8

Intralaminar damage properties are assessed using progressive damage analysis, employing continuum damage mechanics principles and Hashin failure criteria [3]. The progressive damage model utilized in the FEA predicts and assesses damage within the plies, requiring additional parameters such as critical energy release rate. Cohesive Zone Modelling is utilized to model the initiation and growth of delaminations. Specific material parameters for cohesive elements are provided in Table 2, emphasizing the influence of Mode-I fracture on transverse matrix cracking and Mode-II fracture on delamination essential for accurate simulations and structural analysis [4-6].

Table 2. Material properties for the cohesive elements.

Direction	Mode I	Mode II, III
Penalty stiffness ($\frac{N}{m^3}$)	10^{14}	10^{14}
Interface strength (MPa)	60	60
Fracture energy ($\frac{J}{m^2}$)	500	800

2.2. Experimental test methods

In this research, a GFRP pipe with a diameter of 200 mm and average thicknesses of 2.5 mm and 5 mm for two different models is selected for the case study. Initially, the pipe is wound with fibers exclusively in the hoop direction, resulting in a unidirectional configuration. For subsequent tests, pipe sections produced by Superlit Boru San. Inc. using filament winding with 20 layers and alternating winding angles of ±55° and ±45° are used, featuring a nominal thickness of 5 mm.

The experimental study examines filament wound GFRP pipes through various tests. The Ring Compression Test, per ASTM D2412-02 standard [7], is conducted to assess compressive transverse

loading resistance. Compression is applied diametrically, with a 10 mm/min test speed, and ring stiffness is calculated to evaluate ovality resistance.

The Circumferential Tensile Test (Split-disk), following ASTM D2290 [8], evaluates ultimate hoop tensile strength using split-ring tests. Stress concentration is induced by a notch, simulating critical defects. Flexural Test (Four-Point Bending) and Short Beam Shear Test, as per ASTM D7264 [9] and D2344 [10], assess flexural characteristics and shear behavior.

The Double-Notch Shear test (ASTM D 3846) [11] evaluates interlaminar and through-the-thickness shear strength. Specimen geometry, especially notch dimensions, significantly affects failure mechanisms. Lastly, tensile tests on specimens cut in the axial direction are performed according to BS ISO 8513:2016 [12], evaluating properties like tensile strength and elongation percentage. Figure 1 shows the test setup for the ring compression, four-point bending, short beam shear, longitudinal tensile, split disk, and double notch shear test for coupon specimens, respectively.

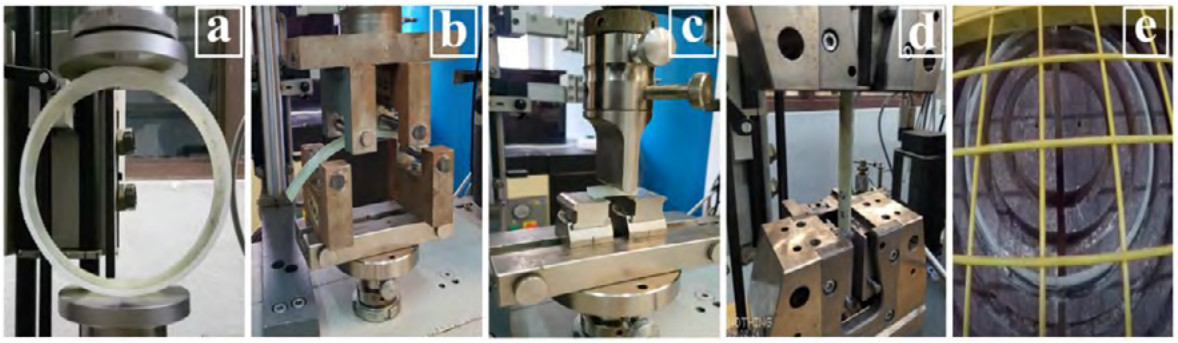


Figure 1. Setup for different tests. (a) Ring Compression fixture, (b) Flexural test with a four-point bending fixture, (c) Short-beam shear test with a three-point bending fixture, (d) Tensile test fixture, (e) Split disc test and Double-notch shear test fixture.

2.3. Damage Analysis using Finite Element Method

ABAQUS software is employed to simulate damage modes across various tests. For ring compression, models represent GFRP pipes with continuum shell elements. Each pipe layer is separately modeled, resulting in 8 and 20-layer pipe specimens with 2.5 and 5 mm thicknesses. Similar modeling approaches are used for flexural, shear, and tensile tests. Longitudinal tensile tests utilize 20 layers of shell elements connected through cohesive zone elements.

Pipe joint simulations assess axial and rotational behavior, incorporating GFRP layers with ±55° angle orientation, an SBR gasket, and a lock ring made of thermoplastic material. Boundary conditions include uniform loads of 600 kN, an inner pipe pressure of 20 bars for axial motions, and a concentrated shear force of 600 kN for rotational movement. General-purpose continuum shell elements ensure an accurate representation of composite behavior.

2.4. Designing of a seismic pipe joint (with locking system)

The spigot and socket pipe ball joint fitting was designed using SOLIDWORKS software, providing resistance to substantial axial and rotational motions while accommodating ground deformation. The design features an EPDM O-ring gasket for sealing, a lock ring for reinforcement, and an assist for rotational freedom. Composite layers are strategically placed for strength, particularly around the lock ring area. The joint's groove for the lock ring is designed to avoid stress concentrations. Figure 2 illustrates the seismic pipe joint model.

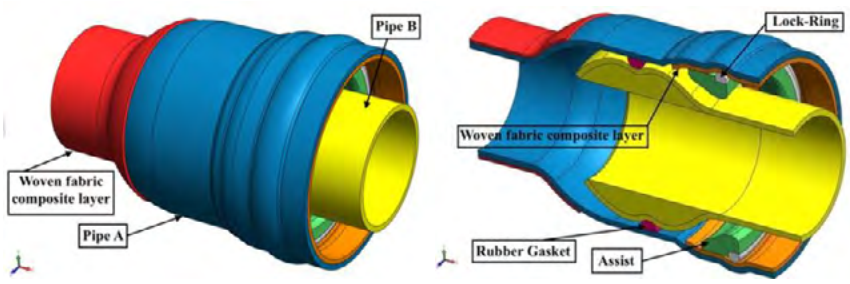


Figure 2. 3D illustration of the seismic pipe joint sleeve model.

The joint allows axial movement and rotation, achieving a secure seal via compression deformation of the rubber ring. The design allows axial flexibility and long-distance deflection, which is crucial for pipeline installation in earthquake susceptible regions. Figure 3 outlines test conditions, demonstrating the joint's ability to withstand diverse forms of deformation. Design parameters include a maximum angle deflection of 12° and an axial extension/contraction deflection of 120 mm, ensuring flexibility without compromising joint integrity.

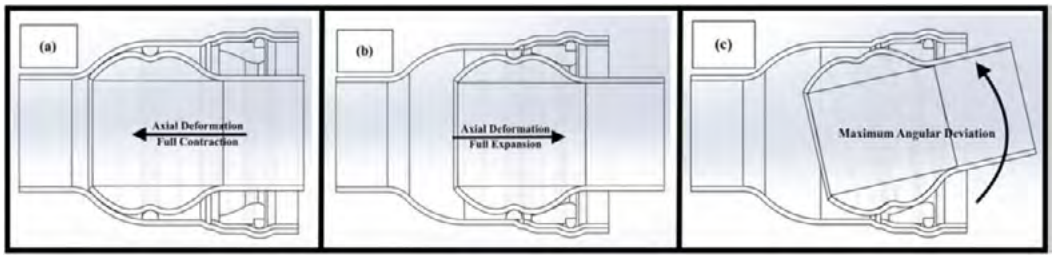


Figure 3. Test conditions (parameters). (a) Full Contraction, (b) Full Expansion, and (c) Maximum Angular Deviation.

3. Results and discussion

Ring compression tests were halted at approximately 50% and 70% diametric deflections for 8T and 20T (UD) specimens, respectively. Visual examination revealed cracking and delamination. The 8T specimen showed extensive delamination within inner plies, starting with matrix cracks and progressing to axial splitting, accentuated by buckling effects. The 20T specimen experienced severe splitting along the fiber winding angle following the pipe's pattern. The reaction force before damage is 1592 N for the 8T model and 6203 N for the 20T (UD) model. For the 20T ± 55° ply orientated model, the inter-ply delamination typically starts from the edges at the top and bottom of the composite pipe before propagating to the sides and other regions of the structure. Upon impact and deformation, buckling and subsequent interlaminar delamination at these regions are observed for all cases. The FEA model estimated the compressive force at damage initiation as 3291 N.

Load-displacement graphs, FEA results, and positions of four diametric deflections for the ±55° ply orientated model are illustrated in Figure 4. Consistency among repeated experimental results across six specimens highlights test reproducibility.

Four-point bending and short-beam shear tests are performed to determine polymer matrix composites' flexural properties and shear behavior. Using three specimens, the flexural tests are conducted on the 20T (UD) model. Table 3 presents the maximum flexural stress, flexural modulus, maximum strain, and short beam strength as determined from experimental and numerical analyses for three composite specimens. Load-displacement graphs are seen in Figure 5 for the 20T (UD) specimens.

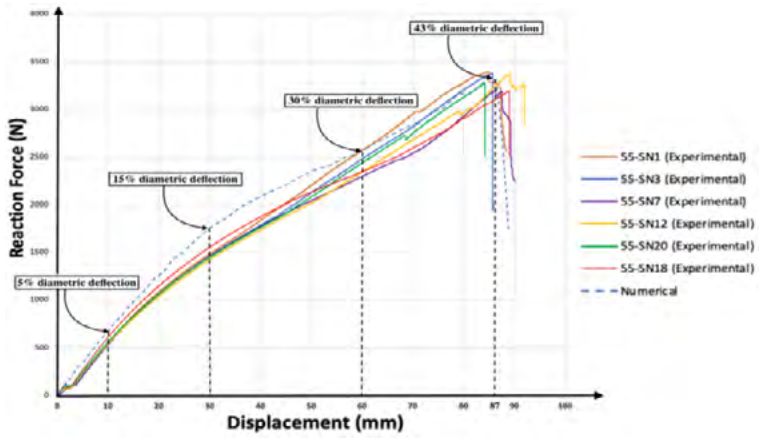


Figure 4. Load-displacement curve for 20T (± 55°) oriented specimens (compression test)

Table 3. Material properties for the 4-Point and Short Beam Shear Tests (UD).

	Flexural Modulus (MPa)	Maximum Flexural Stress (Mpa)	Maximum Strain %	Short Beam Strength (MPa)
20T-1	3497.095	511.95	4.83	49.13
20T-2	3989.872	411.14	4.94	43.35
20T-3	3956.574	419.62	5.72	30.68
Numerical (UD)	4769.37	416.42	4.63	45.41

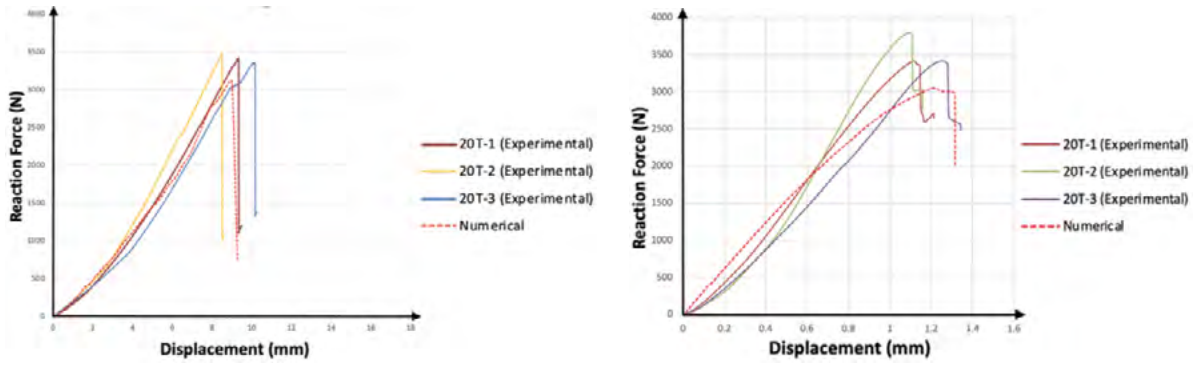


Figure 5. Load-displacement curve. (a) 4-point bending test, (b) 3-point bending test of 20T (UD) model (compression test).

Determining the initial longitudinal tensile strength involves subjecting test pieces, consisting of a specified length of pipe, to longitudinal extension at a constant speed until fracture occurs within a specified timeframe. Observable failure indicators in the tensile test include whitening in the gauge region due to matrix cracks and evident fiber breakage in the test coupons. A comparison of load-displacement curves for experimental and numerical tests is depicted in Figure 6, while Table 4 presents the initial and ultimate tensile strength for the coupon specimens.

The Composite Pipe Split Disc Test is crucial for assessing how well composite pipes withstand internal pressure. Its controlled nature and capability to replicate critical defects make it essential for understanding composite material behavior. In Table 5, there's a comparison of the ultimate hoop tensile stress for ±45° and ±55°orientation between numerical and experimental tests.

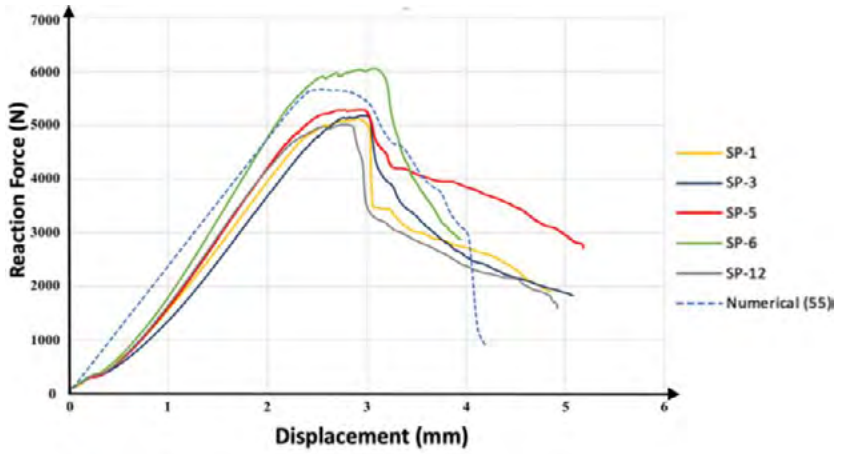


Figure 6. The load-displacement curve for 20T (± 55°) oriented specimens (Tensile test).

Table 4. Tensile test results for for experimental and numerical analysis.

Test Specimen	Initial longitudinal tensile strength (N/mm)	Percentage ultimate elongation (%)	Ultimate tensile Strength (MPa)
SP-1	209.38	1.981	44.54
SP-3	219.61	1.942	42.53
SP-5	219.12	1.921	40.14
SP-6	251.20	1.981	44.07
SP-12	255.45	1.875	41.54
Numerical (±55°)	233.4	-	47.07
Numerical (±45°)	292	-	58.4

Table 5. Material Properties for Pipe Split Disc Test.

Test Specimen	Average thickness (mm)	Average Width (mm)	Average notched width (mm)	Circumferential Tensile Strength (N/mm)	Ultimate Hoop Tensile Strength (MPa)
Experimental	6.44	21.46	11.65	2387.3	368.6
Numerical (±55°)	5	22.5	11.25	1753.5	350.7
Numerical (±45°)	5	22.5	11.25	1600.5	320.1

Similarly, the Double-Notch Shear test assesses interlaminar and through-the-thickness shear strength, with a similar comparison shown in Table 6. This comparison helps validate the accuracy of numerical simulations against real-world experiments.

Table 6. Double-notch shear test results for experimental and numerical analysis.

Test Specimen	Thickness (mm)	Width (mm)	Average Slot 1 thickness (mm)	Average Slot 2 thickness (mm)	Shear zone width (mm)	Shear zone thickness (mm)	Slot distance (inside) (mm)	Slot distance (outside) (mm)	Shear strength (Mpa)
Experimental	5.79	22.05	2.6	2.56	22.08	5.52	12.10	11.95	29.04
Numerical (±55°)	5	25	2.5	2.5	25	5	12.5	13	31.93
Numerical (±45°)	5	25	2.5	2.5	25	5	12.5	13	28.12

Figure 7 depicts the FEM shear damage analysis for Ring compression, Double-Notch Shear, Split-Disk, and Longitudinal tensile test, respectively.

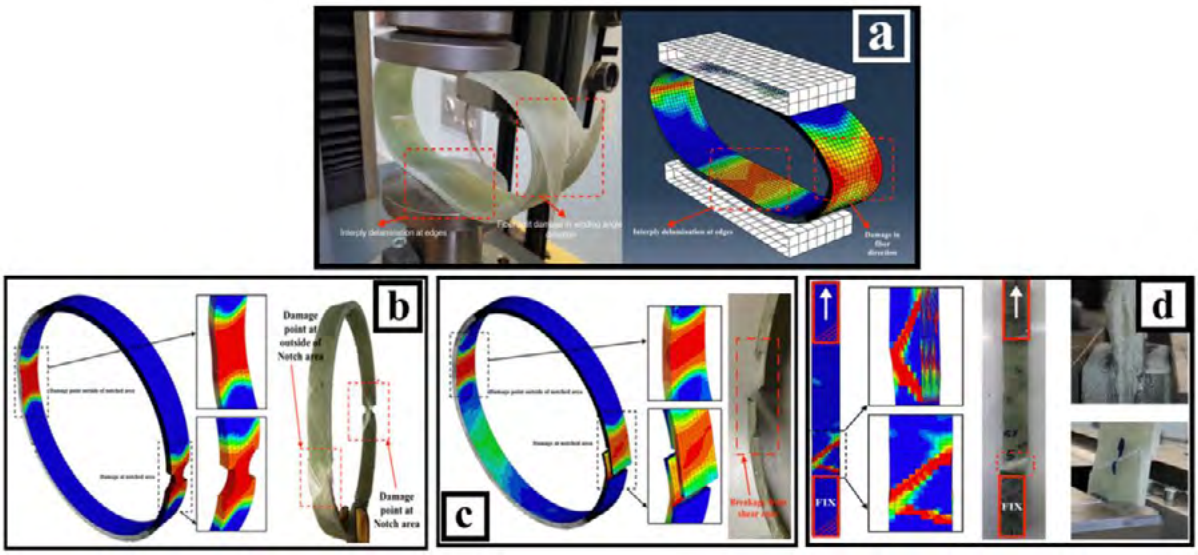


Figure 7. FEM analysis depicting shear damage. (a) Ring-Compression, (b) Double-Notch Shear test, (c) Split-Disk and (d) Longitudinal Tensile test.

Figure 8 depicts the three-dimensional distribution of Hoop stresses for the seismic pipe joint model resulting from a simulation with a 120 mm axial displacement under 600 kN axial load and 20 bar internal pressure for expansion and contraction movements, and 600 kN axial load and 20 bar internal pressure for rotational movement. Vulnerable regions are identified to be around the region where the constriction of the bell pipe's cross-section takes place, along the wall of the pipe bell where the lock ring makes contact for both pull and push movements of the spigot pipe. Examining the stress attributes of the pipeline concerning angular rotation, localized stresses are situated at sensitive locations directly beneath the contact point of the bell mouth with the crown and invert of the spigot. These specific sensitive locations highlight the presence of observable concentrated stress, which shows satisfactory outcomes

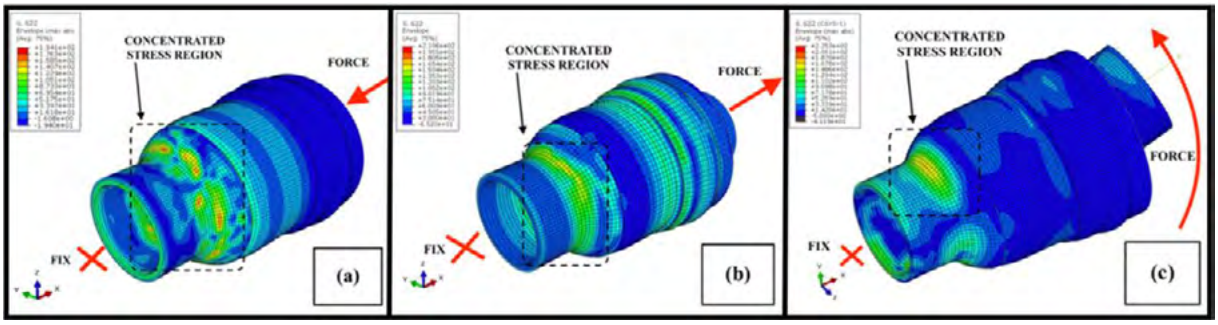


Figure 8. Numerical simulations showing Hoop stress for different movements of the pipe joint. (a) Full Contraction (b) Full Expansion (c) Maximum Angular Deviation.

The tests and results presented here are expected to help tackle some demanding problems related to composite laminate designs, especially for underground composite pipes. Additionally, they aim to emphasize significant challenges and areas of limited understanding in current practices.

4. Conclusions

This research addresses a significant gap in earthquake-resistant composite pipelines by introducing a novel glass fiber-reinforced composite (GRP) pipe connection system. This innovation includes a solution for angular deflection in GRP pipes, enhancing their ability to withstand seismic deformations effectively. Simplifying assembly and disassembly, the system eliminates bolts in joints. The study encompasses the mechanical characterization of composite materials and rings from filament-wound pipes and the structural optimization of earthquake-resistant composite Pipes and Joints. Ring compression tests accurately predict stiffness and strength using finite element models. Integrating composite micromechanics theories and literature, the research refines ply properties through an iterative process validated by comparing simulated outcomes with experimental data. Leveraging these test results, stress analysis via Finite Element Analysis enhances the optimization of pipe joint designs. The proposed socket joints offer advantages in elongation/contraction and rotation during ground deformations, while the absence of bolts in assembly ensures simplicity. The findings of this research contribute to advancing composite laminate designs for subterranean pipelines, addressing significant challenges in existing methodologies, and providing valuable insights for seismic-resilient pipeline engineering. In forthcoming research, the results from numerical analysis used to simulate seismic pipe joints will be further validated through comparison with a physically manufactured model.

5. Acknowledgement

This paper is a part of a university-industry collaborative project between SUPERLIT Boru San. Inc. and Bogazici University, in the context of TUBITAK TEYDEB-1505 funded project (No 5220085).

References

[1] L. A. L. Martins, F. L. Bastian, and T. A. Netto, "Structural and functional failure pressure of filament wound composite tubes," *Materials & Design* (1980-2015), vol. 36, pp. 779-787, 4// 2012.

[2] Kaddour, A. S., Hinton, M. J., Smith, P. A., & Li, S. Mechanical properties and details of composite laminates for the test cases used in the third world-wide failure exercise. *Journal of Composite Materials*, 47, 2427-2442, 2013.

[3] Z. Hashin, A. Rotem, A fatigue criterion for fiber-reinforced materials, *J. Compos*. Mater. 7 448–464, 1973.

[4] Zou, Z., Reid, S. R., Soden, P. D., & Li, S. Measurement of the critical energy release rate GIIc for filament wound GRP pipes. *Composites: Part A*, 32, 271-280, 2001.

[5] Zou, Z., Reid, S. R., Li, S., & Soden, P. D. Applications of a delamination model to laminated composite structures. *Composite Structures*, 56, 375-389, 2002.

[6] Zou, Z., Reid, S. R., & Li, S. A continuum damage model for delamination in laminated composites. *Journal of the Mechanics and Physics of Solids*, 51, 333-356, 2003.

[7] ASTM D2412-02. Standard Test Method for Determination of External Loading Characteristics of Plastic Pipe by Parallel-Plate Loading, *American Society for Testing and Materials*, 2002.

[8] ASTM D2290, Revision 19A,- Standard Test Method for Apparent Hoop Tensile Strength of Plastic or Reinforced Plastic Pipe, 2019.

[9] ASTM D7264/D7264M-15, Standard Test Method for Flexural Properties of Polymer Matrix Composite Materials. *American Society of Testing Materials*, West Conshohocken, 2015.

[10] ASTM D2344/D2344M-16, Standard Test Method for Short-Beam Strength of Polymer Matrix Composite Materials and Their Laminates, 2016.

[11] ASTM D3846-08, Standard Test Method for In-Plane Shear Strength of Reinforced Plastics, ASTM International, West Conshohocken, PA, 2015.

[12] ISO 8513:2016: Plastics piping systems – glass-reinforced thermosetting plastics (GRP) pipes – test methods for the determination of longitudinal tensile properties. ISO, Geneva, Switzerland, 2016.

EXPERIMENTAL EVALUATION OF THE T-STRESS IMPACT ON THE CRACK TRAJECTORY IN THICK ADHESIVE JOINTS UNDER MODE I LOADING

Ali Shivaie Kojouri[1], Javane Karami[1], Kalliopi-Artemi Kalteremidou[1], Jialiang Fan[2], Akash Sharma[3], Anastasios P. Vassilopoulos[4], Veronique Michaud[2], Wim Van Paepegem[3], Danny Van Hemelrijck[1]
1: Department of Mechanics of Materials and Constructions (MeMC), Vrije Universiteit Brussel, Brussels, Belgium
2: Laboratory for Processing of Advanced Composites (LPAC), Institute of Materials (IMX), Ecole Polytechnique Fédérale de Lausanne (EPFL), Lausanne, Switzerland
3: Department of Materials, Textiles and Chemical Engineering, Ghent University, Technologiepark–Zwijnaarde 46, B-9052 Zwijnaarde, Belgium
4: Composite Construction Laboratory (CCLab), Ecole Polytechnique Fédérale de Lausanne (EPFL), Lausanne, Switzerland

Keywords: T-stress, Mode I fracture, Thick adhesive joint, Crack kinking

Abstract

In the present research, pre-cracked double cantilever beam (DCB) thick adhesive joint specimens, manufactured with glass/epoxy composite adherends and a structural adhesive with a bond-line thickness of approximately 10 mm, are tested under pure mode I loading. A Digital Image Correlation (DIC)-assisted in-situ measurement technique is used to determine the T-stress in the test samples, and the crack propagation angles are determined using the second-order crack kinking theory in order to be compared to the experimental values. A good agreement is observed between the experimental and theoretical crack propagation angles. The geometry of the thick adhesive joint causes the T-stress and the crack kinking phenomenon, even if a perfect interface between the adhesive and the adherends exists. In order to validate this observation Polymethyl Methacrylate (PMMA) specimens, in which no interface or voids were present to affect the stress field around the crack tip and cause the crack to deviate from the middle plane of specimens were tested. To accomplish this, two types of specimens, i.e. Compact Tension (CT) and DCB, were manufactured out of (PMMA) and loaded under pure mode I. The same behavior, i.e. deviation of the crack from the middle of the specimen to an oblique path, is observed by changing the specimen geometry from CT to DCB specimens.

1 Introduction

Adhesive joints are used in different industries, including the wind turbine manufacturing, because of their advantages compared to traditional mechanical joining methods. By applying adhesives, there is no need to drill any holes; therefore, the structural integrity of the substrate materials remains intact. Moreover, compared to traditional mechanical joining methods, adhesive joints offer uniform stress distribution as well as more freedom in joining similar and dissimilar materials. In the literature, studies on the fracture behavior of thick adhesive joints are still scarce, even if they are frequently used in the blades of wind turbines. For instance, Miao et al. [1] showed both experimentally and numerically that the crack in thick adhesive joints loaded under pure mode I can initiate in the adhesive; however, the main tendency of the crack is to propagate toward the interface. Similarly, Fernandes et al. [2] and Fan et al. [3] experimentally revealed that the crack trajectory for a joint with a bond-line thickness of about 10 mm is not stable under mode I loading, and that the crack tends to propagate from the middle of the specimen towards the interface. Fan et al. [3] investigated the effect of voids on the performance of thick adhesive joints.

The T-stress is a constant stress acting parallel to the crack plane. It is known that under pure mode I loading, the crack tends to propagate along its initial plane when the T-stress is zero or negative, i.e., the T-stress does not affect the crack trajectory in that condition. A positive T-stress however, causes crack deviation and an unstable crack trajectory [4]. Indeed, finite element simulations were used by Fernandes et al. [5], and it was shown that the positive T-stress in thick adhesive joint specimens is possibly

responsible for the crack kinking from the middle of the specimen. Furthermore, the effect of the specimen geometry on the T-stress and the crack trajectory has been studied by Ayatollahi et al. [6] and Bahadori et al. [7] for notched and cracked DCB specimens made of PMMA. In their analyses, the experimental and analytical predictions were in good agreement regarding the angle of crack propagation.

In-situ measurement approaches based on DIC [8–12] can be used to assess crack tip parameters such as the J-integral, Stress Intensity Factor (SIF), and T-stress for different specimens subjected to mode I loading. These methods, not yet studied for adhesive joints, can be applied in this context to analyze the T-stress of the thick joints under consideration in this study.

Hence, considering the lack of experimental investigations regarding the impact of the T-stress on the unstable crack trajectory in thick adhesive joints, this study employs an in-situ measurement method, validated in [8], to examine the unstable crack path propagation of thick adhesive joints. To do so, the second-order crack kinking theory is used together with experimental data to predict the crack initiation angle. The experimental and analytical methodologies are described hereunder.

2 Materials and methods

A glass fiber reinforced epoxy composite material, manufactured by Vacuum Assisted Resin Transfer Molding (VARTM) and the Sika power®-830 adhesive (Sika Technology AG, Switzerland), were used to prepare the adhesive joints. A unidirectional glass fabric with 425 g/m^2 areal weight was used as the reinforcement, in 0/90 configuration, and the EPIKOTE Resin MGS RIMR 135, together with the EPIKURE Curing Agent MGS RIMH 137, was used as the epoxy resin for manufacturing the composite material. The mechanical properties of the adherend and the adhesive are presented in Table 1 and Table 2, respectively. It has to be noted that, the through-thickness Young's modulus of the composite was estimated based on the test conducted on $[90^o]_8$ specimens. To prepare the joint specimens the procedure outlined in Refs. [3,13] was followed. The specimens had a width of 25.4 mm and a length equal to 356 mm, according to ASTM D3433 [14], and cutting took place using a water-cooled rotating saw. In order to produce pre-cracked specimens, each of them was cut at the middle of the adhesive layer using a thin saw. In the end, the pre-crack was sharpened by a fresh razor blade. Different pre-crack lengths were studied, as will be discussed later. Furthermore, DCB and CT specimens manufactured with PMMA were tested under mode I loading.

Load was applied to the specimens using an Instron universal testing machine (5885). The tests were conducted at a constant crosshead speed of 2 mm/min and DIC was used to monitor the deformation of the specimens during the tests. DIC images were captured both from the undeformed specimens as well as during their loading. After the tests, the images were processed using the VIC3D-9 software [15] to determine the displacement field of the specimens. For that, a subset size of 41*41 pixels was utilized. Section 4 presents the results of the experiments described in this section.

Table 1. Mechanical properties of the adherend

Glass fiber reinforced epoxy	
E_{xx} [GPa]	24.5
E_{yy} [Gpa]	24.5
E_{zz} [Gpa]	12.5
ν_{xy}	0.12

3 Theoretical background

The detailed description of the in-situ measurement method utilized in this study for the evaluation of the J-integral and the higher-order non-singular terms of the Williams' expansion is available in Ref. [8]. Hereafter, a brief explanation of the method is provided for clarity reasons.

Table 2. Mechanical properties of the adherend

Sika power®-830	
Young's modulus [GPa]	2.8
Yield strength [MPa]	33
Ultimate strength [MPa]	40
Poisson's ratio [-]	0.4
Fracture toughness [MPa.m$^{0.5}$]*	2.8
*From reference [16]	

3.1 Theoretical stress field around the crack

The Williams' expansion for the displacement field, considering higher-order singular and non-singular terms, can be expressed as follows [17]:

$$\begin{Bmatrix} u \\ v \end{Bmatrix} = \sum_{n=-(N+2)}^{N} \frac{a_n}{2\mu} r^{\delta_n+1} \begin{Bmatrix} (\kappa + \frac{n}{2} + (-1)^n) cos\left(\frac{n}{2}\theta\right) - (\frac{n}{2}) \cos\left[\left(\frac{n}{2} - 2\right)\theta\right] \\ (\kappa - \frac{n}{2} - (-1)^n) sin\left(\frac{n}{2}\theta\right) + (\frac{n}{2}) \sin\left[\left(\frac{n}{2} - 2\right)\theta\right] \end{Bmatrix} + \sum_{n=-(N+2)}^{N} \frac{b_n}{2\mu} r^{\delta_n+1} \begin{Bmatrix} (-\kappa - \frac{n}{2} + (-1)^n) sin\left(\frac{n}{2}\theta\right) + (\frac{n}{2}) \sin\left[\left(\frac{n}{2} - 2\right)\theta\right] \\ (\kappa - \frac{n}{2} + (-1)^n) cos\left(\frac{n}{2}\theta\right) + (\frac{n}{2}) \cos\left[\left(\frac{n}{2} - 2\right)\theta\right] \end{Bmatrix} \quad (1)$$

in which a_n and b_n are known as Williams' coefficients and are related to mode I and mode II loading conditions, respectively, while u and v represent the displacements in the x and y directions correspondingly, as shown in Figure 1. Moreover, the first-order singular terms, associated with the SIFs K_I and K_{II} are defined as $K_I = \sqrt{2\pi}\, a_1$ and $K_{II} = \sqrt{2\pi}\, b_1$, respectively. Moreover, the T-stress can be derived from the second Williams' expansion as $T = 4a_2$.

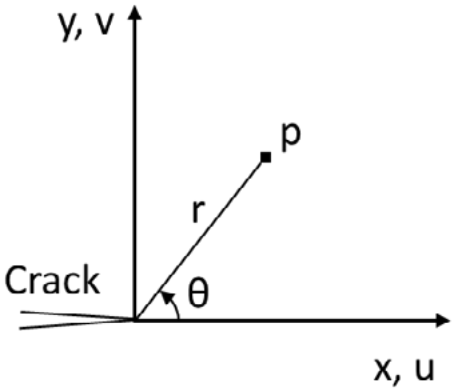


Figure 1. Defined coordinate system at the crack tip

It is worth mentioning that both rigid body translation and rotation are taken into account in Eq. (1), which can be applied to the displacement field derived from DIC [8]. Eq. (1) can be rewritten in a matrix form for a given number of points in the vicinity of the crack as follows:

$$\begin{Bmatrix} u_1 \\ u_2 \\ \vdots \\ u_k \\ v_1 \\ v_2 \\ \vdots \\ v_k \end{Bmatrix} = \begin{bmatrix} F^I_{-(N+2)}(r_1,\theta_1) & \dots & F^I_0(r_1,\theta_1) & \dots & F^I_N(r_1,\theta_1) & F^{II}_{-(N+2)}(r_1,\theta_1) & \dots & F^{II}_0(r_1,\theta_1) & \dots & F^{II}_N(r_1,\theta_1) \\ F^I_{-(N+2)}(r_2,\theta_2) & \dots & F^I_0(r_2,\theta_2) & \dots & F^I_N(r_2,\theta_2) & F^{II}_{-(N+2)}(r_2,\theta_2) & \dots & F^{II}_0(r_2,\theta_2) & \dots & F^{II}_N(r_2,\theta_2) \\ \vdots & \vdots & \vdots & \vdots & \vdots & \vdots & \vdots & \vdots & \vdots & \vdots \\ F^I_{-(N+2)}(r_k,\theta_k) & \dots & F^I_0(r_k,\theta_k) & \dots & F^I_N(r_k,\theta_k) & F^{II}_{-(N+2)}(r_k,\theta_k) & \dots & F^{II}_0(r_k,\theta_k) & \dots & F^{II}_N(r_k,\theta_k) \\ G^I_{-(N+2)}(r_1,\theta_1) & \dots & G^I_0(r_1,\theta_1) & \dots & G^I_N(r_1,\theta_1) & G^{II}_{-(N+2)}(r_1,\theta_1) & \dots & G^{II}_0(r_1,\theta_1) & \dots & G^{II}_N(r_1,\theta_1) \\ G^I_{-(N+2)}(r_2,\theta_2) & \dots & G^I_0(r_2,\theta_2) & \dots & G^I_N(r_2,\theta_2) & G^{II}_{-(N+2)}(r_2,\theta_2) & \dots & G^{II}_0(r_2,\theta_2) & \dots & G^{II}_N(r_2,\theta_2) \\ \vdots & \vdots & \vdots & \vdots & \vdots & \vdots & \vdots & \vdots & \vdots & \vdots \\ G^I_{-(N+2)}(r_k,\theta_k) & \dots & G^I_0(r_k,\theta_k) & \dots & G^I_N(r_k,\theta_k) & G^{II}_{-(N+2)}(r_k,\theta_k) & \dots & G^{II}_0(r_k,\theta_k) & \dots & G^{II}_N(r_k,\theta_k) \end{bmatrix} \begin{Bmatrix} a_{n-2} \\ \vdots \\ a_0 \\ \vdots \\ a_n \\ b_{n-2} \\ \vdots \\ b_0 \\ \vdots \\ b_n \end{Bmatrix} \quad (2)$$

in which k is the number of points or equations, and N is the number of the higher-order non-singular Williams' expansion terms, including the first-order singular term. It has to be noted that Eq. (1) should be written for each point and since each point has a unique coordinate, i.e., (r,θ) therefore for k number of points there are k equations. Considering that each higher-order non-singular term and its complementary singular term are essential in order to determine the J-integral, for N non-singular terms, N-2 higher-order singular terms are needed when calculating the J-integral using Eq. (2). In Eq. (2), u and v are the displacements of the point P(x,y) as obtained by the DIC. Furthermore, F_N^I, F_N^{II}, G_N^I, and G_N^{II} are functions of r and θ. Additionally, (r_k ,θ_k) corresponds to each (x,y) and can be obtained from the DIC data using the following formula:

$$r_k = \sqrt{(x_k - x_0)^2 + (y_k - y_0)^2}; \theta_k = \tan^{-1}\frac{(y_k - y_0)}{(x_k - x_0)} \quad (3)$$

in which x_0 and y_0 are the coordinates of the tip of the crack. Finally, the unknown coefficients of the Williams' expansion, a_n and b_n, can be calculated using matrix operations and the least square approach [18], which is done in this study through a code implemented in MATLAB [19] in order to calculate the J-integral [8].

3.2 Second-order crack kinking theory

For mode I loading, the tangential stress considering the SIF and the T-stress can be expressed as follows [17]:

$$\sigma_{\theta\theta} = \frac{1}{\sqrt{2\pi r}} \mathrm{K}_I \cos^3\frac{\theta}{2} + T\sin^2\theta \quad (4)$$

in which the first term corresponds to the singular term and the second term corresponds to the T-stress in the Williams' expansion. In order to predict the crack propagation angle, the maximum hoop stress theory or the Generalized Maximum Tangential Stress criterion (GMTS) [4,7] can be utilized. According to the GMTS criterion, the crack will propagate when the tangential stress $\sigma_{\theta\theta}$ reaches its critical value $(\sigma_{\theta\theta})_c$ in a critical distance r_c from the crack tip. Thus, the angle θ_c, corresponding to the propagation angle, can be found as follows:

$$\frac{\partial \sigma_{\theta\theta}}{\partial \theta} = 0 \; and \; \left.\frac{\partial^2 \sigma_{\theta\theta}}{\partial \theta^2}\right|_{\theta = \theta_c} < 0 \rightarrow \theta = \theta_c \quad (5)$$

Using Eqs. (4) and (5) considering the singular term K_I and the T-stress, θ_c can be determined by:

$$\theta_c = 0 \text{ or } \theta_c = 2\cos^{-1}\left[\frac{1}{4\,\bar{T}} \pm \sqrt{0.5 + \frac{1}{(4\bar{T})^2}}\right] \quad (6)$$

in which $\bar{T}$ is the normalized T-stress and is defined as:

$$\bar{T} = \frac{8}{3}\frac{T}{\frac{K_I}{\sqrt{2\pi r_c}}} \quad (7)$$

Eq. (6) predicts fracture for any geometry when K_I and T-stress are known. From Eqs. (6) and (7), it can be deduced that determining the critical distance is necessary for predicting the fracture initiation angle. In the present study, the critical distance as defined by Seweryn [20] is used:

$$r_c = \frac{2}{\pi}\left(\frac{K_{Ic}}{\sigma_u}\right)^2 \tag{8}$$

where K_{IC} is the fracture toughness, and σ_u is the ultimate strength, given in

4 Results and discussions

In all tested thick adhesive joint specimens, unstable crack propagation has been observed, wherein the crack instantly jumps to the interface between the adhesive and the adherend, resulting in a sudden decrease in load. Figure 2 displays an example whereby the crack has jumped to the interface.

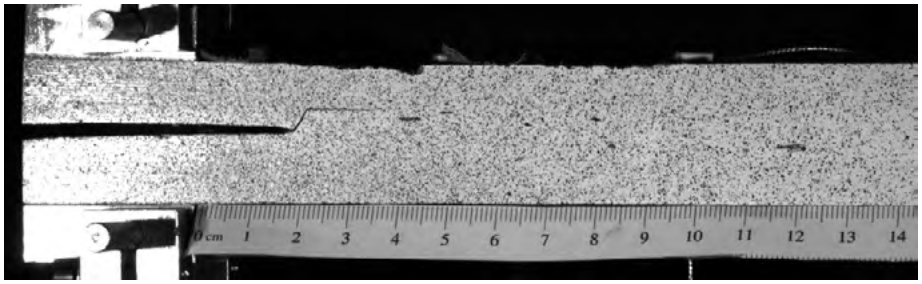


Figure 2. Crack propagation from the middle of the specimen to the interface

The second-order crack kinking theory is employed in this study to predict the crack kinking angle. By employing the Williams' expansion's first and second-order terms, the crack propagation angle of each specimen can be determined and compared with the experimentally measured values. The experimental crack kinking angle values as well as those obtained from the second-order crack kinking theory are presented in Table 3 for each specimen together with the corresponding crack length. Figure 3 shows the crack propagation angle for all specimens, obtained from microscopic observations after the experiment.

Considering the results presented in Table 3, a good correlation can be observed between the experimentally measured values and the theoretical predictions pertaining to the crack propagation angle. Although there are discrepancies between the predicted and measured crack propagation angles, the GMTS criterion indicates the unlikelihood of crack propagation at the middle of the specimen for any crack length.

Table 3. Theoretical and experimental crack kinking angle values

Specimen	Crack length [mm]	Experiment [°]	GMTS [°]
S1	24.0	29	±43
S2	34.0	28	±30
S3	46.5	-40	±37
S4	48.5	39	±62

Each angle is rounded to the closest integer

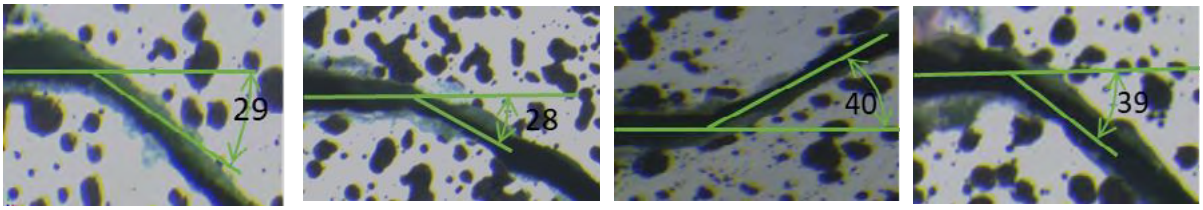


Figure 3. Monitored crack propagation angle of DCB specimens (each experimentally measured angle is rounded to the closest integer)

Ayatollahi et al. [6] investigated the effect of the T-stress on the crack propagation angle on PMMA specimens including CT and DCB as well as Tapered Double Cantilever Beam (TDCB) geometries. They observed that for the DCB specimens, the crack did not propagate in the middle of the specimens under a pure opening mode. In order to reproduce the previous findings DCB and CT specimens made from PMMA are tested. Figure 4 shows DCB and CT PMMA specimens tested in the present research. It can be seen that by changing the geometry, the crack propagation direction under pure mode I loading conditions also changes. Specifically, while the crack propagates at the middle of the CT specimen, it deviates from the middle plane of the DCB specimen and ultimately propagates along an oblique path. The used PMMA specimens did not have any interfaces or voids, which could potentially affect the stress field ahead of the crack tip. Therefore, it is rational to conclude that any deviation of the crack path is due to the geometry.



Figure 4. DCB (left) and CT (right) PMMA specimens under mode I loading

5 Conclusions

The current study investigates the fracture behavior of thick adhesive DCB joints fabricated using composite adherends and subjected to pure mode I loading. It has been observed that in all specimens, the crack propagated instantly from the crack tip towards the interface. It was shown that the positive T-stress at the crack tip due to the DCB geometry is the reason for such a behavior. In order to validate this observation and conclusion and to exclude any effect from voids or other manufacturing defects, DCB and CT PMMA specimens were manufactured and tested under mode I loads. By changing the geometry from CT to DCB in the PMMA specimens, it was observed that the crack tends to deviate from the middle plane of the specimen and then propagates along an oblique path. Hence, it is concluded that the geometry is the primary reason for crack deviations whereas the presence of voids and interfaces in thick adhesive joints can be secondary causes contributing to changes in the crack propagation path. Despite the fact that there are differences between predicted and actual crack propagation angle the GMTS criterion shows that the crack does not tend to propagate at the middle of the specimen for any crack length.

6 Acknowledgments

The authors acknowledge funding under the Lead Agency scheme from the Research Foundation - Flanders (FWO Vlaanderen) through the project grant G031020N and the Swiss National Science Foundation (SNF) through the project grant 200021E_18944/1 with the title "Combined numerical and experimental approach for the development, testing, and analysis of thick adhesive joints in large wind turbine blades". The authors also acknowledge Sika Technology AG for providing materials and support.

7 References

[1] Miao XY, Chen X, Lu R, Eder MA. Multi-site crack initiation in local details of composite adhesive joints. Compos B Eng 2022;242:110055. https://doi.org/10.1016/J.COMPOSITESB.2022.110055.

[2] Lopes Fernandes R, Teixeira de Freitas S, Budzik MK, Poulis JA, Benedictus R. Role of adherend material on the fracture of bi-material composite bonded joints. Compos Struct 2020;252. https://doi.org/10.1016/j.compstruct.2020.112643.

[3] Fan J, Vassilopoulos AP, Michaud V. Mode I fracture of thick adhesively bonded GFRP composite joints for wind turbine rotor blades. Compos Struct 2024;327:117705. https://doi.org/10.1016/J.COMPSTRUCT.2023.117705.

[4] Zehnder AT. Fracture Mechanics. vol. 62. Dordrecht: Springer Netherlands; 2012. https://doi.org/10.1007/978-94-007-2595-9.

[5] Lopes Fernandes R, Budzik MK, Benedictus R, Teixeira de Freitas S. Multi-material adhesive joints with thick bond-lines: Crack onset and crack deflection. Compos Struct 2021;266. https://doi.org/10.1016/j.compstruct.2021.113687.

[6] Ayatollahi MR, Rashidi Moghaddam M, Razavi N, Berto F. Geometry effects on fracture trajectory of PMMA samples under pure mode-I loading. Eng Fract Mech 2016;163:449–61. https://doi.org/10.1016/J.ENGFRACMECH.2016.05.014.

[7] Bahadori R, Ayatollahi MR, Cicero S, Álvarez JA. Geometry Effects on Mode I Brittle Fracture in VO-Notched PMMA Specimens. Polymers 2021, Vol 13, Page 3017 2021;13:3017. https://doi.org/10.3390/POLYM13173017.

[8] Shivaie Kojouri A, Khosravi Rikaee H, Kalteremidou KA, Van Hemelrijck D. Experimental evaluation of J-integral in elastic and elastic–plastic polymers by means of digital image correlation and higher-order eigenfields under mode-I. Eng Fract Mech 2023;291:109534. https://doi.org/10.1016/j.engfracmech.2023.109534.

[9] Eshraghi I, Yadegari Dehnavi MR, Soltani N. Effect of subset parameters selection on the estimation of mode-I stress intensity factor in a cracked PMMA specimen using digital image correlation. Polym Test 2014;37:193–200. https://doi.org/10.1016/j.polymertesting.2014.05.017.

[10] Allaer K, De Baere I, Van Paepegem W, Degrieck J. Direct fracture toughness determination of a ductile epoxy polymer from digital image correlation measurements on a single edge notched bending sample. Polym Test 2015;42:199–207. https://doi.org/10.1016/J.POLYMERTESTING.2015.01.014.

[11] McNeill SR, Peters WH, Sutton MA. Estimation of stress intensity factor by digital image correlation. Eng Fract Mech 1987;28:101–12. https://doi.org/10.1016/0013-7944(87)90124-X.

[12] Lammens B, Portemont G, Berthe J, Seghir R, Réthoré J. Determining singular and non-singular Williams' expansion terms from full-field measurements: Consideration of structural effects on fracture behavior. Theoretical and Applied Fracture Mechanics 2024;130:104304. https://doi.org/10.1016/J.TAFMEC.2024.104304.

[13] Fan J, Karami J, Shivaie Kojouri A, Van Hemelrijck D, Vassilopoulos A, and Véronique M. Investigation of bulk adhesive material and thick adhesive joints for wind turbine applications. 20th European Conference on Composite Materials, 2022.

[14] ASTM D3433-99(2020) Standard Test Method for Fracture Strength in Cleavage of Adhesives in Bonded Metal Joints. Current 2004;98:1–5.

[15] Correlated solutions. VIC 3D n.d.
[16] Karami J, Kojouri AS, Fan J, Kalteremidou K-A, Paepegem W, Vassilopoulos A, Véronique M and Van Hemelrijck D. Investigating the effects of different crack sharpening methods on the mode II and mode II fracture tests of an epoxy resin 2022:1–8.
[17] Williams M. On the Stress Distribution at the Base of a Stationary Crack. Journal of Applied Mechanics, Transactions ASME 1957;24:109–16.
[18] Ayatollahi MR, Nejati M. An over-deterministic method for calculation of coefficients of crack tip asymptotic field from finite element analysis. Fatigue Fract Eng Mater Struct 2011;34:159–76. https://doi.org/10.1111/j.1460-2695.2010.01504.x.
[19] MATLAB. version 2021a 2021.
[20] Seweryn A. Brittle fracture criterion for structures with sharp notches. Eng Fract Mech 1994;47:673–81. https://doi.org/10.1016/0013-7944(94)90158-9.

A double-wall CFPR hydrogen storage and distribution system as a structural component in aircraft applications

N. Sindhe Narayana Rao[1], U. Blass[1], N. Motsch-Eichmann[1], T. Pfaff[1], U. Schmitt[1] and J. Hausmann [1]

[1]Leibniz-Institut für Verbundwerkstoffe GmbH, Component Development, Erwin-Schrödinger-Straße, Geb. 58, 67663 Kaiserslautern
Email: nithya.sindhe@leibniz-ivw.de, Web Page: https://www.ivw.uni-kl.de

Keywords: Liquid hydrogen pipeline, Cryo-compressed hydrogen, load-bearing pipelines, IVW load introduction, Suspension

Abstract
Efficient hydrogen storage and distribution in aircraft require lightweight construction methods, such as fiber-reinforced plastic (FRP) composites produced through efficient processes. Conventional 'Type 4' pressure vessels are made by winding fiber reinforcement over a liner, but these cylindrical vessels cannot be made arbitrarily small in diameter due to the need for a specific winding angle at the dome area for integration of load introduction elements. If lightweight pressure vessels with selectable diameter and length can be economically produced with axial and circumferential layers, they could also serve as structural components in aircraft, like spars and stringers. To increase volumetric storage density, hydrogen can be stored at cryogenic temperatures as liquid hydrogen (LH_2) or Cryo-compressed hydrogen (CcH_2). The main challenge is maintaining hydrogen at -252°C. A pipeline concept for distributing LH_2 and CcH_2 addresses these challenges using a double-wall CFRP construction. The inner pressure tube stores hydrogen and absorbs internal pressure, while the outer shell provides thermal insulation and system connections. The patented 'IVW Load Introduction' method transfers loads from the outer shell's cylindrical area to the dome or fittings. An effective suspension system mechanically decouples the inner vessel and outer shell, allowing the tank and pipeline to function as structural load-bearing components, potentially replacing existing stiffening components in aircraft.

1. Introduction

The development of liquid hydrogen (LH_2) and cryo-compressed (CcH_2) distribution pipelines is a critical advancement for the aerospace industry, particularly for aircraft applications. Hydrogen as an energy carrier offers numerous advantages due to its high energy density by weight, clean combustion, and potential to significantly reduce greenhouse gas emissions. Transitioning to hydrogen-powered aviation is pivotal for achieving sustainable air travel, given the substantial carbon emissions from conventional aviation fuels \cite {Barthelemy2017}. However, hydrogen's low volumetric density at atmospheric conditions necessitates cooling and/or pressurization to enhance its usability \cite{Massaro 2023}.

Transporting hydrogen in its liquid and cryo-compressed states is beneficial as it occupies significantly less volume than its gaseous form \cite {Klier2017}. Integrating such distribution systems in aircraft poses substantial engineering challenges, particularly in maintaining hydrogen at cryogenic temperatures. Heat ingress can cause hydrogen boil-off, diffusion, permeation, and eventual leakage from the tank. Conventional tanks are double-walled, with an inner tank storing hydrogen and an insulating outer jacket. Efficient and lightweight insulation systems are crucial in reducing boil-off losses while minimizing mass added to the overall vehicle structure. Two materials, foams and Vacuum Assisted Multilayer Insulation (VAMLI), recognized for their excellent thermal resistance properties for aircraft applications \cite {Yin2024}.

Conventional tanks are unsuitable as load-bearing components for tensile, compressive, or bending loads due to the absence of purely axial fibers in the load direction. They also cannot be used in limited design spaces, such as aircraft wings, due to the required minimum diameter of around 200 mm for the winding process. The current research project addresses these limitations by developing small-diameter cylindrical pipelines utilizing the novel 'IVW load introduction' method, which involves fibers applied in purely axial (0°) and circumferential (90°) directions \cite{Motsch-Eichmann2023}.
Current research focuses on developing Type 5 pipelines (without liners) for LH2, where the composite material itself acts as a barrier to prevent hydrogen permeation. The development of insulation systems is not the primary focus of this project.

2. Pipeline design concepts

The main goal is to develop leak tight pipelines for distribution of LH_2 and CcH_2. The pipelines are double-walled, cylindrical and mechanically decoupled by a suspension system. The pipelines are designed be integrated as a structural load-bearing component in aircraft for e.g. as spars or stringers in aircraft as shown in Figure 1.

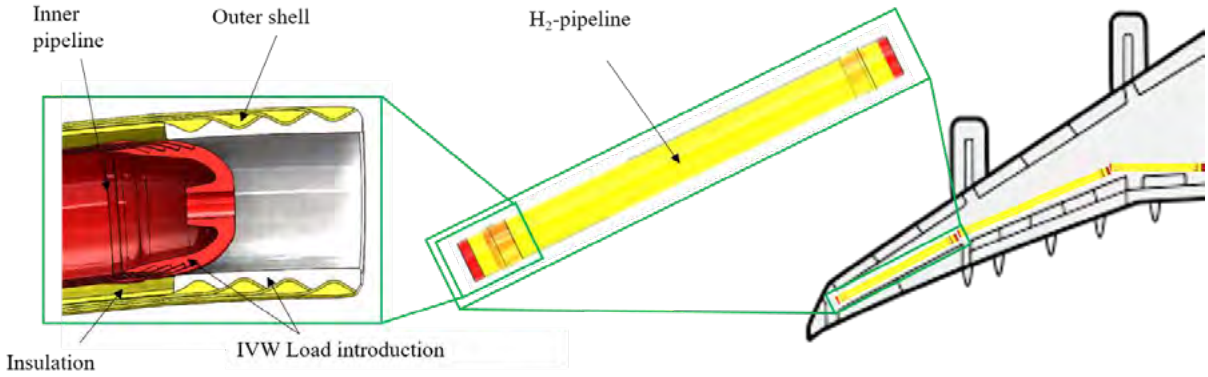


Figure 1. Load-bearing cryogenic hydrogen distribution pipelines.

2.1. Liquid Hydrogen (LH_2) Pipeline

The LH_2 inner pipeline design could incorporate the IVW load introduction, as depicted in Figure 1, but was tailored to meet the geometric and operational specifications outlined in Table 1 (exact dimensions are. Analytical calculations were conducted to determine the requisite minimum wall thickness for the LH_2 inner pipe, utilizing a T300J carbon fiber epoxy laminate with a 60% fiber volume and a strength in fiber direction R_{11} of 1860 MPa. Application of the Boilers formula \cite{Rosen2018} (Eq. 1-3) for pressure vessels yielded a minimum wall thickness requirement of <0.1 mm. While filament winding can achieve such thin wall thickness, stringent attention to manufacturing techniques and quality control is imperative to ensure structural integrity.

Table 1. Geometry and operational specifications for the hydrogen distribution pipeline.

Requirements	Values
Inner Diameter (mm)	35-45
Length (mm)	500
Nominal Pressure LH_2 (bar)	1-10
Nominal Pressure CcH_2 (bar)	200 -350
Operating temperature LH_2 (K)	20
Operating temperature CcH_2 (K)	83

Subsequent investigation explored the viability of a braiding process, reducing the strength in fiber direction R_{11} approximately by 3 times to 500 MPa. This adjustment resulted in a more practical wall thickness of approximately 0.3 mm, a consideration essential for addressing the challenges associated

with connecting metallic end parts to such thin-walled pipes. The first prototype will be produced by biaxial braiding with a braiding angle of ± 54, 7° \cite {Schürmann2005} and Swagelok fitting, which offer reliable vacuum sealing \cite {Glitza2017}.

$$S_{min,u} = \frac{p_i * D_i}{2 * R_{11}} \quad (1)$$

$$S_{min,a} = \frac{p_i * D_i}{4 * R_{11}} \quad (2)$$

$$S_{min,Gesamt} = S_{min,u} + S_{min,a} \quad (3)$$

Due to the applied internal pressure, an axial and a radial load component occurs. Assuming a uniform stress distribution across the cross-section, the stresses for isotropic materials can be determined using the boiler formula (Eq. 4 and 5).

$$\sigma_t = \frac{p_i * D_i}{2 * S} \quad (4)$$

$$\sigma_a = \frac{p_i * D_i}{4 * S} \quad (5)$$

This results in a transverse stress σ_t = 335 MPa and σ_a = 167 MPa.

2.1.1. Outer shell

The outer shell essentially consists of three parts as shown in Figure 2. A metallic boss part, a liner (which in this case acts as a winding aid) and a laminate that absorbs the loads from the boss part. The novel design of the patented IVW load introduction is used \cite{Motsch-Eichmann2023, Nagaraj2022}. The underlying load transfer from the boss part to the laminate works by compressing the axial (0°) layers through the circumferential (90°) layers under the influence of load in axial direction \cite{Motsch-Eichmann2023, Nagaraj2022}.

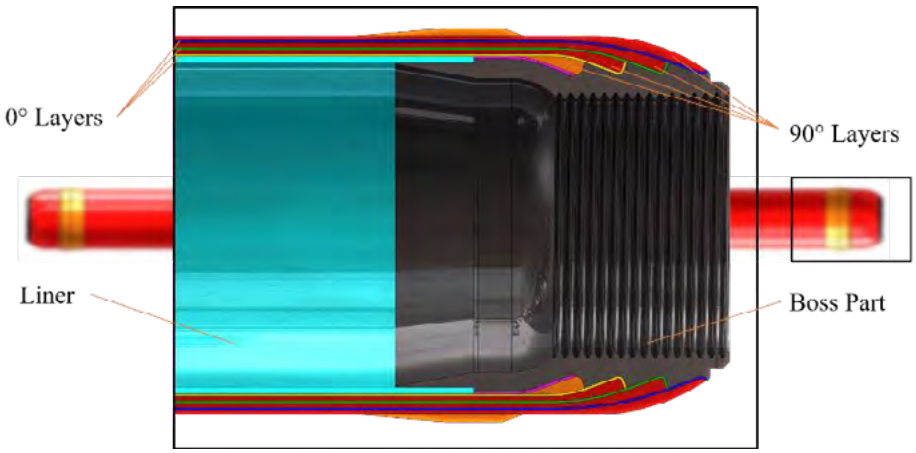


Figure 2. Outer shell for LH_2 and CcH_2 Pipeline employing IVW- load introduction principle. Enclosed view showing the sectional view of the transition area from boss part to CFRP. Adapted from [5] with minor modifications.

Demonstrator production

A demonstrator for the outer shell was produced to assess its load-carrying capacity via initial tensile testing (Figure 4, left view). Aluminum boss parts with IVW load introduction were fabricated and attached to a winding core, which was wrapped with a PVC liner to achieve the desired diameter in the cylindrical area of the pipe. The production process was simplified by employing a unidirectional (UD)

carbon fiber hose, which was pulled over the boss parts and winding core. The UD hose, composed of dry carbon fibers interwoven with an elastomer thread, allows for circumferential stretching and adapts to the contours of the boss parts and winding core. Subsequently, the UD hose was manually impregnated with epoxy resin, and circumferential layers were applied using the wet winding process. Notably, the circumferential layers were applied only in the load introduction area. The results of the tensile test are discussed below.

2.1.2. Suspension concept

The space between the inner tank/pipe and the outer shell is called the interspace, in which the insulation system is installed. The inner diameter of the outer shell depends on the thickness of the required insulation and the geometry of the suspension system. The suspension system is required to keep the mechanical and thermal loads away from being transferred to inner pipe. To this end composite Z-profile springs are designed as shown in Figure 3 to suspend the inner pipe, drawing similarity to the CFRP shell structures developed for pixel detector at CERN \cite {Himmel2003}. As opposed to halfshells in \cite {Himmel2003}, single Z-profile glass fiber laminates will be produced. These individual Z-profiles can be arranged at different points on the surface inner pipe to ensure an effective suspension. The bottom flange of the Z-profile is fixed to the inner tank (for e.g. by gluing). The top flange is flexible and functions like a spring. The Z-profiles are dimensioned such that the flexible top flange can be compressed and pushed into the outer shell where it expands again fixing the inner pipe. The Z-profiles absorb the loads from the outer shell and accommodates the dimensional changes due to its thermal expansion and contraction.

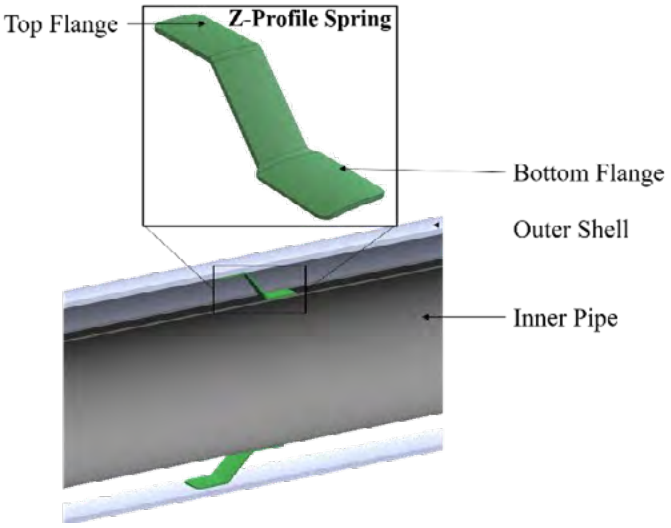


Figure 3. Concept for suspension showing composite Z-profile springs installed at multiple locations on the inner pipe.

2.2. Cryo-compressed Hydrogen (CcH_2) Pipeline

The design of the outer shell can essentially also be used to store or distribute CcH_2. However, the design must be adapted due to the different coefficients of thermal expansion of CFRP and the aluminum boss part. The greater coefficient of thermal expansion of aluminum compared to CFRP would cause the boss part to shrink more than the CFRP when refueling with CcH_2. This would create a gap between the aluminum and CFRP through which the hydrogen could escape. To prevent shrinkage of the boss part, the design of the boss part was revised \cite {Motsch-Eichmann2023}. The revised boss part consists of two parts, an inner cone and an outer cone as shown in Figure 5a. The inner cone design is further modified from \cite {Motsch-Eichmann2023} to enable quick and tightly sealed connection to the On Tank Valve (OTV). No demonstrators are intended to be produced for the CcH_2 pipeline and is only currently considered for a numerical analysis, the results are discussed in this work.

Modelling Approach:
In order to keep the calculation time low, symmetry is utilized and a quarter model is set up in ABAQUS ®. The individual components are meshed using C3D20 Quadratic hexahedral elements. The IMS-65 carbon fiber roving from Teijin and MGS RIMR 135 + MGS RIMH 137 are used as the resin hardener system. The material properties of this composite material are determined from individual components and are shown in Table 2. The liner and metallic boss parts are assigned with material properties of Aluminum 7075. The pressure cylinder model ends shortly after the load introduction as shown in Figure 5. The loads and stresses are evenly distributed in the continuing cylindrical area and therefore are not considered further. The degrees of freedom on the symmetry planes are fixed in the respective directions. The boundary conditions are depicted in Figure 5.

Table 2. Material properties defined in FE-Model.

Material Properties	E_{11} (GPa)	E_{22}, E_{33} (GPa)	E_{33} (GPa)	G_{12}, G_{13}, G_{23} (GPa)	ν_{12}, ν_{13}	ν_{23}	α_{11} (K^{-1})	α_{22}, α_{33} (K^{-1})
CF-Epoxy	192.4	10.6	10.6	7.1	0.25	0.35	1E-06	3E-05
Al-7075	70	-	-	-	0.33	-	2.35E-05	-

3. Results and Discussion

Demonstrator tensile test
The total length of the demonstrator produced was 540 mm with a diameter of 66 mm. A laminate thickness of 2.5 mm was achieved with a resulting demonstrator weight of 910 g including the metallic bosses. The adapters were screwed in to the metallic boss at both ends (Figure 4, left view) and subjected to tensile load until failure. The presence of undulations due to interweaving with elastomeric threads introduces local variations in material properties. The first sings of onset of failure was observed around 245 kN (see graph in Figure 4, right view) at which test was terminated because the max load application limit of the hydraulic cylinder (250 kN) was reached \cite {Nagaraj2022}.There was no failure or fracture observed in the demonstrator.

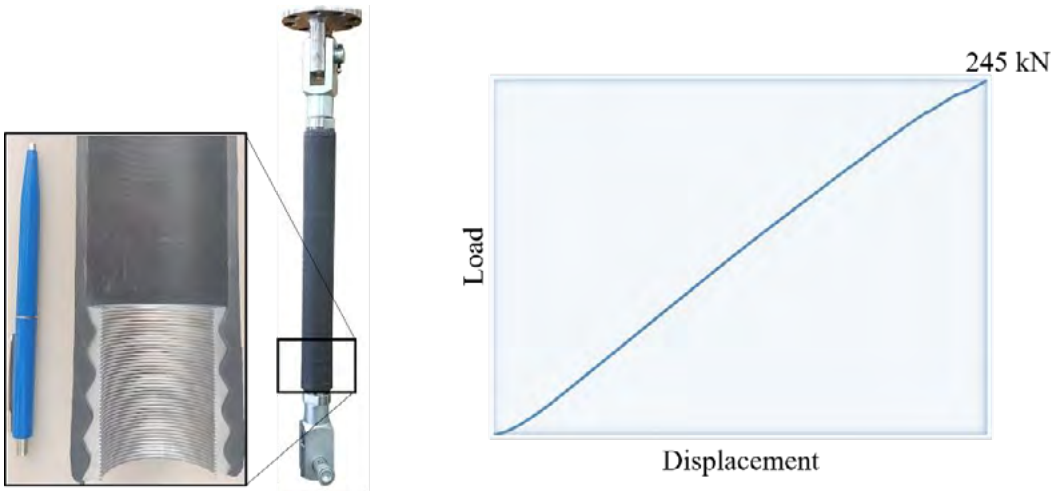


Figure 4. Outer shell demonstrator (left view) with screwed in adapters for the tensile test. Enclosed view showing the sectional view of the load introduction area. Load vs. Displacement curve from the tensile test (right view)

Numerical analysis results for CcH2 pipeline
The numerical analysis consist of four steps. In the first step, the inner cone is displaced relative to the outer cone by an externally applied tensile load. This would be done before installation in the aircraft

(Figure 5b). As a result, the outer cone is stretched in the radial direction and thus also in the circumferential direction. This stretching also elongates the circumferential layers and presses the longitudinal layers against the outer cone. In the second step, the outer tensile load is removed (Figure 5c). Due to the very small angle and the frictional contact between the inner and outer cone, the relative displacement is maintained, and the inner cone does not slip back. The pressure tank or pipeline can now be installed in this pre-stressed state. If the aircraft is now refueled with CcH2 (step three), the hydrogen supply system first cools down before internal pressure builds up. However, the resulting thermal shrinkage of the outer cone is smaller than the expansion caused by the relative displacement between the inner and outer cone. As a result, there is no gap between the CFRP and the outer cone, which means that the tank and the pipeline remain tight throughout (Figure 5d). If the hydrogen supply system continues to be refueled with hydrogen, internal pressure builds up continuously (final step). The internal pressure causes the inner and outer cone to expand in a radial direction and the compression of the longitudinal layers by the circumferential layers increases accordingly. Due to the sufficiently high relative displacement caused by the external load between the inner and outer cone in the first step, there is no further relative movement between the two components during operation (Figure 5e). Consequently, at this pressure, there is no gap between the parts, thereby ensuring that hydrogen leakage is effectively prevented and the pipeline remains leak-proof.

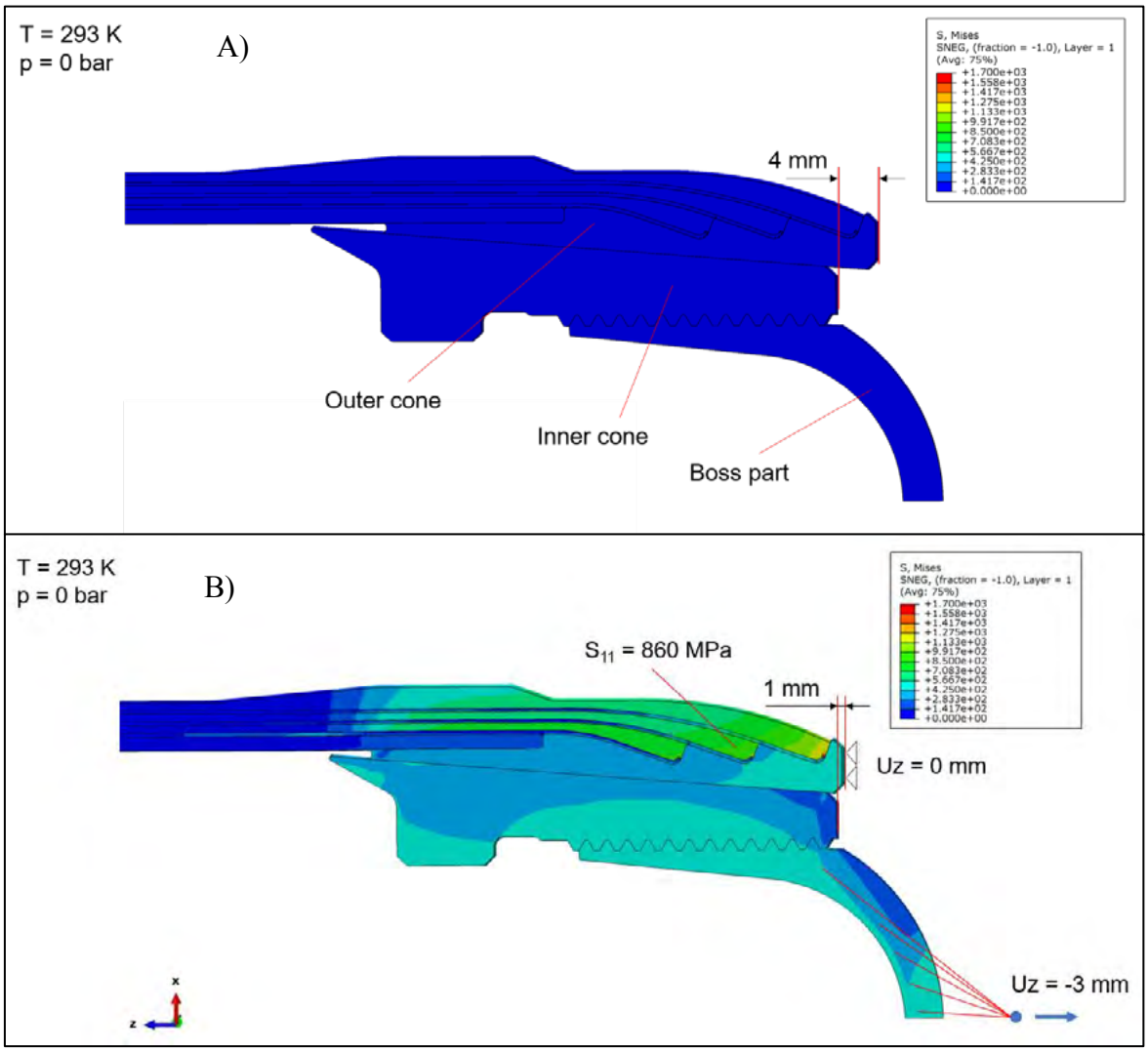
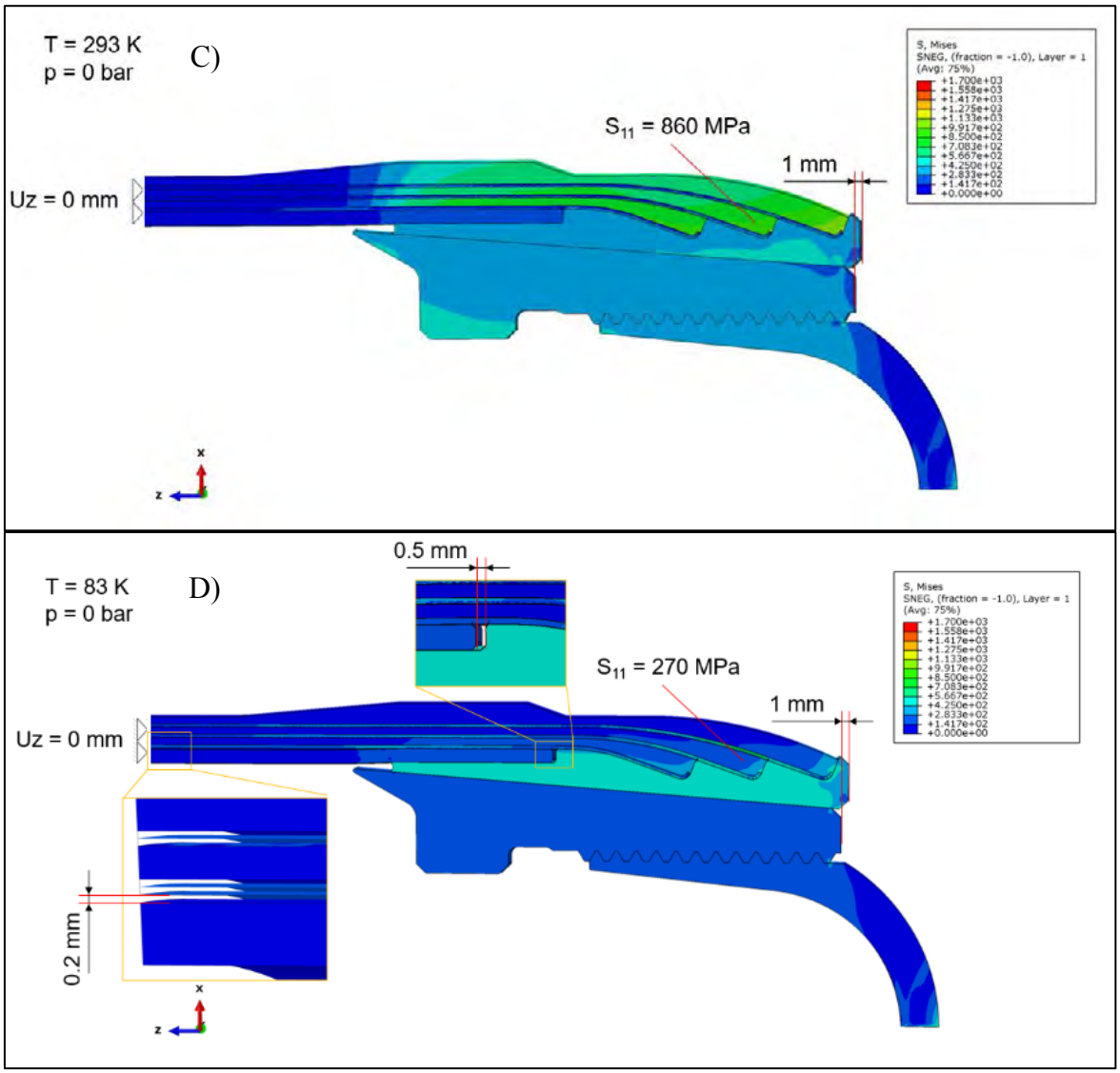
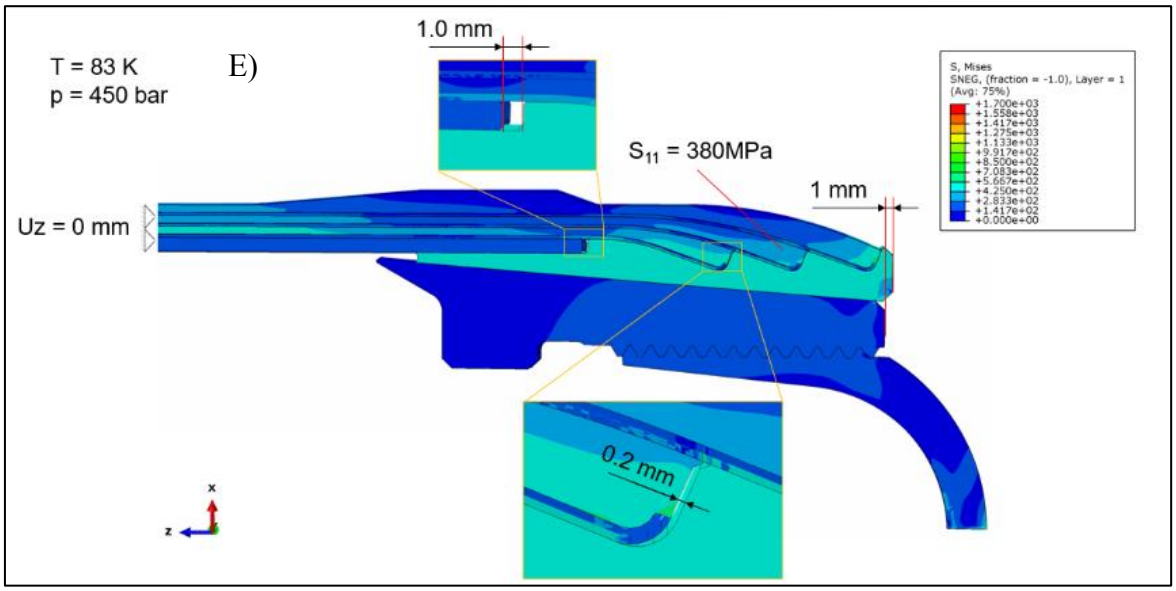


Figure 5. Adapted from [5] with minor modifications. **A):** Further developed design of the boss part [5]. **B):** The inner cone is displaced relative to the outer cone by an external tensile load. As a result, the circumferential layers compress the longitudinal layers.



(Figure 5. Continued): C): The externally applied displacement is released. Due to the relatively flat cone angle, the inner cone does not slip back. **D):** The pressure tank is cooled down during refueling. Due to the pre-tensioning of the outer cone, the thermal shrinkage of the metal parts does not lead to a gap between the CFRP and aluminum.



(Figure 5. Continued): E): The tank is further filled with hydrogen and pressurized. Due to a sufficiently large preload, there is no further relative movement of the two cone parts.

4. Conclusions

As part of the research project, load-bearing hydrogen distribution pipelines are developed. Design concepts for LH_2 and CcH_2 pipelines were presented, utilizing the patented 'IVW load introduction' principle for load transfer. A suspension system with composite Z-profile springs mechanically decouples the inner pipe from the outer shell, enabling its use as a structural load-bearing component in aircraft. Numerical investigations indicate that the developed CcH_2 pipelines can withstand design-operating pressures at cryogenic temperatures. However, further studies under thermo-mechanical cyclic loading at higher temperatures are essential to assess the structure's leak tightness.

Thin-walled braided inner pipes for LH_2 distribution will be produced, followed by burst pressure tests to ensure leak tightness. The first outer shell demonstrator tested with IVW load introduction principle showed high load carrying capacity (245 kN). Production of individual components and bending tests of the double-walled pipelines will be conducted to evaluate the load-bearing capability of the outer shell and the suspension system. Mechanical tests for material characterization at cryogenic temperatures are also planned.

Acknowledgments
The authors would like to express appreciation for the financial support from the Federal Ministry for Economic Affairs and Climate Action within the framework of the Luftfahrtforschungsprogramme (LuFoVI-2) (funding reference 20E2103A). The authors thank all the technical staff and students involved.

References

[1] Barthelemy, H., Weber, M., & Barbier, F. Hydrogen storage: Recent improvements and industrial perspectives. *International Journal of Hydrogen Energy*, 42(11), 7254-7262, 2017.
[2] M. C. Massaro, R. Biga, A. Kolisnichenko, P. Marocco, A. H. A. Monteverde und M. Santarelli. Potential and technical challenges of on-board hydrogen storage technologies coupled with fuel cell systems for aircraft electrification. *Journal of Power Sources*, Jg. 555, S. 232397, 2023.

[3] Klier, J., Rattey, M., Kaiser, G., Klupsch, M., Kade, A., Schneider, M., & Herzog, R. A new cryogenic high-pressure H2 test area: First results. In *Proceedings of the 12th Cryogenics 2012 IIR International Conference, Dresden, Germany*, pp. 11-14, 2012.
[4] Yin, L., Yang, H., & Ju, Y. Review on the key technologies and future development of insulation structure for liquid hydrogen storage tanks. *International Journal of Hydrogen Energy*, 57, 1302-1315, 2024.
[5] N. Motsch-Eichmann, T. Pfaff, U. Blass. Lasttragende Wasserstoffspeicher für Luftfahrtanwendungen. *Deutscher Luft- und Raumfahrtkongress (DLRK2023)*, 19.-21, September 2023.
[6] P. A. Rosen. *Beitrag Zur Optimierung Von Wasserstoffdruckbehältern: Thermische und Geometrische Optimierung Für Die Automobile Anwendung*. Wiesbaden: Springer Fachmedien Wiesbaden GmbH, 2018.
[7] Schürmann, H. *Konstruieren mit faser-kunststoff-verbunden (Vol. 2)*. Springer, Berlin, 2005.
[8] Glitza, K. W., Mättig, P., Sanny, B., Schmitt, U., Siegfanz, A., & Srinivasan, M. Development of diamond powder filled carbon fibre pipes. *Journal of Instrumentation*, *12*(08), T08005, 2017
[9] V.Nagaraj, J.P. Hüppauff, T. Pfaff, N. Motsch-Eichmann, J. Hausmann. Neuartige strukturintegrierte Wasserstoffspeicher für Luftfahrtanwendungen. *Deutsche Gesellschaft für Luft- und Raumfahrt - Lilienthal-Oberth e.V.,* 2022.
[10] N. Himmel, T. Pfaff, U. Schmitt und K.-W. Glitza. Development of high performance CFRP shell structures for the pixel detector in the ATLAS experiment at CERN. *Composites Science and Technology*, Jg. 63, Nr. 14, S. 2013–2028, 2003.

ASSESSMENT OF THE IMPACT PERFORMANCE OF REPAIRED THERMOPLASTIC LAMINATES

Luigi Sorrentino[1], Giuseppe Lama[1], Letizia Verdolotti[1], Maria Oliviero[1], Fabienne Touchard[2], David Mellier[2], Paweł H. Malinowski[3]
[1]Istituto per i Polimeri, Compositi e Biomateriali, Consiglio Nazionale delle Ricerche, P.le E. Fermi 1, 80055 Portici (NA), Italy
Email: luigi.sorrentino@cnr.it (corresponding author), giuseppe.lama@cnr.it, letizia.verdolotti@cnr.it, maria.oliviero@cnr.it
[2]Institut Pprime, CNRS-ISAE-ENSMA-Université de Poitiers, Département Physique et Mécanique des Matériaux, ENSMA, 1 Avenue Clément Ader, 86961 Futuroscope, Chasseneuil, France
Email: fabienne.touchard@ensma.fr, david.mellier@ensma.fr
[3]Institute of Fluid-Flow Machinery, Polish Academy of Sciences, Gdansk, Poland
pmalinowski@imp.gda.pl

Keywords: Repairing; Thermoplastic composites; Impact damage; Scanning laser Doppler vibrometry; Microtomography

Abstract
Thermoplastic composites with 45% by volume of fibres were prepared by using poly(lactic acid) as matrix and basalt woven fabrics as reinforcement. The effect on the laminate performance of a thermal repairing process after non perforating single or consecutive impact events was investigated. The first impact of a series was characterized by a lower value of the peak force, while the following impacts showed a higher peak and a steeper rise of the force, with a substantial superposition of all consecutive impact responses. The laminates showed some energy dissipation after the first impact at all energy levels, while successive impacts didn't show energy dissipation until 8 J.
The damaged laminates were then repaired at 100 °C and 175°C. Scanning laser Doppler vibrometry (SLVD) and microtomography (microCT) were used to assess the laminate damage. Both SLDV and microCT analyses confirmed that matrix continuity and woven fabric planarity were restored at the higher temperature. A second impact testing campaign on the same points demonstrated the complete recovery of the impact resistance after the thermal repairment at 175 °C.

1. Introduction

The composites market is dominated by thermosets composites, due to their high structural properties, but thermoplastic composites are characterized by better performances in damage tolerance and impact resistance, as well as higher productivity [1]. The high sensitivity of composites to hidden defects or damages can give rise to increasing damage during service life [2] and require continuous structural controls and rapid intervention in presence of damages. Cyclic loads or repeated impacts even of low entity, such as during service life or maintenance, can contribute to the onset and propagation of critical damages. The lower sensitivity to impact loads and the higher difficulty for crack growth, which can lead to unexpected laminate failure, is one of the main reasons for the ever growing interest in thermoplastic composites. Other advantages are the recyclability, high specific strength and stiffness, corrosion resistance, enhanced impact toughness, cost effectiveness and flexibility of design [3]. Conventional repairing approaches for damaged laminates make use of bolts, patches, gouges, or on gluing and stitching parts [4]-[10]. These methods can be expensive, and typically are excluded in case of small or barely visible damages, except that in high demanding applications. Thermoplastic composites allow to use conventional repairing methodologies but also exploit new repairing approaches thanks to the possibility to melt their matrix [11],[12].

Non-destructive evaluation (NDE) methods have an important role in post-manufacturing inspection of structures, for identifying damages during service, maintenance, or after repair. Optical inspection is the most simple, albeit very effective, technique [13],[14] but the most diffuse NDE techniques are based on ultrasounds [15]. Among them, scanning laser Doppler vibrometer (SLDV) can detect matrix damages through the excitation of the laminate by means of a surface bonded piezoelectric transducer and measures superficial strain by using a laser beam [14]. SLDV can precisely identify superficial discontinuities, and, with lower precision, estimate the damage extension through the laminate thickness. A very precise detection of through-thickness damages can be achieved by means of X-ray micro-computed tomography (mCT) [16]. In fibre reinforced composites micro-CT is particularly effective in detecting the internal spatial arrangement of fibres, as well as possible damages like delaminations and microcracking [17],[18].

In this paper a thermal treatment is used to recover not-perforating impact damages in the laminate. A reinforced composite based on poly(lactic acid) and basalt fibres woven fabrics was impacted at low energy and multiple times at the same impact point. A compression moulding process was used to repair the thermoplastic composite, and the effect of heating temperature was investigated by means of optical inspection, scanning laser Doppler vibrometry, and micro-computed tomography.

2. Experimental

2.1. Materials

Poly lactic acid - PLA (Luminy L175 from TotalCorbion NV, The Netherlands) was used as matrix. It has a glass transition temperature of 60°C and peak melting temperature of 175°C. The tensile modulus is 3.5 GPa and the tensile strength 50 MPa, as reported in the datasheet [19]. Basalt fibres (type BAS 220.1270.P) were supplied by Basaltex-Flocart NV (Belgium) in the form of a plain weave fabric with surface weight of 220 g/m^2, yarn count of 7.2 ends/cm (warp and weft) [20]. Basalt fibres density was 2.67 g/cm^3, according to the ASTM D792 procedure.

2.2. Composite preparation and repairing

Composite plates were prepared by using the film stacking process. Layers of reinforcing fabric and PLA, 120 mm x 170 mm in size, were alternatively stacked and then pressed by using an hydraulic hot plate press. Laminates consisting of 10 balanced fabric layers 0°/90°, symmetrically arranged with respect to the middle plane of the laminate ([(0/90)5]s configuration), were obtained with a thickness of 1.80 mm and fibre content target of 45% by volume. Compression at 180 °C at 0 MPa for two minutes and 0.5 MPa for five minutes was applied on the stacking sequence to impregnate the fibres. Composite repairing was performed by hot compacting damaged laminates at 100 °C or 175 °C for 5 minutes at near-zero pressure.

2.3. Laminate characterizations

Flexural properties were determined by using a three point bending configuration set according to ASTM D 790. A universal testing machine (mod. 4304 from SANS Shenzen - China, now MTS Inc., USA) equipped with a 5 kN load cell was used. Out-of-plane impact tests were performed by using an instrumented drop-weight impact testing machine (model Fractovis Plus from CEAST – Italy) equipped with a hemispherical tip (diameter 12.7 mm). All tests were performed putting the specimen on a stainless steel annular ring (internal diameter 40 mm, outer diameter 60 mm). The impactor mass was 1.93 kg, and the impact energy, ranging between 1 and 8 J, was set by changing the impact height. Series of 4 consecutive impacts were also applied to investigate the sensitivity to multiple impacts of the composite. Three samples for each impact condition were tested.

2.4. Damage detection

Optical analysis in reflection mode was carried out by using a microscope (model Z16 APO, Leica Microsystems GmbH, Germany) to investigate the superficial damages induced on the composite. The scanning laser Doppler vibrometry (SLDV) acquisition was made with a single head of the PSV-400-3D vibromter from Polytec (Waldbronn, Germany), measuring the vibration velocity of the sample on

the non-impacted surface at grid points spaced about 2.2 mm. The samples were excited with a surface bonded piezoelectric transducers of 10-mm diameter and 0.5-mm thickness (CeramTec, Germany) that was placed on the impacted face at the middle of one of the short edges. The excitation signal (5-cycle long tone burst with 100 kHz central frequency) for the transducer was generated using an arbitrary waveform generator TGA1241 from TTi (Cambridgeshire, England) then amplified using the EPA-104 Piezo Linear Amplifier from Piezo Systems, Inc (Woburn, MA, USA). The sensed wave signals were filtered in the bandwidth 25-300 kHz by a bandpass filter and the signal root mean square (RMS) was calculated for each grid point [21].

Microtomographic image acquisition has been performed using an UltraTom CT scanner manufactured by RX Solutions (France), equipped with a Hamamatsu micro focus sealed X-ray tube operating at 70kV and 428 µA. A 16 µm spatial resolution was used for the acquisitions. The X-ray shadow projections are digitized with 65536 brightness gradations (16 bits) and recorded in TIFF image format. The image acquisition time was about 2h per specimen. For 3D reconstruction, X-ray images were acquired from 1440 rotation views over 360° of rotation (0.25° rotation step).

3. Results and discussion

The average fibre volume content of laminates was 45.8%. All laminates were free of voids. The absence of voids was qualitatively confirmed through optical microscopy and microCT reconstructed volumes. The prepared laminates exhibited a flexural modulus of 18.6 GPa, flexural stress of 213.3 MPa, and strain at break of 1.34 %. The low strain ad break could be related to the possible low interface strength between PLA and basalt fibres, whose sizing treatment was not specifically developed for the used matrix.

Preliminary impact tests on laminates showed a perforation threshold higher than 8 J, hence that was set as limit for testing. Figure 1A shows the impact points at different impact energies. It is evident the increase in size of the damaged area. The force peak during impacts increased with the impact energy as well (Figure 1B). The widening of damaged area can also be associated with the increased energy dissipation during the impact, as evident from the residual value of the energy-displacement curves, which represent the un-recovered energy (Figure 1C).

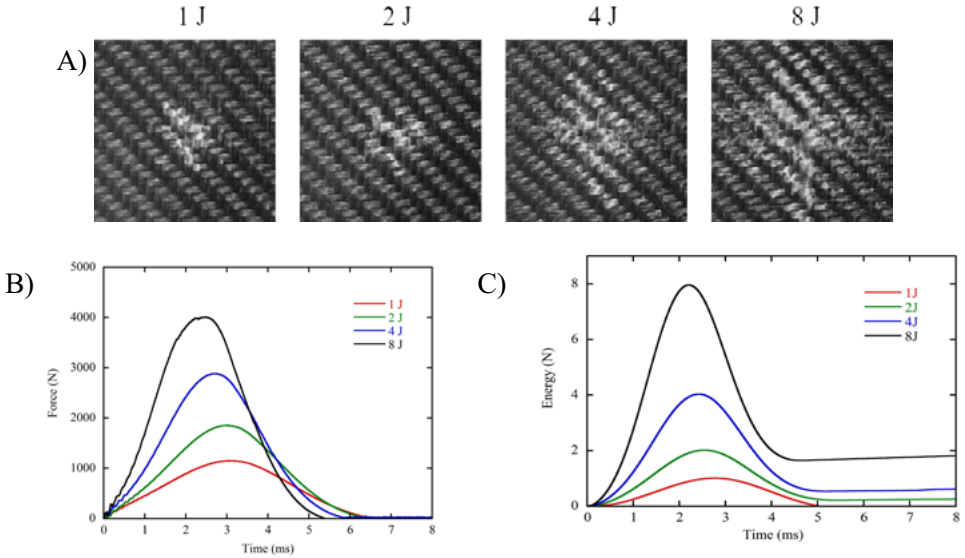


Figure 1. A) Appearance of the impact point at different impact energies; B) Force- and C) Energy-versus time curves as function of the impact energy.

The plots of consecutive impacts show a peculiar behaviour, because the force peak during the first impact is lower than that detected during the subsequent ones (Figure 2A, impacts at 4 J). Additionally, impacts following the first do not show residual dissipated energy up to 4 J (Figure 2B). This verifies at all impact energy values, and has been related to the fact that irreversible phenomena like matrix cracking and delaminations only occur after the first impact, while the subsequent ones do not induce further significant damages until 8 J is used.

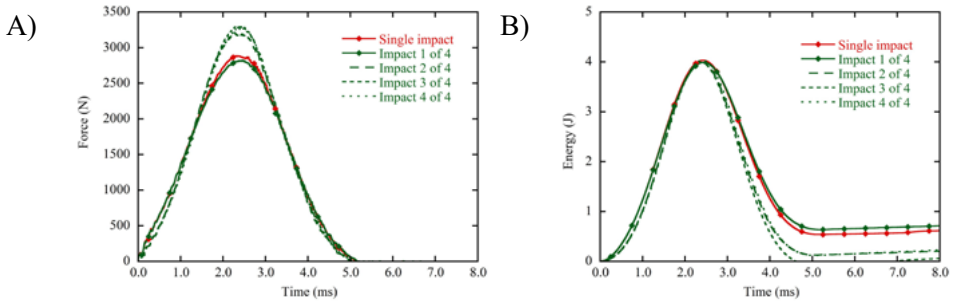


Figure 2. Energy versus time (A) and Force versus time (B) curves after 4 J impacts. Curves from first impacts have a diamond mark.

SLDV analysis evaluated the superficial damaged areas on the impacted surface after one (1x), two (2x) and four (4x) impacts at 4 J (Figure 3A). The damaged area (light grey and white pixels) increases with the impact energy and with the number of consecutive impacts. The optical analysis (Figure 4) shows that laminates processed below the melting temperature of PLA were only able to recover the laminate planarity, while superficial damages were still visible. On the contrary, laminates repaired at 175 °C were completely clean of superficial impact signs. This result is in agreement with the SLDV analysis, which shows residual damages in the laminate repaired at 100 °C (Figure 3B) and no damage pattern in the laminate repaired at 175 °C (Figure 3C). Finally, the microtomographic analysis confirmed the complete recovery of the woven fabrics planarity after both thermal treatments, and no sign of fibres deformation was evident (Figure 5). The combined use of SLDV and microCT results allow to say that thermal treatments were able to recover the reinforcement planarity, but only a temperature high enough to melt the matrix allowed to completely erase any sign of matrix and interface related damages.

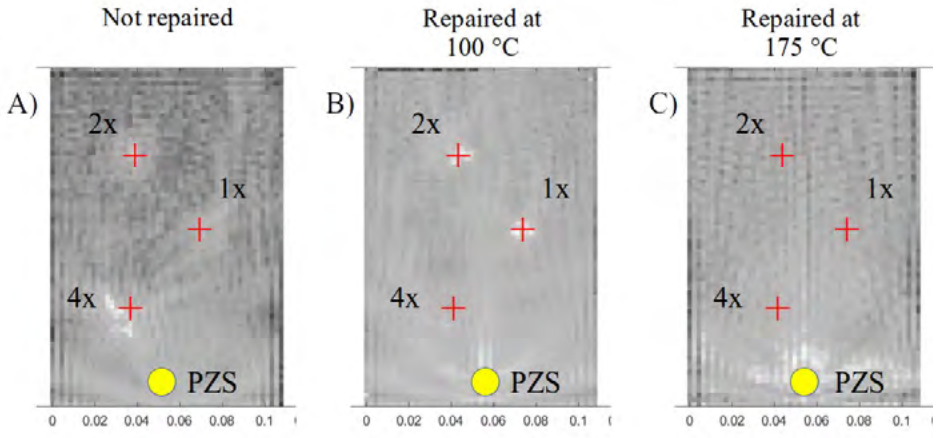


Figure 3. Scanning laser Doppler vibrometric analysis of laminates impacted at 4 J: A) Not repaired, B) repaired at 100 °C, C) repaired at 175 °C. The red cross is the impact point; 1x, 2x and 4x are the number of consecutive impacts. The yellow circle represents the position of the piezoelectric sensor (PZS).

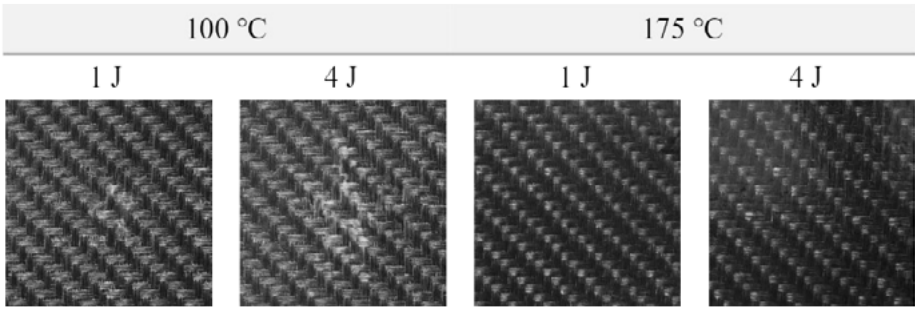


Figure 4. Impact points on front sides of repaired laminates. Square edge is 33 mm.

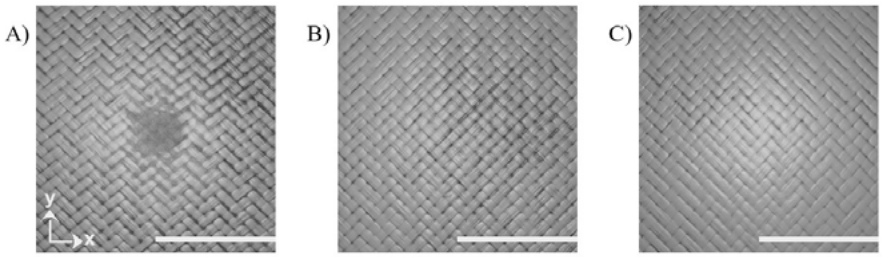


Figure 5. Top surface of microtomographic 3D reconstructions of laminates A) impacted four time at 4 J, b) repaired at 100 °C and c) repaired at 175 °C. White scale bar is 25 mm.

The second impact testing campaign on the same previously impacted points showed that the laminates repaired at 100 °C were still able to show a good performance but force peak values were significantly lower with respect to the first impacts series. On the contrary, the laminates repaired at the matrix melting temperature showed almost the same performances than before repairing, and this is remarkable when considering the fact that each repaired laminate received on each impact point twice the number of impacts with respect to the not repaired laminate.

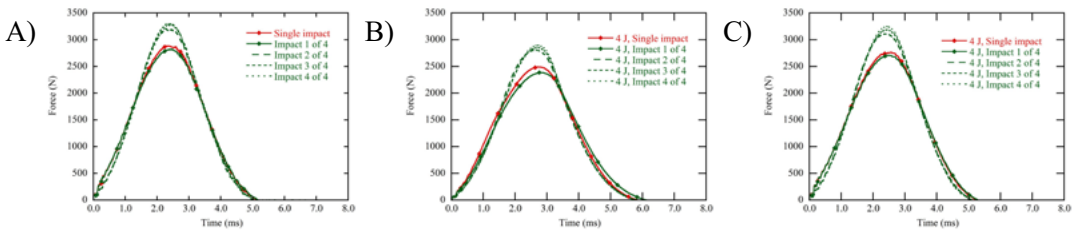


Figure 6. Force versus time curves of laminates impacted at 4 J before and after repairing: A) not repaired, B) repaired at 100 °C, C) repaired at 175 °C.

4. Conclusions

Composites based on PLA and basalt woven fabrics were impact tested at impact energies ranging between 1 and 8 J, and up to four consecutive impacts were delivered. Both front and back surfaces were damaged, and the damaged area increased with the impact energy. The first of each impact series was characterized by a lower peak force and a significant amount of unrecovered energy in proportion to the impact energy. Successive impacts showed a higher peak force and an almost negligible unrecovered energy until impact energy was equal to 8 J.

The laminates were repaired at 100 °C and 175 °C. Microtomographic analysis showed planar woven fabrics at both temperatures. On the contrary, the scanning laser Doppler vibrometry showed that only the higher temperature allowed to erase any visible and instrumental sign of damage. Both techniques combined allowed to assess that a high molecular mobility is needed to successfully restore both matrix continuity and woven fabric planarity.

The effectiveness of the repairing process was finally assessed by a second testing campaign on repaired laminates, and was performed on the previously impacted points. The impact behaviour of laminates repaired at 175 °C was almost superimposed to that of pristine laminates, confirming a complete recovery of the mechanical performance under impact.

Acknowledgments
This study has been carried out within cooperative programme of the agreement on scientific cooperation between the Polish Academy of Sciences (PAS) and the National Research Council of Italy (CNR) within the project “Non-destructive evaluations on repaired fibre reinforced composites (REPCOM)” – Biennium Program 2020-2021 between Institute of Polymers, Composites and Biomaterials, National Research Council (IT) and Institute of Fluid-Flow Machinery, Polish Academy of Sciences (PL).

References

[1] G. Jogur, A. Nawaz Khan, A. Das, P. Mahajan, R. Alagirusamy. Impact properties of thermoplastic composites. *Textile Progress,* (3): 109–183, 2018.
[2] Z. Sun, C. Li,Y. Tie. Experimental and Numerical Investigations on Damage Accumulation and Energy Dissipation of Patch-Repaired CFRP Laminates under Repeated Impacts. *Materials & Design,* 202:109540, 2021.
[3] L. Sorrentino, D. S. De Vasconcellos, M. D’Auria, F. Sarasini, J. Tirillò. Effect of Temperature on Static and Low Velocity Impact Properties of Thermoplastic Composites. *Composites Part B Engineering*, 113:100–110, 2017.
[4] J. Wang, J. Tang, D. Chen, S. Xing, X. Liu, J. Hao. Intrinsic and Extrinsic Self-healing Fiber-reinforced Polymer Composites: A Review. *Polymer Composites*, 44(10):6304–23, 2023.
[5] N. M. Chowdhury, W. K. Chiu, J. Wang, P. Chang. Experimental and Finite Element Studies of Bolted, Bonded and Hybrid Step Lap Joints of Thick Carbon Fibre/Epoxy Panels Used in Aircraft Structures. *Composites Part B Engineering*, 100:68–77, 2016.
[6] N. Encinas, B. R. Oakley, M. A. Belcher, K.Y. Blohowiak, R.G. Dillingham, J. Abenojar, M. A. Martínez. Surface Modification of Aircraft Used Composites for Adhesive Bonding. *International Journal of Adhesion and Adhesives*, 50:157–63, 2014.
[7] P. Cheng, X. J. Gong, D. Hearn, S. Aivazzadeh. Tensile Behaviour of Patch-Repaired CFRP Laminates. *Composite Structures*, 2011;93(2):582–89.
[8] R. S. Pierce, B. G. Falzon. Modelling the Size and Strength Benefits of Optimised Step/Scarf Joints and Repairs in Composite Structures. *Composites Part B Engineering*, 173:107020, 2019.
[9] P. G. Slattery, C. T. McCarthy, R. M. O’Higgins. Assessment of Residual Strength of Repaired Solid Laminate Composite Materials through Mechanical Testing. *Composite Structures*, 147:122–30, 2016.
[10] J. J. Andrew, V. Arumugam, K. Saravanakumar, H. N. Dhakal, C. Santulli. Compression after Impact Strength of Repaired GFRP Composite Laminates under Repeated Impact Loading. *Composite Structures*, 133:911–20, 2015.
[11] J. P. Reis, M. de Moura, S. Samborski. Thermoplastic Composites and Their Promising Applications in Joining and Repair Composites Structures: A Review. *Materials*, 13(24):5832, 2020.
[12] J. Barroeta Robles, M. Dubé, P. Hubert, A. Yousefpour. Repair of thermoplastic composites: an overview. *Advanced Manufacturing: Polymer & Composite Science*, 8(2), 68–96, 2022.
[13] F. Touchard, M. Boustie, L. Chocinski-Arnault, P. P. González, L. Berthe, D. S. De Vasconcellos, L. Sorrentino, P. H. Malinowski, W. Ostachowicz. Mechanical and Laser Impact Effects on Woven Composites with Hemp or Glass Fibres. *International Journal of Structural*

Integrity, 8(3):286–307, 2017.

[14] P. H. Malinowski, W. M. Ostachowicz, F. Touchard, M. Boustie, L. Chocinski-Arnault, P. P. Gonzalez, L. Berthe, D. S. De Vasconcellos, L. Sorrentino. Study of Plant Fibre Composites with Damage Induced by Laser and Mechanical Impacts. *Composites Part B: Engineering,* 152:209–19, 2018.

[15] M. A. Caminero, I. García-Moreno, G. P. Rodríguez, J. M. Chacón. Internal Damage Evaluation of Composite Structures Using Phased Array Ultrasonic Technique: Impact Damage Assessment in CFRP and 3D Printed Reinforced Composites. *Composites Part B: Engineering*, 165:131–42, 2019.

[16] B. Yu, R. S. Bradley, C. Soutis, P. J. Hogg, P. J. Withers. 2D and 3D Imaging of Fatigue Failure Mechanisms of 3D Woven Composites. *Composites Part A: Applied Science and Manufacturing*, 77:37–49, 2015.

[17] L. Sorrentino, F. Sarasini, J. Tirillò, F. Touchard, L. Chocinski-Arnault, D. Mellier, P. Russo. Damage Tolerance Assessment of the Interface Strength Gradation in Thermoplastic Composites. *Composites Part B: Engineering*, 113:111–22, 2017.

[18] Simeoli G, Sorrentino L, Touchard F, Mellier D, Oliviero M, Russo P. Comparison of Falling Dart and Charpy Impacts Performances of Compatibilized and Not Compatibilized Polypropylene/Woven Glass Fibres Composites. *Composites Part B: Engineering*, 165:102–8, 2019.

[19] PLA datasheet: https://www.totalenergies-corbion.com/media/eushodia/pds-luminy-l175-190507.pdf; retrieved on May 20, 2024

[20] Basalt fibre plain weave fabric data retrived from manufacturer website (https://www.basaltex.com/products/woven-fabrics) on May 20, 2024

[21] M. A. Fakih, S. K. Singh, S. Mustapha, M. Radzienski, P. H. Malinowski. A Comprehensive Analysis of Guided-Wave Propagation in 3D-Printed PLA Plates with Different Infill Densities – Experimental Study. *Mechanical Systems and Signal Processing*, 202:110645, 2023.

[22] W. Ostachowicz, M. Radzieński, P. Kudela. 50th Anniversary Article: Comparison Studies of Full Wavefield Signal Processing for Crack Detection. *Strain*, 50(4):275–91, 2014.

[23] L. Sorrentino, D. S. De Vasconcellos, M. D'Auria, J. Tirillò, F. Sarasini. Flexural and Low Velocity Impact Characterization of Thermoplastic Composites Based on PEN and High Performance Woven Fabrics. *Polymer Composites*, 39(8):2942–51, 2018.

[24] L. Sorrentino, D. S. De Vasconcellos, M. D'Auria, F. Sarasini, S. Iannace. Thermoplastic Composites Based on Poly(Ethylene 2,6-Naphthalate) and Basalt Woven Fabrics: Static and Dynamic Mechanical Properties. *Polymer Composites*, 37(7):2549–56, 2016.

INVESTIGATION OF CONTINUOUS FIBER–REINFORCED TRIPLY PERIODIC MINIMAL SURFACES (TPMS) FOR HIGH-PERFORMANCE ENERGY ABSORPTION APPLICATIONS

Bence Szederkényi[1*], Norbert K. Kovács[1,2], Tibor Czigány[1,3]

[1]Department of Polymer Engineering, Faculty of Mechanical Engineering, Budapest University of Technology and Economics, Muegyetem rkp. 3., H-1111 Budapest, Hungary
[2] MTA-BME Lendület Lightweight Polymer Composites Research Group, Muegyetem rkp. 3., H-1111 Budapest, Hungary
[3] HUN-REN-BME Research Group for Composite Science and Technology, Muegyetem rkp. 3., H-1111 Budapest, Hungary
*corresponding author: bszederkenyi@edu.bme.hu

Abstract
Homogeneous and quasi-homogeneous cell structures, including triple-periodic minimal surfaces (TPMS), are crucial in engineering, particularly in lightweight energy absorption applications. While typically made from metals or polymers, the exploration of polymer composites in cellular systems is increasing, driven by additive manufacturing technologies. High-performance energy-absorbing systems often use continuous carbon fiber–reinforced composites embedded in a thermoset matrix. Despite their potential, current literature focuses on short-fiber composites in TPMS systems, with limited studies on continuous fiber placement. We used a Markforged Mark Two 3D printer to explore various cell structures and reinforcement patterns for continuous fibers. The paper investigates the energy absorption capabilities of these structures to enhance their specific energy-absorbing capability, contributing to the development of modern energy-absorbing structures.

Keywords: 3D printed CFRP, Cellular structures, TPMS, Energy absorption, SEA

1. Introduction

The purpose of energy-absorbing structures is to mitigate the momentary, impulse-like effects of dynamic impact by dissipating energy. This process leads to structural deformation, increasing the duration of the load while potentially reducing its intensity significantly by orders of magnitude as energy is absorbed through various structural transformations. The main design parameters for energy-absorbing devices are maximum force and maximum deceleration which the protected objects are capable of withstanding [1]. Currently, energy absorption applications primarily utilize polymer and metal foams and honeycomb structures, exploiting their adjustable porosity and typically plastic properties within these applications. Additionally, with the emergence of additive manufacturing (AM) technologies, tailorable properties of regular cell structures have become a significant research area in energy absorption applications. Cellular structures respond to compressive loads with a consistent plateau phase, offering a predictable maximum force until critical densification. However, a similar characteristic can also be achieved with materials incapable of plastic deformation, such as fiber–reinforced composites [2–5].

1.1. Composites and energy absorption

The application of composites for energy absorption purposes has been a researched area since the 1970s, with its findings applied in numerous critical areas, including helicopter and race car crash zones [6–9]. These structures typically consist of thin-walled, closed-profile systems, primarily tube-like, oriented with their long axis toward the expected impact [10–12]. During crushing, a progressive mechanism can be initiated to stabilize the otherwise catastrophic and unstable response of fiber–reinforced composite specimens. This mechanism advances synchronously with the propagation of the crush zone, a process referred to as fragmentation. The research by Starbuck *et al.* [13] indicates that in the energy-absorption applications of composites, fiber failure is the dominant energy-absorbing mechanism, followed by various crack propagation and fiber bending mechanisms.

1.2. Applications of triply periodic minimal surfaces (TPMS) in energy absorption

In recent years, the utilization of TPMS structures for energy absorption has emerged as a prominent convergence of AM technologies and high-performance, lightweight structures. In these domains, where spatially adjustable properties are increasingly important, TPMS structures have gained significant attention. [14–17]. We selected these cellular systems for our study due to their self-supporting structures, facilitating support-free printing in subsequent processes. Moreover, the mechanical properties of various TPMS structures are extensively documented in the literature [18, 19].

Our objective was to develop hybrid, fiber–reinforced cellular structures that efficiently absorb energy through fragmentation processes, achieved by strategically placed fiber reinforcements. We conducted quasi-dynamic compression tests on various TPMS cell structures using combinations of Markforged's PA6 and Onyx materials alongside continuous carbon fiber to accomplish this. We evaluated the impact of different fiber placement strategies on the energy absorption properties of reinforced structures. We also explored the influence of infill strategies provided by slicing software on unreinforced structures.

2. Methodology

2.1. Selection of test geometry and fiber reinforcement design

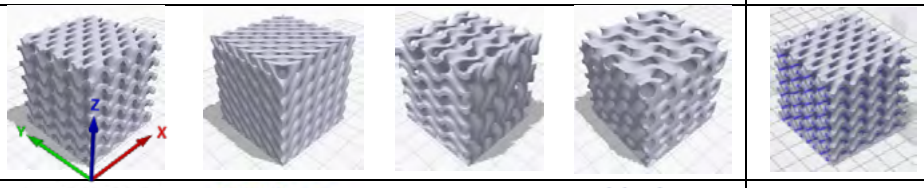
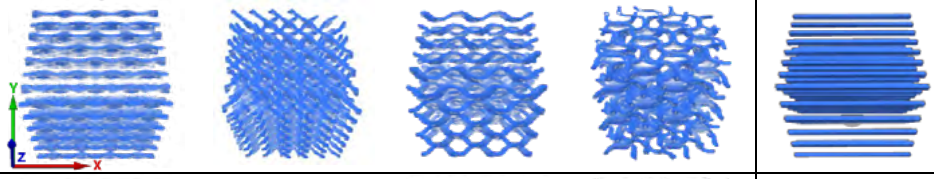
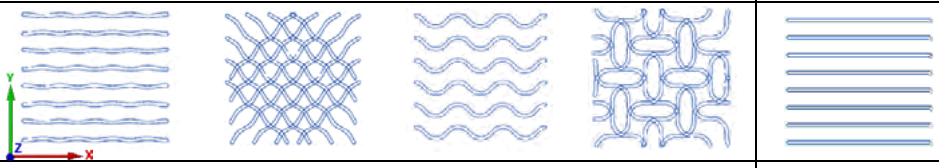
During the TPMS cell structure selection process, we established three key criteria. Firstly, the geometry must be manufacturable without support material, using the chosen material extrusion (MEX) technology. Secondly, the structure should feature longer, uninterrupted cross-sections perpendicular to the main building direction, facilitating continuous fiber placement along its entire length (Table 1). Lastly, we aimed to maximize the geometric energy absorption performance of TPMS cells by selecting structures with optimal specific properties. Building on the research by Kladovasilakis *et al.* [18] and Saleh *et al.* [19], we further analyzed the gyroid (G) and diamond (D) structures to meet these objectives. The compression test specimens were selected as cubes by relevant standards [20]. To mitigate edge effects, we placed 3x3x3 unit cells within these specimens, following literature recommendations [21]. The choice of cube edge length was primarily dictated by the narrowest fiber–reinforced cross-section, determined to be 2.8 mm based on literature data [22] and our own investigations. Consequently, the compression-tested cube had an edge length of 45 mm, with unit cell edges measuring 15 mm, resulting in a relative density of approximately 37%.

Achieving suitable energy absorption characteristics relies on stable, progressive failure processes in the fiber–reinforced region, where continuous fibers break into smaller fragments. In our experiments, we positioned fibers parallel to the loading direction or at angles of ±45 degrees. Fiber placement was restricted to printed layers, ensuring the creation of consistent, identifiable reinforcement with uniform fiber orientation. Thus, for specimens with 0-degree reinforcement, every 60 layers included ten continuous fiber–filled layers spanning the entire cross-section. In specimens reinforced at ±45 degrees, this frequency doubled, with ten continuous fiber–filled layers appearing in every 30 layers, resulting in approximately 8 v% and 16 v% fiber content within the material-filled volume.

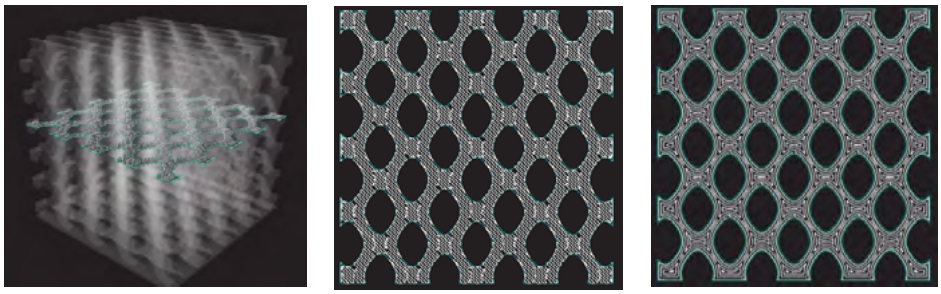
To achieve the desired fiber reinforcement orientation, we rotated the elemental cells of the cell structure, resulting in corresponding rotations of characteristic cross-sections where the reinforcement is placed. Consequently, four different reinforced structures were created (Table 1), labelled as D0, D45, G0, and G45, denoting the cellular structure of Gyroid (G) or Diamond (D) and the dominant fiber direction within each cell type (0 or ±45). Here, the loading direction aligns with the 0-degree fiber direction, coinciding with the X-axis in our notation system.

We hypothesized that the progressive failure mechanism heavily depends on the local curvature of reinforcement paths. Slight waviness induces bending-dominated failure in the structure rather than initiating fragmentation-dominated failure modes, leading to more effective energy absorption characteristics. As shown in Table 1 (G0-D45), reinforcements representing dominant fiber directions exhibit varying degrees of waviness in all cases.

Table 1. Various TPMS structures and fiber reinforcement were examined. The X-axis represents the loading direction, while the Z-axis denotes the printing build direction.

		D0	D45	G0	G45	D0 masked
Weight	PA	52.7 g	51.8 g	43.9 g	44.5 g	-
	Onyx	51.5 g	52.5 g	44.2 g	44.6 g	-
	CCF	52.2 g	51.1 g	43.5 g	43.7 g	52.8 g
Cell structure						
Reinforcement paths within the specimen						
Reinforcement repeating unit/layer inside the specimen						
Fiber content		8.53 v%	15.59 v%	8.82 v%	16.51 v%	14.14 v%

To mitigate this effect and enhance energy absorption, we introduced an additional diamond-based structure (D0_masked), where fiber reinforcement was implemented as a separate geometry within the specimen, forming perfectly straight columns. This was achieved by post-merging the unreinforced and reinforced geometries, created separately in the slicing software and consolidated into G-code.
Alongside specimens with continuous fiber reinforcement, we manufactured a series of pure PA and a series of Onyx (short CF-filled PA) specimens to isolate the effect of fiber reinforcement. Markforged's slicing software, Eiger, a closed industrial system, allows for bare fiber reinforcement placement only if the "exposed infill" beta option is enabled. This feature skips the placement of wall layers and prints only the internal structure of the test specimen, possible with raster infill when using 100% infill (Figure 1 (b)). Consequently, the series without fiber reinforcement was also created with the use of raster infill, with the "exposed infill" option enabled. To further investigate the infill strategy, we made additional test specimens from Onyx with a concentric infill strategy (Figure 1 (c)). The effect of the infill strategy was exclusively examined for the D0 specimens. For the printing parameters, refer to Table 2.



(a) (b) (c)

Figure 1. Infill strategies: A general cross-section (a), which can be filled with a raster (b) or concentric (c) infill pattern.

Table 2. Manufacturing parameters of the compression test specimens

	G0, G45, D0, D0 masked, D45	D0 concentric
Layer thickness	0,125 mm	0,125 mm
Nozzle diameter	0,4 mm	0,4 mm
Infill ratio	100%	100%
Number of walls	0	0
Number of bottom/ top layers	0	0
Reinforcement path-planning strategy	concentric, one loop/-	-
Material deposition strategy in XY plane	raster in ±45°	concentric

2.2. Test environment and parameters

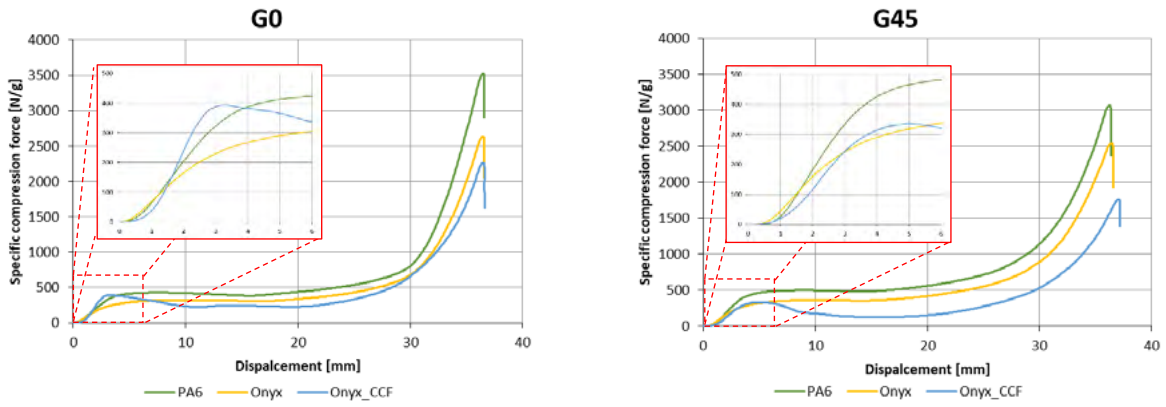
The quasi-dynamic compression tests were conducted on a Zwick Z250 universal testing machine at a maximum achievable loading rate of 600 mm/min. The tests were performed up to 85% engineering strain or a maximum load of 200 kN. The specimens were not conditioned, and air temperature during testing was 21°C with a relative humidity of 48%.
For comparability of the test results, all data is presented normalized to the mass of the respective specimen. Detailed descriptions of the examined parameters can be found in Table 3.

Table 3. Parameters examined during the tests

Designation	Abbreviation	Unit	Determination methodology
Specific energy absorption capability	SEA	J/g	Integration of the force–displacement curve up to the most efficient energy absorption point, followed by normalization with the mass of the specimen (For further information refer to [23])
Specific compression force	F*	N/g	Normalized compressive force with respect to the mass of the specimen.
Specific plateau force	F^*_{plat}	N/g	Average plateau force normalized by the mass of the specimen.
Specific stiffness	E*	MPa/g	The slope of the straight line fitted to the first linear segment of the engineering stress–engineering strain curve, normalized by the mass of the specimen.

3. Results

For better clarity in the presentation of the test results, we depicted the various cell structures on separate diagrams. Additionally, we detailed the initial loading phase in the diagrams. Figure 2 illustrates these compression diagrams.



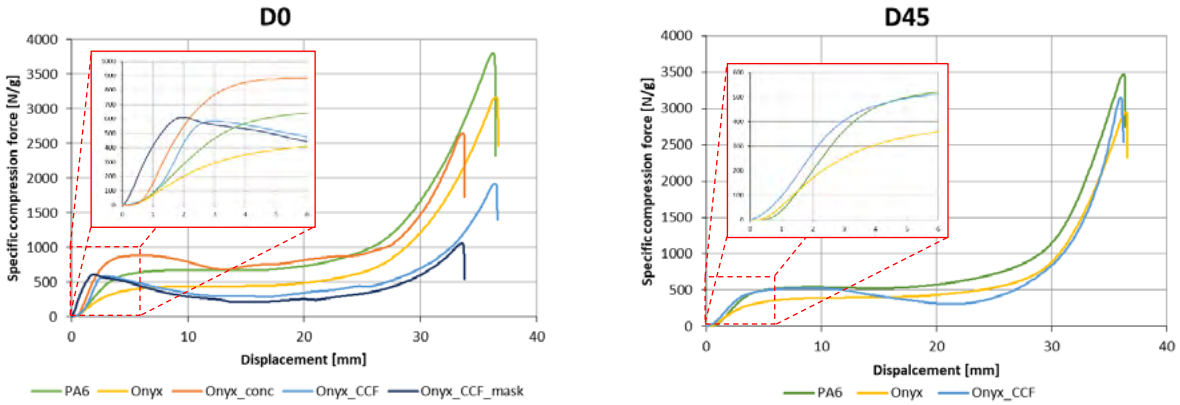


Figure 2. Specific compression force-displacement curves of the test specimens.

From the curves shown in Figure 2, the parameters listed in Table 3 were then calculated for all test specimens. These were then summarized and displayed in the bar chart in Figure 3. To allow for a common diagram, all metrics were expressed as percentages relative to the G0 specimen made of PA6. However, the absolute values were also indicated on the chart in addition to the relative values.

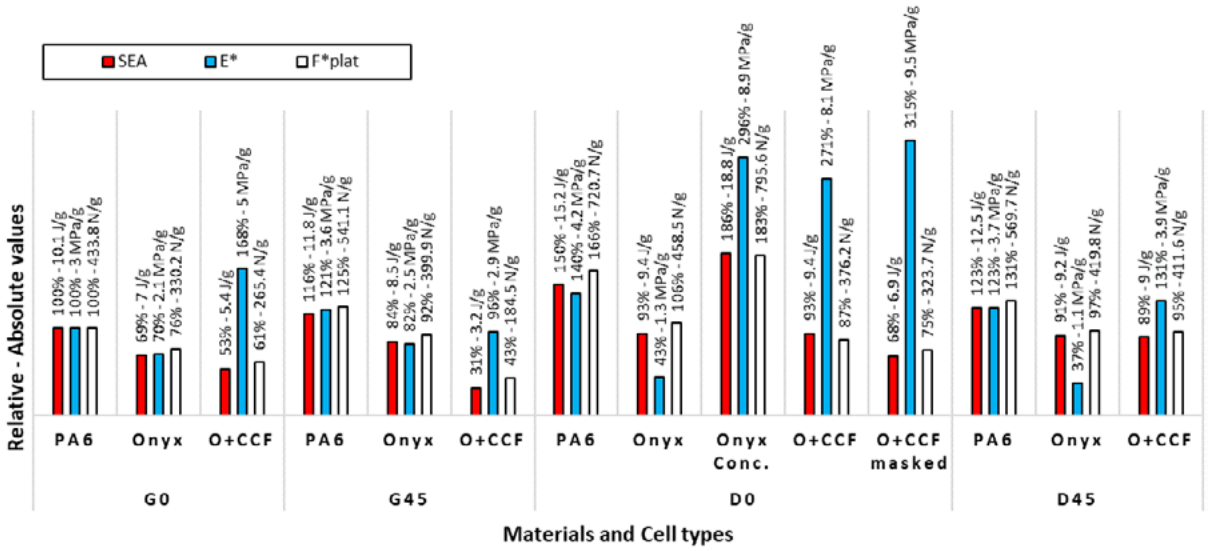
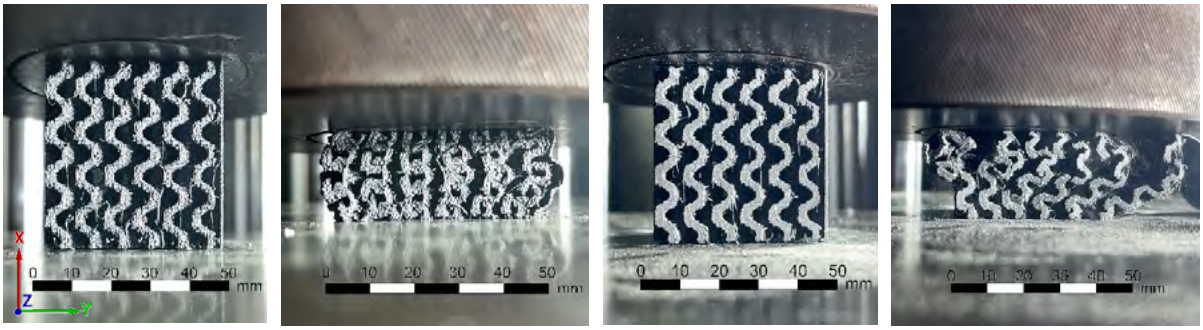


Figure 3. The column chart shows all the results of the tested structures, presenting the relative and absolute performance of each specimen, values normalized to the G0 PA6 structure.

The specimens exhibited consistent failure characteristics across all cell types and orientations, where the PA6 and Onyx specimens remained intact throughout the loading phase, while the fiber–reinforced specimens separated along their length within the reinforced cross-section. Figure 4 illustrates failure typical of matrix-only materials (a, b) compared to the fiber–reinforced structures (c, d).



(a) (b) (c) (d)

Figure 4. Failure characteristic of the axially loaded Schwarz-Diamond cellular structure in the case of short fiber–reinforced PA6 (Onyx) matrix material, where (a) is the undeformed state and (b) shows the ~60% compressive strain state. The axially loaded Schwarz-Diamond cellular structure with continuous fiber reinforcement showed weak interlayer adhesion, where (c) is the undeformed state and (d) shows the ~60% compressive strain state.

4. Discussion and conclusions

Based on the measurement results, the following conclusions were drawn:

1. Clear rankings were established among the examined structural types in cases without continuous fiber reinforcement, extending across all measured parameters. The ranking is as follows: The best was D0, followed by D45, G45 and G0.
2. Fiber–reinforced specimens exhibited a significant average increase of 81% in specific modulus compared to versions made from PA6 for fiber reinforcements corresponding to the 0° loading direction (G0; D0). The structurally regular 0° (D0 masked) fiber–reinforced specimen exhibited an even higher 126% increase in specific modulus.
3. Short-fiber–reinforced Onyx specimens underperformed the pure PA6 structures in terms of all metrics, with average specific modulus reductions of 32% for gyroid (G0, G45) structures and 70% for diamond (D0, D45) structures. In the case of specific plateau forces, this difference averaged 28% across all specimen types while averaging 31% for specific energy absorption. This discrepancy likely stems from the similar ratios between the moduli of pure materials and the lower failure deformation threshold of Onyx, attributed to its high content of inner friction reducers and other additives affecting stiffness.
4. The difference between raster and concentric printing yielded unexpected deviations favoring concentric printing. Among structures made from Onyx material, there was a 585% difference in specific modulus, a 77% difference in specific plateau force, and a 100% difference in SEA values. This significant difference underscores the importance of choosing continuous infill in energy absorption applications, where rasterized infill intermittently builds the cross-section and has a pronounced detrimental effect.
5. The SEA value of the regular 0° (D0 masked) specimen was 37% lower than that of the slightly wavy fiber–reinforced (D0) specimen, likely due to the design created by the combination of two separate pieces on the printing bed during manufacturing, presumably degrading layer adhesion. Additionally, the phenomenon can be explained by the greater lateral force component after stability loss, which caused the structure to separate sooner.
6. Regarding SEA values, the fiber–reinforced specimens consistently underperformed compared to the Onyx and PA6 specimens, with an average value of 47% compared to PA6. This can be explained with the phenomenon presented in Figure 4, where it is clear that while the pure matrix material specimens remained intact throughout the entire loading range, the fiber–reinforced specimens could not resist the simultaneously emerging axial and lateral force components and delaminated and separated due to weak interlayer adhesion. Consequently, they contributed much less to the energy absorption process when deviating from the loading direction. Thus, the desired fiber fragmentation processes fail to initiate properly in the examined specimens,

indicating that continuous fiber reinforcement has not been adequately utilized for energy absorption in the presented cases.

5. Limitations and future improvements

In our study, only one specimen type was manufactured for each test. Thus, our observations and conclusions lack statistical certainty. Supplementary tests would be necessary to establish statistical significance, a task we plan to undertake in the future. Concerning the masked specimen, we relied solely on assumptions regarding interlayer adhesion values, which warrant further investigation under standardized conditions. Moreover, based on the observations outlined in sections 4–6 of Conclusion, it is evident that the most critical parameter requiring development is the integrity of the cellular structure. It ensures adequate support for the fiber reinforcement, even at substantial load states. This may entail enhancing the interfacial adhesion of the fiber reinforcement or implementing macro-level methods, such as radially placed fiber reinforcement. Investigating and improving these parameters could be the foundation for future research.

Acknowledgments

The research reported in this paper was supported by the National Research, Development, and Innovation Office (NRDI, Hungary) through grants OTKA FK134336 and OTKA K 138472.
Project no. TKP-6-6/PALY-2021 has been implemented with the support provided by the Ministry of Culture and Innovation of Hungary from the National Research, Development and Innovation Fund, financed under the TKP2021-NVA funding scheme.
The project 2022-2.1.1-NL-2022-00012 has been implemented with the support provided by the Ministry of Culture and Innovation of Hungary from the National Research, Development and Innovation Fund, financed under the 2022-2.1.1-NL Creation of National Laboratories, Complex Development funding scheme.
Bence Szederkényi expresses appreciation for the support of the Doctoral Excellence Fellowship Programme (DCEP), which is funded by the National Research Development and Innovation Fund of the Ministry of Culture and Innovation and the Budapest University of Technology and Economics under a grant agreement with the National Research, Development and Innovation Office.
Norbert Krisztián Kovács expresses appreciation for the support of the ÚNKP-23-5-BME-466 New National Excellence Program of the Ministry for Culture and Innovation from the source of the National Research, Development and Innovation Fund and the János Bolyai Research Scholarship of the Hungarian Academy of Sciences.

References

[1] Mamalis A. G., Robinson M., Manolakos D. E., Demosthenous G. A., Ioannidis M. B., Carruthers J. Review Crashworthy capability of composite material structures. *Composite Structures*, 37:109–134, 1997.
[2] Özen İ., Gedikli H., Aslan M. Experimental and numerical investigation on energy absorbing characteristics of empty and cellular filled composite crash boxes. *Engineering Structures*, 289:116315, 2023.
[3] Mamalis A. G., Manolakos D. E., Demosthenous G. A., Ioannidis M. B. The static and dynamic axial crumbling of thin-walled fibreglass composite square tubes. *Composites Part B: Engineering*, 28:439–451, 1997.
[4] Ryzińska G., Gieleta R. Effect of Test Velocity on the Specific Energy Absorption under Progressive Crushing of Composite Tubes. *Advances in Science and Technology Research Journal*, 14:94–102, 2020.
[5] Mamalis A. G., Manolakos D. E., Demosthenous G. A., Ioannidis M. B. Analysis of failure mechanisms observed in axial collapse of thin-walled circular fibreglass composite tubes. *Thin-Walled Structures*, 24:335–352, 1996.
[6] Heimbs S., Strobl F. Crash Simulation of an F1 Racing Car Front Impact Structure. *Proceedings of 7th European LS-DYNA Conference*, 1–8, 2009.

[7] Boria S., Obradovic J., Belingardi G. Experimental and numerical investigations of the impact behaviour of composite frontal crash structures. *Composites Part B: Engineering*, 79:20–27, 2015.
[8] Bisagni C., Di Pietro G., Fraschini L., Terletti D. Progressive crushing of fiber-reinforced composite structural components of a Formula One racing car. *Composite Structures*, 68:491–503, 2005.
[9] Kohlgrueber D., Kamoulakos A. Validation of Numerical Simulation of Composite Helicopter Sub-floor Structures under Crash Loading. *Dieter Kohlgrüber German Aerospace Center (DLR) Institute of Structures and Design D-70569 Stuttgart, Germany Argiris Kamoulakos Engineering Systems Int.*, 1998.
[10] Matzenmiller A., Schweizerhof K. Crashworthiness simulations of composite structures - a first step with explicit time integration. In *Nonlinear Computational Mechanics: State of the Art*, Springer, Berlin, 1991.
[11] McGregor C., Zobeiry N., Vaziri R., Poursartip A., Xiao X. Calibration and validation of a continuum damage mechanics model in aid of axial crush simulation of braided composite tubes. *Composites Part A: Applied Science and Manufacturing*, 95:208–219, 2017.
[12] Hull D. A unified approach to progressive crushing of fibre-reinforced composite tubes. *Composites Science and Technology*, 40:377–421, 1991.
[13] Starbuck J. M., Adams D. O., Courteau M. Energy absorbing damage mechanisms in progressive crushing of composite tubes. In *Proceedings of the 32nd Technical Conference of the American Society for Composites*, 2:1419–1432, 2017.
[14] Yang L., Li Y., Wu S., Chen P., Wu H., Su J., Wang H., Liu J., Yan C., Shi Y. Tailorable and predictable mechanical responses of additive manufactured TPMS lattices with graded structures. *Materials Science and Engineering: A*, 843:143109, 2022.
[15] Alkebsi E. A. A., Ameddah H., Outtas T., Almutawakel A. Design of graded lattice structures in turbine blades using topology optimization. *International Journal of Computer Integrated Manufacturing*, 34:370–384, 2021.
[16] Sánchez J. M., Weems E., Hu H. Coupled Field-Driven Design and Numerical Simulation for Engineering Education. *Proceedings of 2023 ASEE Midwest Section Conference*, 2023.
[17] Xu Z., Razavi S. M. J., Ayatollahi M. R. Functionally Graded Lattice Structures: Fabrication Methods, Mechanical Properties, In *Failure Mechanisms and Applications,* Elsevier, New York, 2022.
[18] Kladovasilakis N., Tsongas K., Kostavelis I., Tzovaras D., Tzetzis D. Effective mechanical properties of additive manufactured triply periodic minimal surfaces: experimental and finite element study. *International Journal of Advanced Manufacturing Technology*, 121:7169–7189, 2022.
[19] Saleh M., Anwar S., Al-Ahmari A. M., Alfaify A. Compression Performance and Failure Analysis of 3D-Printed Carbon Fiber/PLA Composite TPMS Lattice Structures. *Polymers*, 14:4595, 2022.
[20] ISO 844: Rigid cellular plastics. Determination of compression properties, 2021.
[21] Peng C. Novel Lattice Structures Based on Triply Periodic Minimal Surfaces. *RMIT University*, College of Science, Technology, Engineering and Maths, School of Engineering College, Phd Thesis, 2022.
[22] Catapano A., Montemurro M., Balcou J.-A., Panettieri E. Rapid Prototyping of Variable Angle-Tow Composites. *Aerotecnica Missili & Spazio*, 98:257–271, 2019.
[23] Lu G., Yu T. *Energy Absorption of Structures and Materials*. CRC Press, Boca Raton, 2003.

A GLOBAL-LOCAL DEFECT AND DAMAGE INITIATION MODEL FOR LAUNCHER COMPOSITE STRUCTURES PRE-SIZING

Alexy TAILLEUR[1], Kévin MATHIS[2], Ange ROGANI[3], Pablo NAVARRO[1], Steven MARGUET[1] and Jean-François FERRERO[1]

[1]Université de Toulouse, Institut Clément Ader, UMR CNRS 5312, Toulouse, France
Email: alexy.tailleur@univ-tlse3.fr - pablo.navarro@univ-tlse3.fr - steven.marguet@univ-tlse3.fr
jean-francois.ferrero@univ-tlse3.fr
[2]CNES Direction Technique et Numérique / Sous-direction Systèmes Transport Spatial, Paris, France
Email: kevin.mathis@cnes.fr,
[3]CT Ingenierie, Toulouse, France
Email: ange.rogani@ctingenierie.com

Keywords: Submodeling, Global-Local, Reissner-Mindlin, Transverse shear, Cohesive zone modeling

Abstract
This paper deals with the development of a numerical approach to study damage initiation in flawed launcher laminated composite structures during pre-sizing phase. It is realised through a novel 2D-3D top-down loose coupling submodeling method adapted to large and complex composite structures. The aim of this numerical strategy is to address defects and damage as early as possible in the development stages of launcher composite structure. A new displacement interpolation based on a fourth order polynomial has been proposed and Reissner-Mindlin theory has been used in addition. Very accurate stress fields are obtained in the local area compared to a refined global model.

1. Introduction

The proportion of composites in Ariane launchers is constantly increasing at each new iteration. Conventional sizing methods of space structures are not suitable for taking into account defects/damage in these structures at the beginning of their development. Indeed, numerical simulations of large damaged composite structures involve high computational costs and are therefore not convenient to rapid pre-sizing loops. Global-local approaches have been developed as a reliable and efficient tool to study the onset and the propagation of damage.

1.1. COLIBRI dimensioning tool

COLIBRI is a platform developed and used by CNES for the design and dimensioning of composite structures for space launch vehicles [16]. This tool sets the critical load threshold before any damage occurs and take into account manufacturing and operational defects via knockdown factors to ensure damage tolerance. More complex methods exist but they come at the end of the development phase, once the architecture is fixed. Therefore, the chosen structure is optimal to meet the specifications but is not necessarily the most efficient to withstand the presence of defects or damage. It is therefore necessary to deal with defects and damage as early as possible in the development phases of the structure.

The composite structures optimised in COLIBRI present large dimensions. In addition, previous studies conducted by CNES and CTI have shown that 3D modeling of the structure, using cohesive elements, is essential to represent damage such as delamination. Due to high computational costs, performing damage calculations on these whole structures is not a feasible solution at the pre-dimensioning stage. In addition, damage initiation and propagation are generally local phenomena that are triggered in stress concentration zones with pre-existing defects such as manufacturing or assembly imperfections, service damage or inadequate maintenance [19].

This dilemma between calculation times adapted to pre-dimensioning and an accurate representation of defects and damage within a composite structure can be addressed by means of submodeling.

1.2. Global-local approach

1.2.1 Global-local methods overview

Widely developed over the last two decades, there are now several categories of global-local approaches. The method most commonly used in industry and commercial software is a top-down loose coupling approach. As shown in Figure 1, it is a two-stage process. First, a simulation is performed on a complete structure with a coarse mesh ("global model"). Then, a new simulation with a refined mesh is carried out on the specific areas to be studied ("local models"). These are two separate models. This is why they are referred to as loose coupling.

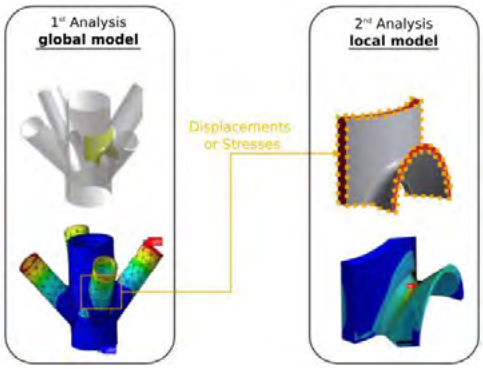


Figure 1. Illustration of top-down approach.

Mechanical quantities are extracted from the global solution and are used as boundary conditions of the local model. Displacements [8, 9, 22] are generally preferred to stresses [15, 30] as prescribed quantities at the boundaries of the local domain because of their higher convergence rate.
Despite its advantages, the top-down approach is limited to cases where the overall response of the structure is not likely to be significantly influenced by the local behaviour. On the other hand, bi-directional submodeling [2, 12, 14, 19, 37] is extremely well suited to damage propagation. Indeed, local information are transferred back to the global model and the global-local process becomes iterative.

1.2.2 Local boundary conditions

After the global static analysis, translations and rotations are known at the global nodes (Figure 2). These data need to be transferred to the local domain interface. The local model has a more refined mesh than the global model. Consequently, intermediate values of displacement along the boundary must be determined. Initially, displacement interpolation was performed using linear shape functions. Later, authors proposed the use of Lagrange interpolation [35] or cubic splines [9].

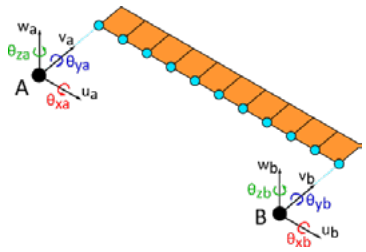


Figure 2. Nodal displacements after global static analysis.

Secondly, the position of the local model boundary is another key point in the success of the global-local approach. As shown by Mao [22], applying displacements at the interface introduces adverse

effects in the accuracy of the solution of the local static problem. They proposed a widely adopted method which involves the use of a transition zone placed around the critical zone, as shown in Figure 3.

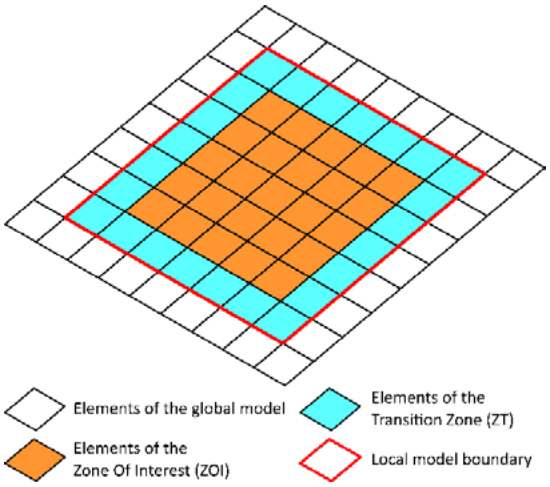


Figure 3. Local model with transition zone.

The suggested size of the transition area is equivalent to a coarse mesh element. As a result, the local model does not correspond exactly to the area of interest, the size of model is increased. [33] studied the effect of interpolation functions on the fidelity of the results obtained for local simulation. Shape functions introduce singularities in the stress field, whereas a cubic spline interpolation generates results in agreement with the exact values. Furthermore, the use of cubic splines would allow to have local boundaries closer to the critical zone. On the contrary, using shape functions would require enlarging the local domain to reduce the impact of singularities at the boundaries.

1.3. Damage modeling

1.3.1 Delamination modeling

Delamination is one of the three main failure mechanisms in laminated composites. This separation of adjacent plies usually occurs in preferred areas and leads to significant decreases in the material strengths. Delamination in composites is often modeled using Virtual Crack Closure Technique (VCCT) or by cohesive interface elements. VCCT is based on linear fracture mechanics and assumes that the energy released during delamination propagation is equal to the work required to close the crack [17, 18, 31]. The main drawback of this technique is that the crack initiation zone must be known in advance, which can be difficult for large complex structures. Cohesive Zone Modeling (CZM), proposed by [4, 20] is another main approach to represent delamination onset and propagation. The behaviour of the cohesive interface is defined by a traction-separation law relating interfacial stresses and displacement jumps at the interface of potential crack. Different forms of cohesive law have been studied in the literature; bilinear, exponential, trapezoidal,...[1, 6, 13]. Both methodologies (VCCT and CZM) have already been studied in the scope of submodeling to represent delamination onset and propagation [2, 5, 17, 34].

1.3.2 Porosity modeling

Voids can be located within a ply (intra-ply voids), as well as in the interface between two plies (inter-ply voids). The presence of voids degrades the mechanical properties dominated by the matrix and the interface [23, 24]. Micro-models are the main category of void modeling [3, 10, 36]. This is mainly because the behaviour of the porous materials is impacted by the location of voids in the laminate but also by their size, shape or distribution [26, 27].
From the point of view of pre-dimensioning, it is not possible to go down to such a small scale and to represent the voids in the material so finely. [20] uses CZM to simulate the presence of inter-ply voids.

Finally, knock-down factors can be used [25] as well as empirical laws to determine the material strength reduction [7, 11, 21, 32].

1.3.3 Matrix cracking modeling

Matrix cracking is one of the first damage modes in composite laminates subjected to mechanical and/or thermal loads. A first way to represent intra-laminar cracking is based on continuous damage mechanics (CDM). Developed over the last two decades, eXtend Finite Element Model (XFEM) allows the modeling of crack initiation and propagation without prior knowledge of the crack path or the need to update the mesh. It has been successfully used in the case of the global-local approach [26, 29]. XFEM can be coupled with CZM, and matrix cracking can also be simulated using cohesive elements [6, 28].

1.4. Objectives

The objectives of the present work is to develop a numerical strategy to take into account the presence of defects and damage in laminated composite structures during pre-sizing stage. The proposed approach allows to go from large dimensional structures represented with 2D shell elements to 3D local areas where defects such as porosity, matrix cracking and delamination have been inserted. Sometimes hard to detect, those damage can lead to a decrease in mechanical properties and a loss of strength. Furthermore, when the structure is loaded, and especially in a reuse scenario, this damage can propagate and lead to final failure with dramatic consequences. For all these reasons, it is important to understand and characterise the behaviour of damaged composite structures:

- At the design level, to improve the performance of structures, challenge mass and cost by accepting to live with damage while avoiding loss of integrity
- At the backup level to be able to confidently predict the propagation of damage and characterise the shape and size of fragments after an accidental event or after neutralisation of the launcher.

This work is a first part in the development of the global/local strategy for modeling damage initiation and propagation in launcher composite structures during pre-sizing phase. The methodology developed focuses therefore on the initiation of damage in the presence of defects.

Most of the works develop their approach via the commercial software Abaqus or use the submodeling module directly implemented in this same software. Here, everything is realized through the numerical solver Nastran only. The automation process is carried out by means of routines written in Python.

2. Developed approach

2.1. Top-down, loose coupling, shell to 3D solid submodeling

The aim of the proposed approach is to detect the onset of damage in laminated composite structures which may have manufacturing or operational defects. Hence the one-way loose coupling global-local methodology is suitable for this problem. As shown in Figure 4, two distinct simulations are performed, one after the other. The information flows from the "global" model to the distinct "local" model.

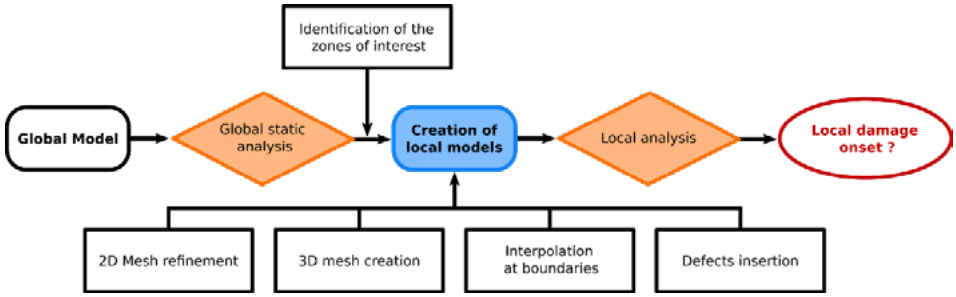


Figure 4. Flowchart of the unidirectional loose coupling procedure.

2.2. Local model's boundary conditions

A key to submodeling is the transfer of information between global and local scales. In the proposed approach, the displacements have been chosen to serve as boundary conditions for the refined local

calculations. The displacements are only known at the nodes of the original mesh. Two steps are then necessary to constrain all the boundaries of the local domain. First, the displacements must be interpolated at the nodes present in the plane on the local mesh boundary. This corresponds to step 1 in Figure 5. In this way, the intermediate values of the displacement between two adjacent nodes of the global mesh (between A and B in the example) are obtained. Because of the three-dimensionality of the local model, a second step is necessary to determine the displacements in the thickness of the boundaries. It is represented in step 2 of Figure 5.

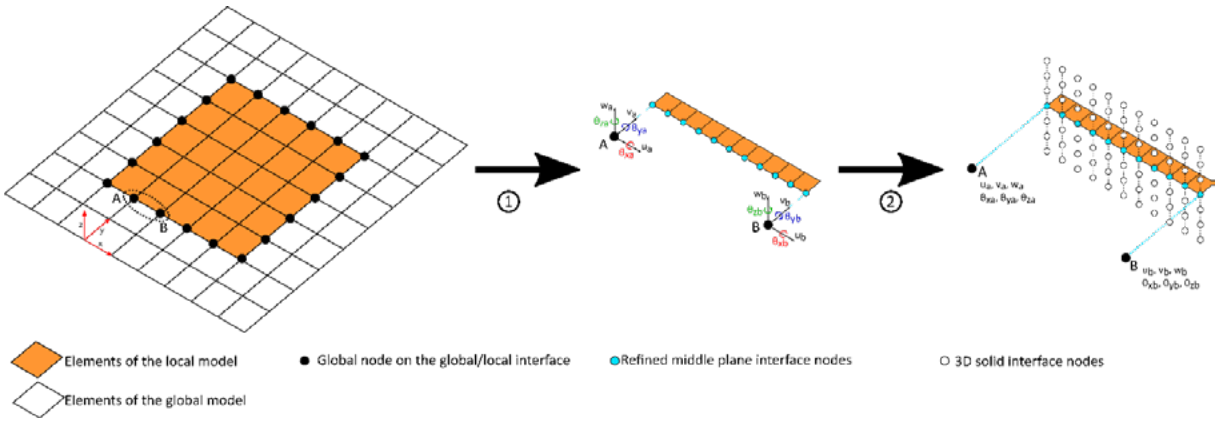


Figure 5. Boundary conditions interpolation steps.

2.2.1 2D shell local model

For the first part of the displacement interpolation, the displacements u and v (in the (x,y) plane) have been linearly interpolated. The interpolation proposed here for out-of-plane displacements w is carried out global element by global element. After the first global simulation, 12 data items are available in each global element: 4 displacements w, 4 rotations around the x axis and 4 rotations around the y axis. A polynomial of order 4 is therefore required to determine w(x,y). As the 4th-order basis is composed of 20 coefficients, truncation was chosen in accordance with the literature:

$$w(x,y)=A_1 x^3 y+A_2 xy^3+B_1 x^3+B_2 y^3+B_3 x^2 y+B_4 xy^2+ C_1 x^2+C_2 y^2+C_3 xy+D_1 x+D_2 y+E \quad (1)$$

According to Reissner-Mindlin theory, the rotations θ_x and θ_y are defined by Eq. 2 and Eq. 3 respectively.

$$\frac{\partial w(x,y)}{\partial y} = k_y \gamma_{yz}^0 + \theta_x \quad (2)$$

$$\frac{\partial w(x,y)}{\partial x} = k_x \gamma_{xz}^0 - \theta_y \quad (3)$$

Where γ_{xz}^0 and γ_{yz}^0 are the mean transverse shear strain of the laminate, k_x and k_y are transverse shear correction coefficients.

2.2.2 3D local model

The proposed approach allows to go from a global model meshed with 2D shell elements to a local model meshed with 3D solid shell Nastran elements. The model will be used in fast optimisation loops during the pre-dimensioning phase of composite structures. Thus, to keep it efficient and to reduce the computational cost, only one 3D element is used in the thickness of a ply. The displacements interpolated at the boundary via the Eq. 1, Eq. 2 and Eq. 3 must then be transformed in pure translational displacement degrees of freedom at each boundary node. For this purpose, the Reissner-Mindlin displacement field defined by Eq. 4 will be used.

$$\begin{cases} u(x,y,z) = u_0 - z\dfrac{\partial w(x,y)}{\partial x} \\ v(x,y,z) = v_0 - z\dfrac{\partial w(x,y)}{\partial x} \\ w(x,y,z) = w_0 \end{cases} \quad (4)$$

Where u_0, v_0 and w_0 are the displacements of the nodes located at the mid-surface.

2.3. Numerical validation

In order to determine the performance of both interpolation steps, multiple simulations have been conducted. Different stacking sequences were studied. The plates were subjected to four loading cases: tension, shear, bending and torsion. All type of loadings are schematized in Figure 6. Local simulations have been carried in presence of transition zone.

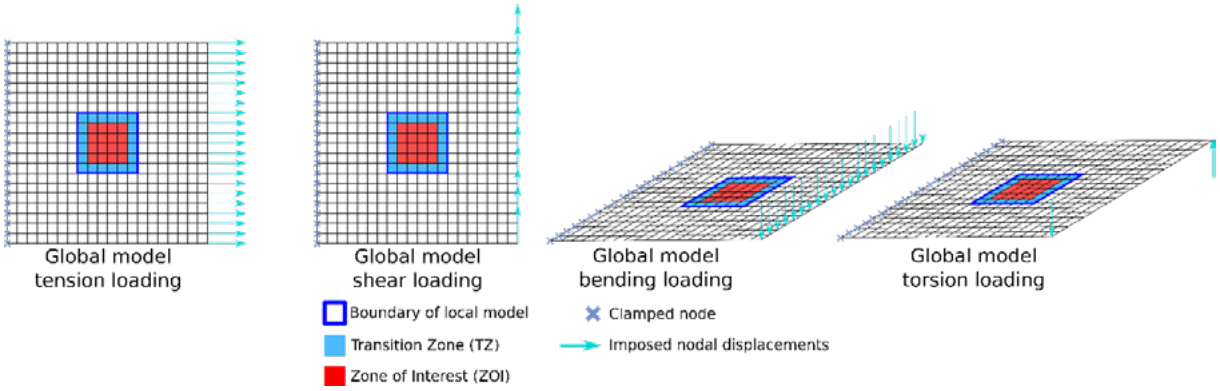


Figure 6. Schematisation of the different modeled loading scenarios.

For each type of solicitations, three models were carried out:

- coarse global model,
- fine global model,
- local model with a mesh size as fine as the fine global model.

The design of experiments was conducted on a 200mmx200mm composite plate meshed with shell elements. The analyses have been done on the following stacking sequences: $[0]_{10}$ and $[45/90/-45/0/0]_s$. The ply thicknesses were all equal to 0,15mm. The material properties are available in the Table 1.

Table 1. Material properties used for analysis.

Material Properties	E_{11} (GPa)	E_{22} (GPa)	E_{33} (GPa)	G_{12} (GPa)	G_{23} (GPa)	G_{13} (GPa)	ν_{12}	ν_{23}	ν_{31}
	160	9.9	9.9	6.1	6.1	3.8	0.33	0.3	0.0178

The elements of the global coarse model have a size of 10mmx10mm. The size of the elements of the fine global model and of the local model is 1mmx1mm. Hence, it corresponds to a factor 10 refinement. The results in the area of interest of the local model were then compared with those of the fine global model. The relative deviation to the ply mean stress has been computed using the Eq. 4.

$$\Delta\sigma_{ij} = \frac{|\sigma_{ij,global}| - |\sigma_{ij,local}|}{|\sigma_{ij,ply,global}|} \quad (4)$$

Where $\Delta\sigma_{ij}$ represents the relative deviations for the stress ij and the index i,j = x,y. $\sigma_{ij,global}$ are the stress ij in the elements of the refined global model and $\sigma_{ij,local}$ are those in the elements of the local model. In this study, the difference is divided by the mean value of the absolute stress in the concerned ply, noted $\overline{|\sigma_{ij,ply,global}|}$. Finaly, $|\overline{\Delta\sigma_{ij}}|$ is the absolute mean values of the concerned $\Delta\sigma_{ij}$. As shown in Table 2, the developed interpolations allows a very satisfying correlation under all types of solicitation

Table 2. Table of relative deviations in stresses for thin 3D model obtained via 3D local and 2D shell fine global simulations for each loading case.

Load cases	Stacking sequences	$\|\overline{\Delta\sigma_x}\|$	$\|\overline{\Delta\sigma_y}\|$	$\|\overline{\Delta\sigma_{xy}}\|$
Tension	$[0]_{10}$	0.002 ± 0.007	X	X
	[45,90,-45,0,0]s	0.04 ± 0.02	0.46 ± 0.41	0.02 ± 0.003
Shear	$[0]_{10}$	1.9 ± 2.47	0.35 ± 0.3	0.04 ± 0.02
	[45,90,-45,0,0]s	0.86 ± 1.36	0.76 ± 1.16	0.82 ± 1.73
Bending	$[0]_{10}$	0.02 ± 0.02	0.16 ± 0.24	16.0 ± 14.6
	[45,90,-45,0,0]s	0.15 ± 0.17	0.37 ± 0.08	0.36 ± 0.44
Torsion	$[0]_{10}$	0.40 ± 0.31	0.39 ± 0.37	0.23 ± 0.04
	[45,90,-45,0,0]s	0.31 ± 0.13	0.29 ± 0.13	0.45 ± 0.43

For instance, the Figure 7 shows the comparison between the stress field σ_x in the zone of interest obtained after a fine global simulation and a 3D local one. The results concern the bending load case of the $[0]_{10}$ plate.

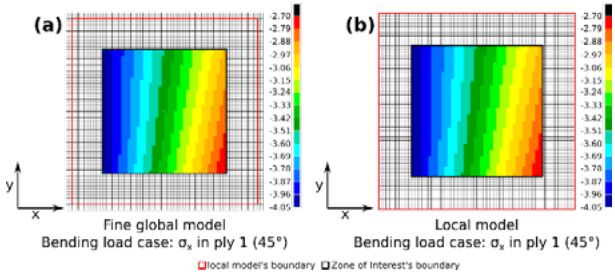


Figure 7. Field σ_x in ply 1 for bending load case

2.4. Local damage introduction

Defects and damage such as porosity, matrix cracking and delamination are inserted into the local model. The onset and progress of delamination will be represented using cohesive elements placed at the interface between plies. These are linear 3D elements with zero thickness. In order to limit the size of the local model, cohesive elements are not inserted between all plies but only at the interfaces where delamination is likely to occur, i.e. between plies of different orientations. Being the most present in the literature, the bilinear cohesive law will been used in the first instance. Currently, porosity and matrix cracking will be modeled via damage variable which will tackle the material properties. Indeed, using cohesive elements to represent matrix cracking could lead to high computational costs and is not in line with the pre-sizing approach. The damage process is automated via Python routines. The proposed approach is illustrated in Figure 8.

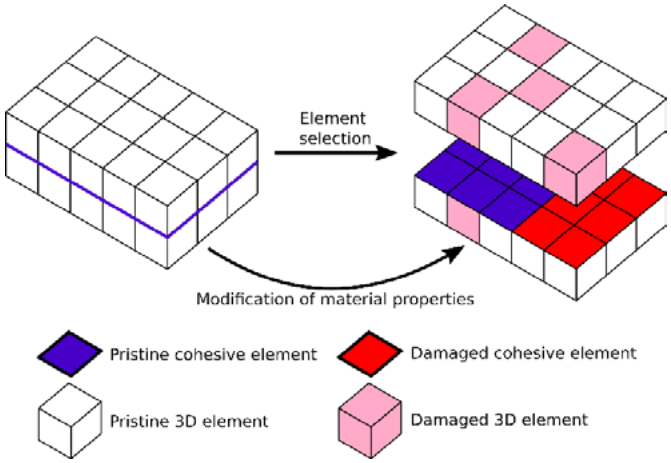


Figure 8. Automated damage process

3. Conclusions

In this paper, a 2D-3D top-down loose coupling submodeling approach adapted to the pre-dimensioning of large composite structures has been formulated. This method is fully compatible with the Nastran solver and allows the local insertion of defects such as porosity, matrix cracking and delamination.
A new displacement interpolation based on a fourth order polynomial and Reissner-Mindlin theory has been proposed. Although this interpolation does not eliminate the need for a transition zone, the very good correlation between the stress fields obtained via the refined global model and the local 3D model demonstrates the effectiveness of the interpolation formulated.
Regarding the insertion of defects and the damage onset, the choice was made to use CZM to represent delamination. Damage variables will be used to model pre-delaminated elements and elements damaged by porosity and matrix cracking.
Finally, the experimental campaign is underway. It will be used to calibrate and validate the insertion of defects into the local model.

References

[1] S. Abrate, J.F. Ferrero and P. Navarro. Cohesive zone models and impact damage predictions for composite structures. *Meccanica* 50, 2587–2620, 2015.
[2] M. Akterskaia, P.P. Camanho, E. Jansen, A. Arteiro and R. Rolfes. Progressive delamination analysis through two-way global-local coupling approach preserving energy dissipation for single-mode and mixed-mode loading. *Composite Structures* 223, 110892, 2019.
[3] D. Ashouri Vajari, C. González, J. Llorca and B.N. Legarth. A numerical study of the influence of microvoids in the transverse mechanical response of unidirectional composites. *Composites Science and Technology* 97, 46–54, 2014.
[4] G.I. Barenblatt. The Mathematical Theory of Equilibrium Cracks in Brittle Fracture. *Advances in Applied Mechanics*. Elsevier, 55–129, 1962.
[5] J. Bertolini, B. Castanié, J.-J. Barrau, J.-P. Navarro and C. Petiot. Multi-level experimental and numerical analysis of composite stiffener debonding. Part 2: Element and panel level. *Composite Structures* 90, 392–403, 2009.
[6] C. Bouvet, 2011. Dommages d'impact sur stratifié composite. In : *JNC17*. 206, 2011.
[7] S.D. Brown, R.B. Biddulph and P.D. Wilcox. A Strength-Porosity Relation Involving Different Pore Geometry and Orientation. *Journal of the American Ceramic Society* 47, 320–322, 1964.
[8] E. Carrera, G.A. Fiordilino, M. Nagaraj, A. Pagani and M. Montemurro. A global/local approach based on CUF for the accurate and efficient analysis of metallic and composite structures. *Engineering Structures* 188, 188–201, 2019.

[9] N.G. Cormier, B.S. Smallwood, G.B. Sinclair and G. Meda Aggressive submodelling of stress concentrations. *Int. J. Numer. Meth. Engng*. 46, 889–909, 1999.
[10] C. Dong. Effects of Process-Induced Voids on the Properties of Fibre Reinforced Composites. *Journal of Materials Science & Technology* 32, 597–604, 2016.
[11] W. Duckworth. Discussion of Ryshkewitch Paper. *J American Ceramic Society* 36, 68–68, 1953.
[12] L. Gendre, O. Allix, P. Gosselet and F. Comte. Non-intrusive and exact global/local techniques for structural problems with local plasticity. *Comput Mech* 44, 233–245, 2009.
[13] V.K. Goyal, V.K., E.R. Johnson and C.G. Dávila. Irreversible constitutive law for modeling the delamination process using interfacial surface discontinuities. *Composite Structures* 65, 289–305, 2004.
[14] S. Hühne, J. Reinoso, E. Jansen and R. Rolfes. A two-way loose coupling procedure for investigating the buckling and damage behaviour of stiffened composite panels. *Composite Structures* 136, 513–525, 2016.
[15] C. C. Jara-Almonte and C.E. Knight. The specified boundary stiffness/force SBSF method for finite element subregion analysis. *Int. J. Numer. Meth. Engng*. 26, 1567–1578, 1988.
[16] C. Julien, F.X. Irisarri, D. Bettebghor, F. Lavelle and K. Mathis. *JEC Composite*, vol. 112, 51-53, 2017.
[17] R. Krueger. The virtual crack closure technique for modeling interlaminar failure and delamination in advanced composite materials. *Numerical Modelling of Failure in Advanced Composite Materials*. Elsevier, pp. 3–53, 2015.
[18] R. Krueger. Virtual crack closure technique: History, approach, and applications. *Applied Mechanics Reviews* 57, 109–143, 2004.
[19] G.N. Labeas, S.D. Belesis, I. Diamantakos and K.I Tserpes. Adaptative Progressive Damage Modeling for Large-scale Composite Structures. *International Journal of Damage Mechanics* 21, 441–462, 2012.
[20] C.S. Lopes, J.J.C. Remmers and Z. Gürdal. Influence of Porosity on the Interlaminar Shear Strength of Fibre-Metal Laminates. *KEM* 383, 35–52, 2008.
[21] B. Madsen and H. Lilholt. Physical and mechanical properties of unidirectional plant fibre composites—an evaluation of the influence of porosity. *Composites Science and Technology* 63, 1265–1272, 2003.
[22] K.M. Mao and C.T. Sun. A refined global-local finite element analysis method. *Int. J. Numer. Meth. Engng*. 32, 29–43, 1991.
[23] L. Maragoni, P.A. Carraro, M. Peron and M. Quaresimin. Fatigue behaviour of glass/epoxy laminates in the presence of voids. *International Journal of Fatigue* 95, 18–28, 2017.
[24] L. Maragoni, P.A. Carraro and M. Quaresimin. Effect of voids on the crack formation in a [45/−45/0]s laminate under cyclic axial tension. *Composites Part A: Applied Science and Manufacturing* 91, 493–500, 2016.
[25] A.J. McMillan, E. Archer, A. McIlhagger and G. Lelong. Strength knock-down assessment of porosity in composites: modelling, characterising and specimen manufacture. *J. Phys.: Conf. Ser*. 382, 012027, 2012.
[26] M. Mehdikhani, N.A. Petrov, I. Straumit, A.R. Melro, S.V. Lomov and L. Gorbatikh. The effect of voids on matrix cracking in composite laminates as revealed by combined computations at the micro- and meso-scales. *Composites Part A: Applied Science and Manufacturing* 117, 180–192, 2019.
[27] P. Olivier, J.P. Cottu and B. Ferret. Effects of cure cycle pressure and voids on some mechanical properties of carbon/epoxy laminates. *Composites* 26, 509–515, 1995.
[28] F. Pascal. Modélisation d'impacts sur structures sandwichs composites : application aux pales d'hélicoptères. *PhD Thesis*. Université Toulouse III - Paul Sabatier, 2016.
[29] N.A. Petrov, L. Gorbatikh and S.V. Lomov. A parametric study assessing performance of eXtended Finite Element Method in application to the cracking process in cross-ply composite laminates. *Composite Structures* 187, 489–497, 2018.
[30] J.B. Ransom and N.F. Knight. Global/local stress analysis of composite panels. *Computers & Structures* 37, 375–395, 1990.

[31] E.F. Rybicki, M.F. Kanninen. A finite element calculation of stress intensity factors by a modified crack closure integral. *Engineering Fracture Mechanics* 9, 931–938, 1977.
[32] E. Ryshkewitch. Compression Strength of Porous Sintered Alumina and Zirconia. *J American Ceramic Society* 36, 65–68, 1953.
[33] G.B. Sinclair and B.P. Epps. On the logarithmic stress singularities induced by the use of displacement shape functions in boundary conditions in submodelling. *Commun. Numer. Meth. Engng.* 18, 121–130, 2002.
[34] R. Vescovini, C.G. Dávila and C. Bisagni. Failure analysis of composite multi-stringer panels using simplified models. *Composites Part B: Engineering* 45, 939–951, 2013.
[35] S.R. Voleti, N. Chandra and J.R. Miller. Global-local analysis of large-scale composite structures using finite element methods. *Computers & Structures* 58, 453–464, 1996.
[36] S.S. Wang. Fracture Mechanics for Delamination Problems in Composite Materials. *Journal of Composite Materials* 17, 210–223, 1983.
[37] J.D. Whitcomb. Iterative global/local finite element analysis. *Computers & Structures* 40, 1027–1031, 1991.

PREDICTION OF MECHANICAL PROPERTIES OF THERMOPLASTIC RESINS CONSIDERING MOLDING CONDITIONS

R. Takashima[1], R. Higuchi[2], S. Oshima[3], T. Yokozeki[4] and T. Aoki[5]

[1]Department of Aeronautics and Astronautics, University of Tokyo, Tokyo, Japan
Email: takashima-risa475@g.ecc.u-tokyo.ac.jp
[2]Department of Aeronautics and Astronautics, University of Tokyo, Tokyo, Japan
Email: higuchi@aastr.t.u-tokyo.ac.jp, Web Page: https://www.aastr.t.u-tokyo.ac.jp/ , https://ais.t.u-tokyo.ac.jp/
[3]Department of Aeronautics and Astronautics, Tokyo Metropolitan University, Tokyo, Japan
Email: s_oshima@tmu.ac.jp, Web Page: https://ais.t.u-tokyo.ac.jp/
[4]Department of Aeronautics and Astronautics, University of Tokyo, Tokyo, Japan
Email: yokozeki@aastr.t.u-tokyo.ac.jp, Web Page: https://www.aastr.t.u-tokyo.ac.jp/ , https://ais.t.u-tokyo.ac.jp/
[5]Department of Aeronautics and Astronautics, University of Tokyo, Tokyo, Japan
Email: aoki@aastr.t.u-tokyo.ac.jp, Web Page: https://ais.t.u-tokyo.ac.jp/

Keywords: Thermoplastics, Phase field method, Finite element analysis, Mechanical property

Abstract
Thermoplastic resins used in thermoplastic composite mostly have semi-crystalline properties. It is known that the microscopic structure changes depending on the crystallization temperature and that the mechanical properties change accordingly. In this study, the mechanical properties of thermoplastic resins are predicted by stepwise analysis combining crystallization simulation based on the phase field method, followed by finite element analysis using the obtained crystalline structure. In the crystallization simulation, the effect of crystallization temperature at the isothermal crystallization process is considered. The constitutive equations are based on the assumption that the amorphous phase exhibits elastic or hyperelastic and perfectly plastic behaviors. In contrast, the crystalline phase behaves as an elastic and perfectly plastic solids. Finally, the accuracy of this method is validated by comparing the simulation result with experimentally obtained Young's modulus, Poisson's ratio, and yield stress.

1. Introduction

Recently used in the aerospace industry, Carbon Fiber Reinforced Plastics (CFRPs) have excellent specific stiffness and specific strength. Resins used as base materials for CFRPs are broadly classified into thermosetting resins and thermoplastic resins. The former irreversibly hardens through a cross-linking reaction by heating, while the latter reversibly softens, melts, and solidifies by heating and cooling. CFRPs using thermoplastic resins have been attracting attention in recent years from the viewpoints of productivity and recyclability. Polyphenylene Sulfide (PPS) and Polyaryl Ether Ketone (PAEK), which are thermoplastic resins used as matrices for CFRPs such as aircraft components, have crystalline properties and crystallize upon cooling. These resins have a semi-crystalline microstructure with a mixture of crystalline and amorphous phases, as shown in Fig. 1[1]. The crystalline structure (degree of crystallinity and grain size) varies depending on molding conditions, including crystallization temperature. In addition to this property, the crystalline and amorphous phases are known to have different material properties [2,3,4]. Therefore, to predict the mechanical properties of semi-crystalline thermoplastics, it is essential to consider the molding conditions, the associated crystal structure, and the mechanical properties of each phase.

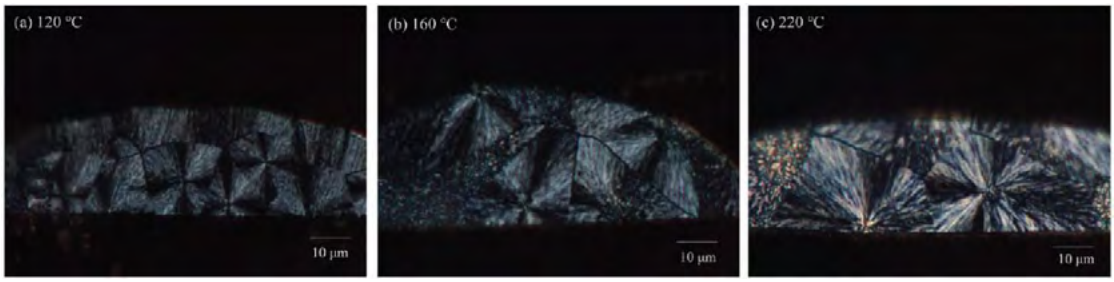


Figure 1. Polarizing optical microscopy image of isothermally melt-crystallized PPS [1].

In this study, PPS, one of the resins with excellent mechanical properties such as stiffness and strength, is studied using a two-step analysis to predict its mechanical properties. First, crystallization simulation with the phase field method is used to obtain the crystal structure that changes with crystallization temperature during the isothermal crystallization process. Next, based on the results of the crystallization analysis, finite element analysis using different material constants for the crystalline and amorphous phases is performed to evaluate the change in mechanical properties as the forming temperature changes. The predicted results are compared with experimental results to verify the validity of the developed method.

2. Crystallization Simulation

2.1. Crystal Growth Model

2.1.1. Phase Field Method

This study uses the phase field method to describe the crystal growth of thermoplastic resin. Interfacial migration is expressed by solving the time evolution equation of ϕ in the phase field method, where $\phi = 0$ is the amorphous phase, $\phi = 1$ is the crystalline phase. This study uses the following governing equations[5,6], where ϕ is a function of position $\boldsymbol{r}$ and time t.

$$\frac{\partial \phi(\boldsymbol{r},t)}{\partial t} = -M_\phi \frac{\delta F(\phi)}{\delta \phi(\boldsymbol{r},t)}. \tag{1}$$

$$F(\phi) = \int f_{\mathrm{cryst}}(\phi) dV = \int \left[f_{\mathrm{local}}(\phi) + f_{\mathrm{grad}}(\phi) \right] dV . \tag{2}$$

$$f_{\mathrm{local}}(\phi, T) = W \int_0^\phi \phi \left(\frac{1}{2} - \phi - m(T) \right) (1-\phi) d\phi . \tag{3}$$

$$f_{\mathrm{grad}}(\phi) = \frac{1}{2} \kappa^2 (\nabla \phi)^2. \tag{4}$$

$F(\phi)$ in Eq. (1) represents the free energy. $f_{\mathrm{local}}(\phi)$ is the local free energy density, $f_{\mathrm{grad}}(\phi)$ is the gradient energy density. M_ϕ in Eq. (1) is the interface mobility, W is a parameter related to the energy barrier, and κ is the gradient coefficient. $m(T)$ is a function of temperature and takes positive values when lower than the melting point. In this analysis, we use the following equation, a dimensionless version of the above equation

$$\tau^* \hat{\varepsilon}^2 \frac{\partial \phi}{\partial t} = \left[\hat{\nabla} \cdot \left(\frac{1}{2} \left(\hat{\nabla} \phi \right)^2 \frac{\partial (\hat{\varepsilon}^2)}{\partial \hat{\nabla} \phi} \right) + \hat{\nabla} \cdot \left(\hat{\varepsilon}^2 \hat{\nabla} \phi \right) - W \phi (\phi - 1) \left(\phi - \frac{1}{2} + m(T) \right) + a \phi (1-\phi) R_{\mathrm{v}} \right] \tag{5}$$

$$\frac{\partial \hat{T}}{\partial \hat{t}} = \hat{\nabla}^2 \hat{T} + \hat{K} \frac{\partial \phi}{\partial \hat{t}}. \tag{6}$$

$$m(\hat{T}) = \frac{a_\mathrm{k}}{\pi} \arctan\left(\gamma(1-\hat{T})\right). \tag{7}$$

with $\hat{T} = (T - T_\mathrm{c})/(T_\mathrm{m} - T_\mathrm{c})$, $\hat{\tau}^* = k_\mathrm{t}/(\rho C_\mathrm{p} \varepsilon M_\phi)$, $\hat{K} = \Delta H_\mathrm{c}/(C_\mathrm{p}(T_\mathrm{m} - T_\mathrm{c}))$, where ρ is density, C_p is constant pressure specific heat, k_t is thermal conductivity, and ΔH_c is latent heat. Also, using representative length D and representative time $\tau = D^2 \rho C_\mathrm{p}/k_\mathrm{t}$, $d\hat{x} = dx/D$, $d\hat{y} = dy/D$, and $d\hat{t} = dt/\tau$ are expressed. $R_\mathrm{v} \in [-1/2, 1/2]$ in Eq. (5) is a random number. $a\phi(1-\phi)R_\mathrm{v}$ denotes the interface noise.

In addition, to introduce the property of temperature dependence of crystallization rate in polymer materials, the simulation model of Bahloul et al [6] is used in Eq. (8). In the analysis, we use the form of Eq. (9), normalized and simplified by the maximum value of the crystallization rate, and treat $\hat{\tau}^*$ and $\hat{K}$ as functions of $\hat{T}$, as shown in Eqs. (10) and (11).

$$G(T_\mathrm{c}) = G_0 \exp\left(-\frac{U}{k(T_\mathrm{c} - T_\infty)}\right) \exp\left(-\frac{K}{T_\mathrm{c}(T_\mathrm{m}^0 - T_\mathrm{c})}\right). \tag{8}$$

$$H(T_\mathrm{c}) = \frac{G(T_\mathrm{c})}{G(T_\mathrm{cmax})} \cong h_0 \exp\left(-\frac{h_1}{T_\mathrm{c} - T_\infty}\right) \exp\left(-\frac{h_2}{T_\mathrm{m}^0 - T_\mathrm{c}}\right). \tag{9}$$

$$\tau^*(T_\mathrm{c}) = \begin{cases} \tau_0^* & (T_\mathrm{g} \le T_\mathrm{c} \le T_\mathrm{cmax}) \\ \tau_0^*/H(T_\mathrm{c}) & (T_{cmax} \le T_\mathrm{c} \le T_\mathrm{m}^0) \end{cases}. \tag{10}$$

$$\hat{K}(T_\mathrm{c}) = \begin{cases} \hat{K}_0/H(T_\mathrm{c}) & (T_\mathrm{g} \le T_\mathrm{c} \le T_\mathrm{cmax}) \\ \hat{K}_0 & (T_\mathrm{cmax} \le T_\mathrm{c} \le T_\mathrm{m}^0) \end{cases}. \tag{11}$$

T_cmax is the temperature at which the crystallization rate reaches its maximum value, and h_1 and h_2 are parameters. The material constants used are shown in Table 1 and the values obtained from the DSC test by Kato et al. were used [7]. Other material constants are taken from a previous study [6].

2.1.2. Parameter Identification

To identify the parameters h_1 and h_2 when using Eq. (9), we first analyzed a single spherical crystal at several crystallization temperatures. For one spherulite with a nucleus placed at the center of the analysis area of 50 μm × 50 μm and mesh size 500 × 500, the average growth rate was obtained from the central nucleus at angles near 0° and 45° to the x-axis as shown in Fig. 2, and $H(T_\mathrm{c})$ was calculated. The Lauritzen-Hoffman equation in Eq. (9), the experimental values from Lovinger et al. [8], and the results of the parameter identification are shown in Fig. 3. In the following analysis, $h_1 = 80$ and $h_2 = 66.73$ obtained from this simulation are used.

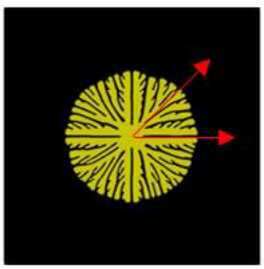


Figure 2. Simulation of PPS crystallization and direction for calculating crystallization rate.

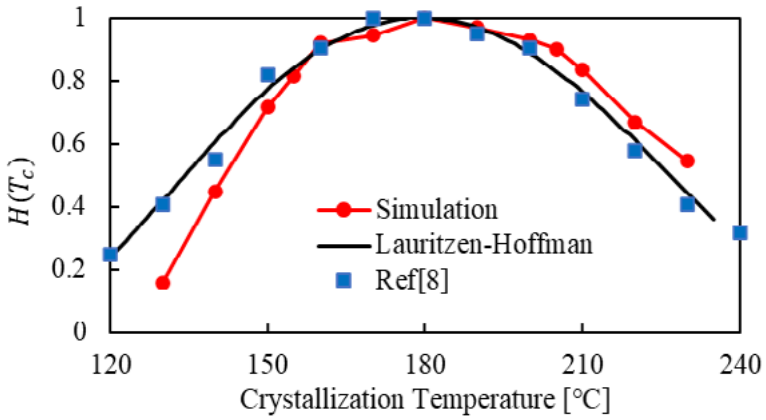


Figure 3. Relationship between crystallization temperature and crystallization rate.

2.2 Multicrystal Simulation

A nucleation model is also introduced since the phase field method can only handle crystal growth. The nucleation rate dN/dt in homogeneous nucleation of polymeric materials is expressed by Eq. (12) using the parameters C_1 for transport of molecular chains and C_2 for primary nucleation [9].

$$\frac{dN(T(t))}{dt} = N_0 \exp\left[-\frac{C_1}{T(t)-T_\infty}\right] \exp\left[-\frac{C_2(T(t)+T_\mathrm{m})}{T(t)^2(T_\mathrm{m}-T(t))}\right]. \tag{12}$$

The nucleation rate is known to affect the size of spherulites as well as the crystallization rate. During isothermal crystallization, spherulites with sizes of 10 μm at $T_\mathrm{c} = 120°\mathrm{C}$, 20 μm at $T_\mathrm{c} = 160°\mathrm{C}$, and 30-40 μm at $T_\mathrm{c} = 220°\mathrm{C}$ have been observed [1], and the values of C_1, C_2, and N_0 obtained by fitting were used in the analysis.

In this study, crystallization analysis is performed on neat PPS. The analysis is performed by discretizing Eqs. (5) and (6) using the finite difference method. The simulation is performed under isothermal conditions at three different temperatures: $T_{\mathrm{cmax}} = 180°\mathrm{C}$, which is the crystallization temperature with the maximum crystallization rate, and $T_\mathrm{c} = 150°\mathrm{C}$ and $210°\mathrm{C}$, which are $T_{\mathrm{cmax}} \pm 30°\mathrm{C}$. The analysis area is $100\ \mu\mathrm{m} \times 100\ \mu\mathrm{m}$ with a mesh size of 1000×1000. Five analyses are performed to account for nucleation and randomness of the crystal structure. Fig. 4(a)-(c) shows results at each crystallization temperature.

3. Finite Element Analysis

Based on the results obtained from the crystallization analysis, homogenized finite element analysis was performed to obtain the mechanical properties. A square mesh was automatically generated using the difference grids used in the crystallization analysis as nodes for FEM.

The results of the crystallization analysis used are those at the time when the change in the average value of the phase field variable over the entire analysis domain is sufficiently small. The dimensioned times t of the results are 1.67×10^{-4} s at $T_\mathrm{c} = 150$ and $210°\mathrm{C}$ and 1.39×10^{-4} s at $T_c = 180°\mathrm{C}$. The mesh size is 1000×1000 and two-dimensional solid elements are used. The finite element method software

Table 1. Material parameters of PPS in crystallization simulation.

$T_\mathrm{g} = 100°\mathrm{C}$	$T_\mathrm{m}^0 = 280.5°\mathrm{C}$	$T_{\mathrm{cmax}} = 180°\mathrm{C}$	$\tau_0^* = 3.0$
$d\hat{t} = 0.1$	$W = 2.0$	$\hat{\varepsilon} = 1/3$	$\hat{K} = 1.4$
$D = 10^{-7}$ m	$a = 0.02$	$a_\mathrm{k} = 0.9$	$\gamma = 10$
$d\hat{x} = d\hat{y} = 1$			

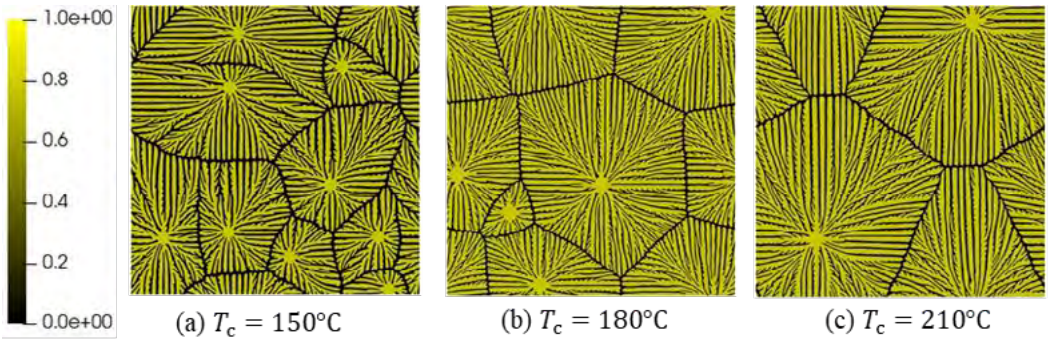


Figure 4. Distribution of phase field variable.
($\phi = 1$ in crystalline phase, and $\phi = 0$ in amorphous phase.)

Abaqus 2019 was used for the analysis.

3.1 Material Model and Boundary Conditions

In the following finite element analysis, the material constants and constitutive equations for the phase field variable $\phi < 0.5$ for the amorphous phase and $\phi \geq 0.5$ for the crystalline phase will be used at each integration point in the finite element.
First, elastic analysis is performed under two assumptions: Model 1: both amorphous and crystalline phases are linearly elastic; Model 2: the amorphous phase is hyperelastic, and the crystalline phase is linearly elastic. The energy density function U is expressed in Eq. (13) using the first-order invariant I_1 of the right Cauchy-Green tensor and the determinant J of the deformation gradient tensor $\boldsymbol{F}$,

$$U = C_{10}(I_1 - 3) + \frac{1}{D_1}(J-1)^2. \tag{13}$$

$$I_1 = \lambda_1^2 + \lambda_2^2 + \lambda_3^2. \tag{14}$$

$$J = \det(\boldsymbol{F}) = \lambda_1\lambda_2\lambda_3. \tag{15}$$

where C_{10} and D_1 are material constants expressed as $C_{10} = G/2$, $D_1 = 2/K_0$ using the initial shear modulus G and volume modulus K_0. Also, λ_i is called the principal stretch and expressed as $\lambda_i = (L_i + u_i)/L_i$ $(i = 1,2,3)$, where L_i is the length before deformation and u_i is the deformation length.
Based on the results of the elastic analysis, the yield stress is obtained by analyzing Model 3: Model 1 with full plasticity based on Mises stress in each phase. Here, 0.2% offset stress is used as the yield stress. Young's modulus to calculate the yield stress is obtained from elastic analysis using the same crystal structure. In both elastic and elastoplastic analyses, the crystal structure is considered to be periodic in a two-dimensional plane, and a periodic boundary condition based on the displacement is added to analyze the plane strain state. In the displacement condition, a macroscopic strain of 3% is applied only in the x- or y-direction. However, if the yield stress could not be obtained in the elastoplastic analysis in the strain range of 3% or less, an macroscopic strain is imposed to the analysis. The macroscopic Young's modulus, Poisson's ratio, and yield stress were obtained from the average stress and macroscopic strain in the analysis region. The material constants used in each finite element analysis are shown in Table 2. The Young's modulus E_c of the crystalline phase was taken from a previous study [10], and the other material constants marked with * were estimated values.

4. Results and Discussion

The relationship between the crystallization temperature and the average values of macroscopic Young's modulus and Poisson's ratio obtained by elastic analysis is shown in Figs. 5(a) and (b). The legend indicates the amorphous/crystalline phase model and the error range indicates the standard deviation.

Table 2. Material parameters of PPS in homogenization simulation.

Amorphous Phase		Crystalline Phase
$E_a^* = 200$ MPa	C_{10}^*=31.25 MPa	$E_c = 28000$ MPa [9]
$\nu_a^* = 0.4$	$D_1^* = 0.006$ MPa^{-1}	ν_c^*=0.3
$\sigma_{Ya}^* = 100$ MPa		$\sigma_{Yc}^* = 400$ MPa

The average values were obtained from the results of x and y tension analyses for each crystallization analyses. Higuchi et al. [11] reported that Young's modulus is higher, and Poisson's ratio is lower at higher crystallization temperatures in experiment. As shown in Fig. 5(a), the tendency that Young's modulus increases with crystallization temperature is consistent to the experiments [11]. The difference grids are used in the crystallization analysis as the nodes for the finite element method. As shown in Fig. 4, the amorphous phase between the spherocrystals at $T_c = 150$ °C is thicker than that at other crystallization temperatures. This cause lower Young's modulus at $T_c = 150$ °C. To solve this, the crystallization analysis needs to be improved. This is a point that needs to be improved in the crystallization analysis. In addition, the large number of spherulite crystals greatly affected the effect of the amorphous phase between the spherulite crystals, resulting in an underestimation of Young's modulus. The Poisson's ratio was greatly affected by the appearance of the spherulites in the analysis region, and the standard deviation was the largest at $T_c = 210$°C, where the number of spherulites was the smallest. We plan to improve this point by expanding the analysis area and using a more coarse-grained model.

The relationship between crystallization temperature and yield stress is shown in Fig. 6(a). The stress-strain diagram obtained from the analysis using Model 3 is shown in Fig. 6(b). In tensile tests [10], it has been reported that yield stress increases as crystallization temperature do. In the present simulation, this tendency was obtained only between $T_c = 150$°C and 180°C. To discuss these results, the phase field variable distribution (crystalline/amorphous phase distribution) is shown in Fig. 4 for each crystallization temperature, one case at each temperature. The total strain, elastic, and plastic strain distributions in the tensile direction are shown in Figs. 7, 8, and 9 respectively. All tensile directions in these results are in the x direction. The yield stresses obtained in simulations are 66.89 MPa at $T_c = 150$°C, 74.85 MPa at $T_c = 180$°C, and 65.02 MPa at $T_c = 210$°C. Areas with compressive strain were found in the amorphous phase between the spherulite lamellae as shown in Figs. 7 and 8. In the amorphous phase between the grains, especially where the amorphous phase is vertically distributed to the tensile direction, the total strain is large, indicating that both elastic and plastic components contribute to the strain. The amorphous phase strain at the spherulitic grain boundaries surrounds the lamellar edge of the neighboring spherulites. On the other hand, the crystalline phase is characterized by a large strain at the nuclei centers of some of the spherulites, where the plastic strain is pronounced.

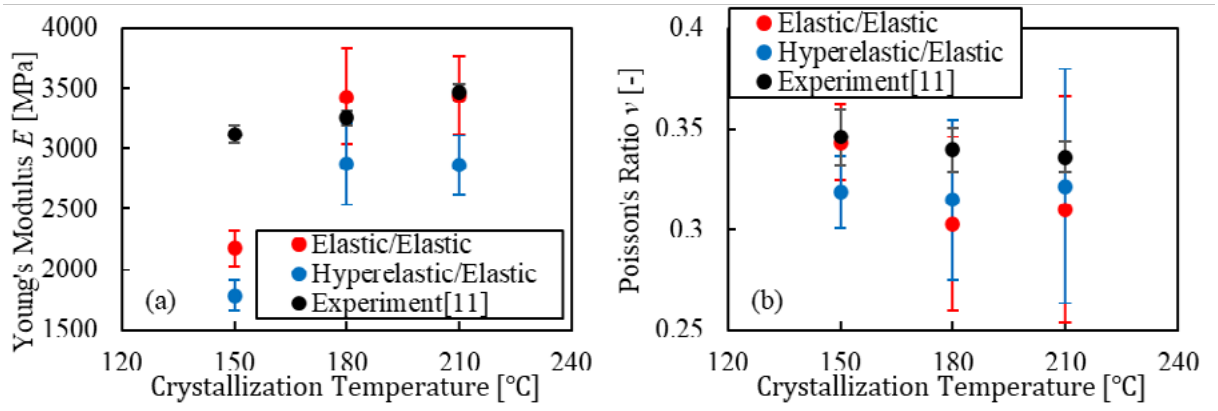


Figure 5. Macroscopic elastic properties gained in FE analysis. (a) Relationship between T_c and Young's modulus (b) Relationship between T_c and Poisson's ratio.

The plastic strain in the spherulite nuclei exists in a direction that connects plastic strain in the nearby amorphous phase. The above confirms the mechanical interaction between the amorphous and crystalline phases. At a crystallization temperature of 210°C, where the yield stress did not match the experimental trend, plastic strain is particularly dominant in the amorphous phase at the grain boundaries due to the low number of spherulites. This causes deformation of the entire region with small plastic deformation of the crystalline phase, resulting in a small increase in stress with increasing strain. This phenomenon is thought to be responsible for the small yield stresses.

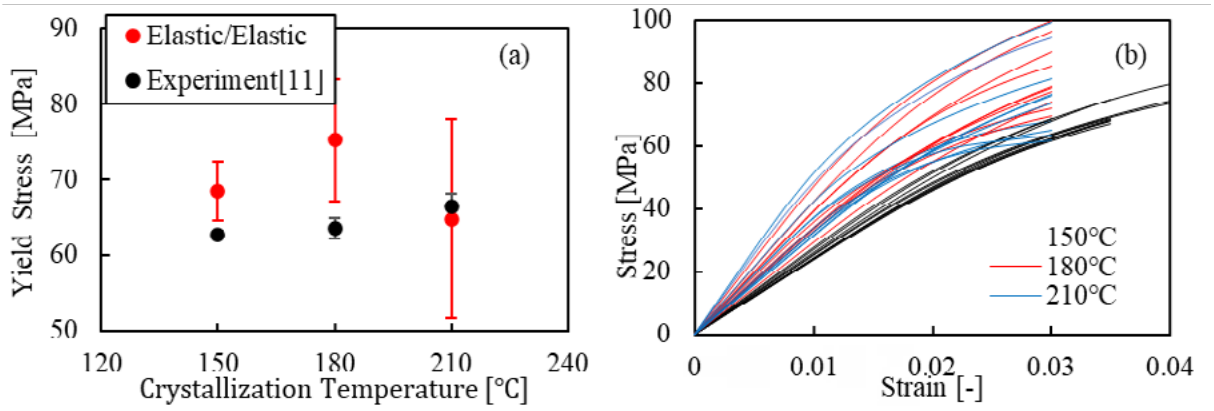


Figure 6. The results of elastoplastic analyses. (a) Relationship between crystallization temperature and yield stress. (b) Stress-strain curves obtained by Model 3.

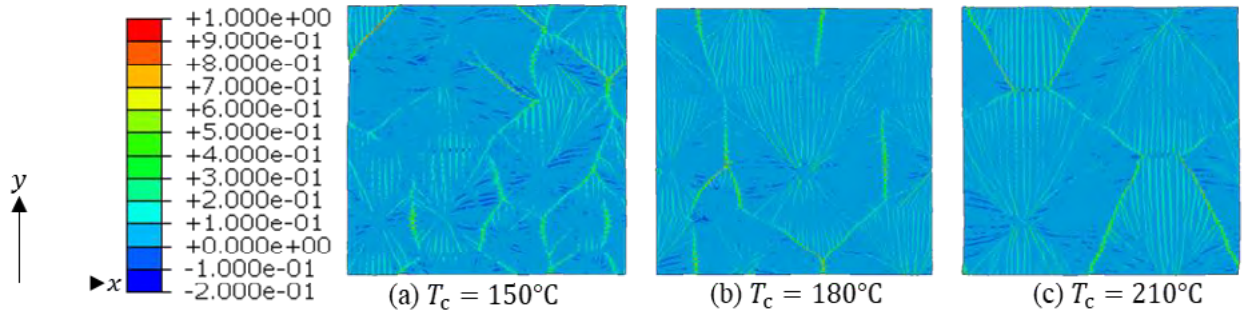


Figure 7. Strain distributions in tension direction at (a) T_c = 150°C, (b) T_c = 180°C, and (c) T_c = 210°C.

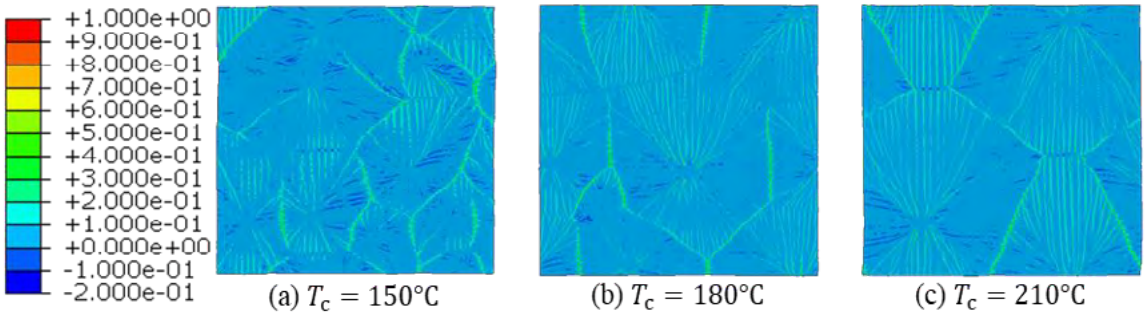


Figure 8. Elastic strain distributions in tension direction at (a) T_c = 150°C, (b) T_c = 180°C, and (c) T_c = 210°C.

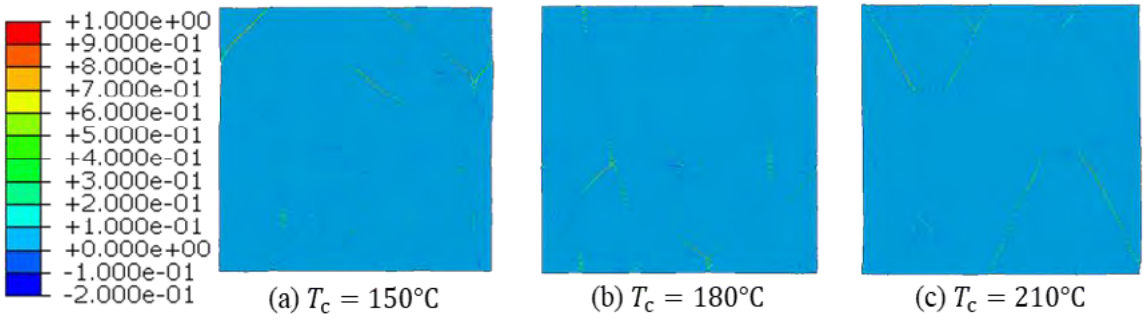


Figure 9. Plastic strain distributions in tension direction at (a) $T_c = 150°C$, (b) $T_c = 180°C$, and (c) $T_c = 210°C$.

5. Conclusion

In this study, isothermal crystallization analysis of PPS, a crystalline thermoplastic resin, was performed at different crystallization temperatures. Parameters related to crystallization and nucleation rate were identified, and the changes in crystal structure with crystallization temperature were captured. Using the microstructures obtained from the crystallization analysis, macroscopic elastoplastic properties were obtained by finite element analysis using different material constants and constitutive equations for the crystalline and amorphous phases. Qualitative agreement with experiments was obtained for Young's modulus concerning crystallization temperature. On the other hand, there were macroscopic mechanical properties and crystallization temperatures that did not capture the trends reported experimentally. In the future, not only crystallization analysis using the phase field method but also the development of constitutive equations used in finite element analysis and the introduction of elastic anisotropy are required to improve the accuracy.

References

[1] Furushima, Y., et al. Crystallization-melting kinetics and morphological analysis of polyphenylene sulfide, *Macromolecular Chemistry and Physics*, volume(219):1700481-1-1700481-7, 2018.
[2] Gao S.L. and Kim J. K. Cooling rate influences in carbon fibre/PEEK composites. Part 1. Crystallinity and interface adhesion. *Composites Part A*, volume(31):517-530, 2000.
[3] Gao S.L. and Kim J. K. Cooling rate influences in carbon fibre/PEEK composites. Part II: interlaminar fracture toughness. *Composites Part A*, volume(32):763-774, 2001.
[4] Gao S.L. and Kim J. K. Cooling rate influences in carbon fibre/PEEK composites. Part III: impact damage performance. *Composites Part A*, volume(32):775-785, 2001.
[5] Kobayashi, R., Modeling and numerical simulations of dendritic crystal growth, *Physica. D, Nonlinear Phenomena,* volume(63):410-423, 1993.
[6] Bahloul A., et al. An enhanced phase field model for the numerical simulation of polymer crystallization. *Polymer Crystallization*, volume(3), 2020.
[7] Kato M., et al. Experimental and Numerical Investigation of the Crystallization Behavior of PPS Resin and CF/PPS. *Journal of the Japan Society for Composite Materials,* volume(50-1):8-18, 2024.
[8] Lovinger A. J., et al. Kinetic analysis of the crystallization of poly (p-phenylene sulphide). *Polymer*, volume(26):1595-1604, 1985.
[9] R. Pantani, et al. Modeling of morphology evolution in the injection molding process of thermoplastic polymers. *Progress in Polymer Science*, volume(30):1185-1222, 2005.
[10] Nishino, T., et al. Elastic modulus of crystalline regions of poly(ether ether ketone), poly(ether ketone) and poly(p-phenylene sulphide), *Polymer*, volume(33-4):736-743, 1992.
[11] Higuchi R, et al. Multiphysics simulation on crystal morphology-dependent material properties of thermoplastic resin and its composites. *In Japan Conference of Composite Materials 14th*, volume v1, 2023.

PRODUCTION OF CONTINUOUS CARBON FIBER REINFORCED THERMOPLASTIC COMPOSITES BY ANISOTROPIC TOPOLOGY OPTIMIZATION AND 3D PRINTING

Ryo Tomuro[1], Naruki Ichihara[2], Sho Kajihara[3] and Tomohiro Yokozeki[4]

[1]Department of Aeronautics and Astronautics, The University of Tokyo,
7-3-1, Hongo, Bunkyo, Tokyo, Janpan, ryotompe@g.ecc.u-tokyo.ac.jp
[2]Department of Mechanical Engineering, College of Science and Technology, Nihon University,
1-8-14, Kandasurugadai, Chiyoda, Tokyo, Japan, ichihara.naruki@nihon-u.ac.jp
[3]Department of Mechanical Engineering, School of Science and Engineering, Meiji University,
1-1-1, Higashimita, Tama, Kawasaki, Japan, kajihara@meiji.ac.jp
[4]Department of Aeronautics and Astronautics, The University of Tokyo,
7-3-1, Hongo, Bunkyo, Tokyo, Janpan, yokozeki@aastr.t.u-tokyo.ac.jp

Keywords: Carbon fibers, Topology optimization, Anisotropy, 3D printing

Abstract
This paper investigated the challenges and methodologies in anisotropic topology optimization for 3D printing, focusing on improving the mechanical properties of structures produced by fused deposition modeling (FDM). The study addressed the significant performance gap between theoretically optimized designs and their physical counterparts. The research adopted a dual optimization approach, utilizing scalar and vector functions to represent topology and fiber orientation, respectively. These functions are smoothed using a Helmholtz type partial differential equation to avoid common problems like checkerboard patterns in design. Optimization targets minimizing compliance to enhance structural stiffness, implemented using finite element methods (FEM). The design variables were updated by the method of moving asymptotes (MMA). Significant findings included the impact of design binarization, where densities were adjusted between solid and void, affecting the structure's compliance. Although a low-density region minimally affected overall compliance, it was critical for global optimal stiffness. The study demonstrated a substantial discrepancy between theoretical and actual design results for 3D printing, suggesting a need for refined optimization and design methods.

1. Introduction

3D printing technology has revolutionized the design and manufacturing fields in terms of its ability to create complex shapes and quickly give shape to ideas by importing CAD data. In particular, the fused deposition modeling (FDM) is one of the most popular methods for manufacturing prototypes. However, structural parts fabricated by the FDM method using polymer and short-fiber reinforced composites have relatively low mechanical properties, limiting their application to structural components [1]. In recent years, continuous fiber-reinforced composites have been focused on in the FDM method to improve mechanical properties.

Carbon fiber-reinforced plastics (CFRP), which have excellent mechanical properties such as specific strength and specific stiffness, have been applied in the aerospace, automotive, and marine fields. Among them, much attention has been paid to designing the structures with continuously varying fiber orientation by anisotropic topology optimization because those structures can effectively utilize the anisotropic nature of composites [2].

However, the design of CFRP in the context of 3D printing spans over different domain such as materials, structures and manufacturing and there are several challenges. One of the challenges is a big gap in mechanical performance between optimized continuous carbon fiber-reinforced composite structures and ones manufactured by the FDM method due to current limitations such as feasible printing curvature of continuous fibers and insufficient impregnation of reinforced fibers by matrix during printing [3]. Therefore, it is necessary to contrive ways to prevent the mismatch and improve the mechanical properties.

This study aims to quantitatively track the mismatch of mechanical properties in a series of design processes of continuous carbon fiber-reinforced composites for manufacturing by 3D printing, and to predict accurate mechanical properties. We hope to provide a new insight for enhancement of mechanical properties from the standpoint of computational mechanics.

2. Formulation

In this section, we first present the topology design representation by using a scalar function and a filter based on a Helmholtz type partial differential equation. Then, we similarly present the orientation design presentation by a vector function. Finally, optimization problem is introduced.

2.1. Topology design representation

To represent the topology, we defined a fixed design domain D and a scalar function $\phi \in [0,1]$ in D. Since ϕ can take arbitrary values for each point, problems such as checkerboard patterns can occur if it is used as a design variable that represents the topology as it is. Therefore, we considered a new scalar function φ that satisfied the following Helmholtz-type partial differential equation and the Neumann boundary condition to smooth the topology. This method is known to have implementation advantages in that it can utilize the already existing framework of finite element methods (FEM) such as geometry and mesh [4, 5].

$$-R_{\varphi}^{2}\nabla^{2}\varphi + \varphi = \phi, \tag{1}$$

$$\frac{\partial \varphi}{\partial \boldsymbol{n}} = 0. \tag{2}$$

R_{φ} is the filter radius with respect to the topology and functions like a low-pass filter by setting an appropriate value for R_{φ} [5]. Also, $\boldsymbol{n}$ is the normal vector to the boundary Γ. Then the material density function ρ can generally obtained by generally introducing a Heaviside function $H \in [0,1]$ and interpolating with a smoothed scalar function φ, so that ρ is forced to approach 0 or 1.

$$\rho(\varphi) = H(\varphi). \tag{3}$$

Since $\phi \in [0,1]$ in this study, $\varphi \in [0,1]$ is satisfied for any φ. Therefore, $H(\varphi)$ was defined by the following equation.

$$H(\varphi) = \varphi. \tag{4}$$

$\rho(\boldsymbol{x}) = 1$ denotes the solid domain Ω_D and $\rho(\boldsymbol{x}) = 0$ denotes the void domain $D \backslash \Omega_D$. The operation to clarify the boundary between 0 and 1 was performed after the optimization calculation, allowing for grayscale.
In addition, the following equation was assumed to hold between the material density $\rho(\boldsymbol{x})$ and the stiffness tensor $\mathbf{C}(\boldsymbol{x})$.

$$\mathbf{C}(\boldsymbol{x}) = \{\varepsilon + (1-\varepsilon)\rho(\boldsymbol{x})^P\}\mathbf{C}_{\boldsymbol{s}}. \tag{5}$$

$\mathbf{C}_{\boldsymbol{s}}$ is the solid stiffness tensor when $\rho(\boldsymbol{x}) = 1$, ε is a very small positive lower bound set for avoiding singularity and P is the density penalty parameter. In this study, $\varepsilon = 10^{-3}$ and $P = 3$ were set.

2.2. Orientation design representation

To represent the orientation design, we defined a vector function $\boldsymbol{\vartheta} = [\xi, \eta]^T, \{\xi,\ \eta \in [-1, 1]\}$ in D. We introduced an isoparametric shape function N and considered a vector function $\tilde{\boldsymbol{\vartheta}}$ that was defined by the following equation to obtain the fiber orientation vector $\boldsymbol{\theta}$.

$$\tilde{\boldsymbol{\vartheta}} = N(\boldsymbol{\vartheta}). \tag{6}$$

An isoparametric shape function N is such a function that transforms a square region in a 2D plane to a circular region in coordinates. The projected vector function $\tilde{\boldsymbol{\vartheta}} = \left[\tilde{\xi}, \tilde{\eta}\right]^T$ satisfies $\tilde{\xi}^2 + \tilde{\eta}^2 \leq 1$. For details on the formulation of this shape function N, please refer to the literature in Nomura [6]. The fiber orientation vector $\boldsymbol{\theta} = [\varsigma, \zeta]^T$ was defined as a vector function satisfying the following Helmholtz-type partial differential equation and the Neumann boundary condition as in the previous section.

$$-R_{\boldsymbol{\theta}}^2\nabla^2\begin{bmatrix}\varsigma\\ \zeta\end{bmatrix} + \begin{bmatrix}\varsigma\\ \zeta\end{bmatrix} = \begin{bmatrix}\tilde{\xi}\\ \tilde{\eta}\end{bmatrix}, \tag{7}$$

$$\frac{\partial \varsigma}{\partial \boldsymbol{n}} = 0, \qquad \frac{\partial \zeta}{\partial \boldsymbol{n}} = 0. \tag{8}$$

R_θ is the filter radius with respect to the fiber orientation. If the fiber orientation angle $\psi \in [0, 2\pi]$ was defined as the angle between $\boldsymbol{\theta}$ and the unit vector $[1, 0]^T$, the stiffness tensor $\tilde{\mathbf{C}}(\boldsymbol{x})$ rotated by ψ around any point $\boldsymbol{x}$ satisfied the following equation.

$$\tilde{\mathbf{C}}(\boldsymbol{x}) = \mathbf{T}(\psi)\mathbf{C}(\boldsymbol{x})\mathbf{T}^{\boldsymbol{T}}(\psi). \tag{9}$$

$\mathbf{T}$ is the rotation tensor. In combination with the previous section, the stiffness tensor $\tilde{\mathbf{C}}(\boldsymbol{x})$ considering anisotropy at a point $\boldsymbol{x}$ is determined by the material density $\rho(\boldsymbol{x})$ and the fiber orientation angle $\psi(\boldsymbol{x})$, and is expressed as

$$\tilde{\mathbf{C}}(\boldsymbol{x}) = \{\varepsilon + (1-\varepsilon)\rho(\boldsymbol{x})^P\}\mathbf{T}(\psi)\mathbf{C}_{\boldsymbol{s}}\mathbf{T}^{\boldsymbol{T}}(\psi). \tag{10}$$

2.3. Optimization problem

The considered optimization problem is the minimization of the compliance, which means the maximization of the global stiffness. The objective is to find a material distribution in the fixed design domain D, which minimizes the compliance for a given set of loads and boundary conditions. The material behavior is liner elastic.

Formulation of the problem is expressed as

$$\min_{\phi,\vartheta} f = \int_D \boldsymbol{\varepsilon} : \tilde{\mathbf{C}} : \boldsymbol{\varepsilon}\, d\Omega, \tag{11}$$

subject to

$$\phi \in [0,1], \tag{12}$$

$$\xi \in [-1,1], \tag{13}$$

$$\eta \in [-1,1], \tag{14}$$

$$\int_D \rho\, d\Omega - \bar{V} \leq 0, \tag{15}$$

$$\begin{cases} -\nabla \cdot \boldsymbol{\sigma} = 0 & \text{in } D \\ \boldsymbol{u} = \bar{\boldsymbol{u}} & \text{in } \Gamma_d \\ \boldsymbol{\sigma} \cdot \boldsymbol{n} = \boldsymbol{t} & \text{in } \Gamma_n \end{cases}, \tag{16}$$

$$\boldsymbol{\sigma} = \tilde{\mathbf{C}} \cdot \boldsymbol{\varepsilon}, \tag{17}$$

$$\boldsymbol{\varepsilon} = \frac{1}{2}(\nabla \boldsymbol{u} + (\nabla \boldsymbol{u})^T), \tag{18}$$

where $\bar{V}$ is the upper boundary for the volume of the material and $\bar{V} = 0.5$ was set in this study. $\boldsymbol{u}$ is the displacement vector fixed as $\boldsymbol{u} = \bar{\boldsymbol{u}}$ on the Dirichlet boundary Γ_d, $\boldsymbol{t}$ is a traction vector defined on the Neumann boundary Γ_n, $\boldsymbol{n}$ is the normal vector to the boundary Γ_n, $\boldsymbol{\sigma}$ is the stress tensor and $\boldsymbol{\varepsilon}$ is the strain tensor.

3. Optimized topology and orientation design

We treated the Messerschmitt-Bolkow-Blohm (MBB) beam problem in 2D plane stress state as a benchmark for single load optimization. In this study, we focused on the process of acquiring the CAD geometry before designing printing path for 3D printing of the structural parts.

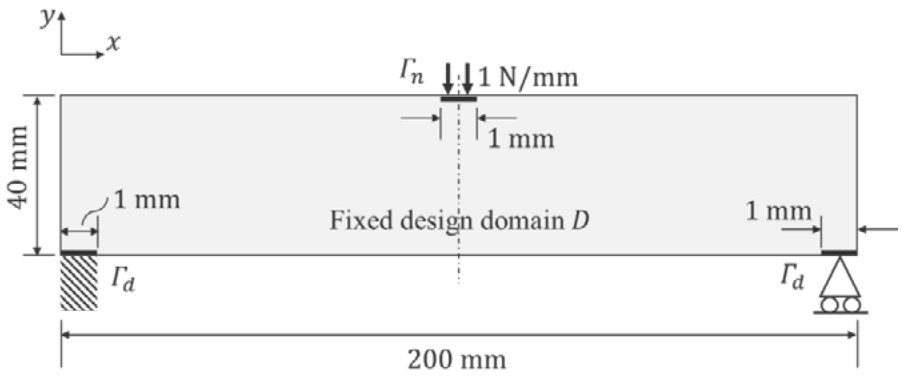


Figure 1. Desing domain and boundary conditions for MBB beam problem.

Table 1. Material properties.

		CF/PA12
E_1 [GPa]	Tensile modulus 0°	130
E_2 [GPa]	Tensile modulus 90°	6.6
G_{12} [GPa]	In-plane shear stiffness	2.2
ν_{12} [-]	In-plane Poisson's ratio	0.33

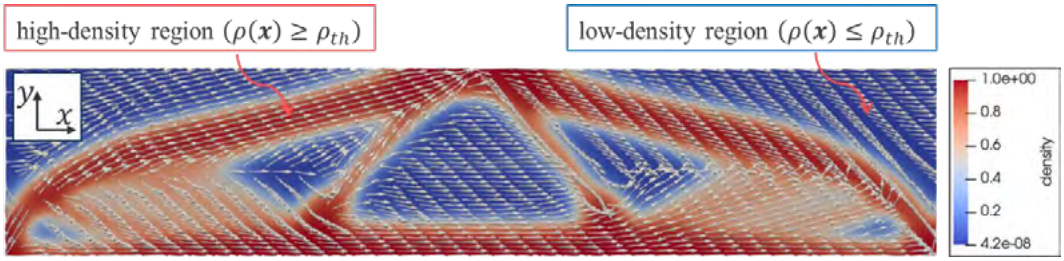


Figure 2. Optimized density and fiber orientation distribution, $f = 0.00293$, Iter.:500.

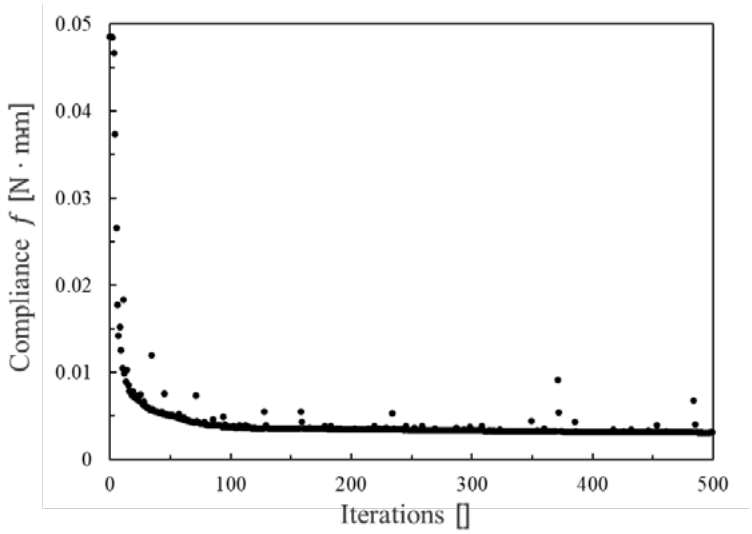


Figure 3. Optimization histories

3.1. Numerical implementation

All formulations were discretized based on the FEM. The design variables were updated by the method of moving asymptotes (MMA), based on the sensitivities of the objective and constraint functions. All of the program was implemented in Python using a combination of FEniCS (a FEA framework), pyadjoint (a generic algorithmic differentiation framework) and nlopt (a library of nonlinear optimization).

Figure 1 shows the fixed design domain D, boundary conditions, and loading conditions of the compliance minimization problem for the MBB beam under volume constraints.
The design domain was divided into (200×40) elements using a square four-node linear element with a side length of 1 mm, consisting of two pasted triangles.
Table 1 shows the material properties used in this study. These are based on the material properties of CF/PA12 at $v_f = 60\%$.

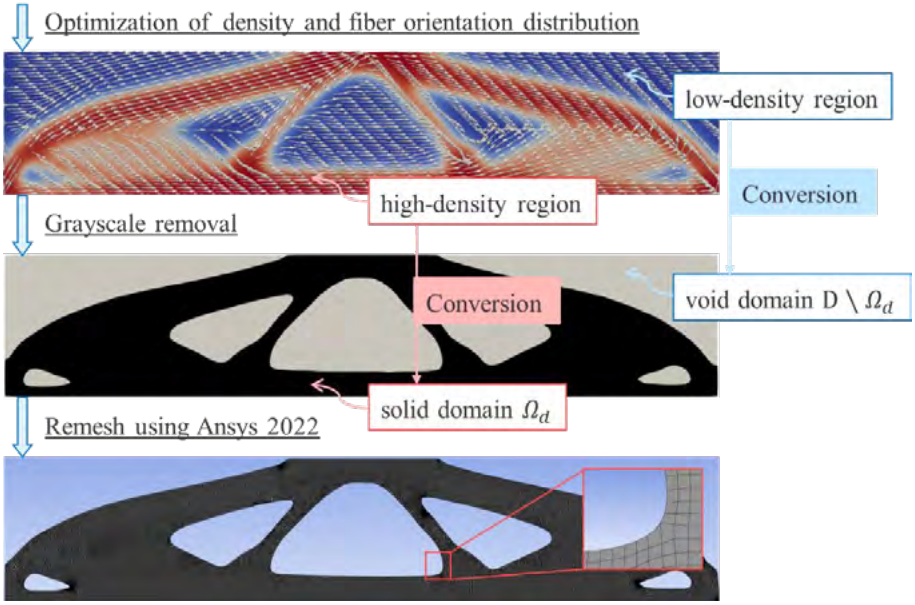


Figure 4. Flow to obtain remesh of the high-density region from optimization results.

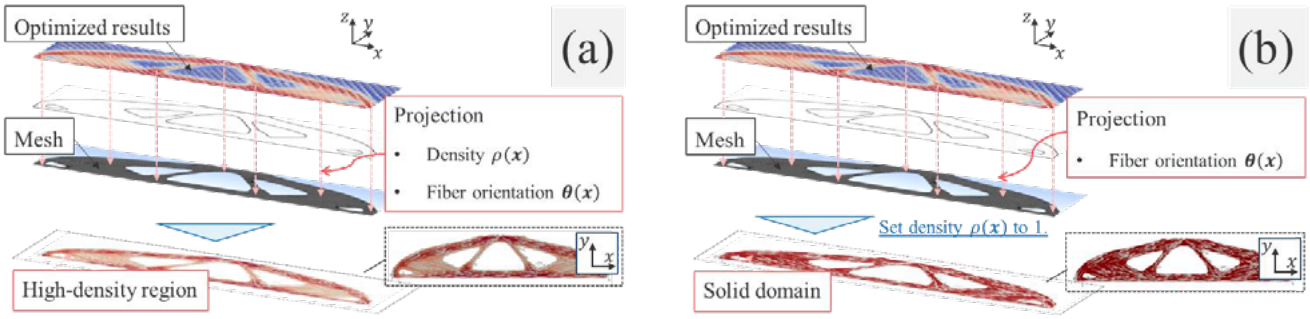


Figure 5. Flow to obtain (a) the remeshed high-density region with the same density and fiber orientation distribution as the optimized results, (b) the remeshed solid domain with the same fiber orientation distribution as the optimized results.

3.2. Optimization results

Figure 2 and 3 show the optimized results for the case where the filter radius R_φ and R_θ were set to (5.0, 5.0). No checkerboard pattern was observed although only the linear elements was used for the discretization.

In order to obtain the CAD geometry, the grayscale of the optimized results at iterations = 500 was removed, which means binarizing densities that take intermediate values between 0 and 1 to 0 or 1. The density threshold for removing grayscale, ρ_{th}, was set to 0.5. Regions with density lower and higher than ρ_{th} were defined as “low-density region” and “high-density region”, respectively, and the low-density region was converted to the void domain and the high-density regions was converted to the solid domain, as shown in Figure 4.

To obtain the mesh of the high-density region, the geometry was imported into Ansys 2022 and automatically remeshed, as shown in Figure 4. The elements were all triangular or rectangular linear elements with 147492 elements and 75415 nodes.

3.3. Discussion about binarization

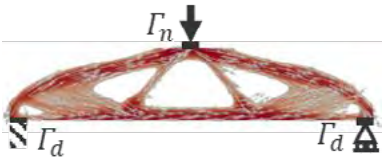
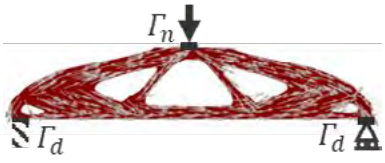
Structural analysis was performed on the two models to investigate the effects of binarization on compliance, as shown in Table 2. One model was the high-density region with the same density and fiber orientation distribution as the optimized results and the other was solid domain with the same fiber orientation distribution as the optimized results. The way to obtain each model from the optimized results is shown in Figure 5. The remeshed high-density region had both optimized density and fiber orientation vectors, while the remeshed solid domain had only the optimized fiber orientation vectors and the density of the entire domain was set to 1. The same boundary and loading conditions as in the problem setup was imposed on both the high-density region and the solid domain models. Here, it was assumed that stiffness was proportional to density. The volume of the material of the high-density region was 8.8 % lower than the upper boundary, $\bar{V} = 0.5$, and the volume of the material of the solid domain 10.6 % was higher than the upper boundary.

The compliance value for the high-density region, 0.00290 N·mm. was higher than that of the solid domain, 0.00261 N·mm. This indicates that the high-density region undergoes slightly more deformation under the same loading conditions, suggesting marginally lower stiffness compared to the solid domain. However, note that the volumes of materials of the two models were different. The volume of material of the solid domain was 22.6% larger than the one of the high-density region, while the compliance of the solid domain was only 10.0% less. This suggests that the solid domain model has the potential to reduce weight.

The maximum and minimum principal stress distribution was comparable between the two models. This suggests that there is no significant difference in their ability to handle tensile and compressive stresses. The high-density region, despite using less material, does not show significant differences in stress distribution compared to the solid domain, indicating that it can effectively handle the applied loads without substantial variations in stress levels.

The discussions so far indicate a large range of gaps from the initial optimization results. These results indicate that binarization has a significant impact on compliance and requires appropriate filtering to reduce the compliance change at each stage of the design process.

Table 2. The comparison of structural analysis results between the high-density region and solid domain.

	High-density region	Solid domain
Volume of the material [%]	45.1	55.3
Boundary conditions		
Compliance f [N·mm]	0.00290	0.00261
Maximum principal stress [MPa]		
Minimum principal stress [MPa]		

4. Conclusions

In this study, anisotropic topology optimization was used to obtain the geometry and fiber orientation distribution, which were then utilized to acquire the CAD geometry for 3D printing of the continuous carbon fiber-reinforced structural parts.
The weight and compliance were investigated during the design process, and it was found that there was a large gap between the initial optimization results and the ones which removed gray scale.
In the future, we will design printing paths based on the geometry, 3D print them and actually test the manufactured structure so as to track the compliance in the whole design and manufacturing process. Another future work is to introduce filtering to binarize the appropriate density to reduce the error of the objective function during the design process.

References

[1] AL ABADI, Haider, et al. Elastic properties of 3D printed fibre-reinforced structures. Composite Structures, 2018, 193: 8-18.
[2] ICHIHARA, Naruki; UEDA, Masahito. 3D-printed high-toughness composite structures by anisotropic topology optimization. Composites Part B: Engineering, 2023, 253: 110572.
[3] CHENG, Ping, et al. 3D printed continuous fiber reinforced composite lightweight structures: A review and outlook. Composites Part B: Engineering, 2023, 250: 110450.
[4] LAZAROV, Boyan Stefanov; SIGMUND, Ole. Filters in topology optimization based on Helmholtz-type differential equations. International journal for numerical methods in engineering, 2011, 86.6: 765-781.
[5] KAWAMOTO, Atsushi, et al. Heaviside projection based topology optimization by a PDE-filtered scalar function. Structural and Multidisciplinary Optimization, 2011, 44: 19-24.
[6] NOMURA, Tsuyoshi, et al. General topology optimization method with continuous and discrete orientation design using isoparametric projection. International Journal for Numerical Methods in Engineering, 2015, 101.8: 571-605.

MICROMECHANICAL CHARACTERIZATION OF FIBRE/MATRIX INTERFACIAL DEBONDING: EFFECTS OF LOADING MODE, TEMPERATURE, AGEING AND FATIGUE

M. Nikforooz[1,2], L. Daelemans [1], K. De Clerck [1], and
W. Van Paepegem [1]

[1]Department of Materials, Textiles and Chemical Engineering (MaTCh), Ghent University, Technologiepark-Zwijnaarde 46/70, B-9052, Zwijnaarde, Belgium

[2]DPI, P.O. Box 902, 5600 AX, Eindhoven, the Netherlands

Keywords: Polymer matrix composites, Mechanical testing, Optical light microscopy, Fibre/matrix interface, Debonding

Abstract
The characteristics of the fibre/matrix interface govern the growth of debonding cracks, which frequently originate from the tips of fibres in short fibre composites. In this regard, off-axis fibres may be exposed to mixed-mode loading, which causes interactive debonding growth in both sliding and opening modes. Polarized light microscopy is a versatile technique to visualize these debonding cracks and their interactions. In this study, single short-fibre specimens were produced by imbedding glass fibres in an epoxy matrix using an innovative manufacturing technique. Utilizing an in-stu micromechanical testing frame, debonding lengths were extracted versus remote stress levels. This method can also be employed in cyclic loading to see the effects of ageing and temperature on debonding progression.

1. Introduction

Since fibre-matrix interface serves an important function in transmitting load from the matrix to the fibre, several studies have been undertaken to investigate its characteristics. Some of the well-known characterization techniques for examining the fibre/matrix interface include the pull-out test [1, 2], the microdroplet test [3, 4], the single fibre fragmentation test [5, 6], the Broutman test [7, 8] and the transverse single fibre test. These tests measure the interfacial shear strength of fibre/matrix interface except the Brutman test and the transverse single fibre test which determine the transverse interfacial strength. Regarding the pull-out test, Nirmal et al. [1] measured the interfacial strength of betelnut fibres in polyester and epoxy matrices using the pull-out test. They examined the effect of different treatment solutions to improve the corresponding interfacial shear strength. Yue et al. [2] evaluated the interfacial shear strength of E-glass/nylon 66 and E-glass/nylon 11 using the single fibre pull-out test and determined the interfacial shear strength, interfacial friction coefficient and matrix shrinkage pressure using this technique. With regard to the microdroplet test, Kang et al. [3] studied the interfacial shear strength of carbon/epoxy using the microdroplet test. They utilized different finite element models of sphere, cylinder and droplet to determine the shear stress distribution at the fibre/matrix interface. Bellil et al. [9] investigated the interfacial shear strength of flax fibres with different polymers using the microdroplet test. They determined the best and worst performing systems as flax/PLA and flax/PP, respectively.

For the transverse single fibre tests, Tandon et al. [10] used different geometries for making transverse fibre specimens including edge-to-edge fibre, short fibre and cruciform specimens. They obtained higher normal interfacial strength values in the cruciform specimens compared to the other geometries. Using cruciform specimens has enabled researchers to examine debonding in the transverse single fiber test

without the problem of specimen edge effects. Foster et al. [11] examined the interfacial strength of steel wire/epoxy using cruciform specimens. They also examined the effect of inter-fibre spacing on the debonding initiation and matrix cavitation using 3D finite element models.
Ogihara and Konayagi [12] employed cruciform specimens with different fibre angles to determine the interfacial shear and normal strength in E-glass/epoxy. They found out that the interfacial shear strength is higher than the interfacial normal strength for this material system. Koyanagi et al. [13] utilized cruciform specimens to determine the effect of temperature on the interfacial strength of glass/epoxy and concluded that this property is independent of testing temperature.

Different techniques can be used to observe the initiation and propagation of debonding cracks such as optical microscopy (OM), scanning electron microscopy (SEM), and transmission electron microscopy (TEM). Optical microscopy has been widely used for examining the debonding initiation and propagation of composites. Scanning electron microscopy has also been utilized to observe the evolution of debonding cracks at specimen edges and surfaces. In this regard, Totten et al. [14] measured the load at the onset of debonding initiation in glass fibre/epoxy composites. They also determined the associated stress state using a 3D finite element model. Bourmaud et al. [15] employed SEM in situ to determine the load at debonding initiation. They captured different failure modes such as void nucleation, debonding and fibre bundle decohesion. Since SEM observation is limited to the specimen surface which is the location of stress singularity, other visualization methods might better represent the damage evolution inside the specimen.
Testing temperature and hydrothermal ageing can affect interfacial bonding in polymer composites. For instance, Thomason and Yang [16] showed that the interfacial shear strength of E-glass/epoxy decreases as testing temperature increases particularly in the glass transition region. They concluded that the interfacial shear strength is affected significantly by compressive residual stresses and static friction between the fibre and matrix. Conversely, Koyanagi and Ogihara [13] studied the effect of temperature on the normal interfacial strength of E-glass/epoxy using cruciform specimens. They concluded that the effect of temperature on the mentioned property is insignificant.
Ageing of fibres and composites can affect debonding evolution. Gaur et al. [17] examined the effect of hydrothermal ageing on the interfacial strength of E-glass, carbon and Kevlar 49 fibres with epoxy as the matrix. They concluded that the interfacial strength of carbon/epoxy is less affected compared to the other material systems. Be et al. [18] investigated the hydrothermal ageing behaviour in E-glass/epoxy composites with different sizing reactivity. They examined the corresponding effect using AFM and DMA.
After reviewing the literature, It was found that most of the research studies on the interface have been focused on the interfacial shear strength of composites. The current paper considers mixed-mode debonding evolution in single fibre E-glass/epoxy composites at different fibre angles, and the effect of ageing and temperature under fatigue loading.

2 Materials and experimental set-up

EPIKOTE™ RIMR 135 and EPIKURE™ RIMH 137 were used as the epoxy resin and its hardener, respectively and mixed at the weight ratio of 10:3. E-glass fibres including StarRov® PR 220 1200 090 from Johns Manville were chopped and compounded with epoxy mixture. The mixture was degassed for 15 min at full vacuum. Short fibre E-glass/epoxy panels with randomly oriented fibres were fabricated. Further details regarding the fabrication process can be found in Refs. [19, 20].

The tensile tests were conducted at a displacement rate of 1 mm/min using an in-house micromechanical tensile stage. A BX51 Olympus microscope was used for the visualization of the fibres and monitoring damages during loading. The setup is shown in Figure 1.

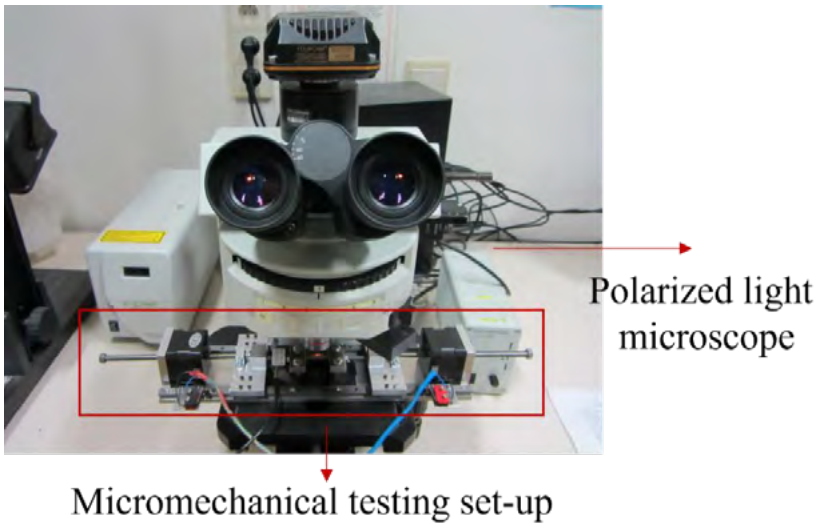


Figure 1. Micromechanical test setup under the polarized light microscope.

The geometry of the specimens and the associated dimensions are indicated in Figure 2 and Table 1, respectively.

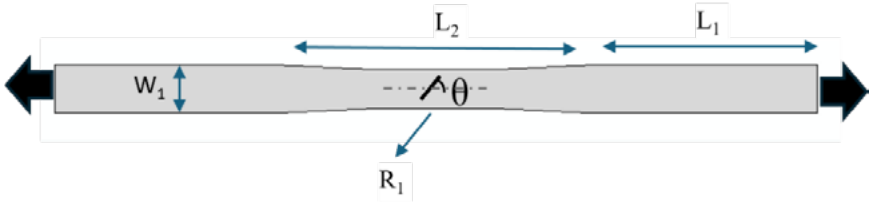


Figure 2. Dog-bone geometry utilized for the micromechanical tensile tests.

Table 1. Dimensions of the dog-bone geometries utilized for short fibre specimens.

Parameter	Value (mm)
L_1	10
L_2	30
R_1	200
W_1	4
W_2	2.9
Thickness	0.18

3. Mechanical testing results and discussion

As the load is applied to the specimen, voids are nucleated at the tips of fibres. Following the void nucleation, debonding cracks are initiated and propagate from the fibre tips and the debonding lengths can be recorded versus remote stress levels. As seen in the figure, the debonding crack is not symmetric relative to the fibre axis and is not cylindrical compared to the debonding cracks in the horizontal fibres in the single fibre fragmentation tests [5].

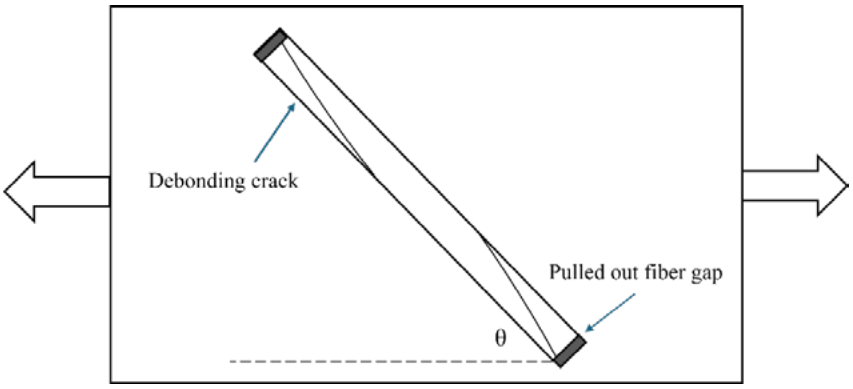


Figure 3. Schematic of debonding growth in an off-axis E-glass/epoxy specimen.

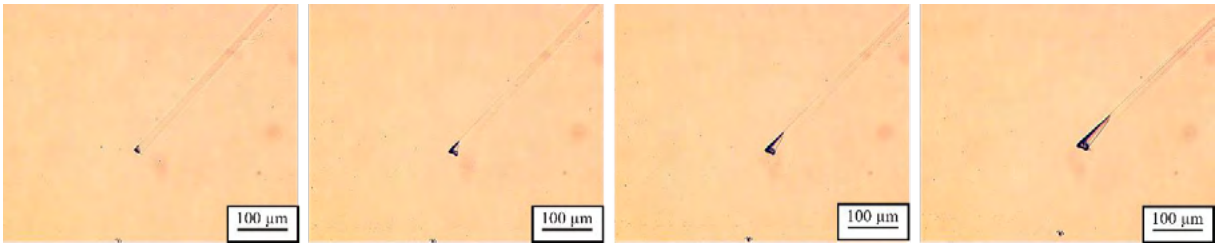


Figure 4. Successive progression of debonding at different remote stress levels for a 45° E-glass/epoxy specimen.

Data on debonding length can be extracted for different remote stress levels. For instance, the plots of debonding lengths versus remote stress levels are shown for (90° and 45°) E-glass/epoxy in Figure 5 and Figure 6. Accordingly, the maximum debonding length is less than 100 µm for the two fibre angles. Meanwhile, the remote stress at void nucleation for the 45° E-glass/epoxy specimens is 44.13 ± 4.01 MPa.

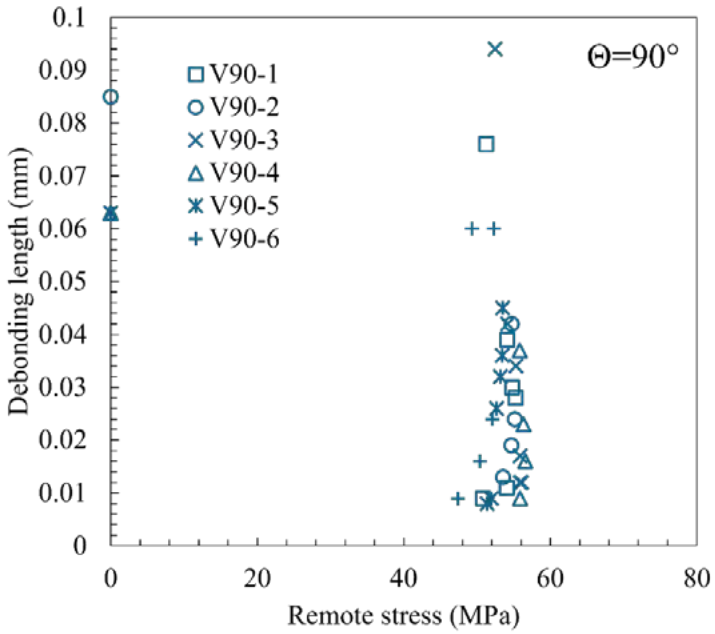


Figure 5. Debonding length versus remote stress for 90° E-glass/epoxy.

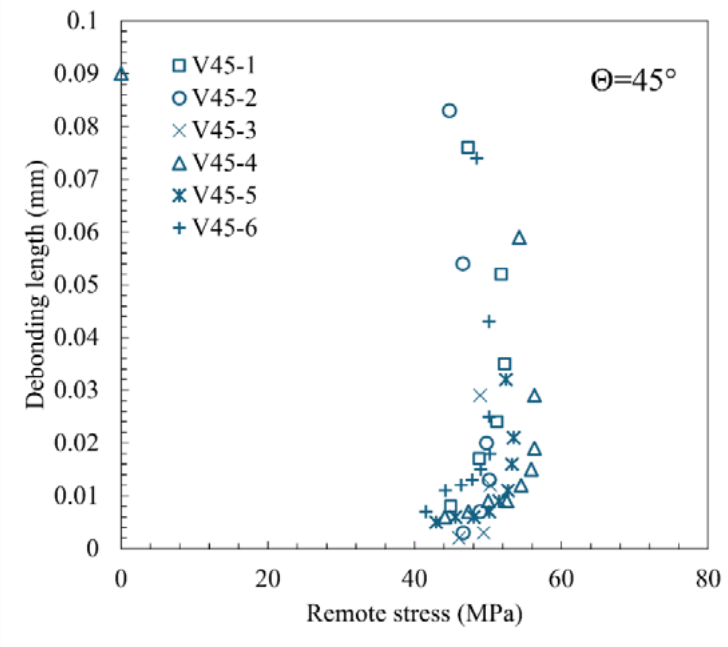


Figure 6. Debonding length versus remote stress for 45° E-glass(090)/epoxy.

For the 0° E-glass/epoxy, debonding cracks are self-similar and symmetrical since the evolution of the cracks occurs in pure shear as seen in Fig. 7 and 8. Pull-out in these specimens is more clear compared to the off-axis fibre specimens.

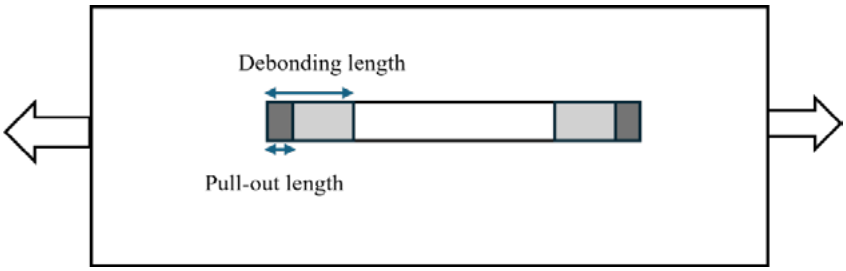


Figure 7. Schematic of debonding growth in a 0° E-glass/epoxy specimen.

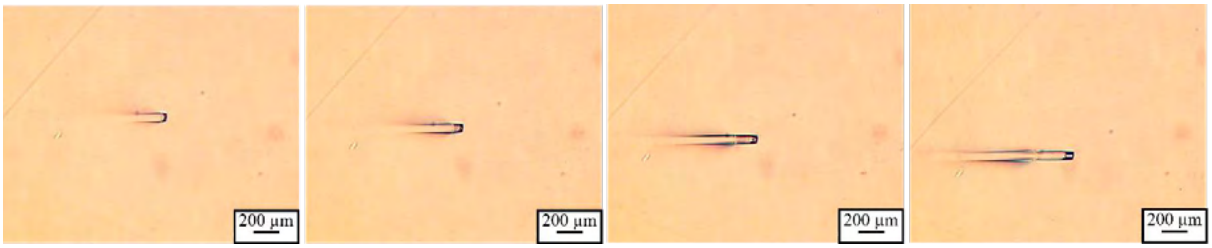


Figure 8. Successive progression of debonding at different remote stress levels for a 0° E-glass/epoxy specimen.

Debonding lengths versus remote stress levels are shown for 0° E-glass/epoxy specimens in Fig. 9. The primary observation in Figs. 5, 6, and 9 is that there are two stages corresponding to the debonding growth: stable and unstable progressions. Debonding growth is relatively slow in the stable phase yet fast in the unstable phase.

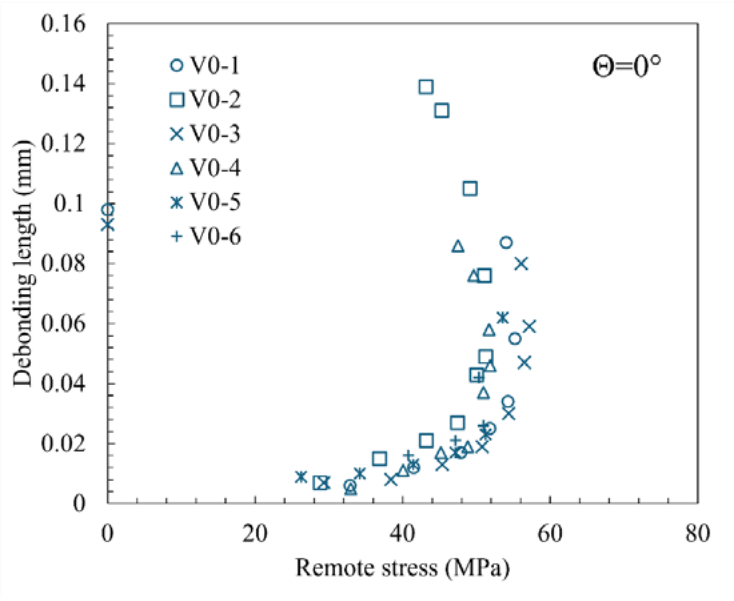


Figure 9. Debonding length versus remote stress for 0° E-glass(090)/epoxy.

Cyclic loading can be utilized to see the effects of fibre ageing on the debonding progression at low stress levels. The progression of debonding cracks at different number of cycles can be clearly seen for virgin (V) and four-week aged fibres (A) in Figure 10(a). An analogous comparison can be performed between 45° virgin E-glass/epoxy at room temperature and 50 °C in Figure 10(b). The difference between the debonding lengths at the two conditions can be readily seen in this Figure.

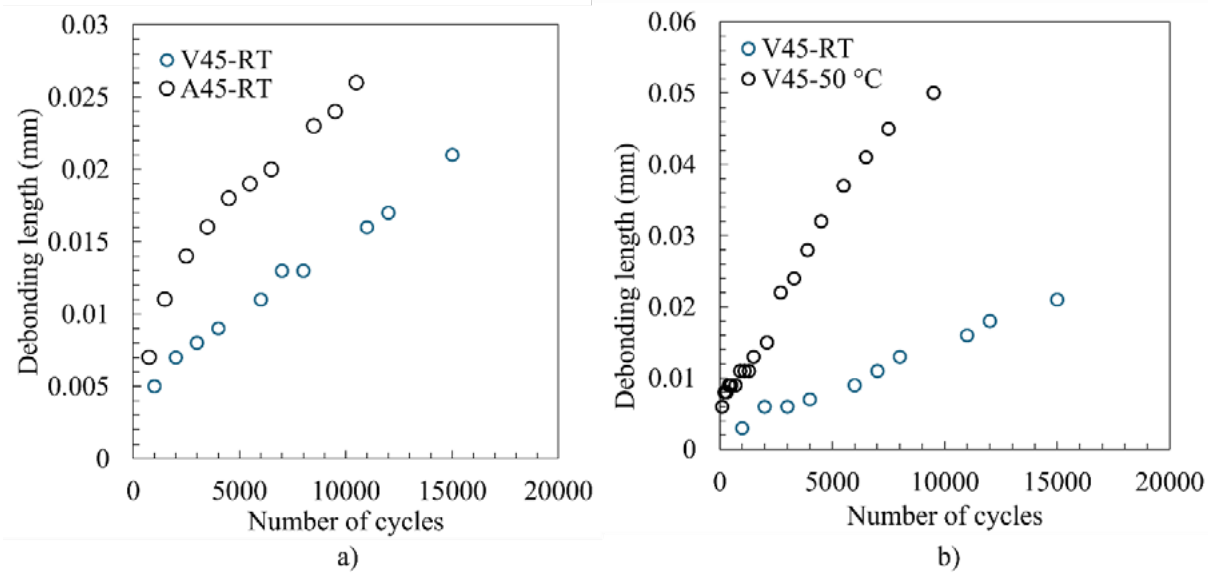


Figure 10. Debonding length versus number of cycles for a) 45° virgin and four-week aged E-glass/epoxy b) 45° virgin E-glass/epoxy at room temperature and 50 °C.

4. Conclusion

Single short fibre E-glass/epoxy specimens were fabricated and loaded under tension using a micromechanical testing setup. Debonding cracks were visualized in real-time using a polarized light microscope. Debonding lengths versus remote stress levels were extracted for 0°, 45° and 90° fibre angles. These debonding lengths can be further utilized by a numerical model to extract the corresponding interfacial strengths and fracture toughness values. This method was also used in cyclic loading to see the effects of ageing and temperature on debonding progression.

Acknowledgments
The work of M. Nikforooz forms part of the research program of DPI, project 812 T17. The authors also acknowledge the financial support of the Energy Transition Fund through the North-C-Blade project and the BOF-project BOF/24J/2023/006 “Development of advanced micro-mechanical test methods for fibre reinforced polymer composites based on in-situ optical and electron microscopy”.

References
[1] U. Nirmal, N. Singh, J. Hashim, S. T. W. Lau, N. Jamil, On the effect of different polymer matrix and fibre treatment on single fibre pullout test using betelnut fibres. *Materials & Design*, 32(5):2717-2726, 2011.
[2] C. Yue, H. Looi, M. Quek, Assessment of fibre-matrix adhesion and interfacial properties using the pull-out test. *International Journal of Adhesion and Adhesives*, 15(2):73-80, 1995.
[3] S. Kang, D. Lee, N. Choi, Fiber/epoxy interfacial shear strength measured by the microdroplet test. *Composites Science and Technology*, 69(2):245-251, 2009.
[4] L. Zhenkun, W. Quan, K. Yilan, Q. Wei, P. Xuemin, Stress transfer in microdroplet tensile test: PVC-coated and uncoated Kevlar-29 single fiber. *Optics and Lasers in Engineering*, 48(11):1089-1095, 2010.
[5] F. A. Ramirez, L. A. Carlsson, B. A. Acha, A method to measure fracture toughness of the fiber/matrix interface using the single-fiber fragmentation test. *Composites Part A: Applied Science and Manufacturing*, 40(6-7):679-686, 2009.
[6] J. Varna, R. Joffe, L. A. Berglund, Interfacial toughness evaluation from the single-fiber fragmentation test. *Composites science and technology*, 56(9):1105-1109, 1996.
[7] C. Ageorges, K. Friedrich, T. Schüller, B. Lauke, Single-fibre Broutman test: fibre–matrix interface transverse debonding. *Composites Part A: Applied Science and Manufacturing*, 30(12):1423-1434, 1999.
[8] T. Schüller, W. Beckert, B. Lauke, C. Ageorges, K. Friedrich, Single fibre transverse debonding: stress analysis of the Broutman test. *Composites Part A: Applied Science and Manufacturing*, 31(7):661-670, 2000.
[9] S. Bellil, D. Pantaloni, D. U. Shah, A. L. Duigou, C. Baley, J. Beaugrand, A. Bourmaud, S. Guessasma, Prediction of interfacial behaviour of single flax fibre bonded to various matrices by simulation of microdroplet test. *Composites Part C: Open Access*, 11, 2023.
[10] G. P. Tandon, R. Y. Kim, S. G. Warrier, B. S. Majumdar, Influence of free edge and corner singularities on interfacial normal strength: application in model unidirectional composites. *Composites Part B: Engineering*, 30(2):115-134, 1999.
[11] D. C. Foster, G. P. Tandon, M. Zoghi, Evaluation of Failure Behavior of Transversely Loaded Unidirectional Model Composites. *Experimental Mechanics*, 46(2):217-243, 2006.
[12] S. Ogihara, J. Koyanagi, Investigation of combined stress state failure criterion for glass fiber/epoxy interface by the cruciform specimen method. *Composites Science and Technology*, 70(1):143-150, 2010.

[13] J. Koyanagi, S. Ogihara, Temperature dependence of glass fiber/epoxy interface normal strength examined by a cruciform specimen method. *Composites Part B: Engineering*, 42(6):1492-1496, 2011.
[14] K. R. Totten, B. Kutub, L. A. Carlsson, In situ determination of the fiber–matrix interface tensile strength *Journal of Composite Materials*, 50(5):589-599.
[15] A. Bourmaud, G. Ausias, G. Lebrun, M. L. Tachon, C. Baley, Observation of the structure of a composite polypropylene/flax and damage mechanisms under stress. *Industrial Crops and Products*, 43:225-236, 2013.
[16] J. L. Thomason, L. Yang, Temperature dependence of the interfacial shear strength in glass–fibre epoxy composites. *Composites Science and Technology*, 96:7-12, 2014.
[17] U. Gaur, C. T. Chou, B. Miller, Effect of hydrothermal ageing on bond strength. *Composites*, 25(7):609-612, 1994.
[18] S. A. Otogo Be, L. Belec, A. Fahs, I. Martin, G. Louarn, J.-F. Chailan, Impact of the sizing reactivity of glass fibers on composites hydrothermal aging. *Polymer Degradation and Stability*, 215, 2023.
[19] M. Nikforooz, O. Verschatse, L. Daelemans, K. De Clerck, W. Van Paepegem, Experimental method for in-situ real-time measurement of mixed mode fibre/matrix interface debonding and comparison of fibre sizings in single short fibre composites. *Composites Science and Technology*, 249, 2024.
[20] M. Nikforooz, O. Verschatse, L. Daelemans, K. De Clerck, W. Van Paepegem, Mixed experimental-numerical method for quantitative measurement of mode II fibre/matrix interface debonding and comparison of fibre sizings in single short fibre composites. *Polymer Testing*:108435, 2024.

THE INFLUENCE OF THE MANUFACTURING PROCESS ON THE DURABILITY OF HIGH IMPACT POLYSTYRENE PARTS MANUFACTURED VIA ADDITIVE MANUFACTURING AND INJECTION MOULDING

Floriane Verceux, Sotirios Grammatikos

ASEMlab – Laboratory of Advanced & Sustainable Engineering Materials, Dept. of Manufacturing & Civil Engineering, NTNU- Norwegian University of Science & Technology, Gjøvik, Norway
Email: floriane.verceux@ntnu.no, grammatikos@outlook.com

Keywords: Recycling, High-Impact Polystyrene, Injection moulding, Additive Manufacturing, Durability, Accelerated aging, Freeze-thaw cyclic aging, Mechanical and Physico-chemical properties

Abstract
Depending on their use, thermoplastic polymers can be processed using different methods, including Additive Manufacturing (AM) and Injection Moulding (IM). This study aims to investigate the impact of the manufacturing process on the behaviour of High-Impact Polystyrene (HIPS) material during service life, simulated via accelerated aging. HIPS is commonly used in different home appliances, such as inner liner in refrigerators. In this work, HIPS coupons were produced by AM and IM, resulting in coupons with different internal structure. To reproduce the real service environment, and by that be able to assess durability, freeze-thaw cyclic aging was adopted. The effects of freeze-thaw aging on the mechanical, physical, and chemical performance of the HIPS material, were assessed by means of tensile testing, assessing the mechanical properties evolution during accelerated aging. To study the evolution of coupon internal structure as a function of aging, a total of 384 freeze-thaw cycles, between -20°C and 50°C were employed, assessing the properties of the material after 3, 6, 12, 24, 48, 96 and 192 days, time intervals. A link between physical, mechanical and chemical properties evolution was developed, in an attempt to develop an understanding of the material's degradation in time and of the effects of the processing method on the durability and long-term performance.

1 Introduction

Plastic production in Europe constantly increases, supported by the evolving needs of consumers and industries. 53,9MT of plastics were produced in 2020, while 57,2MT of plastics were produced in 2021, accompanied by a stagnation of the amount of post-consumer recycled plastics used, close to 10% of the total produced plastic. In 2021, the majority of the plastics produced were used for packaging applications, representing 39,1% of the produced plastics, while the fourth biggest consumption of plastics goes to the industry of electrical and electronics, representing 6,5% of the total produced plastics [1]. Among this 6,5% representing 3,72MT of plastic used for electrical and electronics applications, it was observed that High Impact Polystyrene (HIPS) is the second most used polymer behind ABS, representing 26% of all the polymers found to be used in these applications [2]. The second most used process for plastic manufacturing in any application combined and the first most used in the field of electrical and electronics application is IM, one of the most important processes for mass-production of thermoplastic parts [3-5]. However, traditional manufacturing processes for plastics nowadays give space to AM, a process emerging in different industries for both large and small scale series production. AM is perceived as an emerging manufacturing process with great potential to limit the environmental impact of plastic objects manufacturing, by decreasing the amount of waste and energy consumption [6-8]. This paper focuses on material extrusion Fused Filament Fabrication (FFF) AM. When comparing samples produced in AM or in IM, different properties are obtained after production, in relation to the difference in the parameters used as well as the process itself. For example, F. L. Garcia et al. compared the mechanical properties of Acrylonitrile Butadiene Styrene samples produced by IM and by AM, and found that for an AM sample produced with 100% infill density and 45° printing orientation, the tensile strength and strain were recorded to be 19% higher, for the case of IM samples [6], which render IM samples more resistant to external mechanical loads. In another study comparing AM and IM of

PolyLactic Acid (PLA) material, Acrylonitrile Butadiene Styrene (ABS) and Nylon 6 (PA 6), M. Lay et al. highlighted the lower mechanical properties of AM samples for the three polymers, in comparison to IM produced ones. The tensile strength values were found to be 48, 34 and 37% lower for printed PLA, ABS and Nylon 6, in comparison to the same material produced by IM. This was, according to the authors, attributed to the presence of voids in AM samples observed by Scanning Electron Microscopy (SEM) and through density measurements, but also to the benefit of the injection pressure present during the IM process creating excellent entanglement of the polymers chain and thus ultimately increasing the mechanical performance of the IM samples compared to AM ones [9, 10]. Numerous studies have been reported comparing AM and IM and their impact on the material's properties, as well as studies optimizing AM process parameters to improve the properties of the final produced part. However, no studies have been dedicated to evaluate the impact of the manufacturing process on the sample behaviour throughout its lifetime, by means of accelerated aging.

In this work, we focus on HIPS, and more particularly on HIPS used for refrigerator applications (electronics). As such, freeze-thaw accelerated aging cycles were used to simulate, compare and understand the degradation mechanisms of HIPS produced by AM vs. IM. To understand the impact of the manufacturing process on the polymers' long-term properties, aged coupons were tested in terms of physical, mechanical and chemical properties. Herein, we present preliminary tensile test results of coupons cyclically aged between -20°C and 50°C, for 3, 6, 12, 24, 48, 96 and 192 days intervals. The results presented are preliminary results in the framework of PRecycling Horizon Europe project, aiming to suggest a mechanism of degradation of HIPS material when subjected to different aging conditions.

2 Methodology and materials

2.1 Materials

This work was deployed on recycled HIPS material (rHIPS) supplied by Coolrec, Netherlands, and processed with AM by BIOG3D, Greece and with IM by R-NANO lab, National Technical University of Athens, Greece. For the needs of the study, tensile coupons were manufactured using AM and IM, according to the ISO 527. The AM samples were produced with a 0° orientation, a bed temperature of 60°C, a nozzle temperature of 240°C and a printing speed of 30mm/s. The IM samples were produced with a barrel temperature of 210°C and residence time in the barrel of 10 min to ensure the homogeneous melting of the pellets and a mould temperature of 60°C. The different pressures used at different steps of the process were between 10 and 12 bars.

2.2 Accelerated aging protocol

To simulate real use, freeze-thaw cyclic aging was performed using a Freeze-Thaw Chamber (LIB Industry, China) through repeated cycles, with one cycle corresponding to 6h of exposure to -30°C followed by 6h of exposure at 50°C. Figure 1 illustrates the freeze-thaw cycles performed. All coupons were subjected to freeze-thaw cycles for 3, 6, 12, 24, 48 and 96 days, corresponding to a total of 6, 12, 24, 48 and 192 cycles, respectively.

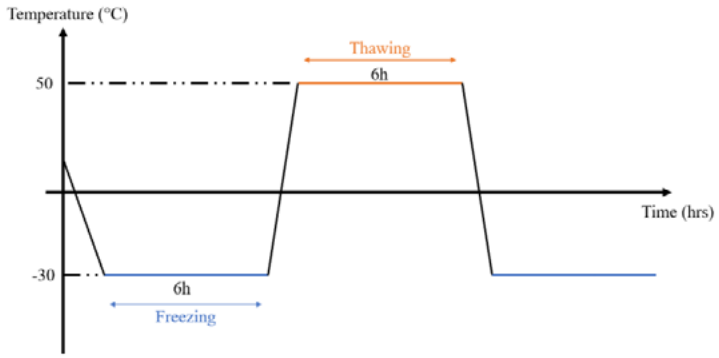


Figure 1. Freeze-thaw cyclic programme

2.3 Material characterisation

After freeze-thaw exposure, coupon's degradation was assessed through the tensile mechanical properties evolution. In specific, preliminary results of the mechanical properties evolution as a function of the aging time are reported, presented changes in Young's modulus evolution and Strain at break values. Uniaxial tensile was performed on coupons following the ISO 527-2 using an Instron 5966 (Instron, Norwood, USA) at a 5mm/min loading rate. An AVE2 video-extensometer was used to measure the mechanical strain. The tensile modulus was determined by analyzing the force-displacement curves. The behaviour of the material was assessed by examining changes in its stiffness (Young's modulus, E) and strain at break.

3 Results and discussion

Preliminary tensile test results are presented as properties retention vs. the number of Freeze-Thaw Cycles (FTC). The average tensile property values obtained for IM and AM samples are presented in Table 1.

Table 2. Average Young's modulus and strain at break for IM and AM samples during FTC

FTC	Injection molding				Additive manufacturing			
	Young's modulus (Gpa)	Standard deviation (Gpa)	Strain at break (mm/mm)	Standard deviation (mm/mm)	Young's modulus (Gpa)	Standard deviation (Gpa)	Strain at break (mm/mm)	Standard deviation (mm/mm)
0	1.736	0.090	0.260	0.026	1.532	0.532	0.064	0.027
12	1.875	0.057	0.259	0.078	1.758	0.131	0.041	0.031
24	2.105	0.516	0.121	0.023	2.600	0.122	0.037	0.013
48	1.958	0.036	0.278	0.092	1.729	0.165	0.027	0.002
96	1.680	0.066	0.255	0.057	1.717	0.219	0.026	0.007
192	1.578	0.037	0.297	0.031	1.535	0.057	0.030	0.005

The results of the mechanical properties presented in Figure 2 show a strong increase in the Young's modulus until 24 FTCs. This stiffness increase is more pronounced for the AM samples than for the IM samples. This can be attributed to a possible crosslinking from radical formation in link to the polymer's oxidation, or a chain relaxation phenomenon resulting in an increase in the crystallinity and embrittlement of the material [11, 12]. It is likely that the HIPS material contains a polybutadiene phase, of which the double bonds are likely to be subjected to oxidation during degradation and this form radicals. However, the stiffness of the material decreases for both AM and IM samples after 24 FTCs, stabilizing around a value close to that of the unaged material. This can be attributed to the polymer chain scission phenomenon occurring through oxidation throughout the degradation process [11-14].

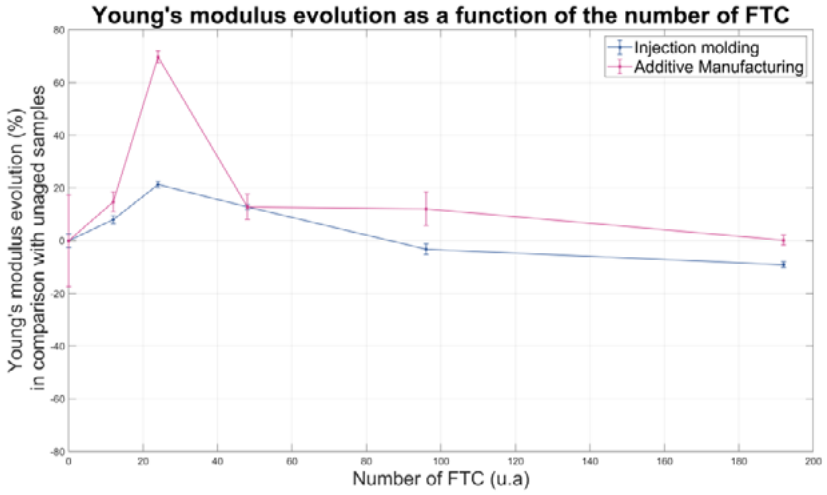


Figure 2. Young's modulus evolution as a function of the number of FTC

In the context of IM samples, the second hypothesis linked to possible chain scission is confirmed by the strain at break values evolution, shown in Figure 3, where the increase in the Young's modulus until 24 FTCs is happening simultaneously with a decrease in the values of strain at break. In this precise case, the chain scission phenomenon occurring with oxidation and radical formation can be observed through the decrease in the strain at break. Later, the decrease in the values of Young's modulus between 24 and 48 FTCs is simultaneous with an increase in the values of strain at break, even if both properties' evolutions are not proportional. The strong increase in the values of strain at break cannot be attributed to a crosslinking reaction, as this increase corresponds to a decrease in the values of Young's modulus. However, other internal structural re-organizations may occur simultaneously. In the case of AM samples, an exponential decrease in the values of strain at break is observed throughout the degradation process highlighting a different impact of FTC aging from this AM process compared to the IM process. The overall decrease in the values of strain at break can for AM samples be attributed to the chain scission phenomenon occurring during the degradation process.

The aging in its globality showcases a more significant and negative impact on the values of strain at break of AM samples than IM samples. The manufacturing process is therefore affecting largely the mechanism of degradation as well as its kinetic and degree.

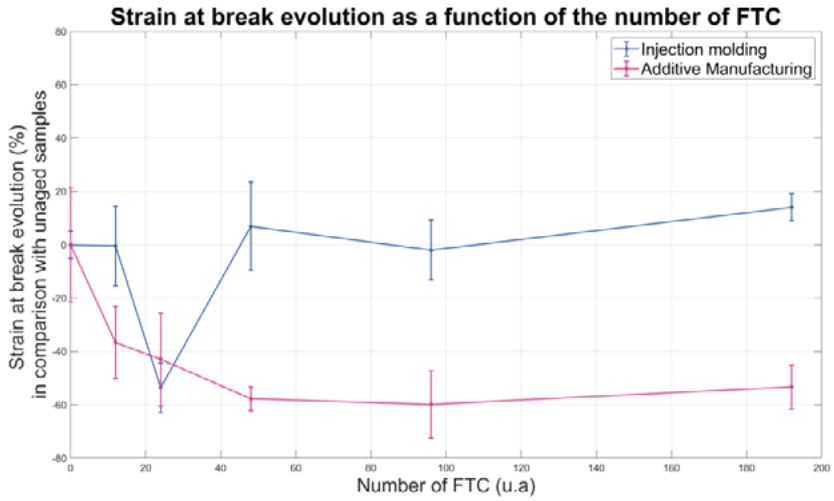


Figure 3. Strain at break evolution as a function of the number of FTC

4 Conclusion

This work focused on the understanding of the impact of the manufacturing process on the durability of additively manufactured and injected moulded recycled HIPS samples. Freeze-thaw aging was used to simulate the real environment and conditions to which HIPS materials are used in white good applications. Preliminary results were shown, presenting the evolution of Young's modulus and strain at break values after FTC aging, highlighting the negative impact of the AM process vs. IM, on the durability of the tested material. An evolution in the Young's modulus values corresponding to an opposite evolution in the strain at break values was observed for both AM and IM samples, highlighting a possible crosslinking followed by a chain scission mechanism. In conclusion, preliminary results on the impact of the manufacturing process on the long term properties of HIPS material were presented, while the degradation mechanism will be further investigated through physico-chemical testing.

Acknowledgments

The authors acknowledge the company Coolrec for the recycled HIPS supply, the National Technical University of Athens (NTUA) for the manufacturing of the IM samples and the company BIOG3D for the manufacturing of the AM samples. This study was part of the PRecycling project funded from the European Union's Horizon Europe research and innovation program under grant agreement No 101058670.

References

1. Europe, P., *Plastics - The facts 2022*, P. Europe, Editor. 2022.
2. Maris, E., et al., *Characterizing plastics originating from WEEE: A case study in France.* Minerals Engineering, 2015. **76**: p. 28-37.
3. Europe, P.R., *Plastic recycling Industry figures 2022*. 2022: https://www.plasticsrecyclers.eu/publications/
4. Kanishka, K. and B. Acherjee, *Revolutionizing manufacturing: A comprehensive overview of additive manufacturing processes, materials, developments, and challenges.* Journal of Manufacturing Processes, 2023. **107**: p. 574-619.
5. Rosato, M. and D. Rosato, *In Injection Molding Handbook*. 2000.
6. Garcia, F.L., et al., *Comparative LCA of conventional manufacturing vs. additive manufacturing: the case of injection moulding for recycled polymers.* International Journal of Sustainable Engineering, 2021. **14**(6): p. 1604-1622.
7. Laverne, F., et al., *Improving resources consumption of additive manufacturing use during early design stages: a case study.* International Journal of Sustainable Engineering, 2019. **12**(6): p. 365-375.
8. Böckin, D. and A.-M. Tillman, *Environmental assessment of additive manufacturing in the automotive industry.* Journal of Cleaner Production, 2019. **226**: p. 977-987.
9. Lay, M., et al., *Comparison of physical and mechanical properties of PLA, ABS and nylon 6 fabricated using fused deposition modeling and injection molding.* Composites Part B: Engineering, 2019. **176**: p. 107341.
10. Weng, Z., et al., *Mechanical and thermal properties of ABS/montmorillonite nanocomposites for fused deposition modeling 3D printing.* Materials & Design, 2016. **102**: p. 276-283.
11. Luzuriaga, S., J. Kovářová, and I. Fortelný, *Degradation of pre-aged polymers exposed to simulated recycling: Properties and thermal stability.* Polymer Degradation and Stability, 2006. **91**(6): p. 1226-1232.
12. Verdu, J., *Effect of Aging on the Mechanical Properties of Polymeric Materials.* Journal of Macromolecular Science, Part A, 1994. **31**(10): p. 1383-1398.
13. Vilaplana, F., A. Ribes-Greus, and S. Karlsson, *Degradation of recycled high-impact polystyrene. Simulation by reprocessing and thermo-oxidation.* Polymer Degradation and Stability, 2006. **91**(9): p. 2163-2170.
14. Cameron, G.G. and G.P. Kerr, *Thermal degradation of polystyrene—I. Chain scission at low temperatures.* European Polymer Journal, 1968. **4**(6): p. 709-717.

TOWARDS HIGHLY HOMOGENEOUS SELF-REGULATING HEATING OF SMART NANOCOMPOSITES

Yushen Wang[1], Bijoy Das[1], Thomas D. S. Thorn[1], Yi Liu[2], Suresh G. Advani[3], Dimitrios G. Papageorgiou[1], Emiliano Bilotti[4], Han Zhang[1]

[1]School of Engineering and Materials Science, Queen Mary University of London, London, UK
[2] Department of Materials, Loughborough University, Loughborough, UK
[3] Department of Mechanical Engineering, University of Delaware, Newark, US
Corresponding author: han.zhang@qmul.ac.uk

Keywords: Positive temperature coefficient (PTC), Conductive polymer nanocomposites (CPCs), Contact resistivity, Thermal management, Resistive heating.

Abstract
Smart self-regulating heating devices utilizing the positive temperature coefficient (PTC) effect have shown great potential in advancing applications across healthcare, soft robotics, and energy-efficient manufacturing. However, achieving homogeneous resistive heating within such temperature self-controllable nanocomposites remains a significant challenge. This study explores and evaluates multiple innovative strategies to enhance the temperature uniformity of PTC nanocomposites. By identifying the primary physical mechanisms behind the inhomogeneous heating observed in conductive polymer composites, we have proposed and evaluated a series of strategies, with an improved temperature uniformity (from 32.6 to 2.7 % variation at 125 °C), providing valuable insights for the design and development of advanced self-regulating heating devices based on conductive polymer nanocomposites.

1. Introduction

The PTC effect in CPCs describes the increase in electrical resistance of conductive nanocomposite upon increased temperature [1]. When utilizing CPC for Joule heating, the passage of electrons through the material generates heat, causing the temperature of the material to increase. As the temperature increases, the material's electrical resistivity also increases due to the mismatched thermal expansion between the polymer matrix and conductive fillers [2], limiting the current flow and reducing the heat generation, hence causing the material to self-regulate its temperature. The temperature of self-regulation is usually determined by the matrix polymer's melting or softening point [1, 3]. The PTC effect in CPCs has been extensively studied for its potential applications in a wide range of industries, including electronics and heating systems, taking advantage of using PTC-CPCs for self-regulating heating and providing precise temperature control in addition to an energy-efficient and cost-effective solution for heating systems [2].

However, a few challenges remain in such self-regulating heating materials that may affect their wider adoption and utilization. One of the most important problems is the temperature uniformity of the self-regulating heating devices. According to the PTC mechanism [1], a conductive filler loading near the percolation threshold can provide the highest PTC intensity, as the number of contact points between the conductive nanofiller particles is relatively low rather than homogeneously distributed throughout the matrix. This results in a non-uniform heat generation, where the heat will be generated mainly along the connected network pathways followed by heat dissipation to other areas. An ideal combination of the filler size and dispersion for homogeneous heating throughout the specimens is often difficult to achieve in practice [3, 4], especially for self-regulating heating films without any high thermal conductivity substrate to homogenize the temperature.

This study addresses the critical issue of temperature non-uniformity that often occurs at the self-regulating heating stage, which is of great importance for practical applications when using such novel materials. Two fundamental interconnected physical mechanisms causing inhomogeneous heating in CPC, namely the mismatch in heat dissipation between the edges and the central areas, and the mismatch in resistivity within the nanocomposites, have been identified and discussed, with a range of strategies proposed and evaluated to address these two challenges towards homogeneous heating of self-regulating heating nanocomposites. By tailoring the materials formulations and utilizing distinct electrode layouts and configurations, an enhanced heating homogeneity with a significantly reduced temperature variation across the heating film can be achieved at the self-regulating heating stage. A systematic analysis and comparison have been performed for all strategies, to provide insightful knowledge and perspectives to design and develop novel self-regulating heating devices based on conductive nanocomposites.

2. Experimental

2.1. Materials

Graphene nanoplatelets from XG Science (GNP, Grade M25) and a relatively high aspect ratio carbon nanotube (CNT) from Nanocyl (NC7000) were used as conductive nanoparticles. Boron nitride (BN) powder with an average particle size of ~1 μm and a purity of 98% from Merck Life Science UK Limited was used as received for thermal conductivity enhancement. The polymer matrix chosen for this research was high-density polyethylene (HDPE) (INEOS, RIGIDEX HD5218EA). Aluminium foil with a thickness of 0.1 mm was used as a 2nd thermal conductive layer in certain strategies. Copper wire with a diameter of 0.15 mm, copper mesh with a wire dimension of 0.056 mm, and recycled carbon fiber veil (Technical Fibre Products Ltd.) were used as electrodes embedded in the nanocomposites.

2.2. Preparation of self-regulating heating film

The nanocomposites were melt-compounded in a Micro Compounder (Xplore MC 15 HT) using a screw speed of 50 rpm at 200 °C with desired filler concentrations as detailed in **Table 1**. The melt-compounded nanocomposite pellets were then compression moulded (Dr Collin GmbH, Presse P300E) at 200 °C with 60 bar to obtain a rectangular shape with a lateral dimension of 100×100×0.15 mm^3. Electrodes were embedded through a 2nd compression moulding with final dimensions in **Figure 1**.

Table 1 Filler concentration and resistivity at room temperature of nanocomposites in each strategy.

No.	Film Strategy	PTC nanocomposites	Resistivity (Ω·m)		Secondary materials	Resistivity (Ω·m)	
			20 °C	120 °C		20 °C	120 °C
Ch1	Challenges	24 wt.% GNP/HDPE	1.47	3.3×10^2	-	-	
Ch2		18 wt.% GNP/HDPE	1.5×10^2	1.5×10^5	-	-	
1	Introducing ZTC materials	30 wt.% GNP/HDPE	0.97	20.2	1.5 wt.% CNT/HDPE	1.84	2.74
2		24 wt.% GNP/HDPE	1.47	3.3×10^2	1.5 wt.% CNT/HDPE	1.84	2.74
3	Increased thickness	24 wt.% GNP/HDPE	1.47	3.3×10^2	-	-	
4	Additional layer	18 wt.% GNP/HDPE	1.5×10^2	1.5×10^5	0.1 mm Al foil	-	
5	Sandwich electrodes	17.1 wt.% GNP/5 wt.% BN/HDPE	2.2×10^2	Not measurable	Cu mesh electrodes	-	
6		17.1 wt.% GNP/5 wt.% BN/HDPE	2.2×10^2	Not measurable	rCF veil electrodes	-	

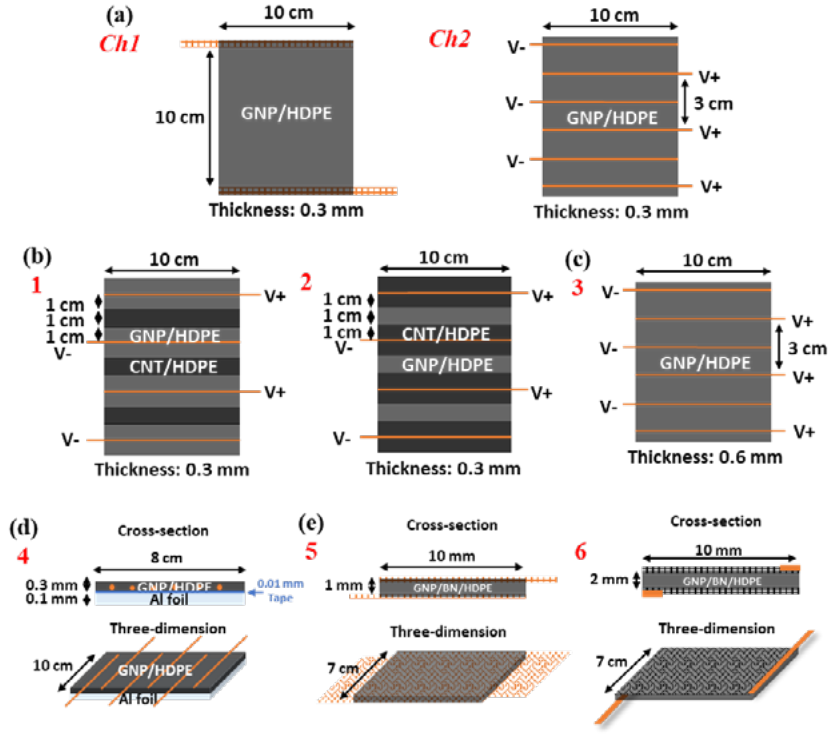


Figure 1 Designs and dimensions of self-regulating heating nanocomposites: (a) Challenge 1&2; (b) Strategy 1-2 with ZTC sections; (c) Strategy 3 with increased thickness; (d) Strategy 4 with additional thermally conductive layer; and (e) Strategy 5-6 with sandwich electrode structures.

2.3. Characterization and Measurements

The electrical conductivity of CPCs and contact resistance at electrodes were measured by a two-point method consisting of a voltage power source (Agilent 6614C) and a picometer (Keithley 6485). The electric current value was measured under an applied voltage range of 0-20 V with a step of 0.5 V. The resistance was then calculated from the I-V curve obtained.

The pyroresistive behavior (temperature-dependent resistance) of nanocomposites was characterized by measuring the electrical resistance of the specimen via a two-probe method inside a convection oven. The electrical resistance of the specimen with dimensions 25 × 5 × 1 mm^3, was measured using a digital multimeter (Agilent 34410 A) and simultaneously recorded by a custom-built LabView program, while the temperature was recorded by a data logger (Pico Technology TC-08).

The Joule heating behavior of the nanocomposites was measured by applying a direct voltage (Fisherbrand PowerPro 300) to the sample with a data logger (Pico Technology TC-08) to record temperature data. A layer of calcium-magnesium silicate thermal insulation wool (Calcium Magnesium Silicate, RS Components, thickness of 38 mm) was placed on the top and bottom of the film. A thermal infrared camera (FLIR, TG165-X) was used to capture thermal images of uncovered CPC.

3. Challenges and Approaches

To achieve a homogeneous Joule heating of conductive polymer nanocomposite films, two interconnected key aspects need to be considered with equal importance: (i) uneven thermal dissipation within the specimen, where the heat preservation area (often the center) reaches the switching temperature first, therefore, leading to a further uneven resistivity; (ii) resistivity distribution among the

specimen, especially at or near the interface between electrodes and conductive polymer composites, which could affect the Joule heating performance at various locations of the film. This is of particular importance for conductive polymer nanocomposites with PTC effect, where sequential heating from the first triggering area can significantly affect the local resistance hence the electric current that goes through other areas, resulting in inhomogeneous heating across the film.

Many heating devices would have electrodes positioned at both ends to maximize the heating areas and materials used (as shown in **Figure 2**a). However, as the heat loss at the edge is normally more pronounced than the central areas of the heating materials, a "hot line" can often be observed near the center of the CPC film (as shown in the IR image in **Figure 2**a). Consequently, the temperature of the hot line would reach the melting point first, resulting in a higher resistivity than other areas during the Joule heating process due to the PTC effect [3], hence further affecting the temperature uniformity of the nanocomposites with reduced heating close to the edges. This uneven heating would be further magnified when the heating devices are scaled up.

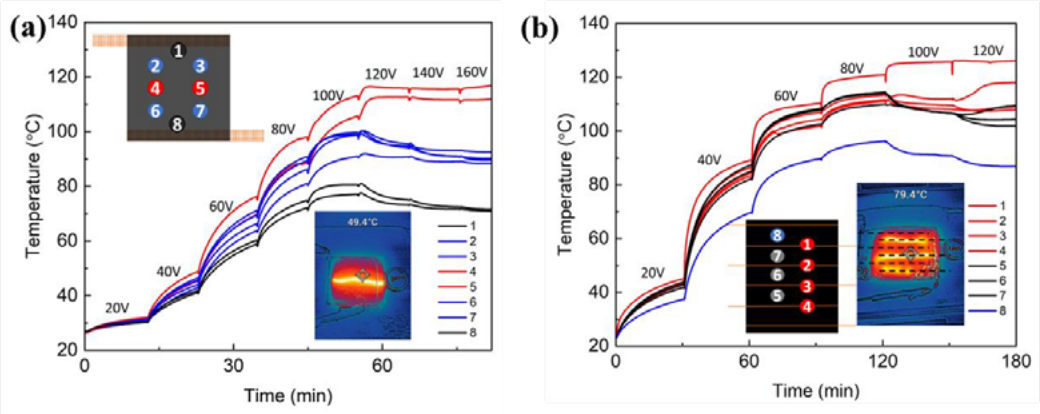


Figure 2: Two main challenges causing the non-uniform heating in GNP/HDPE film: (a) two electrodes with a middle "hot line" resulting from a rapid heat loss at the edges and (b) multiple parallel electrodes with a heat accumulation near copper wire electrodes due to the contact resistance.

With multiple electrodes embedded in the nanocomposite film with reduced distance between electrodes (**Figure 2**b insert), an improved temperature uniformity has been achieved compared to the single pair of end electrodes. However, a clear temperature difference between the maximum and minimum points remains, with multiple hot lines appearing in the IR image. As shown in **Figure 2**b, the temperature of four thermal couples on the copper wire electrodes (red lines of points 1-4) was higher than that of areas between electrodes (black lines of points 5-7), which resulted from the contact resistance between nanocomposites and copper wire electrodes, whereas the lowest temperature was recorded at the edges (blue line of point 8) due to the accumulated effect of rapid heat dissipation. However, with a reduced distance between electrodes, the mismatch of resistance (Ch2) between nanocomposites and electrode contact resistance becomes a dominating factor, resulting in a more pronounced heating close to the copper electrodes.

To address these two challenges causing inhomogeneous heating, several strategies have been proposed and explored: (i) adjusting the resistivity of non-PTC heating areas according to the PTC switching unit at self-regulating temperatures, ensuring sufficient current flow throughout the specimens at elevated temperatures (Strategy 1-2, addressing the sequential heating problem and Ch2); (ii) increasing the film thickness to achieve more consistent resistivity across the film hence to avoid undesirable heating initiation before the temperature equilibrium process (Strategy 3, addressing Ch2); (iii) utilizing additional thermally conductive layers to facilitate the heat transfer (Strategy 4, addressing Ch1); (iv) adjusting and tailoring the initial heating locations to mitigate the heat dissipation issue (Strategy 5,

addressing Ch1); (v) using novel electrode materials to replace copper, reducing the mismatch in electrode contact resistance and nanocomposites (Strategy 6, addressing Ch2).

4. Results and Discussion

4.1. Introducing ZTC heating elements

Considering the pyroresistive feature of the materials, ensuring most areas can be heated before triggering self-regulating heating is essential to allow sufficient heat dissipation to solve the temperature uniformity issue. Therefore, a zero temperature coefficient (ZTC) heating element has been introduced to avoid early triggering of the PTC effect in the central area, which addresses Challenge 1 with the hot line at the center. The sections with a higher resistivity will convert more electrical energy to heat energy, leading to earlier heating once the specimen is subject to an applied current. Therefore, the resistivity of each heating element (CNT/HDPE and GNP/HDPE) at the terminal temperature (120 °C) should be the same to obtain homogeneous heating, while the resistance of CNT/HDPE should be higher than GNP/HDPE at room temperature to initiate the heating (detailed values in **Figure 3**a). In theory, it is expected that the whole system can reach a steady state of self-regulating heating after the GNP/HDPE sections (point 5-6) reach the switching temperature, as shown in Figure 3a, although a temperature drop can be observed in CNT/HDPE sections (point 1-4) due to reduced current from the resistivity increase (PTC effect) in GNP/HDPE units.

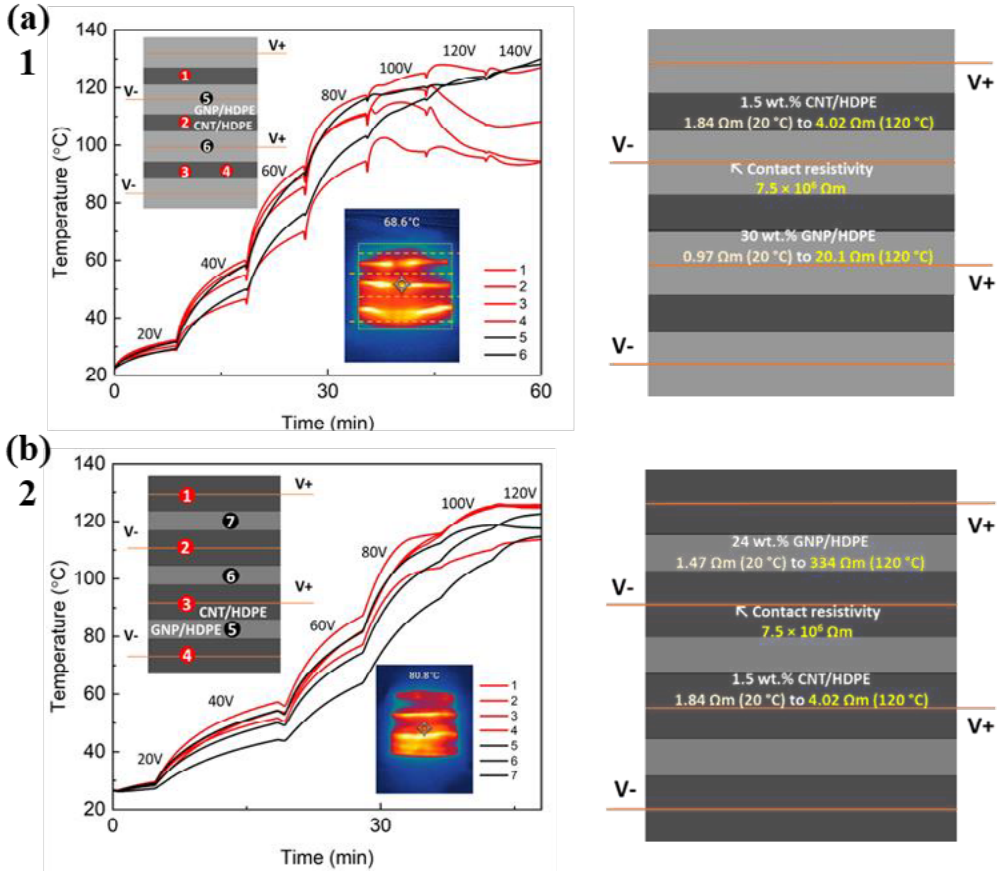


Figure 3 Temperature profile with IR images of self-regulating heating film with resistivity values of each section at room temperature and self-regulating temperature, in introducing ZTC elements strategies with electrodes embedded in either (a) GNP/HDPE sections, or (b) CNT/HDPE sections.

As shown in **Figure 3**a, by embedding electrodes in the GNP/HDPE phase with the CNT/HDPE section joined in between, it is expected that the middle CNT/HDPE ZTC unit with relatively high resistivity (compared with the GNP/HDPE phase) will heat up first, as shown in the three areas between the four dash lines in the IR image. A relatively homogeneous heating process can be found, until the copper wires areas with high contact resistivity in two GNP/HDPE sections (points 5-6, black lines) in between ZTC heating sections reach the switching temperature, triggering the PTC effect and restricting the current with a relatively stabilized temperature apart from two edge sections (point 1, grey line) due to more pronounced heat dissipation. A temperature difference (ΔT) of 56 °C has been recorded across all thermocouples, without improvements compared to previously recorded ΔT of 46 °C in Ch1 and 43 °C in Ch2.

Three different resistance values can be expected, CNT/HDPE, GNP/HDPE, and contact resistance on the copper wire surfaces, which will heat up sequentially. To achieve an ideal process starting with simultaneous heating by contact resistance and CNT/HDPE phase, followed by the GNP/HDPE phase triggered at the end, embedding the electrodes in the CNT/HDPE phase has been explored in Strategy 2 (**Figure 3**b). A significantly reduced ΔT of 12 °C was obtained, achieving an almost 80% reduction compared with Strategy 1. It is worth noticing that the self-regulating performance in Strategy 2 at the switching temperature is also more pronounced than in Strategy 1, attributed to the use of 24 wt.% GNP/HDPE for their desirable resistance range in the design.

4.2. Thickness increase strategy

A slightly increased film thickness has been examined as shown in **Figure 4**a. With applied voltages, all areas in the film started heating with a slight temperature variation, until the first areas reached the melting temperature (points 1, 7, 8, red lines), leading to reduced heating with a temperature equilibrium process. With further increased voltages (from 50V to 90V), a clear self-regulating heating can be observed, with a relatively uniform temperature distribution after the heat transfer.

A significantly reduced ΔT of ~11 °C has been recorded across the surface of the film, especially compared with the same electrode design but thinner 300 µm film in Challenge 2 (**Figure 2**b) with a ΔT of 43 °C. Considering the copper electrode diameter of 150 µm, the current thick film (600 µm) can provide a more consistent film thickness with a well-surrounded area for a more consistent contact resistance. More importantly, heat dissipation through the in-plane direction can facilitate temperature homogeneity in this strategy.

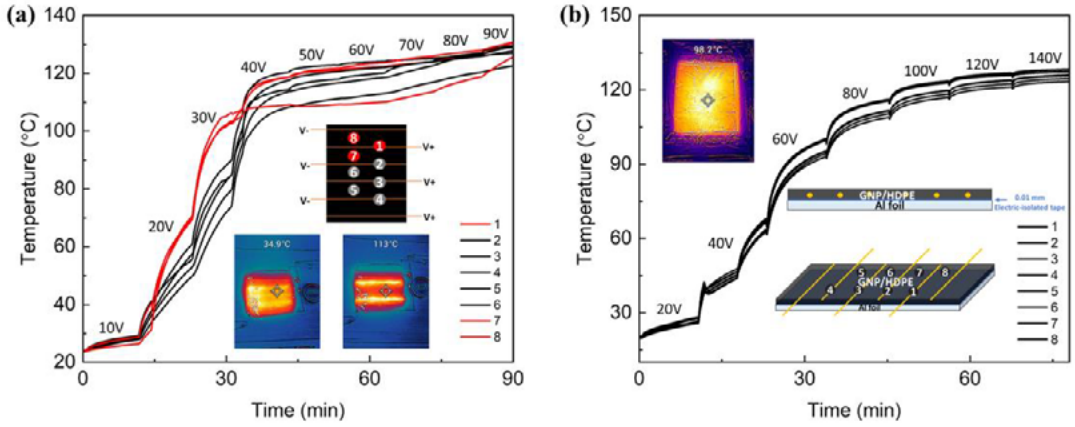


Figure 4 Temperature profile with IR images of the self-regulating heating film in (a) increasing thickness strategy (Strategy 3) and (b) the heating film with 0.1 mm Al foil layer (Strategy 4).

4.3. Additional thermally conductive layer

As indicated by the previous increased thickness strategy, apart from tuning the material compositions and constructions of the PTC and ZTC units, another way to facilitate heat dissipation and temperature homogeneity is to have an efficient heat dissipation layer within (or on top of) the nanocomposite film. Therefore, a heat dissipation layer with a high thermal conductivity has been attached to the nanocomposites, as illustrated in **Figure 4**b insets. This could be an effective alternative to previously examined thick films, especially for end electrode design with relatively large distances between electrodes. A heat-dissipation layer of thin Al foil (100 µm) with a thermal conductivity of ~ 240 W/mK [6], has been attached to previously examined Ch2 nanocomposite films. As shown in **Figure 4**b, an improved temperature uniformity has been achieved with a $\Delta T < 7$ °C. Upon reaching the self-regulating heating stage, a clearer temperature difference has been observed in **Figure 4**b without obvious temperature differences between the contact resistance area near copper wires and the nanocomposites. Despite this fact, a highly thermally conductive layer such as thin Al foil can efficiently facilitate the heat dissipation of the PTC film, achieving more homogeneous heating both before and after the self-regulating stages. This relatively small ΔT agrees with our previous finding when having a continuous layer of materials attached to the heating film for improved heat dissipation [7]. A ΔT of 9 °C has been achieved successfully with clear self-regulating heating observed.

4.4. Sandwich electrode structure

Rather than treating the contact resistance as an uncontrollable heating area, utilizing it as a heat generation area is another approach to address the temperature uniformity problems. **Figure 5**a illustrates a design featuring two layers of copper mesh serving as top and bottom electrodes. As the voltage increased from 80 V to 200 V, the PTC nanocomposites with sandwich-structured electrodes exhibited relatively homogeneous heating and yielded a ΔT of only 11 °C. A stable self-regulating heating can be found, even at increased voltages from 100 V to 200 V, confirming the effective heat dissipation in the current design. However, it is worth noting that although the copper mesh with a wire dimension of only 0.056 mm is relatively flexible, it may result in increased rigidity and additional weight in the sandwiched film for heating devices.

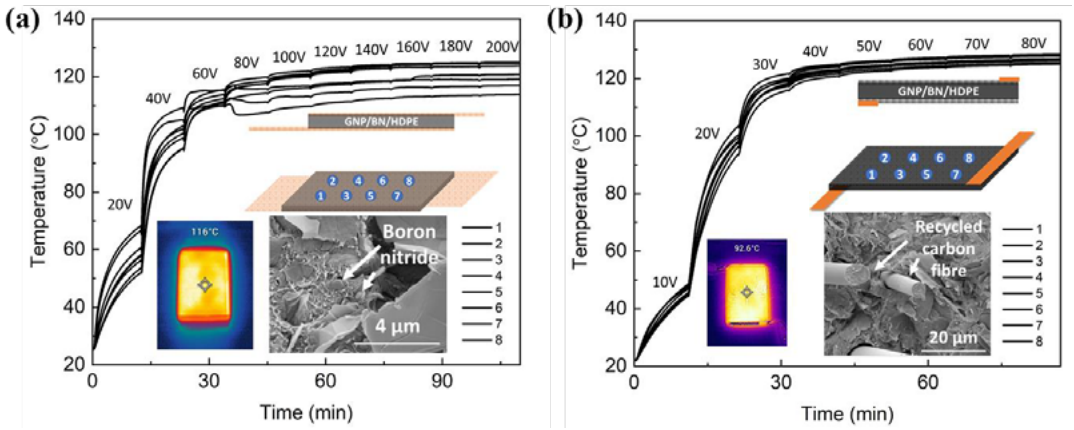


Figure 5: Temperature profile, IR images, schematic illustrations, and morphology images of sandwich electrode strategy with electrodes of (a) copper mesh and (b) rCF veils.

To avoid weight penalty while exploring the potential of upcycling recycled composite wastes as functional and smart materials, lightweight recycled carbon fiber (rCF) veils were evaluated as top and bottom electrodes in sandwich structures. Surprisingly, **Figure 5**b reveals a significantly enhanced heating homogeneity with a minimal ΔT of only 3 °C, surpassing the performance of all previously tested strategies, alongside a stable self-regulating heating with increased voltages from 40 V to 80 V.

Compared to copper mesh electrodes, rCF veils, offers a much larger surface area, leading to a significantly increased total contact area between electrodes and the nanocomposites. In addition, the inherent carbon composition of rCF electrodes contributes to a reduced difference in contact resistance when interfaced with GNP-based PTC nanocomposites.

5. Conclusion

This study aimed to understand and address an issue of inhomogeneous heating which resulted in hot lines in pyroresistive conductive polymer composite heating devices. Two fundamental interconnected physical phenomena causing the inhomogeneous temperature profile have been identified and discussed. Several strategies were proposed and examined to enhance the temperature uniformity of PTC-based self-regulating heating devices, with equivalent simulation performed for most performing strategies. A comprehensive summary showcasing the performance of each strategy has been presented, highlighting the effectiveness of the sandwich electrode structure and the increase in nanocomposite film thickness. A temperature difference of only 3 °C has been achieved successfully at the self-regulating heating stage (125 °C). More interestingly, the use of recycled carbon fibres has been proven an efficient element in smart heating devices, while guidance has been provided for filler selections and electrode designs to enhance the overall functionality of these heating devices.

Acknowledgements

This work was supported by the Engineering and Physical Sciences Research Council (EPSRC) [ESTEEM, grant number EP/V037234/1]. YW is grateful to the China Scholarship Council for its financial support.

References

[1] E. Asare, J. Evans, M. Newton, T. Peijs, and E. Bilotti, "Effect of particle size and shape on positive temperature coefficient (PTC) of conductive polymer composites (CPC)—a model study," *Materials & Design,* vol. 97, pp. 459-463, 2016.

[2] Y. Liu, H. Zhang, H. Porwal, J. J. Busfield, T. Peijs, and E. Bilotti, "Pyroresistivity in conductive polymer composites: a perspective on recent advances and new applications," *Polymer International,* vol. 68, no. 3, pp. 299-305, 2019.

[3] Y. Liu *et al.*, "The effect of conductive network on positive temperature coefficient behaviour in conductive polymer composites," *Composites Part A: Applied Science and Manufacturing,* vol. 139, p. 106074, 2020.

[4] Y. Liu *et al.*, "Tailored pyroresistive performance and flexibility by introducing a secondary thermoplastic elastomeric phase into graphene nanoplatelet (GNP) filled polymer composites for self-regulating heating devices," *Journal of Materials Chemistry C,* vol. 6, no. 11, pp. 2760-2768, 2018.

[5] T. Blecha *et al.*, "Electrical Contact Resistance of Large-Area Graphene on Pre-Patterned Cu and Au Electrodes," *Nanomaterials,* vol. 12, no. 24, p. 4444, 2022.

[6] R. Brandt and G. Neuer, "Electrical resistivity and thermal conductivity of pure aluminum and aluminum alloys up to and above the melting temperature," *International Journal of Thermophysics,* vol. 28, pp. 1429-1446, 2007.

[7] Y. Liu *et al.*, "Sustainable and self-regulating out-of-oven manufacturing of FRPs with integrated multifunctional capabilities," *Composites Science and Technology,* vol. 190, p. 108032, 2020.

INITIAL TESTS OF CCLT – A TIMBER SANDWICH STRUCTURE WITH COMBOO CORE

Jean-Marc Witzmann[1], Andreas Loth[2] and Ralf Förster[3]

[1]Mechanical Engineering, Berliner Hochschule für Technik, Luxemburger Str. 10, 13353 Berlin, Germany
Email: jean-marc.witzmann@bht-berlin.de, Web Page: https://www.bht-berlin.de/viii
[2]Mechatronics, Berliner Hochschule für Technik, Luxemburger Str. 10, 13353 Berlin, Germany
Email: aloth@bht-berlin.de, Web Page: https://www.bht-berlin.de/vii
[3] Mechanical Engineering, Berliner Hochschule für Technik, Luxemburger Str. 10, 13353 Berlin, Germany
Email: rfoerster@bht-berlin.de, Web Page: https://www.bht-berlin.de/viii

Keywords: COMBOO, Bamboo, Honeycomb, Lightweight composite, Sandwich

Abstract
In this paper the results of an initial compression test of the composite sandwich structure CCLT – "COMBOO cross laminated timber", COMBOO being a honeycomb pattern of cut bamboo – compared to conventional CLT are presented and discussed.
CLT is a massive timber plywood usually made of pine boards in several layers aligned under an angle of 90 degrees (fibre orientation) with dimension of up to (W x L x H) 7 m x 13 m x 450 mm. It is widely used in civil engineering and architecture to build even high rise wooden buildings. The consumption of large amounts of timber with its density of 0.45 g/cm^3 can somehow be a disadvantage.
COMBOO has many interesting technical properties and a very low density of 0.2 g/cm^3. The combination of both provides the properties of a sandwich structure and could be an alternative material for CO_2 friendly construction.
The stresses measured ranged from 3.1 - 3.97 MPa at 10% compressive deformation perpendicular to the fibre, an average value of 3.5 MPa, and a standard deviation of 0.36 MPa for CLT samples, and 3.39 - 3.42 MPa, an average value of 3.40 MPa with a standard deviation of 0.01 MPa for conventional CLT samples.

1. Introduction

Composite materials integrate the advantageous properties of various substances to achieve superior functionalities. Often, core layers of sandwich composites include environmentally problematic materials like polymer or metallic foams, aramid honeycomb, or balsa wood. These materials pose significant disposal challenges and carry a heavy CO_2 and energy footprint during production. In response, natural and renewable materials with remarkable mechanical properties are being considered. Bamboo, for instance, not only has a high CO_2 storage capability while growing, akin to timber, but it also grows at the impressive rate of up to one meter per day and can be harvested within about seven years. [1] With its low production energy consumption and non-toxic impact on the environment, bamboo offers a sustainable alternative with a significantly positive ecological footprint.

Earlier research on the combination of a bamboo core layer with outer layers of GFRP as a lightweight structure element for partitioning walls or in transport applications not only showed very promising mechanical properties but also resulted in a decoratively translucent element. The next lightweight component to be tested was a COMBOO core with plywood panels as outer layers. The potentially very interesting combination of properties – a lightweight structure with high stability with respect to

compression and bending based on a renewable material – led to an expansion of scope into the area of civil engineering from partitioning walls to wall and ceiling elements where timber is often used, by envisioning a variation of outer layer material. Integrating the new bamboo structure into elements composed of Cross Laminated Timber (CLT) turned out to be a very promising approach [2, 3, 4, 8].

Bamboo has been a trusted construction material for millennia, praised for its high compressive and tensile strengths. When incorporated into construction materials like CLT, bamboo enhances these composites by leveraging its superior compression strength and lighter density owing to its hollow structure. Bamboo's composition – cellulose, hemicellulose, and lignin – is similar to timber but boasts a more favorable CO_2 impact, stronger material properties, and a lower overall density, enhanced by its rapid growth and short harvest cycle.

COMBOO Cross Laminated Timber (CCLT) innovatively replaces the inner timber layers of CLT with a honeycomb structure made from cut bamboo rings. This creates a lighter yet robust sandwich material with bamboo layers encapsulated by traditional CLT. This composite not only reduces the weight of large-scale construction elements – making it advantageous for high-rise building projects – but also maintains essential mechanical properties. Additionally, substituting timber with bamboo in the honeycomb structure significantly lowers the CO_2 footprint due to the reduced energy requirements and CO_2 emissions associated with bamboo production.

The synergy between timber and bamboo in CCLT allows for environmentally benign construction solutions. By incorporating bamboo, the overall density of construction elements decreases while their crucial characteristics are preserved, demonstrating bamboo's capacity to rival traditional materials like steel in tensile strength and stability thanks to its unique hollow cylindrical structure.

This paper covers the manufacturing of test samples of CCLT as well as conventional CLT and describes the results of first compression tests.

2. Materials and Methods

CLT is composed of an odd number of spruce board layers, beginning at 3 layers, each layer being oriented at an angle of 90° compared to previous/next. For the tests, the number of layers was set to 5, in order to be able to replace the core layer while maintaining the CLT characteristics in the outside layers. The comparison of 5 layered conventional CLT and 5 layered CLT with a COMBOO core layer instead of spruce shows the advantages of the enhanced CLT element compared to its conventional counterpart. In this case only one layer of spruce was replaced by bamboo rings, limiting the weight reduction effect to that layer. The length and diameter of the bamboo rings directly impacts the potential weight reduction. Using a thicker COMBOO layer, with longer bamboo rings and also larger diameters would augment the weight reduction effect even further which may well go beyond 20 percent.

2.1. Manufacturing and Materials

Two types of elements were produced for the compression test: 5-layer CLT, made of 5 layers of spruce boards, and 5-layer CCLT (COMBOO-CLT) in which the middle layer was replaced by a layer of COMBOO. Spruce boards with the dimensions (L x W x H) 450 mm x 150 mm x 20 mm, and bamboo culms of similar diameter were selected for the COMBOO layers, in order to obtain a regular honeycomb structure. Before assembling and gluing the spruce boards, these were processed for smoothing and leveling using a jointer and thickness planer. The bamboo rings were cut using a band saw equipped with a linear guide ensuring a constant length as well as parallel edges. The PU glue used in the production process is certified for the gluing of load-bearing wooden components.

For the 5 layer CLT elements a total of 15 spruce boards was used. The first layer of three spruce boards was placed and arranged on an even and plane surface so as to obtain a square with the dimensions of 450 mm by 450 mm. Glue then was spread over the surface in an approximately 3 mm thick layer and the second layer of boards was placed perpendicularly to the boards in the first layer. After pressing the

boards together manually the second layer of glue was applied and the third layer of boards arranged perpendicularly to the boards below. This procedure was repeated for the last two layers after which a load 1584 kg (block of metal cased concrete) was placed on top for the required hardening time of 60 minutes.

The five layer CCLT elements were made using 12 spruce boards making up four layers of spruce board and cut bamboo rings arranged in a honeycomb structure as the middle layer. The first two layers were made in the same way as for the CLT elements. After applying pressure manually, they were covered with a separator film and the second set of two layers was made in the same manner on top of the first. The load of 1584 kg was then placed on top. During the hardening of the CLT layers (60 minutes) the bamboo with a diameter of approximately 80 mm was cut into rings with a height of slightly more than 20 mm. After the hardening of the two CLT layers, the upper two layers were removed, a layer of glue was applied on top of the remaining two CLT layers, and a total of 34 rings was arranged on top and weighed down individually with weights between 2 and 5 kg instead of using the concrete block because the irregular height of the bamboo rings would not have allowed an even weight distribution. After further 60 minutes of hardening, the weights were removed and the element was placed into a CNC machine and the bamboo ring layer was milled over to remove irregularities and assure an even height of 20 mm. Finally a last layer of glue was applied on the upper side of the bamboo rings and the upper two CLT layers placed on top. For the duration of the hardening the load of 1584 kg was applied.

From these CLT and CCLT elements, a total of 10 test samples with varying dimensions were made: samples 1-3 with the dimensions (L x W x H) 80 mm x 80 mm x 100 mm, samples 4-6 with the dimensions 76 mm x 76 mm x 100 mm, and samples G1-G4 with the dimensions 200 mm x 200 mm x 100 mm. A communication problem with the workshop resulted in the samples 4-6 being cut to the dimensions of 76 mm by 76 mm instead of 80 mm by 80 mm yet an adaptation of the calculations allowed to compensate for the resulting differences.

2.2. Methods – Compression Test

The compression tests were performed in accordance with DIN EN 408 using a compression testing machine by TESTING Bluhm & Feuerherdt GmbH (Berlin, Germany) with a maximal load of 300 kN.

Preliminary tests testing the compressive strength of bamboo rings had resulted in high values [8] which lead to the smaller dimensions of the test samples prepared for the compression test in order to be able to stay below the load-limit of the testing machine during the experiment. Yet the high compressive strength resulted in the bamboo being pressed into the upper and lower CLT layer, so that the samples needed to be re-dimensioned, which led to sample sizes of 200 mm by 200 mm instead of 80 mm by 80 mm.

Before the tests were run, all samples were weighed in order to determine the differences in weight between the CLT and the CCLT samples. In these initial tests with a very limited number of samples weight reduction was about 4.54 % for the small samples (1, 2, 3 vs. 4, 5, 6) and about 8.45 % for the larger ones (G1, G2 vs. G3, G4) [7].

3. Results

The compression tests yielded the following results for the CCLT samples: between 3.1 and 3.97 MPa with an average of 3.5 MPa and a standard deviation of 0,36 MPa for the small samples (samples 1-3), between 3.39 and 3.42 MPa with an average of 3.40 MPa and a standard deviation of 0.01 MPa for the larger ones. In comparison, the testing of the CLT samples yielded between 3.49 and 4.14 MPa with an average of 3.76 MPa and a standard deviation of 0.24 MPa [7].

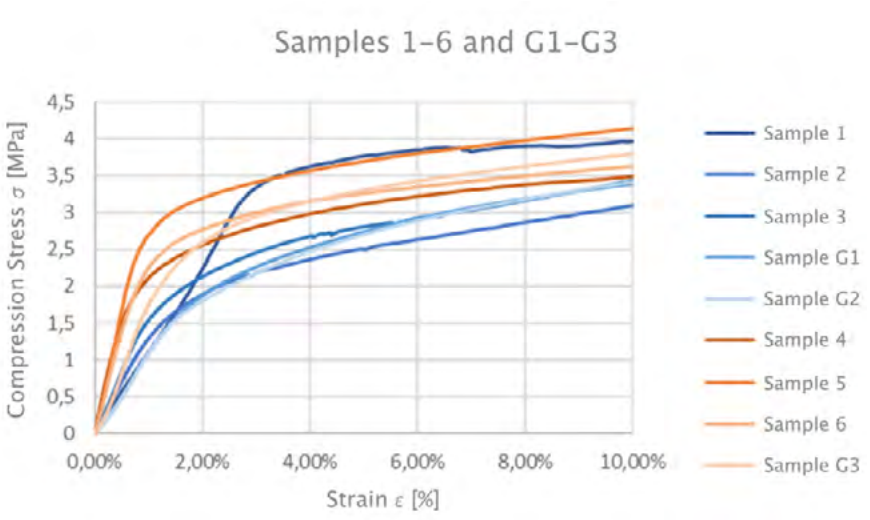


Figure 1. Stress over compression ratio for samples 1-6 and G1-G3 [7, translated into english]

When comparing the samples after the compression tests different failure modes became apparent at 10% compression: penetration of the board layers by the bamboo rings, deformation of board layers, cracks withing the deformed board layers as well as leaked resin from within the boards.

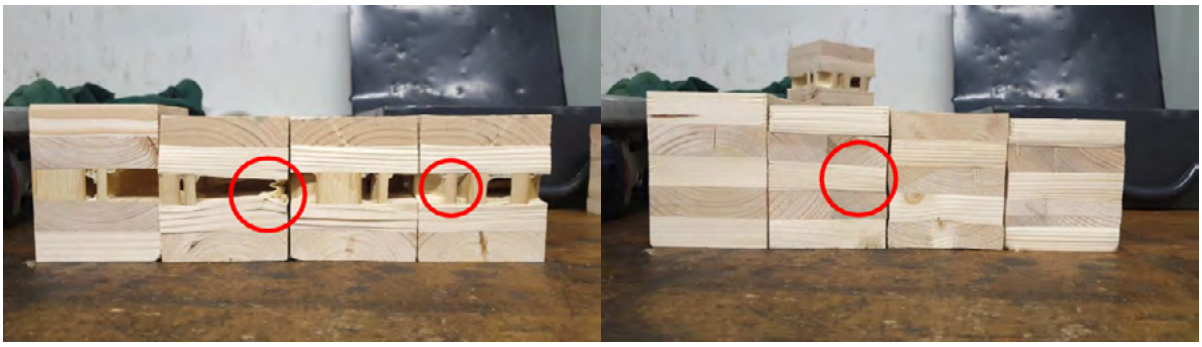


Figure 2. *Deformations in samples 1-3 (left) and 4-6 (right) at 10% compression [7]*

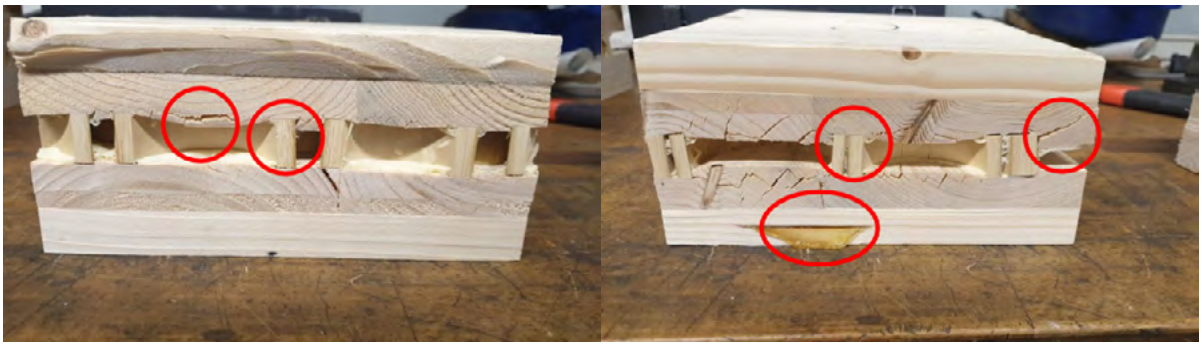


Figure 3. Deformations in sample G1 (left) and G2 (right) at 10% compression [7]

4. Discussion

The obtained results show similar compression strengths of the CLT and the CCLT samples in spite of technical difficulties during sample production. Some of the spruce boards were slightly warped and also the applied pressure using the available load of 1584 kg was much too low compared to what the gluing requirements are: the resulting pressure resulting from the applied load of 1584 kg was at around 0.076 MPa when at least 0.6 MPa would have been required. This probably did not affect the compression test, but might very well affect bending tests, so it is an issue which needs resolving in the future. Additionally the limited available manpower made it impossible to respect the open time of the glue. Considering these difficulties, resulting compression strengths above specification values of industrial CLT (2.7 MPa) are very promising. [6] The compressive strength of the COMBOO layer lies far beyond the compressive strength of the outer CLT layers as it is composed of bamboo rings. The compressive strength of MOSO bamboo which was used to build the COMBOO core reached values between 68.5 MPa and 87 MPa with an average of 75 MPa in earlier compression tests [8], which nearly twentyfold compared to the values obtained for CLT.

5. Conclusion and Outlook

As has already been shown in earlier works involving COMBOO [2, 3, 4], the bamboo layer brings with it the advantages of bamboo, it provides superior mechanical properties when integrated as a core layer into CLT which in this case are high compressive strength, low density due to its hollow structure resulting in lower weight as well as environmental advantages. Ongoing research will provide further insight for example concerning the effect of optimized production processes, on the compression strength and also other properties such as bending strength. Sample production is an issue, which will need to be addressed. This includes an optimized way of applying glue to the bamboo rings within the specified open time, applying a defined pressure to an irregularly shaped surface (when first gluing the bamboo rings to the CLT) in order to be able to apply the required pressure for the gluing process as well as a way to efficiently transfer compressive forces from the COMBOO layer to the CLT layers and vice versa which would allow for even greater compressive strength.

References

[1] Dunkelberg, K., ”Bambus - Bauen mit pflanzlichen Stäben IL 31“, Karl Krämer Stuttgart, 2005.
[2] Loth, A. et al., “Evaluation and comparison of a lightweight bamboo composite”, AIP Conference Proceedings 1769, 170010, 2016
[3] Loth, A., Förster, R., “COMBOO - a novel core material for composite sandwich structures from renewable sources”, ECCM18, Athens, 2018
[4] Loth, A., Förster, R., “First advances of COMBOO, a novel lightweight bamboo based composite material for structural and environmental applications”, Proceedings WCTE 2018, Seoul, pp 6, 2018.
[5] DIN EN 408, “Timber structures - Structural timber and glued laminated timber - Determination of some physical and mechanical properties”, Beuth, 2012
[6] ETA-06/0138, “Europäische Technische Bewertung”, Österreichisches Institut für Bautechnik, 20.02.2017
[7] Baysal, E., ”Vergleich von Holz-Bambus-Sandwichkombinationen mit konventionellen Holzanordnungen“, Bachelor Thesis, BHT Berlin, 2021
[8] Cocaj, S., ”Mechanische Qualifikation von Kernmaterialien für den Leichtbau“, Bachelor Thesis, BHT Berlin, 2018

BIO-INSPIRED 3D-PRINTED MICROSTRUCTURES FOR TOUGHENING BIO-BASED EPOXY MATRIX

Z. Xu[1], R. Tao[1] and S. Teixeira de Freitas[1,2]

[1]Faculty of Aerospace Engineering, Delft University of Technology, Delft, the Netherlands
Email: Z.Xu-8@tudelft.nl, R.Tao@tudelft.nl
[2]IDMEC, Instituto Superior Técnico, Lisbon, Portugal
Email: sofia.teixeira.freitas@tecnico.ulisboa.pt

Keywords: Bio-inspired, 3D printing, sacrificial bonds and hidden lengths, toughness

Abstract

Aiming to aid the sustainable transition to fossil fuel-free epoxy materials and enhance the toughness of bio-based epoxies, here we integrate an overlapping curl microstructure consisting of coiling fiber with sacrificial bonds and hidden lengths into a bio-based epoxy matrix. Inspired by natural material, where exceptional properties are achieved at low environmental cost, the microstructure mimics the molecular structures of spider silk, known for its exceptional fracture resistance. The 3D-printed overlapping curl shows a saw-tooth mechanical response with continuous load-carrying ability thanks to the break of sacrificial bonds and unfolding of the hidden lengths. By embedding the overlapping curl into the compact-tension configuration of the bio-based epoxy, an extrinsic toughening mechanism is triggered as the hidden length unfolds. Experimental results show that a single-sided overlapping curl structure is able to improve the toughness of bio-based epoxy by 19%.

1. Introduction

The demand for a sustainable transition in load-bearing structures in the mobility and energy sector, with low carbon emissions and high safety requirements, drives the need for the replacement of fossil fuel-based materials with bio-based materials. Despite being more sustainable, bio-based epoxies, for example, face strong limitations in engineering applications due to their low mechanical properties such as fracture resistance [1] when compared to their fossil fuel-based counterparts. Through evolution over millions of years, natural materials provide a wealth of sophisticated and hierarchical structures with high fracture resistance at low environmental costs, including spider silk, bone, and nacre [2,3,4]. One of the key features that contribute to the high fracture resistance of these biological materials is the presence of sacrificial bonds and hidden length (SBHL) in their organic structures. Upon stretching, the sacrificial bonds will first break and then the hidden length unfolds, providing a residual load and avoiding the sudden fracture.

Drawing inspiration from these biological structures, this work presents a bio-inspired microstructure named overlapping curl (OC) containing coiling fiber with sacrificial bonds and hidden lengths to mimic SBHL features to delay crack propagation in a bio-based epoxy matrix and improve its intrinsic fracture resistance. Fused filament fabrication 3D-printing was adopted to fabricate OC with polylactide (PLA) material and its mechanical behavior was first characterized through tensile tests. Subsequently, the OC structure was embedded into a bio-based epoxy and tested under Compact tension (CT) tests.

2. Experiments

2.1 3D-printing fabrication of overlapping curl

As shown in Figure 1, the overlapping curl structure containing coiling fibers with sacrificial bonds and hidden lengths was produced using a polylatic acid filament (PLA, ReFormTM – rPLA, Formfutura BV, Nijmegen, Netherlands) with a commercial Prusa i3++ 3D printer. The molten PLA material was firstly extruded from the printer nozzle at the temperature ***T***. With the nozzle moving horizontally with the speed ***F***, the extruded PLA filament coiled under the buckling effect [5] and then intersected itself. By controlling the printing parameters (nozzle height ***Z*** and filament extrusion ***E***) to a specific ratio region, the coiling fibers with different curl sizes and orientations (single-sided and double-sided) can be fabricated and are listed in Table 1.

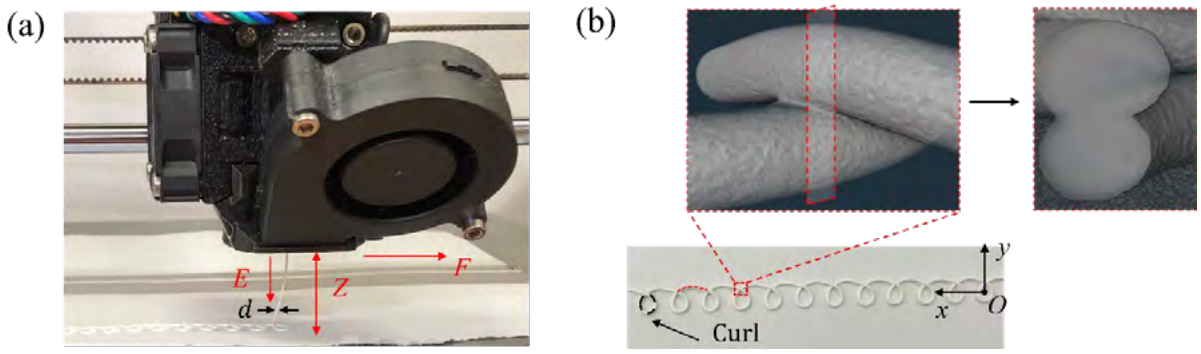


Figure 1. (a) The 3D-printing process and (b) the OC structure contains coiling fiber with sacrificial bonds and hidden lengths.

Table 1. 3D-printing parameters and structures of overlapping curl. ***T***: temperature of the printer nozzle, ***F***: nozzle horizontal speed, ***Z***: nozzle height, and ***E***: filament extrusion.

OC type	***T*** (°C)	***Z*** (mm)	***F*** (mm/min)	***E*** (mm/min)	Structures
Single_Z10	275	10	750	75	
Single_Z5	275	5	750	75	
Double_Z10	275	10	1000	60	
Double_Z5	275	5	1000	60	

2.2 Compact-tension sample manufacturing

A silicon mold was designed for manufacturing compact-tension (CT) samples with consistent geometry shapes, as shown in Figure 2. A two-component bio-based epoxy (SR GreenCast 160) was mixed at a mixing ratio of 1:0.42, before being placed into a vacuum chamber for degassing for around 1 hour. After that, the bio-based epoxy was poured into the mold with the overlapping curl (represented as the blue dashed line in Figure 2) embedded in the vertical direction regarding the crack path and cured for 7 days at room temperature. The thickness of the CT sample was controlled around 8 mm. The CT samples are designated as CT-pure and CT-OC without and with overlapping curl, respectively.

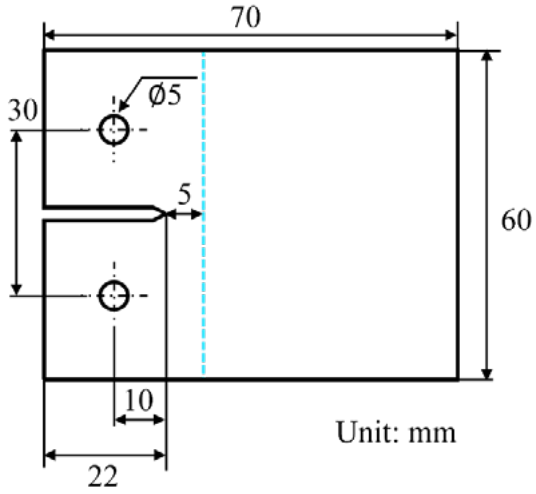


Figure 2. The geometry and dimensions of the CT specimen (thickness of 8 mm). The blue dashed line represents the position of the embedded overlapping curl structure.

2.3 Mechanical testing and characterization

The tensile test and compact-tension test using a universal Zwick loading frame were performed to obtain the corresponding mechanical response of the OC and CT samples. A 100 N load cell was used for loading OC under tensile at a speed of 5 mm/min. During the test, a high-resolution camera is used to capture the deformation process of the OC. Also, a mechanical extensometer is attached to measure the actual separation displacement. For CT tests, a 10 kN load cell is adopted and the tensile loading is applied at a rate of 2 mm/min. Besides, a high-resolution camera and a traveling microscope are set from both sides of CT samples to record the crack advance in the CT testing. The energy release rate (toughness) of the CT samples is obtained from the following equation (Eq. 1) [6],

$$G_I = \frac{P^2}{2t}\frac{dC}{da} \tag{1}$$

Where $\boldsymbol{P}$ is the load, $\boldsymbol{t}$ is the thickness of the sample, $\boldsymbol{C}$ is the fitted compliance of the load-displacement curve, and $\boldsymbol{a}$ is the crack length.

3 Results and discussions

3.1 Overlapping curl mechanical response

Figure 3 shows the representative mechanical response and deformation process of OC under the uniaxial tensile test. With the displacement extension, the load increases until the first sacrificial bond breaks (i) and a load drop happens accordingly. As the curl unfolds (ii), the load rises again reaching the

force limit of the next sacrificial bond (iii). This process continues after all the sacrificial bonds break and a subsequent final failure of the straightened OC (v). This feature leads to the typical saw-tooth curve of the OC structure.

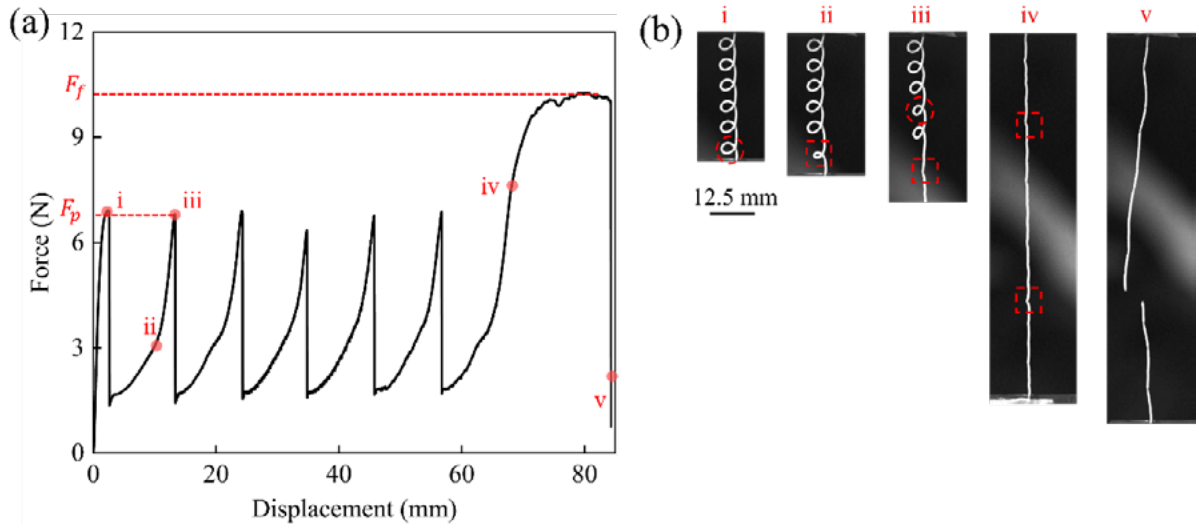


Figure 3. (a) The representative saw-tooth mechanical response curve of Single_Z10 OC and (b) the corresponding deformation process. The red dashed ellipse indicates the broken sacrificial bond and the red dashed rectangle outlines the remaining hidden lengths.

From the load-displacement curves of OC in Figure 4(a), the single-sided overlapping curl structures (Single_Z10 and Single_Z5) show full extension, i.e., all the sacrificial bonds break and hidden lengths unfold. There is also some necking of the filament before the final failure as seen in the final plateau in the load-displacement curve. For the double-sided overlapping curls (Double_Z10 and Double_Z5), they break early, the hidden length is not fully unfolded, and the extension is truncated. To better characterize the mechanical parameters, the sacrificial bonds peak force $\boldsymbol{F_p}$ and failure force $\boldsymbol{F_f}$ of OC, as defined in Figure 3(a), are compared.

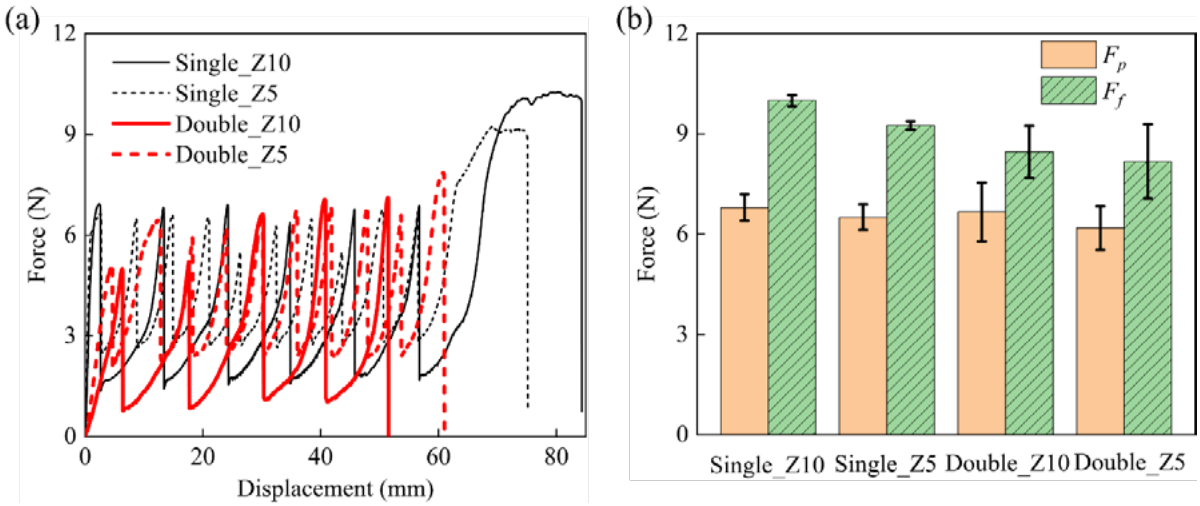


Figure 4. (a) The representative load-displacement curves of the four coiling fiber patterns. (b) The averaged sacrificial bonds peak force $\boldsymbol{F_p}$ and failure force $\boldsymbol{F_f}$ of the coiling fibers.

The average values and standard deviations of F_p and F_f values are shown in Figure 4(b). It can be observed that the F_p values are similar across the four types of structure, while the F_f varies. Both single and double Z5 structures show smaller F_f than their Z10 counterparts. This may be due to the smaller curl size of the Z5 overlapping curl, possibly resulting in more stress concentration while unfolding, causing an early failure and hence lower F_f when compared to Z10. Furthermore, the double-sided structures show lower F_f than the single-sided structures, which may also relate to the higher stress concentration in the double structure since during the manufacturing process, the extruded filament shifts the orientation direction [7].

3.2 Compact-tension test results

To study the effect of the integrated structure on the toughness of bio-based epoxy, CT samples with and without overlapping curl were tested. Figure 5(a) shows the representative load-displacement curves (the load is normalized by the sample thickness). Six typical points in the curve are picked to analyze the OC/epoxy interaction during fracture. Immediately after reaching the peak load, the load decreases faster in the sample with the OC (CT-OC) than without the OC (CT-pure). At point 2 of the CT-OC, the slope in the load-displacement curve changes as the OC starts to affect the crack advance. In Figure 5(b), the delay in crack advance is unnoticeable around point 2 but becomes evident starting from point 3. Figure 5(c) shows the toughness values vs crack length, from point 3 until point 6. An average of 19% toughness improvement is observed. In Figure 6 the fracture process is captured to help illustrate the extrinsic toughening mechanism. Based on Figure 6 - point 2, it can be observed that there is already a gap between the coiling fiber and the epoxy (indicated by the red arrow) indicating that at this point the sacrificial bond has already broken and the hidden length started to unfold. From this point onwards, the OC is believed to start affecting the crack propagation. When the crack tip reaches the position of the overlapping curl (point 3), the hidden length unfolds further, posing a residual load behind the crack tip which delays the crack propagation. The curl completely unfolds at point 4 and breaks at the crack advance of 23mm (point 6). It is also observed an epoxy ligament (highlighted by the red ellipse in Figure 6 - point 6) is also triggered, possibly delaying the crack propagation, and enhancing further the toughness values.

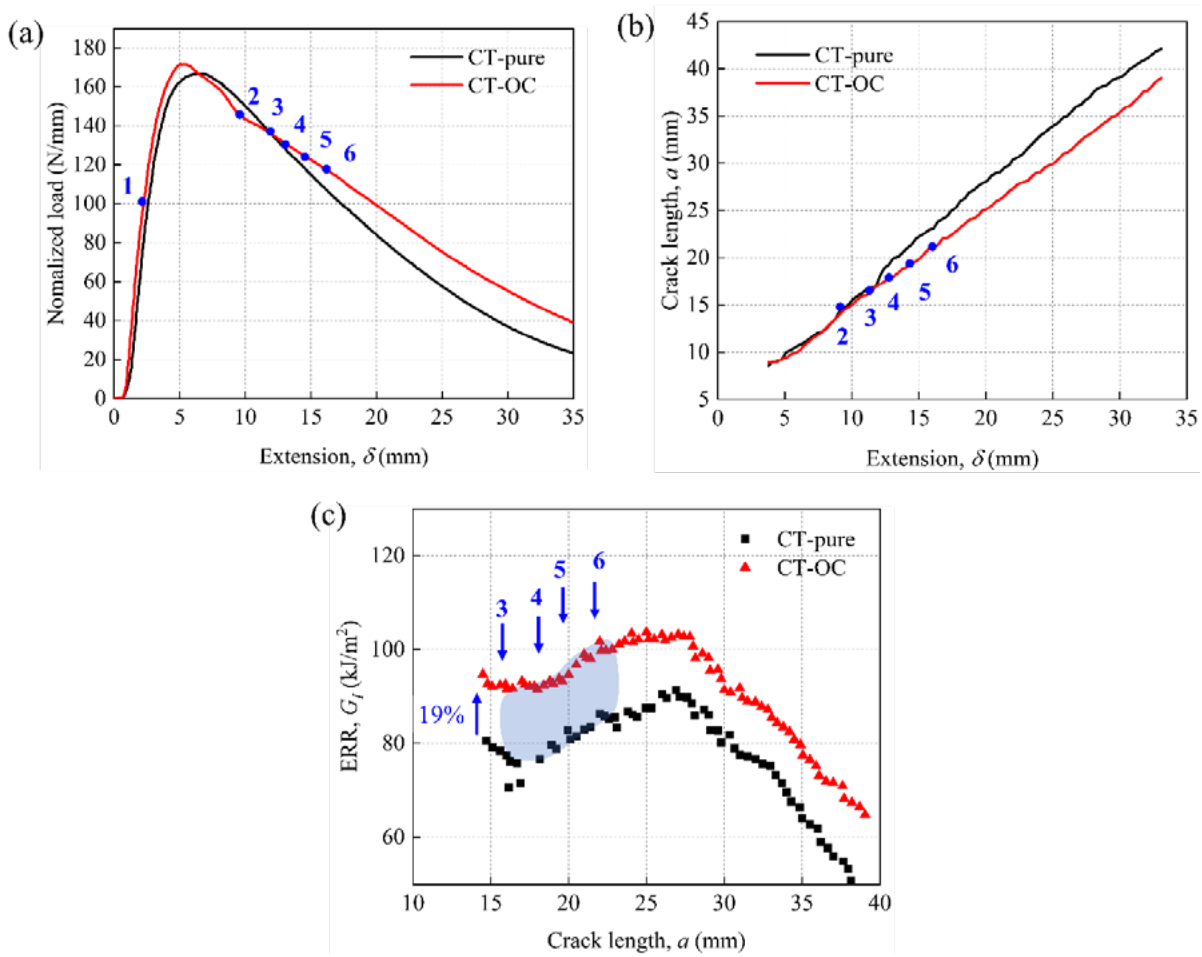


Figure 5. (a) Typical load-displacement curves of CT-pure and CT-OC samples. The load is normalized by the sample thickness. (b) Crack length vs extension curve, and (c) toughness R curve.

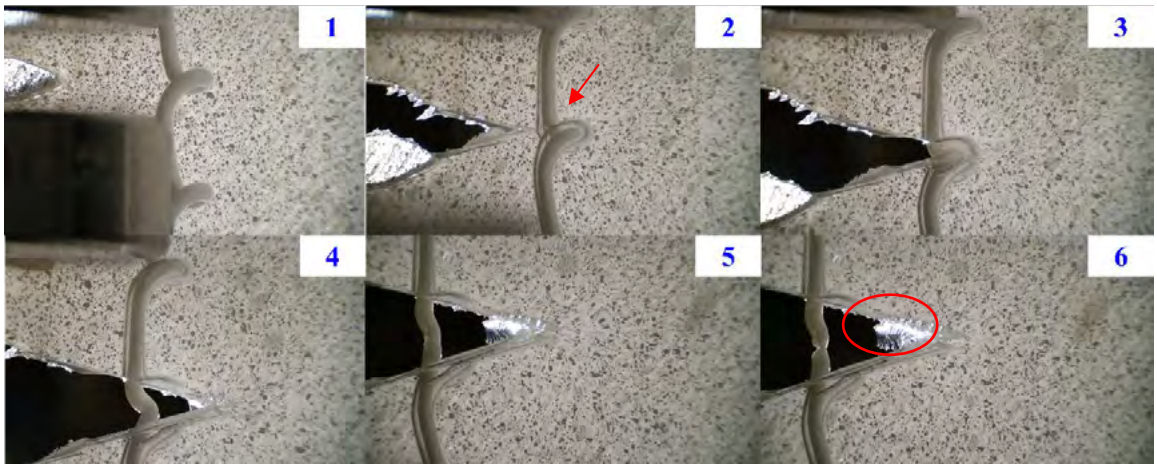


Figure 6. Snapshots during crack propagation of CT-OC sample. The red arrow indicates the gap between the coiling fiber and epoxy. The red ellipse highlights the epoxy ligament.

4. Conclusions

A bio-based epoxy reinforced with a spider silk-inspired overlapping curl consisting of coiling fiber with sacrificial bonds and hidden lengths was designed and tested. The 3D-printed overlapping curl alone shows the typical saw-tooth curve attributed to the break of the sacrificial bonds and unfolding of the hidden lengths. The single-sided overlapping curl structure shows longer extensions than the double-sided ones. Compact tension test of the single-sided overlapping curl structures embedded in the bio-based epoxy shows an average 19% toughness increase when compared to pure bio-based epoxy. As the crack crosses the coiling fibers, and the hidden length unfolds, it is expected that a reinforced load is applied to the crack path delaying crack propagation and contributing to the mechanical performance increase.

Acknowledgments

The authors gratefully acknowledge the financial support from the China Scholarship Council (No.CSC202107720061). This work was also supported by FCT, through IDMEC, under LAETA, project UIDB/50022/2020.

References

[1] Saleh M N, Tomić N Z, Marinković A, et al. The effect of modified tannic acid (TA) eco-epoxy adhesives on mode I fracture toughness of bonded joints. Polymer Testing, 96: 107-122, 2021.
[2] Su I, Buehler M J. Nanomechanics of silk: the fundamentals of a strong, tough and versatile material. Nanotechnology, 27(30): 302001, 2016.
[3] Vagaská B, Bačáková L, Filovaá E, et al. Osteogenic cells on bio-inspired materials for bone tissue engineering. Physiological research, 59: 309-322, 2010.
[4] Yin Z, Hannard F, Barthelat F. Impact-resistant nacre-like transparent materials. Science, 364(6447): 1260-1263, 2019.
[5] Ribe N M, Habibi M, Bonn D. Liquid rope coiling. Annual review of fluid mechanics, 44: 249-266, 2012.
[6] Laffan M J, Pinho S T, Robinson P, et al. Measurement of the in situ ply fracture toughness associated with mode I fiber tensile failure in FRP. Part I: Data reduction. Composites Science and Technology, 70(4): 606-613, 2010.
[7] Brun P T, Audoly B, Ribe N M, et al. Liquid ropes: a geometrical model for thin viscous jet instabilities. Physical review letters, 114(17): 174501, 2015.

MECHANICAL CHARACTERIZATION OF HYBRID REINFORCED POLYPROPYLENE COMPOSITES WITH TALC FILLERS AND CELLULOSE NANOFIBERS

Tatsuto Yamamoto[1], Chao Luo[2], Kouta Ide[3] , Kenji Aoki[4] and Yasutomo Uetsuji[2]

[1] Graduate School, Osaka Institute of Technology, Osaka, Japan
Email: m1m24437@st.oit.ac.jp
[2] Department of Mechanical Engineering, Osaka Institute of Technology, Osaka, Japan
Email: yasutomo.uetsuji@oit.ac.jp
[3] Toyo Resin Corporation, Shizuoka, Japan
Email: kouta-ide@resin.co.jp
[4] Faculty of Global Interdisciplinary Science and Innovation, Shizuoka University, Shizuoka, Japan
Email: aoki.kenji@shizuoka.ac.jp

Keywords: Polypropylene composite, Cellulose nanofiber, Talv filler, 3D printing, Multiscale FEA

Abstract

Hybrid reinforced composites with talc fillers and cellulose nanofibers (CNFs) were proposed as a new fused filament fabrication for polypropylene (PP), which is an important thermoplastic polymer widely used in mass-produced products such as automobiles. The effect of filler addition was clarified by multiscale finite element method (FEM). A multiscale FEM scheme for printed hybrid reinforced PP composites by three-step homogenization was developed in computational simulation. Cross-sections of 3D printed specimens were observed with an optical microscope, and multiscale FEM based on a microstructural model constructed from the binarized images was performed. The effects of voids due to poor filling and interfaces between solidified filaments in the heterogeneous structure formed by printing were quantified, and the mechanism of mechanical property degradation was elucidated.

1. Introduction

Polypropylene (PP) is widely used mainly in the automotive industry because of its excellent mechanical properties and moldability, low cost, thermoplasticity, and high recyclability. In general, PP is reinforced with short glass and carbon fibers, natural fibers such as hemp and yellow hemp, and mineral fillers such as talc and calcium carbonate to improve stiffness and strength. In general, PP products are mass-produced by injection molding. In recent years, however, there has been an increasing demand for prototyping using PP itself instead of alternative materials such as ABS or PLA in the product development process, and for personal production as an alternative to injection molding. PP printing by fused filament fabrication (FFF) is also gaining momentum [1]. However, compared with engineering plastics, PP has lower thermal, electrical, and mechanical properties, and has many points to be improved, such as large warpage after fabrication. In addition, the mechanical properties of PP are lower than those of injection-molded materials due to the generation of internal voids caused by its nature in 3D printer modeling [3]. In order to achieve the multiple objectives of adding desirable properties to the base resin in the 3D printing process and at the same time suppressing the degradation of mechanical properties, it is effective to add multiple fillers with different properties instead of a single filler. In such hybrid reinforced composites, the design parameters of mechanical properties are doubled and the influence of each factor becomes more complex, making the introduction of mathematical and numerical analysis essential. In general, multiscale simulations are effective in characterizing composite materials and elucidating the strengthening mechanism [4-7].

In this study, hybrid reinforced PP composites were proposed as a new PP printing material, and the effects of filler reinforcement were investigated by multiscale finite element analysis based on homogenization theory. Talc, commonly used in the automotive field, was selected as a filler along with CNF, which is increasingly utilized as an environmentally friendly material. Furthermore, by employing a three-step homogenization process, an analytical scheme for the nonlinear mechanical properties of printed hybrid reinforced PP composite structures was developed. The cross section of the 3D printed specimen was observed with an optical microscope, and a multiscale analysis based on the microstructural model constructed from the binarized images was performed. The effects of voids due to poor filling and the interface between melted and solidified filaments on the inhomogeneous structure formed by printing were quantified, and the mechanism of degradation of mechanical properties was elucidated.

2. Computational methods

2.1. Materials

In the creation of hybrid reinforced composite filaments, block PP (J707G, Prime Polymer), a thermoplastic polymer, was employed as the base material, and talc and CNF as reinforcement. For the former, PP masterbatch (MB) mixed with 70% talc was used, and MB mixed with 15% CNF was assumed to be used for the latter. 10 g of talc MB and 10 g of CNF MB were blended with 100 g of MB of PP, and three types of composites, PP/Talc, PP/CNF, and PP/Talc/CNF, were prepared. Three types of composite materials, PP/Talc, PP/CNF, and PP/Talc/CNF, were prepared.

2.2. Multiscale finite element analysis

For hybrid reinforced polymer composites, in addition to heterogeneous structures in which CNF and talc are dispersed, it is necessary to consider heterogeneous structures with inherent voids and interfaces due to printing. Since it is difficult to treat these heterogeneities in a single microstructure, three heterogeneous structures were homogenized hierarchically, as shown in Fig.1. First, we consider the microstructure with talc filler dispersion and the sub-microstructure with CNF dispersion. In the case of injection-molded specimens, the micro- and sub-microstructures are targeted, dealing with homogenized macrostructures in which the microstructures are periodically arranged. On the other hand, in the case of 3D printed specimens, meso-heterogeneous structures formed by melt-glued filaments are also considered. In the meso structure, we consider not only the printed phase, but also the void phase due to poor filling and the interfacial phase between melt-glued filaments. Homogenization theory is employed for scale coupling in macro and meso structures, meso and micro structures, and micro and sub-micro structures. In homogenization theory, scale ratios are introduced and displacements are expressed as asymptotic expansions of the displacements of the global structure and the perturbed displacements of the local structure, allowing the derivation of scale-coupled equations that are mathematically consistent for both structures.

In the first stage of the homogenization process, the homogenization properties of the base material region of the microstructure with talc filler dispersed as the global structure are calculated, with the CNF-dispersed sub-microstructure as the local structure. In the second stage of the homogenization process, the homogenization properties of the printed phase of the 3D printed specimen are obtained using the microstructure with talc filler dispersed as the local structure and the global structure as the global structure. In the third step of the homogenization process, the homogenization properties of the macrostructure are obtained by taking the mesostructure of the 3D printed specimen as the local structure and the global structure as the macrostructure. In addition, the mechanical response of the macrostructure to external loading is analyzed. Multiscale.Sim was used for scale coupled analysis based on homogenization theory, and ANSYS was employed as the FEM solver.

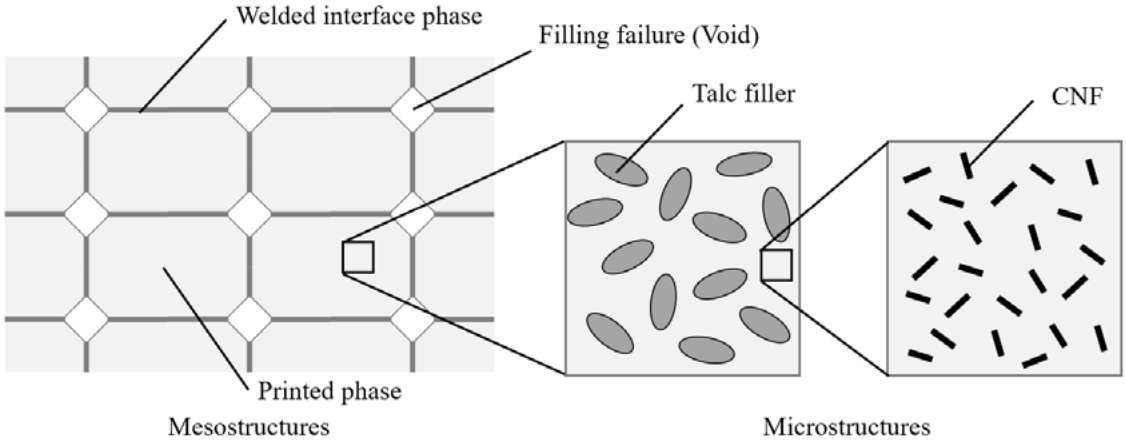


Figure 1. Multiscale modeling of 3D-printed hybrid reinforced composites.

An example of a representative volume element model employed for micro and sub-micro structures is shown in Figure 2. From left to right in the figure below, the RVE models are PP/Talc, PP/CNF, and PP/Talc/CNF. Based on SEM observations of composite cross sections, the Talc shape was a disk with a diameter of 4.0 μm and a thickness of 0.39 μm, and the CNF was 0.03 μm in diameter and 1.5 μm in length based on the published values of the raw material manufacturer. Talc and CNF were assumed to be elastic materials, with Young's modulus of 17.2 GPa and 140 GPa, respectively, and Poisson's ratio of 0.27 and 0.30, respectively, for PP. The mechanical properties of PP/CNF were obtained through the first homogenization process. Next, the obtained mechanical properties of PP/CNF were input to the base material of the RVE model in which only Talc was distributed, and the mechanical properties of PP/Talc/CNF were obtained through a second homogenization process.

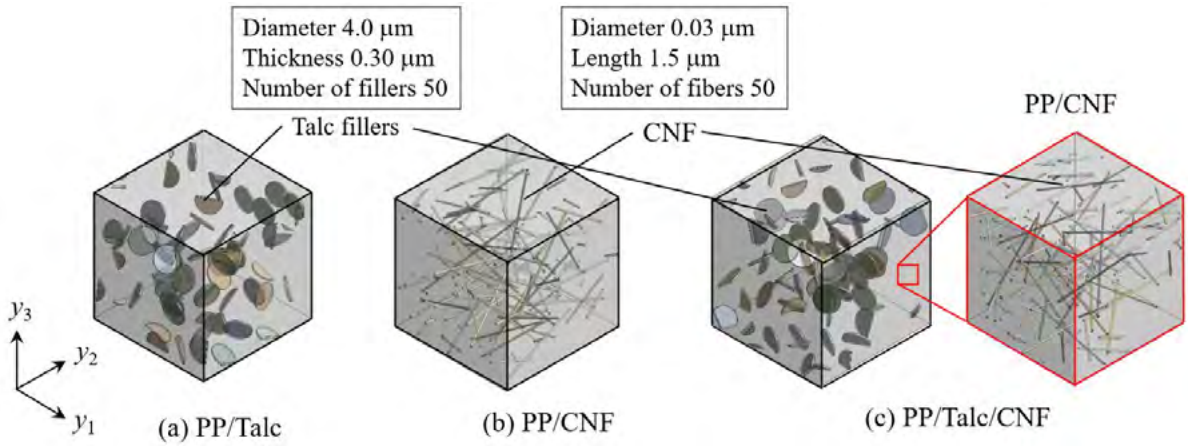


Figure 2. RVE models of PP composites with talc fillers and CNFs dispersed.

3. Result and discussion

Figure 3 shows a microstructure model of a 3D printed body considering the meso-homogeneous structure formed during printing. As shown in (a), an assembly of four melt-glued quarter filaments is considered as the unit cell of the heterogeneous structure, with a diamond-shaped void in the center due to poor filling and an interface phase between the four filaments. First, a general-purpose 3D printer (MF2500EP2, MUTOH) using the FFF method was used to print specimens for cross-sectional observation. The specimens were placed in the xy-plane of the printer table so that the thickness direction coincided with the z-axis in the stacking direction and the longitudinal direction was parallel to the x-axis. The specimens were printed with a fill rate of 100% and a printing angle of 0 degrees, i.e., with the longitudinal direction aligned with the x-axis. A nozzle with a diameter of 0.4 mm was used. After

searching for optimal printing conditions through trial and error, the extrusion nozzle temperature was 235°C, the table temperature was 115°C, the extrusion width was 0.4 mm, and the layer thickness was 0.2 mm. The cross section of the printed specimen was observed under an optical microscope, and the obtained cross-sectional image was binarized to identify void areas. From this, the area percentage and rhombic dimensions of the void areas were statistically calculated and reflected in the unit cell. As shown in (b), the cross section of the unit cell was divided into three regions, A, B, and C, and the possible effects of printing were reflected in these regions as mechanical properties. The PP composite material was set in region A, voids in region B, and one-tenth of the Young's modulus of PP in region C. The interface between the filaments is formed by molten PP, but the degree of entanglement of the PP molecular chains is mild, and a weak interface is assumed to form, different from the original mechanical properties.

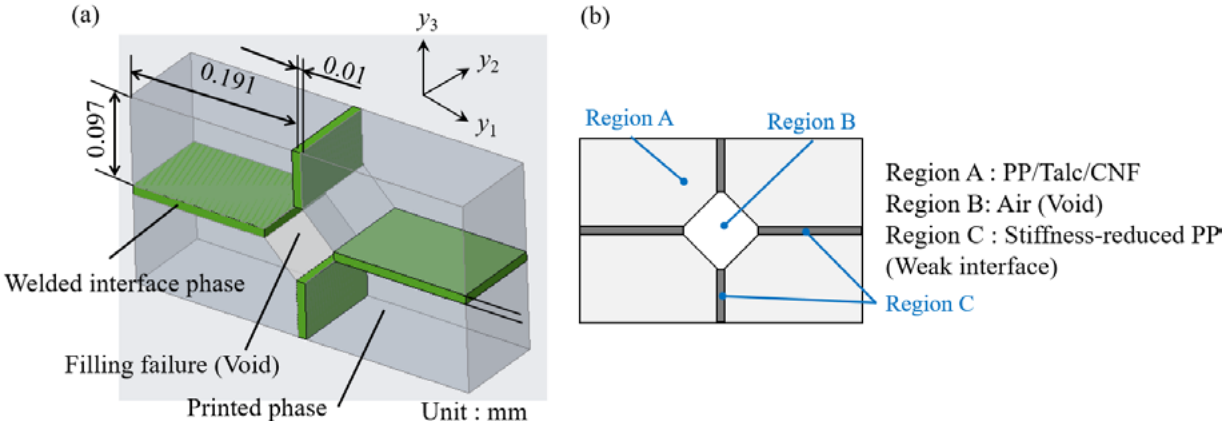


Figure 3. Meso heterogeneous structures formed during printing. (a) Unit cell model and dimensions of the heterogeneous structure; (b) Factors that degrade mechanical properties

Figure 4 shows the stress-strain relationship obtained from multiscale FEA with meso-homogeneous structure in Figure 3 for each of the printed composites. For all composites, the tensile stress increased linearly with increasing applied strain, and then the nonlinearity became significant after the applied strain exceeded 1%. This is because the nonlinear properties obtained from tensile tests of injection-molded PP were input to the base material PP in multi-scale FEA to analyze the mechanical properties of the PP composites. The influence of the filler was significant as the loading increased. At all loading strains, tensile stresses were higher for PP, PP/Talc, PP/CNF, and PP/Talc/CNF in that order, with the hybrid reinforced PP composite having the highest initial modulus and tensile stresses.

To quantitatively confirm the reduction in mechanical properties due to printing, Figure 5 then compares the Young's modulus and tensile strength of the PP composites obtained from the analysis using the injection-molded and 3D-printed models. In (a), Young's modulus of both injection-molded and 3D-printed composites improved in the order of PP, PP/Talc, PP/CNF, and PP/Talc/CNF. The Young's modulus of CNF was about 8 times larger than that of talc filler, which is considered to be due to its greater reinforcing effect. Furthermore, the Young's modulus of the 3D-printed specimens was about 10% lower than that of the injection-molded specimens. The maximum stress of both injection-molded and 3D-printed specimens increased in the order of PP, PP/Talc, PP/CNF, and PP/Talc/CNF in (b), and the maximum stress of the 3D-printed specimens was about 10% lower than that of the injection-molded specimens. These results indicate that voids and fragile interfaces reduce the mechanical properties of the 3D-printed specimens, and that Young's modulus and maximum stress are affected by the printed heterogeneous structure to the same extent.

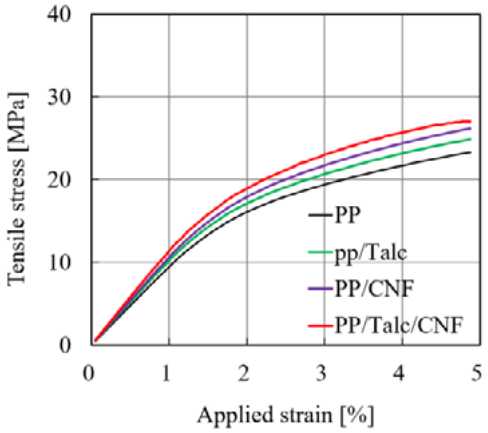


Figure 4. Comparison of computational results of stress-strain relationship of injection molded PP composites.

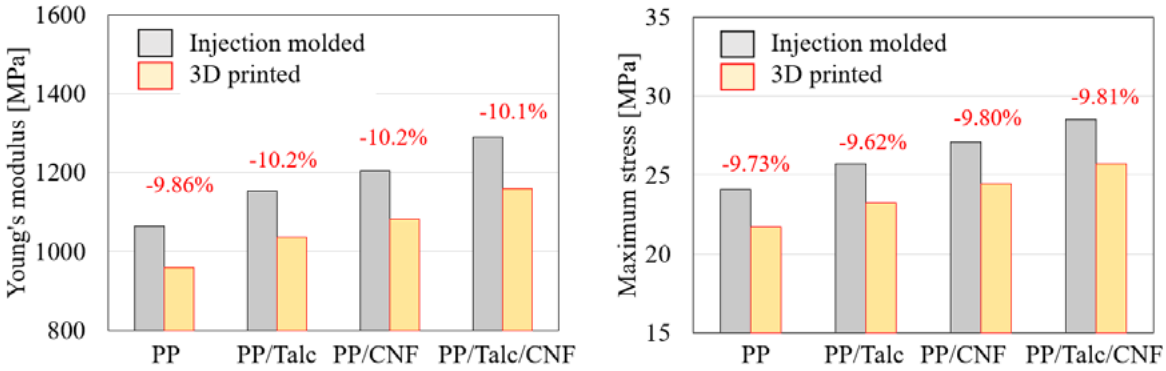


Figure 5. Comparison of mechanical properties of four different injection molded and printed models obtained from the analysis. (a) Young's modulus, (b) Maximum stress.

4. Conclusions

Hybrid reinforced PP composites with talc and CNF were proposed as a new FFF for PP composites, and the effect of filler addition was clarified by multiscale FEA. In the numerical analysis, a multiscale FEM scheme of printed hybrid reinforced PP composites with three-step homogenization was developed. It was found that the addition of talc and CNF was effective in improving Young's modulus and maximum stress, and the hybrid composites with both additions showed further reinforcing effects. For the inhomogeneous structure formed by printing, the effects of voids due to poor filling and the interface between melted and solidified filaments were assumed, and the mechanism of degradation of mechanical properties was clarified.

References

[1] Carneiro OS, Silva AF, Gomes R. Fused deposition modeling with polypropylene. Materials & Design, 83, (2015) 768–76.
[2] Junjiro Shintaku, Report of the New Manufacturing Study Group: Added Value Created by 3D Printers and Two Types of Manufacturing "Data Integration Capability" and "Manufacturing Network", (2014).
[3] Yu-His Huang, Chun-Yi Lin, Measurement of orthotropic material constants and discussion on 3D printing parameters in additive manufacturing, Applied sciences, 12(13), (2022), 6812.
[4] Shogai Yasuda, Yoshikuni Teramoto, Shinji Ogoe, Yasutomo Uetsuji, Fiber contribution on elastic properties of cellulose composites: A multiscale numerical study, Polymer Composites, 43, (2022) , 1656-1664

[5] Yasutomo Uetsuji, Shogai Yasuda, Yoshikuni Teramoto, Effect of fibre aspect ratio and aggregation on nonlinear material property of random cellulose reinforced composites: A multiscale computational study, Composite Structures, 301 (2022) 116201.
[6] Yasutomo Uetsuji, Ryoki Hamamoto, Chao Luo, Yuiciro Tsuyuki, Kazuyoshi Tsuchiya, Ryohei Ikura, Yoshinori Takashima, Fiber morphology design of cellulose composites through multiscale simulation, International Journal of Mechanical Sciences, 258, (2023) 108581.
[7] Taiki Kinoshita, Luo Chao, Kouta Ide, Kenji Aoki, Yasutomo Uetsuji, Mechanical characterization and design of hybrid reinforced polypropylene composites with talc fillers and cellulose fibers", Composites B, 266 (2023) 110971.

Laser ablation mechanism and damage prediction in fiber reinforced polymer composites.

Rishi Raj[1], Chandra Sekher Yerramalli[2]

[1]Indian Institute of Technology, Bombay, Aerospace Engineering Department, Mumbai–400076, Maharashtra, India. Email: 22m0033@iitb.ac.in
[2]Indian Institute of Technology, Bombay, Aerospace Engineering Department, Mumbai – 400076, Maharashtra, India. Email: chandra@aero.iitb.ac.in

Keywords: Laser ablation, Linear regression, Buckingham-Pi, 4D-Imaging, Fiber reinforced polymer composites.

Abstract: The study of laser ablation in fiber-reinforced composites extends beyond machining, offering insights into material behavior in high-heat environments, such as aerodynamic heating in high-speed aircraft, atmospheric re-entry and laser weapon on composite drones, unmanned air vehicles (UAVs) and missiles. Laser ablation, replicating high heat flux rapidly, is pivotal for exploring thermal shock and ablation resistance. Key parameters include ablation depth and the heat-affected zone (HAZ). Initial analysis, utilizing optical microscopy and image processing, revealed a correlation between laser power, energy input, and HAZ size. While HAZ area remains nearly constant with energy input for varying laser power, ablation depth increases proportionally with laser power due to the laser burning off material beyond its diameter, leaving contact with the pit's sidewall. Distinctive heat-affected volumes were observed using a four-dimensional X-ray microscope. The study aims to link ablation performance, material properties, and laser parameters for damage prediction. Methodology focuses on ablation depth and HAZ area, incorporating material properties and non-dimensional terms derived using the Buckingham-pi method. Empirical formulas predicting ablation depth an in GFRP and CFRP was found through linear regression using dimensionless terms.

1. Introduction

Fiber reinforced polymer (FRP) composites is being used extensively in aircraft and drone industry owing to it's high specific strength and stiffness, lightweight design causing fuel savings and lower carbon footprint than traditional material. However, when exposed to high heat flux it undergoes thermal degradation due to low degradation temperature depending upon the type of fiber and matrix used. High heat flux is experienced in cases of laser machining, directed energy system being used to attack UAVs, missiles and during aerodynamic heating in high speed aircraft. The major damage parameter in all of these cases are - heat affected zone and ablation depth. In laser machining of FRPs different laser parameters affect area of heat affected zone and ablation depth, this in turn will affect the quality of machined part [1].

Composite materials were initially used in military aircraft to reduce weight, allowing for increased weapon capacity and extended range. Recently developed directed energy systems are being deployed on battlefields, particularly targeting UAVs and helicopters, with potential for wider adoption as they advance [2]. Carbon-Carbon/Silicon carbide composites are used in hypersonic aircraft and rocket nozzles where they have to withstand sudden extreme heat during their service life, enduring high heat flux for short periods, with the combined effect of aerodynamic forces can cause unprecedented material damage [3,4]. In all these cases, it is evident that there is a need to understand the effect of high heat flux on FRP composites [4]. In laser ablation experiments, high heat flux can be emulated by adjusting both the power and diameter of the laser beam. Therefore, understanding laser material removal and predicting the size of the heat-affected area and depth of material removal is crucial.

In this paper, laser ablation experiments have been conducted on both carbon fiber and glass fiber reinforced polymer composites. The morphological study of the damaged specimen was carried out using four-dimensional X-ray microscope. Non-dimensional framework is introduced that predicts ablation depth (dependent term) given material properties and laser parameters (independent terms).

2. Materials and methods

2.1. Materials

Unidirectional carbon fiber reinforced composite (figure 1(a)) was manufactured using hand lay-up in the composite fabrication lab. It is a 7 layered laminated composite of 5.0 mm thickness. It was made using T-300 carbon fibers with LY 556 epoxy and HY 951 hardener as matrix in 10:1 ratio by weight. The sample was cured for 24 hours under pressure load. It was cut using water jet into rectangular pieces of 100 mm × 20 mm.

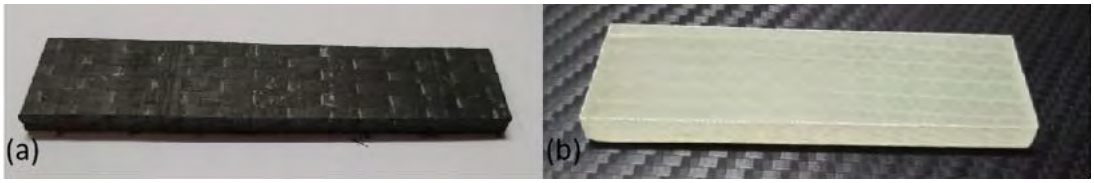


Figure 1. Laminated (a) carbon and (b) glass fiber reinforced composite.

Glass fiber composite (figure 1(b)) was manufactured by Fibrotech Composites. It has e-glass fiber by Owens Cornins and epoxy resin HSC 7600 with hardener HSC 8575 as matrix. It is a unidirectional laminated composite with 6 bundled-layer and a total thickness of 5.0 mm. Each layer has six fiber bundles in it stacked horizontally.

Table 1. Composite material properties

Specimen Type	Density (Kgm^{-3})	Specific heat capacity ($JKg^{-1}K^{-1}$)	Thermal Conductivity ($Wm^{-1}K^{-1}$) (Through thickness)	Melting temperature of fibers(K)
CFRP	1513	1021	0.636	3473
GFRP	2015	672	0.479	1978

2.2. Experimental setup

For the ablation experiment, SIL laser engraving machine and cutting machine AccuCut 1212 model was used. It is a near infrared laser. It has Co_2 DC Glass Laser Tube, pulse laser with a wavelength of 106nm. For ablating UD-GFRP/CFRP composite, laser power was varied as 20W, 26W, 39W, 40W, 52W, 65W while time for irradiation was varied till the laser just ablates through the entire thickness. The laser ablates the composites normal to it's surface. Laser diameter is 0.1 mm.

2.3. Non-dimensional framework

Dimensional analysis is a powerful technique for explaining complex system behaviors, such as laser ablation in polymer composites. It simplifies problems by reducing them to a manageable set of independent variables, offers physical interpretability through dimensionless terms, guides

experiments by identifying key influencing factors, and establishes scaling laws to relate behaviors across different scales. This approach also aids in developing empirical relationships using statistics and machine learning.

Buckingham pi method is one such method that is used to obtain non-dimensionless numbers to explain complex physical phenomenon [5,6,7,8]. The key idea behind the Buckingham Pi theorem is that physical phenomena can often be described by dimensionless groups or parameters, which are combinations of the original variables in a system such that the resulting expression is dimensionless (i.e., it has no units). These dimensionless parameters help in understanding the relative importance of different variables and how they affect the behavior of a physical phenomena [8].

Table 2. Set of fundamental parameters chosen for non-dimensional terms.

Parameters	Symbol	Dimension
Density	p	ML^{-3}
Thermal conductivity (through thickness)	k_1	$MLT^{-3}C^{-1}$
Thermal conductivity (along fibers)	k_2	$MLT^{-3}C^{-1}$
Specific heat	c	$L^2T^{-2}C^{-1}$
Fiber melting temperature	T	C
Material thickness	h	L
Power	P	ML^2T^{-3}
Irradiation time	t	T
Ablation depth (dependent)	d	L

Ablation depth prediction	
Power ratio	$\frac{Thk_1}{P}$
Diffusivity ratio	$\frac{h^2pc}{tk_1}$
Depth ratio	$\frac{d}{h}$
Repeating variable	K_1,h,c,t

Using these set of variables, we end up with 51 sets of π terms for both ablation depth and damage area prediction. To reduce this set of π terms to a unique choice of set that could explain the system behaviour, statistical consideration such as correlation among independent non-dimensional terms, correlation between dependent and independent non-dimensional terms, p-value (significance of independent parameters in predicting dependent terms) and interpretability of the dimensionless terms are considered. The repeating variables in table 2. are not apparent based on the dimensionless numbers since 'Diffusivity ratio' arises due to ratio of two other numbers and 'Conductivity ratio' is dropped due to it's weak correlation with the depth ratio.

3. Results and discussion:

3.1. Experimental:

Area of the heat affected zone (figure 2 (a)) and ablation depth (figure 2 (b)) was calculated in Image J software from the image taken in optical microscope at 16X magnification.

In surface view as shown in figure 3(b), Carbon Fiber Reinforced Polymer (CFRP) exhibits an elliptical profile, while Glass Fiber Reinforced Polymer (GFRP) in figure 3(d) showcases a circular profile. When subjected to damage as shown in Figure 3(a), CFRP typically displays a spheroidal damage profile within the Heat Affected Zone (HAZ), whereas in figure 3(c) GFRP exhibits a conical damage profile within the HAZ. This can be attributed to high thermal conductivity, high melting point of carbon fibers as compared to glass fibers and unidirectional nature of the composites.

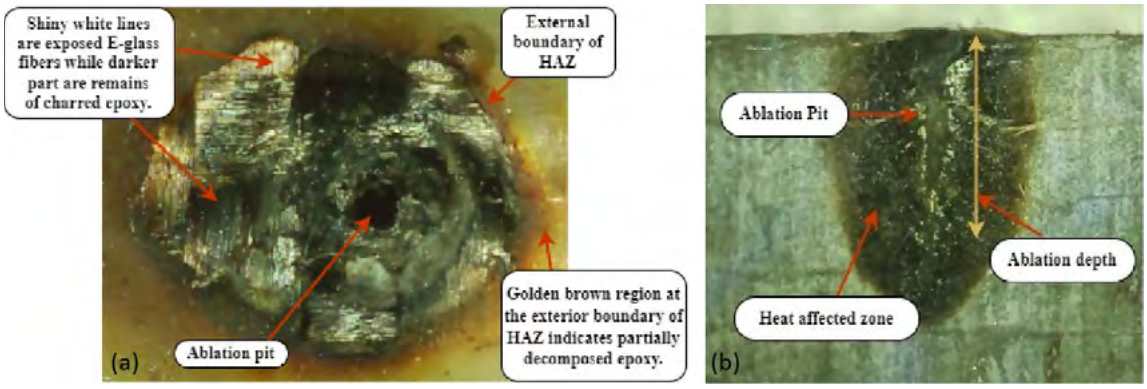


Figure 2. (a) Heat affected zone and (b) ablation pit morphology in case of GFRP.

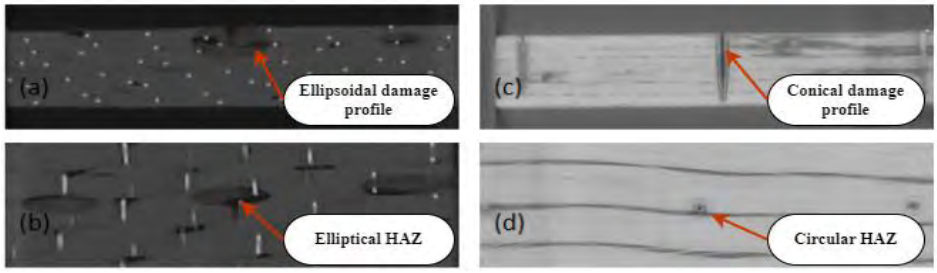


Figure 3. Ablation pit morphology comparison between (a) CFRP & (c) GFRP and heat affected zone profile comparison between (b) CFRP & (d) GFRP.

From figure 4, it can be seen as the area of the heat-affected zone is increasing with increasing power for the same irradiation time because more energy is applied per unit time. For the same power, more irradiation time results in more HAZ area since more energy is being applied. However, for 26W and 39W laser power, after a certain time, the area of HAZ doesn't increase. This could be due to the fact that once more area around the laser diameter region gets vaporized, there is no contact left for heat to be conducted in the in-plane direction of the composite laminate. This is more prominent in the case of low-power lasers since it requires more time to ablate the GFRP laminate completely. This leads to the deepening of the ablation pit without any further increase in the HAZ area. Therefore, in order to observe no further increase in HAZ area with irradiation time for a 52 W laser, we need a thicker composite. For a 65 W laser, the irradiation time to completely ablate the composite is too short; therefore, very few data points are seen in the plot.

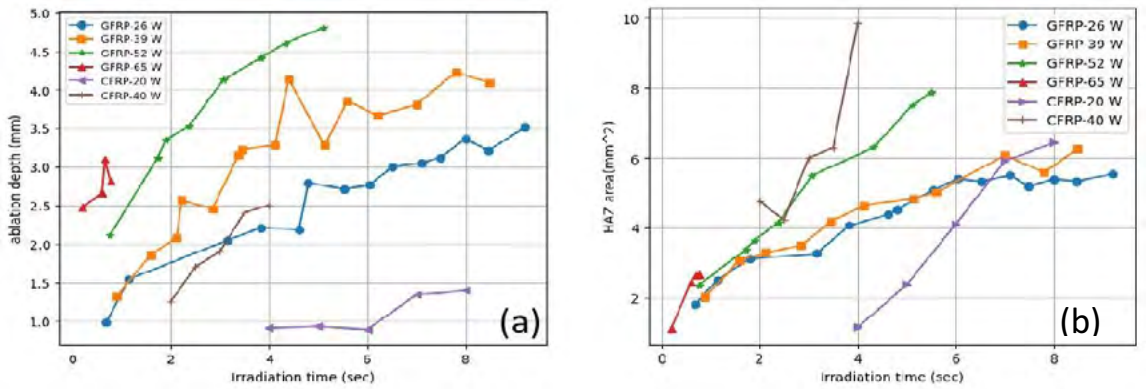


Figure 4. (a) Heat affected zone vs irradiation time plot and (b) ablation depth vs irradiation time for both GFRP and CFRP

For CFRP, higher power does less damage than low power in GFRP. Even a lower laser power will cause a large heat affected zone due to comparatively higher thermal conductivity in the in plane direction along fibers. Any discrepancy with the above-mentioned trend can be attributed to whether laser strikes fibre bundles (more HAZ area) or the interface between the fibre bundles. It is observed that ablation depth is more for higher laser power for the same energy. Here, diameter of the laser is kept the same therefore, higher laser power is also the higher laser intensity which is the critical parameter affecting laser ablation depth. Ablation depth should increase with increasing irradiation time for the same laser power, however, this is not true always in the figure 3(a) for laser power of 26W, 39W and 65W. This results in more depth for lesser time in some of the cases. Another observation that can be made from the figure 3(b) is that as laser power is increasing effective slope of ablation depth vs irradiation time plot is also increasing which suggests that ablation rate is higher for high power laser.

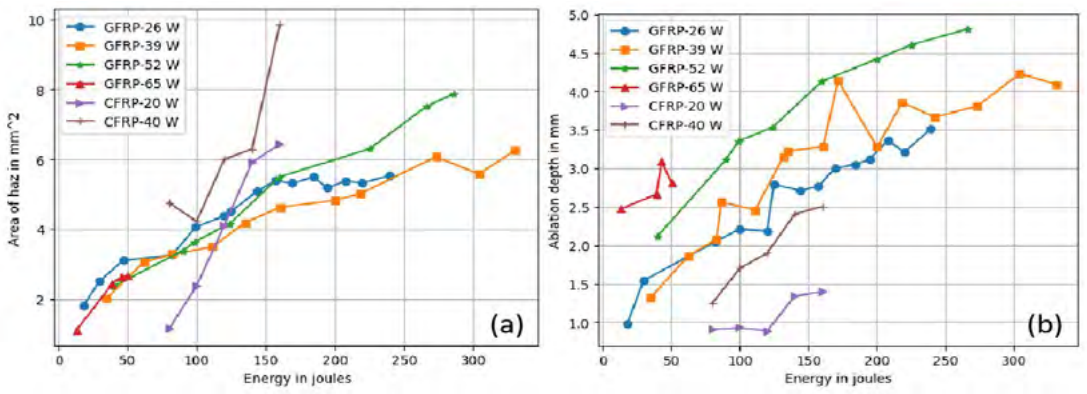


Figure 5. (a) Area of haz at the exposed surface vs energy plot (b) ablation depth vs energy plot for both CFRP and GFRP.

Increasing laser energy increases ablation depth for the same laser power, however ablation depth for high power laser is higher for same energy input. Area of heat affected zone increases with the increase in laser energy. For the same energy, varying laser power level does not change the area of the heat affected zone for GFRP (figure 5(a)) but this cannot be said for the CFRP material (figure 5(b)) owing to less sample points.

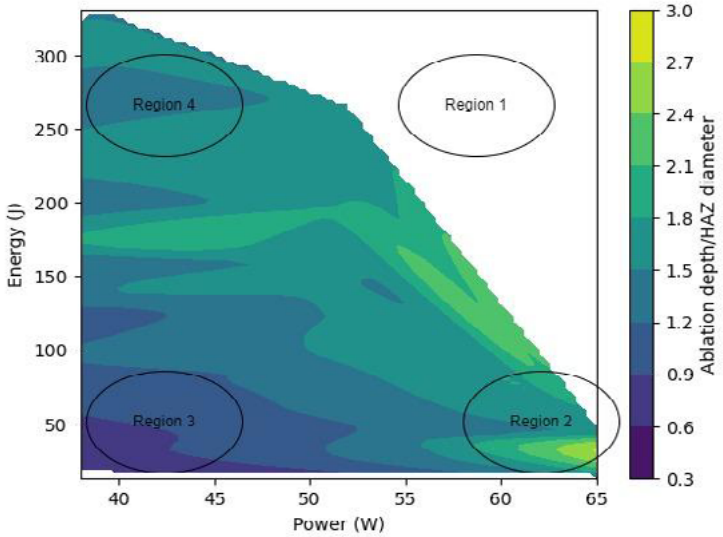


Figure 6. Ablation depth to heat affected zone ratio vs energy input and laser power for GFRP

In figure 6, the plot is divided into 4 regions, region 1 (in white) is for that combination of laser power and energy which results in almost complete ablation of the composite laminate. Region 2 refers to the region of high power and low energy which results in high ablation depth as compared to the width of the heat affected zone. As we move from region 2 (high power) to region 3 (low power) for the same energy, a lower depth to haz diameter ratio is observed since lower power leads to low depth however for large irradiation time (to maintain same energy) results in more heat transfer as melting point of material around laser reaches slowly. From region 3 to region 4, for the same power, energy (irradiation time here) increases which causes ablation depth to dominate as enough time exists for material removal however once material around laser looses contact with laser beam haz stops increasing leading to a higher depth to damage diameter ratio.

3.2. Non-dimensional framework:

For predicting depth ratio, diffusivity ratio and power ratio turns out to be the most important parameters. Linear regression was performed in log-log domain as it linearizes the data that helps to capture non-linear trends by using linear regression which is the simplest model to implement and easily interpretable. Figure 7(a). shows comparison between actual and predicted ablation depth for CFRP and GFRP. The 3D plot in figure 7(b). shows regression plane and scatter points between dependent and independent dimensionless ratios in the log-log domain. The equation for the regression plane for predicting ablation depth is,

$$\frac{d}{h} = 0.286 \times \left(\frac{h^2 pc}{tk_1}\right)^{-0.35} \times \left(\frac{Thk_1}{P}\right)^{-0.7276} \quad (1)$$

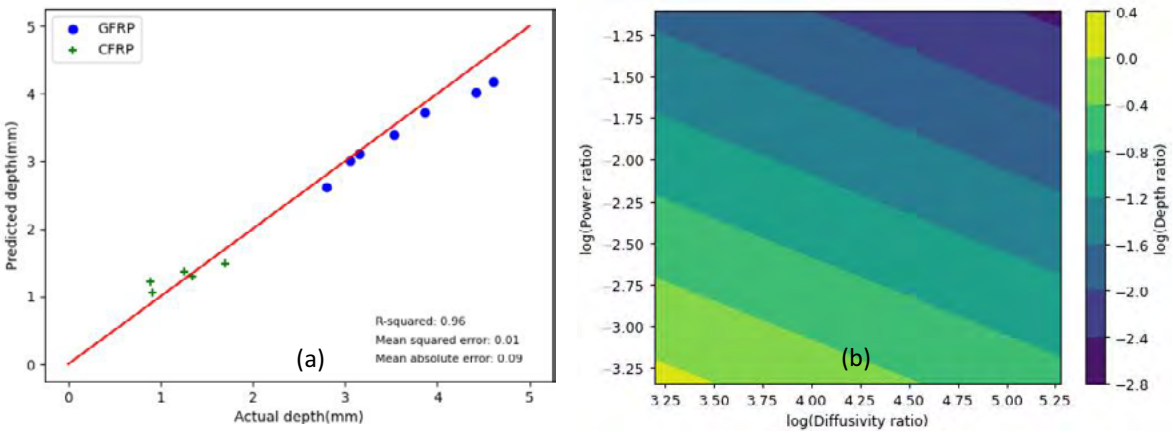


Figure 7. Regression plot (a) predicted depth vs actual depth (b) 2D contour plot for 'Depth ratio' prediction for a combination of 'Diffusivity ratio' and 'Power ratio'.

From figure 7(b) we can observe the parallel shades of colors that represent values of depth ratio for various power and diffusivity ratios. The depth ratio is inversely related to power and diffusivity ratios.

4. Conclusion

Laser ablation damage comprising ablation depth and heat affected zone was investigated for unidirectional carbon and glass fiber reinforced polymer composite. Damage profile was studied under 4D X-ray microscope. Area and depth of the damage was measured in image J software. Experimental data was analyzed to study the effect of laser parameters and material properties on ablation depth and area of heat affected zone. Non dimensional framework was used to predict laser ablation depth. The following conclusions could be drawn:

1. Unidirectional CFRP composite yielded an elliptical heat affected zone surface and ellipsoidal damage profile while unidirectional GFRP composite yielded a circular heat affected zone surface and a conical damage profile.
2. Laser ablation depth increases for the same energy input for the increasing laser power however, area of heat affected zone remains nearly the same for same energy input while laser power is increasing.
3. Ablation depth vs irradiation time plot shows greater slope for higher laser power implying higher ablation rate for high power laser ablation.
4. Buckingham-pi method yielded an empirical formula that relates depth ratio to power and diffusivity ratios.

5. References:

[1] M. H. El-Hofy and H. El-Hofy. Laser beam machining of carbon fiber reinforced composites: a review. The International Journal of Advanced Manufacturing Technology, 101(9-12):2965-2975, 2019.

[2] Y.X. Zhang, Zhi Zhu, Richardson Joseph, and Isfakul Jamal Shihan. Damage to aircraft composite structures caused by directed energy system: A literature review. Defence Technology, 17(1):218-230, 2021.

[3] Jiangtao Wang, Yuzhao Ma, Yuwen Liu, Wu Yuan, Hongwei Song, Chenguang Huang, and Xiaowei Yin. Experimental investigation on laser ablation of C/SiC composites subjected to supersonic airflow. Optics and Laser Technology, 113:358-365, 2019.

[4] Mohammad Zahid and Rajneesh Sharma. Thermal shock resistance of 4D-inplane carbon/carbon composite based on micro-structurally informed effective properties. Materials Today Communications, 24:101637, 2020.

[5] Maximilian Pierzyna, Rudolf Saathof, and Sukanta Basu. Π-ML: A dimensional analysis-based machine learning parameterization of optical turbulence in the atmospheric surface layer. arXiv:2304.12177, 2023.

[6] Rietkerk, R., Heine, A., and Riedel, W. Physics-informed machine learning model for prediction of long-rod penetration depth in a semi-infinite target. International Journal of Impact Engineering, 173:104465, 2023.

[7] Dieter Strobbe, Jean-Pierre Kruth, and Peter Van Puyvelde. Tuning Process Parameters and Polymer Powder Formulation for Laser Sintering; Afstemmen van procesparameters en polymeerpoederformulering voor laser sinteren. PhD Thesis, LIRIAS, 2023.

[8] John F. Mahoney and Sencer Yeralan. Dimensional Analysis. Procedia Manufacturing, 38:694-701, 2019.

COMPREHENSIVE ANALYSIS OF DAMAGE PROGRESSION IN HIGH-PERFORMANCE THERMOPLASTIC COMPOSITES THROUGH MULTI-INSTRUMENTAL STRUCTURAL HEALTH MONITORING APPROACHES

Ceren Yildirim[1,2], Isa Emami Tabrizi [3], Abdulrahman Al-Nadhari [1,2], Serra Topal [1,2] , Bertan Beylergil [4] Mehmet Yildiz [1,2]

[1] Sabanci University Integrated Manufacturing Technologies Research and Application Center & Composite Technologies Center of Excellence, Teknopark Istanbul, Pendik, Istanbul 34906, Turkey
[2] Faculty of Engineering and Natural Sciences, Sabanci University, Tuzla, Istanbul 34956, Turkey
[3] College of Science and Engineering, University of Derby, Kedleston Rd, Derby, DE22 1GB, UK
[4] Faculty of Engineering, Department of Mechanical Engineering, Alanya Alaaddin Keykubat University, 07450, Alanya, Turkey

Presenting author. yildirimceren@sabanciuniv.edu

Keywords: Thermoplastic composites; Automated fiber placement (AFP); Damage characterization; Digital Image Correlation; Acoustic Emission; Thermography

Abstract

The failure behavior of carbon fiber/poly(ether ketone ketone) (CF/PEKK) composites manufactured via automated fiber placement (AFP) followed by subsequent consolidation in autoclave is studied. Multi-instrumental structural health monitoring (SHM) approaches are used to analyze damage development stages and and damage types in high performance thermoplastic composite laminates. Void analysis, and density measurement, and optical microscopy reveal the effect of secondary consolidation through autoclave on the microstructure of the composite laminates. An interlaminar void reduction from 5.65% to 0.46% are observed. Acoustic emission (AE), digital image correlation (DIC), and infrared thermography (IRT) techniques during tensile tests provide complementary understanding of the physics behind the critical damage types occurring in the material, such as edge splitting. Slope of the cumulative AE counts and percentage of total number of hits signify two distinct stages of failure, each associated with a dominant failure mode. Also it is evident that the high energy AE hits are corresponding to macro level damage events which are captured by the IRT in the form of various edge splitting. The initiation of these damage events can be anticipated through concurrent monitoring of DIC strain maps.

1. Introduction

High-performance thermoplastic matrix composites (TPCs) are increasingly favored for aerospace applications due to a multitude of advantages, such as notable strength-to-weight ratios, expedited molding processes, exceptional resistance to environmental factors, recyclability, and the capability for room temperature storage [1,2]. Within the realm of TPCs, Polyetherketoneketone (PEKK) stands out for its remarkable structural advantages, characterized by high mechanical toughness, favorable formability, low moisture absorption, and strong bonding properties [3,4].

Understanding damage onset and evaluation in composites is crucial for ensuring structural integrity and facilitating safer design practices. There is a growing need for alternative and complementary monitoring methods to investigate damage accumulation in composite materials [5,6]. This research integrates a comprehensive structural health monitoring system with mechanical testing to analyze the characterization of damage mechanisms, including their development and classification, in high-performance thermoplastic composites (TPCs) produced through Automated Fiber Placement (AFP) technology, specifically those composed of Carbon Fiber/Polyetherketoneketone (CF/PEKK).

2. Materials and Methods

Three unidirectional laminates are produced using a robotic laser-assisted Automated Fiber Placement (AFP) system (Coriolis C1), with a feed rate of 0.2 m/s and a consolidation force of 400 N (see in **Figure 1a**). The visible nip-point temperature is recorded at 400±10 °C. After the lay-up process, the laminate is cooled down to room temperature and removed. Consolidation of the AFP CF/PEKK thermoplastic lay-up occurs in an autoclave environment using the ASC autoclave system, with a consolidation temperature of 377 °C, heating, and cooling ramps of 5 °C/min and 11 °C/min, and a pressure of 8 bars maintained constant for 40 minutes (see in **Figure 1b**).

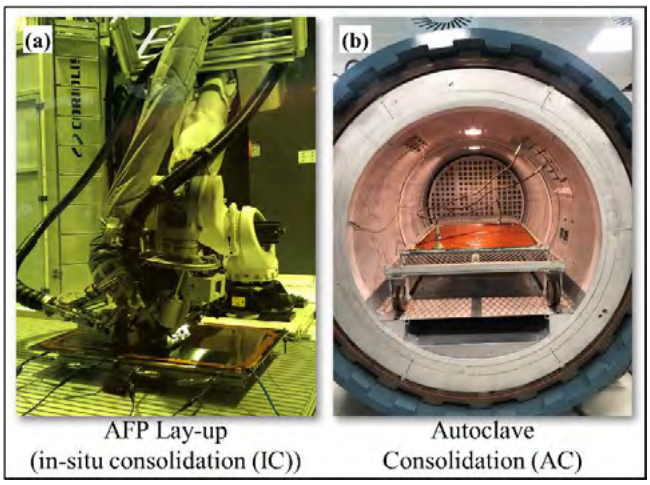


Figure 1. CF/PEKK Composite Manufacturing

To obtain the void content of in-situ and autoclave consolidated CF/PEKK laminates, fiber, matrix, and void contents of these specimens are measured based on the ASTM D3171 standard method 1. Also, the effect of secondary consolidation on the microstructure of the composite is thoroughly investigated using a Nikon, ECLIPSE LV100ND model microscopy.

2.1. Multi-instrument Structural Health Monitoring Techniques

Tensile tests are conducted on CF/PEKK composite specimens at a speed of 1.5 mm/min using an INSTRON 5982 universal testing machine. A bi-axial strain gauge is affixed to the specimen surface to measure the Poisson ratio. Throughout the tests, specimens are monitored using multi-instrument structural health monitoring techniques, including AE, DIC, and passive IRT, as depicted in **Figure 2**.

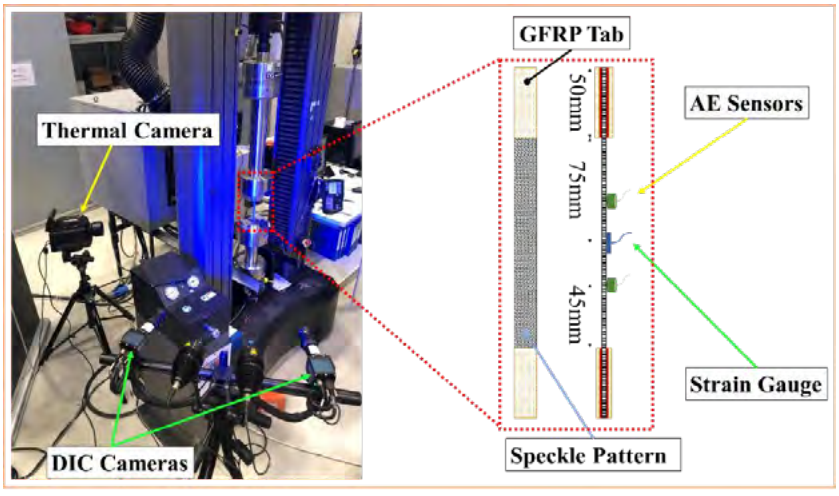


Figure 2. Multi-instrument Structural Health Monitoring.

3. Results

3.1. Impact of secondary consolidation on the microstructure of the composite

The average densities of three samples from in-situ and autoclave consolidated CF/PEKK composite plates are 1.49 and 1.58 g/cm3, respectively. **Table 1** presents the corresponding average weight fractions of fiber (W_f) and matrix (W_m), along with the volume percent contents of fiber (V_f), matrix (V_m), and void (V_v) for both consolidation methods.

Table 1 Fiber, matrix, and void contents of in-situ and autoclave-consolidated laminates.

	W_f (%)	W_m (%)	V_f (%)	V_m (%)	V_v (%)
In-situ consolidated (IC) CF/PEKK	65.04 ± 0.26	34.96 ± 0.26	54.22 ± 0.20	40.13 ± 0.31	5.65 ± 0.13
Autoclave-consolidated (AC) CF/PEKK	65.29 ± 0.14	34.71 ± 0.14	57.47 ± 0.16	42.07 ± 0.15	0.46 ± 0.04

As seen in **Table 1** the void content of autoclave consolidated CF/PEKK composite is less than 1%, i.e. minimum acceptable range in high performance composite laminates. As seen in **Figure 3** the large portion of voids in the microstructure of in-situ consolidated composites are pseudo-interconnected interlaminar voids at intimate contact lines. Autoclave processing not only helps to reduce the size of voids but also provides a network of pathways for removal of trapped air via bleeding. As a result, the void content decreases from 5.65% to 0.46%.

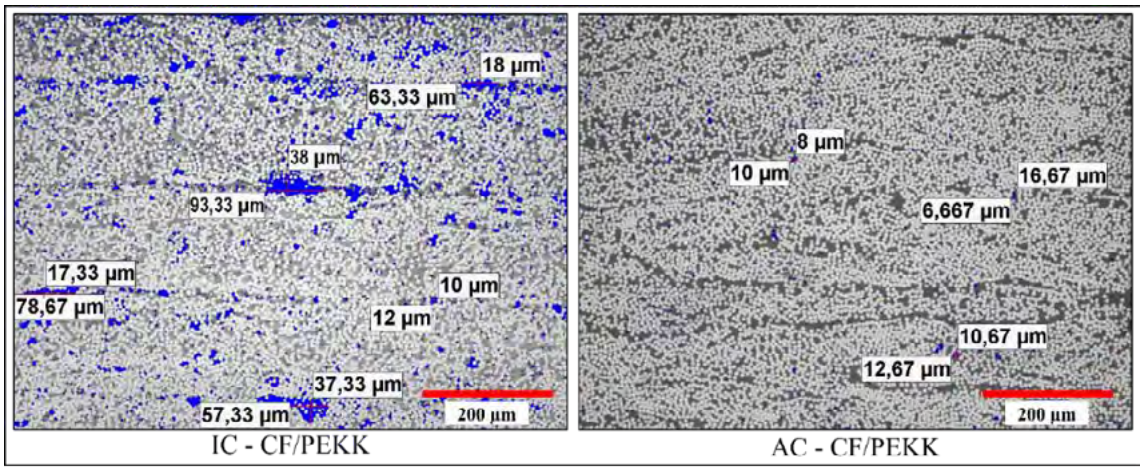


Figure 3. Optical microscope images of in-situ and autoclave consolidated laminate.

3.2. Multi-instrument Nondestructive Monitoring

The identified types of failure have been categorized based on their Weighted Peak Frequency (WPF) [7–9], spanning from low to high, as outlined in **Table 2**. The representative clustering of AE hits tensile samples of CF/PEKK is given in **Figure 4a.** Partial Power 2 indicates to the percentage of signal power in the frequency range of 300–600 kHz. WPF is calculated using Equation (1) as:

$$WPF = (f_c \times f_p)^{1/2} \quad (1)$$

where f_c and f_p indicate the frequency centroidand peak frequency, respectively.

Table 2 WPF range and related failure type.

WPF Range (kHz)	Failure Type
50-190	Matrix Cracking (MC)
190-360	Interface Failure (IF)
360-550	Fiber Failure (FF)

In **Figure 4b**, the amplitude of AE hits and the cumulative AE counts versus time graphs for CF/PEKK composite specimens are depicted. Notably, the cumulative AE count curve reveals two distinct stages called as stage I and stage II, respectively. In the region designated as Stage I, the AE counts demonstrate a linear increase, suggesting a consistent progression of damage within the laminate. In this stage, the AE hits associated with matrix cracking and interface failure exhibit both high and low amplitudes. Contrary to Stage I, Stage II displays a non-linear rise in cumulative AE counts over time, predominantly consisting of low-amplitude AE events. Notably, the frequent incidence of high-amplitude interface failures, such as delamination events observed in Stage I, is absent in Stage II. Although low- and high-amplitude delamination failures are evident in thermoplastic laminates, their occurrence frequency varies depending on the severity of accumulated damage within the material. **Figure 4c** illustrates the percentage of failure in these two stages, indicating a transition from matrix failure to fiber failure.

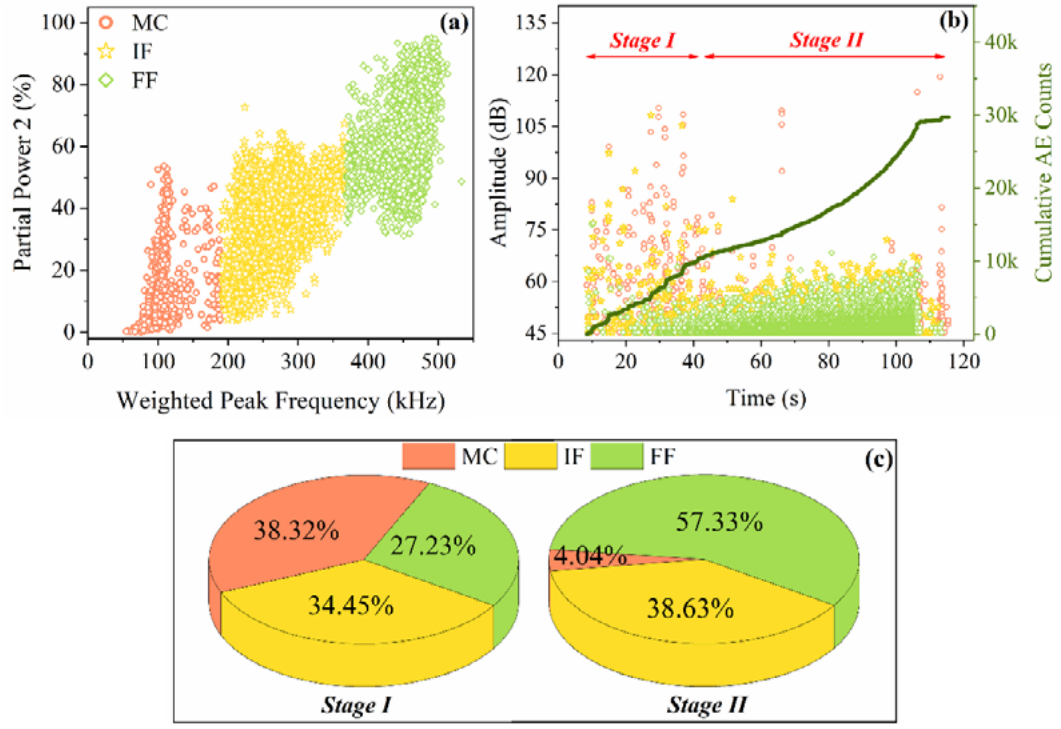


Figure 4. (a) Representative k-means clusters for tensile samples and **(b)** variations of time versus amplitude and cumulative AE counts, and **(c)** number of hits for various damage types

Figure 5 presents the plot of cumulative AE energy and load versus time. The fact that the axial strains-over time obtained from SG and DIC are the same with each other, which means that the DIC method is reliable for this study. Also, there is a deviation between axial strain curves and load curve at the end of the Stage I. At this stage, fiber-dominant failures control the material fracture, concomitant with a reduction in slope observed in the strain-time curve, indicative of an augmented stiffness in the laminates. There are five significant changes in the load versus time curve, marked as i, ii, iii, iv and v. All points (i-v) are also detected by AE, SG, DIC and IRT system, however, after point ii, AE sensor failed to record data.

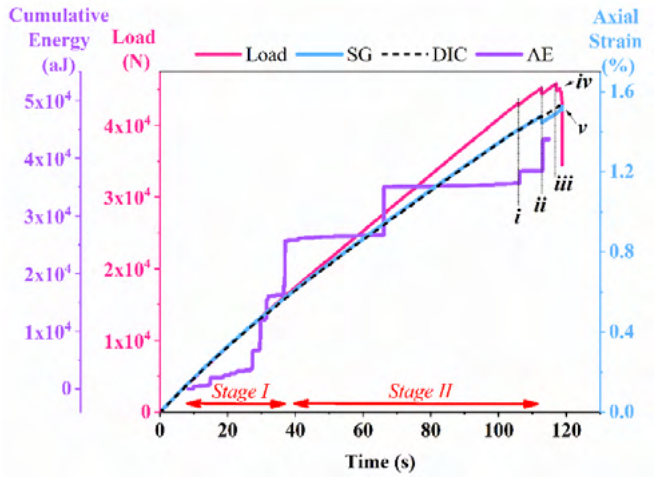


Figure 5. Plots of total AE cumulative energy, load, and axial strain over time. Note: Points (i), (ii), (iii), (iv), and (v) are marked to show the activity at 106, 113, 117, 118 and 119 s, respectively.

Thermal maps and strain maps corresponding to the time intervals (i-v) are depicted in **Figure 6**. Edge splitting, attributed to fiber misalignment at the edges of the composite specimen, is clearly observed from the beginning to the final stages of the tensile test in the IRT maps. Additionally, as depicted in the DIC map, localized high strain regions encircled in the specimen's edges are more pronounced. This suggests that the edge regions of the specimen are more susceptible to damage initiation and growth. Despite the expectation of greater deformation and earlier failure in regions with higher strain regions, it is noteworthy that the top left side of the specimen fails at an early stage, while the lower left region remains unaffected. The comparison between DIC strain maps and corresponding thermal maps indicates that the high strain gradient region at the lower left edge of the sample emerges at 67% of the maximum stress, while thermography maps do not exhibit any relevant activity in the same region until 90% of the ultimate tensile strength is reached. This observation underscores the capability of DIC results to identify failure-prone areas in TPCs well in advance compared to other techniques.

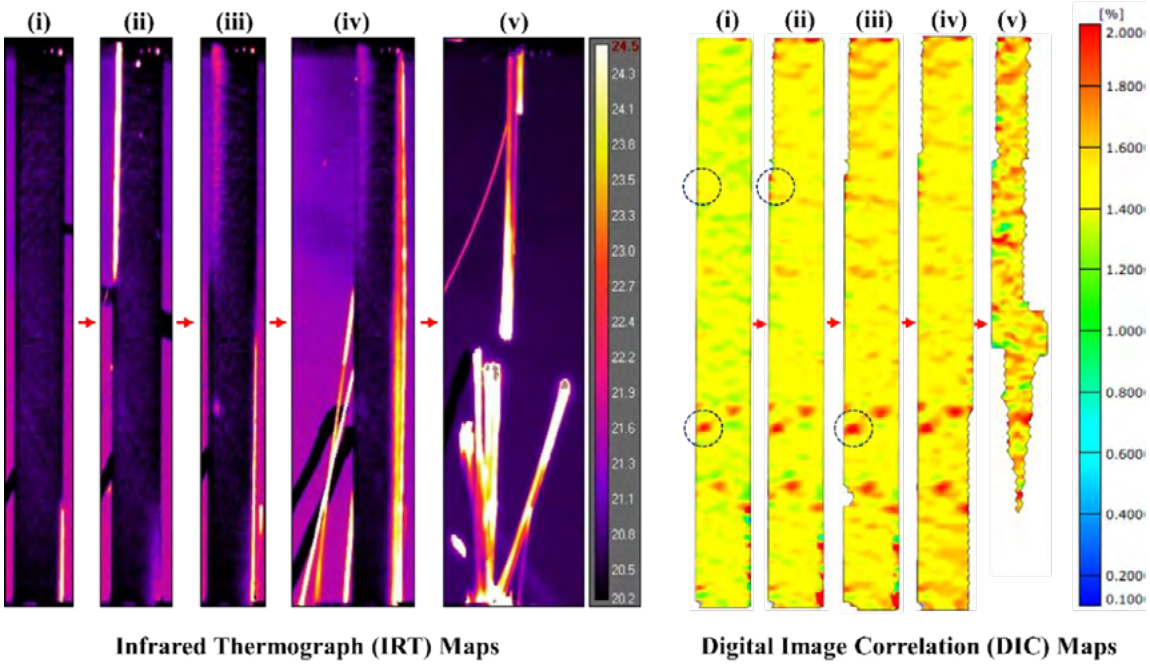


Figure 6. Thermograms and DIC in-plain strain fields for CF/PEKK specimens at (i) 106, (ii) 113, (iii) 117, (iv) 118, and (v) 119 s corresponding to the points marked in **Figure 5.**

4. Conclusions

This study investigates the impact of autoclave consolidation following in-situ consolidation on the microstructural properties of unidirectional CF/PEKK TPCs and examines damage mechanisms under tensile loading using multi-instrumental monitoring techniques. Microscopic observations reveal a reduction in voids within in-situ consolidated laminates post-autoclave consolidation, enhancing material intimacy. Analysis of AE hits and counts demonstrates a shift in tensile failure behavior from matrix-dominant to fiber-dominant failure modes, coinciding with a gradual stiffness increase. This change in AE hits may serve as a damage index in thermoplastic laminates, aiding in assessing composite structure longevity. Correlation between AE energy upsurges and macro-level damage detected by thermal imaging links to edge splitting, predictable through DIC strain maps. However, DIC maps provide insufficient data on the likelihood of these macro damage events due to the stochastic nature of fiber failures in carbon fiber-reinforced laminates. Furthermore, DIC allows susceptible failure areas in thermoplastic materials to be identified much earlier than IRT methodologies.

Acknowledgments
The authors gratefully acknowledge financial support from the Scientific and Technological Research Council of Turkey (TÜB˙ITAK) with project number 218M709C. Yildirim gratefully acknowledges the financial support provided by the European Cooperation in Science & Technology (COST) under Action CA21155 to her attendance at the 21st European Conference on Composite Materials (ECCM21).

References

[1] Hoang VT, Kwon BS, Sung JW, Choe HS, Oh SW, Lee SM, et al. Postprocessing method-induced mechanical properties of carbon fiber-reinforced thermoplastic composites. J Thermoplast Compos Mater 2023;36:432–47. https://doi.org/10.1177/0892705720945376.

[2] Sudhin AU, Remanan M, Ajeesh G, Jayanarayanan K. Comparison of Properties of Carbon Fiber Reinforced Thermoplastic and Thermosetting Composites for Aerospace Applications. Mater. Today Proc., vol. 24, Elsevier; 2020, p. 453–62. https://doi.org/10.1016/j.matpr.2020.04.297.

[3] Yildirim C, Ulus H, Beylergil B, Al-Nadhari A, Topal S, Yildiz M. Tailoring adherend surfaces for enhanced bonding in CF/PEKK composites: Comparative analysis of atmospheric plasma activation and conventional treatments. Compos Part A Appl Sci Manuf 2024:108101. https://doi.org/10.1016/J.COMPOSITESA.2024.108101.

[4] Yildirim C, Ulus H, Beylergil B, Al-Nadhari A, Topal S, Yildiz M. Effect of atmospheric plasma treatment on Mode-I and Mode-II fracture toughness properties of adhesively bonded carbon fiber/PEKK composite joints. Eng Fract Mech 2023;289:109463. https://doi.org/https://doi.org/10.1016/j.engfracmech.2023.109463.

[5] Saeedifar M, Zarouchas D. Damage characterization of laminated composites using acoustic emission: A review. Compos Part B Eng 2020;195:108039. https://doi.org/10.1016/j.compositesb.2020.108039.

[6] Ivanov SG, Beyens D, Gorbatikh L, Lomov S V. Damage development in woven carbon fibre thermoplastic laminates with PPS and PEEK matrices: A comparative study. J Compos Mater 2017;51:637–47. https://doi.org/10.1177/0021998316653460.

[7] Ali HQ, Emami Tabrizi I, Khan RMA, Tufani A, Yildiz M. Microscopic analysis of failure in woven carbon fabric laminates coupled with digital image correlation and acoustic emission. Compos Struct 2019;230. https://doi.org/10.1016/j.compstruct.2019.111515.

[8] Tabrizi IE, Kefal A, Zanjani JSM, Akalin C, Yildiz M. Experimental and numerical investigation on fracture behavior of glass/carbon fiber hybrid composites using acoustic emission method and refined zigzag theory. Compos Struct 2019;223:110971. https://doi.org/10.1016/j.compstruct.2019.110971.

[9] Yildirim C, Tabrizi IE, Al-Nadhari A, Topal S, Beylergil B, Yildiz M. Characterizing damage evolution of CF/PEKK composites under tensile loading through multi-instrument structural health monitoring techniques. Compos Part A Appl Sci Manuf 2023;175:107817. https://doi.org/https://doi.org/10.1016/j.compositesa.2023.107817.

CONTENTS

FAILURE PREDICTION OF INJECTION-MOULDED SHORT-FIBRE COMPOSITES: CHARACTERISATION AND PREDICTION FROM COUPONS TO COMPONENTS

Yuki Fujita[1,2,3], Satoshi Noda[2], Shunta Kimura[2], Junichi Takahashi[2], Emile S. Greenhalgh[3] and Soraia Pimenta[1]

[1] Department of Mechanical Engineering, Imperial College London, South Kensington Campus, SW7 2AZ London, United Kingdom (Email: y.fujita@imperial.ac.uk)
[2] Polymers R&D Planning and Business Development, Asahi Kasei Corporation, 210-0863, 1-3-1, Yako, Kawasaki, Japan
[3] Department of Aeronautics, Imperial College London, South Kensington Campus, SW7 2AZ London, United Kingdom

Keywords: Injection moulded composites, Fracture toughness, Coupled finite element analysis, Cohesive zone modelling, Fractography

Abstract

Injection-moulded short-fibre composites are lightweight materials suitable for high-volume applications; however, current simulation methods for these materials are based on failure initiation criteria only, and cannot yet predict ultimate failure accurately. This work proposes an improved methodology to predict the progressive failure of injection-moulded short-glass-fibre reinforced PA66 composites, from coupon level to component level, based on experimentally-measured properties. The material's fracture toughness was characterised for different fibre orientations and environmental conditions, and these values were used as the input for cohesive zone modelling in Finite Element analyses, coupled with the fibre orientation fields predicted by an injection-moulding process simulation. The coupled process/structural simulations using cohesive zone modelling presents excellent agreement with the expeimental data of the coupons/subcomponents/components, highlighting the importance of accounting for the fracture toughness of the material to accurately predict the ultimate failure of injection-moulded short-fibre reinforced PA66 composites.

1. Introduction

Injection-moulded (IM) short-glass fibre reinforced thermoplastics (SFRPs) have three key advantages over conventional materials: they are lightweight, they have short production cycles, and they can be moulded into complex 3D-shaped components. The injection-moulding process creates a skin-core micro-structure with complex fibre orientation states, as the fibres align along the flow direction in the skin, and along the transverse direction or randomly in the core (as shown in Figure 1). This microstructure leads to anisotropic and heterogeneous mechanical properties and failure modes, which complicate the design of SFRP components.

When designing SFRP components, it is necessary to predict when and where failure will occur. However, existing failure criteria for SFRPs (e.g. based on the Tsai-Hill criterion [1]) underestimate the ultimate failure load of components, because they consider failure initiation only and neglect the finite toughness of the material. The objective of this work is therefore to develop a Finite-Element methodology to predict failure of IM-SFRP subcomponents and components, by accounting for the material's progressive failure using properties measured experimentally from coupon testing.

2. Manufacturing

Polyamide 6.6 reinforced by 50% (wt) glass-fibres (PA66-GF50) from Asahi Kasei Corporation was used to injection-mould plates (Figure 1). Dog-bone specimens (based on ISO8256) and Compact-Tension (CT) specimens (Figure 2) were machined at several angles from the IM-plates [2,3]. Subcomponents (Figure 3(a), representing a simplified geometry of an automotive component [3]), and components (Figure 3(b), representing a real geometry of an automotive engine mount) were also manufactured with the same material as used for IM-plates. These samples were kept dry as moulded (DAM), or conditioned under 50% of relative humidity (RH50, according to ISO1110 [4]).

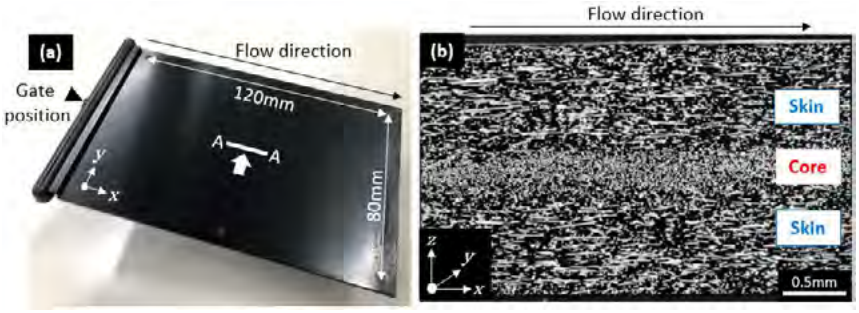


Figure 1. (a) Photograph of an injection-moulded PA66-GF50 plate (2 mm thick). (b) Optical micrograph across the A-A section defined in Subfigure (a) [2,3].

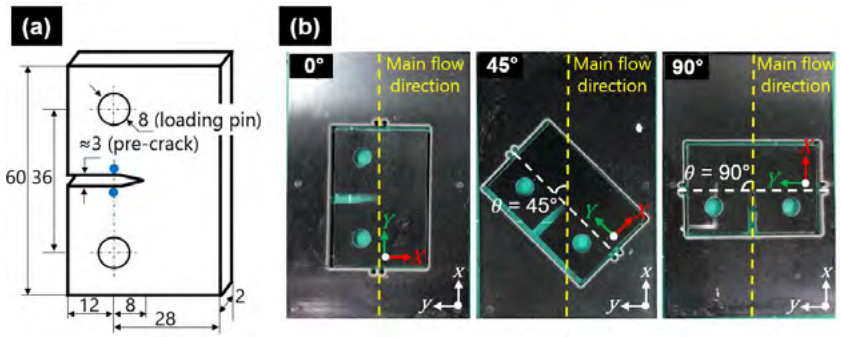


Figure 2. Design of CT specimens: (a) details of the geometry (dimensions: mm), (b) definition of the machining angles [2].

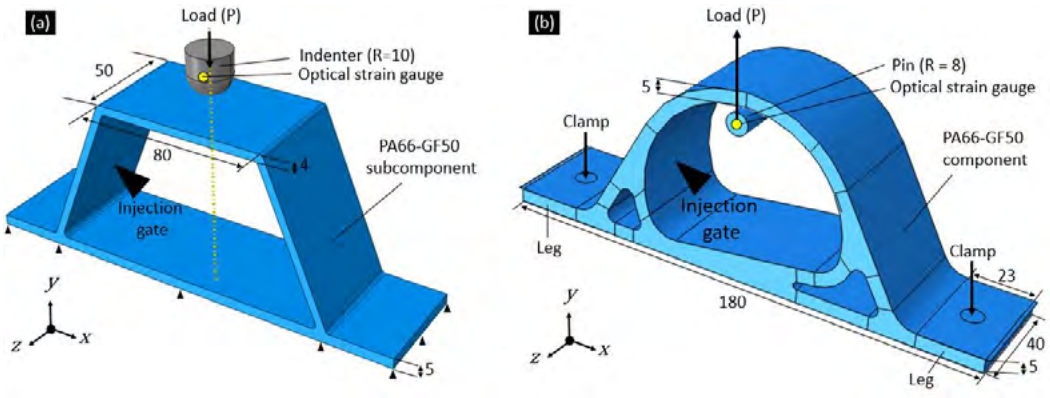


Figure 3. Geometry of (a) subcomponents [3] and (b) components (dimensions: mm).

3. Characterisation of fracture toughness

CT tests were conducted using specimens machined at several angles from the IM plates; all experimental details have been published elsewhere [2]. Representative load-displacement curves of the CT specimens tested at different machining angles and environmental (temperature and moisture) conditions are shown in Figure 4. All specimens exhibited a stable crack propagation (with a gradual decrease in the load after the peak). The value of the peak load was the highest for the specimens machined at a 0° angle, and progressively decreased with increasing machining angles. The value of peak load also decreased with an increase in moisture content or temperature.

These load-displacement curves of CT specimens were transformed into R-curves (using compliance calibration or the J-integral method [2]), and the value of the plateau region in the R-curves were regarded as the overall fracture toughness (or critical strain energy release rate) of the PA66-GF50 material; these are plotted against the machining angles in Figure 5(a). The fracture toughness was maximum at 0° (i.e. for fracture across the preferential fibre orientation direction), and decreased as the machining angle increased up to 90° (i.e. for fracture along the preferential fibre orientation). Moreover, the fracture toughness increased under hotter/wetter conditions. These fracture toughness plots were transformed to functions of the fibre orientation tensor α_{YY} along the loading direction, as shown in Figure 5(b) (the procedure is shown elsewhere [2]).

The fracture surfaces of CT specimens after testing were observed using scanning electron microscopy (SEM) to characterise the damage mechanisms. Representative SEM images (in the skin region) after the tests under 23°C-DAM conditions, for different machining angles, are shown in Figure 6. Large deformation of the PA66 matrix with good interfacial adhesion was observed in all angles. It was also noted that failure mechanisms in the skin region was dominated by fibre tension in the 0° specimens, then shifting to matrix shear failure in the 45° specimens (where the fibres were preferentially aligned diagonally with respect to the crack faces), and to matrix transverse tension failure in the 90° specimens.

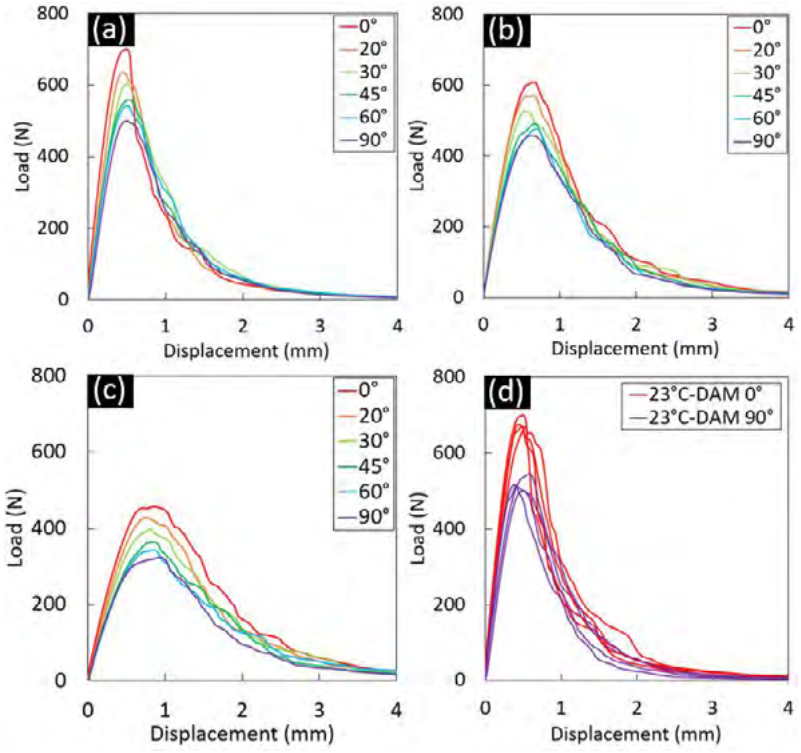


Figure 4. Load-displacement curves of CT specimens: representative curves at different machining tested under (a) 23°C-DAM, (b) 23°C-RH50, and (c) 80°C-RH50; (d) all four load-displacement curves for 0° and 90° tested under 23°C-DAM [2].

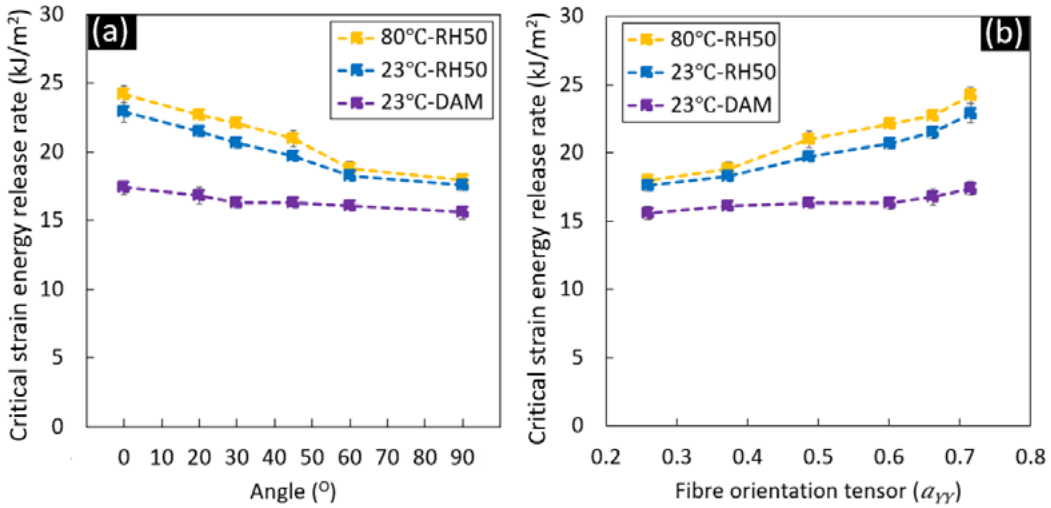


Figure 5. Fracture toughness of PA66-GF50 material as a function of machining angle (a) and fibre orientation tensor along the loading direction a_{YY} (b), under different environmental conditions [2].

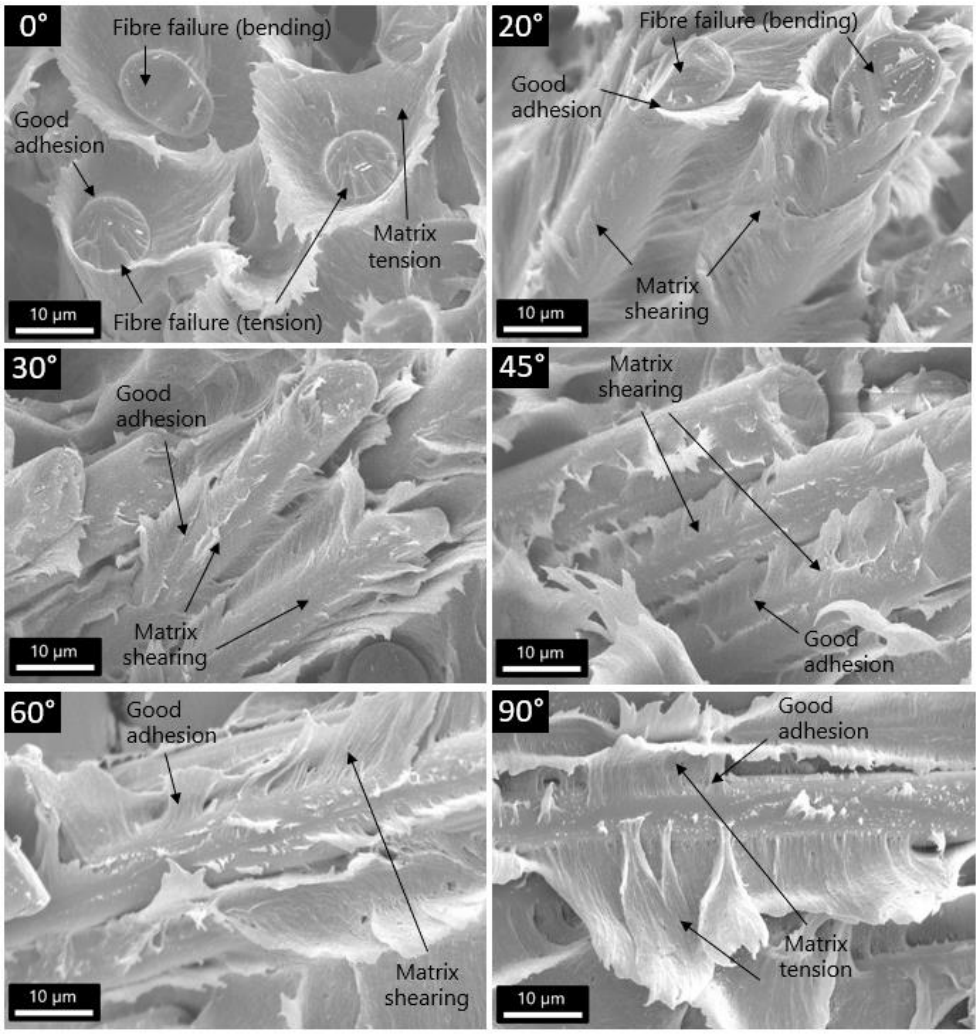


Figure 6. Scanning electron micrographs of the fracture surfaces of CT specimens (in the skin region) after testing under 23°C-DAM conditions: (a) 0°, (b) 20°, (c) 30°, (d) 45°, (e) 60°, (f) 90° [2].

4. Testing and simulations of subcomponents

PA66-GF50 subcomponents (with geometry and loading conditions shown in Figure 3a) were tested under quasi-static conditions at 23°C-DAM, 23°C-RH50 and 80°C-RH50, and the load-displacement curves are shown in Figure 7. A softer and weaker response was observed under wetter or hotter conditions. The crack initiated at the backface of the loading point, then it propagated through-the-thickness along the y-z plane. This crack propagation direction and the fracture plane were consistently observed for all the tested subcomponents regardless of the environmental conditions.

To predict the fibre orientation fields in the subcomponents, the injection-moulding process was simulated using Moldflow software [5]. The obtained fibre orientation tensor fields were then mapped onto an Abaqus [6] Finite Element Analysis (FEA) model of the subcomponent under quasi-static condition, using Digimat-MAP [7]. The PA66-GF50 material was modelled using Digimat's elastic-plastic material model (based on orientation averaging, Mori-Tanaka/Voigt mean-field homogenization and J_2-plasticity model), calibrated with the dogbone tensile testing data under several machining angles, accounting for the anisotropy and material nonlinear-response [7]. We present full details of these coupled process/structural simulations ("coupled FEA") elsewhere [3].

Load-displacement curves of the subcomponents under different environmental conditions from the coupled FEA, using two approaches to predict failure, are also shown in Figure 7:

(i) The conventional approach: failure initiation predicted by the Tsai-Hill ("TH") criterion [1]. The failure point corresponds to the moment when the Tsai-Hill criterion is first met.

(ii) Accounting for the fracture toughness of the material: progressive failure predicted by cohesive zone modelling ("CZM") using the CT test results (Figure 5) as inputs, mapped according to the complex skin-core fibre orientation states predicted by the process simulation (further details are shown elsewhere [3]).

A good agreement was observed regarding the initial stiffness and progressive softening in all simulation results. However, the coupled FEA with the TH criterion predicted onset of failure about 20% earlier than the failure load observed in the tests, under all environmental conditions. These results clearly demonstrate that the failure models currently implemented in commercially-available software, based on failure initiation criteria only, are not sufficient to accurately predict the maximum load in the tests.

To improve failure predictions, the finite fracture toughness of the material (Figure 5) was then introduced in the simulations (in the "FEA (CZM)" approach) of the subcomponents. This approach showed excellent agreement of the failure points between the simulations and the test results, within less than 3% error in the failure load for all environmental conditions.

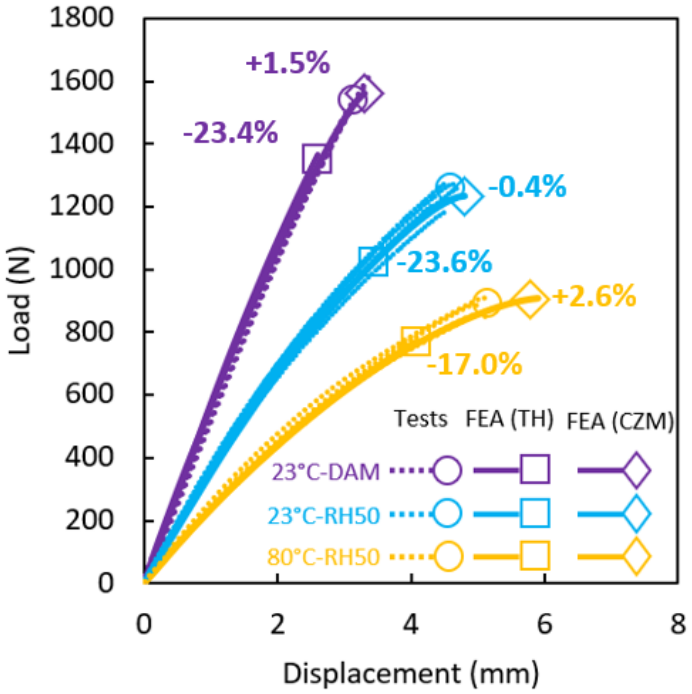


Figure 7. Load-displacement curves of the subcomponents from the tests and the simulations under the three different environmental conditions [3].
The numbers indicate the difference between predictions and experimental results.

5. Testing and simulations of components

PA66-GF50 components (with geometry and loading conditions shown in Figure 3b) were tested under quasi-static conditions at 23°C under DAM conditions, and the load-displacement curves are shown in Figure 8. The crack initiated at the top of the components, from the front edge, and then it propagated through-the-thickness and towards the back of the component (along the *y-z* plane), consistently for all the tests.

The same FE simulation methodologies as used for the subcomponents (with the TH criterion or CZM, described in Section 4) were applied to the PA66-GF50 components; the corresponding outputs are also shown in Figure 8. Both methodologies showed good agreement regarding the initial stiffness and progressive softening compared to the test results; however, the coupled FEA with the TH criterion predicted failure about 14% earlier than observed in the tests. In the coupled FEA with CZM, the predicted failure point showed excellent agreement with the test results (error: -0.6%). This demonstrates that the existing failure initiation criteria are insufficient to simulate the full response of automotive components, and accounting for the finite fracture toughness of the material is essential to accurately predict those maximum failure loads.

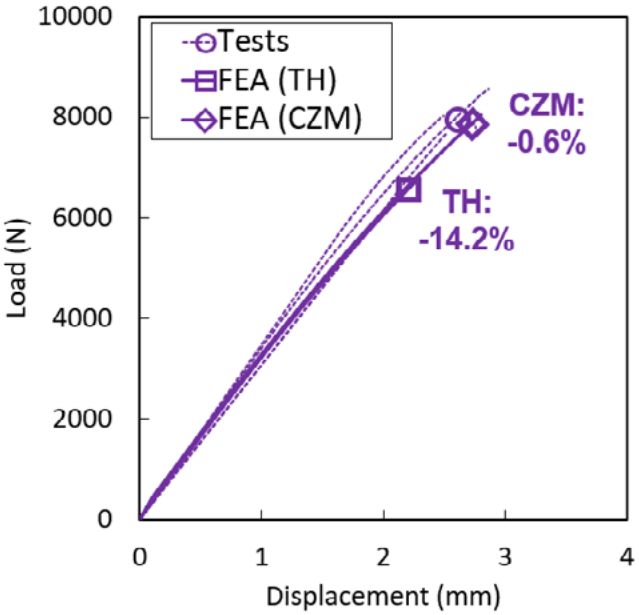


Figure 8. Load-displacement curves of the components from the experimental tests and the simulations. The numbers indicate the difference between predictions and experimental results.

6. Conclusions

PA66-GF50 composite coupons, subcomponents and components were tested under quasi-static conditions; coupled process/structural simulations using CZM calibrated with measured fracture toughness showed excellent agreement of failure points with the test results (within 3% error). This work demonstrates that accounting for the finite fracture toughness of IM-SFRPs is required to overcome the limitations of conventional methodologies, and accurately predict the ultimate failure of IM-SFRP components. The output from this research will provide more confidence in the design of safer and more efficient damage-tolerant IM-SFRP components.

Acknowledgments

This research was funded by Asahi Kasei Corporation under the “Material Modelling of Short-Fibre Reinforced Composites” project.

References

[1] E. Kurkin, M. Spirina, O. Barcenas, E. Kurkina, Calibration of the PA6 short-fiber reinforced material model for 10% to 30% carbon mass fraction mechanical characteristic prediction, *Polymers*, 14, 2022, 1781.
[2] Y. Fujita, S. Noda, J. Takahashi, E.S. Greenhalgh, S. Pimenta, Initiation and propagation fracture toughness of injection-moulded short fibre composites under different environmental conditions, *Composites Science and Technology,* **233**, 2023, 109891.
[3] Y. Fujita, S. Noda, J. Takahashi, E.S. Greenhalgh, S. Pimenta, Predicting failure in injection-moulded short-fibre subcomponents under varied environmental conditions through fracture mechanics, *Composites Part B: Engineering,* **275**, 2024, 111343.
[4] BS EN ISO 1110:2019 Plastics - Polyamides - Accelerated conditioning of test specimens.
[5] Autodesk. Moldflow. Plastic injection and compression mould simulation for design and manufacturing.
[6] Dassault Systemes. Abaqus Analysis User’s Guide Version 6.14
[7] Hexagon. Digimat 2022.2 user’s documentation.

INTERLAMINAR SHEAR FATIGUE OF CARBON/EPOXY LAMINATES

O. Z. Almeida[1,3], N. Carrère[1], M. Le Saux[1], S. Castagnet[2], G. Moreau[3] and Y. Marco[1]

[1]ENSTA Bretagne, UMR CNRS 6027, IRDL, F-29200 Brest, France
Email: otavio.zimmermann@ensta-bretagne.org
[2]ISAE ENSMA, UPR CNRS 3346, Institut PPRIME, F-86170 Poitiers, France
[3]Safran Composites, a technology platform of Safran Tech, 33 avenue de la gare, 91760 Itteville, France

Keywords: interlaminar shear, fatigue, UD laminate, delamination.

Abstract
This work deals with the fatigue of laminates under interlaminar shear stresses. It aims to establish an approach for characterizing the fatigue life of the material using a short beam shear test fixture, identifying the failure mechanisms and establishing a relevant fatigue analysis for such out-of-plane loading conditions. To achieve this objective, high-speed optical camera and digital microscope imaging were used to observe the onset of delamination. Finite element simulations were carried out to refine test analysis.

1. Introduction

Numerous studies have been conducted to characterize the fatigue behavior of carbon/epoxy laminates under in-plane cyclic loadings [1]. However, only few studies address the fatigue of laminates subjected to out-of-plane loadings. Out-of-plane cyclic loadings can occur due to a drastic change in ply orientation in laminates, a complex geometry or the applied loading, and can lead to delamination. A few number of test fixtures are available for such purpose [2-4]. All of them introduce a multiaxial stress state into the laminate, which complicates the interpretation of test results and the adaptation of the test for cyclic loadings. Among them, a 3-point bending short beam shear test fixture is adopted, considering that optical and thermal imaging (for future analysis) are key experimental techniques in this study: fewer metallic pieces are in contact with the sample than for other test standards, reducing friction and heat exchange during cyclic loading, both detrimental to thermal imaging. Short beam shear test fixtures and standards are designed for monotonic loading and, at the day of publication of this paper, no specific standard exists for cyclic loading on laminates. Nonetheless, it has been used in the literature for fatigue testing [5-7], some precautions being needed to correctly analyze test results. The objective of this work is to develop an experimental methodology for characterizing the fatigue of laminates under cyclic interlaminar shear loading using 3-point bending test on a short beam.

2. Material and methods

The material under investigation is a unidirectional (UD) laminate, composed of AS7 carbon fibers and 8552 epoxy resin matrix from Hexcel®. It is approximately 3.27mm thick, and composed of 24 plies stacked in one direction, $[0]_{24}$. The laminate is cured in an autoclave, following the manufacturer's recommended curing cycle. Before curing, a counter plate is placed on top of the stacked plies in order to obtain the same post-cure surface finish on both sides of the panel. The test samples were water-jet-cut, and have dimensions of 30mm x 15mm (length x width). The geometry proportions follow the NF EN 2563 [2] standard. A MTS® servo-hydraulic tension-compression testing machine, with load capacity up to 50kN, was used for testing. A WTF ASTM D790 3-point flexure test fixture is considered.

©2024 | 3_ZIMMERMANN DE ALMEIDA_Otavio_7WJX7.pdf

The distance between the lower loading rollers is half the specimen length (15mm), as recommended in [2] to allow sufficient interlaminar shear and reduce bending stresses in the gauge section. Quasi-static monotonic and fatigue tests were carried out until sample failure. For monotonic loading, a constant crosshead displacement speed of 1mm/min is applied. Cyclic loading is applied in the form of a sinusoidal signal, with a applied compression-compression loading ratio that represents a specimen equivalent stress ratio of $R = \frac{\tau_{13min}}{\tau_{13max}} = 0.1$, where τ_{13min} and τ_{13max} are the minimum and maximum values over the cycle of the maximum out-of-plane shear stress; 1 is the fiber direction and 3 is the out-of-plane direction (**Figure 1**). The number of cycles to failure N is given by the moment where at least one delamination is present in half-length of the specimen. This can be detected as a remarkable variation in the machine loading. The interlaminar shear stress τ_{13} is calculated at the sample neutral axis assuming a parabolic shear stress distribution through the specimen thickness, according to equation (**1**), where P is the load, w the sample width and t the sample thickness. For fatigue testing, a loading frequency of 5Hz is adopted. A Nova FastCam® S9 high-speed camera is used to follow the fast delamination onset during monotonic tests. The lateral surface of the sample observed was painted in white to allow better visualization of cracks. Acquisition frequencies of 1kHz and 10kHz were used. High-speed camera images are linked to the loading cell measurements. They are triggered at a specific force, corresponding to 94% of the mean shear stress at failure measured from monotonic tests. The samples were observed after testing with a Keyence vhx5000® digital microscope.

In order to analyze the results, finite element (FE) simulations of the test were performed using Abaqus®. The specimen mechanical behavior is defined as orthotropic linear elastic; the used coefficients are presented in **Table 1**. Rollers have the same diameter and position of the test fixture. Only half of their volume is represented. Their behavior is isotropic linear elastic, with a Young modulus E_{roller}=210GPa and a Poisson's ratio ν_{roller}=0.3. The lower rollers are clamped. The displacement of the upper roller along the 3 direction is imposed (the displacements along directions 1 and 2 are forbidden). A frictionless contact condition is defined between the rollers and the specimen. Two symmetry planes were used (the first one parallel to the 1-3 plane at half-width, and the second one parallel to the 2-3 plane at half-length) so that only one eighth of the system is modelled. 8-node linear brick elements are used, with an aspect ratio of 4x4x1 (length x width x thickness), each ply having only one element on its thickness.

Table 1. Orthotropic linear elastic ply properties (Ei is the Young's modulus along direction i, Gij is the shear modulus in direction j on the plane whose normal is in direction I, and vij is the Poisson's ratio relative to directions i and j).

E1 (GPa)	E2=E3 (GPa)	G12=G13 (GPa)	G23 (GPa)	ν12= ν13 (-)	ν23 (-)
148	8.7	4.7	4	0.32	0.436

3. Results

May and Hallet [5] have shown that damage initiates inside the specimen and propagates for a certain number of cycles before sample failure (whereas it breaks abruptly under monotonic loading), and that the failure mode differs from quasi-static monotonic tests. The number of cycles between instants when damage is observable inside the specimen and when its failure occurs is into account in this work, but a stress corrective factor is proposed to take into account the difference in failure modes between monotonic and cyclic loading**.**

3.1. Monotonic loading

Eight specimens have been tested under quasi-static monotonic loading, resulting in a mean interlaminar shear strength of τ_{13}^{u}=122MPa. Failure occurs, on average, close to the specimen's mid-height (**Figure 3**). The captured images reveal that delamination initiates inside the specimen and propagates towards

the exterior faces. All delamination occur exclusively on one half of the sample length. The image where delamination is first visible corresponds to the end of the drop on the loading data, and therefore to the point where a damage effect is first detected. In some of the tested specimen, as illustrated in **Figure 1**, two almost simultaneous delaminations appear on the thickness of the sample. For other cases, only one main delamination is visible.

$$\tau_{13} = \frac{3.P}{4.w.t} \quad (1)$$

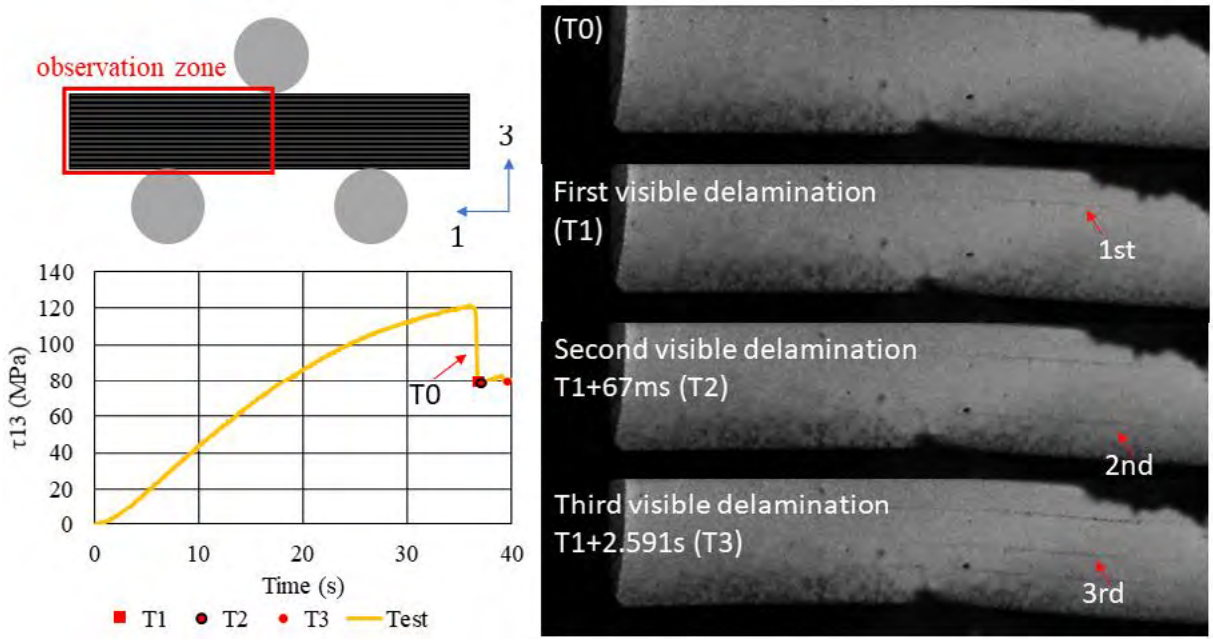


Figure 1. Delamination apparition on the free surface of sample during a monotonic test and comparison with the loading curve.

3.2. Fatigue

Delamination during fatigue tests occurs above the neutral axis, on average. It therefore does not occur in the same place as during monotonic tests (as shown in **Figure 2**). In **Figure 3**, the average position of cracks for each case, with the associated standard deviation, is represented on the observable "length x thickness" face of the FE model: they are named $p_{fatigue}^{delamination}$ for fatigue and $p_{monotonic}^{delamination}$ for monotonic test. The τ_{13} stress distribution shown is calculated through a monotonic loading step up to the equivalent of τ_{13}^{u} in rollers' applied force.

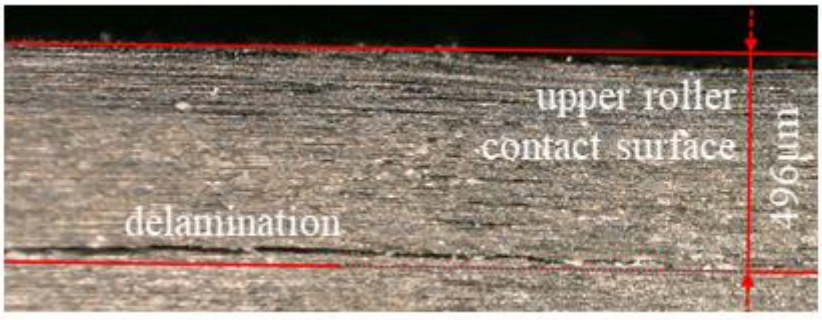


Figure 2. Delamination observed on one length-thickness free surface after fatigue test.

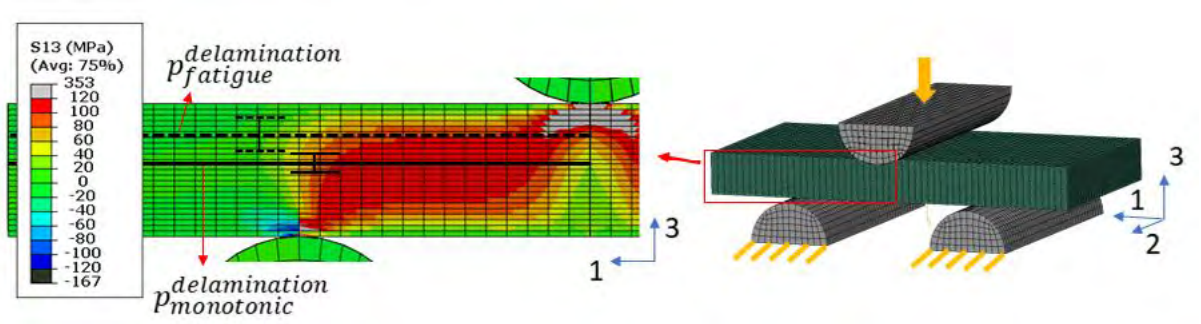


Figure 3. Average delamination location for monotonic and fatigue loadings over an out-of-plane shear stress field calculated by FE simulations.

As the location of delaminations is not the same for monotonic and fatigue tests and the stress distribution over the region of interest is non-homogeneous, fatigue and monotonic data cannot be treated in the same way. The parabolic distribution hypothesis for interlaminar shear stress over the thickness (equation (**1**)) is only valid in the middle of the red zone of the shear stress map seen in **Figure 3**. In order to estimate the effective failure stress $\tau_{13}^{p,fatigue}$ where delamination is observed after fatigue tests from the stress τ_{13} calculated at mid-thickness (equivalent to the stress calculated with equation (**1**)), a stress correction factor is determined from the results of FE simulations: the peak shear stress $\tau_{13}^{p,fatigue}$ in the plane at the position $p_{fatigue}^{delamination}$ is estimated and a constant correction factor f is calculated according to equation (**2**). This correction factor is calculated for all fatigue tests, as the samples were scanned on the microscope and the position $p_{fatigue}^{delamination}$ of each one is known. In **Figure 4**, the stress-corrected S-N curve is compared to the S-N curve obtained when the shear stress is calculated from equation (**1**). For a given number of cycles at failure, the effective maximal interlaminar shear stress is higher than the one calculated near the neutral axis of the sample.

$$f = \frac{\tau_{13}^{p,fatigue}}{\tau_{13}} \quad (2)$$

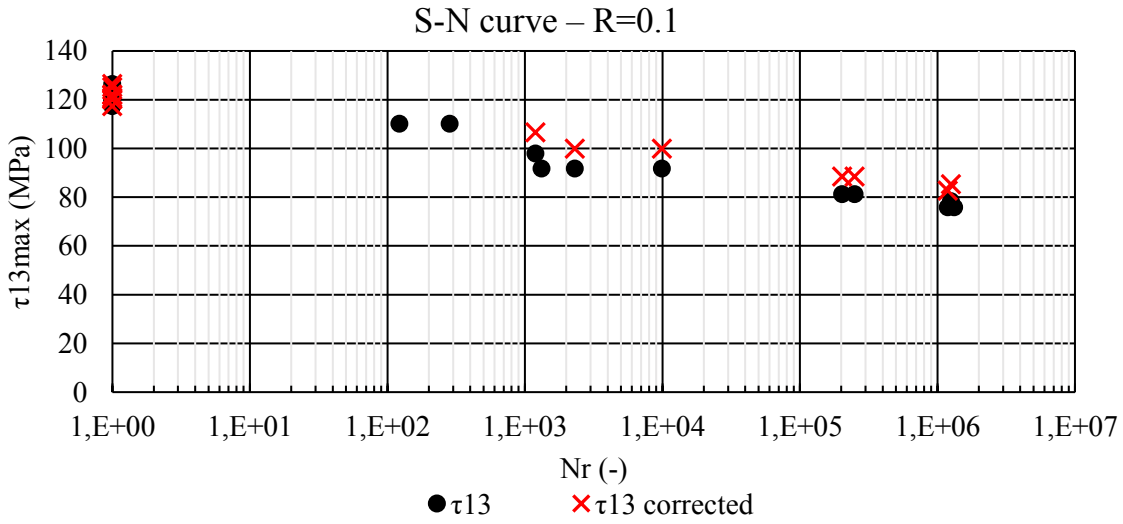


Figure 4. S-N curve considering parabolic stress distribution hypothesis and considering the corrected stress values.

3.3. Discussion of delamination location

Under monotonic loading, delamination occurs on the half-thickness plane, while out-of-plane shear stress is the highest under the upper roller. This could be linked to the significant out-of-plane compression stresses under the roller. Indeed, an increase in the interlaminar shear strength in the presence of out-of-plane compression has been reported in the literature [8,9]. Under cyclic loading, delamination does not occur at mid-height. Cohesive element-based FE simulations have been conducted in [10,11] to explain the difference observed between the failure locations. In this work, an interpretation of the problem is made on the basis of the coupled stress and energy criterion proposed by Leguillon [12]. This criterion has already been used to predict delamination in composites [13]. According to the criterion, for a crack to appear and propagate over a surface ΔS, both stress and energy criterion must be met (**Figure 5**). Under monotonic loading, on the one hand, the stress concentration zone under the upper roller exceeds the critical stress, but the region concerned is too small for the energy developed to be sufficient to reach the critical value. In the half-thickness region, on the other hand, both the stress and energy criteria are met so that crack propagation is expected. Under cyclic loading, the shear stress in the half-thickness plane is never high enough to meet the stress criterion. It is assumed that, over a number of cycles, the stress concentration zone under the upper roller is damaged and the mechanical properties of the matrix degrade, leading to a decrease in the critical strain energy release rate G_c. When the energy release rate meets G_c, delamination occurs.

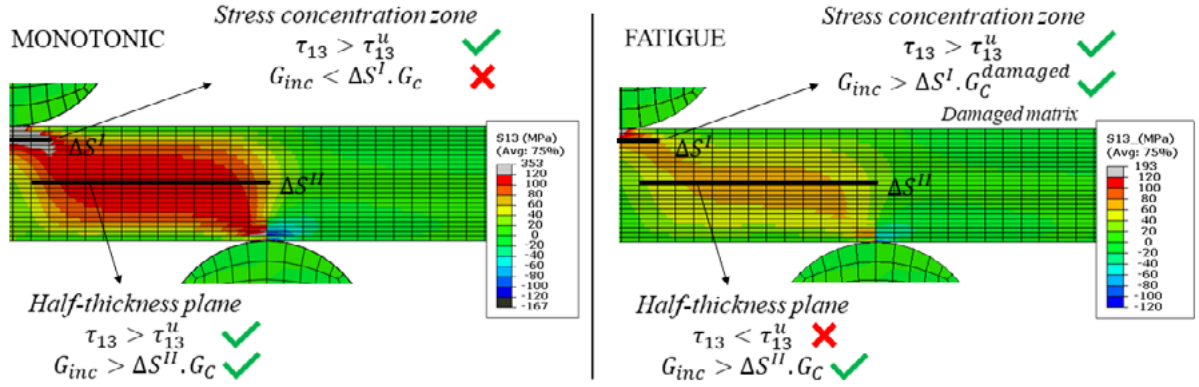


Figure 5. Interpretation of fatigue and monotonic failure cases according to the coupled criterion.

4. Conclusions

The presented work aimed to establish an experimental methodology to characterize the fatigue behavior of an UD laminate under interlaminar shear cyclic loading. A 3-point short beam shear test fixture is used. As observed in the literature, the failure modes induced by monotonic and fatigue loadings are different. High-speed camera films allowed to better understand the process of delamination: where the crack probably starts and how it propagates. *Post-mortem* digital microscope analysis was used to measure the position of delamination over the sample thickness. This information was related to the stress field in the samples calculated using a FE model. These results were used to determine the failure stress at the fatigue crack location from the test data. A S-N curve was then obtained for R=0.1. The difference between failure locations for monotonic and fatigue tests can be explained with the coupled criterion (energy and stress).

Acknowledgments

This study is part of the industrial research chair ANR-Safran-Naval "Self-Heating" (subvention # ANR-20-CHIN-0002), involving the societies Safran, Naval Group, ENSTA Bretagne and Institut PPrime. We would like to acknowledge their support.

References

[1] VASSILOPOULOS, A.P. The history of fiber-reinforced polymer composite laminate fatigue". International Journal of Fatigue, vol. 134, p. 105512, 2020.
[2] NF EN 2563 standard. *Série aérospatiale - Plastiques renforcés de fibres de carbone. Stratifiés unidirectionnels. Détermination de la résistance apparente au cisaillement interlaminaire*. 1997.
[3] SHOKRIEH, Mahmood M. et LESSARD, Larry B. An assessment of the double-notch shear test for interlaminar shear characterization of a unidirectional graphite/epoxy under static and fatigue loading. Applied Composite Materials, 1998, vol. 5, p. 289-304.
[4] CHARRIER, Jean-Sebastien. Développement de méthodologies dédiées à l'analyse robuste de la tenue de structures composites sous chargements complexes tridimensionnels. 2013. Thèse de doctorat. Paris, ENSAM.
[5] MAY, M. et HALLETT, S. R. Analysis of damage evolution in unidirectional carbon/epoxy samples under shear fatigue loading. In : 17th International conference on composite materials. 2009. p. 27-31.
[6] MAKEEV, Andrew. Interlaminar shear fatigue behavior of glass/epoxy and carbon/epoxy composites. Composites Science and Technology, 2013, vol. 80, p. 93-100.
[7] MAY, Michael et HALLETT, Stephen R. An assessment of through-thickness shear tests for initiation of fatigue failure. Composites Part A: Applied Science and Manufacturing, 2010, vol. 41, no 11, p. 1570-1578.
[8] NI, Xinchen, FURTADO, Carolina, KALFON-COHEN, Estelle, et al. Static and fatigue interlaminar shear reinforcement in aligned carbon nanotube-reinforced hierarchical advanced composites. Composites Part A: Applied Science and Manufacturing, 2019, vol. 120, p. 106-115.
[9] LI, Xiangqian, HALLETT, Stephen R., et WISNOM, Michael R. Predicting the effect of through-thickness compressive stress on delamination using interface elements. Composites Part A: Applied Science and Manufacturing, 2008, vol. 39, no 2, p. 218-230.
[10] CUI, Weicheng et WISNOM, Michael R. A combined stress-based and fracture-mechanics-based model for predicting delamination in composites. Composites, 1993, vol. 24, no 6, p. 467-474.
[11] MAY, Michael et HALLETT, Stephen R. A combined model for initiation and propagation of damage under fatigue loading for cohesive interface elements. Composites part A: Applied science and manufacturing, 2010, vol. 41, no 12, p. 1787-1796.
[12] LEGUILLON, Dominique. Strength or toughness? A criterion for crack onset at a notch. European Journal of Mechanics-A/Solids, 2002, vol. 21, no 1, p. 61-72.
[13] MARTIN, E., LEGUILLON, D., et CARRÈRE, N. A twofold strength and toughness criterion for the onset of free-edge shear delamination in angle-ply laminates. International journal of Solids and Structures, 2010, vol. 47, no 9, p. 1297-1305.

©2024 | 3_ZIMMERMANN DE ALMEIDA_Otavio_7WJX7.pdf:6

THE BEHAVIOR OF PAPER COMPOSITES UNDER COMPRESSIVE LOAD

S. Schmidt[1] and A. Büter[2]

Hochschule Darmstadt h_da, Faculty of Mechanical and Plastics Engineering, University of Applied Siences, Schöfferstraße 3, D-64295 Darmstadt, Germany
[1]Email: sandra.schmidt@h-da.de, Web Page: https://fbmk.h-da.de
[2]Email: andreas.bueter@h-da.de, Web Page: https://fbmk.h-da.de

Keywords: natural fiber-reinforced materials, compressive load, laminates

Abstract
Objective of a current research project at the University of Applied Sciences in Darmstadt is to investigating whether paper laminate is a sustainable material for lightweight design. Therefore thick-walled material examined here consists of thin layers and, due to the fiber reinforcement, exhibits a slight anisotropy in relation to the production direction.
Under compressive loads, this material exhibits a complex failure in the form of symmetrical or asymmetrical layer buckling due to its layered structure. In our opinion (thesis), this instability results in a local reduction in stiffness caused by these layer buckling. On the other hand, there is an increase in stiffness with increasing specimen length.
In order to understand the failure behaviour, compression tests in the form of face crush tests with defined strain rates were carried out on air-conditioned, thick-walled samples (50x10 mm) of different lengths. Calculability is generally required of materials used in light weight design.
The paper presents and discusses the test and calculation results obtained. The aim is to generate a first material model for compressive loads that takes into account the special features of the failure of paper composites.

1. Introduction

A current research project at the University of Applied Sciences in Darmstadt is investigating whether paper laminate is a sustainable material for lightweight design. This project continues the work of the LOEWE project BAMP (Building with Paper) founded by the LOEWE program of the State of Hessen. The aim of BAMP was to provide scientific and technical foundations for the use of paper in building applications and to develop new approaches to solutions. One application for paper is columns or beams subjected to pressure loads, which is why this work focuses on compressive loads. For tensile loads, comprehensive investigations and a suitable material model for paper laminates are presented in [4].

2. Experimentell Investigation

2.1. Paper Material and Semifinished Products

Paper fibers are processed for the production of paper, which, according to [2], are mainly obtained from annual plants, thinned wood and sawmill waste. In contrast to other short-fiber-reinforced plastic composites (FRP), in which carbon or glass fibers are usually used, the fibers of paper laminates are renewable and recyclable. As shown in Figure 1, paper is a renewable, random fibre-reinforced material. The investigated material was cut out of an L-shaped angular edge protector (150x150x10mm). The angular edge protector itself consists of glue and approx. 15 layers of paper produced continuously in a rolling/drying process. These thin layers of paper are then cut to size, placed on top of each other and formed into an L-shape and glued together in several steps using a moulding rolling process [5].
Therefore the thick-walled material examined here consists of thin layers and, due to the fiber reinforcement, exhibits a slight anisotropy in relation to the production direction (MD).

2.2. Sample Manufacturing and Preparation

Samples of different lengths were cut from a commercially available angular edge protector in the longitudinal direction (//), i.e. in the production direction (MD) and transverse to the production direction (⊥ or CD) using a band saw or circular saw. The following samples were analysed: 150x50x10mm (//) ; 100x50x10mm (//) ; 50x50x10mm (//) ; 15x50x10mm (//) ; 50x50x10mm (⊥). Figure 1 shows an example of the 50x50x10mm (//) with its microstructure and layer structure.

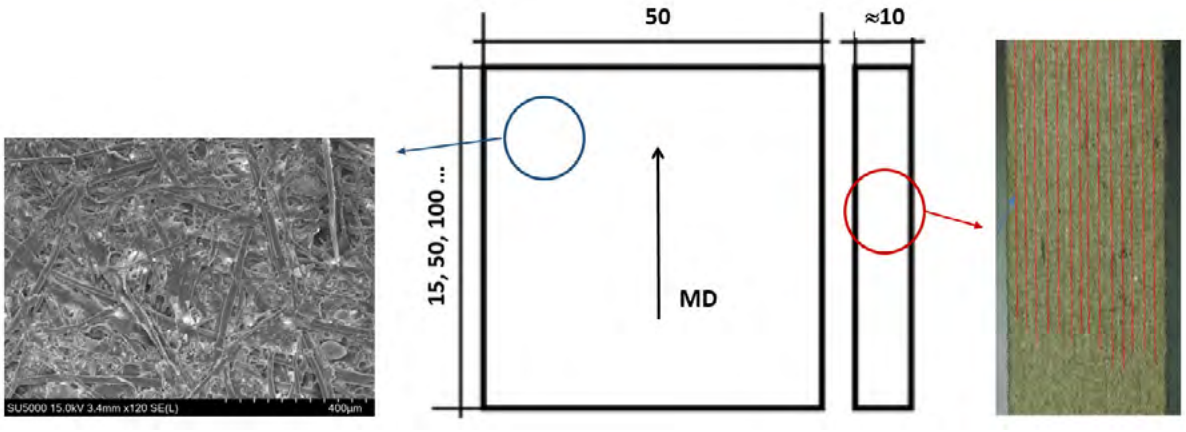


Figure 1. Microstructure of the Paper, the geometry of the 50x50x10mm samples and there layup.

Before carrying out the compression tests, it was necessary to prepare the samples cut from the semi-finished product for the tests. As paper is very hydrophilic and swells as it absorbs moisture, all samples were stored in a climate chamber at 23°C and 50 % relative humidity for a week after being graded, measured regularly and their weight determined. After one week, the weight remained constant, which means that the moisture exchange was complete.

2.3. Carrying out Experiments

Due to the 'column' application, the compression tests were carried out as a forehead compression test using a Zwick&Roell Z050 universal machine in a climatic chamber. DIN EN ISO 604 [3] was used as the basis, although the specimen geometry and test speeds deviated from the standard. The material paper reacts to an applied force, similar to plastics or wood, by yielding to reduce the external stress (creep) [1]. Due to the application as a support with primarily static loads, a rather slow strain rate of 0.0005 was selected for the test series despite the tendency of the paper to creep. The test procedure could explain failure type A due to the transverse strain on the load introduction plates prevented by friction. Figure 2 shows the test setup and failure mode A.

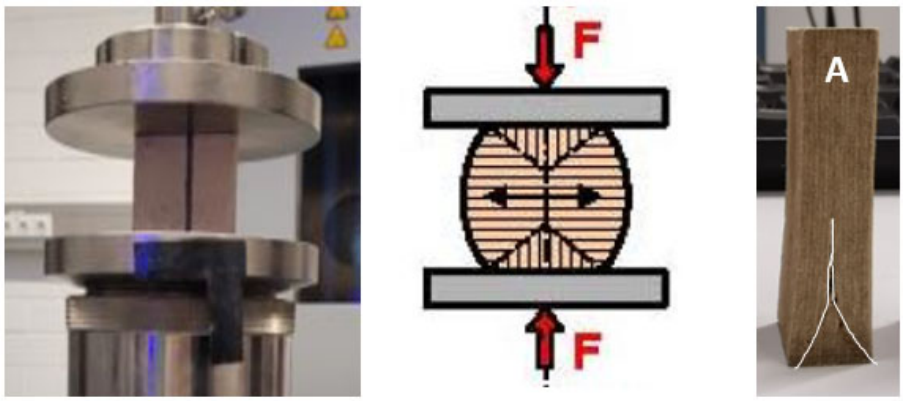


Figure 2. Experimental setup.

2.4. Results of the Experimental Investigations

To determine the optimum specimen geometry and to avoid buckling of the specimens, both the length and the width of the specimens were varied. Figure 3 shows examples, only the length differs here, of the stress-strain curves of specimens measuring 15x50x10 and 50x50x10mm as well as typical damage modes.

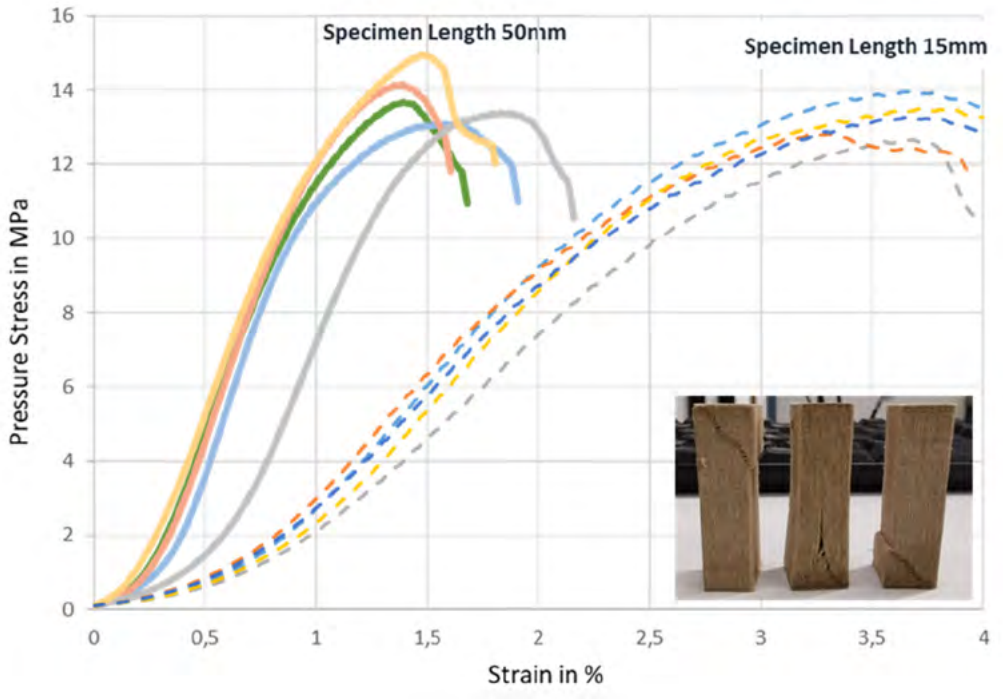


Figure 3. Stress-strain diagrams for samples of different lengths and typical damages modes
First measurement campaign

A comparison of the stress-strain curves shows that the modulus of elasticity increases with length. As far as the strength is concerned, it is on average at the same level for both sample lengths. Furthermore, it can be seen that there is a distinct and in part quite different running-in phase. For the further analyses, the greatest gradient after the running-in phase was determined as the modulus of elasticity.
Figure 4 summarises the moduli of elasticity determined in this way for the first measurement campaigns. The compression modulus of elasticity is compared as a function of the sample length (left) and the sample width (right). The compressive modulus of elasticity increases as the sample length increases. However, a dependence of the modulus of elasticity on the width could not be reliably proven due to the scattering.

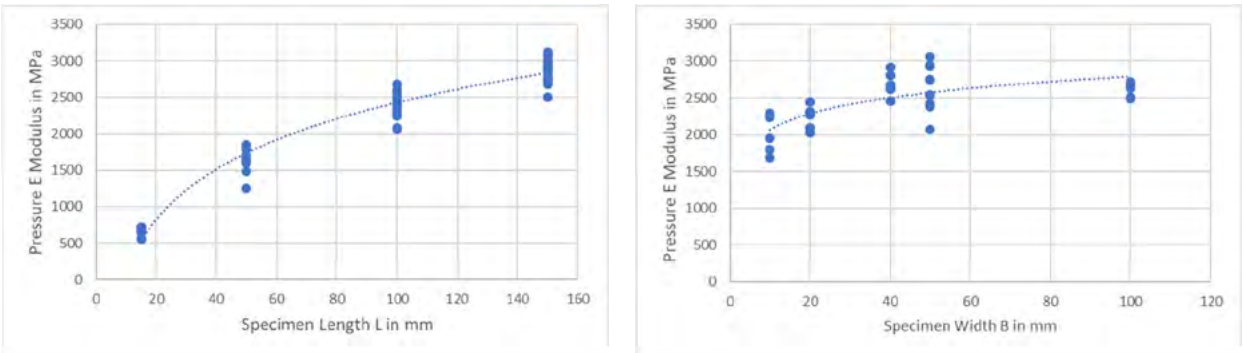


Figure 4. Pressure E-modules: as a function of sample length (left) and sample width (right)
First measurement campaign

The measurement results shown in Figure 5 occurred during further tests of the same delivery batch of the angular edge protector material. With the exception of the tester, an attempt was made to keep all test parameters constant. In relation to the first series of measurements, these measurement results show differences both in the scatter and in the position of the mean values (Figure 6).

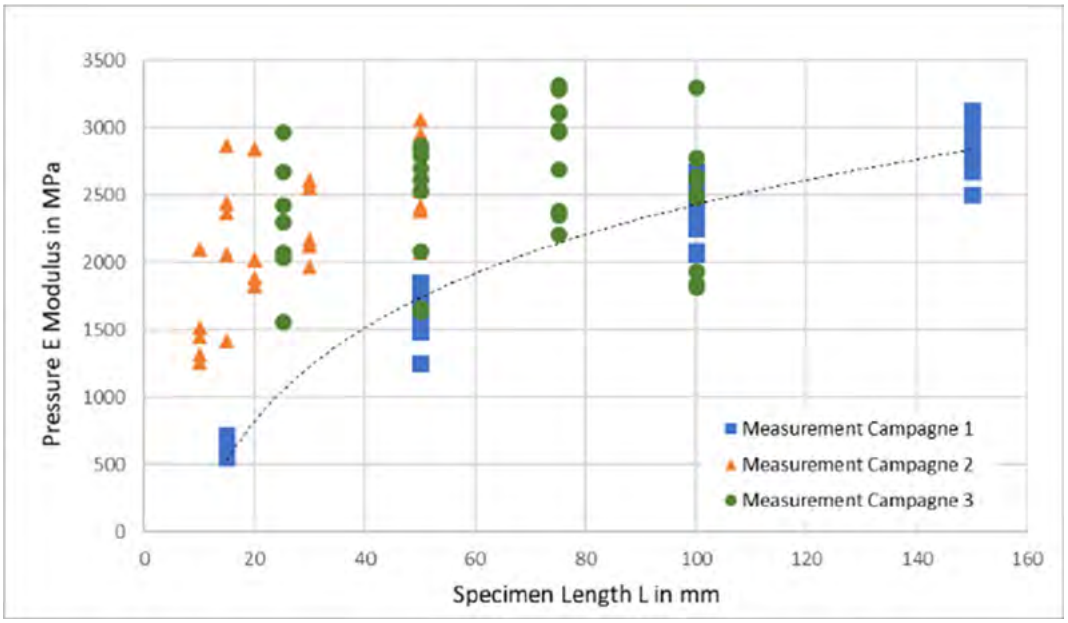


Figure 5. Results of various measurement campaigns

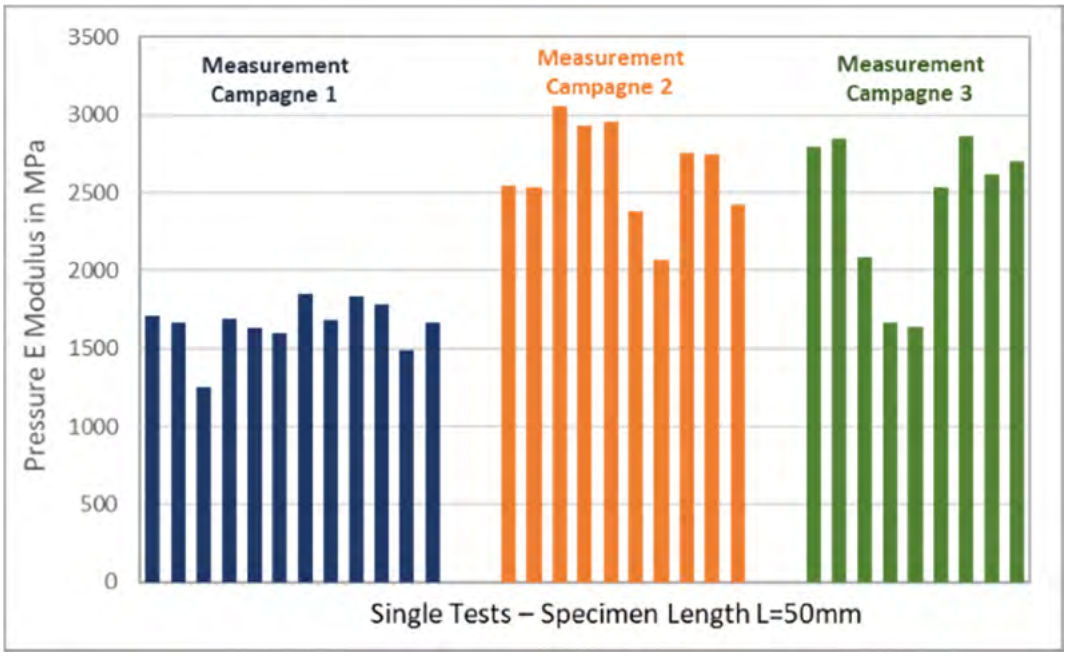


Figure 6. Comparison of the results of various measurement campaigns

3. Material Model based on a "*Spring Approach*"

Even if only indicated by the scattering, one cause of the length dependence of the modulus of elasticity is asymmetrical layer buckling (failure mode B). The layer buckling leads to a reduced stiffness C_f. in

the damaged area. If damage over the entire cross-sectional area is assumed, the total stiffness C_{res} of the specimen can be described by a series connection of the spring stiffness of the damaged area C_f with that of the undamaged area C_{non}, as shown in Figure 7.
The following equation (Eq. 1) describes the series-connected stiffnesses of the specimen (Figure 7) with A for the cross-sectional area, l_f for the length of the damaged area (*right*) and L-l_f as the length of the undamaged area (*left*):

$$C_f = \frac{E_f A}{l_f} \quad \text{and} \quad C_{non} = \frac{E_{non} A}{L - l_f} \tag{1}$$

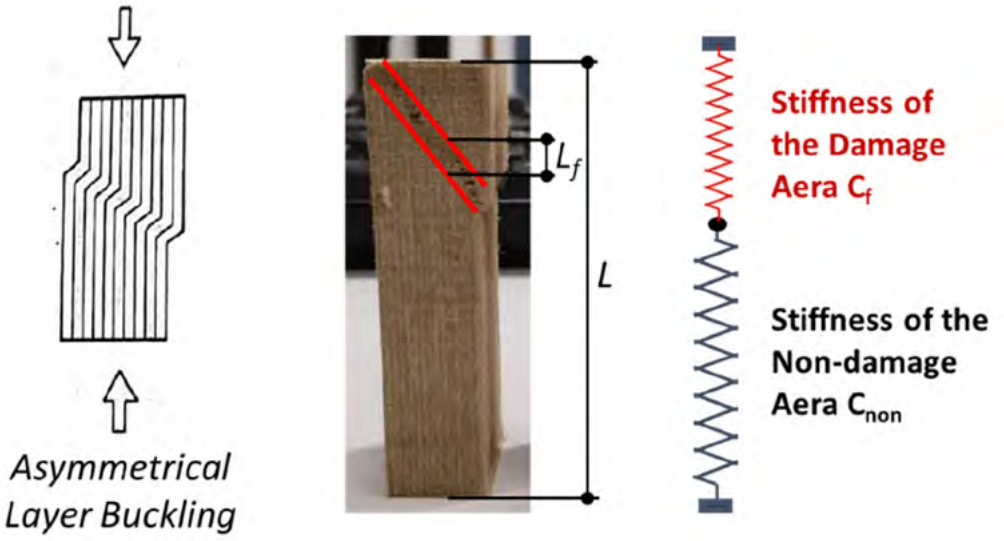


Figure 7. Spring Approach for Asymmetrical Layer Buckling [6].

E_{non} is the modulus of elasticity of the undamaged material and E_f that of the damaged material. Analogous to (Eq. 1), the resulting overall stiffness can also be calculated using L, A and E_{res}, whereby it can also be calculated by connecting the springs specified in (Eq.1) in series:

$$C_{res} = \frac{E_{res} A}{L} = \frac{C_f \; C_{non}}{C_f + C_{non}} \tag{2}$$

If (Eq.1) is set in (Eq.2), ones get Eq.3. (Eq.3) shows the resulting modulus of elasticity of the hole sample E_{res}. This equation can be simplified as a function of L. The parameters a and b are fitting parameters that can be determined from test data.

$$E_{res} = \frac{L \, E_{non}}{L + \left(\frac{E_{non}}{E_f} - 1\right) L_f} = \frac{L \, a}{L - b} \tag{3}$$

Figure 8 shows the test results of the first measurement campaign and the adapted fitting curve. As the measured values can be mapped very well using the two fitting parameters, it can be seen that the series connection approach is very well suited to explaining the length dependence of the modulus of elasticity.

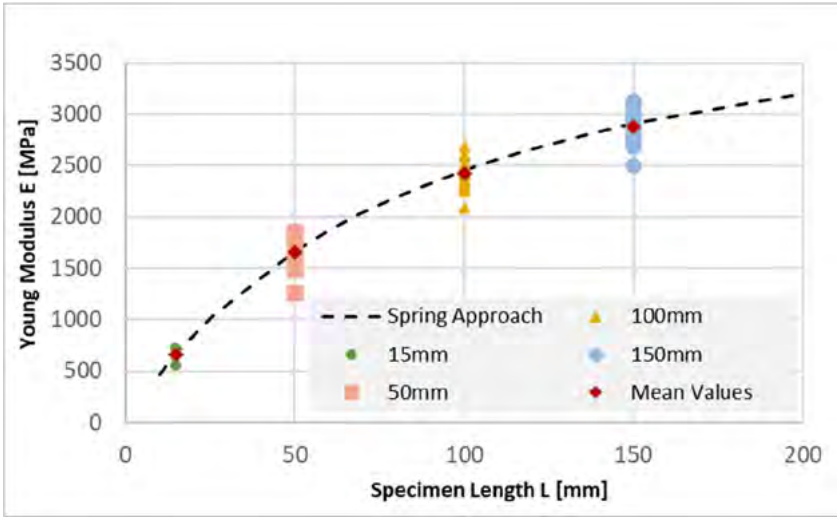


Figure 8. Testing Results fits with adapted fitting curve based on the spring approach.

Furthermore, a reduction factor f_{red} for the modulus of elasticity of the undamaged material can also be derived from (Eq.3).

$$E_{res} = \frac{1}{1+\left(\frac{E_{non}}{E_f} - 1\right)\frac{L_f}{L}} E_{non} = f_{red}\, E_{non} \tag{4}$$

The value (L_f/L) describes the geometric size of the damage in relation to the total length L of the sample. The value (E_{non}/E_f) describes the 'severity' of the damage by the ratio of the modulus of elasticity of the undamaged material to that of the damaged material. If $E_{non}/E_f = 1$, this means that there is no damage. In the case of $E_{non}/E_f = \infty$, this means that the stiffness in the damage area is zero (extreme damage). Figure 9 shows the reduction factor f_{red} over (L_f/L). With a damage length of approx. $l_f = 1$ to 2 mm and the analysed sample lengths of 15 to 150 mm, the values for the factor (L_f/L) are between 0.133 (short samples) and 0.007 (long samples). As we do not know the 'severity of damage' (value: E_{non}/E_f), various values from 1 (no damage) to 100 (damage) were selected. Whether $E_{non}/E_f = 100$ is a realistic damage value is not yet known. Perhaps the value is also greater.

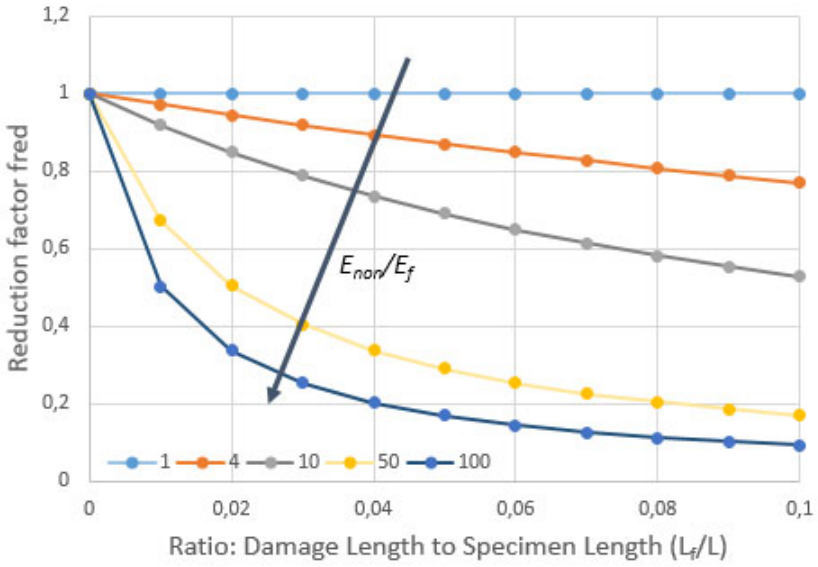


Figure 9. Influence of Damage on the Testing Results.

Figure 9 clearly shows why the short samples in particular scatter strongly. Small differences in the damage (value: E_{non}/E_f) lead to large changes in the reduction factor f_{red} and thus the measured modulus of elasticity.

3. Conclusions

The test results show that this material exhibits a complex failure in the form of symmetrical or asymmetrical layer buckling under compressive load due to its layer structure. In our opinion, this instability leads to a local reduction in stiffness caused by layer buckling. This hypothesis also explains the measured increase in the compressive E-modulus with increasing sample length, as has been shown.

The scattering of the measurement results that occurs with the different measurement campaigns is problematic for the use of paper as a lightweight construction material. One explanation for the scattering of the measured values is the drop in stiffness in the local failure area. How great is the damage (E_{non}/E_f) and what influences it? Subsequent series of tests should shed further light on the reasons for the scattering of the measured values. The aim is to derive measures that reduce the scattering and possibly also improve the performance of the material.

Acknowledgments

First of all, we would like to thank the state of Hesse for the funding that laid the foundation for this work with the LOEWE project BAMP! and enabled further work through the Hessian University Pact 2021-2025. Furthermore, our students: Schneider, Eydt, Kling, Khoder Waffo, Mirza, Tozan, and many others should not go unmentioned, who have made this work possible through their contribution.

References

[1] W. Bergmann: *Werkstofftechnik* - Teil 1: Grundlagen, Carl Hanser Verlag, München, 1984
[2] J. Blechschmidt: *Paper Processing Technology*, Carl Hanser Verlag, 1st edition 17, 2013
[3] DIN EN ISO 604:2003-12: *Kunststoffe - Bestimmung von Druckeigenschaften*; Deutsche Fassung EN ISO 604:2003
[4] N. Kiziltoprak: *On the Bi-Axial In-Plane Behavior of Laminated Paperboard Components in Construction: A Representative Engineering ModelOn the Bi-Axial In-Plane Behavior of Laminated Paperboard Components in Construction*, TUprints, Technische Universität Darmstadt, 2022
[5] U. Knaack, R. Bach, S. Schabel: *Bauen mit Papier: Architektur und Konstruktion* – Kapitel 3: Halbzeuge und Komponenten, Birkhäuser Verlag, 2023
[6] H.Öry; H.G.Reimerdes: Faserverbundwerkstoffe, RWTH Aachen, 1987

ECCM21

02-05 July 2024 | **Nantes - France**

Volume 3

Material and Structural Behavior Simulation & Testing



ISBN: 978-2-912985-01-9
DOI: 10.60691/yj56-np80